INTERNATIONAL TABLES FOR CRYSTALLOGRAPHY

Volume H

POWDER DIFFRACTION

Edited by

C. J. GILMORE, J. A. KADUK AND H. SCHENK

First Edition

Published for
THE INTERNATIONAL UNION OF CRYSTALLOGRAPHY
by
WILEY

2019

Contributing authors

A. J. Allen: National Institute of Standards and Technology (NIST), 100 Bureau Drive, Gaithersburg, MD 20899, USA. [5.8]

A. Altomare: Institute of Crystallography – CNR, Via Amendola 122/o, Bari, I-70126, Italy. [3.4, 4.2]

G. Álvarez-Pinazo: Departamento de Química Inorgánica, Cristalografía y Mineralogía, Universidad de Málaga, 29071 Málaga, Spain, and X-Ray Data Services S.L., Edificio de institutos universitarios, c/ Severo Ochoa 4, Parque technológico de Andalucía, 29590 Málaga, Spain. [3.10]

M. A. G. Aranda: ALBA Synchrotron, Carrer de la Llum 2–26, Cerdanyola, 08290 Barcelona, Spain, and Departamento de Química Inorgánica, Cristalografía y Mineralogía, Universidad de Málaga, 29071 Málaga, Spain. [3.10, 7.12]

R. Arletti: Dipartimento di Scienze della Terra, Università degli Studi di Torino, Via Valperga Caluso 35, I-10125 Torino, Italy. [7.14]

G. Artioli: Dip. Geoscienze, Università di Padova, Via Gradenigo 6, I-35131 Padova, Italy. [7.4]

Ch. Baerlocher: Laboratory of Crystallography, ETH Zurich, HCI, G 509, CH-8093 Zurich, Switzerland. [4.6]

G. Barr: Department of Chemistry, University of Glasgow, University Avenue, Glasgow G12 8QQ, UK. [3.8]

S. Bates: Triclinic Labs, 1201 Cumberland Ave., Suite S, West Lafayette, IN 47906, USA. [5.6]

W. van Beek: Swiss–Norwegian Beamlines at ESRF, CS 40220, 38043 Grenoble Cedex 9, France. [2.9]

J. Bernstein: Department of Chemistry, Ben-Gurion University of the Negev, PO Box 653, Beer Sheva, 84102, Israel. [7.5]

S. J. L. Billinge: Department of Applied Physics and Applied Mathematics, Columbia University, 500 West 120th Street, Room 200 Mudd, MC 4701, New York, NY 10027, USA, and Condensed Matter Physics and Materials Science Department, Brookhaven National Laboratory, PO Box 5000, Upton, NY 11973-5000, USA. [1.1, 5.7]

M. Birkholz: IHP, Im Technologiepark 25, 15236 Frankfurt (Oder), Germany. [5.4]

D. L. Bish: Department of Earth and Atmospheric Sciences, Indiana University, Bloomington, IN 47405, USA. [7.7]

D. Black: National Institute of Standards and Technology, Gaithersburg, Maryland, USA. [3.1]

K. Cenzual: University of Geneva, 24 quai Ernest-Ansermet, CH-1211 Geneva 4, Switzerland. [3.7.5]

R. Černý: Laboratory of Crystallography, DQMP, University of Geneva, 24 quai Ernest-Ansermet, CH-1211 Geneva 4, Switzerland. [4.5]

D. Chateigner: CRISMAT–ENSICAEN, UMR CNRS No. 6508, 6 Boulevard M. Juin, F-14050 Caen, France, and Normandie Université, IUT Mesures-Physiques, Université de Caen Normandie, Caen, France. [5.3]

J. P. Cline: National Institute of Standards and Technology, Gaithersburg, Maryland, USA. [3.1]

G. Cruciani: Department of Physics and Earth Sciences, University of Ferrara, Polo Scientifico-technologico – Bld B, Via G. Saragat 1, I-44122 Ferrara, Italy. [7.14]

A. Cuesta: ALBA Synchrotron, Carrer de la Llum 2–26, Cerdanyola, 08290 Barcelona, Spain. [3.10]

C. Cuocci: Institute of Crystallography – CNR, Via Amendola 122/o, Bari, I-70126, Italy. [3.4, 4.2]

W. I. F. David: ISIS Facility, Rutherford Appleton Laboratory, Chilton OX11 0QX, UK. [4.3]

A. G. De la Torre: Departamento de Química Inorgánica, Cristalografía y Mineralogía, Universidad de Málaga, 29071 Málaga, Spain. [3.10, 7.12]

R. E. Dinnebier: Max Planck Institute for Solid State Research, Heisenbergstrasse 1, D-70569 Stuttgart, Germany. [1.1, 4.8]

W. Dong: Department of Chemistry, University of Glasgow, University Avenue, Glasgow G12 8QQ, UK. [3.8]

H. Ehrenberg: Institut für Angewandte Materialien (IAM-ESS), Karlsruhe Institut für Technologie (KIT), Eggenstein-Leopoldshafen, Germany. [2.8]

V. Favre-Nicolin: ESRF – The European Synchrotron, F-38043 Grenoble, France. [4.5]

F. R. Feret‡: Feret Analytical Consulting, 128, Des Fauvettes, Saint-Colomban, Québec, Canada J5K 0E2. [7.6]

G. Ferraris: Dipartimento di Scienze della Terra, Università degli Studi di Torino, Via Valperga Caluso 35, I-10125 Torino, Italy. [7.14]

A. Fitch: ESRF, 71 Avenue des Martyrs, CS40220, 38043 Grenoble Cedex 9, France. [2.2]

A. J. Florence: Strathclyde Institute of Pharmacy and Biomedical Sciences, University of Strathclyde, Glasgow, UK. [4.4]

H. Fuess: Technische Universität Darmstadt, Darmstadt, Germany. [2.8]

M. García-Maté: Departamento de Química Inorgánica, Cristalografía y Mineralogía, Universidad de Málaga, 29071 Málaga, Spain, and X-Ray Data Services S.L., Edificio de institutos universitarios, c/ Severo Ochoa 4, Parque technológico de Andalucía, 29590 Málaga, Spain. [3.10]

C. J. Gilmore: Department of Chemistry, University of Glasgow, University Avenue, Glasgow G12 8QQ, UK. [3.8, 6.1]

T. E. Gorelik: University of Ulm, Central Facility for Electron Microscopy, Electron Microscopy Group of Materials Science (EMMS), Albert Einstein Allee 11, 89069 Ulm, Germany. [2.4]

S. Gražulis: Institute of Biotechnology, Vilnius University, Saulekekio al. 7, 10257 Vilnius, Lithuania. [3.7.8]

B. B. He: Bruker AXS Inc., 5465 E. Cheryl Parkway, Madison, WI 53711, USA. [2.5]

A. Henins: National Institute of Standards and Technology, Gaithersburg, Maryland, USA. [3.1]

M. Hinterstein: Institut für Angewandte Materialien (IAM-ESS), Karlsruhe Institut für Technologie (KIT), Eggenstein-Leopoldshafen, Germany. [2.8]

C. J. Howard: School of Engineering, University of Newcastle, Callaghan, NSW 2308, Australia. [2.3]

Qingzhen Huang: NIST Center for Neutron Research, National Institute of Standards and Technology, Gaithersburg, Maryland 20899, USA. [7.13]

A. Huq: Chemical and Engineering Materials Division, Spallation Neutron Source, PO Box 2008, MS 6475, Oak Ridge, TN 37831, USA. [2.10]

J. A. Kaduk: Department of Chemistry, Illinois Institute of Technology, 3101 South Dearborn Street, Chicago, IL 60616, USA, Department of Physics, North Central College, 131 South Loomis Street, Naperville, IL 60540, USA, and Poly Crystallography Inc., 423 East Chicago Avenue, Naperville, IL 60540, USA. [2.10, 3.7, 4.9, 6.1, 7.11]

---

‡ Emeritus, Senior Consultant with Arvida R&D Centre of Rio Tinto Alcan in Jonquiere, Quebec, Canada.

A. Katrusiak: Faculty of Chemistry, Adam Mickiewicz University, Poznań, Poland. [2.7]

A. Kern: Bruker AXS, Östliche Rheinbrückenstrasse 49, Karlsruhe 76187, Germany. [2.1]

E. H. Kisi: School of Engineering, University of Newcastle, Callaghan, NSW 2308, Australia. [2.3]

R. Kleeberg: TU Bergakademie Freiberg, Institut für Mineralogie, Brennhausgasse 14, Freiberg, D-09596, Germany. [3.9]

K. Knorr: Bruker AXS GmbH, Oestliche Rheinbrückenstr. 49, 76187 Karlsruhe, Germany. [3.9]

U. Kolb: Institut für Physikalische Chemie, Johannes Gutenberg-Universität Mainz, Welderweg 11, 55099 Mainz, Germany. [2.4]

J. L. Lábár: Institute of Technical Physics and Materials Science, Centre for Energy Research, Hungarian Academy of Sciences, Konkoly Thege M. u. 29–33, H-1121 Budapest, Hungary. [2.4]

A. Le Bail: Université du Maine, Institut des Molécules et Matériaux du Mans, UMR CNRS 6283, Avenue Olivier Messiaen, 72085 Le Mans Cedex 9, France. [3.5]

L. León-Reina: Servicios Centrales de Apoyo a la Investigación, Universidad de Málaga, 29071 Málaga, Spain. [3.10, 7.12]

M. Leoni: Department of Civil, Environmental and Mechanical Engineering, University of Trento, via Mesiano 77, 38123 Trento, Italy. [3.6, 5.1]

L. Lutterotti: Dipartimento di Ingegneria Industriale, Università di Trento, via Sommarive, 9, 38123 Trento, Italy. [5.3]

L. B. McCusker: Laboratory of Crystallography, ETH Zurich, HCI, G 509, CH-8093 Zurich, Switzerland. [4.6]

I. C. Madsen: CSIRO Mineral Resources, Private Bag 10, Clayton South 3169, Victoria, Australia. [3.9]

O. V. Magdysyuk: Max Planck Institute for Solid State Research, Heisenbergstrasse 1, D-70569 Stuttgart, Germany. [4.8]

I. Margiolaki: Department of Biology, Section of Genetics, Cell Biology and Development, University of Patras, GR-26500, Patras, Greece. [7.1]

M. H. Mendenhall: National Institute of Standards and Technology, Gaithersburg, Maryland, USA. [3.1]

S. T. Misture: Inamori School of Engineering, Alfred University, Alfred, NY 14802, USA. [7.9]

A. Moliterni: Institute of Crystallography – CNR, Via Amendola 122/o, Bari, I-70126, Italy. [3.4, 4.2]

M. Morales: CIMAP ENSICAEN, UMR CNRS No. 6252, 6 Boulevard M. Juin, F-14050 Caen, France, and Normandie Université, ESPE Caen, Université de Caen Normandie, Caen, France. [5.3]

P. Pattison: Laboratory for Quantum Magnetism, Institute of Physics, Ecole Polytechnique Federale de Lausanne, CH-1015 Lausanne, Switzerland. [2.9]

N. C. Popa: National Institute of Materials Physics, Atomistilor Str. No. 405A, PO Box MG7, 077125 Magurele, Romania. [5.2]

H. F. Poulsen: Institut for Fysik, Danmarks Tekniske Universitet, Kgs. Lyngby, Denmark. [5.5]

C. A. Reiss: Noordikslaan 51, 7602 CC Almelo, The Netherlands. [2.6]

D. F. Rendle‡: Cranfield Forensic Institute, Department of Engineering & Applied Science, Cranfield University, Shrivenham, Swindon SN6 8LA, Wiltshire, UK. [7.2]

S. M. Reutzel-Edens: Lilly Research Laboratories, Eli Lilly & Company, Indianapolis, IN 46285, USA. [7.5]

R. Rizzi: Institute of Crystallography – CNR, Via Amendola 122/o, Bari, I-70126, Italy. [3.4, 4.2]

M. A. Rodriguez: Materials Characterization and Performance Department, Sandia National Laboratories, Albuquerque, NM 87185–1411, USA. [7.3]

I. Santacruz: Departamento de Química Inorgánica, Cristalografía y Mineralogía, Universidad de Málaga, 29071 Málaga, Spain. [3.10]

N. V. Y. Scarlett: CSIRO Mineral Resources, Private Bag 10, Clayton South 3169, Victoria, Australia. [3.9, 7.7]

H. Schenk: HIMS, FWNI, University of Amsterdam, Postbus 94157, 1090 GD Amsterdam, The Netherlands. [6.1]

M. U. Schmidt: Institut für Anorganische und Analytische Chemie, Johann Wolfgang Goethe-Universität, Max-von-Laue-Strasse, D-60438 Frankfurt am Main, Germany. [7.10]

A. Senyshyn: Technische Universität München, Garching b. München, Germany. [2.8]

K. Shankland: School of Pharmacy, The University of Reading, Whiteknights, PO Box 224, Reading RG6 6AD, UK. [4.1]

S. van Smaalen: Laboratory of Crystallography, University of Bayreuth, Universitätsstrasse 30, D-95447 Bayreuth, Germany. [4.8]

K. Ståhl: Department of Chemistry, Technical University of Denmark, Kemitorvet, Building 207, DK-2800 Kgs. Lyngby, Denmark. [3.7.7.2]

J. K. Stalick: NIST Center for Neutron Research, National Institute of Standards and Technology, 100 Bureau Drive, Gaithersburg, MD 20899, USA. [4.9.3]

P. W. Stephens: Department of Physics and Astronomy, Stony Brook University, Stony Brook, NY 11794–3800, USA. [3.2]

B. H. Toby: Advanced Photon Source, Argonne National Laboratory, Argonne, IL 60439-4856, USA. [4.7, 4.9.2, 4.9.3, 4.10]

O. Vallcorba: ALBA Synchrotron, Carrer de la Llum 2–26, Cerdanyola, 08290 Barcelona, Spain. [3.10]

G. B. M. Vaughan: European Synchrotron Radiation Facility, Grenoble, France. [5.5]

P. Villars: 400 Schwanden, Vitznau, CH-6354 Switzerland. [3.7.5]

R. B. Von Dreele: Advanced Photon Source, Argonne National Laboratory, 9700 S. Cass Avenue, Argonne, IL 60439–4814, USA. [3.3]

P. S. Whitfield: Energy, Mining and Environment Portfolio, National Research Council Canada, 1200 Montreal Road, Ottawa ON K1A 0R6, Canada. [2.10]

D. Windover: National Institute of Standards and Technology, Gaithersburg, Maryland, USA. [3.1]

W. Wong-Ng: Materials Science Measurement Division, National Institute of Standards and Technology, Gaithersburg, MD 20899, USA. [7.8]

J. Zhang: Intel Corporation, Technology Manufacturing Group, 2501 NE Century Boulevard, Hillsboro, OR 97124, USA. [2.4]

J.-M. Zuo: Department of Materials Science and Engineering, University of Illinois, 1304 W. Green Street, Urbana, IL 61801, USA. [2.4]

---

‡ Visiting Fellow.

Contents

PAGE

Preface (C. J. Gilmore, J. A. Kaduk and H. Schenk) xxviii

PART 1. INTRODUCTION 1

1.1. Overview and principles of powder diffraction (R. E. Dinnebier and S. J. L. Billinge) 2

- **1.1.1. Information content of a powder pattern** 2
- **1.1.2. The peak position** 2
  - **1.1.2.1. The Bragg equation derived** 2
  - **1.1.2.2. The Bragg equation from the reciprocal lattice** 4
  - **1.1.2.3. The Bragg equation from the Laue equation** 6
  - **1.1.2.4. The Ewald construction and Debye–Scherrer cones** 7
- **1.1.3. The peak intensity** 9
  - **1.1.3.1. Adding phase-shifted amplitudes** 9
- **1.1.4. The peak profile** 12
  - **1.1.4.1. Sample contributions to the peak profile** 13
- **1.1.5. The background** 15
  - **1.1.5.1. Information content in the background** 15
  - **1.1.5.2. Background from extraneous sources** 15
  - **1.1.5.3. Sources of background from the sample** 16
- **1.1.6. Local and global optimization of crystal structures from powder diffraction data** 19
  - **1.1.6.1. Rietveld refinement** 19
  - **1.1.6.2. Local structure refinement** 22
  - **1.1.6.3. Parametric Rietveld refinement** 22
- **1.1.7. Outlook** 22

PART 2. INSTRUMENTATION AND SAMPLE PREPARATION 25

2.1. Instrumentation for laboratory X-ray scattering techniques (A. Kern) 26

- **2.1.1. Introduction** 26
- **2.1.2. Scope and terminology** 26
- **2.1.3. Historical overview** 26
  - **2.1.3.1. From film cameras to diffractometers** 26
  - **2.1.3.2. Recent years** 28
- **2.1.4. The platform concept – fitting the instrument to the need** 28
  - **2.1.4.1. Basic design principles and instrument geometry considerations** 28
  - **2.1.4.2. Range of hardware** 30
  - **2.1.4.3. Range of applications** 31
- **2.1.5. Goniometer designs** 32
  - **2.1.5.1. Geometrical conventions and scan modes** 32
  - **2.1.5.2. Accuracy and precision** 34
  - **2.1.5.3. Hybrid beam-path systems** 35
- **2.1.6. X-ray sources and optics** 36
  - **2.1.6.1. X-ray beam quality measures** 36
  - **2.1.6.2. X-ray sources** 37
  - **2.1.6.3. X-ray optics** 39
- **2.1.7. X-ray detectors** 45
  - **2.1.7.1. Detector parameters** 45

2.1.7.2. Detector types .. 46

2.1.7.3. Position sensitivity and associated scanning modes .. 49

2.2. Synchrotron radiation and powder diffraction (A. Fitch) .. 51

2.2.1. Introduction .. 51

2.2.2. Production of synchrotron radiation .. 51

2.2.2.1. Bending magnets .. 52

2.2.2.2. Insertion devices .. 53

2.2.3. Optics .. 54

2.2.3.1. Monochromator .. 54

2.2.3.2. Mirror .. 55

2.2.3.3. Compound refractive lens .. 56

2.2.4. Diffractometers .. 56

2.2.4.1. Parallel-beam instruments .. 56

2.2.4.2. Debye–Scherrer instruments .. 58

2.2.4.3. Energy-dispersive instruments .. 59

2.2.5. Considerations for powder-diffraction experiments .. 60

2.2.5.1. Polarization .. 60

2.2.5.2. Radiation damage .. 61

2.2.5.3. Beam heating .. 61

2.2.5.4. Choice of wavelength .. 61

2.2.5.5. Angular resolution .. 62

2.2.5.6. Spatial resolution .. 62

2.2.5.7. Time resolution .. 63

2.2.5.8. Beamline evolution .. 63

2.3. Neutron powder diffraction (C. J. Howard and E. H. Kisi) .. 66

2.3.1. Introduction to the diffraction of thermal neutrons .. 66

2.3.2. Neutrons and neutron diffraction – pertinent details .. 67

2.3.2.1. Properties of the neutron .. 67

2.3.2.2. Neutron scattering lengths .. 68

2.3.2.3. Refractive index for neutrons .. 68

2.3.2.4. Neutron attenuation .. 69

2.3.2.5. Magnetic form factors and magnetic scattering lengths .. 69

2.3.2.6. Structure factors .. 70

2.3.3. Neutron sources .. 70

2.3.3.1. The earliest neutron sources .. 70

2.3.3.2. Fission reactors for neutron-beam research .. 72

2.3.3.3. Spallation neutron sources .. 73

2.3.3.4. Neutron beam tubes and guides .. 77

2.3.4. Diffractometers .. 80

2.3.4.1. Constant-wavelength neutron diffractometers .. 80

2.3.4.2. Time-of-flight (TOF) diffractometers .. 85

2.3.4.3. Variations on a theme .. 88

2.3.4.4. Comparison of CW and TOF diffractometers .. 91

2.3.5. Experimental considerations .. 92

2.3.5.1. Preliminary considerations .. 92

2.3.5.2. Sample-related factors .. 94

2.3.5.3. Sample environment and *in situ* experiments .. 96

2.3.6. Concluding remarks .. 98

2.4. Electron powder diffraction (J.-M. Zuo, J. L. Lábár, J. Zhang, T. E. Gorelik and U. Kolb) 102

2.4.1. Introduction 102

2.4.2. Electron powder diffraction pattern geometry and intensity (J.-M. Zuo and J. L. Lábár) 103

2.4.3. Electron powder diffraction techniques (J.-M. Zuo and J. Zhang) 105

2.4.3.1. Selected-area electron diffraction (SAED) 105

2.4.3.2. Nano-area electron diffraction (NAED) 105

2.4.3.3. Sample preparation 106

2.4.3.4. Diffraction data collection, processing and calibration 107

2.4.4. Phase identification and phase analysis (J. L. Lábár) 108

2.4.5. Texture analysis (J. L. Lábár) 110

2.4.6. Rietveld refinement with electron diffraction data (T. E. Gorelik and U. Kolb) 111

2.4.7. The pair distribution function from electron diffraction data (T. E. Gorelik and U. Kolb) 113

2.4.8. Summary 114

Appendix A2.4.1. Computer programs for electron powder diffraction 114

2.5. Two-dimensional powder diffraction (B. B. He) 118

2.5.1. Introduction 118

2.5.1.1. The diffraction pattern measured by an area detector 118

2.5.1.2. Comparison between 2D-XRD and conventional XRD 118

2.5.1.3. Advantages of two-dimensional X-ray diffraction 118

2.5.2. Fundamentals 119

2.5.2.1. Diffraction space and laboratory coordinates 119

2.5.2.2. Detector space and pixel position 121

2.5.2.3. Sample space and goniometer geometry 122

2.5.2.4. Diffraction-vector transformation 123

2.5.3. Instrumentation 124

2.5.3.1. X-ray source and optics 124

2.5.3.2. 2D detector 125

2.5.3.3. Data corrections and integration 128

2.5.4. Applications 133

2.5.4.1. Phase identification 133

2.5.4.2. Texture analysis 136

2.5.4.3. Stress measurement 140

2.5.4.4. Quantitative analysis 145

2.6. Non-ambient-temperature powder diffraction (C. A. Reiss) 150

2.6.1. Introduction 150

2.6.2. *In situ* powder diffraction 150

2.6.3. Processes of interest 150

2.6.4. General system setup of non-ambient chambers 150

2.6.4.1. Sample stage 150

2.6.4.2. Temperature-control unit, process controller 150

2.6.4.3. Vacuum equipment, gas supply 151

2.6.4.4. Water cooling 151

2.6.4.5. Diffractometer and height-compensation mechanism 151

2.6.5. Specimen properties 151

2.6.6. High-temperature sample stages 151

2.6.6.1. Direct heating: strip heaters 152

2.6.6.2. Environmental heating: the oven 152

2.6.6.3. Environmental heating: lamp furnace 152

2.6.6.4. Domed hot stage 153

2.6.7. Low-temperature sample stages 153

2.6.7.1. Cryogenic cooling stages/cryostat 153

2.6.7.2. Cryogenic cooling stages/cryostream 154

2.6.8. Temperature accuracy 155

2.6.9. Future 155

2.7. High-pressure devices (A. Katrusiak) 156

2.7.1. Introduction 156

2.7.2. Historical perspective 156

2.7.3. Main types of high-pressure environments 157

2.7.4. The diamond-anvil cell (DAC) 159

2.7.5. Variable-temperature high-pressure devices 160

2.7.6. Soft and biomaterials under pressure 161

2.7.7. Completeness of data 161

2.7.8. Single-crystal data collection 162

2.7.9. Powder diffraction with the DAC 163

2.7.10. Sample preparation 164

2.7.11. Hydrostatic conditions 164

2.7.12. High-pressure chamber and gasket in the DAC 165

2.7.13. High-pressure neutron diffraction 166

2.7.14. Pressure determination 166

2.7.15. High-pressure diffraction data corrections 167

2.7.16. Final remarks 168

2.8. Powder diffraction in external electric and magnetic fields (H. Ehrenberg, M. Hinterstein, A. Senyshyn and H. Fuess) 174

2.8.1. Introduction 174

2.8.2. Experimental conditions 174

2.8.2.1. Detectors 175

2.8.2.2. Absorption 176

2.8.2.3. Sample fluorescence and incoherent neutron scattering 177

2.8.3. Examples 177

2.8.3.1. *In situ* studies of ferroelectrics in an external electric field 177

2.8.3.2. *In situ* studies of electrode materials and *in operando* investigations of Li-ion batteries 181

2.8.3.3. Diffraction under a magnetic field 183

2.8.4. Summary 186

2.9. Cells for *in situ* powder-diffraction investigation of chemical reactions (W. van Beek and P. Pattison) .. 189

2.9.1. Introduction 189

2.9.2. Historical perspective 189

2.9.3. Main types of reaction cells 189

2.9.3.1. Introduction 189

2.9.3.2. Capillary cells 190

2.9.3.3. Reactions requiring specialist cells 192

2.9.3.4. Cells specifically for neutrons 195

2.9.4. Complementary methods and future developments 197

2.10. Specimen preparation (P. S. Whitfield, A. Huq and J. A. Kaduk) 200

2.10.1. X-ray powder diffraction 200

2.10.1.1. Powders and particle statistics (granularity) 201

2.10.1.2. Preferred orientation 206

2.10.1.3. Absorption (surface roughness), microabsorption and extinction 209

2.10.1.4. Holders 211

2.10.2. Neutron powder diffraction 218

2.10.2.1. Specimen form 218

2.10.2.2. Sample size 218

2.10.2.3. Specimen containment 218

2.10.2.4. Isotopes, absorption and activation 220

2.10.3. Conclusions 221

PART 3. METHODOLOGY 223

3.1. The optics and alignment of the divergent-beam laboratory X-ray powder diffractometer and its calibration using NIST standard reference materials (J. P. Cline, M. H. Mendenhall, D. Black, D. Windover and A. Henins) 224

3.1.1. Introduction 224

3.1.2. The instrument profile function 224

3.1.3. Instrument alignment 230

3.1.4. SRMs, instrumentation and data-collection procedures 235

3.1.5. Data-analysis methods 238

3.1.6. Instrument calibration 241

3.1.7. Conclusions 250

3.2. The physics of diffraction from powders (P. W. Stephens) 252

3.2.1. Introduction 252

3.2.2. Idealized diffraction from powders 252

3.2.2.1. Peak positions 252

3.2.2.2. Diffraction peak intensities 253

3.2.2.3. Peak shapes 255

3.2.3. Complications due to non-ideal sample or instrument properties 257

3.2.3.1. Absorption within a homogeneous sample 257

3.2.3.2. Absorption with multiphase samples 258

3.2.3.3. Granularity, microabsorption and surface roughness 258

3.2.3.4. Anisotropic strain broadening 259

3.2.3.5. Preferred orientation (texture) 260

3.2.3.6. Extinction 260

3.2.4. The Debye scattering equation 261

3.2.5. Summary 261

3.3. Powder diffraction peak profiles (R. B. Von Dreele) 263

3.3.1. Introduction 263

3.3.2. Peak profiles for constant-wavelength radiation (X-rays and neutrons) 263

3.3.2.1. Introduction – symmetric peak profiles 263

3.3.2.2. Constant-wavelength powder profile asymmetry 264

3.3.2.3. Peak-displacement effects 264

3.3.2.4. Fundamental parameters profile modelling 265

3.3.3. Peak profiles for neutron time-of-flight experiments 265

3.3.3.1. The experiment 265

3.3.3.2. The neutron pulse shape 265

3.3.3.3. The neutron TOF powder peak profile 266

3.3.4. Peak profiles for X-ray energy-dispersive experiments 266

3.3.5. Sample broadening 267

3.3.5.1. Crystallite size broadening .. 267
3.3.5.2. Microstrain broadening .. 267

3.4. Indexing a powder diffraction pattern (A. Altomare, C. Cuocci, A. Moliterni and R. Rizzi) .. 270
3.4.1. Introduction .. 270
3.4.2. The basic concepts of indexing .. 270
3.4.2.1. Figures of merit .. 271
3.4.2.2. Geometrical ambiguities .. 272
3.4.3. Indexing methods .. 273
3.4.3.1. Traditional indexing methods .. 273
3.4.3.2. Non-traditional indexing methods .. 275
3.4.4. Software packages for indexing and examples of their use .. 275
3.4.4.1. Traditional indexing programs .. 276
3.4.4.2. Evolved indexing programs .. 276
3.4.4.3. Non-traditional indexing programs .. 277
3.4.4.4. Crysfire: a suite of indexing programs .. 278
3.4.4.5. Two commercial programs .. 278
3.4.4.6. Examples of applications of indexing programs .. 278
3.4.5. Conclusion .. 280

3.5. Data reduction to $|F_{hkl}|$ values (A. Le Bail) .. 282
3.5.1. Introduction .. 282
3.5.2. Algorithms .. 282
3.5.2.1. Unrestrained cell .. 282
3.5.2.2. Restrained cell .. 283
3.5.3. Pitfalls in the extraction of accurate $|F_{hkl}|$ values using the Pawley and Le Bail methods .. 284
3.5.3.1. Consequences of (exact or accidental) overlap .. 284
3.5.3.2. Preferred-orientation effects .. 284
3.5.3.3. Background-estimation effects .. 285
3.5.4. Applications and by-products .. 285
3.5.4.1. Supporting indexing and space-group determination .. 286
3.5.4.2. Structure solution .. 286
3.5.5. Conclusion .. 286

3.6. Whole powder pattern modelling: microstructure determination from powder diffraction data (M. Leoni) 288
3.6.1. Introduction .. 288
3.6.2. Fourier methods .. 289
3.6.2.1. Definitions .. 289
3.6.2.2. Peak profile and the convolution theorem .. 289
3.6.2.3. The Warren–Averbach method and its variations .. 289
3.6.2.4. Beyond the Warren–Averbach method .. 290
3.6.2.5. Whole powder pattern modelling (WPPM) .. 290
3.6.2.6. Broadening components .. 291
3.6.2.7. Assembling the equations into a peak and modelling the data .. 296
3.6.3. Examples of WPPM analysis .. 298
3.6.3.1. Nanocrystalline ceria .. 298
3.6.3.2. Copper oxide .. 299
Appendix A3.6.1. Functions for profile shapes .. 301

3.7. Crystallographic databases and powder diffraction (J. A. Kaduk) .. 304
3.7.1. Introduction .. 304

3.7.1.1. History of the PDF/ICDD .. 304

3.7.1.2. Search/match .. 304

3.7.2. Powder Diffraction File (PDF) .. 305

3.7.2.1. Sources and formats of the PDF .. 306

3.7.2.2. Quality marks in the PDF .. 306

3.7.2.3. Features of the PDF .. 307

3.7.2.4. Boolean logic in phase identification .. 309

3.7.3. Cambridge Structural Database (CSD) .. 313

3.7.3.1. *Mercury* .. 314

3.7.4. Inorganic Crystal Structure Database (ICSD) .. 314

3.7.4.1. General features of the ICSD .. 315

3.7.4.2. Features particularly useful for powder crystallography .. 315

3.7.5. Pearson's Crystal Data (PCD/LPF) (with P. Villars and K. Cenzual) .. 316

3.7.5.1. General information .. 316

3.7.5.2. Evaluation procedure .. 316

3.7.5.3. Standardized crystallographic data .. 316

3.7.5.4. Consequent prototype assignment .. 317

3.7.5.5. Assigned atom coordinates .. 317

3.7.5.6. External links .. 317

3.7.5.7. Retrievable database fields .. 317

3.7.5.8. Particular software features .. 318

3.7.6. Metals data file (CRYSTMET) .. 318

3.7.7. Protein Data Bank (PDB) .. 318

3.7.7.1. Powder diffraction by proteins .. 318

3.7.7.2. Calculation of protein powder patterns (with K. Ståhl) .. 319

3.7.8. Crystallography Open Database (COD) (with S. Gražulis) .. 320

3.7.9. Other internet databases .. 321

3.8. Clustering and visualization of powder-diffraction data (C. J. GILMORE, G. BARR AND W. DONG) .. 325

3.8.1. Introduction .. 325

3.8.2. Comparing 1D diffraction patterns .. 325

3.8.2.1. Spearman's rank order coefficient .. 325

3.8.2.2. Pearson's *r* coefficient .. 325

3.8.2.3. Combining the correlation coefficients .. 325

3.8.2.4. Full-profile qualitative pattern matching .. 326

3.8.2.5. Generation of the correlation and distance matrices .. 326

3.8.3. Cluster analysis .. 327

3.8.3.1. Dendrograms .. 327

3.8.3.2. Estimating the number of clusters .. 327

3.8.3.3. Metric multidimensional scaling .. 328

3.8.3.4. Principal-component analysis .. 329

3.8.3.5. Choice of clustering method .. 329

3.8.3.6. The most representative sample .. 329

3.8.3.7. Amorphous samples .. 329

3.8.4. Data visualization .. 329

3.8.4.1. Primary data visualization .. 329

3.8.4.2. Secondary visualization using parallel coordinates, the grand tour and minimum spanning trees .. 330

3.8.5. Further validating and visualizing clusters: silhouettes and fuzzy clustering .. 331

3.8.5.1. Silhouettes .. 331

3.8.5.2. Fuzzy clustering .. 333

3.8.5.3. The *PolySNAP* program and *DIFFRAC.EVA* 333

3.8.6. Examples 333

3.8.6.1. Aspirin data 333

3.8.6.2. Phase transitions in ammonium nitrate 335

3.8.7. Quantitative analysis with high-throughput PXRD data without Rietveld refinement 337

3.8.7.1. Example: inorganic mixtures 338

3.8.8. Using spectroscopic data 339

3.8.9. Combining data types: the INDSCAL method 340

3.8.9.1. An example combining PXRD and Raman data 342

3.8.10. Quality control 342

3.8.11. Computer software 342

3.9. Quantitative phase analysis (I. C. Madsen, N. V. Y. Scarlett, R. Kleeberg and K. Knorr) 344

3.9.1. Introduction 344

3.9.2. Phase analysis 344

3.9.3. QPA methodology 345

3.9.3.1. Absorption–diffraction method 345

3.9.3.2. Internal standard method 346

3.9.3.3. Reference intensity ratio methods 347

3.9.3.4. Matrix-flushing method 347

3.9.3.5. Full-pattern fitting methods 348

3.9.3.6. Rietveld-based QPA 348

3.9.4. Demonstration of methods 350

3.9.4.1. Absorption–diffraction method 350

3.9.4.2. Internal standard method 350

3.9.4.3. Reference intensity ratio 351

3.9.4.4. Matrix flushing 352

3.9.4.5. Rietveld-based methods 352

3.9.5. Alternative methods for determination of calibration constants 353

3.9.5.1. Standardless determination of the phase constant *C* 353

3.9.5.2. Demonstration of the Zevin approach 354

3.9.5.3. Experiment constant – a whole-sample approach 355

3.9.6. Quantification of phases with partial or no known crystal structures 356

3.9.6.1. Use of calibrated models 356

3.9.6.2. Modelling of structural disorder 358

3.9.6.3. Quantitative determination of amorphous material 360

3.9.7. QPA from *in situ* experimentation 361

3.9.7.1. Data analysis 361

3.9.8. QPA using neutron diffraction data 362

3.9.9. QPA using energy-dispersive diffraction data 362

3.9.10. Improving accuracy 364

3.9.10.1. Standard deviations and error estimates 364

3.9.10.2. Minimizing systematic errors 364

3.9.10.3. Minimizing sample-related errors 365

3.9.11. Summary 370

3.10. Accuracy in Rietveld quantitative phase analysis with strictly monochromatic Mo and Cu radiations
(L. León-Reina, A. Cuesta, M. García-Maté, G. Álvarez-Pinazo, I. Santacruz, O. Vallcorba,
A. G. De la Torre and M. A. G. Aranda) 374

3.10.1. Introduction 374

3.10.2. Compounds and series .. 375

3.10.2.1. Single phases .. 375

3.10.2.2. Crystalline inorganic series .. 375

3.10.2.3. Crystalline organic series .. 375

3.10.2.4. Variable amorphous content series .. 376

3.10.3. Analytical techniques .. 376

3.10.3.1. Mo $K\alpha_1$ laboratory X-ray powder diffraction (LXRPD) .. 376

3.10.3.2. Cu $K\alpha_1$ laboratory X-ray powder diffraction (LXRPD) .. 376

3.10.3.3. Transmission synchrotron X-ray powder diffraction (SXRPD) .. 376

3.10.4. Powder-diffraction data analysis .. 377

3.10.5. Crystalline single phases .. 377

3.10.6. Limits of detection and quantification .. 379

3.10.7. Increasing inorganic crystalline phase content series .. 381

3.10.8. Increasing crystalline organic phase content series .. 381

3.10.9. Increasing amorphous content series within an inorganic crystalline phase matrix .. 382

3.10.10. Conclusions .. 383

PART 4. STRUCTURE DETERMINATION .. 385

4.1. An overview of currently used structure determination methods for powder diffraction data (K. Shankland) .. 386

4.1.1. Introduction .. 386

4.1.2. Methods used in SDPD .. 386

4.1.3. Conventional direct methods of structure determination .. 387

4.1.4. Modified direct methods of structure determination .. 388

4.1.5. The direct-methods sum function .. 388

4.1.6. The Patterson function .. 388

4.1.7. Resonant (anomalous) scattering .. 388

4.1.8. Isomorphous replacement .. 389

4.1.9. Maximum-entropy methods .. 389

4.1.10. Charge flipping .. 389

4.1.11. Molecular envelopes .. 390

4.1.12. Model building .. 390

4.1.13. Molecular replacement .. 390

4.1.14. Global optimization .. 390

4.1.15. Maximum-likelihood methods .. 391

4.1.16. Local minimization .. 391

4.1.17. Active use of prior information for particular structural classes .. 391

4.1.18. Combined figures of merit .. 392

4.2. Solving crystal structures using reciprocal-space methods (A. Altomare, C. Cuocci, A. Moliterni and R. Rizzi) .. 395

4.2.1. Introduction .. 395

4.2.2. Intensity extraction for RS methods .. 395

4.2.3. Direct methods .. 395

4.2.3.1. Normalized structure factors .. 396

4.2.3.2. Structure invariants .. 397

4.2.3.3. Triplet invariants .. 397

4.2.3.4. How direct methods work .. 397

4.2.4. Improving data normalization .. 399

4.2.4.1. Pseudotranslational symmetry .. 399

- 4.2.4.2. Preferred orientation .. 400
- 4.2.4.3. Systematic decomposition .. 400
- 4.2.5. Patterson methods .. 400
  - 4.2.5.1. The use of the Patterson function for estimating integrated intensities .. 401
- 4.2.6. Charge flipping .. 402
- 4.2.7. Maximum-entropy methods .. 403
- 4.2.8. Optimization of the structure model .. 404
  - 4.2.8.1. Fourier recycling (FR) .. 404
  - 4.2.8.2. Weighted least-squares (WLSQ) refinement .. 405
  - 4.2.8.3. Resolution bias modification (RBM) .. 405
- 4.2.9. Software packages for powder solution .. 406
  - 4.2.9.1. Example of structure solution by *XLENS* .. 406
  - 4.2.9.2. Example of structure solution by *SUPERFLIP* .. 407
  - 4.2.9.3. The input file for a default run of *EXPO* .. 407
  - 4.2.9.4. An example of model optimization by *EXPO* for an inorganic compound .. 407
  - 4.2.9.5. Example of model optimization by *EXPO* for an organic compound .. 408
  - 4.2.9.6. The ALLTRIALS tool in *EXPO*: exploring all the phase sets .. 410
  - 4.2.9.7. Graphical tools in *EXPO* .. 410
- 4.2.10. Conclusions .. 410

4.3. Real-space methods for structure solution from powder-diffraction data: application to molecular structures (W. I. F. DAVID) .. 414

- 4.3.1. Introduction .. 414
- 4.3.2. Real-space structure determination: a global-optimization extension of the Rietveld method .. 416
- 4.3.3. Optimizing the process of real-space structure determination from powder-diffraction data .. 416
  - 4.3.3.1. Introduction .. 416
  - 4.3.3.2. Parameterization of the molecular structure .. 417
- 4.3.4. The nature and magnitude of the global-optimization challenge .. 418
  - 4.3.4.1. Interpretation of the least-squares cost function .. 419
  - 4.3.4.2. The chi-squared hypersurface .. 421
- 4.3.5. Global-optimization algorithms .. 424
  - 4.3.5.1. Stochastic search algorithms .. 426
  - 4.3.5.2. Deterministic search algorithms .. 429
- 4.3.6. Using maximum-likelihood techniques to tackle incomplete structural models .. 430
  - 4.3.6.1. Introduction .. 430
  - 4.3.6.2. Working with incomplete structural models: maximum-likelihood methods .. 430

4.4. The use of supplementary information to solve crystal structures from powder diffraction (A. J. FLORENCE) 433

- 4.4.1. General remarks .. 433
- 4.4.2. Molecular models .. 434
  - 4.4.2.1. Molecular volume .. 434
  - 4.4.2.2. Fragment model selection: bond length and angles .. 434
  - 4.4.2.3. Flexible ring conformations .. 435
  - 4.4.2.4. Torsion-angle constraints .. 436
  - 4.4.2.5. Intermolecular distance constraints .. 438
  - 4.4.2.6. H-atom location in structures solved from X-ray powder data .. 438
  - 4.4.2.7. Crystal-structure prediction and crystal-structure solution .. 439
- 4.4.3. Concluding remarks .. 439
  - 4.4.3.1. Test data for SDPD .. 439

4.5. Solving and refining inorganic structures (R. Černý and V. Favre-Nicolin) 442

4.5.1. The molecular/non-molecular and the organic/inorganic boundaries 442

4.5.2. Modelling of non-molecular compounds 442

4.5.2.1. Principles 442

4.5.2.2. Building units 442

4.5.2.3. Special positions and the sharing of atoms between building units 443

4.5.2.4. Is there a need for precise unit-cell contents? 444

4.5.2.5. Building units and the convergence of the DSM algorithm 444

4.5.2.6. Random *versus* non-random DSM algorithms 444

4.5.2.7. The choice of the cost function in DSM algorithms 445

4.5.3. Solving, refining and completing inorganic structures 445

4.5.3.1. A general problem: poor quality powder data 445

4.5.3.2. Indexing of multiphase samples 445

4.5.3.3. X-rays *versus* neutrons 446

4.5.3.4. Chemical and positional disorder 446

4.5.3.5. Structure validation – theoretical issues 447

4.5.4. Examples 448

4.5.4.1. Polyhedral compounds 448

4.5.4.2. Hybrid compounds 449

4.5.4.3. Close-packed compounds 450

4.6. Zeolites (L. B. McCusker and Ch. Baerlocher) 452

4.6.1. Introduction 452

4.6.2. Framework structure determination 452

4.6.2.1. Preliminary steps 454

4.6.2.2. Model building 454

4.6.2.3. *Focus* 455

4.6.2.4. Direct methods 456

4.6.2.5. Charge flipping 456

4.6.2.6. Using additional information 457

4.6.3. Structure refinement 458

4.6.3.1. Space-group ambiguity 458

4.6.3.2. Geometric restraints 458

4.6.3.3. Disorder 459

4.6.3.4. Locating non-framework species 459

4.6.3.5. Rietveld refinement of SSZ-74 460

4.6.3.6. Locating isomorphously substituted *T* atoms 462

4.6.4. Conclusions 462

4.7. Rietveld refinement (B. H. Toby) 465

4.7.1. History 465

4.7.2. Rietveld *versus* single-crystal refinements 466

4.7.3. Multiphase and multiple data set fitting 466

4.7.4. The mechanism of Rietveld fitting 467

4.7.5. Types of profile functions 467

4.7.6. Observed structure-factor estimates 467

4.7.7. Estimating observed structure factors without a structure 468

4.7.8. Agreement factors 468

4.7.9. Restraints and constraints in Rietveld refinement 469

4.7.10. The order in which to introduce parameters in a fit 470

4.7.11. Examples .. 471

4.7.12. Conclusions .. 471

4.8. Application of the maximum-entropy method to powder-diffraction data (O. V. MAGDYSYUK, S. VAN SMAALEN AND R. E. DINNEBIER) .. 473

4.8.1. Introduction .. 473

4.8.2. The principle of maximum entropy .. 474

4.8.3. Prior densities in MEM calculations .. 475

4.8.4. Crystallographic MEM equations .. 476

4.8.5. MEM algorithms .. 476

4.8.5.1. Exponential modelling algorithm (Gull & Daniell, 1978; Collins, 1982; Collins & Mahar, 1983) .. 476

4.8.5.2. Sakata–Sato algorithm (Sakata & Sato, 1990; Sakata *et al.*, 1990, 1992, 1993; Kumazawa *et al.*, 1995) .. 477

4.8.5.3. Cambridge algorithm (Bryan & Skilling, 1980, 1986; Burch *et al.*, 1983; Skilling & Bryan, 1984; Gull & Skilling, 1987, 1999) .. 477

4.8.5.4. Two-channel MaxEnt method (Papoular & Gillon, 1990; Zheludev *et al.*, 1995; Papoular *et al.*, 1996) .. 477

4.8.5.5. Valence-only MaxEnt method (Roversi *et al.*, 1998) .. 477

4.8.6. Constraints in the MEM based on the measured intensities from powder-diffraction data .. 478

4.8.6.1. *F* and *G* constraints .. 478

4.8.6.2. Constraints using 'partly phased' reflections for anomalous-scattering X-ray powder diffraction .. 479

4.8.6.3. Prior-derived *F* constraints .. 480

4.8.6.4. Observed structure factors .. 480

4.8.7. Analysis of the electron-density distribution from powder-diffraction data .. 480

4.8.7.1. Types of MEM-reconstructed electron-density distribution .. 480

4.8.7.2. MEM-based improvement of the structure model from charge flipping .. 482

4.8.7.3. Combination of MEM and Rietveld refinement (REMEDY cycle) .. 482

4.8.7.4. MEM-assisted structure solution by charge flipping .. 483

4.8.7.5. Disorder and anharmonic atomic displacements .. 484

4.8.7.6. Accurate electron densities .. 485

4.8.8. Extensions of the MEM .. 485

4.8.8.1. Distribution of normalized residuals of the structure factors .. 485

4.8.8.2. Stopping criterion .. 485

4.8.8.3. Generalization of MaxEnt algorithm to *n* dimensions ($n > 3$) and application to powder-diffraction data of aperiodic structures .. 486

4.9. Structure validation (J. A. KADUK) .. 489

4.9.1. Introduction .. 489

4.9.2. Statistical measures (with contributions from B. H. Toby) .. 489

4.9.3. Graphical measures (with contributions from B. H. Toby and J. K. Stalick) .. 490

4.9.4. Chemical reasonableness .. 496

4.9.4.1. Organic compounds .. 496

4.9.4.2. Inorganic compounds .. 503

4.9.5. Working by analogy .. 508

4.9.6. Structure validation in general .. 508

4.9.7. *CheckCIF/PLATON* .. 509

4.10. Use of CIF for powder diffraction data (B. H. TOBY) .. 515

4.10.1. Background .. 515

4.10.2. A brief introduction to CIF .. 515

4.10.3. CIF usage for powder diffraction .. 516

4.10.4. Creation of pdCIF data files .. 517

4.10.5. Creating readers for pdCIF data files .. 518

4.10.5.1. Ordinate .. 518

- 4.10.5.2. Observed intensities 518
- 4.10.5.3. Background intensities 518
- 4.10.5.4. Computed intensities 518
- 4.10.6. CIF software for powder diffraction 518
  - 4.10.6.1. *enCIFer* 519
  - 4.10.6.2. The IUCr *publCIF* application 519
  - 4.10.6.3. The IUCr *checkCIF* web application 519
  - 4.10.6.4. The IUCr *pdCIFplot* application 519
  - 4.10.6.5. International Centre for Diffraction Data (ICDD) *Genie* application 520
  - 4.10.6.6. pdCIF creation in *GSAS-II* 520
- 4.10.7. Conclusions 521

PART 5. DEFECTS, TEXTURE AND MICROSTRUCTURE 523

5.1. Domain size and domain-size distributions (M. Leoni) 524
- 5.1.1. Introduction 524
- 5.1.2. The Scherrer formula and integral-breadth methods 524
- 5.1.3. Fourier methods 526
- 5.1.4. The peak profile and the common volume function (‘ghost’) 526
- 5.1.5. Common volume function for simple shapes 528
- 5.1.6. Calculation of the intensity profile for simple shapes 530
- 5.1.7. Meaning of the size Fourier coefficients: mean size and column-length distribution 531
- 5.1.8. Extension of the Fourier approach to a size distribution 531
- 5.1.9. Analytical distributions 533
- 5.1.10. Histogram (arbitrary) distributions 534
- 5.1.11. Example 534

5.2. Stress and strain (N. C. Popa) 538
- 5.2.1. The importance of determining stress and the diffraction method 538
- 5.2.2. Strain and stress in single crystals, elastic constants and transformations 538
- 5.2.3. Strain and stress in polycrystalline samples 540
  - 5.2.3.1. Types of strains and stresses, and the strain/stress orientation distribution function 540
  - 5.2.3.2. The mean and variance of the observable strain, the peak shift and broadening 541
- 5.2.4. Determining the strain/stress by diffraction 542
  - 5.2.4.1. Determining the macrostrain/stress 542
  - 5.2.4.2. Determining the microstrain 543
- 5.2.5. Macrostrain/stress in isotropic samples: classical approximations 543
  - 5.2.5.1. The Voigt model 544
  - 5.2.5.2. The Reuss model 544
  - 5.2.5.3. The Hill average 545
  - 5.2.5.4. The Kroner model 545
  - 5.2.5.5. The ‘$\sin^2 \Psi$’ method 545
  - 5.2.5.6. Determining the single-crystal elastic constants 546
- 5.2.6. The hydrostatic state in isotropic polycrystals 546
- 5.2.7. Calculating the macroscopic strain/stress using spherical harmonics 547
  - 5.2.7.1. Strain expansion in generalized spherical harmonics: the Popa and Balzar approach 547
  - 5.2.7.2. The selection rules for all Laue classes 548
  - 5.2.7.3. Generalized spherical harmonics of real type, and the WSODF index 548
  - 5.2.7.4. Determining the macrostrain/stress state of the sample 549
  - 5.2.7.5. Simplified (‘short’) harmonics representation of the peak shift, and the ‘mixed’ representation 550
  - 5.2.7.6. Implementation in Rietveld codes 550

5.2.7.7. An application: determining the averaged macroscopic strain and stress tensors in a rolled uranium plate from time-of-flight neutron diffraction data .. 551

5.2.7.8. Limitations of the spherical-harmonics approach and possible further developments .. 552

5.2.8. The spherical-harmonics approach to strain broadening .. 552

5.2.8.1. Ignoring the macrostrain variance .. 552

5.2.8.2. The double-dependent anisotropic strain breadth (DDASB) .. 552

5.2.8.3. The ‘classical’ limit of the DDASB .. 553

5.3. Quantitative texture analysis and combined analysis (D. Chateigner, L. Lutterotti and M. Morales) .. 555

5.3.1. Introduction .. 555

5.3.2. Crystallographic quantitative texture analysis (QTA) .. 555

5.3.2.1. Orientation distribution (OD) .. 555

5.3.2.2. The fundamental equation of quantitative texture analysis .. 558

5.3.2.3. Resolution of the fundamental equation .. 559

5.3.2.4. Inverse pole figures .. 562

5.3.2.5. OD refinement reliability estimators .. 563

5.3.2.6. Texture-strength factors .. 564

5.3.2.7. Texture types .. 564

5.3.2.8. Reciprocal-space mapping .. 566

5.3.3. Magnetic quantitative texture analysis (MQTA) .. 567

5.3.3.1. Magnetization curves and magnetic moment distributions .. 567

5.3.3.2. Magnetic pole figures and magnetic ODs .. 567

5.3.3.3. An example .. 568

5.3.4. Modelling of preferred orientation in the Rietveld method .. 569

5.3.4.1. Rietveld and March approaches .. 569

5.3.4.2. March–Dollase approach .. 569

5.3.4.3. Modified March–Dollase models .. 570

5.3.4.4. Donnet–Jouanneaux function .. 570

5.3.4.5. Modelling by spherical harmonics (and exponential) .. 570

5.3.4.6. The use of standard functions (or texture components) .. 570

5.3.4.7. Remarks .. 570

5.3.5. Combined analysis: structure, texture, microstructure, stress, phase, layering and reflectivity analyses in a single approach .. 571

5.3.5.1. Problems .. 571

5.3.5.2. Intensity of a pattern and general scheme .. 572

5.3.5.3. Minimum experimental requirements .. 572

5.3.5.4. Theoretical implementation .. 572

5.3.5.5. Implementation .. 577

5.3.5.6. Examination of a solution .. 577

5.3.6. Conclusions .. 578

5.4. Thin films and multilayers (M. Birkholz) .. 581

5.4.1. Introduction .. 581

5.4.2. Effects of absorption .. 581

5.4.2.1. Absorption factor .. 581

5.4.2.2. Chemical phase identification .. 582

5.4.2.3. Determination and interpretation of the product μt .. 583

5.4.2.4. Phase inhomogeneities .. 584

5.4.3. Grazing-incidence configurations .. 584

5.4.3.1. Grazing-incidence X-ray diffraction (GIXRD) .. 585

5.4.3.2. Penetration depth and information depth .. 587

5.4.3.3. Depth-dependent properties .. 587

5.4.3.4. Index of refraction for X-rays 588
5.4.3.5. Total external reflection and critical angle 588
5.4.3.6. Use of synchrotron radiation 590
5.4.4. Thin-film textures and their depth dependence 590
5.4.4.1. Texture factors 590
5.4.4.2. Pole-figure scans and analysis 590
5.4.4.3. Texture gradients 592
5.4.5. Stress and strain analysis 593
5.4.6. X-ray reflectivity (XRR) 594
5.4.6.1. Reflectivity from a substrate 594
5.4.6.2. Reflectivity of a single layer 595
5.4.6.3. Reflectivity of multilayers and superlattices 596
5.4.7. Grazing-incidence X-ray scattering (GIXS) 597
5.4.8. Conclusions and perspective 598
5.5. Multigrain crystallography and three-dimensional grain mapping (H. F. Poulsen and G. B. M. Vaughan) 601
5.5.1. List of symbols 601
5.5.2. Introduction 601
5.5.3. Experimental setup 602
5.5.4. Diffraction geometry 603
5.5.4.1. The laboratory and rotated coordinate systems 603
5.5.4.2. Detector coordinate systems 603
5.5.4.3. Diffraction 604
5.5.4.4. Forward projection, no detector tilt 604
5.5.4.5. Forward projection with detector tilt and non-centred sample 605
5.5.5. Indexing 605
5.5.6. Multigrain crystallography 606
5.5.6.1. Monophase materials 606
5.5.6.2. Multiphase materials containing unknown phases 607
5.5.7. Centre-of-mass and stress mapping 607
5.5.8. 3D grain and orientation mapping 608
5.5.8.1. Approach 1: Grain-by-grain volumetric mapping 608
5.5.8.2. Approach 2: Orientation mapping by Monte Carlo optimization 608
5.5.9. Representation of crystallographic orientation 609
5.5.9.1. Euler angles (Bunge definition) 609
5.5.9.2. Rodrigues vectors 610
5.5.9.3. Unit quaternions 611
5.5.9.4. Bounding cubes 612
5.5.10. Representation of elastic strain 613
5.5.10.1. Definition of strain 613
5.5.10.2. Strain-to-stress conversion 613
5.5.11. Crystal symmetry in relation to multigrain samples 613
5.5.11.1. Fundamental zone 614
5.5.11.2. Determining the orientation in the fundamental zone 614
5.5.11.3. Use of symmetry-equivalent orientations for strain and stress characterization 614
5.5.12. Discussion 614
5.6. X-ray diffraction from non-crystalline materials: the Debye model (S. Bates) 617
5.6.1. Outline 617
5.6.2. Crystalline and non-crystalline: an introduction to the Debye model 617

5.6.3. Application of the Debye equation to a single molecule .. 619
5.6.4. The Debye–Menke equation .. 621
5.6.5. Verification of the Debye–Menke intensity function .. 622
5.6.6. Background removal, intensity normalization and choice of X-ray optics .. 623
5.6.7. Application of the Debye normalization to semi-quantitative analysis .. 625
5.6.8. Correction for the instrumental intensity response .. 627
5.6.9. The full Debye normalization procedure .. 631
5.6.10. Application of the Debye normalization procedure .. 633
5.6.11. Universal appearance of non-crystalline powder patterns .. 635
5.6.12. Steps towards an effective lattice model of high-density randomly packed materials .. 638
5.6.13. Practical application of the effective lattice function determination .. 642
5.6.14. Debye diffraction models for larger molecular ensembles .. 645
5.6.15. Conclusions .. 646

5.7. Nanometre-scale structure from powder diffraction: total scattering and atomic pair distribution function analysis (S. J. L. Billinge) .. 649
5.7.1. Introduction .. 649
    5.7.1.1. Types of nanostructure .. 649
5.7.2. Scattering from nanostructures .. 650
    5.7.2.1. The Debye equation .. 650
    5.7.2.2. Correlation functions .. 652
    5.7.2.3. Low-angle scattering intensity .. 654
    5.7.2.4. Calculating $\mathscr{F}(r; Q_{\min})$ from models .. 655
    5.7.2.5. The extent of small-angle scattering .. 657
    5.7.2.6. PDFs from structures with multiple elements .. 657
    5.7.2.7. Differential structure functions .. 658
5.7.3. Collecting data for total-scattering and PDF measurements .. 659
    5.7.3.1. Neutrons .. 659
    5.7.3.2. X-rays .. 660
    5.7.3.3. Electrons .. 661
    5.7.3.4. Q ranges and Q resolutions .. 662
5.7.4. Data reduction .. 663
5.7.5. Extracting structural information .. 664
    5.7.5.1. Obtaining the PDF from a model .. 664
    5.7.5.2. PDFs from multi-element material .. 664
    5.7.5.3. Model-independent information from the PDF .. 664
    5.7.5.4. Modelling approaches .. 665

5.8. Scattering methods for disordered heterogeneous materials (A. J. Allen) .. 673
5.8.1. Introduction and overview .. 673
    5.8.1.1. Amorphous and non-crystalline materials .. 673
    5.8.1.2. Disordered and heterogeneous (and multi-component) materials .. 673
    5.8.1.3. Small-angle and wide-angle scattering tools .. 674
    5.8.1.4. Tabulated summary of quantitative information obtainable .. 674
    5.8.1.5. Different notations .. 675
5.8.2. Recommended measurement tools .. 675
    5.8.2.1. Small-angle scattering using a position-sensitive detector .. 675
    5.8.2.2. Ultra-small-angle scattering using crystal diffraction optics .. 677
    5.8.2.3. Data reduction and calibration of small-angle scattering data .. 679
    5.8.2.4. Reflectivity, grazing-incidence small-angle scattering and diffraction .. 680
    5.8.2.5. Wide-angle scattering and other methods for disordered structures .. 681

5.8.3. Quantitative analysis of disordered heterogeneous materials .. 683
5.8.3.1. Interpretative models for analysis of SAS data .. 683
5.8.3.2. Small-angle scattering effects on wide-angle scattering analysis .. 691
5.8.3.3. Combining information from different methods .. 691
5.8.4. Prospects for future development and recommended further reading .. 692
5.8.4.1. Developments at X-ray synchrotron facilities .. 692
5.8.4.2. Developments at steady-state and pulsed neutron sources .. 693
5.8.4.3. Future prospects .. 693
5.8.4.4. Further reading .. 693

PART 6. SOFTWARE .. 697

6.1. Survey of computer programs for powder diffraction (C. J. Gilmore, J. A. Kaduk and H. Schenk) .. 698

PART 7. APPLICATIONS .. 717

7.1. Macromolecular powder diffraction (I. Margiolaki) .. 718
7.1.1. Introduction .. 718
7.1.2. Sample preparation and handling .. 718
7.1.3. Data collection .. 720
7.1.4. Cryo-cooling protein powder samples and microstructural effects .. 721
7.1.5. Crystal screening .. 723
7.1.6. Improvements in data quality *via* the use of multiple profiles .. 725
7.1.7. Structure solution .. 726
7.1.7.1. Molecular replacement .. 726
7.1.7.2. The isomorphous-replacement method .. 728
7.1.7.3. Emerging powder phasing methods .. 728
7.1.8. Structure refinement .. 729
7.1.8.1. Stereochemical restraints .. 729
7.1.8.2. Rigid-body representation of amino-acid residues .. 731
7.1.9. Related developments .. 731
7.1.10. Concluding remarks .. 732

7.2. Forensic applications of X-ray powder diffraction (D. F. Rendle) .. 737
7.2.1. Introduction .. 737
7.2.1.1. Background information .. 737
7.2.1.2. Preservation of evidence .. 737
7.2.1.3. Versatility .. 737
7.2.1.4. Variable specimen size .. 741
7.2.1.5. Contamination .. 741
7.2.1.6. Identification *versus* comparison .. 741
7.2.1.7. Complementary techniques .. 741
7.2.2. Instrumentation .. 742
7.2.2.1. Choice of instrumentation .. 742
7.2.2.2. Choice of radiation .. 742
7.2.3. Technical procedures .. 742
7.2.3.1. Variety and types of specimen encountered and specimen preparation .. 742
7.2.3.2. Specimen preparation – powders .. 743
7.2.3.3. Specimen preparation – metals and alloys .. 743
7.2.3.4. Specimen preparation – monolithic (polycrystalline) .. 743
7.2.3.5. Sample preparation – single crystal .. 744

7.2.3.6. Interpretation of results: identifications and comparisons, checking procedures .. 744

7.2.3.7. Data archives for statistical and reference purposes .. 744

7.2.3.8. Continuity of evidence .. 745

7.2.3.9. Presentation of evidence to the court .. 745

7.2.4. Examples of forensic casework involving the use of XRPD .. 746

7.2.4.1. Criminal damage to an automobile .. 746

7.2.4.2. Fatal road traffic accident .. 746

7.2.4.3. Attempted murder? .. 747

7.2.4.4. Synthesis of crack cocaine .. 747

7.2.5. Summary .. 747

7.2.5.1. Advantages and limitations of XRPD in forensic science .. 747

7.2.5.2. Thoughts on the future .. 748

7.3. Materials for energy storage and conversion (M. A. RODRIGUEZ) .. 752

7.3.1. Introduction .. 752

7.3.2. Fossil fuel .. 752

7.3.3. Hydrogen storage .. 752

7.3.4. Wind .. 753

7.3.5. Solar .. 753

7.3.6. Battery technology .. 755

7.4. Powder diffraction in art and archaeology (G. ARTIOLI) .. 759

7.4.1. Introduction .. 759

7.4.2. The information provided by diffraction .. 759

7.4.3. Phase identification and quantification .. 760

7.4.4. Crystal structure analysis .. 761

7.4.5. Texture analysis .. 762

7.4.6. Microstructural analysis .. 762

7.4.7. Present trends .. 763

7.5. Powder diffraction and pharmaceuticals (J. BERNSTEIN AND S. M. REUTZEL-EDENS) .. 767

7.5.1. Introduction .. 767

7.5.2. Some basic background and references .. 767

7.5.3. Identification and characterization .. 767

7.5.3.1. Polymorphs, salts, solvates, co-crystals .. 767

7.5.3.2. Indexing .. 768

7.5.3.3. Crystal structure solution .. 769

7.5.4. Quantitation of mixtures by traditional and Rietveld methods .. 769

7.5.5. Characterization of amorphous materials .. 771

7.5.6. Quality control and regulatory aspects .. 773

7.5.7. Creating and protecting intellectual property .. 773

7.5.7.1. Crystal habit .. 776

7.5.8. Counterfeit medicines .. 777

7.5.9. Concluding remarks .. 778

7.6. Selected applications of Rietveld analysis in the aluminium industry (F. R. FERET) .. 782

7.6.1. Introduction .. 782

7.6.2. Bauxite .. 782

7.6.3. Quantification of quartz in bauxite .. 784

7.6.4. Occurrence and characterization of Zn and Mn in bauxite .. 785

7.6.5. Red mud (bauxite residue) .. 785

7.6.6. Alumina .. 787

7.6.7. Scrubber alumina .. 788
7.6.8. Electrolytic bath .. 788
7.6.9. Spent potlining (SPL) .. 790
7.6.10. Dross .. 790
7.6.11. Discussion .. 791

7.7. Mining and mineral processing (N. V. Y. Scarlett and D. L. Bish) .. 793
7.7.1. Introduction .. 793
7.7.2. Use of powder diffraction in mining and mineral processing .. 793
7.7.2.1. Areas of applicability .. 794
7.7.3. Powder-diffraction methodology .. 794
7.7.3.1. Equipment and data collection .. 794
7.7.3.2. Qualitative analysis .. 796
7.7.3.3. Quantitative analysis .. 797
7.7.3.4. Crystal structural analysis .. 797
7.7.3.5. High-throughput and batch processing .. 797
7.7.4. Examples .. 799
7.7.4.1. Exploration .. 799
7.7.4.2. Process control .. 799
7.7.4.3. Research .. 800
7.7.5. Conclusions .. 801

7.8. Ceramic materials (W. Wong-Ng) .. 804
7.8.1. Introduction .. 804
7.8.1.1. Definition .. 804
7.8.1.2. A brief history of ceramic development .. 804
7.8.1.3. Industrial aspects of fine ceramics/advanced ceramics .. 804
7.8.2. Categories of ceramics .. 805
7.8.2.1. Art and archaeological ceramics .. 805
7.8.2.2. Modern technical ceramics .. 805
7.8.3. Applications of powder X-ray diffraction to the studies of ceramics .. 810
7.8.3.1. Phase characterization .. 811
7.8.3.2. Structure and microstructure .. 814
7.8.3.3. Processing and performance .. 819
7.8.4. Summary .. 825

7.9. Applications in glass-ceramics (S. T. Misture) .. 828
7.9.1. Introduction .. 828
7.9.1.1. Devitrification .. 828
7.9.1.2. Applications of powder diffraction .. 829
7.9.2. Methods .. 829
7.9.2.1. Time–temperature profiles .. 829
7.9.3. Qualitative analysis of devitrification .. 829
7.9.4. Kinetics analysis .. 830
7.9.4.1. Theory .. 830
7.9.4.2. Complexities in kinetics measurements .. 831
7.9.4.3. Kinetics analysis example 1: glass to single-phase crystal .. 831
7.9.4.4. Kinetics analysis example 2: glass to crystal to crystal .. 832
7.9.4.5. Kinetics analysis example 3: effects of nucleation .. 832
7.9.5. Remnant glass compositions *via* quantitative analysis .. 833
7.9.6. Summary .. 833

7.10. Industrial organic pigments (M. U. Schmidt) 834

7.10.1. On organic pigments 834

7.10.2. Main applications of X-ray powder diffraction to organic pigments (and other organic compounds) 835

7.10.2.1. Qualitative phase analysis 835

7.10.2.2. Quantitative phase analysis 836

7.10.2.3. Determination of the domain size 837

7.10.2.4. Structure determination from powder-diffraction data 837

7.10.2.5. Determination of the amorphous content 838

7.10.2.6. Investigation of local structures of nanocrystalline and amorphous organic compounds using pair-distribution function analyses 838

7.11. Powder diffraction in the petroleum and petrochemical industries (J. A. Kaduk) 843

7.11.1. Introduction 843

7.11.2. Exploration and production 843

7.11.2.1. Rock properties 843

7.11.2.2. Clay mineralogy and the Reynolds Cup 843

7.11.2.3. Gas hydrates 844

7.11.2.4. Corrosion deposits 844

7.11.3. Refining and petrochemicals 844

7.11.3.1. Corrosion deposits 844

7.11.3.2. Catalysts 846

7.11.4. *In situ* studies 852

7.12. Powder-diffraction characterization of cements (M. A. G. Aranda, A. G. De la Torre and L. León-Reina) 855

7.12.1. An introduction to cements and types of cements 855

7.12.2. Rietveld quantitative phase analysis of cements 855

7.12.2.1. Obtaining crystal-structure information 855

7.12.2.2. Data analysis 856

7.12.3. Phase quantification of Portland cements 856

7.12.3.1. Quantification of Portland clinkers 857

7.12.3.2. Quantification of Portland cements and blended cements 857

7.12.3.3. Online quantification of Portland clinkers and cements 858

7.12.4. Quantification of other cementitious materials 859

7.12.4.1. Calcium aluminate cements 859

7.12.4.2. Calcium sulfoaluminate cements 859

7.12.4.3. Calcium sulfobelite cements 860

7.12.4.4. Materials with pozzolanic activity 860

7.12.4.5. Other cements 861

7.12.5. Powder-diffraction studies on the hydration of cements 861

7.12.5.1. Hydration studies of Portland cements and blended Portland cements 861

7.12.5.2. Hydration studies of alternative cementitious materials 862

7.12.6. The use of synchrotron and neutron powder diffraction for studying cements 863

7.12.7. Conclusions and outlook 864

7.13. Powder diffraction of superconductors (Qingzhen Huang) 868

7.13.1. Introduction 868

7.13.1.1. Properties of superconductors 868

7.13.1.2. A brief description of superconducting systems 868

7.13.2. Advantages of structure analysis from powder diffraction 870

7.13.2.1. Comparison of XPD and NPD 871

7.13.2.2. Choice of radiation 872

7.13.3. Analysis of the chemical and structural features of nonstoichiometric superconductors 872

7.13.3.1. Charge transfer and valence-state manipulation 872

7.13.3.2. Modelling of layer structures 875

7.13.3.3. Structural transformations 876

7.13.4. Magnetic order in superconductors and parent compounds 878

7.13.5. Conclusions 879

Appendix A7.13.1. The study of long-range magnetic order in superconductors 879

A7.13.1.1. Commensurate magnetic ordering and primitive cells 879

A7.13.1.2. The 36 magnetic lattices and 1651 Shubnikov groups 881

A7.13.1.3. Magnetic symmetry and antisymmetry operations 881

A7.13.1.4. Magnetic reflection conditions for centred lattices 881

A7.13.1.5. An example of Rietveld refinement against NPD data for a superconductor 882

7.14. Powder diffraction by minerals (R. Arletti, G. Cruciani and G. Ferraris) 885

7.14.1. Powder diffraction and characterization of new mineral species 885

7.14.2. Mineral physics through *in situ* powder-diffraction experiments 886

7.14.2.1. Thermoelastic behaviour of minerals 886

7.14.2.2. Negative thermal expansion in minerals 887

7.14.2.3. Dehydration of nonporous minerals 887

7.14.2.4. Dehydration and adsorption/desorption mechanisms in porous materials 888

7.14.2.5. High-pressure (HP)-induced reaction/penetration in porous materials 888

7.14.2.6. Phase transitions and spontaneous strain in minerals 888

7.14.2.7. HT studies related to CO_2 sequestration 889

7.14.3. Minerals related to human health, the biosphere and planetary exploration 889

7.14.3.1. Fibrous minerals 889

7.14.3.2. Biominerals 890

7.14.3.3. Mars mineralogy 890

Subject index 895

Preface

International Tables for Crystallography started life in in 1935 as a two-volume set entitled *Internationale Tabellen zur Bestimmung von Kristallstrukturen*, with C. Hermann as editor. We are now in the third series, with eight volumes covering all aspects of crystallography from symmetry to macromolecular crystallography. However, there has always been one glaring omission and one that has become increasingly serious: powder diffraction. This is odd: powder crystallography started as early as 1916 with the seminal work of Debye and Scherrer, and has grown to include quantitative and semi-quantitative analysis, structure solution and refinement, two-dimensional data, comprehensive databases, clustering, and microstructural properties, and is applied to a wide range of problems of both academic and industrial interest. Articles in the International Union of Crystallography's monthly *Journal of Applied Crystallography* are dominated by powder-diffraction papers. In terms of instrumentation, there are more powder diffractometers (~10 000) in use worldwide than any other comparable diffraction instrument. There have also been rapid advances in radiation sources and detectors, and major developments in software, computing power and visualization tools, all of which have made what was once cutting-edge science commonplace.

The methodology that has done more than anything to transform the field treats the measured powder-diffraction data in a comparable way to single-crystal data (albeit with more restrictive conditions) and is generally known as Rietveld refinement. This method will be found everywhere in this volume and was developed in the 1960s by Bert Loopstra (who came up with the concept), Bob van Laar (who worked out the mathematics) and Hugo Rietveld (who wrote the first computer program for it), as discussed in a recent article by van Laar & Schenk [*Acta Cryst.* (2018), A**74**, 88–92].

The field has not been devoid of books: there are excellent books edited by Dinnebier and Billinge [*Powder Diffraction Theory and Practice* (2008), Cambridge: Royal Society of Chemistry], Clearfield, Reibenspies and Bhuvanesh [*Principles and Applications of Powder Diffraction* (2008), Oxford: Wiley] and Mittemeijer and Welzel [*Modern Diffraction Methods* (2013), Weinheim: Wiley-VCH]. These, however, are not completely comprehensive and the need for a volume of *International Tables* dedicated to powder diffraction has become increasingly urgent.

So here it is. As if to emphasize the scale and diversity of the topic, it is one of the larger volumes of *International Tables* with over 900 pages and 54 chapters. The first part is devoted to basic diffraction theory as applied to powder samples, followed by parts on instrumentation and sample preparation, methodology, structure determination, defects, texture and microstructure, and software, and concluding with descriptions of applications over a wide variety of disciplines ranging from ceramics to pharmaceuticals. Even a volume of this size cannot be wholly comprehensive, but the editors hope that it covers a wide range of topics that will be relevant and of interest to most powder diffractionists. We plan to include yet more topics in a second edition.

The volume is intended primarily to be a practical one – when you have a problem in powder analysis this should be the first book you reach for. To this end, the data for many of the examples discussed in the text can be downloaded from https://it.iucr.org, so that readers can try the examples for themselves. We have not (yet) included step-by-step instructions on how to process the data; perhaps that will come in the future. The chapter on software gives information on how to obtain the necessary programs.

A word is needed about notation. A field as diverse as powder diffraction does not have a uniform notation. Texture and stress, for example, use a different nomenclature to structure solution. Our conclusion was that if we were to attempt to impose a uniform notation throughout the volume, it would have made it very difficult to link the chapters to the existing literature. We have to live with diversity.

An enterprise such as this has been a large undertaking, and we thank the authors for their patience. It is important to acknowledge the role of the staff at the IUCr offices in Chester, especially Nicola Ashcroft, Simon Glynn and Peter Strickland. We are very grateful for all their hard work.

Chris Gilmore, Jim Kaduk and Henk Schenk
Editors, *International Tables for Crystallography* Volume H

International Tables for Crystallography (2019). Vol. H, Chapter 1.1, pp. 2–23.

1.1. Overview and principles of powder diffraction

R. E. Dinnebier and S. J. L. Billinge

1.1.1. Information content of a powder pattern

The structures of real materials comprise not only the crystal structure – the time- and space-averaged periodic configuration of atoms on an idealized periodic lattice – but also the microstructure, which is caused by imperfections, dislocations and all kinds of disorder. The microstructure is often responsible for interesting properties of the material. A powder diffraction pattern contains a wealth of information about this microstructure in addition to the average crystal structure, as shown schematically in Fig. 1.1.1.

At each stage of a powder diffraction study, great effort and ingenuity are needed to find the optimal experimental conditions and to understand and analyse the resulting line shapes and signals. As experimental equipment, theoretical understanding and computational tools have improved, it has become possible to tap into the rich information content of the line peak shapes and diffuse background of a typical powder diffraction pattern, yielding unprecedented information about real materials for materials scientists, chemists, physicists, earth scientists and engineers. For example, in the modern practice of whole-pattern modelling, the line profile is calculated from first principles, taking into account all aspects of the state of the sample, such as particle-size distributions, inhomogeneous strains and texture, as well as the experimental setup and aberrations. There is a useful feedback effect in that better profile descriptions result in more accurate determinations of the intensities of the Bragg peaks, which is important to extract accurate structural information (Bragg peaks are introduced in detail in the next section). Similarly, great progress has been made in the extraction of information from the diffuse signal that used to be called the ‘background’. Rather than fitting the background using arbitrary fitting parameters, as is done in a traditional Rietveld refinement, careful corrections can be made for experimental effects such as Compton scattering, fluorescence, multiple scattering and scattering from sample environments. The resulting ‘background’ beneath and between the Bragg peaks of the corrected data is information-rich diffuse scattering from the sample, which contains information about the local structure and how it deviates from the average crystal structure in the form of defects and correlated lattice dynamics (phonons). Total-scattering methods that include both the Bragg and diffuse scattering are only now being fully appreciated, with quantitative analyses being carried out in real space using the atomic pair distribution function (PDF) method, and in reciprocal space with Monte Carlo simulated-annealing-type modelling based on the Debye equation.

In this introductory chapter, the basic physics behind the observation of a powder diffraction pattern is described. In accordance with the scheme in Fig. 1.1.1, the information in a powder diffraction pattern can be described by the Bragg-peak positions, the peak profile, the Bragg-peak intensities and the non-Bragg-scattering contributions to the background. After describing the fundamentals of scattering by a crystalline powder, the chapter is organized such that each of the paths illustrated in Fig. 1.1.1 is followed and described in an introductory way. Detailed descriptions of the state of the art in the kinds of studies covered in Fig. 1.1.1 can be found in following chapters, but here we discuss each aspect of powder diffraction in turn, giving a high-level overview of what information is available from powder diffraction as well as explaining the fundamental origin of the features containing that information. We do not attempt to review applications of the different kinds of studies, leaving that to the following chapters.

In this chapter we have drawn heavily on information within three textbooks (Dinnebier & Billinge, 2008; Mittemeijer & Welzel, 2012; Egami & Billinge, 2013) and references therein.

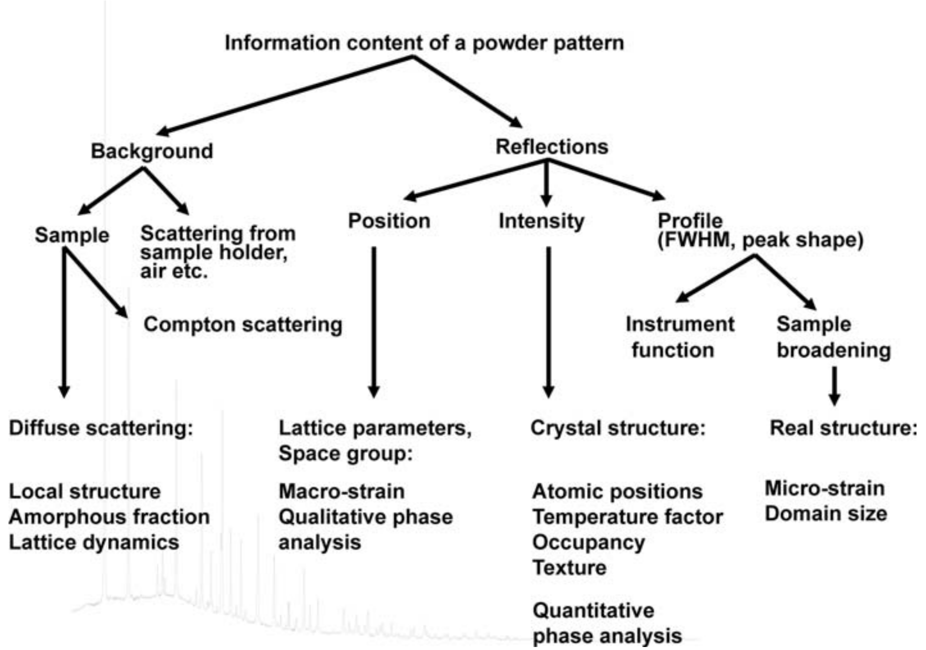

Figure 1.1.1
Schematic picture of the information content of a powder pattern. [Reproduced from Dinnebier & Billinge (2008) with permission from the Royal Society of Chemistry.]

1.1.2. The peak position

1.1.2.1. *The Bragg equation derived*

The easiest way to understand the structural information contained in powder diffraction, and historically one of the first ways in which diffraction was described, is *via* the well known Bragg equation (Bragg, 1913), which describes the principle of X-ray diffraction in terms of the reflection of X-rays by sets of lattice planes.

To understand the concept of a lattice plane, first imagine a three-dimensional periodic lattice of points, for example the corners of an array of cubes stacked in three dimensions. We can imagine a particular plane through the lattice by placing each layer of the stack of cubes on a tray: the tray then defines a lattice plane. Now imagine making the tray thinner and thinner until it

Copyright © 2019 International Union of Crystallography

is infinitely thin, but still goes through the same set of points (the cube corners). What we see is that there is not just a single plane, but a series of equivalent planes: for example, between the top and second layers, the second and third layers, and so on. Each plane is parallel to the others and subsequent planes are separated by the same distance (the height of the cube). This is a set of lattice planes. We can also envisage inserting the trays in other ways. For example, we could place the trays vertically rather than horizontally and running from the left side to the right side of the stack of cubes, or alternatively running from the front of the stack to the back of the stack. Each of these is a different set of lattice planes (Fig. 1.1.2), although in this case they have the same layer spacing, or periodicity. If we were able to insert the tray at different angles to the cubes, for example at 45°, we could find other sets of parallel planes that, when we force them to go through some well defined subset of the points defining the lattice, will have well defined layer spacings or periodicities. Bragg's law showed that the diffraction pattern could be understood in terms of X-rays reflecting specularly off subsequent planes in each of these sets of planes and emerging in phase. (In reality, the actual effect is not specular reflection of light from an abstract plane, but a diffraction effect. However, the combination of diffraction and periodicity results in a selection rule that intense scattering only occurs when this particular specular-reflection condition holds.)

There are actually an infinite number of lattice planes in an infinite lattice, and it is important to have a way of labelling them, which is commonly done using the triplet of indices *hkl*, called Miller indices, where *h*, *k* and *l* are integers, and the separation of the planes is denoted by the distance d_{hkl}. When *h*, *k* and *l* have small values the planes are said to be 'low-order' planes. Low-order planes have the largest interplanar separations, and for a particular symmetry of the lattice there is a direct relationship between the Miller indices and d_{hkl}.

The Bragg equation gives the condition that must hold for specular reflection from subsequent planes in a set to be perfectly in phase, as illustrated in Fig. 1.1.3. It is evident in Fig. 1.1.3 that the wave reflecting off the lower plane travels a longer distance (by PN before and NQ after reflection occurs) than the wave reflecting off the upper plane. The two waves are in phase, resulting in constructive interference, only when $\Delta = |\mathrm{PN}| + |\mathrm{NQ}|$ is a multiple $n = 0, 1, 2, \ldots$ of the wavelength λ,

$$\Delta = n\lambda. \tag{1.1.1}$$

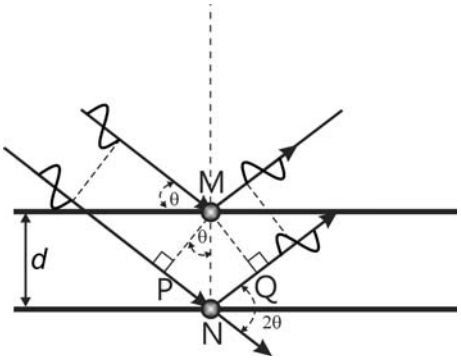

Figure 1.1.3
Illustration of the geometry used for the simplified derivation of Bragg's law. [Reproduced from Dinnebier & Billinge (2008) with permission from the Royal Society of Chemistry.]

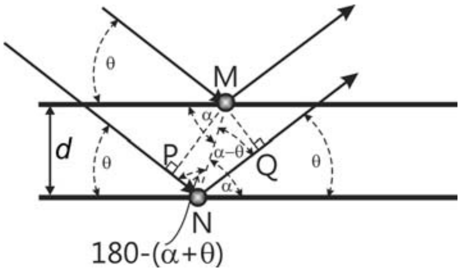

Figure 1.1.4
Illustration of the geometry in the general case where scattering takes place at the position of atoms in consecutive planes. [Reproduced from Dinnebier & Billinge (2008) with permission from the Royal Society of Chemistry.]

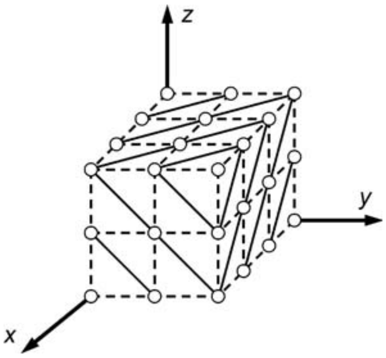

Figure 1.1.2
Schematic drawing of a set of parallel lattice planes (111) passing through all points of the cubic lattice.

In all other cases, destructive interference results, since it is always possible to find a deeper plane, *p*, for which the relation $p\Delta = n\lambda + 1/2$ exactly holds, giving rise to perfect destructive interference. Thus, when a narrow beam of X-rays impinges on a crystalline sample, sharp peaks in the intensity of the scattered X-rays are seen only at the angles for which equation (1.1.1) holds, with no intensity observed at other angles. As can easily be seen from Fig. 1.1.3, geometrically,

$$\Delta = 2d\sin\theta, \tag{1.1.2}$$

where *d* is the interplanar spacing of the parallel lattice planes and 2θ is the diffraction (or 'scattering') angle, the angle between the incoming and outgoing X-ray beams. The angle $\theta = 2\theta/2$ is often called the Bragg angle. Combining equations (1.1.1) and (1.1.2) we get

$$n\lambda = 2d\sin\theta, \tag{1.1.3}$$

which is the Bragg equation (Bragg, 1913).

This simplified derivation of the Bragg equation is often reproduced in textbooks. Although it leads to the correct solution, it has a serious drawback. In reality the X-rays are not reflected by planes, but are scattered by electrons bound to the atoms in the sample. The planes within a crystal are not like shiny optical mirrors, but contain discrete atoms separated by regions of much lower electron density and, in general, the atoms in one plane will not lie exactly above atoms in the plane below as implied by Fig. 1.1.3. How is it then that the simplified picture shown in Fig. 1.1.3 gives the correct result? A more general description shows that equation (1.1.3) is also valid if the atom in the lower lattice plane in Fig. 1.1.3 is shifted by an arbitrary amount within the plane (Fig. 1.1.4).

The phase shift can immediately be deduced from Fig. 1.1.4 as

$$\begin{aligned} n\lambda &= \mathrm{MN}\cos[180^\circ - (\alpha + \theta)] + \mathrm{MN}\cos(\alpha - \theta) \\ &= \mathrm{MN}[-\cos(\alpha + \theta) + \cos(\alpha - \theta)]. \end{aligned} \tag{1.1.4}$$

Using the standard trigonometric results

$$\begin{aligned}\cos(\alpha+\theta)&=\cos\alpha\cos\theta-\sin\alpha\sin\theta,\\ \cos(\alpha-\theta)&=\cos\alpha\cos\theta+\sin\alpha\sin\theta,\end{aligned}\tag{1.1.5}$$

equation (1.1.4) becomes

$$n\lambda=\mathrm{MN}(2\sin\alpha\sin\theta)\tag{1.1.6}$$

with

$$d=\mathrm{MN}\sin\alpha,\tag{1.1.7}$$

which may be substituted to yield the Bragg equation:

$$n\lambda=2d\sin\theta.\tag{1.1.8}$$

The Bragg equation holds for any radiation or particle that is used to probe the structure of the sample: X-rays, neutrons or electrons. Another equivalent, and highly useful, form of the Bragg equation for the particular case of X-rays is

$$Ed=\frac{6.199}{\sin\theta}\ \text{with}\ \lambda=\frac{12.398}{E},\tag{1.1.9}$$

where the energy E of the X-rays is in keV and λ is in ångströms.

The Bragg law results in narrow beams of high intensity that emerge from the crystal in specific directions given by the Bragg equation, resulting in sharp spots on the detector, and there is a one-to-one correspondence between these Bragg spots (often referred to as Bragg reflections) and each set of crystallographic planes. Each Bragg spot is therefore labelled with the same set of Miller indices, *hkl*, as the set of planes that gave rise to it.

It is possible to construct a 'reciprocal space' where the axes of the space are in units of inverse length. The reference coordinate frame of the reciprocal space is defined by a set of basis vectors whose directions are perpendicular to the plane normals of the (100), (010) and (100) planes of the crystal. Thus, a *point* in this reciprocal space corresponds to a *direction* in direct space and every allowed reflection according to the Bragg law is represented by a point in reciprocal space. The set of points arising from the Bragg law forms a lattice in reciprocal space, which is called the 'reciprocal lattice', and each single crystal has its own reciprocal lattice. [See *International Tables for Crystallography* Volume B (Shmueli, 2008) for more details.]

To derive the Bragg equation, we used an assumption of specular reflection, which is borne out by experiment: for a crystalline material, destructive interference eliminates scattered intensity in all directions except where equation (1.1.3) holds. Strictly this holds only for crystals that are infinite in extent and which the incident X-ray beam can penetrate without loss of intensity. This does not sound like a particularly good approximation, but in practice it holds rather well. Even a fairly low energy X-ray beam that only penetrates, say, a micrometre into the material will still probe ~10 000 atomic layers. The condition is not strictly obeyed in the presence of defects and disorder in the material. In such materials the Bragg peaks are modified in their position, their width and their shape, and there is also an additional component of the diffracted intensity that may be observed in all directions, away from reciprocal-lattice points, known as diffuse scattering.

1.1.2.2. *The Bragg equation from the reciprocal lattice*

Here we develop in more detail the mathematics of the reciprocal lattice. The reciprocal lattice has been adopted by crystallographers as a simple and convenient representation of the physics of diffraction by a crystal. It is an extremely useful tool for describing all kinds of diffraction phenomena occurring in powder diffraction.

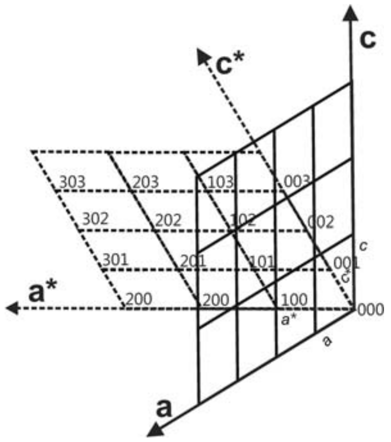

Figure 1.1.5
A two-dimensional monoclinic lattice and its corresponding reciprocal lattice. [Adapted from Dinnebier & Billinge (2008) with permission from the Royal Society of Chemistry.]

Consider a 'normal' crystal lattice with lattice vectors **a**, **b** and **c**, which have lengths a, b and c, respectively, and angles α between **b** and **c**, β between **a** and **c** and γ between **a** and **b**. The unit-cell volume is given by V. A second lattice with lattice parameters a^*, b^*, c^*, α^*, β^*, γ^* and unit-cell volume V^* with the same origin exists such that

$$\begin{aligned}&\mathbf{a}\cdot\mathbf{b}^*=\mathbf{a}\cdot\mathbf{c}^*=\mathbf{b}\cdot\mathbf{c}^*=\mathbf{a}^*\cdot\mathbf{b}=\mathbf{a}^*\cdot\mathbf{c}=\mathbf{b}^*\cdot\mathbf{c}=0,\\ &\mathbf{a}\cdot\mathbf{a}^*=\mathbf{b}\cdot\mathbf{b}^*=\mathbf{c}\cdot\mathbf{c}^*=1.\end{aligned}\tag{1.1.10}$$

This is known as the reciprocal lattice[1] (Fig. 1.1.5), which exists in so-called reciprocal space. As mentioned above, we will see that it turns out that the points in the reciprocal lattice are related to the vectors defining the crystallographic plane normals. There is one point in the reciprocal lattice for each set of crystallographic planes, (*hkl*), separated by distance d_{hkl}, as discussed below. For now, just consider h, k and l to be integers that index a point in the reciprocal lattice. A reciprocal-lattice vector $\mathbf{h}_{hkl}$ is the vector from the origin of reciprocal space to the reciprocal-lattice point for the plane (*hkl*),

$$\mathbf{h}_{hkl}=h\mathbf{a}^*+k\mathbf{b}^*+l\mathbf{c}^*,\quad h,k,l\in\mathbb{Z}.\tag{1.1.11}$$

where $\mathbb{Z}$ is the set of all integers.

The length of the reciprocal basis vector $\mathbf{a}^*$ is defined according to

$$\mathbf{a}^*=x(\mathbf{b}\times\mathbf{c}),\tag{1.1.12}$$

where the scale factor x can easily be deduced, using equations (1.1.12) and (1.1.10), as

$$\mathbf{a}^*\cdot\mathbf{a}=x(\mathbf{b}\times\mathbf{c}\cdot\mathbf{a})=xV\Rightarrow x=\frac{1}{V},\tag{1.1.13}$$

leading to

$$\mathbf{a}^*=\frac{1}{V}(\mathbf{b}\times\mathbf{c}),\quad \mathbf{b}^*=\frac{1}{V}(\mathbf{c}\times\mathbf{a}),\quad \mathbf{c}^*=\frac{1}{V}(\mathbf{a}\times\mathbf{b})\tag{1.1.14}$$

and, *vice versa*,

---

[1] The reciprocal lattice is a commonly used construct in solid-state physics, but with a different normalization: $\mathbf{a}\cdot\mathbf{a}^*=2\pi$.

$$\mathbf{a} = \frac{1}{V^*}(\mathbf{b}^* \times \mathbf{c}^*), \quad \mathbf{b} = \frac{1}{V^*}(\mathbf{c}^* \times \mathbf{a}^*), \quad \mathbf{c} = \frac{1}{V^*}(\mathbf{a}^* \times \mathbf{b}^*). \tag{1.1.15}$$

The relationship between the reciprocal and the real lattice parameters expressed geometrically rather than in the vector formalism used above is

$$\begin{aligned} a^* &= \frac{bc\sin\alpha}{V}, \\ b^* &= \frac{ac\sin\beta}{V}, \\ c^* &= \frac{ab\sin\gamma}{V}, \\ \cos\alpha^* &= \frac{\cos\beta\cos\gamma - \cos\alpha}{\sin\beta\sin\gamma}, \\ \cos\beta^* &= \frac{\cos\alpha\cos\gamma - \cos\beta}{\sin\alpha\sin\gamma}, \\ \cos\gamma^* &= \frac{\cos\alpha\cos\beta - \cos\gamma}{\sin\alpha\sin\beta}, \\ V &= abc\sqrt{1 + 2\cos\alpha\cos\beta\cos\gamma - \cos^2\alpha - \cos^2\beta - \cos^2\gamma}. \end{aligned} \tag{1.1.16}$$

Equation (1.1.16) is the most general expression for non-orthogonal lattices. The expressions simplify considerably for higher-symmetry crystal systems.

We now re-derive Bragg's law using the vector notation introduced above (Fig. 1.1.6). The wave vectors of the incoming and outgoing beams are given by $\mathbf{s}_0$ and $\mathbf{s}$, respectively. They point in the direction of propagation of the wave and their length depends on λ. For elastic scattering (for which there is no change in wavelength on scattering), $\mathbf{s}_0$ and $\mathbf{s}$ have the same length.

We define the scattering vector as

$$\mathbf{h} = (\mathbf{s} - \mathbf{s}_0), \tag{1.1.17}$$

which for a specular reflection is always perpendicular to the scattering plane. The length of $\mathbf{h}$ is given by

$$\frac{h}{s} = 2\sin\theta. \tag{1.1.18}$$

Comparison with the formula for the Bragg equation (1.1.3),

$$\frac{n\lambda}{d} = 2\sin\theta, \tag{1.1.19}$$

gives

$$\frac{n\lambda}{d} = \frac{h}{s}. \tag{1.1.20}$$

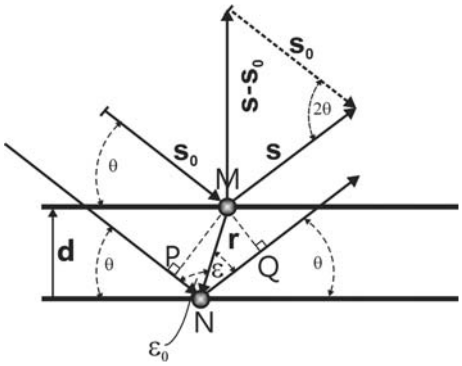

Figure 1.1.6
Illustration of the important wave and scattering vectors in the case of elastic Bragg scattering. [Reproduced from Dinnebier & Billinge (2008) with permission from the Royal Society of Chemistry.]

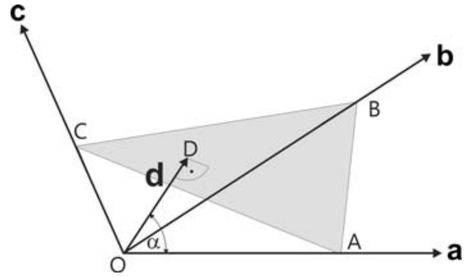

Figure 1.1.7
Geometrical description of a lattice plane in terms of real-space basis vectors. The arc and dot below the letter D indicate a right angle. [Reproduced from Dinnebier & Billinge (2008) with permission from the Royal Society of Chemistry.]

Setting the magnitude of $\mathbf{s}$ to $1/\lambda$, we get the Bragg equation in terms of the magnitude h of the scattering vector,

$$h = \frac{n}{d}. \tag{1.1.21}$$

This shows that diffraction occurs when the magnitude of the scattering vector is an integral number of reciprocal-lattice spacings $1/d$. We define a vector $\mathbf{d}^*$ perpendicular to the lattice planes with length $1/d$. Since $\mathbf{h}$ is perpendicular to the scattering plane, this leads to

$$\mathbf{h} = n\mathbf{d}^*. \tag{1.1.22}$$

Diffraction can occur at different scattering angles 2θ for the same crystallographic plane, giving the different orders n of diffraction. For simplicity, the number n will be incorporated in the indexing of the lattice planes, where

$$d^*_{nh,nk,nl} = nd^*_{hkl}, \tag{1.1.23}$$

e.g., $d^*_{222} = 2d^*_{111}$, and we get an alternative expression for Bragg's equation:

$$\mathbf{h} = \mathbf{d}^*_{hkl}. \tag{1.1.24}$$

The vector $\mathbf{d}^*_{hkl}$ points in a direction perpendicular to a real-space lattice plane. We would like to express this vector in terms of the reciprocal-space basis vectors $\mathbf{a}^*$, $\mathbf{b}^*$, $\mathbf{c}^*$.

First we define $\mathbf{d}_{hkl}$ in terms of the real-space basis vectors $\mathbf{a}$, $\mathbf{b}$, $\mathbf{c}$. Referring to Fig. 1.1.7, we can define

$$\mathbf{OA} = \frac{1}{h}\mathbf{a}, \quad \mathbf{OB} = \frac{1}{k}\mathbf{b}, \quad \mathbf{OC} = \frac{1}{l}\mathbf{c} \tag{1.1.25}$$

with h, k and l being integers, as required by the periodicity of the lattice.

The plane-normal vector $\mathbf{d}_{hkl}$ originates on one plane and terminates on the next parallel plane. Therefore, $\mathbf{OA}\cdot\mathbf{d} = (\mathrm{OA})d\cos\alpha$. From Fig. 1.1.7 we see that, geometrically, $(\mathrm{OA})\cos\alpha = d$. Substituting, we get $\mathbf{OA}\cdot\mathbf{d} = d^2$. Combining this with equation (1.1.25) leads to

$$\frac{1}{h}\mathbf{a}\cdot\mathbf{d} = d^2 \tag{1.1.26}$$

and consequently

$$h = \mathbf{a}\cdot\frac{\mathbf{d}}{d^2}, \quad k = \mathbf{b}\cdot\frac{\mathbf{d}}{d^2}, \quad l = \mathbf{c}\cdot\frac{\mathbf{d}}{d^2}. \tag{1.1.27}$$

By definition, h, k and l are divided by their largest common integer to be Miller indices. The vector $\mathbf{d}^*_{hkl}$, from Bragg's equation (1.1.24), points in the plane-normal direction parallel to $\mathbf{d}$ but with length $1/d$. We can now write $\mathbf{d}^*_{hkl}$ in terms of the vector **d**:

$$\mathbf{d}^*_{hkl} = \frac{\mathbf{d}}{d^2}, \qquad (1.1.28)$$

which gives

$$\mathbf{d}^*_{hkl} = \frac{\mathbf{d}_{hkl}}{d^2} = h\mathbf{a} + k\mathbf{b} + l\mathbf{c}, \qquad (1.1.29)$$

or written in terms of the reciprocal basis

$$\mathbf{d}^*_{hkl} = h\mathbf{a}^* + k\mathbf{b}^* + l\mathbf{c}^*, \qquad (1.1.30)$$

which was obtained using

$$\begin{aligned}
\mathbf{d}^*_{hkl} \cdot \mathbf{a}^* &= h\mathbf{a} \cdot \mathbf{a}^* + k\mathbf{b} \cdot \mathbf{a}^* + l\mathbf{c} \cdot \mathbf{a}^* = h,\\
\mathbf{d}^*_{hkl} \cdot \mathbf{b}^* &= h\mathbf{a} \cdot \mathbf{b}^* + k\mathbf{b} \cdot \mathbf{b}^* + l\mathbf{c} \cdot \mathbf{b}^* = k,\\
\mathbf{d}^*_{hkl} \cdot \mathbf{c}^* &= h\mathbf{a} \cdot \mathbf{c}^* + k\mathbf{b} \cdot \mathbf{c}^* + l\mathbf{c} \cdot \mathbf{c}^* = l. \qquad (1.1.31)
\end{aligned}$$

Comparing equation (1.1.30) with equation (1.1.11) proves the identity of $\mathbf{d}^*_{hkl}$ and the reciprocal-lattice vector $\mathbf{h}_{hkl}$. Bragg's equation, (1.1.24), can be re-stated as

$$\mathbf{h} = \mathbf{h}_{hkl}. \qquad (1.1.32)$$

In other words, diffraction occurs whenever the scattering vector **h** equals a reciprocal-lattice vector $\mathbf{h}_{hkl}$. This powerful result is visualized in the useful Ewald construction, which is described in Section 1.1.2.4.

Useful equivalent variations of the Bragg equation are

$$|\mathbf{h}| = |\mathbf{s} - \mathbf{s}_0| = \frac{2\sin\theta}{\lambda} = \frac{1}{d} \qquad (1.1.33)$$

and

$$|\mathbf{Q}| = \frac{4\pi\sin\theta}{\lambda} = \frac{2\pi}{d}. \qquad (1.1.34)$$

The vector **Q** is the physicist's equivalent of the crystallographer's **h**. The physical meaning of **Q** is the momentum transfer on scattering and it differs from the scattering vector **h** by a factor of 2π.

1.1.2.3. *The Bragg equation from the Laue equation*

Another approach for describing scattering from a material was first described by Laue (von Laue, 1912). The Laue equation can be derived by evaluating the phase relation between two wavefronts after hitting two scatterers that are separated by the vector **r**. The path-length difference $\Delta = |\mathrm{CD}| - |\mathrm{BA}|$ between the two scattered waves introduces a phase shift between the two outgoing waves (Fig. 1.1.8). From Fig. 1.1.8 one immediately sees that the path-length difference is given by

$$\Delta = r\cos\varepsilon - r\cos\varepsilon_0. \qquad (1.1.35)$$

This path-length difference gives rise to a phase shift

$$\varphi = 2\pi\frac{\Delta}{\lambda} = 2\pi\left(\frac{r}{\lambda}\cos\varepsilon - \frac{r}{\lambda}\cos\varepsilon_0\right). \qquad (1.1.36)$$

The term in parentheses is

$$\mathbf{s}\cdot\mathbf{r} - \mathbf{s_0}\cdot\mathbf{r} = (\mathbf{s} - \mathbf{s_0})\cdot\mathbf{r} = \mathbf{h}\cdot\mathbf{r}. \qquad (1.1.37)$$

The amplitude of the scattered wave at a large distance away in the direction of the vector **s** is

$$A(\mathbf{h}) = \exp(2\pi i 0) + \exp(2\pi i \mathbf{h}\cdot\mathbf{r}) \qquad (1.1.38)$$

When we generalize the idea laid out above to n scatterers, we get

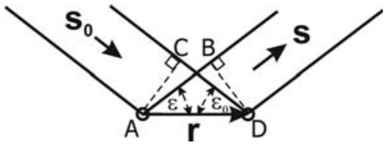

Figure 1.1.8
Scattering from an object consisting of two scatterers separated by **r**.

$$A(\mathbf{h}) = \sum_{j=1}^{n} \exp\big(2\pi i \mathbf{h}\cdot\mathbf{r}_j\big). \qquad (1.1.39)$$

For simplicity, consider the case of an infinite one-dimensional crystal of scatterers that are equally spaced by distance a_i. In this case, $r_j = aj$ and

$$A(h) = \sum_{j=-\infty}^{\infty} \exp(2\pi i h a j). \qquad (1.1.40)$$

Using the definition for a periodic delta function,

$$\lim_{n\to\infty} \sum_{j=-n}^{n} \exp(2\pi i h a j) = \sum_{k=-\infty}^{\infty} \delta(k - ha) \qquad (1.1.41)$$

and

$$A(h) = \sum_{k=-\infty}^{\infty} \delta(k - ha), \qquad (1.1.42)$$

which is a periodic array of delta functions at positions $h = k/a$. This means that sharp peaks of intensity will only appear when this expression holds, which are the reciprocal-lattice points. This is the same result as given by the Bragg equation (1.1.3) in one dimension. Extending to three dimensions, equations (1.1.40) and (1.1.42) become

$$\begin{aligned}
A(\mathbf{h}) = &\sum_{j=-\infty}^{\infty} \exp\big(2\pi i(\mathbf{h}\cdot\hat{\mathbf{a}})aj\big) \sum_{k=-\infty}^{\infty} \exp\big(2\pi i(\mathbf{h}\cdot\hat{\mathbf{b}})bk\big)\\
&\times \sum_{l=-\infty}^{\infty} \exp\big(2\pi i(\mathbf{h}\cdot\hat{\mathbf{c}})cl\big), \qquad (1.1.43)
\end{aligned}$$

where $\hat{\mathbf{a}} = \mathbf{a}/a$, and

$$A(\mathbf{h}) = \sum_{\mu,\nu,\eta=-\infty}^{\infty} \delta[\mu - (\mathbf{h}\cdot\hat{\mathbf{a}})a]\delta[\nu - (\mathbf{h}\cdot\hat{\mathbf{b}})b]\delta[\eta - (\mathbf{h}\cdot\hat{\mathbf{c}})c]. \qquad (1.1.44)$$

Equation (1.1.44) has the same meaning in three dimensions, where intensity appears only when all three delta functions are non-zero. This occurs for the conditions

$$\mathbf{h}\cdot\hat{\mathbf{a}} = \frac{\mu}{a},\ \ \mathbf{h}\cdot\hat{\mathbf{b}} = \frac{\nu}{b} \text{ and } \mathbf{h}\cdot\hat{\mathbf{c}} = \frac{\eta}{c}, \qquad (1.1.45)$$

where μ, ν and η are integers. From this follows

$$\mathbf{h}\cdot\mathbf{a} = \mu,\ \ \mathbf{h}\cdot\mathbf{b} = \nu \text{ and } \mathbf{h}\cdot\mathbf{c} = \eta. \qquad (1.1.46)$$

These conditions are met when

$$\mathbf{h} = \mu\mathbf{a}^* + \nu\mathbf{b}^* + \eta\mathbf{c}^* = \mathbf{d}^*_{\mu\nu\eta}. \qquad (1.1.47)$$

This is exactly Bragg's equation in the form given in equation (1.1.30).

For practical purposes including the indexing of powder patterns and refinement of a structural model, given a set of lattice parameters a, b, c, α, β, γ, the positions for all possible reflections hkl can be calculated according to

$$\begin{aligned}\frac{1}{d_{hkl}} = \frac{1}{V}\Big\{\Big[&h^2b^2c^2\sin^2\alpha + k^2a^2c^2\sin^2\beta + l^2a^2b^2\sin^2\gamma \\ &+ 2hkabc^2(\cos\alpha\cos\beta - \cos\gamma) \\ &+ 2kla^2bc(\cos\beta\cos\gamma - \cos\alpha) \\ &+ 2hlab^2c(\cos\alpha\cos\gamma - \cos\beta)\Big]\Big\}^{1/2}, \qquad (1.1.48)\end{aligned}$$

for the triclinic case. Equation (1.1.48) simplifies considerably with symmetry to, for example,

$$\frac{1}{d_{hkl}} = \frac{\sqrt{h^2 + k^2 + l^2}}{a} \qquad (1.1.49)$$

for the cubic case.

1.1.2.4. *The Ewald construction and Debye–Scherrer cones*

The Bragg equation shows that diffraction occurs when the scattering vector equals a reciprocal-lattice vector. The scattering vector depends on the geometry of the experiment, whereas the reciprocal-lattice vectors are determined by the orientation and the lattice parameters of the crystalline sample. Bragg's law shows the relationship between these vectors in a scattering experiment. Ewald developed a powerful geometric construction that combines these two concepts in an intuitive way (Ewald, 1921). A sphere of radius 1/λ is drawn following the recipe below. The Bragg equation is satisfied and diffraction occurs whenever a reciprocal-lattice point coincides with the surface of the sphere.

The recipe for constructing Ewald's sphere[2] is as follows (Fig. 1.1.9):

(1) Draw the incident wave vector $\mathbf{s}_0$. This points in the direction of the incident beam and has length 1/λ.

(2) Draw a sphere centred on the tail of this vector with radius 1/λ. The incident wave vector $\mathbf{s}_0$ defines the radius of the sphere. The scattered wave vector **s**, also of length 1/λ, points in the direction from the sample to the detector. This vector is also drawn starting from the centre of the sphere and also terminates at a point on the surface of the sphere. The scattering vector $\mathbf{h} = \mathbf{s} - \mathbf{s}_0$ completes the triangle from the tip of **s** to the tip of $\mathbf{s}_0$, both of which lie on the surface of the sphere. Thus the surface of the sphere defines the locus of points in reciprocal space where the scattering vector in our experiment may possibly lie.

(3) Draw the reciprocal lattice with the origin lying at the tip of $\mathbf{s}_0$.

(4) Find all the places on the surface of the sphere where reciprocal-lattice points lie. This gives the set of points in reciprocal space where the expression $\mathbf{h} = \mathbf{h}_{hkl}$ may possibly be satisfied in our experiment.

This construction places a reciprocal-lattice point at one end of **h**. The other end of **h** lies on the surface of the sphere by definition. Thus, Bragg's law is only satisfied when another reciprocal-lattice point coincides with the surface of the sphere. Diffraction can be envisaged as beams of X-rays emanating from the sample in these directions. In order to detect the intensity of these diffracted beams, one simply moves the detector to the right position. Any vector between two reciprocal-lattice points has the potential to produce a Bragg peak. The Ewald-sphere construction indicates which of these possible reflections are experimentally accessible.

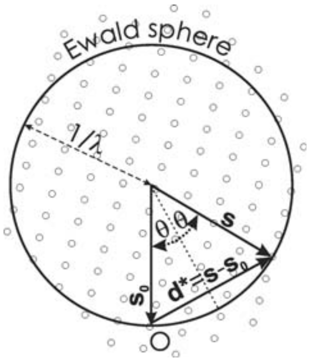

Figure 1.1.9
Simplified representation of the Ewald-sphere construction as a circle in two dimensions. O marks the origin of reciprocal space. The vectors are defined in the text. [Reproduced from Dinnebier & Billinge (2008) with permission from the Royal Society of Chemistry.]

Changing the orientation of the crystal reorients the reciprocal lattice, bringing different reciprocal-lattice points onto the surface of the Ewald sphere. In a single-crystal experiment it is necessary to repeatedly reorient the crystal to bring new reciprocal-lattice points onto the surface of the Ewald sphere, and then to reorient the detector in such a way as to measure the scattering from each particular reflection on the surface. This is done in a highly automated fashion these days. Once a diffraction pattern has been indexed so that the lattice vectors and the orientation matrix (the relation of the lattice vectors to the laboratory coordinate frame) are found, then all of the diffractometer settings that are required to collect all the Bragg peaks are fully determined and this process can be accomplished automatically.

In this chapter we are considering scattering from powders. An ideal powder contains individual crystallites in all possible orientations with equal probability. The powder experiment is equivalent to placing a detector at a fixed position and rotating a single crystal through every orientation, spending an equal amount of time in each orientation. The first powder experiment was reported by Debye & Scherrer in 1916, and independently by Hull in 1917. In the Ewald construction, this is the same as

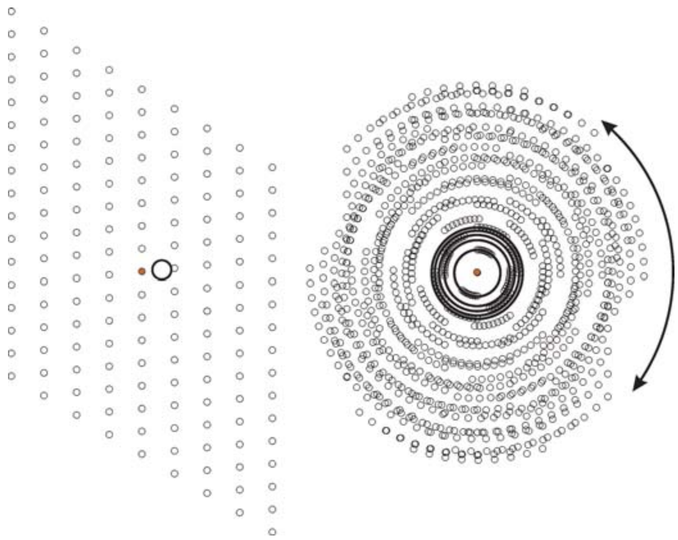

Figure 1.1.10
Illustration of the reciprocal lattice associated with a single-crystal lattice (left) and a large number of randomly oriented crystallites (right). A real powder consists of so many grains that the dots of the reciprocal lattice form into continuous lines. [Reproduced from Dinnebier & Billinge (2008) with permission from the Royal Society of Chemistry.]

---

[2] For practical reasons, plots of the Ewald 'sphere' are circular cuts through the sphere and the corresponding slice of reciprocal space.

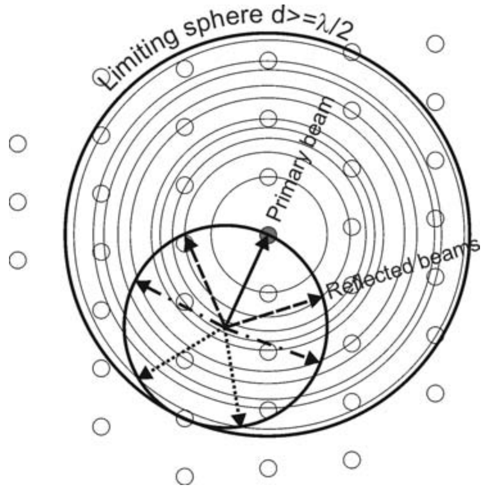

Figure 1.1.11
Simplified representation of the Ewald-sphere construction as a circle in two dimensions. Illustration of the region of reciprocal space that is accessible in a powder diffraction experiment. The smaller circle represents the Ewald sphere. As shown in Fig. 1.1.10, a powder sample has crystallites in all possible orientations, which is modelled by rotating the reciprocal lattice to sample all orientations. An equivalent operation is to rotate the Ewald sphere in all possible orientations around the origin of reciprocal space. The volume swept out is the region of reciprocal space accessible in the experiment. [Reproduced from Dinnebier & Billinge (2008) with permission from the Royal Society of Chemistry.]

smearing out every reciprocal-lattice point over the surface of a sphere centred on the origin of reciprocal space. This is illustrated in Fig. 1.1.10. The orientation of the $\mathbf{d}^*_{hkl}$ vector is lost and the three-dimensional vector space is reduced to one dimension with the independent variable being the modulus of the vector $|\mathbf{d}^*_{hkl}| = 1/d$.

These spherical shells intersect the surface of the Ewald sphere in circles. A two-dimensional projection is shown in Fig. 1.1.11. Diffracted beams can be envisaged as emanating from the sample in, and only in, the directions where the thin circles from the smeared reciprocal lattice intersect the thick circle of the Ewald sphere. A few representative diffraction beams are indicated by the dashed, dotted and dash-dotted arrows.

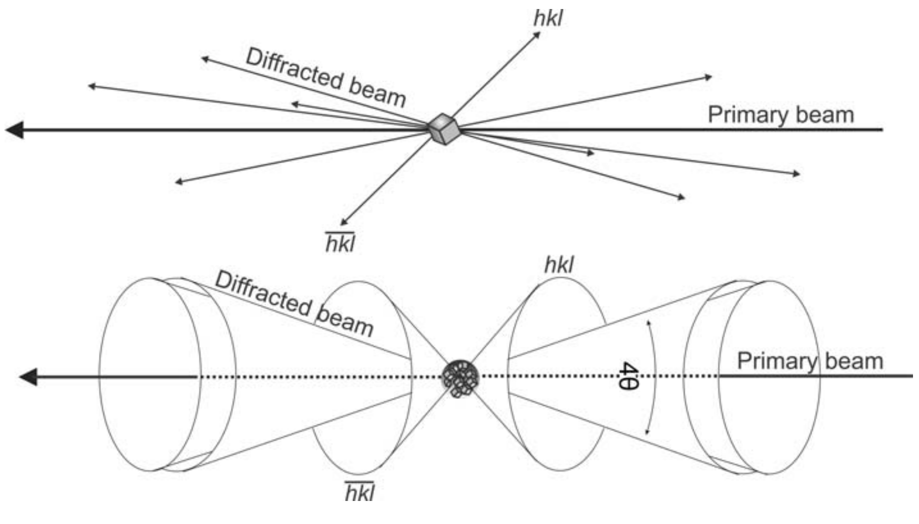

Figure 1.1.12
Comparison between the scattered beams originating from a single crystal (top) and a powder (bottom). For the latter, some Debye–Scherrer cones are drawn in reciprocal space. [Reproduced from Dinnebier & Billinge (2008) with permission from the Royal Society of Chemistry.]

The reflections from planes with the smallest d-spacing that are accessible in the experiment are determined by the diameter of the Ewald sphere, which is $2/\lambda$. In order to increase the number of reflections that can be detected, one must decrease the incident wavelength. In the case of an energy-dispersive experiment such as a time-of-flight neutron powder diffraction experiment, which makes use of a continuous distribution of wavelengths from $\lambda_{\min}$ to $\lambda_{\max}$ at fixed angle, all reflections that lie in the cone-shaped region of reciprocal space between the two limiting Ewald spheres at $2/\lambda_{\min}$ and $2/\lambda_{\max}$ will be detected.

As mentioned above, in a powder the reciprocal-lattice points get smeared into a spherical surface, which intersects the Ewald sphere as a circle. This means that, in three dimensions, the resulting diffracted radiation associated with the reflection hkl forms a cone emanating from the sample on an axis given by the direct beam, the so-called Debye–Scherrer cone. Different reciprocal-lattice points, at different values of $1/d_{hkl}$, give rise to coaxial cones of scattering. This is illustrated in Fig. 1.1.12.

The smearing of reciprocal space in a powder experiment makes the measurement of a powder diffraction pattern easier than the measurement of a set of single-crystal data, because the sample does not have to be repeatedly re-oriented, but this comes at the cost of a loss of information. At first sight the loss of information seems to be the directional information about the points in the reciprocal lattice. However, once the lattice is indexed (*i.e.* its basis vectors are known) the directional information in the pattern can be recovered without difficulty, which is why three-dimensional structures can be determined from the one-dimensional diffraction information in a powder pattern. The loss of information comes from the fact that reflections from lattice planes whose vectors lie in different directions but which have the same d-spacing overlap. These reflections cannot be resolved by the measurement and so the intensity in each of the peaks is not known. The peak-overlap problem becomes increasingly worse with increasing scattering angle as the number of diffraction planes in a particular d-spacing range increases and their separation decreases.

Some of these overlaps are dictated by symmetry (systematic overlaps) and others are accidental. Systematic overlaps are less problematic because the number of equivalent reflections (the multiplicity) is known from the symmetry, and, by symmetry, each of the overlapping peaks has the same intensity. For highly crystalline samples, the number of accidental overlaps can be reduced by making measurements with higher resolution, since this allows similar but not identical d-spacings to be separated.

To obtain the maximum amount of information, a spherical-shell detector would be desirable, although this is currently impractical. Often, a flat two-dimensional detector, either film, an image plate or a charge-coupled device (CCD), is placed perpendicular to the direct beam, or offset to one side to increase the angular range of the data collected. In this case, the Debye–Scherrer cones appear as circles, as shown in Fig. 1.1.13, or as ellipses if the detector is at an angle to the direct beam.

For an ideal powder, the intensity distribution around the rings is uniform. In a traditional powder diffraction experiment using a point detector, for example a scintillator detector behind a receiving slit that defines the angular resolution of the measurement, at each position the detector samples a point on the two-dimensional diffraction pattern shown in Fig. 1.1.13. As the detector is moved to higher 2θ angles the locus of the points that are sampled is a horizontal or vertical (depending on whether the detector is moving in the horizontal or the vertical plane) line across the two-dimensional image. The intensity that is detected is low except where the detector crosses the circles of high intensity. This type of measurement is preferred for obtaining the highest resolution, especially if a highly perfect analyser crystal is used instead of a slit for defining the angle of the scattered beam. However, if the full rings, or fractions of them, are detected with two-dimensional detectors, the counting statistics can be improved enormously by integrating azimuthally around the rings at constant $|\mathbf{h}|$. This mode is becoming very popular for time-resolved, *in situ* and parametric studies where rapid throughput is more important than high resolution. It is also useful for samples that are weakly scattering and for nanometre-sized crystals or defective crystals, which may not show sharper peaks even when measured at higher resolution.

If the powder is non-ideal, the intensity distribution around the ring is no longer uniform, as illustrated in the right part of Fig. 1.1.13, and a one-dimensional scan will give arbitrary intensities for the reflections. To check for this in a conventional measurement it is possible to measure a rocking curve by keeping the detector positioned so that the Bragg condition for a reflection is satisfied and then taking measurements while the sample is rotated. If the powder is ideal, *i.e.* it is uniform and fine-grained enough to sample every orientation uniformly, this will result in a constant intensity as a function of sample angle, while large fluctuations in intensity will suggest a poor powder average. To improve powder statistics, powder samples may be rotated during a single measurement exposure, both for conventional point measurements and for measurements with two-dimensional detectors. Additional averaging of the signal also occurs during the azimuthal integration in the case of two-dimensional detectors. Outlier intensities can be identified and excluded from the integration. On the other hand, the intensity variation around the rings can give important information about the sample, such as preferred orientation of the crystallites or texture.

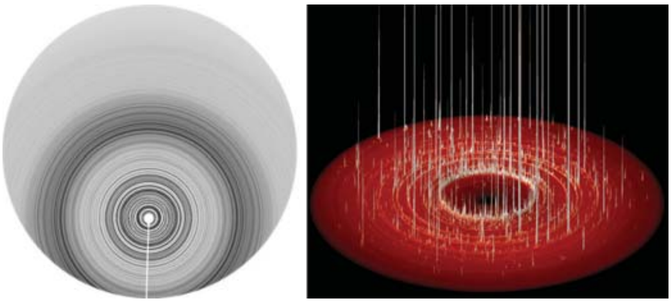

Figure 1.1.13
Left: Debye–Scherrer rings from an ideal fine-grained powder sample of a protein (courtesy Bob Von Dreele). Right: perspective view of Debye–Scherrer rings from a grainy powder sample of $BiBO_3$ at high pressure in a diamond anvil cell.

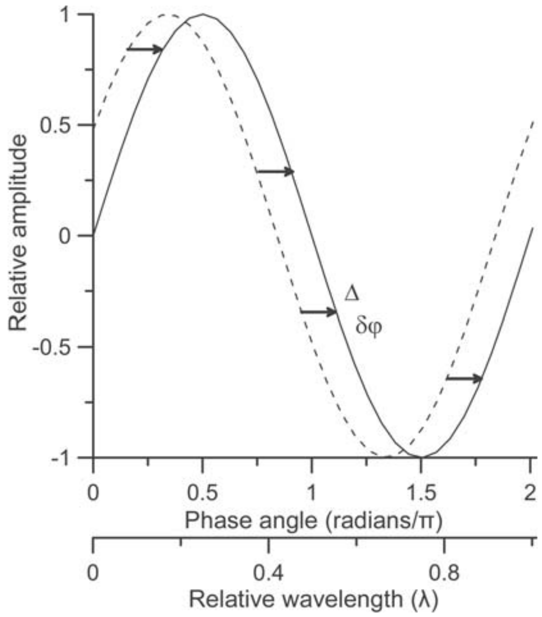

Figure 1.1.14
Graphical illustration of the phase shift between two sine waves of equal amplitude. [Reproduced from Dinnebier & Billinge (2008) with permission from the Royal Society of Chemistry.]

The d-spacings that are calculated from a powder diffraction pattern will include measurement errors, and it is important to minimize these as much as possible. These can come from uncertainty in the position of the sample, the zero point of 2θ, the angle of the detector or the angle of a pixel on a two-dimensional detector, uncertainties in the wavelength and so on. These effects will be dealt with in detail in later chapters. These aberrations often have a well defined angular dependence which can be included in fits to the data so that the correct underlying Bragg-peak positions can be determined with high accuracy.

1.1.3. The peak intensity

1.1.3.1. *Adding phase-shifted amplitudes*

Bragg's law gives the *positions* at which diffraction by a crystal will lead to sharp peaks (known as Bragg peaks) in diffracted intensity. We now want to investigate the factors that determine the intensities of these peaks.

X-rays are electromagnetic (EM) waves with a much shorter wavelength than visible light, typically of the order of 1 Å ($= 10^{-10}$ m). The physics of EM waves is well understood and excellent introductions to the subject are found in every textbook on optics. Here we briefly review the results that are most important in understanding the intensities of Bragg peaks.

Classical EM waves can be described by a sine wave of wavelength λ that repeats every 2π radians. If two identical waves are not coincident, they are said to have a phase shift, which is either measured as a shift, Δ, on a length scale in units of the wavelength, or equivalently as a shift in the phase, $\delta\varphi$, on an angular scale, such that

$$\frac{\Delta}{\lambda} = \frac{\delta\varphi}{2\pi} \Rightarrow \delta\varphi = \frac{2\pi}{\lambda}\Delta. \qquad (1.1.50)$$

This is shown in Fig. 1.1.14.

The detected intensity, I, is proportional to the square of the amplitude, A, of the sine wave. With two waves present that are coherent and can interfere, the amplitude of the resultant wave is not just the sum of the individual amplitudes, but depends on the phase shift $\delta\varphi$. The two extremes occur when $\delta\varphi = 0$ (constructive interference), where $I \simeq (A_1 + A_2)^2$, and $\delta\varphi = \pi$ (destructive interference), where $I \simeq (A_1 - A_2)^2$. In general, $I \simeq \left[A_1 + A_2 \exp(i\delta\varphi)\right]^2$. When more than two waves are present, this equation becomes

$$I \simeq \left[\sum_j A_j \exp\left(i\varphi_j\right)\right]^2, \qquad (1.1.51)$$

where the sum is over all the sine waves present and the phases, φ_j, are measured with respect to some origin.

Measuring X-ray diffraction involves the measurement of the intensity of X-rays scattered from electrons bound to atoms. Waves scattered by atoms at different positions arrive at the detector with a relative phase shift. Therefore, the measured intensities yield information about the relative atomic positions.

In the case of X-ray diffraction, the Fraunhofer approximation is valid. This is a far-field approximation, where the distances L_1 from the source to the place where scattering occurs (the sample) and L_2 from the sample to the detector are much larger than the separation, D, of the scatterers. This is an excellent approximation, since in this case $D/L_1 \simeq D/L_2 \simeq 10^{-10}$. The Fraunhofer approximation greatly simplifies the mathematics. The incident X-rays come from a distant source and form a wavefront of constant phase that is a plane wave. X-rays scattered by single electrons are outgoing spherical waves, which again appear as plane waves in the far field. This allows us to express the intensity of the diffracted X-rays using equations (1.1.51) and (1.1.39).

This is the origin of equation (1.1.39), which gives the amplitude of the scattered radiation in terms of the scattering vector, $\mathbf{h} = \mathbf{s}_0 - \mathbf{s}$, and the atomic positions, $\mathbf{r}_j$. In fact, the amplitude of the scattered radiation is only proportional to this expression. The actual intensity depends on the amplitude of the incident wave and also on the absolute scattering power of the scatterers. If we neglect for now the incident intensity and assume that our measured intensities are normalized to the incident beam intensity, we get

$$A(\mathbf{h}) = \sum_{j=1}^{n} f_j(h) \exp\left(2\pi i \mathbf{h} \cdot \mathbf{r}_j\right), \qquad (1.1.52)$$

where $f_j(h)$ is the atomic form factor and $h = |\mathbf{h}|$ is the magnitude of the scattering vector, and is described in more detail in *International Tables for Crystallography*, Volume C, Part 6. This is a measure of the strength of scattering from the jth atom. At $h = 0$, scattering is in the forward direction with all electrons scattering in phase. As a result, $f_j(0)$ equals the number of electrons bound to the atom (in units of the Thomson scattering cross section for an electron), usually taken to be the atomic number of the atomic species at the jth site. An additional h-dependent reduction of the amplitude comes from positional disorder of the atoms. A Gaussian blurring is used with a width that is often falsely called the 'temperature factor', but is more correctly known as the atomic displacement parameter (ADP). The Gaussian is known as the Debye–Waller factor, which is discussed below. More information can be found in Chapter 4.7.

The crystal structure consists of periodic arrangements of atoms. The simplest structures have one atom in a periodically repeated unit cell. However, in general, there is a well defined group of atoms that forms a structural motif that is periodically repeated. This motif can range from one atom to thousands of atoms in complex protein structures. Solving the crystal structure consists of finding the unit-cell parameters and determining the positions in the unit cell of the atoms in the structural motif. In this sense, the structure of the infinite crystal can be thought of mathematically as a convolution of the periodic lattice that we discussed above with the structural motif. This results in a perfect, orientationally ordered copy of the structural motif in every unit cell translated in three-dimensional space.

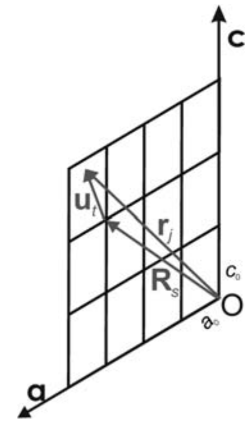

Figure 1.1.15
The position vector of the jth atom $\mathbf{r}_j$ can be decomposed into a vector $\mathbf{R}_s$ from the origin of the crystal to the origin of the unit cell containing the jth atom, and the vector $\mathbf{u}_t$ from the unit cell origin to the jth atom.

As we discussed above, the direct-space lattice has a reciprocal lattice associated with it which determines the positions of the Bragg peaks, or allowed delta functions of scattered intensity. The reciprocal lattice is actually a Fourier transform of the periodic lattice in direct space. The convolution theorem of Fourier transforms tells us that a convolution of two functions in direct space will result in a product of the Fourier transforms of those functions in the Fourier space. Since the structure is a convolution of the direct-space lattice with the structural motif, the reciprocal lattice will be *multiplied* by the Fourier transform of the structural motif. This Fourier transform of the structural motif is called the crystallographic structure factor, F_{hkl}.

This result can be readily derived from equation (1.1.52). In this equation $\mathbf{r}_j$ is the vector from the (arbitrary but fixed) origin to the jth atom in the material. If we now think of the crystal as consisting of n identical cells, each containing an identical structural motif consisting of m atoms, we can write $\mathbf{r}_j$ as a sum of two vectors: a vector that goes from the origin to the corner of the sth unit cell that contains the jth atom, and a second vector that goes from the corner of the sth cell to the position of the jth atom. This is illustrated in Fig. 1.1.15.

Equation (1.1.52) can then be written as

$$A(\mathbf{h}) = \sum_{s=1}^{n} \sum_{t=1}^{m} f_t(h) \exp\left(2\pi i \mathbf{h} \cdot (\mathbf{R}_s + \mathbf{u}_t)\right), \qquad (1.1.53)$$

where it is readily seen that the first sum is taken over all the cells in the crystal and the second sum is taken over the m atoms in the structural motif. The equation is readily factored as follows:

$$A(\mathbf{h}) = \sum_{s=1}^{n} \exp(2\pi i \mathbf{h} \cdot \mathbf{R}_s) \sum_{t=1}^{m} f_t(h) \exp(2\pi i \mathbf{h} \cdot \mathbf{u}_t). \qquad (1.1.54)$$

Taking n to infinity, we immediately recognise the first sum as the lattice sum of equation (1.1.43), and we can therefore rewrite equation (1.1.54) as

$$\begin{aligned} A(\mathbf{h}) &= \sum_{t=1}^{m} f_t(h) \exp(2\pi i \mathbf{h} \cdot \mathbf{u}_t) \\ &\quad \times \sum_{\mu,\nu,\eta=-\infty}^{\infty} \delta\left[\mu - (\mathbf{h} \cdot \hat{\mathbf{a}})a\right] \delta\left[\nu - (\mathbf{h} \cdot \hat{\mathbf{b}})b\right] \delta\left[\eta - (\mathbf{h} \cdot \hat{\mathbf{c}})c\right], \\ A(\mathbf{h}) &= F_{hkl} \sum_{\mu,\nu,\eta=-\infty}^{\infty} \delta\left[\mu - (\mathbf{h} \cdot \hat{\mathbf{a}})a\right] \delta\left[\nu - (\mathbf{h} \cdot \hat{\mathbf{b}})b\right] \delta\left[\eta - (\mathbf{h} \cdot \hat{\mathbf{c}})c\right]. \end{aligned} \qquad (1.1.55)$$

The delta functions determine the positions of the reciprocal-

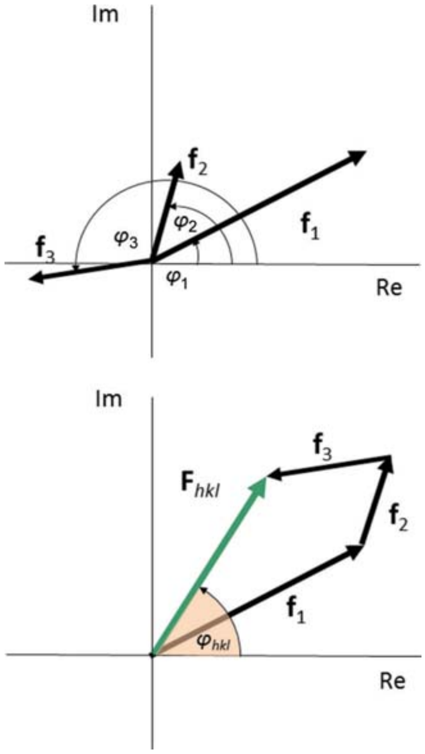

Figure 1.1.16
Graphical illustration of the summation of scattered wave amplitudes $\mathbf{f}_t$ in the complex plane, accounting for the phase shifts coming from the different positions of the atoms in the unit cell.

lattice points (directions of the Bragg peaks), and their intensities are multiplied by a factor, the crystallographic structure factor,

$$F_{hkl} = \sum_{t=1}^{m} f_t(h)\exp(2\pi i\mathbf{h}\cdot\mathbf{u}_t). \qquad (1.1.56)$$

If we write each term as a complex number denoted $\mathbf{f}_t$, we can represent this complex sum as a vector sum in the complex plane, as illustrated in Fig. 1.1.16, where the $\varphi_t = 2\pi\mathbf{h}\cdot\mathbf{u}_t$. The intensity of the Bragg peak depends only on the length of the $\mathbf{F}_{hkl}$, not its direction. However, its length depends on both the lengths *and the phases* of each contribution, which in turn depend on the positions of the atoms within the unit cell. This is the phase information that is 'lost' in a diffraction experiment. Given a structure, we can directly calculate all the Bragg-peak intensities (the 'forward problem'). However, given all the Bragg-peak intensities, we cannot directly calculate the structure (the 'inverse problem'). Structure determination uses the measured intensities and reconstructs the lost phase information using various iterative methods and algorithms.

In fact, the intensity of a Bragg reflection *hkl* is given by the squared absolute value of the structure-factor amplitude F_{hkl},

$$\left|F_{hkl}\right|^2 = \sum_{t,t'=1}^{m} f_t(h) f_{t'}^*(h)\exp\left(2\pi i\mathbf{h}\cdot(\mathbf{u}_t-\mathbf{u}_{t'})\right), \qquad (1.1.57)$$

where * indicates the complex conjugate. This analysis shows that the *positions* of the Bragg peaks determine the geometry of the periodic lattice (the size and shape of the unit cell, for example), but the *intensities* of the Bragg peaks are determined by the relative positions of atoms within the unit cell, scaled by their respective scattering power. To solve the internal structure of the structural motif within the unit cell, it is necessary to measure quantitatively the intensities of many Bragg peaks and use some kind of iterative procedure to move the atoms within the cell until the calculated structure factors self-consistently reproduce the intensities of all the measured Bragg peaks.

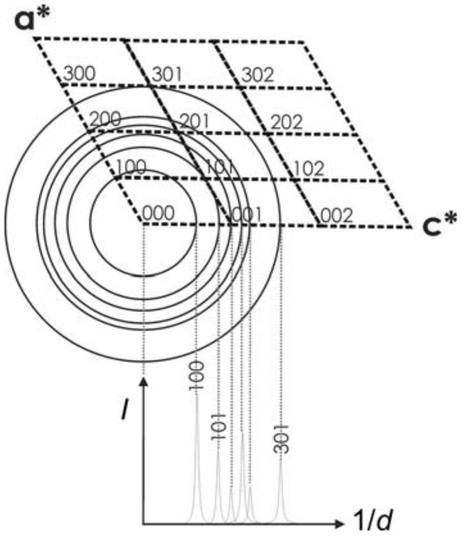

Figure 1.1.17
Schematic illustration of the projection of the reciprocal **a*****c*** plane (representing the three-dimensional reciprocal-lattice space) into the one-dimensional powder pattern.

The situation is not fundamentally different in a powder diffraction experiment from the single-crystal case, except that the Bragg peaks in three-dimensional reciprocal space are projected into one dimension, as shown in Fig. 1.1.17.

'Indexing' is the term used for deriving the lattice parameters from the positions of the Bragg peaks (see Chapter 3.4). Once the size and shape of the reciprocal lattice is determined, Miller indices can be assigned to each of the Bragg peaks in a one-dimensional powder pattern. If it is possible to extract the intensities of those peaks from the pattern, diffraction data from a powder can be used to reconstruct the three-dimensional structure in exactly the same way as is done with data from a single crystal. This process is known as structure solution from powder diffraction, and is often successful, although it is less well automated than structure solution from data from single crystals. As mentioned above, the main problem with powder data is a loss of information due to systematic and accidental peak overlap, but this can often be overcome.

There are various methods for extracting quantitative peak intensities from indexed powder patterns by computer fitting of profiles to the Bragg peaks at their known positions. Two of the most common are Pawley refinement (Pawley, 1981) and Le Bail refinement (Le Bail *et al.*, 1988), as discussed in Chapter 3.5.

In general, the intensities of the Bragg reflections must be corrected by the product K_{hkl} of various correction factors. Some common correction factors are given by

$$K_{hkl} = M_{hkl}\mathrm{Abs}_{hkl}\mathrm{Ext}_{hkl}\mathrm{LP}_{hkl}\mathrm{PO}_{hkl}\ldots, \qquad (1.1.58)$$

where M_{hkl} is the multiplicity, Abs_{hkl} is an absorption correction, Ext_{hkl} is an extinction correction, LP_{hkl} is the geometrical Lorentz–polarization correction and PO_{hkl} is a correction for preferred orientation (see Chapter 4.7).

If there is more than one crystalline phase present in the sample, and the structures of all the crystalline phases are known, then we can find a scale factor for each phase in the mixture which reproduces the data. This is then a way of determining the proportion of each phase in the sample. This is called quantitative phase analysis (see Chapter 3.9).

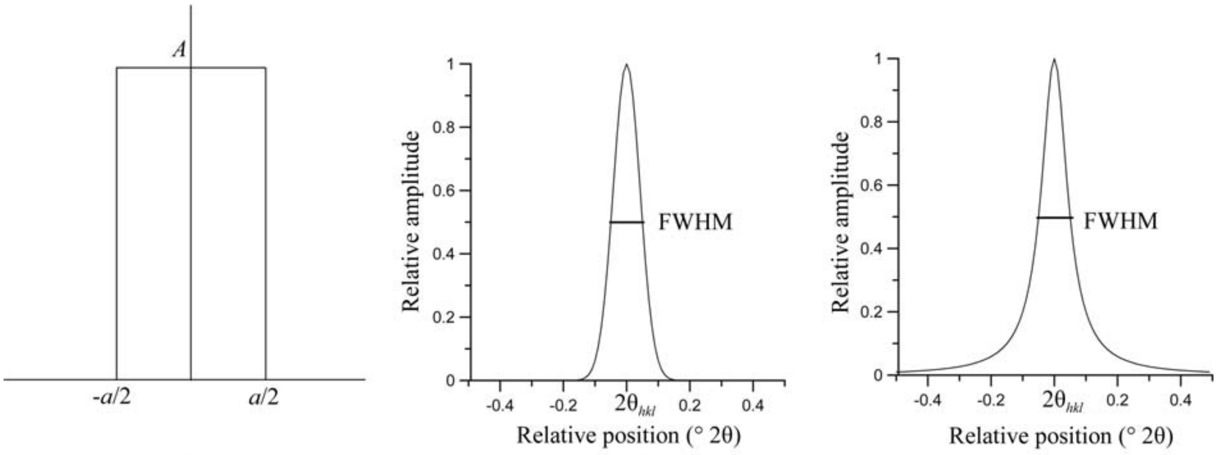

(*a*) (*b*) (*c*)

Figure 1.1.18
Normalized peak-shape functions. (*a*) The hat function, (*b*) the Gaussian function and (*c*) the Lorentzian function.

1.1.4. The peak profile

The peak profile refers to the shape of the measured Bragg peak. In the treatment above, the Bragg peaks from a perfect infinite crystal were delta functions and therefore infinitely narrow. In reality, the finite size of the crystal, the finite resolution of the measurement and defects in the material that result in inhomogeneous strains all broaden the delta function, giving it a finite width and some characteristic shape. When fitting a model to the measured diffraction pattern we should correctly account for these effects in order to obtain correct values for the Bragg-peak intensities. On the other hand, a careful study of the peak shapes yields important information about the size of the crystallites in the sample and defects that they contain. With recent improvements in instrumentation and computational data-analysis methods, this latter type of study has become more important and is having considerable scientific and technological impact.

The convolution theorem of the Fourier transform that was introduced in the derivation of the crystallographic structure factor above is also very useful in understanding the peak profile. In this case, the measured Bragg peak can be thought of as a delta function convoluted with a profile (Klug & Alexander, 1974). The profile of the Bragg reflection *hkl*, Φ_{hkl}, can be written as

$$\Phi_{hkl}(2\theta_i - 2\theta_{hkl}) = \mathrm{EP}(2\theta_i) \otimes \mathrm{IP}(2\theta_i) \otimes \mathrm{MS}(2\theta_i - 2\theta_{hkl}), \tag{1.1.59}$$

where $\mathrm{EP}(2\theta_i)$ is the emission profile of the X-ray source (tube or synchrotron), $\mathrm{IP}(2\theta_i)$ contains additional contributions to the profile from the instrument and $\mathrm{MS}(2\theta_i - 2\theta_{hkl})$ is the contribution from the microstructure of the sample. The symbol $\otimes$ denotes convolution.

The convolution of two functions $f(t)$ and $g(t)$ in real space is defined as

$$(f \otimes g)(t) = \int\limits_{\tau=-\infty}^{\infty} f(\tau) g(t-\tau)\,\mathrm{d}\tau. \tag{1.1.60}$$

The convolution theorem tells us that the Fourier transform (FT) of two convoluted functions is the product of the Fourier transforms of those functions:

$$\mathrm{FT}(f \otimes g)(t) = \big(\mathrm{FT}(f)\big)\big(\mathrm{FT}(g)\big). \tag{1.1.61}$$

Normalization of the transform leads to scaling factors like 2π which have been omitted here for simplicity.

In practice, numerical integrations are almost always required, as many of the instrument aberration functions cannot be convoluted analytically. This convolution approach is the basis of the so-called fundamental-parameter (FP) approach (Cheary & Coelho, 1992) and has proven to be superior to other more empirical or phenomenological methods. The idea behind the FP approach is to build up the profile from first principles, exclusively using measurable physical quantities like slit widths, slit lengths, Soller-slit opening angles *etc*. The process of convolution from a fundamental-parameters perspective is an approximation whereby second- and higher-order effects are typically neglected for computational speed and simplicity. The instrumental profile is usually fully characterized by measuring a line-profile standard such as NIST SRM 660c $\mathrm{LaB_6}$, which is expected to contain only small microstructural contributions, and comparing the calculated diffraction pattern to the measured one. Once the instrumental part of the profile is sufficiently well determined, it can be assumed that the remaining contributions to the 'real' profile are purely sample dependent (*e.g.* domain size, strain).

In general, it is desirable to keep the number of functions that are used to describe the peak profile to a minimum. Typical examples of mathematical functions which are convoluted to form the profile of a Bragg reflection include:

(*a*) the hat function H (*e.g.* for all kinds of rectangular slits),

$$H(2\theta - 2\theta_{hkl}) = \begin{cases} A \text{ for } -a/2 < (2\theta - 2\theta_{hkl}) < a/2, \\ 0 \text{ for } (2\theta - 2\theta_{hkl}) \le -a/2 \\ \quad \text{and } (2\theta - 2\theta_{hkl}) \ge -a/2 \end{cases} \tag{1.1.62}$$

(Fig. 1.1.18*a*);

(*b*) the normalized Gaussian G (*e.g.* for microstrain broadening),

$$G(2\theta - 2\theta_{hkl}) = \left(\frac{2\sqrt{\ln(2)/\pi}}{\mathrm{FWHM}}\right) \exp\left(\frac{-4\ln(2)(2\theta - 2\theta_{hkl})^2}{\mathrm{FWHM}^2}\right), \tag{1.1.63}$$

(Fig. 1.1.18*b*), where FWHM denotes the full width at half maximum of the Gaussian function in ° 2θ; and

(*c*) the Lorentzian function L (*e.g.* for the emission profile),

$$L(2\theta - 2\theta_{hkl}) = \frac{1}{2\pi}\left(\frac{\mathrm{FWHM}}{(2\theta - 2\theta_{hkl}) + \mathrm{FWHM}^2/4}\right), \tag{1.1.64}$$

(Fig. 1.1.18*c*).

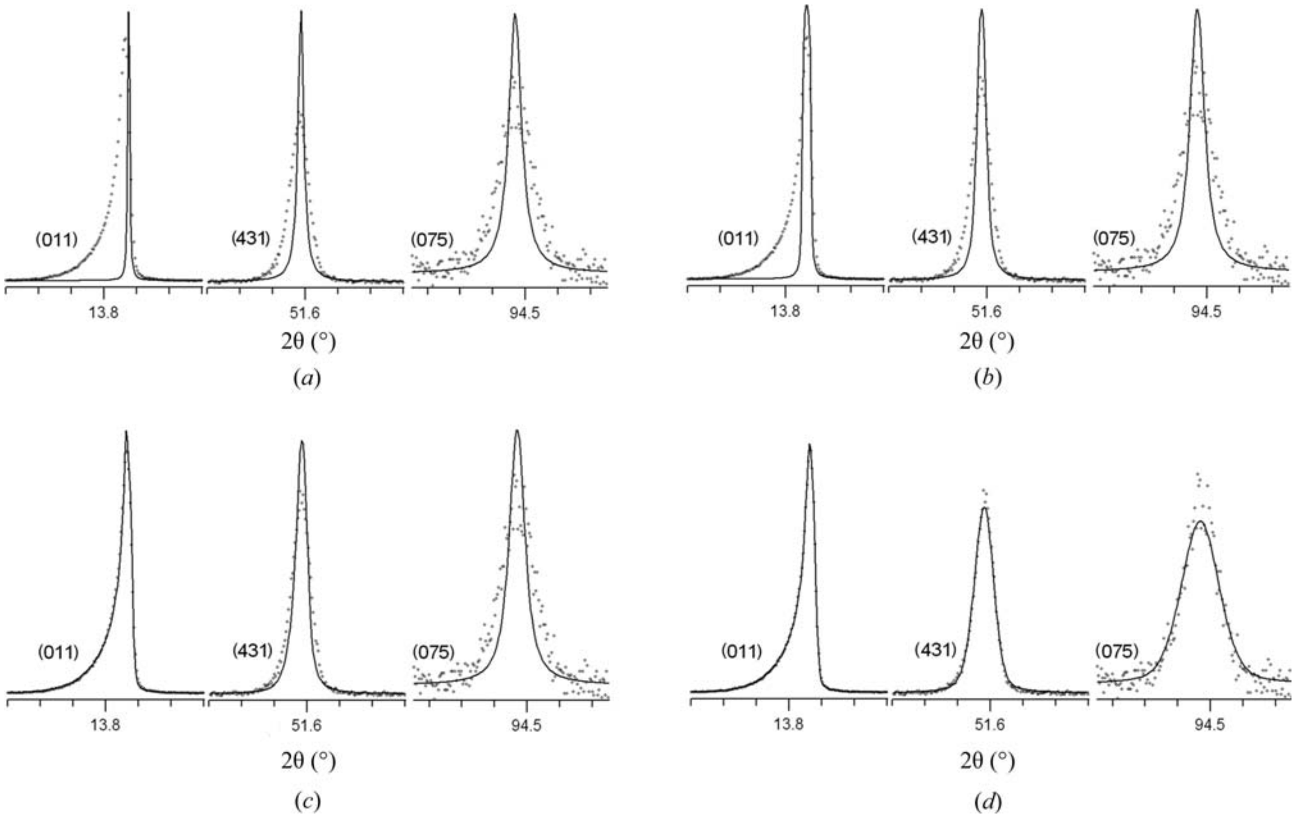

Figure 1.1.19
Peak fits of three selected reflections for an $\mathrm{LaB_6}$ standard measured with Mo $K\alpha_1$ radiation (λ = 0.7093 Å) from a Ge(220) monochromator in Debye–Scherrer geometry using the fundamental-parameter approach. (*a*) A pure Lorentzian emission profile with a half width of 0.2695 mÅ is applied, refining the peak position and intensity only; (*b*) additionally, a hat shape function of the receiving slit in the equatorial plane with a width of 0.1 mm has been convoluted into the profile; (*c*) additionally, an axial convolution with filament-, sample- and receiving-slit lengths of 8 mm each and a secondary Soller slit with an opening angle of 2.5° has been convoluted into the profile; (*d*) additionally a small contribution of Gaussian broadening coming from the position-sensitive detector is convoluted into the profile. [From Mittemeijer & Welzel (2012). Copyright Wiley-VCH Verlag GmbH & Co. KGaA. Reproduced with permission.]

These functions can be convoluted sequentially as needed, first with the delta-function Bragg peak, and subsequently with the existing profile from the previous convolutions, each time resulting in a new profile that can become quite complex (Fig. 1.1.19). It is often the case that for a particular resolution effect the angular dependence of the profile function is known from the geometry of the measurement, and the convolution function for each peak is determined with only a very small number of parameters.

1.1.4.1. *Sample contributions to the peak profile*

Features of the sample that affect the peak profile include crystallite domain size and shape, dislocations, disclinations, twin and stacking faults, antiphase domains, microstrains, grain surface relaxations, and compositional fluctuations. Here we reproduce some basic results as examples; they also illustrate some fundamental aspects of diffraction from real crystals.

1.1.4.1.1. *Crystallite size*

The starting point for the analysis of finite size effects is the Laue equation, equation (1.1.39), which is reproduced here for a one-dimensional crystal:

$$A(h)=\sum_{j=0}^{n}\exp(2\pi iajh). \qquad (1.1.65)$$

When we were deriving the Bragg equation from the Laue equation we assumed an infinite crystal, and the sum taken to infinity resulted in delta functions at the reciprocal-lattice points. Now we want to consider a finite crystal with n unit cells. There is an analytic form for this sum which, using Euler's identity, is given by

$$\begin{aligned}A(h)&=\frac{\exp\big(2\pi i(n+1)ah\big)-1}{\exp(2\pi iah)-1}\\&=\frac{\exp\big(i\pi(n+1)ah\big)}{\exp(i\pi ah)}\frac{\exp\big(i\pi(n+1)ah\big)-\exp\big(-i\pi(n+1)ah\big)}{\exp(i\pi ah)-\exp(-i\pi ah)}\\&=\exp(i\pi nah)\frac{\sin\big(\pi(n+1)ah\big)}{\sin(\pi ah)}. \qquad (1.1.66)\end{aligned}$$

The intensity is obtained by taking the modulus squared of this complex function, resulting in

$$I(h)=\frac{\sin^2\big(\pi(n+1)ah\big)}{\sin^2(\pi ah)}. \qquad (1.1.67)$$

This function has sharp maxima when $h = \nu(1/a)$, where ν is an integer. This large central maximum falls off with a width proportional to $1/n^2$ with oscillating tails of intensity where the frequency of the oscillations increases with increasing n. This is illustrated in Fig. 1.1.20 for two different values of n but the same value of a.

In general, the Fourier transforms of periodic patterns become sharper with increasing number of unit cells. The expression $\sin(\pi(n+1)ah)/\sin(\pi ah)$ is also called the geometric factor of the structure amplitude.

This size broadening is often modelled in practice by using an equation due to Scherrer. We now reproduce the simple deri-

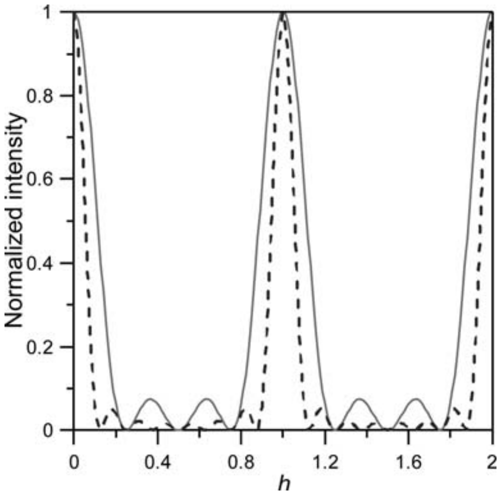

Figure 1.1.20
Normalized intensity from a finite lattice with $n = 3$ (solid curve) and $n = 8$ (dashed line), demonstrating the sharpening of peaks with increasing number of unit cells n. The normalization was done such that the peaks have the same peak maximum rather than the same integrated intensity for a clearer comparison of the relative peak widths.

vation of the Scherrer equation following Klug & Alexander (1974).

Fig. 1.1.21 shows the path-length difference *versus* the depth of the lattice plane. When the angle between the incoming beam and the lattice plane θ is different by an amount ε from the Bragg condition, it is always possible to find a lattice plane inside an infinite crystal where the extra path is $\Delta = \lambda(n + \frac{1}{2})$ for n integer, producing destructive interference. For a thick crystal this is true for arbitrarily small ε, which explains the sharp Bragg reflections. In the case of a crystal with finite dimensions, for small ε the plane for which $\Delta = \lambda(n + \frac{1}{2})$ holds will not be reached, thus leading to an intensity distribution over some small angular range. We can use this idea to estimate the broadening of a Bragg reflection due to size effects.

The thickness of a crystallite in the direction perpendicular to p planes of separation d_{hkl} (Fig. 1.1.21) is

$$L_{hkl} = p d_{hkl}. \tag{1.1.68}$$

The additional beam path between consecutive lattice planes at the angle $\theta + \varepsilon$ is

$$\begin{aligned}\Delta &= 2d\sin(\theta+\varepsilon)\\ &= 2d(\sin\theta\cos\varepsilon + \cos\theta\sin\varepsilon)\\ &= n\lambda\cos\varepsilon + 2d\sin\varepsilon\cos\theta\\ &\simeq n\lambda + 2d\sin\varepsilon\cos\theta.\end{aligned} \tag{1.1.69}$$

The corresponding phase difference is then

$$\delta\varphi = 2\pi\frac{\Delta}{\lambda} = 2\pi n + \frac{4\pi}{\lambda}\varepsilon d\cos\theta = \frac{4\pi\varepsilon d\cos\theta}{\lambda} \tag{1.1.70}$$

and the phase difference between the top and the bottom layer (layer p) is then

$$p\delta\varphi = p\frac{4\pi\varepsilon d\cos\theta}{\lambda} = \frac{4\pi L_{hkl}\varepsilon\cos\theta}{\lambda}. \tag{1.1.71}$$

Rearranging equation (1.1.71) leads to

$$\varepsilon = \frac{\lambda\delta\varphi}{4\pi L_{hkl}\cos\theta}, \tag{1.1.72}$$

which gives an expression for the misalignment angle in terms of the crystallite size L_{hkl} and the phase difference $\delta\varphi$ between the reflections originating from the top plane and the bottom plane. Clearly, the scattered intensity is at a maximum for $\delta\varphi = 0$ ($\varepsilon = 0$). With increasing ε the intensity decreases, giving rise to a peak of finite width. Perfect cancellation of the waves from the top and bottom planes occurs for a phase difference of $\delta\varphi = \pm\pi$, at which point $\varepsilon = \pm\lambda/(4L_{hkl}\cos\theta)$. On a 2θ scale, the measured angular width between these points is

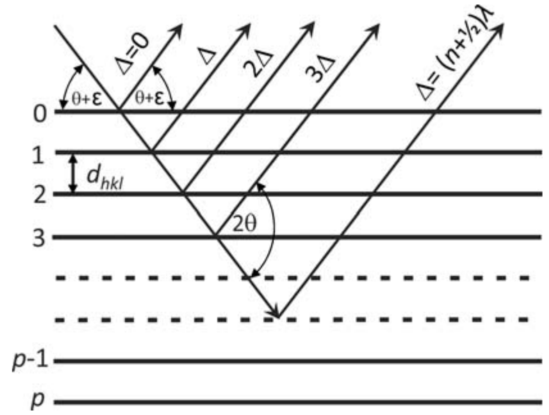

Figure 1.1.21
Path-length difference of the scattered ray *versus* the depth of the lattice plane in the crystal. [Reproduced from Dinnebier & Billinge (2008) with permission from the Royal Society of Chemistry.]

$$\beta_{hkl} = 4\varepsilon = \frac{\lambda}{L_{hkl}\cos\theta}, \tag{1.1.73}$$

giving us some measure of the peak width in radians that results from the finite particle size. A full treatment taking into account the correct form for the intensity distribution gives

$$\beta_{hkl} = \frac{K\lambda}{L_{hkl}\cos\theta}, \tag{1.1.74}$$

with a scale factor of $K = 0.89$ for perfect spheres. In general K depends on the shape of the grains (*e.g.* K is 0.94 for cube-shaped grains), but it is always close to unity. This equation is not valid for crystallites[3] that are too large or too small. In the case of large crystallites the peak width is governed by the coherence of the incident beam and not by particle size. For nanometre-sized crystallites, Bragg's law fails and the Debye equation needs to be used instead. The Debye equation (see Section 1.1.5.3) gives the scattering from an isotropically scattering sample such as a glass, liquid or powder, and does not presume that the sample is periodic.

1.1.4.1.2. *Microstrain*

Several important relationships in crystallography, including the effect of strain and microstrain on Bragg peaks, follow directly from a derivative of the Bragg equation (1.1.3). First we rewrite Bragg's law making the d-spacing the subject of the equation:

$$d = \frac{n\lambda}{2\sin\theta}. \tag{1.1.75}$$

The uncertainty of the measured lattice spacing is given by the total derivative dd,

$$\mathrm{d}d = \frac{\partial d}{\partial\theta}\mathrm{d}\theta + \frac{\partial d}{\partial\lambda}\mathrm{d}\lambda, \tag{1.1.76}$$

---

[3] Strictly speaking, the term crystallite size here refers to the dimension of a coherently scattering domain. Only in a perfect crystal is this the grain size.

Table 1.1.1
Types of scattering from a sample

Type of scattering	Coherent	Incoherent
Elastic	Bragg scattering Magnetic Bragg scattering Bragg scattering from ferroelectric/magnetic order Diffuse scattering from static defects Diffuse signal from small nanoparticles (<10 nm) Scattering from amorphous material (except excitations) Multiple scattering (coherent)	Laue monotonic diffuse scattering Neutron incoherent scattering Multiple scattering (incoherent)
Inelastic	Thermal diffuse scattering Spin-wave scattering Paraelectric/paramagnetic scattering Scattering from liquids	Compton scattering Fluorescence Incoherent scattering from hydrogen

leading to

$$\mathrm{d}d = -\frac{n\lambda}{2\sin\theta}\frac{\cos\theta}{\sin\theta}\mathrm{d}\theta + \frac{n}{2\sin\theta}\mathrm{d}\lambda \qquad (1.1.77)$$

and finally

$$\frac{\mathrm{d}d}{d} = -\frac{\mathrm{d}\theta}{\tan\theta} + \frac{\mathrm{d}\lambda}{\lambda}. \qquad (1.1.78)$$

When a crystal is strained, the d-spacings vary. A *macroscopic* strain changes the interplanar spacing by Δd_{hkl}, giving rise to a shift of $\Delta\theta$ in the *average* position of the diffraction peak. On the other hand, *microscopic* strains result in a distribution of d-spacings of width δd_{hkl}, which has the effect of *broadening* the diffraction peak by $\delta\theta$. Equation (1.1.78) gives an expression for the amount of Bragg-peak broadening that occurs for a given δd_{hkl}.

1.1.5. The background

1.1.5.1. *Information content in the background*

As discussed above, the elastic scattering from a crystalline powder consists of sharp rings, or peaks, of scattering at the 2θ angles where the Bragg or von Laue laws are satisfied. In general these sharp peaks sit on top of a 'background' which is broad and somewhat featureless. There are two components to this background, illustrated in Fig. 1.1.1: extraneous counts in the detector from things other than the sample, and non-Bragg scattering from the sample itself. The former are rarely of interest scientifically and the objective of a good experimental design is to minimize them as far as possible, or explicitly measure and subtract them, and then account well in any model or data interpretation for the part that cannot be eliminated from the measurement. Historically, the diffuse-scattering signals from the sample itself were also considered to be an inconvenience to be minimized and removed, and indeed in many cases this is still the best course of action (for example, sample fluorescence can be eliminated by choosing to work at an X-ray energy that lies below the absorption edge of a constituent atom). However, the diffuse 'background' from the sample can contain crucial information about defects, disorder and nanoscale order in the sample, and increasingly we are interested in studying it in order to understand the properties of the material that is under investigation. In some cases, such as glasses, liquids and samples of small nanoparticles, there is no Bragg scattering at all and only a diffuse scattering signal (see Chapter 5.6).

All the intensity scattered by the sample can be categorized as either coherent or incoherent and as elastic or inelastic, which are defined as follows. The coherency of the signal derives from whether or not the scattered waves interfere with each other constructively, and the resulting intensities are different in each case. For coherent scattering, the waves contributing to the signal are all summed first, before the wave amplitude is squared, to find the intensity distribution, which is the modulus squared of the resulting wave. For incoherent waves, one simply squares the amplitude of each wave to get its intensity and sums these together to get the total intensity. Switching to a consideration of the elasticity of the scattering, we define the scattering as elastic if the incident and scattered waves have the same energy, in which case no energy was exchanged during the scattering process between the incident wave and the sample, and inelastic scattering as the opposite. Inelastic scattering may result in a gain or a loss of energy of the scattered particle depending on the nature of the scattering, which results in a change in the wavelength of the scattered particle. There are also some non-scattering processes that can take place, such as absorption and fluorescence, but emissions resulting from these processes can also be categorized by whether or not they are coherent and elastic. It should be noted that the total energy of the system must be conserved during the scattering process, and so when a scattered wave gains or loses energy it exchanges it with the sample. This is used as a way of probing excitations in a material. Table 1.1.1 summarizes many of the types of diffuse scattering coming from a sample and categorizes them by their coherency and elasticity.

1.1.5.2. *Background from extraneous sources*

The most commonly observed extraneous, or parasitic, scattering is from the sample container (such as a capillary) that holds the sample during the measurement. Another large contribution may come from air scattering, which originates principally from scattering of the direct beam by molecules in the air in the beam path, both before and after the sample. Air-scattering effects can be minimized by enclosing as much of the beam path as possible in a tube which may be evacuated or where the air is replaced by a weakly scattering gas (such as He in the case of X-rays). Air scattering that is detected by the detector can also be reduced by careful collimation of the beams and then shielding the detector from detecting radiation that does not originate from the sample position. Collimating the incident beam is straightforward and results in a big reduction in air scattering. For point detectors it is also straightforward to collimate the scattered beam, but the modern trend towards using linear and area detectors makes this more difficult. There is sometimes a trade-off between collimating the scattered beam to reduce background and having uniform backgrounds that do not vary with angle because of incomplete angle-dependent collimation. Incomplete angle-dependent collimation can be very difficult to correct when trying to measure diffuse scattering quantitatively and the current trend is to have minimal secondary collimation.

There is increasing interest in carrying out *in situ* experiments under extreme conditions of pressure, temperature, magnetic field and so on (see Chapters 2.6 to 2.8). These experiments inevitably introduce additional scattering from the environment. Again, there is a balance between finding creative ways to reduce these backgrounds, and simply making them less problematic in the data analysis. For example, in a diamond-anvil cell, where the beam accesses the sample through the diamond, one can drill a hole part way through the diamond to accommodate the direct beam and make the direct beam small enough to fit in the hole. This increases the complexity of the measurement as alignment becomes harder, but it is usually worth it. Shielding structural parts of the environment cell with an absorbing material, such as lead for X-rays or a borated material for neutrons, can help to reduce unwanted background intensity a lot, as can making thin, transparent windows for the incident and scattered beams.

An additional source of background in the signal does not come from scattering at all, but from electrical noise in the detector electronics. For some types of detectors it may be important to measure 'dark' exposures with the X-rays turned off and subtract these carefully from the experimental data. It is also possible to detect signals from cosmic rays, which can leave tracks in two-dimensional detector signals.

1.1.5.3. *Sources of background from the sample*

1.1.5.3.1. *Elastic coherent diffuse scattering*

As discussed in Section 1.1.4.1.1, decreasing the size of a crystal leads to an increase in the width of the Bragg peaks. When the size of the crystallite becomes very small, as a rule of thumb below 10 nm in diameter for typical unit cells, the widths of the Bragg peaks become so large that they merge and overlap, and it does not make sense to use delta-function Bragg peaks as the starting point for the analysis. At this point the coherent diffraction is completely diffuse in nature. Nonetheless, it still contains structural information. To see this we begin again with the Laue equation before we assumed periodicity [equation (1.1.39)]. For the simple case of a diatomic gas such as N_2, the sum would be taken only over two atoms, since scattering from a single molecule will be coherent but that from different molecules will be incoherent. In that case we have

$$\begin{aligned} A(\mathbf{h}) &= \sum_{j=1}^{2} f_j(h)\exp(2\pi i\mathbf{h}\cdot\mathbf{r}_j),\\ A(\mathbf{h}) &= f_1\exp(2\pi i\mathbf{h}\cdot\mathbf{r}_1)+f_2\exp(2\pi i\mathbf{h}\cdot\mathbf{r}_2), \end{aligned} \tag{1.1.79}$$

and the intensity is proportional to

$$\begin{aligned} I(\mathbf{h}) = (f_1f_1^*+f_2f_2^*) &+ f_1f_2^*\exp\left(2\pi i\mathbf{h}\cdot\mathbf{r}_{12}\right)\\ &+ f_2f_1^*\exp\left(-2\pi i\mathbf{h}\cdot\mathbf{r}_{12}\right), \end{aligned} \tag{1.1.80}$$

where $\mathbf{r}_{12} = \mathbf{r}_1 - \mathbf{r}_2$. For a diatomic molecule where both atoms are the same $f_1 = f_2$ and

$$I(\mathbf{h}) = f^*f\cos^2(\pi\mathbf{h}\cdot\mathbf{r}_{12}). \tag{1.1.81}$$

The scattering from a diatomic molecule of an element is simply a single-component cosine wave with a wavelength that depends on the separation of the atoms in the molecule. In an actual experiment there will be scattering from all the molecules that have every orientation with equal probability, so it is necessary to take an orientational average of the scattering. How this is done is shown in Chapter 5.7 on PDF analysis, but the result is the Debye equation (Debye, 1915),

$$I(h) = \frac{1}{N\langle f\rangle^2}\sum_{i,j} f_j^*f_i\left[\frac{\sin(Qr_{ij})}{Qr_{ij}}\right], \tag{1.1.82}$$

where N is the total number of atoms. For our diatomic molecule this becomes

$$I(h) = \frac{1}{N}\left[\frac{\sin(Qr_{ij})}{Qr_{ij}}\right]. \tag{1.1.83}$$

For clusters of atoms such as larger molecules or small nanoparticles that are intermediate in size between a diatomic molecule and a small chunk of crystal, the Debye equation is exact and may be used to calculate the intensity of the scattering. As the clusters get larger and the structure more periodic, such as small chunks of crystal, the scattering calculated from the Debye equation crosses smoothly to that obtained from the periodic Laue equation. The finite size broadened crystallographic model works well as a starting point for calculating scattering from well ordered crystals down to nanoparticle sizes of 10 nm, but loses accuracy rapidly below this particle size. The Debye equation is accurate for all particle sizes, but becomes computationally intractable for larger clusters much above 10 nm.

1.1.5.3.2. *Total-scattering and atomic pair distribution function analysis*

An alternative approach to the analysis of diffuse scattering from nanostructures is to Fourier transform the data to obtain the atomic pair distribution function, or PDF. In fact, the Fourier transform does not depend on whether the structure is periodic or not, and it is also possible to Fourier transform the Bragg scattering from crystals. If there is no nanoscale disorder in the crystal there are few real benefits in doing this rather than using the powerful crystallographic methods described elsewhere in this chapter. However, the PDF approach utilizes both the Bragg *and* diffuse components, and yields additional information about the structure that is particularly valuable when the crystal contains some kind of nanoscale domains. The presence of such domains was rarely considered in the past, but we now know that they are often found in materials. In the sense that both Bragg and diffuse scattering data are used without prejudice, and also that the data are measured over a wide range of the scattering vector so that, as far as possible, the coherent scattering in all of the reciprocal space is measured, this method is known as 'total-scattering analysis', and as 'PDF analysis' when the data are Fourier transformed and studied in real space.

The powder diffraction data for total-scattering studies are measured in much the same way as in a regular powder diffraction experiment. However, explicit corrections are made for extrinsic contributions to the background intensity from such effects as Compton scattering, fluorescence, scattering from the sample holder and so on. The resulting coherent scattering function $I(Q)$ is a continuous function of $Q = |\mathbf{Q}| = 2h = 4\pi\sin\theta/\lambda$, with sharp peaks where there are Bragg reflections and broad features in between. In general it is usual to work with a normalized version of this scattering intensity, $S(Q)$. This is the intensity normalized by the incident flux per atom in the sample. $S(Q)$ is called the total-scattering structure function. It is a dimensionless quantity and the normalization is such that the average value $\langle S(Q)\rangle = 1$. In short, $S(Q)$ is nothing other than the powder diffraction pattern that

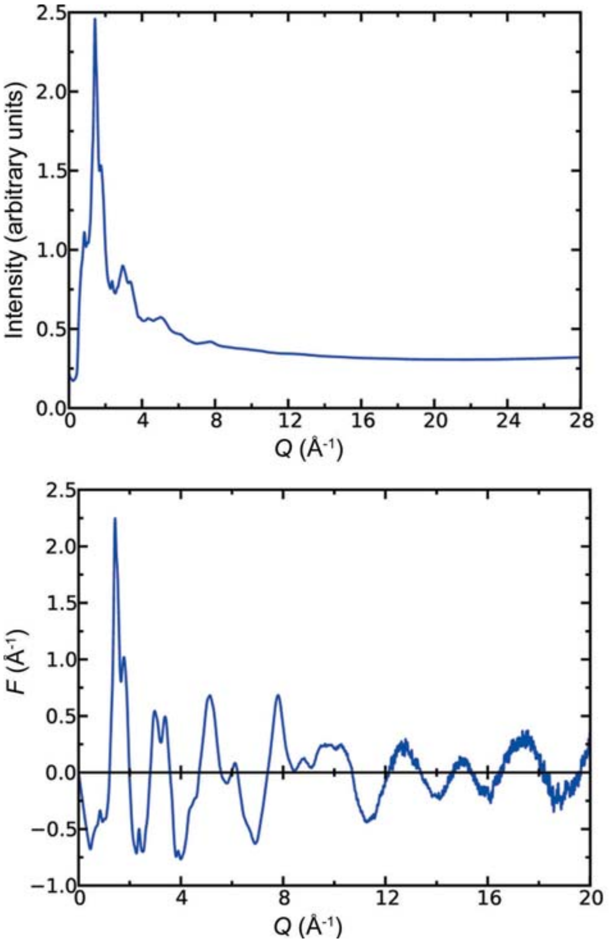

Figure 1.1.22

Comparison of raw data and the normalized reduced total-scattering structure function $F(Q) = Q[S(Q) - 1]$. The sample is a powder of 2 nm diameter CdSe nanoparticles and the data are X-ray data from beamline 6ID-D at the Advanced Photon Source at Argonne National Laboratory. The raw data are shown in the top panel. The high-Q data in the region $Q > 9$ Å^{-1} appear smooth and featureless. However, after normalizing and dividing by the square of the atomic form factor, important diffuse scattering is evident in this region of the diffraction pattern (bottom panel).

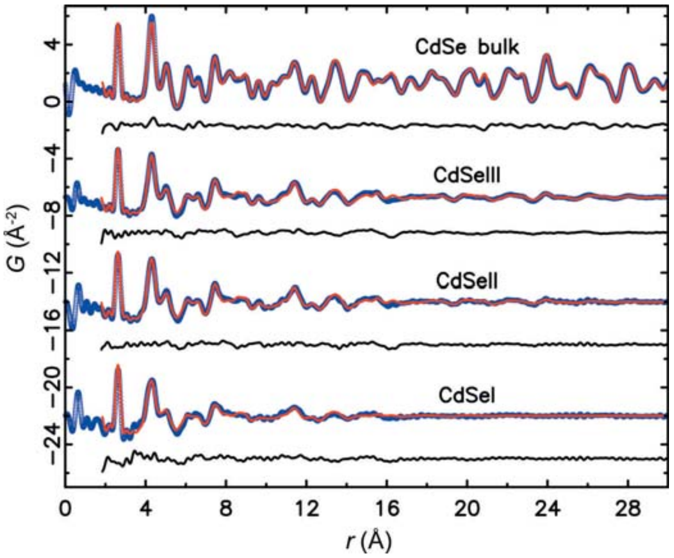

Figure 1.1.23

PDFs in the form of $G(r)$ from bulk CdSe and from a series of CdSe nanoparticles. The blue curve at the bottom is the PDF obtained from the data shown in Figure 1.1.22. The blue symbols are from the data and the thin red lines on top are from models of the local structure in these nanoparticles. Offset below are difference curves between the model and the data. [Reprinted with permission from Masadeh *et al.* (2007). Copyright (2007) by the American Physical Society.]

has been corrected for experimental artifacts and suitably normalized (Egami & Billinge, 2013).

Measuring over a wide range of Q values yields better resolution in real space, as well as yielding more information, and is desirable. The coherent intensity (the features) in $S(Q)$ dies out with increasing Q because of the Debye–Waller factor (which comes from thermal and quantum zero-point motion of the atoms), as well as any static displacive disorder in the material and, for X-ray measuerments, because of the X-ray form factor. In a neutron measurement, the atomic displacement effects are still present, but the neutron has no form factor and the scattering length is constant in Q. By a Q value of 30–50 Å^{-1} (depending on the temperature and the stiffness of the bonding in the sample) there are no more features in $S(Q)$ and there is no need to measure data to higher Q. Still, this is a much higher maximum value of Q than is measured in conventional powder diffraction experiments using laboratory X-rays or reactor neutrons. The maximum value of Q attainable in back scattering from a Cu $K\alpha$ tube is around 8 Å^{-1} and from an Mo $K\alpha$ tube it is around 16 Å^{-1}. Routine total-scattering measurements can be made using laboratory sources with Mo or Ag tubes; however, for the highest real-space resolution, and the smallest statistical uncertainties, synchrotron data are preferred. In the case of neutron scattering, spallation neutron sources are ideal for total-scattering experiments.

The total-scattering function $S(Q)$ appears to be different from the function measured in a standard powder diffraction experiment because of the Q range studied, and also because of an important aspect of the normalization: the measured intensity is divided by the total scattering cross section of the sample. In the case of X-ray scattering, the sample scattering cross section is the square of the atomic form factor, $\langle f(Q)\rangle^2$, which becomes very small at high Q. Thus, during the normalization process the data at high Q are amplified (by being divided by a small number), which has the effect that even rather weak intensities at high Q, which are totally neglected in a conventional analysis of the data, become rather important in a total-scattering experiment. Because the signal at high Q is weak it is important to collect the data in that region with good statistics. This is illustrated in Fig. 1.1.22.

The Fourier transform of the total-scattering data is the reduced pair distribution function, $G(r)$, which is related to $S(Q)$ through a sine Fourier transform according to

$$G(r) = \frac{2}{\pi} \int\limits_{Q_{\min}}^{Q_{\max}} Q[S(Q) - 1] \sin(Qr)\,\mathrm{d}Q. \qquad (1.1.84)$$

Examples of $G(r)$ functions from small nanoparticles of CdSe are shown in Fig. 1.1.23.

$G(r)$ has peaks at positions, r, that separate pairs of atoms in the solid with high probability. For example, there are no physically meaningful peaks below the nearest-neighbour peak at ~2.5 Å, which is the Cd–Se separation in CdSe. However, in addition to the nearest-neighbour information, valuable structural information is contained in the pair correlations that extend to much higher values of r. In fact, with data to a high resolution in Q, PDFs can be measured out to hundreds of nanometres (*i.e.*, thousands of ångströms) and the structural information that can be obtained from the data remains quantitatively reliable (Levashov *et al.*, 2005).

The function $G(r)$ is related to the atomic density. However, it is not the atomic density itself, but its autocorrelation. This is obtained by taking the atomic density of the molecule or cluster (which are the atoms at their respective positions) and convoluting it with a replica of the same thing. This object is then orientationally averaged to obtain the PDF. It is not a particularly intuitive object, but it is straightforward to calculate it from a given structural model. The inverse problem, calculating the structure from a PDF, is not possible directly, although in favourable cases, as with structure solution from powder diffraction, it is possible to obtain a unique structure solution from a PDF (Juhás *et al.*, 2006).

We described above how to obtain $G(r)$ from powder data. Here we briefly describe how to calculate a PDF from a structural model. To do this we have to introduce a related function to the PDF, the radial distribution function (RDF), $R(r)$, which is related to $G(r)$ by

$$G(r) = \frac{R(r)}{r} - 4\pi r \rho_0, \qquad (1.1.85)$$

where ρ_0 is the atomic number density (Egami & Billinge, 2013).

The function $R(r)$ is important because it is more closely related to the physical structure than $G(r)$, since $R(r)\,\mathrm{d}r$ gives the number of atoms in an annulus of thickness $\mathrm{d}r$ at distance r from another atom. For example, the coordination number (or the number of neighbours) of an atom, N_C, is given by

$$N_\mathrm{C} = \int\limits_{r_1}^{r_2} R(r)\,\mathrm{d}r, \qquad (1.1.86)$$

where r_1 and r_2 define the start and end positions of the RDF peak corresponding to the coordination shell in question. This suggests a scheme for calculating PDFs from atomic models. Consider a model consisting of a large number of atoms situated at positions $\mathbf{r}_\nu$ with respect to some origin. Expressed mathematically, this amounts to a series of delta functions, $\delta(\mathbf{r} - \mathbf{r}_\nu)$. The RDF is then given as

$$R(r) = \frac{1}{N}\sum_\nu \sum_\mu \delta(r - r_{\nu\mu}), \qquad (1.1.87)$$

where $r_{\nu\mu} = |\mathbf{r}_\nu - \mathbf{r}_\mu|$ is the magnitude of the separation of the νth and μth ions, and the double sum runs twice over all atoms in the sample. In Chapter 5.7 on PDF analysis we address explicitly samples with more than one type of atom, but for completeness we give here the expression for $R(r)$ in this case:

$$R(r) = \frac{1}{N}\sum_\nu \sum_\mu \frac{f_\nu f_\mu}{\langle f\rangle^2} \delta(r - r_{\nu\mu}), \qquad (1.1.88)$$

where f_ν and f_μ are the form factors, evaluated at $Q = h = 0$, for the νth and μth atoms, respectively, and $\langle f\rangle$ is the sample-average form factor.

1.1.5.3.3. *Inelastic coherent diffuse scattering*

Scattering events must conserve energy and momentum. When a wave is scattered it changes direction and therefore changes its momentum. To satisfy conservation, this momentum, $\mathbf{Q} = 2\pi\mathbf{h} = 2\pi(\mathbf{s} - \mathbf{s}_0)$, must be transferred to the material. When radiation is scattered by a crystal, the mass of the crystal is so large that this produces a negligible acceleration and the scattering is elastic. However, scattering from free atoms or fluids will produce a recoil, which results from a transfer of energy to the atom and the scattering is strictly inelastic. Even within a bulk crystal, there are lattice excitation modes (phonons) which may be created during a particular scattering event and the resulting scattering is inelastic. In an X-ray experiment, the energy resolution of the measurement usually is much too poor to separate this from the elastic scattering and it all appears mixed together (and is often simply referred to as 'elastic scattering'). As the excitation energies of internal modes of the system have energies of the order of meV (10^{-3} eV) and the X-ray energy is of the order of keV (10^3 eV), resolving the inelastic modes would require an energy resolution of $\Delta E/E = 10^{-6}$, which is often unachievable. Nonetheless, such experiments are now carried out at synchrotron sources and provide important scientific insights, although the experiments are very slow and very specialized (Burkel, 1991).

These experiments are rarely carried out on powders. If the inelastic scattering is not resolved during the measurement, as is usually the case, it appears as a diffuse-scattering component in the signal from the powder or single crystal and it can be interpreted and modelled to extract information. In powder diffraction, when the scattering occurs from lattice vibrations, or phonons, the diffuse signal is called 'thermal diffuse scattering' or TDS (Warren, 1990). Over the last 50–60 years, a number of attempts have been made to extract information about phonon energies and phonon dispersions from TDS with varying amounts of success (Warren, 1990; Jeong *et al.*, 1999; Graf *et al.*, 2003; Goodwin *et al.*, 2005). In the case of PDF analysis, the information in the TDS manifests itself in real space as correlated motion, and it is observed that the low-r peaks are sharper than the high-r peaks. This is because closely bonded atoms tend to move together: if an atom moves to the right it tends to push its neighbour also over to the right, so the motion is correlated. There is useful information in the TDS and the r dependence of the PDF peak broadening, but this is at best a very indirect way of measuring lattice-dynamical effects.

When the energy transfer is not resolved it is hard to separate the cases of scattering arising from phonons (which are dynamic atomic displacements) and scattering arising from static atomic displacements. To some extent these can be disentangled by studying the temperature dependence of the atomic displacement parameters (ADPs) obtained from modelling the data either in reciprocal space or real space (Billinge *et al.*, 1991). This is often done by using a Debye model (Debye, 1912), where the temperature dependence of the mean-square ADP is given by

$$\overline{u^2} = \left(\frac{3h^2 T}{4\pi^2 M k_B \theta_D^2}\right)\left[\varphi\left(\frac{\theta_D}{T}\right) + \frac{1}{4}\frac{\theta_D}{T}\right] + A_\mathrm{offset}, \qquad (1.1.89)$$

where

$$\varphi\left(\frac{\theta_D}{T}\right) = \frac{T}{\theta_D}\int\limits_0^{\theta_D/T}\left[\frac{x}{\exp(x) - 1}\right]\mathrm{d}x, \qquad (1.1.90)$$

is the Debye integral. Here, θ_D is the Debye temperature, which is a measure of the stiffness of the bonding, h and k_B are Planck's and Boltzmann's constants, respectively, and M is the mass of the oscillating atom. The constant A_offset is a temperature-independent offset that is generally needed in the model to account for static distortions. The Debye model is rather crude but surprisingly useful and works well in many cases.

As in the case of phonons, if the scatterer couples to something else in the solid that has an excitation spectrum, this can be studied too. The case of neutrons scattered by magnetic moments is the best known example. Inelastic scattering gives direct information about the magnon dispersion curves. Information about magnetic excitations may also be obtained indirectly from

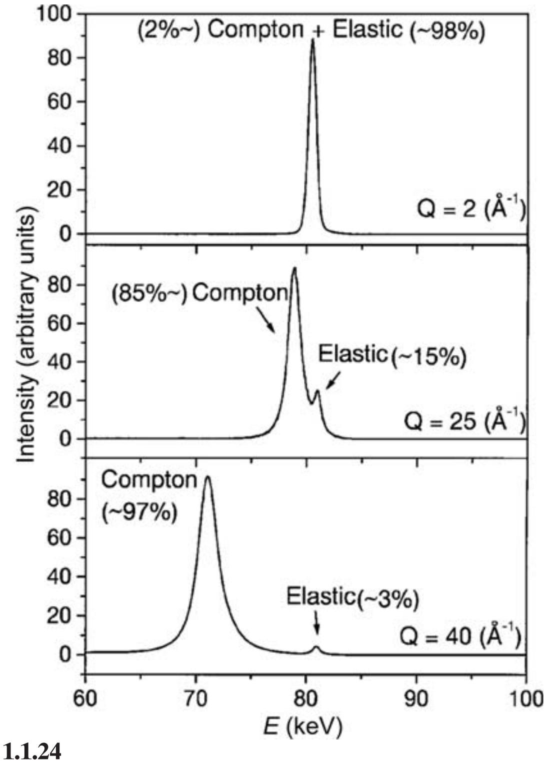

Figure 1.1.24
Spectrum from an energy-resolving detector that shows the elastic and Compton signals as a function of scattering vector **Q**. [Reprinted with permission from Petkov *et al.* (2000). Copyright (2007) by the American Physical Society.]

the non-energy-resolved magnetic diffuse scattering signal. Magnetic PDF is now possible (Frandsen & Billinge, 2015) as described in Chapter 5.7, as well as reciprocal-space studies of magnetic diffuse scattering (Paddison & Goodwin, 2012).

1.1.5.3.4. *Incoherent scattering*

Incoherent scattering does not contain any structural information, and cannot be used to study structure in a diffraction experiment since the intensities of the scattered waves do not depend on the position of the scatterers. This does not mean that all incoherent scattering intensity is useless. The fluorescence intensity is incoherent, but may be used in EXAFS experiments to yield structural information. This is because coherent scattering of the photoexcited electron during an absorption event modulates the absorption cross section and therefore the incoherent fluorescence intensity, so a coherent scattering process leaves a measurable response in an incoherent intensity. Incoherent scattering can also be used to measure excitations, although all momentum-transfer information is lost so it is not possible to measure, for example, dispersions of excitations such as phonons and magnons. Even if the scattering process is incoherent, the energy exchanged between the probe and the sample can be measured by the change in wavelength of the scattered wave, and the amplitude of the scattering at each energy transfer is proportional to the density of states of the excitation being probed. In the case of neutrons, the very large incoherent cross section for scattering by hydrogen ($\sim$100× the scattering cross section of most atoms) provides a strong signal for studying low-probability inelastic scattering events. Measuring inelastic scattering from powders can be a rapid way of determining the density of states of phonons, magnons and so on, which is very useful for determining the thermodynamic properties of materials, even though it is less precise than measurement of the full set of dispersion curves.

Another type of incoherent scattering that can be observed in X-ray experiments is Compton scattering (Compton, 1923; Cooper *et al.*, 2004), which is an inelastic incoherent process where the scattering atom recoils during the scattering event. An example of Compton scattering measured in the spectrum from an energy-resolving detector is shown in Fig. 1.1.24.

The Compton scattering is strong in this experiment because the incident X-ray energy is high (80 keV) and the sample is a low-atomic-number alumina-silicate glass. Both the high X-ray energy and the low atomic numbers of the atoms in the sample increase the Compton cross section with respect to the coherent elastic scattering. As the magnitude of the scattering vector, Q, is increased the Compton scattering moves to lower energy and increases in intensity, but the elastic line stays fixed in energy and its intensity decreases because of form-factor and Debye–Waller effects. Momentum as well as energy is conserved in this process and the Compton scattering can be used to measure the momentum distribution of electrons in a material, although this kind of experiment is not widespread these days.

Elastic incoherent scattering provides no information about the sample, and simply degrades the signal-to-noise ratio of the measurement. As such, it is just inconvenient and cannot be easily removed. Monotonic Laue diffuse scattering originates from different chemical species with different scattering powers residing on different sites in the crystal, and when a destructive interference condition is satisfied the resulting intensity does not go to zero but is proportional to $[f_i(h) - f_j(h)]^2$ (Warren, 1990). In pure elements in an X-ray experiment, the atoms on every site are the same and there is no Laue diffuse scattering. This is not true in neutron experiments where different nuclei have different scattering powers and most elements contain a range of isotopes in their natural form (the 'natural abundance'; Squires, 1996). This results in Laue diffuse scattering even in an element, although it is normally not referred to in these terms but is encompassed by a so-called 'incoherent neutron cross section' that is defined and tabulated (see Table 4.4.4.1 in *International Tables for Crystallography*, Volume C) for each element. This is not the only source of incoherent scattering in neutron diffraction, since the scattering power also depends on the relative orientation of the neutron and nuclear spins. In general these spins are all orientationally disordered (and fluctuating) and the result is an additional scattering-event-dependent contribution to the incoherent scattering from the sample, again encompassed by the 'incoherent neutron cross section' of the element. Where necessary, it may be possible to make isotopically enriched samples for neutron experiments so that the proportion of isotopes with large incoherent scattering cross sections is minimized (or the isotopes are removed altogether), and the range of isotopes can also be reduced, which further reduces the incoherent component of the signal. However, the cost and difficulty of doing this means that it is rarely done.

1.1.6. Local and global optimization of crystal structures from powder diffraction data

1.1.6.1. *Rietveld refinement*

More than 40 years have passed since the publication of the pioneering papers by Hugo Rietveld (Rietveld, 1967, 1969), in which he described a method for the refinement of crystal structures from neutron powder diffraction data. Neutron data sets from reactor sources were more amenable than X-ray data sets to this method because the line profiles are quite Gaussian.

However, it was not long before the method was extended to X-ray powder diffraction. The quality of the data and the computation power available these days have allowed the technique to develop enormously, to the point that even the (successful) Rietveld refinement of small protein structures from synchrotron powder diffraction data is now possible (see Chapter 7.1). Another development is the extension of the Rietveld method towards parametric refinement on large numbers of complimentary data sets with various as-yet unexplored new applications. Rietveld refinement is so important it is described in detail in Chapter 4.7, but we describe a number of important fundamentals of the method here by way of introduction.

The basic idea behind the Rietveld method is simple: Instead of extracting the integrated intensities of Bragg peaks and fitting models to these, as would be done in single-crystal and early powder diffraction studies, the full powder pattern, for example available as step-scanned intensity data, is fitted using a model whose parameters are refined using a least-squares procedure. The model parameters are varied in such a way as to minimize the sum of the squares of the difference between the n observed $Y\mathrm{obs}_i$ and n calculated $Y\mathrm{calc}_i(\{p\})$ step-scan intensities in the powder pattern, where the latter are calculated from a model containing a set of parameters $\{p\}$. The function that is minimized is usually the profile-weighted residual function, or R factor, given by

$$R_w = \sum_{i=1}^{n} w_i\big(Y\mathrm{obs}_i(2\theta) - Y\mathrm{calc}_i(2\theta;\,\{p\})\big)^2. \qquad (1.1.91)$$

The weight w_i is derived from the variance of the values of $Y\mathrm{obs}_i$, while all covariances between different $Y\mathrm{obs}_i$ values are assumed to be zero.

The calculated intensity $Y\mathrm{calc}_i$ is expressed by combinations of mostly nonlinear and analytic or non-analytic functions as

$$Y\mathrm{calc}_i = \sum_{ph=1}^{\mathrm{phases}}\left(S_{ph}\sum_{hkl(ph)}\left(K_{hkl(ph)}\left|F_{hkl(ph)}\right|^2\Phi_{hkl(ph)}\big(2\theta_i - 2\theta_{hkl(ph)}\big)\right)\right) + b_i(\mathrm{obs}). \qquad (1.1.92)$$

The outer sum runs over all phases ph present in the powder pattern, while the inner sum runs over all reflections hkl of a phase ph that contribute to the intensity at the position i in the powder pattern. A scaling factor S_{ph} is assigned to the reflection intensities for each phase; the scaling factor is proportional to the weight fraction of the phase. $K_{hkl(ph)}$ represents the product of various correction factors to the square of the structure-factor amplitudes, $\left|F_{hkl(ph)}\right|^2$, which may depend on the diffraction geometry and/or individual reflections. The value of the profile function $\Phi_{hkl}(2\theta_i - 2\theta_{hkl})$ is given for the profile point $(2\theta_i - 2\theta_{hkl})$ relative to the position of the Bragg reflection hkl. The observed background at position i in the powder pattern is denoted as $b_i(\mathrm{obs})$. Parameters in the model such as atomic positions, lattice parameters and experimental factors that affect peak shape and background are varied, using a least-squares approach, until the agreement between the calculated and measured diffraction profiles is optimized. In a least-squares approach, optimization consists of minimizing a cost function that is the weighted sum of the squared differences. This is a refinement method: a good initial guess at, or knowledge of, the structure is required and this model is refined by small adjustments.

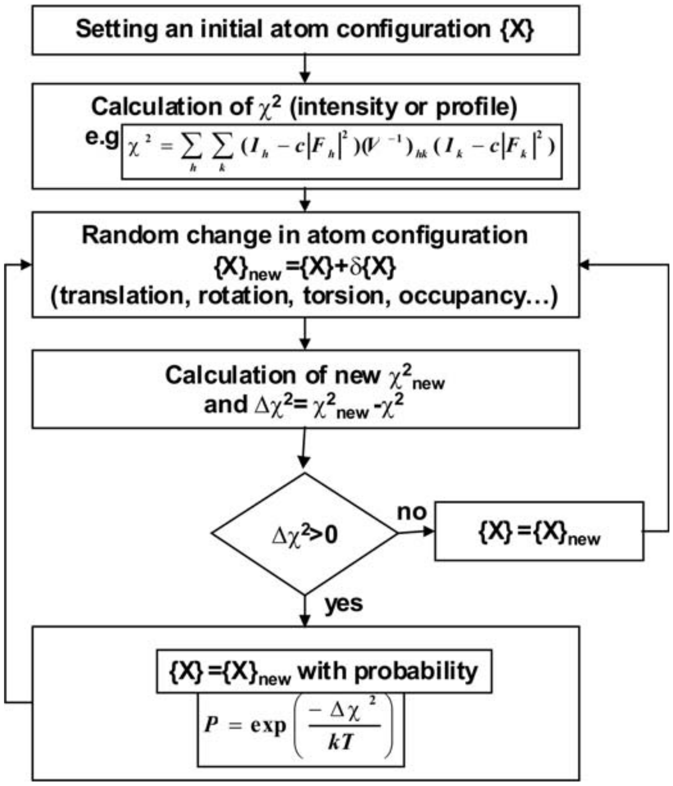
Setting an initial atom configuration {X}
Calculation of χ^2 (intensity or profile)
e.g $\chi^2 = \sum_h \sum_k (I_h - c|F_h|^2)(V^{-1})_{hk}(I_k - c|F_k|^2)$
Random change in atom configuration
$\{X\}_{new} = \{X\} + \delta\{X\}$
(translation, rotation, torsion, occupancy...)
Calculation of new χ^2_{new}
and $\Delta\chi^2 = \chi^2_{new} - \chi^2$
$\Delta\chi^2 > 0$
no
$\{X\} = \{X\}_{new}$
yes
$\{X\} = \{X\}_{new}$ with probability
$P = \exp\left(\frac{-\Delta\chi^2}{kT}\right)$

Figure 1.1.25

Flow diagram of a simulated-annealing procedure used for structure determination from powder diffraction data (from Mittemeijer & Welzel, 2012). F in the double sum is the structure factor from the structural model at each step of the optimization. Each sum runs over all reflections. h and k are summation indices representing hkl and $h'k'l'$, respectively.

This approach requires the modelling of the *entire* powder pattern. To simplify this complex task, the information content of the powder pattern can be divided into several parts (Fig. 1.1.1), allowing the separation of groups of parameters with respect to their origin:

(*a*) the peak intensity $\left|F_{hkl(ph)}\right|^2$ – the time- and space-averaged crystal structure and geometrical contributions;
(*b*) the peak position – crystallographic lattice and symmetry, and instrumental contributions;
(*c*) the peak shape $\Phi_{hkl}(2\theta_i - 2\theta_{hkl})$ – microstructural parameters and instrument profile;
(*d*) the background $b_i(\mathrm{obs})$ – local structure and instrumental conditions.

Each part contains contributions from the sample and the instrument.

Rietveld refinement is a nonlinear least-squares process and requires starting values for all parameters. It is generally implemented with a local, rather than a global, optimizer and it is important for the starting parameters to be close to those of the actual solution to ensure that it is in the valley in parameter space that contains the global minimum. It is usual to guide the refinement into the (relatively narrow) range of convergence by hand by adding the parameters to the refinement sequentially. In this sense, Rietveld refinement takes some time to learn, but with care it can provide robust quantitative structures and a wealth of information can be extracted from the data.

Of course, there is no reason (other than computational efficiency) why the minimization algorithm could not be a more robust global optimizer, and this is now starting to be implemented in modern Rietveld codes. The most common and most easily implemented global optimizer, though one of the least efficient, is the Metropolis or simulated-annealing (SA) algo-

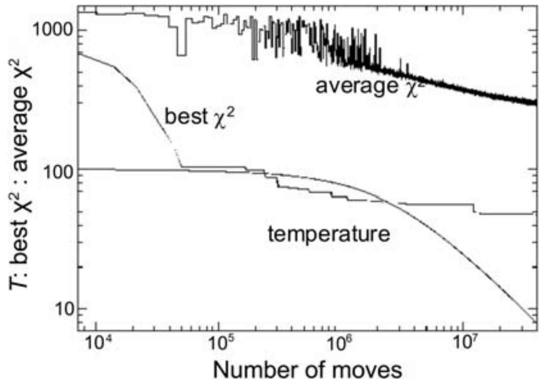

Figure 1.1.26
χ^2 (cost function) and 'temperature' dependence of the number of moves during a simulated-annealing run. [From Mittemeijer & Welzel (2012). Copyright Wiley-VCH Verlag GmbH & Co. KGaA. Reproduced with permission.]

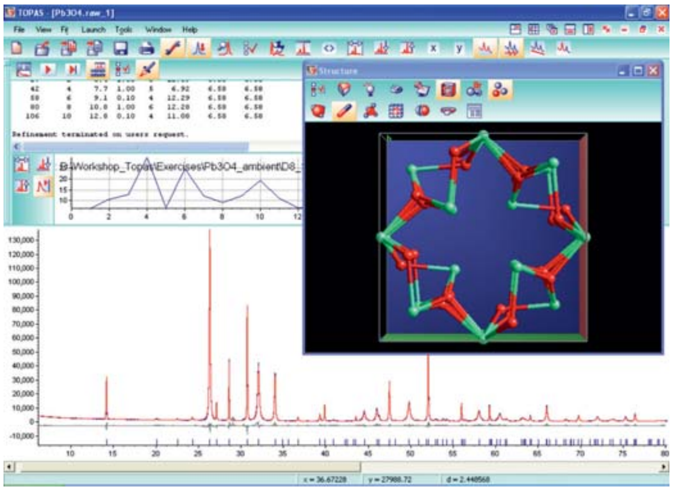
TOPAS - [Pb3O4.raw_1]
File View Fit Launch Tools Window Help
Structure
B:\Workshop_Topas\Exercises\Pb3O4_ambient\D8_
x = 36.67228
y = 27988.72
d = 2.448568

```
    42     4     7.7  1.00   5    6.92    6.58    6.58
    58     6     9.1  0.10   4   12.29    6.58    6.58
    80     8    10.8  1.00   6   12.28    6.58    6.58
   106    10    12.0  0.10   4   11.00    6.58    6.58

Refinement terminated on users request.
```

Figure 1.1.27
Screen shot (*TOPAS* 4.1; Bruker-AXS, 2007) of a simulated-annealing run on Pb_3O_4 measured with a D8 advance diffractometer in Bragg–Brentano geometry. [From Mittemeijer & Welzel (2012). Copyright Wiley-VCH Verlag GmbH & Co. KGaA. Reproduced with permission.]

rithm. The most usual implementation is actually as a 'regional' optimizer where the updates to parameters such as atomic position are constrained to be not too far from the previous values in such a way that the algorithm makes a random walk through the parameter space. This algorithm can avoid being trapped in a local minimum by 'walking uphill', since changes to the parameters that produce a worse agreement may be accepted with a probability based on the Boltzmann criterion, $\exp(-\Delta R/kT)$. The temperature in this expression is fictitious (*i.e.*, it does not refer to any real temperature) and ΔR is the change in the agreement produced by the trial update. The temperature plays the role of tuning the probability of accepting a bad move. It is initially chosen to have a high value, giving a high probability of escaping a minimum and allowing the algorithm to explore more of the parameter space. Later in the run the temperature is lowered, trapping the solution into successively finer valleys in the parameter space until it settles into (hopefully) the global minimum (Fig. 1.1.26). The calculation of R can be based on the entire profile, or on integrated intensities. For the latter, the correlation between partially or fully overlapping reflections must be taken into account (as shown schematically in Fig. 1.1.25).

A flow diagram of a typical SA algorithm as used for structure determination from powder diffraction data is shown in Fig. 1.1.25. Parameters that can be varied during the SA runs include internal and external degrees of freedom like translations (fractional coordinates or rigid-body locations), rotations (Cartesian angles, Eulerian angles or quaternions, describing the orientation of molecular entities), torsion angles, fractional occupancies, displacement parameters *etc*. Fig. 1.1.26 shows the results of a typical simulated-annealing run in which the cost function, χ^2, falls dramatically in the first few thousand moves, indicating that the scattering is dominated by the positioning of heavier atoms or globular molecules. Several million trial structures are usually generated before a minimum can be reached. At the end of the simulated-annealing run, Rietveld refinement is used to find the bottom of the global minimum valley.

Special algorithms are not usually used to prevent close contact of atoms or molecules during the global-optimization procedure, as in general these have not been found to be necessary, as the fit to the intensities alone quickly moves the molecules to regions of the unit cell where they do not grossly overlap with neighbouring molecules. A subsequent Rietveld refinement in which only the scale and overall displacement parameters are refined will immediately show whether further refinement of bond lengths and bond angles is necessary. Since unconstrained refinement often results in severe distortions from the ideal molecular geometry, either rigid bodies or soft constraints on bond lengths, the planarity of flat groups and bond angles can be used to stabilize the refinement. Another advantage of the simulated-annealing technique is that hydrogen atoms can often be included at calculated positions from the beginning if their relative position with respect to other atoms can be anticipated, which is often the case for molecular structures.

For inorganic crystal structures in particular, the identification of special positions or the merging of defined rigid bodies is useful during the final stages of structure solution. This can be accomplished by a so-called 'occupancy-merge' procedure as proposed by Favre-Nicolin & Černý (2004; see also Chapter 4.5). Here, the occupancies of the sites are modified as a function of the fractional coordinates, *i.e.* they are changed when the atoms get 'too close' to a special position. The sites are thought of as spheres with a radius r. In this way any number of sites can be merged when their distances are less than $2r$. As an example, the crystal structure solution of minium (Pb_3O_4) is shown in Fig. 1.1.27. In this example, special positions are identified when two oxygen or lead atoms approach within a distance less than the sum of their respective merging radii, which is estimated as 0.7 Å. The occupancies of the sites then become: 1/(1 + intersection fractional volumes).

The power of the Rietveld approach lies in its ability to extract the maximum information from the region of the data where peaks overlap. Since peak overlap is a significant problem even at moderate d-spacings, this method revolutionized powder diffraction to the point where the quantitative results are often trusted more than those coming from refinements of single-crystal data, since they are less sensitive to factors such as extinction that can affect single-crystal structure refinements. Single-crystal data are still preferred for structure solution, but Rietveld refinement is often the method of choice for obtaining the fine quantitative details of the structure after a solution has been found. However, the Rietveld method has also opened the door to using powder data for structure solution. In structure-solution methods, the structure factors are calculated from the intensities of all the available peaks, and algorithms are used to find the missing phases for each of these peaks and therefore the positions of the atoms in the unit cell. As mentioned above, full profile fitting following the Rietveld method can be carried out without a model, where the ‘parameters’ are the Bragg-peak intensities themselves; this is known as Pawley or Le Bail refinement, depending on details of the approach used (see Chapter 3.5). This allows more accurate determination of the structure factors from Bragg peaks in regions where there is significant peak overlap.

These days, with high-quality data from synchrotron X-ray sources and excellent algorithms (either direct methods or global-optimization methods in direct space), determination of even quite complex crystal structures from powder diffraction data is becoming a routine method in almost all branches of natural sciences and engineering. The success rate mainly depends on three parameters: the choice of measurement device, how well the pattern profile is described and how good the structure-solving algorithm is. It is becoming increasingly evident that the use of highly monochromatic parallel-beam synchrotron radiation is a huge advantage for obtaining accuracy in the atomic parameters, which allows for the interpretation of bonding and reaction mechanisms. In some cases, even details like rotational disorder can be extracted from powder diffraction data if maximum-entropy methods are combined with high-resolution synchrotron data.

1.1.6.2. *Local structure refinement*

As described in Section 1.1.5.3.2, similar full-profile-fitting strategies are now also carried out on total-scattering data that include diffuse-scattering intensity residing in what used to be considered as the ‘background’. This is either done by taking a structural model, which may be similar to the crystal model used in the Rietveld method (but the crystallographic symmetry of the model could also be reduced) or be a discrete cluster or molecule. As with the Rietveld method, structural parameters are varied in such as way as to obtain a good fit of the calculated function to the measured one. These methods go beyond the average structure and yield information about the local structure in the material, which may be different from the long-range ordered (LRO) crystal structure (or indeed there may be no LRO structure, as is the case in liquids and glasses). They are becoming more popular as data quality and computational power increase.

Solving the structures of nanoparticles from PDF data is less well developed, although it has been demonstrated for some simple structures such as C_{60} and simple inorganic crystalline compounds. We expect that this will grow in importance in the coming years, following the trend of the Rietveld method and structure solution from powders.

1.1.6.3. *Parametric Rietveld refinement*

The conventional approach to analysing a set of powder patterns is to treat each powder pattern independently, thus refining the entire set of all relevant parameters for each pattern separately. Further analysis of the values of these parameters, for example fitting with empirical or physics-based functions such as fitting the temperature dependence of the ADPs with a Debye model, is then performed after the Rietveld refinements. Alternatively, all powder patterns can be subjected to refinement simultaneously, which allows the refinement of the functional dependence of external variables instead of deriving the parameters of the function from the individual Rietveld refinements afterwards. This so-called parametric or surface Rietveld refinement was first introduced by Stinton & Evans (2007). Parametric refinement offers several advantages over the traditional sequential refinement approach because the correlation between parameters and the final standard uncertainty can be reduced by introducing simple and physically meaningful constraints and restraints. Furthermore, it is possible to refine noncrystallographic parameters such as rate constants or temperatures directly from Rietveld refinement (Stinton & Evans, 2007). Of course, introducing external constraints in this way may introduce bias into the refinement if the constraint is not valid. For example, if there is anharmonicity in the motion and the temperature dependence of the ADPs does not follow the Debye law, carrying out a parametric refinement where the Debye law is presumed will result in biased refinements. However, with careful application, this is a potentially powerful approach to maximizing the quantitative information available from powder data in complex systems. In the following, the basic concept of parametric refinement is illustrated with several examples.

If we assume a set of $p_{\max}$ powder patterns from a single sample that have been measured as a function of the value of an external variable, *e.g.* time, temperature or pressure, equation (1.1.92) can be formally written for each powder pattern separately:

$$\begin{aligned}
&Y\mathrm{calc}_{i,\mathrm{pattern}(1)} = \mathrm{function}(p_{1,\mathrm{pattern}(1)}, p_{2,\mathrm{pattern}(1)}, \ldots, p_{m,\mathrm{pattern}(1)})\\
&Y\mathrm{calc}_{i,\mathrm{pattern}(2)} = \mathrm{function}(p_{1,\mathrm{pattern}(2)}, p_{2,\mathrm{pattern}(2)}, \ldots, p_{m,\mathrm{pattern}(2)})\\
&Y\mathrm{calc}_{i,\mathrm{pattern}(p_{\max})}\\
&\quad = \mathrm{function}(p_{1,\mathrm{pattern}(p_{\max})}, p_{2,\mathrm{pattern}(p_{\max})}, \ldots, p_{m,\mathrm{pattern}(p_{\max})}).
\end{aligned} \tag{1.1.93}$$

If a functional dependency of some of the parameters p on external variables T exists, these parameters may be expressed as functions of these variables, for example T. This functional relationship can be used to constrain together the p parameters for individual patterns measured at different temperatures, drastically reducing the number of global parameters. Equation (1.1.93) can thus be written as

$$\begin{aligned}
&Y\mathrm{calc}_{i,\mathrm{pattern}(1)}\\
&= \mathrm{function}\big(p_{1,\mathrm{pattern}(1)}, p_{2,\mathrm{pattern}(1)} = f(T_1, T_2, \ldots, T_t), \ldots, p_{m,\mathrm{pattern}(1)}\big)\\
&Y\mathrm{calc}_{i,\mathrm{pattern}(2)}\\
&= \mathrm{function}\big(p_{1,\mathrm{pattern}(2)}, p_{2,\mathrm{pattern}(2)} = f(T_1, T_2, \ldots, T_t), \ldots, p_{m,\mathrm{pattern}(2)}\big)\\
&\vdots\\
&Y\mathrm{calc}_{i,\mathrm{pattern}(p_{\max})}\\
&= \mathrm{function}\big(p_{1,\mathrm{pattern}(p_{\max})}, p_{2,\mathrm{pattern}(p_{\max})} = f(T_1, T_2, \ldots, T_t),\\
&\qquad \ldots, p_{m,\mathrm{pattern}(p_{\max})}\big).
\end{aligned} \tag{1.1.94}$$

The cost function (1.1.91) to be minimized changes accordingly:

$$R_w = \sum_{\mathrm{pattern}=1}^{p_{\max}} \left(\sum_{i=0}^{n-1} \left(w_{i,\mathrm{pattern}} \big(Y\mathrm{obs}_{i,\mathrm{pattern}} - Y\mathrm{calc}_{i,\mathrm{pattern}} \big)^2 \right) \right). \tag{1.1.95}$$

1.1.7. Outlook

As is evident from the above, the information content in a powder diffraction pattern is enormous. This chapter gives only an overview of the types of information about materials that can be obtained from powder diffraction data, and the various approaches mentioned here are described in greater detail in the rest of this volume. The powder community is growing, as is the number of applications of powder diffraction in all the materials sciences as instrumentation and computer modelling become ever more powerful. Although intense modern X-ray and electron sources can measure data from tiny single crystals (of a size approaching that of a single powder grain), this does not diminish the usefulness and impact of powder diffraction, as powder diffraction is much more than just crystal structure solution. It probes real materials in real environments, yielding information about defects, texture, nanostructure, strain, phase composition, kinetics, phase transformations, size and shape distributions, and heterogeneity. In short, crystallography gives us the structure, but powder diffraction allows us to study the 'materials science', of materials.

References

Billinge, S. J. L., Davies, P. K., Egami, T. & Catlow, C. R. A. (1991). *Deviations from planarity of copper-oxygen sheet in* $Ca_{0.85}Sr_{0.15}CuO_2$. *Phys. Rev. B*, **43**, 10340–10352.

Bragg, W. L. (1913). *The diffraction of short electromagnetic waves by a crystal*. *Proc. Camb. Philos. Soc.* **17**, 43–57.

Bruker-AXS (2007). *TOPAS* version 4.1. Bruker-AXS, Karlsruhe, Germany.

Burkel, E. (1991). *Inelastic Scattering of X-rays With Very High Energy Resolution*. Springer Tracts in Modern Physics. Amsterdam: Springer-Verlag.

Cheary, R. W. & Coelho, A. (1992). *A fundamental parameters approach to X-ray line-profile fitting*. *J. Appl. Cryst.* **25**, 109–121.

Compton, A. H. (1923). *A quantum theory of the scattering of X-rays by light elements*. *Phys. Rev. Lett.* **21**, 483.

Cooper, M. J., Mijnarends, P. E., Shiotani, N., Sakai, N. & Bansil, A. (2004). *X-ray Compton Scattering*. Oxford University Press.

Debye, P. (1912). *Zur Theorie der spezifischen Wärmen*. *Ann. Phys.* **344**, 789–839.

Debye, P. (1915). *Dispersion of Röntgen rays*. *Ann. Phys.* **46**, 809–823.

Debye, P. & Scherrer, P. (1916). *Interferenzen an regellos orientierten Teilchen im Röntgenlicht*. *Nachr. Ges. Wiss. Göttingen*. **29**, 1–15.

Dinnebier, R. E. & Billinge, S. J. L. (2008). Editors. *Powder Diffraction: Theory and Practice*, 1st ed. London: Royal Society of Chemistry.

Egami, T. & Billinge, S. J. L. (2013). *Underneath the Bragg Peaks: Structural Analysis of Complex Materials*, 2nd ed. Amsterdam: Elsevier.

Ewald, P. P. (1921). *Das reziproke Gitter in der Strukturtheorie*. *Z. Kristallogr.* **56**, 129–156.

Favre-Nicolin, V. & Černý, R. (2004). *Fox: Modular approach to crystal structure determination from powder diffraction*. *Mater. Sci. Forum*, **443–444**, 35–38.

Frandsen, B. A. & Billinge, S. J. L. (2015). *Magnetic structure determination from the magnetic pair distribution function (mPDF): ground state of MnO*. *Acta Cryst.* A**71**, 325–334.

Goodwin, A. L., Tucker, M. G., Cope, E. R., Dove, M. T. & Keen, D. A. (2005). *Model-independent extraction of dynamical information from powder diffraction data*. *Phys. Rev. B*, **72**, 214304.

Graf, M. J., Jeong, I. K., Starr, D. L. & Heffner, R. H. (2003). *Limits on phonon information extracted from neutron pair-density functions*. *Phys. Rev. B*, **68**, 064305.

Hull, A. W. (1917). *A new method of X-ray crystal analysis*. *Phys. Rev.* **10**, 661–696.

Jeong, I.-K., Proffen, T., Mohiuddin-Jacobs, F. & Billinge, S. J. L. (1999). *Measuring correlated atomic motion using X-ray diffraction*. *J. Phys. Chem. A*, **103**, 921–924.

Juhás, P., Cherba, D. M., Duxbury, P. M., Punch, W. F. & Billinge, S. J. L. (2006). *Ab initio determination of solid-state nanostructure*. *Nature*, **440**, 655–658.

Klug, H. P. & Alexander, L. E. (1974). *X-ray Diffraction Procedures*, 2nd ed. New York: John Wiley.

Laue, M. von (1912). *Eine quantitative Prüfung der Theorie für die Interferenz-Erscheinungen bei Röntgenstrahlen*. *Sitzungsber. K. Bayer. Akad. Wiss.* pp. 363–373. [Reprinted in *Ann. Phys.* (1913), **41**, 989–1002.]

Le Bail, A., Duroy, H. & Fourquet, J. L. (1988). *Ab-initio structure determination of* $LiSbWO_6$ *by X-ray powder diffraction*. *Mater. Res. Bull.* **23**, 447–452.

Levashov, V. A., Billinge, S. J. L. & Thorpe, M. F. (2005). *Density fluctuations and the pair distribution function*. *Phys. Rev. B*, **72**, 024111.

Masadeh, A. S., Božin, E. S., Farrow, C. L., Paglia, G., Juhás, P., Billinge, S. J. L., Karkamkar, A. & Kanatzidis, M. G. (2007). *Quantitative size-dependent structure and strain determination of CdSe nanoparticles using atomic pair distribution function analysis*. *Phys. Rev. B*, **76**, 115413.

Mittemeijer, E. J. & Welzel, U. (2012). Editors. *Modern Diffraction Methods*. Weinheim: Wiley-VCH Verlag GmbH.

Paddison, J. A. M. & Goodwin, A. L. (2012). *Empirical magnetic structure solution of frustrated spin systems*. *Phys. Rev. Lett.* **108**, 017204.

Pawley, G. S. (1981). *Unit-cell refinement from powder diffraction scans*. *J. Appl. Cryst.* **14**, 357–361.

Petkov, V., Billinge, S. J. L., Shastri, S. D. & Himmel, B. (2000). *Polyhedral units and network connectivity in calcium aluminosilicate glasses from high-energy X-ray diffraction*. *Phys. Rev. Lett.* **85**, 3436–3439.

Rietveld, H. M. (1967). *Line profiles of neutron powder-diffraction peaks for structure refinement*. *Acta Cryst.* **22**, 151–152.

Rietveld, H. M. (1969). *A profile refinement method for nuclear and magnetic structures*. *J. Appl. Cryst.* **2**, 65–71.

Shmueli, U. (2008). Editor. *International Tables for Crystallography*, Vol. B, *Reciprocal Space*, 3rd ed. Chichester: Wiley.

Squires, G. L. (1996). *Introduction to the Theory of Thermal Neutron Scattering*. New York: Dover Publications.

Stinton, G. W. & Evans, J. S. O. (2007). *Parametric Rietveld refinement*. *J. Appl. Cryst.* **40**, 87–95.

Warren, B. E. (1990). *X-ray Diffraction*. New York: Dover Publications.

International Tables for Crystallography (2019). Vol. H, Chapter 2.1, pp. 26–50.

2.1. Instrumentation for laboratory X-ray scattering techniques

A. Kern

2.1.1. Introduction

X-ray scattering techniques are among the most essential means of characterizing materials, as they are the most direct analytical methods for providing structural information for a material. In particular, X-ray powder diffraction has become one of the most important techniques in materials science, since many materials are first formed or are only available or used as powders or other polycrystalline forms.

The ever-increasing need for materials characterization, from basic research to industrial quality control, has led to a multitude of evolutionary and revolutionary instrument and application developments. In the past two decades, the capabilities and thus the range of application of laboratory X-ray diffractometers have increased exponentially.

The present chapter covers the full range of commonly used instrumentation for home-laboratory X-ray scattering analyses as detailed in Section 2.1.2, with the focus on powder diffraction. The scope is limited to recent and commercial designs, available off-the-shelf from the major manufacturers. Neither technologically obsolete nor niche instrumentation will be discussed. A short description of the history of X-ray instrumentation is given in Section 2.1.3, illustrating the significant technological advances made since 1985. Sections 2.1.4 to 2.1.7 describe the components of the diverse range of currently available home-laboratory X-ray powder diffractometers. The most important concepts are discussed here; for technological details the reader is referred to the original literature or to textbooks.

In order to maintain neutrality as well as timeliness, the use of brand names and photos of real equipment has been avoided.

2.1.2. Scope and terminology

An X-ray (powder) diffractometer is by definition an instrument for measuring X-ray diffraction phenomena (from powders), where ‘diffraction’ is defined as elastic, coherent scattering of X-rays from a crystal lattice (in the crystallographic literature, the terms ‘diffraction’, ‘X-ray diffraction’ and ‘Bragg diffraction’ are frequently used synonymously). In recent texts, a ‘powder’ is frequently defined as a ‘solid containing small crystallites or particles that will flow when agitated’ in accordance to the usual sense of the word in colloquial speech.

Such definitions for ‘X-ray diffractometer’ and ‘powder’ are problematic, as their scope is too narrow and arbitrarily limited. They are probably the result of the historical development of the methodology and the lack of interaction between groups representing different application areas, such as X-ray scattering, emission or absorption techniques. The application range and thus capabilities of today’s instrumentation are neither comprehensively nor even appropriately described by their implicit limitation to measuring X-ray diffraction phenomena of crystalline solids in powdered form.

It is well known that scattering and thus interference phenomena will occur with any type of waves and obstacles, and are by no means restricted to X-rays or perfectly regular arrays of atoms exhibiting long-range order (X-ray diffraction). In general, X-ray scattering can provide information on the arrangement of atoms or particles in materials with short-range order or no order at all, like gases, liquids and amorphous solids. For this reason it is obvious that X-ray diffractometers are intrinsically suited (and are actually used) for a wide range of X-ray techniques beyond X-ray diffraction as defined above. These techniques not only comprise X-ray scattering from any solids or liquids with any degree of order, but also X-ray absorption (radiography) or X-ray emission (XRF) techniques, see also Section 2.1.4.3. Consequently, the following terminology will be used throughout the remainder of this chapter:

A *sample* is the object or quantity of material to be investigated, while the *specimen* is the representative portion of the sample that is actually prepared and analysed. Specimen properties such as microstructure and packing density may differ from the properties of the sample as a result of specimen preparation. This must be taken into account for selection of the appropriate instrument configuration, data acquisition and evaluation.

A *powder* is defined in EN-1330-11 (2007) as a ‘large number of crystallites and/or particles (*i.e.* grains, agglomerates or aggregates; crystalline or non-crystalline) irrespective of any adhesion between them’ and thus can be a loose powder (in the sense of common language), a solid block, a thin film or even a liquid. An *ideal powder* is represented by a virtually unlimited number of sufficiently sized, randomly oriented and spherical crystallites.

The term *X-ray diffractometer* will refer to an instrument that, in principle, is capable of doing any of the X-ray techniques mentioned above, further detailed in Section 2.1.4.3. Instrument components will be described independently of applications, as they are not exclusive to any application area. Note that the term X-ray diffractometer also explicitly includes ‘film cameras’. This is worth mentioning, as even recent texts still differentiate between (i) cameras, originally characterized by the use of X-ray films, and (ii) diffractometers, originally defined as an instrument derived from a camera in which the film had been replaced by a point detector. In principle, any so-called cameras and any diffractometers can be equipped with any type of today’s point, linear and area detectors, so the former distinction between cameras and diffractometers, which arose from the historical development of X-ray instrumentation, is completely obsolete.

2.1.3. Historical overview

2.1.3.1. *From film cameras to diffractometers*

2.1.3.1.1. *Film cameras*

Powder diffraction analysis started with the development of simple film cameras, right after von Laue formulated his basic diffraction theory and the Braggs, father and son, laid down the foundations of crystal structure analysis, in the years 1912–1914. The first and simplest cameras were developed independently by Debye & Scherrer (1916) and Hull (1917), using a film to detect the scattered X-rays, with the instrument geometry termed ‘Debye–Scherrer geometry’. The basic drawback of Debye–Scherrer cameras was their lack of resolution. Consequently,

Copyright © 2019 International Union of Crystallography

since standard X-ray tubes readily produce divergent beams, the next evolutionary step was to employ self-focusing geometries, as first proposed independently by Seemann (1919) and Bohlin (1920), termed 'Seemann–Bohlin geometry'. In addition to significantly improved resolution, the intensity was also greatly increased by using a para-focusing arrangement using an X-ray source and specimen with finite width (line focus). Guinier (1937) extended the Seemann–Bohlin geometry using an incident-beam monochromator. Although the monochromator significantly reduced the intensity, this disadvantage was overcompensated for by improved beam conditioning, leading to unparalleled resolution at that time and elimination of the $K\alpha_2$ component of the radiation. This made the Guinier camera the best-performing film camera at that time and it therefore enjoyed high popularity.

The idea of using powder diffraction for phase identification of substances in pure form or in mixtures, originally suggested by Hull (1919) and then formalized by Hanawalt *et al.* (1938), attracted enormous interest, and developed into the powder diffraction method, making it a fundamental tool for material scientists. However, while classic film cameras laid down the historical foundation for the success of polycrystalline diffraction, their use was mostly limited to phase identification, semi-quantitative phase analysis and macroscopic stress measurements. Inherent difficulties included, but were not limited to, obtaining reliable intensities (because of film grain size and nonlinearity of the film response), very limited flexibility in terms of hardware extensions such as non-ambient specimen stages, and lack of diffracted-beam conditioning (*e.g.* the use of diffracted-beam monochromators).

Detailed descriptions of the many camera types as well as their use are given in a large number of texts. The interested reader is specifically referred to the textbook of Klug & Alexander (1974), which also contains an extensive bibliography.

2.1.3.1.2. *Diffractometers*

Photographic films have two important weaknesses: the detection efficiency is low and quantification of the diffracted intensities, including the line-profile shapes, is indirect and cumbersome. These shortcomings led to the idea of replacing the film with a photon counter (most commonly utilizing the Geiger–Müller counter at that time) and thus to the development of a device called a 'diffractometer'. The design resembled that of the Bragg ionization spectrometer, but dispersed monochromatic radiation from lattice planes rather than a spectrum of X-ray wavelengths. The first diffractometer developed by Le Galley (1935) was a non-focusing arrangement using a point-focus X-ray tube, making use of the cylindrical geometry of a normal film camera. In subsequent instrument designs focusing geometries were adopted, mostly the 'Bragg–Brentano geometry' (Brentano, 1924), a modification of the Seemann–Bohlin geometry, first introduced by Lindemann & Trost (1940) and Friedmann (1945).

The introduction of the first commercial focusing diffractometer in the early 1950s resulted in another major advance of the polycrystalline diffraction method, and may be largely credited to Parrish and co-workers (*e.g.* Parrish, 1949). This instrument consisted of a fixed-anode X-ray tube and a mechanical goniometer, operating in Bragg–Brentano geometry. The initial replacement of photographic film by the Geiger–Müller counter, and soon after by scintillation and lithium-drifted silicon detectors, allowed accurate intensities and line-profile shapes with high resolution to be recorded. The large space around the specimen permitted the design of various interchangeable stages for specimen rotation and translation, automatic specimen changing and non-ambient analyses. As a consequence, powder diffraction found many new applications beyond phase identification, including, but not limited to, quantitative analysis of crystalline and amorphous phases, microstructure analysis, and texture and strain analysis, at ambient and non-ambient conditions.

In the following decades, diffractometers were fully automated, fully digitized, and electronically and mechanically stabilized. The data quality they delivered became generally superior to that of film cameras, including in terms of resolution, eventually even facilitating structure determination and refinement from powders. Attempts to improve Guinier or Seemann–Bohlin cameras by replacing the film with image plates or any other stationary or scanning detectors did not produce competitive instrumentation in terms of instrument flexibility and mechanical simplicity. As a result, film cameras were steadily replaced by automated diffractometers using the Bragg–Brentano geometry. Since the 1990s, classic film cameras as well as other Guinier- or Seemann–Bohlin-based instruments are no longer used in practical polycrystalline diffraction analysis and thus lost any commercial relevance, apart from for a few niche applications. The Bragg–Brentano geometry, as developed in the 1940s, became the dominating instrument geometry and accounted for more than 90% of all instruments sold. The remainder almost exclusively used Debye–Scherrer-type arrangements, either employing focusing incident-beam monochromators for flat-plate or capillary transmission setups, or parallel-beam setups based on (pinhole) slits and/or Soller collimators and/or channel-cut monochromators for microdiffraction, small-angle X-ray scattering and the characterization of thin films.

While powder diffractometers have changed little in their construction and geometry since the 1940s, considerable advances have made in X-ray detection and X-ray beam conditioning (X-ray optics).

Significant detector developments include one- and two-dimensional position-sensitive detectors (PSDs) based on gas proportional counter technology, and especially that of the scanning one-dimensional PSD (Göbel, 1980). The replacement of a point detector by a scanning one-dimensional PSD allowed the measurement time required to record a full pattern to be reduced down to minutes without significant compromise on resolution. This enabled time-critical applications (such as non-ambient and high-throughput analyses), or compensation of the intensity loss when employing incident-beam monochromators.

The introduction of laterally graded multilayers on figured reflectors, so-called 'Göbel mirrors' (Schuster & Göbel, 1996), allowed the conversion of a convergent beam into a parallel beam, and thus added a new dimension to laboratory beam conditioning – at a time when X-ray techniques were expanding into the now very rapidly growing area of thin-film characterization, sparking a renaissance of the Debye–Scherrer geometry.

Until the late 1980s and early 1990s, traditional powder diffraction and thin-film characterization were seen as two different techniques with diverse requirements. As a consequence, thin-film techniques formed a different X-ray diffraction application sector, served by different and specialized instrumentation, in addition to the already existing distinction between single-crystal and powder diffraction applications and instrumentation. The X-ray powder diffraction market was characterized by dedicated (and separately marketed) instruments for traditional powder diffraction, usually based on the Bragg–

Brentano geometry, and for thin-film analysis, usually based on the Debye–Scherrer geometry.

2.1.3.2. *Recent years*

In the 1990s, more and more laboratories started to deal with a full range of materials and related applications - from powders through polycrystalline thin films to epitaxial thin films. Dedicated and inflexible instruments were no longer economic for serving the increasing range of applications and also their increasing data-quality requirements.

The growing need for multipurpose instrumentation led to a new generation of X-ray diffractometers in the late 1990s, from all of the major manufacturers, based on a platform concept covering all relevant beam-path components including X-ray sources, optics, specimen stages and detectors. This concept, described in Section 2.1.4, allowed for a faster development of more and more differentiated instrumentation to optimally meet the requirements of all possible applications and sample types. Particularly successful were design improvements that allow the user to transform an instrument on-site by changing beam-path components, often without any need for alignment or even tools, to cover a larger range of applications and sample types using a single instrument.

A major contribution to the platform concept came from the continued development of beam conditioners based on multilayers, resulting in a wealth of X-ray beam optics for different applications. Advanced sputtering techniques allow the fabrication of multilayer optics with virtually arbitrary beam divergence, which can be used to generate focusing, parallel and divergent beams for both point- and line-focus applications.

The introduction of a series of new detector technologies in the early 2000s represented another technological quantum leap, which completely changed the X-ray detection landscape for laboratory diffraction. Within only a few years, detectors based on silicon micro-strip, silicon pixel and micro-gap technologies reached a market share of more than 90% in newly sold systems. Proportional and scintillation point detectors will probably become obsolete in only a few years from now, but can still be found, usually in lower-budget systems.

Today's instruments, with their different possible configurations of beam-path components, are now capable of performing a wider range of X-ray scattering applications than ever (see Section 2.1.4.3). Not surprisingly, the platform concept has become so successful that all modern X-ray diffractometers are now, at least to some extent, equipped with interchange capabilities for beam-path components. However, the fundamental principles remain the same and date back to the first film cameras and diffractometers, no matter how advanced today's instrumentation is.

2.1.4. The platform concept – fitting the instrument to the need

Modern X-ray diffractometers are highly modular assembly systems based on a platform concept, with a shared set of major components over a number of distinct diffractometer models, serving different X-ray scattering application areas. Such a platform concept has two important advantages. Firstly, a common design allows differentiated instruments to be developed faster, and eases the integration of new or improved beam-path components, potentially over the whole model range. Secondly, it enables the design of an X-ray optical bench with on-site interchange capabilities, allowing the mounting of selected beam-path components to meet specific application and specimen-property requirements.

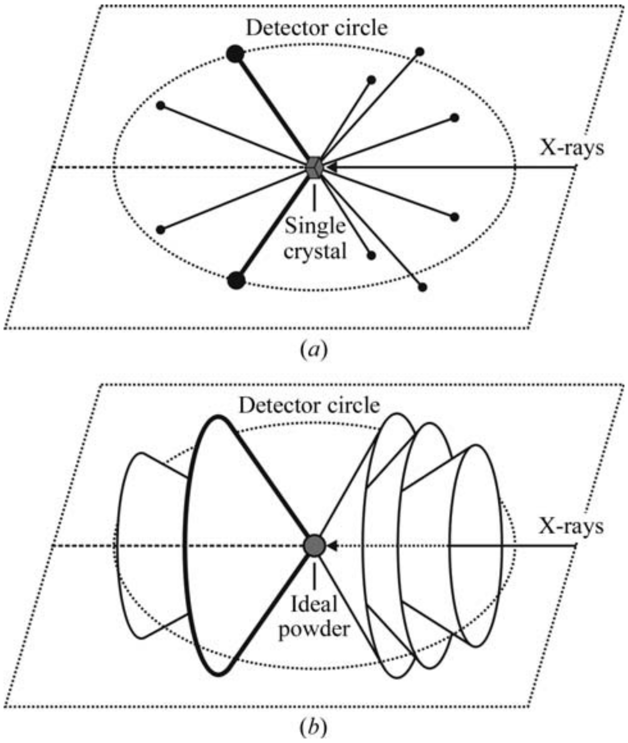

Figure 2.1.1

Diffraction of X-rays by (*a*) a rotating single crystal and (*b*) an ideal powder. The scattered intensity may be measured by a detector placed on the detector circle.

2.1.4.1. *Basic design principles and instrument geometry considerations*

X-ray scattering data are generally recorded in what is virtually the simplest possible manner, where the scattered intensity is measured by a detector mounted at some distance from the specimen. This is illustrated in Fig. 2.1.1, where a narrow, essentially monochromatic beam illuminates a small spherical specimen. For a rotating single crystal, the diffracted beams point in discrete directions in space as given by Bragg's law for each lattice vector d_{hkl} (Fig. 2.1.1*a*). For an ideal powder consisting of a virtually unlimited number of randomly oriented crystallites, the diffracted beams will form concentric cones ('Debye cones') with a semi-apex angle of 2θ, representing all randomly oriented identical lattice vectors d_{hkl} (Fig. 2.1.1*b*). Note that in contrast to a single crystal, an ideal powder does not need to be rotated to obtain a complete powder diffraction pattern.

Most instruments are built around a central specimen and consist of the following beam-path components, the numbering of which is consistent with the mounting positions shown in Fig. 2.1.2:

(1) X-ray source;
(2) incident-beam optics;
(3) goniometer base or specimen stage;
(4) diffracted-beam optics;
(5) detector.

The directions of the *incident* and *diffracted beams* (also called 'primary' and 'secondary' beams) form the *diffraction plane* (also called the 'equatorial plane' or 'scattering plane'). The goniometer base can be mounted horizontally (horizontal diffraction plane) or vertically (vertical diffraction plane). The direction perpendicular to the equatorial plane is known as the *axial*

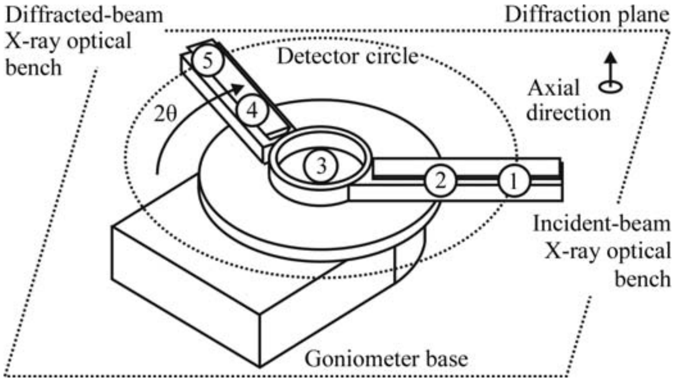

Figure 2.1.2
The basic design principle of modern diffractometers. Currently available instruments are built around a centrally mounted specimen and represent an X-ray optical bench with mounting positions for any (1) X-ray sources, (2) incident-beam optics, (3) specimen stages, (4) diffracted-beam optics and (5) detectors. The 2θ position of the scattered-X-ray optical bench refers to the 2θ angle of the Debye cone shown in bold in Fig. 2.1.1(*b*).

direction. The *detector circle* (also called the 'goniometer circle' or 'diffractometer circle') is defined either by the centre of the active window of a stationary detector, or, in most cases, by a detector moving around the specimen, and is coplanar to the diffraction plane. The 2θ angle of both the diffracted beam in Fig. 2.1.1(*a*) and the Debye cone in Fig. 2.1.1(*b*) (shown in bold) refers to the 2θ position of the diffracted-beam X-ray optical bench in Fig. 2.1.2. It is obvious from Figs. 2.1.1 and 2.1.2 that, in principle, diffraction from single crystals and (ideal) powders can be measured using the same instrument.

An instrument design with a centrally mounted specimen has the important advantage that it implicitly allows the operation of one and the same instrument in both Bragg–Brentano and Debye–Scherrer geometry, depending on the beam divergence chosen. The actual instrument geometry is thus a function of the actual beam propagation angle (divergent, parallel or convergent), making the X-ray optics the most important part of any instrument-geometry conversion. The relationship between the two geometries and their implementation in a single instrument using an incident-beam X-ray optical bench is illustrated in Fig. 2.1.3.

As laboratory X-ray sources invariably produce divergent beams, the 'natural' instrument geometry is self-focusing, 'automatically' leading to the Bragg–Brentano geometry as shown in Fig. 2.1.3(*a*). In this geometry the angle of both the incident and the diffracted beam is θ with respect to the specimen surface. The X-ray-source-to-specimen and the specimen-to-detector distances are equal. The diffraction pattern is collected by varying the incidence angle of the incident beam by θ and the diffracted-beam angle by 2θ. The focusing circle is defined as positioned tangentially to the specimen surface. The focusing condition is fulfilled at the points where the goniometer circle intersects the focusing circle, and thus requires measurements in reflection mode.

The Bragg–Brentano geometry may be extended by an incident- or a diffracted-beam monochromator. In the case of an incident-beam monochromator as shown in Fig. 2.1.3(*b*), the focus of the X-ray source is replaced by the focus of the monochromator crystal. This involves mounting the monochromator crystal (and the X-ray source) a certain distance away along the incident-beam X-ray optical bench, as given by the focusing length of the monochromator crystal (the dotted line in Fig. 2.1.3*b*). For a diffracted-beam monochromator or mirror, the geometry shown in Fig. 2.1.3(*b*) can be thought of as reversed (simply consider the X-ray source and detector switching their positions).

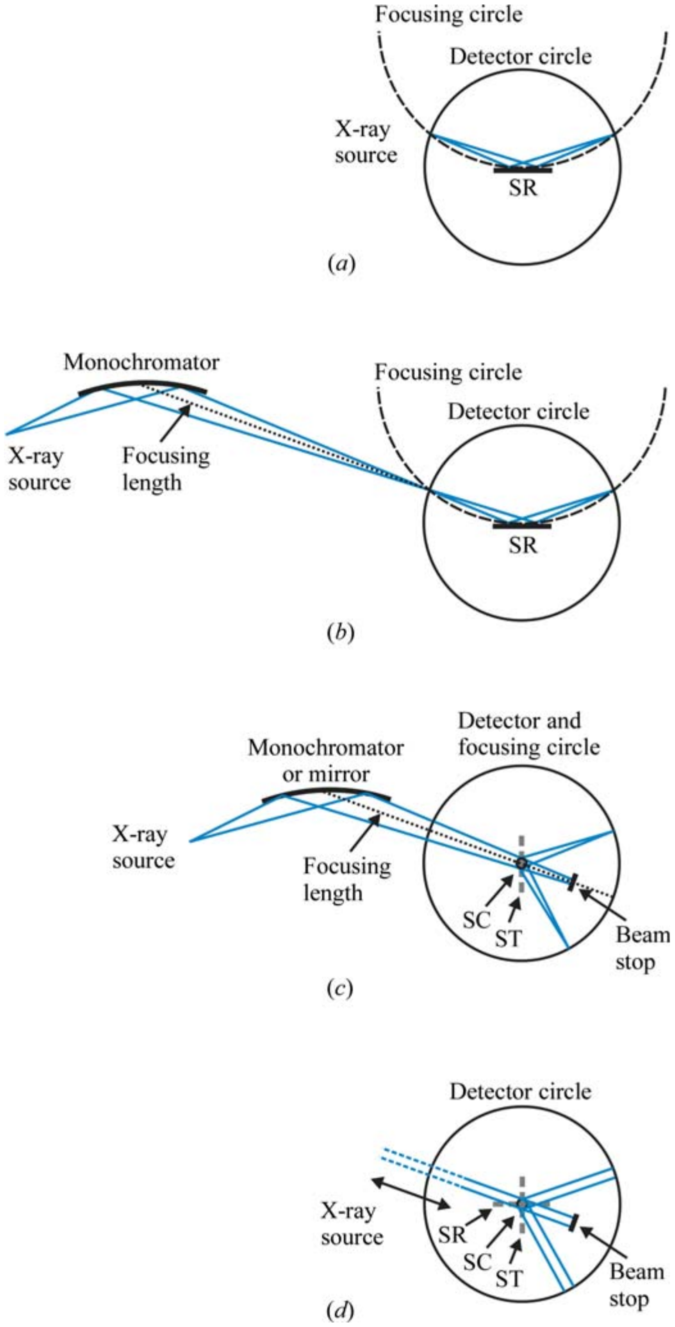

Figure 2.1.3
Transformation between the Bragg–Brentano and Debye–Scherrer geometries using a incident-beam X-ray optical bench. SR: flat specimen, reflection mode; SC: capillary specimen, transmission mode; ST: flat specimen, transmission mode. The actual instrument geometry is a function of the actual beam-propagation angle, making the X-ray optics the most important part of any instrument-geometry conversion. (*a*) Divergent beam: Bragg–Brentano geometry, (*b*) divergent beam: Bragg–Brentano geometry extended by an incident-beam monochromator. (*c*) Convergent beam: focusing Debye–Scherrer geometry, (*d*) parallel beam: Debye–Scherrer geometry. Transformation is achieved by mounting the X-ray tube and pre-aligned optical components at pre-defined positions of the optical bench. None of the figures are to scale.

The conversion from Bragg–Brentano to Debye–Scherrer geometry involves the mounting of some kind of optics designed to convert the divergent beam coming from the X-ray source into a focusing or parallel beam; this is shown in Figs. 2.1.3(*c*) and (*d*), respectively.

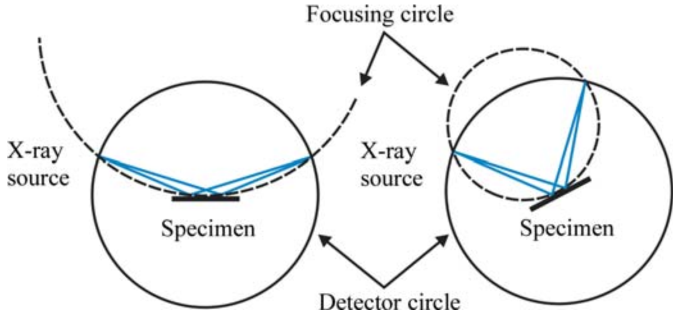

Figure 2.1.4
Bragg–Brentano geometry. The focusing circle, given for two different angles 2θ, is tangential to the specimen surface. Its diameter is given by the intersections between the detector and the focusing circles and is thus 2θ dependent.

In a focusing Debye–Scherrer geometry setup, as shown in Fig. 2.1.3(*c*), the divergent beam coming from the X-ray source is normally focused on the detector circle (for highest resolution) by means of an incident-beam monochromator or a focusing mirror. The focusing circle is identical to the detector circle and the focusing condition requires measurements in transmission mode. When employing an incident-beam monochromator with sufficient focusing length, then conversion between the Bragg–Brentano geometry and the focusing Debye–Scherrer geometry involves a shift of the monochromator crystal (and the X-ray source) along the incident-beam X-ray optical bench (note the identical focusing length of the monochromator shown in Figs. 2.1.3*b* and *c*).

For a parallel-beam setup, as shown in Fig. 2.1.3(*d*), parallelization of the divergent beam coming from the X-ray source may be achieved by different means, such as collimators (classic Debye–Scherrer geometry) or reflective optics such as mirrors or capillaries. In principle, the X-ray source and the detector may be placed at any distance from the specimen, as there are no focusing requirements. As a consequence, measurements can be performed in both reflection and transmission mode.

In a simplified scheme, conversion between the geometries discussed above involves repositioning of the X-ray source, together with mounting of X-ray optics with suitable beam divergence. To make this possible, the incident-beam optical X-ray bench offers the necessary predefined mounting positions including relevant translationary and rotationary degrees of freedom.

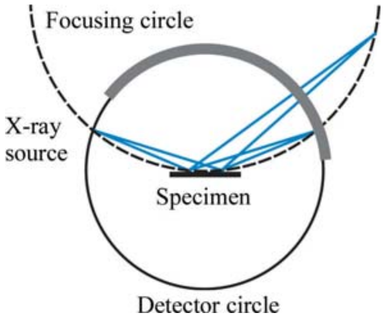

Figure 2.1.5
Bragg–Brentano geometry. While all diffracted beams focus on the (variable-diameter) focusing circle (here shown for two beams), focusing on the detector circle is only achieved at the X-ray source and detector positions (located at the intersections between the detector and the focusing circles). This prevents the use of larger position-sensitive detectors because of defocusing, as indicated by the hypothetical large position-sensitive detector represented by the bold grey line.

An important aspect directly related to the choice of the instrument geometry is the geometric compatibility with position-sensitive detectors. In contrast to Debye–Scherrer geometry, large line and area detectors may not be used in Bragg–Brentano geometry. This is an important limitation of the latter, as the focusing circle does not coincide with the detector circle and has a 2θ-dependent diameter, as illustrated in Fig. 2.1.4. As a consequence, the diffracted beam is only focused on a single point of the goniometer circle, as shown in Fig. 2.1.5. However, small position-sensitive detectors with an angular coverage of not more than about 10° 2θ are used with great success, as defocusing can be ignored at diffraction angles larger than about 20° 2θ if high angular accuracy and resolution are not required. For measurements at smaller 2θ angles, or for highest angular accuracy and resolution, the active window size of a position-sensitive detector may be reduced by means of slits and/or electronically down to a point, allowing the use of this detector as a point detector.

2.1.4.2. *Range of hardware*

An X-ray diffractometer is generally characterized by the relationship between a conditioned beam, the specimen orientation and the subsequent interception of the diffracted beams by a detector of given geometry and imaging properties. There are only a very few instrument configurations that will be ideal for any two application areas, or every conceivable sample within a single application area. It is the user's responsibility to match the instrument to the specimen properties, which can be challenging, particularly in multi-user environments with a large variety of sample types. The platform and the X-ray optical-bench concepts allow the user to choose and mount the most appropriate beam-path components in order to optimize an instrument with respect to a specific application and specimen-property requirements. Table 2.1.1 provides an overview of the currently available types of beam-path components from the X-ray source through to the detector.

The length of available X-ray optical benches varies, and is typically in the range of about 15 cm up to 100 cm. Larger benches allow mounting of bulky components (*e.g.* moving-target X-ray sources or large detectors) as well as mounting of several X-ray optics in a row (*e.g.* combinations of mirrors and channel-cut monochromators). Some diffractometer models allow mounting of two incident- and/or diffracted-beam X-ray optical benches to mount different beam-path components in parallel, *e.g.* X-ray sources with different wavelengths or beam shapes (very popular in single-crystal diffraction), X-ray optics with different beam divergence (*e.g.* to switch between Bragg–Brentano and Debye–Scherrer geometry), and different detector types.

While Table 2.1.1 and the above may imply an enormous combinatorial diversity, in practice this is not entirely the case. In general, beam-path components have to be compatible with the selected instrument geometry, which is dictated by the choice of the X-ray source (point or line), the beam characteristics (wavelength distribution, divergence) and the detector (point, linear or area). This automatically narrows down the range of combinations. As an obvious example, many crystal monochromators and X-ray mirrors are only compatible with a particular wavelength. Also, the size and weight of bulky components, such as moving-target X-ray sources, large specimen stages and large two-dimensional detectors, may impose practical constraints that require consideration. For example, the acces-

Table 2.1.1
Types of beam-path components available in laboratory X-ray powder diffraction

The column numbering corresponds to the positions indicated in Fig. 2.1.2 at which individual components can be mounted.

Position 1	Positions 2 and 4	Position 3		Position 5
X-ray sources	X-ray optics	Goniometer base	Specimen stages	Detectors
Fixed target Moving target (rotating anodes, liquid-metal jets)	Absorptive (apertures, metal filters) Diffractive (monochromators, analysers) Reflective (multilayer mirrors, capillary optics)	Vertical [ω–θ (θ–θ), ω–2θ (θ–2θ)] Horizontal [ω–θ (θ–θ), ω–2θ (θ–2θ)]	Fixed, rotating Specimen changer Eulerian cradles Kappa stages Tilt/fixed χ stages *XYZ* stages Flow-through cells Non-ambient (low temperature, high temperature, humidity, high pressure)	Scintillation Gas ionization (metal wire, micro-gap) Semiconductor (SiLi, strip/pixel, CCD/CMOS)

sible angular range may be limited for large components owing to collision issues, while heavy loads on vertical goniometers may impede alignment and lead to early wear and tear. Restrictions will be discussed in Sections 2.1.5 to 2.1.7 for the individual components.

These days, the exchange of lighter components, such as most X-ray optics, specimen stages and detectors, does not require any tools at all (such as when a snap-lock mechanism is employed) or more than a few screws for fixing. Alignment is normally not required when components are factory pre-aligned and handled with care, and when mounts are manufactured with good quality. Intrinsic changes of the beam direction (*e.g.* focusing crystal monochromators or X-ray mirrors) or beam offsets (*e.g.* two-bounce channel-cut monochromators) need compensating translation and/or rotation of the components involved.

The exchange of large, heavy components, or complicated rebuildings such as the conversion of a goniometer (vertical ↔ horizontal, θ–θ ↔ θ–2θ *etc.*), may be still possible for technically skilled users. However, special tools may be necessary, requiring shipment of the component(s), or even the instrument, back into the factory. In addition, X-ray, machine and electrical safety directives by the local authorities have to be obeyed, and conversions may require updating approval to use the instrument. In such cases it may be more economic to operate two dedicated instruments instead.

The instrument control software plays a particularly important role in the context of instrument configuration and automated instrument conversion. In modern instruments, each beam-path component is equipped with an identification chip or hole masks read out by light barriers, which uniquely identify the respective component and link it with all its individual stored or coded properties. This information may range from part numbers, usage history or alignment information such as beam offsets, through to a virtually unlimited wealth of any physical data required to configure and operate that particular component. This ‘component recognition’ feature provides for completely new and important capabilities of laboratory powder diffractometers, the most important of which are:

(*a*) Any beam-path components, and each change of status, can be automatically detected, validated and configured, allowing true ‘plug & play’ operation.

(*b*) Real-time conflict detection: detection of incompatible, incorrectly mounted or missing instrument components. This feature can also help the user in choosing compatible instrument components, as already discussed above.

(*c*) Automatic, motorized adjustments of beam direction or beam-offset changes, based on the information stored in the related components’ ID chips, as individually determined at the factory *via* pre-alignment.

(*d*) Every instrument detail can be saved together with the measurement data, providing for a complete and accurate documentation of the experiment. In principle, every measurement can be exactly reproduced even years later.

(*e*) Measurement instructions can include instrument information. For example, manufacturers or users can configure the measurement software to propose instrument configurations deemed best for particular applications. A user with appropriate rights can choose to enforce a certain instrument configuration so that measurements will not start unless the instrument has detected the required configuration.

Both the platform concept and the huge advances in instrumentation and instrument control software have dramatically changed the laboratory X-ray instrumentation landscape in the past few years. The ease with which an instrument configuration can be changed is not only useful for less-skilled users. Probably even more importantly, it allows the use of the same instrument, in different configurations, for different X-ray application areas. It can generally be said that laboratory X-ray instrumentation has overcome the (mostly historical) dividing lines between different applications, which were mostly between single-crystal diffraction, powder diffraction and thin-film analysis. As far as differences still remain, these are usually solely the consequence of dedicated instrument components for meeting specific application requirements, resulting in specialized measurement and data-evaluation software, which is rarely included with each instrument.

2.1.4.3. *Range of applications*

It is the flexibility of today’s X-ray diffractometers that leads to their usefulness for a wide range of X-ray scattering techniques beyond traditional X-ray powder ‘Bragg diffraction’. Table 2.1.2 provides an overview.

X-ray scattering techniques represent the vast majority of techniques that X-ray diffractometers are used for. Properly configured, however, the same instrument can also be used to collect X-ray absorption (X-ray radiography) or X-ray emission (X-ray fluorescence) data, even if the achievable data quality cannot compete with dedicated instruments.

For X-ray radiography, an instrument will be configured in transmission geometry with the X-rays projected towards a

Table 2.1.2
X-ray applications for with modern X-ray diffractometers

- **X-ray scattering**
  - Powder diffraction
    - Qualitative (phase identification) and quantitative phase analysis
    - Indexing, structure determination and structure refinement from powder data
    - Microstructure analysis (texture, size, strain, microstrain, disorder and other defects)
    - Pair distribution function analysis ('total scattering')
  - Thin-film analysis
    - Grazing incidence X-ray diffraction (GIXRD)
    - X-ray reflectometry
    - Stress and texture
    - High-resolution X-ray diffraction
    - Reciprocal-space mapping
    - In-plane GIXRD
  - Single-crystal diffraction
    - Chemical crystallography
    - Protein crystallography
  - Small-angle X-ray scattering
  - X-ray topography

- **X-ray absorption**
  - X-ray radiography (X-ray-absorption-based imaging)

- **X-ray emission**
  - X-ray fluorescence

specimen. X-rays that pass through the specimen can be detected to give a two-dimensional representation of the absorption contrast within the specimen. For tomography, the X-ray source and detector will be moved to blur out structures not in the focal plane. Multiple images can be used to generate a three-dimensional representation of the specimen by means of computed tomography. Obvious disadvantages are the large effective focal spot size of the X-ray sources and the relatively low resolution of the detectors that are typically used for powder diffraction, which, in combination with a limited adjustability of both the X-ray-source-to-specimen and specimen-to-detector distances, lead to substantial unsharpness issues and poor resolution. High-quality images can be achieved when using microfocus X-ray sources and charge-coupled device (CCD) detectors with focus and pixel sizes smaller than 10 µm, respectively, but such an instrument configuration is not suitable for applications requiring ideal powders (see also Sections 2.1.6 and 2.1.7).

Collecting X-ray fluorescence data is comparatively straightforward. Data can be collected simultaneously to X-ray scattering data when employing a suitable detector, such as an energy-dispersive detector (Section 2.1.7.2.3). There are a couple of disadvantages to be considered, such as absorption issues (the specimen will be normally measured in air rather than in vacuum, hampering the analysis of light elements) and the inefficiency of excitation by the characteristic line energies of the X-ray source anode materials typically used for diffraction (hampering the analysis of elements with higher atomic numbers than that of the anode material).

2.1.5. Goniometer designs

A goniometer, by definition, is an instrument that either measures an angle or allows an object to be rotated to a precise angular position. In an X-ray diffractometer the purpose of the goniometer is to move the X-ray source, specimen and detector in relation to each other. Goniometers are usually categorized by the number of axes available for X-ray source, specimen and detector rotation, and are thus called one-, two-, three-, ..., *n*-axis (or -circle) goniometers.

Because of practical reasons, most goniometers consist of two distinct components, a goniometer base and a specimen stage, with the specimen stage mounted on the goniometer base.

The goniometer base typically offers two axes, one axis to rotate the X-ray source or the specimen stage, the other axis to rotate the detector. In some designs goniometer bases are omitted, specifically if there is no need to move the X-ray source and the detector, such as in Debye–Scherrer-type diffractometers with large detectors. Such machines are usually dedicated to a particular application without the need for high flexibility.

Depending on the requirements of the application, additional rotational and translational degrees of freedom may be needed to rotate and translate a specimen in space; these are usually implemented in the specimen stage. More rotational degrees of freedom may include the rotation of the X-ray source line focus or a rotation of the detector out of the diffraction plane to measure diffraction by lattice planes (nearly) perpendicular to the specimen surface, so-called non-coplanar diffraction.

2.1.5.1. *Geometrical conventions and scan modes*

In the literature there is some inconsistency related to the naming of axes and the choice of signs for angles (left- *versus* right-handed). A comprehensive treatment of geometrical conventions has recently been given by He (2009); in the following these conventions will be adhered to.

In many texts the notations θ–2θ and θ–θ rather than ω–2θ and ω–θ are used, mostly because of historical reasons. The first diffractometers operated in Bragg–Brentano geometry (see Section 2.1.3.1.2) and were equipped with single-axis goniometers. In such a goniometer the single axis drives two shafts which are mechanically coupled 1:2 or 1:1; thus the notations θ–2θ and θ–θ were coined. Today, the majority of all goniometer bases allow coupled as well as uncoupled rotation of the ω and θ axes. Therefore the ω–2θ and ω–θ notations should be generally preferred, as they represent the more general notations.

2.1.5.1.1. *Goniometer base*

A typical goniometer base provides two coaxial and independently driven axes, ω and 2θ, mounted perpendicular to the diffraction plane. These two axes are the main axes of a goniometer, since they have the most effect on the accuracy and precision of measured Bragg angles. The diffraction plane and the axes are generally described by a right-handed Cartesian coordinate system, as illustrated in Fig. 2.1.6, where the direct X-ray beam propagates along the X_L axis. Z_L is up and coincident with the ω and 2θ axes, and X_L–Y_L define the diffraction plane with the detector circle coplanar to it. Since X_L is coincident with the incident X-ray beam, it is also the axis of the Debye cones. The semi-apex angles of the cones are determined by the 2θ values given by the Bragg equation. The angles 2θ and γ describe the direction of scattering vectors in space (compare Fig. 2.1.1), where γ is defined as the azimuthal angle from the origin at $-Z_L$ with a right-hand rotation axis along the opposite direction of the incident beam ($-X_L$ direction).

The ω and 2θ axes are mechanically arranged as the inner circle and outer circle, respectively. The inner circle usually carries either the specimen stage or the X-ray source, while the detector is mounted on the outer circle. As a consequence, there are two common base goniometer configurations in use: In the ω–2θ (or θ–2θ with $\omega = \theta$) configuration, the incident-beam direction is

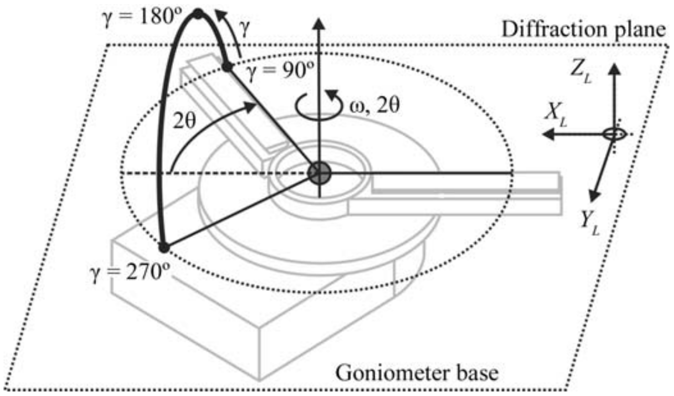

Figure 2.1.6
Laboratory coordinates and geometric definition of the coaxial goniometer axes ω and 2θ. If the azimuthal angle γ takes all values from 0 to 360° at a given Bragg angle 2θ, the trace of the diffracted beams forms a Debye cone (compare with Fig. 2.1.1).

mechanically fixed. The ω axis rotates the specimen stage, while the 2θ axis rotates the detector. In the ω–θ (or θ–θ with $\omega = \theta$) configuration, the ω axis defines the incident-beam angle by rotating the X-ray source, while the other axis scans the detector. In this configuration the specimen stage is mechanically fixed. Both configurations allow identical positioning of the X-ray source, specimen and detector relative to each other.

The goniometer base orientation is defined by the diffraction plane, which can be either horizontal or vertical. Vertical-base goniometers in ω–θ configuration are particularly popular, as the specimen is always kept horizontal, effectively preventing it from falling off. However, heavy specimens and beam-path components require particular attention in both the goniometer base design and choice of orientation, as they have a strong impact on goniometer accuracy, precision and early wear and tear (see also Section 2.1.5.2). Where loads exceed the maximum specifications for a vertically mounted goniometer base, and whenever horizontal specimen positioning is not imperative, either a vertical goniometer base in ω–2θ configuration or a horizontal goniometer should be chosen.

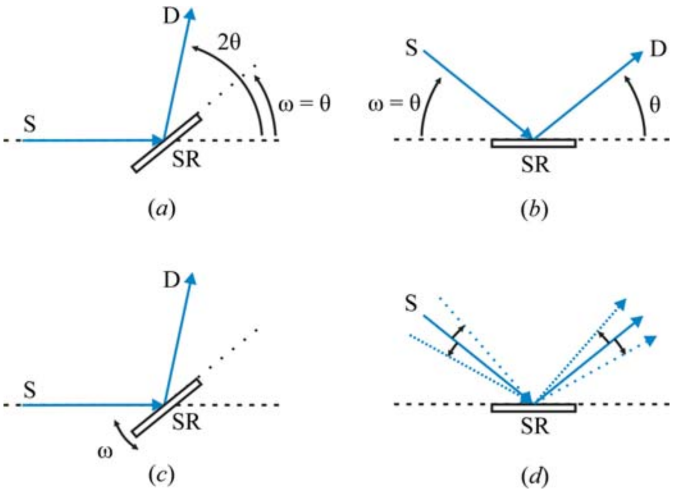

Figure 2.1.7
Goniometer base configurations and scan modes suitable for both Bragg–Brentano or Debye–Scherrer geometry. Symmetric beam path setup in (*a*) ω–2θ and (*b*) ω–θ configuration. Rocking curve setup in (*c*) ω–2θ and (*d*) ω–θ configuration. Only the central beams are shown for clarity, rotations are indicated by arrows. S: X-ray source, D: detector, SR: flat specimen, reflection mode.

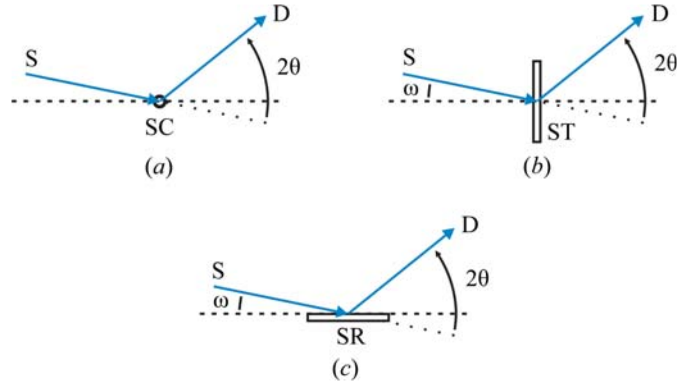

Figure 2.1.8
Goniometer base configurations and scan modes suitable for the Debye–Scherrer geometry only. Only the central beams are shown for clarity. (*a*) Capillary specimen in transmission mode, (*b*) flat specimen in transmission mode, (*c*) flat specimen in reflection mode, grazing incidence with fixed ω. S: X-ray source, D: detector, SR: flat specimen, reflection mode; SC: capillary specimen, transmission mode; ST: flat specimen, transmission mode.

In Figs. 2.1.7 and 2.1.8 a range of typical goniometer base configurations and scan modes are illustrated.

A symmetric beam-path setup in reflection mode, where both the incident and diffracted beam form an angle of θ with respect to the specimen surface, is mandatory for instruments operating in Bragg–Brentano geometry to maintain the focusing condition (see Section 2.1.4.1), but is also commonly used in Debye–Scherrer geometry. Scanning involves coupling of the ω (with $\omega = \theta$) and 2θ axes in a ratio of 1:2 for the ω–2θ configuration (Fig. 2.1.7*a*) and 1:1 for the ω–θ configuration (Fig. 2.1.7*b*), but only allows probing of lattice planes essentially parallel to the specimen surface. Where determination of a texture parameter is sought, a so-called 'rocking-curve' measurement can be performed by rocking either the specimen or the X-ray source and detector around the position of a Bragg peak. Two scenarios need to be considered and are illustrated in Fig. 2.1.7(*c*) and Fig. 2.1.7(*d*). In the ω–2θ configuration with fixed X-ray source (Fig. 2.1.7*c*), the detector will be fixed at the 2θ position of a selected Bragg peak, while the specimen is rotated ('rocked') independently, to perform a so-called 'ω-scan'. To achieve the same in an ω–θ configuration with fixed specimen, the X-ray source and the detector will be coupled 1:−1 or −1:1 to perform a clockwise or anticlockwise scan while maintaining the selected 2θ position, respectively, as illustrated in Fig. 2.1.7(*d*).

In Debye–Scherrer geometry there is no geometrical restraint requiring coupled scans to maintain 2θ-dependent focusing conditions, as is the case in the Bragg–Brentano geometry, providing high flexibility. Specimens can be measured in both reflection as well as transmission mode. In principle, the incident-beam direction may be any relative to the specimen surface, and can be fixed or variable, while the detector performs a 'detector scan'. The ω and 2θ axes may be coupled or not. Choices solely depend on the specimen properties and the requirements of the application. This is demonstrated in Fig. 2.1.8 for a few representative examples. The classic Debye–Scherrer geometry using a capillary specimen is shown in Fig. 2.1.8(*a*). The capillary specimen can be readily exchanged for a flat-plate specimen as shown in Fig. 2.1.8(*b*) and Fig. 2.1.8(*c*) for flat-plate transmission and reflection, respectively. ω can be set to different angles or perform a coupled scan to allow access to higher 2θ angles (Fig. 2.1.8*b*) or can be set to a different angle for grazing-incidence measurements (Fig. 2.1.8*c*). In some applications it may be beneficial to perform a (usually coupled) scan of both ω and 2θ to

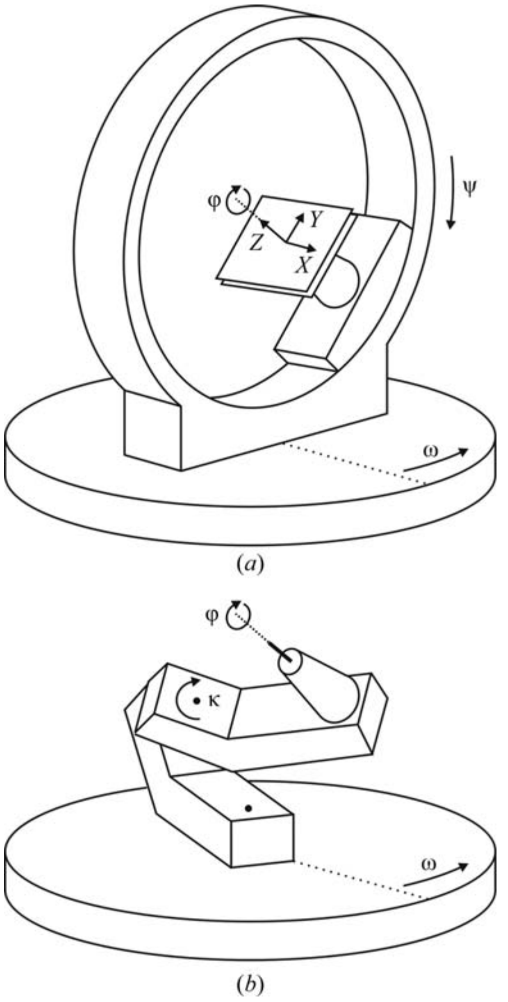

Figure 2.1.9
Geometric definition of the Eulerian and kappa geometries with identical specimen orientation in space. (*a*) Specimen rotation and translation in a Eulerian cradle equipped with an *XYZ* stage, (*b*) specimen rotation on a kappa stage.

improve particle statistics ('wobbling'). Obviously, all the setups shown in Fig. 2.1.8 will work for the full range of X-ray scattering and absorption techniques as discussed in Section 2.1.4.3, leading to the renaissance of the Debye–Scherrer geometry within the past 20 years.

2.1.5.1.2. *Specimen stage*

Depending on the requirements of the application, the specimen stage may offer additional degrees of freedom for specimen rotation as well as X, Y, Z translation. The goniometer base may be configured as ω–2θ as well as ω–θ, and may be oriented vertically as well as horizontally.

To orient a specimen in all possible orientations in space, the specimen stage will offer two more rotational degrees of freedom in addition to the ω and 2θ axes provided by the goniometer base. Such goniometers are known as four-axis diffractometers, with two basic geometries in common use for specimen orientation: Eulerian geometry and kappa geometry.

In the Eulerian geometry the specimen is oriented through the three Euler angles ω (defined by the ω axis of the goniometer base), ψ (psi), and φ (phi). The relationship between the laboratory and rotation axes is shown in Fig. 2.1.9(*a*) for a typical Eulerian cradle. The ω angle is defined as a right-handed rotation about the ω (or Z_L) axis. The ψ angle is a right-hand rotation about the ψ axis, which lies in the diffraction plane and runs parallel to the bisectrix between the incident and diffracted beams. The φ angle defines a left-handed rotation about an axis on the specimen, typically the normal to a flat specimen surface. In some texts the angle χ (chi) is used instead of ψ, with the relationship between the two angles defined as $\psi = 90 - \chi$. Eulerian cradles have the advantage of high mechanical stability and are often integrated with *XYZ* stages to handle bulky specimens. The geometrical definitions of specimen X, Y, Z translations are also shown in Fig. 2.1.9(*a*).

The kappa (κ) geometry shown in Fig. 2.1.9(*b*) represents an alternative way to orient a specimen in space. The ψ axis of the Eulerian geometry is replaced by the κ axis, which is tilted at 50° relative to the diffraction plane. It supports an arm carrying the specimen, with the φ axis tilted at 50° to κ. The role of the Eulerian ψ rotation is fulfilled by means of combined rotation along κ and φ, which allows Eulerian ψ angles in the range -100 to +100° to be obtained. The absence of the (bulky) ψ circle of Eulerian cradles allows an unobstructed view of the specimen and unhindered access from 'above', for example to mount a cooling device without risk of collision. These two advantages made the kappa geometry popular in single-crystal work. On the other hand, it is not possible to move the specimen to an 'upside-down' position, *i.e.* equivalent to Eulerian ψ angles less than -100° or greater than 100°.

Most goniometers do not offer all six rotational and translational degrees of freedom. The majority of these are actually three-axis goniometers, where the specimen stage offers one additional axis for specimen rotation.

A comprehensive overview of commercially available specimen stages is beyond the scope of this chapter owing to the huge number of dedicated specimen stages available for different kinds of specimen types, levels of automation and non-ambient analyses. The most complete and most current information will be found in manufacturers' product information.

2.1.5.2. *Accuracy and precision*

Particularly high demands are made on goniometer accuracy and precision in Bragg-angle positioning (goniometer base) and specimen orientation (specimen stage). These are usually expressed by the angular accuracy and precision of the goniometer-base axes (ω, 2θ) and the sphere of confusion of specimen positioning in space. A detailed discussion is given by He (2009).

Depending on the application and the actual instrument configuration, additional requirements may be imposed on goniometers, and may limit the maximum accuracy and precision that are achievable. Typical requirements, often not compatible with each other, are:

(*a*) mounting of heavy and bulky beam-path components and specimens;
(*b*) variable goniometer radii, typically ranging from about 15 to 60 cm; and
(*c*) vertical goniometer operation to prevent specimens from falling off the holder.

Each of these requirements may have an impact on goniometer accuracy and precision, and potential early wear and tear. Typical loads range from several kg for fixed-target X-ray sources up to 50 kg and more for moving-target X-ray sources. Small detectors such as point and one-dimensional detectors range from less than 1 kg up to a few kg, while large two-dimensional detectors may weigh up to 50 kg and sometimes even more.

For vertical goniometers, the loads on the main axis bearings can be effectively reduced by counterbalances, as shown in Fig.

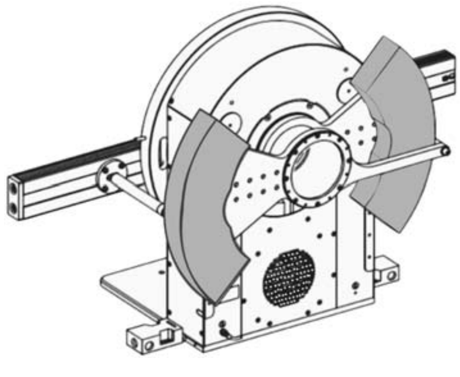

Figure 2.1.10
Example of counterbalancing of a vertical θ–θ goniometer. The counterweights (grey parts) are located at positions matching the weights and locations of the X-ray source and detector. Mounting of different beam-path components with significantly different weight or moving of, for example, the X-ray source and/or the detector to change the respective radii may require repositioning of the counterweights to maintain goniometer accuracy and instrument alignment.

2.1.10 for a goniometer in the ω–θ configuration. Heavy specimen stages may also be supported from below or mounted directly on the bench, disconnected from the goniometer base. However, for heavy beam-path components and larger goniometer radii there is the additional issue of high torques on the incident- and/or the diffracted-beam X-ray optical benches, leading to torsions along the benches. These may significantly deteriorate both the angular accuracy of a goniometer and instrument alignment. For heavy incident-beam-path components such as moving-target X-ray sources, a vertical goniometer base in the ω–2θ configuration is commonly used, as the incident-beam optical X-ray bench is mechanically fixed. For heavy incident- and diffracted-beam-path components a horizontal goniometer base is preferred.

Modern goniometers are equipped with stepping motors and optical encoders, and feature life-span lubrication for maintenance-free operation. The typical accuracy of the two goniometer base axes (ω, 2θ) is of the order of a few thousandths of a degree, with a precision of the order of a few tens of thousandths of a degree. The ψ and φ axes of the specimen stage are mostly used for specimen orientation; the typical angular accuracy and precision are in the range of about 0.01°.

The sphere of confusion of a goniometer is the result of a superposition of all axes and represents the minimum spherical volume covering all possible locations of an infinitely small specimen at all possible orientations. The size of the sphere of confusion depends on issues such as individual axis accuracy and precision, mechanical tolerances, thermal-expansion mismatches, and the weights of the specimen and beam-path components. The sphere of confusion for a two-axis goniometer or a four-axis goniometer with a kappa stage is typically less than 10 µm, and for a four-axis goniometer with a Eulerian cradle less than 50 µm; both values are without a specimen loaded.

Note that the final accuracy of the Bragg angles of the measurement data is mostly determined by instrument alignment, and not by the accuracy specifically of the two goniometer base axes. Optical encoders can measure and control axis positions, but they cannot detect any misaligned or even loose beam-path components. The final data accuracy is determined by the adjustability of an X-ray diffractometer with all its beam-path components. A modern X-ray diffractometer can be aligned to an angular accuracy of equal or better than 0.01° 2θ, which can be checked using suitable standard reference materials (see Chapter 3.1).

2.1.5.3. *Hybrid beam-path systems*

The trend towards multipurpose instrumentation as well as specific application requirements has led to a few specialized goniometer designs. Two major representatives of such designs are (1) multiple-beam-path systems and (2) systems with additional rotational degrees of freedom of beam-path components, such as is required for non-coplanar grazing-incidence diffraction (GID).

2.1.5.3.1. *Multiple-beam-path systems*

Multiple-beam-path systems are usually characterized by integrating more than one beam path on a single goniometer, employing different, complementary beam-path components to meet different application and specimen-property requirements. Mounting two different fixed-target X-ray sources (usually microsources) with different wavelengths (Cu, Mo) is very popular in single-crystal crystallography. Double detector arms are used to mount different types of detectors, most frequently one-dimensional detectors in combination with point detectors. Different X-ray optics can be used to implement different instrument geometries.

A significant driving force behind such multipurpose instrumentation is convenience, *i.e.* to serve a maximum range of applications and specimen types, ideally without the need to manually change the instrument configuration. Indeed, switching between different, preconfigured beam paths may often only require the push of a single software button. However, parallel mounting of different beam-path components raises issues related to the goniometer load and to limitations of angular scan ranges owing to collision issues.

In more recent designs, different X-ray optics have been combined into single motorized modules, allowing switching between different beam paths. Such 'combi-optics' are described in Section 2.1.6.3.4.

2.1.5.3.2. *Non-coplanar beam-path systems*

Non-coplanar (or 'in-plane') grazing-incidence diffraction is a technique for investigating the near-surface region of specimens (ten or fewer nanometres beneath the air–specimen interface). It exploits the high intensity of the total external reflection condition while simultaneously involving Bragg diffraction from planes that are nearly perpendicular to the specimen surface.

As illustrated in Fig. 2.1.11, the incident beam is set at an angle α_I, enabling total external reflection in the coplanar direction (that is coplanar to the diffraction plane); related applications include reflectometry and grazing-incidence small-angle X-ray scattering (GISAXS). 'In-plane' grazing-incidence diffraction

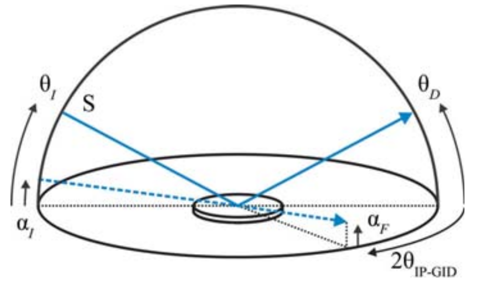

Figure 2.1.11
Illustration of coplanar and in-plane diffraction. S: X-ray source. θ_I, θ_D: incident and diffracted beams for coplanar diffraction. α_I, α_F, $2\theta_{\text{IP-GID}}$: incident-beam angle, exit angle and diffracted-beam angle, respectively, for in-plane grazing-incidence diffraction.

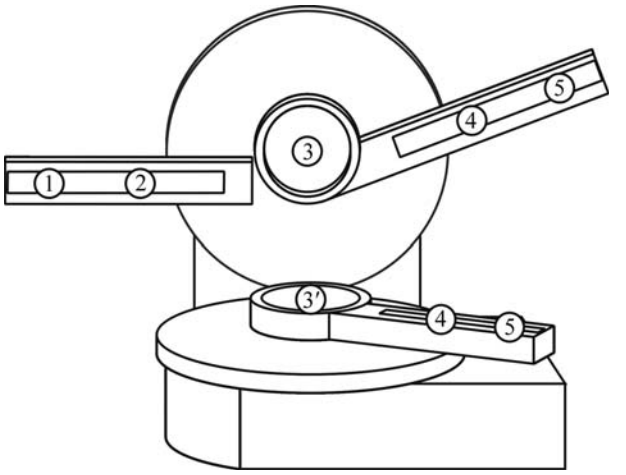

Figure 2.1.12
Sophisticated IP-GID implementation by placing two goniometers vertically with respect to each other, allowing simultaneous coplanar and in-plane measurements using two independent scattered-beam optical X-ray benches (compare with Fig. 2.1.2). The sample stage may be mounted at position 3 or 3′.

(IP-GID) may be measured at angles $2\theta_{\text{IP-GID}}$ in the non-coplanar direction at an exit angle α_F.

There are two principal instrument designs implementing coplanar and in-plane data collection. Firstly, as is obvious from Fig. 2.1.11, a dual-goniometer system may be employed. The most sophisticated implementation has two goniometers placed vertically one above the other, allowing simultaneous coplanar and in-plane measurements using two independent scattered-beam optical X-ray benches as shown in Fig. 2.1.12. Alternatively, the second goniometer may be integrated into the scattered-beam optical X-ray bench, allowing sequential coplanar and in-plane measurements. As a further alternative, a single goniometer may be used, with a Eulerian cradle mounted at the detector position, allowing the detector to be moved around the specimen to perform in-plane measurements. Secondly, a single goniometer equipped with a Eulerian cradle may be used, where the specimen is simply turned by 90° in ψ. As line focus is usually employed for IP-GID measurements, the X-ray source is also turned by 90° to increase the flux.

For all systems, the diffracted-beam optical X-ray benches may be equipped as for multiple beam-path systems, as described in Section 2.1.5.3.1, providing extremely high flexibility. The choice of the most appropriate design depends on issues such as specimen size and weight, the weight of any components in the diffracted-beam path, related spheres of confusion, and the potential need to measure the specimen in a horizontal position.

2.1.6. X-ray sources and optics

This section covers both the generation as well as the conditioning of X-ray beams. All types of X-ray sources, whether laboratory or synchrotron sources, emit a wide range of wavelengths with a characteristic beam divergence and with an intensity related to the power load applied. The function of the incident- and diffracted-beam X-ray optics is to condition the emitted beam in terms of desired wavelength spread, divergence, cross-section size, and shape, and to conserve as much intensity as possible. To achieve maximum performance in terms of intensity and angular resolution, it is essential to design the X-ray optics so that their properties match the characteristics of the X-ray source. Important parameters are the X-ray source beam size and shape, as well as the acceptance angle of the optics given by their design and the distance to the X-ray source.

The optimum choice of an X-ray source and the X-ray optics always depends on the properties of the specimen and the requirements of the applications. Applications requiring high spatial resolution (*e.g.* small single crystals or microdiffraction) or low-angle scattering (*e.g.* thin-film analysis or SAXS) usually require parallel and narrow beams, while diffraction by ideal powders usually works best with larger and slightly divergent beams. As X-ray sources are hardly ever used without X-ray optics, all the components should be seen as one unit determining the beam characteristics at the specimen and eventually at the detector position.

2.1.6.1. *X-ray beam quality measures*

An X-ray beam is characterized by its intensity, wavelength spread, divergence, cross-section size, homogeneity and shape. Simple means for quantifying the quality of an X-ray beam are often useful, and can be used to design an optimal measurement setup by appropriate choice of a combination of X-ray source and X-ray optics. The quantities that are typically used are flux, flux density, brightness and brilliance, all within a 0.1% bandwidth represented by a wavelength range, $\Delta\lambda$, centred around a specific wavelength λ, *i.e.* $\Delta\lambda$ is equal to 1/1000 of λ. While flux, flux density, brightness and brilliance are inter-related, they are distinct and one thus has to consider all of these when comparing X-ray beam characteristics.

Flux represents the integrated intensity of an X-ray beam and is defined as the number of X-ray photons emitted per unit time. The unit for flux is photons per second (p.p.s.).

Flux density is defined as the flux passing through a unit area. The unit is p.p.s. mm^{-2}. Flux density is an appropriate parameter for measuring local counting rates and is synonymous to the term ‘intensity’ as used in colloquial speech.

Brightness takes the beam divergence into account, and is defined as the flux per unit of solid angle of the radiation cone. The unit is p.p.s. mrad^{-2}. Brightness is an appropriate parameter to use when comparing two X-ray sources with identical focal spot size, as the definition does not contain a unit area.

Brilliance additionally takes the beam dimensions into account and is defined as brightness per mm^2. The unit is p.p.s. $\text{mm}^{-2}\,\text{mrad}^{-2}$. Brilliance is maximized by making the beam size and divergence as small as possible, and the photon flux as large as possible. Two X-ray beams may have the same flux density but different brilliance if the two beams have different beam divergence. Brilliance is thus an appropriate parameter to use when comparing two X-ray sources with different focal spot sizes.

Note that the X-ray source brilliance is an invariant quantity, *i.e.* the brilliance at the specimen position cannot be improved by any optical techniques, but only by increasing the brilliance of the X-ray source. This is a consequence of Liouville’s theorem, which states that phase space is conserved. Accordingly, focusing the beam to a smaller size by means of any diffractive or reflective optics will necessarily increase the flux density and the divergence of the X-ray beam, and *vice versa*. Additionally, any diffractive or reflective optics lose flux owing to their reflectivity, which usually is $\leq$90%. Apertures such as slits can help to reduce beam size and divergence, but only at the expense of flux.

Brilliance is more important than flux for experiments with small specimens (*e.g.* single crystals) or small regions of interest (*e.g.* microdiffraction), where it is generally desirable to work

Table 2.1.3

Characteristic wavelengths and absorption edges of metal filters in common use

These data are taken from *International Tables for Crystallography* Vol. C (2004). Metal filters are discussed in Section 2.1.6.3.1.2.

Anode material	$K\alpha_2$	$K\alpha_1$	$K\beta_3$	$K\beta_1$	Metal filter	K absorption edge (Å)
Cr	2.2936510 (30)	2.2897260 (30)	2.0848810 (40)	2.0848810 (40)	V	2.269211 (21)
Co	1.7928350 (10)	1.7889960 (10)	1.6208260 (30)	1.6208260 (30)	Fe	1.7436170 (49)
Cu	1.54442740 (50)	1.54059290 (50)	1.3922340 (60)	1.3922340 (60)	Ni	1.4881401 (36)
Ga†	1.3440260 (40)	1.3401270 (96)	1.208390 (75)	1.207930 (34)		
Mo	0.713607 (12)	0.70931715 (41)	0.632887 (13)	0.632303 (13)	Zr Nb	0.6889591 (31) 0.6531341 (14)
Ag	0.5638131 (26)	0.55942178 (76)	0.4976977 (60)	0.4970817 (60)	Rh Pd	0.5339086 (69) 0.5091212 (42)

† Currently used with dedicated Montel optics only.

with a beam of low divergence and to match the incident beam size to the size of the specimen or the region of interest.

The illumination of larger specimen areas is particularly important for any applications involving polycrystalline specimens, where focusing of the diffracted beam has an advantage over parallel-beam optics in terms of higher beam flux and divergence in that the angular resolution in the diffraction pattern increases. Using an X-ray beam with too small a cross section and/or divergence will result in a smaller or even too small number of diffracting crystallites. This will generally lead to a loss in the diffracted intensity, and may additionally lead to an inhomogeneous intensity distribution in space, leading to random and uncorrectable intensity errors (known as 'particle statistics error', 'spottiness error' or 'granularity error'), and needs to be avoided by all means.

The combination of an appropriate X-ray source with appropriate X-ray optics thus depends on the properties of the specimen and the requirements of the application, and contributes most to the attainable data quality. This is in full agreement with the statement made earlier that there are only a few instrument configurations that will be ideal for any two application areas, or every conceivable sample within a single application area. While changes of most X-ray optics are extremely easy these days, changing between different types of X-ray sources may require significant effort. The choice of the most appropriate X-ray source therefore requires, at the time of instrument acquisition, careful consideration of the types of specimen in relation to the analyses to be conducted.

2.1.6.2. *X-ray sources*

In this section the general concepts of the commonest types of X-ray sources will be described. The physics of X-ray generation and the properties of X-rays have been extensively covered in the literature. More detailed information can be found in, for example, *International Tables for Crystallography* Vol. C (2004) as well as in the textbooks by Pecharsky & Zavalij (2009), Clearfield *et al.* (2008), Jenkins & Snyder (1996), and Klug & Alexander (1974).

2.1.6.2.1. *Generation of X-rays and the X-ray spectrum*

In laboratory X-ray sources, X-rays are produced by a multi-keV electron beam impinging on a metallic target. The X-ray spectrum that is obtained is characterized by a broad band of continuous radiation, accompanied by a number of discrete spectral lines characteristic of the target material. The continuous part of the spectrum ('*Bremsstrahlung*') is generated by the rapid deceleration of the electrons within the target, ranging from lowest energies as a result of gradual deceleration through to a cutoff wavelength whose energy corresponds to the initial kinetic energy of the electron, as a result of instantaneous deceleration. The discrete spectral lines ('characteristic radiation') are the result of electrons knocking out core electrons from the target material. This results in emission of 'fluorescent' X-rays when the perturbed atom relaxes to its ground state by filling up the energy levels of the electrons that have been knocked-out by means of electron transitions from higher electron shells. The energy of the fluorescent radiation is characteristic of the atomic energy levels of the target material. The most commonly used characteristic radiation is that of $K\alpha$, representing the transition of a $2p$ electron (L shell) filling a hole in a $1s$ (K) shell.

The target materials that are commonly in use strongly depend on the application and the type of X-ray source used. The most commonly used target materials range from Cr through to Co, Cu, Mo and Ag. With the recent introduction of liquid-metal targets, see Section 2.1.6.2.2.2(*b*), Ga will find increasing use in applications requiring the smallest spot sizes and highest brilliance. A list of characteristic wavelengths and absorption edges of commonly used metal ($K\beta$) filters is given in Table 2.1.3.

Today's laboratory X-ray sources can be classified as shown in Table 2.1.1, and are described in Section 2.1.6.2.2. For performance considerations see Section 2.1.6.2.3.

2.1.6.2.2. *Types of X-ray sources*

The performance of X-ray sources is usually characterized *via* brilliance as a measure for the quality of the emitted X-rays. The brilliance of an X-ray source is determined by several factors such as electron power density and the take-off angle.

The electron power density is the most important factor. Only a small fraction of <1% of the applied electron energy is converted into X-rays, so most of the incident energy is dissipated within the target as heat. The maximum power density and thus brightness of the X-ray source is limited by the melting or evaporation temperature of solid or liquid metal targets, respectively, and the efficiency with which the heat is removed from the area on which the electrons impact.

The take-off angle describes the angle under which the focal spot is viewed, and typically ranges from 3° to 7°, but may be up to 45°, depending on the type of X-ray source. The actual take-off angle that is chosen represents a compromise. On the one hand, it should be as small as possible to minimize the effectively seen

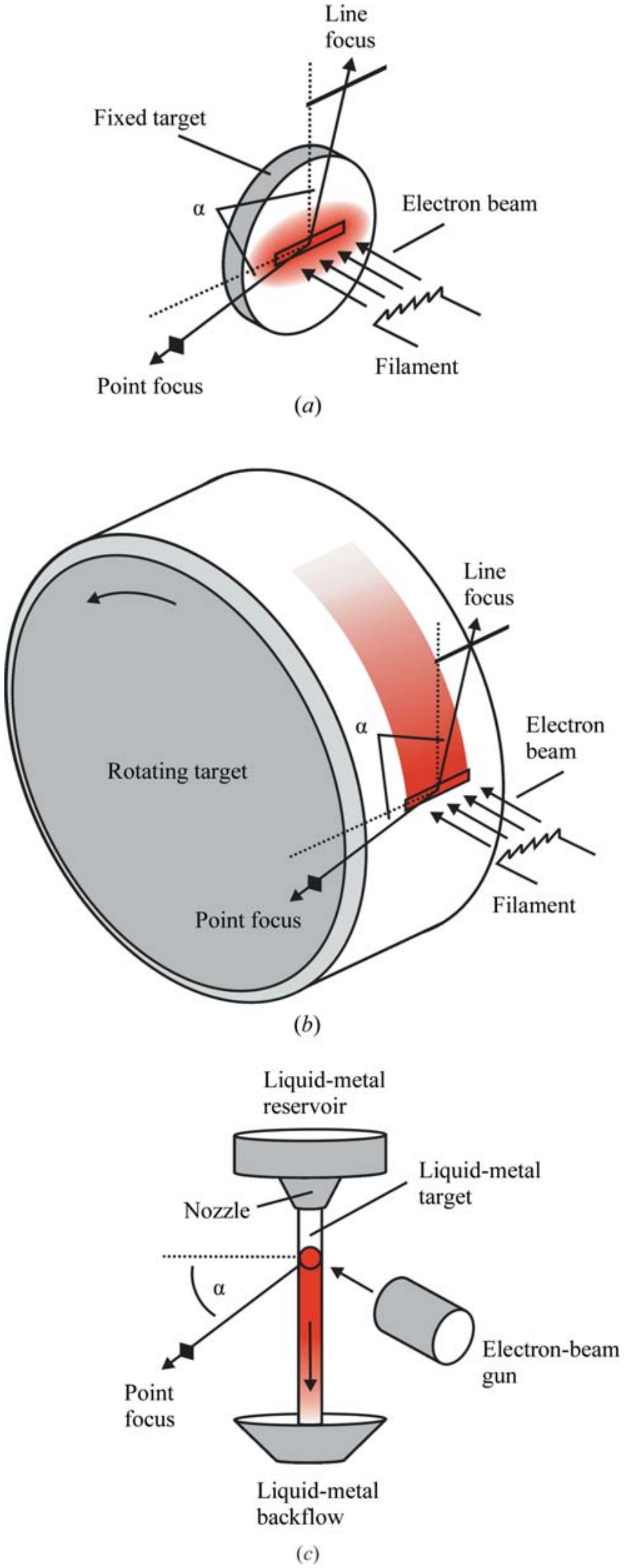

Figure 2.1.13
Illustration of the working principle of laboratory X-ray sources: (*a*) fixed target, (*b*) rotating target, (*c*) liquid-metal jet. α: take-off angle. For fixed targets (*a*) the heat mainly flows towards the cooled back end of the target. For moving targets (*b*, *c*) cold parts of the target are moved into the electron beam continously, providing an extremely large effective cooling efficiency.

width of the focal spot to increase resolution. On the other hand, it cannot be made arbitrarily small to avoid self-absorption by the metal target due to the finite depth in which the X-ray radiation is produced. The higher the tube voltage the larger the take-off angle should be to avoid intensity losses by self-absorption.

In the history of laboratory X-ray source development, most effort has probably been concentrated on techniques for removing the heat from the metal target as efficiently as possible, as illustrated in Fig. 2.1.13, leading to two different categories of X-ray sources for laboratory use: fixed- and moving-target X-ray sources.

2.1.6.2.2.1. Fixed-target X-ray sources

Fixed-target X-ray sources are used in more than 90% of all X-ray diffractometer installations (Fig. 2.1.13*a*). Electrons are generated by heating a filament (cathode) and accelerated towards the metal target (anode) by means of a high potential, typically of the order of 30–60 kV.

In conventional X-ray sources the electrons are focused by an electrostatic lens onto the anode to form the focal spot. Typical power ratings range from several hundred watts up to about 3 kW. The anode is water-cooled from the back. Focal spots are of rectangular shape, and can be viewed at the two long and the two short faces, giving two line and two point foci, respectively. This allows up to four instruments to be operated with a single X-ray source. However, the vast majority of all today's X-ray diffractometers are equipped with an individual X-ray source (and sometimes two, see Section 2.1.5.3.1). This significantly eases alignment as there is no need to align the instrument with respect to the X-ray source, and allows instrument configurations with moving X-ray sources. Modern X-ray-source stage designs allow switching between point and line focus by rotating the X-ray source 90° without alignment and even without the need to disconnect the powder cables and water supply.

Conventional X-ray sources have long and wide electron beams so that a large area of the target is heated (Fig. 2.1.13*a*). The heat generated in the middle of this area can mainly flow in just one direction: towards the water-cooled back of the anode. Heat flow parallel to the surface is minimal, thus limiting the cooling efficiency. It is for this reason that conventional X-ray sources achieve the lowest brilliance of any laboratory X-ray source. Conventional X-ray sources are usually coupled with relatively simple optics and are cheap compared to moving-target systems. In addition they are maintenance-free, apart from periodic changes of the X-ray source owing to ageing.

'Micro-focus' X-ray sources represent another category of X-ray source and are characterized by very small focal spot sizes ranging from a few µm up to about 50 µm. In this type of X-ray source, the improved focusing of the electron beam is achieved by very fine electrostatic or magnetic lenses. Power requirements are significantly less than conventional X-ray sources, ranging from a few watts up to some hundred watts, depending on focal spot size; water cooling is frequently not required. Again, there is no maintenance required beyond periodic tube changes.

As the focal spot area is very small, heat can also flow sideways, improving the thermal cooling efficiency and thus allowing this type of X-ray-source tube to achieve significantly higher brilliance than conventional X-ray sources. To benefit from this increased performance, relatively large optics of the reflective type (see Section 2.1.6.3.3) are required, making micro-focus X-ray source systems significantly more expensive than conventional systems.

The lifetime of a fixed-target X-ray source depends on many factors, of which operation of the source within specifications (such as specific loading and cooling) is particularly important. The 'useful' lifetime may be significantly shorter, even though the X-ray source still operates. Deposition of tungsten from the filament on the anode and on the inner beryllium window surfaces leads to spectral contamination and substantial loss of intensity with time. Increasing deterioration of the filament may change its position relative to the electrostatic lens used for focusing and result in beam inhomogeneity and additional intensity losses. Further intensity losses and beam inhomogeneity may arise from pitting of the anode surface as a result of the intense electron flux on the anode surface.

2.1.6.2.2.2. *Moving-target X-ray sources*

(*a*) *Rotating-target X-ray sources*. Rotating-target X-ray sources are able to remove heat more efficiently than fixed-target sources, and can thereby sustain higher fluxes of X-ray photons (Fig. 2.1.13*b*). This is achieved by rotating a cooled anode, with a typical diameter ranging from about 10 to 30 cm, at about 6000–12 000 revolutions per minute. The maximum power loads depend on the focal spot size, and can range up to 18 kW for conventional rotating-target X-ray sources, and 3 kW for micro-focus rotating-target X-ray sources. Rotating-target X-ray sources are thus inherently more brilliant, and gain up to an order of magnitude in brilliance compared to their respective fixed-target counterparts.

Rotating-target systems do require routine maintenance such as periodic anode refurbishment and changes of the filament, bearings and seals. The maintenance requirements of micro-focus systems are significantly lower than those of conventional rotating-target systems because of the lower total power loading.

(*b*) *Liquid-metal-jet X-ray sources*. A very recent development is that of liquid-metal-jet micro-focus X-ray sources (Fig. 2.1.13*c*), where a jet of liquid metal acts as the electron-beam target (Hemberg *et al.*, 2003). A thin (<100–225 μm) high-speed (>50 m s^{-1}) liquid-metal jet is injected into vacuum by applying a backing pressure of about 200 bar and is targeted by a focused electron beam with a beam power of up to 200 W and a focal spot size of down to 6 μm. The focal spot is viewed at a take-off angle of about 45° to obtain a symmetric beam usually coupled into Montel optics. (Montel optics are described in Section 2.1.6.3.3.1.)

Ideal materials for use in liquid-jet anodes are electrically conductive to avoid charging and have low vapour pressure to simplify vacuum operation. Among a few materials currently being evaluated, Galinstan (a eutectic mixture of 68.5% Ga, 21.5% In and 10% Sn by weight) is particularly suited for laboratory X-ray analyses, as it is liquid at room temperature (melting point 254 K), with the most intense Ga $K\alpha$ line at 9.25 keV, and less intense In $K\alpha$ and Sn $K\alpha$ lines at 24 and 25.3 keV, respectively.

The obvious advantage of a metal-jet anode is that the maximum electron-beam power density can be significantly increased compared to solid-metal anodes and thus the brilliance can be increased by up to an order of magnitude.

2.1.6.2.3. *Performance of X-ray sources*

The single most important property of an X-ray source is its brilliance, which is proportional to the maximum target loading per unit area of the focal spot, also referred to as the specific loading.

In Table 2.1.4 the maximum target loading and specific loading (relative brilliance) for some typical sealed tubes and some rotating-anode sources with a Cu target are compared. Also listed are data for the liquid-metal jet with Ga as a target. Micro-focus fixed-target X-ray sources have up to two orders of magnitude higher specific loadings compared to conventional fixed target tubes, and even 2 to 5 times higher specific loadings compared to conventional rotating-anode systems. In contrast to fixed-target micro-focus X-ray sources, where the specific loading can only be increased by reducing the source size, moving-target X-ray sources are also made brighter by increasing the speed of the target relative to the electron beam. Moving-target X-ray sources are thus inherently brighter than stationary targets. The liquid-gallium jet has a higher (by a further order of magnitude) specific loading than the most brilliant rotating-anode systems, and now rivals the intensity of second-generation synchrotron beamlines.

Table 2.1.4
Maximum target loading and specific loading for some selected fixed- and moving-target X-ray sources

X-ray source	Focal spot (mm^2)	Maximum load (kW)	Specific loading (kW mm^{-2})
Fixed target			
Broad focus (Cu)	2 × 10	3	0.15
Normal focus (Cu)	1 × 10	2.5	0.25
Long fine focus (Cu)	0.4 × 12	2.2	0.5
Micro-focus (Cu)	0.01–0.05	<0.05	5–50
Moving target			
Rotating anode (Cu)	0.5 × 10 0.3 × 3 0.2 × 2 0.1 × 1	18 5.4 3 1.2	3.6 6 7.5 12
Micro-focus rotating anode (Cu)	0.1	2.7	27
Liquid-metal jet (Ga)	0.02 × 0.02	0.2	>500

2.1.6.3. *X-ray optics*

The purpose of X-ray optical elements is to condition the beam emitted by an X-ray source in terms of desired wavelength spread, divergence, cross-section size and shape, and to conserve as much intensity as possible. X-ray optics currently employed in laboratory X-ray diffractometers may be classified as absorptive, diffractive and reflective, as shown in Table 2.1.1.

Absorptive and diffractive X-ray optics represent selective beam-conditioning techniques, where parts of the beam are eliminated to achieve a particular wavelength distribution and divergence. In contrast to this, reflective optics modify the beam divergence to direct the full beam to the specimen or to the detector. The extremely large number of X-ray optical elements available allows for an enormous range of incident and diffracted beam-path configurations. Choosing the most appropriate X-ray optics and X-ray optics combination for a particular experiment is a challenge for the user. The general rule to be obeyed in order to obtain the best data quality is that the beam dimension, wavelength distribution and divergence should compare to the specimen dimension and angular spread of the structural features to be resolved.

In this section the most common features of X-ray optics in current use will be discussed. A comprehensive survey cannot be given, since there exists an incredible multitude of variants of the basic X-ray optic types listed in Table 2.1.1. X-ray optics have been extensively covered in the literature, for example in *International Tables for Crystallography* Vol. C (2004) and in the textbooks by He (2009), Pecharsky & Zavalij (2009), Paganin

(2006), Fewster (2003), Bowen & Tanner (1998), Jenkins & Snyder (1996), Klug & Alexander (1974), and Peiser *et al.* (1955). An extensive discussion of the principles of combining X-ray optics to optimally suit a wide range of different powder diffraction as well as thin-film applications has been given in the textbook by Fewster (2003).

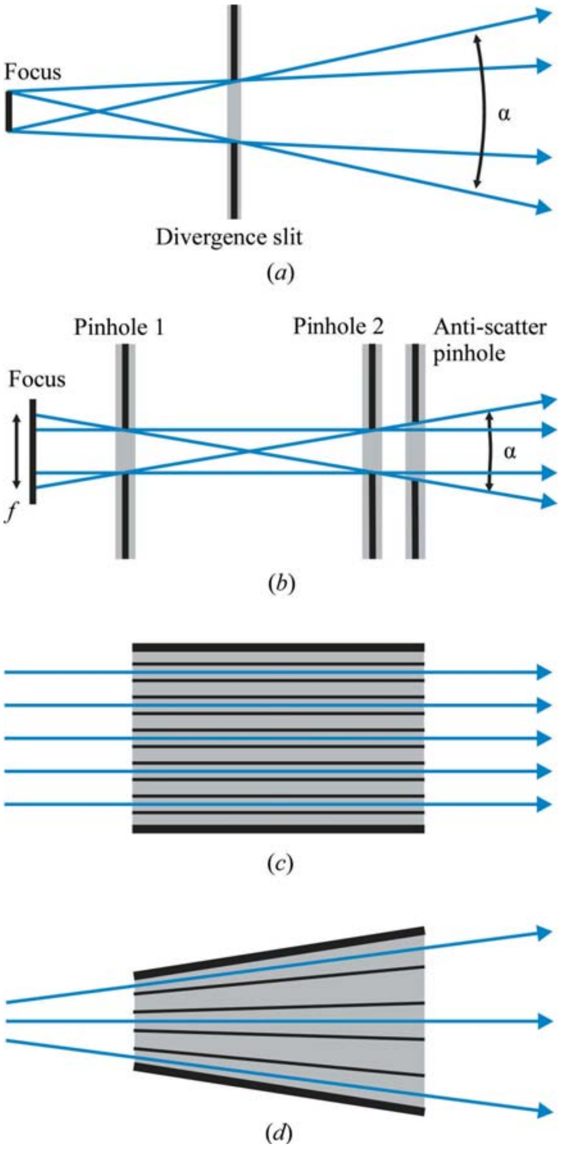

Figure 2.1.14
Apertures used for beam collimation. α: divergence angle, f: virtual focus. (*a*) Single slit or pinhole, (*b*) parallelization through double slits or pinholes, (*c*) parallelization through a parallel-plate collimator, (*d*) a radial plate collimator.

2.1.6.3.1. *Absorptive X-ray optics*

2.1.6.3.1.1. Apertures

The simplest way of beam conditioning is to place apertures such as slits (line focus) or pinholes (point focus) into the incident and/or diffracted beam to control beam divergence and shape, and to reduce unwanted scattering from air or any beam-path components. Apertures are ‘shadow-casting’ optics and thus cannot increase flux density. Reducing beam divergence and beam dimensions by means of apertures invariably results in a loss of intensity that is inversely proportional to the slit aperture.

The principles are shown in Fig. 2.1.14. The divergence of a beam is established by the dimensions of the focal spot as well as the aperture and the distance of the aperture from the source (Fig. 2.1.14*a*). The divergence in the diffraction plane is usually called ‘equatorial divergence’ and the divergence in the axial direction ‘axial divergence’. Apertures can be of the plug-in type requiring manual changes of the aperture to obtain different divergence angles, or – usually only for equatorial divergence slits – motorized. Motorized slits are mostly used in the Bragg–Brentano geometry to limit equatorial divergence, which can be arbitrarily chosen and either be kept constant to keep the diffracting specimen volume constant (as is invariably the case with plug-in slits), or varied as a function of 2θ to keep the illuminated specimen length constant. Typical aperture angles range from 0.1–1°.

To provide additional collimation, a second aperture may be placed at some distance away from the first (Fig. 2.1.14*b*). When using the same aperture, an almost-parallel beam may be obtained from a divergent beam at the cost of high intensity losses. A third aperture is often used to reduce scattering by the second slit. In laboratory X-ray diffractometers dedicated for SAXS analysis such collimation systems may reach lengths of more than 1 m.

Another way to parallelize radiation is to use a parallel-plate collimator (PPC), which is manufactured from sets of parallel, equally spaced thin metal plates, as shown in Fig. 2.1.14(*c*). Each pair of neighbouring plates works like a double-aperture arrangement as shown in Fig. 2.1.14(*b*). In contrast to simple slits and pinholes, PPCs do not change the shape of the beam. PPCs arranged parallel to the diffraction plane are usually called ‘Soller slits’ and are used to control axial divergence. Such devices can be used for focusing as well as parallel-beam geometries with typical aperture angles ranging from 1–5°. Soller slits are usually mounted on both the incident- and diffracted-beam sides of the specimen. PPCs arranged parallel to the diffraction plane are specifically used in parallel-beam geometries to minimize equatorial beam divergence, with typical aperture angles ranging from 0.1–0.5°.

The ways in which the diffracted beam can be conditioned are limited when employing one- or two-dimensional detectors. A particular issue related to these types of detectors is unwanted scattering from air or any beam-path components. Ideally, a closed, evacuated or He-flushed beam path will be used, but this is often not feasible owing to collision issues. For smaller detectors it is possible to place the anti-scatter aperture closer to the specimen surface. Alternatively, a knife edge may be placed on top of the specimen. As knife edges may interfere with divergent beams at higher 2θ angles, it is necessary to move them away from the specimen at higher 2θ angles. Another possibility, limited to one-dimensional detectors, is to use radial Soller slits as shown in Fig. 2.1.14(*d*).

2.1.6.3.1.2. Metal filters

Metal filters are the most frequently used devices for monochromatization of X-rays in laboratory diffractometers. Metal filters represent single-band bandpass devices where monochromatization is based on the K absorption edge of the filter material to selectively allow transmission of the $K\alpha$ characteristic lines while filtering white radiation, $K\beta$ radiation (hence they are frequently known as ‘$K\beta$ filters’), and other characteristic lines.

A properly selected metal filter has its K absorption edge right between the energies of the $K\alpha$ and $K\beta$ characteristic lines of the source. As a rule of thumb, this is achieved by choosing an element just one atomic number less than the X-ray source target material in the periodic table. For heavy target materials such as

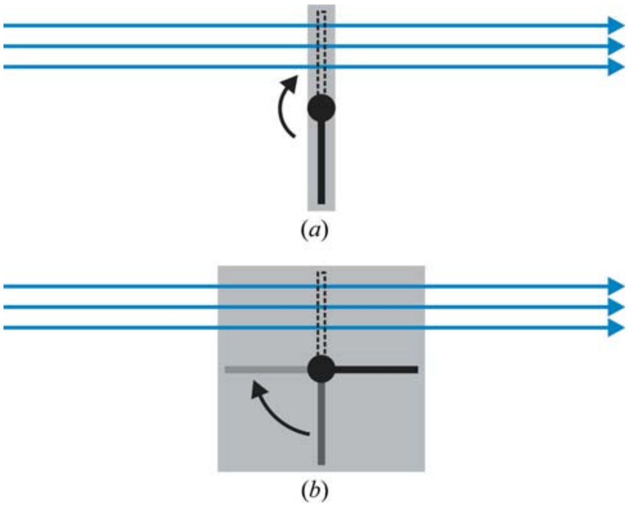

Figure 2.1.15
Motorized switchable (*a*) and rotating (*b*) absorbers.

Mo or Ag, this rule can be extended to two atomic numbers. A list of metal filters suitable for the most commonly used target materials is given in Table 2.1.3.

A major disadvantage of metal filters is that they cannot completely eliminate $K\beta$ radiation at bearable intensity losses. In addition, they introduce absorption edges at the high-energy (low-angle) side of diffraction peaks, the magnitudes of these being dependent on the wavelength as well as on the filter material and its thickness. While for point detectors absorption edges are usually obscured by counting statistics, they are much more readily visible to position-sensitive detectors owing to the high number of counts that are typically collected.

Positioning of the metal filter does not make a difference in terms of filtering of $K\beta$ or white radiation, but can in the case of specimen fluorescence. Placing the metal filter in the diffracted beam can filter some fluorescence radiation, unless the specimen contains the same element as the metal filter. Taking Cu radiation as an example, most fluorescence radiation excited by Ni in the specimen will pass through a diffracted-beam Ni filter. In this instance, the $K\beta$ filter should be mounted in the incident beam to suppress Cu $K\beta$ radiation, which is very efficient at exciting Ni fluorescence. Balanced-filter techniques, employing two (or more) filters that have absorption edges just above and below $K\alpha$, are no longer in use as the resulting bandpass is still much wider than that of crystal monochromators at even higher intensity losses.

Metal filters are generally supplemented by some energy discrimination by the detector to remove the high-energy white radiation from the X-ray source. The effectiveness of this white-radiation removal depends upon the energy resolution of the detector, and is discussed in Section 2.1.7 for the different detector technologies currently in use. Recent improvements in the energy-discrimination capabilities for silicon strip detectors now even allow filtering of $K\beta$ radiation, completely eliminating the need for metal filters (see Section 2.1.7.2.3.2). As a consequence, the use of metal filters is likely to decline.

Another type of metal filter is represented by absorbers, *e.g.* Cu foils, which are used at high intensities to avoid detector saturation or even damage. Absorbers can be motorized and switched in and out automatically depending on the actual count rates that are detected (Fig. 2.1.15*a*). Several absorbers with different thickness may be combined in the form of motorized rotating absorbers (Fig. 2.1.15*b*).

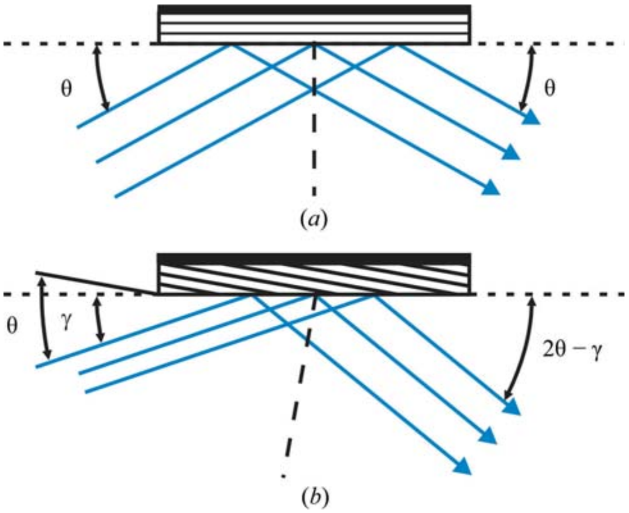

Figure 2.1.16
Illustration of flat single-reflection monochromators. (*a*) Symmetrically cut crystal, (*b*) asymmetrically cut crystal with an angle γ between the reflecting lattice planes and the crystal surface.

2.1.6.3.2. *Diffractive X-ray optics*

Single crystals or highly textured polycrystals (mosaic crystals) represent effective beam conditioners by allowing the spectral bandwidth as well as the X-ray beam divergence to be modified. When they are placed at a specific angle with respect to the incident and diffracted beams, according to Bragg's law, only a small spectral bandwidth will be transmitted depending on the divergence of the incident beam and the rocking angle (mosaic spread) of the crystal. Higher harmonics ($\lambda/2$, $\lambda/3, \ldots$) are diffracted as well, but can be successfully suppressed by using materials with small higher-order structure factors and *via* energy discrimination by the detector. Depending on the application, a crystal monochromator can be either used as a spectral filter ('monochromator'), typically used in the incident beam, or as an angular filter ('analyser'), typically used in the diffracted beam to restrict the angular acceptance of the detector.

It is likely that all monochromators currently employed in laboratory X-ray diffractometers are of the reflective type ('Bragg geometry'). Transmission-type monochromators ('Laue geometry') play no role in laboratory powder diffraction. Two designs are in common use and are described below: (*a*) single-reflection monochromators and (*b*) multiple-reflection monochromators.

2.1.6.3.2.1. Single-reflection monochromators

The most common types of single-reflection monochromators are illustrated in Figs. 2.1.16 and 2.1.17. Flat crystals (Fig. 2.1.16) are used in parallel-beam geometry and curved crystals in focusing geometries (Fig. 2.1.17). A beam reflected from a flat crystal with the reflecting lattice planes parallel to its surface (symmetric cut) is nearly parallel (Fig. 2.1.16*a*). If the crystal is cut at an angle to the reflecting lattice planes (asymmetric cut), then the beam will be expanded (Fig. 2.1.16*b*), or compressed if reversed (Fankuchen, 1937). Monochromators can be curved (Johann, 1931) or curved and ground (Johannson, 1933), and may be cut symmetrically (Fig. 2.1.17*a*) or asymmetrically (Fig. 2.1.17*b*). The latter has the particular advantage of providing different focal lengths for the incident and diffracted beam. A shortened incident beam allows the monochromator to be mounted closer to the X-ray source to capture a larger solid angle of the emitted beam. If the diffracted-beam focusing length is

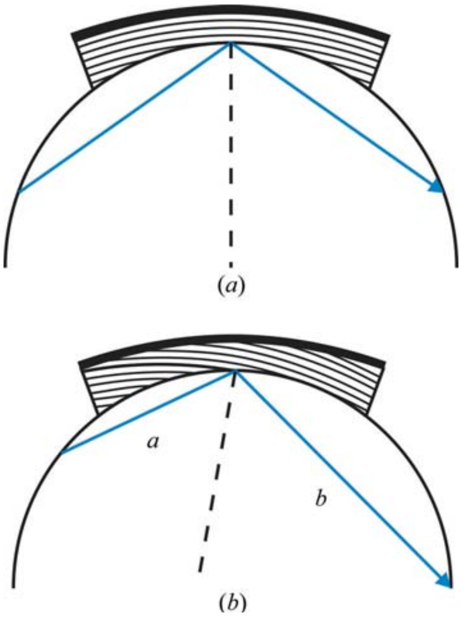

Figure 2.1.17
Illustration of curved and ground single-reflection monochromators. Only the central beam is shown for clarity. (*a*) Symmetrically cut crystal, (*b*) asymmetrically cut crystal with two different focal lengths *a* and *b*.

sufficiently large, then the instrument geometry can be converted between the Bragg–Brentano and the focusing Debye–Scherrer geometries by shifting the monochromator crystal and the X-ray source along the incident-beam X-ray optical bench (see Section 2.1.4.1 and Fig. 2.1.3).

The most commonly used monochromator crystal materials are germanium and quartz, which have very small mosaic spreads and are able to separate the $K\alpha_1/K\alpha_2$ doublet. In contrast to germanium and quartz crystals, graphite and lithium fluoride have large mosaic spreads and thus high reflectivity, but cannot suppress $K\alpha_2$. In principle, any of these monochromators can be mounted in the incident as well as the diffracted beam; the choice mostly depends on the purpose of the monochromator. Germanium and quartz monochromators are typically used as incident-beam monochromators to produce pure $K\alpha_1$ radiation. Graphite (focusing geometries) and lithium fluoride (parallel-beam geometry) are often used as diffracted-beam monochromators to suppress fluorescence radiation. Germanium and quartz can also be used as diffracted-beam monochromators, but are usually not because of their lower reflectivity. Where mounting of diffracted-beam monochromators is difficult or impossible, which is specifically true for one- and two-dimensional detector applications, curved graphite monochromators are frequently used as incident-beam monochromators.

The use of diffracted-beam monochromators – at least in powder X-ray diffraction – is declining steeply because of the geometric incompatibility issues with one- and two-dimensional detector systems (which, since 2010, have been sold with more than 90% of all diffractometers; see Section 2.1.3.2). With the recent improvements of energy-discrimination capabilities for silicon micro-strip detectors, the need for diffracted-beam monochromators will further diminish (see Section 2.1.7.2.3).

2.1.6.3.2.2. Multiple-reflection monochromators

Multiple-reflection monochromators can reduce the wavelength dispersion $\Delta\lambda\,/\lambda$ significantly more than single-reflection monochromators. Multiple-reflection monochromators are often made of monolithically grooved single crystals and are also known as channel-cut monochromators (Bonse & Hart, 1965). In Fig. 2.1.18 an overview is given of the most common channel-cut monochromator types; for a detailed discussion see *e.g.* Hart (1971) and Bowen & Tanner (1998). Successive reflection of the X-ray beam at the channel walls by the same lattice planes causes a strong reduction of the X-ray intensity contained in the tails of the beam. Depending on the number of reflections, multiple-reflection monochromators are denoted as two-bounce, three-bounce *etc.* channel-cut monochromators. The Bartels monochromator (Bartels, 1983) comprises two two-bounce channel-cut crystals. For Cu radiation, such a monochromator results in a wavelength spread which is less than the natural line width of the Cu $K\alpha_1$ line. The most commonly used crystal material is germanium, which delivers higher intensity than silicon, using the 400, 220, or 440 reflections. Crystals may be cut symmetrically or asymmetrically. In Table 2.1.5 several types of

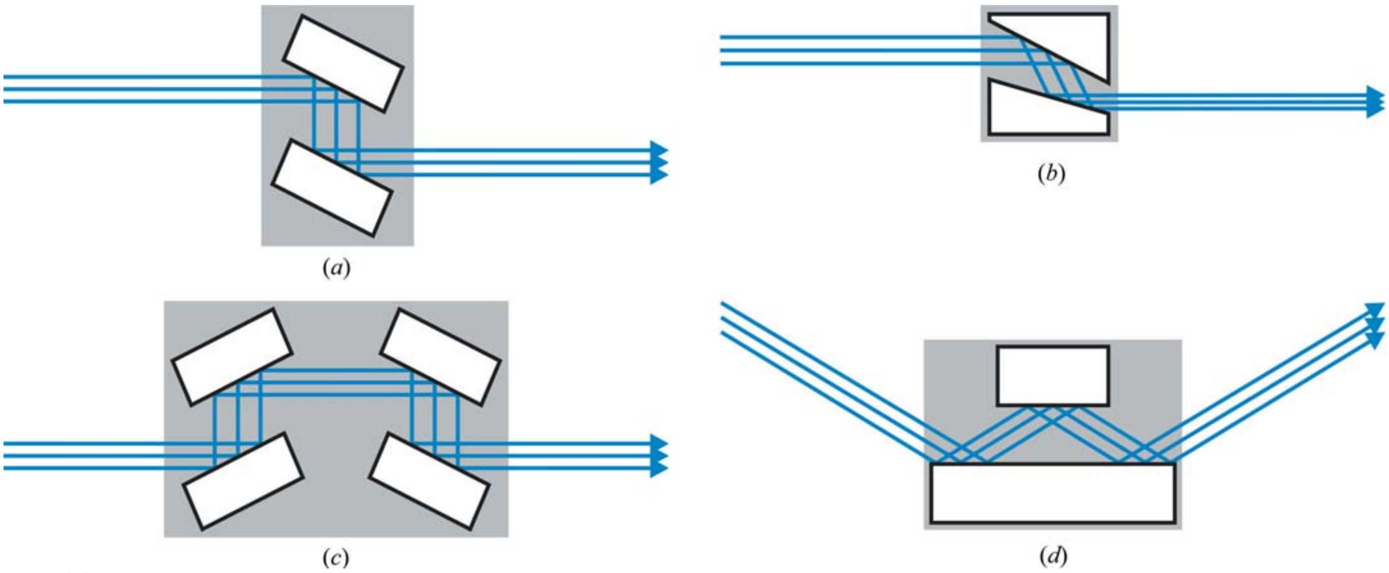

Figure 2.1.18
Illustration of multiple-reflection monochromators. (*a*) Symmetrically cut two-bounce channel-cut monochromator, (*b*) asymmetrically cut two-bounce channel-cut monochromator for beam compression, or, if reversed, for beam expansion, (*c*) symmetrically or asymmetrically cut four-bounce channel-cut monochromator, (*d*) symmetrically cut three-bounce channel-cut monochromator.

Table 2.1.5
Comparison of divergence and intensity for several types of germanium channel-cut monochromators

In each case, the monochromator is coupled with a graded multilayer providing 3×10^9 counts per second at <0.028° beam divergence. The values in parentheses denote the percentage of intensity diffracted by the respective monochromator crystals.

Type	(*hkl*)	Divergence (°)	Intensity
Two-bounce	220, symmetric	<0.0052	5.0×10^7 (~1.5%)
Two-bounce	220, asymmetric	<0.0085	3.3×10^8 (~10%)
Two-bounce	400, asymmetric	<0.0045	4.8×10^7 (~1.5%)
Four-bounce	220, symmetric	<0.0035	6.5×10^6 (~0.2%)
Four-bounce	220, asymmetric	<0.0080	2.7×10^7 (~1%)
Four-bounce	440, symmetric	<0.0015	2.2×10^5 (~0.075%)

germanium channel-cut monochromators are compared in terms of divergence and intensity.

Switching between different channel-cut monochromators is extremely easy these days and can be accomplished without the need for any tools and without realignment. This is also true for cases where a beam offset is introduced, *e.g.* by switching between two- and four-bounce channel-cut monochromators. In sophisticated instruments such an offset can be compensated fully automatically by a software-controlled motor.

The combination of different types of channel-cut monochromators in both the incident and diffracted beam allows the construction of advanced diffractometer configurations with extremely high resolution capabilities. It should be emphasized that laboratory X-ray diffractometers can have identical optical configurations to diffractometers operated at synchrotron beamlines. The important and obvious difference, however, is the extremely low flux coming from laboratory X-ray sources, which is further diminished by each reflection in a channel-cut monochromator (Table 2.1.5). While such configurations work perfectly for strongly scattering single-crystal layers in thin films, for example, analysis of ideal powders is normally not possible.

2.1.6.3.3. *Reflective X-ray optics*

2.1.6.3.3.1. Multilayer mirrors

Multilayer mirrors used in laboratory X-ray diffractometers are efficient beam conditioners, using total reflection as well as Bragg reflection on inner interfaces of a multilayer structure to modify beam divergence, cross-section size, shape and – to some extent – spectral bandwidth. A comprehensive description of current mirror designs and important mirror properties is found in the VDI/VDE Guideline 5575 Part 4 (2011).

Multilayer mirrors consist of a multilayer coating deposited on a flat or curved substrate. The *imaging* characteristics are mostly determined by the contour of the mirror surface as defined by the substrate surface. The most common contours include planes, ellipsoids, paraboloids, elliptic cylinders or parabolic cylinders. The *spectral reflection* properties are determined by the coating, which may consist of some 10 up to 1000 alternating layers of amorphous low-density ('spacer') and high-density ('reflector') materials, with a period of a few nanometres. The first curved mirrors were produced by depositing the multilayers on a flat substrate that was subsequently bent to the desired contour, yielding typical r.m.s. slope errors of about 15 arcsec. By using prefigured substrates with r.m.s. slope errors below 1.7 arcsec, significantly improved reflectivity and lower beam divergence are obtained. Laterally graded multilayer mirrors (so-called 'Göbel mirrors') have a layer thickness gradient parallel to the surface (Schuster & Göbel, 1996), which, when combined with a planar, parabolic or elliptic substrate contour, produce a divergent, parallel or focusing beam. Fig. 2.1.19 illustrates graded multilayer mirrors for parallelization and focusing in the plane of diffraction.

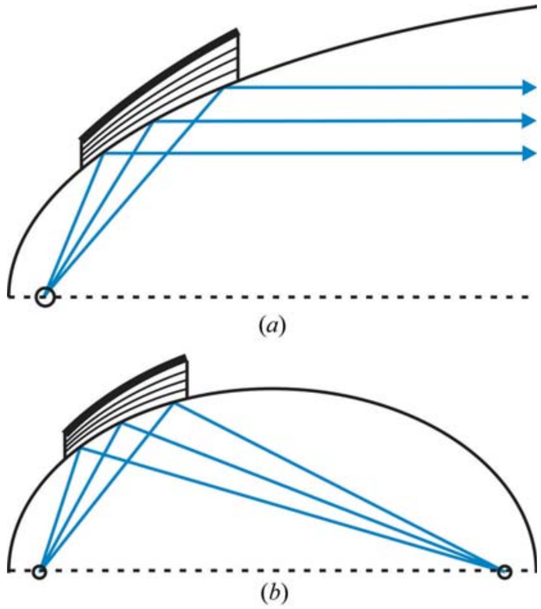

Figure 2.1.19
Schematic of graded multilayer mirrors. (*a*) Parabolic mirror for parallelization of a divergent beam, or, if reversed, focusing of a parallel beam. In the latter case the mirror will also filter some specimen fluorescence. (*b*) Elliptical mirror for focusing of a divergent beam.

For beam conditioning in two perpendicular directions, two perpendicularly oriented curved mirrors may be used, as illustrated in Fig. 2.1.20. In the Kirkpatrick–Baez scheme (Kirkpatrick & Baez, 1948), two mirrors are cross-coupled as shown in Fig. 2.1.20(*a*). This setup has some issues related to the inherently different capture angles and magnification of both mirrors, resulting in less flux from smaller sources and in different divergences in both directions for elliptical mirrors. The Montel optics (Montel, 1957) shown in Fig. 2.1.20(*b*) overcome these issues by arranging both mirrors in a 'side-by-side' configuration.

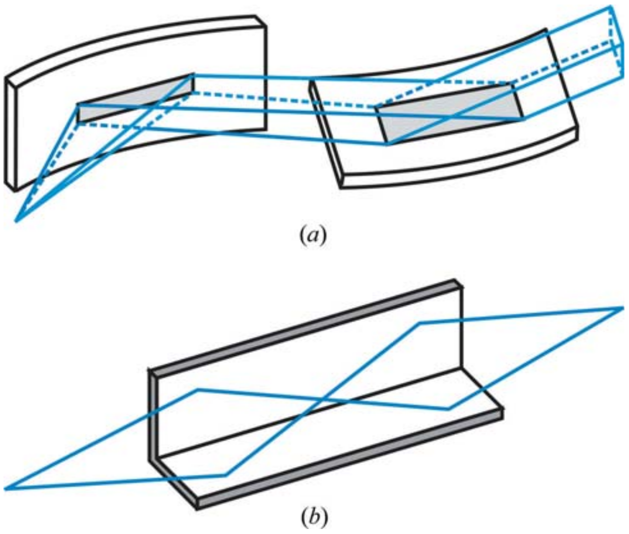

Figure 2.1.20
Examples for orthogonally positioned curved mirrors for beam conditioning. (*a*) Kirkpatrick–Baez scheme employing two parabolic mirrors to create a parallel beam, (*b*) Montel optics employing two elliptical mirrors side-by-side to create a focusing beam.

Mirrors are available for all characteristic wavelengths used in laboratory X-ray powder diffractometers. A wealth of different materials are being used as double layers (reflector/spacer), including but not limited to W/Si, W/B_4C, Ni/C, Ru/B_4C, Ti/B_4C, V/B_4C, Cr/B_4C and Mo/B_4C. The double-layer materials may be selected according to the energies of their absorption edges to make the mirror act as a filter as well. While none of these mirrors is strictly speaking a monochromator, appropriate selection of the double-layer materials, depending on the wavelength used, will allow monochromatization of the radiation to $K\alpha$ while $K\beta$ and *Bremsstrahlung* are suppressed.

Within the past two decades mirror systems have become invaluable for all applications requiring a small and/or highly parallel beam. In particular, coupling of a parallel-beam mirror with multiple-reflection channel-cut monochromators allows the use of a wider solid-angle range of the X-ray source and a gain of nearly two orders of magnitude in intensity (Schuster & Göbel, 1995). For applications requiring ideal powders, however, too-small as well as too-parallel beams may result in too small a number of diffracting crystallites, which will generally reduce the diffracted intensity, and may additionally lead to particle statistics errors (see also Section 2.1.6.1).

Today, advanced sputtering techniques allow the fabrication of a wealth of different multilayer optics with virtually arbitrary beam divergences to generate focusing, parallel and divergent beams, for both point- and line-focus applications. The most comprehensive overview of currently available mirrors and up-to-date specifications will be found in manufacturers' brochures.

2.1.6.3.3.2. *Capillaries*

X-ray capillary optics are finding increasing use in applications where a small focused beam with high intensity is required. Their design, important properties and applications are discussed by *e.g.* Bilderback (2003), He (2009), and the VDI/VDE Guideline 5575 Part 3 (2011).

X-ray capillary optics employ total external reflection by the inner surface of hollow glass tubes to guide and shape X-ray radiation. For incidence angles lower than the critical angle of total reflection the X-ray radiation is guided through the optics at very low losses. The transmission efficiency depends upon the X-ray energy, the capillary materials, reflection surface smoothness, the number of reflections, the capillary inner diameter and the incident beam divergence, and is thus determined by the particular design of the given optics. Generally, the transmission efficiency decreases with increasing X-ray energy owing to the decreasing critical angle of total reflection. The role of X-ray capillary optics as energy filters is insignificant, therefore capillaries are usually used in combination with monochromatization devices such as metal filters, incident-beam graphite monochromators or graded multilayers. Gains in flux density of more than two orders of magnitude compared to pinhole systems have been reported. The most common X-ray capillary optics currently used in laboratory X-ray powder diffractometers can be categorized as either monocapillaries or polycapillaries.

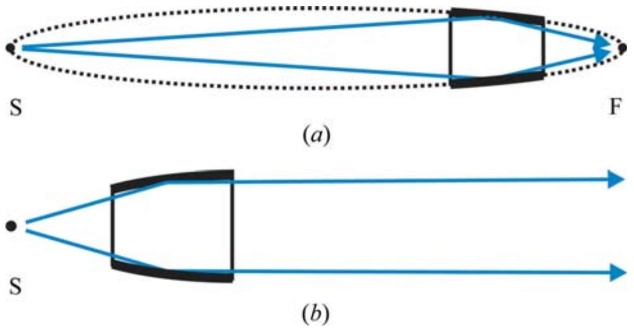

Figure 2.1.21
Schematic of monocapillary optics. (*a*) Elliptical and (*b*) parabolic monocapillary. S = source; F = focal point.

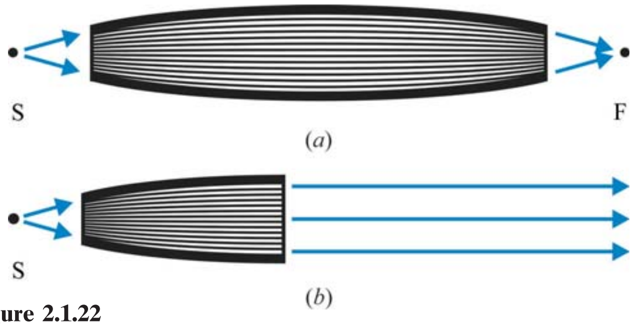

Figure 2.1.22
Schematic of polycapillary optics. (*a*) Focusing and (*b*) parallel-beam polycapillary. S = source; F = focal point.

Monocapillaries consist of ellipsoidal or paraboloidal capillaries for focusing or parallelizing X-rays by means of single or multiple total reflections, as illustrated in Fig. 2.1.21. The exit-beam divergence is controlled by the capillary diameter and length as well as the critical angle of total reflection; typical spot sizes range from some 20 mm down to less than 1 µm. Single-reflection monocapillaries are achromatic and almost 100% efficient. Their most important limitations are figure slope errors limiting the spot size. Multi-reflection monocapillaries can have the smallest spot sizes, which do not depend on the source size. An important drawback is that the beam is smallest at the capillary tip. In order to obtain the smallest possible spot size the sample has to be positioned to within 10–100 times the diameter of the tip exit size, *e.g.* 10–100 µm for a capillary with a 1 µm tip exit size.

Polycapillaries (*e.g.* Kumakhov & Komarov, 1990) are monolithic systems of micro-structured glass consisting of thousands up to several millions of channels, which are tapered at one or both ends to form desired beam profiles as illustrated in Fig. 2.1.22. A single channel can efficiently turn an 8 keV beam by up to 30° by multiple total reflections. Polycapillaries can collect a very large solid angle up to 20°, resulting in very high intensity gains. Typical spot sizes range from some 20 mm down to about 10 µm and are energy dependent, getting larger at lower energies.

2.1.6.3.4. *Combi-optics*

The steadily growing trend towards multipurpose instrumentation has led to a multitude of X-ray optics combined in single modules to eliminate reassembling and realignment. Such 'combi-optics' are usually motorized and allow a fully automatic, software-controlled switch between different beam paths to switch between different instrument geometries or to optimize beam conditioning (*e.g.* high flux *versus* high resolution).

A frequent requirement is the ability to switch between the divergent-beam Bragg–Brentano and parallel-beam Debye–Scherrer geometries, which can be achieved by two combi-optics as illustrated in Fig. 2.1.23. In this example, the incident-beam combi-optics consist of a variable slit and a Göbel mirror. When operating as a variable slit (Fig. 2.1.23*a*), the parallel-beam path is blocked by the variable slit. Turning the variable slit parallel to the divergent beam (Fig. 2.1.23*b*) enables the parallel beam and blocks the divergent beam. The diffracted-beam combi-optics consist of a set of two parallel-plate collimators, which are

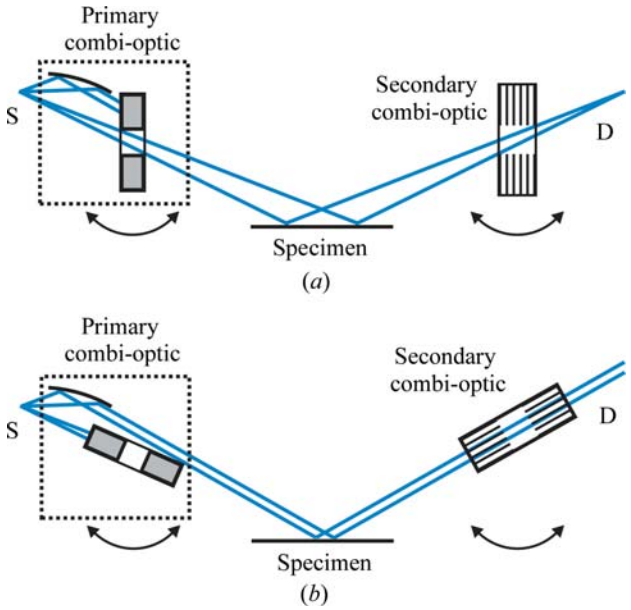

Figure 2.1.23
Incident and diffracted beam combi-optics for switching between (*a*) the Bragg–Brentano geometry and (*b*) the parallel-beam geometry. S: X-ray source; D: detector.

separated by a small gap. When turning the two parallel-plate collimators into the beam direction, only those diffracted rays running parallel to the collimator plates will reach the detector (Fig. 2.1.23*b*). When turning the collimators by approximately 90°, the gap between the two collimators acts as a variable slit enabling a divergent beam (Fig. 2.1.23*a*).

Significantly more sophisticated combi-optics are used in X-ray diffractometers that are mostly used for thin-film analysis. In Fig. 2.1.24 an example for two different incident-beam and four different diffracted-beam paths is shown, providing the choice between eight different beam paths depending on the properties of the specimen and the application requirements. The incident beam path is characterized by a fixed-target X-ray source equipped with a Göbel mirror, attached on a motorized mount. By rotating this arrangement by about 5°, the beam travels either through a rotary absorber followed by a two-bounce channel-cut monochromator and a slit (upper beam path, high-resolution setting), or just through a single slit (lower beam path, high-flux setting). The diffracted beam path represents a double-detector setup, typically consisting of a point detector (D1) and a position-sensitive detector (D2). For the point detector three different beam paths can be chosen by means of a switchable slit, which either sends the beam through a three-bounce channel-cut analyser, or through the same two-parallel-plate-collimator arrangement already discussed in Fig. 2.1.23, either acting as a parallel-plate collimator or a variable slit. A fourth beam path without any diffracted-beam X-ray optics allows use of the position-sensitive detector.

2.1.7. X-ray detectors

The general concepts of X-ray detectors are described here with the focus on practical aspects. The physics of X-ray detection and the individual detector technologies are extensively covered in the literature. He (2009) gives a comprehensive discussion that also includes the most recent detector technologies. Additional detailed descriptions are found in *International Tables for Crystallography* Vol. C (2004), as well as in the textbooks by Pecharsky & Zavalij (2009), Clearfield *et al.* (2008), Paganin (2006), Jenkins & Snyder (1996), and Klug & Alexander (1974).

2.1.7.1. *Detector parameters*

There are many ways to characterize the properties and performance of an X-ray detector.

Ideally, in a given detector operated under appropriate conditions, (1) each photon will produce a detectable signal and (2) the signal recorded is proportional to the number of photons detected. If both conditions are fulfilled then the detector has unit *quantum efficiency*. The *detective quantum efficiency* (DQE) may be defined as the squared ratio of the output signal-to-noise ratio to the input signal-to-noise ratio, expressed as a percentage. A detector's DQE is generally less than 100% because there is always detector noise and not every photon is detected. The DQE thus depends on the characteristics of the detector (*e.g.* transmission of the detector window, count rates and dead time, *etc.*) and varies with the X-ray energy for the same detector.

The *detector linearity* determines the accuracy of intensity measurements and depends on the ratio between the photon

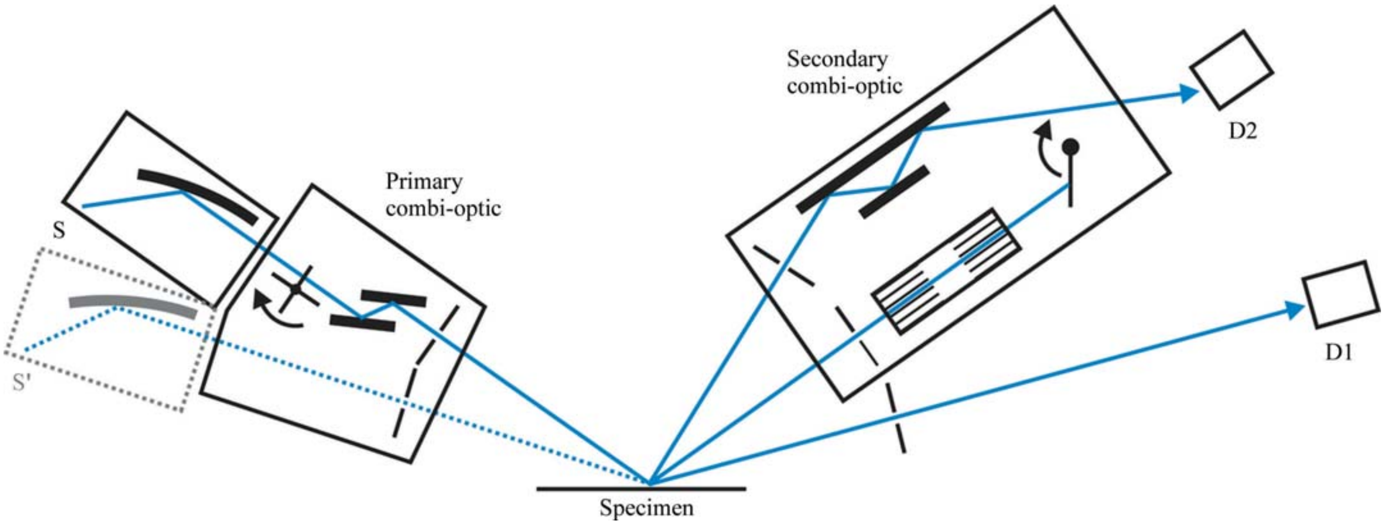

Figure 2.1.24
Example of the use of highly sophisticated incident- and diffracted-beam combi-optics in combination with a rotatable X-ray source and a double detector arm. This setup enables two different incident-beam and four different diffracted-beam paths, and thus provides a choice between eight different beam paths, depending on the properties of the specimen and the requirements of the application. S: X-ray source, S′: X-ray source rotated by about 5°, D1, D2: detectors.

count rate and the rate of signals generated and registered by the detector. In any detector it takes some time to process the conversion of an individual photon to a voltage pulse, which is related to the detector *dead time*: photons arriving while the detector is still processing the previous photon conversion may be lost. The detector dead time is related to the physical characteristics of the detector, *e.g.* the drift time in a gas-ionization detector, or the read-out time of the counting electronics, *e.g.* the shaping time of the amplifier. The effect of dead time becomes a substantial issue at high photon count rates, when the dead time becomes a significant part of the average time separation between two arriving photons, leading to increasing intensity losses at higher count rates. Detectors can be categorized as being non-paralysable or paralysable with respect to dead time. A non-paralysable detector is dead for a fixed time after each count, but not influenced by photons arriving during the dead time. Counting losses increase with increasing count rates, but the true count rate of a nonparalysable detector can be corrected unless the maximum observed count rate is equal to the inverse of the dead time. In a paralysable detector, a second photon arriving within the dead time can not be counted but will extend the dead time up to a point where the detector will be incapable of collecting any counts at all (saturation point). Modern detectors can stand the count rates obtained in powder diffraction experiments using fixed-target X-ray sources. At very high count rates, *e.g.* those obtained in thin-film experiments such as reflectometry, it may be necessary to attenuate the beam. Sophisticated instruments are equipped with an electronic feedback system and automatic absorbers (see Section 2.1.6.3.1.2) to ensure that detector saturation is avoided.

The *dynamic range* of a detector may be defined as the range between the smallest detectable photon count rates (determined by inherent detector noise such as readout and dark noise) to the largest acceptable photon count rates (determined by the dead time).

Energy resolution is the ability of a detector to resolve two photons that have different energies. Energy resolution is typically characterized by the size of the detector energy window, ΔE, in electron volts, as determined by the full width at half maximum (FWHM) of the detector-efficiency curve as a function of energy, with the detector and counting electronics set to a specific wavelength. Another frequently used expression for energy resolution is the ratio of the detector energy window size to the energy of the monochromatic X-ray beam, E, expressed as $\Delta E/E$.

The *proportionality* of the detector determines how the size of the generated voltage pulse is related to the energy of the absorbed X-ray photons, and electronic methods (pulse-height selection) can be used to discriminate between different energies. An accurate proportionality thus allows the use of *energy discrimination* as a form of monochromatization, where the energy is filtered by the detector rather than by an optical element such as a metal filter, crystal or mirror; see Section 2.1.6.3. Signals corresponding to photons with too high or too low energies are discarded.

The size and weight of detectors may impose several practical constraints, see also Section 2.1.4.2. For large detectors the accessible angular range may be limited owing to collision issues. For heavy detectors a horizontal goniometer may be preferred over a vertical goniometer (unless horizontal specimen positioning is imperative) in order to minimize the goniometer load.

X-ray detectors may be broadly classified as *counting detectors* or *integrating detectors*. Counting (digital) detectors are able to detect and count individual photons. The number of pulses counted per unit time is proportional to the incident X-ray flux. Integrating (or analogue) detectors accumulate photon-induced signals for a given period of time, prior to the integrated signal being read out and converted into an (analogue) electrical signal. The signal size is proportional to the flux density of the incident X-rays.

Counting and integrating detectors each have their clear advantages and disadvantages. Counting detectors normally have a greater dynamic range than integrating detectors, while integrating detectors normally have better spatial resolution (Section 2.1.7.3). Energy resolution is only possible for counting detectors. Readout and dark noise are usually higher for integrating detectors. Integrating detectors are not limited by the photon count rate as there is no dead time; nevertheless, the measurement time has to be kept sufficiently small to avoid saturation.

2.1.7.2. *Detector types*

Counting and integrating detectors can be further distinguished by their working principle, and are represented by scintillation, gas-ionization and semiconductor detectors. The most commonly used detector types and their properties are listed in Tables 2.1.1 and 2.1.6, respectively.

At the end of the 1990s the types of detectors in use were scintillation, gas-ionization, Si(Li) and image-plate detectors, with the scintillation counter being the most common by far. Usage of photographic film had already greatly diminished by that time. With the introduction of a series of new one- and two-dimensional detector technologies since the late 1990s, the X-ray detection landscape changed completely. New semiconductor-based detectors (silicon micro-strip, silicon pixel) as well as gas-ionization-based detectors (micro-gap) reached a market share of >90% in newly sold X-ray powder diffractometers within only a few years. As a consequence, classical metal-wire-based proportional counters and scintillation counters will probably become obsolete before 2020. The same is expected for CCD-based detectors, which will be replaced by the very recently introduced complementary metal–oxide–semiconductor (CMOS) active pixel sensor technology.

In the following the working principles of currently available detector types will be briefly described. Matters that are specific to zero- (0D), one- (1D) and two-dimensional (2D) detection are discussed in Section 2.1.7.3. While image plates are still in use, their market share in newly sold systems has become insignificant. Photographic film techniques are totally obsolete. For these reasons, these two detector types will not be taken into further consideration.

2.1.7.2.1. *Scintillation counters*

Scintillation counters are constructed from a scintillator crystal optically coupled to a photomultiplier tube. The crystal is typically made of sodium iodide (NaI) doped with about 1% thallium, frequently denoted as NaI(Tl). When irradiated by X-ray radiation, blue light (~415 nm) is emitted and converted to electrons in a photomultiplier and amplified; the resulting pulses are registered as photon counts.

The height of the outgoing pulses is proportional to the energy of the incoming X-ray photons. This permits the use of pulse-height selection but only allows for poor energy resolution. The relatively high count rate and a moderate noise level result in a moderate dynamic range. These characteristics are the reason for the formerly wide-ranging acceptance of the scintillation counter

Table 2.1.6
Important detector properties at 8 keV as reported by various vendors

Only typical values are given to allow approximate comparisons. Detector properties strongly depend on individual detector designs and are subject to high development rates.

		Gas ionization (Xe/CO_2 gas filling)		
	Scintillation	Wire based (0D)	Wire based (1D/2D)	Micro-gap (1D/2D)
DQE	$\sim$95%	$\sim$95%	$\sim$80%	$\sim$80%
Dynamic range	$>6 \times 10^6$	$>10^6$	$>10^4$ (1D) $>10^6$ (2D)	$>8 \times 10^7$ (1D) $>10^9$ (2D)
Maximum global count rate	$>2 \times 10^6$ c.p.s.	$>7.5 \times 10^5$	$>10^5$ (1D) $>4 \times 10^4$ c.p.s. (2D)	$>8 \times 10^5$ (1D) $>1.6 \times 10^6$ c.p.s. (2D)
Maximum local count rate	n/a	n/a	$>10^4$ (1D) $>10^4$ c.p.s. mm^{-2} (2D)	$>9 \times 10^5$ c.p.s. mm^{-2} (1D, 2D)
Noise	$\sim$0.3 c.p.s.	$\sim$1 c.p.s.	$\sim$1 c.p.s. (1D) $<5 \times 10^{-4}$ c.p.s. mm^{-2} (2D)	<0.01 c.p.s. (1D) $<5 \times 10^{-4}$ c.p.s. mm^{-2} (2D)
Energy resolution	$\sim$3500 eV ($\sim$45%)	$\sim$1600 eV ($\sim$20%)	$\sim$1600 eV ($\sim$20%)	$\sim$1600 eV ($\sim$20%)
Detection mode	Photon counting	Photon counting	Photon counting	Photon counting

	Semiconductor				
	Si(Li)	Strip	Pixel	CCD	CMOS
DQE	>98%	>98%	>98%	$\sim$20–60%	$\sim$75%
Dynamic range	$>10^6$	$>7 \times 10^6$ per strip	$>10^9$	$>5 \times 10^4$	$>1.6 \times 10^4$
Maximum global count rate	$>10^5$ c.p.s.	$>10^8$ c.p.s	$>10^7$ c.p.s. mm^{-2}	n/a	n/a
Maximum local count rate	n/a	$>7 \times 10^5$ c.p.s. per strip	$>10^4$ per pixel	n/a	n/a
Noise	$\sim$0.1 c.p.s.	$\sim$0.1 c.p.s. per strip	$\sim 2.5 \times 10^{-3}$ c.p.s. mm^{-2}	<0.1 c.p.s. per pixel	<0.05 c.p.s. per pixel
Energy resolution	$\sim$200 eV ($\sim$4%)	$\sim$1600 eV ($\sim$20%)†	>1000 eV ($\sim$12.5%)	n/a‡	n/a
Detection mode	Photon counting	Photon counting	Photon counting	Integrating§	Integrating

† $\sim$380 eV/$\sim$5%; Wiacek *et al.* (2015). ‡ >300 eV/>6% in photon-counting mode, see text. § Photon-counting mode possible, see text.

as the detector of choice. An important disadvantage these days is the limitation to 0D detection.

2.1.7.2.2. *Gas-ionization detectors*

The gas-ionization detectors in current use are proportional counters and can be of the 0D, 1D or 2D detection type. Common to all proportional counters is a gas-filled chamber permeated by a non-uniform electric field between positive and negative electrodes, held at a constant potential difference relative to each other. Typically the noble gases Ar or Xe are used as gas fill, mixed with a small amount of quenching gas such as CH_4 or CO_2 to limit discharges. When an X-ray photon travels through the gas-filled volume, it may be absorbed by a noble-gas atom, resulting in the ejection of an electron (photoelectric and Compton recoil). This electron, accelerated by the electric field towards the anode, will cause an avalanche by subsequent ionization along its path (gas amplification), generating an electric pulse which can be registered. The height of the generated pulse is proportional to the energy of the incoming X-ray photon and permits the use of pulse-height selection to achieve moderate energy resolution.

2.1.7.2.2.1. Wire-based proportional counters

In a point proportional detector (0D detection), the pulses generated are measured at one end of a wire (or a knife edge). Position-sensitive (1D and 2D detection) proportional detectors have the added capability of detecting the location of an X-ray photon absorption event. In a 1D proportional detector, pulses are detected at both ends of the wire. Thus the time difference between the measurements of a given pulse can be used to determine the location of the discharge. 2D proportional counters consist of three arrays of wires (multiwire proportional counter, MWPC; Sauli, 1977; Charpak *et al.*, 1968), where one array forming the anode plane is placed between two cathode arrays with their wires oriented parallel and orthogonal to the anode-plane wires, respectively.

Low count rates and low-to-moderate detector noise result in low-to-moderate dynamic ranges. Wire-based proportional counters are not competitive with micro-gap and semiconductor detectors, as can be seen in Table 2.1.6, and are therefore being driven out of the market.

2.1.7.2.2.2. Micro-gap detectors

The maximum count rates in ‘classical’ metal-wire-based proportional counters are severely limited by the long ion-drift times in the chamber (which typically have a cathode to anode spacing of $\sim$10 mm). This issue has been successfully addressed by so-called micro-gap technology using parallel-plate avalanche chambers with a readout electrode separated from a resistive anode. The key feature is the resistive anode, which allows a very small amplification gap (1–2 mm cathode to anode spacing) at an increased average electric field intensity, while preventing discharges (Durst *et al.*, 2003; Khazins *et al.*, 2004). As a result, micro-gap detectors can achieve count rates several orders of magnitude higher than classical proportional counters at higher position sensitivity. Micro-gap detectors of the 1D and 2D detection type are available. Moderate count rates and very small noise levels result in very high dynamic ranges. Notably, in contrast to wire detectors, micro-gap detectors are not likely to be damaged by accidental exposure to a high-intensity direct beam, as a patterned anode plane is used rather than wires.

2.1.7.2.3. *Semiconductor detectors*

Semiconductor (or solid-state) detectors are solid-state ionization devices in which electron–hole pairs instead of electron–ion pairs are generated by incoming photons, and they are sensitive to the entire electromagnetic spectrum from visible light to X-rays. The energy required for production of an electron–hole pair is very low compared to the energy required for production of paired ions in a noble-gas-filled detector. As a consequence, a larger number of charge pairs with a smaller statistical variation are generated in semiconductor detectors, resulting in intrinsically higher energy-resolution capabilities. The efficiency of semiconductor detectors is very high due to the high absorption of the semiconductor materials, usually reaching 100%, but may decline at higher photon energies if the photons are not fully absorbed in the semiconductor *e.g.* because of insufficient thickness.

2.1.7.2.3.1. The Si(Li) detector

The Si(Li) detector sensor consists of a lithium-drifted silicon crystal which must be cooled to prevent lithium diffusion and to reduce dark noise. An important advantage of this detector is its excellent energy resolution of even better than 200 eV (4%) at 8 keV (Cu radiation), allowing very effective filtering of Kβ and fluorescence radiation and thus operation without a metal filter or a diffracted-beam monochromator. As Peltier cooling is sufficient, the Si(Li) detector type has found wide interest for applications benefitting from high energy resolution, unlike energy-dispersive detectors requiring operation under cryogenic conditions [*e.g.* Ge(Li)]. In particular, the Si(Li) detector significantly extends the application range of today's X-ray diffractometers by allowing energy-dispersive X-ray powder diffraction (EDXRD) as well as – to some extent – XRF (see Section 2.1.4.3).

An important disadvantage of Si(Li) detectors is their large dead time, which prohibits the handling of higher count rates. Moderate noise levels result in low-to-moderate dynamic ranges. An additional important disadvantage is the limitation to 0D detection.

2.1.7.2.3.2. Silicon micro-strip and silicon pixel detectors

Silicon micro-strip and silicon pixel detectors employ silicon sensors, which are one- or two-dimensional arrays of p–n diodes in the form of strips or pixels, respectively, individually connected to an array of readout channels. The development of this type of detector technology has obviously been driven by the idea of massive parallelism: each strip or pixel actually represents an individual detector. Accordingly, the silicon micro-strip and silicon pixel detectors are therefore of the 1D and 2D detection type, respectively.

Count rates recorded by silicon micro-strip and silicon pixel detectors are very high with very low noise levels, resulting in very large dynamic ranges. The energy resolution of most silicon micro-strip and silicon pixel detectors is of the order of 1600 eV (20%) at 8 keV (Cu radiation). Recently, a silicon micro-strip detector with an energy resolution of better than 380 eV at 8 keV has been introduced (Wiacek *et al.*, 2015). At such high energy resolution Cu $K\beta$ is filtered out to below the detection limit while Mn, Fe and Co fluorescence is filtered completely, allowing this detector to be operated without a metal filter or a diffracted-beam monochromator for most applications.

2.1.7.2.3.3. CCD and CMOS detectors

Charge-coupled device (CCD) detectors are represented by one- or two-dimensional arrays of square or rectangular pixels consisting of metal–oxide–semiconductor (MOS) capacitors, and can detect X-ray photons directly or indirectly. The pixel size may be less than 10 µm. The majority of detectors use indirect detection, where the incoming X-ray photons are first converted to visible-light photons by a phosphor layer. CCD detectors employ the 'bucket brigade' readout method, in which charge is shifted one pixel at a time by phasing the bias on the gate electrodes that overlay each pixel until it reaches the output, resulting in relatively large readout times ranging from a few tenths of a second up to several seconds per frame. Cooling (Peltier-type) is required to reduce the dark-current noise representing the dominant noise source for long exposures. In some detector designs fibre-optic demagnification is used to increase the effective active detector area, resulting in an imaging area larger than the active area of the CCD chip at the cost of detector sensitivity and spatial resolution.

CCD detectors are usually operated as integrating detectors. As such, they have no dead time and therefore provide excellent linearity over a moderate dynamic range, but cannot have energy resolution. CCD detectors are the detectors of choice for single-crystal diffraction and imaging, but are not favourable for applications with weak diffraction signals, such as powder X-ray diffraction, owing to the relatively large dark-current noise.

CCD detectors may also function as counting detectors by making the exposure time sufficiently short. In single-event mode the energy of each photon can be determined, providing an energy resolution down to about 300 eV at 8 keV (Cu radiation) and allowing a spectrum at each pixel of the CCD array to be built up by a series of consecutive measurements. Such a detector can record energy-dispersive X-ray powder diffraction (EDXRD) as well as – to some extent – XRF (see Section 2.1.4.3); however, owing to the readout time, count rates are extremely low with high statistical noise.

Unlike the bucket-brigade readout of a CCD, the complementary metal–oxide–semiconductor (CMOS) active-pixel sensor (He *et al.*, 2011) uses a completely different architecture in which each pixel incorporates a readout preamplifier and is then read out through a bus, as in random-access memory (He *et al.*, 2011). Cooling is not required. CMOS detectors are immune to the blooming effect (in which a light source overloads the sensitivity of the sensor, causing the signal to bleed vertically into surrounding pixels forming vertical streaks). Additionally, they offer the very significant advantage of shutter-free operation, that is dead-time-free continuous scans which improve the efficiency of data collection and also improve data quality by eliminating shutter-timing jitter.

As a consequence of these characteristics, CMOS-detector active-pixel sensors are now replacing CCD chips in a number of high-end applications (*e.g.* professional digital photography and high-definition television), and have reached a level of performance where they are also starting to displace CCD chips in the most demanding scientific applications.

2.1.7.3. *Position sensitivity and associated scanning modes*

2.1.7.3.1. *Pixel size, spatial resolution and angular resolution*

Detectors of the line (1D) or area (2D) type have the important property of position sensitivity, which is characterized by the two parameters pixel size and spatial resolution.

The pixel size of a position-sensitive detector (PSD) can be represented either by the intrinsic size of the smallest addressable sensitive component of a detector (*e.g.* the actual size of the diodes), which can be binned to form larger pixels, or is set by the readout electronics (*e.g.* for wire-based detectors such as proportional counters). The spatial resolution is determined by the actual pixel size, the point-spread function (PSF) and parallax. The PSF represents the spread of a signal produced by a single photon over several pixels by mapping the probability density that a photon is recorded by a pixel in the vicinity of the point that the photon hit. Parallax will lead to an additional smearing if the photon travels at an angle to the detector normal. The final angular resolution of a detector system is given by the spatial detector resolution and the specimen-to-detector distance.

Point (0D) detectors do not provide position sensitivity, regardless of the actual size of the active window (representing a single pixel). Simply speaking, in analogy to PSDs, the spatial resolution of a point detector is determined by the goniometer step size representing the actual pixel size, and the size of the detector slit representing the PSF. As for PSDs, the angular resolution is given by the spatial resolution and the specimen-to-detector distance.

Detectors can be operated in fixed as well as in (2θ) scanning mode, where the step size is usually determined by the detector pixel size. Subsampling, that is scanning using an angular step size smaller than the angular pixel resolution, may be used to improve observed line profile shapes if the pixel resolution is too small. As a rule of thumb some 5–8 data points need be collected over the FWHM of a diffraction peak to allow for an appropriate description of the line-profile shape.

2.1.7.3.2. *Dimensionality*

Area detectors can be operated as line or point detectors. Electronic binning of the pixels into columns will form a line detector, while binning all pixels together will form a point detector, each associated with improvements of count rates and thus dynamic ranges. Alternatively, 1D or 0D 'regions of interest' can be defined electronically and/or by mounting suitable diffracted-beam-path X-ray optics. Area detectors – when operated as such – require point-focus operation.

Line detectors can be used as point detectors, which may be formed in several ways. One way is to only use one or more central pixels by either electronically switching off outer pixels and/or by mounting suitable X-ray optics. Another way is to turn the detector by 90° and to bin all pixels, leading to an improved count rate and thus dynamic range.

Obviously, when turning a line detector by 90°, it will function as an area detector if it is scanned over an angular range; the trace of the scan will form a cylindrical surface that is a two-dimensional diffraction image (He, 2009). This scan mode may be associated with a few advantages, in addition to lower costs. For example, the elimination of parallax and the possibility of using diffracted-beam-path optics improve the angular resolution in the 2θ direction and allow air scattering to be reduced.

2.1.7.3.3. *Size and shape*

PSDs are available in different sizes with flat (1D, 2D), curved (1D), cylindrical (2D) and spherical (2D) detection surfaces. Curved, cylindrical and spherical detectors are designed for focusing or parallel-beam geometries with a fixed specimen-to-detector distance, and cannot normally be used with the Bragg–Brentano geometry because of its 2θ-dependent focusing circle (Section 2.1.4.1). Flat detectors can be used at different specimen-to-detector distances, with either high angular resolution at a large distance or large angular coverage at a short distance. For large flat detectors, parallax errors must be addressed. Small flat detectors are perfectly suited for operation in Bragg–Brentano geometry but the angular coverage should not exceed about 10° 2θ (Section 2.1.4.1) to minimize defocusing, particularly at small 2θ angles.

References

Bartels, W. J. (1983). *Characterization of thin layers on perfect crystals with a multipurpose high resolution X-ray diffractometer*. *J. Vac. Sci. Technol. B*, **1**, 338–345.

Bilderback, D. H. (2003). *Review of capillary X-ray optics from the 2nd International Capillary Optics Meeting*. *X-ray Spectrom.* **32**, 195–207.

Bohlin, H. (1920). *Eine neue Anordnung für röntgenkristallographische Untersuchungen von Kristallpulver*. *Ann. Phys.* **366**, 421–439.

Bonse, U. & Hart, M. (1965). *Tailless X-ray single crystal reflection curves obtained by multiple reflection*. *Appl. Phys. Lett.* **7**, 238–240.

Bowen, D. K. & Tanner, B. K. (1998). *High Resolution X-ray Diffractometry and Topography*. London: Taylor & Francis.

Brentano, J. C. M. (1924). *Focussing method of crystal powder analysis by X-rays*. *Proc. Phys. Soc.* **37**, 184–193.

Charpak, G., Bouclier, R., Bressani, T., Favier, J. & Zupančič, Č. (1968). *The use of multiwire proportional counters to select and localize charged particles*. *Nucl. Instrum. Methods*, **62**, 262–268.

Clearfield, A., Reibenspiess, J. & Bhuvanesh, N. (2008). *Principles and Applications of Powder Diffraction*. New York: Wiley.

Debye, P. & Scherrer, P. (1916). *Interference of X-rays, employing amorphous substances*. *Phys. Z.* **17**, 277–283.

Durst, R. D., Diawara, Y., Khazins, D. M., Medved, S., Becker, B. L. & Thorson, T. A. (2003). *Novel, photon counting X-ray detectors*. *Powder Diffr.* **18**, 103–105.

EN 1330–11 (2007). *Non-Destructive Testing*. Part 11. *Terms used in X-ray Diffraction from Polycrystalline and Amorphous Materials*. Brussels: European Committee for Standardization (CEN).

Fankuchen, I. (1937). *A condensing monochromator for X-rays*. *Nature (London)*, **139**, 193–194.

Fewster, P. F. (2003). *X-ray Scattering from Semiconductors*. London: Imperial College Press.

Friedmann, H. (1945). *Geiger counter spectrometer for industrial research*. *Electronics*, **18**, 132–137.

Göbel, H. E. (1980). *The use and accuracy of continuously scanning position-sensitive detector data in X-ray powder diffraction*. *Adv. X-ray Anal.* **24**, 123–138.

Guinier, A. (1937). *Arrangement for obtaining intense diffraction diagrams of crystalline powders with monochromatic radiation*. *C. R. Acad. Sci. Paris*, **204**, 1115–1116.

Hanawalt, J. D., Rinn, H. W. & Frevel, L. K. (1938). *Chemical analysis by X-ray diffraction*. *Ind. Eng. Chem. Anal.* **10**, 457–512.

Hart, M. (1971). *Bragg-reflection X-ray optics*. *Rep. Prog. Phys.* **34**, 435–490.

He, B. B. (2009). *Two-Dimensional X-ray Diffraction*. New York: Wiley.

He, T., Durst, R. D., Becker, B. L., Kaercher, J. & Wachter, G. (2011). *A large area X-ray imager with online linearization and noise suppression*. *Proc. SPIE*, **8142**, 81421Q.

Hemberg, O. E., Otendal, M. & Hertz, H. M. (2003). *Liquid-metal-jet anode electron-impact X-ray source*. *Appl. Phys. Lett.* **83**, 1483–1485.

Hull, A. W. (1917). *A new method of X-ray crystal analysis*. *Phys. Rev.* **10**, 661–696.

Hull, A. W. (1919). *A new method of chemical analysis*. *J. Am. Chem. Soc.* **41**, 1168–1175.

International Tables for Crystallography (2004). Volume C, 3rd ed., edited by E. Prince. Dordrecht: Kluwer Academic Publishers.

Jenkins, R. & Snyder, B. (1996). *Introduction to X-ray Powder Diffractometry*. New York: Wiley.

Johann, H. H. (1931). *Die Erzeugung lichtstarker Röntgenspektren mit Hilfe von Konkavkristallen*. *Z. Phys.* **69**, 185–206.

Johannson, T. (1933). *Über ein neuartiges, genau fokussierendes Röntgenspektrometer*. *Z. Phys.* **82**, 507–528.

Khazins, D. M., Becker, B. L., Diawara, Y., Durst, R. D., He, B. B., Medved, S. A., Sedov, V. & Thorson, T. A. (2004). *A parallel-plate resistive-anode gaseous detector for X-ray imaging*. *IEEE Trans. Nucl. Sci.* **51**, 943–947.

Kirkpatrick, P. & Baez, A. V. (1948). *Formation of optical images by X-rays*. *J. Opt. Soc. Am.* **38**, 766–774.

Klug, H. P. & Alexander, L. E. (1974). *X-ray Diffraction Procedures for Polycrystalline and Amorphous Materials*, 2nd ed. New York: Wiley.

Kumakhov, M. A. & Komarov, F. F. (1990). *Multiple reflection from surface X-ray optics*. *Phys. Rep.* **191**, 289–350.

Le Galley, D. P. (1935). *A type of Geiger–Müller counter suitable for the measurement of diffracted X-rays*. *Rev. Sci. Instrum.* **6**, 279–283.

Lindemann, R. & Trost, A. (1940). *Das Interferenz-Zählrohr als Hilfsmittel der Feinstrukturforschung mit Röntgenstrahlen*. *Z. Phys.* **115**, 456–468.

Montel, M. (1957). *X-ray microscopy with catamegonic roof-shaped objective*. In *X-ray Microscopy and Microradiography*, pp. 177–185. New York: Academic Press.

Paganin, D. M. (2006). *Coherent X-ray Optics*. Oxford University Press.

Parrish, W. (1949). *X-ray powder diffraction analysis: film and Geiger counter techniques*. *Science*, **110**, 368–371.

Pecharsky, V. K. & Zavalij, P. Y. (2009). *Fundamentals of Powder Diffraction and Structural Characterisation of Materials*, 2nd ed. New York: Springer.

Peiser, M. A., Rooksby, H. P. & Wilson, A. J. C. (1955). *X-ray Diffraction by Polycrystalline Materials*. London: Institute of Physics.

Sauli, F. (1977). *Principle of operation of multi-wire proportional and drift chambers*. CERN 77–09, May 1977.

Schuster, M. & Göbel, H. (1995). *Parallel-beam coupling into channel-cut monochromators using curved graded multilayers*. *J. Phys. D Appl. Phys.* **28**, A270–A275.

Schuster, M. & Göbel, H. (1996). *Application of graded multilayer optics in X-ray diffraction*. *Adv. X-ray Anal.* **39**, 57–72.

Seemann, H. (1919). *Eine fokussierende röntgenspektroskopische Anordnung für Kristallpulver*. *Ann. Phys.* **364**, 455–464.

VDI/VDE Guideline 5575 Part 3 (2011). *X-ray Optical Systems: Capillary X-ray Lenses*. Berlin: Beuth.

VDI/VDE Guideline 5575 Part 4 (2011). *X-ray Optical Systems: X-ray Mirrors. Total Reflection Mirrors and Multilayer Mirrors*. Berlin: Beuth.

Wiacek, P., Dabrowski, W., Fink, J., Fiutowski, T., Krane, H.-G., Loyer, F., Schwamberger, A., Świentek, K. & Venanzi, C. (2015). *Position sensitive and energy dispersive X-ray detector based on silicon strip detector technology*. *J. Instrumen.* **10**, P04002.

International Tables for Crystallography (2019). Vol. H, Chapter 2.2, pp. 51–65.

2.2. Synchrotron radiation and powder diffraction

A. Fitch

2.2.1. Introduction

X-rays produced at a synchrotron source are exploited in a wide range of applications in crystallography and structural science, and this includes studies by powder diffraction. Many synchrotron-radiation facilities have one or more dedicated powder-diffraction beamlines or end stations in regular user service. The high intensity, collimation and wavelength tunability of the radiation allow instruments to be designed whose performance and flexibility surpass what is possible with conventional laboratory apparatus. The majority of instruments operate with monochromatic radiation and an angle-dispersive diffractometer, but the polychromatic nature of synchrotron radiation means that an energy-dispersive setup is also possible. The general properties of synchrotron radiation include:

(*a*) High brightness, *i.e.* a highly collimated, intense X-ray beam and small source size.

(*b*) High flux of photons delivered to the sample.

(*c*) A range of wavelengths is available, possibly extending from the soft to the hard X-ray regimes, depending on the facility.

(*d*) Polarized source: synchrotron radiation is linearly polarized with the electric vector lying in the plane of the synchrotron orbit, but becomes progressively less polarized out of the plane.

(*e*) Pulsed source: the distribution of the bunches of electrons circulating in the storage ring allows the time structure to be exploited for specialized experiments.

Further information about the nature of synchrotron radiation can be found in texts by, for example, Margaritondo (1988), Als-Nielsen & McMorrow (2001) and Kim (2001).

Synchrotrons are usually user facilities, where scientists from external laboratories visit to perform experiments that have been approved by a peer-review or other procedure, and are supported by the scientific and technical staff for the beamlines. Most facilities have regular rounds in which users submit proposals for beam time, with special arrangements for access to carry out proprietary research. Arrangements can also usually be made for urgent access to the facility (when justified), and some beamlines run a routine mail-in service, allowing samples to be measured under defined conditions without the user needing to attend.

For any powder X-ray diffraction experiment, the wavelength of the radiation to be used is of high importance. The wavelength, λ, is a measure of the photon energy, ε, and the terms 'photon energy' and 'wavelength' tend to be used interchangeably at synchrotron beamlines. They can readily be converted by

$$\varepsilon = h\nu = hc/\lambda,$$

where h is the Planck constant, ν is the frequency of the radiation and c is the speed of light. If expressed in convenient units with λ in Å and ε in keV then

$$\varepsilon\ [\text{keV}] = hc/e\lambda \times 10^7\ [\text{Å}] \simeq 12.3984/\lambda\ [\text{Å}] \simeq 12.4/\lambda\ [\text{Å}],$$

where e is the elementary charge.

2.2.2. Production of synchrotron radiation

Synchrotron radiation is emitted by charged particles travelling at relativistic speeds when they are accelerated to move in a curved trajectory. In a modern synchrotron facility dedicated to the production of X-ray beams for scientific experiments, electrons are circulated in a closed horizontal orbit in a storage ring at an energy of several GeV, steered by magnetic fields from bending magnets. The overall circumference of the orbit can be several hundred metres depending on the design and specifications of an individual ring. The synchrotron ring is built up of cells (Fig. 2.2.1) comprising a straight section and a bending magnet by which the electrons are guided into the following straight section. Beamlines emerge tangentially from the bending magnets where synchrotron radiation is emitted by the electrons as they curve from one straight section into the next. Beamlines are also constructed on the straight sections where insertion devices, arrays of magnets providing an alternating magnetic field, are placed to cause the path of the electrons to oscillate and so also emit synchrotron radiation. By choosing the period of the magnetic array and by varying the strength of the magnetic field, the wavelength distribution and divergence of the X-rays emitted from an insertion device can be controlled. A straight section may accommodate more than one insertion device in series, allowing greater intensity or flexibility in the emitted radiation for the associated beamline. In the storage ring, the energy that the electrons lose by emitting synchrotron radiation is replaced by coupling the electrons to radio-frequency radiation supplied from klystrons or solid-state devices. Thus the synchrotron facility converts electrical energy, *via* radio waves and relativistic electrons, into powerful beams of electromagnetic radiation.

One key parameter of a storage ring is the energy of the circulating electrons. The energy of an electron moving with

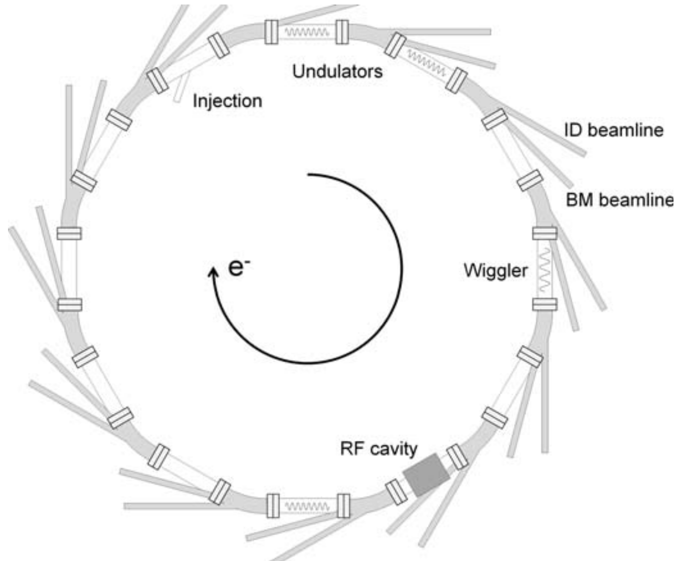

Figure 2.2.1
Schematic representation of a synchrotron storage ring with beamlines radiating tangentially from the bending magnets and in line with the straight sections. ID = insertion device, BM = bending magnet; RF = radio-frequency.

Copyright © 2019 International Union of Crystallography

speed v is

$$E_e = \frac{m_e c^2}{(1 - v^2/c^2)^{1/2}} = \gamma m_e c^2,$$

where m_e is the rest mass of the electron, 9.10938356 (11) $\times$ 10^{-31} kg. The term $1/(1 - v^2/c^2)^{1/2}$ is referred to as γ and is the factor by which the mass of the electron increases from its rest mass because of its relativistic speed. Expressed in eV (the conversion factor from kg to eV is c^2/e), the electron rest mass is 5.109989461 (31) $\times$ 10^5 eV, so that

$$\gamma \simeq 1957 E_e \text{ [GeV]}$$

when E_e is given in the customary units of GeV. Thus for a 3-GeV machine, a common energy for a synchrotron-radiation source, γ has the value of 5871. The mass of an electron with energy 3 GeV is therefore 3.22 atomic mass units, so around 7% more massive than a stationary atom of ^{3}H or ^{3}He.

Electrons do not circulate individually in the storage ring but in a series of bunches that are in phase with the accelerating radio frequency. Radiation is therefore emitted in pulses as each bunch passes through a bending magnet or insertion device. Thus the number and distribution of the electron bunches around the orbit determine the time structure of the emitted radiation. For most powder-diffraction applications using synchrotron radiation, the pulsed nature of the source can be neglected and the radiation can be regarded as continuous, although attention should also be paid to the performance of detectors that are more susceptible to pulse pile-up problems when the radiation arrives at very high average rates or in concentrated bursts (Cousins, 1994; Laundy & Collins, 2003; Honkimäki & Suortti, 2007), which can happen with certain bunch-filling modes. Certain specialized experiments requiring very fast time resolution can exploit the time structure of the source. In such experiments the longitudinal dimension of the bunches controls the pulse duration, which is usually a few tens of picoseconds.

In discussing the performance of different beamlines, the spectral brightness (Mills *et al.*, 2005) is often quoted for the source and is defined as

spectral brightness =
photons per second per 0.1% bandwidth per mrad^2 per mm^2,

where '0.1% bandwidth' represents $\delta\lambda/\lambda = 0.001$, the mrad^2 term expresses the solid-angle of the emission of the X-rays from the source and the mm^2 term relates to the cross-sectional area of the source. Thus a source of high spectral brightness emits many photons per second of the specified energy, into a narrow solid angle, with a small source size. The source size, which may well differ in the horizontal and vertical directions, is an important consideration as source size and beam divergence ultimately limit the performance of the beamline optical system in terms of collimation, energy resolution and focal spot size.

2.2.2.1. *Bending magnets*

A bending magnet provides a vertical magnetic field to deflect the electrons laterally in the horizontal plane from a straight-line trajectory, and thereby causes the emission of synchrotron radiation (see Fig. 2.2.2). The lateral Lorentz force, F, acting on an electron travelling at velocity v in a magnetic field B is mutually perpendicular to both the magnetic field and the direction of travel of the electron, and is given by

$$F = evB.$$

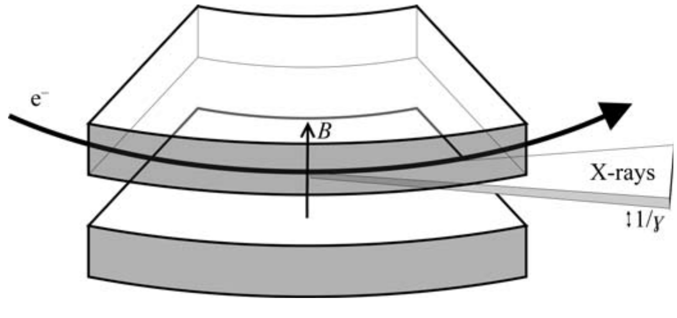

Figure 2.2.2
Emission of a fan of radiation by the electron beam as it curves in a bending magnet from one straight section of the ring to the next.

In a bending magnet the magnetic field is applied over an extended distance leading to a curved path of radius ρ. The centripetal acceleration is $F/\gamma m_e$, which for circular motion is equal to v^2/ρ. Since $v \simeq c$,

$$\rho = \frac{\gamma m_e c}{eB},$$

so the radius of curvature decreases with magnetic field strength and increases with machine energy *via* increased γ. With the electron energy expressed in GeV, this can be approximated to $\rho \simeq 3.34 E_e \text{ [GeV]}/B$ (where $10^9/c \simeq 3.34$).

Synchrotron radiation is emitted in a forward cone tangential to the direction of the electrons' motion (Fig. 2.2.3) with a nominal Gaussian distribution and an opening angle of the order of $1/\gamma$. Thus the radiation is highly collimated in the vertical plane. In the horizontal plane, synchrotron radiation is emitted in a broad fan, tangential to the curved trajectory of the electrons as they sweep through the bending magnet. Only a fraction of the radiation emitted by a bending magnet enters the associated beamline *via* a cooled aperture defining a horizontal acceptance angle of a few mrad. The radiation is polarized in the plane of the synchrotron orbit. Sometimes, more than one beamline can be built on a bending magnet with a suitable angular separation between them.

Photons are emitted over a broad spectral range. The critical photon energy, ε_c, divides the emitted power into equal halves and is given by

$$\varepsilon_c = \frac{3\hbar c \gamma^3}{2\rho} = \frac{3\hbar \gamma^2 eB}{2m_e} = \frac{3\hbar e E_e^2 B}{2m_e^3 c^4} = 4.151 E_e^2 B,$$

or, with photon and electron energies in keV and GeV, respectively,

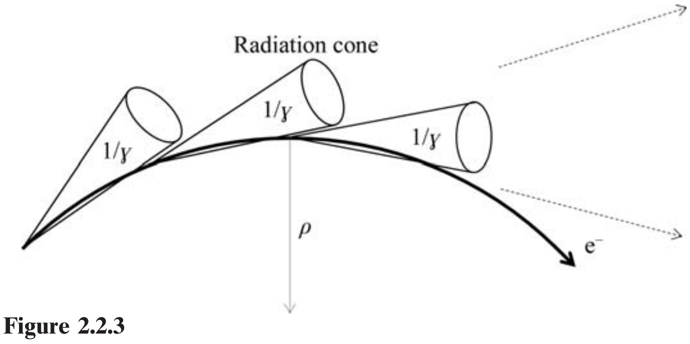

Figure 2.2.3
Synchrotron radiation is emitted in a cone of opening angle of the order of $1/\gamma$ tangential to the electrons as they follow a curved trajectory through the bending magnet.

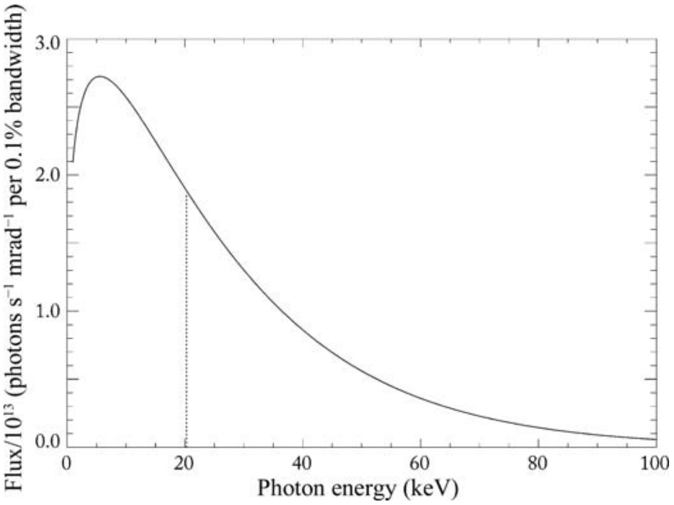

Figure 2.2.4
Spectrum of a bending magnet (B = 0.85 T) at the ESRF with an electron energy of 6 GeV (γ = 11 742), shown as flux per horizontal mrad for a 0.1% energy bandwidth at a storage-ring current of 200 mA. The critical energy of 20.3 keV divides the emitted power into equal halves.

$$\varepsilon\ [\mathrm{keV}] = 0.665 E_e^2\ [\mathrm{GeV}] B.$$

The higher the critical energy, the greater the number of photons produced with short X-ray wavelengths. As an example, consider a bending magnet at the ESRF in Grenoble, France, which has a 6-GeV storage ring and bending magnets with a field of 0.85 T. The bending radius is 23.5 m and the critical photon energy is 20.3 keV (equivalent to a wavelength of 0.61 Å). The spectrum of such a device is shown in Fig. 2.2.4.

The vertical collimation of the radiation varies with photon energy in a nonlinear manner (Kim, 2001). Nevertheless, the divergence decreases with increased photon energy, so beams with the shortest wavelengths are the most vertically collimated. Various approximations can be written to describe the variation, such as for a single electron (Margaritondo, 1988),

$$\sigma_v(\varepsilon) \simeq \frac{0.565}{\gamma} \left(\frac{\varepsilon_c}{\varepsilon}\right)^{0.425},$$

where $\sigma_v(\varepsilon)$ is the standard deviation of the vertical-divergence distribution of photons of energy ε. For a population of electrons circulating in a storage ring, the distribution of the trajectories with respect to the plane of the orbit (of the order µrad) must also be considered, as these add to the vertical emission distribution. An approximation such as

$$\Psi_v(\varepsilon) = 2\sigma_v(\varepsilon) \simeq \frac{1.2}{\gamma} \left(\frac{\varepsilon_c}{\varepsilon}\right)^{1/2}$$

will often be adequate to estimate the vertical divergence Ψ_v in the vicinity of ε_c. Thus for the bending magnet illustrated in Fig. 2.2.4, photons at the critical energy of 20.3 keV will have a vertical divergence of ~100 µrad. A beamline would probably accept less than this, *e.g.* a 1.5-mm-high slit at 25 m from the source defining the beam onto a monochromator crystal defines an angle of ~60 µrad.

2.2.2.2. *Insertion devices*

Insertion devices can be classified into two main types, termed 'wigglers' and 'undulators', illustrated in Fig. 2.2.5. A wiggler has a relatively long magnetic period and the radiation from each oscillation is emitted like a series of powerful bending magnets, summing together to provide increased intensity. An undulator has a relatively short magnetic period and the radiation from sequential oscillations interferes coherently to give modified beam characteristics.

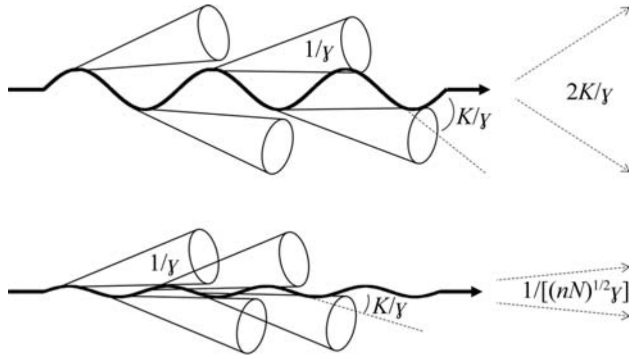

Figure 2.2.5
Schematic illustration of a wiggler (upper) and an undulator (lower).

For insertion devices the magnetic field acting on the electrons varies sinusoidally along the device,

$$B(z) = B_0 \sin(2\pi z/\lambda_u),$$

where B_0 is the peak magnetic field, z is the distance along the insertion-device axis and λ_u is the magnetic period. With a vertical field, the alternating magnetic field causes the electron path to oscillate in the horizontal plane. Note that the radiation is emitted mainly towards the outsides of the oscillations where the electrons change transverse direction, and where the magnetic field and beam-path curvature are highest. The maximum angular deflection of an electron from the axis of the insertion device is K/γ, where the deflection parameter K is given by

$$K = \frac{eB_0\lambda_u}{2\pi m_e c},$$

which simplifies to K = $0.0934 B_0 \lambda_u$ [mm] with λ_u expressed in mm. K is a crucial parameter that determines the behaviour of the insertion device.

2.2.2.2.1. *Wigglers*

If K is large (10 or above), the insertion device is a wiggler and the electrons oscillate with an amplitude significantly greater than the emitted radiation's natural opening angle $1/\gamma$. Every oscillation along the device produces a burst of synchrotron radiation and these add together incoherently so increasing the flux in proportion to the number of magnetic periods. The radiation emerges from the wiggler in a horizontal fan with a horizontal opening angle $\sim 2K/\gamma$. The intensity of a wiggler-based beamline can be very high because each oscillation produces synchrotron radiation, and this radiation is directed close to the axis of the device. Like a bending magnet, wigglers produce a continuous spectrum but with the critical energy shifted to harder energies because the magnetic field is (usually) greater. Thus for a wiggler at a 6-GeV source, with a magnetic field of 1.2 T and a magnetic period of 125 mm, K is 14, the maximum deflection of the electrons from the straight-line path is 1.2 mrad and the critical photon energy is 28.7 keV. Magnetic fields of several tesla can be exploited using superconducting magnets to obtain even higher critical photon energies.

2.2.2.2.2. *Undulators*

If the value of K is 2 or less, the insertion device is an undulator. The deflection of the electrons is comparable to the natural opening angle of the emitted radiation $1/\gamma$. Radiation emitted from sequential oscillations interferes coherently, and the beam

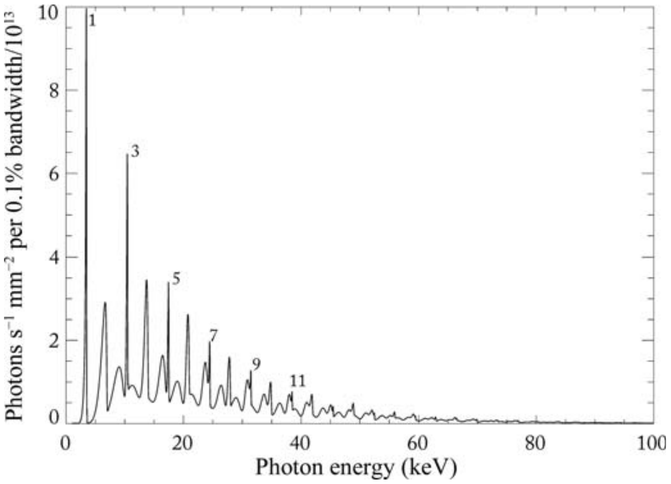

Figure 2.2.6
Photon flux *versus* energy through a 1-mm^2 aperture 30 m from the source, 0.1% bandwidth, for an ESRF u35 undulator (magnetic periodicity 35 mm, 1.6 m long, magnetic gap of 11 mm, peak magnetic field B_0 = 0.71 T, electron energy 6 GeV, K = 2.31, storage-ring current 200 mA). Odd-numbered harmonics are labelled, which are those usually employed for powder-diffraction experiments as they have maximum intensity on axis.

becomes highly collimated in the horizontal and vertical directions. Thus, the radiation from an undulator is concentrated into a central on-axis cone (fundamental and odd harmonics), surrounded by rings from higher-order even harmonics. The flux density arriving on a small sample from this central cone is therefore very high. With high on-axis intensity, it is therefore the undulators that provide the beams with the highest spectral brightness at any synchrotron-radiation source. The interference also modifies the spectrum of the device, which has a series of harmonics derived from a fundamental energy. At a horizontal angle θ to the axis of the insertion device, the wavelength of harmonic n is given by

$$\lambda_n = \frac{1 + (K^2/2) + \gamma^2\theta^2}{2n\gamma^2}\lambda_u,$$

which can be simplified on axis (θ = 0) to

$$\lambda_n \ [\text{Å}] = 1.3056\,\frac{1 + K^2/2}{nE_e^2 \ [\text{GeV}]}\lambda_u \ [\text{mm}]$$

or

$$\varepsilon_n \ [\text{keV}] = 9.50\,\frac{nE_e^2 \ [\text{GeV}]}{\lambda_u \ [\text{mm}](1 + K^2/2)}.$$

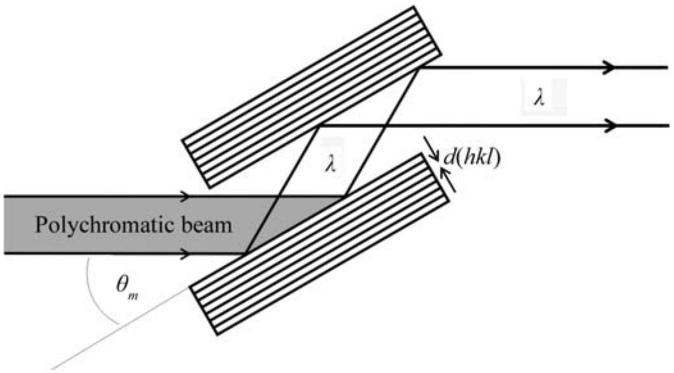

Figure 2.2.7
Double-crystal monochromator arrangement.

On axis, only odd-numbered harmonics are emitted and it is these that are usually employed in a powder-diffraction experiment. The horizontal and vertical divergence of the radiation emerging from an undulator is of the order of $1/[(nN)^{1/2}\gamma]$, where N is the number of magnetic periods making up the device. The spectrum of an undulator at a 6-GeV source with a 35-mm magnetic period is shown in Fig. 2.2.6. By carefully shimming the magnetic lattice so that it is highly regular, the higher-order harmonics persist, allowing the undulator to be a powerful source of high-energy X-rays. Any imperfections in the magnetic periodicity cause the higher-order harmonics to broaden and fade away, reducing the utility of the device at higher energies.

2.2.2.2.3. *Tuning*

For insertion devices the magnetic field can be modified by changing the vertical distance between the magnetic poles. By opening the gap, the magnetic field and K decrease following

$$B_0 \simeq B_r \exp(-\pi G/\lambda_u),$$

where B_r is proportional to the remanent magnetic field, which depends upon the nature of the magnets used in the insertion device, and G is the magnetic gap. Decreasing K for an undulator means that the energy of the fundamental harmonic increases; however, this is at the expense of the intensities of the higher harmonics. Thus the insertion device can be tuned to produce high intensity at the wavelength most suitable for a particular measurement. The smallest gap possible for a device depends on the design of the storage-ring vacuum vessel in which the electrons circulate. It is difficult to have a vessel smaller than about 10 mm high, and hence for an externally applied field a minimum magnetic gap of about 11 mm is to be expected. For smaller gaps, the magnets must be taken into the vacuum of the storage ring, a so-called ‘in-vacuum’ insertion device.

2.2.3. Optics

The intense polychromatic beam from the source needs to be conditioned before hitting the sample and diffracting. In the simplest experimental configuration, the white beam is used in an energy-dispersive experiment, and conditioning may involve no more than using slits to define the horizontal and vertical beam sizes and suppress background scattering. More usually, monochromatic radiation is employed, and the desired wavelength is chosen from the source by a monochromator. A monochromator consists of a perfect crystal, or a pair of crystals, set to select the chosen wavelength by Bragg diffraction. Additional optical elements can also be incorporated into the beamline for focusing, collimation, or for filtering out unwanted photons to reduce heat loads or remove higher-order wavelengths transmitted by the monochromator.

2.2.3.1. *Monochromator*

The monochromator is a crucial optical component in any angle-dispersive powder-diffraction beamline, and consists of one or a pair of perfect crystals (*e.g.* Beaumont & Hart, 1974), Fig. 2.2.7, set to a particular angle to the incident beam, θ_m, that transmits by diffraction wavelengths that satisfy the Bragg equation, $n\lambda = 2d(hkl)\sin\theta_m$, where $d(hkl)$ is the lattice spacing of the chosen reflection. Note that photons from higher-order reflections can also be transmitted, corresponding to wavelengths λ/n, depending on the structure factor of the nth-order reflection and its Darwin width, but these can be eliminated by use of a mirror (see Section 2.2.3.2), or by adjusting the electronic acceptance windows of the detector system, if possible. They can also be suppressed to some extent by slightly detuning the second crystal from the first, because the Darwin width of a higher-order reflection is narrower than that of a lower-order reflection, and is thus more seriously affected by the mismatch between Bragg angles.

For a given reflection, a crystal does not transmit a unique single wavelength but a narrow distribution. The width of the distribution, $\delta\lambda$, is determined by the effective divergence of the incident beam Ψ (which corresponds to a range of values for θ_m) and the Darwin width of the reflection, ω, at the chosen wavelength. The energy resolution of a monochromator crystal can be estimated *via*

$$\delta\varepsilon/\varepsilon = \delta\lambda/\lambda = \cot\theta_m(\Psi^2 + \omega^2)^{1/2}.$$

With a highly collimated beam incident on a crystal and with a narrow Darwin width, high energy resolution is achieved. The Darwin width of a reflection can be calculated from dynamical theory [Zachariasen (1945); Chapter 5.1 of *International Tables for Crystallography*, Volume B (Authier, 2006)] *via*

$$\omega = \frac{2r_e\lambda^2}{\pi V}|F(\mathbf{h})|\frac{K}{\sin 2\theta_m},$$

where r_e is the classical electron radius (~2.818 fm), V is the volume of the unit cell, $F(\mathbf{h})$ is the structure factor and K the polarization factor (1 for reflection in the vertical plane, $\cos 2\theta_m$ for the horizontal plane). Thus for Si(111), with $d(111)$ = 3.1356 Å and $F(\mathbf{h}) \simeq 59$, a Darwin width of about 8.3 µrad is obtained at 31 keV (λ = 0.4 Å). With an effective beam divergence of say 25 µrad (delivering a beam 1.1 mm high at 44 m from the source), an energy resolution of 4.8×10^{-4} is obtained. Even better energy resolution can be obtained by increasing the collimation of the beam before the monochromator, *e.g.* with a curved mirror.

Energy resolution is an important quantity to control. Its value needs to be known when modelling powder-diffraction peak shapes *via* a fundamental-parameters approach, and it affects the angular resolution of the powder-diffraction pattern, broadening the peaks as 2θ increases, as can be seen by differentiating the Bragg equation to yield

$$\frac{\delta\lambda}{\lambda} = \cot\theta\,\delta\theta \quad \text{or} \quad \delta\theta = \frac{\delta\lambda}{\lambda}\tan\theta. \qquad (2.2.1)$$

Thus powder-diffraction peaks broaden towards higher 2θ angles because of this effect.

Silicon is a common choice for a monochromator; it forms large, perfect single crystals, with dimensions of cm if required, has appropriate mechanical, diffraction and thermal properties, and can resist prolonged exposure to an intense radiation source. A monochromator crystal absorbs a large fraction of the energy incident upon it, and hence must be cooled. Even when cooled, the high power density (tens or even more than a hundred W mm^{-2} at normal incidence) can cause local heating of the surface, which leads to distortion of the lattice planes *via* thermal expansion. This degrades the performance, as a heat bump increases the range of θ_m values, broadening the energy band transmitted by the crystal. With a double-crystal arrangement, this bump cannot be matched by the second crystal, which has a much lower heat load so is flat, with the result that photons from the first crystal are not transmitted by the second, thus losing intensity from the monochromatic beam. By cooling to cryogenic temperatures, the thermal expansion of Si can be reduced to a very small value, going through zero at around 120 K (Bilderback, 1986; Glazov & Pashinkin, 2001) and thereby alleviating the heat-bump problem. Thus cryogenically cooled monochromators can be found at high-performance synchrotron beamlines. Other crystals employed as monochromators are germanium and diamond, the latter in transmission because of the small size of available diamond crystals.

Although a monochromator assembly can employ only one crystal, for example deflecting the beam horizontally into a side branch of a beamline, a double-crystal arrangement (Fig. 2.2.7) is more usually used to conserve the direction of the beam from the storage ring. This can exploit either a channel-cut crystal or two crystals, with a number of adjustments in the position and orientation of the second crystal to allow it to be aligned optimally to transmit the wavelength envelope defined by the first crystal. In some cases, the second crystal can be bent sagittally to focus X-rays horizontally onto the sample. Although this increases the divergence of the beam arriving at the sample and so affects the 2θ resolution of the powder pattern, it can lead to a significant increase in intensity, and is useful to capture more radiation from a horizontally divergent source such as a bending magnet or wiggler.

2.2.3.2. *Mirror*

Some powder-diffraction beamlines are equipped with X-ray mirrors, which can be used to focus or to improve the collimation of the already highly collimated beam, and to act as a high-energy filter for photons with energies above a certain value, *e.g.* to remove higher-order wavelengths transmitted by the monochromator. Usually reflecting in the vertical plane, a mirror consists of a highly polished substrate (*e.g.* Si) with a thin metal coating, such as Pt or Rh, set at grazing incidence. The nature of the coating and the graze angle determine the energy cutoff, where the reflectivity falls to very low values following

$$\theta_c\ [\text{mrad}] = 2.324(\rho Z/A)^{1/2}\lambda\ [\text{Å}],$$

where θ_c is the critical graze angle for X-rays of wavelength λ, ρ is the density, Z is the atomic number and A is the atomic weight of the metal coating. As an example, an Rh-coated mirror set at a grazing incidence of 2 mrad will only reflect X-rays with a wavelength longer than around 0.37 Å. A Pt-coated mirror set at the same graze angle will transmit shorter wavelengths, down to 0.30 Å. The wavelength cutoff for a particular mirror can be adjusted by changing the angle of grazing incidence. However, this then entails realignment of the beamline downstream of the mirror. To avoid this, some beamlines have mirrors with stripes of different metals, allowing adjustment of the cutoff by simply translating the mirror sideways to change the coating while keeping the graze angle constant.

Curving a mirror concavely as shown in Fig. 2.2.8 allows focusing or collimation, following

$$R = \frac{2L_1L_2}{(L_1 + L_2)\sin\alpha},$$

where R is the radius of curvature, L_1 is the source-to-mirror distance, L_2 is the mirror-to-focus distance and α is the angle of grazing incidence. For collimation ($L_2 = \infty$), this reduces to $R = 2L_1/\sin\alpha$. Thus a mirror 25 m from the source set at a graze angle of 2 mrad must be curved to a radius of 25 km to collimate the beam. As noted above, silicon is frequently chosen as a substrate for a mirror as it is sufficiently stiff to help minimize the intrinsic

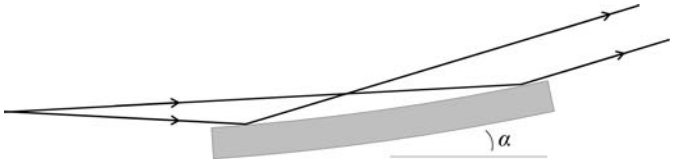

Figure 2.2.8
Curved mirror set to collimate the beam.

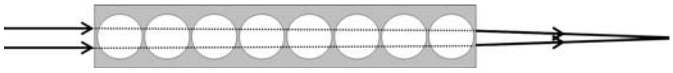

Figure 2.2.9
Schematic diagram of a set of refractive lenses.

curvature of the mirror caused by its own weight. Even then, very careful mounting and precise mechanics are required to achieve this level of accuracy. If placed in the polychromatic beam directly from the source, cooling of the mirror will be necessary.

Other mirror arrangements can be employed, such as a horizontal and vertical pair of focusing mirrors in a Kirkpatrick–Baez (Kirkpatrick & Baez, 1948) arrangement. Such a device might be used to produce a small focal spot for powder-diffraction measurements from a sample in a diamond anvil cell. Multilayer mirrors can also be found in service on certain beamlines.

2.2.3.3. *Compound refractive lens*

The refractive index n of a material for X-rays is given (Gullikson, 2001; Spiller, 2000) by

$$n = 1 - \delta - i\beta = 1 - \frac{r_e}{2\pi}\lambda^2 \sum_n N_n f_n,$$

where $f_n = f_1 + if_2$ is the complex scattering factor for forward scattering for atom n and N_n is the number of atoms of type n per unit volume. δ and β are known as the refractive index decrement and the absorption index, respectively, and vary with photon energy depending on the proximity of an absorption edge. The real part of the refractive index is therefore slightly less than 1, with δ typically of the order 10^{-6}–10^{-9} depending on the energy. Thus a hole drilled in a piece of metal can act like a conventional convex lens, as the hole has a higher refractive index than the surrounding metal. With such a small difference in n between hole and metal, the focusing power is very slight; however, a series of holes (Fig. 2.2.9) can be used to focus the X-ray beam over a reasonable distance (Snigirev *et al.*, 1997, 1998). For a series of cylindrical lenses, the focal length, f, is given by $f = r/2N\delta$, where r is the radius of the hole and N is the number of holes.

Note that further away from the axis of the device the X-ray beam must pass through increasing amounts of material which absorb the radiation. Hence, only relatively small holes and apertures are possible (a maximum of a few mm in diameter) and weakly absorbing metals such as Be and Al are preferred. With hard-energy photons, Ni lenses are possible, and indeed the construction of such a device is a compromise between refractive power, absorption, aperture and the desired focal length. Such devices can be placed in the monochromatic beam or in a polychromatic beam with cooling.

Many variants of the basic scheme exist, with lenses pressed from foil with a parabolic form to eliminate spherical aberrations, with axial symmetry to focus in both the horizontal and vertical simultaneously (Lengeler *et al.*, 1999), etched *via* lithography from plastic or other material, or with a more complex profile to minimize the amount of redundant material attenuating the transmitted beam by absorption and so allowing a larger aperture. A 'transfocator' can be constructed whereby series of lenses can be accurately inserted or removed from the beam path, thus allowing the focusing power to be adjusted depending on the desired focal distance and the wavelength of the experiment (Vaughan *et al.*, 2011).

2.2.4. Diffractometers

Most powder-diffraction beamlines are angle dispersive, operating with monochromatic radiation. When scanning a detector arm or employing a curved position-sensitive detector (PSD), detection is normally in the vertical plane because the polarization of the radiation in the plane of the synchrotron orbit means there is very little effect on the intensities due to polarization. By contrast, if diffracting in the horizontal plane, the projection of the electric vector onto the direction of the diffracted beam means that the intensity is reduced by a factor of $\cos^2 2\theta$, going to zero at $2\theta = 90^\circ$, and so horizontal detection is less useful unless working at hard energies when 2θ angles are correspondingly small. In addition, for the highest angular resolution, the natural beam divergence in the vertical plane is usually lower than in the horizontal plane, particularly if the instrument has a bending magnet or wiggler as its source.

In general, diffractometers are heavy-duty pieces of equipment and are designed to have excellent angular accuracy while working with substantial loads. A high degree of mechanical accuracy is required to match the high optical accuracy inherent in the techniques employed. The calibration of the incident wavelength and any 2θ zero-point error is best done by measuring the diffraction pattern from a sample such as NIST standard Si (640 series), each of which has a certified lattice parameter (see Chapter 3.1). It is also good practice to measure the diffraction pattern of a standard sample regularly and whenever the instrument is realigned or the wavelength changed, to be sure that everything is working as expected.

Monochromatic instruments can have an analyser crystal or long parallel-foil collimators in the diffracted beam (a so-called parallel-beam arrangement), or can scan a receiving slit, or possess a one- or two-dimensional PSD, similar to Debye–Scherrer or Laue front-reflection geometry. Instruments equipped with a PSD can collect data much faster than those with a scanning diffractometer, so are exploited especially for time-resolved measurements. They may also have advantages for rapid data collection if the sample is sensitive to radiation, or be helpful if the sample is prone to granularity or texture to assess the extent of the problem.

Instruments can also be equipped with a sample changer, allowing measurements on a series of specimens, perhaps prepared by systematically changing the conditions of synthesis or the composition in a combinatorial approach. The use of beam time can be optimized with minimal downtime due to interventions around the instrument, and with the possibility to control the data acquisition remotely if desired.

2.2.4.1. *Parallel-beam instruments*

Cox *et al.* (1983, 1986), Hastings *et al.* (1984) and Thompson *et al.* (1987) described the basic ideas behind these instruments *via* their pioneering work at CHESS (Cornell, USA) and NSLS (Brookhaven, USA). The highly collimated monochromatic incident beam is diffracted by the sample and passes *via* a perfect analyser crystal [such as Si or Ge(111)] to the detector. The analyser crystal defines a very narrow angular acceptance for the diffracted radiation, determined by its Darwin width. The combination of the collimation of the incident radiation, its highly monochromatic nature and the stringent angular acceptance defines the instrument's excellent angular resolution. The detector arm supporting the analyser is scanned through the desired range of 2θ angles either in a step-scan mode or continuously, reading out at very short intervals the electronic modules that accumulate the detector counts.

To be transmitted by the analyser crystal, a photon must be incident on the crystal at the correct angle θ_a that satisfies the Bragg condition. The analyser crystal defines therefore a true direction (2θ angle) for the diffracted beam irrespective of where in the sample it originates from. This removes a number of aberrations that affect diffractometers with a scanning slit or PSD where the 2θ angle is inferred from the position of the slit or detecting pixel. Thus, with a capillary specimen, peak widths are independent of the capillary diameter, so a fat capillary of non-absorbing sample can be used to optimize diffracted intensity, and any modest misalignment of the sample from the diffractometer axis, or specimen transparency or surface roughness for flat-plate samples, does not lead to shifts in the peak positions. Modest movement of the sample with temperature changes in a furnace *etc*. does not cause shifts in peak positions. These instruments are therefore highly accurate, and are ideal for obtaining peak positions for indexing a diffraction pattern of a material of unknown unit cell (the first step in the solution of a structure from powder data), or following the evolution of lattice parameter with temperature *etc*. For flat samples, the $\theta/2\theta$ parafocusing condition does not need to be satisfied to have high resolution. The peak width does not therefore depend on sample orientation, which is useful for measurements of residual strain by the $\sin^2\psi$ technique or for studying surfaces and surface layers by grazing-incidence diffraction. Interchange between capillary and flat-plate samples can easily be done as required without major realignment of the instrument. The stringent acceptance conditions also help to suppress parasitic scattering originating from sample-environment windows *etc*. and inelastic scattering such as fluorescence and Compton scattering.

On the other hand, at any 2θ angle only a tiny fraction of the diffracted photons can be transmitted by an analyser crystal, so this is a technique that consumes a lot of photons, and the high incident flux is essential to keep scan times to reasonable values. To overcome this, at least to some extent, Hodeau *et al.* (1998) devised a system of multiple analyser crystals, with nine channels mounted in parallel, each separated from the next by 2° (Fig. 2.2.10). In effect, as the detector arm is scanned, nine high-resolution powder-diffraction patterns are measured in parallel, each offset from the next by 2°. If the data from the channels are to be combined, which is the usual procedure, the detectors must be calibrated with respect to each other, in terms of counting efficiency and exact angular offset, by comparing regions of the diffraction pattern scanned by several detectors (Wright *et al.*, 2003). A multianalyser system speeds up data collection significantly and can be found in various modified forms at a number of powder-diffraction beamlines (*e.g.* Lee, Shu *et al.*, 2008).

The multianalyser approach is best suited to capillary samples because of the axial symmetry of the arrangement. With flat plates in reflection, only one detector can be in the $\theta/2\theta$ condition where the effect of specimen absorption (for a sufficiently thick sample) is isotropic. Corrections must therefore be made to the intensities from the other channels (Lipson, 1967; Koopmans & Rieck, 1968). For a capillary, choosing the wavelength and the diameter allows absorption to be kept to an acceptable value. Maximum diffracted intensity is expected at $\mu r = 1$ (where μ is the linear absorption coefficient and r the radius of the capillary), and below this value simple absorption corrections can be applied (Hewat, 1979; Sabine *et al.*, 1998). A value of μr greater than 1.5 begins to degrade the quality of the pattern significantly. If a sample with high absorption is unavoidable, such as when working close to an absorption edge of an element, *e.g.* the K edge of Mn at 6.539 keV (1.896 Å), then it can be preferable to stick a thin layer of sample on the outside of a 1-mm-diameter capillary. The shell-like nature of the sample has no effect on the peak shape or resolution because of the use of analyser crystals.

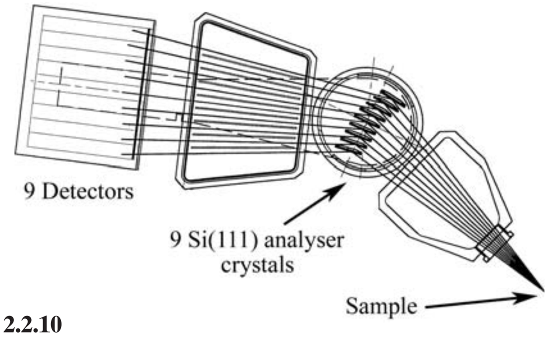

Figure 2.2.10
Multianalyser stage, nine channels separated by 2°, devised by Hodeau *et al.* (1998), originally installed on the BM16 bending-magnet beamline at the ESRF with Ge(111) analyser crystals. With an undulator source, the greatly increased flux allows use of Si(111), which has a narrower Darwin width (by a factor of ~2.4) and thus improved 2θ resolution, but with a lower fraction of the diffracted radiation accepted.

Capillaries also have the advantage that preferred orientation can be significantly less as compared to a flat sample, where there is a tendency for crystallites to align in the surface layers, especially if compressed to hold the powder in place. Spinning or otherwise moving the sample is necessary, whether capillary or flat plate, to increase the number of crystallites appropriately oriented to fulfil the Bragg condition and avoid a spotty diffraction pattern, the likelihood of which is exacerbated by the highly collimated nature of the incident radiation.

2.2.4.1.1. *Angular resolution*

Various authors (*e.g.* Sabine, 1987*a*,*b*; Wroblewski, 1991; Masson *et al.*, 2003; Gozzo *et al.*, 2006) have discussed the resolution of a synchrotron-based diffractometer equipped with a double-crystal monochromator and an analyser crystal. The most usual setting of the diffracting crystals, ignoring any mirrors or other optical devices, is non-dispersive, alternatively described as parallel or (1, −1, 1, −1).

The approach developed by Sabine (1987*a*,*b*) involves modelling the vertical divergence of the source and the angular acceptance of the monochromator and analyser crystals as Gaussian distributions with the same full width at half-maximum (FWHM) as the real distributions, and considering a powder as a crystal with an infinite mosaic spread. The rocking curve of the analyser crystal (equivalent to rocking 2θ) is given by

$$I(\beta) = \int\int \mathrm{d}\alpha\,\mathrm{d}\delta\,\exp\left\{-\left[\left(\frac{\alpha}{\alpha'_m}\right)^2 + 2\left(\frac{\delta-\alpha}{\Delta'_m}\right)^2 + \left(\frac{b\delta+\alpha-\beta}{\Delta'_a}\right)^2\right]\right\},$$

where

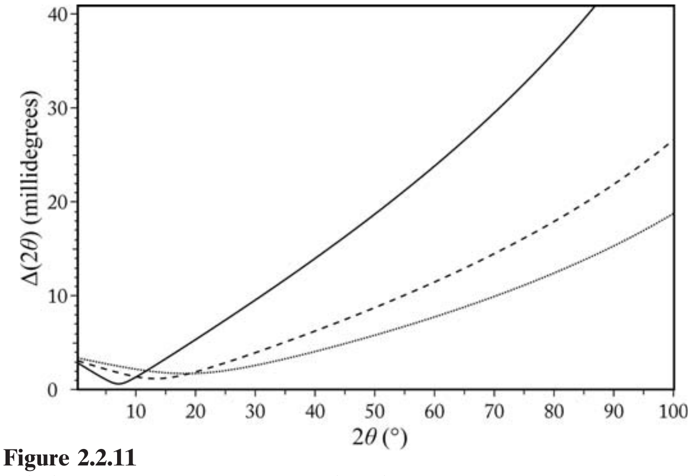

Figure 2.2.11
$\Delta(2\theta)$ calculated from equation (2.2.2) for a beamline with a double-crystal Si(111) monochromator, an Si(111) analyser ($\Delta_m = \Delta_a$ and $\theta_m = \theta_a$) and an FWHM vertical divergence of 25 µrad at $\lambda = 0.4$ Å (solid line: $\Delta_m \simeq 8.3$ µrad, $\theta_m = 3.6571°$), $\lambda = 0.8$ Å (dashed line: $\Delta_m \simeq 16.6$ µrad, $\theta_m = 7.3292°$) and $\lambda = 1.2$ Å (dotted line: $\Delta_m \simeq 25.2$ µrad, $\theta_m = 11.0319°$).

$$b = \tan\theta_a / \tan\theta_m - 2\tan\theta / \tan\theta_m.$$

Here α represents the vertical divergence from the source, δ is the difference between the Bragg angles of a central ray reflected from the monochromator at the angle θ_m and of another ray at angle θ'_m such that $\delta = \theta'_m - \theta_m$, and θ_a is the Bragg angle of the analyser crystal. The terms α'_m, Δ'_m and Δ'_a are related to the FWHM of the Gaussians representing the vertical divergence distribution or the Darwin widths of the monochromator and analyser crystals, α_m, Δ_m and Δ_a, respectively, with

$$\alpha'_m = \alpha_m / 2(\ln 2)^{1/2}, \quad \Delta'_m = \Delta_m / 2(\ln 2)^{1/2}, \quad \Delta'_a = \Delta_a / 2(\ln 2)^{1/2}.$$

From the above equation, the intrinsic FWHM of the Gaussian-approximated peaks of the powder-diffraction pattern can be obtained as

$$\Delta^2(2\theta) = \alpha_m^2\left(\frac{\tan\theta_a}{\tan\theta_m} - 2\frac{\tan\theta}{\tan\theta_m} + 1\right)^2 + \tfrac{1}{2}\Delta_m^2\left(\frac{\tan\theta_a}{\tan\theta_m} - 2\frac{\tan\theta}{\tan\theta_m}\right) + \Delta_a^2. \quad (2.2.2)$$

Note that the true peak shape is not Gaussian, and a pseudo-Voigt (*e.g.* as described by Thompson *et al.*, 1987), Voigt (*e.g.* Langford, 1978; David & Matthewman, 1985; Balzar & Ledbetter, 1993) or other function modelled from first principles (*e.g.* Cheary & Coelho, 1992; Ida *et al.*, 2001, 2003) is usually better. Examples of FWHM curves calculated from equation (2.2.2) are plotted in Fig. 2.2.11 at three wavelengths. Differentiating the Bragg equation gives $\Delta d/d = -\cot\theta\,\Delta(\theta)$, where θ is in radians.

Gozzo *et al.* (2006) have extended the formulation of Sabine to include the effects of collimating and focusing mirrors in the overall scheme. Axial (horizontal) divergence of the beam between the sample and the detector causes shifts and broadening of the peaks, as well as the well known low-angle peak asymmetry due to the curvature of the Debye–Scherrer cones. Sabine (1987*b*), based on the work of Hewat (1975) and Hastings *et al.* (1984), suggests the magnitude of the broadening, $B(2\theta)$, due to horizontal divergence Φ can be estimated *via*

$$B(2\theta) = (\tfrac{1}{4}\Phi)^2(\cot 2\theta + \tan\theta_a),$$

where B and Φ are in radians. This value is added to $\Delta(2\theta)$.

2.2.4.1.2. *Hart–Parrish design*

A variant of the parallel-beam scheme replaces the analyser crystal with a set of long, fine Soller collimators (Parrish *et al.*, 1986; Parrish & Hart, 1987; Parrish, 1988; Cernik *et al.*, 1990; Collins *et al.*, 1992) (Fig. 2.2.12). The collimators define a true angle of diffraction, but with lower 2θ resolution than an analyser crystal because their acceptance angle is necessarily much larger and so the transmitted intensity is greater. They are not particularly suitable for fine capillary specimens, as the separation between foils may be similar to the capillary diameter, resulting in problems of shadowing of the diffracted beam. However, they are achromatic, and so do not need to be reoriented at each change of wavelength, which may have advantages when performing anomalous-scattering studies around an element's absorption edge. Unlike an analyser crystal, however, they do not suppress fluorescence. Peak shapes and resolution can be influenced by reflection of X-rays from the surface of the foils, or any imperfections in their manufacture, *e.g.* if the blades are not straight and flat. The theoretical resolution curve of such an instrument can be obtained from equation (2.2.2) by setting $\tan\theta_a$ to zero and replacing the angular acceptance of the analyser crystal Δ_a with the angular acceptance of the collimator Δ_c.

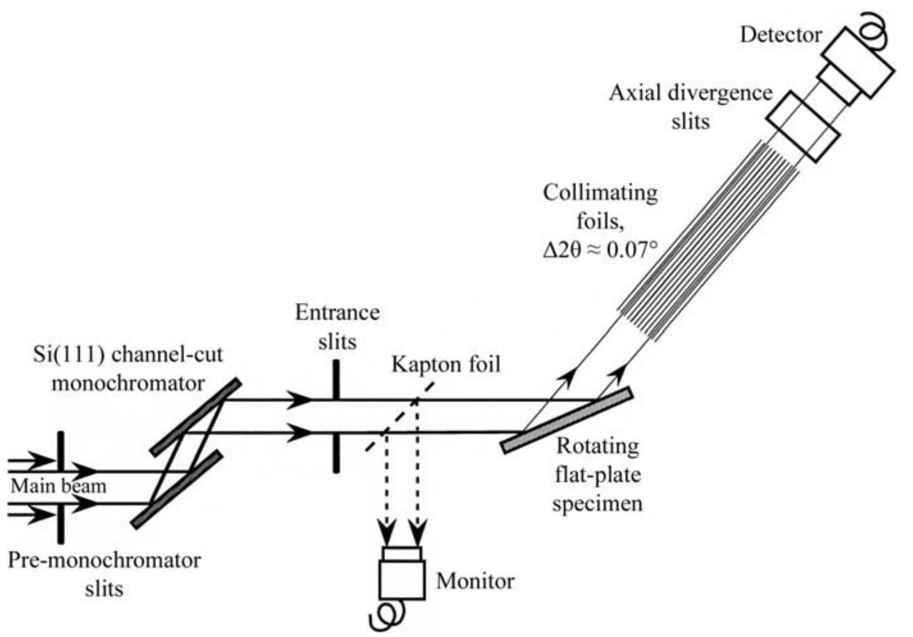

Figure 2.2.12
Schematic representation of a parallel-beam diffractometer of the Hart–Parrish design. The collimators installed on Stations 8.3 and 2.3 at the SRS Daresbury (Cernik *et al.*, 1990; Collins *et al.*, 1992) had steel blades 50 µm thick, 355 mm long, separated by 0.2 mm spacers, defining a theoretical opening angle (FWHM Δ_c) of 0.032° and a transmission of 80%.

2.2.4.2. *Debye–Scherrer instruments*

The simplest diffractometer has a receiving slit at a convenient distance from the sample in front of a point detector such as a scintillation counter. The height of the slit should match the capillary diameter, or incident beam height for flat plates. A slightly larger antiscatter slit near the sample should also be employed to reduce

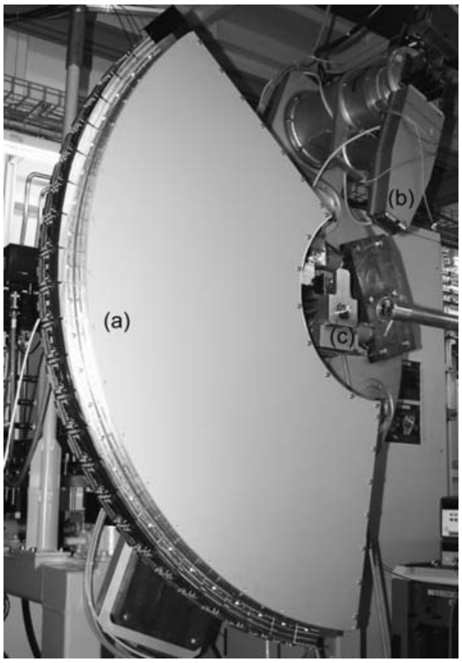

Figure 2.2.13
(*a*) 120° Mythen detector box, containing helium, mounted on the powder diffractometer of the materials science beamline at the Swiss Light Source. (*b*) Multianalyser detector stage. (*c*) Capillary spinner. (Bergamaschi *et al.*, 2009, 2010.)

background. The detector arm is scanned and a powder pattern recorded. This arrangement can be used for narrow capillary samples on lower-flux sources, avoiding the loss of intensity that use of an analyser crystal entails. The resolution is largely determined by the opening angle defined by the capillary and the receiving slit. Despite the simplicity of such an instrument, high-quality high-resolution data can be obtained.

For much faster data acquisition, a one-dimensional (1D) PSD or an area detector can be employed. Any sort of 1D detector with an appropriate number of channels, channel separation, efficiency, count rate (in an individual channel and overall) and speed of read out can be employed. Technology evolves and detectors make continual progress in performance. At the time of writing the most advanced 1D detector is the Mythen module developed by the Swiss Light Source (SLS). Mythen modules are based on semiconducting silicon technology and have 1280 8-mm-wide strips with a 50 µm pitch (64 × 8 mm^2). They can be combined to form very large curved detectors such as that on the powder diffractometer of the materials science beamline at the SLS (Fig. 2.2.13). This detector consists of 24 modules, 30 720 channels, set on a radius of 760 mm, covering 120° 2θ. Detector elements are therefore separated by ~0.004°. The whole detector can be read out in 250 µs. Being Si based, its efficiency falls off above 20–25 keV, where the absorbing power of Si falls to very small values. Nevertheless, at intermediate and low energies a full powder-diffraction pattern for structural analysis can be measured in just seconds, or even faster if the intention is to follow a dynamic process.

Two-dimensional (2D) detectors are generally flat, so cannot extend to the same 2θ values as a curved multistrip detector unless scanned on a detector arm. This is possible, but usually a short wavelength is used with a fixed detector. This allows an adequate data range to be recorded, particularly if the detector is positioned with the direct beam ($2\theta = 0$) near an edge. A 2D detector records complete or partial Debye–Scherrer rings, which increases the counting efficiency with respect to scanning an analyser crystal by several orders of magnitude. In addition, if the rings do not appear smooth and homogeneous, this indicates problems with the sample, such as preferred orientation or granularity, both of which can seriously affect diffraction intensities when measuring just a thin vertical strip. Detectors that have been used are diverse and include image plates, though these have slow read out, charge-coupled devices (CCDs) or Si-based photon-counting pixel detectors used for single-crystal diffraction or protein crystallography (*e.g.* Broennimann *et al.*, 2006), and medical-imaging detectors, which are designed for hard-energy operation. Examples include the CCD-based Frelon camera, developed at the ESRF (Labiche *et al.*, 2007), and commercially available large flat-panel medical-imaging detectors up to 41 × 41 cm^2, based on scintillator-coated amorphous silicon, which have been exploited at speeds of up to 60 Hz for selected read-out areas (Chupas, Chapman & Lee, 2007; Lee, Aydiner *et al.*, 2008; Daniels & Drakopoulos, 2009).

Note that a 2D detector can be used as a 1D detector by applying a mask and reading out only a narrow strip, which can enhance the rate of data acquisition. For CCD chips, the electronic image can be rapidly transferred to pixels behind the masked part of the detector from where it can be read out while the active area is re-exposed. Translating an image plate behind a mask is a simple way of acquiring a series of diffraction patterns for following a process with modest time resolution.

These instruments are vulnerable to aberrations that cause systematic shifts in peak positions, such as misalignment of the capillary or surface of the sample from the diffractometer axis, and specimen transparency, which also affects the peak width and shape. The peak width also depends on whether a flat sample is in the $\theta/2\theta$ condition, or on the diameter of a capillary sample, *etc*. Focusing the incident beam onto the detector decreases the peak width, as fewer pixels are illuminated compared to using a highly collimated incident beam. PSDs are much more open detectors than those behind an analyser crystal or set of slits, so are more susceptible to background and parasitic scatter from sample environments *etc*. However, the speed and efficiency of data acquisition usually outweigh such concerns.

2.2.4.3. *Energy-dispersive instruments*

The broad, continuous spectrum from a wiggler or bending magnet is suitable for energy-dispersive diffraction (EDD). Here, the detector is fixed at an angle 2θ and the detector determines the energy, ε, of each arriving photon scattered by the sample (Fig. 2.2.14). The energy [keV] can be converted to d-spacing [Å] *via*

$$d \simeq 12.3984/2\varepsilon \sin\theta.$$

The detector usually consists of a cryogenically cooled semi-conducting Ge diode. An absorbed X-ray photon promotes electrons to the conduction band in proportion to its energy. By

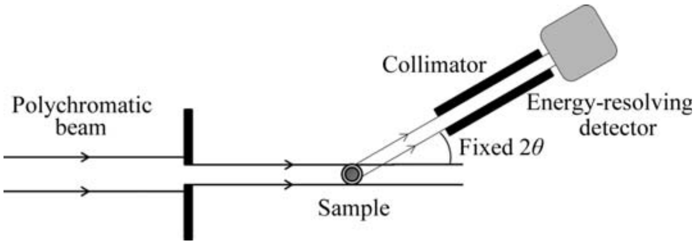

Figure 2.2.14
Schematic representation of an energy-dispersive diffraction arrangement.

analysing the size of the charge pulse produced, the energy of the photon is determined. The powder-diffraction pattern is recorded as a function of energy (typically somewhere within the range 10–150 keV, depending on the source) *via* a multichannel analyser (MCA). Instruments may have multiple detectors, at different 2θ angles covering different ranges in *d*-spacing (Barnes *et al.*, 1998), or arranged around a Debye–Scherrer ring, as in the 23-element semi-annular detector at beamline I12 at Diamond Light Source (Korsunsky *et al.*, 2010; Rowles *et al.*, 2012).

Prior to performing the EDD experiment, the detector and MCA system must be calibrated, *e.g.* by measuring signals from sources of known energy, such as ^{241}Am (59.5412 keV) or ^{57}Co (122.06014 and 136.4743 keV) at hard energies, and/or from the fluorescence lines of elements such as Mo, Ag, Ba *etc*. The 2θ angle also needs to be calibrated if accurate *d*-spacings are desired. This should be done by measuring the diffraction pattern of a standard sample with known *d* values.

The detector angle is typically chosen in the range 2–6° 2θ and influences the range of *d*-spacings accessible *via* the term $1/\sin\theta$, *i.e.* the lower the angle, the higher the energy needed to access any particular *d*. Normally, the range of most interest should be matched to the incident spectrum, taking account also of sample absorption and fluorescence, to produce peaks with high intensity. More than one detector at different angles can also be employed. Energy-sensitive Ge detectors do not count particularly fast, up to 50 kHz being a typical value compared to possibly 1–2 MHz with a scintillation detector. Hence they are relatively sensitive to pulse pile-up and other effects of high count rates (Cousins, 1994; Laundy & Collins, 2003; Honkimäki & Suortti, 2007), particularly if the synchrotron is operating in a mode with a few large electron bunches giving very intense pulses of X-rays on the sample.

The energy resolution of the detector is of the order of 2%, which dominates the overall resolution of the technique. Its main uses are where a fixed geometry with penetrating X-rays is required, *e.g.* in high-pressure cells, for *in situ* studies (Häusermann & Barnes, 1992), *e.g.* of chemical reactions under hydrothermal conditions (Walton & O'Hare, 2000; Evans *et al.*, 1995), electrochemistry (*e.g.* Scarlett *et al.*, 2009; Rijssenbeek *et al.*, 2011; Rowles *et al.*, 2012), or measurements of residual strain (Korsunsky *et al.*, 2010). Owing to the use of polychromatic radiation, the technique has very high flux on the sample and can be used for high-speed data collection, following rapid processes *in situ*. However, accurate modelling of the intensities of the powder-diffraction pattern for structural or phase analysis is difficult because of the need to take several energy-dependent effects into account, *e.g.* absorption and scattering factors, the incident X-ray spectrum, and the detector response. Nevertheless, examples where this has been successfully carried out have been published (*e.g.* Yamanaka & Ogata, 1991; Scarlett *et al.*, 2009).

A higher-resolution variant of the energy-dispersive technique can be performed by using a standard detector behind a collimator at fixed 2θ scanning the incident energy *via* the monochromator. The Hart–Parrish design with long parallel foils is suitable. Such an approach has been demonstrated in principle (Parrish, 1988), but is rarely used in practice. The advantage is to be able to measure data of improved *d*-spacing resolution, as compared to using an energy-dispersive detector, from sample environments with highly restricted access. In principle, as a further variant, white incident radiation could be used with scanning of θ_a, the angle of the analyser crystal, and associated detector at $2\theta_a$, all at fixed 2θ.

2.2.5. Considerations for powder-diffraction experiments

Synchrotron radiation allows considerable flexibility for a powder-diffraction experiment, offering choice and optimization of a number of quantities such as the wavelength, with high energy resolution, range in *d*-spacing, angular resolution, angular accuracy, and spatial or time resolution (but not all of these can necessarily be optimized at the same time). Increasingly, powder-diffraction experiments at synchrotrons are combined with complementary measurements, simultaneously applying techniques such as Raman spectroscopy (Boccaleri *et al.*, 2007; Newton & van Beek, 2010), particularly when carrying out *in situ* studies of an evolving system. In this respect, the open nature of a synchrotron instrument, with space around the sample to position auxiliary equipment, is an advantage.

2.2.5.1. *Polarization*

Assuming the beam is 100% polarized in the horizontal plane of the synchrotron orbit and with detection in the vertical plane, there is no need for any polarization correction to the diffracted intensities. However, if a small amount of vertical polarization of the beam does need to be taken into account (possibly up to a few per cent depending on the source), the polarization factor that describes its effect on the intensity of the diffracted beam can be derived, following the approach of Azároff (1955) and Yao & Jinno (1982), as

$$P = \frac{1 - dp + dp\cos^2 2\theta\cos^2 2\theta_a}{1 - dp + dp\cos^2 2\theta_a} = \frac{1 - dp + dp\cos^2 2\theta\cos^2 2\theta_a}{1 - dp\sin^2 2\theta_a}, \tag{2.2.3}$$

where *dp* is the depolarization fraction (*i.e.* the fraction of the total intensity incident on the sample that is vertically polarized), $2\theta_a$ is the Bragg angle of the analyser crystal (if any), and the denominator scales *P* to unity at 2θ equal to zero (Dwiggins, 1983) and is a constant for any particular experimental setup. If there is no analyser crystal, or we ignore the effect it would have (*i.e.* by putting $2\theta_a = 0$), then

$$P = 1 - dp\sin^2 2\theta.$$

Beamline staff can usually advise on the appropriate values to use. These expressions reduce to the usual polarization factor for unpolarized ($dp = 0.5$) laboratory X-rays without a monochromator or analyser crystal, $\frac{1}{2}(1 + \cos^2 2\theta)$.

An alternative formulation of equation (2.2.3) considers the ratio of the vertical to horizontal polarization,

$$rp = \frac{dp}{1 - dp} \quad \text{and} \quad dp = \frac{rp}{1 + rp},$$

so that

$$P = \frac{1 + rp\cos^2 2\theta\cos^2 2\theta_a}{1 + rp\cos^2 \theta_a}. \tag{2.2.4}$$

Note that $rp = 1.0$ for unpolarized (laboratory) X-rays. In reality, because the synchrotron beam is near 100% plane polarized, *dp* and *rp* have similar values. The same expressions can be used if diffracting and analysing in the horizontal plane, except that now the value of *dp* or *rp* is replaced with the value of $(1 - dp)$ or $1/rp$, respectively.

For Debye–Scherrer rings detected on a 2D detector, the azimuthal angle around the ring needs to be taken into account, yielding

$$P = (1 - dp)(\cos^2 2\theta \sin^2 \kappa + \cos^2 \kappa) + dp(\cos^2 2\theta \cos^2 \kappa + \sin^2 \kappa)$$

or

$$P = \frac{(\cos^2 2\theta \sin^2 \kappa + \cos^2 \kappa) + rp(\cos^2 2\theta \cos^2 \kappa + \sin^2 \kappa)}{1 + rp},$$

where κ is the azimuthal angle (zero in the vertical direction) (Rowles *et al.*, 2012).

2.2.5.2. *Radiation damage*

The intensity of the incident beam can be so high that radiation damage becomes a real concern, particularly for samples containing organic molecules, such as pharmaceuticals, or organometallic materials. Radiation damage manifests itself by progressive shifts (often anisotropic) in the peak positions, a general reduction in peak intensities and peak broadening as the sample's crystallinity degrades. With high-resolution data, the effects are easily seen and can appear after only a few seconds in the worst cases. In such circumstances it may be better to use a 1D or 2D PSD to collect data of sufficient statistical quality before the damage is too severe. However, if the highest-resolution data are required, *via* scanning an analyser crystal, then the problem can be alleviated by filling a long capillary with sample and translating it between scans to expose fresh sample to the beam, thus acquiring multiple data sets which can be summed together. Such an approach necessarily requires a sufficient amount of disposable sample. If attempting to study the evolution of a particular part of the sample, *e.g.* undergoing heat treatment in the beam, then substituting fresh sample is not necessarily an option, and radiation damage can be a frustrating hindrance.

2.2.5.3. *Beam heating*

With a photon intensity of the order 10^{12} photons mm^{-2} s^{-1} incident on the sample – a possible value for the unfocused beam on a beamline based on an insertion device at a modern third-generation source – the power in the beam corresponds to a few mW mm^{-2}. If a small fraction is absorbed by the sample this can represent a significant heat load that becomes troublesome when trying to work with samples at cryogenic temperatures, where heat capacities are relatively low.

As an example, consider a sample of microcrystalline silicon, composed of cubic 1 µm^3 grains irradiated by a 31 keV beam (0.4 Å wavelength) with 10^{12} photons mm^{-2} s^{-1}. The power of the beam is 5 mW mm^{-2} ($31 \times 10^3\, e \times 10^{12}$ W mm^{-2}). The mass absorption coefficient of Si at 0.4 Å wavelength $\mu/\rho \simeq 1.32$ cm^2 g^{-1} (Milledge, 1968) leading to a linear absorption coefficient of 3.1 cm^{-1} (density of Si = 2.33 g cm^{-3}). Any problems with absorption by such a sample might usually be discounted; for a 1-mm-diameter capillary the value of μr is 0.1, assuming the powder density is 2/3 of the theoretical density.

A single 1-µm^3 grain of cross section 1 µm^2 is hit by 10^6 photons s^{-1}, of which a small fraction are absorbed,

$$\begin{aligned}\text{photons absorbed} &= 10^6[1 - \exp(-3.1 \times 10^{-4})]\\ &= 310 \text{ photons s}^{-1},\end{aligned}$$

corresponding to an absorbed power of 1.54×10^{-12} W. Not all this energy is retained; significant amounts are lost as fluorescence, Compton scatter *etc*. Consultation of tables of mass attenuation coefficients and mass energy-absorption coefficients (Hubbell, 1982; Seltzer, 1993) indicates that for Si at 31 keV about 80% of the energy is retained, thus a net heating power of 1.2×10^{-12} W. The mass of the Si grain is 2.33×10^{-15} kg. At ambient temperature, where the specific heat capacity of Si is 704.6 J kg^{-1} K^{-1}, this leads to an instantaneous tendency to increase the temperature by ∼0.7 K s^{-1}. At cryogenic temperatures, *e.g.* 10 K, the specific heat capacity is over three orders of magnitude lower, 0.28 J kg^{-1} K^{-1} (Desai, 1986), leading to a very strong tendency for the temperature to rise (1840 K s^{-1}). The extent of the potential problem varies depending on the real net absorption of energy of the sample at the wavelength being used. However, it is clear that to prevent local beam-heating effects, the absorbed energy must be removed from the sample as efficiently as possible, *i.e.* by having excellent thermal contact between the grains of the sample and the external medium. At cryogenic temperatures this can be accomplished *via* the He exchange gas in the cryostat. Thus, if using a capillary sample, the capillary must either be left unsealed, to allow the He to permeate between the grains of sample, or it must be sealed under He, allowing transport of the heat to the walls of the capillary. Sealing under air, nitrogen, argon or other atmosphere leads to a loss of heat-transport capability when the gas solidifies, with consequent unpredictable behaviour for the sample caused by the beam-heating effects. This can involve significant shifts in peak positions and peak broadening depending on the instantaneous local temperature gradients. The problems tend to be worse at softer energies, where X-ray absorption is generally higher. Notwithstanding the potential problems, good-quality low-temperature data can be measured with appropriate care.

2.2.5.4. *Choice of wavelength*

The tunability of synchrotron radiation allows the wavelength best suited to the measurements to be selected. The collimation of the beam from the source combined with a perfect crystal monochromator lead automatically to high energy resolution, with a narrow wavelength distribution about a mean value. Consequently there are no issues to contend with such as α_1, α_2 doublets or other effects due to a composite incident spectrum, contributing to a relatively simple instrumental peak-shape function. High energy resolution is essential for high 2θ resolution, because, as shown in equation (2.2.1), the effect of the energy envelope is to broaden the diffraction peaks as 2θ increases.

In choosing the wavelength for an experiment, factors to consider include:

(*a*) The optimum operational range for the beamline to be used, which will principally depend on the characteristics of the source.

(*b*) Absorption: choosing a sufficiently hard energy generally reduces absorption and allows the use of a capillary specimen in transmission for a wide range of compounds, *e.g.* those containing transition metals or heavier elements, thus minimizing preferred orientation. Selecting the energy a little way below (in energy) the K or $L_{\rm III}$ absorption edge of an element in the sample may help minimize sample absorption. For any sample or series of samples, it is good practice in the planning of the experiment to calculate the linear absorption coefficient to assess the optimum capillary diameter, the wavelength to use and those to avoid.

(*c*) The use of hard energies can be advantageous for penetration through sample environments, although these should normally, as much as possible, be designed with appropriate X-ray windows *etc*. However, when absorbing environments are unavoidable, such as containing a sample in a spinning Pt

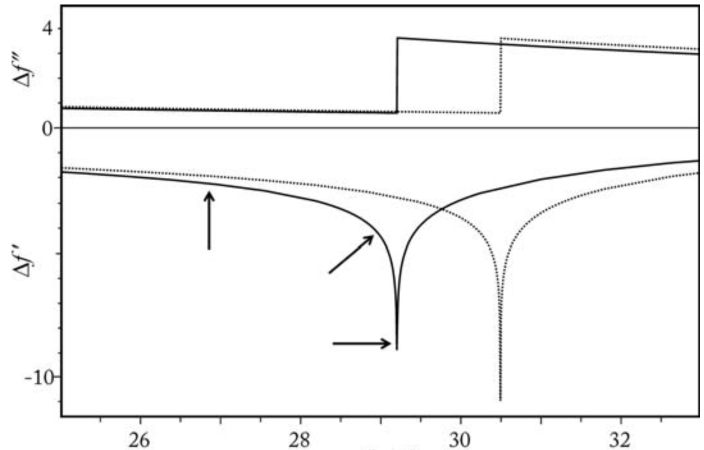

Figure 2.2.15
Variation of $\Delta f'$ and $\Delta f''$ with photon energy for Sn (solid line) and Sb (dotted line) in the vicinity of their K absorption edges (from the tables of Sasaki, 1989). An anomalous-scattering experiment seeking to distinguish the arrangement of the two elements could make measurements at the Sn edge (29.2001 keV), at a few eV below the edge and at an energy significantly removed from the edge (arrows). Equivalent measurements could be made at the Sb edge (30.4912 keV), but as this is above the energy of the Sn edge careful attention must be paid to the increase in the sample's absorption (reflected in the values of $\Delta f''$).

capillary for heating to very high temperatures, then high energy can be a major benefit.

(*d*) Hard energies are essential to measure to high Q values, where $Q = 4\pi \sin\theta/\lambda = 2\pi/d$. For pair distribution function (PDF) analysis, data to $Q > 25$ Å^{-1} ($d < 0.25$ Å) or more are required, with patterns of good statistical quality. Such Q values are not possible with Mo or Ag radiation (Ag $K\alpha$, λ = 0.56 Å, $Q \simeq 22$ Å^{-1} at $2\theta = 160°$), but are easily accessible at λ = 0.4 Å (31 keV) by scanning to $2\theta = 106°$. At 80.7 keV (0.154 Å, ten times shorter than Cu $K\alpha$) patterns to $Q \simeq 35$ Å^{-1} can be obtained in minutes (even seconds) with a large stationary medical-imaging flat-panel detector (Lee, Aydiner *et al.*, 2008). Even for more classical powder-diffraction experiments, access to data for high Q values can be advantageous for Rietveld refinement of crystal structures, or for measuring several orders of reflections for peak-shape analysis in the investigation of microstructure.

(*e*) Anomalous scattering: performing measurements near the absorption edge of an element in a sample and away from that edge gives element-specific changes in the diffraction intensities, enhancing the experiment's sensitivity to that element (Fig. 2.2.15). The approach can be complimentary to isotopic substitution in a neutron-diffraction experiment or may be the only option when no suitable isotope is available. Good energy resolution is important for these experiments. The values of $\Delta f'$ and $\Delta f''$ vary sharply over only a few eV at the edge, so poor energy resolution would average the abruptly changing values over too broad a range to the detriment of elemental sensitivity and sample absorption if part of the wavelength envelope strays above the edge. Moreover, it is necessary to know accurately where on the edge the measurement is being made to allow the correct values of $\Delta f'$ and $\Delta f''$ to be used in the data analysis. Tables of values have been calculated (*e.g.* Sasaki, 1989), but these do not take account of shifts in an edge due to the oxidation state(s) and chemical environment(s) of the elements. It is advisable to measure the fluorescence of the sample as the energy is scanned through the edge (by varying the monochromator angle θ_m) and then use the Kramers–Kronig relation to calculate the variation of $\Delta f'$ and $\Delta f''$ with energy. A program such as *CHOOCH* (Evans & Pettifer, 2001) allows this to be done.

(*f*) A wavelength greater than 1 Å may be best when working with large unit cells, such as found for proteins, organic molecules or organometallic compounds. Using a long wavelength helps by moving the diffraction pattern to higher 2θ values, away from the zone most affected by background air scatter or masked by the beam stop, and to where the peak asymmetry due to axial beam divergence is less severe. Longer wavelengths are also useful when working in reflection with plate samples to minimize beam penetration and thus enhance sensitivity to the surface regions, *e.g.* in the study of surfaces or coatings.

(*g*) The broad continuous spectrum available from a bending magnet or wiggler allows powder-diffraction measurements *via* the energy-dispersive approach, which is exploited when geometric considerations of the sample or environment mean that a restricted range of 2θ values is accessible or when attempting to obtain the maximum time resolution from a source, as a larger fraction of the photons from the source can be exploited.

2.2.5.5. *Angular resolution*

The highest angular resolution is obtained from a diffractometer equipped with an analyser crystal such as Si(111) or Ge(111). This also gives the robust parallel-beam optical configuration so that peak positions are accurately determined. For well crystallized high-quality samples, peak FWHMs of a few millidegrees are possible, thus maximizing the resolution of reflections with similar d-spacings. For less ideal samples, which represent the majority, microstructural effects broaden the peaks, and indeed high-resolution synchrotron data are exploited for detailed investigation of peak shapes and characterization of a range of properties such as crystallite size, microstrain (Chapter 5.2), defects, chemical homogeneity *etc*. Accurate high-resolution data are particularly useful for solving crystal structures from powders (Chapter 4.1), increasing the possibilities for indexing the powder diffraction pattern (Chapter 3.4), assessing the choice of possible space groups, and providing high-quality data for the structural solution and refinement steps. With a high-resolution pattern, the maximum amount of information is stored in the complex profile composed from the overlapping peaks.

2.2.5.6. *Spatial resolution*

Focusing the X-ray beam gives improved spatial resolution, *e.g.* for studying a small sample contained in a diamond anvil cell at high pressure. A beam with dimensions of a few µm can be obtained, though at the expense of the divergence of the beam arriving at the sample. In such cases the use of a 2D detector to record the entire Debye–Scherrer rings will be required to accumulate the diffraction pattern in a reasonable time and to reveal any problems with preferred orientation or granularity in the sample. With a very small sample only a few grains may be correctly oriented to provide each powder reflection. Alternatively, provided the intensity of the beam is high enough, simply cutting down the beam size with slits may be appropriate, *e.g.* to map residual strain in a weld or mechanical component where a spatial resolution on the 50–100 µm scale may be required. Smaller beam sizes may not be useful if they are comparable to the intrinsic grain size of the material, thus leading to a poor statistical average of grain orientations and a spotty diffraction pattern.

2.2.5.7. *Time resolution*

The high flux allows powder-diffraction patterns to be measured quickly, opening up the possibilities for time-resolved studies, following the evolution of samples on a timescale, if appropriate, down to milliseconds, *e.g.* to investigate the kinetics and the mechanism of a phase transition caused by a change of the temperature, pressure or other external condition, or a chemical reaction taking place in the sample, such as self-propagating combustion synthesis (Labiche *et al.*, 2007). Many instruments allow great flexibility in the design of experiments to study systems *in situ*, helped by the availability of hard radiation to penetrate through sample environments and reduce the angular range that must be accessed to measure enough diffraction peaks to yield the desired information.

2.2.5.7.1. *Using fast detectors*

Scanning a detector through the *d*-spacing range of interest necessarily takes a few seconds, so is too slow to measure the fastest processes. Thus, for speed, a multichannel detector system is required that acquires the full diffraction pattern synchronously and that can be read out rapidly, such as *via* a fast PSD or using the energy-dispersive approach. Many different types of detector systems have been exploited for fast powder-diffraction studies using the monochromatic Debye–Scherrer configuration (Section 2.2.4.2), including 1D photodiode arrays (Pennartz *et al.*, 1992; Wong *et al.*, 2006; Palmer *et al.*, 2004), the Mythen curved 1D PSD (Fadenberger *et al.*, 2010), pixel detectors (Yonemura *et al.*, 2006; Terasaki & Komizo, 2011), CCD-based detectors (Malard *et al.*, 2011; Elmer *et al.*, 2007), and medical-imaging detectors (Chupas, Chapman, Jennings *et al.*, 2007; Newton *et al.*, 2010). The former of these last two studies shows that these large detectors working at hard X-ray energies above 60 keV register a wide enough Q range in a single cycle to allow PDF analysis to be made, thus allowing the conduct of time-resolved PDF analysis of, for example, catalytic systems composed of evolving nanoparticles. For the latter study, the diffraction measurements were combined with simultaneous monitoring of the reacting system with the acquisition of complementary mass and diffuse reflectance infrared Fourier transform spectra (DRIFTS).

2.2.5.7.2. *Using the pulse structure*

For investigating very fast, reversible processes, use can be made of the bunch structure of the synchrotron source and the stroboscopic measurement approach. The time for an orbit of an electron circulating in a synchrotron is (circumference/c) s. For a synchrotron such as at the ESRF (with a circumference of 844.4 m), this corresponds to 2.82 µs (*i.e.* a frequency of 355036 Hz). Thus when operating with 16 electron bunches distributed evenly around the ring, there is a burst of X-rays delivered to a beamline every 176 ns, and because of the longitudinal dimension of the electron bunch (~20 mm), each burst lasts ~70 ps. Such a pulsed source can be used in pump–probe powder-diffraction experiments, whereby a sample is excited by a short laser pulse (~100 fs duration) then probed by the X-ray beam a chosen delay time later. The scattered X-rays are recorded with a suitable (probably 2D) detector and the process is repeated, with the statistical quality of the diffraction pattern building up over a number of cycles, after which the detector is read out. A high-speed chopper in the X-ray beam can be used to select the pulse frequency desired for any particular set of measurements. By varying the delay time the evolution of the sample as a function of time after the initial excitation can be investigated. The whole experiment needs fast, accurate electronics to correlate the timing of the firing of the laser, the arrival of the X-ray pulse and the phasing of the chopper.

Examples include the study of 4-(dimethylamino)benzonitrile and 4-(diisopropylamino)benzonitrile (Davaasambuu *et al.*, 2004; Techert & Zachariasse, 2004), whose fluorescence properties indicate that photoexcitation leads to the formation of an intramolecular charge-transfer state. Powder-diffraction patterns were collected over 10-minute periods at a frequency of 897 Hz at delay times ranging from −150 ps (as a reference before the laser excitation) to +2500 ps after excitation. Only about 5% of the molecules are excited by the laser, so the powder-diffraction pattern is from a sample containing both excited and ground-state molecules. Rietveld refinement of the structures from the diffraction patterns gave the fraction of excited molecules as a function of delay time, and the nature of the structural change induced by the photoexcitation. For the isopropyl analogue, an exponential relaxation time of 6.3 (±2.8) ns was observed for the excited molecules (compared to 3.28 ns seen spectroscopically). The main distortion to the molecules was a change in the torsion angle between the diisopropylamino group and the benzene ring, from 13–14° determined from the pre-excitation patterns (14.3° *via* single-crystal analysis) to 10 (±1–2)°.

2.2.5.8. *Beamline evolution*

A beamline at a synchrotron source will certainly evolve in its specifications and capabilities. Users and prospective users should follow updates on a facility's website, or contact the beamline staff, for information concerning possibilities for experiments.

References

Als-Nielsen, J. & McMorrow, D. (2001). *Elements of Modern X-ray Physics*. New York: Wiley.

Authier, A. (2006). *Dynamical theory of X-ray diffraction. International Tables for Crystallography*, Vol. B, *Reciprocal Space*, 1st online ed., ch. 5.1. Chester: International Union of Crystallography.

Azároff, L. V. (1955). *Polarization correction for crystal-monochromatized X-radiation*. *Acta Cryst.* **8**, 701–704.

Balzar, D. & Ledbetter, H. (1993). *Voigt-function modeling in Fourier analysis of size- and strain-broadened X-ray diffraction peaks*. *J. Appl. Cryst.* **26**, 97–103.

Barnes, P., Jupe, A. C., Colston, S. L., Jacques, S. D., Grant, A., Rathbone, T., Miller, M., Clark, S. M. & Cernik, R. J. (1998). *A new three-angle energy-dispersive diffractometer*. *Nucl. Instrum. Methods Phys. Res. B*, **134**, 310–313.

Beaumont, J. H. & Hart, M. (1974). *Multiple Bragg reflection monochromators for synchrotron X radiation*. *J. Phys. E Sci. Instrum.* **7**, 823–829.

Bergamaschi, A., Cervellino, A., Dinapoli, R., Gozzo, F., Henrich, B., Johnson, I., Kraft, P., Mozzanica, A., Schmitt, B. & Shi, X. (2009). *Photon counting microstrip detector for time resolved powder diffraction experiments*. *Nucl. Instrum. Methods Phys. Res. A*, **604**, 136–139.

Bergamaschi, A., Cervellino, A., Dinapoli, R., Gozzo, F., Henrich, B., Johnson, I., Kraft, P., Mozzanica, A., Schmitt, B. & Shi, X. (2010). *The MYTHEN detector for X-ray powder diffraction experiments at the Swiss Light Source*. *J. Synchrotron Rad.* **17**, 653–668.

Bilderback, D. H. (1986). *The potential of cryogenic silicon and germanium X-ray monochromators for use with large synchrotron heat loads*. *Nucl. Instrum. Methods Phys. Res. A*, **246**, 434–436.

Boccaleri, E., Carniato, F., Croce, G., Viterbo, D., van Beek, W., Emerich, H. & Milanesio, M. (2007). *In situ simultaneous Raman/high-resolution X-ray powder diffraction study of transformations occurring in materials at non-ambient conditions*. *J. Appl. Cryst.* **40**, 684–693.

Broennimann, Ch., Eikenberry, E. F., Henrich, B., Horisberger, R., Huelsen, G., Pohl, E., Schmitt, B., Schulze-Briese, C., Suzuki, M., Tomizaki, T., Toyokawa, H. & Wagner, A. (2006). *The PILATUS 1m detector*. *J. Synchrotron Rad.* **13**, 120–130.

Cernik, R. J., Murray, P. K., Pattison, P. & Fitch, A. N. (1990). *A two-circle powder diffractometer for synchrotron radiation with a closed loop encoder feedback system*. *J. Appl. Cryst.* **23**, 292–296.

Cheary, R. W. & Coelho, A. (1992). *A fundamental parameters approach to X-ray line-profile fitting*. *J. Appl. Cryst.* **25**, 109–121.

Chupas, P. J., Chapman, K. W., Jennings, G., Lee, P. L. & Grey, C. P. (2007). *Watching nanoparticles grow: the mechanism and kinetics for the formation of TiO_2-supported platinum nanoparticles*. *J. Am. Chem. Soc.* **129**, 13822–13824.

Chupas, P. J., Chapman, K. W. & Lee, P. L. (2007). *Applications of an amorphous silicon-based area detector for high-resolution, high-sensitivity and fast time-resolved pair distribution function measurements*. *J. Appl. Cryst.* **40**, 463–470.

Collins, S. P., Cernik, R. J., Pattison, P., Bell, A. M. T. & Fitch, A. N. (1992). *A two-circle powder diffractometer for synchrotron radiation on Station 2.3 at the SRS*. *Rev. Sci. Instrum.* **63**, 1013–1014.

Cousins, C. S. G. (1994). *High-resolution diffraction at synchrotron sources: correction for counting losses*. *J. Appl. Cryst.* **27**, 159–163.

Cox, D. E., Hastings, J. B., Cardoso, L. P. & Finger, L. W. (1986). *Synchrotron X-ray powder diffraction at X13A: a dedicated powder diffractometer at the National Synchrotron Light Source*. *Mater. Sci. Forum*, **9**, 1–20.

Cox, D. E., Hastings, J. B., Thomlinson, W. & Prewitt, C. T. (1983). *Application of synchrotron radiation to high resolution powder diffraction and Rietveld refinement*. *Nucl. Instrum. Methods*, **208**, 573–578.

Daniels, J. E. & Drakopoulos, M. (2009). *High-energy X-ray diffraction using the Pixium 4700 flat-panel detector*. *J. Synchrotron Rad.* **16**, 463–468.

Davaasambuu, J., Durand, P. & Techert, S. (2004). *Experimental requirements for light-induced reactions in powders investigated by time-resolved X-ray diffraction*. *J. Synchrotron Rad*. **11**, 483–489.

David, W. I. F. & Matthewman, J. C. (1985). *Profile refinement of powder diffraction patterns using the Voigt function*. *J. Appl. Cryst.* **18**, 461–466.

Desai, P. D. (1986). *Thermodynamic properties of iron and silicon. J. Phys. Chem. Ref. Data*, **15**, 967–983.

Dwiggins, C. W. Jr (1983). *General calculation of the polarization factor for multiple coherent scattering of unpolarized and plane-polarized X-rays*. *Acta Cryst.* A**39**, 773–777.

Elmer, J. W., Palmer, T. A. & Specht, E. D. (2007). *In situ observations of sigma phase dissolution in 2205 duplex stainless steel using synchrotron X-ray diffraction*. *Mat. Sci. Eng. A*, **459**, 151–155.

Evans, G. & Pettifer, R. F. (2001). *CHOOCH: a program for deriving anomalous-scattering factors from X-ray fluorescence spectra*. *J. Appl. Cryst.* **34**, 82–86.

Evans, J. S. O., Francis, R. J., O'Hare, D., Price, S. J., Clark, S. M., Flaherty, J., Gordon, J., Nield, A. & Tang, C. C. (1995). *An apparatus for the study of the kinetics and mechanism of hydrothermal reactions by in situ energy dispersive x-ray diffraction*. *Rev. Sci. Instrum.* **66**, 2442–2445.

Fadenberger, K., Gunduz, I. E., Tsotsos, C., Kokonou, M., Gravani, S., Brandstetter, S., Bergamaschi, A., Schmitt, B., Mayrhofer, P. H., Doumanidis, C. C. & Rebholz, C. (2010). *In situ observation of rapid reactions in nanoscale Ni–Al multilayer foils using synchrotron radiation*. *Appl. Phys. Lett.* **97**, 144101.

Glazov, V. M. & Pashinkin, A. S. (2001). *The thermophysical properties (heat capacity and thermal expansion) of single-crystal silicon*. *High Temp.* **39**, 413–419.

Gozzo, F., De Caro, L., Giannini, C., Guagliardi, A., Schmitt, B. & Prodi, A. (2006). *The instrumental resolution function of synchrotron radiation powder diffractometers in the presence of focusing optics*. *J. Appl. Cryst.* **39**, 347–357.

Gullikson, E. M. (2001). *Atomic scattering factors*. *X-ray Data Booklet*, edited by A. C. Thompson & D. Vaughan. Lawrence Berkeley National Laboratory, USA. http://xdb.lbl.gov/Section1/Sec_1-7.pdf.

Hastings, J. B., Thomlinson, W. & Cox, D. E. (1984). *Synchrotron X-ray powder diffraction*. *J. Appl. Cryst.* **17**, 85–95.

Häusermann, D. & Barnes, P. (1992). *Energy-dispersive diffraction with synchrotron radiation: optimization of the technique for dynamic studies of transformations*. *Phase Transit.* **39**, 99–115.

Hewat, A. W. (1975). *Design for a conventional high-resolution neutron powder diffractometer*. *Nucl. Instrum. Methods*, **127**, 361–370.

Hewat, A. W. (1979). *Absorption corrections for neutron diffraction*. *Acta Cryst.* A**35**, 248.

Hodeau, J.-L., Bordet, P., Anne, M., Prat, A., Fitch, A. N., Dooryhée, E., Vaughan, G. & Freund, A. (1998). *Nine-crystal multianalyzer stage for high-resolution powder diffraction between 6 keV and 40 keV*. *Proc. SPIE*, **3448**, 353–361.

Honkimäki, V. & Suortti, P. (2007). *Energy-dispersive diffraction with synchrotron radiation and a germanium detector*. *J. Synchrotron Rad.* **14**, 331–338.

Hubbell, J. H. (1982). *Photon mass attenuation and energy-absorption coefficients*. *Int. J. Appl. Radiat. Isot.* **33**, 1269–1290.

Ida, T., Hibino, H. & Toraya, H. (2001). *Peak profile function for synchrotron X-ray diffractometry*. *J. Appl. Cryst.* **34**, 144–151.

Ida, T., Hibino, H. & Toraya, H. (2003). *Deconvolution of instrumental aberrations for synchrotron powder X-ray diffractometry*. *J. Appl. Cryst.* **36**, 181–187.

Kim, K.-J. (2001). *Characteristics of synchrotron radiation*. *X-ray Data Booklet*, edited by A. C. Thompson & D. Vaughan. Lawrence Berkeley National Laboratory, USA. http://xdb.lbl.gov/Section2/Sec_2-1.html.

Kirkpatrick, P. & Baez, A. V. (1948). *Formation of optical images by X-rays*. *J. Opt. Soc. Am.* **38**, 766–774.

Koopmans, K. & Rieck, G. D. (1968). *International Tables for X-ray Crystallography*, Vol. III, edited by C. H. MacGillavry & G. D. Rieck, pp. 194–195. Birmingham: Kynoch Press.

Korsunsky, A. M., Song, X., Hofmann, F., Abbey, B., Xie, M., Connolley, T., Reinhard, C. R. C., Atwood, R. C., Connor, L. & Drakopoulos, M. (2010). *Polycrystal deformation analysis by high energy synchrotron X-ray diffraction on the I12 JEEP beamline at Diamond Light Source*. *Mater. Lett.* **64**, 1724–1727.

Labiche, J.-C., Mathon, O., Pascarelli, S., Newton, M. A., Ferre, G. G., Curfs, C., Vaughan, G., Homs, A. & Carreiras, D. F. (2007). *The fast readout low noise camera as a versatile X-ray detector for time resolved dispersive extended X-ray absorption fine structure and diffraction studies of dynamic problems in materials science, chemistry, and catalysis*. *Rev. Sci. Instrum.* **78**, 091301–1–11.

Langford, J. I. (1978). *A rapid method for analysing the breadths of diffraction and spectral lines using the Voigt function*. *J. Appl. Cryst.* **11**, 10–14.

Laundy, D. & Collins, S. (2003). *Counting statistics of X-ray detectors at high counting rates*. *J. Synchrotron Rad.* **10**, 214–218.

Lee, J. H., Aydiner, C. C., Almer, J., Bernier, J., Chapman, K. W., Chupas, P. J., Haeffner, D., Kump, K., Lee, P. L., Lienert, U., Miceli, A. & Vera, G. (2008). *Synchrotron applications of an amorphous silicon flat-panel detector*. *J. Synchrotron Rad.* **15**, 477–488.

Lee, P. L., Shu, D., Ramanathan, M., Preissner, C., Wang, J., Beno, M. A., Von Dreele, R. B., Ribaud, L., Kurtz, C., Antao, S. M., Jiao, X. & Toby, B. H. (2008). *A twelve-analyzer detector system for high-resolution powder diffraction*. *J. Synchrotron Rad.* **15**, 427–432.

Lengeler, B., Schroer, C., Tümmler, J., Benner, B., Richwin, M., Snigirev, A., Snigireva, I. & Drakopoulos, M. (1999). *Imaging by parabolic refractive lenses in the hard X-ray range*. *J. Synchrotron Rad.* **6**, 1153–1167.

Lipson, H. (1967). *International Tables for X-ray Crystallography*, Vol. II, edited by J. S. Kasper & K. Lonsdale, pp. 291–292. Birmingham: Kynoch Press.

Malard, B., Pilch, J., Sittner, P., Delville, R. & Curfs, C. (2011). *In situ investigation of the fast microstructure evolution during electropulse treatment of cold drawn NiTi wires*. *Acta Mater.* **59**, 1542–1556.

Margaritondo, G. (1988). *Introduction to Synchrotron Radiation.* Oxford University Press.

Masson, O., Dooryhée, E. & Fitch, A. N. (2003). *Instrument line-profile synthesis in high-resolution synchrotron powder diffraction*. *J. Appl. Cryst.* **36**, 286–294.

Milledge, H. J. (1968). *International Tables for X-ray Crystallography*, Volume III, *Physical and Chemical Tables*, edited by C. H. MacGillavry, G. D. Rieck & K. Lonsdale, pp. 175–192. Birmingham: Kynoch Press.

Mills, D. M., Helliwell, J. R., Kvick, Å., Ohta, T., Robinson, I. A. & Authier, A. (2005). *Report of the Working Group on Synchrotron Radiation Nomenclature - brightness, spectral brightness or brilliance?* *J. Synchrotron Rad.* **12**, 385.

Newton, M. A., Di Michiel, M., Kubacka, A. & Fernández-García, M. (2010). *Combining time-resolved hard X-ray diffraction and diffuse* *reflectance infrared spectroscopy to illuminate CO dissociation and transient carbon storage by supported Pd nanoparticles during CO/NO cycling*. *J. Am. Chem. Soc.* **132**, 4540–4541.

Newton, M. A. & van Beek, W. (2010). *Combining synchrotron-based X-ray techniques with vibrational spectroscopies for the in situ study of heterogeneous catalysts: a view from a bridge*. *Chem. Soc. Rev.* **39**, 4845–4863.

Palmer, T. A., Elmer, J. W. & Babu, S. S. (2004). *Observation of ferrite/austenite transformations in the heat affected zone of 2205 duplex stainless steel spot welds using time resolved X-ray diffraction*. *Mater. Sci. Eng. A*, **374**, 307–321.

Parrish, W. (1988). *Advances in synchrotron X-ray polycrystalline diffraction*. *Aust. J. Phys.* **41**, 101–112.

Parrish, W. & Hart, M. (1987). *Advantages of synchrotron radiation for polycrystalline diffractometry*. *Z. Kristallogr.* **179**, 161–173.

Parrish, W., Hart, M., Erickson, C. G., Masciocchi, N. & Huang, T. C. (1986). *Instrumentation for synchrotron X-ray powder diffractometry*. *Adv. X-ray Anal.* **29**, 243–250.

Pennartz, P. U., Löchner, U., Fuess, H. & Wroblewski, T. (1992). *Powder diffraction in the range of milliseconds*. *J. Appl. Cryst.* **25**, 571–577.

Rijssenbeek, J., Gao, Y., Zhong, Z., Croft, M., Jisrawi, N., Ignatov, A. & Tsakalakos, T. (2011). *In situ X-ray diffraction of prototype sodium metal halide cells: time and space electrochemical profiling*. *J. Power Sources*, **196**, 2332–2339.

Rowles, M. R., Styles, M. J., Madsen, I. C., Scarlett, N. V. Y., McGregor, K., Riley, D. P., Snook, G. A., Urban, A. J., Connolley, T. & Reinhard, C. (2012). *Quantification of passivation layer growth in inert anodes for molten salt electrochemistry by in situ energy-dispersive diffraction*. *J. Appl. Cryst.* **45**, 28–37.

Sabine, T. M. (1987*a*). *The N-crystal spectrometer*. *J. Appl. Cryst.* **20**, 23–27.

Sabine, T. M. (1987*b*). *A powder diffractometer for a synchrotron source*. *J. Appl. Cryst.* **20**, 173–178.

Sabine, T. M., Hunter, B. A., Sabine, W. R. & Ball, C. J. (1998). *Analytical expressions for the transmission factor and peak shift in absorbing cylindrical specimens*. *J. Appl. Cryst.* **31**, 47–51.

Sasaki, S. (1989). *Numerical Tables of Anomalous Scattering Factors Calculated by the Cromer and Liberman Method*. KEK Report, 88–14, 1–136.

Scarlett, N. V. Y., Madsen, I. C., Evans, J. S. O., Coelho, A. A., McGregor, K., Rowles, M., Lanyon, M. R. & Urban, A. J. (2009). *Energy-dispersive diffraction studies of inert anodes*. *J. Appl. Cryst.* **42**, 502–512.

Seltzer, S. M. (1993). *Calculation of photon mass energy-transfer and mass energy-absorption coefficients*. *Radiat. Res.* **136**, 147–170.

Snigirev, A. A., Filseth, B., Elleaume, P., Klocke, Th., Kohn, V., Lengeler, B., Snigireva, I., Souvorov, A. & Tuemmler, J. (1997). *Refractive lenses for high-energy X-ray focusing*. *Proc. SPIE*, **3151**, 164–170.

Snigirev, A., Kohn, V., Snigireva, I., Souvorov, A. & Lengeler, B. (1998). *Focusing high-energy X rays by compound refractive lenses*. *Appl. Opt.* **37**, 653–662.

Spiller, E. (2000). *X-ray optics*. *Adv. X-ray Anal.* **42**, 297–307.

Techert, S. & Zachariasse, K. A. (2004). *Structure determination of the intramolecular charge transfer state in crystalline 4-(diisopropylamino) benzonitrile from picosecond X-ray diffraction*. *J. Am. Chem. Soc.* **126**, 5593–5600.

Terasaki, H. & Komizo, Y. (2011). *Diffusional and displacive transformation behaviour in low carbon-low alloy steels studied by a hybrid in situ observation system*. *Scr. Mater.* **64**, 29–32.

Thompson, P., Cox, D. E. & Hastings, J. B. (1987). *Rietveld refinement of Debye–Scherrer synchrotron X-ray data from* Al_2O_3. *J. Appl. Cryst.* **20**, 79–83.

Vaughan, G. B. M., Wright, J. P., Bytchkov, A., Rossat, M., Gleyzolle, H., Snigireva, I. & Snigirev, A. (2011). *X-ray transfocators: focusing devices based on compound refractive lenses*. *J. Synchrotron Rad.* **18**, 125–133.

Walton, R. I. & O'Hare, D. (2000). *Watching solids crystallise using in situ powder diffraction*. *Chem. Commun.* pp. 2283–2291.

Wong, J., Larson, E. M., Waide, P. A. & Frahm, R. (2006). *Combustion front dynamics in the combustion synthesis of refractory metal carbides and di-borides using time-resolved X-ray diffraction*. *J. Synchrotron Rad.* **13**, 326–335.

Wright, J., Vaughan, G. & Fitch, A. (2003). *Merging data from a multi-detector continuous scanning powder diffraction system*. *International Union of Crystallography Commission on Crystallographic Computing Newsletter*, **1**, 92–96.

Wroblewski, T. (1991). *Resolution functions of powder diffractometers at a synchrotron-radiation source*. *Acta Cryst.* A**47**, 571–577.

Yamanaka, T. & Ogata, K. (1991). *Structure refinement of* GeO_2 *polymorphs at high pressures and temperatures by energy-dispersive spectra of powder diffraction*. *J. Appl. Cryst.* **24**, 111–118.

Yao, T. & Jinno, H. (1982). *Polarization factor for the X-ray powder diffraction method with a single-crystal monochromator*. *Acta Cryst.* A**38**, 287–288.

Yonemura, M., Osuki, T., Terasaki, H., Komizo, Y., Sato, M. & Toyokawa, H. (2006). *Two-dimensional time-resolved X-ray diffraction study of directional solidification in steels*. *Mater. Trans.* **47**, 2292–2298.

Zachariasen, W. H. (1945). *Theory of X-ray Diffraction in Crystals*. Dover Publications Inc.

International Tables for Crystallography (2019). Vol. H, Chapter 2.3, pp. 66–101.

2.3. Neutron powder diffraction

C. J. Howard and E. H. Kisi

2.3.1. Introduction to the diffraction of thermal neutrons

Diffraction of neutrons occurs by virtue of their wave character, the de Broglie wavelength λ being

$$\lambda = \frac{h}{mv} = \frac{h}{(2mE)^{1/2}}, \qquad (2.3.1)$$

where m, v and E are the mass, speed and energy of the neutron, respectively, and h is Planck's constant. It may be convenient to express the neutron energy in meV, in which case the wavelength in ångströms is given by

$$\lambda\ (\text{Å}) = 9.045/(E)^{1/2}\ (\text{meV}). \qquad (2.3.2)$$

Thermal neutrons produced by a fission reactor have a representative energy of 25 meV, and accordingly a wavelength of 1.809 Å, which is well suited to the study of condensed matter since it is of the order of the interatomic spacings therein.

Neutrons have a number of distinctive properties making neutron diffraction uniquely powerful in several applications. They may be scattered by nuclei or by magnetic entities in the sample under study.

(*a*) *Scattering by nuclei*: The atomic nucleus is tiny compared with the atomic electron cloud, which is the entity that scatters X-rays and electrons. The scattering cross section for a particular nucleus is written as

$$\sigma = 4\pi b^2, \qquad (2.3.3)$$

where σ is typically of the order of 10^{-28} m^2 (1×10^{-28} m^2 = 1 barn) and b, which is termed the *scattering length*, is of the order of femtometres. The small size of the nucleus relative to the wavelength of interest means that the scattering is isotropic – there is no angle-dependent form factor, as occurs in the X-ray case (*cf.* Section 1.1.3.1). This confers advantages in studies aimed at determining atomic displacement parameters (ADPs),[1] and indeed for the total-scattering studies requiring data over a large Q range ($Q = 4\pi \sin\theta/\lambda$) that are described in Chapter 5.7. Importantly, scattering lengths vary somewhat erratically with atomic number Z; this is in marked contrast to the X-ray case in which the form factor increases monotonically with Z (see Figs. 2.3.1 and 2.3.2). This can make it much easier to detect the scattering from light (low-Z) elements in the presence of much heavier ones; it also makes it easier to distinguish scattering from elements adjacent in the periodic table, *e.g.* Cu with Z = 29, b = 7.718 fm and Zn with Z = 30, b = 5.680 fm. The scattering length is also different for different isotopes of the same element,[2] *e.g.* for ^{1}H b = −3.741 fm, whereas for ^{2}H b = 6.671 fm, so that sometimes isotopic substitution can be employed to obtain contrast as desired.

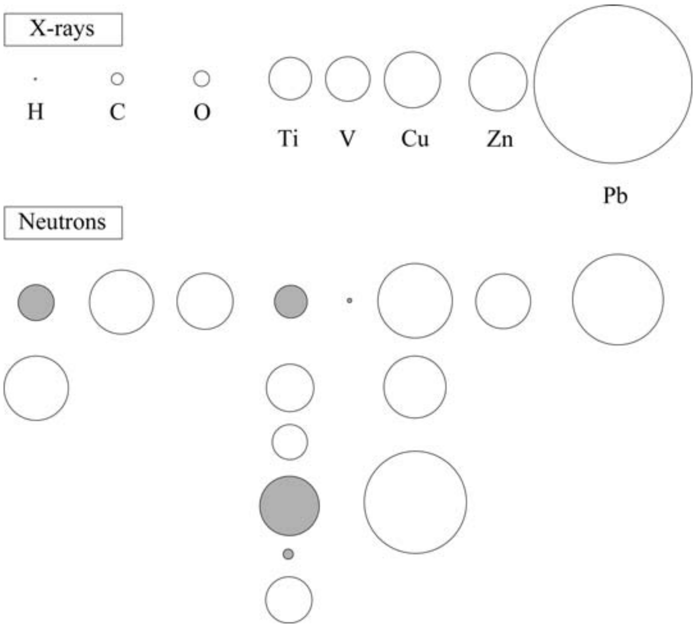

Figure 2.3.1
Representations of the scattering of X-rays and neutrons by selected elements. The scattering cross sections are proportional to the areas of the circles shown. For the neutron case, separate entries appear for the different isotopes and negative scattering lengths are indicated by shading. The figure is not intended to imply a relationship between the X-ray and neutron cross sections.

(*b*) *Scattering by magnetic entities*: The neutron carries a magnetic moment of $-1.913\,\mu_N$ (where μ_N is the nuclear magneton) and accordingly it interacts with magnetic entities in the sample. These may be nuclei, with magnetic moments of the order of the nuclear magneton, or atoms with much larger magnetic moments, of the order of the Bohr magneton (μ_B). If the magnetic entities are disordered, then the result is magnetic diffuse scattering, but if they are in some way ordered then the magnetic structure can be studied *via* the magnetic Bragg reflections that arise. (These may not be so obvious if they coincide with the nuclear Bragg reflections.) The magnetic moment of the neutron interacts with atomic magnetic moments, attributable to unpaired electrons in the atoms. These electrons tend to be the outer electrons, spread over dimensions comparable with atomic spacings and hence with the wavelengths used for diffraction; a consequence is that magnetic scattering is characterized by a magnetic form factor which falls off with Q more rapidly than does the form factor for the X-ray case (Fig. 2.3.3). The confirmation of the antiferromagnetic ordering in MnO below its ordering (Néel) temperature of 120 K (Fig. 2.3.4; Shull *et al.*, 1951) was the first of numerous studies of magnetic structure by neutron powder diffraction that have continued to the present day (Izyumov & Ozerov, 1970; Chatterji, 2006; Chapter 7 in Kisi & Howard, 2008). Investigations of nuclear moments are more challenging largely because the smaller moments mean extremely low ordering temperatures; nevertheless neutron diffraction has been used, for example, to study the ordering

---

[1] The atomic displacements (*e.g.* thermal vibrations) smear the scattering sites to an extent that is likely to be considerably smaller than the atom itself, but very much larger than the nucleus.

[2] If the nucleus in question carries spin, the scattering length also depends on the relative orientation of the neutron and nuclear spins.

Copyright © 2019 International Union of Crystallography

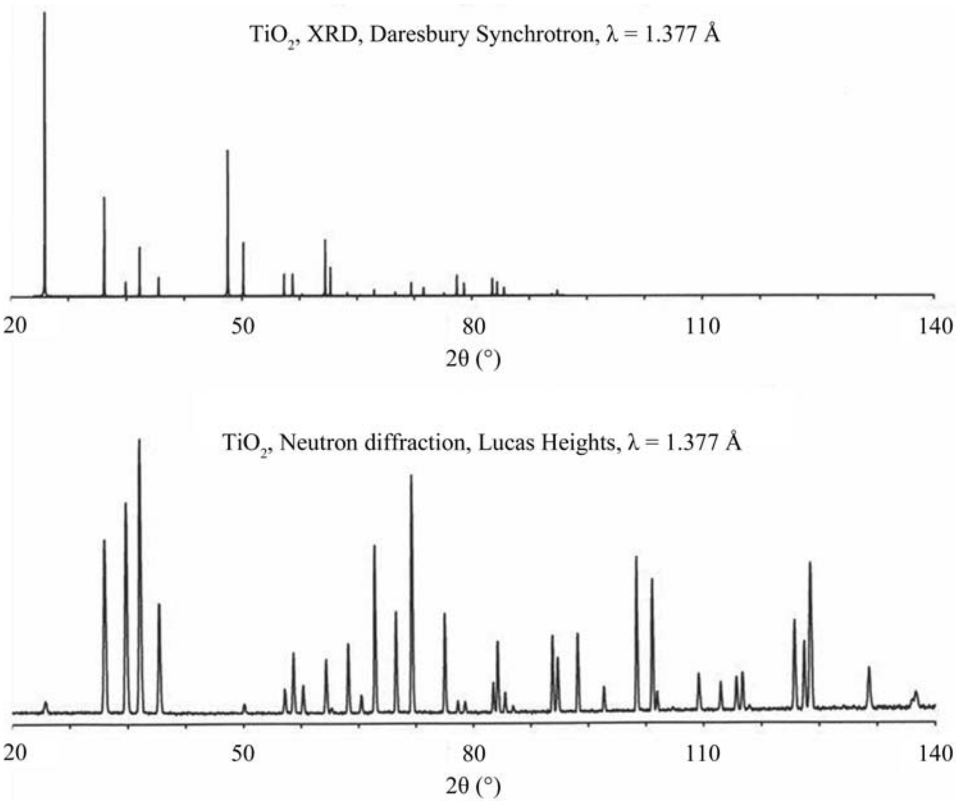

Figure 2.3.2
Comparison of X-ray and neutron powder-diffraction patterns from rutile, TiO$_2$. The patterns were recorded at the same wavelength, 1.377 Å. The differences between form factors and scattering lengths give rise to large differences in the relative intensities of the different peaks; note also that the fall off in the form factor evident in the X-ray case does not occur for neutrons.

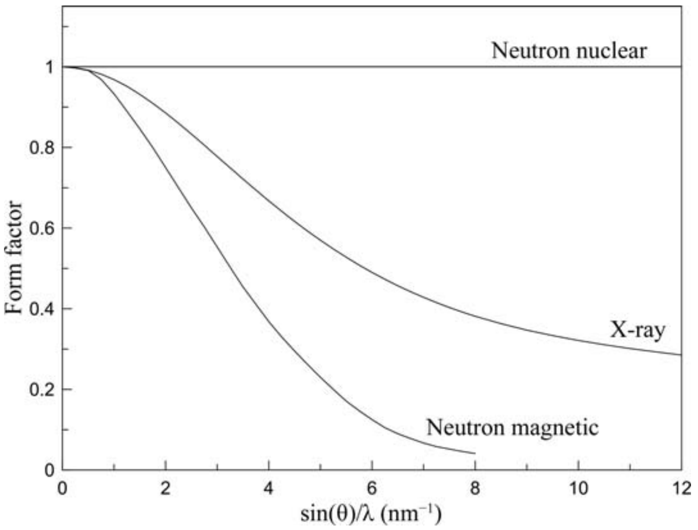

Figure 2.3.3
The magnetic form factor for Mn^{2+} compared with the normalized X-ray form factor and the normalized neutron nuclear scattering length.

of nuclear moments in metallic copper (^{65}Cu) at temperatures below 60 nK (Hakonen *et al.*, 1991).[3]

(*c*) *Low attenuation*: The combination of the small scattering cross sections and generally low cross sections for absorption (notable exceptions are B, Cd and Gd) gives thermal neutrons the ability to penetrate quite deeply into most materials. Indeed, the linear attenuation coefficient for thermal (25 meV) neutrons in Fe is 110 m^{-1}, and for neutrons in Al it is only about 9.8 m^{-1}; the implication is that it takes about 10 cm of Al to reduce the intensity by a factor 1/*e*. The fact that neutrons are so little attenuated by these materials makes it easier to design large and complex sample-environment chambers which may be used for *in situ* studies at high temperature, under pressure or stress, in magnetic fields, and in reaction cells (Chapters 2.6–2.9; Chapter 3 in Kisi & Howard, 2008). Neutron powder diffraction is well suited to quantitative phase analysis (QPA, see Chapter 3.9 and Chapter 8 in Kisi & Howard, 2008); as pointed out in Chapter 8, Section 8 of Kisi & Howard (2008), neutron QPA provides a better sampling ability and is less prone to microabsorption errors than the X-ray technique; indeed, neutron diffraction was the method employed in one of the earliest and most convincing demonstrations of the Rietveld method in QPA (Hill & Howard, 1987). Another advantage conferred by the deep penetration of neutrons is the ability to probe below the surface of samples to measure such aspects as structure, phase composition and stress; a particular example is the application to the analysis of zirconia ceramics (Kisi *et al.*, 1989) where the surface composition (as would be measured by X-rays) is unrepresentative of the bulk. A downside of the small scattering cross sections (along with neutron sources of limited 'brightness') is that relatively large samples may be required.

(*d*) *Low energy*: We note from equation (2.3.1) that, for a specified wavelength, the energy of the neutron is much less than that for lighter probes, such as electrons or photons. This is critically important for studying inelastic processes (*e.g.* measurement of phonon dispersion curves), but is usually not a factor in neutron powder diffraction.[4]

Neutron sources, in common with synchrotrons, are large national or international facilities, set up to cater for scientists from external laboratories. There are usually well defined access procedures, involving the submission and peer review of research proposals. Visiting users are usually assisted in their experiments by in-house staff. In some cases external users can mail in their samples for collection of diffraction data by the resident staff.

2.3.2. Neutrons and neutron diffraction – pertinent details

2.3.2.1. *Properties of the neutron*

The basic properties of the neutron are summarized in Table 2.3.1.

---

[3] This study depends on the spin-dependent scattering lengths rather than magnetic scattering *per se*.

[4] However, if the incident beam is monochromatic, a crystal monochromator placed in the diffracted beam can be used to exclude inelastic scattering from the 'background'.

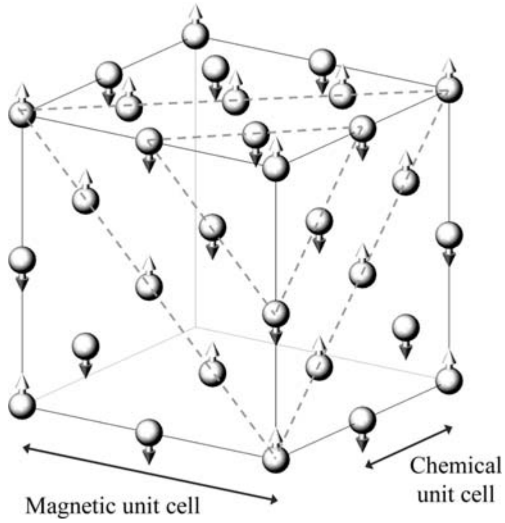

Figure 2.3.4
Magnetic structure for MnO proposed by Shull *et al.* (1951). The figure shows only the Mn atoms, and indeed only those Mn atoms located on the visible faces of the cubic cell. [From Shull *et al.* (1951), redrawn using *ATOMS* (Dowty, 1999).]

2.3.2.2. *Neutron scattering lengths*

The scattering lengths of most interest in neutron powder diffraction are those for coherent elastic scattering, $b_{\rm coh}$, often abbreviated to b. As already mentioned, there is no angle (Q) dependence, since the scattering from the nucleus is isotropic. A selection of scattering lengths for different isotopes and different elements is given in Table 2.3.2.

The first thing to note is the variation in scattering length from element to element and indeed from isotope to isotope. The scattering lengths are in most cases positive real numbers, in which case there is a phase reversal of the neutron on scattering, but for some isotopes the scattering lengths are negative, so there is no change in phase on scattering. The scattering lengths are determined by the details of the neutron–nucleus interaction (Squires, 1978).[5] In the event that the neutron–nucleus system is close to a resonance, such as it is for ^{10}B, ^{155}Gd and ^{157}Gd, scattering lengths will be complex quantities and the scattered neutron will have some different phase relationship with the incident one. The imaginary components imply absorption, which is reflected in the very high absorption cross sections, σ_a, for these isotopes.

The total scattering cross section, σ_s, is given by $\sigma_s = 4\pi b^2_{\rm coh}$ when only coherent scattering from a single isotope is involved, which is very nearly the case for oxygen since 99.76% of naturally occurring oxygen is zero-spin ^{16}O. In most cases there is a more substantial contribution from incoherent scattering, which may be either spin or isotope incoherent scattering. Spin incoherent scattering arises because the scattering length depends on the relative orientation of the neutron and nuclear spins, parallel and antiparallel arrangements giving rise to scattering lengths b_+ and b_-, respectively. Isotope incoherent scattering arises because of the different scattering of neutrons from different isotopes of the same element. In almost all circumstances (except, for example, at the extraordinarily low temperatures mentioned in Section 2.3.1) the distributions of spins and isotopes are truly random, which means that there is no angle dependence in this scattering: this is sometimes described as Laue monotonic scattering.

Table 2.3.1
Properties of the neutron (adapted from Kisi & Howard, 2008)

Mass (m)	1.675×10^{-27} kg
Charge	0
Spin	$\frac{1}{2}$
Magnetic moment (μ_n)	$-1.913\ \mu_N$
Wavelength (λ)	h/mv
Wavevector ($\mathbf{k}$)	Magnitude $2\pi/\lambda$
Momentum ($\mathbf{p}$)	$\hbar\mathbf{k}$
Energy (E)	$(1/2)mv^2 = h^2/2m\lambda^2$

When b varies from nucleus to nucleus (even considering just a single element), the coherent scattering is determined by the average value of b, that is $b_{\rm coh} = \overline{b}$, $\sigma_{\rm coh} = 4\pi(\overline{b})^2$, and the average incoherent cross section is given by $\sigma_{\rm inc} = 4\pi[\overline{b^2} - (\overline{b})^2]$. The total scattering cross section σ_s is the sum of the two cross sections (Squires, 1978; see also Section 2.3.2 in Kisi & Howard, 2008). For the particular case of a nucleus with spin I, the states $I + 1/2$ and $I - 1/2$ give scattering determined by b_+ and b_-, respectively, and have multiplicities $2I + 2$ and $2I$, respectively, from which it follows that

$$b_{\rm coh} = \overline{b} = \frac{I+1}{2I+1} b_+ + \frac{I}{2I+1} b_-,$$
$$b^2_{\rm inc} = \left[\overline{b^2} - (\overline{b})^2\right] = \frac{I(I+1)}{(2I+1)^2}(b_+ - b_-)^2.$$

More information, including a comprehensive listing of scattering lengths, can be found in Section 4.4.4 of *International Tables for Crystallography* Volume C (Sears, 2006). This listing presents the spin-dependent scattering lengths *via* $b_{\rm coh}$ and $b_{\rm inc}$ as just defined. Other compilations can be found in the *Neutron Data Booklet* (Rauch & Waschkowski, 2003), and online through the Atominstitut der Österreichischen Universitäten, Vienna, at http://www.ati.ac.at/~neutropt/scattering/table.html. In addition, the majority of computer programs used for the analysis of data from neutron diffraction incorporate, for convenience, a list of $b_{\rm coh}$ values for the elements.

2.3.2.3. *Refractive index for neutrons*

The coherent scattering lengths of the nuclei determine the refractive index for neutrons through the relationship (Squires, 1978)

$$n = 1 - \frac{1}{2\pi}\lambda^2 N b_{\rm coh}, \qquad (2.3.4)$$

where N is the number of nuclei per unit volume. For elements with positive values of the coherent scattering length the refractive index is slightly less than one, and that leads to the possibility of total external reflection of the neutrons by the element in question. In fact, when the coherent scattering length is positive, neutrons will undergo total external reflection for glancing angles less than a critical angle γ_c given by

$$\cos\gamma_c = n = 1 - \frac{1}{2\pi}\lambda^2 N b_{\rm coh}, \qquad (2.3.5)$$

which, since γ_c is small, reduces to

$$\gamma_c = \lambda\left(\frac{N b_{\rm coh}}{\pi}\right)^{1/2}. \qquad (2.3.6)$$

It can be seen that the pertinent material quantity is $Nb_{\rm coh}$, the 'coherent scattering length density'; for materials comprising more than one element this is the quantity that would be

---

[5] It is evident from Fig. 2.3 in this reference that even for an attractive interaction between neutron and nucleus positive scattering lengths will predominate.

Table 2.3.2

Coherent scattering lengths and absorption cross sections (for 25 meV neutrons) for selected isotopes

Data are taken from Section 4.4.4 of Volume C (Sears, 2006). Where not stated, the values are for the natural isotopic mix. The X-ray atomic form factors, f, evaluated at $Q = 1.2\pi$ Å^{-1}, are included for comparison.

Element	Isotope	$b_{\rm coh}$ (fm)	$\sigma_{s({\rm tot})}$ (10^{-24}cm^2)	σ_a (10^{-24}cm^2)	f	Isotopic abundance (%)
H		−3.7390 (11)	82.02 (6)	0.3326 (7)	0.25	
	1	−3.7406 (11)	82.03 (6)	0.3326 (7)		99.985
	2	6.671 (4)	7.64 (3)	0.000519 (7)		0.015
	3	4.792 (27)	3.03 (5)	0		—
B		5.30 (4) − 0.213 (2)i	5.24 (11)	767 (8)	1.99	
	10	−0.1 (3) − 1.066 (3)i	3.1 (4)	3835 (9)		20.0
	11	6.65 (4)	5.78 (9)	0.0055 (33)		80.0
C		6.6460 (12)	5.551 (3)	0.00350 (7)	2.50	
	12	6.6511 (16)	5.559 (3)	0.00353 (7)		98.90
	13	6.19 (9)	4.84 (14)	0.00137 (4)		1.10
O		5.803 (4)	4.232 (6)	0.00019 (2)	4.09	
Ti		−3.370 (13)	4.06 (3)	6.43 (6)	13.2	
	46	4.725 (5)	2.80 (6)	0.59 (18)		8.2
	47	3.53 (7)	3.1 (2)	1.7 (2)		7.4
	48	−5.86 (2)	4.32 (3)	8.30 (9)		73.8
	49	0.98 (5)	3.4 (3)	2.2 (3)		5.4
	50	5.88 (10)	4.34 (15)	0.179 (3)		5.2
V		−0.3824 (12)	5.10 (6)	5.08 (2)	14.0	
Ni		10.3 (1)	18.5 (3)	4.49 (16)	18.7	
	58	14.4 (1)	26.1 (4)	4.6 (3)		68.27
	60	2.8 (1)	0.99 (7)	2.9 (2)		26.10
	61	7.60 (6)	9.2 (3)	2.5 (8)		1.13
	62	−8.7 (2)	9.5 (4)	14.5 (3)		3.59
	64	−0.37 (7)	0.017 (7)	1.52 (3)		0.91
Cu		7.718 (4)	8.03 (3)	3.78 (2)	19.9	
	63	6.43 (15)	5.2 (2)	4.50 (2)		69.17
	65	10.61 (19)	14.5 (5)	2.17 (3)		30.83
Zn		5.680 (5)	4.131 (10)	1.11 (2)	20.8	
Zr		7.16 (3)	6.46 (14)	0.185 (3)	27.0	
Gd		6.5 (5)	180 (2)	49700 (125)	45.9	
	155	6.0 (1) − 17.0 (1)i	66 (6)	61100 (400)		14.8
	157	−1.14 (2) − 71.9 (2)i	1044 (8)	259000 (700)		15.7
Pb		9.405 (3)	11.118 (7)	0.171 (2)	60.9	

computed. Since the critical angle for total external reflection is proportional to the neutron wavelength, it is convenient to express this as degrees per ångstrom of neutron wavelength. These are important considerations in the design and development of neutron guides (Section 2.3.3.4).

2.3.2.4. *Neutron attenuation*

Neutron beams are attenuated by coherent scattering, incoherent scattering and true absorption. The cross sections for all these processes are included in the tables cited above. For powder diffraction, the coherent scattering is usually small because it takes place only in that small fraction of crystallites correctly oriented for Bragg reflection; the other processes, however, take place throughout the sample.

If a particular scattering entity i with scattering cross sections $(\sigma_i)_{\rm inc}$ and $(\sigma_i)_{\rm abs}$ is present at a number density N_i, then the contribution it makes to the linear attenuation coefficient μ is $\mu_i = N_i[(\sigma_i)_{\rm inc} + (\sigma_i)_{\rm abs}]$. If the mass is M_i, then the density is simply $\rho_i = N_iM_i$, so we have the means to evaluate the mass absorption coefficient $(\mu/\rho)_i$. The calculation of absorption for elements, compounds and mixtures commonly proceeds by the manipulation of mass absorption coefficients, in the same manner as is employed for X-rays (see Section 2.4.2 in Kisi & Howard, 2008).

2.3.2.5. *Magnetic form factors and magnetic scattering lengths*

For a complete treatment of the magnetic interaction between the neutron and an atom carrying a magnetic moment, and the resulting scattering, the reader is referred elsewhere [Marshall & Lovesey, 1971; Squires, 1978; Section 6.1.2 of Volume C (Brown, 2006*a*)]. The magnetic moment of an atom is associated with unpaired electrons, but may comprise both spin and orbital contributions. The magnetic interaction between the neutron and the atom depends on the directions of the scattering vector and the magnetic moment vector according to a triple vector product. The direction of polarization of the neutron must also be taken into account. For an unpolarized incident beam, the usual case in neutron powder diffraction, it is a useful consequence of the triple vector product that the magnetic scattering depends on the sine of the angle that the scattering vector makes with the magnetic moment on the scattering atom (see Section 2.3.4 and Chapter 7 in Kisi & Howard, 2008). The extent of the unpaired electron distribution (usually outer electrons) implies that the scattering diminishes as a function of Q, an effect that can be described by a magnetic form factor. For a well defined direction for the magnetic moment $\mathbf{M}$, and with a distribution of moment that can be described by a normalized scalar $m(\mathbf{r})$, the form factor as a function of the scattering vector $\mathbf{h}$ [defined in equation (1.1.17) in Chapter 1.1][6] is the Fourier transform of $m(\mathbf{r})$,

$$f(\mathbf{h}) = \int m(\mathbf{r}) \exp(2\pi i \mathbf{h}\cdot\mathbf{r})\,\mathrm{d}\mathbf{r},$$

where $m(\mathbf{r})$ can comprise both spin and orbital contributions [Section 6.1.2 of Volume C (Brown, 2006*a*)]. The tabulated form factors are based on the assumption that the electron distributions are spherically symmetric, so that $m(\mathbf{r}) = m(r) = U^2(r)$, where $U(r)$ is the radial part of the wave function for the unpaired electron. In the expansion of the plane-wave function $\exp(2\pi i\mathbf{h}\cdot\mathbf{r})$ in terms of spherical Bessel functions, we find that the leading term is just the zeroth-order spherical Bessel function $j_0(2\pi hr)$ with a Fourier transform

$$\langle j_0(h)\rangle = 4\pi \int\limits_0^\infty U^2(r) j_0(2\pi hr) r^2\,\mathrm{d}r.$$

This quantity is inherently normalized to unity at $h = 0$, and may suffice to describe the form factor for spherical spin-only cases. In other cases it may be necessary to include additional terms in the expansion, and these have Fourier transforms of the form

$$\langle j_l(h)\rangle = 4\pi \int\limits_0^\infty U^2(r) j_l(2\pi hr) r^2\,\mathrm{d}r$$

with l even; these terms are zero at $h = 0$ (Brown, 2006*a*). In practice these quantities are evaluated using theoretical calculations of the radial distribution functions for the unpaired electrons [Section 4.4.5 of Volume C (Brown, 2006*b*)].

Form factors can be obtained from data tabulated in Section 4.4.5 of Volume C (Brown, 2006*b*). Data are available for elements and ions in the 3*d*- and 4*d*-block transition series, for rare-earth ions and for actinide ions. These data are provided by way of the coefficients of analytical approximations to $\langle j_l(h)\rangle$, the analytical approximations being

$$\langle j_0(s)\rangle = A\exp(-as^2) + B\exp(-bs^2) + C\exp(-cs^2) + D$$

and for $l \neq 0$

$$\langle j_l(s)\rangle = s^2\left[A\exp(-as^2) + B\exp(-bs^2) + C\exp(-cs^2) + D\right],$$

where $s = h/2$ in Å^{-1}. These approximations, with the appropriate coefficients, are expected to be coded in to any computer program purporting to analyse magnetic structures. Although the tabulated form factors are based on theoretical wave functions, it is worth noting that the incoherent scattering from an ideally disordered (*i.e.*, paramagnetic) magnetic system will display the magnetic form factor directly.

It is often convenient to define a (Q-dependent) magnetic scattering length

$$p = \left(\frac{e^2\gamma}{2m_e c^2}\right) gJf,$$

where m_e and e are the mass and charge of the electron, γ (= μ_n) is the magnetic moment of the neutron, c is the speed of light, J is the total angular momentum quantum number, and g is the Landé splitting factor given in terms of the spin S, orbital angular momentum L, and total angular momentum quantum numbers by

$$g = 1 + \frac{J(J+1) + S(S+1) - L(L+1)}{2J(J+1)}.$$

For the spin-only case, $L = 0$, $J = S$, so $g = 2$. The differential magnetic scattering cross section per atom is then given by q^2p^2 where $|q| = \sin\alpha$, α being the angle between the scattering vector and the direction of the magnetic moment. This geometrical factor is very important, since it can help in the determination of the orientation of the moment of interest; there is no signal, for example, when the moment is parallel to the scattering vector. Further discussion appears in Chapters 2 (Section 2.3.4) and 7 in Kisi & Howard (2008).

2.3.2.6. *Structure factors*

The locations of the Bragg peaks for neutrons are calculated as they are for X-rays[7] (Section 1.1.2), and the intensities of these peaks are determined by a structure factor, which in the nuclear case is [*cf.* Chapter 1.1, equation (1.1.56)]

$$F_{hkl}^{\rm nuc} = \sum_{i=1}^{m} b_i T_i \exp(2\pi i\mathbf{h}\cdot\mathbf{u}_i), \qquad (2.3.7)$$

where b_i here denotes the coherent scattering length, T_i has been introduced to represent the effect of atomic displacements (thermal or otherwise, see Section 2.4.1 in Kisi & Howard, 2008), $\mathbf{h}$ is the scattering vector for the *hkl* reflection, and the vectors $\mathbf{u}_i$ represent the positions of the m atoms in the unit cell.

For coherent magnetic scattering, the structure factor reads

$$F_{hkl}^{\rm mag} = \sum_{i=1}^{m} p_i \mathbf{q}_i T_i \exp(2\pi i\mathbf{h}\cdot\mathbf{u}_i), \qquad (2.3.8)$$

where p_i is the magnetic scattering length. The vector $\mathbf{q}_i$ is the 'magnetic interaction vector' and is defined by a triple vector product (Section 2.3.4 in Kisi & Howard, 2008), and has modulus $\sin\alpha$ as already mentioned. In this case the sum needs to be taken over the magnetic atoms only.

As expected by analogy with the X-ray case, the intensity of purely nuclear scattering is proportional to the square of the modulus of the structure factor $|F_{hkl}^{\rm nuc}|^2$. In the simplest case of a collinear magnetic structure and an unpolarized incident neutron beam, the intensity contributed by the magnetic scattering is proportional to $|F_{hkl}^{\rm mag}|^2$, and the nuclear and magnetic contributions are additive.

2.3.3. Neutron sources

2.3.3.1. *The earliest neutron sources*

The earliest neutron source appears to have been beryllium irradiated with α-particles (helium nuclei), as emitted for example by polonium or radon. First described as 'beryllium radiation', the radiation from a Po/Be source was identified by

---

[6] To reiterate, $\mathbf{h} = \mathbf{s} - \mathbf{s}_0$, where $\mathbf{s}_0$ and $\mathbf{s}$ are vectors, each of magnitude $1/\lambda$, defining the incident and scattered beams. Note that $\mathbf{Q} = 2\pi\mathbf{h}$.

[7] The nuclear unit cell is expected to coincide with the X-ray unit cell, but the magnetic unit cell may be larger. So, although the methods of calculation are the same, the larger magnetic cell may give rise to additional (magnetic) Bragg peaks.

Chadwick (1932) as comprising neutrons:

$$^{4}_{2}\mathrm{He} + ^{9}_{4}\mathrm{Be} \rightarrow ^{12}_{6}\mathrm{C} + ^{1}_{0}\mathrm{n}.$$

It was soon found (Szilard & Chalmers, 1934) that the disintegration of beryllium under irradiation by the γ-rays from radium also led to the release of neutrons; this represented an alternative neutron source. The first demonstrations of the diffraction of neutrons (Mitchell & Powers, 1936; von Halban & Preiswerk, 1936) made use of Rn/Be sources, analogous to Chadwick's Po/Be source. These were now surrounded by paraffin to reduce the energy ('moderate') and hence increase the de Broglie wavelength of the neutrons, and so provide a reasonable match to the atomic spacings in the crystalline samples; in the Mitchell & Powers' demonstration the reflection of neutrons of estimated wavelength 1.6 Å from (100) planes in large single crystals of MgO, the separation of these planes being 4.2 Å, showed a dependence on crystal orientation that was indicative of Bragg reflection. The intensities available from these sources, however, were not sufficient to allow the observation of diffraction from polycrystalline (powder) samples.

A source based on the bombardment of Be by cyclotron-accelerated MeV deuterons (nuclei of deuterium)

$$^{2}_{1}\mathrm{H} + ^{9}_{4}\mathrm{Be} \rightarrow ^{10}_{5}\mathrm{B} + ^{1}_{0}\mathrm{n}$$

was also employed in early work, notably by Alvarez & Bloch (1940) in their determination of the neutron magnetic moment.

The further development of neutron diffraction, and indeed the first observation of neutron powder diffraction, awaited the development of much more intense neutron sources; the first suitably intense neutron sources were nuclear reactors. The neutron-induced fission of uranium isotope $^{235}_{92}\mathrm{U}$ was observed in 1938 and reported early in 1939 (Hahn & Strassmann, 1939; Meitner & Frisch, 1939; Anderson *et al.*, 1939). By this time Fermi and his co-workers (Fermi, Amaldi, D'Agostino *et al.*, 1934; Fermi, Amaldi, Pontecorvo *et al.*, 1934) had already carried out studies on neutron activation, in the course of which they found that neutrons could be moderated by hydrogenous materials, providing 'slow' neutrons for which the activation cross sections were enhanced. Once it was established that the neutron-induced fission of a $^{235}_{92}\mathrm{U}$ nucleus also led to the release of ~2–3 'fast' neutrons plus energy (von Halban *et al.*, 1939; Zinn & Szilard, 1939), then a self-sustaining 'chain reaction' based on the fission of $^{235}_{92}\mathrm{U}$ by a slow neutron, the slowing in a moderator of the several fast neutrons released, followed by the slow-neutron-induced fission of additional $^{235}_{92}\mathrm{U}$ nuclei, became a realistic possibility. The translation of this possibility into reality was given great impetus by the military potential of the chain reaction; the reader is referred to Mason *et al.* (2013) for the history of this development. The first self-sustaining chain reaction took place in Chicago Pile 1 (CP-1) on 2 December 1942. CP-1 made use of uranium oxide mixed with some metallic uranium as fuel, high-purity graphite as the neutron moderator and rods of neutron-absorbing cadmium for control. CP-1 was located on a squash court under the spectator stand at a sports field at the University of Chicago; remarkably, its construction took less than a month. In November 1943, an essentially scaled up version of this reactor, the X-10 pile (also known as the Oak Ridge Graphite Reactor) achieved criticality. The fuel was now metallic uranium, and the greater power (1 MW as compared with the 200 W of CP-1) necessitated an air cooling system; the neutron flux[8] was a creditable 10^{12} n cm^{-2} s^{-1} and the main purpose was the production of plutonium. May 1944 saw the completion of yet another reactor, Chicago Pile 3 (CP-3), outside Chicago at the site of the present Argonne laboratories. This was a 300 kW reactor, using natural uranium fuel, with heavy water serving as both moderator and coolant; this also provided a flux of 10^{12} n cm^{-2} s^{-1}.

Early diffraction experiments using reactor neutrons were carried out 'in the wings of the Manhattan project' (Mason *et al.*, 2013). Evidently, Wollan & Borst (1945) obtained rocking curves when collimated thermal neutrons from X-10 were beamed onto single crystals of gypsum and rocksalt, while Zinn was able to reflect neutrons from a calcite crystal [see, for example, the post-war publication by Zinn (1947)]; much of the wartime interest was in using these crystals for neutron spectrometry. However, the potential use of these copious sources of neutrons was recognized, so by the early months of 1946 (according to Shull, 1995) the first neutron powder-diffraction patterns, from polycrystalline NaCl and from light and heavy water, had been recorded. Wollan and co-workers (Wollan & Shull, 1948; Shull *et al.*, 1948) published a number of these early diffraction patterns, along with a schematic of the diffractometer employed.

Although accelerator-based neutron sources had been around as early as 1940 (see above), the development of such sources, at least for diffraction applications, proceeded at a relatively slower pace. Indeed, it was not until 1968 that the first reports of neutron powder diffraction using accelerator-based sources appeared in the literature (Moore *et al.*, 1968; Kimura *et al.*, 1969; Day & Sinclair, 1969). All this work involved the use of linear electron accelerators (LINACs) delivering pulses of ~150 MeV electrons onto a heavy-metal target; the deceleration results in *Bremsstrahlung* radiation (photons) of sufficient energy to bring about the release of neutrons from the target. These fast neutrons were moderated, and the result was a pulsed source of thermal neutrons. Diffraction patterns were recorded by time-of-flight methods which had already been developed on reactor sources (Buras & Leciejewicz, 1964).

It may be helpful to describe one of these experiments in more detail (Kimura *et al.*, 1969). A tungsten target immersed in water was bombarded by 2.5 µs pulses of 250 MeV electrons from the Tohoku LINAC; the water, which served as a moderator, was also 'poisoned' by the addition of neutron-absorbing boric acid. The thermal neutron pulses were of 30–50 µs duration. It is a fundamental problem that the time taken to moderate the fast neutrons produced at an accelerator-based source degrades the time structure, and the addition of boron here was one method to counteract this effect. Kimura *et al.* presented a selection of time-of-flight diffraction patterns, from Al at different temperatures, as well as from Si, Ni, ZnO, $\mathrm{CaFe_2O_4}$ and α-$\mathrm{Fe_2O_3}$.

The next generation of accelerator-based sources were spallation sources, based on the breaking up of heavy target elements by bombardment with 10–1000 MeV protons; up to ~30 neutrons are ejected in each spallation event; such sources can be operated in either a pulsed mode or continuously. The first spallation sources were ZING-P (100 nA of 300 MeV protons, pulsed at 30 Hz, target Pb, moderator polyethylene) and ZING-P′ (3 µA of 500 MeV protons, 30 Hz, target W/natural U, moderator polyethylene/liquid hydrogen), both at the Argonne National Laboratory (Carpenter, 1977), and at the TRIUMF laboratory (400 µA of 500 MeV protons, steady, target liquid Pb/Bi, moderator light/heavy water) in Vancouver. The KENS facility (operational from 1980 to 2005, 9 µA of 500 MeV protons, 20 Hz, target W, moderator solid methane/ice) in Tsukuba, Japan, and the Intense Pulsed Neutron Source (IPNS) at the Argonne National Laboratory (operational from 1981 to 2008, 15 µA of 450 MeV protons, 30 Hz, target depleted U, moderator solid/liquid methane) are both worthy of mention for their work on techniques and applications at pulsed neutron sources; notable are contributions from IPNS on the subjects of high-temperature superconductors (Jorgensen *et al.*, 1987) and colossal magnetoresistance (Radaelli *et al.*, 1997).

---

[8] The powers and fluxes given here are taken from a presentation by T. E. Mason at the Bragg Symposium, Adelaide, 6 December 2012.

The specifications and performance of modern currently operating spallation neutron sources will be presented in Section 2.3.3.3.

2.3.3.2. *Fission reactors for neutron-beam research*

Reactors used for neutron-beam research all rely on the fissile uranium isotope[9] $^{235}_{92}$U. This constitutes only about 0.7% of natural uranium; however, enrichment in this isotope is possible. A representative fission event would be

$$^{1}_{0}\mathrm{n} + {}^{235}_{92}\mathrm{U} \rightarrow {}^{236}_{92}\mathrm{U} \rightarrow {}^{141}_{56}\mathrm{Ba} + {}^{92}_{36}\mathrm{Kr} + 3^{1}_{0}\mathrm{n} + 170\ \mathrm{MeV}.$$

This equation indicates that a neutron of thermal energy is captured by ^{235}U to form ^{236}U in an unstable state, and in the majority of cases (88%) this breaks up almost instantly to yield fission products of intermediate mass, fast neutrons and energy. The unstable ^{236}U can break up in many different ways – there are usually products of intermediate but unequal masses, with masses distributed around 95 and 135 (Burcham, 1979), with the release of usually 2 or 3 neutrons (average 2.5; one of these neutrons is needed to initiate the next fission event), and of different amounts of energy (average around 200 MeV). As explained in Section 2.3.3.1, a chain reaction becomes possible if the fast neutrons released in the fission process are moderated to thermal energies so that they can be captured by another ^{235}U nucleus. Neutrons will lose energy most rapidly through collisions with nuclei of mass equal to the neutron mass, namely nuclei of hydrogen atoms, but collisions with other light nuclei are also quite effective. Hydrogenous substances are evidently useful, and water would seem ideal; however, there is some absorption of neutrons in water, so in some reactors, heavy water (D_2O, where D is $^{2}_{1}$H) is used since, as can be seen from the absorption cross sections (Table 2.3.2), thermal neutron capture in D is orders of magnitude less than for H. It has not been possible to achieve a self-sustaining chain reaction using natural uranium and light water as a moderator – for this reason uranium fuel enriched in ^{235}U and/or heavy-water moderators are in use. Adjacent to the reactor core is a so-called reflector, which is simply in place to moderate neutrons and prevent their premature escape. The energy released in the fission process ends up as heat, which must be dissipated (or used), so cooling is required – where light or heavy water is used as the moderator it can also serve as the coolant. Control rods are also essential – these are rods containing highly neutron absorbing materials, such as boron, cadmium or hafnium, which can be inserted into or withdrawn from the reactor to increase, maintain or reduce the thermal neutron flux as required. These control rods provide the means for reactor shutdown.

The neutrons in a reactor core range from the fast neutrons (~1 MeV) released in the fission process, through epithermal neutrons (in the range eV to keV), which are neutrons in the process of slowing down, to thermal neutrons (~25 meV), which are neutrons in equilibrium with the moderator (see Carlile, 2003). Evidently, for sustaining the chain reaction and for providing neutrons for diffraction instruments, the thermal neutrons are of the greatest interest. Neutrons in thermal equilibrium with the moderator have a Maxwellian distribution of energies, such that the number of neutrons with energies between E and $E + \mathrm{d}E$ is given by $N(E)\,\mathrm{d}E$, where

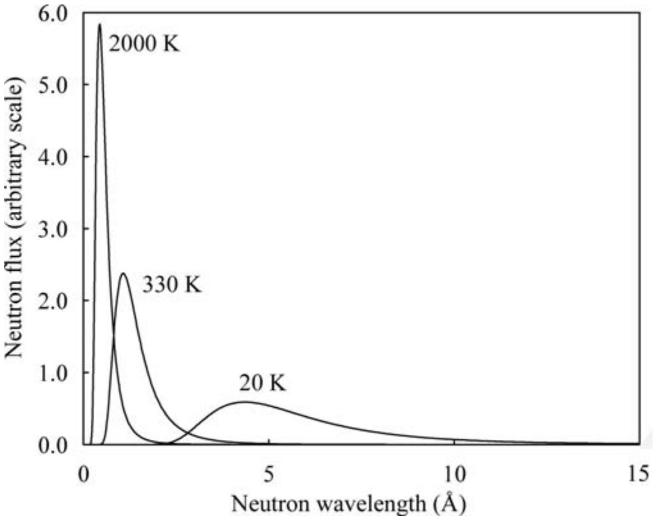

Figure 2.3.5
The Maxwellian distribution of neutron wavelengths produced within moderators at different temperatures. Reproduced from Kisi & Howard (2008) by permission of Oxford University Press.

$$N(E) = \frac{2\pi N_0}{(\pi k_B T)^{3/2}} (E)^{1/2} \exp(-E/k_B T). \qquad (2.3.9)$$

Here N_0 is the total number of neutrons, T is the temperature (in kelvin) of the moderator, and k_B is Boltzmann's constant. The neutron flux is the product of the neutron density with the neutron speed, so the energy dependence of the flux distribution takes the form

$$\varphi(E) = \varphi_0 \frac{E}{(k_B T)^{3/2}} \exp(-E/k_B T). \qquad (2.3.10)$$

This distribution takes its peak value at $E = k_B T$; for a temperature of 293 K, this leads to a peak in the flux distribution at 25.2 meV (*cf.* Section 2.3.1). In the diffraction context the wavelength dependence of the flux is of more interest. Making use of the relationships $E = h^2/2m\lambda^2$ and $\mathrm{d}E/\mathrm{d}\lambda = -h^2/m\lambda^3$, we find that the variation of flux with wavelength can be described by $\varphi(\lambda)\,\mathrm{d}\lambda$, where

$$\varphi(\lambda) \propto \lambda^{-5} \exp(-h^2/2m\lambda^2 k_B T). \qquad (2.3.11)$$

This distribution peaks at $\lambda = h/(5mk_B T)^{1/2}$; at 293 K the peak in this wavelength distribution is at 1.15 Å. For some applications of neutron diffraction it may be desirable to have a greater neutron flux at shorter or longer wavelengths; as indicated in Fig. 2.3.5 this can be achieved by cooling or heating strategically placed special moderators.

As one specific example of a research reactor, we consider the NBSR located at the National Institute of Standards and Technology, Gaithersburg, USA. This reactor uses highly enriched (93% ^{235}U) uranium in U_3O_8-Al as fuel, and heavy water as moderator and coolant. The thermal neutron flux in this reactor is 4×10^{14} n cm^{-2} s$^{\ 1}$. It uses four cadmium control blades. An early plan view of this reactor and a cutaway view of the core assembly

---

[9] Bombardment with >1 MeV neutrons can cause the fission of the predominant uranium isotope ^{238}U; however, there are too few neutrons at these energies to support a chain reaction based on this isotope.

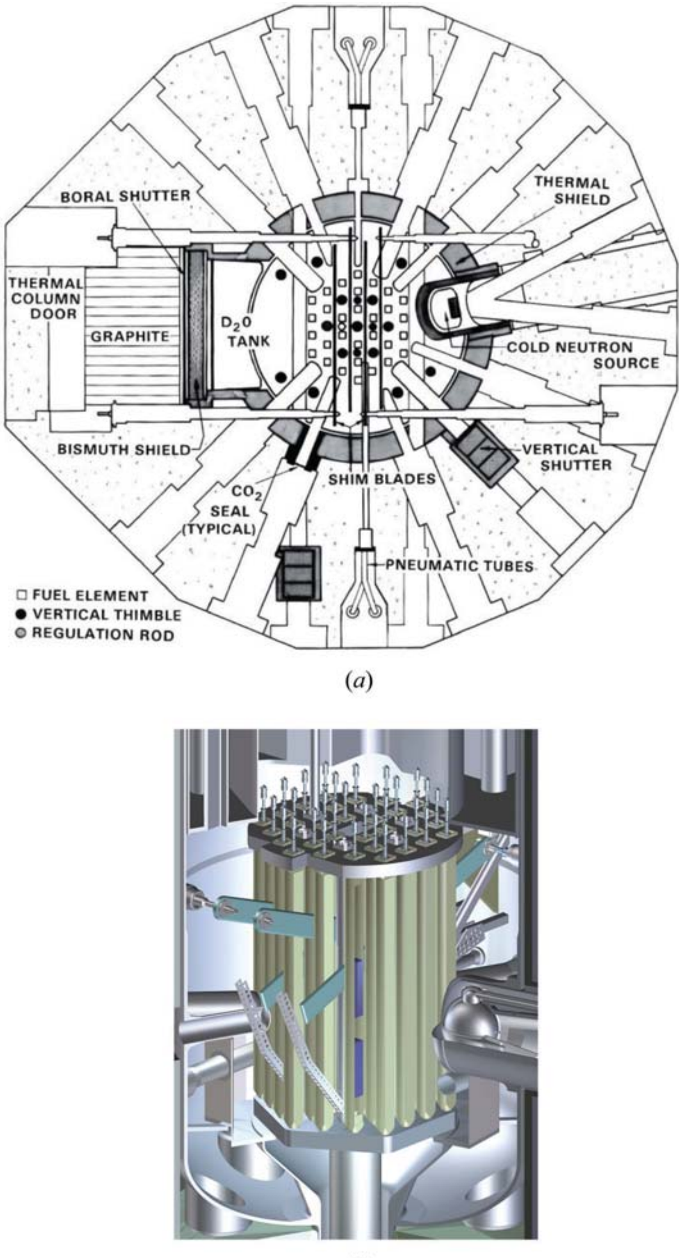

(*a*)

(*b*)

Figure 2.3.6
The NBSR at the National Institute of Standards and Technology Center for Neutron Research. Part (*a*) is a plan view (reproduced from Rush & Cappelletti, 2011) while (*b*) is a recent cutaway view of the reactor core showing the liquid-hydrogen cold source on the right-hand side.

are shown in Fig. 2.3.6. Note the presence of numerous beam tubes that allow neutrons to be taken out from the vicinity of the reactor core. This view of the NBSR (Fig. 2.3.6*a*) shows provision for a cold neutron source, and for beam tubes to transport cold neutrons to experiments, but it was years before any cold neutron source was installed. The first cold source, installed in 1987, was frozen heavy water; this was replaced in 1995 by a liquid-hydrogen cold source, and that was upgraded in turn in 2003. The NBSR first went critical in December 1967; the history of its subsequent development and use in neutron-beam research has been recounted by Rush & Cappelletti (2011).

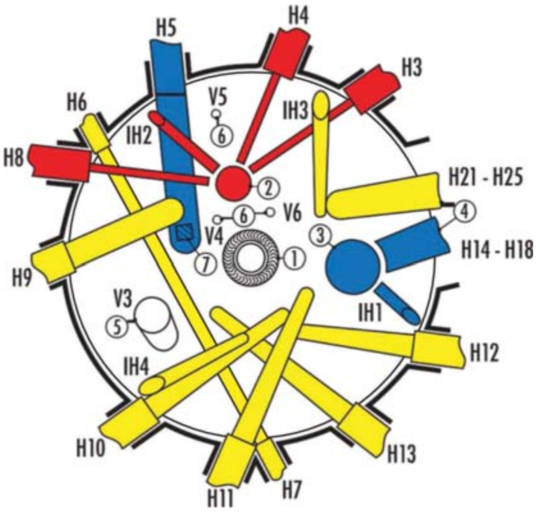

Figure 2.3.7
Schematic diagram of the HFR operated by the Institut Laue–Langevin in Grenoble, France. It has a compact core – the beam tubes avoid viewing the central core in favour of the surrounding moderator. This reactor also features hot (red) and cold (blue) sources. (Diagram reproduced with permission from the ILL from The Yellow Book 2008, https://www.ill.eu/fileadmin/users_files/Other_Sites/Yellow-Book2008CDRom/index.htm.)

The HFR at the Institut Laue–Langevin (ILL), considered to be the premier source for reactor-based neutron-beam research, serves as our second example. It too uses highly enriched uranium, here in a single centrally located U_3Al_x-Al fuel element, and it relies on heavy water for moderator and coolant. It operates at 58 MW and the thermal neutron flux is 1.5 × 10^{15} n cm^{-2} s^{-1}. The reactor incorporates two liquid-deuterium cold sources, operating at 20 K, and a graphite hot source operating at 2000 K. In the HFR, being of modern design and purpose-built for neutron-beam research, the beam tubes do not view the core directly, but are 'tangential' to it (Fig. 2.3.7); this reduces the unwelcome fast-neutron component of the emerging beams. The HFR achieved criticality in July 1971. More details on this reactor can be found in the 'Yellow Book' which is maintained on the ILL web site, https://www.ill.eu.

From the opening paragraph of this section, it might be concluded that the more heavy water deployed, and the more highly is the uranium enriched in the fissile isotope ^{235}U, the greater the neutron fluxes that can be obtained. This conclusion would be correct, but concerns about nuclear proliferation have brought a shift to the use of low-enrichment uranium (LEU) in which the ^{235}U is enriched to less than 20%; however, in some reactors highly enriched uranium (HEU) with enrichment levels greater than 90% remains in use. Table 2.3.3 gives pertinent details on a number of research reactors important for neutron diffraction. Additional reactors are listed by Kisi & Howard (2008) in their Table 3.1, and a complete listing is available from the International Atomic Energy Agency Research Reactor Database (IAEA RRDB, https://nucleus.iaea.org/RRDB/RR/ReactorSearch.aspx).

2.3.3.3. *Spallation neutron sources*

The bombardment of heavy-element nuclei by high-energy protons, *i.e.* protons in the energy range 100 MeV to GeV, causes the nuclei to break up with the release of large numbers of neutrons. The word 'spallation' might suggest that neutrons are simply being chipped off the target nucleus, and indeed neutrons can be ejected by protons in a direct collision process with transfer of the full proton energy, but such simple events are relatively rare. In most cases there is a sequence involving incorporation of the bombarding proton into the nucleus, intra- and internuclear cascades accompanied by the ejection of assorted high-energy particles, including neutrons, and then an 'evaporation' process releasing neutrons from excited nuclei with

Table 2.3.3
Details on selected research reactors

The primary source of data is the IAEA Research Reactor Database (RRDB). The publicly accessible RRDB does not include information on fuel: limited information on this has been found from other internet sources.

Reactor (type)	Power (MW)	Location	Fuel (see text)	Moderator/ coolant	Reflector	Thermal flux (n cm^{-2} s^{-1})	Cold/hot neutron sources
CARR (tank in pool)	60	CIAE, Beijing, China	U_3Si_2-Al, LEU 19.75%	Light water	Heavy water	8×10^{14}	1 cold
FRM-II (pool)	20	TUM, Garching, Germany	U_3Si_2-Al, HEU	Light water	Heavy water	8×10^{14}	1 cold, 1 hot
HANARO (pool)	30	KAERI, Daejeon, Korea	U_3Si, LEU 19.75%	Light water	Heavy water	4.5×10^{14}	1 cold
HFIR (tank)	85	ORNL, Oak Ridge, USA	U_3O_8-Al, HEU 93%	Light water	Beryllium	2.5×10^{15}	1 cold
HFR (heavy water)	58.3	ILL, Grenoble, France	U_3Al_x-Al, HEU	Heavy water	Heavy water	1.5×10^{15}	2 cold, 1 hot
JRR-3M† (pool)	20	JAEA, Tokai, Japan	U_3O_8-Al, U_3Si_2-Al, LEU	Light water	Light water, heavy water, beryllium	2.7×10^{14}	1 cold
NBSR (heavy water)	20	NIST, Gaithersburg, USA	U_3O_8-Al HEU 93%	Heavy water	Heavy water	4×10^{14}	1 cold
OPAL (pool)	20	ANSTO, Sydney, Australia	U_3Si_2-Al, LEU 19.75%	Light water	Heavy water	2×10^{14}	1 cold

† This reactor has been temporarily shut down.

energies comparable to those released in the fission process (Carpenter, 1977; Carlile, 2003; Arai & Crawford, 2009). The numbers of neutrons released in these various processes depend on the proton energies and the target materials employed; for 1 GeV protons on a Pb target, around 25 neutrons are released per bombarding proton (Arai & Crawford, 2009). Target materials in use include Hg, Pb, W, Ta and ^{238}U (depleted uranium). The yield of neutrons per proton for non-fissionable target materials is approximated by $0.1(E - 0.12)(A + 20)$ where E is the proton energy in GeV and A is the atomic number of the target nucleus; for a target such as ^{238}U that is fissionable under bombardment by high-energy neutrons the yield is almost double that. Generally, the energy to be dissipated as heat in the spallation process will be no more than the energy of the bombarding proton, so for the example of 1 GeV protons on Pb it should not exceed 40 MeV per neutron produced. Nevertheless, cooling requires attention. The use of liquid targets such as Hg, and Pb either in pure form or in a Pb-Bi eutectic alloy, facilitates the dissipation of heat. Solid targets are usually water cooled. The fast neutrons from spallation need to be moderated, not in this case for sustaining the process, but simply to make them useful for diffraction and other applications. Moderators in common use include water, heavy water, liquid or solid methane (CH_4), and liquid hydrogen (H_2). The volumes of moderator are usually small, for reasons that will be explained below.

Most spallation neutron sources, though by no means all, operate in 'short-pulse mode', then employ time-of-flight methods in their instrumentation. The duration of the neutron pulse is critical in determining the time-of-flight resolution. Short-pulse operation depends first of all on a short-pulse structure of the bombarding protons. This is inherent in proton-accelerating systems that incorporate synchrotron accelerators or accumulator rings, since the protons become bunched[10] while travelling around these rings, and pulses of duration <1 μs are delivered. The frequency of these pulses is modest, say 50 Hz, in part to reduce power requirements, but also to avoid the situation in which the desired thermal (or cold) neutrons from one pulse are overtaken by fast neutrons from the next. For short-pulse operation, the proton pulse must be translated into a still-short pulse of moderated neutrons; this has significant implications for moderator design (Tamura *et al.*, 2003; Arai, 2008; Arai & Crawford, 2009; Batkov *et al.*, 2013; Zhao *et al.*, 2013; Thomsen, 2014). The normal processes of moderation – neutrons giving up energy in collisions with nuclei in the moderator until thermal equilibrium is achieved – need to be to some extent curtailed. One means to curtail these processes is to use only a small volume of moderator, so neutrons escape before spending excessive time in it. Another is to place neutron absorbers – cadmium or gadolinium – around the moderator, or indeed incorporate these absorbing materials into it, so that the slow neutrons remaining in the moderator are absorbed before the pulse length becomes excessive; in this case the moderator is said to be 'decoupled' from the target. For cold-neutron moderators on short-pulse spallation sources the use of an ambient-temperature 'pre-moderator' may be advantageous. Whatever the means to limit the dwell time in the moderator, the emerging neutrons will be under-moderated, hence their spectrum will contain more epithermal neutrons (*i.e.* neutrons with energies of the order of eV to keV) than fully moderated neutrons from a continuous source. Fig. 2.3.8 shows the results for energy spectra and pulse length, from Monte Carlo calculations, for different cryogenic moderators for the J-PARC spallation neutron source, Tokai, Japan. The neutron dwell time and therefore the pulse length are calculated to be smaller in the decoupled moderators (Fig. 2.3.8*b*), but comparison with the coupled moderator (Fig. 2.3.8*a*) shows that intensity is sacrificed. The pulse length in the high-energy region, and at lower energies for the poisoned moderators, varies as roughly $1/(E)^{1/2}$; from equation (2.3.1) this makes the pulse length Δt proportional to the wavelength λ. In a time-of-flight analysis we measure the flight time t over a length L; noting that $v = L/t$ and using that same equation we find that t is also proportional to λ, *viz.* $t = (mL/h)\lambda$. The result is that the time resolution $\Delta t/t$

---

[10] At the ISIS spallation neutron source, for example, the protons are injected into the synchrotron in 200 μs bursts, where they form two bunches each only 100 ns wide (detail from https://www.isis.stfc.ac.uk/Pages/How-ISIS-works–in-depth.aspx).

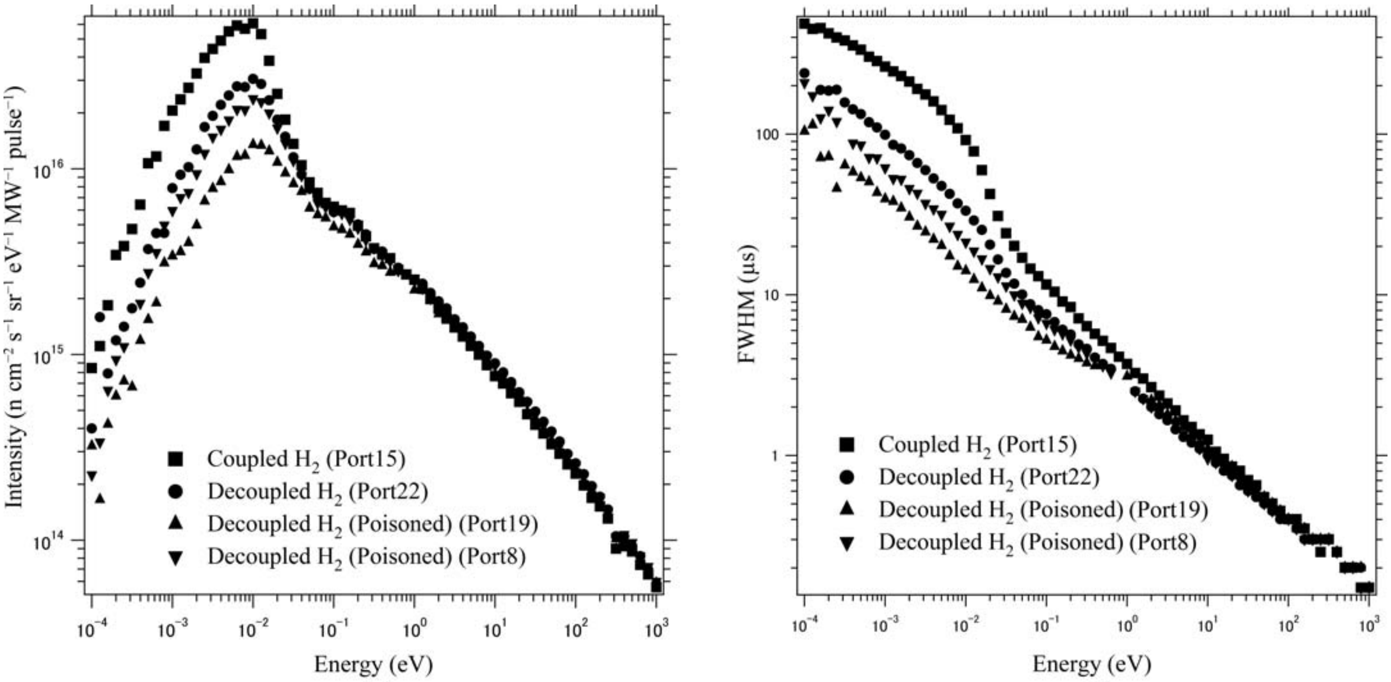

(*a*) (*b*)

Figure 2.3.8

(*a*) The neutron energy distribution (flux) of the J-PARC neutron source for coupled, decoupled and poisoned decoupled moderators. The flux consists of a Maxwell distribution at low energies and a $1/E$ region at higher energies. (*b*) Pulse duration as a function of energy calculated for the same moderators. For the decoupled moderators, the peak widths vary approximately as $1/E^{1/2}$. Reproduced from Tamura *et al.* (2003).

is independent of flight time (or wavelength), which is a very satisfactory state of affairs (see Section 2.3.4.2.1).

As mentioned earlier, there is the problem for time-of-flight analysis that the slower neutrons from one pulse might be overtaken by the first arrivals from the next – a problem known as 'frame overlap'. Taking the example of 25 meV thermal neutrons, at a speed of 2190 m s^{-1} and a 50 Hz pulse repetition frequency, the neutrons from one pulse will have travelled 44 m when the next pulse occurs. If instrument flight paths are longer than this, or indeed if slower neutrons are involved, then the frame-overlap problem is encountered. A conceptually simple approach is to reduce the pulse frequency, and this has been implemented at the UK's ISIS neutron facility where Target Station 2 takes just one pulse in five from the proton-acceleration system, reducing the effective pulse frequency to 10 Hz; the other four pulses are directed to Target Station 1. Neutron choppers provide an alternative means to address this problem. The simplest kind of chopper is a disc (Fig. 2.3.9), usually of aluminium, nickel alloy or carbon fibre, coated in part with neutron-absorbing material such as boron, cadmium or gadolinium, rotating in a synchronous relationship with the source. A chopper located near to the source can be adjusted to block the fast neutrons and γ-rays that emerge immediately, but allow through neutrons in a restricted time window, from T_0 to $T_0 + \Delta T$, measured from the time of the pulse. Evidently, time $T_0 + \Delta T$ cannot exceed the time for a single rotation of the disc; when the disc is rotating at the pulse-repetition frequency this is the time between pulses. If the disc-rotation frequency is a submultiple of the pulse frequency, *i.e.* the rotation frequency is the pulse frequency divided by n, then the time window ΔT can be set to select only every nth pulse from the source. A two-chopper arrangement is used, for example, in the 96 m flight path of the High Resolution Powder Diffractometer (HRPD) at the ISIS facility; the first chopper at 6 m from the source runs at the pulse frequency and the second at 9 m from the source runs at one-fifth or one-tenth of that frequency, so that only every fifth or tenth pulse is used (HRPD user manual, http://www.isis.stfc.ac.uk/Pages/hrpd-manual.pdf).

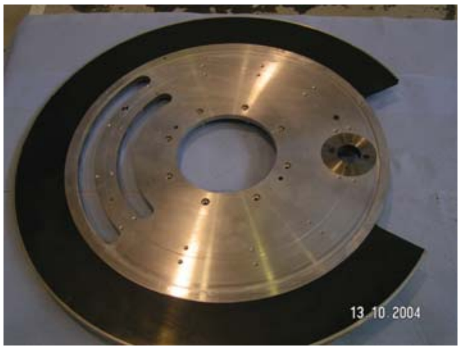

Figure 2.3.9

One of the disc choppers in use at the ISIS neutron facility. This is an aluminium (2014A) alloy disc, and the neutron-absorbing coating (the darker region) is boron carbide in a resin. The cut-out on the right-hand side provides the aperture for neutrons. (Credit: STFC.)

Although we have introduced neutron choppers in the context of spallation sources, we should acknowledge that mechanical choppers and velocity selectors have a long history, dating back long before the advent of spallation sources. In fact, the first report on a velocity selector (Dunning *et al.*, 1935) pre-dates even the earliest demonstrations of neutron diffraction. Mechanical systems have long been used at continuous neutron sources to act as velocity (wavelength) selectors, and/or to tailor pulses of neutrons suitable for time-of-flight studies. Two disc choppers can be arranged to serve both purposes – the first chopper has a limited aperture transmitting a short pulse of neutrons, and the second chopper, with a similar aperture and located at some distance from the first, is phased so as to allow through only those neutrons with a particular velocity. This arrangement can provide short pulses of more-or-less monochromatic neutrons to an experiment. The helical velocity selector (Friedrich *et al.*, 1989) is conceptually somewhat similar. This takes the form of a cylinder,

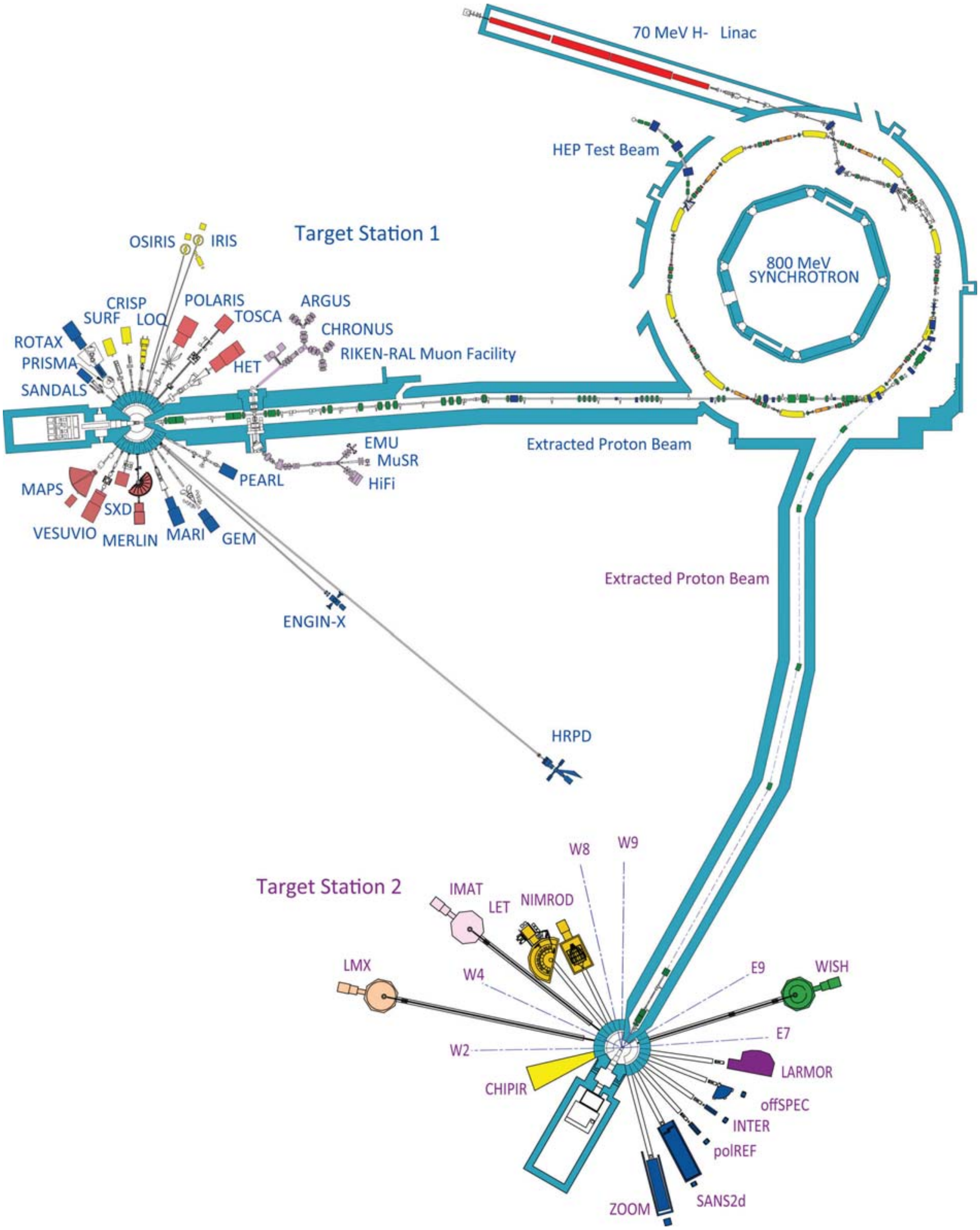
70 MeV H- Linac
HEP Test Beam
800 MeV SYNCHROTRON
Target Station 1
OSIRIS
IRIS
CRISP
SURF
LOQ
POLARIS
TOSCA
ARGUS
CHRONUS
RIKEN-RAL Muon Facility
ROTAX
PRISMA
SANDALS
HET
EMU
MuSR
HiFi
PEARL
MAPS
SXD
VESUVIO
MERLIN
MARI
GEM
Extracted Proton Beam
ENGIN-X
HRPD
Extracted Proton Beam
Target Station 2
W8
W9
IMAT
LET
NIMROD
LMX
W4
E9
WISH
E7
W2
LARMOR
CHIPIR
offSPEC
INTER
polREF
ZOOM
SANS2d

Figure 2.3.10
Layout of the ISIS spallation neutron source. (Credit: STFC.)

or indeed a stack of discs, rotating around an axis parallel to the neutron beam, with helical slits such that exits are offset from the entrance apertures in much the same manner as described above; the difference from the two-chopper arrangement is that there are apertures located all around the cylinder, giving closely spaced pulses unsuitable for time-of-flight studies. The purpose of mechanical wavelength selection at a continuous source is to select longer wavelengths and a broader range of wavelengths than a crystal monochromator (Section 2.3.4.1.2) could provide. Also worthy of mention is the Fermi chopper (Fermi *et al.*, 1947), comprising a package of neutron-transmitting slits set into a cylinder that rotates at rates of some hundreds of hertz around an axis in the plane of the slits, coincident with the cylinder axis, and perpendicular to the neutron beam. Neutrons above a threshold velocity are transmitted for the brief periods in which the slits are suitably aligned, so short (µs) but frequent pulses of neutrons are delivered. In a variation of the Fermi chopper (Marseguerra & Pauli, 1959), the transmitting slits are curved, providing for the transmission of rather slower neutrons while preventing the transmission of faster ones; in this variant the chopper not only delivers short pulses of neutrons but acts as a velocity selector as well. Neutron choppers are used in various combinations at both continuous and pulsed neutron sources; the Fermi chopper in particular can be used for ‘shaping’ the pulses at long-pulse spallation neutron sources (Peters *et al.*, 2006).

As an initial case study, we consider the ISIS neutron facility, located in Oxfordshire, England, at the Rutherford Appleton Laboratory. This is a well established neutron spallation source supporting a strong programme of research using neutron beams. Of particular note are the excellent facilities for powder diffraction. First neutrons were delivered in 1984, but there have been upgrades since then, including the commissioning of a second target station in 2009. Fig. 2.3.10 is a schematic showing the layout of this facility. Some details about its operation are available on the ISIS web site, at https://www.isis.stfc.ac.uk/Pages/How-ISIS-works.aspx. Briefly, an ion source and radio-frequency quadrupole accelerator (not shown) inject bunches of negative hydrogen ions, H^-, into the linear accelerator where they are accelerated to 70 MeV. These are passed through aluminium foil, which strips them of their electrons, so they become protons, H^+, which are then accelerated to 800 MeV in the proton synchrotron. The protons, then travelling in two 100 ns bunches 230 ns apart, are kicked out of their synchrotron orbits and directed toward the targets. The whole process is repeated at a frequency of 50 Hz; the kickers are arranged to send one pulse in five to Target Station 2 (so that the pulse frequency there is just 10 Hz), and the remainder to Target Station 1. Both targets are made of tantalum-coated tungsten, as a stack of water-cooled plates in Target Station 1 and as a heavy-water surface-cooled cylinder in Target Station 2. As explained earlier, the fast neutrons produced in the spallation process must be moderated, and for this purpose moderators are located adjacent to the targets: two water moderators at 300 K, one liquid-methane moderator at 100 K and one liquid-hydrogen moderator at 20 K at Target Station 1; and one decoupled solid-methane moderator at 26 K and one coupled liquid-hydrogen/methane moderator at 26 K at Target Station 2. The widths of the pulses of the moderated neutrons are typically 30–50 µs, but 300 µs for the coupled moderator at Target Station 2. The target/moderator assemblies are surrounded, apart from beam exit ports, by beryllium reflectors. The schematic of Fig. 2.3.10 indicates the placement of the various neutron-beam instruments around the target stations.

The Swiss neutron spallation source, SINQ, located at the Paul Scherrer Institute in Villigen, is the only spallation source operating in continuous mode. SINQ reached full power in 1997. Since there is no time structure to be preserved, more generous quantities of moderator can be used; in fact the target, which becomes the source of neutrons, is located centrally in a moderator tank. The situation here is not very different from that in a medium-flux research reactor. The target comprises lead rods in Zircaloy tubes, the moderator is heavy water and there is a light-water reflector outside the moderator tank. Protons accelerated first by a Cockroft–Walton accelerator, then to 72 MeV by an injector cyclotron, and finally to 590 MeV in a proton ring cyclotron are directed onto the target from below (Fig. 2.3.11). The proton current is initially 2.4 mA, but this is reduced in muon production, so that only about 1.65 mA reaches the spallation target. The power is thus close to 1.0 MW. A horizontal insert in the moderator tank houses a liquid-deuterium cold source at 25 K.

As a final example we describe the 5 MW long-pulse European Spallation Source, now under construction in Lund, Sweden (see Fig. 2.3.12). A more detailed description is available at the ESS web site, https://europeanspallationsource.se/technology. The proton-acceleration system, although comprising a number of different components, will be linear. The protons from the ion source will be accelerated through a radio-frequency quadrupole and drift tube LINAC up to 90 MeV, then through a series of superconducting cavities up to the final energy of 2 GeV. This system will deliver proton pulses of 2.86 ms duration at a 14 Hz repetition rate; the average current will be 6.26 mA and hence the total power 5 MW. The target material will be helium-cooled tungsten encased in stainless steel, in the form of a 2.5 m-diameter rotating wheel. Such an arrangement assists in dissipation of the heat deposited in the target. Coupled liquid-hydrogen moderators will be located above and below the rotating wheel, and this assembly will be partially surrounded by a water pre-moderator and beryllium reflector. Neutron choppers will be used to shape the neutron pulses as required, and neutron optical systems will deliver neutrons to the experiments. First beam on target is expected in 2019.

Characteristics of these and other neutron spallation sources are recorded in Table 2.3.4. The information included there has been taken from the respective facility web sites.

2.3.3.4. *Neutron beam tubes and guides*

Ideally, neutron diffractometers should be designed following a holistic approach, designing the source of moderated neutrons, through the delivery system, to the instrument itself. This is not often possible in practice; for example the source must often be taken as a given, and in some cases the delivery of the neutrons as well. The holistic approach is commonly a very large Monte Carlo simulation, not suitable for purposes of description; in this chapter, therefore, we provide separate descriptions of these different components.

The simplest delivery system is a neutron beam tube or collimator. A collimator could comprise just two pinholes of diameters a_1 and a_2 cut into neutron-absorbing material, and placed at a distance L apart; this limits the divergence of the beam to (full angle) $2\alpha = (a_1 + a_2)/L$. It is of course possible to use apertures of different cross section, for example rectangular slits, if the divergence must be smaller in one direction than another.

Neutron guides are now widely used at both reactor and spallation neutron sources. These are able to transport neutrons over distances ranging to 100 m or more. They are evacuated tubes, normally of rectangular cross section, and transmission depends on the reflection of glancing-angle neutrons from the walls of the guide. The guides are constructed from glass plates with a reflective coating deposited on the internal surfaces.

Initially, total external reflection (Section 2.3.2.3) provided the basis for reflection; the coating was nickel, or preferably ^{58}Ni. Given that nickel has a face-centred cubic structure (4 atoms per unit cell) with lattice parameter 3.524 Å, and taking the scattering lengths from Table 2.3.2, we find from equation (2.3.6) that the critical glancing angles per unit wavelength for total external reflection are 0.10° Å^{-1} and 0.12° Å^{-1} for nickel and ^{58}Ni, respectively. Taking wavelengths of 0.4, 1.2 and 5 Å as representative of hot, thermal and cold neutrons, respectively (*cf.* Fig. 2.3.5), these angles for a nickel mirror are just 0.04, 0.12 and 0.5°. Consequently, these guides are most useful for transmitting cold neutrons and are moderately useful for thermal neutrons, but are not used for hot neutrons. The small glancing angles are demanding, not only on the precision of manufacture, but also because it is highly desirable to use a curved guide tube so there is no direct line of sight to the source (as in Fig. 2.3.13); this is a way of preventing fast neutrons and γ-radiation from impacting on the experiment. The guide tube still transmits a range of wave-

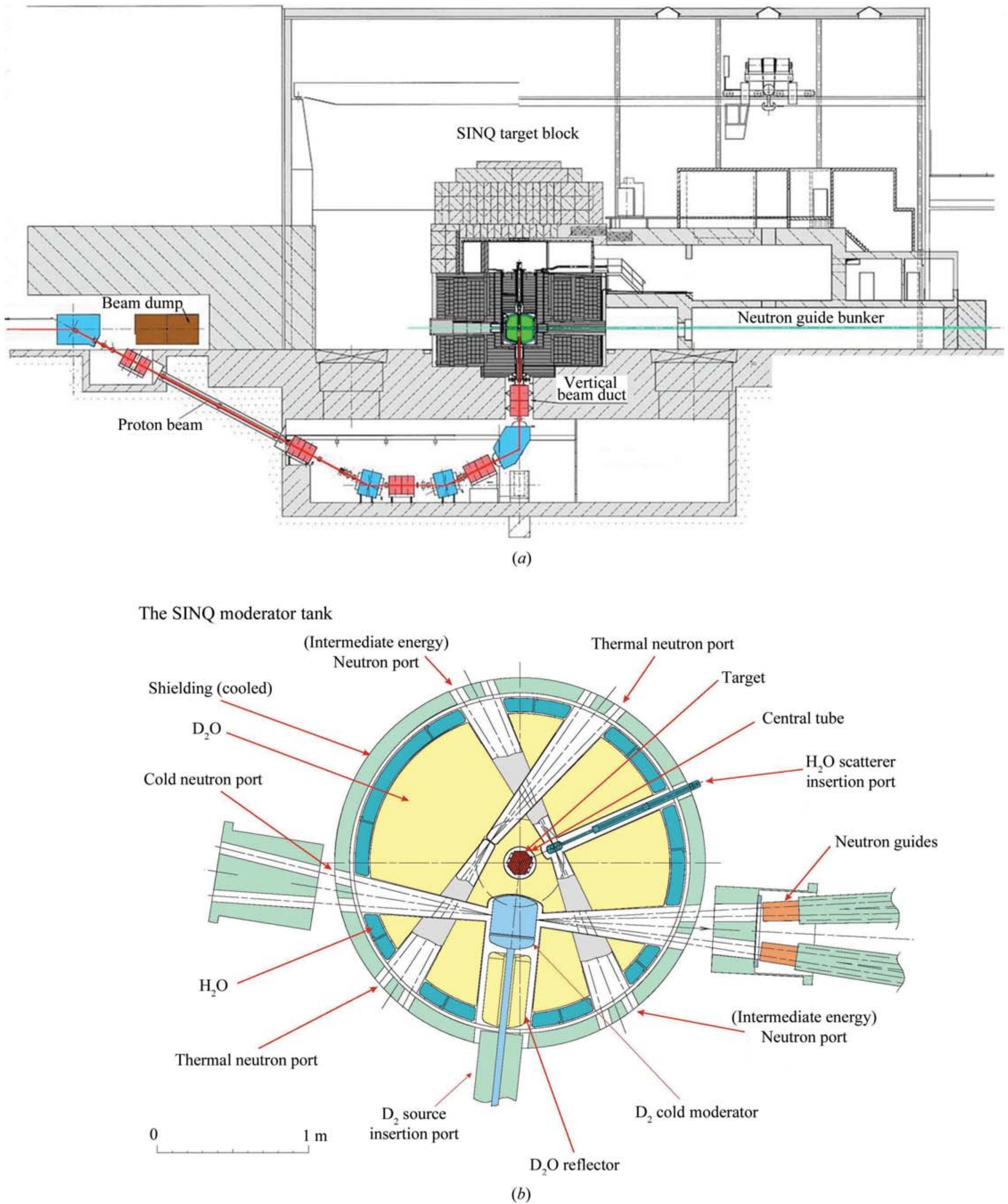
SINQ target block
Beam dump
Neutron guide bunker
Vertical beam duct
Proton beam
(a)
The SINQ moderator tank
(Intermediate energy) Neutron port
Thermal neutron port
Target
Shielding (cooled)
Central tube
D_2O
H_2O scatterer insertion port
Cold neutron port
Neutron guides
H_2O
(Intermediate energy) Neutron port
Thermal neutron port
D_2 source insertion port
D_2 cold moderator
0
1 m
D_2O reflector
(b)

Figure 2.3.11
Layout at the SINQ neutron source. (*a*) Elevation: the target is located in the moderator tank, the high-energy protons being delivered from below. (*b*) Plan: showing the location of guide tubes relative to this central target. (Courtesy: Dr Bertrand Blau, Paul Scherrer Insitut.)

lengths, although only the longest wavelengths can travel by the zig-zag path indicated in Fig. 2.3.13. If the guide width is a, and its radius of curvature ρ (see Fig. 2.3.13), then the minimum length to avoid direct transmission is $(8a\rho)^{1/2}$. Critical to the transmission of a guide tube is the angle θ^*, which is the minimum glancing angle of incidence onto the outer surface that permits subsequent reflection from the inner surface, and is given by $\theta^* = (2a/\rho)^{1/2}$. The shortest wavelength, then, that can be transmitted involving reflection from the inner surface is given by [*cf.* equation (2.3.6)]

Table 2.3.4
Details of selected spallation neutron sources

Source	Type	Location	Proton energy	Current	Average power	Target(s)	Repetition rate (Hz)	Moderator(s)
CSNS†	Short pulse	Institute of High Energy Physics, Guangdong, China	1.6 GeV	62.5 µA	100 kW	Tungsten	25	Water, 2 × liquid hydrogen
ESS†	Long pulse	European Spallation Source, Lund, Sweden	2 GeV	2.5 mA	5 MW	Tungsten wheel (helium cooled)	14	2 × Liquid hydrogen (pancake geometry)
ISIS	Short pulse	Rutherford Appleton Laboratory, Oxfordshire, UK	800 MeV	200 µA	160 kW	2 × Tungsten	50 10	2 × Water, liquid methane, liquid hydrogen Hydrogen/methane, solid methane at 26 K
JSNS‡	Short pulse	J-Parc Centre, Tokai-mura, Japan	3 GeV	333 µA	1 MW	Liquid mercury	25	Supercritical hydrogen
LANSCE	Long pulse	Los Alamos National Laboratory, Los Alamos, USA	800 MeV	125 µA	100 kW	Tungsten	20	Water, 2 × liquid hydrogen
SINQ	Continuous	Paul Scherrer Institute, Villigen, Switzerland	590 MeV	1.64 mA§	0.97 MW	Lead	—	Heavy water; cold source: liquid deuterium at 20 K
SNS	Short pulse	Oak Ridge National Laboratory, Oak Ridge, USA	1 GeV	1.4 mA	1.4 MW	Liquid mercury	60	2 × Water, 2 × liquid hydrogen

† Under construction. ‡ Currently operating at <0.5 MW. § Current reaching spallation target after attenuation in muon source.

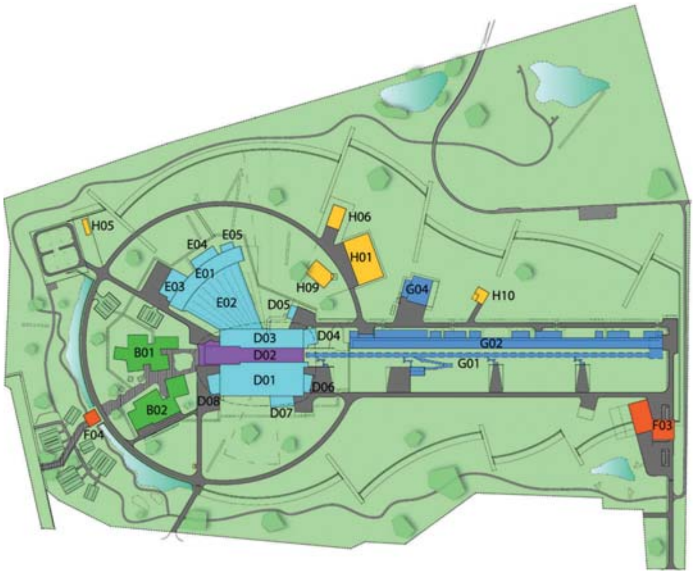

Figure 2.3.12
Schematic diagram of the ESS facility. The proton beam enters at the right, strikes the target and liberates neutrons for instruments in the three neutron experiment halls. (Image courtesy of the ESS.)

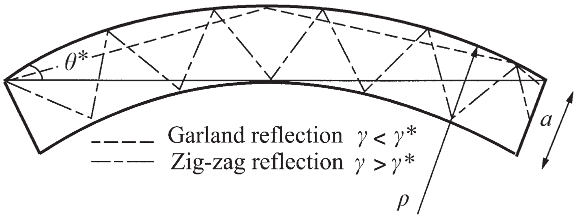

Figure 2.3.13
Plan of a curved neutron guide, indicating different possible neutron paths, labelled 'garland' and 'zig-zag'. Only the longer-wavelength neutrons can travel the zig-zag path because the glancing angles on this path (which must be less than the critical angle) are greater. In this schematic, the glancing angles, the width and the curvature have all been exaggerated. [From Section 4.4.2 of Volume C (Anderson & Schärpf, 2006).]

$$\lambda^* = \theta^* \left(\frac{\pi}{Nb_{\rm coh}}\right)^{1/2}. \tag{2.3.12}$$

This is known as the 'characteristic' wavelength of the guide [see Section 4.4.2 of Volume C by Anderson & Schärpf (2006)]; the majority of transmitted neutrons will have longer wavelengths than this.

The desire to use guides for shorter (*e.g.* thermal-neutron) wavelengths, and for retaining more neutrons at a given wavelength, has motivated the development of mirrors capable of reflecting neutrons incident at greater glancing angle. The earliest such mirrors were in fact monochromating mirrors obtained by laying down alternate layers of metals with contrasting coherent-scattering-length densities (Fig. 2.3.14). For a bilayer thickness d and angle of incidence θ these would select wavelengths according to Bragg's law [equation (1.1.3)],

$$\lambda = 2d\sin(\theta).$$

In an early implementation (Schoenborn *et al.*, 1974), the metals were Ge and Mn (which have coherent scattering lengths opposite in sign) and the bilayer thickness was of the order of 100 Å; this is a larger d-spacing giving access to longer wave-

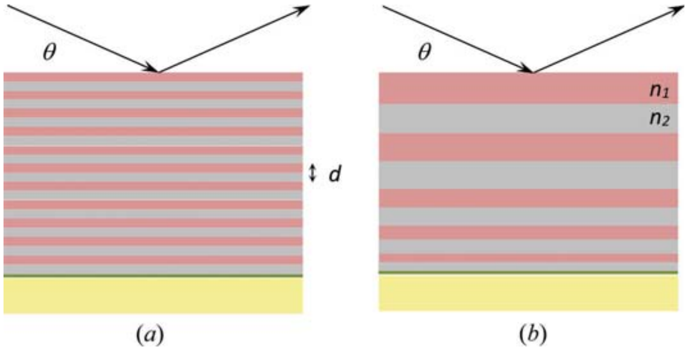

Figure 2.3.14
Schematic diagrams of (*a*) a multilayer monochromator and (*b*) a neutron supermirror.

lengths than would be accessible with the usual crystal monochromator (Section 2.3.4.1.2). The idea of supermirrors, comprising bilayers of graduated thickness, and in effect increasing the critical angle, was suggested by Turchin (1967) and Mezei (1976). For a perhaps simplistic explanation, we note first that since the bilayer dimension d is large compared with the neutron wavelength, we can approximate the above equation for reflection as

$$\theta \simeq \lambda \frac{1}{2d},$$

in which form it is reminiscent of equation (2.3.6). If we take $d_{\min}$ to be the thickness of the thinnest bilayer, then we can propose that the critical angle for reflection by the supermirror should be

$$\theta_c^{\rm SM} \simeq \lambda \frac{1}{2d_{\min}}. \qquad (2.3.13)$$

In order to ensure that all neutrons incident at angles less than this critical angle should be reflected, we need to incorporate a more-or-less continuous range of thicker bilayers into the supermirror (Fig. 2.3.14*b*). A more rigorous treatment (Hayter & Mook, 1989; Masalovich, 2013) takes account of the transmission and reflection at each interface, and lays down a prescription as to how the thicknesses should be varied. The most common pairing for the bilayer is now Ni with Ti; the coherent scattering cross sections are of opposite sign (see Table 2.3.2). The performance of a supermirror is normally quoted as the ratio m of the critical angle for the supermirror, $\theta_c^{\rm SM}$, to that for natural nickel, $\theta_c^{\rm Ni}$; a high value for reflectivity is also important. Supermirrors to m of 2 or 3 are in quite common use, while now Ni/Ti supermirrors with m up to 7 are offered for purchase (Swiss Neutronics AG; see also Maruyama *et al.*, 2007).

Consideration is currently being given to the variation of the cross section of the guide along its length. There is some loss on reflection by supermirrors, so these studies aim to reduce the number of reflections involved in transmission along the guide. One suggestion (also attributable to Mezei, 1997) is to use a 'ballistic guide', in which neutrons from the source travel through a taper of widening cross section into a length of larger guide, then through a taper of narrowing cross section to restore the original cross section at the exit. This is said to reduce the number of reflections suffered by the neutron by a factor of $(w_0/w)^2$, where w_0 is the width at entrance and exit and w the larger width along the main part of the guide (Häse *et al.*, 2002). Such a guide has been installed and is operating successfully on the vertical cold source at the Institut Laue–Langevin (Abele *et al.*, 2006). An extension of this idea is based on the well known property of ellipses that a ray emanating from one focus is reflected (just one bounce) to pass through the other; so if the guide cross section could be varied to give a very long ellipse, a source of neutrons placed at one focus, and the target point at the other, then perhaps the neutrons could be transmitted along the guide with just a single reflection (Schanzer *et al.*, 2004; Rodriguez *et al.*, 2011). Accordingly a number of neutron facilities have installed elliptical guides, and indeed a number of neutron powder diffractometers now are located on elliptical guides; these include diffractometer POWTEX at FRM-II, the high-resolution diffractometers HRPD and WISH at ISIS, and Super-HRPD at JSNS. Computer simulation by Cussen *et al.* (2013), however, questions whether, given the practicalities of finite source sizes and the approximation of elliptical variation by a number of linear segments, the theoretical improvement is fully realized.

2.3.4. Diffractometers

Put simply, the diffracted neutron beams associated with the different d-spacings in the sample under study satisfy Bragg's law,

$$\lambda = 2d\sin(\theta). \qquad (2.3.14)$$

As always, λ is the wavelength of the incident neutrons, and these neutrons are scattered through an angle 2θ.

There are basically two ways of exploiting this relationship. The first is to use a single wavelength for the investigation, in which case diffracted neutrons are observed at different angles 2θ corresponding to different d-spacings in the sample. A neutron powder diffractometer designed to carry out an investigation by this means we choose to call a 'constant wavelength' (CW) diffractometer. The other means is to fix the angle 2θ, illuminate the specimen with a range of wavelengths, and note the different wavelengths that are diffracted. In this case, we determine the wavelengths of the diffracted neutrons *via* their speed $\lambda = h/(mv)$ [equation (2.3.1)], and that in turn is measured by their flight time t over a path of length L, $v = L/t$; this leads to

$$\lambda = \frac{ht}{mL}. \qquad (2.3.15)$$

A diffractometer designed to carry out such an analysis of wavelengths we call a 'time-of-flight (TOF) diffractometer'.

The distinction between these two modes of operation can also be indicated *via* the Ewald construction in reciprocal space (Section 1.1.2.4). In this, the ideal powder is represented by concentric spheres in reciprocal space. In the constant-wavelength situation, the primary beam is fixed in direction and the Ewald sphere has a fixed radius; diffracted (reflected) beams are observed at any angle at which the surface of the Ewald sphere intersects one of the concentric spheres mentioned just above. In the wavelength-analysis (time-of-flight) situation, the directions of the primary and diffracted beams are fixed, but the radius of the Ewald sphere ($1/\lambda$) is variable through a range; diffracted beams are observed whenever the wavelength is such that the tip of the vector representing the reflected beam lies on one of the concentric spheres.

2.3.4.1. *Constant-wavelength neutron diffractometers*

The salient features of a constant-wavelength diffractometer are perhaps most easily explained by reference to a particular example; for this purpose we consider the High Resolution Powder diffractometer for Thermal neutrons (HRPT) installed at the SINQ continuous spallation source (Fischer *et al.*, 2000). Neutrons from the source travel through a guide tube to the crystal monochromator, which directs neutrons of a selected wavelength toward the sample. The diffracted neutrons are registered in a detector or detectors that cover a range of angles of scattering from the sample. Collimation is used to better define the directions of the neutron beams; in this instance a primary collimator is included in the guide tube and additional collimation is included between the sample and the position-sensitive detector. The various components will be described in more detail below.

2.3.4.1.1. *Collimation*

There need to be restrictions on the angular divergences of the neutron beams. The divergence of the beam impinging upon the crystal monochromator must be limited to better define the wavelength of the neutrons directed to the sample, whereas the divergences of the beams incident upon and diffracted from

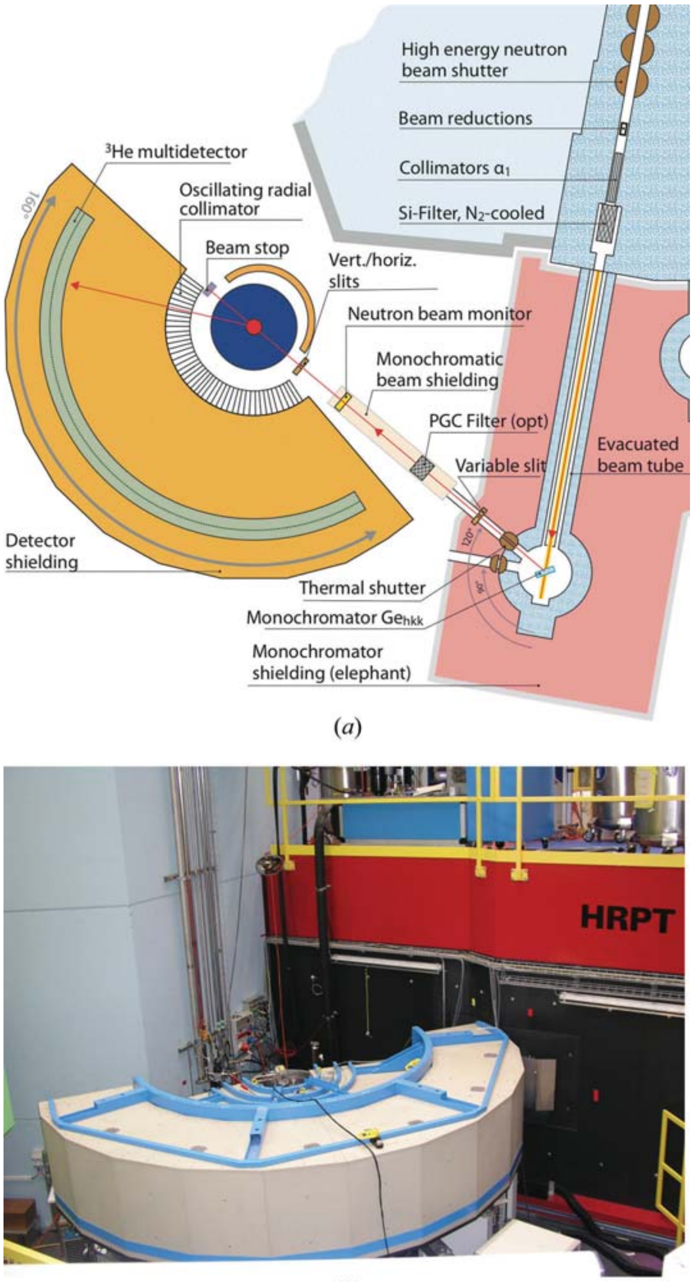

(*a*)

(*b*)

Figure 2.3.15
A constant-wavelength neutron powder diffractometer. This figure shows (*a*) a layout diagram and (*b*) the physical appearance (dominated by the monochromator and detector shieldings) for the HRPT diffractometer installed at the SINQ continuous spallation source. (Figures from https://www.psi.ch/sinq/hrpt/.)

the sample will control the precision with which the scattering angle 2θ can be determined. For a diffractometer detecting neutrons and measuring scattering angles in the horizontal plane (as shown in Fig. 2.3.15) the horizontal divergences are critical, the vertical divergences less so.[11] Indeed, the horizontal divergences are key parameters in the determination of resolution and intensity (Section 2.3.4.1.4); for this reason we denote by α_1, α_2 and α_3 the (half-angle) angular divergences of the primary beam (*i.e.* the beam onto the monochromator), the monochromatic beam (from monochromator to sample) and the diffracted beam (from sample to detector), respectively.

The divergences are limited by various forms of collimation. The divergence of the primary beam will be limited in the first instance by the delivery system. For delivery through a simple beam tube of length L, with entrance and exit apertures of dimensions a_1 and a_2, respectively, the angular divergence (half-angle) is given by (as already noted in Section 2.3.3.4)

$$\alpha_1 = \frac{a_1 + a_2}{2L}. \qquad (2.3.16)$$

Neutrons emerging from a guide tube would have divergence equal to the critical angle of the guide, $\alpha_1 = \theta_c$. Soller collimators (see below) can be used if there is a need to further reduce the horizontal divergence of the primary beam. The divergence of the monochromatic beam may be limited by slits, or a beam tube. The divergence of the diffracted beam, α_3, is often defined using another Soller collimator. Sometimes this divergence is limited just by the dimensions of the sample and the detecting elements; equation (2.3.16) gives α_3 if it now references the sample and detector element dimensions and the distance between them. Even in this circumstance (as in HRPT), Soller collimators may be used in front of the detector to reduce scattering from ancillary equipment and other background contributions.

Soller collimators (Soller, 1924) are used to transmit beams of large cross section while limiting (for example) horizontal divergence. They are in effect narrow but tall rectangular collimators stacked side by side; in practice they comprise thin neutron-absorbing blades equally spaced in a mounting box. It should be evident from equation (2.3.16) that if the length of the collimator is L and the separation between the blades is a, then the (half-angle) horizontal divergence is a/L. The transmission function for a Soller collimator is ideally triangular. It is technologically challenging to make compact Soller collimators, since, for a given collimation, a shorter collimator needs a smaller blade spacing. One very successful approach, due to Carlile *et al.* (1977), has been to make the neutron-absorbing blades from Mylar, stretched on thin steel or aluminium alloy frames, and subsequently coated with gadolinium oxide paint; these blades are stacked and connected *via* the frames which become the spacers in the final product. The collimators made by Carlile *et al.* were 34 cm long, and the blade spacing was 1 mm, giving a horizontal divergence of 0.17°. Compact Soller collimators of this type (Fig. 2.3.16) are now commercially available, with blade spacings down to 0.5 mm.

Even more compact collimators can be produced by eliminating the gaps in favour of solid layers of neutron-transmitting material; for example, a collimator only 2.75 cm long made by stacking 0.16 mm thick gadolinium-coated silicon wafers gave a divergence of 0.33° (Cussen *et al.*, 2001). Microchannel plates (Wilkins *et al.*, 1989) may offer additional possibilities for collimation and focusing.

2.3.4.1.2. *Monochromators*

The wavelength in a constant-wavelength powder diffractometer is almost invariably selected by a single-crystal monochromator. If the primary beam is incident onto the monochromator in such a way as to make an angle θ_M with a chosen set of planes in the crystal, then the wavelength that will be reflected from these planes is given by Bragg's law,

$$\lambda = 2d\sin(\theta_M),$$

where d is the spacing of the chosen planes. A spread of angles of incidence represented by $\Delta\theta_M$ will result in the selection of a

---

[11] For this reason large vertical divergences are employed to increase intensity; they do however have second-order impacts on the shapes (asymmetry) and positions of diffraction peaks (Howard, 1982; Finger *et al.*, 1994; see also Section 4.2 in Kisi & Howard, 2008).

Figure 2.3.16
Commercially available compact Soller collimators. (Reproduced with permission from Eurocollimators Ltd, UK.)

band of wavelengths $\Delta\lambda$ given by

$$\frac{\Delta\lambda}{\lambda} = \cot\theta_M \Delta\theta_M. \tag{2.3.17}$$

For high-resolution performance we need a rather precisely defined wavelength, so $\Delta\lambda$ should be small; if, on the other hand, intensity is an issue then a wider band of wavelengths needs to be accepted. It should be evident from equation (2.3.17) that a high-resolution diffractometer will operate with a take-off angle from the monochromator, $2\theta_M$, as high (*i.e.* as close to 180°) as practicable, and with tight primary collimation α_1.

It might be noticed that the integer n appearing on the right-hand side of equation (1.1.3) has been omitted from our formulation of Bragg's law. If the Miller indices of the chosen planes are *hkl*, if the spacing of these planes is d_{hkl}, and if we introduce $d_{nh,nk,nl} = d_{hkl}/n$ [*cf.* equation (1.1.23)], then the factor n is effectively restored. This means that, as well as reflecting the selected wavelength through the *hkl* reflection, the monochromator has the potential to reflect unwanted harmonics λ/n of the desired wavelength through the *nh*,*nk*,*nl* reflections. This problem can be largely overcome using the *hkl* planes with h, k, l all odd in crystals with the diamond structure, such as silicon and germanium; for this structure the structure factors [equation (2.3.7)] for the $2h$,$2k$,$2l$ reflections are zero so that there is no contamination by $\lambda/2$, and at the shorter wavelengths, $\lambda/3$ and so on, there are very few neutrons in the thermal neutron spectrum (Fig. 2.3.5).

Since 'perfect' crystals (of silicon and germanium, for example) have low reflectivity, for monochromator applications imperfect or 'mosaic' crystals are usually preferred. A mosaic crystal can be pictured as comprising small blocks of crystal with slightly differing orientations, the distribution in angle of these blocks being characterized by a full-width at half-maximum angle, β, known as the 'mosaic spread'. In addition to improving the intensity markedly,[12] this 'mosaic spread' will also increase the range of wavelengths obtained. Crystals intended for use as monochromators are very often deliberately deformed to achieve the desired mosaic structure. Further gains in intensity are sought by using vertically focusing monochromators, since the vertical divergence can be increased without serious detriment to the diffraction patterns. Vertically focusing monochromators usually comprise a number of separate monochromator crystals either individually adjustable (Fig. 2.3.17) or in fixed mountings on a bendable plate.

It is not common to find polarized neutrons being used in neutron powder diffractometers. Nevertheless, we think it appropriate to mention here that one means to obtain a polarized neutron beam is to use an appropriate polarizing crystal monochromator.[13] The 111 reflection from the ferromagnetic Heusler alloy Cu_2MnAl is commonly used for this purpose; the nuclear and magnetic structure factors [equations (2.3.7) and (2.3.8)] are of similar magnitude and they add or subtract depending on whether the neutron spin is antiparallel or parallel to the magnetization of the alloy. The beam reflected from such a monochromator can be polarized to better than 99%.

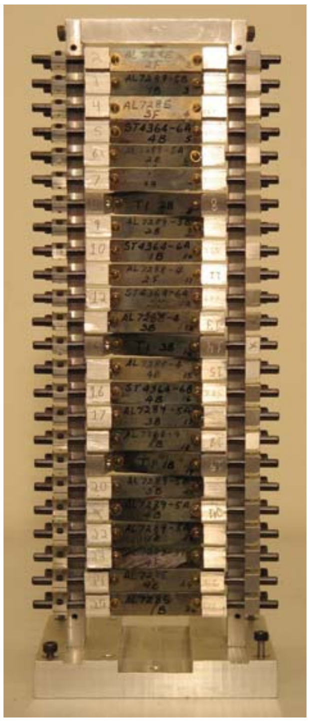

Figure 2.3.17
The vertically focusing monochromator constructed at the Brookhaven National Laboratory (Vogt *et al.*, 1994) and now used by the high-resolution powder diffractometer ECHIDNA at OPAL. The 24 monochromating elements are individually adjustable, and each of these is a 30-high stack of 0.3 mm thick Ge wafers, deformed to yield a suitable mosaic structure and then brazed together. (Reproduced with permission from ANSTO.)

The reader is referred to Section 4.4.2 of Volume C (Anderson & Schärpf, 2006) and to Kisi & Howard (2008) Sections 3.2.1 and 12.3 for further details.

2.3.4.1.3. *Neutron detectors*

Neutrons, being electrically neutral, do not themselves cause ionization and so cannot be detected directly; their detection and counting therefore depend on their capture by specific nuclei and the production of readily detectable ionizing radiation in the ensuing nuclear reaction. Only a limited number of neutron-capture reactions are useful for neutron detection [see Chapter 7.3 of Volume C (Convert & Chieux, 2006)]; they include

$$\begin{aligned}
{}^1_0\mathrm{n} + {}^3_2\mathrm{He} &\rightarrow {}^1_1\mathrm{H} + {}^3_1\mathrm{H} + 0.76\ \mathrm{MeV}\\
{}^1_0\mathrm{n} + {}^6_3\mathrm{Li} &\rightarrow {}^3_1\mathrm{H} + {}^4_2\mathrm{He} + 4.79\ \mathrm{MeV}\\
{}^1_0\mathrm{n} + {}^{10}_5\mathrm{B} &\rightarrow {}^7_3\mathrm{Li} + {}^4_2\mathrm{He} + 2.8\ \mathrm{MeV}\\
{}^1_0\mathrm{n} + {}^{157}_{64}\mathrm{Gd} &\rightarrow {}^{158}_{64}\mathrm{Gd} + \gamma\text{-rays} + \text{conversion electrons}\\
&\qquad + \leq 0.18\ \mathrm{MeV}\\
{}^1_0\mathrm{n} + {}^{235}_{92}\mathrm{U} &\rightarrow \text{fission fragments} + {\sim}200\,\mathrm{MeV}
\end{aligned}$$

(*cf.* Section 2.3.3.2).

---

[12] Most of the improvement is due to a change from a 'dynamical' to a 'kinematic' scattering regime.

[13] Polarized beams can also be produced using suitable mirrors or filters [see Section 4.4.2 of Volume C by Anderson & Schärpf (2006)].

The attenuation of neutrons in these materials (Section 2.3.2.4) will be dominated by the high absorption (by capture) cross sections (Table 2.3.2), so the linear attenuation coefficient will be given by $\mu = N\sigma_{\rm abs}$ where N is the number of absorbing nuclei per unit volume. We remark that absorption cross sections, with the exception of Gd, increase linearly with wavelength. The factor by which the neutron beam is diminished in a detector of thickness x is $\exp(-\mu x) = \exp(-N\sigma_{\rm abs}x)$. The detector efficiency, then, given by the fraction of neutrons absorbed (captured) in the detector, is $1 - \exp(-N\sigma_{\rm abs}x)$. In most cases the aim is to have high detector efficiency; however, in some circumstances it is desirable to monitor an incident neutron beam, in which case attenuation should be kept to a minimum. The account of neutron detection given here will be kept relatively brief since much has been written on this subject elsewhere [Oed, 2003; Chapter 7.3 of Volume C (Convert & Chieux, 2006)].

The task, following the neutron-capture reaction, is to detect the various charged particles or ionizing radiations that are produced. These are registered by the electrical signals they generate in a gas-filled proportional counter or ionization chamber, or in a semiconductor detector, recorded on film, or detected from the flashes of light they produce in a scintillator, for example ZnS. It is well worth noting that the secondary radiation carries no record of the energy of the detected neutrons; so whatever the means of detection, detectors can count neutrons but can provide no information on their energy distribution.

The gas-filled radiation detectors are essentially Geiger counters, comprising a gas-filled tube with a fine anode wire running along its centre. The anode collects the electrons released by ionization of the gas; if the anode voltage is high enough, there is a cascade of ionization providing amplification of the signal.[14] Detectors filled with boron trifluoride, $^{10}BF_3$, and helium-3, ^3He, have high efficiencies and are in common use; in these the nucleus designated to capture neutrons is incorporated in the filling gas. Such detectors operate with pulse-height discrimination, not in any attempt to determine neutron energy, but to discriminate against lower-voltage signals from γ-rays and other unwanted background. Another approach is to have a thin solid layer[15] of neutron-absorbing material, ^{235}U for example, releasing secondary radiation, in this case fission products, into a gas proportional counter filled with a standard argon/methane mixture; this would represent a low-efficiency neutron detector suitable for use as an incident-beam neutron monitor. Neutron detection based on semiconductor particle detectors is still in the developmental stage. The main problem is that the semiconductors used for charged-particle detection do not contain neutron-absorbing isotopes. Semiconductor particle detectors could be used to register the secondary radiation from an abutting layer of neutron-absorbing solid, but that layer would need to be thin, and another low-efficiency neutron detector would result. Scintillation detectors involve the placement of neutron-absorbing materials, such as ^6LiF, adjacent to a scintillator such as a ZnS screen, or perhaps the use of a Ce-doped lithium silicate glass, and counting the flashes of light that are produced. These light flashes can be recorded by photomultiplier tubes or on film. Scintillation detectors are, however, not used in constant-wavelength diffractometers because of their sensitivity to γ-radiation. They are used in time-of-flight diffractometers at spallation sources by exploiting the fact that the unwanted fast neutrons and γ-rays, and the thermal neutrons of interest, are separated in time (Section 2.3.4.2.2).

Much of the preceding description refers to single neutron counters, although it should be noted that there is a position-sensitive capability inherent in a film or scintillator screen. The earliest CW diffractometers employed just a single detector set on an arm that scanned through the scattering angle 2θ; the deployment of a Soller collimator just in front of the detector was advantageous. Conceptually the simplest but not necessarily the cheapest means for improvement was to mount a number of collimator/detector pairs on the detector arms. Such an improvement was made to diffractometer D1A at the Institut Laue–Langevin (Hewat & Bailey, 1976) by mounting ten sets of 10′ divergence Soller collimators/^3He detectors at intervals of 6°. The BT-1 diffractometer at NBSR operates with 32 ^3He detectors set at 5° intervals, so a scan through 5° covers a total angular range of 160°. The ultimate level for this kind of development was reached when D2B at the Institut Laue–Langevin operated in its former mode, with 64 detectors set at 2.5° intervals, each with its own 5′ Mylar Soller collimator; this required a scan through only 2.5° to record 160° of diffraction.

The alternative to using large numbers of individual detectors is to make use of position-sensitive neutron detectors (PSDs), and these have been in use for quite some time. The technology is that of the position-sensitive detection of charged particles, the important issue for neutrons being that the charged-particle detection should be located close to the neutron-capture event so that positional information is retained. A gas-filled ^3He detector with a single anode wire can serve as a linear PSD, for example by comparing the charges collected, after the capture event, at the opposite ends of the wire. The D2B diffractometer at the Institut Laue–Langevin has now been upgraded to ‘SuperD2B’, which uses 128 linear PSDs with their axes (anode wires) vertical, at 2θ intervals of 1.25°; this operates as a quasi-two-dimensional PSD. Diffractometers SPODI at FRM-II (80 detectors) and ECHIDNA at OPAL (128 detectors) are fitted with similar detector arrays. A single gas-filled chamber containing a number of separate parallel vertically aligned anodes, termed a multi-wire proportional counter (MWPC), provides another approach; the electronics needs to register at which of the wires the capture event occurred. This technology has extended from the first multi-wire PSD with 400 wires at 5 mm (0.2°) separation, used on the D1B diffractometer at the Institut Laue–Langevin in the 1970s, to a PSD with 1600 wires at 0.1° separation now in use on HRPT at SINQ (Fig. 2.3.15). A further advance is the development of the micro-strip gas chamber (MSGC) detector (Oed, 1988). In this detector the anodes and the cathodes are printed circuits on glass substrates, which are then mounted into the chamber. With this arrangement, an anode separation of 1 mm is achievable and the stability is excellent. The high-intensity diffractometer D20 at the Institut Laue–Langevin has a detector assembled from plates of micro-strip detectors and achieves 1600 anodes at 0.1° angle separation.

As pointed out above, the detection systems on SuperD2B, SPODI and ECHIDNA achieve a quasi-two-dimensional position capability by using banks of linear PSDs located side by side. An MWPC detector can achieve two-dimensional capability in a very similar manner, using the anode position to locate in the horizontal direction and charge division measurements at the ends of each anode wire to find the vertical position. An MWPC detector can also be fitted with segmented cathodes, either side of the anodes, one returning positional information in the horizontal direction and the other giving the vertical position. A detector of this kind is used on the WOMBAT diffractometer at the OPAL reactor. MSGC detectors can also be adapted to provide two-dimensional positional information after printing a set of cathodes orthogonal to the primary set on the back surface of the glass.

---

[14] Strictly speaking, the term ‘Geiger counter’ should be reserved for detectors operating in this amplification regime.

[15] The layer must be thin so that the secondary radiation, which has a short range in solids, can escape into the charged-particle detector.

A few general comments about detecting systems are in order. The time for a detector to recover after registering a neutron count is known as the dead time, and this may be significant when count rates are high, in which case corrections are needed [Chapter 7.3 of Volume C (Convert & Chieux, 2006)]. For banks of detectors, and also for position-sensitive detectors, calibration for position and sensitivity becomes a critical issue. In the case of a smaller bank of detectors, it may be possible to scan the detector bank so the same diffraction pattern is recorded in the different detectors, in which case the relative positions and efficiencies of the different detectors can be determined quite well (see Section 4.1 of Kisi & Howard, 2008). For more extensive banks or large position-sensitive detectors, detector sensitivity calibration is performed by examining the very nearly isotropic incoherent scattering from vanadium. In this case checking for angular accuracy can be more difficult. The time taken to register a neutron count cannot be said to be a fundamental issue in CW powder diffraction, since in some applications it is scarcely relevant, although in other applications, such in the study of very fast reaction kinetics (Riley *et al.*, 2002), the constraints on time are very demanding.

2.3.4.1.4. *Resolution and intensity*

The resolution and intensity of a CW powder diffractometer are strongly influenced by the divergences α_1, α_2 and α_3 of the primary, monochromatic and diffracted beams, respectively, along with the mosaic spread β of the crystal monochromator. The situation was analysed by Caglioti *et al.* (1958) on the basis that the triangular transmission factor of each collimator, total width 2α, could be approximated by a Gaussian with full-width at half-maximum (FWHM) α, that the mosaic distribution of the monochromator could also be described by a Gaussian with FWHM β, but that there was no sample contribution to the peak widths. On this basis the diffraction peaks were found to be Gaussian, with the FWHM of the diffraction peak occurring at scattering angle 2θ given by (Hewat, 1975)

$$\mathrm{FWHM}^2 = U\tan^2\theta + V\tan\theta + W, \qquad (2.3.18)$$

where

$$U = \frac{4(\alpha_1^2\alpha_2^2 + \alpha_1^2\beta^2 + \alpha_2^2\beta^2)}{\tan^2\theta_M(\alpha_1^2 + \alpha_2^2 + 4\beta^2)}, \qquad (2.3.18a)$$

$$V = \frac{-4\alpha_2^2(\alpha_1^2 + 2\beta^2)}{\tan\theta_M(\alpha_1^2 + \alpha_2^2 + 4\beta^2)}, \qquad (2.3.18b)$$

$$W = \frac{\alpha_1^2\alpha_2^2 + \alpha_1^2\alpha_3^2 + \alpha_2^2\alpha_3^2 + 4\beta^2(\alpha_2^2 + \alpha_3^2)}{\alpha_1^2 + \alpha_2^2 + 4\beta^2} \qquad (2.3.18c)$$

and θ_M is the Bragg angle ($2\theta_M$ is the take-off angle) at the monochromator. Under these conditions the total (integrated) intensity in the diffraction peak is given by

$$L \propto \frac{\alpha_1\alpha_2\alpha_3\beta}{(\alpha_1^2 + \alpha_2^2 + 4\beta^2)^{1/2}}. \qquad (2.3.19)$$

These equations have important implications and accordingly have received a good deal of attention. They return at once the well known resolution advantage in setting up the diffractometer in the parallel configuration (that seen in Fig. 2.3.15, in this configuration θ_M taken to be positive). Caglioti *et al.* (1958) deduced that for the simple case of $\alpha_1 = \alpha_2 = \alpha_3 = \beta = \alpha$ equations (2.3.18) and (2.3.19) reduce to

$$\mathrm{FWHM} = \alpha\left(\frac{11 - 12a + 12a^2}{6}\right)^{1/2} \text{ and } L \propto \alpha^3/(6)^{1/2},$$

where $a = \tan\theta/\tan\theta_M$; they went on to record results for a number of other combinations. In his design for a high-resolution diffractometer, Hewat (1975) considered the case $\alpha_2 = 2\beta > \alpha_1 \simeq \alpha_3$. Under these conditions, the peak widths are close to their minimum around the parallel focusing condition $\theta = \theta_M$, their widths there are given by

$$\mathrm{FWHM}^2 = (\alpha_1^2 + \alpha_3^2) - \frac{\alpha_1^4}{\alpha_1^2 + \alpha_2^2 + 4\beta^2} \simeq \alpha_1^2 + \alpha_3^2,$$

and the total intensity is approximately

$$L \propto \alpha_1\alpha_3\beta/(2)^{1/2}.$$

Hewat's conclusions, put briefly, were that good resolution could be obtained by keeping divergences α_1 and α_3 small, while intensity could be somewhat recovered by adopting relatively large values for the monochromator mosaic spread β and divergence α_2 of the monochromatic beam. Hewat also argued for a high monochromator take-off angle $2\theta_M$, not only to reduce peak widths [through the term $\cot\theta_M$ appearing in equation (2.3.17) and reappearing in equations (2.3.18)], but also to match the region of best resolution to that of the most closely spaced peaks in the diffraction pattern. Hewat's design was implemented in the D1A diffractometer at the Institut Laue–Langevin (Hewat & Bailey, 1976), subsequently in the D2B diffractometer at the same establishment, and elsewhere. In a version installed at the (now retired) HIFAR reactor in Sydney, Howard *et al.* (1983), using an Al_2O_3 (corundum) ceramic sample, reported a peak-width variation in close agreement with that calculated from equation (2.3.18). Although more sophisticated analyses are available in the literature (Cussen, 2000), this result would suggest that equations (2.3.18) still provide a good starting point.

The usual trade-off between intensity and resolution applies, and since neutron sources are rather less intense than X-ray sources, this is an important consideration. Intensity is sacrificed by using high monochromator take-off angles to limit the wavelength spread [equation (2.3.17)], and by using tight collimation [equation (2.3.19)]. Evidently intensities could be increased by relaxing these constraints. These days it is more common to build diffractometers of good-to-high resolution, and then to seek other means to improve data-collection rates. Focusing monochromators, such as described in Section 2.3.4.1.2, serve to increase the neutron intensity at the sample position without seriously degrading the resolution. In addition, the use of multi-detector banks and the development and deployment of position-sensitive detectors, as described in Section 2.3.4.1.3, has been very much driven by the desire to increase the speed of data collection. As mentioned earlier, the design and analysis of neutron powder diffractometers should be treated in a holistic fashion, and although some advanced analytical methods have been applied (Cussen, 2016 and references therein), Monte Carlo analyses using programs such as *McStas* (Willendrup *et al.*, 2014) and *VITESS* (Zendler *et al.*, 2014) to track large numbers of neutrons from the source right through to the neutron detectors are now widely employed.

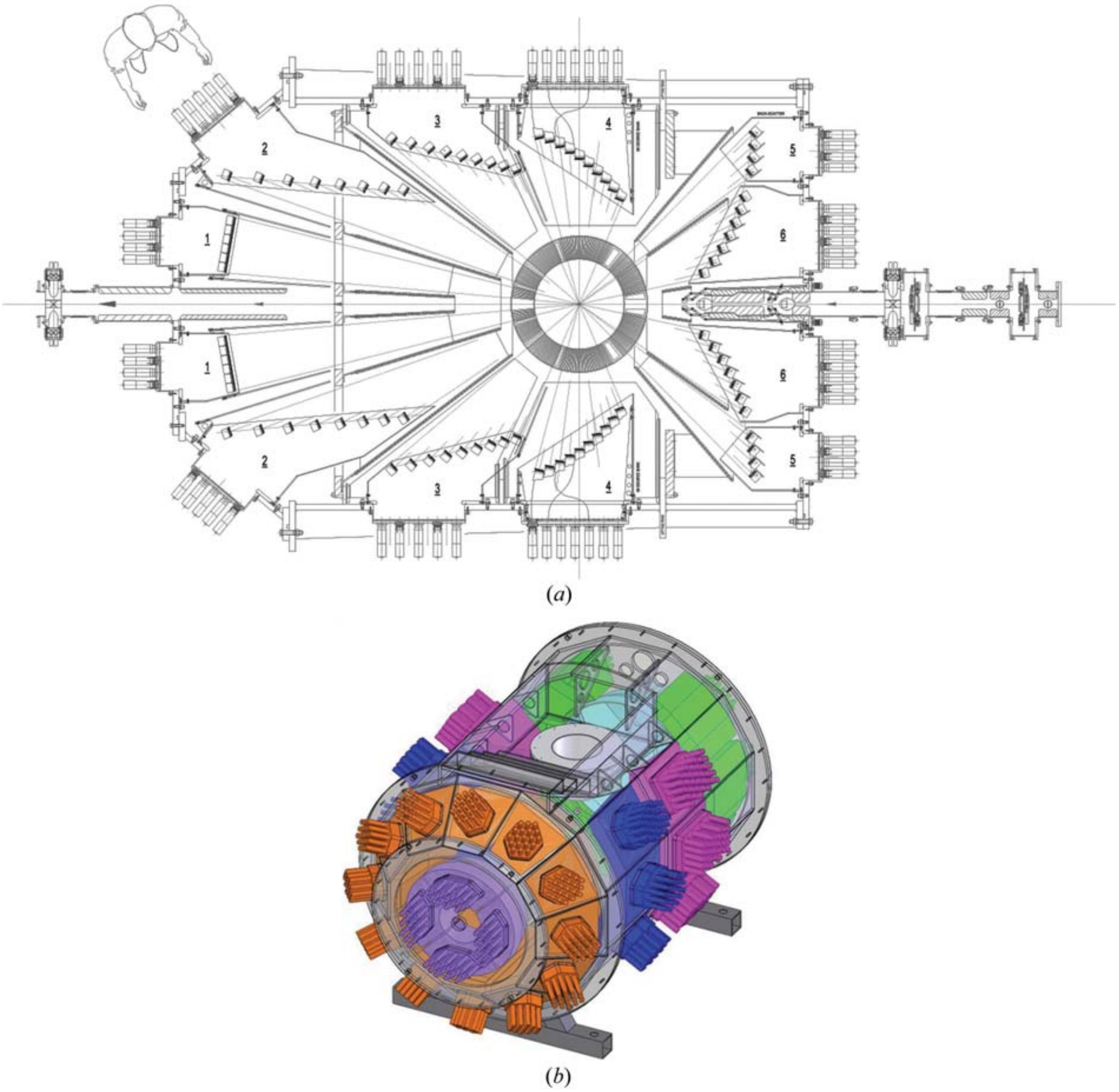

Figure 2.3.18
(*a*) Schematic cross section of the POLARIS diffractometer at the ISIS facility, UK, and (*b*) a three-dimensional solid model of the detector chamber. (Credit: STFC.)

2.3.4.2. *Time-of-flight (TOF) diffractometers*

Time-of-flight (TOF) diffractometers differ substantially from CW diffractometers. Neutrons delivered to the instrument are already partially collimated and TOF instruments have no monochromator and consequently no moving parts. The full incident neutron spectrum is utilized and needs to be well characterized in order to extract meaningful intensities; in addition the wavelength dependence of detector efficiencies needs to be taken into account. In principle, measurements from an incoherently (therefore isotropic and wavelength-independent) scattering sample such as V or H_2O provide the required characterization.[16] In practice, however, incident spectra are usually recorded using a low-efficiency detector (beam monitor) in the incident beam. Data from V are still required to correct for the relative efficiency of individual detectors or detector elements and their wavelength dependence (Soper *et al.*, 2000).

The basic components of a TOF powder diffractometer are the flight tube from the neutron source or a neutron guide, a precisely located sample position, banks of detectors at various positions around the sample position and a neutron-absorbing beam stop. In early TOF diffractometers, detector banks were relatively localized typically in forward scattering, close to $2\theta = 90^\circ$ and backscattering locations. More modern diffractometers have very extensive detector arrays such as the newly upgraded POLARIS instrument at the ISIS facility, which is illustrated in Fig. 2.3.18. Neutrons enter the diffractometer at the right of Fig. 2.3.18(*a*) through a number of adjustable neutron-absorbing jaws which trim the beam size to match the sample size. The beam is then incident on the sample, which is located within the chamber where the detectors, arranged in numbered banks, are housed. The entire sample/detector chamber (and flight tube) is evacuated during data collection in order to reduce absorption and scattering of the incident neutron beam by air, effects which both decrease the intensity of the neutrons incident on the sample and increase the background scattering. A human figure in Fig. 2.3.18(*a*) indicates the large scale of the device and it should be noted that the substantial neutron shielding surrounding the detector chamber (known as the blockhouse) is not shown.

---

[16] The much larger incoherent scattering cross section of H allows normalization data to be recorded much more quickly using H_2O; however, the small amount of additional moderation of the beam that occurs is usually considered undesirable.

2.3.4.2.1. *Instrument resolution and design*

In a TOF instrument, all of the incident spectrum of neutron wavelengths is utilized, appropriately trimmed by the chopper system as previously described. The different wavelengths (λ) are identified through their time-of-flight (t) according to equation (2.3.15). Substituting that equation into Bragg's law, we obtain

$$\begin{aligned} d_{hkl} &= \frac{ht}{2mL\sin\theta} \\ &= \frac{t}{505.554L\sin\theta} \end{aligned} \tag{2.3.20}$$

for t in microseconds, d in ångstroms and L in metres.

The resolution of a TOF diffractometer is defined by the uncertainty in the d-spacing (Δd) relative to its absolute value d. Apparent as the width of the diffraction peaks, the resolution is given primarily by (Buras & Holas, 1968; Worlton *et al.*, 1976)

$$\frac{\Delta d}{d} = \left[\Delta\theta^2\cot^2\theta + \left(\frac{\Delta t}{t}\right)^2 + \left(\frac{\Delta L}{L}\right)^2\right]^{1/2}. \tag{2.3.21}$$

There are a number of important things to note concerning this equation:

(i) The terms $\Delta\theta\cot\theta$ and $\Delta L/L$ are fixed and independent of flight time once the diffractometer is constructed; in addition, as we have already noted (Section 2.3.3.3), for a spallation source with a suitably poisoned moderator the time resolution $\Delta t/t$ is practically constant. Thus the resolution of a TOF diffraction pattern is virtually constant across the entire range of d-spacing explored in a given detector bank.[17]

(ii) Uncertainties in the neutron path length, ΔL, can arise due to measurement uncertainty in determining L; however, these are usually overshadowed by the uncertainty that arises because neutrons can emerge into the neutron guide from any position within the finite-sized moderator and this uncertainty constitutes the major contribution to ΔL.

(iii) As ΔL is a constant, a linear improvement in resolution can be achieved merely by making the instrument longer, such as HRPD at ISIS and S-HRPD at J-PARC, which are almost 100 m long.

(iv) The contribution of the diffraction angle 2θ to resolution is considerable. For a fixed angular uncertainty (detector positioning and finite width) the $\cot\theta$ term varies from infinite at $2\theta = 0$ to zero at $2\theta = 180°$. Therefore, the higher the detector angle, the better the resolution.

With these matters considered, we can return to our example of a modern TOF diffractometer in Fig. 2.3.18 and in particular the arrangement of the detectors. The strategy employed is to group multiple individual detector elements into a number of discrete banks. It may be seen from equation (2.3.21) that decreasing 2θ and increasing L have opposing effects on resolution. By appropriate manipulation of the equation and by expressing the overall neutron flight path as $L = L_1 + L_2$ where L_1 is the moderator-to-sample distance and L_2 is that from the sample to the detector, it is straightforward to obtain

$$L_2 = \Delta L\left[\left(\frac{\Delta d}{d}\right)^2 - \left(\frac{\Delta\theta}{\tan\theta}\right)^2 - \left(\frac{\Delta t}{t}\right)^2\right]^{-1/2} - L_1. \tag{2.3.22}$$

Therefore by adjusting 2θ and L_2 correctly, it is possible to construct banks of detectors covering a range of 2θ, for which the resolution is identical. This allows neutrons recorded in the entire detector bank to be 'focused' into a single diffraction pattern. The resulting curved detector arrangement is obvious in the high-resolution detector bank labelled 5 and 6 in Fig. 2.3.18(*a*). For a fixed (small) value of $\Delta d/d$, eventually space limitations impose restrictions on L_2 and a new, lower-resolution detector bank (4) commences. As the benefits of a curved arrangement become insignificant, the appropriate curve is approximated by a straight arrangement in the lower-angle banks and dispensed with altogether in the very low angle bank. In Fig. 2.3.18 the backscattering (5, 6), 90° (4), two separate low-angle (2 & 3) and the very low angle (1) detector banks of POLARIS are identified. These have average 2θ angles of 146.72, 92.59, 52.21, 25.99 and 10.40°, respectively.

Raw diffraction patterns recorded in the various detector banks are compared in Fig. 2.3.19. Note that the curved background due to the incident spectrum is flattened when the patterns are normalized. A logarithmic scale is necessary to display the very wide range of d-spacings accessible across the whole instrument and this scale emphasises the near-constant resolution across each pattern. In keeping with equations (2.3.21) and (2.3.20), the effects of changing the detector angle are obviously greater resolution and access to shorter d-spacings as 2θ increases. Each detector bank can provide data for a different purpose according to its resolution and d-spacing coverage. For example, the combination of good resolution (4×10^{-3}) and a wide range of d-spacing (0.2–2.7 Å) makes data from the backscattering bank (Fig. 2.3.19*e*) ideal for the refinement of medium- to large-scale crystal structures. The 90° bank (Fig. 2.3.19*d*) is optimized for use with complex sample environments such as high-pressure cells or reaction vessels, as this geometry combined with appropriate collimation of the incident and scattered neutron beams enables diffraction patterns to be collected that only contain Bragg reflections from the sample being studied. It can be used to obtain good-resolution data (7×10^{-3}) during a variety of *in situ* studies. The low-angle and very low angle banks with their access to very large d-spacings up to 20 Å are invaluable in determining unknown crystal structures and complex magnetic structures by allowing the indexing of low-index reflections and determining reflection conditions.

In order to reduce unwanted background counts and give better localization of the diffraction pattern from the sample, *i.e.* to better exclude sample environments such as cryostats or furnaces, the instrument is fitted with a radial collimator surrounding the sample position.[18] For more common sample environments, *e.g.* furnaces, this collimation allows all detector banks to view the sample unimpeded. The detector banks are contained within the large vacuum vessel shown in Fig. 2.3.18(*b*). This reduces attenuation and background due to scattering by air. The detector coverage on such an instrument is very large, in the case of POLARIS up to 45% of the available solid angle is covered. A full description of this instrument may be found in Smith *et al.* (2018).

---

[17] A small effect due to a time-dependent component of $\Delta t/t$ might be observed depending on the source and instrument configuration.

[18] Although typically constructed from planar vanes which are oscillated to average their shadow across all the detectors, the POLARIS collimator vanes are stationary, and are conical to follow the Debye–Scherrer cones of the diffracted neutrons.

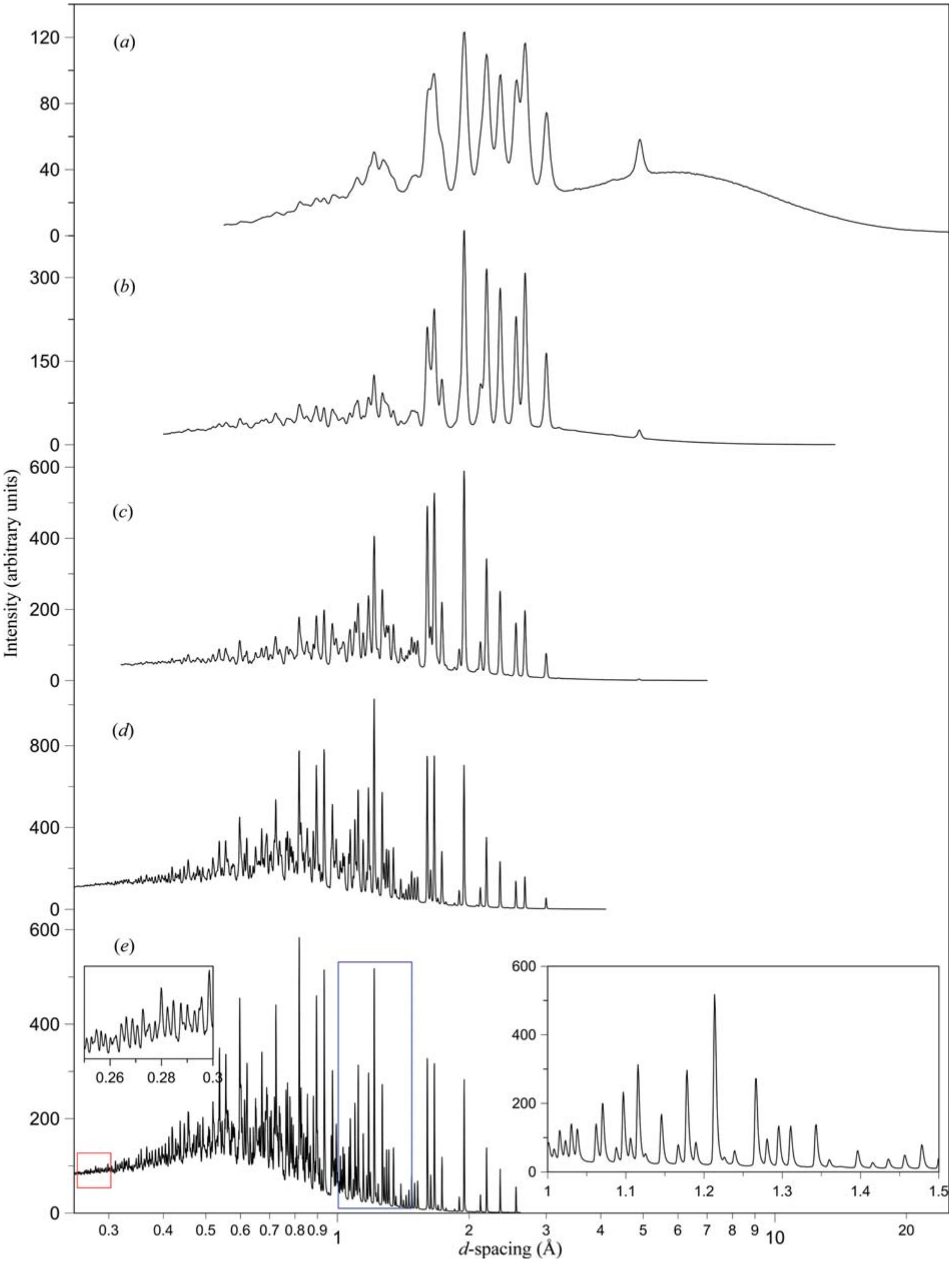

Figure 2.3.19

Raw neutron diffraction patterns from $Y_3Al_5O_{12}$ (YAG). Patterns from the five POLARIS detector banks, (*a*) very low angle, (*b*) low angle 1, (*c*) low angle 2, (*d*) 90° and (*e*) backscattering, are shown separately. Note that the very wide range of *d*-spacings accessible (~0.2–25 Å) necessitates the use of a $\log_{10}$ scale. Insets for the backscattering bank illustrate that useful data are obtained even at very small *d*-spacing (red) and that the resolution is very good (blue). Note the asymmetric peak shape that results from a rapid rise, followed by a slower exponential decay, in the number of neutrons emerging from the moderator after each incident proton pulse.

2.3.4.2.2. *Detection*

All the neutron detector types discussed in Section 2.3.4.1.3 are capable of detecting the scattered neutrons in a TOF pattern. Gas-filled proportional counters such as BF_3 and ^3He detectors have efficiencies governed by the neutron energy (or wavelength). Detectors on CW diffractometers are optimized for the narrow band of wavelengths available when using a crystal monochromator, say 1–2.4 Å. The wavelength range in TOF diffraction is generally much wider; as much as 0.2–6 Å or more, and proportional detectors need to be specifically optimized. There is of course the added complexity of tracking the arrival time of each neutron and this has worked against the use of multiwire proportional detectors and microstrip detectors as described in Section 2.3.4.1.3. Instead, there is extensive use of scintillation detectors, which are usually based on the ^{6}Li(n;t,α) reaction (Section 2.3.4.1.3). When doped into the ZnS film of a scintillator, the ^{6}Li provides excellent detection sensitivity and energy range. Discrimination against fast neutrons and γ-ray contamination in the incident beam is easily accommodated as these have different velocities to the thermal and epithermal neutrons used for TOF diffraction and are therefore readily excluded by the chopper system and detector electronics.

The detector electronics on older instruments recorded the diffraction pattern in a fixed set of time channels or bins; typically 1024 to begin with and progressively more as electronic and computational advances occurred. More recently, the technique has shifted to recording the data to memory in a continuous stream known as event mode, where the arrival time of each neutron is recorded. The user may then bin (and re-bin) the data into time channels to suit the resolution of the diffraction pattern, which may differ significantly from the instrument resolution because of microstructural features of the sample. Such features are discussed at length in Chapters 5.1 and 5.2.

In a new development, a neutron-sensitive microchannel plate detector has been developed (Tremsin, McPhate, Vallerga, Siegmund, Feller *et al.*, 2011). Microchannel plate detectors (MCPs) are divided into discrete pixels and record the arrival time of each neutron in each pixel. Initially used for high-resolution radiography at pulsed neutron sources, it was quickly realized that MCP detectors can be used for diffraction *via* the Bragg-edge phenomenon (Tremsin, McPhate, Vallerga, Siegmund, Kockelmann *et al.*, 2011). The resolution is typically 55 μm due to the data-acquisition electronics but can be sharpened to less than 15 μm using centroiding techniques. This type of detector opens the door to spatially resolved neutron powder diffraction in materials as well as strain-imaging applications on TOF neutron diffractometers.

2.3.4.3. *Variations on a theme*

The diffractometers HRPT (Fig. 2.3.15) and POLARIS (Fig. 2.3.18) are general-purpose instruments suitable for solving and studying medium-sized crystal structures under a range of non-ambient conditions and in some cases the study of non-crystalline or poorly crystalline materials. There are several such diffractometers at reactors [HB-2A at Oak Ridge (https://neutrons.ornl.gov/powder), D1B at ILL (https://www.ill.eu/instruments-support/instruments-groups/instruments/d1b/description/instrument-layout/), HRPD at KAERI (http://www.kaeri.re.kr:8080/english/sub/sub03_04_01_01.jsp), C2 at CINS (http://cins.ca/get-beam-time/beamline-specs/c2/)] and spallation sources around the world [POWGEN and NOMAD at SNS (https://neutrons.ornl.gov/powgen; https://neutrons.ornl.gov/nomad), GEM at ISIS (http://www.isis.stfc.ac.uk/instruments/gem/gem2467.html), iMATERIA at J-PARC (https://j-parc.jp/researcher/MatLife/en/instrumentation/images/BL20.gif) *etc*].

A more specialized type of TOF powder diffractometer is the High Resolution Powder Diffractometer (HRPD) at ISIS (https://www.isis.stfc.ac.uk/Pages/Hrpd.aspx) and a similar instrument, Super-HRPD at J-PARC (https://j-parc.jp/researcher/MatLife/en/instrumentation/images/BL08.jpg). Although both of these instruments have 90° and low-angle detector banks, their overall design has strongly centred on extremes of resolution, attaining $\Delta d/d$ values of 4×10^{-4} and 3×10^{-4}, respectively. Such extremes of resolution are attained primarily through making the flight path of both instruments nearly 100 m long and placing detectors at very high Bragg angles (150–176°). Data from these can supply individual peak positions to a precision of approximately 5 parts per million and whole pattern fitting can give correspondingly precise lattice parameters. Recalling that in TOF powder diffraction the resolution is constant across the whole pattern, this makes the instruments ideal for the solution of large crystal structures in which a great many diffraction peaks need to be resolved, for tracking phase transitions, and for solving structures involving pseudo-symmetry, which even in relatively small structures (*e.g.* perovskites) can be a challenge for lower-resolution instruments. Example diffraction patterns are shown in Fig. 2.3.20 for the structural transitions in $SrZrO_3$ (Howard *et al.*, 2000).

At the other extreme of instrument design are the very high intensity diffractometers exemplified by the CW instruments D20 at ILL (https://www.ill.eu/instruments-support/instruments-groups/instruments/d20/) and WOMBAT at ANSTO (http://www.ansto.gov.au/ResearchHub/Bragg/Facilities/Instruments/Wombat/). These diffractometers use a large degree of vertical focusing to greatly increase the incident flux on the sample and are fitted with large position-sensitive detectors from which the data can be stored at 1 MHz or faster. If there is a periodic time structure to the phenomenon under study due to some driving stimulus (*e.g.* a periodic laser, electric or magnetic field pulse), then the data can be analysed stroboscopically by synchronizing with the driving stimulus, giving an effective time resolution in the MHz range. Even in the absence of a periodic stimulus, useful diffraction patterns on these diffractometers can in favourable circumstances be stored at rates of 2, 10 or with a large enough sample even 50 Hz (Fig. 2.3.21).

It should be noted that for TOF diffractometers, the time structure imposed by the pulsed neutron source and chopper system places absolute limitations on the most rapid diffraction pattern that can be recorded. This is typically ~0.1 s at sources such as ISIS, J-PARC or SNS. An additional time penalty is often paid due to the time taken to save such large amounts of data (typically between 10 and 30 s). There is therefore no TOF equivalent of the very rapid stroboscopic mode of operation.

Other forms of specialized neutron powder diffractometer have also been developed. Among these are the engineering or residual stress diffractometers, exemplified by the TOF diffractometers ENGIN-X at ISIS (https://www.isis.stfc.ac.uk/Pages/Engin-X.aspx), VULCAN at SNS (https://neutrons.ornl.gov/vulcan), TAKUMI at J-PARC (https://j-parc.jp/researcher/MatLife/en/instrumentation/ns.html) and the CW diffractometers SALSA at ILL (https://www.ill.eu/instruments-support/instruments-groups/instruments/salsa/description/instrument-layout) and KOWARI at ANSTO (http://www.ansto.gov.au/ResearchHub/Bragg/Facilities/Instruments/Kowari/). The purpose of these diffractometers is to measure accurate interplanar spacing (d) within a small gauge volume defined by the intersection of incident and diffracted beams inside a larger sample, as illustrated for constant wavelength in Fig. 2.3.22.

Variations in the d-spacing relative to a strain-free reference value (d_o) represent the average strain in the gauge volume parallel to the scattering vector (*i.e.* perpendicular to the diffracting planes) as is also illustrated in Fig. 2.3.22. By determining strains in several directions, it is possible to reconstruct the full strain tensor within each gauge volume, and

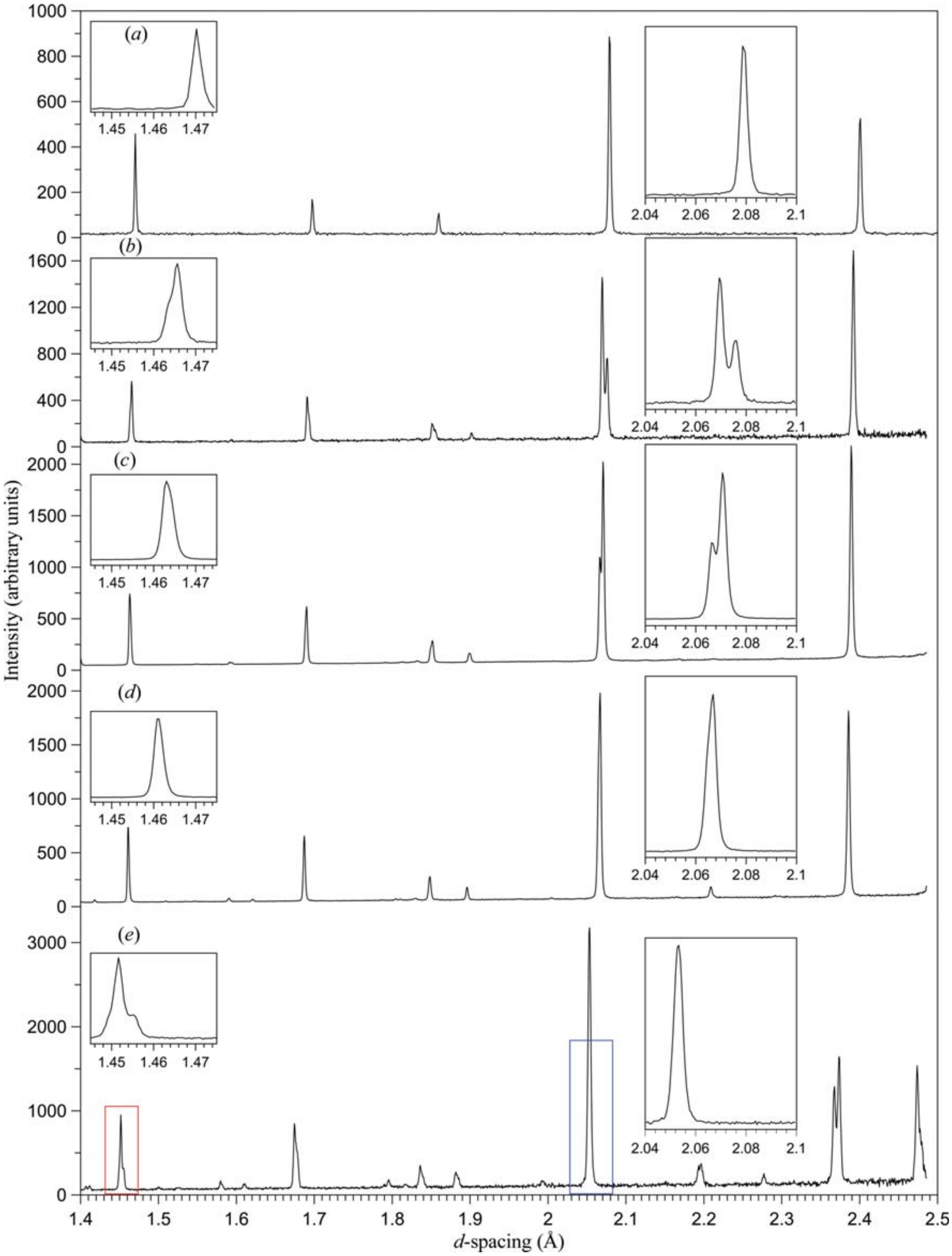

Figure 2.3.20

Parts of the very high resolution neutron powder-diffraction patterns recorded by the backscattering detector bank on the instrument HRPD at ISIS from $SrZrO_3$ at (*a*) 1403, (*b*) 1153, (*c*) 1053, (*d*) 933 and (*e*) 293 K. Insets to the left and right show subtle changes to the reflection shapes and splitting of reflections due to phase transitions from the cubic ($Pm\bar{3}m$) in pattern (*a*), to the tetragonal phase ($I4/mcm$) in (*b*), an orthorhombic phase (*Imma*) in (*c*) and a second orthorhombic phase (*Pnma*) in (*d*) and (*e*). Note the intensity reversal in the 002 reflection (right insets), which was pivotal in finding and solving the orthorhombic phase in *Imma* (Howard *et al.*, 2000).

this may be converted into the stress tensor, the desired outcome for engineering purposes (Noyan & Cohen, 1987; Fitzpatrick & Lodini, 2003; Kisi & Howard, 2008). This procedure is widely used in residual stress analysis to study stress distributions in fabricated or welded components and also to observe the internal stress distribution due to an externally imposed load. An example is illustrated in Fig. 2.3.23 in relation to *in situ* experiments and the stress distribution in granular materials.

The required localization of the gauge volume is achieved by shaping the incident and diffracted beams with slits/collimators and is greatly assisted by fixing the diffraction angle 2θ at $\pm 90^\circ$. In CW instruments, the need for high resolution and good intensity is met by using a focusing (bent Si) monochromator and a small area detector to record the data. This generally limits the investigation to a single Bragg peak (reflection), the position of which is carefully mapped over the sampled area for each strain component under investigation.

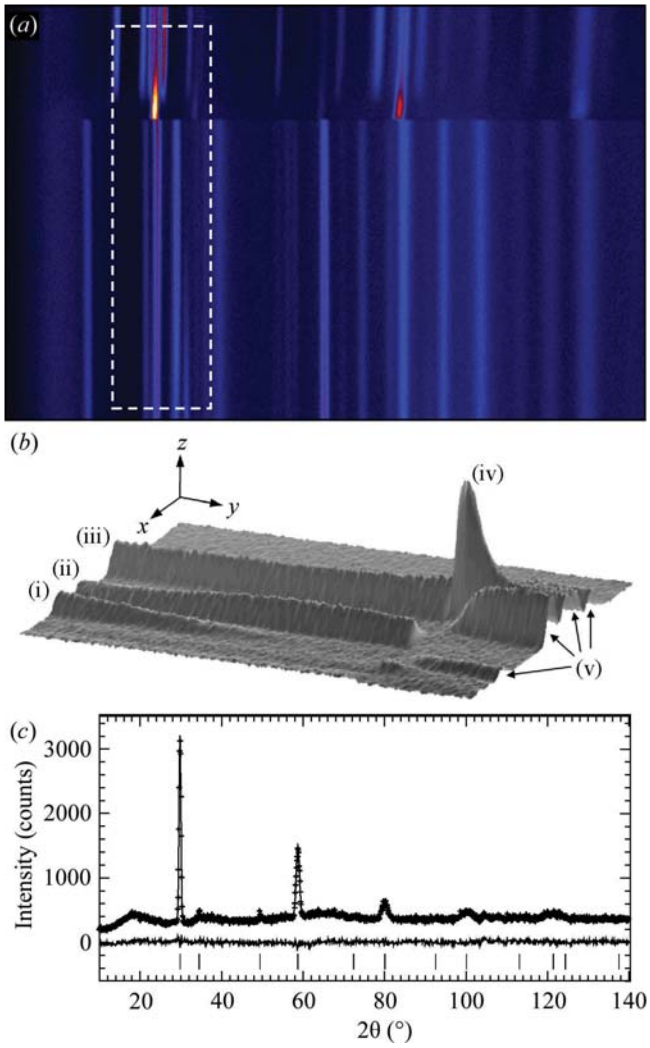

Figure 2.3.21
Neutron powder-diffraction patterns during combustion synthesis of Ti_3SiC_2 recorded in 400 ms each on the diffractometer D20 at ILL (Riley *et al.*, 2002). Panel (*a*) shows an overview of the reaction process with time vertical, diffraction angle horizontal and intensity as colour/brightness. Panel (*b*) is a three-dimensional view of the portion enclosed by dashed lines in (*a*), representing 140 s of reaction, wherein the numbered reflections show (i), (ii) a phase change in Ti, (iii) SiC, (iv) formation of an intermediate phase Ti(Si,C) and (v) growth of the Ti_3SiC_2 product. Panel (*c*) illustrates *via* Rietveld refinement the high quality of diffraction patterns even on this short timescale.

TOF engineering diffractometers record a full diffraction pattern at each position. Localization of the gauge volume is achieved using symmetric detector banks and radial collimators on either side of the sample position (Fig. 2.3.24). All other instrument-design criteria are generally secondary to this, as a parallelepiped-shaped gauge volume allows a seamless strain (stress) map to be obtained. These instruments are usually 40–50 m long and have moderately high resolution, which allows peak positions and hence strains to be measured to a precision of 5×10^{-5} in favourable circumstances. In common engineering materials (steels, aluminium alloys *etc.*) this equates to an absolute minimum stress uncertainty of 4–10 MPa. The extreme resolution that would be available using very high resolution designs like HRPD and Super-HRPD (above) is sacrificed in order to obtain data on a reasonable timescale given the generally small gauge volume (0.5–30 mm^3) and the need to map the strain field piecewise over an extended region of the sample.

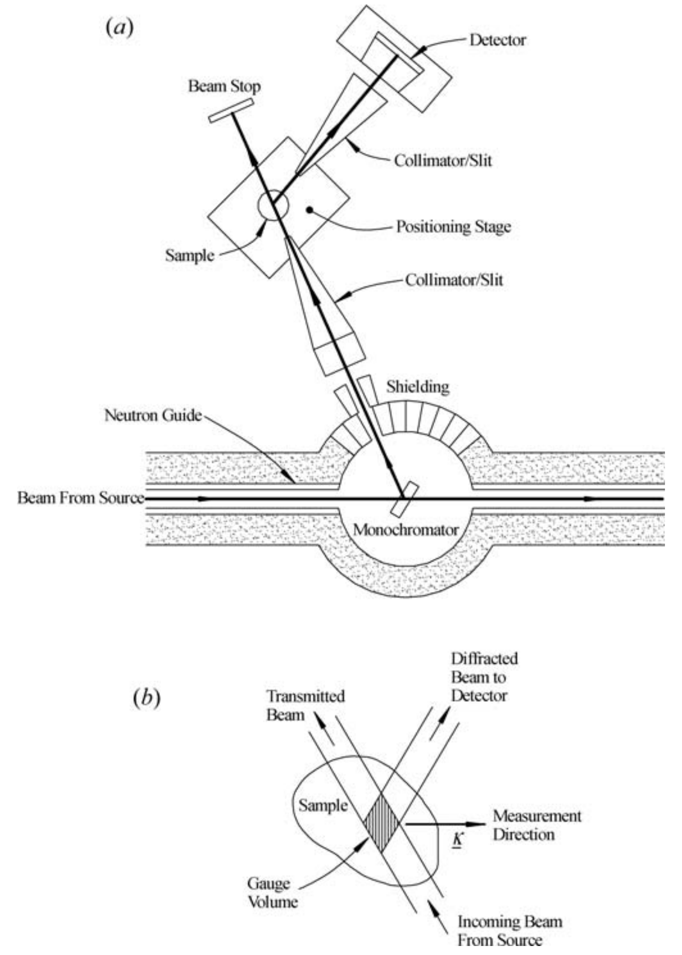

Figure 2.3.22
Illustrating (*a*) a CW engineering diffractometer and (*b*) the formation of a gauge volume at the intersection of the incident and diffracted beams.

Although it is not usual for instruments to be specifically designed for the purpose, neutron diffraction is also particularly useful for studying crystallographic texture in materials, as the neutron-diffraction pattern is not distorted by surface coatings or preparation methods. In principle, any diffractometer can be used for measuring texture simply by recording a large number of diffraction patterns with the sample rastered in small angular intervals (5° is common) about two mutually perpendicular axes to form a grid over all orientations. This is extremely time consuming on a conventional CW diffractometer, although the whole pattern is captured each time, as the intensity recorded for the different reflections is subject to different corrections. This can be greatly sped up by using a CW engineering diffractometer (SALSA, KOWARI) with an intense, well collimated incident beam and fitted with an area detector. For example, on KOWARI, the detector spans 15° in both horizontal and vertical directions and so the sample needs to be re-positioned far fewer times. An added advantage is that the diffraction geometry is identical for each sample position and almost so for each reflection studied, and so a pure (*i.e.* model-independent) texture measurement is obtained. Texture measurements on modern TOF diffractometers (*e.g.* GEM, POLARIS, POWGEN, NOMAD and iMATERIA) are in principle quite straightforward. Because there are detectors in many positions all around the sample, the scattering vector and hence orientation of diffracting planes (crystal orientation) is sampled in many orientations all in one data collection. If data from the individual detectors are not 'focused' into composite diffraction patterns as for crystal-structure studies, then very few re-orientations are required to record data representing the full texture. However, since each reflection in each detector bank is sampled using

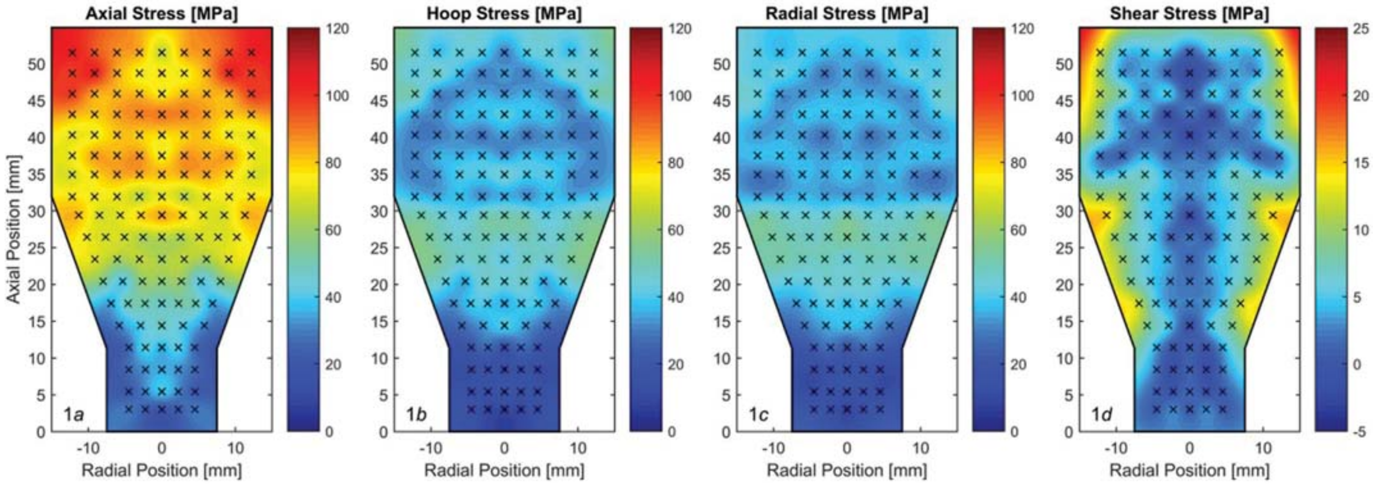

Figure 2.3.23
Stress distribution for four stress components in an iron powder compacted within a convergent die (see also Zhang *et al.*, 2016).

neutrons of different wavelength, each is recorded under different conditions for attenuation and extinction. In addition, to make full use of all the data, whole pattern or Rietveld analysis using a preferred-orientation (texture) model has to be conducted for each of the multitude of diffraction patterns recorded. As well as being time consuming, the reliability of the resultant pole figures and orientation density function is governed by the quality of all the individual models (for background, peak shape, peak width, sample centring, attenuation *etc.*) within the Rietveld refinement as well as the ability of the preferred-orientation model in the Rietveld program to accurately fit the real texture. A pure model-independent texture measurement can only be obtained using CW or TOF single-peak methods.

The instrument WISH at ISIS represents a departure from the normal TOF diffractometer design in that it receives *long wavelength* neutrons (1.5–15 Å) from a cold neutron source at Target Station 2. Ballistic supermirror neutron guides and three choppers deliver neutrons in an active bandwidth of 8 Å for a given chopper setting (https://www.isis.stfc.ac.uk/Pages/Wish.aspx). The pixelated ^{3}He detectors cover Bragg angles in the very wide range 10–170°. WISH is designed for the study of complex magnetic structures and large-unit-cell structures in chemistry and biology. Polarization analysis is available to assist the former.

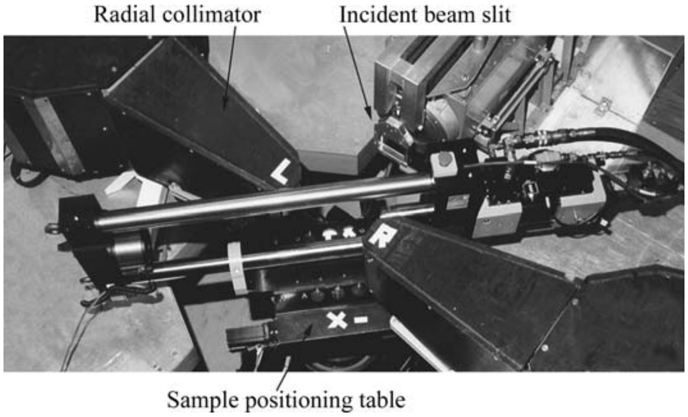

Figure 2.3.24
The engineering diffractometer ENGIN-X at ISIS. The incident beam enters through the flight tube at the top and the left (L) and right (R) 90° detector banks simultaneously record patterns with the scattering vector perpendicular and parallel to the sample axis, respectively. A mechanical testing machine used for *in situ* application of loads is also shown (https://www.isis.stfc.ac.uk). (Credit: STFC.)

The concept of long-wavelength neutron powder diffraction will be taken a step further in the DREAM instrument planned for the European Spallation Source (ESS, https://europeanspallationsource.se/realizing-dream-versatile-powder-diffractometer). This instrument will receive neutrons simultaneously from *thermal* and *cold* neutron moderators. It will have a complex array of choppers to shape the incident pulse prior to arrival at the sample. Modelling has indicated that intensity gains of a factor of 10–30 are to be expected and that the instrument may be able to deliver $\Delta d/d$ as low as 4×10^{-5}, albeit at very long wavelengths. More typically the projection is that $\Delta d/d$ as low as 1×10^{-4} could be achieved with more conventional wavelengths. Perhaps the major advantage of the instrument will not be its absolute resolution but the ability to change resolution over the full range during the experiment by simply altering the chopper settings. Therefore unexpected phenomena (phase transitions *etc.*) can be tracked during the initial experiment with no time lost by having to prepare a proposal for a different higher-resolution instrument.

2.3.4.4. *Comparison of CW and TOF diffractometers*

The preceding discussion has demonstrated that, although not necessarily the case for other types of neutron scattering, powder diffraction can be very successfully conducted on either CW or TOF instruments. Their relative advantages for the various types of powder-diffraction experiment are embedded in the discussion above and summarized in Table 2.3.5.

Plotting and summarizing the approximate intensity and resolution of different types of neutron diffractometer may be of assistance in assessing the options (Fig. 2.3.25). In the figure, resolution is shown as the inverse of the FWHM ($\Delta d/d$) and intensity is shown as the inverse of the time in seconds taken to record a single diffraction pattern, so that improvements follow the positive x and y axes.

There are two particular cases where the distinction between CW and TOF instruments can determine the success or failure of a neutron powder-diffraction experiment. The first is where crystal structures or phase transitions involving extreme pseudosymmetry are being studied. In this case, the very high resolution available over the entire Q-range (d-spacing range) using high-resolution TOF instruments such as HRPD at the ISIS

Table 2.3.5
Advantages of CW and TOF instruments (modified from Kisi & Howard, 2008)

CW	TOF
(1) Incident beam may be essentially monochromatic, in which case the spectrum is well characterized	(1) The whole incident spectrum is utilized, but it needs to be carefully characterized if intensity data are to be used
(2) Large *d*-spacings are easily accessible for study of complex magnetic and large-unit-cell structures	(2) Data are collected to very large Q values (small *d*-spacings)
	(3) Few cold neutron instruments are available for study of complex magnetic and large-unit-cell structures
(3) Can fine tune the resolution during an experiment	(4) Resolution is constant across the whole pattern
	(5) Very high resolution is readily attained by using long flight paths
(4) More common	(6) Complex sample environments are very readily used if 90° detector banks are available
(5) Peak shapes are simpler to model	
(6) Absorption and extinction corrections are relatively straightforward	(7) Simpler to intersect a large proportion of the Debye–Scherrer cones with large detector banks
(7) Data storage and reduction is simpler	
(8) Extremely rapid data collection and stroboscopic measurements are feasible	(8) Very fast data collection is feasible
(9) Engineering diffractometers are very well suited for strain scanning in complex objects	(9) Engineering diffractometers use an extended diffraction pattern, ideal for *in situ* loading and/or heating
(10) Texture is straightforward to measure on engineering diffractometers	(10) Texture can be measured on universal instruments

facility (UK) or SuperHRPD at J-PARC confers a particular advantage. The CW equivalent high-resolution powder diffractometers such as D2B at ILL and ECHIDNA at ANSTO can almost match the absolute resolution of the TOF instruments, D2B achieving $\Delta d/d$ of 5.6×10^{-4}; however, the resolution function for a CW diffractometer [equation (2.3.18)] has a strong minimum and so this resolution can only be achieved over a restricted range of *d*-spacing. The reflections appearing in the highest-resolution zone can be shifted by wavelength changes, which of necessity require re-recording of the pattern.

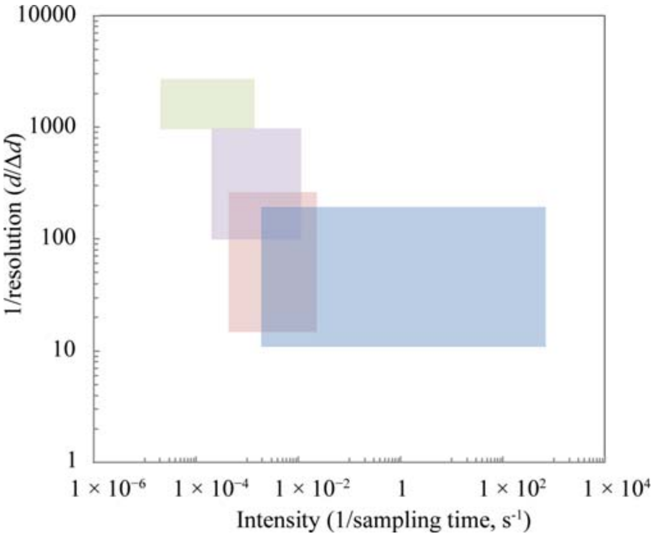

Figure 2.3.25
Schematic showing regions of intensity–resolution space in which different diffractometer types typically operate. High-resolution TOF diffractometers operate in the green area, engineering diffractometers (TOF or CW) in the purple area, multi-purpose TOF diffractometers such as POLARIS in the orange area and very high intensity CW diffractometers in the blue area.

The second extreme case is when rapid kinetic behaviours are to be studied. In this case, a small number of CW diffractometers (*e.g.* D20 at the Institut Laue–Langevin or WOMBAT at ANSTO) have a distinct advantage. Therefore at this time, processes that occur reproducibly and uniformly over a large sample on sub-1 s timescales are best suited to stroboscopic studies using one of the very rapid CW diffractometers available. There are nonetheless a great number of processes that can be studied on the timescales accessible using TOF, where near-constant resolution across the entire diffraction pattern lends considerable advantage.

If unaffected by extremes of resolution, intensity or highly specialized data types (stress, texture *etc.*), the choice between a CW or TOF instrument can be made based more casually on proximity to neutron sources and the access arrangements for national or regional neutron users.

2.3.5. Experimental considerations

2.3.5.1. *Preliminary considerations*

Neutron-diffraction studies are motivated by a desire to exploit the unique properties of neutrons as listed in Sections 2.3.1 and 2.3.2. As access to neutron diffraction is carefully regulated through an experiment proposal system, considerable planning is required in order to write a successful proposal. Owing to the expense of operating a neutron source and pressure on instrument time, there is an onus on the experimental team to make the best use of neutron beam time. Consideration should be given to the type of instrument required, the resolution that is needed, the *d*-spacing range of interest, how long each pattern will take to record, the requirement (or not) for standard samples and whether a special sample environment is needed.

Table 2.3.6
Suitability of problems to high-resolution or high-intensity diffractometers

Reproduced from Kisi & Howard (2008) by permission of Oxford University Press.

Problem	High resolution	High intensity (medium resolution)
Solve a complex crystal or magnetic structure	Essential, especially in the presence of pseudosymmetry	Not usually suitable†‡
Refine a complex crystal or magnetic structure	Essential. Will benefit from a high *Q*-range if available	Not usually suitable†‡
Solve or refine small inorganic structures	Beneficial, but not usually essential unless pseudosymmetry is present	Usually adequate
Quantitative phase analysis	Only required when peaks from the different phases are heavily overlapped	Usually adequate. Allows phase quantities to be tracked in fine environmental variable steps (*T*, *P*, *E*, *H* *etc.*) during *in situ* experiments
Phase transitions	Depends on the nature of the transition and complexity of the structures. Essential for transitions involving subtle unit-cell distortions and pseudosymmetry	Often adequate for small inorganic structure transitions and order–disorder transitions. Allows fine steps in an environmental variable (*T*, *P*, *E*, *H* *etc.*)
Line-broadening analysis	Essential for complex line broadening such as from a combination of strain and particle size, dislocations, stacking faults *etc.*	Adequate for tracking changes in severe line broadening as a function of an environmental variable (*T*, *P* *etc.*) especially if the pure instrumental peak shape is well characterized
Rapid kinetic studies	Not appropriate	Essential

† In some cases the symmetry and lattice parameters are such that the diffraction peaks are well spaced and not severely overlapped even at modest resolution. ‡ May be necessary to supplement high-resolution data to observe weak superlattice reflections in the presence of very subtle or incomplete order–disorder transitions.

Table 2.3.7
Guidance on choice of wavelength/detector bank

Reproduced from Kisi & Howard (2008) by permission of Oxford University Press.

Problem	Choice	Reasons
Solve complex or low-symmetry structures	Longer wavelength	Increase *d*-spacing resolution to allow correct symmetry and space group to be assigned
Refine a large or complex crystal structure	Shorter wavelength	Ensure that the number of peaks greatly exceeds the number of parameters. Improve determination of site occupancies and displacement parameters
Solve or refine magnetic structures	Longer wavelength	Ensure that large *d*-spacing peaks are observed. Spread the magnetic form factor over the entire diffraction pattern
Quantitative phase analysis	Usually shorter wavelength	Improve the accuracy of the determination. Longer wavelengths only required if peak overlap is severe
Phase transitions	Shorter wavelength	Ensures adequate data for order–disorder or other unit-cell-enlarging transitions
	Longer wavelength	Subtle unit-cell distortion or pseudosymmetric structures

In the general case, there is competition between the resolution and the intensity of diffractometers, although some of the modern TOF diffractometers (*e.g.* POLARIS, GEM, POWGEN, NOMAD and iMATERIA) simultaneously record patterns of moderate resolution and intensity, and high-intensity patterns at low resolution, in different detector banks. For the purposes of this chapter, high resolution is defined as a minimum diffraction peak width at half maximum height corresponding to $\Delta d/d \leq 10^{-3}$. This is the resolution typically required to observe lattice-parameter differences [*e.g.* $(a - b)/a$] of as little as 4×10^{-5} or so in the absence of sample-related peak broadening. Such a diffractometer is typically of the order of 10 to 1000 times slower than corresponding high-intensity diffractometers at the same neutron source. The decision to opt for a high-resolution diffractometer or a high-intensity diffractometer will depend critically on the nature of the problem under study. This situation was considered in Kisi & Howard (2008) and their conclusions are reproduced in Table 2.3.6.

It might be expected that the total information content in a diffraction pattern correlates with the *d*-spacing range covered and therefore this should be maximized. However, this expectation overlooks the different purposes for which powder-diffraction patterns are used. A greater density of diffraction peaks (*e.g.* in a CW pattern recorded using a short neutron wavelength) makes the detailed refinement of complex crystal structures more precise; however, it makes the determination of unit cell and systematic absences *more* difficult as well as reducing access to information contained within the peak shapes concerning the sample microstructure. Table 2.3.7 summarizes these effects. It should be noted that in this context parallels exist between a short-wavelength CW diffraction pattern and a low-angle-detector-bank TOF pattern; and between a longer-wavelength CW pattern and a high-angle-detector-bank TOF pattern, subject to limitations imposed by the wavelength distribution in the incident spectrum.

A decision must be made on how long to spend recording each diffraction pattern, such that the greatest number of patterns (samples) may be studied without compromising the information content of each pattern. Since counting is governed by Poisson statistics, the statistical precision of N counts in a radiation detector (X-ray, electron or neutron) is represented by the standard deviation σ:

$$\sigma = N^{1/2}. \qquad (2.3.23)$$

This is true regardless of whether a single count is made or multiple counts are summed to give an integrated intensity or a total count from several detectors. For a relatively constant arrival rate of neutrons, the precision of each data point will increase with counting time t in proportion to $t^{1/2}$, and this will be reflected in the agreement indices (*e.g.* $R_{\rm wp}$; Chapter 4.7) between the observed and calculated neutron intensities during structure refinements (*e.g.* Rietveld refinement) as well as in the estimated standard deviation (e.s.d.) of the refined crystal structure and other parameters. It has been shown by Hill & Madsen (1984) using CW X-ray powder-diffraction patterns that this is the case for small counting time; however, the agreement and e.s.d.'s quickly attain a plateau for counting times where 2000–5000 counts are recorded at the top of the largest diffraction peak. Beyond this, systematic errors in the models used for peak shapes, background *etc.* begin to dominate the fitting procedure. An important consequence is that since the expected values of the parameter e.s.d.'s fall in proportion to $t^{-0.5}$ whereas their actual values plateau, the statistical χ^2 increases for patterns recorded beyond the limit suggested by Hill & Madsen. A number of recommendations may be derived from these results:

(i) It is of no benefit for routine crystal structure refinements to record data beyond the point where the strongest peak has 5000 or so counts at its apex and to do so may render parameter e.s.d.'s invalid.

(ii) Counting for longer times *is* however recommended for problems that hinge upon weak superlattice or magnetic peaks. Similarly, it may be of benefit when minor phases are of interest, such as in complex engineering materials, in samples undergoing phase transitions or in multi-component geological materials.

(iii) An equally important result from Hill & Madsen is that respectable refined parameter estimates could be obtained using powder-diffraction patterns with only 200–500 counts at the apex of the strongest peak. This is extremely useful when assessing counting times in rapid kinetic studies where the shortest acceptable counting time is preferred. Modern data-acquisition electronics are often configured to allow very short acquisition times or 'event-mode operation' (Section 2.3.4.2.2) with patterns subsequently added together to obtain the required statistical and/or time resolution. In this case, the shortest time step available should be used provided sufficient data storage capacity is at hand.

In CW measurements with a detector bank scanned in small angular steps, similar arguments to those above apply to the sampling interval. This too has been investigated by Hill & Madsen (1986) and again, improvements to the agreement between the calculated and observed patterns and indeed improvements to refined parameter e.s.d.'s were only observed until systematic errors begin to dominate the fit. As a general rule of thumb, once the applicable counting *time* has been established, the counting interval should be adjusted to give at least 2 (but typically around 5) sampling points in the top half of the diffraction peak for routine crystal structure refinements. Finer sampling intervals are however beneficial in the case of:

(i) subtle symmetry changes that manifest in the peak shape well before peak splitting is observable,

(ii) following the evolution of a minor phase during an *in situ* experiment, or

(iii) peak-shape analyses to explore the sample microstructure (crystallite size, strain distribution, dislocation density, stacking-fault probability *etc.*).

CW measurements using instruments with a fixed position-sensitive detector and TOF measurements both have their raw sampling interval fixed by the instrument architecture, which cannot be varied. The recorded patterns can be subsequently re-binned to a larger sampling interval, although this would usually only be considered to reduce serial correlations during profile refinement (Hill & Madsen, 1986).

2.3.5.2. *Sample-related factors*

Recording a neutron powder-diffraction pattern is in itself a simple operation. There are, however, a number of sample-related variables that can affect the accuracy or the precision of the resulting patterns, or the ability to analyse them. It is worth mentioning here that neutron-diffraction samples are often large, in the range 1–40 g, to compensate for the lower incident fluxes and scattering cross sections as compared with the X-ray case. Large sample size has a strong mitigating effect on many of the sample-induced problems to be discussed in Chapter 2.10 and below.

The absolute *accuracy* of the position, intensity and shape of neutron powder-diffraction peaks is primarily determined by:

(i) *How representative the whole sample is of the whole system.* Known as disproportionation, this problem results from any non-random factor during sampling. For example, within rocks there is spatial variability in the mineral content (where to sample), hardness differences (different mineral particle sizes) and differing density (settling effects). Similar considerations apply to multiphase ceramic materials and metal alloys. With highly penetrating neutrons, this can be greatly reduced by using the polycrystalline solid sample provided that the crystallite size is relatively small [see (iii) below]. Disproportionation primarily influences quantitative phase analysis studies. Crystal-structure results are unaffected provided there is enough of each phase of interest to give a high-quality diffraction pattern.

(ii) *How representative the irradiated part of the sample is of the whole system.* Although ideally the entire sample is bathed in the incident beam, for highly focused neutron beams on high-intensity and/or strain-scanning diffractometers, the beam–sample interaction volume is smaller than the whole sample. In such cases, if a gradient in an experimental variable such as temperature, pressure or composition is present, then the irradiated portion of the sample can be quite unrepresentative and this needs to be addressed in the overall experiment plan.

(iii) *How representative the diffracting part of the sample is of the whole sample.* There are two circumstances in which the observed diffraction pattern may be unrepresentative of the irradiated portion of the sample. First, very large crystallite size leads to the phenomenon of *granularity*, which is dealt with in detail in Section 2.10.1.1. Crystallites diffract only when the Bragg condition is met, so if the crystallite size is a sizable fraction of the irradiated part of the sample, only a small number of crystallites are aligned for diffraction. With only relatively few crystals diffracting, the peak shapes, intensities and apparent *d*-spacings are strongly distorted. Second, when there is amorphous material present, it is visible in the diffraction pattern only as structure in the background signal and is not analysed using standard crystallographic techniques.

(iv) *How representative the recorded pattern is of the sample.* There are two other factors that can affect accuracy of the diffraction pattern.

The first is that the crystallites may have preferred (rather than random) orientations, so that some sets of atomic planes are overrepresented and others underrepresented in the diffraction pattern. This effect and the means to overcome it in X-ray diffraction measurements are covered in Section 2.10.1.2. Neutron powder diffraction, by using large samples on a rotating sample holder in transmission geometry, is generally far less susceptible to preferred orientation than X-ray diffraction. In cases where preferred orientation is unavoidable, it is generally of a simple axial form due to the sample rotation. Quite good analytical means for modelling preferred orientation of this type are available in the various refinement programs described in Chapter 4.7.

The second effect is attenuation. For most materials, thermal neutrons are attenuated comparably by true absorption and scattering, the overall effect being very minor. For a small number of elements (*e.g.* B, Cd, Gd – see Table 2.3.2) the absorption is high, and in an even smaller number of isotopes (*e.g.* H) the incoherent scattering is high enough to give significant attenuation. Details of these processes are dealt with in Section 2.10.2.4 as well as in Sections 2.4.2 and 3.5.3 of Kisi & Howard (2008). In summary, when using transmission geometry and absorbing samples, diffraction peaks at low angle (CW) are attenuated more than those at higher angles. An additional linear dependence on neutron wavelength occurs in TOF patterns. Therefore the relative intensities are incorrect and during structure refinements unreasonable (often negative) displacement parameters will result. When strongly attenuating elements or isotopes are present three approaches are available; the data can be recorded in reflection geometry, the capillary-coating method can be adapted from X-ray diffraction, or the sample can be diluted with a large amount of a weakly absorbing material. The latter two methods are explained in Section 2.10.1.4.2.2.

Sample-related factors that interact with the precision of various crystallographic and microstructural parameters determined from a given diffraction pattern are:

(i) *The crystallite size within the sample.* As discussed at length in Chapter 2.10, the ideal size for crystallites in a powder-diffraction measurement is 2–5 µm. The upper limit is determined by onset of granularity [see (iii) above]. The lower limit is set by the onset of detectable crystallite size broadening (Chapter 5.1). To first order, the broadening of diffraction peaks due to small crystallite size is well understood. It has negligible effect on the measured intensity of diffraction peaks and does not affect the numerical value of the peak positions (hence *d*-spacings); however, the precision or standard error of such measured positions is strongly affected. In addition, the precision (standard error) of measurements of other microstructural features such as strain distributions, dislocation density or stacking-fault probability are strongly affected. Powdered samples should be sized to lie within the range 2–5 µm with the lower limit being the more important in this case. The crystallite size within solid polycrystalline samples is an inherent part of the system. Forming a material with a fine grain size is a universal method for strengthening metals and ceramics alike. In systems undergoing phase transitions the crystallites typically subdivide into small portions during the transition. Consequently, crystallite size broadening is often an inevitable part of a powder-diffraction experiment.

(ii) *How ideal the crystal structure is within the crystallites.* The preparation of powder samples can induce several types of lattice defects (dislocations, stacking faults, twin faults *etc.*) into the material under study. Each of these leads to changes to the peak positions, shapes and breadths. Likewise, in solid polycrystalline samples, thermal-expansion anisotropy and mismatch between different phases cause intergranular strains which manifest themselves in broadened peaks. Each new source of broadening strongly affects the precision with which other microstructural features of the sample can be determined from peak-shape analysis. In ground powders, it is sometimes possible to relieve stresses and repair defects by annealing, but only if it is certain that no detrimental changes to the material occur under the annealing conditions.

A common prerequisite for the detailed analysis of diffraction patterns is a good understanding of the instrument's characteristic peak shapes and widths, *i.e.* the resolution function (Sections 2.3.4.1.4 and 2.3.4.2.1). The parameters of the resolution function are needed to enable Rietveld (Chapter 4.7) or whole-pattern (Chapter 3.6) analysis of the diffraction patterns. A good description for the instrument resolution function is important in the study of sample microstructure (*e.g.* crystallite size, strain distribution or dislocation studies) and may be established using standard samples. Early versions of the NIST LaB_6 lattice-parameter and peak-shape standards (SRM 660) were unsuitable because of the high neutron absorption of natural boron. More recently, NIST has developed LaB_6 standards SRM 660b and 660c made with ^{11}B that can be used for neutron diffraction (see Section 3.1.4). Suitable air- and moisture-stable alternatives with a closely regulated crystallite size and a moderate density of diffraction peaks include Al_2O_3, CeO_2, Y_2O_3 and some intermetallic compounds such as Cu_9Al_4 and Cu_5Zn_8.

One's ability to successfully analyse a diffraction pattern is then strongly affected by:

(i) *Smooth and locally monotonic peak shapes.* The two primary causes of failing to meet this requirement are granularity (crystallites significantly above the preferred 2–5 µm size) and unusual sample shapes such as hollow samples. Examples of the former may be seen in Figs. 2.10.2 and 2.10.3, where large single crystals in the sample each give a discrete diffraction peak, the composite of which looks nothing like the true powder peak shape. The case of hollow samples is rarely seen unless the 'capillary-coating' technique (see Section 2.10.1.4.2.2) is adopted for a highly absorbing sample or diffraction peaks from a hollow sample container are also to be analysed. In this case, the peak shape will have a depression in the centre due to the non-uniform distribution of diffracting matter across the specimen.

(ii) *Crystallite perfection.* For crystal-structure studies, it is preferred that the crystallites in the sample be as near perfect[19] as possible. However, materials of interest are often far from perfect, containing stacking faults, domain walls, antiphase boundaries, compositional gradients, strain gradients *etc*. Fig. 9.22 in Kisi & Howard (2008) illustrates this for a ferroelectric material. Here the individual crystallites are subdivided into ferroelectric domains with different orientations defined by the symmetry relationship between the parent (cubic) and daughter (tetragonal) structures. Where differently oriented domains abut, there is a strain gradient over a finite portion of crystal. This is visible in the diffraction pattern as a plateau between twin-related pairs of peaks such as the 200/002 pair shown, because in the strain gradient all d-spacings between d_{200} and d_{002} are present.

(iii) *Sample perfection.* The major types of imperfection in sampling are described under *accuracy* in the preceding discussion. Our main interest here is in the preferred orientation of crystallites, which means some diffraction peaks are exaggerated and others underrepresented in the diffraction pattern. Methods for avoiding or reducing preferred orientation are dealt with in Section 2.10.1.2. In addition, whole-pattern fitting and reasonably robust mathematical models for preferred orientation, principally the March–Dollase model (Dollase, 1986) and models based on spherical harmonics (Ahtee *et al.*, 1989), have reduced the effect of preferred orientation on crystal-structure parameters and quantitative phase analyses derived from powder-diffraction patterns. In a small number of cases of severe and/or multi-axis preferred orientation, these models can fail and efforts to reduce the effect within the sample need to be revisited.

2.3.5.3. *Sample environment and in situ experiments*

It is more often the case with neutron diffraction than with X-ray or electron diffraction that the purpose is an experimental study involving rather more than a simple room-temperature data collection.[20] As such, there are a great variety and complexity of sample environments available, relating to studies: at room temperature, cryogenic temperatures, high temperature and high pressure; under magnetic fields, electric fields or applied stress; during gas–solid, liquid–solid, solid–solid or electrochemical reactions; and almost any combination of these. There are several other chapters in this volume that include descriptions of sample environments for neutron powder-diffraction experiments under high (hydrostatic) pressure (Chapter 2.7), electric and magnetic fields (Chapter 2.8) and chemical and electrochemical reactions (Chapter 2.9). Some general guidance on the mounting of samples is also given in Chapter 2.10. Additional information concerning sample containers for non-ambient studies, as well as sample environments not expressly covered in these chapters, will be presented briefly below.

2.3.5.3.1. *Sample containers*

Solid polycrystalline samples can be directly mounted on the diffractometer; however, powder samples require careful containment. Powder spillage must be avoided because samples may become activated in the neutron beam and spilled powders present a radiological hazard. Owing to the low neutron attenuation by most materials, neutron diffraction patterns are generally recorded in transmission (Debye–Scherrer) geometry. Therefore sample containers that do not contribute significantly to the diffraction pattern are required. Fortunately there are several materials that have essentially zero coherent neutron scattering length, *i.e.* they give no discernible diffraction peaks and minimal contribution to the background. Most versatile is elemental vanadium, which has a scattering length of just −0.3824 fm (Table 2.3.2), making its diffraction pattern 100–750 times weaker than most other metals. Coupled with excellent room-temperature resistance to atmospheric corrosion, it is not surprising that it is the material that is used most often for neutron powder diffraction sample holders. Typical designs are discussed in Section 2.10.2.3. Another useful material for room-temperature containment is Al, which has very low attenuation and few diffraction peaks of its own. This is especially useful in cases where only the large d-spacing peaks are of interest, for example with magnetic materials or large-scale structures, or where a fine radial collimator is able to exclude diffraction from the sample container.

Sample containers for specialized sample environments vary greatly. Low-temperature studies routinely use V or Al cans, as for room-temperature studies. High-temperature studies of powders can use V cans up to approximately 1073 K provided that an inert gas or vacuum environment is present. At higher temperatures, thin-walled fused silica (silica glass) can be used as it has several advantages: it is amorphous and therefore gives no sharp diffraction peaks; it is vacuum tight and relatively easy to seal to vacuum fittings *via* O-rings outside or graded glass–metal seals within the hot zone of the furnace; it is transparent, so the state of the sample can be viewed during loading and after the experiment; and it is immune to thermal shock. Silica can survive at temperatures up to 1473 K and for short periods can resist temperatures up to 1673 K, although some devitrification may occur. Care should be exercised since although fused silica has no sharp diffraction peaks, its short-range order does give a structured background which has to be carefully treated in subsequent analyses. Containers for still higher temperatures can be made from other ceramics such as alumina or from refractory metals such as Nb, Ta or W in increasing order of temperature resistance. Noble metals such as Pt may seem to have some advantages; however, they are extremely weak and fragile after high-temperature annealing. All high-temperature sample-container materials are able to chemically react with *some* samples at high temperature and great care must be taken when selecting them. If possible, a trial heating should be conducted off-line prior to the experiment.

2.3.5.3.2. *Non-ambient temperature*

As neutron powder diffraction is routinely conducted in transmission geometry, non-ambient sample environments have many common features. They are typically cylindrical in shape, with the sample can loaded centrally from above on a ‘sample stick’, which goes by various names in different fields.

An example is the liquid-helium cryostat developed at the Institut Laue–Langevin, shown in Fig. 2.3.26. The internal space is evacuated and heat is removed from the sample *via* conduction through the sample stick to cold reservoirs in contact with the liquid-helium tank. The sample protrudes below the helium and nitrogen tanks into the ‘tails’, which are thin-walled Al or V

---

[19] If the crystallites are too perfect, then diffracted intensities might be affected by ‘extinction’ (Sabine, 1985), so an ‘ideally imperfect’ crystallite is to be preferred.

[20] For example, more than 90% of recent neutron powder-diffraction proposals to Oak Ridge have requested non-ambient conditions (Kaduk, personal communication).

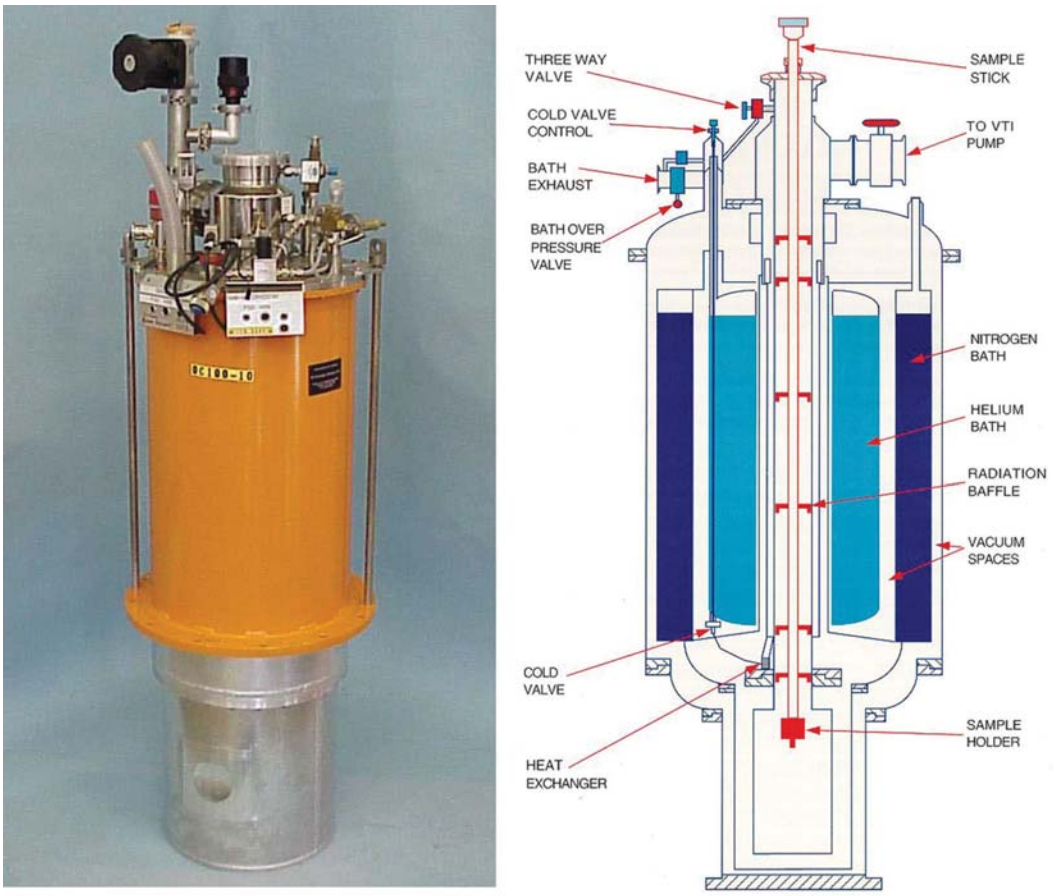

(*a*) (*b*)

Figure 2.3.26
(*a*) Exterior and (*b*) interior of the standard ILL liquid-helium cryostat for cooling samples in the range 1.8–295 K. An internal heater allows samples to be studied without interruption from 1.8–430 K. Reproduced with permission from the ILL.

cylindrical sections that allow ready transmission of neutrons but preserve the vacuum and exclude radiant heat from the outside world. Liquid-helium cryostats can generally attain base temperatures of 4.2 K (He alone) or 1.9 K if pumped. Liquid-nitrogen cryostats are limited to 77 K. A second type of low-temperature device is the closed-cycle He refrigerator, commonly referred to by the trade name Displex. These are more compact than a liquid-helium cryostat and do not require refilling. Depending on the number of stages and internal design, refrigerators with base temperatures as low as 4 K are available.

Samples are typically first cooled to base temperature and then studied at the chosen sequence of increasing temperatures. This is achieved through a small electric resistance heater and control system. As heat transfer to and from the sample is deliberately poor in these devices, sufficient time should be allowed for the (often large) sample to reach thermal equilibrium before recording its neutron-diffraction pattern. It is worth noting that the attainment of thermal equilibrium does not guarantee that the sample has attained thermodynamic equilibrium. Some phase transitions are notoriously slow, for example the ordering of hydrogen (or deuterium) in Pd metal at 55 K and 75 K, which can take up to a month (Kennedy *et al.*, 1995; Wu *et al.*, 1996), or the ordering of C in TiC_x ($0.6 < x < 0.9$) around 973 K, which can take a week to complete (Moisy-Maurice *et al.*, 1982; Tashmetov *et al.*, 2002).

Raising samples to above ambient temperature is, for X-ray diffraction, the subject of a separate chapter (Chapter 2.6); however, neutron-diffraction high-temperature devices are somewhat different. Most commonly used and most versatile is the foil element resistance furnace, in which Cu bus bars transfer electric current to a cylindrical metal foil which heats up as a result of its electrical resistance. Foil elements are typically 30–60 mm in diameter and up to 200 or 250 mm long so as to provide a long hot zone of uniform temperature within the furnace. The sample is located, *via* a sample stick from above or occasionally *via* a pedestal support from below, in the centre of the foil heating element, ensuring that it is uniformly bathed in radiant heat. Concentric metal-foil heat shields greatly reduce heat loss to the exterior by radiation, while convective losses are avoided by evacuating the interior of the furnace to $\sim 10^{-5}$ mbar. Metals for manufacture of the foil elements include V, which has almost no coherent diffraction pattern and can operate continuously up to 1173 K or intermittently to 1273 K. For temperatures above this, progressively more refractory metals are chosen such as Nb (<1773 K), Ta (<2473 K) or W (2773 K). These materials will contribute some small diffraction peaks to the observed patterns, which requires the recording of reference patterns from the empty furnace before commencing. Owing to the internal vacuum, some types of sample are at risk of subliming, decomposing or disproportioning during the experiment. In such cases, sample cans that extend outside the hot zone, where they can be coupled to a gas-handling system and filled with an internal atmosphere of air, an inert gas or a reactive gas of interest as required, are used.

Alternatives to foil furnaces include variations of the wire-wound laboratory furnace with a split winding and reduced insulating material in the neutron beam path, Peltier devices, hot-air blowers and induction heaters. The first three of these are discussed by Kisi & Howard (2008).

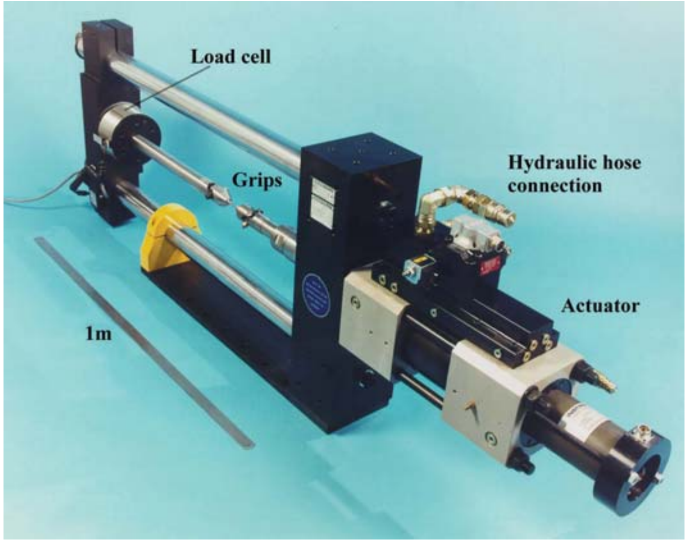

Figure 2.3.27
Elements of a typical mechanical testing machine used for applying uniaxial stress (pressure) to samples on an engineering neutron diffractometer. This example of a 100 kN device is from the instrument ENGIN-X at the ISIS facility, UK. (Credit: STFC.)

Non-ambient temperature devices are usually designed for operation either below or above ambient temperature. However, there are a large number of phase transitions and other phenomena that span from below to above ambient temperature. In order to avoid transferring samples from one sample environment to another mid-experiment, a useful hybrid device is the cryo-furnace. Cryo-furnaces are based around the liquid-helium cryostat and are equipped with more powerful heaters, allowing temperatures typically in the range 4–600 K to be covered.

2.3.5.3.3. *Uniaxial stress*

There are two major applications of *in situ* uniaxial loading. In the first, stress-induced phase transitions, ferroelasticity or simply mechanical response are studied throughout the whole sample as a function of applied stress. This may be undertaken on any powder diffractometer with a reasonable data-collection rate, depending on the resolution required. Parameters typically monitored are the relative phase proportions of parent and daughter structures, lattice parameters, individual peak shifts, which can yield the single-crystal elastic constants (Howard & Kisi, 1999), peak widths, which can indicate the breadth of strain distributions, and preferred-orientation parameters, which can indicate the degree of ferroelasticity (Kisi *et al.*, 1997; Ma *et al.*, 2001; Forrester & Kisi, 2004; Forrester *et al.*, 2005). The second application involves strain scanning using an engineering diffractometer as described in Section 2.3.4.3; however, in this instance an external load is applied to the object under study. This technique can be used to validate finite element analysis simulations of complex components with or without internal residual stresses.

Devices for the *in situ* application of uniaxial stress include adaptations of laboratory universal testing machines such as the 100 kN hydraulic load frame shown in Fig. 2.3.27. Devices such as this may be used in tension, compression, fatigue or even creep conditions depending on the sample and the problem under study.

For more specialized applications, it is sometimes possible to create a more compact device. A recent adaptation of strain scanning is to study the stress distribution within granular materials subjected to a variety of load cases as either the average stresses shown in Fig. 2.3.23 (Wensrich *et al.*, 2012; Kisi *et al.*, 2014), or the stress tensor in individual particles throughout a granular material bed. The latter provides insight into inhomogeneous stress distributions such as force chains (Wensrich *et al.*, 2014). The device that was used in these studies (Fig. 2.3.28) is a self-loading die within which a granular material is compacted while diffraction studies are conducted.

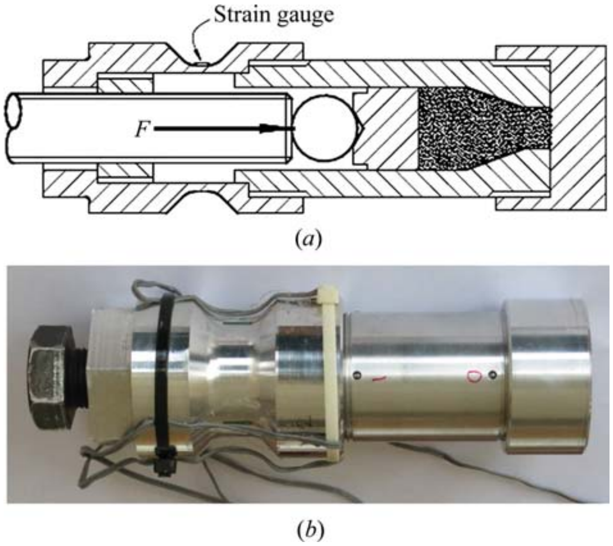

Figure 2.3.28
(*a*) Cross section and (*b*) exterior of a self-loading die for the study of stresses in granular materials.

2.3.6. Concluding remarks

Neutron powder diffraction is just one of many neutron-scattering techniques available; however, it is one that is very commonly used. In fact, the demand for this particular neutron technique is rivalled only by that for small-angle neutron scattering. The close analogy with X-ray powder diffraction makes the technique very familiar to many practitioners of that technique. The differences from X-rays are also critical (Sections 2.3.1 and 2.3.2), since these are the means by which neutron diffraction can obtain information not otherwise accessible. In this chapter we have included descriptions of the various types of neutron source, the neutron powder diffractometers installed at these sources, and a selection of routine and more specialized applications. Demand for the technique is expected to continue, buoyed by further developments in instrumentation and the exploration of new applications.

The authors thank Judith Stalick (NIST), Masatoshi Arai (ESS), Peter Galsworthy (ISIS), Philip King (STFC), Bertrand Blau (PSI), Oliver Kirstein (ESS), Vladimir Pomjakushin (PSI) and Ron Smith (ISIS) for their assistance in organizing Figs. 2.3.6, 2.3.8, 2.3.9, 2.3.10, 2.3.11, 2.3.12, 2.3.15 and 2.3.18, respectively. Ron Smith also provided the data for Fig. 2.3.19. The authors are also grateful for selected proof reading and specialized advice from Greg Storr (ANSTO) as well as Bertrand Blau, Oliver Kirstein and Ron Smith. The authors are particularly appreciative of the efforts of Mark Senn (Oxford) in reading the entire chapter and offering useful constructive comment.

References

Abele, H., Dubbers, D., Häse, H., Klein, M., Knöpfler, A., Kreuz, M., Lauer, T., Märkisch, B., Mund, D., Nesvizhevsky, V., Petoukhov, A., Schmidt, C., Schumann, M. & Soldner, T. (2006). *Characterization of a ballistic supermirror neutron guide*. *Nucl. Instrum. Methods Phys. Res. A*, **562**, 407–417.

Ahtee, M., Nurmela, M., Suortti, P. & Järvinen, M. (1989). *Correction for preferred orientation in Rietveld refinement*. *J. Appl. Cryst.* **22**, 261–268.

Alvarez, L. W. & Bloch, F. (1940). *A quantitative determination of the neutron moment in absolute nuclear magnetons*. *Phys. Rev.* **57**, 111–122.

Anderson, H. L., Booth, E. T., Dunning, J. R., Fermi, E., Glasoe, G. N. & Slack, F. G. (1939). *The fission of uranium*. *Phys. Rev.* **55**, 511–512.

Anderson, I. S. & Schärpf, O. (2006). *International Tables for Crystallography*, Volume C, *Mathematical, Physical and Chemical Tables*, 1st online ed., edited by E. Prince, pp. 431–432. Chester: International Union of Crystallography.

Arai, M. (2008). *J-Parc and the prospective neutron sciences. Pramana J. Phys.* **71**, 629–638.

Arai, M. & Crawford, K. (2009). *Neutron sources and facilties. Neutron Imaging and Applications: a Reference for the Imaging Community*, ch. 2. Springer.

Batkov, K., Takibayev, A., Zanini, L. & Mezei, F. (2013). *Unperturbed moderator brightness in pulsed neutron sources*. *Nucl. Instrum. Methods Phys. Res. A*, **729**, 500–505.

Brown, P. J. (2006*a*). *Magnetic scattering of neutrons*. *International Tables for Crystallography*, Volume C, *Mathematical, Physical and Chemical Tables*, 1st online ed., edited by E. Prince, pp. 590–593. Chester: International Union of Crystallography.

Brown, P. J. (2006*b*). *Magnetic form factors*. *International Tables for Crystallography*, Volume C, *Mathematical, Physical and Chemical Tables*, 1st online ed., edited by E. Prince, pp. 454–461. Chester: International Union of Crystallography.

Buras, B. & Holas, A. (1968). *Intensity and resolution in neutron time-of-flight powder diffractometry*. *Nukleonika*, **13**, 591–619.

Buras, B. & Leciejewicz, J. (1964). *A new method for neutron diffraction crystal structure investigations*. *Phys. Status Solidi B*, **4**, 349–355.

Burcham, W. E. (1979). *Elements of Nuclear Physics*, in particular §11.7.2 and p. 353. New York: Longman.

Caglioti, G., Paoletti, A. & Ricci, F. P. (1958). *Choice of collimators for a crystal spectrometer for neutron diffraction*. *Nucl. Instrum.* **3**, 223–228.

Carlile, C. J. (2003). *The production of neutrons*. *Neutron Data Booklet*, 2nd ed., edited by A. J. Dianoux & G. Lander, §3.1. Grenoble: Institut Laue–Langevin.

Carlile, C. J., Hey, P. D. & Mack, B. (1977). *High-efficiency Soller slit collimators for thermal neutrons*. *J. Phys. E Sci. Instrum.* **10**, 543–546.

Carpenter, J. M. (1977). *Pulsed spallation neutron sources for slow neutron scattering*. *Nucl. Instrum. Methods*, **145**, 91–113.

Chadwick, J. (1932). *The existence of a neutron*. *Proc. R. Soc. London Ser. A*, **136**, 692–708.

Chatterji, T. (2006). Editor. *Neutron Scattering from Magnetic Materials.* Amsterdam: Elsevier BV.

Convert, P. & Chieux, P. (2006). *Thermal neutron detection*. *International Tables for Crystallography*, Volume C, *Mathematical, Physical and Chemical Tables*, 1st online ed., edited by E. Prince, pp. 644–652. Chester: International Union of Crystallography.

Cussen, L. D. (2000). *Resolution calculations for novel neutron beam elements*. *J. Appl. Cryst.* **33**, 1393–1398.

Cussen, L. D. (2016). *Optimizing constant wavelength neutron powder diffractometers*. *Nucl. Instrum. Methods Phys. Res. A*, **821**, 122–135.

Cussen, L. D., Nekrassov, D., Zendler, C. & Lieutenant, K. (2013). *Multiple reflections in elliptic neutron guide tubes*. *Nucl. Instrum. Methods Phys. Res. A*, **705**, 121–131.

Cussen, L. D., Vale, C. J., Anderson, I. S. & Høghoj, P. (2001). *Tests of a silicon wafer based neutron collimator*. *Nucl. Instrum. Methods Phys. Res. A*, **471**, 392–397.

Day, D. H. & Sinclair, R. N. (1969). *A pulsed neutron diffraction measurement of preferred orientation in pressed powder compacts of bismuth seleno-telluride*. *J. Phys. C Solid State Phys.* **2**, 870–873.

Dollase, W. A. (1986). *Correction of intensities for preferred orientation in powder diffractometry: application of the March model*. *J. Appl. Cryst.* **19**, 267–272.

Dowty, E. (1999). *ATOMS*. Version 5.0.7. Shape Software, Kingsport, Tennessee, USA.

Dunning, J. R., Pegram, G. B., Fink, G. A., Mitchell, D. P. & Segrè, E. (1935). *Velocity of slow neutrons by mechanical velocity selector*. *Phys. Rev.* **48**, 704.

Fermi, E., Amaldi, E., D'Agostino, O., Rasetti, F. & Segrè, E. (1934). *Artificial radioactivity produced by neutron bombardment*. *Proc. R. Soc. London Ser. A*, **146**, 483–500.

Fermi, E., Amaldi, E., D'Agostino, O., Pontecorvo, B., Rasetti, F. & Segrè, E. (1934). *Azione di sostanze idrogenate sulla radioattivita provocata da neutroni. I. Ric. Sci.* **5**, 282–283.

Fermi, E., Marshall, J. & Marshall, L. (1947). *A thermal neutron velocity selector and its application to the measurement of the cross section of boron*. *Phys. Rev.* **72**, 193–196.

Finger, L. W., Cox, D. E. & Jephcoat, A. P. (1994). *A correction for powder diffraction peak asymmetry due to axial divergence*. *J. Appl. Cryst.* **27**, 892–900.

Fischer, P., Frey, G., Koch, M., Könnecke, M., Pomjakushin, V., Schefer, J., Thut, R., Schlumpf, N., Bürge, R., Greuter, U., Bondt, S. & Berruyer, E. (2000). *High-resolution powder diffractometer HRPT for thermal neutrons at SINQ Physica B*, **276–278**, 146–147.

Fitzpatrick, M. E. & Lodini, A. (2003). *Analysis of Residual Stress by Diffraction Using Neutron and Synchrotron Radiation*. Boca Raton: CRC Press.

Forrester, J. S. & Kisi, E. H. (2004). *Ferroelastic switching in a soft lead zirconate titanate*. *J. Eur. Ceram. Soc.* **24**, 595–602.

Forrester, J. S., Kisi, E. H. & Studer, A. J. (2005). *Direct observation of ferroelastic domain switching in polycrystalline $BaTiO_3$ using in situ neutron diffraction*. *J. Eur. Ceram. Soc.* **25**, 447–454.

Friedrich, H., Wagner, V. & Wille, P. (1989). *A high-performance neutron velocity selector*. *Physica B*, **156–157**, 547–549.

Hahn, O. & Strassmann, F. (1939). *Über den Nachweis und das Verhalten der bei der Bestrahlung des Urans mittels Neutronen entstehenden Erdalkalimetalle*. *Naturwissenschaften*, **27**, 11–15.

Hakonen, P., Lounasmaa, O. V. & Oja, A. (1991). *Spontaneous nuclear magnetic ordering in copper and silver at nano- and picokelvin temperatures*. *J. Magn. Magn. Mater.* **100**, 394–412.

Halban, H. von, Joliot, F. & Kowarski, L. (1939). *Number of neutrons liberated in the nuclear fission of uranium*. *Nature*, **143**, 680.

Halban, H. von & Preiswerk, P. (1936). *Preuve expérimentale de la diffraction des neutrons. C. R. Acad. Sci. Paris*, **203**, 73.

Häse, H., Knöpfler, A., Fiederer, K., Schmidt, U., Dubbers, D. & Kaiser, W. (2002). *A long ballistic supermirror guide for cold neutrons at ILL*. *Nucl. Instrum. Methods Phys. Res. A*, **485**, 453–457.

Hayter, J. B. & Mook, H. A. (1989). *Discrete thin-film multilayer design for X-ray and neutron supermirrors*. *J. Appl. Cryst.* **22**, 35–41.

Hewat, A. W. (1975). *Design for a conventional high-resolution neutron powder diffractometer*. *Nucl. Instrum. Methods*, **127**, 361–370.

Hewat, A. W. & Bailey, I. (1976). *D1A, a high resolution neutron powder diffractometer with a bank of Mylar collimators*. *Nucl. Instrum. Methods*, **137**, 463–471.

Hill, R. J. & Howard, C. J. (1987). *Quantitative phase analysis from neutron powder diffraction data using the Rietveld method*. *J. Appl. Cryst.* **20**, 467–474.

Hill, R. J. & Madsen, I. C. (1984). *The effect of profile-step counting time on the determination of crystal structure parameters by X-ray Rietveld analysis*. *J. Appl. Cryst.* **17**, 297–306.

Hill, R. J. & Madsen, I. C. (1986). *The effect of profile step width on the determination of crystal structure parameters and estimated standard deviations by X-ray Rietveld analysis*. *J. Appl. Cryst.* **19**, 10–18.

Howard, C. J. (1982). *The approximation of asymmetric neutron powder diffraction peaks by sums of Gaussians*. *J. Appl. Cryst.* **15**, 615–620.

Howard, C. J., Ball, C. J., Davis, R. L. & Elcombe, M. M. (1983). *The Australian high resolution neutron powder diffractometer*. *Aust. J. Phys.* **36**, 507–518.

Howard, C. J. & Kisi, E. H. (1999). *Measurement of single-crystal elastic constants by neutron diffraction from polycrystals*. *J. Appl. Cryst.* **32**, 624–633.

Howard, C. J., Knight, K. S., Kennedy, B. J. & Kisi, E. H. (2000). *The structural phase transitions in strontium zirconate revisited*. *J. Phys. Condens. Matter*, **12**, L677–L683.

Izyumov, Y. A. & Ozerov, R. P. (1970). *Magnetic Neutron Diffraction*. New York: Plenum Press.

Jorgensen, J. D., Beno, M. A., Hinks, D. G., Soderholm, L., Volin, K. J., Hitterman, R. L., Grace, J. D., Schuller, I. K., Segre, C. U., Zhang, K. & Kleefisch, M. S. (1987). *Oxygen ordering and the orthorhombic-to-*

tetragonal phase transition in $YBa_2Cu_3O_{7-x}$. Phys. Rev. B, **36**, 3608–3616.

Kennedy, S. J., Wu, E., Kisi, E. H., Gray, E. M. & Kennedy, B. J. (1995). *Ordering of deuterium in $PdD_{0.65}$ at 54 K. J. Phys. Condens. Matter*, **7**, L33–L40.

Kimura, M., Sugawara, M., Oyamada, M., Yamada, Y., Tomiyoshi, S., Suzuki, T., Watanabe, N. & Takeda, S. (1969). *Neutron Debye–Scherrer diffraction works using a linear electron accelerator. Nucl. Instrum. Methods*, **71**, 102–110.

Kisi, E. H. & Howard, C. J. (2008). *Applications of Neutron Powder Diffraction*. Oxford University Press.

Kisi, E. H., Howard, C. J. & Hill, R. J. (1989). *Crystal structure of orthorhombic zirconia in partially stabilized zirconia. J. Am. Ceram. Soc.* **72**, 1757–1760.

Kisi, E. H., Kennedy, S. J. & Howard, C. J. (1997). *Neutron diffraction observations of ferroelastic domain switching and tetragonal-to-monoclinic transformation in Ce-TZP. J. Am. Ceram. Soc.* **80**, 621–628.

Kisi, E. H., Wensrich, C. M., Luzin, V. & Kirstein, O. (2014). *Stress distribution in iron powder during die compaction. Mater. Sci. Forum*, **777**, 243–248.

Ma, Y., Kisi, E. H. & Kennedy, S. J. (2001). *Neutron diffraction study of ferroelasticity in a 3 mol% Y_2O_3-ZrO_2. J. Am. Ceram. Soc.* **84**, 399–405.

Marseguerra, M. & Pauli, G. (1959). *Neutron transmission probability through a curved revolving slit. Nucl. Instrum. Methods*, **4**, 140–150.

Marshall, W. & Lovesey, S. W. (1971). *Theory of Thermal Neutron Scattering: The Use of Neutrons for the Investigation of Condensed Matter*. Oxford: Clarendon Press.

Maruyama, R., Yamazaki, D., Ebisawa, T., Hino, M. & Soyama, K. (2007). *Development of neutron supermirrors with large critical angle. Thin Solid Films*, **515**, 5704–5706.

Masalovich, S. (2013). *Analysis and design of multilayer structures for neutron monochromators and supermirrors. Nucl. Instrum. Methods Phys. Res. A*, **722**, 71–81.

Mason, T. E., Gawne, T. J., Nagler, S. E., Nestor, M. B. & Carpenter, J. M. (2013). *The early development of neutron diffraction: science in the wings of the Manhattan Project. Acta Cryst.* A**69**, 37–44.

Meitner, L. & Frisch, O. R. (1939). *Disintegration of uranium by neutrons: a new type of nuclear reaction. Nature*, **143**, 239–240.

Mezei, F. (1976). *Novel polarized neutron devices: supermirror and spin component amplifier. Commun. Phys.* **1**, 81–85.

Mezei, F. (1997). *The raison d'être of long pulse spallation sources. J. Neutron Res.* **6**, 3–32.

Mitchell, D. P. & Powers, P. N. (1936). *Bragg reflection of slow neutrons. Phys. Rev.* **50**, 486–487.

Moisy-Maurice, V. N., Lorenzelli, N., De Novion, C. H. & Convert, P. (1982). *High temperature neutron diffraction study of the order–disorder transition in TiC_{1-x}. Acta Metall.* **30**, 1769–1779.

Moore, M. J., Kasper, J. S. & Menzel, J. H. (1968). *Pulsed LINAC neutron diffraction. Nature*, **219**, 848–849.

Noyan, I. C. & Cohen, J. B. (1987). *Residual Stress: Measurement by Diffraction and Interpretation*. New York: Springer.

Oed, A. (1988). *Position-sensitive detector with microstrip anode for electron multiplication with gases. Nucl. Instrum. Methods Phys. Res. A*, **263**, 351–359.

Oed, A. (2003). *Detectors for thermal neutrons. Neutron Data Booklet*, 2nd ed., edited by A. J. Dianoux & G. Lander, §3.3. Grenoble: Institut Laue–Langevin.

Peters, J., Champion, J. D. M., Zsigmond, G., Bordallo, H. N. & Mezei, F. (2006). *Using Fermi choppers to shape the neutron pulse. Nucl. Instrum. Methods Phys. Res. A*, **557**, 580–584.

Radaelli, P. G., Iannone, G., Marezio, M., Hwang, H. Y., Cheong, S. W., Jorgensen, J. D. & Argyriou, D. N. (1997). *Structural effects on the magnetic and transport properties of perovskite $A_{(1-x)}A_{(x)}'MnO_3$ (x = 0.25, 0.30). Phys. Rev. B*, **56**, 8265–8276.

Rauch, H. & Waschkowski, W. (2003). *Neutron scattering lengths. Neutron Data Booklet*, 2nd ed., edited by A. J. Dianoux & G. Lander, §1.1. Grenoble: Institut Laue–Langevin.

Riley, D. P., Kisi, E. H., Hansen, T. C. & Hewat, A. W. (2002). *Self-propagating high-temperature synthesis of Ti_3SiC_2: I, ultra-high-speed neutron diffraction study of the reaction mechanism. J. Am. Ceram. Soc.* **85**, 2417–2424.

Rodriguez, D. M., Kennedy, S. J. & Bentley, P. M. (2011). *Properties of elliptical guides for neutron beam transport and applications for new instrumentation concepts. J. Appl. Cryst.* **44**, 727–737.

Rush, J. J. & Cappelletti, R. L. (2011). *The NIST Center for Neutron Research: Over 40 Years Serving NIST/NBS and the Nation*. National Institute of Standards Special Publication (NIST SP) 1120. National Institute of Standards, Gaithersburg, Maryland, USA.

Sabine, T. M. (1985). *Extinction in polycrystalline materials. Aust. J. Phys.* **38**, 507–518.

Schanzer, C., Böni, P., Filges, U. & Hils, T. (2004). *Advanced geometries for ballistic neutron guides. Nucl. Instrum. Methods Phys. Res. A*, **529**, 63–68.

Schoenborn, B. P., Caspar, D. L. D. & Kammerer, O. F. (1974). *A novel neutron monochromator. J. Appl. Cryst.* **7**, 508–510.

Sears, V. F. (2006). *Scattering lengths for neutrons. International Tables for Crystallography*, Volume C, *Mathematical, Physical and Chemical Tables*, 1st online ed., edited by E. Prince, pp. 444–454. Chester: International Union of Crystallography.

Shull, C. G. (1995). *Early development of neutron scattering. Rev. Mod. Phys.* **67**, 753–757.

Shull, C. G., Strauser, W. A. & Wollan, E. O. (1951). *Neutron diffraction by paramagnetic and antiferromagnetic substances. Phys. Rev.* **83**, 333–345.

Shull, C. G., Wollan, E. O., Morton, G. A. & Davidson, W. L. (1948). *Neutron diffraction studies of NaH and NaD. Phys. Rev.* **73**, 842–847.

Smith, R. I. *et al.* (2018). In preparation.

Soller, W. (1924). *A new precision X-ray spectrometer. Phys. Rev.* **24**, 158–167.

Soper, A. K., Howells, W. S., Hannon, A. C., Turner, J. Z. & Bowron, D. T. (2000). *ATLAS – analysis of time-of-flight diffractometer data from liquid and amorphous samples*. http://wwwisis2.isis.rl.ac.uk/Disordered/Manuals/ATLAS%20manual%20and%20SSG.pdf.

Squires, G. L. (1978). *Introduction to the Theory of Thermal Neutron Scattering.* Cambridge University Press.

Szilard, L. & Chalmers, T. A. (1934). *Detection of neutrons liberated from beryllium by gamma rays: a new technique for inducing radioactivity. Nature*, **134**, 494–495.

Tamura, I., Aizawa, K., Harada, M., Shibata, K., Maekawa, F., Soyama, K. & Arai, M. (2003). *Simulation for developing new pulse neutron spectrometers: creation of new McStas components of moderators of JSNS*. JAERI Research Report 2003-008. JAERI, Japan.

Tashmetov, M. Y., Em, V. T. E., Lee, C. H., Shim, H. S., Choi, Y. N. & Lee, J. S. (2002). *Neutron diffraction study of the ordered structures of nonstoichiometric titanium carbide. Physica B*, **311**, 318–325.

Thomsen, K. (2014). *Conceptual proposal for compound moderators with preferential emission directions. Phys. Procedia*, **60**, 278–293.

Tremsin, A. S., McPhate, J. B., Vallerga, J. V., Siegmund, O. H. W., Feller, W. B., Lehmann, E., Butler, L. G. & Dawson, M. (2011). *High-resolution neutron microtomography with noiseless neutron counting detector. Nucl. Instrum. Methods Phys. Res. A*, **652**, 400–403.

Tremsin, A. S., McPhate, J. B., Vallerga, J. V., Siegmund, O. H. W., Kockelmann, A., Steuwer, A. & Feller, W. B. (2011). *High-resolution neutron counting sensor in strain mapping through transmission Bragg edge diffraction. IEEE Sens. J.* **11**, 3433–3436.

Turchin, V. F. (1967). Deposited Paper, USSR Atomic Energy, 1967, p. 22.

Vogt, T., Passell, L., Cheung, S. & Axe, J. D. (1994). *Using wafer stacks as neutron monochromators. Nucl. Instrum. Methods Phys. Res. A*, **338**, 71–77.

Wensrich, C. M., Kisi, E. H., Luzin, V., Garbe, U., Kirstein, O., Smith, A. L. & Zhang, J. F. (2014). *Force chains in monodisperse spherical particle assemblies: three-dimensional measurements using neutrons. Phys. Rev. E*, **90**, 042203.

Wensrich, C. M., Kisi, E. H., Zhang, J. F. & Kirstein, O. (2012). *Measurement and analysis of the stress distribution during die compaction using neutron diffraction. Granular Matter*, **14**, 67–680.

Wilkins, S. W., Stevenson, A. W., Nugent, K. A., Chapman, H. & Steenstrup, S. (1989). *On the concentration, focusing, and collimation of x-rays and neutrons using microchannel plates and configurations of holes. Rev. Sci. Instrum.* **60**, 1026–1036.

Willendrup, P., Farhi, E., Knudsen, E., Filges, U. & Lefmann, K. (2014). *McStas: Past, present and future. J. Neutron Res.* **17**, 35–43.

Wollan, E. O. & Borst, L. B. (1945). *Physics Section III Monthly Report for the Period Ending December 31, 1944*, p. 37. Metallurgical Project Report No. M-CP-2222. Clinton Laboratories, Oak Ridge, Tennessee, USA.

Wollan, E. O. & Shull, C. G. (1948). *The diffraction of neutrons by crystalline powders*. *Phys. Rev.* **73**, 830–841.

Worlton, T. G., Jorgensen, J. D., Beyerlein, R. A. & Decker, D. L. (1976). *Multicomponent profile refinement of time-of-flight neutron powder diffraction data*. *Nucl. Instrum. Methods*, **137**, 331–337.

Wu, E., Kennedy, S. J., Gray, E. M. & Kisi, E. H. (1996). *The ordered structure of* $PdD_{0.78}$ *at 70–75K*. *J. Phys. Condens. Matter*, **8**, 2807–2813.

Zendler, C., Lieutenant, K., Nekrassov, D. & Fromme, M. (2014). *VITESS 3 – virtual instrumentation tool for the European Spallation Source*. *J. Phys. Conf. Ser.* **528**, 012036.

Zhang, J. F., Wensrich, C. M., Kisi, E. H., Luzin, V., Kirstein, O. & Smith, A. L. (2016). *Stress distributions in compacted powders in convergent and stepped dies*. *Powder Technol.* **292**, 23–30.

Zhao, J. K., Robertson, J. L., Herwig, K. W., Gallmeier, F. X. & Riemer, B. W. (2013). *Optimizing moderator dimensions for neutron scattering at the spallation neutron source*. *Rev. Sci. Instrum.* **84**, 125104.

Zinn, W. H. (1947). *Diffraction of neutrons by a single crystal*. *Phys. Rev.* **71**, 752–757.

Zinn, W. H. & Szilard, L. (1939). *Emission of neutrons by uranium*. *Phys. Rev.* **56**, 619–624.

International Tables for Crystallography (2019). Vol. H, Chapter 2.4, pp. 102–117.

2.4. Electron powder diffraction

J.-M. Zuo, J. L. Lábár, J. Zhang, T. E. Gorelik and U. Kolb

2.4.1. Introduction

Electron powder diffraction is commonly performed in transmission geometry inside a transmission electron microscope using ∼80–300 kV high-energy electrons with wavelengths from 0.0418 to 0.0197 Å (Cowley, 1992; Peng *et al.*, 2004). The incident electron beam can be as small as a few nm or as large as tens of µm in diameter. Transmission electron powder diffraction can be obtained from randomly oriented nanocrystalline or amorphous materials. The short electron wavelengths allow the observation of powder diffraction rings over a large range of S (= $\sin\theta/\lambda$). Electron powder diffraction can also be performed using the Bragg reflection geometry in reflection high-energy electron diffraction (RHEED) with 10–30 kV electrons (Ichimiya & Cohen, 2004). RHEED has a limited penetration depth and therefore is mostly used for the study of supported nanoparticles.

Because the electron beam can be formed into a small probe using electromagnetic lenses in a transmission electron microscope, electron diffraction has the advantage of being able to address individual particles in a powder as single crystals. Single-crystal electron diffraction data are often used for the determination of unit-cell parameters (Zuo, 1993; Zuo *et al.*, 1998; Gramm *et al.*, 2006; Sun *et al.*, 2009; Kolb *et al.*, 2006; Zhuang *et al.*, 2011), phase identification (Gramm *et al.*, 2006) or quantitative structural analysis (Vincent & Exelby, 1991; Jansen *et al.*, 1998; Tsuda & Tanaka, 1999; Hovmoller *et al.*, 2002; Sun *et al.*, 2009; Gorelik *et al.*, 2010; Mugnaioli *et al.*, 2012), or in combination with X-ray and neutron powder diffraction for structure determination (Wu *et al.*, 2006; Baerlocher *et al.*, 2007; McCusker & Baerlocher, 2009).

The principle of electron diffraction is similar to that of X-ray diffraction. Both use atomic scattering and interference of the scattered waves to probe the atomic structure. The difference is that electrons are charged particles and interact with both the electrons and nucleus of the atom with a large elastic scattering cross section (several orders of magnitude larger than that of X-rays). The combination of short wavelength, the large scattering cross section and the small electron beam makes electron powder diffraction a powerful technique for the analysis of amorphous or nanocrystalline thin films, nanoparticles and ‘small’ crystals in general (see Fig. 2.4.1 for an example).

A drawback of the strong interaction of electrons with matter is the presence of multiple-scattering effects. In X-ray diffraction, the measured integrated intensity is often less than predicted by the theory for an ideally imperfect crystal (because of extinction) but larger than predicted by the theory for an ideal perfect crystal. There are two types of extinction: primary and secondary. Primary extinction describes the multiple scattering within a single mosaic block. Primary extinction diminishes the intensity when the mosaic blocks are so large that they behave as fragments of perfect crystals. The effect of electron multiple scattering is similar to primary extinction in X-ray diffraction, except the electron extinction length is short and comparable with the sample thickness. Strong extinction can be an issue when analysis based on kinematical diffraction (single-scattering) theory, as in X-ray powder diffraction, is used for electron diffraction intensities; thus dynamic theory, which takes into account multiple scattering of the incident and diffracted waves inside a crystal, is necessary. Secondary extinction also occurs in electron powder diffraction. However, so far there is no satisfactory treatment of this effect in electron diffraction. For small nanoparticles or nanocrystalline thin films the electron multiple-scattering effects are typically reduced, so quantitative structural information can be extracted from electron powder diffraction using the kinematical approximation (Cockayne & McKenzie, 1988; Ishimaru *et al.*, 2002; Chen & Zuo, 2007; Cockayne, 2007). Recent studies have demonstrated that multiple-scattering effects can be significantly reduced by averaging over a range of crystal orientations using precession electron diffraction (Vincent & Midgley, 1994; Gjonnes *et al.*, 1998; Gemmi *et al.*, 2003; Own *et al.*, 2006; Oleynikov & Hovmoller, 2007). The same benefit is expected in electron powder diffraction with 360° orientation averaging.

The quality of electron powder diffraction work has also benefited from the development of TEM (transmission electron microscopy) technologies. The adoption of field emission guns (FEGs) in conventional transmission electron microscopes led to the development of electron sources with high brightness, small probe size and improved coherence. Electron energy filters, such as the in-column Ω energy filter, allow a reduction of the inelastic background due to plasmon scattering, or higher electron energy losses, with an energy resolution of a few eV (Rose & Krahl, 1995). The development of array detectors, such as charge-coupled device (CCD) cameras or image plates, enables the recording of entire powder diffraction patterns and direct quantification of diffraction intensities over a large dynamic range that was not possible earlier (Zuo, 2000). The latest

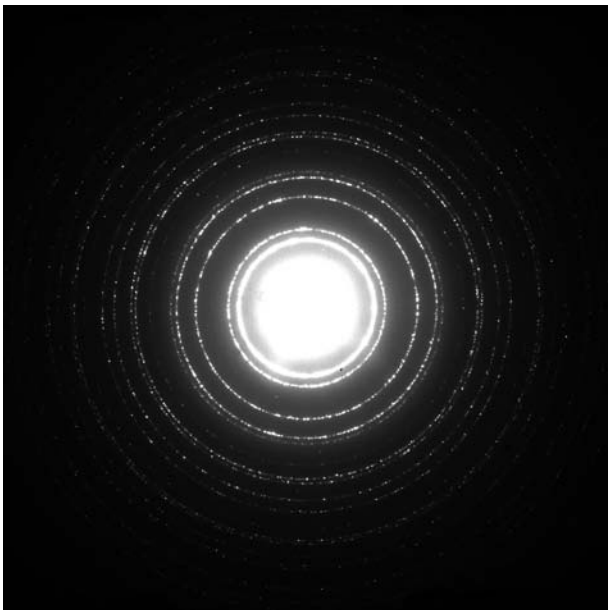

Figure 2.4.1
An electron powder diffraction pattern recorded on an imaging plate from a polycrystalline Al thin film using selected-area electron diffraction geometry with 200 kV electrons.

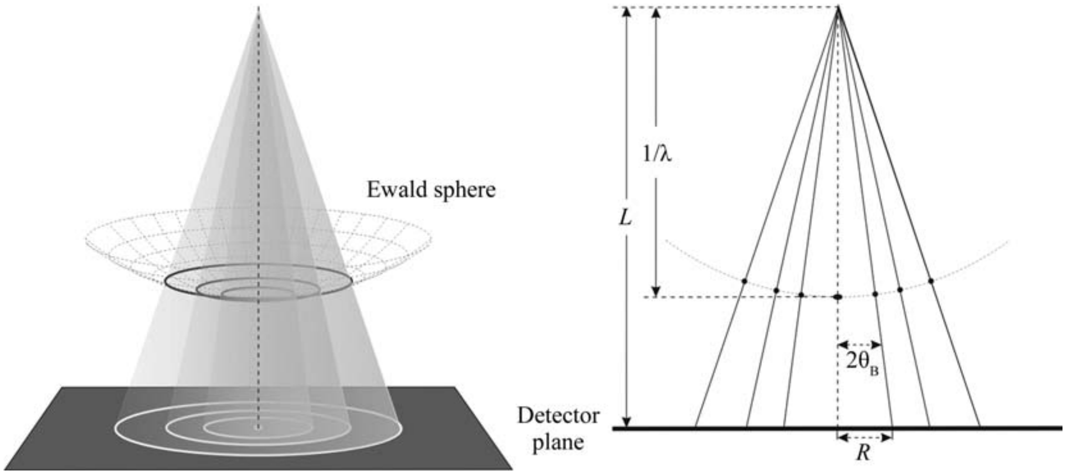

Figure 2.4.2
Schematic diagram of the Ewald sphere construction and the geometry for recording electron diffraction patterns.

development in time-resolved electron diffraction at a time resolution approaching femtoseconds (Elsayedali & Herman, 1990; Siwick *et al.*, 2003) will significantly improve the ability to interrogate structures at high spatial and time resolution.

Irradiation of both organic and inorganic materials with an electron beam can cause severe modification of the structure. The amount of energy deposited into the material can be estimated through the ratio of the elastic and inelastic scattering cross sections. For carbon the ratio for electrons (300 keV) and X-rays (with a wavelength of less than 1 Å) is comparable, meaning that the radiation damage caused by these sources is on the same scale (Henderson, 1995). Electron radiation damage is caused by all kinds of ionization processes, including bond breakdown and subsequent recombination of radicals and active molecular species. Inorganic materials can show knock-on damage (atomic displacement) or sputtering effects (loss of atoms). This damage may lead to a total structural collapse. The collective damage due to electron radiation is quantified using the electron dose and electron dose rates. In many cases the damage can be reduced by minimizing the electron dose received by the sample, cryo-protection, or deposition of a protective conductive layer (Reimer & Kohl, 2008).

This chapter covers the practical issues and theory of electron powder diffraction as well as applications for material analysis. A fundamental description of electron diffraction can be found in *International Tables for Crystallography*, Vol. C (2004) and the book by Zuo & Spence (2017). The present chapter is subdivided into seven sections. Sections 2.4.2 and 2.4.3 cover the theory and the experimental setup of an electron powder diffraction experiment using transmission electron microscopes, respectively. Sections 2.4.4 and 2.4.5 discuss the application of electron powder diffraction data to phase and texture analysis and related techniques. Rietveld refinement with electron powder diffraction data is a relatively new field; this is discussed in Section 2.4.6. The last section reviews pair distribution function (PDF) analysis using electron diffraction data.

2.4.2. Electron powder diffraction pattern geometry and intensity

By J.-M. Zuo and J. L. Lábár

The powder diffraction rings in transmission geometry appear where the cone of diffracted electron beams intersects the Ewald sphere. The intersection creates a ring of diffracted beams, which is then projected onto the planar detector (see Fig. 2.4.2) with a radius (R) according to

$$R = L \tan 2\theta_{\rm B}. \tag{2.4.1}$$

Here $\theta_{\rm B}$ is the Bragg diffraction angle and L is the camera length.

The d-spacing can be obtained by measuring the length of R in an experimental diffraction pattern using

$$d = \frac{\lambda}{2\sin\theta_{\rm B}}. \tag{2.4.2}$$

The electron wavelength is determined by the electron accelerating voltage (Φ), in volts:

$$\lambda = \frac{h}{(2m_e\Phi)^{1/2}} \simeq \frac{1.226}{[\Phi(1+0.97845\times10^{-6}\Phi)]^{1/2}}. \tag{2.4.3}$$

The wavelength of high-energy electrons is relatively short. For 200 kV electrons, the wavelength is 0.025 Å and the Bragg angle is very small. For example, for d = 2.5 Å the electron scattering angle θ is 5 mrad. For a small Bragg angle one can use the approximation $\sin\theta \simeq \tan\theta \simeq \theta$. This gives the relationship

$$d \simeq \frac{L\lambda}{Rd}. \tag{2.4.4}$$

At large scattering angles with $\sin\theta/\lambda$ 2 Å^{-1} or greater, a better approximation is given by (Cowley & Hewat, 2004)

$$d \simeq \frac{L\lambda}{R}\left(1+\frac{3R^2}{8L^2}\right). \tag{2.4.5}$$

The camera length L can be determined using a sample with known d-spacings, while the electron wavelength or acceleration voltage can be calibrated using high-order Laue zone (HOLZ) lines in convergent-beam electron diffraction (CBED) patterns (Zuo, 1993).

For a small parallelepiped crystal fully illuminated by a coherent electron beam of intensity I_0, the kinematic diffraction intensity is given by

$$I_{\rm SC} = I_0\frac{|F_{hkl}|^2}{L^2}\left\{\frac{\sin[\pi\mathbf{S}_{hkl}\cdot N_1\mathbf{a}]}{\sin[\pi\mathbf{S}_{hkl}\cdot\mathbf{a}]}\,\frac{\sin[\pi\mathbf{S}_{hkl}\cdot N_2\mathbf{b}]}{\sin[\pi\mathbf{S}_{hkl}\cdot\mathbf{b}]}\,\frac{\sin[\pi\mathbf{S}_{hkl}\cdot N_3\mathbf{c}]}{\sin[\pi\mathbf{S}_{hkl}\cdot\mathbf{c}]}\right\}^2, \tag{2.4.6}$$

where N_1, N_2 and N_3 are the number of unit cells along the three axis directions, and F_{hkl} is the electron structure factor of the hkl reflection:

$$F_{hkl} = \sum_{i=1}^{n} f_i^e T_i \exp[2\pi i(hx_i + ky_i + lz_i)]. \qquad (2.4.7)$$

Here T is the atomic displacement factor, which accounts for atomic thermal vibrations, and the electron atomic scattering factor f_i^e is defined by equation (4.3.1.13) in *International Tables for Crystallography*, Vol. C (2004). For a reflection with the scattering vector $\mathbf{g}_{hkl}$ the deviation from the Bragg condition of the *hkl* reflection is expressed by the excitation error $\mathbf{S}_{hkl}$:

$$\mathbf{k} - \mathbf{k}_0 = \mathbf{g}_{hkl} + \mathbf{S}_{hkl}. \qquad (2.4.8)$$

The diffraction intensity recorded in a powder diffraction pattern is the integrated intensity over the crystal orientation and the detector area. A change in crystal orientation leads to a change in the excitation error normal to the diffracted beam in the plane of Bragg reflection. The integration in these three directions is equivalent to integration over the reciprocal-space volume around the Bragg peak. The result gives the diffraction power of a sample with a large number of crystallites for the *hkl* reflection as (Warren, 1990)

$$P_{hkl} = I_0 \frac{\lambda^2 m_{hkl} V_{\rm sample} d_{hkl}}{2V_c^2} \left|F_{hkl}\right|^2, \qquad (2.4.9)$$

where $V_{\rm sample}$ is the sample volume, m_{hkl} is the multiplicity of the reflection based on the symmetry-equivalent number of *hkl* reflections, and V_c is the volume of the unit cell. For randomly oriented powder samples, the diffraction power is uniformly distributed over the bottom edge of a cone of half apex angle $2\theta_{hkl}$ and height L, and the peak intensity is more appropriately described by the power per unit length of the diffraction circle (Vainshtein, 1964):

$$I_k = \frac{P_{hkl}}{2\pi L \sin 2\theta_{hkl}} = \frac{I_0}{4\pi L} \frac{\lambda d_{hkl}^2 m_{hkl} V_{\rm sample}}{V_c^2 \cos\theta_{hkl}} \left|F_{hkl}\right|^2. \qquad (2.4.10)$$

Here $\cos\theta_{hkl} \simeq 1$ is a good approximation for electron diffraction and this formula is presented in equation (2.4.1.3) in *International Tables for Crystallography*, Vol. C (2004).

The kinematic approximation in electron diffraction is valid only for very small crystals. Defining the validity of the kinematic approximation for different crystals has been difficult and the subject of extensive debate (Blackman, 1939; Vainshtein, 1964; Turner & Cowley, 1969; Cowley, 1995). For single-crystal electron diffraction, numerous studies using CBED have demonstrated an almost perfect fit to experimental diffraction intensities using dynamic theory. Using this fitting approach, experimental structure-factor amplitudes and phases can be measured through a refinement process with high accuracy (Saunders *et al.*, 1995; Tsuda *et al.*, 2002; Zuo, 2004). However, this approach requires knowledge of the approximate crystal structure and can rarely be used for powder electron diffraction, where unknown crystal structures are often studied. In developing a theory for the integrated intensity for powder electron diffraction, the magnitude of the dynamic effect and its dependence on crystal orientations, defects, thickness variations and crystal shape must be considered. In X-ray and neutron diffraction, the combination of these factors led to the highly successful kinematical theory of ideal imperfect crystals with randomly distributed mosaic blocks. For electron diffraction, an all-encompassing theory of integrated intensity has been elusive because of the small electron coherence length, which is much less than the size of typical mosaic blocks detected by X-ray and neutron diffraction, and strong scattering. An approximation has been developed to take account of dynamical scattering using the two-beam theory (Blackman, 1939). Under this approximation, the integrated dynamic intensity I_d over a large range of excitation is given by the expression

$$I_d \propto \left|F_{hkl}\right| \int_0^{A_{hkl}} J_0(2x)\,{\rm d}x. \qquad (2.4.11)$$

Here

$$A_{hkl} = \frac{\lambda\gamma\left|F_{hkl}\right|t}{V_c \cos\theta_{hkl}} \simeq \frac{\lambda\gamma\left|F_{hkl}\right|t}{V_c}, \qquad (2.4.12)$$

where t is the thickness of the crystallite along the electron-beam direction, γ is the relativistic constant of electrons and $J_0(2x)$ is the zero-order Bessel function. For a very small value of A_{hkl} the Bessel function $J_0(2x)$ is nearly constant with a value of 1 and the diffraction intensity approaches that of the kinematical limit. From this, the following formula can be derived for the dynamical intensity:

$$I_d = \frac{I_0}{4\pi L} \frac{d_{hkl}^2 m_{hkl} V_{\rm sample}}{V_c \gamma t} \left|F_{hkl}\right| \int_0^{A_{hkl}} J_0(2x)\,{\rm d}x. \qquad (2.4.13)$$

For very large A_{hkl}, the integral over the Bessel function approaches the value of 1/2 and in this case the diffraction intensity is proportional to the structure-factor amplitude instead of its square as predicted by kinematical theory.

The extent of dynamic effects that can be reduced by averaging over crystal orientations has been demonstrated by precession electron diffraction (PED). This technique was originally developed by Vincent & Midgley (1994) to improve the single-crystal electron diffraction intensities for structural analysis. In PED, the incident electron beam is tilted and precessed along a conical surface that is centred on the electron optical axis. Below the crystal, the diffraction pattern is tilted back with the position of the direct beam remaining approximately constant during precession. The diffraction pattern then generally appears similar to a conventional electron diffraction pattern. The measured diffraction intensity, however, is a double integration over the two-dimensional detector and the incident-beam angles defined by the precession cone surface. Experimental and theoretical studies of PED integrated intensities have shown an overall 'more kinematical' behaviour with less sensitivity to crystal thickness and exact orientation than for conventional electron diffraction patterns. Simulations also showed that the dynamical effects are still present in the PED integrated intensities, but the extent of the dynamic effect as measured by the correlation between the integrated intensity and the squared amplitude of the structure factor follows the empirical rules:

(i) The correlation increases with the precession angle.
(ii) The correlation is more pronounced for higher-order reflections than lower-order ones, for which the integration over the different excitation error is less complete.
(iii) The correlation also improves as the crystal thickness decreases.

In the electron powder diffraction of randomly oriented crystals, the angular integration is performed over the entire solid angle. Zone-axis patterns with enhanced dynamical interaction between the diffracted beams are also included in this solid angle. However, the overall probability for a crystal to be in exact zone-axis orientation is very small, even if the zone axis is defined within a wedge of tens of milliradians. Thus, powder electron data generally tend to be more kinematical than single-crystal data.

2.4.3. Electron powder diffraction techniques

By J.-M. Zuo and J. Zhang

The basic setup for electron powder diffraction uses a transmission electron microscope equipped with an area electron detector (photographic film, CCD camera *etc.*). Thin films, such as amorphous carbon or holey carbon films supported on metal grids, are typically used to support powder samples, which are then mounted and inserted into the transmission electron microscope inside a TEM sample holder. Solid free-standing thin films can be placed directly on top of a metal grid.

The electron beam used for a powder electron diffraction experiment is shaped using electromagnetic lenses. A modern transmission electron microscope uses at least three sets of magnetic lenses for the illumination system: condensers I and II, and the objective prefield. The prefield is part of the objective lens system before the sample acting as a lens. Some transmission electron microscopes come with an additional condenser lens (condenser III, or condenser mini-lens), which can be used for nanodiffraction. These lenses are used in various combinations to set up electron illumination for selected-area electron diffraction (SAED) or nano-area electron diffraction (NAED) (Zuo, 2004). The major difference between these two is the area of illumination, which is controlled by the strength (or focal length) of the condensers II and III.

An issue to be considered during setup of the electron beam for powder diffraction is the electron lateral coherence length. In a transmission electron microscope, the electron coherence is defined by the coherence length seen at the condenser aperture. According to the Zernike–Van Cittert theorem, the degree of coherence between electron wavefunctions at two different points far away from a monochromatic electron source is given by the Fourier transform of the source intensity distribution (Cowley, 1999). If we assume that the source has a uniform intensity within a circular disc, the coherence function is then given by $\lambda J_1(\pi\beta r/\lambda)/\beta r$ with J_1 being the first-order Bessel function, r the radial distance at the aperture and β the angle sustained by the electron source. The lateral coherence length L, which is often referred to in the literature, is defined by r at the first zero of J_1, which has the value of $L = 1.2\lambda/\beta$. The source seen by the condenser aperture inside a transmission electron microscope is the source image formed after the condenser-I lens. For a Schottky emission source, the emission diameter is between 20 and 30 nm according to Botton (2007). For a condenser aperture placed 10 cm away from the electron source image, a factor of 10 source demagnification provides a coherence length from 100 to 150 µm. When a smaller condenser aperture is used, such as in NAED, the electron beam can be considered as approximately coherent and the lateral coherence length on the same is limited by the beam convergence angle α with $L_{\rm sample} = 1.2\lambda/\alpha$.

2.4.3.1. *Selected-area electron diffraction (SAED)*

SAED is formed using the transmission electron microscope illumination, which is spread out over a large area of the specimen to minimize the beam convergence angle. The diffraction pattern is first formed at the back focal plane of the objective lens and then magnified by the intermediate and projector lenses (only one is shown) onto the screen or electron detector (Fig. 2.4.3). The recorded diffraction pattern is from an area of interest selected by placing an aperture in the conjugate (imaging) plane of the objective lens. Only electron beams passing through this aperture contribute to the diffraction pattern. For a perfect lens without aberrations, electron beams recorded in the diffraction pattern come from an area that is defined by the image of the selected-area aperture at the specimen plane. The aperture image is demagnified by the objective lens. In a conventional electron microscope, rays at an angle to the optic axis are displaced away from the centre because of the spherical aberration of the objective lens (C_s) as shown in Fig. 2.4.3. The displacement is proportional to $C_s\alpha^3$, where α is twice the Bragg angle. The smallest area that can be selected in SAED is thus limited by the objective lens aberrations. This limitation is removed by using an electron microscope equipped with a transmission electron microscope aberration corrector placed after the objective lens (Haider *et al.*, 1998).

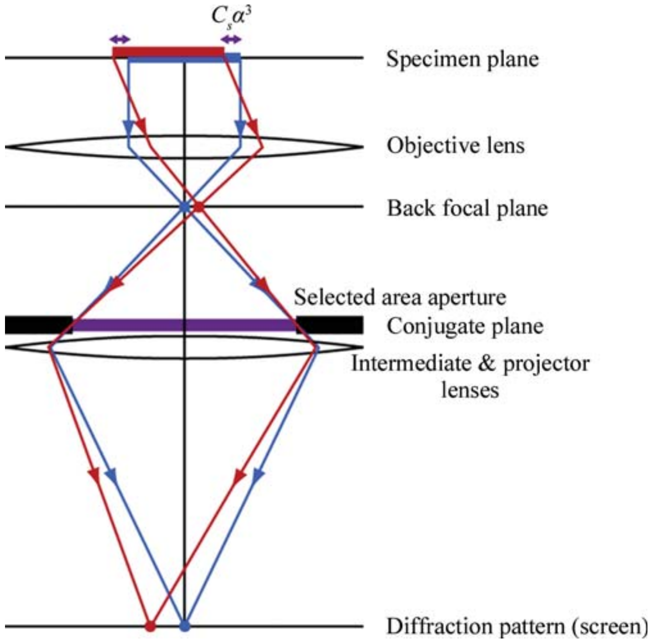

Figure 2.4.3
Schematic illustration of selected-area electron diffraction in conventional TEM. (Provided by Jun Yamasaki of Nagoya University, Japan.)

The major feature of SAED is that it provides a large illumination area, which is beneficial for recording diffraction patterns from polycrystalline samples as it leads to averaging over a large volume (for example, a large number of nanoparticles). SAED can also be used for low-dose electron diffraction, which is required for studying radiation-sensitive materials such as organic thin films.

2.4.3.2. *Nano-area electron diffraction (NAED)*

NAED uses a small (nanometre-sized) parallel illumination with the condenser/objective setup shown in Fig. 2.4.4 (Zuo *et al.*, 2004). The small beam is achieved by reducing the convergence angle of the condenser-II crossover and placing it at the focal plane of the objective prefield, which then forms a parallel-beam illumination on the sample for an ideal lens. A third condenser lens, or a mini-lens, is required for the formation of a nanometre-sized parallel beam. For a condenser aperture of 10 µm in diameter, the probe diameter is ~50 nm with an overall magnification factor of 1/200 in the JEOL 2010 electron microscopes (JEOL, USA). The smallest beam convergence angle in NAED is

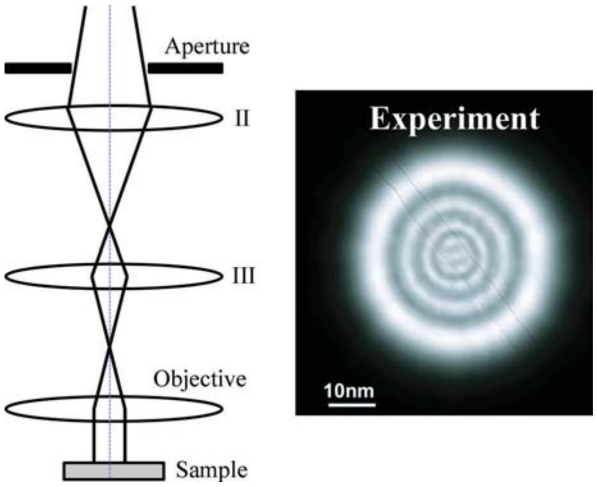

Figure 2.4.4
Schematic illustration of electron nanoprobe formation using a combination of condenser lenses (II and III) and the objective lens. The beam divergence angle is kept at a minimum by forming a crossover at the front focal plane of the objective lens. An image of an experimental electron nanoprobe is shown on the right with a carbon nanotube contained inside the probe.

limited by the aberrations of the illumination lenses. A beam convergence angle as small as ~0.05 mrad has been reported (Zuo *et al.*, 2004). A diffraction pattern recorded using NAED is similar to one recorded by SAED. The major difference is that the diffraction volume is defined directly by the electron probe in NAED. Since all electrons illuminating the sample are recorded in the diffraction pattern, NAED in an FEG microscope also provides higher beam intensity than SAED (the probe current intensity using a 10 µm condenser-II aperture in a JEOL 2010F is $\sim10^5$ e s^{-1} nm^{-2}) (Zuo *et al.*, 2004).

The small probe size is most useful for studying a small section of thin films or for selection of nanoparticles for powder diffraction. The small beam size reduces the background in the electron diffraction pattern from the surrounding materials.

2.4.3.3. *Sample preparation*

The success of an electron powder diffraction experiment to a large extent depends on sample preparation. The powder sample has to be suitable for electron-beam observation, and the sample also needs to be compatible with the vacuum environment of the microscope. *In situ* experiments can be carried out using special holders for cooling, heating and cryogenic or environmental transfer. Special microscopes are also available to provide a gaseous or ultra high vacuum environment for the investigation of structures under a gas or at ultra low pressure, or *in situ* sample preparation.

The observed area of the sample must be electron transparent, *i.e.* have a thickness of less than or comparable to the inelastic mean free path of electrons. The inelastic mean free path increases with the electron voltage (Egerton, 2011). The typical sample thickness ranges from a few tens to hundreds of nanometres for 200 kV high-energy electrons (see Table F.1 in Zuo & Spence, 2017).

The sample-preparation techniques can be divided into three categories: (i) bulk-based for bulky materials and supported thin films, (ii) powder-based techniques and (iii) free-standing thin films over a supporting grid prepared by vacuum evaporation or sputtering.

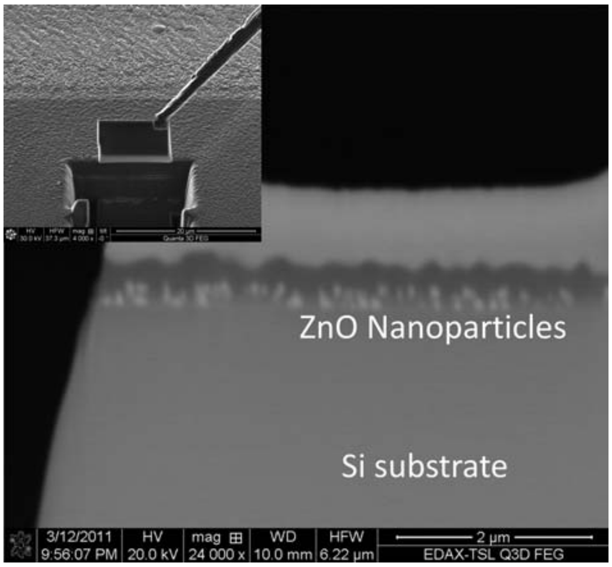

Figure 2.4.5
Sample preparation and lift-out using a focused ion beam (FIB). A thin section of the sample is cut out using the FIB and attached to a mechanical probe for lift-out (inset). The image shows the lift-out section containing ZnO nanoparticles in bright dot-like contrast supported on an Si substrate.

The bulk-based techniques involve mechanical cutting, thinning/polishing and perforation. An ion beam is typically used in the last step of perforation to create a thin area around the edge of a hole for electron-beam observation. Chemical and electrolytic methods are also often used for preparing electron-transparent samples. While these methods have been applied to a broad range of materials, they are mostly used for metals or semiconductors to create smooth sample surfaces free from defects or sample heating caused by ion-beam irradiation. Mechanical thinning and polishing are sometimes done with a wedge angle with the help of a tripod. The thin region next to the edge only requires a brief ion-beam bombardment to make it electron transparent. A detailed description of traditional sample-preparation techniques for TEM can be found in Barna & Pécz (1997). The above techniques are applicable to both thin films and bulk nanocrystalline materials. The powder-based techniques use dispersion of powders on thin supporting films placed on metal grids specially made for TEM observations. This technique is most suitable for nanoparticles. For micron or larger-sized powders, additional grinding is used to produce smaller particles. The most commonly used supporting films are continuous amorphous carbon films, holey carbon films, networked carbon fibres (lacey carbon), amorphous silicon nitride and SiO_x. For amorphous carbon films, an ultra thin version is available which is especially useful for nanoparticle samples.

A recent development in TEM sample preparation is the use of a focused ion beam of Ga^+ ions for cross-sectioning a sample. The focused ion beam can drill a precise hole in the sample. The same ion beam can also be scanned over a sample surface to form an image by collecting the secondary electrons or ions generated by the beam. The ion column can be integrated into an electron column in a scanning electron microscope in the so-called dual-beam configuration. An image can be formed using either electrons or ions. Most often the electron beam is used for sample inspection, while the ion beam is used for patterning and milling. This allows precise control over the position and thickness of the cross section, which is very practical for characterization of semiconductor devices or failure analysis in general (Fig. 2.4.5). Further details about ion-beam techniques can be found in Lábár & Egerton (1999) and Orloff *et al.* (2002). For a comprehensive review of sample-preparation techniques for TEM, see Őzdöl *et al.* (2012).

2.4.3.4. *Diffraction data collection, processing and calibration*

Experimental electron powder diffraction data are collected using two-dimensional area electron detectors. Experimental issues involved in the diffraction-pattern recording procedure are electron optical alignment, diffraction-pattern collection and calibration, with particular care taken in adjusting the specimen height position (eucentric position), selection of a suitable illumination-beam convergence angle and diffraction-camera length, and finally projector-lens focusing. The diffraction-camera length is determined by the setting of intermediate and projector lenses in combination with the objective lens. To calibrate the diffraction-camera length, a standard sample is placed in the eucentric position of the objective lens at the standard focus. At this setting, the specimen plane is conjugate to the selected-area aperture (Fig. 2.4.3) and the sample image appears in focus. To obtain a sharp diffraction pattern, the detector plane must be conjugate to the back focal plane of the objective lens. This can be achieved by setting up a parallel-beam illumination and adjusting the intermediate-lens focus length to bring the direct beam into a sharp focus.

Currently available area electron detectors are CCD and CMOS cameras, imaging plates (IPs) and photographic film. While photographic film has a long history of use in electron microscopy, its limited dynamic range makes it less useful for electron diffraction data collection. Both CCD cameras and IPs are digital recorders capable of collecting electron intensity over a large dynamic range. The crucial characteristics of digital recording systems are the gain (g), linearity, resolution, detector quantum efficiency (DQE) and the dynamic range. The gain of a CCD or CMOS camera can be normalized using a flat-field illumination; the gain in IPs is assumed to be constant. The detector resolution is characterized by the point-spread function (PSF), which is roughly the detector's response to a point-like illumination. These characteristics for CCDs and IPs have been compared by Zuo (2000). The intensity of an electron diffraction pattern recorded with a digital detector is given by

$$I^{\text{recorded}}(i,j) = g(i,j)H(i,j) \otimes I^{\text{original}}(i,j) + n(i,j), \qquad (2.4.14)$$

where $g(i, j)$ is the detector gain image, H is the PSF of the detector, n is the detector noise and I^{original} is the intensity of scattered electron beams originally received by the detector. The i and j are the pixel coordinates of the detector. The PSF is experimentally characterized and measured by the amplitude of its Fourier transform, or the so-called modulated transfer function (MTF). The effects of the PSF can be removed by deconvolution. The Richardson–Lucy method is specifically targeted for Poisson processes, which can be applied to CCD images (Zuo, 2000). The alternative to the removal of the PSF is to treat it as part of the peak broadening that can be used to fit the powder pattern.

The noise in the experimental data is characterized by the DQE:

$$\text{var}(I) = \frac{m\bar{g}I}{\text{DQE}(I)}. \qquad (2.4.15)$$

Here I is the experimentally measured intensity, var stands for the variance, m is the area under the MTF and $\bar{g}$ is the average gain of the detector. Once the DQE is known, this expression allows an estimation of the variance in measured intensity, which is essential for quantitative intensity analysis where the variance is often used as the weight for comparing experimental and fitted data.

The performances of CCDs and IPs for electron diffraction pattern recording are different at different electron dose rates. At low dose rates, the DQE of the CCD camera is limited by the readout noise and the dark current of the CCD. IPs have better performance in the low dose range due to the low dark current and low readout noise of the photomultipliers used in IP readers. At medium and high dose rates, the IP signal is affected mostly by the linear noise due to the granular variation in the phosphor and instability in the readout system, while for CCDs the noise is mostly linear noise in the gain image.

Electromagnetic lenses are not perfect and have aberrations affecting the collected data. In most transmission electron microscopes, electron diffraction patterns are produced using the post-specimen magnetic lenses. For electron diffraction, the most important aberration is the distortion of the projector lens, causing a shift of an image point. There is no blurring in diffraction patterns associated with the lens distortion. However, the distortion affects the overall shape of diffraction patterns. The distortion is most obvious at low camera lengths, where the pattern may seem stretched or twisted at high scattering angles. There are three types of distortion of the same order as the spherical aberration of the lens. They are called pin-cushion, barrel and spiral distortions (Reimer, 1984). A distortion can also arise from the use of an electron energy filter, where a lower order of distortion can be introduced with the use of non-spherical lenses (Rose & Krahl, 1995).

For quantitative analysis an electron powder diffraction pattern recorded on an area detector needs to be integrated into one-dimensional powder diffraction data (Fig. 2.4.6). The integration involves four separate steps: (i) identifying areas of the diffraction pattern for integration, (ii) centring the diffraction pattern, (iii) applying a diffraction pattern distortion correction, if there is any, and (iv) integrating intensities for a constant diffraction angle. Electron powder diffraction patterns can be recorded on a crystalline support film, which gives sharp diffraction spots distinct from the powder diffraction rings. The sharp diffraction patterns from the support film can be excluded from the powder diffraction intensity integration in step (i) by using a mask. The same approach can be used to eliminate any alien features from a diffraction pattern caused, for instance, by the aperture or the energy filter. The diffraction pattern centring is based on the analysis of the transmitted beam in the centre of the pattern. As the transmitted beam is usually very strong and is often overexposed, finding its centre may be a non-trivial task. In order to prevent detector damage in the area of the transmitted beam a beam stop is often used. In this case, the central area in the pattern may have an irregular shape not suitable for the centring procedure. Non-distorted diffraction patterns can be centred by finding the centre of the concentric diffraction rings either by locating the position of the maximum diffraction peak intensity along the ring and using these positions to determine the centre of the ring, or by searching for the centre that gives the maximum correlation between $I(g)$ and $I(-g)$. For distorted diffraction patterns, the centring and the distortion correction must be carried out simultaneously.

The distortion correction requires a powder sample with known d-spacings. The amount of distortion can be obtained by

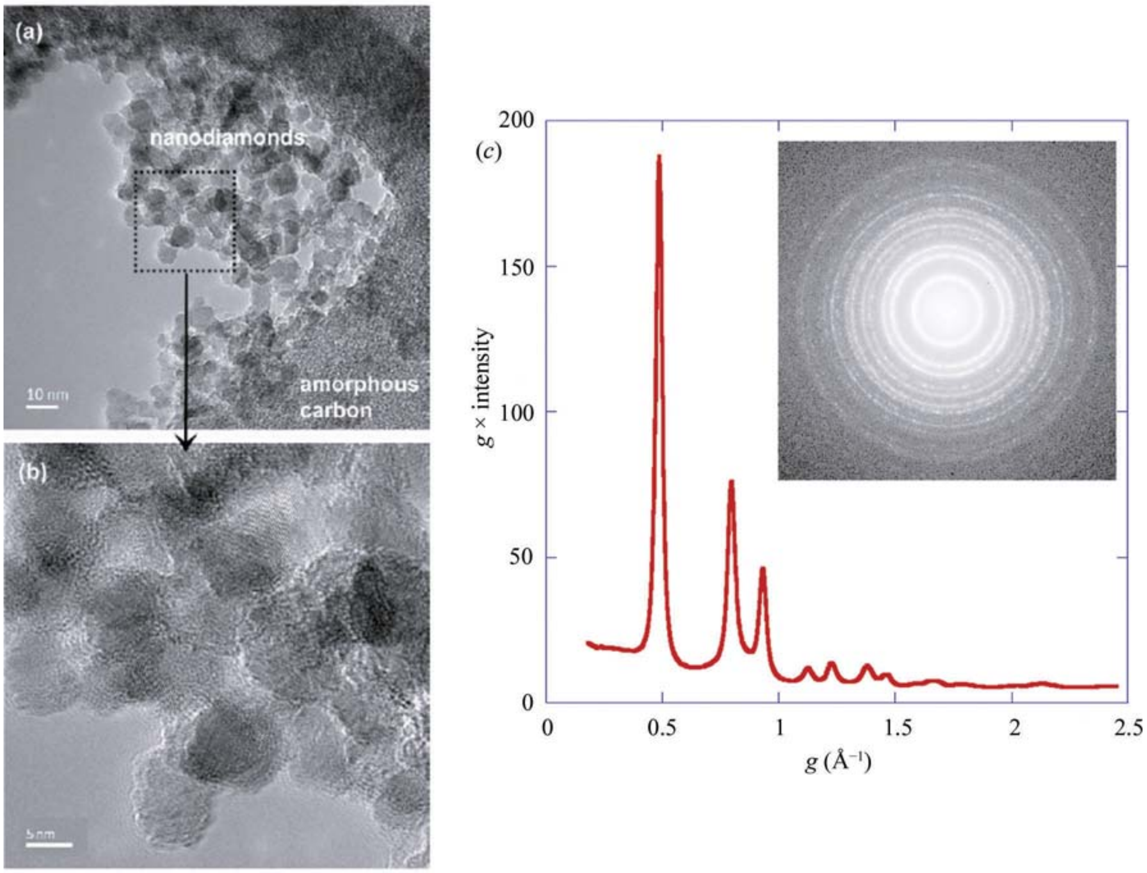

Figure 2.4.6
An example of electron powder diffraction recording for nanodiamonds. (*a*) A TEM image showing nanodiamond particles supported on amorphous carbon, (*b*) the magnified image from the boxed region of (*a*), and (*c*) the recorded electron powder diffraction pattern from nanodiamond particles and the obtained radial intensity profile.

fitting the diffraction ring position $R_d(\varphi)$ using a cosine expansion with

$$R_d(\varphi) = R + \sum_{n=1}^{N} \Delta R_n \cos n(\varphi - \varphi_n), \tag{2.4.16}$$

where R is the average radius (zero order) of the diffraction ring, ΔR represents the amplitude of distortion of order n and φ is the azimuthal angle. Once the distortion is calibrated and excluded from the data, the diffraction intensity integration can be simply carried out by summing the recorded diffraction intensity according to the radius using

$$I_n = \frac{1}{N} \sum I[i, j], \tag{2.4.17}$$

where the sum is taken over $R(i, j, i_0, j_0, \Delta R) \in \{n\delta, (n+1)\delta\}$. Here the powder diffraction intensity is integrated in fine discrete steps along the radius of a diffraction pattern (corresponding to increasing scattering angle) with an interval of δ, the summation is done over all diffraction pixels that fall between the radius of $n\delta$ and $(n + 1)\delta$ and N is the number of these pixels.

Filtering the inelastic background is an option for electron microscopes equipped with an electron energy filter. A major contribution to the inelastic background in electron diffraction patterns comes from bulk plasmon excitation (Egerton, 2011). This can be filtered out by dispersing the electrons according to their energies using magnetic or electrostatic fields inside an electron energy filter and using a slit of a few eV in width around the elastic (zero-loss) electron beam. For use with an area electron detector for electron diffraction, the filter must also have a double focusing capability to function as an imaging lens. There are two types of electron imaging energy filters that are currently employed: one is the in-column Ω energy filter and the other is the post-column Gatan imaging filter (GIF). The in-column Ω filter is placed between the transmission electron microscope's intermediate and projector lenses and can be used in combination with IPs, as well as with a CCD or CMOS camera. The GIF is placed after the projector lens and the use of a GIF for electron diffraction typically requires the transmission electron microscope to be switched to a special low-camera-length setting. For electron diffraction, geometric distortions, isochromaticity and the angular acceptance are important characteristics of the imaging filter (Rose & Krahl, 1995). Geometrical distortions arise from the use of non-cylindrical lenses inside the energy filter. The distortion can be caused by optical misalignment, which is an issue with the GIF with its low camera-length setting. The amount of distortion can be measured using a standard calibration sample and corrected using numerical methods. Isochromaticity defines the range of electron energies for each detector position. Ideally, this should be the same across the whole detector area. The angular acceptance defines the maximum range of diffraction angles that can be recorded on the detector without a significant loss of isochromaticity (Rose & Krahl, 1995).

2.4.4. Phase identification and phase analysis

By J. L. Lábár

For known structures, powder diffraction patterns can be used for identification of the crystalline phases and quantification of their volume fraction for samples containing multiple phases. These procedures are usually performed in two steps. First, the candidate phases must be selected to produce a shortlist of the structures that may be present in the sample. Preparation of the shortlist generally relies on *a priori* chemical information [obtained *e.g.* from energy-dispersive X-ray spectroscopy (EDS) or electron energy-loss spectrometry (EELS)] to reduce the number of candidate phases (crystalline structures) that are searched for (Lábár & Adamik, 2001; Lábár, 2006) in a comprehensive database such as the Powder Diffraction File (Faber & Fawcett, 2002). The identification of the crystalline phases in the experimental data is done through pattern fingerprinting. Final confirmation of phase identification is provided by the success of quantitative or semi-quantitative phase analysis, which determines the phase fractions and amount of texture.

In principle, the Le Bail structure-factor extraction (decomposition) method (see Chapter 3.5) could also be used for electron diffraction ring patterns from nanocrystals that are small enough to scatter kinematically or quasi-kinematically (Moeck & Fraundorf, 2007). The main advantage of this approach would be that no assumptions about the structure have to be made. However, none of the methods available for electron diffraction data follow this approach and identification of crystalline phases generally follows a different route [qualitative phase analysis (Lábár & Adamik, 2001) or traditional structural fingerprinting (Moeck & Rouvimov, 2010)].

After a two-dimensional ring pattern is integrated into a one-dimensional intensity distribution, the positions and intensities of peaks are extracted. The positions of the diffraction peaks are used as minimum information for fingerprinting. For successful phase identification the largest *d* values (at the smallest scattering angles) are crucial. Unfortunately, they are not always listed in the X-ray diffraction databases (Moeck & Fraundorf, 2007). Use of diffraction-peak intensities for fingerprinting has limited validity due to the deviation of electron diffraction intensities from the kinematic scattering formalism and the possible presence of texture in the sample. Phase analysis (fingerprinting) is complete when only one (set of) model structure(s) remains (out of several candidates listed in the previous step) on the basis of best fit between the model and the measured diffraction patterns. The addition of features to the Powder Diffraction File to make it more useful for phase identification using electron diffraction data is an active area of development.

Once a structural model is selected, the quantitative fit of diffraction intensities is performed. The quantitative modelling requires knowledge of the atomic positions within the unit cell. Atomic coordinates are not listed in the older PDF-2 database, but are given for many phases in the PDF-4+ database that combines five collections provided by different institutions. There are also open databases, like COD (http://www.crystallography.net/cod/), NIMS_MatNavi (http://crystdb.nims.go.jp/index_en.html) or AMCDS (http://rruff.geo.arizona.edu/AMS/periodictable.php). They also list atomic coordinates and can export structure data as CIF files.

For calculation of the electron structure factors, the electron atomic scattering factors are given in *International Tables for Crystallography*, Vol. C (2004). In the case of kinematical scattering, the intensity is proportional to the square of the electron structure factor F_{hkl}. If necessary, an absorption correction can be performed using the Weickenmeier & Kohl (1991) formalism.

Application of the quasi-kinematic formalism paves the way to giving an estimate of grain size in the beam direction (Lábár *et al.*, 2012). However, there is no straightforward correlation of this value with the actual crystal size or the thickness of the TEM sample. The grain size coming from the quasi-kinematic formula is also different from the size of the coherently scattering domains that could be determined from the broadening of the diffraction peaks (Ungár *et al.*, 2001), which is related to the lateral size of the crystallites (grains, particles) in the TEM sample.

In addition to peak positions and intensities, the peak shape and the background intensity have to be fitted. The pseudo-Voigt peak shape is most frequently used in electron diffraction phase analysis. The background intensity distribution in powder electron diffraction patterns is modelled empirically. The width of the diffraction peaks is an empirical parameter in the present implementation of phase analysis (Lábár, 2009). A Williamson–Hall type analysis of the variation of the experimentally observed peak width with the diffraction vector is also possible for simple profiles with well separated peaks (Gammer *et al.*, 2010); however, so far it has only been done for single-phase diffraction profiles with a known material without an attempt to combine it with phase analysis. Making the peak width dependent on grain size and defect structure (Ungár *et al.*, 2001) would in principle also be possible for phase analysis from powder electron diffraction data, but has not been implemented so far.

Selection of the appropriate structure model is done based on the value of the goodness-of-fit (GOF) criterion. For a one-dimensional electron diffraction profile recorded for *n* pixels, the GOF is given by

$$\mathrm{GOF} = \frac{1}{n-p} \sum_{k=n_0}^{n} \frac{1}{w_k} (I_k^{\mathrm{exp}} - I_k^{\mathrm{calc}})^2, \qquad (2.4.18)$$

where p is the number of parameters used in fitting, w_k is a relative weight of the intensity value at the kth pixel, and I_k^{exp} and I_k^{calc} are the experimentally measured and calculated intensity values for the kth pixel, respectively.

Structure models are described in parametric form (including experimental parameters, peak-shape parameters together with volume fractions of the phases and their fibre-textured components: p parameters altogether) and the p-dimensional parameter space is explored to calculate the GOF. The model with the smallest GOF is accepted. In phase analysis the best match is searched for by using the downhill simplex algorithm (Nelder & Mead, 1965). The semi-global simplex was found to be robust and allowed easy escape from local minima (Zuo & Spence, 1991) when used for fitting CBED patterns.

For polyphasic diffraction profiles, the volume fraction of phases is calculated at the end of the fitting procedure. It is assumed that the net diffraction intensity in each pixel is a linear combination of contributions of the individual phases (random and textured fractions are treated as independent model components). The over-determined set of equations is solved using least-squares minimization. The number of equations is reduced, while keeping the information content of all equations, by forming matrix **A** as

$$a_{i,j} = \sum_k \mathrm{Model}_k(i)\mathrm{Model}_k(j), \qquad (2.4.19)$$

where summation is performed for all pixels k for the model functions of the ith and jth phases, and vector **b** as

$$b_i = \sum_k (\mathrm{Measured}_k - \mathrm{Background}_k)\mathrm{Model}_k(i). \qquad (2.4.20)$$

The coefficients of the linear combination are obtained by solving for vector **x** the matrix equation **Ax** = **b** using matrix inversion.

The coefficients of this linear combination $[x(i)]$ put the intensities of the peaks in phase i on the absolute scale. $I_{\max}(i)$, the intensity calculated on the absolute scale for the strongest (100%) diffraction peak of phase i, gives the intensity diffracted by one unit cell (structure factors are calculated for the atoms of one unit cell). Then $x(i)/I_{\max}(i)$ is the number of unit cells of phase i in the analysed volume. Consequently, the volume extended by phase i in the analysed volume is $V(i)x(i)/I_{\max}(i)$, where $V(i)$ is the volume of the unit cell of phase i. The volume fraction of phase f_i is then given by

$$f_i = \frac{V(i)x(i)}{I_{\max}(i)} \bigg/ \sum_i \frac{V(i)x(i)}{I_{\max}(i)}. \qquad (2.4.21)$$

In addition to volume fractions of phases and their fibre-textured components, the same method can determine the variation (contraction, dilation, distortions) of the unit cell, provided experimental parameters specific to electron diffraction (*e.g.* the camera length and pattern distortion) are properly calibrated. The reliability of the camera-length calibration (systematic error) is usually around 2% (Williams & Carter, 2009); in the best cases accuracy of better than 0.3% has been reported (Lábár *et al.*, 2012). Consequently, only large variations in the lattice parameter can be determined reliably from powder electron diffraction data and the typical accuracy of powder X-ray diffraction cannot be attained.

There are two main advantages of phase analysis from powders by electron diffraction compared with X-ray diffraction. First, much smaller volumes can be studied. Diffraction information can be collected from thin layers of a few tens of nanometres thickness, enabling precise identification of the inspected volume. If needed, different lateral sections from different depths of a bulk sample can be studied by TEM, thus providing three-dimensional information about the sample. In a non-homogeneous sample, electron diffraction data can be collected from different areas, allowing detection of different phases or texture components at a spatial resolution and sensitivity superior to X-ray diffraction methods (Lábár *et al.*, 2012).

The accuracy of the phase-content identification in a mixture for the major components is around 10–15% (Lábár *et al.*, 2012). The detection limit depends on the scattering power of the component. A weakly scattering phase of Cr in a strongly scattering matrix of Ag could only be detected at the content of 2%, while the presence of 5% Ag in a relatively weakly scattering Ni matrix allowed full quantification of the two phases (Lábár *et al.*, 2012). Thus, generally 5% (by volume) is accepted as the detection limit for powder electron diffraction experiments.

2.4.5. Texture analysis

By J. L. Lábár

The orientation distribution in a polycrystalline (nanocrystalline) TEM sample (used for powder electron diffraction) can either be random or a large fraction of grains can favour a special direction, *i.e.* the sample is textured. The texture can originate from the non-spherical shape of the particles (as in sedimentation geology or drop-drying of a suspension of nanoparticles on a TEM grid) or from energetic and/or kinetic conditions during nucleation and growth of grains in the formation of polycrystalline thin films on a substrate or, alternatively, the texture can be a result of mechanical deformation (as in drawing wires or rolling sheets of metals). Although the distribution of the preferred orientations can be very different, a few general types are frequently observed.

In the simplest case only one preferred-orientation vector characterizes the sample and the orientations of the grains are distributed arbitrarily around that direction. This situation is called *fibre texture* (single-axis texture). The most typical representatives of this texture class are sedimentation platy particles on a flat surface where the preferred-orientation vector is normal to the flat face of the particles, or a drawn metal wire where the preferred-orientation vector is directed along the wire axis. Another texture type frequently observed in the sedimentation of rod-shaped particles is described by the preferred-orientation vector being confined within a plane, but being arbitrarily oriented within this plane. Rolling of metal sheets results in other, more complex, but well characterized texture types: 'copper-type', 'brass-type' and 'S-type' (Mecking, 1985).

There are different ways to handle texture with electron diffraction. One approach is to collect the orientation information from individual nanograins in an automated area scan and reconstruct pole figures and inverse pole figures on a medium-sized population of grains (Rauch *et al.*, 2008). In principle, this is a single-crystal method analysing the information from an assembly of crystals. The Russian crystallography group developed the theory of arcs in oblique texture and used such textured patterns in structure analysis (Vainshtein, 1964; Vainshtein & Zvyagin, 1992). The *TexPat* software (Oleynikov & Hovmoller, 2004) was designed and effectively applied to determining unit-cell parameters and refining structure from oblique textured electron diffraction patterns. Tang *et al.* (1996) developed a method to determine the axis of texture and distribution of directions around that axis. The March–Dollase model (Dollase, 1986) for the description of pole densities was adapted for electron diffraction and used for the simulation of ring patterns (Li, 2010); however, no attempt was made to determine the phase fractions or textured fractions automatically.

A simplified automatic treatment of texture was implemented in the *ProcessDiffraction* software (Lábár, 2008, 2009). Partial texture is approximated by a linear combination of an ideally sharp fibre texture and a random distribution of components. Both the textured and the random components are treated as separately determined volume fractions during quantitative phase analysis (see Section 2.4.4). The advantage of the method is that the determination of the textured fraction is combined with simultaneous handling of a quasi-kinematic scattering by the Blackman approximation, and these two effects, which both modify the relative intensities, are treated simultaneously on a unified platform.

The application of the most general method for determining texture from powder electron diffraction patterns is restricted to the thinnest samples where kinematic scattering holds (Gemmi, Voltolini *et al.*, 2011). The method consists of recording a set of powder electron diffraction patterns at defined tilt steps of the two-axis goniometer, covering a considerable part of the solid-angle range usually used for recording pole figures. Azimuthal sections are integrated separately in 10° steps. The resulting large three-dimensional data set is fed into a variant of the Rietveld method called *MAUD* (Lutterotti *et al.*, 1997), which has built-in scattering factors for electrons. The orientation density function (ODF) is determined from the measured data by discretization of the orientation space. For texture fitting the *EWIMV* algorithm is used (Lutterotti *et al.*, 2004), which can be applied with irregular pole figure coverage and includes smoothing methods based on a concept of the tube projection. Pole figures from the smoothed

ODF were obtained for both sediment aggregates and evaporated thin films (Gemmi, Voltolini *et al.*, 2011).

2.4.6. Rietveld refinement with electron diffraction data

By T. E. Gorelik and U. Kolb

The Rietveld refinement method was initially developed for neutron diffraction data (Rietveld, 1967, 1969). It has now become a standard technique which is extensively used with neutron, laboratory X-ray and synchrotron diffraction data. A detailed description of the method can be found in Chapter 4.7.

Compared with the popularity of Rietveld refinement in X-ray and neutron powder diffraction, its application to powder electron diffraction data is very limited. So far, Rietveld refinement with electron diffraction data has only been done for nanocrystalline Al, α-MnS (Gemmi, Fischer *et al.*, 2011), hydroxyapatite (Song *et al.*, 2012), intermetallic AuFe (Luo *et al.*, 2011), TiO_2 (Weirich *et al.*, 2000; Tonejc *et al.*, 2002; Djerdj & Tonejc, 2005, 2006) and $MnFe_2O_4$ (Kim *et al.*, 2009). An example of a fit with powder electron diffraction data obtained by Rietveld refinement for hydroxyapatite is shown in Fig. 2.4.7.

Two major factors limit the application of Rietveld refinement to electron powder diffraction. First, electron powder diffraction data are collected from a sample volume far smaller than that used in an X-ray experiment. Therefore, the average statistics are poor compared with those of X-ray data. Nevertheless, electron powder diffraction data from a small sample area or thin films can give specific information which is difficult to obtain using other methods. Second, the presence of dynamical effects in the electron diffraction data hinders quantitative assessment of reflection intensities. Dynamical effects are strongest in zone-axis electron diffraction geometry, when many beams belonging to the same systematic rows are excited simultaneously. In powder electron diffraction crystals are randomly oriented towards the electron beam, thus making the fraction of zonal patterns low, thereby reducing the dynamical scattering in the data (see Section 2.4.2 for a more detailed discussion).

Within the limit of kinematical diffraction, the principle of Rietveld refinement is the same for electrons and X-rays, except the electron atomic scattering factors are different. The refinement procedure can thus be performed using existing programs if it is possible to input the scattering factors for electrons. Most of the reported Rietveld refinements on electron powder diffraction data have been performed using *FullProf* (Rodríguez-Carvajal, 1993); a refinement in *MAUD* (Lutterotti *et al.*, 1999) has also been reported (Gemmi, Voltolini *et al.*, 2011).

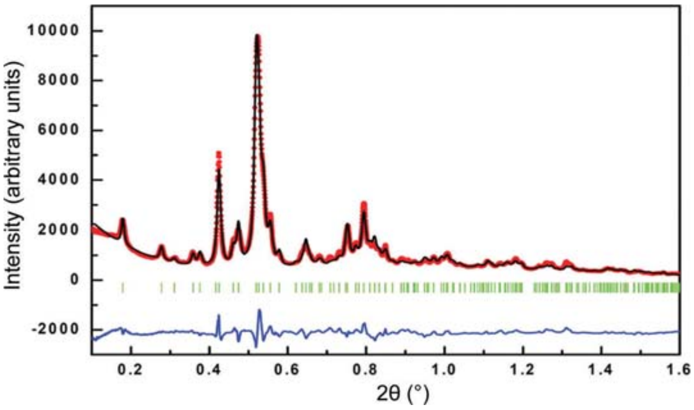

Figure 2.4.7
Rietveld analysis result with powder electron diffraction data of hydroxyapatite. Reproduced from Song *et al.* (2012) with permission from Oxford University Press.

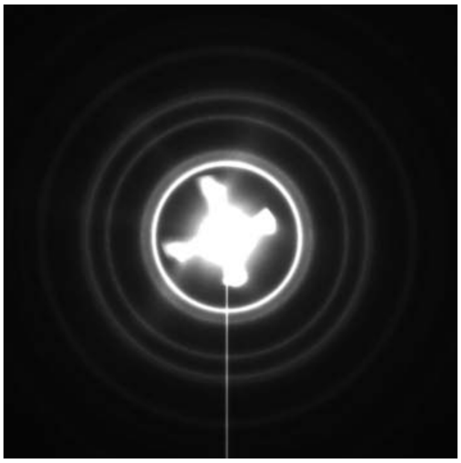

Figure 2.4.8
Powder electron diffraction pattern of nanocrystalline gold demonstrating non-symmetrical background features.

Electron powder diffraction patterns are recorded on an area detector. For a Rietveld refinement the two-dimensional diffraction patterns have to be integrated into one-dimensional profiles. The zero shift is treated as for the X-ray data integrated from a two-dimensional position-sensitive detector. Details about electron diffraction data processing and calibration are given in Section 2.4.3.4.

The background in electron powder patterns is a complex combination of inelastic scattering, scattering from the supporting film (when it is present) and other factors. For the Rietveld refinement procedure the background of a one-dimensional integrated profile is fitted by a polynomial function. If a supporting thin amorphous carbon film is used, the background can include broad rings, which after the one-dimensional integration can produce pronounced broad peaks. These peaks are difficult to subtract using a model based on a polynomial function; therefore, these intensities may hamper the powder diffraction profile matching (Kim *et al.*, 2009). In some cases, the background can even include radially non-symmetric features originating from the shape of the tip within the electron source (see Fig. 2.4.8); it can have blooming due to oversaturated CCD pixels, or streak shadows due to the fast transmission electron microscope beam-shutter movement. In these cases, a diffraction pattern from the adjacent 'empty' area of the sample can be acquired and subtracted from the diffraction pattern of the material prior to the integration into one dimension. This procedure allows elimination of some of the artifacts discussed above, which otherwise after the one-dimensional integration may be falsely interpreted as diffraction peaks, and are generally more difficult to fit.

Unit-cell parameters are mostly subject to the error due to the accuracy of the electron diffraction camera-length calibration. Although examples have been published showing 0.3% accuracy of the camera-length calibration, in most cases accuracy of about 2% can be achieved (Williams & Carter, 2009). The effective camera length depends on many instrumental parameters such as the convergence of the electron beam, the diffraction lens focus, the mechanical position of the sample within the objective lens, or the hysteresis of the electromagnetic lenses. Thus, while the ratio of the lattice parameters within one aligned diffraction pattern can be very precise, the absolute values might not be.

Atomic displacement parameters can be refined from electron powder diffraction data; however, the interpretation of the results can be manifold. For nanocrystalline materials, which have a relatively high surface-to-volume ratio, the surface effect can be enhanced compared with that of the bulk. Thus, the average atomic displacement factors can increase because of the high fraction of near-surface relaxed atoms. Consequently, the isotropic displacement parameter B resulting from the Rietveld refinement can be relatively high. Local heating (Reimer, 1984) during the electron illumination may also contribute to higher average displacement parameters. Finally, if the electron beam exceeds a material-dependent threshold acceleration voltage, it can cause knock-on damage (Williams & Carter, 2009) in both organic and inorganic materials. This is a dynamical process which can cause both material loss and rearrangement of atoms. The presence of defects resulting from the rearrangement of atoms may lead to an increase in the average displacement factors. Nevertheless, the refinement using polycrystalline anatase data showed the expected displacement parameters of 1.4 (1) Å^2 for Ti and 1.9 (2) Å^2 for oxygen (Weirich *et al.*, 2000). Of all the parameters used during Rietveld refinement, the displacement parameters and atomic coordinates are probably the most sensitive to a possible dynamical-scattering contribution in the data. It is noticeable that after the refinement of the anatase structure the atomic coordinates converged to reasonable positions: $[0, \frac{1}{4}, 0.1656\,(5)]$ for oxygen (Weirich *et al.*, 2000) compared with the previous range obtained in neutron diffraction studies of $[0, \frac{1}{4}, 0.16686\,(5)]$ (Burdett *et al.*, 1987) to $[0, \frac{1}{4}, 0.20806\,(5)]$ (Howard *et al.*, 1991).

The relative ratio of two components in a mixture can be determined using the Hill–Howard approach (Hill & Howard, 1987): the relative weight of a phase in a mixture of phases is proportional to the scaling factor of the phase given by the Rietveld refinement combined with the mass and the volume of the unit cell of the component. The relative content of a mixture of anatase and brookite was successfully determined from electron powder diffraction data (Djerdj & Tonejc, 2005, 2006).

For the modelling of the Bragg reflection shape the Pearson VII function can be used (Weirich *et al.*, 2000; Kim *et al.*, 2009), although recently the more popular pseudo-Voigt peak shape function has been used (Tonejc *et al.*, 2002; Djerdj & Tonejc, 2005, 2006) and provides a satisfactory fit between the experimental and calculated data.

The average crystalline domain size can be determined using line-broadening analysis. The measured intensity profile is a convolution of the physical line profile given by the sample with the instrumental profile broadening. When expressed in terms of the scattering angle θ, the width of the electron diffraction peaks is much smaller than that for X-rays. On the other hand, electrons generally have a smaller coherence length than X-rays. As a result, for the same material, the effective peak width for electron diffraction is larger than that for powder X-ray data (Song *et al.*, 2012). Because of this, it is sometimes difficult to separate the domain size and the instrumental contributions to the peak broadening. Therefore, the average domain size obtained after the refinement procedure should be cross-checked with the domain size determined from TEM images obtained, for instance, using the dark-field technique (Williams & Carter, 2009).

In electron diffraction various instrumental parameters can affect the peak width. The energy spread of the electrons causes additional broadening of diffracted spots. This effect can be partially reduced by energy filtering of the diffraction patterns (Kim *et al.*, 2009; Egerton, 2011). Finally, the electron diffraction camera length must be large enough that the detector broadening is much smaller than the peak width, as demonstrated in Fig. 2.4.9: large values of the camera length (‘zoomed in’ diffraction patterns) result in thinner, better separated peaks.

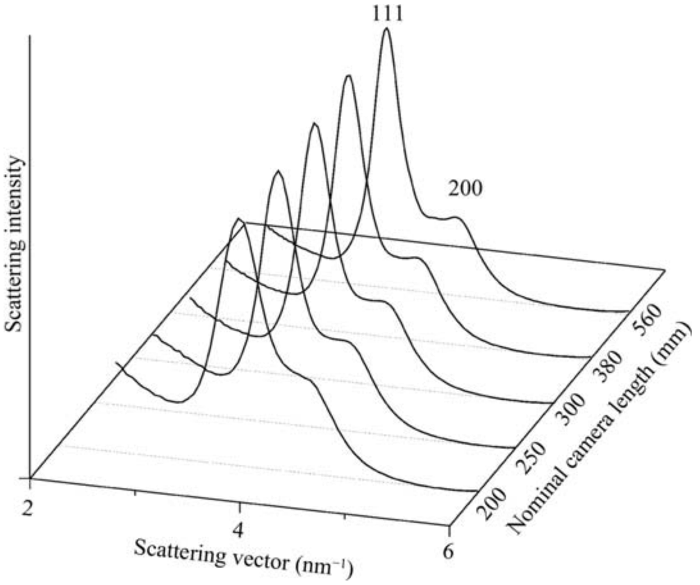

Figure 2.4.9
Electron powder diffraction profiles of gold nanoparticles (range 2–6 nm^{-1}) recorded at different electron diffraction camera lengths.

Preferred orientation can be an issue for electron powder diffraction: when the powder material is supported on a thin film, the crystals tend to orient themselves with their most developed facet facing the support. As a result, the relative intensities of the diffracted peaks are modified (Kim *et al.*, 2009). Texture within nanocrystalline powders introduced by the sample preparation on a support for TEM can be analysed using electron powder diffraction patterns recorded at different tilt positions of the sample. Refinement of the preferred orientation of two different materials – nanocrystalline aluminium and α-MnS powders – showed that the aluminium particles tend to have strong preferred orientation due to their facet morphology, while α-MnS particles are randomly oriented (Gemmi, Fischer *et al.*, 2011).

Although dynamical effects are believed to be reduced for nanocrystalline materials and additionally reduced by data collection from non-oriented crystals, the dynamical component of the scattering cannot be neglected. For the dynamical correction using the two-beam approximation formalism of equation (2.4.12), the reader is referred to Section 2.4.2. For a range of electron-beam energies from 20 to 50 kV it has been shown that polycrystalline electron diffraction patterns of aluminium crystals smaller than 9 nm have a dynamical scattering component below 10% (Horstmann & Meyer, 1962). For polycrystalline $MnFe_2O_4$ with an average crystal size of 11 nm measured using a 120 kV electron beam, the ratio of the kinematical to dynamical contributions in the structure factor was about 1:1.5 (Kim *et al.*, 2009). The application of the small (less than 3%) correction for the dynamical component during Rietveld refinement of nanocrystalline intermetallic Au_3Fe_{1-x} improved the refined long-range order parameter of the alloy (Luo *et al.*, 2011).

In summary, the Rietveld refinement technique applied to electron powder diffraction data is a new area of research. It can be successfully carried out for small volumes of nanocrystalline materials, for which the small electron beam is an advantage. Results obtained from Rietveld analysis of electron powder diffraction data of nanocrystalline materials are encouraging. The refinement for powders containing large crystal grains is problematic because of dynamical scattering present in the data. There are also uncertainties caused by instrumental effects. The dynamical effects can be accounted for using the Blackman formalism, while the influence of diverse instrumental parameters needs further systematic study.

2.4.7. The pair distribution function from electron diffraction data

By T. E. Gorelik and U. Kolb

An extensive description of pair distribution function (PDF) analysis covering data acquisition, reduction and interpretation can be found in Chapter 5.7. Here, only a short outline is presented, concentrating on aspects that are specific to PDFs obtained by electron diffraction.

Poorly crystalline and amorphous materials exhibit no long-range order and therefore show no pronounced Bragg peaks in diffraction patterns. Nevertheless, owing to defined bonding geometry, these materials do have a specific local arrangement of atoms, denoted as short-range order. The short-range order can be analysed using the PDF obtained from the total scattering profile. The PDF can provide general information about the degree of order, the character of local atomic packing and the size of the correlation domains. The total scattering function is collected over a wide range of reciprocal space and includes not only the Bragg reflections (if present), but also the diffuse scattering information between them (Egami & Billinge, 2003).

The PDF $G(r)$ represents the probability of finding a pair of atoms with an interatomic distance r, weighted by the scattering power of the individual atoms. After normalization and suitable corrections, the reduced scattering function $F(Q)$ is derived. [In the PDF analysis, the scattering vector Q, which is related to the scattering angle θ as $Q = (4\pi \sin\theta)/\lambda$ is used, instead of $S = \sin\theta/\lambda$.] The PDF can be calculated by the Fourier transformation of $F(Q)$ into direct space (Warren, 1990; Egami & Billinge, 2003; Farrow & Billinge, 2009).

Powder diffraction data for PDF analysis should be measured over a sufficiently large range of the scattering angle θ; therefore, neutron or synchrotron sources or laboratory X-ray data with a short-wavelength source (Mo or Ag anode) are used. Powder electron diffraction data, with their flexibility in electron diffraction camera length, short wavelength and nuclear scattering at large scattering angles, can also cover the desired large range of scattering angles and are therefore highly suitable for PDF analysis. In addition, atoms have a much larger scattering cross section for electrons than for X-rays or neutrons, allowing sufficient signal collection from very small volumes. Finally, electrons can be focused with lenses down to a few nanometres. All these reasons make electron diffraction analysis attractive for the study of the structure of nanovolumes. The electron PDF is therefore a powerful tool for the investigation of the structures of amorphous or poorly crystalline thin films, or for small sample volumes of inhomogeneous samples.

There are several practical issues to consider when collecting electron diffraction data for PDF analysis:

Energy filtering. Traditionally, electron diffraction data for PDF analysis are collected using energy filtering in order to exclude the inelastic scattering contribution. However, quantitative or semi-quantitative electron PDFs can be obtained without filtering (Abeykoon *et al.*, 2012).

Multiple scattering/dynamical effects. In order to keep the contribution of non-kinematic scattering low, the sample thickness and the nanoparticle size should be as small as possible. Generally, particles 10 nm and smaller should scatter kinematically, and this is the size range that benefits most from PDF analysis (Abeykoon *et al.*, 2012).

Powder average. Proper statistics are important for PDF analysis. In order to decrease measurement errors one can increase the illumination area on the sample (or the selected-area aperture in the case of SAED), collect several diffraction patterns from different areas and average them.

Scattering angle range. A large θ range is essential for PDF analysis. An electron diffraction experiment offers significant flexibility in selecting the scattering range through the adjustment of the electron diffraction camera length and illumination wavelengths. Additionally, in order to enhance the data quality, merging of different scattering ranges recorded in a set of diffraction patterns is possible (Petersen *et al.*, 2005).

An electron diffraction pattern is a combination of signals produced by *elastically* and *inelastically* scattered electrons. The inelastic component is a result of electron energy loss due to plasmon or inner-shell excitation, electron Compton or thermal diffuse scattering (Egerton, 2011). For crystalline materials with distinct Bragg peaks the inelastic scattering is not particularly critical, as it mainly contributes to the background in diffraction patterns and can be neglected when only the intensities of the Bragg peaks are analysed. For PDF analysis the total scattering profile is used; thus, the inelastic scattering, which can significantly modify the scattering profile, needs to be considered (Ishimaru, 2006). Two strategies are followed in this respect: (i) energy filtering of diffraction patterns, which is the more accurate approach but demands specific instrumentation, and (ii) subtraction of the background scattering taken from an area adjacent to the sample (*i.e.* from the supporting film), which assumes that the main inelastic scattering component originates from the support, and the contribution from the sample can be neglected (Cockayne, 2007). The validity of this approximation depends on the level of quantification intended in the particular study.

The PDF formalism presented above is based on the single-scattering approximation. Multiple scattering, which is much stronger in electron diffraction than for X-rays and neutrons, significantly affects the total scattering profile and therefore the PDF. The multiple-scattering effects can modify the peak positions in the PDF as well as the relative intensities of the peaks, the latter being more sensitive to multiple scattering (Anstis *et al.*, 1988). It has been shown that for amorphous materials, owing to the contribution of the multiple scattering, the total scattering profile depends on the thickness of the foil (Childs & Misell, 1972; Rez, 1983). Knowledge of the film thickness allows extraction of the single-scattering distribution. An improved agreement with the expected PDF was shown for hydrogenated amorphous silicon (Anstis *et al.*, 1988) and amorphous germanium (Ankele *et al.*, 2005) using the single-scattering profile.

Experimentally, it is difficult to determine the sample thickness along the incident-electron-beam direction. In this case, the thickness parameter employed in calculations can be varied, adjusting the amplitudes of the PDF. An estimate for the sample thickness is found when the optimal fit is obtained. Different input values of the thickness result in different principal gradients of the oscillations. Once a reasonable fit is found, the correct thickness is determined and the contribution of multiple scattering can be eliminated (Ankele *et al.*, 2005). This method was applied to amorphous NiNb alloy, allowing an estimate of the foil thickness, and thereafter improved the fit to the PDF obtained from Ag-anode X-ray scattering experiments (Ankele *et al.*, 2005).

Alternatively, the wavelength dependence of the multiple-scattering term can be used. A set of diffraction patterns of a glassy carbon film was collected from the same sample (apparently having the same thickness) using different wavelengths (Petersen *et al.*, 2005). These patterns were then processed in order to retrieve the single-scattering profile of tetrahedral amorphous carbon, which showed an improved fit to the reduced scattering function obtained with neutrons (Petersen *et al.*, 2005). This method can be applied to materials for which significant multiple scattering is expected and the thickness of the foil cannot be determined *a priori*. For very thin films the contribution of the multiple scattering is very low and, therefore, often neglected.

The PDF of elemental materials arising from only one contributing atomic scattering function can be directly interpreted in terms of coordination numbers and allows conclusions to be drawn about the local structure. PDF analysis of amorphous silicon prepared by deposition showed the existence of voids in the structure (Moss & Graczyk, 1969) which anneal on progressive heating. PDF investigation of amorphous carbon films prepared by arc plasma deposition showed that the material mainly consists of tetrahedrally coordinated carbon rather than having a graphitic structure (McKenzie *et al.*, 1991).

For ZrNi and ZrCu metallic glasses, partial PDFs were obtained by reverse Monte Carlo simulation (McGreevy & Pusztai, 1988) and fitted to the experimentally obtained electron scattering data. The analysis of the polyhedral statistics showed that the average coordination number of Cu was 11, while for Ni it was less than 10 (Hirata *et al.*, 2007). Study of amorphous FeB alloys (Hirata *et al.*, 2006) and $Fe_{90}Zr_7B_3$ (Hirotsu *et al.*, 2003) by PDF analysis allowed detection of nanoscale phase separation resulting in the formation of a mixture of different clusters.

Nanocrystals can be efficiently analysed by electron PDF analysis, giving information complementary to TEM imaging. The electron PDF of detonation nanodiamonds (DND) was used to estimate the average domain size (Zhang, 2011). Studies of phase separation in AgCu alloys showed the complex behaviour of the material with variation of temperature (Chen & Zuo, 2007). In the first stage, the nanodomains of the two terminal phases (Ag- and Cu-rich) are built; in the second stage, dewetting of the thin film and formation of large Ag and Cu grains occur. A comparison of electron PDFs from nanocrystalline, partially ordered and amorphous parts of silica glasses (Kovács Kis *et al.*, 2006) allowed the estimation of the degree of order developed by changing the connectivity and orientation of the undistorted SiO_4 tetrahedra. Indirect detection of hydrogen atoms was performed from a modified distribution of atomic distances in soot samples using electron PDF analysis (Kis *et al.*, 2006).

With an increase in the particle size the deviations from the kinematical scattering become severe. Nevertheless, the electron PDF calculated for 100 nm Au crystals reproduced the simulated data quite well: the peak positions and relative amplitudes were not significantly modified (Abeykoon *et al.*, 2012).

2.4.8. Summary

Powder electron diffraction can be used for materials structural characterization, just as is routinely done using X-rays and neutrons. The specific characteristics of electron scattering result in both benefits and drawbacks to using electron diffraction data. Strong scattering of electrons allows collection of a sufficient signal from nanovolumes of material, thus offering the possibility of studying small amounts of material and thin films. The opportunity to couple the diffraction information with imaging gives the unique possibility of performing a structural study on the nanoscale in a controlled way. The strong interaction of electrons with matter leads to dynamical-scattering effects that result in deviation of the electron diffraction intensities from the kinematical model. Since the amount of the dynamical-scattering component in a powder sample is difficult to quantify, the quantitative use of electron diffraction intensity data is limited. For large crystals, the dynamical treatment of electron diffraction data is efficiently done in CBED analysis, providing exclusive information about the structure. For nanocrystalline or amorphous materials, an increasing number of sets of experimental data show that quantitative structure information can be obtained using electron powder diffraction. This encourages further applications of different kinds of electron diffraction data, giving new perspectives for the quantitative use of electron diffraction in general.

APPENDIX A2.4.1

Computer programs for electron powder diffraction

CHECKCELL is a graphical powder-pattern indexing helper and space-group-assignment program that links into the *CRYSFIRE* powder indexing suite. More information and the program are available at http://www.ccp14.ac.uk/tutorial/lmgp/achekcelld.htm.

CRYSFIRE is a powder-pattern indexing system for DOS/Windows for unit-cell parameter determination from powder data (free for academic use). More information and the program are available at http://www.ccp14.ac.uk/tutorial/crys/.

ELD is a commercial program for calibrating and integrating two-dimensional electron diffraction patterns. The program is commercially available from Calidris, Sweden. More information is available from http://www.calidris-em.com/eld.php.

Electron diffraction pattern atlas. The website of Professor Jean-Paul Morniroli (http://electron-diffraction.fr/) provides an atlas of electron diffraction patterns that can be used to identify the space group of a crystal from observation of a few typical PED and CBED zone-axis patterns.

FIT2D is a general-purpose image and diffraction processing program, designed for use with synchrotron data, that integrates pre-selected sections of either one-dimensional or two-dimensional data. Corrections for geometrical distortion and for nonlinearity of intensity are included. It is available both for the Windows operating system (and DOS window) and for Macintosh OSX. The program is freely available for academic users. More information and the program are available at http://www.esrf.eu/computing/scientific/FIT2D/.

JEMS is a popular suite of simulation routines for a variety of platforms, mainly used for simulating high-resolution TEM (HRTEM), CBED, PED and SAED patterns. Simulation of powder diffraction rings is also included. The student version is free of charge. A licence is available from the author: http://www.jems-saas.ch/.

PCED is a program for the simulation of polycrystalline electron diffraction patterns (Li, 2010). A licence file is needed to unlock the program for loading input data files. More information is available at http://www.unl.edu/ncmn-cfem/xzli/.

PDFgui and *PDFfit2* are programs for full-profile fitting of the atomic PDF derived from X-ray or neutron diffraction data. *PDFgui* is a graphical front end for the *PDFfit2* refinement program, with built-in graphical and structure-visualization capabilities. *PDFgui* is currently in beta release and it is distributed as part of the DiffPy library. More information and the program are available at http://www.diffpy.org.

Process Diffraction is designed for processing of SAED and NAED patterns. It includes quantitative determination of phase fractions and texture from ring patterns recorded from nanocrystalline thin films in TEM. More information and the program are available at http://www.energia.mta.hu/~labar/ProcDif.htm.

QPCED and *PCED* are Java-based software for digitization, processing, quantification and simulation of powder electron diffraction patterns. For information contact Dr X. Z. Li (xzli@unl.edu) or visit http://www.unl.edu/ncmn-cfem/xzli.

TexPat is a program for quantification of texture (preferred orientation) from a tilt series of ring patterns recorded from nanocrystalline thin films in TEM (Oleynikov & Hovmoller, 2004).

WebEMAPS is a suite of computer programs that can be obtained at http://cbed.matse.illinois.edu/software_emaps.html. The programs include functions for visualization of crystal structures, simulation of single-crystal diffraction patterns, dynamic electron diffraction simulation, and calculations of electron structure factors and lattice *d*-spacings.

WinPLOTR is a peak-search program for plotting powder diffraction patterns and can be used as a graphical user interface for several programs used frequently in powder diffraction data analysis (*e.g. FullProf*, *DicVOL*, *SuperCELL*). *WinPLOTR* has been developed to run on PCs with a 32-bit Microsoft Windows operating system. More information and the program are available at http://www.cdifx.univ-rennes1.fr/winplotr/readme.htm.

References

Abeykoon, M. C. D., Malliakas, C. D., Juhás, P., Bozin, E. S., Kanatzidis, M. G. & Billinge, S. J. L. (2012). *Quantitative nanostructure characterization using atomic pair distribution functions obtained from laboratory electron microscopes. Z. Kristallogr.* **227**, 248–256.

Ankele, J., Mayer, J., Lamparter, P. & Steeb, S. (2005). *Quantitative electron diffraction data of amorphous materials. Z. Naturforsch. A*, **60**, 459–468.

Anstis, G. R. Z., Liu, Z. & Lake, M. (1988). *Investigation of amorphous materials by electron diffraction – the effects of multiple scattering. Ultramicroscopy*, **26**, 65–69.

Baerlocher, C., Gramm, F., Massüger, L., McCusker, L. B., He, Z., Hovmöller, S. & Zou, X. (2007). *Structure of the polycrystalline zeolite catalyst IM-5 solved by enhanced charge flipping. Science*, **315**, 1113–1116.

Barna, Á. & Pécz, B. (1997). *Preparation techniques for transmission electron microscopy.* In *Handbook of Microscopy*, edited by S. Amelinckx, D. van Dyck, J. van Landuyt & G. van Tendeloo, Vol. 3, pp. 751–801. Weinheim: Wiley-VCH Verlag GmbH.

Blackman, M. (1939). *On the intensities of electron diffraction rings. Proc. R. Soc. London Ser. A*, **173**, 68–82.

Botton, G. (2007). *Analytical electron microscopy*. In *Science of Microscopy*, edited by P. Hawkes & J. C. H. Spence, pp. 273–405. New York: Springer.

Burdett, J. K. T., Hughbanks, T., Miller, G. J., Richardson, J. W. & Smith, J. V. (1987). *Structural–electronic relationships in inorganic solids: powder neutron diffraction studies of the rutile and anatase polymorphs of titanium dioxide at 15 and 295 K. J. Am. Chem. Soc.* **109**, 3639–3646.

Chen, H. & Zuo, J. M. (2007). *Structure and phase separation of Ag–Cu alloy thin films. Acta Mater.* **55**, 1617–1628.

Childs, P. A. & Misell, D. L. (1972). *Some aspects of elastic plural scattering of electrons by atoms. J. Phys. D Appl. Phys.* **5**, 2095.

Cockayne, D. J. H. (2007). *The study of nanovolumes of amorphous materials using electron scattering. Annu. Rev. Mater. Res.* **37**, 159–187.

Cockayne, D. J. H. & McKenzie, D. R. (1988). *Electron diffraction analysis of polycrystalline and amorphous thin films. Acta Cryst.* A**44**, 870–878.

Cowley, J. M. (1992). *Electron Diffraction Techniques*. International Union of Crystallography Monographs on Crystallography. Oxford: IUCr/Oxford University Press.

Cowley, J. M. (1995). *Diffraction Physics*. Amsterdam: Elsevier Science BV.

Cowley, J. M. (1999). *Electron nanodiffraction. Microsc. Res. Tech.* **46**, 75–97.

Cowley, J. M. & Hewat, A. W. (2004). *Powder and related techniques: electron and neutron techniques*. *International Tables for Crystallography* Vol. C, pp. 80–83. Dordrecht: Kluwer Academic Publishers.

Djerdj, I. & Tonejc, A. M. (2005). *Transmission electron microscopy studies of nanostructured TiO_2 films on various substrates. Vacuum*, **80**, 371–378.

Djerdj, I. & Tonejc, A. M. (2006). *Structural investigations of nanocrystalline TiO_2 samples. J. Alloys Compd.* **413**, 159–174.

Dollase, W. A. (1986). *Correction of intensities for preferred orientation in powder diffractometry: application of the March model. J. Appl. Cryst.* **19**, 267–272.

Egami, T. & Billinge, S. J. L. (2003). *Underneath the Bragg Peaks: Structural Analysis of Complex Materials*. Oxford: Pergamon.

Egerton, R. F. (2011). *Electron Energy-Loss Spectroscopy in the Electron Microscope*. New York: Plenum Press.

Elsayedali, H. E. & Herman, J. W. (1990). *Ultrahigh vacuum picosecond laser-driven electron diffraction system. Rev. Sci. Instrum.* **61**, 1636–1647.

Faber, J. & Fawcett, T. (2002). *The Powder Diffraction File: present and future. Acta Cryst.* B**58**, 325–332.

Farrow, C. L. & Billinge, S. J. L. (2009). *Relationship between the atomic pair distribution function and small-angle scattering: implications for modeling of nanoparticles. Acta Cryst.* A**65**, 232–239.

Gammer, C. C., Mangler, C., Rentenberger, C. & Karnthaler, H. P. (2010). *Quantitative local profile analysis of nanomaterials by electron diffraction. Scr. Mater.* **63**, 312–315.

Gemmi, M. J., Fischer, J., Merlini, M., Poli, S., Fumagalli, P., Mugnaioli, E. & Kolb, U. (2011). *A new hydrous Al-bearing pyroxene as a water carrier in subduction zones. Earth Planet. Sci. Lett.* **310**, 422–428.

Gemmi, M., Voltolini, M., Ferretti, A. M. & Ponti, A. (2011). *Quantitative texture analysis from powder-like electron diffraction data. J. Appl. Cryst.* **44**, 454–461.

Gemmi, M., Zou, X. D., Hovmöller, S., Migliori, A., Vennström, M. & Andersson, Y. (2003). *Structure of Ti_2P solved by three-dimensional electron diffraction data collected with the precession technique and high-resolution electron microscopy. Acta Cryst.* A**59**, 117–126.

Gjonnes, K., Cheng, Y., Berg, B. S. & Hansen, V. (1998). *Corrections for multiple scattering in integrated electron diffraction intensities. Application to determination of structure factors in the [001] projection of Al_mFe. Acta Cryst.* A**54**, 102–119.

Gorelik, T., Matveeva, G., Kolb, U., Schleuss, T., Kilbinger, A. F. M., van de Streek, J., Bohled, A. & Brunklaus, G. (2010). *H-bonding schemes of di- and tri-p-benzamides assessed by a combination of electron diffraction, X-ray powder diffraction and solid-state NMR. CrystEngComm*, **12**, 1824–1832.

Gramm, F. C., Baerlocher, C., McCusker, L. B., Warrender, S. J., Wright, P. A., Han, B., Hong, S. B., Liu, Z., Ohsuna, T. & Terasaki, O. (2006). *Complex zeolite structure solved by combining powder diffraction and electron microscopy. Nature*, **444**, 79–81.

Haider, M. H., Rose, H., Uhlemann, S., Schwan, E., Kabius, B. & Urban, K. (1998). *A spherical-aberration-corrected 200 kV transmission electron microscope. Ultramicroscopy*, **75**, 53–60.

Henderson, R. (1995). *The potential and limitations of neutrons, electrons and X-rays for atomic resolution microscopy of unstained biological molecules. Q. Rev. Biophys.* **28**, 171–193.

Hill, R. J. & Howard, C. J. (1987). *Quantitative phase analysis from neutron powder diffraction data using the Rietveld method. J. Appl. Cryst.* **20**, 467–474.

Hirata, A., Hirotsu, Y., Ohkubo, T., Hanada, T. & Bengus, V. Z. (2006). *Compositional dependence of local atomic structures in amorphous $Fe_{100-x}B_x$ (x = 14, 17, 20) alloys studied by electron diffraction and high-resolution electron microscopy. Phys. Rev. B*, **74**, 214206.

Hirata, A. T., Morino, T., Hirotsu, Y., Itoh, K. & Fukunaga, T. (2007). *Local atomic structure analysis of Zr-Ni and Zr-Cu metallic glasses using electron diffraction. Mater. Trans.* **48**, 1299–1303.

Hirotsu, Y. T., Ohkubo, T., Bae, I.-T. & Ishimaru, M. (2003). *Electron diffraction structure analysis for amorphous materials. Mater. Chem. Phys.* **81**, 360–363.

Horstmann, M. & Meyer, G. (1962). *Messung der elastischen Elektronenbeugungsintensitäten polykristalliner Aluminium-Schichten. Acta Cryst.* **15**, 271–281.

Hovmoller, S., Zou, X. & Weirich, T. E. (2002). *Crystal structure determination from EM images and electron diffraction patterns. Adv. Imaging Electron Phys.* **123**, 257–289.

Howard, C. J., Sabine, T. M. & Dickson, F. (1991). *Structural and thermal parameters for rutile and anatase. Acta Cryst.* B**47**, 462–468.

Ichimiya, A. & Cohen, P. I. (2004). *Reflection High-Energy Electron Diffraction*. Cambridge University Press.

International Tables for Crystallography (2004). Volume C, *Mathematical, Physical and Chemical Tables*, edited by E. Prince. Dordrecht: Kluwer Academic Publishers.

Ishimaru, M. (2006). *Electron-beam radial distribution analysis of irradiation-induced amorphous SiC. Nucl. Instrum. Methods Phys. Res. Sect. B*, **250**, 309–314.

Ishimaru, M., Bae, I.-T., Hirotsu, Y., Matsumura, S. & Sickafus, K. E. (2002). *Structural relaxation of amorphous silicon carbide. Phys. Rev. Lett.* **89**, 055502.

Jansen, J., Tang, D., Zandbergen, H. W. & Schenk, H. (1998). *MSLS, a least-squares procedure for accurate crystal structure refinement from dynamical electron diffraction patterns. Acta Cryst.* A**54**, 91–101.

Kim, J. G., Seo, J. W., Cheon, J. & Kim, Y. J. (2009). *Rietveld analysis of nano-crystalline $MnFe_2O_4$ with electron powder diffraction. Bull. Korean Chem. Soc.* **30**, 183–187.

Kis, V. K. M., Posfai, M. & Labar, J. (2006). *Nanostructure of atmospheric soot particles. Atmos. Environ.* **40**, 5533–5542.

Kolb, U. K., Büscher, K., Helm, C. A., Lindner, A., Thünemann, A. F., Menzel, M., Higuchi, M. & Kurth, D. G. (2006). *The solid-state architecture of a metallosupramolecular polyelectrolyte. Proc. Natl Acad. Sci. USA*, **103**, 10202–10206.

Kovács Kis, V., Dódony, I. & Lábár, J. L. (2006). *Amorphous and partly ordered structures in SiO_2 rich volcanic glasses. An ED study. Eur. J. Mineral.* **18**, 745–752.

Lábár, J. L. (2006). *Phase identification by combining local composition from EDX with information from diffraction database.* In *Electron Crystallography*, edited by T. E. Weirich, J. L. Lábár & X. Zou, Nato Science Series II, Vol. 211, pp. 207–218. Dordrecht: Springer.

Lábár, J. L. (2008). *Electron diffraction based analysis of phase fractions and texture in nanocrystalline thin films, part I: principles. Microsc. Microanal.* **14**, 287–295.

Lábár, J. L. (2009). *Electron diffraction based analysis of phase fractions and texture in nanocrystalline thin films, part II: implementation. Microsc. Microanal.* **15**, 20–29.

Lábár, J. L. & Adamik, M. (2001). *ProcessDiffraction V1.2: new possibilities in manipulating electron diffraction ring patterns. Microsc. Microanal.* **7** (Suppl. 2), 372–373.

Lábár, J. L. M., Adamik, M., Barna, B. P., Czigány, Z., Fogarassy, Z., Horváth, Z. E., Geszti, O., Misják, F., Morgiel, J., Radnóczi, G., Sáfrán, G., Székely, L. & Szüts, T. (2012). *Electron diffraction based analysis of phase fractions and texture in nanocrystalline thin films, part III: application examples. Microsc. Microanal.* **18**, 406–420.

Lábár, J. L. & Egerton, R. (1999). *Special issue on ion beam techniques. Micron*, **30**, 195–196.

Li, X. Z. (2010). *PCED2.0 – a computer program for the simulation of polycrystalline electron diffraction pattern. Ultramicroscopy*, **110**, 297–304.

Luo, Z., Vasquez, Y., Bondi, J. F. & Schaak, R. E. (2011). *Pawley and Rietveld refinements using electron diffraction from $L1_2$-type intermetallic Au_3Fe_{1-x} nanocrystals during their in-situ order–disorder transition. Ultramicroscopy*, **111**, 1295–1304.

Lutterotti, L. D., Chateigner, D., Ferrari, S. & Ricote, J. (2004). *Texture, residual stress and structural analysis of thin films using a combined X-ray analysis. Thin Solid Films*, **450**, 34–41.

Lutterotti, L., Matthies, S. & Wenk, H. R. (1999). *MAUD: a friendly Java program for Material Analysis Using Diffraction. IUCr CPD Newsletters*, **21**, May 1999. http://www.mx.iucr.org/iucr-top/comm/cpd/Newsletters/no21may1999/art17/art17.htm.

Lutterotti, L. S., Matthies, S., Wenk, H.-R., Schultz, A. S. & Richardson, J. W. Jr (1997). *Combined texture and structure analysis of deformed limestone from time-of-flight neutron diffraction spectra. J. Appl. Phys.* **81**, 594–600.

McCusker, L. B. & Baerlocher, C. (2009). *Using electron microscopy to complement X-ray powder diffraction data to solve complex crystal structures. Chem. Commun.* pp. 1439–1451.

McGreevy, R. L. & Pusztai, L. (1988). *Reverse Monte Carlo simulation: a new technique for the determination of disordered structures. Mol. Simul.* **1**, 359–367.

McKenzie, D. R., Muller, D., Pailthorpe, B. A., Wang, Z. H., Kravtchinskaia, E., Segal, D., Lukins, P. B., Swift, P. D., Martin, P. J., Amaratunga, G., Gaskell, P. H. & Saeed, A. (1991). *Properties of tetrahedral amorphous carbon prepared by vacuum arc deposition. Diamond Relat. Mater.* **1**, 51–59.

Mecking, H. (1985). *Textures of metals*. In *Preferred Orientation in Deformed Metals and Rocks: An Introduction to Modern Texture Analysis*, edited by H.-R. Wenk, pp. 267–306. Orlando/London: Academic Press Inc.

Moeck, P. & Fraundorf, P. (2007). *Structural fingerprinting in the transmission electron microscope: overview and opportunities to implement enhanced strategies for nanocrystal identification. Z. Kristallogr.* **222**, 634–645.

Moeck, P. & Rouvimov, S. (2010). *Precession electron diffraction and its advantages for structural fingerprinting in the transmission electron microscope. Z. Kristallogr.* **225**, 110–124.

Moss, S. C. & Graczyk, J. F. (1969). *Evidence of voids within the as-deposited structure of glassy silicon. Phys. Rev. Lett.* **23**, 1167–1171.

Mugnaioli, E., Andrusenko, I., Schüler, T., Loges, N., Dinnebier, R. E., Panthöfer, M., Tremel, W. & Kolb, U. (2012). *Ab initio structure determination of vaterite by automated electron diffraction. Angew. Chem.* **51**, 7041–7045.

Nelder, J. A. & Mead, R. (1965). *A simplex method for function minimization. Comput. J.* **7**, 308–313.

Oleynikov, P. & Hovmoller, S. (2004). *TexPat – a program for quantitative analysis of oblique texture electron diffraction patterns. Z. Kristallogr.* **219**, 12–19.

Oleynikov, P. & Hovmoller, S. (2007). *Precession electron diffraction: observed and calculated intensities. Ultramicroscopy*, **107**, 523–533.

Orloff, J., Swanson, L. & Utlaut, M. (2002). *High Resolution Focused Ion Beams: FIB and Applications*. New York: Springer.

Own, C. S., Marks, L. D. & Sinkler, W. (2006). *Precession electron diffraction 1: multislice simulation. Acta Cryst.* A**62**, 434–443.

Őzdöl, V. B., Srot, V. & van Aken, P. A. (2012). *Sample preparation for transmission electron microscopy.* In *Handbook of Nanoscopy*, edited by G. Van Tendeloo, D. Van Dyck & S. J. Pennycook. Weinheim: Wiley.

Peng, L. M., Dudarev, S. L. & Whelan, M. J. (2004). *High-Energy Electron Diffraction and Microscopy*. USA: Oxford University Press.

Petersen, T. C., McBride, W., McCulloch, D. G., Snook, I. K. & Yarovsky, I. (2005). *Refinements in the collection of energy filtered diffraction patterns from disordered materials. Ultramicroscopy*, **103**, 275–283.

Rauch, E. F., Váron, M., Portillo, J., Bultreys, D., Maniette, Y. & Nicolopoulos, S. (2008). *Automatic crystal orientation and phase mapping in TEM by precession diffraction. Microsc. Anal.* **22**, S5–S8.

Reimer, L. (1984). *Transmission Electron Microscopy – Physics of Image Formation and Microanalysis*. Heidelberg: Springer-Verlag.

Reimer, L. & Kohl, H. (2008). *Transmission Electron Microscopy: Physics of Image Formation*. New York: Springer.

Rez, P. (1983). *A transport-equation theory of beam spreading in the electron microscope. Ultramicroscopy*, **12**, 29–38.

Rietveld, H. M. (1967). *Line profiles of neutron powder-diffraction peaks for structure refinement. Acta Cryst.* **22**, 151–152.

Rietveld, H. M. (1969). *A profile refinement method for nuclear and magnetic structures. J. Appl. Cryst.* **2**, 65–71.

Rodríguez-Carvajal, J. (1993). *Recent advances in magnetic structure determination by neutron powder diffraction. Physica B*, **192**, 55–69.

Rose, H. & Krahl, D. (1995). *Electron optics of imaging energy filters.* In *Energy-Filtering Transmission Electron Microscopy*, edited by L. Reimer, pp. 43–149. Berlin: Springer.

Saunders, M., Bird, D. M., Zaluzec, N. J., Burgess, W. G., Preston, A. R. & Humphreys, C. J. (1995). *Measurement of low-order structure factors for silicon from zone-axis CBED patterns. Ultramicroscopy*, **60**, 311–323.

Siwick, B. J., Dwyer, J. R., Jordan, R. E. & Miller, R. J. D. (2003). *An atomic-level view of melting using femtosecond electron diffraction. Science*, **302**, 1382–1385.

Song, K. Y. J., Kim, Y.-J., Kim, Y.-I. & Kim, J.-G. (2012). *Application of theta-scan precession electron diffraction to structure analysis of hydroxyapatite nanopowder. J. Electron Microsc.* **61**, 9–15.

Sun, J., Bonneau, C., Cantín, A., Corma, A., Díaz-Cabañas, M. J., Moliner, M., Zhang, D., Li, M. & Zou, X. (2009). *The ITQ-37 mesoporous chiral zeolite. Nature*, **458**, 1154–1157.

Tang, L., Feng, Y. C., Lee, L.-L. & Laughlin, D. E. (1996). *Electron diffraction patterns of fibrous and lamellar textured polycrystalline thin films. II. Applications. J. Appl. Cryst.* **29**, 419–426.

Tonejc, A. M., Djerdj, I. & Tonejc, A. (2002). *An analysis of evolution of grain size-lattice parameters dependence in nanocrystalline* TiO_2 *anatase. Mater. Sci. Eng. C*, **19**, 85–89.

Tsuda, K., Ogata, Y., Takagi, K., Hashimoto, T. & Tanaka, M. (2002). *Refinement of crystal structural parameters and charge density using convergent-beam electron diffraction – the rhombohedral phase of* $LaCrO_3$*. Acta Cryst.* A**58**, 514–525.

Tsuda, K. & Tanaka, M. (1999). *Refinement of crystal structural parameters using two-dimensional energy-filtered CBED patterns. Acta Cryst.* A**55**, 939–954.

Turner, P. S. & Cowley, J. M. (1969). *The effects of N-beam dynamical diffraction on electron diffraction intensities from polycrystalline materials. Acta Cryst.* A**25**, 475–481.

Ungár, T., Gubicza, J., Ribárik, G. & Borbély, A. (2001). *Crystallite size distribution and dislocation structure determined by diffraction profile analysis: principles and practical application to cubic and hexagonal crystals. J. Appl. Cryst.* **34**, 298–310.

Vainshtein, B. K. (1964). *Structure Analysis by Electron Diffraction*. Oxford: Pergamon Press.

Vainshtein, B. K., Zvyagin, B. B. & Avilov, A. S. (1992). *Electron diffraction structure analysis.* In *Electron Diffraction Techniques*, Vol. 1, edited by J. M. Cowley, pp. 216–312. Oxford University Press.

Vincent, R. & Exelby, D. R. (1991). *Structure of metastable Al–Ge phases determined from HOLZ Patterson transforms. Philos. Mag. Lett.* **63**, 31–38.

Vincent, R. & Midgley, P. A. (1994). *Double conical beam-rocking system for measurement of integrated electron diffraction intensities. Ultramicroscopy*, **53**, 271–282.

Warren, B. E. (1990). *X-ray Diffraction*. New York: Dover Publications.

Weickenmeier, A. & Kohl, H. (1991). *Computation of absorptive form factors for high-energy electron diffraction. Acta Cryst.* A**47**, 590–597.

Weirich, T. E. M., Winterer, M., Seifried, S., Hahn, H. & Fuess, H. (2000). *Rietveld analysis of electron powder diffraction data from nanocrystalline anatase,* TiO_2*. Ultramicroscopy*, **81**, 263–270.

Williams, D. B. & Carter, C. B. (2009). *Transmission Electron Microscopy: a Textbook for Materials Science*. New York: Springer.

Wu, J. S. K., Leinenweber, K., Spence, J. C. H. & O'Keeffe, M. (2006). *Ab initio phasing of X-ray powder diffraction patterns by charge flipping. Nat. Mater.* **5**, 647–652.

Zhang, J. (2011). *Atomic structures of carbon nanomaterials studied by coherent electron diffraction.* PhD thesis, University of Illinois, USA.

Zhuang, J. L. K., Lommel, K., Ceglarek, D., Andrusenko, I., Kolb, U., Maracke, S., Sazama, U., Fröba, M. & Terfort, A. (2011). *Synthesis of a new copper-azobenzene dicarboxylate framework in the form of hierarchical bulk solids and thin films without and with patterning. Chem. Mater.* **23**, 5366–5374.

Zuo, J. M. (1993). *New method of Bravais lattice determination. Ultramicroscopy*, **52**, 459–464.

Zuo, J. M. (2000). *Electron detection characteristics of a slow-scan CCD camera, imaging plates and film, and electron image restoration. Microsc. Res. Tech.* **49**, 245–268.

Zuo, J. M. (2004). *Measurements of electron densities in solids: a real-space view of electronic structure and bonding in inorganic crystals. Rep. Prog. Phys.* **67**, 2053–2103.

Zuo, J. M., Gao, M., Tao, J., Li, B. Q., Twesten, R. & Petrov, I. (2004). *Coherent nano-area electron diffraction. Microsc. Res. Tech.* **64**, 347–355.

Zuo, J. M., Kim, M. & Holmestad, R. (1998). *A new approach to lattice parameter measurements using dynamic electron diffraction and pattern matching. J. Electron Microsc.* **47**, 121–127.

Zuo, J. M. & Spence, J. C. H. (1991). *Automated structure factor refinement from convergent-beam patterns. Ultramicroscopy*, **35**, 185–196.

Zuo, J. M. & Spence, J. C. H. (2017). *Advanced Transmission Electron Microscopy: Imaging and Diffraction in Nanoscience*. New York: Springer.

International Tables for Crystallography (2019). Vol. H, Chapter 2.5, pp. 118–149.

2.5. Two-dimensional powder diffraction

B. B. He

2.5.1. Introduction

2.5.1.1. *The diffraction pattern measured by an area detector*

The diffracted X-rays from a polycrystalline or powder sample form a series of cones in three-dimensional space, since large numbers of crystals oriented randomly in the space are covered by the incident X-ray beam. Each diffraction cone corresponds to the diffraction from the same family of crystal planes in all the participating grains. The apex angles of cones are given by Bragg's law for the corresponding crystal interplanar *d*-spacing. A conventional X-ray powder-diffraction pattern is collected by scanning a point or linear detector along the 2θ angle. The diffraction pattern is displayed as scattering intensity *versus* 2θ angle (Klug & Alexander, 1974; Cullity, 1978; Warren, 1990; Jenkins & Snyder, 1996; Pecharsky & Zavalij, 2003). In recent years, use of two-dimensional (2D) detectors for powder diffraction has dramatically increased in academic and industrial research (Sulyanov *et al.*, 1994; Rudolf & Landes, 1994; He, 2003, 2009). When a 2D detector is used for X-ray powder diffraction, the diffraction cones are intercepted by the area detector and the X-ray intensity distribution on the sensing area is converted to an image-like diffraction pattern, also referred to as a frame. Since the diffraction pattern collected with a 2D detector is typically given as an intensity distribution over a two-dimensional region, so X-ray diffraction with a 2D detector is also referred to as two-dimensional X-ray diffraction (2D-XRD) or 2D powder diffraction. A 2D diffraction pattern contains far more information than a conventional diffraction pattern, and therefore demands a special data-collection strategy and data-evaluation algorithms. This chapter covers the basic concepts and recent progress in 2D-XRD theory and technologies, including geometry conventions, X-ray source and optics, 2D detectors, diffraction-data interpretation, and various applications, such as phase identification and texture, stress, crystallinity and crystallite-size analysis. The concepts and algorithms of this chapter apply to both laboratory and synchrotron diffractometers equipped with 2D detectors.

2.5.1.2. *Comparison between 2D-XRD and conventional XRD*

Fig. 2.5.1 is a schematic of X-ray diffraction from a powder (polycrystalline) sample. For simplicity, it shows only two diffraction cones; one represents forward diffraction ($2\theta \leq 90^\circ$) and one represents backward diffraction ($2\theta > 90^\circ$). The diffraction measurement in a conventional diffractometer is confined within a plane, here referred to as the diffractometer plane. A point (0D) detector makes a 2θ scan along a detection circle. If a line (1D) detector is used in the diffractometer, it will be mounted on the detection circle. Since the variations in the diffraction pattern in the direction (**Z**) perpendicular to the diffractometer plane are not considered in a conventional diffractometer, the X-ray beam is normally extended in the Z direction (line focus). Since the diffraction data out of the diffractometer plane are not detected, the structures in the material that are represented by the missing diffraction data will either be ignored, or extra sample rotation and time are needed to complete the measurement.

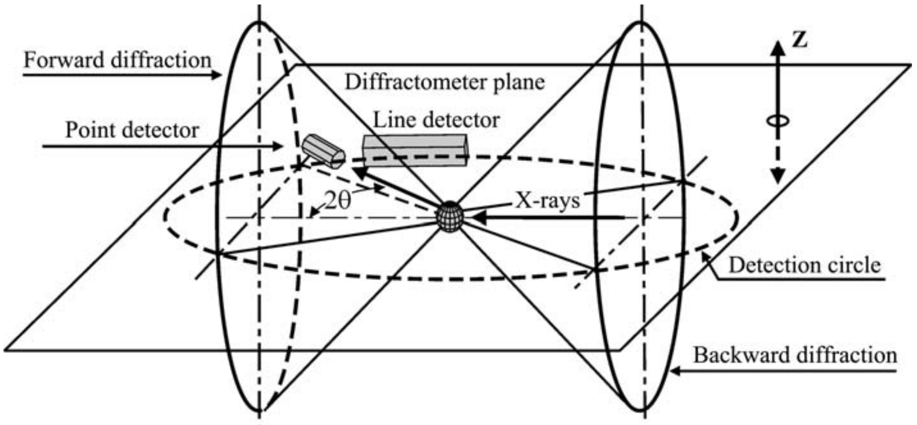

Figure 2.5.1
Diffraction patterns in 3D space from a powder sample and the diffractometer plane.

With a 2D detector, the diffraction measurement is no longer limited to the diffractometer plane. Depending on the detector size, the distance to the sample and the detector position, the whole or a large portion of the diffraction rings can be measured simultaneously. Diffraction patterns out of the diffractometer plane have for a long time been recorded using Debye–Scherrer cameras, so the diffraction rings are referred to as Debye rings. However, when a Debye–Scherrer camera is used, only the position of the arches in the 2θ direction and their relative intensities are measured for powder-diffraction analysis. The diffraction rings collected with a large 2D detector extend further in the 'vertical' direction and the intensity variation in the vertical direction is also used for data evaluation. Therefore, the terms 'diffraction cone' and 'diffraction ring' will be often be used in this chapter as alternatives to 'Debye cone' and 'Debye ring'.

2.5.1.3. *Advantages of two-dimensional X-ray diffraction*

A 2D diffraction frame contains far more information than a diffraction pattern measured using a conventional diffraction system with a point detector or a linear position-sensitive detector. In addition to the significantly higher data-collection speed, the intensity and 2θ variation along the diffraction rings can reveal abundant structural information typically not available from a conventional diffraction pattern. Fig. 2.5.2 shows a 2D pattern collected from a battery component containing multiple layers of different phases. Some diffraction rings have strong intensity variation due to preferred orientation, and the spotty diffraction rings are from a phase that contains large crystal grains. It is apparent that different diffraction-ring patterns are from different phases. 2D-XRD analyses commonly performed on polycrystalline materials include phase identification, quantitative phase analysis, preferred-orientation quantification and characterization of residual stresses.

Phase identification (phase ID) can be done by integration in a selected 2θ range along the diffraction rings (Hammersley *et al.*,

Copyright © 2019 International Union of Crystallography

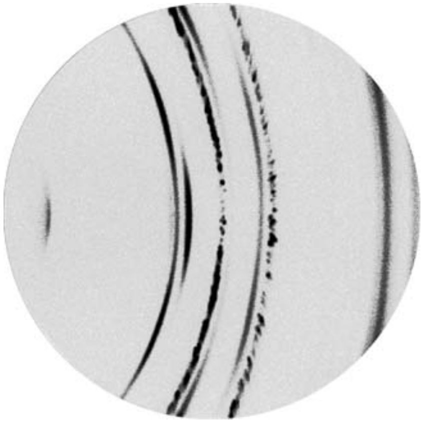

Figure 2.5.2
Diffraction pattern from a battery component containing multiple layers.

1996; Rodriguez-Navarro, 2006). The integrated data give better intensity and statistics for phase ID and quantitative analysis, especially for those samples with texture or large grain sizes, or where the sample is small. Then the integrated diffraction profiles can be analysed with existing algorithms and methods: profile fitting with conventional peak shapes and fundamental parameters, quantification of phases, and lattice-parameter indexing and refinement. The results can be used to search and match to entries in a powder-diffraction database, typically the Powder Diffraction File.

Texture measurement with 2D-XRD is extremely fast compared to measurement using a point or linear detector. The area detector collects texture data and background values simultaneously for multiple poles and multiple directions. Owing to the high measurement speed, pole figures can be measured at very fine steps, allowing detection of very sharp textures (Smith & Ortega, 1993; Bunge & Klein, 1996; He, 2009).

Stress measurement with 2D-XRD is based on a direct relationship between the stress tensor and distortion of the diffraction cones. Since the whole or a part of the diffraction ring is used for stress calculation, 2D-XRD can measure stress with high sensitivity, high speed and high accuracy (He & Smith, 1997; He, 2000). It is highly suitable for samples containing large crystals and textures. Simultaneous measurement of stress and texture is also possible, since 2D data contain both stress and texture information.

Concentrations of crystalline phases can be measured faster and more accurately with data analysis over 2D frames, especially for samples with an anisotropic distribution of crystallite orientations and/or amorphous content. The amorphous region can be defined by the user to consist of regions with no Bragg peaks, or the amorphous region can be defined with the crystalline region included when the crystalline region and the amorphous region overlap.

Microdiffraction data are collected with speed and accuracy. Collection of X-ray diffraction data from small sample amounts or small sample areas has always been a slow process because of limited beam intensity. The 2D detector captures whole or a large portion of the diffraction rings, so spotty, textured or weak diffraction data can be integrated over the selected diffraction rings (Winter & Squires, 1995; Bergese *et al.*, 2001; Tissot, 2003; Bhuvanesh & Reibenspies, 2003; He, 2004). The point beam used for microdiffraction allows diffraction mapping with fine space resolution, even on a curved surface (Allahkarami & Hanan, 2011).

Data can be collected from thin-film samples containing a mixture of single-crystal and polycrystalline layers with random orientation distributions, and highly textured layers, with all the features appearing simultaneously in diffraction frames (Dickerson *et al.*, 2002; He, 2006). The pole figures from different layers and the substrate can be overlapped to reveal the orientation relationships. The use of a 2D detector can dramatically speed up the data collection for reciprocal-space mapping on an in-plane reciprocal-lattice point (Schmidbauer *et al.*, 2008).

Because of the penetrating power of the X-ray beam, fast nondestructive data collection and the abundant information about atomic structure, two-dimensional X-ray diffraction can be used to screen a library of materials with high speed and high accuracy. Two-dimensional X-ray diffraction systems dedicated for combinatorial screening are widely used in the pharmaceutical industry for drug discovery and process analysis (Klein *et al.*, 1998; He *et al.*, 2001).

Forensic science and archaeology have benefited from using two-dimensional X-ray diffraction for identifying materials and structures from small specimens (Kugler, 2003; Bontempi *et al.*, 2008). It is nondestructive and does not require special sample treatment, so the original evidence or sample can be preserved. Two-dimensional diffraction patterns contain abundant information and are easy to observe and explain in the courtroom.

2.5.2. Fundamentals

A conventional powder-diffraction pattern is displayed as the scattering intensity *versus* scattering angle 2θ or d-spacing. A 2D-XRD pattern contains the scattering-intensity distribution as a function of two orthogonal dimensions. One dimension can be expressed in 2θ, which can be interpreted by Bragg's law. The distribution in the dimension orthogonal to 2θ contains additional information, such as the orientation distribution, strain states, and crystallite-size and -shape distribution. In order to understand and analyse 2D diffraction data, new geometry conventions and algorithms are introduced. The geometry conventions and algorithms used for 2D-XRD should also be consistent with conventional XRD, so that many existing concepts and algorithms are still valid when 2D diffraction data are used.

The geometry of a 2D-XRD system can be explained using three distinguishable and interrelated geometry spaces, each defined by a set of parameters (He, 2003). The three geometry spaces are the diffraction space, detector space and sample space. The laboratory coordinate system $\mathbf{X}_L$, $\mathbf{Y}_L$, $\mathbf{Z}_L$ is the basis of all three spaces. Although the three spaces are interrelated, the definitions and corresponding parameters should not be confused. Except for a few parameters introduced specifically for 2D-XRD, many of these parameters are used in conventional X-ray diffraction systems. Therefore, the same definitions are maintained for consistency. The three-circle goniometer in Eulerian geometry is the most commonly used, and all the algorithms for data interpretation and analysis in this chapter are based on Eulerian geometry. The algorithms can be developed for the geometries of other types (such as kappa) by following the same strategies.

2.5.2.1. *Diffraction space and laboratory coordinates*

2.5.2.1.1. *Diffraction cones in laboratory coordinates*

Fig. 2.5.3(*a*) describes the geometric definition of diffraction cones in the laboratory coordinate system $\mathbf{X}_L$, $\mathbf{Y}_L$, $\mathbf{Z}_L$. The laboratory coordinate system is a Cartesian coordinate system.

The plane given by X_L and Y_L is the diffractometer plane. The axis Z_L is perpendicular to the diffractometer plane. The axes X_L, Y_L and Z_L form a right-handed rectangular coordinate system with the origin at the instrument centre. The incident X-ray beam propagates along the X_L axis, which is also the rotation axis of all diffraction cones. The apex angles of the cones are determined by the 2θ values given by the Bragg equation. The apex angles are twice the 2θ values for forward reflection ($2\theta \leq 90^\circ$) and twice the value of $180^\circ - 2\theta$ for backward reflection ($2\theta > 90^\circ$). For clarity, only one diffraction cone of forward reflection is displayed. The γ angle is the azimuthal angle from the origin at the six o'clock direction with a right-handed rotation axis along the opposite direction of incident beam ($-X_L$ direction). A given γ value defines a half plane with the X_L axis as the edge; this will be referred to as the γ plane hereafter. The diffractometer plane consists of two γ planes at $\gamma = 90^\circ$ and $\gamma = 270^\circ$. Therefore many equations developed for 2D-XRD should also apply to conventional XRD if the γ angle is given as a constant of 90° or 270°. A pair of γ and 2θ values represents the direction of a diffracted beam. The γ angle takes a value of 0 to 360° for a complete diffraction ring with a constant 2θ value. The γ and 2θ angles form a spherical coordinate system which covers all the directions from the origin of sample (instrument centre). The γ–2θ system is fixed in the laboratory system $\mathbf{X}_L$, $\mathbf{Y}_L$, $\mathbf{Z}_L$, which is independent of the sample orientation and detector position in the goniometer. 2θ and γ are referred to as the diffraction-space parameters. In the laboratory coordinate system $\mathbf{X}_L$, $\mathbf{Y}_L$, $\mathbf{Z}_L$, the surface of a diffraction cone can be mathematically expressed as

$$y_L^2 + z_L^2 = x_L^2 \tan^2 2\theta, \qquad (2.5.1)$$

with $x_L \geq 0$ or $2\theta \leq 90^\circ$ for forward-diffraction cones and $x_L < 0$ or $2\theta > 90^\circ$ for backward-diffraction cones.

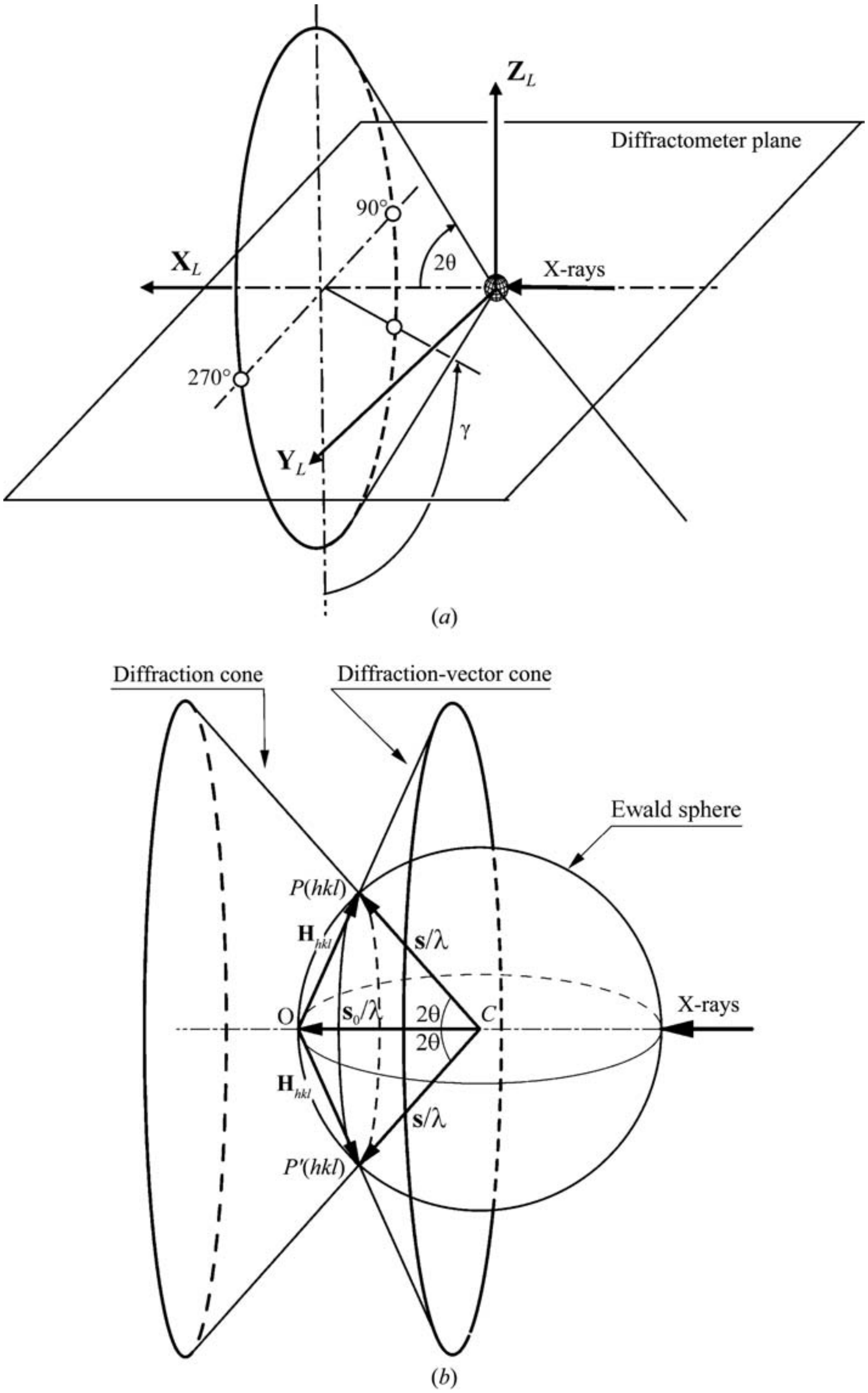

Figure 2.5.3
The diffraction cone and the corresponding diffraction-vector cone.

2.5.2.1.2. *Diffraction-vector cones in laboratory coordinates*

Fig. 2.5.3(b) shows the diffraction-vector cone corresponding to the diffraction cone in the laboratory coordinate system. C is the centre of the Ewald sphere. The diffraction condition can be given by the Laue equation as

$$\frac{\mathbf{s} - \mathbf{s}_0}{\lambda} = \mathbf{H}_{hkl}, \qquad (2.5.2)$$

where $\mathbf{s}_0$ is the unit vector representing the incident beam, $\mathbf{s}$ is the unit vector representing the diffracted beam and $\mathbf{H}_{hkl}$ is the reciprocal-lattice vector. Its magnitude is given as

$$\left|\frac{\mathbf{s} - \mathbf{s}_0}{\lambda}\right| = \frac{2\sin\theta}{\lambda} = \left|\mathbf{H}_{hkl}\right| = \frac{1}{d_{hkl}}, \qquad (2.5.3)$$

in which d_{hkl} is the d-spacing of the crystal planes (hkl). It can be easily seen that it is the Bragg law in a different form. Therefore, equation (2.5.2) is the Bragg law in vector form. In the Bragg condition, the vectors $\mathbf{s}_0/\lambda$ and $\mathbf{s}/\lambda$ make angles θ with the diffracting planes (hkl) and $\mathbf{H}_{hkl}$ is normal to the (hkl) crystal plane. In order to analyse all the X-rays measured by a 2D detector, we extend the concept to all scattered X-rays from a sample regardless of the Bragg condition. Therefore, the index (hkl) can be removed from the above expression. $\mathbf{H}$ is then a vector which takes the direction bisecting the incident beam and the scattered beam, and has dimensions of inverse length given by $2\sin\theta/\lambda$. Here 2θ is the scattering angle from the incident beam. The vector $\mathbf{H}$ is referred to as the scattering vector or, alternatively, the diffraction vector. When the Bragg condition is satisfied, the diffraction vector is normal to the diffracting lattice planes and its magnitude is reciprocal to the d-spacing of the lattice planes. In this case, the diffraction vector is equivalent to the reciprocal-lattice vector. Each pixel in a 2D detector measures scattered X-rays in a given direction with respect to the incident beam. We can calculate a diffraction vector for any pixel, even if the pixel is not measuring Bragg scattering. Use of the term 'diffracted beam' hereafter in this chapter does not necessarily imply that it arises from Bragg scattering.

For two-dimensional diffraction, the incident beam can be expressed by the vector $\mathbf{s}_0/\lambda$, but the diffracted beam is no longer in a single direction, but follows the diffraction cone. Since the direction of a diffraction vector is a bisector of the angle between the incident and diffracted beams corresponding to each diffraction cone, the trace of the diffraction vectors forms a cone. This cone is referred to as the diffraction-vector cone. The angle between the diffraction vector and the incident X-ray beam is 90° + θ and the apex angle of a vector cone is 90° − θ. It is apparent that diffraction-vector cones can only exists on the $-X_L$ side of the diffraction space.

For two-dimensional diffraction, the diffraction vector is a function of both the γ and 2θ angles, and is given in laboratory coordinates as

$$\mathbf{H} = \frac{\mathbf{s} - \mathbf{s}_0}{\lambda} = \frac{1}{\lambda}\begin{bmatrix} \cos 2\theta - 1 \\ -\sin 2\theta \sin\gamma \\ -\sin 2\theta \cos\gamma \end{bmatrix}. \qquad (2.5.4)$$

The direction of the diffraction vector can be represented by its unit vector, given by

$$\mathbf{h}_L = \frac{\mathbf{H}}{|\mathbf{H}|} = \begin{bmatrix} h_x \\ h_y \\ h_z \end{bmatrix} = \begin{bmatrix} -\sin\theta \\ -\cos\theta \sin\gamma \\ -\cos\theta\cos\gamma \end{bmatrix}, \qquad (2.5.5)$$

where $\mathbf{h}_L$ is a unit vector expressed in laboratory coordinates and the three components in the square brackets are the projections of the unit vector on the three axes of the laboratory coordinates, respectively. If γ takes all values from 0 to 360° at a given Bragg angle 2θ, the trace of the diffraction vector forms a diffraction-vector cone. Since the possible values of θ lie within the range 0 to 90°, h_x takes only negative values.

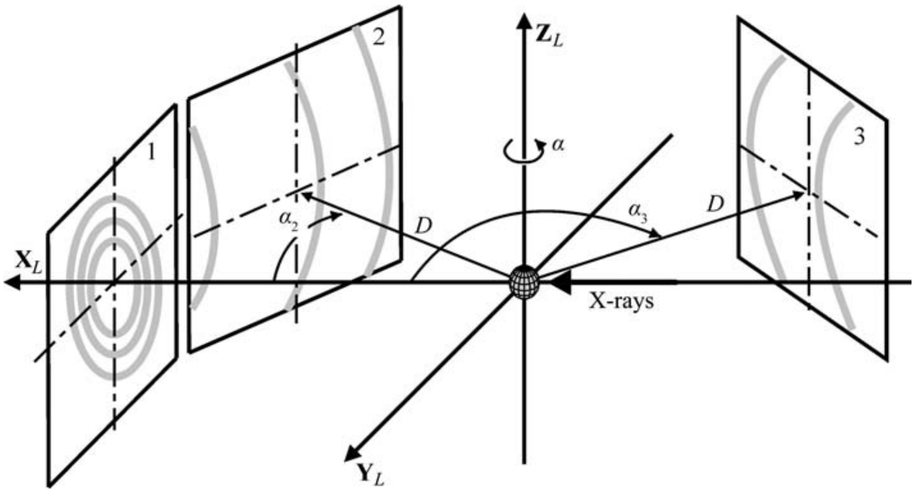

Figure 2.5.4
Detector positions in the laboratory-system coordinates.

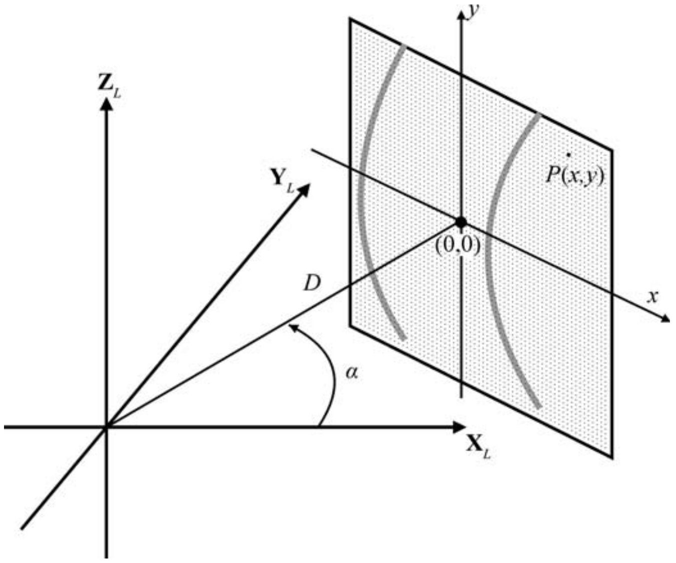

Figure 2.5.5
Relationship between a pixel P and detector position in the laboratory coordinates.

2.5.2.2. *Detector space and pixel position*

A typical 2D detector has a limited detection surface, and the detection surface can be spherical, cylindrical or flat. Spherical or cylindrical detectors are normally designed for a fixed sample-to-detector distance, while a flat detector has the flexibility to be used at different sample-to-detector distances so as to choose either high resolution at a large distance or large angular coverage at a short distance.

2.5.2.2.1. *Detector position in the laboratory system*

The position of a flat detector is defined by the sample-to-detector distance D and the detector swing angle α. D and α are referred to as the detector-space parameters. D is the perpendicular distance from the goniometer centre to the detection plane and α is a right-handed rotation angle about the Z_L axis. Detectors at different positions in the laboratory coordinates X_L, Y_L, Z_L are shown in Fig. 2.5.4. The centre of detector 1 is right on the positive side of the X_L axis (on-axis), $\alpha = 0$. Both detectors 2 and 3 are rotated away from the X_L axis with negative swing angles ($\alpha_2 < 0$ and $\alpha_3 < 0$). The detection surface of a flat 2D detector can be considered as a plane, which intersects the diffraction cone to form a conic section. Depending on the swing angle α and the 2θ angle, the conic section can appear as a circle, an ellipse, a parabola or a hyperbola.

2.5.2.2.2. *Pixel position in diffraction space for a flat detector*

The values of 2θ and γ can be calculated for each pixel in the frame. The calculation is based on the detector-space parameters and the pixel position in the detector. Fig. 2.5.5 shows the relationship of a pixel $P(x, y)$ to the laboratory coordinates X_L, Y_L, Z_L. The position of a pixel in the detector is defined by the (x, y) coordinates, where the detector centre is defined as $x = y = 0$. The diffraction-space coordinates $(2\theta, \gamma)$ for a pixel at $P(x, y)$ are given by

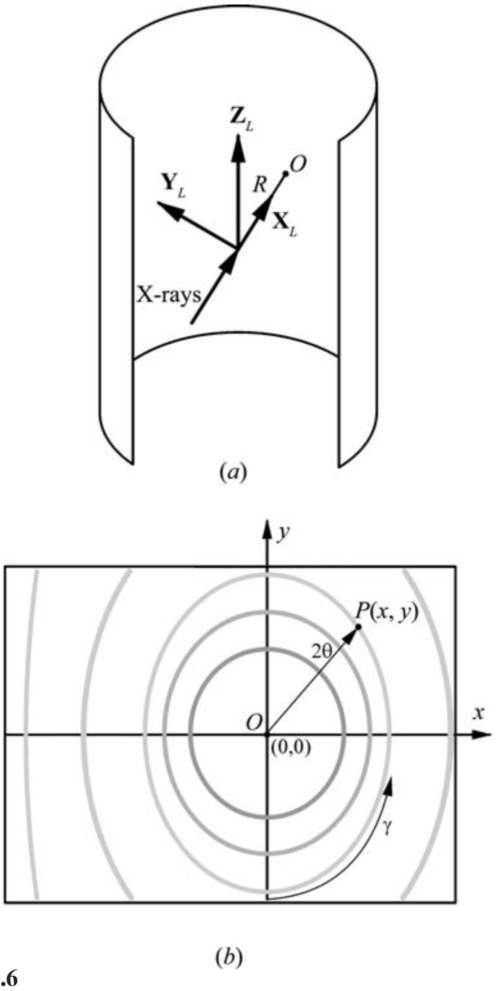

Figure 2.5.6
Cylinder-shaped detector in vertical direction: (*a*) detector position in the laboratory coordinates; (*b*) pixel position in the flattened image.

$$2\theta = \arccos \frac{x\sin\alpha + D\cos\alpha}{(D^2+x^2+y^2)^{1/2}} \quad (0 < 2\theta < \pi), \tag{2.5.6}$$

$$\gamma = \frac{x\cos\alpha - D\sin\alpha}{|x\cos\alpha - D\sin\alpha|} \arccos \frac{-y}{[y^2 + (x\cos\alpha - D\sin\alpha)^2)]^{1/2}} \quad (-\pi < \gamma \le \pi). \tag{2.5.7}$$

2.5.2.2.3. *Pixel position in diffraction space for a curved detector*

The conic sections of the diffraction cones with a curved detector depend on the shape of the detector. The most common curved detectors are cylinder-shaped detectors. The diffraction frame measured by a cylindrical detector can be displayed as a flat frame, typically a rectangle. Fig. 2.5.6(*a*) shows a cylindrical detector in the vertical direction and the corresponding laboratory coordinates X_L, Y_L, Z_L. The sample is located at the origin of the laboratory coordinates inside the cylinder. The incident X-rays strike the detector at a point O if there is no sample or beam stop to block the direct beam. The radius of the cylinder is R. Fig. 2.5.6(*b*) illustrates the 2D diffraction image collected with the cylindrical detector. We take the point O as the origin of the pixel position (0, 0). The diffraction-space coordinates (2θ, γ) for a pixel at $P(x, y)$ are given by

$$2\theta = \arccos\left[R\cos\left(\frac{x}{R}\right)\Big/(R^2+y^2)^{1/2}\right], \tag{2.5.8}$$

$$\gamma = \frac{x}{|x|}\arccos\left\{-y\Big/\left[y^2 + R^2\sin^2\left(\frac{x}{R}\right)\right]^{1/2}\right\} \quad (-\pi < \gamma \le \pi). \tag{2.5.9}$$

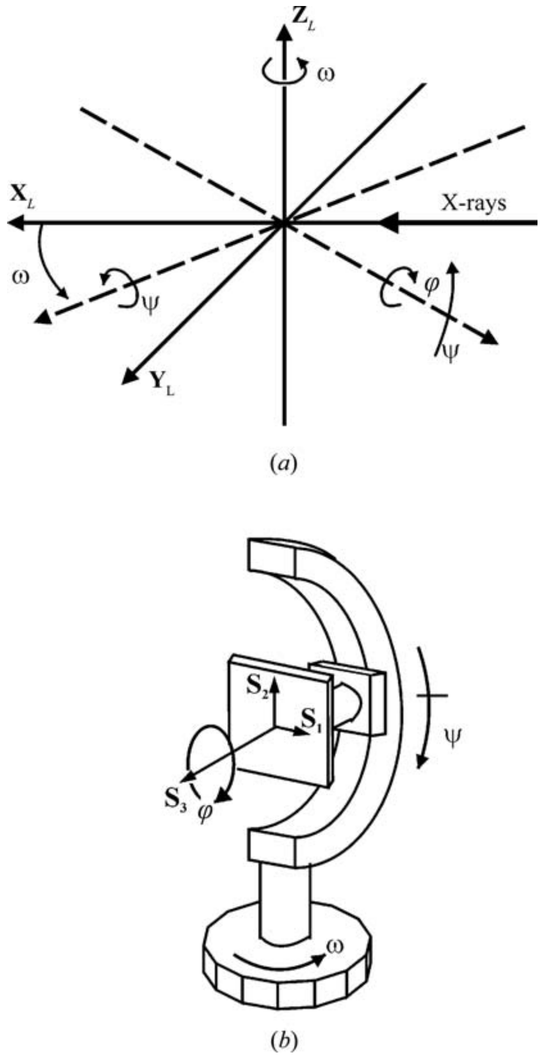

Figure 2.5.7
Sample rotation and translation. (*a*) Three rotation axes in laboratory coordinates; (*b*) rotation axes (ω, ψ, φ) and sample coordinates.

The pixel-position-to-(2θ, γ) conversion for detectors of other shapes can also be derived. Once the diffraction-space coordinates (2θ, γ) of each pixel in the curved 2D detector are determined, most data-analysis algorithms developed for flat detectors are applicable to a curved detector as well.

2.5.2.3. *Sample space and goniometer geometry*

2.5.2.3.1. *Sample rotations and translations in Eulerian geometry*

In a 2D-XRD system, three rotation angles are necessary to define the orientation of a sample in the diffractometer. These three rotation angles can be achieved either by a Eulerian geometry, a kappa (κ) geometry or another kind of geometry. The three angles in Eulerian geometry are ω (omega), ψ (psi) and φ (phi). Fig. 2.5.7(*a*) shows the relationship between rotation axes (ω, ψ, φ) in the laboratory system $\mathbf{X}_L$, $\mathbf{Y}_L$, $\mathbf{Z}_L$. The ω angle is defined as a right-handed rotation about the Z_L axis. The ω axis is fixed in the laboratory coordinates. The ψ angle is a right-handed rotation about a horizontal axis. The angle between the ψ axis and the X_L axis is given by ω. The ψ axis lies on X_L when ω is set at zero. The φ angle defines a left-handed rotation about an axis on the sample, typically the normal of a flat sample. The φ axis lies on the Y_L axis when $\omega = \psi = 0$. In an aligned diffraction system, all three rotation axes and the primary X-ray beam cross at the origin of the X_L, Y_L, Z_L coordinates. This cross point is also known as the goniometer centre or instrument centre.

Fig. 2.5.7(*b*) shows the relationship and stacking sequence among all rotation axes (ω, ψ, φ) and the sample coordinates S_1, S_2, S_3. ω is the base rotation; all other rotations and translations are on top of this rotation. The next rotation above ω is the ψ rotation. The next rotation above ω and ψ is the φ rotation. The sample coordinates S_1, S_2, S_3 are fixed to the sample regardless of the particular sample orientation given by the rotation angles (ω, ψ, φ). The φ rotation in the goniometer is intentionally chosen as a left-handed rotation so that the diffraction vectors will make a right-hand rotation observed in the sample coordinates S_1, S_2, S_3.

2.5.2.4. *Diffraction-vector transformation*

2.5.2.4.1. *Diffraction unit vector in diffraction space and sample space*

In 2D-XRD data analysis, it is crucial to know the diffraction-vector distribution in terms of the sample coordinates S_1, S_2, S_3. However, the diffraction-vector distribution corresponding to the measured 2D data is always given in terms of the laboratory coordinates X_L, Y_L, Z_L because the diffraction space is fixed to the laboratory coordinates. Fig. 2.5.8 shows the unit vector of a diffraction vector in both (*a*) the laboratory coordinates X_L, Y_L, Z_L and (*b*) the sample coordinates S_1, S_2, S_3. In Fig. 2.5.8(*a*) the unit vector $\mathbf{h}_L$ is projected to the X_L, Y_L and Z_L axes as h_x, h_y and h_z, respectively. The three components are given by equation (2.5.5). In order to analyse the diffraction results relative to the sample orientation, it is necessary to transform the unit vector to the sample coordinates S_1, S_2, S_3. Fig. 2.5.8(*b*) shows the same unit vector, denoted by $\mathbf{h}_s$ projected to S_1, S_2 and S_3 as h_1, h_2 and h_3, respectively.

2.5.2.4.2. *Transformation from diffraction space to sample space*

The transformation of the unit diffraction vector from the laboratory coordinates X_L, Y_L, Z_L to the sample coordinates S_1, S_2, S_3 is given by

$$\mathbf{h}_s = \boldsymbol{A}\mathbf{h}_L, \tag{2.5.10}$$

where $\boldsymbol{A}$ is the transformation matrix. For Eulerian geometry in matrix form, we have

$$\begin{aligned}\begin{bmatrix}h_1\\h_2\\h_3\end{bmatrix} &= \begin{bmatrix}a_{11}&a_{12}&a_{13}\\a_{21}&a_{22}&a_{23}\\a_{31}&a_{32}&a_{33}\end{bmatrix}\begin{bmatrix}h_x\\h_y\\h_z\end{bmatrix}\\ &= \begin{bmatrix}-\sin\omega\sin\psi\sin\varphi - \cos\omega\cos\varphi & \cos\omega\sin\psi\sin\varphi - \sin\omega\cos\varphi & -\cos\psi\sin\varphi\\ \sin\omega\sin\psi\cos\varphi - \cos\omega\sin\varphi & -\cos\omega\sin\psi\cos\varphi - \sin\omega\sin\varphi & \cos\psi\cos\varphi\\ -\sin\omega\cos\psi & \cos\omega\cos\psi & \sin\psi\end{bmatrix}\\ &\quad\times\begin{bmatrix}-\sin\theta\\-\cos\theta\sin\gamma\\-\cos\theta\cos\gamma\end{bmatrix}.\end{aligned} \tag{2.5.11}$$

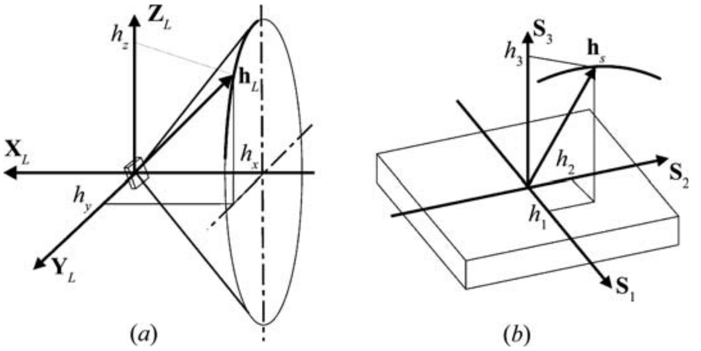

Figure 2.5.8
Unit diffraction vector in (*a*) the laboratory coordinates and (*b*) the sample coordinates.

In expanded form:

$$\begin{aligned}h_1 &= \sin\theta(\sin\varphi\sin\psi\sin\omega + \cos\varphi\cos\omega) + \cos\theta\cos\gamma\sin\varphi\cos\psi\\ &\quad - \cos\theta\sin\gamma(\sin\varphi\sin\psi\cos\omega - \cos\varphi\sin\omega)\\ h_2 &= -\sin\theta(\cos\varphi\sin\psi\sin\omega - \sin\varphi\cos\omega)\\ &\quad - \cos\theta\cos\gamma\cos\varphi\cos\psi\\ &\quad + \cos\theta\sin\gamma(\cos\varphi\sin\psi\cos\omega + \sin\varphi\sin\omega)\\ h_3 &= \sin\theta\cos\psi\sin\omega - \cos\theta\sin\gamma\cos\psi\cos\omega - \cos\theta\cos\gamma\sin\psi\end{aligned} \tag{2.5.12}$$

In addition to the diffraction intensity and Bragg angle corresponding to each data point on the diffraction ring, the unit vector $\mathbf{h}_s\{h_1, h_2, h_3\}$ provides orientation information in the sample space. The transformation matrix of any other goniometer geometry, such as kappa geometry (Paciorek *et al.*, 1999), can be introduced into equation (2.5.10) so that the unit vector $\mathbf{h}_s\{h_1, h_2, h_3\}$ can be expressed in terms of the specified geometry. All equations using the unit vector $\mathbf{h}_s\{h_1, h_2, h_3\}$ in this chapter, such as in data treatment, texture analysis and stress measurement, are applicable to all goniometer geometries provided that the unit-vector components are generated from the corresponding transformation matrix from diffraction space to the sample space.

2.5.2.4.3. *Transformation from detector space to reciprocal space*

Reciprocal-space mapping is commonly used to analyse the diffraction patterns from highly oriented structures, diffuse scattering from crystal defects, and thin films (Hanna & Windle, 1995; Mudie *et al.*, 2004; Smilgies & Blasini, 2007; Schmidbauer *et al.*, 2008). The equations of the unit-vector calculation given above can also be used to transform the diffraction intensity from the diffraction space to the reciprocal space with respect to the sample coordinates. The direction of the scattering vector is given by the unit vector $\mathbf{h}_s\{h_1, h_2, h_3\}$ and the magnitude of the scattering vector is given by $2\sin\theta/\lambda$, so that the scattering vector corresponding to a pixel is given by

$$\mathbf{H} = \frac{2\sin\theta}{\lambda}\mathbf{h}_s. \tag{2.5.13}$$

The three-dimensional reciprocal-space mapping can be obtained by applying the normalized pixel intensities to the corresponding reciprocal points. With various sample orientations, all pixels on the detector can be mapped into a 3D reciprocal space.

2.5.3. Instrumentation

2.5.3.1. *X-ray source and optics*

2.5.3.1.1. *Beam path in a diffractometer equipped with a 2D detector*

The Bragg–Brentano (B-B) parafocusing geometry is most commonly used in conventional X-ray diffractometers with a point detector (Cullity, 1978; Jenkins & Snyder, 1996). In the Bragg–Brentano geometry, the sample surface normal is always a bisector between the incident beam and the diffracted beam. A divergent incident beam hits the sample surface with an incident angle θ. The area of the irradiated region depends on the incident angle θ and the size of the divergence slit. The diffracted rays leave the sample at an angle 2θ, pass through the anti-scatter slit and receiving slit, and reach the point detector. Soller slits are used on both the primary side and secondary side to minimize the effects of axial divergence due to the line-focus beam. The primary line-focus beam sliced by the Soller slits can also be considered as an array of point beams parallel to the diffractometer planes. Each of these point beams will produce a diffraction cone from the sample. The overlap of all the diffraction cones will create a smeared diffraction peak. The Soller slits on the receiving side allow only those diffracted beams nearly parallel to the diffractometer plane to pass through, so the smearing effect is minimized. In another words, the so-called 'line-focus geometry' in conventional diffractometry is actually a superposition of many layers of 'spot-focus geometry'.

The beam path in a diffractometer equipped with a 2D detector is different from that in a conventional diffractometer in many respects (He & Preckwinkel, 2002). In a 2D-XRD system the whole or a large portion of the diffraction rings are measured simultaneously, and neither slits nor monochromator can be used between the sample and detector. Therefore, the X-ray source and optics for 2D-XRD systems have different requirements in terms of the beam spectral purity, divergence and beam cross-section profile. Fig. 2.5.9 shows the beam path in a 2D-XRD system with the θ–θ configuration. The geometry for the θ–2θ configuration is equivalent. The X-ray tube, monochromator and collimator assembly are all mounted on the primary side. The incident-beam assembly rotates about the instrument centre and makes an incident angle θ_1 to the sample surface. The first main axis is also called the θ_1 axis. The diffracted beams travel in all directions and some are intercepted by a 2D detector. The detector is mounted on the other main axis, θ_2. The detector position is determined by the sample-to-detector distance D and the detector swing angle α (= $\theta_1 + \theta_2$).

All the components and space between the focal spot of the X-ray tube and sample are collectively referred to as the primary beam path. The primary beam path in a 2D-XRD system is typically sheltered by optical components except between the exit of the collimator and the sample. The X-rays travelling through this open incident-beam path are scattered by the air with two adverse effects. One is the attenuation of the primary beam intensity. The more harmful effect is that the scattered X-rays travel in all directions and some reach the detector, as is shown by the dashed lines with arrows in Fig. 2.5.9. This air scatter introduces a background over the diffraction pattern. Weak diffraction patterns may be buried under the background. Obviously, the air scatter from the incident beam is significantly stronger than that from diffracted X-rays. The intensity of the air scatter from the incident beam is proportional to the length of the open incident-beam path. The effect of air scatter also depends on the wavelength of the X-rays. The longer the wavelength is, the more severe is the air scatter. The secondary beam path is the space between the sample and the 2D detector. The diffracted X-rays are also scattered by air and the diffraction pattern is both attenuated and blurred by the air scattering. In a conventional diffractometer, one can use an anti-scatter slit, diffracted-beam monochromator or detector Soller slits to remove most of the air scatter that is not travelling in the diffracted-beam direction. These measures cannot be used for a 2D-XRD system, which requires an open space between the sample and the 2D detector. Therefore, the open incident-beam path should be kept as small as possible. In order to reduce the air attenuation and air scatter of the incident beam, a helium-purged beam path or a vacuum beam path are sometimes used in a diffractometer. The air scatter from the diffracted X-rays is relatively weak and the effect depends on sample-to-detector distance. It is typically not necessary to take measures to remove air scatter from the diffracted X-rays between the sample and 2D detector if the sample-to-detector distance is 30 cm or less with Cu $K\alpha$ radiation. However, if the sample-to-detector distance is larger than 30 cm or longer-wavelength radiation, such as Co $K\alpha$ or Cr $K\alpha$, is used, it is then necessary to use an He beam path or vacuum beam path to reduce the air scatter.

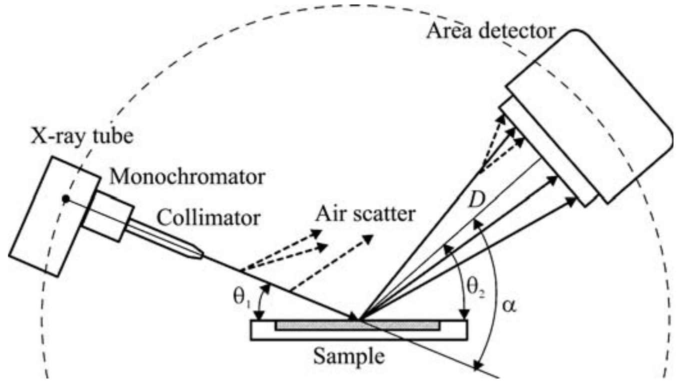

Figure 2.5.9
X-ray beam path in a two-dimensional X-ray diffraction system.

2.5.3.1.2. *Liouville's theorem*

Liouville's theorem can be used to describe the nature of the X-ray source, the X-ray optics and the coupling of the source and optics (Arndt, 1990). Liouville's theorem can be stated in a variety of ways, but for X-ray optics the best known form is

$$S_1\alpha = S_2\beta, \qquad (2.5.14)$$

where S_1 is the effective size of the X-ray source and α is the capture angle determined by the effective size of the X-ray optics and the distance between the source and optics. S_2 is the size of the image focus. β is the convergence angle of the X-ray beam from the optics, which is also determined by the effective size of the X-ray optics and the distance between the optics and the image focus. The β angle is also called the crossfire of the X-ray beam. S_2 and β are typically determined by experimental requirements such as beam size and divergence. Therefore, the product $S_1\alpha$ is also determined by experimental conditions. In another expression of Liouville's theorem, the space volume containing the X-ray photons cannot be reduced with time along the trajectories of the system. Therefore, the brilliance of an X-ray source cannot be increased by optics, but may be reduced because of the loss of X-ray photons passing through the optics. In practice, no optics can have 100% reflectivity or transmission.

Considering this, Liouville's theorem given in equation (2.5.14) should be expressed as

$$S_1\alpha \leq S_2\beta. \qquad (2.5.15)$$

This states that the product of the divergence and image size can be equal to or greater than the product of the capture angle and source size. If the X-ray source is a point with zero area, the focus image from focusing optics or the cross section of a parallel beam can be any chosen size. For focusing optics, the source size must be considerably smaller than the output beam size in order to achieve a gain in flux. In this case, the flux gain is from the increased capture angle. For parallel optics, the divergence angle β is infinitely small by definition, so it is necessary to use an X-ray source as small as possible to achieve a parallel beam. Focusing optics have an advantage over parallel optics in terms of beam flux. Using an X-ray beam with a divergence much smaller than the mosaicity of the specimen crystal does not improve the resolution, but does sacrifice diffraction intensity. For many X-ray diffraction applications with polycrystalline materials, a large crossfire is acceptable as long as the diffraction peaks concerned can be resolved. The improved peak profile and counting statistics can most often compensate for the peak broadening due to large crossfire.

2.5.3.1.3. *X-ray source*

A variety of X-ray sources, from sealed X-ray tubes and rotating-anode generators to synchrotron radiation, can be used for 2D powder diffraction. The history and principles of X-ray generation can be found in many references (Klug & Alexander, 1974; Cullity, 1978). The X-ray beam intensity depends on the X-ray optics, the focal-spot brightness and the focal-spot profile. The focal-spot brightness is determined by the maximum target loading per unit area of the focal spot, also referred to as the specific loading. A microfocus sealed tube (Bloomer & Arndt, 1999; Wiesmann *et al.*, 2007), which has a very small focal spot size (10–50 µm), can deliver a brilliance as much as one to two orders of magnitude higher than a conventional fine-focus sealed tube. The tube, which is also called a 'microsource', is typically air cooled because the X-ray generator power is less than 50 W. The X-ray optics for a microsource, either a multilayer mirror or a polycapillary, are typically mounted very close to the focal spot so as to maximize the gain on the capture angle. A microsource is highly suitable for 2D-XRD because of its spot focus and high brilliance.

If the X-rays used for diffraction have a wavelength slightly shorter than the *K* absorption edge of the sample material, a significant amount of fluorescent radiation is produced, which spreads over the diffraction pattern as a high background. In a conventional diffractometer with a point detector, the fluorescent background can be mostly removed by either a receiving monochromator mounted in front of the detector or by using a point detector with sufficient energy resolution. However, it is impossible to add a monochromator in front of a 2D detector and most area detectors have insufficient energy resolution. In order to avoid intense fluorescence, the wavelength of the X-ray-tube $K\alpha$ line should either be longer than the *K* absorption edge of the sample or far away from the *K* absorption edge. For example, Cu $K\alpha$ should not be used for samples containing significant amounts of the elements iron or cobalt. Since the $K\alpha$ line of an element cannot excite fluorescence of the same element, it is safe to use an anode of the same metallic element as the sample if the X-ray tube is available, for instance Co $K\alpha$ for Co samples. In general, intense fluorescence is produced when the atomic number of the anode material is 2, 3, or 4 larger than that of an element in the sample. When the sample contains Co, Fe or Mn (or Ni or Cu), the use of Cu $K\alpha$ radiation should be avoided; similarly, one should avoid using Co $K\alpha$ radiation if the sample contains Mn, Cr or V, and avoid using Cr $K\alpha$ radiation if the sample contains Ti, Sc or Ca. The effect is reduced when the atomic-number difference increases.

2.5.3.1.4. *X-ray optics*

The function of the X-ray optics is to condition the primary X-ray beam into the required wavelength, beam focus size, beam profile and divergence. Since the secondary beam path in a 2D-XRD system is an open space, almost all X-ray optics components are on the primary side. The X-ray optics components commonly used for 2D-XRD systems include a β-filter, a crystal monochromator, a pinhole collimator, cross-coupled multilayer mirrors, a Montel mirror, a polycapillary and a monocapillary. Detailed descriptions of these optic devices can be found in Chapter 2.1. In principle, the cross-sectional shape of the X-ray beam used in a 2D diffraction system should be small and round. In data-analysis algorithms, the beam size is typically considered to be a point. In practice, the beam cross section can be either round, square or another shape with a limited size. Such an X-ray beam is typically collimated or conditioned by the X-ray optics in two perpendicular directions, so that the X-ray optics used for the point beam are often called 'two-dimensional X-ray optics'.

A pinhole collimator is normally used to control the beam size and divergence in addition to other optic devices. The choice of beam size is often a trade-off between intensity and the ability to illuminate small regions or resolve closely spaced sample features. Smaller beam sizes, such as 50 µm and 100 µm, are preferred for microdiffraction and large beam sizes, such as 0.5 mm or 1 mm, are typically used for quantitative analysis, or texture or crystallinity measurements. In the case of quantitative analysis and texture measurements, using too small a collimator can actually be a detriment, causing poor grain-sampling statistics. The smaller the collimator, the longer the data-collection time. The beam divergence is typically determined by both the collimator and the coupling optic device. Lower divergence is typically associated with a long beam path. At the same time, the beam flux is inversely proportional to the square of the distance between the source and the sample. There are two main factors determining the length of the primary beam path: the first is the required distance for collimating the beam into the required divergence, the second is the space required for the primary X-ray optics, the sample stage and the detector. On the condition that the above two factors are satisfied, the primary X-ray beam path should be kept as short as possible.

2.5.3.2. *2D detector*

Two-dimensional (2D) detectors, also referred to as area detectors, are the core of 2D-XRD. The advances in area-detector technologies have inspired applications both in X-ray imaging and X-ray diffraction. A 2D detector contains a two-dimensional array of detection elements which typically have identical shape, size and characteristics. A 2D detector can simultaneously measure both dimensions of the two-dimensional distribution of the diffracted X-rays. Therefore, a 2D detector may also be referred to as an X-ray camera or imager. There are many technologies for area detectors (Arndt, 1986; Krause & Phillips, 1992; Eatough *et al.*, 1997; Giomatartis, 1998; Westbrook, 1999; Durst *et al.*, 2002; Blanton, 2003; Khazins *et al.*, 2004). X-ray photographic plates and films were the first generation of two-dimensional X-ray detectors. Now, multiwire proportional counters (MWPCs), image plates (IPs), charge-coupled devices (CCDs) and microgap detectors are the most commonly used large area detectors. Recent developments in area detectors include X-ray pixel array detectors (PADs), silicon drift diodes (SDDs) and complementary metal-oxide semiconductor (CMOS) detectors (Ercan *et al.*, 2006; Lutz, 2006; Yagi & Inoue, 2007; He *et al.*, 2011). Each detector type has its advantages over the other types. In order to make the right choice of area detector for a 2D-XRD system and applications, it is necessary to characterize area detectors with consistent and comparable parameters. Chapter 2.1 has more comprehensive coverage on X-ray detectors, including area detectors. This section will cover the characteristics specifically relevant to area detectors.

2.5.3.2.1. *Active area and pixel size*

A 2D detector has a limited detection surface and the detection surface can be spherical, cylindrical or flat. The detection-surface shape is also determined by the detector technology. For example, a CCD detector is made from a large semiconductor wafer, so that only a flat CCD is available, while an image plate is flexible so that it is easily bent to a cylindrical shape. The area of the detection surface, also referred to as the active area, is one of the most important parameters of a 2D detector. The larger the active area of a detector, the larger the solid angle that can be covered at the same sample-to-detector distance. This is especially important when the instrumentation or sample size forbid a short sample-to-detector distance. The active area is also limited by the detector technology. For instance, the active area of a CCD detector is limited by the semiconductor wafer size and fabrication facility. A large active area can be achieved by using a large demagnification optical lens or fibre-optical lens. Stacking several CCD chips side-by-side to build a so-called mosaic CCD detector is another way to achieve a large active area.

In addition to the active area, the overall weight and dimensions are also very important factors in the performance of a 2D detector. The weight of the detector has to be supported by the goniometer, so a heavy detector means high demands on the size and power of the goniometer. In a vertical configuration, a heavy detector also requires a heavy counterweight to balance the driving gear. The overall dimensions of a 2D detector include the height, width and depth. These dimensions determine the manoeuvrability of the detector within a diffractometer, especially when a diffractometer is loaded with many accessories, such as a video microscope and sample-loading mechanism. Another important parameter of a 2D detector that tends to be ignored by most users is the blank margin surrounding the active area of the detector. Fig. 2.5.10 shows the relationship between the maximum measurable 2θ angle and the detector blank margin. For high 2θ angle measurements, the detector swing angle is set so that the incident X-ray optics are set as closely as possible to the detector. The unmeasurable blank angle is the sum of the detector margin m and the dimension from the incident X-ray beam to the outer surface of the optic device h. The maximum measurable angle is given by

$$2\theta_{\max} = \pi - \frac{m+h}{D}. \tag{2.5.16}$$

It can be seen that either reducing the detector blank margin or optics blank margin can increase the maximum measurable angle.

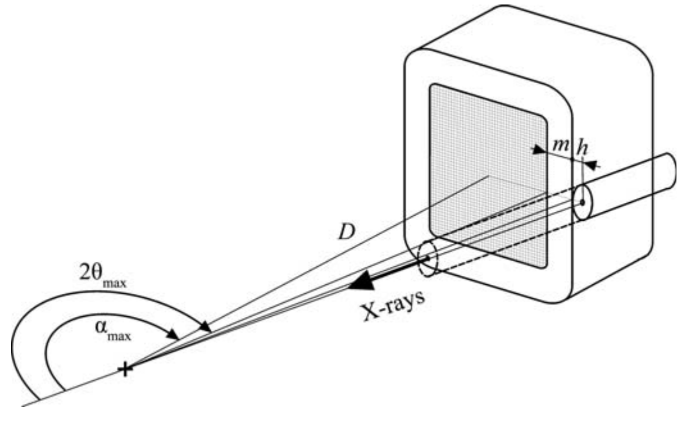

Figure 2.5.10
Detector dimensions and maximum measurable 2θ.

The solid angle covered by a pixel in a flat detector is dependent on the sample-to-detector distance and the location of the pixel in the detector. Fig. 2.5.11 illustrates the relationship between the solid angle covered by a pixel and its location in a flat area detector. The symbol S may represent a sample or a calibration source at the instrument centre. The distance between the sample S and the detector is D. The distance between any arbitrary pixel $P(x, y)$ and the detector centre pixel $P(0, 0)$ is r. The pixel size is Δx and Δy (assuming $\Delta x = \Delta y$). The distance between the sample S and the pixel is R. The angular ranges covered by this pixel are $\Delta\alpha$ and $\Delta\beta$ in the x and y directions, respectively. The solid angle covered by this pixel, $\Delta\Omega$, is then given as

$$\Delta\Omega = \Delta\alpha\Delta\beta = \frac{D}{R^3}\Delta y\Delta x = \frac{D}{R^3}\Delta A, \tag{2.5.17}$$

where $\Delta A = \Delta x\Delta y$ is the area of the pixel and R is given by

$$R = (D^2 + x^2 + y^2)^{1/2} = (D^2 + r^2)^{1/2}. \tag{2.5.18}$$

When a homogeneous calibration source is used, the flux to a pixel at $P(x, y)$ is given as

$$F(x, y) = \Delta\Omega B = \frac{\Delta ADB}{R^3} = \frac{\Delta ADB}{(D^2 + x^2 + y^2)^{3/2}}, \tag{2.5.19}$$

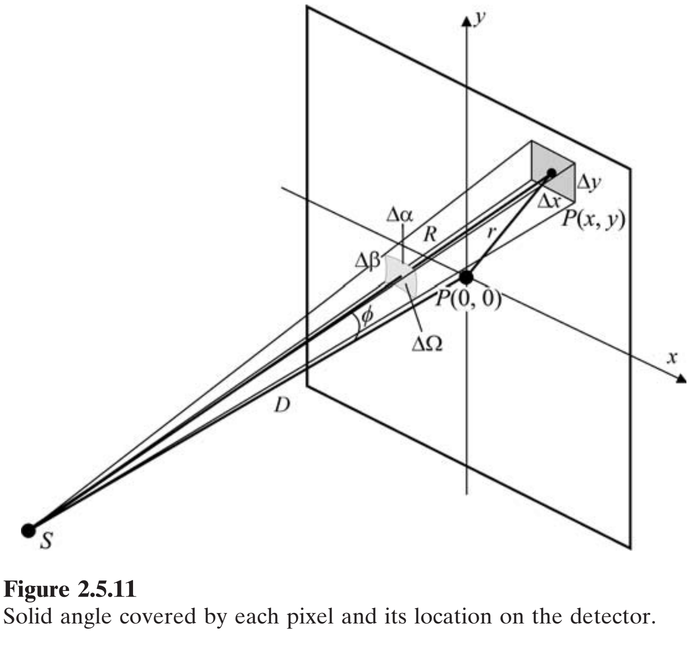

Figure 2.5.11
Solid angle covered by each pixel and its location on the detector.

where $F(x, y)$ is the flux (in photons s^{-1}) intercepted by the pixel and B is the brightness of the source (in photons $\mathrm{s}^{-1}\ \mathrm{mrad}^{-2}$) or scattering from the sample. The ratio of the flux in pixel $P(x, y)$ to that in the centre pixel $P(0, 0)$ is then given as

$$\frac{F(x,y)}{F(0,0)}=\frac{D^3}{R^3}=\frac{D^3}{(D^2+x^2+y^2)^{3/2}}=\cos^3\phi, \qquad (2.5.20)$$

where ϕ is the angle between the X-rays to the pixel $P(x, y)$ and the line from S to the detector in perpendicular direction. It can be seen that the greater the sample-to-detector distance, the smaller the difference between the centre pixel and the edge pixel in terms of the flux from the homogeneous source. This is the main reason why a data frame collected at a short sample-to-detector distance has a higher contrast between the edge and centre than one collected at a long sample-to-detector distance.

2.5.3.2.2. *Spatial resolution of area detectors*

In a 2D diffraction frame, each pixel contains the X-ray intensity collected by the detector corresponding to the pixel element. The pixel size of a 2D detector can be determined by or related to the actual feature sizes of the detector structure, or artificially determined by the readout electronics or data-acquisition software. Many detector techniques allow multiple settings for variable pixel size, for instance a frame of 2048 × 2048 pixels or 512 × 512 pixels. Then the pixel size in 512 mode is 16 (4 × 4) times that of a pixel in 2048 mode. The pixel size of a 2D detector determines the space between two adjacent pixels and also the minimum angular steps in the diffraction data, therefore the pixel size is also referred to as pixel resolution.

The pixel size does not necessarily represent the true spatial resolution or the angular resolution of the detector. The resolving power of a 2D detector is also limited by its point-spread function (PSF) (Bourgeois *et al.*, 1994). The PSF is the two-dimensional response of a 2D detector to a parallel point beam smaller than one pixel. When the sharp parallel point beam strikes the detector, not only does the pixel directly hit by the beam record counts, but the surrounding pixels may also record some counts. The phenomenon is observed as if the point beam has spread over a certain region adjacent to the pixel. In other words, the PSF gives a mapping of the probability density that an X-ray photon is recorded by a pixel in the vicinity of the point where the X-ray beam hits the detector. Therefore, the PSF is also referred to as the spatial redistribution function. Fig. 2.5.12(*a*) shows the PSF produced from a parallel point beam. A plane at half the maximum intensity defines a cross-sectional region within the PSF. The FWHM can be measured at any direction crossing the centroid of the cross section. Generally, the PSF is isotropic, so the FWHMs measured in any direction should be the same.

Measuring the PSF directly by using a small parallel point beam is difficult because the small PSF spot covers a few pixels and it is hard to establish the distribution profile. Instead, the line-spread function (LSF) can be measured with a sharp line beam from a narrow slit (Ponchut, 2006). Fig. 2.5.12(*b*) is the intensity profile of the image from a sharp line beam. The LSF can be obtained by integrating the image from the line beam along the direction of the line. The FWHM of the integrated profile can be used to describe the LSF. Theoretically, LSF and PSF profiles are not equivalent, but in practice they are not distinguished and may be referenced by the detector specification interchangeably. For accurate LSF measurement, the line beam is intentionally positioned with a tilt angle from the orthogonal direction of the pixel array so that the LSF can have smaller steps in the integrated profile (Fujita *et al.*, 1992).

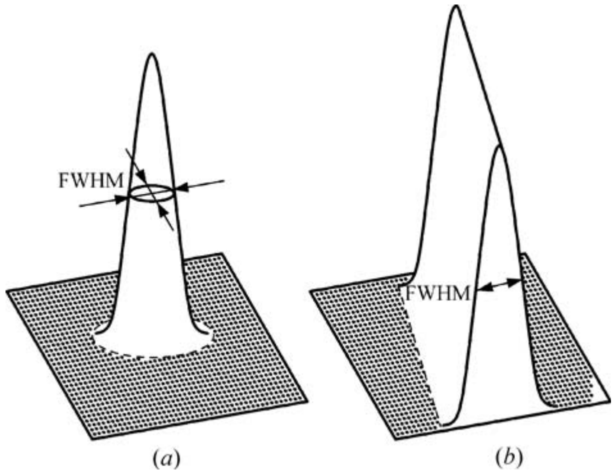

Figure 2.5.12
(*a*) Point-spread function (PSF) from a parallel point beam; (*b*) line-spread function (LSF) from a sharp line beam.

The RMS (root-mean-square) of the distribution of counts is another parameter often used to describe the PSF. The normal distribution, also called the Gaussian distribution, is the most common shape of a PSF. The RMS of a Gaussian distribution is its standard deviation, σ. Therefore, the FWHM and RMS have the following relation, assuming that the PSF has a Gaussian distribution:

$$\mathrm{FWHM}=2[-2\ln(1/2)]^{1/2}\mathrm{RMS}=2.3548\times\mathrm{RMS}. \qquad (2.5.21)$$

The values of the FWHM and RMS are significantly different, so it is important to be precise about which parameter is used when the value is given for a PSF.

For most area detectors, the pixel size is smaller than the FWHM of the PSF. The pixel size should be small enough that at least a 50% drop in counts from the centre of the PSF can be observed by the pixel adjacent to the centre pixel. In practice, an FWHM of 3 to 6 times the pixel size is a reasonable choice if use of a smaller pixel does not have other detrimental effects. A further reduction in pixel size does not necessarily improve the resolution. Some 2D detectors, such as pixel-array detectors, can achieve a single-pixel PSF. In this case, the spatial resolution is determined by the pixel size.

2.5.3.2.3. *Detective quantum efficiency and energy range*

The detective quantum efficiency (DQE), also referred to as the detector quantum efficiency or quantum counting efficiency, is measured by the percentage of incident photons that are converted by the detector into electrons that constitute a measurable signal. For an ideal detector, in which every X-ray photon is converted to a detectable signal without additional noise added, the DQE is 100%. The DQE of a real detector is less than 100% because not every incident X-ray photon is detected, and because there is always some detector noise. The DQE is a parameter defined as the square of the ratio of the output and input signal-to-noise ratios (SNRs) (Stanton *et al.*, 1992):

$$\mathrm{DQE}=\left(\frac{(S/N)_{\mathrm{out}}}{(S/N)_{\mathrm{in}}}\right)^2. \qquad (2.5.22)$$

The DQE of a detector is affected by many variables, for example the X-ray photon energy and the counting rate. The dependence of the DQE on the X-ray photon energy defines the energy range of a detector. The DQE drops significantly if a detector is used out of its energy range. For instance, the energy range of MWPC and microgap detectors is about 3 to 15 keV. The DQE with Cu $K\alpha$ radiation (8.06 keV) is about 80%, but drops gradually when approaching the lower or higher energy limits. The energy range of imaging plates is much wider (4–48 keV). The energy range of a CCD, depending on the phosphor, covers from 5 keV up to the hard X-ray region.

2.5.3.2.4. *Detection limit and dynamic range*

The detection limit is the lowest number of counts that can be distinguished from the absence of true counts within a specified confidence level. The detection limit is estimated from the mean of the noise, the standard deviation of the noise and some confidence factor. In order to have the incoming X-ray photons counted with a reasonable statistical certainty, the counts produced by the X-ray photons should be above the detector background-noise counts.

The dynamic range is defined as the range extending from the detection limit to the maximum count measured in the same length of counting time. The linear dynamic range is the dynamic range within which the maximum counts are collected within the specified linearity. For X-ray detectors, the dynamic range most often refers to linear dynamic range, since only a diffraction pattern collected within the linear dynamic range can be correctly interpreted and analysed. When the detection limit in count rate approaches the noise rate at extended counting time, the dynamic range can be approximated by the ratio of the maximum count rate to the noise rate.

Dynamic range is very often confused with the maximum count rate, but must be distinguished. With a low noise rate, a detector can achieve a dynamic range much higher than its count rate. For example, if a detector has a maximum linear count rate of 10^5 s^{-1} with a noise rate of 10^{-3} s^{-1}, the dynamic range can approach 10^8 for an extended measurement time. The dynamic range for a 2D detector has the same definition as for a point detector, except that with a 2D detector the whole dynamic range extending from the detection limit to the maximum count can be observed from different pixels simultaneously. In order to record the entire two-dimensional diffraction pattern, it is necessary for the dynamic range of the detector to be at least the dynamic range of the diffraction pattern, which is typically in the range 10^2 to 10^6 for most applications. If the range of reflection intensities exceeds the dynamic range of the detector, then the detector will either saturate or have low-intensity patterns truncated. Therefore, it is desirable that the detector has as large a dynamic range as possible.

2.5.3.2.5. *Types of 2D detectors*

2D detectors can be classified into two broad categories: photon-counting detectors and integrating detectors (Lewis, 1994). Photon-counting area detectors can detect a single X-ray photon entering the active area. In a photon-counting detector, each X-ray photon is absorbed and converted to an electrical pulse. The number of pulses counted per unit time is proportional to the incident X-ray flux. Photon-counting detectors typically have high counting efficiency, approaching 100% at low count rate. The most commonly used photon-counting 2D detectors include MWPCs, Si-pixel arrays and microgap detectors. Integrating area detectors, also referred to as analogue X-ray imagers, record the X-ray intensity by measuring the analogue electrical signals converted from the incoming X-ray flux. The signal size of each pixel is proportional to the fluence of incident X-rays. The most commonly used integrating 2D detectors include image plates (IPs) and charge-coupled devices (CCDs).

The selection of an appropriate 2D detector depends on the X-ray diffraction application, the sample condition and the X-ray beam intensity. In addition to geometry features, such as the active area and pixel format, the most important performance characteristics of a detector are its sensitivity, dynamic range, spatial resolution and background noise. The detector type, either photon-counting or integrating, also leads to important differences in performance. Photon-counting 2D detectors typically have high counting efficiency at low count rate, while integrating 2D detectors are not so efficient at low count rate because of the relatively high noise background. An MWPC has a high DQE of about 0.8 when exposed to incoming local fluence from single photons up to about 10^3 photons s^{-1} mm^{-2}. The diffracted X-ray intensities from a polycrystalline or powder sample with a typical laboratory X-ray source fall into this fluence range. This is especially true with microdiffraction, where high sensitivity and low noise are crucial to reveal the weak diffraction pattern. Owing to the counting losses at a high count rate, the DQE of an MWPC decreases with increasing count rate and quickly saturates above 10^3 photons s^{-1} mm^{-2}. Therefore, an MWPC is not suitable for collecting strong diffraction patterns or for use with high intensity sources, such as synchrotron X-ray sources. An IP can be used in a large fluence range from 10 photons s^{-1} mm^{-2} and up with a DQE of 0.2 or lower. An IP is suitable for strong diffraction from single crystals with high-intensity X-ray sources, such as a rotating-anode generator or synchrotron X-ray source. With weak diffraction signals, the image plate cannot resolve the diffraction data near the noise floor. A CCD detector can also be used over a large X-ray fluence range from 10 photons s^{-1} mm^{-2} to very high fluence with a much higher DQE of 0.7 or higher. It is suitable for collecting diffraction of medium to strong intensity from single-crystal or polycrystalline samples. Owing to the relatively high sensitivity and high local count rate, CCDs can be used in systems with either sealed-tube X-ray sources, rotating-anode generators or synchrotron X-ray sources. With a low DQE at low fluence and the presence of dark-current noise, a CCD is not a good choice for applications with weak diffraction signals. A microgap detector has the best combination of high DQE, low noise and high count rate. It has a DQE of about 0.8 at an X-ray fluence from single photons up to about 10^5 photons s^{-1} mm^2. It is suitable for microdiffraction when high sensitivity and low noise are crucial to reveal weak diffraction patterns. It can also handle high X-ray fluence from strong diffraction patterns or be used with high-intensity sources, such as rotating-anode generators or synchrotron X-ray sources.

2.5.3.3. *Data corrections and integration*

2D diffraction patterns contain abundant information. In order to interpret and analyse 2D patterns accurately it is necessary to apply some data-treatment processes (Sulyanov *et al.*, 1994; Scheidegger *et al.*, 2000; Cervellino *et al.*, 2006; Boesecke, 2007; Rowe, 2009). Most data-treatment processes can be categorized as having one of the following four purposes: to eliminate or reduce errors caused by detector defects; to remove undesirable effects of instrument and sample geometry; to transfer a 2D frame into a format such that the data can be presented or further analysed by conventional means and software; and cosmetic treatment, such as smoothing a frame for reports and publications.

2.5.3.3.1. *Nonuniform response correction*

A 2D detector can be considered as an array of point detectors. Each pixel may have its own response, and thus a 2D detector may exhibit some nonuniformity in intensity measurement when exposed to an isotropic source. The nonuniform response can be caused by manufacturing defects, inadequate design or limitations of the detector technology. For instance, a nonuniform phosphor screen or coupling fibre optic for a CCD detector may cause nonuniformity in quantum efficiency (Tate *et al.*, 1995). A gas-filled detector may have a different intensity response between the detector edge and centre due to the variation in the electric field from the centre to the edge. A thorough correction to the nonuniformity of the intensity response can be performed if the detector counting curves of all pixels are given. In practice, this is extremely difficult or impossible, because the behaviour of a pixel may be affected by the condition of the adjacent pixels and the whole detector. The practical way to correct the nonuniformity of the intensity response is to collect an X-ray image from an isotropic point source at the instrument centre and use the image data frame to generate a correction table for the future diffraction frames. The frame collected with the isotropic source is commonly referred to as a 'flood-field' frame or a flat-field image, and the correction is also called a flood-field correction or flat-field correction (Stanton *et al.*, 1992). Another type of correction for a nonuniform response is background correction. Background correction is done by subtracting a background frame from the data frame. The background frame is collected without X-ray exposure. Integrating detectors, such as image plates or CCDs, have a strong background which must be considered in nonuniform response correction. Photon-counting detectors, such as MWPC and microgap detectors, have negligible background, so background correction is not necessary.

The X-ray source for calibration for flood-field correction should be a uniform, spherically radiating point source. Identical brightness should be observed at any pixel on the detector. The radiation strength of the source should match the intensity of the diffraction data to be collected. The photon energy of the source should be the same as or close to the X-ray beam used for diffraction-data collection so that the detector behaves the same way during calibration and data collection.

There are many choices of calibration sources, including X-ray tubes, radioactive sources, diffuse scattering or X-ray fluorescence. The radioactive source Fe-55 (^{55}Fe) is the most commonly used calibration source for a diffraction system because of its major photon energy level of 5.9 keV. X-ray fluorescence is an alternative to a radioactive source. Fluorescence emission is generated by placing a fluorescent material into the X-ray beam. Fluorescence radiation is an isotopic point source if the irradiated area is a small point-like area. For example, Cu $K\alpha$ can produce intense fluorescence from materials containing significant amounts of iron or cobalt and Mo $K\alpha$ can produce intense fluorescence from materials containing yttrium. In order to avoid a high localized intensity contribution from X-ray diffraction, the fluorescent material should be amorphous, such as a glassy iron foil. An alternative to a glassy alloy foil is amorphous lithium borate glass doped with the selected fluorescent element up to a 10% concentration (Moy *et al.*, 1996).

There are many algorithms available for flood-field correction depending on the nature of the 2D detector. The correction is based on the flood-field frame collected from the calibration source. The simplest flood-field correction is to normalize the counts of all pixels to the same level assuming that all pixels have the same response curve. The corrected frame from an isotropic source is not flat, but maintains the $\cos^3\phi$ falloff effect, which will be considered in the frame integration. For gas-filled detectors, such as MWPC and microgap detectors, the pixel intensity response is not independent, but is affected by X-ray exposure to surrounding pixels and the whole detector. Flood-field correction is carried out by applying a normalization factor to each pixel in which a 'rubber-sheet' kind of stretching and shrinking in regions along the x and y detector axes slightly alters the size of each pixel (He, 2009). The total number of counts remains the same after the correction but is redistributed throughout the pixels so that the image from an isotropic source is uniformly distributed across the detector. The flood-field calibration must be done with the same sample-to-detector distance as for the diffraction-data collection.<

2.5.3.3.2. *Spatial correction*

In an ideal flat 2D detector, not only does each pixel have the same intensity response, but also an accurate position. The pixels are aligned in the x and y directions with equal spacing. In most cases we assume that the detective area is completely filled by pixels, so the distance between two neighbouring pixels is equivalent to the pixel size. The deviation from this perfect pixel array is called spatial distortion. The extent of spatial distortion is dependent on the nature and limitation of the detector technology. A CCD detector with 1:1 demagnification may have a negligible spatial distortion, but the barrel distortion in the coupling fibre-optic taper can introduce substantial spatial distortion. An image-plate system may have spatial distortion caused by imperfections in the scanning system (Campbell *et al.*, 1995). MWPC detectors typically exhibit more severe spatial distortion due to the window curvature and imperfections in the wire anode (Derewenda & Helliwell, 1989).

The spatial distortion is measured from X-ray images collected with a uniformly radiating point source positioned at the instrument centre and a fiducial plate fastened to the front surface of the detector. The source for spatial correction should have a very accurate position, point-like shape and small size. The fiducial plate is a metal plate with accurately distributed pinholes in the x and y directions. The X-ray image collected with this setup contains sharp peaks corresponding to the pinhole pattern of the fiducial plate. Since accurate positions of the peaks are given by the fiducial plate, the spatially corrected image is a projection of the collected image to this plane. Therefore, the detector plane is defined as the contacting plane between the fiducial plate and detector front face.

Spatial correction restores the spatially distorted diffraction frame into a frame with correct pixel positions. Many algorithms have been suggested for spatial correction (Sulyanov *et al.*, 1994; Tate *et al.*, 1995; Stanton *et al.*, 1992; Campbell *et al.*, 1995). In the spatially corrected frame each pixel is generated by computing the pixel count from the corresponding pixels based on a spatial-correction look-up table. In a typical spatial-correction process, an image containing the spots from the calibration source passing through the fiducial plate is collected. The distortion of the image is revealed by the fiducial spots. Based on the known positions of the corresponding pinholes in the fiducial plate, the distortion of each fiducial spot can be determined. The spatial correction for all pixels can be calculated and stored as a look-up table. Assuming that the detector behaves the same way in the real diffraction-data collection, the look-up table generated from the fiducial image can then be applied to the real diffraction frames.

The spatial calibration must be done at the same sample-to-detector distance as the diffraction-data collection.

2.5.3.3.3. *Frame integration*

2D frame integration is a data-reduction process which converts a two-dimensional frame into a one-dimensional intensity profile. Two forms of integration are generally of interest in the analysis of a 2D diffraction frame from polycrystalline materials: γ integration and 2θ integration. γ integration sums the counts in 2θ steps ($\Delta 2\theta$) along constant 2θ conic lines and between two constant γ values. γ integration produces a data set with intensity as a function of 2θ. 2θ integration sums the counts in γ steps ($\Delta\gamma$) along constant γ lines and between two constant 2θ conic lines. 2θ integration produces a data set with intensity as a function of γ. γ integration may also be carried out with the integration range in the vertical direction as a constant number of pixels. This type of γ integration may also be referred to as slice integration. A diffraction profile analogous to the conventional diffraction result can be obtained by either γ integration or slice integration over a selected 2θ range. Phase ID can then be done with conventional search/match methods. 2θ integration is of interest for evaluating the intensity variation along γ angles, such as for texture analysis, and is discussed in more depth in Chapter 5.3.

The γ integration can be expressed as

$$I(2\theta) = \int\limits_{\gamma_1}^{\gamma_2} J(2\theta, \gamma)\,\mathrm{d}\gamma, \quad 2\theta_1 \le 2\theta \le 2\theta_2, \tag{2.5.23}$$

where $J(2\theta, \gamma)$ represents the two-dimensional intensity distribution in the 2D frame and $I(2\theta)$ is the integration result as a function of intensity *versus* 2θ. γ_1 and γ_2 are the lower limit and upper limit of integration, respectively, which are constants for γ integration. Fig. 2.5.13 shows a 2D diffraction frame collected from corundum (α-Al_2O_3) powder. The 2θ range is from 20 to 60° and the 2θ integration step size is 0.05°. The γ-integration range is from 60 to 120°. In order to reduce or eliminate the dependence of the integrated intensity on the integration interval, the integrated value at each 2θ step is normalized by the number of pixels, the arc length or the solid angle. γ integration with normalization by the solid angle can be expressed as

$$I(2\theta) = \frac{\int_{\gamma_1}^{\gamma_2} J(2\theta, \gamma)(\Delta 2\theta)\,\mathrm{d}\gamma}{\int_{\gamma_1}^{\gamma_2} (\Delta 2\theta)\,\mathrm{d}\gamma}, \quad 2\theta_1 \le 2\theta \le 2\theta_2. \tag{2.5.24}$$

Since the $\Delta 2\theta$ step is a constant, the above equation becomes

$$I(2\theta) = \frac{\int_{\gamma_1}^{\gamma_2} J(2\theta, \gamma)\,\mathrm{d}\gamma}{\gamma_2 - \gamma_1}, \quad 2\theta_1 \le 2\theta \le 2\theta_2. \tag{2.5.25}$$

There are many integration software packages and algorithms available for reducing 2D frames into 1D diffraction patterns for polycrystalline materials (Cervellino *et al.*, 2006; Rodriguez-Navarro, 2006; Boesecke, 2007). With the availability of tremendous computer power today, a relatively new method is the bin method, which treats pixels as having a continuous distribution in the detector. It demands more computer power than older methods, but delivers much more accurate and smoother results even with $\Delta 2\theta$ integration steps significantly smaller than the pixel size. Depending on the relative size of $\Delta 2\theta$ to the pixel size, each contributing pixel is divided into several 2θ 'bins'. The intensity counts of all pixels within the $\Delta 2\theta$ step are summarized. All the normalization methods in the above integration, either by pixel, arc or solid angle, result in an intensity level of one pixel or unit solid angle. Since a pixel is much smaller than the active area of a typical point detector, the normalized integration tends to result in a diffraction pattern with fictitiously low intensity counts, even though the true counts in the corresponding $\Delta 2\theta$ range are significantly higher. In order to avoid this misleading outcome, it is reasonable to introduce a scaling factor. However, there is no accurate formula for making the integrated profile from a 2D frame comparable to that from a conventional point-detector scan. The best practice is to be aware of the differences and to try not to make direct comparisons purely based on misleading intensity levels. Generally speaking, for the same exposure time, the total counting statistics from a 2D detector are significantly better than from a 0D or 1D detector.

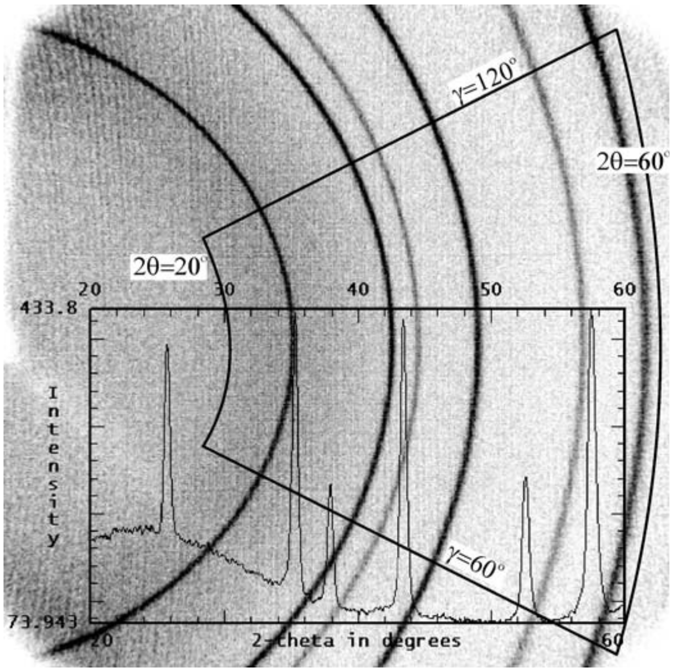

Figure 2.5.13
A 2D frame showing γ integration.

2.5.3.3.4. *Lorentz, polarization and absorption corrections*

Lorentz and polarization corrections may be applied to the diffraction frame to remove their effect on the relative intensities of Bragg peaks and background. The 2θ angular dependence of the relative intensity is commonly given as a Lorentz–polarization factor, which is a combination of Lorentz and polarization factors. In 2D diffraction, the polarization factor is a function of both 2θ and γ, therefore it should be treated in the 2D frames, while the Lorentz factor is a function of 2θ only. The Lorentz correction can be done either on the 2D frames or on the integrated profile. In order to obtain relative intensities equivalent to a conventional diffractometer with a point detector, reverse Lorentz and polarization corrections may be applied to the frame or integrated profile.

The Lorentz factor is the same as for a conventional diffractometer. For a sample with a completely random orientation distribution of crystallites, the Lorentz factor is given as

$$L = \frac{\cos\theta}{\sin^2 2\theta} = \frac{1}{4\sin^2\theta\cos\theta}. \tag{2.5.26}$$

The Lorentz factor may be given by a different equation for a different diffraction geometry (Klug & Alexander, 1974). The forward and reverse Lorentz corrections are exactly reciprocal

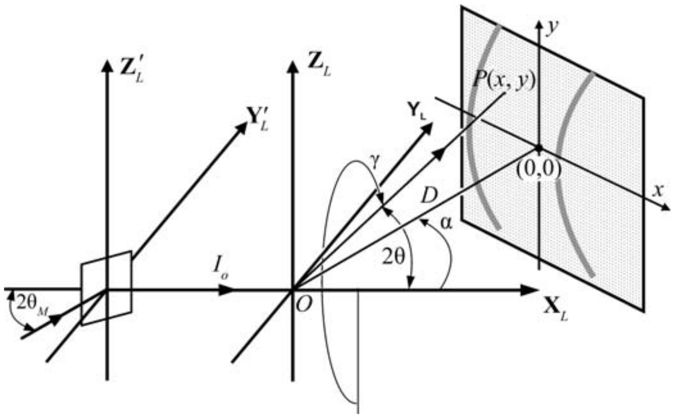

Figure 2.5.14
Geometric relationship between the monochromator and detector in the laboratory coordinates.

and effectively cancel each other. Therefore, it is not necessary to perform the Lorentz correction to the frame before integration if relative intensities equivalent to a conventional Bragg–Brentano diffractometer are expected. The Lorentz correction can be done on the integrated diffraction profiles in the same way as on the diffraction profiles collected with conventional diffractometers.

When a non-polarized X-ray beam is scattered by matter, the scattered X-rays are polarized. The intensity of the diffracted beam is affected by the polarization; this effect is expressed by the polarization factor. In two-dimensional X-ray diffraction the diffraction vectors of the monochromator diffraction and sample crystal diffraction are not necessarily in the same plane or perpendicular planes. Therefore, the overall polarization factor is a function of both 2θ and γ. Fig. 2.5.14 illustrates the geometric relationship between the monochromator and detector in the laboratory coordinates, X_L, Y_L, Z_L. The monochromator is located at the coordinates X_L, Y'_L, Z'_L, which is a translation of the laboratory coordinates along the X_L axis in the negative direction. The monochromator crystal is rotated about the Z'_L axis and $2\theta_M$ is the Bragg angle of the monochromator crystal. The diffracted beam from the monochromator propagates along the X_L direction. This is the incident beam to the sample located at the instrument centre O. The 2D detector location is given by the sample-to-detector distance D and swing angle α. The pixel $P(x, y)$ represents an arbitrary pixel on the detector. 2θ and γ are the corresponding diffraction-space parameters for the pixel. Since a monochromator or other beam-conditioning optics can only be used on the incident beam, the polarization factor for 2D-XRD can then be given as a function of both θ and γ:

$$P(\theta, \gamma) = \frac{(1+\cos^2 2\theta_M \cos^2 2\theta)\sin^2\gamma + (\cos^2 2\theta_M + \cos^2 2\theta)\cos^2\gamma}{1+\cos^2 2\theta_M}. \tag{2.5.27}$$

If the crystal monochromator rotates about the Y'_L axis, *i.e.* the incident plane is perpendicular to the diffractometer plane, the polarization factor for two-dimensional X-ray diffraction can be given as

$$P(\theta, \gamma) = \frac{(1+\cos^2 2\theta_M \cos^2 2\theta)\cos^2\gamma + (\cos^2 2\theta_M + \cos^2 2\theta)\sin^2\gamma}{1+\cos^2 2\theta_M}. \tag{2.5.28}$$

In the above equations, the term $\cos^2 2\theta_M$ can be replaced by $|\cos^n 2\theta_M|$ for different monochromator crystals. For a mosaic crystal, such as a graphite crystal, $n = 2$. For most real monochromator crystals, the exponent n takes a value between 1 and 2. For near perfect monochromator crystals, n approaches 1 (Kerr & Ashmore, 1974). All the above equations for polarization factors may apply to multilayer optics. However, since multilayer optics have very low Bragg angles, $|\cos^n 2\theta_M|$ approximates to unity. The γ dependence of the polarization factor diminishes in this case. The polarization factor approaches

$$P(\theta, \gamma) \simeq \frac{1+\cos^2 2\theta}{2}. \tag{2.5.29}$$

2.5.3.3.5. *Air scatter*

X-rays are scattered by air molecules in the beam path between the X-ray source and detector. Air scatter results in two effects: one is the attenuation of the X-ray intensity, the other is added background in the diffraction pattern. Air scatter within the enclosed primary beam path – for instance, in the mirror, monochromator housing or collimator – results in attenuation of only the incident beam. The enclosed beam path can be purged by helium gas or kept in vacuum to reduce the attenuation so that no correction is necessary for this part of the air scatter. The open beam between the tip of the collimator and the sample generates an air-scatter background pattern, which is the major part of the air scatter. In the secondary beam path, the air scatter from the diffracted beam may generate background too, but the main effect of the air scatter is inhomogeneous attenuation of the diffraction pattern due to the different beam path lengths between the centre and the edge of the detector.

The background generated by air scattering from the open incident-beam path has a strong 2θ dependence. The specific scattering curve depends on the length of the open primary beam path, the beam size and the wavelength of the incident beam. There are two approaches to correct air scatter. One is to collect an air-scatter background frame under the same conditions as the diffraction frame except without a sample. The background frame is then subtracted from the diffraction frame. Another approach is to remove the background from the integrated profile, since the background is 2θ dependent.

The attenuation of the diffracted beam by air absorption depends on the distance between the sample and pixel. For a flat detector, air absorption can be corrected by

$$p_c(x, y) = p_o(x, y)\exp\left[\mu_{\rm air}(D^2 + x^2 + y^2)^{1/2}\right], \tag{2.5.30}$$

where $p_o(x, y)$ is the original pixel intensity of the pixel $P(x, y)$ and $p_c(x, y)$ is the corrected intensity. The detector centre is given by (0, 0). $\mu_{\rm air}$ is the linear absorption coefficient of air. The value of $\mu_{\rm air}$ is determined by the radiation wavelength. By approximation, for air with 80% N_2 and 20% O_2 at sea level and at 293 K, $\mu_{\rm air} = 0.01$ cm^{-1} for Cu $K\alpha$ radiation. Air scatter and absorption increases with increasing wavelength. For example, $\mu_{\rm air} = 0.015$ cm^{-1} for Co $K\alpha$ radiation and 0.032 cm^{-1} for Cr $K\alpha$ radiation. The absorption coefficient for Mo $K\alpha$ radiation, $\mu_{\rm air} = 0.001$ cm^{-1}, is only one-tenth of that for Cu $K\alpha$ radiation, so an air-absorption correction is not necessary. Alternatively, the absorption correction may be normalized to the absorption level in the beam centre as

$$p_c(x, y) = p_o(x, y)\exp\left\{\mu_{\rm air}\left[(D^2 + x^2 + y^2)^{1/2} - D\right]\right\}. \tag{2.5.31}$$

In this normalized correction the attenuation by air scatter is not fully corrected for each pixel, but rather corrected to the same attenuation level as the pixel in the detector centre. This means that the effect of path-length differences between the detector centre pixel and other pixels are eliminated.

2.5.3.3.6. *Sample absorption*

The absorption of X-rays by the sample reduces the diffracted intensity. Many approaches are used to calculate and correct the absorption effect for various sample shapes and geometries [*International Tables for Crystallography* Volume C, Chapter 6.3 (Maslen, 1992); Ross, 1992; Pitschke *et al.*, 1996; Zuev, 2006]. The sample absorption can be measured by the transmission coefficient (also referred to as the absorption factor):

$$A = (1/V) \int_V \exp(-\mu\tau)\,\mathrm{d}V, \qquad (2.5.32)$$

where A is the transmission coefficient, μ is the linear absorption coefficient and τ is the total beam path in the sample, which includes the incident-beam path and diffracted-beam path. Fig. 2.5.15(*a*) shows reflection-mode diffraction with a flat-plate sample. The thickness of the plate is t. z is the distance of the element dV from the sample surface. The normal to the reflection surface is **n**. The incident beam is represented by the unit vector $\mathbf{s}_o$ and the diffracted beam by the unit vector **s**. The transmission coefficient is given as (Maslen, 1992)

$$A = \frac{1-\exp\{-\mu t[(1/\cos\eta)+(1/\cos\zeta)]\}}{\mu[(\cos\zeta/\cos\eta)+1]}, \qquad (2.5.33)$$

where η is the angle between the incident beam and the normal to the sample surface, and ζ is the angle between the diffracted beam and the sample normal. For two-dimensional X-ray diffraction, there is a single incident-beam direction at a time, but various diffracted-beam directions simultaneously, so

$$\cos\eta = \sin\omega\cos\psi \qquad (2.5.34)$$

and

$$\begin{aligned}\cos\zeta = &-\cos 2\theta\sin\omega\cos\psi - \sin 2\theta\sin\gamma\cos\omega\cos\psi\\ &-\sin 2\theta\cos\gamma\sin\psi. \end{aligned}\qquad (2.5.35)$$

The transmission coefficient from equation (2.5.33) contains a length unit, which creates ambiguity if such transmission coefficients are used to correct the intensity pixel-by-pixel. In order to make the relative intensity comparable to the results from Bragg–Brentano geometry, we introduce a new transmission coefficient, which is normalized by the transmission coefficient of the Bragg–Brentano geometry, $A_{\rm BB} = 1/(2\mu)$. This normalized transmission coefficient is also a numerical factor without units. The transmission coefficient with normalization will be denoted by T hereafter in this chapter. The transmission coefficient for reflection-mode diffraction with a flat sample of thickness t is then given as

$$T = A/A_{\rm BB} = \frac{2\cos\eta\big(1-\exp\{-\mu t[(1/\cos\eta)+(1/\cos\zeta)]\}\big)}{\cos\eta+\cos\zeta}. \qquad (2.5.36)$$

For a thick plate or material with a very high linear absorption coefficient, the transmission through the sample thickness is negligible and the above equation becomes

$$T = \frac{2\cos\eta}{\cos\eta+\cos\zeta}. \qquad (2.5.37)$$

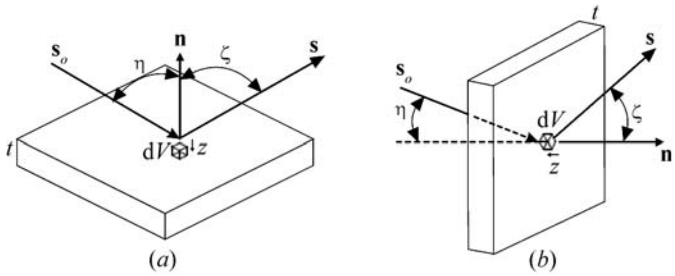

Figure 2.5.15
Absorption correction for a flat slab: (*a*) reflection; (*b*) transmission.

Fig. 2.5.15(*b*) shows transmission-mode diffraction with a flat-plate sample. The thickness of the plate is t. The normal to the reflection surface is represented by the unit vector **n**. The incident beam is represented by the unit vector $\mathbf{s}_o$ and the diffracted beam by the unit vector **s**. η is the angle between the incident beam and the normal of the sample surface, and ζ is the angle between the diffracted beam and the sample normal.

The transmission coefficient normalized by $A_{\rm BB} = 1/(2\mu)$ is given by (Maslen, 1992; Ross, 1992)

$$T = \frac{2\sec\eta[\exp(-\mu t\sec\eta)-\exp(-\mu t\sec\zeta)]}{\sec\zeta-\sec\eta} \quad \text{for } \sec\zeta \neq \sec\eta. \qquad (2.5.38)$$

For two-dimensional X-ray diffraction in transmission mode

$$\cos\eta = \sin\omega\sin\psi\sin\varphi + \cos\omega\cos\varphi \qquad (2.5.39)$$

and

$$\begin{aligned}\cos\zeta = &(\sin\omega\sin\psi\sin\varphi+\cos\omega\cos\varphi)\cos 2\theta\\ &+(\cos\omega\sin\psi\sin\varphi-\sin\omega\cos\varphi)\sin 2\theta\sin\gamma\\ &-\cos\psi\sin\varphi\sin 2\theta\cos\gamma.\end{aligned} \qquad (2.5.40)$$

It is very common practice to set the incident angle perpendicular to the sample surface, *i.e.* $\eta = 0$. For most transmission-mode data collection, equation (2.5.40) becomes

$$T = \frac{2[\exp(-\mu t)-\exp(-\mu t\sec\zeta)]}{\sec\zeta-1}. \qquad (2.5.41)$$

When $\eta = \zeta$, both the numerator and denominator approach zero, and the transmission coefficient should be given by

$$T = 2\mu t\sec\zeta\exp(-\mu t\sec\zeta). \qquad (2.5.42)$$

It is common practice to load the sample perpendicular to the incident X-ray beam at the goniometer angles $\omega = \psi = \varphi = 0$. Therefore, $\cos\eta = 1$ and $\cos\zeta = \cos 2\theta$, and the transmission coefficient becomes

$$T = \frac{2\cos 2\theta[\exp(-\mu t)-\exp(-\mu t/\cos 2\theta)]}{1-\cos 2\theta}. \qquad (2.5.43)$$

The maximum scattered intensity occurs when

$$t = \frac{\cos 2\theta\ln\cos 2\theta}{\mu(\cos 2\theta - 1)}. \qquad (2.5.44)$$

This equation can be used to select the optimum sample thickness for transmission-mode diffraction. For example, if the measurement 2θ range is between 3 and 50°, the preferred sample thickness should be given by μt = 0.8–1.0.

2.5.4. Applications

2.5.4.1. *Phase identification*

In materials science, a phase is defined as a region that has uniform chemical composition and physical properties, including crystal structure. Therefore, every phase should give a unique diffraction pattern. A sample for X-ray diffraction may contain a single phase or multiple phases. Analysis of the diffraction pattern can accurately and precisely determine the contents of the sample. This qualitative analysis is called phase identification (phase ID). One of the most efficient methods of phase identification is to compare the diffraction pattern from an unknown material to those in a database of a large number of standard diffraction patterns. The most comprehensive database is the Powder Diffraction File (PDF), updated annually by the International Centre for Diffraction Data (ICDD).

Two-dimensional X-ray diffraction has enhanced phase identification in many respects (Rudolf & Landes, 1994; Sulyanov *et al.*, 1994; Hinrichsen, 2007). Because of its ability to collect diffracted X-rays in a large angular range in both the 2θ and γ directions, it can collect diffraction data with high speed and better sampling statistics than obtained by conventional diffraction. Owing to point-beam illumination on the sample, a relatively small sample size is required for phase identification. The large 2D detector allows for a large 2θ range to be analysed without any movement of the sample and detector. This makes it possible to perform *in situ* phase investigation on samples during phase transformations, chemical reactions and deformations. The diffraction information in the γ direction allows accurate phase identification of samples with large grains and preferred orientation.

In the Bragg–Brentano geometry, the 2θ resolution is controlled by the selection of the divergence slit and receiving slit in the diffractometer plane, and the axial divergence is controlled by Soller slits, while in a diffractometer with a 2D detector, the 2θ resolution is mainly determined by the spatial resolution of the detector and the sample-to-detector distance. The relative peak intensity in a diffraction pattern from a sample with texture measured with a 2D detector can be significantly different from the results measured with Bragg–Brentano geometry. It is imperative to study the nature of these discrepancies so that the diffraction patterns collected with 2D detectors can be used for phase ID with proper understanding and correction if necessary.

When two-dimensional diffraction is used for phase identification, the first step is to integrate the 2D diffraction frame into a diffraction profile resembling the diffraction pattern collected with a conventional diffractometer (Cervellino *et al.*, 2006; Rodriguez-Navarro, 2006; Boesecke, 2007; Fuentes-Montero *et al.*, 2011; Hammersley, 2016). The integrated diffraction profiles can be analysed with all existing algorithms and methods, including profile fitting with conventional peak shapes and fundamental parameters, quantification of phases, and lattice-parameter determination and refinement (Ning & Flemming, 2005; Flemming, 2007; Jabeen *et al.*, 2011). The results can be used to search a powder-diffraction database to find possible matches. Since there is a great deal of literature covering these topics (Cullity, 1978; Jenkins & Snyder, 1996; Pecharsky & Zavalij, 2003), this section will focus on the special characteristics of two-dimensional X-ray diffraction as well as system geometry, data-collection strategies and data analysis in dealing with relative peak intensities, 2θ resolution, grain size and distribution, and preferred orientation. Many factors and correction algorithms described here can help in understanding the characteristics of two-dimensional diffraction. In most applications, however, the γ-integrated profile can be used for phase identification without these corrections.

2.5.4.1.1. *Relative intensity*

The integrated intensity diffracted from polycrystalline materials with a random orientation distribution is given by

$$I_{hkl} = k_I \frac{p_{hkl}}{v^2} (\mathrm{LPA}) \lambda^3 F_{hkl}^2 g_{hkl}(\alpha, \beta) \exp(-2M_t - 2M_s), \quad (2.5.45)$$

where k_I is an instrument constant that is a scaling factor between the experimental observed intensities and the calculated intensity, p_{hkl} is the multiplicity factor of the crystal plane (hkl), v is the volume of the unit cell, (LPA) is the Lorentz–polarization and absorption factors, λ is the X-ray wavelength, F_{hkl} is the structure factor for the crystal plane (hkl), $g_{hkl}(\alpha, \beta)$ is the normalized pole-density distribution function and $\exp(-2M_t - 2M_s)$ is the attenuation factor due to lattice thermal vibrations and weak static displacements (Warren, 1990; He *et al.*, 1994). Except for the texture effect, all the factors in the above equation are either discussed in the previous sections or have the same definitions and values as in conventional diffraction.

Phase-identification studies by XRD are preferably carried out on powders or polycrystalline samples with a random orientation distribution of crystallites. Preferred orientation causes relative intensities to deviate from theoretical calculations or those reported in reference databases. In practice, a sample with a perfectly random orientation distribution of crystallites is very hard to fabricate and most polycrystalline samples have a preferred orientation to a certain extent. Discrepancies in the relative peak intensities between conventional diffraction and 2D-XRD are largely due to texture effects. For B-B geometry, the diffraction vector is always perpendicular to the sample surface. With a strong texture, it is possible that the pole density of certain reflections in the sample normal direction is very low or even approaches zero. In this case, the peak does not appear in the diffraction pattern collected in B-B geometry. In 2D-XRD, several diffraction rings may be measured with a single incident beam; the corresponding diffraction vectors are not necessarily in the sample normal direction. The diffraction profiles from 2D frames are produced by γ integration, therefore the texture factor $g_{hkl}(\alpha, \beta)$ should be replaced by the average normalized pole-density function within the γ integration range $\langle g_{hkl}(\Delta\gamma)\rangle$. The relation between (α, β) and $(2\theta, \gamma)$ is given in Chapter 5.4. The chance of having zero pole density over the entire γ-integration range is extremely small. Therefore, phase identification with 2D-XRD is much more reliable than with conventional diffraction.

2.5.4.1.2. *Detector distance and resolution*

The 2θ resolution with B-B geometry is controlled by the size of the slits. Smaller apertures of the divergence slit are used for higher 2θ resolution and larger apertures for fast data collection. With a two-dimensional X-ray diffraction system, the 2θ resolution is achieved with different approaches. A flat 2D detector has the flexibility to be used at different sample-to-detector distances. The detector resolution is determined by the pixel size and point-spread function. For the same detector resolution and detector active area, a higher resolution can be achieved at larger distance, and higher angular coverage at shorter distance. The sample-to-detector distance should be optimized depending on the 2θ measurement range and required resolution. In situations where the 2θ range of one frame is not enough, several frames at

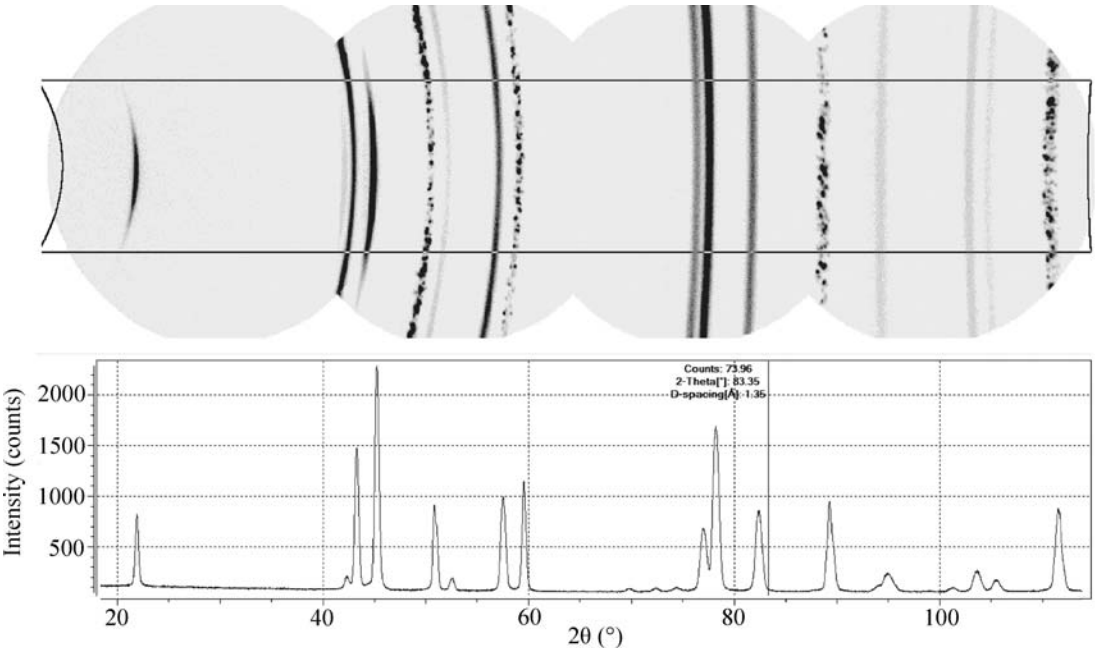

Figure 2.5.16
Diffraction pattern merged from four 2D frames collected from a battery material.

sequential 2θ ranges can be collected. The integrated profiles can then be merged to achieve a large 2θ range. Fig. 2.5.16 shows four 2D frames collected from a battery material with a microgap detector. The slice integration region is defined by two conic lines and two horizontal lines. The diffraction profile integrated from the merged frames is displayed below.

2.5.4.1.3. *Defocusing effect*

A 2D diffraction pattern over a range of 2θ is measured simultaneously with a single incident angle, so the incident angle has to be lower than the minimum 2θ angle. Since the reflected angle cannot always be the same as the incident angle, geometric aberrations are observed. The defocusing effect occurs when the incident angle is lower than the reflection angle. At low incident angles, the incident beam spreads over the sample surface into an area much larger than the size of the original X-ray beam. The observed diffracted beam size is magnified by the defocusing effect if the diffracted beam makes an angle larger than the incident angle. The defocusing effect for reflection-mode diffraction can be expressed as

$$\frac{B}{b}=\frac{\sin\theta_2}{\sin\theta_1}=\frac{\sin(2\theta-\omega)}{\sin\omega}, \qquad (2.5.46)$$

where θ_1 is the incident angle, b is the incident beam size and B is diffracted beam size. The ratio of B to b is a measurement of the geometric aberration and will be referred to as the defocusing factor. In principle, defocusing occurs only when B/b is larger than 1. The reflected beam is actually focused to the detector when $\theta_2 < \theta_1$. The defocusing effect occurs when $\theta_2 > \theta_1$ and the defocusing factor increases with increasing θ_2 or decreasing θ_1. The maximum defocusing appears at $\theta_2 = 90°$. For the θ–2θ configuration, the incident angle ω (= θ_1) is used in the equation.

For B-B geometry with a divergent slit and receiving slit of the same size the defocusing factor is always 1. With a 2D detector the defocusing factor varies with the 2θ angle. If a large 2θ range is measured on a flat sample in reflection mode, it is always desirable to collect several frames at different incident angles for each 2θ range so as to improve the 2θ resolution. A cylindrical detector may collect a diffraction pattern over a large 2θ range (Gelfi *et al.*, 2005). However, the defocusing effect prevents it from being used for a large 2θ range for a flat sample. Fig. 2.5.17 compares the effect for a flat detector and a cylindrical detector. Fig. 2.5.17(*a*) shows a cylindrical detector being used to collect a diffraction pattern from a flat sample for a 2θ range of 5 to 80°. The incident angle must be kept at 5° or lower. Fig. 2.5.17(*b*) shows a flat detector being used to collect the diffraction pattern over the same 2θ range. In order to minimize the defocusing effect, the data collection is done at four different incident angles (5, 15, 25 and 35°) with four corresponding detector swing angles (10, 30, 50 and 70°). Fig. 2.5.17(*c*) compares the defocusing factors of the two configurations. The horizontal dot-dashed line with defocusing factor B/b = 1 represents the situation with B-B geometry. The defocusing factor continues to increase with 2θ angle up to B/b = 11 for cylindrical detector. That means that the 2θ resolution would be 10 times worse than for the B-B geometry. For the diffraction pattern collected with a flat detector in four steps, the defocusing factor fluctuates above 1, with the worst value being less than 3. Another approach to avoiding defocusing is to collect the diffraction pattern in transmission mode. There is no defocusing effect in transmission when the incident beam is perpendicular to the sample surface. Therefore, the transmission pattern has significantly better 2θ resolution. Transmission-mode diffraction also has other advantages. For instance, the air scattering from the primary beam may be blocked by a flat sample, therefore lowering the background from air scattering. However, transmission-mode diffraction data can only be collected from samples with limited thickness, and the maximum scattering intensity is achieved at low 2θ angles with a sample thickness of $t = 1/\mu$, where μ is the linear absorption coefficient. The scattering intensity drops dramatically when the thickness increases.

2.5.4.1.4. *Sampling statistics*

In powder X-ray diffraction, the number of crystallites contributing to each reflection must be sufficiently large to generate reproducible integrated peak intensities (see Chapter 2.10). A larger number of contributing crystallites gives better precision or sampling statistics (also referred to as particle

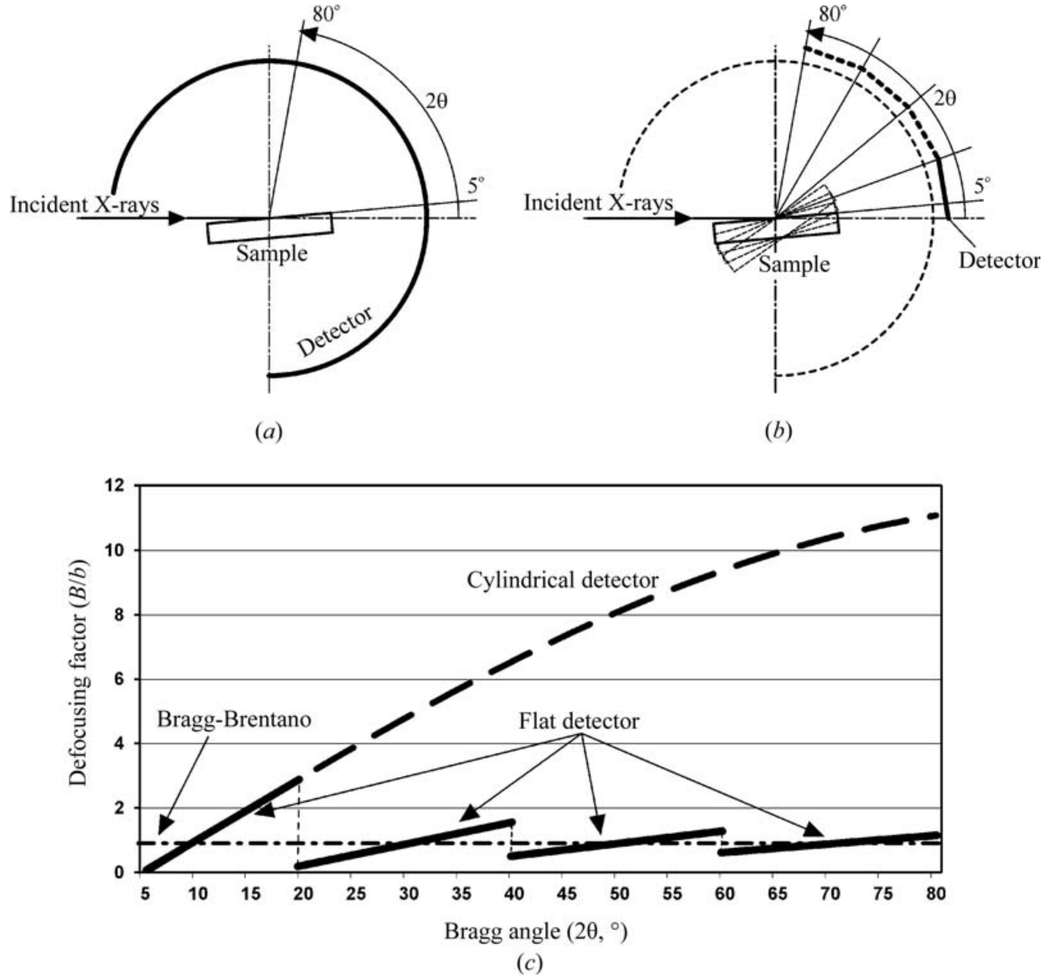

Figure 2.5.17
Defocusing effects: (*a*) cylindrical detector; (*b*) flat detector at various incident angles and detector swing angles; (*c*) comparison of defocusing factors.

statistics). Sampling statistics are determined by both the structure of the sample and the instrumentation. For a powder sample in which the crystallites are perfectly randomly oriented, the number of contributing crystallites for a diffraction peak can be given as

$$N_s = p_{hkl}\frac{Vf_i}{v_i}\frac{\Omega}{4\pi}, \tag{2.5.47}$$

where p_{hkl} is the multiplicity of the diffracting planes, V is the effective sampling volume, f_i is the volume fraction of the measuring crystallites ($f_i = 1$ for single-phase materials), v_i is the volume of individual crystallites and Ω is the angular window of the instrument (given as a solid angle). The multiplicity term, p_{hkl}, effectively increases the number of crystallites contributing to the integrated intensity from a particular set of (*hkl*) planes. The volume of individual crystallites, v_i, is an average of various crystallite sizes. The combination of the effective sampling volume and the angular window makes up the instrumental window, which determines the total volume of polycrystalline material making a contribution to a Bragg reflection. For 2D-XRD, the instrumental window is not only determined by the incident beam size and divergence, but also by the detective area and the sample-to-detector distance (γ angular coverage).

In B-B geometry, the effective irradiated volume is a constant,

$$V_{\rm BB} = A_oA_{\rm BB} = A_o/2\mu, \tag{2.5.48}$$

where A_o is the cross-section area of the incident beam measured on the sample surface, $A_{\rm BB} = 1/(2\mu)$ is the transmission coefficient for B-B geometry, and μ is the linear absorption coefficient. For 2D-XRD, the effective volume is given as

$$V = A_oA = A_oT/2\mu, \tag{2.5.49}$$

where A is the transmission coefficient and T is the transmission coefficient with B-B normalization for either transmission or reflection as given previously.

The angular window is given as a solid angle. The incident beam has a divergence angle of β_1 within the diffraction plane and β_2 in the perpendicular direction. The angular window corresponding to the incident-beam divergence is given by

$$\Omega = \beta_1\beta_2/\sin\theta \text{ or } \Omega = \beta^2/\sin\theta \text{ if } \beta = \beta_1 = \beta_2. \tag{2.5.50}$$

For 2D-XRD, the angular window is not only determined by the incident-beam divergence, but also significantly increased by γ integration. When γ integration is used to generate the diffraction profile, it actually integrates the data collected over a range of various diffraction vectors. Since the effect of γ integration on sampling statistics is equivalent to the angular oscillation on the ψ axis in a conventional diffractometer, the effect is referred to as virtual oscillation and $\Delta\psi$ is the virtual oscillation angle. In conventional oscillation, mechanical movement may result in some sample-position error. Since there is no actual physical movement of the sample stage during data collection, virtual oscillation can avoid this error. This is crucial for microdiffraction. The angular window with the contributions of both the incident-beam divergence and the virtual oscillation is

$$\Omega = \beta\Delta\psi = 2\beta\arcsin[\cos\theta\sin(\Delta\gamma/2)], \tag{2.5.51}$$

where β is the divergence of the incident beam. While increasing the divergence angle β may introduce instrumental broadening which deteriorates the 2θ resolution, virtual oscillation improves sampling statistics without introducing instrumental broadening.

In the cases of materials with a large grain size or preferred orientation, or of microdiffraction with a small X-ray beam size, it can be difficult to determine the 2θ position because of poor counting statistics. In these cases, some kind of sample oscillation, either by translation or rotation, can bring more crystallites into the diffraction condition. Angular oscillation is an enhancement to the angular window of the instrument. The effect is that the angular window scans over the oscillation angle. Any of the three rotation angles (ω, ψ, φ) or their combinations can be used as oscillation angles. Angular oscillation can effectively improve the sampling statistics for both large grain size and preferred orientation. As an extreme example, a powder-diffraction pattern can be generated from single-crystal sample if a sufficient angular window can be achieved by sample rotation in such as way as to simulate a Gandolfi camera (Guggenheim, 2005). Sample oscillation is not always necessary if virtual oscillation can achieve sufficient sampling statistics.

2.5.4.2. *Texture analysis*

Most natural or artificial solid materials are polycrystalline, consisting of many crystallites (also called grains) of various sizes, shapes and orientations. When the orientations of the crystallites in a material have a random distribution, it presents isotropic properties. The anisotropic orientation distribution of crystallites is referred to as preferred orientation or texture. Depending on the degree of the preferred orientation, a sample is referred to as having a weak, moderate or strong texture. Many electrical, optical or mechanical properties of materials are affected or determined by their texture. The determination and interpretation of textures are therefore of fundamental importance in materials science and technology (Bunge, 1983).

When a conventional X-ray diffractometer with a point detector is used for texture measurement, the crystallite orientation distribution in one direction is measured at a time, and full texture information is measured by rotating the sample to all the desired orientations. When a two-dimensional X-ray diffraction system is used for texture measurement, the orientation distributions of several crystallographic planes over a range of angles can be measured simultaneously so as to get better measurement results in a shorter data-collection time (Smith & Ortega, 1993; Blanton, 1994; Bunge & Klein, 1996; Helming *et al.*, 2003; Wenk & Grigull, 2003; He, 2009). The orientation relationships between different phases or between different layers of thin films and substrates can also be easily revealed. The texture effect may be observed and evaluated directly from the 2D diffraction frames without data processing.

2.5.4.2.1. *Pole density and pole figures*

XRD results from an 'ideal' powder in which the crystallites are randomly oriented normally serve as a basis for determining the relative intensity of each diffraction peak. The deviation of the grain orientation distribution of a polycrystalline material from that of an ideal powder is measured as texture. The pole figure for a particular crystallographic plane is normally used to represent the texture of a sample. Assuming that all grains have the same volume, each 'pole' represents a grain that satisfies the Bragg condition. The number of grains satisfying the Bragg condition at a particular sample orientation can be larger or smaller than the number of grains for an ideal sample, and likewise for the integrated intensity of that peak. The measured 2D diffraction pattern contains two very important parameters at each γ angle: the partially integrated intensity I and the Bragg angle 2θ. Fig. 2.5.18 shows a 2D frame for a Cu thin film on an Si wafer collected with a microgap 2D detector. It contains four Cu lines and one Si spot. The diffraction intensity varies along γ because of the anisotropic pole-density distribution. For each diffraction ring, the intensity is a function of γ and the sample orientation (ω, ψ, φ), *i.e.* $I = I(\gamma, \omega, \psi, \varphi)$.

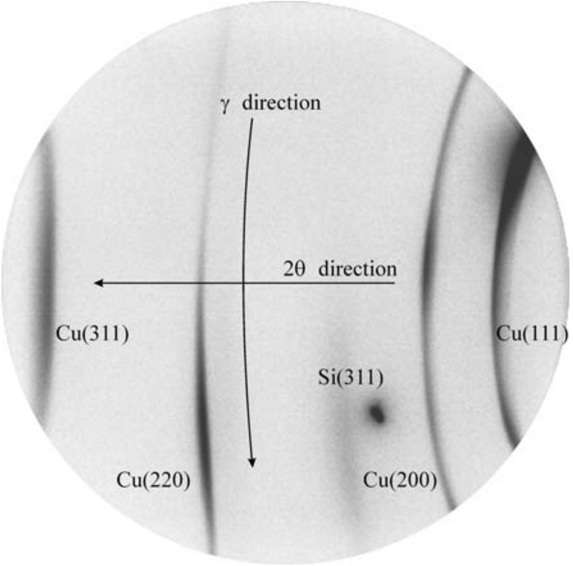

Figure 2.5.18
Diffraction frame collected from a Cu film on an Si substrate showing intensity variation along γ due to texture.

Plotting the intensity of each (hkl) line with respect to the sample coordinates in a stereographic projection gives a qualitative view of the orientation of the crystallites with respect to a sample direction. These stereographic projection plots are called pole figures. As is shown in Fig. 2.5.19(a), the sample orientation is defined by the sample coordinates S_1, S_2 and S_3. For metals with rolling texture, the axes S_1, S_2 and S_3 correspond to the transverse direction (TD), rolling direction (RD) and normal direction (ND), respectively. Let us consider a sphere with unit radius and the origin at O. A unit vector representing an arbitrary pole direction starts from the origin O and ends at the point P on the sphere. The pole direction is defined by the radial angle α and azimuthal angle β. The pole density at the point P projects to the point P' on the equatorial plane through a straight line from P to the point S. The pole densities at all directions are mapped onto the equatorial plane by stereographic projection as shown in Fig. 2.5.19(b). This two-dimensional mapping of the pole density onto the equatorial plane is called a pole figure. The azimuthal angle β projects to the pole figure as a rotation angle about the centre of the pole figure from the sample direction S_1. When plotting the pole density into a pole figure of radius R, the location of the point P' in the pole figure should be given by β and

$$r = R\tan\left(\frac{\pi}{4} - \frac{\alpha}{2}\right) = R\tan\frac{\chi}{2}. \qquad (2.5.52)$$

For easy computer plotting and easy angular readout from the pole figure, the radial angle α may be plotted on an equally spaced angular scale, similar to a two-dimensional polar coordinate system. Other pole-figure mapping styles may be used, but must be properly noted to avoid confusion (Birkholz, 2006).

2.5.4.2.2. *Fundamental equations*

The α and β angles are functions of γ, ω, ψ, φ and 2θ. As shown in Fig. 2.5.19(*a*), a pole has three components h_1, h_2 and h_3, parallel to the three sample coordinates S_1, S_2 and S_3, respectively. The pole-figure angles (α, β) can be calculated from the unit-vector components by the following pole-mapping equations:

$$\alpha = \sin^{-1}|h_3| = \cos^{-1}(h_1^2 + h_2^2)^{1/2}, \qquad (2.5.53)$$

$$\beta = \pm\cos^{-1}\frac{h_1}{(h_1^2 + h_2^2)^{1/2}} \qquad \begin{cases} \beta \geq 0^\circ \text{ if } h_2 \geq 0 \\ \beta < 0^\circ \text{ if } h_2 < 0 \end{cases}, \qquad (2.5.54)$$

where α takes a value between 0 and 90° ($0^\circ \leq \alpha \leq 90^\circ$) and β takes values in two ranges ($0^\circ \leq \beta \leq 180^\circ$ when $h_2 > 0$ and $-180^\circ \leq \beta < 0^\circ$ when $h_2 < 0$). The condition for reflection-mode diffraction is $h_3 > 0$. For transmission diffraction it is possible that $h_3 < 0$. In this case, the pole with mirror symmetry about the S_1S_2 plane to the diffraction vector is used for the pole-figure mapping. The absolute value of h_3 is then used in the equation for the α angle. When $h_2 = 0$ in the above equation, β takes one of two values depending on the value of h_1 ($\beta = 0^\circ$ when $h_1 \geq 0$ and $\beta = 180^\circ$ when $h_1 < 0$). For Eulerian geometry, the unit-vector components $\{h_1, h_2, h_3\}$ are given by equation (2.5.11).

The 2θ integrated intensity along the diffraction ring is then converted to the pole-density distribution along a curve on the pole figure. The α and β angles at each point of this curve are calculated from ω, ψ, φ, γ and 2θ. The sample orientation (ω, ψ, φ) and 2θ for a particular diffraction ring are constants; only γ takes a range of values depending on the detector size and distance.

For a textured sample, the 2θ-integrated intensity of a diffraction ring from a family of (*hkl*) planes is a function of γ and the sample orientation (ω, ψ, φ), *i.e.* $I_{hkl} = I_{hkl}(\omega, \psi, \varphi, \gamma, \theta)$. From the pole-figure angle-mapping equations, we can obtain the integrated intensity in terms of pole-figure angles as

$$I_{hkl}(\alpha, \beta) = I_{hkl}(\omega, \psi, \varphi, \gamma, \theta). \qquad (2.5.55)$$

The pole density at the pole-figure angles (α, β) is proportional to the integrated intensity at the same angles:

$$P_{hkl}(\alpha, \beta) = K_{hkl}(\alpha, \beta) I_{hkl}(\alpha, \beta), \qquad (2.5.56)$$

where $I_{hkl}(\alpha, \beta)$ is the 2θ-integrated intensity of the (*hkl*) peak corresponding to the pole direction (α, β), $K_{hkl}(\alpha, \beta)$ is the scaling factor covering the absorption, polarization, background corrections and various instrument factors if these factors are included in the integrated intensities, and $P_{hkl}(\alpha, \beta)$ is the pole-density distribution function. Background correction can be done during the 2θ integration and will be discussed in Section 2.5.4.2.4. The pole figure is obtained by plotting the pole-density function based on the stereographic projection.

The pole-density function can be normalized such that it represents a fraction of the total diffracted intensity integrated over the pole sphere. The normalized pole-density distribution function is given by

$$g_{hkl}(\alpha, \beta) = \frac{2\pi P_{hkl}(\alpha, \beta)}{\int_0^{2\pi} \int_0^{\pi/2} P_{hkl}(\alpha, \beta) \cos\alpha \, \mathrm{d}\alpha \, \mathrm{d}\beta}. \qquad (2.5.57)$$

The pole-density distribution function is a constant for a sample with a random orientation distribution. Assuming that the sample and instrument conditions are the same except for the pole-density distribution, we can obtain the normalized pole-density function by

$$g_{hkl}(\alpha, \beta) = \frac{I_{hkl}(\alpha, \beta)}{I_{hkl}^{\text{random}}(\alpha, \beta)}. \qquad (2.5.58)$$

The integrated intensity from the textured sample without any correction can be plotted according to the stereographic projection as an ‘uncorrected’ pole figure. The same can be done for the sample with a random orientation distribution to form a ‘correction’ pole figure that contains only the factors to be corrected. The normalized pole figure is then obtained by dividing the ‘uncorrected’ pole figure by the ‘correction’ pole figure. This experimental approach is feasible only if a similar sample with a random orientation distribution is available.

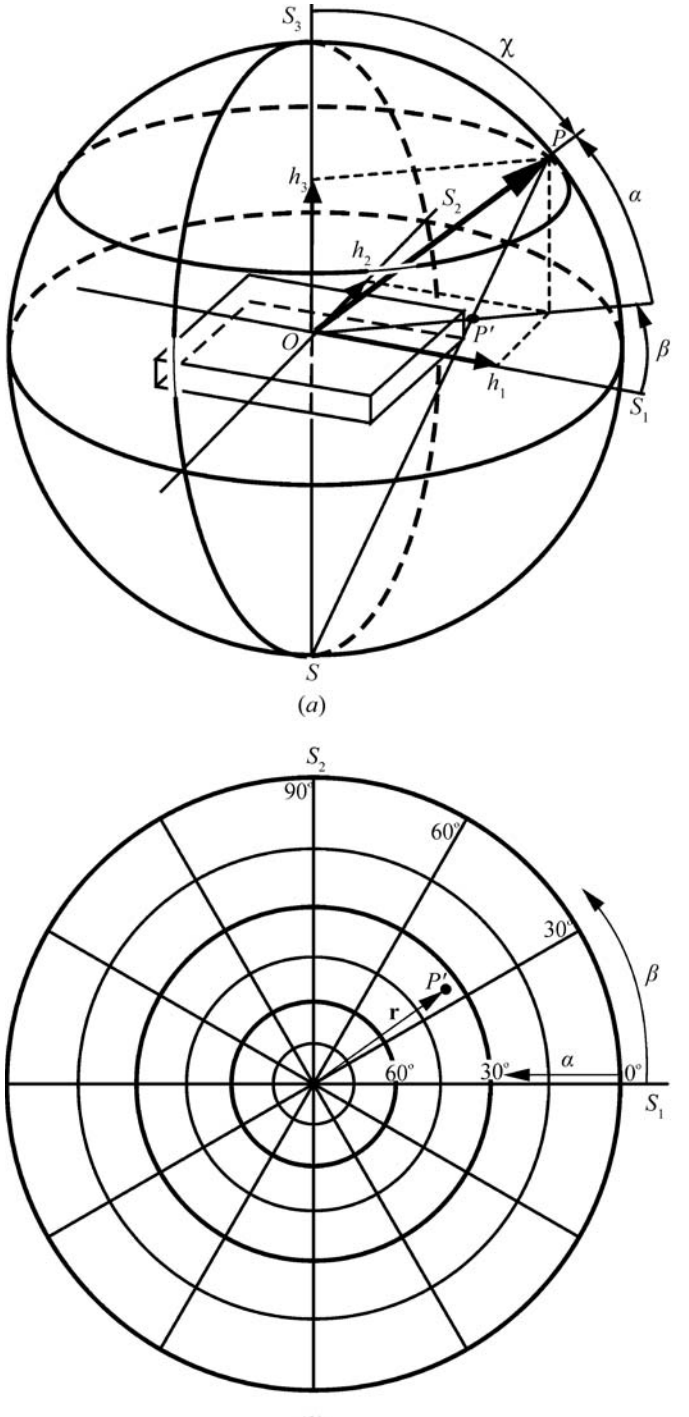

(*a*)

(*b*)

Figure 2.5.19
(*a*) Definition of pole direction angles α and β; (*b*) stereographic projection in a pole figure.

If the texture has a rotational symmetry with respect to an axis of the sample, the texture is referred to as a fibre texture and the axis is referred to as the fibre axis. The sample orientation containing the symmetry axis is referred to as the fibre axis. The fibre texture is mostly observed in two types of materials: metal wires or rods formed by drawing or extrusion, and thin films formed by physical or chemical deposition. The fibre axis is the wire axis for a wire and normal to the sample surface for thin films. Fibre texture can also be artificially formed by rotating a sample about its normal. If the fibre axis is aligned to the S_3 direction, the pole-density distribution function becomes independent of the azimuthal angle β. For samples with fibre texture, or artificially formed fibre texture by rotating, the pole-density function is conveniently expressed as a function of a single variable, $g_{hkl}(\chi)$. Here, χ is the angle between the sample normal and pole direction.

$$\chi = 90^\circ - \alpha \text{ or } \chi = \cos^{-1}|h_3|. \qquad (2.5.59)$$

The pole-density function for fibre texture can be expressed as a fibre plot. The fibre plot $g_{hkl}(\chi)$ can be calculated from the relative intensity of several peaks (He, 1992; He *et al.*, 1994) and artificial fibre texture can be achieved by sample spinning during data collection.

2.5.4.2.3. *Data-collection strategy*

Since a one-dimensional pole-density mapping is created from each 2D frame, it is important to lay out a data-collection strategy so as to have the optimum pole-figure coverage and minimum redundancy in data collection. The pole-figure coverage can be simulated from the diffraction 2θ angle, detector swing angle, detector distance, goniometer angles and scanning steps. When a large 2D detector is placed close to the sample, it is possible to collect a pole figure with a single φ scan. Fig. 2.5.20(*a*) shows an example of a scheme generated by a single φ scan of 5° steps with a detector 10.5 cm in diameter and D = 7 cm. The data collected with a single exposure at φ = 0° would generate a one-dimensional pole figure as shown in the curve marked by A and B. The pole figure can be generated by a full-circle rotation of 360°. The pole density at the centre represents the diffraction vector perpendicular to the sample surface. It is important to have the pole-density information in the centre region of the pole figure, especially for fibre texture. The pole-figure angle at the centre is α = 90°, and the best strategy is to put point A at the centre of pole figure. That is

$$h_3^A = \sin\theta\cos\psi\sin\omega - \cos\theta\sin\gamma_A\cos\psi\cos\omega - \cos\theta\cos\gamma_A\sin\psi = 1. \qquad (2.5.60)$$

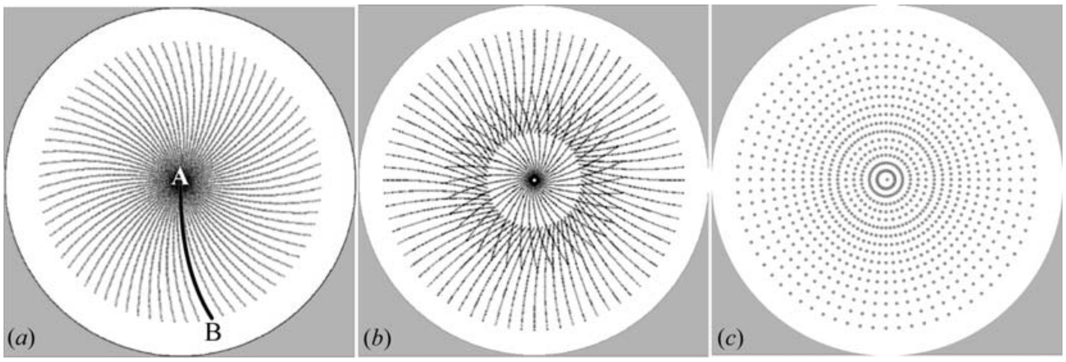

Figure 2.5.20
Data-collection strategy: (*a*) 2D detector with D = 7 cm; (*b*) 2D detector with D = 10 cm; (c) point detector.

In some cases, a single φ scan is not enough to cover sufficient pole-figure angles because of a large detector distance or limited detector area, so it is necessary to collect a set of data with φ scans at several different sample tilt angles. Fig. 2.5.20(*b*) illustrates the data-collection scheme with a detector that is 10.5 cm in diameter and D = 10 cm for the (111) plane of a Cu thin film. In this case, each pole figure requires two φ scans at different sample orientations. The data-collection strategy should also be optimized for several crystallographic planes if all can be covered in a frame. The step size of the data-collection scan depends highly on the strength of the texture and the purpose of the texture measurements. For a weak texture, or quality control for metal parts, φ (or ω, or ψ) scan steps of 5° may be sufficient. For strong textures, such as thin films with epitaxial structure, scan steps of 1° or smaller may be necessary.

The effectiveness of two-dimensional data collection for a texture can be compared with that using a point detector with the data-collection strategy of the Cu thin film as an example. Fig. 2.5.20(*c*) shows the pole-figure data-collection strategy with a point detector. For the same pole-figure resolution, significantly more exposures are required with a point detector. Considering that several diffraction rings are measured simultaneously with a 2D detector, the pole-figure measurement is typically 10 to 100 times faster than with a point detector. Therefore, quantitative high-resolution pole-figure measurements are only practical with a 2D-XRD system (Bunge & Klein, 1996).

2.5.4.2.4. *Texture-data processing*

For a specific diffraction ring, 2θ is a constant or at least assumed to be constant for texture analysis, and the sample-orientation angles (ω, ψ, φ) for a frame are also constants. Therefore, the pole-density information is given by the diffraction-intensity distribution as a function of γ only, or $I = I(\gamma)$. Integration of the diffraction intensities in the 2θ direction converts 2D information into the function $I(\gamma)$.

Fig. 2.5.21(*a*) shows a 2D diffraction ring for texture analysis. The low and high background and diffraction-ring 2θ–γ range are defined by three boxes, noted as B_L, B_H and $I(\gamma)$, respectively. All three boxes have the same γ range from γ_1 to γ_2. The 2θ ranges for the diffraction ring, low background and high background should be determined based on the width of the 2θ peak and available background between adjacent peaks. Assuming a normal distribution, a 2θ range of 2 times the FWHM covers 98% of the intensity peak, and 3 times the FWHM covers more than 99.9%. The 2θ range should also be broad enough to cover the possible 2θ shifts caused by residual stresses in the sample. Fig. 2.5.21(*b*) is the 2θ profile integrated over the section $\Delta\gamma$ in Fig. 2.5.21(*a*). The background ranges on the low and high 2θ sides are given by $2\theta_{L1}$–$2\theta_{L2}$ and $2\theta_{H1}$–$2\theta_{H2}$, respectively. The 2θ-integrated diffraction intensities as a function of γ are plotted in Fig. 2.5.21(*c*). The background can be calculated and removed from the intensity values of the low and high backgrounds or ignored if the contribution of the background is very small.

2θ integration without a background correction can be

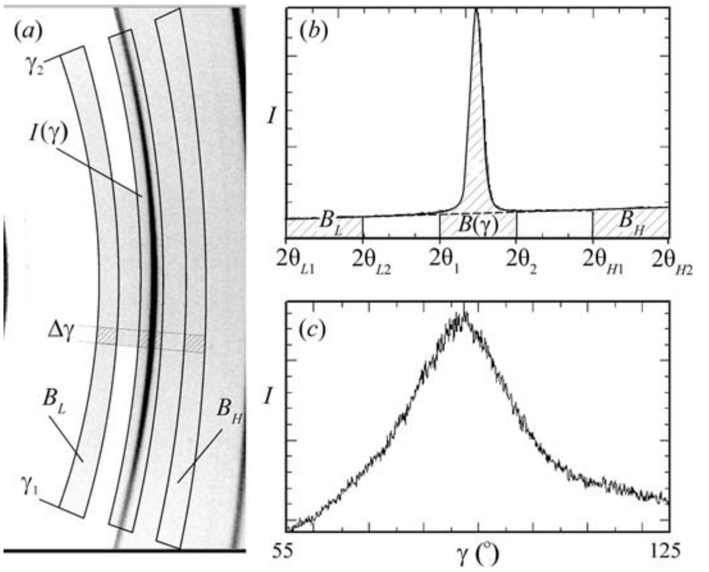

Figure 2.5.21
Pole-figure data processing: (*a*) a frame with the 2θ integration ranges for the (220) ring; (*b*) 2θ profile showing the background and peak; (*c*) integrated intensity distribution as a function of γ.

expressed as

$$I(\gamma) = \int_{2\theta_1}^{2\theta_2} J(2\theta, \gamma)\, \mathrm{d}(2\theta), \quad \gamma_1 \le \gamma \le \gamma_2. \tag{2.5.61}$$

A similar equation can be used for 2θ integration of the low and high backgrounds $B_L(\gamma)$ and $B_H(\gamma)$. Assuming a linear background change in the vicinity of the 2θ peak, the background under the peak, $B(\gamma)$, is then given by

$$\begin{aligned} B(\gamma) = {} & B_L(\gamma)\frac{(2\theta_2 - 2\theta_1)(2\theta_{H2} + 2\theta_{H1} - 2\theta_2 - 2\theta_1)}{(2\theta_{L2} - 2\theta_{L1})(2\theta_{H2} + 2\theta_{H1} - 2\theta_{L2} - 2\theta_{L1})} \\ & + B_H(\gamma)\frac{(2\theta_2 - 2\theta_1)(2\theta_2 + 2\theta_1 - 2\theta_{L2} - 2\theta_{L1})}{(2\theta_{H2} - 2\theta_{H1})(2\theta_{H2} + 2\theta_{H1} - 2\theta_{L2} - 2\theta_{L1})}. \end{aligned} \tag{2.5.62}$$

Then the background $B(\gamma)$ can be subtracted from the integrated intensity distribution $I(\gamma)$.

The algorithms of γ integration given in Section 2.5.4.2.3 can be easily modified for 2θ integration by exchanging γ and 2θ in the equations. Algorithms with solid-angle normalization should be used to get consistent integrated intensity over all areas of the detector. The 2θ-integrated intensity distribution can then be mapped onto a pole figure based on the fundamental equations (2.5.53) and (2.5.54). When a pole-figure pixel is overlapped by more than one data point from different scans, as shown in the region covered by two scans in Fig. 2.5.20(*b*), the average value should be mapped to that pole-figure pixel. Fig. 2.5.22(*a*) shows pole-density mappings on the pole figure. There are big gaps between the measured pole-density data points due to the large φ-scan steps of 5°.

All factors affecting relative intensities, such as Lorentz, polarization, air scattering, and Be-window and sample absorption, will have an effect on the measured pole densities for the pole figures. Some or all these corrections may be applied to the diffraction frames before 2θ integration if the texture study demands high accuracy in the relative pole densities. Among these factors, the most important factor is sample absorption, since data sets for pole figures are typically collected at several different incident angles. A ridge between the pole-density regions covered by two different incident angles may be observed if sample absorption is not properly corrected.

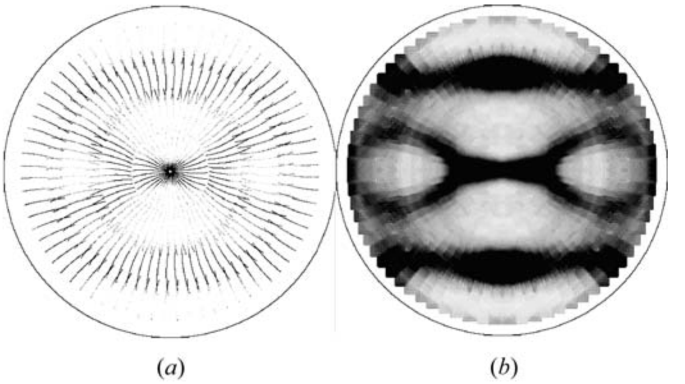

Figure 2.5.22
Pole-figure processing: (*a*) $I(\gamma)$ mapped to the pole figure; (*b*) Pole figure after interpolation and symmetry processing.

2.5.4.2.5. *Pole-figure interpolation and use of symmetry*

The pole figure is stored and displayed as a bitmap image. The pole-density data from the data set may not fill up all the pixels of the pole-figure image. In order to generate a smooth pole figure, the unmapped pixels are filled with values generated from the interpolation of the surrounding pixels. A linear interpolation within a defined box is sufficient to fill the unmapped pixels. The size of the box should be properly chosen. A box that is too small may not be able to fill all unmapped pixels and a box that is too big may have a smearing effect on the pole figure, especially if a sharp pole figure is processed. All the gaps between the measured pole-density points are filled after this interpolation. For a sample with sharp texture, smaller φ-scan steps should be used.

All pole figures possess symmetry as a consequence of the Laue symmetry of the crystallites in the sample. This symmetry can be used to fill in values for pixels in the pole figure for which data were not measured, or to smooth the pole figure. For example, orthorhombic materials exhibit *mmm* symmetry, thus one needs to collect only an octant or quadrant of the pole sphere to generate the entire pole figure. The pole figures of materials with higher symmetry may be treated by using lower symmetry in the processing. For instance, one can use 2/*m* or *mmm* symmetry for hexagonal materials and *mmm* for cubic materials. In symmetry processing, all the symmetry-equivalent pole-figure pixels are filled by the average value of the measured pixels. For the unmeasured pole-figure pixels, this symmetry processing fills in a value from the average of all the equivalent pixels. For the measured pixels, this average processing serves as a smoothing function. Fig. 2.5.22(*b*) shows the results after both interpolation and use of symmetry.

2.5.4.2.6. *Orientation relationship*

A 2D-XRD system can measure texture from a sample containing a single phase, multiple phases or single crystals. The orientation relationship between different phases, or thin films and substrates, can be revealed because data are collected from all phases of the sample simultaneously. One example is the measurement of pole figures for a magnetron sputter-deposited Cu film on an Si wafer (He *et al.*, 2005). Fig. 2.5.23 shows the overlapped pole figures of the Cu (111) film and Si (400) substrate in a 2D pole figure (*a*) and 3D surface plot (*b*). The three sharp spots from the (400) spots of the Si wafer show the wafer cut orientation of (111). The Cu (111) pole density maxi-

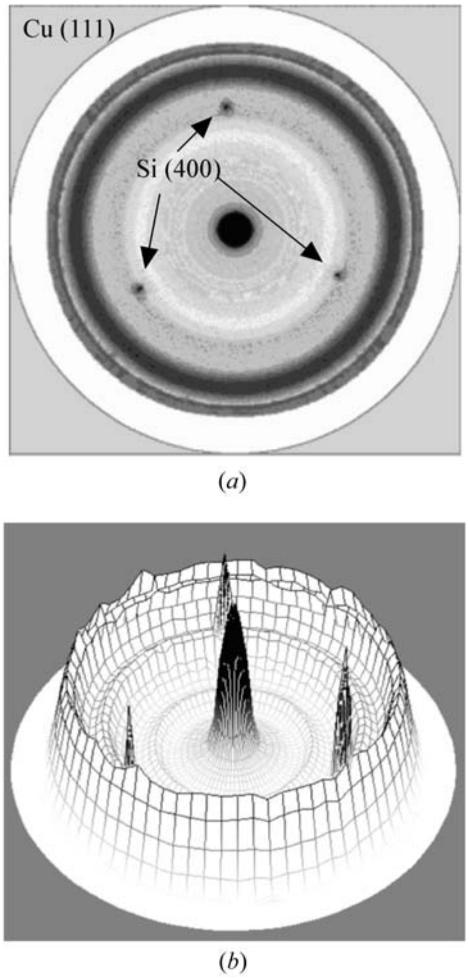

Figure 2.5.23
Combined pole figure of a Cu (111) film on an Si (400) substrate: (*a*) regular 2D projection; (*b*) 3D surface plot.

mized in the centre of the pole figure shows a strong (111) fibre texture. The orientation relationship between the film fibre axis and the substrate is clearly described by the combined pole figures. For samples containing multiple thin-film layers, the orientation relationships between the different layers of the films and substrate can be revealed by superimposing their pole figures.

2.5.4.3. *Stress measurement*

When a solid material is elastically deformed by a force, each crystallite in it changes shape or size. Assuming that the stresses in each crystallite represent the stresses in the solid, the stresses can be measured by measuring the lattice *d*-spacing changes in the crystallites. These *d*-spacing changes can be measured by the changes in diffraction-peak positions based on Bragg's law. In this case, the *d*-spacing serves as a gauge of the deformation. Stress measurement by X-ray diffraction is typically done using a point detector or line detector (Walter, 1971; James & Cohen, 1980; Noyan & Cohen, 1987; Lu, 1996); this will be referred to as the conventional method. The stress or stress tensor is calculated from many strain measurements from diffraction-peak 2θ shifts of a specific lattice-plane family. With a point or line detector, only a small cross section of the diffraction cone is measured at one sample orientation (ψ, φ). Compared to using a conventional detector, 2D detectors have many advantages in stress measurement (Borgonovi, 1984; Korhonen *et al.*, 1989; Yoshioka & Ohya, 1992; Fujii & Kozaki, 1993; He & Smith, 1997; Kämpfe *et al.*, 1999; Hanan *et al.*, 2004). Since a 2D diffraction pattern covers the whole or a large portion of the diffraction rings, it can be used to measure stress with higher accuracy and can be collected in a shorter time than a conventional diffraction pattern, especially when dealing with highly textured materials, large grain sizes, small sample areas, weak diffraction, stress mapping and stress-tensor measurement. The 2D method for stress measurement is based on the fundamental relationship between the stress tensor and the diffraction-cone distortion (He & Smith, 1997; He, 2000; European Standard, 2008).

There are two kinds of stresses, which depend on the source of the loading forces that produce them. One kind is applied stress, caused by external forces acting on the solid object. Applied stress changes when the loading forces change and it disappears once the forces are removed. The stresses measured by X-ray diffraction method are mostly residual stresses. Residual stress is caused by internal forces between different parts of a solid body. Residual stress exists without external forces or remains after the external forces have been removed. The net force and moment on a solid body in equilibrium must be zero, so the residual stresses in the body must be balanced within the body. This means that a compressive stress in one part of the body must come with a tensile stress in another part of the body. For example, the residual stress in a thin film is balanced by the stresses in the substrate. When residual stress in a solid body is mentioned it typically refers to a specific location.

Residual stresses are generally categorized as macroscopic or microscopic depending on the range over which the stresses are balanced. The macroscopic residual stress is the stress measured over a large number of grains. This kind of stress can be measured by X-ray diffraction through the shift of the Bragg peaks. The microscopic stress is the stress measured over one or a few grains, or as small a range as micro- or nanometres. This kind of stress alone will not cause a detectable shift of diffraction peaks, but is reflected in the peak profiles. In this chapter, we will focus on the X-ray diffraction method for stress measurement at the macroscopic level.

2.5.4.3.1. *Stress and strain relation*

Stress is a measure of the deforming force applied to a solid per unit area. The stress on an elemental volume in the sample coordinates S_1, S_2, S_3 contains nine components, given by

$$\sigma_{ij} = \begin{bmatrix} \sigma_{11} & \sigma_{12} & \sigma_{13} \\ \sigma_{21} & \sigma_{22} & \sigma_{23} \\ \sigma_{31} & \sigma_{32} & \sigma_{33} \end{bmatrix}. \qquad (2.5.63)$$

A component is normal stress when the two indices are identical, or shear stress when the two indices differ. The group of the nine stress components is called the stress tensor. The stress tensor is a tensor of the second order. Under equilibrium conditions, the shear components must maintain the following relations:

$$\sigma_{12} = \sigma_{21},\ \ \sigma_{23} = \sigma_{32} \text{ and } \sigma_{31} = \sigma_{13}. \qquad (2.5.64)$$

Therefore, only six independent components define the stress state in a solid. The following stress states are typically measured:

Uniaxial: all stress components are zero except one normal stress component.

Biaxial: all nonzero components are within the S_1S_2 plane.

Biaxial with shear: $\sigma_{33} = 0$, all other components are not necessarily zero.

Equibiaxial: a special case of biaxial stress where $\sigma_{11} = \sigma_{22} = \sigma$.

Triaxial: all components are not necessarily zero.

Equitriaxial: a special case of triaxial stress where $\sigma_{11} = \sigma_{22} = \sigma_{33} = \sigma$.

Strain is a measure of the resulting deformation of a solid body caused by stress. Strain is calculated from the change in the size and shape of the deformed solid due to stress. Analogous to normal stresses and shear stresses are normal strains and shear strains. The normal strain is calculated from the change in length of the solid body along the corresponding normal stress direction. Like the stress tensor, the strain tensor contains nine components:

$$\varepsilon_{ij} = \begin{bmatrix} \varepsilon_{11} & \varepsilon_{12} & \varepsilon_{13} \\ \varepsilon_{21} & \varepsilon_{22} & \varepsilon_{23} \\ \varepsilon_{31} & \varepsilon_{32} & \varepsilon_{33} \end{bmatrix}. \tag{2.5.65}$$

The directions of all strain components are defined in the same way as for the stress tensor. Similarly, there are six independent components in the strain tensor. Strictly speaking, X-ray diffraction does not measure stresses directly, but strains. The stresses are calculated from the measured strains based on the elasticity of the materials. The stress–strain relations are given by the generalized form of Hooke's law:

$$\sigma_{ij} = C_{ijkl}\varepsilon_{kl}, \tag{2.5.66}$$

where C_{ijkl} are elastic stiffness coefficients. The stress–strain relations can also be expressed as

$$\varepsilon_{ij} = S_{ijkl}\sigma_{kl}, \tag{2.5.67}$$

where S_{ijkl} are the elastic compliances. For most polycrystalline materials without texture or with weak texture, it is practical and reasonable to consider the elastic behaviour to be isotropic and the structure to be homogeneous on a macroscopic scale. In these cases, the stress–strain relationship takes a much simpler form. Therefore, the Young's modulus E and Poisson's ratio ν are sufficient to describe the stress and strain relations for homogeneous isotropic materials:

$$\begin{aligned} \varepsilon_{11} &= \frac{1}{E}[\sigma_{11} - \nu(\sigma_{22} + \sigma_{33})], \\ \varepsilon_{22} &= \frac{1}{E}[\sigma_{22} - \nu(\sigma_{33} + \sigma_{11})], \\ \varepsilon_{33} &= \frac{1}{E}[\sigma_{33} - \nu(\sigma_{11} + \sigma_{22})], \\ \varepsilon_{12} &= \frac{1+\nu}{E}\sigma_{12}, \quad \varepsilon_{23} = \frac{1+\nu}{E}\sigma_{23}, \quad \varepsilon_{31} = \frac{1+\nu}{E}\sigma_{31}. \end{aligned} \tag{2.5.68}$$

It is customary in the field of stress measurement by X-ray diffraction to use another set of macroscopic elastic constants, S_1 and $\frac{1}{2}S_2$, which are given by

$$\tfrac{1}{2}S_2 = (1+\nu)/E \text{ and } S_1 = -\nu/E. \tag{2.5.69}$$

Although polycrystalline materials on a macroscopic level can be considered isotropic, residual stress measurement by X-ray diffraction is done by measuring the strain in a specific crystal orientation of the crystallites that satisfies the Bragg condition. The stresses measured from diffracting crystallographic planes may have different values because of their elastic anisotropy. In such cases, the macroscopic elasticity constants should be replaced by a set of crystallographic plane-specific elasticity constants, $S_1^{\{hkl\}}$ and $\frac{1}{2}S_2^{\{hkl\}}$, called X-ray elastic constants (XECs). XECs for many materials can be found in the literature, measured or calculated from microscopic elasticity constants (Lu, 1996). In the case of materials with cubic crystal symmetry, the equations for calculating the XECs from the macroscopic elasticity constants $\frac{1}{2}S_2$ and S_1 are

$$\begin{aligned} \tfrac{1}{2}S_2^{\{hkl\}} &= \tfrac{1}{2}S_2[1 + 3(0.2 - \Gamma(hkl))\Delta] \\ S_1^{\{hkl\}} &= S_1 - \tfrac{1}{2}S_2[0.2 - \Gamma(hkl)]\Delta, \end{aligned} \tag{2.5.70}$$

where

$$\Gamma(hkl) = \frac{h^2k^2 + k^2l^2 + l^2h^2}{(h^2+k^2+l^2)^2} \text{ and } \Delta = \frac{5(A_{\rm RX} - 1)}{3 + 2A_{\rm RX}}.$$

In the equations for stress measurement hereafter, either the macroscopic elasticity constants $\frac{1}{2}S_2$ and S_1 or the XECs $S_1^{\{hkl\}}$ and $\frac{1}{2}S_2^{\{hkl\}}$ are used in the expression, but either set of elastic constants can be used depending on the requirements of the application. The factor of anisotropy ($A_{\rm RX}$) is a measure of the elastic anisotropy of a material (He, 2009).

2.5.4.3.2. *Fundamental equations*

Fig. 2.5.24 illustrates two diffraction cones for backward diffraction. The regular diffraction cone (dashed lines) is from the powder sample with no stress, so the 2θ angles are constant at all γ angles. The diffraction ring shown as a solid line is the cross section of a diffraction cone that is distorted as a result of stresses. For a stressed sample, 2θ becomes a function of γ and the sample orientation (ω, ψ, φ), *i.e.* $2\theta = 2\theta(\gamma, \omega, \psi, \varphi)$. This function is uniquely determined by the stress tensor. The strain measured by the 2θ shift at a point on the diffraction ring is $\varepsilon^{\{hkl\}}_{(\gamma,\omega,\psi,\varphi)}$, based on the true strain definition

$$\varepsilon^{\{hkl\}}_{(\gamma,\omega,\psi,\varphi)} = \ln\frac{d}{d_o} = \ln\frac{\sin\theta_o}{\sin\theta} = \ln\frac{\lambda}{2d_o\sin\theta}, \tag{2.5.71}$$

where d_o and θ_o are the stress-free values and d and θ are measured values from a point on the diffraction ring corresponding to (γ, ω, ψ, φ). The direction of $\varepsilon^{\{hkl\}}_{(\gamma,\omega,\psi,\varphi)}$ in the sample coordinates S_1, S_2, S_3 can be given by the unit-vector components h_1, h_2 and h_3. As a second-order tensor, the relationship between the measured strain and the strain-tensor components is then given by

$$\varepsilon^{\{hkl\}}_{(\gamma,\omega,\psi,\varphi)} = \varepsilon_{ij} \cdot h_i \cdot h_j. \tag{2.5.72}$$

The scalar product of the strain tensor with the unit vector in the above equation is the sum of all components in the tensor multiplied by the components in the unit vector corresponding to the first and the second indices. The expansion of this equation for i and j values of 1, 2 and 3 results in

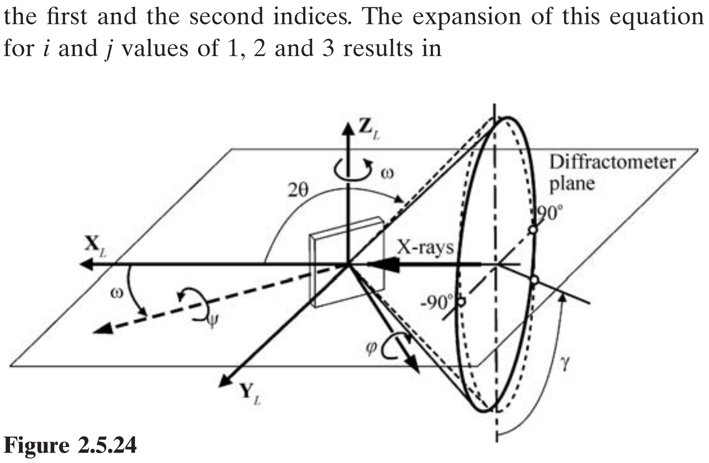

Figure 2.5.24
Diffraction-cone distortion due to stresses.

$$\varepsilon^{\{hkl\}}_{(\gamma,\omega,\psi,\varphi)} = h_1^2\varepsilon_{11} + 2h_1h_2\varepsilon_{12} + h_2^2\varepsilon_{22} + 2h_1h_3\varepsilon_{13} + 2h_2h_3\varepsilon_{23} + h_3^2\varepsilon_{33}. \tag{2.5.73}$$

Or, taking the true strain definition,

$$h_1^2\varepsilon_{11} + 2h_1h_2\varepsilon_{12} + h_2^2\varepsilon_{22} + 2h_1h_3\varepsilon_{13} + 2h_2h_3\varepsilon_{23} + h_3^2\varepsilon_{33} = \ln\left(\frac{\sin\theta_0}{\sin\theta}\right), \tag{2.5.74}$$

where θ_o corresponds to the stress-free d-spacing and θ are measured values from a point on the diffraction ring. Both θ and $\{h_1, h_2, h_3\}$ are functions of $(\gamma, \omega, \psi, \varphi)$. By taking γ values from 0 to 360°, equation (2.5.74) establishes the relationship between the diffraction-cone distortion and the strain tensor. Therefore, equation (2.5.74) is the fundamental equation for strain measurement with two-dimensional X-ray diffraction.

Introducing the elasticity of materials, one obtains

$$\begin{aligned}&-\frac{\nu}{E}(\sigma_{11}+\sigma_{22}+\sigma_{33})\\ &\quad+\frac{1+\nu}{E}(\sigma_{11}h_1^2+\sigma_{22}h_2^2+\sigma_{33}h_3^2+2\sigma_{12}h_1h_2+2\sigma_{13}h_1h_3+2\sigma_{23}h_2h_3)\\ &\quad=\ln\left(\frac{\sin\theta_0}{\sin\theta}\right)\end{aligned} \tag{2.5.75}$$

or

$$\begin{aligned}&S_1(\sigma_{11}+\sigma_{22}+\sigma_{33})\\ &\quad+\tfrac{1}{2}S_2(\sigma_{11}h_1^2+\sigma_{22}h_2^2+\sigma_{33}h_3^2+2\sigma_{12}h_1h_2+2\sigma_{13}h_1h_3+2\sigma_{23}h_2h_3)\\ &\quad=\ln\left(\frac{\sin\theta_0}{\sin\theta}\right).\end{aligned} \tag{2.5.76}$$

It is convenient to express the fundamental equation in a clear linear form:

$$p_{11}\sigma_{11}+p_{12}\sigma_{12}+p_{22}\sigma_{22}+p_{13}\sigma_{13}+p_{23}\sigma_{23}+p_{33}\sigma_{33}=\ln\left(\frac{\sin\theta_0}{\sin\theta}\right), \tag{2.5.77}$$

where p_{ij} are stress coefficients given by

$$p_{ij}=\begin{cases}(1/E)[(1+\nu)h_i^2-\nu]=\tfrac{1}{2}S_2h_i^2+S_1 & \text{if } i=j,\\ 2(1/E)(1+\nu)h_ih_j=2\tfrac{1}{2}S_2h_ih_j & \text{if } i\neq j.\end{cases} \tag{2.5.78}$$

In the equations for the stress measurement above and hereafter, the macroscopic elastic constants $\frac{1}{2}S_2$ and S_1 are used for simplicity, but they can always be replaced by the XECs for the specific lattice plane $\{hkl\}$, $S_1^{\{hkl\}}$ and $\frac{1}{2}S_2^{\{hkl\}}$, if the anisotropic nature of the crystallites should be considered. For instance, equation (2.5.76) can be expressed with the XECs as

$$\begin{aligned}&S_1^{\{hkl\}}(\sigma_{11}+\sigma_{22}+\sigma_{33})\\ &\quad+\tfrac{1}{2}S_2^{\{hkl\}}(\sigma_{11}h_1^2+\sigma_{22}h_2^2+\sigma_{33}h_3^2+2\sigma_{12}h_1h_2+2\sigma_{13}h_1h_3+2\sigma_{23}h_2h_3)\\ &\quad=\ln\left(\frac{\sin\theta_0}{\sin\theta}\right).\end{aligned} \tag{2.5.79}$$

The fundamental equation (2.5.74) may be used to derive many other equations based on the stress–strain relationship, stress state and special conditions. The fundamental equation and the derived equations are referred to as 2D equations hereafter to distinguish them from the conventional equations. These equations can be used in two ways. One is to calculate the stress or stress-tensor components from the measured strain (2θ-shift) values in various directions. The fundamental equation for stress measurement with 2D-XRD is a linear function of the stress-tensor components. The stress tensor can be obtained by solving the linear equations if six independent strains are measured or by linear least-squares regression if more than six independent measured strains are available. In order to get a reliable solution from the linear equations or least-squares analysis, the independent strain should be measured at significantly different orientations. Another function of the fundamental equation is to calculate the diffraction-ring distortion for a given stress tensor at a particular sample orientation (ω, ψ, φ) (He & Smith, 1998). The fundamental equation for stress measurement by the conventional X-ray diffraction method can also be derived from the 2D fundamental equation (He, 2009).

2.5.4.3.3. *Equations for various stress states*

The general triaxial stress state is not typically measured by X-ray diffraction because of low penetration. For most applications, the stresses in a very thin layer of material on the surface are measured by X-ray diffraction. It is reasonable to assume that the average normal stress in the surface-normal direction is zero within such a thin layer. Therefore, $\sigma_{33}=0$, and the stress tensor has five nonzero components. In some of the literature this stress state is denoted as triaxial. In order to distinguish this from the general triaxial stress state, here we name this stress state as the 'biaxial stress state with shear'. In this case, we can obtain the linear equation for the biaxial stress state with shear:

$$p_{11}\sigma_{11}+p_{12}\sigma_{12}+p_{22}\sigma_{22}+p_{13}\sigma_{13}+p_{23}\sigma_{23}+p_{\rm ph}\sigma_{\rm ph}=\ln\left(\frac{\sin\theta_0}{\sin\theta}\right), \tag{2.5.80}$$

where the coefficient $p_{\rm ph}=\frac{1}{2}S_2+3S_1$ and $\sigma_{\rm ph}$ is the pseudo-hydrostatic stress component introduced by the error in the stress-free d-spacing. In this case, the stresses can be measured without the accurate stress-free d-spacing, since this error is included in $\sigma_{\rm ph}$. The value of $\sigma_{\rm ph}$ is considered as one of the unknowns to be determined by the linear system. With the measured stress-tensor components, the general normal stress (σ_φ) and shear stress (τ_φ) at any arbitrary angle φ can be given by

$$\sigma_\varphi=\sigma_{11}\cos^2\varphi+\sigma_{12}\sin2\varphi+\sigma_{22}\sin^2\varphi, \tag{2.5.81}$$

$$\tau_\varphi=\sigma_{13}\cos\varphi+\sigma_{23}\sin\varphi. \tag{2.5.82}$$

Equation (2.5.81) can also be used for other stress states by removing the terms for stress components that are zero. For instance, in the biaxial stress state $\sigma_{33}=\sigma_{13}=\sigma_{23}=0$, so we have

$$p_{11}\sigma_{11}+p_{12}\sigma_{12}+p_{22}\sigma_{22}+p_{\rm ph}\sigma_{\rm ph}=\ln\left(\frac{\sin\theta_0}{\sin\theta}\right). \tag{2.5.83}$$

In the 2D stress equations for any stress state with $\sigma_{33}=0$, we can calculate stress with an approximation of d_o (or $2\theta_o$). Any error in d_o (or $2\theta_o$) will contribute only to a pseudo-hydrostatic term $\sigma_{\rm ph}$. The measured stresses are independent of the input d_o (or $2\theta_o$) values (He, 2003). If we use d_0' to represent the initial input, then the true d_o (or $2\theta_o$) can be calculated from $\sigma_{\rm ph}$ with

$$d_0=d_0'\exp\left(\frac{1-2\nu}{E}\sigma_{\rm ph}\right), \tag{2.5.84}$$

$$\theta_0=\arcsin\left[\sin\theta_0'\exp\left(\frac{1-2\nu}{E}\sigma_{\rm ph}\right)\right]. \tag{2.5.85}$$

Care must be taken that the $\sigma_{\rm ph}$ value also includes the measurement error. If the purpose of the experiment is to determine the stress-free d-spacing d_o, the instrument should be first calibrated with a stress-free standard of a similar material.

2.5.4.3.4. *Data-collection strategy*

The practice of stress analysis with 2D-XRD involves the selection of the diffraction-system configuration and the data-collection strategy, frame correction and integration, and stress calculation from the processed data points. Most concepts and strategies developed for a conventional diffractometer are still valid for 2D-XRD. We will focus on the new concepts and practices due to the nature of the 2D detectors.

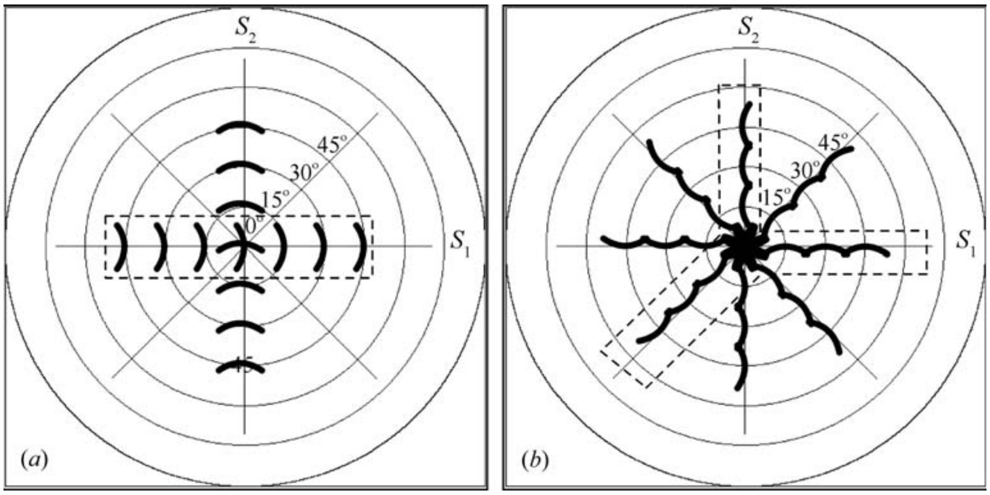

Figure 2.5.25
Data-collection strategy schemes: (a) $\omega + \varphi$ scan; (b) $\psi + \varphi$ scan.

The diffraction vector is in the normal direction to the measured crystalline planes. It is not always possible to have the diffraction vector in the desired measurement direction. In reflection mode, it is easy to have the diffraction vector normal to the sample surface, or tilted away from the normal, but impossible to have the vector on the surface plane. The stress on the surface plane, or biaxial stress, is calculated by elasticity theory from the measured strain in other directions. The final stress-measurement results can be considered as an extrapolation from the measured values. In the conventional $\sin^2\psi$ method, several ψ-tilt angles are required, typically at 15° steps from −45° to +45°. The same is true with a 2D-XRD system. The diffraction vectors corresponding to the data scan can be projected onto a 2D plot in the same way as the pole-density distribution in a pole figure. The 2D plot is called a data-collection strategy scheme.

By evaluating the scheme, one can generate a data-collection strategy suitable for the measurement of the intended stress components. Fig. 2.5.25 illustrates two schemes for data collection. In the bisecting condition ($\omega = \theta$ or $\theta_1 = \theta$ and $\psi = 0°$), the trace of the diffraction vector falls in the vicinity of the scheme centre. Either an ω tilt or a ψ tilt can move the vectors away from the centre. The circles on the scheme are labelled with the tilt angle of 15°, 30° and 45°. Scheme (a) is for an ω tilt of 0°, ±15°, ±30° and ±45° with the φ angle at 0° and 90°. It is obvious that this set of data would be suitable for calculating the biaxial-stress tensor. The data set with $\varphi = 0°$, as shown within the box enclosed by the dashed lines, would be sufficient on its own to calculate σ_{11}. Since the diffraction-ring distortion at $\varphi = 0°$ or $\varphi = 90°$ is not sensitive to the stress component σ_{12}, strategy (a) is suitable for the equibiaxial stress state, but is not able to determine σ_{12} accurately. In scheme (b), the ψ scan covers 0° to 45° with 15° steps at eight φ angles with 45° intervals. This scheme produces comprehensive coverage on the scheme chart in a symmetric distribution. The data set collected with this strategy can be used to calculate the complete biaxial-stress tensor components and shear stress (σ_{11}, σ_{12}, σ_{22}, σ_{13}, σ_{23}). The scheme indicated by the boxes enclosed by the dashed lines is a time-saving alternative to scheme (b). The rings on two φ angles are aligned to S_1 and S_2 and the rings on the third φ angle make 135° angles to the other two arrays of rings. This is analogous to the configuration of a stress-gauge rosette. The three φ angles can also be separated equally by 120° steps. Suitable schemes for a particular experiment should be determined by considering the stress components of interest, the goniometer, the sample size, the detector size and resolution, the desired measurement accuracy and the data-collection time.

2.5.4.3.5. *Data integration and peak evaluation*

The purpose of data integration and peak evaluation is to generate a set of data points along distorted diffraction rings. Data integration for stress analysis is γ integration over several defined segments so as to generate diffraction profiles representing the corresponding segments. The peak position can be determined by fitting the diffraction profile to a given analytic function. Fig. 2.5.26 illustrates data integration over a diffraction frame. The total integration region is defined by $2\theta_1$, $2\theta_2$, γ_1 and γ_2. The integration region is divided into segments given by $\Delta\gamma$. One data point on the distorted diffraction ring is generated from each segment. The γ value in the centre (denoted by the dot-dashed line) of each segment is taken as the γ value of the data point. γ integration of the segment produces a diffraction profile and the 2θ value is determined from the profile. The number of segments and the segment size ($\Delta\gamma$) are selected based on the quality of the data frame. The larger the segment size $\Delta\gamma$ is, the better the integrated diffraction profile as more counts are being integrated. γ integration also produces a smearing effect on the diffraction-ring distortion because the counts collected within the segment size $\Delta\gamma$ are considered as a single γ value at the segment

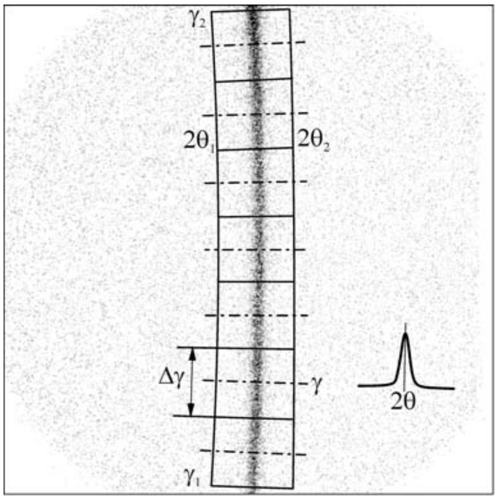

Figure 2.5.26
Data integration for stress measurement.

centre. The 2θ shift in the segment is averaged. The segment size $\Delta\gamma$ should be sufficient to produce a smooth diffraction profile, but not so large as to introduce too much smearing. For data frames containing high pixel counts, the integration segment can be small, *e.g.* $\Delta\gamma \leq 2^\circ$, and still have a smooth profile for each segment. For data frames having low pixel counts, for example the frames collected from a micron-sized area, from a sample with large grains or with a short data-collection time, it is critical to choose a sufficiently large segment size. The segment size can be determined by observing the smoothness of the integrated profile.

Peak evaluation in each segment can be done using the same algorithm used in the conventional method. The corrections to the integrated profiles are performed before or during the peak evaluation. Absorption correction eliminates the influence of the irradiated area and the diffraction geometry on the measured intensity distribution. The absorption for a given material and radiation level depends on the incident angle to the sample and the reflected angle from the sample. For 2D-XRD, the reflected angle is a function of γ for each frame. The polarization effect is also a function of γ. Therefore, the correction for polarization and absorption should be applied to the frame before integration. (Details of these corrections were discussed in Section 2.5.4.3.4.) The polarization and absorption correction is not always necessary if the error caused by absorption can be tolerated for the application, or if the data-collection strategy involves only ψ and φ scans.

In most cases, $K\alpha$ radiation is used for stress measurement, in which case the weighted average wavelength of $K\alpha_1$ and $K\alpha_2$ radiation is used in the calculations. For samples with a broad peak width, diffraction of $K\alpha_1$ and $K\alpha_2$ radiation is merged together as a single peak profile, and the profile can be evaluated as if there is a single $K\alpha$ line without introducing much error to the measured *d*-spacing. For samples with a relatively narrow peak width, the diffraction profile shows strong asymmetry or may even reveal two peaks corresponding to the $K\alpha_1$ and $K\alpha_2$ lines, especially at high 2θ angles. In this case the profile fitting should include contributions from both the $K\alpha_1$ and $K\alpha_2$ lines. It is common practice to use the peak position from the $K\alpha_1$ line and the $K\alpha_1$ wavelength to calculate the *d*-spacing after $K\alpha_2$ stripping.

Background correction is necessary if there is a strong background or the peak-evaluation algorithms are sensitive to the background, such as in $K\alpha_2$ stripping, peak fitting, and peak-intensity and integrated-intensity evaluations. Background correction is performed by subtracting a linear intensity distribution based on the background intensities at the lower 2θ side and the higher 2θ side of the diffraction peak. The background region should be sufficiently far from the 2θ peak so that the correction will not truncate the diffraction profile. The 2θ ranges of the low background and high background should be determined based on the width of the 2θ peak and available background in the profile. Based on a normal distribution, a 2θ range of 2 times the FWHM covers 98% of the peak intensity, and 3 times the FWHM covers more than 99.9%, so the background intensity should be determined at more than 1 to 1.5 times the FWHM away from the peak position. The background correction can be neglected for a profile with a low background or if the error caused by the background is tolerable for the application. The peak position can be evaluated by various methods, such as gravity, sliding gravity, and profile fitting by parabolic, pseudo-Voigt or Pearson-VII functions (Lu, 1996; Sprauel & Michaud, 2002).

2.5.4.3.6. *Stress calculation*

The final data set after integration and peak evaluation should contain many data points describing the diffraction-ring shape for all collected frames. Each measured data point contains three goniometer angles (ω, ψ, φ) and the diffraction-ring position (γ, 2θ). The peak intensity or integrated intensity of the diffraction profile is another value to be determined and may be used in the stress calculation. In most cases the number of data points is more than the number of unknown stress components, so a linear least-squares method can be used to calculate the stresses. In a general least-squares regression, the residual for the *i*th data point is defined as

$$r_i = y_i - \hat{y}_i, \tag{2.5.86}$$

where y_i is the observed response value, $\hat{y}_i$ is the fitted response value and r_i is the residual, which is defined as the difference between the observed value and the fitted value. The summed square of residuals is given by

$$S = \sum_{i=1}^{n} r_i^2 = \sum_{i=1}^{n} (y_i - \hat{y}_i)^2, \tag{2.5.87}$$

where n is the number of data points and S is the sum-of-squares error to be minimized in the least-squares regression. For stress calculation, the observed response value is the measured strain at each data point,

$$y_i = \ln\left(\frac{\sin\theta_0}{\sin\theta_i}\right), \tag{2.5.88}$$

and the fitted response value is given by the fundamental equation as

$$\hat{y}_i = p_{11}\sigma_{11} + p_{12}\sigma_{12} + p_{22}\sigma_{22} + p_{13}\sigma_{13} + p_{23}\sigma_{23} + p_{33}\sigma_{33} + p_{\rm ph}\sigma_{\rm ph}, \tag{2.5.89}$$

where all possible stress components and stress coefficients are listed as a generalized linear equation. Since the response-value function is a linear equation of unknown stress components, the least-squares problem can be solved by a linear least-squares regression. In order to reduce the impact of texture, large grains or weak diffraction on the results of the stress determination, the standard error of profile fitting and the integrated intensity of each profile may be introduced as a weight factor for the least-squares regression (He, 2009).

2.5.4.3.7. *Comparison between the 2D method and the conventional method*

Stress measurement on a polycrystalline material by X-ray diffraction is based on the strain measurements in a single or in several sample orientations. Each measured strain is calculated from the average *d*-spacing of specific lattice planes $\{hkl\}$ over many crystallites (grains). A larger number of contributing crystallites gives better accuracy and sampling statistics (also referred to as particle statistics). The sampling statistics are determined by both the crystal structure and the instrumentation. The instrument window is mainly determined by the divergence of the incident X-ray beam. Lattice-plane families with high multiplicity will also effectively improve the sampling statistics. The number of contributing crystallites measured by a conventional diffractometer is limited by the sizes and divergences of the incident and diffracted beams to the point detector. In a two-

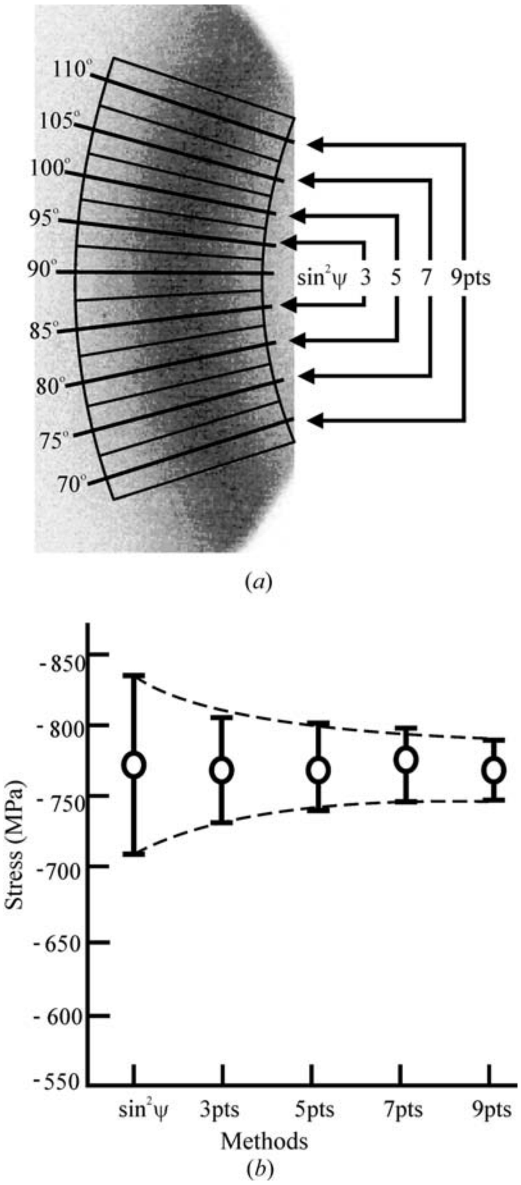

Figure 2.5.27
Stress calculation with the 2D method and the $\sin^2\psi$ method: (*a*) nine data points (abbreviated as pts) on the diffraction ring; (*b*) measured stress and standard deviation by different methods.

dimensional diffraction system, more crystallites can contribute to the diffraction because of the larger γ range.

An example of a stress calculation is provided by the measurement of the residual stress on the end surface of a carbon steel roller. One of the seven frames taken with an ω scan is shown in Fig. 2.5.27(*a*). The (211) ring covering the γ range 67.5 to 112.5° was used for stress analysis. First, the frame data were integrated along γ with an interval of $\Delta\gamma = 5°$. A total of nine diffraction profiles were obtained from γ integration. The peak position 2θ for each γ angle was then obtained by fitting the profile with a Pearson-VII function. A total of 63 data points can be obtained from the seven frames. The data points at $\gamma = 90°$ from seven frames, a typical data set for an ω diffractometer, were used to calculate the stress with the conventional $\sin^2\psi$ method. In order to compare the gain from having increased data points with the 2D method, the stress was calculated from 3, 5, 7 and 9 data points on each frame. The results from the conventional $\sin^2\psi$ method and the 2D method are compared in Fig. 2.5.27(*b*). The measured residual stress is compressive and the stress values from different methods agree very well. With the data taken from the same measurement (seven frames), the 2D method gives a lower standard error and the error decreases with increasing number of data points from the diffraction ring.

2.5.4.4. *Quantitative analysis*

2.5.4.4.1. *Crystallinity*

The crystallinity of a material influences many of its characteristics, including mechanical strength, opacity and thermal properties. Crystallinity measurement provides valuable information for both materials research and quality control in materials processing. The diffraction pattern from a material containing both amorphous and crystalline solids has a broad feature from the amorphous phase and sharp peaks from the crystalline phase. The weight percentage of the crystalline phases in a material containing both crystalline and amorphous phases can be determined by X-ray diffraction (Chung & Scott, 1973; Alexander, 1985; Murthy & Barton, 2000; Kasai & Kakudo, 2005). Assuming that the X-ray scattering intensity from each phase in such a material is proportional to its weight percentage, and that the scattering intensities from all phases can be measured within a given 2θ range, the per cent crystallinity is given by

$$x_{\rm pc} = 100\% \frac{I_{\rm crystal}}{I_{\rm crystal} + I_{\rm amorphous}}, \qquad (2.5.90)$$

where $x_{\rm pc}$ is the per cent crystallinity, $I_{\rm crystal}$ is the integrated intensity of all crystalline peaks and $I_{\rm amorphous}$ is the integrated intensity of the amorphous scattering. The accuracy of the measured per cent crystallinity depends on the integrated diffraction profile. Since most crystalline samples have a preferred orientation, it is very difficult to obtain a consistent measurement of crystallinity with a conventional diffractometer. Fig. 2.5.28 shows a 2D diffraction frame collected from an oriented polycrystalline sample. The diffraction is in transmission mode with the X-ray beam perpendicular to the plate sample surface. Fig. 2.5.28(*a*) shows a diffraction profile integrated from a horizontal region analogous to a profile collected with a conventional diffractometer. Only one peak from the crystalline phase can be observed in the profile. It is also possible that a different peak or no peak is measured if the sample is loaded in other orientations. Fig. 2.5.28(*b*) is the diffraction profile integrated from the region covering all peaks from the crystalline phase over almost all azimuthal angles. A total of four peaks from the crystalline phase are observed. This shows that a 2D-XRD system can measure per cent crystallinity more accurately and with more consistent results (Pople *et al.*, 1997; Bruker, 2000) than a conventional system.

2.5.4.4.2. *Crystallite size*

The size of the crystallites in a polycrystalline material has a significant effect on many of its properties, such as its thermal, mechanical, electrical, magnetic and chemical properties. X-ray diffraction has been used for crystallite-size measurement for many years. Most methods are based on diffraction-line broadening and line-profile analysis (Wilson, 1971; Klug & Alexander, 1974; Ungár, 2000). Another approach to crystallite-size measurement is based on the spotty diffraction rings collected with two-dimensional detectors when a small X-ray beam is used (Cullity, 1978; He, 2009). Line-profile analysis is based on the

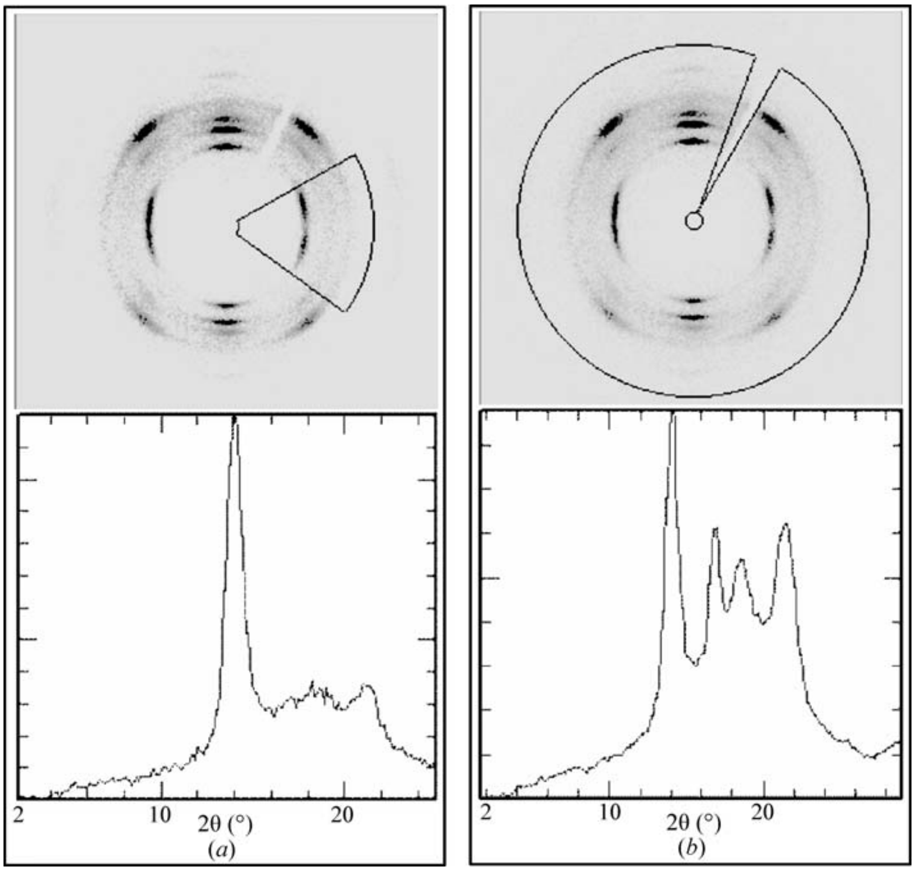

Figure 2.5.28
2D diffraction pattern from an oriented polycrystalline polymer sample. (*a*) Diffraction profile integrated from a horizontal region analogous to a profile collected with point detector. (*b*) Diffraction profile integrated from all parts of the 2D frame.

diffraction profile in the 2θ direction, while crystallite-size analysis with a spotty 2D diffraction pattern is based on the diffraction profile in the γ direction. The latter may be referred to as γ-profile analysis.

Fig. 2.5.29(*a*) shows a diffraction profile collected from gold nanoparticles and regular gold metal. The 2θ profile from the gold nanoparticles is significantly broader than the profile from regular gold metal. The crystallite size can be calculated by measuring the broadening and using the Scherrer equation:

$$B = \frac{C\lambda}{t\cos\theta}, \qquad (2.5.91)$$

where λ is the X-ray wavelength (in Å), B is the full width at half maximum (FWHM) of the peak (in radians) corrected for instrumental broadening and strain broadening, θ is the Bragg angle, C is a factor, typically from 0.9 to 1.0, depending on the crystallite shape (Klug & Alexander, 1974), and t is the crystallite size (also in Å). This equation shows an inverse relationship between crystallite size and peak-profile width. The wider the peak is, the smaller the crystallites. The 2θ diffraction profiles can be obtained either by using a conventional diffractometer with a point or line detector, or by γ integration from a diffraction pattern collected with 2D detector. When a 2D detector is used, a long sample-to-detector distance should be used to maximize the resolution. A small beam size and low convergence should also be used to reduce instrument broadening.

Fig. 2.5.29(*b*) shows a frame collected from an SRM660a (LaB_6) sample with a 2D-XRD system. The spotty diffraction rings are observed with average crystallite size of 3.5 µm. The number of spots in each diffraction ring is determined by the crystallite size and diffraction volume. Introducing a scaling factor covering all the numeric constants,

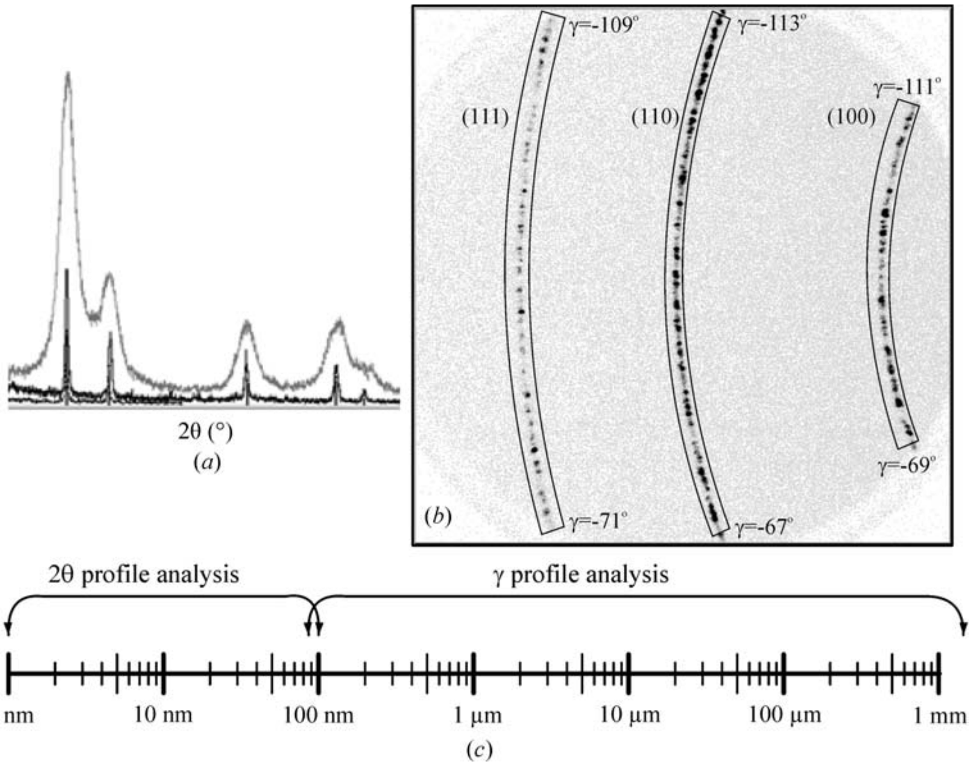

Figure 2.5.29
Crystallite-size analysis: (*a*) 2θ profile of a gold nanoparticle (grey) and regular gold metal (black); (*b*) γ profile of LaB_6; (*c*) measurement range.

the incident-beam divergence and the calibration factor for the instrument, we obtain an equation for the crystallite size as measured in reflection mode:

$$d = k\left\{\frac{p_{hkl}b^2 \arcsin[\cos\theta \sin(\Delta\gamma/2)]}{\mu N_s}\right\}^{1/3}, \qquad (2.5.92)$$

where d is the diameter of the crystallite particles, p_{hkl} is the multiplicity of the diffracting planes, b is the size of the incident beam (*i.e.* its diameter), $\Delta\gamma$ is the γ range of the diffraction ring, μ is the linear absorption coefficient and N_s is the number of spots within $\Delta\gamma$. For transmission mode, we have

$$d = k\left\{\frac{p_{hkl}b^2 t \arcsin[\cos\theta \sin(\Delta\gamma/2)]}{N_s}\right\}^{1/3}, \qquad (2.5.93)$$

where t is the sample thickness. In transmission mode with the incident beam perpendicular to the sample surface, the linear absorption coefficient affects the relative scattering intensity, but not the actual sampling volume. In other words, all the sample volume irradiated by the incident beam contributes to the diffraction. Therefore, it is reasonable to ignore the absorption effect $\exp(\mu t)$ for crystallite-size analysis as long as the sample is thin enough for transmission-mode diffraction. The effective sampling volume reaches a maximum for transmission-mode diffraction when $t = 1/\mu$.

For both reflection and transmission,

$$k = \left(\frac{3\beta}{8\pi}\right)^{1/3}, \qquad (2.5.94)$$

where β is the divergence of the incident beam. Without knowing the precise instrumental broadening, k can be treated as a calibration factor determined from the 2D diffraction pattern of a known standard. Since only a limited number of spots along the diffraction ring can be resolved, it can be seen from equation (2.5.94) that a smaller X-ray beam size and low-multiplicity peak should be used if a smaller crystallite size is to be determined.

Fig. 2.5.29(*c*) shows the measurement ranges of 2θ-profile and γ-profile analysis. The 2θ-profile analysis is suitable for crystallite sizes below 100 nm (1000 Å), while γ-profile analysis is suitable for crystallite sizes from as large as tens of µm down to 100 nm with a small X-ray beam size. By increasing the effective diffraction volume by translating the sample during data collection or multiple sample integration (or integrating data from multiple samples), the measurement range can be increased up to millimetres. Multiple sample integration can deal with large crystallite sizes without recalibration. The new calibration factor is given as

$$k_n = n^{1/3}k, \qquad (2.5.95)$$

where n is the number of targets that are integrated. The number of crystallites can be counted by the number of intersections of the γ profile with a threshold line. Every two intersections of the γ profile with this horizontal line represents a crystallite. In order to cancel out the effects of preferred orientation and other material and instrumental factors on the overall intensity fluctuation along the γ profile, one can use a trend line fitted to the γ profile by a second-order polynomial. It is always necessary to calibrate the system with a known standard, preferably with a comparable sample geometry and crystallite size. For reflection mode, it is critical to have a standard with a comparable linear absorption coefficient so as to have similar penetration.

References

Alexander, L. E. (1985). *X-ray Diffraction Methods in Polymer Science*. Malabar: Krieger Publishing Company.

Allahkarami, M. & Hanan, J. C. (2011). *X-ray diffraction mapping on a curved surface*. *J. Appl. Cryst.* **44**, 1211–1216.

Arndt, U. W. (1986). *X-ray position-sensitive detectors*. *J. Appl. Cryst.* **19**, 145–163.

Arndt, U. W. (1990). *Focusing optics for laboratory sources in X-ray crystallography*. *J. Appl. Cryst.* **23**, 161–168.

Bergese, P., Bontempi, E., Colombo, I. & Depero, L. E. (2001). *Micro X-ray diffraction on capillary powder samples: a novel and effective technique for overcoming preferred orientation*. *J. Appl. Cryst.* **34**, 663–665.

Bhuvanesh, N. S. P. & Reibenspies, J. H. (2003). *A novel approach to micro-sample X-ray powder diffraction using nylon loops*. *J. Appl. Cryst.* **36**, 1480–1481.

Birkholz, M. (2006). *Thin Film Analysis by X-ray Scattering*, pp. 191–195. Weinheim: Wiley-VCH.

Blanton, T. N. (1994). *X-ray diffraction orientation studies using two-dimensional detectors*. *Adv. X-ray Anal.* **37**, 367–373.

Blanton, T. N. (2003). *X-ray film as a two-dimensional detector for X-ray diffraction analysis*. *Powder Diffr.* **18**, 91–98.

Bloomer, A. C. & Arndt, U. W. (1999). *Experiences and expectations of a novel X-ray microsource with focusing mirror. I*. *Acta Cryst.* D**55**, 1672–1680.

Boesecke, P. (2007). *Reduction of two-dimensional small- and wide-angle X-ray scattering data*. *J. Appl. Cryst.* **40**, s423–s427.

Bontempi, E., Benedetti, D., Massardi, A., Zacco, A., Borgese, L. & Depero, L. E. (2008). *Laboratory two-dimensional X-ray microdiffraction technique: a support for authentication of an unknown Ghirlandaio painting*. *Appl. Phys. A*, **92**, 155–159.

Borgonovi, G. M. (1984). *Determination of residual stress from two-dimensional diffraction pattern*. *Nondestructive Methods for Material Property Determination*, edited by C. O. Ruud & R. E. Green Jr, pp. 47–57. New York: Plenum Publishing Corporation.

Bourgeois, D., Moy, J. P., Svensson, S. O. & Kvick, Å. (1994). *The point-spread function of X-ray image-intensifiers/CCD-camera and imaging-plate systems in crystallography: assessment and consequences for the dynamic range*. *J. Appl. Cryst.* **27**, 868–877.

Bruker (2000). *Percent crystallinity in polymer*. Bruker AXS Lab Report No. L86-E00005.

Bunge, H. J. (1983). *Texture Analysis in Materials Science*. London: Butterworth.

Bunge, H. J. & Klein, H. (1996). *Determination of quantitative, high-resolution pole-figures with the area detector*. *Z. Metallkd.* **87**(6), 465–475.

Campbell, J. W., Harding, M. M. & Kariuki, B. (1995). *Spatial-distortion corrections, for Laue diffraction patterns recorded on image plates, modelled using polynomial functions*. *J. Appl. Cryst.* **28**, 43–48.

Cervellino, A., Giannini, C., Guagliardi, A. & Ladisa, M. (2006). *Folding a two-dimensional powder diffraction image into a one-dimensional scan: a new procedure*. *J. Appl. Cryst.* **39**, 745–748.

Chung, F. H. & Scott, R. W. (1973). *A new approach to the determination of crystallinity of polymers by X-ray diffraction*. *J. Appl. Cryst.* **6**, 225–230.

Cullity, B. D. (1978). *Elements of X-ray Diffraction*, 2nd ed. Reading, MA: Addison-Wesley.

Derewenda, Z. & Helliwell, J. R. (1989). *Calibration tests and use of a Nicolet/Xentronics imaging proportional chamber mounted on a conventional source for protein crystallography*. *J. Appl. Cryst.* **22**, 123–137.

Dickerson, M. B., Pathak, K., Sandhage, K. H., Snyder, R. L., Balachandran, U., Ma, B., Blaugher, R. D. & Bhattacharya, R. N. (2002). *Applications of 2D detectors in x-ray analysis*. *Adv. X-ray Anal.* **45**, 338–344.

Durst, R. D., Carney, S. N., Diawara, Y. & Shuvalov, R. (2002). *Readout structure and technique for electron cloud avalanche detectors*. US Patent No. 6, 340, 819.

Eatough, M. O., Rodriguez, M. A., Blanton, T. N. & Tissot, R. G. (1997). *A comparison of detectors used for microdiffraction applications*. *Adv. X-ray Anal.* **41**, 319–326.

Ercan, A., Tate, M. W. & Gruner, S. M. (2006). *Analog pixel array detectors*. *J. Synchrotron Rad.* **13**, 110–119.

European Standard (2008). *Non-destructive Testing – Test Method for Residual Stress Analysis by X-ray Diffraction*. EN15305–2008.

Flemming, R. L. (2007). *Micro X-ray diffraction (µXRD): a versatile technique for characterization of Earth and planetary materials*. *Can. J. Earth Sci.* **44**, 1333–1346.

Fuentes-Montero, L., Montero-Cabrera, M. E. & Fuentes-Cobas, L. (2011). *The software package ANAELU for X-ray diffraction analysis using two-dimensional patterns*. *J. Appl. Cryst.* **44**, 241–246.

Fujii, N. & Kozaki, S. (1993). *Highly sensitive x-ray stress measurement in small area*. *Adv. X-ray Anal.* **36**, 505–513.

Fujita, H., Tsai, D.-Y., Itoh, T., Doi, K., Morishita, J., Ueda, K. & Ohtsuka, A. (1992). *A simple method for determining the modulation transfer function in digital radiography*. *IEEE Trans. Med. Imag.* **11**, 34–39.

Gelfi, M., La Vecchia, G. M., Lecis, N. & Troglio, S. (2005). *Relationship between through-thickness residual stress of CrN-PVD coatings and fatigue nucleation sites*. *Surf. Coat. Technol.* **192**, 263–268.

Giomatartis, Y. (1998). *Development and prospects of the new gaseous detector 'Micromegas'*. *Nucl. Instrum. Methods A*, **419**, 239.

Guggenheim, S. (2005). *Simulations of Debye–Scherrer and Gandolfi patterns using a Bruker Smart Apex diffractometer system*. Bruker AXS Application Note 373.

Hammersley, A. P. (2016). *FIT2D: a multi-purpose data reduction, analysis and visualization program*. *J. Appl. Cryst.* **49**, 646–652.

Hammersley, A. P., Svensson, S. O., Hanfland, M., Fitch, A. N. & Häusermann, D. (1996). *Two-dimensional detector software: From real detector to idealised image or two-theta scan*. *High Pressure Res*. **14**, 235–248.

Hanan, J., Űstündag, E. & Almer, J. D. (2004). *A new analysis method for two-dimensional X-ray data*. *Adv. X-ray Anal.* **47**, 174–180.

Hanna, S. & Windle, A. H. (1995). *A novel polymer fibre diffractometer, based on a scanning X-ray-sensitive charge-coupled device*. *J. Appl. Cryst.* **28**, 673–689.

He, B. (1992). *X-ray Diffraction from Point-Like Imperfection*. PhD dissertation, Virginia Tech, USA.

He, B. B. (2000). *Residual stress measurement with two-dimensional diffraction*. *The 20th ASM Heat Treating Society Conference Proceedings*, Vol. 1, pp. 408–417. St Louis, USA.

He, B. B. (2003). *Introduction to two-dimensional X-ray diffraction*. *Powder Diffr.* **18**, 71–85.

He, B. B. (2004). *Microdiffraction using two-dimensional detectors*. *Powder Diffr.* **19**, 110–118.

He, B. B. (2006). *Measurement of residual stresses in thin films by two-dimensional XRD*. *Mater. Sci. Forum*, **524–525**, 613–618.

He, B. B. (2009). *Two-dimensional X-ray Diffraction*. New York: John Wiley & Sons.

He, B. B., Anzelmo, J., LaPuma, P., Preckwinkel, U. & Smith, K. (2001). *XRD rapid screening system for combinatorial chemistry*. *Adv. X-ray Anal.* **44**, 1–5.

He, T., Durst, R. D., Becker, B. L., Kaercher, J. & Wachter, G. (2011). *A large area X-ray imager with online linearization and noise suppression*. *Proc. SPIE*, **8142**, 81421Q.

He, B. B. & Preckwinkel, U. (2002). *X-ray optics for two-dimensional x-ray diffraction*. *Adv. X-ray Anal.* **45**, 332–337.

He, B., Rao, S. & Houska, C. R. (1994). *A simplified procedure for obtaining relative x-ray intensities when a texture and atomic displacements are present*. *J. Appl. Phys.* **75**, 4456–4464.

He, B. B. & Smith, K. L. (1997). *Strain and stress measurement with two-dimensional detector*. *Adv. X-ray Anal.* **41**, 501–508.

He, B. B. & Smith, K. L. (1998). *Computer simulation of diffraction stress measurement with 2D detectors*. *Proceedings of 1998 SEM Spring Conference on Experimental and Applied Mechanics*, Houston, USA.

He, B. B., Xu, K., Wang, F. & Huang, P. (2005). *Two-dimensional X-ray diffraction for structure and stress analysis*. *Mater. Sci. Forum*, **490–491**, 1–6.

Helming, K., Lyubchenko, M., He, B. & Preckwinkel, U. (2003). *A new method for texture measurements using a general area detector diffraction system*. *Powder Diffr.* **18**, 99–102.

Hinrichsen, B. (2007). *Two-dimensional X-ray powder diffraction*. PhD dissertation, University of Stuttgart, Germany.

Jabeen, S., Raza, S. M., Ahmed, M. A., Zai, M. Y. & Erlacher, K. (2011). *Two dimensional X-ray diffraction (2D-XRD) studies on olivine of U. S. A*. *J. Chem. Soc. Pak.* **33**(5), 612–618.

James, M. R. & Cohen, J. B. (1980). *The measurement of residual stresses by x-ray diffraction techniques*. *Treatise on Materials Science and Technology*, **19A**, edited by H. Herman. New York: Academic Press.

Jenkins, R. & Snyder, R. L. (1996). *Introduction to X-ray Powder Diffractometry*. New York: John Wiley & Sons.

Kämpfe, A., Kämpfe, B., Goldenbogen, S., Eigenmann, B., Macherauch, E. & Löhe, D. (1999). *X-ray stress analysis on polycrystalline materials using two-dimensional detectors*. *Adv. X-ray Anal.* **43**, 54–65.

Kasai, N. & Kakudo, M. (2005). *X-ray Diffraction by Macromolecules*, pp. 393–417. Tokyo: Kodansha/Springer.

Kerr, K. A. & Ashmore, J. P. (1974). *Systematic errors in polarization corrections for crystal-monochromatized radiation*. *Acta Cryst.* A**30**, 176–179.

Khazins, D. M., Becker, B. L., Diawara, Y., Durst, R. D., He, B. B., Medved, S. A., Sedov, V. & Thorson, T. A. (2004). *A parallel-plate resistive-anode gaseous detector for X-ray imaging*. *IEEE Trans. Nucl. Sci.* **51**, 943–947.

Klein, J., Lehmann, C. W., Schmidt, H.-W. & Maier, W. F. (1998). *Combinatorial material libraries on the microgram scale with an example of hydrothermal synthesis*. *Angew. Chem. Int. Ed.* **37**, 3369–3372.

Klug, H. P. & Alexander, L. E. (1974). *X-ray Diffraction Procedures for Polycrystalline and Amorphous Materials*. New York: John Wiley & Sons.

Korhonen, M. A., Lindroos, V. K. & Suominen, L. S. (1989). *Application of a new solid state x-ray camera to stress measurement*. *Adv. X-ray Anal.* **32**, 407–413.

Krause, K. L. & Phillips, G. N. (1992). *Experience with commercial area detectors: a 'buyer's' perspective*. *J. Appl. Cryst.* **25**, 146–154.

Kugler, W. (2003). *X-ray diffraction analysis in the forensic science: the last resort in many criminal cases*. *Adv. X-ray Anal.* **46**, 1–16.

Lewis, R. (1994). *Multiwire gas proportional counters: decrepit antiques or classic performers?* *J. Synchrotron Rad.* **1**, 43–53.

Lu, J. (1996). *Handbook of Measurement of Residual Stress*. Society for Experimental Mechanics. Lilburn: The Fairmont Press.

Lutz, G. (2006). *Silicon drift and pixel devices for X-ray imaging and spectroscopy*. *J. Synchrotron Rad.* **13**, 99–109.

Maslen, E. N. (1992). *X-ray absorption*. *International Tables for Crystallography*, Vol. C, edited by A. J. C. Wilson, pp. 520–529. Dordrecht: Kluwer Academic Publishers.

Moy, J. P., Hammersley, A. P., Svensson, S. O., Thompson, A., Brown, K., Claustre, L., Gonzalez, A. & McSweeney, S. (1996). *A novel technique for accurate intensity calibration of area X-ray detectors at almost arbitrary energy*. *J. Synchrotron Rad.* **3**, 1–5.

Mudie, S. T., Pavlov, K. M., Morgan, M. J., Hester, J. R., Tabuchi, M. & Takeda, Y. (2004). *Collection of reciprocal space maps using imaging plates at the Australian National Beamline Facility at the Photon Factory*. *J. Synchrotron Rad.* **11**, 406–413.

Murthy, N. S. & Barton, R. Jr (2000). *Polymer industry*. *Industrial Applications of X-ray Diffraction*, edited by F. H. Chung & D. K. Smith, pp. 495–509. New York: Marcel Dekker.

Ning, G. & Flemming, R. L. (2005). *Rietveld refinement of LaB_6: data from µXRD*. *J. Appl. Cryst.* **38**, 757–759.

Noyan, I. C. & Cohen, J. B. (1987). *Residual Stress*. New York: Springer-Verlag.

Paciorek, W. A., Meyer, M. & Chapuis, G. (1999). *On the geometry of a modern imaging diffractometer*. *Acta Cryst.* A**55**, 543–557.

Pecharsky, V. K. & Zavalij, P. Y. (2003). *Fundamentals of Powder Diffraction and Structure Characterization of Materials*. Boston: Kluwer Academic Publishers.

Pitschke, W., Collazo, J. A. L., Hermann, H. & Hildenbrand, V. D. (1996). *Absorption corrections of powder diffraction intensities recorded in transmission geometry*. *J. Appl. Cryst.* **29**, 561–567.

Ponchut, C. (2006). *Characterization of X-ray area detectors for synchrotron beamlines*. *J. Synchrotron Rad.* **13**, 195–203.

Pople, J. A., Keates, P. A. & Mitchell, G. R. (1997). *A two-dimensional X-ray scattering system for in-situ time-resolving studies of polymer structures subjected to controlled deformations*. *J. Synchrotron Rad.* **4**, 267–278.

Rodriguez-Navarro, A. B. (2006). *XRD2DScan: new software for polycrystalline materials characterization using two-dimensional X-ray diffraction*. *J. Appl. Cryst.* **39**, 905–909.

Ross, C. R. (1992). *Measurement of powder diffraction sample absorption coefficients using monochromated radiation and transmission geometry*. *J. Appl. Cryst.* **25**, 628–631.

Rowe, R. (2009). *New statistical calibration approach for Bruker AXS D8 Discover microdiffractometer with Hi-Star detector using GADDS software*. *Powder Diffr.* **24**, 263–271.

Rudolf, P. R. & Landes, B. G. (1994). *Two-dimensional X-ray diffraction and scattering of microcrystalline and polymeric materials*. *Spectroscopy*, **9**(6), 22–33.

Scheidegger, S., Estermann, M. A. & Steurer, W. (2000). *Correction of specimen absorption in X-ray diffuse scattering experiments with area-detector systems*. *J. Appl. Cryst.* **33**, 35–48.

Schmidbauer, M., Schäfer, P., Besedin, S., Grigoriev, D., Köhler, R. & Hanke, M. (2008). *A novel multi-detection technique for three-dimensional reciprocal-space mapping in grazing-incidence X-ray diffraction*. *J. Synchrotron Rad.* **15**, 549–557.

Smilgies, D.-M. & Blasini, D. R. (2007). *Indexation scheme for oriented molecular thin films studied with grazing-incidence reciprocal-space mapping*. *J. Appl. Cryst.* **40**, 716–718.

Smith, K. L. & Ortega, R. B. (1993). *Use of a two-dimensional, position sensitive detector for collecting pole figures*. *Adv. X-ray Anal.* **36**, 641–647.

Sprauel, J. M. & Michaud, H. (2002). *Global X-ray method for the determination of stress profiles*. *Mater. Sci. Forum*, **404–407**, 19–24.

Stanton, M., Phillips, W. C., Li, Y. & Kalata, K. (1992). *Correcting spatial distortions and nonuniform response in area detectors*. *J. Appl. Cryst.* **25**, 549–558.

Sulyanov, S. N., Popov, A. N. & Kheiker, D. M. (1994). *Using a two-dimensional detector for X-ray powder diffractometry*. *J. Appl. Cryst.* **27**, 934–942.

Tate, M. W., Eikenberry, E. F., Barna, S. L., Wall, M. E., Lowrance, J. L. & Gruner, S. M. (1995). *A large-format high-resolution area X-ray detector based on a fiber-optically bonded charge-coupled device (CCD)*. *J. Appl. Cryst.* **28**, 196–205.

Tissot, R. G. (2003). *Microdiffraction applications utilizing a two-dimensional proportional detector*. *Powder Diffr.* **18**, 86–90.

Ungár, T. (2000). *Warren–Averbach applications*. *Industrial Applications of X-ray Diffraction*, edited by F. H. Chung & D. K. Smith, pp. 847–867. New York: Marcel Dekker.

Walter, N. M. (1971). *Residual Stress Measurement by X-ray Diffraction* – SAE J784a. Society of Automotive Engineering.

Warren, B. E. (1990). *X-ray Diffraction*. New York: Dover Publications.

Wenk, H.-R. & Grigull, S. (2003). *Synchrotron texture analysis with area detectors*. *J. Appl. Cryst.* **36**, 1040–1049.

Westbrook, E. M. (1999). *Performance characteristics needed for protein crystal diffraction X-ray detectors*. *Proc. SPIE*, **3774**, 2–16.

Wiesmann, J., Graf, J., Hoffmann, C. & Michaelsen, C. (2007). *New possibilities for x-ray diffractometry*. *Physics meets Industry*, edited by J. Gegner & F. Haider. Renningen: ExpertVerlag. ISBN 978–3-8169–2740-2.

Wilson, A. J. C. (1971). *Some further considerations in particle-size broadening*. *J. Appl. Cryst.* **4**, 440–443.

Winter, D. J. & Squires, B. A. (1995). *A new approach in performing microdiffraction analysis*. *Adv. X-ray Anal.* **38**, 551–556.

Yagi, N. & Inoue, K. (2007). *CMOS flatpanel detectors for SAXS/WAXS experiments*. *J. Appl. Cryst.* **40**, s439–s441.

Yoshioka, Y. & Ohya, S. (1992). *X-ray analysis of stress in a localized area by use of image plate*. *Adv. X-ray Anal.* **35**, 537–543.

Zuev, A. D. (2006). *Calculation of the instrumental function in X-ray powder diffraction*. *J. Appl. Cryst.* **39**, 304–314.

International Tables for Crystallography (2019). Vol. H, Chapter 2.6, pp. 150–155.

2.6. Non-ambient-temperature powder diffraction

C. A. Reiss

2.6.1. Introduction

X-ray powder diffraction (XRPD) is a powerful tool for the *in situ* investigation of the evolution of a specimen during a non-ambient experiment and for studying structural changes such as lattice expansions and contractions, phase transformations, phase composition, material stability, and alterations in crystallite size. X-rays (and neutrons) are more penetrating than other analytical probes and thus are ideally suited to carrying out *in situ* studies. Many (if not most) polycrystalline materials undergo transformations under non-ambient conditions. If the aim of an experiment is to discover structure–property correlations, it is crucial that the correct structure be used; thus *in situ* diffraction experiments are almost mandatory. This chapter highlights the best ways to perform non-ambient experiments, describing the different equipment for slightly and heavily absorbing materials and the corresponding optical pathways.

The focus is on commercially available equipment for laboratory diffractometers and not on special equipment built at synchrotrons and neutron facilities.

2.6.2. *In situ* powder diffraction

The Latin phrase '*in situ*' literally means 'in position', but it is used in many contexts. In the field of X-ray powder diffraction there is no strict definition of this phrase. If the phrase is taken literally, all non-ambient experiments are *in situ*; the material stays 'in position' during the non-ambient experiment. The environment changes while transforming the sample by outside influences (Norby & Schwarz, 2008). Temperature changes give rise to many processes that can be monitored with or without different gas environments. The main processes that are monitored are the formation of new compounds, phase transformations, and structural changes such as lattice expansions and contractions. Increasingly, surface-layer properties such as stress and texture are studied. The characterization of variations in the crystallite size of nanomaterials is a more recent application.

In situ X-ray diffraction is still a growing research field owing to the introduction of line detectors and area detectors (see Chapter 2.5). These make it possible to measure a large part of the diffraction pattern at once, making the scanning time much shorter compared with a point detector. This speed significantly improves the data quality and reduces the risk of collecting uninterpretable data because of changes in the material under study during the measurement. Another advantage of these detectors is that static detector measurements can be performed, making time-resolved and/or temperature-resolved studies possible.

2.6.3. Processes of interest

Many applications of XRPD contribute to industrial and environmental process development. Some typical application areas are heat treatment and annealing, which are frequently used in the production of alloys, ceramics and polymers; the annealing process affects the strength and/or hardness of materials through microstructural changes. Calcination and sintering are used in the fields of catalysts, building materials and zeolites. Dehydration processes in pharmaceuticals are studied to determine the influence of local environment on the microstructure of drugs and how time affects the availability or preservation of the active pharmaceutical ingredient. These very important topics can be investigated in the case of hydration or dehydration with a humidity chamber. Such chambers control the relative humidity at the same time as the temperature, and are commercially available. Another important topic for the pharmaceutical industry (see Chapter 7.5) is the polymorphic transformations that occur under near- and non-ambient conditions. In nearly all fields from alloys to drugs, from building materials to catalysts, and from nanomaterials to single-crystal materials, structure and phase changes are studied during the operation of processes. Increasingly, non-ambient studies also include other parameters besides temperature and gas environment, for example pressure and humidity. Processes such as the charging and discharging of batteries (see Chapter 7.3) can also be seen as a non-ambient or perhaps better as an '*in operando*' process.

2.6.4. General system setup of non-ambient chambers

2.6.4.1. *Sample stage*

The main requirement for a good non-ambient chamber is that the specimen is cooled/heated homogeneously at a controllable rate. The temperature of the goniometer and other parts of the diffractometer should not be affected while operating the temperature stage. Different sample-stage designs are possible: direct heating/cooling *via* a strip or plate, or surround heating/cooling with an oven or gas convection for a capillary. The advantage of an environmental heater/cooler is the good temperature homogeneity, as there is heat transfer from all sides by radiation and gas convection around the sample or capillary. In contrast, when using a direct heater such as a heating/cooling strip or plate only one-side heat transfer to the sample is possible through the contact surface. An advantage of direct heaters/coolers is the ability to achieve very high and low temperatures and rapid temperature changes. Other differences are the more accurate sample-temperature measurement in an oven compared with a strip heater, where temperature gradients can be present in the strip and the sample attached to the strip heater. For high-temperature measurements with capillaries, the best choice is fused silica ('quartz') glass with a melting point of ∼1973 K; for low-temperature measurements borosilicate glass capillaries are used. A typical hardware setup for a non-ambient X-ray diffraction experiment is shown in Fig. 2.6.1.

2.6.4.2. *Temperature-control unit, process controller*

To control the temperature, a temperature controller with an integrated process controller is needed. For controlled heating/cooling it is necessary to continuously measure the actual temperature and compare it with the set temperature. Often, a standard industrial process controller is used to convert the signal from the temperature sensor into a temperature value, to display

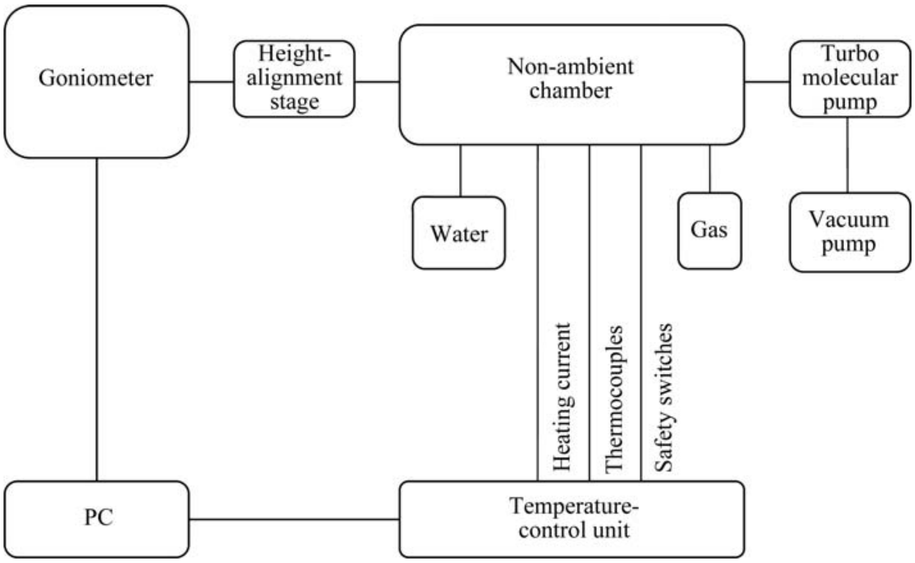

Figure 2.6.1
Typical hardware setup for a non-ambient X-ray diffraction experiment as described in Section 2.6.4; non-ambient chamber, temperature/process-control unit, vacuum/gas equipment, cooling water and goniometer with height-alignment stage connected to a PC.

the value, to send it to the control PC and to control the power for heating/cooling. In addition to controlling the sample conditions, the temperature-control unit (TCU) usually monitors other instrument components such as the cooling of the sample-stage housing and safety devices.

2.6.4.3. *Vacuum equipment, gas supply*

High-temperature X-ray diffraction measurements are often performed in vacuum or in an inert-gas atmosphere to avoid oxidation of the specimen or the sample support. Systems with a rotary pump typically achieve a vacuum of 10^{-2} mbar (where 1 mbar = 100 Pa); when adding a turbo molecular pump to the rotary pump, a vacuum of about 10^{-4} mbar can be reached. A low vacuum or a completely dry gas atmosphere, *e.g.* pure nitrogen (or helium, which has the advantage of a lower background in the diffraction patterns), is also needed for low-temperature experiments to avoid icing problems. Best practice is not to vent the flow of inert gas into the diffractometer enclosure or the laboratory atmosphere, but into the ventilation system (fume hood). Some local safety authorities may require such venting.

2.6.4.4. *Water cooling*

The housing of the sample stage must be kept close to room temperature to avoid heat transfer to the diffractometer and to ensure user safety. In most cases, water is used for this purpose, and the cooling water can be shared with the diffractometer.

2.6.4.5. *Diffractometer and height-compensation mechanism*

The non-ambient chamber has to be interfaced to the goniometer. Interfaces are available without and with a height-compensation mechanism; the latter can be manual or motorized.

When heating/cooling a specimen in an environmental heater, sample displacement is virtually unavoidable, mainly owing to the thermal expansion/contraction of the sample holder. It is possible to correct the temperature-dependent change of the sample position with a height-compensation mechanism (motorized z stage) or to model the displacement in the refinement software. When using a z stage that is controlled *via* software, the shifts in peak positions are only caused by the thermal lattice expansion/contraction of the sample under study. If no such mechanism is available, a parallel X-ray beam (which is not sensitive to sample displacement) can be used, but the resolution may be worse compared with measurements in para-focusing Bragg–Brentano geometry, and granularity may be significant. For strip heaters the displacement of the sample due to the strip is not so pronounced. If a peak of the material of the strip is visible in the diffractogram this can be used as a reference for height compensation if the thermal expansion of the strip material is also taken into account.

2.6.5. Specimen properties

In designing a non-ambient experiment the specimen properties must be taken into account; the holder material should not react with the sample. For flat sample geometry it is preferable that the specimen completely absorbs the X-ray beam. If the specimen is highly transparent, one can either use a thin specimen on a zero-background sample holder or use a capillary. For capillary measurements the X-ray beam must penetrate the capillary completely; if this is not the case, higher energy X-rays (such as Mo or Ag) can be used (Section 2.6.7.2). Every sample is unique, and a suitable solution must be devised.

2.6.6. High-temperature sample stages

A typical laboratory non-ambient setup consists of a non-ambient sample stage, often called a temperature chamber. The sample stage is mounted on a goniometer, preferably in a θ–θ configuration (Fig. 2.6.2). In this case the sample stays horizontal and there is no need to fear melting of the sample with the possibility of it dripping off/out of the sample holder.

A temperature-control unit, vacuum equipment, gas supply and water cooling have to be added to the system before it can be operational.

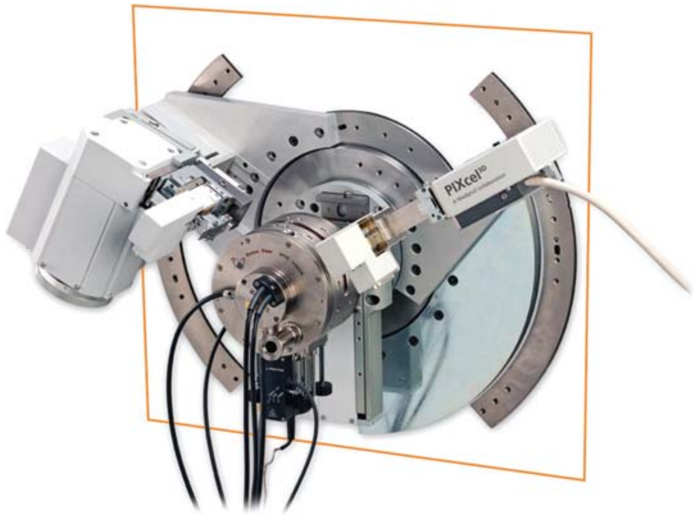

Figure 2.6.2
An Anton Paar HTK 1200N high-temperature oven chamber on a PANalytical Empyrean system equipped with a PIXcel3D detector.

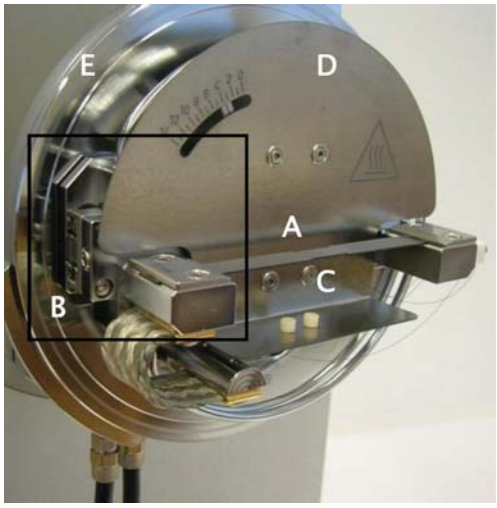

Figure 2.6.3
The interior of a typical strip-heater sample stage (Anton Paar HTK 2000N) with heating strip (A), mechanics to compensate strip expansion (B), thermocouple wires (C), heat shield (D) and water-cooled base plate (E).

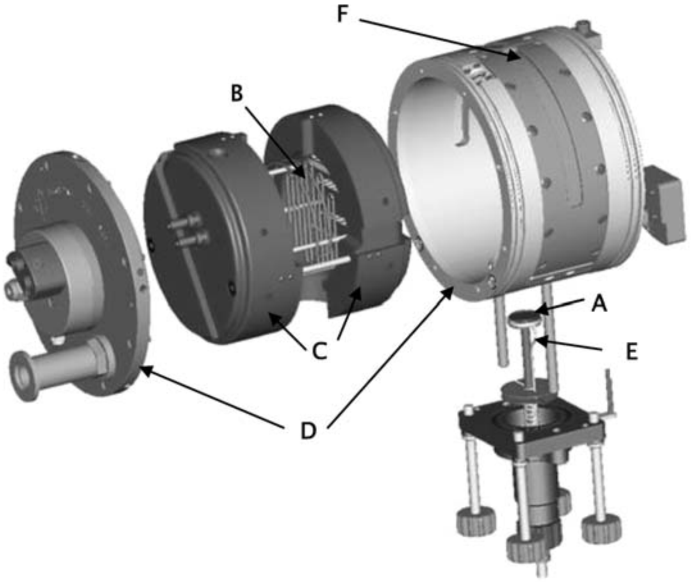

Figure 2.6.4
A typical furnace heater (Anton Paar HTK 1200N) consisting of sample holder (A), heater (B), thermal insulation (C), water-cooled housing (D), thermocouple (E) and X-ray window (F).

2.6.6.1. *Direct heating: strip heaters*

The highest temperatures can be reached with so-called strip heaters (Fig. 2.6.3). Commercial stages that can heat to up to 2573 K are available. Sample heating is performed with a high-current resistance heater. The specimen is placed directly on the strip or in a crucible on the strip. Typical strip materials are platinum (which can be heated in air to up to 1873 K) and tungsten (maximum temperature 2673 K), which requires a vacuum or an inert-gas atmosphere. Less common strip materials which have to be operated in vacuum or in an inert-gas atmosphere are graphite (maximum 1773 K), molybdenum (maximum 2173 K) and tantalum (maximum 2873 K). In addition to very high temperatures, these heaters offer very fast heating and cooling. The HTK 2000N from Anton Paar, for example, can reach up to 2573 K in 3 min. The temperature is measured with a thermocouple, which is usually welded to the heating strip. The main disadvantages of strip heaters are possible chemical reactions between the heating strip and sample, difficulties in measuring the sample temperature accurately and difficult sample preparation. Often, it is not the starting material that reacts but the products that form during heating. Another strip material can be chosen if reactions are known to occur. Inaccurate temperature measurements can be minimized by placing a second temperature sensor on top of the sample.

2.6.6.2. *Environmental heating: the oven*

The second common type of sample stage for high temperatures are oven heaters, also called environmental heaters (Fig. 2.6.4). An electrically heated wire is formed into a cage, which is surrounded with thermal insulation. The heater and insulation form a furnace which almost completely surrounds the sample, creating a very uniform temperature distribution on the inside and minimizing the heat transfer to the housing of the sample stage. Heat is transferred *via* radiation and convection to the sample. The sample is placed on a sample holder in the centre of the furnace, without direct contact with the heater. The sample temperature is measured with a thermocouple located close to the sample, providing accurate measurement of the sample temperature. In addition, it is possible to oscillate the sample to improve the data quality (by reducing granularity), and the user can measure (polycrystalline) solid samples as well as powder samples. In most cases, a long sample holder must be used to place the sample in the centre of the furnace. The thermal expansion of the sample holder while heating must be compensated for by z adjustment to avoid sample displacement (see Section 2.6.4.5). Windows for letting the X-rays enter and leave the chamber should preferably have no influence on the diffraction process. Different materials are available depending on the requirements of the non-ambient measurements. Kapton is the most commonly used window material, followed by graphite, aluminium and beryllium. Environmental heating is also one of two methods used to heat capillaries for X-ray diffraction with transmission geometry. The other option is heating the capillary with a gas flow.

Example: Cement. Cement consists of different calcium silicates (see Chapter 7.12). The exact phases that are present and their abundances determine important physical properties of a cement such as its strength. One of the phases in cement, belite (Ca_2SiO_4), exhibits rapid phase transitions. Fast transitions require good time resolution to detect short-lived intermediate phases and to follow the kinetics of fast phase transformations. An Anton Paar HTK 1200N oven was used for this experiment together with a PIXcel3D detector in static mode using a radius-reduction interface to allow snapshots to be taken over a 2θ range of 6° within a time frame of less than 1 min. Bragg–Brentano geometry was used to achieve a good resolution in 2θ and, to compensate for thermal expansion of the sample holder, an automatic height compensation was applied. On heating $CaCO_3$ with amorphous SiO_2 at 10 K min^{-1}, a solid-state reaction was seen at 853 K; α'_L-Ca_2SiO_4 is formed together with CO_2 (Fig. 2.6.5*a*). Dicalcium silicate exists in five polymorphic forms (Odler, 2000). During cooling, one of the other polymorphs of dicalcium silicate, β-Ca_2SiO_4, is formed, which has a different crystal structure and optical properties (Fig. 2.6.5*b*).

2.6.6.3. *Environmental heating: lamp furnace*

Another approach to designing an environmental chamber is the quadrupole lamp furnace developed by W. M. Kriven (Sarin

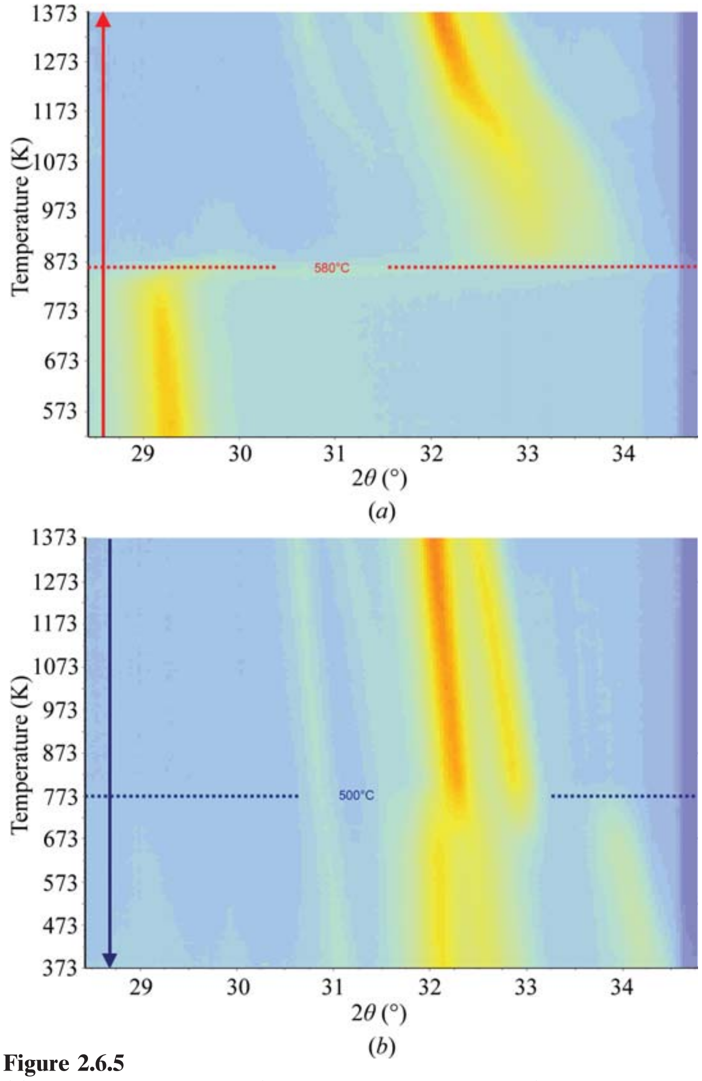

Figure 2.6.5
(*a*) Upon heating, $CaCO_3$ (the peak at about 29.3° in 2θ) reacts with SiO_2 (amorphous); at 853 K the new phase α'_L-Ca_2SiO_4 is formed (the peak between 33 and 32° in 2θ). (*b*) During cooling α'_L-Ca_2SiO_4 (the two peaks between 33 and 32° in 2θ), a different dicalcium silicate polymorph is formed at 773 K; this is β-Ca_2SiO_4.

et al., 2006). Such a furnace can heat a specimen to >2000 K in air. A recent application of this furnace is the characterization of high-temperature phase transitions in $Zr_2P_2O_9$ (Angelkort *et al.*, 2013).

2.6.6.4. *Domed hot stage*

Sample stages with an X-ray transparent dome, such as the DHS 1100 domed hot stage manufactured by Anton Paar (Fig. 2.6.6), give another dimension to polycrystalline diffraction. The dome is made of highly transparent graphite. The transmission of the primary and diffracted beams depends on the wavelength used, and for Cu *Kα* radiation 65% is transmitted. The dome can be used on most of the commercially available modern multipurpose X-ray diffractometers with linear or two-dimensional detectors. Mounted on an *XYZ* table or a cradle, these sample stages can be used to study texture, stress/strain and other phase-induced changes in (for example) thin-film layers under non-ambient conditions.

Example: thin films. A great deal of research has been devoted to the development of gallium nitride (GaN)-based high-electron-mobility transistor (HEMT) structures (Kelekci *et al.*, 2012; Butté *et al.*, 2007). The structural quality of the layers and their interfaces is critical for the performance of the device (Teke *et al.*, 2009). Detailed knowledge of the effects of further process steps, such as thermal annealing, on these parameters is crucial. X-ray reflectivity can be used for monitoring, among other things, the layer thickness and (interface) roughness (Daillant & Gibaud, 2009). To monitor the annealing process, a wurtzite-type AlInN/AlN/GaN/ heterostructure was mounted on a DHS 1100 domed hot stage; 26 scans were made, each of which lasted 1 h and 59 min at a temperature of 823 K (Fig. 2.6.7). From these reflectivity measurements the activation energy could be calculated and compared with the results from X-ray diffraction data from a nominally identical structure (Grieger *et al.*, 2013). The same value was found for both experiments within 5%, giving valuable information about heterostructure layer and interface stability.

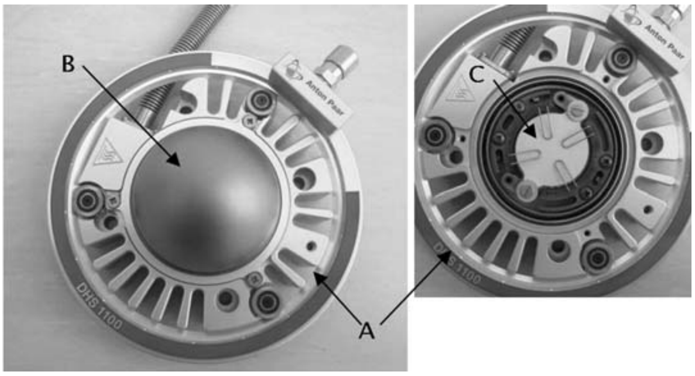

Figure 2.6.6
Sample-heating stage (Anton Paar DHS 1100) with lightweight, air-cooled housing (A), dome-shaped X-ray window (B) and heating plate with sample fixation (C).

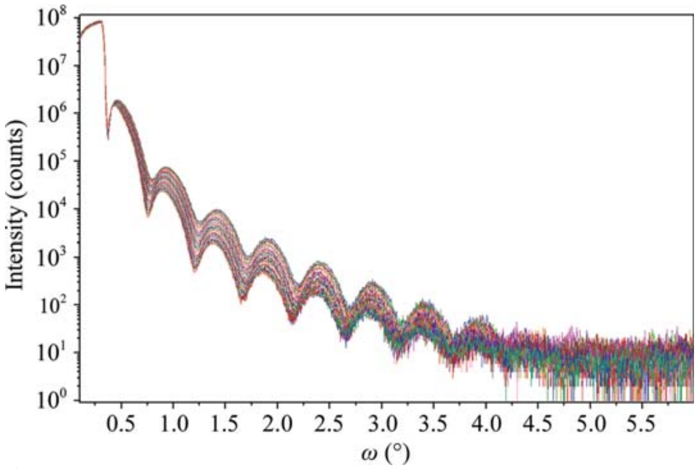

Figure 2.6.7
Monitoring of layer thickness and roughness by X-ray reflectivity measurements during annealing at 823 K.

2.6.7. Low-temperature sample stages

2.6.7.1. *Cryogenic cooling stages/cryostat*

For cryogenic experiments, liquid nitrogen (boiling point 77.4 K at 1 atm, where 1 atm = 101 325 Pa) or liquid helium (boiling point 4.3 K at 1 atm) is required (Weast, 1980). The most common types of chambers for medium-to-low temperatures are chambers with continuous-flow cooling. Here, a continuous flow of liquid nitrogen is provided from a Dewar storage vessel and the cooling process is controlled by a liquid-nitrogen controller. For lower temperatures helium is used. Helium is an expensive gas, and therefore a more economic method is to use a closed-

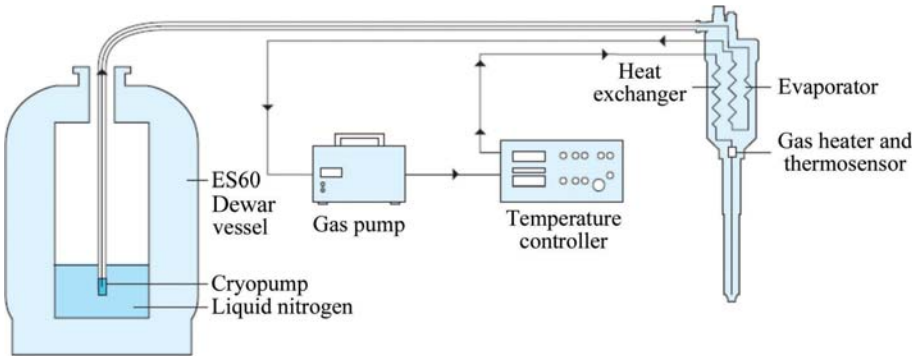

Figure 2.6.8
Schematic drawing of the Oxford Cryosystems cryostream setup.

cycle cryostat. This has the disadvantage that it consumes relatively large amounts of energy, but it does not need a continuous flow of helium and is also easy to use. The PheniX cryostat from Oxford Cryosystems is an example of such a chamber, which makes it possible to cool flat-plate powder samples to 20 K in just 35 min and to as low as about 12 K after a further 25 min. Recently, a group using beamline L11 at the Diamond Light Source synchrotron made some modifications to the PheniX cryostat to enable it to perform low-temperature Debye–Scherrer powder diffraction (Potter *et al.*, 2013). The original flat-plate sample holder in the cryostat was changed to a capillary sample holder.

2.6.7.2. *Cryogenic cooling stages/cryostream*

The cryostream from Oxford Cryosystems (Cosier & Glazer, 1986) cools the sample in a different way (Fig. 2.6.8). Originally developed for single-crystal X-ray diffraction experiments, it is currently also used to cool/heat capillaries in Debye–Scherrer experiments (Fig. 2.6.9). To prevent atmospheric moisture from freezing on the capillary, the cryogenic nitrogen-gas stream is shrouded in a second dry gas stream. When the two flows are balanced, the outer stream protects the inner nitrogen stream and temperatures as low as 80 K can be reached without ice formation on the capillary. The main advantage of measuring a powder sample in a capillary (transmission geometry) in contrast to flat-plate reflection geometry is minimization of preferred orientation of the sample. Attention must be paid, as in all non-ambient measurements, to temperature gradients in the sample. A short capillary is therefore advisable to minimize the occurrence of a gradient along the capillary.

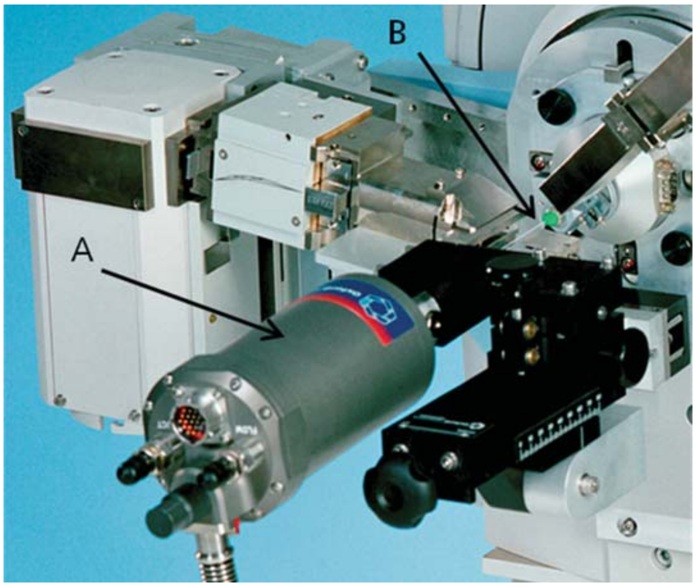

Figure 2.6.9
Oxford Cryostream (A) mounted on a PANalytical diffractometer for cooling a capillary (B).

For absorbing samples, hard radiation must be used to completely penetrate the capillary. Another possibility is to use capillaries with very small diameters, but this is not always very easy and filling them can be time consuming.

Example: buckminsterfullerene. An example that demonstrates the capability of the pair distribution function (PDF) method to independently probe the short-range and long-range atomic ordering in materials is C_{60}, also known as (C_{60}-I_h)[5,6]fullerene, fullerene or buckyball (Egami & Billinge, 2003). A buckyball molecule consists of 60 C atoms arranged on the vertices of a soccer-ball-like frame. At room temperature the C_{60} molecules are arranged in a face-centred cubic (f.c.c.) lattice and they assume completely random orientations as a result of thermal energy.

For long-range atomic order to be present, the atoms of the C_{60} molecules must remain in the same crystallographic position, which is not the case at room temperature. The time-averaged structure of the material can be represented as an f.c.c. structure, with space group $Fm\bar{3}m$, of uniform hollow balls with a diameter of about 7.1 Å. On cooling through 260 K a first-order structural phase transition occurs; the random rotation of each C_{60} molecule becomes slower and is now best described as a librational motion (Brown *et al.*, 2005). The phase transition is accompanied by a sudden contraction of the cubic lattice parameter and the long-range order can be described with a primitive cubic lattice (space group $Pa\bar{3}$).

Fig. 2.6.10 shows the atomic PDF at room and low temperature; only the short distances within the balls are clearly observed at room temperature (Reiss *et al.*, 2012). The correlation between atoms of neighbouring molecules cannot be seen, but ball–ball correlations are visible at larger distances. The low-temperature measurement shows similar peaks below 7.1 Å as the ambient measurement, but above 7.1 Å peaks are visible that result from distances from C atoms in one C_{60} molecule to C atoms in another C_{60} molecule.

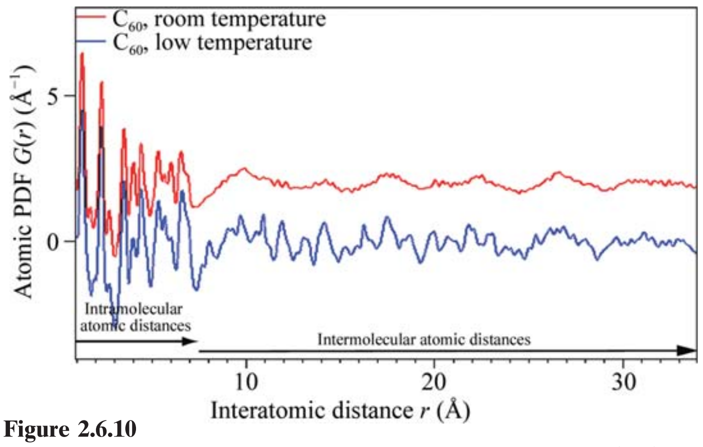

Figure 2.6.10
Atomic pair distribution function of C_{60} at room temperature (red) and at 100 K (blue).

2.6.8. Temperature accuracy

The accuracy of the temperature measurement of a non-ambient device has to be determined before starting a non-ambient experiment. At present no certified temperature standards for X-ray powder diffraction are available, only commonly used reference materials. A list of these materials can be found at https://www.xrayforum.co.uk/ and https://bl831.als.lbl.gov/~jamesh/pickup/Snell_SG_change_table.pdf.

A common method for validation of a non-ambient chamber is by determining the thermal expansion coefficient of a reference material as a function of temperature. Another is to determine the transition temperature of well known phase transformations. A third method is the so-called 'differential thermal expansion' method (Drews, 2001). This method utilizes the relative thermal expansion of two diffraction peaks. These peaks can be from the same or different reference material(s) but must be found in a narrow angular range and have different thermal expansion behaviour. Using only the relative separations of the peaks that are closely spaced eliminates the need for full pattern refinement to take into account geometrical aberrations and makes this method fast.

2.6.9. Future

A whole new field of non-ambient experiments has opened up with the study of new applications such as non-ambient PDF (see Section 2.6.7.2) and non-ambient SAXS measurements. And what happens in the nano world when large-scale models no longer hold at ambient and non-ambient temperatures? The future will tell; non-ambient diffraction/scattering experiments are more relevant now than ever before.

References

Angelkort, J., Apostolov, Z. D., Jones, Z. A., Letourneau, S. & Kriven, W. M. (2013). *Thermal properties and phase transition of $2ZrO_2{\cdot}P_2O_5$ studied by in situ synchrotron X-ray diffraction. J. Am. Ceram. Soc.* **96**, 1292–1299.

Brown, C., Copley, J. & Qiu, Y. (2005). *The orientational order/disorder transition in buckminsterfullerene (C_{60}): an experiment using the NCNR Disk Chopper Spectrometer*. Gaithersburg: NIST Center for Neutron Research. https://www.ncnr.nist.gov/summerschool/ss05/C60_EXPT_05.pdf.

Butté, R., *et al.* (2007). *Current status of AlInN layers lattice-matched to GaN for photonics and electronics. J. Phys. D Appl. Phys.* **40**, 6328–6344.

Cosier, J. & Glazer, A. M. (1986). *A nitrogen-gas-stream cryostat for general X-ray diffraction studies. J. Appl. Cryst.* **19**, 105–107.

Daillant, J. & Gibaud, A. (2009). Editors. *X-ray and Neutron Reflectivity: Principles and Applications.* Berlin, Heidelberg: Springer.

Drews, A. R. (2001). *Calibration of a high temperature X-ray diffraction stage by differential thermal expansion. Adv. X-ray Anal.* **44**, 44–49.

Egami, T. & Billinge, S. J. L. (2003). *Underneath the Bragg Peaks: Structural Analysis of Complex Materials.* Oxford: Pergamon.

Grieger, L., Kharchenko, L., Heuken, M. & Woitok, J. F. (2013). *15th European Workshop on Metalorganic Vapour Phase Epitaxy (EWMOVPE XV)*, Extended abstracts, pp. 51–54. Jülich: Forschungszentrum Jülich.

Kelekci, O., Tasli, P., Cetin, S. S., Kasap, M., Ozcelik, S. & Ozbay, E. (2012). *Investigation of AlInN HEMT structures with different AlGaN buffer layers grown on sapphire substrates by MOCVD. Curr. Appl. Phys.* **12**, 1600–1605.

Norby, P. & Schwarz, U. (2008). *Powder Diffraction: Theory and Practice*, edited by R. E. Dinnerbier & S. J. L. Billinge, pp. 439–463. Cambridge: Royal Society of Chemistry.

Odler, I. (2000). *Special Inorganic Cements*. London: CRC Press.

Potter, J., Parker, J. E., Lennie, A. R., Thompson, S. P. & Tang, C. C. (2013). *Low-temperature Debye–Scherrer powder diffraction on Beamline I11 at Diamond. J. Appl. Cryst.* **46**, 826–828.

Reiss, C. A., Kharchenko, A. & Gateshki, M. (2012). *On the use of laboratory X-ray diffraction equipment for pair distribution function (PDF) studies. Z. Kristallogr.* **227**, 256–261.

Sarin, P., Yoon, W., Jurkschat, K., Zschack, P. & Kriven, W. M. (2006). *Quadrupole lamp furnace for high temperature (up to 2050 K) synchrotron powder X-ray diffraction studies in air in reflection geometry. Rev. Sci. Instrum.* **77**, 092906.

Teke, A., Gökden, S., Tülek, R., Leach, J. H., Fan, Q., Xie, J., Özgür, Ü., Morkoç, H., Lisesivdin, S. B. & Özbay, E. (2009). *The effect of AlN interlayer thicknesses on scattering processes in lattice-matched AlInN/GaN two-dimensional electron gas heterostructures. New J. Phys.* **11**, 063031.

Weast, R. C. (1980). *CRC Handbook of Chemistry and Physics*, 61st ed. Boca Raton: CRC Press.

International Tables for Crystallography (2019). Vol. H, Chapter 2.7, pp. 156–173.

2.7. High-pressure devices

A. Katrusiak

2.7.1. Introduction

Although life in the biosphere of Earth exists within narrow limits of temperature and pressure, these thermodynamic conditions are unusual *on* Earth and in the Universe. Most of the matter in the Universe is contained in black holes, stars and planets, where it is exposed to extreme temperature and pressure. On the other hand, interstellar space constitutes most of the Universe's volume, where both pressure and temperature are close to their absolute-zero values. On Earth's surface at sea level, atmospheric pressure is about 1000 hPa [1 atm = kG cm^{-2} = 9.807×10^4 Pa $\simeq$ 0.1 MPa; currently, the pascal (abbreviated Pa) is the generally accepted pressure unit recommended by the International System of Units]. Under water on Earth, the pressure increases by 0.1 MPa for every 10 m depth, and rises to 120 MPa at the bottom of the Mariana Trench, 11 km below the sea's surface. A relatively low pressure change, to about 0.3 MPa at a depth of 20 m, affects the dissolution of nitrogen in human blood and can lead to decompression sickness (caisson disease); at 300 m in the oceans (3 MPa) and 288 K, methane forms stable hydrates, which constitute the most abundant deposits of carbon on Earth. All geological deposits are exposed to some pressure; at a depth of 1000 m this is about 300 MPa. Consequently, the structure and properties of very many minerals, formed and deposited in the crust, can transform considerably after their exposure to the surface. The syntheses of numerous minerals require high-pressure conditions. Thus, high-pressure experiments can provide indispensable information about the geological and stellar mechanisms, transformations and properties governing the matter forms, properties and distribution inside stars and planets.

Therefore, the pressure dependence of crystal structures is of primary interest to geologists, planetologists and astrophysicists (Hazen, 1999; Merlini *et al.*, 2012). The most cited examples of the effects of extreme conditions are thermonuclear synthesis, the formation of diamond (the dielectric carbon allotrope), the formation of stishovite (the dense form of SiO_2) and the propagation of seismic waves through the Earth's crust. The understanding of these and other phenomena requires that extreme conditions be reproduced and crystal structures investigated in laboratories. Most importantly, the conditions that are ubiquitous across the Universe are viewed as extreme only from our perspective of a narrow thermodynamic space, of a few tens of kelvin and a few megapascals around the triple point of water. From this narrow thermodynamic space, most of our knowledge of materials science has been developed. Extreme conditions allow theories to be verified and developed to a more general level. Moreover, extreme conditions can be utilized to produce new materials with desired properties (Hanfland *et al.*, 2011; Senyshyn *et al.*, 2009), including diamond or its other super-hard substitutes, or new forms of pharmaceutical drugs (Boldyreva, 2010; Boldyreva *et al.*, 2002, 2006; Fabbiani, 2010; Fabbiani & Pulham, 2006; Fabbiani *et al.*, 2004, 2005, 2009). The key element for such research is a sample-environment device for generating high pressure in the laboratory.

The pressure at the centre of Earth is about 364 GPa, one order of magnitude higher again inside the giant planets Jupiter and Saturn, and over 1 000 000 GPa (*i.e.* 1000 TPa) inside small stars like the Sun. Structural determinations under varied thermodynamic conditions are essential for the general understanding of physical and chemical phenomena, and to gain knowledge about the properties of materials and to describe the world around us. Indeed, the biosphere where we live is confined to a range from 0.33 atm (0.033 MPa) at the top of Chomolungma (Mt Everest), 8848 m above sea level, to about 1200 atm (120 MPa). The most commonly discussed and studied thermodynamic parameters are temperature (T), pressure (P) and composition (X). In principle, they affect the structure of matter differently. For example, the primary change induced by temperature is in the energy of atomic, molecular and lattice vibrations, whereas increasing pressure always reduces the volume. These changes are interdependent, and the compression of a structure can also reduce its thermal vibrations, change the types of cohesion forces and reverse the balance between competing compounds of different composition. This concerns all compounds, not only minerals deep under the Earth's surface. An exciting example of a molecular compound undergoing such transformations is water, transforming between at least ten polymorphic structures at high pressure, and also forming hydrates, depending on the thermodynamic conditions. Hence, pressure is now utilized to generate new polymorphs and solvates that cannot be obtained under normal conditions (Patyk *et al.*, 2012; Tomkowiak *et al.*, 2013; Fabbiani, 2010; Boldyreva, 2010).

For these reasons, high-pressure techniques have been developed dynamically, and the breakthrough invention of the diamond-anvil cell and its development in the second half of the 20th century greatly intensified high-pressure research. Today, the effects of high pressure on various materials and their reactions are studied both in small laboratories in universities and at large facilities, which provide powerful beams of X-rays from synchrotrons and beams of neutrons from reactors and spallation targets. The large facilities are either international initiatives, like the European Synchrotron Radiation Facility (ESRF) and Institute Laue–Langevin (ILL) in Grenoble, France, or national ones, like the Diamond Light Source and ISIS at the Rutherford Appleton Laboratory in Oxfordshire, UK, the Deutsches Elektronen Synchrotron (DESY) in Hamburg, Germany, the Photon Factory in Tsukuba, SPring-8 (Super Photon ring – 8 GeV) in Hyōgo Prefecture and the Japan Proton Accelerator Research Complex (J-PARC) in Tokal near Tokyo, Japan, the National Synchrotron Light Source (NSLS) at Brookhaven National Laboratory, USA, the Advanced Photon Source (APS) at Argonne National Laboratory and Los Alamos National Laboratory (LANL), New Mexico, USA, the Lawrence Livermore National Laboratory, California, USA, the Joint Institute for Nuclear Research (JINR) in Dubna, Russian Federation, the Spallation Neutron Source (SNS) at Oak Ridge National Laboratory, USA, and others. They provide access to the beams and high-pressure equipment to the general scientific community.

2.7.2. Historical perspective

The earliest concepts of pressure are often associated with Evangelista Torricelli's famous statement '*Noi viviamo sommersi nel fondo d'un pelago d'aria*' ('We live submerged at the bottom of an ocean of air') in 1643, Otto von Guericke's experiment pitting the force of six horses against atmospheric pressure acting to squeeze together two hemispheres evacuated using the vacuum pump he had constructed in Magdeburg in 1654, and Blaise Pascal's measurements of pressure differences at different altitudes and his demonstrations of barrels being blown up by the force of water poured in through a tall pipe. The subsequently developed high-pressure devices were mainly of the piston-and-cylinder type.

At the beginning of the 19th century, pressures of about 400 MPa could be obtained, and at the beginning of the 20th century, often referred to as the end of the pre-Bridgman era, pressures up to about 2 GPa could be achieved. Then Percy W. Bridgman's remarkable inventions extended the pressure range greatly, to over 10 GPa (Bridgman, 1964). He devised new techniques for sealing pressure chambers, developed the opposed-anvils apparatus and introduced methods for the controlled measurement of various phenomena. Moreover, he used his new methods to describe a vast number of observations and properties of matter at high-pressure ranges hitherto unexplored. Bridgman's ingenious designs of high-pressure devices, such as the opposed-anvils apparatus, paved the path for future researchers. His scientific achievements won him the Nobel Prize in Physics in 1946.

The Bridgman era in high-pressure research ended in the late 1950s, when the diamond-anvil cell, often abbreviated to DAC, was invented (Weir *et al.*, 1959; Jamieson *et al.*, 1959; Piermarini, 2001). Soon after, the DAC became the main tool of high-pressure researchers; it gradually increased the range of attainable pressure by more than an order of magnitude, and under laboratory conditions it surpassed the pressure level at the centre of the Earth. Most importantly, the DAC allowed many new measuring techniques, particularly X-ray diffraction and optical spectroscopy, to be utilized. Before that, spectroscopic studies were limited to about 0.5 GPa. High-pressure X-ray diffraction, pioneered by Cohen (1933) in Berkeley for powders and by Vereshchagin *et al.* (1958) in Moscow for a single crystal of halite at 0.4 GPa in a beryllium high-pressure vessel, had been expensive, inefficient and inaccurate.

The DAC has become commonly available because of its low cost and easy operation. Today, the DAC continues to be the main and most versatile piece of laboratory pressure equipment and a record-breaking high-pressure apparatus. However, other sample environments provide complementary means of structural studies. For example, the large-volume press can be advantageous for neutron diffraction studies and in experiments where very stable high-pressure/high-temperature conditions are required. Naturally, the success of many high-pressure methods would not be possible without the development of other sciences and technologies, including computers, powerful sources of X-rays and neutrons and their detectors, and lasers.

2.7.3. Main types of high-pressure environments

High-pressure methods can be classified as dynamic or static. In the traditional dynamic methods, the pressure is generated for microseconds, usually at an explosion epicentre or at targets where ultra-fast bullets or gas guns are fired at the sample. The explosions are carried out either in special chambers or in bores underground (Batsanov, 2004; Ahrens, 1980, 1987; Keller *et al.*, 2012).

Even shorter, of a few nanoseconds' duration, the shock compression generated in targets using laser drivers coupled to the powerful X-ray pulses of a free-electron laser, or an otherwise generated X-ray beam, can further extend the attainable pressure limits. While this laser shock generates both high pressure and high temperature in the sample (the so-called Hugoniot compression path), in the ramp compression, also termed the off-Hugoniot path, the signal of the designed profile from an optical laser affords terapascal compression and approximates isothermal conditions (Wicks *et al.*, 2018; Smith *et al.*, 2014; Wang *et al.*, 2016).

The advantage of the gas and laser shock-wave and ramp-compression methods is that the attainable pressure is not limited by the tensile strength of the pressure chamber. Disadvantages include the inhomogeneous pressure, difficulties in controlling the temperature, the requirement for very fast analytical methods and the very high cost. The kinetic products generated during the explosion and in the shock waves can be different from the products recovered after the explosion, and different again from those formed under stable conditions. In most cases the laser-generated shock annihilates the sample.

Static methods are at present more suitable for crystallographic studies. The first variable-temperature sample-environment devices for structural studies of liquids and solids were designed soon after the inception of X-ray diffraction analysis. Structural investigations at high and low temperature at ambient pressure were mainly performed either by blowing a stream of heated or cooled gas onto a small sample (Abrahams *et al.*, 1950) or by placing the sample inside an oven or a cryostat. At present, a variety of attachments for temperature control are commercially available as standard equipment for X-ray and neutron diffractometers. Open-flow coolers using gaseous nitrogen and helium are capable of maintaining temperatures of about 90 K and a few kelvin, respectively, for days and weeks. They are easy to operate and pose no difficulties for centring the sample crystal, because the crystal is mounted, as in routine experiments, on a goniometer head with adjustable *x*–*y*–*z* translations and is visible at all positions through a microscope attached to the diffractometer. Cryostats and furnaces obscure the visibility of the sample and are usually heavy, and hence require strong goniometers; however, they often have the advantage of higher stability, a larger homogeneous area in the sample and a larger range of temperature (see Chapter 2.6).

Devices for static high-pressure generation are more difficult to construct because of the obvious requirement for strong walls capable of withstanding the high pressure applied to the sample. There are several types of high-pressure device and they can be classified in several ways. The piston-and-cylinder (PaC) press is the oldest type of pressure generator. However, the pressure range is limited in most advanced constructions (of multilayer negatively strained cylinders, like one shown in Fig. 2.7.1) to 3.0 GPa (Baranowski & Bujnowski, 1970; Besson, 1997; Dziubek & Katrusiak, 2014). PaC presses are ideal for volumetric measurements on a sample enclosed in the cylinder and for generating pressure in a hydrostatic medium transmitted through a capillary to other external high-pressure chambers containing the sample and optimized for a chosen measurement method, usually optical spectroscopy and diffraction. The external devices include chambers for loading the PaC with gas, which is either the hydrostatic medium or the sample itself (Tkacz, 1995; Rivers *et al.*, 2008; Couzinet *et al.*, 2003; Mills *et al.*, 1980; Yagi *et al.*, 1996; Kenichi *et al.*, 2001). In some pressure generators, a cascade of two or three PaC presses is applied for highly compressible pressure-transmitting media (gases) before the final setup stage.

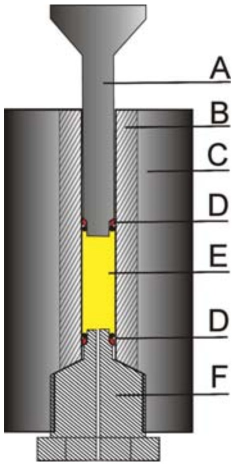

Figure 2.7.1
A cross section through a piston-and-cylinder device with a shrink-fitted double cylinder. In this design, the bottom piston (stopper F) is in the fixed position and only the top piston (A) is pushed into the cylinder by a hydraulic press. The main components of the device are: piston (A), inner cylinder (B), outer supporting shell (C), brass and rubber sealing rings (D), sample (E) and stopper (F).

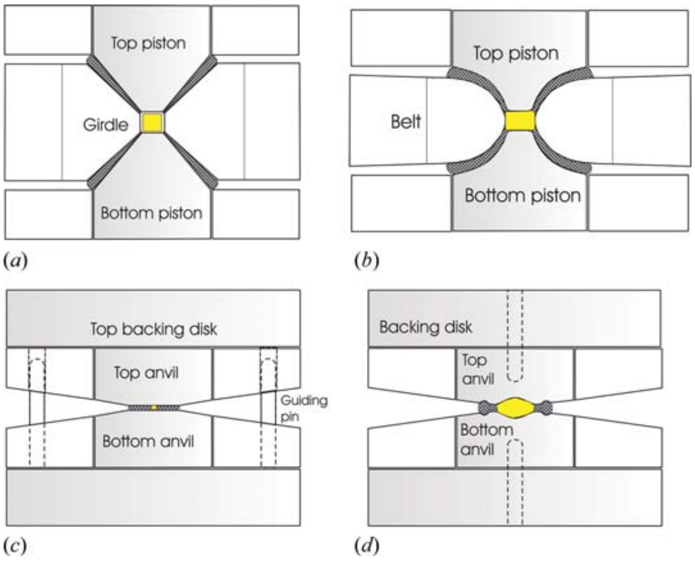

Figure 2.7.2
Cross sections of (*a*) the girdle anvil, (*b*) the belt anvil, (*c*) the Bridgman anvil and (*d*) the toroid anvil. The gaskets are dark grey, the tungsten carbide elements are pale grey and the sample chamber is yellow.

The PaC press can be considered as the prototype of other large-volume presses (LVPs). The PaC press consists of a cylinder closed at both ends with pistons, sealed with gaskets. The attainable pressure depends mainly on the tensile strength of the cylinder and of the gasket. The cylinder can be strengthened by the process of frettage, *i.e.* inducing tensile strain in the outer part and compressive strain inside (Onodera & Amita, 1991). This can be achieved by autofrettage, when a one-block cylinder is purposely overstrained to the point of plastic deformation and the deformation residues result in the required strain. Likewise, the cylinder can be built of shrink-fitted inner and outer tubes (the outer diameter of the inner tube is slightly larger than the inner diameter of the outer tube, which must be heated to assemble the cylinder) or of cone-shaped tubes (with a cone half-angle of *ca* 1°) pushed into one another to generate the frettaging strains. Alternatively, a coil of several layers of strained wire or tape can be wound around the cylinder, or the cylinder can be compressed externally to counteract its tensile strain simultaneously with the load being applied to the pistons (Baranowski & Bujnowski, 1970). The load against the cylinder walls can be reduced by containing the sample in a capsule of soft incompressible material, usually lead (Bridgman, 1964). Cylinder chambers with externally generated pressures up to 0.4 GPa (Blaschko & Ernst, 1974) and PaC cells capable of generating 2 GPa (Bloch *et al.*, 1976; McWhan *et al.*, 1974) have been used for neutron diffraction, and a beryllium cylinder has been used for X-ray diffraction on protein crystals to 100 MPa (Kundrot & Richards, 1986). The range of pressure up to a few hundred megapascals is often described as medium pressure. There are sample-environment chambers with externally generated medium pressure that are designed for in-house powder diffractometers operating in the Bragg–Brentano geometry (Koster van Groos *et al.*, 2003; Whitfield *et al.*, 2008).

If the cylinder length is reduced and the gasket reinforced by compression of the conical pistons, the girdle press is obtained (Fig. 2.7.2*a*). Its optimized modification is the belt apparatus (Fig. 2.7.2*b*). The girdle and belt presses generate pressures of about 10 GPa and can be internally heated to about 1500 K, and hence they have been used widely to synthesise materials. However, the opacity of the girdle/belt and anvils allows no access for X-ray or neutron beams between the anvils. This disadvantage is alleviated in the opposed-anvils press, operating on the massive-support principle, where the beams can pass through the gasket material. After the first record of a simple version of the opposed-anvils experiment in the mid 19th century performed in order to measure the effect of medium pressure on the electric conductibility of wires by Wartmann (1859), the opposed anvils were extensively developed and applied to much higher pressure by Bridgman (1935, 1941, 1952). He also equipped them with a pyrophyllite gasket separating the anvil faces (Bridgman, 1935), and in this form they are commonly known as Bridgman anvils (Fig. 2.7.2*c*). In the 1960s, the flat faces of the Bridgman anvils were modified to so-called toroidal anvils (Fig. 2.7.2*d*), where the sample space is considerably increased by hemispherical depressions at the anvil centre and surrounded by a groove supporting the gasket and preventing its extrusion (Khvostantsev, 1984; Khvostantsev *et al.*, 1977, 2004; Ivanov *et al.*, 1995). Anvils with a spherical sample cavity only, so-called Chechevitsa anvils, preceded the construction of toroidal anvils. Toroidal anvils were optimized for neutron diffraction by adding a small pneumatic press called the Paris–Edinburgh cell (Besson *et al.*, 1992). Toroidal anvils enabled neutron diffraction studies up to 50 GPa and 3000 K (Kunz, 2001; Zhao *et al.*, 1999, 2000; Redfern, 2002). Experiments on magnetic systems in a similar pressure range and at low temperature were performed in a very different design of opposed anvils, the sapphire Kurchatov–LBB cell, shown in Fig. 2.7.3 (Goncharenko & Mirebeau, 1998; Goncharenko, 2004).

More complex LVPs have been based on multi-anvil presses (Liebermann, 2011). These are usually very large devices capable of containing tens of cubic centimetres of sample. The sample is encapsulated and pressurized between anvils sealed with some kind of gasket. The attainable pressure depends on a number of factors, including the applied load and the strength of the anvils, which are made of steel, tungsten carbide, sapphire or sintered diamond; the maximum pressure depends inversely on the sample volume. Multi-anvil presses (Huppertz, 2004; Liebermann, 2011) – tetrahedral, trigonal–bipyramidal, cubic (Akimoto *et al.*, 1987) and octahedral (Onodera, 1987) – are optimized for larger sample volumes and for the high temperatures required for the synthesis of hard materials, especially diamond (Hazen, 1999). The multi-anvil presses are used for diffraction studies.

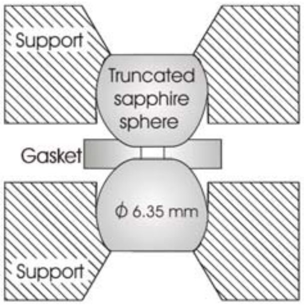

Figure 2.7.3
A schematic view of the opposed-sapphire anvil of the Kurchatov–LBB cell designed for neutron diffraction on magnetic materials (Goncharenko, 2004).

The sample can be either contained in a capsule or mixed with a pressure-transmitting pseudo-hydrostatic medium, which is inert and a weak absorber of X-rays. The sample is accessed by the X-ray beam between the anvils through a weakly absorbing sealing material, such as amorphous boron, magnesium oxide, corundum or pyrophyllite. Like the opposed-anvil presses, multi-anvil LVPs can be used effectively for X-ray diffraction at synchrotrons and neutron sources. However, these large installations also require (apart from intense primary beams) powerful translations for their precise centring relative to the primary beam and diffractometer axes. The main advantage of an LVP is stable and homogenous internal heating up to about 2000 K (Besson, 1997). Such stable conditions are particularly valuable for high-pressure synthesis and crystallization, for example of diamonds (Hazen, 1999).

2.7.4. The diamond-anvil cell (DAC)

The invention of the DAC revolutionized high-pressure studies, diversified their scope, greatly simplified the experimental procedures, increased the range of pressure and temperature, and initiated constant growth in the number of high-pressure structural studies, starting in the 1960s and continuing up to today. The DAC is built from a pair of opposing diamond anvils and a vice to generate their thrust. The sample is compressed between the culets of the anvils. Since its inception, the DAC has been modified and redesigned frequently, in order to adapt it to new experimental techniques or to take advantage of the parallel progress in scientific equipment. The original DAC built at the National Bureau of Standards (Maryland, USA) was used for infrared spectroscopy. Another DAC designed for powder diffraction experiments was made of beryllium, a relatively strong metal which weakly absorbs short-wavelength X-rays (Weir *et al.*, 1959; Bassett, 2009). The DAC, with steel frames and beryllium discs supporting the anvils, is still in use today.

The original and most efficient concept applied in the operation of the DAC was that the incident beam enters the pressure chamber through one diamond anvil and the reflections leave through the other anvil; this mode of operation is often referred to as transmission geometry. Together with the diamond anvils, Be discs constitute windows for the X-rays. However, beryllium has several disadvantages. It is the softest and weakest of the materials used in DAC construction, it softens at about 470 K, beryllium oxide is poisonous, and machining beryllium is difficult and expensive. Therefore, except for the pioneering DAC design by Weir *et al.* (1959), Be parts were initially limited to disc supports for the anvils. Moreover, polycrystalline Be discs produce broad reflection rings and a strong background, and the small central hole in the disc obscured optical observation of the sample. In many modern DACs the beryllium discs have been completely eliminated, and the diamond anvils are directly supported by steel or tungsten carbide platelets (Konno *et al.*, 1989; Ahsbahs, 2004; Boehler & De Hantsetters, 2004; Katrusiak, 2008). For this purpose new diamond anvils, exemplified in Fig. 2.7.4, were designed. Anvils of different sizes, culet dimensions, height-to-diameter ratios and other dimensions can be adjusted for the experimental requirements, such as the planned pressure range and the opening angles of the access windows.

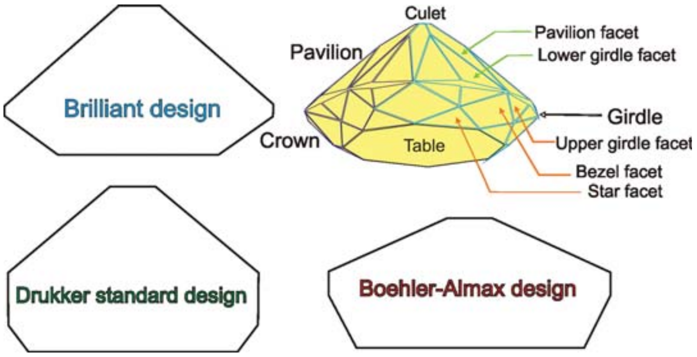

Figure 2.7.4
Cross sections of three types of diamond anvil used in high-pressure cells: the brilliant design (supported either on the table or on the crown rim), the Drukker design (supported on the table and crown) and the Boehler–Almax design (supported on the crown).

Another DAC was independently designed for X-ray powder diffraction by Jamieson *et al.* (1959). In their DAC, the incident beam was perpendicular to the axis through the opposed anvils, and the primary beam passed along the sample contained and squeezed directly (no gasket was used) between the culets. The reflections were recorded on photographic film located on the other side of the DAC, perpendicular to the incident beam. This geometry was described as either panoramic, perpendicular or transverse. The transverse geometry is also used with beryllium or other weakly absorbing gaskets (Mao *et al.*, 1998). Other DACs, for example where both the incident beam and the reflections pass through one diamond anvil, were also designed (Denner *et al.*, 1978; Malinowski, 1987); however, the transmission geometry is most common owing to its advantages. In the transmission geometry the uniaxial support of the anvils leaves a window for optical observation of the sample, as well as for spectroscopic and diffractometric experiments along the cylindrical pressure chamber. Therefore, at present most DAC designs operate in transmission geometry.

The DAC construction can generally be described as a small vice generating thrust between opposed anvils. In the first DACs designed in the late 1950s, no gasket nor hydrostatic fluids were used and the sample was exposed to strong anisotropic stresses. Van Valkenburg (1962) enclosed the sample in a hole in a metal gasket, filled the hole with hydrostatic fluid and sealed it between the culets of the anvils. This most significant development of the miniature high-pressure chamber opened new possibilities for all sorts of studies under hydrostatic conditions, in particular powder and single-crystal diffraction studies. Since then, the gaskets have become an intrinsic part of the DAC. The hydrostatic conditions in the DAC have been used to grow *in situ* single crystals from the melts of neat compounds (Fourme, 1968; Piermarini *et al.*, 1969) and from solutions (Van Valkenburg *et al.*, 1971*a*,*b*). Now it is a common method for *in situ* crystallization under isothermal and isochoric conditions (Dziubek & Katrusiak, 2004; Bujak *et al.*, 2004; Fabbiani *et al.*, 2004; Fabbiani & Pulham, 2006; Budzianowski & Katrusiak, 2006*a*,*b*; Dziubek *et al.*, 2007; Paliwoda *et al.*, 2012; Sikora & Katrusiak, 2013).

The original designs of the DAC (Weir *et al.*, 1959; Jamieson *et al.*, 1959) were later adapted to various purposes. Significant modifications take advantage of new designs of diamond anvils and their supports. Initially, the brilliant-cut diamonds of traditional design, but with the culet ground off to form a flat thrust surface parallel to the table, were used (Fig. 2.7.4). Culets of 0.8 mm in size can be used to about 10 GPa, 0.4 mm culets to about 50 GPa, 0.1 mm culets to about 100 GPa and 0.02 mm (20 μm in diameter) or even smaller (Akahama *et al.*, 2014; Akahama & Kawamura, 2010; Dalladay-Simpson *et al.*, 2016) culets can be used for the megabar 200–400 GPa range. The megabar range requires bevels on the culets to protect their edges from very high strain and damage. The bevels are about 6–7° off the culet plane and the ratio of bevel-to-culet diameters is between 10 and 20. Also, the gasket material, the hole diameter and its height, being a fraction of the hole diameter, are of primary importance. Double bevels can be used to release the strain further, but it appears that a value of about 400 GPa is the maximum pressure attainable in the conventional DAC (c-DAC).

The pressure limits of the c-DAC are surpassed in a double-stage DAC (ds-DAC), in a toroidal DAC (t-DAC) or by shock compression. In the ds-DAC a pair of small anvils, constituting a microscopic DAC (m-DAC, also described as second-stage anvils), is contained inside the c-DAC. The micro-anvils are prepared from diamond or amorphous diamond using the focused ion-beam technique (Sakai *et al.*, 2015, 2018). For another type of ds-DAC, employing microscopic diamond hemispheres (Dubrovinsky *et al.*, 2012; Dubrovinskaia *et al.*, 2016), pressures exceeding 1 TPa have been reported. In the t-DAC, each diamond culet is modified in such a way that an ion-beam-eroded groove surrounds the central micro culet (Dewaele *et al.*, 2018; Jenei *et al.*, 2018; Mao *et al.*, 2018).

At present, the DAC most commonly applied in laboratories is a miniature Merrill–Bassett DAC, where the anvils are installed on two triangular frames driven by three screws along three sliding pins (Merrill & Bassett, 1974). Analogous designs with two or four thrust-generating screws are also in use. The original Merrill–Bassett DAC was equipped with a pair of brilliant-cut 0.2 carat diamonds with polished culets (Fig. 2.7.4) and the anvils were supported on Be discs. The Merrill–Bassett DAC is optimized for use with automatic diffractometers. It contains no rocking blocks but allows translation of one of the anvils. The light weight and small size allow the Merrill–Bassett cell to be routinely used on single-crystal diffractometers. This simple DAC design is suitable for experiments up to about 10 GPa. Dedicated DACs for higher pressure have rocking supports for the diamonds, in the form of either hemispheres or half-cylinders (Fig. 2.7.5).

A very fine adjustment of the anvils and fine and remote pressure control can be obtained in a membrane DAC, where the thrust is generated by a metal membrane operated with gaseous helium or nitrogen (Letoullec *et al.*, 1988; Chervin *et al.*, 1995). Owing to the ideally coaxial thrust generation by the membrane and the stable supports of the anvils, usually in the form of a piston and cylinder, the membrane DAC is suitable for generating pressures of hundreds of gigapascals. The membrane DAC can be operated remotely through a flexible metal capillary, which is advantageous for spectroscopy and both powder and single-crystal diffraction experiments at synchrotrons.

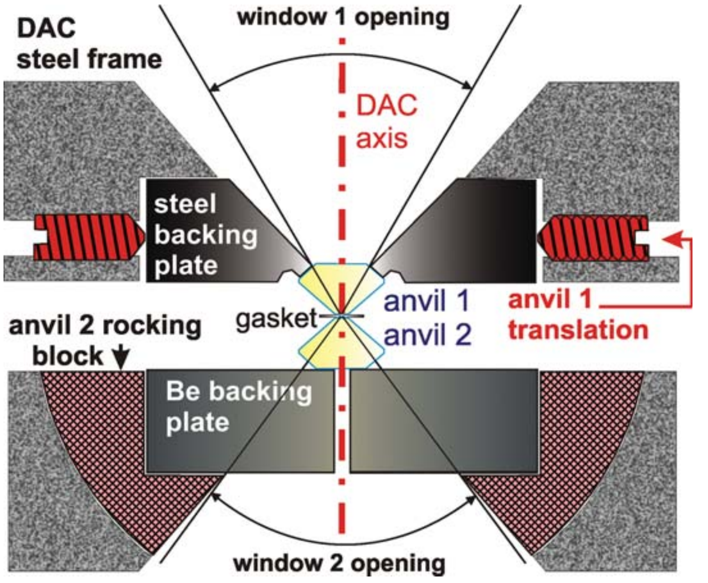

Figure 2.7.5
A cross section through the central part of a diamond-anvil cell, schematically showing the main elements applied in various designs. Usually, either beryllium backing plates or steel/tungsten carbide backing plates with conical windows are used. One of the plates can be translated and the other rocked in all directions (the hemispherical rocking mechanism). In other designs, one of the anvils can be rocked around and translated along one axis, and the other anvil rocked and translated in the perpendicular direction (two perpendicular hemi-cylindrical mechanisms). The usual thickness of the beryllium plate is 3 mm or more, and most constructions allow a window opening of about 40° to the DAC axis. The thickness of the diamond window (the table-to-culet distance) is usually about 1.5 mm.

2.7.5. Variable-temperature high-pressure devices

One of the most common interests in extreme conditions combines high pressure and high temperature. Several techniques for simultaneously controlling both pressure and temperature have been developed (Fei & Wang, 2000). The DAC can be heated externally (with respect to the sample chamber between the anvils' culets) when the entire DAC is placed in an oven or in a hot stream of air from an electrical heater (Fourme, 1968; Allan & Clark, 1999; Podsiadło & Katrusiak, 2008; Bujak *et al.*, 2008). External resistance-wire heaters placed immediately around the diamond anvils and the gasket are often used (Bassett & Takahashi, 1965; Takahashi *et al.*, 1982; Adams & Christy, 1992; Eremets, 1996; Moore *et al.*, 1970; Hazen & Finger, 1982; Besson, 1997; Dubrovinskaia & Dubrovinsky, 2003; Fei & Wang, 2000). External heating can routinely operate up to about 673 K. Its main advantages are stability, reliable measurement of temperature and high homogeneity of temperature in the chamber. The disadvantages include the relatively low temperature range and the large mass of the DAC mechanical parts that are heated. Their thermal expansion can cause loss of pressure. This does not apply to the membrane DAC, where a constant thrust from the membrane is transmitted to the anvils. A sophisticated externally heated DAC in an atmosphere of inert gases is capable of operating between 83 and 1473 K (Bassett *et al.*, 1993).

A very small turnbuckle DAC, about 6 mm in diameter, was originally constructed of plastic and hardened beryllium–copper alloy (BERYLCO 25) in order to perform magnetic measurements at low temperature in the small bore of a superconductive quantum interference device (SQUID) (Graf *et al.*, 2011; Giriat *et al.*, 2010). These are at present the smallest designs that can be used for X-ray diffraction studies, with the whole DAC cooled by commercial low-temperature gas-stream attachments. Alireza & Lonzarich (2009) built another miniature DAC for high-pressure magnetic measurements in a SQUID.

Temperatures of several thousand kelvin can be achieved by internal heating, where the sample absorbs the focused light beam of a laser (Bassett, 2001; Ming & Bassett, 1974; Shen *et al.*, 1996) or is heated by a thin wire passing through the chamber or its immediate surroundings, either in the gasket walls (Boehler *et al.*, 1986; Mao *et al.*, 1987; Zha & Bassett, 2003; Dubrovinsky *et al.*, 1998) or in the culets of intelligent diamond anvils (Bureau *et al.*, 2006). Composite resistance gaskets, with a platinum chamber wall acting as a 35 W resistance heater, can increase the temperature to over 2273 K (Miletich *et al.*, 2000, 2009). Laser beam(s) focused through the DAC anvil(s) onto the sample (Boehler *et al.*, 2001) can heat it to over 3273 K. This requires that the laser beam, or several beams, or a fraction of their energy, be absorbed in the sample. In order to increase the absorption, the sample can be mixed with another compound, for example gold powder. The main disadvantage of laser heating is inhomogeneous distribution of the temperature within the sample.

Much smaller temperature gradients, of a few kelvin at 2773 K, can be obtained in large-volume presses (LVPs). The multi-anvil LVP has traditionally been applied for the synthesis of diamond, which requires stable conditions of both high pressure and high temperature (Hazen, 1999; Liebermann, 2011). In the LVP, a resistance heater installed inside the chamber can provide stable control of the temperature for days, while the pressure is controlled by a hydraulic press. Owing to the large sample volume, the diffraction pattern can be quickly recorded. Most often, energy-dispersive diffraction is applied for the beams entering and leaving the pressure chamber through the gasket material between the anvils. LVPs are generally very large and heavy, which contrasts with the compact construction of the Paris–Edinburgh and Kurchatov–LLB pressure cells (Besson *et al.*, 1992; Goncharenko, 2004, 2006). Both these opposed-anvil cells can be placed in cryostats, and they can be used for either energy- or angle-dispersive diffraction of neutrons or X-rays. The Kurchatov–LLB cell has been optimized for neutron diffraction studies of magnetic structures at high pressure and low temperature (Goncharenko & Mirebeau, 1998; Goncharenko *et al.*, 1995).

2.7.6. Soft and biomaterials under pressure

Interest in the effects of pressure on biological materials is connected to the processing of food and the search for methods of modifying the structure of living tissue and its functions. Soft biological compounds, including proteins, membranes, surfactants, lipids, polymer mesophases and other macromolecular assemblies present in living tissue, are susceptible to pressure, which can affect the molecular conformation and arrangement with relatively low energies of transformation (Royer, 2002). Medium pressure suffices for protein coagulation, as observed for egg white at 0.5 GPa by Bridgman (1914). However, single crystals of egg-white lysozyme survived a pressure of several gigapascals (Katrusiak & Dauter, 1996; Fourme *et al.*, 2004), which was connected to the concentration of the mother liquor used as the hydrostatic fluid. Cells with externally generated pressures up to about 200 MPa for diffraction measurements on single crystals in a beryllium capsule (Kundrot & Richards, 1986) and on powders contained between beryllium windows (So *et al.*, 1992) have been built. Powder diffraction studies have also been performed on samples frozen under high pressure and recovered to ambient pressure (Gruner, 2004). High-pressure studies can be conveniently performed in the DAC, but because of the usually weak scattering of macromolecular samples, synchrotron radiation is preferred for such experiments (Fourme *et al.*, 2004; Katrusiak & Dauter, 1996).

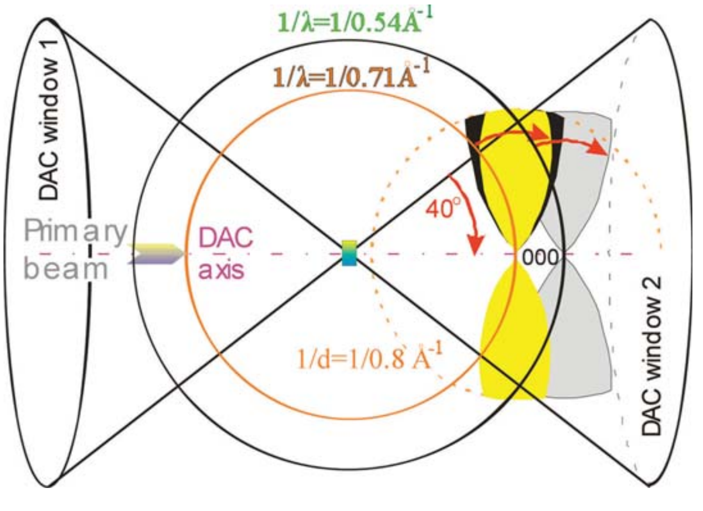

Figure 2.7.6
A diamond-anvil cell, showing the 40° half-angle opening of the conical windows and the reciprocal space accessed for a single-crystal sample and Mo $K\alpha$ or Ag $K\alpha$ radiation. In this schematic drawing, the window cones intersect at the disc-shaped sample (yellow–blue shaded rectangle) and around it the Ewald spheres of reciprocal radii corresponding to Mo $K\alpha$ and Ag $K\alpha$ wavelengths are drawn. The shape of the two yellow profiles meeting at the reciprocal 000 node is the cross section through the torus-like accessible volume of reciprocal space for Mo $K\alpha$ radiation; this torus is circularly symmetric about the DAC axis. The grey shape is likewise the accessible space for Ag $K\alpha$ radiation. Both are at the same resolution of $1/d_{hkl} = 1/0.8$ Å^{-1} (corresponding to θ angles of 26.4° for Mo $K\alpha$ radiation and 19.7° for Ag $K\alpha$). For a powdered sample, all reciprocal-space nodes contained within the resolution sphere (dotted circle) can be recorded. The DAC windows and the sample are shown at the initial ‘zero’ position, when the DAC axis coincides with the primary beam; the red arrows indicate the rotation of the DAC, sample and Ewald sphere to the limiting 40° angle.

2.7.7. Completeness of data

The steel parts of the DAC can restrict access of the incident beam to the sample and can obscure the exit of reflections. For a typical DAC working in transmission mode, the incident beam can be inclined to the DAC axis by up to about 25–40°, for the full opening of the window of 50–80°, respectively. In most DACs the collimator and detector sides are symmetric, so the opposing conical windows have the same opening angle. This limited access to the sample can affect the completeness of diffraction data for low-symmetry crystals, which can then pose considerable difficulties in solving and refining crystal structures from single-crystal measurements.

The restricted access of the primary and diffracted beams to the sample can conveniently be described by the concept of the reciprocal lattice (Fig. 2.7.6). The initial orientation of the crystal in the DAC defines the accessible region of the reciprocal lattice in such a way that the Ewald sphere can be inclined to the initial direction of the incident beam by up to the maximum window opening angle, denoted α_M. The sample can be accessed from both sides of the DAC (by rotating the DAC by 180°) and thus the accessible region of reciprocal space has the form of a round flat cushion, with surfaces touching at the cushion centre [described as a donut cake by Merrill & Bassett (1974)], as shown in Fig. 2.7.6. In the directions perpendicular to the DAC axis, the maximum coordinate $d^*_{yz} = 2\lambda^{-1}\sin\alpha_M$ of reciprocal vectors is for many crystals larger than the resolution of the data (for a typical DAC, $\alpha_M = 40°$, which for organic crystals or other weakly scattering substances is less than required, as the data measured with Mo $K\alpha$ radiation for molecular crystals often extend up to a maximum θ of only about 25°). However, access to the reciprocal lattice is significantly limited along the DAC axis (perpendicular to the flat cushion). In this direction, only those reflections can be accessed for which

$$d^*_x = 2\lambda^{-1}\sin^2(\alpha_M/2),$$

where d^*_x is the maximum coordinate of accessible reciprocal vectors along the x_L axis running from the sample to the radiation source in the laboratory reference system, λ is the wavelength, and α_M is the opening angle of the window measured from the DAC axis (or the maximum inclination of the DAC axis to the incident beam). For example, a DAC with a full window opening angle of $2\alpha_M = 60°$ limits the laboratory reciprocal x coordinate to 0.1885 Å^{-1} when λ(Mo $K\alpha$) = 0.71073 Å is used; if the crystal x^* axis is aligned along the laboratory x_L axis, and if the crystal a^* = 0.10 Å^{-1}, then the maximum Bragg reflection index $|h|$ is 1. If the wavelength is decreased to λ(Ag $K\alpha$) = 0.56 Å, the maximum d_x increases to 0.2392 Å^{-1} and reflections with index h = 2 can be recorded.

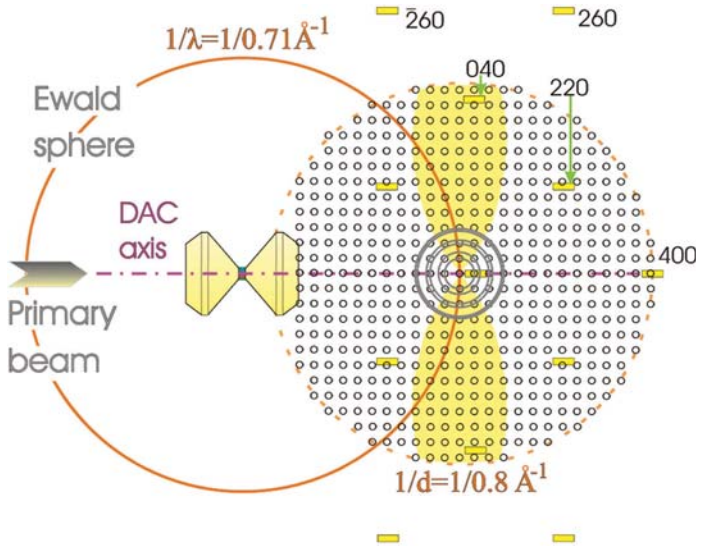

Figure 2.7.7
A schematic illustration of the reciprocal space associated with a sample enclosed in a diamond-anvil cell (DAC). For clarity, the sizes of the sample and diamond anvils have been increased. The Ewald sphere is drawn for the sample only and cubic symmetry with an a parameter of 10 Å has been assumed. Of the reciprocal lattice of the sample, only the layer of $hk0$ nodes is shown as small circles within the resolution limit of $1/d_{hkl}$ = 1/0.8 Å^{-1}. The Ewald spheres of the diamond anvils have been omitted, and only the layer of nodes $hk0$ of the detector anvil is shown as yellow rectangles. Owing to its short unit-cell parameter of 3.57 Å and $Fd\bar{3}m$ symmetry, there are few diamond reflections in the pattern. Note the displaced origins of the reciprocal lattices of the sample and of the detector anvil (the anvil on the detector side) as a result of the off-centre positions of the anvil. For a powdered sample, each node is distributed on a sphere. In this drawing, the spheres are represented by circles only for nodes 100, 110, 200, 210, 220 and 300. The other node spheres contained within the chosen resolution limit have been omitted for clarity; for a triclinic sample, the $hk0$ layer would include 266 powder reflections.

Although the accessible region of the reciprocal lattice depends strongly on the DAC design, the final completeness of the data also depends on several other factors: (i) the symmetry of the sample crystal; (ii) the sample orientation; and (iii) the wavelength of the X-ray radiation. Therefore, the DAC is ideally suited to high-pressure studies of simple and high-symmetry crystals. The Laue-class symmetry of cubic crystals is either $m\bar{3}$ or $m\bar{3}m$, and in most cases the whole of the required resolution falls within the accessible flat-cushion reciprocal region. Thus, the completeness in high-pressure experiments on cubic samples mounted in the chamber at a random orientation is not limited. For hexagonal and tetragonal samples, the crystal orientation is very significant. The maximum completeness can be obtained when the hexagonal or tetragonal axis is perpendicular to the DAC axis. Then the sample reciprocal axis c^* is located along the flat-cushion plane. When two axes of a monoclinic or orthorhombic crystal are at 90° to the DAC axis, a considerable portion of the symmetry-independent part of the reciprocal lattice is not accessible. This reduces the completeness of the data, even though the redundancy of the data is increased. Optimum orientation of the sample can double the completeness compared with experiments measured for the same sample with its axes aligned along the DAC axis and plane.

The completeness of the data can be increased by collecting several data sets for samples oriented differently in the DAC and merging these data (Patyk *et al.*, 2012). This purpose can also be achieved by placing several crystal grains at different orientations in the high-pressure chamber, and then separating their reflections, indexing them and merging.

When the powder diffraction method is used, this problem of completeness is irrelevant. As shown in Fig. 2.7.7, for an ideal powder with randomly oriented grains all reciprocal-lattice nodes can be represented as spheres and they all satisfy the Bragg diffraction condition. The main problem occurring for samples with low symmetry and long lattice constants is overlapping reflections. The intensity of the powder reflection rings is low, because only a small fraction of the sample volume, less than one part per million, contributes to the intensity at a specific point on the reflection ring. Furthermore, the sample volume in the DAC is very small. For these reasons, powder X-ray diffraction in the laboratory usually provides only qualitative information. After the introduction of synchrotron radiation and area detectors, powder diffraction became one of most efficient methods of high-pressure structural studies.

2.7.8. Single-crystal data collection

It is essential that a crystal sample is centred precisely on the diffractometer. Optical centring of a crystal is hampered by the limited view of the sample through the DAC windows in one direction only and by the strong refractive index of diamonds. Consequently, diffractometric methods of crystal centring are more precise for DAC centring. Hamilton's method comparing the diffractometer setting angles of reflections at equivalent positions (Hamilton, 1974) was modified for the purpose of the DAC by King & Finger (1979) and then generalized for any reflections, not necessarily at equivalent positions (Dera & Katrusiak, 1999). These methods are very precise, but they require the approximate orientation matrix (UB matrix) of the sample crystal (Busing & Levy, 1967) to be known and the reflections to be indexed. This information was determined at the beginning of an experiment when traditional diffractometers with a point detector were used. However, nowadays diffractometers with area detectors are used, and generally the crystal orientation is not determined before collecting the diffraction data. To meet these requirements, a new efficient and semi-automatic method was devised, whereby the diffractometer measures a sequence of shadows of the gasket on the CCD detector and calculates the required corrections to the DAC position along the goniometer-head translations (Budzianowski & Katrusiak, 2004). Precise centring can only be achieved for very stable goniometer heads that do not yield under the weight of the DAC (Katrusiak, 1999).

The mode of data collection for a sample enclosed in a DAC can affect the data quality considerably. Data for a bare crystal on a four-circle diffractometer with a scintillation point detector were measured in the so-called bisecting mode, where the ω angle [diffractometer-axes positioning angles ω, χ, φ and θ of the Eulerian cradle will be used here (Busing & Levy, 1967), unless otherwise noted] was fixed to 0° and not used in the process of crystal positioning. In other words, the shaft φ and circle χ lie in the plane bisecting the angle formed by the incident beam and the reflection actually measured. The bisecting mode was optimal for avoiding collisions between the diffractometer shafts and detector, and also minimized absorption effects for most vertically mounted samples. However, these features are irrelevant for samples enclosed in a DAC. It was shown by Finger & King (1978) that the DAC absorption of the incident and reflected beams is a minimum when the Eulerian goniometer φ axis is not used and is always set to 0°. Hence, this is called the $\varphi = 0°$ mode. The $\varphi = 0°$ mode also minimizes the effect of the sample being shadowed by the gasket edges (Katrusiak, 2008). Moreover, in the $\varphi = 0°$ mode the DAC axis always lies in the diffraction plane of the diffractometer, which gives maximum access to the reciprocal-lattice nodes (Fig. 2.7.6).

The advent of area detectors facilitated high-pressure experiments considerably and extended the range of attainable conditions to simultaneous very high pressure and temperatures of several thousand kelvin. Single-crystal experiments are easier because the diffraction data can be recorded before the orientation matrix UB of the crystal is determined (Busing & Levy, 1967; Finger & King, 1978). The recorded data can thus be analysed after the experiment and all relevant structural models can be tested. The use of area detectors shortens the data-collection times for both single-crystal and powder diffraction measurements, and this is particularly efficient with the extremely intense X-ray beams provided by synchrotrons. In single-crystal experiments, several or even tens of reflections are partly scanned through or fully recorded in one image. Although these reflections are not each recorded at their optimum diffractometer settings, corresponding to the $\varphi = 0°$ mode setting described above, the redundancy of the data is increased and the intensities can be corrected for the absorption coefficients derived from differences between equivalent reflections. It is also advantageous that simultaneous diffraction events in the sample crystal and in one or both of the diamonds, which occur sporadically and weaken the recorded reflections, can be eliminated by comparing the intensities of the same reflection measured at several ψ angle positions as well as the equivalent reflections. Equivalent reflections measured at different positions are particularly useful for eliminating systematic errors in the data collection.

It is important that the so called 'run list', defining the diffractometer setting angles and scan directions for the detector exposures, takes into account the $\varphi = 0°$ mode of the DAC orientations, for which access to the DAC is still on average at its widest and the DAC absorption and gasket-shadowing effects are on average the smallest. Most importantly, such an optimum setting can be executed with a four-circle diffractometer, and cannot be done on simplified diffractometers with the φ shaft fixed at a χ angle of about 50°. Even fewer reflections can be accessed when the DAC is rotated about one axis only, which is still the case for some laboratory and synchrotron diffractometers.

2.7.9. Powder diffraction with the DAC

The DAC is often described as the workhorse of high-pressure research, owing to its versatile applications, low cost, easy operation and unrivalled attainable static pressure. However, the small size of the DAC chamber, containing sample volumes between 0.025 mm^3 for pressure to about 5 GPa, 0.005 mm^3 to about 10 GPa and less than 3×10^{-6} mm^3 for the megabar range, can be disadvantageous for powder diffraction studies. The disadvantages include the inhomogeneous distribution of temperature within the sample (particularly as it remains in contact with a diamond, which is the best known thermal conductor) and nonhydrostatic strain (often due to the technique of generating pressure by uniaxial compression of the chamber). In some samples close to the melting curve some grains increase in size at the expense of others, partly or fully dissolving, so the number of grains may be insufficient for obtaining good-quality powder diffraction patterns. This difficulty can be partly circumvented by rocking the DAC during the experiment about the ω axis. On the other hand, for a sample consisting of tens of grains it is possible to perform multi-grain analysis by merging the diffraction patterns to give the equivalent of single-crystal data. High-pressure powder diffraction patterns can also be affected by a low signal-to-noise ratio, too few crystal grains, and their preferential orientation in the DAC uniaxially compressed chamber. The preferential orientation is particularly significant when the grains are elongated and their compressibility is anisotropic; these effects can be further aggravated by the nonhydrostatic environment. Powder reflections are much weaker in intensity than the equivalent single-crystal reflections from the same sample volume. Small sample volumes are compensated for by the powerful beams available at synchrotrons. At present, high-pressure powder diffraction experiments are mainly carried out at synchrotrons by energy-dispersive (Buras *et al.*, 1997*a*,*b*; Baublitz *et al.*, 1981; Brister *et al.*, 1986; Xia *et al.*, 1990; Oehzelt *et al.*, 2002) and angle-dispersive methods (Jephcoat *et al.*, 1992; Nelmes & McMahon, 1994; Fiquet & Andrault, 1999; Crichton & Mezouar, 2005; Mezouar *et al.*, 2005; Hammersley *et al.*, 1996). Angle-dispersive methods are currently preferred to the energy-dispersive method owing to their higher resolution and simpler data processing. However, the energy-dispersive method requires less access for the X-ray beams probing the sample, and hence it is often preferred for studies in the megabar range (hundreds of gigapascals). For high-pressure powder diffraction studies in the laboratory, energy-dispersive methods are still preferred (Tkacz, 1998; Palasyuk & Tkacz, 2007; Palasyuk *et al.*, 2004). The main advantages of experiments at synchrotrons are:

(i) They have a very intense beam compared with traditional sealed X-ray tubes and modern micro-focus sources;

(ii) They offer the possibility of very narrow collimation of the beam, to a diameter of one or a few micrometres;

(iii) Very quick collection of high-quality diffraction data is possible, which is most useful for high-pressure and very high temperature data collections;

(iv) It is possible to measure diffraction data from very small samples, to reduce the dimensions of the DAC chamber and hence to increase the attainable pressure, which is inversely proportional to the chamber diameter;

(v) The microbeam can illuminate a small selected portion of the sample chosen for the investigation, which can be used to perform single-crystal diffraction on a selected grain or for X-ray tomography of the sample and its inclusions;

(vi) The beam diameter is smaller than the diameter of the chamber, which minimizes or even eliminates the effects of beam shadowing;

(vii) The X-ray wavelength is tuneable down to about 0.3 Å. This considerably increases the data completeness and reduces absorption effects in the sample and DAC.

Owing to these features, synchrotron beams are ideally suited for high-pressure diffraction experiments and some researchers have completely stopped using in-house laboratory equipment with sealed X-ray tubes. Historically, the first use of synchrotron radiation for high-pressure studies was reported by Buras, Olsen & Gerward (1977) and Buras, Olsen, Gerward *et al.* (1977). Conventional diffractometers with sealed X-ray tubes can be effectively used for preliminary powder diffraction experiments. For example, a new high-pressure phase of (+)-sucrose was found in this way (Patyk *et al.*, 2012), although the data were insufficient for any structural refinements.

Diffraction data are collected in single and multiple exposures, and the pressure is controlled remotely by inflating a membrane through a gas system. Currently assembled high-pressure powder diffraction synchrotron beamlines incorporate on-line pressure calibration using ruby fluorescence and, often, Raman spectroscopy.

2.7.10. Sample preparation

Several basic techniques can be used to prepare a sample for a high-pressure experiment, for example:

(i) A solid sample can be mounted under ambient conditions in the high-pressure chamber together with the hydrostatic fluid, then sealed and pressurized;

(ii) A solid sample can be mounted under ambient conditions in the high-pressure chamber, condensed gas loaded at elevated pressure (Tkacz, 1995; Rivers *et al.*, 2008; Couzinet *et al.*, 2003; Mills *et al.*, 1980; Yagi *et al.*, 1996; Kenichi *et al.*, 2001) or under cryogenic conditions, and the sample sealed and further pressurized by gasket compression;

(iii) A liquid sample can fill the whole chamber volume under ambient conditions, or condensed gases or their mixtures can be loaded at elevated pressure, and after sealing the DAC the sample is frozen under isothermal conditions;

(iv) A crystal of the pure compound or of a solvate can precipitate from the mixture (solution) when compressed isothermally – the crystal can be in the form of a single crystal or a powder, fully or partly filling the DAC chamber;

(v) Samples completely filling the DAC chamber can be compressed isothermally or undergo isochoric treatment, but strains can be generated in a single crystal or in the grains of a compressed powder conglomerate by anisotropic thermal contraction/expansion; this strain can be avoided by having an excess of the hydrostatic component of the mixture;

(vi) A solid powdered sample can be mixed with a powder of another compound, which is much softer than the sample and is used as a pseudo-hydrostatic medium (halite and MgO are often used for this purpose) – this technique is mainly used for cubic or isotropic samples in large-volume presses, where (pseudo)isotropic strain and pseudo-spherical compression minimize the effect of preferential orientation in the sample.

Preferential orientation can significantly hamper the quality of powder diffraction data, and corrections for this effect should be applied in the Rietveld refinement. All Rietveld refinement programs include preferential orientation models, which fit the data with satisfactory results (McMahon, 2004, 2005; Filinchuk, 2010).

2.7.11. Hydrostatic conditions

Hydrostatic conditions in the sample chamber are essential for good-quality high-pressure diffraction data. They are equally important for single-crystal and powder diffraction experiments. To secure hydrostaticity, the sample is submerged in a hydrostatic medium. The pressure and temperature ranges of the planned experiment depend on the hydrostatic properties of the applied medium. Eventually all substances solidify because of crystallization or vitrification (Piermarini *et al.*, 1973; Eggert *et al.*, 1992; Grocholski & Jeanloz, 2005), which can lead to damage of single crystals, anisotropic strain in powder grains and inhomogeneity of pressure across the sample. It is also important to protect a solid sample from dissolution in the hydrostatic fluid. The dissolved sample can lose its required features (such as shape, polymorphic form or chemical composition) and recrystallize at higher pressure in an undesired form. For example, a fine powder may recrystallize into a few large and preferentially oriented grains. Another potential problem can arise from reactions between the sample and the hydrostatic medium. For example, a pure compound can form solvates incorporating molecules of the hydrostatic fluid (Olejniczak & Katrusiak, 2010, 2011; Andrzejewski *et al.*, 2011; Tomkowiak *et al.*, 2013; Boldyreva *et al.*, 2002; Fabbiani & Pulham, 2006). This has also been observed for helium and argon penetrating into the structures of the fullerenes C_{60} and C_{70} (Samara *et al.*, 1993) and into arsenolite As_4O_6 (Guńka *et al.*, 2015). High-pressure crystallization of water in the presence of helium leads to an inclusion compound interpreted as ice XII. Therefore, the hydrostatic medium should be carefully chosen for a specific experiment, depending on the sample solubility, the pressure range and the type of investigation, whether a mounted-sample study, or *in situ* crystallization or reaction (Sobczak *et al.*, 2018; Półrolniczak *et al.*, 2018).

Many minerals and inorganic samples hardly dissolve at all and a commonly applied pressure-transmitting medium is a mixture of methanol, ethanol and water (16:3:1 by volume), hydrostatic to over 10 GPa at 296 K (see Table 2.7.1); separately, pure methanol crystallizes at 3.5 GPa, ethanol at 1.8 GPa and water at 1.0 GPa. If a sample dissolves well in methanol, ethanol and water, other fluids can be selected (Piermarini *et al.*, 1973; Angel *et al.*, 2007). Liquids like glycerine (hydrostatic to 3 GPa) and special inert fluids, such as silicone oil (Shen *et al.*, 2004; Ragan *et al.*, 1996), Daphne oil (Yokogawa *et al.*, 2007; Murata *et al.*, 2008; Klotz *et al.*, 2009), or condensed gases, like helium, argon and hydrogen (Tkacz, 1995; Dewaele & Loubeyre, 2007), can be used. Alternatively, a saturated solution of the sample compound, for example in a methanol–enthanol–water mixture, can prevent sample dissolution, but on increasing the pressure the compound can precipitate in the form of a powder or single crystals. One can choose to load an excess of the sample into the chamber before filling it up with the hydrostatic fluid, which would dissolve only some of the sample.

Table 2.7.1
The (pseudo)hydrostatic limits of selected media at 296 K (Holzapfel, 1997; Miletich *et al.*, 2000)

Medium	Freezing point (GPa)	(Pseudo)hydrostatic limit (GPa)	Reference
4:1 Methanol:ethanol	–	9.8	Angel *et al.* (2007)
16:3:1 Methanol:ethanol:water	–	10.5	Angel *et al.* (2007)
Anhydrous propan-2-ol	–	4.2	Angel *et al.* (2007)
Neon	4.7	19	Klotz *et al.* (2009)
Argon	1.2	9/35	Bell & Mao (1981)/You *et al.* (2009)
Helium	11.8	70/150	Bell & Mao (1981)/Dewaele & Loubeyre (2007)
Hydrogen	5.7	177	Mao & Bell (1979)
Nitrogen	2.4	13	LeSar *et al.* (1979)
Glycerol	–	1.4	Angel *et al.* (2007)
Glycerin	–	3.0	Hazen & Finger (1982)
Glycerin		4.0	Tateiwa & Haga (2010)
Fluorinert FC84/87	–	7.0	Klotz *et al.* (2009)
Petroleum ether	–	6.0	Mao & Bell (1979)
Isopropyl alcohol		4.3	Piermarini *et al.* (1973)
1:1 Pentane:isopentane	–	7.4	Piermarini *et al.* (1973)
Silicone oil, viscosity 0.65 cSt	–	0.9	Angel *et al.* (2007)
Silicone oil	–	14	Klotz *et al.* (2009)
Daphne oil 7373		2.3	Murata *et al.* (2008)
Daphne oil 7474		3.7 at 296 K/6.7 at 273 K	Klotz *et al.* (2009)/Tateiwa & Haga (2010)
Vaseline	–	2.0	Tateiwa & Haga (2010)
NaCl	–	0.05/25	Tateiwa & Haga (2010)/You *et al.* (2009)

In situ crystallization at high pressure requires good, though not necessarily very good, solvents. Also, co-crystallizations can be performed in the DAC, and in this case the product that is obtained can depend on the solvents used and their concentration. Pressure effectively modifies intermolecular interactions, and new solvates can be obtained depending on the concentration of the substrates. It can be tricky to avoid co-crystallization of some compounds; in these cases a range of hydrostatic fluids has to be tried. A mixture of petroleum ethers, silicone or Daphne oils can be a good choice. Daphne oil, consisting mainly of alkylsilane (Murata *et al.*, 2008), has the rare feature of negligible thermal expansion, which is particularly useful for low-temperature high-pressure experiments: the DAC can be loaded under normal conditions and then pressurized and cooled to the required temperature, *e.g.* in a cryostat, without significant loss of pressure due to contraction of the medium.

The hydrostatic conditions can be checked by inspecting the width of reflections from the sample (full width at half-maximum, FWHM, is usually plotted), the width of the ruby fluorescence R_1 line and the R_1–R_2 line separation (You *et al.*, 2009). The pressure homogeneity can be checked by measurements for several ruby chips mounted across the DAC chamber. Nonhydrostatic conditions can cause inconsistent results and difficulties in their interpretation, which can prompt the researcher to consider changing the hydrostatic medium.

For hard samples, some departure from hydrostatic conditions is often acceptable. It is assumed that for a hard sample the nonhydrostatic compression component is small in a much softer medium, for example, hard corundum studied in soft NaCl. On the other hand, it may be easier to prepare a sample under normal conditions by uniformly mixing the powder of the specimen with a pseudo-hydrostatic medium, rather than using hydrostatic liquids or gases. The diffraction from the pseudo-hydrostatic medium powder can be used to monitor the pressure and measure non-hydrostaticity effects. Pseudo-hydrostatic solid media are often used for multi-anvil presses, where a solid sample facilitates loading and the uniaxial stress is not as drastic as in the opposed-anvil presses. Also, in high-temperature experiments the process of annealing reduces non-hydrostatic strain.

A relatively low nonhydrostatic effect was reported for argon frozen at 1.9 GPa: its pressure gradient up to 1% only is supported at 9 GPa (Bell & Mao, 1981) and up to 1.5% at 80 GPa (Liu *et al.*, 1990). This illustrates how the pseudo-hydrostaticity limit can be extended depending on the hardness of the specimen, the type of high-pressure device and the acceptance of deviatoric stress in the sample.

At very high pressure, exceeding 60 GPa, no compounds persisting as liquids are known (*cf.* Table 2.7.1). Diffraction data must then be corrected for a deviatoric stress component, causing the broadening of reflection rings and affecting their $2\theta_{\rm Bragg}$ positions, when the uniaxial stress is not collinear with the incident beam (Singh, 1993; Singh & Balasingh, 1994; Singh *et al.*, 1998; Mao *et al.*, 1998). The effect of uniaxial stress can be reduced or eliminated by sample annealing, which is often applied to improve the hydrostaticity of the sample.

2.7.12. High-pressure chamber and gasket in the DAC

A high-pressure device should be adjusted to the experiments planned, and in particular to the chemical activity of the sample. Gaseous hydrogen penetrates and dissolves in most metals, and therefore special alloys, such as beryllium bronze, have to be used for hydrogen setups. For some experiments non-metallic gaskets can be used, for example amorphous boron, corundum or diamond powders mixed with a resin. Owing to the insulating properties of such a gasket, the pressure dependence of the electric, dielectric and magnetic properties of the sample can be measured. Chemically aggressive samples can interact with the gasket material of the DAC chamber, and even with the diamond anvils, and this effect usually intensifies at high temperature and pressure. Consequently, both the sample and the high-pressure device can be affected. The erosion caused by an aggressive liquid can be considerably slowed down by its crystallization, which freezes the diffusion of molecules into the gasket. For example, *in situ* crystallization of halogen derivatives of acetic acid could only be performed in a DAC chamber with tungsten gaskets (Gajda & Katrusiak, 2009). In these experiments, the gasket was gradually eroded by the acid, but after its crystallization the measurements could be performed over several days. In order fully to prevent erosion of the gasket, it can be coated with a layer of inert material, for example gold or platinum. Alternatively, a composite chamber can be prepared: after pre-indenting the gasket and drilling a hole at the centre of the indentation, a piece of gold wire can be fitted to the hole, and after pressing into a hole in the DAC again, a smaller hole can be drilled through this inset. A DAC chamber formed in this way has a gold lining and can be resistant to aggressive compounds.

2.7.13. High-pressure neutron diffraction

Neutron scattering is an indispensable and complementary technique in materials research (see Chapter 2.3), particularly for compounds containing heavy elements that strongly absorb X-rays, or light-atom weak X-ray scatterers (*e.g.* see Goncharenko & Loubeyre, 2005). However, the flux of neutron sources, both reactors and spallation targets, is several orders of magnitude lower than that of X-rays, even from traditional sealed X-ray tubes. Moreover, the scattering cross sections of neutrons are on average two orders of magnitude smaller than for X-rays (Bacon, 1975). These two considerations conflict with the requirement of small sample volume preferred for high-pressure devices. Consequently, a prohibitively long measurement time would be required to obtain meaningful neutron diffraction data from the DAC in its original form and size-optimized for X-ray studies. Therefore, initially, the designs of high-pressure devices for neutron scattering studies were based on typical large-volume presses: gas bombs with external multi-stage pressure generators, and piston-and-cylinder, multi-anvil and belt presses (Worlton & Decker, 1968; Bloch *et al.*, 1976; McWhan *et al.*, 1974; Srinivasa *et al.*, 1977; Besson, 1997; Klotz, 2012). The sample volume in the Bridgman-type opposed-anvil press, with flat anvils separated by a gasket of pipestone, was increased severalfold by making a recess at the centre of the pressure chamber of the so-called Chechevitsa anvils (Stishov & Popova, 1961*a*,*b*). The sample volume was further increased in toroid anvils by grooves supporting the gasket around the central recess (Khvostantsev *et al.*, 1977). This made them ideal for powder diffraction neutron measurements on samples of about 100 mm^3 to above 10 GPa in a Paris–Edinburgh hydraulic press (Besson *et al.*, 1992; Besson, 1997). The application of sintered diamond anvils increased this pressure range. High-pressure cells in a form optimized for neutron diffraction can contain between several cubic millimetres and a few cubic centimetres of sample volume. Such a large sample volume naturally limits the pressure range of cells used for neutron diffraction, compared with the DAC used for X-rays. However, the pressure range has increased considerably for neutron diffraction experiments during recent decades, to over 20 GPa in a moissanite anvil cell (Xu *et al.*, 2004; Dinga *et al.*, 2005), and to 40 GPa in a high-pressure cell capable of operating in helium cryostats at 0.1 K and in magnetic fields up to 7.5 T (Goncharenko, 2006; Goncharenko *et al.*, 1995). High-pressure high-temperature cells for neutron diffraction are usually equipped with internal heaters capable of exceeding 1500 K (Zhao *et al.*, 1999, 2000; Le Godec *et al.*, 2001, 2002).

It is particularly advantageous for the construction of large presses for neutron studies that most of the materials used have very low absorption of neutrons. There are also metals (vanadium, aluminium) with very low scattering lengths, and it is possible to obtain alloys ($Ti_{66}Zr_{34}$) with the scattering length scaled to zero. This allows access of the neutron beam to the sample and exit of reflections. In a Paris–Edinburgh cell operating in the time-of-flight mode, the incident beam enters the pressure chamber through the tungsten carbide anvil, along its axis, and the reflections leave the chamber through the gasket along the slit between the anvils with approximately ±6° opening (Besson *et al.*, 1992; Takahashi *et al.*, 1996). In this operation mode, highly neutron-absorbing anvils made of sintered cubic boron nitride (cBN) can also be used (Klotz, 2012). Alternatively, the monochromatic angle-dispersive mode of operation, with the incident and diffracted beams passing through the slit between the anvils, is possible but it is less efficient with regard to the use of the full spectrum of neutrons. The application of a focused neutron beam and the time-of-flight technique allow the use of small sample volumes of a fraction of a cubic millimetre in compact opposed-anvil high-pressure cells (Okuchi *et al.*, 2012). Two DACs were recently optimized for neutron diffraction on single crystals. Owing to the application of a white neutron beam, the structure of a crystal 0.005 mm^3 in volume was determined. All reflections could be recorded because of the smaller Merrill & Bassett (1974) design made of neutron-transparent beryllium–copper alloy (Binns *et al.*, 2016). Another design with a wide access to the sample for the primary and diffracted beams has been successfully used at a hot-neutron source (Grzechnik *et al.*, 2018).

2.7.14. Pressure determination

Pressure determination inside a high-pressure sample chamber is most straightforward in piston-and-cylinder devices, where the force applied to the piston and its surface area are known. Pressure is the force per unit area, with corrections for the friction between the cylinder wall and the piston (particularly significant above 1 GPa) and for the buoyancy of the piston, marginally important for all high pressures. Several types of mechanical pressure gauge are available. In the Bourdon gauge, a spiral metal tube that is pressurized inside unwinds and moves a pointer around a precise scale. Electrical resistance gauges are most often based on a manganin alloy sensor. The resistance of manganin changes at the rate of $2.4 \times 10^{-5}\,\mathrm{GPa}^{-1}$, although precise calibration depends on the alloy composition and it changes with the age of the sensor. The resistance of manganin depends only very weakly on temperature.

The most common pressure calibration method used for the DAC is the fluorescence pressure scale of the ruby R_1 (λ_{R1} at 0.1 MPa is the reference; $\lambda_0 = 694.2$ nm) and R_2 (at 0.1 MPa, $\lambda_{R2} = 692.8$ nm) lines (Forman *et al.*, 1972; Barnett *et al.*, 1973; Syassen, 2008; Gao & Li, 2012). Synthetic ruby with a Cr^{3+} concentration of 3000–5500 p.p.m., illuminated with green laser light, is commonly used. Inclusions of spinels make natural ruby unsuitable as a pressure gauge. A piece of ruby is usually crushed into small pieces and one or several small chips are placed in the DAC chamber close to the sample (Hazen & Finger, 1982). Alternatively, small ruby spheres can be used for this purpose (Chervin *et al.*, 2001).

The linear pressure dependence of the ruby R_1 fluorescence line was established according to the equation of state (EOS) of NaCl to 19.5 GPa:

$$P\,(\mathrm{GPa}) = 2.74\Delta\lambda\,(\mathrm{nm}),$$

where $\Delta\lambda = \lambda_{R1} - \lambda_0$ (Piermarini *et al.*, 1975). The extension of the pressure range to 180 GPa, according to the equations of state of copper, gold and other metals, showed that $P(\Delta\lambda)$ is quasi-linear:

Table 2.7.2

Luminescence pressure sensors, their electronic transition types (s = singlet, d = doublet) and rates of spectral shifts (after Holzapfel, 1997)

Sensor	Transition	λ_0 (Å)	$d\lambda/dP$ (Å GPa^{-1})	$d\lambda/dT$ ($\times 10^{-2}$ Å K^{-1})	$(d\lambda/dP)/\Gamma$ (Å GPa^{-1})	$(d\lambda/dT)/(d\lambda/dP)$ ($\times 10^{-2}$ GPa K^{-1})
Cr^{3+}:Al_2O_3	$^2E{\downarrow}^4A_2$/d	6942	3.65 (9)	6.2 (3)	4.9	17.0
Sm^{2+}:SrB_4O_7	$^5D_0{\downarrow}^7F_0$/s	6854	2.55	−0.1	17.0	−0.4
Sm^{2+}:BaFCl	$^5D_0{\downarrow}^7F_0$/s	6876	11.0	−1.6	4.8	−1.5
Sm^{2+}:SrFCl	$^5D_0{\downarrow}^7F_0$/s	6903	11.2 (3)	−2.36 (3)	5.8	−2.1
Eu^{3+}:LaOCl	$^5D_0{\downarrow}^7F_0$/s	5787	2.5	−0.5	1.0	−2.0
Eu^{3+}:YAG	$^5D_0{\downarrow}^7F_1$/d	5906	1.97	−0.5	0.7	−2.5

Table 2.7.3

Parameters recommended for pressure determination by EOS measurements

Various face-centred cubic (f.c.c.) and body-centred cubic (b.c.c.) metals are used as calibrants, with the EOS given by equation (2.7.1) and the reference temperature T_R = 300 K (after Holzapfel, 1997).

Metal	a_{0R} (pm)	K_{0R} (GPa)	K'_{0R}	α_{0R} ($\times 10^6$ K)	$\delta_{\alpha R}$
Al	404.98 (1)	72.5 (4)	4.8 (2)	23.0 (4)	5.5 (11)
Cu	361.55 (1)	133.2 (2)	5.4 (2)	16.6 (3)	6.1 (6)
Ag	408.62 (1)	101.0 (2)	6.2 (2)	19.2 (4)	7.1 (6)
Au	407.84 (1)	166.7 (2)	6.3 (2)	14.2 (2)	7.2 (6)
Pd	388.99 (1)	189 (3)	5.3 (2)	11.6 (4)	6.0 (11)
Pt	392.32 (1)	277 (5)	5.2 (2)	8.9 (4)	5.9 (11)
Mo	314.73 (1)	261 (5)	4.5 (5)	5.0 (4)	5.2 (14)
W	316.47 (1)	308 (2)	4.0 (2)	4.5 (4)	4.7 (11)

Table 2.7.4

Pressure fixed points at ambient temperature (after Holzapfel, 1997; Hall, 1980)

P (GPa)	Element transition
0.7569 (2)†	Hg freezing at 273 K
1.2 (1)†	Hg freezing at 298 K
2.55 (6)†	Bi I–II at 298 K
3.67 (3)†	Tl h.c.p.–f.c.c.
2.40 (10)†	Cs I–II
4.25 (1)†	Cs II–III
4.30 (1)†	Cs III–IV
5.5 (1)‡	Ba I–II
7.7 (2)‡	Bi III–IV
9.4 (3)†	Sn I–II
12.3 (5)†	Ba II–III
13.4 (6)†	Pb I–II

† Onset of forward transition. ‡ Centre of hysteresis.

$$P = 1904[(\lambda/\lambda_0)^B - 1]/B,$$

where B = 7.665 for quasi-hydrostatic and 5.0 for non-hydrostatic conditions (Mao *et al.*, 1986, 1978; Bell *et al.*, 1986).

The ruby fluorescence depends strongly on temperature (Barnett *et al.*, 1973; Vos & Schouten, 1991; Yamaoka *et al.*, 2012) and a temperature change of about 6 K causes R_1 line shifts equivalent to 0.1 GPa. The fluorescence-line dependence on temperature is much weaker for Sm^{2+}:SrB_4O_7 (Lacam & Chateau, 1989; Lacam, 1990; Datchi *et al.*, 1997) and the other rare-earth-doped sensors listed in Table 2.7.2. These sensors can be more sensitive to pressure than ruby, and together with ruby can be used simultaneously for both temperature and pressure calibration.

The calibration of most pressure gauges is based on comparisons of theoretical and shock-wave data (Holzapfel, 1997), so the derived equations of state are used with an accuracy of about 5% up to 1 TPa. The EOS recommended by Holzapfel (1997) is

$$P = [3K_0(1-x)/x^5]\exp[c_0(1-x)], \tag{2.7.1}$$

where $x = a/a_0 = (V/V_0)^{1/3}$, $c_0 = 3(K_0' - 3)/2$, a is the unit-cell dimension, V is the unit-cell volume, a_{0R} and V_{0R} are the reference parameters under ambient conditions (Table 2.7.3), α_{0R} is the thermal expansion coefficient, K_{0R} is the bulk modulus, and $K_0' = dK_0/dP$. $dK_0/dT = -3\alpha_{0R}K_0\delta_{\alpha R}$, where $\delta_{\alpha R} = \partial(\ln\alpha)/\partial(\ln V)_{TR}$. Pressure can be computed by assuming constant K_0' and linear temperature relations for T close to or higher than T_R = 300 K:

$$\begin{aligned} a_0(T) &= a_{0R}[1 + \alpha_{0R}(T - T_R)],\\ V_0(T) &= V_{0R}[1 + 3\alpha_{0R}(T - T_R)],\\ K_0(T) &= K_{0R}[1 - \alpha_{0R}\delta_{\alpha R}(T - T_R)]. \end{aligned}$$

The details of the parameterization are explained by Holzapfel (1991, 1994) and listed for the simple face-centred (f.c.c.) and body-centred (b.c.c.) cubic metals in Table 2.7.3 (Holzapfel, 1997). Powders of these metals can be mixed with the sample and its pressure can be calibrated according to the unit-cell dimension of the standard. The well known compressibilities of NaCl, CaF_2 and MgO, in the form of either powders or single crystals, are also often used as internal pressure standards (Dorfman *et al.*, 2010, 2012; Dorogokupets & Dewaele, 2007).

An independent pressure assessment can be obtained from standard materials undergoing pressure-induced phase transitions (Table 2.7.4). This method is limited to just a few pressure points (Holzapfel, 1997), but they can provide a useful verification of other pressure gauges.

Other methods of pressure calibration are still being developed. For example, it has been shown that very high pressure can be determined from the Raman shift of strained diamond-anvil culets (Akahama & Kawamura, 2004). The strong piezochromic effect of visible colour changes in soft coordination polymers allows pressure calibration without spectrometers. These changes can proceed gradually (Andrzejewski & Katrusiak, 2017*a*) and abruptly at phase transitions (Andrzejewski & Katrusiak, 2017*b*). Another method of pressure calibration is based on the luminescence lifetime of lanthanide nanocrystals (Runowski *et al.*, 2017).

2.7.15. High-pressure diffraction data corrections

Apart from the Lorentz and polarization (Lp) corrections routinely applied to reflection intensities measured for bare crystals (*i.e.* crystals not enclosed in environment devices), as well as other corrections like extinction and absorption in the sample, the effects of the high-pressure cell should additionally be accounted for. These effects mainly include absorption in the pressure-vessel walls, shadowing of the sample by the pressure-cell opaque elements and elimination of the reflections of the diamond anvils for measurements in a DAC. The set of corrections is usually described for the specific pressure vessel. For a typical DAC with the anvils (about 1.7 mm high) supported directly on the edges of conical steel or tungsten carbide windows, and for Mo *K* radiation, the absorption is quite uniform and varies between about 0.50 and 0.60, for the beams passing close to the DAC axis and those close to the conical window edge, respectively. This absorption is even smaller at the shorter wavelengths used for high-pressure X-ray diffraction studies at synchrotrons. For this reason the absorption correction for the DAC is often neglected.

The sample-shadowing correction accounts for the loss of intensity due to the sample being partly shadowed by the gasket edges. This effect can be avoided by choosing a sufficiently small crystal or by applying a sufficiently narrow beam, which would illuminate only the central part of the sample. Such microbeams are now routinely used at synchrotrons. For these reasons, synchrotron data are often used straightforwardly after applying just the Lp corrections and incident-beam variation and eliminating the diamond reflections. In fact there are very few diamond reflections because of the small unit cell and many systematic absences, and the DAC can be treated as a low-background cuvette for powder diffraction.

The corrections for absorption and gasket shadowing are very important for high-pressure data collection in the laboratory, where a sealed X-ray tube is used. Its beam is relatively weak and for this reason the quality of the data (signal-to-background ratio) is low, but can be improved by increasing the sample volume. Ideally, a sample that completely fills the DAC chamber secures the highest intensity of reflections. However, for large samples the shadowing of the incident and diffracted beams by the gasket is very significant and should be corrected for (Katrusiak, 2004*a*,*b*).

The calculation of the so-called analytical corrections, obtained by dividing the high-pressure chamber into small pixels and calculating the beam's trajectory to and off each pixel, through all the DAC components (beryllium discs, if present, diamond anvils, hydrostatic fluid and sample) can precisely eliminate errors. Having the correct reflection intensities simplifies the structure solution of new phases and increases the accuracy of the refined structure. It has been shown that some incompleteness of accurate data does not cause systematic errors in the structural parameters (Dziubek & Katrusiak, 2002). In most calculations of reflection intensity corrections, the cylindrical symmetry of the DAC about its axis is assumed (Katrusiak, 2001, 2004*a*,*b*; Hazen & Finger, 1982; Angel, 2004; Kuhs *et al.*, 1996; Miletich *et al.*, 2000).

Diffraction measurements with area detectors have the advantage of collecting data with a considerable redundancy factor, which is often routinely used to calculate the so-called empirical absorption corrections, which are sometimes applied to a sample in a DAC. The intensities of powder diffraction reflections measured at synchrotrons with microbeams are often not corrected, particularly when the DAC axis is not significantly moved from the primary beam during data collection. The redundancy of the data also considerably reduces the effect of simultaneous diffraction events by the sample and one or two of the diamond anvils.

The most significant systematic errors in the diffraction of a sample in a DAC may be due to preferential orientation of the grains, which can occur for an anisotropic sample and non-hydrostatic conditions in the chamber. This effect can be accounted for in the process of Rietveld refinement (McMahon, 2004; Filinchuk, 2010), or may require repetition of the measurement after reloading a new sample into the DAC.

2.7.16. Final remarks

During the last 100 years, and particularly during the last few decades, high-pressure diffractometric techniques have been developed covering a broad range of research in different fields of science. It is simply impossible to present all aspects of high-pressure methodology in one chapter. Many books, book chapters and scientific papers have been written on high-pressure research and therefore I have chosen to present a 'flavour' of high-pressure crystallography, rather than concentrating on all its aspects. Readers interested in specific subjects can find the required information in a number of instructive books (Hazen & Finger, 1982; Eremets, 1996; Holzapfel, 1997; Katrusiak & McMillan, 2004; Boldyreva & Dera, 2010; McMahon, 2012) and in numerous articles in research journals. This chapter is only an introduction and gives some useful reference information for high-pressure crystallographers.

It should be stressed that the sample-preparation techniques for high-pressure studies are relatively demanding. Therefore, diffraction studies are often 'adjusted' to the form of the sample obtained in the high-pressure device. In particular, powder diffraction, single-crystal and spectroscopic measurements can be conducted on some synchrotron beamlines (see *e.g.* Dera *et al.*, 2013). Many experimental techniques complementary to high-pressure crystallographic studies have not been mentioned here.

It can be concluded that, over the years, high-pressure research has become quite popular in materials science and at present all over the world there are hundreds or even thousands of scientists capable of performing high-pressure experiments. Their scientific output is significant, and can be used as a guide for those interested in specific types of high-pressure research.

References

Abrahams, S. C., Collin, R. L., Lipscomb, W. N. & Reed, T. B. (1950). *Further techniques in single-crystal X-ray diffraction studies at low temperatures. Rev. Sci. Instrum.* **21**, 396–397.

Adams, D. M. & Christy, A. G. (1992). *Materials for high-temperature diamond-anvil cells. High Press. Res.* **8**, 685–689.

Ahrens, T. J. (1980). *Dynamic compression of Earth materials. Science*, **207**, 1035–1041.

Ahrens, T. J. (1987). *Shock wave techniques for geophysics and planetary physics.* In *Methods of Experimental Physics*, Vol. 24A, edited by C. G. Sammis & T. L. Henyey, pp. 185–235. New York: Academic Press.

Ahsbahs, H. (2004). *New pressure cell for single-crystal X-ray investigations on diffractometers with area detectors. Z. Kristallogr.* **219**, 305–308.

Akahama, Y., Hirao, N., Ohishi, Y. & Singh, A. K. (2014). *Equation of state of bcc-Mo by static volume compression to 410 GPa. J. Appl. Phys.* **116**, 223504.

Akahama, Y. & Kawamura, H. (2004). *High-pressure Raman spectroscopy of diamond anvils to 250 GPa: method for pressure determination in the multimegabar pressure range. J. Appl. Phys.* **96**, 3748–3751.

Akahama, Y. & Kawamura, H. (2010). *Pressure calibration of diamond anvil Raman gauge to 410 GPa. J. Phys. Conf. Ser.* **215**, 012195.

Akimoto, S., Suzuki, T., Yagi, T. & Shimomura, O. (1987). *Phase diagram of iron determined by high-pressure/temperature X-ray diffraction using synchrotron radiation*. In *High-Pressure Research in Mineral Physics*, Geophysics Monograph Series, Vol. 39, edited by M. H. Manghnani & Y. Syono, pp. 149–154. Washington, DC: AGU.

Alireza, P. L. & Lonzarich, G. G. (2009). *Miniature anvil cell for high-pressure measurements in a commercial superconducting quantum interference device magnetometer. Rev. Sci. Instrum.* **80**, 023906.

Allan, D. R. & Clark, S. J. (1999). *Impeded dimer formation in the high-pressure crystal structure of formic acid. Phys. Rev. Lett.* **82**, 3464–3467.

Andrzejewski, M. & Katrusiak, A. (2017*a*). *Piezochromic porous metal–organic framework. J. Phys. Chem. Lett.* **8**, 279–284.

Andrzejewski, M. &. Katrusiak, A. (2017*b*). *Piezochromic topology switch in a coordination polymer. J. Phys. Chem. Lett.* **8**, 929–935.

Andrzejewski, M., Olejniczak, A. & Katrusiak, A. (2011). *Humidity control of isostructural dehydration and pressure-induced polymorphism in 1,4-diazabicyclo[2.2.2]octane dihydrobromide monohydrate. Cryst. Growth Des.* **11**, 4892–4899.

Angel, R. J. (2004). *Absorption corrections for diamond-anvil pressure cells implemented in the software package Absorb6.0. J. Appl. Cryst.* **37**, 486–492.

Angel, R. J., Bujak, M., Zhao, J., Gatta, G. D. & Jacobsen, S. D. (2007). *Effective hydrostatic limits of pressure media for high-pressure crystallographic studies. J. Appl. Cryst.* **40**, 26–32.

Bacon, G. E. (1975). *Neutron Diffraction*. Oxford University Press.

Baranowski, B. & Bujnowski, W. (1970). *A device for generation of hydrogen pressure to 25000 at. Ann. Soc. Chim. Polonarum*, **44**, 2271–2273.

Barnett, J. D., Block, S. & Piermarini, G. J. (1973). *An optical fluorescence system for quantitative pressure measurement in the diamond-anvil cell. Rev. Sci. Instrum.* **44**, 1–9.

Bassett, W. A. (2001). *The birth and development of laser heating in diamond anvil cells. Rev. Sci. Instrum.* **72**, 1270–1272.

Bassett, W. A. (2009). *Diamond anvil cell, 50th birthday. High Press. Res.* **29**, 163–186.

Bassett, W. A., Shen, A. H., Bucknum, M. & Chou, I.-M. (1993). *A new diamond anvil cell for hydrothermal studies to 2.5 GPa and from −190 to 1200°C. Rev. Sci. Instrum.* **64**, 2340–2345.

Bassett, W. A. & Takahashi, T. (1965). *Silver iodide polymorphs. Am. Mineral*. **50**, 1576–1594.

Batsanov, S. S. (2004). *Solid phase transformations under high dynamic pressure.* In *High-Pressure Crystallography*, edited by A. Katrusiak & P. F. McMillan, pp. 353–366. Dordrecht: Kluwer.

Baublitz, M. A., Arnold, V. & Ruoff, A. L. (1981). *Energy dispersive X-ray diffraction from high pressure polycrystalline specimens using synchrotron radiation. Rev. Sci. Instrum.* **52**, 1616–1624.

Bell, P. M. & Mao, H.-K. (1981). *Degree of hydrostaticity in He, Ne, and Ar pressure-transmitting media. Carnegie Inst. Washington Yearb.* **80**, 404–406.

Bell, P. M., Xu, J. A. & Mao, H.-K. (1986). *Static compression of gold and copper and calibration of the ruby pressure scale to pressures to 1.8 megabars.* In *Shock Waves in Condensed Matter*, edited by Y. M. Gupta, pp. 125–130. New York: Plenum Press.

Besson, J. M. (1997). *Pressure generation.* In *High-Pressure Techniques in Chemistry and Physics. A Practical Approach*, edited by W. B. Holzapfel & N. S. Isaacs, pp. 1–45. Oxford University Press.

Besson, J. M., Nelmes, R. J., Hamel, G., Loveday, J. S., Weill, G. & Hull, S. (1992). *Neutron powder diffraction above 10 GPa. Physica B*, **180–181**, 907–910.

Binns, J., Kamenev, K. V., McIntyre, G. J., Moggach, S. A. & Parsons, S. (2016). *Use of a miniature diamond-anvil cell in high-pressure single-crystal neutron Laue diffraction. IUCrJ*, **3**, 168–179.

Blaschko, O. & Ernst, G. (1974). *Autofrettaged high pressure chamber for use in inelastic neutron scattering. Rev. Sci. Instrum.* **45**, 526–528.

Bloch, D., Paureau, J., Voiron, J. & Parisot, G. (1976). *Neutron scattering at high pressure. Rev. Sci. Instrum.* **47**, 296–298.

Boehler, R. & De Hantsetters, K. (2004). *New anvil designs in diamond-cells. High Press. Res*. **24**, 391–396.

Boehler, R., Nicol, M., Zha, C. S. & Jonson, M. L. (1986). *Resistance heating of Fe and W in diamond anvil cells. Physica B*, **139–140**, 916–918.

Boehler, R., Ross, M. P. & Boercker, D. B. (2001). *High-pressure melting curves of argon, krypton, and xenon: deviation from corresponding states theory. Phys. Rev. Lett*. **86**, 5731–5734.

Boldyreva, E. V. (2010). *High-pressure studies of pharmaceuticals and biomimetics. Fundamentals and applications. A general introduction.* In *High-Pressure Crystallography. From Fundamental Phenomena to Technological Applications*, edited by E. Boldyreva & P. Dera, pp. 533–543. Dordrecht: Springer.

Boldyreva, E. V. & Dera, P. (2010). Editors. *High-Pressure Crystallography: From Fundamental Phenomena to Technological Applications*. Dordrecht: Springer.

Boldyreva, E. V., Dmitriev, V. P. & Hancock, B. C. (2006). *Effect of pressure up to 5.5 GPa on dry powder samples of chlorpropamide form-A. Int. J. Pharm.* **327**, 51–57.

Boldyreva, E. V., Shakhtshneider, T. P., Ahsbahs, H., Sowa, H. & Uchtmann, H. (2002). *Effect of high pressure on the polymorphs of paracetamol. J. Therm. Anal. Cal.* **68**, 437–452.

Bridgman, P. W. (1914). *The coagulation of albumen by pressure. J. Biol. Chem.* **19**, 511–512.

Bridgman, P. W. (1935). *Effects of high shearing stress combined with high hydrostatic pressure. Phys. Rev.* **48**, 825–847.

Bridgman, P. W. (1941). *Explorations toward the limit of utilizable pressures. J. Appl. Phys.* **12**, 461–469.

Bridgman, P. W. (1952). *The resistance of 72 elements, alloys and compounds to 100,000* kg/cm^2*. Proc. Am. Acad. Arts Sci.* **81**, 167–251.

Bridgman, P. W. (1964). *Collected Experimental Papers*, Volumes I–VII. Cambridge, MA: Harvard University Press.

Brister, K. E., Vohra, Y. K. & Ruoff, A. L. (1986). *Microcollimated energy-dispersive X-ray diffraction apparatus for studies at megabar pressures with a synchrotron source. Rev. Sci. Instrum.* **57**, 2560–2563.

Budzianowski, A. & Katrusiak, A. (2004). *High-pressure crystallographic experiments with a CCD detector.* In *High-Pressure Crystallography*, edited by A. Katrusiak & P. F. McMillan, pp. 101–112. Dordrecht: Kluwer.

Budzianowski, A. & Katrusiak, A. (2006*a*). *Pressure tuning between NH···N hydrogen-bonded ice analogue and NH···Br polar dabcoHBr complexes. J. Phys. Chem. B*, **110**, 9755–9758.

Budzianowski, A. & Katrusiak, A. (2006*b*). *Pressure-frozen benzene I revisited. Acta Cryst.* B**62**, 94–101.

Bujak, M., Budzianowski, A. & Katrusiak, A. (2004). *High-pressure in-situ crystallization, structure and phase transitions in 1,2-dichloroethane. Z. Kristallogr.* **219**, 573–579.

Bujak, M., Podsiadło, M. & Katrusiak, A. (2008). *Energetics of conformational conversion between 1,1,2-trichloroethane polymorphs. Chem. Commun.* pp. 4439–4441.

Buras, B., Olsen, J. S. & Gerward, L. (1977). *White beam, X-ray, energy-dispersive diffractometry using synchrotron radiation. Nucl. Instrum. Methods*, **152**, 293–296.

Buras, B., Olsen, J. S., Gerward, L., Will, G. & Hinze, E. (1977). *X-ray energy-dispersive diffractometry using synchrotron radiation. J. Appl. Cryst.* **10**, 431–438.

Bureau, H., Burchard, M., Kubsky, S., Henry, S., Gonde, C., Zaitsev, A. & Meijer, J. (2006). *Intelligent anvils applied to experimental investigations: state of the art. High Press. Res*. **26**, 251–265.

Busing, W. R. & Levy, H. A. (1967). *Angle calculations for 3- and 4-circle X-ray and neutron diffractometers. Acta Cryst.* **22**, 457–464.

Chervin, J. C., Canny, B., Besson, J. M. & Pruzan, Ph. (1995). *A diamond anvil cell for IR microspectroscopy. Rev. Sci. Instrum.* **66**, 2595–2598.

Chervin, J. C., Canny, B. & Mancinelli, M. (2001). *Ruby-spheres as pressure gauge for optically transparent high pressure cells. High Press. Res*. **21**, 305–314.

Cohen, W. M. (1933). *X-ray investigations at high pressures. Phys. Rev.* **44**, 326–327.

Couzinet, B., Dahan, N., Hamel, G. & Chervin, J.-C. (2003). *Optically monitored high-pressure gas loading apparatus for diamond anvil cells. High Press. Res.* **23**, 409–415.

Crichton, W. A. & Mezouar, M. (2004). *Methods and application of the Paris–Edinburgh press to X-ray diffraction structure solution with large-volume samples at high pressures and temperatures.* In *Advances in High-Pressure Technology for Geophysical Applications*, edited by J. Chen, Y. Wang, T. S. Duffy, G. Shen & L. F. Dobrzhinetskaya, pp. 353–369. Amsterdam: Elsevier.

Dalladay-Simpson, P., Howie, R. T. & Gregoryanz, E. (2016). *Evidence for a new phase of dense hydrogen above 325 gigapascals. Nature*, **529**, 63–67.

Datchi, F., LeToullec, R. & Loubeyre, P. (1997). *Improved calibration of the* $SrB_4O_7{:}Sm^{2+}$ *optical pressure gauge: advantages at very high pressures and high temperatures. J. Appl. Phys.* **81**, 3333–3339.

Denner, W., Schulz, H. & d'Amour, H. (1978). *A new measuring procedure for data collection with a high-pressure cell on an X-ray four-circle diffractometer. J. Appl. Cryst.* **11**, 260–264.

Dera, P. & Katrusiak, A. (1999). *Diffractometric crystal centering. J. Appl. Cryst.* **32**, 510–515.

Dera, P., Zhuravlev, K., Prakapenka, V., Rivers, M. L., Finkelstein, G. F., Grubor-Urosevic, O., Tschauner, O., Clark, S. M. & Downs, R. T. (2013). *High pressure single-crystal micro X-ray diffraction analysis with GSE_ADA/RSV software. High Press. Res*. **33**, 466–484.

Dewaele, A. & Loubeyre, P. (2007). *Pressurizing conditions in helium-pressure-transmitting medium. High. Press. Res.* **27**, 419–429.

Dewaele, A., Loubeyre, P., Florent Occelli, F., Marie O. & Mezouar, M. (2018). *Toroidal diamond anvil cell for detailed measurements under extreme static pressures. Nat. Commun.* **9**, 2913.

Dinga, Y., Xu, J., Prewitt, Ch. T., Hemley, R. J., Mao, H., Cowan, J. A., Zhang, J., Qian, J., Vogel, S. C., Lokshin, K. & Zhao, Y. (2005). *Variable pressure–temperature neutron diffraction of wüstite, $Fe_{1-x}O$: absence of long-range magnetic order to 20 GPa. Appl. Phys. Lett.* **86**, 052505.

Dorfman, S. M., Jiang, F., Mao, Z., Kubo, A., Meng, Y., Prakapenka, V. B. & Duffy, T. S. (2010). *Phase transitions and equations of state of alkaline earth fluorides CaF_2, SrF_2, and BaF_2 to Mbar pressures. Phys. Rev. B*, **81**, 174121.

Dorfman, S. M., Prakapenka, V. B., Meng, Y. & Duffy, T. S. (2012). *Intercomparison of pressure standards (Au, Pt, Mo, MgO, NaCl and Ne) to 2.5 Mbar. J. Geophys. Res.* **117**, B08210.

Dorogokupets, P. I. & Dewaele, A. (2007). *Equations of state of MgO, Au, Pt, NaCl-B1, and NaCl-B2: internally consistent high-temperature pressure scales. High Press. Res.* **27**, 431–446.

Dubrovinskaia, N. & Dubrovinsky, L. S. (2003). *Whole-cell heater for the diamond anvil cell. Rev. Sci. Instrum.* **74**, 3433–3437.

Dubrovinskaia, N., Dubrovinsky, L., Solopova, N. A., Abakumov, A., Turner, S., Hanfland, M., Bykova, E., Bykov, M., Prescher, C., Prakapenka, V. B., Petitgirard, S., Chuvashova, I., Gasharova, B., Mathis, Y.-L., Ershov, P., Snigireva, I. & Snigirev, A. (2016). *Terapascal static pressure generation with ultrahigh yield strength nanodiamond. Sci. Adv.* **2**, e1600341.

Dubrovinsky, L., Dubrovinskaia, N., Prakapenka, V. B. & Abakumov, A. M. (2012). *Implementation of micro-ball nanodiamond anvils for high-pressure studies above 6 Mbar. Nat. Commun.* **3**, 1163.

Dubrovinsky, L. S., Saxena, S. K. & Lazor, P. (1998). *High-pressure and high-temperature in situ X-ray diffraction study of iron and corundum to 68 GPa using an internally heated diamond anvil cell. Phys. Chem. Miner.* **25**, 434–441.

Dziubek, K. & Katrusiak, A. (2002). *Structural refinements on restricted intensity data collected in high-pressure diffraction experiments. Defect Diffus. Forum*, **208–209**, 319–322.

Dziubek, K. F. & Katrusiak, A. (2004). *Compression of intermolecular interactions in CS_2 crystal. J. Phys. Chem. B*, **108**, 19089–19092.

Dziubek, K. F. & Katrusiak, A. (2014). *Complementing diffraction data with volumetric measurements. Z. Kristallogr.* **229**, 129–134.

Dziubek, K., Podsiadło, M. & Katrusiak, A. (2007). *Nearly isostructural polymorphs of ethynylbenzene: resolution of $\equiv$CH$\cdots\pi$(arene) and cooperative $\equiv$CH$\cdots\pi$(C$\equiv$C) interactions by pressure freezing. J. Am. Chem. Soc.* **129**, 12620–12621.

Eggert, J. H., Xu, L. W., Che, R. Z., Chen, L. C. & Wang, J. F. (1992). *High pressure refractive-index measurements of 4/1 methanol–ethanol. J. Appl. Phys.* **72**, 2453–2461.

Eremets, M. (1996). *High Pressure Experimental Methods*. New York: Oxford University Press.

Fabbiani, F. P. A. (2010). *New frontiers in physical form discovery: high-pressure recrystallization of pharmaceutical and other molecular compounds.* In *High-Pressure Crystallography. From Fundamental Phenomena to Technological Applications*, edited by E. Boldyreva & P. Dera, pp. 545–558. Dordrecht: Springer.

Fabbiani, F. P. A., Allan, D. R., David, W. I. F., Moggach, S. A., Parsons, S. & Pulham, C. R. (2004). *High-pressure recrystallization – a route to new polymorphs and solvates. CrystEngComm*, **6**, 504–511.

Fabbiani, F. P. A., Allan, D. R., Parsons, S. & Pulham, C. R. (2005). *An exploration of the polymorphism of piracetam using high pressure. CrystEngComm*, **7**, 179–186.

Fabbiani, F. P. A., Dittrich, B., Florence, A. J., Gelbrich, T., Hursthouse, M. B., Kuhs, W. F., Shankland, N. & Sowa, H. (2009). *Crystal structures with a challenge: high-pressure crystallisation of ciprofloxacin sodium salts and their recovery to ambient pressure. CrystEngComm*, **11**, 1396–1406.

Fabbiani, F. P. A. & Pulham, C. R. (2006). *High-pressure studies of pharmaceutical compounds and energetic materials. Chem. Soc. Rev.* **35**, 932–942.

Fei, Y. & Wang, Y. (2000). *High-pressure and high-temperature powder diffraction. Rev. Mineral. Geochem.* **41**, 521–557.

Filinchuk, Y. (2010). *Light metal hydrates under non-ambient conditions: probing chemistry by diffraction?* In *High-Pressure Crystallography. From Fundamental Phenomena to Technological Applications*, edited by E. Boldyreva & P. Dera, pp. 281–291. Dordrecht: Springer.

Finger, L. W. & King, H. E. (1978). *A revised method of operation of the single-crystal diamond cell and refinement of the structure of NaCl at 32 kbar. Am. Mineral*. **63**, 337–342.

Fiquet, G. & Andrault, D. (1999). *Powder X-ray diffraction under extreme conditions of pressure and temperature. J. Synchrotron Rad.* **6**, 81–86.

Forman, R. A., Piermarini, G. J., Barnett, J. D. & Block, S. (1972). *Pressure measurement made by the utilization of ruby sharp-line luminescence. Science*, **176**, 284–285.

Fourme, R. (1968). *Appareillage pour études radiocristallographiques sous pression et à température variable. J. Appl. Cryst.* **1**, 23–30.

Fourme, R. E., Girard, R., Kahn, I., Ascone, M., Mezouar, T., Lin, J. E. & Johnson (2004). *State of the art and prospects of macromolecular X-ray crystallography at high hydrostatic pressure.* In *High-Pressure Crystallography*, edited by A. Katrusiak & P. F. McMillan, pp. 527–542. Dordrecht: Kluwer.

Gajda, R. & Katrusiak, A. (2009). *Electrostatic matching versus close-packing molecular arrangement in compressed dimethyl sulfoxide (DMSO) polymorphs. J. Phys. Chem. B*, **113**, 2436–2442.

Gao, R. & Li, H. (2012). *Pressure measurement using the R fluorescence peaks and 417 cm^{-1} Raman peak of an anvil in a sapphire-anvil cell. High Press. Res*. **32**, 176–185.

Giriat, G., Wang, W., Attfield, J. P., Huxley, A. D. & Kamenev, K. V. (2010). *Turnbuckle diamond anvil cell for high-pressure measurements in a superconducting quantum interference device magnetometer. Rev. Sci. Instrum.* **81**, 073905.

Goncharenko, I. N. (2004). *Magnetic properties of crystals and their studies at high pressure conditions.* In *High-Pressure Crystallography*, edited by A. Katrusiak & P. F. McMillan, pp. 321–340. Dordrecht: Kluwer.

Goncharenko, I. N. (2006). *Magnetic and crystal structures probed by neutrons in 40 GPa pressure range. Acta Cryst.* A**62**, s95.

Goncharenko, I. & Loubeyre, P. (2005). *Neutron and X-ray diffraction study of the broken symmetry phase transition in solid deuterium. Nature*, **435**, 1206–1209.

Goncharenko, I. N., Mignot, J.-M., Andre, G., Lavrova, O. A., Mirebeau, I. & Somenkov, V. A. (1995). *Neutron diffraction studies of magnetic structure and phase transitions at very high pressures. High Press. Res*. **14**, 41–53.

Goncharenko, I. N. & Mirebeau, I. (1998). *Magnetic neutron diffraction under very high pressures. Study of europium monochalcogenides. Rev. High Press. Sci. Technol*. **7**, 475–480.

Graf, D. E., Stillwell, R. L., Purcell, K. M. & Tozer, S. W. (2011). *Nonmetallic gasket and miniature plastic turnbuckle diamond anvil cell for pulsed magnetic field studies at cryogenic temperatures. High Press. Res*. **31**, 533–543.

Grocholski, B. & Jeanloz, R. (2005). *High-pressure and -temperature viscosity measurements of methanol and 4:1 methanol:ethanol solution. J. Chem. Phys.* **123**, 204503.

Gruner, S. M. (2004). *Soft materials and biomaterials under pressure.* In *High-Pressure Crystallography*, edited by A. Katrusiak & P. F. McMillan, pp. 543–556. Dordrecht: Kluwer.

Grzechnik, A., Meven, M. & Friese, K. (2018). *Single-crystal neutron diffraction in diamond anvil cells with hot neutrons. J. Appl. Cryst.* **51**, 351–356.

Guńka, P. A., Dziubek, K. F., Gładysiak, A., Dranka, M., Piechota, J., Hanfland, M., Katrusiak, A. & Zachara, J. (2015). *Compressed arsenolite As_4O_6 and its helium clathrate $As_4O_{62}He$. Cryst. Growth Des.* **15**, 3740–3745.

Hall, H. T. (1980). *High pressure techniques*. In *Chemical Experimentation under Extreme Conditions, Techniques of Chemistry*, Vol. IX, ch. II, edited by A. Weissberger & B. Rossiter, pp. 9–72. Chichester: John Wiley & Sons.

Hamilton, W. C. (1974). *International Tables for X-ray Crystallography*, Vol. IV, pp. 273–284. Birmingham: Kynoch Press.

Hammersley, A. P., Svensson, S. O., Hanfland, M., Fitch, A. N. & Hauessermann, D. (1996). *Two-dimensional detector systems. From real detector to idealised image of two-theta scan. High Press. Res.* **14**, 235–248.

Hanfland, M., Proctor, J. E., Guillaume, Ch. L., Degtyareva, O. & Gregoryanz, E. (2011). *High-pressure synthesis, amorphization, and decomposition of silane. Phys. Rev. Lett.* **106**, 095503.

Hazen, R. M. (1999). *The Diamond Makers*. Cambridge Unversity Press.

Hazen, R. M. & Finger, L. (1982). *Comparative Crystal Chemistry*. New York: John Wiley & Sons.

Holzapfel, W. B. (1991). *Equations of state for strong compression. High. Press. Res.* **7**, 290–292.

Holzapfel, W. B. (1994). *Approximate equations of state for solids from limited data sets. J. Phys. Chem. Solids*, **55**, 711–719.

Holzapfel, W. B. (1997). *Pressure determination.* In *High-Pressure Techniques in Chemistry and Physics. A Practical Approach*, edited by W. B. Holzapfel & N. S. Isaacs, pp. 47–55. Oxford University Press.

Huppertz, H. (2004). *Multianvil high-pressure/high-temperature synthesis in solid state chemistry. Z. Kristallogr*. **219**, 330–338.

Ivanov, A. N., Nikolaev, N. A., Pashkin, N. V., Savenko, B. N., Smirnov, L. S. & Taran, Y. V. (1995). *Ceramic high pressure cell with profiled anvils for neutron diffraction investigations (up to 7 GPa). High-Press. Res.* **14**, 203–208.

Jamieson, J. C., Lawson, A. W. & Nachtrieb, N. D. (1959). *New device for obtaining X-ray diffraction patterns from substances exposed to high pressure. Rev. Sci. Instrum.* **30**, 1016–1019.

Jenei, Zs., O'Bannon, E. F., Weir, S. T., Cynn, H., Lipp, M. J. & Evans, W. J. (2018). *Single crystal toroidal diamond anvils for high pressure experiments beyond 5 megabar. Nat. Commun.* **9**, 3563.

Jephcoat, A. P., Finger, L. W. & Cox, D. E. (1992). *High pressure, high resolution synchrotron X-ray powder diffraction with a position-sensitive detector. High Press. Res*. **8**, 667–676.

Katrusiak, A. (1999). *A hinge goniometer head. J. Appl. Cryst.* **32**, 576–578.

Katrusiak, A. (2001). *Absorption correction for crystal-environment attachments from direction cosines. Z. Kristallogr.* **216**, 646–647.

Katrusiak, A. (2004*a*). *Shadowing and absorption corrections of single-crystal high-pressure data. Z. Kristallogr.* **219**, 461–467.

Katrusiak, A. (2004*b*). *Shadowing and absorption corrections of high-pressure powder diffraction data: toward accurate electron-density determinations. Acta Cryst.* A**60**, 409–417.

Katrusiak, A. (2008). *High-pressure crystallography. Acta Cryst.* A**64**, 135–148.

Katrusiak, A. & Dauter, Z. (1996). *Compressibility of lysozyme protein crystals by X-ray diffraction. Acta Cryst.* D**52**, 607–608.

Katrusiak, A. & McMillan, P. F. (2004). Editors. *High Pressure Crystallography*. Dordrecht: Kluwer Academic Press.

Keller, K., Schlothauer, T., Schwarz, M., Heide, G. & Kroke, E. (2012). *Shock wave synthesis of aluminium nitride with rocksalt structure. High Press. Res.* **32**, 23–29.

Kenichi, T., Sahu, P. Ch., Yoshiyasu, K. & Yasuo, T. (2001). *Versatile gas-loading system for diamond-anvil cells. Rev. Sci. Instrum.* **72**, 3873–3876.

Khvostantsev, L. G. (1984). *A verkh-niz (up-down) device of toroid type for generation of high pressure. High Temp. High Press.* **16**, 165–169.

Khvostantsev, L. G., Slesarev, V. N. & Brazhkin, V. V. (2004). *Toroid type high-pressure device: history and prospects. High Press. Res*. **24**, 371–383.

Khvostantsev, L. G., Vereshchagin, L. F. & Novikov, A. P. (1977). *Device of toroid type for high pressure generation. High Temp. High Press.* **9**, 637–639.

King, H. E. & Finger, L. W. (1979). *Diffracted beam crystal centering and its application to high-pressure crystallography. J. Appl. Cryst.* **12**, 374–378.

Klotz, S. (2012). *Techniques in High Pressure Neutron Scattering*. Boca Raton: CRC Press.

Klotz, S., Chervin, J.-C., Munsch, P. & Le Marchand, G. (2009). *Hydrostatic limits of 11 pressure transmitting media. J. Phys. D Appl. Phys.* **42**, 075413.

Konno, M., Okamoto, T. & Shirotani, I. (1989). *Structure changes and proton transfer between O$\cdots$O in bis(dimethylglyoximato)platinum(II) at low temperature (150 K) and at high pressures (2.39 and 3.14 GPa). Acta Cryst.* B**45**, 142–147.

Koster van Groos, A. F., Guggenheim, S. & Cornell, C. (2003). *Environmental chamber for powder X-ray diffractometers for use at elevated pressures and low temperatures. Rev. Sci. Instrum.* **74**, 273–275.

Kuhs, W. F., Bauer, F. C., Hausmann, R., Ahsbahs, H., Dorwarth, R. & Hölzer, K. (1996). *Single crystal diffraction with X-rays and neutrons: high quality at high pressure? High Press. Res.* **14**, 341–352.

Kundrot, C. E. & Richards, F. M. (1986). *Collection and processing of X-ray diffraction data from protein crystals at high pressure. J. Appl. Cryst.* **19**, 208–213.

Kunz, M. (2001). *High pressure phase transformations.* In *Phase Transformations in Materials*, edited by G. Kostorz, pp. 655–695. Weinheim: Wiley-VCH Verlag.

Lacam, A. (1990). *The SrB_4O_7:Sm^{2+} optical sensor and the pressure homogenization through thermal cycles in diamond anvil cells. High Press. Res*. **5**, 782–784.

Lacam, A. & Chateau, C. (1989). *High-pressure measurements at moderate temperatures in a diamond anvil cell with a new optical sensor: SrB_4O_7:Sm^{2+}. J. Appl. Phys.* **66**, 366–372.

Le Godec, Y., Dove, M. T., Francis, D. J., Kohn, S. C., Marshall, W. G., Pawley, A. R., Price, G. D., Redfern, S. A. T., Rhodes, N., Ross, N. L., Schofield, P. F., Schooneveld, E., Syfosse, G., Tucker, M. G. & Welch, M. D. (2001). *Neutron diffraction at simultaneous high temperatures and pressures, with measurement of temperature by neutron radiography. Min. Mag.* **65**, 749–760.

Le Godec, Y., Dove, M. T., Redfern, S. A. T., Marshall, W. G., Tucker, M. G., Syfosse, G. & Besson, J. M. (2002). *A new high P–T cell for neutron diffraction up to 7 GPa and 2000 K with measurement of temperature by neutron radiography. High Press. Res.* **65**, 737–748.

LeSar, R., Ekberg, S. A., Jones, L. H., Mills, R. L., Schwalbe, L. A. & Schiferl, D. (1979). *Raman spectroscopy of solid nitrogen up to 374 kbar. Solid State Commun.* **32**, 131–134.

Letoullec, R., Pinceaux, J. P. & Loubeyre, P. (1988). *The membrane diamond anvil cell: a new device for generating continuous pressure and temperature variations. High Press. Res.* **1**, 77–90.

Liebermann, R. C. (2011). *Multi-anvil, high pressure apparatus: a half-century of development and progress. High Press. Res*. **31**, 493–532.

Liu, Z. X., Cui, Q. L. & Zou, G. T. (1990). *Disappearance of the ruby R-line fluorescence under quasihydrostatic pressure and valid pressure range of ruby gauge. Phys. Lett. A*, **143**, 79–82.

McMahon, M. I. (2004). *High pressure diffraction from good powders, poor powders and poor single crystals.* In *High-Pressure Crystallography*, edited by A. Katrusiak & P. F. McMillan, pp. 1–20. Dordrecht: Kluwer.

McMahon, M. I. (2005). *Structures from powders and poor-quality single crystals at high pressure. J. Synchrotron Rad.* **12**, 549–553.

McMahon, M. I. (2012). *High-pressure crystallography. Top. Curr. Chem.* **315**, 69–109.

McWhan, D. B., Bloch, D. & Parisot, G. (1974). *Apparatus for neutron diffraction at high pressure. Rev. Sci. Instrum.* **45**, 643–646.

Malinowski, M. (1987). *A diamond-anvil high-pressure cell for X-ray diffraction on a single crystal. J. Appl. Cryst.* **20**, 379–382.

Mao, H. K. & Bell, P. M. (1979). *Observations of hydrogen at room temperature (25°C) and high pressure (to 500 kilobars). Science*, **203**, 1004–1006.

Mao, H. K., Bell, P. & Hadidiacos, C. (1987). *Experimental phase relations in iron to 360 kbar, 1400°C, determined in an internally heated diamond-anvil apparatus.* In *High-Pressure Research in Mineral Physics*, edited by M. H. Manghnani & Y. Syono, pp. 135–138. San Francisco: Terrapub/AGU.

Mao, H.-K., Bell, B. M., Shaner, J. W. & Steinberg, D. J. (1978). *Specific volume measurements of Cu, Mo, Pd, and Ag and calibration of the ruby R_1 fluorescence pressure gauge from 0.06 to 1 mbar. J. Appl. Phys.* **49**, 3276–3283.

Mao, H.-K., Chen, X.-J., Ding, Y., Li, B. & Wang, L. (2018). *Solids, liquids and gases under high pressure. Rev. Mod. Phys.* **90**, 015007.

Mao, H. K., Shu, J., Shen, G. Y., Hemley, R. J., Li, B. S. & Singh, A. K. (1998). *Elasticity and rheology of iron above 220 GPa and the nature of the Earth's inner core. Nature*, **396**, 741–743.

Mao, H.-K., Xu, J. & Bell, P. M. (1986). *Calibration of the ruby pressure gauge to 800 kbar under quasi-hydrostatic conditions. J. Geophys. Res.* **91**, 4673–4676.

Merlini, M., Crichton, W. A., Hanfland, M., Gemmi, M., Müller, H., Kupenko, I. & Dubrovinsky, L. (2012). *Structures of dolomite at ultrahigh pressure and their influence on the deep carbon cycle. Proc. Natl Acad. Sci. USA*, **109**, 13509–13514.

Merrill, L. & Bassett, W. A. (1974). *Miniature diamond anvil pressure cell for single crystal X-ray diffraction studies. Rev. Sci. Instrum.* **45**, 290–294.

Mezouar, M., Crichton, W. A., Bauchau, S., Thurel, F., Witsch, H., Torrecillas, F., Blattmann, G., Marion, P., Dabin, Y., Chavanne, J., Hignette, O., Morawe, C. & Borel, C. (2005). *Development of a new state-of-the-art beamline optimized for monochromatic single-crystal and powder X-ray diffraction under extreme conditions at the ESRF. J. Synchrotron Rad.* **12**, 659–664.

Miletich, R., Allan, D. R. & Kuhs, W. F. (2000). *High-pressure single crystal techniques. Rev. Mineral. Geochem.* **41**, 445–519.

Miletich, R., Cinato, D. & Johänntgen, S. (2009). *An internally heated composite gasket for diamond-anvil cells using the pressure chamber wall as the heating element. High Press. Res.* **29**, 290–305.

Mills, R. L., Liebenberg, D. H., Bronson, J. C. & Schmidt, L. C. (1980). *Procedure for loading diamond cells with high-pressure gas. Rev. Sci. Instrum.* **51**, 891–895.

Ming, L. C. & Bassett, W. A. (1974). *Laser heating in the diamond anvil press up to 2000°C sustained and 3000°C pulsed at pressures up to 260 kilobars. Rev. Sci. Instrum.* **45**, 1115–1118.

Moore, M. J., Sorensen, D. B. & DeVries, R. C. (1970). *A simple heating device for diamond anvil high pressure cells. Rev. Sci. Instrum.* **41**, 1665–1666.

Murata, K., Yokogawa, K., Yoshino, H., Klotz, S., Munsch, P., Irizawa, A., Nishiyama, M., Iizuka, K., Nanba, T., Okada, T., Shiraga, Y. & Aoyama, S. (2008). *Pressure transmitting medium Daphne 7474 solidifying at 3.7 GPa at room temperature. Rev. Sci. Instrum.* **79**, 085101.

Nelmes, R. J. & McMahon, M. I. (1994). *High-pressure powder diffraction on synchrotron sources. J. Synchrotron Rad.* **1**, 69–73.

Oehzelt, M., Weinmeier, K., Heimel, G., Pusching, P., Resel, R., Ambrosch-Draxl, C., Porsch, F. & Nakayama, A. (2002). *Structural properties of anthracene under high pressure. High Press. Res.* **22**, 343–347.

Okuchi, T., Sasaki, S., Ohno, Y., Abe, J., Arima, H., Osakabe, T., Hattori, T., Sano-Furukawa, A., Komatsu, K., Kagi, H., Utsumi, W., Harjo, S., Ito, T. & Aizawa, K. (2012). *Neutron powder diffraction of small-volume samples at high pressure using compact opposed-anvil cells and focused beam. J. Phys. Conf. Ser.* **377**, 012013.

Olejniczak, A. & Katrusiak, A. (2010). *Pressure induced transformations of 1,4-diazabicyclo[2.2.2]octane (dabco) hydroiodide: diprotonation of dabco, its N-methylation and co-crystallization with methanol. CrystEngComm*, **12**, 2528–2532.

Olejniczak, A. & Katrusiak, A. (2011). *Pressure-induced hydration of 1,4-diazabicyclo[2.2.2]octane hydroiodide (dabcoHI). Cryst. Growth Des.* **11**, 2250–2256.

Onodera, A. (1987). *Octahedral-anvil high-pressure press. High Temp. High Press.* **19**, 579–609.

Onodera, A. & Amita, F. (1991). *Apparatus and operation.* In *Organic Synthesis at High Pressures*, edited by K. Matsumoto & R. M. Acheson. Chichester: John Wiley & Sons.

Palasyuk, T., Figiel, H. & Tkacz, M. (2004). *High pressure studies of GdMn$_2$ and its hydrides. J. Alloys Compd.* **375**, 62–66.

Palasyuk, T. & Tkacz, M. (2007). *Pressure-induced structural phase transition in rare earth trihydrides. Part II. SmH$_3$ and compressibility systematics. Solid State Commun*. **141**, 5, 302–305.

Paliwoda, D. K., Dziubek, K. F. & Katrusiak, A. (2012). *Imidazole hidden polar phase. Cryst. Growth Des.* **12**, 4302–4305.

Patyk, E., Skumiel, J., Podsiadło, M. & Katrusiak, A. (2012). *High-pressure (+)-sucrose polymorph. Angew. Chem. Int. Ed.* **51**, 2146–2150.

Piermarini, G. J. (2001). *High pressure X-ray crystallography with the diamond cell at NIST/NBS. J. Res. Natl Inst. Stand. Technol.* **106**, 889–920.

Piermarini, G. J., Block, S. & Barnett, J. D. (1973). *Hydrostatic limits in liquids and solids to 100 kbar. J. Appl. Phys.* **44**, 5377–5382.

Piermarini, G. J., Block, S., Barnett, J. D. & Forman, R. A. (1975). *Calibration of the pressure dependence of the R$_1$ ruby fluorescence line to 195 kbar. J. Appl. Phys.* **46**, 2774–2780.

Piermarini, G. J., Mighell, A. D., Weir, C. E. & Block, S. (1969). *Crystal structure of benzene II at 25 kilobars. Science*, **165**, 1250–1255.

Podsiadło, M. & Katrusiak, A. (2008). *Isostructural relations in dihalomethanes and disproportionation of bromoiodomethane. CrystEngComm*, **10**, 1436–1442.

Półrolniczak, A., Sobczak, S. & Katrusiak, A. (2018). *Solid-state associative reactions and the coordination compression mechanism. Inorg. Chem.* **57**, 8942–8950.

Ragan, D. D., Clarke, D. R. & Schiferl, D. (1996). *Silicone fluid as a high-pressure medium in diamond anvil cells. Rev. Sci. Instrum.* **67**, 494–496.

Redfern, S. A. T. (2002). *Neutron powder diffraction of minerals at high pressures and temperatures: some recent technical developments and scientific applications. Eur. J. Mineral*. **14**, 251–261.

Rivers, M., Prakapenka, V. B., Kubo, A., Pullins, C., Holl, Ch. M. & Jacobsen, S. D. (2008). *The COMPRES/GSECARS gas-loading system for diamond anvil cells at the Advanced Photon Source. High Press. Res.* **28**, 273–292.

Royer, C. A. (2002). *Revisiting volume changes in pressure-induced protein unfolding. Biochim. Biophys. Acta*, **1595**, 201–209.

Runowski, M., Marciniak, J., Grzyb. T., Przybylska, D., Shyichuk, A., Barszcz, B., Katrusiak, A. & Lis, S. (2017). *Lifetime nanomanometry – high-pressure luminescence of up-converting lathanide nanocrystals – SrF$_2$:Yb^{3+},Er^{3+}. Nanoscale*, **9**, 16030–16037.

Sakai, T., Yagi, T., Irifune, T., Kadobayashi, H., Hirao, N., Kunimoto, T., Ohfuji, H., Kawagushi-Imada, S., Ohishi, Y., Tateno, Sh. & Hirose, K. (2018). *High pressure generation using double-stage diamond anvil technique: problems and equations of state of rhenium. High Press. Res.* **38**, 107–119.

Sakai, T., Yagi, T., Ohfuji, H., Irifune, T., Ohishi, Y., Hirao, N., Suzuki, Y., Kuroda, Y., Asakawa, T. & Kanemura, T. (2015). *High-pressure generation using double stage micro-paired diamond anvils shaped by focused ion beam. Rev. Sci. Instrum.* **86**, 033905.

Samara, G. A., Hansen, L. V., Assink, R. A., Morosin, B., Schirber, J. E. & Loy, D. (1993). *Effects of pressure and ambient species on the orientational ordering in solid C$_{60}$. Phys. Rev. B*, **47**, 4756–4764.

Senyshyn, A., Engel, J. M., Oswald, I. D. H., Vasylechko, L. & Berkowski, M. (2009). *Powder diffraction studies of pressure-induced instabilities in orthorhombic LnGaO$_3$. Z. Kristallogr. Suppl.* **30**, 341–346.

Shen, G., Mao, H. K. & Hemley, R. J. (1996). *Laser-heated diamond anvil cell technique: double-sided heating with multimode Nd:YAG laser. Proceedings of the 3rd NIRIM International Symposium on Advanced Materials, ISAM'96*, 4–8 March 1996, Tsukuba, Japan, pp. 149–152. Tsukuba: National Institute for Research in Inorganic Materials.

Shen, Y., Kumar, R. S., Pravica, M. & Nicol, M. F. (2004). *Characteristics of silicone fluid as a pressure transmitting medium in diamond anvil cells. Rev. Sci. Instrum.* **75**, 4450–4454.

Sikora, M. & Katrusiak, A. (2013). *Pressure-controlled neutral–ionic transition and disordering of NH···N hydrogen bonds in pyrazole. J. Phys. Chem. C*, **117**, 10661–10668.

Singh, A. K. (1993). *The lattice strains in a specimen (cubic system) compressed nonhydrostatically in an opposed anvil device. J. Appl. Phys.* **73**, 4278–4286.

Singh, A. K. & Balasingh, C. (1994). *The lattice strains in a specimen (hexagonal system) compressed nonhydrostatically in an opposed anvil high pressure setup. J. Appl. Phys.* **75**, 4956–4962.

Singh, A. K., Balasingh, C., Mao, H. K., Hemley, R. J. & Shu, J. (1998). *Analysis of lattice strains measured under nonhydrostatic pressure. J. Appl. Phys.* **83**, 7567–7575.

Smith, R. F., Eggert, J. H., Jeanloz, R., Duffy, T. S., Braun, D. G., Patterson, J. R., Rudd, R. E., Biener, J., Lazicki, A. E., Hamza, A. V., Wang, J., Braun, T., Benedict, L. X., Celliers, P. M. & Collins G. W. (2014). *Ramp compression of diamond to five terapascals. Nature*, **511**, 330–333.

So, P. T. C., Gruner, S. M. & Shyamsunder, E. (1992). *Automated pressure and temperature control apparatus for X-ray powder diffraction studies. Rev. Sci. Instrum.* **63**, 1763–1770.

Sobczak, S., Drożdż, W., Lampronti, G. I., Belenguer, A. M., Katrusiak, A. & Stefankiewicz, A. R. (2018). *Dynamic covalent chemistry under high pressure: a new route to disulfide metathesis. Chem. Eur. J.* **24**, 8769–8773.

Srinivasa, S. R., Cartz, L., Jorgensen, J. D., Worlton, T. G., Beyerlein, R. A. & Billy, M. (1977). *High-pressure neutron diffraction study of Si$_2$N$_2$O. J. Appl. Cryst.* **10**, 167–171.

Stishov, S. M. & Popova, S. V. (1961*a*). *New dense polymorphic modification of silica. Geokhimiya*, **10**, 837–839.

Stishov, S. M. & Popova, S. V. (1961*b*). *New dense polymorphic modification of silica. Geochemistry*, **10**, 923–926.

Syassen, K. (2008). *Ruby under pressure. High Press. Res.* **28**, 75–126.

Takahashi, H., Mori, N., Matsumoto, T., Kamiyama, T. & Asano, H. (1996). *Neutron powder diffraction studies at high pressure using a pulsed neutron source. High Press. Res.* **14**, 295–302.

Takahashi, E., Yamada, H. & Ito, E. (1982). *An ultrahigh-pressure furnace assembly to 100 kbar and 1500°C with minimum temperature uncertainty. Geophys. Res. Lett.* **9**, 805–807.

Tateiwa, N. & Haga, Y. (2010). *Appropriate pressure-transmitting media for cryogenic experiment in the diamond anvil cell up to 10 GPa. J. Phys. Conf. Ser.* **215**, 012178.

Tkacz, M. (1995). *Novel high-pressure technique for loading diamond anvil cell with hydrogen. Pol. J. Chem.* **69**, 1205.

Tkacz, M. (1998). *High pressure studies of the rhodium–hydrogen system in diamond anvil cell. J. Chem. Phys.* **108**, 2084–2087.

Tomkowiak, H., Olejniczak, A. & Katrusiak, A. (2013). *Pressure-dependent formation and decomposition of thiourea hydrates. Cryst. Growth Des.* **13**, 121–125.

Van Valkenburg, A. (1962). *Visual observations of high pressure transitions. Rev. Sci. Instrum.* **33**, 1462.

Van Valkenburg, A., Mao, H.-K. & Bell, P. M. (1971*a*). *Solubility of minerals at high water pressures. Carnegie Inst. Washington Yearb.* **70**, 233–237.

Van Valkenburg, A., Mao, H.-K. & Bell, P. M. (1971*b*). *Ikaite ($CaCO_3$·$6H_2O$), a phase more stable than calcite and aragonite ($CaCO_3$) at high water pressure. Carnegie Inst. Washington Yearb.* **70**, 237–238.

Vereshchagin, L. F., Kabalkina, S. S. & Evdokimova, V. V. (1958). *Kamera dlya rentgenostrukturnykh issledovanii monokristallov pod vysokim davleniem. (A camera for X-ray diffraction studies of single crystals at high pressure). Prib. Tekh. Eksp.* **3**, 90–92.

Vos, W. L. & Schouten, J. A. (1991). *On the temperature correction to the ruby pressure scale. J. Appl. Phys.* **69**, 6744–6746.

Wang, J., Coppari, F., Smith, R. F., Eggert, J. H., Lazicki, A. E., Fratanduono, D. E., Rygg, J. R., Boehly, T. R., Collins, G. W. & Duffy, T. S. (2016). *X-ray diffraction of molybdenum under ramp compression to 1 TPa. Phys. Rev. B*, **94**, 104102.

Wartmann, E. (1859). *On the effect of pressure on the electric conductibility of metallic wires. Philos. Mag.* **17**, 441–442.

Wicks, J. K., Smith, R. F., Fratanduono, D. E., Coppari, F., Kraus, R. G., Newman, M. G., Rygg, J. R., Eggert, J. H. & Duffy, T. S. (2018). *Crystal structure and equation of state of Fe–Si alloys at super-Earth core conditions. Sci. Adv.* **4**, eaao5864.

Weir, C. E., Lippincott, E. R., Van Valkenburg, A. & Bunting, N. E. (1959). *Infrared studies in the 1–15-micron region to 30,000 atmospheres. J. Res. Natl Bur. Stand. USA*, **63A**, 5–62.

Whitfield, P. S., Nawaby, A. V., Blak, B. & Ross, J. (2008). *Modified design and use of a high-pressure environmental stage for laboratory X-ray powder diffractometers. J. Appl. Cryst.* **41**, 350–355.

Worlton, T. G. & Decker, D. L. (1968). *Neutron diffraction study of the magnetic structure of hematite to 41 kbar. Phys. Rev.* **171**, 596–599.

Xia, H., Duclos, S. J., Ruoff, A. L. & Vohra, Y. K. (1990). *New high-pressure phase transition in zirconium metal. Phys. Rev. Lett.* **64**, 204–207.

Xu, J., Mao, H. K., Hemley, R. J. & Hines, E. (2004). *Large volume high-pressure cell with supported moissanite anvils. Rev. Sci. Instrum.* **75**, 1034–1038.

Yagi, T., Yusa, H. & Yamakata, M. (1996). *An apparatus to load gaseous materials to the diamond-anvil cell. Rev. Sci. Instrum.* **67**, 2981–2984.

Yamaoka, H., Zekko, Y., Jarrige, I., Lin, J.-F., Hiraoka N., Ishii, H., Tsuei, K. D. & Mizuki, J. (2012). *Ruby pressure scale in a low-temperature diamond anvil cell. J. Appl. Phys.* **112**, 124503.

Yokogawa, K., Murata, K., Yoshino, H. & Aoyama, Sh. (2007). *Solidification of high-pressure medium Daphne 7373. Jpn. J. Appl. Phys.* **46**, 3636–3639.

You, Sh.-J., Chen, L.-Ch. & Jin, Ch.-Q. (2009). *Hydrostaticity of pressure media in diamond anvil cells. Chin. Phys. Lett.* **26**, 096202.

Zha, C. S. & Bassett, W. A. (2003). *Internal resistive heating in diamond anvil cell for in situ X-ray diffraction and Raman scattering. Rev. Sci. Instrum.* **74**, 1255–1262.

Zhao, Y. S., Lawson, A. C., Zhang, J. Z., Bennett, B. I. & Von Dreele, R. B. (2000). *Thermoelastic equation of state of molybdenum. Phys. Rev. B*, **62**, 8766–8776.

Zhao, Y. S., Von Dreele, R. B. & Morgan, J. G. (1999). *A high P–T cell assembly for neutron diffraction up to 10 GPa and 1500 K. High Press. Res.* **16**, 161–177.

International Tables for Crystallography (2019). Vol. H, Chapter 2.8, pp. 174–188.

2.8. Powder diffraction in external electric and magnetic fields

H. Ehrenberg, M. Hinterstein, A. Senyshyn and H. Fuess

2.8.1. Introduction

The functionality of materials depends strongly on the crystalline structure and structural changes during operation. The term ‘structure’ usually refers to the ideal structure, which specifies the positions of the atoms in a lattice, and thus the distances and angles between them. This idealized model is, however, far too simple to describe the full functionality of a material in a device. Many types of defects, such as point defects, dislocations or grain boundaries, are essential to the functionality and have to be taken into account. As the length scales of defects range from atomic bond lengths *via* nanometres to micrometres, different methods have to be used for comprehensive structural characterization. High-resolution transmission electron microscopy (HRTEM) is the ideal tool for studying a material at the atomic scale, as it gives direct evidence of the arrangement of atoms. In addition, information on the chemical composition can be provided through X-ray or electron spectroscopies. However, in many cases electron microscopy requires a tremendous effort in sample preparation. Furthermore, the application of electric fields in a TEM column is a serious challenge with significant limitations. While electron microscopy will provide information on small sample volumes, diffraction methods probe larger quantities of samples, but give average information. In general, diffraction methods are based on electromagnetic or particle waves. X-ray photons with energies in the keV range have wavelengths similar to interatomic distances and, therefore, X-rays from laboratory sources or synchrotrons are the most widely used. Thermal neutrons with meV energies have complementary properties suited for other applications. While electrons are usually used for microscopy techniques, the field of electron crystallography has developed in recent years. However, given the very small size of an electron beam, its short wavelength (*circa* 0.03 Å) and high absorption, most particles studied by electron crystallography can be considered as single crystals. The combination of electron crystallography and powder diffraction is a powerful tool for tiny crystalline samples, especially inclusions (Weirich *et al.*, 2006).

In the field of *in situ* materials research, multiparametric measurements as functions of three or more external parameters, *e.g.* temperature–magnetic field–pressure or temperature–magnetic field–electric field, have been reported. However, the majority of so-called *in situ* studies are carried out as a function of temperature and sometimes of external pressure. Studies of structural changes under electric fields are relatively rare. Studies of changes due to magnetic fields almost entirely lie in the domain of neutron scattering, where single-crystal experiments usually give more details on the evolution of the magnetic structure. The challenges, necessary instrumentation and some examples of *in situ* diffraction measurements are described in Chapter 16 of the book *Modern Diffraction Methods* (Mittemeijer & Welzel, 2012).

2.8.2. Experimental conditions

Several challenges have to be overcome for experiments under external fields, so the exerimental conditions have to be adapted accordingly. As all these experiments are based on time-dependent conditions, the first requirement is a detecting system that allows fast data acquisition. Considerable progress in recent years has made time resolution of the order of nanoseconds possible (Schmitt *et al.*, 2007), thus enabling stroboscopic diffraction experiments. Higher time resolutions are possible with careful synchronization of the experiment with the time structure of a synchrotron X-ray beam. The electron bunches in a synchrotron are usually separated by several tens to hundreds of nanoseconds and have a width in the range of picoseconds. Once the gating window of an experiment is smaller than the time between successive bunches, the time resolution immediately reaches the width of a bunch. Structural responses to external stimuli are related to displacements of atoms and changes in unit-cell distortion (*i.e.* lattice parameters). The displacements are fairly small and thus very high sensitivity is a prerequisite. In order to study small unit-cell distortions, very good angular resolution is mandatory. The potential angular resolution that is possible in synchrotron experiments is very often not reached for powder samples, as the half-widths of the reflections are mainly determined by the microstructure.

In monochromatic neutron diffraction, the greater divergence of a neutron beam compared to a synchrotron beam and its spectral width ($\Delta\lambda/\lambda$) usually only allow a resolution in the range $\Delta d/d \simeq 10^{-2}$ to be achieved with medium-resolution (high-intensity) diffractometers; this can be tuned down to $\Delta d/d \simeq 10^{-3}$ by tightening the beam collimation at high-resolution monochromatic instruments. Significantly better resolution of $\Delta d/d \simeq 4 \times 10^{-4}$ can be achieved by combining the neutron time-of-flight technique with long neutron flight paths (*circa* 100 m) in backscattering geometry. Even higher $\Delta d/d$ values (potentially down to 10^{-6}) can be obtained using the spin-echo-based neutron-scattering technique called Larmor diffraction (Repper *et al.*, 2009). The advantages of neutrons over X-rays are that they penetrate more deeply through materials, their scattering form factors are nearly independent of momentum transfer, and they are sensitive to the isotopic composition of a material, enabling accurate location of light elements in the presence of heavy ones, as well as the ability to distinguish between neighbouring elements in the periodic table. Whereas both synchrotron radiation and neutron scattering may be used to elucidate crystal structures under an electric field, neutrons can also be used to study magnetic order and its modification under a magnetic field. Therefore, the examples listed here for studies under electric fields use both kinds of radiation, whereas the examples of studies involving magnetic fields mainly use neutron scattering.

The properties of the materials discussed in this chapter are intimately related to their crystal structures; hence, any change in crystal structure is immediately reflected in the properties. The examples we have chosen are dominated by ferroelectric ceramics and lithium-ion battery materials on the one hand and multiferroic materials on the other.

Most reports in the literature on *in situ* or *in operando* studies deal either with the kinetics of chemical reactions (intercalation, crystallization, catalysis) or structural changes of materials under varying external conditions (temperature, pressure *etc.*). This

Copyright © 2019 International Union of Crystallography

chapter is devoted to structural modifications under external fields, both electric and magnetic. The application of external fields requires dedicated sample environments; these often result in an increase in absorption and contribute to the scattering. Furthermore, some components of the devices used for these studies can cause inhomogeneity in the sample or texture. Challenges can be presented by, for example, the deposition of metallic contacts on ferroelectric ceramics, the pronounced materials interaction and mass transport accompanied by changes in electrode volumes in Li-ion batteries, and the housing of magnets.

2.8.2.1. *Detectors*

For an *in situ* or *in operando* study, the choice of detector depends on the specific demands of the study with respect to angular resolution and speed of data collection. High angular resolution is needed to investigate small changes in reflection profiles, resulting from tiny modifications in the microstructure. Fast data collection is generally desirable, but is particularly important when monitoring metastable states in fast and irreversible processes. For a general overview of commonly used X-ray detector systems see Chapter 2.1. The following is a detailed overview of detector systems with high angular or time resolution for X-ray as well as neutron powder diffraction.

For synchrotron X-ray diffraction, analyser crystals between the sample and detector allow angular resolutions to be achieved at the physical limit. Detection is performed point by point, or with a set of point detectors in a multi-analyser crystal detector (MAD) (Toraya *et al.*, 1996; Hodeau *et al.*, 1998; Lee *et al.*, 2008; Peral *et al.*, 2011). The angular resolution of these detectors is only limited by the Darwin width of the analyser crystals, the energy bandwidth of the monochromator and the divergence of the incoming beam.

Gas counters or neutron scintillators are usually used for the detection of thermal neutrons. Because of the shortage of ^{3}He for research applications, alternative technologies are undergoing rapid development, including ^{10}B-based detectors such as Cascade (Köhli *et al.*, 2016), Jalousie (Stefanescu *et al.*, 2017) and Multigrid (Anastasopoulos *et al.*, 2017). However, owing to their relatively low efficiency for thermal neutrons compared with ^{3}He gas counters, neutron detectors that involve $^{10}\mathrm{B}(\mathrm{n},\alpha)^7\mathrm{Li}$ conversion are mainly used for neutron non-diffraction applications. Even though an analyser setup would in theory be possible for neutron diffraction experiments, the drastically increased time that would be required for data acquisition means that it is not feasible. Alternative concepts have evolved for the use of monochromatic neutrons in powder diffraction with high angular resolution. Multidetectors consist of 80 (SPODI, Hoelzel *et al.*, 2007) or 128 (ECHIDNA, Liss *et al.*, 2006; D2B, Suard & Hewat, 2001) detection units [1/3, 1/2 or 1 inch (where 1 inch = 2.54 cm) diameter ^{3}He tubes, either position-sensitive or not] separated by a small angle and with Soller collimators installed in front. This requires a stepwise re-positioning of the detector bank in order to collect data for complete patterns. The angular resolution of these instruments is limited by the beam divergence, the energy bandwidth of the monochromator and grain-size effects (Liss *et al.*, 2006). A reduction in the divergence of a neutron beam is associated with a considerable loss of intensity. The prerequisites of low divergence and high take-off angle of the monochromator have to be optimized in combination with a two-dimensional detector system. The height of the detectors is limited, however, by the 'umbrella' effect, which produces a broadening of the Debye–Scherrer rings. This effect may be partially compensated for during the numerical data-reduction process (Hoelzel *et al.*, 2012). On the other hand, the detection of some extended sections of the Debye–Scherrer rings provides additional information on strain and texturing.

For a compromise of high angular resolution and fast data acquisition, one-dimensional strip detectors have become popular. These detectors allow data collection in one shot and thus no re-positioning is required. However, if more than one module is used, the gaps between the modules have to be filled by measuring two different positions. Silicon microstrip sensors are used for detecting X-rays (Bergamaschi *et al.*, 2009). The MYTHEN II detector system consists of a set of modules, each consisting of 1280 50 µm-pitch strips, which are wirebonded to the photon-counting readout (Bergamaschi *et al.*, 2009). In combination with a set of vertically focusing mirrors and a sagittally focusing second monochromator crystal, high angular resolution can be achieved together with short acquisition times (for example at the materials science beamline X04SA at the Swiss Light Source) (Patterson *et al.*, 2005). In order to cope with instantaneous many-photon deposition, which is typical of X-ray free-electron lasers (XFELs), a similar system based on the charge-integration principle has been developed (GOTTHARD, Cartier *et al.*, 2014).

For detecting neutrons, microstrip detectors are used, which consist of thin-film metallic strips of anodes and cathodes, deposited on electrically conducting Fe-containing 'black' glass in a ^{3}He gas chamber (*e.g.* D20, Hansen *et al.*, 2008). Similar specifications can be realized with a multiwire setup in ^{3}He gas chambers (WOMBAT, Studer *et al.*, 2006). The multiwire detector has the advantage of being fully two-dimensionally sensitive. This allows for a larger aperture along the wires. The angular resolution can be maintained in the data-reduction process through straightening of the Debye–Scherrer rings. As Soller collimators cannot be used in front of a multiwire or multistrip detector, the effects of sample environments are eliminated by radial oscillating collimators. Multiwire and multistrip detectors are usually installed at high-throughput instruments, whereas high-resolution powder diffractometers are equipped with multidetector systems.

In materials science the investigation of real structure effects can be important. These can include texturing, where the orientation of the sample with respect to the scattering vector is crucial, or diffuse scattering in crystalline materials, and where a large dynamic intensity range has to be covered. The most efficient way of detecting these effects is to use two-dimensional detectors. In most cases the detector is mounted on a set of translational stages, so that the setup can be optimized for either high angular resolution or a wide angular range (Herklotz *et al.*, 2013).

When high-energy X-rays are used, two-dimensional detectors based on digital flat-panel technology are the best choice. They combine an amorphous Si panel with a CsI:Tl or various $\mathrm{Gd_2O_2S}$:Tb scintillators. Pixel sizes of 200 × 200 µm (Perkin Elmer 1621N ES, Herklotz *et al.*, 2013) or 154 × 154 µm (Pixium 4700, Daniels & Drakopoulos, 2009) together with frame rates of up to 60 frames per second overcome several drawbacks of the high-energy detectors that were previously available.

For soft X-rays a range of two-dimensional detectors has been developed. The PILATUS detector (Kraft *et al.*, 2009) is a silicon-based hybrid pixel detector system, similar to the MYTHEN strip detector. Instead of a one-dimensional strip setup, individual modules with 487 × 195 pixels of identical pitch (172 × 172 µm) are combined into a detector array of up to 6 224 001 pixels. A further development of the PILATUS detector is the EIGER detector (Johnson *et al.*, 2014). The system consists of single-photon-counting modules of 256 × 256 pixels with a significantly reduced pitch of only 75 × 75 µm. Like GOTTHARD, the charge-integrating equivalent of MYTHEN, the JUNGFRAU detector (Mozzanica *et al.*, 2014) was developed as a charge-integrating equivalent to the PILATUS and EIGER detectors.

Even smaller pixel sizes of 55 × 55 µm have been achieved for the hybrid pixel detector Medipix3 (Ballabriga *et al.*, 2007). Modules of 256 × 256 pixels can be combined into large arrays. The electronics are highly configurable and allow charge summing, programmable binary counter and continuous count–read modes.

In principle, fast data collection seems to be desirable, but it has to be adjusted to the process that is being investigated. In most cases for a continuous frame rate the limiting factor is the data rate. The MYTHEN II detector (Schmitt *et al.*, 2003) installed at the Swiss Light Source allows a frame rate of 10–90 Hz, depending on the desired dynamic range (24–4 bits), and thus observations in the time range below 1 s to 10 ms. The two-dimensional detectors for high-energy X-rays can operate at a maximum of 30 Hz (Perkin Elmer) or 60 Hz (Pixium). In this context it is also worth mentioning the PILATUS detectors – a series of silicon pixel detectors also developed at the Swiss Light Source and further commercialized by Dectris. These detectors possess a high dynamic range over five orders of magnitude along with a rate capability of $>2 \times 10^6$ photons s^{-1} pixel^{-1} and excellent detection efficiency of nearly single-photon counting (99% at 8 keV and 55% at 15 keV). The use of 1000 µm-thick CdTe instead of silicon enables >90% quantum efficiency at 20 keV, 81% at 40 keV, 90% at 60 keV, 77% at 80 keV and 56% at 100 keV. Complex detectors are often characterized by a long readout time of a large number of two-dimensional pixels, *e.g.* for PILATUS detectors the readout time per module is ∼2.7 ms.

Semiconductor-based detectors can operate at significantly higher frame rates. The EIGER detector can operate at a maximum frame rate of 24 kHz, while GOTTHARD can reach 40 kHz. In a special burst mode of 128 frames, a frame rate of 800 kHz is possible, reaching a single exposure time of 1.25 µs. The Timepix3 detector (Poikela *et al.*, 2014), which is a further development of the Medipix3 detector, can theoretically sustain continuous frame rates of up to 200 kHz, as long as the overall hit rate is less than 80 MHz.

In order to collect enough intensity for fast processes or to investigate even shorter timescales, stroboscopic measurements are useful. Thus, timescales in the range of milliseconds down to nanoseconds may be followed using a pump–probe setup. In this technique, the reaction is first triggered (pump) and after a specific time delay the diffraction pattern is collected (probed). The use of rapidly rotating choppers in the incoming beam is an attractive alternative to pump–probe experiments (Yoo *et al.*, 2011). Time resolution in the microsecond regime is routinely obtained in synchrotron experiments (Hinterstein, 2011; Hinterstein *et al.*, 2014) and in about the millisecond regime in neutron diffraction (Eckold *et al.*, 2010). When these experiments are conducted at a synchrotron and the periodic excitation of the sample is synchronized with the bunch clock of the synchrotron, the time resolution can be increased significantly. For a time resolution smaller than the temporal separation of the particle bunches (typically 8–200 ns), the time resolution suddenly drops to the bunch width, which is in the range of picoseconds. For neutron diffraction, the limiting factor for time resolution can be calculated from the energy bandwidth and the speed of the neutrons, which is dependent on the wavelength. The lower limit is typically in the range of 25 µs. These time ranges can be reached by multistrip or multiwire detectors in a stroboscopic setup.

In situ and *in operando* measurements require a specific sample environment, which is normally built using a different material to the sample and leads to additional contributions to the diffraction pattern. The use of strongly scattering materials such as thin metallic foils (Al foil in batteries, Ag or Au films as electrodes) or single crystals (sapphire capillaries for high-temperature experiments or diamonds in high-pressure experiments) may seriously bias data collection or damage the detector. If it is not possible to eliminate them by masking, they have to be taken into account by Rietveld analysis or profile matching. A correct treatment of the contributions from the sample environment has to take into consideration the fact that the additional scattering is normally off the diffractometer centre and this sample shift produces a non-linear shift in 2θ of the corresponding reflections in the pattern.

2.8.2.2. *Absorption*

Additional equipment is required for *in situ* experiments. The necessary parts are quite often constructed from metallic components. Light metals like aluminium are preferred for shielding parts within the beam for neutrons and X-rays. Vanadium is a suitable choice in neutron experiments, as it has a very small scattering cross section, so produces almost no coherent scattering. In most cases a suitable absorption correction is mandatory. For X-rays the energy dependence of the linear absorption coefficient $\mu(E)$ is very pronounced, especially close to X-ray absorption edges. Away from an absorption edge, higher energies lead to lower absorption. As an example, the linear absorption coefficient μ for steel (α-Fe) at 45 keV is 0.18 cm^{-1} and at 60 keV it is 0.076 cm^{-1}. The transmitted intensity after a beam has penetrated 1 mm steel with 100% packing density twice (once for the incoming and once for the outgoing beam) is therefore 2.7% for 45 keV but 22% for 60 keV. For one of the examples treated later, the piezoceramic $\text{Pb(Zr}_{0.5}\text{Ti}_{0.5}\text{)O}_3$, the calculation for a sample diameter of 1 mm and a typical packing density of 60% in a powder leads to beam transmission of 3% (45 keV) and 21% (60 keV). Therefore, using high-energy X-rays enables transmission diffraction experiments that are not feasible with lower energies. The gain in measured intensities by decreasing absorption normally overcompensates for the decrease in scattering at shorter wavelengths, which is proportional to λ^3 within kinematical theory. The linear absorption coefficient of thermal neutrons (with wavelengths from 1 to about 3 Å) is small for most elements and scales in proportion to the wavelength, $\lambda = h/p = h/(2mE)^{1/2}$, *i.e.* λ (Å) = $9.045/E^{1/2}$ (meV) = $3956/v$ (m s^{-1}). However, the absorption cross sections for different isotopes of the same element may be very different. Numerical values are listed in Sears (1992) and *International Tables for Crystallography* Volume C, Table 4.4.4.1. For ferroelectric $\text{Pb(Zr}_{0.5}\text{Ti}_{0.5}\text{)O}_3$, the linear neutron absorption coefficient at a wavelength λ = 1.5 Å and for a packing density of 60% is 0.026 cm^{-1}, significantly smaller than for X-rays; it is mainly determined by the Ti content.

As both the scattering and the absorption cross section for neutrons are in most cases much smaller than for X-rays, bigger samples are required. On the one hand, this leads to the advantage of better averaging over many particles. On the other hand, the spatial resolution is significantly affected by the sample dimensions because of self-collimation. The appropriate choice of diffraction method is defined by the particular scientific challenge and has to take into consideration the different amount of sample that is needed for each experiment.

Very high absorption cross sections are desirable for shielding purposes. In X-ray diffraction, lead or tungsten are widely used. Only a few isotopes have a nuclear resonance in the thermal neutron range and thus a high absorption cross section. The most prominent are ^{10}B, ^{113}Cd and ^{157}Gd, which are used in neutron optics as collimators, attenuators and beam-shaping devices.

2.8.2.3. *Sample fluorescence and incoherent neutron scattering*

Sample fluorescence is a common problem for laboratory X-ray powder diffractometers, which are neither equipped with an analyser nor use detectors with a narrow energy resolution. In powder diffraction using synchrotron radiation, this problem is often solved either by adjusting the energy of the incident beam or by an adjustment of the dynamic range of the detector, or by a combination of both.

Like absorption cross sections, the incoherent neutron scattering lengths for different elements and isotopes do not vary in any obviously systematic way throughout the periodic table. Among the known stable isotopes, ^{1}H has the largest incoherent scattering length (25.274 fm) and has a small and negative coherent one (−3.7406 fm). The situation is very different for ^{2}H (deuterium), for which the incoherent and coherent scattering lengths are 4.04 and 6.671 fm, respectively. Differences between the coherent scattering lengths of hydrogen and deuterium form the basis of the isotopic labelling technique, called contrast matching; this is particularly important in applications of neutron scattering to hydrogen storage, structural biology and polymer science. Deuteration of samples is a challenging task, but obtaining high-quality powder diffraction data from hydrogenated samples is far more difficult. Use of neutron polarization analysis is a reliable way to subtract the incoherent scattering contribution from the diffraction data (Mikhailova *et al.*, 2012), but it is often accompanied by significant losses of incident neutron flux and, consequently, of data quality. Both sample fluorescence and incoherent neutron scattering are isotropic and, therefore, are often considered as a background in powder diffraction experiments.

2.8.3. Examples

2.8.3.1. *In situ studies of ferroelectrics in an external electric field*

The function of ferroelectrics as stress sensors, high-frequency microphones, medical injectors or large strain actuators is based on electric poling. A polycrystalline material exhibits a zero net polarization. When an electric field is applied to the sample, the spontaneous electric polarization of the ferroelectric material is reoriented along the electric field vector. This occurs by a reorientation of domains. Additional polarization is obtained by an increase of the spontaneous polarization induced by the applied electric field. With *in situ* experiments, the field-induced changes in the powder diffraction reflections are measured. Fig. 2.8.1 is a schematic representation of some *in situ* sample geometries. The electric field is applied *via* electrodes on the sample surface.

Many of these ferroelectric materials crystallize in a structure derived from the cubic perovskite type, but in a crystal system with lower symmetry and with a non-centrosymmetric space group. The most widely used material is lead zirconate-titanate ($PbZr_{1-x}Ti_xO_3$, PZT), which exhibits the highest strain response at the so-called morphotropic phase boundary with a composition of about 50% for Ti and Zr. It is generally accepted that the phase on the Ti-rich side of the PZT phase diagram has a tetragonal structure with space group *P*4*mm*. On the rhombohedral Zr-rich side, two ferroelectric phases can be identified, with space groups *R*3*m* for high and *R*3*c* for low temperatures. A considerable amount of work has been devoted to the elucidation of the crystal structure of the material close to the morphotropic phase boundary. Neutron and synchrotron diffraction detected monoclinic symmetry at low temperatures and nanometre-sized regions (the so-called polar nanoregions) were inferred from diffuse scattering (Noheda *et al.*, 2000; Hirota *et al.*, 2006). Alternative interpretations explained the new reflection found in the pattern between the 111_C and 200_C reflections (where the subscript 'C' corresponds to the cubic archetype structure) as diffuse scattering from diffuse incoherent scattering by small domains (Jin *et al.*, 2003).

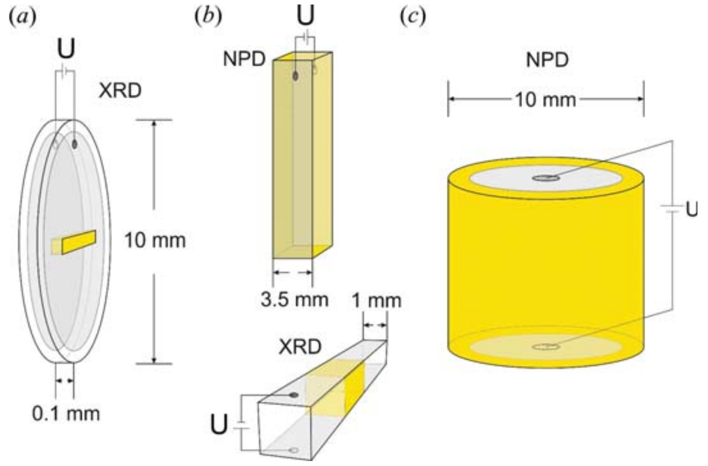

Figure 2.8.1
Sample geometries for *in situ* experiments with an applied electric field. Samples are poled *via* an applied voltage (U) at the sample electrodes (grey). Different sample geometries are necessary to account for different beam sizes, absorption and detector concepts. Yellow indicates the irradiated sample volume. (*a*) Flat-plate samples for X-ray experiments with strip detectors, limiting photon energies to around 30 keV. (*b*) Bar-shaped samples for high-intensity neutron powder diffraction (NPD) or high-energy X-ray diffraction (XRD). (*c*) Cylinder-shaped samples for high-resolution neutron diffraction with fixed detector collimators.

Unique information on structural changes during poling is obtained from *in situ* studies in applied external electric fields (Hoffmann *et al.*, 2001). Fig. 2.8.2 displays two groups of powder reflections (Schönau, Schmitt *et al.*, 2007) observed by synchrotron X-ray diffraction. They are directly compared with the domain structure from TEM observations (Schmitt *et al.*, 2007) for a range of compositions near the morphotropic phase boundary. One group of reflections is derived from the cubic 111_C reflection, the other from the archetype 200_C reflection. The transition from the rhombohedral splitting to the tetragonal one with increasing Zr content is correlated with the forms of ferroelectric domains in TEM. Close to the morphotropic phase boundary, nanodomains (ranging in width from 20 to 200 nm) are observed in addition to the well known microdomains. The nanodomains react immediately under the influence of an electric field to become microdomains. Fig. 2.8.3 shows the intensity changes observed for the 110_C group of reflections. The changes under an electric field are pronounced and depend on the *c*/*a* ratio (Schönau, Knapp *et al.*, 2007), the formation and disappearance of nanodomains, and the local symmetry of these domains.

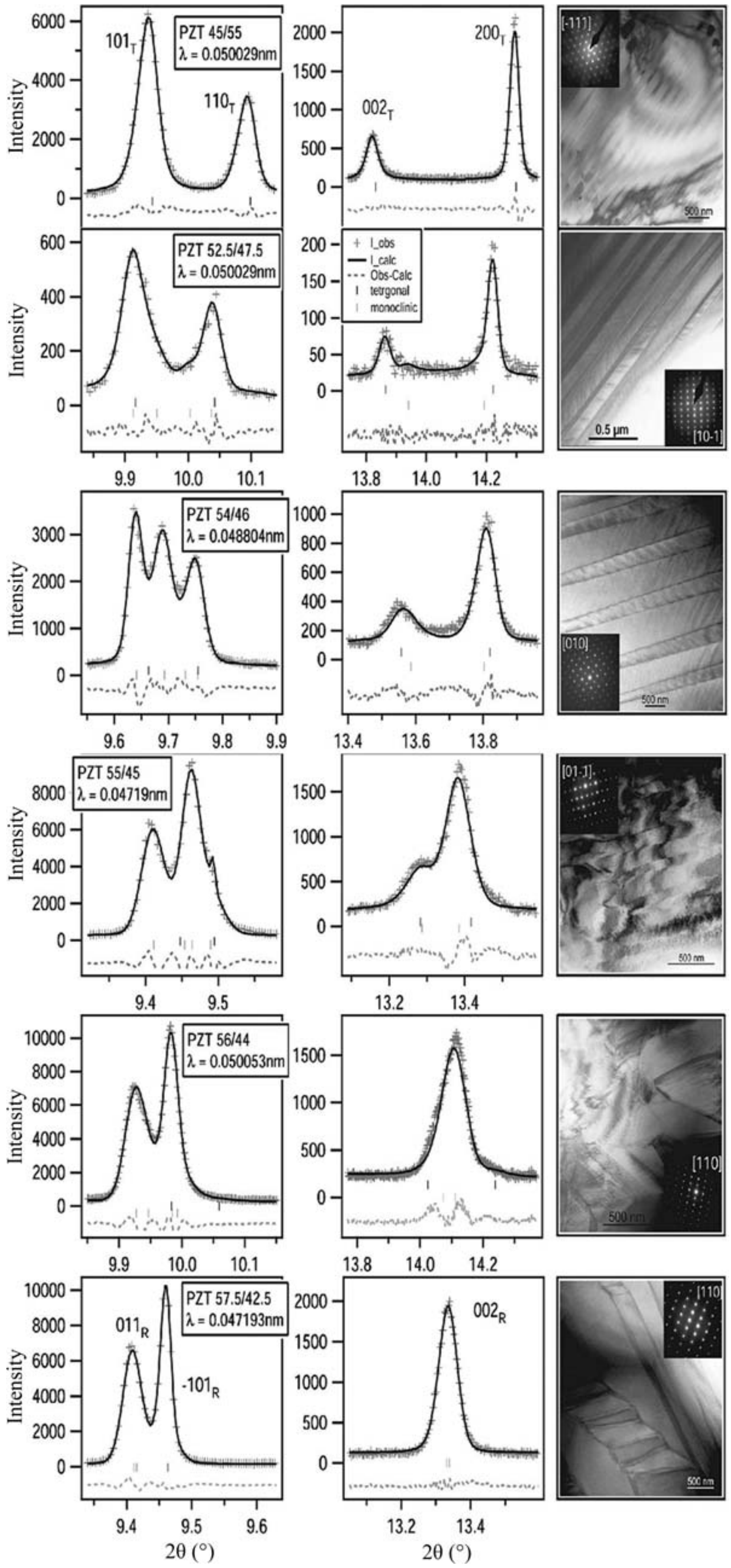

Figure 2.8.2

(*a*), (*b*) High-resolution synchrotron X-ray powder diffraction patterns and TEM imaging of PZT with a varying Zr/Ti ratio. An increase in broadening is seen in changes in shape and width of the 002_T reflection between the samples PZT 45/55, 52.5/47.5 and 54/46. The asymmetry and width of the tetragonal 101_T reflection not only change, but also evolve into a new peak between 101_T and 110_T in sample PZT 54/46, which gains in intensity towards PZT 57.5/42.5. This rise is accompanied by a decrease in intensity of the visible 110_T reflection, which then seems to be absent or overlapped in sample PZT 56/44. The domain structure changes from a lamellar tetragonal configuration *via* nanodomains to a rhombohedral herringbone structure. Reproduced with permission from Schönau, Schmitt *et al.* (2007). Copyright (2007) by the American Physical Society.

The different poling mechanisms can be studied in transmission geometry, which allows variation of the angle between the electric field vector **E** and the direction of the incident X-ray beam **k** from 0° to about 45° (Fig. 2.8.4) (Hinterstein *et al.*, 2011). Two sputtered electrodes (Ag, Pt) were used for polarization.

An extensive study under an electric field has been carried out on the commercially available sintered PZT material named PIC, in which Ti is partially replaced by Ni and Sb [$Pb_{0.99}Zr_{0.45}Ti_{0.47}(Ni_{0.33}Sb_{0.67})_{0.08}O_3$], in transmission geometry. The angle between the electric field perpendicular to the flat sample surface and the incident beam was varied between 0 and 45°. The effect of domain switching in tetragonal symmetry mainly affects the $\{h00\}_C$ reflections, whereas the piezoelectric effect predominantly influences the $\{hhh\}_C$ reflections. Thus, the reflection pair 111_C and 200_C are the only reflections analysed in most studies. Fig. 2.8.5 displays just these reflections, with 200_C split into 002_T and 200_T, where the subscript 'T' refers to the tetragonal distorted cell, which is *translationengleich* to the cubic one (*i.e.* they have the same group of translations). The shift to higher angles of 111_C under an applied field indicates a decrease in volume. This is explained by the large angle between the electric field vector and the vector of spontaneous polarization for the unit cells contributing to 111_C. This induced compression remains in the remanent state.

While analysis of single reflections or orientations can yield valuable information on textured functional materials, a more sophisticated approach involves coupling the Eulerian angles to the diffraction patterns and modelling all observable mechanisms within a single refinement. By applying this method to a technically applied actuator material, Hinterstein, Hoelzel *et al.* (2015) could quantify all strain mechanisms and calculate the macroscopic response to an applied electric field with a structure model at the atomic scale.

The function of piezoceramics is related to periodic cycling of the polarization, accompanied by periodic changes of macroscopic strain. Fatigue in piezoceramic materials means that this strain is reduced as a result of the cycling; this has been studied with respect to the underlying structural changes (Hinterstein *et al.*, 2011, 2014).

Whereas strain is related to texturing, no preferred orientation is observed in fatigued samples. The orientation of nanodomains is demonstrated in different patterns: in Fig. 2.8.6 the two reflections are shown for the remanent state (0 kV mm^{-1}) at different diffraction angles and in Fig. 2.8.7 for values of the external field ranging from 0 to 2 kV mm^{-1}.

The diffuse scattering between the split 200_C reflections in the fatigued sample is reduced and the texturing increases after static poling for a few seconds. Thus, the fatigued samples show a more tetragonal appearance after cycling. The energy of the electric field induces a transition of well oriented nanodomains with preferred orientation along the field vector, leading to texturing for $\omega = 0°$. At a certain point the system will no longer respond to the electric field because of crack formation and a decrease in the volume of switchable nanodomains. From that point, the diffraction pattern recorded under a field is no different to the diffraction pattern recorded without a field.

Cyclic loading with high frequencies is required in real applications of ferroelectric ceramics. Exposure times

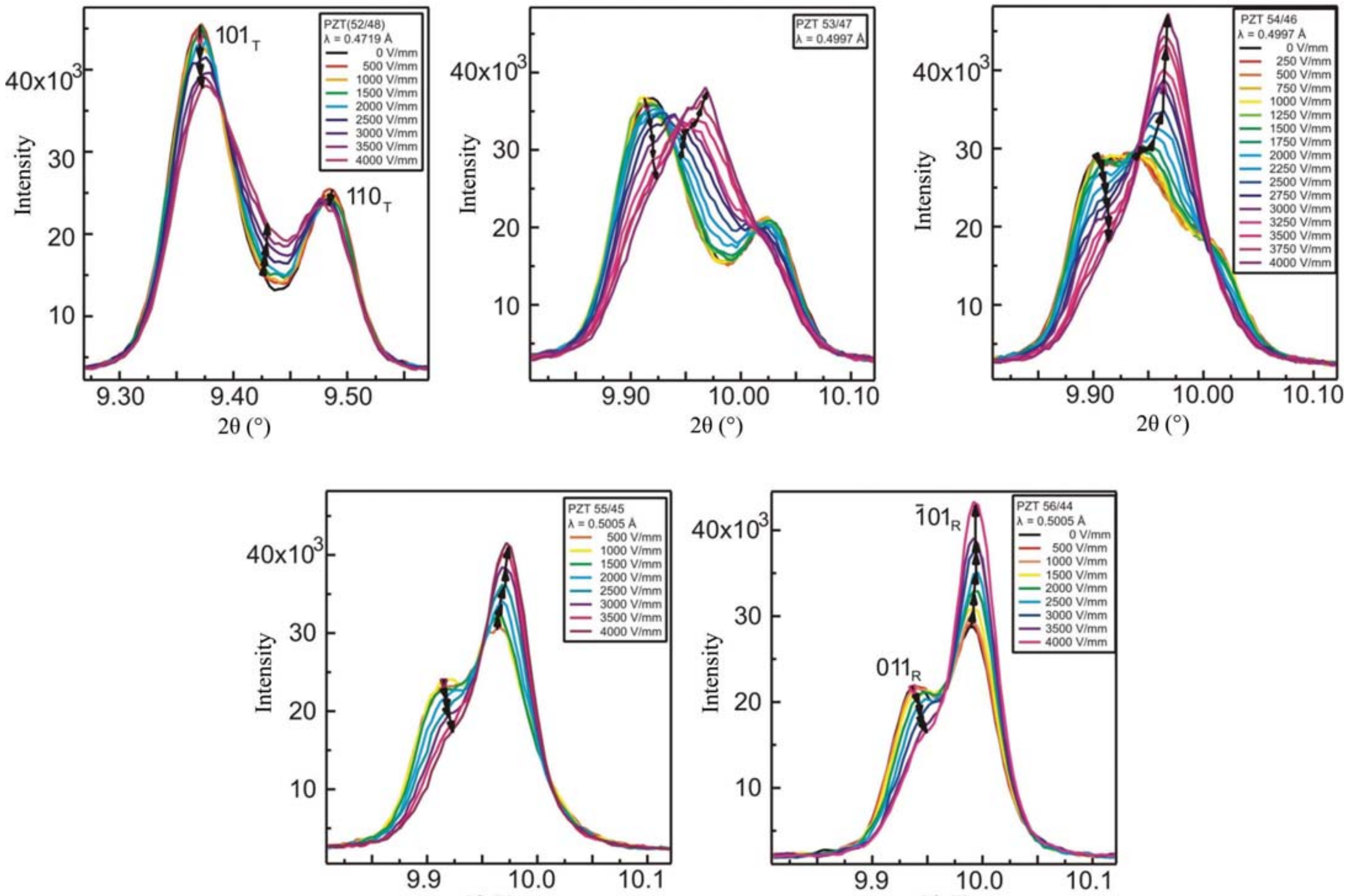

Figure 2.8.3
Diffraction patterns of the tetragonal 101_T /110_T reflection pairs of PZT 52/48, PZT 53/47, PZT 54/46, PZT 55/45 and PZT 56/44 recorded *in situ* under an electric field for the first poling cycle of up to 4 kV mm^{-1}. Reproduced with permission from Schönau, Knapp *et al.* (2007). Copyright (2007) by the American Physical Society.

in the range of seconds are necessary to ensure sufficient statistics for single diffraction experiments in the subsecond regime. Stroboscopic measurements can be used to achieve this.

Absolutely reversible processes are necessary for a successful stroboscopic analysis. The stability of the system is achieved by pre-cycling *circa* 10^5 times. Time resolutions in the range of several tens of milliseconds are possible with modern X-ray detectors. By repeating the excitation and summing the intensities, proper statistics can be achieved (Choe *et al.*, 2015; Hinterstein *et al.*, 2014).

The use of the stroboscopic data-collection technique and cyclic fields in neutron diffraction experiments enabled a direct measurement of non-180° domain wall motion during the application of subcoercive cyclic electric fields (Fig. 2.8.8) (Jones *et al.*, 2006, 2007; Jones, 2007; Daniels *et al.*, 2007). It was shown that the non-180° domain switching contributes 34% of the macroscopically measured strain during cycling with half of the coercive field.

The highest time resolutions are obtained in a pump–probe setup. Under the influence of an electric field of 2 kV mm^{-1}, the switching kinetics can be investigated directly. With a time

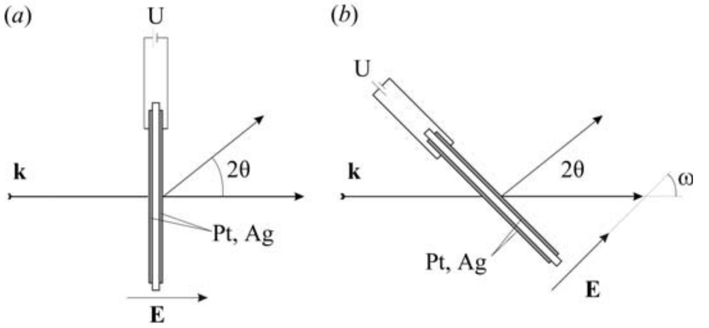

Figure 2.8.4
In situ transmission geometry developed by Schönau, Schmitt *et al.* (2007) with the electric field vector perpendicular to the flat-plate sample surface. The electric field results from an applied voltage U between two opposing sputtered electrodes (Ag, Pt) with a thickness of about 15 nm. (*a*) $\omega = 0^\circ$ and (*b*) $\omega = 45^\circ$.

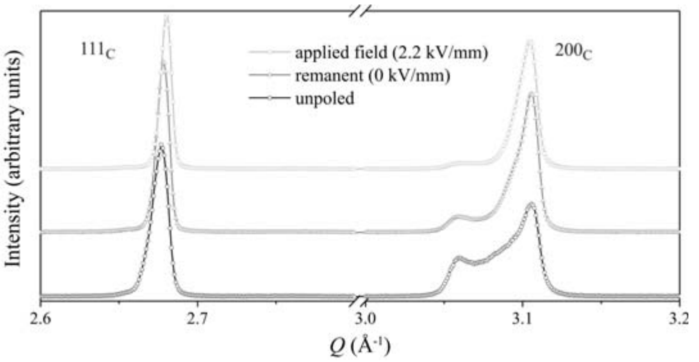

Figure 2.8.5
111_C and 200_C reflections of the unpoled, remanent and applied field state of PIC 151 at $\omega = 0^\circ$. Owing to the piezoelectric effect, the 111_C reflection is shifted. The preferred orientation of the 200_C reflection indicates tetragonal 90° domain switching.

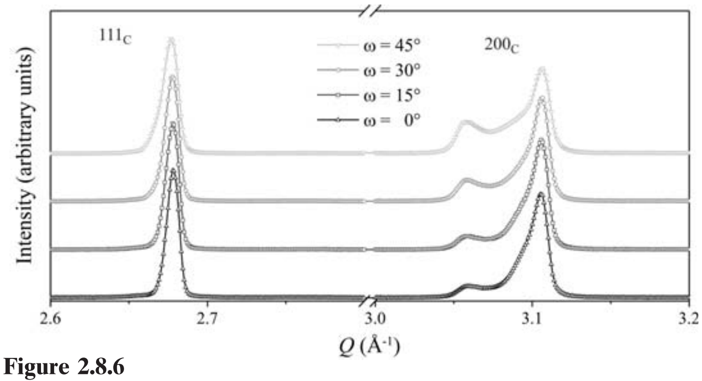

Figure 2.8.6
111_C and 200_C reflections of bipolar fatigued PIC 151 (50 Hz, 10^7 cycles) in the remanent state (0 kV mm^{-1} at ω = 0°, 15°, 30° and 45°).

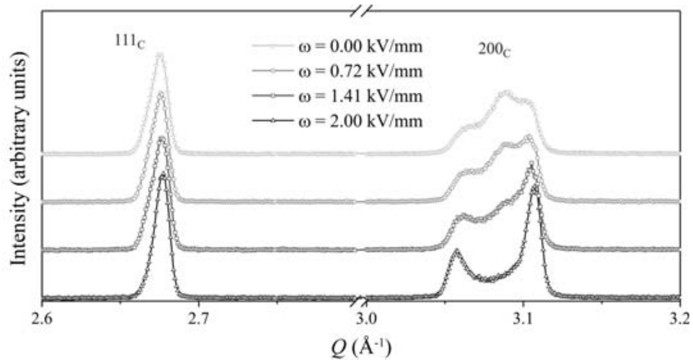

Figure 2.8.7
111_C and 200_C reflections of bipolar fatigued PIC 151 (50 Hz, 10^7 cycles) at ω = 45° with 0.0, 0.72, 1.41 and 2.0 kV mm^{-1}.

resolution of 1 ms only one intermediate step is observed (Fig. 2.8.9*a*). With a time resolution of 250 µs a significant number of intermediate steps can be studied (Fig. 2.8.9*b*). The commercially available soft-doped PZT material EC-65 has also been observed under the application of an electric field and mechanical stress. Lattice strains were measured under cyclic electric fields at times as short as 30 µs (Pramanick *et al.*, 2010).

The use of lead-containing materials may in the future be banned because of environmental concerns, hence considerable efforts are being made to find materials with properties similar to PZT. Only a few elements (Ba, Bi, Na, K, Nb, Ti) seem to be suitable. Nevertheless, a combination of the relevant oxides of these leads to a large variety of potential materials. $(Bi_{0.5}Na_{0.5})$-TiO_3–$BaTiO_3$ (BNT–BT) (Hinterstein, Schmitt *et al.*, 2015), $(Bi_{0.5}Na_{0.5})TiO_3$–$(Bi_{0.5}K_{0.5})TiO_3$ (BNT–BKT) (Levin *et al.*, 2013),

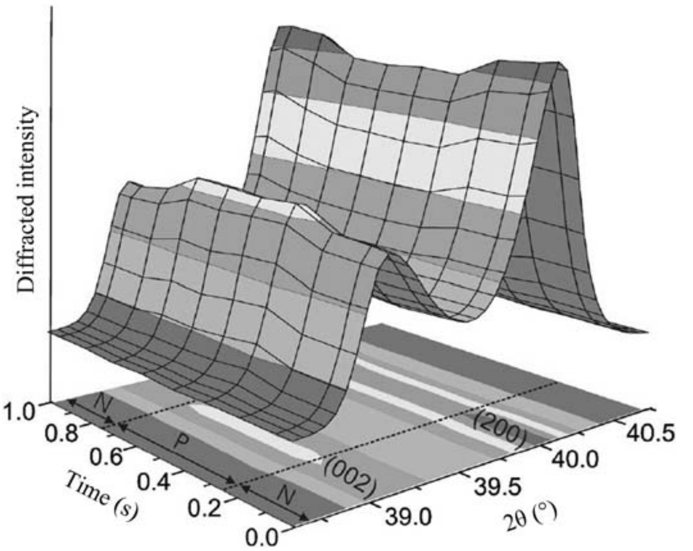

Figure 2.8.8
Diffracted intensities of the pseudo-cubic 002 reflections as a function of 2θ and time during application of a square, bipolar electric field waveform of frequency 1 Hz and amplitude of plus or minus half the coercive field. The timescale is described using eight steps. The positive (P) state of the electric field is applied between 0.25 and 0.75 s, which is bounded on either side by the negative (N) field state. The diffraction vectors 002 and 200 are parallel to the applied electric field. Reproduced with permission from Jones *et al.* (2006). Copyright (2006) AIP Publishing.

BNT–BT–$K_{0.5}Na_{0.5}NbO_3$ (BNT–BT–KNN) (Schmitt *et al.*, 2010), BNT–BKT–KNN (Anton *et al.*, 2012) and BNT–KNN (Liu *et al.*, 2017) are the focus of most attention. The materials in the $(1 - x - y)$BNT–xBT–yKNN system exhibit remarkable piezoelectric properties over a narrow composition range $0.05 \le x \le 0.07$ and $0.01 \le y \le 0.03$ (Zhang *et al.*, 2007). Daniels *et al.* (2010) proposed a combinatorial approach to studying a range of compositions in a single sample, where different stoichiometries created a compositional gradient in the sample. A limited number of bulk homogeneous samples were prepared for comparison. Microfocus X-ray beams from a synchrotron allowed investigation of the gradient material under a field.

Fig. 2.8.10 displays the diffraction patterns under an external electric field up to 5.5 kV mm^{-1}. Data analysis was performed by fitting the data of the pseudo-cubic 002 reflection to distorted pseudo-cubic and tetragonal symmetry for each composition and electric field. Whereas in the 0.86BNT–0.14KNN composition only a distorted pseudo-cubic behaviour is observed

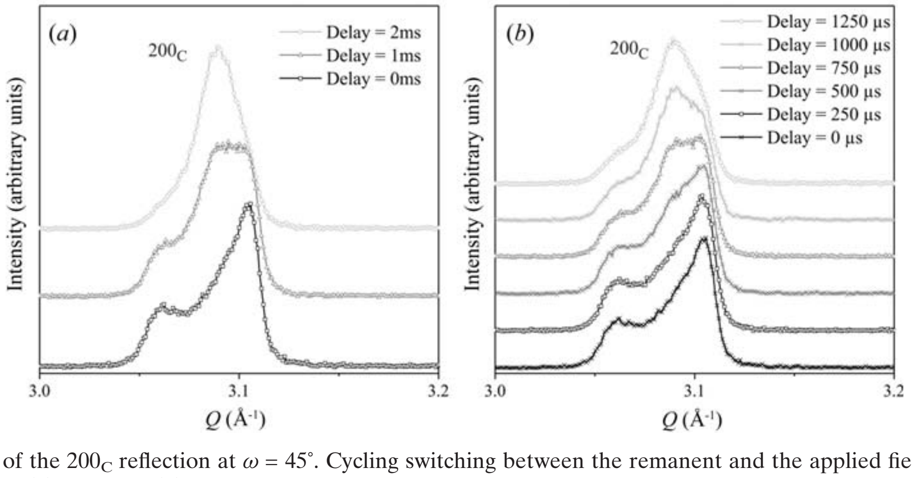

Figure 2.8.9
Pump–probe measurements of the 200_C reflection at ω = 45°. Cycling switching between the remanent and the applied field state at 2 kV mm^{-1} with 50 Hz and a time resolution of (*a*) 1 ms and (*b*) 250 µs. Only a time resolution of 250 µs results in sufficient intermediate steps between the remanent and the poled state to study the processes during poling.

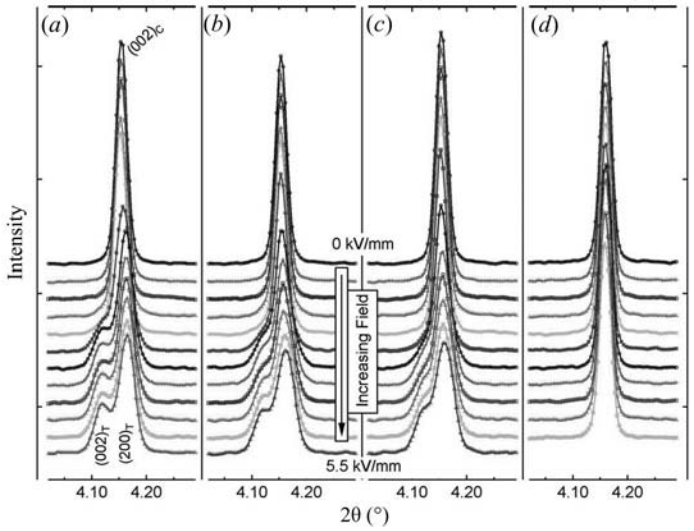

Figure 2.8.10

The pseudo-cubic 002 reflection of (*a*) 0.93BNT–0.07BT end member, (*b*) 0.938BNT–0.053BT–0.009KNN, (*c*) 0.932BNT–0.045BT–0.023KNN and (*d*) 0.86BNT–0.14KNN end member as a function of electric field from the initial zero-field state (top) to an applied field of 5.5 kV mm^{-1} (bottom). The sample orientation is such that the scattering vector is parallel to the electric field. Reproduced with permission from Daniels *et al.* (2010). Copyright (2010) Elsevier.

above a threshold of 0.5 kV mm^{-1}, a very pronounced distortion is observed for 0.93BNT–0.07BT, which eventually above 2 kV mm^{-1} develops into a tetragonal structure. In addition to the combination of various compositions, the authors simultaneously measured the X-ray fluorescence spectra, thus confirming the actual composition.

Fig. 2.8.11 depicts a Rietveld refinement of a lead-free ferroelectric material with the composition $0.92Ba_{0.5}Na_{0.5}TiO_3$–$0.06BaTiO_3$–$0.02K_{0.5}Na_{0.5}NbO_3$. New superstructure reflections (Fig. 2.8.11*b*, arrows) and a lattice distortion (Fig. 2.8.11*b*, circled) were observed due to a transition from space group *P*4*bm* to *R*3*c* (Hinterstein *et al.*, 2010).

In an overview, Jones summarized the use of diffraction techniques. Along with the importance of microdiffraction, diffuse scattering and texture effects, the importance of time-resolved studies including stroboscopy was acknowledged (Jones, 2007).

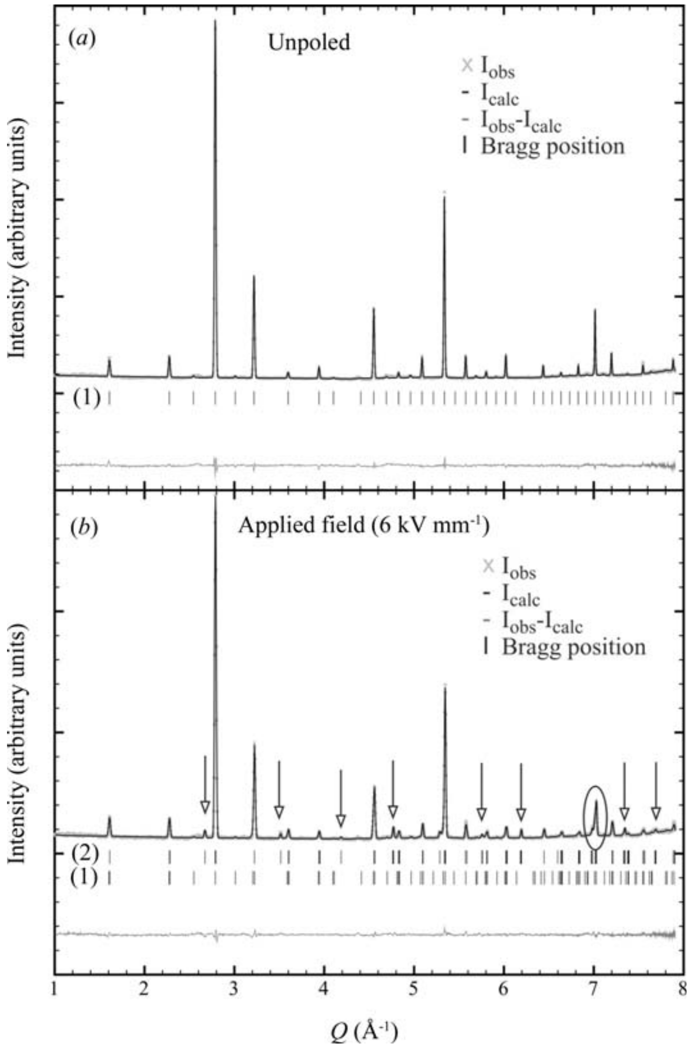

Figure 2.8.11

Rietveld refinement based on different patterns of $0.92Bi_{0.5}Na_{0.5}TiO_3$–$0.06BaTiO_3$–$0.02K_{0.5}NbO_3$ (*a*) in the unpoled and (*b*) in the applied field state at 6 kV mm^{-1}. Experimental data are shown by grey crosses, black lines denote calculated profiles, and the lower plot shows their difference. Calculated positions of Bragg reflections are shown by vertical tick marks, where the different rows correspond to the initial tetragonal phase with space group *P*4*bm* (1) and the field-induced rhombohedral phase with space group *R*3*c* (2). Arrows mark superlattice reflections of type $\frac{1}{2}\{ooe\}$ and the circle highlights the rhombohedral split 331_C reflection.

2.8.3.2. *In situ studies of electrode materials and in operando investigations of Li-ion batteries*

Rechargeable energy sources in mobile electronics are mainly based on lithium-ion batteries. Their application relies on the mobility of the small Li ions, which move from the cathode through an electrolyte to the anode during charge and back during discharge. Intensive research is underway to improve the performance of such energy-storage technology. High gravimetric and volumetric energy and power densities are required. Other additional challenges are safety, lifetime, the temperature range of stable operation and production costs per unit energy at the battery level. Knowledge of the correlation between the electrochemical functionality and the structure of the electrode materials during Li exchange is essential in order to interpret the underlying mechanisms and degradation processes and to find a promising approach to better materials. The high reactivity of the cell components and the very strong interactions between materials inside an electrochemical cell require studies on complete operational devices by non-invasive *in operando* methods. So-called electrochemical ‘half cells’ are often studied to follow structural changes in electrode materials. These are complete operational cells, but the electrode is cycled against an Li-metal counter electrode. Such half-cell studies are sometimes described as *in situ* studies. Limitations might occur with respect to fatigue studies and at very high charge and discharge rates, when the performance is determined by the Li-metal electrode. The classification of *in situ* and *in operando* methods is not unambiguous in structural studies on battery materials. Sometimes the term *quasi in situ* is used for studies where specific states of the materials are prepared electrochemically and handled in an Ar atmosphere with complete protection against humidity and air, but actually investigated *ex situ* (Oswald *et al.*, 2009).

Some early *in situ* setups have been described for neutron diffraction (Bergstöm, Andersson *et al.*, 1998) and transmission X-ray diffraction (Bergström, Gustafsson & Thomas, 1998), and also at elevated temperatures (Eriksson *et al.*, 2001). Today, for example, good-quality full diffraction patterns can be obtained with exposure times well below 100 ms using synchrotron radiation (Herklotz *et al.*, 2013). Capillary-based micro-battery cells allow for *in situ* X-ray powder diffraction studies on one single electrode (Johnsen & Norby, 2013). Even spatially resolved neutron diffraction studies are possible on commercial cylindrical Li-ion batteries (Senyshyn *et al.*, 2015).

The mechanism of Li extraction and insertion differs for different types of electrodes. In intercalation-type electrodes the topology of the host structure remains mainly unchanged, and suitable sites in the structure are either occupied by Li or are vacant in the delithiated state. This use of intercalation chemistry for electrochemical energy storage was established for a battery based on Li metal as the negative electrode and TiS_2 as the positive electrode (Whittingham, 1976). In commercial cells today the negative electrode is also based on intercalation and consists of layered graphite, which hosts Li during the charge cycle up to the composition LiC_6. Another working mechanism for negative electrodes is electrochemical alloying with Li. The most promising examples involve Si, Al and Sn. These electrode concepts suffer from extreme volume changes: 100% for Al → LiAl or even 300% for Si → $Li_{21}Si_5$. In combination with the brittleness of these materials, the particles break down and become amorphous during successive charging and discharging, accompanied by contact losses and resulting pronounced fade in capacity. Two other mechanisms have also received considerable attention as they allow higher specific capacities. In a replacement reaction, one transition metal is replaced by Li while the topology of the structure is mainly preserved. During a conversion or displacement reaction the initial structures of transition-metal compounds, for example nanometre-sized oxides (Poizot *et al.*, 2000) or other binary compounds (Cabana *et al.*, 2010), are believed to be destroyed completely by either amorphization or phase transitions. The transition-metal ions are reduced to metallic nanoparticles, which are embedded in a complex network of Li_2O and reaction products from the electrolyte. In spite of the loss of long-range order, an important short-range structure remains. This has been shown in detail for ternary Cu–Fe oxides (Adam *et al.*, 2013). The reduction of Cu^{2+} from CuO takes place through the formation of a Cu_2O/Li_2O composite, in which Cu_2O reacts further to form Cu metal and Li_2O. Spinel-type $CuFe_2O_4$ and $CuFeO_2$ react to form α-$LiFeO_2$ with the extrusion of metallic Cu and Fe nanoparticles. At even lower potentials against Li^+/Li between 0.8 and 1.0 V, α-$LiFeO_2$ is further reduced into metallic Fe nanoparticles and Li_2O. While most of these displacement reactions suffer from very poor reversibility, good cycling stability was shown for $Cu_{2.33}V_4O_{11}$ (Morcrette *et al.*, 2003). During cell discharge Li penetrates into the well crystallized copper vanadate, forming a solid solution up to an Li content of $x = 0.6$, when Bragg peaks of metallic copper were observed. The end result was a composite electrode of an amorphous Li–V–O matrix with dispersed metallic copper. The essential point is the reversibility, with the disappearance of the metallic copper and the recrystallization of the initial $Cu_{2.33}V_4O_{11}$.

Two more examples belong to the class of intercalation materials: graphite as used for the negative electrode, and $LiNiO_2$ as a candidate for the positive electrode. 'Positive' and 'negative' electrodes are the preferred terms for secondary batteries instead of 'cathode' and 'anode', because anode and cathode reactions match only for discharge (interchange between the two electrodes occurs for the charge process). A comprehensive summary of structure reports on lithiated graphite can be found in Johnsen & Norby (2013). From the voltage plateau in cyclovoltammograms four distinct lithiated graphite phases have been postulated. However, only for two of them have complete structure models been reported and confirmed. The first is LiC_{12}, *P*6/*mmm* (space group No. 191), $a = 4.29$, $c = 7.03$ Å, with C on the 12*n* site with $x = 0.33$ and $z = 0.25$ and Li on the 1*a* site; the second is LiC_6, also *P*6/*mmm*, $a = 4.31$, $c = 3.70$ Å with C on the 6*k* site with $x = 0.33$ and Li again on the 1*a* site. According to the number of graphene layers that are needed for the smallest unit repeated by translational symmetry along the sixfold rotation axis, these structures are described as stage-II (LiC_{12}) and stage-I (LiC_6) compounds, like graphites intercalated with other alkaline elements. Note that in these phases the graphene layers are not shifted with respect to each other (*AA* sequence), in contrast to graphite (*AB* sequence). For a lower Li content, a much more complex structural behaviour was observed, including incommensurate Li distributions between the graphene layers, which were described as twisted bilayers (Senyshyn *et al.*, 2013). Higher-order reflections were observed for these phases and allowed indexing with a propagation vector (α, α, 0). Different structure models were discussed, but a complete description of the Li distribution is still lacking. Therefore, it is still an open question as to where the Li atoms in lithiated graphite are at low Li contents (below 1 Li per 12 C).

$LiNiO_2$ is considered to be a promising positive electrode material (Ohzuku *et al.*, 1993). However, it has some limitations, which are directly linked to the underlying structure. A high degree of cation disorder, *i.e.* Li on the Ni site and *vice versa*, hinders Li transport within the layers. Furthermore, Li and Ni exchange takes place rather easily, in contrast to $LiCoO_2$, because of a more favourable transport process through a tetrahedral interstitial site for Ni than for Co. In the cases of Li excess, $Li_{1+\delta}NiO_2$, or Ni excess, $(Li_{1-\delta}Ni_\delta)NiO_2$, some Ni^{2+} ions exist, which have a very similar ionic radius to that of Li^+. Therefore, it is nearly impossible to prepare stoichiometric $LiNiO_2$ with perfect separation of Li and Ni onto distinct layers. The best samples with respect to cation order are obtained from $NaNiO_2$ by successive Na → Li ion-exchange reactions. These drawbacks have prevented the commercial application of $LiNiO_2$, and more complex materials like $Li(Ni,Co,Al)O_2$ (NCA) and $Li(Ni,Co,Mn)O_2$ (NCM) are increasingly replacing $LiCoO_2$. Fig. 2.8.12 shows the structural changes in $LiNiO_2$ during the first charge and discharge. The detailed experimental conditions are the same as those described by Nikolowski *et al.* (2005) for $Li(Ni_{0.8}Co_{0.2})O_2$. One of the most characteristic features of the structural response to Li extraction and insertion is the pronounced change in the lattice parameters, shown by the changes in the *c*/*a* ratio for the rhombohedral structure. During Li extraction the *c* parameter increases, because there are fewer Li ions between (repulsive) O-atom layers. However, at lower Li contents, some of the O ions become oxidized, and the repulsion between the O-atom layers is weaker, resulting in shorter *c*-axis parameters. As a general rule, all layered oxides $LiMO_2$, with M = Mn, Co and/or Ni, become intrinsically unstable in the highly delithiated states beyond the maximum in the *c*/*a* ratio. Note that the as-prepared material has a very high degree of cation disorder (9.3% Ni on the Li site) and very poor capacity retention in the second cycle. The initial phase (*A*) gradually disappears and apparently transforms into a second phase (*B*) with a much lower degree of cation disorder (less than 3%). Note that this phase sequence does not necessarily reflect equilibrium conditions, but depends strongly on the chemical composition (Li or Ni excess), microstructure (size and strain) and the experimental conditions (charge rate, temperature, electrode formulation and more).

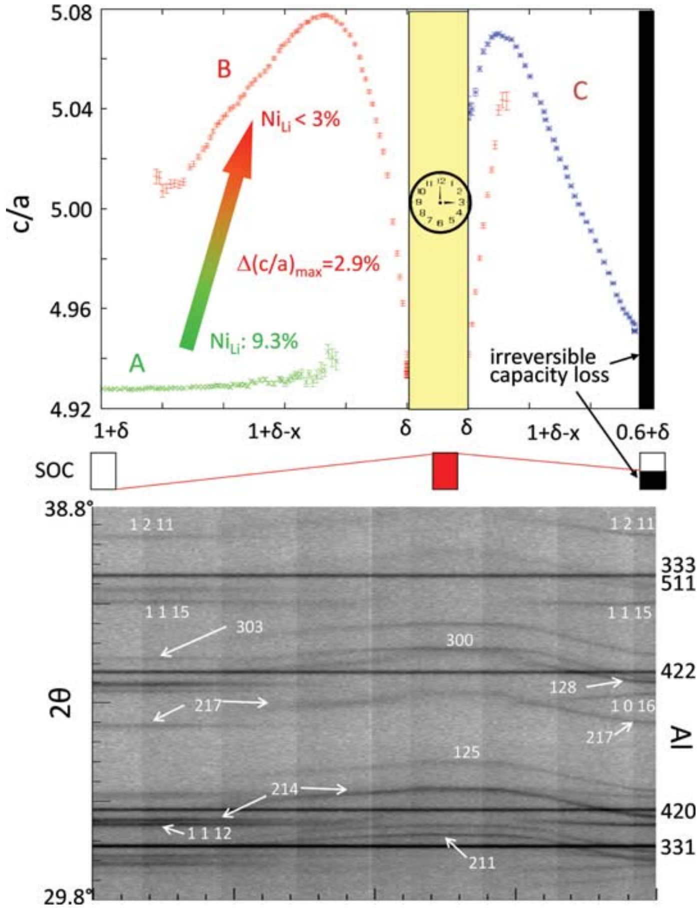

Figure 2.8.12
$Li_{1+\delta}NiO_2$ during charge and discharge. From about 210 complete diffraction patterns [a small section is shown below (λ = 0.499366 Å)], the structural response to Li extraction and insertion was monitored. In addition to changes in the unit-cell metric, the distribution of Li and Ni onto layers becomes more ordered during the first highly charged state. A pronounced capacity loss is observed during discharge after a holding time of 3 h in this overcharged state. A, B and C are three successively appearing phases. SOC = state of charge.

Such *in situ* studies are very important for elucidating the working mechanism and degradation processes for intercalation electrodes (Senyshyn *et al.*, 2012). Nevertheless, complementary methods are also essential for providing all the necessary information, especially about the surface near-interface region between the electrode and electrolyte, which has to be studied with surface-sensitive and local methods.

2.8.3.3. *Diffraction under a magnetic field*

2.8.3.3.1. *General remarks*

The majority of synchrotron and neutron experiments are currently limited to superconducting magnets with fields of 5–16 T. When higher fields are required there are essentially two possible solutions: pulsed resistive or steady-field resistive (or hybrid: resistive inner coil, superconducting outer coil) magnets. Pulsed fields are often used when signals are strong and the signal-to-noise ratio is good, whereas steady fields are primarily used for techniques with relatively long counting times and many data points. The relatively short pulse duration (from microseconds to milliseconds) along with the rather large sample volume required severely limit the use of pulsed magnetic fields in powder diffraction applications as well as more exotic methods of achieving high magnetic fields, *e.g.* magnetic flux compression or single-turn coils (Schneider-Muntau *et al.*, 2006). Furthermore, because of the large stresses, the lifetime of a resistive/pulsed magnet is finite: pulsed magnets have typical lifetimes of 500 shots at 95% of the design field, and their lifetimes are virtually independent of pulse duration.

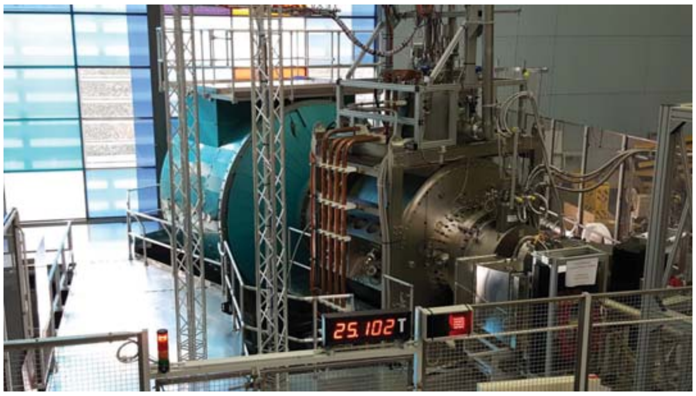

Figure 2.8.13
The High Magnetic Field Facility for Neutron Scattering at the Helmholtz-Zentrum Berlin has two main components: the High Field Magnet (HFM) and the Extreme Environment Diffractometer (EXED). Courtesy of Dr O. Prokhnenko.

At present, the maximum field for technical superconductors is 23 T and modern developments in superconductor design along with robust magnet manufacturing techniques have made possible high-flux-density magnets for neutron scattering studies up to 16 T. For resistive magnets, there are in principle no limitations to the generation of the highest continuous fields apart from economics, as approximately 1 MW of electric power is consumed per 1 T field strength. Therefore, in order to reduce the running costs (*i.e.* the required power per unit magnetic field), hybrid magnets are becoming increasingly popular. In this context we mention the joint developments between the National High Magnetic Field Laboratory (Tallahassee, FL, USA), the Spallation Neutron Source (Oak Ridge, TN, USA) and Helmholtz-Zentrum Berlin (Germany) in the development of high-steady-field (25 T with a 4 MW resistive insert, 30 T with an 8 MW resistive insert) hybrid magnets for neutron scattering (Bird *et al.*, 2009). A high-field magnet has been installed and is in routine user operation (Fig. 2.8.13) at the Extreme Environment Diffractometer (HFM-EXED) of Helmholtz-Zentrum Berlin (Prokhnenko *et al.*, 2015).

On the other hand, it is quite simple to produce magnetic flux density uniformity or homogeneity over the required sample volume down to the p.p.m. level with a solenoid magnet. However, the majority take the form of split-pair solenoids. With this setup, the access to the sample environment (along the magnetic axis) can be orthogonal to the beam-access plane. The split-coil setup is the most popular in neutron scattering, but the geometry constraints imposed by the neutron aperture make the creation of very uniform flux density much more difficult. In general, for a typical neutron-scattering sample volume of 1 cm^3, the magnetic field homogeneity is normally limited to the range 0.1 to 5%. As the available current density for a given conductor decreases with increasing flux density, the flux density seen by the superconductor inside the magnet windings is greater than the ‘nominal’ central value. This is particularly the case for split-pair magnets, where the ratio of the two can be large, *e.g.* for a central value of 9 T, a ratio of 1.6 gives a maximum flux density of 14.3 T (Brown, 2010).

As already pointed out, diffraction studies under a magnetic field are almost always performed with neutrons. However, Mitsui *et al.* (2009) have developed a device that includes a cryocooled split-pair NbTi superconducting magnet and a sample furnace, for high fields and temperatures above room temperature, respectively, which can be installed on a laboratory X-ray diffractometer. The magnetic field generated goes up to 5 T at the centre of a 50 mm vertical and 10 mm horizontal bore, with a field homogeneity of 0.1%. The first results of studies on the martensitic phase transition in the shape memory system $Ni_{40}Co_{10}Mn_{34}Al_{16}$ in a field of 5 T and at temperatures up to 473 K have been reported for powders (Mitsui *et al.*, 2009).

Synchrotron radiation can be used to study specific properties such as orbital contributions and their separation from the spin values. Diffraction studies with unpolarized neutrons are common at a constant field to elucidate simple magnetic structures: no confident conclusion about the spin direction can be obtained if the configurational symmetry is cubic, and in the case of uniaxial symmetry (either tetragonal, hexagonal or rhombohedral) only the angle with the unique axis of the magnetic structure can be defined (Shirane, 1959). The sensitivity of nonpolarized neutron powder diffraction (the magnetic detection limit) is by a few orders of magnitude less than that of superconducting quantum interference device (SQUID) magnetometry, muon spin rotation or magnetic dichroism spectroscopy. In an antiferromagnetically ordered system the determination of magnetic moments below 0.1 μ_B per magnetic atom presents severe challenges, which become even more pronounced for the localization of weak ferromagnetic components. Less frequent are *in situ* investigations to determine magnetic phase diagrams. The use of powder samples at high magnetic fields is often limited by the redistribution of grains and texture effects.

Experiments with polarized neutrons are normally performed with single crystals. Out of the variety of compounds that have been studied, we have chosen materials with particular properties and report on *in situ* studies of them under magnetic fields.

2.8.3.3.2. *Frustrated magnetic systems*

Multiferroic systems (or more precisely magnetoelectric materials) have gained considerable attention because of their potential applications in devices. In fact, the efficient control of magnetism by an electric field allows magnetic information to be written electrically (with low energy consumption) and read magnetically. A real application, however, requires both phenomena to occur at room temperature. There are very few compounds that fulfil this requirement; examples include $BiFeO_3$ and β-$NaFeO_2$.

Magnetoelectric properties have been observed in many compounds with different structures and chemical compositions. However, they all have a geometrical magnetic frustration in common, which induces competition among multiple magnetic ground states. Furthermore, a magnetic phase transition is thought to be an essential ingredient for realizing a non-linear colossal response in the electric properties. In the colossal effect, the two properties not only coexist but couple strongly in their order parameter. Most novel multiferroic materials exhibit a cycloidal component to the magnetic structure; this has been considered as a guiding principle for tailoring new materials based on the non-collinearity of the spins. Many cycloidal compounds exhibit a small ferromagnetic component in their antiferromagnetic order, giving rise to the Dzyaloshinskii–Moriya interaction. We shall concentrate here on two systems linked by frustration in the magnetic ordering, namely orthovanadates and the manganites of the rare earths.

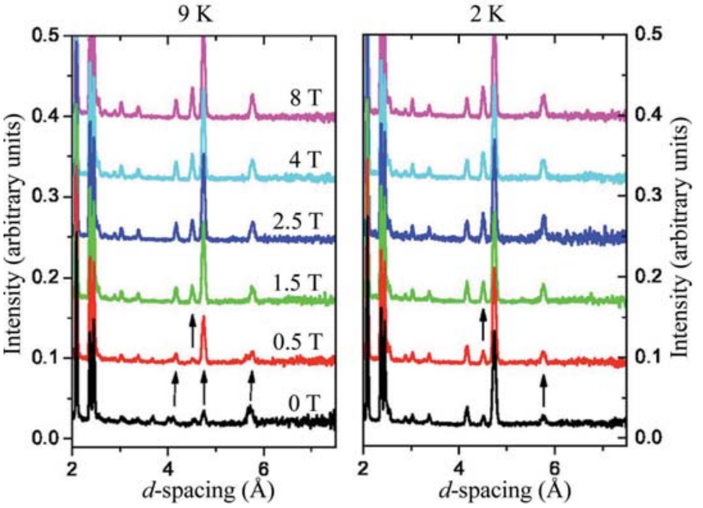

Figure 2.8.14
Neutron powder diffraction data for $Co_3V_2O_8$ at 9 K (left) and 2 K (right) under magnetic fields of 0, 0.5, 1.5, 2.5, 4.0 and 8.0 T. Data from a bank of detectors situated at the scattering angle 35° are shown. The arrows indicate the changes between the data at different fields. Individual curves are offset arbitrarily for display purposes. Reprinted with permission from Wilson *et al.* (2007). Copyright (2007) by the American Physical Society.

2.8.3.3.2.1. *Kagomé staircase systems*

Among the orthovanadates of 3*d* metals, $Co_3V_2O_8$ and $Ni_3V_2O_8$ have been identified as kagomé staircase magnetic structures, which exhibit a considerable number of phase transitions at low temperature. Their crystal structure was determined by Fuess *et al.* (1970) as orthorhombic (space group *Cmca*). Ferromagnetic order was found for the cobalt compound and an indication of antiferromagnetism for the nickel compound at 4.2 K. The crystal structure is characterized by edge-sharing CoO_6 octahedra forming buckled layers of corner-sharing triangles, called kagomé staircases, separated by VO_4 tetrahedra. The magnetic ions (Co or Ni) are situated at the corners of triangles, thus leading to spin frustration. Therefore, if a small amount of energy is supplied by an external magnetic field, a whole sequence of magnetic phase transitions can be introduced. The previously determined ferromagnetic order as the ground state for $Co_3V_2O_8$ was confirmed by Wilson *et al.* (2007). They also reported field-dependent neutron powder diffraction studies under a field of 8 T at 2 and 9 K (Fig. 2.8.14). At 9 K the system has an incommensurate magnetic structure. At a field as low as 0.5 T, new magnetic peaks indexed in a commensurate structure occur, accompanied by a shift in the position of others. The incommensurate ordering disappears completely at a higher field and a purely ferromagnetic behaviour is observed, similar to the low-temperature ground state at zero field. At 2 K and 8 T no additional magnetic reflections are observed but changes in the intensity of several existing ones are seen. The refinement of the magnetic structure based on these data indicated a change of the spin direction in the ferromagnetic arrangement as compared with the zero-field low-temperature structure. Furthermore, the magnetic moments on the two different Co sites in the structure are aligned under the field and reach the same value of 3.15 μ_B on both sites, which is similar to the spin-only moment of cobalt.

The reorientation of spins and the complete magnetic field *versus* temperature (*H*–*T*) phase diagram of the multiferroic $Ni_3V_2O_8$ has been reported (Kenzelmann *et al.*, 2006). The inversion symmetry of space group *Cmca* is broken at low temperature and a commensurate phase is observed. Thus, over a

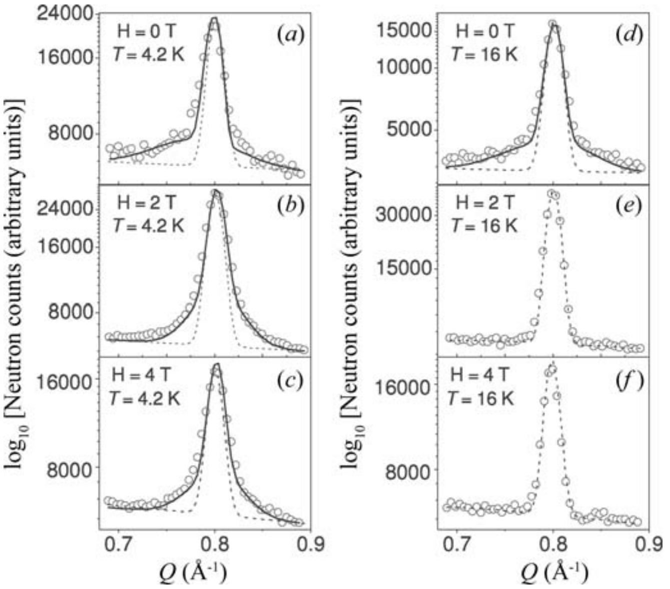

Figure 2.8.15
The observed Bragg reflection 100 (open circles) under an applied field of (*a*) 0 T, (*b*) 2 T and (*c*) 4 T at 4.2 K and (*d*) 0 T, (*e*) 2 T and (*f*) 4 T at 16 K (taken from Yusuf *et al.*, 2013). Copyright IOP Publishing. Reproduced with permission. All rights reserved.

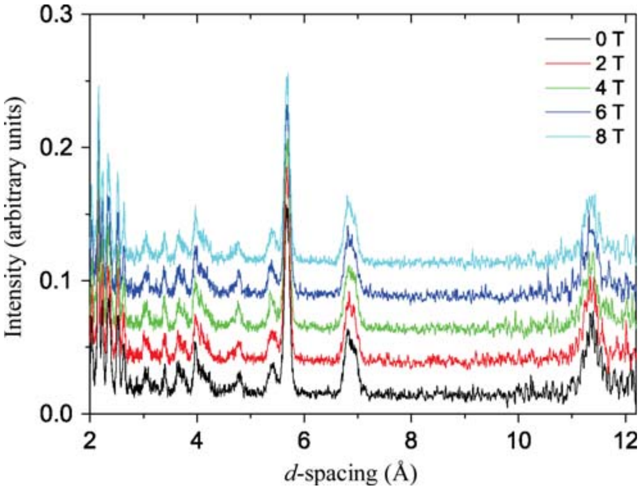

Figure 2.8.16
Time-of-flight diffraction patterns of YMn_2O_5 at 1.6 K under magnetic fields between 0 and 8 T (taken from Radaelli & Chapon, 2008). Copyright IOP Publishing. Reproduced with permission. All rights reserved.

narrow temperature range a macroscopic polar vector leads to a multiferroic behaviour. As this study was based on single-crystal neutron measurements, no further details are given here. Frustrated triangular-lattice Ising antiferromagnets have degenerate magnetic ground states, which give rise to very complex magnetic structures. As there are only small differences in the competing exchange interaction in such frustrated triangular-lattice compounds, a sequence of phase transitions is introduced by changes in temperature or magnetic field. The compound $Ca_3Co_2O_6$ is another example of a frustrated system. Field-dependent powder diffraction patterns were reported for the doped system $Ca_3Co_{1.8}Fe_{0.2}O_6$ by Yusuf *et al.* (2013). They distinguished the short-range magnetic order (SRO), reflected in the half-width of the Bragg reflections (Fig. 2.8.15), from the long-range order as given by the Bragg positions. They stated that even under magnetic fields up to 4 T the broadening of Bragg reflections indicates the persistence of SRO. In a field of 2 T, the observed change in the structure from incommensurate to commensurate indicates a reduction of spin frustration. In fields of 4 T, a ferrimagnetic system is introduced, followed by a ferromagnetic one above 5 T.

2.8.3.3.2.2. *Manganite systems*

Like the vanadates, in the class of rare-earth manganites of the type RMn_2O_5 successive magnetic phase transitions between commensurate (CO) and incommensurate phases (ICP) can occur. Intensive investigations have been undertaken to understand the relationship between their magnetic and dielectric properties. The spontaneous electric polarization is induced by a magnetic transition. Thus the primary order parameter is magnetic rather than structural. Among the rare-earth compounds, those containing Nd or an element lighter than Nd do not exhibit ferroelectricity. In all these materials a broken magnetic symmetry at lower temperatures leads to a polar symmetry group. In addition, a cycloidal component indicates a common underlying mechanism. The Mn^{3+} and Mn^{4+} ions are fully charge-ordered. Neutron diffraction studies of these phases have been performed by Radaelli & Chapon (2008), who also analysed the possible exchange pathways. In $TbMn_2O_5$ the *H*–*T* phase diagram of the commensurate–low-temperature–incommensurate (CO–LT–ICP) magnetic transitions shows an upward jump in the transition temperature from ~25 K at zero field to 27 K at 9 T. The low-temperature ICP phase is stabilized under an external field for $TbMn_2O_5$ and the dielectric constant is enhanced. It was concluded that Tb and Mn order independently, implying the absence of coupling terms between them. Strong support for this suggestion was provided by an in-field neutron study on the analogue YMn_2O_5. Neither the positions nor the intensities of the magnetic Bragg reflections were affected by the magnetic field (Fig. 2.8.16). The magnetic low-temperature ICP phase in the Tb compound was stabilized under a magnetic field. This is in contrast to observations on $HoMn_2O_5$ by Kimura *et al.* (2007), using single crystals. In both cases, however, the neutron data correlate directly with the results obtained by dielectric measurements under a magnetic field. The difference in the behaviours is thus confirmed. The two studies also reveal different magnetic order at low temperatures. The same magnetic sequence at low temperatures as for Tb was observed in YMn_2O_5, which does not contain a magnetic rare-earth element. Under fields up to 8 T the positions and the intensities of the magnetic Bragg reflections remained unchanged, showing that the antiferromagnetic structure of the manganese sublattice is extremely stable. As in the vanadates, the main reason for the sequence of magnetic structures is frustration of the manganese spins. Without going too deeply into the details of the different exchange pathways and orbital occupancies, one factor behind this behaviour is the Jahn–Teller effect of the Mn^{3+} ion, which is also relevant in the multiferroic $TbMnO_3$ as part of the $RMnO_3$ family (Kimura *et al.*, 2003). Another feature often found in multiferroic systems is the small ferromagnetic component caused by small spin canting due to Dzyaloshinskii–Moriya interactions. This property strongly influences the low-temperature magnetism in RMn_2O_5 (Kimura *et al.*, 2009).

2.8.3.3.3. *Additional systems and scattering techniques*

Information about the anisotropy of the local magnetic susceptibility at different magnetic sites has been extracted from diffraction patterns for a $Tb_2Sn_2O_7$ powder measured using polarized neutrons under magnetic fields of 1 and 5 T (Gukasov

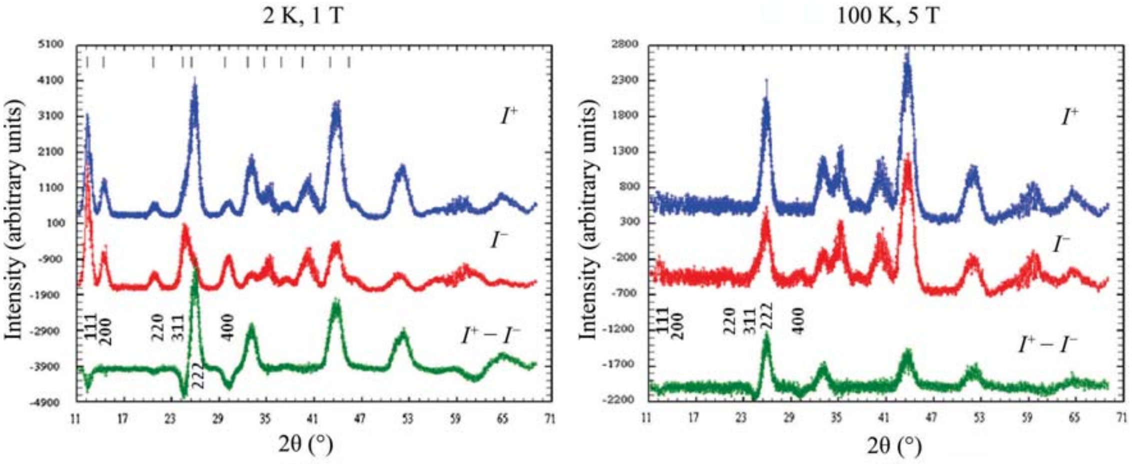

(*a*) (*b*)

Figure 2.8.17
Polarized neutron diffraction patterns for $Tb_2Sn_2O_7$ at 2 K and 1 T (*a*) and 100 K and 5 T (*b*). I^+ and I^- are the intensities for spin-up and spin-down neutrons, respectively. Taken from Gukasov & Brown (2010). Copyright IOP Publishing. Reproduced with permission. All rights reserved.

& Brown, 2010). No magnetic contribution to the diffracted intensities was observed at 2 K in the absence of an external field. However, applying a field led to considerable changes in the diffraction pattern (Fig. 2.8.17). At 100 K and 5 T, the intensities of the reflections that are allowed for the cubic space group $Fd\overline{3}m$ increase considerably. Furthermore, they were found to depend strongly on the polarization of the incoming neutrons, as shown by the difference pattern in Fig. 2.8.17. At a field of 1 T, new reflections appear (Fig. 2.8.17*a*) that are forbidden for the occupied sites in $Fd\overline{3}m$ symmetry, such as 200, 222 and 240. The intensities of these new reflections do not change with the polarization of the neutrons, as demonstrated in the difference plot, hence they are purely magnetic. In conclusion, information on local anisotropic magnetic susceptibility at different sites can be obtained by using a combination of unpolarized and polarized neutron powder patterns. This demonstrates the usefulness of polarized neutron scattering, even for polycrystalline samples.

We now return to X-ray investigations of magnetic materials. A laboratory device for fields up to 5 T and temperatures above room temperature was mentioned in Section 2.8.3.3.1. The corresponding low-temperature apparatus (Koyama *et al.*, 2013) has produced results on magneto-caloric compounds of MnFeP-type materials. Substitution of P in $MnFeP_{1-x}Z_x$ with Z = As or Ge produces materials that exhibit a large magneto-caloric effect and thus allows control of the Curie temperature by chemical composition. Studies under magnetic fields are mandatory, as the refrigerants are working under a field. For two different compositions of the As compound the lattice parameters change drastically and the cell volume decreases with increasing magnetic field strength. In $MnFeP_{0.78}Ge_{0.22}$ a field-induced ferromagnetic phase was observed near the Curie temperature at 280 K. This phase is, however, not identical to the low-temperature ferromagnetic one (Koyama *et al.*, 2013).

2.8.3.3.4. *Concluding remarks*

Despite some shortcomings, powder diffraction studies as a function of magnetic fields are valuable for the qualitative and sometimes even quantitative interpretation of magnetic materials. Unpolarized neutrons are used in most experiments, but the additional information from polarized neutrons has also been exploited. X-rays do not interact directly with the magnetic moments, but structural changes as a consequence of magnetic phase transitions have been observed in several cases. *In situ* powder diffraction under magnetic fields reaching 4 T on an X-ray diffractometer with a rotating anode revealed details of lattice parameters and atomic positions in rare-earth alloys with a higher precision than that accessible by neutron diffraction (Pecharsky *et al.*, 2007). Furthermore, the two test-case compounds studied, Gd_5Ge_4 and $DyCo_2$, contain the rare-earth elements Gd and Dy with the highest absorption cross sections for neutrons in their natural isotope abundance. The data were used to refine the underlying structure models by Rietveld analysis. Advances in X-ray and neutron sources and optics delivered higher resolution and flux to the samples, which in combination with rapid computing made real-time experiments feasible.

2.8.4. Summary

We have shown here that *in situ* studies under electric and magnetic fields are in a well advanced state. Laboratory equipment can be used for diverse experiments where changes occur on a timescale that can be followed with an exposure time of minutes. Real progress is, however, achieved by using high-energy synchrotron radiation and by using neutrons, which can penetrate larger volumes. Thus *in operando* studies of real devices are feasible. In addition to such diffraction experiments, which provide average information on a macroscopic length scale, complementary experiments like electron microscopy are vital for revealing local structural information. Only the combination of several methods can give sufficient insight into structure–property relationships and the functionality of materials.

References

Adam, R., Wadewitz, D., Gruner, W., Klemm, V., Ehrenberg, H. & Rafaja, D. (2013). *Phase and microstructure development in the conversion type electrodes for Li-ion batteries based on the Cu-Fe-O system. J. Electrochem. Soc.* **160**, A1594–A1603.

Anastasopoulos, M., Bebb, R., Berry, K., Birch, J., Bryś, T., Buffet, J.-C., Clergeau, J.-F., Deen, P. P., Ehlers, G., van Esch, P., Everett, S. M., Guerard, B., Hall-Wilton, R., Herwig, K., Hultman, L., Höglund, C., Iruretagoiena, I., Issa, F., Jensen, J., Khaplanov, A., Kirstein, O., Higuera, I. L., Piscitelli, F., Robinson, L., Schmidt, S. & Stefanescu, I. (2017). *Multi-grid detector for neutron spectroscopy: results obtained on time-of-flight spectrometer CNCS. J. Instrum.* **12**, P04030.

Anton, E.-M., Schmitt, L. A., Hinterstein, M., Trodahl, J., Kowalski, B., Jo, W., Kleebe, H.-J., Rödel, J. & Jones, J. L. (2012). *Structure and temperature-dependent phase transitions of lead-free $Bi_{1/2}Na_{1/2}TiO_3$–$Bi_{1/2}K_{1/2}TiO_3$–$K_{0.5}Na_{0.5}NbO_3$ piezoceramics. J. Mater. Res.* **27**, 2466–2478.

Ballabriga, R., Campbell, M., Heijne, E. H. M., Llopart, X. & Tlustos, L. (2007). *The Medipix3 prototype, a pixel readout chip working in single photon counting mode with improved spectrometric performance. IEEE Trans. Nucl. Sci.* **54**, 1824–1829.

Bergamaschi, A., Cervellino, A., Dinapoli, R., Gozzo, F., Henrich, B., Johnson, I., Kraft, P., Mozzanica, A., Schmitt, B. & Shi, X. (2009). *Photon counting microstrip detector for time resolved powder diffraction experiments. Nucl. Instrum. Methods Phys. Res. A*, **604**, 136–139.

Bergstöm, Ö., Andersson, A. M., Edström, K. & Gustafsson, T. (1998). *A neutron diffraction cell for studying lithium-insertion processes in electrode materials. J. Appl. Cryst.* **31**, 823–825.

Bergström, O., Gustafsson, T. & Thomas, J. O. (1998). *An X-ray powder diffraction attachment for in situ studies of ion insertion processes in electrode materials. J. Appl. Cryst.* **31**, 103–105.

Bird, M. D., Hongyu Bai, Bole, S., Jingping Chen, Dixon, I. R., Ehmler, H., Gavrilin, A. V., Painter, T. A., Smeibidl, P., Toth, J., Weijers, H., Ting Xu & Zhai, Y. (2009). *The NHMFL hybrid magnet projects. IEEE Trans. Appl. Supercond.* **19**, 1612–1616.

Brown, F. J. (2010). *Aspects of superconducting magnet design for neutron scattering sample environments. J. Phys. Conf. Ser.* **251**, 012093.

Cabana, J., Monconduit, L., Larcher, D. & Palacín, M. (2010). *Beyond intercalation-based Li-ion batteries: the state of the art and challenges of electrode materials reacting through conversion reactions. Adv. Mater.* **22**, E170–E192.

Cartier, S., Bergamaschi, A., Dinapoli, R., Greiffenberg, D., Johnson, I., Jungmann, J. H., Mezza, D., Mozzanica, A., Schmitt, B., Shi, X., Stampanoni, M., Sun, J. & Tinti, G. (2014). *Micron resolution of MÖNCH and GOTTHARD, small pitch charge integrating detectors with single photon sensitivity. J. Instrum.* **9**, C05027.

Choe, H., Gorfman, S., Hinterstein, M., Ziolkowski, M., Knapp, M., Heidbrink, S., Vogt, M., Bednarcik, J., Berghäuser, A., Ehrenberg, H. & Pietsch, U. (2015). *Combining high time and angular resolutions: time-resolved X-ray powder diffraction using a multi-channel analyser detector. J. Appl. Cryst.* **48**, 970–974.

Daniels, J. E. & Drakopoulos, M. (2009). *High-energy X-ray diffraction using the Pixium 4700 flat-panel detector. J. Synchrotron Rad.* **16**, 463–468.

Daniels, J. E., Finlayson, T. R., Studer, A. J., Hoffman, M. & Jones, J. L. (2007). *Time-resolved diffraction measurements of electric-field-induced strain in tetragonal lead zirconate titanate. J. Appl. Phys.* **101**, 094104.

Daniels, J. E., Jo, W., Rödel, J., Honkimäki, V. & Jones, J. L. (2010). *Electric-field-induced phase-change behavior in* $(Bi_{0.5}Na_{0.5})TiO_3$–$BaTiO_3$–$(K_{0.5}Na_{0.5})NbO_3$*: a combinatorial investigation. Acta Mater.* **58**, 2103–2111.

Eckold, G., Schober, H. & Nagler, S. E. (2010). Editors. *Studying Kinetics with Neutrons. Springer Series in Solid State Sciences.* Berlin, Heidelberg: Springer.

Eriksson, T., Andersson, A. M., Bergström, Ö., Edström, K., Gustafsson, T. & Thomas, J. O. (2001). *A furnace for in situ X-ray diffraction studies of insertion processes in electrode materials at elevated temperatures. J. Appl. Cryst.* **34**, 654–657.

Fuess, H., Bertaut, E. F., Pauthenet, R. & Durif, A. (1970). *Structure aux rayons X, neutrons et propriétés magnétiques des orthovanadates de nickel et de cobalt. Acta Cryst.* B**26**, 2036–2046.

Gukasov, A. & Brown, P. J. (2010). *Determination of atomic site susceptibility tensors from neutron diffraction data on polycrystalline samples. J. Phys. Condens. Matter*, **22**, 502201.

Hansen, T. C., Henry, P. F., Fischer, H. E., Torregrossa, J. & Convert, P. (2008). *The D20 instrument at the ILL: a versatile high-intensity two-axis neutron diffractometer. Meas. Sci. Technol.* **19**, 034001.

Herklotz, M., Scheiba, F., Hinterstein, M., Nikolowski, K., Knapp, M., Dippel, A.-C., Giebeler, L., Eckert, J. & Ehrenberg, H. (2013). *Advances in in situ powder diffraction of battery materials: a case study of the new beamline P02.1 at DESY, Hamburg. J. Appl. Cryst.* **46**, 1117–1127.

Hinterstein, M. (2011). *Mikrostrukturanalyse von Piezokeramiken mit Hilfe von Synchrotron- und Neutronenstrahlung*. Goettingen: Sierke Verlag.

Hinterstein, M., Hoelzel, M., Rouquette, J., Haines, J., Glaum, J., Kungl, H. & Hoffman, M. (2015). *Interplay of strain mechanisms in morphotropic piezoceramics. Acta Mater.* **94**, 319–327.

Hinterstein, M., Knapp, M., Hölzel, M., Jo, W., Cervellino, A., Ehrenberg, H. & Fuess, H. (2010). *Field-induced phase transition in* $Bi_{1/2}Na_{1/2}TiO_3$*-based lead-free piezoelectric ceramics. J. Appl. Cryst.* **43**, 1314–1321.

Hinterstein, M., Rouquette, J., Haines, J., Papet, P., Glaum, J., Knapp, M., Eckert, J. & Hoffman, M. (2014). *Structural contribution to the ferroelectric fatigue in lead zirconate titanate ceramics. Phys. Rev. B*, **90**, 094113.

Hinterstein, M., Rouquette, J., Haines, J., Papet, Ph., Knapp, M., Glaum, J. & Fuess, H. (2011). *Structural description of the macroscopic piezo- and ferroelectric properties of lead zirconate titanate. Phys. Rev. Lett.* **107**, 077602.

Hinterstein, M., Schmitt, L. A., Hoelzel, M., Jo, W., Rödel, J., Kleebe, H.-J. & Hoffman, M. (2015). *Cyclic electric field response of morphotropic* $Bi_{1/2}Na_{1/2}TiO_3$-$BaTiO_3$ *piezoceramics. Appl. Phys. Lett.* **106**, 222904.

Hirota, K., Wakimoto, S. & Cox, D. E. (2006). *Neutron and X-ray scattering studies of relaxors. J. Phys. Soc. Jpn*, **75**, 111006.

Hodeau, J. L., Bordet, P., Anne, M., Prat, A., Fitch, A. N., Dooryheé, E., Vaughan, G. & Freund, A. (1998). *Nine-crystal multianalyzer stage for high-resolution powder diffraction between 6 keV and 40 keV. Proc. SPIE*, **3448**, 353–361.

Hoelzel, M., Senyshyn, A., Gilles, R., Boysen, H. & Fuess, H. (2007). *Scientific review: the structure powder diffractometer SPODI. Neutron News*, **18**, 23–26.

Hoelzel, M., Senyshyn, A., Juenke, N., Boysen, H., Schmahl, W. & Fuess, H. (2012). *High-resolution neutron powder diffractometer SPODI at research reactor FRM II. Nucl. Instrum. Methods Phys. Res. A*, **667**, 32–37.

Hoffmann, M. J., Hammer, M., Endriss, A. & Lupascu, D. C. (2001). *Correlation between microstructure, strain behavior, and acoustic emission of soft PZT ceramics. Acta Mater.* **49**, 1301–1310.

Jin, Y. M., Wang, Y. U., Khachaturyan, A. G., Li, J. E. & Viehland, D. (2003). *Conformal miniaturization of domains with low domain-wall energy: monoclinic ferroelectric states near the morphotropic phase boundaries. Phys. Rev. Lett.* **91**, 197601.

Johnsen, R. E. & Norby, P. (2013). *Capillary-based micro-battery cell for in situ X-ray powder diffraction studies of working batteries: a study of the initial intercalation and deintercalation of lithium into graphite. J. Appl. Cryst.* **46**, 1537–1543.

Johnson, I., Bergamaschi, A., Billich, H., Cartier, S., Dinapoli, R., Greiffenberg, D., Guizar-Sicairos, M., Henrich, B., Jungmann, J., Mezza, D., Mozzanica, A., Schmitt, B., Shi, X. & Tinti, G. (2014). *Eiger: a single-photon counting X-ray detector. J. Instrum.* **9**, C05032.

Jones, J. L. (2007). *The use of diffraction in the characterization of piezoelectric materials. J. Electroceram.* **19**, 69–81.

Jones, J., Hoffman, M., Daniels, J. E. & Studer, A. J. (2006). *Direct measurement of the domain switching contribution to the dynamic piezoelectric response in ferroelectric ceramics. Appl. Phys. Lett.* **89**, 092901.

Jones, J. L., Pramanick, A., Nino, J. C., Maziar Motahari, S., Üstündag, E., Daymond, M. R. & Oliver, E. C. (2007). *Time-resolved and orientation-dependent electric-field-induced strains in lead zirconate titanate ceramics. Appl. Phys. Lett.* **90**, 172909.

Kenzelmann, M., Harris, A. B., Aharony, A., Entin-Wohlman, O., Yildirim, T., Huang, Q., Park, S., Lawes, G., Broholm, C., Rogado, N., Cava, R. J., Kim, K. H., Jorge, G. & Ramirez, A. P. (2006). *Field dependence of magnetic ordering in kagomé-staircase compound. Phys. Rev. B*, **74**, 014429.

Kimura, H., Kamada, Y., Noda, Y., Wakimoto, S., Kaneko, K., Metoki, N., Kakurai, K. & Kohn, K. (2007). *Field-induced dielectric and magnetic phase transitions in multiferroic compounds of* RMn_2O_5 *(R = Er, Ho). J. Korean Phys. Soc.* **51**, 870–873.

Kimura, H., Noda, Y. & Kohn, K. (2009). *Spin-driven ferroelectricity in the multiferroic compounds of* RMn_2O_5*. J. Magn. Magn. Mater.* **321**, 854–857.

Kimura, T., Goto, T., Shintani, H., Ishizaka, K., Arima, T. & Tokura, Y. (2003). *Magnetic control of ferroelectric polarization. Nature*, **426**, 55–58.

Köhli, M., Allmendinger, F., Häussler, W., Schröder, T., Klein, M., Meven, M. & Schmidt, U. (2016). *Efficiency and spatial resolution of the CASCADE thermal neutron detector. Nucl. Instrum. Methods Phys. Res. A*, **828**, 242–249.

Koyama, K., Watanabe, K., Tegus, O., Brück, E., Buschow, K. H. J. & de Boer, F. R. (2013). *X-ray powder diffraction studies on* $MnFeP_{0.78}Ge_{0.22}$ *in high magnetic fields. J. Low Temp. Phys.* **170**, 279–284.

Kraft, P., Bergamaschi, A., Bronnimann, Ch., Dinapoli, R., Eikenberry, E. F., Graafsma, H., Henrich, B., Johnson, I., Kobas, M., Mozzanica, A., Schleputz, C. M. & Schmitt, B. (2009). *Characterization and calibration of PILATUS detectors. IEEE Trans. Nucl. Sci.* **56**, 758–764.

Lee, P. L., Shu, D., Ramanathan, M., Preissner, C., Wang, J., Beno, M. A., Von Dreele, R. B., Ribaud, L., Kurtz, C., Antao, S. M., Jiao, X. & Toby, B. H. (2008). *A twelve-analyzer detector system for high-resolution powder diffraction. J. Synchrotron Rad.* **15**, 427–432.

Levin, I., Reaney, I. M., Anton, E.-M., Jo, W., Rödel, J., Pokorny, J., Schmitt, L. A., Kleebe, H.-J., Hinterstein, M. & Jones, J. L. (2013). *Local structure, pseudosymmetry, and phase transitions in* $Na_{1/2}Bi_{1/2}TiO_3$–$K_{1/2}Bi_{1/2}TiO_3$ *ceramics. Phys. Rev. B*, **87**, 024113.

Liss, K. D., Hunter, B., Hagen, M., Noakes, T. & Kennedy, S. (2006). *Echidna – the new high-resolution powder diffractometer being built at OPAL. Physica B*, **385–386**, 1010–1012.

Liu, L., Knapp, M., Ehrenberg, H., Fang, L., Fan, H., Schmitt, L. A., Fuess, H., Hoelzel, M., Dammak, H., Thi, M. P. & Hinterstein, M. (2017). *Average vs. local structure and composition-property phase diagram of* $K_{0.5}Na_{0.5}NbO_3$–$Bi_{1/2}Na_{1/2}TiO_3$ *system. J. Eur. Ceram. Soc.* **37**, 1387–1399.

Mikhailova, D., Schwarz, B., Senyshyn, A., Bell, A. M. T., Skourski, Y., Ehrenberg, H., Tsirlin, A. A., Agrestini, S., Rotter, M., Reichel, P., Chen, J. M., Hu, Z., Li, Z. M., Li, Z. F. & Tjeng, L. H. (2012). *Magnetic properties and crystal structure of SrCoIrO and SrNiIrO. Phys. Rev. B*, **86**, 134409.

Mitsui, Y., Koyama, K. & Watanabe, K. (2009). *X-ray diffraction measurements in high magnetic fields and at high temperatures. Sci. Technol. Adv. Mater.* **10**, 014612.

Mittemeijer, E. J. & Welzel, U. (2012). Editors. *Modern Diffraction Methods*. Weinheim: Wiley-VCH.

Morcrette, M., Rozier, P., Dupont, L., Mugnier, E., Sannier, L., Galy, J. & Tarascon, J.-M. (2003). *A reversible copper extrusion–insertion electrode for rechargeable Li batteries. Nat. Mater.* **2**, 755–761.

Mozzanica, A., Bergamaschi, A., Cartier, S., Dinapoli, R., Greiffenberg, D., Johnson, I., Jungmann, J., Maliakal, D., Mezza, D., Ruder, C., Schaedler, L., Schmitt, B., Shi, X. & Tinti, G. (2014). *Prototype characterization of the JUNGFRAU pixel detector for SwissFEL. J. Instrum.* **9**, C05010.

Nikolowski, K., Baehtz, C., Bramnik, N. N. & Ehrenberg, H. (2005). *A Swagelok-type in situ cell for battery investigations using synchrotron radiation. J. Appl. Cryst.* **38**, 851–853.

Noheda, B., Gonzalo, J. A., Cross, L. E., Guo, R., Park, S. E., Cox, D. E. & Shirane, G. (2000). *Tetragonal-to-monoclinic phase transition in a ferroelectric perovskite: the structure of* $PbZr_{0.52}Ti_{0.48}O_3$. *Phys. Rev. B*, **61**, 8687–8695.

Ohzuku, T., Ueda, A. & Nagayama, M. (1993). *Electrochemistry and structural chemistry of* $LiNiO_2$ *(R3m) for 4 volt secondary lithium cells. J. Electrochem. Soc.* **140**, 1862–1870.

Oswald, S., Nikolowski, K. & Ehrenberg, H. (2009). *Quasi in situ XPS investigations on intercalation mechanisms in Li-ion battery materials. Anal. Bioanal. Chem.* **393**, 1871–1877.

Patterson, B. D., Brönnimann, C., Maden, D., Gozzo, F., Groso, A., Schmitt, B., Stampanoni, M. & Willmott, P. R. (2005). *The materials science beamline at the Swiss Light Source. Nucl. Instrum. Methods Phys. Res. B*, **238**, 224–228.

Pecharsky, V. K., Mudryk, Ya. & Gschneidner, K. A. Jr (2007). *In-situ powder diffraction in high magnetic fields. Z. Kristallogr. Suppl.* **26**, 139–145.

Peral, I., McKinlay, J., Knapp, M. & Ferrer, S. (2011). *Design and construction of multicrystal analyser detectors using Rowland circles: application to MAD26 at ALBA. J. Synchrotron Rad.* **18**, 842–850.

Poikela, T., Plosila, J., Westerlund, T., Campbell, M., Gaspari, M. D., Llopart, X., Gromov, V., Kluit, R., van Beuzekom, M., Zappon, F., Zivkovic, V., Brezina, C., Desch, K., Fu, Y. & Kruth, A. (2014). *Timepix3: a 65k channel hybrid pixel readout chip with simultaneous ToA/ToT and sparse readout. J. Instrum.* **9**, C05013.

Poizot, P., Laruelle, S., Grugeon, S., Dupont, L. & Tarascon, J.-M. (2000). *Nano-sized transition-metal oxides as negative-electrode materials for lithium-ion batteries. Nature*, **407**, 496–499.

Pramanick, A., Prewitt, A. D., Cottrell, M. A., Lee, W., Studer, A. J., An, K., Hubbard, C. R. & Jones, J. L. (2010). *In situ neutron diffraction studies of a commercial, soft lead zirconate titanate ceramic: response to electric fields and mechanical stress. Appl. Phys. A*, **99**, 557–564.

Prokhnenko, O., Stein, W.-D., Bleif, H.-J., Fromme, M., Bartkowiak, M. & Wilpert, T. (2015). *Time-of-flight extreme environment diffractometer at the Helmholtz-Zentrum Berlin. Rev. Sci. Instrum.* **86**, 033102.

Radaelli, P. G. & Chapon, L. C. (2008). *A neutron diffraction study of* RMn_2O_5 *multiferroics. J. Phys. Condens. Matter*, **20**, 434213.

Repper, J., Keller, T., Hofmann, M., Krempaszky, C., Werner, E. & Petry, W. (2009). *Neutron Larmor diffraction for the determination of absolute lattice spacing Adv. X-ray Anal.* **52**, 201–208.

Schmitt, B., Broennimann, C., Eikenberry, E. F., Gozzo, F., Hoermann, C., Horisberger, R. & Patterson, B. (2003). *Mythen detector system. Nucl. Instrum. Methods Phys. Res. A*, **501**, 267–272.

Schmitt, L. A., Hinterstein, M., Kleebe, H.-J. & Fuess, H. (2010). *Comparative study of two lead-free piezoceramics using diffraction techniques. J. Appl. Cryst.* **43**, 805–810.

Schmitt, L. A., Schönau, K. A., Theissmann, R., Fuess, H., Kungl, H. & Hoffmann, M. J. (2007). *Composition dependence of the domain configuration and size in* $Pb[Zr_{1-x}Ti_x]O_3$ *ceramics. J. Appl. Phys.* **101**, 074107.

Schneider-Muntau, H.-J., Gavrilin, A. V. & Swenson, C. A. (2006). *Magnet technology beyond 50 T. IEEE Trans. Appl. Supercond.* **16**, 926–933.

Schönau, K. A., Knapp, M., Kungl, H., Hoffmann, M. J. & Fuess, H. (2007). *In situ synchrotron diffraction investigation of morphotropic Pb* $[Zr_{1-x}Ti_x]O_3$ *under an applied electric field. Phys. Rev. B*, **76**, 144112.

Schönau, K. A., Schmitt, L. A., Knapp, M., Fuess, H., Eichel, R., Kungl, H. & Hoffmann, M. J. (2007). *Nanodomain structure of Pb* $[Zr_{1-x}Ti_x]O_3$ *at its morphotropic phase boundary: investigations from local to average structure. Phys. Rev. B*, **75**, 184117.

Sears, V. F. (1992). *Neutron scattering lengths and cross sections. Neutron News*, **3**, 26–37.

Senyshyn, A., Dolotko, O., Mühlbauer, M. J., Nikolowski, K., Fuess, H. & Ehrenberg, H. (2013). *Lithium intercalation into graphitic carbons revisited: experimental evidence for twisted bilayer behavior. J. Electrochem. Soc.* **160**, A3198–A3205.

Senyshyn, A., Mühlbauer, M. J., Dolotko, O., Hofmann, M. & Ehrenberg, H. (2015). *Homogeneity of lithium distribution in cylinder-type Li-ion batteries. Sci. Rep.* **5**, 18380.

Senyshyn, A., Mühlbauer, M. J., Nikolowski, K., Pirling, T. & Ehrenberg, H. (2012). *'In-operando' neutron scattering studies on Li-ion batteries. J. Power Sources*, **203**, 126–129.

Shirane, G. (1959). *A note on the magnetic intensities of powder neutron diffraction. Acta Cryst.* **12**, 282–285.

Stefanescu, I., Christensen, M., Fenske, J., Hall-Wilton, R., Henry, P. F., Kirstein, O., Müller, M., Nowak, G., Pooley, D., Raspino, D., Rhodes, N., Šaroun, J., Schefer, J., Schooneveld, E., Sykora, J. & Schweika, W. (2017). *Neutron detectors for the ESS diffractometers. J. Instrum.* **12**, P01019.

Studer, A. J., Hagen, M. E. & Noakes, T. J. (2006). *Wombat: the high-intensity powder diffractometer at the OPAL reactor. Physica B*, **385–386**, 1013–1015.

Suard, E. & Hewat, A. (2001). *The super-D2B project at the ILL. Neutron News*, **12**, 30–33.

Toraya, H., Hibino, H. & Ohsumi, K. (1996). *A new powder diffractometer for synchrotron radiation with a multiple-detector system. J. Synchrotron Rad.* **3**, 75–83.

Weirich, T. E., Lábár, J. L. & Zuo, X. (2006). Editors. *Electron Crystallography. Nato Science Series, Series II: Mathematics, Physics and Chemistry*, Vol. 211. Heidelberg: Springer-Verlag.

Whittingham, M. S. (1976). *Electrical energy storage and intercalation chemistry. Science*, **192**, 1126–1127.

Wilson, N. R., Petrenko, O. A. & Chapon, L. C. (2007). *Magnetic phases in the kagomé staircase compound studied using powder neutron diffraction. Phys. Rev. B*, **75**, 094432.

Yoo, C.-S., Wei, H., Chen, J.-Y., Shen, G., Chow, P. & Xiao, Y. (2011). *Time- and angle-resolved X-ray diffraction to probe structural and chemical evolution during Al-Ni intermetallic reactions. Rev. Sci. Instrum.* **82**, 113901.

Yusuf, S. M., Jain, A. & Keller, L. (2013). *Field induced incommensurate-to-commensurate magnetic phase transition in* $Ca_3Co_{1.8}Fe_{0.2}O_6$*: a neutron diffraction study. J. Phys. Condens. Matter*, **25**, 146001.

Zhang, S. T., Kounga, A. B., Aulbach, E., Ehrenberg, H. & Rödel, J. (2007). *Giant strain in lead-free piezoceramics* $Bi_{0.5}Na_{0.5}TiO_3$–$BaTiO_3$–$K_{0.5}Na_{0.5}NbO_3$ *system. Appl. Phys. Lett.* **91**, 112906.

International Tables for Crystallography (2019). Vol. H, Chapter 2.9, pp. 189–199.

2.9. Cells for *in situ* powder-diffraction investigation of chemical reactions

W. van Beek and P. Pattison

2.9.1. Introduction

In a time-resolved powder-diffraction experiment performed *in situ* (sometimes also called non-ambient diffraction), the aim is to follow the behaviour of a sample as a function of one or more external stimuli. The use of this technique can be roughly divided into two fields: academic research and industrial applications. In academic research, the goal is generally to understand the structure–property relationship of the studied material and then to use this understanding in order to improve the design of materials, pharmaceutical products, synthesis routes, reaction conditions *etc.* In the industrial world, one typically wants to learn whether a particular phase, phase mixture or polymorph arrives at a certain time in a production process. Reaction cells that are well suited to industrial applications may well be inadequate for academic research and *vice versa*. Owing to the huge variety of applications, it is impossible to come up with a generic cell design. In this chapter, we show what information content is accessible for a given combination of X-ray or neutron source and *in situ* cell through various case studies. The enabling technology that has driven these recent developments will be outlined in the next section, followed by an overview of the different types of reaction cells in use at home laboratories and at synchrotron and neutron facilities. Finally, we indicate some areas in which new developments can be expected.

2.9.2. Historical perspective

Within a decade of the discovery of the Bragg law, Westgren & Lindh (1921) had already observed several different polymorphs of iron as a function of temperature using powder diffraction. We have recently celebrated the centenary of the founding of X-ray crystallography, and during this time the use of *in situ* powder diffraction has become immensely popular. Although most of the pioneering powder-diffraction experiments were performed with X-ray tubes and scanning point detectors or with neutrons and an array of detectors, the real breakthrough came with the advent of synchrotron sources, providing high-energy penetrating X-rays, in combination with area detectors. This combination of source and detector type allowed diffraction experiments to be performed with both good angular and time resolution, thus opening up many new applications in chemical, physical, material and biological sciences. The topic of *in situ* cells for chemical reactions is therefore an enormous field and we cannot claim to provide an exhaustive list of instruments. We rather intend to point out the major cell designs, and to provide the reader with an overview to allow them to select the appropriate device for their application and available diffraction apparatus. We have tried to select where possible *in situ* case studies that use the full power of crystallography by solving structures and/or performing Rietveld refinements. A large number of review articles and book chapters written by some of the pioneers in this field have appeared during the last two decades with some overlap but slightly different emphasis. Walton & O'Hare (2000) describe many aspects of the crystallization of inorganic solids. Norby (2006) looks at zeolite synthesis, including an excellent commented reference list. Evans & Radosavljelić Evans (2004) focus on what can be performed with conventional equipment available in many university departments. Majuste *et al.* (2013) illustrate reactions relevant to hydrometallurgy studied with *in situ* synchrotron X-ray diffraction (XRD). Parise *et al.* (2000) also concentrate on synchrotron-based examples, and already foresee the abundance of data coming from modern third-generation powder-diffraction beamlines. Automated analysis tools are still underdeveloped, and we will comment on possible future developments in this area. Norby & Schwarz (2008) discuss powder diffraction under non-ambient conditions using X-ray sources, cells and diamond-anvil cell work. *In situ* gas–solid reactions are discussed by Møller *et al.* (2014), and Sharma *et al.* (2015) review the rapidly growing field of crystallographic–electrochemical investigations for both X-rays and neutrons. References to review articles for neutrons are given below (see Section 2.9.3.4).

2.9.3. Main types of reaction cells

2.9.3.1. *Introduction*

Powder-diffraction experiments can be performed either in transmission or reflection geometries. The diffraction signals can be collected in angular- or energy-dispersive mode with parallel or focused X-ray or neutron beams. Dedicated reaction cells have been developed for all possible permutations of the above variables. Each setup has its own trade-off in terms of time, angular and crystallographic resolution, and intrinsic limitations in data quality. In the last two decades, enormous progress has been made in instrumentation for diffraction experiments. A good example is the development of X-ray detectors where, as a direct consequence of the use of linear or area detectors, a time resolution of seconds or even shorter is now feasible in angular-dispersive mode. These and many other developments, such as more intense laboratory X-ray sources, have redefined the ways in which one can best perform *in situ* experiments. Energy-dispersive systems have lost some of their early advantages with respect to angular-dispersive geometries; nevertheless, there are still good grounds for selecting the energy-dispersive technique for some applications. Similarly, reflection-geometry flat-plate reactors have lost a lot of their early popularity because of well known problems with the diffraction geometry during heating. On the other hand, flat-plate strip heaters can reach thermal ramp rates that are hard to obtain otherwise. Flat-plate reflection-geometry reactors remain the main workhorses in academic and industrial home laboratories (mainly because of the good diffraction intensities which they provide) and several commercial vendors sell these units. Commercial and home-laboratory-developed cells, such as that from Moury *et al.* (2015) for high-pressure hydrogenation experiments, often provide the basis for further studies at central facilities. In this chapter, we intend rather to focus on new types of cells and their use with modern linear and area detectors, also indicating the level of information that can obtained. Microreactors in the form of capillary cells are popular for many different kinds of *in situ* diffraction experiments, and we therefore will review their use in some detail.

Copyright © 2019 International Union of Crystallography

2.9.3.2. *Capillary cells*

Capillary cells, also called microreactors, exist in many variations. Depending on the application (temperature, pressure and chemical environment), capillaries may be made of polyimide, glass, quartz, single-crystal sapphire or steel. They are simple and extremely efficient devices which can accommodate a large number of different applications. The impetus for their development has mainly come from catalysis research, but they have also been successfully employed to perform *in situ* reactions on intercalation, ion exchange, gas sorption/desorption, cement hardening, hydration–dehydration, light-induced transitions, crystallization processes and polymorphism, to name a few. Capillary cells are almost always used together with temperature- and/or gas-handling (static pressure or flow) devices. In open geometry, or with simple heat shields, one can easily obtain temperatures ranging from 80 to 1000 K with cryogenic and hot-air blowers or resistive heaters close to the sample. Static gas pressures can be as high as 30 MPa and in flow cells 2 MPa is commonly reached, as well as vacuum conditions. Capillary cells were first applied by Clausen (1991) and have been adapted numerous times (Brunelli & Fitch, 2003; Chupas *et al.*, 2008; Jensen *et al.*, 2010; Madsen *et al.*, 2005; Norby *et al.*, 1998, 2000; Palancher *et al.*, 2005) together with gas-handling systems (Eu *et al.*, 2009; Hill, 2013; Krogh Andersen *et al.*, 1998; Llewellyn *et al.*, 2009), with large 6 mm-diameter samples (Andrieux *et al.*, 2014), with supercritical solvents up to 40 MPa with a swing-in blower for rapid heating (Becker *et al.*, 2010) or with pulsed supercritical flows (Mi *et al.*, 2014) for following synthesis reactions. A recent review of several capillary cells for high-pressure reactions (Hansen *et al.*, 2015) also contains useful information on how to calculate burst pressures.

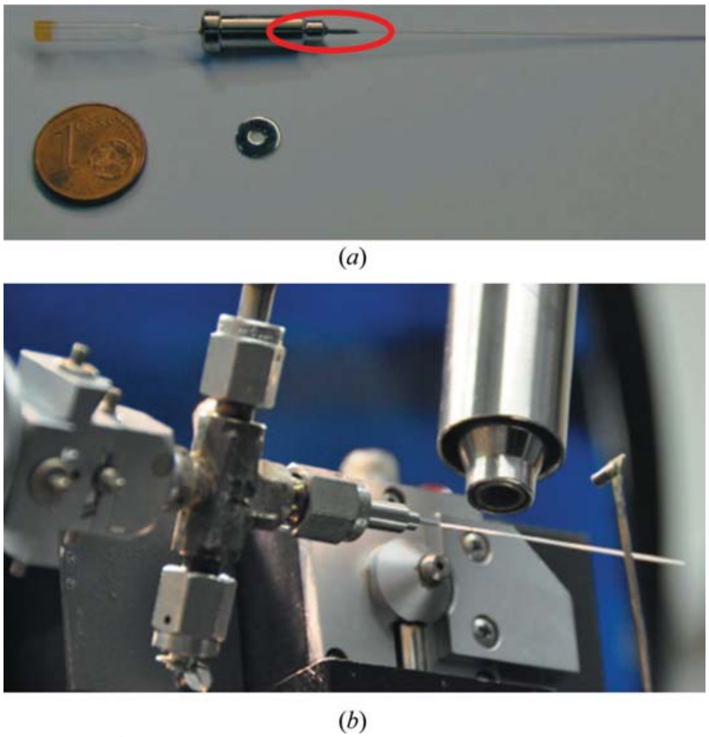
(*a*)

(*b*)

Figure 2.9.1
(*a*) Swagelock VCR gland with an epoxy-glued capillary (red ellipse). (*b*) VCR capillary cell on a beamline with a cryostream (adapted from Jensen *et al.*, 2010).

One of the most critical issues is how to create a reliable leak-tight connection between the capillary and the metallic or polyether ether ketone (PEEK) gas/liquid supply line(s). For fragile capillaries there are basically two strategies: either to glue the capillary to a metal support with high-temperature epoxy (see Fig. 2.9.1), or to use ferules. When both ends of a capillary have to be tightened with thin-walled capillaries, the use of ferrules needs some skill (see Fig. 2.9.2).

If the working temperature permits, it is easy and reliable to use a stainless-steel bracket in which capillaries are glued such that all mechanical forces are transferred to the support instead of being taken up by the thin (glass) capillaries (van Beek *et al.*, 2011), as in Fig. 2.9.3. Gas systems are typically constructed from a combination of pressure reducers, mass-flow meters, valves and a manifold which supplies gases to the cell at controlled pressures and flow rates. It is worth pointing out the less-common back-pressure regulator used in Fig. 2.9.3. This unit allows 2 MPa of pressure to be maintained on the sample during flow experiments. Backpressure regulators for much higher pressures are commercially available, but these have so far not been used for *in situ* work. *In situ* diffraction has been coupled with stable-isotope analysis to correlate isotope fractionation with crystal structure. For this, a nonmetallic flowthrough capillary cell that avoids any contamination from the components of the cell itself was designed (Wall *et al.*, 2011). Many hundreds of studies have been performed over the last two decades with capillary devices in the above-mentioned fields.

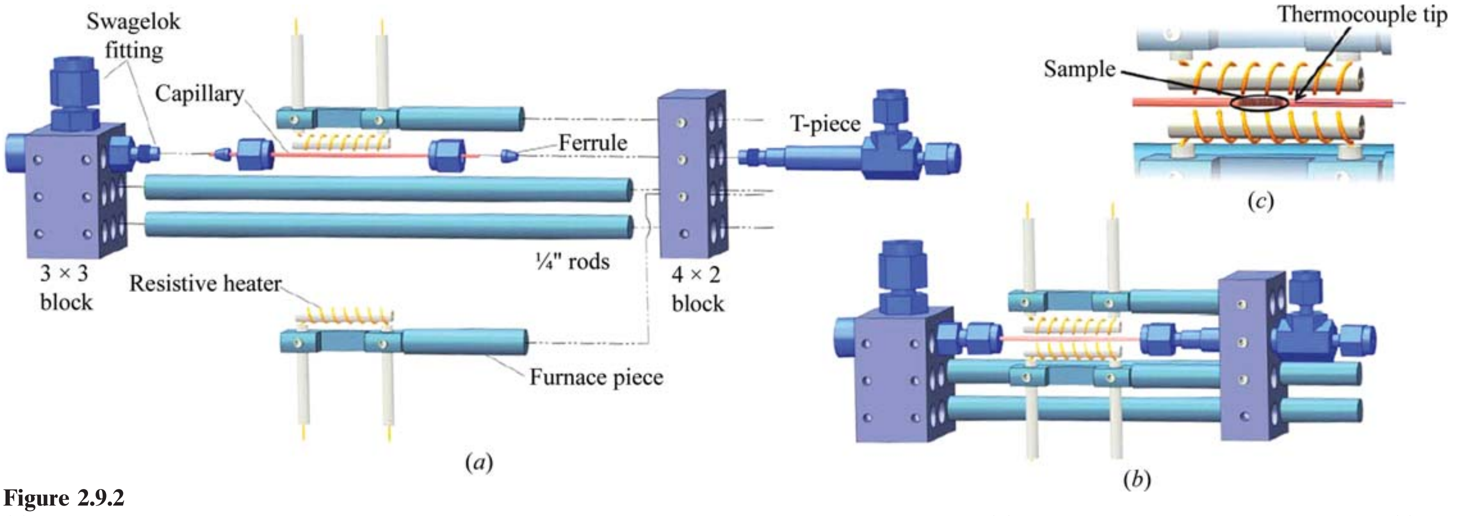

Figure 2.9.2
(*a*) An exploded representation of the flow-cell/furnace components, indicating how they fit together. (*b*) The fully assembled flow cell/furnace. (*c*) An expanded view of the sample region, indicating the relative position of the sample and thermocouple tip within the furnace hot zone (adapted from Chupas *et al.*, 2008).

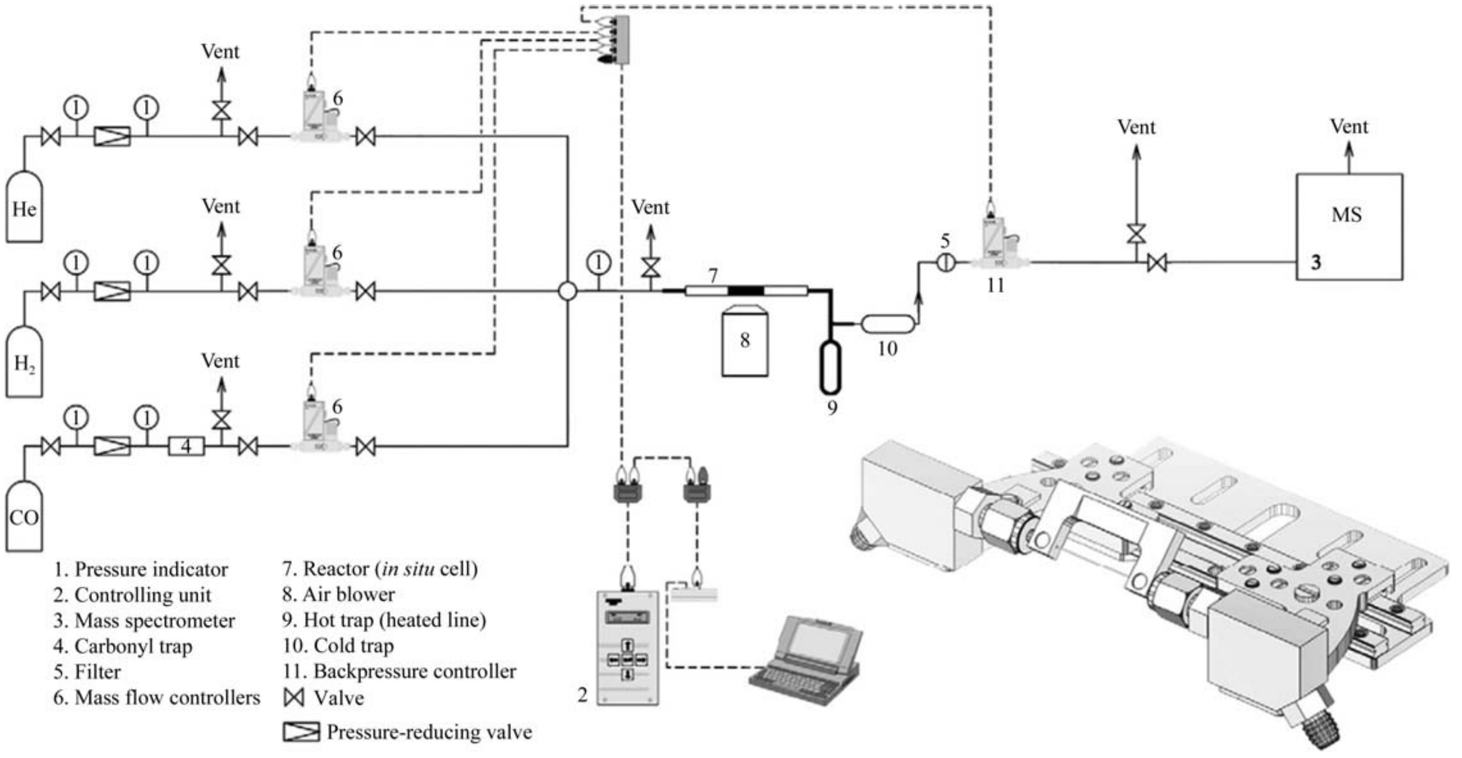

Figure 2.9.3
Sketch of a typical experimental setup and a three-dimensional drawing of the *in situ* flow cell. Note the strain-relief bracket over the capillary. Adapted from Tsakoumis *et al.* (2012), with permission from Elsevier.

Above 800 K, open capillary systems have severe heat loss and the use of insulation or reflectors around the sample or mirror furnaces is more appropriate. See Lorenz *et al.* (1993), Margulies *et al.* (1999), Proffen *et al.* (1995), Riello *et al.* (2013) and Yashima & Tanaka (2004) for special designs to minimize heat loss. Finally, it is worth mentioning the recent work of Figueroa *et al.* (2013), which combines the strong points of the various capillary designs, and also work by Johnsen & Norby (2013), who managed to create and study a working battery in a capillary.

In any powder-diffraction experiment (Warren, 1990), but particularly when using capillary cells, the experimentalist needs to take special care in order to obtain sufficient averaging in terms of grain statistics and to avoid preferred orientation. Typically *ex situ* capillaries are spun, but when gas lines are attached to the sample, spinning is not possible and only rocking or stationary geometry can be used. In addition, a fine (ground) polycrystalline powder giving perfect homogenous Debye–Scherrer rings, even without spinning, often results in an excessive pressure drop due to its high density and packing. In such cases, the sample may need to be pressed into a pellet and then crushed again to obtain larger agglomerates that allow sufficient gas flow through the sample (Jacques *et al.*, 2009). However, relatively large agglomerates, while reducing the packing density, might still give nonhomogeneous powder rings, which affects the intensities, especially on one-dimensional detector systems (strip detectors or crystal-analyser high-resolution systems). For all of these reasons it is not always straightforward to acquire reliable intensities under *in situ* conditions. If, however, proper care is taken, then precise structural parameters can indeed be refined from *in situ* data. For example, Milanesio *et al.* (2003) obtained a detailed view of the structural rearrangements induced by the template-burning process from 350 to 1000 K on a zeolitic MFI framework. Oxygen flowed through a rocking sample and diffraction data were collected on a translating two-dimensional image plate capable of verifying the reliability of the measured

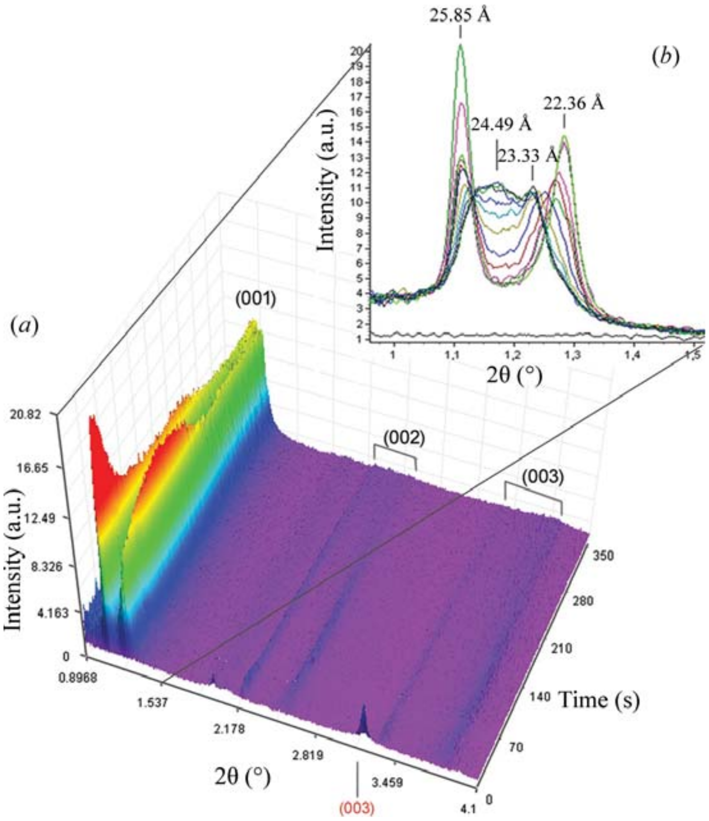

Figure 2.9.4
(*a*) *In situ* three-dimensional stacked plot of the intercalation of ibuprofen into an LDH. Miller indices are shown in black for the intercalation product peaks and in red for the LDH nitrate starting material peaks. (*b*) Two-dimensional patterns showing the low-angle peaks during the first instance of the reaction. Adapted with permission from Conterosito *et al.* (2013). Copyright (2013) American Chemical Society.

intensities with a time resolution of several minutes (Meneghini *et al.*, 2001). From the temperature-dependent *in situ* data, the authors were able to extract the overall template occupancy in the framework. This allowed a definition of the key steps in the template-removal process, namely the start of the template decomposition, the start of the template burning and the end of the template burning. These three steps were then used to explain the cell-parameter evolution and atomic displacement parameters of the Si-framework atoms. Kinetic analysis performed on the results from the Rietveld refinements suggested a diffusion-limited reaction of the volatile products of the template leaving the framework (Milanesio *et al.*, 2003).

Conterosito *et al.* (2013) reduced the time resolution to 100 ms per image using a Pilatus 300 K-W (Kraft *et al.*, 2009) pixel detector installed on an ESRF bending-magnet beamline in combination with a capillary reactor. In these experiments, a mechano-chemical method for fast and clean preparation of exchanged layered double hydroxides (LDHs) was investigated. The inorganic anion in the interlayer region (chloride or nitrate) was exchanged with a series of organic pharmaceutically important molecules. In Fig. 2.9.4, one can see the diffraction patterns of the intercalation process of ibuprofen into an LDH, which allowed the complex mechanism to be understood. Firstly, it is striking to note that the signal from the LDH starting material (the 003 reflection, in red) decreases, while the products and intermediates (001 reflections in black) grow already immediately after the first 100 ms image. Secondly, one can see that the low-angle peaks (<1.5°) show a different behaviour in time, suggesting a two-stage process with an intermediate phase and, thirdly, one sees that the intercalation process is over in ∼4 min. The reliability of the *in situ* procedure was confirmed by comparing the production yield of *ex situ* and *in situ* experiments. Owing to the complex two-stage process, kinetic analysis was not possible in the case of ibuprofen. In the same article, however, it was shown that it was possible to perform a full kinetic analysis on single-stage intercalation processes with different molecules reacting at comparable speeds. It is hard to imagine that so much detail on such timescales could be obtained using other techniques. For example, related intercalation experiments performed with energy-dispersive diffraction (Williams *et al.*, 2009) were, at that time, still limited to 10 s per pattern. Hence it was not possible to study the kinetics of such fast intercalation processes by other means.

Care must be taken to ensure that, when performing experiments at microgram or microlitre levels inside capillaries, the results are still representative of the bulk reaction. Therefore, when studying *in situ* catalytic reactions, it has become common practice to measure the activity or selectivity of the sample with gas chromotography or mass spectrometry (see Fig. 2.9.3) at the same time. It is also well known from reactor engineering that pressured drops, diffusion effects and flow disturbance are important parameters to take into account (Nauman, 2008). The term *operando* was introduced by Bañares (2005) during a discussion with colleagues (Weckhuysen, 2002) for these combined experiments coupling structure with the sample activity.

If the miniaturization turns out to be problematic, one could consider measuring bulky (∼1 cm or more) samples and/or using larger reaction vessels in combination with either energy-dispersive diffraction or extremely high X-ray energies (Tschentscher & Suortti, 1998). This gives the additional advantage that identical sample volumes to those for neutron studies can be used. Hence, one often needs to utilize reaction cells that are specifically designed for the application, as explained in the following section.

2.9.3.3. *Reactions requiring specialist cells*

2.9.3.3.1. *Cells for electrochemistry*

With ever-increasing standards of living, the world is becoming more and more dependent on energy. As natural resources (coal, gas and petrol) are limited, there has been a large impetus towards developing alternative ways of producing and storing energy, while also taking into account environmental issues. Despite many decades of research and tremendous progress in

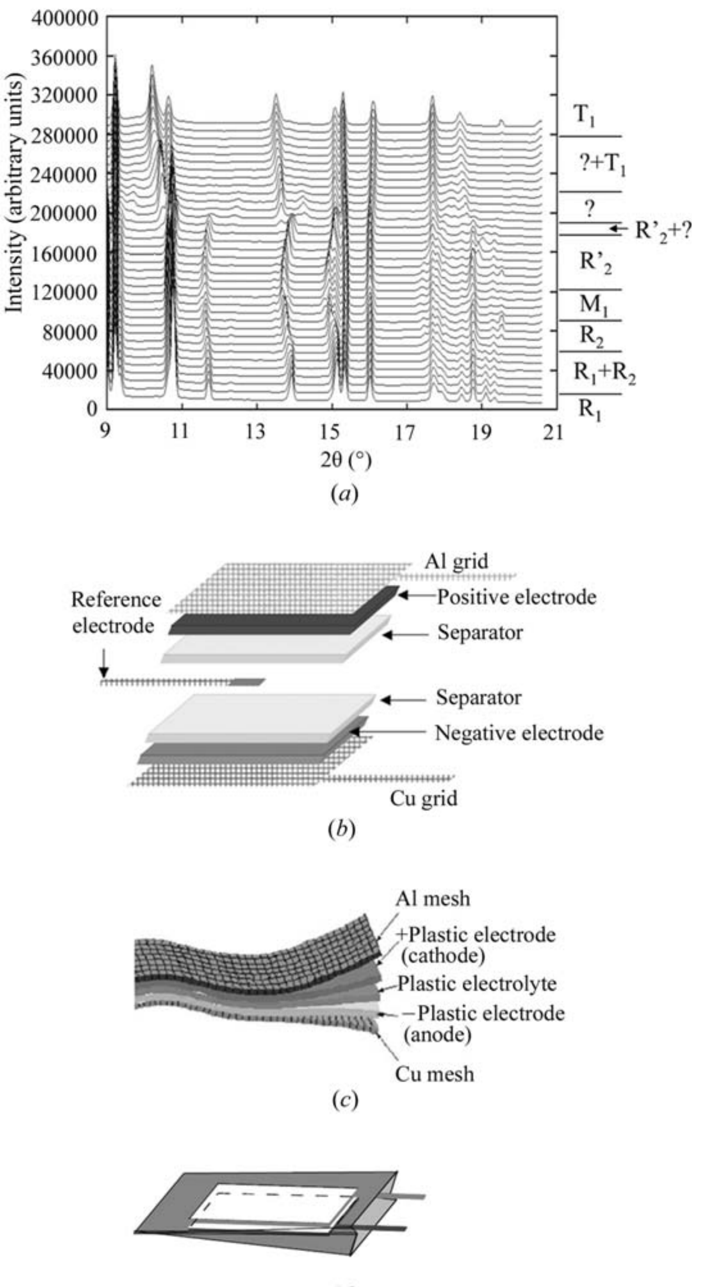

Figure 2.9.5

(*a*) *In situ* synchrotron diffraction patterns (selected region) of an $LiCoO_2$/Li cell collected during cell charging. Below: overview of a Bellcore flat three-electrode plastic Li-ion cell (*b*) with an enlargement (*c*) of the assembly steps during which all the separated laminates are brought together by a thermal fusion process *via* a laminator. The thicknesses of the plastic Li-ion cells assembled for *in situ* X-ray experiments were about 0.4/0.5 mm. A derived version of the Bellcore plastic Li-ion battery with a beryllium window thermally glued to the packing envelope on one side is shown in (*d*). Adapted from Morcrette *et al.* (2002) with permission from Elsevier.

this field, *in situ* diffraction was only adapted for electrochemical research in the 1990s. Nevertheless, this field now has the largest variety of cells. It is impossible to give a comprehensive overview of this complex subject here, and therefore the reader is referred to the articles by Brant *et al.* (2013), De Marco & Veder (2010) and Morcrette *et al.* (2002), which describe how to design and reference most existing miniaturized *in situ* cells. The recent work by Johnsen & Norby (2013), who have developed a capillary-based micro-battery cell, is not included in these reviews. The main advantage of this cell is that it allows diffraction data to be obtained from a single electrode. The recent work on electrochemical cells using conventional diffractometers (Shen *et al.*, 2014) and high-throughput cells for synchrotron applications (Herklotz *et al.*, 2013, 2016) is also relevant. When planning experiments on central facilities, not only appropriate cells but also dedicated ancillary equipment (*e.g.* a glove box) for cell loading owing to air sensitivity of the electrode material (*e.g.* lithium) are essential. In centralized facilities, this may lead to conflicts due to the incompatibility of liquid electrolytes with samples from other users, and dedicated electrochemistry glove boxes have started to appear. As an example of the use of an electrochemical cell, Morcrette *et al.* (2002) managed to perform structural Rietveld refinement during delithiation of an $LiCoO_2$ electrode. In order to obtain reliable intensities, five diffraction images at six different positions in the cell were averaged for each point in the charge cycle. Owing to the amount and quality of the data, six different structural phases could be determined, including lattice parameters, space group, atomic positions and *R* factors (see Fig. 2.9.5). As the potentiostat or galvanostat is driving and measuring the performance of the battery, the structure–activity relationship is obtained automatically. This is a similar concept to the *operando* methodology in catalysis research that uses a mass spectrometer to measure activity.

In analogy with microcapillary cells, miniaturized electrochemistry cells are extremely efficient for studying many aspects of an operational battery despite the fact that a fundamental understanding of electrochemical systems is inherently challenging. All the components of a cell influence each other at the interfaces during the cyclic charge-transfer process. It is also crucial to be able to establish the critical factors that determine the lifetime of the battery. To make efficient use of beamtime, it is common practice to construct many cells within one frame, all operating in parallel. The whole batch of cells is then mounted on translation stages on a diffractometer and measurements are taken periodically. However, miniature cells will never provide a complete picture, and there will always be a need to study large prototype or production cells (Rijssenbeek *et al.*, 2011) of the types discussed in Sections 2.9.3.3.3 and 2.9.3.4.3.

2.9.3.3.2. *Cells with humidity control*

Humidity is a relevant parameter in many areas of research. For instance, the interlayer spacing in clays, corrosion, pharmaceutical processes, cement hardening, phase transitions in minerals or proton conductors and crystal growth of salts are all dependent on relative humidity, often in combination with high temperatures.

Most work so far has been carried out in home laboratories with flat-plate commercial chambers connected to a manifold with a gas mass-flow controller and liquid mass-flow controllers, thus providing an air flow with controlled humidity (Chipera *et al.*, 1997; Kühnel & van der Gaast, 1993; Watanabe & Sato, 1988). In addition, capillary cells have also successfully been used (Walspurger *et al.*, 2010) on synchrotrons. It is imperative to have very good thermal stability and to avoid temperature gradients throughout the system. The dew point of water is strongly affected by temperature, and unwanted condensation of water can easily occur on colder parts of the system. Fig. 2.9.6 shows a schematic of a humidity-control system developed by Linnow *et al.* (2006). The thermal management in this design has been optimized to avoid condensation.

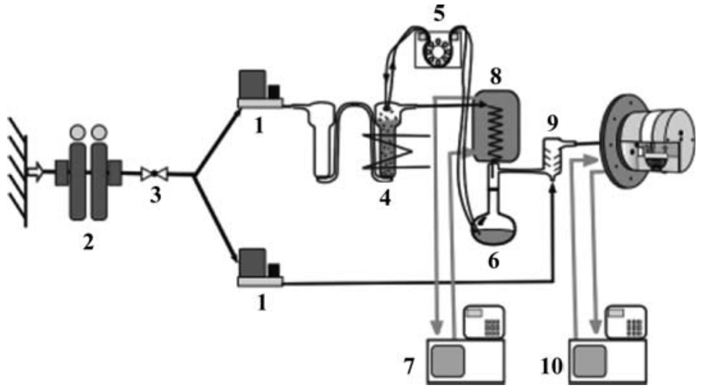

Figure 2.9.6
Schematic drawing of the humidity-control system: (1) mass-flow controller, (2) adsorption dryer, (3) pressure regulator, (4) heated bubbler, (5) peristaltic pump, (6) water reservoir, (7) thermostat, (8) condensation trap, (9) mixing chamber and (10) thermostat. Adapted with permission from Linnow *et al.* (2006). Copyright (2006) American Chemical Society.

Linnow *et al.* (2006) and Steiger *et al.* (2008) have used the system in Fig. 2.9.6 to investigate the crystal growth of various salts, which is considered to be the cause of many failures in building materials (stone, brick, concrete). In order to do so, they scanned through the relative humidity (RH) *versus* temperature phase diagrams of these salts in various porous materials used in the building industry. Diffraction experiments revealed differences in reaction pathways and stress in both host and guest materials.

The NASA Phoenix Mars Lander has discovered perchlorate anions on Mars. This is important, since they could possibly be used as indicators for hydrological cycles. Robertson & Bish (2010) studied a magnesium perchlorate hydrate system, $Mg(ClO_4)_2{\cdot}nH_2O$, with the aim of solving the various unknown crystal structures as a function of water content *n*. Fig. 2.9.7 shows *in situ* diffraction data collected during dehydration in a

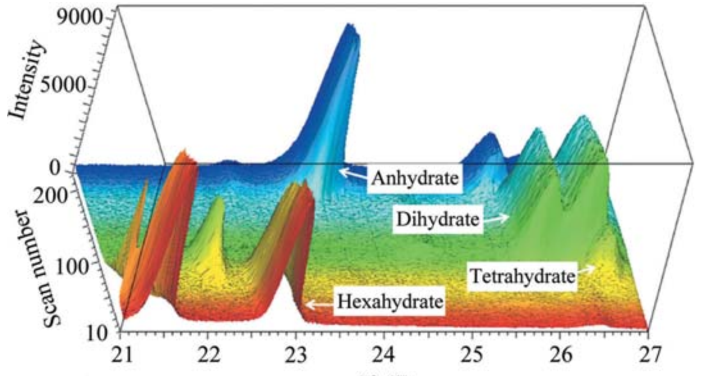

Figure 2.9.7
Sequence of XRD measurements between 21 and 27° 2θ. On heating at a rate of 2° min^{-1} at <1% RH, sequential dehydration was observed, with the anhydrate observed at the highest temperature. The vertical axis represents intensity. The ‘time’ (scan number) axis represents temperature from 298 to 498 K in 2° min^{-1} increments. Adapted from Robertson & Bish (2010).

commercial Anton Paar flat-plate heating stage connected to an automated RH control system similar to that shown in Fig. 2.9.6. The rapidly collected *in situ* data (30 s per scan, with a position-sensitive detector) were crucial to define at what temperatures longer data collections had to be taken in order to acquire single-phase, high-quality powder patterns suitable for crystal structure solution. Robertson & Bish (2010) managed to index and solve the dihydrate and tetrahydrate phases by charge flipping. Although the tetrahydrate structure was later revised by Solovyov (2012) using the exact same data, this example clearly indicates the level of complexity that can be studied in local laboratories under *in situ* conditions. In this case, this task included understanding the dehydration pathway, solving the structure of $Cl_2H_4MgO_{10}$ with two molecules in the unit cell and refining anisotropic displacement parameters using Rietveld refinement.

2.9.3.3.3. *Large-volume cells for energy-dispersive diffraction*

Large-volume cells have been used to date with great success almost exclusively with energy-dispersive diffraction (EDXRD). Early work on this was carried out by Munn *et al.* (1992) and He *et al.* (1992) using the synchrotron source at Daresbury Laboratory. Walton & O'Hare (2000), who continued the pioneering work, provide a good historical overview of the kinds of studies that can be performed. Norby (2006) also provides excellent references to and explanations of work in this field. In brief, the main advantages of EDXRD are that the X-ray high energies (*i.e.* 50–120 keV) present in the beam can penetrate and probe into large vessels. Furthermore, only minor modifications to create small entrance and exit windows on commercial autoclaves, which are standard equipment in many laboratories, are necessary in order to turn them into extreme-condition *in situ* reaction vessels. An additional advantage arises from the fact that there is no bias due to volume differences between the laboratory experiments and *in situ* reactions studied at the synchrotron (see Fig. 2.9.8).

The variety of scientific applications is huge: pressure-induced phase transitions of inorganic solids, hydrothermal synthesis of microporous solids, intercalation, growth of layered perovskites and breathing in metal-organic frameworks, to name a few examples (see Walton & O'Hare, 2000). Extreme conditions can be reached in terms of temperature (~1273 K) in an autoclave with subsecond XRD time resolution. EDXRD in combination with large-volume autoclaves has provided otherwise-inaccessible information on many processes: intermediates in crystallization routes, activation energies for reactions, and kinetic parameters crucial for their understanding and optimization. The major disadvantage of EDXRD is that the resolution in the diffraction pattern is limited, since it is defined by the energy resolution of the solid-state detector. This effectively excludes all access to precise structural information. However, recent efforts have allowed quantitative phase analysis (Rowles, 2011; Rowles *et al.*, 2012). With the advent of third-generation synchrotrons, which provide orders of magnitude more flux at high energies, and the availability of high-energy flat-panel detectors, angular-dispersive diffraction data can successfully be collected from samples in large-volume cells. Their use expands the available information dramatically. To date, however, there are very few high-energy angular-dispersive beamlines, and the use of the large-volume cells in combination with EDXRD remains an active field and has recently been developed further by, for example, Moorhouse *et al.* (2012) at the Diamond Light Source. The cell there can be equipped with various reaction vessels made of alumina, steel, PTFE-lined steel or glassy carbon tubes depending on the chemical reaction to be studied. It can achieve temperatures as high as 1473 K with infrared lamps and has a magnetic stirrer to avoid sedimentation of the reaction products. In addition, Styles *et al.* (2012) have developed a large furnace and *in situ* cell for salt electrolysis.

Rijssenbeek *et al.* (2011) have studied a full-size battery cell with EDXRD (see Fig. 2.9.9). Diffraction data were collected during charge/discharge at high temperature of the sodium metal halide (Na/$M$$Cl_2$, M = Ni and/or Fe) cells. They were able to assess the charge-state variations as a function of space and time in the cell during many charge/discharge cycles, and identify local crystal structures and phase distributions. The data confirm the propagation of a known well-defined chemical reaction front beginning at the ceramic separator and proceeding inward.

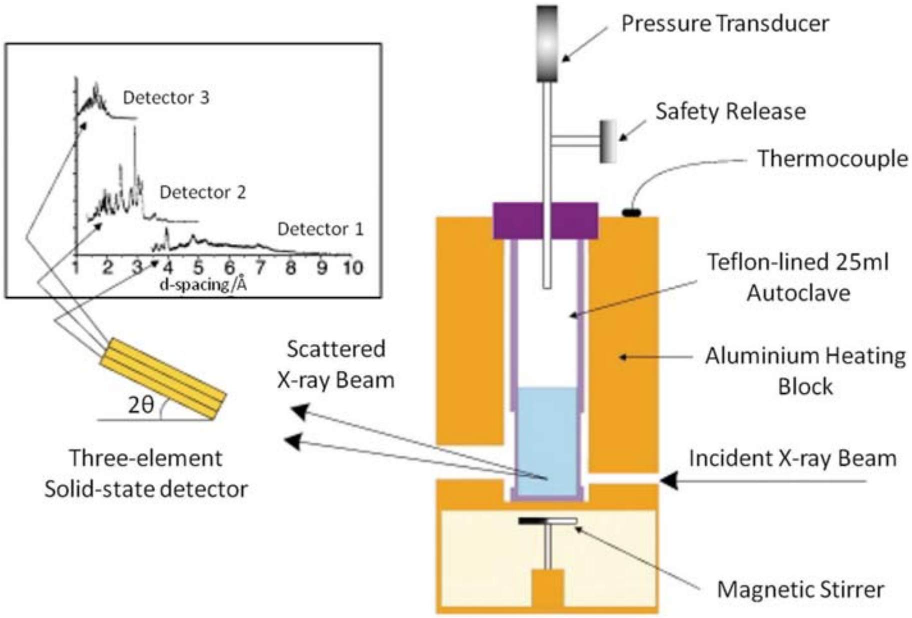

Figure 2.9.8
A schematic of the Oxford/Daresbury hydrothermal autoclave used for energy-dispersive X-ray diffraction studies. Adapted from Walton & O'Hare (2000) with permission of The Royal Society of Chemistry.

2.9.3.3.4. *Large-volume cells for angular-dispersive diffraction*

This application implies the use of monochromatic X-rays with extremely high energies (70 keV and above). Such energies can be easily reached on third-generation synchrotrons with in-vacuum undulators, thus providing sufficient flux for angular-dispersive diffraction experiments. The challenge with these experiments is to have a sufficiently high X-ray energy to penetrate large sample-cell vessels while maintaining reasonably good angular resolution in the diffraction pattern. When using large *in situ* cells with low-energy diffraction, there is a severe peak-broadening effect resulting in a deterioration of the data quality. At high energies, however, where the scattering angles are small, the sample thickness has little effect on the angular resolution provided that the area detector is positioned at a sufficient distance from the sample.

O'Brien *et al.* (2011) explain the trade-offs for such experiments in detail and have shown that it is possible to extract useful structural information. Large-volume cells that used to be exclusively the domain of neutron diffraction and EDXRD have now also been adapted for angular-dispersive powder diffraction with, in some cases, increased speed and information content. For instance, Wragg *et al.* (2012) studed an industrial methanol-to-olefin conversion process with *operando* time- and space-resolved diffraction. The sample is rapidly scanned up and down to provide one-dimensional spatial information. The results complement earlier experiments performed with a microreactor. Jacques *et al.* (2011) extracted three-dimensional information by using dynamic X-ray diffraction computed tomography (XRD-CT). They measured over 50 000 diffraction patterns on beamline ID15 at the ESRF with different sample orientations, positions and temperatures. From this huge amount of data, they reconstructed the catalyst body in three dimensions with a diffraction pattern assigned to each volume unit within the sample as a function of time. With this information, they were able to follow the evolution of the catalytically active phase throughout the sample. Wragg *et al.* (2015) have since performed Rietveld analysis on voxels from the XRD-CT data for a methanol-to-olefin reactor bed. It is also worth mentioning work by Jensen *et al.* (2007), performed on beamline 1-ID at APS Argonne National Laboratory, investigating the kinetics of nanoparticle formation involving a sol–gel reaction in supercritical CO_2 at 10 MPa. The reaction was studied with XRD and small-angle X-ray scattering (SAXS) in a large 30 ml vessel. In a different application, Friščić *et al.* (2013) mounted a laboratory-scale 10 ml ball mill on the ID15 beamline in order to study mechanochemical reactions, which are used in numerous industrial production processes. By averaging ten 400 ms frames, they obtained sufficiently good data to perform full-pattern refinements and kinetic analysis, providing information about otherwise completely inaccessible processes. We therefore foresee a bright future for such extreme high-energy applications together with large-volume studies, since they provide a useful bridge between the academic and industrial worlds.

2.9.3.4. *Cells specifically for neutrons*

2.9.3.4.1. *Introduction*

The special characteristics of neutrons imply both advantages and challenges for the design of *in situ* experiments and their associated equipment. The differences in penetration depths between X-rays and neutrons and the correspondingly smaller scattering cross sections for neutrons, together with the much lower flux densities, imply that cells for neutrons are quite different from the miniature capillary cells for X-rays described in the previous sections. Above all, the sample volume is by necessity often much larger than the equivalent volume required for a laboratory X-ray or synchrotron experiment. However, the ability of neutrons to penetrate deep into sample environments has been of great importance for studying samples at very low temperature, under high pressure or within strong magnetic fields. Similarly, reaction cells for *in situ* investigations profit from the ability of neutrons to penetrate through thick-walled vessels, for example for studying gas–solid reactions under high pressure. Only relatively recently, with the availability of high-energy synchrotron beamlines (>100 keV), can X-rays effectively compete with neutrons in this domain. Even in these cases, the very different scattering properties of neutrons (*e.g.* the strong variation of cross section with isotope) means that some measurements that are challenging, if not impossible, with X-rays can become quite feasible with neutrons. The solid–gas reaction of intermetallic phases with H_2 gas is a good example, where the positions of the interstitial H atoms can be located within a heavy-metal hydride (Kamazawa *et al.*, 2013). Similarly, the hydration of cement has been investigated many times, with improved time resolution resulting from developments in neutron optics and detector performance. *In situ* studies of oxidation reactions have also benefited from the better ability of

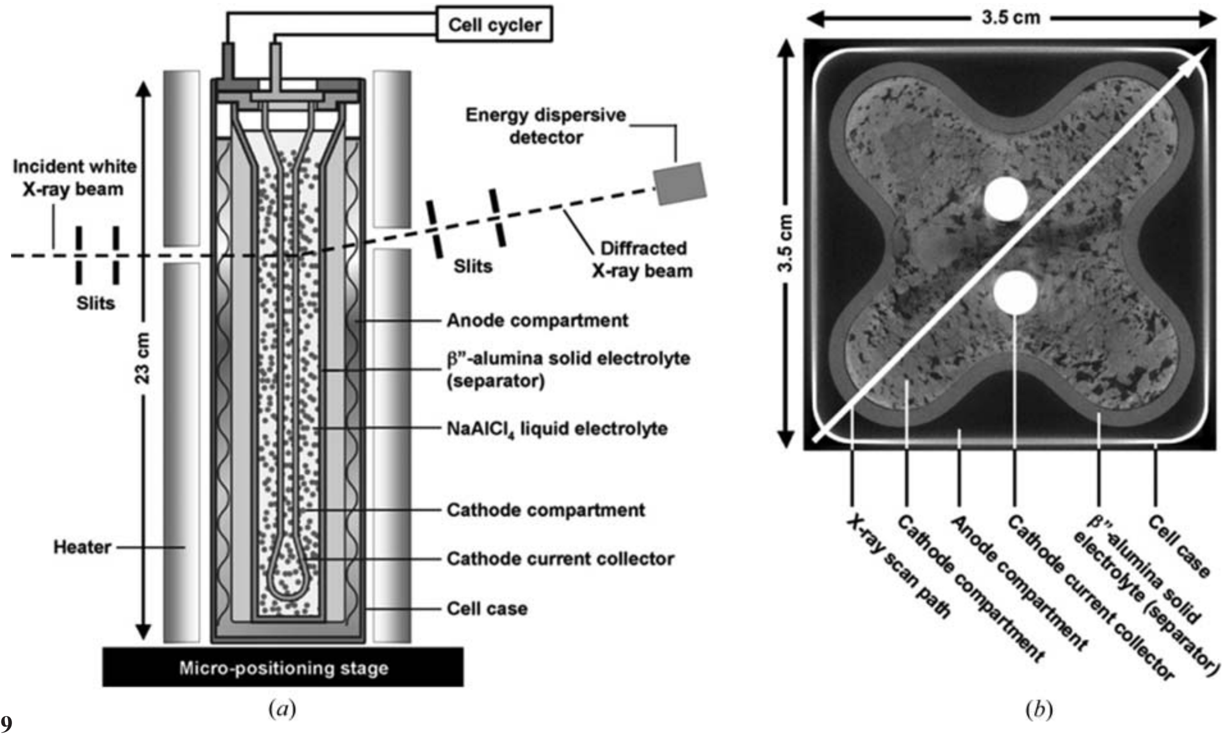
Cell cycler
Energy dispersive detector
Incident white X-ray beam
Slits
Slits
Diffracted X-ray beam
23 cm
Anode compartment
β"-alumina solid electrolyte (separator)
NaAlCl$_4$ liquid electrolyte
Cathode compartment
Cathode current collector
Cell case
Heater
Micro-positioning stage
3.5 cm
3.5 cm
X-ray scan path
Cathode compartment
Anode compartment
Cathode current collector
β"-alumina solid electrolyte (separator)
Cell case
(*a*)
(*b*)

Figure 2.9.9

(*a*) Schematic of a sodium-halide cell in an *in situ* synchrotron EDXRD experimental setup. (*b*) Cross-sectional computed tomography image of a cell. The arrow along the cell diagonal denotes the path of the X-ray line scans used in this work. This corresponds to an X-ray penetration depth of up to 50 mm. Adapted from Rijssenbeek *et al.* (2011) with permission from Elsevier.

neutrons to determine the atomic positions of oxygen during synthesis (Bianchini *et al.*, 2013). The investigation of chemical processes in the electrodes of batteries has, for example, been particularly fruitful. Once again, specialist cells for electrochemistry have been developed that take advantage of the penetration power of the neutrons in order to reveal bulk behaviour within the electrode material. Examples of these and other applications are given in an extensive review of *in situ* and time-resolved neutron scattering (Isnard, 2007) and in the more recent articles by Hansen & Kohlmann (2014), Sharma *et al.* (2015) and Pang & Peterson (2015). It should also be noted that different geometrical arrangements are used in angular-dispersive monochromatic neutron diffraction or when using a fixed-angle detector bank for time-of-flight neutron diffraction, which can have important implications for the cell design. In the following sections, we will examine some of these specialist cells in more detail.

2.9.3.4.2. *Solid–gas reactions*

Suitable storage media for hydrogen and other small molecules include hydrides, hydrates, clathrates and other microporous materials [*e.g.* metal-organic frameworks (MOFs)]. *In situ* neutron powder diffraction has been the method of choice to investigate solid–gas reactions involving light molecules reacting with these types of framework structures, and a wide variety of *in situ* cells have been developed for this purpose. The design of the cell can be quite primitive, yet still be very successful for this kind of application. As a simple example, we consider the study of the reduction of a perovskite-related oxide under flowing hydrogen carried out at D20 at the Institut Laue–Langevin (ILL) in Grenoble (Tonus *et al.*, 2009). The powder sample was loaded into a quartz tube (12 mm diameter) and mounted in the standard D20 furnace. The tube was connected to a flow of reducing gas controlled by a needle valve. High-quality data could be collected in a short time (a few minutes) at high temperature under flowing H_2 gas, in this case up to a maximum temperature of 973 K. Occupancy factors for the different oxygen sites could be refined as a function of temperature under reducing and oxidizing conditions.

In another example, the goal was to investigate solid–gas reactions under pressures of 16 MPa and temperatures up to 673 K (Widenmeyer *et al.*, 2013). Since the use of thin-walled single-crystal sapphire capillaries has become routine in synchrotron powder X-ray diffraction, the authors decided to adopt a similar strategy for the neutron-diffraction experiment. In this case, they selected a 6 mm diameter sapphire tube with steel end caps and metal seals. Pressures of 16 MPa could be achieved over periods of days without measurable pressure loss, and the powder data were of high quality, allowing Rietveld refinement of crystal structures including light-atom positions, displacement parameters and site occupancies. In addition to providing good-quality data and a low background, the sapphire tube also has the advantage of being chemically very robust and hence avoiding, for example, the problem of hydrogen embrittlement.

2.9.3.4.3. *Electrochemistry using neutron diffraction*

The advantages of high penetration and sensitivity to light elements such as hydrogen, oxygen and lithium make neutron powder diffraction an interesting tool for investigating processes occurring within complex electrochemical systems. Lithium-ion batteries are one of the most widely used portable energy sources. These devices rely on the insertion of lithium ions into both positive and negative electrodes. A proper understanding of the structural processes that occur at the electrodes can only be obtained from *in situ* diffraction experiments performed during electrochemical charging and discharging. A suitable electrochemical cell for this type of measurement has been reported by Rosciano *et al.* (2008). The challenge for the design of this type of cell is to enable the neutron-diffraction data to be collected with the minimum of hindrance, while allowing electrochemical characterization to be performed at the same time. In addition, the fact that most separators and polycarbonate-based electrolyte solutions contain large amounts of hydrogen presents problems due to the large incoherent neutron-scattering cross section of hydrogen, which results in a deterioration in the signal-to-background ratio. However, as pointed out by Sharma *et al.* (2011), designs have been developed that minimize the amount of electrolyte required, and, where possible, deuterated solution can be used. Using a home-made design of a rollover, cylindrical cell that mimicked the geometry of commercial batteries, Sharma *et al.* (2011) were able to probe structural changes in real time (5 min per pattern) as a function of electrochemical cycling using the Wombat powder diffractometer (ANSTO). Sharma *et al.* (2015) have since reviewed both synchrotron and neutron electrochemistry cells. Pang & Peterson (2015) provide an overview of all lithium-ion and sodium-ion battery materials studied by neutron powder diffraction *in situ* since 1998.

Battery materials and fuel cells are extensively used in a vast variety of applications in energy conversion and storage, and there is no doubt that *in situ* neutron powder diffraction will continue to play an important role in the efforts to further improve the performance of these materials. In Japan, for example, a new neutron-diffraction instrument (SPICA at the J-PARC spallation source) will be used to analyse atomic structures and the behaviour of batteries during their charge cycle. Both at spallation and reactor-based neutron sources, improvements in neutron optics and detector performance have reduced both the volume of sample needed for *in situ* experiments and the time required to collect each powder pattern.

2.9.3.4.4. *Hydrothermal reaction cells*

Many materials with potential applications in technologically important fields can only be prepared by the supercritical hydrothermal synthesis method. A detailed knowledge of the reaction mechanisms is lacking, mainly because the processes take place within sealed and thick-walled reaction vessels. A technique is required that can penetrate the walls of the vessel during the reaction, and can reveal the kinetics and mechanism of bulk sample synthesis. Neutron diffraction is the ideal tool for this task. For example, Ok *et al.* (2010) constructed a relatively simple chemical-reaction cell for investigating syntheses, even under extreme supercritical conditions, using of time-of-flight techniques. The cell itself was machined from a single ingot of Inconel, and had a maximum wall thickness of 4.0 mm. Thinner sections of 2.7 mm thickness were used in parts of the cell to reduce attenuation of the incident and scattered neutron beams. The vessel had a normal working pressure and temperature of 40 MPa at 723 K. The experiments were carried out on the POLARIS diffractometer at the ISIS pulsed spallation neutron source.

Another example of a hydrothermal reaction cell of somewhat different design is that used by Xia *et al.* (2010). In this case, a large sample volume was chosen (320 ml internal volume) to allow bulk properties to be investigated. The cell had a dumbbell configuration, assembled from commercial stainless-steel components, that held most of the hydrothermal liquid, and a zero-scattering Ti–Zr alloy sample compartment with a 0.4 mm wall thickness. This choice of material and wall thickness for the sample cell dramatically reduced the background scattering from the container, but limited the operational range to temperatures up to 573 K and pressures up to 9 MPa. The cell was commissioned at the Wombat neutron powder diffractometer at ANSTO, using the *in situ* kinetic study of the hydrothermal phase transformations from leucite ($KAlSi_2O_4$) to analcime ($NaAlSi_2O_6{\cdot}H_2O$) as a demonstration of the capabilities of the equipment.

2.9.4. Complementary methods and future developments

Standard crystallographic powder-diffraction methods can provide information about component phases and particle size, and can also be used to determine crystal structure, but the data quality required means that long-range crystalline order needs to be present. However, many real systems have amorphous components or demonstrate various degrees of disorder. In order to provide complementary information on the disordered components, alternative techniques are needed. In the early 1990s, Couves and co-workers started to combine XRD with XAFS in one setup in order to complement the XRD data (Couves *et al.*, 1991); they were quickly followed by Clausen and co-workers (Clausen *et al.*, 1993). Shortly afterwards, small-angle scattering (Dokter *et al.*, 1994) and vibrational spectroscopic techniques such as infrared and Raman were also added to complement the diffraction information (Newton & van Beek, 2010). More recently, a very old technique (Tarasov & Warren, 1936) based on the pair distribution function (PDF) has become immensely popular with the advent of high X-ray energies and efficient detectors (Chupas *et al.*, 2003). The PDF technique does not depend upon any assumptions about long-range crystalline order and can therefore be used to extract information on amorphous materials, defect structures and the structures of nanoparticles (see Chapter 5.7). It has the same huge variety of applications as traditional diffraction methods, and provides complementary information. Several of the *in situ* cells described above can also be used for combined techniques and PDF experiments at synchrotrons. One of the many reasons behind the rapid success of the PDF method is the availability of well developed software for data analysis (Juhás *et al.*, 2013) and modelling (Neder & Proffen, 2008).

We have seen in some of the examples above that acquisition times are reaching down into the millisecond range and the quantity of data being delivered by modern systems is becoming increasingly difficult to analyse. There is progress in automated sequential and parallel parametric refinements with traditional data-analysis software. However, we believe new strategies are necessary in order to make better, more efficient use of modern detectors. There are efforts in this direction in automated chemometric methods (Burley *et al.*, 2011) stemming from spectroscopy. However, these algorithms are not always well adapted to analyse data derived from powder-diffraction measurements. Chernyshov *et al.* (2011) have performed theoretical and experimental work taking the interference nature of diffraction into account in their method, which is based on modulation. Nevertheless, improvements in data analysis are still trailing far behind experimental progress and much effort will be necessary in this area. Choe *et al.* (2015) have even performed stroboscopic high-resolution powder diffraction on piezoelectric ceramics, detecting sub-millidegree shifts with microsecond time resolution.

In contrast to the pursuit of speed, the Diamond Light Source have decided to extend their powder-diffraction beamline and make it suitable for experiments lasting several months or even more, by moving slowly aging samples automatically into the measurement position at regular intervals (hours, days or even weeks) in a long-duration experiment (LDE) facility. Relevant applications are in batteries, fuel cells, crystallization, gas storage, mineral evolution, seasonal effects, thermal and electrical power cycling, and corrosion science.

In addition to the developments in instrumentation presented here, the availability of new radiation sources is opening up many interesting possibilities for studying chemical reactions. Not only are more, and better equipped, synchrotron beamlines becoming operational, but there are new facilities in planning or under construction that will dramatically change the way in which chemical processes can be investigated. New spallation sources and free-electron lasers (FELs) open up new possibilities in the time and space domains. In particular, FELs will facilitate the study of reactions on sub-picosecond timescales. Preliminary experiments using picosecond to nanosecond time resolution have already been carried out on synchrotron beamlines to investigate transient structural changes in organic powders (Techert *et al.*, 2001). It is evident that the huge increase in flux per pulse and the much shorter pulse length available from FELs will open up completely new dimensions in the field of *in situ* experiments.

References

Andrieux, J., Chabert, C., Mauro, A., Vitoux, H., Gorges, B., Buslaps, T. & Honkimäki, V. (2014). *A high-pressure and high-temperature gas-loading system for the study of conventional to real industrial sized samples in catalysed gas/solid and liquid/solid reactions. J. Appl. Cryst.* **47**, 245–255.

Bañares, M. A. (2005). *Operando methodology: combination of in situ spectroscopy and simultaneous activity measurements under catalytic reaction conditions. Catal. Today*, **100**, 71–77.

Becker, J., Bremholm, M., Tyrsted, C., Pauw, B., Jensen, K. M. Ø., Eltzholt, J., Christensen, M. & Iversen, B. B. (2010). *Experimental setup for in situ X-ray SAXS/WAXS/PDF studies of the formation and growth of nanoparticles in near- and supercritical fluids. J. Appl. Cryst.* **43**, 729–736.

Beek, W. van, Safonova, O. V., Wiker, G. & Emerich, H. (2011). *SNBL, a dedicated beamline for combined in situ X-ray diffraction, X-ray absorption and Raman scattering experiments. Phase Transit.* **84**, 726–732.

Bianchini, M., Leriche, J. B., Laborier, J.-L., Gendrin, L., Suard, E., Croguennec, L. & Masquelier, C. (2013). *A new null matrix electrochemical cell for Rietveld refinements of in-situ or operando neutron powder diffraction data. J. Electrochem. Soc.* **160**, A2176–A2183.

Brant, W. R., Schmid, S., Du, G., Gu, Q. & Sharma, N. (2013). *A simple electrochemical cell for in-situ fundamental structural analysis using synchrotron X-ray powder diffraction. J. Power Sources*, **244**, 109–114.

Brunelli, M. & Fitch, A. N. (2003). *A glass capillary cell for in situ powder X-ray diffraction of condensed volatile compounds. Solid HCFC-123a and HCFC-124. J. Synchrotron Rad.* **10**, 337–339.

Burley, J. C., O'Hare, D. & Williams, G. R. (2011). *The application of statistical methodology to the analysis of time-resolved X-ray diffraction data. Anal. Methods*, **3**, 814–821.

Chernyshov, D., van Beek, W., Emerich, H., Milanesio, M., Urakawa, A., Viterbo, D., Palin, L. & Caliandro, R. (2011). *Kinematic diffraction on a structure with periodically varying scattering function. Acta Cryst.* A**67**, 327–335.

Chipera, S. J., Carey, J. W. & Bish, D. L. (1997). *Controlled-humidity XRD analyses: application to the study of smectite expansion/contraction. Adv. X-ray Anal.* **39**, 713–722.

Choe, H., Gorfman, S., Hinterstein, M., Ziolkowski, M., Knapp, M., Heidbrink, S., Vogt, M., Bednarcik, J., Berghäuser, A., Ehrenberg, H. & Pietsch, U. (2015). *Combining high time and angular resolutions: time-resolved X-ray powder diffraction using a multi-channel analyser detector. J. Appl. Cryst.* **48**, 970–974.

Chupas, P. J., Chapman, K. W., Kurtz, C., Hanson, J. C., Lee, P. L. & Grey, C. P. (2008). *A versatile sample-environment cell for non-ambient X-ray scattering experiments. J. Appl. Cryst.* **41**, 822–824.

Chupas, P. J., Qiu, X., Hanson, J. C., Lee, P. L., Grey, C. P. & Billinge, S. J. L. (2003). *Rapid-acquisition pair distribution function (RA-PDF) analysis. J. Appl. Cryst.* **36**, 1342–1347.

Clausen, B. S. (1991). *In situ cell for combined XRD and on-line catalysis tests: studies of Cu-based water gas shift and methanol catalysts. J. Catal.* **132**, 524–535.

Clausen, B. S., Gråbaek, L., Steffensen, G., Hansen, P. L. & Topsøe, H. (1993). *A combined QEXAFS/XRD method for on-line, in situ studies of catalysts: examples of dynamic measurements of Cu-based methanol catalysts. Catal. Lett.* **20**, 23–36.

Conterosito, E., Van Beek, W., Palin, L., Croce, G., Perioli, L., Viterbo, D., Gatti, G. & Milanesio, M. (2013). *Development of a fast and clean intercalation method for organic molecules into layered double hydroxides. Cryst. Growth Des.* **13**, 1162–1169.

Couves, J. W., Thomas, J. M., Waller, D., Jones, R. H., Dent, A. J., Derbyshire, G. E. & Greaves, A. N. (1991). *Nature (London)*, **354**, 465–468.

De Marco, R. & Veder, J.-P. (2010). *In situ structural characterization of electrochemical systems using synchrotron-radiation techniques. TrAC Trends Anal. Chem.* **29**, 528–537.

Dokter, W. H., Beelen, T. P. M., van Garderen, H. F., van Santen, R. A., Bras, W., Derbyshire, G. E. & Mant, G. R. (1994). *Simultaneous monitoring of amorphous and crystalline phases in silicalite precursor gels. An in situ hydrothermal and time-resolved small- and wide-angle X-ray scattering study. J. Appl. Cryst.* **27**, 901–906.

Eu, W. S., Cheung, W. H. & Valix, M. (2009). *Design and application of a high-temperature microfurnace for an in situ X-ray diffraction study of phase transformation. J. Synchrotron Rad.* **16**, 842–848.

Evans, J. S. O. & Radosavljević Evans, I. (2004). *Beyond classical applications of powder diffraction. Chem. Soc. Rev.* **33**, 539–547.

Figueroa, S. J. A., Gibson, D., Mairs, T., Pasternak, S., Newton, M. A., Di Michiel, M., Andrieux, J., Christoforidis, K. C., Iglesias-Juez, A., Fernandez-Garcia, M. & Prestipino, C. (2013). *Innovative insights in a plug flow microreactor for operando X-ray studies. J. Appl. Cryst.* **46**, 1523–1527.

Friščić, T., Halasz, I., Beldon, P. J., Belenguer, A. M., Adams, F., Kimber, S. A. J., Honkimäki, V. & Dinnebier, R. E. (2013). *Real-time and in situ monitoring of mechanochemical milling reactions. Nat. Chem.* **5**, 66–73.

Hansen, B. R. S., Møller, K. T., Paskevicius, M., Dippel, A.-C., Walter, P., Webb, C. J., Pistidda, C., Bergemann, N., Dornheim, M., Klassen, T., Jørgensen, J.-E. & Jensen, T. R. (2015). *In situ X-ray diffraction environments for high-pressure reactions. J. Appl. Cryst.* **48**, 1234–1241.

Hansen, T. C. & Kohlmann, H. (2014). *Chemical reactions followed by in situ neutron powder diffraction. Z. Anorg. Allg. Chem.* **640**, 3044–3063.

He, H., Barnes, P., Munn, J., Turrillas, X. & Klinowski, J. (1992). *Autoclave synthesis and thermal transformations of the aluminophosphate molecular sieve VPI-5: an in situ X-ray diffraction study. Chem. Phys. Lett.* **196**, 267–273.

Herklotz, M., Scheiba, F., Hinterstein, M., Nikolowski, K., Knapp, M., Dippel, A.-C., Giebeler, L., Eckert, J. & Ehrenberg, H. (2013). *Advances in in situ powder diffraction of battery materials: a case study of the new beamline P02.1 at DESY, Hamburg. J. Appl. Cryst.* **46**, 1117–1127.

Herklotz, M., Weiss, J., Ahrens, E., Yavuz, M., Mereacre, L., Kiziltas-Yavuz, N., Dräger, C., Ehrenberg, H., Eckert, J., Fauth, F., Giebeler, L. & Knapp, M. (2016). *A novel high-throughput setup for in situ powder diffraction on coin cell batteries. J. Appl. Cryst.* **49**, 340–345.

Hill, A. H. (2013). *A new gas system for automated in situ powder diffraction studies at the European Synchrotron Radiation Facility. J. Appl. Cryst.* **46**, 570–572.

Isnard, O. (2007). *A review of in situ and/or time resolved neutron scattering. C. R. Phys.* **8**, 789–805.

Jacques, S. D. M., Di Michiel, M., Beale, A. M., Sochi, T., O'Brien, M. G., Espinosa-Alonso, L., Weckhuysen, B. M. & Barnes, P. (2011). *Dynamic X-ray diffraction computed tomography reveals real-time insight into catalyst active phase evolution. Angew. Chem. Int. Ed.* **50**, 10148–10152.

Jacques, S. D. M., Leynaud, O., Strusevich, D., Stukas, P., Barnes, P., Sankar, G., Sheehy, M., O'Brien, M. G., Iglesias-Juez, A. & Beale, A. M. (2009). *Recent progress in the use of in situ X-ray methods for the study of heterogeneous catalysts in packed-bed capillary reactors. Catal. Today*, **145**, 204–212.

Jensen, H., Bremholm, M., Nielsen, R. P., Joensen, K. D., Pedersen, J., Birkedal, H., Chen, Y.-S., Almer, J., Søgaard, E., Iversen, S. & Iversen, B. (2007). *In situ high-energy synchrotron radiation study of sol–gel nanoparticle formation in supercritical fluids. Angew. Chem. Int. Ed.* **46**, 1113–1116.

Jensen, T. R., Nielsen, T. K., Filinchuk, Y., Jørgensen, J.-E., Cerenius, Y., Gray, E. M. & Webb, C. J. (2010). *Versatile in situ powder X-ray diffraction cells for solid-gas investigations. J. Appl. Cryst.* **43**, 1456–1463.

Johnsen, R. E. & Norby, P. (2013). *Capillary-based micro-battery cell for in situ X-ray powder diffraction studies of working batteries: a study of the initial intercalation and deintercalation of lithium into graphite. J. Appl. Cryst.* **46**, 1537–1543.

Juhás, P., Davis, T., Farrow, C. L. & Billinge, S. J. L. (2013). *PDFgetX3: a rapid and highly automatable program for processing powder diffraction data into total scattering pair distribution functions. J. Appl. Cryst.* **46**, 560–566.

Kamazawa, K., Aoki, M., Noritake, T., Miwa, K., Sugiyama, J., Towata, S., Ishikiriyama, M., Callear, S. K., Jones, M. O. & David, W. I. F. (2013). *In-operando neutron diffraction studies of transition metal hydrogen storage materials. Adv. Energ. Mater.* **3**, 39–42.

Kraft, P., Bergamaschi, A., Broennimann, C., Dinapoli, R., Eikenberry, E. F., Henrich, B., Johnson, I., Mozzanica, A., Schlepütz, C. M., Willmott, P. R. & Schmitt, B. (2009). *Performance of single-photon-counting PILATUS detector modules. J. Synchrotron Rad.* **16**, 368–375.

Krogh Andersen, E., Krogh Andersen, I. G., Norby, P. & Hanson, J. C. (1998). *Kinetics of oxidation of fuel cell cathode materials lanthanum strontium manganates(III)(IV) at actual working conditions: in situ powder diffraction studies. J. Solid State Chem.* **141**, 235–240.

Kühnel, R. & van der Gaast, S. J. (1993). *Humidity controlled diffractometry and its application. Adv. X-ray Anal.* **36**, 439–449.

Linnow, K., Zeunert, A. & Steiger, M. (2006). *Investigation of sodium sulfate phase transitions in a porous material using humidity- and temperature-controlled X-ray diffraction. Anal. Chem.* **78**, 4683–4689.

Llewellyn, P. L., Horcajada, P., Maurin, G., Devic, T., Rosenbach, N., Bourrelly, S., Serre, C., Vincent, D., Loera-Serna, S., Filinchuk, Y. & Férey, G. (2009). *Complex adsorption of short linear alkanes in the flexible metal-organic-framework MIL-53(Fe). J. Am. Chem. Soc.* **131**, 13002–13008.

Lorenz, G., Neder, R. B., Marxreiter, J., Frey, F. & Schneider, J. (1993). *A mirror furnace for neutron diffraction up to 2300 K. J. Appl. Cryst.* **26**, 632–635.

Madsen, I. C., Scarlett, N. V. Y. & Whittington, B. I. (2005). *Pressure acid leaching of nickel laterite ores: an in situ diffraction study of the mechanism and rate of reaction. J. Appl. Cryst.* **38**, 927–933.

Majuste, D., Ciminelli, V. S. T., Eng, P. J. & Osseo-Asare, K. (2013). *Applications of in situ synchrotron XRD in hydrometallurgy: literature review and investigation of chalcopyrite dissolution. Hydrometallurgy*, **131–132**, 54–66.

Margulies, L., Kramer, M. J., McCallum, R. W., Kycia, S., Haeffner, D. R., Lang, J. C. & Goldman, A. I. (1999). *New high temperature furnace for structure refinement by powder diffraction in controlled atmospheres using synchrotron radiation. Rev. Sci. Instrum.* **70**, 3554–3561.

Meneghini, C., Artioli, G., Balerna, A., Gualtieri, A. F., Norby, P. & Mobilio, S. (2001). *Multipurpose imaging-plate camera for in situ powder XRD at the GILDA beamline. J. Synchrotron Rad.* **8**, 1162–1166.

Mi, J. L., Shen, Y., Becker, J., Bremholm, M. & Iversen, B. B. (2014). *Controlling allotropism in ruthenium nanoparticles: a pulsed-flow supercritical synthesis and in situ synchrotron X-ray diffraction study. J. Phys. Chem. C*, **118**, 11104–11110.

Milanesio, M., Artioli, G., Gualtieri, A. F., Palin, L. & Lamberti, C. (2003). *Template burning inside TS-1 and Fe-MFI molecular sieves: an in situ XRPD study. J. Am. Chem. Soc.* **125**, 14549–14558.

Møller, K. T., Hansen, B. R. S., Dippel, A.-C., Jørgensen, J.-E. & Jensen, T. R. (2014). *Characterization of gas-solid reactions using in situ powder X-ray diffraction. Z. Anorg. Allg. Chem.* **640**, 3029–3043.

Moorhouse, S. J., Vranješ, N., Jupe, A., Drakopoulos, M. & O'Hare, D. (2012). *The Oxford–Diamond in situ cell for studying chemical* *reactions using time-resolved X-ray diffraction. Rev. Sci. Instrum.* **83**, 084101.

Morcrette, M., Chabre, Y., Vaughan, G., Amatucci, G., Leriche, J.-B., Patoux, S., Masquelier, C. & Tarascon, J.-M. (2002). *In situ X-ray diffraction techniques as a powerful tool to study battery electrode materials. Electrochim. Acta*, **47**, 3137–3149.

Moury, R., Hauschild, K., Kersten, W., Ternieden, J., Felderhoff, M. & Weidenthaler, C. (2015). *An in situ powder diffraction cell for high-pressure hydrogenation experiments using laboratory X-ray diffractometers. J. Appl. Cryst.* **48**, 79–84.

Munn, J., Barnes, P., Haüsermann, D., Axon, S. A. & Klinowski, J. (1992). *In-situ studies of the hydrothermal synthesis of zeolites using synchrotron energy-dispersive X-ray diffraction. J. Phase Transit.* **39**, 129–134.

Nauman, E. B. (2008). *Chemical Reactor Design, Optimization, and Scaleup.* Hoboken: John Wiley & Sons.

Neder, R. B. & Proffen, T. (2008). *Diffuse Scattering and Defect Structure Simulations.* Oxford University Press.

Newton, M. A. & van Beek, W. (2010). *Combining synchrotron-based X-ray techniques with vibrational spectroscopies for the in situ study of heterogeneous catalysts: a view from a bridge. Chem. Soc. Rev.* **39**, 4845–4863.

Norby, P. (2006). *In-situ XRD as a tool to understanding zeolite crystallization. Curr. Opin. Colloid Interf. Sci.* **11**, 118–125.

Norby, P., Cahill, C., Koleda, C. & Parise, J. B. (1998). *A reaction cell for in situ studies of hydrothermal titration. J. Appl. Cryst.* **31**, 481–483.

Norby, P., Hanson, J. C., Fitch, A. N., Vaughan, G., Flaks, L. & Gualtieri, A. (2000). *Formation of α-eucryptite, $LiAlSiO_4$: an in-situ synchrotron X-ray powder diffraction study of a high temperature hydrothermal synthesis. Chem. Mater.* **12**, 1473–1479.

Norby, P. & Schwarz, U. (2008). *Powder Diffraction, Theory and Practice*, edited by R. E. Dinnebier & S. J. L. Billinge, pp. 439–463. Cambridge: The Royal Society of Chemistry.

O'Brien, M. G., Beale, A. M., Jacques, S. D. M., Di Michiel, M. & Weckhuysen, M. (2011). *Closing the operando gap: the application of high energy photons for studying catalytic solids at work. Appl. Catal. A Gen.* **391**, 468–476.

Ok, K. M., O'Hare, D., Smith, R. I., Chowdhury, M. & Fikremariam, H. (2010). *New large volume hydrothermal reaction cell for studying chemical processes under supercritical hydrothermal conditions using time-resolved in situ neutron diffraction. Rev. Sci. Instrum.* **81**, 125107.

Palancher, H., Pichon, C., Rebours, B., Hodeau, J. L., Lynch, J., Berar, J. F., Prevot, S., Conan, G. & Bouchard, C. (2005). *A cell for in situ dynamic X-ray diffraction studies: application to the dehydration of zeolite SrX. J. Appl. Cryst.* **38**, 370–373.

Pang, W. K. & Peterson, V. K. (2015). *A custom battery for operando neutron powder diffraction studies of electrode structure. J. Appl. Cryst.* **48**, 280–290.

Parise, J. B., Cahill, C. L. & Lee, Y. (2000). *Dynamic powder crystallography with synchrotron X-ray sources. Can. Mineral.* **38**, 777–800.

Proffen, T., Frey, F., Plöckl, H. & Krane, H. G. (1995). *A mirror furnace for synchrotron diffraction experiments up to 1600 K. J. Synchrotron Rad.* **2**, 229–232.

Riello, P., Lausi, A., Macleod, J., Plaisier, J. R., Zerauschek, G. & Fornasiero, P. (2013). *In situ reaction furnace for real-time XRD studies. J. Synchrotron Rad.* **20**, 194–196.

Rijssenbeek, J., Gao, Y., Zhong, Z., Croft, M., Jisrawi, N., Ignatov, A. & Tsakalakos, T. (2011). *In situ X-ray diffraction of prototype sodium metal halide cells: time and space electrochemical profiling. J. Power Sources*, **196**, 2332–2339.

Robertson, K. & Bish, D. (2010). *Determination of the crystal structure of magnesium perchlorate hydrates by X-ray powder diffraction and the charge-flipping method. Acta Cryst.* B**66**, 579–584.

Rosciano, F., Holzapfel, M., Scheifele, W. & Novák, P. (2008). *A novel electrochemical cell for in situ neutron diffraction studies of electrode materials for lithium-ion batteries. J. Appl. Cryst.* **41**, 690–694.

Rowles, M. R. (2011). *On the calculation of the gauge volume size for energy-dispersive X-ray diffraction. J. Synchrotron Rad.* **18**, 938–941.

Rowles, M. R., Styles, M. J., Madsen, I. C., Scarlett, N. V. Y., McGregor, K., Riley, D. P., Snook, G. A., Urban, A. J., Connolley, T. & Reinhard, C. (2012). *Quantification of passivation layer growth in inert anodes for molten salt electrochemistry by in situ energy-dispersive diffraction. J. Appl. Cryst.* **45**, 28–37.

Sharma, N., Du, G., Studer, A. J., Guo, Z. & Peterson, V. K. (2011). *In-situ neutron diffraction study of the MoS_2 anode using a custom-built Li-ion battery. Solid State Ionics*, **199–200**, 37–43.

Sharma, N., Pang, W. K., Guo, Z. & Peterson, V. K. (2015). *In situ powder diffraction studies of electrode materials in rechargeable batteries. ChemSusChem*, **8**, 2826–2853.

Shen, Y., Pedersen, E. E., Christensen, M. & Iversen, B. B. (2014). *An electrochemical cell for in operando studies of lithium/sodium batteries using a conventional X-ray powder diffractometer. Rev. Sci. Instrum.* **85**, 084101.

Solovyov, L. A. (2012). *Revision of the $Mg(ClO_4)_2{\cdot}4H_2O$ crystal structure. Acta Cryst.* B**68**, 89–90.

Steiger, M., Linnow, K., Juling, H., Gülker, G., Jarad, A. E., Brüggerhoff, S. & Kirchner, D. (2008). *Hydration of $MgSO_4{\cdot}H_2O$ and generation of stress in porous materials. Cryst. Growth Des.* **8**, 336–343.

Styles, M. J., Rowles, M. R., Madsen, I. C., McGregor, K., Urban, A. J., Snook, G. A., Scarlett, N. V. Y. & Riley, D. P. (2012). *A furnace and environmental cell for the in situ investigation of molten salt electrolysis using high-energy X-ray diffraction. J. Synchrotron Rad.* **19**, 39–47.

Tarasov, L. P. & Warren, B. E. (1936). *X-ray diffraction study of liquid sodium. J. Chem. Phys.* **4**, 236–238.

Techert, S., Schotte, F. & Wulff, M. (2001). *Picosecond X-ray diffraction probed transient structural changes in organic solids. Phys. Rev. Lett.* **86**, 2030–2033.

Tonus, F., Bahout, M., Henry, P. F., Dutton, S. E., Roisnel, T. & Battle, P. D. (2009). *Use of in situ neutron diffraction to monitor high-temperature, solid/H_2-gas reactions. Chem. Commun.* pp. 2556–2558.

Tsakoumis, N. E., Voronov, A., Rønning, M., van Beek, W., Borg, Ø., Rytter, E. & Holmen, A. (2012). *Fischer–Tropsch synthesis: an XAS/XRPD combined in situ study from catalyst activation to deactivation. J. Catal.* **291**, 138–148.

Tschentscher, Th. & Suortti, P. (1998). *Experiments with very high energy synchrotron radiation. J. Synchrotron Rad.* **5**, 286–292.

Wall, A. J., Heaney, P. J., Mathur, R., Post, J. E., Hanson, J. C. & Eng, P. J. (2011). *J. Appl. Cryst.* **44**, 429–432.

Walspurger, S., Cobden, P. D., Haije, W. G., Westerwaal, R., Elzinga, G. D. & Safonova, O. V. (2010). *In situ XRD detection of reversible dawsonite formation on alkali promoted alumina: a cheap sorbent for CO_2 capture. Eur. J. Inorg. Chem.* **2010**, 2461–2464.

Walton, R. I. & O'Hare, D. (2000). *Watching solids crystallise using in situ powder diffraction. Chem. Commun.* pp. 2283–2291.

Warren, B. E. (1990). *X-ray Diffraction.* New York: Dover.

Watanabe, T. & Sato, T. (1988). *Expansion characteristics of montmorillonite and saponite under various relative humidity conditions. Clay Sci.* **7**, 129–138.

Weckhuysen, B. M. (2002). *Snapshots of a working catalyst: possibilities and limitations of in situ spectroscopy in the field of heterogeneous catalysis. Chem. Commun.* pp. 97–110.

Westgren, A. & Lindh, A. E. (1921). *Zur Kristallbau des Eisens und Stahl. I. Z. Phys. Chem.* **98**, 181.

Widenmeyer, M., Niewa, R., Hansen, T. C. & Kohlmann, H. (2013). *In situ neutron diffraction as a probe on formation and decomposition of nitrides and hydrides: a case study. Z. Anorg. Allg. Chem.* **639**, 285–295.

Williams, G. R., Khan, A. I. & O'Hare, D. (2009). *Mechanistic and kinetic studies of guest ion intercalation into layered double hydroxides using time-resolved, in-situ X-ray powder diffraction. Struct. Bond.* **119**, 161–192.

Wragg, D. S., O'Brien, M. G., Bleken, F. L., Di Michiel, M., Olsbye, U. & Fjellvåg, H. (2012). *Watching the methanol-to-olefin process with time- and space-resolved high-energy operando X-ray diffraction. Angew. Chem. Int. Ed.* **51**, 7956–7959.

Wragg, D. S., O'Brien, M. G., Di Michiel, M. & Lønstad-Bleken, F. (2015). *Rietveld analysis of computed tomography and its application to methanol to olefin reactor beds. J. Appl. Cryst.* **48**, 1719–1728.

Xia, F., Qian, G., Brugger, J., Studer, A., Olsen, S. & Pring, A. (2010). *A large volume cell for in situ neutron diffraction studies of hydrothermal crystallizations. Rev. Sci. Instrum.* **81**, 105107.

Yashima, M. & Tanaka, M. (2004). *Performance of a new furnace for high-resolution synchrotron powder diffraction up to 1900 K: application to determine electron density distribution of the cubic $CaTiO_3$ perovskite at 1674 K. J. Appl. Cryst.* **37**, 786–790.

International Tables for Crystallography (2019). Vol. H, Chapter 2.10, pp. 200–222.

2.10. Specimen preparation

P. S. Whitfield, A. Huq and J. A. Kaduk

Powder X-ray diffraction is a popular technique, as it is quick and easy to obtain a data set in a non-destructive manner. However, the old adage ‘garbage in, garbage out’ is as applicable to powder diffraction as to any other technique. Obtaining a high-quality data set is often not straightforward, and it can be impossible to distinguish visually a poor data set from a good one prior to attempting an analysis. This can be problematic if someone collects poor data and then spends days in a fruitless attempt to analyse it – or even worse unknowingly produces erroneous results. Specimen preparation is a key element in the quest to produce good data.

One of the tasks of the analyst is to determine what is required for a ‘fit-for-purpose’ data set. Practically, in the interests of time and instrument efficiency one might not need to aim for perfection in the preparation of every specimen. The majority of analyses carried out in most laboratories are for phase identification, whose minimum requirements for sample preparation are less stringent than for quantitative phase analysis or structure refinement. However, the need for more detailed analysis is never clear at the outset, and if the specimen has been altered or destroyed by other analyses, any economy in specimen preparation will turn out to have been false.

Although the laboratory instrument appears to be very different from synchrotron or neutron diffractometers at large central facilities, many of the concepts in the collection of powder diffraction data are common. Whether in the home institution with a basic laboratory system or in a huge instrument hall at a central facility, the basic concepts of specimen preparation are very similar (although neutrons have some unique issues). The imposing surroundings at large facilities may make specimen preparation seem like an unimportant distraction, but it is worth bearing in mind that repeating experiments if the data are poor may be impossible with limited beam time available. At the risk of overusing everyday sayings, ‘if it’s worth doing, it’s worth doing right’. One common scenario is a user trying to replicate what has been seen in a literature paper without assessing critically whether the authors took the necessary care to collect accurate data.

Many of the problems that occur with powder diffraction specimens are related to size in some form – most often crystallite size, but sometimes particle size as well. Although the problems relating to size are described separately for the sake of clarity, where one of the issues exists the others are likely to follow. The first size-related problem to be described is particle statistics (granularity). Although theoretical models of varying success exist for the other issues of preferential orientation, microabsorption and extinction, no such model is possible when the data suffer from poor particle statistics. Consequently the message here is ‘prevention through proper specimen preparation’; taking steps in specimen preparation to improve particle statistics will automatically reduce the effects of other potential problems.

The classic work on preparation of X-ray diffraction specimens is Buhrke *et al.* (1998). This book should be on the shelf of every powder diffractionist. It provides an excellent discussion on sampling, a discussion which is not necessary to repeat here. This chapter attempts to update and expand the advice given there on specimen preparation.

2.10.1. X-ray powder diffraction

Most people first encounter X-ray powder diffraction with laboratory instrumentation, but concepts applying to laboratory systems are also applicable to synchrotron and neutron beamlines. The scattering mechanisms of X-rays in the laboratory and at a synchrotron are the same, and apparent differences are usually due to specifics of the wavelength used or beamline/instrument geometry. Differences and similarities between synchrotron and laboratory experiments will be highlighted where they are significant. For example, differences in the polarization factor result in different intensities from the same specimen on laboratory and synchrotron instruments (Fig. 2.10.1). Issues specific to neutron powder diffraction will be covered in Section 2.10.2.

A typical laboratory instrument has the Bragg–Brentano reflection geometry, either with θ–θ (fixed specimen) or θ–2θ (fixed tube) setup. Other laboratory configurations are possible, such as transmission (capillary or flat plate) and spot focus with area detectors. Some of the concepts described affect both reflection and transmission, but some will be more important for one geometry over the other. Synchrotron beamlines can also be operated in reflection or transmission geometry, but capillary transmission geometry is much more common than in the laboratory. Some of the apparent differences are due to the

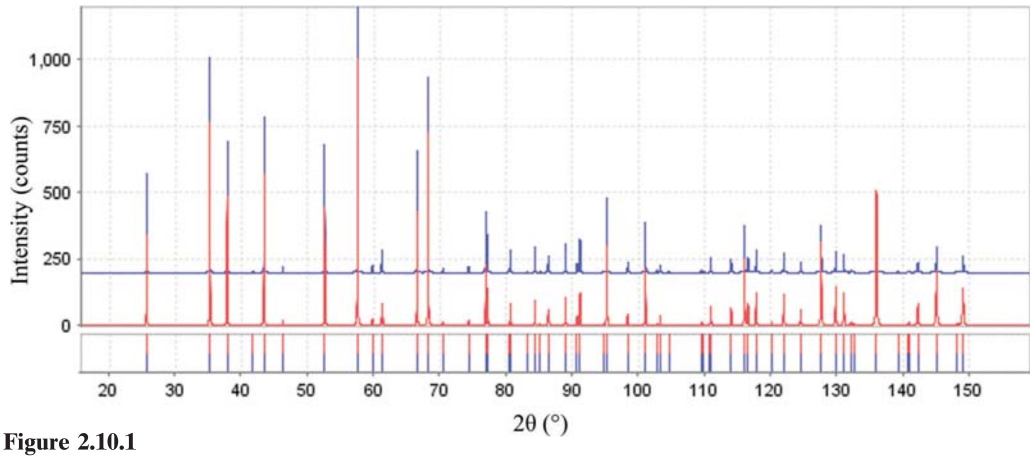

Figure 2.10.1
Calculated corundum powder patterns using the structure of Lewis *et al.* (1982; PDF entry 04–004-2852) for laboratory and synchrotron instruments, using the default profile settings from the Powder Diffraction File. The synchrotron pattern is displaced by 200 intensity units for clarity.

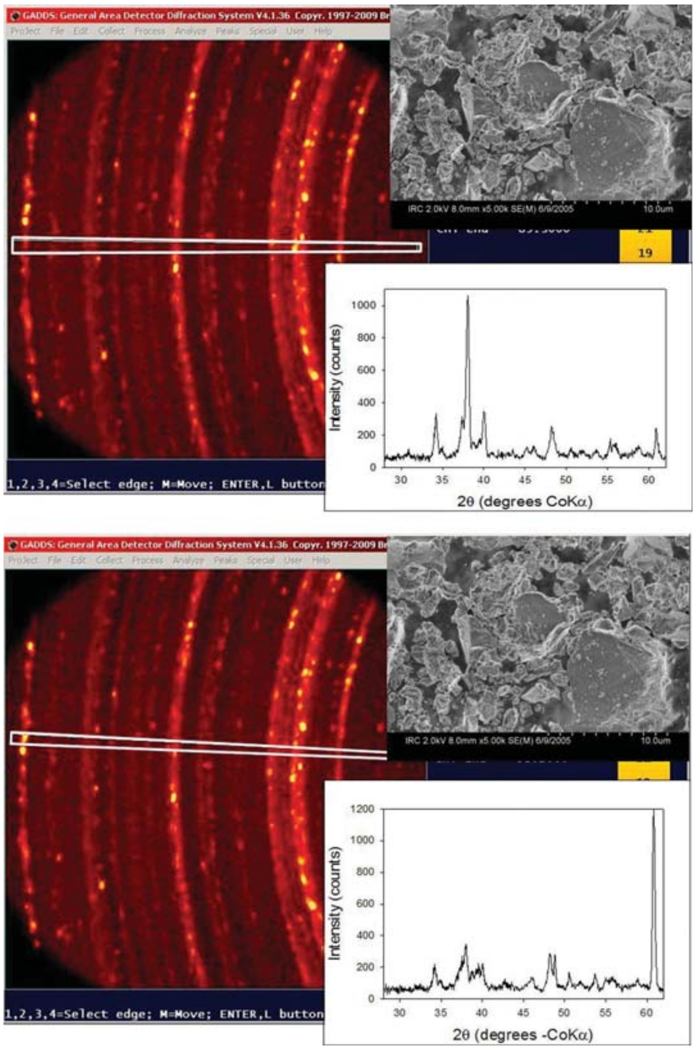
GADDS: General Area Detector Diffraction System V4.1.36 Copyr. 1997-2009
IRC 2.0kV 8.0mm x5.00k SE(M) 6/9/2005 10.0um
19
Intensity (counts)
2θ (degrees CoKα)
2θ (degrees -CoKα)
1,2,3,4=Select edge; M=Move; ENTER,L button

Figure 2.10.2
2D images of the spotty Debye rings of a coarse (~35 μm) cement powder using a Co *Kα* radiation 1 mm point source. Overlaid are SEMs of the sample material and integrated patterns from the thin slices indicated in the 2D patterns to illustrate what a point or 1D detector would see. Note: in these 2D data sets the low 2θ rings are on the right-hand side.

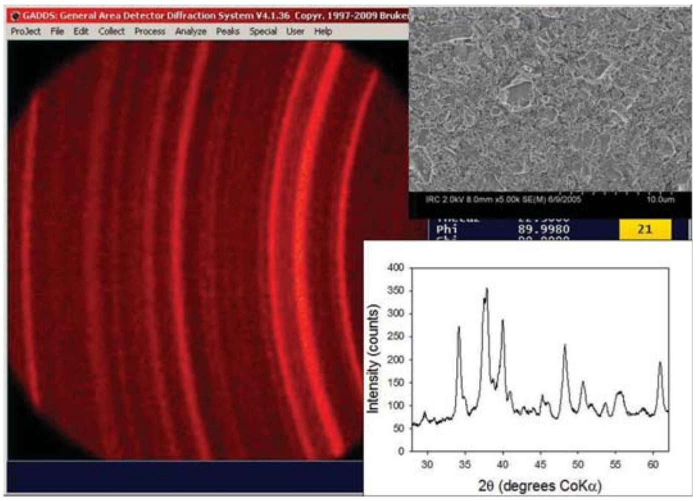
GADDS: General Area Detector Diffraction System V4.1.36 Copyr. 1997-2009 Bruker
Project File Edit Collect Process Analyze Peaks Special User Help
IRC 2.0kV 8.0mm x5.00k SE(M) 6/9/2005 10.0um
Phi 89.9980
21
Intensity (counts)
2θ (degrees CoKα)

Figure 2.10.3
2D image from the same sample after reducing the crystallites down to a few μm, together with the properly averaged integrated data.

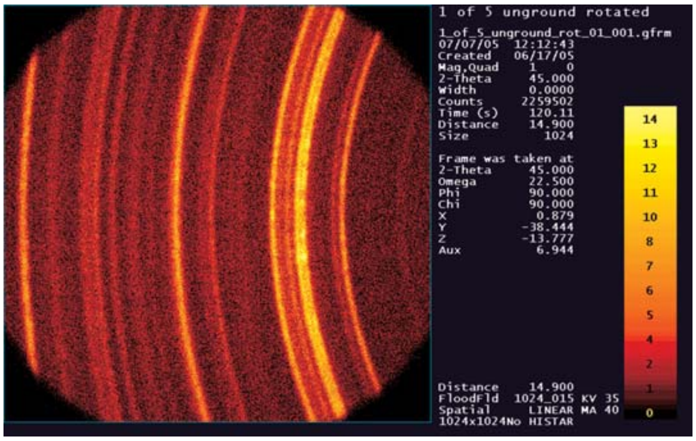

```
1 of 5 unground rotated
1_of_5_unground_rot_01_001.gfrm
07/07/05   12:12:43
Created    06/17/05
Mag,Quad      1     0
2-Theta       45.000
Width         0.0000
Counts       2259502
Time (s)      120.11
Distance      14.900
Size            1024

Frame was taken at
2-Theta       45.000
Omega         22.500
Phi           90.000
Chi           90.000
X              0.879
Y            -38.444
Z            -13.777
Aux            6.944

Distance      14.900
FloodFld   1024_015 KV 35
Spatial       LINEAR MA 40
1024x1024No HISTAR
```

14
13
12
11
10
8
7
6
5
4
2
1
0

Figure 2.10.4
2D image showing the Debye rings when the unmilled sample from Fig. 2.10.2 is rotated. The slight spottiness shows that the quality is not as good as the milled sample, even when not rotated, as shown in Fig. 2.10.3.

typically very small beam divergence, and the tunable wavelength can be very helpful in circumventing some problems.

It will become apparent that many problems relating to specimen preparation and data quality are directly and indirectly the result of samples being too coarse to produce a random powder. The word 'powder' forms part of the name of the technique, but what makes a powder a powder?

2.10.1.1. *Powders and particle statistics (granularity)*

The question of when a powder is a 'true' powder is not new. It was dealt with in Klug & Alexander (1954) and Alexander & Klug (1948), and more recently by Smith (Smith, 2001; Buhrke *et al.*, 1998). The short answer is that at least 50 000 crystallites in the illuminated volume are necessary to obtain a random powder pattern.

The classic Debye rings of powder diffraction are formed by the random orientation of a large number of single crystallites, which are either physically separate or part of larger agglomerates. These rings used to be a common sight when film cameras were the norm, but can still be seen where two-dimensional (2D) or area detectors are used, most often on microdiffraction systems or synchrotron beamlines. Where there are sufficient crystallites diffracting, the spots from the crystallites merge into smooth rings. Problems with insufficient crystallites are often indicated by the presence of high-intensity spots in the Debye rings. When using 2D data sets, part or all of the intensity in the Debye rings may be integrated to produce an average 1D powder pattern.

More serious problems can arise in cases where 0D or 1D detectors are used. Most modern laboratory powder diffractometers use some form of 0D point detector (*e.g.* a scintillation counter) or 1D position-sensitive detector (PSD). When collecting data, these detectors pass through the Debye rings along a radius vector. Should the Debye ring be spotty, it is purely down to chance whether the detector will intersect with a spot of higher intensity or low intensity within the ring. An example of how spotty Debye rings can have an adverse effect on the integrated pattern can be seen in Fig. 2.10.2. Unfortunately there is usually no indication of the problem in the resulting integrated 1D pattern. The uncertainty with regard to the intensity of the Bragg reflections is something that must be minimized should accurate relative intensities be required for an analysis. This reproducibility is the concern when the term 'particle statistics' is used in relation to powder diffraction. The desirable smooth Debye rings shown in Fig. 2.10.3 were produced after reducing

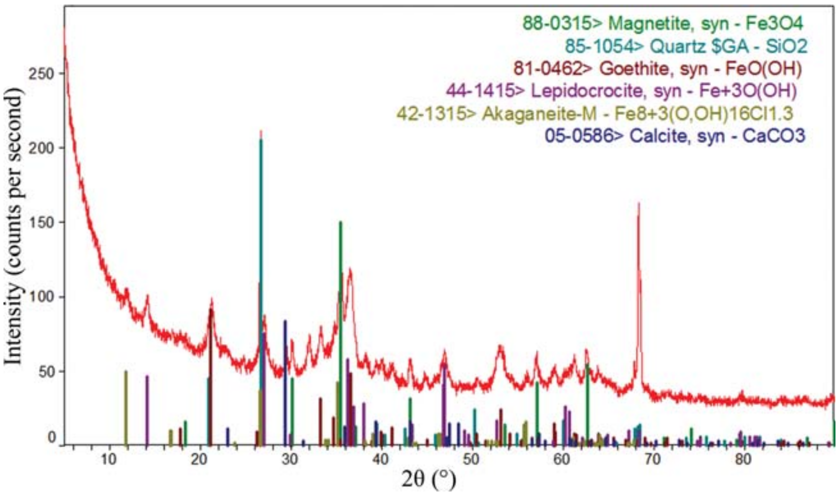

Figure 2.10.5
The appearance of specimen granularity in a hand-ground specimen of a railroad tank car corrosion deposit. The pattern was measured using a point detector. The intense sharp peak at ~68° 2θ turned out to come from a single crystal grain of sand at the surface of the specimen. The grain was detected by examination (after the measurement) in an optical microscope.

the crystallites to less than a few μm by milling. As shown in Fig. 2.10.4, rotating the coarse unmilled sample greatly improves the Debye rings compared with those seen in Fig. 2.10.2, but they are still not as uniform as those from the static milled sample in Fig. 2.10.3.

When using a point detector, granularity often manifests itself in the presence of a sharp (instrumental width) peak at relatively high diffraction angle. After a sharp peak at ~68° 2θ was observed in the pattern of a railroad tank car corrosion deposit (Fig. 2.10.5), examination of the specimen in an optical microscope indicated the presence of a single crystal grain of sand (quartz) on the surface. Re-grinding the specimen removed this artifact. Such sharp peaks tend to occur at relatively high diffraction angles, because at such angles the illuminated specimen area is smaller than at low angles, and the presence of a single crystal grain at the surface is relatively more important than when a larger area is illuminated.

An extreme example of granularity is provided by a hand-ground specimen of Scott's Moss Control Granules (Fig. 2.10.6). The even spacing of the strong peaks suggested severe preferred orientation, but examination of the specimen in an optical microscope (Fig. 2.10.7) revealed the presence of grains several tens of μm in size. Regrinding the sample in a McCrone micronizing mill reduced the crystallite size to a few μm (Fig. 2.10.7), and resulted in random powder data which could be used successfully in a Rietveld refinement (Fig. 2.10.8) and quantitative phase analysis.

An example of granularity at a synchrotron beamline is provided by $(Ba_{0.7}Sr_{1.3})TiO_4$ (Fig. 2.10.9). A Rietveld refinement using data collected from a static capillary specimen was unsuccessful. In an attempt to understand why, the diffractometer was driven to the 2θ angle of a strong peak, and a φ scan was carried out (rotating the capillary in steps). The intensity varied by a factor of five, as individual crystallites came into and out of diffracting position. Clearly, the intensities from such a measurement are not meaningful. When the capillary was rotated rapidly during a repeated φ scan, the intensity was constant and reliable.

Granularity can be encountered even in highly transparent organic specimens. A synchrotron pattern of 17α-estradiol showed that the sample was a mixture of the α-polymorph and an additional phase. Indexing the unknown peaks yielded the cell of the β-polymorph, the structure of which was unknown. The structure of the β-polymorph was solved using Monte Carlo simulated-annealing techniques, but the Rietveld refinement (Fig. 2.10.10) was not nearly as good as a Le Bail fit using the same cell and profile. The errors were then clearly in the structural model and/or the data. Examination of the specimen under an optical microscope revealed the presence of needles ~50 × 50 × 150–200 μm in size. Even the rapid rotation of the capillary specimen was not sufficient to obtain a powder average of such large crystallites.

Although granularity is normally considered to affect only the intensities of peaks, in extreme cases it can also affect the shapes. This is easily seen in a pattern from very coarse crystalline quartz in Fig. 2.10.11. The strange looking 101 reflection at 26.6° contains contributions from individual single crystals. When a wider view is taken, the relative intensities are distorted from those expected, similar to that seen in Fig. 2.10.2. Flat-plate data from highly-parallel-beam synchrotron beamlines are more (as opposed to less) susceptible, as shown by the comparison between flat-plate and capillary data of LaB_6 from the Australian Synchrotron in Fig. 2.10.12. Despite the use of ω-rocking and a Mythen position-sensitive detector, the flat-plate synchrotron data with 2–5 μm SRM660a LaB_6 crystallites show worse splitting of the Bragg peaks than lower-resolution laboratory data with 100 μm quartz crystallites.

The quantitative effect of particle statistics on diffraction results can be seen in Table 2.10.1. In the 15–50 μm sample the intensity varied from 4823 to 11 123 counts, which is a huge variation when trying to extract reliable intensities for analysis. Averaging over ten samples, the mean deviation was reduced from 18.2% to 1.2% when the smallest fraction of <5 μm was used. The absolute intensities of the largest fraction are significantly lower, which was attributed to extinction effects.

The source of this huge variation in errors can be understood more clearly when the theoretical treatment for quartz from

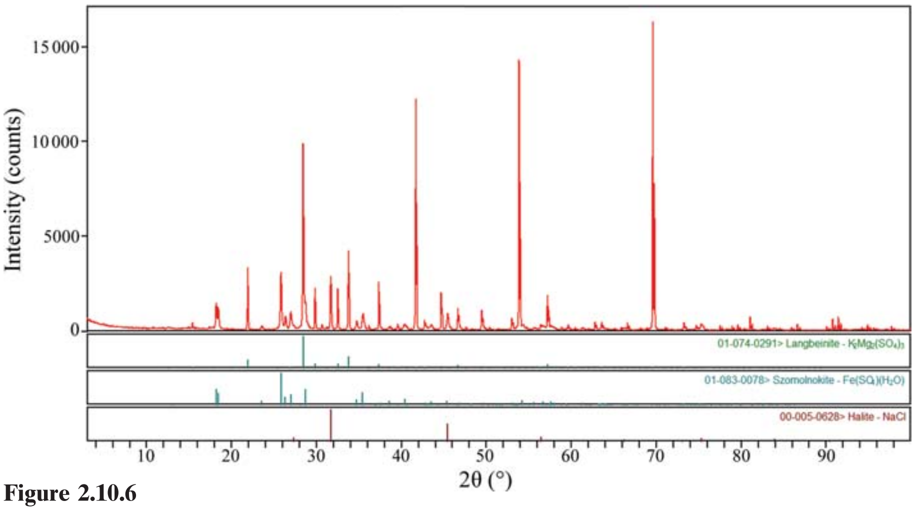

Figure 2.10.6
An extreme example of granularity. The pattern is of a hand-ground specimen of Scott's Moss Control Granules. No preferred orientation model could fit the langbeinite peaks.

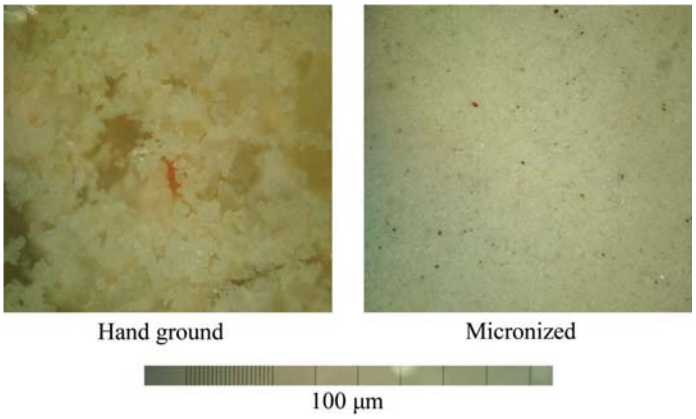

Figure 2.10.7
Optical microscope images of the surfaces of the hand-ground and micronized specimens of Scott's Moss Control Granules. The full length of the bar at the bottom is 100 µm. The hand-ground specimen contains grains much too large to yield a random powder pattern. Courtesy of B. J. Huggins, BP Analytical.

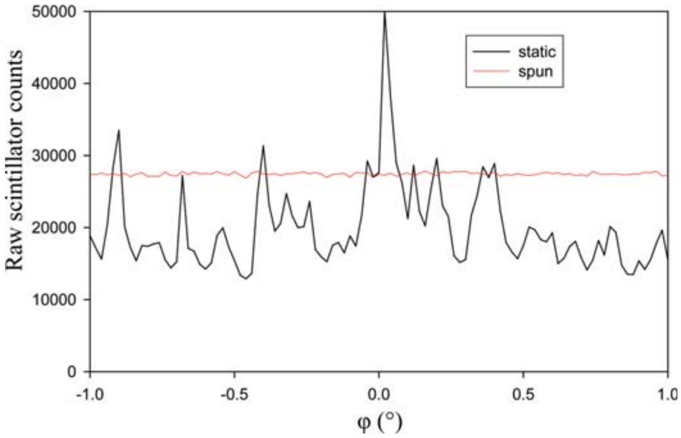

Figure 2.10.9
A rocking curve (φ scan) of $(Ba_{0.7}Sr_{1.3})TiO_4$, with the detector fixed at 9.647° 2θ, the top of a strong peak in the synchrotron pattern. The jagged plot is from a static specimen, and shows individual grains moving in and out of diffracting position. The flat curve is from a rotating specimen, and indicates that a powder average was obtained.

Smith (Smith, 2001; Buhrke *et al.*, 1998) is considered, which followed principles first described by de Wolff (1958). By considering the effects of crystallite size, illuminated volume and beam divergence, for a monodisperse 40 µm specimen Smith calculated that only 12 crystallites would be in the diffracting condition (assuming a point detector). Obviously this is nowhere near enough to create the desired smooth Debye rings. To obtain a standard error of less than 1% the number of diffracting crystallites should be over 52 900, which even the 1 µm sample fails to meet.

Why then does a powder diffraction experiment work? A number of factors may affect the effective number of crystallites, many of which will be mentioned in the following paragraphs. One that isn't is the multiplicity due to the crystal symmetry, meaning that there are always at least two equivalent orientations of each crystallite that would meet the diffraction condition, up to 48 for some cubic reflections. It is worth remembering that these figures relate to a single phase, so the impact on the errors in quantitative phase analysis can be considerable. For low-concentration phases, the number of crystallites is automatically smaller than those of the major phases, so the effects of granularity might be more pronounced.

When considering the granularity of a particular specimen there are a few things to consider. The number of diffracting crystallites depends on the illuminated volume (V), the size of the crystallites (s), the packing density (ρ) and the probability that a crystallite is in the correct orientation (P).

The illuminated volume V depends on a combination of instrument geometry, specimen geometry and the X-ray absorption of the sample. The footprint of the X-rays on a specimen in reflection depends on the beam width, beam length, the beam divergence (if any) and the diffraction angle. The effective beam width at the tube window with a typical long-fine-focus X-ray tube is 0.04 mm, with a length of 12 mm. The beam width may be increased up to 0.2 mm by using a broad-focus tube (Jenkins & Snyder, 1996), but these are rarely used in modern powder diffractometers. With Bragg–Brentano geometry the beam divergence may be increased to cover the available specimen, but large divergence angles degrade the peak resolution. A parallel-beam primary optic produces negligible beam divergence. The beam width may be reduced using an exit slit, but the largest beam width attainable is dependent on the characteristics of the mirror.

Additionally, V also depends on how deeply the X-rays can penetrate into the sample. This depends on the linear absorption coefficient of the specimen for the particular radiation being used, and is given (Klug & Alexander, 1954) by $t = (3.2\rho \sin\theta)/(\mu\rho')$, in which μ is the linear absorption coefficient, ρ is the crystal density and ρ' is the packing density. In the absence of other information, a reasonable assumption for the value of ρ'/ρ is 0.5. The penetration with Cu $K\alpha$ radiation can range from >1 mm for an organic material to a few µm for heavily absorbing specimens. With Bragg–Brentano geometry this leads to a potential trade-off between improving particle statistics and the peak shifts resulting from sample transparency. As a rule, doubling the diffracting volume will reduce the errors in intensity by about 1.5 times (Zevin &

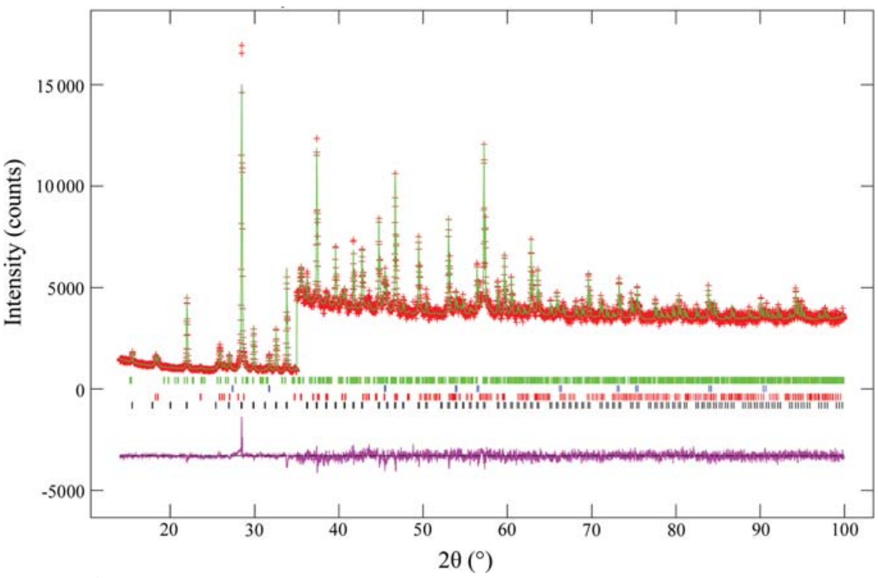

Figure 2.10.8
Rietveld refinement plot for micronized Scott's Moss Control Granules. No preferred orientation correction was necessary, and the specimen scattered as a random powder. For angles > 35° the vertical scale has been multipled by a factor of 5.

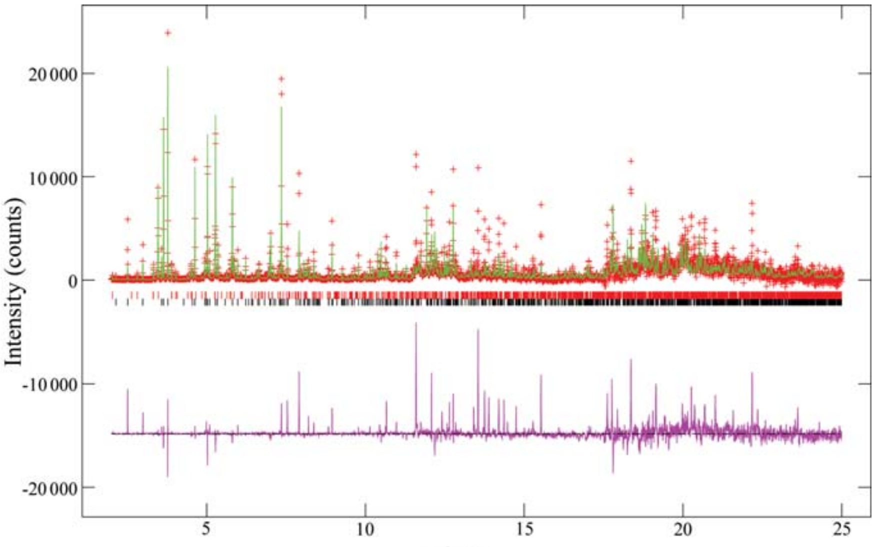

Figure 2.10.10
Rietveld plot of a mixture of β-17α-estradiol hemihydrate and α-17α-estradiol. The largest errors occur at the peaks of the β phase. Examination of the sample with an optical microscope revealed the presence of large single crystals. The rapid specimen rotation at the synchrotron beamline could not yield a powder average from such a coarse sample.

Kimmel, 1995), so is rarely sufficient on its own to solve problematic particle statistics.

Both the experimental data and theoretical treatment shown in Tables 2.10.1 and 2.10.2 show that with a typical laboratory setup, crystallites should ideally be in the range of a few μm in size to produce accurate intensity data. Reducing the crystallites to below 1 μm will improve the statistics further but may also induce crystallite-size and/or microstrain broadening depending on the instrument resolution. It is important to note that the crystallites must be uniformly small. Mineralogists often refer to 'rocks in dust', where there are a small number of very large crystallites scattered among the sample. Scattering of X-rays is sensitive to statistics by *volume*. A few very large crystallites will dominate (and probably distort) the resulting pattern, so the 'rocks in dust' scenario should be avoided whenever possible by correct specimen-preparation techniques.

As we have seen previously, the granularity can be seen visually in a 2D data set. If the researcher has access to a 2D detector this is the quickest way to assess a sample. However, where such a system is not available, an alternative is to use φ scans. In simple terms this involves taking data sets of a static specimen but rotating the specimen by a particular angle between data sets, for example at 0, 90, 180 and 270° in φ. Ideally the patterns should overlap exactly, although in practice one is looking for reproducible relative intensities, as the absolute intensities may change slightly. The examples used here are the so-called 'five fingers' of quartz. Although they are relatively weak reflections in the quartz pattern, three overlapping $K\alpha_{1,2}$ doublets provide a conveniently compact example. The three data sets shown in Fig. 2.10.13 are -400-mesh quartz (<38 μm), a commercial quartz with a size less than 15 μm and a sample milled to less than 5 μm. Optical micrographs of the -400 mesh and milled quartz samples are shown in Fig. 2.10.14.

The most obvious feature of the φ scans is that the reproducibility of the relative intensities is poor with the -400 mesh quartz sample. This has obvious consequences for any analytical technique relying on accurate peak intensities. All eight of the patterns from the micronized sample have practically identical relative peak intensities. It is worth comparing the similar results in the variability visible in Fig. 2.10.13 with the tabulated errors for the different methodology used for the data in Table 2.10.1.

The final approach to improving statistics is to increase the probability P that a crystallite is in the diffracting condition and visible to the detector. The latter is relevant today with 1D PSD detectors becoming more common, as the detector can simultaneously see multiple crystallite orientations at a particular incident beam angle, as shown in Fig. 2.10.15. P also increases with beam divergence; although there are many advantages of parallel-beam geometry, improving particle statistics is not one of them.

P is much higher with capillary transmission geometry than for reflection geometry. By rotating the specimen about an axis normal to the beam the effective number of orientations 'seen' by the detector increases greatly. This is the reason why a powder passing a 325-mesh sieve (<45 μm) almost always yields smooth

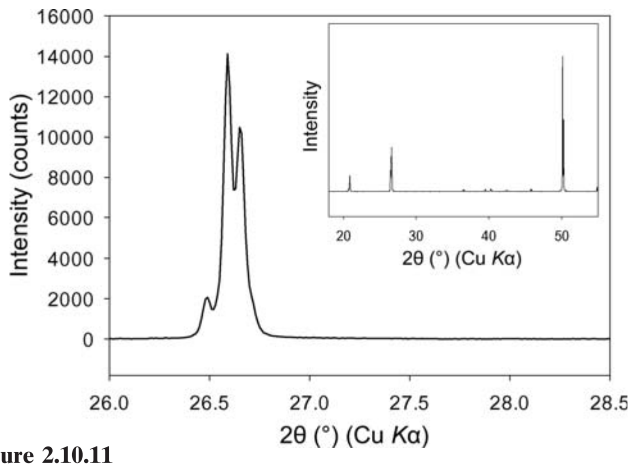

Figure 2.10.11
The main 101 reflection in data collected from a very coarse (~100 μm) highly crystalline quartz. The strange peak splitting is characteristic where there are very large crystallites present in the sample. The inset shows the diffraction pattern over a wider range and the strangely high intensity at 50° 2θ is caused by the detector intersecting a very intense diffraction spot similar to that seen in the lower part of Fig. 2.10.2.

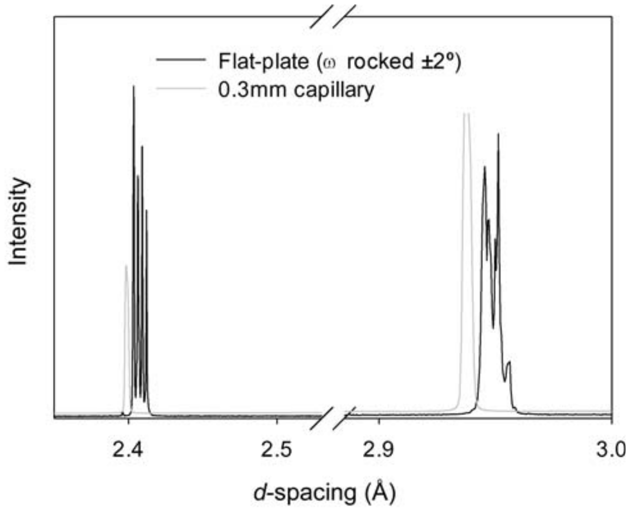

Figure 2.10.12
Comparison between capillary (0.3 mm, 0.8265 Å) and rocking flat-plate (strip heater, 1.2386 Å, ω ±2°) data from the Australian Synchrotron. Data courtesy of Ian Madsen, CSIRO.

Table 2.10.1
Intensity (counts) and mean deviation in intensity of the main quartz 101 reflection with a stationary sample of -325 mesh quartz powder

Data from Alexander *et al.* (1948) and Klug & Alexander (1954).

	Crystallite size			
Data set	15–50 μm	5–50 μm	5–15 μm	<5 μm
1	7612	8688	10841	11055
2	8373	9040	11336	11040
3	8255	10232	11046	11386
4	9333	9333	11597	11212
5	4823	8530	11541	11460
6	11123	8617	11336	11260
7	11051	11598	11686	11241
8	5773	7818	11288	11428
9	8527	8021	11126	11406
10	10255	10190	10878	11444
Mean % deviation	18.2	10.1	2.1	1.2

Table 2.10.2
Theoretical behaviour of different crystallite sizes of quartz in a volume of 20 mm^3

Data from Smith (2001).

Crystallite diameter (μm)	40	10	1
Crystallites per 20 mm^3	5.97×10^5	3.82×10^7	3.82×10^{10}
No. of diffracting crystallites	12	760	38 000

Debye rings in a capillary (Klug & Alexander, 1954), while the pattern would be granular in reflection. Specimen rotation has also been long employed in reflection geometry (de Wolff, 1958; de Wolff *et al.*, 1959), and a sample spinner is now a standard attachment for commercial diffractometers. When properly applied, the use of a spinner can reduce the standard deviation of the integrated intensity by a factor of approximately 4–5 (~7–8 for peak intensities) (de Wolff *et al.*, 1959), corresponding to a reduction in the effective crystallite size by a factor of 3 (Zevin & Kimmel, 1995). However, depending on the sample, as seen in Table 2.10.2 this can be insufficient on its own as it rotates the specimen only in a single plane. Where a spinner is used in conjunction with a point counter, it is important that the spinner must complete at least one rotation during each step to maximize its effectiveness. In order to further improve the particle statistics it is possible to construct spinners that tilt back and forth along an axis normal to the beam (similar to the capillary concept) in addition to the normal axis of rotation. This is effective in improving particle statistics but adversely affects the parafocusing condition in Bragg–Brentano geometry. It is important to note that specimen rotation improves grain-sampling statistics, but does nothing to alter preferred orientation.

The term 'micronized' is one that is frequently seen in papers on quantitative phase analysis. Potentially any kind of mill could be used to reduce the crystallites down to the desirable μm size range (such as shown in Fig. 2.10.14*a* and *b*). However, most mills use high-energy percussion-like impacts between the grinding media and the sample, which tend to damage the crystal structure in softer materials and induce microstrain into the material. In extreme cases the sample can become completely amorphous. There is also the potential problem of modifying the polymorph with samples susceptible to such changes. The mill produced by McCrone (http://www.mccrone.com) was designed specifically for the preparation of X-ray diffraction and X-ray fluorescence samples, and the shearing milling mechanism minimizes damage *versus* conventional impact milling. It is necessary to use wet milling to produce the best results, so it is up to the analyst to choose the best media compatible with both the sample and the polymer micronizing vials. Commonly used are ethanol, isopropyl alcohol, *n*-hexane and water; it is not advisable to use acetone, as this solvent dissolves the polymer jars supplied with this mill. A limitation of most forms of milling is the requirement for a relatively large amount of sample. In the McCrone mill a volume of >1 ml is usually required, although desperate scientists have been known to dilute the specimen with amorphous material, such as silica gel. The analyst should also be aware of the possible contamination of samples by degrading and eroding grinding

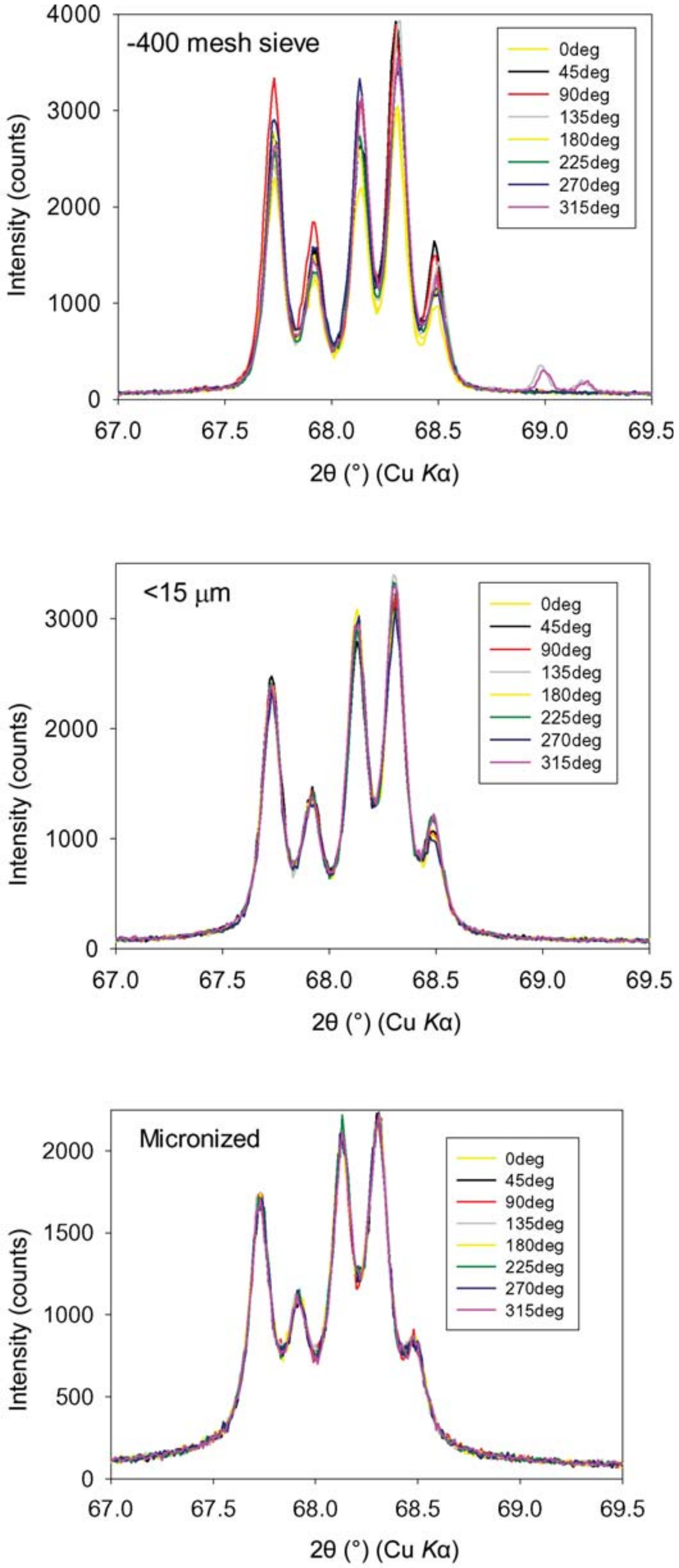

Figure 2.10.13
φ scans of the five fingers of quartz for (*a*) <38 μm, (*b*) <15 μm and (*c*) micronized samples.

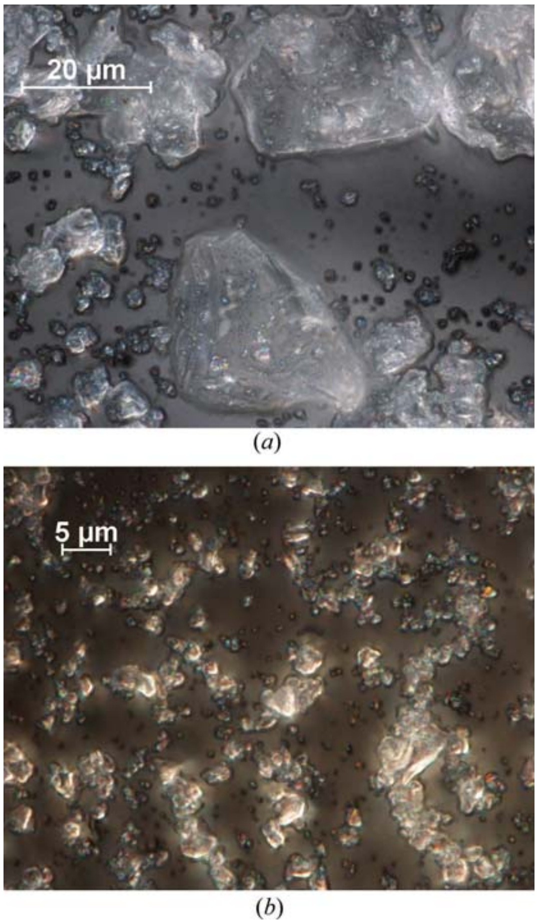

Figure 2.10.14
Optical micrographs of (*a*) -400 mesh quartz at 100× magnification and (*b*) quartz milled in a McCrone micronizer for 15 min in isopropyl alcohol at 150× magnification.

elements (corundum or agate in the micronizing mill; possibly iron, WC, SiC *etc*. in other types of mill).

Obviously, a reduction of the crystallite size to the µm-sized region will produce size broadening if the instrument has sufficient resolution to detect it. It is worth bearing in mind that micronizing does not guarantee a problem-free sample. Micronized specimens almost always exhibit some microstrain broadening. In principle, this could be decreased by an annealing treatment, but this step is rarely practiced. When a mixture contains both very hard and very soft phases, the hard phases may not mill properly. This has been observed in mixtures containing organics and a minor quartz fraction. Despite milling for 30 min or more, the classical split 101 quartz reflection (such as seen in Fig. 2.10.11) was still visible in some data sets, an indication of the 'rocks in dust' phenomenon. Although the McCrone mill is designed to minimize microstructural damage to samples, damage can still occur with very soft materials, and ductile materials may weld as opposed to mill. With very soft and pliable materials a possible alternative could be to cryo-mill the samples, taking advantage of the increased brittleness of materials at low temperature.

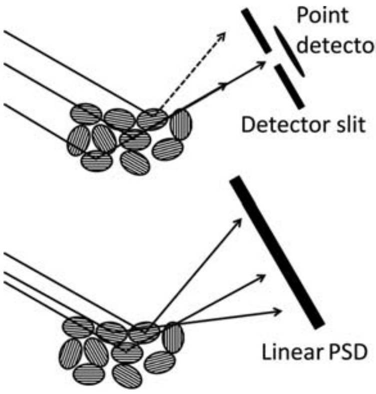

Figure 2.10.15
Diagram showing the source of improved particle statistics in reflection geometry using a 1D position sensitive detector (PSD) *versus* a point detector.

2.10.1.2. *Preferred orientation*

Preferred orientation is usually undesirable in a powder diffraction pattern, although sometimes it *is* the information required, as in texture studies. One of the exceptions is the analysis of clays, where orientation is deliberately induced to identify related reflections. Preferred orientation manifests itself as continuous but non-uniform intensity in the Debye rings, and so is easily characterized with 2D detectors. Preferred orientation does not change the total diffracted intensity, but renormalizes some classes of reflections with respect to others.

Reference is commonly made to a preferred-orientation 'correction'. Strictly speaking, what is done is 'modelling' of the preferred orientation. The proper way to correct preferred orientation is through better specimen preparation.

Models for preferred orientation exist in many analysis packages, specifically the March–Dollase (Dollase, 1986) and spherical-harmonics (Järvinen, 1993) formalisms. Apparent severe preferred orientation may be a sign of large crystallites, which may result in one or more of the other problems outlined in this section.

Additional care must be taken where software corrections are used during quantitative phase analysis, where overlapping reflections can cause serious correlations and erroneous results. The March–Dollase correction is less prone to this, as an orientation direction must be supplied by the analyst. The spherical-harmonics correction has no such constraint. It behaves properly where peak overlap is not extensive, but negative peak intensities are not uncommon (especially when too high an order is used) when applying it without thought in complex mixtures. Negative peak intensities are obviously impossible, so the results of such an analysis must be viewed with great suspicion.

The presence of preferred orientation can be most easily discerned by comparing the observed pattern to a calculated pattern (random) of the same phase from the Powder Diffraction File or other source. The likelihood of preferred orientation can be assessed by calculating the Bravais–Friedel–Donnay–Harker (Bravais, 1866; Friedel, 1907; Donnay & Harker, 1937) morphology from the crystal structure using *Mercury* (Sykes *et al.*, 2011) or other tools.

Orientation tends to occur in materials where the crystallites have either a needle or plate-like morphology. Plates are common in the analysis of mineral samples, such as the commercial phlogopite mica used here as an example. Conventional top-loading of such samples can result in very few reflections being visible because of almost perfect orientation of the plates during pressing, as seen in Fig. 2.10.16. Where the aspect ratio of the crystallites is large, micronizing the sample does not reduce the preferred orientation significantly (Fig. 2.10.17).

The most common approach to decrease preferred orientation of troublesome samples such as this mica is a technique known as back-loading. [Others are discussed in Buhrke *et al.* (1998).] The concept is that the surface of the sample is not subjected to

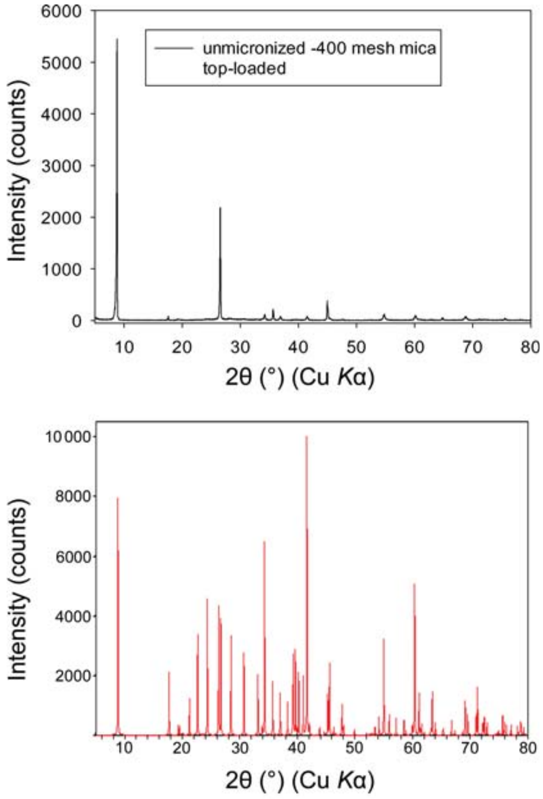

Figure 2.10.16
Top: diffraction pattern of top-loaded 400 mesh phlogopite mica. Bottom: calculated random pattern.

significant compression, yet remains flat. An example of a commercial back-loading holder is shown in Fig. 2.10.34. These holders are filled while upside down with the back removed. The cavity is filled with sample using minimal pressing, the back of the holder is replaced, and then the whole assembly including specimen is flipped the right way up. Generally, the deeper the holder the lower the compressive force on the analysed surface, but the trade-off is the requirement for large amounts of sample. Many of the samples exhibiting plate-like morphology possess low-angle reflections (such as mica and illite) so the sample area cannot be reduced too much to reduce sample volume, or beam overspill may occur.

A variation of the back-loading sample holder is the side-loading sample holder. These are less common, although the sample is still loaded against some surface in the same fashion as the back-loading variant. As the name implies, the difference is that the sample is introduced from a hole in the side as opposed to the back, and the hole is then plugged after filling.

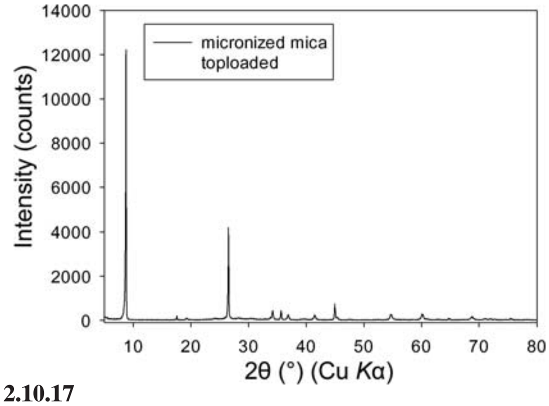

Figure 2.10.17
Diffraction pattern of top-loaded miconized phlogopite mica.

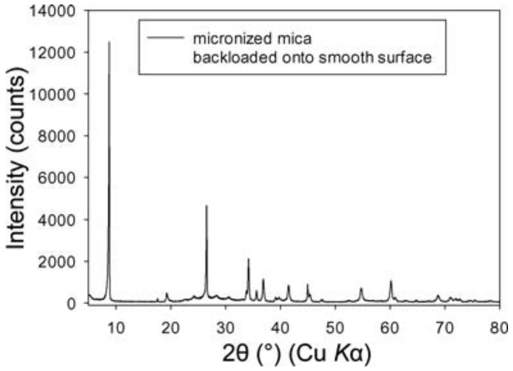

Figure 2.10.18
Diffraction pattern of miconized phlogopite mica when back-loaded onto a smooth surface.

Simple back-loading of samples in itself is not always sufficient for very platy samples such as the high-aspect-ratio mica used here. Fig. 2.10.18 shows the result from back-loading a micronized sample of the mica onto a smooth surface.

Although the result is improved, the specimen is still not a random powder. A useful approach in these circumstances is to make the surface of a back-loaded sample deliberately rough to break up the orientation of the plates. An easy way to achieve this is to load the sample onto the surface of sandpaper or a coarse ground glass slide. Sandpaper has the advantage of being disposable so avoiding cross-contamination among samples. Not all sandpaper has the desired jagged surface, so it may be necessary to experiment to find the best. The paper used for the data shown here was a 400-grit carborundum paper, the surface morphology of which is shown in Fig. 2.10.19. The rough surface will cause some slight defocusing in a parafocusing setup and reduce the count rates somewhat, but in many cases the advantages outweigh the disadvantages.

The result of back-loading the micronized mica onto the 400-grit carborundum paper is shown in Fig. 2.10.20. The dominance of the 00*l* reflections is reduced even further than when mounted onto a smooth surface. The approach is simple enough that it is used routinely in at least one laboratory dealing with large numbers of mining and mineral samples (Raudsepp, 2012). Back-loading samples is more time consuming than top-loading. Consequently, where high sample throughput is required, back-loading can be reserved for those samples where orientation is a problem.

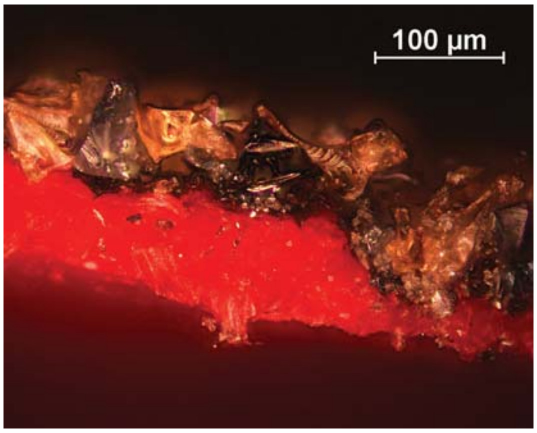

Figure 2.10.19
20× optical micrograph of a cross section of the 400-grit carborundum paper used for back-loaded mica.

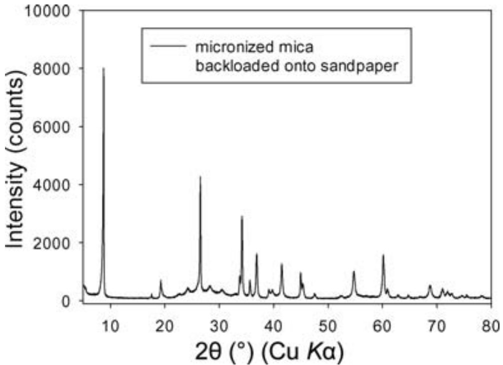

Figure 2.10.20
Diffraction pattern of micronized phlogopite mica when back-loaded onto 400-grit carborundum paper.

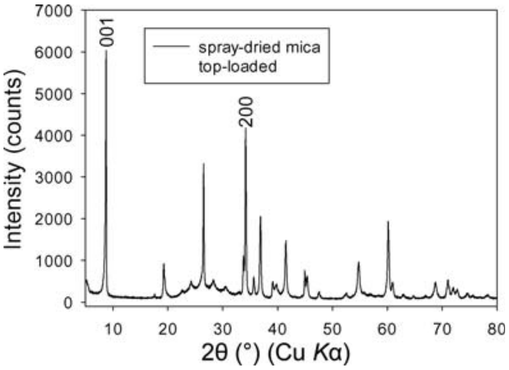

Figure 2.10.21
Diffraction pattern of top-loaded spray-dried phlogopite mica. The sample was not pressed; instead, a flat surface was produced by lightly scraping off excess material with a microspatula.

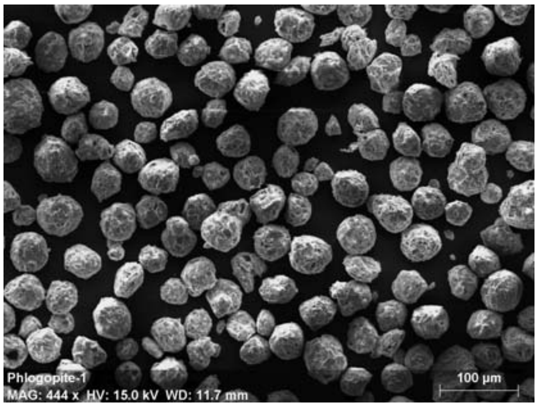

Figure 2.10.22
SEM micrograph of spray-dried micronized phlogopite mica (courtesy of M. Raudsepp, University of British Columbia).

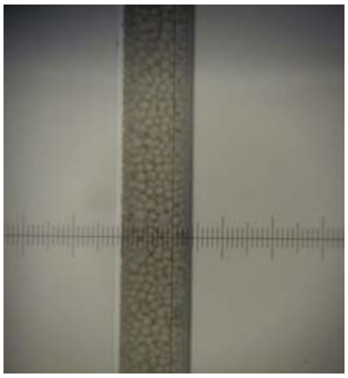

Figure 2.10.23
View through the alignment scope of the spherical spray-dried mica inside a 0.5 mm capillary.

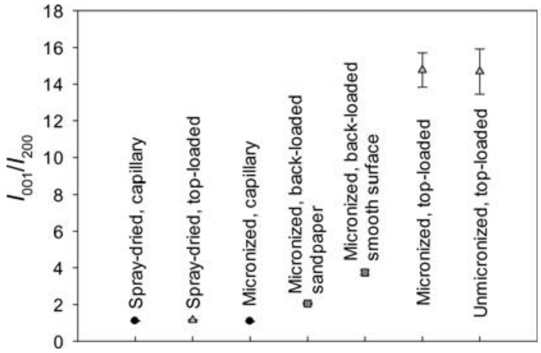

Figure 2.10.24
Plot of the ratio of the integrated intensities of the 001/200 reflections of the mica using different sample-preparation techniques.

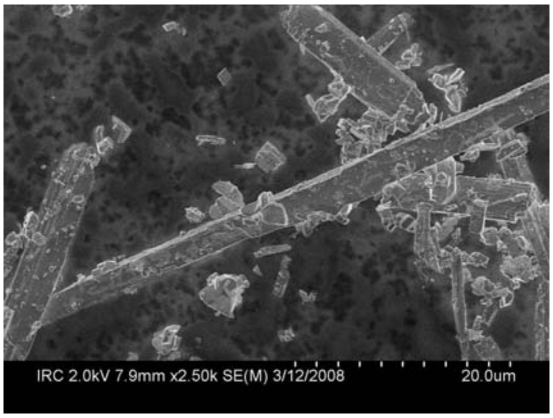

Figure 2.10.25
SEM micrograph of wollastonite needles.

Without resorting to transmission measurements, preferred orientation from platy samples may be almost, if not completely, eliminated by spray drying micronized samples (Hillier, 1999, 2002; see Fig. 2.10.21). This process produces spherical agglomerates (Fig. 2.10.22) that have no tendency to orient if handled gently. The disadvantage is that a relatively large amount of sample is often required because of inefficient sample recovery. Equipment optimized to reduce sample loss for spray-dried XRD samples may be bought in kit form (http://www.claysandminerals.com/spraydrykit), or constructed in house using a small air-brush and heated oven.

One potential practical problem when using spray-dried material with $\theta-2\theta$ geometry instruments is that the spherical particles can start to roll out of the specimen holder at higher 2θ angles (Raudsepp, 2012). The effectiveness of spray drying can be seen as the relative intensities from the top-loaded spray-dried material are almost identical to those in data obtained from the capillary experiments. The spray-dried spheres are very delicate and pressing of the sample must be avoided where possible.

It is worth noting that the platy nature of this mica was so extreme that the micronized mica tended to orient slightly inside the capillary if too much energy was applied during the filling process (*e.g.* using ultrasonics). Arguably, a capillary measurement using a spray-dried material is the ultimate precaution against preferred orientation effects, and the excellent flow characteristics of the spheres mean that the agglomerates remain

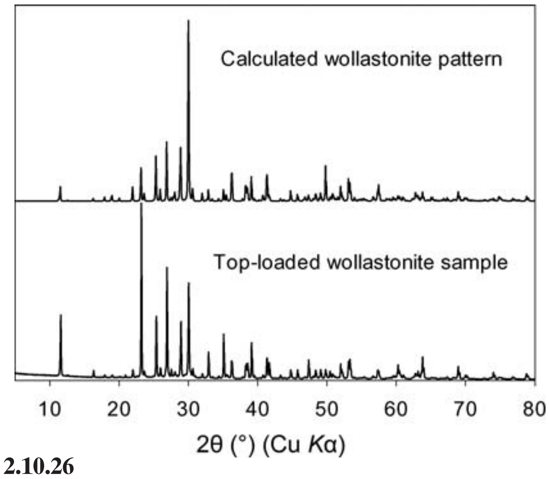

Figure 2.10.26
Effect of preferential orientation on data from top-loaded wollastonite compared with the calculated pattern from the literature wollastonite-1A structure (Ohashi, 1984).

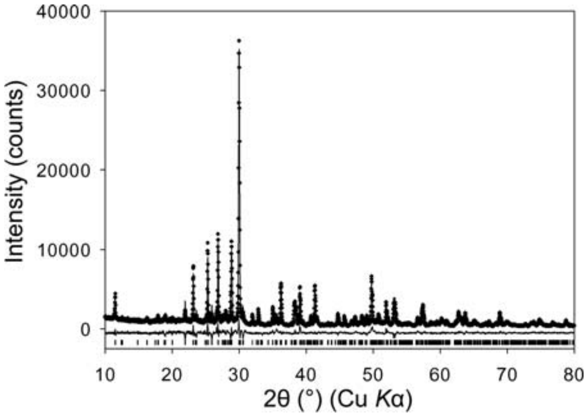

Figure 2.10.27
Rietveld refinement fit to the literature wollastonite-1A structure (Ohashi, 1984) with data from a 0.3 mm capillary with no orientation corrections.

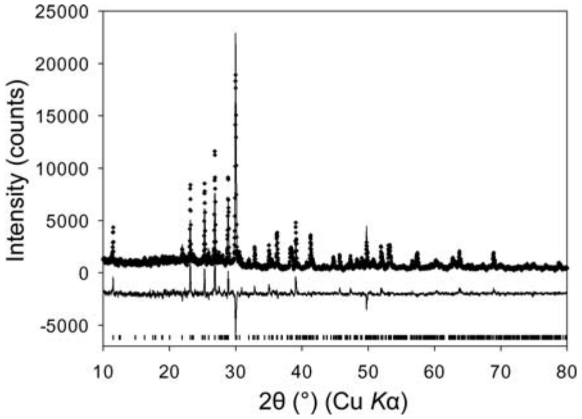

Figure 2.10.28
Rietveld refinement fit to the literature wollastonite-1A structure (Ohashi, 1984) with data from a 0.2 mm capillary with no orientation corrections.

intact while filling the capillary (Fig. 2.10.23). Fig. 2.10.24 gives a summary of the effectiveness of the different sample-preparation techniques for this particular mica sample in terms of the ratio of the integrated intensities of the 001 and 200 reflections. The spray-dried sample with careful top loading can produce a pattern practically equivalent to the capillary data set.

Plates are not the only problematic morphology. Needle-shaped crystallites such as those exhibited by wollastonite (Fig. 2.10.25) and some organic compounds can also show significant problems when top-loaded. In fact, lath-like crystallites such as wollastonite can orient in two directions at the same time, so the behaviour can be more complicated than that of materials with plate-like morphology (see Figs 2.10.26, 2.10.27 and 2.10.28).

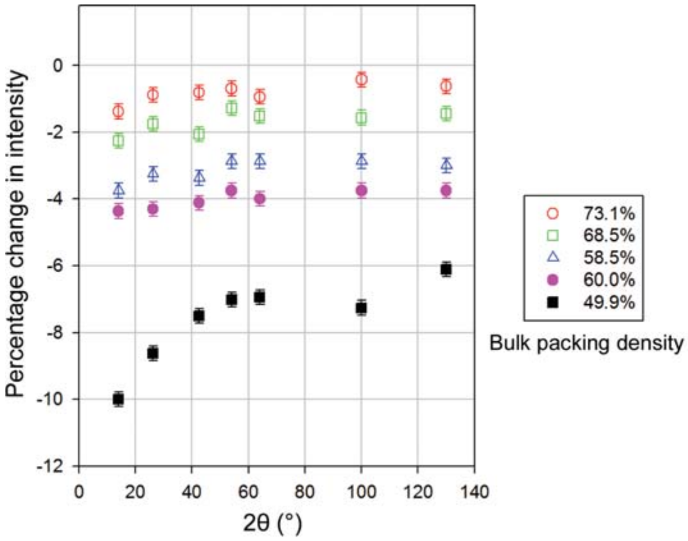

Figure 2.10.29
The effect of surface roughness on the intensity compared to that of a bulk copper specimen. Data from Suortti *et al.* (1972).

2.10.1.3. *Absorption (surface roughness), microabsorption and extinction*

Absorption, microabsorption and extinction effects all alter peak intensities, although particularly low absorption (*e.g.* from organics) can give rise to sample transparency in reflection geometry (as discussed in the section on the choice of sample mounting), where a peak shift and change in profiles can occur. Microabsorption and extinction solely affect the peak intensities.

Microabsorption (also known as absorption contrast) and extinction are effects that complicate quantitative phase analysis. They are both still related to size – particles in the case of microabsorption and crystallites in the case of extinction.

2.10.1.3.1. *Absorption (surface roughness)*

Absorption is an obvious issue when using capillaries in transmission (a convenient calculator is available on the 11-BM web site, http://11bm.xray.aps.anl.gov), but absorption can also affect data obtained in reflection using Bragg–Brentano geometry through the mechanism commonly described as 'surface roughness'. In essence, the increasing packing density with depth leads to lower intensities at low diffraction angles, leading to anomalously low or negative displacement parameters (much as absorption does in capillaries). There are two components to the effect (Fig. 2.10.29, Suortti, 1972). The constant decrease in intensity is generally incorporated into the refined scale factor. The angle-dependent portion becomes more significant as the packing density is reduced.

The effect is greatest with strongly absorbing materials analysed in reflection geometry, so care should be taken to produce a sample with a smooth surface and uniform density where possible. An example is provided by the patterns (Fig. 2.10.30) of a commercial cobalt silicate (which turned out to consist of a mixture of phases). A pattern from a slurry deposited on a zero-background cell – a technique useful for small samples, but which produces a rough surface – yielded significantly lower

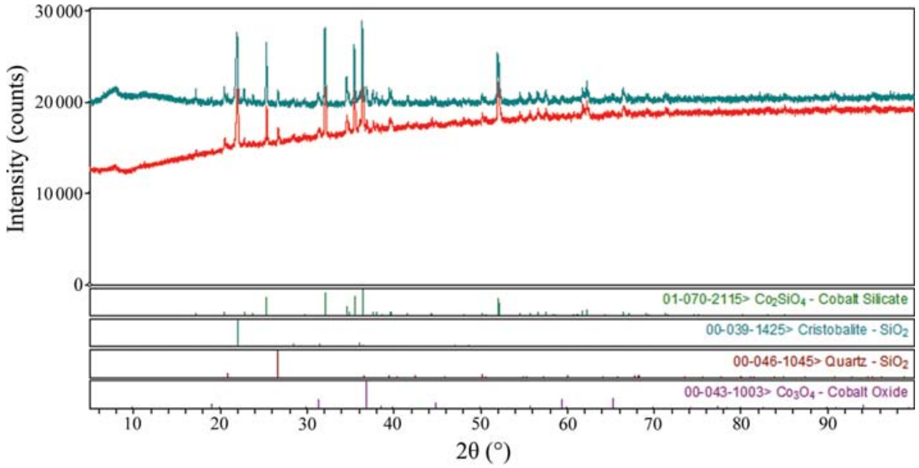

Figure 2.10.30

Powder patterns of a commercial cobalt silicate sample, measured from a (rough) slurry-mounted specimen (red) and from a (flat) conventional front-packed specimen (green). The surface roughness decreases the intensities of the low-angle peaks and background.

peak and background intensities at low angles than a conventionally front-packed specimen. Refinement using the 'rough' data yielded unreasonably negative displacement coefficients. Including a surface-roughness model in the refinement resulted in reasonable displacement coefficients, identical to those obtained using the 'flat' data.

Models by Suortti (1972) and Pitschke *et al.* (1993) exist in most analysis software. They both yield similar results, but the Suortti correction is generally regarded as slightly more stable at 2θ angles below 20°.

2.10.1.3.2. *Microabsorption*

Microabsorption is widely regarded as the greatest impediment to the application of quantitative phase analysis with powder X-ray diffraction data. Misapplication of a microabsorption correction can degrade accuracy (Scarlett *et al.*, 2002). The infamous sample 4 in the Commission for Powder Diffraction quantitative phase analysis round robin (Scarlett *et al.*, 2002) was deliberately designed to be difficult to analyse accurately using any wavelengths available to a laboratory X-ray diffractometer because of microabsorption effects.

Brindley (1945) published a theoretical correction (model) for microabsorption, but the range for an appropriate application can be easily exceeded. In the absence of such a correction, relative concentration errors can commonly be 20–30%. The extent of microabsorption for a phase was described by Brindley in terms of μD, where μ is the linear absorption coefficient and D is the particle (not crystallite) diameter. While a crystallite size can be estimated from the profile widths, determining the particle size requires additional information, such as laser light-scattering measurements. Where $\mu D > 0.1$ the Brindley correction may not be accurate, and ideally μD for every phase present should be less than 0.01, where microabsorption can safely be ignored. Brindley also suggested a rule-of-thumb for the maximum acceptable particle size for quantitative phase analysis, where $D_{\max} = 1/(100\mu)$.

The terms μ and D show that microabsorption can be affected by X-ray wavelength and particle size. The easiest approach for the analyst with a troublesome sample is to reduce the particle size by micronizing the sample. Some in-house laboratories may have multiple systems or the flexibility to change wavelengths. As a rule the linear absorption coefficient decreases with increasing energy, but users should beware of absorption edges that can create a serious discontinuity in this trend. Synchrotron beamlines have more flexibility for avoiding absorption edges and can achieve higher energies that are not practical in laboratory systems. Even when using this high-energy 'sledgehammer' approach there is still a benefit to reducing the crystallite size to avoid some of the other effects mentioned in this chapter.

Microabsorption results from differences in linear absorption coefficients and particle sizes, and can sometimes arise in unexpected situations. Adding a NIST SRM 640b silicon internal standard to a micronized mullite sample (Kaduk, 2009) in order to quantify the amorphous content resulted in a significant microabsorption effect, the result of differences in both particle size and absorption coefficients. The microabsorption could be overcome by micronizing the mullite/Si blend.

Even in cases where the absorption contrast is small, large differences in particle size can result in significant microabsorption effects. For anatase/rutile mixtures (μ = 489.4 and 534.2 cm^{-1}, respectively) in which the anatase and rutile particle sizes were 3 and 150 µm, respectively, concentration errors of 20% relative were observed. The errors were corrected by micronizing the mixtures (Kaduk, 2013). Similarly, mixtures of large-particle (23 µm) MFI zeolite (μ = 65.66 cm^{-1}) and a quartz internal standard (μ = 96.39 cm^{-1}, 10 µm) resulted in relative concentration errors of 5%; these errors were corrected by micronizing the mixtures.

Neutrons are absorbed much less than X-rays, which means that microabsorption is practically nonexistent in neutron diffraction data. The lack of microabsorption is why neutron diffraction is often regarded as the 'gold standard' for quantitative phase analysis, although the beamline proposal process tends to make its application in conventional quantitative phase analysis uncommon. The application of quantitative phase analysis using neutron diffraction data is most often seen when studying phase evolution in an *in situ* experiment. Microabsorption is an issue specific to quantitative phase analysis and a more detailed discussion of the problem is given in Chapter 3.9.

2.10.1.3.3. *Extinction*

Extinction effects are not common in X-ray powder diffraction but may be significant when using neutrons. Extinction is dependent on the size/shape of the coherently diffracting domains, and is a multiple-scattering phenomenon. Primary extinction occurs when a second diffracting event occurs within a single crystallite. Secondary extinction occurs in mosaic crystals and is not seen in powders. When primary extinction occurs, the re-diffracted beam will continue in the same direction as the incident beam but interfere destructively with it. Re-diffraction within a crystallite is not likely to occur where imperfections disrupt the ordering of a crystallite. Consequently, primary extinction is usually only seen in powders of highly ordered and crystalline materials. A classic example is powdered single-crystal silicon as used in studies on extinction such as that by Cline & Snyder (1987). The most commonly encountered phase that can exhibit primary extinction is high-quality natural quartz.

Zachariasen (1945) described an extinction correction (model) including terms relating to crystallite size, wavelength, structure factor and scattering angle. Extinction effects will be apparent with large crystallites and long wavelengths. Extinction effects are also greater for the more intense (low-angle) reflections, so extinction mimics the effects of small displacement parameters. In a single-phase system, unexpectedly low or even negative displacement parameters may be the only sign that extinction effects are present. In a multiphase system the effects of extinction will reduce the apparent phase fraction of the affected phase with respect to the rest of the sample. In fact, studying extinction experimentally is often done by using its effects on quantitative phase analysis to untangle the different effects (Cline & Snyder, 1987). The frequently high quality of natural quartz makes the quantitative phase analysis of mineral samples the most likely scenario for the appearance of extinction in a practical laboratory setting.

The wide range of wavelengths and wide range of $(\sin\theta)/\lambda$ used in time-of-flight (TOF) neutron diffraction makes extinction effects particularly pronounced. Consequently TOF data often require the application of an extinction correction (Sabine *et al.*, 1988). Constant-wavelength neutron diffraction frequently uses longer wavelengths than normally used in the laboratory or synchrotron beamlines, so the user must be aware of possible problems.

Despite the danger of 'message fatigue', the dependence of primary extinction on crystallite size adds yet another reason to reduce the crystallite sizes to the order of 1 µm or so. Theoretically, single-crystal silicon will exhibit extinction with copper radiation with crystallite sizes of 5 µm.

2.10.1.4. *Holders*

2.10.1.4.1. *Reflection sample holders*

In a laboratory setting these are the most common type of holders – normally for use in a Bragg–Brentano instrument. A wide variety of sample holders for different applications are available. Several different holders and techniques will be described, but there are some issues common to all holders in reflection geometry, particularly with Bragg-–Brentano geometry.

In Bragg–Brentano parafocusing geometry care should be taken that the surface of the sample is flat. If the surface is not flat the parafocusing condition is violated and will degrade the peak resolution and positions; in addition, surface roughness can affect the intensities. Where there is a cavity it seems straightforward to make sure that the sample surface is level with the top surface of the holder. The peak positions obtained in Bragg–Brentano geometry are very sensitive to specimen displacement; a vertical displacement of 20 µm in a typical diffractometer will shift the peaks by approximately 0.01° 2θ. The derivation of the equation for the effect of displacement on peak position is given in Fig. 2.10.31. The minus sign in the equation reflects the convention that the displacement is positive if it increases the radius of the diffracting circle, *i.e.* the sample is too low. Front-packed specimens are almost always too high, so the analyst needs to refine his/her technique to minimize the displacement errors.

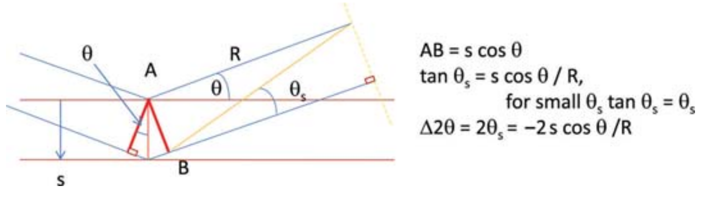

Figure 2.10.31
Derivation of the equation relating peak displacement to sample displacement (s) in parafocusing geometry. R is the goniometer radius.

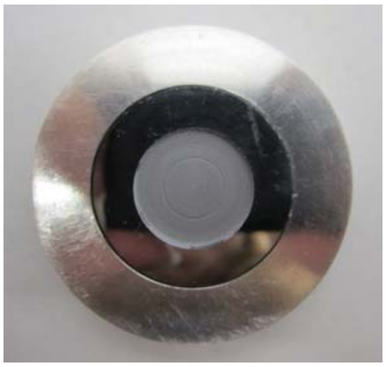

Figure 2.10.32
A home-made top-loading zero-background silicon holder with a 0.5 mm deep cavity.

The sensitivity to specimen displacement is such that even dirt between the reference surface of the sample stage and the holder can produce a detectable peak shift. Dust accumulation inside a powder diffractometer is almost inevitable, so occasionally cleaning these surfaces is recommended.

Parallel-beam-geometry diffractometers have become popular in many laboratories because some of these problems are avoided. Although there are often some disadvantages in terms of peak resolution and grain sampling, they allow more flexibility in the mounting of specimens. For instance, rough sample surfaces and displacements do not cause the aberrations that are apparent in data from conventional parafocusing diffractometers when the same samples are analysed with a parallel-beam system.

Many different types of holders for reflection geometry are available commercially from the instrument vendors, but often home-made holders can be equally effective and customized for specific tasks. Most common are the different types of top-loading sample holders made from plastic or metal, often with a cavity to hold the sample. Commonly the cavities are larger or smaller than those offered by the vendors. The cavity may include some form of zero-background plate such as specially cut single-crystal silicon (Fig. 2.10.32) or quartz, although this does add a significant cost. Some quartz plates may exhibit forbidden reflections or contain inclusions, so they should be tested before use in a sample spinner.

In addition to the standard holders, more specialized holders may be bought or built, or indeed fabricated using a 3D printer. These include holders for air-sensitive samples (Fig. 2.10.33), back-loading (Fig. 2.10.34) and side-loading holders, holders for filter papers, clay samples *etc*. Any laboratory with a competent workshop can construct a wide variety of holders, including those for complex *in situ* work, which is discussed in Chapter 2.9. One common theme is that any material in the X-ray beam path must be kept to a minimum to reduce attenuation. Ideally any such material (such as the polymer dome of the air-sensitive holder shown in Fig. 2.10.33) should be as far away from the diffracting plane as possible. A secondary monochromator can be effective in stopping the parasitic scattering from reaching the detector, but with a PSD there is greater reliance on good design to reduce it as much as possible. A common approach with home-designed and -constructed sample holders for air- or moisture-sensitive samples is to cover the sample with a thin Kapton or Mylar film attached with a bead of silicone grease.

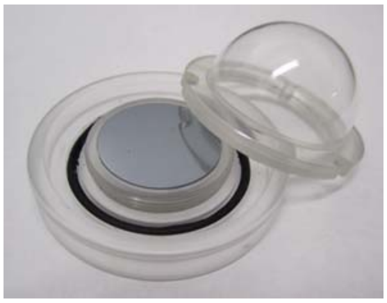

Figure 2.10.33
Commercial holder for air-sensitive samples. This particular holder for small samples has a flat silicon zero-background plate and a polymer dome which screws down against a rubber o-ring seal.

One of the most common questions asked by users of laboratory instruments is how to deal with small sample sizes. In an ideal world, a specialist microdiffraction system or capillary geometry could be used, but many laboratories do not have access to such equipment. How problematic such samples can be depends to some extent on the mass absorption coefficient of the sample. Conventional powder diffraction data relies on having a sample with an ‘infinite sample depth’. However, that depth can be very small for samples with very high absorption coefficients. In those cases, spreading the sample in a very thin layer can still yield reasonable relative intensities across a large range of 2θ angles. With low-absorbing samples such as organics the relative intensities will drop off at higher angles as the sample is no longer ‘infinitely thick’, as shown in Fig. 2.10.35. However, the peak positions will be more accurate than with deeper samples because of the lack of transparency effects in thin samples. Consequently, it is not uncommon to obtain two data sets from such samples: from a thin sample to obtain good peak positions, and from a deep one to obtain better relative intensities. The details of sample penetration are given in Chapter 5.4.

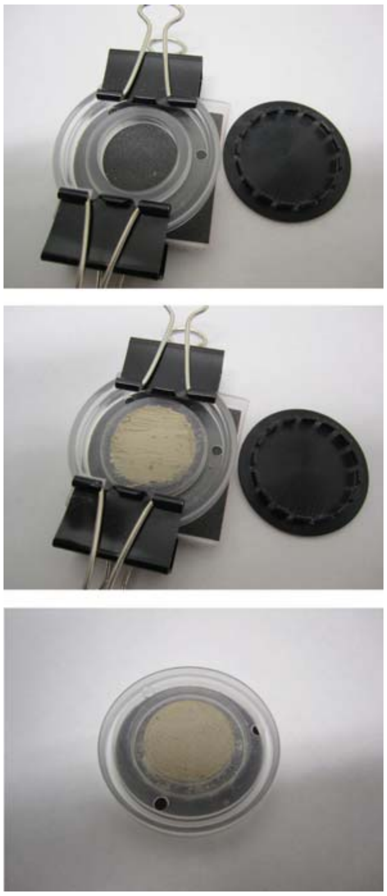

Figure 2.10.34
Filling a commercial back-loading sample holder. The holder is held against a base surface (sandpaper in this case) while filling, the back is replaced and then the holder is flipped over to reveal the sample surface once the clips are removed.

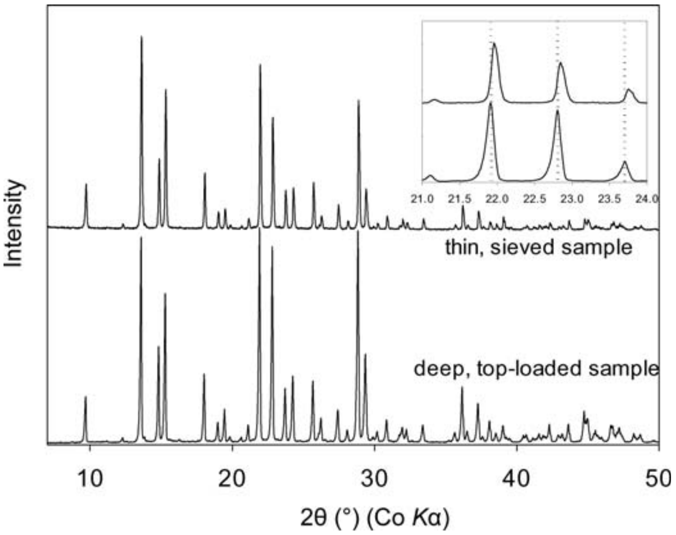

Figure 2.10.35
Data from powdered sucrose on a Bragg–Brentano instrument, with the peak intensities normalized to the first reflection. The thin sample was prepared by sieving onto a low-background silicon plate made slightly tacky using hairspray. The inset shows that there is a slight peak shift between the two data sets as well as the predicted decay in relative intensities with the thin sample with 2θ angle.

Most modern holders are circular and the specimen is often loaded into a round cavity. As the beam ‘footprint’ is rectangular, this is not the most efficient use of the material, as a significant portion will always remain outside the beam. Prior to the introduction of sample spinners, square and rectangular cavities were quite common. It is good practice to know the footprint of the beam at various diffraction angles by observing the illuminated area of a fluorescent specimen. Should the material be in particularly short supply and sample spinning is not absolutely necessary, the powder may be mounted in the minimum rectangular shape to be illuminated by the incident beam. Such an approach may be combined with the use of motorized divergence slits to maintain a constant beam length on the sample. Although most analysis software assumes constant divergence slits, the correction is well known and implemented in most commercial software.

In order to avoid background from the sample holder, thin specimens are usually mounted on flat zero-background plates. It is useful to have the surface of the plate lower than the reference surface (50 µm is a common value) to minimize specimen displacement effects. In practical terms, thin samples are historically referred to as smear mounts. Slurry mounting using ethanol or acetone often yields a self-adhesive specimen, but it is tricky to obtain the correct slurry rheology to produce a non-lumpy, thin and even layer across the surface; surface roughness is often apparent in the pattern. Loose, friable samples may be problematic with spinning specimens or the tilting specimens in $\theta{-}2\theta$ geometry. A number of materials have been used over the years to adhere thin powder samples to flat plates; common ones are thin smears of Vaseline or grease, but analysts often have their own favourites. The particular material used to stick the sample to the surface is often the result of testing a large number

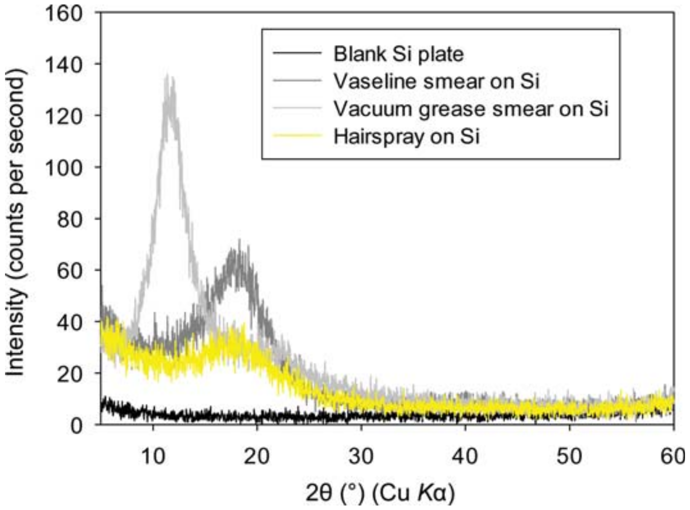

Figure 2.10.36
Diffraction pattern from a silicon-wafer zero-background holder, smears of Vaseline and Corning high-vacuum grease, and the surface treated with hairspray.

of options to find the one with the lowest background and fewest non-Bragg reflections. An unusual alternative is hairspray, which produces a tacky surface when applied correctly whilst having a minimal effect on the resulting diffraction pattern. The medium chosen may also depend on whether the sample must be recovered intact, as contamination with grease might not be acceptable. The effect on the background of different adhesion materials can be seen in Fig. 2.10.36. The Vaseline and vacuum grease smears add broad reflections at approx. 19 and 11° 2θ, respectively, with Cu $K\alpha$ radiation. Where data collection starts above the main portion of the peak the effect may be hardly noticeable, but could be problematic when starting at low 2θ angles. Such broad patterns are straightforward to model with a Debye (diffuse scattering) function, and it is not necessary to subtract them from the raw data.

Should the instrument have parallel-beam geometry, an alternative approach is to use a fixed incident-beam angle, more commonly known as grazing-incidence geometry. In this way the volume of sample illuminated is constant with angle, so in the absence of secondary diffractometer optics the relative intensities will match those expected with conventional geometry. An unfortunate effect of conventional grazing-incidence geometry with long slits is that the peak widths degrade significantly at lower incident angles (Toraya & Yoshino, 1994). It is possible to model the peak broadening in a Rietveld refinement (Rowles & Madsen, 2010) but it is not straightforward. Use of an appropriate secondary optic can avoid the peak-broadening problem but introduces a complex, geometry-dependent intensity correction (Toraya *et al.*, 1993).

2.10.1.4.2. *Transmission sample holders*

Transmission geometry of any type is best suited to samples with low absorption such as organics and polymers, and is preferred for such samples when available. Transmission geometry has advantages when data are required at low diffracting angles. While the beam often has to be stopped-down in reflection geometry to avoid overspilling the sample, this undesired attenuation of the beam is not required for transmission geometry. Another advantage common to both the foil and capillary transmission techniques is that a small quantity of a powdered sample is usually sufficient. Samples small enough to be problematic with reflection geometry will often be perfectly adequate for transmission.

Data collection in transmission geometry is best done with either a parallel-beam or focusing geometry; the focus should be at the detector. Data can be collected using a divergent-beam setup, but the intensities obtained are very low and the resolution is usually poor. Parallel-beam geometry has the advantage that it is able to perform reflection and transmission measurements equally well.

2.10.1.4.2.1. Flat foils

Although less commonly used with modern diffractometers, the foil-type transmission sample mounting was quite common in some older-style X-ray cameras. Sprinkling powders onto single-sided Scotch tape was sometimes used with instrumentation such as Hägg–Guinier cameras, but care should be taken as the quality of the tapes as diffraction substrates can vary wildly; the crystallinity of the polymer can be high or low, and the adhesive sometimes contains mineral inclusions, such as talc. In the modern diffractometer, foil-type transmission data can sometimes be collected using the same rotating sample stage as for reflection measurements. Simply turning the stage by 90° and using a different holder can be sufficient if the optical configuration is suitable for both reflection and transmission. For solid organic samples such as polymers this foil transmission geometry has significant advantages because of the lack of transparency effects. It is worth noting, however, that the processing of polymers can induce significant texture, such that the data collected from a film in reflection geometry will not necessarily be identical to those collected in transmission. Should a reproducible pattern independent of geometry be required, then steps should be taken to reduce the sample to a true random powder and/or a 2D detector should be used.

With powder samples the technique requires the use of a transparent substrate, usually in the form of a thin polymer film or foil. In an analytical laboratory the easiest place to find such a substrate is the X-ray fluorescence laboratory, where very thin X-ray transparent polymer films are used for both sample supports and covers for liquid cells. Some of the materials used in these applications are familiar in the diffraction community as windows, *i.e.* Mylar and Kapton, but others such as polypropylene are not. The substrate will obviously add to the background, but a good substrate from a diffraction standpoint combines transparency with a lack of sharp features in the diffraction pattern. This makes fitting the background much easier. Any holder must be capable of stretching or holding the film flat across an opening for the X-ray beam. A commercial version of a foil-type holder is shown prior to assembly in Fig. 2.10.37. Example data from three different XRF films are shown in Fig. 2.10.38, together with that from a thicker Kapton foil commonly used as window material. It is notable that, despite the two 7.6 µm Kapton films being almost twice as thick as the Mylar or polypropylene films, the scattering from them is almost identical. The lack of any distinctive, sharp features above 6° 2θ in the Kapton films makes them attractive in this region, but for low-angle data Mylar is probably the better choice. Although giving a generally higher background, the thicker 50 µm Kapton foils can be used very successfully (see Fig. 2.10.39). Despite the greater attenuation they are much easier to handle, as their greater stiffness and weight makes them less susceptible to static electricity.

One advantage of transmission foil mounts is the small amount of sample required. In a similar way to producing smear mounts

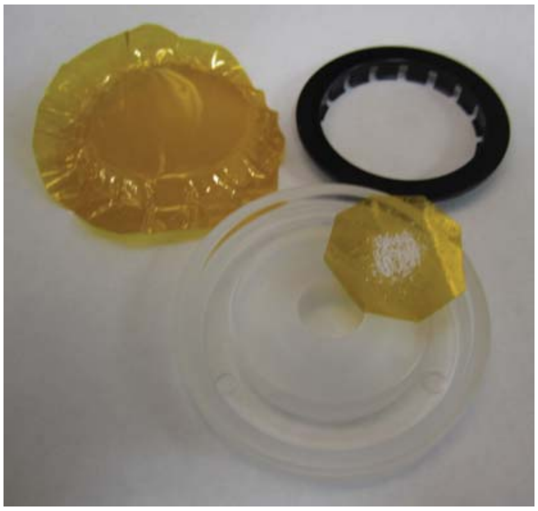

Figure 2.10.37
Parts prior to assembly of a transmission foil sample in the holder. In this instance, micronized quartz is held as a loose powder between two 50 μm Kapton foils while the upper foil is stretched into place by the black clip.

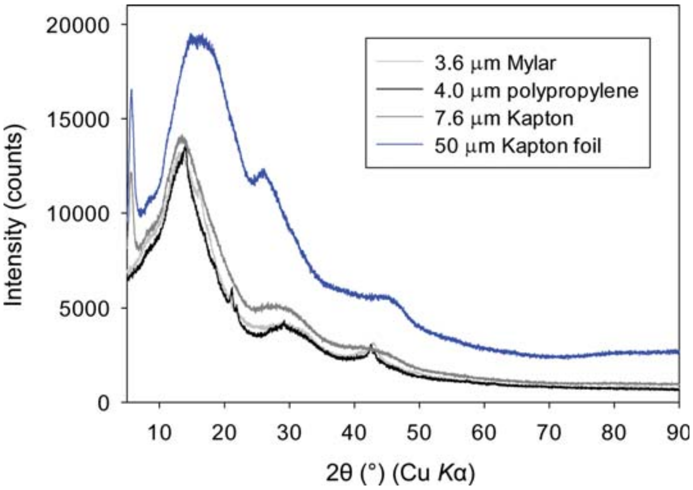

Figure 2.10.38
Transmission data from double layers (as used for powder samples) of different polymer substrate films. They include 3.6 μm Mylar, 4.0 μm polypropylene and 7.6 μm XRF films, and a thicker 50 μm Kapton foil.

for reflection geometry, there are a number of ways to prepare the thin layer required. Loose powders may be trapped between two foils as in Fig. 2.10.39, or alternatively a slurry or smear mount may be used in a similar way to reflection geometry. Although the sample may adhere sufficiently such that a single foil can be used, it may be necessary to use a sandwich in the same way as a loose powder. For instance, slurries do not usually adhere well to Kapton foils, so it is often better to sacrifice a little intensity from the additional Kapton attenuation and ensure the sample does not fall away during data collection. Lack of adhesion could be regarded as an advantage with regard to recovery of valuable samples. Where an adhesive is used, the same considerations as with a smear mount in reflection still apply with regard to background *etc*.

Ideally the sample thickness should be perfectly uniform, but in practice this will rarely be achieved. Commonly a specimen in visible light transmission will appear something like that seen in Fig. 2.10.40. Rotation is used to average out inhomogeneity in the specimen.

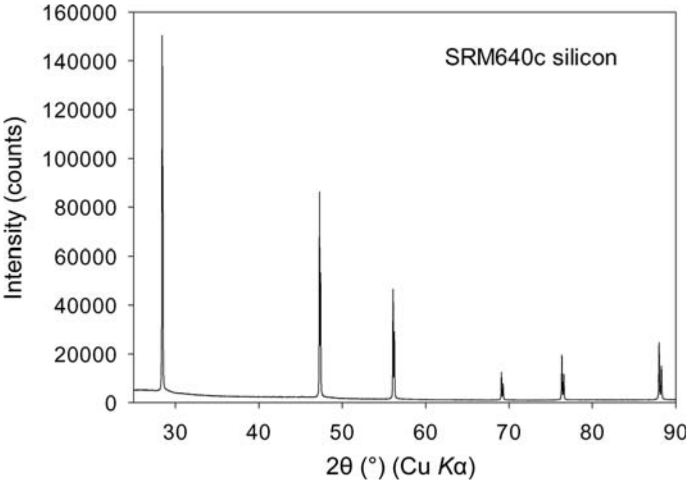

Figure 2.10.39
Diffraction pattern from loose SRM640c powder between two 50 μm Kapton foils.

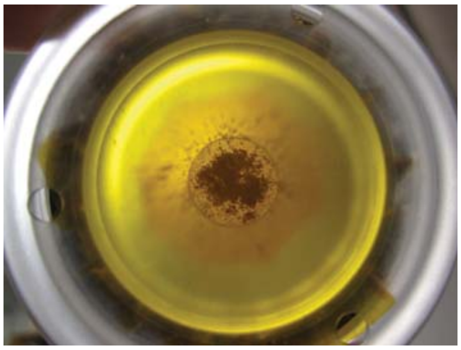

Figure 2.10.40
Transmitted light view of a micronized quartz sample through 50 μm Kapton foils.

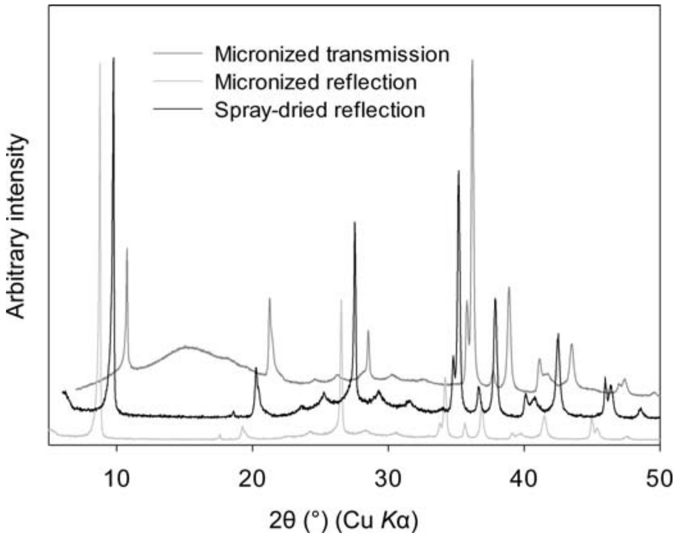

Figure 2.10.41
Comparison of data from micronized 40S mica taken in reflection and transmission geometry, and spray-dried material in reflection geometry. For improved clarity the spray-dried and transmission data sets are translated by +1° and +2° 2θ respectively.

Sedimentation during slurry mounting and compression of powders between two foils can lead to preferential orientation in foil transmission samples just as with flat-plate reflection specimens. Although the physical effect is the same for plate-like crystallites, it should be remembered that the crystallite orientation with respect to the beam is rotated by 90°, so the resulting diffraction patterns will not look the same. This becomes very apparent when comparing the foil transmission and reflection patterns from the micronized mica in Fig. 2.10.41.

Foil transmission specimens are usually rotated in a similar fashion to a reflection sample, but the improvement in statistics falls short of that found in the capillary geometry described in the next section.

One thing worth considering is that there is an inherent angular intensity aberration due to the plate transmission geometry. Owing to geometrical considerations, the path length through the specimen (and support) increases with angle with a resulting increase in absorption. For refinement work, a $1/\cos\theta$ correction can be applied.

2.10.1.4.2.2. Capillaries

Capillaries are particularly suitable for small samples, air- and moisture-sensitive samples and organics where the absorption is low enough to cause transparency effects in reflection data. They are also commonly used for materials with platy morphologies such as clays to eliminate or greatly reduce preferred-orientation effects. They are less effective at reducing preferred orientation in materials with needle-like morphologies but are still useful, a possible analogy being that the crystallites pack into the capillary like a handful of pencils in a glass. The extent of the problems with needles depends on the aspect ratio of the needles and the diameter of the capillary used – smaller diameter capillaries usually being more problematic. Figs. 2.10.27 and 2.10.28 show the example of wollastonite powder mounted in 0.3 and 0.2 mm capillaries, respectively, where orientation effects become pronounced in the 0.2 mm capillary. Fortunately, needle-like morphology is observed more often in organic crystallites, where larger-diameter capillaries can be tolerated.

Glass and fused silica (‘quartz’) capillaries can be bought commercially in a range of diameters between 0.1 and 2 mm. Different compositions of glass are available that have varying absorption characteristics (Table 2.10.3). The softer glass has a greater tendency to splinter but can be heat-sealed very easily by melting. Quartz tends to be stiffer and often breaks more cleanly when scored using a cutting stone, but requires a hydrogen flame for heat-sealing because of its high melting point. Alternative methods of sealing the open end of capillaries include using molten wax, epoxy and nail varnish. The choice may be restricted by the environment in which the capillary is being filled. In an argon-filled glove box the use of a flame or solvent-based method may not be feasible or desirable, whereas wax sealing with a heated filament is acceptable.

The small size and delicate nature of capillaries can make them extremely frustrating to fill, especially in environments such as glove boxes. Patience is an absolute must, especially with valuable or small samples where capillary breakage and sample loss are unacceptable. It is very important to make sure that the sample is fine enough to pass into the capillary without jamming. Even if it is fine enough, different powders can vary considerably in their tendency to aggregate. For example, NIST 640d silicon contains fine crystallites and flows extremely well, making it very easy to load into a capillary. However, some rutile powders can be very fine but don’t flow well, making them difficult to load into smaller capillaries.

Once the small amount of material is in the capillary funnel (assuming it is a commercial capillary), it must be coaxed to drop to the bottom. This is usually done using some form of vibration. Anything from dedicated capillary-filling machines to ultrasonic baths, test-tube vibrators and nail files can be used. A common strategy is to drop the capillary down a vertical 50 cm glass tube, and allow the bouncing when the capillary hits the bottom to vibrate the sample. However, with very small and/or valuable samples the risk of the sample being vibrated out of the funnel may be too great to use automated techniques. In this case, very gently stroking the capillary using a fingernail to induce a low-frequency vibration may be the best option, changing the position at which the capillary is held to alter the vibration frequency as required. Agglomerates blocking a capillary can be very difficult to break up by vibrating the capillary manually, but an ultrasonic bath can often break up loosely bound agglomerates. Using a smaller-diameter quartz capillary or wire to tamp down a clog is possible, but riskier than using an ultrasonic bath.

Table 2.10.3
Absorption and physical characteristics of the capillaries whose data are shown in Fig. 2.10.46

Material	Linear absorption, Cu $K\alpha$ (cm^{-1})	Wall thickness (μm)	Outside diameter (mm)
Quartz (Hampton Research)	76	10	0.50
Soda lime glass (Hampton Research)	126	10	0.50
PET (Advanced Polymers)	10	19	0.58
Polyimide (Cole-Palmer)	9	25	0.55

The most commonly used capillaries range between 0.3 and 0.8 mm in diameter. Capillaries with a diameter less than 0.3 mm are extremely difficult to fill and very large ones can cause unwanted artifacts. For moisture-sensitive materials it is worth noting that significant moisture can adhere to the interior surface of commercial glass and quartz capillaries, so heating them in an oven prior to use is recommended.

The interplay between the sample absorption, radiation and optics can make the choice of capillary material and diameter a dynamic one. The capillary absorption is measured using the term μR, where μ is the effective linear absorption coefficient (taking account of the sample density) and R is the capillary radius. A convenient tool for estimating capillary absorption is available on the 11-BM web site (http://11bm.xray.aps.anl.gov). Ideally, the value of μR should be less than 3 for the absorption corrections in most software packages to adequately cope with the effect of absorption. A recent analytical correction has been shown to be effective to $\mu R = 10$ (Lobanov & Alte de Viega, 1998), but is not yet implemented in all current analysis software. A pre-analysis correction is always possible but not ideal. The effect of high capillary absorption can be seen visually by a reduction in peak intensity at lower angles, which correlates with the displacement parameters in a structure refinement. The easiest way to change μR is by changing the capillary diameter. More heavily absorbing samples usually require smaller capillaries, although using an alternative radiation such as Mo $K\alpha$ to change the linear absorption coefficient is a possible alternative. Determining an accurate sample packing density experimentally can be tricky. There can be significant variability between supposedly identical capillaries, so ideally the empty portion of the actual capillary being used should be measured. The packing density generally ranges from 20–50% depending on the morphology of the crystallites and the amount of energy applied in vibrating the sample into the capillary (*e.g.* sonicating the sample will increase the packing density).

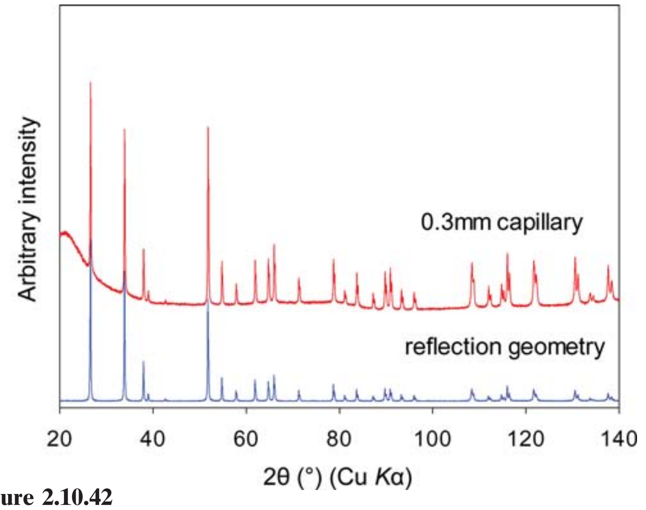

Figure 2.10.42
Comparison of the diffraction patterns of pure SnO_2 from a 0.3 mm quartz capillary in transmission and reflection geometries with Cu *Kα* radiation. The very high absorption of SnO_2 leads to severe attenuation of the lower-angle reflections in the transmission data.

Where contaminating the sample is acceptable, another option is to dilute the sample with a material with very low absorption to reduce the overall sample absorption. There are two options here: either an amorphous material or a crystalline one. The addition of an amorphous material such as fumed silica (others could include amorphous boron, carbon black *etc*.) does not add any additional reflections to the pattern but will increase the background. Given that the backgrounds of capillaries using Cu *Kα* radiation are often quite high already, this may not be desirable. Alternatively, a material such as diamond powder can be used, which will add a small number of lines at high angles but does not add to the background. The closely defined crystallite sizes of diamond polishing powder can also improve the flow characteristics of materials that tend to agglomerate. The phase purity of polishing media is not relevant to their intended use, and some diamond polishing powders can contain some SiC, corundum or quartz. Check the phase purity of any diluting phase before use.

Fig. 2.10.42 shows the pattern from a 0.3 mm capillary of pure SnO_2 (cassiterite) taken with Cu *Kα* radiation compared with that from reflection geometry. The linear absorption coefficient of SnO_2 with Cu *Kα* radiation is ~1400 cm^{-1}. Assuming a 50% packing density, μR with a 0.3 mm diameter capillary is 10.5, which is much higher than can be tolerated in any structural analysis. Absorption attenuates the lower-angle reflections as the X-rays cannot penetrate properly compared to the high angles. However, in addressing capillary absorption, less really can be more. Fig. 2.10.43 shows data sets from SnO_2 diluted with 8000 grit diamond powder and with amorphous carbon black. As expected, the background is higher with the amorphous carbon but without the additional reflections from the diamond powder. Despite there being only approximately 10 vol% SnO_2 in each of the sample mixtures, the raw low-angle intensities are much higher, and the relative intensities are comparable with those from the reflection data in Fig. 2.10.42. Assuming a 50% packing density for the mixture, the value of μR with a 0.3 mm capillary would be approximately 2.3, which is in the acceptable range for structural analysis.

The relative intensities are such that a good-quality Rietveld refinement of a heavily absorbing compound such as SnO_2 with Cu *Kα* laboratory data can be easily carried out. Fig. 2.10.44 shows the fit of the diamond-diluted sample to the literature cassiterite SnO_2 structure. With very high dilution factors one should be careful not to compromise the particle statistics too much. Utilizing the full width of the detector with a full capillary will maximize the available statistics.

An alternative approach to dilution of heavily absorbing samples inside a capillary is to coat the outside (or inside) of a capillary. An appropriate absorption correction for annular samples does exist (Bowden & Ryan, 2010), so this is not an impediment. However, it is not available in common software packages so may have to be applied to the raw data prior to a structural analysis. One requirement is that a known thickness of sample needs to be applied to the surface of the capillary as uniformly as possible. This can be difficult to achieve and may require the use of an adhesive to bond the sample sufficiently to the capillary while spinning. The additional effect of an adhesive on the background should be considered in the same way as for a smear mount. Similar results to dilution may be achieved if done with care, as shown in Fig. 2.10.45.

Depending on the instrument geometry, a large diameter capillary can have an additional effect. Where an instrument does not have a focusing geometry (either primary or secondary), the peak resolution is degraded with increasing capillary diameter. With organic samples this can lead the analyst to use a smaller

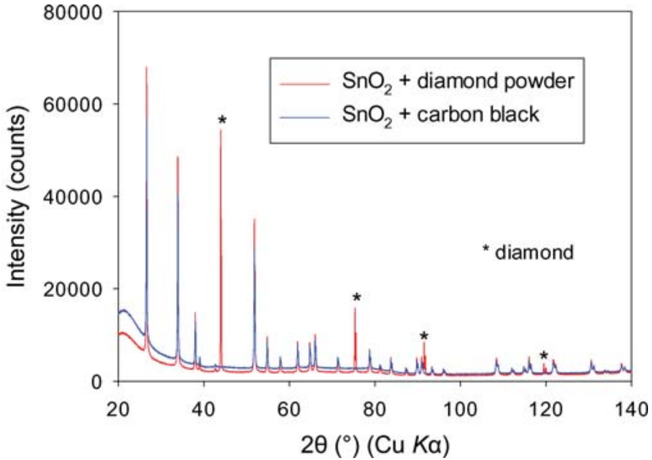

Figure 2.10.43
Raw diffraction data from 0.3 mm capillaries of SnO_2 diluted with 8000 grit diamond powder and carbon black. In each case the capillaries had approximately the same packing density of SnO_2, so yielded almost identical intensities.

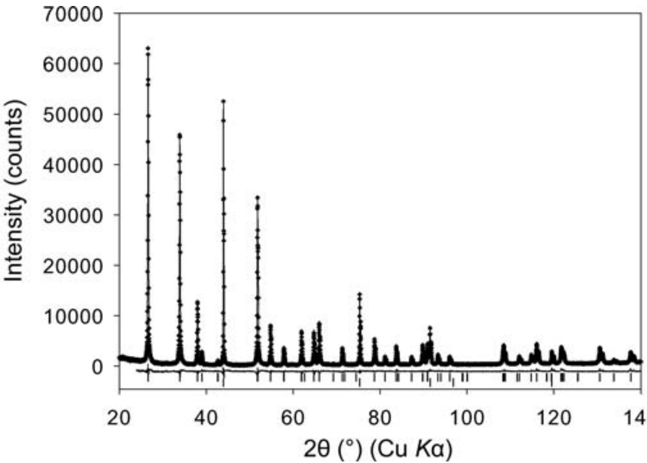

Figure 2.10.44
Rietveld refinement of the diamond-diluted data with the SnO_2 cassiterite structure. The capillary background was subtracted prior to the fitting whilst maintaining the correct counting statistics. The R_{wp} value for this fit was 8.4%.

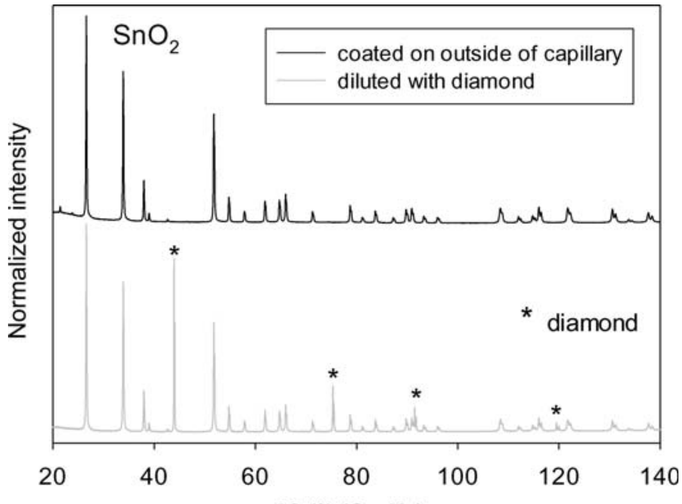

Figure 2.10.45
Comparison of data from SnO$_2$ when diluted with diamond inside a 0.3 mm capillary and pure SnO$_2$ coated on the outside of a 0.3 mm capillary.

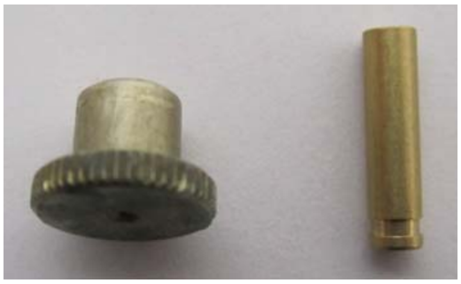

Figure 2.10.47
Platform and pin mounts for capillary samples.

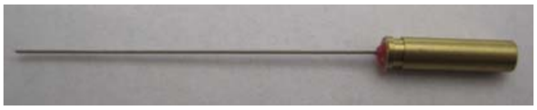

Figure 2.10.48
A 0.5mm capillary secured into a standard brass capillary pin using dental wax at both ends of the pin.

diameter capillary than optimal to retain reasonable resolution. Consequently, with organic samples where capillaries of 0.8 mm diameter are commonly used, it is highly recommended that an instrument with a primary focusing monochromator (or mirror) is used; the focus should be at the detector. Where the diffractometer is $\theta-\theta$ geometry it is best to still collect capillary data as if it were a $\theta-2\theta$ Debye–Scherrer instrument, simply by collecting ‘detector scans’ or the equivalent in the data-collection software. This has no effect on the data in a perfect situation, but it means that the sample illumination is constant over all diffracting angles even if there is a misalignment of the primary beam with respect to the capillary axis (caused either by misaligned optics, a misaligned capillary stage, or both). In addition, a correction for capillary displacement can be applied to data collected in conventional Debye–Scherrer geometry (Klug & Alexander, 1954) as the x and y displacements relative to the incident beam are constant over all 2θ angles.

Polymer capillaries are becoming increasingly common and are the standard at many synchrotron beamlines. They are easy to seal, but the lack of a funnel can make smaller sizes trickier to fill. A number of polymers can be used for capillaries, *e.g.* Mylar [poly(ethylene terephthalate) – PET] and Kapton [poly(oxydiphenylene pyromellitimide)]. The background from the capillary material itself is often more noticeable with a laboratory diffractometer than for higher-energy synchrotron instruments. A comparison of the background with a Cu *Kα* focusing mirror laboratory diffractometer from 0.5 mm quartz, soda lime glass, PET and polyimide capillaries is shown in Fig. 2.10.46. A study of the different options for polymer capillaries in the laboratory environment was published by Reibenspies & Bhuvanesh (2006), which highlighted the awkward reflection with polyimide visible just above 5° 2θ in Fig. 2.10.46. It is also worth noting that the walls of polymer capillaries are not as stiff as those of quartz capillaries. If a low-temperature or other experiment might produce an internal vacuum (*i.e.* freezing a liquid sample), a polymer capillary can deform from a perfect cylinder, which may cause problems.

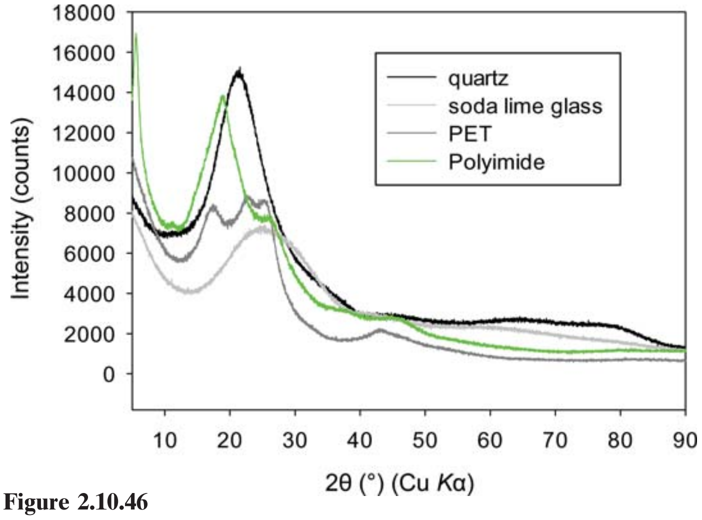

Figure 2.10.46
Comparison of the background from four different 0.5 mm-diameter capillaries. The quartz and glass capillaries are commercial capillaries for diffraction analysis. PET and Kapton capillary tubing are available from a number of different suppliers and are not made specifically for diffraction.

Mounting the filled capillary on the goniometer head can be achieved in different ways. Most commonly a hollow brass pin is used, but flat platforms are available (Fig. 2.10.47). The various pins/platforms are a standard size, so they should fit no matter where they are sourced from. The flat platforms have a hole in the middle, but it is only suitable for inserting small-diameter capillaries. Large-diameter capillaries must be affixed to the platform surface with wax and are vulnerable to sagging with horizontal goniometers because of the lack of support. The brass pins will accept larger capillaries and are to be preferred with respect to improved support for the capillary where the capillary is held at both ends of the brass pin (Fig. 2.10.48). Fixing the capillary onto the base is often done using wax or clay, although epoxy may be preferable if elevated temperatures are to be used. Coarse alignment is usually performed using a small desktop microscope before final alignment on the system. It is important to try to get the capillary rotating as straight as possible before mounting on the system, as removing tilt errors is much more difficult with the higher-magnification alignment scope mounted on the goniometer. Final alignment of a capillary is an exercise requiring patience. Never try to align out errors in two directions at once. Even if repeated attempts are necessary to stop the goniometer head in the correct position (Fig. 2.10.49), only correct errors perpendicular to the view in the scope. Ideally, the final alignment should only require correction of a side-to-side

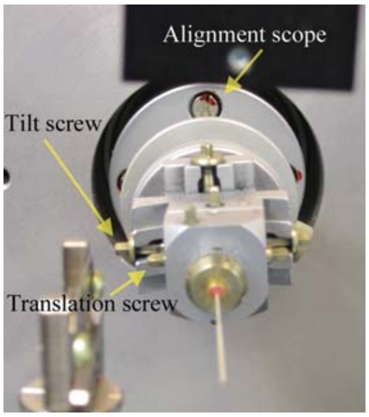

Figure 2.10.49
Goniometer head position in relation to the goniometer-mounted alignment scope.

movement rather than any wobble from tilt misalignment. However, it can still take some time. For systems where the goniometer spinning is controlled by computer software a wireless computer mouse is a very good investment, as it allows the person performing the alignment to stop the spinning capillary without taking their eyes off the sample.

2.10.2. Neutron powder diffraction

2.10.2.1. *Specimen form*

Large penetration depth and sensitivity to lighter elements (especially mobile species such as hydrogen, lithium and oxygen) in the presence of heavier elements make neutron diffraction a powerful and complementary technique to X-ray diffraction for structural studies. Because neutrons are highly penetrating and large sample volumes can be used, sometimes no specimen preparation is needed at all; sintered ceramic pellets, fish otoliths and renal calculi can be placed directly in the beam. However, the most traditional sample holder for standard neutron powder diffraction (Debye–Scherrer geometry) is cylindrical and is usually made of vanadium. If the diffraction instrument has reflection geometry, however, one has to use flat plates. Diffractometers built for the study of engineering materials can accommodate various shapes and forms because they can isolate small volumes within the sample.

2.10.2.2. *Sample size*

Traditionally, a large amount of sample was needed for neutron powder diffraction because of the limited flux available at various neutron sources. However, significant advances have been made in source power and detector technology, making it possible to do standard diffraction experiments with relatively small quantities of samples, both at reactor and spallation sources. There are multiple factors that have to be taken into account to determine how much sample is required. These include source power, detector coverage of the instrument, source-to-sample distance, the scattering power of the sample, beam size, available time and information sought from the measurement. Neutron powder diffraction instruments often have to trade intensity for resolution, and so often a larger quantity of sample is needed for high-resolution instruments. Sample mass can vary from milligrammes to several grammes, so it is always advisable to contact the scientists responsible for the particular instrument to determine the quantity needed for the proposed measurements.

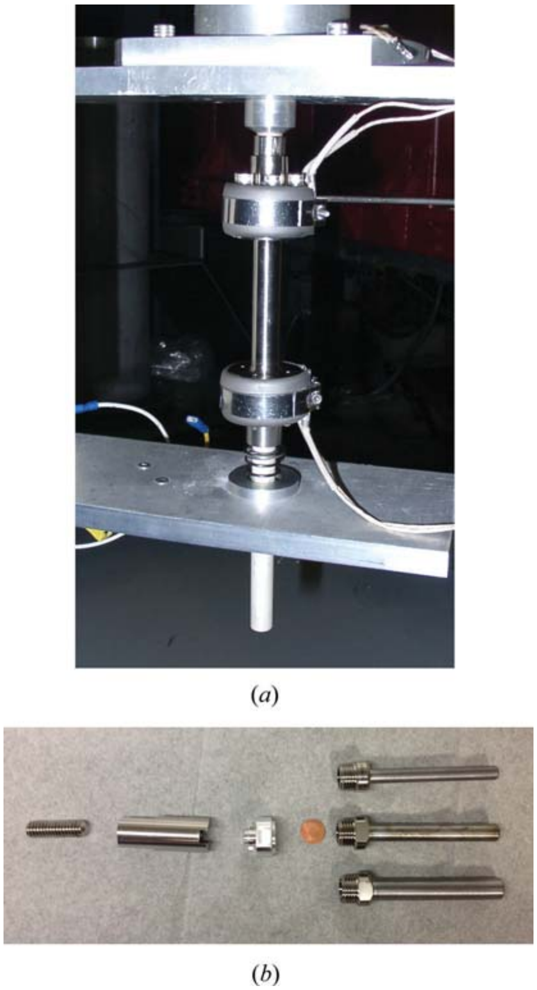
(*a*)
(*b*)

Figure 2.10.50
Two examples of sample holders used in neutron powder diffraction. (*a*) A cell made of Inconel used for hydrogen absorption studies in Li_3N (Huq *et al.*, 2007). (*b*) Vanadium holders that were specially made for a sample changer built for the Powgen diffractometer located at Oak Ridge National Laboratory.

2.10.2.3. *Specimen containment*

The choice of materials for designing sample holders usually depends on the type of experiments, temperature or pressure conditions, the type of neutron source (constant-wavelength or time-of-flight), the presence or absence of fine radial collimators in the instrument and finally the sample. The scattering of vanadium ($\sigma_{\rm coh}$ = 0.0184 b) or a TiZr alloy (a null scatterer, because of exact matching of the negative scattering length of titanium and the positive scattering length of zirconium) is almost purely incoherent, making it ideal for sample containment for diffraction measurements. Although the coherent scattering of vanadium is small, in careful work it should not be a surprise to find weak peaks from V (space group $Im\bar{3}m$, a = 3.027 Å) in the powder pattern. Examples of vanadium sample cans are shown in Fig. 2.10.50(*b*). At a reactor source aluminium is even better if low-angle (large *d*-spacing) reflections are of interest, as in the case of many magnetic structural studies, because the aluminium incoherent scattering cross section is three orders of magnitude less than that of vanadium. At elevated temperatures, vanadium easily forms oxides or hydrides in the presence of air or hydrogen, making the cell brittle, so its use is limited to low-temperature studies or in vacuum furnaces. At temperatures higher than 1273 K one often has to use boron nitride caps and molybdenum screws for vanadium sample holders to avoid eutectic formation (an example is shown in Fig. 2.10.51*b*). For

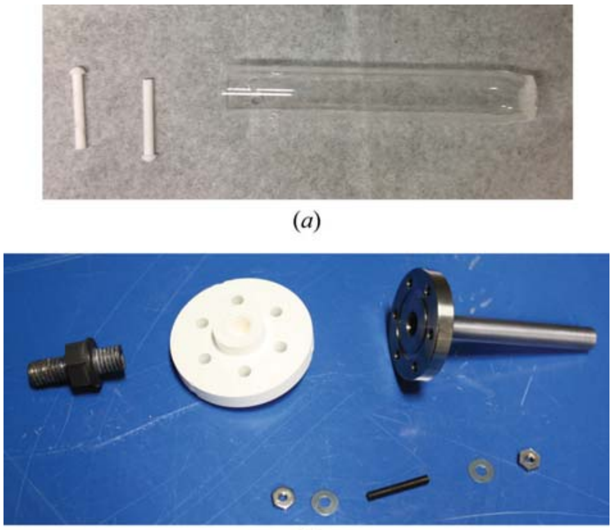

Figure 2.10.51
Two sample holders used for high-temperature studies. (*a*) A cell made of quartz with frits at the bottom to allow gas flow through the sample. (*b*) A holder on the right made of vanadium but using a boron nitride top with molybdenum bolt, nuts and washers to avoid melting due to eutectic formation. The fitting on the far left, which is made of stainless steel, is used to attach the boron nitride cap to the stick.

samples that react with vanadium, a thin layer of a noble metal such as gold can be vacuum deposited inside a vanadium can to stop it from reacting with the sample (Turner *et al.*, 1999). If this approach is used, it should be remembered that the melting point of gold is 1337 K, and when it is irradiated by neutrons it becomes activated with a half-life of 2.7 days. For experiments requiring hydrogen pressure at elevated temperature, Inconel (Fig. 2.10.50*a*) is often the material of choice (Bailey *et al.*, 2004). However, in this case for diffraction measurements one has to either exclude the Inconel peaks or make use of radial collimators to reduce the signal from the vessel itself. In spallation sources with large detector area coverage one can also do an experiment where only detectors at a scattering angle of 90° are used. For gas-absorption experiments at low temperatures, however, vanadium is still the material of choice. For pressure measurement in anvil-type cells, TiZr is used for the gasket.

For opposed-anvil pressure experiments the anvil materials can be either cubic tungsten carbide or boron nitride. The latter is preferred as boron is highly absorbing and does not contribute anvil reflections to the sample measurement, so therefore effectively works as an incident-beam collimator. The use of tungsten carbide is reserved for techniques where a ‘through-gasket’ approach is required, such as furnace measurements with a graphite heater where the use of a null scattering alloy as a gasket material is not possible. A recent development in high-pressure neutron scattering is the use of sintered diamond anvils, also called PCDs (from polycrystalline diamond). They allow the accessible pressure range to be doubled at the cost of adding very strong diamond reflections to the pattern.

However, for gas pressure cells aluminium is often used, as it can withstand higher pressure and Al absorbs neutrons only weakly as the absorption cross section of aluminium, $\sigma_{\rm abs}$ = 0.231 b for a wavelength of 1.8 Å, is small. For high-temperature gas-flow experiments fused silica (‘quartz’) glass is generally used for sample containment. These holders can also have glass frits attached at one or both ends for easy flow of gas through the sample, as shown in Fig. 2.10.51(*a*).

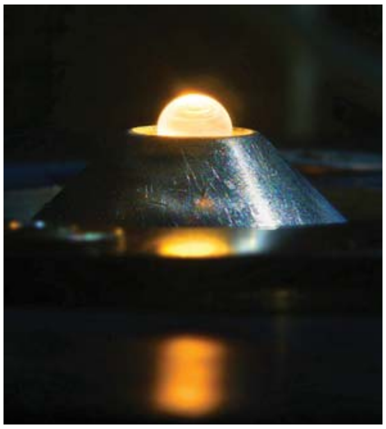

Figure 2.10.52
Aerodynamic levitation system to suspend melts at temperatures to 2773 K and beyond for neutron diffraction measurements.

A few very high intensity instruments are now able to carry out powder diffraction from milligramme quantities of sample. For these measurements vanadium cans produce too much background, as there is more vanadium in the beam than the sample. The use of thin-walled silica/glass or Kapton capillaries maybe more appropriate in those circumstances.

It is also important to remember that an exchange medium is used for low-temperature (heat transfer) and pressure (pressure transfer) measurements. Helium gas is generally used as a low-temperature exchange medium. Typically, cans are sealed with a flange and lid that supports an indium (or other soft metal) gasket. If the sample is air sensitive and has to be loaded in a glove box, one should try to use a helium-filled glove box. Argon- or nitrogen-filled glove boxes are more common but the freezing temperatures of argon and nitrogen are 84 K and 77 K, respectively. They will no longer work as exchange gases below these temperatures and, because of their rather large neutron-scattering lengths, new diffraction peaks will emerge at or below these temperatures. Similarly one should ensure that a pressure medium will remain hydrostatic for the pressure range for which it is being considered (Varga *et al.*, 2003).

It is also worth noting that cooling powder samples below 1 K relies entirely on thermal conduction through the walls of the sample holder and to the specimen itself. If great care is not taken, the specimen temperature may be far higher than that reported by a thermometer attached to the sample holder. At a minimum, the holder lid should be made from copper, as it is expected that the superconducting transitions in aluminium and vanadium would cause the walls of the sample holder to become thermally insulating and greatly reduce their ability to cool the sample. Of course, properly sealing the loose powder under an atmosphere of ^{4}He is equally important. It is essential that the indium seal be installed correctly, as ^{4}He undergoes a transition to a superfluid at 2.17 K and has effectively zero viscosity, and can easily escape from a poorly sealed can.

Levitation methods (*e.g.* gas flow, acoustic, electrostatic) as shown in Fig. 2.10.52 offer a containerless method, which eliminates altogether sample–container reaction problems and diffraction or additional background scattering from a sample container (Weber *et al.*, 2014). Levitated samples are typically used in conjunction with laser heating to achieve high temperatures, *in situ* melting of samples and prevention of heterogeneous nucleation.

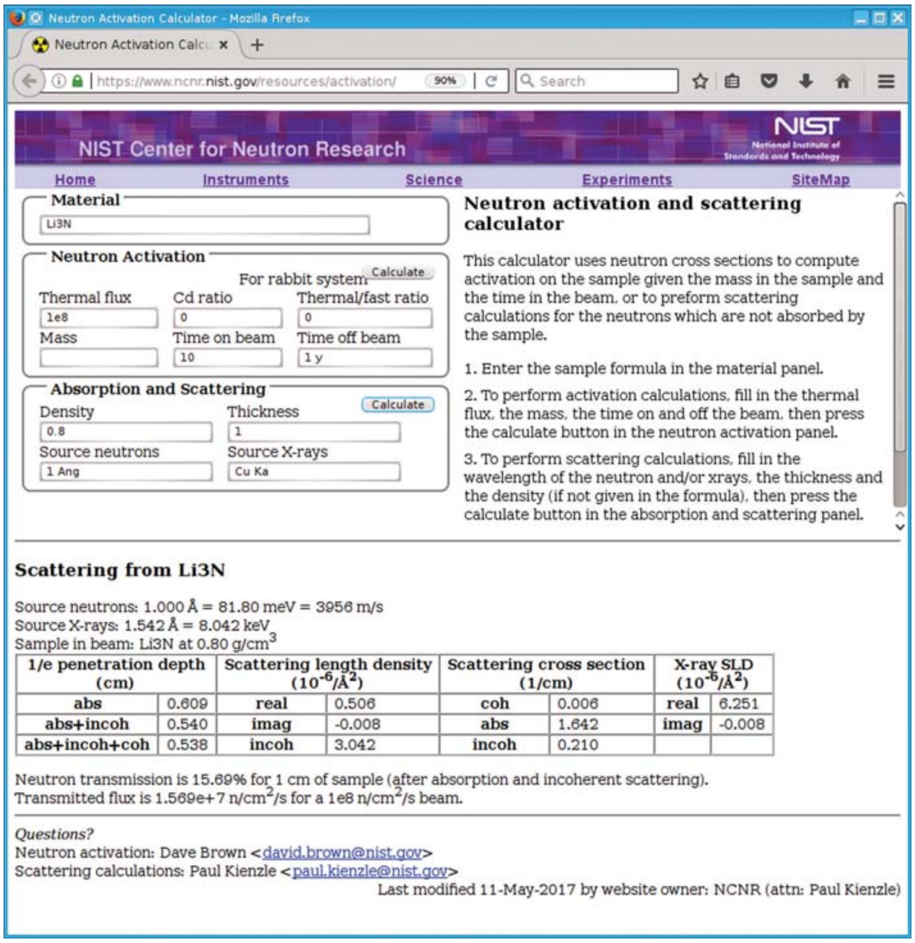
Neutron Activation Calculator - Mozilla Firefox
Neutron Activation Calc
https://www.ncnr.nist.gov/resources/activation/
90%
Search
NIST Center for Neutron Research
NIST
National Institute of Standards and Technology
Home
Instruments
Science
Experiments
SiteMap
Calculate
Calculate

Material

Li3N

Neutron Activation

For rabbit system

Thermal flux: 1e8
Cd ratio: 0
Thermal/fast ratio: 0
Mass:
Time on beam: 10
Time off beam: 1 y

Absorption and Scattering

Density: 0.8
Thickness: 1
Source neutrons: 1 Ang
Source X-rays: Cu Ka

Neutron activation and scattering calculator

This calculator uses neutron cross sections to compute activation on the sample given the mass in the sample and the time in the beam, or to preform scattering calculations for the neutrons which are not absorbed by the sample.

1. Enter the sample formula in the material panel.

2. To perform activation calculations, fill in the thermal flux, the mass, the time on and off the beam, then press the calculate button in the neutron activation panel.

3. To perform scattering calculations, fill in the wavelength of the neutron and/or xrays, the thickness and the density (if not given in the formula), then press the calculate button in the absorption and scattering panel.

Scattering from Li3N

Source neutrons: 1.000 Å = 81.80 meV = 3956 m/s
Source X-rays: 1.542 Å = 8.042 keV
Sample in beam: Li3N at 0.80 g/cm^3

1/e penetration depth (cm)		Scattering length density (10^{-6}/Å^2)		Scattering cross section (1/cm)		X-ray SLD (10^{-6}/Å^2)	
abs	0.609	**real**	0.506	**coh**	0.006	**real**	6.251
abs+incoh	0.540	**imag**	-0.008	**abs**	1.642	**imag**	-0.008
abs+incoh+coh	0.538	**incoh**	3.042	**incoh**	0.210		

Neutron transmission is 15.69% for 1 cm of sample (after absorption and incoherent scattering).
Transmitted flux is 1.569e+7 n/cm^2/s for a 1e8 n/cm^2/s beam.

Questions?
Neutron activation: Dave Brown <david.brown@nist.gov>
Scattering calculations: Paul Kienzle <paul.kienzle@nist.gov>
Last modified 11-May-2017 by website owner: NCNR (attn: Paul Kienzle)

Figure 2.10.53
Calculation of the penetration of neutrons into Li_3N using the online tool at https://www.ncnr.nist.gov/resources/activation/.

2.10.2.4. *Isotopes, absorption and activation*

There are usually multiple sizes of vanadium cans available, the most common sizes being 6, 8 and 10 mm diameter. The choice of can depends on the quantity of sample available and the nature of the elements. Some elements such as cadmium, gadolinium and boron have extremely large absorption for neutrons and may not be feasible for measurements. Some elements have high absorption for the naturally occurring isotope mixes, but by choosing an alternative isotope one can often reduce or eliminate the absorption problem completely. For example, natural lithium is mostly ^{7}Li and has an absorption cross section of 70.5 b. However, pure ^{7}Li has an absorption cross section of 0.0454 b. The difference is due to the small amount of highly absorbing ^{6}Li (absorption cross section = 940 b) present in naturally occurring lithium. With commercially sourced lithium salts it is not always safe to assume a natural abundance of lithium isotopes. ^{6}Li is used in the production of tritium and, depending on their history, commercial lithium salts may be deficient in ^{6}Li. Given the significantly different scattering lengths of ^{6}Li and ^{7}Li, this can have serious consequences for a structure refinement, so it may be necessary to perform an isotopic analysis to verify the ^{6}Li:^{7}Li ratio. The various neutron scattering cross sections are available on the NIST website http://www.ncnr.nist.gov/resources/n-lengths/ and in Table 4.4.4.1 in *International Tables for Crystallography* Volume C (2006). If the sample contains any element with a large absorption and is not isotopically substituted, it is prudent to calculate by how much the neutrons will penetrate the sample. Tools are available at the NIST website http://www.ncnr.nist.gov/resources/activation/ to carry out this calculation. The input information is the composition of the compound, the density (generally a 50% packing fraction and hence $\frac{1}{2}$ of the calculated density is a good approximation for planning purposes) and the wavelength of the neutrons used. Fig. 2.10.53 shows a calculation for Li_3N. Natural lithium has a quite large absorption, but in this case 1 Å neutrons will penetrate through 5 mm and so the use of a 6-mm diameter can is appropriate.

However, if the penetration depth 1/*e* is 1–2 mm, one has to reconsider the choice of sample holder. For a high-intensity beamline capillaries can be considered. The other option is to use an annular holder made using co-axial, thin-walled vanadium or aluminium cylinders, or flat-plate mounts based on aluminium foils where the total depth of the sample is approximately the calculated 1/*e*. Perhaps the best way to maximize the transmission and improve the signal-to-noise ratio is to use silicon flat-wafer sample holders. When loading a can it is also important to record the weight and height of the sample in the can so that the absorption correction for the sample can be calculated. Alternatively, the neutron transmission through the sample can be measured using a pinhole mask and a detector downstream from the sample.

One of the other factors to keep in mind for neutron sample preparation is that hydrogen is a very special element in terms of its interaction with neutrons. Hydrogen has a very large incoherent scattering cross section ($\sigma_{\rm inc}$) of 80.26 b, while its coherent cross section ($\sigma_{\rm coh}$) is 1.758 b. In comparison, for deuterium $\sigma_{\rm inc}$ = 2.05 b and $\sigma_{\rm coh}$ = 5.59 b. If the scattering nuclei contain a mixture of isotopes or have a non-zero nuclear spin, the neutron scattering length consists of a coherent component, which is the average over all spins, and an incoherent part, which gives the deviation from this average value. In other words, coherent scattering describes interference between waves produced by the scattering of a single neutron from all the neutrons in the nuclei of the sample. On the other hand, incoherent scattering involves correlations between the position of an atom *j* at time zero and the position of the same atom at time *t*, and so the scattered waves from different nuclei no longer interfere. Thus incoherent scattering provides an excellent tool for studying processes involving atomic diffusion, but produces large backgrounds for diffraction experiments. Based on the available flux at the instrument of choice and the atom% hydrogen present in the sample, complete or partial deuteration of the sample may be necessary.

When illuminated by a neutron beam, some nuclei are converted into other radioactive nuclei (activated). Thus it may not be possible to return the specimen to the home laboratory, but it may have to be treated as radioactive waste. A sample-activation calculator is also available at http://www.ncnr.nist.gov/resources/activation/.

2.10.3. Conclusions

Powder diffraction as a technique encompasses a wide range of possible experimental setups. Diverse though they are, specimen-preparation methods are a key component in obtaining the best possible data for the best possible analysis. Many issues are common whether X-rays or neutrons are the probe of choice (*e.g.* particle statistics, preferred orientation), but neutrons do pose some unique issues such as sample activation and isotope-dependent scattering behaviour. Given that X-ray and neutron diffraction are frequently used in a joint analysis, some forethought may be required if the desired situation of the same sample being used for both is to be achieved.

For the common laboratory setups a recurring theme should be apparent through this overview – specimens should ideally have crystallite sizes of the order of a few µm. If this is the case, then many of the issues mentioned (particle statistics, preferred orientation, extinction) will either disappear or be significantly reduced. The same is true for microabsorption, except in this case it is particle as opposed to crystallite sizes that are the issue. Grinding or milling can easily reduce crystallite size to this range, but the milling action should be chosen so as to avoid damaging the crystal structure of the sample or possibly amorphizing it completely.

Ideally, the in-house laboratory should have the flexibility to tailor the experiment to the sample, using transmission or reflection geometry depending on the nature of the sample. Unfortunately, in many instances this is not possible. ‘Coping strategies’ for non-ideal samples such as diluting samples in capillaries or using very thin organic specimens on flat plates are available, but their limitations and compromises should be understood by the person receiving the data.

In many instances, the experimental configuration at a central facility, such as a synchrotron or neutron source, can be customized for a particular experiment. However, the need for high throughput for rapid-access mail-in services may dictate a more standardized setup.

In summary, specimen preparation is the foundation upon which powder diffraction measurements are built. Good specimen preparation will not guarantee excellent data, but poor preparation can pretty much guarantee poor data.

We would like to acknowledge the assistance of Mati Raudsepp of the Department of Earth and Ocean Sciences, University of British Columbia, for the production and SEM micrograph of the spray-dried mica sample. Ashfia Huq acknowledges support by the US Department of Energy (DE-AC05–00OR22725) with UT-Battelle, LLC. R.

References

Alexander, L. E. & Klug, H. P. (1948). *Basic aspects of X-ray absorption in quantitative diffraction analysis of powder mixture*. *Anal. Chem.* **20**, 886–894.

Alexander, L., Klug, H. P. & Kummer, E. (1948). *Statistical factors affecting the intensity of X-rays diffracted by crystalline powders*. *J. Appl. Phys.* **19**, 742–753.

Bailey, I. F., Done, R., Dreyer, J. W. & Gray, E. M. (2004). *A high-temperature high-pressure gas-handling cell for neutron scattering measurements*. *High Press. Res.* **24**, 309–315.

Bowden, M. & Ryan, M. (2010). *Absorption correction for cylindrical and annular specimens and their containers or supports*. *J. Appl. Cryst.* **43**, 693–698.

Bravais, A. (1866). *Etudes Cristallographiques*. Paris: Gauthier Villars.

Brindley, G. W. (1945). *The effect of grain or particle size on X-ray reflections from mixed powders and alloys, considered in relation to the quantitative determination of crystalline substances by X-ray methods*. *London Edinb. Dubl. Philos. Mag. J. Sci.* **36**, 347–369.

Buhrke, V. E., Jenkins, R. & Smith, D. K. (1998). *A Practical Guide for the Preparation of Specimens for X-ray Fluorescence and X-ray Diffraction Analysis*. New York: Wiley-VCH.

Cline, J. P. & Snyder, R. L. (1987). *The effects of extinction on X-ray powder diffraction intensities*. *Adv. X-ray Anal.* **30**, 447–456.

Dollase, W. A. (1986). *Correction of intensities for preferred orientation in powder diffractometry: application of the March model*. *J. Appl. Cryst.* **19**, 267–272.

Donnay, J. D. H. & Harker, D. (1937). *A new law of crystal morphology extending the law of Bravais*. *Am. Mineral.* **22**, 446–467.

Friedel, G. (1907). *Etudes sur la loi de Bravais*. *Bull. Soc. Fr. Mineral.* **30**, 326–455.

Hillier, S. (1999). *Use of an air brush to spray dry samples for X-ray powder diffraction*. *Clay Miner.* **34**, 127–135.

Hillier, S. (2002). *Spray drying for X-ray powder diffraction specimen preparation*. IUCr Commission on Powder Diffraction Newsletter, **27**, 7–9. http://www.iucr.org/__data/assets/pdf_file/0017/21626/cpd27.pdf.

Huq, A., Richardson, J. W., Maxey, E. R., Chandra, D. & Chien, W. (2007). *Structural studies of Li_3N using neutron powder diffraction*. *J. Alloys Compd.* **436**, 256–260.

International Tables for Crystallography (2006). Volume C, *Mathematical, Physical and Chemical Tables*, 1st online edition, edited by E. Prince. Chester: International Union of Crystalloagraphy. doi:10.1107/97809553602060000103.

Järvinen, M. (1993). *Application of symmetrized harmonics expansion to correction of the preferred orientation effect*. *J. Appl. Cryst.* **26**, 525–531.

Jenkins, R. & Snyder, R. (1996). *Introduction to X-ray Powder Diffractometry*. New York: Wiley-Interscience.

Kaduk, J. A. (2009). *A Rietveld tutorial – mullite*. *Powder Diffr.* **24**, 351–361.

Kaduk, J. A. (2013). Personal communication.

Klug, H. P. & Alexander, L. E. (1954). *X-ray Diffraction Procedures for Polycrystalline and Amorphous Materials*. New York: Wiley-Interscience.

Lewis, J., Schwarzenbach, D. & Flack, H. D. (1982). *Electric field gradients and charge density in corundum, α-Al_2O_3*. *Acta Cryst.* A**38**, 733–739.

Lobanov, N. N. & Alte de Viega, L. (1998). *Analytic absorption correction factors for cylinders to an accuracy of .5%*. Abstract P 2–16, 6th European Powder Diffraction Conference, Budapest, Hungary, 22–25 August. Zurich: Trans Tech Publications.

Ohashi, Y. (1984). *Polysynthetically-twinned structures of enstatite and wollastonite*. *Phys. Chem. Miner.* **10**, 217–229.

Pitschke, W., Hermann, H. & Mattern, N. (1993). *The influence of surface roughness on diffracted X-ray intensities in Bragg–Brentano geometry and its effect on the structure determination by means of Rietveld analysis*. *Powder Diffr.* **8**, 74–83.

Raudsepp, M. (2012). Personal communication.

Reibenspies, J. H. & Bhuvanesh, N. (2006). *Capillaries prepared from thin-walled heat-shrink poly(ethylene terephthalate) (PET) tubing for X-ray powder diffraction analysis*. *Powder Diffr.* **21**, 323–325.

Rowles, M. R. & Madsen, I. C. (2010). *Whole-pattern profile fitting of powder diffraction data collected in parallel-beam flat-plate asymmetric reflection geometry*. *J. Appl. Cryst.* **43**, 632–634.

Sabine, T. M., Von Dreele, R. B. & Jørgensen, J.-E. (1988). *Extinction in time-of-flight neutron powder diffractometry*. *Acta Cryst.* A**44**, 374–379.

Scarlett, N. V. Y., Madsen, I. C., Cranswick, L. M. D., Lwin, T., Groleau, E., Stephenson, G., Aylmore, M. & Agron-Olshina, N. (2002). *Outcomes of the International Union of Crystallography Commission on Powder Diffraction Round Robin on Quantitative Phase Analysis: samples 2, 3, 4, synthetic bauxite, natural granodiorite and pharmaceuticals*. *J. Appl. Cryst.* **35**, 383–400.

Smith, D. K. (2001). *Particle statistics and whole-pattern methods in quantitative X-ray powder diffraction analysis*. *Powder Diffr.* **16**, 186–191.

Suortti, P. (1972). *Effects of porosity and surface roughness on the X-ray intensity reflected from a powder specimen*. *J. Appl. Cryst.* **5**, 325–331.

Sykes, R. A., McCabe, P., Allen, F. H., Battle, G. M., Bruno, I. J. & Wood, P. A. (2011). *New software for statistical analysis of Cambridge Structural Database data*. *J. Appl. Cryst.* **44**, 882–886.

Toraya, H., Huang, T. C. & Wu, Y. (1993). *Intensity enhancement in asymmetric diffraction with parallel-beam synchrotron radiation*. *J. Appl. Cryst.* **26**, 774–777.

Toraya, H. & Yoshino, J. (1994). *Profiles in asymmetric diffraction with pseudo-parallel-beam geometry*. *J. Appl. Cryst.* **27**, 961–966.

Turner, J. F. C., Done, R., Dreyer, J., David, W. I. F. & Catlow, C. R. A. (1999). *On apparatus for studying catalysts and catalytic processes using neutron scattering*. *Rev. Sci. Instrum.* **70**, 2325–2330.

Varga, T., Wilkinson, A. P. & Angel, R. J. (2003). *Fluorinert as a pressure-transmitting medium for high-pressure diffraction studies*. *Rev. Sci. Instrum.* **74**, 4564–4566.

Weber, J. K. R., Benmore, C. J., Skinner, L. B., Neuefeind, J., Tumber, S. K., Jennings, G., Santodonato, L. J., Jin, D., Du, J. & Parise, J. B. (2014). *Measurements of liquid and glass structures using aerodynamic levitation and in-situ high energy X-ray and neutron scattering*. *J. Non-Cryst. Solids*, **383**, 49–51.

Wolff, P. M. de (1958). *Particle statistics in X-ray diffractometry*. *Appl. Sci. Res.* **7**, 102–112.

Wolff, P. M. de, Taylor, J. M. & Parrish, W. (1959). *Experimental study of effect of crystallite size statistics on X-ray diffractometer intensities*. *J. Appl. Phys.* **30**, 63–69.

Zachariasen, W. H. (1945). *Theory of X-ray Diffraction in Crystals*. New York: Dover Publications Inc.

Zevin, L. S. & Kimmel, G. (1995). *Quantitative X-ray Diffractometry*. New York: Springer-Verlag.

International Tables for Crystallography (2019). Vol. H, Chapter 3.1, pp. 224–251.

3.1. The optics and alignment of the divergent-beam laboratory X-ray powder diffractometer and its calibration using NIST standard reference materials

J. P. Cline, M. H. Mendenhall, D. Black, D. Windover and A. Henins

3.1.1. Introduction

The laboratory X-ray powder diffractometer has several virtues that have made it a principal characterization device for providing critical data for a range of technical disciplines involving crystalline materials. The specimen is typically composed of small crystallites (5–30 µm), which is a form that is suitable for a wide variety of materials. A continuous set of reflections can be collected with a single scan in θ–2θ angle space. Not only can timely qualitative analyses be carried out, but with the more advanced data-analysis methods a wealth of quantitative information may be extracted. Modern commercial instruments may include features that include focusing mirror optics and the ability to change quickly between various experimental configurations. In this chapter, we discuss results from a NIST-built diffractometer with features specific to the collection of data that complement the NIST effort in standard reference materials (SRMs) for powder diffraction. While this machine can be configured with focusing optics, here we consider only those configurations that use a divergent beam in Bragg–Brentano, para-focusing geometry.

A principal advantage of the divergent-beam X-ray powder diffractometer is that a relatively large number of crystallites are illuminated, providing a strong diffraction signal from a representative portion of the sample. However, the para-focusing optics of laboratory diffractometers produce patterns that display profiles of a very complex shape. The observed 2θ position of maximum diffraction intensity does not necessarily reflect the true spacing of the lattice planes (*hkl*). While advanced data-analysis methods can be used to model the various aberrations and account for the observed profile shape and position, there are a number of instrumental effects for which there is not enough information for reliable, *a priori* modelling of the performance of the instrument. The task may be further compounded when instruments are set up incorrectly, because the resultant additional errors are convoluted into the already complex set of aberrations. Therefore, the results are often confounding, as the origin of the difficulty is problematic to discern. The preferred method for avoiding these situations is the use of SRMs to calibrate the instrument performance. We will describe the various methods with which NIST SRMs may be used to determine sources of measurement error, as well as the procedures that can be used to properly calibrate the laboratory X-ray powder diffraction (XRPD) instrument.

The software discussed throughout this manuscript will include commercial as well as public-domain programs, some of which were used for the certification of NIST SRMs. In addition to the NIST disclaimer concerning the use of commercially available resources,[1] we emphasize that some of the software presented here was also developed to a certain extent through longstanding collaborative relationships between the first author and the respective developers of the codes. The codes that will be discussed include: *GSAS* (Larson & Von Dreele, 2004), the PANalytical software *HighScore Plus* (Degen *et al.*, 2014), the Bruker codes *TOPAS* (version 4.2) (Bruker AXS, 2014) and *DIFFRAC.EVA* (version 3), and the Rigaku code *PDXL 2* (version 2.2) (Rigaku, 2014). The fundamental-parameters approach (FPA; Cheary & Coelho, 1992) for modelling X-ray powder diffraction line profiles, as implemented in *TOPAS*, has been used since the late 1990s for the certification of NIST SRMs. To examine the efficacy of the FPA models, as well as their implementation in *TOPAS*, we have developed a Python-based code, the NIST Fundamental Parameters Approach Python Code (*FPAPC*), that replicates the FPA method in the computation of X-ray powder diffraction line profiles (Mendenhall *et al.*, 2015). This FPA capability is to be incorporated into *GSASII* (Toby & Von Dreele, 2013).

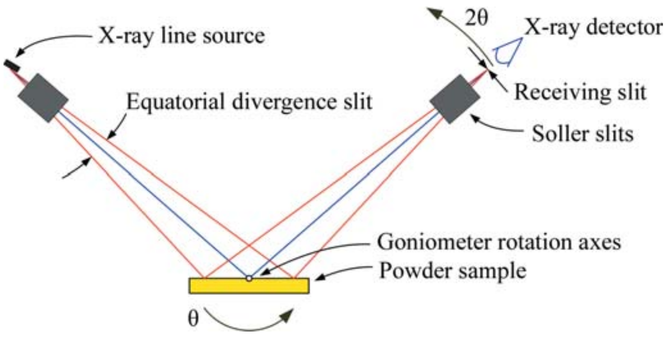

Figure 3.1.1
A schematic diagram illustrating the operation and optical components of a Bragg–Brentano X-ray powder diffractometer.

3.1.2. The instrument profile function

The instrument profile function (IPF) describes the profile shape and displacement as a function of 2θ that is the intrinsic instrumental response imparted to any data collected with that specific instrument. It is a function of the radiation used, the instrument geometry and configuration, slit sizes *etc.*[2] The basic optical layout of a divergent-beam X-ray powder diffractometer of Bragg–Brentano, para-focusing geometry using a tube anode in a line-source configuration is illustrated in Fig. 3.1.1. This figure shows the various optical components in the plane of diffraction, or equatorial plane. The dimensions of the optical components shown in Fig. 3.1.1 and the dimensions of the goniometer itself determine the resolution of the diffractometer. The divergent nature of the X-ray beam will increase the number of crystallites giving rise to the diffraction signal; the incident-beam slit defines an angular range within which crystallites will be oriented such that their diffraction is registered. One of the manifestations of this geometry is that knowledge of both the diffraction angle and

---

[1] Certain commercial equipment, instruments, or materials are identified in this in order to adequately specify the experimental procedure. Such identification does not imply recommendation or endorsement by the National Institute of Standards and Technology, nor does it imply that the materials or equipment identified are necessarily the best available for the purpose.

[2] See Chapters 3.6 and 5.1 for details of contributions to the profile shape from the sample.

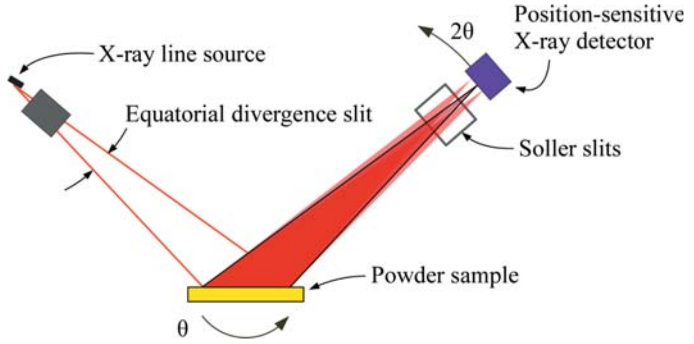

Figure 3.1.2
A schematic diagram illustrating the operation and optical components of a Bragg–Brentano X-ray diffractometer equipped with a position-sensitive detector. Only the rays striking the centre line of the PSD, outlined in black, are in accordance with Bragg–Brentano focusing.

specimen position are critical for the correct interpretation of the data. The goniometer radius is the distance between the rotation axes and the X-ray source (R_1), or the distance between the rotation axes and receiving slit (R_2), as shown in Fig. 3.1.1; these two distances must be equal. The specimen surface is presumed to be on the rotation axes; however, this condition is rarely realized and it is common to have to consider a specimen-displacement error.

Goniometer assemblies themselves can be set up in several configurations. Invariably, two rotation stages are utilized. Fig. 3.1.1 illustrates a machine of $\theta/2\theta$ geometry: the tube is stationary while one stage rotates the specimen through angle θ, sometimes referred to as the angle Ω, while a second stage rotates the detector through angle 2θ. Another popular configuration is θ/θ geometry, where the specimen remains stationary and both the tube and detector rotate through angle θ. However, the diffraction optics themselves do not vary with regard to how the goniometer is set up.

The detector illustrated in Fig. 3.1.1 simply reads any photons arriving at its entrance window as the diffracted signal is analysed by the receiving slit. Such detectors, which often use a scintillation crystal, are typically referred to as point detectors. A diffracted-beam post-sample monochromator is often added to the beam path after the receiving slit to filter out any fluorescence from the sample. The crystal optic of these monochromators typically consists of pyrolytic graphite with a high level of mosaicity that is bent to a radius in rough correspondence to that of the goniometer. This imposes a relatively broad energy bandpass of approximately 200 eV (with 8 keV Cu $K\alpha$ radiation) in width on the diffracted beam. This window is centred so as to straddle that of the energy of the source radiation being used, thereby filtering fluorescent and other spurious radiation from the detector while transmitting the primary features of the emission spectrum, presumably without distortion.

Within the last decade, however, the popularity of this geometry has fallen markedly, as the use of the post-sample monochromator/point-detector assembly has been largely displaced by the use of a position-sensitive detector (PSD). This geometry is illustrated in Fig. 3.1.2. A line detector replaces the point detector, and offers the ability to discriminate with respect to the position of arriving X-rays within the entrance window of the PSD. A multichannel analyser is typically used to map the arriving photons from the PSD window into 2θ space. Depending on the size of the PSD entrance window, increases in the counting rate by two orders of magnitude relative to a point detector can be easily achieved. Furthermore, this is accomplished by including the signal from additional crystallites, mitigating any problems with particle-counting statistics (Fig. 3.1.2). A drawback to the PSD is that the increased intensity is achieved with the inclusion of signals that are not within the Bragg–Brentano focusing regimen (compare Figs. 3.1.1 and 3.1.2), leading to a broadening of the line profiles. The level of broadening is proportional to the size of the PSD entrance window and inversely proportional to 2θ angle. The move to PSDs has been further augmented by the development of solid-state, silicon strip detectors that offer the advantages of a PSD without the maintenance issues of the early gas-flow proportional PSDs. Fluorescence can be problematic with a PSD; however, the problem can be countered with the use of filters. More recent developments in electronics have improved the ability of these PSDs to discriminate with respect to energy. We discuss only this newer class of solid-state linear PSDs in this chapter.

A monochromator can also be used to condition the incident beam so that it will consist exclusively of $K\alpha_1$ radiation. Monochromators of this nature are inserted into the beam path prior to the beam's arrival at the incident-beam slit shown in Fig. 3.1.1. These devices typically use a Ge(111) crystal as the optic; Ge monochromators have a much smaller energy bandpass than graphite monochromators. They are, therefore, much more complex and difficult to align. Here we discuss an incident-beam monochromator (IBM) using a Johansson focusing optic (Johansson, 1933), as shown in Fig. 3.1.3. When incorporating an IBM assembly into a powder diffractometer using reflection geometry, the focal line of the optic must be positioned on the goniometer radius as per the line source of the tube anode in a conventional setup, shown in the right-hand

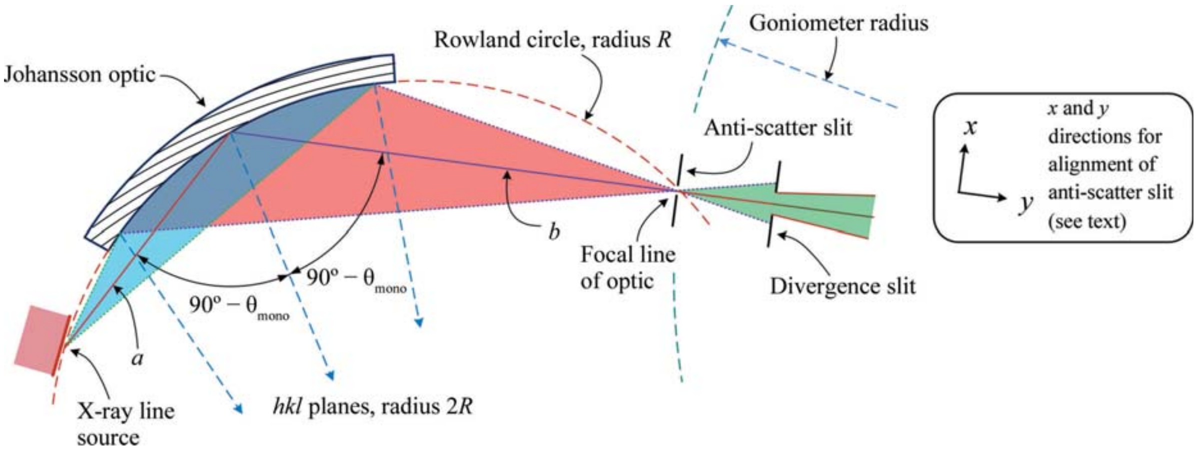

Figure 3.1.3
A schematic diagram illustrating the geometry of a Johansson incident-beam monochromator.

Table 3.1.1
Aberrations comprising the geometric component of the IPF

Aberration	Controlling parameters	Impact
X-ray source width (w_x)	Angle subtended by source: w_x/R	Symmetric broadening
Receiving-slit width or PSD strip width (w_r)	Angle subtended by slit/strip: w_r/R	Symmetric broadening
Flat specimen error/equatorial divergence	Angle of divergence slit: α	Asymmetric broadening to low 2θ, with decreasing 2θ
PSD defocusing	PSD window width, angle of divergence slit: α	Symmetric broadening with $1/(\tan\theta)$
Axial divergence		Below $\sim 100^\circ$:
Case 1: no Soller slits	Axial lengths of the X-ray source (L_x), sample (L_s) and receiving slit (L_r) relative to goniometer radius (R)	asymmetric broadening to low 2θ, with decreasing 2θ
Case 2: Soller slits define divergence angle	Acceptance angles Δ_I and Δ_D of the incident- and diffracted-beam Soller slits	else to high 2θ, with increasing 2θ
Specimen transparency	Penetration factor relative to diffractometer radius $1/\mu R$	Asymmetric broadening to low 2θ, with $\sin(2\theta)$
Specimen displacement z height	Displacement of specimen surface from goniometer rotation axes	Displacement of profiles with $\cos\theta$

side of Fig. 3.1.3. In this way, a Johansson optic provides a monochromatic X-ray source, passing some portion of the $K\alpha_1$ emission spectrum, while preserving the divergent-beam Bragg–Brentano geometry as shown in Figs. 3.1.1 and 3.1.2. The use of an IBM reduces the number of spectral contributions to the observed line shape and results in an IPF that is more readily modelled with conventional profile fitting. Furthermore, equipping such a machine with a PSD affords all of its advantages, while the elimination of the *Bremsstrahlung* by the IBM reduces the impact of fluorescence that can otherwise be problematic with a PSD.

Throughout this manuscript we use the terms ‘width’ and ‘length’ when referring to the optics. Width expresses extent in the equatorial plane. Length is used to denote a physical dimension parallel to the rotation axes of the goniometer as defined in Fig. 3.1.1. The designation of the axial divergence angle, as well as the specifications concerning Soller slits, will be considered in terms of the double angle, both for incoming and outgoing X-rays. This is in contrast to the generally accepted single-angle definition shown in Klug & Alexander (1974); hence the axial-divergence angles reported throughout this chapter are twice those that are often encountered elsewhere.

The observed line shape in powder diffraction consists of a convolution of contributions from the instrument optics (referred to as the geometric profile), the emission spectrum and the specimen, as shown diagrammatically for divergent-beam XRPD in Fig. 3.1.4. The specimen contribution is often the dominant one in a given experiment; however, we do not consider it to any great extent in this discussion. The factors comprising the geometric profile are listed in Table 3.1.1. Technically, neither of the last two items (specimen transparency and displacement) are components of the geometric profile of the instrument. They are functions of the specimen and the manner in which it was mounted. However, it is not possible to use a whole-pattern data-analysis method without considering these two factors; as they play a critical role in the modelling of the observed profile positions and shapes they are included in this discussion. The convolution of the components of the geometric profile and emission spectrum forms the IPF. As will be discussed, both of these contributions are complex in nature, leading to the well known difficulty in modelling the IPF from Bragg–Brentano equipment. This complexity, and the relatively limited q-space (momentum space) range accessible with laboratory equipment, tends to drive the structure solution and refinement community, with their expertise in the development of data-analysis procedures, towards the use of synchrotron and neutron sources. A significant number of the models and analytical functions discussed here were developed for, and are better suited to, powder-diffraction equipment using such nonconventional sources.

We now consider the geometric profile with an examination of the aberrations listed in Table 3.1.1. Figs. 3.1.5–3.1.10 illustrate simulations of the aberration function associated with the factors listed in Table 3.1.1. The first two of these, the source and receiving-slit width or silicon strip width with a PSD, simply cause symmetric broadening, constant with 2θ angle, and are typically described with ‘impulse’ or ‘top-hat’ functions. The flat specimen error is due to defocusing in the equatorial plane. One can see from Fig. 3.1.1 that for any beam that is not on the centre line of the goniometer, R_1 is not equal to R_2. The magnitude of the effect is directly

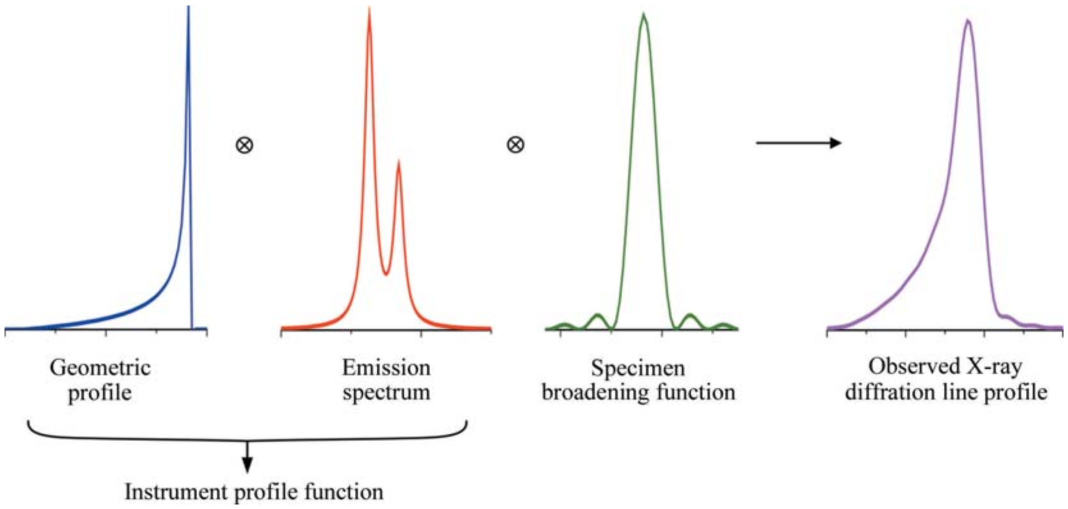
⊗
⊗
Geometric profile
Emission spectrum
Specimen broadening function
Observed X-ray diffration line profile
Instrument profile function

Figure 3.1.4
Diagrammatic representations of convolutions leading to the observed XRPD profile.

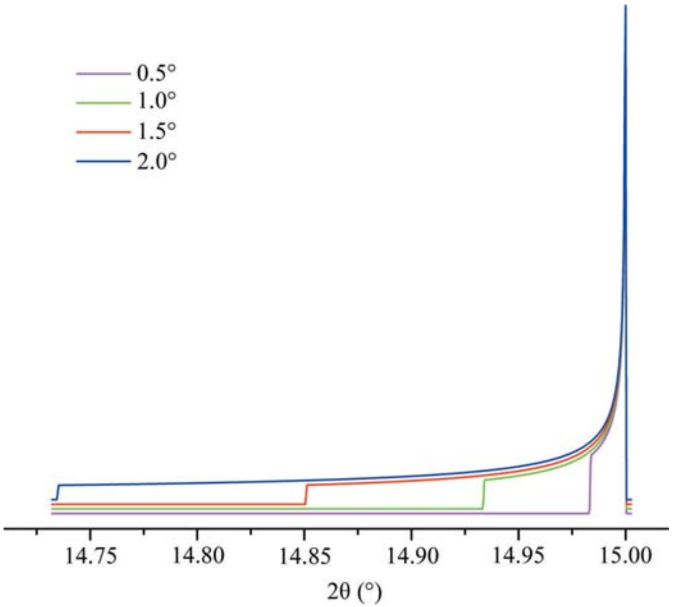

Figure 3.1.5
The flat specimen error aberration profile as a function of incident-slit size (R = 217.5 mm).

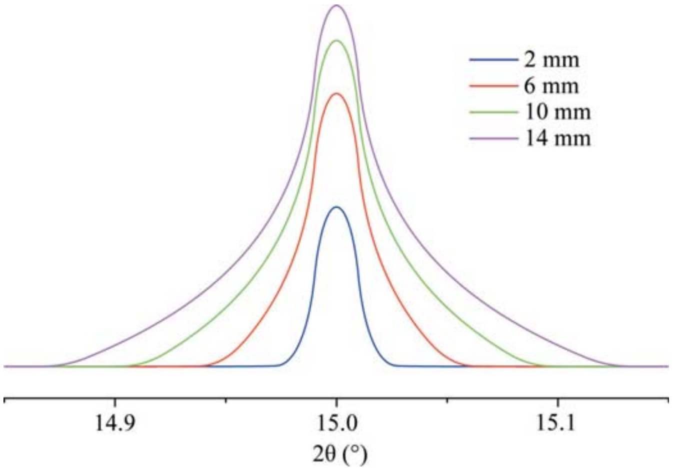

Figure 3.1.7
The PSD defocusing error aberration profiles for a silicon strip PSD as a function of window width (R = 217.5 mm, incident slit = 1° and strip width = 75 µm).

proportional to the divergent slit size as shown in Fig. 3.1.5. Its functional dependence on 2θ angle, *i.e.* $1/\tan\theta$, is illustrated in Fig. 3.1.6. The flat specimen error leads to asymmetric profile broadening on the low-angle side, accentuated at decreasing values of 2θ. The functional dependence of this aberration on 2θ, shown in Fig. 3.1.6, is for a fixed slit; the use of a variable-divergence incident-beam slit to obtain a constant area of illumination reduces this dependence on the 2θ angle.

The broadening imparted to diffraction line profiles from the early gas-flow proportional PSDs was due to defocusing originating from both the equatorial width of the PSD window and parallax within the gas-filled counting chamber. Early models for these effects (Cheary & Coelho, 1994) included two parameters: one for the window width and a second for the parallax. The modern silicon strip PSDs do not need this second term as there is effectively no parallax effect. The aberration profile imparted to the data from a modern PSD (Mendenhall *et al.*, 2015) is illustrated in Fig. 3.1.7 as a function of window width. The profiles are symmetric about the centre line, exhibiting both increasing intensity and breadth as the window width is increased. The profile consists of two components: a central peak with a width independent of 2θ, which is due to the pixel strip width of the detector, and wings which are due to the defocusing. The breadths of the wings shown in Fig. 3.1.7 vary in proportion to the incident slit size and as $1/\tan\theta$, and therefore are largely unobservable at high 2θ angles.

Cheary & Coelho (1998*a*,*b*) have modelled axial divergence effects in the context of two geometric cases. Case 1 is the situation in which the axial divergence is limited solely by the width of the beam path as determined by the length of the tube filament, the receiving slit and the size of the sample. The aberration function in which these parameters are 12 mm, 15 mm and 15 mm, respectively, is illustrated in Fig. 3.1.8; the extent of broadening is nearly 1° in 2θ at a 2θ angle of 15°. The other plots of Fig. 3.1.8 refer to a 'case 2' situation where axial divergence is limited by the inclusion of Soller slits in the incident- and diffracted-beam paths. One also has to consider the impact of a including a graphite post-monochromator. This would increase

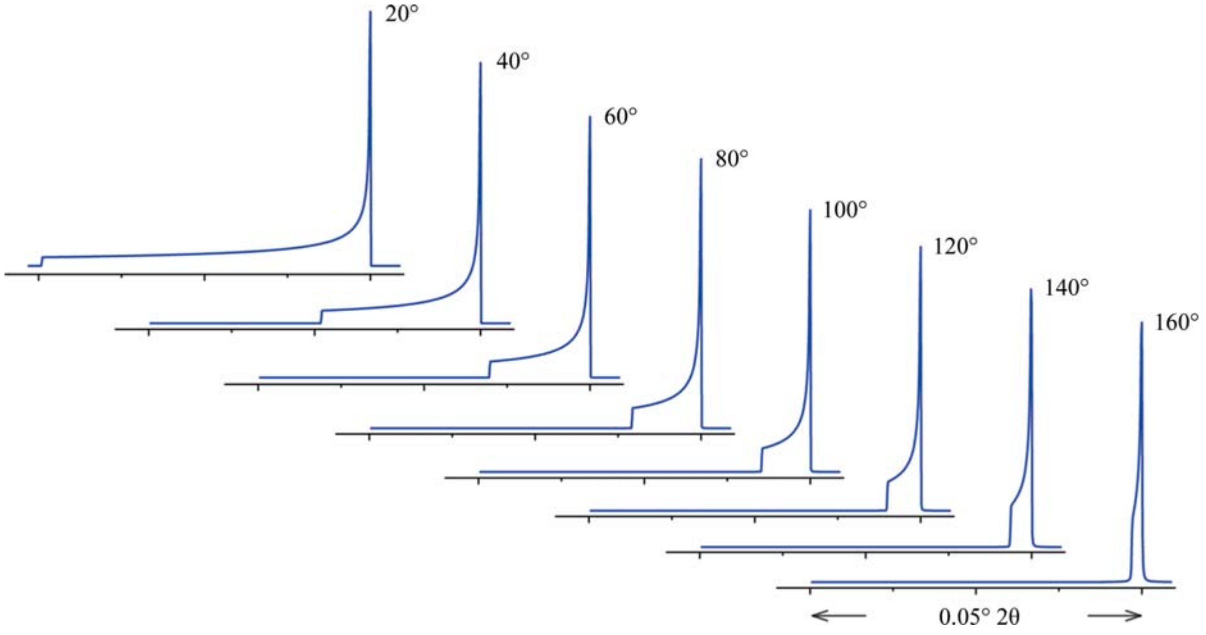

Figure 3.1.6
The flat specimen error aberration profiles for a 1° incident slit as a function 2θ (R = 217.5 mm).

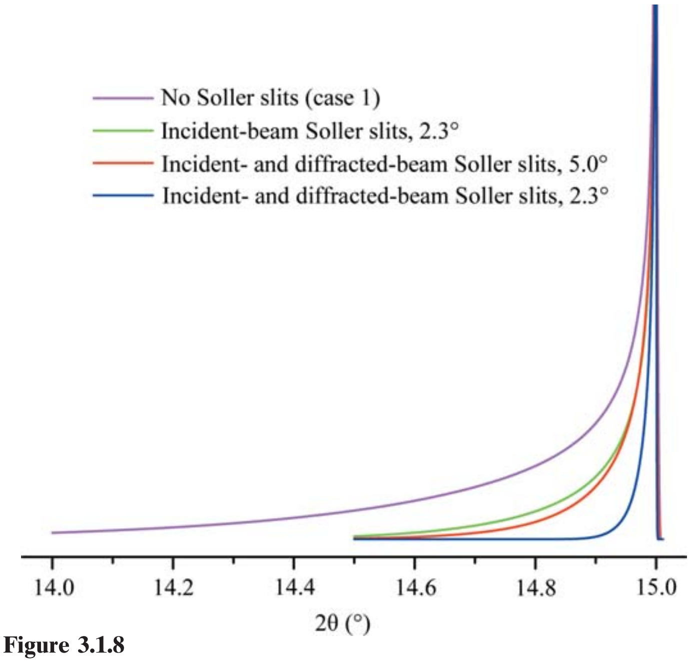

Figure 3.1.8
Axial divergence aberration profiles shown for several levels of axial divergence. Case 1 (of Table 3.1.1) is computed for a source length of 12 mm and a sample and receiving-slit length of 15 mm. The remaining three simulations include are of case 2, where Soller slits limit the axial divergence (R = 217.5 mm).

the path length of the diffracted beam by 10 to 15 cm, reducing axial divergence effects substantially and effectively functioning as a Soller slit. Cheary & Cline (1995) determined that the inclusion of a Soller slit with a post-monochromator did result in a slight improvement in resolution; however, this was at the cost of a threefold reduction in intensity. We do not use Soller slits in the diffracted beam when using a post-monochromator. The 5° primary and secondary Soller slit aberration profile of Fig. 3.1.8 corresponds to an instrument with a primary Soller slit and a graphite post-monochromator. The profiles shown for the two 2.3° Soller-slit configurations actually constitute a fairly high level of collimation given the double-angle definition of the specifications. Fig. 3.1.9 shows the functional dependence of the aberration profile for two 2.3° Soller slits on 2θ. Below approximately 100°, the effect increases with decreasing 2θ. Approximate symmetry is observed at 100°, while asymmetry to high angle increases thereafter. The aberration profile associated with specimen transparency to the X-ray beam is illustrated in Fig. 3.1.10. The figure shows the impact at 90° 2θ where the effect is at its maximum. The observed profile is broadened asymmetrically to low 2θ; the effect drops off in a largely symmetric manner with 2θ on either side of 90°.

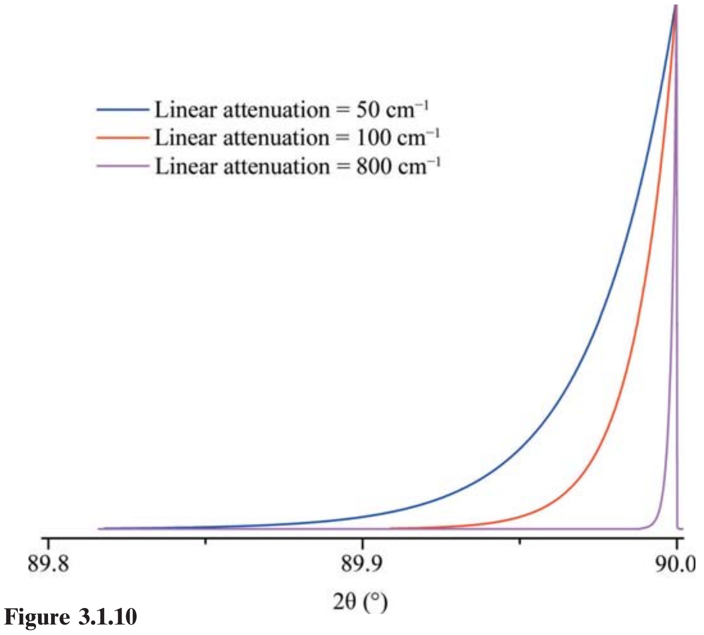

Figure 3.1.10
Linear attenuation aberration profiles that would roughly correspond to SRMs 676a (50 cm^{-1}), 640e and 1976b (100 cm^{-1}), and 660c (800 cm^{-1}) at 90° 2θ, where the transparency effect is at a maximum (R = 217.5 mm).

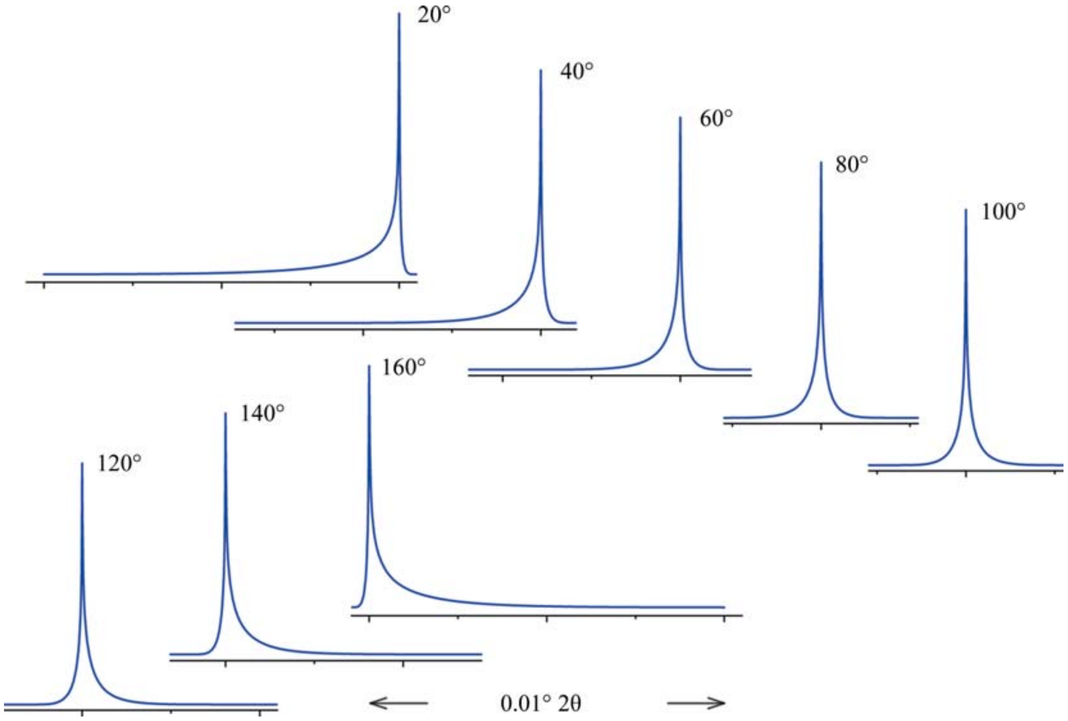

Figure 3.1.9
Axial divergence aberration profiles for primary and secondary Soller slits of 2.3° as a function of 2θ (R = 217.5 mm).

The wavelength profile or emission spectrum with its characterization on an absolute energy scale provides the traceability of the diffraction measurement to the International System of Units (SI) (BIPM, 2006). The currently accepted characterization of the emission spectrum of Cu $K\alpha$ radiation is provided by Hölzer *et al.* (1997) and is shown in Fig. 3.1.11. The spectrum is modelled with four Lorentzian profile shape functions (PSFs): two large ones for the primary $K\alpha_1$ and $K\alpha_2$ profiles, and two smaller ones displaced slightly to lower energy to account for the asymmetry in the observed line shape. The data shown in Fig. 3.1.11 are in energy space and are transformed into 2θ space with the dispersion relation. This is obtained by differentiating

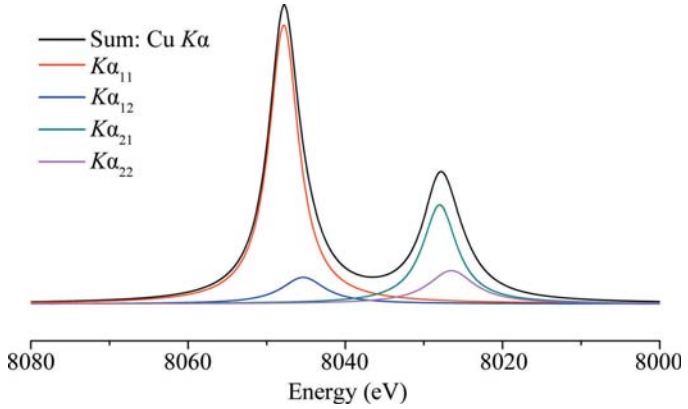

Figure 3.1.11
The emission spectrum of Cu $K\alpha$ radiation as provided by Hölzer *et al.* (1997), represented by four Lorentzian profiles: two primary ones and a pair of smaller ones to account for the observed asymmetry. The satellite lines, often referred to as the $K\alpha_3$ lines, are not displayed.

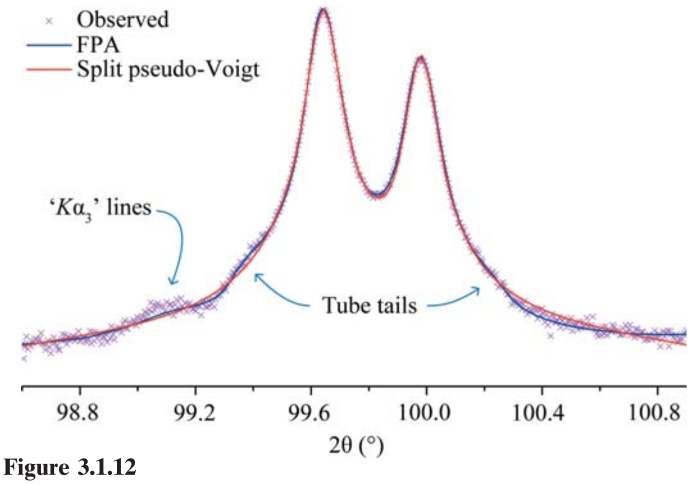

Figure 3.1.12
Illustration of the $K\alpha_3$ lines and tube-tails contributions to an observed profile on a log scale, shown with two fits: the fundamental-parameters approach, which includes these features, and the split pseudo-Voigt PSF, which does not.

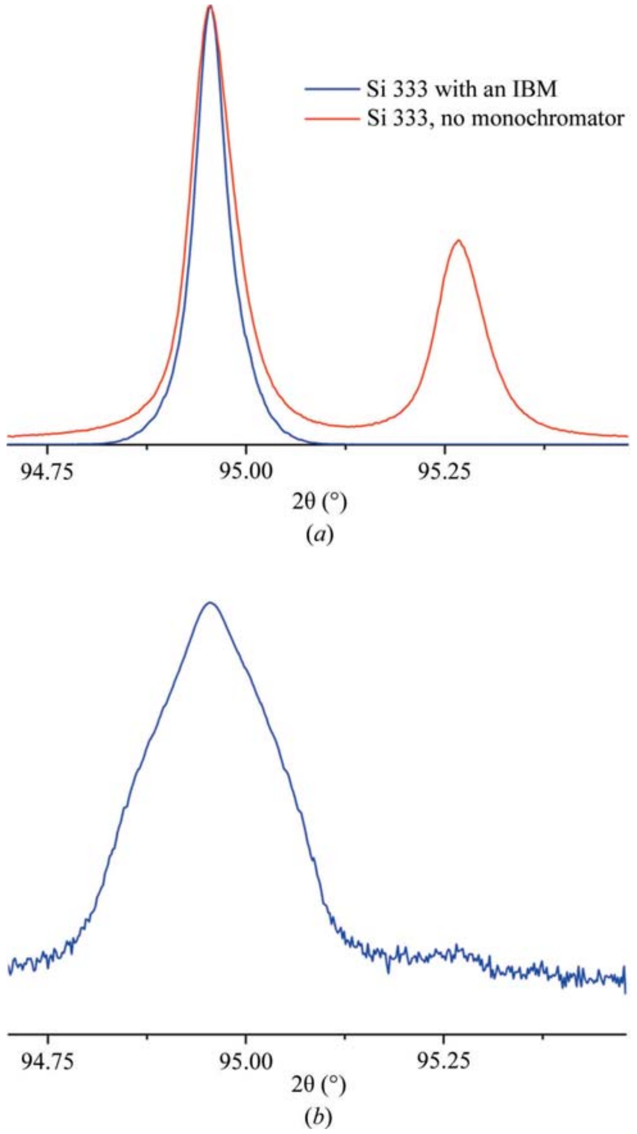

Figure 3.1.13
Illustration of the effect of the Johansson optic on the Cu $K\alpha$ emission spectrum. (*a*) Data collected for the Si 333 single-crystal reflection on a linear scale. (*b*) Analogous data from Johansson optic alone on a log scale. Both data sets were collected with 0.05 mm incident and receiving slits. The near absence of the $K\alpha_2$ scatter displayed in (*b*) can only be realized with the use of a properly aligned anti-scatter slit located at the focal line of the optic.

Bragg's law to obtain $d\theta/d\lambda$. The dominant term in the result is $\tan\theta$, which leads to the well known 'stretching' of the wavelength distribution with respect to 2θ. Maskil & Deutsch (1988) characterized a series of satellite lines in the Cu $K\alpha$ spectrum with an energy centred around 8080 eV and an intensity relative to the $K\alpha_1$ line of 6×10^{-3}. These are sometimes referred to as the $K\alpha_3$ lines, and are typically modelled with a single Lorentzian within the FPA. The 'tube tails' as reported by Bergmann *et al.* (2000) are a contribution that is strictly an artifact of how X-rays are produced in the vast majority of laboratory diffractometers. With the operation of an X-ray tube, off-axis electrons are also accelerated into the anode and produce X-rays that originate from positions other than the desired line source. They are not within the expected trajectory of para-focusing X-ray optics and produce tails on either side of a line profile as illustrated, along with the $K\alpha_3$ lines, in Fig. 3.1.12. Lastly, the energy bandpass of the pyrolytic graphite crystals used in post-monochromators is not a top-hat (or square-wave) function. Thus, the inclusion of a post-monochromator influences the observed emission spectrum.

A Johansson IBM dramatically reduces the complexity of the IPF by largely removing the $K\alpha_2$, $K\alpha_3$ and tube-tails contributions to the observed profile shape. The vast majority of the *Bremsstrahlung* is also removed. Furthermore, the inclusion of the IBM increases the path length of the incident beam by 25 to 30 cm. This substantially reduces the contribution of axial divergence to the observed profile shape. The crystals used are almost exclusively germanium (the 111 reflection), and are ground and bent to the Johansson focusing geometry, as shown in Fig. 3.1.3. They can be symmetric, with the source-to-crystal distance *a* and the crystal-to-focal point distance *b* being equal, in which case they will exhibit a bandpass of the order of 8 eV. They will slice a central portion out of the $K\alpha_1$ line, clipping the tails, to transmit perhaps 70% of the original width of the Cu $K\alpha_1$ emission spectrum. This yields a symmetric profile shape of relatively high resolution, or reduced profile breadth (other parameters being equal). The crystals can also be asymmetric, with the distance *a* being ~60% of the distance *b*. These optics will exhibit a bandpass of the order of 15 eV, in which case they transmit most of the $K\alpha_1$ line for a higher intensity, but with a lower resolution. The optic discussed here is of the latter geometry, as shown in Fig. 3.1.3.

A potential drawback to the use of an IBM concerns the nature of the $K\alpha_1$ emission spectrum it transmits, which may preclude the use of data-analysis methods that are based upon an accurate

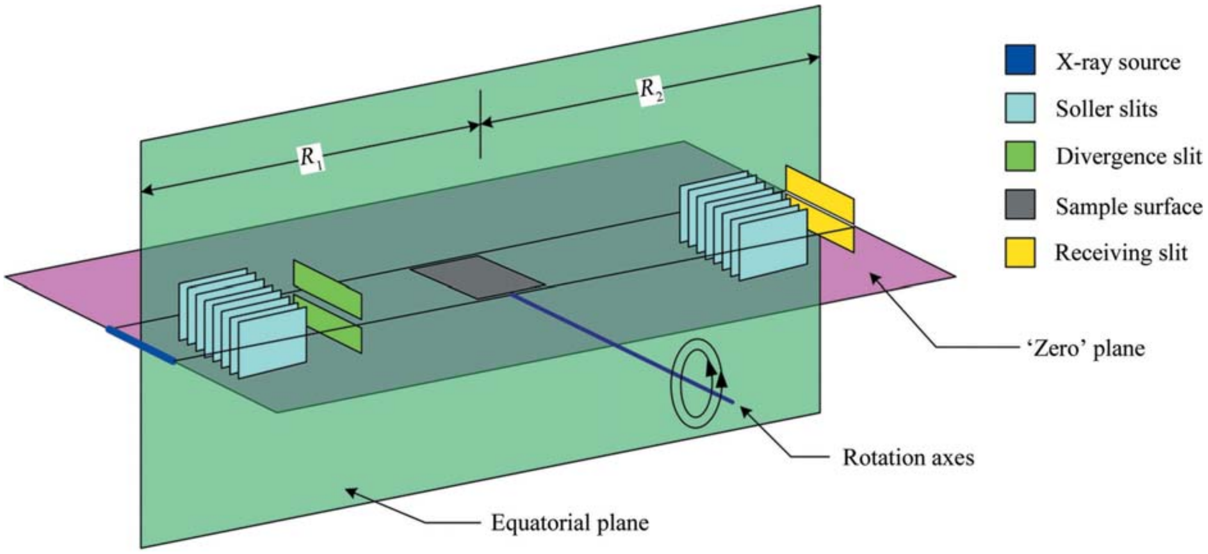

Figure 3.1.14
Diagrammatic explanation of the conditions necessary to realize a properly aligned X-ray powder diffractometer.

mathematical description of an incident spectrum. At best, a 'perfect' focusing crystal will impose an uncharacterized, though somewhat Gaussian, energy filter on the beam it diffracts. However, in certain optics the required bend radius of Johansson geometry is realized by clamping the crystal onto a curved form. The clamping restraint exists only at the edges of the optic, not in the central, active area where it is illuminated by the X-ray beam. The crystal itself however, can minimize internal stress by remaining flat; in this case an anticlastic curvature of the optic results. A 'saddle' distortion across the surface of the diffracting region of the crystal results in a complex asymmetric $K\alpha_1$ spectrum that defies accurate mathematical description. Johansson optics, however, can be bent by cementing the crystals into a preform, yielding an optic of superior perfection in curvature. Fig. 3.1.13 shows data collected from such an optic using an Si single crystal, 333 reflection, as an analyser. Parallel-beam conditions were approximated in this experiment with the use of very fine 0.05 mm incident and receiving slits. The observed symmetric emission profile of Fig. 3.1.13(*a*) can be modelled with a combination of several Gaussians. However, a Johansson optic will scatter 1–2% of high-energy radiation to a higher 2θ angle than the $K\alpha_1$ focal line of the optic. This unwanted scatter is dominated by, but not exclusive to, the $K\alpha_2$ spectrum. Louër (1992) indicated that it can be largely blocked with a knife edge aligned to just 'contact' the high-angle side of the optic's focal line. Alternatively, the NIST method is to use a slit aligned to straddle the focal line. Proper alignment of this anti-scatter slit is critical to achieving a good level of performance with the absence of '$K\alpha_2$' scatter, as illustrated in Fig. 3.1.13(*b*). As will be demonstrated, with use of any Johansson optic the elimination of the $K\alpha_2$ line is of substantial benefit in fitting the observed peaks with analytical profile-shape functions.

3.1.3. Instrument alignment

Modern instruments embody the drive towards interchangeable pre-aligned or self-aligning optics, which, in turn, has led to several approaches to obtaining proper alignment with minimum effort on the part of the user. We will not review these approaches, but instead we decribe here the methods used at NIST, which could be used to check the alignment of newer equipment. With the use of calibration methods that simply characterize the performance (which includes the errors) of the machine in an empirical manner and apply corrections, the quality of the instrument alignment may be surprisingly uncritical for a number of basic applications such as lattice-parameter refinement. However, with the use of the more advanced methods for characterization of the IPF that are based on the use of model functions, the proper alignment of the machine is critical. The models invariably include refineable parameter(s) that characterize the extent to which the given aberration affects the data; the correction is applied, and the results are therefore 'correct'. However, if the instrument is not aligned properly, the analysis attempts to model the errors due to misalignment as if they were an expected aberration. The corrections applied are therefore incorrect in degree and nature and an erroneous result is obtained.

The conditions for proper alignment of a Bragg–Brentano diffractometer (see Fig. 3.1.14) are:

1. the goniometer radius, defined by the source-to-rotation-axes distance, R_1, equals that defined by the rotation-axes-to-receiving-slit distance, R_2 (to ±0.25 mm);
2. the X-ray line source, sample and receiving slit are centred in the equatorial plane of diffraction (to ±0.25 mm);
3. the goniometer rotation axes are co-axial and parallel (to ±5 µm and <10 arc seconds);
4. the X-ray line source, specimen surface, detector slit and goniometer rotation axes are co-planar, in the 'zero' plane, at the zero angle of θ and 2θ (to ±5 µm and ±0.001°); and
5. the incident beam is centred on both the equatorial and 'zero' planes (to ±0.05°).

The first three conditions are established with the X-rays off, while conditions (4) and (5) are achieved with the beam present, as it is actively used in the alignment procedure. Neither incident- nor diffracted-beam monochromators are considered; they are simply added on to the Bragg–Brentano arrangement and have no effect on the issues outlined here. Also, in order to execute this procedure, a sample stage that can be rotated by 180° in θ is required. However, this does not need to be the sample stage used for data collection. Before any concerted effort to achieve proper alignment, it is advisable to check the mechanical integrity of the equipment. Firmly but gently grasp a given component of the diffractometer, such as the tube shield, receiving-slit assembly or sample stage, and try to move it in a manner inconsistent with its proper mounting and function. The number of defects, loose bolts *etc.*, that can be found this way, even with quite familiar equipment, can be surprising.

Let us briefly review the development of diffraction equipment and the subsequent impact on alignment procedures. The goniometer assemblies used for powder diffractometers utilize a worm/ring gear to achieve rotation of the θ and 2θ axes while allowing for the $\sim 0.002^\circ$ resolution with the use of a stepper or servo motor actuating the worm gear. 'Home' switches, with a coarse one on the ring gear and a fine one on the worm shaft, allow the software to locate the reference angle(s) of the goniometer assembly to a repeatability of the stepper motor resolution. With the first generation of these automated goniometers, the zero angles were fixed relative to the home positions. With such a design the invariant reference was the receiving slit, and the operator adjusted the height of the tube shield and the angle of the θ stage to realize alignment condition (4). Second-generation machines offered the ability to set the zero angles relative to the home positions (or those of optical encoders) *via* software, in which case the exact angular position of either the X-ray tube focal line or of the receiving slit in θ–2θ space is arbitrary. The operator simply determines the positions where the θ and 2θ angles are zero, and then sets them there. There is no technical reason why the older designs cannot be aligned to the accuracy of newer ones. In practice, however, with older equipment the patience of the operator tends to become exhausted, and a less accurate alignment is accepted. An important consideration in evaluating modern equipment is that it is often the incident optic, not the X-ray source (focal line), that is used as the reference. Which situation is the case can be readily discerned with an inspection of the hardware: if the incident optic is anchored to the instrument chassis, then it is the reference. If it is attached to the tube shield, however, then the source establishes the reference. The NIST equipment has the latter design.

Condition (1) is that the goniometer radius, defined by the source-to-rotation-axis distance, R_1, equals that defined by the rotation-axis-to-receiving-slit distance, R_2. This condition is required for proper focusing and is generally realized with the use of rulers to achieve a maximum permissible error of $R \pm 0.25$ mm for a nominal $R = 200$ mm diffractometer. Condition (2) concerns the centring of the components in the plane of diffraction or equatorial plane. This condition is assured with the use of straightedges and rulers and, again for a line focus with an 8 to 12 mm source length, the maximum permissible error for deviations along the equatorial plane is ± 0.25 mm. One can also consider the takeoff angle at this time; this is the angle between the surface of the X-ray tube anode and the equatorial centre line of the diffractometer incident-beam path. As this angle decreases the resolution is improved at the expense of signal intensity, and *vice versa*, as a consequence of the variation in the size of the source that the specimen 'sees'. However, with modern fine-focus tubes, this is not a major effect. Qualitative experiments at NIST indicate that the exact angle is not critical; a 6° takeoff angle is reasonable.

The third issue concerns the concentricity of the θ and 2θ rotation axes of the goniometer assembly; this is a matter of underappreciated concern. It is not, however, one over which the end user has a great deal of control. Measurement of axes centricity requires the construction of some fairly complex and stiff structures capable of measuring displacements of the order of 1 to 2 μm and rotations of seconds of arc. The objective is to measure both the offset between the two axes and the angle between them. Concentricity errors affect XRPD data in a manner analogous to that of sample displacement; hence a 5 μm concentricity error is of concern. Worse yet is the possibility that some degree of precession occurs between the two axes with the operation of the goniometer. In this case, the performance of the machine will challenge description using established models.

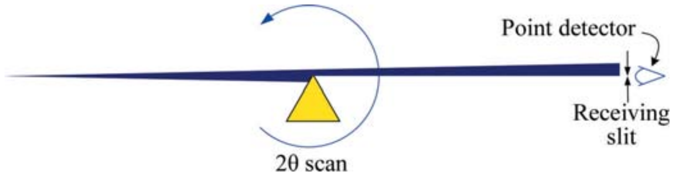

Figure 3.1.15
Diagrammatic view illustrating the use of a knife edge to determine the 2θ zero angle.

Subsequent experiments are performed with the X-rays present in order to achieve conditions (4) and (5). The criteria for proper alignment are universal, but there is a range of experimental approaches by which they can be realized. The specific approach may well be based on the age and make of the equipment as well as the inclinations of the operator. The essence of the experimental design remains constant, however: the operator uses optics mounted in the sample position that will either pass or block the X-ray beam in such a way as to tell the operator if and when the desired alignment condition has been realized. One approach is to use a knife edge mounted as shown in Fig. 3.1.15; a 2θ scan is performed using a point detector with a narrow receiving slit. When the intensity reaches 50% of the maximum, the X-ray source (focal line), the rotation axes of the goniometer and the 2θ (zero) angle are coplanar. However, the problematic presumption here is that the sample stage is aligned so exactly that the rotation axes of the goniometer assembly bisect the specimen surface, and therefore the knife edge, to within a few micrometres. This is equivalent to the z height being zero. The verification of this level of accuracy in stage alignment would be exceedingly difficult *via* direct measurements on the sample stage itself. While many would be inclined to trust the instrument manufacturer to have correctly aligned the stage, at NIST we use an alternative approach.

A straightforward means of addressing this problem is to use a stage that can be inverted, and perform the 2θ zero angle experiment in both orientations. 2θ scans of a knife edge in the normal and inverted positions can be compared to determine the true 2θ zero angle, independent of any z-height issue associated with the stage. It is often useful to draw a diagram of the results in order to avoid confusion; half the difference between the two measured zero angles yields the true one. With this information, the final alignment involves adjusting the specimen z height in the desired stage, which need not be invertible, until what is known to be the true 2θ zero angle is realized. The knife edge can also be used to centre the beam on the rotation axes, as per condition (5). Determination of the θ stage zero angle can be performed using a precision ground flat. An alternative optic to the knife edge is a rectangular 'tunnel' through which the X-ray beam passes. The entrance window of said tunnel may measure 20 to 40 μm in height and 10 mm in width, while the tunnel itself is 5 cm long. It is mounted in the beam path as illustrated in Fig. 3.1.16, with the 20 to 40 μm dimension defining the width of the beam and the 10 mm dimension describing the beam's length. Optics like this can be made of metal but are often made of glass. This optic will pass an X-ray beam only if it is parallel to the direction of the tunnel and can be used to determine both θ and 2θ zero angles. These are the optics used at NIST, *via* an experimental approach that will be discussed below.

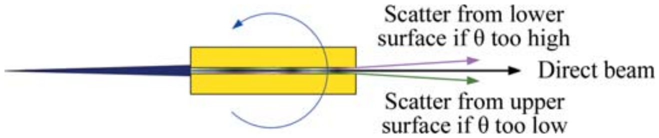
Scatter from lower surface if θ too high
Direct beam
Scatter from upper surface if θ too low

Figure 3.1.16
Diagrammatic view of the glass tunnel for determination of θ and 2θ zero angles.

If a diffractometer is being commissioned for the first time, or if major components have been replaced, it is appropriate to use fluorescent screens to achieve a rough alignment and to ensure that the incident beam does indeed cross the goniometer rotation axes and enter the detector; otherwise one may waste time looking for the beam. It is critical that these experiments are performed with the tube at operating power and that the equipment is at thermal equilibrium. Thermal effects will cause the anode to expand and contract, which will typically cause the position of the source to change. This is particularly critical when using optics to prepare the incident beam, as the performance of the optics can change markedly with movement of the source.

The objective of the first experiment using X-rays is to achieve parallelism between the line source of the tube anode, or focal line of the Johansson optic, and the receiving slit. A 5 μm platinum pinhole, which was originally manufactured as an aperture for transmission electron microscopy, is mounted in the sample position and used to image the focal line of the source onto the receiving slit (Fig. 3.1.17). This experiment is the one exception to the operating-power rule, as otherwise *Bremsstrahlung* will penetrate the platinum foil of the pinhole and produce confounding results. Success can be realized with settings of 20 kV and 10 mA; these reduced power settings are not thought to affect the angle between the tube anode and receiving slit (which is the issue addressed in this experiment). The incident slit is opened to the point at which the line source itself is imaged, not the incident slit. The Soller slits, and the post-monochromator if there is one, must also be removed to allow for the axial divergence that is needed for the success of this experiment. The pinhole images the line source onto the receiving slit; as the angle between the two decreases, progressively larger lengths of the receiving slit are illuminated during a 2θ scan. The tilt of the X-ray tube shield is varied and sequential 2θ scans are collected. As parallelism is approached, the profiles will exhibit a progressive increase in the maximum intensity value, with corresponding decreases in breadth. Conclusive results are shown in Fig. 3.1.18. It should be noted that this is a very difficult experiment to perform because the beam is essentially open and scatter is abundant. Shielding must be installed such that the detector can see only the signal that passes through the pinhole. The pinhole itself should also be shielded to minimize the area of (relatively transparent) platinum exposed to the direct beam.

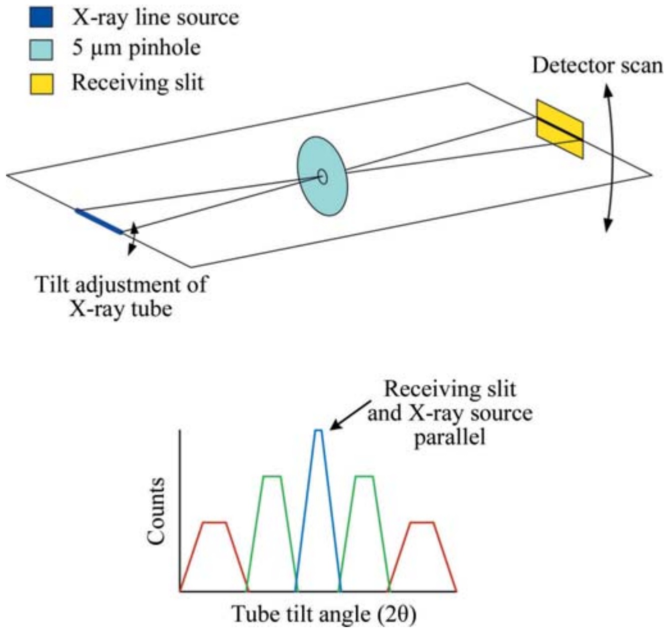

Figure 3.1.17
Design of experiments using a pinhole optic to align the X-ray source with the receiving slit.

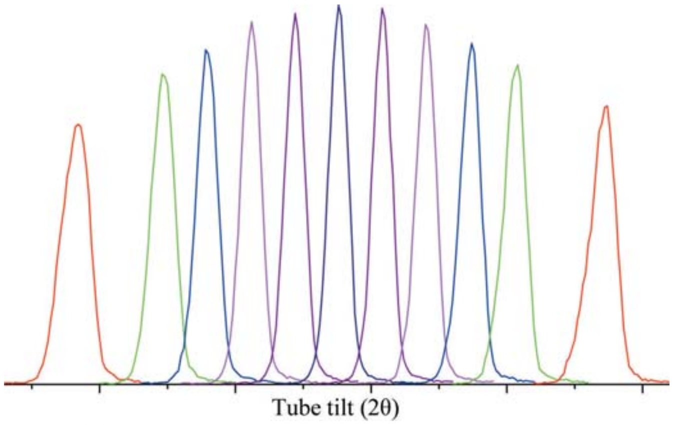

Figure 3.1.18
Successful results from the pinhole experiment showing variation in profile shape with successive adjustment of tube tilt; the central peak of highest intensity indicates the state of parallelism between the source and the receiving slit.

We now proceed to determine the θ and 2θ zero angles using the glass-tunnel optic. Initial experiments should be performed without a post-monochromator, as its presence tends to complicate finding the beam. However, it should be installed as experiments progress, as it will lead to an increase in resolution; it may alter the wavelength distribution slightly and its mass will change the torque moment on the 2θ axis. The latter two factors may alter the apparent 2θ zero by several hundredths of a degree. It is best to use a minimum slit size for the incident beam that will fully illuminate the entrance to the tunnel optic to avoid undue levels of scatter. The receiving slit should be the smallest size available, 0.05 mm in our case. The first experiment will determine a first approximation of the zero angle of θ. The tunnel optic is used, with a θ scan being performed with an open detector. Once an approximate zero angle of θ is determined, the receiving slit is installed and a 2θ scan is performed with θ at its zero point. Thus, we now have a qualitative idea of both zero angles. Then an experiment is performed as shown in Fig. 3.1.19; sequential 2θ scans are performed as θ is stepped through its zero point by very small steps (0.004° in the case of our experiment). The tunnel scatters radiation from its upper and lower surfaces when it is not parallel to the central portion of the beam, resulting in a lobe on each side of the direct beam in Fig. 3.1.19. When θ is at the desired zero angle, the direct beam is transmitted with minimum intensity in the lobes.

Once the zero positions of the θ and 2θ angles are determined, the stage is inverted and this set of experiments is repeated. It is desirable to drive the stage by 180°; however, remounting the stage in an inverted position is acceptable if the mounting structure centres the stage to within a few micrometres. Again, it is often useful to draw a diagram of the results from these two zero-angle determinations to ensure that the data are interpreted

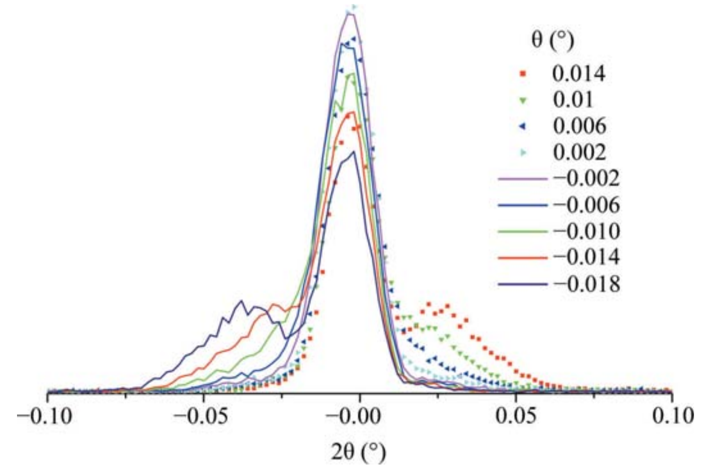

Figure 3.1.19
Results from 2θ scans at successive θ angles using the glass tunnel to determine the θ and 2θ zero angles.

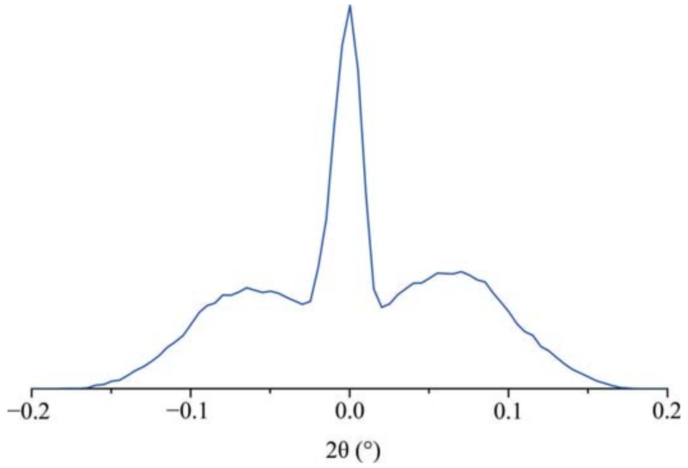

Figure 3.1.21
Final results from a θ–2θ scan using the glass tunnel, indicating the correct determination of θ and 2θ zero angles.

correctly, as shown in Fig. 3.1.20. In this example, the sample height is displaced in the positive z direction, otherwise the positions of orientation 1 and 180° from orientation 1 would be reversed. The operator should verify that fully self-consistent results are obtained with respect to the four zero angles shown in Fig. 3.1.20. Because the beam is divergent, the difference between the two θ zero angles will not be precisely 180°, as shown in Fig. 3.1.20. Again, half the difference between the two measured 2θ zero angles yields the true one, with respect only to the locations of the X-ray source and the goniometer rotation axes. Using the data of Fig. 3.1.20 and the goniometer radius, the z-height error on the stage in question could be computed and an adjustment made; this should be followed by repeating the two zero-angle measurements and checking for self-consistency to provide additional confidence in the alignment.

The final task is to mount the stage to be used in subsequent data collection and adjust its sample height until the known true 2θ zero angle is obtained. The final experiment is a θ–2θ scan of the tunnel optic to yield data of the kind shown in Fig. 3.1.21. The symmetry of the lobes on each side of the peak from the direct beam is indicative of the correct θ zero angle setting. This final high-resolution experiment is an excellent indicator of the state of the alignment of the instrument. These experiments, when used in conjunction with profile fitting, can yield measurements of the zero angles with an uncertainty for θ and 2θ of ±0.001°. Given the high certainty with which the zero angles are determined, they would then not be refined in subsequent data analyses. The alignment of the incident-beam slit, issue (5), is accomplished with a scan of the direct beam. If the machine is equipped with a variable-divergence incident-beam slit, it is important to evaluate it at several settings because changes in the centre line of the beam may occur as the divergence angle is altered. Use of an excessively narrow receiving slit should be avoided for scans of the direct beam, since the thickness of the metal blades used for the slit itself may be larger than the width of the slit, leading to a directional selectivity as the scan is performed.

The alignment presented here was carried out using a scintillation detector; however, much of it could be performed using a PSD in 'picture-taking' mode. In any case, the count rates have to be monitored to ensure that they are within the linear range of the detector (5000 to 10 000 counts per second), otherwise anomalous results are obtained. Attenuating foils that are flat and in good condition can be used to reduce the intensity. It should also be stressed that if the observations made during the experiments do not meet expectations, something is wrong and the desired outcome, *i.e.* the correct alignment, will not be realized. Drawing a diagram of the X-ray beam path can be very useful for discovering the cause of apparently unexplainable observations. Also, throughout these experiments it is appropriate for the operator to try various additional settings to ensure that the machine is operating as expected. Anomalous observations can almost always be explained in a quantitative manner with appropriate investigation. Patience is required.

In the past, achieving acceptable performance with a Johansson optic was considered so problematic that they were under-used, despite the improvements in the data quality they provided. Modern instrumentation can provide their advantages with dramatically reduced effort. The NIST Johansson IBM, however, was derived from an older design that was originally supplied with a Siemens D500, *circa* 1987. It uses a Huber 611 monochromator housing that provides 5 degrees of freedom in the positioning of the optic: the a distance, the takeoff angle, crystal 2θ, tilt and azimuth. For aforementioned reasons, we installed a modern Johansson optic manufactured by Crismatec (now part of Saint Gobain). There are two stages to the procedure for aligning the machine equipped with the IBM: first, the crystal optic itself is aligned

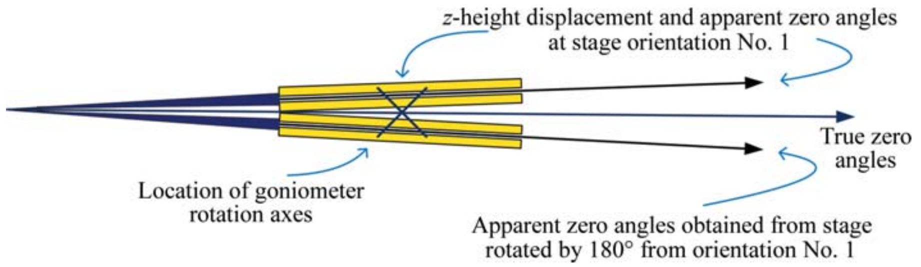
z-height displacement and apparent zero angles at stage orientation No. 1
True zero angles
Location of goniometer rotation axes
Apparent zero angles obtained from stage rotated by 180° from orientation No. 1

Figure 3.1.20
Diagram of hypothetical results from two zero-angle measurements (Fig. 3.1.19) with the sample stage in the normal and inverted positions to determine the true 2θ zero angle of the goniometer assembly in the absence of a z-height error from sample-stage misalignment.

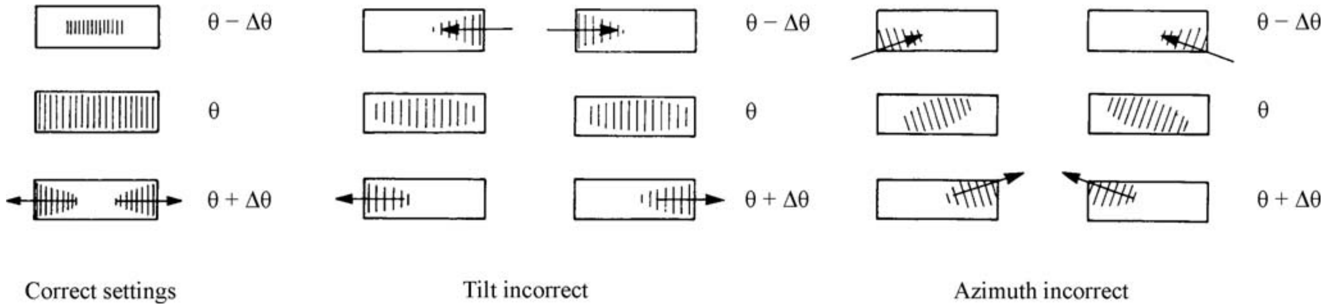

Figure 3.1.22
Figures found within the instructions for a Siemens D500 incident-beam monochromator in a Huber 611 monochromator housing, illustrating image formation and movement for correct and incorrect settings of tilt and azimuth angles (reproduced with verbal permission from Huber).

with the line source of the tube anode, and then the tube shield/IBM assembly is aligned with the goniometer. The second stage is analogous to the instrument alignment described above, so here we will discuss only the first stage (although not exhaustively).

The alignment of the Johansson optic to the X-ray source is done largely with the X-rays present. The crystal tilt and azimuth are set by using a fluorescent screen or camera to observe the diffraction images from the optic as it is rotated through its diffraction angle. Fig. 3.1.22, which is reproduced from the instructions supplied by Siemens, shows how the images form and move, informing the operator of necessary adjustments. Initially, a set of hex-drive extensions was used to drive the optic remotely through its 2θ angle. The source was operated at full power while the movement of the image was observed through a lead-impregnated window. Later, a motor drive was installed onto the 2θ actuator of the 611 housing. In the end, the incident-beam intensity realized from the optic is dependent upon the operator's ability to discern the subtleties in the image movement (Fig. 3.1.22). Blocking the axially divergent signals from the optic with a high-resolution 0.05° Soller slit dramatically improves the sensitivity of this observation to the setting of the tilt and azimuth angles. The inclusion of the Soller slit, however, will reduce the intensity markedly. A complete darkening of the room, including blocking of the shutter lights, as well as allowing time for pupil dilation, can be helpful. However, the use of an X-ray imager or a PSD in picture-taking mode improves the quality of the alignment by allowing for a more accurate interpretation of the observations.

The goal is the formation of an image in the centre of the beam path that splits symmetrically out to the edges with increasing crystal 2θ angle (Fig. 3.1.22). The directions supplied by Siemens and Huber allude to the fine adjustment [see Huber (2014) for movies] of the tilt and azimuth by examining the structure of the diffracted beam at the optic's focal point. A fluorescent screen located at the focal point and set at a 6° angle to the beam path is used to image the beam structure. With the use of the Soller slit for coarse alignment of tilt and azimuth, the desired final image for the fine-adjustment mode was, indeed, obtained. But it was not possible, even with a deliberate mis-setting of tilt and azimuth angles, to use the defective images at the focal point as a source of feedback for correcting the settings because they were too diffuse.

The Johansson optic is supplied with a and b distances that correspond to the angle of asymmetry in the diffraction planes and the bend radius. The instructions indicate that an incorrect setting in a will cause the optic's diffraction image to move up or down in the plane of diffraction with variation of the crystal 2θ angle. Again, a lack of sensitivity prevents the use of this effect as a feedback loop to set a. Alternative experiments for the optimization of the distance a of the optic were time consuming and not conclusive, so we decided to accept the supplied value for a. As before, we set the takeoff angle at 6°. A critical and quite difficult problem is the alignment of the slit located between the X-ray tube and the crystal optic (not shown in Fig. 3.1.3). This slit centres the beam onto the active area of the optic; misalignment leads to unwanted scatter from the optic's edges. It is aligned with the X-ray beam present, yielding an image of the shadow cast by the optic itself on one side, and one edge of the slit on the other. The optic is rotated in 2θ so that its surface is parallel to the X-ray beam, *i.e.* shadowing is minimized. The shadow from the second edge of the slit is obscured by the optic. Geometric considerations are used in conjunction with knowledge of the radius of curvature of the optic to obtain the correct location for the slit. A drawing is highly useful in this instance. After the installation of this slit, it is appropriate to re-check the tilt and azimuth settings, as the alignment of the optic is nearly complete.

The setting of the crystal 2θ is performed by evaluation of the direct beam, either with scans using a scintillation detector or by taking pictures with a PSD. With increasing crystal 2θ, the beam diffracted by the optic will build in the centre forming a broad profile; then the intensity on either side of the initial profile will rise, leading to the desired box form; and then intensity at the centre of the box will fall, followed lastly by the intensity at either side of the centre. This is consistent with Fig. 3.1.22. The process will repeat at half the $K\alpha_1$ intensity for the $K\alpha_2$ line. (Avoid tuning to the wrong line.) The crystal 2θ setting should be checked at regular intervals with a scan of the direct beam; this is the only setting on the IBM that has been observed to drift with time.

The final step in alignment of the IBM is the installation of the anti-scatter slit located at the focal line of the optic (Fig. 3.1.3). This is performed after the IBM assembly is aligned to the goniometer. Optimal performance of the anti-scatter slit can be expected only if it is located precisely at the focal line, which itself constitutes the smallest region within which a maximum of X-ray flux is transmitted. Therefore, the NIST alignment procedure includes an experiment using a narrow slit positioned by an x–y translator to evaluate the relative flux of the beam in the vicinity of the focal line. The y direction is parallel to the b direction (Fig. 3.1.3). A 0.05 mm slit is translated across the beam in the x direction, while intensity readings are recorded from an open detector. This process is repeated for a sequence of y distances. A plot of the recorded intensity *versus* x at a sequence of y settings will yield a set of profiles which broaden on either side of the true value of b; the narrowest, highest-intensity profile will indicate the location of the focal line. Thus, the experiment determines both the true b distance and the location in the x direction of the focal line. Once b is known, translational adjustment of the IBM assembly may be required to locate the focal line precisely on the goniometer radius. The experiment also effectively measures the size of the focal line, in our case this was 0.15 mm. A slit of this dimension was fabricated, and the *x*–*y* translator was replaced with a standard slit retainer positioned at the desired location. The results are shown in Fig. 3.1.13.

3.1.4. SRMs, instrumentation and data-collection procedures

NIST maintains a suite of SRMs suitable for calibration of powder-diffraction equipment and measurements (NIST, 2015*a*,*b*,*c*,*d*). These SRMs can be divided into various categories based on the characteristic they are best at calibrating for: line position, line shape, instrument response or quantitative analysis, although some degree of overlap exists. The powder SRMs are certified in batches, typically consisting of several kilograms of feedstock, that are homogenized, riffled and bottled prior to the certification. A representative sample of the bottle population, typically consisting of ten bottles, undergoes certification measurements. The specific size of each lot is based on expected sales rates, mass of material per unit and an anticipated re-certification interval of 5 to 7 years. When the stocks of a given certification are exhausted, a new batch of the SRM is certified and a letter is appended to the code to indicate the new certification. Hence SRM 640e (2015) is the sixth certification of SRM 640, originally certified in 1973. The microstructural character of the SRM artifact and/or the certification procedure itself are expected to change (improve) with each renewal.

To understand the role of an SRM in the calibration of XRPD measurements and equipment, it is helpful to discuss briefly the documentation accompanying an SRM [see also Taylor & Kuyatt (1994), GUM (JCGM, 2008*a*) and VIM (JCGM, 2008*b*)]. NIST SRMs are known internationally as certified reference materials. Accompanying an SRM is a certificate of analysis (CoA), which contains both certified and non-certified quantity values and their stated uncertainties. Certified quantity values are determined by NIST to have metrological traceability to a measurement unit – often a direct linkage to the SI. Non-certified values (those lacking the word certified, as presented within a NIST CoA) are defined by NIST as best estimates of the true value provided by NIST where all known or suspected sources of bias have not been fully investigated. Both certified and non-certified quantity values are stated with an accompanying combined expanded (k = 2) uncertainty. Expanded uncertainty is defined as the combined standard uncertainty values for a given certified value multiplied by a coverage factor, k, of 2 and represents a 95% confidence interval for a given value. The combined standard uncertainties are determined by applying standard procedures for the propagation of uncertainty. The distinguishing characteristic of a NIST-certified quantity value is that all known instrumental measurement uncertainties have been considered, including the uncertainties from the metrological traceability chain. NIST defines uncertainties in two contexts: type A and type B. Type A are the random uncertainties determined by statistical methods, for example the standard deviation of a set of measurements. Type B uncertainties are systematic in nature and their extent is usually based on scientific judgment using all relevant information available on possible biases of the experiment. Assessing the technical origin and magnitude of these type-B uncertainties is a dominant part of the NIST X-ray metrology program.

XRPD SRM-certified quantity values are used primarily for calibration of XRPD measurement systems. The calibration data collected on test instruments also contain the two types of errors: random and systematic. It is the systematic measurement errors, or so-called instrument bias, that can be corrected with a calibration. Calibration is a multi-step process. First, certified quantity values are related to test instrument data. This is done by computing, from these values, what would constitute an ‘ideal’ data set from the ‘measurement method’ to be calibrated. The ‘method’ in this case would include the test instrument, its configuration settings and the data-analysis method to be used in subsequent measurements. Then a data set from the SRM is collected and analysed under the conditions of the method. Lastly, a calibration curve is generated by comparing the ‘ideal’ data set to the measured one. This would establish a correction to the instrument data and yield a calibrated measurement result. For XRPD, this correction has classically taken the form of a calibration function shifting the apparent 2θ indications. There is also the possibility that comparing the ‘ideal’ instrument response with the observed one indicates a mechanical, optical or electrical malfunction of the instrument. This, of course, requires further investigation and repair, rather than simply applying a calibration curve.

The generation of a calibration curve as just described can be thought of as a ‘classical’ calibration, and is applicable when the data-analysis procedure(s) use empirical methods to parameterize the observations. More recent, advanced methods such as the FPA use model functions that relate the form of the data directly to the characteristics of the diffraction experiment. The parameters of the model describing the experiment are refined in a least-squares context in order to minimize the difference between a computed pattern and the observed one. With the use of methods that use model functions, the calibration takes on a different form, as the collection and analysis of data can be thought of as replacing the aforementioned multi-step process. The calibration is completed by comparing the results of the refinement with certified quantity values from an appropriately chosen SRM and the known physical-parameter values that describe the optical configuration of the test instrument.

Random measurement error, describing the variation of data for a large set of measurements, can be estimated by repeating measurements over an extended period and computing the variance in the data. Furthermore, over time, one could recalibrate the system and look at the variance of the systematic bias for a given instrument, *i.e.* the rate of drift in the instrument. One would also have to investigate the sensitivity of both the random error and the variance in the systematic bias to environmental variables such as ambient temperature, power fluctuations *etc*. This systematic error variance, combined with the prior determined random error variance and the certified value and its uncertainty, provides an instrumental measurement uncertainty that can be applied to all measurements from a given instrument. Such an in-field study, however, would take years to complete. Instead, the instrumental measurement uncertainties for a given commercial XRPD measurement system are typically provided by the manufacturer, with the stated caveat that periodic calibrations should be performed *via* factory specifications. The instrumental measurement uncertainties determined through such a study are invariably much larger than those of the NIST-certified quantity values, as they contain both the instrument measurement errors (systematic and random) combined with certified quantity value uncertainties.

NIST maintains a suite of more than a dozen SRMs for powder diffraction. However, one often encounters discussions of non-institutionally-certified standards such as ‘NAC’ ($Na_2Ca_3Al_2F_{14}$), annealed yttrium oxide and silver behenate. Our discussions here principally concern SRMs 640e (silicon), 660b (NIST, 2010) (lanthanum hexaboride), 1976b (2012) (a sintered alumina disc) and 676a (NIST, 2008) (alumina). SRM 660b has since been renewed as SRM 660c (2014). Most of the work presented here was performed using SRM 660b; however, SRM 660c could be used in any of these applications with identical results. SRMs certified to address the calibration of line position, such as SRMs 640e, 660c and 1976b, are certified in an SI-traceable manner with respect to lattice parameter. SRM 1976b is also certified with respect to 14 relative intensity values throughout the full 2θ range accessible with Cu $K\alpha$ radiation. As such, it is used to verify the correct operation of a diffractometer with respect to diffraction intensity as a function of 2θ angle, *i.e.* instrument sensitivity (Jenkins, 1992) or instrument response. SRM 676a is a quantitative-analysis SRM certified with respect to phase purity (Cline *et al.*, 2011). While SRM 676a is certified for use as a quantitative-analysis SRM, it is also certified with respect to lattice parameters.

Starting with the certification of SRM 640c in 2000, the 640*x* SRMs have been prepared in a way that minimizes sample-induced line broadening. These powders consist of single-crystal particles that were annealed after comminution in accordance to the method described by van Berkum *et al.* (1995). Their crystallite-size distributions (as determined by laser scattering) have a maximum probable size of approximately 4 µm with 10% of the population being above 8 µm and 10% of the population being below 2.5 µm (with trace quantities below 1 µm). With Cu $K\alpha$ radiation, silicon has a linear attenuation of 148 cm^{-1}, which is a relatively low value. SRMs 660*x* consist of lanthanum hexaboride, which was prepared to display a minimal level of both size and microstrain broadening. With the release of SRM 660a, high-resolution diffraction using synchrotron radiation must be used to detect microstructural broadening. However, the use of lanthanum hexaboride by the neutron-diffraction community is problematic, as the naturally abundant isotope ^{10}B has an extremely high neutron absorption cross section. Lanthanum hexaboride made from ^{10}B is essentially opaque to neutrons, rendering it unsuitable for neutron experiments. This problem was addressed with SRMs 660b and 660c by means of a dedicated processing run using a boron carbide precursor enriched with the ^{11}B isotope to a nominal 99% concentration. As such, SRMs 660b and 660c are suitable for neutron experiments; they display a miniscule reduction in microstrain broadening relative to 660a. SRMs 660b and 660c were prepared at the same time using identical procedures and equipment, but in different lots. Lanthanum hexaboride has a relatively high linear attenuation of 1125 cm^{-1} with Cu $K\alpha$ radiation. This linear attenuation virtually eliminates the contribution of specimen transparency to the observed data; as such it offers a more accurate assessment of the IPF for a machine of Bragg–Brentano geometry than is available from other SRMs in the suite. The powders of the SRM 660*x* series consist of aggregates, with the crystallite size being approximately 1 µm and the aggregate size distribution being centred at approximately 8 µm for SRM 660a and 10 µm for 660b and 660c. SRM 676a consists of a fine-grained, equi-axial, high-phase-purity α-alumina powder that does not display the effects of preferred orientation. It consists of approximately 1.5 µm-diameter aggregates with a broad crystallite-size distribution centred at 75 nm. Therefore, the diffraction lines from SRM 676a display a considerable degree of Lorentzian size broadening, with a $1/\cos\theta$ dependence.

SRM 1976b consists of a sintered alumina disc; this format eliminates the variable of sample-loading procedure from the diffraction data collected from this SRM. The alumina powder precursor for SRMs 1976, 1976a and 1976b consists of a ‘tabular’ alumina that has been calcined to a high temperature, approximately 1773 K. This calcination results in a phase-pure α-alumina powder with a plate-like crystal morphology, approximately 10 µm in diameter by 2 to 3 µm in thickness, leading to the texture displayed by these SRMs. The feedstock for SRMs 1976, 1976a and 1976b was manufactured with a common processing procedure: the compacts are liquid-phase sintered using a 3 to 5% anorthite glass matrix; hot forging was used to achieve a compact of approximately 97% of theoretical density. A unique outcome of the hot-forging operation used to manufacture these pieces was the axi-symmetric texture imparted to the microstructure. This axi-symmetric nature permits mounting of the sample in any orientation about the surface normal. Furthermore, as the sintered compacts cool, the viscosity of anorthite steadily increases, solidifying at approximately 1073 K. This permits intergranular movement during cooling, at least until 1073 K, and reduces the level of microstrain that would otherwise build between the grains due to the anisotropic thermal expansion behaviour of alumina. However, despite this relaxation mechanism, SRM 1976*x* still displays a discernable level of Gaussian microstrain broadening. SRMs 1976a and 1976b were manufactured in a single custom production run, and display a much more uniform level of texture than SRM 1976. This fact is reflected in the considerably smaller uncertainty bounds on the certified relative intensity values of SRMs 1976a and 1976b compared to the original SRM 1976.

Mounting of powder specimens for analysis using Bragg–Brentano geometry is a non-trivial process that typically requires 20 to 30 min. The objective is to achieve a maximum in packing density of the powder with a smooth, flat surface. A 5 µm displacement error in the position of the sample surface will have a noticeable impact on the data collected. Side-drifted mounts allow for realization of a flat surface with relative ease, though maximizing the density of the compact can be challenging. Top-mounted specimens can be compacted using a glass plate or bar that allows the operator to see the sample surface through the glass and, in real time, determine the success or failure in obtaining the desired outcome. Some powders, such as that of SRM 640e, ‘flow’ in the mount with the oscillation of the glass plate across the sample surface. Others, such as SRM 676a do not flow at all, but can be ‘chopped’ into the holder and compacted with a single compression. Several attempts may be necessary to realize a high-quality mount. A low-wetting-angle, low-viscosity silicone-based liquid resin, such as those marketed as vacuum-leak sealants for high-vacuum operations, can be used to infiltrate the compact once it is mounted; this results in a stable sample that will survive some degree of rough handling.

The diffractometer discussed in this work is a NIST-built instrument with a conventional optical layout, although it has several features that are atypical of equipment of this nature. It was designed and built to produce measurement data of the highest quality. This outcome is not only consistent with the certification of SRMs, but is also requisite to critical evaluation of modern data-analysis methods (another goal of this work), as discussed below. The essence of the instrument is a superior goniometer assembly that is both stiff and accurate in angle measurement, in conjunction with standard but thoroughly evaluated optics. The tube shield and incident-beam optics are mounted on a removable platform that is located *via* conical pins that constitute a semi-kinematic mount. This feature allows rapid interchange between various optical geometries. Fig. 3.1.23 shows

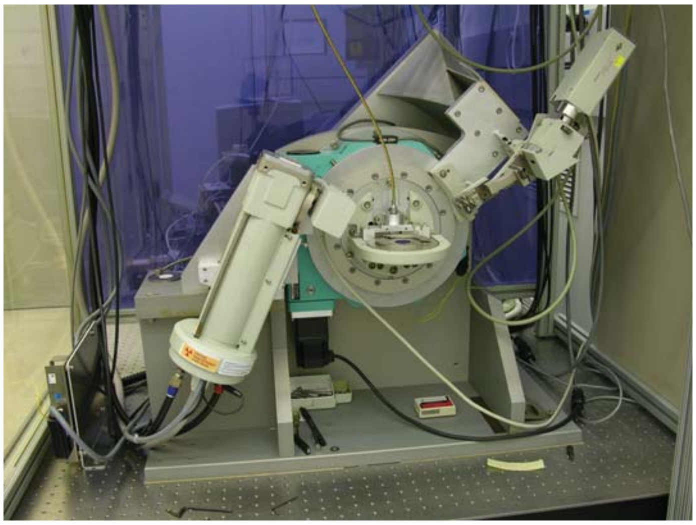

Figure 3.1.23
The X-ray powder diffractometer designed and fabricated at NIST, in conventional divergent-beam format.

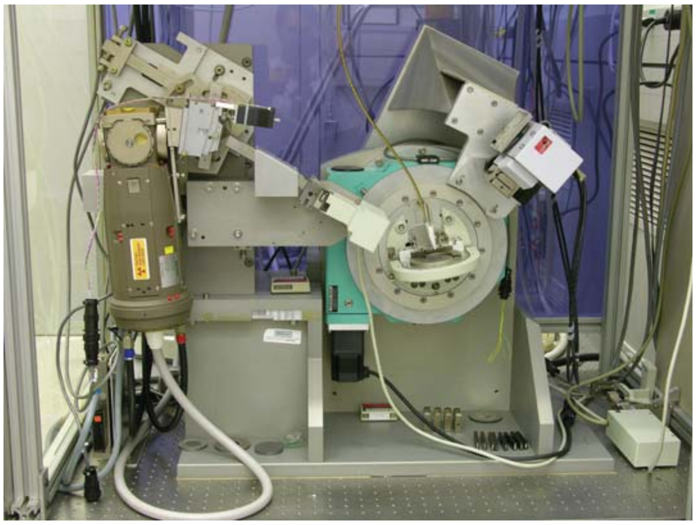

Figure 3.1.24
The NIST-built powder diffractometer configured with the Johansson incident-beam monochromator and a position-sensitive detector.

the instrument set up in conventional geometry with a post-monochromator and point detector, while Fig. 3.1.24 shows the setup with a Johansson IBM and a PSD. Data from these two configurations are discussed below.

The goniometer assembly, which is of θ–2θ geometry, uses a pair of Huber 420 rotation stages mounted concentrically with the rotation axes horizontal. The stage that provides the θ motion faces forward while the 2θ stage faces rearward; they are both mounted on a common aluminium monolith, visible in Figs. 3.1.23 and 3.1.24, which forms the basis of the chassis for the instrument. Both stages incorporate Heidenhain 800 series optical encoders mounted so as to measure the angle of the ring gear. With 4096-fold interpolation provided by IK220 electronics, an angle measurement to within ±0.00028° (1 arc second) was realized for both axes. The stages are driven by five-phase stepper motors that incorporate gear reducers of 10:1 for the θ stage and 5:1 for the 2θ stage, yielding step sizes of 0.0002° and 0.0004°, respectively. The manufacturer's specifications for the Huber 420 rotation stage claim an eccentricity of less than 3 μm and a wobble of less than 0.0008° (3 arc seconds). The construction of the goniometer assembly necessitated the development of a specialized jig to align the two 420 rotation stages with regard to both the concentricity (eccentricity) and parallelism (wobble) of their rotation axes. The result was that the overall eccentricity and wobble of the assembly met the specifications cited for the individual stages. The flexing of the detector arm, attached to the rearward-facing 2θ stage, was minimized by fabricating a honeycombed aluminium structure, 7.6 cm deep, which maximized stiffness while minimizing weight. Furthermore, the entire detector-arm assembly, including the various detectors, was balanced on three axes to minimize off-axis stress on the 2θ rotation stage (Black *et al.*, 2011). Thus, the goniometer assembly is exceedingly stiff and offers high-accuracy measurement and control of both the θ and 2θ angles.

The optics, graphite post-monochromator, sample spinner, X-ray generator and tube shield of the machine were originally components of a Siemens D5000 diffractometer, *circa* 1992. As previously discussed, the parts for the IBM configuration were obtained primarily from a Siemens D500, *circa* 1987. Both configurations include a variable-divergence incident-beam slit from a D5000. The PSD used in this work was a Bruker LynxEye XE. The cable attached to the sample spinner (as seen in Figs. 3.1.23 and 3.1.24) is a flexible drive for the spinner itself; the remote location of the drive motor (not shown) isolates the sample and machinery from the thermal influence of the motor. The machine was positioned on an optical table within a temperature-controlled (±0.1 K) space. The temperature of the water used for cooling the X-ray tube and generator was regulated to within ±0.01 K. Operation of the machine was provided through control software written in *LabVIEW*. Data were recorded in true x–y format using the angular measurement data from the optical encoders.

In conventional configuration, the 2.2 kW copper tube of long fine-focus geometry was operated at a power of 1.8 kW. This tube gives a source size of nominally 12 × 0.04 mm, while the goniometer radius is 217.5 mm. The variable-divergence slit was set to ~0.9° for the collection of the data discussed here. This results in a beam width, or footprint at the lowest θ angle, on the sample of about 20 mm, conservatively smaller than the sample size of 25 mm. A Soller slit with a divergence of 4.4° defined the axial divergence of the incident beam. A 2 mm anti-scatter slit was placed approximately 113 mm in front of the 0.2 mm (0.05°) receiving slit. The total path length of the scattered radiation (the goniometer radius plus the traverse through the post-monochromator) was approximately 330 mm. This setup reflects what is thought to be a medium-resolution diffractometer that would be suitable for a fairly broad range of applications and is therefore a reasonable starting point for a study of instrument calibration. With the IBM, the 1.5 kW copper tube of fine-focus geometry was operated at a power of 1.2 kW. This tube had a source size of nominally 8 × 0.04 mm. The variable-divergence incident slit was also set to 0.9° with a 0.2 mm (0.05°) receiving slit. The receiving optics were fitted with a 4.4° Soller slit. The total beam-path length was about 480 mm.

With the scintillation detector, data were collected using two methods, both of which encompassed the full 2θ range available with these instruments and for which the SRMs show Bragg reflections. The first involves data collection in peak regions only, as illustrated in Table 3.1.2 for SRM 660b. The run-time parameters listed in Table 3.1.2 reflect the fact that the data-collection efficiency can be optimized by collecting data in several regions, as both the intensity and breadth vary systematically with respect to 2θ. This was the manner in which data were collected for the certification measurements of SRMs 660c, 640e and 1976b. The

Table 3.1.2
Run-time parameters used for collection of the data used for certification of SRM 660b

The ‘overhead time’ associated with the operation of the goniometer is included.

hkl	Start angle (°)	End angle (°)	Step width (°)	Count time (s)	Total peak time (min)
100	20.3	22.2	0.01	2	6.3
110	29.1	31.4	0.01	1	3.8
111	36.4	38.4	0.01	3	10.0
200	42.7	44.4	0.01	5	14.2
210	48	50	0.008	2	8.3
211	53.2	54.896	0.008	5	17.7
110	62.5	64.204	0.008	11	39.0
300	66.7	68.596	0.008	4	15.8
310	70.9	72.7	0.008	6	22.5
311	75	76.904	0.008	9	35.7
222	79.3	80.804	0.008	47	147.3
320	83	84.904	0.008	15	59.5
321	86.9	88.9	0.008	8	33.3
400	95	96.704	0.008	42	149.1
410	98.6	100.8	0.008	9	41.3
330	102.7	104.9	0.008	12	55.0
331	106.9	108.9	0.01	27	90.0
420	111.1	113.1	0.01	20	66.7
421	115.3	117.6	0.01	10	38.3
332	119.9	122.1	0.01	19	69.7
422	129.6	131.796	0.012	32	97.6
500	134.9	137.396	0.012	27	93.6
510	140.5	144	0.014	7	29.2
511	147.5	150.908	0.016	15	53.2
Total time = 20.0 hours					

second involved a simple continuous scan of fixed step width and count time. It is generally accepted that a step width should be chosen so as to collect a minimum of five data points above the full-width-at-half-maximum (FWHM) to obtain data of sufficient quality for a Rietveld analysis (Rietveld, 1967, 1969; McCusker *et al.*, 1999). This does not, however, constitute any sort of threshold; collecting data of a finer step width can, with proper data analysis, result in a superior characterization of the IPF. However, one must consider the angular range of acceptance of the receiving slit that is chosen. For a slit of 0.05° a step width of 0.005° would add only 10% ‘new’ information, so selecting this step width would not be worth the extra data-collection time. We did, however, collect some data sets we refer to as ‘ultra-high-quality’ data; the step widths for these were half those shown in Table 3.1.2 and the count times were approximately three times higher than those in Table 3.1.2. For the reported instrument and configuration, the run-time parameters of Table 3.1.2 result in a minimum of 8 to 10 points above the FWHM. Count times were selected to obtain a uniform number of counts for each profile. It should be noted that it is probably not worth spending time collecting quality data from the 222 line of LaB_6, as it is of low intensity and relatively close to other lines of higher intensity; however, this is not the case with the 400 line. Selection of the run-time parameters can be an iterative process; the total width of each profile scan was set to include at least 0.3° 2θ of apparent background on either side of the profile. Except for the data for SRM 676a, the continuous scans discussed were collected with a step width of 0.008° 2θ and a count time of 4 s to result in a scan time of roughly 24 h. The scans of 676a were collected with 0.01° 2θ step width and 5 s count time.

The PSD used on the NIST diffractometer was a one-dimensional silicon strip detector operated in picture-taking mode for all data collection. It has an active window length of 14.4 mm that is divided into 192 strips for a resolution of 75 µm. With a goniometer radius of 217.5 mm this constitutes an active angular range of 3.80° with 0.020° per strip. Slits that would limit the angular range of the PSD window were not used; with each step the counts from all 192 channels were recorded. The PSD was stepped at 0.005° 2θ, for 25% new information per strip; however, to reduce the data-collection time a second coarse step was also included. Therefore, the data-collection algorithm includes the selection of three parameters: a fine step of 0.005°, the number of fine steps between coarse steps (4), and the size of a coarse step (typically 0.1° or 0.2° 2θ). This approach allows for the collection of high-resolution data without stepping through the entire pattern at the high-resolution setting. Data were collected with four fine steps per detector pixel and a coarse step of 0.1° 2θ. They were processed to generate *x*–*y* data for subsequent analysis. The operator can select the portion of the 192 channels, centred in the detector window, to be included in the generation of the *x*–*y* file. The PSD was fitted with a 1.5° Soller slit for collection of the data presented here.

3.1.5. Data-analysis methods

Data-analysis procedures can range from the entirely non-physical, using arbitrary analytical functions that have been observed to yield reasonable fits to the observation, to those that exclusively use model functions, derived to specifically represent the effect of some physical aspect of the experiment. The non-physical methods serve to parameterize the performance of the instrument in a descriptive manner. The origins of two of the most common measures of instrument performance are illustrated in Fig. 3.1.25. The first is the difference between the apparent position, in 2θ, of the profile maximum and the position of the Bragg reflection computed from the certified lattice parameter. These data are plotted *versus* 2θ to yield a $\Delta(2\theta)$ curve; a typical example is shown in Fig. 3.1.26. An illustration of the half-width-at-half-maximum (HWHM), which is defined as the width of either the right or left half of the profile at one half the value of maximum intensity after background subtraction, is also shown in Fig. 3.1.25. These values can be summed to yield the FWHM, and plotted *versus* 2θ to yield an indication of the profile breadth as it varies with 2θ (Fig. 3.1.27). In addition, the left and right HWHM values of Fig. 3.1.28 gauge the variation of profile asymmetry with 2θ; additional parameters of interest, such as the degree of Lorentzian and Gaussian contribution to profile shape,

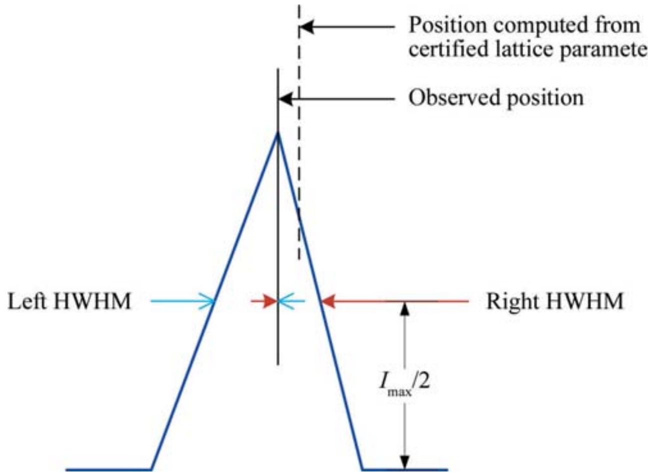

Figure 3.1.25
Diagrammatic representation of a powder-diffraction line profile, illustrating the metrics $\Delta(2\theta)$ and half-width-at-half-maximum (HWHM). The full-width-at-half-maximum (FWHM) = left HWHM + right HWHM.

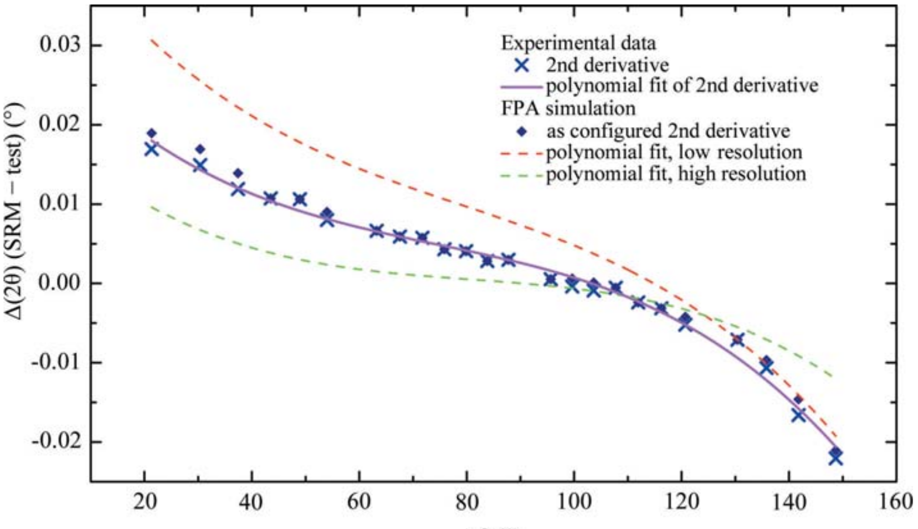

Figure 3.1.26
$\Delta(2\theta)$ curve using SRM 660b illustrating the peak-position shifts as function of 2θ. The peak positions were determined *via* a second-derivative algorithm, and $\Delta(2\theta)$ values (SRM − test) were fitted with a third-order polynomial. Simulated data are from *FPAPC* and were analysed *via* the second-derivative algorithm and polynomial fits as per the experimental data.

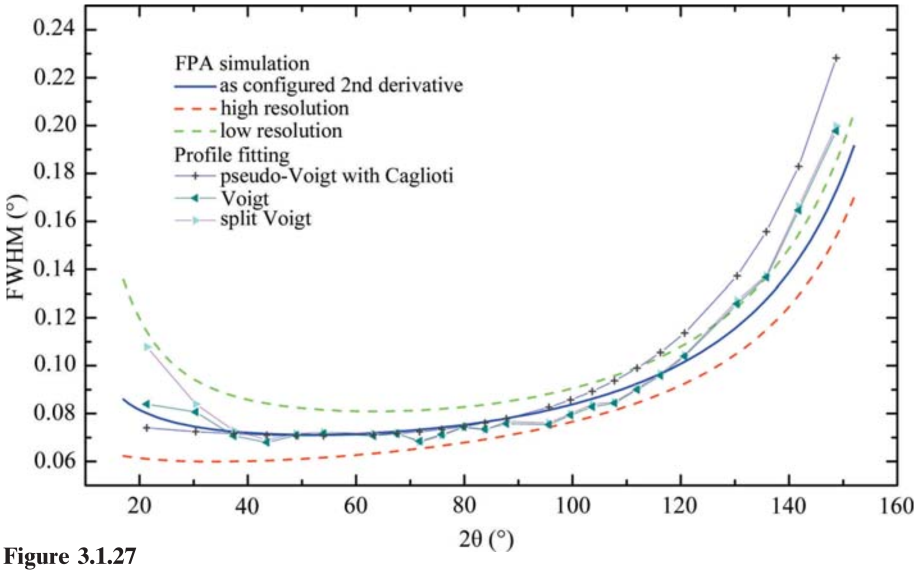

Figure 3.1.27
Simulated and actual FWHM data from SRM 660b using the two Voigt PSFs with (‘with Caglioti’) and without constraints.

can be plotted *versus* 2θ to describe the instrument and evaluate its performance.

The least computationally intensive methods for the analysis of XRPD data, which have been available since the onset of automated powder diffraction, are based on first- or second-derivative algorithms. These methods report peak positions as the 2θ value at which a local maximum in diffraction intensity is detected in the raw data. Typical software provides ‘tuning’ parameters so that the operation of these algorithms can be optimized for the noise level, step width and profile width of the raw data. These methods are highly mature and offer a quick and reliable means of analysing data in a manner suitable for qualitative analysis and lattice-parameter refinement. However, they only give information about the position of the top of the peak. Calibration of the diffractometer *via* this method is useful only for subsequent analyses that also use such peak-location methods.

Profile fitting with an analytical profile-shape function offers the potential for greater accuracy, because the entire profile is used in the analysis. As with the derivative-based methods, profile fitting also reports the observed 2θ position of maximum intensity, in addition to parameters describing profile shape and breadth. The discussion of the IPF in Section 3.1.1, as well as a quick look at Figs. 3.1.26–3.1.28, shows the complexity in the line profile shape from a Bragg–Brentano instrument. The profiles are symmetric only in a limited region of 2θ; in other regions, the degree and direction of profile asymmetry also vary as a function of 2θ. To a first approximation, the optics of an instrument contribute to the Gaussian nature of the profiles; this Gaussian nature will be constant with respect to 2θ. The Lorentzian contribution is primarily from the emission spectrum; given the dominance of angular-dispersion effects at high angle, one can expect to see an increase in the Lorentzian character of the profiles with increasing 2θ. While it can be argued that it is physically valid to model specific contributions to the IPF with Gaussian and Lorentzian PSFs, either of these two analytical functions alone cannot be expected to fit the complexities of the IPF and yield useful results. Combinations of these two functions, however, using shape parameters that vary as a function of 2θ, have given credible results for fitting of data from the Bragg–Brentano diffractometer and have been widely incorporated into Rietveld structure-refinement software. The Voigt function is a convolution of a Gaussian with a Lorentzian, while the pseudo-Voigt is the sum of the two. The parameters that are refined consist of an FWHM and shape parameter that indicates the ratio of the Gaussian to Lorentzian character. The Voigt, being a true convolution, is the more desirable PSF as it is more physically realistic; the pseudo-Voigt tends to be favoured as it is less computationally intensive and the differences between the two PSFs have been demonstrated to be minimal (Hastings *et al.*, 1984), although there is not universal agreement about this.

Refining the profile shapes independently invariably leads to errors when analysing patterns with peak overlap, as correlations

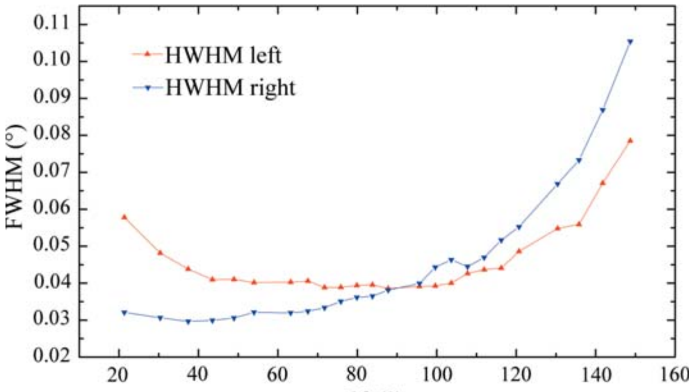

Figure 3.1.28
Left and right HWHM data from SRM 660b using the split pseudo-Voigt PSF fitted with uniform weighting.

occur between shape parameters of neighbouring profiles. This problem can be addressed by constraining the shape parameters to follow some functional form with respect to 2θ. Caglioti *et al.* (1958) developed such a function specifically for constant-wavelength neutron powder diffractometers; it has been incorporated in many Rietveld codes for use with XRPD data. It constrains the FWHM of the Gaussian contribution to the Voigt or pseudo-Voigt PSF:

$$\mathrm{FWHM}^2 = U\tan^2\theta + V\tan\theta + W, \qquad (3.1.1)$$

where the refineable parameters are U, V and W. The term U can be seen to correspond with microstrain broadening from the sample, and broadening due to the angular-dispersion component of the IPF. In *GSAS* an additional term, GP, in $1/\cos\theta$, is included to account for Gaussian size broadening. The Lorentzian FWHM in *GSAS* can vary as

$$\mathrm{FWHM} = \frac{LX}{\cos\theta} + LY\tan\theta, \qquad (3.1.2)$$

where LX and LY are the refineable parameters. Here LX varies with size broadening while LY is the Lorentzian microstrain and angular-dispersion term. Given that the emission spectrum is described with Lorentzian profiles, we would expect the LY term to model the effects of angular dispersion. Within the code *HighScore Plus*, the Lorentzian contribution is allowed to vary as

$$\mathrm{FWHM} = \gamma_1 + \gamma_2(2\theta) + \gamma_3(2\theta)^2, \qquad (3.1.3)$$

where γ_1, γ_2, and γ_3 are the refineable parameters. Alternatives to the Caglioti function have been proposed that are arguably more appropriate for describing the FWHM data from a Bragg–Brentano instrument (Louër & Langford, 1988; Cheary & Cline, 1995). However, they have not yet been incorporated into many computer codes.

The asymmetry in the observed profiles can be fitted with the use of a split profile, where the two sides of the PSF are refined with independent shape and HWHM parameters. This approach will improve the quality of the fit to the observations; however, it is empirical in nature. The more physically valid approach is the use of models to account for the origins of profile asymmetry. The Finger *et al.* (1994) model for axial divergence has been widely implemented in various Rietveld codes. It is formulated to model the axial-divergence effects of a synchrotron powder diffraction experiment where the incident beam is essentially parallel. The two refineable parameters, S/L and H/L, refer to the ratios of sample and receiving-slit length, relative to the goniometer radius; they define the level of axial divergence in the diffracted beam. This model is not in precise correspondence with the optics of a Bragg–Brentano diffractometer where both the incident and diffracted beams exhibit divergence in the axial direction. It does, however, give quality fits to such data. The use of such a model, as opposed to the sole use of a symmetric or split PSF, will yield peak positions and/or lattice parameters that are ‘corrected’ for the effects of the aberration in question. Therefore, results from the use of model(s) cannot be directly compared with empirical methods that simply characterize the form of the observation. In the case of the Bragg–Brentano experiment, the correction that the Finger model applies is not rigorously correct. However, the impact of axial divergence, regardless of the details of diffractometer optics, is universal; as such the use of the Finger model results in a more accurate assessment of ‘true’ peak position and, therefore, lattice parameters.

A third PSF that is in common use is the Pearson VII, or split Pearson VII, that was proposed by Hall *et al.* (1977) for fitting X-ray line profiles. No *a priori* physical justification exists for the use of this PSF. The refineable parameters are the FWHM, or HWHM, and an exponent, m. The exponent can range from 1, approximating a Lorentzian PSF, to infinity, where the function tends to a Gaussian. Owing to the lack of a clear physical justification for use of this PSF, it is not often used in Rietveld analysis software.

Convolution-based profile fitting, as shown in Fig. 3.1.4, was proposed by Klug and Alexander in 1954 (see Klug & Alexander, 1974) and much of the formalism of the aberration functions shown in Table 3.1.1 was developed by Wilson (1963). However, limitations in computing capability largely prevented the realization of the full fundamental-parameters approach method until 1992, with the work of Cheary & Coelho. This was made available to the community through the public-domain programs *Xfit*, and later *KoalaRiet* (Cheary & Coelho, 1996) and more recently *via* *TOPAS*. Other FPA programs are available, most notably *BGMN* (Bergman *et al.*, 1998); more recently, *PDXL 2* has had some FPA models incorporated. Within the FPA there are no PSFs other than the Lorentzians used to describe the emission spectrum, the shapes of which are not typically refined. All other aspects of the observation are characterized with the use of model functions that yield parameters descriptive of the experiment. Plausibility of the analysis is determined through evaluation of these parameters with respect to known or expected values. Direct comparison of the results from an FPA to those from methods using analytical PSFs is difficult because of the fundamental difference in the output from the techniques; for example, FWHM values are not obtained directly from the FPA method. However, the NIST program *FPAPC* can be used to determine FWHM values numerically.

The FPA models of *TOPAS*, *BGMN* and *PDXL 2* were developed specifically for the analysis of data from a laboratory diffractometer of Bragg–Brentano geometry. Analyses using this method would be expected to result in the lowest possible residual error terms that characterize the difference between calculation and observation. As has been discussed, the various aberrations affecting the diffraction line shape are such that the observed profile maxima do not necessarily correspond to the d-spacing of the diffracting plane (hkl), except perhaps in a limited region of 2θ, emphasizing the need for physically valid modelling of the observed line shape to realize a credible value for the lattice parameter. At NIST, we are particularly interested in the capabilities of the FPA method, as one of the primary interests of the NIST X-ray metrology program is obtaining the correct values for lattice parameters. Furthermore, experience has demonstrated that the refined parameters obtained through the use of FPA models can be used in a ‘feedback loop’ to isolate problems and anomalies with the equipment.

The instrument response, *i.e.* the diffracted intensity as a function of 2θ, is measured by Rietveld analysis using models for intensity-sensitive parameters such as crystal-structure parameters and Lorentz–polarization factors. The extraction of plausible crystal-structure parameters from standards *via* a Rietveld analysis serves as an effective and independently verifiable means of calibrating instrument performance. Considering these refined values provides an effective way to detect defects that vary smoothly over the full range of 2θ. However, errors that are only observable within limited regions of 2θ may be difficult to detect with a whole-pattern method; these should be investigated with second-derivative or profile-fitting methods. SRM

676a (alumina) is well suited to assessing instrument response because it is non-orienting and of high purity. Alumina is of lower symmetry than either silicon or lanthanum hexaboride; it has a considerable number of diffraction lines and has well established structure parameters. A Rietveld analysis of SRM 660c, however, yields the IPF in terms of code-specific profile shape terms and verifies that peak-position-specific aspects of the equipment and analysis are working correctly.

The instrument response may be evaluated with the more conventional data-analysis methods with use of SRM 1976b. Measurements of peak intensities are obtained from the test instrument, typically by profile fitting, and compared with the certified values. However, the use of SRM 1976b with diffraction equipment with different optical configurations may require the application of a bias to the certified values to render them appropriate for the machine to be qualified. This bias is needed to account for differences in the polarization effects from the presence, absence and character of crystal monochromators. The polarization factor for a diffractometer that is not equipped with a monochromator is (Guinier, 1994)

$$\frac{1+\cos^2 2\theta}{2}. \tag{3.1.4}$$

The polarization factor for a diffractometer equipped with only an incident-beam monochromator is (Azároff, 1955)

$$\frac{1+\cos^2 2\theta_m \cos^2 2\theta}{1+\cos^2 2\theta_m}, \tag{3.1.5}$$

where $2\theta_m$ is the 2θ angle of diffraction for the monochromator crystal. The polarization factor for a diffractometer equipped with only a diffracted-beam post-monochromator is (Yao & Jinno, 1982)

$$\frac{1+\cos^2 2\theta_m \cos^2 2\theta}{2}, \tag{3.1.6}$$

where $2\theta_m$ is the 2θ angle of the monochromator crystal. Equations (3.1.5) and (3.1.6) are appropriate when the crystal has an ideal mosaic structure, *i.e.* the diffracting domains are uniformly small and, therefore, the crystal is diffracting in the kinematic limit. This is in contrast to a 'perfect' crystal, which would diffract in accordance with dynamical scattering theory. Note that equations (3.1.5) and (3.1.6) both have the $\cos^2 2\theta_m$ multiplier operating on the $\cos^2 2\theta$ term. Since this multiplier is less than unity, the intensity change on machines equipped with a monochromator exhibits a weaker angular dependence.

The certification data for SRM 1976b were collected with the NIST machine equipped with the Johansson IBM and a scintillation detector. The simplified IPF of this machine is advantageous for the accurate fitting of the profiles and, therefore, intensity measurement. The validity of the 'ideal mosaic' assumption embodied in equation (3.1.5) was evaluated using this diffractometer; the validity of equation (3.1.6) was evaluated with data from the machine configured with the post-monochromator. With respect to equation (3.1.5), for a Ge crystal (111) reflection, $2\theta_m$ was set to 27.3°; with regard to equation (3.1.6), for a pyrolytic graphite crystal (0002) basal-plane reflection, $2\theta_m$ was set to 26.6°. Rietveld analyses of data from SRMs 660b, 1976b and 676a included a refinement of the polarization factor, modelled according to equations (3.1.5) and (3.1.6) in *TOPAS*, and yielded fits of high quality, indicating that these models were appropriate for these crystals and configurations. Equations (3.1.4), (3.1.5) and (3.1.6) were used to bias the certified values to correspond to those of alternative configurations. These values are included in the SRM 1976b CoA as ancillary data.

3.1.6. Instrument calibration

The calibration procedure has traditionally involved the comparison of measurements from a reference (an SRM) with those of the test instrument. However, the exact form of this comparison depends upon the data-analysis procedure to be used. A classical calibration, permitting qualitative analyses and lattice-parameter refinement, can be readily performed as per Fig. 3.1.26. These data are fitted with a polynomial that describes the 2θ error correction that is then applied to subsequent unknown samples. Furthermore, with this calibration method, the actual form of the curve of Fig. 3.1.26 is largely irrelevant. As the data-analysis methods become more advanced, physical models are chosen to replace analytical PSFs. The calibration is then based upon the observation that the machine performance does indeed correspond to the models used, and that acceptable values for refined parameters describing the experiment are obtained from an analysis of data from an SRM. A systematic approach to instrument calibration with a full evaluation of the data, including those obtained from the empirical methods shown in Figs. 3.1.26 and 3.1.27, results in the ability to use the advanced methods in a rational manner and obtain results in which one can have confidence. The advanced methods, while more complex to use and requiring a much more extensive instrument calibration process, reward the user with a sample characterization of greater breadth and reduced measurement uncertainty.

Consider the $\Delta(2\theta)$ curve illustrated in Fig. 3.1.26. The y-axis values are the differences between the peak positions computed from the certified lattice parameter of SRM 660b and those of each observed profile determined *via* a second-derivative-based peak-location algorithm. Therefore, each of the $\Delta(2\theta)$ data points plotted on Fig. 3.1.26 were determined independently. It is immediately apparent that the data follow a smooth, monotonic curve with no substantive outliers. Discontinuities or non-monotonicity would typically indicate mechanical difficulties with the equipment, such as loose components or problems with the goniometer assembly. Evaluation of independently determined data such as these is critical to verifying that there are no 'high-frequency' difficulties with the equipment that would otherwise be hidden or smoothed out with the use of methods that apply models or constraints across the entire 2θ range, such as a Rietveld analysis. The $\Delta(2\theta)$ values were fitted with a third-order polynomial that is also illustrated in Fig. 3.1.26. Consideration of the deviation values between the observations and the third-order fit indicates a random or 'top hat' distribution with a maximum excursion of ±0.0025° 2θ; this provides further evidence that a machine is operating properly.

FPAPC was used to generate simulated data, which were then analysed using the same second-derivative algorithm as was applied to the raw data. The aforementioned optical setup of the NIST instrument was used in the as-configured simulation (see the caption for Fig. 3.1.26), while the high-resolution and low-resolution data were simulated with a 50% increase or decrease of the incident and Soller slit angles. For the 'high-resolution' and 'low-resolution' data, third-order polynomial fits to the $\Delta(2\theta)$ values are displayed in Fig. 3.1.26; for the 'as-configured' data, the Δ values themselves are indicated. The correspondence between the simulation and observation indicates that trends in the data can be readily explained in the context of the aberration functions discussed in Section 3.1.1 and that such a machine can

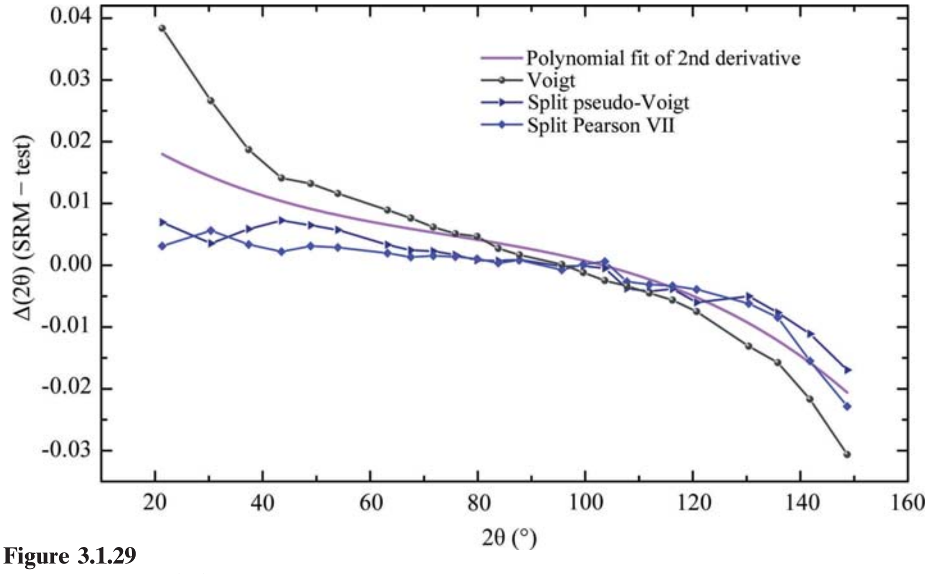

Figure 3.1.29
Comparison of Δ(2*θ*) curves determined with profile fitting of SRM 660b data without the use of any constraints, as a function of 2*θ*.

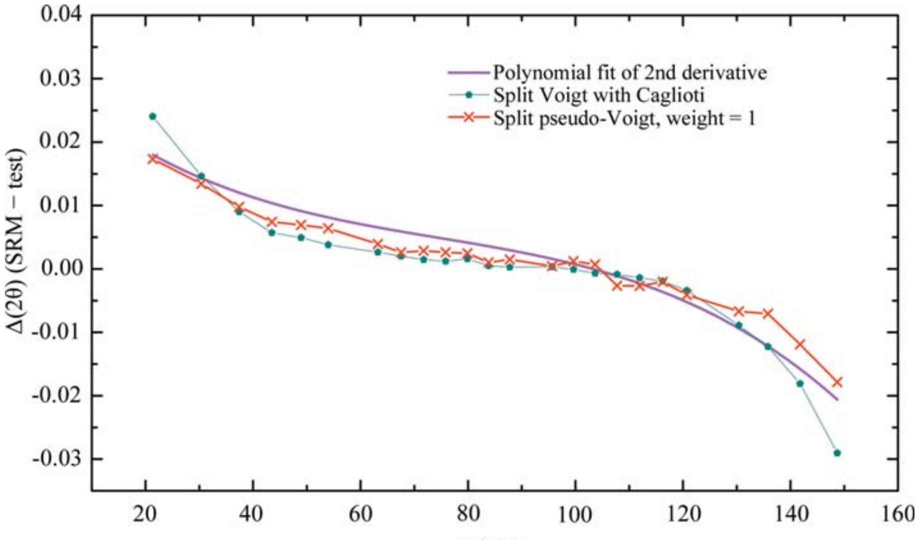

Figure 3.1.30
Δ(2*θ*) curves from SRM 660b determined with profile fitting using the Caglioti function and the unconstrained split pseudo-Voigt PSF with uniform weighting.

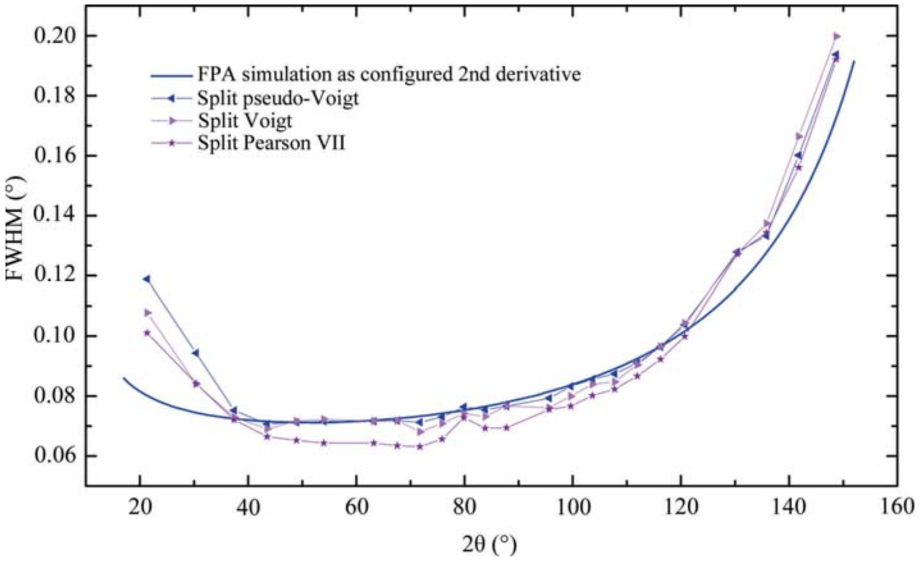

Figure 3.1.31
FWHM data from SRM 660b using various split PSFs fitted without constraints.

generate data for successful analysis with the FPA method, *i.e.* the metrological loop is closed. At low 2*θ* the profiles are displaced to low angle by the effects of the flat specimen error and axial divergence. The Δ(2*θ*) curve crosses the zero point at approximately 100° 2*θ* where the profiles are largely symmetric; the slight asymmetry to low angle caused by the flat specimen error is somewhat offset by asymmetry of the emission spectrum at high angles. At higher 2*θ* the profiles are displaced to high angle by the combined effects of axial divergence and the asymmetry of the emission spectrum. As illustrated with the simulations at lower and higher resolution, the experimental curve of Fig. 3.1.26 would either flatten out or become steeper, respectively, with changes in instrument resolution. Given the uniformity of the data and overall plausibility of this Δ(2*θ*) curve, the third-order polynomial fit is used as a reference against which the merits of other techniques can be judged.

It should also be noted that the data and method shown Fig. 3.1.26 constitute the 'low-hanging fruit' of powder diffraction. Data analogous to those of Fig. 3.1.26 can be used to correct peak positions of unknowns *via* either the internal- or external-standard method using a polynomial fit. The external-standard method, however, cannot account for specimen displacement or sample-transparency effects; these require use of the internal-standard method, which is the same procedure but applied to a standard admixed with the unknown. Either of these methods will correct for instrumental aberrations regardless of their form; the nature of the curve of Fig. 3.1.26 need only be continuous to permit modelling with a low-order polynomial. Studies performed in conjunction with the International Centre for Diffraction Data (ICDD) demonstrate that the use of the internal-standard method routinely yields results that are accurate to parts in 10^4 (Edmonds *et al.*, 1986). Fawcett *et al.* (2004) demonstrated the direct relationship between the use of standards, with the vast majority of analyses being performed *via* the internal- or external-standard methods, and the number of high-quality starred patterns in the ICDD database. Thus, the community's collective ability to perform the most routine of XRPD analyses, qualitative analysis, has been greatly enhanced over the past 30 or so years by these most basic methods and the use of SRMs.

The Δ(2*θ*) and FWHM calibration curves shown in Figs. 3.1.27–3.1.31 were determined *via* profile fitting, using several PSFs,

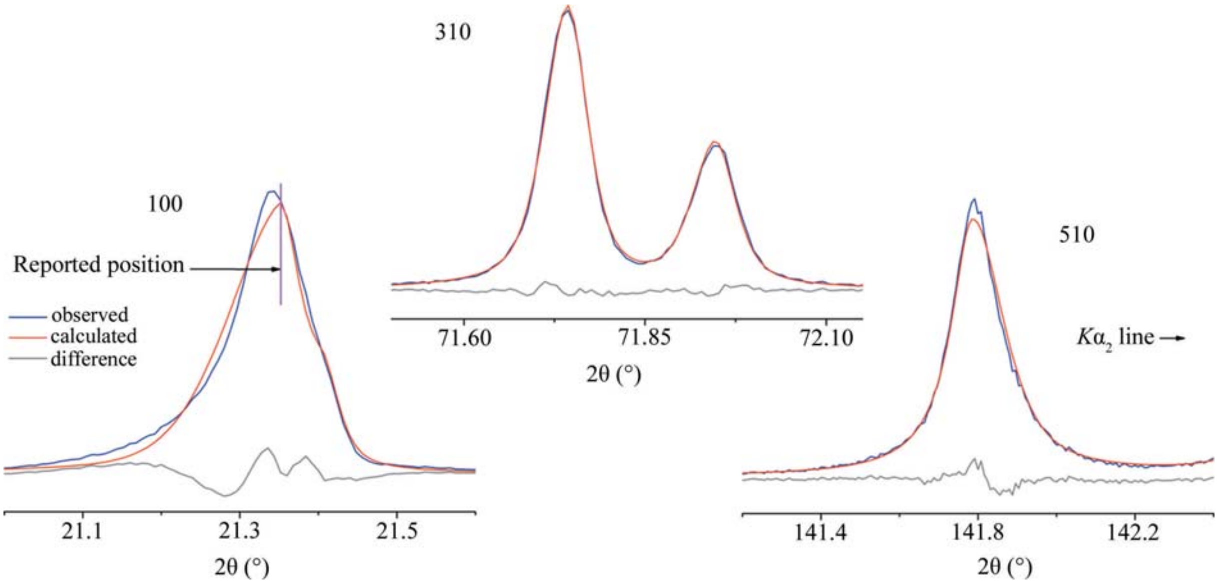

Figure 3.1.32
Fits of the split pseudo-Voigt PSF to the low-angle 100, mid-angle 310 and high-angle 510 lines from SRM 660b illustrating the erroneous peak position and FWHM value reported for the 100 and 510 lines, respectively.

of the same raw data from SRM 660b used to generate Fig. 3.1.26. In general, results from the three commercial codes were in close correspondence. When used on a split PSF, the Caglioti function was applied independently to the left and right FWHM values. A five- to seven-term Chebyshev polynomial was used for modelling the background in these refinements. The goodness of fit (GoF) (which is the square root of reduced χ^2) residual error term of the refinements ranged from 1.6 to 1.9, with the unconstrained refinements yielding the slightly improved fits to the data. Fig. 3.1.32 illustrates the fit quality of typical results using the split pseudo-Voigt PSF. However, as will be demonstrated, the more plausible parameters, particularly in the context of the FWHM values, were often obtained with the more constrained refinements.

The results from the fitting of the Voigt PSF provide a reference for consideration of the $\Delta(2\theta)$ data of Fig. 3.1.29. The use of any of the symmetric PSFs considered here, with or without the Caglioti constraint, resulted in curves virtually identical to the one displayed in Fig. 3.1.29 for the Voigt PSF. Not surprisingly, the symmetric PSF performs quite well in the mid-angle region where the profiles are symmetric but will report an erroneous position in the direction of the asymmetry, when it is present. However, the opposite effect was observed with the use of any of the split PSFs, as can be seen in Figs. 3.1.29 and 3.1.32. When two HWHM values are refined, the larger HWHM value will shift the reported peak position in the direction of the smaller one. This effect can be readily observed in the fit quality of the low-angle 100 reflection displayed in Fig. 3.1.32. The spilt PSFs yield results that reflect an overly asymmetric profile; thus the reported peak positions are displaced to high angle at 2θ angles below 100°, and to low angle at 2θ angles above 100°. Curiously this effect was markedly reduced in one of the commercial computer codes (not shown) and was the sole difference observed between them when the models were equivalent. It is apparent that subtleties in implementation of an ostensibly identical PSF and minimization algorithm (the Marquardt algorithm) can result in dramatic differences in results. Careful examination of the fit quality is required to assess the reliability of profile-fitting results. The data of Fig. 3.1.29 indicate that errors in peak position of up to 0.015° 2θ are plausible with profile fitting of these data with these PSFs. In contrast to its use with symmetric PSFs, the Caglioti function will improve results when using split PSFs (Fig. 3.1.30).

Consideration of the issues related to profile fitting shown in Fig. 3.1.32 led to the conjecture that fitting the data with a uniform weighting as opposed to Poisson statistical weighting might result in more accurate determination of the peak position and FWHM parameters. (In the vast majority of circumstances this approach would never be used, because the integrated intensity is a critical metric.) This was tried, and resulted in considerable success. Fig. 3.1.30 displays data from the use of split pseudo-Voigt that are in very good agreement with second-derivative values.

Experimental and simulated values of the FWHM are displayed in Figs. 3.1.27 and 3.1.31. Data from the profile refinements performed without the use of the Caglioti function, displayed in Figs. 3.1.27 and 3.1.31, yield independently determined measures of the FWHM. Again, the lack of scatter and the continuity of these FWHM values are consistent with proper operation of the instrument, *i.e.* an absence of 'high-frequency' problems. The basic trends are also consistent with the instrument optics: at low 2θ the observed increase in FWHM is due to both the flat specimen and axial divergence aberrations, while at high 2θ angular dispersion dominates and a substantial increase in FWHM with $\tan\theta$ is apparent. The FPA simulations were performed using the settings for high and low resolution. The FWHM values were determined numerically from the simulated patterns; no PSF was used. As shown with the simulated data, the degree of upturn at low 2θ increases with a decrease in instrument resolution and *vice versa*. Angular-dispersion effects, however, are less dependent on the instrument configuration; FWHM values tend towards convergence at high 2θ (Fig. 3.1.27).

As seen in Fig. 3.1.27, above 40° 2θ the Voigt and split-Voigt PSFs give similar values for the FWHM and a fairly accurate representation of instrument performance. It was observed that with regard to the correlation between FWHM values for split *versus* symmetric PSFs, the other PSFs behaved in an analogous manner to the Voigt (not shown): above 40° 2θ the values reported for the FWHM from split *versus* symmetric PSFs are nearly identical. From Fig. 3.1.31, the split Pearson VII PSF underestimates the FWHM throughout the mid-angle region; this error was duplicated with the use of the symmetric Pearson VII

PSF (not shown). When fitted with uniform weighting, however, these FWHM data from the Pearson VII PSF fell quite precisely (not shown) on the simulated curve. Below 40° 2θ, a split PSF will provide results that overestimate true FWHM values, as shown in Figs. 3.1.27 and 3.1.31. The cause for this is analogous to that discussed for the $\Delta(2\theta)$ values, and can be readily observed in the fit quality displayed in Fig. 3.1.32 for the low-angle 100 reflection. In accounting for the asymmetry to low angle, the FWHM of the observed profile is substantially overestimated by the calculated one. With all PSFs, the high-angle FWHM values are observed to be overestimated, as shown in Figs. 3.1.27 and 3.1.31; the problem is exacerbated with the use of the Caglioti function. Inspection of the fit quality of the high-angle 510 line shown in Fig. 3.1.32 indicates that there are two contributions to this effect: one is that the PSF cannot model the shape of the high side of the profile; the other is that the height of the profile is underestimated. These two effects, particularly the inability of the PSF to correctly model the height of the profile, were observed with all of the other PSFs considered here.

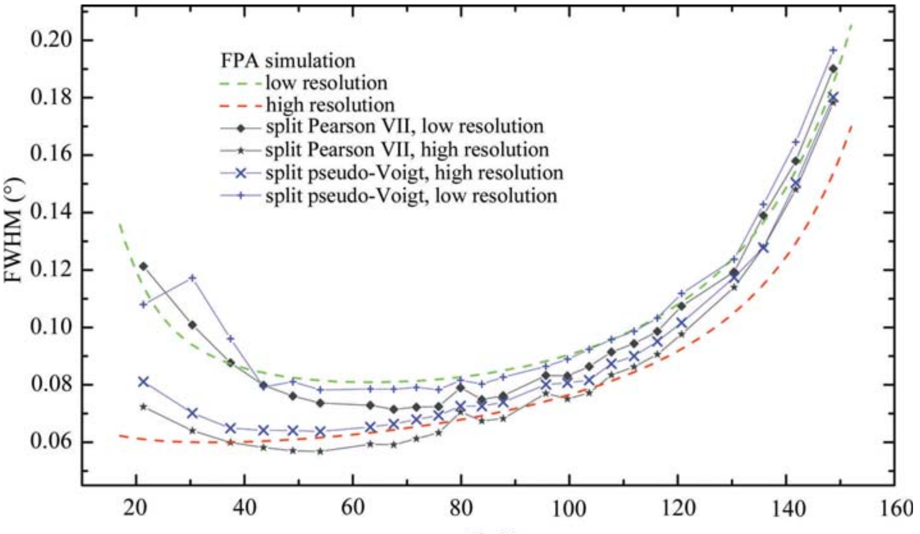

Figure 3.1.33

FWHM data from fits of the split pseudo-Voigt and split Pearson VII PSFs to simulated low- and high-resolution data.

The use of the pseudo-Voigt PSF with the Caglioti function results in a reasonable fit to the FWHM values of the observation; however, the breadth of the high-angle lines is overestimated. The U, V and W terms of the Caglioti function vary in a specific manner to account for various physical effects (*e.g.* see Fig. 3.1.27): the U term, in $\tan\theta$, accounts for angular dispersion; the W term describes the 'floor' and the V term accounts for the reduction of the FWHM values in the mid-2θ region. Therefore, the U and W terms should refine to positive values, while the V term should tend to a negative value; negative values for V were, indeed, obtained in these analyses. V should be constrained to negative values or set to zero, as positive values for V are nonphysical. With an instrument configured for high resolution, however, values of $V = 0$ are entirely reasonable as the trend towards an upturn in FWHM at low 2θ angle will be suppressed.

To some extent, the difficulties in determining profile positions through the use of these PSFs can be ascribed to the Cu $K\alpha_1/K\alpha_2$ doublet as it is stretched by angular dispersion. The pattern can be thought of as divided into three regions, each of which will confound fitting procedures in a different manner: the low-2θ range, where profiles can be considered as a peak with a shoulder, the mid-2θ range (perhaps 40 to 110° 2θ), where the profiles can be considered as a doublet, and the high-angle region where they are two distinct peaks. This 'three-region' consideration is compounded by the direction and severity of the asymmetry in these profiles. The data shown in Fig. 3.1.27 largely correspond to the problematic effects of angular dispersion in the context of these three 2θ regions. These effects are particularly apparent, as shown in Fig. 3.1.31, with the use of the Pearson VII function: over-estimation of FWHM values occurs at low 2θ, underestimation occurs in the mid-2θ region, and credible values are obtained at high angle. The use of the Caglioti function is effective in addressing the more extreme excursions from plausible FWHM values. Fig. 3.1.28 shows the left and right HWHM values for SRM 660b using the split pseudo-Voigt PSF refined with uniform weighting. For reasons discussed in Section 3.1.2, the degree, direction and point of crossover in the profile asymmetry indicated in Fig. 3.1.28 are in correspondence with expectation and the previously discussed results from these data from SRM 660b.

To consider the impact of instrument resolution on the use of analytical PSFs for the determination of FWHM values, the simulated high-resolution and low-resolution data were analysed *via* profile fitting. Fig. 3.1.33 shows the results from the use of the split Pearson VII and spilt pseudo-Voigt PSFs. The data of Fig. 3.1.33 indicate an effect that is dependent on the PSF used. The performance of the split Pearson VII PSF is observed to improve with instrument resolution; FWHM values from the narrower profiles are observed to correspond with expectation in the low- and mid-angle regions, while substantial deviation is noted with the broader profiles. This is counter to expectation, as broader profiles are generally easier to fit than narrow ones. The performance of the split pseudo-Voigt PSF is observed to degrade marginally with either an increase or decrease in instrument resolution. Curiously, the breadths of the profiles in the high-resolution data are overestimated, while those in low-resolution data are largely underestimated. Both PSFs do quite poorly in fitting the high-angle data from the high-resolution setting. These observations emphasize the need to scrutinize the results with an examination of the fit quality, as per Fig. 3.1.32.

When the IPF is simplified with the use of a Johansson IBM, analytical PSFs can provide an excellent fit to the observations. Fig. 3.1.34 shows the fit quality of the split Pearson VII PSF to (high-quality) peak-scan data. The split Pearson VII PSF consistently provides a better fit to IBM data than either the split Voigt or split pseudo-Voigt PSFs. Note that the asymmetry exhibited by the profiles follows the same trends as were outlined previously, but to a much reduced extent because of the extended incident-beam path length and the resulting reduction in the effects of axial divergence. Fig. 3.1.35 shows the $\Delta(2\theta)$ calibration curves that were obtained as per the procedures outlined for Fig. 3.1.29. Indeed, the trends that are followed, and the reasons why, are largely analogous to those of Fig. 3.1.29, but to a much reduced extent because of the reduced profile asymmetry. Use of symmetric PSFs yields reported peak positions that are shifted in the direction of the asymmetry, while use of split PSFs yields positions shifted in the opposite direction owing to the fitted profiles displaying excessive levels of asymmetry. One notes the complete failure of the split pseudo-Voigt, split Voigt (not shown)

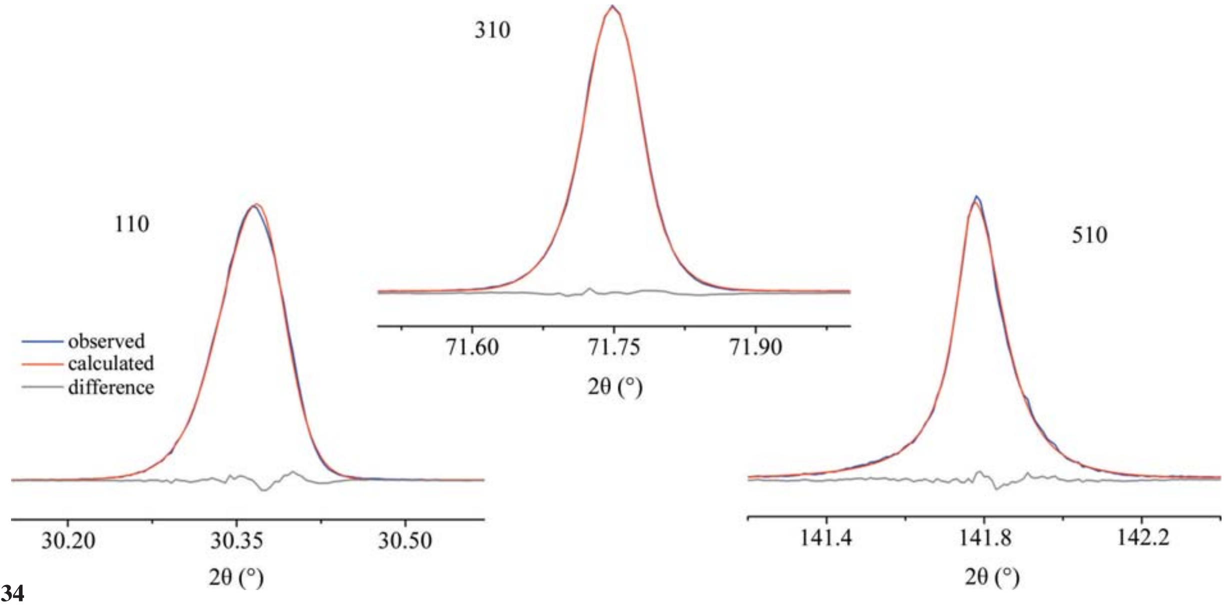

Figure 3.1.34
Fits of a split Pearson VII PSF to data from SRM 660b collected using a Johansson IBM.

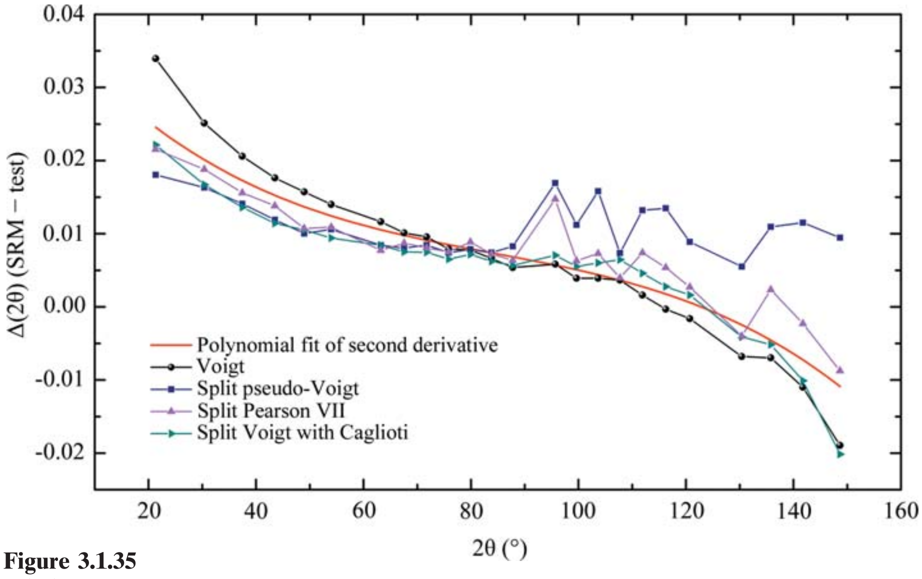

Figure 3.1.35
Δ(2θ) curves from the NIST machine configured with a Johansson IBM, illustrating a comparison of results from second-derivative and various profile-fitting methods. Data are from SRM 660b.

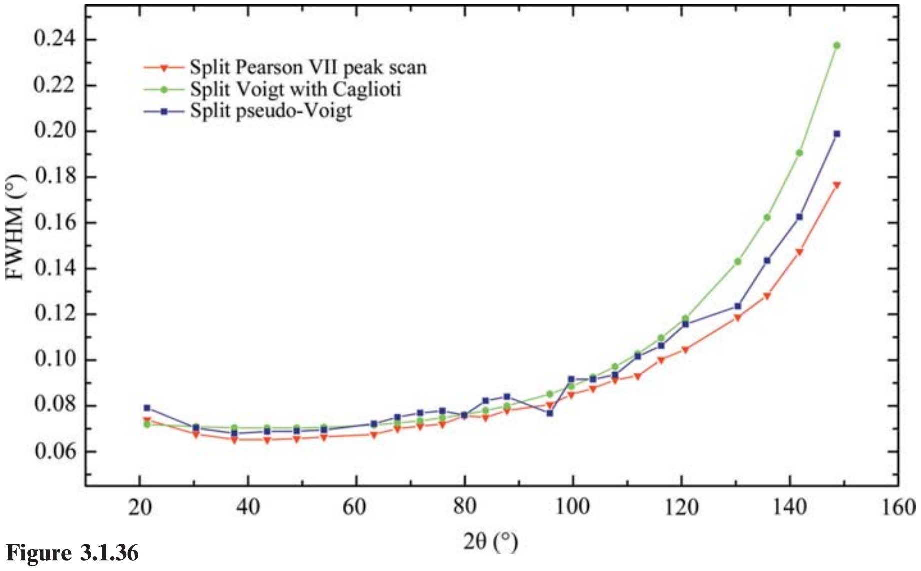

Figure 3.1.36
FWHM data from SRM 660b collected using the NIST machine configured with a Johansson IBM, illustrating a comparison of results from various profile-fitting and data-collection methods.

and, to a lesser extent, the split Pearson VII PSFs at high angle. However, the more accurate peak positions are obtained from the more intense reflections, indicating that higher-quality data may improve the results. Improvements in FWHM determination with the use of an IBM are illustrated in Fig. 3.1.36, where it can be seen that the pseudo-Voigt and Pearson VII yield values for the FWHM that differ in a systematic manner, but to a reduced extent than with the conventional data. The virtues of the peak-scan data are illustrated by the continuity of the FWHM values of Fig. 3.1.36 relative to the discontinuities observed in the corresponding data from the conventional scans that were fitted with the pseudo-Voigt PSF. The results from the use of the Caglioti function in Fig. 3.1.36 illustrate that otherwise noisy FWHM data are effectively smoothed out, but a significant bias at high angle is indicated.

FWHM values from the machine equipped with the IBM and PSD are shown Fig. 3.1.37, again with data from SRM 660b. These values were obtained from fits of the split Pearson VII PSF using uniform weighting. The resolution improvement from the use of the PSD is due to the 75 µm strip width, as opposed to the 200 µm receiving slit used with the scintillation detector. This is analogous to a reduction in the width of the top-hat function used to model the impact of the receiving slit or silicon strip width as discussed in Section 3.1.2. The impact is greatest at low 2θ angles where the other contributions to the overall breadth are small. With increasing 2θ angle, the contribution of a top-hat function to overall breadth is reduced because it is being convoluted with profiles influenced by ever-increasing spectral dispersion. The improve-

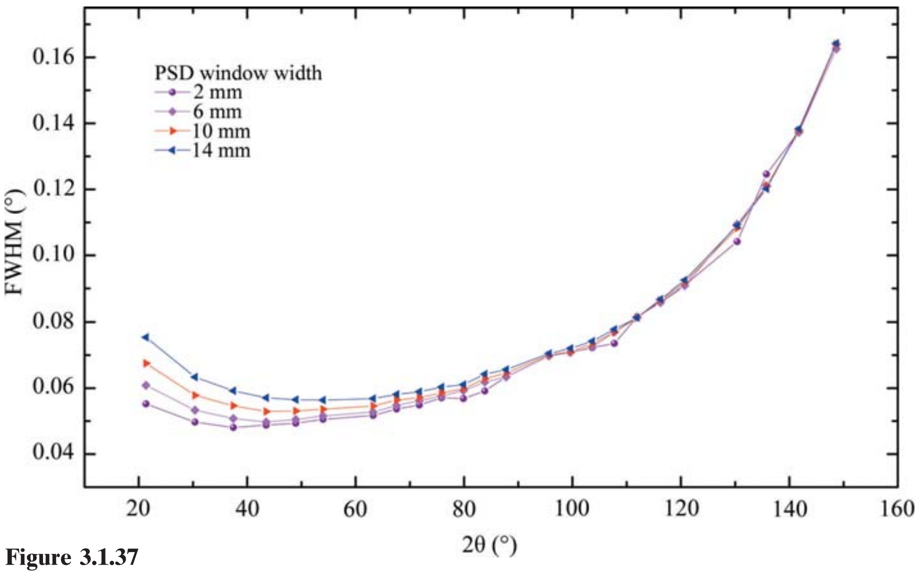

Figure 3.1.37
FWHM data from SRM 660b collected using the NIST machine configured with a Johansson IBM and PSD, illustrating the contribution to defocusing at low angles with increasing window width.

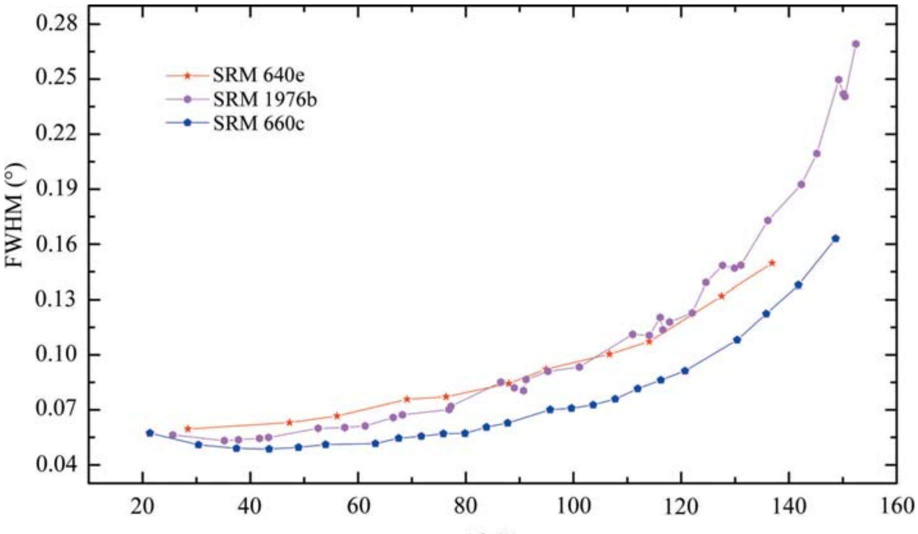

Figure 3.1.38
FWHM data from SRMs 640e, 1976b and 660c collected with the IBM and PSD (4 mm window) and fitted using the split Pearson VII PSF with uniform weighting.

ment in resolution with the reduction in the width of the PSD window is apparent, and is in accordance with expectations as per Fig. 3.1.7 of Section 3.1.2. Also, because of the 1/tan θ dependence of this broadening effect, the impact of the window size nearly vanishes above 100° 2θ.

Fig. 3.1.38 shows FWHM data obtained for SRMs 640e, 1976b and 660c using the split Pearson VII PSF, fitted using uniform weighting on data collected with the IBM and PSD with a 4 mm window. The 660c data set, which exhibits the lowest FWHM values, will be discussed first. The FPA analysis performed in the certifications of SRM 660b and 660c included a Lorentzian FWHM with a 1/cos θ dependence to account for size-induced broadening; a domain size of approximately 0.7 to 0.8 µm was indicated. There is a high level of uncertainty in these values, as they are reflective of an exceedingly small degree of broadening, the detection of which is near the resolution limit of the equipment. The term varying as tan θ, interpreted as microstrain, refined to zero. These values are found in the CoA for the SRMs. The linear attenuation coefficient for a compact of LaB_6, with an intrinsic linear attenuation of 1125 cm^{-1} and a particle-packing factor of 60 to 70%, would be approximately 800 cm^{-1}. Therefore, the contribution to the observed FWHM from specimen transparency with SRM 660c is negligible, as illustrated in Fig. 3.1.10. Likewise, the FPA analysis performed for the certification of SRM 640e included size and microstrain terms; a smaller crystallite size of 0.6 µm was obtained with a very slight amount of microstrain broadening. However, the linear attenuation coefficient for silicon is 148 cm^{-1}; for a powder compact it would be approximately 100 cm^{-1}. The transparency of this specimen would lead to significant broadening. (See Fig. 3.1.10 for the effect of an attenuation of 100 cm^{-1}.) Therefore, these three effects, in combination, would be expected to lead to a small degree of broadening throughout the 2θ range for SRM 640e, but with a substantial effect in the mid-angle region because of the sin 2θ dependence of the transparency aberration. Lastly, SRM 1976b is a sintered compact of near theoretical density; therefore, considering the linear attenuation coefficient for alumina, 126 cm^{-1}, a value for the actual SRM 1976b specimen of somewhat less than this is expected. An FPA analysis of SRM 1976b indicates a domain size of 1 µm, but with a significant degree of Gaussian microstrain broadening; this is evident in the observed increase in FWHM with 2θ angle shown in Fig. 3.1.38. We conclude that the FWHM data from all three SRMs shown in Fig. 3.1.38 are in correspondence with expectations and can be used to select which SRM is best suited for a given application. We do not, however, recommend using an SRM other than SRM 660*x* for a microstructure analysis. It should be added that fitting the profiles of SRM 1976b is complicated by the fact that many of them overlap; this leads to the oscillations in the FWHM values shown in Fig. 3.1.38 for this SRM. The origins of this difficulty were discussed in Section 3.1.5 and can be addressed with the use of the Caglioti function.

With the use of model-based methods for calibration and subsequent data analysis, it is appropriate to consider a strategy for the refinement of the available parameters. The successful refinement will yield the right answer and, with the use of models that make sound physical sense with respect to the experimental design, a good fit to the observation. The refinement strategies for both FPA and Rietveld analyses can be based on a consideration of which terms are specific to the IPF and the manner in which they can be determined. Several parameters can be measured explicitly from experiments other than the diffraction experiment under examination. Examples of these 'well determined' parameters include the goniometer zero angles and the incident- and receiving-slit sizes. Conversely, indeterminate metrics that can only be determined through the diffraction experiment itself include the impact of the post-monochromator on the Cu $K\alpha_1/K\alpha_2$ ratio and the degree of axial divergence. Indeterminate parameters specific to the IPF are only refined using high-quality data from standards and are fixed for subse-

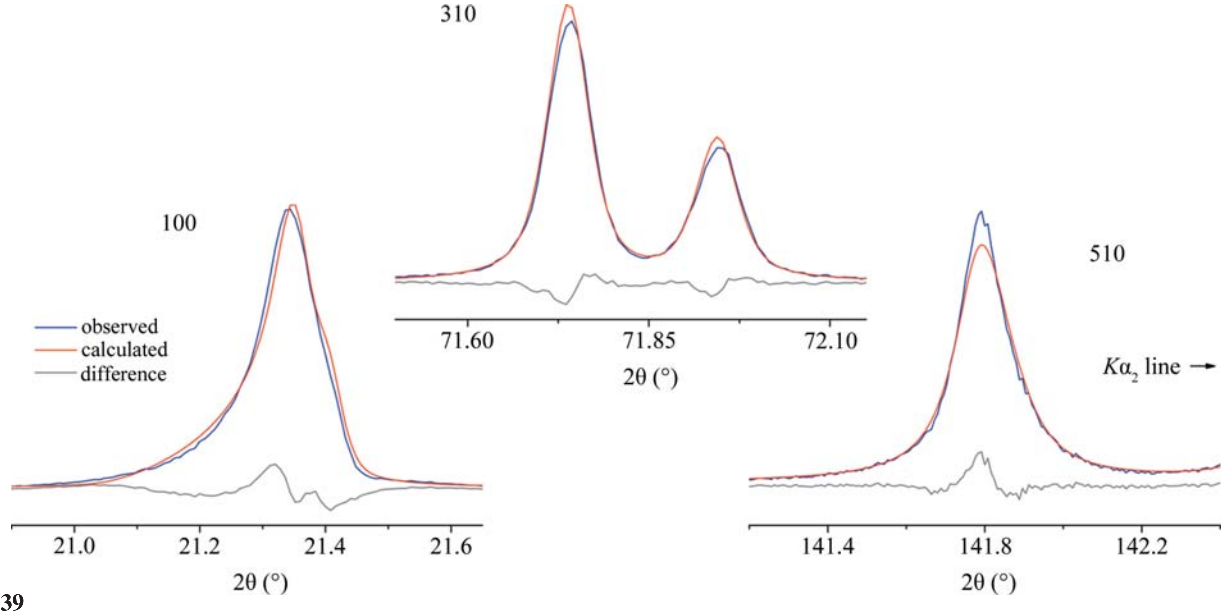

Figure 3.1.39

Fits of three SRM 660b lines obtained with a Rietveld analysis using the Thompson, Cox and Hastings formalism of the pseudo-Voigt PSF and the Finger model for asymmetry. *TOPAS* was used for the analysis.

quent analyses of unknowns. This approach tends to result in stable and robust refinements. Parameters can, therefore, be considered as falling into three groups: those that are specific to any given sample and are always refined, ones that are specific to the IPF and are refined using only high-quality data from standards, and lastly the highly determined parameters that are refined only as a basic test of the model.

To consider the Thompson, Cox & Hastings (1987) (TCH) formalism of the pseudo-Voigt PSF with the Finger model for asymmetry, which is common to many Rietveld codes, a Rietveld analysis of SRM 660b was performed using *GSAS* (using the type-3 PSF) and *TOPAS* (using the PV_TCHZ peak type). The TCH formalism allows for the direct refinement of the Gaussian and Lorentzian FWHM values. The Caglioti function was used; Lorentzian terms were constrained as per equation (3.1.2). The *S*/*L* and *H*/*L* terms are highly correlated; *S*/*L* was refined, while *H*/*L* was adjusted manually so that the two terms were nearly equal. Additional parameters that were refined included the lattice parameters, sample displacement and transparency terms, Chebyshev polynomial terms (typically 5 to 7) to represent the background, scale factors, the type-0 Lorentz–polarization term (*GSAS*), the Cu $K\alpha_1/K\alpha_2$ ratio, and structural parameters. With this strategy, the sample shift and transparency aberration functions, in conjunction with the Finger asymmetry model, were used to model the data of Fig. 3.1.26. Given that the Finger model is not entirely appropriate for divergent-beam laboratory data, the sample shift and transparency terms may refine to non-physical values. They will, however, correctly indicate relative values for sample z height and transparency. The model for specimen transparency in *TOPAS* is the asymmetric function illustrated in Fig. 3.1.10, while the model in *GSAS* consists of a profile displacement in $\sin 2\theta$. The TCH/Finger formalism of *TOPAS* reproduced the certified lattice parameter and resulted in a GoF of 1.5, whereas the GoF value realized with *GSAS* was 1.85. Fig. 3.1.39 displays the fit quality of the 100, 310 and 510 reflections obtained with *TOPAS*. The fit to the asymmetry of the 100 reflection is reasonable, with a 0.007° shift in position. The fit to the 510 reflection is not dissimilar to that shown in Fig. 3.1.32, indicating that the Caglioti function is working analogously to the manner previously discussed. The improvement in fit with the *TOPAS* implementation was most notable around the 70 to 90° 2θ region, where the transparency effects are at a maximum. These results validate the TCH/Finger formalism and constitute a valid calibration for this equipment and data-analysis method; the utility of the aberration function for specimen transparency as documented by Cheary & Coelho (1992) is demonstrated.

Differentiating between the profile-shape terms that are specific to the IPF and those refined to consider the microstructure of unknowns yields a stable refinement strategy when using the TCH/Finger formalism. The profile parameters *GU*, *GV*, *GW*, *LX*, *LY*, *S*/*L* and *H*/*L* as determined from SRM 660b constitute the IPF and are fixed, or used as floors, in subsequent refinements (Cline, 2000). The IPF for the NIST machine was described with only the *GW*, *LX* and *LY* parameters. In subsequent analyses only the *GP*, *GU*, *LX* and *LY* terms were refined to represent Gaussian size and microstrain and Lorentzian size and microstrain broadening, respectively, and thus yield microstructural information from the sample. Parameters that tend to values less than the IPF were fixed at IPF values. The Finger asymmetry parameters determined from the standard need not be refined with unknowns; it has, however, been observed that doing so will neither substantially improve the quality of the fit, nor will it result in instability. Additional parameters that are always refined with unknowns include: scale factors, lattice parameters, specimen displacement and transparency terms, background terms, and structural parameters.

While an analysis of SRM 660x permits the calibration of the instrument with respect to profile shape and position, it is also desirable to evaluate parameters related to the diffraction intensity. However, the analysis of data from high-symmetry materials such as silicon and lanthanum hexaboride may result in some degree of instability with the refinement of the intensity-specific parameters, perhaps because of the relatively small number of lines. Use of SRM 676a addresses this difficulty (Fig. 3.1.40). With this analysis, the Lorentz–polarization factor refined to a credible value and structure parameters were within the bounds of those obtained from the high-q-range experiments performed in the certification of SRM 676a (Cline *et al.*, 2011).

We start the discussion on the FPA method for instrument calibration by listing the parameters specific to the IPF that

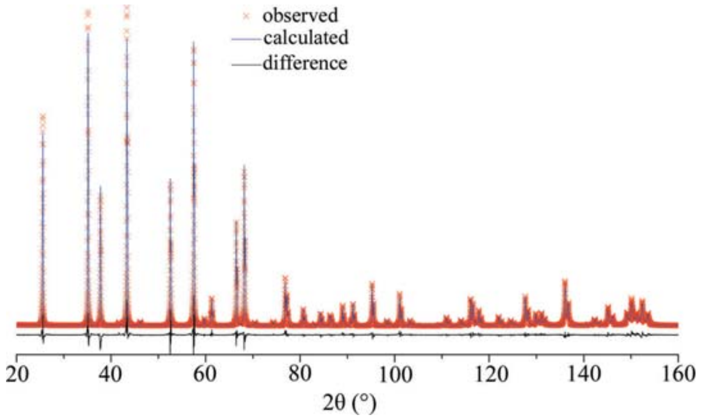

Figure 3.1.40
Fits of SRM 676a obtained from a Rietveld analysis using *GSAS* with the Thompson, Cox and Hastings formalism of the pseudo-Voigt PSF and the Finger model for asymmetry.

would have to be refined with a most basic calibration using an analysis of an SRM. The parameters to be refined for the emission spectrum include the positions and intensities of the $K\alpha_2$ profile, the satellite components and the tube tails. When addressing the $K\alpha_2$ profile, the relative positions and intensity ratios of the $K\alpha_{21}$ and $K\alpha_{22}$ Lorentzian profiles were constrained so as to preserve the overall shape as characterized by Hölzer *et al.* (1997). For the geometric profile, a single Soller-slit angle was refined, characterizing the degree of axial divergence and using the case-2 axial-divergence model applied to both the incident and diffracted beams. Other parameters of the geometric profile were fixed at known values. Additional parameters included a Lorentzian size-broadening term, background terms, and profile intensities and positions. A Gaussian microstrain term was included for analyses of SRM 1976b. Fig. 3.1.41 shows the quality of the fits obtained from an FPA analysis of SRM 660b. These fits present a substantial improvement over those using any of the analytical PSFs (Figs. 3.1.32 and 3.1.39). Furthermore, the GoF residual error term for an FPA profile analysis of a continuous scan of SRM 660b was 1.08, while the corresponding terms from analyses of the same data using the split pseudo-Voigt and split Pearson VII PSFs were 1.65 and 1.43, respectively (these three analyses were all from *TOPAS*). The FPA method can account for subtleties in the observed X-ray line profiles that analytical PSFs could never be expected to fit. In subsequent analyses of unknowns, it is not imprudent to fix parameters associated with the IPF; refining them, however, is typically not problematic with the FPA.

There were indications that the breadths of the profiles of the Cu $K\alpha$ emission spectrum as characterized by Hölzer *et al.* (1997) were in excess of those of our observations. This was investigated using the ultra-high-quality data. The FWHM ratios of the two pairs of Lorentzian profiles, the $K\alpha_{11}$ *versus* the $K\alpha_{12}$ and the $K\alpha_{21}$ *versus* the $K\alpha_{22}$, were constrained to those reported by Hölzer *et al.* (1997). The positions and intensities of the $K\alpha_2$ doublet were also refined, again with constraints applied to preserve the shape as per Hölzer *et al.* (1997). These refinements indicated that the breadths given by Hölzer *et al.* (1997) were significantly in excess of those that gave the best fit to the data. After an extensive investigation, this observation was confirmed to originate with the performance of the post-monochromator. Several graphite monochromator crystals were investigated using a beam diffracted from an Si single crystal (333 reflection) mounted in the specimen position. The graphite crystals that were manufactured within the last 15 years all gave identical results: after an alignment procedure to optimize the intensity of the $K\alpha_1$ line, they do clip the breadths of the profiles of the emission spectrum by approximately 20%. They also alter the position of diffraction lines by perhaps 0.01° in 2θ; therefore, the goniometer zero angles must be determined with the monochromator installed. We therefore used a reduced-breadth Hölzer emission spectrum in our FPA analysis. Note that these breadths vary with $\tan\theta$ because of angular dispersion, as does microstrain; therefore, only a microstrain-free specimen can be used for an analysis of the impact of a monochromator on the emission spectrum. We found that both SRMs 660c and 640e were suitable for this analysis.

The refinement strategy for the case-2 Soller-slit angle was also investigated with the ultra-high-quality data. Technically, the axial divergence of the incident beam, with the inclusion of the Soller slit, is less than that of the diffracted beam, which is limited by its extended beam-path length through the monochromator. Several strategies were investigated, some of which may have represented a more accurate physical model than that of a single divergence value applied to both beams, but none resulted in any improvement in the fit quality. Lastly, it was observed that the

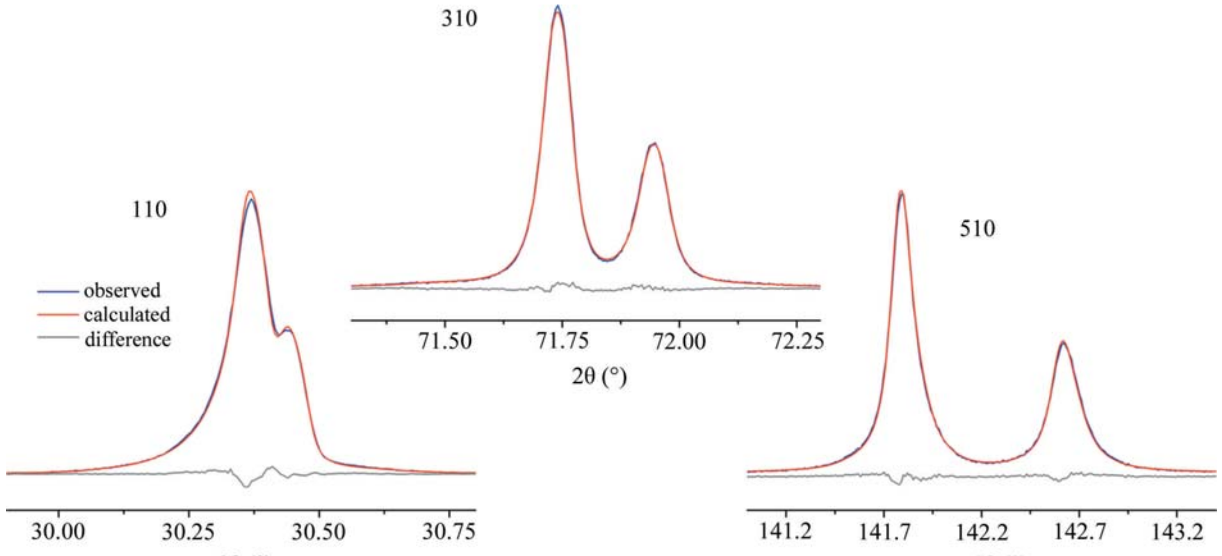

Figure 3.1.41
Fit quality realized with a fundamental-parameters-approach analysis of SRM 660b peak-scan data using *TOPAS*.

value for the width of the divergence slit, particularly with the use of the IBM, refined to values in excess of the known value. This observation will be discussed further.

With the certification of SRMs 640e, 660c and 1878b (respirable quartz, 2014), global refinements were set up allowing for the simultaneous analysis of the 20 high-quality data sets collected for the certification of each SRM. With this approach, the analyses could be carried out in the context of highly favourable Poisson counting statistics and permitted a robust analysis of FPA models that would otherwise be problematic because of parameter correlation. Data were collected from two samples from each bottle. With SRMs 640e and 660c, the machine was configured as per the work of this study with the post-monochromator; for 1878b, the machine was configured likewise with the IBM and scintillation detector. For SRM 660c the data were collected in accordance to the run-time parameters of Table 3.1.2, and in an analogous manner for SRM 640e. For SRM 1878b, the data were collected on mixtures of 50% SRM 1878b and 50% SRM 676a in continuous, 24 h scans. Concurrent with the effort to certify SRMs 640e and 660c, the agreement between the results from *FPAPC* and *TOPAS* was established, indicating that both codes operated in accordance with published FPA models (Mendenhall *et al.*, 2015). Initially with *FPAPC* and later with *TOPAS*, the data from these three SRMs were analysed using the global refinement strategy.

The global refinements were used to investigate possible difficulties with the FPA models. First, the global refinements were used to determine more robust values for the breadths of the emission spectrum as influenced by the post-monochromator. The issue concerning the refined value for the incident slit size was revisited with the global refinements. Values of 25% in excess of the known size were observed in refinements of IBM data from several materials using *TOPAS*. While these refinements were quite robust, corresponding analysis of ultra-high-quality post-monochromator data sets resulted in a slow increase in the slit value with little change in residual error terms, indicating a shallow χ^2 minimization surface. With the global analysis of the SRM 660c, 640e and 1878b data, however, the incident slit value refined to a value of 15 to 25% in excess of the known value in a robust manner. The reduced correlations between models with the global refinements led to this improved ability to reach the minimum in error space for both data types. An investigation into the sensitivity of the lattice-parameter value and GoF on the incident slit size was consistent with the shallow χ^2 minimization surface; changes in lattice parameters were less than 2 fm and only small changes in GoF were noted. The lowest-angle lines used in our analyses were at 18°; given the 1/tan θ dependence of the incident-slit correction, lower-angle lines are required for robust use of this model for refinement of incident-slit size. A second observation of concern was the low values for sample attenuation refined from data for SRM 660*x*. As previously stated, a reasonable value for a compact of LaB_6 would be 800 cm^{-1}, yet the fits were giving values in the 400 cm^{-1} range. Again, a sensitivity study indicated little dependence of either the lattice parameter or the GoF on the attenuation values when they are this large. In contrast, sensitivity studies on SRM 640*x* (silicon in the 80 to 100 cm^{-1} range) indicated a high level of response to changes in attenuation values. Again, in the range where the model is active, results are in correspondence with expectations; where there is little impact on the refinement, parameter values may differ from true values with little impact on the refinement as a whole. We are continuing to investigate the issue of the non-physical values obtained for the refined divergence-slit width.

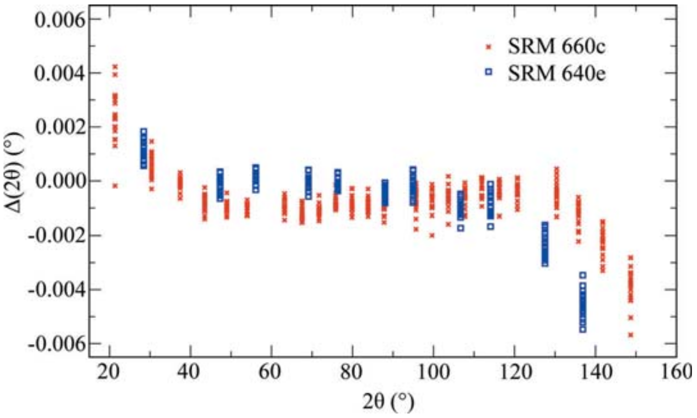

Figure 3.1.42
$\Delta(2\theta)$ data from the 20 data sets collected for the certification of SRMs 660c and 640e, determined *via* FPA analyses using *TOPAS*.

The $\Delta(2\theta)$ data shown in Fig. 3.1.42 illustrate results from an FPA analysis of the 20 data sets collected for the certification of SRMs 660c and 640e. The $\Delta(2\theta)$ values were generated using the certified lattice parameters of SRMs 660c and 640e to compute 'SRM' or reference peak positions, and the unconstrained profile positions from the FPA analysis were used as the 'test' data. The analyses were performed using *TOPAS* with the divergence-slit width fixed at the known value. The data in Fig. 3.1.42 clearly reflect the efficacy of the FPA method. The certification data for these SRMs were collected on the machine set up as for Fig. 3.1.26; the trends of the peak position for these data are identical to those of Fig. 3.1.26. Yet the FPA has corrected the profile positions to a degree indiscernible from the 'true' positions in the 40 to 120° 2θ region. The trends observed otherwise in these data are consistent with prior observations discussed at length above, albeit in 2θ regions limited to below 40° and above 120° and to a vastly reduced level. These deviations are consistent with shortcomings in the model, although the deviations are so small that it may be difficult to work out their origin. The unequivocal technical justification for use of the FPA in SRM certification is also apparent in Fig. 3.1.42; when properly used, the method is capable of reporting the 'true' *d*-spacing for profiles located in the 40 to 120° 2θ region.

Using SRM 1976b for calibration of the instrument response entails determining the integrated intensity of 14 profiles from the test instrument and comparing them with certified values. However, the test instrument in this case was the NIST instrument equipped with the graphite post-monochromator. Therefore, the relative intensity values used for comparison were the ones biased to account for the effects of polarization. They were obtained from Table 4 of the SRM 1976b CoA. Fig. 3.1.43 shows the results from various data-analysis techniques performed on a common raw data set from the test instrument. With the noteworthy exception of the split Pearson VII PSF, all methods gave an acceptable result. It can be seen that when intensity measurement is the issue, the use of unconstrained PSFs is more effective than the analyses described earlier, which were intended to determine the profile position or FWHM. With the use of *GSAS*, the pattern was fitted with a Rietveld analysis using a sixth-order spherical harmonic to model the texture. The reported relative intensity data are computed from the observed structure factors using the *GSAS* utility *REFLIST*. This approach is identical to that used for the certification of SRM 1976b, except the certification data were collected on the NIST instrument setup with the IBM.

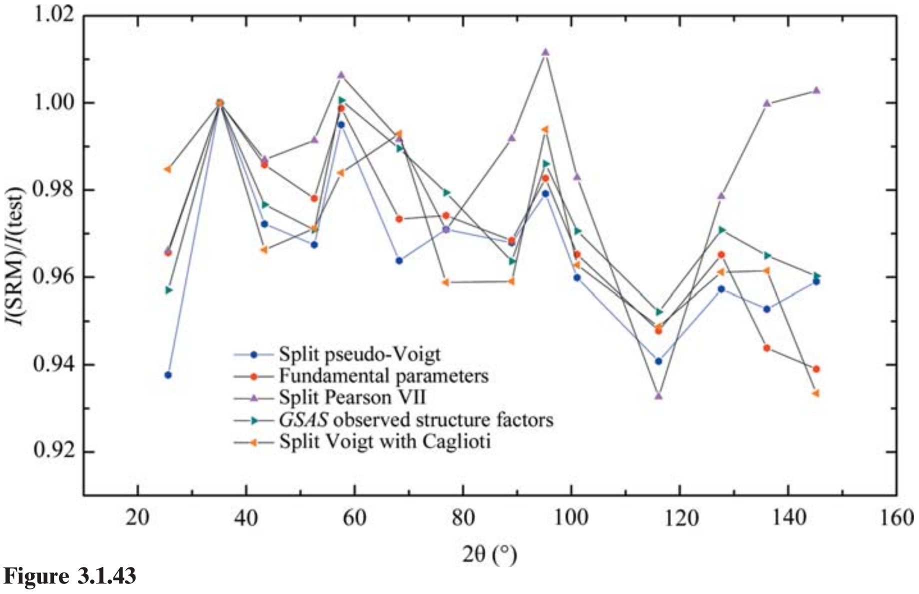

Figure 3.1.43
Qualification of a machine using SRM 1976b. The data were analysed using several PSFs.

The structure common to all the data sets of Fig. 3.1.43 is as yet unexplained. With any of these methods, modelling the background is of critical concern. The intensity scale of the fitted pattern must be expanded to allow for inspection of the background fit alone. The weak amorphous peak at approximately 25° 2θ, which is associated with the anorthite glass matrix phase, complicates the matter. Certain refinement programs allow for the insertion of a broad peak to account for this. Alternatively an 11- to 13-term Chebyshev polynomial could be used. Keeping the number of these terms to a minimum is consistent with preventing the background function from interfering with the modelling of the profiles. Lastly, the use of $K\beta$ filters in conjunction with a PSD can be problematic for the calibration of instrument response using SRM 1976b. Such filters typically impart an absorption edge in the background on the low-energy side of the profiles. With the use of a high-count-rate PSD, this effect can be quite pronounced and can cause difficulties in fitting the background and, therefore, erroneous determination of the profile intensity.

3.1.7. Conclusions

In this chapter, we reviewed the theoretical background behind the well known complexity of X-ray powder diffraction line profiles. A divergent-beam laboratory X-ray diffractometer with a conventional layout was used to rigorously examine the full range of procedures that have been developed for the analysis of the instrument profile function. The machine featured superlative accuracy in angle measurement, and attention was paid to the precision and stability of the optical components and sample positioning. The instrument was aligned in accordance with first-principles methods and was shown to exhibit an optical performance that conformed with the expectations of established theories for powder-diffraction optics.

Data-analysis methods can be divided into two categories that require fundamentally different approaches to instrument calibration. Empirical profile-analysis methods, either based on second-derivative algorithms or profile fitting using analytical profile-shape functions, seek to characterize the instrument performance in terms of shape and position parameters that are used in subsequent analysis for determining the character of the specimen. These methods, however, provide no information about the origins of the peak shift or profile shape that they describe. Model-based methods seek to link the observation directly to the character of the entire experiment. The calibration procedure for the first category can be regarded as a 'classical' calibration where a correction curve is developed through the use of an SRM and applied to subsequent unknowns. With model-based methods, it is the user's responsibility to calibrate the instrument in a manner that ensures that the models that are being used correctly correspond to the experiment. This is best accomplished through the analysis of results from empirical methods, particularly $\Delta(2\theta)$ curves, as well as the analysis of data from an SRM followed by a critical examination of the refined parameters.

Second-derivative-based algorithms for determining peak locations are able to provide the 2θ positions (the positions of the maxima in the observed profile intensity) to within ±0.0025° 2θ. Profile fitting using analytical profile-shape functions to determine the peak position was shown to be problematic; errors of up to 0.015° 2θ were noted. The use of uniform weighting in the refinements resulted in improved accuracy in the reported peak positions and FWHM values. Using a Johansson incident-beam monochromator led to high-quality fits of diffraction data using analytical profile shape functions. The Caglioti function can be used to improve the reliability of FWHM values.

The fundamental-parameters approach was found to be effective in modelling the performance of the Bragg–Brentano divergent-beam X-ray diffractometer. The form of the $\Delta(2\theta)$ curve, determined *via* a second-derivative algorithm, can be explained quantitatively through an examination of FPA models. Furthermore, FPA simulations of diffraction data, computed from the instrument configuration using both commercial and NIST FPA codes, and analysed using the same second-derivative algorithm, reproduced the $\Delta(2\theta)$ results from the experimental data. This self-consistency verified the correct operation of both the instrument and the FPA models. Using the FPA for modelling the diffraction profiles provided the best fits to the observations and the most accurate results for the 'true' reported peak positions. The TCH/Finger models for profile shape yielded credible results for refinement of lattice parameters *via* the Rietveld method.

This chapter is based on an article published in the *Journal of Research of the National Institute of Standards and Technology* (Cline *et al.*, 2015).

References

Azároff, L. V. (1955). *Polarization correction for crystal-monochromatized X-radiation*. *Acta Cryst.* **8**, 701–704.

Bergmann, J., Friedel, P. & Kleeberg, R. (1998). *BGMN – a new fundamental parameters based Rietveld program for laboratory X-ray sources, it's use in quantitative analysis and structure investigations*. *IUCr Commission on Powder Diffraction Newsletter*, **20**, 5–8. http://www.iucr.org/resources/commissions/powder-diffraction/newsletter/.

Bergmann, J., Kleeberg, R., Haase, A. & Breidenstein, B. (2000). *Advanced fundamental parameters model for improved profile analysis*. In *Proceedings of the Fifth European Conference on Residual Stresses*, edited by A. J. Böttger, R. Delhez & E. J. Mittemeijer, *Mater.*

Sci. Forum, **347–349**, 303–308. Zürich Uetikon, Switzerland: Trans Tech. Publications.

Berkum, J. G. M. van, Sprong, G. J. M., de Keijser, T. H., Delhez, R. & Sonneveld, E. J. (1995). *The optimum standard specimen for X-ray diffraction line-profile analysis. Powder Diffr.* **10**, 129–139.

BIPM (2006). *The International System of Units (SI)*, 8th ed. Sèvres: Bureau International des Poids et Mesures. http://www.bipm.org/utils/common/pdf/si_brochure_8_en.pdf.

Black, D. R., Windover, D., Henins, A., Filliben, J. & Cline, J. P. (2011). *Certification of standard reference material 660b*. *Powder Diffr.* **26** (Special Issue 02), 155–158.

Bruker AXS (2014). *TOPAS Software*. https://www.bruker.com/products/x-ray-diffraction-and-elemental-analysis/x-ray-diffraction/xrd-software/topas.html.

Caglioti, G., Paoletti, A. & Ricci, F. (1958). *Choice of collimators for a crystal spectrometer for neutron diffraction*. *Nucl. Instrum.* **3**, 223–228.

Cheary, R. W. & Cline, J. P. (1995). *An analysis of the effect of different instrumental conditions on the shapes of X-ray line profiles*. *Adv. X-ray Anal.* **38**, 75–82.

Cheary, R. W. & Coelho, A. (1992). *A fundamental parameters approach to X-ray line-profile fitting*. *J. Appl. Cryst.* **25**, 109–121.

Cheary, R. W. & Coelho, A. (1994). *Synthesizing and fitting linear position-sensitive detector step-scanned line profiles*. *J. Appl. Cryst.* **27**, 673–681.

Cheary, R. W. & Coelho, A. A. (1996). Programs *XFIT* and *FOURYA*. CCP14 Powder Diffraction Library, Engineering and Physical Sciences Research Council, Daresbury Laboratory, UK. http://www.ccp14.ac.uk/.

Cheary, R. W. & Coelho, A. A. (1998*a*). *Axial divergence in a conventional X-ray powder diffractometer. I. Theoretical foundations*. *J. Appl. Cryst.* **31**, 851–861.

Cheary, R. W. & Coelho, A. A. (1998*b*). *Axial divergence in a conventional X-ray powder diffractometer. II. Realization and evaluation in a fundamental-parameter profile fitting procedure*. *J. Appl. Cryst.* **31**, 862–868.

Cline, J. P. (2000). *Use of NIST standard reference materials for characterization of instrument performance*. In *Industrial Applications of X-ray Diffraction*, edited by F. H. Chung & D. K. Smith, pp. 903–917. New York: Marcel Dekker, Inc.

Cline, J. P., Mendenhall, M. H., Black, D., Windover, D. & Henins, A. (2015). *The optics and alignment of the divergent beam laboratory X-ray powder diffractometer and its calibration using NIST standard reference materials*. *J. Res. NIST*, **120**, 173–222. http://nvlpubs.nist.gov/nistpubs/jres/120/jres.120.013.pdf.

Cline, J. P., Von Dreele, R. B., Winburn, R., Stephens, P. W. & Filliben, J. J. (2011). *Addressing the amorphous content issue in quantitative phase analysis: the certification of NIST standard reference material 676a*. *Acta Cryst.* A**67**, 357–367.

Degen, T., Sadki, M., Bron, E., König, U. & Nénert, G. (2014). *Powder Diffr.* **29**, S13–S18.

Edmonds, J., Brown, A., Fischer, G., Foris, C., Goehner, R., Hubbard, C., Evans, E., Jenkins, R., Schreiner, W. N. & Visser, J. (1986). *JCPDS – International Centre for Diffraction Data Task Group on Cell Parameter Refinement. Powder Diffr.* **1**, 66–76.

Fawcett, T. G., Kabbekodu, S. N., Faber, J., Needham, F. & McClune, F. (2004). *Evaluating experimental methods and techniques in X-ray diffraction using 280,000 data sets in the Powder Diffraction File*. *Powder Diffr.* **19**, 20–25.

Finger, L. W., Cox, D. E. & Jephcoat, A. P. (1994). *A correction for powder diffraction peak asymmetry due to axial divergence*. *J. Appl. Cryst.* **27**, 892–900.

Guinier, A. (1994). *X-ray Diffraction in Crystals, Imperfect Crystals, and Amorphous Bodies*. N. Chelmsford, USA: Courier Dover Publications.

Hall, M. M., Veeraraghavan, V. G., Rubin, H. & Winchell, P. G. (1977). *The approximation of symmetric X-ray peaks by Pearson type VII distributions*. *J. Appl. Cryst.* **10**, 66–68.

Hastings, J. B., Thomlinson, W. & Cox, D. E. (1984). *Synchrotron X-ray powder diffraction*. *J. Appl. Cryst.* **17**, 85–95.

Hölzer, G., Fritsch, M., Deutsch, M., Härtwig, J. & Förster, E. (1997). *$K\alpha_{1,2}$ and $K\beta_{1,3}$ X-ray emission lines of the 3d transition metals*. *Phys. Rev. A*, **56**, 4554–4568.

Huber (2014). Monochromator 611 manual. http://www.xhuber.de/fileadmin/user_upload/downloads/usermanuals/Guinier_Monochromator_611_online.pdf.

JCGM (2008*a*). *Uncertainty of Measurement – Part 3: Guide to the expression of uncertainty in measurement* (JCGM 100:2008, GUM: 1995). Tech. Rep. Joint Committee for Guides in Metrology. http://www.iso.org/sites/JCGM/GUM-introduction.htm.

JCGM (2008*b*). *International vocabulary of metrology – basic and general concepts and associated terms (VIM)*. Tech. Rep. Joint Committee for Guides in Metrology. http://www.bipm.org/en/publications/guides/vim.html.

Jenkins, R. (1992). *Round robin on powder diffractometer sensitivity*. ICDD Workshop at *Accuracy in Powder Diffraction II*, May 26–29, NIST, Gaithersburg, USA.

Johansson, T. (1933). *Über ein neuartiges, genau fokussierendes Röntgenspektrometer*. *Z. Phys.* **82**, 507–528.

Klug, H. P. & Alexander, L. E. (1974). *X-ray Diffraction Procedures*, 2nd ed. New York: John Wiley & Sons.

Larson, A. C. & Von Dreele, R. B. (2004). *General Structure Analysis System (GSAS)*. Tech. Rep. Los Alamos National Laboratory, New Mexico, USA.

Louër, D. (1992). Personal communication.

Louër, D. & Langford, J. I. (1988). *Peak shape and resolution in conventional diffractometry with monochromatic X-rays*. *J. Appl. Cryst.* **21**, 430–437.

McCusker, L. B., Von Dreele, R. B., Cox, D. E., Louër, D. & Scardi, P. (1999). *Rietveld refinement guidelines*. *J. Appl. Cryst.* **32**, 36–50.

Maskil, N. & Deutsch, M. (1988). *X-ray $K\alpha$ satellites of copper*. *Phys. Rev. A*, **38**, 3467–3472.

Mendenhall, M. H., Mullen, K. & Cline, J. P. (2015). *An implementation of the fundamental parameters approach for analysis of X-ray powder diffraction line profiles*. *J. Res. NIST*, **120**, 223–251.

NIST (2008). *Standard Reference Material 676a: Alumina Internal Standard for Quantitative Analysis by X-ray Powder Diffraction*. SRM certificate. NIST, U. S. Department of Commerce, Gaithersburg, MD, USA. https://www-s.nist.gov/srmors/view_detail.cfm?srm=676a.

NIST (2010). *Standard Reference Material 660b: Lanthanum Hexaboride – Powder Line Position and Line Shape Standard for Powder Diffraction*. SRM certificate. NIST, U. S. Department of Commerce, Gaithersburg, MD, USA. https://www-s.nist.gov/srmors/view_detail.cfm?srm=660b.

NIST (2015*a*). *209.1 – X-ray Diffraction (powder and solid forms)*. SRM catalog. NIST, U. S. Department of Commerce, Gaithersburg, MD, USA. https://www-s.nist.gov/srmors/viewTableV.cfm?tableid=149.

NIST (2015*b*). *Standard Reference Material 1976b: Instrument Response Standard for X-ray Powder Diffraction*. SRM certificate. NIST, U. S. Department of Commerce, Gaithersburg, MD, USA. https://www-s.nist.gov/srmors/view_detail.cfm?srm=1976B.

NIST (2015*c*). *Standard Reference Material 640e: Line Position and Line Shape Standard for Powder Diffraction (Silicon Powder)*. SRM certificate. NIST, U. S. Department of Commerce, Gaithersburg, MD, USA. https://www-s.nist.gov/srmors/view_detail.cfm?srm=640E.

NIST (2015*d*). *Standard Reference Material 660c: Line Position and Line Shape Standard for Powder Diffraction (Lanthanum Hexaboride Powder)*. SRM certificate. NIST, U. S. Department of Commerce, Gaithersburg, MD, USA. https://www-s.nist.gov/srmors/view_detail.cfm?srm=660c.

Rietveld, H. M. (1967). *Line profiles of neutron powder-diffraction peaks for structure refinement*. *Acta Cryst.* **22**, 151–152.

Rietveld, H. M. (1969). *A profile refinement method for nuclear and magnetic structures*. *J. Appl. Cryst.* **2**, 65–71.

Rigaku (2014). *PDXL 2, Rigaku powder diffraction data analysis software version 2.2*. Rigaku Corporation, Tokyo, Japan.

Taylor, B. & Kuyatt, C. (1994). *TN1297: Guidelines for Evaluating and Expressing the Uncertainty of NIST Measurement Results*. Tech. Rep. NIST. Washington, DC: U. S. Government Printing Office. http://physics.nist.gov/cuu/Uncertainty/index.html.

Thompson, P., Cox, D. E. & Hastings, J. B. (1987). *Rietveld refinement of Debye–Scherrer synchrotron X-ray data from Al_2O_3*. *J. Appl. Cryst.* **20**, 79–83.

Toby, B. H. & Von Dreele, R. B. (2013). *GSAS-II: the genesis of a modern open-source all purpose crystallography software package*. *J. Appl. Cryst.* **46**, 544–549.

Wilson, A. J. C. (1963). *Mathematical Theory of X-ray Powder Diffractometry*. New York: Gordon & Breach.

Yao, T. & Jinno, H. (1982). *Polarization factor for the X-ray powder diffraction method with a single-crystal monochromator*. *Acta Cryst.* A**38**, 287–288.

International Tables for Crystallography (2019). Vol. H, Chapter 3.2, pp. 252–262.

3.2. The physics of diffraction from powders

P. W. Stephens

3.2.1. Introduction

The term powder is used here as a label for polycrystalline samples, but they may not be powdery at all, *e.g.*, metallurgical samples or chocolate. The central premise of powder diffraction is that the sample consists of a sufficiently large number of independent particles (Smith, 2001). In that case, the diffraction pattern will consist of a series of peaks corresponding to the Bragg reflections from each component of the sample. This chapter starts with an idealized description of the data collected in a powder-diffraction measurement and how it relates to the physical properties of the sample and the diffractometer. In real experiments, many of the idealizations of this description are not satisfied, and the influence of those deviations from simple model behaviour are discussed in turn. To a greater or lesser extent, those confounding factors are under the control of the experimenter, and so it is important to understand how they can be optimized or avoided in the experimental design, as well as how to deal with situations where they cannot be (or have not been) avoided and deal with them in real data that have been collected.

The diffraction probes discussed here are X-rays and neutrons. Bragg's equation, $\lambda = 2d\sin\theta$, relates properties of the measurement (wavelength of the diffracted radiation λ and scattering angle 2θ) with a property of the sample (the d-spacing of the particular reflection observed). Data may be collected with radiation of fixed wavelength as a function of angle, or as energy-dispersive measurements at fixed angle. The former case is perhaps the most familiar, exemplified by a laboratory powder diffractometer using characteristic radiation from an X-ray tube, but it is frequently performed with X-rays or neutrons from a continuum source (*e.g.*, storage ring or nuclear reactor) selected by a suitable monochromator. Energy-dispersive X-ray experiments are performed by illuminating the sample with a continuum spectrum from a synchrotron source or *Bremsstrahlung* from an X-ray tube, whereas time-of-flight methods are in use at pulsed spallation neutron sources. Convenient conversions are that X-rays of energy E (keV) have wavelength λ (Å) = $12.398/E$, and neutrons with a speed v (m s^{-1}) have wavelength λ (Å) = $3956/v$.

3.2.2. Idealized diffraction from powders

From an experimental measurement, powder-diffraction data generally consist of detected intensity *versus* an experimental parameter (angle, time of flight, photon energy), where the latter can be related to the d-spacing of a Bragg reflection in the sample. Unless the sample is severely disordered, these data takes the form of a series of peaks which may or may not be distinctly separated. (In a severely disordered sample, the concept of a discrete set of Bragg peaks may not be applicable, and the Debye scattering equation, mentioned in Section 3.2.4 and more thoroughly covered in Chapters 3.6, 5.6 and 5.7, may be more appropriate.) The attributes of those peaks are their positions, integrated intensities and shapes. Their positions will depend on the dimensions of the crystal lattice, their relative intensities will depend on the crystallographic structure factors of the reflections, and their shapes will depend on aspects of the sample (*e.g.* grain size and internal strain) and on the configuration of the instrument on which the pattern is measured. We consider each of these in turn in the following sections.

In addition, there is generally a relatively smooth background (Riello *et al.*, 1995) due to a number of effects, such as fluorescence (X-rays), thermal diffuse scattering, multiple scattering within the sample, incoherent scattering, small-angle scattering, parasitic scattering from the atmosphere, the sample holder and/or the windows of environmental chambers, *etc.*

3.2.2.1. *Peak positions*

Starting with a single crystal, the lattice is described by non-coplanar translation vectors $\mathbf{a}, \mathbf{b}$ and $\mathbf{c}$, with magnitudes a, b and c, respectively, and angles α between $\mathbf{b}$ and $\mathbf{c}$, β between $\mathbf{c}$ and $\mathbf{a}$, and γ between $\mathbf{a}$ and $\mathbf{b}$. Diffraction peak positions are governed by the reciprocal lattice, spanned by vectors $\mathbf{a}^* = \mathbf{b}\times\mathbf{c}/(\mathbf{a}\cdot\mathbf{b}\times\mathbf{c})$ and cyclic permutations. These have the property that $\mathbf{a}^*\cdot\mathbf{a} = 1$, $\mathbf{b}^*\cdot\mathbf{a} = 0$ *etc.* (This is the 'crystallographic' convention; the scattering community usually defines reciprocal-lattice vectors as larger by a factor of 2π.) The reciprocal lattice is indexed by Miller indices (hkl), so that each vector in the reciprocal lattice is given by $\mathbf{G} = h\mathbf{a}^* + k\mathbf{b}^* + l\mathbf{c}^*$.

Incoming and diffracted radiation are described by wave vectors $\mathbf{k}_i$ and $\mathbf{k}_f$, both of magnitude $1/\lambda$, and separated by the angle 2θ. The condition for a particular Bragg reflection to be observed is $\mathbf{G}_{hkl} = \mathbf{k}_f - \mathbf{k}_i$. Note that this requires that the diffracting crystal be correctly oriented relative to the incident beam. For a given reflection $\mathbf{G}_{hkl}$, the d-spacing between reflecting planes is given by $d = 1/|\mathbf{G}|$. (Again, in the scattering convention, incident and diffracted beams have wave vectors of magnitude $2\pi/\lambda$, and $d = 2\pi/|\mathbf{G}|$.) In either case, this allows the Bragg condition to be written in the scalar form $\lambda = 2d\sin\theta$.

If the sample is a powder instead of a single crystal, some large number of crystallites will be aligned to meet the (vector) Bragg condition with the incident radiation, and then the diffracted radiation will take the form of a cone of opening half-angle 2θ.

It is often convenient to work with equations written for scalars, *viz.*

$$\begin{aligned} a^* &= bc\sin\alpha/V,\\ \sin\alpha^* &= V/(abc\sin\beta\sin\gamma) \text{ or equivalently}\\ \cos\alpha^* &= \frac{\cos\beta\cos\gamma - \cos\alpha}{\sin\beta\sin\gamma},\end{aligned}$$

with cyclic permutations. Here the unit-cell volume is given by

$$V = abc(1-\cos^2\alpha-\cos^2\beta-\cos^2\gamma+2\cos\alpha\cos\beta\cos\gamma)^{1/2}.$$

Note that the volume of the reciprocal cell is $V^* = 1/V$, and that the equations above are valid upon exchanging starred and unstarred variables.

For powder samples, using only scalars, the Bragg condition may be written as

$$\frac{4\sin^2\theta}{\lambda^2} = d^{-2} = Ah^2 + Bk^2 + Cl^2 + Dkl + Ehl + Fhk, \qquad (3.2.1)$$

where $A = a^{*2}$, $B = b^{*2}$, $C = c^{*2}$, $D = 2b^*c^*\cos\alpha^*$, $E = 2c^*a^*\cos\beta^*$ and $F = 2a^*b^*\cos\gamma^*$. Crystal symmetries higher than triclinic lead to significant simplifications in the above, *e.g.* in the orthorhombic system, $a^* = 1/a$, $A = 1/a^2$ *etc.*, $\alpha^* = \beta^* = \gamma^* = 90^\circ$, and $D = E = F = 0$. See Chapter 1.1, *Reciprocal space in crystallography*, in Volume B of *International Tables for Crystallography* for more details.

3.2.2.2. *Diffraction peak intensities*

3.2.2.2.1. *X-rays*

Consider a polycrystalline sample of randomly oriented grains of a single crystalline phase, containing a total number of atoms N, illuminated by an X-ray beam of wavelength λ. Each reciprocal-lattice vector with magnitude $|\mathbf{G}| < 2/\lambda$ will produce a cone of diffracted radiation with opening half-angle $2\theta = 2\sin^{-1}(\lambda|\mathbf{G}|/2)$. Regarding the diffraction lines as perfectly sharp delta-functions, the differential cross section for one powder Bragg peak is (Marshall & Lovesey, 1971)

$$\frac{\mathrm{d}\sigma}{\mathrm{d}\Omega} = \frac{N\lambda^3 r_e^2}{16\pi V}\frac{Pm_{hkl}}{\sin\theta\sin 2\theta}|A_{hkl}|^2\delta\left(2\theta - 2\sin^{-1}\frac{\lambda}{2d}\right). \qquad (3.2.2)$$

In this equation, $r_e = 2.82 \times 10^{-15}$ m is the classical electron radius and V is the unit-cell volume; the polarization factor P, multiplicity m_{hkl} and structure factor A_{hkl} are discussed below. Finite crystallite size, strain and other factors discussed below will broaden the peak, but the integrated intensity of each peak will be given by the factors before the delta-function.

Before continuing, note that this result is correct within the approximation that the entire sample is uniformly bathed in radiation (*i.e.*, there is no absorption) and the kinematic approximation that the scattering power is very weak, so that further interaction of the scattered radiation with the sample may be neglected. The latter is equivalent to the Born approximation of elementary quantum mechanics, and its failure is referred to as extinction; it is discussed below in Section 3.2.3.6. It should also be noted here that equation (3.2.2) refers only to diffraction in Bragg peaks, and not to thermal diffuse scattering or scattered radiation due to static distortions from an ideal crystal lattice (Huang scattering; Krivoglaz, 1969).

Returning to the terms in equation (3.2.2), for X-rays the polarization factor P accounts for the polarization dependence of the Thomson scattering cross section from a free electron. For a completely polarized incident beam: $P = 1$ for S polarization (polarization perpendicular to the scattering plane); $P = \cos^2 2\theta$ for P polarization (in the scattering plane). For unpolarized X-rays (no monochromator), $P = (1 + \cos^2 2\theta)/2$. For horizontally polarized X-rays from a synchrotron-radiation source, diffracted vertically, the polarization factor is very close to unity, and so P can generally be taken as 1. If there is a crystal monochromator (deflection angle $2\theta_m$) coplanar with the diffractometer and an unpolarized source, $P = (1 + \cos^2 2\theta_m \cos^2 2\theta)/(1 + \cos^2 2\theta_m)$. If there is a polarization-sensitive analyser crystal following the sample, its relative transmission of X-rays polarized within or perpendicular to its plane of scattering must also be taken into account.

The multiplicity factor m_{hkl} accounts for the number of symmetry-equivalent reflections in the crystal structure, *i.e.*, the number of distinct reflections that have the same structure factor. Note that the equivalence of Bragg reflections depends on the Laue group of the sample. For example, in the cubic space group $Fm\bar{3}m$, reflections (hkl) and (khl) are equivalent, whereas they are not in space group $Fm\bar{3}$. If the atomic scattering factors are purely real or the structure is centrosymmetric, the intensities of Friedel pairs hkl and $h\bar{k}\bar{l}$ are equal. However, in an acentric structure with significant imaginary component of any of the atomic scattering factors (see below), Friedel pairs cannot be treated as symmetry equivalent.

The (dimensionless) X-ray structure factor is given by

$$\begin{aligned} A_{hkl} &= \sum_n f_n \exp(2\pi i\mathbf{G}_{hkl}\cdot\mathbf{r}_n)\exp(-W_n) \\ &= \sum_n f_n \exp[2\pi i(hx_n + ky_n + lz_n)]\exp(-W_n), \end{aligned} \qquad (3.2.3)$$

where the sum runs over all atoms in the unit cell. In the first form of this equation, $\mathbf{r}_n$ is the vector from the origin of the unit cell to the nth atom; in the second form, x_n, y_n and z_n are fractional coordinates of the nth atom in the unit cell such that $\mathbf{r}_n = x_n\mathbf{a} + y_n\mathbf{b} + z_n\mathbf{c}$.

The term $\exp(-W_n)$ is called the Debye–Waller factor, and it accounts for random dynamical motion of the nth atom away from its equilibrium position. This may be due to thermal fluctuations or (at low temperature) the quantum zero-point motion. If the atomic motion is isotropic, this term takes the form

$$W_n = B\sin^2\theta/\lambda^2 = 8\pi^2 U_n \sin^2\theta/\lambda^2, \qquad (3.2.4)$$

where $U_n = \langle u_n^2\rangle$ is the mean-square fluctuation of the atom's distance from its equilibrium position (in three dimensions). Observed values of B are generally in the range of 0.5 to 1 Å^2 for inorganic crystals, and as large as 5 Å^2 for organic crystals.

A more general treatment of the Debye–Waller factor considers the probability density of the centre of the atom to be a three-dimensional ellipsoidal Gaussian function. Then for a given diffraction peak, it takes the form

$$\begin{aligned} W = 2\pi^2(&U_{11}a^{*2}h^2 + U_{22}b^{*2}k^2 + U_{33}c^{*2}l^2 \\ &+ 2U_{12}a^*b^*hk + 2U_{23}b^*c^*kl + 2U_{13}a^*c^*hl). \end{aligned} \qquad (3.2.5)$$

The parameters U_{ij} that define the displacement ellipsoid are constrained to match the point symmetry of the site. For example, an atom that lies on a site of mmm symmetry will have the cross terms $U_{12} = U_{23} = U_{13} = 0$.

In equation (3.2.3), f_n is the atomic scattering factor, which arises because X-rays interact with the electrons in the sample, and the strength of that interaction depends both on the magnitude of the scattering vector and the X-ray frequency (wavelength). The electrons are distributed around the nucleus, and so their scattering power decreases with increasing magnitude of the scattering vector. There is also a dependence of the phase and amplitude of the scattering factor on the X-ray energy, which is especially significant near resonance with atomic transition energies. These factors are gathered into the atomic scattering factor f_n, which is commonly written as

$$f_n = f_n^0(\sin\theta/\lambda) + f'(\lambda) + if''(\lambda). \qquad (3.2.6)$$

f^0 is the Fourier transform of the electron number density, so that $f^0(0)$ is equal to the number of electrons in the atom or ion. These factors are tabulated in *International Tables for Crystallography*, Volume C, Chapter 6.1 and https://physics.nist.gov/PhysRefData/FFast/html/form.html and http://henke.lbl.gov/optical_constants/asf.html. Values of atomic scattering factors are normally incorporated into data-analysis programs that require them, so the user does not often have to worry about them.

Equation (3.2.3) above is premised on the assumption that the distribution of electrons in the sample is confined to spherically symmetric atoms, *i.e.,* ignoring charge density in bonds and the deformation of core electron density. For the purposes of phase identification and structure refinement, this is generally a good approximation. X-ray determination of non-spherical charge densities goes beyond the scope of this introduction; for further information, see *e.g.* Coppens (1997) and Bindzus *et al.* (2014).

In energy-dispersive X-ray measurements, the detector sits at a fixed 2θ and collects diffracted radiation from a continuum source. The independent variable of the measurement can be taken as the X-ray energy, $E = hc/\lambda$. With the appropriate change of variables, equation (3.2.2) can be written as

$$\frac{\mathrm{d}\sigma}{\mathrm{d}\Omega} = \frac{Nr_e^2}{16\pi V}\frac{h^3c^3Pm_{hkl}}{E^2\sin^3\theta}|A_{hkl}|^2\delta\left(E - \frac{hc}{2d\sin\theta}\right). \qquad (3.2.7)$$

Recall that hc = 12.398 KeV Å in convenient units. Again, instrument resolution and sample effects will broaden the peak, but its integrated area is given by the terms preceding the delta-function. Of course, the diffracted intensity must be normalized to the incident spectrum as a function of energy; this may be a rather complicated undertaking as it involves energy-dependent corrections for such factors as detector sensitivity, absorption in the sample *etc.*

3.2.2.2.2. *Neutrons and nuclear scattering*

Neutrons interact with the sample in two ways: the strong interaction with the atomic nuclei, and the magnetic interaction between the neutron's dipole moment and magnetization density in the sample. We consider here only unpolarized neutrons; the use of polarized neutrons permits separation between nuclear and magnetic scattering as well as direct observation of the interference between the two; details are beyond the scope of this chapter. Nuclear scattering is very similar to the X-ray case discussed above, except that the atomic scattering amplitude r_ef_n is replaced by the nuclear coherent scattering length $\bar{b}_n$ (given in *International Tables for Crystallography*, Volume C, Table 4.4.4.1), which is generally independent of neutron energy.

Unlike X-rays, the strength of the neutron–nucleus interaction is not a smooth function of atomic number. This creates opportunities to use neutrons to distinguish atoms with nearly identical X-ray scattering amplitudes, but it also makes certain elements very difficult to study with neutrons. The interaction between neutrons and the nuclei in the sample depends on the isotope and possibly the spin angular momentum of the neutron–nucleus system. This means that incoherent scattering can be significantly larger than the (coherent) diffracted signal for certain atoms, notably hydrogen (^{1}H); see Chapter 2.3 of this volume for further details. For wavelengths of interest in crystallography, the nucleus is essentially a point, and so there is no atomic form factor. This generally leads to greater intensity relative to X-rays at increasing scattering vector (decreasing d-spacing).

Neutron diffractometers operate in one of two ways: angle dispersive or energy dispersive. The configuration for angle-dispersive diffraction measurements is conceptually similar to that used for X-rays; a monochromatic beam of neutrons impinges on the sample and a detector measures the distribution of neutrons *versus* scattering angle. For Bragg neutron diffraction from nuclei,

$$\frac{\mathrm{d}\sigma}{\mathrm{d}\Omega} = \frac{N\lambda^3}{16\pi V}\frac{m_{hkl}}{\sin\theta\sin2\theta}|A_{hkl}^{(n)}|^2\delta\left(2\theta - 2\sin^{-1}\frac{\lambda}{2d}\right), \qquad (3.2.8)$$

where the neutron nuclear structure factor is defined as

$$A_{hkl}^{(n)} = \sum_n \bar{b}_n\exp(2\pi i\mathbf{G}\cdot\mathbf{r}_n)\exp(-W). \qquad (3.2.9)$$

Time-of-flight neutron diffractometers, generally based at pulsed spallation sources, operate by measuring the time from the creation of the pulse of neutrons at the target until they appear in a given detector. If the total path length from source to detector is L and the detector is situated at an angle 2θ, a neutron with time of flight t had speed L/t and wavelength $\lambda = ht/m_nL$. Here h is Planck's constant and m_n is the mass of the neutron. This provides a measurement of the d-spacing within the sample, $d = ht/(2m_nL\sin\theta)$. Another change of variables from equation (3.2.2) yields

$$\frac{\mathrm{d}\sigma}{\mathrm{d}\Omega} = \frac{N}{64\pi V}\left(\frac{h}{m_nL}\right)^3\frac{t^4}{\sin^2\theta}m_{hkl}|A_{hkl}|^2\delta(t - 2d\sin\theta Lm_n/h). \qquad (3.2.10)$$

In practice, a large number of detectors surround the sample and counts from the same d-spacing (appropriately normalized for incident-beam intensity and detector solid angle) are binned together. In convenient units, m_n/h = 253 µs m^{-1} Å^{-1}.

3.2.2.2.3. *Neutrons and magnetic scattering*

Magnetic neutron scattering is also described through a structure factor which is, however, a vector. The magnetic moment of the neutron interacts with the magnetization density of unpaired electrons in the sample, which may possess spin and/or orbital angular momentum. The magnetic interaction is only sensitive to the component of magnetization perpendicular to the scattering vector. When discussing magnetic scattering, it is more common to use the scattering vector $\mathbf{Q} = 2\pi\mathbf{G}$. The magnetic structure factor is defined as

$$\mathbf{A_Q}^{\mathrm{mag}} = (\gamma r_e/2)\sum_n f_n(Q)(\hat{\mathbf{Q}}\times\mathbf{m}_n\times\hat{\mathbf{Q}})\exp(i\mathbf{Q}\cdot\mathbf{r_n})\exp(-W). \qquad (3.2.11)$$

Here γ = 1.9132 is the neutron gyromagnetic factor, $f_n(Q)$ is the atomic magnetic form factor, $\mathbf{m}_n$ is the magnetization of the nth site in units of the Bohr magneton and $\hat{\mathbf{Q}}$ is the unit vector in the direction of $\mathbf{Q}$. The double cross product isolates the component of magnetization perpendicular to $\mathbf{Q}$.

Note that many magnetically ordered materials have a magnetic cell which is larger than the chemical cell. Indeed, many magnetic phases are incommensurately modulated, *i.e.*, the magnetic structure is not periodic with any combination of the chemical unit cell translation vectors. Such matters are beyond the scope of this introduction, and are handled in Chapter 7.13 of this volume.

For unpolarized neutron measurements (*i.e.*, an average over all polarization states of the incoming and diffracted beam), the intensities of the nuclear and magnetic diffraction peaks may be computed separately and then added to determine the overall diffraction pattern. In cases where the chemical and magnetic cells are identical (*e.g.* simple ferromagnets) the nuclear and magnetic diffraction patterns overlap, and so one observes only intensity differences upon magnetic ordering. In the case of antiferromagnets, new magnetic diffraction peaks appear at positions not allowed for the chemical unit cell.

Note also that the magnetic form factor depends on the spin density in the magnetic orbitals, which are typically of greater spatial extent than either the total charge density or the nuclear density. Therefore, the intensity of magnetic neutron diffraction peaks falls off much more rapidly with (sin θ)/λ than do nuclear neutron diffraction peaks.

3.2.2.3. *Peak shapes*

The shape of a powder-diffraction peak is a convolution of the intrinsic line shape due to the microscopic structure of the sample crystallites (*e.g.* size and strain) and the configuration of the instrument used to record the pattern. A major goal of powder-diffraction analysis is to be able to separate the contributions of instrument and sample, so that information about the microstructure of the sample can be extracted reliably. On the other hand, in some cases one simply wants to be able to model the combined influence of instrument and sample, to obtain a functional form that permits the most accurate way of apportioning intensities to partially overlapping peaks.

Consider first the sample-dependent factors. The following division into size and strain effects is somewhat artificial, insofar as lattice strains affect the size of the coherently diffracting domain. Nevertheless, it is common to make a distinction between the two, as size broadening produces a peak width proportional to $1/\cos\theta$ in angle-dispersive measurements, whereas the peak width is proportional to $\tan\theta$ for strain broadening.

3.2.2.3.1. *Domain size*

In very general terms, diffraction peaks from an object of linear size L will have a width in Q of the order of $1/L$. As formulated by Scherrer (1918), in an angle-dispersive measurement, the full width at half-maximum (FWHM) in 2θ, measured in radians, is given by

$$\Gamma = \frac{K\lambda}{L\cos\theta}, \qquad (3.2.12)$$

where K is called the shape factor and is a number of the order of unity whose precise value depends on the shape of the particles, which are assumed to be of uniform size and shape. The FWHM shape factor for a spherical particle is $K = 0.829$ (Patterson, 1939). Note that if a powder sample is polydisperse (*i.e.*, it contains a distribution of grain sizes), the average grain size is not necessarily given by the Scherrer equation.

Perhaps a more useful measure of the width of a peak is the integral breadth. In an angle-dispersive measurement, the integral breadth of a given peak centred at $2\theta_0$ is defined as

$$\beta = \frac{1}{I(2\theta_0)}\int I(2\theta)\,\mathrm{d}2\theta.$$

From a technical point of view, measurement of the integral breadth requires accurate measurement of the intensity in the wings of the diffraction peak, which in turn depends on accurate knowledge of the background intensity.

For any crystallite shape, it can be shown that the integral breadth is related to the volume-average thickness of the crystallite in the direction of the diffraction vector, *viz.*

$$L_V = \frac{\lambda}{\beta\cos\theta} = \frac{1}{V}\int \mathrm{d}^3\mathbf{r}\,T(\mathbf{r},\mathbf{G}),$$

where V is the volume of the crystallite and $T(\mathbf{r},\mathbf{G})$ is the length of the line inside the crystallite parallel to $\mathbf{G}$ and passing through the point $\mathbf{r}$. For example, if one writes an integral-breadth version of the Scherrer equation,

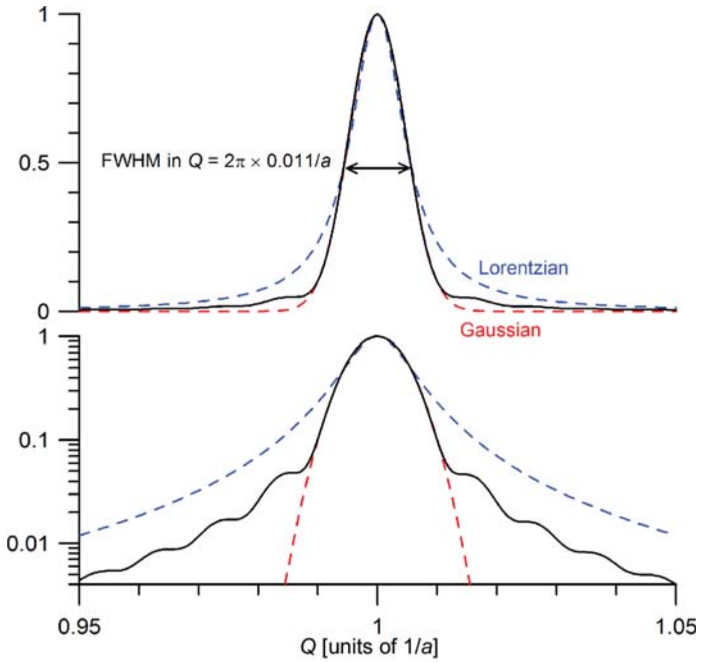

Figure 3.2.1
Computed powder line shape from an ensemble of spherical particles of diameter 100a, including comparison to Gaussian and Lorentzian line shapes of equal FWHM.

$$\beta = \frac{K_\beta\lambda}{L\cos\theta},$$

the shape factor K_β is unity for (00l) reflections from cube-shaped crystals of size L. $K_\beta = 1.075$ for a sphere of diameter L.

An important feature of the integral breadth is that it has a well defined meaning for a polydisperse sample of crystallites. Assuming that the crystallites all have the same shape,

$$\beta = \frac{K_\beta\lambda\langle L^3\rangle}{\cos\theta\langle L^4\rangle},$$

where $\langle L^3\rangle$ and $\langle L^4\rangle$ are the third and fourth moments of the size distribution (Langford & Wilson, 1978).

In many applications such as Rietveld or profile refinement, it is important to treat the full shape of the diffraction peak instead of merely its width (Loopstra & Rietveld, 1969; Rietveld, 1969). By way of illustration, Fig. 3.2.1 shows one Bragg peak of the computed powder-diffraction pattern from an ensemble of spherical particles of point scatterers in a simple cubic lattice. The lattice parameter is a, and the diameter of the particles is chosen to be 100a, so that each crystallite consists of approximately 5.2×10^5 'atoms'. (This line shape was calculated using the Debye equation, described in Section 3.2.4.)

Several different analytical functions are frequently used in powder diffraction. In terms of the independent variable x, centred at x_0 with FWHM Γ, the normalized Gaussian function is

$$G(x - x_0) = \pi^{-1/2}\sigma^{-1}\exp -\left(\frac{x - x_0}{\sigma}\right)^2,$$

with $\sigma = \Gamma/2(\ln 2)^{1/2}$. The normalized Lorentzian is

$$L(x - x_0) = \frac{\Gamma/2\pi}{(x - x_0)^2 + (\Gamma/2)^2}.$$

The symmetric Pearson-VII function is a generalization of the Lorentzian, written as

$$P(x-x_0)=\frac{a}{\Gamma}\left[1+b\left(\frac{x-x_0}{\Gamma}\right)^2\right]^{-m}.$$

Here m is a parameter that governs the line shape (essentially the strength of the wings *versus* the peak), and the numerical parameters $b = 4(2^{1/m} - 1)$ and $a = (b/\pi)^{1/2}\Gamma(m)/\Gamma(m - 1/2)$. (Note the gamma function in the definition of a; the FWHM does not appear in that expression.) The Pearson-VII function with $m = 1$ is a Lorentzian, and it is a Gaussian in the limit $m \to \infty$.

It must be emphasized that none of these functions has any theoretical justification whatsoever. However, in loose powders size broadening is almost always Lorentzian, while Gaussian size broadening is more commonly observed in dense polycrystalline specimens (such as bulk metals).

The Lorentzian and Gaussian functions are also plotted in the same figure for comparison to the actual powder-diffraction line shape of a spherical particle. It can be seen that the correct function has stronger tails than the Gaussian, but the Lorentzian line shape seriously overestimates the intensity in the wings. Both the Gaussian and the Pearson VII fail to capture the general feature that any compact object with a sharp boundary will give a diffraction line shape with tails that asymptotically decay as $(x-x_0)^{-2}$.

One approach to obtaining a more accurate phenomenological description to diffraction line shapes is the Voigt function, which is a convolution of a Gaussian and Lorentzian,

$$V(x-x_0)=\textstyle\int \mathrm{d}x'\, G(x'-x_0)L(x-x').$$

The presence of two shape parameters, the independent widths of the Gaussian and Lorentzian functions, provide independent parameters to control the width and the strength of the wings in the Voigt line shape. The Voigt is more computationally expensive than any elementary function, and so a commonly used approximation is the pseudo-Voigt,

$$\mathrm{PV}(x-x_0;\,\Gamma)=\eta L(x-x_0;\,\Gamma)+(1-\eta)G(x-x_0;\,\Gamma),$$

which is a mixture of Gaussian and Lorentzian functions of the same width. The parameter η controls the shape (strength of the wings) of the pseudo-Voigt line-shape function, independent of its width. There is a computationally convenient approximate relation between Voigt line-shape parameters Γ_L and Γ_G and the pseudo-Voigt Γ and η (Thompson *et al.*, 1987).

3.2.2.3.2. *Strain*

An individual crystal in a sample may be subject to lattice deformation, either due to forces external to that crystal, or to internal factors such as substitutional disorder and dislocations. A comprehensive treatment of microstructural properties and their effects on powder-diffraction peak shapes is given in Chapter 3.6 of this volume; this section gives a general overview from a phenomenological basis.

The simplest description of strain broadening imagines an ensemble of independent crystallites with different lattice parameters. If the crystallites have an isometric distribution of lattice parameters with a fractional width $\delta a/a$, that will be reflected in the range of d-spacings for each reflection. In an angle-dispersive measurement, this will lead to an angular width $\delta 2\theta = 2\tan\theta\;\delta a/a$ (radians).

Physically plausible mechanisms for a distribution of strains in a powder sample include random inter-grain forces arising during crystallization and the elastic response to internal defects such as dislocations. In practice, these effects often give rise to peak widths which likewise grow as $\tan\theta$. However, there is no *a priori* basis for expecting any particular functional form for that distribution. Frequent practice is to assume a Gaussian, Lorentzian, Voigt, or pseudo-Voigt form for an isotropic strain broadening, with an adjustable parameter ε representing the FWHM of the strain distribution. The FWHM Γ of the chosen functional form is then $\Gamma_{2\theta}=2\varepsilon\tan\theta$ for angle-dispersive measurements, $\Gamma_E=\varepsilon E$ for energy-dispersive X-ray measurements and $\Gamma_t=\varepsilon t$ for neutron time-of-flight measurements.

3.2.2.3.3. *Instrumental contributions*

The instrument used to collect diffraction data affects the observed line shape in many ways. A complete discussion is beyond the scope of this article (but see Chapter 3.1, and would have to consider many different diffraction geometries separately. One approach, generally known as fundamental parameters, is to model the effect of every optical element on the peak shape. The instrumental response function is then the convolution of all of these individual contributions.

The simplest (and most widely successful) application of fundamental parameters arises from the analysis of Caglioti *et al.* (1958, 1960) on the instrument response function of a step-scanning powder diffractometer at a reactor neutron source. Neutrons pass through a parallel-blade collimator to a monochromator crystal, through a second collimator to the sample, and then through a third collimator into the detector. It is a fair approximation to assume that the transmission functions of the collimators and the mosaicity of the monochromator are all Gaussians. In that case, the instrument response function produces diffraction peaks which are also Gaussians, with a width that depends on the diffraction angle as

$$\Gamma=\left(U\tan^2\theta+V\tan\theta+W\right)^{1/2}, \qquad (3.2.13)$$

where the parameters U, V and W can be expressed in closed form as functions of the collimator acceptances and monochromator angle and mosaicity (Caglioti *et al.*, 1958, 1960). Indeed, it was this simple form of the line-shape function that allowed Rietveld and co-workers to develop the important methodology of data analysis commonly known as the Rietveld or profile method (Loopstra & Rietveld, 1969; Rietveld, 1969).

The functional form used to describe the shape of the pulse that emerges from the moderator of a spallation neutron source, and the numerical values of the parameters which go into it, determine the peak shapes observed in the powder diffractometer at such an instrument. The treatment of such matters lies beyond this introduction; documentation of the widely used *GSAS* software includes a detailed description (Larson & Von Dreele, 2004; see also Chapter 3.3).

Analytical treatment of the resolution of X-ray diffractometers is generally complicated by the fact that the various contributions are more difficult to model, especially in the case of the parafocusing Bragg–Brentano geometry most commonly used in laboratory X-ray diffractometers. In the diffractometer, one generally considers factors that affect the line shape separately in the equatorial plane (the plane containing the source, sample and detector) and the axial direction (perpendicular to the equatorial plane, *i.e.*, parallel to the diffractometer axis). In the equatorial plane the resolution is primarily governed by the divergence of the X-ray beam illuminating the sample and by the width of the receiving slit, but there are numerous contributions to the diffraction peak width and shape from such factors as nonconformance of the flat sample surface to the focusing circle, partial transparency of the sample and misalignment of the diffractometer (Cheary & Coelho, 1992). Even if a monochromator is used to select only the $K\alpha_1$ line, the radiation spectrum from an X-ray tube consists of several Lorentzian functions owing to satellite transitions.

Axial divergence produces a pronounced asymmetry of low-angle diffraction peaks to the low-angle direction (and on the high-angle side of peaks with 2θ near 180°). If the incident or diffracted rays are out of the equatorial plane, they will be intercepted at a detector setting below (above) the actual diffraction angle if it is small (close to 180°), respectively. The effect can be minimized, but not completely eliminated, by narrowing the beam-defining apertures in the equatorial direction, or by introduction of parallel-blade Soller (1924) slits. The full treatment of the effect of axial divergence in a Bragg–Brentano diffractometer has been presented in a computationally convenient form (Cheary & Coelho, 1998).

It is generally easier to model the instrumental response function of a powder X-ray diffractometer based on a synchrotron-radiation source with an analyser crystal, because the transfer functions of the various optical elements are simpler to express. One approach is to approximate the wavelength- and angle-dependent reflectivity of monochromator and analyser crystals by Gaussians, and derive a closed-form expression for the width of the instrument response function (Sabine, 1987). This has been extended to include collimating and focusing (in the scattering plane) mirrors (Gozzo *et al.*, 2006); see Chapter 3.1 for a full description of the relevant optical configurations. A shortcoming of this analytical approach is that the correct single-crystal reflectivity function is not a Gaussian, so it cannot account for the correct line shape, only provide an estimate of its width. Numerical convolutions to accurately model the line-shape function have been performed, and produce excellent agreement with measured profiles (Masson *et al.*, 2003).

Instead of the analytical approach described in the previous few paragraphs, one frequently writes a parametrized function for the measured line shape without concern for the connection between the numerical values of the parameters and the microscopic properties of the sample or the geometry of the diffractometer. For example, one can use the Caglioti form for diffraction peak width [equation (3.2.13)] on any diffractometer, and adjust the parameters U, V and W to some measured standard sample. If size and strain contributions to sample-dependent broadening are both regarded as Lorentzians, they could be combined as $\Gamma = X/\cos\theta + Y\tan\theta$. (Here we make use of the fact that the convolution of two Lorentzians is a Lorentzian whose width is the sum of the individual widths. For Gaussians, the widths combine in quadrature, *i.e.*, $\Gamma^2 = \Gamma_1^2 + \Gamma_2^2$.) In the general case, where neither the instrumental response function nor the sample broadening is purely a Gaussian or Lorentzian function, one can write an empirical line shape as the approximate convolution of a Gaussian and a Lorentzian, with widths given by

$$\begin{aligned}\Gamma_G &= (U\tan^2\theta + V\tan\theta + W + P/\cos^2\theta)^{1/2},\\ \Gamma_L &= X/\cos\theta + Y\tan\theta.\end{aligned} \qquad (3.2.14)$$

This is one of the flexible line-shape models available in the widely used program *GSAS* (Larson & Von Dreele, 2004). It is still possible to make a semi-quantitative statement about sample properties by comparing refined parameters against a standard sample; for example, size broadening will increase the P and X parameters, and strain will increase U and Y. A similar model is used in the *FullProf* software (Rodríguez-Carvajal, 1993, 2001; Kaduk & Reid, 2011).

3.2.3. Complications due to non-ideal sample or instrument properties

In this section, we consider various factors that modify powder X-ray diffraction data relative to the idealized situation described above.

3.2.3.1. *Absorption within a homogeneous sample*

In equations (3.2.2) and (3.2.10), it was assumed that the neither the incident nor the diffracted radiation is absorbed within the sample. However, it is generally the case that neutrons or X-rays are attenuated as they travel through any material, such that the fraction of original intensity surviving after a distance x is $I(x)/I(0) = \exp(-\mu x)$. Here μ is the linear absorption coefficient, which generally depends strongly on the composition of the sample and the X-ray wavelength.

X-ray attenuation coefficients for elements are often given as mass attenuation coefficients, μ/ρ, in units of cm^2 g^{-1}. These are available in various sources, such as *International Tables for Crystallography*, Volume C, Table 4.2.4.3, or from internet resources such as http://11bm.xray.aps.anl.gov/absorb/absorb.php. The exact positions of X-ray absorption edges can depend on the chemical environment of the atom, and so tabulated or computed atomic absorption coefficients are not entirely trustworthy within about ±100 eV of an absorption edge. The X-ray mass attenuation coefficient is related to the imaginary part of the atomic scattering factor [equation (3.2.6)] as $\mu_m = 2r_e\lambda f''/m$, where m is the atomic mass. For a compound or other mixture of elements of total density ρ in which the (dimensionless) mass fraction of element i is g_m^i, the X-ray linear absorption constant is given by

$$\mu_{\text{X-ray}} = \rho\sum_i g_m^i(\mu_m/\rho)^i.$$

In the case of neutrons used for powder diffraction, the absorption cross section is typically tabulated in barns (1 barn = 10^{-24} cm^2); see Table 4.4.4.1 in *International Tables for Crystallography*, Volume C or websites such as http://www.ncnr.nist.gov/resources/n-lengths/list.html. The neutron absorption cross section is generally inversely proportional to velocity, and values are usually tabulated for neutrons with a speed of 2200 m s^{-1} (*i.e.*, 25.3 meV kinetic energy, 1.80 Å wavelength). For neutrons, the equivalent expression with absorption cross sections depends on the number densities g_n^i (atoms/volume) of each element:

$$\mu_{\text{neutron}} = \sum_i g_n^i(\sigma_{\text{abs}}^i + \sigma_{\text{inc}}^i).$$

Considering absorption, the effective volume is given by an integral over the sample,

$$V_{\text{eff}} = \int \mathrm{d}^3\,\mathbf{R}\exp[-\mu(L_{\text{in}} + L_{\text{out}})], \qquad (3.2.15)$$

where L_{in} and L_{out} are the paths of the incident and diffracted radiation to the point $\mathbf{R}$ within the sample, respectively.

The simplest case is of a sample in the form of a flat plate, with a thickness significantly greater than $1/\mu$, in the dividing position so that the angles of incidence and diffraction from the plane of the sample are both equal to θ. Let the dimensions of the beam be W in the equatorial direction (in the diffraction plane) and H in the axial direction (parallel to the diffractometer axis, *i.e.*, perpendicular to the scattering plane) as shown in Fig. 3.2.2.

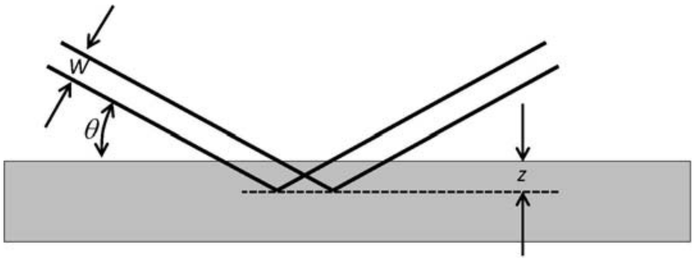

Figure 3.2.2
Sketch illustrating symmetrical diffraction from a flat sample.

Assume that the detector is large enough in the equatorial direction that all diffracted radiation is captured (*i.e.*, no loss of signal due to parallax). Radiation scattered from a volume element a distance z below the surface of the sample will have a total path length $2z/\sin\theta$; integration yields an effective sample volume of $WH/2\mu$, independent of diffraction angle. The situation is more complicated if a flat sample is not optically deep or if the sample is shorter than $W/\sin\theta$; in either case, computation of the effective volume is straightforward, as long as the sample geometry is known with sufficient accuracy. The calculations are described in detail in Chapter 5.4 of this volume.

Another important case is that of a cylindrical sample, such as a Lindemann capillary for X-rays or a can of appropriate material (often vanadium) for neutrons. The integration for $V_{\rm eff}$ above is given in convenient form for computation by Ida (2010), and is tabulated in *International Tables for Crystallography*, Volume C, Section 6.3.3.2. In the case of monochromatic radiation (neutrons or X-rays), for a given absorption constant μ, $V_{\rm eff}$ is an increasing function of diffraction angle 2θ so that higher-angle peaks will appear relatively stronger. Weak-to-moderate absorption from a cylindrical sample affects the observed intensities in essentially the same algebraic form as a negative effective Debye–Waller factor (Hewat, 1979), leading to significantly underestimated (perhaps even negative) measured Debye–Waller factors. In the case of pulsed neutrons, the effect is compounded by the fact that the absorption cross section is generally inversely proportional to the neutron velocity; consequently, in a given detector, faster neutrons, representing larger $|\mathbf{G}|$, will suffer less attenuation in the sample.

3.2.3.2. *Absorption with multiphase samples*

One important application of powder diffraction is the quantitative analysis of mixtures. Quantitative phase analysis is covered in detail in Chapter 3.9 of this volume; here we set the stage. If a sample is a mixture of several phases, the powder-diffraction pattern will be the sum of the patterns of each phase, weighted by the fraction of the illuminated volume occupied by that phase. The most common configuration for quantitative analysis by X-ray diffraction is reflection from an optically deep flat-plate sample. In this case, the integrated intensity of a particular reflection from the jth phase is

$$I_{hkl}(j) = I_0 LP(\theta)\frac{m_{hkl}(j)|A_{hkl}(j)|^2}{V^2(j)}\frac{w_m(j)}{\rho(j)\overline{\mu}}, \qquad (3.2.16)$$

where $V(j)$, $w_m(j)$ and $\rho(j)$ are the unit-cell volumes, mass fraction and density of phase j, respectively. Here I_0 is an overall intensity scale factor, $LP(\theta)$ is the Lorentz and polarization factor common to all phases, and $\bar{\mu} = \sum_j w_m(j)\mu(j)$ is the absorption coefficient of all solid phases in the sample. The summation includes all solid phases, even amorphous materials.

Note that the intensity of peaks from a particular phase is not simply proportional to the fraction of that phase present. For example, if there are two phases A and B, the intensity of A peaks will be proportional to

$$\frac{w_m(A)}{w_m(A)[\mu(A)-\mu(B)]+\mu(B)}.$$

3.2.3.3. *Granularity, microabsorption and surface roughness*

The above discussion of absorption in a powder sample is premised on the assumption that the powder sample is sufficiently fine that the beam traverses a large number of grains, *i.e.*, that $\mu\ell \ll 1$, where μ is the absorption coefficient in the solid material and ℓ is a characteristic linear grain dimension. In that case, the effective linear absorption constant is $\bar{\mu} = \mu\rho_{\rm powder}/\rho_{\rm solid}$, independent of the path that the radiation follows through the sample. However, if $\mu\ell$ is not very small, the simple picture of an average absorption length in the sample breaks down, leading to changes in the diffracted intensity.

There have been several treatments of microabsorption due to porosity and surface roughness. Rather than reviewing the literature, this section summarizes work of Hermann & Ermrich (1987) on a flat sample in the symmetrical reflection geometry discussed above. The single-phase sample is taken to be a collection of random polyhedra of average chord length ℓ with packing fraction α_0. The surface has the same lateral correlation length, but the average packing fraction rises from zero at the surface with characteristic dimension t_s, *i.e.*, $\alpha(z) = \alpha_0[1-\exp(-z/t_s)]$, where z is the distance from the surface into the sample. $t_s = 0$ represents an abrupt termination of the bulk porous material.

Hermann & Ermrich find that the diffracted intensity is reduced from the fine powder limit by a factor of $1 - P_{\rm bulk} - P_{\rm surface}$, where

$$\begin{aligned}P_{\rm bulk} &\simeq 2\mu\ell(1-\alpha_0)^2,\\ P_{\rm surface} &\simeq \frac{2\mu\alpha_0 t_s}{\sin\theta}\left(1-\frac{t_s}{\ell(1-\alpha_0)\sin\theta}\right).\end{aligned}$$

If surface roughness is small, there is no dependence on diffraction angle 2θ, and the only effect is an overall reduction of diffracted intensity. Excess surface roughness ($t_s > 0$), as might be produced by allowing a granular powder to settle against a flat surface, leads to additional diminution of diffracted intensity at low angles. The expression for $P_{\rm surface}$ given above is to leading order in $1/\sin\theta$, and is therefore not valid for small grazing angles of incidence. Note that both the surface and bulk correction factors approach zero as $\mu\ell \to 0$. This analysis is in general agreement with analysis and measurements performed by Suortti (1972).

An additional effect of microabsorption in multi-component powders has been considered by Brindley (1945). The principle is illustrated in Fig. 3.2.3. An X-ray propagating through the sample (depicted by the broken line) suffers absorption according to the weighted average $\bar{\mu}$, but an X-ray diffracted in a grain of phase a has travelled further in that phase than average (solid line). If its path in the diffracting grain is x and the total path through the sample is L, absorption will reduce its intensity by a factor

$$\exp(-\mu_a x)\exp[-\overline{\mu}(L-x)].$$

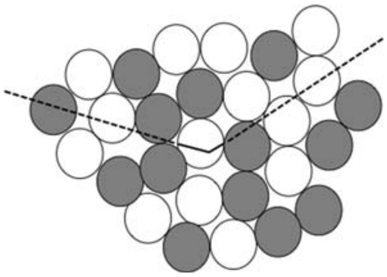

Figure 3.2.3
Sketch illustrating an X-ray propagating through a mixture of two kinds of particles.

This leads to a weaker observed reflection from a phase a with larger absorption constant μ_a if the particle size is an appreciable fraction of $1/(\mu_a - \bar{\mu})$.

Averaging over the particle volume, we see that the observed intensity of phase a will be lowered from its value in a fine powder by a factor

$$\tau = V_a^{-1} \int \exp[-(\mu_a - \overline{\mu})x]\,\mathrm{d}V_a,$$

where the integral is taken over one representative grain of phase a. This is exactly the integral of equation (3.2.15), and if one assumes monodisperse spherical particles, it is tabulated in *International Tables for Crystallography*, Volume C, Section 6.3.3.2 and elsewhere, with $\mu_a - \bar{\mu}$ replacing μ. One hitch is that the tabulations are for $\mu > 0$, whereas $\mu_a - \bar{\mu} < 0$ for the less absorbing phases in a mixture. Brindley handles this with a series expansion and provides a table of τ *versus* $(\mu_a - \bar{\mu})R$.

By way of illustration, consider a mixture of equal weight fractions of corundum, magnetite and zircon powders, analysed with Cu $K\alpha$ radiation. Fig. 3.2.4 shows the weight fractions that would be measured from such a sample as a function of particle radius (assumed equal for all three phases). In this case, microabsorption biases the result by about 10% for particles of 10 µm diameter, and misses by a factor of two if the diameter is 70 µm.

In considering microabsorption, there are several important points to note. This entire analysis is only valid for $\mu R \ll 1$, since otherwise the concept of an average absorption length becomes ill defined. That means that the Brindley analysis breaks down precisely when it becomes significant. Of course, the Brindley assumption of monodisperse spherical particles is unrealistic for most real samples. Both the surface roughness and Brindley corrections depend on diffraction angle as well as μR, but, as noted above, for moderate absorption, the angle dependence appears as an effective Debye–Waller factor. The parameter R is the radius of the grain of material, which is commonly very much larger than the size of a coherently diffracting region; a Scherrer analysis of particle size through line broadening does not provide a useful estimate of R. Most importantly, unless one has an accurate independent measurement of the size and shape of the grains, microabsorption corrections should be taken as a sign of impending trouble, not a quantitative correction.

3.2.3.4. *Anisotropic strain broadening*

Strain broadening is often observed not to be monotonically dependent on the magnitude of the d-spacing, but to have a more complicated dependence on the direction of the diffraction vector **G**. An illustration of the effect in cubic Rb_3C_{60} is shown in Fig. 3.2.5 (Stephens, 1999). The lower part of the figure shows an apparently irregular trend of diffraction peak widths on diffraction angle 2θ.

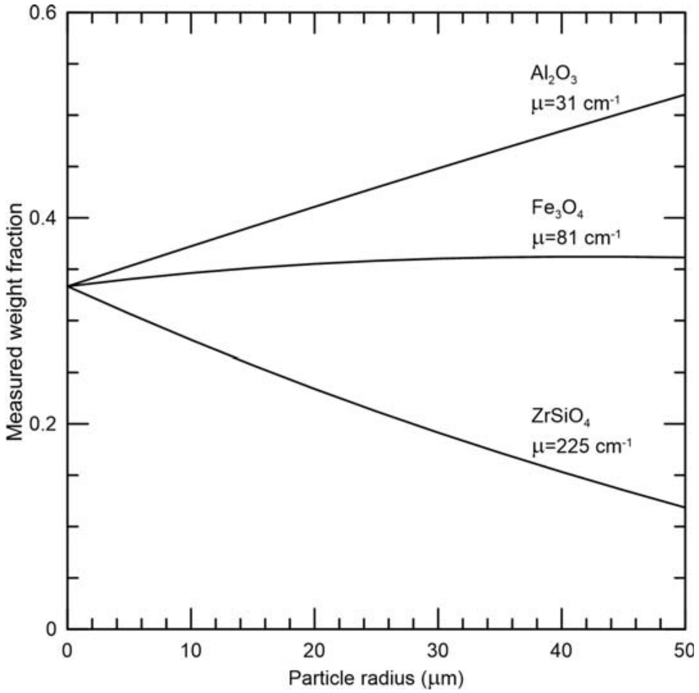

Figure 3.2.4
Weight fractions that would be measured from a mixture of equal parts of three phases with Cu $K\alpha$ radiation.

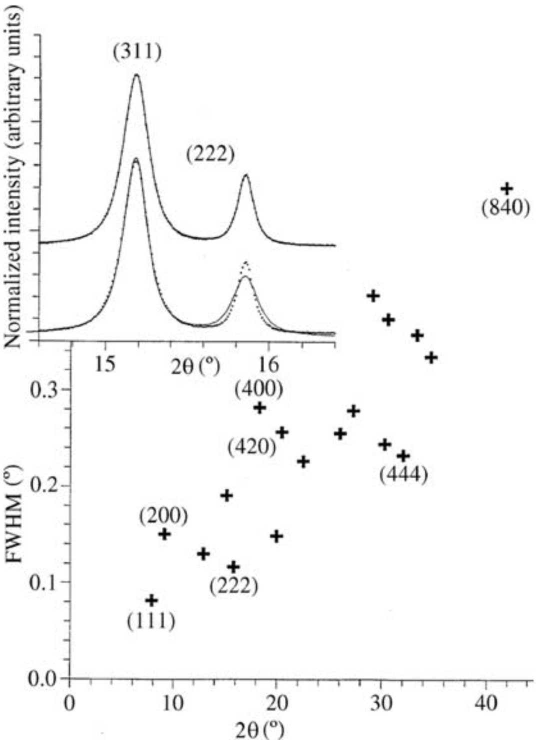

Figure 3.2.5
Diffraction peak width *versus* diffraction angle from a powder pattern of face-centred cubic Rb_3C_{60} (Stephens, 1999). The inset at the top shows a limited range of the data, fitted by a model with two different peak widths (upper trace) and with the widths constrained to be equal (lower trace).

Whatever the nature of random internal stresses and strains, it can be argued on general grounds that strain broadening depends on a combination of fourth-rank tensors. On the assumption that the distribution of random strains is Gaussian, each diffraction peak has Gaussian shape, and the variance of the inverse d-spacing squared is a quartic form in the reflection indices (hkl). This can be expressed as

$$\sigma^2 = \langle d_{hkl}^{-4} \rangle - \langle d_{hkl}^{-2} \rangle^{-2} = \sum_{HKL} S_{HKL} h^H k^K l^L, \qquad (3.2.17)$$

where the sum is over terms with $H + K + L = 4$. This leads to a contribution to the width of a diffraction peak proportional to $\Gamma_{2\theta} = d^2 \sqrt{\sigma^2} \tan \theta$ for angle-dispersive measurements, and $\Gamma_t = t d^2 \sqrt{\sigma^2}$ for time-of-flight neutron measurements. Strain broadening in real samples frequently leads to peak shapes that are closer to Lorentzian than Gaussian, and the justification of this expression breaks down because the second moment of the distribution of d^{-2} is then not defined. Nevertheless, this method is often successful at modelling the phenomenology of anisotropic peak broadening.

The parameters S_{HKL} arise from the nature of the strain and the values of elastic constants for any particular sample. Typically, they must therefore be regarded as phenomenological, and can be adjusted in fitting a model to observed data. They are constrained by the symmetry of the Laue group of the sample, which leads to restrictions on the S_{HKL} terms for the various Laue classes, listed in Table 3.2.1 (Popa, 1998).

Table 3.2.1
Restrictions and reflections of anisotropic strain parameters for the various Laue classes

$\bar{3}, \bar{3}m1, \bar{3}1m$: hexagonal indices.

Class	$\langle 1/d^2 \rangle^2$
$\bar{1}$	$S_{400}h^4 + S_{040}k^4 + S_{004}l^4 + S_{220}h^2k^2 + S_{202}h^2l^2$ $+ S_{022}k^2l^2 + S_{310}h^3k + S_{130}hl^3 + S_{301}h^3l + S_{103}hl^3$ $+ S_{031}k^3l + S_{013}kl^3 + S_{211}h^2kl + S_{121}hk^2l + S_{112}hkl^2$
2/*m* (*b*-axis unique)	$S_{400}h^4 + S_{040}k^4 + S_{004}l^4 + S_{220}h^2k^2 + S_{202}h^2l^2$ $+ S_{022}k^2l^2 + S_{301}h^3l + S_{103}hl^3 + S_{121}hk^2l$
2/*mmm*	$S_{400}h^4 + S_{040}k^4 + S_{004}l^4 + S_{220}h^2k^2 + S_{202}h^2l^2 + S_{022}k^2l^2$
4/*m*	$S_{400}(h^4 + k^4) + S_{004}l^4 + S_{220}h^2k^2 + S_{202}(h^2 + k^2)l^2$ $+ S_{310}(h^3k - hk^3)$
4/*mmm*	$S_{400}(h^4 + k^4) + S_{004}l^4 + S_{220}h^2k^2 + S_{202}(h^2 + k^2)l^2$
$\bar{3}$	$S_{400}(h^2 + k^2 + hk)^2 + S_{202}(h^2 + k^2 + hk)l^2 + S_{004}l^4$ $+ S_{211}(h^3 - k^3 + 3h^2k)l + S_{121}(-h^3 + k^3 + 3hk^2)l$
$\bar{3}m1$	$S_{400}(h^2 + k^2 + hk)^2 + S_{202}(h^2 + k^2 + hk)l^2 + S_{004}l^4$ $+ S_{301}(2h^3 + 3h^2k - 3hk^2 - 2k^3)l$
$\bar{3}1m$	$S_{400}(h^2 + k^2 + hk)^2 + S_{202}(h^2 + k^2 + hk)l^2 + S_{004}l^4$ $+ S_{211}(h^2k + hk^2)l$
Hexagonal	$S_{400}(h^2 + k^2 + hk)^2 + S_{202}(h^2 + k^2 + hk)l^2 + S_{004}l^4$
Cubic	$S_{400}(h^4 + k^4 + l^4) + S_{220}(h^2k^2 + h^2l^2 + k^2l^2)$

3.2.3.5. *Preferred orientation (texture)*

The discussion of diffraction-peak intensities in Section 3.2.2.2 above presumes that the sample is a random powder, with every orientation equally probable. Real samples frequently exhibit some deviation from that ideal case, perhaps because of the way that grains of platy or acicular (needle-like) habit settle into a sample holder, or because a solid polycrystalline sample crystallized or grew anisotropically, or was formed or worked as a solid. The latter case is generally called texture, and can provide a fruitful basis for understanding the history or mechanical properties of a sample. The topic is further discussed in Chapter 5.3 of this volume. For the present purposes, deviation from a collection of randomly oriented grains will be regarded as an artifact to be minimized and/or modelled.

The distribution of orientations of crystallites in a sample can be studied using pole figures. For a given reflection **G**, the pole figure is defined as the probability density over a spherical surface that **G** falls in a particular direction relative to the sample. For a random powder, all pole figures would be uniform; for a single crystal, each pole figure would be a set of delta functions. Modelling of preferred orientation in the sample is accomplished by multiplying the theoretical intensity by the pole-figure density in the direction of the diffraction vector. Here we discuss two different treatments of preferred orientation.

The symmetrized spherical-harmonic approach follows Järvinen (1993), considering samples that are axially symmetric about some axis **P**. Experimentally, this can be ensured by rotating the sample about **P** during data collection. Take α to be the angle between **P** and the diffraction vector: α is zero for a conventional symmetrical flat plate and 90° for Debye–Scherrer geometry.

For a given reflection *hkl*, the polar-axis density in the diffraction direction may be expanded in spherical harmonics as

$$A(hkl, \alpha) = \sum_{ij} C_{ij} Y_{ij}(\theta_{hkl}, \varphi_{hkl}) P_i(\cos \alpha),$$

where Y_{ij} and P_i are the usual spherical harmonics and Legendre polynomials, and θ_{hkl} and φ_{hkl} are the spherical coordinates of the *hkl* reflection relative to some chosen axis of the crystal.

In general, there will be several reflections equivalent to *hkl* by the Laue symmetry of the crystalline phase, and so symmetry-adapted functions should replace the spherical harmonics in the above equation. Only even orders *i* are considered, because of the inversion symmetry of diffraction (neglecting imaginary atomic scattering amplitudes). The Laue symmetry of the crystalline phase implies that certain of the harmonics are zero; see the original article by Järvinen (1993) for explicit functional forms of the harmonics and a tabulation of which are allowed for each Laue group.

The second approach considered here is the widely used March (1932)–Dollase (1986) model, which is applicable to the most common powder-diffraction sample geometries of axial symmetry either along the diffraction vector or perpendicular to the diffraction plane, for samples whose preferred orientation arises from the settling of either disc- or rod-shaped crystallites in the sample holder. The cylinder axis **H** governs the preferred orientation. For any Bragg reflection **G**, the pole density in the diffraction direction is hypothesized to be a particular function of the angle α between **H** and **G**, *viz*.

$$A(G) = (R^2 \cos^2 \alpha + \sin^2 \alpha / R)^{-3/2}.$$

Here R is a parameter describing the degree of preferred orientation; it is less than unity for maximum pole density at $\alpha = 0$, *i.e.*, $\mathbf{H} \parallel \mathbf{G}$, as would be found for disc-like samples preferentially lying in the reflection plane. $R > 1$ corresponds to maximum pole density at $\alpha = 90°$, as might be found for acicular crystallites in either a flat-plate or Debye–Scherrer geometry. The particular functional form has some theoretical justification as a model for grain rotation in settling of a granular sample, as well as being properly normalized, suitable for oblate or prolate grains with a single parameter, and in agreement with pole distributions observed in many samples. To apply this model to powder-diffraction data, one must find the appropriate axis **H**, either through prior knowledge of growth habit or by trial and error.

3.2.3.6. *Extinction*

The analysis of diffracted intensities in this chapter has been premised on the assumption that the diffracted beam produced by each crystallite is much weaker than the incident beam, known

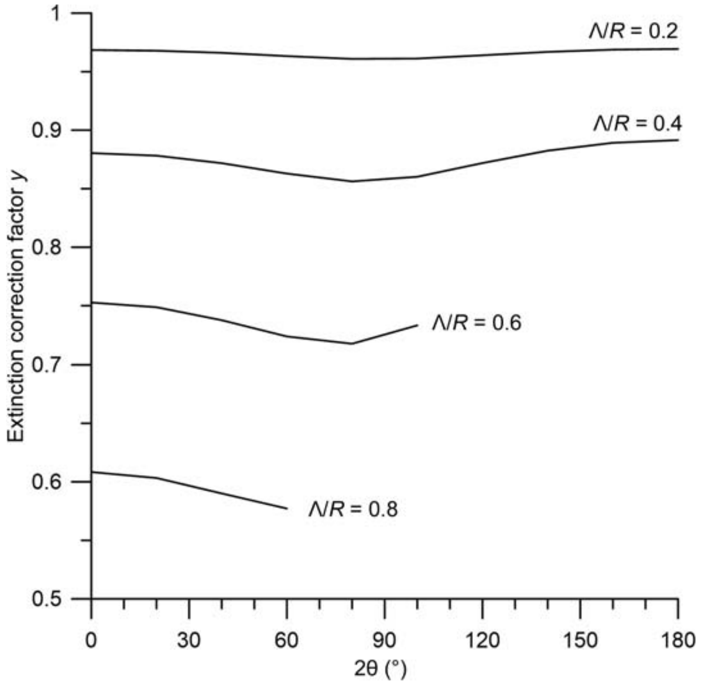

Figure 3.2.6
Extinction correction for spherical particles according to Thorkildsen & Larsen (1998).

as the kinematic approximation. This is a consequence of the Born approximation, whereby the diffracted intensity from one grain is proportional to the number of atoms within it. However, as the size of the crystallite grows, so will the intensity of the diffracted wave within it. The diffracted radiation will be re-diffracted back into the incident beam, leading to a measured integrated intensity less than the kinematic value, by a ratio $y(\mathbf{G}) = I_{\rm obs}(\mathbf{G})/I_{\rm kinematic}(\mathbf{G})$, which depends on the particular Bragg reflection **G**. This is the phenomenon of primary extinction, which can be understood within the framework of the dynamical theory of diffraction. The following discussion ignores absorption.

The relevant physical parameter is the extinction length Λ. For X-rays,

$$\Lambda(\mathbf{G}) = \frac{V}{r_e \lambda P |A_{\mathbf{G}}|},$$

where V is the unit-cell volume, $r_e = 2.82 \times 10^{-15}$ m, $A_{\mathbf{G}}$ is the structure factor, and P is the polarization factor: 1 or $\cos^2 2\theta$ for S or P polarization, respectively. For neutrons,

$$\Lambda(\mathbf{G}) = \frac{V}{\lambda |A^{(n)}_{\mathbf{G}}|}.$$

As an example, the 111 reflection of Si has an extinction length of 7.2 µm for 1.54 Å X-rays and 50 µm for 1.59 Å neutrons. Intensities from the kinematic theory are correct in the limit that the coherent grain size is much less than Λ. Note that extinction is most significant for the strongest reflections in a powder-diffraction pattern.

There are no exact calculations of extinction available for sample geometries applicable to powder samples, but Thorkildsen and Larsen have obtained a rigorous series solution for spherical particles of radius R in powers of Λ/R (Thorkildsen & Larsen, 1998). To lowest order,

$$\begin{aligned} y &= 1 - (R/\Lambda)^2 f_1(\theta), \text{ where} \\ f_1(\theta) &= \frac{8}{5\pi \sin 2\theta}(1 + \pi\theta - 4\theta^2 - \cos 4\theta - \theta \sin 4\theta) \\ &\quad \text{for } 0 \le \theta \le \pi/4 \\ &= \frac{4}{5\pi \sin 2\theta}(2 - \pi^2 + 6\pi\theta - 8\theta^2 - 2\cos 4\theta + \pi \sin 4\theta \\ &\quad - 2\theta \sin 4\theta) \text{ for } \pi/4 \le \theta \le \pi/2. \end{aligned}$$

This first term gives y accurate to 3% for $R/\Lambda \le 0.4$. Fig. 3.2.6 shows their calculated result up to fifth order.

3.2.4. The Debye scattering equation

The Debye scattering equation is an alternative method to compute the diffraction pattern of a collection of solid grains, which does not rely on a requirement of crystalline periodicity (Debye, 1915). Consequently, it is useful for cases where the grains of the sample are not fragments of idealized crystals, such as are frequently observed in nanoparticles. For a collection of identical grains, each containing N atoms having individual scattering amplitude b_j, $1 \le j \le N$, the orientation-average cross section per grain is given by

$$\left\langle \frac{{\rm d}\sigma}{{\rm d}\Omega} \right\rangle_{\rm orientation} = \sum_j^N b_j^2 + \sum_j^N \sum_{k \ne j}^N b_j b_k \frac{\sin(2\pi q r_{ij})}{2\pi q r_{ij}},$$

where r_{jk} is the distance between atoms j and k, and the scattering vector $q = 2\sin\theta/\lambda$. For neutrons, b_j is the scattering length; in the case of multiple isotopes of a given atomic species, one may use the coherent scattering length to obtain the coherent elastic cross section. For X-rays, $b_j = r_e f_j(\sin\theta/\lambda)$, the classical electron radius times the atomic scattering factor, and the cross section must be multiplied by the polarization factor as described in Section 3.2.2.2.1. This topic is treated in much greater detail in Chapters 3.6, 5.6 and 5.7 of this volume.

3.2.5. Summary

Although a powder-diffraction experiment is simple experimentally, considerable physics goes into determining the actual experimental data. Any user attempting to extract the maximum information from the diffraction data (especially through a Rietveld refinement) ultimately needs to understand all of the factors that affect the experimental data. This chapter provides a succinct summary of the major factors that contribute to the experimental data. Many of these factors are explored in more detail in other chapters of this volume.

References

Bindzus, N., Straasø, T., Wahlberg, N., Becker, J., Bjerg, L., Lock, N., Dippel, A.-C. & Iversen, B. B. (2014). *Experimental determination of core electron deformation in diamond*. *Acta Cryst.* A**70**, 39–48.

Brindley, G. W. (1945). *The effect of grain or particle size on x-ray reflections from mixed powders and alloys, considered in relation to the quantitative determination of crystalline substances by x-ray methods*. *Philos. Mag.* **36**, 347–369.

Caglioti, G., Paoletti, A. T. & Ricci, F. P. (1958). *Choice of collimators for a crystal spectrometer for neutron diffraction*. *Nucl. Instrum. Methods*, **3**, 223–228.

Caglioti, G., Paoletti, A. & Ricci, F. P. (1960). *On resolution and luminosity of a neutron diffraction spectrometer for single crystal analysis*. *Nucl. Instrum. Methods*, **9**, 195–198.

Cheary, R. W. & Coelho, A. (1992). *A fundamental parameters approach to X-ray line-profile fitting*. *J. Appl. Cryst.* **25**, 109–121.

Cheary, R. W. & Coelho, A. A. (1998). *Axial divergence in a conventional X-ray powder diffractometer. I. Theoretical foundations*. *J. Appl. Cryst.* **31**, 851–861.

Coppens, P. (1997). *X-ray charge densities and chemical bonding*. Oxford: International Union of Crystallography/Oxford University Press.

Debye, P. (1915). *Zerstreuung von Röntgenstrahlen. Ann. Phys.* **351**, 809–823.

Dollase, W. A. (1986). *Correction of intensities for preferred orientation in powder diffractometry: application of the March model*. *J. Appl. Cryst.* **19**, 267–272.

Gozzo, F., De Caro, L., Giannini, C., Guagliardi, A., Schmitt, B. & Prodi, A. (2006). *The instrumental resolution function of synchrotron radiation powder diffractometers in the presence of focusing optics*. *J. Appl. Cryst.* **39**, 347–357.

Hermann, H. & Ermrich, M. (1987). *Microabsorption of X-ray intensity in randomly packed powder specimens*. *Acta Cryst.* A**43**, 401–405.

Hewat, A. W. (1979). *Absorption corrections for neutron diffraction*. *Acta Cryst.* A**35**, 248.

Ida, T. (2010). *Efficiency in the calculation of absorption corrections for cylinders*. *J. Appl. Cryst.* **43**, 1124–1125.

Järvinen, M. (1993). *Application of symmetrized harmonics expansion to correction of the preferred orientation effect*. *J. Appl. Cryst.* **26**, 525–531.

Kaduk, J. A. & Reid, J. (2011). *Typical values of Rietveld instrument profile coefficients*. *Powder Diffr.* **26**, 88–93.

Krivoglaz, M. A. (1969). *Theory of X-ray and thermal-neutron scattering by real crystals.* New York: Plenum Press. (Translated from the Russian by S. Moss.)

Langford, J. I. & Wilson, A. J. C. (1978). *Scherrer after sixty years: a survey and some new results in the determination of crystallite size*. *J. Appl. Cryst.* **11**, 102–113.

Larson, A. C. & Von Dreele, R. B. (2004). *General Structure Analysis System (GSAS)*. Los Alamos National Laboratory Report LAUR 86–748. Los Alamos, USA.

Loopstra, B. O. & Rietveld, H. M. (1969). *The structure of some alkaline-earth uranates. Acta Cryst.* B**25**, 787–791.

March, A. (1932). *Mathematische Theorie der Regelung nach der Korngestah bei affiner Deformation*. *Z. Kristallogr.* **81**, 285–297.

Marshall, W. & Lovesey, S. W. (1971). *Theory of Thermal Neutron Scattering.* Oxford: Clarendon.

Masson, O., Dooryhée, E. & Fitch, A. N. (2003). *Instrument line-profile synthesis in high-resolution synchrotron powder diffraction*. *J. Appl. Cryst.* **36**, 286–294.

Patterson, A. L. (1939). *The Scherrer formula for X-ray particle size determination*. *Phys. Rev.* **56**, 978–982.

Popa, N. C. (1998). *The (hkl) dependence of diffraction-line broadening caused by strain and size for all Laue groups in Rietveld refinement*. *J. Appl. Cryst.* **31**, 176–180.

Riello, P., Fagherazzi, G., Clemente, D. & Canton, P. (1995). *X-ray Rietveld analysis with a physically based background*. *J. Appl. Cryst.* **28**, 115–120.

Rietveld, H. M. (1969). *A profile refinement method for nuclear and magnetic structures*. *J. Appl. Cryst.* **2**, 65–71.

Rodríguez-Carvajal, J. (1993). *Recent advances in magnetic structure determination by neutron powder diffraction*. *Phys. B Condens. Matter*, **192**, 55–69.

Rodríguez-Carvajal, J. (2001). *Recent developments of the program FULLPROF. IUCr Commission on Powder Diffraction Newsletter*, **26**, 12–19.

Sabine, T. M. (1987). *The N-crystal spectrometer*. *J. Appl. Cryst.* **20**, 23–27.

Scherrer, P. (1918). *Bestimmung der Grösse und der inneren Struktur von Kolloidteilchen mittels Röntgenstrahlen. Nachr. Ges. Wiss. Göttingen*, pp. 98–100.

Smith, D. K. (2001). *Particle statistics and whole-pattern methods in quantitative X-ray powder diffraction analysis*. *Powder Diffr.* **16**, 186–191.

Soller, W. (1924). *A new precision X-ray spectrometer*. *Phys. Rev.* **24**, 158–167.

Stephens, P. W. (1999). *Phenomenological model of anisotropic peak broadening in powder diffraction*. *J. Appl. Cryst.* **32**, 281–289.

Suortti, P. (1972). *Effects of porosity and surface roughness on the X-ray intensity reflected from a powder specimen*. *J. Appl. Cryst.* **5**, 325–331.

Thompson, P., Cox, D. E. & Hastings, J. B. (1987). *Rietveld refinement of Debye–Scherrer synchrotron X-ray data from Al_2O_3*. *J. Appl. Cryst.* **20**, 79–83.

Thorkildsen, G. & Larsen, H. B. (1998). *Primary extinction in cylinders and spheres*. *Acta Cryst.* A**54**, 172–185.

International Tables for Crystallography (2019). Vol. H, Chapter 3.3, pp. 263–269.

3.3. Powder diffraction peak profiles

R. B. Von Dreele

3.3.1. Introduction

The analysis of a powder diffraction pattern usually involves the fitting of a model to the set of peaks that are found in that pattern. The desired result may be accurate peak positions to be used as input for an indexing procedure, or extraction of the suite of reflection intensities for crystal structure determination or a Rietveld refinement. In any case, a good description of the shape of the powder peak profile and how it varies across the entire pattern is of paramount importance for obtaining the highest-quality results, and this topic was briefly reviewed in Volume C of *International Tables for Crystallography* (Parrish, 1992).

The fitting is a least-squares procedure in which the model used to calculate the intensity of the profile is

$$Y(x) = \sum_j I_j P_j(\Delta) + B(x), \qquad (3.3.1)$$

where I_j is the integrated intensity of the jth peak and P is the shape function for that peak, which depends on the offset ($\Delta = x - T_j$) of its position T_j from the observation point x. The sum is over all reflections that could contribute to the profile and $B(x)$ is a background intensity function. The observed shape of the peaks arises from a convolution of the intrinsic source profile (G_λ), the various instrumental profile contributions (G_I) (*e.g.* from slits and monochromators, discussed in Chapter 3.1) and the characteristics of the sample (G_S) that broaden the idealized reciprocal-space points (see Chapter 3.6):

$$P(\Delta) = G_\lambda * G_I * G_S. \qquad (3.3.2)$$

In practice, the peak profile function is usually developed by either selecting a peak-shape function that has the required shape characteristics to fit the experimental peak profiles (the semi-empirical function approach, or SFA) or by selecting a number of contributing functions and doing the requisite convolutions (the fundamental parameters approach, or FPA) (Cheary & Coelho, 1998*b*).

Both approaches have been used for the analysis of constant-wavelength neutron and X-ray powder diffraction data and for neutron time-of-flight (energy-dispersive) powder data. In addition, the peaks can be seen to be displaced from their expected positions given by Bragg's law. As we will see, this displacement is partially a consequence of some geometric features of the experiment but is also dependent upon the particular description of the peak profile.

3.3.2. Peak profiles for constant-wavelength radiation (X-rays and neutrons)

3.3.2.1. *Introduction – symmetric peak profiles*

The realization that the neutron powder diffractometer at the Reactor Centrum Nederland, Petten, produced powder peak profiles that were Gaussian in shape led Rietveld (1967) to develop a full-pattern method for crystal structure refinement (Rietveld, 1967, 1969), now known as the Rietveld refinement method. The Gaussian is formulated as

$$\begin{aligned} P_G(\Delta, \Gamma_G \text{ or } \sigma^2) &= \frac{(8\ln 2)^{1/2}}{\Gamma_G (2\pi)^{1/2}} \exp\left(\frac{-4\ln 2\Delta^2}{\Gamma_G^2}\right) \\ &= \frac{1}{(2\pi\sigma^2)^{1/2}} \exp\left(\frac{-\Delta^2}{2\sigma^2}\right), \end{aligned} \qquad (3.3.3)$$

where the width of the peak is expressed as either the full width at half-maximum (FWHM = Γ_G) or as the variance (σ^2). Rietveld also recognized the earlier analysis of the resolution of a neutron powder diffractometer by Caglioti *et al.* (1958), who showed that the contributions from the source size, collimators and monochromator crystal mosaic spread and scattering angle could be combined analytically to give

$$\Gamma_G^2 = U\tan^2\theta + V\tan\theta + W \qquad (3.3.4)$$

with U, V and W adjustable during the Rietveld refinement. A modified form of this may have more stability in refinement (attributed to E. Prince by Young & Wiles, 1982):

$$\Gamma_G^2 = U'(\tan\theta - K_0)^2 + V'(\tan\theta - K_0) + W', \qquad (3.3.5)$$

where K_0 is arbitrarily chosen as 0.6.

Improvements in the resolution of neutron powder diffractometers and (more importantly) attempts to apply the Rietveld method to X-ray powder diffraction data required the development of new powder profile functions (Malmros & Thomas, 1977; Young *et al.*, 1977; Young & Wiles, 1982); this is because the Gaussian function [equation (3.3.3)] gave poor fits to observed peak profiles, partially because of the Lorentzian emission line profile (G_λ) from laboratory X-ray tubes. Many functions were considered, including Lorentzian ('Cauchy'), various modified Lorentzians, Pearson VII and pseudo-Voigt. Of these the last two performed (on individual peak fits) about equally well; functional forms are:

Lorentzian 'Cauchy' function

$$P_L(\Delta, \Gamma_L) = \left(\frac{\Gamma_L}{2\pi}\right)\left\{\frac{4}{\left[\Gamma_L^2 + (2\Delta)^2\right]}\right\}, \qquad (3.3.6)$$

Pearson VII function

$$P_{\rm P7}(\Delta, \xi, \mu) = \frac{\Gamma(\mu)}{\xi\Gamma\left(\mu - \frac{1}{2}\right)(\mu\pi)^{1/2}} \Big/ \left(1 + \frac{\Delta^2}{\mu\xi^2}\right)^{\mu}, \qquad (3.3.7)$$

pseudo-Voigt function

$$P_{\rm PV}(\Delta, \Gamma, \eta) = \eta P_L(\Delta, \Gamma) + (1 - \eta) P_G(\Delta, \Gamma), \qquad (3.3.8)$$

where Γ_L is the FWHM of the Lorentzian peak and $\Gamma(\mu)$ in the Pearson VII function is the Gamma function; μ may vary between 0 and ∞, and μ is the half width at $(1 + 1/\mu)^{-\mu}$ of the peak height (David, 1986); $P_{\rm P7}(\Delta, \Gamma, 1) \simeq P_L(\Delta, \Gamma)$ and $P_{\rm P7}(\Delta, \Gamma, \infty) \simeq P_G(\Delta, \Gamma)$. Although the Pearson VII function performs well in individual peak fits, it is of little use for Rietveld refinements because of the difficulty in relating its coefficients to physically meaningful characteristics of the sample and will not be considered further in this discussion.

Copyright © 2019 International Union of Crystallography

The pseudo-Voigt function is an approximation to the Voigt function, which is the convolution of a Gaussian and a Lorentzian:

Voigt function

$$P_V(\Delta, \Gamma_L, \Gamma_G) = \int\limits_{-\infty}^{\infty} P_L(\Delta, \Gamma_l) P_G(\Delta - \delta, \Gamma_G)\, \mathrm{d}\delta$$
$$= \left(\frac{4 \ln 2}{\pi \Gamma_G^2}\right)^{1/2} \mathrm{Re}[\exp(-z^2) \mathrm{erfc}(-iz)], \qquad (3.3.9)$$

where $z = \alpha + i\beta$, $\alpha = (4 \ln 2)^{1/2} \Delta/\Gamma_G$ and $\beta = (\ln 2)^{1/2} \Gamma_L/\Gamma_G$.

A number of formulations have been proposed for the pseudo-Voigt coefficients to make the best fit to the corresponding Voigt function (Hastings *et al.*, 1984; David, 1986; Thompson *et al.*, 1987). The latter is most commonly used and gives overall the FWHM, Γ and the mixing coefficient, η, to be used in equation (3.3.8) as functions of the individual FWHMs Γ_G and Γ_L:

$$\Gamma = [(\Gamma_G^5 + 2.69269\Gamma_G^4\Gamma_L + 2.42843\Gamma_G^3\Gamma_L^2 + 4.47163\Gamma_G^2\Gamma_L^3 + 0.07842\Gamma_G\Gamma_L^4 + \Gamma_L^5)]^{1/5}, \qquad (3.3.10)$$

$$\eta = 1.36603(\Gamma_L/\Gamma) - 0.47719(\Gamma_L/\Gamma)^2 + 0.11116(\Gamma_L/\Gamma)^3. \qquad (3.3.11)$$

The alternative given by David (1986) uses a more generalized version of the pseudo-Voigt function,

$$\begin{aligned}
P_{\rm PV}(\Delta, W_G, W_L, \eta_G, \eta_L) &= \eta_L P_L(\Delta, W_L) + \eta_G P_G(\Delta, W_G),\\
\eta_G &= 0.00268\rho_1 + 0.75458\rho_1^2 + 2.88898\rho_1^3 - 3.85144\rho_1^4\\
&\quad - 0.55765\rho_1^5 + 3.03824\rho_1^6 - 1.27539\rho_1^7,\\
\eta_L &= 1.35248\rho_2 + 0.41168\rho_2^2 - 2.18731\rho_2^3 + 6.42452\rho_2^4\\
&\quad - 10.29036\rho_2^5 + 6.88093\rho_2^6 - 1.59194\rho_2^7,\\
W_G &= \Gamma(1 - 0.50734\rho_2 - 0.22744\rho_2^2 + 1.63804\rho_2^3\\
&\quad - 2.28532\rho_2^4 + 1.31943\rho_2^5),\\
W_L &= \Gamma(1 - 0.99725\rho_1 + 1.14594\rho_1^2 + 2.56150\rho_1^3\\
&\quad - 6.52088\rho_1^4 + 5.82647\rho_1^5 - 1.91086\rho_1^6),
\end{aligned} \qquad (3.3.12)$$

where $\Gamma = \Gamma_G + \Gamma_L$, $\rho_1 = \Gamma_G/\Gamma$ and $\rho_2 = \Gamma_L/\Gamma$; this is claimed to match the Voigt function to better than 0.3%.

3.3.2.2. *Constant-wavelength powder profile asymmetry*

Rietveld (1969) noted that at very low scattering angles the peaks displayed some asymmetry, which shifted the peak maximum to lower angles. He ascribed the effect to 'vertical divergence' and proposed a purely empirical correction for it. Subsequent authors (Cooper & Sayer, 1975; Howard, 1982; Hastings *et al.*, 1984) offered semi-empirical treatments of the profile shape that results from the intersection of a Debye–Scherrer cone with a finite receiving slit, which is described as 'axial divergence'. A more complete analysis of the problem in neutron powder diffraction was offered by van Laar & Yelon (1984), who considered the effect of a finite vertical slit ($2H$) intercepting a set of Bragg diffraction cones generated from a finite sample length ($2S$) within the incident beam for a goniometer radius (L). As seen in Fig. 3.3.1, this gives peak intensity beginning at $2\varphi_{\rm min} < 2\theta$ *via* scattering from only the ends of the sample; at $2\varphi_{\rm infl}$ the entire sample scatters into the detector. The resulting intensity profile is then convoluted with a Gaussian function to give the resulting asymmetric powder line profile (Fig. 3.3.2). This approach was then considered by Finger *et al.* (1994) for synchrotron powder diffraction and they created a Fortran code that was subsequently adopted *via* convolution with a pseudo-Voigt function [equation (3.3.12)] for use by many Rietveld refinement codes. Although originally formulated for parallel-beam neutron optics, it was shown by Finger *et al.* (1994) that it could be equally well applied to diverging X-ray and neutron optics by allowing the sample length to vary during the Rietveld refinement. They also showed that it could be applied to the asymmetry observed at low angles with Bragg–Brentano instrumentation. In that case the detector height is defined by the diffracted-beam Soller slits.

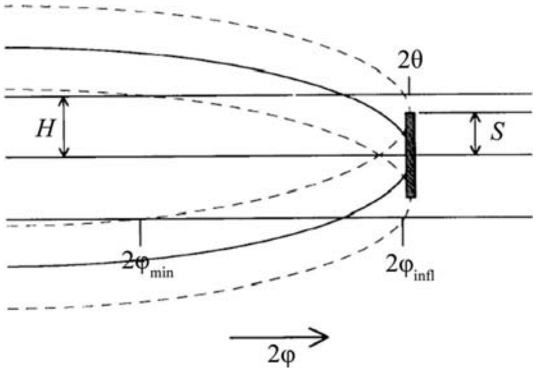

Figure 3.3.1
The band of intensity diffracted by a sample with height $2S$, as seen by a detector with opening $2H$ and a detector angle 2φ moving in the detector cylinder. For angles below $2\varphi_{\rm min}$ no intensity is seen. For angles between $2\varphi_{\rm infl}$ and 2θ, scattering from the entire sample can be seen by the detector. Figure and caption adapted from Finger *et al.* (1994).

Clearly, this asymmetric peak-shape function properly represents the offset of the peak top from the peak position, in contrast to functions such as the split Pearson VII function. Consequently, single peak fits using this function will give peak positions that are more readily indexed using methods such as those described in Chapter 3.4.

3.3.2.3. *Peak-displacement effects*

The position of the peak is also affected by various instrumental and geometric effects. For example, the sample position in a Bragg–Brentano experiment is ideally tangent to the focusing circle (Parrish, 1992). A radial displacement, *s*, of the sample will shift the Bragg peaks according to

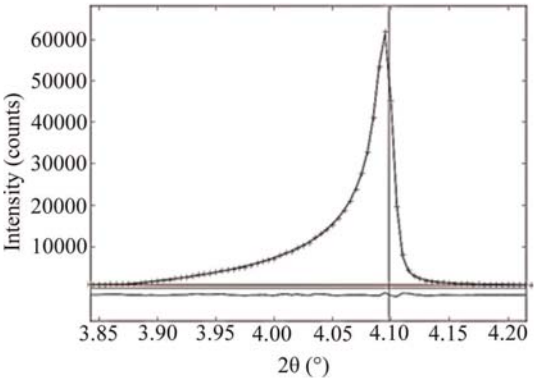

Figure 3.3.2
Low-angle synchrotron powder diffraction line ($2\theta \simeq 4.1°$) fitted by the Finger *et al.* (1994) axial divergence powder line-shape function. The observed points (+), calculated curve, background and difference curves are shown. Note the offset of the peak top from the Bragg 2θ position (vertical line).

$$\Delta 2\theta = 360 s \cos\theta / \pi R, \qquad (3.3.13)$$

where R is the goniometer radius. This is the major peak-displacement effect and can be detected for sample displacements as small as 10 µm.

A similar effect can be observed for Debye–Scherrer instrumentation when the goniometer axis is not coincident with the sample axis; this is a more common problem for neutron powder diffraction instruments where accurate placement of very massive goniometers can be difficult. In this case the peak displacement is

$$\Delta 2\theta = \frac{180}{\pi R}(s_x \cos 2\theta + s_y \sin 2\theta), \qquad (3.3.14)$$

where s_x and s_y are displacements perpendicular and parallel to the incident beam, respectively, all in the diffraction plane.

In high-resolution instrumentation (even at a synchrotron) goniometer axis displacements less than 10 µm can be detected.

Specimen transparency in Bragg–Brentano diffraction can also cause peak displacements arising from the shift in effective sample position to below the surface at high scattering angles. This shift for a thick specimen is

$$\Delta 2\theta = 90 \sin 2\theta / \mu_{\rm eff} \pi R, \qquad (3.3.15)$$

where $\mu_{\rm eff}$ is the effective sample absorption coefficient taking into account the packing density.

3.3.2.4. *Fundamental parameters profile modelling*

An alternative method for describing the source and instrumental part of the powder peak profile is to develop a set of individual functions that form the part of the profile arising from each of the instrumental components that shape the beam profile (Cheary & Coelho, 1992, 1998*a*,*b*). Ideally, each function is parameterized in terms of the physical parameters of the corresponding instrument component (*e.g.* slit width and height, sample dimensions and absorption, source size and emission characteristics, *etc.*), which are known from direct measurement. The set of functions are then convoluted *via* fast mathematical procedures to produce a line profile that matches the observed one. Any remaining profile-broadening parameters (*e.g.* for sample crystallite size and microstrain, see Section 3.3.5 for details) are then allowed to adjust during a Rietveld refinement. By employing this fundamental parameters (FP) approach, these parameters are unaffected by any instrumental parameterization.

The FP method offers two clear advantages over the more empirical approach outlined in Sections 3.3.2.1–3.3.2.3 above: (i) it can more closely describe the actual instrumental effects that contribute to the profile shape, thus improving the precision of the fit to the observed data and (ii) it can be used to describe a source characteristic or an instrumental arrangement that is outside the normally used configuration, yielding a result that would be difficult to obtain otherwise (Cheary *et al.*, 2004).

3.3.3. Peak profiles for neutron time-of-flight experiments

3.3.3.1. *The experiment*

The neutron source in a time-of-flight (TOF) powder diffraction experiment produces pulses of polychromatic neutrons; these travel over the distance from the source to the sample and then to the detectors which are placed at fixed scattering angles about the sample position; the travel times are of the order of 1–100 ms. This has been briefly described in Volume C of *International Tables for Crystallography* (Jorgensen *et al.*, 1992). Because neutrons of differing velocities (v) have differing wavelengths (λ) according to the de Broglie relationship ($\lambda = h/mv$) given Planck's constant (h) and the neutron mass (m), they will sort themselves out in their time of arrival at the detector. The powder pattern appears as a function of TOF *via* Bragg's law ($\lambda = 2d\sin\theta$) in which the wavelength is varied and θ is fixed. The approximate relationship between TOF, wavelength and d-spacing observed in a particular detector can be derived from the de Broglie relationship and Bragg's law to give

$$\mathrm{TOF} = 252.7784 L\lambda = 505.5568 L d \sin\theta. \qquad (3.3.16)$$

The constants are such that given λ in ångströms and the total neutron flight path length L in metres, then the TOF will be in µs. An analysis of the possible variances in these components then gives an estimate of the powder diffraction peak widths:

$$\Delta d/d = [(\Delta t/t)^2 + (\Delta\theta \cot\theta)^2 + (\Delta L/L)^2]^{1/2}, \qquad (3.3.17)$$

where Δd, Δt, $\Delta\theta$ and ΔL are, respectively, the uncertainties in d-spacing, TOF, scattering angle θ and total flight path L (Jorgensen & Rotella, 1982). Consequently, these three terms also determine the instrumental contribution to the neutron TOF powder peak profile.

3.3.3.2. *The neutron pulse shape*

The neutron pulse shape depends on the mode of production. Early studies (Buras & Holas, 1968; Turberfield, 1970) used one or more choppers to define a polychromatic pulse from a reactor source, resulting in essentially Gaussian powder peak profiles whose FWHM (Γ_G) is nearly constant ($B \simeq 0$):

$$\Gamma_G^2 = A + Bd^2, \qquad (3.3.18)$$

so that the Rietveld technique can easily be used (*e.g.* Worlton *et al.*, 1976). Unfortunately, this approach gave very low intensities and relatively low resolution powder patterns.

A more useful approach uses a spallation source to produce the pulsed neutron beam. Neutrons are produced when a high-energy proton beam (>500 MeV) strikes a heavy metal target (usually W, U or liquid Hg) *via* a spallation process (Carpenter *et al.*, 1984). These very high energy neutrons strike small containers of moderating material (usually H_2O, liquid CH_4 or liquid H_2) which then comprise the neutron source seen by the powder diffraction instrument. The entire target/moderator system is encased in a neutron-reflective material (usually Be) to enhance the neutron flux and then further encased in a biological shield. Each moderator may be encased on the sides away from the instrument (*e.g.* powder diffractometer) in a thin neutron absorber (*e.g.* Cd or Gd) and may also contain an inner absorber layer ('poison') to sharpen the resulting pulse of thermal neutrons. These sources produce a polychromatic neutron beam that is rich in both thermal (<300 meV) and epithermal (>300 meV) neutrons. The proton pulses can have a very short duration (∼200 ns) (from a 'short-pulse' source, *e.g.* ISIS, Rutherford Laboratory, UK or LANSCE, Los Alamos National Laboratory, USA) or a much longer duration (>500 ns) (a 'long-pulse' source, *e.g.* SNS, Oak Ridge National Laboratory, USA or ESS, European Spallation Source, Sweden); the pulse repetition rate at these sources is 10–60 Hz. These characteristics are largely dictated by the proton accelerator and neutron source design. The resulting neutron pulse results from complex down-scattering and thermalization processes in the whole target/moderator assembly; it may be further shaped by choppers,

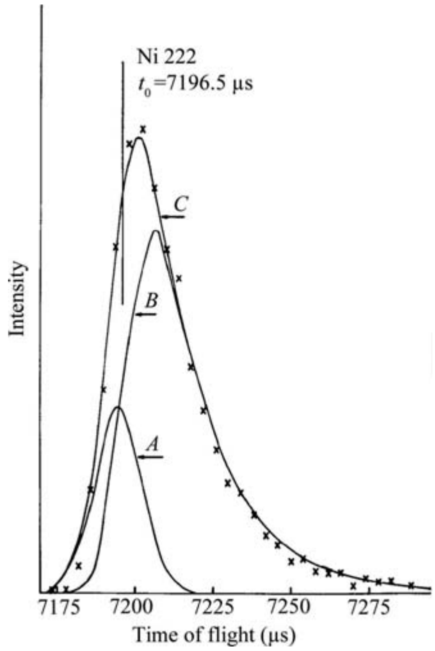

Figure 3.3.3
The observed and calculated Ni 222 diffraction line profile from the Back Scattering Spectrometer, Harwell Laboratory, Chilton, UK. The curves *A* and *B* are computed from the two terms in equation (3.3.19) and curve *C* is the sum (from Von Dreele *et al.*, 1982).

particularly for long-pulse sources, to give what is seen at the powder diffractometer.

Consequently, the neutron pulse structure from these sources has a complex and asymmetric shape, usually characterized by a very sharp rise and a slower decay, both of which are dependent on the neutron wavelength. The resulting powder diffraction peak profile (Fig. 3.3.3) is then the convolution [equation (3.3.2)] of this pulse shape (G_λ) with symmetric functions (G_I) arising from beamline components (*e.g.* slits and choppers) and the sample characteristics (G_S).

3.3.3.3. *The neutron TOF powder peak profile*

An early attempt at representing the TOF peak profile used a piecewise approach combining a leading-edge Gaussian, a peak-top Gaussian and an exponential decay for the tail (Cole & Windsor, 1980). Although single peaks could be fitted well with this function, the variation with TOF was complex and required many arbitrary coefficients.

A more successful approach empirically represented the pulse shape by a pair of back-to-back exponentials which were then convoluted with a Gaussian (Jorgensen *et al.*, 1978; Von Dreele *et al.*, 1982) to give

$$P(\Delta) = \frac{\alpha\beta}{\alpha+\beta}\left\{\exp\left[\frac{\alpha}{2}(\alpha\sigma^2+2\Delta)\right]\operatorname{erfc}\left[\frac{\alpha\sigma^2+\Delta}{\sigma(2^{1/2})}\right] + \exp\left[\frac{\beta}{2}(\beta\sigma^2-2\Delta)\right]\operatorname{erfc}\left[\frac{\beta\sigma^2-\Delta}{\sigma(2^{1/2})}\right]\right\}, \tag{3.3.19}$$

where α and β are, respectively, the coefficients for the exponential rise and decay functions; erfc is the complementary error function. Analysis of the data that were available then gave empirical relations for α, β and σ as

$$\alpha = \alpha_1/d; \quad \beta = \beta_0 + (\beta_1/d^4); \quad \sigma = \sigma_1 d. \tag{3.3.20}$$

The two terms in this function are shown in Fig. 3.3.3. The junction of the two exponentials defines the peak position (shown as a vertical line in Fig. 3.3.3); it is offset to the low side of the peak maximum. This arbitrary choice of peak position then affects the relationship between the TOF and reflection d-spacing; an empirical relationship (Von Dreele *et al.*, 1982) was found to suffice:

$$\mathrm{TOF} = Cd + Ad^2 + Z, \tag{3.3.21}$$

with three adjustable coefficients (C, A, Z) established *via* fitting to the pattern from a standard reference material.

Although this profile description was adequate for room-temperature moderators (H_2O or polyethylene) at low-power spallation sources, it does not describe well the wavelength dependence for cold moderators feeding neutron guides used at higher-power sources. An alternative description, employing a switch function to account for the fundamental change in the neutron leakage profile from the moderator between epithermal and thermal neutrons, was proposed (Ikeda & Carpenter, 1985; Robinson & Carpenter, 1990) to accommodate the profiles seen from liquid CH_4 or H_2 moderators. A drawback of this description is that the pulse profile is defined with the peak position at the low TOF edge; convolution with G_I and G_S results in a function where the peak position is far below the peak top. An empirical approach by Avdeev *et al.* (2007) simply requires tables to be established from individual peak fits to a standard material powder pattern for the values of α, β and TOF in place of the expressions given in equations (3.3.20) and (3.3.21); this establishes the G_λ and G_I contributions to the TOF line shape. More recently, some simple extensions (Toby & Von Dreele, 2013) to the empirical functions [equations (3.3.22) and (3.3.23)] appear to better cover the deviations arising from the enhanced epithermal contribution to the cold moderator spectrum:

$$\mathrm{TOF} = Cd + Ad^2 + B/d + Z, \tag{3.3.22}$$

$$\alpha = \frac{\alpha_1}{d}; \quad \beta = \beta_0 + \frac{\beta_1}{d^4} + \frac{\beta_2}{d^2}; \quad \sigma = \sigma_0 + \sigma_1 d^2 + \sigma_2 d^4 + \frac{\sigma_3}{d^2}. \tag{3.3.23}$$

3.3.4. Peak profiles for X-ray energy-dispersive experiments

In an X-ray dispersive powder diffraction experiment, a detector with good energy-discrimination capability is placed at a fixed scattering angle while the sample is illuminated by a ‘white’ beam of radiation. The detector response is binned into discrete energies by a multichannel analyser (MCA) (Glazer *et al.*, 1978). Typically these instruments display peaks that are purely Gaussian in shape with quite low resolution ($\Delta E/E \simeq 1\%$) and have widths that are proportional to the energy:

$$\Gamma_G = UE + W. \tag{3.3.24}$$

This is most useful for experiments with very limited angular access (*e.g.* high-pressure multi-anvil setups, as described in Chapter 2.7) using synchrotron radiation and can give very high data collection rates on very small samples. Glazer *et al.* (1978) showed that simple crystal structures can be modelled with the Rietveld technique after suitable corrections to account for the variation in source intensity, detector response and sample absorption effects. Otto (1997) expanded the peak-profile description to include possible sample-broadening effects *via* a Voigt profile; this extended the expression in equation (3.3.24) by adding a second-order term in energy and allowed extraction of size and microstrain sample-broadening effects in cases where these were large.

A related alternative technique (Wang *et al.*, 2004) collects multiple energy-dispersive powder patterns over a narrow and coarse angular step scan; this is easily done in a typical multi-anvil high-pressure setup. The array of spectra are binned as multiple angle-dispersive patterns which are then combined into a single refinement; the complex corrections required for pure energy-dispersive patterns reduce to refinable scaling factors. Typically a scan over 10° 2θ with 0.1–0.2° steps suffices to give suitable data; binning into $\Delta E/E \simeq 20\%$ energy bands gives data that are used in a conventional multiple-data-set Rietveld refinement.

3.3.5. Sample broadening

Very often, particularly for synchrotron-radiation experiments, the powder diffraction peak profile is dominated by broadening effects from the sample, *e.g.*

$$P(\Delta) = G_\lambda * G_I * G_S \simeq G_S. \qquad (3.3.25)$$

For the cases considered here, the focus will be on sample-broadening models that allow improved fits within the context of a Rietveld refinement; a more detailed treatment aimed at extracting sample characteristics (*e.g.* crystallite size distributions) is covered in Chapter 5.1.

Two mechanisms for sample broadening are considered here: crystallite size and 'microstrain' broadening; each will be discussed in turn.

3.3.5.1. *Crystallite size broadening*

The reciprocal space associated with an ideal large crystal will consist of a periodic array of infinitely sharp δ functions, one for each of the structure factors, as expected from the Fourier transform of the essentially infinite and periodic crystal lattice. For real crystals, this limit is reached for crystal dimensions exceeding *circa* 10 µm. The Fourier transform of a crystal lattice that is smaller than this will show a profile that follows the form described by the $\mathrm{sinc}(x) = \sin(\pi x)/\pi x$ function. Any dispersion in the crystal sizes in a powder sample will smear this into a form intermediate between a Gaussian and a Lorentzian, which is well described by either a Voigt [equation (3.3.9)], a pseudo-Voigt [equation (3.3.8)] or the less-useful Pearson VII [equation (3.3.7)] function. The physical process used to form the powder will influence the details of the size distribution; usually this will approximate a log-normal distribution and the resulting peak-shape contribution from crystallite size effects will be largely Lorentzian with a width $\Gamma_{\rm SL}$. Predominantly Gaussian size broadening can only occur if the size distribution is very tightly monodisperse. Then, for isotropic crystal dimensions this broadening is uniformly the same everywhere in reciprocal space; *e.g.* $\Delta d^* = \text{constant} \simeq 1/p$, where p is the crystallite size. Transformation *via* Bragg's law to the typical measurement of a powder pattern as a function of 2θ gives this Lorentzian width as

$$\Gamma_{pL} = \frac{180}{\pi}\frac{K\lambda}{p\cos\theta} \qquad (3.3.26)$$

expressed in degrees and the Scherrer constant, K, which depends on the shape of the crystallites; *e.g.* $K = 1$ for spheres, 0.89 for cubes *etc.* (see Table 5.1.1 in Chapter 5.1). A similar expression for the crystallite size from a neutron TOF experiment is

$$\Gamma_{pL} = \frac{CK}{p}, \qquad (3.3.27)$$

where C is defined by equation (3.3.21). In some cases the crystallites have anisotropic shapes (*e.g.* plates or needles), in which case the peak broadening will be dependent on the respective direction in reciprocal space for each reflection. Many Rietveld refinement programs implement various models for this anisotropy.

3.3.5.2. *Microstrain broadening*

The existence of imperfections (*e.g.* deformation faults) within the crystal lattice produces local distortions of the lattice and thus a broadening of the points in reciprocal space. To a first approximation these points are broadened proportionally to their distance from the origin, *e.g.* $\Delta d^*/d^* = \Delta d/d \simeq \text{constant}$.

As for crystallite size, there is normally dispersion in the density of defects and thus the peak shape will be intermediate between a Gaussian and a Lorentzian form, and it is well described by the Voigt, pseudo-Voigt or Pearson VII functions. Usually, the Lorentzian form dominates this type of broadening and it is the most common form of sample broadening in powder diffraction. It usually arises because of defects introduced during sample preparation (especially during grinding). The Lorentzian width contribution from microstrain broadening is

$$\Gamma_{sL} = \frac{180}{\pi} s \tan\theta, \qquad (3.3.28)$$

where s is the dimensionless microstrain; it is frequently multiplied by 10^6. A similar expression for neutron TOF is

$$\Gamma_{sL} = Csd, \qquad (3.3.29)$$

where C is defined by equation (3.3.21).

In many cases, the microstrain broadening is not isotropic; presumably this is a consequence of the interaction between the defects and the elastic properties of the crystals. A phenomenological description of these effects by Popa (1998) and Stephens (1999) is obtained by considering the variance of

$$\frac{1}{d^2} = M_{hkl} = \alpha_1 h^2 + \alpha_2 k^2 + \alpha_3 l^2 + \alpha_4 kl + \alpha_5 hl + \alpha_6 hk \qquad (3.3.30)$$

with respect to each of the coefficients α_i.

$$\Gamma_{sL}^2 = \sum_{i,j} S_{ij} \frac{\partial M}{\partial \alpha_i}\frac{\partial M}{\partial \alpha_j} \qquad (3.3.31)$$

where

$$\frac{\partial M}{\partial \alpha_i}\frac{\partial M}{\partial \alpha_j} = \begin{bmatrix} h^4 & h^2k^2 & h^2l^2 & h^2kl & h^3l & h^3k \\ h^2k^2 & k^4 & k^2l^2 & k^3l & hk^2l & hk^3 \\ h^2l^2 & k^2l^2 & l^4 & kl^3 & hl^3 & hkl^2 \\ h^2kl & k^3l & kl^3 & k^2l^2 & hkl^2 & hk^2l \\ h^3l & hk^2l & hl^3 & hkl^2 & h^2l^2 & h^2kl \\ h^3k & hk^3 & hkl^2 & hk^2l & h^2kl & h^2k^2 \end{bmatrix}. \qquad (3.3.32)$$

Examination of this sum for the triclinic case collects terms to give

$$\begin{aligned} \Gamma_{sL}^2 = {} & S_{400}h^4 + S_{040}k^4 + S_{004}l^4 + 3(S_{220}h^2k^2 + S_{202}h^2l^2 + S_{022}k^2l^2) \\ & + 2(S_{310}h^3k + S_{103}hl^3 + S_{031}k^3l + S_{130}hk^3 + S_{301}h^3l + S_{013}kl^3) \\ & + 4(S_{211}h^2kl + S_{121}hk^2l + S_{112}hkl^2) \qquad (3.3.33) \end{aligned}$$

with 15 coefficients S_{hkl}. The subscript hkl in S_{hkl} refers to the powers used for h, k, l in equations (3.3.33)–(3.3.44).

For Laue symmetries other than triclinic, there are restrictions on the allowed S_{hkl} terms and, as a practical matter, additional equivalences from symmetry-forced reflection overlaps for trigonal and tetragonal Laue symmetries.

Monoclinic ($2/m$, b axis unique; others similar, nine coefficients):

$$\begin{aligned}\Gamma^2_{sL} &= S_{400}h^4 + S_{040}k^4 + S_{004}l^4 + 3S_{202}h^2l^2 \\ &\quad + 3(S_{220}h^2k^2 + S_{022}k^2l^2) + 2(S_{301}h^3l + S_{103}hl^3) \\ &\quad + 4S_{121}hk^2l. \end{aligned} \tag{3.3.34}$$

Orthorhombic (mmm, six coefficients):

$$\Gamma^2_{sL} = S_{400}h^4 + S_{040}k^4 + S_{004}l^4 + 3(S_{220}h^2k^2 + S_{202}h^2l^2 + S_{022}k^2l^2). \tag{3.3.35}$$

Tetragonal ($4/m$, five coefficients):

$$\begin{aligned}\Gamma^2_{sL} &= S_{400}(h^4 + k^4) + S_{004}l^4 + 3S_{220}h^2k^2 \\ &\quad + 3S_{202}(h^2l^2 + k^2l^2) + 2S_{310}(h^3k - hk^3). \end{aligned} \tag{3.3.36}$$

The last coefficient (S_{310}) cannot normally be determined owing to exact reflection overlaps. Thus, equation (3.3.37) is normally used for both $4/m$ and $4/mmm$ Laue symmetries:

Tetragonal ($4/mmm$, four coefficients):

$$\Gamma^2_{sL} = S_{400}(h^4 + k^4) + S_{004}l^4 + 3S_{220}h^2k^2 + 3S_{202}(h^2l^2 + k^2l^2). \tag{3.3.37}$$

Trigonal ($\bar{3}$, rhombohedral setting, five coefficients):

$$\begin{aligned}\Gamma^2_{sL} &= S_{400}(h^4 + k^4 + l^4) + 3S_{220}(h^2k^2 + h^2l^2 + k^2l^2) \\ &\quad + 2S_{310}(h^3k + k^3l + hl^3) + 2S_{130}(h^3l + kl^3 + hl^3) \\ &\quad + 4S_{211}(h^2kl + hk^2l + hkl^2). \end{aligned} \tag{3.3.38}$$

The pair of coefficients S_{310} and S_{130} cannot normally be independently determined owing to exact reflection overlaps. Thus, equation (3.3.39) is normally used for both rhombohedral symmetries:

Trigonal ($\bar{3}m$, rhombohedral setting, four coefficients):

$$\begin{aligned}\Gamma^2_{sL} &= S_{400}(h^4 + k^4 + l^4) + 3S_{220}(h^2k^2 + h^2l^2 + k^2l^2) \\ &\quad + 2S_{310}(h^3k + k^3l + hl^3 + h^3l + kl^3 + hl^3) \\ &\quad + 4S_{211}(h^2kl + hk^2l + hkl^2). \end{aligned} \tag{3.3.39}$$

Trigonal ($\bar{3}$, five coefficients):

$$\begin{aligned}\Gamma^2_{sL} &= S_{400}(h^4 + k^4 + 2h^3k + 2hk^3 + 3h^2k^2) + S_{004}l^4 \\ &\quad + 3S_{202}(h^2l^2 + k^2l^2 + hkl^2) + S_{301}(2h^3l - 2k^3l - 6hk^2l) \\ &\quad + 4S_{211}(h^2kl + hk^2l). \end{aligned} \tag{3.3.40}$$

The coefficient S_{301} cannot normally be independently determined owing to exact reflection overlaps. Thus, equation (3.3.42) is normally used for $\bar{3}$ Laue symmetry.

Trigonal ($\bar{3}m1$, four coefficients):

$$\begin{aligned}\Gamma^2_{sL} &= S_{400}(h^4 + k^4 + 2h^3k + 2hk^3 + 3h^2k^2) + S_{004}l^4 \\ &\quad + 3S_{202}(h^2l^2 + k^2l^2 + hkl^2) \\ &\quad + S_{301}(3h^2kl - 3hk^2l + 2h^3l - 2k^3l). \end{aligned} \tag{3.3.41}$$

The coefficient S_{301} cannot normally be independently determined due to exact reflection overlaps. Thus, equation (3.3.43) is normally used for $\bar{3}m1$ Laue symmetry.

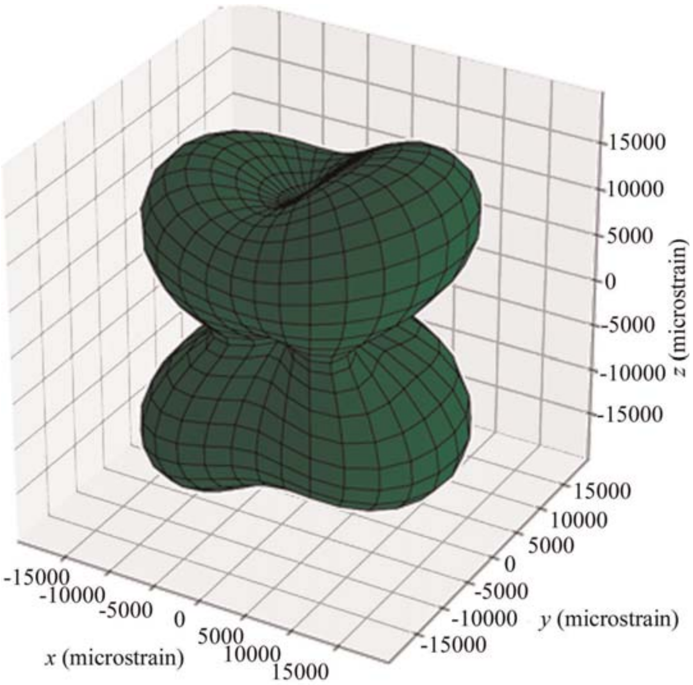

Figure 3.3.4
Microstrain surface for sodium parahydroxybenzoate multiplied by 10^6.

Trigonal ($\bar{3}1m$, four coefficients):

$$\begin{aligned}\Gamma^2_{sL} &= S_{400}(h^4 + k^4 + 2h^3k + 2hk^3 + 3h^2k^2) + S_{004}l^4 \\ &\quad + 3S_{202}(h^2l^2 + k^2l^2 + hkl^2) + 4S_{211}(h^2kl + hk^2l). \end{aligned} \tag{3.3.42}$$

Hexagonal ($6/m$ and $6/mmm$, three coefficients):

$$\begin{aligned}\Gamma^2_{sL} &= S_{400}(h^4 + k^4 + 2h^3k + 2hk^3 + 3h^2k^2) + S_{004}l^4 \\ &\quad + 3S_{202}(h^2l^2 + k^2l^2 + hkl^2). \end{aligned} \tag{3.3.43}$$

Cubic ($m\bar{3}$ and $m\bar{3}m$, two coefficients):

$$\Gamma^2_{sL} = S_{400}(h^4 + k^4 + l^4) + 3S_{220}(h^2k^2 + h^2l^2 + k^2l^2). \tag{3.3.44}$$

These equations can be used with the refined values of the coefficients to produce a surface representing the extent of the microstrain in reciprocal space. The surface resulting from Stephens' (1999) analysis of powder diffraction data from sodium parahydroxybenzoate is shown Fig. 3.3.4. At the present time, the connection between the elastic properties and defects with these microstrain surface models is unclear. Some aspects of this for cubic and hexagonal systems are discussed in Chapter 5.1.

References

Avdeev, M., Jorgensen, J., Short, S. & Von Dreele, R. B. (2007). *On the numerical corrections of time-of-flight neutron powder diffraction data. J. Appl. Cryst.* **40**, 710–715.

Buras, B. & Holas, A. (1968). *Nukleonika*, **13**, 591–620.

Caglioti, G., Paoletti, A. & Ricci, F. P. (1958). *Choice of collimators for a crystal spectrometer for neutron diffraction. Nucl. Instrum.* **3**, 223–228.

Carpenter, J. M., Lander, G. H. & Windsor, C. G. (1984). *Instrumentation at pulsed neutron sources. Rev. Sci. Instrum.* **55**, 1019–1043.

Cheary, R. W. & Coelho, A. A. (1998*a*). *Axial divergence in a conventional X-ray powder diffractometer. I. Theoretical foundations. J. Appl. Cryst.* **31**, 851–861.

Cheary, R. W. & Coelho, A. A. (1998*b*). *Axial divergence in a conventional X-ray powder diffractometer. II. Realization and evalua-*

tion in a fundamental-parameter profile fitting procedure. J. Appl. Cryst. **31**, 862–868.

Cheary, R. W. & Coelho, A. (1992). *A fundamental parameters approach to X-ray line-profile fitting. J. Appl. Cryst.* **25**, 109–121.

Cheary, R. W., Coelho, A. A. & Cline, J. P. (2004). *Fundamental parameters line profile fitting in laboratory diffractometers. J. Res. Natl Inst. Stand. Technol.* **109**, 1–25.

Cole, I. & Windsor, C. G. (1980). *The lineshapes in pulsed neutron powder diffraction. Nucl. Instrum. Methods*, **171**, 107–113.

Cooper, M. J. & Sayer, J. P. (1975). *The asymmetry of neutron powder diffraction peaks. J. Appl. Cryst.* **8**, 615–618.

David, W. I. F. (1986). *Powder diffraction peak shapes. Parameterization of the pseudo-Voigt as a Voigt function. J. Appl. Cryst.* **19**, 63–64.

Finger, L. W., Cox, D. E. & Jephcoat, A. P. (1994). *A correction for powder diffraction peak asymmetry due to axial divergence. J. Appl. Cryst.* **27**, 892–900.

Glazer, A. M., Hidaka, M. & Bordas, J. (1978). *Energy-dispersive powder profile refinement using synchrotron radiation. J. Appl. Cryst.* **11**, 165–172.

Hastings, J. B., Thomlinson, W. & Cox, D. E. (1984). *Synchrotron X-ray powder diffraction. J. Appl. Cryst.* **17**, 85–95.

Howard, C. J. (1982). *The approximation of asymmetric neutron powder diffraction peaks by sums of Gaussians. J. Appl. Cryst.* **15**, 615–620.

Ikeda, S. & Carpenter, J. M. (1985). *Wide-energy-range, high-resolution measurements of neutron pulse shapes of polyethylene moderators. Nucl. Instrum. Methods Phys. Res. Sect. A*, **239**, 536–544.

Jorgensen, J. D., David, W. I. F. & Willis, B. T. M. (1992). *White-beam and time-of-flight neutron diffraction*. In *International Tables for Crystallography*, Vol. C, edited by A. J. C. Wilson. Dordrecht: Kluwer.

Jorgensen, J. D., Johnson, D. H., Mueller, M. H., Peterson, S. W., Worlton, J. G. & Von Dreele, R. B. (1978). *Profile analysis of pulsed-source neutron powder diffraction data*. Proceedings of the Conference on Diffraction Profile Analysis, Cracow 14–15 August 1978, pp. 20–22.

Jorgensen, J. D. & Rotella, F. J. (1982). *High-resolution time-of-flight powder diffractometer at the ZING-P$''$ pulsed neutron source. J. Appl. Cryst.* **15**, 27–34.

Laar, B. van & Yelon, W. B. (1984). *The peak in neutron powder diffraction. J. Appl. Cryst.* **17**, 47–54.

Malmros, G. & Thomas, J. O. (1977). *Least-squares structure refinement based on profile analysis of powder film intensity data measured on an automatic microdensitometer. J. Appl. Cryst.* **10**, 7–11.

Otto, J. W. (1997). *On the peak profiles in energy-dispersive powder X-ray diffraction with synchrotron radiation. J. Appl. Cryst.* **30**, 1008–1015.

Parrish, W. (1992). *Powder and related techniques: X-ray techniques*. In *International Tables for Crystallography*, Vol. C, edited by A. J. C. Wilson, ch. 2.3. Dordrecht: Kluwer.

Popa, N. C. (1998). *The (hkl) dependence of diffraction-line broadening caused by strain and size for all Laue groups in Rietveld refinement. J. Appl. Cryst.* **31**, 176–180.

Rietveld, H. M. (1967). *Line profiles of neutron powder-diffraction peaks for structure refinement. Acta Cryst.* **22**, 151–152.

Rietveld, H. M. (1969). *A profile refinement method for nuclear and magnetic structures. J. Appl. Cryst.* **2**, 65–71.

Robinson, R. A. & Carpenter, J. M. (1990). *On the use of switch functions in describing pulsed moderators*. Report LAUR 90-3125. Los Alamos National Laboratory, USA.

Stephens, P. W. (1999). *Phenomenological model of anisotropic peak broadening in powder diffraction. J. Appl. Cryst.* **32**, 281–289.

Thompson, P., Cox, D. E. & Hastings, J. B. (1987). *Rietveld refinement of Debye–Scherrer synchrotron X-ray data from Al_2O_3. J. Appl. Cryst.* **20**, 79–83.

Toby, B. H. & Von Dreele, R. B. (2013). *GSAS-II: the genesis of a modern open-source all-purpose crystallographic software package. J. Appl. Cryst.* **46**, 544–549.

Turberfield, K. C. (1970). *Time-of-flight neutron diffractometry*. In *Thermal Neutron Diffraction*, edited by B. T. M. Willis. Oxford University Press.

Von Dreele, R. B., Jorgensen, J. D. & Windsor, C. G. (1982). *Rietveld refinement with spallation neutron powder diffraction data. J. Appl. Cryst.* **15**, 581–589.

Wang, Y., Uchida, T., Von Dreele, R., Rivers, M. L., Nishiyama, N., Funakoshi, K., Nozawa, A. & Kaneko, H. (2004). *A new technique for angle-dispersive powder diffraction using an energy-dispersive setup and synchrotron radiation. J. Appl. Cryst.* **37**, 947–956.

Worlton, J. G., Jorgensen, J. D., Beyerlein, R. A. & Decker, D. L. (1976). *Multicomponent profile refinement of time-of-flight neutron diffraction data. Nucl. Instrum. Methods*, **137**, 331–337.

Young, R. A., Mackie, P. E. & von Dreele, R. B. (1977). *Application of the pattern-fitting structure-refinement method of X-ray powder diffractometer patterns. J. Appl. Cryst.* **10**, 262–269.

Young, R. A. & Wiles, D. B. (1982). *Profile shape functions in Rietveld refinements. J. Appl. Cryst.* **15**, 430–438.

International Tables for Crystallography (2019). Vol. H, Chapter 3.4, pp. 270–281.

3.4. Indexing a powder diffraction pattern

A. Altomare, C. Cuocci, A. Moliterni and R. Rizzi

3.4.1. Introduction

The crystal structure solution process presupposes that the crystal cell and the space group are known. In other words, the first step in the solution pathway is the identification of the unit-cell parameters. Knowledge of the crystal structure strongly depends on the determination of the cell: a cell incorrectly defined does not lead to the solution. The cell-determination process (which operates in a 6-dimensional continuous parameter space) is also called 'indexing' because it consists of assigning the appropriate triple (*hkl*) of Miller indices of the lattice plane to each of the N_l experimental diffraction lines (in a $3N_l$-dimensional integer-valued index space) (Shirley, 2003). (In this chapter, 'line' and 'peak' are used synonymously.) In the case of powder diffraction, the determination of the cell parameters is not a trivial task, and it is much more difficult than in the single-crystal case. This is because the information about the three-dimensional reciprocal space is compressed into the one-dimensional experimental powder pattern. Whatever the method used, working in the parameter or index space, powder pattern indexing aims to recover the three-dimensional information from the positions of the diffraction peaks in the observed profile. In particular, the experimental information used for carrying out the indexing process is the d_{hkl} interplanar spacings, which are related to the diffraction angles by the well known Bragg law:

$$2d_{hkl}\sin\theta_{hkl}=\lambda.$$

In theory, if we had available an experimental pattern at infinite resolution with well resolved peaks with no overlapping, the determination of the six cell parameters corresponding to a problem with six degrees of freedom would be easy (Shirley, 2003). In practice, only the first 20–30 observed lines are useful for two main reasons: (1) they are less sensitive to small changes in the cell parameters than the higher-angle lines; and (2) higher-angle lines (even if they seem to be single peaks) actually often consist of more than one overlapping peak and their positions cannot be accurately evaluated. Using higher-angle lines is therefore unwise. The successful outcome of powder pattern indexing is correlated to which and how many d_{hkl} values derived from the peaks in the diffraction pattern are selected and how reliable they are. Precision and accuracy in detecting peak positions are essential conditions for successful indexing (Altomare *et al.*, 2008). Unfortunately they can be degraded by different sources of errors: peak overlap, poor peak resolution, 2θ zero shift, errors in measurement, and a low peak-to-background ratio. Moreover, impurity lines (*i.e.* peaks from a different chemical phase in the sample to the compound being studied) can hinder the attainment of the correct result. The history of indexing, having its origin in the early 20th century (Runge, 1917), has produced several methods and software packages (Shirley, 2003; Werner, 2002) with surprising progress in strengthening and automating the cell-determination process. Innovative approaches that aim to reduce the dependence on the d_{hkl} values (by avoiding the peak-search step and considering the full information contained in the diffraction pattern) have also been developed. Despite great advances, powder pattern indexing is still a challenge in many cases. Factors that affect the success or failure of the process include: the presence of diffraction peaks from unexpected phases, the precision in the peak-position value, the size of the unit cell to be identified (indexing is easier if the unit cell is not too big) and the symmetry (indexing a pattern from a compound with high symmetry is generally more reliable than for a compound with lower symmetry). Before the zeroth step of the indexing process (the searching for peaks in the experimental pattern) it is always necessary to obtain good-quality diffraction data. Of course, the use of synchrotron radiation is preferable, but conventional laboratory X-ray data are usually suitable. Whether automated or manual, the peak search and each successive step of the indexing process must be carefully checked. For example, in a first attempt the positions that correspond to overlapping peaks could be set aside. If one attempt fails, the most useful tactic is to try another software package, since the programs available at present are based on different approaches.

The aim of this chapter is first to illustrate the background of the topic and the main theoretical approaches used to carry out the powder pattern indexing, and then to give some examples of applications. Section 3.4.2 is mainly devoted to the basic concepts of a crystalline lattice, the main indexing equations and figures of merits; Section 3.4.3 discusses the traditional and non-traditional methods developed for indexing a powder pattern, and Section 3.4.4 discusses some applications, referring to the most widely used indexing programs.

3.4.2. The basic concepts of indexing

We now describe some concepts that are fundamental in crystallography and useful for understanding the indexing process. The measured diffraction intensities correspond to the reciprocal-lattice points

$$\mathbf{r}^*_{hkl}=h\mathbf{a}^*+k\mathbf{b}^*+l\mathbf{c}^*.$$

The Miller indices (*hkl*) identify the plane of the direct lattice and $\mathbf{a}^*$, $\mathbf{b}^*$ and $\mathbf{c}^*$ are the three vectors of the reciprocal lattice, which are related to the direct lattice by

$$\mathbf{a}=\frac{\mathbf{b}^*\times\mathbf{c}^*}{V^*},\quad \mathbf{b}=\frac{\mathbf{c}^*\times\mathbf{a}^*}{V^*},\quad \mathbf{c}=\frac{\mathbf{a}^*\times\mathbf{b}^*}{V^*},$$

where

$$V^*=\mathbf{a}^*\cdot\mathbf{b}^*\times\mathbf{c}^*$$

is the reciprocal-cell volume (V^* is the inverse of the direct-unit-cell volume V).

In case of single-crystal data, the three-dimensional nature of the experimental diffraction data makes it easy to identify $\mathbf{a}^*, \mathbf{b}^*, \mathbf{c}^*$, from which the direct-space unit-cell vectors are derived (Giacovazzo, 2011).

In case of powder diffraction, the three-dimensional nature of the diffraction data is compressed into one dimension in the experimental pattern, and the accessible experimental information is the d_{hkl} values involved in the Bragg law and related to the

Copyright © 2019 International Union of Crystallography

Table 3.4.1
Expressions for $Q(hkl)$ for different types of symmetry

Symmetry	$Q(hkl)$
Cubic	$(h^2 + k^2 + l^2)A_{11}$
Tetragonal	$(h^2 + k^2)A_{11} + l^2A_{33}$
Hexagonal	$(h^2 + hk + k^2)A_{11} + l^2A_{33}$
Orthorhombic	$h^2A_{11} + k^2A_{22} + l^2A_{33}$
Monoclinic	$h^2A_{11} + k^2A_{22} + l^2A_{33} + hlA_{13}$
Triclinic	$h^2A_{11} + k^2A_{22} + l^2A_{33} + hkA_{12} + hlA_{13} + klA_{23}$

diffraction angles by

$$d_{hkl} = \lambda/(2\sin\theta_{hkl}).$$

d_{hkl}, the spacing of the planes (hkl) in the direct lattice, is obtained by the dot products of the reciprocal-lattice vectors with themselves:

$$(\mathbf{r}^*_{hkl})^2 = \frac{1}{d^2_{hkl}} = h^2a^{*2} + k^2b^{*2} + l^2c^{*2} + 2hka^*b^*\cos\gamma^* + 2hla^*c^*\cos\beta^* + 2klb^*c^*\cos\alpha^*, \quad (3.4.1)$$

where α^* is the angle between $\mathbf{b}^*$ and $\mathbf{c}^*$, β^* is the angle between $\mathbf{c}^*$ and $\mathbf{a}^*$, and γ^* is the angle between $\mathbf{a}^*$ and $\mathbf{b}^*$. If we introduce

$$Q(hkl) = \frac{10^4}{d^2_{hkl}}$$

[where $Q(hkl)$ differs from $\sin^2\theta_{hkl}$ by a scale factor of $(200/\lambda)^2$], (3.4.1) becomes

$$Q(hkl) = h^2A_{11} + k^2A_{22} + l^2A_{33} + hkA_{12} + hlA_{13} + klA_{23}, \quad (3.4.2)$$

where

$$A_{11} = 10^4a^{*2},\ A_{22} = 10^4b^{*2},\ A_{33} = 10^4c^{*2},$$
$$A_{12} = 2\times10^4a^*b^*\cos\gamma^*,\ A_{13} = 2\times10^4a^*c^*\cos\beta^*,$$
$$A_{23} = 2\times10^4b^*c^*\cos\alpha^*.$$

The number of parameters A_{ij} in (3.4.2) depends on the type of symmetry: from 1 in the case of cubic symmetry to 6 for triclinic symmetry (see Table 3.4.1).

The quadratic form (3.4.2) relates the observed $Q(hkl)$ values to the reciprocal cell parameters and, consequently, to the direct cell. It is the basic equation used in powder-indexing procedures. Therefore the indexing problem (Werner, 2002) is to find A_{ij} and, for each observed $Q(hkl)$ value, three crystallographic indices (hkl) satisfying (3.4.2) within a suitable tolerance parameter Δ:

$$Q(hkl) - \Delta < h^2A_{11} + k^2A_{22} + l^2A_{33} + hkA_{12} + hlA_{13} + klA_{23} < Q(hkl) + \Delta. \quad (3.4.3)$$

The importance of using accurate $Q(hkl)$ values in (3.4.3) is obvious. Moreover, it is worth noticing that (3.4.3) must lead to physically reasonable indexing – low-angle peaks should correspond to small integer values for h, k and l and the values of the cell parameters and cell volume should be reasonable.

3.4.2.1. *Figures of merit*

An important task is the introduction of a figure of merit (FOM) that is able to (*a*) describe the physical plausibility of a trial cell and its agreement with the observed pattern, and (*b*) select the best cell among different possible ones. de Wolff (1968) made an important contribution in this direction. He developed the M_{20} figure of merit defined by

$$M_{20} = \frac{Q_{20}}{2\langle\varepsilon\rangle N_{20}}, \quad (3.4.4)$$

where Q_{20} is the Q value corresponding to the 20th observed and indexed peak, N_{20} is the number of different calculated Q values up to Q_{20}, and $\langle\varepsilon\rangle$ is the average absolute discrepancy between the observed and the calculated Q values for the 20 indexed peaks; the factor 2 is a result of statistics, explained by the larger chance for an observed line to sit in a large interval as compared with sitting in a small interval. The rationale behind M_{20} is as follows: the better the agreement between the calculated and the observed peak positions (the smaller the $\langle\varepsilon\rangle$ value) and the smaller the volume of the unit cell (the smaller the N_{20} value), the larger the M_{20} value and consequently the confidence in the proposed unit cell. A rule of thumb for M_{20} is that if the number of unindexed peaks whose Q values are less than Q_{20} is not larger than 2 and if $M_{20} > 10$, then the indexing process is physically reasonable (de Wolff, 1968; Werner, 2002). This rule is often valid, but exceptions occur. The use of the first 20 peaks is a compromise (coming from experience) between introducing a quite large number of observed peaks (depending on the number of parameters of the unit cell) and avoiding the use of high-angle peak positions, which are more affected by errors. M_{20} is statistically expected to be 1 in case of completely arbitrary indexing. It has no upper limit (it can be very large when $\langle\varepsilon\rangle$ is very small).

Smith & Snyder (1979) proposed the F_N criterion in order to overcome the limits of M_{20} with respect to its dependence on the 20 lines and on crystal class and space group. The F_N figure of merit is given by

$$F_N = \frac{1}{\langle|\Delta2\theta|\rangle}\frac{N}{N_{\rm poss}},$$

where $\langle|\Delta2\theta|\rangle$ is the average absolute discrepancy between the observed and calculated 2θ peak position values and $N_{\rm poss}$ is the number of possible diffraction lines up to the Nth observed line. The values of $\langle|\Delta2\theta|\rangle$ and $N_{\rm poss}$, $(\langle|\Delta2\theta|\rangle, N_{\rm poss})$, are usually given with F_N. With respect to M_{20}, F_N is more suitable for ranking the trial solutions and less for indicating their physical plausibility (Werner, 2002).

Both M_{20} and F_N, being based on the discrepancies between observed and calculated lines, are less reliable if there are impurity peaks; if the information about the unindexed lines is not taken into account, the risk of obtaining false solutions increases. Alternative FOMs based on joint probability have also been proposed (Ishida & Watanabe, 1967, 1971). Among the recently developed FOMs, we mention:

(1) $Q_{\rm partial}$ (Bergmann, 2007):

$$Q_{\rm partial} = \sum_i \min\left[w_i, \left(\frac{x_i - \hat{x}_i}{\delta_i}\right)^2\right],$$

where the summation is over the number of observed lines, w_i is the observed weight of line i, x and $\hat{x}_i$ are the observed and simulated line positions, respectively, and δ_i is the observed random error of line i. $Q_{\rm partial}$ is multiplied by a factor that depends on the symmetry of the simulated lattice (triclinic, …, cubic), on the unit cell volume and on the number of ignored peaks.

(2) McM_{20} (Le Bail, 2008):

$$McM_{20} = [100/(R_pN_{20})]B_rS_y,$$

where N_{20} is the number of possible lines that might exist up to the 20th observed line (for a primitive P lattice). R_p is the profile R factor (Young, 1993). B_r is a factor arbitrarily set to 6 for F and R Bravais lattices, 4 for I, 2 for A, B and C, and 1 for P. S_y is a factor equal to 6 for a cubic or a rhombohedral cell, 4 for a trigonal, hexagonal or tetragonal cell, 2 for an orthorhombic cell, and 1 for a monoclinic or triclinic cell.

(3) WRIP20 (Altomare *et al.*, 2009):

$$\mathrm{WRIP20} = \mathrm{RAT}^2_{Rp} \times \mathrm{RAT}_{\mathrm{Ind}} \times \mathrm{RAT}_{\mathrm{Pres}} \times w_u \times \mathrm{RAT}^{1/2}_{M20}. \tag{3.4.5}$$

Based on M_{20} (M_{20} and F_N remain the most widely used FOMs), WRIP20 has been developed for exploiting the full information contained in the diffraction profile. The factors that appear in (3.4.5) are

$$\mathrm{RAT}_{Rp} = \frac{1 - R_p}{1 - (R_p)_{\min}}, \quad \mathrm{RAT}_{\mathrm{Ind}} = \frac{\mathrm{PERC}_{\mathrm{Ind}}}{(\mathrm{PERC}_{\mathrm{Ind}})_{\max}},$$

$$\mathrm{RAT}_{\mathrm{Pres}} = \frac{(\mathrm{PERC}_{\mathrm{Pres}})_{\min}}{\mathrm{PERC}_{\mathrm{Pres}}}, \quad w_u = (N_{\mathrm{obs}} - N_u)/N_{\mathrm{obs}},$$

$$\mathrm{RAT}_{M20} = \frac{M_{20}}{(M_{20})_{\max}}, \quad \mathrm{PERC}_{\mathrm{Pres}} = \sum_{\mathrm{Pres}} \mathrm{mult} / \sum_{\mathrm{all}} \mathrm{mult}.$$

R_p is the profile-fitting agreement calculated after the Le Bail (Chapter 3.5) decomposition of the full pattern using the space group with the highest Laue symmetry compatible with the geometry of the current unit cell and no extinction conditions. $\mathrm{PERC}_{\mathrm{Ind}}$, the percentage of independent observations in the experimental profile, is estimated according to Altomare *et al.* (1995). For each extinction symbol compatible with the lattice geometry of the current unit cell, normalized intensities are calculated and subjected to statistical analysis in order to obtain a probability value associated with each extinction symbol in accordance with Altomare *et al.* (2004, 2005). For the extinction symbol with the highest probability value, the value of $\mathrm{PERC}_{\mathrm{Pres}}$ is calculated: $\sum_{\mathrm{all}} \mathrm{mult}$ is the total number of reflections (symmetry-equivalent included) for the space group having the highest Laue symmetry and no extinction conditions. (It varies with the volume of the unit cell and the data resolution.) $\sum_{\mathrm{Pres}} \mathrm{mult}$, which varies according to the extinction rules of the current extinction symbol, coincides with the number of non-systematically absent reflections (with the symmetry equivalents included). The subscripts min and max mark the minimum and the maximum values of each factor respectively, calculated for the possible unit cells that are to be ranked. N_{obs} and N_u are the number of observed and unindexed lines, respectively. All the terms in (3.4.5) are between 0 and 1, so ensuring that WRIP20 also lies between 0 and 1. In addition, WRIP20 has the following properties: (*a*) it is continuous, that is, definable in any interval of the experimental pattern; (*b*) it takes into account the peak intensities, the number of generated peaks and their overlap, and the systematically absent reflections (through the extinction-symbol test); and (*c*) it is not very sensitive to the presence of impurity lines (these usually have low intensities). WRIP20 is effective in finding the correct cell among a number of possible ones and selecting the corresponding most probable extinction symbol (see Example 3 in Section 3.4.4.6.2).

(4) Two new figures of merit based on de Wolff's method, the reversed figure of merit (M_n^{Rev}) and the symmetric figure of merit (M_n^{Sym}), have recently been proposed (Oishi-Tomiyasu, 2013). As observed by Oishi-Tomiyasu, the de Wolff figure of merit M_n does not use the observed and calculated lines in a symmetrical way, consequently it is (*a*) insensitive to computed but unobserved lines (*i.e.*, extinct peaks) and (*b*) sensitive to unindexed observed lines (*e.g.*, impurity peaks). M_n^{Rev} and M_n^{Sym} aim to compensate for the disadvantages of M_n. In particular, M_n^{Rev} has characteristics opposite to those of M_n with regard to sensitivity to extinct reflections and impurity peaks, and M_n^{Sym} has intermediate properties between M_n and M_n^{Rev}. They prove useful in selecting the correct solution, particularly in case of presence of impurity peaks. (See also Section 3.4.4.3.)

3.4.2.2. *Geometrical ambiguities*

Before discussing the concept of geometrical ambiguity in indexing, it is useful to introduce the definition of a reduced cell. While a unit cell defines the lattice, a lattice can be described by an unlimited number of cells. The Niggli reduced cell (Niggli, 1928) is a special cell able to uniquely define a lattice. Methods and algorithms have been derived for identifying the reduced cell starting from an arbitrary one (Buerger, 1957, 1960; Santoro & Mighell, 1970; Mighell, 1976, 2001). The reduced cell has the advantage of introducing a definitive classification, making a rigorous comparison of two lattices possible in order to establish whether they are identical or related (Santoro *et al.*, 1980). An algorithm based on the converse-transformation theory has been developed and implemented in the Fortran program *NIST*LATTICE* for checking relationships between any two cells (Karen & Mighell, 1991).

It is very important to recognize that two lattices are derivative of each other, because many crystallographic problems (twinning, indexing of powder patterns, single-crystal diffractometry) stem from the derivative properties of the lattices. Derivative lattices are classified as super-, sub- or composite according to the transformation matrices that relate them to the lattice from which they are derived (Santoro & Mighell, 1972).

A further obstacle to the correct indexing of a powder pattern is the problem of geometrical ambiguities. It may occur when '*two or more different lattices, characterized by different reduced forms, may give calculated powder patterns with the identical number of distinct lines in identical 2θ positions*' (Mighell & Santoro, 1975). The number of planes (*hkl*) contributing to each reflection may differ, however. Such ambiguity, due to the fact that the powder diffraction pattern only contains information about the length of the reciprocal-lattice vector and not the three-dimensional vector itself, is geometrical. It mainly occurs for high-symmetry cells (from orthorhombic up). The lattices having this property are related to each other by rotational transformation matrices. In Table 3.4.2 some examples of lattices giving geometrical ambiguities and the corresponding transformation matrices are given (Altomare *et al.*, 2008). Where there are geometrical ambiguities, additional prior information (*e.g.*, a single-crystal study) may be useful in order to choose one of the two possible lattices.

A recent procedure developed by Kroll *et al.* (2011) aims to reveal numerical and geometrical relationships between different reciprocal lattices and unit cells. The procedure is based on the assumption that distinct unit cells with lines in the same 2θ positions are derivatives of each other. However, two non-derivative lattices can have identical peak positions. Very recently, Oishi-Tomiyasu (2014*a*, 2016) has developed a new algorithm able to obtain all lattices with computed lines in the same positions as a given lattice. (See also Section 3.4.4.3.)

Table 3.4.2
Examples of lattices leading to geometrical ambiguities

$\boldsymbol{P} = \{P_{ij}\}$ is the transformation matrix from lattice I to lattice II, described by the vectors $\{\mathbf{a}_i\}$ and $\{\mathbf{b}_i\}$, respectively, with $\mathbf{b}_i = \sum_j P_{ij}\mathbf{a}_j$.

Lattice I	Lattice II	***P***
Cubic *P*	Tetragonal *P*	$\begin{pmatrix} 0 & -1/2 & 1/2 \\ 0 & 1/2 & 1/2 \\ -1 & 0 & 0 \end{pmatrix}$
Cubic *I*	Tetragonal *P*	$\begin{pmatrix} 0 & -1/2 & 1/2 \\ 0 & -1/2 & -1/2 \\ 1/2 & 0 & 0 \end{pmatrix}$
	Orthorhombic *F*	$\begin{pmatrix} -1/3 & -1/3 & 0 \\ 0 & 0 & -1 \\ 1 & -1 & 0 \end{pmatrix}$
	Orthorhombic *P*	$\begin{pmatrix} 1/4 & -1/4 & 0 \\ 0 & 0 & 1/2 \\ -1/2 & -1/2 & 0 \end{pmatrix}$
Cubic *F*	Orthorhombic *C*	$\begin{pmatrix} -1/2 & 0 & 1/2 \\ 0 & 1 & 0 \\ -1/4 & 0 & -1/4 \end{pmatrix}$
	Orthorhombic *I*	$\begin{pmatrix} -1/6 & 0 & -1/6 \\ 1/2 & 0 & -1/2 \\ 0 & -1 & 0 \end{pmatrix}$
Hexagonal	Orthorhombic *P*	$\begin{pmatrix} 1/2 & 1/2 & 0 \\ 1/2 & -1/2 & 0 \\ 0 & 0 & -1 \end{pmatrix}$
Rhombohedral	Monoclinic *P*	$\begin{pmatrix} -1/2 & 0 & -1/2 \\ 1/2 & 0 & -1/2 \\ 0 & -1 & 0 \end{pmatrix}$

3.4.3. Indexing methods

Indexing methods aim to reconstruct the three-dimensional direct lattice from the one-dimensional distribution of d_{hkl} values. Systematic or accidental peak overlap, inaccuracy of peak positions, zero shift in the $2\theta_{hkl}$ Bragg angles and/or the presence of impurity peaks make the reconstruction difficult. Data accuracy is fundamental for increasing the probability of success; as emphasized by de Wolff: '*The 'indexing problem' is essentially a puzzle: it cannot be stated in rigorous terms (...). It would be quite an easy puzzle if errors of measurements did not exist*' (de Wolff, 1957).

Different approaches have been proposed for solving the indexing puzzle since the pioneering work of Runge (1917). As suggested by Shirley (2003), indexing procedures work in parameter space, or in index space, or in both spaces. As a general consideration, the parameter space allows the inclusion of the cell information and constraints, while the index space is more suitable in cases where there are accidental or systematic absences (Shirley, 1980). In this section an outline of the strategies and search methods adopted by the main traditional and non-traditional indexing approaches is given. For more details see the papers by Shirley (2003) and Bergmann *et al.* (2004).

Among the main indexing procedures, zone indexing (Section 3.4.3.1.1), SIW heuristic (Section 3.4.3.1.2), successive dichotomy (Section 3.4.3.1.5), the topographs method (Section 3.4.3.2.1) and global-optimization methods (Section 3.4.3.2.2) operate in the parameter space; index heuristics (Section 3.4.3.1.3) and index permutation (Section 3.4.3.1.4) work in the index space; and scan/covariance (Bergmann, 2007) operates both in index and parameter space. Each method can be classified as exhaustive or not. An exhaustive method systematically and rigorously searches in the solution space; a non-exhaustive method exploits coincidences and relations between the observed lines with the aim of finding the solution quickly. The classification is not rigorous: approaches that try to combine rigour and speed can be defined as semi-exhaustive (Table 3.4.3).

Indexing procedures can also be classified as traditional and non-traditional. Each indexing method generates a list of possible cells. Their reliability is assessed by FOMs with the aim of selecting the correct one (see Section 3.4.2.1).

3.4.3.1. *Traditional indexing methods*

The traditional indexing approaches adopted over the last century are based on the following strategies and search methods: (1) zone indexing, (2) SIW heuristic, (3) index heuristics, (4) index permutation and (5) successive dichotomy. All of them exploit information about a limited number of observed peak positions.

3.4.3.1.1. *Zone-indexing strategy*

The zone-indexing strategy was originally developed by Runge (1917), successively proposed by Ito (1949, 1950), generalized by de Wolff (1957, 1958) and enhanced by Visser (1969). This approach is based on the search for zones, *i.e.*, crystallographic planes, in the reciprocal lattice, defined by the origin O and two lattice points. If $\mathbf{r}^*_{hkl}$ and $\mathbf{r}^*_{h'k'l'}$ are two vectors in reciprocal space, *i.e.* the positional vectors of the lattice points A and A′, they describe a zone containing any lattice point B whose positional vector is of type $m\mathbf{r}^*_{hkl} \pm n\mathbf{r}^*_{h'k'l'}$, where m and n are positive integers. If ω is the angle between $\mathbf{r}^*_{hkl}$ and $\mathbf{r}^*_{h'k'l'}$, the squared distance of B from O (*i.e.*, $Q_{m,n}$) can be expressed by (de Wolff, 1958; Visser, 1969)

$$Q_{m,n} = m^2 Q_{\rm A} + n^2 Q_{\rm A'} \pm mnR, \qquad (3.4.6)$$

where $Q_{\rm A} = Q(hkl)$ and $Q_{\rm A'} = Q(h'k'l')$ are the squared distances of A and A′ from O, respectively, and $R = 2(Q_{\rm A}Q_{\rm A'})^{1/2}\cos\omega$. R can be derived as

$$R = |Q_{m,n} - m^2 Q_{\rm A} - n^2 Q_{\rm A'}|/mn. \qquad (3.4.7)$$

The method is applied as follows: $Q_{\rm A}$ and $Q_{\rm A'}$ are chosen among the first experimental Q_i values; the $\{Q_i\}$, up to a reasonable resolution, are introduced in (3.4.7) in place of $Q_{m,n}$; and a few positive integer values are assigned to m and n. Equation (3.4.7) provides a large number of R values; equal R values (within error limits) define a zone, for which the ω angle can easily be calculated. The search for zones is performed using different $(Q_{\rm A}, Q_{\rm A'})$ pairs. The R values that are obtained many times identify the most important crystallographic zones. The zones are sorted according to a quality figure, enabling selection of the best ones. In order to find the lattice, all possible combinations of the best zones are tried. For every pair of zones the intersection line is found, then the angle between them is determined and the lattice is obtained.

The method has the advantage of being very efficient for indexing low-symmetry patterns. The main disadvantage is its sensitivity to errors in the peak positions, particularly in the low 2θ region.

3.4.3.1.2. *Shirley–Ishida–Watanabe (SIW) heuristic strategy*

This needs only one single well-established zone, then it arbitrarily chooses the 001 line from the first-level lines. The indexing problem is thus lowered to two dimensions and an exhaustive search is carried out.

3.4.3.1.3. *Index-heuristics strategy*

The index-heuristics strategy searches for the correct cell *via* a trial-and-error approach, assigning tentative Miller indices to a few experimental peak positions (basis lines), usually belonging to the low 2θ region of the experimental pattern. It was first proposed by Werner (1964), then successively refined (Werner *et al.*, 1985) and made more robust and effective (Altomare *et al.*, 2000, 2008, 2009). This approach, which works in the index space, was defined by Shirley as semi-exhaustive (Shirley, 1980). The search starts from the highest-symmetry crystal system (cubic) and, if no plausible solution is found, it is extended to lower symmetry down to triclinic. The number of selected basis lines increases as the crystal symmetry lowers. A dominant zone occurs when one cell axis is significantly shorter than the other two; in this case most of the first observed lines (in terms of increasing $2\theta_{hkl}$ values) can be indexed with a common zero Miller index. Special short-axis tests, aimed at finding two-dimensional lattices, have been proposed for monoclinic symmetry in order to detect the presence of dominant zones (Werner *et al.*, 1985). The index-heuristics method is based on the main indexing equation [see equation (3.4.2)] that can be rewritten (Werner *et al.*, 1985) as

$$Q(hkl) = h^2x_1 + k^2x_2 + l^2x_3 + hkx_4 + hlx_5 + klx_6,$$

where $\{x_i\} = X$ is the vector of unknown parameters, which are derived by solving a system of linear equations

$$\mathbf{MX} = \mathbf{Q}, \tag{3.4.8}$$

where $\mathbf{M}$ is a matrix of Miller indices and $\mathbf{Q}$ is the vector of the selected $Q(hkl)$ values corresponding to the basis lines. The dimensions of $\mathbf{M}$, $\mathbf{X}$ and $\mathbf{Q}$ change according to the assumed symmetry. From the inverse matrix $\mathbf{M}^{-1}$ the corresponding $\mathbf{X}$ is obtained *via* $\mathbf{X} = \mathbf{M}^{-1}\mathbf{Q}$. In the case of monoclinic and higher symmetry, $\{x_i\}$ are calculated by Cramer's rule. Different $\mathbf{X}$ vectors are derived by using a different selection of basis lines. The possible solutions are checked by using the full list of peak positions (up to the first 25 experimental lines). The method is sensitive to errors on peak positions and to the presence of impurities (the presence of only one impurity peak is not critical). The correctness of the $\{x_i\}$ strongly depends on the accuracy of the observed Q values, especially for low-2θ region lines, which are the most dominant ones for this indexing procedure. The possibility of testing different combinations of basis-line sets enables the correct cell to be found by bypassing the cases for which errors in the basis lines occur.

The method has been recently enhanced (Altomare *et al.*, 2000, 2009) by introducing new procedures that are able to increase the probability of successful indexing (see Section 3.4.4.2.1); among them are: (1) a correction for systematic errors in the experimental 2θ values (positive and negative trial 2θ zero shifts are taken into account); this correction should, in principle, describe a real diffractometer error; in practice, it also approximates the specimen displacement error well (perhaps coupled with transparency for organic samples); (2) a more intensive search in solution space for orthorhombic and monoclinic systems; (3) an improvement of the triclinic search; (4) a new figure of merit, WRIP20, which is more powerful than M_{20} in identifying the correct solution among a set of possible ones (see Section 3.4.2.1); (5) a check for geometrical ambiguities; (6) an automatic refinement of the possible cells; and (7) a statistical study of the parity of the Miller indices, performed at the end of the cell refinement, aimed at detecting doubled axes or additional lattice points (for *A*-, *B*-, *C*-, *I*-, *R*- or *F*-centred cells) (such information is used in the successive steps).

3.4.3.1.4. *Index-permutation strategy*

This strategy was proposed by Taupin (1973), and is based on a systematic permutation of indices associated to observed lines for obtaining candidate cells. Because this trial-and-error strategy is similar to the index-heuristics approach, we do not describe it here.

3.4.3.1.5. *Successive-dichotomy search method*

The successive-dichotomy method, first developed by Louër & Louër (1972), is based on an exhaustive strategy working in direct space (except for triclinic systems, where it operates in reciprocal space) by varying the lengths of the cell axes and the interaxial angles within finite intervals. The search for the correct cell is performed in an n-dimensional domain D (where n is the number of cell parameters to be determined). If no solution belongs to D, the domain is discarded and the ranges for the allowed values of cell parameters are increased; on the contrary, if D contains a possible solution, it is explored further by dividing the domain into 2^n subdomains *via* a successive-dichotomy procedure. Each subdomain is analysed and discarded if it does not contain a solution. The method was originally applied to orthorhombic and higher-symmetry systems (Louër & Louër, 1972), but it has been successively extended to monoclinic (Louër & Vargas, 1982) and to triclinic systems (Boultif & Louër, 1991). The search can be performed starting from cubic then moving down to lower symmetries (except for triclinic) by partitioning the space into shells of volume ΔV = 400 A^3. For triclinic symmetry ΔV is related to the volume $V_{\rm est}$ suggested by the method proposed by Smith (1977), which is able to estimate the unit-cell volume from only one line in the pattern:

$$V_{\rm est} \simeq \frac{0.60 d_N^3}{\frac{1}{N} - 0.0052},$$

where d_N is the value for the Nth observed line; in the case $N = 20$ the triclinic cell volume is $V_{\rm est} \simeq 13.39 d_{20}^3$.

Let us consider, as an example, the monoclinic case; in terms of direct cell parameters, $Q(hkl)$ is given by (Boultif & Louër, 1991)

$$Q(hkl) = f(A, C, \beta) + g(B),$$

where $f(A, C, \beta) = h^2/A^2 + l^2/C^2 - 2hl\cos\beta/(AC)$, $A = a\sin\beta$, $C = c\sin\beta$, $g(B) = k^2/B^2$ and $B = b$. The search using the successive-dichotomy method is performed in a four-dimensional space that is covered by increasing the integer values i, l, m and n in the intervals $[A_-, A_+] = [A_- = A_0 + ip, A_+ = A_- + p]$, $[B_-, B_+] = [B_- = B_0 + lp, B_+ = B_- + p]$, $[C_-, C_+] = [C_- = C_0 + mp, C_+ = C_- + p]$ and $[\beta_-, \beta_+] = [\beta_- = 90 + n\theta, \beta_+ = \beta_- + \theta]$, where the step values of p and θ are 0.4 Å and 5°, respectively, and A_0, B_0 and C_0 are the lowest values of A, B and C (based on the positions of the lowest-angle peaks), respectively. Each quartet of intervals defines a domain D and, by taking into account the current limits for the parameters A, B, C and β, a calculated pattern is generated, not in terms of discrete $Q(hkl)$ values but of allowed intervals $[Q_-(hkl), Q_+(hkl)]$. D is retained only if the observed Q_i values belong to the range $[Q_-(hkl) - \Delta Q_i, Q_+(hkl) + \Delta Q_i]$, where ΔQ_i is the absolute error of the observed lines (*i.e.*, impurity lines are not tolerated). If D has been accepted, it is divided into 2^4 subdomains by halving the original intervals $[A_-, A_+]$, $[B_-, B_+]$, $[C_-, C_+]$ and $[\beta_-, \beta_+]$ and new limits $[Q_-(hkl), Q_+(hkl)]$ are calculated; if a possible solution is found, the dichotomy method is applied iteratively. In case of triclinic symmetry the expression for $Q(hkl)$ in terms of direct cell parameters is too complicated to be treated *via* the successive-dichotomy method; therefore the basic indexing equation (3.4.2) is used. In this case, the $[Q_-(hkl), Q_+(hkl)]$ intervals are set in reciprocal space according to the A_{ij} parameters of (3.4.2). To reduce computing time the following restrictions are put on the (hkl) Miller indices associated with the observed lines: (1) maximum h, k, l values equal to 2 in case of the first five lines; (2) $h + k + l < 3$ for the first two lines.

The outcome of the successive-dichotomy method is not strongly influenced by the presence of a dominant zone. New approaches have been devoted to overcome the limitations of the method with a strict dependence on data accuracy and on impurities (Boultif & Louër, 2004; Louër & Boultif, 2006, 2007), see Section 3.4.4.2).

3.4.3.2. *Non-traditional indexing methods*

New indexing procedures that provide alternatives to the traditional approaches outlined in Section 3.4.3.1 have recently been proposed.

3.4.3.2.1. *The topographs method*

This method (Oishi *et al.*, 2009) is based on the Ito equation (de Wolff, 1957):

$$Q(\mathbf{h}_1 + \mathbf{h}_2) + Q(\mathbf{h}_1 - \mathbf{h}_2) = 2[Q(\mathbf{h}_1) + Q(\mathbf{h}_2)], \qquad (3.4.9)$$

where $Q(\mathbf{h})$ is the length of the reciprocal vector $\mathbf{r}^*_{hkl}$ corresponding to the Miller index vector $\mathbf{h} = (hkl)$. It uses Conway's topograph (Conway & Fung, 1997), a connected tree obtained by associating a graph to each equation of type (3.4.9) and consisting of infinite directed edges. According to Ito's method, if quadrupoles (Q_1, Q_2, Q_3, Q_4) detected among the observed Q_i values satisfy the condition $2(Q_1 + Q_2) = Q_3 + Q_4$, two Miller-index vectors $\mathbf{h}_1$ and $\mathbf{h}_2$ are expected to exist such that $Q_1 = Q(\mathbf{h}_1)$, $Q_2 = Q(\mathbf{h}_2)$, $Q_3 = Q(\mathbf{h}_1 - \mathbf{h}_2)$ and $Q_4 = Q(\mathbf{h}_1 + \mathbf{h}_2)$. If an additional value Q_5 satisfying the condition $2(Q_1 + Q_4) = Q_2 + Q_5$ is found, the graph of the quadrupole (Q_1, Q_2, Q_3, Q_4) grows *via* the addition of the Q_5 contribution; this procedure is iterated. If topographs share a Q value that corresponds to the same reciprocal-lattice vector, then a three-dimensional lattice is derived containing the two-dimensional lattices associated with the original topographs. Three-dimensional lattices are also obtained by combining topographs. The probability that topographs correspond to the correct cell increases with the number of edges of the graph structure. The method is claimed by the authors to be insensitive to the presence of impurity peaks.

3.4.3.2.2. *Global-optimization methods*

Global-optimization methods, widely adopted for solving crystal structures from powder data, have also been successfully applied to indexing. Among them, we provide brief descriptions of genetic algorithms, and Monte Carlo and grid-search methods.

3.4.3.2.2.1. *Genetic-algorithm search method*

The use of genetic algorithms (GAs) for solving the indexing problem was proposed by Tam & Compton (1995) and Paszkowicz (1996). Since then, Kariuki and co-workers (Kariuki *et al.*, 1999) have combined GAs with a whole-profile-fitting procedure for indexing powder diffraction patterns. This approach exploits the information of the full powder diffraction pattern. It is inspired by the Darwinian evolutionary principle based on mating, mutation and natural selection of the member of a population that survives and evolves to improve future generations. The initial population consists of a set of trial cell parameters, chosen randomly within a given volume range; a full pattern-decomposition process is performed using the Le Bail algorithm (Chapter 3.5) and the agreement between the calculated and observed profiles is derived and used for assessing the goodness of an individual member (*i.e.*, a set of unit-cell parameters). The most plausible cell is therefore found by exploring a six-dimensional hypersurface $R'_{wp}(a, b, c, \alpha, \beta, \gamma)$ and searching for the global minimum of R'_{wp} (see Section 3.4.4.3.2). In contrast to the main traditional methods, whose outcomes depend on the reliability of a set of peak positions, this procedure has the advantage of being insensitive to the presence of small impurity peaks that have a negligible influence on the agreement factor between the experimental and calculated profiles: the global minimum of R'_{wp} is reached if the majority phase is correctly indexed. The main disadvantage of the method is the computing time required, in particular in the case of low symmetry.

3.4.3.2.2.2. *Monte Carlo search method*

The Monte Carlo approach has also been applied to indexing powder diffraction patterns (Le Bail, 2004; Bergmann *et al.*, 2004; Le Bail, 2008). It exploits all the information contained in the full pattern, randomly generates and selects trial cell parameters, and calculates peak positions to which it assigns the corresponding Miller indices. An idealized powder pattern consisting of peak positions d and extracted intensities I is considered to test the trial cell. The cell reliability is assessed by suitable figures of merit (*e.g.* R_p and McM_{20}, see Section 3.4.2.1). The main drawback of this approach is the significant computing time required, in particular for triclinic systems.

3.4.3.2.2.3. *Grid-search method*

This performs an iterated 'step-and-repeat search' in the parameter space. It has the advantage of being flexible, exhaustive and not particularly sensitive to impurities or errors, and the disadvantage of being slow (Shirley, 2003).

3.4.4. Software packages for indexing and examples of their use

The different strategies and methods described in Section 3.4.3 have been implemented in a variety of automatic indexing programs (Bergman *et al.*, 2004). Almost all use one of the two different approaches working in parameter space (*i.e.*, unit-cell parameters) or index space (*i.e.*, reflection indices). Only the *EFLECH/INDEX* program (Bergman, 2007), applying the scan/covariance strategy, works in both spaces: in parameter space from cubic down to monoclinic, switching to index space for triclinic. The different indexing methods are classified according to Shirley (2003) in Table 3.4.3. Alternative classifications can be

Table 3.4.3
Classification of indexing methods

Method (strategy/search)	Space	Exhaustive
Zone indexing	Parameter	No
SIW heuristic	Parameter	Semi
Scan/covariance	Parameter (for cubic to monoclinic); index (for triclinic)	To monoclinic
Index heuristics	Index	Semi
Index permutation	Index	Yes
Successive dichotomy	Parameter	Yes
Grid search	Parameter	Yes
Genetic algorithms	Parameter	No
Monte Carlo	Parameter	No

made by considering whether a program works in direct or reciprocal space, or uses Bragg diffraction line positions or the whole experimental diffraction profile. Using the whole experimental diffraction profile requires a lot of computing time, but has become possible as a consequence of recent increases in the speed of computers. In the following, descriptions of the principal (default) steps of the most widely used indexing programs are given. Several non-default options are available for each program. The chances of success of the indexing step increase if more than one program is used.

3.4.4.1. *Traditional indexing programs*

3.4.4.1.1. *ITO (Visser, 1969)*

This program is based on the zone-indexing strategy and uses the Runge–Ito–de Wolff–Visser method of decomposition of the reciprocal space into zones, as described in Section 3.4.3.1.1.

The following steps are executed by the program:

1. The potential zones are found always using the 20 lowest Bragg angle peaks. The program does not work with fewer peaks.
2. All possible combinations of the six best zones (including the combination of each zone with itself) are found by searching for trial zones that share a row of common points. For every pair of such zones, the angle between them is found, thus giving a trial reciprocal lattice.
3. The reduction of the resulting unit cells is carried out using the Delaunay–Ito method (Pecharsky & Zavalij, 2009).
4. The program tries to index the first 20 lines and repeats this check after least-squares refinement of the unit-cell parameters.
5. The figures of merit are calculated to assess the quality of each trial unit cell and the four best lattices are provided.

ITO is very efficient at indexing patterns with low symmetry and is only weakly sensitive to impurity peaks, if they occur at high angles. The most frequent causes of failure are inaccuracy or incompleteness of the input data.

3.4.4.1.2. *TREOR90 (Werner et al., 1985)*

Classified by Shirley (1980, 2003) as semi-exhaustive, *TREOR90* is based on the index-heuristics strategy (see Section 3.4.3.1.3) and uses a trial-and-error approach. It performs the following steps:

1. Some basis lines are selected among the experimental d values, generally from the low-2θ region of the powder diffraction pattern. Five sets of basis lines are generally sufficient for orthorhombic tests, whereas more than seven sets may be necessary for the monoclinic system. At least 20–25 experimental d values are potentially required.
2. The trial unit cells in the index space are searched by varying the Miller indices that are tentatively assigned to the basis lines.
3. The analysis starts with cubic symmetry and, in a stepwise manner, tests for lower-symmetry crystal systems are performed. In the case of monoclinic symmetry, a special short-axis test is carried out.
4. The solution of the linear system in equation (3.4.8) gives the possible cell parameters. Different combinations of the basis lines are tested.
5. Each possible solution is checked by using the full list of experimental lines.
6. The quality of the trial cell parameters is mainly assessed by using the M_{20} figure of merit [see equation (3.4.4)]. An effective rule for identifying a reliable solution is $M_{20} > 10$ and no more than one unindexed line.

The success of the program is related to the use of some suitable standard sets of parameter values (maximum unit-cell volume, maximum cell axis, tolerance of values *etc.*) arising from the accumulated experience of the authors; they can be easily changed by the user *via* suitable keywords in the input file.

3.4.4.1.3. *DICVOL91 (Boultif & Louër, 1991)*

This program works in direct space (down to the monoclinic system) by using the successive-dichotomy search method (see Section 3.4.3.1.5), which was introduced for the automatic indexing of powder diffraction patterns by Louër & Louër (1972). *DICVOL91* has been defined as exhaustive by Shirley (1980, 2003). Its main steps are:

1. The unit-cell volume is partitioned by moving from high to low symmetry. Shells of 400 Å^3 of volume are scanned for all the symmetry systems except for triclinic; for the triclinic system the shells are based on the definition of volume proposed by Smith (1977) (see Section 3.4.3.1.5).
2. A search using the successive-dichotomy method, based on suitable intervals (see Section 3.4.3.1.5), is carried out. In the case of the triclinic system the general expression for $Q(hkl)$ as function of the direct cell parameters is too complicated, and the reciprocal-space parameters in equation (3.4.2) are used for setting the intervals.
3. The derived cell parameters are refined using the least-squares method.
4. The quality of each trial unit cell is evaluated by using the M_N and F_N figures of merit (see Section 3.4.2.1).

The program is fast at performing exhaustive searches in parameter space (except for the triclinic case); on the other hand, its efficiency is strongly related to the quality of the data and to the presence of impurities (in fact, impurities are not permitted).

3.4.4.2. *Evolved indexing programs*

3.4.4.2.1. *N-TREOR09 (Altomare et al., 2009)*

Implemented in the *EXPO* program (Altomare *et al.*, 2013) to perform the powder pattern indexing step, *N-TREOR09* is an update of *N-TREOR* (Altomare *et al.*, 2000), which in turn is an evolution of *TREOR90*, and preserves the main strategies with some changes introduced to make the program more exhaustive and powerful. In particular:

(*a*) If the default indexing process fails, the unit-cell search is automatically repeated by changing some default choices, *e.g.*, increasing the tolerance value on the observed *d* values. If still no solution is obtained, the maximum (*hkl*) Miller indices assigned to the orthorhombic or monoclinic base lines are increased and the tolerance limits of the default values are halved in order to avoid the generation of wrong large unit cells.

(*b*) At the end of the first run, whatever the obtained results, a possible 2θ zero-position shift is taken into account: the indexing process starts again by applying positive and negative 2θ zero-position shifts to the original peak search result.

(*c*) An exhaustive triclinic search is performed. The dominant-zone tests that are usually carried out for the monoclinic system have been extended to include the triclinic case.

(*d*) A new figure of merit, WRIP20, more powerful than the classical M_{20}, is used. It is calculated when more than one possible cell is found and takes into account the M_{20} value, the full experimental pattern, the degree of reflection overlap, the systematically absent reflections and the number of unindexed lines (see Section 3.4.2.1).

This program is also able to index powder patterns from small proteins: see Example 4 in Section 3.4.4.6.2.

3.4.4.2.2. *DICVOL06 (Louër & Boultif, 2006, 2007) and DICVOL14 (Louër & Boultif, 2014)*

The most recent of a series of versions, *DICVOL14* is the successor of *DICVOL04* (Boultif & Louër, 2004) and *DICVOL06*. *DICVOL06* includes *DICVOL04* with its optimized search procedure and an extended search in shells of volumes. *DICVOL04* represented an improvement of *DICVOL91*. Among the features of *DICVOL06* are:

(*a*) A tolerance for unindexed lines that can result from the presence of unwanted additional phases or inaccurately measured peaks. The program can tolerate a user-defined number of unindexed lines. Care must be taken when using this option to avoid the possibility of generating erroneous cells. It is worth noting that the inclusion of the possibility of at least one unindexed peak has markedly increased the success rate of *DICVOL06*.

(*b*) A correction of the zero-point error in the measured data. *Via* an *a priori* zero-origin evaluation, two different approaches can be followed: (i) if there is a non-negligible zero shift (*i.e.*, ~0.1°), the reflection-pair method is adopted (Dong *et al.*, 1999); (ii) if the shift is small (<0.03°), a refinement of the experimental data zero point together with the cell parameters is carried out as soon as a solution is found. In the monoclinic and triclinic systems, a reduced-cell analysis is performed to choose among equivalent solutions.

(*c*) When a solution is found in a 400 Å^3 shell of volume, the exhaustive search is extended to the whole domain.

No formal limits on the number of input Bragg peaks have been established but, for reliable indexing, it is recommended that 20 or more peaks (in the low-2θ region) are used.

Compared to *DICVOL04*/*DICVOL06*, *DICVOL14* includes: an optimization of filters in the final stages of the convergence of the successive dichotomy process; an optimization and extension of scanning limits for the triclinic case; a new approach for zero-point offset evaluation; a detailed review of the input data from the resulting unit cells; and cell centring tests. *DICVOL14* has been improved particularly for triclinic cases, which are generally the most difficult to solve with the dichotomy algorithm.

3.4.4.3. *Non-traditional indexing programs*

The indexing programs described above are based on using, for a limited number of lines, the measured positions of peak maxima as directly obtained from the experimental powder diffraction pattern. *Conograph* (Oishi-Tomiyasu, 2014*b*), which has been more recently proposed, also belongs to that group of programs. A brief description of *Conograph* follows

3.4.4.3.1. *Conograph: indexing via the topographs method*

Conograph is based on the topographs method, and its main functions are the determination of the primitive unit cell and lattice symmetry, and refinement of lattice parameters. Among the main features we note:

(1) A new Bravais-lattice determination algorithm (Oishi-Tomiyasu, 2012), which has been proved to be stable with respect to peak-position errors under very general conditions. The algorithm applies the Minkowski reduction to primitive cells and the Delaunay reduction (Delaunay, 1933) to face-centred, body-centred, rhombohedral and base-centred cells in such a way that the computational efficiency of the process is better than the Andrews & Bernstein (1988) method.

(2) The two figures of merit $M_n^{\rm Rev}$ and $M_n^{\rm Sym}$ proposed by Oishi-Tomiyasu (2013) are used for for selecting the true unit cells. They are also used to estimate the zero-point shift.

(3) The use of many observed peaks in the default setting, which aims to make *Conograph* robust against dominant zones and missing or false peaks (Oishi-Tomiyasu, 2014*b*).

(4) The method for exhaustively searching unit cells that involve geometrical ambiguity (Oishi-Tomiyasu, 2014*a*, 2016). The geometrical ambiguities that are detected also include lattices with very similar calculated lines, because of the error tolerance in the *d* spacings.

Programs that use only the measured positions of peak maxima are particularly vulnerable to experimental errors in the measured peak positions and to the presence of impurity peaks. For these reasons, at the end of the 1990s new indexing strategies were developed that do not require the peak locations in the experimental pattern. These approaches are completely different from the methods described above because they use the whole diffraction profile. They try to explore the parameter space (direct space) exhaustively by applying different optimization techniques in order to find the cells in best agreement with the experimental powder diffraction pattern. Some of the most widely used indexing programs in direct space are described here.

3.4.4.3.2. *GAIN: indexing via a genetic-algorithm search method*

The use of genetic algorithms (GAs) for indexing powder diffraction data by exploiting the diffraction geometry (as in the traditional indexing methods) was firstly proposed by Tam & Compton (1995) and Paszkowicz (1996). Subsequently, Kariuki *et al.* (1999) applied GA techniques by using whole profile fitting with the aim of exploring the parameter space $\{a, b, c, \alpha, \beta, \gamma\}$ and finding the global minimum of the *R*-factor $\{a, b, c, \alpha, \beta, \gamma\}$ hypersurface, yielding the parameter set able to generate the best agreement between the observed and calculated powder diffraction patterns.

This new strategy has been implemented in the program *GAIN* (Harris *et al.*, 2000), whose main features are:

(1) Starting from a population of N_p sets of lattice parameters and using the evolutionary operations of mating, mutation and natural selection, the population is allowed to evolve

through several generations, with the aim of generating sets of possible trial cell parameters.

(2) The search procedure, using a GA, is performed in restricted, sensible cell-volume ranges consistent with the knowledge of the system under study.

(3) For each set of trial parameters a calculated powder diffraction pattern is constructed. The peak positions and parameters describing the shape and width of each peak are used in the Le Bail profile-fitting procedure (Chapter 3.5).

(4) The pattern is split into different regions (defined by the user), and the weighted profile *R* factor is calculated for each region; all the values are summed to obtain the overall $R'_{\rm wp}$:

$$R'_{\rm wp} = \sum_{\rm regions} \left[\frac{\sum_i w_i (y_i - y_{ci})^2}{\sum_i w_i y_i^2} \right]^{1/2},$$

where the summation is over the regions, i runs over the experimental points belonging to each region and y_i and y_{ci} are the observed and calculated profile at the ith experimental step, respectively. *Via* the $R'_{\rm wp}$ formula the residual for each region is scaled according to the total intensity in the region, so a region with only low-intensity peaks can make an important contribution to $R'_{\rm wp}$.

This approach is robust at handling the problems that may affect the experimental powder pattern: peak overlap, (*hkl*)-dependent effects and zero-point errors. It is time consuming (particularly in the case of low symmetry) but not very sensitive to the presence of minority impurity phases.

3.4.4.3.3. *McMaille: indexing via a Monte Carlo search method*

The information in the whole powder diffraction profile is exploited by the program *McMaille* (Le Bail, 2004), which is based on the random generation of cell parameters and uses the Monte Carlo optimization technique. Once the trial cell parameters have been generated and the Miller indices and the peak positions have been calculated, the quality of the cell is assessed by using, as figure of merit, the conventional Rietveld profile reliability factor R_p (Young, 1993) or McM_{20} (see Section 3.4.2.1). The program uses some tricks that can increase the success of the Monte Carlo algorithm:

(1) Only the trial cells corresponding to a value of R_p that is smaller than a user-defined value (~50%) are retained for successive refinement.

(2) If all the observed peaks, except for a user-defined number of tolerated impurity peaks, are 'explained' whatever the R_p value, the cell is retained for successive examination.

(3) If either of the conditions (1) or (2) is fulfilled, the cell parameters are randomly changed in 200 to 5000 attempts (for cubic to triclinic cases, respectively) in which small random parameter variations *via* the Monte Carlo algorithm are carried out. The new parameters are preserved if an improvement of R_p is verified in 85% of the attempts.

This procedure is not sensitive to impurity lines, provided that the sum of their intensities is less than 10–15% of the total intensity. A zero-point error up to 0.05° is tolerated. To reduce the long computing time required to successfully complete the procedure, a significant increase in speed has been obtained by using idealized profiles generated by applying simplified line profiles to extracted line positions. A parallelized version of *McMaille* has also been developed. The indexing problem can usually be solved in few minutes if: (*a*) no triclinic symmetry is handled (because this requires more computing time); (*b*) the cell volume is less than 2000 Å^3; (*c*) no cell length is longer than 20 Å.

3.4.4.4. *Crysfire: a suite of indexing programs*

The *Crysfire* suite (Shirley, 2002) is a multi-program indexing facility. It can perform a self-calibration, which is aimed at detecting and correcting 2θ zero errors, and is able to strip out weak lines. Its single unified user interface and data-file format make a wide set of indexing packages accessible with minimal effort (especially to non-specialists). *Crysfire* provides a list of the possible cells suggested by each indexing program, suitably ranked. The *Crysfire* 2003 suite supports a total of 11 programs (Bergmann *et al.*, 2004), among which are *ITO*, *TREOR90*, *DICVOL91* and *McMaille*. The possibility of using different indexing programs, working in parameter space or index space and adopting different indexing approaches increases the probability of finding the correct cell.

3.4.4.5. *Two commercial programs*

3.4.4.5.1. *SVD-Index*

This commercial indexing program (Coelho, 2003*a*), which uses the Monte Carlo method, is part of the *TOPAS* (Coelho, 2003*b*) suite from Bruker AXS. The reciprocal-cell parameters in equation (3.4.2) are found by using, in an iterative way, the singular value decomposition (SVD) approach (Nash, 1990) to solve linear equations relating (*hkl*) values to *d* spacings. The method is particularly useful in cases for which there are more equations than variables. All the observed lines in the powder pattern are involved in the indexing procedure. It is claimed that the program is relatively insensitive to impurity peaks and missing high *d* spacings; it performs well on data with large diffractometer zero errors.

More recently, two indexing methods have been introduced in *TOPAS*: LSI (least-squares iteration), an iterative least-squares process which operates on the *d*-spacing values extracted from reasonable-quality powder diffraction data, and LP-Search (lattice parameter search), a Monte Carlo based whole-powder-pattern decomposition approach independent of the knowledge of the *d*-spacings (Coelho & Kern, 2005).

3.4.4.5.2. *X-CELL*

This commercial program is part of the *Materials Studio* suite from Accelrys (Neumann, 2003). To perform an exhaustive search, like *DICVOL*, the program uses the successive-dichotomy approach. Its principal features are:

(1) the user can define how many impurity lines can be tolerated;

(2) a search for the zero-point shift of the diffraction pattern; and

(3) systematic absences are taken into account.

The program is described as 'virtually exhaustive'; it is expected to work well when faced with missing lines, impurities and errors.

3.4.4.6. *Examples of applications of indexing programs*

3.4.4.6.1. *Indexing using DICVOL06*

The program *DICVOL06*, as implemented in the *WinPLOTR*/*FULLPROF* suite (Roisnel & Rodríquez-Carvajal, 2001) and recently introduced into *EXPO*, was applied to two experimental diffraction patterns.

Example 1

Norbornene (Brunelli *et al.*, 2001). Published information: C_7H_{10}, monoclinic, a = 7.6063 (9), b = 8.6220 (1), c = 8.749 (1) Å, β = 97.24 (1)°, $P2_1/c$, experimental range 5–60° 2θ, λ = 0.85041 Å, RES = 1.0 Å (where RES is the data resolution), synchrotron data, indexed by *Fzon* (Visser, 1969).

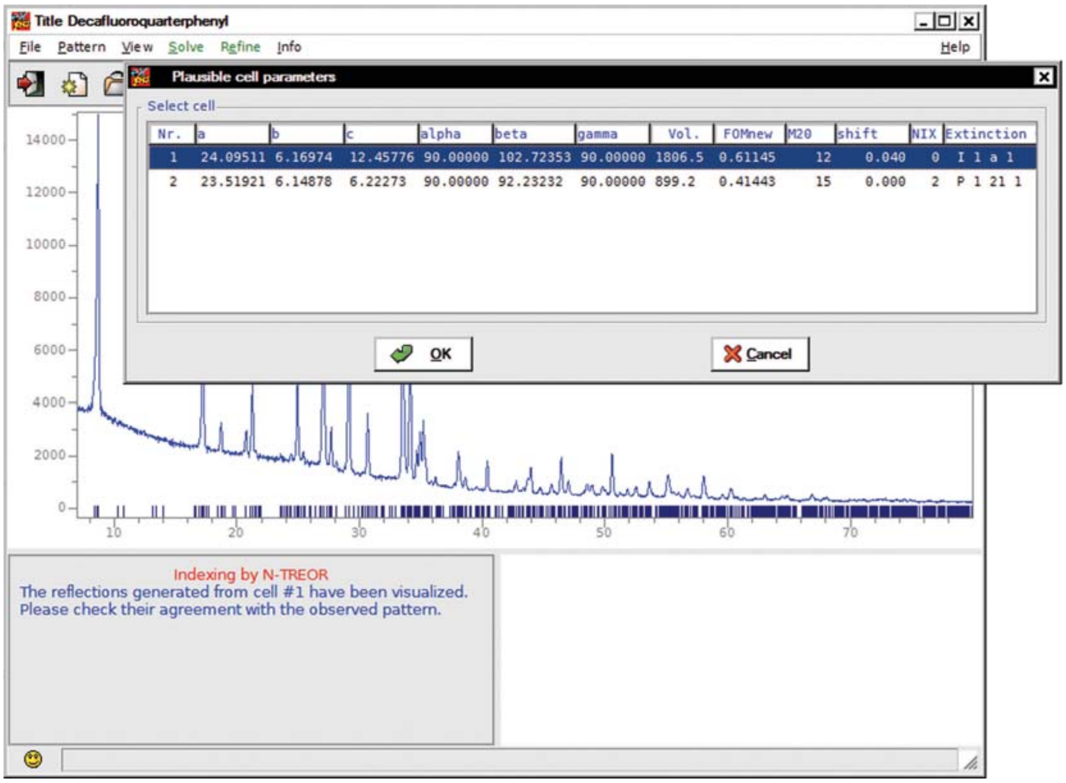

Nr.	a	b	c	alpha	beta	gamma	Vol.	FOMnew	M20	shift	NIX	Extinction
1	24.09511	6.16974	12.45776	90.00000	102.72353	90.00000	1806.5	0.61145	12	0.040	0	I 1 a 1
2	23.51921	6.14878	6.22273	90.00000	92.23232	90.00000	899.2	0.41443	15	0.000	2	P 1 21 1

Indexing by N-TREOR
The reflections generated from cell #1 have been visualized.
Please check their agreement with the observed pattern.

Figure 3.4.1
The list of possible cells for the decafluoroquarterphenyl structure automatically found using *N-TREOR09*.

The 2θ values of the first 25 peaks, in the range 5–25°, were determined by *WinPLOTR* and supplied to *DICVOL06*. The first 20 peaks were used for searching for the solution. No plausible cell was found when assuming that no impurity was present and exploring all the systems (from cubic to triclinic). *DICVOL06* was also unsuccessful when the non-default strategies of extended search and data correction for zero-point error were considered (by setting some flags to 1 in the input file). If it was supposed that two impurity lines might be present among the peaks (by setting the flag corresponding to the maximum number of accepted impurity/spurious lines to 2), *DICVOL06* was able to find the following monoclinic cell: a = 8.7480 (36), b = 8.6313 (32), c = 7.6077 (26) Å, β = 97.201 (33)°, with two unindexed lines, M_{18} = 41.5, F_{18} = 125(0.0041, 35). The refinement of the cell by considering all the 25 lines gave a = 7.6087 (26), b = 8.6295 (30), c = 8.7459 (34) Å, β = 97.201 (34)°, which is very similar to the published one; 23 indexed lines, M_{20} = 30.1, F_{20} = 102.6(0.0048, 41). The presence of the two impurity lines has been ascribed by the authors to a small amount of hexagonal plastic phase.

Example 2

Cu(II)–Schiff base complex (Banerjee *et al.*, 2002). Published information: $Cu(C_{15}H_{12}NO_2)_2$, triclinic, a = 11.928 (4), b = 12.210 (5), c = 9.330 (5) Å, α = 102.54 (4), β = 111.16 (5), γ = 86.16 (4)°, $P\bar{1}$, experimental range 6–100° 2θ, λ = 1.54056 Å, RES = 1.22 Å, high-quality X-ray laboratory data, indexed by *DICVOL91*. The 2θ values of the first 30 peaks, in the range 6–25°, were determined by *WinPLOTR* and supplied to *DICVOL06*. The first 20 peaks were used for searching for the solution. If it was assumed that no impurity was present, no plausible cell was found down to the monoclinic system. When the triclinic system was explored, *DICVOL06* suggested only one plausible solution: a = 12.2157 (73), b = 12.2031 (77), c = 9.3071 (41) Å, α = 65.798 (46), β = 102.572 (59), γ = 95.711 (61)°, with no unindexed lines, M_{20} = 27.0, F_{20} = 77.0(0.010, 26). The refinement of the cell considering all the 30 lines gave a = 12.2125 (65), b = 12.1989 (61), c = 9.3016 (32) Å, α = 65.826 (33), β = 102.569 (40), γ = 97.755 (44)°, no unindexed lines, M_{20} = 27.9, F_{20} = 72.8(0.0106, 26). For this, the corresponding conventional cell is a = 11.93313 (61), b = 12.2125 (65), c = 9.3016 (32) Å, α = 102.569 (40), β = 111.152 (33), γ = 86.151 (44)°, similar to the published one.

3.4.4.6.2. *Indexing using N-TREOR09*

Two examples of powder diffraction pattern indexing by using *N-TREOR09*, as implemented in the *EXPO* program, will be described. To activate the procedure some specific instructions must be given to *EXPO via* the input file or the graphical interface. As a first step, the peak-search procedure is automatically performed on the experimental powder pattern and the list of corresponding d values are supplied to *N-TREOR09*. During the indexing process a correction for zero-point error is automatically carried out (positive and negative shifts are taken into account). Both the examples below were successfully indexed by a default run of *EXPO*.

Example 3

Decafluoroquarterphenyl (Smrčok *et al.*, 2001). Published information: $C_{24}H_8F_{10}$, monoclinic, a = 24.0519 (9), b = 6.1529 (3), c = 12.4207 (5) Å, β = 102.755 (2)°, $I2/a$, experimental range 7–80° 2θ, λ = 1.79 Å, RES = 1.39 Å, medium-quality X-ray laboratory data. The first 43 peaks (in the range 7–67°) with intensities greater than a default threshold were selected (an intensity-based criterion is automatically adopted). The first 25 lines were used to find a possible cell that was then refined by considering all the 43 peaks. At the end of the automatic indexing procedure, *N-TREOR09* suggested two possible cells ranked according to WRIP20 [equation (3.4.5)], as shown in Fig. 3.4.1 (WRIP20 is denoted as

FOMnew in *N-TREOR09*). The first one in the list is the correct cell. It is worth mentioning that the classical M_{20} figure of merit was not able to pick up the solution. The best cell parameters, found according to FOMnew, were a = 24.0951 (50), b = 6.1697 (21), c = 12.4578 (37) Å, β = 102.724 (18)°, similar to those reported in the literature, with FOMnew = 0.61, M_{20} = 12; all the lines in the pattern were indexed. The program provided the solution thanks to its automatic check for a zero-point correction (2θ zero shift = 0.04°) and was able to correctly identify the extinction group (*I_a_*). For the second suggested cell (the wrong solution) FOMnew = 0.41, M_{20} = 15, and two lines were unindexed.

Example 4

Hexagonal turkey egg-white lysozyme (Margiolaki *et al.*, 2005). Published information: hexagonal, a = 71.0862 (3), c = 85.0276 (5) Å, $P6_122$, experimental range 0.4–12° 2θ, RES = 3.35 Å, synchrotron data. The first 94 peaks (in the range 0.4–6°, λ = 0.700667 Å) with intensities greater than a default threshold were selected. An intensity-based criterion was automatically adopted. The first 25 lines were used to find possible cells that were then refined by considering all 94 peaks. Five possible unit cells were automatically suggested by the program in the following systems: hexagonal (1), orthorhombic (1) and monoclinic (3). The highest value for WRIP20 was 0.99, and was for the correct hexagonal cell parameters: a = 71.0922 (4), c = 85.0269 (7) Å, which are similar to those reported in the literature; all the 94 selected lines in the pattern were indexed. For this cell, the program detected a geometrical ambiguity (see Section 3.4.2.2) between hexagonal and orthorhombic lattices and automatically selected the higher-symmetry one.

3.4.5. Conclusion

Indexing a powder diffraction pattern is sometimes described as a ‘gateway technology’, because the determination of the cell parameters is so fundamental: if no cell has been identified the execution of the subsequent steps of the structure solution process is impossible, and if a wrong cell has been used the correct solution is unreachable. Therefore extremely close attention must be paid to the indexing step of the process. From the early 1970s, the increasing interest in powder pattern indexing and the progress seen, in terms of both methods and algorithms, have strongly contributed to opening the door to modern applications of powder diffraction techniques. The availability of a quite large number of software packages, based on different indexing strategies, enables the scientist interested in solving crystal structures to switch from one program to another when the first fails, so increasing the possibility of success. In some cases indexing is still a challenging process. Good-quality data are necessary and careful inspection of each indexing step, in particular in the selection of the experimental peak positions to be used, is advisable.

References

Altomare, A., Caliandro, R., Camalli, M., Cuocci, C., da Silva, I., Giacovazzo, C., Moliterni, A. G. G. & Spagna, R. (2004). *Space-group determination from powder diffraction data: a probabilistic approach*. *J. Appl. Cryst.* **37**, 957–966.

Altomare, A., Camalli, M., Cuocci, C., da Silva, I., Giacovazzo, C., Moliterni, A. G. G. & Rizzi, R. (2005). *Space group determination: improvements in EXPO2004*. *J. Appl. Cryst.* **38**, 760–767.

Altomare, A., Campi, G., Cuocci, C., Eriksson, L., Giacovazzo, C., Moliterni, A., Rizzi, R. & Werner, P.-E. (2009). *Advances in powder diffraction pattern indexing: N-TREOR09*. *J. Appl. Cryst.* **42**, 768–775.

Altomare, A., Cascarano, G., Giacovazzo, C., Guagliardi, A., Moliterni, A. G. G., Burla, M. C. & Polidori, G. (1995). *On the number of statistically independent observations in a powder diffraction pattern*. *J. Appl. Cryst.* **28**, 738–744.

Altomare, A., Cuocci, C., Giacovazzo, C., Moliterni, A., Rizzi, R., Corriero, N. & Falcicchio, A. (2013). *EXPO2013: a kit of tools for phasing crystal structures from powder data*. *J. Appl. Cryst.* **46**, 1231–1235.

Altomare, A., Giacovazzo, C., Guagliardi, A., Moliterni, A. G. G., Rizzi, R. & Werner, P.-E. (2000). *New techniques for indexing: N-TREOR in EXPO*. *J. Appl. Cryst.* **33**, 1180–1186.

Altomare, A., Giacovazzo, C. & Moliterni, A. (2008). *Indexing and space group determination*. In *Powder Diffraction Theory and Practice*, edited by R. E. Dinnebier & S. J. L. Billinge, pp. 206–226. Cambridge: RSC Publishing.

Andrews, L. C. & Bernstein, H. J. (1988). *Lattices and reduced cells as points in 6-space and selection of Bravais lattice type by projections*. *Acta Cryst.* A**44**, 1009–1018.

Banerjee, S., Mukherjee, A., Neumann, M. A. & Louër, D. (2002). *Ab-initio structure determination of a Cu(II)-Schiff base complex from X-ray powder diffraction data*. *Acta Cryst.* A**58**, c264.

Bergmann, J. (2007). *EFLECH/INDEX – another try of whole pattern indexing*. *Z. Kristallogr. Suppl.* **26**, 197–202.

Bergmann, J., Le Bail, A., Shirley, R. & Zlokazov, V. (2004). *Renewed interest in powder diffraction data indexing*. *Z. Kristallogr.* **219**, 783–790.

Boultif, A. & Louër, D. (1991). *Indexing of powder diffraction patterns for low-symmetry lattices by the successive dichotomy method*. *J. Appl. Cryst.* **24**, 987–993.

Boultif, A. & Louër, D. (2004). *Powder pattern indexing with the dichotomy method*. *J. Appl. Cryst.* **37**, 724–731.

Brunelli, M., Fitch, A. N., Jouanneaux, A. & Mora, A. J. (2001). *Crystal and molecular structures of norbornene*. *Z. Kristallogr.* **216**, 51–55.

Buerger, M. J. (1957). *Reduced cells*. *Z. Kristallogr.* **109**, 42–60.

Buerger, M. J. (1960). *Note on reduced cells*. *Z. Kristallogr.* **113**, 52–56.

Coelho, A. A. (2003*a*). *Indexing of powder diffraction patterns by iterative use of singular value decomposition*. *J. Appl. Cryst.* **36**, 86–95.

Coelho, A. A. (2003*b*). *TOPAS. Version 3.1 User’s Manual*. Bruker AXS GmbH, Karlsruhe, Germany.

Coelho, A. A. & Kern, A. (2005). *Discussion of the indexing algorithms within TOPAS*. *IUCr Commission on Powder Diffraction Newsletter*, **32**, 43–45.

Conway, J. H. & Fung, F. Y. C. (1997). *The Sensual (Quadratic) Form*. Washington, DC: The Mathematical Association of America.

Delaunay, B. (1933). *Neue Darstellung der geometrischen Kristallographie*. *Z. Kristallogr.* **84**, 109–149.

Dong, C., Wu, F. & Chen, H. (1999). *Correction of zero shift in powder diffraction patterns using the reflection-pair method*. *J. Appl. Cryst.* **32**, 850–853.

Giacovazzo, C. (2011). *Crystallographic computing*. In *Fundamentals of Crystallography*, 3rd ed., edited by C. Giacovazzo, pp. 66–156. Oxford: IUCr/Oxford University Press.

Harris, K. D. M., Johnston, R. L., Chao, M. H., Kariuki, B. M., Tedesco, E. & Turner, G. W. (2000). *Genetic algorithm for indexing powder diffraction data*. University of Birmingham, UK.

Ishida, T. & Watanabe, Y. (1967). *Probability computer method of determining the lattice parameters from powder diffraction data*. *J. Phys. Soc. Jpn*, **23**, 556–565.

Ishida, T. & Watanabe, Y. (1971). *Analysis of powder diffraction patterns of monoclinic and triclinic crystals*. *J. Appl. Cryst.* **4**, 311–316.

Ito, T. (1949). *A general powder X-ray photography*. *Nature*, **164**, 755–756.

Ito, T. (1950). *X-ray Studies on Polymorphism*. Tokyo: Maruzen Company.

Karen, V. L. & Mighell, A. D. (1991). *Converse-transformation analysis*. *J. Appl. Cryst.* **24**, 1076–1078.

Kariuki, B. M., Belmonte, S. A., McMahon, M. I., Johnston, R. L., Harris, K. D. M. & Nelmes, R. J. (1999). *A new approach for indexing powder* *diffraction data based on whole-profile fitting and global optimization using a genetic algorithm*. *J. Synchrotron Rad.* **6**, 87–92.

Kroll, H., Stöckelmann, D. & Heinemann, R. (2011). *Analysis of multiple solutions in powder pattern indexing: the common reciprocal metric tensor approach*. *J. Appl. Cryst.* **44**, 812–819.

Le Bail, A. (2004). *Monte Carlo indexing with McMaille*. *Powder Diffr.* **19**, 249–254.

Le Bail, A. (2008). *Structure solution*. In *Principles and Applications of Powder Diffraction*, edited by A. Clearfield, J. H. Reibenspies & N. Bhuvanesh, pp. 261–309. Oxford: Wiley-Blackwell.

Louër, D. & Boultif, A. (2006). *Indexing with the successive dichotomy method, DICVOL04*. *Z. Kristallogr. Suppl.* **23**, 225–230.

Louër, D. & Boultif, A. (2007). *Powder pattern indexing and the dichotomy algorithm*. *Z. Kristallogr. Suppl.* **26**, 191–196.

Louër, D. & Boultif, A. (2014). *Some further considerations in powder diffraction pattern indexing with the dichotomy method. Powder Diffr.* **29**, S2, S7–S12.

Louër, D. & Louër, M. (1972). *Méthode d'essais et erreurs pour l'indexation automatique des diagrammes de poudre*. *J. Appl. Cryst.* **5**, 271–275.

Louër, D. & Vargas, R. (1982). *Indexation automatique des diagrammes de poudre par dichotomies successives*. *J. Appl. Cryst.* **15**, 542–545.

Margiolaki, I., Wright, J. P., Fitch, A. N., Fox, G. C. & Von Dreele, R. B. (2005). *Synchrotron X-ray powder diffraction study of hexagonal turkey egg-white lysozyme*. *Acta Cryst.* D**61**, 423–432.

Mighell, A. D. (1976). *The reduced cell: its use in the identification of crystalline materials*. *J. Appl. Cryst.* **9**, 491–498.

Mighell, A. D. (2001). *Lattice symmetry and identification – the fundamental role of reduced cells in materials characterization*. *J. Res. Natl Inst. Stand. Technol.* **106**, 983–995.

Mighell, A. D. & Santoro, A. (1975). *Geometrical ambiguities in the indexing of powder patterns*. *J. Appl. Cryst.* **8**, 372–374.

Nash, J. C. (1990). *Compact Numerical Methods for Computers: Linear Algebra and Function Minimisation*, 2nd ed. Bristol: Adam Hilger.

Neumann, M. A. (2003). *X-cell: a novel indexing algorithm for routine tasks and difficult cases*. *J. Appl. Cryst.* **36**, 356–365.

Niggli, P. (1928). *Handbuch der Experimentalphysik*, Vol. 7, Part 1. Leipzig: Akademische Verlagsgesellschaft.

Oishi, R., Yonemura, M., Hoshikawa, A., Ishigaki, T., Mori, K., Torii, S., Morishima, T. & Kamiyama, T. (2009). *New approach to the indexing of powder diffraction patterns using topographs*. *Z. Kristallogr. Suppl.* **30**, 15–20.

Oishi-Tomiyasu, R. (2012). *Rapid Bravais-lattice determination algorithm for lattice parameters containing large observation errors*. *Acta Cryst.* A**68**, 525–535.

Oishi-Tomiyasu, R. (2013). *Reversed de Wolff figure of merit and its application to powder indexing solutions*. *J. Appl. Cryst.* **46**, 1277–1282.

Oishi-Tomiyasu, R. (2014*a*). *Method to generate all the geometrical ambiguities of powder indexing solutions*. *J. Appl. Cryst.* **47**, 2055–2059.

Oishi-Tomiyasu, R. (2014*b*). *Robust powder auto-indexing using many peaks*. *J. Appl. Cryst.* **47**, 593–598.

Oishi-Tomiyasu, R. (2016). *A table of geometrical ambiguities in powder indexing obtained by exhaustive search*. *Acta Cryst.* A**72**, 73–80.

Paszkowicz, W. (1996). *Application of the smooth genetic algorithm for indexing powder patterns – tests for the orthorhombic system*. *Mater. Sci. Forum*, **228–231**, 19–24.

Pecharsky, V. K. & Zavalij, P. Y. (2009). *Determination and refinement of the unit cell*. In *Fundamentals of Powder Diffraction and Structural Characterization of Materials*, 2nd ed., pp. 407–495. New York: Springer.

Roisnel, T. & Rodríquez-Carvajal, J. (2001). *WinPLOTR: a windows tool for powder diffraction pattern analysis*. *Mater. Sci. Forum*, **378–381**, 118–123.

Runge, C. (1917). *Die Bestimmung eines Kristallsystems durch Rontgenstrahlen*. *Phys. Z.* **18**, 509–515.

Santoro, A. & Mighell, A. D. (1970). *Determination of reduced cells*. *Acta Cryst.* A**26**, 124–127.

Santoro, A. & Mighell, A. D. (1972). *Properties of crystal lattices: the derivative lattices and their determination*. *Acta Cryst.* A**28**, 284–287.

Santoro, A., Mighell, A. D. & Rodgers, J. R. (1980). *The determination of the relationship between derivative lattices*. *Acta Cryst.* A**36**, 796–800.

Shirley, R. (1980). *Data accuracy for powder indexing*. In *Accuracy in Powder Diffraction*, edited by S. Block & C. R. Hubbard, *NBS Spec. Publ.* **567**, 361–382.

Shirley, R. (2002). *User Manual, The Crysfire 2002 system for Automatic Powder Indexing*. Guildford: Lattice Press.

Shirley, R. (2003). *Overview of powder-indexing program algorithms (history and strengths and weaknesses)*. *IUCr Comput. Comm. Newsl.* **2**, 48–54. http://www.iucr.org/resources/commissions/crystallographic-computing/newsletters/2.

Smith, G. S. (1977). *Estimating the unit-cell volume from one line in a powder diffraction pattern: the triclinic case*. *J. Appl. Cryst.* **10**, 252–255.

Smith, G. S. & Snyder, R. L. (1979). *F_N: a criterion for rating powder diffraction patterns and evaluating the reliability of powder-pattern indexing*. *J. Appl. Cryst.* **12**, 60–65.

Smrčok, L., Koppelhuber-Bitschau, B., Shankland, K., David, W. I. F., Tunega, D. & Resel, R. (2001). *Decafluoroquarterphenyl – crystal and molecular structure solved from X-ray powder data*. *Z. Kristallogr.* **216**, 63–66.

Tam, K. Y. & Compton, R. G. (1995). *GAMATCH – a genetic algorithm-based program for indexing crystal faces*. *J. Appl. Cryst.* **28**, 640–645.

Taupin, D. (1973). *A powder-diagram automatic-indexing routine*. *J. Appl. Cryst.* **6**, 380–385.

Visser, J. W. (1969). *A fully automatic program for finding the unit cell from powder data*. *J. Appl. Cryst.* **2**, 89–95.

Werner, P.-E. (1964). *Trial-and-error computer methods for the indexing of unknown powder patterns*. *Z. Kristallogr.* **120**, 375–387.

Werner, P.-E. (2002). *Autoindexing*. In *Structure Determination from Powder Diffraction Data*, edited by W. I. F. David, K. Shankland, L. B. McCusker & Ch. Baerlocher, pp. 118–135. Oxford University Press.

Werner, P.-E., Eriksson, L. & Westdahl, M. (1985). *TREOR, a semi-exhaustive trial-and-error powder indexing program for all symmetries*. *J. Appl. Cryst.* **18**, 367–370.

Wolff, P. M. de (1957). *On the determination of unit-cell dimensions from powder diffraction patterns*. *Acta Cryst.* **10**, 590–595.

Wolff, P. M. de (1958). *Detection of simultaneous zone relations among powder diffraction lines*. *Acta Cryst.* **11**, 664–665.

Wolff, P. M. de (1968). *A simplified criterion for the reliability of a powder pattern indexing*. *J. Appl. Cryst.* **1**, 108–113.

Young, R. A. (1993). *Introduction to the Rietveld method*. In *The Rietveld Method*, edited by R. A. Young, pp. 1–38. Oxford: IUCr/Oxford University Press.

International Tables for Crystallography (2019). Vol. H, Chapter 3.5, pp. 282–287.

3.5. Data reduction to $|F_{hkl}|$ values

A. Le Bail

3.5.1. Introduction

Collecting the structure-factor amplitudes $|F_{hkl}|$ is the key step leading to structure solution from powder-diffraction data, just as from single-crystal data. However, there are specific difficulties and pitfalls associated with powder data, mainly because of diffraction-peak overlap. Once indexing is realized, data reduction to $|F_{hkl}|$ is a fast process, using whole-powder-pattern decomposition (WPPD) methods. This comfortable situation was not attained without past efforts, which are reviewed in this chapter. The introduction of modern WPPD methods occurred slowly and progressively over the past 30 years, thanks to increases in computer power, improvements in graphical user interfaces, diffractometer data digitalization, the availability of synchrotron and neutron radiation, and last but not least, the proposition of new algorithms. Innovations were not instantly accepted, this also being true for the Rietveld (1969) method, or could not be applied immediately to every type of powder data. Predecessors of the current WPPD methods extracted peak intensities without restraining the cell, so that each peak position was a parameter to be refined (as well as the peak intensity, and the peak shape and width). This is still useful if the aim is to obtain peak positions for indexing, although simple derivative methods can make searching for peak positions faster. Taking advantage of the indexing (Bergmann *et al.*, 2004), new WPPD methods that applied cell restraints to the peak positions opened the door to a long list of new possibilities and applications (including first indexing confirmation and manual or automatic space-group estimation) which are detailed in this chapter. A partial review of the applications realized in thousands of published papers is given, and the evolution of the methods will be discussed. Additional information on the topic of reduction to $|F_{hkl}|$ values can be found in the books by Young (1993), Giacovazzo (1998), David *et al.* (2002), Pecharsky & Zavalij (2003), Clearfield *et al.* (2008) and Dinnebier & Billinge (2008) or in selected reviews (Toraya, 1994; Langford & Louër, 1996; Le Bail, 2005).

3.5.2. Algorithms

Whole-powder-pattern fitting (WPPF) is a general definition including WPPD as well as the Rietveld method (Rietveld, 1969). In the latter method, the atomic coordinates are required for the intensity calculations, and the sum of all the peak contributions produces a calculated powder pattern which is compared to the observed one, allowing the least-squares refinement of profile and structural parameters. The Rietveld method historically preceded modern WPPD methods, though the latter are applicable without atomic coordinates. Of course, one may use WPPD methods if the structure is known, but in some cases one does not want to use that knowledge (not wanting to restrain the peak intensities by the structural model, for instance, nevertheless believing in the indexing or wanting to confirm it, using the restraint of the cell parameters). Any WPPF approach should be able to model the peak shape and width variations with diffraction angle (complications not considered here may occur in the case of anisotropic broadening intrinsic to the sample). This can be done by fitting some analytical profile shape and width parameters in a semi-empirical approach. The angular variation of these parameters is generally controlled by refining the U, V and W terms in the Caglioti *et al.* (1958) expression [$(\text{FWHM})^2 = U\tan^2\theta + V\tan\theta + W$] or a variation (where FWHM = full width at half maximum). The alternative is to use the fundamental parameter approach (FPA) (Cheary & Coelho, 1992). However, some of the original computer programs did not apply any cell restraint or even any restraint at all.

3.5.2.1. *Unrestrained cell*

Without a cell hypothesis, no $|F_{hkl}|$ values can be extracted; the intensity values collected will be noted by $I(i)$ until Miller indices are attributed, enabling the multiplicity correction. Obtaining all the peak positions, areas, breadths and shape parameters as independent values for a whole powder pattern is limited to simple cases where there is not too much peak overlap. With such an approach (both cell and space group unknown or unused) one has to estimate the number of peaks to be fitted, so that the fit of a complex group of peaks will lead to large uncertainties. However, knowing the cell and space group provides at least the correct number of peaks and an estimate of their starting positions. Such calculations were made as an alternative to the Rietveld method, during the first stage of the so-called two-stage method for refinement of crystal structures (Cooper *et al.*, 1981). In the case of X-ray data, the profile shapes applied in the Rietveld method (Gaussian at the beginning for neutron data) evolved a great deal (Wiles & Young, 1981), and on the WPPD side happened to be described in these two-stage approaches by a sum of Lorentzian curves, or double Gaussians (Will *et al.*, 1983, 1987). The computer program *PROFIT* (Scott, 1987), derived from software for individual profile fitting (Sonneveld & Visser, 1975) and extended to the whole pattern, was applied to the study of crystallite size and strain in zinc oxide (Langford *et al.*, 1986) and for the characterization of line broadening in copper oxide (Langford & Louër, 1991). Studying a whole pattern can also be done in simple cases by using software designed for the characterization of single or small groups of peaks; an example is a ZnO study (Langford *et al.*, 1993) using the computer program *FIT* (Socabim/Bruker). WPPD on complex cases is mostly realized today by using peak positions controlled by the cell parameters, with the benefit of stronger accuracy of the $|F_{hkl}|$ values, even if the lost degrees of freedom may lead to slightly worse fits, increasing the profile R factors. Before 1987, close to thirty structure determinations by powder diffractometry (SDPDs) were achieved using intensities extracted by using these old WPPD methods without cell constraints (see the SDPD database; Le Bail, 2007). It can be argued that freeing the peak positions allows one to take into account subtle effects in position displacement (in stressed samples, for example). But systematic discrepancy of observed peak positions with regard to the theoretical position, as expected from the cell parameters, can be modelled as well in modern WPPD methods or in the Rietveld method.

Copyright © 2019 International Union of Crystallography

3.5.2.2. *Restrained cell*

WPPD methods that strictly applied the peak positions calculated from a cell (hypothesized from indexing results) marked a great step forward in the quest for improving the SDPD success rate. This is essentially because the quality of the estimated intensities increased, and even if the main handicap of powder diffraction (peak overlap) could not be completely circumvented, it was at least more clearly delimited. Today two generic names are retained for such cell-restrained WPPD methods that can produce a set of extracted $|F_{hkl}|$ values suitable for attempting a structure solution: the Pawley and Le Bail methods. Both were derived from the Rietveld (1969) method, so they share with it many equations which will not be restated here (see Chapter 4.7).

3.5.2.2.1. *Pawley method*

The idea of removing the crystal structure refinement part in a Rietveld program and adding the potential to refine an individual intensity for every expected Bragg peak produced a new software package (named *ALLHKL*) allowing refinement of the cell parameters very precisely and extraction of a set of structure-factor amplitudes (Pawley, 1981). The process was much later called the 'Pawley method'. Overcoming the least-squares ill conditioning due to peak overlap was achieved by using slack constraints (Waser, 1963). Pawley clearly insisted on the usefulness of the procedure for the confirmation of the indexing of a powder pattern of an unknown. Nevertheless, the structure of the C_6F_{10} (at 4.2 K) test case selected for demonstration purposes remained unsolved (but see Section 3.5.4.2 below). No SDPD of an unknown was realized using the Pawley method for several years (although successful tests were published corresponding to redeterminations of previously known structures). The first real SDPD of an unknown using the Pawley method seems to be that of I_2O_4 (Lehmann *et al.*, 1987); its powder pattern had been previously indexed, but the structure not determined because of the lack of a suitable single crystal. During these pioneering years, *ALLHKL* could not extract the intensities for more than 300 peaks, so that, in more complex cases, it was necessary to subdivide the pattern into several parts. Moreover, it was rather difficult to avoid completely the ill conditioning due to overlapping peaks. Successful fits yielded equipartitioned intensities (*i.e.*, equal structure factors for those Bragg peaks with exact overlap). Unsuccessful fits could easily produce negative intensities which, combined with positive ones for other peak(s) at the same angle, reproduced the global positive value. Moreover, the first version to apply Gaussian peak shapes could not easily produce any SDPD because of the relatively poor resolution of constant-wavelength neutron data, so that it needed to be adapted to X-ray data, with the implementation of more complex peak shapes. Several programs were subsequently developed, based on the same principles as the original Pawley method. The first of them, by Toraya (1986), extended the use to X-ray data with non-Gaussian profile shapes, and introduced two narrow band matrices instead of a large triangular matrix, saving both computation time and memory space in a program named *WPPF*. Some programs were used to produce intensities in order to apply the so-called two-stage method (Cooper *et al.*, 1981) for structure refinement, such as *PROFIT* (Scott, 1987) and *PROFIN* (Will, 1988) (no slack constraints, but equal division of the intensity between expected peaks when the overlap was severe). There was intense continuing activity on Pawley-like software with other programs such as *FULFIT* (Jansen *et al.*, 1988), *LSQPROF* (Jansen *et al.*, 1992) and *POLISH* (Byrom & Lucas, 1993). Estimation of intensities of overlapping reflections was improved in *LSQPROF* by applying relations between structure-factor amplitudes derived from direct methods, and the Patterson function was considered in the satellite program *DOREES* (Jansen *et al.*, 1992). The question of how to determine the intensities of completely (or largely) overlapping reflections (either systematic overlap due to symmetry or fortuitous overlap) from a single powder pattern cannot have a definite simple answer, but continues to be discussed, since it is essential for improving our ability to solve structures. An early view with a probabilistic approach was given by David (1987), later introducing Bayesian statistics (Sivia & David, 1994) into the Pawley method. Early detection of preferred orientation on the basis of analysis of the *E*-value distribution was another way (Peschar *et al.*, 1995) to improve the structure-factor-amplitude estimate. New computer programs based on the Pawley method continue to be written even today.

3.5.2.2.2. *Le Bail method*

In order to be able to estimate *R* factors related to integrated intensities, Rietveld (1969) stated [see also the book *The Rietveld Method* edited by Young (1993)]: 'a fair approximation to the observed integrated intensities can be made by separating the peaks according to the calculated values of the integrated intensities,' *i.e.*

$$I_{hkl}(\text{obs}) = \sum_j [w_{j,hkl} S_{hkl}^2(\text{calc}) y_j(\text{obs})/y_j(\text{calc})], \qquad (3.5.1)$$

where $w_{j,hkl}$ is a measure of the contribution of the Bragg peak at position $2\theta_{hkl}$ to the diffraction profile y_j at position $2\theta_j$ [corresponding to equation 7 in Rietveld (1969)]. S_{hkl}^2 is the sum of the nuclear and magnetic contributions for neutron diffraction, or is more simply F_{hkl}^2 for X-rays. The sum is over all y_j(obs) that can theoretically contribute to the integrated intensity I_{hkl}(obs). Bias is introduced here by apportioning the intensities according to the calculated intensities; this is why the observed intensities are said to be 'observed', in quotation marks, in the Rietveld method. These 'observed' intensities are used in the R_B and R_F calculations (residuals on intensities and structure-factor amplitudes, respectively). They are also required for Fourier-map estimations, which, as a consequence, are less reliable than those from single-crystal data.

A process using the Rietveld decomposition formula iteratively for WPPD purposes was first applied in 1988 (Le Bail *et al.*, 1988) and much later was called the 'Le Bail method' or 'Le Bail fit', or 'pattern matching' as well as 'profile matching' in the *FULLPROF* Rietveld program (Rodriguez-Carvajal, 1990). In the original computer program (named *ARITB*), arbitrarily all equal S_{hkl}^2(calc) values are first entered in the above equation, instead of using structure factors calculated from the atomic coordinates, resulting in 'I_{hkl}(obs)' which are then re-entered as new S_{hkl}^2(calc) values at the next iteration, while the usual profile and cell parameters (but not the scale) are refined by least squares (*ARITB* used profile shapes represented by Fourier series, either analytical or learned from experimental data, providing an easy way to realize convolution by broadening functions modelling size–strain sample effects, possibly anisotropic). Equipartition of exactly overlapping reflections comes from the strictly equal result from equation (3.5.1) for Bragg peaks at the same angles which would have equal starting calculated intensities. Not starting from a set of all equal S_{hkl}^2(calc) values avoids equipartition for the exactly overlapping reflections but produces I_{hkl}(obs) keeping the same original ratio as the S^2_{hkl}(calc) ones. It is understandable that such an iterative process requires starting cell and profile parameters as good as the Rietveld method itself. The process is easier to incorporate within an existing Rietveld code than the Pawley method, so that most Rietveld codes now include structure-factor amplitudes extraction as an option (generally multiphase), with the possibility of combining Rietveld refinement(s) together with Le Bail fit(s).

A non-exhaustive list of programs applying this method (either exclusively or added within a Rietveld code) includes *MPROF* (Jouanneaux *et al.*, 1990), later renamed *WinMPROF*; *FULLPROF* (Rodriguez-Carvajal, 1990); *EXTRACT* (Baerlocher, 1990); *EXTRA* (Altomare *et al.*, 1995); *EXPO* (Altomare *et al.*, 1999), which is the integration of *EXTRA* and *SIRPOW.92* for solution and refinement of crystal structures; and *RIETAN* (Izumi & Ikeda, 2000). Then followed most well known Rietveld codes (*BGMN*, *GSAS*, *MAUD*, *TOPAS etc.*) or standalone programs (*AJUST* by Rius *et al.*, 1996). In the work of the Giacovazzo group, many modifications of the $|F_{hkl}|$ values for SDPD purposes were applied before or after the extraction and were integrated in *EXPO2011* (Altomare *et al.*, 2011): obtaining information about the possible presence of preferred orientation by statistical analysis of the normalized structure-factor moduli; using the positivity of the Patterson function in the decomposition process, this having been considered previously (David, 1987; Estermann & Gramlich, 1993); characterization of pseudotranslational symmetry used as prior information in the pattern-decomposition process; multiple Le Bail fits with random attribution of intensity to the overlapping reflections, instead of equipartition, followed by application of direct methods to large numbers of such data sets; use of a located structure fragment for improving the pattern-decomposition process; and use of probability (triplet-invariant distribution functions) integrated with the Le Bail algorithm. Another approach for solving the overlapping problem was proposed by using maximum-entropy coupled with likelihood evaluation (Dong & Gilmore, 1998). The list of structure solutions made from intensities extracted by using the Pawley and Le Bail methods is too long to be given here; a partial list (>1000 first cases, including those using $|F_{hkl}|$ values extracted by other methods) can be found on the web (Le Bail, 2007). The first application of the Le Bail method was to the structure solution of $LiSbWO_6$ (Le Bail *et al.*, 1988) using the *ARITB* software.

3.5.3. Pitfalls in the extraction of accurate $|F_{hkl}|$ values using the Pawley and Le Bail methods

In the Rietveld refinement guidelines published by the IUCr Commission on Powder Diffraction (McCusker *et al.*, 1999), it is said that the Rietveld $R_{\rm wp}$ value should approach the value obtained in a structure-free refinement (*i.e.* using WPPD methods). Such a refinement is recommended for the estimation of initial values of the Rietveld profile parameters. Consequently, $|F_{hkl}|$ values extracted by WPPD can be used to make a good reproduction of the experimental powder pattern if the cell is correct (which is ultimately only proven if the structure is solved and refined). Pitfalls can occur during post-treatment and application of the $|F_{hkl}|$ data if one neglects the possible errors that are inherently present due to exact or accidental overlap, preferred orientation effects or wrong background estimations, citing only three of the main possible causes of errors in these $|F_{hkl}|$ values.

3.5.3.1. *Consequences of (exact or accidental) overlap*

The uncertainties of the $|F_{hkl}|$ values of overlapped reflections cannot be overcome in a single powder-diffraction experiment. This problem has led to various approaches, all being more or less inefficient: equipartition, non-equipartition by random distribution *etc.* If direct methods are applied, the trend is to multiply the number of solution attempts, trying to identify the most convincing one by using structural arguments (such as atoms in chemically reasonable positions). When applying real-space methods (which require chemical knowledge, such as the three-dimensional molecular structure or the presence of definite polyhedra) one generally chooses to work either directly on the raw powder pattern or on a pseudo pattern built from the extracted $|F_{hkl}|$ values, so that wrong individual values are less of a problem, since only the sums of the contributions in overlapping regions are checked during the search for the molecule, polyhedra or atom positions. Indeed, working on the raw powder pattern does not need reduction to $|F_{hkl}|$ values in theory, but in practice either the Pawley or Le Bail methods are applied first in order to fix the zero point, background, cell and profile parameters which will then be applied during the structure model checking, and to speed the calculations. The extracted $|F_{hkl}|$ values can be used in mathematical expressions defining correlations induced by the overlap. These equations were developed by David *et al.* (1998) for the Pawley method in the real-space structure solution program *DASH* and by Pagola *et al.* (2000) for the Le Bail method in *PSSP*. Regenerating a powder pattern from the extracted $|F_{hkl}|$ values was carried out in the *ESPOIR* real-space computer program (Le Bail, 2001) using a simple Gaussian peak shape whose width follows the Caglioti relation established from the raw pattern. With such a pseudo powder pattern (without profile asymmetry, background *etc.*), the calculations are much faster than if the raw pattern is used. When using direct methods instead of real-space methods, the approaches are different, because direct methods require a more complete data set (up to d = 1 Å) of accurate $|F_{hkl}|$ values. However, removing up to half of them (those with too much overlap, *i.e.* where the overlap is greater than half the FWHM, for instance) can lead to success with direct methods. One can even remove up to 70–80% of the data if the Patterson method is applied and if only a small number of heavy atoms are to be located.

3.5.3.2. *Preferred-orientation effects*

One has to ensure that preferred orientation is minimized during the recording of the powder pattern if the extracted $|F_{hkl}|$ values are to be used for structure solution. In transmission geometry with a capillary specimen (provided that it is not composed of long needle-shaped particles that are all aligned), there is generally no problem. But in reflection geometry with samples pressed on the holder, preferred orientation is not rare, even if it is not obvious in the data. Collecting a second pattern from a sample dusted onto the holder through a fine sieve can be informative. However, some WPPD applications may not be sensitive to such a problem. If only the cell parameters have to be accurately estimated for thermal-expansion studies (Evans *et al.*, 1996), it can be much faster to use WPPD rather than the Rietveld method. However, it is not recommended to do this systematically, especially if the structure is complex and the resolution is low [see the warnings in Peterson (2005)].

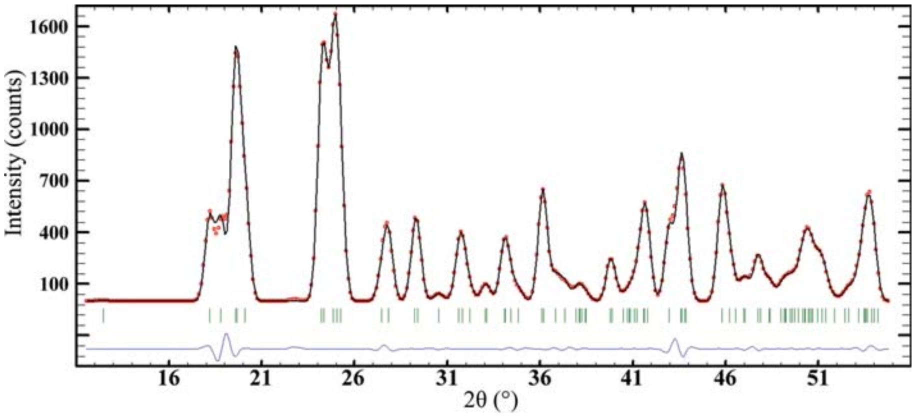

Figure 3.5.1
Data reduction to $|F_{hkl}|$ values for the C_6F_{10} Pawley (1981) test case by the Le Bail method using *FULLPROF*. The neutron powder pattern (4.2 K) was rebuilt (λ = 1.909 Å) from the intensities given in the original paper ($P2/m$). The extraction of $|F_{hkl}|$ values was carried out in the space group $P2_1/n$.

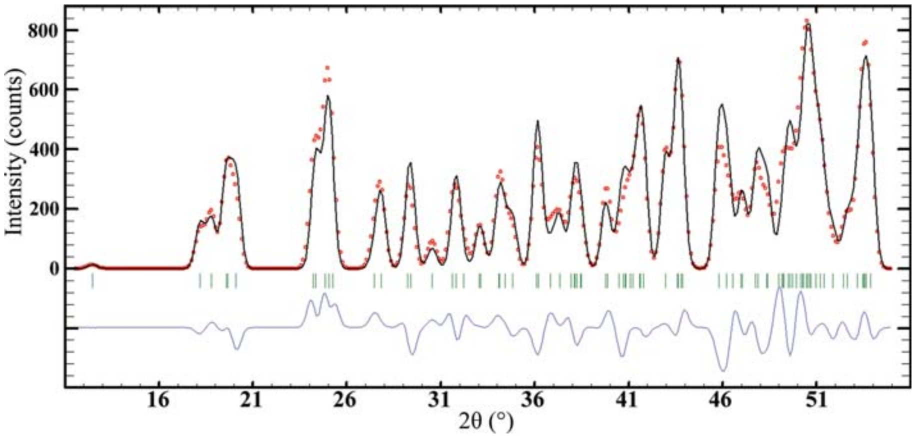

Figure 3.5.2
The C_6F_{10} Monte Carlo molecule positioning by the real-space *ESPOIR* program produces that best fit (R_p = 13.6%) of the pseudo powder pattern built from the previously extracted $|F_{hkl}|$ values (Fig. 3.5.1), overcoming the equipartition problem at the reduction stage. Compared to Fig. 3.5.1, which shows intensities, the multiplicity and geometrical factors are removed, leading to structure-factor amplitudes.

3.5.3.3. *Background-estimation effects*

Logically, a background value will never be higher than the observed intensity at the diffraction angle where it is visually estimated. In the first refinement cycles by the Pawley or Le Bail methods, it is preferable to keep the background fixed as well as the cell parameters, which assumes that the starting values have been carefully estimated or even (in the cell-parameter case) have already been refined from the peak positions that were used for indexing. This is because all refinement processes need to start from parameters close to the final values. Selecting background values leading to negative intensities after background removal could result in negative $|F_{hkl}|$ values if the software does not account for this.

3.5.4. Applications and by-products

The first modern WPPD method with cell restraints was developed for neutron data by Pawley (1981), 12 years after the publication of the paper that described the Rietveld (1969) method. In Le Bail *et al.* (1988) a new WPPD approach was used to extract intensities, making use of iterations of the Rietveld decomposition formula. It is clear that both these WPPD methods are children of the Rietveld method. Today most users of the Rietveld method do not cite the original Rietveld papers, but only refer to the computer program that they used. This is also now increasingly the case for the WPPD methods.

From the Thomson Reuters ISI citation index consulted in May 2015, the papers for the Pawley and Le Bail methods scored 892 and 1425 direct citations, respectively. There are several highly cited papers that then cite these two papers. The most highly cited paper (>5100 times) that cites both WPPD methods concerns use of the Le Bail intensity-extraction method by *FULLPROF* for solving magnetic structures (Rodriguez-Carvajal, 1993). This paper is also given as a reference for *FULLPROF* used in more standard Rietveld refinements. This suggests that the impact of WPPD methods is higher than commonly believed. The list of possible WPPD applications includes phase identification, quantitative phase analysis, measurement of crystallite sizes and strains, creation of Fourier maps for partially solved structures, structure refinement by the two-step method, studies of electron-density distribution, and characterization of pole figures, using either the Pawley or Le Bail methods. All routes to SDPD use at least one of them. WPPD has even entered into the indexing step, with Kariuki *et al.* (1999) using the Le Bail fit for testing cell hypotheses (for which it is faster than the Pawley method) in a new computer program that uses a genetic algorithm. But the main applications of the WPPD methods are to provide support for cell-parameter refinement and the determination of the space group, as a prelude to the full use of the extracted $|F_{hkl}|$ values for *ab initio* structure solution.

3.5.4.1. *Supporting indexing and space-group determination*

As they yield the smallest possible profile R_p and $R_{\rm wp}$ factors (smaller than from the Rietveld method, which is limited by the crystal-structure refinement), the Pawley and Le Bail methods provide strong support for both the proposed indexing and the determination of the space group. Some computer programs provide an automated suggestion for the latter. This support is needed to show that it is worth attempting to solve the structure. Once the structure is solved, the structure constraint will remove the ambiguity between intensities of close Bragg peaks and necessarily improve the quality of the cell parameters. If the structure is already known, the best approach is the Rietveld method. There is a progression in the precision of the refined cell parameters from the lowest level (least squares from individually extracted peak positions) to a medium level (WPPD with cell restraint) to the highest possible level (Rietveld, adding the structure constraint). With both Pawley and Le Bail methods, the fit quality is checked using agreement factors which are the same as with the Rietveld method: R_p and $R_{\rm wp}$ (moreover, a careful visual check is recommended). The reliabilities relative to the structure (R_B and R_F), which can still be calculated, are meaningless (WPPD programs tending to obtain a value close to zero for both of them).

3.5.4.2. *Structure solution*

SDPD can be undertaken by various approaches, depending on the chemical knowledge of the sample (formula, molecular formula, presence of defined polyhedra . . .), either directly using the $|F_{hkl}|$ values for structure solution by direct or Patterson methods, or by rebuilding a pseudo powder pattern from them, or by applying fixed profile parameters from the Pawley or Le Bail fits during whole-powder-pattern fitting wherein the structure solution is attempted by real-space methods. In order to illustrate the power of WPPD methods and to show the progress realized over the last 30 years, the decafluorocyclohexene structure that was unsolved in the Pawley method paper of 1981 is reconsidered. As stated by Pawley, from plausible extinctions the space group of the C_6F_{10} crystal structure at 4.2 K could well be $P2_1/n$. The $|F_{hkl}|$ values were extracted from the rebuilt neutron powder pattern by applying the Le Bail method and used for attempting the structure solution by real-space methods. The neutron powder pattern was rebuilt from the 109 intensities extracted up to 54° 2θ, in space group $P2/m$, given in Table 2 of the original paper. The fit (using *FULLPROF*) in $P2_1/n$ of the data rebuilt in $P2/m$ is satisfactory (Fig. 3.5.1). The three-dimensional C_6F_{10} molecule was rotated and translated (six degrees of freedom) in the cell using the *ESPOIR* (Le Bail, 2001) Monte Carlo program, leading to a plausible starting model (R_p = 13.6%) ready for Rietveld refinement. This program builds a pseudo powder pattern from the extracted $|F_{hkl}|$ values, which is then compared to the data calculated from the model (Fig. 3.5.2). Unrefined atomic coordinates are available from the Crystallography Open Database (COD, CIF No. 3500009) (Grazulis *et al.*, 2009); a projection of the corresponding structure is shown in Fig. 3.5.3. The true crystal structure is apparently more complex (Solovyov *et al.*, 2014). Final resolution of the structure will require collection of a better experimental powder pattern. However, the coordinates have been refined by energy minimization in the solid state (Smrčok *et al.*, 2013).

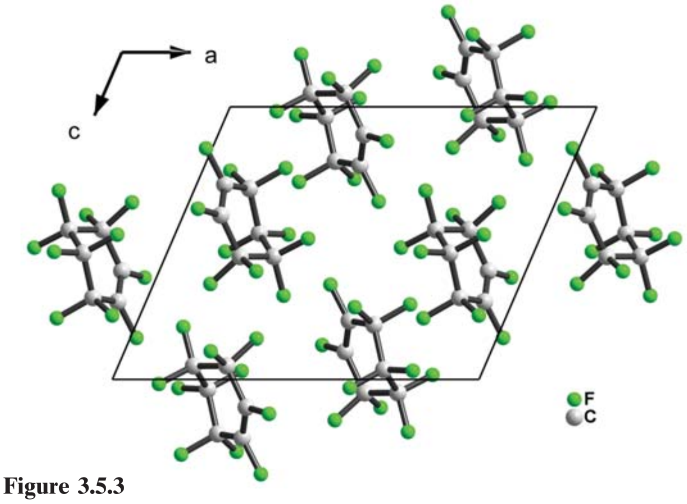

Figure 3.5.3
Projection along the *b* axis of the C_6F_{10} structure model in $P2_1/n$ before Rietveld refinement.

3.5.5. Conclusion

'Which is best: the Pawley or the Le Bail method?' is not a question with a simple conclusive answer. The fact is that both methods are able to estimate structure-factor amplitudes, which can lead to structure solution from powder-diffraction data in a more efficient way than was previously possible, even if the problem of peak overlap precludes attaining single-crystal quality data from only one powder pattern. The advantage of the Le Bail method over the Pawley method is its speed, which becomes apparent when several thousands of $|F_{hkl}|$ values have to be extracted, for instance from high-resolution synchrotron data of a complex compound, since no more than about ten parameters have to be refined instead of thousands. Chemical knowledge may reduce the number of $|F_{hkl}|$ values necessary for solving a structure to the first 100 Bragg peaks at low diffraction angles, as shown in the above example. Moreover, the small number of successful participants in the three SDPD round robins held in 1998, 2002 and 2008 (Le Bail *et al.*, 2009) did not allow us to conclude whether one approach is really better than the other, or even to be sure if all the further modifications of the extracted $|F_{hkl}|$ values in particular computer programs are really decisive improvements (the conclusion was that SDPD 'on demand' was still not an easy task). WPPD is not the only reef on the SDPD journey; indexing remains a considerable bottleneck for complex materials and low-resolution data.

References

Altomare, A., Burla, M. C., Camalli, M., Carrozzini, B., Cascarano, G. L., Giacovazzo, C., Guagliardi, A., Moliterni, A. G. G., Polidori, G. & Rizzi, R. (1999). *EXPO: a program for full powder pattern decomposition and crystal structure solution*. *J. Appl. Cryst.* **32**, 339–340.

Altomare, A., Burla, M. C., Cascarano, G., Giacovazzo, C., Guagliardi, A., Moliterni, A. G. G. & Polidori, G. (1995). *EXTRA: a program for extracting structure-factor amplitudes from powder diffraction data. J. Appl. Cryst.* **28**, 842–846.

Altomare, A., Cuocci, C., Giacovazzo, C., Moliterni, A. G. G. & Rizzi, R. (2011). *Obtaining models suitable for Rietveld refinement: the EXPO2011 techniques*. *Z. Kristallogr.* **226**, 869–881.

Baerlocher, Ch. (1990). *EXTRACT, a Fortran program for the extraction of integrated intensities from a powder pattern.* Institut für Kristallographie, ETH, Zürich, Switzerland.

Bergmann, J., Le Bail, A., Shirley, R. & Zlokazov, V. (2004). *Renewed interest in powder diffraction data indexing*. *Z. Kristallogr.* **219**, 783–790.

Byrom, P. G. & Lucas, B. W. (1993). *POLISH: computer program for improving the accuracy of structure-factor magnitudes obtained from powder data. J. Appl. Cryst.* **26**, 137–139.

Caglioti, G., Paoletti, A. & Ricci, F. P. (1958). *Choice of collimators for a crystal spectrometer for neutron diffraction. Nucl. Instrum.* **3**, 223–228.

Cheary, R. W. & Coelho, A. (1992). *A fundamental parameters approach to X-ray line-profile fitting. J. Appl. Cryst.* **25**, 109–121.

Clearfield, C., Reibenspies, J. & Bhuvanesh, N. (2008). *Principles and applications of powder diffraction*, pp. 261–309. Oxford: Wiley.

Cooper, M. J., Rouse, K. D. & Sakata, M. (1981). *An alternative to the Rietveld profile refinement method. Z. Kristallogr.*, **157**, 101–117.

David, W. I. F. (1987). *The probabilistic determination of intensities of completely overlapping reflections in powder diffraction patterns. J. Appl. Cryst.* **20**, 316–319.

David, W. I. F., Shankland, K., McCusker, L. B. & Baerlocher, Ch. (2002). *Structure Determination from Powder Diffraction Data*, IUCr Monographs on Crystallography, Vol 13. New York: Oxford University Press.

David, W. I. F., Shankland, K. & Shankland, N. (1998). *Routine determination of molecular crystal structures from powder diffraction data. Chem. Commun.* pp. 931–932.

Dinnebier, R. E. & Billinge, S. J. L. (2008). *Powder diffraction: theory and practice*, pp. 134–165. Cambridge: RSC Publishing.

Dong, W. & Gilmore, C. J. (1998). *The ab initio solution of structures from powder diffraction data: the use of maximum entropy and likelihood to determine the relative amplitudes of overlapped reflections using the pseudophase concept. Acta Cryst.* A**54**, 438–446.

Estermann, M. A. & Gramlich, V. (1993). *Improved treatment of severely or exactly overlapping Bragg reflections for the application of direct methods to powder data. J. Appl. Cryst.* **26**, 396–404.

Evans, J. S. O., Mary, T. A., Vogt, T., Subramanian, M. A. & Sleight, A. W. (1996). *Negative thermal expansion in ZrW_2O_8 and HfW_2O_8. Chem. Mater.* **8**, 2809–2823.

Giacovazzo, C. (1998). *Direct Phasing in Crystallography: Fundamentals and Applications*, IUCr Monographs on Crystallography, Vol. 8, pp. 410–444. New York: Oxford University Press.

Grazulis, S., Chateigner, D., Downs, R. T., Yokochi, A. F. T., Quirós, M., Lutterotti, L., Manakova, E., Butkus, J., Moeck, P. & Le Bail, A. (2009). *Crystallography Open Database - an open-access collection of crystal structures. J. Appl. Cryst.* **42**, 726–729.

Izumi, F. & Ikeda, T. (2000). *A Rietveld-analysis program RIETAN-98 and its applications to zeolites. Mater. Sci. Forum*, **321–324**, 198–205.

Jansen, E., Schäfer, W. & Will, G. (1988). *Profile fitting and the two-stage method in neutron powder diffractometry for structure and texture analysis. J. Appl. Cryst.* **21**, 228–239.

Jansen, J., Peschar, R. & Schenk, H. (1992). *On the determination of accurate intensities from powder diffraction data. I. Whole-pattern fitting with a least-squares procedure. J. Appl. Cryst.* **25**, 231–236.

Jouanneaux, A., Murray, A. D. & Fitch, A. N. (1990). *MPROF: a multipattern Rietveld refinement program for neutron, X-ray and synchrotron radiation*. SERC Daresbury Laboratory, Warrington, England.

Kariuki, B. M., Belmonte, S. A., McMahon, M. I., Johnston, R. L., Harris, K. D. M. & Nelmes, R. J. (1999). *A new approach for indexing powder diffraction data based on whole-profile fitting and global optimization using a genetic algorithm. J. Synchrotron Rad.* **6**, 87–92.

Langford, J. I., Boultif, A., Auffrédic, J. P. & Louër, D. (1993). *The use of pattern decomposition to study the combined X-ray diffraction effects of crystallite size and stacking faults in ex-oxalate zinc oxide. J. Appl. Cryst.* **26**, 22–33.

Langford, J. I. & Louër, D. (1991). *High-resolution powder diffraction studies of copper(II) oxide. J. Appl. Cryst.* **24**, 149–155.

Langford, J. I. & Louër, D. (1996). *Powder diffraction. Rep. Prog. Phys.* **59**, 131–234.

Langford, J. I., Louër, D., Sonneveld, E. J. & Visser, J. W. (1986). *Applications of total pattern fitting to a study of crystallite size and strain in zinc oxide powder. Powder Diffr.* **1**, 211–221.

Le Bail, A. (2001). *ESPOIR: A program for solving structures by Monte Carlo analysis of powder diffraction data. Mater. Sci. Forum*, **378**, 65–70.

Le Bail, A. (2005). *Whole powder pattern decomposition methods and applications: A retrospection. Powder Diffr.* **20**, 316–326.

Le Bail, A. (2007). *Structure Determination from Powder Diffraction Database – SDPD*. http://www.cristal.org/iniref.html.

Le Bail, A., Cranswick, L. M. D., Adil, K., Altomare, A., Avdeev, M., Cerny, R., Cuocci, C., Giacovazzo, C., Halasz, I., Lapidus, S. H., Louwen, J. N., Moliterni, A., Palatinus, L., Rizzi, R., Schilder, E. C., Stephens, P. W., Stone, K. H. & van Mechelen, J. (2009). *Third structure determination by powder diffractometry round robin (SDPDRR-3). Powder Diffr.* **24**, 254–262.

Le Bail, A., Duroy, H. & Fourquet, J. L. (1988). *Ab-initio structure determination of $LiSbWO_6$ by X-ray powder diffraction. Mater. Res. Bull.* **23**, 447–452.

Lehmann, M. S., Christensen, A. N., Fjellvåg, H., Feidenhans'l, R. & Nielsen, M. (1987). *Structure determination by use of pattern decomposition and the Rietveld method on synchrotron X-ray and neutron powder data; the structures of $Al_2Y_4O_9$ and I_2O_4. J. Appl. Cryst.* **20**, 123–129.

McCusker, L. B., Von Dreele, R. B., Cox, D. E., Louër, D. & Scardi, P. (1999). *Rietveld refinement guidelines. J. Appl. Cryst.* **32**, 36–50.

Pagola, S., Stephens, P. W., Bohle, D. S., Kosar, A. D. & Madsen, S. K. (2000). *The structure of malaria pigment beta-haematin. Nature*, **404**, 307–310.

Pawley, G. S. (1981). *Unit-cell refinement from powder diffraction scans. J. Appl. Cryst.* **14**, 357–361.

Pecharsky, V. K. & Zavalij, P. Y. (2003). *Fundamentals of powder diffraction and structural characterization of materials*. New York: Springer.

Peschar, R., Schenk, H. & Capkova, P. (1995). *Preferred-orientation correction and normalization procedure for ab initio structure determination from powder data. J. Appl. Cryst.* **28**, 127–140.

Peterson, V. K. (2005). *Lattice parameter measurement using Le Bail versus structural (Rietveld) refinement: a caution for complex, low symmetry systems. Powder Diffr.* **20**, 14–17.

Rietveld, H. M. (1969). *A profile refinement method for nuclear and magnetic structures. J. Appl. Cryst.* **2**, 65–71.

Rius, J., Sane, J., Miravitlles, C., Amigo, J. M., Reventos, M. M. & Louër, D. (1996). *Determination of crystal structures from powder diffraction data by direct methods: extraction of integrated intensities from partially overlapping Bragg reflections. Anal. Quim.* **92**, 223–227.

Rodriguez-Carvajal, J. (1990). *FULLPROF: a program for Rietveld refinement and pattern-matching analysis*. Abstracts of the meeting Powder Diffraction, Toulouse, France, pp. 127–128.

Rodriguez-Carvajal, J. (1993). *Recent advances in magnetic structure detemination by neutron powder diffraction. Physica B*, **192**, 55–69.

Scott, H. G. (1987). *PROFIT – a peak-fitting program for powder diffraction profile*. IUCr Satellite Meeting on X-ray Powder Diffractometry, 20–23 August 1987, Fremantle, Western Australia. Abstract P28.

Sivia, D. S. & David, W. I. F. (1994). *A Bayesian approach to extracting structure-factor amplitudes from powder diffraction data. Acta Cryst.* A**50**, 703–714.

Smrčok, Ľ., Mach, P. & Le Bail, A. (2013). *Decafluorocyclohex-1-ene at 4.2 K – crystal structure and theoretical analysis of weak interactions. Acta Cryst.* B**69**, 395–404.

Solovyov, L. A., Fedorov, A. S. & Kuzubov, A. A. (2014). *Complete crystal structure of decafluorocyclohex-1-ene at 4.2 K from original neutron diffraction data. Acta Cryst.* B**70**, 395–397.

Sonneveld, E. J. & Visser, J. W. (1975). *Automatic collection of powder data from photographs. J. Appl. Cryst.* **8**, 1–7.

Toraya, H. (1986). *Whole-powder-pattern fitting without reference to a structural model: application to X-ray powder diffraction data. J. Appl. Cryst.* **19**, 440–447.

Toraya, H. (1994). *Applications of whole-powder-pattern fitting technique in materials characterization. Mater. Charact. Adv. X-ray Anal.* **37**, 37–47.

Waser, J. (1963). *Least-squares refinement with subsidiary conditions. Acta Cryst.* **16**, 1091–1094.

Wiles, D. B. & Young, R. A. (1981). *A new computer program for Rietveld analysis of X-ray powder diffraction patterns. J. Appl. Cryst.* **14**, 149–151.

Will, G. (1988). *Crystal structure analysis and refinement using integrated intensities from accurate profile fits. Aust. J. Phys.* **41**, 283–296.

Will, G., Masciocchi, N., Parrish, W. & Hart, M. (1987). *Refinement of simple crystal structures from synchrotron radiation powder diffraction data. J. Appl. Cryst.* **20**, 394–401.

Will, G., Parrish, W. & Huang, T. C. (1983). *Crystal-structure refinement by profile fitting and least-squares analysis of powder diffractometer data. J. Appl. Cryst.* **16**, 611–622.

Young, R. A. (1993). *The Rietveld Method*. IUCr Monographs on Crystallography, Vol. 5. New York: Oxford University Press.

International Tables for Crystallography (2019). Vol. H, Chapter 3.6, pp. 288–303.

3.6. Whole powder pattern modelling: microstructure determination from powder diffraction data

M. Leoni

3.6.1. Introduction

X-ray diffraction is a very simple technique, but is one of the most flexible and powerful tools for the analysis of materials. The diffraction pattern carries information about the atomic arrangement and motion at both the short and the long range; for nanostructured materials this means that a single technique can simultaneously provide structural and microstructural information.

Microstructure analysis *via* X-ray powder diffraction (XRD), often termed line-profile analysis (LPA), is mostly performed through the Scherrer (1918) formula. Just a few years after the discovery of X-ray diffraction, Scherrer derived a very simple relationship between the width of the diffraction peaks and the size of the so-called *Kristallchen* (translated as crystallites), the coherently scattering (nanocrystalline) domains composing the colloids that he was studying (the formula is rewritten here using an updated notation):

$$\langle D\rangle = \frac{K_w \lambda}{\mathrm{FWHM}_{hkl}\cos\theta_{hkl}}. \qquad (3.6.1)$$

The calculation of an 'average size' $\langle D\rangle$ is therefore immediate once the position and full-width at half-maximum of a peak ($2\theta_{hkl}$ and FWHM_{hkl}, respectively), measured with X-rays of wavelength λ, are available. The constant K_w (the Scherrer constant) carries information on the shape of the domains and has an order of magnitude of 1. Values of the Scherrer constant can be found in the literature for both isotropic and anisotropic shapes (in the latter case leading to different sizes for different reflections *hkl*): Table 3.6.1 contains the data of Langford & Wilson (1978) for common domain shapes. An elegant derivation of the Scherrer formula can be found in the work of Patterson (1939) and Warren (1990); a summary is also presented in Chapter 5.1.

Its simple mathematical nature is probably the main reason for the widespread (ab)use of equation (3.6.1). Simple, in fact, does not mean accurate.

The Scherrer formula and its variants are based on strong assumptions about the peak shape. In the original derivation [equation (3.6.1)] the peak was assumed to be Gaussian (see Appendix A3.6.1 for the definition of a unit-area Gaussian); in subsequent derivations, the peak-shape information is lost, as the peak is transformed into an equivalent rectangle *via* the use of the integral breadth (IB) $\beta = A/I$, where A and I are the area and the maximum intensity of the peak, respectively (see Table 3.6.1 for the corresponding Scherrer constant values). Together with this, we should consider that the size of the domains in a real specimen is always disperse; it can be easily proven that the quantity $\langle D\rangle$, which is called the 'average size' or 'mean size', is actually not the mean (first moment) of the size distribution, but is related to its third moment (*i.e.* it is volume-weighted). If we add that the finite size of the domains is not the only source of peak broadening, we immediately see where the abuse of the Scherrer formula can lie.

Table 3.6.1
Scherrer constants (K_w and K_β) for various domain shapes (Langford & Wilson, 1978)

Shape	K_w (FWHM)	K_β (integral breadth)
Sphere	0.89	1.07
Cube	0.83–0.91	1.00–1.16
Tetrahedron	0.73–1.03	0.94–1.39
Octahedron	0.82–0.94	1.04–1.14

To try to sort some of those issues out, Williamson & Hall (1953) proposed plotting the FWHM (or the IB) *versus* the reciprocal of the lattice spacing ($d^*_{hkl} = 1/d_{hkl} = 2\sin\theta_{hkl}/\lambda$). For spherical domains (*i.e.* size independent of the direction), a horizontal line is expected. An anisotropic shape would cause a scattering of the points, whereas other sources of broadening might also change the slope. Following the findings of Stokes & Wilson (1944), Williamson and Hall proposed writing the integral breadth in reciprocal space (reciprocal-space variable d^*) as a combination of the Scherrer formula with the differential of Bragg's law:

$$\beta(d^*) = \frac{K_\beta}{\langle D\rangle} + 2ed^*. \qquad (3.6.2)$$

Equation (3.6.2) describes a line for which the intercept (extrapolation of the integral breadth to the origin of the reciprocal space, *i.e.* to $d\to\infty$) is related to the reciprocal of the Scherrer size, and the slope parameter e accounts for the distribution of local strain inside the domains. For a Gaussian distribution of this local strain, the root-mean strain (also known as microstrain) $\langle\varepsilon^2\rangle^{1/2} = e\sqrt{2/\pi}$ can be obtained. The microstrain, which is mostly caused by the presence of imperfections, is often quoted together with the average size.

Even though the Williamson–Hall idea is straightforward, there is no physical reason why the two terms in equation (3.6.2) should be added: the only case where breadths are additive is when the peaks are Lorentzian (see Appendix A3.6.1 for the definition of a unit-area Lorentzian). The Williamson–Hall equation is therefore valid for Lorentzian peaks and under the condition that both the size and strain contributions are Lorentzian as well. We therefore immediately envisage a problem here, as the size contribution, described by the Scherrer equation, was derived in the Gaussian limit. This inconsistency is seldom reported or considered in the literature. The fact that, in the end, the profiles are often highly Lorentzian in character mathematically justifies the separation of a size and a strain term, but dilutes the quantitative meaning of the result.

Modification of the Williamson–Hall approach to remove the inconsistency of the size- and strain-broadening terms has been extensively discussed by Balzar & Popović (1996). Using Voigtians (*i.e.* the convolution of a Gaussian G and a Lorentzian L; see Appendix A3.6.1) to describe a profile, four combinations are possible for the size and strain terms: *L–L*, *L–G*, *G–L* and *G–G*. The Williamson–Hall method corresponds to the *L–L* case, whereas the combinations involving a Gaussian size term are more compatible with the Scherrer formula. Even in those cases, though, 'The pure-Gauss size-broadened profile is incompatible

Copyright © 2019 International Union of Crystallography

with the definitions of surface-weighted domain size and column-length distribution function' (Balzar & Popović, 1996): integral breadth methods are therefore intrinsically limited for the microstructure analysis of real materials. This is in stark contrast to the fact that equation (3.6.2) is used, for example, by a large number of Rietveld refinement codes to describe the observed trend in line-profile broadening (and to perform a rough microstructure analysis). This situation can be improved a little by properly considering at least the anisotropic broadening component, as performed, for example, in the modified Williamson–Hall method (MWH; Ungár & Borbély, 1996; Ungár, 2001; Scardi *et al.*, 2004). The results are more accurate and related to some physical quantities (a dislocation density and a stacking fault probability), but they are still tightly bound to a Voigtian profile approximation.

An alternative to the integral breadth methods was developed by Warren & Averbach (1950, 1952) almost simultaneously with the idea of Williamson and Hall, but took longer to be fully employed owing to the lack of fast computing tools. It is based on the extensive use of Fourier transforms and represents the starting point of modern line-profile analysis techniques. The whole profile carries information on the microstructure, as each point in reciprocal space is related to the Fourier transform of real space (and thus to the size and shape of the domains and also the deviation from perfect three-dimensional periodicity). Each profile also contributes to a better picture of the microstructure, as it samples along a different direction in space.

For decades, these Fourier methods were only used in a very small number of scientific areas; the availability of fast computers and the fast Fourier transform has contributed greatly to their further diffusion. It is, however, only in recent years that the full power of the Fourier approach has been unveiled, with the development of whole-pattern methods and the extension of most models to a wider range of materials.

3.6.2. Fourier methods

3.6.2.1. *Definitions*

In the following, the diffraction peaks for a powder will be described in reciprocal space with reference to the Bragg position $d^*_{\{hkl\}}$ expected for the $\{hkl\}$ reflection family in the absence of any type of defect. The coordinate s, where

$$s = d^* - d^*_{\{hkl\}} = \frac{2}{\lambda}\left(\sin\theta - \sin\theta_{\{hkl\}}\right), \qquad (3.6.3)$$

will be employed. Moving from reciprocal to diffraction space ('2θ space') involves a trivial but nonlinear change of variables: peaks that are symmetrical in reciprocal space will become asymmetrical in 2θ space and *vice versa*.

3.6.2.2. *Peak profile and the convolution theorem*

Each peak profile $h(s)$ in a powder diffraction pattern can be described as the convolution of an instrumental profile $g(s)$ with a function $f(s)$ accounting for sample-related effects (microstructure; see, for example, Jones, 1938; Alexander, 1954; Klug & Alexander, 1974; and references therein):

$$h(s) = \int\limits_{-\infty}^{\infty} f(y)g(s-y)\,\mathrm{d}y = f \otimes g(s). \qquad (3.6.4)$$

The calculation of the integral in equation (3.6.4) can be simplified through the use of a Fourier transform (FT). In fact, the convolution theorem states that the FT of a convolution is the product of the Fourier transforms of the functions to be folded:

$$\mathcal{C}(L) = \mathrm{FT}[h(s)] = \mathrm{FT}[f(s)] \times \mathrm{FT}[g(s)]. \qquad (3.6.5)$$

In this equation, L is the (real) Fourier variable conjugate to s. The properties of the Fourier transform allow equation (3.6.4) to be rewritten as

$$h(s) = \mathrm{FT}^{-1}[\mathcal{C}(L)] = \mathrm{FT}^{-1}\big[\mathrm{FT}[h(s)]\big] = \mathrm{FT}^{-1}\big[\mathrm{FT}[f(s)]\mathrm{FT}[g(s)]\big]. \qquad (3.6.6)$$

This equation is the basis of the Warren–Averbach approach and also of all modern LPA methods.

3.6.2.3. *The Warren–Averbach method and its variations*

The convolution theorem can be employed to disentangle the specimen-related broadening contributions described by $f(s)$. In fact, let us suppose, as in the Williamson–Hall method, that size and microstrain are the only two sources of specimen-related broadening. We call the Fourier transform of the profiles broadened by size and distortion effects only $A^S_{hkl}(L)$ and $A^D_{hkl}(L)$, respectively. As the size and distortion profiles are folded into $f(s)$, the following holds:

$$A(L) = \mathrm{FT}[f(s)] = \mathrm{FT}[h(s)]/\mathrm{FT}[g(s)] = A^S_{hkl}(L)A^D_{hkl}(L). \qquad (3.6.7)$$

The separation of the size and distortion terms is straightforward for spherical domains: the size effects for a sphere are independent of the reflection order, whereas those related to distortions (causing the change in the slope of the Williamson–Hall plot) are order-dependent. To describe the distortion term it is convenient to follow the idea of Bertaut (1949*a*,*b*, 1950), considering the specimen as made of columns of cells along the **c** direction. The profile due to distortions is calculated by taking the average phase shift along the column due to the presence of defects. The analytical formula for the distortion term is thus of the type $A^D_{hkl}(L) = \langle\exp(2\pi iLn\varepsilon_L)\rangle$, where $\varepsilon_L = \Delta L/L$ is the average strain along **c** calculated for a correlation distance (*i.e.* Fourier length) L.

As a first-order approximation, the distortion terms give no profile asymmetry; $A^D_{hkl}(L)$ is just a cosine Fourier transform. We can thus expand it as (Warren, 1990)

$$A^D_{hkl}(L) = \langle\cos(2\pi Ln\varepsilon_L)\rangle = 1 - 2\pi^2L^2n^2\langle\varepsilon^2_L\rangle. \qquad (3.6.8)$$

If we now rewrite equation (3.6.7) on a log scale, taking equation (3.6.8) into account, we obtain

$$\begin{aligned}\ln[A_{hkl}(L)] &= \ln[A^S_{hkl}(L)] + \ln[A^D_{hkl}(L)]\\ &= \ln[A^S_{hkl}(L)] + \ln[1 - 2\pi 2L^2n^2\langle\varepsilon^2_L\rangle]\\ &= \ln[A^S_{hkl}(L)] - 2\pi^2L^2n^2\langle\varepsilon^2_L\rangle. \qquad (3.6.9)\end{aligned}$$

Equation (3.6.9) represents a line in the variable n^2: the intercepts at increasing L values provide the logarithm of the Fourier size term, whereas the slopes give the microstrain directly (Warren, 1990). From the size coefficients, we can obtain an average size, again following the idea of Bertaut (1949*a*, 1950), related to the properties of the Fourier transform:

$$\langle D\rangle = \left[-\left.\frac{\partial A^S_{hkl}(L)}{\partial L}\right|_{L=0}\right]^{-1}. \qquad (3.6.10)$$

This average size is thus related to the initial slope of the Fourier coefficients [assuming that they are well behaved, *i.e.* that the tangent is always below the $A^S_{hkl}(L)$ curve].

A long chain of operations is needed to obtain the size and the strain contributions; there is thus a risk that the final result will no longer be compatible with the experimental data. Only a few years after the introduction of this method, Garrod *et al.* (1954) wrote

> Hence, in any attempt to distinguish between particle size or strain broadening from a particular material, the use of the one or the other of these functions [Gaussian and Lorentzian] (together with the appropriate relationship between B, b, and β) involves an intrinsic initial assumption about the cause of the broadening, when the object of the investigation is to discover the cause. Such an assumption must inevitably weight the experimental results, partially at least, in favour of one or the other of the two effects. In this connexion it is therefore perhaps significant that in most previous work on the cause of line broadening from cold-worked metals, those investigators who have used the Warren relationship between B, b, and β have concluded that lattice distortion was the predominant factor, whilst those who have employed the Scherrer correction found that particle size was the main cause. The best procedure in such work therefore is to make no assumptions at all about the shape of the experimental line profiles . . .

This is owing to the fact that a direct connection between the experimental data and the final microstructural result does not really exist in those methods and that the whole information contained in the pattern is not exploited.

3.6.2.4. *Beyond the Warren–Averbach method*

The work of Alexander (see, for example, Alexander, 1954; Klug & Alexander, 1974; and references therein) was definitely pioneering here. Alexander proposed a set of formulae for the synthesis of the instrumental profile, with the aim of obtaining a correction curve to subtract the instrumental contribution to the measured breadth of the profiles (thus improving the accuracy of the size determination). The true power of this idea was not fully exploited, as the Scherrer formula was still used for microstructure analysis. A few decades later, Adler, Houska and Smith (Adler & Houska, 1979; Houska & Smith, 1981) proposed the use of simplified analytical functions to describe the instrument, size and strain broadening and to perform the convolution of the equation numerically *via* Gauss–Legendre quadrature. Rao & Houska (1986) improved the procedure by carrying out part of the integration analytically (for monodisperse spheres). The microstructure parameters are directly obtained from a fit of this numerical peak to the experimental data. The fit partly solves the problem of peak overlap: in traditional methods it is in fact impossible to establish the extent of overlap between the peaks and therefore to correctly extract the area or maximum intensity. The method is a major step forward, but is still related to the Warren–Averbach approach, as just two multiple-order peaks are considered.

Cheary & Coelho (1992, 1994, 1998*a*,*b*) pushed the idea forward with the fundamental parameters approach (FPA). The FPA is based on the intuition of Alexander (1954) and the general idea of the Rietveld (1969) method: the calculation speed is greatly improved to facilitate widespread use. The convolution is performed directly in 2θ space, where instrumental aberrations, which were extensively explored by these researchers, occur. Very simplistic models were employed to describe the broadening due to the specimen; the whole pattern (and therefore all of the measured information) is considered in place of one or more peaks and of the extracted information. For structural analysis and for the Rietveld method, the FPA is a huge step forward, as it allows a more accurate determination of lattice parameters and integrated intensities. Moreover, it enables some line-profile analysis on low-quality patterns or on data affected by strong peak asymmetry.

3.6.2.5. *Whole powder pattern modelling (WPPM)*

The techniques briefly illustrated in the previous section, as well as other alternatives appearing in the literature before the beginning of this century, lack full completeness for quantitative microstructure analysis. The whole powder pattern modelling method attempted to fill this gap. Starting with the same ideas as in Section 3.6.2.1 (*i.e.* peaks as convolution), it uses equations (3.6.5) and (3.6.6) to generate the peaks within a fully convolutional approach. The peak profiles are therefore generated from the Fourier transform of each broadening component; the resulting $h(x)$ function accounts just for the shape of the profile, which in turn can be represented as (Scardi & Leoni, 2002)

$$I_{\{hkl\}}(s) = k(d^*)h(s) = k(d^*)\int\limits_{-\infty}^{\infty} \mathcal{C}(L)\exp(2\pi iLs)\,\mathrm{d}L, \tag{3.6.11}$$

where $k(d^*)$ includes all constant or known functions of d^* (*e.g.* structure factor, Lorentz–polarization factor *etc.*), whereas $\mathcal{C}(L)$ is the Fourier transform of the peak profile. The term k is a function of d^*; it is not necessarily a function of s, as the peak is actually centred in $d^*_{\{hkl\}}$.

Equation (3.6.11) assumes that the broadening sources act on the entire family of symmetry-equivalent reflections $\{hkl\}$ and therefore that a multiplicity term [included in $k(d^*)$] can be used: however, certain types of defects (*e.g.* faults) can act independently on each of the symmetry-equivalent reflections. Equation (3.6.11) then becomes more correctly

$$I_{\{hkl\}}(s) = k(d^*)\sum_{hkl} w_{hkl} I_{hkl}(s_{hkl}) = k(d^*)\sum_{hkl} w_{hkl} I_{hkl}(s-\delta_{hkl}), \tag{3.6.12}$$

where w_{hkl} is a weight function depending on the lattice symmetry and actual broadening source, $s_{hkl} = d^* - (d^*_{\{hkl\}} + \delta_{hkl}) = s - \delta_{hkl}$ is the distance, in reciprocal space, from the centroid of the peak hkl, and δ_{hkl} is the shift from $d^*_{\{hkl\}}$, the Bragg position in the absence of defects. The sum is over independent profile subcomponents selected on the basis of the specific defects (*e.g.* two for the $\{111\}$ family in f.c.c. when faults are present; selection is based on the value of $|L_0| = |h + k + l|$, *i.e.* 3 or 1).

According to equation (3.6.5), the function $\mathcal{C}(L)$ is the product of the Fourier transforms of the broadening contributions. In a real material, broadening is mostly due to the specific nature of the instrument, to the finite size of the coherently diffracting domain (size effect) and to the presence of defects such as, for example, dislocations and faults (Cheary & Coelho, 1992; van Berkum, 1994; Scardi & Leoni, 2002). Taking these into account,

$$\mathcal{C}(L) = T^{\mathrm{IP}}(L)A^{S}_{hkl}(L)\langle\exp[2\pi i\psi_{hkl}(L)]\rangle\langle\exp[2\pi i\varphi_{hkl}(L)]\rangle\ldots, \tag{3.6.13}$$

where $T^{\mathrm{IP}}(L)$ and $A^{S}_{hkl}(L)$ are the FTs of the instrumental and domain-size components, respectively, whereas the terms in angle brackets $\langle\,\rangle$ are average phase factors related to lattice distortions (ψ_{hkl}) and faulting (φ_{hkl}).

Equation (3.6.13) is the core of the WPPM method: as indicated by the ellipsis, any other broadening source can easily be considered by including the corresponding (complex) Fourier transform (*i.e.* the corresponding average phase factor) in equation (3.6.13). Expressions are known for several cases of practical interest (see, for example, Scardi & Leoni, 2002, 2004, 2005; Leoni & Scardi, 2004; Leineweber & Mittemeijer, 2004; van Berkum, 1994; Cheary & Coelho, 1992).

The approach is strictly valid when the broadening sources can be considered as diluted and independent (*i.e.* uncorrelated defects). If this does not apply, then cross-terms should be considered and the whole approach revised. In fact, here we assume that the structure factor can be factored and the lattice is fully periodic in three dimensions: under these conditions, structure (peak intensity) and microstructure (peak shape) can be decoupled as the peak positions can be determined in a straightforward way. Extended defects (*e.g.* faults) cause the appearance of diffuse effects and the displacement of the Bragg peaks: in order to calculate the diffraction pattern, the structure and the microstructure must be simultaneously known (see, for example, Drits & Tchoubar, 1990).

3.6.2.6. *Broadening components*

A brief account is given of the main sources of broadening that can be encountered in practice. An accent will be placed on X-rays, but extension to electrons and neutrons is in most cases straightforward. Concerning electron diffraction, precession data can be used in a straightforward way, whereas for traditional data, containing dynamical effects, further calculations, for example of the intensity, are in principle needed.

3.6.2.6.1. *Instrument*

Each of the components of the diffraction instrument (*i.e.* source, optics, specimen stage, measurement geometry and detector) can have a dramatic impact both on the position and the broadening of the peaks. Axial divergence, for instance, introduces both an asymmetric broadening and an apparent shift of the low-angle peaks. When microstructure (*i.e.* specimen-related effects) is the focus of the analysis, the primary recommendation is to try to limit the instrumental influence. Alternatively, it is preferred to have an instrumental profile (no matter how complex) that can be well described and properly simulated: for instance the profile of an instrument with a $K\alpha_1$ primary monochromator (apparently advantageous) might be hard to model if the $K\alpha_2$ removal is not perfect. This becomes more and more important when the instrumental effects are of the same order of magnitude as the specimen-related broadening.

Two possible paths can be followed when dealing with the instrumental contribution: modelling using the fundamental parameters approach (see, for example, Cheary & Coelho, 1992; Kern & Coelho, 1998) or parameterization of the pattern of an ideal specimen. In the fundamental parameters approach, the geometry of the instrument and the effects of each optical component on the peak profile are described mathematically in 2θ. Most of the formulae for the various optical elements can be found, for example, in the work of Wilson (1963), Klug & Alexander (1974) and Cheary & Coelho (1992, 1994, 1998*a*,*b*). The aberration profiles are folded into the (X-ray) source emission profile (Hölzer *et al.*, 1997; Deutsch *et al.*, 2004) to generate a combined instrumental profile.

When no information on the instrument is available, it is possible to predict the instrumental profile just by using the nominal data for the optical components. It is however advised, whenever possible, to tune the instrumental parameters using the pattern of a line-profile standard [*e.g.* NIST LaB$_6$ SRM 660(x) series; Cline *et al.*, 2010] showing negligible specimen effects. These instrument-only parameters must then be kept fixed for any subsequent microstructure refinement. It is of paramount importance that all instrumental features are well reproduced when dealing with microstructure effects. Provided that this condition is met, we can therefore employ any arbitrary function to describe the instrumental profile. Thus, as an alternative to FPA, we can either 'learn' the instrumental profile from a standard (Bergmann & Kleeberg, 2001) or use a Voigtian to model it. The Voigtian is particularly convenient as it can be defined directly in L space and thus directly enter the Fourier product of equation (3.6.13).

3.6.2.6.2. *Source emission profile*

For X-rays, the source emission profile at an energy E_l can be well described by a Lorentzian of energy width Γ_l (Hölzer *et al.*, 1997; Deutsch *et al.*, 2004),

$$I_l(E) = \frac{2}{\Gamma_l \pi}\left[1 + 4\left(\frac{E - E_l}{\Gamma_l}\right)^2\right]^{-1}. \qquad (3.6.14)$$

As dE/E = dλ/λ = ds/s, the function can also be represented as a function of s:

$$I^{\rm IP}_{hkl,l}(s, d^*_{hkl}) = \frac{2}{\pi}\frac{E_l}{d^*_{hkl}\Gamma_l}\left[1 + 4\left(\frac{s_{hkl}}{d^*_{hkl}\Gamma_l/E_l}\right)^2\right]^{-1}. \qquad (3.6.15)$$

For a laboratory tube emitting simultaneously a set of N_λ wavelengths, we have

$$I^{\rm IP}_{hkl}(s, d^*_{hkl}) = \sum_{l=1}^{N_\lambda} w_l I^{\rm IP}_{hkl,l}(s, d^*_{hkl}), \qquad (3.6.16)$$

where w_l is the relative intensity of the lth wavelength component (referred, for example, to $w_1 = 1$). The corresponding Fourier transform entering (3.6.13) can be written as

$$\begin{aligned} T^{\rm IP}(L) &= \sum_{l=1}^{N_\lambda} \exp\left[2\pi i d^*_{hkl}\left(1 - \frac{\Gamma_l}{E_l}\right)L\right]\exp\left(-2\pi s_{hkl}\frac{\Gamma_l}{E_l}L\right) \\ &= \sum_{l=1}^{N_\lambda}\left\{\cos\left[2\pi d^*_{hkl}\left(1 - \frac{\Gamma_l}{E_l}\right)L\right] + i\sin\left[2\pi d^*_{hkl}\left(1 - \frac{\Gamma_l}{E_l}\right)L\right]\right\} \\ &\quad \times \exp\left(-2\pi s_{hkl}\frac{\Gamma_l}{E_l}L\right). \end{aligned} \qquad (3.6.17)$$

The complex term in (3.6.17) accounts for the shift of each emission component with respect to the reference one. For more flexibility (for example to consider the non-ideal behaviour of the instrument), we can use a pseudo-Voigt (pV) in place of the Lorentzian in equation (3.6.14).

3.6.2.6.3. *Optical elements*

The equation of Caglioti *et al.* (1958), modified by Rietveld (1969) and originally developed for constant-wavelength neutron diffraction, is frequently employed for parameterization of the instrumental profile. The FWHM and the pV mixing parameter η (replacing the Lorentzian and Gaussian widths of the Voigt) are then parameterized according to functions in $\tan(\theta)$ and θ, respectively (Caglioti *et al.*, 1958; Leoni *et al.*, 1998; Scardi & Leoni, 1999),

$$\mathrm{FWHM}^2 = U\tan^2\theta + V\tan\theta + W, \qquad (3.6.18)$$

$$\eta = a + b\theta + c\theta^2. \qquad (3.6.19)$$

The parameters of the Fourier transform of a Voigt or pseudo-Voigt are then constrained to those of equations (3.6.18) and

(3.6.19). This is particularly convenient, as the Fourier transform of a Voigtian is analytical. In fact, for the pV case we have

$$T^{\rm IP}_{\rm pV}(L) = (1-k)\exp(-\pi^2\sigma^2L^2/\ln 2) + k\exp(-2\pi\sigma L), \tag{3.6.20}$$

where σ = FWHM/2 and where (Langford & Louër, 1982; Scardi & Leoni, 1999)

$$k = \left[1 + (1-\eta)/\left(\eta\sqrt{\pi\ln 2}\right)\right]^{-1}. \tag{3.6.21}$$

Equation (3.6.18) can be found in the literature in a different form and with additional terms accounting, for example, for size effects: besides forcing a symmetry of the profile in 2θ space, these extra terms are a contradiction as they have nothing to do with the instrument itself.

3.6.2.6.4. *Domain size and shape*

In nanostructured materials, the finite size of the scattering domains is usually the dominant source of line-profile broadening. Actually, when dealing with size, we should consider a size and a shape distribution of the domains. In most cases, one or more distributions of similar objects are considered. For an up-to-date description of issues related to size broadening, see Chapter 5.1. The domain shape is not a property of the material and therefore the use of symmetry constraints [*e.g.* spherical harmonics to describe the shape of the scattering object as in the model of Popa (1998) or as a size extension of Stephens' (1999) work] is not justified in the general case (Nye, 1987). Exceptions, however, exist.

The size-broadening contribution in WPPM follows the ideas of Bertaut (1949*a*,*b*, 1950) and of Stokes & Wilson (1942). Bertaut proposed the division of the domains into columns and the analysis of the independent scattering of these columns. The column-length distribution can always be extracted from the data: more complex models involving given shapes or distributions simply modify the way in which the columns are rearranged. Stokes and Wilson introduced the concept of a *ghost* to calculate the Fourier transform for a given shape: the volume common to a domain of shape c and its ghost, *i.e.* a copy of the same domain displaced by a quantity L along the scattering direction hkl, is proportional to the (size) Fourier transform $A^S_{c,hkl}(L,D)$ for the given domain. The calculation has been already carried out analytically for several simple shapes characterized by a single length parameter (Stokes & Wilson, 1942; Lele & Anantharaman, 1966; Wilson, 1969; Langford & Louër, 1982; Vargas *et al.*, 1983; Grebille & Bérar, 1985; Scardi & Leoni, 2001), and can be performed numerically in the general case (Leonardi *et al.*, 2012). It is possible to relate the Fourier coefficients to the size values obtained from traditional methods. In particular, the area-weighted average size $\langle L\rangle_S$ (Warren–Averbach method) and the volume-weighted average size $\langle L\rangle_V$ (Williamson–Hall method) are obtained as

$$\langle L\rangle_S = -\left[dA^S_c(L,D)/dL\big|_{L=0}\right]^{-1} = D/K_k = -D/H_1, \tag{3.6.22}$$

$$\langle L\rangle_V = [\beta(s)]^{-1} = 2\int\limits_0^{D/K} A^S_c(L,D)\,{\rm d}L = D/K_\beta, \tag{3.6.23}$$

where $\beta(s)$ is the integral breadth and K_k and K_β are the initial slope and integral breadth Scherrer constants, respectively (Langford & Wilson, 1978; Scardi & Leoni, 2001).

The average size might have little physical significance in real cases: the size (and shape) distribution can in fact play a key role in determining both the properties and the diffraction line-profile shapes of the powder under analysis. Fortunately, the Fourier coefficients for the polydisperse case can be easily calculated for any given distribution: the log-normal and the gamma distributions are the most common (and the most flexible). The equations and the corresponding moments are

$$\begin{aligned} g_l(D) &= \frac{1}{D\sigma_l\sqrt{2\pi}}\exp\left[-\frac{(\ln D-\mu_l)^2}{2\sigma_l^2}\right],\\ M_{l,n} &= \exp\left(n\mu_l + \frac{n^2}{2}\sigma_l^2\right), \end{aligned} \tag{3.6.24}$$

$$\begin{aligned} g_g(D) &= \frac{\sigma_p}{\mu_g\Gamma(\sigma_g)}\left(\frac{\sigma_g D}{\mu_g}\right)^{\sigma_g-1}\exp\left(-\frac{\sigma_g D}{\mu_g}\right),\\ M_{g,n} &= \left(\frac{\mu_g}{\sigma_g}\right)^n\frac{\Gamma(n+\sigma_g)}{\Gamma(\sigma_g)}. \end{aligned} \tag{3.6.25}$$

The scattered intensity for the given distribution g_i, and the given shape c, is

$$\begin{aligned} I_{c,hkl}(s) &\propto \frac{\int\limits_0^\infty\left[\int\limits_{L=0}^{D/K_{hkl}} A^S_{c,hkl}(L,D)\exp(2\pi iLs)\,{\rm d}L\right]w(D)\,{\rm d}D}{\int\limits_0^\infty w(D)\,{\rm d}D}\\ &\propto \int\limits_{L=0}^\infty\left[\frac{\int\limits_{D=LK_{hkl}}^\infty A^S_{c,hkl}(L,D)w(D)\,{\rm d}D}{\int\limits_0^\infty w(D)\,{\rm d}D}\right]\exp(2\pi iLs)\,{\rm d}L\\ &\propto \int\limits_{L=0}^\infty A^S_{hkl}(L)\exp(2\pi iLs)\,{\rm d}L, \end{aligned} \tag{3.6.26}$$

where $w(D) = g_i(D)V_c(D)$ and where

$$A^S_{hkl}(L) = \frac{\int\limits_{D=LK_{hkl}}^\infty A^S_{c,hkl}(L,D)w(D)\,{\rm d}D}{\int\limits_0^\infty w(D)\,{\rm d}D}. \tag{3.6.27}$$

With a suitable definition of the Fourier coefficients, the polydisperse case therefore becomes analogous to the monodisperse case. Analytic expressions can be obtained in particular cases. For instance, the Fourier coefficients for the log-normal and gamma distributions (Scardi & Leoni, 2001) are

$$A^S_l(L) = \sum_{n=0}^{3}{\rm erfc}\left[\frac{\ln(LK_c)-\mu_l-(3-n)\sigma_l^2}{\sigma_l\sqrt{2}}\right]\frac{M_{l,3-n}}{2M_{l,3}}H^c_nL^n \tag{3.6.28}$$

and

$$A^S_g(L) = \sum_{n=0}^{3}\left(\frac{\sigma_g}{M_{g,1}}\right)^n\frac{\Gamma[\sigma_g+(3-n),K_cL\sigma_g/M_{g,1}]}{\Gamma(\sigma_g+3)}H^c_nL^n, \tag{3.6.29}$$

respectively, where

$$\begin{aligned} \Gamma(x,a) &= \int\limits_a^\infty y^{x-1}\exp(-y)\,{\rm d}y,\\ \Gamma(x) &= \Gamma(x,0),\\ {\rm erfc}(x) &= 2\pi^{-1/2}\int\limits_x^\infty\exp(-y^2)\,{\rm d}y, \end{aligned}$$

with the definitions already given in equations (3.6.24) and (3.6.25).

The functional forms of equations (3.6.28) and (3.6.29) clearly suggest that the profile for a log-normal distribution of domains (which is frequently encountered in practice) is not Voigtian: all traditional line-profile analysis methods (based on Voigt or pseudo-Voigt functions) are therefore unable to correctly deal with a log-normally dispersed powder.

By analogy to the monodisperse case, it is possible to relate the parameters of the polydisperse system to the size obtained with traditional methods (Warren–Averbach and Williamson–Hall, respectively). The following holds (Krill & Birringer, 1998; Scardi & Leoni, 2001):

$$\langle L\rangle_S = \frac{1}{K_k}\frac{M_{i,3}}{M_{i,2}}, \quad \langle L\rangle_V = \frac{1}{K_\beta}\frac{M_{i,4}}{M_{i,3}}. \tag{3.6.30}$$

Here, it is clear that diffraction does not provide the first moment of the distribution directly: ratios between high-order moments are involved.

Using an analytical expression for the description of a size distribution can help in stabilizing the results (as the size distribution curve is forced to be zero at very small and very large size values). Some doubts can, however, arise as to the physical validity of this forcing. An example is the case of a multimodal system. The traditional LPA techniques are unable to directly deal with multimodal size distributions. In cases where the multimodal character is clear and the various distribution are well behaved (*i.e.* when they can be modelled with analytical functions), the pattern can be usually modelled by considering the material as made of different fractions, each of them characterized by a different size distribution.

A possible alternative has been proposed in the literature: replacing the analytical distribution with a histogram. The ability of this model to fit the experimental data has been demonstrated (Leoni & Scardi, 2004; Matěj *et al.*, 2011); a regularization might be necessary to stabilize the shape and/or smoothness of the size distribution. The quality of the measurement and the availability of models describing all contributions to the peak broadening are in most cases the limiting factors for extensive use of the histogram model: correlations of small sizes with the background and with features such as thermal diffuse scattering (Beyerlein *et al.*, 2012) can in fact occur. So far, this is the only available method for exploring cases where the analytical models are unable to correctly describe the observed broadening.

3.6.2.6.5. *Strain broadening (lattice distortions)*

A local variation of the lattice spacing (due, for example, to the presence of a defect) leads to an average phase term that, in general, is a complex quantity:

$$\begin{aligned}\langle \exp[2\pi i\psi_{hkl}(L)]\rangle &= \langle \cos[(2\pi L d^*_{\{hkl\}}\varepsilon_{\{hkl\}}(L)]\rangle \\ &\quad + i\langle \sin[2\pi L d^*_{\{hkl\}}\varepsilon_{\{hkl\}}(L)]\rangle \\ &= A^D_{\{hkl\}}(L) + iB^D_{\{hkl\}}(L).\end{aligned} \tag{3.6.31}$$

The strain $\varepsilon_{\{hkl\}}(L)$ represents the relative displacement of atoms at a (coherence) distance L along the scattering vector *hkl*. Knowledge of the actual source of distortion allows the explicit calculation of the various terms (van Berkum, 1994). It is quite customary to assume that the strain is the same for symmetry-equivalent reflections [$\varepsilon_{hkl}(L) = \varepsilon_{\{hkl\}}(L)$]: this is a reasonable hypothesis for a powder, where we assume that any configuration is equally probable.

Traditional LPA methods such as the Warren–Averbach method (Warren & Averbach, 1950, 1952; Warren, 1990) take a first-order MacLaurin expansion of equation (3.6.31) to extract the microstrain contribution from the measured data:

$$A^D_{\{hkl\}}(L) \cong 1 - 2\pi^2 L^2 d^{*2}_{\{hkl\}}\langle \varepsilon^2_{\{hkl\}}(L)\rangle, \tag{3.6.32}$$

$$B^D_{\{hkl\}}(L) \cong -\frac{4}{3}\pi^3 L^3 d^{*3}_{\{hkl\}}\langle \varepsilon^3_{\{hkl\}}(L)\rangle. \tag{3.6.33}$$

The term in equation (3.6.33) would cause peak asymmetry. However, we usually consider only the second-order moment of the strain distribution (*root-mean strain* or *microstrain*) and thus symmetric peaks. Owing to the anisotropy of the elastic properties, the broadening described by equation (3.6.32) is in general anisotropic: an extensive discussion of strain anisotropy and of the order dependence of strain broadening can be found, for example, in Leineweber & Mittemeijer (2010) and Leineweber (2011). It should be stressed that in their original form, traditional line-profile methods are unable to deal with this anisotropy (corrections have been proposed for particular cases, for example, in the so-called modified Williamson–Hall (MWH) and modified Warren–Averbach (MWA) analyses; Ungár & Borbély, 1996).

3.6.2.6.6. *Dislocations*

Dislocations are often the main source of strain broadening. The magnitude of this broadening depends not only on the elastic anisotropy of the material, but also on the relative orientation of the Burgers and diffraction vectors with respect to the dislocation line (Wilkens, 1970*a*,*b*). This problem was analysed in the 1960s by Krivoglaz and Ryaboshapka (Krivoglaz & Ryaboshapka, 1963; Krivoglaz, 1969) and then subsequently reprised and completed by Wilkens (1970*a*,*b*). Further elements have been added to put it into the present form (see, for example, Krivoglaz *et al.*, 1983; Groma *et al.*, 1988; Klimanek & Kuzel, 1988; van Berkum, 1994; Kamminga & Delhez, 2000). For the purpose of WPPM, the distortion Fourier coefficients caused by dislocations can be written as

$$A^D_{\{hkl\}}(L) = \exp[-\tfrac{1}{2}\pi b^2 \overline{C}_{\{hkl\}}\rho d^{*2}_{\{hkl\}} L^2 f(L/R'_e)], \tag{3.6.34}$$

where b is the modulus of the Burgers vector, $\overline{C}_{\{hkl\}}$ is the so-called average contrast factor of the dislocations, ρ is the density of the dislocations and R'_e is an effective outer cutoff radius. Only the low-L trend of equation (3.6.34) is well reproduced by Wilkens' theory: a decaying function $f(L/R'_e)$ has thus been introduced to guarantee a proper convergence to zero of the Fourier coefficients for increasing L. Actually, the function $f^*(\eta)$ is mostly quoted in place of (L/R'_e), where $\eta = (e^{-1/4}/2)L/R'_e$: the multiplicative term can however be dropped, considering that the cutoff radius is an effective value [some discussion of the meaning of the f and f^* functions and of the effective cutoff radius can be found in Scardi & Leoni (2004), Armstrong *et al.* (2006) and Kaganer & Sabelfeld, 2010)].

The most complete definition of $f^*(\eta)$ is from Wilkens (1970*a*,*b*):

$$f^*(\eta) = -\ln\eta + \frac{7}{4} - \ln 2 + \frac{256}{45\pi\eta} + \frac{2}{\pi}\left(1 - \frac{1}{4\eta^2}\right)\int_0^\eta \frac{\arcsin y}{y}\,\mathrm{d}y$$
$$- \frac{1}{\pi}\left(\frac{769}{180\eta} + \frac{41}{90}\eta + \frac{\eta^3}{45}\right)(1-\eta^2)^{1/2}$$
$$- \frac{1}{\pi}\left(\frac{11}{12\eta^2} + \frac{7}{2} + \frac{\eta^2}{3}\right)\arcsin\eta + \frac{\eta^2}{6}, \qquad \eta \le 1, \tag{3.6.35}$$

$$f^*(\eta) = \frac{256}{45\pi\eta} - \left(\frac{11}{24} + \frac{1}{4}\ln 2\eta\right)\frac{1}{\eta^2}, \qquad \eta \ge 1. \tag{3.6.36}$$

For $\eta < 1$, the integral in (3.6.35) can be calculated in terms of special functions as

$$\int_0^\eta \frac{\arcsin y}{y}\,\mathrm{d}y$$
$$= \frac{i}{12}\left\{\pi^2 - 6\arcsin^2\eta - 12i\ln\left[2\eta\left(\eta - i\sqrt{1-\eta^2}\right)\right]\arcsin\eta\right.$$
$$\left. - 6\mathrm{Li}_2\left(1 - 2\eta^2 + 2i\eta\sqrt{1-\eta^2}\right)\right\}$$
$$= \ln(2\eta)\arcsin\eta + \frac{1}{2}\mathrm{Im}\left[\mathrm{Li}_2\left(1 - 2\eta^2 + 2i\eta\sqrt{1-\eta^2}\right)\right]$$
$$= \ln(2\eta)\arcsin\eta + \frac{1}{2}\mathrm{Cl}_2(2\arcsin\eta), \tag{3.6.37}$$

where $\mathrm{Li}_2(z)$ and $\mathrm{Cl}_2(z)$ are the dilogarithm function (Spence's function) and the Clausen integral, respectively:

$$\mathrm{Li}_2(z) = \sum_{k=1}^{\infty} z^k/k^2, \tag{3.6.38}$$

$$\mathrm{Cl}_2(z) = \sum_{k=1}^{\infty} \sin(kz)/z^2 = -\int_0^x \ln[2\sin(t/2)]\,\mathrm{d}t. \tag{3.6.39}$$

The approximation proposed by van Berkum (1994) for (3.6.35) and (3.6.36),

$$f^*(\eta) = \begin{cases} -\ln\eta + \dfrac{7}{4} - \ln 2 + \dfrac{\eta^2}{6} - \dfrac{32\eta^3}{225\pi}, & \eta \le 1 \\ \dfrac{256}{45\pi\eta} - \left(\dfrac{11}{24} + \dfrac{1}{4}\ln 2\eta\right)\dfrac{1}{\eta^2}, & \eta \ge 1, \end{cases} \tag{3.6.40}$$

should not be employed, as the derivative is discontinuous at $\eta = 1$. A simpler approximation, valid over the whole η range, was provided by Kaganer & Sabelfeld (2010):

$$f^*(\eta) = -\ln\left(\frac{\eta}{\eta_0 + \eta}\right). \tag{3.6.41}$$

With $\eta_0 = 2.2$, the results of equation (3.6.41) are similar to those of (3.6.35) and (3.6.36).

Together with dislocation density and outer cutoff radius, a parameter traditionally quoted for the dislocations ensemble is Wilkens' dislocation arrangement parameter $M = R_e\sqrt{\rho}$ (Wilkens, 1970*a*). By combining the information on dislocation screening and dislocation distance, it gives an idea of the interaction of dislocations (strength of the dipole character; Ungár, 2001). A value close to or below unity indicates highly interacting dislocations (for example, dipole configurations or dislocation walls), whereas a large value is typical of a system with randomly dispersed dislocations (weak dipole character).

The anisotropic broadening caused by the presence of dislocations is mainly taken into account by the contrast (or orientation) factor C_{hkl}. The contrast factor depends on the strain field of the dislocation and therefore on the elastic anisotropy and orientation of the scattering vector with respect to the slip system considered. The average of the contrast factor over all equivalent slip systems, $\overline{C}_{hkl}$, is often used in the analysis of powders. The averaging is usually performed under the assumption that all equivalent slip systems are equally populated. The calculation of the contrast factor can be lengthy: full details can be found in the literature (Wilkens, 1970*a*,*b*, 1987; Krivoglaz *et al.*, 1983; Kamminga & Delhez, 2000; Groma *et al.*, 1988; Klimanek & Kuzel, 1988; Kuzel & Klimanek, 1989) for the cubic and hexagonal cases. For a generalization, the reader is referred to the recent work of Martinez-Garcia *et al.* (2007, 2008, 2009). It is possible to show that the contrast factor of a given material has the same functional form as the fourth-order invariant of the Laue class (Popa, 1998; Leoni *et al.*, 2007):

$$d^4_{\{hkl\}}C_{\{hkl\}}$$
$$= E_1h^4 + E_2k^4 + E_3l^4 + 2(E_4h^2k^2 + E_5k^2l^2 + E_6h^2l^2)$$
$$+ 4(E_7h^3k + E_8h^3l + E_9k^3h + E_{10}k^3l + E_{11}l^3h + E_{12}l^3k)$$
$$+ 4(E_{13}h^2kl + E_{14}k^2hl + E_{15}l^2hk). \tag{3.6.42}$$

In the general case, 15 coefficients are thus needed to describe the strain anisotropy effects. Symmetry reduces the number of independent coefficients: for instance, two coefficients survive in the cubic case, and the average contrast factor is (Stokes & Wilson, 1944; Popa, 1998; Scardi & Leoni, 1999)

$$\overline{C}_{\{hkl\}} = (A + BH) = A + B\frac{h^2k^2 + h^2l^2 + k^2l^2}{(h^2 + k^2 + l^2)^2}. \tag{3.6.43}$$

The values of A and B can be calculated from the elastic constants and slip system according to the literature (Klimanek & Kuzel, 1988; Kuzel & Klimanek, 1989; Martinez-Garcia *et al.*, 2007, 2008, 2009). Excluding the case of $\overline{C}_{\{h00\}} = 0$, the parameterization $\overline{C}_{\{hkl\}} = \overline{C}_{\{h00\}}(1 + qH)$ proposed by Ungár & Tichy (1999) can also be used. Some calculated values for cubic and hexagonal materials can be found in Ungár *et al.* (1999) and Dragomir & Ungár (2002), respectively.

As the calculation of the contrast factor for a dislocation of general character is not trivial, it is customary to evaluate it for the screw and edge case and to refine an effective dislocation character φ (Ungár *et al.*, 1999),

$$\overline{C}_{\{hkl\}} = [\varphi\overline{C}_{E,\{hkl\}} + (1-\varphi)\overline{C}_{S,\{hkl\}}]$$
$$= [\varphi A_E + (1-\varphi)A_S] + [\varphi B_E + (1-\varphi)B_S]H, \tag{3.6.44}$$

where the geometric term H is the same as in equation (3.6.43). Although not completely correct, the approach proposed in equation (3.6.44) allows the case where a mixture of dislocations of varying character are acting on equivalent slip systems to be dealt with. For a proper refinement, however, the active slip systems as well as the contrast factors of the edge and screw dislocations should be known.

It is worth mentioning that the invariant form proposed by Popa (1998) has been reprised by Stephens (1999) to describe the strain-broadening anisotropy, for example, within the Rietveld method: the formula correctly accounts for the relative broadening (*i.e.* for the anisotropy), but it does not give any information on the actual shape of the profiles. This is the major reason why the Stephens model can be considered as only phenomenological (it captures the trend but not the details): when the source of microstrain broadening is known, we can obtain the functional form of the profile (as proposed, for example, here for dislocations) and the model can become exact.

3.6.2.6.7. *Twin and deformation faults*

Planar defects, *i.e.* a mismatch in the regular stacking of crystallographic planes, are quite frequent in a vast family of technologically important materials and, in some cases, are responsible for their macroscopic properties. In the general case, the analysis of faulting using a Bragg-type method is troublesome. The local change in the structure causes the appearance of diffuse scattering (*i.e.* extra intensity) between the Bragg spots. This can be handled in the single-crystal case (Welberry, 2004), but can be challenging in a powder, where the reciprocal space is rotationally averaged and the (weak) diffuse scattering is lost in the background. The handling of diffuse phenomena is the main difference between the Rietveld (1969) and the pair distribution function (PDF) (Billinge, 2008) methods.

A simple description of the broadening effects of faulting, useful for WPPM, is available only for a restricted class of systems, namely face-centred cubic (f.c.c.) ($Fm\bar{3}m$), body-centred cubic (b.c.c.) ($Im\bar{3}m$) and hexagonal close packed (h.c.p.) ($P6_3/mmc$) lattices. Monatomic metals with f.c.c. (*e.g.* Cu, Ni and Au), h.c.p. (*e.g.* Ti, Co and Zr) and b.c.c. (*e.g.* W and Mo) structures fall into this list. Faulting in the wurtzite structure ($P6_3mc$) leading to a local transformation into sphalerite ($F\bar{4}3m$) can be handled with rules completely analogous to those for the h.c.p./f.c.c. case. The main types of faults in all of these systems are the so-called deformation and twin faults: looking at the planes on the two sides of the faulting, a deformation fault appears as a shear, whereas twinning causes a mirroring of the atomic positions. The effect of these defects can be modelled using recurrence equations for the stacking. Initially proposed for the h.c.p. case by Wilson (Edwards & Lipson, 1942; Wilson, 1942), this idea was then extended to the f.c.c. case (Paterson, 1952; Gevers, 1954*a*,*b*; Warren, 1959, 1963). More recently, Estevez-Rams *et al.* (2003, 2008) improved the accuracy and extended the validity range by including all terms in the stacking probability formulae, whereas Velterop *et al.* (2000) corrected the formalism to properly take the various *hkl* components of a peak into account.

In an f.c.c. system, reliable information can be obtained up to a few per cent of faults on the {111} plane. The trick is to describe the lattice with hexagonal axes, effectively transforming the problem into that of ⟨001⟩ stacking on the {111} plane. Under these hypotheses, the average phase term due to faulting can be written as

$$\left\langle \exp\left[2\pi i\varphi(L; d^*_{\{hkl\}}, L_0/h_0^2)\right]\right\rangle = A^F_{hkl}(L) + iB^F_{hkl}(L), \qquad (3.6.45)$$

where $L_0 = h + k + l$ and $h_0^2 = h^2 + k^2 + l^2$. The lattice symmetry influences the definitions of these two parameters. Faulting is one of the typical cases where a complex (sine) term is present, as peak shift and asymmetry in the profiles is expected (unless twin faults are absent). Following the treatment of Warren (see, for example, Warren, 1963), a set of recurrence equations can be written for the probability of the occurrence of faulting. The solution of the recurrence equations is used to generate the Fourier coefficients for faulting. In particular, if the probabilities of deformation and twin fault are α and β, respectively, then

$$\begin{aligned} S^2 &= 3 - 12\alpha - 6\beta + 12\alpha^2 - \beta^2 + 24\alpha\beta(1-\alpha), \\ Z &= \sqrt{(1-\beta^2) + S^2}/2 \end{aligned} \qquad (3.6.46)$$

and, introducing the sign function,

$$\sigma_{L_0} = \begin{cases} +1 & \text{for } L_0 = 3N+1 \\ 0 & \text{for } L_0 = 3N \\ -1 & \text{for } L_0 = 3N-1 \end{cases} \qquad N = 0, \pm1, \pm2, \ldots, \qquad (3.6.47)$$

the Fourier coefficients can be obtained as

$$A^F_{hkl}(L) = \exp\left[\tfrac{1}{2}\ln(Z)|Ld^*_{\{hkl\}}\sigma_{L_0}L_0/h_0^2|\right], \qquad (3.6.48)$$

$$B^F_{hkl}(L) = -\sigma_{L_0}\frac{L}{|L|}\frac{L_0}{|L_0|}\frac{\beta}{S}A^F_{hkl}(L). \qquad (3.6.49)$$

Besides being asymmetric, each profile subcomponent can also be shifted with respect to the average Bragg position. For the subcomponent *hkl* the shift is

$$\delta_{hkl} = -\left[\frac{1}{2\pi}\arctan\left(\frac{s}{1-\beta}\right) - \frac{1}{6}\right]d^*_{\{hkl\}}\frac{L_0}{h_0^2}\sigma_{L_0}. \qquad (3.6.50)$$

In a given reflection family {*hkl*}, reflections affected and unaffected by faulting coexist, leading to peculiar shapes of the corresponding peak profiles.

Analogous formulae can be obtained for the b.c.c. and h.c.p. cases. In the former, the selection rule becomes $L_0 = -h - k + 2l$, whereas for the latter $L_0 = l$ and the condition for faulting is based on $h - k = 3N \pm 1$. Implementation requires the application of the proper formula to the particular reflection *hkl* considered in the analysis.

Analysing faults by observing just the peak shift, as in the original treatment of Warren (1959, 1963) or within the Warren–Averbach method (Warren & Averbach, 1950, 1952), would be erroneous, as it does not take the fine details of the broadening into account.

An alternative to the adoption of Warren's formalism was proposed by Balogh *et al.* (2006). Instead of performing the calculation explicitly, the authors parameterized the profiles obtained from the *DIFFaX* software (Treacy *et al.*, 1991) calculated for increasing quantities of faulting. The *DIFFaX* software is based on a recursive description of the stacking: the intensity is calculated along rods in reciprocal space using the tangent cylinder approximation. The parameterization, which is performed in terms of a sum of Lorentzian curves, is then employed for the evaluation of the fault-broadening profile at any angle. The modelling should be performed on a profile that contains a faulting-only contribution: note that for high faulting probabilities, it becomes arbitrary whether to assign the diffuse scattering part to one or another Bragg reflection. This introduces some arbitrariness in the subsequent (directional) convolution of the faulting profile with the other broadening effects. When applicable, however, this parameterization has several advantages: it takes the actual shape of the reciprocal-space rods into account (in an effective way), it does not necessitate any *hkl* selection rule and an analytical treatment can be employed, as the Lorentzian has an analytical transform. With the above caveats, it is in principle not even necessary to decompose the *DIFFaX*-generated profile if a numerical convolution is employed. This would also correspond to an extension of WPPM to the *DIFFaX*+ idea (Leoni, Gualtieri & Roveri, 2004; Leoni, 2008), or *vice versa*, where *DIFFaX*+ uses a corrected and improved version of the recursive approach of *DIFFaX* to generate the profiles, but allows the refinement of all model parameters. [*DIFFaX+* is available from the author (matteo.leoni@unitn.it) on request.]

3.6.2.6.8. *Antiphase domain boundaries*

In the diffraction pattern of an ordered alloy, a dissimilar broadening can often be observed for structure and superstructure peaks (with the former being present in both the ordered and disordered states). The superstructure peaks, in fact, bear microstructural information on the interface between the ordered regions in the material: broadening occurs when domains meet out of phase, creating an antiphase domain boundary (APB or APDB). A general formula for APDB-related broadening does not exist: for a given ordered structure, the Fourier coefficients correspond to the normalized value of $A_{\mathrm{APDB},hkl}(L) = \overline{F(0)F^{*}(L)}$, where $F(0)$ is the structure factor of a cell positioned at $L = 0$ and $F^{*}(L)$ is the complex conjugate of the structure factor of a cell at a distance L along the direction $[hkl]$. Being the result of a combination of probabilities, the peak is always expected to be Lorentzian.

Explicit formulae have been derived for the Cu_3Au ordered alloy ($L1_2$ phase; Wilson, 1943; Wilson & Zsoldos, 1966; Scardi & Leoni, 2005). Several types of boundaries can form, depending on the way that the domains meet: the broadening depends both on the boundary plane and on the local arrangement of Au atoms leading to conservative (no Au atoms in contact) or nonconservative (Au atoms in contact) boundaries. By arranging the indices in such a way that $h \geq k \geq l$ and that l is always the unpaired index, the broadening of the superstructure reflections can be described as (Scardi & Leoni, 2005)

$$A^{\mathrm{APDB}}(L) = \exp[-2L\delta f(h,k,l)]. \qquad (3.6.51)$$

In this formula, $\delta = \gamma_{\mathrm{APDB}}/a_0$ is the probability of occurrence of an APDB, a_0 is the unit-cell parameter and $f(h, k, l)$ is a function of hkl defined in Table 3.6.2, obtained from the results of Wilson (1943) and Wilson & Zsoldos (1966).

The average distance between two APDBs is given by $1/\delta$. For a random distribution of faults, the broadening is Lorentzian and $A^{\mathrm{APDB}} = \exp(-4L\delta/3)$.

3.6.2.7. *Assembling the equations into a peak and modelling the data*

As previously mentioned, the broadening contributions briefly illustrated in the previous sections are employed to generate the powder peak profile for reflections from the set of planes $\{hkl\}$ using equations (3.6.11) and (3.6.12) and where

$$\begin{aligned} I_{hkl}(s) &= k(d^{*}) \int\limits_{-\infty}^{\infty} C(L)\exp(2\pi iLs)\,\mathrm{d}L \\ &= k(s) \int\limits_{-\infty}^{\infty} T^{\mathrm{IP}}_{\mathrm{pV}}(L)A^{S}_{hkl}(L)[A^{D}_{hkl}(L)\cos(2\pi Ls) + iB^{D}_{hkl}(L)\sin(2\pi Ls)] \\ &\quad \times \ldots \times [A^{F}_{hkl}(L)\cos(2\pi Ls) + iB^{F}_{hkl}(L)\sin(2\pi Ls)]\,\mathrm{d}L. \end{aligned} \qquad (3.6.52)$$

Table 3.6.2
Models for antiphase domain boundaries for the Cu_3Au case

$N = h^2 + k^2 + l^2$.

ID	Model	$f(h, k, l)$
1	Random	2/3
2	{100} planes	$\frac{2}{3}\frac{h+k+l}{\sqrt{N}}$
2.I	{100} planes, no Au–Au contacts	$(k+l)/\sqrt{N}$ if h is the unpaired index $(h+l)/\sqrt{N}$ if k is the unpaired index $(h+k)/\sqrt{N}$ if l is the unpaired index
2.II	{100} planes, only Au–Au contacts	$\frac{2h+k+l}{2\sqrt{N}}$ if h is the unpaired index $\frac{h+2k+l}{2\sqrt{N}}$ if k is the unpaired index $\frac{h+k+2l}{2\sqrt{N}}$ if l is the unpaired index
3	{110} planes	$\frac{2}{3}\frac{4h+2k}{\sqrt{2N}}$
3.I	{110} planes, Au displacement parallel or perpendicular to plane normal	$\frac{4h}{\sqrt{2N}}$ if h is the unpaired index $\frac{2h+2k}{\sqrt{2N}}$ otherwise
3.II	{110} planes, Au displacement at 60° to plane normal	$\frac{2h+2k}{\sqrt{2N}}$ if h is the unpaired index $\frac{3h+k}{\sqrt{2N}}$ otherwise
4	{111} planes	$\frac{8h}{3\sqrt{3N}}$ if $h \geq (k+l)$ $\frac{4(h+k+l)}{3\sqrt{3N}}$ otherwise

Equation (3.6.52) represents an asymmetrical peak profile (the asymmetry is given by the sine terms). Fast Fourier transform and space remapping (usually s to 2θ) are then employed to generate the peaks in the measurement space; intensities are multiplied by the Lorentz and, if needed, polarization terms, and a background is added to the whole pattern. Other aberrations (affecting the position, the intensity or the shape of the peak) can be included as needed.

The various reflections are then positioned on the basis of the (reference) Bragg angle $2\theta_{\rm B}$ calculated from the unit-cell parameters, and a background (for example, a Chebychev polynomial) is suitably added. For completeness, thermal diffuse scattering should be included, as it can contribute to the broadening near the peak tails (see, for example, Beyerlein *et al.*, 2012). In addition, small-angle scattering can be considered to improve the WPPM result and to account for the observed increase in the background at low angle (Scardi *et al.*, 2011). The final equation is thus similar to that of the Rietveld (1969) or the Pawley (1981) methods,

$$I(2\theta) = {\rm SAXS} + {\rm TDS} + {\rm bkg} + k(2\theta)LP\sum_{hkl} I_{\{hkl\}}(x), \qquad (3.6.53)$$

the main difference being in the focus of the analysis and in the way that the profiles are generated.

The model parameters are then refined using a nonlinear least-squares routine (*e.g.* based on the Marquardt algorithm or suitable modifications, as proposed, for example, by Coelho, 2005) to directly match the synthesized pattern to the experimental data. The usual weight, related to Poisson counting statistics, is employed.

As the shape of each peak is bound to the underlying physical models, the number of parameters to be refined is usually quite limited. Compared with the four parameters per peak (intensity, width, shape and position) necessary for a Scherrer-type analysis, in WPPM we refine, for example, two parameters for a domain-size distribution, three parameters for dislocations (ρ, R'_e and φ), two parameters for faulting (α and β), at most six lattice parameters, a few background parameters (*e.g.* four parameters) and one parameter (intensity) per peak. In addition, we can also refine some further specimen-related parameters such as a misalignment error. No atomic coordinates are involved.

A flexible software package implementing WPPM (*PM2K*: Leoni *et al.*, 2006) is available from the author on request (matteo.leoni@unitn.it): the software includes all of the broadening models illustrated here. The user can work with any type and any simultaneous set of diffraction data (X-ray, neutrons or electrons) and build their own model with no *a priori* restriction on the quantity and type of parameters, the number of phases, the models or the relationships between the parameters. The WPPM method has also been implemented in the *TOPAS* refinement software [version 5 (Coelho, 2009; Bruker, 2009)] using the flexible macro language provided.[1]

3.6.2.7.1. *Alternative approaches*

Convolutional multiple whole profile fitting (CMWP; Ribárik *et al.*, 2004) and extended convolutional multiple whole profile fitting (eCMWP; Balogh *et al.*, 2006) have been developed to solve the same problem.

CMWP, introduced as a convolutive version of multiple whole profile fitting (MWP; Ungár *et al.*, 2001; Ribárik, 2008), is very similar to the WPPM. The notable differences are:

(i) The instrumental profile is employed directly without interpolation and the profile of the instrumental peak closest to the peak under analysis is used. The instrumental profile imposes conditions on the range of L used in profile modelling.

(ii) In CMWP a subset of data points is used for speed.

(iii) The background is given by the user (as a spline or Legendre polynomial).

(iv) All points of a given (generated) peak are weighted by the same value related to the maximum intensity. However, the correct weighting scheme with individual weights for data points is available as an option.

The authors also suggest using the MWP procedure in other cases, for example separately measured profiles or single crystals. The MWP procedure works in Fourier space so there is no direct possibility of checking the agreement between the model and data.

In the extended version (Balogh *et al.*, 2006), (e)CMWP introduces an interesting model for faults based on a parameterization of the profiles simulated with the *DIFFaX* software (Treacy *et al.*, 1991). This simulates the diffraction pattern of a faulted structure within the tangent cylinder approximation. The proposed parameterization allows more complex faulting models, at the expense of the calculation and parameterization of the profiles for any new, intermediate or mixed case or for any peak lying outside the parameterized range. The application of (e)CMWP is limited to cubic, hexagonal and orthorhombic powders with spherical or ellipsoidal domain shapes and assumes the presence of dislocations and faults.

It is worth mentioning two more alternative approaches: the Debye scattering equation (Debye, 1915; for some applications, see, for example, Cervellino *et al.*, 2003; Cozzoli *et al.*, 2006) and the total scattering (TS) approach [also known as pair distribution function (PDF) analysis; Egami & Billinge, 2003; Billinge, 2008; see also Chapter 5.7]. Both techniques work in real space: the first creates the pattern directly from atomic positions and the other extracts the real-space information (the PDF) from the diffraction data. As the information content does not change on moving from reciprocal (measured) to direct space, provided that similar hypotheses are employed (similar microstructure and, if necessary, structure), real-space and reciprocal-space methods should give similar results. Of course there are differences, related to the way that the data are handled. For instance, it is easier to visualize the anisotropic effects in reciprocal space, as the information is contained in the peak broadening (different peaks show different breadths): in the PDF this information is sparser as it should be reflected in a variation in the correlation lengths, but also (highly integrated) in a variation of the decay of the curve. Conversely, information on the atomic arrangement (*i.e.* on possible defects) appears more clearly in the PDF, where variations in the distances and in coordination are well localized, contrary to the diffraction pattern, where the information is contained in the (weak) diffuse signal, in the broadening and in the peak position.

Direct-space and reciprocal-space methods thus each have their own advantages and disadvantages. Combined or comparative modelling, whenever possible, is therefore always the best solution: we can match the flexibility and immediacy of a real-space approach with the possibility of working directly with the measured data as typical in reciprocal-space methods.

---

[1] Some small errors are present in some versions of the WPPM macros implemented in *TOPAS*. An example of a corrected macro for a lognormal distribution of spheres is given in the supporting information. The implementation using the mean and variance of the distribution *versus* the lognormal mean and variance is straightforward. Please refer to Chapter 5.1 for corrected versions of the Fourier coefficients and ancillary equations that should be present in the macros.

3.6.3. Examples of WPPM analysis

To illustrate the power of the WPPM approach, a few examples are provided based both on simulated and on real data. The analyses were performed using the *PM2K* software (Leoni *et al.*, 2006). Similar results are obtained using the WPPM implementation in the commercial program *TOPAS*.

3.6.3.1. *Nanocrystalline ceria*

The first example concerns a nanocrystalline ceria powder obtained by the calcination of a cerium isopropoxide gel (Leoni, Di Maggio *et al.*, 2004; Leoni & Scardi, 2004; Scardi *et al.*, 2004). A large amount of XRD and transmisson electron microscopy (TEM) data have been collected on the same system (and specimen), starting from the xerogel and following calcination (Scardi *et al.*, 2010). Fig. 3.6.1(*a*) shows the X-ray powder diffraction pattern of the gel calcined for 1 h at 673 K measured with Cu radiation (40 kV, 45 mA) on a Rigaku PMG/VH diffractometer.

The data were collected over the 2θ range 18–154° (with a step of 0.05°) with a counting time of 60 s per step: a wide angular range and a high signal-to-noise ratio (SNR) are prerequisites for a proper line-profile analysis. The large span in reciprocal space is important for the complete characterization of any anisotropy in the broadening (a large set of independent directions in reciprocal space needs to be sampled), whereas the high SNR guarantees the collection of data at peak tails where the differences between similar microstructure models manifest themselves. The log scale employed in Fig. 3.6.1(*a*) highlights the low level of noise present in the pattern.

The diffractometer had 0.5° divergence and 2° Soller slits mounted on the primary arm and 0.15 mm antiscatter, 0.5° receiving and 2° Soller slits and a curved graphite analyser crystal mounted on the secondary arm. This setup provided a narrow and symmetrical instrumental profile that could be described by a pseudo-Voigt curve and was thus ideal for line-profile analysis studies. The Caglioti *et al.* (1958) parameterization of the instrumental profile [*cf.* equations (3.6.18) and (3.6.19)] performed on the profiles of the NIST SRM 660a standard (LaB_6) is shown in Fig. 3.6.2.

Analysis of the pattern using traditional methods (see Scardi *et al.*, 2004) required 59 parameters, 53 of which were actually refined:

(i) one unit-cell parameter (a_0),
(ii) six (fixed) parameters defining the instrumental contribution [five parameters for the Caglioti parameterization (U, V, W, a and b) and one for the $K\alpha_2$ intensity ratio],
(iii) three parameters for the background,
(iv) one parameter for the specimen displacement,
(v) 48 parameters for the peaks (intensity, FWHM and shape for 16 peaks).

An analysis using traditional analysis methods resulted in an 'average domain size' of 3.65 (10) nm using the (modified) Warren–Averbach method and in the range from 4.95 (10) to 5.3 (1) nm using a (modified) Williamson–Hall approach. A discussion of the meaning and accuracy of the results can be found in Scardi *et al.* (2004).

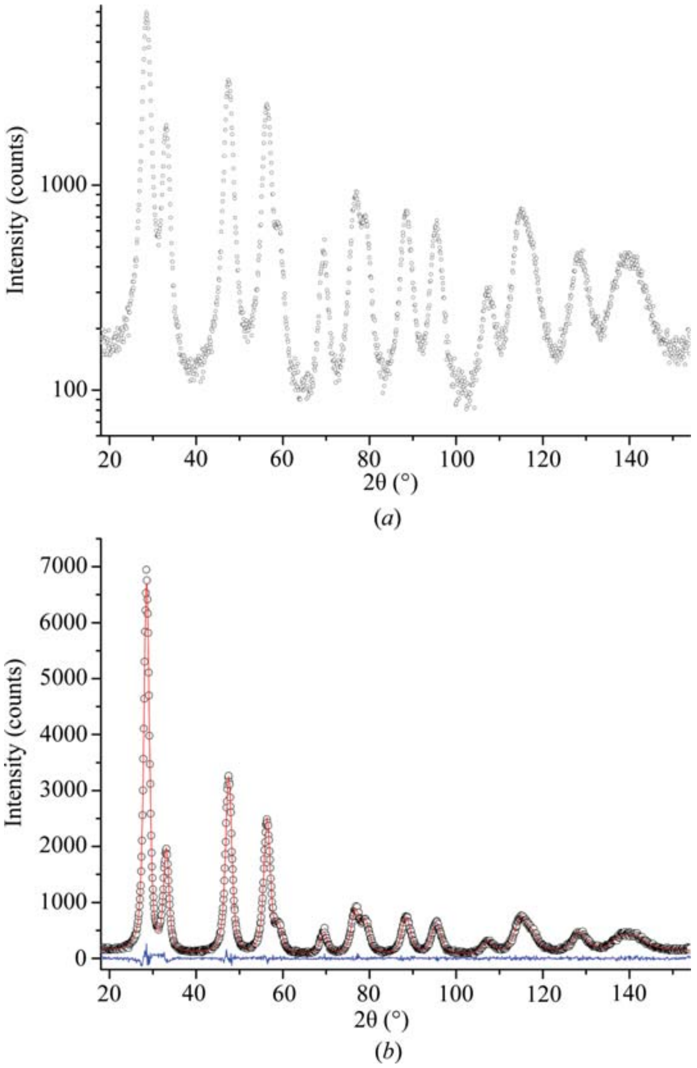

Figure 3.6.1
X-ray powder diffraction pattern of nanocrystalline ceria calcined at 673 K. In (*a*) the pattern is shown on a log scale to highlight the weak features in the data. In (*b*) the results of WPPM are shown: raw data (dots), model (line) and difference (lower line).

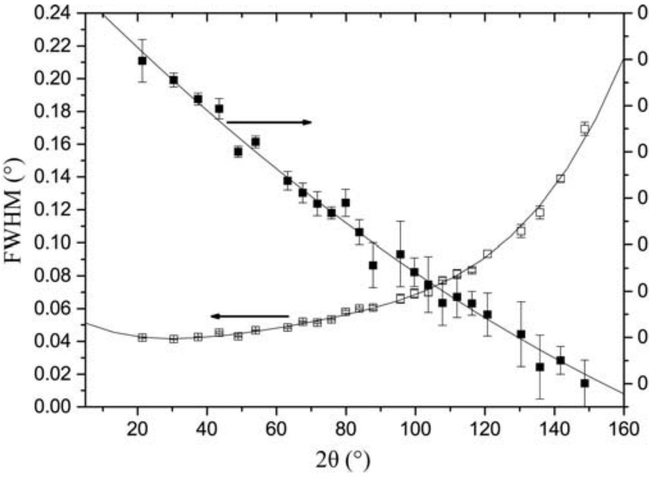

Figure 3.6.2
Parameterization of the instrumental resolution function using a pseudo-Voigt and the relationship of Caglioti *et al.* (1958).

The WPPM result, shown in Fig. 3.6.1(*b*), matches the experiment quite well: this is remarkable considering that the whole pattern (1800 data points) is modelled using just 32 parameters (26 free parameters):

(i) one unit-cell parameter (a_0),
(ii) six (fixed) parameters defining the instrumental contribution [five parameters for the Caglioti parameterization (U, V, W, a and b) and one for the $K\alpha_2$ intensity ratio],

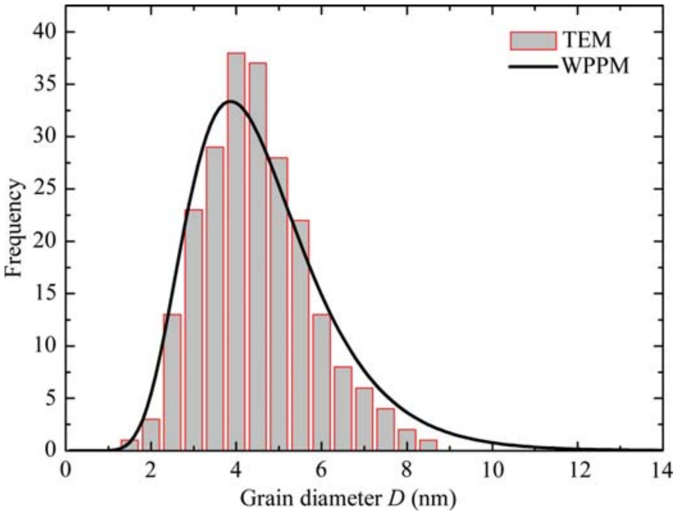

Figure 3.6.3
Size distribution of the ceria powder: WPPM (line) and TEM (histogram).

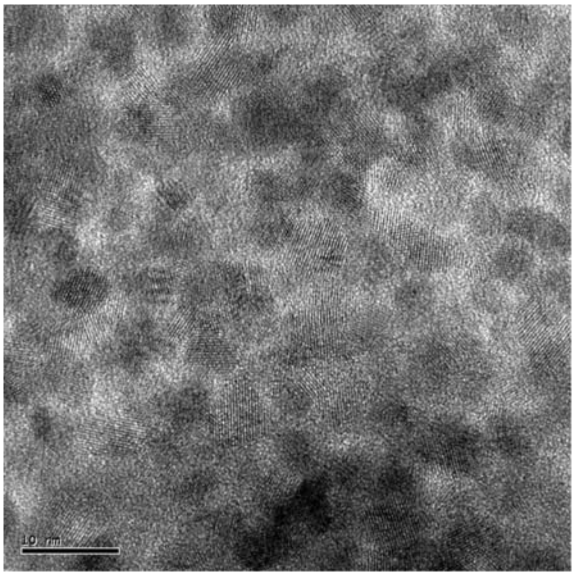

Figure 3.6.4
TEM micrograph of the calcined ceria powder. The scale bar represents 10 nm.

(iii) two parameters for the log-normal size distribution (μ and σ),
(iv) three parameters for the dislocation contributions (ρ, R_e and the mixing parameter f_e),
(v) three parameters for the background,
(vi) one parameter for the specimen displacement,
(vii) 16 parameters for the intensity of the peaks.

It is therefore possible to obtain more complete results with a number of parameters that is dramatically lower than that needed for the traditional analysis: the shapes of the peaks are interlinked *via* the microstructure models. It is suggested that the parameters are initialized with values providing a minimal but measurable effect (*i.e.*, for instance, $\mu = 2$, $\sigma = 0.4$, $\rho = 10^{15}$ m^{-2}, $f_e = 0.5$) to favour a rapid convergence.

By way of a check, Fig. 3.6.3 shows the good agreement between the size distribution obtained by WPPM and that obtained on the same specimen from the analysis of a large set of TEM micrographs (800 grains surveyed; Fig. 3.6.4). The data were collected on a 300 kV JEOL 3010 microscope (0.17 nm point-to-point resolution) equipped with a Gatan slow-scan 974 CCD camera (Leoni, Di Maggio *et al.*, 2004). Even if the particles are well separated, the analysis is quite tedious and prone to bias from the operator. The large and small particles are in fact easily missed, and overlapping particles are hard to separate and are usually not considered. Moreover, only the cross section is measured, as the transverse direction is difficult to access.

The statistical validity of the WPPM result is quite clear: a few million grains are probed by the X-rays *versus* the few hundred actually considered in microscopy. The WPPM result allows not only the mean (first moment) and variance to be obtained from the refined size distribution, but also the recovery of the most probable values for the traditional results (we know the shape and we can weight the column-length distribution by the surface or by the volume). In this case the numerical mean is ~4.3 nm: we can immediately understand the risk of placing faith in the results of a traditional analysis. The agreement between TEM and XRD is in any case excellent. The residual differences may be due both to the issues related to sizing under the microscope and to the simplified treatment employed in the WPPM (perfectly spherical domains, monodisperse shape, absence of surface relaxation *etc.*). A more complex model (accounting, for example, for surface relaxation effects) can be considered (see Scardi & Leoni, 2002; Leoni & Scardi, 2004), but the effects on the distribution are minimal.

The possibility of extracting information on the type of defects (*e.g.* dislocations, faults and APDBs) and on their amount is definitely a major advantage of WPPM over traditional methods and over TEM. For the determination of the dislocation density, the average contrast factor is needed; the actual expressions can be readily obtained from the single-crystal elastic constants (c_{11} = 403, c_{12} = 105 and c_{44} = 60 GPa; Nakajima *et al.*, 1994) as

$$\overline{C}_{\mathrm{CeO}_2,e} = 0.122945 + 0.358092\,\frac{h^2k^2 + k^2l^2 + h^2l^2}{(h^2 + k^2 + l^2)^2}, \qquad (3.6.54)$$

$$\overline{C}_{\mathrm{CeO}_2,s} = 0.105762 + 0.207999\,\frac{h^2k^2 + k^2l^2 + h^2l^2}{(h^2 + k^2 + l^2)^2} \qquad (3.6.55)$$

for edge and screw dislocations, respectively.

A dislocation density of 1.4 × 10^{16} m^{-2} was obtained for the specimen analysed here. This dislocation density immediately appears to be quite high when compared with the number of dislocations that can be identified in high-resolution TEM micrographs, as it corresponds to approximately one dislocation every couple of grains (Leoni & Scardi, 2004). However, the dislocations visible in the micrographs are just a small fraction of the total: if a dislocation is not properly aligned with the zone axis, it is in fact invisible (its presence can only be inferred from the effects of the distortion field). It is true that a sufficiently large number of dislocations must be present in order to give appreciable effects on the diffraction pattern, and TEM is still the better technique if the density of dislocations is below, for example, 10^{14} m^{-2}.

3.6.3.2. *Copper oxide*

The true power of WPPM, and of diffraction in general, can be appreciated in multi-phase systems. The unequivocal assignment of a structure to each grain is definitely impossible using TEM, unless each grain is individually sampled and carefully analysed. It is therefore quite hard to identify the phases present in the specimen and to characterize their microstructure independently from a micrograph alone. Conversely, information on the various phases is well separated in a diffraction pattern. The various (known) phases in a specimen can easily be identified (for

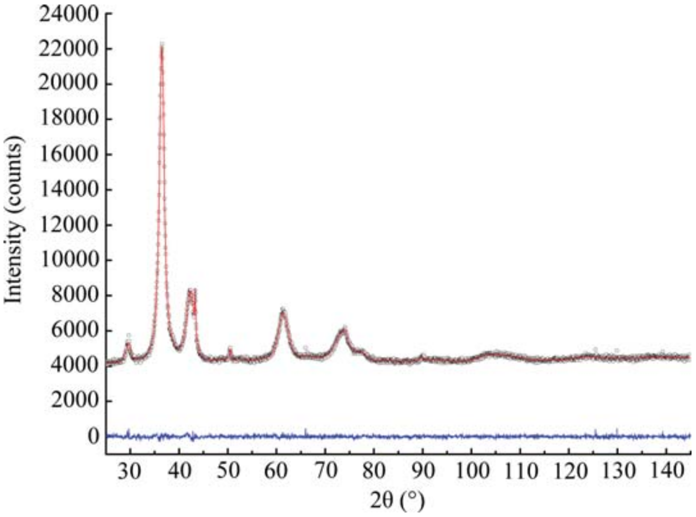

Figure 3.6.5
Result of WPPM of ball-milled Cu_2O: raw data (dots), model (line) and difference (lower line).

example by search/match in a large database such as the ICDD Powder Diffraction File): each diffraction peak belongs to a well defined phase and bears information on the microstructure of that phase.

As an example, Fig. 3.6.5 shows the diffraction pattern of a Cu_2O powder specimen obtained by grinding commercial Cu_2O powder (Carlo Erba) in a high-energy shatter mill (Fritsch Pulverisette 9). To limit the heating of the cup that would lead to dynamic recrystallization, milling was performed in 30 steps consisting of 10 s milling followed by 120 s room-temperature cooling (Martinez-Garcia *et al.*, 2007). The powder diffraction pattern was collected on the same diffractometer that was used for the analysis of the ceria powder. To obtain a sufficient SNR, the data were collected in the 18–154° 2θ range with a step size of 0.1° and a fixed acquisition time of 150 s per point. The fluorescence of the Cu present in the specimen is responsible for the large background that was not eliminated by the crystal analyser. From a quick comparison of Figs. 3.6.5 and 3.6.1, we notice a large difference at high angle: high strain effects (due to dislocations) are expected in this specimen as an effect of the extensive cold-work deformation introduced by the milling process.

A search match signals the presence of not just Cu_2O (cuprite, $Pn\bar{3}m$) but also metallic Cu (f.c.c. copper, $Fm\bar{3}m$) and CuO (tenorite, Cc) as minor phases, presumably due to reduction of the higher oxide. WPPM of the diffraction pattern, performed by considering all three observed phases, shows a flat residual (see Fig. 3.6.5). The severe peak overlap and the large broadening at high angle do not help in the analysis: the intensities of tenorite peaks (minor and broadened phase) were then constrained by a structural model (only a scale parameter was refined). Atomic coordinates and Debye–Waller factors for CuO were taken from the ICSD file (FIZ#69094; Brese *et al.*, 1990) and were considered to be constant.

Spherical domains were chosen for all phases. A log-normal distribution was used to model the minor phases. A histogram distribution was chosen for cuprite instead: the peaks clearly have a peculiar shape with a rather sharp tip, possibly indicating a wide, bimodal or odd size distribution (Leoni & Scardi, 2004). The size distribution resulting from the WPPM analysis is shown in Fig. 3.6.6(*a*): in this case it would be impossible for a traditional method to provide a physically sound result. The breadth of the profile is not fully informative: as the diffraction signal is proportional to the volume of matter, the actual distribution 'seen' in the experiment is that of Fig. 3.6.6(*b*), obtained by multiplying the result of Fig. 3.6.5(*a*) by D^3.

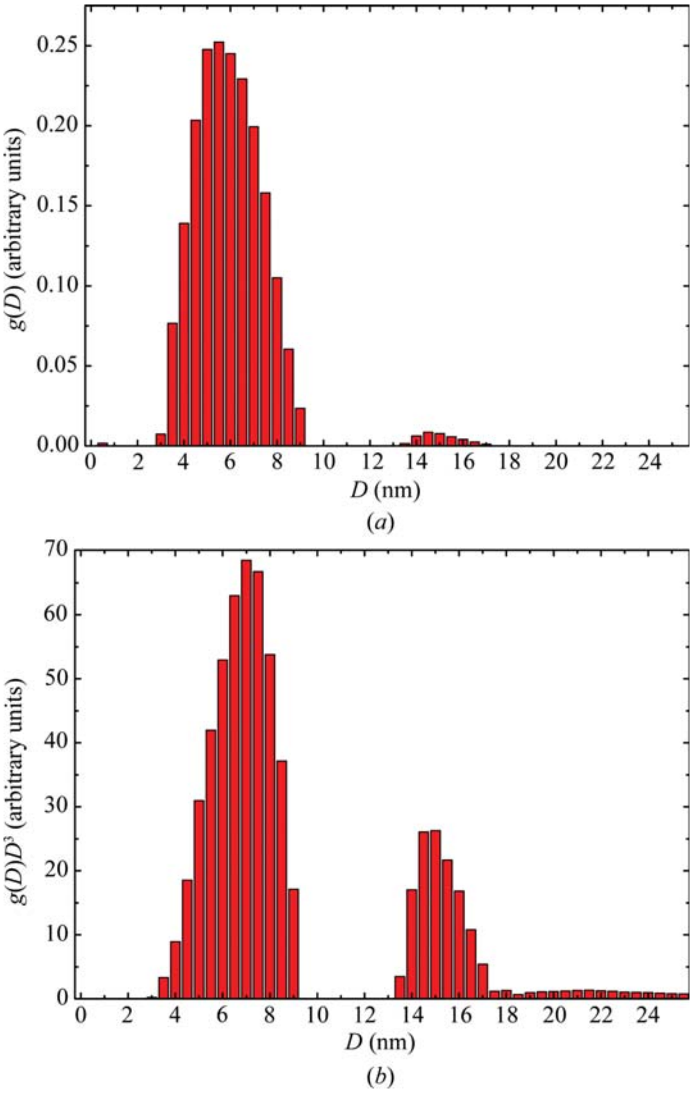

(*a*)

(*b*)

Figure 3.6.6
Domain-size distribution of cuprite: (*a*) WPPM result and (*b*) distribution multiplied by D^3.

The larger size fraction therefore makes a non-negligible contribution to the pattern: as a rule of thumb, the smaller the domains and the wider the distribution, the stronger the contribution of the large domains. This problem of 'visibility' of small domains is attenuated when an analytical distribution (*e.g.* a log normal) can be used as the function goes smoothly to zero at zero size.

Dislocations can also be observed in these specimens: their quantification by TEM is nearly impossible due to the high defect density. The anisotropy term, *i.e.* the average contrast factor, has to be calculated for each of the three phases (Scardi *et al.*, 2007).

The slip system for Cu (c_{11} = 169, c_{12} =122, c_{44} = 75.3 GPa; Every & McCurdy, 1992*a*) is $\frac{1}{2}\langle 1\bar{1}0\rangle\{111\}$ and the corresponding average contrast factor (for edge and screw dislocations, respectively), is

$$\overline{C}_{\mathrm{Cu},e} = 0.304062 - 0.500211\frac{h^2k^2 + k^2l^2 + h^2l^2}{(h^2 + k^2 + l^2)^2}, \qquad (3.6.56)$$

$$\overline{C}_{\mathrm{Cu},s} = 0.298340 - 0.708805\frac{h^2k^2 + k^2l^2 + h^2l^2}{(h^2 + k^2 + l^2)^2}. \qquad (3.6.57)$$

For cuprite, the literature (Tromans & Meech, 2001) suggests that the main slip system is $\langle 001\rangle\{100\}$. The contrast factor can be calculated analytically from the single-crystal elastic constants of cuprite (c_{11} = 121, c_{12} = 105 and c_{44} = 12.1 GPa; Every & McCurdy, 1992*b*) following Martinez-Garcia *et al.* (2007):

$$\overline{C}_{\mathrm{Cu_2O},e} = 0.355963 - 0.609491\,\frac{h^2k^2 + k^2l^2 + h^2l^2}{(h^2 + k^2 + l^2)^2}, \qquad (3.6.58)$$

$$\overline{C}_{\mathrm{Cu_2O},s} = \frac{2}{3}\frac{h^2k^2 + k^2l^2 + h^2l^2}{(h^2 + k^2 + l^2)^2}. \qquad (3.6.59)$$

For tenorite, a different approach was followed. The phase is minor and the single-crystal elastic constants are not readily available: we can therefore use the contrast factor in an effective way by refining the coefficients of the corresponding invariant [see equation (3.6.42)]. This preserves the profile shape determined by Wilkens' theory and just dilutes the meaning of the dislocation density. The average contrast factor is

$$\begin{aligned}&\overline{C}_{\mathrm{CuO},\{hkl\}}\\ &= \Big\{4\big[E_1h^4 + E_2k^4 + E_3l^4 + 2(E_4h^2k^2 + E_5k^2l^2 + E_6h^2l^2)\\ &\quad + 4(E_7h^3k + E_8h^3l + E_9k^3h)\big)\big]Y^4Z^4\sin^4\beta\Big\}\\ &\quad \times \left(\left\{k^2Z^2 + 2Y^2(l^2 + h^2Z^2) - Z[4hlY^2\cos(\beta) + k^2Z\cos(2\beta)]\right\}^2\right)^{-1},\end{aligned} \qquad (3.6.60)$$

where a, b, c and β are the unit-cell parameters of tenorite, $Y = b/a$ and $Z = c/a$.

The dislocation density in Cu_2O is quite high [ρ = 2.8 (5) × 10^{16} m^{-2}]: dislocations are more of the edge character [f_E = 0.85 (3)] and the outer cutoff radius R_e = 9 (3) nm leads to a Wilkens' parameter of approximately 1.5, suggesting a strong dislocation interaction. The high dislocation density in this material is justified by the very low shear modulus (G = 10.3 GPa; Every & McCurdy, 1992*b*), whereas the high dislocation interaction is the result of the severe deformation induced by the milling.

APPENDIX A3.6.1
Functions for profile shapes

The unit-area Gaussian $G(x, \omega)$ and Lorentzian $L(x, \omega)$ functions are defined as

$$G(x,\omega) = \frac{2\sqrt{\ln 2/\pi}}{\omega}\exp\left(-\frac{4x^2\ln 2}{\omega^2}\right), \qquad (3.6.61)$$

$$L(x,\omega) = \frac{2}{\pi\omega}\left(\frac{1}{1 + 4x^2/\omega^2}\right), \qquad (3.6.62)$$

where x is the running variable and ω is the full-width at half-maximum. Based on these definitions, the Voigt and pseudo-Voigt are

$$V(x,\omega_L,\omega_G) = L(x,\omega_L) \otimes G(x,\omega_G) \qquad (3.6.63)$$

and

$$\mathrm{pV}(x,\omega_L,\omega_G) = \eta L(x,\omega_L) + (1-\eta)G(x,\omega_G), \qquad (3.6.64)$$

respectively, where η is the mixing parameter (ranging between 0 and 1) and w_L and w_G are the width of the Lorentzian and Gaussian components, respectively.

References

Adler, T. & Houska, C. R. (1979). *Simplifications in the X-ray line-shape analysis. J. Appl. Phys.* **50**, 3282–3287.

Alexander, L. (1954). *The synthesis of X-ray spectrometer line profiles with application to crystallite size measurements. J. Appl. Phys.* **25**, 155–161.

Armstrong, N., Leoni, M. & Scardi, P. (2006). *Considerations concerning Wilkens' theory of dislocation line-broadening. Z. Kristallogr. Suppl.* **23**, 81–86.

Balogh, L., Ribárik, G. & Ungár, T. (2006). *Stacking faults and twin boundaries in fcc crystals determined by X-ray diffraction profile analysis. J. Appl. Phys.* **100**, 023512.

Balzar, D. & Popović, S. (1996). *Reliability of the simplified integral-breadth methods in diffraction line-broadening analysis. J. Appl. Cryst.* **29**, 16–23.

Bergmann, J. & Kleeberg, R. (2001). *Fundamental parameters versus learnt profiles using the Rietveld program BGMN. Mater. Sci. Forum*, **378–381**, 30–37.

Berkum, J. G. M. van (1994). *Strain Fields in Crystalline Materials*. PhD thesis, Technische Universiteit Delft, Delft, The Netherlands.

Bertaut, E. F. (1949*a*). *Etude aux rayons X de la répartition des dimensions des cristallites dans une poudre cristalline. C. R. Acad. Sci.* **228**, 492–494.

Bertaut, E. F. (1949*b*). *Signification de la dimension cristalline mesurée d'apres la largeur de raie Debye-Scherrer. C. R. Acad. Sci.* **228**, 187–189.

Bertaut, E. F. (1950). *Raies de Debye–Scherrer et repartition des dimensions des domaines de Bragg dans les poudres polycristallines. Acta Cryst.* **3**, 14–18.

Beyerlein, K. R., Leoni, M. & Scardi, P. (2012). *Temperature diffuse scattering of nanocrystals. Acta Cryst.* A**68**, 382–392.

Billinge, S. J. L. (2008). *Local structure from total scattering and atomic pair distribution function (PDF) analysis.* In *Powder Diffraction: Theory and Practice*, edited by R. E. Dinnebier & S. J. L. Billinge. London: Royal Society of Chemistry.

Brese, N. E., O'Keeffe, M., Ramakrishna, B. L. & Von Dreele, R. B. (1990). *Low-temperature structures of CuO and AgO and their relationships to those of MgO and PdO. J. Solid State Chem.* **89**, 184–190.

Bruker (2009). *DIFFRAC.SUITE TOPAS*, *Total Pattern Analysis Solution.* Version 5. Bruker AXS, Karlsruhe, Germany.

Caglioti, G., Paoletti, A. & Ricci, F. P. (1958). *Choice of collimator for a crystal spectrometer for neutron diffraction. Nucl. Instrum.* **3**, 223–228.

Cervellino, A., Giannini, C. & Guagliardi, A. (2003). *Determination of nanoparticle structure type, size and strain distribution from X-ray data for monatomic f.c.c.-derived non-crystallographic nanoclusters. J. Appl. Cryst.* **36**, 1148–1158.

Cheary, R. W. & Coelho, A. (1992). *A fundamental parameters approach to X-ray line-profile fitting. J. Appl. Cryst.* **25**, 109–121.

Cheary, R. W. & Coelho, A. (1994). *Synthesizing and fitting linear position-sensitive detector step-scanned line profiles. J. Appl. Cryst.* **27**, 673–681.

Cheary, R. W. & Coelho, A. A. (1998*a*). *Axial divergence in a conventional X-ray powder diffractometer. I. Theoretical foundations. J. Appl. Cryst.* **31**, 851–861.

Cheary, R. W. & Coelho, A. A. (1998*b*). *Axial divergence in a conventional X-ray powder diffractometer. II. Realization and evaluation in a fundamental-parameter profile fitting procedure. J. Appl. Cryst.* **31**, 862–868.

Cline, J. P., Black, D., Windover, D. & Henins, A. (2010). *SRM 660b – Line Position and Line Shape Standard for Powder Diffraction.* https://www-s.nist.gov/srmors/view_detail.cfm?srm=660b.

Coelho, A. A. (2005). *A bound constrained conjugate gradient solution method as applied to crystallographic refinement problems. J. Appl. Cryst.* **38**, 455–461.

Coelho, A. A. (2009). *TOPAS Academic.* Version 5. http://www.topas-academic.net/.

Cozzoli, P. D., Snoeck, E., Garcia, M. A., Giannini, C., Guagliardi, A., Cervellino, A., Gozzo, F., Hernando, A., Achterhold, K., Ciobanu, N., Parak, F. G., Cingolani, R. & Manna, L. (2006). *Colloidal synthesis and characterization of tetrapod-shaped magnetic nanocrystals. Nano Lett.* **6**, 1966–1972.

Debye, P. (1915). *Zerstreuung von Röntgenstrahlen. Ann. Phys.* **351**, 809–823.

Deutsch, M., Forster, E., Holzer, G., Hartwig, J., Hämäläinen, K., Kao, C.-C., Huotari, S. & Diamant, R. (2004). *X-ray spectrometry of copper: new results on an old subject. J. Res. Natl Inst. Stand. Technol.* **109**, 75–98.

Dragomir, I. C. & Ungár, T. (2002). *Contrast factors of dislocations in the hexagonal crystal system. J. Appl. Cryst.* **35**, 556–564.

Drits, V. A. & Tchoubar, C. (1990). *X-ray Diffraction by Disordered Lamellar Structures: Theory and Applications to Microdivided Silicates and Carbons.* Berlin: Springer-Verlag.

Edwards, O. S. & Lipson, H. (1942). *Imperfections in the structure of cobalt. I. Experimental work and proposed structure. Proc. R. Soc. Lond. Ser. A*, **180**, 268–277.

Egami, T. & Billinge, S. J. L. (2003). *Underneath the Bragg Peaks. Structural Analysis of Complex Materials.* Oxford: Elsevier.

Estevez-Rams, E., Leoni, M., Scardi, P., Aragon-Fernandez, B. & Fuess, H. (2003). *On the powder diffraction pattern of crystals with stacking faults. Philos. Mag.* **83**, 4045–4057.

Estevez-Rams, E., Welzel, U., Pentón Madrigal, A. & Mittemeijer, E. J. (2008). *Stacking and twin faults in close-packed crystal structures: exact description of random faulting statistics for the full range of faulting probabilities. Acta Cryst.* A**64**, 537–548.

Every, A. G. & McCurdy, A. K. (1992*a*). *Landolt–Börnstein: Crystal and Solid State Physics New Series*, Group III, Vol. 29, edited by D. F. Nelson, p. 12. Berlin: Springer.

Every, A. G. & McCurdy, A. K. (1992*b*). *Landolt–Börnstein: Crystal and Solid State Physics New Series*, Group III, Vol. 29, edited by D. F. Nelson, p. 68. Berlin: Springer.

Garrod, R. I., Brett, J. F. & MacDonald, J. A. (1954). *X-ray line broadening and pure diffraction contours. Aust. J. Phys.* **7**, 77–95.

Gevers, R. (1954*a*). *X-ray diffraction by close-packed crystals with 'growth stacking faults' assuming an 'N-layer influence'. Acta Cryst.* **7**, 492–494.

Gevers, R. (1954*b*). *X-ray diffraction by close-packed crystals with 'growth-' and 'deformation or transformation stacking faults' assuming an 'N-layer influence'. Acta Cryst.* **7**, 740–744.

Grebille, D. & Bérar, J.-F. (1985). *Calculation of diffraction line profiles in the case of a major size effect: application to boehmite AlOOH. J. Appl. Cryst.* **18**, 301–307.

Groma, I., Ungár, T. & Wilkens, M. (1988). *Asymmetric X-ray line broadening of plastically deformed crystals. I. Theory. J. Appl. Cryst.* **21**, 47–54.

Hölzer, G., Fritsch, M., Deutsch, M., Härtwig, J. & Förster, E. (1997). *$K\alpha_{1,2}$ and $K\beta_{1,3}$ X-ray emission lines of the 3d transition metals. Phys. Rev. A*, **56**, 4554–4568.

Houska, C. R. & Smith, T. M. (1981). *Least-squares analysis of X-ray diffraction line shapes with analytic functions. J. Appl. Phys.* **52**, 748.

Jones, F. W. (1938). *The measurement of particle size by the X-ray method. Proc. R. Soc. Lond. Ser. A*, **166**, 16–43.

Kaganer, V. M. & Sabelfeld, K. K. (2010). *X-ray diffraction peaks from correlated dislocations: Monte Carlo study of dislocation screening. Acta Cryst.* A**66**, 703–716.

Kamminga, J.-D. & Delhez, R. (2000). *Calculation of diffraction line profiles from specimens with dislocations. A comparison of analytical models with computer simulations. J. Appl. Cryst.* **33**, 1122–1127.

Kern, A. A. & Coelho, A. A. (1998). *A new fundamental parameters approach in profile analysis of powder data.* New Delhi: Allied Publishers.

Klimanek, P. & Kuzel, R. (1988). *X-ray diffraction line broadening due to dislocations in non-cubic materials. I. General considerations and the case of elastic isotropy applied to hexagonal crystals. J. Appl. Cryst.* **21**, 59–66.

Klug, H. P. & Alexander, L. E. (1974). *X-ray Diffraction Procedures for Polycrystalline and Amorphous Materials*, 2nd ed. New York: Wiley.

Krill, C. E. & Birringer, R. (1998). *Estimating grain-size distributions in nanocrystalline materials from X-ray diffraction profile analysis. Philos. Mag. A*, **77**, 621–640.

Krivoglaz, M. A. (1969). *Theory of X-ray and Thermal Neutron Scattering by Real Crystals.* New York: Plenum Press.

Krivoglaz, M. A., Martynenko, O. V. & Ryaboshapka, K. P. (1983). *Influence of correlation in position of dislocations on X-ray diffraction by deformed crystals. Phys. Met. Metall.* **55**, 1–12.

Krivoglaz, M. A. & Ryaboshapka, K. P. (1963). *Theory of X-ray scattering by crystals containing dislocations. Screw and edge dislocations randomly distributed throughout the crystal. Phys. Met. Metall.* **15**, 14–26.

Kuzel, R. & Klimanek, P. (1989). *X-ray diffraction line broadening due to dislocations in non-cubic crystalline materials. III. Experimental results for plastically deformed zirconium. J. Appl. Cryst.* **22**, 299–307.

Langford, J. I. & Louër, D. (1982). *Diffraction line profiles and Scherrer constants for materials with cylindrical crystallites. J. Appl. Cryst.* **15**, 20–26.

Langford, J. I. & Wilson, A. J. C. (1978). *Scherrer after sixty years: a survey and some new results in the determination of crystallite size. J. Appl. Cryst.* **11**, 102–113.

Leineweber, A. (2011). *Understanding anisotropic microstrain broadening in Rietveld refinement. Z. Kristallogr.* **226**, 905–923.

Leineweber, A. & Mittemeijer, E. J. (2004). *Diffraction line broadening due to lattice-parameter variations caused by a spatially varying scalar variable: its orientation dependence caused by locally varying nitrogen content in ε-FeN$_{0.433}$. J. Appl. Cryst.* **37**, 123–135.

Leineweber, A. & Mittemeijer, E. J. (2010). *Notes on the order-of-reflection dependence of microstrain broadening. J. Appl. Cryst.* **43**, 981–989.

Lele, S. & Anantharaman, T. R. (1966). *Influence of crystallite shape on particle size broadening of Debye–Scherrer reflections. Proc. Indian Acad. Sci. A*, **64**, 261–274.

Leonardi, A., Leoni, M., Siboni, S. & Scardi, P. (2012). *Common volume functions and diffraction line profiles of polyhedral domains. J. Appl. Cryst.* **45**, 1162–1172.

Leoni, M. (2008). *Diffraction analysis of layer disorder. Z. Kristallogr.* **223**, 561–568.

Leoni, M., Confente, T. & Scardi, P. (2006). *PM2K: a flexible program implementing whole powder pattern modelling. Z. Kristallogr. Suppl.* **23**, 249–254.

Leoni, M., Di Maggio, R., Polizzi, S. & Scardi, P. (2004). *X-ray diffraction methodology for the microstructural analysis of nanocrystalline powders: application to cerium oxide. J. Am. Ceram. Soc.* **87**, 1133–1140.

Leoni, M., Gualtieri, A. F. & Roveri, N. (2004). *Simultaneous refinement of structure and microstructure of layered materials. J. Appl. Cryst.* **37**, 166–173.

Leoni, M., Martinez-Garcia, J. & Scardi, P. (2007). *Dislocation effects in powder diffraction. J. Appl. Cryst.* **40**, 719–724.

Leoni, M. & Scardi, P. (2004). *Nanocrystalline domain size distributions from powder diffraction data. J. Appl. Cryst.* **37**, 629–634.

Leoni, M., Scardi, P. & Langford, J. I. (1998). *Characterization of standard reference materials for obtaining instrumental line profiles. Powder Diffr.* **13**, 210–215.

Martinez-Garcia, J., Leoni, M. & Scardi, P. (2007). *Analytical expression for the dislocation contrast factor of the ⟨001⟩{100} cubic slip-system: Application to Cu$_2$O. Phys. Rev. B*, **76**, 174117.

Martinez-Garcia, J., Leoni, M. & Scardi, P. (2008). *Analytical contrast factor of dislocations along orthogonal diad axes. Philos. Mag. Lett.* **88**, 443–451.

Martinez-Garcia, J., Leoni, M. & Scardi, P. (2009). *A general approach for determining the diffraction contrast factor of straight-line dislocations. Acta Cryst.* A**65**, 109–119.

Matěj, Z., Matějová, L., Novotný, F., Drahokoupil, J. & Kuzel, R. (2011). *Determination of crystallite size distribution histogram in nanocrystalline anatase powders by XRD. Z. Kristallogr. Proc.* **1**, 87–92.

Nakajima, A., Yoshihara, A. & Ishigame, M. (1994). *Defect-induced Raman spectra in doped CeO$_2$. Phys. Rev. B*, **50**, 13297–13307.

Nye, J. F. (1987). *Physical Properties of Crystals: Their Representation by Tensors and Matrices*, reprint edition. Oxford University Press.

Paterson, M. S. (1952). *X-ray diffraction by face-centered cubic crystals with deformation faults. J. Appl. Phys.* **23**, 805–811.

Patterson, A. L. (1939). *The Scherrer formula for X-ray particle size determination. Phys. Rev.* **56**, 978–982.

Pawley, G. S. (1981). *Unit-cell refinement from powder diffraction scans. J. Appl. Cryst.* **14**, 357–361.

Popa, N. C. (1998). *The (hkl) dependence of diffraction-line broadening caused by strain and size for all Laue groups in Rietveld refinement. J. Appl. Cryst.* **31**, 176–180.

Rao, S. & Houska, C. R. (1986). *X-ray diffraction profiles described by refined analytical functions. Acta Cryst.* A**42**, 14–19.

Ribárik, G. (2008). *Modeling of Diffraction Patterns Properties.* PhD thesis, Eötvös University, Budapest.

Ribárik, G., Gubicza, J. & Ungár, T. (2004). *Correlation between strength and microstructure of ball-milled Al–Mg alloys determined by X-ray diffraction. Mater. Sci. Eng. A Struct. Mater.* **387–389**, 343–347.

Rietveld, H. M. (1969). *A profile refinement method for nuclear and magnetic structures. J. Appl. Cryst.* **2**, 65–71.

Scardi, P. & Leoni, M. (1999). *Fourier modelling of the anisotropic line broadening of X-ray diffraction profiles due to line and plane lattice defects. J. Appl. Cryst.* **32**, 671–682.

Scardi, P. & Leoni, M. (2001). *Diffraction line profiles from polydisperse crystalline systems. Acta Cryst.* A**57**, 604–613.

Scardi, P. & Leoni, M. (2002). *Whole powder pattern modelling. Acta Cryst.* A**58**, 190–200.

Scardi, P. & Leoni, M. (2004). *Whole powder pattern modelling: theory and application.* In *Diffraction Analysis of the Microstructure of Materials*, edited by E. J. Mittemeijer & P. Scardi, pp. 51–91. Berlin: Springer-Verlag.

Scardi, P. & Leoni, M. (2005). *Diffraction whole-pattern modelling study of anti-phase domains in Cu_3Au. Acta Mater.* **53**, 5229–5239.

Scardi, P., Leoni, M. & Beyerlein, K. R. (2011). *On the modelling of the powder pattern from a nanocrystalline material. Z. Kristallogr.* **226**, 924–933.

Scardi, P., Leoni, M. & Delhez, R. (2004). *Line broadening analysis using integral breadth methods: a critical review. J. Appl. Cryst.* **37**, 381–390.

Scardi, P., Leoni, M., Müller, M. & Di Maggio, R. (2010). *In situ size-strain analysis of nanocrystalline ceria growth. Mater. Sci. Eng. A Struct. Mater.* **528**, 77–82.

Scardi, P., Leoni, M., Straffelini, G. & Giudici, G. D. (2007). *Microstructure of Cu–Be alloy triboxidative wear debris. Acta Mater.* **55**, 2531–2538.

Scherrer, P. (1918). *Bestimmung der Grösse und der inneren Struktur von Kolloidteilchen mittels Röntgenstrahlen. Nachr. Ges. Wiss. Göttingen*, pp. 98–100.

Stephens, P. W. (1999). *Phenomenological model of anisotropic peak broadening in powder diffraction. J. Appl. Cryst.* **32**, 281–289.

Stokes, A. R. & Wilson, A. J. C. (1942). *A method of calculating the integral breadths of Debye–Scherrer lines. Math. Proc. Cambridge Philos. Soc.* **38**, 313–322.

Stokes, A. R. & Wilson, A. J. C. (1944). *The diffraction of X-rays by distorted crystal aggregates – I. Proc. Phys. Soc.* **56**, 174–181.

Treacy, M. M. J., Newsam, J. M. & Deem, M. W. (1991). *A general recursion method for calculating diffracted intensities from crystals containing planar faults. Proc. R. Soc. Lond. Ser. A*, **433**, 499–520.

Tromans, D. & Meech, J. A. (2001). *Enhanced dissolution of minerals: stored energy, amorphism and mechanical activation. Miner. Eng.* **14**, 1359–1377.

Ungár, T. (2001). *Dislocation densities, arrangements and character from X-ray diffraction experiments. Mater. Sci. Eng. A Struct. Mater.* **309–310**, 14–22.

Ungár, T. & Borbély, A. (1996). *The effect of dislocation contrast on X-ray line broadening: a new approach to line profile analysis. Appl. Phys. Lett.* **69**, 3173.

Ungár, T., Dragomir, I., Révész, Á. & Borbély, A. (1999). *The contrast factors of dislocations in cubic crystals: the dislocation model of strain anisotropy in practice. J. Appl. Cryst.* **32**, 992–1002.

Ungár, T., Gubicza, J., Ribárik, G. & Borbély, A. (2001). *Crystallite size distribution and dislocation structure determined by diffraction profile analysis: principles and practical application to cubic and hexagonal crystals. J. Appl. Cryst.* **34**, 298–310.

Ungár, T. & Tichy, G. (1999). *The effect of dislocation contrast on X-ray line profiles in untextured polycrystals. Phys. Stat. Solidi A Appl. Res.* **171**, 425–434.

Vargas, R., Louër, D. & Langford, J. I. (1983). *Diffraction line profiles and Scherrer constants for materials with hexagonal crystallites. J. Appl. Cryst.* **16**, 512–518.

Velterop, L., Delhez, R., de Keijser, Th. H., Mittemeijer, E. J. & Reefman, D. (2000). *X-ray diffraction analysis of stacking and twin faults in f.c.c. metals: a revision and allowance for texture and non-uniform fault probabilities. J. Appl. Cryst.* **33**, 296–306.

Warren, B. E. (1959). *X-ray studies of deformed metals. Progr. Met. Phys.* **8**, 147–202.

Warren, B. E. (1963). *Single- and double-deformation faults in face-centered cubic crystals. J. Appl. Phys.* **34**, 1973–1975.

Warren, B. E. (1990). *X-ray Diffraction.* New York: Dover Publications. (Unabridged reprint of the original 1969 book.)

Warren, B. E. & Averbach, B. L. (1950). *The effect of cold-work distortion on X-ray patterns. J. Appl. Phys.* **21**, 595–599.

Warren, B. E. & Averbach, B. L. (1952). *The separation of cold-work distortion and particle size broadening in X-ray patterns. J. Appl. Phys.* **23**, 492.

Welberry, T.R. (2004). *Diffuse X-ray Scattering and Models of Disorder.* Oxford University Press.

Wilkens, M. (1970*a*). *The determination of density and distribution of dislocations in deformed single crystals from broadened X-ray diffraction profiles. Phys. Stat. Solidi A Appl. Res.* **2**, 359–370.

Wilkens, M. (1970*b*). *Fundamental Aspects of Dislocation Theory*, edited by J. A. Simmons, R. de Wit & R. Bullough, Vol. II, pp. 1195–1221. Washington DC: National Institute of Standards and Technology.

Wilkens, M. (1987). *X-ray line broadening and mean square strains of straight dislocations in elastically anisotropic crystals of cubic symmetry. Phys. Stat. Solidi A Appl. Res.* **104**, K1–K6.

Williamson, G. K. & Hall, W. H. (1953). *X-ray line broadening from filed aluminium and wolfram. Acta Metall.* **1**, 22–31.

Wilson, A. J. C. (1942). *Imperfections in the structure of cobalt. II. Mathematical treatment of proposed structures. Proc. R. Soc. Lond. Ser. A*, **180**, 277–285.

Wilson, A. J. C. (1943). *The reflexion of X-rays from the 'anti-phase nuclei' of $AuCu_3$. Proc. R. Soc. Lond. Ser. A*, **181**, 360–368.

Wilson, A. J. C. (1963). *Mathematical Theory of X-ray Powder Diffractometry.* New York: Gordon & Breach.

Wilson, A. J. C. (1969). *Variance apparent particle sizes for cylinders, prisms and hemispheres. J. Appl. Cryst.* **2**, 181–183.

Wilson, A. J. C. & Zsoldos, L. (1966). *The reflexion of X-rays from the 'anti-phase nuclei' of $AuCu_3$. II. Proc. R. Soc. Lond. Ser. A*, **290**, 508–514.

International Tables for Crystallography (2019). Vol. H, Chapter 3.7, pp. 304–324.

3.7. Crystallographic databases and powder diffraction

J. A. Kaduk

3.7.1. Introduction

Identifying compounds using powder-diffraction data requires a comparison of the current experimental pattern with essentially all previous crystallographic information. This information is incorporated into the Powder Diffraction File (Fawcett *et al.*, 2017), which is traditionally the primary tool for phase identification, but other databases are important to the process, as well as being the repositories of the atom coordinates necessary for Rietveld refinements. This chapter summarizes the characteristics of the various databases that the author has found useful in the practice of powder diffraction. It also provides several examples of the thought processes and capabilities which can be used to identify phases.

3.7.1.1. *History of the PDF/ICDD*

Although powder-diffraction experiments date from the beginning of the 20th century (Debye & Scherrer, 1916, 1917; Hull, 1919), what we now know as the Powder Diffraction File and the International Centre for Diffraction Data date from two papers from the Dow Chemical Company (Hanawalt & Rinn, 1936; Hanawalt *et al.*, 1938). The importance of these papers lies not only in the compilation of a database but also in a method for the identification of materials, and how the database was organized to work with the method. Discussion among industrial and academic scientists made the need for a central collection of powder-diffraction patterns apparent. The Joint Committee for Chemical Analysis by Powder Diffraction Methods was founded in 1941. It produced a primary reference of X-ray powder diffraction data, which became known as the Powder Diffraction File (PDF). This effort was supported initially by Committee E-4 of the American Society for Testing and Materials (ASTM). Over the next two decades, other professional bodies added their support, culminating in 1969 with the establishment of the Joint Committee on Powder Diffraction Standards (JCPDS). The JCPDS was incorporated as a separate nonprofit corporation to continue the mission of maintaining the PDF. In 1978 the name was changed to the International Centre for Diffraction Data to highlight the global nature of this scientific endeavour. Additional information on the history of the powder method is given in Parrish (1983) and on the early history of the Powder Diffraction File in Hanawalt (1983).

3.7.1.2. *Search/match*

What is now known as the Hanawalt search method (Hanawalt & Rinn, 1936; Hanawalt *et al.*, 1938) is an empirical scheme which was based on earlier ideas (Hull, 1919; Davey, 1922, 1934; Winchell, 1927; Waldo, 1935; Boldyrev *et al.*, 1938). The basic ideas behind the scheme have been summarized in more modern language by Hanawalt (1986). Other discussions of the method can be found in Jenkins & Rose (1990) and Hull (1983).

The patterns in the PDF are divided into 40 groups according to the *d*-spacing of the strongest peak and including error limits on the *d*-spacing. The entries within each group are sorted by the position of the second strongest peak. Because the peak intensities can be more difficult to measure than the positions and may vary from sample to sample, PDF entries appear in the index multiple times (‘rotations’ in the current nomenclature). All patterns appear at least once. Patterns appear twice when $I_2/I_1 > 0.75$ and $I_3/I_1 \le 0.75$, three times when $I_3/I_1 > 0.75$ and $I_4/I_1 \le 0.75$, and four times when $I_4/I_1 > 0.75$ (where I_1 is the strongest peak, I_2 is the second strongest and so on). There are four more rules, dealing with things such as low-angle peaks, rounding of *d*-spacings and closely spaced peaks.

The phase-identification process actually involves several steps. This was realized by Hanawalt, Rinn and Frevel even in 1938. The first step is to *search* the experimental data against an index (a structured subset of a database) to identify potential compounds. The printed *Hanawalt Search Manual* was such an index, and contemporary search/match programs all generate indices to enhance the speed of the phase-identification process. The second step is the *match* of the full PDF entry against the full experimental pattern to use all peaks in the identification process. Typically, the quality of the match is evaluated at this point to rank the potential candidate match among the others in the list; the hit list is sorted on goodness of match, similarity index, figure of merit or some similar quantity generated by the program. The third step is to *identify* the phase (generally by computer, but best with some human judgement). The pattern of the identified phase is then subtracted from the experimental pattern and the process is repeated to identify additional phases. The final step in the process is often quantification of the concentrations. Ultimately, the errors introduced during the subtractions limit the number of phases which can be identified in a mixture, and additional techniques are required to identify minor or trace phases. As specimen-preparation methods and equipment and standardized reference data have improved with time (over decades), the residual errors in the subtraction process have diminished, generally increasing the number of phases that can be identified when appropriate techniques are applied.

An early computer version of the Hanawalt search algorithm was implemented by Frevel (Frevel, 1965; Frevel *et al.*, 1976). This program used a 300-phase microfile database of common phases resulting from empirical work performed over decades at the Dow Chemical Company. Another early computer implementation of the Hanawalt search algorithm was developed by Snyder (1981). The index file stored the d/I pairs in the PDF as 16-bit integers: 11 bits for $1/d$ and five bits for I. The index file was an indexed sequential file with the PDF entries sorted on d_1 (the *d*-spacing of the strongest peak). Each PDF set was indexed separately, and smaller MICRO (300 phases) and MINI (2500 common phases) index files were also generated to permit faster searches on the slow computers of the day. After input of the d/I list for the experimental pattern, the program located PDF entries whose d_1 values lay within $\pm 0.1^\circ\ 2\theta$ (copper radiation) of the observed d_1. If the reference pattern passed three tests – it was a member of a user-specified subfile, all PDF entry peaks with $I \ge 50$ were present in the unknown pattern and user-specified chemical constraints were satisfied – a figure of merit (FOM) was calculated. The pattern with the highest FOM was saved for the match step, and the process was repeated for d_2 and d_3. If no hits were obtained, larger error windows and then weaker peaks were used.

The FOM was calculated as

$$\mathrm{FOM} = d_R I_R^2 d_U, \tag{3.7.1}$$

where d_R is the percentage of the reference peaks which match the unknown (within the error window) and have I greater than that of the lowest-intensity matched peak, I_R is the percentage of the reference intensity ($I_{\rm ref}$) matched and d_U is the percentage of the unknown peaks (with intensities $I_{\rm unk}$) matched.

PDF hits were considered for the match step if the FOM was >10. For the hit with the highest FOM, an I-weighted linear regression between $I_{\rm ref}$ and $I_{\rm unk}$ was carried out. Peaks with $I_{\rm calc} < I_{\rm obs} - 5$ were assigned as overlapped, and the least-squares scale factor was recalculated using only the non-overlapped peaks. The scaled PDF entry was subtracted from the unknown pattern and the residual was sent back to the search step.

Several commercial search/match programs have been developed, not from Snyder's implementation of the Hanawalt algorithm, but from the Johnson–Vand algorithm (Johnson & Vand, 1967, 1968; Cherukuri *et al.*, 1983). This algorithm used constant error windows in $1/d$ and $\log(I)$ and used integer arithmetic. The d/I pairs were packed into characteristic integers PSI = $(1000/d) \times 10 + 5\log_{10} I_3$. An inverted PDF was created, an index which contained the characteristic integers of the strongest lines of the reference patterns (PSI, PDF No. pairs) sorted by decreasing PSI. The input d/I list was compared with the index. All patterns that contained the characteristic integers within the bandpass were considered as potential hits. The full PDF was used to compare observed and reference patterns. A Davey minimum concentration (DMC) was calculated; this was the largest value in the range $0 \le \mathrm{DMC} \le 1$ for which $I_{\rm PDF}\mathrm{DMC} \le I_{\rm unk}$ for all peaks. The PDF entry was then subtracted from the unknown pattern and the process was repeated. Initially, there were no chemistry or user filters; these appeared in later versions.

The Johnson–Vand figure of merit,

$$\mathrm{FOM} = A\left[1 - \frac{\sum_N |\Delta D|}{(IW)N}\right]\left[1 - \frac{\sum_N |\Delta I| - K}{\sum_N I}\right], \tag{3.7.2}$$

was calculated, in which A is the percentage of peak match in the d-space range considered (above the background), $\Delta D = d_{\rm unk} - d_{\rm ref}$ (integer), N is the number of peaks under consideration, $\Delta I = I_{\rm unk} - I_{\rm ref}$, K is a scale factor and $IW = d$ is the error window (integer).

A derivative of the Johnson–Vand program was $\mu PDSM$ (Marquart *et al.*, 1979; Marquart, 1986). This program also used the integer $1000/d$ internally, and considered the probability of the occurrence of a d-spacing in calculating its figure of merit. It used the 15 strongest peaks of the reference patterns in the search step and was the first to make extensive use of pre-screens (especially chemistry) to speed up the search. In addition to the similarity index, other measures of the quality of a match were the numbers of matched and missing lines.

Sometimes, references to 'generations' of search/match programs will be encountered. The first-generation programs include those of Johnson & Vand (1967, 1968), Nichols (1966), Frevel *et al.* (1976), Marquart *et al.* (1979) and O'Connor & Bagliani (1976). The distinction between first- and second-generation programs (Snyder, 1981; Jobst & Goebel, 1982; Huang & Parrish, 1982; Schreiner *et al.*, 1982; Goehner & Garbauskas, 1984; Toby *et al.*, 1990; Caussin *et al.*, 1988) is fuzzy, and is partially a matter of timing and features. Contemporary third-generation programs such as *Jade* (Materials Data, 2016), *EVA* (Caussin *et al.*, 1989; Nusinovici & Bertelmann, 1993; Nusinovici & Winter, 1994), *HighScore* (Degen *et al.*, 2014), *Match!* (Crystal Impact, 2012), *Crystallographica Search-Match* (Oxford Cryosystems, 2012) and *Siroquant* (Sietronics, 2012) are distinguished mainly by the ability to use raw data in addition to peak lists. The presence and absence of peaks in particular regions are both considered in the calculation of the figure of merit. The width of the peak profiles serves as an error window. After the mid-1990s, there is virtually nothing in the open literature about search/match programs, and we are forced to rely on the help documentation of the commercial programs. Occasionally, one will encounter references to a fourth-generation program such as *SNAP* (Barr *et al.*, 2004; Gilmore *et al.*, 2004), *PolySNAP* (Barr *et al.*, 2009) or *FULLPAT* (Chipera & Bish, 2002). There is current development in using similarity indices as a complementary method for the analysis of noncrystalline materials, as these methods depend on whole-pattern fitting instead of peak location and intensity. These methods also cluster isotypical and isostructural crystalline materials, and can be applied to nanomaterial analyses, where there is frequently severe peak overlap.

Originally developed for use with both electron and/or X-ray diffraction data, the Fink search (Bigelow & Smith, 1964) uses the d-spacings of the eight strongest peaks in the pattern, but does not otherwise use the intensities. The justification for not using the intensities was that electron-diffraction intensities were not very reliable, often as a result of poor counting statistics in the small areas analysed in a typical electron-diffraction attachment to a scanning or transmission electron microscope coupled with the effects of dynamical scattering and sample decomposition in the electron beam. The search was named in honour of William H. Fink, a long-time chairman of the JCPDS/ICDD. In the current *SIeve+* module of the PDF, all eight rotations (considering each of the eight peaks as the strongest in turn) are commonly used. *SIeve+* also incorporates a 'Long 8' search, which uses the eight lowest-angle peaks. Fundamentally, searches using electron-diffraction data have deviated from traditional powder-diffraction searches because of the unreliability of both the intensities and the peak locations often brought about by the limited space within an electron microscope. Most modern electron-diffraction searches incorporate elemental data as an integral part of the method. As for X-ray diffraction, there are various generations that integrate elemental composition data, d-spacings or crystallographic data into a search/match process. The *SIeve+* program can also incorporate composition data into the search process.

3.7.2. Powder Diffraction File (PDF)

The PDF is a collection of single-phase X-ray powder patterns in the form of tables of characteristic interplanar spacings and corresponding relative intensities, along with other pertinent physical, chemical and crystallographic properties. The PDF contains various subfiles, which include alkaloids, amino acids, peptides and complexes, battery materials, bioactive compounds, carbohydrates, cement materials, ceramics (bioceramics, ferroelectrics, microwave materials, perovskites and semiconductors), common phases, education, explosives, forensic, hydrogen-storage materials, inorganics, intercalates, ionic conductors, Merck Index compounds, metals and alloys, meso- and microporous (clathrates, metal–organic frameworks and zeolites), mineral-related (minerals, gems, natural and synthetic), modulated structures, nucleosides and nucleotides, organics, pharmaceuticals, pigments and dyes, polymers, porphyrins, corrins and complexes, steroids, superconducting materials (conventional superconductors, superconductor reaction products, superconductor-related and high-T_c superconductors), terpenes and thermoelectric materials. There is an educational package for classroom use, and the complete PDF is available for educational use on a time-limited basis. A primary purpose of the subfile system is to limit the size of the search universe by applying prior knowledge of the system being studied. This greatly reduces the number of false positives in a database that contains hundreds of thousands of materials. Field experts are consulted to guide the criteria for subfile selection, allowing novices to use the subfiles without being a subject expert.

3.7.2.1. *Sources and formats of the PDF*

The data incorporated into the Powder Diffraction File are acquired through contributions from individual scientists, corporate laboratories, literature surveys and a Grant-in-Aid programme. Approximately 200 leading scientific journals are searched manually for powder-diffraction data. Additional literature surveys covering patents, dissertations and the remaining open literature are performed using various online resources and search techniques.

Release 2019 (the current release as of this writing) contains more than 893 400 unique material data sets. The large size and comprehensive coverage of the PDF is achieved through the ICDD's historical sources of powder data (searches of the original literature, contributions and the Grant-in-Aid programme) as well as current and historic collaborations with crystallographic database organizations. Each PDF entry is assigned a unique identifying number of the format *ss-mmm-nnnn*. The integer *ss* indicates the source of the data: 00, ICDD location/generation of powder data; 01, Inorganic Crystal Structure Database; 02, Cambridge Structural Database; 03, NIST (a short-term collaboration focused on metals and alloys); 04, Pearson's Crystal Data; 05, ICDD extraction of atomic coordinates from published sources (including incommensurate/modulated structures). Powder-diffraction data for sources 01 through 05 are computed from the crystal structures provided by these sources.

The Powder Diffraction File is designed and produced in several different formats in order to serve different groups of users. The PDF-2 database is designed for phase identification of inorganic materials; many common organic materials have also been added to this database. The PDF-4+ database is the most advanced database and is designed for both phase identification and quantitative analysis. This database has comprehensive coverage of inorganic materials and contains numerous additional features such as digitized (raw) patterns, molecular graphics and atomic coordinates to facilitate Rietveld refinements. The PDF-4+ database is also available as a portable full-function WEBPDF-4+ version. The PDF-4/Minerals database is a subset of the PDF-4+ database, and is the most comprehensive collection of mineral diffraction data. The PDF-4/Organics database is designed for phase identification of organic and coordination compounds. It contains data from ICDD sources (both experimental powder patterns and extraction of coordinates) as well as patterns calculated from CSD entries.

Advances in hardware, software and computing power have led to the collection of higher-quality powder data, and thus have necessitated higher-quality reference data to perform more complex multiphase analyses and total-pattern analyses. The PDF now includes tools that permit users to evaluate different types of data collected using different types of detectors and different sources, including X-rays, neutrons and electrons. The goal is to include ideal specimen patterns in the PDF, patterns that can be modified by the user to correspond to the current experiment. The user can select the wavelength type and various instrumental parameters to simulate the whole diffraction pattern. A crystallite size calculation was added in 2007 and an orientation function in 2011.

Since 2006, the ICDD has begun to include several types of less-crystalline materials in the database, materials for which too much information is lost when reducing the raw data to a list of *d*-spacings and intensities. These materials include clays and other layered materials, mixed-crystallinity polymers, amorphous materials and nanomaterials.

Nanomaterials often contain crystalline and amorphous fractions, and their powder patterns are difficult to generate from an ideal crystal structure. The ICDD has developed quality-evaluation methods for noncrystalline materials, and has established two additional quality marks: 'good' (G) and 'minimal acceptable' (M). These marks reflect the quality of the supporting data used to characterize the material. An amorphous material with a G quality mark has been characterized by independent analyses verifying the stated composition or thermogravimetric/differential scanning calorimetry analyses confirming the physical stability or the presence of a glass transition. A G quality mark indicates that the editors are satisfied that the pattern is representative of both the diffraction conditions and the stated chemistry and have confidence that the user can reproduce the pattern using similar conditions. The quality mark M indicates that the ICDD received some supporting documentation but it was insufficient for structural interpretation and classification of the material.

Great care needs to be taken in interpreting the patterns of mixtures of crystalline and amorphous phases, particularly in the definition and subtraction of the background. Significant work is under way to develop and adapt numerical techniques for processing full patterns of low-crystallinity materials.

3.7.2.2. *Quality marks in the PDF*

All data are critically reviewed and evaluated by the PDF editorial staff. Each pattern must pass through a four-tiered editorial review process before it can be included in the PDF. As technology evolves, the quality requirements for reference data also evolve. As a result, the information in the PDF is continuously reviewed and upgraded for accuracy and quality.

For many years, a quality mark has been assigned to each experimental PDF entry. A Star (*/S) pattern represents high-quality diffractometer or Guinier data. Several criteria must be satisfied for a pattern to be assigned a Star quality mark:

(i) The chemical composition must be well characterized.
(ii) The intensities must have been measured objectively; no visual estimation is allowed.
(iii) The pattern has a good range and an even spread of intensities.
(iv) The completeness of the pattern is sensible.
(v) The *d*-spacing of each reflection with $d \leq 2.500$ Å is given to at least three decimal places. The *d*-spacings of reflections with $d \leq 1.2000$ Å are given to at least four decimal places.
(vi) No serious systematic errors exist.
(vii) The $|\Delta 2\theta|$ value (*i.e.* the difference between the observed peak position and the position calculated from the unit

cell) of a qualifying reflection is $\leq 0.05^\circ$. In the case of multiply-indexed reflections, only the minimum absolute $\Delta 2\theta$ is considered.

(viii) The average $|\Delta 2\theta| \leq 0.03^\circ$ for qualifying reflections.

(ix) No unindexed, space-group-extinct or impurity reflections are present.

An Indexed (I) quality mark indicates that the pattern has been indexed; therefore, the material is almost certainly single-phase. There is a reasonable range and spread of intensities, and the completeness of the pattern is sensible. The d-spacings of reflections with $d \leq 2.000$ Å have at least three significant figures after the decimal point. No serious systematic errors exist. No qualifying reflection has $|\Delta 2\theta| \geq 0.20^\circ$ and the average $|\Delta 2\theta|$ is $\leq 0.06^\circ$. The maximum number of unindexed, space-group-extinct or impurity reflections is two, but none of these reflections are among the eight strongest lines.

A Blank (B) quality mark represents a mid-range quality. An O quality mark means that the data have been obtained from a poorly characterized material or that the data are known (or are suspected) to be of low precision and accuracy. Such patterns include those from multiphase mixtures or from a phase that is poorly characterized chemically. The O mark is commonly assigned to patterns for which no unit cell is reported, unless qualifying information indicates a single-phase material. Usually, the editor will have inserted a comment to explain why the O mark was assigned. For patterns with a unit cell, the following criteria are used to suggest the presence of two or more phases: the number of unindexed, space-group-extinct or impurity reflections is ≥ 3, or one of the three strongest peaks is unindexed.

Beginning with Release 2006, the quality-mark system was extended to patterns calculated from structural data supplied by ICDD partners. The focus of the quality mark is to determine the confidence level of the structural model used and its impact on the calculated pattern (especially for the purpose of phase identification). The major step involves several crystallographic and editorial checks by the ICDD, followed by extraction and flagging of the warnings/comments in the structural databases. The resulting calculated patterns are classified based on the significance and nature of the warnings. Any possible corrections that can be applied to resolve the errors are performed before publishing the calculated pattern.

The crystallographic checking rules are designed based on the expected quality of a contemporary crystal structure. An estimate of the missing electron density is made based on the difference between the reported composition and the structural composition. Transformations of nonstandard space groups are checked; the reported site multiplicities must match those generated by the symmetry operators. All of the eigenvalues of the anisotropic tensor matrix for each atomic displacement must be positive. All anisotropic tensor coefficients must be permitted by the site symmetry. Displacement coefficients should fall in the range $0.001 < U < 0.1$ Å^2. Isotropic displacement coefficients must be positive. Mixed displacement coefficients are converted to a standard type. The reported value of Z must be consistent with the sum of the site multiplicities. Lattice parameters are checked for missing decimal points, missing standard uncertainties and the magnitudes of the uncertainties. R factors close to the theoretical limits (0.83 for centrosymmetric structures and 0.59 for non-centrosymmetric structures) are signs of potential errors in the conversion to/from absolute/percentage values. Site occupancies cannot be greater than 1. Refining part of the structure as a group without locating the positions of the constituent atoms (for example, in C_{60}) will generate a warning. Possible typographical errors in element symbols are checked by comparing the chemical formula, atomic coordinate list and chemical name. When a measured density is available, the percentage difference between the measured and calculated density is determined.

Many warnings/comments from the collaborating databases are used in assignment of the quality mark. Editorial comments on unusually short or long bond lengths or questionable bond angles are considered; the comment needs to be very specific for structures exhibiting disorder or partial/mixed occupancies. A listing of other types of comments considered is contained in the PDF-4+ database help documentation. Entries are assigned a quality mark of * (no warning found during data evaluation), I (minor warning), B (significant warning found), O (major warning), P (the structure was assigned by the editor based on a prototype) or H (hypothetical) according to the criteria in Table 3.7.1.

3.7.2.3. *Features of the PDF*

Most users access the PDF through the software provided by their instrument manufacturer, but it is a powerful standalone database. The PDF is a large relational database consisting of many linked tables. The complete set of features can be accessed through the PDF front end supplied by the ICDD. It is possible to directly access a PDF entry by entering its PDF number. However, one can search for an entry or a class of entries through a series of search tabs. Queries from multiple tabs can be combined in a single search, or individual searches can be saved in a history and combined using Boolean operations. The results of such searches can be analysed as a group or can be used as subfiles for *SIeve*, the search/index phase-identification add-on for the PDF.

Selections on the main search screen permit selection by the source of data, quality mark, primary/alternate, ambient/non-ambient and subfile or subclass. The comprehensive nature of the PDF means that there are often many entries for an individual material. The ICDD editorial staff and volunteer task groups assign one experimental and one calculated entry (if present) as primary entries for each phase so that the user can avoid the duplication if desired. The other entries are designated as alternates. The subfiles and subclasses provide a convenient means for the user to limit the size of the search universe based on prior knowledge and result in faster searches and fewer false-positive matches.

Perhaps the most commonly used screen is the Periodic Table tab for chemistry searches. Individual elements, groups, periods and pre-defined selections (nonmetals, semimetals *etc.*) can be selected and combined in various ways. The ‘and’ operation requires that all selected elements be present in the entries in the selection set, but other elements can also be present. The ‘or’ operation requires at least one of the selected elements to be present. The ‘only’ operation requires that all of the selected elements, and only those elements, be present in the hit. The ‘just’ operation results in a hit list of entries that contain the selected elements in all combinations: elements, binaries, ternaries *etc.* The results of these four types of element searches can also be combined using Boolean operations. An alternative way of using periodic-table screening is through the labelling of each element with ‘yes’, ‘no’ or ‘maybe’ to indicate elements that are known to be present, absent or unsure in the specimen.

The Formula/Name tab facilitates searches on formula, empirical formula, structural formula and formula type ANX [as in the Inorganic Crystal Structure Database (ICSD)]. The formulae may be exact or contain individual elements or strings.

Table 3.7.1

Criteria for the assignment of quality marks to calculated patterns in the Powder Diffraction File

A Star (*/S) pattern has no warnings.

Minor warning (I)	Significant warning (B)	Major warning (O)
Density calculated from reported and calculated compositions differ ($1\% < x < 3\%$)	Density calculated from reported and calculated compositions differ ($1\% < x < 15\%$)	Density calculated from reported and calculated compositions differ ($15\% < x$)
No e.s.d. reported/abstracted on cell dimensions	Lattice parameters taken from figure (approximated)	Incorrect lattice parameters
Magnitude of e.s.d.s on lattice parameters > 1000 p.p.m.	Missing decimal point in lattice parameter	Incorrect space group
$0.07 < R < 0.12$ (single crystal), $0.10 < R < 0.15$ (powder)	$0.12 < R$ (single crystal), $0.15 < R$ (powder)	Incommensurate/modulated structure. Only average structure of the subcell is given.
No R reported/abstracted	Anisotropic displacement tensor is non-positive definite	Published atomic coordinates are wrong
Reported Z is inconsistent with the sum of the site multiplicities	Anisotropic tensor coefficient not permitted by site symmetry	Structural database removed the entry corresponding to a published calculated pattern
Type of experiment (single crystal/powder) is not mentioned	Magnitude of displacement coefficients outside the range $0.001 < U < 0.1$ Å^2	
Structure corrected by the editor	$U_{\rm iso} < 0.0$	
Difference between measured and calculated density > 2%	Source-database warning on bond length/angle	
Misprint in original paper corrected in database	Average structure of a modulated structure	
Site occupation factor > 1.0	Probable site-occupation factor deduced from the nominal composition	
	Part of the structure was refined as a group without locating the constituent atoms	
	Comments containing a reference to a contradicting structure exist	
	Structure determined from projections	
	Structure determined using electron diffraction	

Searches on the number of elements present in the compound, as well as composition searches (by weight or atom per cent, *i.e.* wt% or at.%), are also possible.

The Formula/Name tab also permits searches on compound name, common name, mineral name and all names. It is also the screen from which searches on zeolite structure-type code (the International Zeolite Association codes are used) and mineral classification (according to the International Mineralogical Association) are performed.

Under the Reference tab, searches on author, journal name, CODEN, year, volume and title of the paper are possible. The titles were not originally included in PDF entries, but have been added to all entries in recent years. Also possible from this tab are searches on the Chemical Abstracts Service Registry Number (CASRN). Such searches are very powerful for organic compounds, with their complicated nomenclature. CASRNs are present for many, but not all, PDF entries.

The Classification and Crystallography tabs contain searches on Pearson symbol code, space group and space-group number, prototype structure, centrosymmetric/noncentrosymmetric and whether the entry contains atomic coordinates. Searches on the authors' cell, the Pearson's Crystal Data cell or the reduced cell are also possible. I find it useful to use fairly large tolerances (say 0.3–0.5 Å on edges) in such searches. I prefer to examine a longer list of potential matches which contains the correct phase, rather than risk missing an identification.

The Diffraction tab includes searches on the longest (lowest-angle or highest *d*-spacing) and strongest lines in the pattern. A line can be specified to be one of the three longest/strongest, or the first, second or third. This screen also includes searches on density, I/I_c (which is $I/I_{\rm corundum}$, a measure of the inherent scattering power of a phase and useful in quantitative phase analysis), melting point, R value, colour and Smith–Snyder figure of merit. There are check boxes to select whether the entries in the hit list include 'PD3' patterns (raw data) and property sheets. These property sheets are PDF documents embedded in an entry. These sheets are starting to be included for materials in subfiles that are defined by a particular property, such as superconductivity or thermoelectricity. These sheets are generated by groups of ICDD consulting editors.

Once a hit list has been generated, an individual entry can be selected (double clicked) to bring up the complete PDF entry. The results display can be customized using the Preferences menu (or by right clicking in the entry). The powder pattern can be plotted and additional PDF entries and/or raw data can be overlaid and scaled. In the Plot window, a PDF entry can be exported to several formats. The most useful is a CIF; the crystal structure described by the CIF can then be imported into to the user's graphics or Rietveld package.

Free-text searches of the comments are also included on this screen. These are particularly useful, as ICSD collection codes and CSD refcodes are included in the comments. If the user has the CSD installed on the same machine as the PDF, the PDF entry links live to the coordinates in the CSD entry.

By using the Results menu option when a hit list is displayed, ranges of cells in the spreadsheet can be selected and simple descriptive statistics (mean, median and estimated standard deviation) can be generated. Also under Results is a Graph Fields option. The variables used for the x and y axes of the plot can be selected and both scatter plots and histograms can be generated. Each of the points in such a plot is 'live' and can be clicked to display the full PDF entry. Fig. 3.7.1 shows a plot of the cubic lattice parameter with respect to at.% Fe in FeO (Fe and O only, space group No. 225) under ambient conditions. From such data it is easy to generate a correlation between the Fe stoichiometry and the lattice parameter.

An optional add-on module to the PDF is *SIeve* (Search Index). This is a peak-based search/match program which enables the use of a manually entered (or imported) peak list or derives a peak list from imported ASCII raw powder-diffraction data in several formats. It also has a flexible ASCII data-import module. Hanawalt, Fink, Long8 (the eight lowest-angle peaks in the pattern) or electron-diffraction searches can be carried out. Again, there is a Preferences option to customize the searches. A particularly useful (and easy-to-use) feature is the ability to apply a filter to the search/match. This filter can be selected from several pre-defined filters and/or any previous search in the session (stored in a history list). The combination of conventional search/match and Boolean searches can be very powerful, as illustrated in the next section.

3.7.2.4. *Boolean logic in phase identification*

Most phase identifications are carried out using the peak-based or full-pattern algorithms supplied by the instrument vendor. These often work well for major phases and can be customized to improve their success in identifying minor/trace phases. The native capabilities of the PDF (not all of which are accessible through some vendors' software) can be very powerful in identifying those extra peaks that result from a Rietveld difference plot (or any difference plot from pattern-fitting software) using the major phases. Below we use examples to illustrate several strategies.

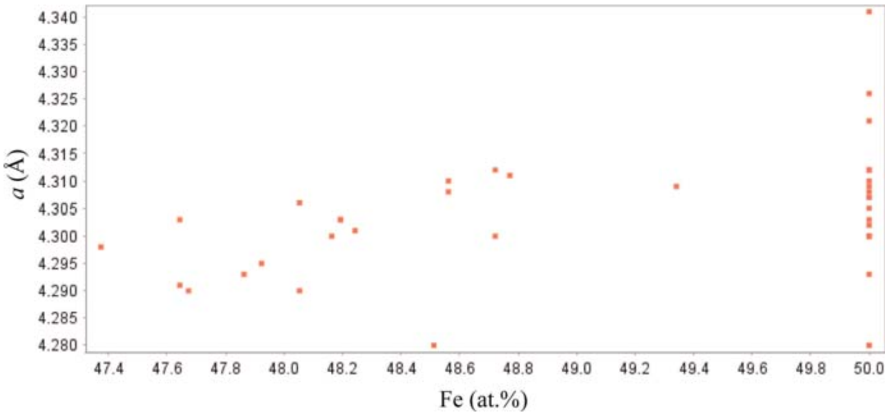

Figure 3.7.1
A plot generated by the Results/Graph Fields function in the Powder Diffraction File. The search was for entries containing only Fe and O and with space group No. 225 (resulting in FeO entries) measured under ambient conditions. One outlier was removed from the hit list manually. The trend in the cubic a lattice parameter with Fe content is apparent, as well as the large number of apparently stoichiometric FeO entries, some of which may not be correctly characterized.

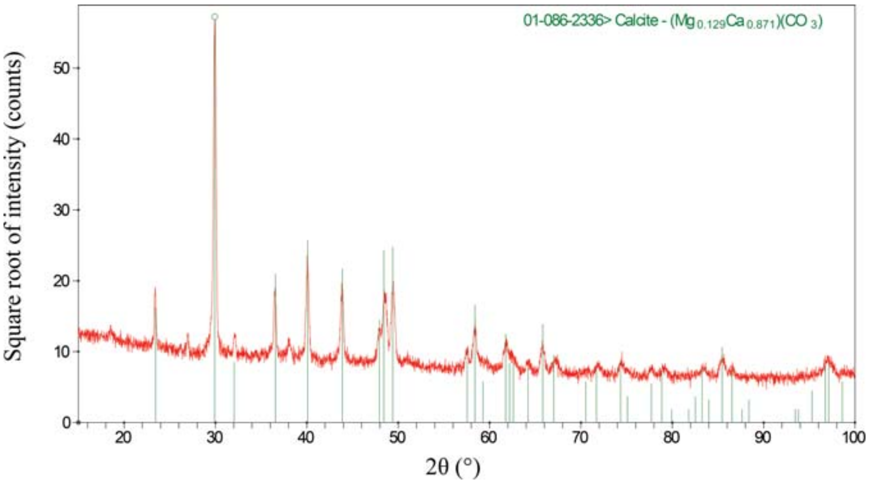

Figure 3.7.2
The result of applying a commercial search/match program (*Jade* 9.5; Materials Data, 2012) to the powder pattern of a water-still scale. Weak peaks not accounted for by the major magnesian calcite phase are apparent and additional tools in the Powder Diffraction File were needed to identify the additional phases.

3.7.2.4.1. *Water-still deposit*

A water still in my home eventually generates scale, much of which flakes off the walls, permitting easy analysis in the powder diffractometer. Any commercial search/match program will easily identify magnesian calcite (Fig. 3.7.2; files kadu1389.gsas, kadu1389.raw and iitd26_0510.prm, available in the supporting information). There are, however, three additional weak peaks at d/I = 4.788/38, 3.3089/51 and 2.3697/56. In Naperville, Illinois, the tap water comes from Lake Michigan. The bedrock underlying the Chicago region is the Racine Dolomite. Given the identity of the major phase in the scale and the source of the water, it seems likely that any minor phases will be mineral-related and contain some combination of the elements Ca, Mg, C, O and H (to include the possibility of hydrates and hydroxides). Accordingly, a search of mineral-related entries containing 'just' the elements Ca, Mg, C, O and H was performed and used as a filter in a Hanawalt search using these three peaks. This limits the search universe to 692 of the 328 660 entries in the PDF-4+ in 2012. The seven highest goodness-of-match entries in the hit list were brucite, $Mg(OH)_2$. This phase was added to the Rietveld refinement. Analysis of the difference plot indicated an unaccounted-for peak at a d-spacing of 3.3089 Å. A search for mineral-related entries with the same chemistry and having one of their three strongest peaks in the range 3.309 (30) Å yielded the vaterite polymorph of $CaCO_3$ as the hit with the highest goodness of match. This phase was added to the Rietveld refinement. The final quantitative phase analysis was: 94.7 (1) wt% $Ca_{0.84}Mg_{0.16}(CO_3)$, 5.2 (4) wt% $Mg(OH)_2$ and 0.2 (1) wt% vaterite.

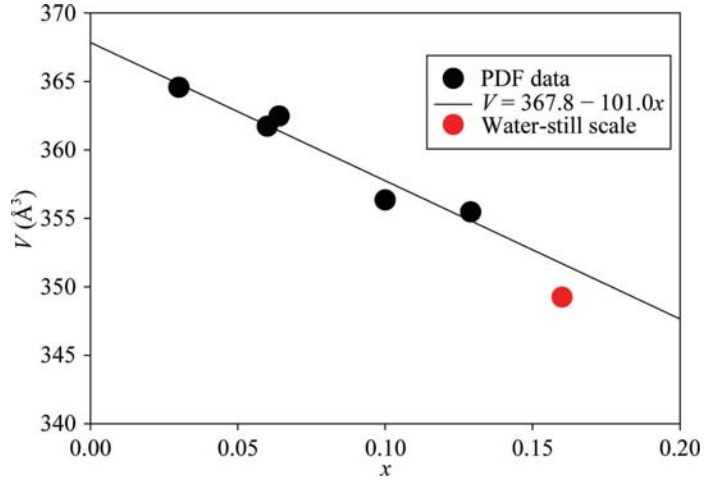

Figure 3.7.3
Variation of the unit-cell volume with the magnesium content in magnesian calcites in the Powder Diffraction File.

The composition of the major phase was refined, constraining the sum of the Ca and Mg site occupancies to equal 1.0. To understand how this fitted with previous magnesian calcites, a search for compounds containing only Ca, Mg, C and O, ambient conditions and space group No. 167 was carried out. Some manual editing of the hit list was required. Adjusting the preferences to include the display of composition in at.% and the unit-cell volume made it convenient to plot the variation in unit-cell volume as a function of Mg content x in $Ca_{1-x}Mg_x(CO_3)$ (Fig. 3.7.3). This magnesian calcite in the water-still scale has a higher Mg concentration than most, but falls close to the trend line. The flexibility and content of the Powder Diffraction File makes such data mining relatively straightforward.

3.7.2.4.2. *Vanadium phosphate butane-oxidation catalyst*

Vanadyl pyrophosphate [$(VO)_2P_2O_7$] catalysts are used commercially for the selective oxidation of butane to maleic anhydride. Modern third-generation search/match programs [using the background-subtracted, $K\alpha_2$-stripped data (files goed80.gsas, GOED80.raw and d8v3.prm); Fig. 3.7.4] had no trouble in identifying the desired major phase $(VO)_2P_2O_7$, but had difficulty with the minor phases that were clearly present. Unless the display of duplicate entries is turned off, most programs will yield several duplicate hits at the top of the list. Both 00-050-0380 and 04-009-2740 are Star quality, but only the Linus Pauling File (LPF) entry 04-009-2740 contains atom coordinates for a Rietveld refinement. Entry 01-070-8726 has the lower-quality B mark.

The native capabilities of the PDF proved helpful in identifying the minor phases. The lowest-angle peak not accounted for by the major phase is at a d-spacing of 7.2107 Å. A search for phases containing just the elements V, P, O and H (known from the synthesis procedure) and having one of their three strongest peaks in the range 7.21 ± 0.05 Å (an estimated range) yielded only the single hit 00-047-0967: $H_4V_3P_3O_{16.5}(H_2O)_2$. This is a low-precision (O quality mark) pattern from a US Patent (Harju & Pasek, 1983), and the pattern contains only four lines. The comments in the PDF entry indicate that this hydrated phase was formed by exposing a catalyst to ambient conditions, so it seems chemically reasonable but poorly defined.

To see whether this phase had been better characterized by a crystal structure, the four peaks were entered into *SIeve+* and a Hanawalt search using a wider than default tolerance of 0.3° on the peak positions and the 'just' chemistry filter V, P, O and H was carried out. As expected, PDF entry 00-047-0967 was at the top of the hit list, but close to the top was entry 04-017-1008 (Shpeizer *et al.*, 2001): $[H_{0.6}(VO)_3(PO_4)_3(H_2O)_3](H_2O)_4$. The article by Shpeizer *et al.* (2001) indicates that this phase was formed from an anhydrous precursor by exposing it to ambient conditions. The single-crystal structure was obtained at 173 K. The similarity of the two PDF entries (Fig. 3.7.5) and the difference in data-collection temperatures makes it clear that these correspond to the same phase, and that the structure of $[H_{0.6}(VO)_3(PO_4)_3(H_2O)_3](H_2O)_4$ could be used in a Rietveld refinement.

There were still unaccounted-for peaks at 3.5823 and 3.0760 Å. Under the assumption that these came from a single phase, two separate searches for phases containing just V, P, O and H and with one of their three strongest lines in the ranges 3.58 ± 0.03 and 3.08 ± 0.03 Å were carried out and then combined (using the History option) with a Boolean 'and' operation. All five of the entries on the hit list corresponded to α-$VOPO_4$. This yellow V^{5+} compound was consistent with the altered colour of the V^{4+}-based catalyst, and is a common impurity.

Close examination of the Rietveld difference plot from a refinement including these three phases indicated that there was a weak shoulder at a d-spacing of 3.985 Å. A search for phases containing just V, P, O and H and having a strong peak near this d-spacing yielded β-$(VO)(PO_3)_2$, another common catalyst impurity (Fig. 3.7.6). Including this compound as a fourth phase yielded a satisfactory Rietveld refinement and a quantitative analysis of 84.8 (1) wt% $(VO)_2P_2O_7$, 5.9 (1) wt% $[H_{0.6}(VO)_3(PO_4)_3(H_2O)_3](H_2O)_4$, 5.6 (1) wt% α-$VOPO_4$ and 3.7 (1) wt% β-$VO(PO_3)_2$.

3.7.2.4.3. *Valve deposit from a piston aviation engine*

Applying a commercial search/match program to the diffraction pattern of a deposit from a valve in a gasoline-powered aircraft engine easily identified quartz and corundum. The specimen was scraped from the valve seat and micronized. The corundum represents abrasion from the elements of the micronizing mill, as it was not present in the pattern of the as-scraped sample. Metal particles were visibly present in the deposit, so one could reasonably guess the presence of both ferrite and austenite (Fig. 3.7.7; files maso04.gsas, maso04.rd and padv.prm). A Rietveld refinement using these four phases was carried out.

Six peaks picked from the difference plot were entered into *SIeve+* and a Hanawalt search was carried out. No chemically reasonable simple compounds were near the top of the hit list, so extra information was sought. An XPS analysis indicated the presence of Pb, Br, Fe, P, O and C (and H assumed). Aviation gasoline is still leaded, and ethylene dibromide is sometimes added as a lead scavenger. The result of a 'just' chemistry search using these seven elements (6543/328 660 entries) was applied as a filter to the Hanawalt search. Near the top of the hit list was $PbBr_2$. Although apparently surprising, this phase is reasonable given our chemical knowledge. Lead bromide was added to the Rietveld refinement. Further analysis of the difference pattern using the same techniques indicated the presence of cohenite, Fe_3C, from the steel, and $Fe_3Fe_4(PO_4)_6$, the reaction product of the steel with a phosphate fuel additive. The final Rietveld refinement yielded a quantitative analysis of 26.5 (4) wt% austenite (γ-Fe, stainless steel), 47.9 (4) wt% ferrite (α-Fe, carbon steel), 17.7 (4) wt% quartz (sand/dirt), 2.9 (2) wt% $PbBr_2$, 2.6 (2) wt% $Fe_3Fe_4(PO_4)_6$ and 2.2 (2) wt% cohenite (Fig. 3.7.8).

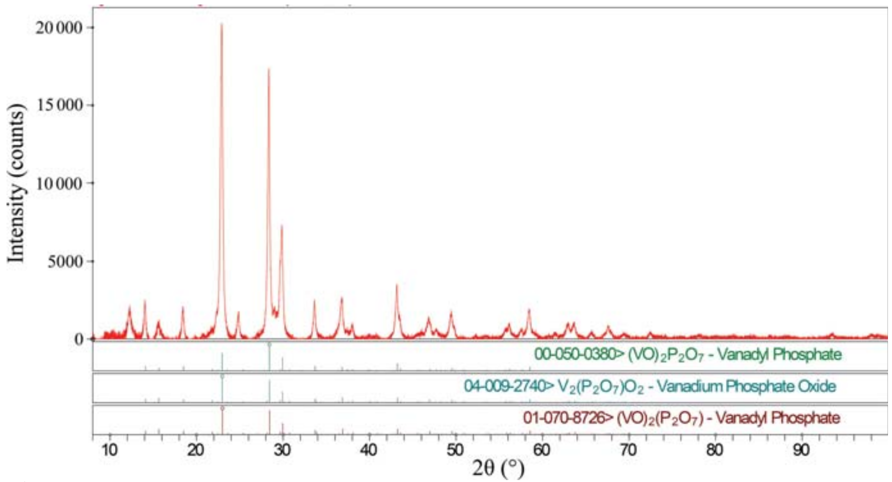

Figure 3.7.4
The results of applying a commercial search/match program (*Jade* 9.5; Materials Data, 2012) to the (background-subtracted, $K\alpha_2$-stripped) powder pattern of a butane-oxidation catalyst. The first three patterns in the hit list had equivalent figures of merit. The PDF entries 00-050-0380 and 04-009-2740 had Star quality marks and 04-009-2740 contained the atomic coordinates necessary for a Rietveld refinement. Additional peaks are apparent. The phases that give rise to them were identified using the native capabilities of the Powder Diffraction File.

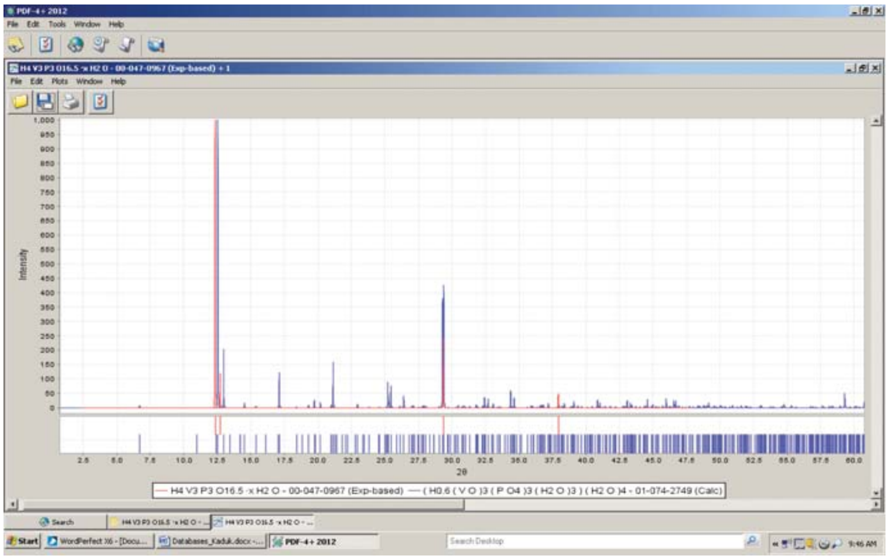
PDF-4+ 2012
File Edit Tools Window Help
H4 V3 P3 O16.5 ·x H2 O - 00-047-0967 (Exp-based) + 1
File Edit Plots Window Help
Intensity
1,000
0
2.5
5.0
7.5
10.0
12.5
15.0
17.5
20.0
22.5
25.0
27.5
30.0
32.5
35.0
37.5
40.0
42.5
45.0
47.5
50.0
52.5
55.0
57.5
60.0
2θ
H4 V3 P3 O16.5 ·x H2 O - 00-047-0967 (Exp-based) — (H0.6 (V O)3 (P O4)3 (H2 O)3) (H2 O)4 - 01-074-2749 (Calc)
Search
Start
WordPerfect X6 - [Docu...
Databases_Kaduk.docx -...
PDF-4+ 2012
Search Desktop
9:46 AM

Figure 3.7.5
Comparison of the low-quality experimental PDF entry 00-047-0967 with the high-quality calculated pattern 01-074-2749 located by searching the experimental pattern against the rest of the PDF. The similarity in patterns and chemistry demonstrated that the two phases were the same and that the coordinates used to calculate entry 01-074-2749 could be used in a Rietveld refinement of a butane-oxidation catalyst.

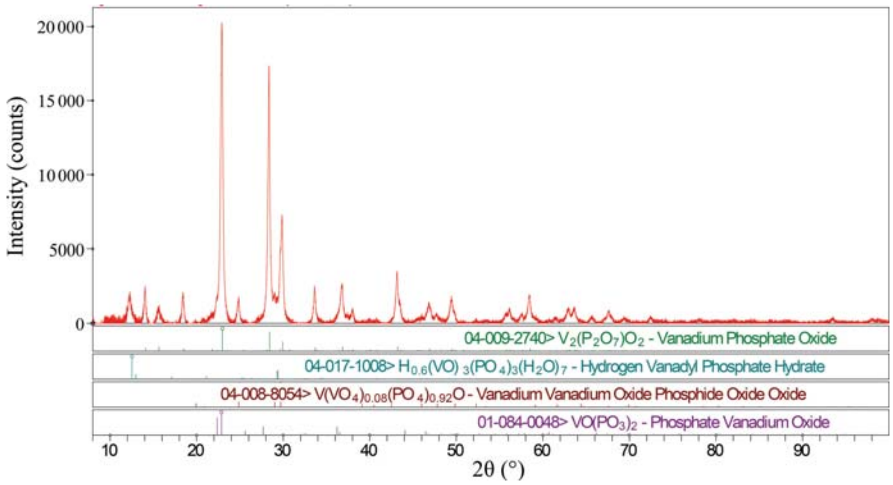

Figure 3.7.6
The four crystalline phases identified in a butane-oxidation catalyst.

3.7.2.4.4. *Isocracker sludge*

An isocracker is a refinery unit which simultaneously carries out cracking and isomerization reactions to produce more high-octane gasoline. A black deposit isolated from such a unit was surprisingly crystalline (Fig. 3.7.9; files NALK157.gsas, NALK157.raw and padv.prm). It was easy to identify small concentrations of elemental sulfur, pyrrhotite-4M (now called pyrrhotite-4C), haematite, lepidocrocite and dolomite, but the major peaks did not match well those of any entry in the PDF.

It seemed likely that a mineral-related phase would serve as a structural prototype for an apparently new phase, so two separate searches for mineral-related phases with one of their three strongest peaks in the *d*-spacing ranges 7.09 ± 0.03 and 5.57 ± 0.03 Å were combined. The two hits in the search list were both uranium minerals. These seemed unlikely in a refinery deposit(!). Widening the search ranges to 7.09 ± 0.10 and 5.57 ± 0.07 Å yielded rasvumite, KFe_2S_3 (PDF entry 00-033-1018), as the second entry in the hit list.

The fit to the major peaks in the deposit was reasonable, but there should not be any potassium in a refinery deposit and none was detected in a bulk chemical analysis. When the jar containing the deposit was opened, it smelled strongly of ammonia. Ammonium and potassium ions are about the same size and often form isostructural compounds. The infrared spectrum of the deposit was dominated by bands of ammonium ions.

The potassium in the structure of rasvumite (PDF entry 01-083-1322, used as a reference) was replaced by nitrogen. Analysis of potential hydrogen-bonding interactions yielded approximate hydrogen positions in the ammonium ion. These positions were refined using a density-functional geometry optimization. This model yielded a satisfactory Rietveld refinement (Fig. 3.7.10) and the quantitative analysis 45.7 (2) wt% $(NH_4)Fe_2S_3$, 12.8 (4) wt% S_8, 22.0 (6) wt% lepidocrocite (γ-FeOOH), 5.5 (5) wt% haematite (α-Fe_2O_3), 6.6 (3) wt% pyrrhotite-4C (Fe_7S_8) and 6.6 (3) wt% dolomite [$CaMg(CO_3)_2$; limestone environmental dust]. The powder pattern and crystal structure of $(NH_4)Fe_2S_3$ are now included in the PDF as entry 00-055-0533.

3.7.2.4.5. *Amoxicillin*

The amoxicillin powder from a commercial antibiotic capsule was highly crystalline. Its powder pattern (files kadu918.gsas, KADU918.raw, d8v3.prm and KADU921.rd) was matched well by the PDF entries 00-039-1832 and 00-033-1528 for amoxicillin trihydrate, but there was an additional peak at a *d*-spacing of 16.47 Å (5.37° 2θ). With such a low-angle peak, it seemed prudent to measure the pattern again

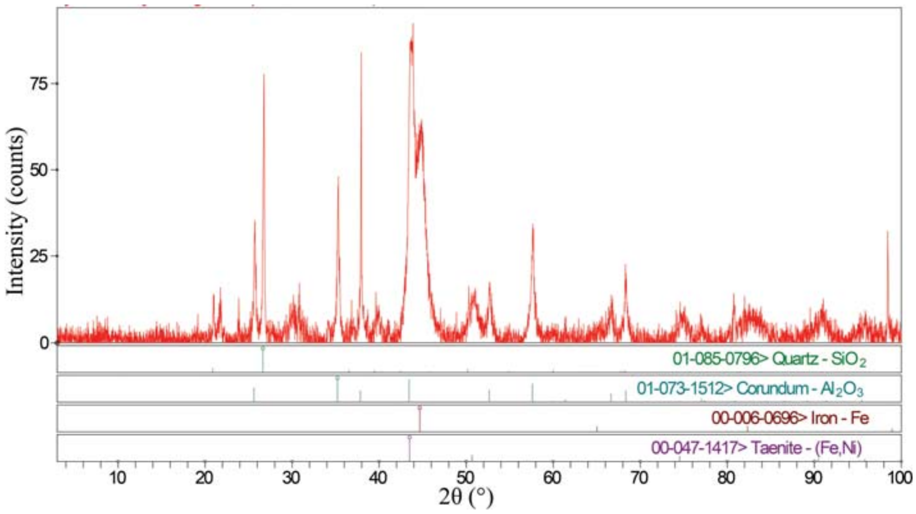

Figure 3.7.7
The four phases identified in a valve deposit from an aircraft engine by automated search/match methods and guessing based on the appearance of the sample. The pattern has had the background and $K\alpha_2$ peaks removed.

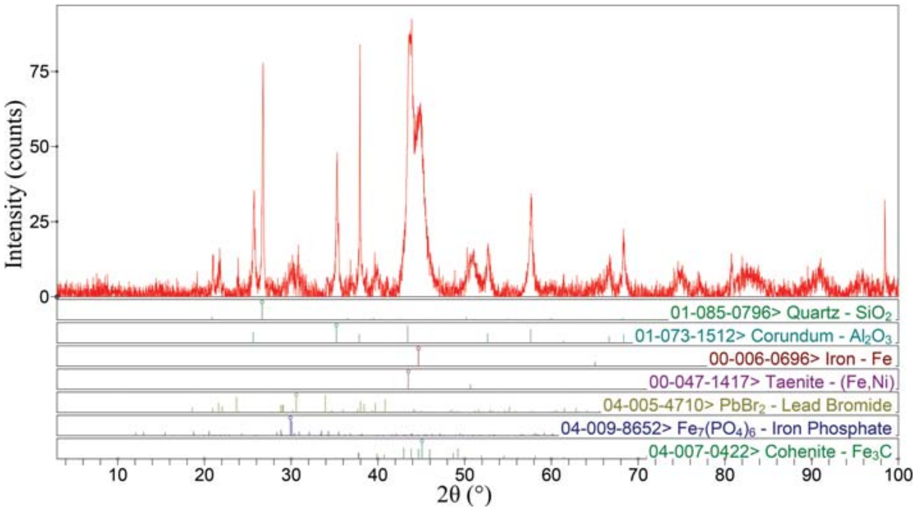

Figure 3.7.8
The seven phases identified in the valve deposit from an aircraft engine.

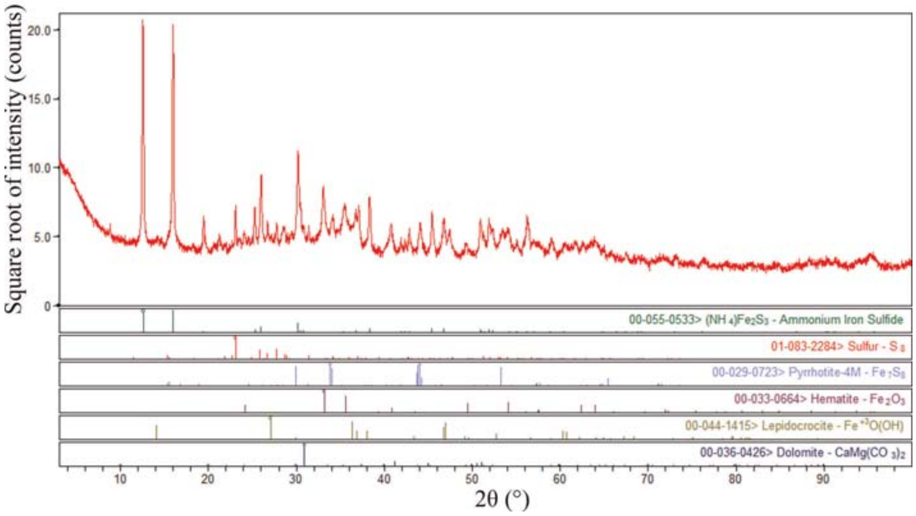

Figure 3.7.9
The phases identified in a deposit from a refinery isocracker. At the time, the $(NH_4)Fe_2S_3$ was a new phase, identified by analogy to KFe_2S_3, rasvumite.

starting at 3°, and another peak was observed at d = 24.80 Å (3.56° 2θ).

A search of the PDF-4/Organics 2013 for phases having two such peaks among their longest (lowest-angle) peaks yielded entry 00-005-0010 for calcium stearate at the top of the hit list, as well as two lead stearates. We can safely assume that lead stearate is not present in a pharmaceutical. Calcium stearate, however, has its strongest peak at 1.76°, so another pattern was measured starting at 1.5° 2θ. This peak is indeed present (Fig. 3.7.11).

The primary literature suggests that the compound in PDF entry 00-005-0010 is really calcium stearate monohydrate, and that its structure (like those of many other stearate salts) has not yet been determined. The CSD entry for amoxicillin trihydrate (AMOXCT10; Boles *et al.*, 1978) contained some incorrect H-atom positions and was missing an H atom, so these were corrected before a Rietveld refinement was carried out.

3.7.2.4.6. *Pseudoephedrine*

As P. W. Stephens was measuring the powder pattern of a commercial pseudoephedrine-based decongestant on beamline X16C at the National Synchrotron Light Source at Brookhaven National Laboratory, he noted that extra peaks were present. The lowest-angle peak was at a d-spacing of 12.73 Å, and other peaks occurred at 5.74, 4.62 (strongest) and 4.407 Å. A search in the PDF-4/Organics for compounds having the string ‘ephed’ in the name, a long line at 12.73 ± 0.05 Å and a strong line at 4.62 ± 0.02 Å yielded the single hit 00-041-1946, pseudoephedrine hydrochloride, a reasonable impurity in pseudoephedrine.

3.7.2.4.7. *Commercial multivitamin: Centrum A to Zn*

Commercial multivitamins are challenging phase-identification problems because they contain small concentrations of many different components. The application of a commercial search/match program to a pattern of Centrum A to Zn collected on beamline ID-32 at the Advanced Photon Source at Argonne National Laboratory using a wavelength of 0.495850 Å (files centrum.gsas and id320304.prm) easily identified brushite, $CaHPO_4(H_2O)_2$, and sylvite, KCl (Fig. 3.7.12).

To identify additional phases, 64 peaks with d > 1.91 Å were picked from the plot and entered into *SIeve+* in the PDF-4/Organics 2013 database. The PDF-4/Organics database was used to enhance the success in identifying organic compounds, and the relatively short d-spacing limit was used to ease the identification of the simple inorganic compounds which are often present in commercial vitamins.

A Hanawalt search using these peaks easily identified iron fumarate (00-062-1294), szmikite [$MnSO_4(H_2O)$; 00-033-0906], L-ascorbic acid (02-063-2295), monetite ($CaHPO_4$; 01-070-0359) and calcite ($CaCO_3$; 00-005-0586). Note that these hits come from four different data sources; searches based on just one source would not have identified all of these compounds.

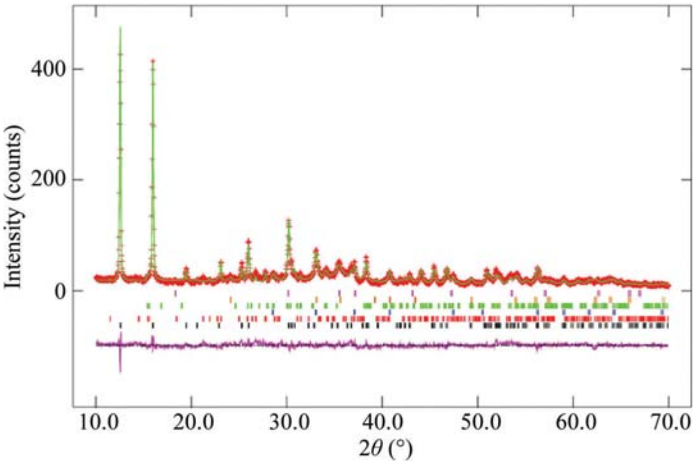

Figure 3.7.10
The final Rietveld plot from refinement of the isocracker deposit.

There were strong high-angle peaks that had not yet been accounted for at *d*-spacings of 2.4762, 2.1068, 1.4900 and 1.4783 Å. These four peaks were entered into a new Hanawalt search, which identified periclase (MgO; 01-071-3631) and zincite (ZnO; 01-075-9742).

Superimposing the peaks for all of these compounds onto the raw data made it clear that there were broad peaks in the pattern at *d*-spacings of approximately 5.8750, 5.3273, 4.3277 and 3.9217 Å. Since the lowest and highest angles of these four were the best defined, separate searches for compounds having each of these peaks as one of their three strongest lines were combined using a Boolean ‘and’. Among the hit list was cellulose I_β (00-060-1502), which is a common constituent of pharmaceuticals. The structure model from PDF entry 00-056-1718 was added to the Rietveld refinement as a ninth phase.

One last peak at 5.9915 Å was unaccounted for. A search for pharmaceutical-related compounds with this peak as one of the three strongest included nicotinamide (02-063-5340; niacin or vitamin B_3). Ten phases were thus identified and these account for all of the peaks in the pattern.

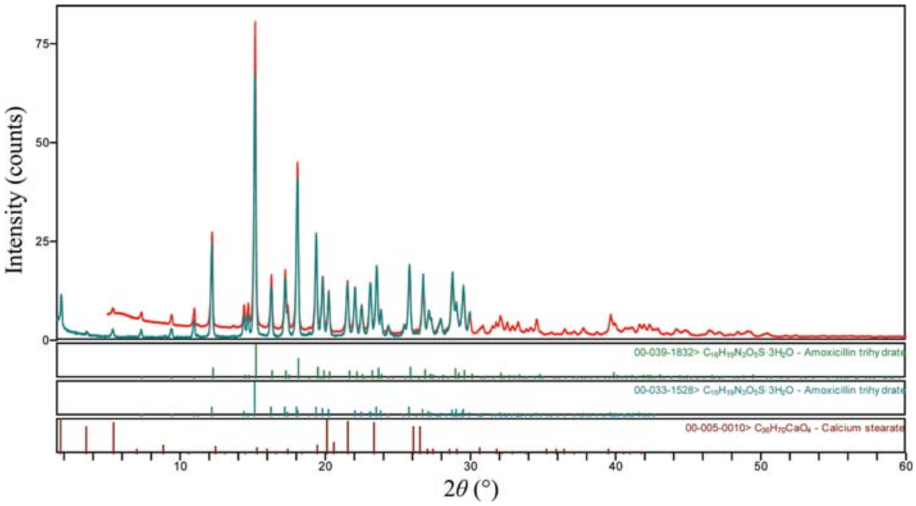

Figure 3.7.11
Phases identified in amoxicillin powder from a commercial capsule.

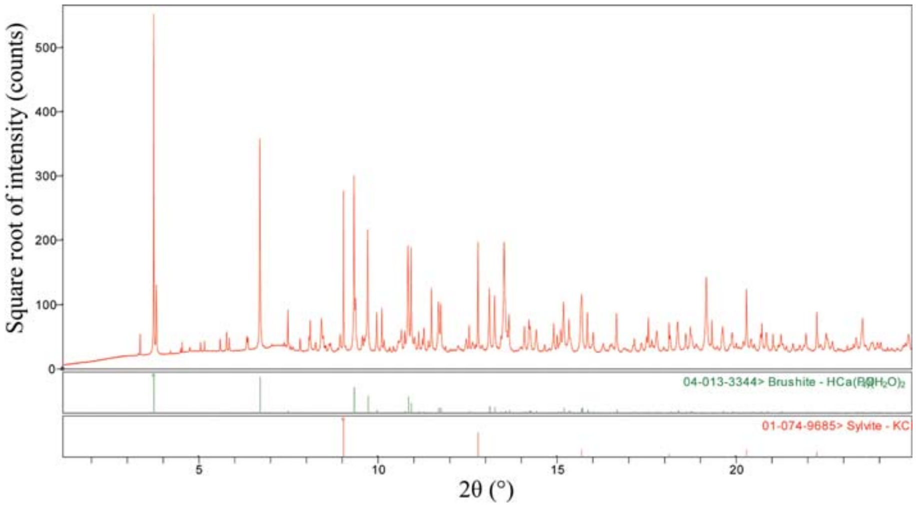

Figure 3.7.12
Phases identified by automated search/match in a Centrum A to Zn multivitamin tablet. Additional phases were identified using the native capabilities of the Powder Diffraction File.

3.7.3. Cambridge Structural Database (CSD)

Some features of the Cambridge Structural Database system (CSD; https://www.ccdc.cam.ac.uk; Groom *et al.*, 2016) are described in Chapter 22.5 of *International Tables for Crystallography* Volume F (Allen *et al.*, 2011). The CSD contains X-ray and neutron diffraction analyses of carbon-containing molecules with up to 1000 atoms (including hydrogens), including organic compounds, compounds of the main-group elements, organometallic compounds and metal complexes. The CSD covers peptides of up to 24 residues; higher polymers are covered by the Protein Data Bank. The CSD also covers mononucleotides, dinucleotides and trinucleotides; higher oligomers are covered by the Nucleic Acid Database (http://ndbserver.rutgers.edu). There is a small overlap between the CSD and the Inorganic Crystal Structure Database in the area of molecular inorganics.

Capabilities particularly useful for structure validation are covered in Chapter 4.9 of this volume. This discussion will not attempt a comprehensive description of the capabilities of the CSD, but will concentrate on features that are particularly relevant to powder diffraction.

The principal interface to the CSD is the program *ConQuest* (Bruno *et al.*, 2002). Its most distinctive feature is the ability to draw molecular structures and fragments and carry out substructure searches. Such searches eliminate the ambiguities that can arise when searching by compound name or other text-based properties. These chemical-connectivity searches can include the number of H atoms bonded to a particular atom, the charge, the number of bonded atoms and whether the atom is part of a ring. In addition, three-dimensional quantities can be defined, tabulated and analysed. These quantities can be analysed in *Mercury* (Macrae *et al.*, 2008) and *Mogul* (Bruno *et al.*, 2004). Such analyses are useful for defining geometrical restraints in a Rietveld refinement. A general practice is to use the mean and standard deviations directly output by *Mogul* for the restraints. It is important to understand the CSD conventions for defining bond types to obtain successful results.

In *ConQuest*, searches can be carried out on author and/or journal name, as well as the normal bibliographic characteristics. Compounds can be located by chemical and/or common names, but such searches should be complemented by chemical-connectivity searches. It is possible to limit the search universe by chemical class, including carbohydrates, nucleosides and nucleotides, amino acids, peptides and complexes, porphyrins, corrins and complexes, steroids, terpenes, alkaloids and organic polymers. Searches on elements and formulae are possible, as well as searches on space groups and crystal systems. Particularly useful in searching for structure analogues are reduced-cell searches. Queries on Z, Z' and density are useful in data mining. A wide variety of searches on experimental parameters are possible; there is an option to exclude powder structures. Searches on both pre-defined terms and general text searches are possible. Particularly convenient for users of the PDF-4/Organics database is the retrieval of individual refcodes; the refcode from the PDF entry can be input directly into *ConQuest*. Starting with the 2013 release of the PDF-4/Organics database this link is live; the display of a PDF entry will result in import of the coordinates from the CSD entry. Boolean operations can be used to combine search queries in many flexible ways.

In recent years, many (if not most) single-crystal structures have been determined at low temperatures, while most powder-diffraction measurements are made under ambient conditions. Thermal expansion (often anisotropic) can result in differences between the observed peak positions and those in a PDF-4/Organics entry calculated from a CSD entry. For successful phase identification, larger than default tolerances must often be used in the search/match process. Transparency effects in pure organic compounds can also lead to significant peak shifts to lower angles, as well as significant asymmetry, so wider search windows may be necessary for phase identification.

3.7.3.1. *Mercury*

The structure-visualization program *Mercury* (Macrae *et al.*, 2008) is available as a free version and as a version with the CSD which has additional capabilities that are useful for powder diffraction. *Mercury* reads and writes a variety of molecular and crystal structure file formats, but is most commonly used with CIFs. Structures can be edited, and among the edit options is Normalize Hydrogens. This is particularly useful to improve the approximate H-atom positions that are often used in the early and intermediate stages of a Rietveld refinement. It is always worth including the H atoms in the structure model (in at least approximate positions) because better residuals and improved molecular geometry are obtained.

The Display Symmetry Elements tool is particularly useful for teaching symmetry. The Display Voids tool is useful in validating structures after solution. For most materials (zeolites and metal–organic frameworks are notable exceptions) we do not expect empty spaces in the crystal structure, so the presence of voids suggests the presence of an incomplete structure model and/or errors.

Among the options in the Calculate menu is Powder Pattern. The calculation can be customized by the user to match the desired instrumental configuration. The calculated pattern can be saved in several formats for comparison in the user's instrument software. *Mercury* expects the displacement coefficients to be given as U values. CIFs can come from many sources and can use different conventions for the displacement coefficients or may be missing them entirely. Manual editing of the input CIF is often required, otherwise strange powder patterns can be calculated.

Among the CSD-Materials/Calculations options is BFDH morphology (Bravais, 1866; Friedel, 1907; Donnay & Harker, 1937). Although a simple calculation, it is often realistic enough to suggest the likelihood of profile anisotropy and preferred orientation, along with expected directions. The calculation can thus save guessing about preferred directions.

The Structure Overlay and Molecule Overlay options are very useful for comparing structures quantitatively. There is also an interface to the semi-empirical code *MOPAC*, which can also be a useful tool for assessing structural reasonableness. The H-Bonds and Short Contacts options are useful in completing a structure solved using powder data, as often the 'interesting' H-atom positions have to be deduced. There is a relatively new Solid Form menu, which contains several tools for analysing crystal structures.

3.7.4. Inorganic Crystal Structure Database (ICSD)

The Inorganic Crystal Structure Database (ICSD; https://icsd.fiz-karlsruhe.de; Bergerhoff & Brown, 1987; Belsky *et al.*, 2002; Hellenbrandt, 2004) strives to contain an exhaustive collection of inorganic crystal structures published since 1913, including their atomic coordinates. It is a joint project between FIZ Karlsruhe and NIST. The database is accessed through the online WebICSD or the locally-installed program *FINDIT*. Typical interatomic distances in inorganic compounds derived from the ICSD have been collected in Chapter 9.4 of *International Tables for Crystallography* Volume C (Bergerhoff & Brandenburg, 1999). Applications of the ICSD have been discussed by Kaduk (2002), Behrens & Luksch (2006) and Allmann & Hinek (2007).

The ICSD began as an inorganic crystal structure database of published structures with atomic coordinates. The scope was gradually extended to include intermetallic compounds. Since 2003, FIZ Karlsruhe has started to fill in the gaps, and the aim is for the ICSD to include all published intermetallic compounds. Originally the ICSD did not contain structures with C—H or C—C bonds. After 2003, this rule was modified so that new entries should not contain both C—H and C—C bonds; compounds containing tetramethylammmonium and oxalate ions are now included.

The ICSD contains fully determined structures with atomic coordinates. Coordinates of light atoms (such as H atoms) or extra-framework species (such as in zeolites) may be missing. Structures described as isotypic to other structures, but without determination of the atomic coordinates, are included using the coordinates from the corresponding structure-type prototype. Such entries get a special remark/comment: 'Cell and Type only determined by the author(s). Coordinates estimated by the editor in analogy to isotypic compounds.' Currently there are more than

26 000 entries with derived coordinates. At present, the ICSD contains more than 187 000 entries, including 2033 crystal structures of elements, 34 785 records for binary compounds, 68 730 records for ternary compounds and 68 083 records for quaternary and quintenary compounds. About 149 000 entries have been assigned a structure type; there are currently 9093 structure prototypes.

Most of the structures contained in the ICSD are from published journal articles, although private communications are also accepted. The entries are tested for formal errors, plausibility and logical consistency. The data are stored as published; the authors' settings of space groups are considered to be valuable information which should not be changed. Only some 'exotic' space groups are transformed. In addition, for each entry in the ICSD the structure is standardized using the program *STRUCTURE TIDY* by Gelato & Parthé (1987). The published cell, standardized cell and reduced cell are all searchable. Since 2003, FIZ Kalrsruhe has been assigning structure-type classifications (Allmann & Hinek, 2007). In the future, this feature will enable easier searches for compounds that are closely related in structure.

3.7.4.1. *General features of the ICSD*

The chemical name is given in English following IUPAC rules, with the oxidation state in roman numerals. The formula upon which the name is based is calculated from all atoms with defined coordinates. Phase (polymorph) designations are given after a hyphen. Mineral names and group names are given for all entries that correspond to minerals. Details of the origin are given after a hyphen. The formula is coded as a structural formula, which provides the opportunity to search for typical structure units (such as SiO_4). Such searches can be useful, but can easily miss structurally similar compounds, and should be used with caution.

The title of the publication is given in English, French or German. There can be several citations, but an author list is only given for the first reference. I have encountered truncated author lists. Authors' surnames can vary when the original publication uses a non-roman alphabet. In some cases, the first and last names of Chinese authors may be interchanged.

The Hermann–Mauguin space-group symbol is given according to the conventions of *International Tables for Crystallography* Volume A. If different origin choices are available, those space groups with the origin at a centre of symmetry (origin choice 2) are characterized by an additional '*z*', while an additional '*s*' is used for special origins (origin choice 1). Thus, the space group for magnetite may be reported as *Fd*-3*mz* or *Fd*-3*ms*, depending on which origin the authors used. Since all contemporary Rietveld programs use origin choice 2, care must be taken when importing coordinates.

Along with the fractional coordinates, atom identifiers are reported. These are principally running numbers and may differ from those reported by the authors. The oxidation state is given with a sign. When importing coordinates into a Rietveld program these oxidation states can influence which scattering factors are used, and so should be examined by the user. Both site multiplicities and Wyckoff positions are generated for all atoms.

The ICSD archives displacement coefficients (both isotropic and aniostropic) according to what the authors reported. Isotropic displacement coefficients can be given as either *B* or *U* values and anisotropic coefficients can be given as *β*, *B* or *U* values (or, in rare cases, using other conventions). Displacement coefficients imported into a Rietveld program should always be checked, as it is common for the program to interpret *B* as *U* and *vice versa*. Such wrong displacement coefficients can make Rietveld refinements hard to perform. There are a number of standard remarks and standard test codes; these text fields can be useful for limiting the universe of the search (such as for neutron-diffraction structures).

3.7.4.2. *Features particularly useful for powder crystallography*

A field which is particularly useful for identifying structural analogues is the ANX formula. This formula is generated according to the following rules:

(i) H^+ is not taken into account, even if coordinates are available.
(ii) The coordinates of all sites of all other atoms must be determined.
(iii) Different atom types on the same positions (for example, in solid solutions) are treated as a single atom type.
(iv) An exception: if cations and anions occupy the same site they will not be treated as one atom type.
(v) All sites occupied by the same atom type are combined, unless the oxidation state is different. Thus, $Fe^{2+}(Fe^{3+})_2O_4$ yields AB2X4, while $(Fe^{2.667+})_3O_4$ yields A3X4.
(vi) For each atom type, the multiplicities are multiplied by the site-occupancy factors and the products are added. The sums are rounded and divided by the greatest common divisor.
(vii) If the rounded sum equals zero, all sums are multiplied by a common factor so that the smallest sum equals unity, so no element will be omitted.
(viii) Cations are assigned the symbols A–M, neutral atoms are assigned N–R and anions are assigned X, Y, Z and S–W.
(ix) The symbols are sorted alphabetically and the characters are assigned according to ascending indices: AB2X4, not A2BX4.
(x) All ANX symbols with more than four cation symbols, three neutral atom symbols or three anion symbols are deleted.

The utility of these symbols is illustrated by the fact that the three garnets $Mg_3Al_2(SiO_4)_3$, $Ca_3(Al_{1.34}Fe_{0.66})Si_3O_{12}$ and $(Mg_{2.7}Fe_{0.3})(Al_{1.7}Cr_{0.3})Si_3O_{12}$ all yield ANX = A2B3C3X12.

Reduced-cell searches [see *International Tables for Crystallography* Volume A, Section 3.1.3 (de Wolff, 2016)] are particularly easy to carry out in the 'Cell' section of Advanced Searches. Once a unit cell has been determined by indexing the powder pattern, it is always worth carrying out a reduced-cell search to identify potential isostructural compounds using lattice-matching techniques. It is often wise to first carry out such a search using relatively narrow tolerances (say, 1% on the lattice parameters) and then carry out additional searches using larger tolerances. Systematic searches of the subcells and supercells of a given unit cell, as could be carried out using the *NBS*LATTICE* program with the NIST Crystal Data Identification File (Mighell & Himes, 1986; Mighell, 2003), are not yet implemented.

Under the 'Crystal Chemistry' section it is possible to search for crystal structures that contain bonds between particular atom types in a distance range. Such searches are particularly valuable in assessing the chemical reasonableness of crystal structures, such as the study by Sidey (2013) on the shortest $B^{III}-O$ bonds.

Because the ICDD Powder Diffraction File '01' entries contain the ICSD collection code in the comments, searching for the collection code of a hit in a search/match is particularly easy in the 'DB Information' section. In this way, the relevant ICSD entry can be located without any ambiguity and the best structure for the problem at hand can be used to start the Rietveld refinement.

3.7.5. Pearson's Crystal Data (PCD/LPF) (with Pierre Villars and Karen Cenzual)

3.7.5.1. *General information*

The Pearson's Crystal Data database (PCD; Villars & Cenzual, 2013) is an outgrowth of the (Linus) Pauling File (LPF; Villars *et al.*, 1998; http://www.paulingfile.com), which was designed to combine crystal structures, phase diagrams and physical properties under the same computer framework to form a tool useful for materials design. PCD is the result of a collaboration between Material Phases Data Systems (Vitznau, Switzerland) and ASM International (Materials Park, Ohio, USA). The retrieval software was developed by Crystal Impact (Bonn, Germany). As suggested by the name, Pearson's Crystal Data is a follow-up product to *Pearson's Handbook: Crystallographic Data for Intermetallic Phases* (Villars & Calvert, 1985, 1991; Villars, 1997). However, in contrast to the latter, it also covers oxides and halides, which represent about 80% of the compounds with more than four chemical elements.

The 2016/2017 release of Pearson's Crystal Data contains more than 288 000 data sets for more than 165 300 different chemical formulae, representing over 53 000 distinct chemical systems. To achieve this, the editors have processed over 93 500 original publications; recent literature is surveyed in a cover-to-cover approach, including about 250 journal titles. Over 153 000 database entries contain refined atom coordinates, as well as isotropic and/or anisotropic displacement parameters when published, whereas more than 72 000 data sets contain atom coordinates corresponding to the structure prototype assigned by the authors of the original publication or by the database editors. Approximately 15 000 data sets contain only crystallographic data such as the lattice parameters and possibly a space group.

When available in the original publications, each data set contains comprehensive information on the sample-preparation and experimental procedure, as well as on the stability of the phase with respect to temperature, pressure and composition. The presence of plots (cell parameters or diffraction patterns) in the original paper is indicated, and over 30 000 descriptions of the variation of the cell parameters as a function of temperature, pressure or composition are proposed. Roughly 18 300 experimental diffraction patterns are reported.

The Linus Pauling File was designed as a phase-oriented, fully relational database system. This required the creation of a 'distinct phases' table, with internal links between the three parts of the database. In practice, this means that the senior editors have evaluated the distinct phases existing in the system for every chemical system using all information available in the LPF. Each structure entry in Pearson's Crystal Data has been linked to such a distinct phase, which allows a rapid overview of a particular chemical system.

3.7.5.2. *Evaluation procedure*

Extensive efforts have been made to ensure the quality and reliability of the crystallographic data. Pearson's Crystal Data is checked for consistency by professional crystallographers, assisted by an original software package, *ESDD* (*Evaluation, Standardization and Derived Data*), containing more than 60 different modules (Cenzual *et al.*, 2000). The checking is carried out progressively, level by level. The following checks are made.

Individual database fields:

(i) order of magnitude of numerical values;
(ii) Hermann–Mauguin symbols, Pearson symbols;
(iii) consistency of journal CODEN, year, volume, first page, last page;
(iv) formatting of chemical formulae;
(v) neutrality of oxides and halides;
(vi) spelling.

Consistency within individual data sets:

(i) atom coordinates, Wyckoff letters, site multiplicities;
(ii) chemical elements in different database fields;
(iii) computed, published values (cell volume, density, absorption coefficient, *d*-spacings);
(iv) Pearson symbol, space group, cell parameters;
(v) Bravais lattice, Miller indices;
(vi) site symmetry, anisotropic displacement parameters.

Particular crystal-structure checks:

(i) interatomic distances, sum of atomic radii;
(ii) geometry of functional groups;
(iii) search for overlooked symmetry elements;
(iv) composition from refinement, chemical formula.

Consistency within the database:

(i) comparison of cell-parameter ratios for isotypic entries;
(ii) comparison of atom coordinates for isotypic entries with refined coordinates;
(iii) comparison of densities;
(iv) thorough search for duplicates, also considering translated references.

Wherever possible, misprints have been corrected based on arguments explained in remarks; as a result, more than 13 000 crystallographic data sets are accompanied by at least one erratum. In other cases remarks drawing the attention to discrepancies or unexpected features have been added.

The *ESDD* software package also produces derived data such as the Niggli reduced cell, equivalent isotropic displacement parameters, density and formula weight.

3.7.5.3. *Standardized crystallographic data*

The crystallographic data in Pearson's Crystal Data are presented as published, respecting the original site labels, but are also standardized following the method proposed by Parthé and Gelato (Parthé & Gelato, 1984, 1985; Parthé *et al.*, 1993). This second presentation of the same data has been further adjusted so that compounds crystallizing with the same prototype structure (isotypic compounds) can be easily compared. It is prepared in a three-step procedure as follows.

(i) The crystallographic data are checked for the presence of overlooked symmetry elements. Whenever it is possible to describe the structure in a higher-symmetry space group, or with a smaller unit cell, without any approximations, this is performed.
(ii) In the next step, the crystallographic data are standardized using the program *STRUCTURE TIDY* (Gelato & Parthé, 1987).
(iii) The resulting data are compared with the standardized data of the type-defining data set and, if relevant, adjusted using an *ESDD* module based on the program *COMPARE* (Berndt, 1994).

For data sets with no published coordinates, the cell parameters are standardized following the criteria defined for the unit-cell and space-group setting. For data sets with unknown space group, the cell parameters have been standardized assuming the space group of lowest symmetry in agreement with the Pearson symbol, *e.g.* *P*222 for *oP** or *o***.

Standardized data are described with respect to the standard settings described in *International Tables for Crystallography* Volume A, with the following additional restraints: inversion centre at the origin, unique *b* axis and 'best' cell for monoclinic structures (Parthé & Gelato, 1985), triple-hexagonal cell for rhombohedral structures or Niggli reduced cell for triclinic structures. As a consequence, they can easily be incorporated into any program handling crystallographic data. The systematic standardization of the crystallographic data also greatly simplifies the classification of crystal structures into different prototypes.

A conversion tool to standardize cell parameters and/or compute the Niggli reduced cell is included in the software of Pearson's Crystal Data.

3.7.5.4. *Consequent prototype assignment*

The prototype is a well known concept in inorganic chemistry, where a large number of compounds often crystallize with very similar atom arrangements. The compilation *Strukturbericht* started to catalogue crystal structures into types named by codes such as A1, B1 or A15. These notations are still in use; however, today prototypes are generally referred to by the name of the compound for which this particular kind of atom arrangement was first identified, *i.e.* Cu, NaCl and Cr_3Si for the types enumerated above. Pearson's Crystal Data uses a longer notation which also includes the Pearson symbol and the space-group number: Cu,cF4,225, NaCl,cF8,225 and Cr_3Si,cP8,223. In a few cases several prototypes correspond to the same code, for example several polytypes of CdI_2 have the same notation. A similar situation occurs for the wrong and the correct structure proposals for FeB, which have the same Pearson code and space group. In these cases a letter is added after the type-defining compound, for example the correct FeB type will be referred to as FeB-b,oP8,62.

Each prototype is defined on a particular PCD database entry. In principle, this data set represents a recent refinement of the structure of the type-defining compound, but no effort has been made to find or use the most recent determination.

All of the data sets with published coordinates in Pearson's Crystal Data have been classified into prototypes following the criteria defined in *TYPIX* (Parthé *et al.*, 1993, 1994). According to this definition, isotypic compounds must crystallize in the same space group and have similar cell-parameter ratios; the atoms should occupy the same Wyckoff positions in the standardized description and have similar positional coordinates. If all of these criteria are fulfilled, the atomic environments should be similar. Note that H^+ (protonic hydrogen) is ignored in the assignment of the prototype as well as in the Wyckoff sequence, Pearson symbol/code and atomic environments. Isopointal substitution variants are usually distinguished; however, no distinction is made between structures with fully and partly occupied atom sites. At present, 29 470 prototypes are represented.

When possible, a prototype has also been assigned to data sets without published atom coordinates. The prototype is often stated in the publication; in other cases the editors have assigned it. The editor will have added the exact space-group setting to which the cell parameters refer when this was not published. It is important to note that a prototype has been assigned at two different levels. The first is intimately related to the published data (entry level), whereas the second is assigned at the phase level and may, in some cases, be inconsistent with the crystallographic data listed below.

For partly investigated structures, the available structural information is given using a similar way, for example the complete Pearson symbol may be replaced by *t*** (tetragonal) or *cI** (cubic body-centred) and the place of the type-defining compound is occupied by an asterisk.

3.7.5.5. *Assigned atom coordinates*

In order to give an approximate idea of the actual structure, a complete set of positional coordinates and site occupancies is proposed for data sets where a prototype could be assigned but the atom coordinates were not determined. The coordinates of the type-defining entry are proposed as a first approximation. The atom distribution is inserted by an *ESDD* module that compares the chemical formula of the type-defining entry with the chemical formula of the isotypic compound where the chemical elements have been reordered by the editor so that the first element is expected to occupy the same atom sites as the first element in the type-defining formula, and so on. Depending on the character of the prototype, substitutions and/or vacancies are either distributed over all atom sites occupied by the corresponding element or are expected to occur selectively on particular atom sites.

For this category of database entries, structure drawings, diffraction patterns and interatomic distances have also been computed. The structural portion of the database is thus more extensive than the primary literature.

3.7.5.6. *External links*

When relevant, the database entries contain links to external data sources, including ASM International Alloys Phase Diagrams Centre Online, SpringerMaterials (The Landolt–Börnstein Database incorporating Inorganic Solid Phases PAULING FILE Multinaries Edition – 2010 in SpringerMaterials) and the original publication (through https://www.crossref.org/). A (static) reference to the Powder Diffraction File entry number is provided for database entries that are included in the PDF4+ product.

3.7.5.7. *Retrievable database fields*

In addition to bibliographic (*e.g.* a particular institute) and chemical (*e.g.* sulfates) searches, many characteristics of the experiment and data processing (*e.g.* single crystal, neutron diffraction, range of temperature or reliability factors) or additional studies (*e.g.* pressure-dependence studies, magnetic structure) can be used as search criteria. Published crystal data, standardized crystal data and the Niggli reduced cells can be searched, as well as crystallographic classifications such as crystal class, Pearson symbol, Pearson code, Wyckoff sequence, structure prototype or structure class. Such searches can be very valuable in identifying a structural model for a new composition and saving the work of an *ab initio* structure determination.

The Quick Search pane includes commonly used searches on chemical elements (including cations in a particular oxidation state for oxides and halides), the number of elements and functional groups. The chemical selection (and/or/not) can be combined with selection on structure prototypes, space-group numbers and symbols or the crystal system. Retrieval on cell parameters (with ranges) and bibliographic information is also possible and the desired level of structural studies (*e.g.* complete) may be specified.

Many more searches can be carried out in the complete Search Dialog. Particularly useful are searches on atomic environments and interatomic distances. The atomic environment is defined by the coordination number, the geometry of the coordination polyhedron and the identities of the central and peripheral atoms. Searches on the number of different atomic environment types in the same structure can also be carried out. Specifying a pair of elements makes it possible to select a range of interatomic distances to be included in the search. These histograms are also useful in assessing the reasonableness of a particular distance in a Rietveld refinement.

3.7.5.8. *Particular software features*

All searches use the 'Perpetual Restraining' feature, which updates the selection set in real time as a new query is introduced, so that the progress of the search scheme can easily be monitored. The complete Search Dialog offers a large variety of features that make the retrieval and presentation of information extremely flexible.

The Chemical System Matrix View makes it easy to locate phases in binary, ternary, quaternary and pseudo-quaternary systems. The Phases List View collects a selection set into its 'distinct' phases. From the individual database entry it is particularly easy to find all database entries with the same prototype structure and plot the unit-cell volume as a function of selected atomic radii. The standard display of an entry includes a short summary about the phase, structural, bibliographic, experimental and editorial data, as well as a structure drawing, a powder pattern and a table of interatomic distances.

The software for producing structure drawings offers the visualization of atomic environments (coordination polyhedra), the statistics of interatomic distances and the calculation of selected distances and angles. Four different models are available (ball and stick, wires, sticks and space-filling), with on-the-fly rotation controlled by the mouse. The nearest-neighbour histogram of a selected atom is compared with a statistical plot containing all distances in the database involving the same chemical elements, and the atomic environments can be instantaneously modified by clicking on the nearest-neighbour histogram.

Powder-diffraction patterns can be computed for any user-defined wavelength and the visualization includes a tool for zoom-in/out tracking. Patterns based on published lists of interplanar spacings can also be visualized. It is further possible to export database entries as CIF files, tables (*e.g.* powder-diffraction pattern, distances and angles) or graphics (*e.g.* structure drawings; BMP, GIF, JPG, PNG, TIFF or Diamond documents), and individually tailored dossiers can be designed and printed.

3.7.6. Metals data file (CRYSTMET)

CRYSTMET (White *et al.*, 2002) began as a database of critically evaluated crystallographic data for metals, including alloys, intermetallics and minerals, and has grown to include inorganic compounds in general. It was started in 1960 by Cromer and Larson at Los Alamos National Laboratory, and its development was continued by the National Research Council of Canada. In 1996, the production and dissemination was transferred to Toth Information Systems.

CRYSTMET contains chemical, crystallographic and bibliographic data, together with comments regarding experimental details for each study. Using these data, a number of associated data files are generated, with the major one being a file of calculated powder patterns. Entry into CRYSTMET is *via* a number of search screens, including chemistry, bibliographic information, unit cell and reduced cell, powder patterns (using the positions of the strongest peaks as input), formula, structure type, Pearson symbol and space group. The results of queries reside in sets, which can be further manipulated using logical operations.

The results are displayed as a series of screens, which include crystallographic data, distances and angles, and the powder pattern. There is some ability to customize the calculation of the powder pattern of an entry; the calculation is performed for Debye–Scherrer geometry. Included on the Results tabs is a direct interface to the *MISSYM* program (Le Page, 1987, 1988), which searches the reported structure for additional symmetry elements. This is a very useful tool for detecting missed symmetry.

3.7.7. Protein Data Bank (PDB)

The Protein Data Bank is described in Chapter 24.1 of *International Tables for Crystallography* Volume F (Berman *et al.*, 2011). Current information is available on the web at https://www.wwpdb.org/.

3.7.7.1. *Powder diffraction by proteins*

Although powder-diffraction techniques had been applied to proteins as long ago as 1936 (Wyckoff & Corey, 1936; Corey & Wyckoff, 1936), and proof-of-principle experiments had been carried out (Rotella *et al.*, 1998, 2000), real progress in protein powder crystallography began with the work of Von Dreele (Von Dreele, 1998, 1999, 2003; Von Dreele *et al.*, 2000).

Progress in powder crystallography on macromolecules has been reviewed by Margiolaki & Wright (2008) and is also discussed in Chapter 7.1 of this volume. Notable studies include the characterization of the binding of *N*-acetylglucosamine oligosaccharides to hen egg-white lysozyme (Von Dreele, 2007*a*) and determination of the second SH3 domain of ponsin (Margiolaki *et al.*, 2007).

As with all powder diffraction, peak overlap ultimately limits the information available. Multi-pattern strategies to overcome the overlap problem have been investigated by Von Dreele (2007*b*). Multiple-pattern resonant-diffraction experiments have enabled study of the binding of PtBr_6^{2-} ions to lysozyme (Helliwell *et al.*, 2010). A bootstrap approach has been used to determine the structure of bacteriorhodopsin to 7 Å resolution (Dilanian *et al.*, 2011). Parametric resonant-scattering experiments have been used to determine the secondary structures of lysozyme derivatives (Basso *et al.*, 2010). Powder-diffraction experiments have also been used to gain insight into the general features of a nonstructural protein 3 (nsp3) macro domain (Papageorgiou *et al.*, 2010).

The structure of a five-residue peptide has been determined *ab initio* using laboratory powder data (Fujii *et al.*, 2011). We can expect further useful results at this interface between small-molecule and protein powder crystallography.

As is typical in other areas of science, powder diffraction has proven to be useful in more practical features of protein processing. It has been used to identify insulin (Norrman *et al.*, 2006) and GB1 (Frericks Schmidt *et al.*, 2007) polymorphs and lot-to-lot variations in lyophilized protein formulations (Hirakura *et al.*, 2007), and has been explored for use in structure-based generic assays (Allaire *et al.*, 2009).

3.7.7.2. *Calculation of protein powder patterns (with Kenny Ståhl)*

The Powder Diffraction File contains a few experimental powder patterns of proteins. These include silk fibroin protein (00-054-1394), tubulin (00-036-1547 and 00-036-1548), insulin (00-060-1360 through 00-060-1368), tomato bushy stunt virus (00-003-0001) and tobacco mosaic virus (00-003-0003 and 00-003-0004). Patterns have not yet been calculated from the structures in the Protein Data Bank because the calculated intensities generally fit poorly to those in experimental patterns.

Protein structures in the PDB do not generally contain H-atom positions, and the contributions from the disordered solvent in the solvent channels (which is the major source of the discrepancy) is not described (Hartmann *et al.*, 2010). The conventional Lorentz factor tends to infinity when approaching $2\theta = 0°$. Differences in data-collection temperatures and solvent content between powder and single-crystal specimens often mean that the lattice parameters differ. The relatively poor scattering from the protein and the large scattering from the mother liquor and sample holder result in significant background contributions to experimental powder patterns.

Optimization of the lattice parameters is generally straightforward and is important because most protein crystal structures are determined at low temperatures, while powder data are collected under ambient conditions. Protein crystals contain 30–80% disordered solvent. The solvent contribution to the diffraction pattern is most important for the low-angle powder data. In conventional protein crystallography several correction models have been developed (Moews & Kretsinger, 1975; Phillips, 1980; Jiang & Brünger, 1994), but the flat bulk-solvent model is the simplest one which yields a realistic correction (Jiang & Brünger, 1994; Hartmann *et al.*, 2010). This model includes two parameters: $k_{\rm sol}$, which defines the level of electron density in the solvent region, and $B_{\rm sol}$, which defines the steepness of the border between the solvent and macromolecular regions. These parameters are typically refined in contemporary software and cluster around $k_{\rm sol} = 0.35\ {\rm e\ Å^{-3}}$ and $B_{\rm sol} = 46\ {\rm Å^2}$ (Fokine & Urzhumtsev, 2002).

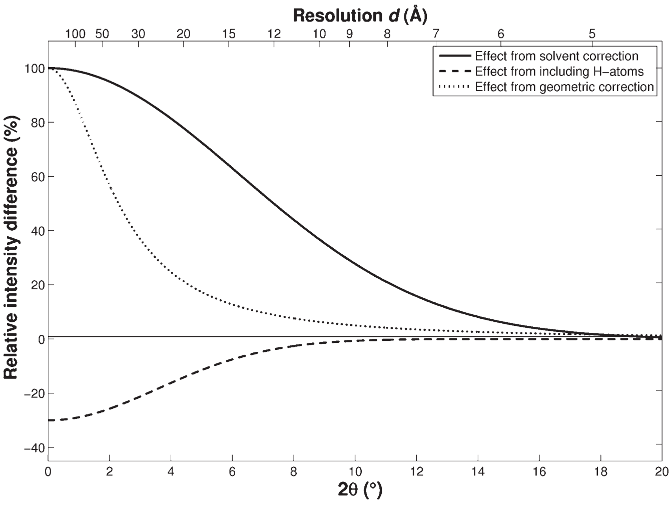

Figure 3.7.13

Overview of the trends from the different corrections. The effects are shown as the relative intensity difference $(I_{\rm non\text{-}corr} - I_{\rm corr})/I_{\rm non\text{-}corr}$ plotted as functions of the scattering angle 2θ (using Cu $K\alpha_1$) and resolution $d = \lambda/(2\sin\theta)$. The curves are based on average corrections of lysozyme and insulin data. $I_{\rm non\text{-}corr}$ is the raw intensity from a calculated pattern which has only been Lorentz corrected. The geometric correction curve was calculated using $\eta = 0.045\ {\rm Å^{-1}}$. From Hartmann *et al.* (2010).

The flat bulk-solvent correction can be applied using *phenix.pdbtools* (Adams *et al.*, 2010), which requires a PDB coordinate file and values of $k_{\rm sol}$ and $B_{\rm sol}$ as input. Average values can be used, but refined values or values from the Electron Density Server (EDS; Kleywegt *et al.*, 2004) can improve the results. The bulk-solvent correction is highly anisotropic, and both parameters affect the anisotropy.

The ideal H-atom positions can be calculated using *phenix.pdbtools*. The solvent and hydrogen contributions to the pattern can be significant (Fig. 3.7.13).

The Lorentz factor L describes the fraction of a reflection that is in the diffracting condition. For Bragg–Brentano and Debye–Scherrer geometries it is given by

$$L = \frac{1}{\sin 2\theta}\frac{1}{\sin\theta}. \qquad (3.7.3)$$

This equation assumes ideal crystals, resulting in infinitesimally small reciprocal-lattice points. The true size of the lattice points depends on the crystallite size and imperfections (strain). This smearing needs to be included in the Lorentz factor at low angles. A revised Lorentz factor for protein powder diffraction has been derived (Hartmann *et al.*, 2010),

$$L_{\rm rev} = \frac{1}{\sin 2\theta}\frac{1}{\sin\theta}\frac{\sin^2\theta}{(\sin^2\theta + \lambda^2\eta^2/12)}, \qquad (3.7.4)$$

in which η reflects the distribution of scattering-vector amplitudes. For Guinier geometry these equations become more complex (Hartmann *et al.*, 2010). Fig. 3.7.14 shows that the Lorentz factor has a smaller effect than the solvent and H atoms, but that it is still significant. By applying these corrections it should be possible for the ICDD editorial staff to calculate useful powder patterns from PDB entries that could be included in the Powder Diffraction File.

Separating the background from the diffraction pattern is not straightforward (Frankaer *et al.*, 2011). Estimation of the background is greatly assisted by a correct calculated pattern. The calculated pattern can be scaled to the experimental data using *PROTPOW* (http://www.kemi.dtu.dk/english/Research/PhysicalChemistry/Protein_og_roentgenkrystallografi/Protpow).

Ståhl *et al.* (2013) have demonstrated that existing search/match procedures can be used to identify proteins using their powder patterns, and that powder patterns calculated from Protein Data Bank coordinates with proper care can be added to a database and included in the search/match procedure. Several problems can be foreseen when including large amounts of protein data into the Powder Diffraction File. It may be worthwhile including powder patterns with several levels of solvent correction, rather than just an average value. Asymmetry from instrumental effects and specimen transparency, which can affect the peak positions, needs to be taken into account. The use of an average thermal expansion coefficient may be sufficient to account for the differences in lattice parameters between low-temperature single-crystal structures and powder patterns measured under ambient conditions.

3.7.8. Crystallography Open Database (COD) (with Saulius Gražulis)

The Crystallography Open Database (COD) project (http://www.crystallography.net/cod/; Gražulis *et al.*, 2009, 2012) aims at collecting in a single open-access database all organic, inorganic and organometallic structures, except for the structures of biological macromolecules, which are available in the Protein Data Bank (Berman *et al.*, 2003, 2011). The database was founded by Armel Le Bail, Lachlan Cranswick, Michael Berndt, Luca Lutterotti and Robert M. Downs in February 2003 as a response to Michael Berndt's letter published on the Structure Determination by Powder Diffractometry (SDPD) mailing list (Berndt, 2003). Since December 2007, the main database server has been maintained and new software has been developed by Saulius Gražulis and Andrius Merkys at the Institute of Biotechnology of Vilnius University (VU). Currently, the database includes more than 376 000 entries describing structures of small molecules and small-to-medium-sized unit-cell materials as published in IUCr journals and other major crystallographic and peer-reviewed journals, as well as contributions by crystallographers from major laboratories. Most of the mineral data are obtained from the American Mineralogist Structure Database (Rajan *et al.*, 2006) and are donated by its maintainer and COD co-founder Robert M. Downs.

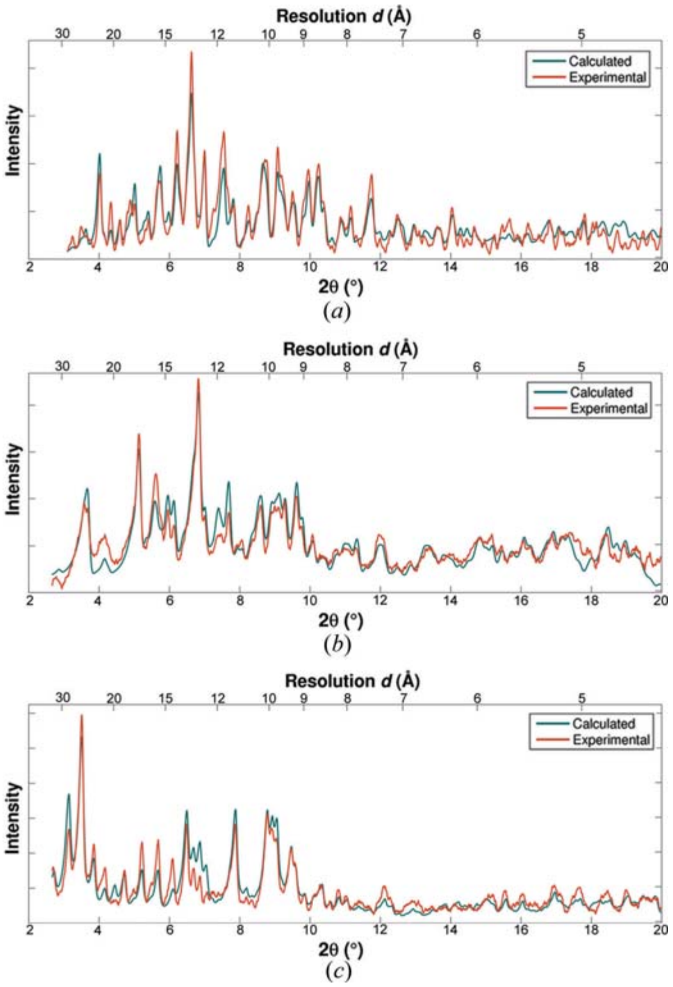

(*a*)

(*b*)

(*c*)

Figure 3.7.14
Calculated and experimental powder patterns for (*a*) lysozyme, (*b*) trigonal insulin and (*c*) cubic insulin. The calculated patterns (blue) are corrected for bulk-solvent and geometrical effects using the revised Lorentz factor. From Hartmann *et al.* (2010).

The database is an internet resource (Fig. 3.7.15) with data-search and download capabilities designed by Armel Le Bail and Michael Berndt. In addition, registered users may deposit new data, whether from previous publications or as personal communications, using the deposition web site designed at VU by

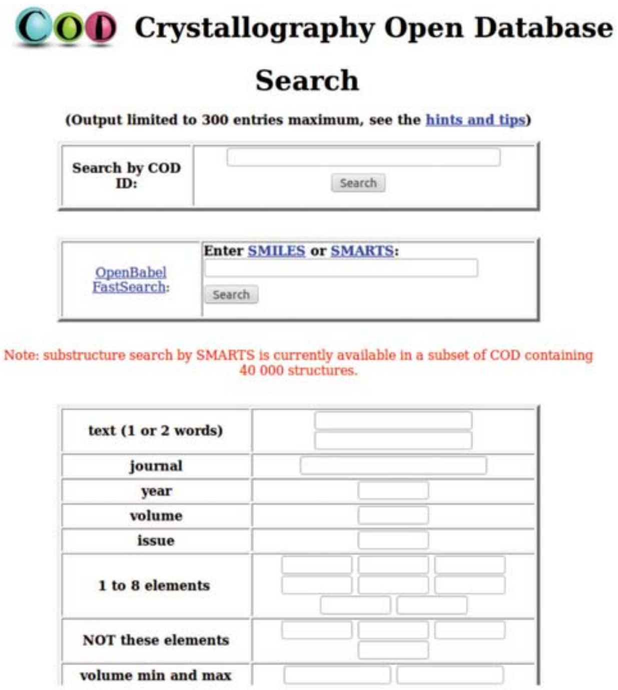

Crystallography Open Database

Search

(Output limited to 300 entries maximum, see the hints and tips)

Search by COD ID:

Enter SMILES or SMARTS:

Note: substructure search by SMARTS is currently available in a subset of COD containing 40 000 structures.

text (1 or 2 words)

journal

year

volume

issue

1 to 8 elements

NOT these elements

volume min and max

(*a*)

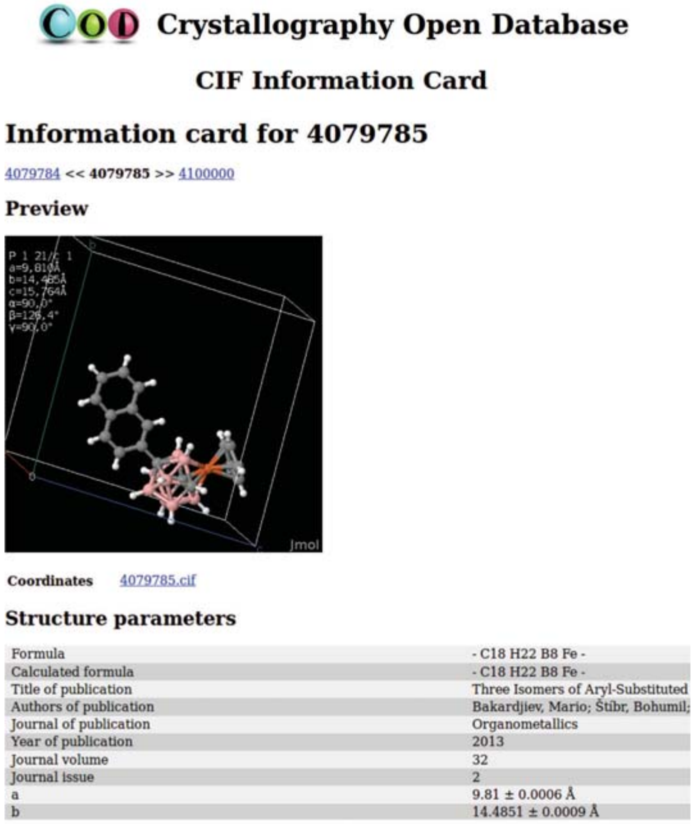

Crystallography Open Database

CIF Information Card

Information card for 4079785

4079784 << 4079785 >> 4100000

Preview

Coordinates 4079785.cif

Structure parameters

Formula	- C18 H22 B8 Fe -
Calculated formula	- C18 H22 B8 Fe -
Title of publication	Three Isomers of Aryl-Substituted
Authors of publication	Bakardjiev, Mario; Štíbr, Bohumil;
Journal of publication	Organometallics
Year of publication	2013
Journal volume	32
Journal issue	2
a	9.81 ± 0.0006 Å
b	14.4851 ± 0.0009 Å

(*b*)

Figure 3.7.15
(*a*) The website and search interface of the Crystallography Open Database (COD) permits searches of crystallographic data by a range of parameters and unrestricted retrieval of the found data. (*b*) Data can be viewed online in the interactive *Jmol* applet (Hanson, 2010, 2013) or downloaded for further processing either one record at a time or in bulk.

Saulius Gražulis, Justas Butkus and Andrius Merkys. The deposition software performs rigorous checks of syntax and semantics.

The COD website allows searching on COD numerical identifier, unit-cell parameters, chemical composition and bibliographic data. Substructure searches using SMILES and SMARTS strings have been implemented. The free software package *OpenBabel* (O'Boyle *et al.*, 2011; Hutchison, 2007) is used for both the CIF-to-SMILES transformation and the actual search.

The retrieved records can be viewed online or downloaded for further processing. For massive data mining, COD permits downloads and updates of the whole database using Subversion, Rsync or http protocols. The ease of access to the COD data and its open nature has spurred the use of this resource for software testing (Grosse-Kunstleve & Gildea, 2011), teaching (Moeck, 2004) and research (First & Floudas, 2013). Multiple mirrors around the globe (Quirós-Olozábal, 2006; Gražulis, 2007; Moeck, 2007*a*; Chateigner, 2010) ensure data preservation, provide off-site backups, offer improved search interfaces (Moeck, 2007*b*) and increase reliability.

For the powder-diffraction community, the COD is interesting not only as an archive of structures solved by powder-diffraction methods, but also as a possibility for use in search/match procedures to identify crystalline compounds. Recently, the development of an open full-pattern search/match internet tool was launched by the COD developers. It allows phase quantifications from X-ray, neutron and electron powder patterns (with high- or medium-resolution instruments) provided that the structures are already in the COD. This tool is particularly suited to nanocrystalline powders, in which severe line broadening appears, precluding phase identification from only peak positions (Lutterotti *et al.*, 2012). COD-derived databases are also offered for software produced by several diffractometer vendors (Rigaku, 2011; PANalytical, 2012*a*,*b*; Bruker, 2013). In addition to the COD, searches and matches can be performed against its sister database, the PCOD, which contains structures predicted by the *GRINSP* program (Le Bail, 2005) and hypothetical zeolites (Pophale *et al.*, 2013). The power of such an approach is demonstrated by PCOD entry 3102887 (formulated as SiO_2). It was recently identified as corresponding structurally to a new phosphorus(V) oxonitride polymorph δ-PON (Baumann *et al.*, 2012).

3.7.9. Other internet databases

Other useful databases include the following:

(i) The American Mineralogist Crystal Structure Database (http://rruff.geo.arizona.edu/AMSamcsd.php).
(ii) The Mineralogy Database (http://webmineral.com).
(iii) MinCryst (http://database.iem.ac.ru/mincryst/index.php).
(iv) The International Zeolite Association Database of Zeolite Structures (http://www.iza-structure.org/databases).
(v) The Incommensurate Structures Database (http://webbdcrista1.ehu.es/incstrdb/).
(vi) The Nucleic Acid Database (http://ndbserver.rutgers.edu).

I thank Timothy G. Fawcett and Cyrus Crowder of the International Centre for Diffraction Data, Colin Groom of CCDC, Stephan Ruehl of FIZ Karlsruhe, Pierre Villars and Karen Cenzual of Material Phases Data Systems, and Saulius Gražulis of Vilnius University Institute of Biotechnology for their valuable comments and additions.

References

Adams, P. D., Afonine, P. V., Bunkóczi, G., Chen, V. B., Davis, I. W., Echols, N., Headd, J. J., Hung, L.-W., Kapral, G. J., Grosse-Kunstleve, R. W., McCoy, A. J., Moriarty, N. W., Oeffner, R., Read, R. J., Richardson, D. C., Richardson, J. S., Terwilliger, T. C. & Zwart, P. H. (2010). *PHENIX: a comprehensive Python-based system for macromolecular structure solution. Acta Cryst.* D**66**, 213–221.

Allaire, M., Moiseeva, N., Botez, C. E., Engel, M. A. & Stephens, P. W. (2009). *On the possibility of using polycrystalline material in the development of structure-based generic assays. Acta Cryst.* D**65**, 379–382.

Allen, F. H., Cole, J. C. & Verdonk, M. L. (2011). *The relevance of the Cambridge Structural Database in protein crystallography. International Tables for Crystallography*, Vol. F, 2nd ed., edited by E. Arnold, D. M. Himmel & M. G. Rossmann, pp. 736–748. Chichester: Wiley.

Allmann, R. & Hinek, R. (2007). *The introduction of structure types into the Inorganic Crystal Structure Database ICSD. Acta Cryst.* A**63**, 412–417.

Barr, G., Dong, W. & Gilmore, C. J. (2009). *PolySNAP3: a computer program for analysing and visualizing high-throughput data from diffraction and spectroscopic sources. J. Appl. Cryst.* **42**, 965–974.

Barr, G., Gilmore, C. J. & Paisley, J. (2004). *SNAP-1D: a computer program for qualitative and quantitative powder diffraction pattern analysis using the full pattern profile. J. Appl. Cryst.* **37**, 665–668.

Basso, S., Besnard, C., Wright, J. P., Margiolaki, I., Fitch, A., Pattison, P. & Schiltz, M. (2010). *Features of the secondary structure of a protein molecule from powder diffraction data. Acta Cryst.* D**66**, 756–761.

Baumann, D., Sedlmaier, S. J. & Schnick, W. (2012). *An unprecedented AB_2 tetrahedra network structure type in a high-pressure phase of phosphorus oxonitride (PON). Angew. Chem. Int. Ed.* **51**, 4707–4709.

Behrens, H. & Luksch, P. (2006). *A bibliometric study in crystallography. Acta Cryst.* B**62**, 993–1001.

Belsky, A., Hellenbrandt, M., Karen, V. L. & Luksch, P. (2002). *New developments in the Inorganic Crystal Structure Database (ICSD): accessibility in support of materials research and design. Acta Cryst.* B**58**, 364–369.

Bergerhoff, G. & Brandenburg, K. (1999). *Typical interatomic distances: inorganic compounds. International Tables for Crystallography*, Vol. C, edited by E. Prince, pp. 770–781. Dordrecht: Kluwer Academic Publishers.

Bergerhoff, G. & Brown, I. D. (1987). *Crystallographic Databases*, edited by F. H. Allen, G. Bergerhoff & R. Sievers. Chester: International Union of Crystallography.

Berman, H. M., Henrick, K., Kleywegt, G., Nakamura, H. & Markley, J. (2011). *The Worldwide Protein Data Bank. International Tables for Crystallography*, Vol. F, 2nd ed., edited by E. Arnold, D. M. Himmel & M. G. Rossmann, pp. 827–832. Chichester: Wiley.

Berman, H., Henrick, K. & Nakamura, H. (2003). *Announcing the Worldwide Protein Data Bank. Nature Struct. Mol. Biol.* **10**, 980.

Berndt, M. (1994). Thesis, University of Bonn, Germany. Updates by O. Shcherban, SCC Structure-Properties Ltd, Lviv, Ukraine.

Berndt, M. (2003). *Open crystallographic database – a role for whom?* http://www.cristal.org/SDPD-list/2003/msg00025.html.

Bigelow, W. C. & Smith, J. V. (1964). *Two new indexes to the Powder Diffraction File. ASTM Spec. Tech. Publ.* STP372, 54. https://doi.org/10.1520/STP48334S.

Boldyrev, A. K., Mikheev, V. I., Dubinina, V. N. & Dovalev, G. A. (1938). *X-ray determination tables for minerals, Ft. I. Ann. Inst. Mines Leningrad*, **11**, 1–157.

Boles, M. O., Girven, R. J. & Gane, P. A. C. (1978). *The structure of amoxycillin trihydrate and a comparison with the structures of ampicillin. Acta Cryst.* B**34**, 461–466.

Bravais, A. (1866). *Etudes Cristallographiques*. Paris: Gathier Villars.

Bruker-AXS (2013). Crystallography Open Database for DIFFRAC.EVA. https://www.bruker.com/products/x-ray-diffraction-and-elemental-analysis/x-ray-diffraction/xrd-software/eva/cod.html.

Bruno, I. J., Cole, J. C., Edgington, P. R., Kessler, M., Macrae, C. F., McCabe, P., Pearson, J. & Taylor, R. (2002). *New software for searching the Cambridge Structural Database and visualizing crystal structures. Acta Cryst.* B**58**, 389–397.

Bruno, I. J., Cole, J. C., Kessler, M., Luo, J., Motherwell, W. D. S., Purkis, L. H., Smith, B. R., Taylor, R., Cooper, R. I., Harris, S. E. & Orpen, A. G. (2004). *J. Chem. Inf. Comput. Sci.* **44**, 2133–2144.

Caussin, P., Nusinovici, J. & Beard, D. W. (1988). *Using digitized X-ray powder diffraction scans as input for a new PC-At search/match program. Adv. X-ray Anal.* **31**, 423–430.

Caussin, P., Nusinovici, J. & Beard, D. W. (1989). *Specific data handling techniques and new enhancements in a search-match program. Adv. X-ray Anal.* **32**, 531–538.

Cenzual, K., Berndt, M., Brandenburg, K., Luong, V., Flack, E. & Villars, P. (2000). *ESDD* software package. Updates by O. Shcherban, SCC Structure-Properties Ltd, Lviv, Ukraine.

Chateigner, D. (2010). *Crystallography Open Database Mirror at ENSICAEN*. http://cod.ensicaen.fr.

Cherukuri, S. C., Snyder, R. L. & Beard, D. W. (1983). *Comparison of the Hanawalt and Johnson–Vand computer search/match strategies. Adv. X-ray Anal.* **26**, 99–104.

Chipera, S. J. & Bish, D. L. (2002). *FULLPAT: a full-pattern quantitative analysis program for X-ray powder diffraction using measured and calculated patterns. J. Appl. Cryst.* **35**, 744–749.

Corey, R. B. & Wyckoff, R. W. G. (1936). *Long spacings in macromolecular solids. J. Biol. Chem*. **114**, 407–414.

Crystal Impact (2012). *Match!* v.2. Crystal Impact, Bonn, Germany.

Davey, W. P. (1922). *A new X-ray diffraction apparatus. Gen. Elec. Rev.* **25**, 565.

Davey, W. P. (1934). *Study of Crystal Structure and Its Applications*. New York: McGraw-Hill.

Debye, P. & Scherrer, P. (1916). *Interference on inordinate orientated particles in Roentgen light. Phys. Z.* **17**, 277–283.

Debye, P. & Scherrer, P. (1917). *Interference on inordinate orientated particles in X-ray light. III. Phys. Z.* **18**, 291–301.

Degen, T., Sadki, M., Bron, E., König, U. & Nénert, G. (2014). *The HighScore suite. Powder Diffr.* **29**, S13–S18.

Dilanian, R. A., Darmanin, C., Varghese, J. N., Wilkins, S. W., Oka, T., Yagi, N., Quiney, H. M. & Nugent, K. A. (2011). *A new approach for structure analysis of two-dimensional membrane protein crystals using X-ray powder diffraction data. Protein Sci.* **20**, 457–464.

Donnay, J. D. H. & Harker, D. (1937). *A new law of crystal morphology extending the law of Bravais. Am. Mineral.* **22**, 463–467.

Fawcett, T. G., Kabekkodu, S. N., Blanton, J. R. & Blanton, T. N. (2017). *Chemical analysis by diffraction: the Powder Diffraction File. Powder Diffr.* **32**, 63–71.

First, E. L. & Floudas, C. A. (2013). *MOFomics: computational pore characterization of metal–organic frameworks. Microporous Mesoporous Mater.* **165**, 32–39.

Fokine, A. & Urzhumtsev, A. (2002). *Flat bulk-solvent model: obtaining optimal parameters. Acta Cryst.* D**58**, 1387–1392.

Frankaer, C. G., Harris, P. & Ståhl, K. (2011). *A sample holder for in-house X-ray powder diffraction studies of protein powders. J. Appl. Cryst.* **44**, 1288–1290.

Frericks Schmidt, H. L., Sperling, L. J., Gao, Y. G., Wylie, B. J., Boettcher, J. M., Wilson, S. R. & Rienstra, C. M. (2007). *Crystal polymorphism of protein GB1 examined by solid-state NMR spectroscopy and X-ray diffraction. J. Phys. Chem. B*, **111**, 14362–14369.

Frevel, L. K. (1965). *Computational aids for identifying crystalline phases by powder diffraction. Anal. Chem.* **37**, 471–482.

Frevel, L. K., Adams, C. E. & Ruhberg, L. R. (1976). *A fast search-match program for powder diffraction analysis. J. Appl. Cryst.* **9**, 199–204.

Friedel, G. (1907). *Etudes sur la loi de Bravais. Bull. Soc. Fr. Miner.* **30**, 326–455.

Fujii, K., Young, M. T. & Harris, K. D. M. (2011). *Exploiting powder X-ray diffraction for direct structure determination in structural biology: the P2X4 receptor trafficking motif YEQGL. J. Struct. Biol.* **174**, 461–467.

Gelato, L. M. & Parthé, E. (1987). *STRUCTURE TIDY – a computer program to standardize crystal structure data. J. Appl. Cryst.* **20**, 139–143.

Gilmore, C. J., Barr, G. & Paisley, J. (2004). *High-throughput powder diffraction. I. A new approach to qualitative and quantitative powder diffraction pattern analysis using full pattern profiles. J. Appl. Cryst.* **37**, 231–242.

Goehner, R. P. & Garbauskas, M. F. (1984). *PDIDENT – a set of programs for powder diffraction phase identification. X-ray Spectrom.* **13**, 172–179.

Gražulis, S. (2007). *COD Mirror in Vilnius*. http://cod.ibt.lt/cod/.

Gražulis, S., Chateigner, D., Downs, R. T., Yokochi, A. F. T., Quirós, M., Lutterotti, L., Manakova, E., Butkus, J., Moeck, P. & Le Bail, A. (2009). *Crystallography Open Database – an open-access collection of crystal structures. J. Appl. Cryst.* **42**, 726–729.

Gražulis, S., Daškevič, A., Merkys, A., Chateigner, D., Lutterotti, L., Quirós, M., Serebryanaya, N. R., Moeck, P., Downs, R. T. & Le Bail, A. (2012). *Crystallography Open Database (COD): an open-access collection of crystal structures and platform for world-wide collaboration. Nucleic Acids Res.* **40**, D420–D427.

Groom, C. R., Bruno, I. J., Lightfoot, M. P. & Ward, S. C. (2016). *The Cambridge Structural Database. Acta Cryst.* B**72**, 171–179.

Grosse-Kunstleve, R. & Gildea, R. (2011). *Computational Crystallography Initiative: COD stats.* http://cci.lbl.gov/cod_stats.

Hanawalt, J. D. (1983). *History of the Powder Diffraction File (PDF). Crystallography in North America*, edited by D. McLachlan & J. P. Glusker, pp. 215–219. Buffalo: American Crystallographic Association.

Hanawalt, J. D. (1986). *Manual search/match methods for powder diffraction in 1986. Powder Diffr.* **1**, 7–13.

Hanawalt, J. D. & Rinn, H. W. (1936). *Identification of crystalline materials. Ind. Eng. Chem. Anal. Ed.* **8**, 244–247.

Hanawalt, J. D., Rinn, H. W. & Frevel, L. K. (1938). *Chemical analysis by X-ray diffraction. Ind. Eng. Chem. Anal. Ed.* **10**, 457–512.

Hanson, R. M. (2010). *Jmol – a paradigm shift in crystallographic visualization. J. Appl. Cryst.* **43**, 1250–1260.

Hanson, R. M. (2013). *Jmol: an open-source Java viewer for chemical structures in 3D.* http://www.jmol.org.

Harju, P. & Pasek, P. (1983). *Vanadium–hydrogen–phosphorus–oxygen catalytic material.* US Patent 4374756; PDF entry 00-047-0967.

Hartmann, C. G., Nielsen, O. F., Ståhl, K. & Harris, P. (2010). *In-house characterization of protein powder. J. Appl. Cryst.* **43**, 876–882.

Hellenbrandt, M. (2004). *The Inorganic Crystal Structure Database (ICSD) – present and future. Crystallogr. Rev.* **10**, 17–22.

Helliwell, J. R., Bell, A. M. T., Pryant, P., Fisher, S. J., Habash, G., Helliwell, M., Margiolaki, I., Kaenket, S., Watier, Y., Wright, J. P. & Yalamanchilli, S. (2010). *Time-dependent analysis of K_2PtBr_6 binding to lysozyme studied by protein powder and single crystal X-ray analysis. Z. Kristallogr.* **225**, 570–575.

Hirakura, Y., Yamaguchi, H., Mizuno, M., Miyanishi, H., Ueda, S. & Kitamura, S. (2007). *Detection of lot-to-lot variations in the amorphous microstructure of lyophilized protein formulations. Int. J. Pharm.* **340**, 34–41.

Huang, T. C. & Parrish, W. (1982). *A new computer algorithm for qualitative X-ray powder diffraction analysis. Adv. X-ray Anal.* **25**, 213–219.

Hull, A. W. (1919). *A new method of chemical analysis. J. Am. Chem. Soc.* **41**, 1168–1175.

Hull, A. W. (1983). *An account of early studies at Schenectady. Crystallography in North America*, edited by D. McLachlan & J. P. Glusker, p. 32. Buffalo: American Crystallographic Association.

Hutchison, G. R. (2007). *OpenBabel: The Open Source Chemistry Toolbox.* http://openbabel.org.

ICDD (2016). *PDF-4+ 2016 (Database)*. Newtown Square: International Centre for Diffraction Data. http://www.icdd.com.

Jenkins, R. & Rose, R. N. (1990). *Don Hanawalt – early days and his contribution to qualitative powder diffractometry. Powder Diffr.* **5**, 70–75.

Jiang, J.-S. & Brünger, A. T. (1994). *Protein hydration observed by X-ray diffraction. Solvation properties of penicillopepsin and neuraminidase crystal structures. J. Mol. Biol.* **243**, 100–115.

Jobst, B. A. & Goebel, H. E. (1982). *IDENT – a versatile microfile-based system for fast interactive XRPD phase analysis. Adv. X-ray Anal.* **25**, 273–282.

Johnson, G. G. Jr & Vand, V. (1967). *A computerized powder diffraction identification system. Ind. Eng. Chem.* **59**, 19–31.

Johnson, G. G. Jr & Vand, V. (1968). *Computerized multiphase X-ray powder diffraction identification system. Adv. X-ray Anal.* **11**, 376–384.

Kaduk, J. A. (2002). *Use of the Inorganic Crystal Structure Database as a problem solving tool. Acta Cryst.* B**58**, 370–379.

Kleywegt, G. J., Harris, M. R., Zou, J., Taylor, T. C., Wählby, A. & Jones, T. A. (2004). *The Uppsala Electron-Density Server. Acta Cryst.* D**60**, 2240–2249.

Le Bail, A. (2005). *Inorganic structure prediction with GRINSP. J. Appl. Cryst.* **38**, 389–395.

Le Page, Y. (1987). *Computer derivation of the symmetry elements implied in a structure description. J. Appl. Cryst.* **20**, 264–269.

Le Page, Y. (1988). *MISSYM1.1 – a flexible new release. J. Appl. Cryst.* **21**, 983–984.

Lutterotti, L. (2012). *Qualitative Phase Analysis: Method Developments.* In *Uniting Electron Crystallography and Powder Diffraction*, pp. 233–242. Dordrecht: Springer.

Macrae, C. F., Bruno, I. J., Chisholm, J. A., Edgington, P. R., McCabe, P., Pidcock, E., Rodriguez-Monge, L., Taylor, R., van de Streek, J. & Wood, P. A. (2008). *Mercury CSD 2.0 – new features for the visualization and investigation of crystal structures. J. Appl. Cryst.* **41**, 466–470.

Margiolaki, I. & Wright, J. P. (2008). *Powder crystallography on macromolecules. Acta Cryst.* A**64**, 169–180.

Margiolaki, I., Wright, J. P., Wilmanns, M., Fitch, A. N. & Pinotsis, N. (2007). *Second SH3 domain of ponsin solved from powder diffraction. J. Am. Chem. Soc.* **129**, 11865–11871.

Marquart, R. G. (1986). *μPDSM: mainframe search/match on an IBM PC. Powder Diffr.* **1**, 34–39.

Marquart, R. G., Katsnelson, I., Milne, G. W. A., Heller, S. R., Johnson, G. G. & Jenkins, R. (1979). *A search-match system for X-ray powder diffraction data. J. Appl. Cryst.* **12**, 629–634.

Materials Data (2016). *Jade* 9.6. Livermore: Materials Data Inc. https://materialsdata.com/.

Mighell, A. D. (2003). *The normalized reduced form and cell mathematical tools for lattice analysis – symmetry and similarity. J. Res. Natl Inst. Stand. Technol.* **108**, 447–452.

Mighell, A. D. & Himes, V. L. (1986). *Compound identification and characterization using lattice-formula matching techniques. Acta Cryst.* A**42**, 101–105.

Moeck, P. (2004). *EDU-COD: Educational Subset of COD.* http://nanocrystallography.research.pdx.edu/search/edu.

Moeck, P. (2007*a*). *Crystallography Open Database Mirror in North America.* http://nanocrystallography.org.

Moeck, P. (2007*b*). *Alternative COD search interface at Portland State University.* http://nanocrystallography.research.pdx.edu/search/codmirror.

Moews, P. C. & Kretsinger, R. H. (1975). *Refinement of the structure of carp muscle calcium-binding parvalbumin by model building and difference Fourier analysis. J. Mol. Biol.* **91**, 201–225.

Nichols, M. (1966). *A Fortran Program for the Identification of X-ray Powder Diffraction Patterns*. Report UCRL-70078, Lawrence Livermore National Laboratory, USA.

Norrman, M., Ståhl, K., Schluckebier, G. & Al-Karadaghi, S. (2006). *Characterization of insulin microcrystals using powder diffraction and multivariate data analysis. J. Appl. Cryst.* **39**, 391–400.

Nusinovici, J. & Bertelmann, D. (1993). *Practical determination of the acceptable 2θ error for non-ambiguous identification of pure phases with DIFFRAC-AT. Adv. X-ray Anal.* **36**, 327–332.

Nusinovici, J. & Winter, M. J. (1994). *Diffrac-At search: search/match using full traces as input. Adv. X-ray Anal.* **37**, 59–66.

O'Boyle, N. M., Banck, M., James, C. A., Morley, C., Vandermeersch, T. & Hutchison, G. R. (2011). *Open Babel: an open chemical toolbox. J. Cheminf.* **3**, 33.

O'Connor, B. H. & Bagliani, F. (1976). *A semi-automated system for identifying crystalline materials with powder diffraction data. J. Appl. Cryst.* **9**, 419–423.

Oxford Cryosystems (2012). *Crystallographica Search-Match (CSM)*. Oxford: Oxford Cryosystems Ltd. http://www.oxcryo.com/software/.

PANalytical (2012*a*). *HighScore Plus*. Almelo: PANalytical B.V.

PANalytical (2012*b*). *The COD database files for the PANalytical HighScore or HighScore Plus software packages*. http://www.crystallography.net/archives/2012/PANalytical.

Papageorgiou, N., Watier, Y., Saunders, L., Coutard, B., Lantez, V., Gould, E. A., Fitch, A. N., Wright, J. P., Canard, B. & Margiolaki, I. (2010). *Preliminary insights into the non structural protein 3 macro domain of the Mayaro virus by powder diffraction. Z. Kristallogr.* **225**, 576–580.

Parrish, W. (1983). *History of the X-ray powder method in the USA. Crystallography in North America*, edited by D. McLachlan & J. P. Glusker, pp. 201–214. Buffalo: American Crystallographic Association.

Parthé, E., Cenzual, K. & Gladyshevskii, R. (1993). *Standardization of crystal structure data as an aid to the classification of crystal structure types. J. Alloys Compd*, **197**, 291–301.

Parthé, E. & Gelato, L. M. (1984). *The standardization of inorganic crystal-structure data. Acta Cryst.* A**40**, 169–183.

Parthé, E. & Gelato, L. M. (1985). *The 'best' unit cell for monoclinic structures consistent with b axis unique and cell choice 1 of International Tables for Crystallography (1983). Acta Cryst.* A**41**, 142–151.

Parthé, E., Gelato, L., Chabot, B., Penzo, M., Cenzual K. & Gladyshevskii, R. (1993, 1994). *TYPIX – Standardized Data and Crystal Chemical Characterization of Inorganic Structure Types.* Heidelberg: Springer. https://doi.org/10.1007/978-3-662-10641-9.

Phillips, S. E. V. (1980). *Structure and refinement of oxymyoglobin at 1.6 Å resolution. J. Mol. Biol.* **142**, 531–554.

Pophale, R., Daeyaert, F. & Deem, M. W. (2013). *Computational prediction of chemically-synthesizable organic structure directing agents for zeolites. J. Mater. Chem. A*, **1**, 6750–6760.

Quirós-Olozábal, M. (2006). *COD Mirror of Granada University.* http://qiserver.ugr.es/cod.

Rajan, H., Uchida, H., Bryan, D., Swaminathan, R., Downs, R. M. & Hall-Wallace, M. (2006). *Building the American Mineralogist Crystal Structure Database: A recipe for construction of a small internet database. Geoinformatics: Data to Knowledge*, edited by A. Sinha. McLean: Geological Society of America. https://doi.org/10.1130/2006.2397(06).

Rigaku (2011). *COD for PDXL: Integrated Powder X-ray Diffraction Software.* http://www.crystallography.net/archives/2011/Rigaku.

Rotella, F. J., Duke, N. & Kaduk, J. A. (1998). *X-ray powder diffraction from biological macromolecules. What do we see? What can we tell? American Crystallographic Association Meeting Abstracts, Washington DC, 18–23 July*. Buffalo: American Crystallographic Association.

Rotella, F. J., Duke, N. & Kaduk, J. A. (2000). *Powder diffraction from biological macromolecules using synchrotron X-rays. American Crystallographic Association Meeting Abstracts, St Paul MN, 22–27 July*. Buffalo: American Crystallographic Association.

Schreiner, W. N., Surdukowski, C. & Jenkins, R. (1982). *A new minicomputer search/match/identify program for qualitative phase analysis with the powder diffractometer. J. Appl. Cryst.* **15**, 513–523.

Shpeizer, B., Ouyang, X., Heising, J. M. & Clearfield, A. (2001). *Synthesis and crystal structure of a new vanadyl phosphate $[H_{0.6}(VO)_3(PO_4)_3(H_2O)_3].4H_2O$ and its conversion to porous products. Chem. Mater.* **13**, 2288–2296.

Sidey, V. (2013). *On the shortest $B^{III}-O$ bonds. Acta Cryst.* B**69**, 86–89.

Sietronics (2012). *Siroquant* v.4. Canberra: Sietronics. http://www.siroquant.com.

Snyder, R. L. (1981). *A Hanawalt type phase identification procedure for a minicomputer. Adv. X-ray Anal.* **24**, 83–90.

Ståhl, K., Frankaer, C. G., Petersen, J. & Harris, P. (2013). *Monitoring protein precipitates by in-house X-ray powder diffraction. Powder Diffr.* **28**, S448–S457.

Toby, B. H., Harlow, R. L. & Holomany, M. A. (1990). *The POWDER SUITE: computer programs for searching and accessing the JCPDS-ICDD powder diffraction database. Powder Diffr.* **5**, 2–7.

Villars, P. (1997). *Pearson's Desk Edition*, Vols. 1–2. Materials Park: ASM International.

Villars, P. & Calvert, L. D. (1985). *Pearson's Handbook of Crystallographic Data for Intermetallic Phases*, 1st Ed., Vols. 1–3. Materials Park: ASM International.

Villars, P. & Calvert, L. D. (1991). *Pearson's Handbook of Crystallographic Data for Intermetallic Phases*, 2nd Ed., Vols. 1–4. Materials Park: ASM International.

Villars, P. & Cenzual, K. (2013). *Pearson's Crystal Data: Crystal Structure Database for Inorganic Compounds* (CD-ROM). Materials Park: ASM International.

Villars, P., Onodera, N. & Iwata, S. (1998). *The Linus Pauling File (LPF) and its application to materials design. J. Alloys Compd*, **279**, 1–7.

Von Dreele, R. B. (1998). *Protein structures by powder diffraction? Abstr. Pap. Am. Chem. Soc.* **215**, U759.

Von Dreele, R. B. (1999). *Combined Rietveld and stereochemical restraint refinement of a protein crystal structure. J. Appl. Cryst.* **32**, 1084–1089.

Von Dreele, R. B. (2003). *Protein crystal structure analysis from high-resolution X-ray powder-diffraction data. Methods Enzymol.* **368**, 254–267.

Von Dreele, R. B. (2007*a*). *Binding of N-acetylglucosamine oligosaccharides to hen egg-white lysozyme: a powder diffraction study. Acta Cryst.* D**61**, 22–32.

Von Dreele, R. B. (2007*b*). *Multipattern Rietveld refinement of protein powder data: an approach to higher resolution. J. Appl. Cryst.* **40**, 133–143.

Von Dreele, R. B., Stephens, P. W., Smith, G. D. & Blessing, R. H. (2000). *The first protein crystal structure determined from high-resolution X-ray powder diffraction data: a variant of T_3R_3 human insulin–zinc complex produced by grinding. Acta Cryst.* D**56**, 1549–1553.

Waldo, A. W. (1935). *Identification of the copper ore minerals by means of X-ray powder diffraction patterns. Am. Mineral.* **20**, 575–597.

White, P. S., Rodgers, J. R. & Le Page, Y. (2002). *CRYSTMET: a database of the structures and powder patterns of metals and intermetallics. Acta Cryst.* B**58**, 343–348.

Winchell, A. N. (1927). *Further studies in the mica group. Am. Mineral.* **12**, 267–279.

Wolff, P. M. de (2016). *International Tables for Crystallography*, Vol. A, 6th ed., edited by M. I. Aroyo, pp. 709–714. Chichester: Wiley.

Wyckoff, R. W. G. & Corey, R. B. (1936). *X-ray diffraction patterns of crystalline tobacco mosaic proteins. J. Biol. Chem.* **116**, 51–55.

International Tables for Crystallography (2019). Vol. H, Chapter 3.8, pp. 325–343.

3.8. Clustering and visualization of powder-diffraction data

C. J. Gilmore, G. Barr and W. Dong

3.8.1. Introduction

In high-throughput crystallography, crystallization experiments using robotics coupled with automatic sample changers and two-dimensional (2D) detectors can generate and measure over 1000 powder-diffraction patterns on a series of related compounds, often polymorphs or salts, in a day (Storey *et al.*, 2004). It is also possible to simultaneously measure spectroscopic data, especially Raman (Alvarez *et al.*, 2009). The analysis of these patterns poses a difficult statistical problem: a need to classify the data by putting the samples into clusters based on diffraction-pattern similarity so that unusual samples can be readily identified. At the same time, suitable visualization tools to help in the data-classification process are required; the techniques of classification and visualization go hand-in-hand. Interestingly, the techniques developed for large data sets with poor-quality data also have great value when looking at smaller data sets, and the visualization tools developed for high-throughput studies are especially useful when looking at phase transitions, mixtures *etc.*

In this chapter the methods for comparing whole patterns will be described. The mathematics of cluster analysis will then be explained, followed by a discussion of the associated visualization tools. Examples using small data sets from pharmaceuticals, inorganics and phase transitions will be given; the techniques used can be readily scaled up for handling large, high-throughput data sets. The same methods also work for spectroscopic data and the use of such information with and without powder X-ray diffraction (PXRD) data will be discussed. Finally, the use of visualization tools in quality control is demonstrated.

3.8.2. Comparing 1D diffraction patterns

Comparing 1D diffraction patterns or spectra cannot be done by simply using the peaks and their relative intensities for a number of reasons:

(1) The accurate determinations of the peak positions may be difficult, especially in cases where peak overlap occurs or there is significant peak asymmetry.
(2) The hardware and the way in which the sample is prepared can also affect the *d*-spacing (or 2θ value) that is recorded for the peak. Shoulders to main peaks and broad peaks can also be problematic.
(3) There is a subjective element to deciding how many peaks there are in the pattern, especially for weak peaks and noisy data.
(4) Weak peaks may be discarded. This can affect the quantitative analysis of mixtures if one component diffracts weakly or is present only in small amounts.
(5) Differences in sample preparation and instrumentation can lead to significant differences in the powder-diffraction patterns of near-identical samples.
(6) Preferred orientation may be present: this is a very difficult and common problem.
(7) The reduction of the pattern to point functions can also make it difficult to design effective algorithms.

In order to use the information contained within the full profile, algorithms are required that utilize each measured data point in the analysis. We use two correlation coefficients for the purpose of comparing PXRD patterns: the Pearson and the Spearman coefficients.

3.8.2.1. *Spearman's rank order coefficient*

Consider two diffraction patterns, *i* and *j*, each with *n* measured points $n((x_1, y_1), \ldots, (x_n, y_n))$. These are transformed to ranks $R(x_k)$ and $R(y_k)$. The Spearman test (Spearman, 1904) then gives a correlation coefficient (Press *et al.*, 2007),

$$R_{ij} = \frac{\sum\limits_{k=1}^{n} R(x_k)R(y_k) - n\left(\frac{n+1}{2}\right)^2}{\left(\sum\limits_{k=1}^{n} R(x_k)^2 - n\left(\frac{n+1}{2}\right)^2\right)^{1/2} \left(\sum\limits_{k=1}^{n} R(y_k)^2 - n\left(\frac{n+1}{2}\right)^2\right)^{1/2}}, \tag{3.8.1}$$

where $-1 \le R_{ij} \le 1$.

3.8.2.2. *Pearson's r coefficient*

Pearson's *r* is a parametric linear correlation coefficient widely used in crystallography. It has a similar form to Spearman's test, except that the data values themselves, and not their ranks, are used:

$$r_{ij} = \frac{\sum\limits_{k=1}^{n} (x_k - \overline{x})(y_k - \overline{y})}{\left[\sum\limits_{k=1}^{n} (x_k - \overline{x})^2 \sum\limits_{k=1}^{n} (y_k - \overline{y})^2\right]^{1/2}}, \tag{3.8.2}$$

where $\overline{x}$ and $\overline{y}$ are the means of intensities taken over the full diffraction pattern. Again, *r* can lie between −1.0 and +1.0.

Fig. 3.8.1 shows the use of the Pearson and Spearman correlation coefficients (Barr *et al.*, 2004*a*). In Fig. 3.8.1(*a*) $r = 0.93$ and $R = 0.68$. The high parametric coefficient arises from the perfect match of the two biggest peaks, but the much lower Spearman coefficient acts as a warning that there are unmatched regions in the two patterns. In Fig. 3.8.1(*b*) the situation is reversed: $r = 0.79$, whereas $R = 0.90$, and it can be seen that there is a strong measure of association with the two patterns, although there are some discrepancies in the region 15–35°. In Fig. 3.8.1(*c*) $r = 0.66$ and $R = 0.22$; in this case the Spearman test is again warning of missing match regions. Thus, the use of the two coefficients acts as a valuable balance of their respective properties when processing complete patterns. The Spearman coefficient is also robust in the statistical sense and useful in the case of preferred orientation.

3.8.2.3. *Combining the correlation coefficients*

Correlation coefficients are not additive, so it is invalid to average them directly; they need to be transformed into the Fisher *Z* value to give

Copyright © 2019 International Union of Crystallography

$$\rho_{ij} = \tanh\left[\left(\tanh^{-1} R_{ij} + \tanh^{-1} r_{ij}\right)/2\right]. \qquad (3.8.3)$$

3.8.2.4. *Full-profile qualitative pattern matching*

Before performing pattern matching, some data pre-processing may be necessary. In order not to produce artefacts, this should be minimized. Typical pre-processing activities are:

(1) The data are normalized such that the maximum peak intensity is 1.0.

(2) The patterns need to be interpolated if necessary to have common increments in 2θ. High-order polynomials using Neville's algorithm can be used for this (Press *et al.*, 2007).

(3) If backgrounds are large they should be removed. High-throughput data are often very noisy because of low counting times and the sample itself. If this is the case, smoothing of the data can be carried out. The SURE (Stein's Unbiased Risk Estimate) thresholding procedure (Donoho & Johnstone, 1995; Ogden, 1997) employing wavelets is ideal for this task since it does not introduce potentially damaging artefacts, for example ringing around peaks (Barr *et al.,* 2004*a*; Smrčok *et al.*, 1999).

After pre-processing, which needs to be carried out in an identical way for each sample, the following steps are carried out:

(1) The intersecting 2θ range of the two data sets is calculated, and each of the pattern correlation coefficients is calculated using only this region.

(2) A minimum intensity is set, below which profile data are set to zero. This reduces the contribution of background noise to the matching process without reducing the discriminating power of the method. We usually set this to $0.1I_{\max}$ as a default, where $I_{\max}$ is the maximum measured intensity.

(3) The Pearson correlation coefficient is calculated.

(4) The Spearman R is computed in the same way.

(5) An overall ρ value is calculated using (3.8.3).

(6) A shift in 2θ values between patterns is often observed, arising from equipment settings and data-collection protocols. Three possible simple corrections are

$$\Delta(2\theta) = a_0 + a_1 \cos\theta, \qquad (3.8.4)$$

which corrects for the zero-point error *via* the a_0 term and, *via* the $a_1 \cos\theta$ term, for varying sample heights in reflection mode, or

$$\Delta(2\theta) = a_0 + a_1 \sin\theta, \qquad (3.8.5)$$

which corrects for transparency errors, for example, and

$$\Delta(2\theta) = a_0 + a_1 \sin 2\theta, \qquad (3.8.6)$$

which provides transparency coupled with thick specimen error corrections, where a_0 and a_1 are constants that can be determined by shifting patterns to maximize their overlap as measured by ρ. It is difficult to obtain suitable expressions for the derivatives $\partial a_0/\partial\rho_{ij}$ and $\partial a_1/\partial\rho_{ij}$ for use in the optimization, so we use the downhill simplex method (Nelder & Mead, 1965), which does not require their calculation.

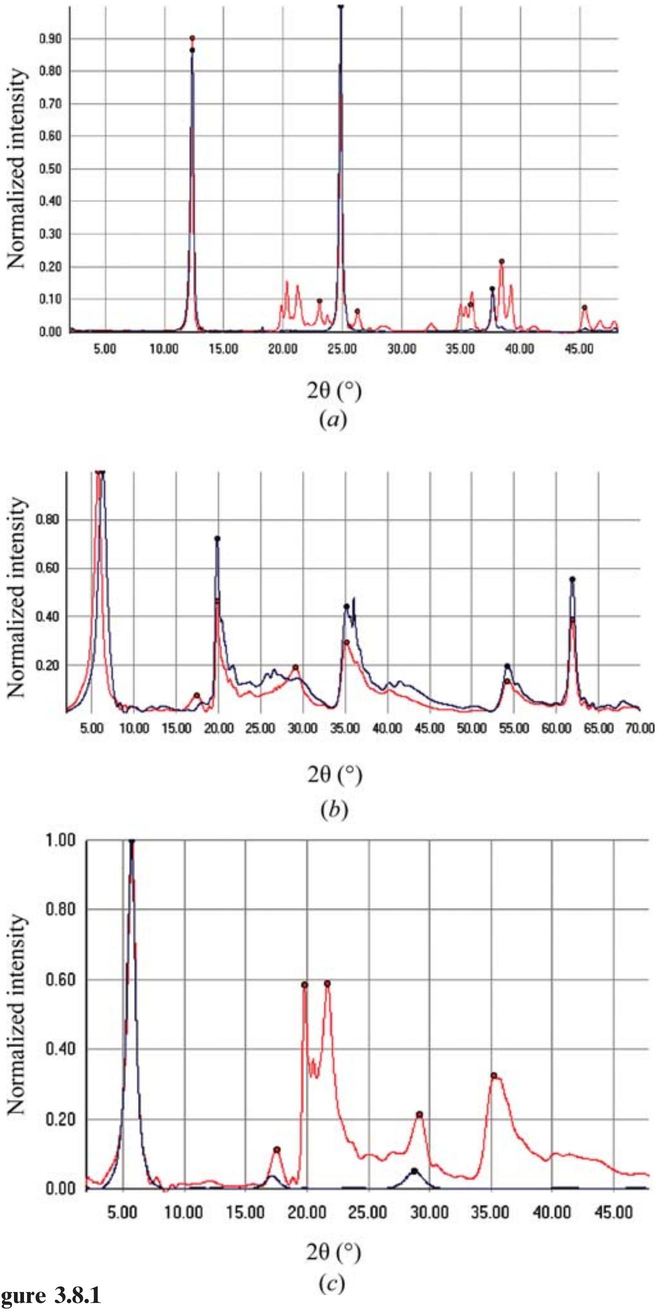

Figure 3.8.1
The use of the Pearson (r) and Spearman (R) correlation coefficients to quantitatively match powder patterns: (*a*) $r = 0.93$, $R = 0.68$; (*b*) $r = 0.79$, $R = 0.90$; (*c*) $r = 0.66$, $R = 0.22$.

3.8.2.5. *Generation of the correlation and distance matrices*

Using equation (3.8.3), a correlation matrix is generated in which a set of n patterns is matched with every other to give a symmetric ($n \times n$) correlation matrix $\boldsymbol{\rho}$ with unit diagonal. The matrix $\boldsymbol{\rho}$ can be converted to a Euclidean distance matrix, $\mathbf{d}$, of the same dimensions *via*

$$\mathbf{d} = 0.5(1.0 - \boldsymbol{\rho}) \qquad (3.8.7)$$

or a distance-squared matrix,

$$\mathbf{D} = 0.25(1 - \boldsymbol{\rho})^2 \qquad (3.8.8)$$

for each entry i, j in $\mathbf{d}$, $0.0 \le d_{ij} \le 1.0$. A correlation coefficient of 1.0 translates to a distance of 0.0, a coefficient of −1.0 to 1.0, and zero to 0.5. There are other methods of generating a distance matrix from $\boldsymbol{\rho}$ (see, for example, Gordon, 1981, 1999), but we have found this to be both simple and as effective as any other.

For other purposes a dissimilarity matrix $\mathbf{s}$ is also needed, whose elements are defined *via*

$$s_{ij} = 1 - d_{ij}/d^{\max}, \qquad (3.8.9)$$

where $d^{\max}$ is the maximum distance in matrix $\mathbf{d}$. A dissimilarity matrix, $\boldsymbol{\delta}$, is also generated with elements

$$\delta_{ij} = d_{ij}/d_{ij}^{\max}. \qquad (3.8.10)$$

Table 3.8.1
Six commonly used clustering methods

For each method, the coefficients α_i, β and γ in equation (3.8.11) are given.

Method	α_i	β	γ
Single link	$\frac{1}{2}$	0	$-\frac{1}{2}$
Complete link	$\frac{1}{2}$	0	$\frac{1}{2}$
Average link	$n_i/(n_i + n_j)$	0	0
Weighted-average link	$\frac{1}{2}$	0	0
Centroid	$n_i/(n_i + n_j)$	$-n_in_j/(n_i + n_j)^2$	0
Sum of squares	$(n_i + n_k)/(n_i + n_j + n_k)$	$-n_k/(n_i + n_j + n_k)$	0

In some cases it can be advantageous to use $I^{1/2}$ in the distance-matrix generation; this can enhance the sensitivity of the clustering to weak peaks (Butler *et al.*, 2019).

3.8.3. Cluster analysis

Cluster analysis uses **d** (or **s**, or $\boldsymbol{\delta}$) to partition the patterns into groups based on the similarity of their diffraction profiles. Associated with cluster are a number of important ancillary techniques all of which will be discussed here. A flowchart of these methods is shown in Fig. 3.8.4.

3.8.3.1. *Dendrograms*

Using **d** and **s**, agglomerative, hierarchical cluster analysis is now carried out, in which the patterns are put into clusters as defined by their distances from each other. [Gordon (1981, 1999) and Everitt *et al.* (2001) provide excellent and detailed introductions to the subject. Note that the two editions of Gordon's monograph are quite distinct and complementary.] The method begins with a situation in which each pattern is considered to be in a separate cluster. It then searches for the two patterns with the shortest distance between then, and joins them into a single cluster. This continues in a stepwise fashion until all the patterns form a single cluster. When two clusters (C_i and C_j) are merged, there is the problem of defining the distance between the newly formed cluster $C_i \cup C_j$ and any other cluster C_k. There are a number of different ways of doing this, and each one gives rise to a different clustering of the patterns, although often the difference can be quite small. A general algorithm has been proposed by Lance & Williams (1967), and is summarized in a simplified form by Gordon (1981). The distance from the new cluster formed by merging C_i and C_j to any other cluster C_k is given by

$$\begin{aligned} d(C_i \cup C_j,\ C_k) &= \alpha_i d(C_i,\ C_k) + \alpha_j d(C_j,\ C_k) + \beta d(C_i,\ C_j) \\ &\quad + \gamma\left|d(C_i,\ C_k) - d(C_j,\ C_k)\right|. \end{aligned} \tag{3.8.11}$$

There are many possible clustering methods. Table 3.8.1 defines six commonly used clustering methods, defined in terms of the parameters α, β and γ. All these methods can be used with powder data; in general, the group-average-link or single-link formalism is the most effective, although differences between the methods are often slight.

The results of cluster analysis are usually displayed as a dendrogram, a typical example of which is shown in Fig. 3.8.6(a), where a set of 13 powder patterns is analysed using the centroid method. Each pattern begins at the bottom of the plot as a separate cluster, and these amalgamate in stepwise fashion linked by horizontal tie bars. The height of the tie bar represents a similarity measure as measured by the relevant distance. As an indication of the differences that can be expected in the various algorithms used for dendrogram generation, Fig. 3.8.6(e) shows the same data analysed using the single-link method: the resulting clustering is slightly different: the similarity measures are larger, and, in consequence, the tie bars are higher on the graph. [For further examples see Barr *et al.* (2004b,c) and Barr, Dong, Gilmore & Faber (2004).]

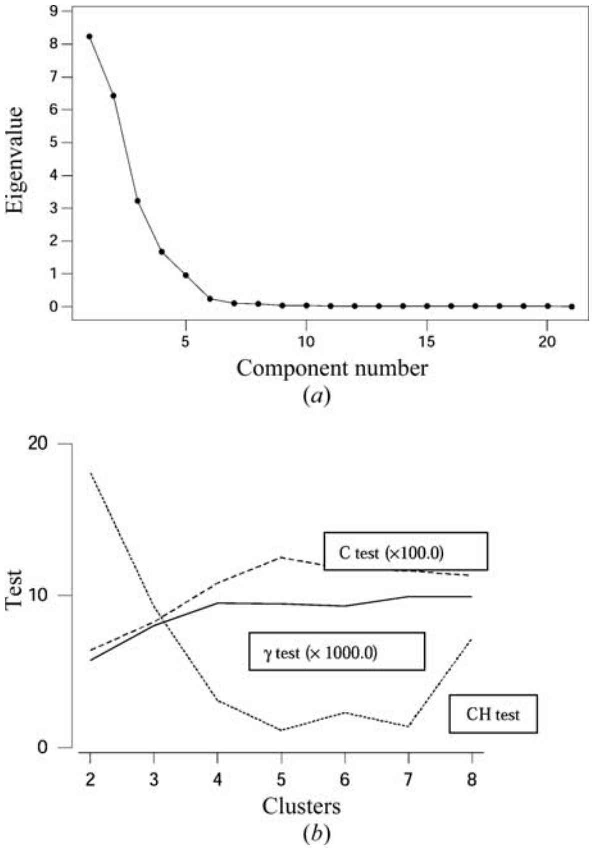

Figure 3.8.2
Four different methods of estimating the number of clusters present in a set of 23 powder patterns for the drug doxazosin. A total of five polymorphs are present, as well as two mixtures of these polymorphs. (a) A scree plot from the eigenvalue analysis of the correlation matrix; (b) the use of the C test (the coefficients have been multiplied by 100.0), which gives an estimate of five clusters using its local maximum. The γ test estimates that there are seven clusters and the CH test has a local maximum at seven clusters. Numerical details are given in Table 3.8.2.

3.8.3.2. *Estimating the number of clusters*

An estimate of the number of clusters present in the data set is needed. In terms of the dendrogram, this is equivalent to 'cutting the dendrogram' *i.e.* the placement of a horizontal line across it such that all the clusters as defined by tie lines above this line remain independent and unlinked. The estimation of the number of clusters is an unsolved problem in classification methods. It is easy to see why: the problem depends on how similar the patterns need to be in order to be classed as the same, and how much variability is allowed within a cluster. We use two approaches: (a) eigenvalue analysis of matrices $\boldsymbol{\rho}$ and **A**, and (b) those based on cluster analysis.

Eigenvalue analysis is a well used technique: the eigenvalues of the relevant matrix are sorted in descending order and when a fixed percentage (typically 95%) of the data variability has been accounted for, the number of eigenvalues is selected. This is shown graphically *via* a scree plot, an example of which is shown in Fig. 3.8.2.

We carry out eigenvalue analysis on the following:

(1) Matrix $\boldsymbol{\rho}$.

(2) Matrix **A**, as described in Section 3.8.3.3.

(3) A transformed form of $\boldsymbol{\rho}$ in which $\boldsymbol{\rho}$ is standardized to give $\boldsymbol{\rho}_s$ in which the rows and columns have zero mean and unit variance. The matrix $\boldsymbol{\rho}_s\boldsymbol{\rho}_s^T$ is then computed and subjected to eigenanalysis. It tends to give a lower estimate of cluster numbers than (1).

The most detailed study on cluster counting is that of Milligan & Cooper (1985), and is summarized by Gordon (1999). From this we have selected three tests that seem to operate effectively with powder data:

(4) The Calinški & Harabasz (1974) (CH) test:

$$\mathrm{CH}(c) = \left[B/(c-1)\right]/\left[W/(n-c)\right]. \tag{3.8.12}$$

A centroid is defined for each cluster. W denotes the total within-cluster sum of squared distances about the cluster centroids, and B is the total between-cluster sum of squared distances. Parameter c is the number of clusters chosen to maximize CH.

(5) A variant of Goodman & Kruskal's (1954) γ test, as described by Gordon (1999). The dissimilarity matrix is used. A comparison is made between all the within-cluster dissimilarities and all the between-cluster dissimilarities. Such a comparison is marked as concordant if the within-cluster dissimilarity is less than the between-cluster dissimilarity, and discrepant otherwise. Equalities, which are unusual, are disregarded. If S_+ is the number of concordant and S_- the number of discrepant comparisons, then

$$\gamma(c) = \left(S_+ - S_-\right)/\left(S_+ + S_-\right). \tag{3.8.13}$$

A maximum in γ is sought by an appropriate choice of cluster numbers.

(6) The C test (Milligan & Cooper, 1985). This chooses the value of c that minimizes

$$\mathrm{C}(c) = \left[W(c) - W_{\min}\right]/(W_{\max} - W_{\min}). \tag{3.8.14}$$

$W(c)$ is the sum of all the within-cluster dissimilarities. If the partition has a total of r such dissimilarities, then $W_{\min}$ is the sum of the r smallest dissimilarities and $W_{\max}$ is the sum of the r largest.

The results of tests (4)–(6) depend on the clustering method being used. To reduce the bias towards a given dendrogram method, these tests are carried out on four different clustering methods: the single-link, the group-average, the sum-of-squares and the complete-link methods. Thus there are 12 semi-independent estimates of the number of clusters from clustering methods, and three from eigenanalysis, making 15 in all.

A composite algorithm is used to combine these estimates. The maximum and minimum values of the number of clusters ($c_{\max}$ and $c_{\min}$, respectively) given by the eigenanalysis results [(1)–(3) above] define the primary search range; tests (4)–(6) are then used in the range $\min(c_{\max} + 3, n) \leq c \leq \max(c_{\min} - 3, 0)$ to find local maxima or minima as appropriate. The results are averaged, any outliers are removed, and a weighted mean value is taken of the remaining indicators, then this is used as the final estimate of the number of clusters. Confidence levels for c are also defined by the estimates of the maximum and minimum cluster numbers after any outliers have been removed.

A typical set of results for the PXRD data from 23 powder patterns for doxazosin (an anti-hypertension drug) in which five polymorphs are present, as well as two mixtures of polymorphs, is shown in Fig. 3.8.2(a) and (b) (see also Table 3.8.2). The scree plot arising from the eigenanalysis of the correlation matrix indicates that 95% of the variability can be accounted for by five components, and this is shown in Fig. 3.8.2(a). Eigenvalues from other matrices indicate that four clusters are appropriate. A search for local optima in the CH, γ and C tests is then initiated in the range 2–8 possible clusters. Four different clustering methods are tried, and the results indicate a range of 4–7 clusters. There are no outliers, and the final weighted mean value of 5 is calculated. As Fig. 3.8.2(b) shows, the optimum points for the C and γ tests are often quite weakly defined (Barr *et al.*, 2004*b*).

Table 3.8.2

Estimate of the number of clusters for the 23 sample data set for doxazosin

There are five polymorphs present, plus two mixtures of these polymorphs. The maximum estimate is 7; the minimum estimate is 4; the combined weighted estimate of the number of clusters is 6, and the median value is 5. The dendrogram cut level is set to give 5 clusters, and the lower and upper confidence limits are 4 and 7, respectively.

Method	No. of clusters
Principal-component analysis (non-transformed matrix)	5
Principal-component analysis (transformed matrix)	4
Multidimensional metric scaling	4
γ statistic using single linkage	7
CH statistic using single linkage	7
C statistic using single linkage	—
γ statistic using group averages	7
CH statistic using group averages	5
C statistic using group averages	—
γ statistic using sum of squares	—
CH statistic using sum of squares	5
C statistic using sum of squares	—
γ statistic using complete linkage	—
CH statistic using complete linkage	5
C statistic using complete linkage	—

3.8.3.3. *Metric multidimensional scaling*

This is, in its essentials, the particle-in-a-box problem. Each powder pattern is represented as a single sphere, and these spheres are placed in a cubic box of unit dimensions such that the positions of the spheres reproduce as closely as possible the distance matrix, **d**, generated from correlating the patterns. The spheres have an arbitrary orientation in the box.

To do this, the $(n \times n)$ distance matrix **d** is used in conjunction with metric multidimensional scaling (MMDS) to define a set of p underlying dimensions that yield a Euclidean distance matrix, $\mathbf{d}^{\mathrm{calc}}$, whose elements are equivalent to or closely approximate the elements of **d**.

The method works as follows (Cox & Cox, 2000; Gower, 1966; Gower & Dijksterhuis, 2004).

The matrix **d** has zero diagonal elements, and so is not positive semidefinite. A positive definite matrix, $\mathbf{A}(n \times n)$ can be constructed, however, by computing

$$\mathbf{A} = -\frac{1}{2}\left[\mathbf{I}_n - \frac{1}{n}\mathbf{i}_n\mathbf{i}_n'\right]\mathbf{D}\left[\mathbf{I}_n - \frac{1}{n}\mathbf{i}_n\mathbf{i}_n'\right], \tag{3.8.15}$$

where $\mathbf{I}_n$ is an $(n \times n)$ identity matrix, $\mathbf{i}_n$ is an $(n \times 1)$ vector of unities and **D** is defined in equation (3.8.8). The matrix $[\mathbf{I}_n - (1/n)\mathbf{i}_n\mathbf{i}_n']$ is called a centring matrix, since **A** has been derived from **D** by centring the rows and columns.

The eigenvectors $\mathbf{v}_1, \mathbf{v}_2, \ldots, \mathbf{v}_n$ and the corresponding eigenvalues $\lambda_1, \lambda_2, \ldots, \lambda_n$ are then obtained. A total of p eigenvalues of **A** are positive and the remaining $(n - p)$ will be zero. For the p

non-zero eigenvalues a set of coordinates can be defined *via* the matrix $\mathbf{X}(n \times p)$,

$$\mathbf{X} = \mathbf{V}\Lambda^{1/2}, \tag{3.8.16}$$

where $\boldsymbol{\Lambda}$ is the vector of eigenvalues.

If $p = 3$, then we are working in three dimensions, and the $\mathbf{X}(n \times 3)$ matrix can be used to plot each pattern as a single point in a 3D graph. This assumes that the dimensionality of the problem can be reduced in this way while still retaining the essential features of the data. As a check, a distance matrix $\mathbf{d}^{\rm calc}$ can be calculated from $\mathbf{X}(n \times 3)$ and correlated with the observed matrix $\mathbf{d}$ using both the Pearson and Spearman correlation coefficients. In general the MMDS method works well, and correlation coefficients greater than 0.95 are common. For large data sets this can reduce to ~0.7, which is still sufficiently high to suggest the viability of the procedure. Parallel coordinates based on the MMDS analysis can also be used, and this is discussed in Sections 3.8.4.2.1 and 3.8.4.2.2.

There are occasions in which the underlying dimensionality of the data is 1 or 2, and in these circumstances the data project onto a plane or a line in an obvious way without any problems.

An example of an MMDS plot is shown in Fig. 3.8.6(*b*), which is linked to the dendrogram in Fig. 3.8.6(*a*).

3.8.3.4. *Principal-component analysis*

It is also possible to carry out principal-component analysis (PCA) on the correlation matrix. The eigenvalues of the correlation matrix can be used to estimate the number of clusters present *via* a scree plot, as shown in Fig. 3.8.2(*a*), and the eigenvectors can be used to generate a score plot, which is an $\mathbf{X}(n \times 3)$ matrix and can be used as a visualization tool in exactly the same way as the MMDS method to indicate which patterns belong to which class. Score plots traditionally use two components with the data thus projected on to a plane; we use 3D plots in which three components are represented. In general, we find that the MMDS representation of the data is nearly always superior to the PCA analysis for powder and spectroscopic data.

3.8.3.5. *Choice of clustering method*

It is possible to use the MMDS plot (or, alternatively, PCA score plots) to assist in the choice of clustering method, since the two methods operate semi-independently. The philosophy here is to choose a technique that results in the tightest, most isolated clusters as follows:

1. The MMDS formalism is used to derive a set of three-dimensional coordinates stored in matrix $\mathbf{X}(n \times 3)$.
2. The number of clusters, c, is estimated as described in Section 3.8.3.2.
3. Each of six dendrogram methods (see Table 3.8.1) is employed in turn, stopping when c clusters have been generated. Each entry in $\mathbf{X}$ can now be assigned to a cluster.
4. A sphere is drawn around each point in $\mathbf{X}$ and the average between-cluster overlap of the spheres is calculated for each of the N clusters C_1 to C_N. If the total number of overlaps is m, this can be written as

$$S = \sum_{i=1}^{n} \sum_{\substack{j=1,n \\ j\neq i}}^{n} \left(\int_V s_{i\in C_i} s_{j\in C_j} \,{\rm d}s \right) \Big/ m. \tag{3.8.17}$$

If the clusters are well defined then S should be a minimum. Conversely, poorly defined clusters will tend to have large values of S. In the algorithm used in *PolySNAP* (Barr, Dong & Gilmore, 2009) and *DIFFRAC.EVA* (Bruker, 2018), the sphere size depends on the number of diffraction patterns.

5. The tightness of each cluster is also estimated by computing the mean within-cluster distance. This should also be a minimum for well defined, tight clusters.
6. The mean within-cluster distance from the centroid of the cluster can also be computed, which should also be a minimum.
7. Steps (4)–(6) are repeated using coordinates derived from PCA 3D score plots.
8. Tests (4)–(7) are combined in a weighted, suitably scaled mean to give an overall figure of merit (FOM); the minimum is used to select which dendrogram method to use (Barr *et al.*, 2004*b*).

3.8.3.6. *The most representative sample*

Similar techniques can be used to identify the most representative sample in a cluster. This is defined as the sample that has the minimum mean distance from every other sample in the clusters, *i.e.* for cluster J containing m patterns, the most representative sample, i, is defined as that which gives

$$\min\left(\sum_{\substack{j=1 \\ i,j\in J}}^{m} d(i,j)/m \right). \tag{3.8.18}$$

The most representative sample is useful in visualization and can, with care, be used to create a database of known phases (Barr *et al.*, 2004*b*).

3.8.3.7. *Amorphous samples*

Amorphous samples are an inevitable consequence of high-throughput experiments, and need to be handled correctly if they are not to lead to erroneous indications of clustering. To identify amorphous samples the total background for each pattern is estimated and its intensity integrated; the integrated intensity of the non-background signal is then calculated. If the ratio falls below a preset limit (usually 5%, but this may vary with the type of samples under study) the sample is treated as amorphous. The distance matrix is then modified so that each amorphous sample is given a distance and dissimilarity of 1.0 from every other sample, and a correlation coefficient of zero. This automatically excludes the samples from the clustering until the last amalgamation steps, and also limits their effect on the estimation of the number of clusters (Barr *et al.*, 2004*b*). Of course, the question of amorphous samples is not a binary (yes/no) one: there are usually varying degrees of amorphous content, which further complicates matters.

3.8.4. Data visualization

3.8.4.1. *Primary data visualization*

It is important when dealing with large data sets to have suitable visualization tools. These tools are also a valuable resource for exploring smaller data sets. This methodology provides four primary aids:

1. A pie chart is produced for each sample, corresponding to the sample wells used in the data-collection process, in which each well is given a colour as defined by the dendrogram. If mixtures of known phases are detected, the pie charts give the relative proportions of the pure samples as estimated by quantitative analysis (see Section 3.8.7).

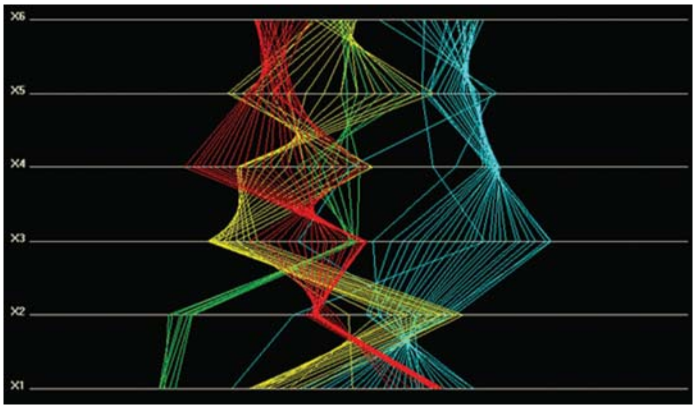

Figure 3.8.3
Example of a parallel-coordinates plot in six dimensions, with axes labeled X1, X2, . . . , X6, for a set of 80 organic PXRD samples partitioned into four clusters. The plot shows that the clustering looks realistic and that it is maintained when the data are examined in six dimensions.

(2) The dendrogram gives the clusters, the degree of association within the clusters and the differential between a given cluster and its neighbours. Different colours are used to distinguish each cluster. The cut line is also drawn along with the associated confidence levels. The dendrogram is the primary visualization tool.

(3) The MMDS method reproduces the data as a 3D plot in which each point represents a single powder pattern. The colour for each point is taken from the dendrogram. The most representative sample for each cluster is marked with a cross.

(4) Similarly, the eigenvalues from principal-component analysis can be used to generate a 3D score plot in which each point also represents a powder pattern. Just as in the MMDS formalism, the colour for each point is taken from the dendrogram, and the most representative sample is marked with a cross.

These aids give graphical views of the data that are semi-independent and thus can be used to check for consistency and discrepancies in the clustering. They are also interactive. No one method is optimal, and a combination of mathematical and visualization techniques is required, techniques that often need tuning for each individual application (Barr, Cunningham *et al.*, 2009; Barr, Dong & Gilmore, 2009).

3.8.4.2. *Secondary visualization using parallel coordinates, the grand tour and minimum spanning trees*

In the MMDS and PCA methods $p = 3$ [equation (3.8.16)] to work in three dimensions; the **X** matrix can then be used to plot each pattern as a single point in a 3D graph. However, this has reduced the dimensionality of the data to three, and the question arises as to the validity of this: are three dimensions sufficient? The use of parallel-coordinates plots coupled with the grand tour can assist here as well as giving us an alternative view of the data.

3.8.4.2.1. *Parallel-coordinates plots*

A parallel-coordinates plot is a graphical data-analysis technique for plotting multivariate data. Usually orthogonal axes are used when doing this, but in parallel-coordinates plots orthogonality is abandoned and replaced with a set of N equidistant parallel axes, one for each variable and labelled X1, X2, X3, . . . , XN (Inselberg, 1985, 2009; Wegman, 1990). Each data point is plotted on each axis and the points are joined *via* a line connecting each data point. The data now become a set of lines. The lines are given the colours of the cluster to which they belong as defined by the current dendrogram. A parallel-coordinates display can be interpreted as a generalization of a two-dimensional scatterplot, and it allows the display of an arbitrary number of dimensions. The method can also be used to validate the clustering itself without using dendrograms. Using this technique it is possible to determine whether the clustering shown by the MMDS (or PCA) plot in three dimensions continues in higher dimensions.

Fig. 3.8.3 shows a typical example for a set of 80 organic samples partitioned into four clusters (Barr, Dong & Gilmore, 2009). The plot shows that the clustering looks realistic when

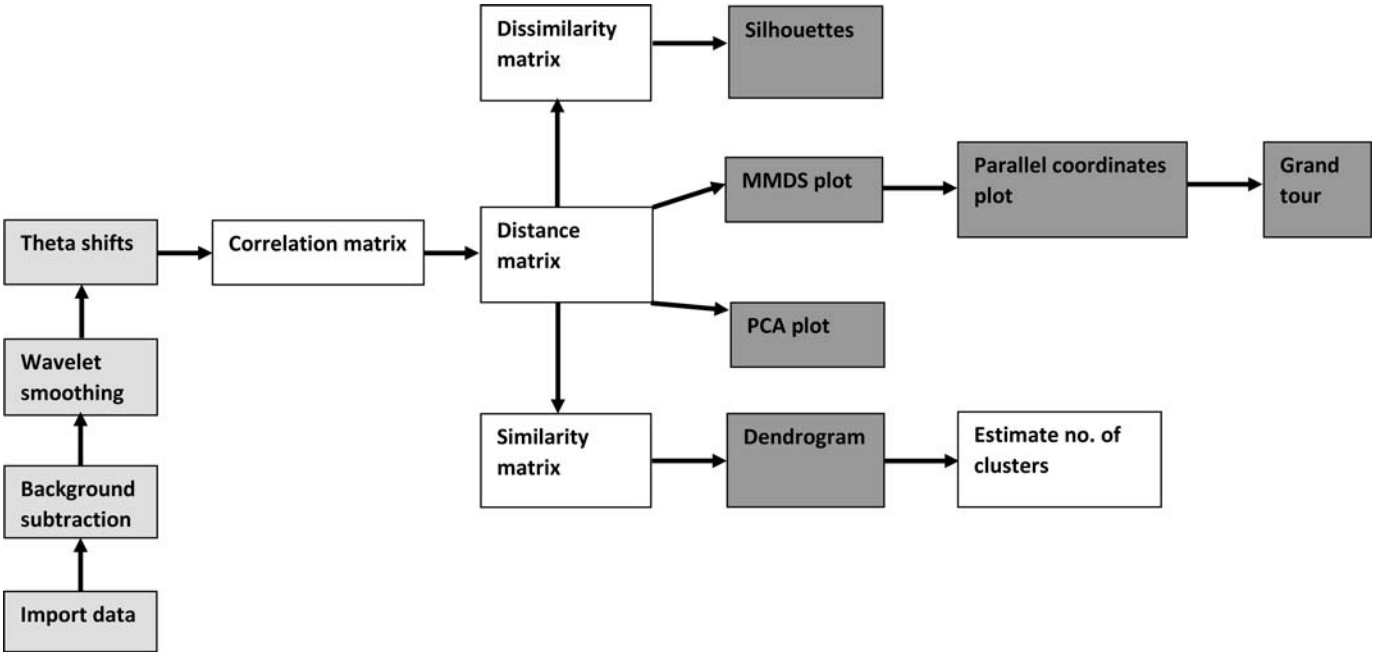

Figure 3.8.4
Flowchart for the cluster-analysis and data-visualization procedure described in this chapter. The light grey boxes denote data-visualization elements and the dark grey objects are optional data pre-processing operations.

viewed in this way and that it is maintained when the data are examined in six dimensions.

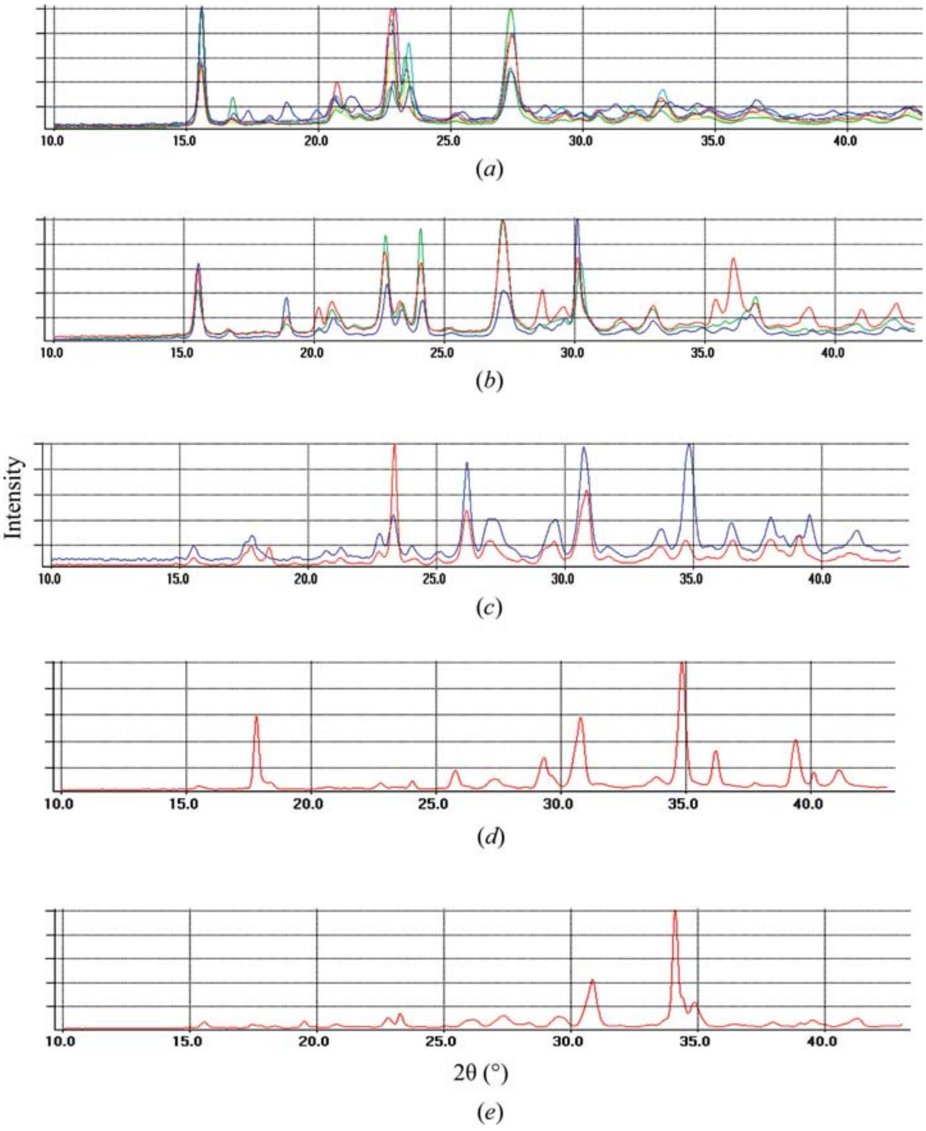

Figure 3.8.5

Powder patterns for 13 commercial aspirin samples partitioned into five sets. The patterns are in highly correlated sets: (*a*) comprises patterns 1, 3, 5, 6, 9 and 12; (*b*) comprises patterns 10, 11 and 13; (*c*) contains patterns 2 and 4; (*d*) contains pattern 7 and (*e*) contains pattern 8.

3.8.4.2.2. *The grand tour*

The grand tour is a method of animating the parallel-coordinates plot to examine it from all possible viewpoints. Consider a 3D data plot using orthogonal axes: a grand tour takes 2D sections through these data and displays them in parallel-coordinates plots in a way that explores the entire space in a continuous way. The former is important, because the data can be seen from all points of view, and the latter allows the user the follow the data without abrupt discontinuities. This concept was devised by Asimov (1985) and further developed by Wegman (1990). In more than three dimensions it becomes a generalized rotation of all the coordinate axes. A *d*-dimensional tour is a continuous geometric transformation of a *d*-dimensional coordinate system such that all possible orientations of the coordinate axes are eventually achieved. The algorithm for generating a smooth and complete view of the data is described by Asimov (1985).

To do this, the restriction of $p = 3$ in the MMDS calculation is relaxed to 6, so that there is now a 6D data set with six orthogonal axes. The choice of six is somewhat arbitrary – more can be used, but six is sufficient to see whether the clustering is maintained without generating unduly complex plots and requiring extensive computing resources. The data are plotted as a parallel-coordinates plot. The grand-tour method is then applied by a continuous geometric transformation of the 6D coordinate system such that all possible orientations of the axes are achieved. Each orientation is reproduced as a parallel-coordinates plot using six axes.

Figs. 3.8.9(*j*) and (*k*) show an example from the clustering of the 13 aspirin samples using PXRD data. Fig. 3.8.9(*j*) shows the default parallel-coordinates plot. Fig. 3.8.9(*k*) shows alternative views of the data taken from the grand tour. In Fig. 3.8.9(*j*) there appears to be considerable overlap between clusters in the 4th, 5th and 6th dimensions (X4, X5 and X6), but the alternative view given in Fig. 3.8.9(*k*) show that the clustering is actually well defined in all six dimensions (Barr, Dong & Gilmore, 2009).

3.8.4.2.3. *Powder data as a tree: the minimum spanning trees*

The minimum spanning tree (MST) displays the MMDS plot as a tree whose points are the data from the MMDS calculation (in three dimensions) and whose weights are the distances between these points. The minimum-spanning-tree problem is that of joining the points with a minimum total edge weight. (As an example, airlines use minimum spanning trees to work out their basic route systems: the best set of routes taking into account airport hubs, passenger numbers, fuel costs *etc.* is the minimum spanning tree.) Because a tree is used, each point is only allowed a maximum of three connections to other points.

To do this Kruskal's (1956) algorithm can be used, in which the lowest weight edge is always added to see if it builds a spanning tree; if so, it is added or otherwise discarded. This process continues until the tree is constructed. An example is shown in Figs. 3.8.7 for the 13-sample aspirin data. A complete tree for this data set using three dimensions and the MMDS-derived coordinates is shown in Fig. 3.8.7(*a*). This has 12 links between the 13 data points. Reducing the number of links to 10 gives Fig. 3.8.7(*b*).

3.8.5. Further validating and visualizing clusters: silhouettes and fuzzy clustering

Other techniques exist to validate the clusters, and these are discussed here.

3.8.5.1. *Silhouettes*

Silhouettes (Rousseeuw, 1987; Kaufman & Rousseeuw, 1990) are a property of every member of a cluster and define a coef-

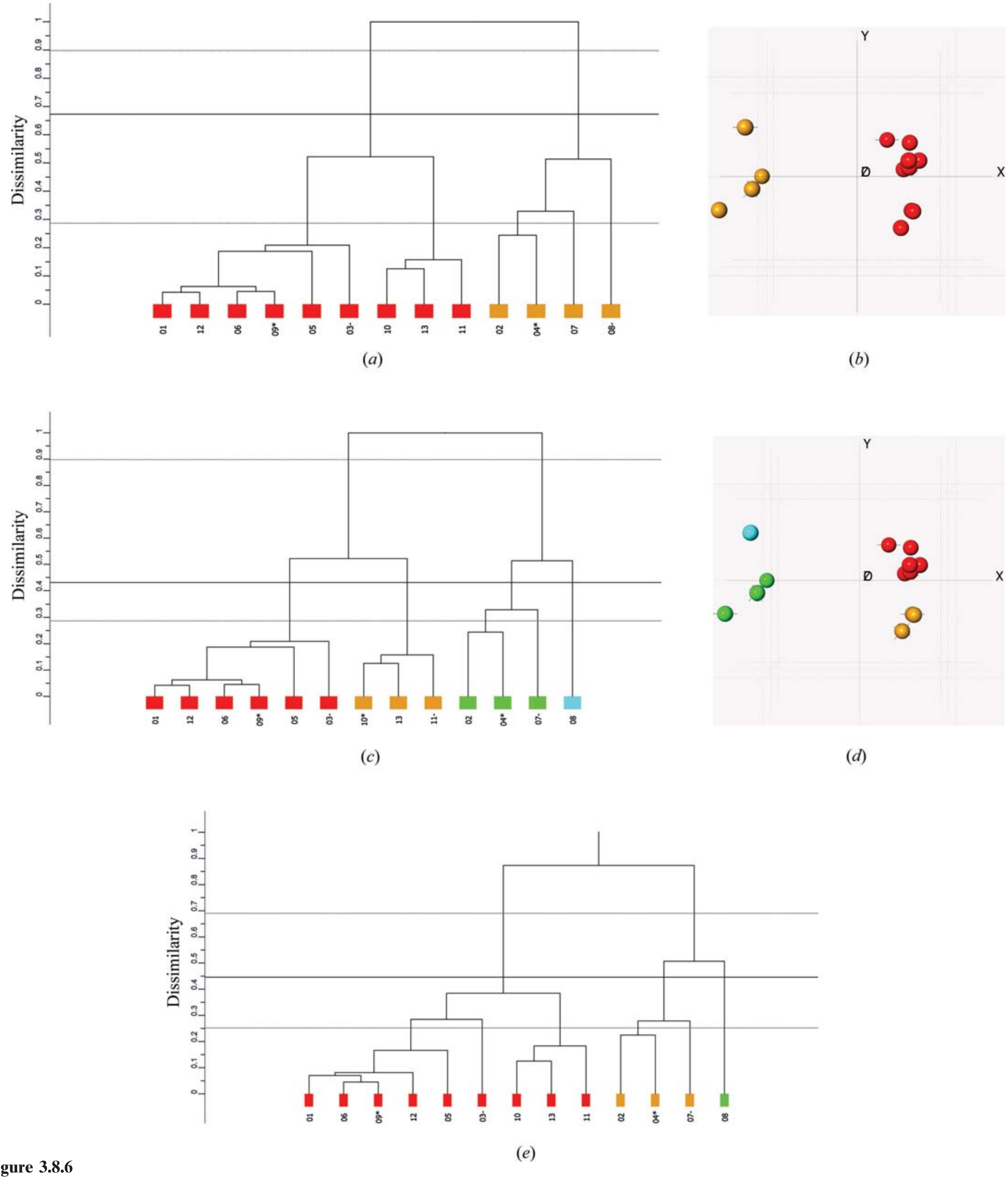

Figure 3.8.6
(*a*) The initial default dendrogram using the centroid clustering method on 13 PXRD patterns from 13 commercial aspirin samples. (*b*) The corresponding MMDS plot. It can be seen that both clusters have a natural break in them and should be partitioned into two clusters. (*c*) The dendrogram cut line is reduced. (*d*) The corresponding MMDS plot. The red cluster is now partitioned into two; the remaining patterns are a light-blue singleton and a green triplet cluster. (*e*) The default dendrogram using the single-link method.

ficient of cluster membership. To compute them, the dissimilarity matrix, $\boldsymbol{\delta}$, is used. If the pattern i belongs to cluster C_r which contains n_r patterns, we define

$$a_i = \sum_{\substack{j\in C_r\\ j\neq i}} \delta_{ij}/(n_r - 1). \tag{3.8.19}$$

This defines the average dissimilarity of pattern i to all the other patterns in cluster C_r. Further define

$$b_i = \min_{s\neq r}\left\{\sum_{j\in C_s} \delta_{ij}/n_s\right\}. \tag{3.8.20}$$

The silhouette for pattern i is then

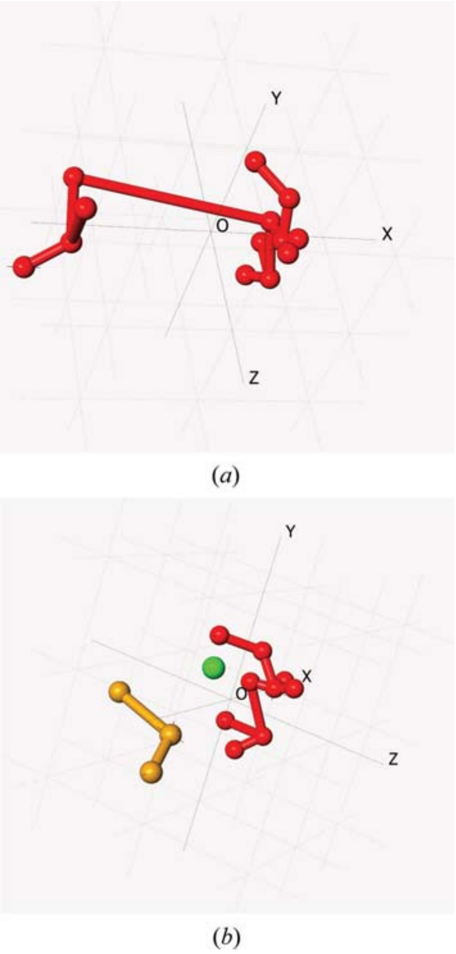

(*a*)

(*b*)

Figure 3.8.7
The use of minimum spanning trees (MSTs). (*a*) The MST with 12 links. (*b*) The MST with 10 links; three clusters are now present.

$$h_i = \frac{b_i - a_i}{\max(a_i,\ b_i)}. \qquad (3.8.21)$$

Clearly $-1 \le h_i \le 1.0$. It is not possible to define silhouettes for clusters with only one member (singleton clusters). Silhouettes are displayed such that each cluster is represented as a histogram of frequency plotted against silhouette values so that one can look for outliers or poorly connected plots.

From our experience with powder data collected in reflection mode on both organic and inorganic samples (Barr *et al.*, 2004*b*), we conclude that for any given pattern

(1) $h_i > 0.5$ implies that pattern i is probably correctly classified;
(2) $0.2 < h_i < 0.5$ implies that pattern i should be inspected, since it may belong to a different or new cluster;
(3) $h_i < 0.2$ implies that pattern i belongs to a different or new cluster.

The use of silhouettes in defining the details of the clustering is shown for the aspirin data in Fig. 3.8.8. The silhouettes for the red cluster corresponding to the dendrogram in Fig. 3.8.6(*a*) are shown in Fig. 3.8.8(*a*) and those for the corresponding orange cluster are shown in Fig. 3.8.8(*b*). Both sets of silhouettes have values < 0.5, which indicates that the clustering is not optimally defined. When the cut line is moved to give the dendrogram in Fig. 3.8.6(*c*), the silhouettes for the red cluster are shown in Fig. 3.8.8(*c*). The entry centred on a silhouette value of 0.15 is pattern 3. This implies that pattern 3 is only loosely connected to the cluster and this is demonstrated in Fig. 3.8.8(*d*) where pattern 3 and the most representative pattern for the cluster (No. 9) are superimposed. Although there is a general sense of similarity there are significant differences and the combined correlation coefficient is only 0.62. In Fig. 3.8.8(*e*), the silhouettes for the orange cluster are shown. They imply that this is a single cluster without outliers. The silhouettes for the green cluster corresponding to the dendrogram in Fig. 3.8.6(*c*) are shown in Fig. 3.8.8(*f*). The clustering is poorly defined here.

3.8.5.2. *Fuzzy clustering*

In standard clustering methods a set of n diffraction patterns are partitioned into c disjoint clusters. Cluster membership is defined *via* a membership matrix $\mathbf{U}(n \times c)$, where individual coefficients, u_{ik}, represent the membership of pattern i of cluster k. The coefficients are equal to unity if i belongs to c and zero otherwise, *i.e.*

$$u_{ik} \in [0, 1] \quad (i = 1, \ldots, n;\ k = 1, \ldots, c). \qquad (3.8.22)$$

If these constraints are relaxed, such that

$$0 \le u_{ik} \le 1 \quad (i = 1, \ldots, n;\ k = 1, \ldots, c), \qquad (3.8.23)$$

$$0 < \sum_{i=1}^{n} u_{ik} < n \quad (k = 1, \ldots, c) \qquad (3.8.24)$$

and

$$\sum_{k=1}^{c} u_{ik} = 1, \qquad (3.8.25)$$

then fuzzy clusters are generated, in which there is the possibility that a pattern can belong to more than one cluster (see, for example, Everitt *et al.*, 2001; Sato *et al.*, 1966). Such a situation is quite feasible in the case of powder diffraction, for example, when mixtures can be involved. It is described in detail by Barr *et al.* (2004*b*).

3.8.5.3. *The PolySNAP program and DIFFRAC.EVA*

All these techniques have been incorporated into the *PolySNAP* computer program (Barr *et al.*, 2004*a*,*b*,*c*; Barr, Dong, Gilmore & Faber, 2004; Barr, Dong & Gilmore, 2009), which was developed from the *SNAP-D* software (Barr, Gilmore & Paisley, 2004). *PolySNAP* has subsequently been incorporated into the Bruker *DIFFRAC.EVA* program (Bruker, 2018), and the following sections are based on its use.

3.8.6. Examples

All the elements for clustering and visualization are now in place. Fig. 3.8.4 shows this as a flowchart. Hitherto we have looked at elements of the aspirin data to demonstrate how methods work; we now examine the aspirin data in detail as a single analysis.

3.8.6.1. *Aspirin data*

In this example we use 13 powder patterns from commercial aspirin samples collected in reflection mode on a Bruker D8 diffractometer. Since these samples include fillers, the active pharmaceutical ingredient (API) and other formulations, it is not surprising that peak widths are high: ~0.5° full width at half maximum (FWHM). The data-collection range was 10–43° in 2θ using Cu $K\alpha$ radiation. The 13 powder data sets are shown in Fig. 3.8.5 arranged into groups based on similarity. We have already described the methods of analysis and have shown typical results in Figs. 3.8.6 to 3.8.8, and now present detailed examples. The correlation matrix derived from equation (3.8.3) is shown in Fig.

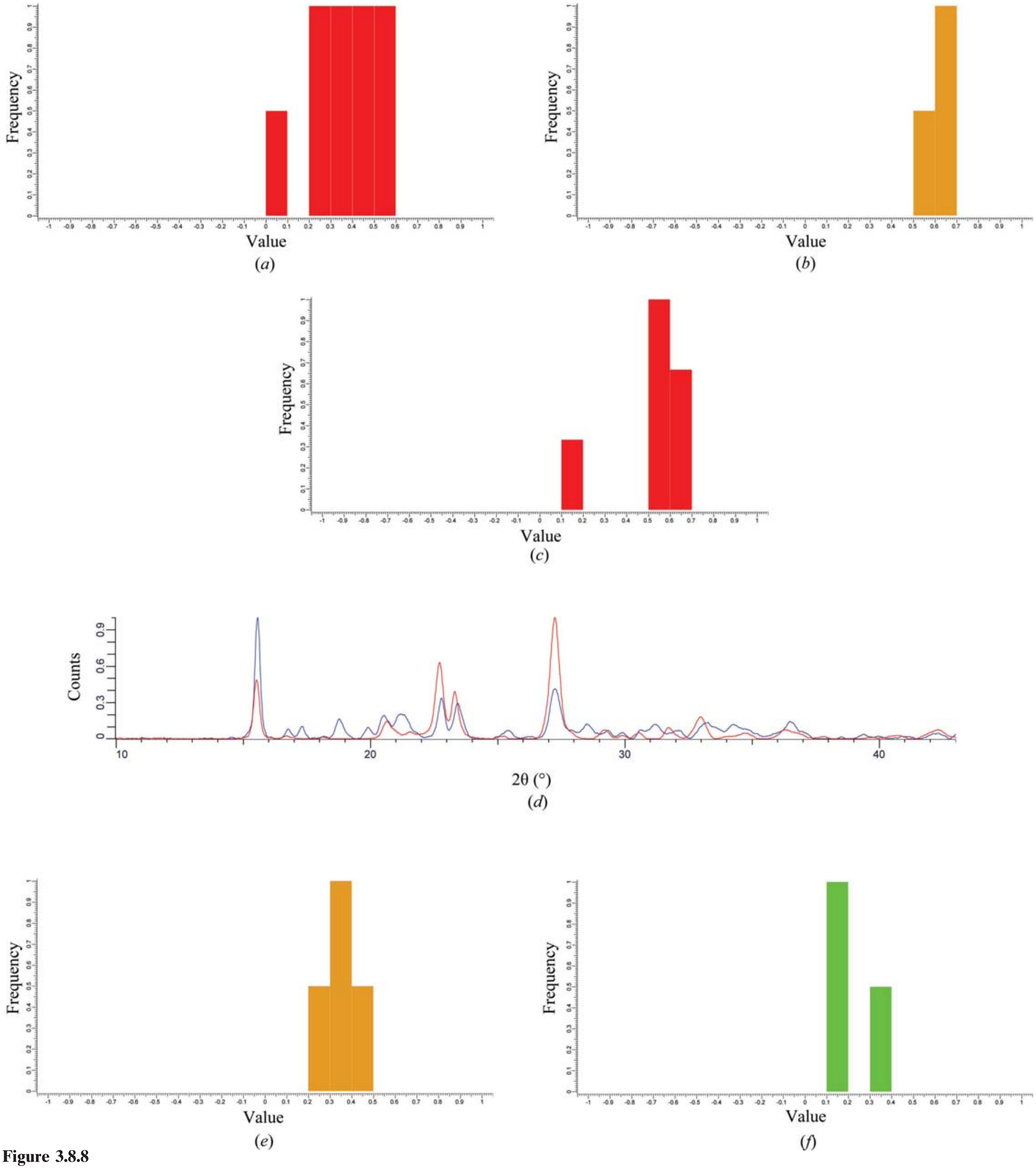

Figure 3.8.8
The use of silhouettes in defining the details of the clustering. (*a*) The silhouettes for the red cluster in the dendrogram from Fig. 3.8.6(*a*). (*b*) The corresponding orange cluster. Both sets of silhouettes have values that are less than 0.5, which indicates that the clustering is not well defined. (*c*) The silhouettes for the red cluster corresponding to the dendrogram in Fig. 3.8.6(*c*). The entry centred on a silhouette value of 0.15 is pattern 3. This implies that pattern 3 is only loosely connected to the cluster and this is demonstrated in part (*d*), where pattern 3 and the most representative pattern for the cluster (No. 9) are superimposed. Although there is a general sense of similarity there are significant differences and the combined correlation coefficient is only 0.62. (*e*) The silhouettes for the orange cluster corresponding to the dendrogram in Fig. 3.8.6(*c*). The silhouettes imply that this is a single cluster without outliers. (*f*) The silhouettes for the green cluster corresponding to the dendrogram in Fig. 3.8.6(*c*). The clustering is poorly defined here.

3.8.9(*a*), colour coded to reflect the values of the coefficients; the darker the shade, the higher the correlation. The resulting dendrogram and MMDS plot are shown in Figs. 3.8.9(*b*) and (*c*), respectively. Four clusters are identified in the dendrogram and these have been appropriately coloured. Other visualization tools are now shown. In Fig. 3.8.9(*d*) the pie chart is displayed; the number of rows can be adjusted to reflect the arrangement of the samples in a multiple sample holder. Fig. 3.8.9(*e*) shows the default minimum spanning tree with 12 links. In Fig. 3.8.9(*f*) the scree plot indicates that three clusters will account for more than 95% of the data variability. The steep initial slope is a clear indication of good cluster estimation. The silhouettes are shown in Fig. 3.8.9(*g*–*i*). These were discussed in Section 3.8.5.1. In Fig. 3.8.9(*j*) the default parallel-coordinates plot for the same data is shown, and in Fig. 3.8.9(*k*) there is another view taken from the grand tour. These two plots validate the clustering and also indicate that there is no significant error introduced into the MMDS plot by truncating it into three dimensions.

3.8.6.1.1. *Aspirin data with amorphous samples included*

As a demonstration of the handling of data from amorphous samples, five patterns for amorphous samples were included in the aspirin data and the clustering calculation was repeated. The results are shown in Fig. 3.8.10. Fig. 3.8.10(*a*) shows the dendrogram. It can be seen that the amorphous samples are positioned as isolated clusters on the right-hand end. They also appear as an isolated cluster in the MMDS plot and the parallel-coordinates plots, as shown in Figs. 3.8.10(*b*) and (*c*). It could be argued that these samples should be treated as a single, five-membered cluster rather than five individuals, but we have found that this confuses the clustering algorithms, and it is clearer to the user if the data from amorphous samples are presented as separate classes.

3.8.6.2. *Phase transitions in ammonium nitrate*

Ammonium nitrate exhibits temperature-induced phase transformations. Between 256 and 305 K it crystallizes in the orthorhombic space group *Pmmm* with $a = 5.745$, $b = 5.438$, $c = 4.942$ Å and $Z = 2$; from 305 to 357 K it crystallizes in *Pbnm* with

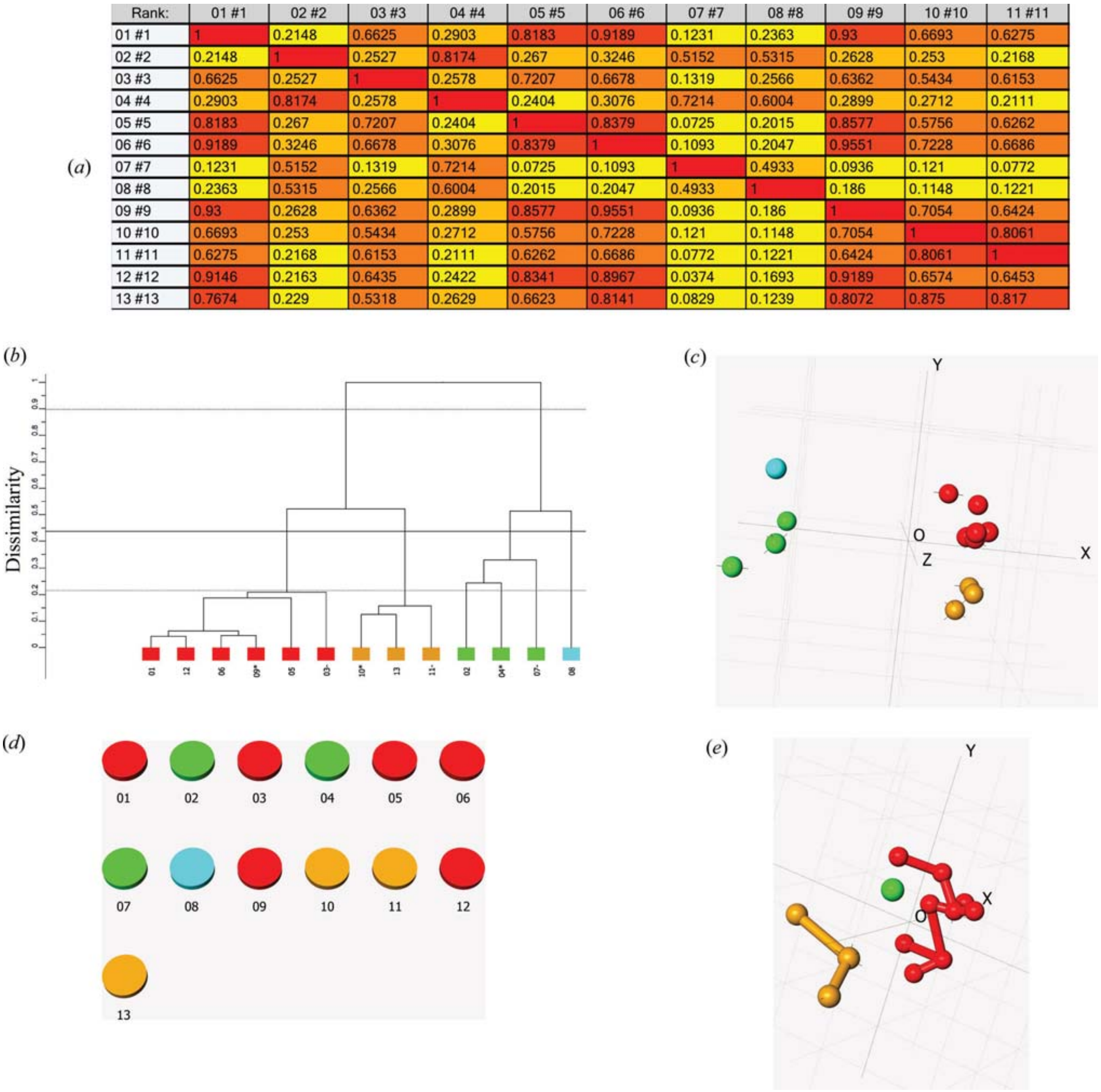

Rank:	01 #1	02 #2	03 #3	04 #4	05 #5	06 #6	07 #7	08 #8	09 #9	10 #10	11 #11
01 #1	1	0.2148	0.6625	0.2903	0.8183	0.9189	0.1231	0.2363	0.93	0.6693	0.6275
02 #2	0.2148	1	0.2527	0.8174	0.267	0.3246	0.5152	0.5315	0.2628	0.253	0.2168
03 #3	0.6625	0.2527	1	0.2578	0.7207	0.6678	0.1319	0.2566	0.6362	0.5434	0.6153
04 #4	0.2903	0.8174	0.2578	1	0.2404	0.3076	0.7214	0.6004	0.2899	0.2712	0.2111
05 #5	0.8183	0.267	0.7207	0.2404	1	0.8379	0.0725	0.2015	0.8577	0.5756	0.6262
06 #6	0.9189	0.3246	0.6678	0.3076	0.8379	1	0.1093	0.2047	0.9551	0.7228	0.6686
07 #7	0.1231	0.5152	0.1319	0.7214	0.0725	0.1093	1	0.4933	0.0936	0.121	0.0772
08 #8	0.2363	0.5315	0.2566	0.6004	0.2015	0.2047	0.4933	1	0.186	0.1148	0.1221
09 #9	0.93	0.2628	0.6362	0.2899	0.8577	0.9551	0.0936	0.186	1	0.7054	0.6424
10 #10	0.6693	0.253	0.5434	0.2712	0.5756	0.7228	0.121	0.1148	0.7054	1	0.8061
11 #11	0.6275	0.2168	0.6153	0.2111	0.6262	0.6686	0.0772	0.1221	0.6424	0.8061	1
12 #12	0.9146	0.2163	0.6435	0.2422	0.8341	0.8967	0.0374	0.1693	0.9189	0.6574	0.6453
13 #13	0.7674	0.229	0.5318	0.2629	0.6623	0.8141	0.0829	0.1239	0.8072	0.875	0.817

Figure 3.8.9
The complete cluster analysis for the aspirin samples. (*a*) The correlation matrix, which is the source of all the clustering results. The entries are colour coded: the darker the shade, the higher the correlation. (*b*) The dendrogram. The colours assigned to the samples are used in all the visualization tools. (*c*) The corresponding MMDS plot. The clustering defined by the dendrogram is well defined. (*d*) The pie-chart view. (*e*) The minimum spanning tree.

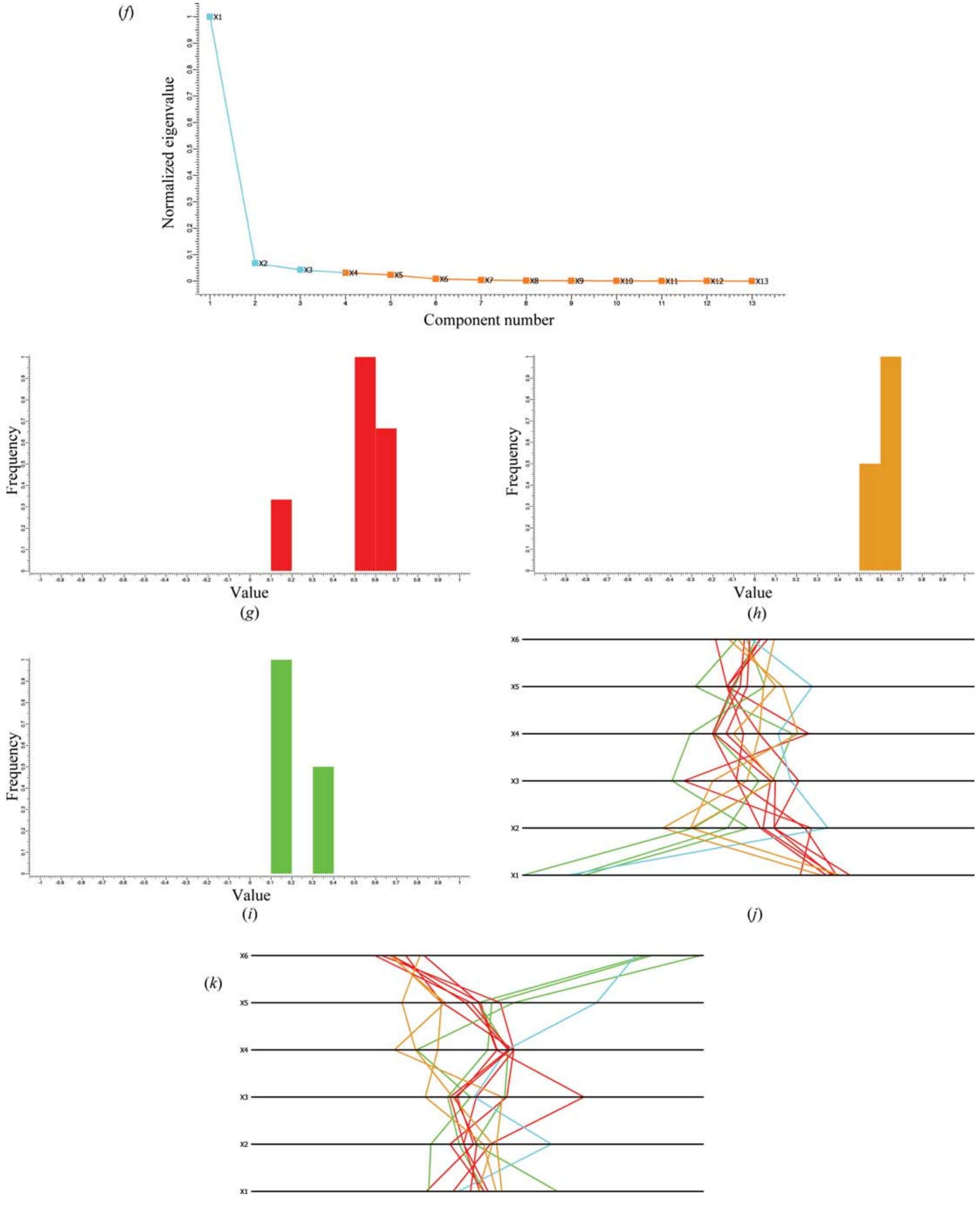

Figure 3.8.9 (continued)
The complete cluster analysis for the aspirin samples (continued). (*f*) The scree plot. It indicates that three clusters explain 95% of the variance of the distance matrix derived from (*a*). (*g–i*) The silhouettes for the red, the orange and the green clusters, respectively. These are discussed in detail in the caption to Fig. 3.8.8. (*j*) The default parallel-coordinates plot. The clusters are well maintained into the 4th, 5th and 6th dimensions. (*k*) Another view of the parallel coordinates using the grand tour. The clustering remains well maintained in higher dimensions.

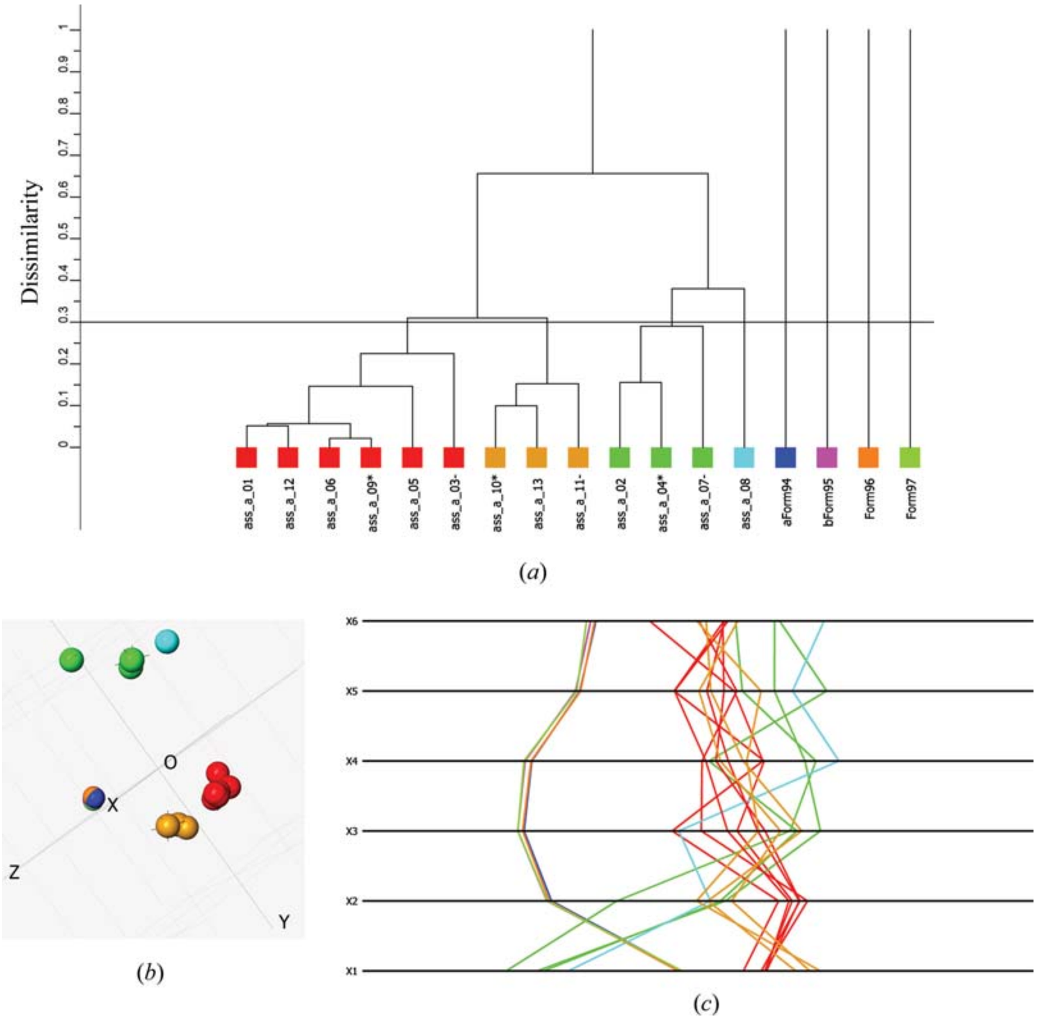

Figure 3.8.10
The aspirin data including data from five amorphous samples. (*a*) The resulting dendrogram and (*b*) the corresponding MMDS plot. (*c*) The parallel-coordinates plot.

$a = 7.14$, $b = 7.65$, $c = 5.83$ Å with $Z = 4$; between 357 and 398 K it crystallizes in the tetragonal space group $P\overline{4}2_1m$ with $a = 5.719$, $c = 4.932$ Å, $Z = 2$, and above 398 K it transforms to the cubic space group $Pm\overline{3}m$ with $a = 4.40$ Å and $Z = 1$. PXRD data containing 75 powder patterns taken at intervals of 3 K starting at 203 K using a D5000 Siemens diffractometer and Cu $K\alpha$ radiation with a 2θ range of 10–100° were used (Herrmann & Engel, 1997). Fig. 3.8.11(*a*) shows the data in the 2θ range 17–45°.

The visualization of these data following cluster analysis is shown in Fig. 3.8.11(*b*) using an MMDS plot on which has been superimposed a line showing the route followed by the temperature increments. The purple line follows the transition from a mixture of forms IV and V at low temperature (red) through form IV (yellow), form II (blue) and finally form I at high temperature (green). This is an elegant and concise representation of the data in a single diagram.

3.8.7. Quantitative analysis with high-throughput PXRD data without Rietveld refinement

Since mixtures are so common in high-throughput experiments, and indeed in many situations with multiple data sets, it is useful to have a method of automatic quantitative analysis. The quality of data that results from high-throughput crystallography makes it unlikely that an accuracy better than 5–10% can be achieved but, nonetheless, the identification of mixtures can be carried out by whole-profile matching. First a database of N pure phases is created, or, if that is not possible, then the most representative patterns with appropriate safeguards can be used. Assume that there is a sample pattern, S, which is considered to be a mixture of up to N components. S comprises m data points, $S_1, S_2, \ldots, S_m$. The N patterns can be considered to make up fractions $p_1, p_2, p_3, \ldots, p_N$ of the sample pattern. The best possible combination of the database patterns to fit the sample pattern is required. A system of linear equations can be constructed in which x_{11} is measurement point 1 of pattern 1 *etc.*:

$$\begin{aligned} x_{11}p_1 + x_{12}p_2 + x_{13}p_3 + \ldots + x_{1N}p_N &= S_1, \\ x_{21}p_1 + x_{22}p_2 + x_{23}p_3 + \ldots + x_{2N}p_N &= S_2, \\ &\vdots \\ x_{m1}p_1 + x_{m2}p_2 + x_{m3}p_3 + \ldots + x_{mN}p_N &= S_m. \end{aligned} \tag{3.8.26}$$

Writing these in matrix form, we get

$$\begin{bmatrix} x_{11} & x_{12} & x_{13} & \ldots & x_{1N} \\ x_{21} & x_{22} & x_{23} & \ldots & x_{2N} \\ \vdots & \vdots & \vdots & \ddots & \vdots \\ x_{m1} & x_{m2} & x_{m3} & \ldots & x_{mN} \end{bmatrix} \begin{bmatrix} p_1 \\ p_2 \\ \vdots \\ p_N \end{bmatrix} = \begin{bmatrix} S_1 \\ S_2 \\ \vdots \\ S_N \end{bmatrix} \tag{3.8.27}$$

or

$$\mathbf{xp} = \mathbf{S}. \tag{3.8.28}$$

A solution for S that minimizes

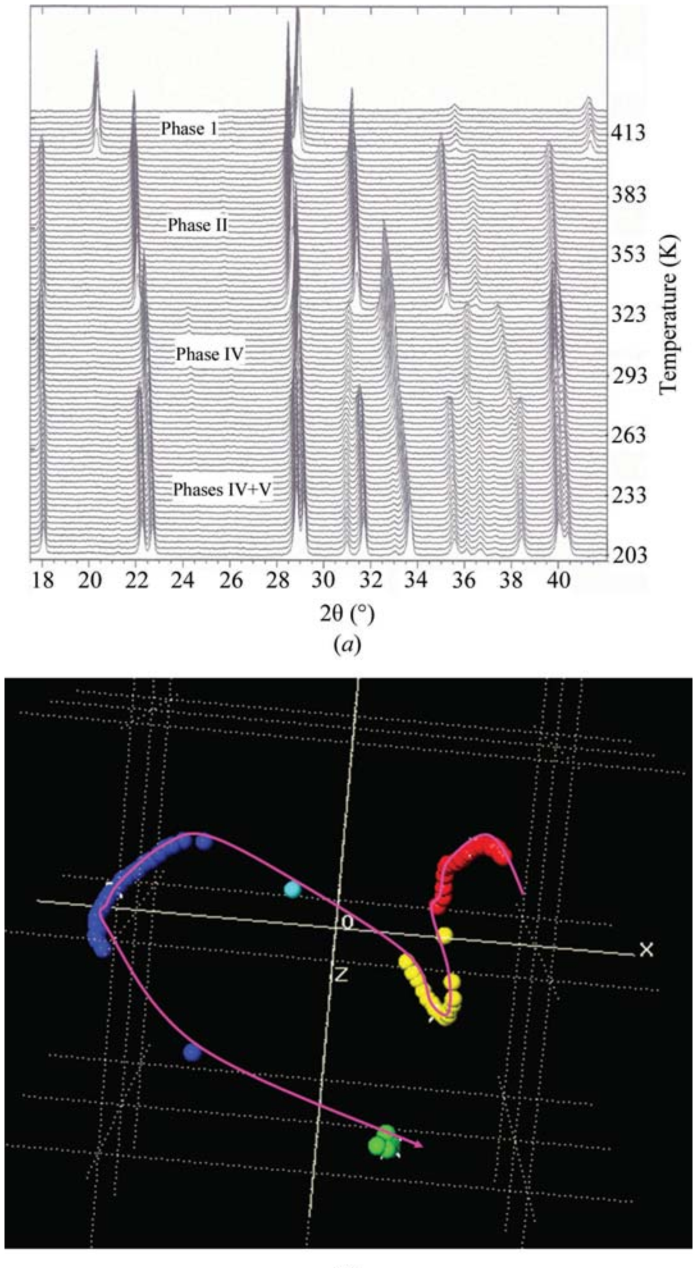

(*a*)

(*b*)

Figure 3.8.11
Ammonium nitrate phase transitions. (*a*) The raw powder data measured between 203 and 425 K. Reproduced with permission from Herrmann & Engel (1997). Copyright (1997) John Wiley and Sons. (*b*) The MMDS plot. The purple line follows the temperature change from 203 to 425 K.

$$\chi^2 = \left|\mathbf{xp} - \mathbf{S}\right|^2. \tag{3.8.29}$$

is required. Since $N \ll m$, the system is heavily overdetermined, and least-squares or singular value decomposition can be used to solve (3.8.29) for the fractional percentages arising from the scattering power of the component mixtures, $s_1, s_2, \ldots, s_N$. The values of s can be used to calculate a weight fraction for that particular phase provided that the atomic absorption coefficients are known, and this in turn requires the unit-cell dimensions and cell contents, but not the atomic coordinates (Smith *et al.*, 1988; Cressey & Schofield, 1996). The general formula for the weight fraction of component n in a mixture comprising N components is (Leroux *et al.*, 1953)

$$c_n = p_n \frac{\mu^*}{\mu_n^*}, \tag{3.8.30}$$

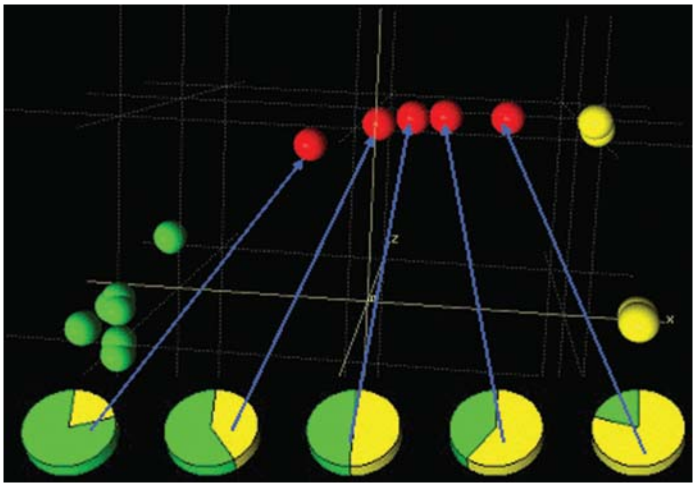

Figure 3.8.12
Identifying mixtures using lanthanum strontium copper oxide and caesium thiocyanate diffraction data taken from the ICDD Clay Minerals database. The green spheres represent pure phases of lanthanum strontium copper oxide and the yellow pure caesium thiocyanate. The red spheres represent mixtures of the two in the relative proportions of lanthanum strontium copper oxide/caesium thiocyanate 80/20, 60/40, 50/50, 40/60 and 20/80 in an arc commencing on the left-hand side of the diagram. The pie charts give the results of an independent quantitative calculation in which lanthanum strontium copper oxide and caesium thiocyanate have been included as pure phases in a reference database.

where

$$\mu^* = \sum_{j=1}^{N} c_j \mu_j^* \tag{3.8.31}$$

and

$$\mu_j^* = \mu_j / \rho_j, \tag{3.8.32}$$

where μ_j is the atomic X-ray absorption coefficient and ρ_j is the density of component j. For polymorphs, the absorption coefficients are sufficiently close and the method sufficiently approximate that the effects of absorption can be ignored.

3.8.7.1. *Example: inorganic mixtures*

As an example, a set of 19 patterns from set 78 of the ICDD database for inorganic compounds (ICDD, 2018) was imported into *DIFFRAC.EVA*. To this was added some simulated mixture data generated by adding the patterns for lanthanum strontium copper oxide and caesium thiocyanate in the proportions 80/20, 60/40, 50/50, 40/60 and 20/80. Two calculations were performed: an analysis without the pure-phase database and a second where the pure phases of lanthanum strontium copper oxide and caesium thiocyanate were present.

The results are shown in Fig. 3.8.12. In the MMDS plot the green spheres represent pure lanthanum strontium copper oxide while the yellow are pure caesium thiocyanate. The red spheres represent mixtures of the two. The latter form an arc between the green and yellow clusters. The distance of the spheres representing mixtures from the lanthanum strontium copper oxide and caesium thiocyanate spheres gives a semi-quantitative representation of the mixture contents. Running the analysis in quantitative mode gives the pie charts also shown in Fig. 3.8.12; they reproduce exactly the relative proportions of the three components.

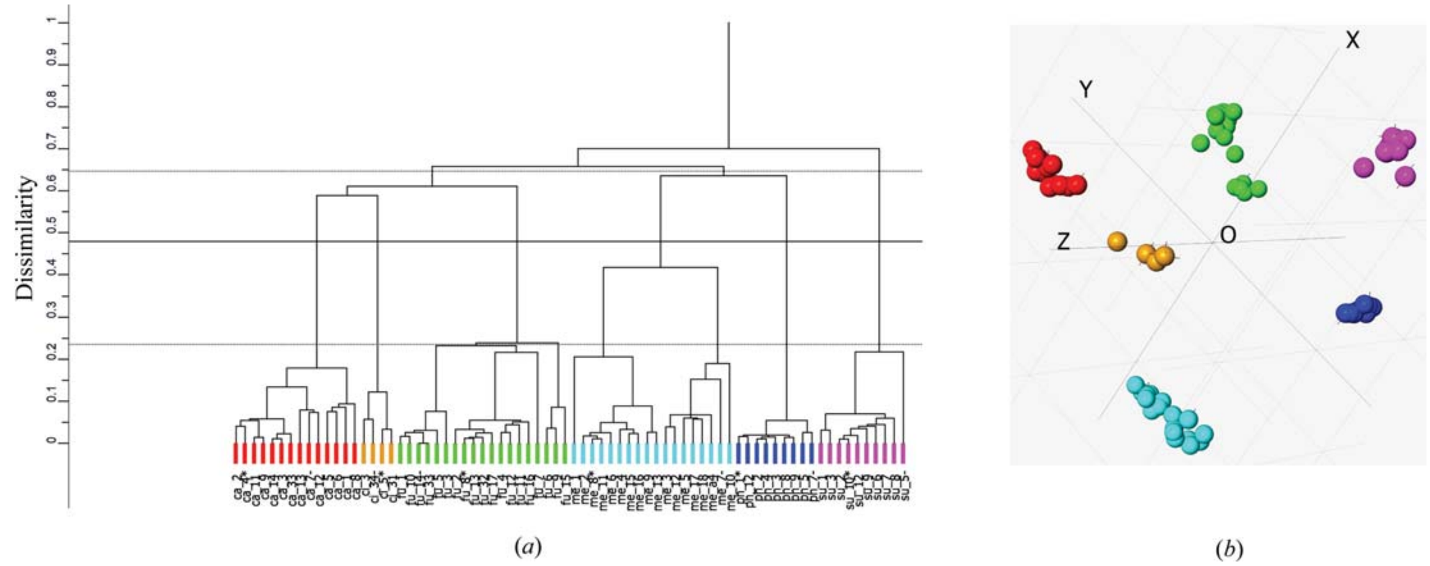

Figure 3.8.13
(*a*) The dendrogram generated from 74 Raman spectra without background corrections applied. Labelling from the left-hand side, the red samples are carbamazepine, the orange are cimetidene, the green are two forms of furosemide, the light blue is mefenamic acid, the dark blue is phenilbutazone and the purple at the right-hand side is sulfamerazine. (*b*) The MMDS plot. The sphere colours are taken from the dendrogram. This representation shows clearly discrete clusters in correspondence with those generated by the dendrogram.

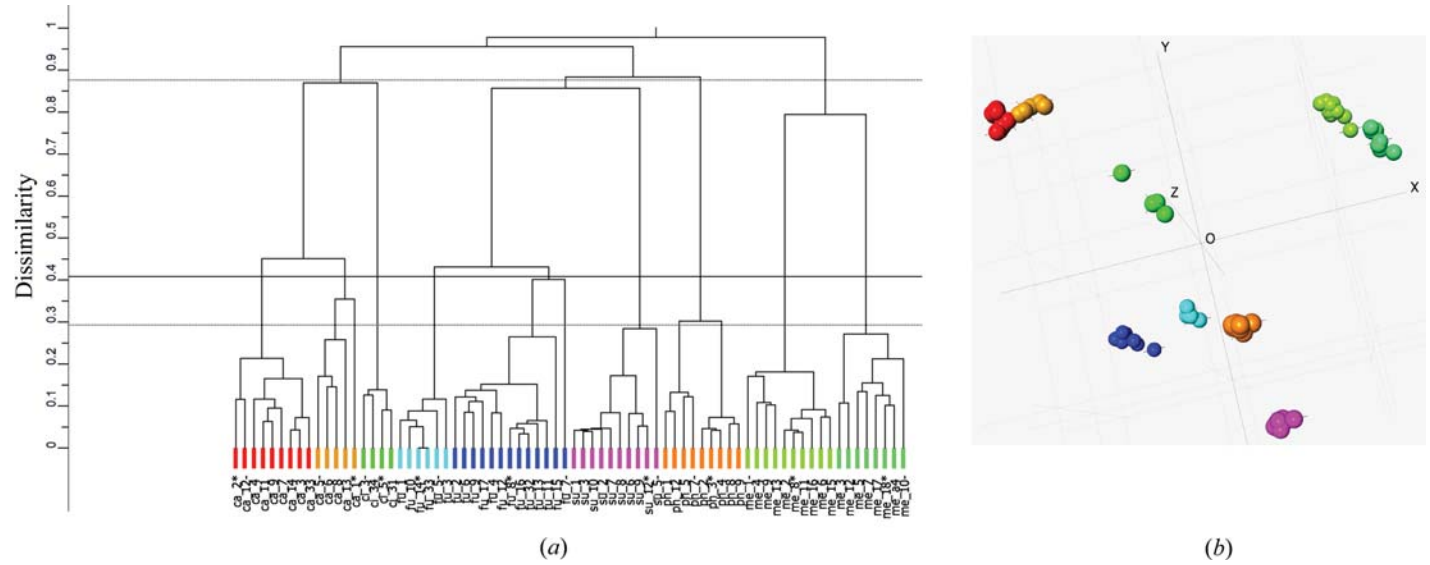

Figure 3.8.14
Clustering the 74 Raman spectra without background corrections applied using first-derivative data. (*a*) The dendrogram. Labelling from the left-hand side, the red and orange entries are carbamazepine; the green are cimetidene; the light blue and dark blue are two forms of furosemide; the purple are sulfamerazine; the brown are phenilbutazone and the right-hand light and dark green are two forms of mefenamic acid. (*b*) The MMDS plot. The clusters are well defined but the orange and red (both carbamazepine) are very close to each other.

For further details of this method with organic samples, see Dong *et al.* (2008).

3.8.8. Using spectroscopic data

There is no reason why the methodology described in this chapter cannot be used for other 1D data sets, *e.g.* Raman, IR, NMR and near-IR spectroscopies, although different data pre-processing is usually required. Raman spectroscopy is well suited to high-throughput screening: good-quality spectra can be collected in a few minutes, and sample preparation is straightforward and flexible, although the resulting spectra are not always as distinct as the PXRD equivalents (Mehrens *et al.*, 2005; Boccaleri *et al.*, 2007).

As an example we show the results of cluster analysis carried out on samples of carbamazepine, cimetidene, furosemide, mefenamic acid, phenilbutazone and sulfamerazine using Raman spectroscopy. A total of 74 samples were measured on a LabRam HR-800/HTS-Multiwell spectrometer at room temperature, equipped with a backscattering light path system of a light-emitting diode laser (785 nm, 300 mW) as an excitation source and an air-cooled charge-coupled device detector. A 20-fold superlong working distance objective lens was used to collect the backscattered light. The spectra were acquired with 5.84 cm^{-1} spectral width and at least 30 s exposure (Kojima *et al.*, 2006). The spectra had backgrounds subtracted but no other corrections were carried out.

The initial clustering is shown in Fig. 3.8.13(*a*) with the default cut level in the dendrogram. There are six clusters: labelling from the left-hand side, the red are three polymorphs of carbamazepine; the orange are cimetidene; the green cluster contains three polymorphs of furosemide; the light blue contains three poly-

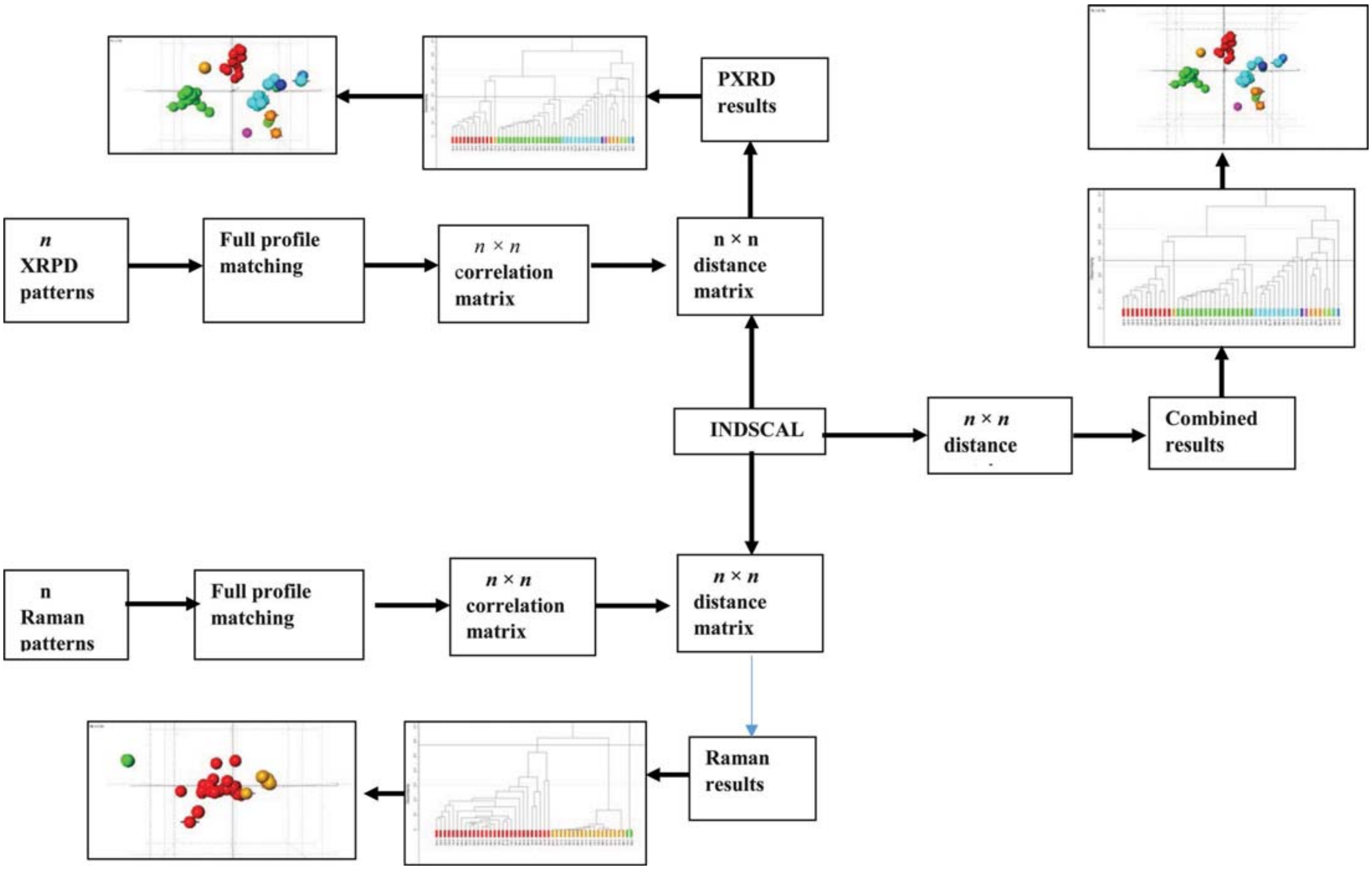

Figure 3.8.15
A flowchart for the INDSCAL method using Raman and PXRD data. Note that any combination of any 1D data can be used here.

morphs of mefenamic acid; the dark blue contains phenilbutazone; and finally the purple cluster contains sulfamerazine. The MMDS plot gives a complementary visualization of the data that supports the clustering.

It is also possible to use derivative data in place of the original spectra for clustering. The results of this for the 74 Raman spectra without initial background subtraction followed by the generation of first-derivative data are shown in Fig. 3.8.14. The clusters are well defined but now the carbamazepine data have split into two clusters. These correspond to forms I and III of carbamazepine, although the differences in the Raman spectra for these three species are small (O'Brien *et al.*, 2004). At the same time, both furosemide and mefenamic acid are each split into two groups. This is probably the best description of the data in terms of clustering and cluster membership corresponding to the chemical differences in the samples. The dendrogram also has the feature that the tie bars between samples are higher, *i.e.* the similarities are lower, reflecting the fact that the use of first derivatives accentuates small differences in the data.

It is interesting to note that, in general, PXRD works less well with derivative data. The reason for this is not clear, but possibly the presence of partial overlapping peaks and the associated issues of peak shape are partly responsible.

3.8.9. Combining data types: the INDSCAL method

It is now common to collect more than one data type, and some instruments now exist for collecting spectroscopic and PXRD data on the same samples, for example the Bruker D8 Screenlab, which combines PXRD and Raman measurement for high-throughput screening (Boccaleri *et al.*, 2007).

A technique for combining the results of more than one data type is needed. One method would be to take individual distance matrices from each data type and generate an average distance matrix using equation (3.8.3), but this leaves open the question of how best to define the associated weights in an optimal, objective way. Should, for example, PXRD be given a higher weight than Raman data? The individual differences scaling method (INDSCAL) of Carroll & Chang (1970) provides an unbiased solution to this problem by, as the name suggests, scaling the differences between individual distance matrices.

In this method, let $\mathbf{D}_k$ be the squared distance matrix of dimension $(n \times n)$ for data type k with a total of K data types. For example, if we have PXRD, Raman and differential scanning calorimetry (DSC) data for each of n samples, then $K = 3$. A group-average matrix $\mathbf{G}$ (which we will specify in two dimensions) is required that best represents the combination of the K data types. To do this, the $\mathbf{D}$ matrices are first put into inner-product form by the double-centring operation to give

$$\mathbf{B}_k = -\tfrac{1}{2}(\mathbf{I} - \mathbf{N})\mathbf{D}_k(\mathbf{I} - \mathbf{N}), \qquad (3.8.33)$$

where $\mathbf{I}$ is the identity matrix and $\mathbf{N}$ is the centring matrix $I - \mathbf{11}'/N$; $\mathbf{1}$ is a column vector of ones. The inner-product matrices thus generated are matched to the weighted form of the group average, $\mathbf{G}$, which is unknown. To do this the function

$$S = \sum_{1}^{K} \left\| \mathbf{B}_k - \mathbf{G}\mathbf{W}_k^2\mathbf{G}' \right\| \qquad (3.8.34)$$

is minimized. The weight matrices, $\mathbf{W}_k$, are scaled such that

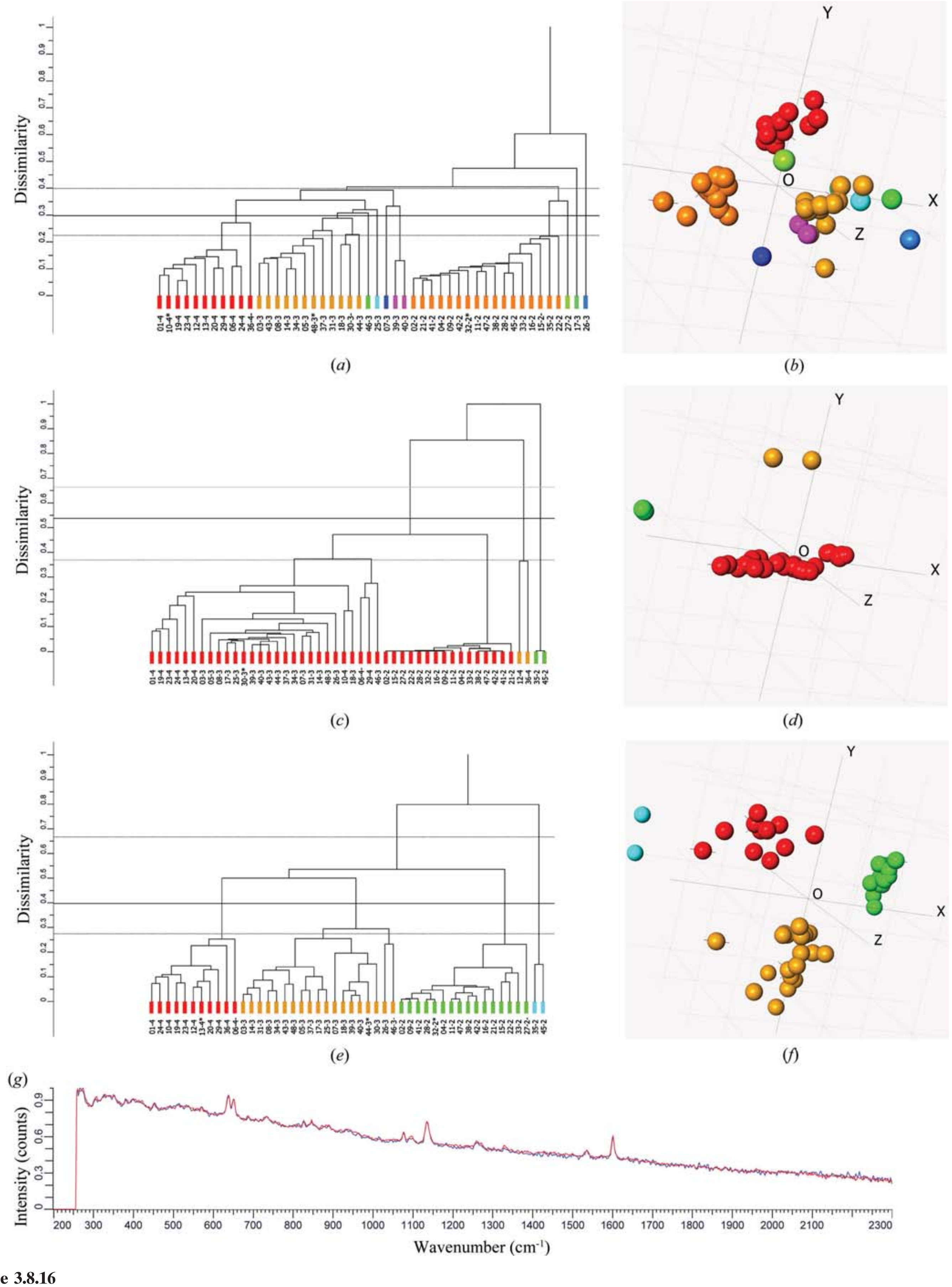

(*a*) (*b*)

(*c*) (*d*)

(*e*) (*f*)

Figure 3.8.16

Clustering 48 PXRD spectra with background corrections applied for three polymorphs of sulfathiazole. (*a*) The dendrogram. Each sample is identified by a four-digit code. The first two digits are the well number, and the last digit defines whether the sample is form 2, 3 or 4 of sulfathiazole. (*b*) The MMDS plot: the red cluster is well defined but the rest of the spheres are diffuse and intermingled. (*c*) The dendrogram derived from clustering 48 Raman spectra of sulfathiazole with background corrections applied. (*d*) The corresponding MMDS plot. The clusters are poorly defined. (*e*) The results of the INDSCAL method. The dendrogram is shown with the default cut level. The clustering is correct; all the samples are placed in the correct group except for patterns 35-2 and 45-2. (*f*) The MMDS plot validates the dendrogram. (*g*) The Raman patterns for 35-2 and 45-2 superimposed. They are primarily background noise.

$$\sum_{k=1}^{K} \mathbf{W}_k^2 = K\mathbf{I}. \qquad (3.8.35)$$

The INDSCAL method employs an iterative technique to solve equation (3.8.7) in which one parameter is kept fixed whilst the other is determined by least-squares refinement. An initial estimate for **G** is taken either from the average of the **D** matrices for each sample or as a random matrix. This is then used to estimate the weight matrices, and the whole process repeated until a minimum value of S is obtained. The algorithm derived by Carroll and Chang was used in the example below. When random matrices are used to generate the initial **G** matrix, the INDSCAL procedure is repeated 100 times and the solution with the minimum value of S is kept. In practice, there is very little difference in the results of these two procedures. The resulting **G** matrix is used as a standard-distance matrix, and used in the standard way to generate dendrograms, MMDS plots *etc*. The method has the property that where data types show samples to be very similar this is reinforced, whereas where there are considerable variations the differences are accentuated in the final **G** matrix. For a fuller description of the INDSCAL method with examples see Gower & Dijksterhuis (2004), Section 13.2, and for a useful geometric interpretation see Husson & Pagès (2006).

3.8.9.1. *An example combining PXRD and Raman data*

We now present an example of the INDSCAL method applied to data collected on sulfathiazole using PXRD and Raman spectroscopy (Barr, Cunningham *et al.*, 2009). A flowchart is shown in Fig. 3.8.15. Three polymorphs of sulfathiazole were prepared and PXRD data were collected on a Bruker C2 GADDS system. Each sample was run for 2 min over a 3–30° range in 2θ using Cu $K\alpha$ radiation. Raman data were collected on a Bruker SENTINEL. The Raman probe was integrated into the PXRD instrument.

The only data pre-processing performed was background removal. Fig. 3.8.16(*a*) shows the resulting dendrogram (with the default cut level) and Fig. 3.8.16(*b*) shows the corresponding MMDS plot. To identify each sample they are numbered *via* a four-digit code: the first two digits are the well number, and the last digit defines whether the sample is form 2, 3 or 4 of sulfathiazole. It can be seen that the clustering is only partly successful: form 4 (red) is correctly clustered; form 3 (orange) gives five clusters and form 2 gives three clusters.

Fig. 3.8.16(*c*) shows the clustering from the Raman spectra. The results are poor: most of form 2 is correctly clustered, but forms 4 and 3 are intermixed, and the MMDS plot in Fig. 3.8.16(*d*) is diffuse with little structure.

The INDSCAL method is now applied starting from random **G** matrices and the results are shown in Fig. 3.8.16(*e*) and (*f*) with the dendrogram cut level at its default value. The clustering is almost correct; all the samples are placed in the correct groups except that there are two outliers coloured in blue. Fig. 3.8.16(*g*) shows the Raman patterns for these samples: they are primarily background with very little usable signal.

3.8.10. Quality control

Quality control (Gilmore, Barr & Paisley, 2009) is designed for situations where the stability of a material is being monitored over time, for example as part of a production-line system, or for periodic equipment alignment. A set of reference patterns is collected that represents acceptable measurements – any measurement sufficiently close to these references represents a good measurement. Various sample patterns are then imported and compared with those reference patterns, and any that vary significantly from the ideal are noted and highlighted.

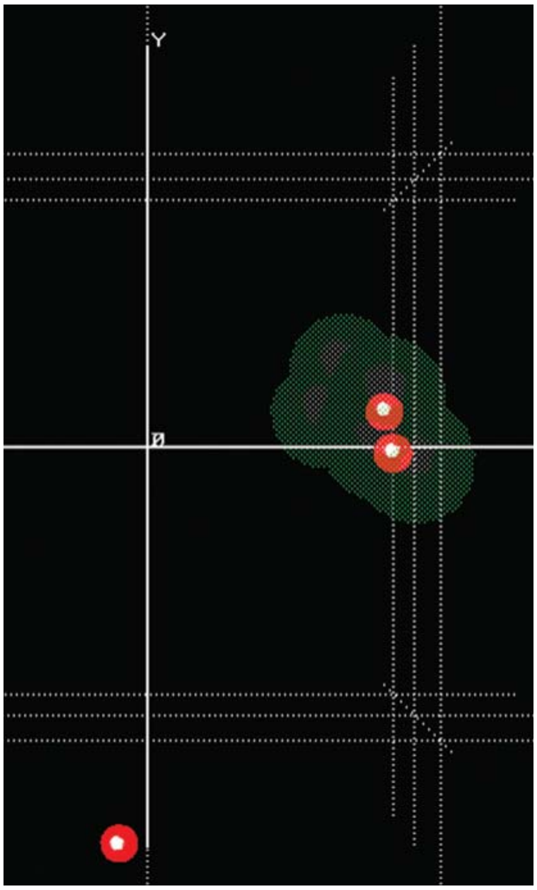

Figure 3.8.17
Visualization tools for quality-control procedures using a modified MMDS plot. The red outlier is a sample unacceptably far from the cluster of reference measurements.

The results are best displayed graphically using a variant of the MMDS method, of which an example is shown in Fig. 3.8.17. The reference patterns define a green shaded surface with acceptable sample patterns, coloured red, shown within it, and potentially problematic sample patterns appearing outside it. The volume of the green shape is defined by intersecting spheres around each reference sample and these can be altered to allow more- or less-stringent quality control.

3.8.11. Computer software

These calculations can be carried out using MATLAB (http://www.mathworks.co.uk/products/matlab/) or the open-source R software (http://www.r-project.org/; Crawley, 2007) with graphics using the *GGobi* software (Cook & Swayne, 2007). There are four commercial packages for handling powder data: *DIFFRAC.EVA* and *PolySNAP 3*, both from Bruker (http://www.bruker.com/; Gilmore, Barr & Paisley, 2004; Barr, Dong & Gilmore, 2009), *Jade* from Materials Data Inc. (http://www.materialsdata.com) and *HighScore* from Malvern PANalytical (http://www.panalytical.com/).

Data were kindly provided by Gordon Cunningham at Glasgow University, Arnt Kern of Bruker AXS in Karlsruhe and Michael Herrman at the Fraunhofer Institute, Germany.

References

Alvarez, A. J., Singh, A. & Myerson, A. S. (2009). *Polymorph screening: comparing a semi-automated approach with a high throughput method. Cryst. Growth Des.* **9**, 4181–4188.

Asimov, D. (1985). *The grand tour: a tool for viewing multidimensional data. SIAM J. Sci. Stat. Comput.* **6**, 128–143.

Barr, G., Cunningham, G., Dong, W., Gilmore, C. J. & Kojima, T. (2009). *High-throughput powder diffraction V: the use of Raman spectroscopy with and without X-ray powder diffraction data. J. Appl. Cryst.* **42**, 706–714.

Barr, G., Dong, W. & Gilmore, C. J. (2004*a*). *High-throughput powder diffraction. II. Applications of clustering methods and multivariate data analysis. J. Appl. Cryst.* **37**, 243–252.

Barr, G., Dong, W. & Gilmore, C. J. (2004*b*). *High-throughput powder diffraction. IV. Cluster validation using silhouettes and fuzzy clustering. J. Appl. Cryst.* **37**, 874–882.

Barr, G., Dong, W. & Gilmore, C. J. (2004*c*). *PolySNAP: a computer program for analysing high-throughput powder diffraction data. J. Appl. Cryst.* **37**, 658–664.

Barr, G., Dong, W. & Gilmore, C. J. (2009). *PolySNAP3: a computer program for analysing and visualizing high-throughput data from diffraction and spectroscopic sources. J. Appl. Cryst.* **42**, 965–974.

Barr, G., Dong, W., Gilmore, C. & Faber, J. (2004). *High-throughput powder diffraction. III. The application of full-profile pattern matching and multivariate statistical analysis to round-robin-type data sets. J. Appl. Cryst.* **37**, 635–642.

Barr, G., Gilmore, C. J. & Paisley, J. (2004). *SNAP-1D: a computer program for qualitative and quantitative powder diffraction pattern analysis using the full pattern profile. J. Appl. Cryst.* **37**, 665–668.

Boccaleri, E., Carniato, F., Croce, G., Viterbo, D., van Beek, W., Emerich, H. & Milanesio, M. (2007). *In situ simultaneous Raman/high-resolution X-ray powder diffraction study of transformations occurring in materials at non-ambient conditions. J. Appl. Cryst.* **40**, 684–693.

Bruker (2018). *DIFFRAC.EVA: software to evaluate X-ray diffraction data*. Version 4.3. https://www.bruker.com/eva.

Butler, B. M., Sila, A., Nyambura, K. D., Gilmore, C. J., Kourkoumelis, N. & Hillier, S. (2019). *Pre-treatment of soil X-ray powder diffraction data for cluster analysis. Geoderma*, **337**, 413–424.

Calinški, T. & Harabasz, J. (1974). *A dendritic method for cluster analysis. Commun. Stat.* **3**, 1–27.

Carroll, J. D. & Chang, J. J. (1970). *Analysis of individual differences in multidimensional scaling via n-way generalization of 'Eckhart–Young' decomposition. Psychometria*, **35**, 283–319.

Cook, D. & Swayne, D. F. (2007). *Interactive and Dynamic Graphics for Data Analysis with R and GGobi*. New York: Springer.

Cox, T. F. & Cox, M. A. A. (2000). *Multidimensional Scaling*, 2nd ed. Boca Raton: Chapman & Hall/CRC.

Crawley, M. J. (2007). *The R Book*. Chichester: Wiley.

Cressey, G. & Schofield, P. F. (1996). *Rapid whole-pattern profile-stripping method for the quantification of multiphase samples. Powder Diffr.* **11**, 35–39.

Dong, W., Gilmore, C., Barr, G., Dallman, C., Feeder, N. & Terry, S. (2008). *A quick method for the quantitative analysis of mixtures. 1. Powder X-ray diffraction. J. Pharm. Sci.* **97**, 2260–2276.

Donoho, D. L. & Johnstone, I. M. (1995). *Adapting to unknown smoothness via wavelet shrinkage. J. Am. Stat. Assoc.* **90**, 1200–1224.

Everitt, B. S., Landau, S. & Leese, M. (2001). *Cluster Analysis*, 4th ed. London: Arnold.

Gilmore, C. J., Barr, G. & Paisley, W. (2004). *High-throughput powder diffraction. I. A new approach to qualitative and quantitative powder diffraction pattern analysis using full pattern profiles. J. Appl. Cryst.* **37**, 231–242.

Goodman, L. A. & Kruskal, W. H. (1954). *Measures of association for cross-classifications. J. Am. Stat. Assoc.* **49**, 732–764.

Gordon, A. D. (1981). *Classification*, 1st ed., pp. 46–49. London: Chapman and Hall.

Gordon, A. D. (1999). *Classification*, 2nd ed. Boca Raton: Chapman and Hall/CRC.

Gower, J. C. (1966). *Some distance properties of latent root and vector methods used in multivariate analysis. Biometrika*, **53**, 325–328.

Gower, J. C. & Dijksterhuis, G. B. (2004). *Procrustes Problems*. Oxford University Press.

Herrmann, M. J. & Engel, W. (1997). *Phase transitions and lattice dynamics of ammonium nitrate. Propellants Explos. Pyrotech.* **22**, 143–147.

Husson, F. & Pagès, J. (2006). *INDSCAL model: geometrical interpretation and methodology. Comput. Stat. Data Anal.* **50**, 358–378.

ICDD (2018). *The Powder Diffraction File*. International Centre for Diffraction Data, 12 Campus Boulevard, Newton Square, Pennsylvania 19073-3273, USA.

Inselberg, A. (1985). *The plane with parallel coordinates. Vis. Comput.* **1**, 69–91.

Inselberg, A. (2009). *Parallel Coordinates. Visual multidimensional geometry and its applications.* New York: Springer.

Kaufman, L. & Rousseeuw, P. J. (1990). *Finding Groups in Data*. New York: Wiley.

Kojima, T., Onoue, S., Murase, N., Katoh, F., Mano, T. & Matsuda, Y. (2006). *Crystalline form information from multiwell plate salt screening by use of Raman microscopy. Pharm. Res.* **23**, 806–812.

Kruskal, J. B. (1956). *On the shortest spanning subtree of a graph and the traveling salesman problem. Proc. Am. Math. Soc.* **7**, 48–50.

Lance, G. N. & Williams, W. T. (1967). *A general theory of classificatory sorting strategies: 1. Hierarchical systems. Comput. J.* **9**, 373–380.

Leroux, J., Lennox, D. H. & Kay, K. (1953). *Direct quantitative X-ray analysis by diffraction absorption technique. Anal. Chem.* **25**, 740–743.

Mehrens, S. M., Kale, U. J. & Qu, X. (2005). *Statistical analysis of differences in the Raman spectra of polymorphs. J. Pharm. Sci.* **94**, 1354–1367.

Milligan, G. W. & Cooper, M. C. (1985). *An examination of procedures for determining the number of clusters in a data set. Psychometrika*, **50**, 159–179.

Nelder, J. A. & Mead, R. (1965). *A simplex method for function minimization. Comput. J.* **7**, 308–313.

O'Brien, L. E., Timmins, P., Williams, A. C. & York, P. (2004). *Use of in situ FT-Raman spectroscopy to study the kinetics of the transformation of carbamazepine polymorphs. J. Pharm. Biomed. Anal.* **36**, 335–340.

Ogden, R. T. (1997). *Essential Wavelets for Statistical Applications and Data Analysis*, pp. 144–148. Boston: Birkhäuser.

Press, W. H., Teukolsky, S. A., Vetterling, W. T. & Flannery, B. P. (2007). *Numerical Recipes*. 3rd ed. Cambridge University Press..

Rousseeuw, P. J. (1987). *Silhouettes: a graphical aid to the interpretation and validation of cluster analysis. J. Comput. Appl. Math.* **20**, 53–65.

Sato, M., Sato, Y. & Jain, L. C. (1966). *Fuzzy Clustering Models and Applications*. New York: Physica-Verlag.

Smith, D. K., Johnson, G. G. & Wims, A. M. (1988). *Use of full diffraction spectra, both experimental and calculated, in quantitative powder diffraction analysis. Aust. J. Phys.* **41**, 311–321.

Smrčok, Ĺ., Ďurík, M. & Jorík, V. (1999). *Wavelet denoising of powder diffraction patterns. Powder Diffr.* **14**, 300–304.

Spearman, C. (1904). *The proof and measurement of association between two things. Am. J. Psychol.* **15**, 72–101.

Storey, R., Docherty, R., Higginson, P., Dallman, C., Gilmore, C., Barr, G. & Dong, W. (2004). *Automation of solid form screening procedures in the pharmaceutical industry–how to avoid the bottlenecks. Crystallogr. Rev.* **10**, 45–56.

Wegman, E. J. (1990). *Hyperdimensional data analysis using parallel coordinates. J. Am. Stat. Assoc.* **85**, 664–675.

International Tables for Crystallography (2019). Vol. H, Chapter 3.9, pp. 344–373.

3.9. Quantitative phase analysis

I. C. Madsen, N. V. Y. Scarlett, R. Kleeberg and K. Knorr

3.9.1. Introduction

The field of quantitative phase analysis (QPA) from powder diffraction data is almost as old powder diffraction itself. Debye and Scherrer first developed the method around 1916 (Debye & Scherrer, 1916, 1917) and between 1917 and 1925 Hull (1917, 1919) and Navias (1925) were reporting studies of QPA related to the new technique. However, further developments in QPA were relatively slow, as much of the activity in X-ray diffraction (XRD) at the time was dedicated to the solution of crystal structures rather than the extraction of other information present in a powder diffraction pattern. While a small number of QPA applications continued to be published in the intervening years, it was not until the advent of scanning diffractometers around 1947 (Langford, 2004, Parrish, 1965) and the work of Alexander and Klug in 1948 (Alexander & Klug, 1948), which provided the formal methodology and a practical approach, that the field began to expand.

Since those original developments, which utilized the intensity of individual peaks or a small group of peaks in the diffraction pattern, there have been extensions to the methodology that use whole-pattern approaches. These methods operate *via* the summation of either (i) patterns collected from pure components or (ii) component contributions calculated from their crystal structures. There are a number of benefits accruing from the whole-pattern approaches since all reflections in the pattern, which may number in the hundreds or thousands, now contribute to the final analysis.

The mathematical basis of QPA is well established and, ideally, QPA should be a relatively straightforward science. However, there are a significant number of factors, many of them experimental, that serve to decrease the accuracy that can be obtained (Chung & Smith, 2000). Some of these, such as accuracy and precision in measurement of peak position and intensity, resolution of overlapping peaks and counting statistics, relate to instrument geometry and data-collection conditions. Other sources of error derive from sample-related issues and include effects such as (i) preferred orientation (which distorts the observed relative intensities from those expected for a randomly oriented powder); (ii) crystallite size and strain broadening (leading to increased peak width and hence overlap); (iii) the grain-size effect (where there may be too few crystallites contributing to the diffraction process to ensure that a representative powder pattern can be measured);[1] and (iv) microabsorption (where phases that strongly absorb the incident and diffracted beams are underestimated with respect to weakly absorbing phases). Of these, microabsorption remains the largest impediment to accurate QPA and is more pronounced in X-ray diffraction than in neutron-based studies.

While there is a very broad scope for the application of diffraction-based estimation of phase abundance, the perceived difficulty involved in developing and using these methods often deters non-specialist users. Consequently, they may resort to other, non-diffraction, material characterization techniques that are more readily implemented.

Analytical techniques for most of the 92 naturally occurring elements are generally well established and, in many cases, the subject of internationally accepted standards. However, the physical properties of minerals and materials formed by these elements, and the manner in which they react, is not solely dependent on their chemical composition but also on how the constituent elements are arranged; that is, their crystal structures. This finite number of known elements combines in an almost infinite array within the 230 crystallographic space groups. Further variability is induced by factors such as solid solution, degree of crystallinity and morphology, thus making QPA by diffraction methods considerably more difficult to implement.

In industry, many manufacturing or processing lines are controlled by measurement of elemental composition alone, simply because these values can be readily obtained to a high degree of accuracy and precision. For example, a plant extracting Cu from an ore body might measure the Cu content of the feed ore and the concentrate, and the plant conditions are optimized based on efficiency of extraction. However, if the mineralogical form of the Cu changes in the feed, then it may not behave in the same manner during grinding, flotation and density separation, and this will affect the recovery. Frequently, where knowledge of the mineralogy or phase abundance is actually used in plant optimization and control, it is derived from bulk or micro-compositional analysis rather than being measured directly. This is often achieved by normative calculation, where the results of element composition analysis are assigned to specific phases based on an assumed knowledge of individual phase composition. Further details of this approach can be found in Chapter 7.7.

In materials science, new compounds are being synthesized at a rapidly increasing rate with techniques such as high-throughput synthesis capable of generating hundreds of new variants in a single experiment. Such techniques are being used in fields ranging from drug discovery, catalyst synthesis and new metal alloy design. The properties of these materials, and their suitability for their designed purpose, are not only dependent on their structural form but, for multiphase materials, on the amount of each component present. In this case, accurate, or at the very least reproducible, QPA is crucial to the screening process.

This chapter focuses on the application of QPA techniques for the extraction of phase abundance from diffraction data. While there is extensive coverage of the QPA methodology in other texts (Klug & Alexander, 1974; Smith *et al.*, 1987; Snyder & Bish, 1989; Zevin & Kimmel, 1995), some of the more commonly used approaches will be described here along with examples of their use in practical applications.

3.9.2. Phase analysis

There are a number of traditional methods for the estimation of phase abundance in multiphase materials (Zevin & Kimmel, 1995). In summary, these can be divided into two groups:

---

[1] It is worth noting that the grain-size effect becomes even more of an issue as the divergence of the instrument is decreased with, for example, high-resolution laboratory or synchrotron-based instruments, since fewer crystallites are likely to meet the diffraction condition.

Copyright © 2019 International Union of Crystallography

(1) *Indirect methods* – these are usually based on the measurement of total chemical composition, which is then apportioned according to an assumed composition for each phase. A very widely used form of this normative calculation approach is the Bogue method (Bogue, 1929) for the quantitative estimation of Portland cement phases. The limitations in this approach arise when the actual compositions of individual phases vary from those assumed in the calculation. This frequently occurs in the cement industry, where variance in local materials and production conditions can affect detailed phase compositions. Normative calculation has the potential to be unstable when a number of phases in the mixture have similar chemical composition and it cannot be used at all for the limiting case of polymorphs that have identical chemical composition.

(2) *Direct methods* – these are based on a property that is specific to phases of interest in the sample. These methods are often not generally applicable to the entire sample, but are useful in estimating abundances of selected components. Examples include:

   (*a*) Magnetic susceptibility – this is applicable to samples in which component phases have different magnetic properties. The magnetic component can be separated and weighed to determine its weight fraction in the starting material. This approach assumes that the magnetic phase is well separated from non-magnetic phases and accuracy will be reduced when there is a fine inseparable intergrowth of magnetic and non-magnetic components.

   (*b*) Selective dissolution – where the rate and extent of dissolution can be phase dependent, and the weight fraction of the residue is used to determine the fractions of soluble and insoluble components.

   (*c*) Density – involves the physical separation of phases with different densities. As with magnetic separation, this approach assumes that the phase of interest is well separated from other phases.

   (*d*) Image analysis – optical microscopy using thin sections is still frequently used for the analysis of mineralogical samples. Thin sections can be time consuming to prepare and analyse, and the observations can be highly subjective depending on the analyst's experience. While automated image analysis of optical and electron-beam images brings more consistency to the estimation of phase abundance, issues in stereology may still affect the determined phase abundances.

   (*e*) Thermal analysis – where the magnitude of endo- and exothermic features during phase transitions are proportional to the amount of the phases present. This can be effective for well known and characterized phases, but is less useful for new phases or complex multiphase samples where there may be significant overlap in the features in the observed patterns. There may also be difficulty in distinguishing features related to individual minerals, for example H_2O evolution from co-existing hydrated minerals.

   (*f*) Infrared (IR) techniques – these are gaining in popularity, especially in mineral exploration environments because of their portability, speed and ability to measure directly from a cleaned drill core or section. However, because the IR beam only penetrates 1–2 µm into the sample, it is a surface-analysis technique providing a semi-quantitative analysis at best. To work effectively, the method needs to be calibrated using other techniques such as diffraction-based phase analysis.

   (*g*) Powder diffraction may be included in the direct-methods category, as it distinguishes and quantifies phases on the basis of their unique crystal structures, giving the technique broad applicability for crystalline materials.

Quantification from powder diffraction data is reliant on determination of the contribution to the final pattern of each component phase in a mixture. Commonly used methods can be divided into two distinct groups:

(1) The traditional 'single-peak' methods, which rely on the measurement of the intensity of a peak, or group of peaks, for each phase of interest and assumes that the intensity of these peaks is representative of the abundance of the individual phases. This is often not the case because of peak overlap and phase-dependent factors, such as preferred orientation and microabsorption, which affect the relative observed intensities.

(2) Whole-pattern methods, which rely on the comparison of observed diffraction data over a wide range of 2θ with a calculated pattern formed from the summation of individual phase components which have either been (i) measured from pure phase samples, or (ii) calculated from crystal-structure information.

3.9.3. QPA methodology

The integrated intensity $I_{(hkl)\alpha}$ of reflection *hkl* for phase α in a multiphase mixture, measured on a flat-plate sample of infinite thickness using a diffractometer with Bragg–Brentano geometry, is given by (Snyder & Bish, 1989; Zevin & Kimmel, 1995; Madsen *et al.*, 2013)

$$\begin{aligned} I_{(hkl)\alpha} = {} & \left[\frac{I_0\lambda^3}{32\pi r}\frac{e^4}{m_e^2c^4}\right] \\ & \times \left[\frac{M_{hkl}}{2V_\alpha^2}\left|F_{(hkl)\alpha}\right|^2\left(\frac{1+\cos^2 2\theta\cos^2 2\theta_m}{\sin^2\theta\cos\theta}\right)\exp\left(-2B(\sin\theta/\lambda)^2\right)\right] \\ & \times \left[\frac{W_\alpha}{\rho_\alpha\mu_m^*}\right], \qquad (3.9.1) \end{aligned}$$

where I_0 is the incident-beam intensity, λ is the wavelength, e is the charge on an electron, m_e is the mass of an electron, r is the distance from the scattering electron to the detector and c is the speed of light. M_{hkl} and F_{hkl} are the multiplicity and structure factor of the *hkl* reflection, respectively, V_α is the unit-cell volume of phase α, and θ and θ_m are the diffraction angles for the *hkl* reflection and the monochromator (if present), respectively. B is the mean atomic displacement parameter (ADP). W_α and ρ_α are the weight fraction and density of phase α respectively, while μ_m^* is the mass absorption coefficient of the entire sample.

3.9.3.1. *Absorption–diffraction method*

The various terms in equation (3.9.1) are related to the (i) instrument configuration (first set of square brackets), (ii) crystal-structure-related parameters for reflection *hkl* of phase α (second set of square brackets), and (iii) phase-specific and whole-sample parameters including the weight fraction W_α for phase α (last set of square brackets).

The instrument-related and phase-dependent parameters, including phase density, can be grouped together and defined as a constant $C_{i\alpha}$ for the ith reflection of phase α for a specific set of measurement conditions. This greatly simplifies the relationship between reflection intensity and weight fraction to

$$I_{i\alpha} = C_{i\alpha}\frac{W_\alpha}{\mu_m^*}. \quad (3.9.2)$$

On rearrangement, the weight fraction can be derived from

$$W_\alpha = \frac{I_{i\alpha}\mu_m^*}{C_{i\alpha}}. \quad (3.9.3)$$

Application of equation (3.9.3) (Klug & Alexander, 1974), referred to as the absorption–diffraction method, requires:

(1) the determination of $C_{i\alpha}$ using a rearranged equation (3.9.3) by (i) the preparation of standards with known additions W of phase α_α, (ii) measurement of peak intensity $I_{i\alpha}$ for the standards, and (iii) estimation of the standard sample mass absorption coefficient μ_m^*;

(2) measurement of $I_{i\alpha}$ and estimation of μ_m^* for the unknown samples; and

(3) calculation of W_α *via* equation (3.9.3).

The value of μ_m^* can be estimated by direct measurement of the beam intensity through a sample of known thickness t in a beam of the same wavelength as that used in the XRD data collection. Following measurement of the beam intensity with the sample in (I) and removed from (I_0) the beam, μ_m^* can be calculated using

$$\frac{I}{I_0} = \exp(-\mu_m^*\rho_m t). \quad (3.9.4)$$

However, this usually involves (i) the preparation of an additional, thinner, sample for presentation to the X-ray beam, (ii) in some cases, the addition of a diluent with a low mass absorption coefficient to produce I/I_0 ratios in a range where reasonable accuracy can be achieved, and (iii) knowledge of the 'mass thickness' $\rho_m t$. It should also be noted that there are few commercially available instruments that would be suitable for such measurements due to safety-related issues in accessing the X-ray beam path.

An alternative approach is to calculate μ_m^* from the sum of the products of the theoretical mass absorption coefficient (μ_j^*) of each element (or phase) and the weight fractions (W_j) of all n elements (or phases) in the sample. The elemental composition may be determined, for example, by X-ray fluorescence (XRF) measurement and its use is more accurate than the use of phase composition as it takes into account any amorphous material not represented by peaks in the diffraction pattern but which still contributes to μ_m^*,

$$\mu_m^* = \sum_{j=1}^{n}\mu_j^* W_j. \quad (3.9.5)$$

3.9.3.2. *Internal standard method*

A more general, and experimentally simpler, approach is to eliminate μ_m^* from the analysis altogether *via* the inclusion of an internal standard s in known weight fraction W_s. Substitution of the measured intensity of the jth peak (or group of peaks) of the standard phase, I_{js}, into equation (3.9.2) yields

$$I_{js} = C_{js}\frac{W_s}{\mu_m^*}. \quad (3.9.6)$$

The ratio of equations (3.9.2) and (3.9.6) gives

$$\frac{I_{i\alpha}}{I_{js}} = \frac{C_{i\alpha}}{C_{js}}\frac{W_\alpha}{W_s}. \quad (3.9.7)$$

Since μ_m^* now appears both in the numerator and denominator, its effect on the analysis, and hence the need to measure or calculate it, is removed from the calculation. Rearrangement of equation (3.9.7) yields

$$\frac{I_{i\alpha}}{I_{js}}\frac{W_s}{W_\alpha} = \frac{C_{i\alpha}}{C_{js}} = C_{js}^{i\alpha}, \quad (3.9.8)$$

where $C_{js}^{i\alpha}$ is a calibration constant specific to the phase and internal standard used. Once $C_{js}^{i\alpha}$ has been determined, the weight fraction of the unknown, W_α, can then be determined from

$$W_\alpha = \frac{W_s}{C_{\alpha s}^{ij}}\frac{I_{i\alpha}}{I_{js}}. \quad (3.9.9)$$

This approach, referred to as the *internal standard method*, relies on the determination of $C_{\alpha s}^{ij}$ using known mixtures of standard and analyte phases. The value of $C_{\alpha s}^{ij}$ will be specific to the diffraction peaks used in its determination; if other lines are used in subsequent analysis, then an appropriate value of C will have to be redetermined.

It should be noted that the presence of systematic errors (such as preferred orientation and microabsorption) that influence the measurement of intensity and vary as a function of W_α will not be detected through application of equation (3.9.9). The use of consistent sample-preparation and presentation techniques is required to minimize the effect of these aberrations on the analysis (Zevin & Kimmel, 1995).

3.9.3.2.1. *Selection of an internal standard*

The selection of an appropriate material for use as an internal standard for QPA is not always straightforward. Ideally, the material selected should:

(1) Have a simple diffraction pattern resulting in minimal overlap with peaks of interest in the sample.

(2) Have a mass absorption coefficient similar to that of the sample to avoid introducing microabsorption effects and thus reducing accuracy.

(3) Have minimal sample-related aberrations that may affect observed intensities. For example, it should be fine-grained to ensure minimal grain-size effects on the observed intensities and not be subject to preferred orientation. Importantly, it should have 100% (or known) crystallinity.

(4) Be stable over an extended time and be unreactive, especially for *in situ* studies where it may be subjected to extreme conditions.

Some possibilities for use as internal standard include α-Al_2O_3 (corundum), TiO_2 (rutile), ZnO (zincite), Cr_2O_3 (eskolaite), α-Fe_2O_3 (haematite), CeO_2 (cerianite), CaF_2 (fluorite) and C (diamond). Cline *et al.* (2011) have described the certification of the standard reference material SRM 676a with accurately known amorphous content for use as an internal standard for QPA (see Chapter 3.1). Alternatively, it is possible to use an independent measure (*e.g.* chemical analysis) to derive the concentration of a phase already present in the sample and then to designate it as the internal standard.

Selection of the amount of internal standard to add is often based on folklore or local practices with reported additions ranging from 5 to 50 wt%. Westphal *et al.* (2009) have described the mathematical basis for selecting the optimal internal standard addition in the context of amorphous phase determination. The amount of internal standard added has a strong influence on the precision of the determination of amorphous content and ‘a poor choice can make determination impossible, while a clever choice can enhance the precision’.

With the exception of diamond, all of the phases listed above tend to have absorption coefficients that are too high for use with organic materials. The development and verification of a suitable low-absorption-coefficient standard material that meets the criteria given above remains an important area of research.

3.9.3.3. *Reference intensity ratio methods*

The reference intensity ratio (RIR) (Hubbard *et al.*, 1976; Hubbard & Snyder, 1988) is an instrument-independent phase constant developed specifically for use in quantitative phase analysis and is defined as the ratio of strongest peak of phase α to the strongest peak of standard s. The RIR can be derived directly from equation (3.9.8):

$$\mathrm{RIR}_{\alpha s} = C_{js}^{i\alpha} = \frac{I_{i\alpha}}{I_{js}} \frac{W_s}{W_\alpha}. \tag{3.9.10}$$

In some cases, the strongest lines of either the standard or phase of interest may not be accessible for measurement if, for example, they strongly overlap with peaks from another phase or if they are out of the 2θ range considered. Equation (3.9.10) can be generalized (Hubbard & Snyder, 1988) to use less intense peaks while keeping the same value of RIR:

$$\frac{I_{i\alpha}}{I_{js}} \frac{I_{js}^{\mathrm{rel}}}{I_{i\alpha}^{\mathrm{rel}}} \frac{W_s}{W_\alpha} = \mathrm{RIR}_{\alpha s}, \tag{3.9.11}$$

where I^{rel} is the ratio of the intensity of the peak used for analysis to the most intense peak for the phase. $\mathrm{RIR}_{\alpha,s}$ is now the generalized reference intensity ratio for phase α with respect to standard s.

Quantification of the unknown phase in the presence of a known standard addition can be achieved by the rearrangement of equation (3.9.11):

$$W_\alpha = \frac{I_{i\alpha}}{I_{js}} \frac{I_{js}^{\mathrm{rel}}}{I_{i\alpha}^{\mathrm{rel}}} \frac{W_s}{\mathrm{RIR}_{\alpha s}}. \tag{3.9.12}$$

The generally accepted reference material for QPA *via* the RIR method is corundum because of its relatively simple diffraction pattern, stability and availability as a highly crystalline and pure single phase. If corundum is used, the RIR equates to I/I_c (or ‘I over I corundum’) for the phase; these are the most commonly reported values in the literature.

RIRs can be determined either by (i) calculation using published crystal-structure information with Rietveld analysis software set to pattern-calculation mode, or (ii) direct measurement by taking the ratio of the strongest peak of the pattern to the intensity of the strongest peak of corundum in a 50/50 weight mixture [or through use of equation (3.9.11) for non-equal proportions]. However, for some phases, there can be ambiguity about which peak is the most intense. For example, the 104 (2.551 Å) and 113 (2.085 Å) peaks of corundum have very similar observed intensities, as do the 111 (3.154 Å) and 022 (1.932 Å) peaks of fluorite. This may lead the analyst to select a peak different from that chosen for reported RIR values.

Collated lists of RIR values for frequently encountered phases can be found in the ICDD database (Fawcett *et al.*, 2017) and Smith *et al.* (1987). It is important to note, however, that the user must be very careful when selecting an appropriate RIR value for their particular experiment. The values of RIR will depend upon the data-collection and measurement strategy employed (for example, peak height, integrated peak area, whole pattern, X-ray wavelength employed and so on) in their derivation. This must match the conditions used in the experiment to which the value is to be applied. In general, RIR values should be determined for the material currently being studied using the methodologies employed rather than relying on published values. Greater accuracy will be achieved if the relative intensities are determined as part of the calibration process using pure samples of the phase and standard or, preferably, samples in which the phases of interest have high and known concentration. If published values of RIR are used, then the determined phase abundances must be referred to as being only semi-quantitative.

3.9.3.4. *Matrix-flushing method*

An important feature of RIR-based techniques is that, once the RIRs are determined for the analyte phases of interest, the standard phase does not need to be present in the sample. The effect of the sample mass absorption coefficient is also removed by taking the ratio of the intensity of phase α to another unknown phase β. Hence the ratio of the weight fractions of the two phases can be derived from

$$\frac{W_\alpha}{W_\beta} = \frac{I_{i\alpha}}{I_{j\beta}} \frac{I_{j\beta}^{\mathrm{rel}}}{I_{i\alpha}^{\mathrm{rel}}} \frac{\mathrm{RIR}_{\beta s}}{\mathrm{RIR}_{\alpha s}}. \tag{3.9.13}$$

For a system comprising n phases, equation (3.9.13) allows the derivation of $n-1$ weight fraction ratios. Chung (1974*a*,*b*) has demonstrated that, if all components are crystalline and included in the analysis, an additional constraint of the following form can be included:

$$\sum_{k=1}^{n} W_k = 1.0. \tag{3.9.14}$$

This forms a system of n linear equations which can be solved to give the weight fractions of all components in the analysis according to (Chung, 1974*a*,*b*; Snyder & Bish, 1989)

$$W_\alpha = \frac{I_\alpha}{\mathrm{RIR}_{\alpha s} I_\alpha^{\mathrm{rel}}} \left(\sum_{k=1}^{n} \frac{I_k}{\mathrm{RIR}_{ks} I_k^{\mathrm{rel}}} \right)^{-1}. \tag{3.9.15}$$

The weight fractions analysed *via* this method are correct relative to each other but may not be correct in an absolute sense if unidentified or amorphous materials are present in the sample. In this case, the reported phase abundances will be overestimated. The addition of an internal standard to the system, or knowledge of the amount of a component phase determined by another technique, allows calculation of the absolute amount $W_{\alpha(\mathrm{abs})}$ of each phase [equation (3.9.16)] and thus the derivation of the amount W_{unk} of unknown (amorphous and/or unidentified) components [equation (3.9.17)].

$$W_{\alpha(\mathrm{abs})} = W_\alpha \times \frac{W_{\mathrm{std(known)}}}{W_{\mathrm{std(meas)}}}, \tag{3.9.16}$$

$$W_{\mathrm{unk}} = 1.0 - \sum_{k=1}^{n} W_{k(\mathrm{abs})}, \tag{3.9.17}$$

where $W_{\alpha(\mathrm{abs})}$ is the absolute weight fraction of phase α, $W_{\mathrm{std(known)}}$ is the known weight fraction of the standard added to the sample, $W_{\mathrm{std(meas)}}$ is the weight fraction of the standard reported by equation (3.9.15) and $W_{\rm unk}$ is the weight fraction of the unidentified and/or amorphous component in the mixture.

If an internal standard has been used, then initial calculation of its concentration *via* equation (3.9.15) may be:

(i) the same as the weighed amount, indicating that there are unlikely to be amorphous or unidentified phases present;

(ii) greater than the weighed amount, indicating that amorphous or unidentified phases may be present; or

(iii) less than the weighed amount, indicating operator error or the use of invalid RIR or $I^{\rm rel}$ values.

3.9.3.5. *Full-pattern fitting methods*

The quantitative XRD techniques described above have traditionally been applied using phase intensity estimates derived from either single peaks or a small group of peaks. This approach can be effective when there is minimal peak overlap but becomes less useful in complex phase systems where it may be difficult to identify freestanding peaks in the pattern. In addition, the presence of sample-related effects such as preferred orientation skew the measured intensities from what would be expected from an ideal powder diffraction pattern, thus reducing the expected accuracy.

Some of these effects can be partially overcome by using full-pattern fitting methods (Smith *et al.*, 1987; Batchelder & Cressey, 1998; Chipera & Bish, 2002, 2013; Eberl, 2003; Toraya & Tsusaka, 1995; Cressey & Schofield, 1996), where wide-range diffraction patterns of phases of interest are scaled, summed and compared with the observed diffraction data in a least-squares minimization process. The method relies on the generation of a library of standard patterns for each phase expected in the analysis collected under the same instrumental conditions as those used in subsequent analyses. The selection of standards that are a good match for the phases in the unknown sample is a critically important step. While the library will normally contain patterns of well ordered phases, it can also include patterns for less well ordered material such as glasses, polymers, clay minerals and gels, thus allowing their direct quantification. Where it is not possible to obtain a measured pattern, calculated patterns may also be included in the library.

Weight fractions are obtained by the solution of simultaneous equations that take into account the scale factors of the individual components and the mass absorption coefficients derived from knowledge of the elemental composition of each phase.

Alternatively, the contribution of library patterns to observed data can be normalized by scaling phases to an internal standard, typically corundum, using an RIR approach. Given the compositional and structural variability of some phases, especially in mineralogical applications, RIRs measured using the same minerals as those to be analysed are preferred to reported RIRs. Toraya (Toraya 2016*a*,*b*) has devised a QPA method which uses observed integrated peaks intensities measured of a wide 2θ range. Phase calibration constants are calculated using only their chemical formula weight and the sum of the square of the number of electrons in the formula unit. While the method is effective for wide-range data, it cannot be applied to single-peak data or data that cover only a limited 2θ range.

The full-pattern fitting method is relatively easy to use and can be applied to difficult samples containing highly disordered materials. For some disordered phases where no crystal structure is available and where peak overlap means that individual peak intensities cannot be measured, full-pattern fitting may be the most appropriate approach to QPA. The major limitations of the method include the need (i) to define and subtract the pattern background, with a subsequent impact on QPA, and (ii) to obtain or generate a library of standard patterns of the phases of interest. The use of an internal standard is recommended and the method is best applied when all standard patterns have first been normalized to an internal standard intensity (Chipera & Bish, 2002, 2013).

3.9.3.6. *Rietveld-based QPA*

The advent of the Rietveld method (Rietveld, 1969) and its extension into the field of QPA (Bish & Howard, 1988; Hill, 1983; Hill & Howard, 1987; O'Connor & Raven, 1988; Taylor, 1991) has brought some significant benefits when compared with the conventional single-peak and pattern-addition methods. Recent surveys (Madsen *et al.*, 2001; Scarlett *et al.*, 2002) show that the majority of participants, greater than 75%, use a Rietveld-based approach for QPA. The benefits derive from (Hill, 1991; Kaduk, 2000):

(i) The use of the entire diffraction pattern. Depending on the 2θ range of the data and the crystallography of the component phases, this may involve hundreds or thousands of reflections rather than the few peaks in conventional methods. This helps to minimize the impact of some systematic sample-related effects such as preferred orientation and extinction.

(ii) The ability to accurately deconvolute overlapping peaks to extract the component intensities, thus allowing more complex patterns to be analysed. The development of fundamental-parameters models (Bergmann *et al.*, 1998, 2000; Cheary & Coelho, 1992; Cheary *et al.*, 2004), which aim to distinguish instrument from sample contributions to the diffraction pattern, minimizes the number of profile parameters that need to be refined, further enhancing this profile-fitting step.

(iii) Refinement of the crystal structure, when supported by the data, to minimize differences between the intensities in the calculated and observed patterns. This brings additional information such as systematic changes in structure parameters from published data.

(iv) The ability to model some remaining systematic effects such as preferred orientation or anisotropic crystallite size/strain peak broadening.

The Rietveld method uses a least-squares procedure to minimize the difference between a calculated pattern and the measured data. The calculated pattern is derived from a model containing crystal-structure information for each phase included in the analysis, convoluted with expressions describing peak shape and width, along with functions to correct systematic variances such as preferred orientation. The calculated pattern is multiplied by an overall scaling factor which may be equated to the peak intensities ($I_{i\alpha}$) considered by the single-peak methods. The Rietveld scale factor for phase α, S_α, can be defined as (Bish & Howard, 1988; Hill, 1991; Hill & Howard, 1987; O'Connor & Raven, 1988)

$$S_\alpha = \left[\frac{K}{V_\alpha^2}\right]\left[\frac{W_\alpha}{\rho_\alpha}\right]\frac{1}{2\mu_m^*}, \qquad (3.9.18)$$

where K is an 'experiment constant' used to put W_α on an absolute basis, and V_α, W_α and ρ_α are the volume of the unit cell, the weight fraction and the density for phase α, respectively.

Since equation (3.9.18) inherently contains the weight-fraction information, it can be rearranged to derive W_α:

$$W_\alpha = \frac{S_\alpha \rho_\alpha V_\alpha^2 \mu_m^*}{K}. \qquad (3.9.19)$$

O'Connor & Raven (1988) and Bish & Howard (1988) have shown that K is dependent only on the instrumental conditions and is independent of individual phase and overall sample-related parameters. Therefore a single measurement is sufficient to determine K for a given instrument configuration and set of data-collection conditions. Determination of K may be carried out by (i) a measurement of either a pure phase, or a phase of known proportion in a mixture, separately from the measurement of the actual unknown mixture, or (ii) using a phase that is present in the sample in a known amount. The value of K calculated in this way will be appropriate for the calibration of subsequent measurements as long as all instrumental and data-collection conditions remain the same as those used in its determination.

For each phase, the density ρ_α can be calculated from the published (or refined) crystal-structure information using

$$\rho_\alpha = \frac{ZM_\alpha}{V_\alpha}, \qquad (3.9.20)$$

where ZM is the mass of the unit-cell contents (Z is the number of formula units in the unit cell and M is the molecular mass of the formula unit) and V is the unit-cell volume.[2]

Substitution of equation (3.9.20) in equation (3.9.19) shows that

$$W_\alpha = \frac{S_\alpha (ZMV)_\alpha \mu_m^*}{K}. \qquad (3.9.21)$$

In this context, $(ZMV)_\alpha$ is the 'phase constant' and can be calculated from published or refined crystal-structure information alone. It is worth noting that, if the crystal structure is refined as part of the analysis, ZMV is updated and hence becomes a dynamic phase constant.

The methodology embodied in equation (3.9.21) is important in many applications in that it produces, within the limits of experimental error, *absolute phase abundances* and is referred to hereafter as the *external standard* approach. While the use of a phase that already exists within the sample to determine K may be considered as an internal standard approach, in some applications, including *in situ* studies, that phase may be removed from the system through, for example, decomposition or dissolution. However, the value of K remains valid for subsequent determination of phase abundances provided that the instrumental and data-collection conditions do not change.

Equation (3.9.21) is directly applicable to the analysis of those phases for which detailed crystal-structure information is available. For phases where only a partial structure (for example, an indexed unit cell but no atom coordinates or site-occupation factors) is available, an empirical ZMV can be derived using mixtures of the phase of interest with known amounts of a well characterized standard (Scarlett & Madsen, 2006). QPA of phases with partial structure is also possible through the use of equation (3.9.19), but an estimate of the phase density, obtained through direct measurement, is required.

The limitations of the approach embodied in equations (3.9.19) and (3.9.21) derive from the need to (i) conduct a measurement of K and (ii) estimate the value of the mass absorption coefficient μ_m^* for the sample(s) used to determine K, as well as for each sample of interest. However, similar to the earlier discussion about the single-peak methods, μ_m^* can be determined by direct measurement or calculation using equations (3.9.4) or (3.9.5), respectively. The benefits that can be derived from the extraction of the absolute, rather than relative, phase abundances, make it worth pursuing in many analytical situations. For example, in time-resolved studies where phases transform and material is lost in the course of reaction, the calculation of relative abundances summed to 100% may give a misleading impression of increased amounts of the remaining phases.

In some diffraction instruments, there may be decay in the incident-beam intensity during the course of measurement. This may happen on the timescale of months for a laboratory-based instrument owing to X-ray tube ageing, or on the scale of minutes at a synchrotron instrument where the storage-ring current is only refreshed once or twice per day. In this case, the change in incident intensity can be taken into account by incorporating an additional term into equation (3.9.21):

$$W_{\alpha i} = \frac{S_{\alpha i} (ZMV)_\alpha \mu_m^*}{K} \frac{I_0}{I_i}, \qquad (3.9.22)$$

where I_0 and I_i are the incident beam intensities present during the determination of K and the collection of data set i, respectively.

The need to measure K, and measure or calculate μ_m^*, serves to increase the overall experimental difficulty and can be eliminated in ways analogous to those used in the single-peak methodology described earlier. For a simple two-phase mixture where both phases, α and β, are 100% crystalline, the sum of their weight fractions W_α and W_β equals unity and can be expressed as (Bish & Howard, 1988)

$$W_\alpha = \frac{W_\alpha}{W_\alpha + W_\beta}. \qquad (3.9.23)$$

Substitution of equation (3.9.21) for phases α and β in equation (3.9.23) results in

$$W_\alpha = \frac{S_\alpha (ZMV)_\alpha}{S_\alpha (ZMV)_\alpha + S_\beta (ZMV)_\beta}. \qquad (3.9.24)$$

Alternatively, in a multiphase sample, the addition of an internal standard s in known amount W_s and taking the ratio of equation (3.9.21) for analyte and standard phases provides the relationship

$$W_\alpha = W_s \frac{S_\alpha (ZMV)_\alpha}{S_s (ZMV)_s}. \qquad (3.9.25)$$

The method embodied in equation (3.9.25) is analogous to the *internal standard* approach in equation (3.9.9) and also serves to produce *absolute phase abundances* $W_{\alpha(\text{abs})}$. Once again, the benefit accruing from the use of absolute phase abundances is the ability to estimate the presence and amount of any amorphous and/or unidentified phases $W_{(\text{unk})}$ through application of equations (3.9.16) and (3.9.17).

Hill & Howard (1987) and Bish & Howard (1988) have adapted the matrix-flushing method of Chung (1974*a*,*b*) to the Rietveld analysis context. By constraining the sum of the analysed weight fractions to the assumed concentration of the crystalline components (usually unity), the weight fraction of phase α in an n-phase mixture is given by the relationship[3]

---

[2] When calculating phase density from crystallographic parameters, a factor of $1.6604 = 10^{24}/6.022 \times 10^{23}$ is needed to convert ρ in a.m.u. Å^{-3} to g cm^{-3}.

[3] It should be noted that the implementation of the matrix-flushing method by Bish and Howard retains the use of phase density, but their approach is essentially the same as that of Hill and Howard.

$$W_\alpha = \frac{S_\alpha(ZMV)_\alpha}{\sum_{k=1}^{n} S_k(ZMV)_k}. \qquad (3.9.26)$$

The use of equation (3.9.26) in QPA again eliminates the need to measure the instrument calibration constant and estimate the sample mass absorption coefficient. However, the necessity of normalizing the sum of the analysed weight fractions to unity only produces the correct *relative phase abundances*. This approach is the most widely used in Rietveld-based QPA and is almost universally coded into Rietveld analysis programs. If the sample contains amorphous phases and/or minor amounts of unidentified crystalline phases, the analysed weight fractions will be overestimated. Where absolute phase abundances are required in, for example, the derivation of reaction mechanisms in *in situ* studies, then one of the methods that produces absolute phase abundances must be used.

3.9.4. Demonstration of methods

The sample 1 suite from the IUCr Commission on Powder Diffraction (CPD) round robin on QPA (Madsen *et al.*, 2001) provides a useful basis for demonstrating the applicability some of the methods described above. Sample 1 was designed to provide a relatively simple analytical system in order to determine the levels of accuracy and precision that could be expected under ideal conditions. The key design criteria required that the phases exhibit little peak overlap in the low-angle region of the diffraction pattern and the samples have at least one freestanding peak for each phase in the *d*-spacing range 3.7 to 1.9 Å.

The three components (corundum, α-Al_2O_3; fluorite, CaF_2; and zincite, ZnO) were prepared in a ternary design to provide a total of eight different mixtures in order to cover as wide a range of composition as possible for each phase. The result is that each phase is present in the suite with concentrations of approximately 1, 4, 15, 33, 55 and 95 wt%. The exact compositions (Madsen *et al.*, 2001) can be found in Table 3.9.1. The unique chemical composition of the component phases also allowed the weighed compositions to be confirmed by measurement of total elemental composition using X-ray fluorescence (XRF) methods.

Data sets were collected from three replicates of the eight mixtures using a Philips X'Pert diffractometer equipped with a Cu long fine focus tube operated at 40 kV and 40 mA. The beam path was defined with 1° divergence, 0.3 mm receiving and 1° scatter slits. A curved graphite post-diffraction monochromator was fitted to eliminate $K\beta$ radiation. Data were collected from 15 to 145° 2θ in increments of 0.02° using a counting time of 1.5 s per step. These data sets are available as supporting information from http://it.iucr.org/ for any reader wishing to develop and test their skills in various methods.

For the single-peak methods, the net intensity for all peaks in the range 22 to 65° 2θ was extracted using a fundamental-parameters approach to peak fitting coded in the *TOPAS* software package (Bruker AXS, 2013). The choice of peak profile type is important, since any misfit will be reflected in the estimation of peak area and hence in the QPA. Unless otherwise stated, QPA was undertaken using the strongest peak in the pattern for each phase (corundum 113, d = 2.085 Å; fluorite 022, d = 1.932 Å; zincite 011, d = 2.476 Å). The average values for these peaks can be found in Table 3.9.2. For those methods requiring knowledge of the mass absorption coefficient, μ_m^* for each sample was calculated from the XRF chemical analysis results.

Table 3.9.1
Weighed composition (weight fraction) of the eight mixtures comprising sample 1 in the IUCr CPD round robin on QPA (Madsen *et al.*, 2001)

Sample	Corundum	Fluorite	Zincite
1A	0.0115	0.9481	0.0404
1B	0.9431	0.0433	0.0136
1C	0.0504	0.0136	0.9359
1D	0.1353	0.5358	0.3289
1E	0.5512	0.2962	0.1525
1F	0.2706	0.1772	0.5522
1G	0.3137	0.3442	0.3421
1H	0.3512	0.3469	0.3019

Table 3.9.2
Average values (n = 3) of net peak intensity derived using profile fitting for the strongest peaks of corundum (113), fluorite (022) and zincite (011)

The figures in parentheses are the standard deviations of the means. The sample mass absorption coefficient μ_m^* was calculated from the XRF-L determined composition.

Sample	Corundum	Fluorite	Zincite	μ_m^* (cm^2 g^{-1})
1A	34.8 (0.6)	8958.7 (33.0)	509.9 (6.0)	93.02
1B	6561.3 (28.6)	1095.5 (7.1)	474.3 (3.8)	34.45
1C	244.4 (0.9)	250.9 (10.1)	22898.0 (37.0)	49.03
1D	474.5 (3.5)	6559.6 (2.8)	5468.5 (9.5)	71.71
1E	2525.3 (27.9)	4835.5 (27.0)	3370.7 (16.3)	53.17
1F	1251.3 (7.8)	2935.8 (9.0)	12494.9 (22.4)	52.67
1G	1295.0 (8.7)	5041.7 (17.0)	6787.9 (26.6)	59.64
1H	1436.5 (7.3)	5132.0 (13.6)	5996.8 (59.5)	59.10

3.9.4.1. *Absorption–diffraction method*

In this method, the QPA of each phase is conducted independently of the others. For each phase, the determination of a specific calibration constant, C, was achieved using a rearranged equation (3.9.3). The sample where the relevant phase was present at about 55 wt% (sample 1E for corundum, 1D for fluorite and 1F for zincite) was taken to be the calibration sample.

For fluorite the determination of C proceeded using

$$C_{i,\alpha} = I_{i,\alpha}\frac{\mu_m^*}{W_\alpha} = 6559.6 \times \frac{71.71}{0.5358} = 877\,919. \qquad (3.9.27)$$

All data sets were then analysed using equation (3.9.3), as demonstrated here using sample 1H.

$$W_\alpha = I_{i,\alpha}\frac{\mu_m^*}{C_{i,\alpha}} = 5132.0 \times \frac{59.1}{877919} = 0.3455, \qquad (3.9.28)$$

compared with a value of 0.3469 added to the sample by weight. Fig. 3.9.1 shows the analysed concentration for all 24 fluorite measurements along with the bias from the known values. The bias (analysed − known) all fall within the range −0.3 to 0.5 wt% with no systematic bias as a function of concentration. The similar results achieved for corundum and zincite demonstrate the validity of the approach where there is minimal peak overlap.

3.9.4.2. *Internal standard method*

Application of the internal standard method normally requires the addition of an appropriate phase in known amount to each sample to be analysed. In order to use this data for demonstration of the internal standard method, it is necessary to designate one of the existing phases as the internal standard. Sample 1H has been used to derive the calibration constant, with fluorite considered to be the phase of interest while zincite is designated as the internal standard. The intensities (Table 3.9.2) and known concentrations (Table 3.9.1) of these phases can then be used to derive $C^{ij}_{\alpha s}$ from equation (3.9.8) to eliminate the need to know or measure μ^*_m for the sample.

$$\frac{I_{\text{fluorite}}}{I_{\text{zincite}}}\frac{W_{\text{zincite}}}{W_{\text{fluorite}}} = C^{ij}_{\alpha s} = \frac{5132.0}{5996.8}\times\frac{0.3019}{0.3469} = 0.7448. \qquad (3.9.29)$$

Analysis of the unknowns (Fig. 3.9.2) then proceeds *via* equation (3.9.9) and is demonstrated here using sample 1D:

$$W_{\text{fluorite}} = \frac{W_{\text{zincite}}}{C^{ij}_{\alpha s}}\frac{I_{\text{fluorite}}}{I_{\text{zincite}}} = \frac{0.3289}{0.7448}\frac{6559.6}{5468.5} = 0.5297, \qquad (3.9.30)$$

compared with a value of 0.5358 added to the sample by weight.

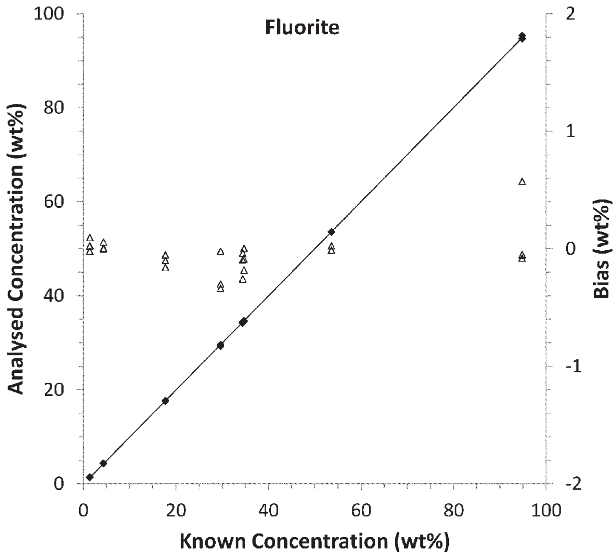

Figure 3.9.1
Plot of the analysed concentration (black diamonds – left axis) and the bias (open triangles – right axis) expressed as wt% for fluorite using the absorption–diffraction method. The analysis was calibrated using sample 1D, which has a fluorite concentration of 53.58 wt%.

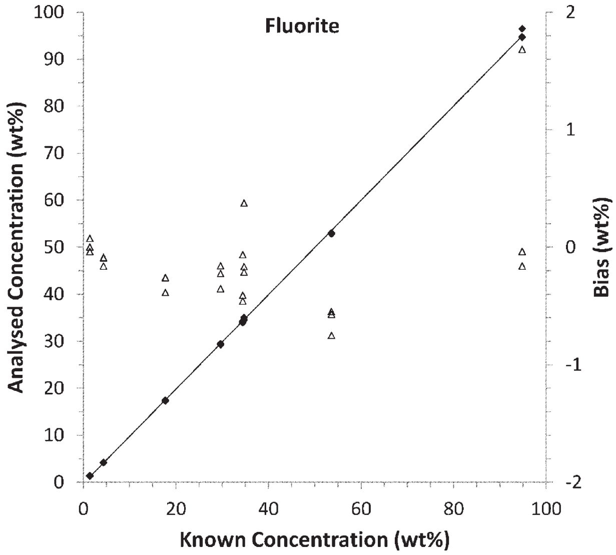

Figure 3.9.2
Plot of the analysed concentration (black diamonds – left axis) and the bias (open triangles – right axis) expressed as wt% for fluorite using the internal standard method with zincite designated as the internal standard. The analysis was calibrated using sample 1H where the fluorite and zincite concentrations are 34.69 and 30.19 wt%, respectively.

3.9.4.3. *Reference intensity ratio*

For this exercise, the peak intensities and phase concentrations in Tables 3.9.1 and 3.9.2 for sample 1H can be used to determine the RIRs for fluorite and zincite.

$$\text{RIR}_{\text{fluorite}} = \frac{5132.0}{1436.5}\times\frac{0.3512}{0.3469} = 3.617, \qquad (3.9.31)$$

$$\text{RIR}_{\text{zincite}} = \frac{5996.8}{1436.5}\times\frac{0.3512}{0.3019} = 4.856. \qquad (3.9.32)$$

These RIRs should be compared with reported values for fluorite in the ICDD database (ICDD, 2015) which have an average of 3.83 (n = 33) but range from 2.40 to 4.21. For zincite the reported RIR values have an average of 5.24 (n = 50) and range from 4.50 to 5.87. The discrepancies in the various reported values of the RIRs highlight the need to determine them under the same conditions as the samples being analysed if the highest accuracy is to be achieved.

Fig. 3.9.3 shows the RIR values calculated from all 24 (eight samples, three replicates each) measurements for fluorite and zincite plotted as a function of corundum concentration. At intermediate concentrations there is quite good agreement between the determined values. However, there are significant deviations at low corundum concentration, resulting in insufficient measured intensity in the corundum peak to ensure sufficient accuracy in the RIR. Hence, care should be taken to ensure that there are sufficient counts in the peaks used to determine the RIR. In addition, a low concentration automatically means that there are fewer grains contributing to the diffraction process; hence particle statistics may also present a significant problem.

The presence of other sample-related aberrations that affect the measured intensities also needs to be considered. For example, microabsorption may affect measured RIR values differently in different concentration ranges. The impact of such effects on the analysis is reduced by their inclusion in the measured RIR provided that variation induced by, for example, sample preparation can be kept to a minimum.

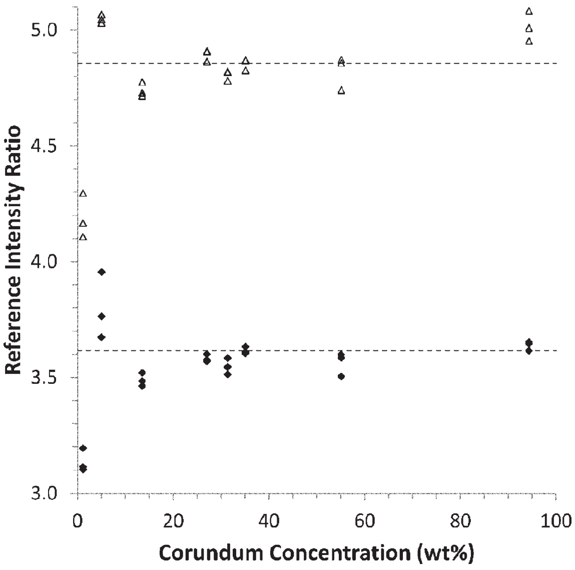

Figure 3.9.3
Plot of the 24 determined RIR values for fluorite (black diamonds) and zincite (open triangles) as a function of corundum concentration. The dashed lines represent the average RIR values for fluorite (lower) and zincite (upper) determined from the three replicates of sample 1H where all phases have approximately equal concentration.

3.9.4.4. *Matrix flushing*

Once the correct value of RIR is determined for each phase, the matrix-flushing method can be applied using equation (3.9.15). For fluorite in sample 1D, the calculation proceeds as follows:

$$\begin{aligned} W_{\rm fluorite} &= \frac{I_{\rm fluorite}/{\rm RIR}_{\rm fluorite}}{\sum_{k=1}^{n} I_k/{\rm RIR}_{ks}} \\ &= \frac{6559.6/3.617}{474.5/1.0 + 6559.6/3.617 + 5468.5/4.856} = 0.5312, \end{aligned} \tag{3.9.33}$$

compared with a value of 0.5358 added to the sample by weight. Fig. 3.9.4 shows the bias for fluorite in all samples analysed by the matrix-flushing method. Once again, there is good agreement between the weighed and analysed amounts. However, it is worth reiterating that this method normalizes the sum of all analysed weight fractions to unity. If amorphous or non-analysed phases are present in the sample, then the weight fractions will be overestimated relative to their absolute abundances.

3.9.4.5. *Rietveld-based methods*

The strengths and weaknesses of some of the methods described in Section 3.9.3 are highlighted through a study of the mechanism and kinetics of nucleation and crystal growth in the context of the Bayer process for the extraction of aluminium from bauxite ores (Webster *et al.*, 2010). Specifically, the experiments utilize synthetic Bayer liquors, consisting of Al-loaded caustic solutions to which a variety of seed material is added. Several polymorphs of $Al(OH)_3$ (gibbsite, bayerite and nordstrandite) crystallize from solution onto the seed material. The rate of crystallization and the ratio of the phases formed depend on the sample conditions used, including the Al and caustic concentrations in solution, as well as sample temperature.

The mechanism and rate of crystallization were followed by collecting XRD data at the powder-diffraction beamline of the Australian Synchrotron[4] over a period of about 3 h. The diffractometer incorporates a Mythen detector (Schmitt *et al.*, 2003) which allows for the simultaneous collection of 80° 2θ of the diffraction pattern. A wavelength of 0.826 Å was used to ensure adequate penetration of the beam in the sample. The sample environment (Madsen *et al.*, 2005; Norby *et al.*, 1998) consisted of a 1-mm quartz glass capillary containing a slurry of the seed and Bayer liquor heated to temperatures between 333 and 348 K using a hot-air blower.

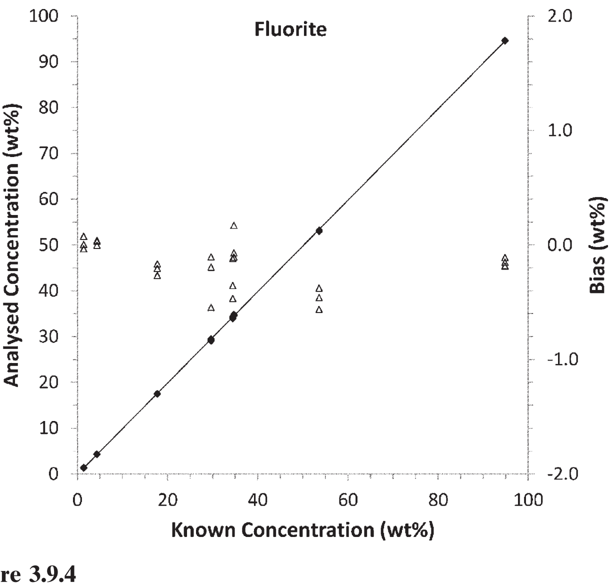

Figure 3.9.4
Plot of the analysed concentration (black diamonds – left axis) and the bias (open triangles – right axis) expressed as wt% for fluorite using the matrix-flushing method with RIRs of 1.0, 3.617 and 4.856 for corundum, fluorite and zincite, respectively. The RIRs were determined using sample 1H where the corundum, fluorite and zincite concentrations are 35.12, 34.69 and 30.19 wt%, respectively.

The data were analysed using *TOPAS* (Bruker AXS, 2013), where a learned-profile approach to peak modelling was used with an empirical instrument width and shape contribution determined using the NIST SRM660 LaB_6 profile standard. For the samples in the study, refined parameters included 2θ zero offset, a Chebychev polynomial pattern background and, for each phase, the Rietveld scale factor, crystallite size and strain, and unit-cell dimensions.

A number of different approaches were used to extract the phase abundances at each stage of the reaction. Initially, QPA was derived using equation (3.9.26); the value that many Rietveld analysis programs output as their first estimate of phase abundance. Fig. 3.9.5 shows the QPA output from an *in situ* experiment in which goethite (FeOOH) was added as the seed.

At the start of the experiment, prior to the crystallization of any of the $Al(OH)_3$ polymorphs, Fig. 3.9.5 shows that the reported concentration of the goethite seed is 100 wt% since it is the only phase represented in the analysis at that time. On formation of gibbsite, bayerite and nordstrandite, the goethite concentration appears to decrease progressively to about 65 wt% while the total $Al(OH)_3$ concentration reaches about 35 wt% at the end of the experiment. However, these figures are in disagreement with (i) the fact that goethite is unlikely to dissolve or otherwise be consumed in this system (Murray *et al.*, 2009), (ii) the known addition of goethite to the sample (14.13 wt%) and (iii) the total amount of $Al(OH)_3$ available from solution (15.92 wt%). The problem with the QPA in this case arises from the fact that only the crystalline components are considered in the analysis and that equation (3.9.26) normalizes the sum of their analysed weight fractions to unity. However, aluminium, which is in solution at the start of the run, forms crystalline phases continuously throughout the reaction after an initial induction period. In order to overcome the anomalies in the QPA results, it is necessary to consider the sample as a whole; that is, the concentration of both the solid and liquid components in the X-ray beam for the duration of the experiment.

In this sample, the concentration of the goethite seed was 14.13 wt% in the slurry injected into the sample capillary. If the assumption is made that, in this environment, goethite is unreactive and its concentration will not change during the reaction, it can be used as an internal standard to put the $Al(OH)_3$ concentrations on an absolute basis. The QPA results derived using the internal standard or 'spiked' approach in equation (3.9.25) are shown in Fig. 3.9.6.

The goethite concentration is fixed at the known addition (14.13 wt%) at the start of the experiment. However, the concentrations of the $Al(OH)_3$ polymorphs are now put on an absolute scale, thus allowing derivation of more meaningful reaction mechanisms.

If, however, there is residual doubt about the reactivity of the goethite, it may be necessary to use the external standard approach embodied in equation (3.9.21). In this case, the value for the instrument constant, K, can be derived using the Rietveld scale factor, ZMV and the known addition of goethite in a rearranged equation (3.9.21). For this determination, the goethite scale factor from the first few data sets, prior to the start of the reaction, was averaged to minimize any errors that may be introduced by counting statistics. The value of the sample mass absorption coefficient μ_m^* was set to an arbitrary value of unity for both the determination of K and all subsequent analyses, since the overall chemical content of the capillary, and hence the attenuation of the X-ray beam, does not change during the reaction.

---

[4] Australian Synchrotron beamtime award number AS091/PD1035.

This experimental work was conducted at the Australian Synchrotron where the storage-ring current was boosted every 12 h. Between these times the current, and hence the incident-beam intensity, decays, resulting in what amounts to a change in the 'instrument configuration'. This requires a modification of the K value and subsequent calculation of concentration to compensate for the changing incident intensity using equation (3.9.22).

Fig. 3.9.7 now shows the results of QPA derived from equation (3.9.22). In this case the concentrations of the $Al(OH)_3$ polymorphs are similar to those in Fig. 3.9.6. However, since the phase abundances are derived using an external standard approach, any changes in the apparent goethite concentration can now be monitored. Fig. 3.9.7 shows that the goethite concentration did not change significantly in the early stages of the experiment ($t < 10$ min) before $Al(OH)_3$ crystallization was observed but there is a small, systematic decrease in the apparent goethite concentration as the experiment progresses. At the end of the experiment, the goethite concentration appears to be lower by about 1% relative to the concentration at the start.

This apparent decrease could be due to a number of causes including (i) poor correction for beam-intensity changes or (ii) solid material moving about in the capillary with some movement out of the X-ray beam. Alternatively, the decrease could be attributed to the 'shielding' of the goethite from the X-ray beam by the $Al(OH)_3$ phases as they form and coat the goethite particles. This decrease could then be used to obtain an average thickness of the $Al(OH)_3$ phases on the seed particles. This layer was calculated to be about 5.5 µm (assuming a linear absorption coefficient of $9.5\ \text{cm}^{-1}$ for gibbsite at 0.826 Å) resulting in an overall particle size of about 11 µm at the end of the run (the goethite particles are about 0.2 × 2 µm and hence do not contribute significantly to the overall particle size). These values are in good agreement with independent studies (Webster *et al.*, 2010) where the gibbsite was examined using scanning electron microscopy (SEM) techniques (Fig. 3.9.8) following crystallization under similar conditions to those used here.

3.9.5. Alternative methods for determination of calibration constants

3.9.5.1. *Standardless determination of the phase constant C*

In order to determine the phase calibration constant C, it is common to obtain (i) a pure sample of the phase of interest that accurately reflects the form of the phase in the samples to be analysed, or (ii) a multiphase sample in which the phase concentration is known by other means (for example, chemical analysis or point counting). In some systems, there may be insufficient sample available to risk 'contaminating' it with an internal standard, especially if the material needs to be analysed using other techniques. The addition of an internal standard may also introduce microabsorption problems or increase the complexity of patterns that are already highly overlapped. For other situations, the time frame demanded for the analysis may prohibit the time-consuming procedures of standard addition, data collection and separate determination of the phase calibration constant.

Zevin & Kimmel (1995) have described an approach to the derivation of phase constants which relies on having a suite of samples to be analysed that (i) have the same phases present in all samples and (ii) exhibit a wide range of composition of these phases in various samples in order to stabilize the analysis. If we reconsider the relationship between the weight fraction W_α and the observed intensity [equation (3.9.3)],

$$W_\alpha = \frac{I_\alpha \mu_m^*}{C_\alpha}, \tag{3.9.34}$$

and assume that all phases in the system are known and included in the analysis, we can introduce the additional constraint that the sum of all W_α's is unity (or at least a known value):

$$\sum_{j=1}^{n} W_j = 1.0. \tag{3.9.35}$$

In a system of n samples containing m phases, we can explicitly write the relationships expressed in equations (3.9.34) and (3.9.35) as a set of simultaneous equations:

$$\begin{aligned}
1.0 &= \frac{1}{C_1} I_{11}\mu_1^* + \frac{1}{C_2} I_{12}\mu_1^* + \ldots + \frac{1}{C_m} I_{1m}\mu_1^*,\\
1.0 &= \frac{1}{C_1} I_{21}\mu_2^* + \frac{1}{C_2} I_{22}\mu_2^* + \ldots + \frac{1}{C_m} I_{2m}\mu_2^*,\\
1.0 &= \frac{1}{C_1} I_{n1}\mu_n^* + \frac{1}{C_2} I_{n2}\mu_n^* + \ldots + \frac{1}{C_m} I_{nm}\mu_n^*,
\end{aligned} \tag{3.9.36}$$

where μ_n^* is the mass absorption coefficient for the nth sample.

Knudsen (1981) has described a modification to this approach by including an internal standard in each of the samples to be analysed and using the ratio of intensities of the analyte and internal standard phases in place of the I_{nm} in equation (3.9.36). While this eliminates the need to determine and use the mass absorption coefficient, the tedious procedure of adding and mixing an internal standard is required for each sample and for reasons described above may not be appropriate.

The relationships embodied in equations (3.9.36) can be expressed more simply in matrix notation as

$$\mathbf{L}' = \mathbf{I}'\mathbf{C}', \tag{3.9.37}$$

where $\mathbf{L}'$ is a column vector (dimensions $1 \times n$) containing the known (or assumed) sum of weight fractions for each sample (unity in this case), $\mathbf{C}'$ is a column vector (dimensions $1 \times m$) containing the calibration constants for each phase and $\mathbf{I}'$ is a rectangular matrix (dimensions n rows × m columns) containing the measured peak intensities (or scale factors) for each phase multiplied by the sample mass absorption coefficient.

A least-squares solution of equation (3.9.37) to derive the value for C for each phase can be calculated using matrix-manipulation methods (Knudsen, 1981):

$$\mathbf{C}' = \left(\mathbf{I}'^T\mathbf{I}'\right)^{-1}\mathbf{I}'^T\mathbf{L}', \tag{3.9.38}$$

where the superscripts T and -1 represent the transpose and inverse matrix functions, respectively.

Accuracy in the calculation of the individual values of C is improved by having (i) phases of the same or similar composition in all samples and (ii) a wide range of concentrations of each phase across the sample suite. These conditions may be met in,

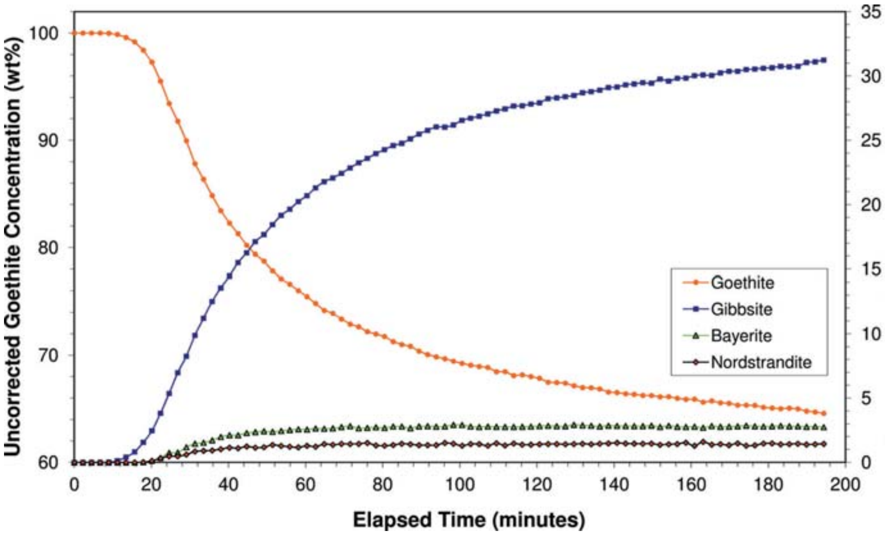

Figure 3.9.5
The results of QPA of the *in situ* XRD data collected during the seeding experiments of Webster *et al.* (2010). The values were derived using the Hill/Howard (Hill & Howard, 1987) relationship in equation (3.9.26). Note the decrease in apparent goethite concentration (left axis) as the polymorphs of Al(OH)$_3$ (right axis) crystallize from solution.

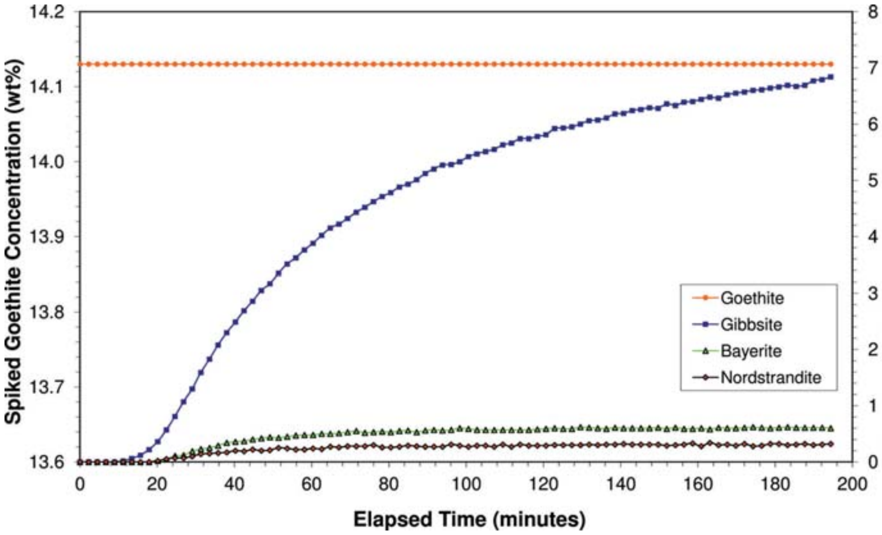

Figure 3.9.6
The results of QPA of the *in situ* XRD data collected during the seeding experiments of Webster *et al.* (2010).The values are absolute phase abundances derived using the internal standard relationship in equation (3.9.25).

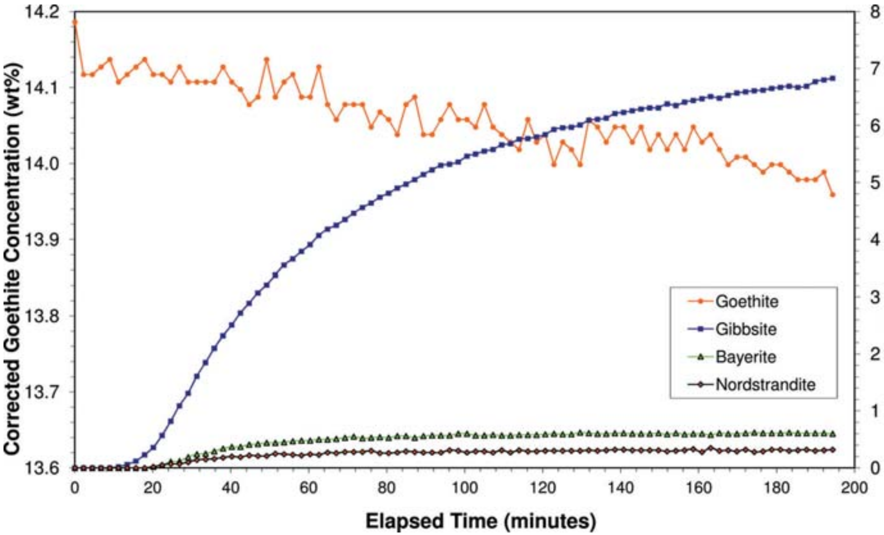

Figure 3.9.7
The results of QPA of the *in situ* XRD data collected during the seeding experiments of Webster *et al.* (2010). The values are absolute phase abundances derived using the external standard relationship in equation (3.9.22). Note the slight decrease in the goethite concentration (left axis) during the run.

for example, mineral exploration samples where a limited number of phases are present in a drill core but their abundance varies as a function of depth. In mineral processing or industrially based material manufacture, the goal is usually to control the system to minimize compositional variation in the product. The side effect of this is that the values of intensity in matrix **I** have too little variation, resulting in large errors in the derived values for C. In the limiting case, the system may become indeterminate with no unique solution available. To overcome this, forced or accidental changes to processing conditions may introduce sufficient compositional variation to stabilize the determination of the C values through equation (3.9.38). Alternatively, physical or chemical separation of selected components may be sufficient to provide the required compositional variation. Knudsen (1981) provides a detailed statistical analysis used in the determination of the errors in the phase constants.

While Zevin (Zevin & Kimmel, 1995) and Knudsen (1981) have demonstrated the application of this approach for single-peak methods, it is equally applicable if scale factors derived from whole-pattern fitting or Rietveld-based methods are used.

3.9.5.2. *Demonstration of the Zevin approach*

The sample 1 suite from the IUCr CPD round robin on QPA again provides an ideal platform for demonstrating the applicability of this method due to the wide variation of concentration of the constituent phases. A measure of intensity was derived using an hkl_phase (see Section 3.9.6) in which the peak positions were constrained to the space group and unit-cell parameters but the individual peak intensities were refined to empirical values using a pure sub-sample of each of the three phases. For the analysis of the samples, the relative peak intensities were fixed and an overall scale factor S for each phase in each sample (eight samples, three replicates, three phases), multiplied by the mass absorption coefficient calculated from the XRF-determined composition, was used as the measure of intensity. These $S\mu_m^*$ values then formed the intensity matrix **I** in equations (3.9.37) and (3.9.38) while all values in the vector **L** were assumed to be 1.0 (*i.e.* all samples were assumed to be fully crystalline). Microsoft Excel provides a useful platform for these calculations since it contains all of the matrix-manipulation functions required by equation (3.9.38). The determined values for C for the three phases are given in Table 3.9.3. The values in the C/C_{corundum} column should be compared with the values derived in Section 3.9.4.3 above.

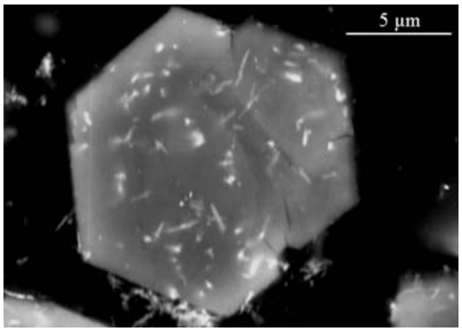

Figure 3.9.8
SEM image of $Al(OH)_3$ (grey hexagon) which has crystallized on goethite seed (light grey needles) (Webster *et al.*, 2010).

Application of these C values to the analysis of all samples *via* equation (3.9.34) yields the results given in Fig. 3.9.9. The results, displayed as bias from the known values, show that at all concentration ranges the analyses are within about ±1% of the weighed values. The important point to note here is that there has been *no prior calibration* conducted to obtain this result; the system is self-calibrating and has only relied on having a wide range of concentrations of the three phases in the sample suite. The only prior knowledge used in the analysis is (i) a measure of peak intensity embodied in the empirical phase scale factor and (ii) an estimate of μ_m^* for each sample calculated from the elemental composition.

3.9.5.3. *Experiment constant – a whole-sample approach*

Earlier discussion has noted that the experiment constant K used in equation (3.9.21) can be determined using (i) a standard pure phase or mixture measured separately from the measurement of the actual unknown mixture being analysed, or (ii) using a phase that is present in the sample in a known amount. However, in some cases, these approaches are not always effective in producing reliable values of K because the methodology assumes that the mass of sample contributing to the diffraction process is constant. While this condition is true for infinitely thick samples in Bragg–Brentano geometry, it is unlikely to be true for capillary or flat-plate samples in transmission geometry. In these cases, the sample thickness and packing density will have a significant influence on the amount of sample contributing to the diffraction process and hence on the observed intensity and the derived values of K. Therefore, a K value determined from one capillary sample is unlikely to be applicable to another capillary even though all other instrumental conditions remain the same. However, for *in situ* studies, a K value determined at the start of an experiment should remain valid as the analysis proceeds.

K can also be determined using the whole sample, rather than an individual phase. Since the determined value of K then applies equally to all phases in the sample, equation (3.9.21) can be summed over all analysed components thus:

$$\sum_{i=1}^{n} W_i = (\mu_m^*/K) \sum_{i=1}^{n} S_i(ZMV)_i. \tag{3.9.39}$$

If the crystallinity of the sample is known (or can safely be assumed), then individual phase abundances are not required and K can be calculated from

$$K = \frac{\mu_m^* \sum_{i=1}^{n} S_i(ZMV)_i}{\sum_{i=1}^{n} W_i}, \tag{3.9.40}$$

where $\sum W_i$ is the assumed crystallinity of the entire sample.

Table 3.9.3
Phase calibration constants for corundum, fluorite and zincite determined using the Zevin (Zevin & Kimmel, 1995) and Knudsen (Knudsen, 1981) method

The RIR values were derived earlier in this chapter.

Phase	C	$C/C_{\rm corundum}$	RIR
Corundum	240.91	1.0	1.0
Fluorite	874.27	3.629	3.617
Zincite	1190.81	4.943	4.856

For a sample that is 100% crystalline and all components included in the analysis, then the denominator is unity and K is simply the sum of the product of the scale factors and their respective ZMV's multiplied by the mass absorption coefficient of the entire sample.

For *in situ* studies where a reaction or process is examined dynamically, sealed capillary sample geometry is frequently used. In this environment, the *chemical* composition of the capillary contents will not change during the course of the reaction even though individual phases may be undergoing transformation. Equation (3.9.40) can be further simplified since the overall sample mass absorption coefficient remains constant throughout the reaction and can therefore be deleted and its effect incorporated into K.

This whole-sample approach to the determination of K is also useful in systems where there are residual errors that may not be evident when equation (3.9.21) is used with the concentration of a single phase. By way of demonstration, the sample 1 suite from the IUCr CPD round robin on QPA has been used to calculate K in two distinct ways:

(1) *Phase specific*: Three replicate measurements of the eight mixtures were analysed using a Rietveld-based surface-analysis approach (Stinton & Evans, 2007). This approach refines a single model to all data sets in the suite simultaneously allowing parameters that are common to all samples to be determined with a greater degree of certainty. Since the sample suite contains corundum, fluorite and zincite in a wide range of concentrations, application of a rearranged equation (3.9.21) using the refined scale factors results in 72 separate determinations of K. The value of μ_m^* for each sample was derived from XRF-determined compositions using equation (3.9.5), while the values for W_i were taken from the known weight additions.

(2) *Whole sample*: Equation (3.9.40) was applied to each of the 24 data sets (*i.e.* three replicates each of the eight samples) assuming (i) that all phases were known and fully crystalline, *i.e.* $\sum W_i = 1$; and (ii) μ_m^* for each sample was derived in the manner described above.

Fig. 3.9.10 shows the 72 individual determinations of K from the phase-specific method as a function of known phase concentration. At high concentrations, the values for K derived from each of the three phases are similar indicating that, for effectively pure phase samples, the approach embodied in equation (3.9.21) is valid. However, if K is determined using the known concentration of a single phase at a lower concentration in a multiphase sample, then residual errors in the measurement of pattern intensity serve to reduce its accuracy. At lower concentrations of corundum, there is a systematic increase in the determined value of K resulting from a small microabsorption effect present in these samples. Since corundum has the lowest mass absorption coefficient of the three phases in this system its intensity, and hence Rietveld scale factor, is slightly

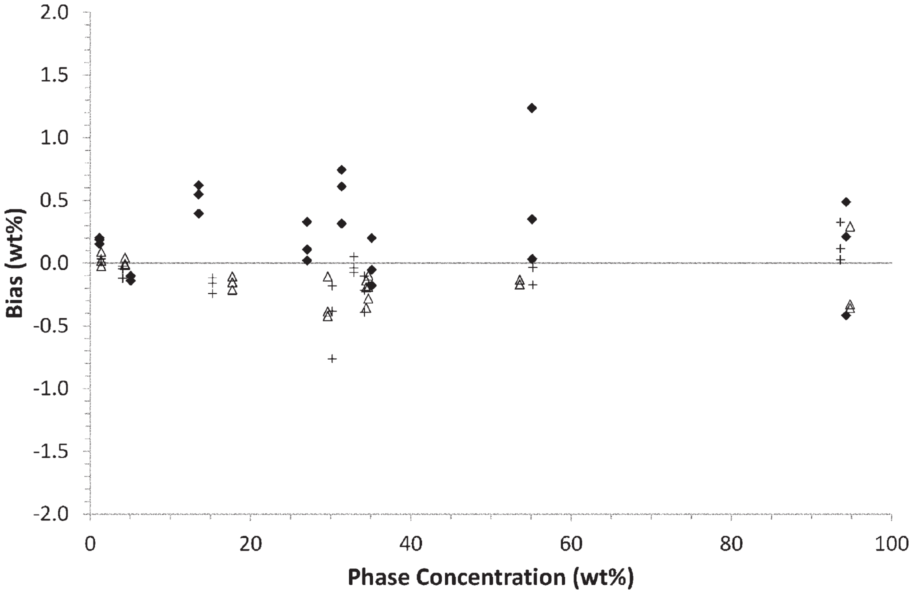

Figure 3.9.9
Plot of the bias (known − determined) in the analysed phase abundances using the Zevin & Kimmel (1995) approach for corundum (black diamonds), fluorite (open triangles) and zincite (crosses). The 72 determinations derive from three replicates of eight mixtures containing three phases each.

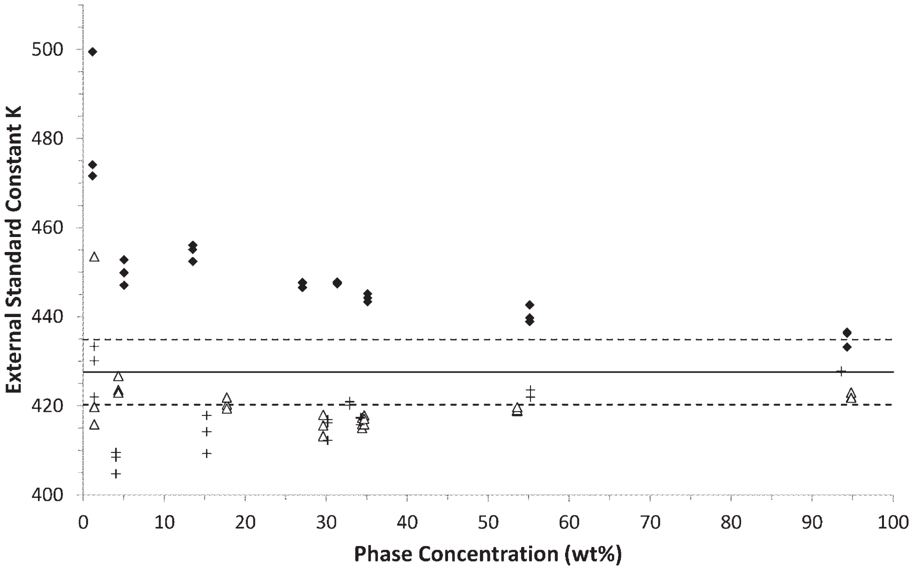

Figure 3.9.10
Plot of the experiment constant K as a function of known phase concentration for corundum (closed diamonds), fluorite (open triangles) and zincite (crosses) using the phase-specific method. The 72 determinations derive from three replicates of eight mixtures containing each of the three phases. The solid line is the mean of 24 values determined using the whole-sample approach. The dashed lines represent ±2 standard deviations about this mean.

overestimated relative to the fluorite and zincite. This results in an overestimation of the value of K relative to an ideal sample; the magnitude of this difference is about 5% relative. Use of these values for subsequent analysis will result in an underestimation of phase concentrations using equation (3.9.21). The converse is true if fluorite or zincite is used to determine K.

However, if the whole-sample approach embodied in equation (3.9.40) is used for the determination of K, these residual sample-related aberrations can be eliminated; the results of the determination of 24 values of K using this approach are also included in Fig. 3.9.10. The mean of all 24 determinations is 427.6 (3.7) representing a relative error of <0.8%. The important point to note here is that knowledge of the individual phase concentrations is not needed; the only assumption needed relates to the total crystallinity of each sample.

For *in situ* studies, using equation (3.9.40) to calculate K at each step i in the reaction (defined as K_i) can be useful in deriving details of the reaction mechanism. If K_i increases as the reaction progresses, this may be indicative of increasing crystallinity in the sample. Reductions in K_i during the reaction may point to the formation of intermediate amorphous material or unidentified crystalline components, the total concentration of which can be readily calculated using

$$\mathrm{wt\%}_{\mathrm{amorphous}} = 100\left(1 - \frac{K_i}{K}\right). \qquad (3.9.41)$$

Application of this can be demonstrated using sample 3 from the QPA round robin (Scarlett *et al.*, 2002), as it contains the same three crystalline phases as the sample 1 suite with the addition of 29.47 wt% amorphous silica flour. Calculation of K_i for sample 3, based only on the three crystalline phases, results in a value of 301.8. Substituting this into equation (3.9.41) along with the previously determined value of K (427.6) gives a measured amorphous content of 29.42 wt% – this is in good agreement with the known weighed amount. The important point to note here is that the data for sample 3 were collected at the same time, and under the same instrumental conditions, as for sample 1, which ensured that the true value of K was the same for all data.

3.9.6. Quantification of phases with partial or no known crystal structures

While the Rietveld-based methods described in Section 3.9.3.6 work for well ordered phases with known crystal structures, they are limited when published structure data do not accurately represent the phase actually present in the sample, are incomplete or do not exist. Poor agreement with published structure data is a common occurrence in mineralogical research where disorder exists and observed diffraction data deviate significantly from the ideal; this situation occurs with many of the clay minerals. The issue of incomplete or non-existent structure data can occur in almost any area where new materials are either synthesized or discovered. The growing demand for the analysis of materials from the nanotechnology community, where phases are at the boundary of what can be considered crystalline, serves to further highlight these limitations. Recent developments in diffraction methods have sought to address these issues and have used approaches that include the development of calibrated models or, where appropriate, the extension of existing structure data to incorporate systematic disorder such as stacking faults in clay minerals.

3.9.6.1. *Use of calibrated models*

Calibrated models are generally developed in one of two ways. The first (which uses what is referred to hereafter as an hkl_phase) is obtained *via* the use of partial structure information. Here the peak positions are constrained by a unit cell and space group but the relative intensities, in the absence of atom types and locations in the unit cell, are determined empirically from a pure sample or one where the phase is present in a mixture at a known concentration. The second method involves the use of a discrete set of peaks whose positions, intensities, width and shape are all determined empirically. Once determined using a standard sample, this group of peaks may then be scaled as a single unit and is referred to hereafter as a peaks_phase.

The software *SIROQUANT* (Taylor & Rui, 1992) employs the simultaneous use of observed and calculated standard profiles within the framework of the Rietveld method. It draws on a library of structures that are stored as lists of reflections and intensities (hkl files). These are calculated on a cycle-by-cycle basis for well described crystalline materials but are read directly from the hkl files for poorly defined materials such as clay minerals. This method still requires some knowledge of the crystal chemistry of all phases involved and that they be included within the programme's database. By the inclusion of reflection information in this way some aberrations such as preferred orientation may be allowed for. This approach to clay mineralogy also provides for the refinement of two sets of halfwidth parameters in order to model the co-existing sharp and broad reflections generated by such minerals.

A subsequent development of the whole-pattern approach is the 'partial or no known crystal structure' (PONKCS) method (Scarlett & Madsen, 2006). This method operates within the framework of the Rietveld method but replaces the traditional crystal structure of the phases in question with an empirical set of peaks (either as an hkl_phase or a peaks_phase). These can then be scaled as a single unit in the course of refinement in similar fashion to the set of structure factors derived from a crystal structure. Since the full structure information is not available, it is not possible to calculate the *ZMV* phase constant normally required for quantification *via* equation (3.9.26) (Hill & Howard, 1987); hence, an empirical value must be derived through calibration.

3.9.6.1.1. *Generation of calibrated PONKCS models*

The generation of a suitable PONKCS model requires that:

(1) The unknown phase is available as either a pure specimen or as a component of a mixture where its abundance is known (in some instances, this may be achieved by other means, such as the measurement of bulk and/or microchemical composition.)

(2) The unknown phase does not vary considerably from the material used to derive the relative intensities of the model. Preferred orientation and other sample-related effects may be compensated for based upon an indexed diffraction pattern.

The initial step in the generation of a PONKCS model is to describe the contribution to the diffraction pattern of the phase with a series of peaks. If the phase of interest has been indexed, the Le Bail or Pawley methods (see Chapter 3.5) can be used to constrain peak positions to the space group and unit-cell parameters while the individual reflection intensities are allowed to vary to best match the observed peaks (*i.e.* an hkl_phase). If the phase has not been indexed, a series of unrelated peaks can be refined using a standard material and scaled as a group during analysis (*i.e.* a peaks_phase). While this approach is effective in most cases, it restricts the refinable parameters that may be used in the treatment of systematic errors such as preferred orientation.

The next step is to calibrate the hkl_phase or peaks_phase and derive a 'phase constant' that is equivalent to the *ZMV* value in crystal-structure-based quantification. This is achieved by the preparation of a mixture in which there are known amounts W_α and W_s of the unknown and standard, respectively. Recalling equation (3.9.25), the ratio of the weight fractions is then given by

$$\frac{W_\alpha}{W_s} = \frac{S_\alpha (ZMV)_\alpha}{S_s (ZMV)_s}, \qquad (3.9.42)$$

where S_α and S_s are the refined scale factors for the unknown and standard, respectively.

Rearrangement of equation (3.9.42) then provides the means for determining an empirical value of $(ZMV)_\alpha$, which is required for the calibration of a peaks_phase:

$$(ZMV)_\alpha = \frac{W_\alpha}{W_s}\frac{S_s}{S_\alpha}(ZMV)_s. \qquad (3.9.43)$$

For an hkl_phase the value of V can be determined from the refined unit-cell parameters and hence can be removed from the phase constant resulting in

$$(ZM)_\alpha = \frac{W_\alpha}{W_s}\frac{S_s}{S_\alpha}\frac{(ZMV)_s}{V_\alpha}. \qquad (3.9.44)$$

Unlike the *ZMV* value derived from the unit-cell contents of a crystal structure, the phase constants derived using equations (3.9.43) and (3.9.44) have no physical meaning, since they have been derived by empirical measurement. For an hkl_phase, a more physically meaningful value of *ZM* can be obtained by deriving the true unit-cell mass from the measured phase density according to

$$(ZM)_{\alpha(\rm true)} = \frac{\rho_\alpha V_\alpha}{1.6604}. \qquad (3.9.45)$$

The empirical 'structure factor' values in the hkl_phase could then be scaled according to the relation $ZM_{\alpha(\rm true)}/ZM_\alpha$, making them approximate 'real' structure factors for the material. Note that this final step is not necessary for quantification, but may make the method more generally applicable.

3.9.6.1.2. *Application of the model*

The PONKCS method is applicable to any mixture in which there are one or more phases that are not fully characterized crystallographically, including essentially amorphous material, provided appropriate calibration samples can be obtained. In the mineralogical context, it may not be possible to obtain pure phase specimens typical of those found in the bulk mixtures, but it may be possible to concentrate them to a point where they can be used. Methods of achieving this may include gravity or magnetic separation, or selective chemical dissolution.

The original paper describing this method (Scarlett & Madsen, 2006) gives a detailed example based upon sample 1 from the IUCr CPD round robin on QPA (Madsen *et al.*, 2001; Scarlett *et al.*, 2002). There, corundum was regarded as the unknown phase, fluorite as an impurity of known crystal structure and zincite a standard material added at known weight fraction. In the same paper, there is a more realistic example regarding the poorly ordered clay mineral nontronite, which is of commercial significance but difficult to quantify *via* traditional structure-based Rietveld methodology. Further details regarding quantification of this mineral *via* the PONKCS method is given in articles detailing its importance in low-grade nickel laterite ores (Scarlett *et al.*, 2008; Wang *et al.*, 2011).

A calibration-based method such as PONKCS may also find increasing application with phases that have a known crystal structure. It has the greatest potential for accuracy, as the calibration process may obviate residual aberrations in the data such as microabsorption. Assuming that the sample suite has the same absorption characteristics as that used for calibration, such aberrations will be included in the calibration function and require no further correction during the sample analysis. This is a realistic scenario for routine analyses in industries as diverse as mineral processing, cement production and pharmaceutical production.

3.9.6.2. *Modelling of structural disorder*

One major challenge for QPA is the treatment of stacking disorder. An alternative to the use of calibrated models is to develop extended structure models that more effectively represent the phases present in the sample than the simple structure models. Stacking disorder occurs in layered structures where long-range order is present within the layers but there is only partial or even no relationship from one layer to another. It is a commonly occurring type of microstructure and is of great interest in various fields including mineralogy and material science.

The most common types of stacking faults in lamellar structures are:

(i) translational stacking faults, characterized by well defined translation vectors between successive layers;
(ii) rotational stacking faults, characterized by irregular but well defined rotation of adjacent layers in a stack; and
(iii) random stacking faults (turbostratic stacking), where there is no registry from one layer to another. This can be readily visualized as a stack of playing cards lying flat on top of each other but with no alignment between the edges (Fig. 3.9.11).

Mixed-layer (interstratified) systems contain different types of layers in a single stack, hence it is necessary to distinguish these from the types above. In this case, the layer types have different basal spacings and atomic coordinates (for example, illite–smectite interstratifications; Reynolds & Hower, 1970). Combinations of several of these types of disorder frequently occur in natural clay minerals. Intricate structural analysis using modelling techniques can give a reliable picture of the disorder of selected pure clay minerals, but such information is difficult to obtain from multiphase samples. Therefore, the type and degree of disorder of the components in natural rocks is one of the major unknowns when starting a quantitative analysis of such samples. The field of clay mineralogy represents a discipline where QPA has a long tradition, but has struggled with issues arising from a wide variety of disorder types. This complexity has led practitioners away from the use of crystallographic models and encouraged modification of the classical methods of quantitative analysis to incorporate empirical, calibration-based techniques such as those described earlier in this section.

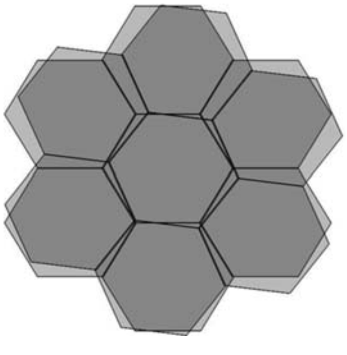

Figure 3.9.11
Turbostratic disorder, illustrated by the stacking of two hexagonal layers rotated by 7°.

An alternative approach is the application of a robust mathematical description of the observed features in the diffraction pattern, thus minimizing their impact on the QPA. In QPA, the existence of disorder contributes to inaccuracy through line broadening and shifting, which results in difficulties in the extraction of integral intensities or scale factors. A range of tools for the modelling of diffraction patterns of disordered layer structures has existed since the middle of the last century (Hendricks & Teller, 1942; Warren, 1941); these have been summarized by Drits & Tchoubar (1990).

In clay mineralogy, highly oriented samples are used for phase identification and characterization. One-dimensional diffraction patterns are collected initially from these, commonly air-dried, oriented samples and contain the information along **c*** that is characteristic of the type, composition and sequence of the layers comprising the clay. Based on this information, the clay minerals are classified into layer types, a classification which is a precursor to more precise identification of mineral species. Diffraction patterns are often collected again following various treatments of the oriented samples (*e.g.* solvation with ethylene glycol, heating to predetermined temperatures for specified times, wetting and drying cycles). Changes in peak positions, shapes and intensities between treatments are also diagnostic for identification of the clay mineral type present.

From a mathematical point of view, the one-dimensional calculation of intensities is much less laborious than a three-dimensional one, because only z coordinates are used and a–b translations and rotations are not considered. In 1985 Reynolds introduced the software package *NEWMOD* for the simulation of one-dimensional diffraction patterns for the study of interstratified systems of two clay minerals (Reynolds, 1985). This simulation was based upon a suite of parameters including instrumental, chemical and structural factors, and has been widely applied to the QPA of interstratified clays *via* the 'pattern-mixing' approach. An updated version (*NEWMOD+*; Yuan & Bish, 2010) has since been developed that incorporates improvements in clay-structure modelling, an improved GUI and the calculation of various fitting parameters that improve the operator's ability to estimate the quality of the profile fit.

The principal drawback of one-dimensional pattern approaches to QPA is that they are limited to the quantification of the ratio of layered structures only. Other minerals within the sample cannot be quantified at the same time. The degree of preferred orientation achieved in the oriented specimens may also differ between the mineral species present depending upon the method of sample preparation (Lippmann, 1970; Taylor & Norrish, 1966; Zevin & Viaene, 1990). This will affect the intensities of the observed peaks, which in turn affects the modelling of the relative proportions of the constituent minerals (Dohrmann *et al.*, 2009; Reynolds, 1989). Therefore, the quantification of minerals from severely oriented samples such as these is frequently inaccurate, as existing correction models are unable to describe the intensity aberrations adequately (Reynolds, 1989).

Quantification of clay minerals within multiphase specimens requires the modelling of the three-dimensional pattern of the randomly ordered clay. There are a number of approaches incorporated in various software packages for the calculation of these three-dimensional diffraction patterns of disordered structures. *WILDFIRE* (Reynolds, 1994) calculates three-dimensional diffraction patterns of randomly oriented illite and illite–smectite powders with various types and quantities of rotational disorder. This is limited, however, to specific mineral types (the procedure has provided much information about the structural disorder of illite, for example) and is computationally demanding. Another approach is the general recursive method of Treacy *et al.* (1991), which simulates diffraction effects from any crystal with stacking disorder. This uses the intensity calculations of Hendricks & Teller (1942) and Cowley (1976) along with Michalski's recurrence relations describing disorder (Michalski, 1988; Michalski *et al.*, 1988). The calculation process for this method is less time consuming than that of *WILDFIRE*, but has the drawback of requiring the user to define the complete stacking sequence including stacking-transition probabilities and interlayer vectors. The original software for this method, *DIFFAX* (Treacy *et al.*, 1991), was extended by a refinement algorithm to *DIFFAX*+ (Leoni *et al.*, 2004) and *FAULTS* (Casas-Cabanas *et al.*, 2006), but multiphase analysis is not possible within either package.

The application of Rietveld-based methods is widespread with many industrial applications, but their application to samples containing disordered materials is not yet routine. As the classical Rietveld method is based on the calculation of intensity for discrete reflections, the question of how the diffraction patterns of disordered phases may be modelled arises.

In principle, every atomic arrangement can be described in the space group $P1$ if the cell parameters are sufficiently large and a reflection-intensity calculation using the Rietveld method could then be performed. But the absence of symmetry in such 'large cell' models makes them inflexible, and parameters describing probabilities of translational and rotational stacking faults and layer-type stacking may not be directly included and refined. Nevertheless, some applications of such externally generated, large-cell structures in Rietveld phase analysis have been published; for example the phase analysis of montmorillonite (Gualtieri *et al.*, 2001).

The use of small, ideal cells in a traditional Rietveld approach for the calculation of diffraction patterns is hampered by the fact that the number of reflections generated by such models is insufficient to fit the asymmetric peak shapes of disordered layer structures. Standard anisotropic line-broadening models exist, such as ellipsoids (Le Bail & Jouanneaux, 1997), spherical harmonics (Popa, 1998) or the distribution of lattice metric parameters (Stephens, 1999), but these are typically unable to fit the patterns of disordered layered structures. They may also become unstable when physically unrealistic parameters are introduced, such as higher-order spherical harmonics. The application of such standard broadening models to clay minerals has therefore not proved successful.

Other Rietveld-based methods attempt to approximate the diffraction features of disordered layered materials by empirical enhancement of the number of reflections. The simplest method is the splitting of the reflections of a traditional cell into two or three separate reflections that can be separately broadened and shifted, following prescribed rules (Bergmann & Kleeberg, 1998). In this way, the broadening of special classes of peaks, for example reflections with $k \neq 3n$, can be modelled. This method is particularly suitable for structures showing well defined stacking faults, such as **b**/3 translations or multiples of 120° rotations. However, when structures show more complex disorder, such as turbostratic stacking, simple geometric dependencies of broadening and shifting are not sufficient to approximate their diffraction patterns.

Turbostratically disordered structures can be depicted in reciprocal space as infinite rods perpendicular to the *ab* plane and parallel to $\mathbf{c}^*$; see Fig. 3.9.12 (Ufer *et al.*, 2004). The diffraction features from such disordered materials consist of two-dimensional asymmetric bands, as can be observed typically for smectites and some other clay minerals (Brindley, 1980). One method for approximating the diffraction effects along the reciprocal-lattice rods within the Rietveld method is *via* the 'single-layer' approach (Ufer *et al.*, 2004). Here, a single layer is placed in a cell elongated along $\mathbf{c}^*$, which is effectively a 'supercell'. In doing this, an enhanced number of discrete lattice points are generated along the rods, according to the factor of elongation of the cell. This elongation generates a continuous distribution of additional *hkl* positions on the reciprocal rods. The inclusion of only a single layer in the supercell destroys periodicity, which is lacking in turbostratically disordered structures. By treating the pseudo-peaks of the supercell in the same manner as other structures within the Rietveld method (*i.e.*, introducing additional broadening, scaling the intensity) and separately calculating the peaks of the $00l$ series, the patterns of turbostratic structures like smectites can be reliably fitted. The model generated in this fashion can be used directly in phase quantification (Ufer, Kleeberg *et al.*, 2008; Ufer, Stanjek *et al.*, 2008).

However, this approach is limited to the turbostratic case. Moreover, the basal $00l$ series points are conventionally calculated, assuming rational diffraction from constant basal spacings in the stack. So the method cannot be applied to mixed-layered structures.

In order to overcome this limitation, Ufer *et al.* (Ufer, Kleeberg *et al.*, 2008; Ufer *et al.*, 2012) combined the recursive calculation method of Treacy *et al.* (1991) and the supercell approach in the structure-description code of the Rietveld software *BGMN* (Bergmann *et al.*, 1998). In this method a supercell is used to generate numerous discrete *hkl* spots along $\mathbf{c}^*$, but the partial structure factors are calculated by the recursive algorithm. This allows the refinement of structural parameters of mixed-layered structures and simultaneous Rietveld QPA to be performed (Ufer *et al.*, 2012). A broader introduction of such models in Rietveld phase analysis can be expected with the

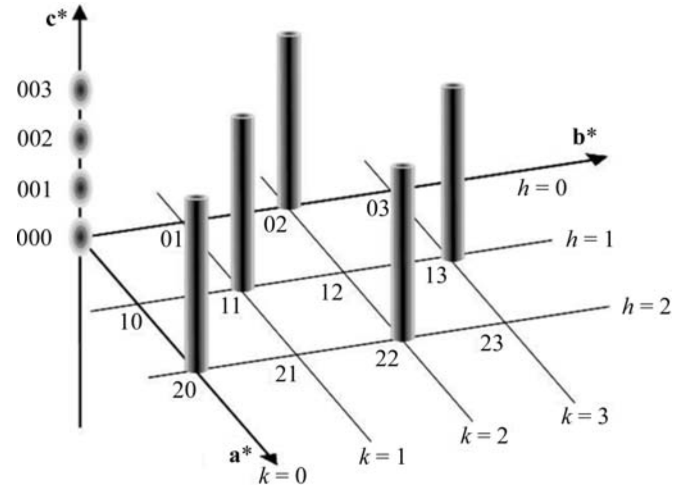

Figure 3.9.12
Section of the reciprocal lattice of a turbostratically disordered pseudo-hexagonal *C*-centred structure.

development of reliable structure models and enhanced computational power (Coelho *et al.*, 2016, 2015; Bette *et al.*, 2015).

3.9.6.3. *Quantitative determination of amorphous material*

Traditionally, most activity in diffraction-based QPA has been concerned with the assessment of the crystalline components. However, all materials possess a non-diffracting surface layer with some degree of disorder or contain some surface reaction products and adsorbed species. While such a layer can easily account for ~1 wt% of the entire sample in a finely divided solid, the fraction of this surface layer will increase as the particle size decreases (Cline *et al.*, 2011). In addition, some materials can contain separate phases that may be amorphous or at least poorly crystalline. The advent of nanotechnology has served to further blur the boundaries between what is defined by powder XRD as crystalline or amorphous.

During *in situ* studies, some phases undergo transformations *via* amorphous intermediate components; the presence of these phases has the potential to influence our understanding of reaction mechanisms. Given the potential for these amorphous components to influence bulk-material properties, the need to quantify them is an increasingly important issue for analysts using diffraction-based methods. Many of the traditional phase-quantification techniques described in this chapter fail to take into account the occurrence of amorphous material in the sample and, without careful attention by the analyst, its presence may remain undetected.

Madsen *et al.* (2011) recently reviewed a range of techniques for the determination of amorphous content and assessed their applicability for various analytical situations. The study used both single-peak and whole-pattern methodology and applied it in two distinct ways.

(1) The first method used an indirect approach; the crystalline components were quantified and put onto an absolute scale using either an internal- or external-standard method. The amorphous content was then determined by subtracting the sum of the absolute weight fractions of the crystalline components from unity.

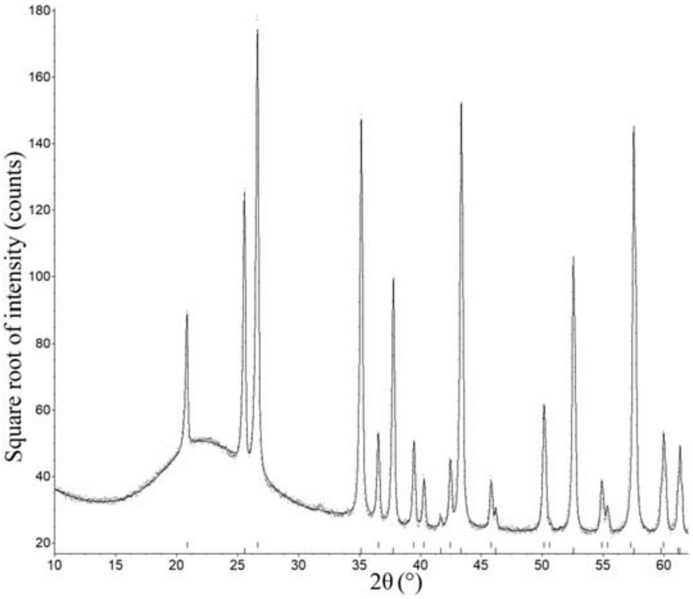

Figure 3.9.13
Output of Rietveld refinement of XRD data (Cu *Kα* radiation) for a synthetic sample containing a mixture crystalline and amorphous phases. The observed data are represented as grey dots and the calculated pattern as the solid black line overlaying them. The broad peak centred at ~22° 2θ is due to amorphous silica flour. The rows of tick marks at the bottom represent the positions of the Bragg reflections for quartz (upper) and corundum (lower).

(2) The second method used a direct approach; it relied on being able to 'see' the amorphous contribution in the diffraction and being able to obtain an estimate of its intensity during analysis (Fig. 3.9.13). Intensity contributions of amorphous phases are not always evident in the diffraction pattern, especially at low concentrations. Even when their presence is apparent, it can be difficult to resolve their contribution from other components of the diffraction pattern such as pattern background. However, once an intensity estimate is obtained, and an appropriate calibration constant derived, the amorphous phase can be included in the analysis along with the crystalline components.

In general, for the determination of amorphous material the problem will dictate the method(s) used. All methods discussed in the study of Madsen *et al.* (2011) are, in principle, capable of determining the concentration of amorphous material in mixtures with similar levels of accuracy and precision as is possible for crystalline phases (down to ~1% absolute or better). The limitations are similar to those for the QPA of crystalline phases, and are dictated by sample properties and the analytical techniques used.

A summary of the recommendations resulting from the study include:

(1) Where the intensity contribution of the amorphous content to the diffraction pattern is not evident, one of the indirect methods (internal or external standard) should be used. For indirect methods, any errors in the analysis of the crystalline phases will decrease the overall accuracy attainable since the amorphous phase abundance is determined by difference.

(2) Where intensity contributions of amorphous phases are evident in the diffraction pattern, any method based on the direct modelling of the amorphous component provides improved accuracy relative to the indirect methods.

(3) Calibration-based methods usually have the potential to achieve the highest accuracy, as residual aberrations in the data, such as microabsorption, are included in the calibration function. Caution is advised here as the magnitudes of these residual errors may change with different sample suites, and so a calibration function derived for one sample suite may not be generally applicable.

(4) A sample of pure amorphous material, or a sample where the amorphous content is high and its concentration known, is normally required to establish an accurate model for the direct methods.

Some materials contain more than one amorphous phase and there may be a desire to quantify these separately rather than as a group. This provides a significant challenge since their broad diffraction patterns will be highly overlapped, thus leading to a high degree of correlation during analysis. However, Williams *et al.* (2011) have demonstrated that, with careful experimentation and data analysis, it is possible to provide QPA for two poorly crystalline components in geopolymers.

Phase abundances reported in the literature are often provided in a manner that suggests they are absolute values. Where no specific allowance for amorphous content has been made and reported, it is better to assume that the reported phase abundances are correct relative to one another, but may be overestimated in an absolute sense. Therefore, standard practice in QPA should be to use methodology which produces *absolute* rather than *relative* phase abundances. Any positive difference between unity and the sum of the absolute weight fractions will alert the analyst to the presence of non-analysed material in the sample.

3.9.7. QPA from *in situ* experimentation

In situ analysis is a growth area in the field of powder diffraction (Ehrenberg *et al.*, 2013) and is dealt with in depth elsewhere in this volume (see Chapter 2.9). The technique is unparalleled in providing information about reaction mechanisms and kinetics under simulated operational conditions and without the artefacts potentially associated with post-mortem sampling or *ex situ* methods.

An *in situ* experiment collects dynamic, time-resolved data, which present unique challenges for QPA. The phase assemblages formed in such experiments may be quite complex and change dramatically over the course of the experiment. In addition, the data are generally of lower quality than those collected for *ex situ* samples at ambient conditions. This may be due to poor counting statistics resulting from the rapid counting times needed to follow various phase transitions. Data for *in situ* studies are often collected using area detectors, some of which are not photon-counting devices. Care should be taken in the error propagation and hence the weighting used during data analysis.

The data quality may also be affected by components in the sample chamber that are required in order to achieve the environmental conditions (temperature, pressure, solution or gaseous atmosphere, and so on) necessary for the experiment: these components may either attenuate the incident and diffracted beams or contribute features to the pattern resulting from scattering of the beam.

One very important issue that arises from *in situ* studies is the large number of data sets generated. The rapid counting times available at modern synchrotron and neutron facilities mean that hundreds or thousands of diffraction patterns can be collected over the duration of the *in situ* experiment.

3.9.7.1. *Data analysis*

There are usually a series of steps involved in the analysis of *in situ* diffraction data. Given the large number of data sets collected, it is generally not practicable to undertake detailed analysis of every pattern individually. Since any changes to the component phases are transitions generally observed in a sequence of patterns, data analysis focused on extracting QPA could be undertaken using the following steps:

(1) Cluster the data into a number of groups necessary to describe the major phase regions present during the reaction. This can be achieved (i) visually, using software that allows the plotting of three-dimensional data sets of the type shown in Fig. 3.9.14, or (ii) through the use of automatic clustering algorithms using, for example, principal-component analysis.

(2) Select the 'most typical' pattern of each cluster as well as the two 'least typical' patterns at the extreme ends of the cluster. These patterns are often identified by clustering software based on the statistical similarity between patterns in the cluster.

(3) Identify the phases present in each cluster using the most typical pattern. This is not always a trivial task since (i) new phases that are not currently present in databases may have been generated; (ii) effects such as thermal expansion or variation of chemical composition may have changed the peak positions so that search/match procedures are no longer successful; or (iii) impurity elements may have stabilized phases that are not expected from related phase-diagram studies.

(4) For the discussion here, it will be assumed that the quantification process will be *via* a whole-pattern method.
   (*a*) Develop appropriate (crystal structure or PONKCS) models for every phase observed within the data suite.
   (*b*) Optimize the pattern and phase-analysis parameters using the most typical pattern selected from each cluster.
   (*c*) Set the relevant parameter refinement limits using the least typical patterns. It is necessary to limit the range over which refined parameters can vary to avoid the return of physically unrealistic values.

(5) Owing to the large number of data sets, analysis for QPA will generally be approached as a batch process with limited refinement of structural parameters. This limitation on the total number of refinable parameters is necessary during batch processing in order to avoid instability in the refined values as the phases progress from major to minor concentration.

(6) Batch processing of data suites may be conducted in a variety of ways including:
   (*a*) Sequential refinement, beginning with either the first or final pattern of the suite and including all phases present in the entire suite. This methodology must be tempered by a means to either remove or severely restrict refinement of any phases that are not present in all patterns of the suite in order to avoid the reporting of 'false positives' where absent phases have been included. Some software packages allow phases to be removed from the analysis if their abundance is below a selected level or has an error that exceeds some predefined criteria (Bruker AXS, 2013).
   (*b*) Parametric Rietveld refinement (Stinton & Evans, 2007), where the entire suite of diffraction data is analysed simultaneously. Selected parameters are constrained to the applied external variable (*e.g.* temperature) with a function describing their evolution throughout the data sequence. For example, the unit-cell parameters for a phase can be constrained to vary according to their thermal coefficients of expansion. This method can bring stability to refined parameters and allows the refinement of noncrystallographic parameters such as temperature and reaction rate constants directly from the diffraction data. This methodology is particularly suited to relatively simple phase systems, but is difficult to develop for complex multiphase mineralogical systems.

(7) In selecting a model for use in QPA, it is highly recommended that one of the approaches that generate absolute phase abundances is used. Many reactions generate intermediate amorphous phases that convert to crystalline components later in the reaction. If relative phase abundances [such as those produced by the *ZMV* approach embodied in equation (3.9.26)] are used, the amounts of the crystalline phases will be overestimated and this will give misleading indications about the reaction mechanism and kinetics.

Whichever method is employed, it is always necessary to examine a sample of individual results as a test of veracity rather than just accepting the suite of numbers for parameter values and QPA resulting from batch processing.

The study of Webster *et al.* (2013) demonstrates many of these points by following the formation mechanisms of the iron-ore

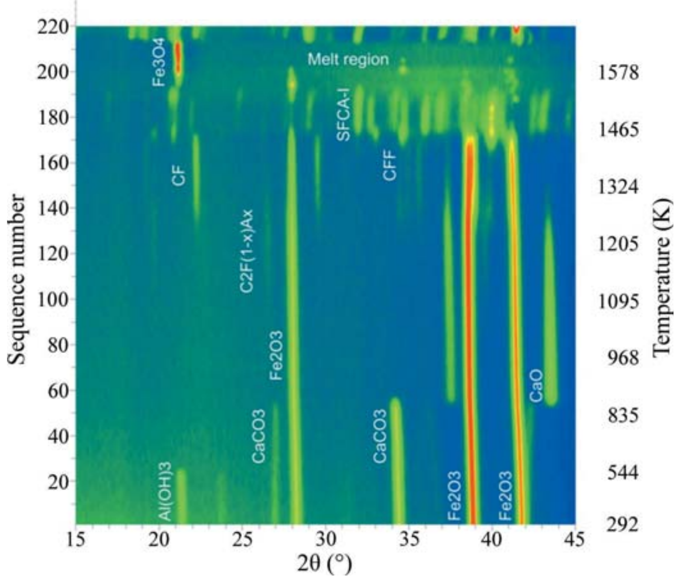

Figure 3.9.14
Raw *in situ* XRD data (Co $K\alpha$ radiation) collected during the synthesis of the iron-ore sinter bonding phase SFCA-I (Webster *et al.*, 2013). The data, collected as a function of heating temperature, are viewed down the intensity axis with red representing the highest intensity and blue the lowest intensity. The identified phases include gibbsite $Al(OH)_3$, calcite $CaCO_3$, haematite Fe_2O_3, lime CaO, calcium ferrites CF and CFF, calcium alumina-ferrite $C_2F_{1-x}A_x$, magnetite Fe_3O_4, and SFCA-I.

sinter bonding phase, SFCA-I, where SFCA = silico-ferrite of calcium and aluminium (Scarlett, Madsen *et al.*, 2004; Scarlett, Pownceby *et al.*, 2004; Webster *et al.*, 2013). The starting material, comprising a synthetic mixture of gibbsite, $Al(OH)_3$, haematite, Fe_2O_3, and calcite, $CaCO_3$, was heated to about 1573 K using an Anton Paar heating stage. The laboratory-based XRD data, collected using an Inel CPS120 diffractometer, are shown in Fig. 3.9.14, while the QPA results are shown in Fig. 3.9.15. Both figures show that there are several phase changes, including the formation of transient intermediate phases before the final production of SFCA.

In Fig. 3.9.15(*a*) the QPA results are derived using the Hill/Howard algorithm (Hill & Howard, 1987) in equation (3.9.26): this is the 'default' value reported by most Rietveld analysis software and normalizes the sum of the analysed components to 100 wt%. The apparent increase in haematite concentration at about 533 and 868 K results from the decomposition of gibbsite and calcite, respectively. There are no possible mechanisms in this system that could lead to an increase in haematite concentration at these temperatures; the reported increases are an artefact derived from normalizing the sum of all analysed phases to 100 wt%. Fig. 3.9.15(*b*) shows the correct result derived using the external-standard approach (O'Connor & Raven, 1988) embodied in equation (3.9.21), which has placed the values on an absolute scale. Fig. 3.9.15 demonstrates the importance of putting the derived phase abundances on an absolute scale for a realistic derivation of reaction mechanism and kinetics.

3.9.8. QPA using neutron diffraction data

One of the early papers detailing the application of the Rietveld method to quantitative phase analysis used neutron diffraction (ND) data (Hill & Howard, 1987). The reasons stated within this work define many of the advantages of neutrons over X-rays for diffraction in general and QPA in particular. One of the most significant advantages for QPA derives from the fact that neutrons interact weakly with matter, hence there is very little microabsorption with ND even in samples comprising a mixture of high- and low-atomic-number materials.

The high penetration capability of neutrons also enables the use of larger sample environments in *in situ* studies, thus enabling studies to be undertaken at, for example, higher pressures than would be possible with many X-ray sources. In addition, larger sample volumes can be investigated, which in turn produces better particle statistics and makes the technique less sensitive to grain size. It also makes ND a bulk technique in comparison with XRD, which is effectively surface-specific with a penetration depth of the order of microns or tens of microns.

The different strengths of ND and XRD mean that they can be exploited in combination to provide complementary information. For example, XRD generally has higher angular resolution and is therefore better at resolving small lattice distortions and heavily overlapped phases. However, the observed intensities in ND do not decrease as strongly with decreasing *d*-spacing. This results in ND providing more accurate determination of atomic displacement parameters and therefore the Rietveld scale factors; this then improves the accuracy of QPA derived from these scale factors (Madsen *et al.*, 2011).

Hill *et al.* (1991) have investigated the phase composition of Mg-PSZ (partially stabilized zirconia) using both ND and XRD. The surfaces of these materials were subjected to various treatments, which meant that they were no longer representative of the bulk. From the more highly penetrating ND data they obtained bulk properties including crystal structure and size and strain parameters of the components along with QPA. From XRD they were able to examine the surface of the samples to investigate the effects of surface grinding and polishing.

The majority of Rietveld-based QPA still relies on the use of accurate crystal structure models; consequently, it is of increasing importance that powder diffraction methods used for structure solution be robust and reliable. Combining laboratory or synchrotron XRD and ND has been shown to be of considerable benefit in the solution of complex structures *via* powder diffraction (Morris *et al.*, 1992). This joint-refinement approach has been used to determine the crystal structure of a component phase of Portland cement (De La Torre *et al.*, 2002) for subsequent use in Rietveld-based QPA.

One of the disadvantages of neutron sources is that they are much less accessible than laboratory X-ray sources and of much lower flux than either laboratory or synchrotron X-rays sources. In addition, larger samples are generally required; this is not always practical in the investigation of many materials.

In many phase systems, the presence of severe microabsorption in XRD data serves to limit the accuracy that can be obtained. The collection of ND data, where microabsorption is virtually absent, from selected samples provides more accurate QPA; selected ND-based values can therefore act as a benchmark for the more routine XRD-based studies.

3.9.9. QPA using energy-dispersive diffraction data

Energy-dispersive diffraction (EDD) involves the use of high-energy white-beam radiation, often from a synchrotron source. This provides very high penetration and is, therefore, ideal as a probe to examine the internal features of relatively large objects (Barnes *et al.*, 2000; Cernik *et al.*, 2011; Hall *et al.*, 1998, 2000). In an experimental arrangement such as that in Fig. 3.9.16, diffraction data can be measured by energy-dispersive detec-

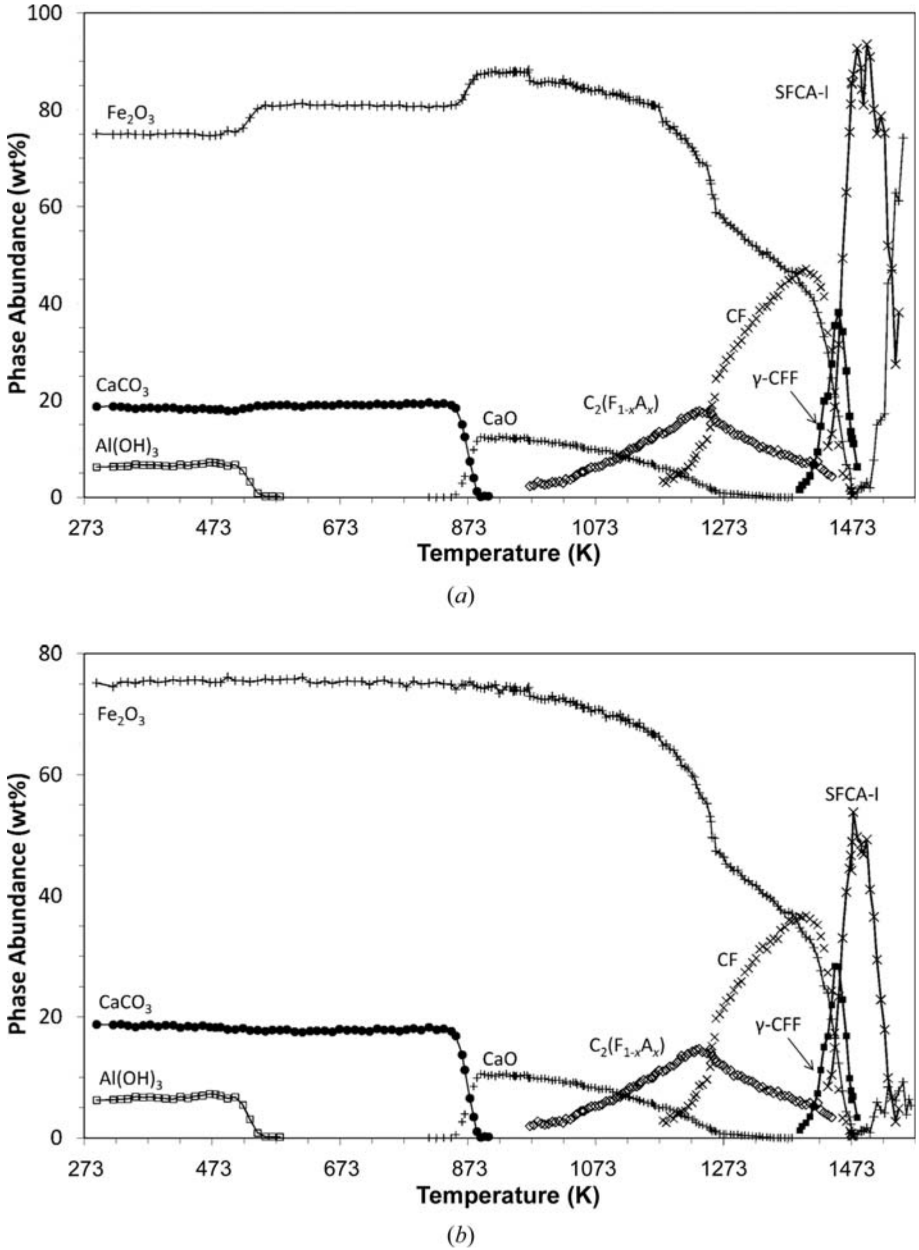

(*a*)

(*b*)

Figure 3.9.15
Results of Rietveld-based QPA of the *in situ* data sequence shown in Fig. 3.9.14 (Webster *et al.*, 2013). The relative phase abundances (upper) are derived using the Hill/Howard algorithm (Hill & Howard, 1987) in equation (3.9.26), while the absolute phase abundances (lower) have been derived from the external-standard approach (O'Connor & Raven, 1988) embodied in equation (3.9.21).

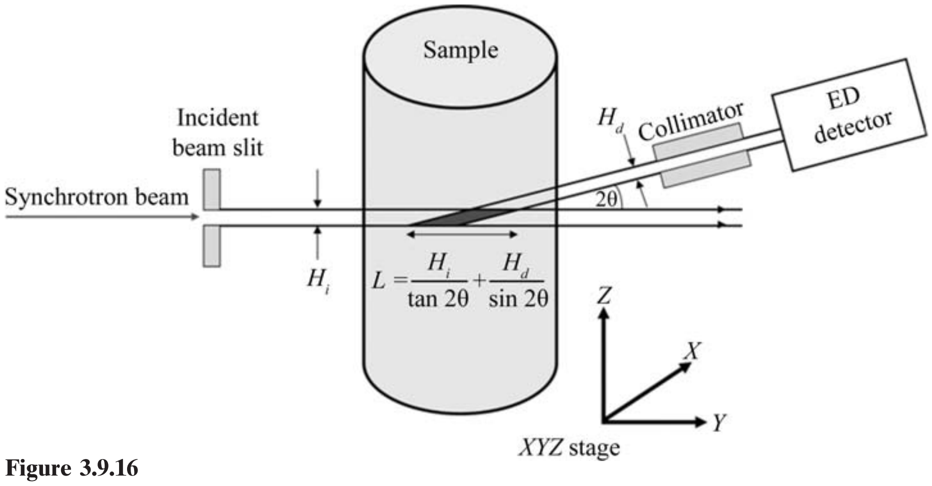

Figure 3.9.16
Basic experimental arrangement for energy-dispersive diffraction. The length of the active area or lozenge (dark grey region), L, is given by the function relating the incident- and diffracted-beam heights (H_i and H_d, respectively) and the angle of diffraction (2θ).

tors producing a spectrum of diffracted intensity as a function of energy.

Traditional angle-dispersive diffraction (ADD) satisfies Bragg's law by using a fixed wavelength and varying 2θ to map the d-spacings. In contrast, EDD data are collected directly on an energy scale at a constant 2θ and the energy is measured to map the d-spacings. This impinges upon the use of Rietveld methodology for QPA since, in contrast to ADD, the structure factors now vary as a function of energy. Energy is related to wavelength *via*

$$E\ (\mathrm{keV}) = \frac{hc}{\lambda} \simeq \frac{12.395}{\lambda}, \qquad (3.9.46)$$

where E is the energy of the incident radiation in keV, h is Planck's constant, c is the speed of light and λ is the wavelength associated with that energy in ångstroms. Rearrangement of equation (3.9.46) and substitution for λ in Bragg's law enables the mapping of the measured energy scale to d-spacings:

$$E\ (\mathrm{keV}) = \frac{6.197}{d \sin\theta}, \qquad (3.9.47)$$

where 2θ is the angle between the incident beam and the detector slit.

EDD data can be analysed using structureless profile-fitting methods such as those of Le Bail *et al.* (see Chapter 3.5) once the energy scale has been converted to a d-spacing scale (Frost & Fei, 1999; Larson & Von Dreele, 2004; Zhao *et al.*, 1997). If the distribution of intensities in the incident spectrum can be measured, it is possible to normalize the EDD data, correct for absorption and convert the pattern to an ADD form using a 'dummy' wavelength (Ballirano & Caminiti, 2001). Access to the incident spectrum, however, is not always possible, especially at synchrotron-radiation sources where the highly intense incident beam could damage the detector.

An alternative approach is to model the pattern directly on the energy scale *via* equation (3.9.47) (Rowles *et al.*, 2012; Scarlett *et al.*, 2009) and extract phase abundances using the methodologies described earlier in this chapter.

However, the major impediment to achieving this is the nonlinearity of the intensity distribution in the incident spectrum. This is due to (i) the nonlinear distribution of intensity as a function of energy in the incident beam, (ii) nonlinear detector responses (Bordas *et al.*, 1977) and (iii) absorption along the beam path (by the sample and air), which skews the energy distribution to the higher energies. This overall nonlinearity can be modelled empirically by functions such a lognormal curve (Bordas *et al.*, 1977; Buras *et al.*, 1979) or by an expansion of a power function (Glazer *et al.*, 1978). Alternatively, it may be determined experimentally by the use of standards measured under the same conditions as the experiment (Scarlett *et al.*, 2009). This latter approach allows some separation of the contributions from the instrument and the sample, and allows some degrees of freedom in the refinement of sample-related parameters that may be of benefit in dynamic experiments. Other contributions to the diffraction pattern that must also be accounted for include any fluorescence peaks arising from the sample or shielding or collimators, and any detector escape peaks from both diffracted and fluorescence peaks. Fluorescence peak positions and relative intensities should be constant throughout the measurement and may therefore be modelled using a fixed 'peak group' whose overall intensity can be refined during analysis. Escape peaks can be accounted for by the inclusion of a second phase identical to the parent phase but with an independent scale factor and a constant energy offset determined by the nature of the detector (Rowles *et al.*, 2012).

Currently, few Rietveld software packages are capable of dealing directly with the differences between EDD and ADD, specifically (i) the variance of structure factors as a function of energy, (ii) the nonlinear distribution of intensity in the incident beam as a function of energy further modified by a nonlinear detector response, and (iii) the preferential absorption of lower-energy X-rays by the sample/air. *TOPAS* (Bruker AXS, 2013) embodies algorithms that allow the pattern to be modelled directly on the energy scale and also the inclusion of equations to account for intensity variations arising from the experimental conditions. This allows quantification from such data to be achieved directly using Rietveld-based crystal-structure modelling incorporating the Hill and Howard algorithm in equation (3.9.26) (Hill & Howard, 1987). The application of *TOPAS* to a complex EDD experiment investigating the changes to the anode during molten-salt electrochemistry conducted in molten $CaCl_2$ at about 1223 K has been described by Rowles *et al.* (2012) and Styles *et al.* (2012).

3.9.10. Improving accuracy

There are many factors that influence the accuracy and precision of QPA results where (i) accuracy is defined as the agreement between the analytical result and the true value, and (ii) precision is the agreement between results if the analysis is repeated under the same conditions. Precision may further be split into (i) repeatability, which is the agreement between repeated measurement and analysis of the same specimen, and (ii) reproducibility, which additionally includes re-preparation, measurement and analysis of the sample.

3.9.10.1. *Standard deviations and error estimates*

Determination of the actual accuracy of an analysis is not a trivial task in a standardless method. In fact, it cannot be achieved without recourse to another measure of the sample that does incorporate standards. Too often, analysts will report Rietveld errors calculated in the course of refinement as the errors in the final quantification. However, these numbers relate purely to the mathematical fit of the model and have no bearing on the accuracy of the quantification itself.

Consider, for example, a three-phase mixture of corundum, magnetite and zircon. Such a sample was presented as sample 4 in the IUCr CPD round robin on QPA (Scarlett *et al.*, 2002). Its components were chosen with the deliberate aim of creating a sample in which severe sample-related aberrations occur. Table 3.9.4 shows the weighed amounts of each component and the results of replicate analyses of three different sub-samples of this material.

Table 3.9.4
Comparison of errors generated during the analysis of XRD data (Cu $K\alpha$ radiation) from three sub-samples of sample 4 from the IUCr CPD round robin on QPA (Scarlett *et al.*, 2002)

The bias values are (measured − weighed) while the values denoted XRF are the phase abundances generated from elemental concentrations measured by X-ray fluorescence methods.

	Phase		
$n = 3$	Corundum	Magnetite	Zircon
Weighed	50.46	19.46	29.90
Mean XRD measured wt%	56.52	17.06	26.42
Mean of Rietveld errors	0.15	0.11	0.11
Standard deviation of measured wt%	0.63	0.41	0.35
Mean of bias	6.06	−2.58	−3.48
XRF	50.4(2)	19.6(1)	29.5(1)

It is apparent that the standard deviation of the mean abundances of the three replicates, which represents the expected precision in the analysis, is 3 to 4 times greater than the errors reported by the Rietveld software. The good level of fit achieved in conducting these analyses (evidenced by low *R* factors) could lead the analyst to conclude that the mean value ± the standard deviation of the mean is an adequate measure of the phase abundances and their errors.

However, both the Rietveld errors and the precision are at least an order of magnitude smaller than the bias. The large bias, in this case due to the presence of severe microabsorption, represents the true accuracy that can be achieved in this example. Unfortunately, there is nothing in the XRD data and Rietveld analysis process that indicates that there may be a problem. It is only when the QPA is compared with other estimates, in this case derived from XRF chemical-analysis results, that the problem becomes apparent. The analyst must take further steps to identify sample-preparation and/or data-collection protocols that may improve accuracy and, importantly, seek ways to verify the results.

3.9.10.2. *Minimizing systematic errors*

The fundamental measured quantities in a diffraction pattern are the integrated intensities of the observed peaks. The precision of these measurements can be improved by: (i) increasing the primary intensity of the diffractometer using optics or higher-power X-ray sources; (ii) using scanning linear detectors (see Chapter 2.1), which have multiple detector elements to collect individual intensities many times; these are then summed to achieve higher accumulated counts; (iii) increasing the number of counts accumulated at each step, that is increasing the step counting time *T*; and (iv) increasing the number of points, *N*, measured across the peak.

Often, the temptation is to collect data with large values of *N* and *T* to maximize counting statistics. However, the resulting increased precision is only useful up to the point where counting variance becomes negligible in relation to other sources of error; thereafter data-collection time is wasted. For example, if the sample is affected by the presence of severe sample-related aberrations, the collection of highly precise data will not improve the accuracy of the resulting analysis significantly.

Therefore, the most important approach to improving the accuracy of an analysis is to eliminate the systematic errors. Given that the largest sources of error in QPA are experimental (Chung & Smith, 2000) and relate to sampling and specimen preparation, then this is the area on which the most careful attention needs to be focused. A detailed discussion of sample preparation and data-collection procedures is beyond the scope of this chapter but further details can be found in Chapter 2.10, and in Hill & Madsen (2002) and Buhrke *et al.* (1998).

3.9.10.3. *Minimizing sample-related errors*

3.9.10.3.1. *Crystallite-size issues*

Crystallite size is considered here as the length of a coherent scattering domain and should not be confused with the terms grain or particle size used frequently in powder diffraction to describe the macroscopic size of the components in the sample. The macroscopic size of the particle is somewhat irrelevant (as in ceramics or other solid pieces of samples) as long as the crystallites (or domains) that comprise the particle are (i) sufficiently small to ensure that there are enough crystallites contributing to the diffraction process (Smith, 1992) and (ii) randomly oriented, thus ensuring a true powder-average representation of intensities. However, for large domains or crystallites this assumption is usually not fulfilled and therefore it is necessary to reduce the crystallite size by reducing the size of the particles or grains that constitute the macroscopic objects of a powder.

Most issues in sample preparation are related to crystallite size and preferred orientation of the particles in the sample holder. For QPA a representative sampling of all possible orientations of crystallites with respect to the diffraction geometry is required. Rotation of the sample improves the particle statistics, since more crystallites can satisfy the diffraction condition (Elton & Salt, 1996).

Large-crystallite issues are easily detected using two-dimensional (2D) detectors, where the Debye rings show a 'spotty' intensity distribution. However, most QPA measurements are performed using 0D (point) or 1D (strip) detectors. The effect of large crystallites in a 1D pattern is that a few crystallites may contribute to irregularly high intensities for selected reflections. In the diffraction pattern, this situation is usually identified by intense reflections having a sharp peak profile compared with the surrounding peaks in the pattern. Furthermore, in a Rietveld refinement this situation is manifested by large intensity differences between the observed and calculated pattern that may not be associated with a particular crystallographic direction and hence to preferred orientation. Another way of detecting inhomogeneous crystallite distributions is to measure a series of scans from the same specimen at various rotation angles and comparing the relative peak intensities. It is worth noting that the push towards ever higher resolution in both laboratory and synchrotron instruments serves to further exacerbate the crystallite-size issue. This arises from the use of beams with decreased divergence, resulting in fewer crystallites likely to satisfy the diffraction condition.

There is no simple mathematical correction for large-crystallite issues and the effect is often misinterpreted in Rietveld refinement as preferred orientation. In this case, the correction would typically involve use of several directions for March–Dollase-type functions (Dollase, 1986) or an increasing order of spherical-harmonics coefficients (Ahtee *et al.*, 1989). In any case, this is an improper use of these corrections and the necessity to do so clearly points to deficiencies in the sample preparation and data-collection regime.

The best way to minimize the large-crystallite issue is to reduce the crystallite size through grinding of the sample. However, size-reduction methods need to be carefully assessed, since overgrinding can cause peak broadening due to (i) a decrease of long-range order and hence crystallite size and (ii) the introduction of microstrain (Hill & Madsen, 2002). The practical effect of peak broadening is increasing peak overlap, which may complicate the phase identification. For whole-pattern-based QPA, overgrinding is not as serious as long as it does not yield nanometre-sized particles or amorphous materials. This is because the integral intensity of the peaks is preserved. It should be noted that some phases can undergo transformation to other polymorphs or decompose to other phases during grinding (Hill & Madsen, 2002).

In practice, there is no generally applicable comminution strategy. For each material, a suitable milling device and grinding strategy needs to be identified. Inhomogeneous materials such as ores, concentrates and other mineralogical materials may have very different comminution properties for their constituents, leading to size fractionation during grinding. Large-crystallite issues are frequently observed for hard minerals (*e.g.* quartz, feldspar) while the grain size of soft minerals (*e.g.* talc) is reduced more rapidly.

A practical way of finding a best compromise for the milling conditions of a mixture may be the analysis of a series of samples of the same material where, for example, the grinding time is successively increased and the quantification results are compared. Fig. 3.9.17 shows the variation of analysed wt% with grinding time for two minerals: a stable result is eventually obtained.

There is a more extensive discussion of the impact of large-crystallite size on observed diffraction data (Smith, 1992) and ways to minimize its effect (Elton & Salt, 1996) in the published literature.

3.9.10.3.2. *Preferred orientation*

In order to generate peak intensities that accurately represent the intensity-weighted reciprocal lattice, the crystallites in the powder must not only be sufficient in number, but they must also be randomly oriented. In other words, each crystal orientation should have the same probability of diffracting. Preferred orientation can arise when particles align in the sample holder according to their morphology. This is most common with platy or

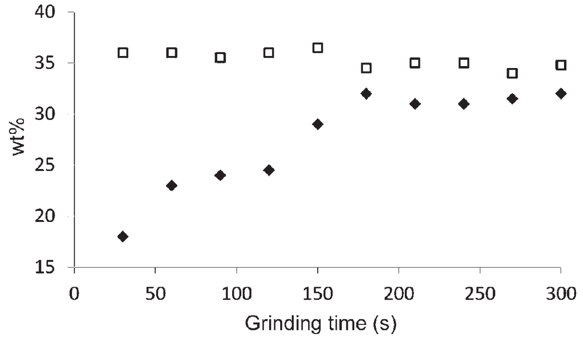

Figure 3.9.17
Variation of the magnetite (filled diamonds) and quartz (open squares) concentration of an iron-ore sample with grinding time. Stable conditions are obtained after about 180 s. Data courtesy ThyssenKrupp – Resource Technologies (Knorr & Bornefeld, 2013).

needle-like materials and the effect on the diffraction pattern is the observation of enhanced intensity along specific crystallographic directions with a subsequent decrease of intensity along other directions.

A number of sample-presentation methods can be used to minimize preferred orientation. For flat specimens, back pressing and side drifting into the sample holder can be effective. These methods tend to produce much less preferred orientation than front-mounted samples, but tend not to be very effective for chronic preferred orientation such as that exhibited by phases like clays, feldspars and chlorite. Reducing the size of the crystallites improves the probability of achieving random alignment of the crystallites in the sample holder. Gradually milling a sample and monitoring the preferred-orientation coefficients as a function of grinding time may again help to find the correct, or at least reproducible, grinding conditions (Fig. 3.9.18).

A major advantage of whole-pattern-based QPA over single-peak methods is that all classes of reflections are considered in the calculation. In this sense, the method is less prone to preferred orientation of a particular class of peaks. Furthermore, orientation effects may be corrected by applying March–Dollase (Dollase, 1986) or spherical-harmonics (Ahtee *et al.*, 1989) corrections. A properly applied correction may be of high importance for QPA in cases where a phase is present at low concentration and only a few peaks can clearly be identified in the pattern. If those peak(s) are affected by preferred orientation, the March–Dollase coefficient correlates strongly with scale factors and leads to biased QPA results. Examples of this effect occur with layered materials that have sheet-like morphology perpendicular to the *c* axis, including mica and clay minerals, which typically show stronger than expected intensity for the $00l$ reflections.

The crucial factor seems to be to what extent the orientation parameters correlate with the Rietveld scale factor. An example where the correlation is only minor is sample 2 from the IUCr CPD round robin on QPA (Scarlett *et al.*, 2002). In that example, brucite [$Mg(OH)_2$] shows strong preferred orientation along the $00l$ direction. This may be corrected by the March–Dollase model, which returns a refined value of 0.66. However, the introduction of this preferred-orientation correction only changes the brucite concentration from 35 to 36 wt% (weighed = 36.36 wt%); this is surprising because the orientation is strong and the weighted residual $R_{\rm wp}$ changes from 30 to 15%. Close examination of the correlations reveals a strong correlation between the brucite scale factor and preferred-orientation factor. However, the correlation of the brucite preferred-orientation parameter to the other scale factors (zincite, corundum and fluorite) is close to zero; this explains why in this example the QPA is not highly dependent on preferred orientation. In cases of strong correlation between the orientation parameter of one phase and the scale factors of other phases, preferred orientation should probably not be refined, or at least it should be verified carefully. It is worth noting that, in all Rietveld-based analyses, users should examine the correlation matrix as a matter of general practice to establish which parameters might be affecting parameters of interest.

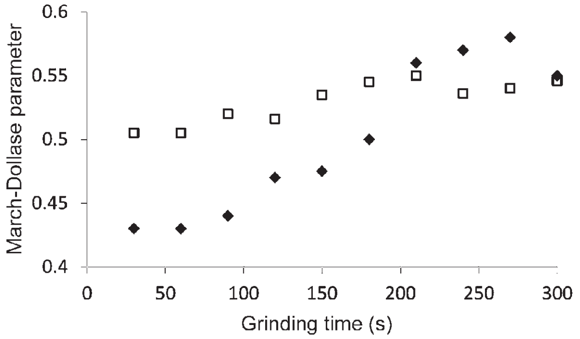

Figure 3.9.18
Increase of the March–Dollase (Dollase, 1986) parameter and related decrease of the degree of preferred orientation with grinding time for the two amphibole species actinolite (filled diamonds) and grunerite (open squares) in an iron ore. Data courtesy ThyssenKrupp – Resource Technologies (Knorr & Bornefeld, 2013).

It should be noted that sample rotation around the scattering vector (typically employed in flat-plate Bragg–Brentano geometry) during the scan does not reduce preferred orientation, since there is no change between the preferred-orientation direction and the diffraction vector. Using capillaries in transmission geometry assists in the reduction of preferred orientation, but the time-consuming nature of packing capillaries makes this technique infeasible in industrial applications where diffraction-based QPA is used for routine quality control.

3.9.10.3.3. *Microabsorption*

The strongest on-going impediment to accuracy in QPA using XRD data is microabsorption. The microabsorption effect occurs when a multiphase sample contains both low- and highly absorbing phases. For the highly absorbing phases, the X-ray beam is more likely to be absorbed in the surface layers of the grain; thus, the fraction of the grain contributing to the diffraction pattern will decrease as the size of the grain increases above the beam-penetration depth. For the low-absorbing phases, the beam penetrates further into the particle resulting in a greater likelihood of the desired 'volume diffraction' occurring (Brindley, 1945). The overall effect is the observation of a disproportionate amount of observed intensity from individual grains relative to what would be expected for the average absorption of the sample; the highly absorbing phases are under-represented relative to the low-absorbing phases. There is extensive discussion of the microabsorption issue in Zevin & Kimmel (1995).

Brindley (1945) has described the particle absorption contrast factor τ_α as

$$\tau_\alpha = (1/V)\int\limits_0^V \exp\left(-(\mu_\alpha - \bar{\mu})\right) {\rm d}v, \qquad (3.9.48)$$

where V is the particle volume, and μ_α and $\bar{\mu}$ are the linear absorption coefficients of phase α and the entire sample, respectively. While it is relatively easy to calculate the absorption coefficients, equation (3.9.48) implies knowledge of the *particle* size of each component; this information is only available through independent microscope or light-scattering characterization.

This correction term is commonly incorporated into QPA through a modification to equation (3.9.26) of the form

$$W_\alpha = \frac{S_\alpha(ZMV)_\alpha/\tau_\alpha}{\sum_{k=1}^n S_k(ZMV)_k/\tau_k}. \qquad (3.9.49)$$

Brindley has also devised criteria by which to assess whether a microabsorption problem is likely to be present or not. Calculation of μD (where μ is the linear absorption coefficient and D is the particle diameter) yields the following criteria:

(i) $\mu D < 0.01$ – fine powder. There is negligible microabsorption and hence no correction is necessary.

Table 3.9.5

Calculated values of μD (where μ is the linear absorption coefficient and D is the particle diameter) for Cu $K\alpha$ X-rays for corundum, magnetite and zircon with a range of particle sizes

Diameter (µm)	μD		
	Corundum, Al_2O_3 (μ = 125 cm^{-1})	Magnetite, Fe_3O_4 (μ = 1167 cm^{-1})	Zircon, $ZrSiO_4$ (μ = 380 cm^{-1})
0.1	0.001	0.012	0.004
0.2	0.003	0.023	0.008
0.5	0.006	0.058	0.019
1	0.013	0.117	0.038
2	0.025	0.233	0.076
5	0.063	0.584	0.190
10	0.125	1.167	0.380
20	0.251	2.334	0.759

(ii) $0.01 < \mu D < 0.1$ – medium powder. Microabsorption is likely to be present and the normal Brindley correction model can be applied.

(iii) $0.1 < \mu D < 1.0$ – coarse powder. A large microabsorption effect is present. The Brindley model can only be used to provide an approximate correction provided that μD is closer to the lower limit of the range.

(iv) $\mu D > 1.0$ – very coarse powder. This indicates that severe microabsorption is likely to be present and that any correction is well beyond the limits of the model.

It is difficult for the analyst encountering a new sample to determine whether a correction for microabsorption is required without first obtaining additional information. A minimum requirement should be to calculate μD for each phase present. However, this requires knowledge of the particle size which, in a multiphase sample, can be very difficult to obtain unambiguously. Even when the particle size is measured by, for example, dynamic light scattering or optical or SEM image analysis, the applicability of the correction can still be unclear. In addition, the correction factor embodied in equations (3.9.48) and (3.9.49) makes the assumption that the particles of the phase of interest are spherical and of uniform size. This assumption is unrealistic in almost all samples; in reality, each phase is likely to be present at a wide range of particle sizes and the particles are highly unlikely to be spherical.

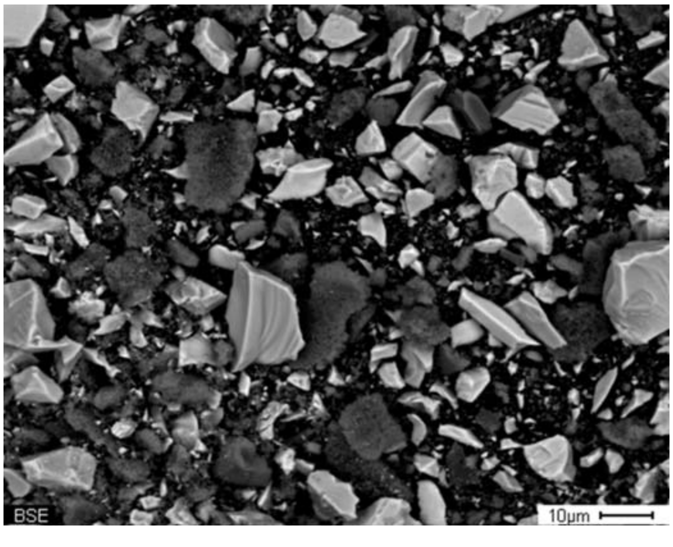

Figure 3.9.19

Backscattered-electron SEM image of a mixture of approximately equal amounts of corundum (dark grey), magnetite and zircon (lighter grey). Note the wide range of particle sizes present for each of the three phases.

Table 3.9.5 shows the calculated values of μD for Cu $K\alpha$ radiation for some commonly encountered phases in mineralogical analysis. For the least absorbing phase (corundum), the upper range of applicability of the Brindley model (medium powder) is reached at about 5 µm; by 8 µm, the coarse powder criterion has been reached and the correction model is no longer applicable. For magnetite, these limits are reached an order of magnitude earlier at about 0.5 and 0.9 µm, respectively.

Fig. 3.9.19 shows an SEM image of a mixture of approximately equal amounts of corundum, magnetite and zircon. The individual components of the sample were weighed and the mixture ground in ethanol in a McCrone micronizing mill (McCrone Research Associates, London) for 10 min g^{-1}. This approach to sample preparation is generally accepted as best practice for powder XRD because it minimizes structural damage during grinding (Hill & Madsen, 2002). After decanting and drying, the sample was back-packed into a cavity sample holder for XRD data collection; the same sample was then used to obtain the SEM image in Fig. 3.9.19. Visual observation shows a wide range of particle sizes (from submicron to greater than 10 µm) and shapes that do not even approximate spheres. Even if this information is obtained, selection of a particle size that best represents each individual phase is a difficult task. In addition, in many sample suites, the component phases exhibit a range of hardness resulting in different rates of grinding and hence difference size ranges. Regrettably, what happens too often in practice is that analysts will micronize the sample and then select an arbitrary particle size in order to derive a 'preferred' value for the final analysis. Therefore, caution is advised in the application of these correction models. The IUCr CPD round robin on QPA (Madsen *et al.*, 2001; Scarlett *et al.*, 2002) showed that many participants severely degraded their results by applying a correction when none was necessary.

Equation (3.9.48) shows that there two ways to minimize microabsorption. The first is to reduce the absorption contrast by, for example, changing the X-ray wavelength. While corundum and magnetite have very different linear absorption coefficients for Cu $K\alpha$ radiation (126 and 1123 cm^{-1}, respectively), the difference is reduced to 196 and 231 cm^{-1}, respectively, for Co $K\alpha$ radiation. The second approach is to reduce the particle size in order to meet Brindley's fine- or medium-powder criteria.

However, even these steps may not be sufficient to eliminate the microabsorption effect. Slightly different absorption coefficients, or different particle sizes for phases with the same absorption coefficients, may still introduce a bias between expected and analysed concentrations. In this situation, it may be better to use a calibrated hkl_phase or peaks_phase (Section 3.9.6) instead of a Rietveld, structure-based phase. The calibration step involved in the generation of such a phase incorporates the microabsorption problem into the calibration constant.

Fig. 3.9.20 shows the bias between known concentrations (derived from chemical analysis) and QPA-determined concentrations for a series of salt samples. The samples contain halite (NaCl), sylvite (KCl) and kieserite ($MgSO_4{\cdot}H_2O$) as major phases and small amounts of anhydrite ($CaSO_4$), langbeinite [$K_2Mg_2(SO_4)_3$] and carnallite [$KMgCl_3{\cdot}6(H_2O)$]. The linear absorption coefficient of sylvite (254 cm^{-1}) is much higher than halite (165 cm^{-1}). Using crystal-structure-based analysis, there is a systematic deviation of up to 3% with an overestimation of the low absorber (halite) and an underestimation of the high absorber (sylvite). After replacing sylvite by a calibrated hkl_phase, the bias is reduced to about 1% and does not show systematic deviations.

It should be noted, however, that the phase constants developed using such a calibration approach will only be applicable to the sample suite and preparation conditions for which it was developed. The calibration process will need to be repeated if there are significant changes to the sample suite or sample-preparation conditions.

3.9.10.3.4. *Whole-pattern-refinement effects*

One of the distinct advantages of structure-based whole-pattern fitting for QPA is that no standards need to be prepared because the structure for each phase provides the phase constant *ZMV*; the unit-cell dimensions allow the calculation of the cell volume *V* and the unit-cell contents provide the mass *ZM* (Bish & Howard, 1988; Hill & Howard, 1987). These values are used, along with the Rietveld scale factor *S*, in equation (3.9.26) to derive the phase abundance. This is especially useful for complex systems where the preparation of multiple standards would add considerably to the analytical complexity.

An additional advantage is the ability to refine the crystal structure (unit-cell dimensions and site-occupation factors, for example), when the data are of sufficiently high quality, in order to obtain the best fit between observed and calculated patterns. In addition to updating the *ZMV* value, the site occupancies are contained in the structure-factor calculation and, therefore, will change the relative reflection intensities and have an impact on the scale factor and QPA. Other structural parameters that have a strong effect on the scale factor and QPA are the atomic displacement parameters (ADPs). Strong correlation between the ADPs and amorphous material concentration has been shown by Gualtieri (2000) and Madsen *et al.* (2011).

This leads to the question: which crystal structure should be selected for QPA? Databases contain multiple entries for the same phase with the structures determined using different methods. While ADPs and site-occupation factors determined using neutron diffraction and single-crystal analysis should be favoured over those determined using X-ray powder data, many database entries do not have refined ADPs for all (and in some cases, any) atoms. Often, arbitrarily chosen default values of 0.5 or 1.0 Å^2 for $B_{\rm eq}$ are entered for all atoms, but this should be viewed or used with great caution. There is clearly a need to carefully evaluate the crystal-structure data used for QPA. This is particularly worth mentioning in view of the advent of new 'user-friendly' software that automatically assigns crystal structures after having performed the phase identification.

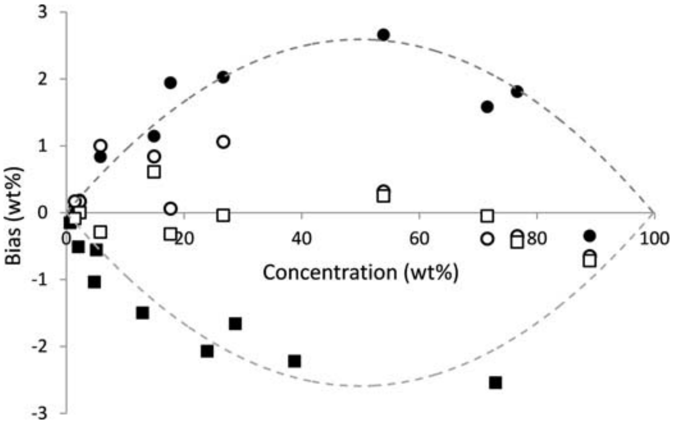

Figure 3.9.20
Bias as a function of phase concentration for industrial salt samples for (i) structure-based QPA (filled symbols) and (ii) calibrated hkl_phase (open symbols) for halite (circles) and sylvite (squares). The broken lines indicate the trend of the bias for structure-based QPA. Data are courtesy of K+S AG, Germany.

Empirical profile-shape models contribute significantly to the complexity (and correlations) of whole-powder-pattern fitting for QPA because of the large number of phases and multiple parameters required to model the profile shape of each phase. The use of convolution-based profile fitting [in, for example, *BGMN* (Bergmann *et al.*, 1998, 2000) and *TOPAS* (Bruker AXS, 2013)] greatly reduces the number of parameters, because the instrument-resolution function (which is constant for a given setup) can be separated from sample-related peak broadening. The instrument component can be refined using a standard and then fixed for subsequent analysis. The sample contribution to peak width and shape can then be related directly to crystallite size and microstrain using a minimal number of parameters. The reduction of the total number of parameters reduces the refinement complexity and the chance of parameter correlation.

The choice of the function used to model the pattern background may also have a strong influence on amorphous content (Gualtieri, 2000; Madsen *et al.*, 2011). Given that the intensities of both the background and the amorphous contribution vary slowly as a function of 2θ, it is inevitable that there will be a high degree of correlation between them. Hence, any errors in determining the true background will result in errors in amorphous phase determination. A simple approach is to use a background function with a minimal number of parameters. A more exact approach requires the separation of the amorphous contribution from background components such as Compton scattering and parasitic scattering by the sample environment and air in the beam path. This is routinely done in pair distribution function (PDF) analysis; details can be found in Chapter 5.7 in this volume and in Egami & Billinge (2003).

Another parameter that correlates with the pattern background is the width of broad peaks for phases of low concentration. If allowed to refine to very large width values, the peaks are 'smeared' over a broad range of the pattern with no clear distinction between peaks and background. The same issue applies when there is a high degree of peak overlap, particularly at high angles, leading to severe under- or over-estimation of the phase. The careful use of limits for either crystallite size or corresponding parameters in empirical peak-shape modelling assists in minimizing this effect.

There can be a subtle interplay between the profile-shape function and the pattern background that has an impact on whole-pattern fitting (Hill, 1992). The data in Fig. 3.9.21, collected using a Cu tube and an Ni $K\beta$ filter, exhibit low-angle truncation of the peak tails at the β-filter absorption edge. On the high-angle side, the anatase peak displays a wide tail which extends to the position of the strongest rutile peak at about 27.5° 2θ. In this case, rutile is present as a minor phase and the error in the background determination using conventional peak-profile modelling (Fig. 3.9.21*a*) introduces about 0.5% bias in the rutile QPA. The use of a more accurate profile model that incorporates the effect of the β-filter absorption edge (Fig. 3.9.21*b*) serves to improve the accuracy (Bruker AXS, 2013).

3.9.10.3.5. *Element analytical standards*

XRD-based derivation of elemental abundances relies on (i) the QPA abundances, and (ii) the assumed or measured stoichiometry of the crystalline phases. The accuracy of the QPA

Table 3.9.6

Compositional analysis of the Dillinger Hütte iron-ore certified reference material SX 11–14, (i) derived from QPA results, taking into account the nominal stoichiometry of the phases (XRD) and (ii) the certified analyses (Cert) (Knorr & Bornefeld, 2013)

Phase	wt%		Fe	FeO	SiO_2	Al_2O_3	MgO	CaO	K_2O	Na_2O	C
Haematite	0.37		0.26	—	—	—	—	—	—	—	—
Goethite	3.86		2.43	—	—	—	—	—	—	—	—
Magnetite	85.97		62.21	26.68	—	—	—	—	—	—	—
Quartz	5.73		—	—	5.73	—	—	—	—	—	—
Gibbsite	0.71		—	—	—	0.46	—	—	—	—	—
Talc	1.79		—	—	1.13	—	0.57	—	—	—	—
Orthoclase	0.30		—	—	0.19	0.05	—	—	0.05	—	—
Albite	0.89		—	—	0.60	0.18	—	—	—	0.10	—
Calcite	0.40		—	—	—	—	—	0.22	—	—	0.19
			Fe	FeO	SiO_2	Al_2O_3	MgO	CaO	K_2O	Na_2O	C
		XRD	64.89	26.68	7.66	0.70	0.57	0.22	0.05	0.10	0.19
		Cert	65.55	27.20	7.47	0.27	0.56	0.42	0.06	0.08	0.12
		Bias	−0.66	−0.52	0.19	0.43	0.01	−0.20	−0.01	0.02	0.07

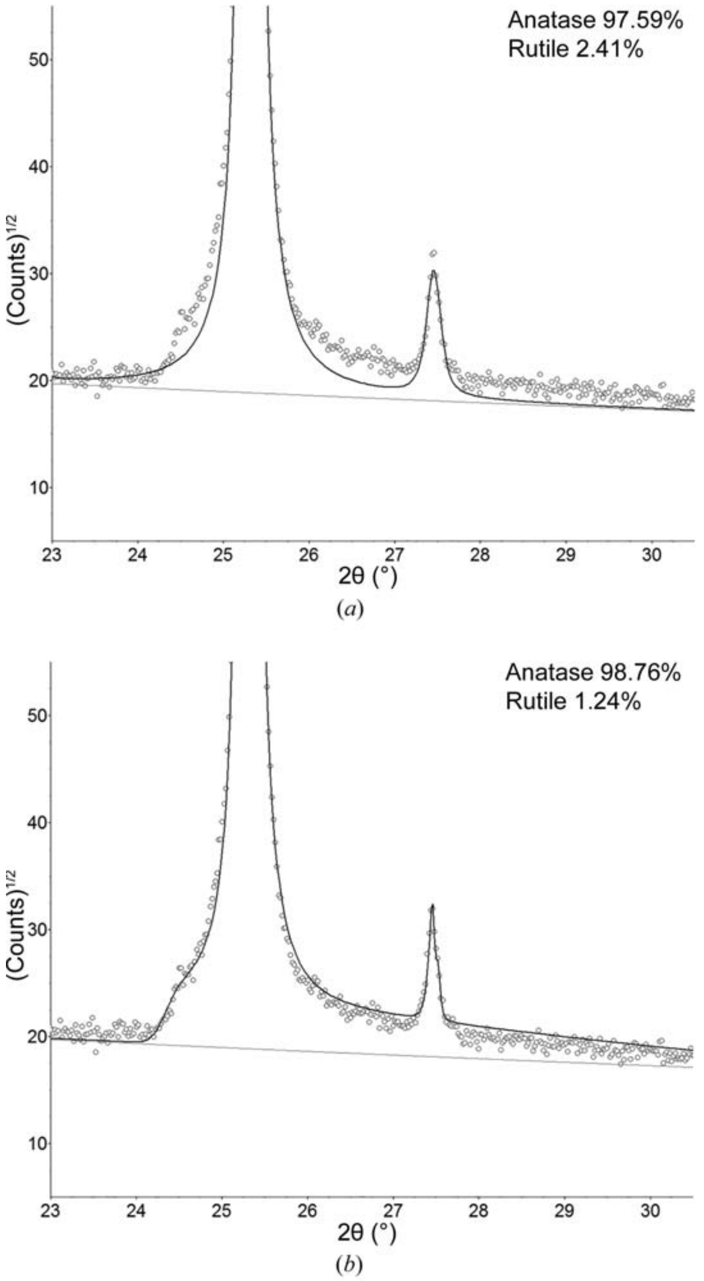

(*a*)

(*b*)

Figure 3.9.21

Profile fit of anatase and rutile (*a*) without and (*b*) with a $K\beta$ filter absorption-edge correction.

result may then be evaluated by comparing the calculated elemental abundances with those determined by traditional chemical-analysis techniques. However, for the best level of agreement, this method requires that the composition of the crystalline phases be well defined. A complication, in particular for minerals, is that idealized compositions may be reported but do not necessarily match the actual composition of the species present in the sample. Where possible, detailed phase analysis using microbeam techniques should be undertaken to establish the true composition for each phase. A complication that serves to decrease the agreement is that chemically based compositional analysis does not distinguish between crystalline and amorphous phase content, while the diffraction-based QPA usually measures only the crystalline phases. Generally, the composition of amorphous phases may not be known accurately and even highly crystalline material can contain amorphous components because of non-diffracting surface layers of the grains (Cline *et al.*, 2011).

An example demonstrating the level of agreement that can be achieved is that of the iron-ore certified reference material SX 11–14 from Dillinger Hütte (Fig. 3.9.22). The material is moderately complex and consists of nine distinct mineral species. The data were measured with Co $K\alpha$ radiation and analysed using Rietveld-based QPA in *TOPAS* (Bruker AXS, 2013). The phase abundances are converted to elemental and oxide compositions for comparison with the certified elemental analyses (Table 3.9.6). There is excellent agreement between the XRD results and the chemical analysis with bias values better than ±1 wt%.

3.9.10.3.6. *Phase-specific methods: diffraction SRMs, round-robin samples and synthetic mixtures*

In contrast to elemental compositional analysis, where standard reference materials (SRMs) are widespread, there are only a very limited number of SRMs available for diffraction-based QPA. Prominent examples are SRMs for the cement industry [NIST reference material clinker 8486 (Stutzman & Leigh, 2000) and ordinary Portland cement NIST SRM 2686] or ceramics materials (silicon nitride CRM BAM-S001) (Peplinski *et al.*, 2004). Similar to elemental standards, the certified values do not necessarily represent the true composition. Rather, they are published values that are typically averaged over the results from different independent methods, instruments and laboratories. Therefore, confidence limits of concentrations are provided that may be much larger than estimated standard deviations of concentrations within a single laboratory.

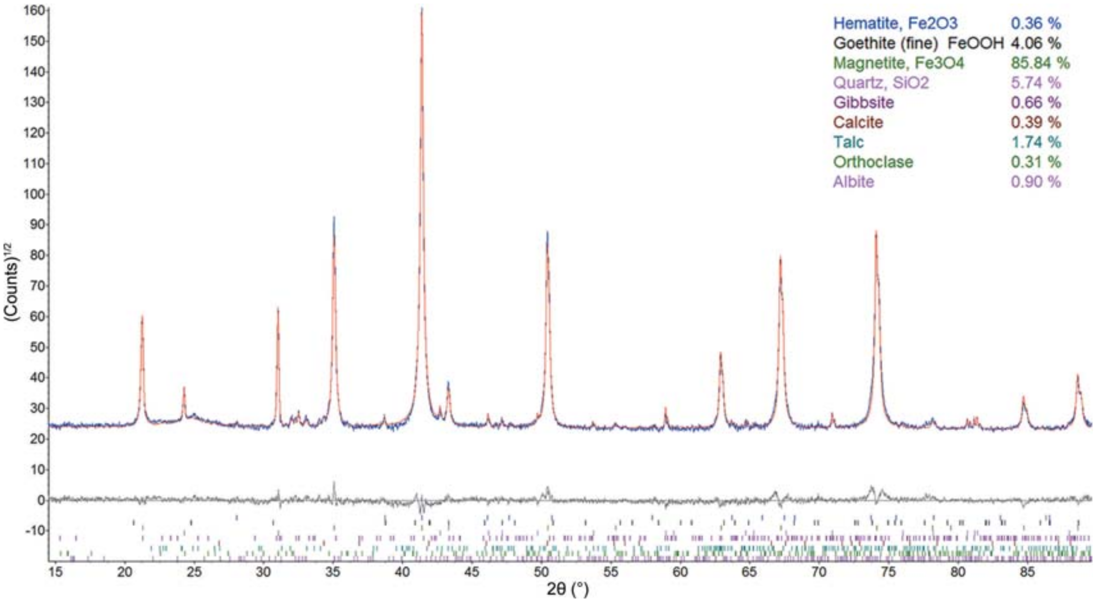

Figure 3.9.22

Output of Rietveld refinement and results of QPA for the iron-ore certified reference material SX 11–14 from Dillinger Hütte. The data were measured with Co $K\alpha$ radiation.

Finally, a number of inter-laboratory tests, or round robins, have been conducted on synthetic mixtures in order to set benchmarks for particular materials and/or the application of methods. Examples range from well ordered, high-symmetry phases discussed in earlier sections of this chapter (Madsen *et al.*, 2001; Scarlett *et al.*, 2002) to standard mixtures of geological material, granite and bauxites (Bish & Post, 1993), and technical products like artificial Portland cements (De la Torre & Aranda, 2003) where relative biases of 2–3% for the main phases and 5–10% for minor phases were found.

Very recently, the precision and accuracy of QPA for the analysis of Portland clinker and cement were determined for synthetic mixtures and commercial samples. The scatter of the results from the inter-laboratory comparison, and the fact that individual errors are much smaller than the standard deviations of all submitted results, points to the widespread presence of user-dependent systematic errors (Léon-Reina *et al.*, 2009).

One of the most challenging round robins is the Reynolds Cup (Ottner *et al.*, 2000; McCarty, 2002; Kleeberg, 2005; Omotoso *et al.*, 2006; Raven & Self, 2017), organized biannually since the year 2000 by the Clay Minerals Society. Synthetic mixtures representing typical sedimentary rock types are analysed and require a very high level of sample preparation and analytical skills because of the presence of a variety of clay minerals.

While most round robins have dealt with inorganic materials, one for pharmaceutical materials was organised by the International Centre for Diffraction Data (ICDD) together with the Pharmaceutical Powder XRD symposium series (PPXRD) (Fawcett *et al.*, 2010). A major outcome was the identification of operator errors in all steps of the analysis to be the largest source of error. This highlights the importance of reducing systematic errors for improving accuracy in QPA.

As a concluding remark, a variety of factors may influence the precision and accuracy of QPA. Nonetheless, better than 1 wt% agreement may be achieved for simple systems of well crystallized material. Moderately complex mixtures such as those routinely observed in cement plants and in the mining industry can be typically analysed at a 1 wt% level of accuracy provided that the analyst chooses the most appropriate sample-preparation, data-collection and analysis methodologies for the samples in question.

3.9.11. Summary

The value in using diffraction-based methods for the determination of phase abundance arises from the fact that the observed data are derived directly from the crystal structure of each phase. Knowledge of phase abundance is valuable in many fields including (i) mineral exploration, where the type and amount of major minerals serve as indicators for valuable minor minerals, (ii) mineral extraction, where the performance of the process line is governed by the mineralogy, not the commonly used elemental compositions, (iii) *in situ* studies, where the mechanism and kinetics of phase evolution resulting from the application of an external variable can be examined and (iv) the optimization of production conditions for advanced materials.

The methodology of QPA is fraught with difficulties, many of which are experimental or derive from sample-related issues. Hence, it is necessary to verify diffraction-based phase abundances against independent methods. This should include calculation of the expected sample element composition (using the QPA and an assumed or measured composition of each phase) and comparing these values with the measured element composition. In those circumstances where this is not possible, the QPA values should be regarded only as semi-quantitative. While such values may be useful for deriving trends within a particular system, they cannot be regarded as an absolute measure.

References

Ahtee, M., Nurmela, M., Suortti, P. & Järvinen, M. (1989). *Correction for preferred orientation in Rietveld refinement. J. Appl. Cryst.* **22**, 261–268.

Alexander, L. E. & Klug, H. P. (1948). *Basic aspects of X-ray absorption in quantitative diffraction analysis of powder mixtures. Anal. Chem.* **20**, 886–889.

Ballirano, P. & Caminiti, R. (2001). *Rietveld refinements on laboratory energy dispersive X-ray diffraction (EDXD) data. J. Appl. Cryst.* **34**, 757–762.

Barnes, P., Colston, S., Craster, B., Hall, C., Jupe, A., Jacques, S., Cockcroft, J., Morgan, S., Johnson, M., O'Connor, D. & Bellotto, M.

(2000). *Time- and space-resolved dynamic studies on ceramic and cementitious materials. J. Synchrotron Rad.* **7**, 167–177.

Batchelder, M. & Cressey, G. (1998). *Rapid, accurate phase quantification of clay-bearing samples using a position-sensitive X-ray detector. Clays Clay Miner.* **46**, 183–194.

Bergmann, J., Friedel, P. & Kleeberg, R. (1998). *Bgmn – a new fundamental parameters based Rietveld program for laboratory X-ray sources; its use in quantitative analysis and structure investigations. IUCr Commission on Powder Diffraction Newsletter*, **20**, 5–8.

Bergmann, J. & Kleeberg, R. (1998). *Rietveld analysis of disordered layer silicates. Mater. Sci. Forum*, **278–281**, 300–305.

Bergmann, J., Kleeberg, R., Haase, A. & Breidenstein, B. (2000). *Advanced fundamental parameters model for improved profile analysis. Mater. Sci. Forum*, **347–349**, 303–308.

Bette, S., Dinnebier, R. E. & Freyer, D. (2015). *Structure solution and refinement of stacking-faulted NiCl(OH). J. Appl. Cryst.* **48**, 1706–1718.

Bish, D. L. & Howard, S. A. (1988). *Quantitative phase analysis using the Rietveld method. J. Appl. Cryst.* **21**, 86–91.

Bish, D. L. & Post, J. E. (1993). *Quantitative mineralogical analysis using the Rietveld full-pattern fitting method. Am. Mineral.* **78**, 932–940.

Bogue, R. H. (1929). *Calculation of the compounds in Portland cement. Ind. Eng. Chem. Anal. Ed.* **1**, 192–197.

Bordas, J., Glazer, A. M., Howard, C. J. & Bourdillon, A. J. (1977). *Energy-dispersive diffraction from polycrystalline materials using synchrotron radiation. Philos. Mag.* **35**, 311–323.

Brindley, G. W. (1945). *The effect of grain or particle size on X-ray reflections from mixed powders and alloys, considered in relation to the quantitative determination of crystalline substances by X-ray methods. London Edinb. Dubl. Philos. Mag. J. Sci.* **36**, 347–369.

Brindley, G. W. (1980). *Crystal structures of clay minerals and their X-ray identification*. Mineralogical Society Monograph No. 5, edited by G. W. Brindley & G. Brown, pp. 125–195. London: Mineralogical Society.

Bruker AXS (2013). *Topas v5: General profile and structure analysis software for powder diffraction data*. Version 5. https://www.bruker.com/topas.

Buhrke, V. E., Jenkins, R. & Smith, D. K. (1998). *A Practical Guide for the Preparation of Specimens for X-Ray Fluorescence and X-ray Diffraction Analysis*. New York: Wiley-VCH.

Buras, B., Gerward, L., Glazer, A. M., Hidaka, M. & Staun Olsen, J. (1979). *Quantitative structural studies by means of the energy-dispersive method with X-rays from a storage ring. J. Appl. Cryst.* **12**, 531–536.

Casas-Cabanas, M., Rodríguez-Carvajal, J. & Palacín, M. R. (2006). *FAULTS, a new program for refinement of powder diffraction patterns from layered structures. Z. Kristallogr. Suppl.* **23**, 243–248.

Cernik, R. J., Hansson, C. C. T., Martin, C. M., Preuss, M., Attallah, M., Korsunsky, A. M., Belnoue, J. P., Jun, T. S., Barnes, P., Jacques, S., Sochi, T. & Lazzari, O. (2011). *A synchrotron tomographic energy-dispersive diffraction imaging study of the aerospace alloy Ti 6246. J. Appl. Cryst.* **44**, 150–157.

Cheary, R. W. & Coelho, A. (1992). *A fundamental parameters approach to X-ray line-profile fitting. J. Appl. Cryst.* **25**, 109–121.

Cheary, R. W., Coelho, A. A. & Cline, J. P. (2004). *Fundamental parameters line profile fitting in laboratory diffractometers. J. Res. Natl Inst. Stand. Technol.* **109**, 1–25.

Chipera, S. J. & Bish, D. L. (2002). *FULLPAT: a full-pattern quantitative analysis program for X-ray powder diffraction using measured and calculated patterns. J. Appl. Cryst.* **35**, 744–749.

Chipera, S. J. & Bish, D. L. (2013). *Fitting full X-ray diffraction patterns for quantitative analysis: a method for readily quantifying crystalline and disordered phases. Adv. Mater. Phys. Chem.* **3**, 47–53.

Chung, F. H. (1974*a*). *Quantitative interpretation of X-ray diffraction patterns of mixtures. I. Matrix-flushing method for quantitative multicomponent analysis. J. Appl. Cryst.* **7**, 519–525.

Chung, F. H. (1974*b*). *Quantitative interpretation of X-ray diffraction patterns of mixtures. II. Adiabatic principle of X-ray diffraction analysis of mixtures. J. Appl. Cryst.* **7**, 526–531.

Chung, F. H. & Smith, D. K. (2000). *Industrial Applications of X-ray Diffraction*, edited by F. H. Chung & D. K. Smith, ch. 1, pp. 3–10, and ch. 2, pp. 13–32. New York: Marcel Dekker.

Cline, J. P., Von Dreele, R. B., Winburn, R., Stephens, P. W. & Filliben, J. J. (2011). *Addressing the amorphous content issue in quantitative phase analysis: the certification of NIST standard reference material 676a. Acta Cryst.* A**67**, 357–367.

Coelho, A. A., Evans, J. S. O. & Lewis, J. W. (2016). *Averaging the intensity of many-layered structures for accurate stacking-fault analysis using Rietveld refinement. J. Appl. Cryst.* **49**, 1740–1749.

Coelho, A. A., Chater, P. A. and Kern, A. (2015). *Fast synthesis and refinement of the atomic pair distribution function. J. Appl. Cryst.* **48**, 869–875

Cowley, J. M. (1976). *Diffraction by crystals with planar faults. I. General theory. Acta Cryst.* A**32**, 83–87.

Cressey, G. & Schofield, P. F. (1996). *Rapid whole-pattern profile-stripping method for the quantification of multiphase samples. Powder Diffr.* **11**, 35–39.

De La Torre, A. G., Ángeles, G., Bruque, S., Campo, J. & Aranda, M. A. G. (2002). *The superstructure of C3S from synchrotron and neutron powder diffraction and its role in quantitative phase analyses. Cem. Concr. Res.* **32**, 1347–1356.

De la Torre, A. G. & Aranda, M. A. G. (2003). *Accuracy in Rietveld quantitative phase analysis of Portland cements. J. Appl. Cryst.* **36**, 1169–1176.

Debye, P. & Scherrer, P. (1916). *Interferenzen an regellos orientierten Teilchen im Röntgenlicht Phys. Z.* **17**, 277–283.

Debye, P. & Scherrer, P. (1917). *X-ray interference produced by irregularly oriented particles: Constitution of graphite and amorphous C. Phys. Z.* **18**, 291–301.

Dohrmann, R., Rüping, K. B., Kleber, M., Ufer, K. & Jahn, R. (2009). *Variation of preferred orientation in oriented clay mounts as a result of sample preparation and composition. Clays Clay Miner.* **57**, 686–694.

Dollase, W. A. (1986). *Correction of intensities for preferred orientation in powder diffractometry: application of the March model. J. Appl. Cryst.* **19**, 267–272.

Drits, V. A. & Tchoubar, C. (1990). *X-ray diffraction by disordered lamellar structures: Theory and application to microdivided silicates and carbons*. Heidelberg: Springer Verlag.

Eberl, D. D. (2003). *User's guide to rockjock - a program for determining quantitative mineralogy from powder x-ray diffraction data.* U.S. Geological Survey Open-File Report 2003–78. http://pubs.er.usgs.gov/publication/ofr200378.

Egami, T. & Billinge, S. J. L. (2003). *Underneath the Bragg Peaks: Structural Analysis of Complex Materials*. Oxford: Elsevier.

Ehrenberg, H., Senyshyn, A., Hinterstein, M. & Fuess, H. (2013). *Modern Diffraction Methods*, edited by E. J. Mittemeijer & U. Welzel, pp. 491–517. Weinheim: Wiley-VCH Verlag GMBH & Co.

Elton, N. J. & Salt, P. D. (1996). *Particle statistics in quantitative X-ray diffractometry. Powder Diffr.* **11**, 218–229.

Fawcett, T. G., Kabekkodu, S. N., Blanton, J. R. & Blanton, T. N. (2017). *Chemical analysis by diffraction: the Powder Diffraction File. Powder Diffr.* 32, 63–71.

Fawcett, T. G., Needham, F., Faber, J. & Crowder, C. E. (2010). *International Centre for Diffraction Data round robin on quantitative Rietveld phase analysis of pharmaceuticals. Powder Diffr.* **25**, 60–67.

Frost, D. J. & Fei, Y. (1999). *Static compression of the hydrous magnesium silicate phase d to 30 GPa at room temperature. Phys. Chem. Miner.* **26**, 415–418.

Glazer, A. M., Hidaka, M. & Bordas, J. (1978). *Energy-dispersive powder profile refinement using synchrotron radiation. J. Appl. Cryst.* **11**, 165–172.

Gualtieri, A. F. (2000). *Accuracy of XRPD QPA using the combined Rietveld–RIR method. J. Appl. Cryst.* **33**, 267–278.

Gualtieri, A. F., Viani, A., Banchio, G. & Artioli, G. (2001). *Quantitative phase analysis of natural raw materials containing montmorillonite. Mater. Sci. Forum*, **378–381**, 702–709.

Hall, C., Barnes, P., Cockcroft, J. K., Colston, S. L., Häusermann, D., Jacques, S. D. M., Jupe, A. C. & Kunz, M. (1998). *Synchrotron energy-dispersive X-ray diffraction tomography. Nucl. Instrum. Methods Phys. Res. B*, **140**, 253–257.

Hall, C., Colston, S. L., Jupe, A. C., Jacques, S. D. M., Livingston, R., Ramadan, A. O. A., Amde, A. W. & Barnes, P. (2000). *Non-destructive tomographic energy-dispersive diffraction imaging of the interior of bulk concrete. Cem. Concr. Res.* **30**, 491–495.

Hendricks, S. & Teller, E. (1942). *X-ray interference in partially ordered layer lattices. J. Chem. Phys.* **10**, 147–167.

Hill, R. J. (1983). *Calculated X-ray powder diffraction data for phases encountered in lead/acid battery plates. J. Power Sources*, **9**, 55–71.

Hill, R. J. (1991). *Expanded use of the Rietveld method in studies of phase abundance in multiphase mixtures. Powder Diffr.* **6**, 74–77.

Hill, R. J. (1992). *The background in X-ray powder diffractograms: a case study of Rietveld analysis of minor phases using Ni-filtered and graphite-monochromated radiation. Powder Diffr.* **7**, 63–70.

Hill, R. J. & Howard, C. J. (1987). *Quantitative phase analysis from neutron powder diffraction data using the Rietveld method. J. Appl. Cryst.* **20**, 467–474.

Hill, R. J., Howard, C. J. & Reichert, B. E. (1991). *Quantitative phase abundance in Mg-PSZ by Rietveld analysis of neutron and X-ray diffraction data. Mater. Sci. Forum*, **34–36**, 159–163.

Hill, R. J. & Madsen, I. C. (2002). *Structure Determination from Powder Diffraction Data*, edited by W. David, K. Shankland, L. McCusker & C. Baerlocher, ch. 6, pp. 98–116. Oxford University Press.

Hubbard, C. R., Evans, E. H. & Smith, D. K. (1976). *The reference intensity ratio, I/Ic, for computer simulated powder patterns. J. Appl. Cryst.* **9**, 169–174.

Hubbard, C. R. & Snyder, R. L. (1988). *RIR – measurement and use in quantitative XRD. Powder Diffr.* **3**, 74–77.

Hull, A. W. (1917). *A new method of X-ray crystal analysis. Phys. Rev.* **10**, 661–696.

Hull, A. W. (1919). *A new method of chemical analysis. J. Am. Chem. Soc.* **41**, 1168–1175.

ICDD (2015). The Powder Diffraction File, database of the International Centre for Diffraction Data, release PDF4+, 2015. ICDD, 12 Campus Boulevard, Newton Square, Pennsylvania 19073–3273, USA.

Kaduk, J. A. (2000). In *Industrial Applications of X-ray Diffraction*, edited by F. H. Chung & D. K. Smith, pp. 207–253. New York: Marcel Dekker.

Kleeberg, R. (2005). *Results of the second Reynolds Cup contest in quantitative mineral analysis*. IUCr Commission on Powder Diffraction Newsletter, **30**, 22–26.

Klug, H. P. & Alexander, L. E. (1974). *X-ray Diffraction Procedures: For Polycrystalline and Amorphous Materials*. New York: Wiley.

Knorr, K. & Bornefeld, M. (2013). Proceedings of Process Mineralogy '12, 7–9 November 2012. Cape Town, South Africa, pp. 651–652. http://www.proceedings.com/16755.html.

Knudsen, T. (1981). *Quantitative X-ray diffraction analysis with qualitative control of calibration samples. X-ray Spectrom.* **10**, 54–56.

Langford, J. I. (2004). In *Diffraction Analysis of the Microstructure of Materials*, edited by E. J. Mittemeijer & P. Scardi, pp. 3–11. Berlin: Springer-Verlag.

Larson, A. C. & Von Dreele, R. B. (2004). *General Structure Analysis System (GSAS)*. Report LAUR 86–748, Los Alamos National Laboratory, New Mexico, USA.

Le Bail, A., Duroy, H. & Fourquet, J. L. (1988). *Ab-initio structure determination of $LiSbWO_6$ by X-ray powder diffraction. Mater. Res. Bull.* **23**, 447–452.

Le Bail, A. & Jouanneaux, A. (1997). *A qualitative account for anisotropic broadening in whole-powder-diffraction-pattern fitting by second-rank tensors. J. Appl. Cryst.* **30**, 265–271.

León-Reina, L., De la Torre, A. G., Porras-Vázquez, J. M., Cruz, M., Ordonez, L. M., Alcobé, X., Gispert-Guirado, F., Larrañaga-Varga, A., Paul, M., Fuellmann, T., Schmidt, R. & Aranda, M. A. G. (2009). *Round robin on Rietveld quantitative phase analysis of Portland cements. J. Appl. Cryst.* **42**, 906–916.

Leoni, M., Gualtieri, A. F. & Roveri, N. (2004). *Simultaneous refinement of structure and microstructure of layered materials. J. Appl. Cryst.* **37**, 166–173.

Lippmann, F. (1970). *Functions describing preferred orientation in flat aggregates of flake-like clay minerals and in other axially symmetric fabrics. Contr. Miner. Petrol.* **25**, 77–94.

McCarty, D. K. (2002). *Quantitative mineral analysis of clay-bearing mixtures: The 'Reynolds Cup' contest*. IUCr Commission on Powder Diffraction Newsletter, **27** 12–16.

Madsen, I. C., Scarlett, N. V. Y., Cranswick, L. M. D. & Lwin, T. (2001). *Outcomes of the International Union of Crystallography Commission on Powder Diffraction Round Robin on Quantitative Phase Analysis: samples 1a to 1h. J. Appl. Cryst.* **34**, 409–426.

Madsen, I. C., Scarlett, N. V. Y. & Kern, A. (2011). *Description and survey of methodologies for the determination of amorphous content via x-ray powder diffraction. Z. Kristallogr.* **226**, 944–955.

Madsen, I. C., Scarlett, N. V. Y., Riley, D. P. & Raven, M. D. (2013). *Modern Powder Diffraction*, edited by E. J. Mittemeijer & U. Welzel, pp. 283–320. Weinheim: Wiley-VCH.

Madsen, I. C., Scarlett, N. V. Y. & Whittington, B. I. (2005). *Pressure acid leaching of nickel laterite ores: an in situ diffraction study of the mechanism and rate of reaction. J. Appl. Cryst.* **38**, 927–933.

Michalski, E. (1988). *The diffraction of X-rays by close-packed polytypic crystals containing single stacking faults. I. General theory. Acta Cryst.* A**44**, 640–649.

Michalski, E., Kaczmarek, S. M. & Demianiuk, M. (1988). *The diffraction of X-rays by close-packed polytypic crystals containing single stacking faults. II. Theory for hexagonal and rhombohedral structures. Acta Cryst.* A**44**, 650–657.

Morris, R. E., Harrison, W. T. A., Nicol, J. M., Wilkinson, A. P. & Cheetham, A. K. (1992). *Determination of complex structures by combined neutron and synchrotron X-ray powder diffraction. Nature*, **359**, 519–522.

Murray, J., Kirwan, L., Loan, M. & Hodnett, B. K. (2009). *In-situ synchrotron diffraction study of the hydrothermal transformation of goethite to hematite in sodium aluminate solutions. Hydrometallurgy*, **95**, 239–246.

Navias, L. (1925). *Quantitative determination of the development of mullite in fired clays by an X-ray method. J. Am. Ceram. Soc.* **8**, 296–302.

Norby, P., Cahill, C., Koleda, C. & Parise, J. B. (1998). *A reaction cell for in situ studies of hydrothermal titration. J. Appl. Cryst.* **31**, 481–483.

O'Connor, B. H. & Raven, M. D. (1988). *Application of the Rietveld refinement procedure in assaying powdered mixtures. Powder Diffr.* **3**, 2–6.

Omotoso, O., McCarty, D. K., Hillier, S. & Kleeberg, R. (2006). *Some successful approaches to quantitative mineral analysis as revealed by the 3rd Reynolds Cup contest. Clays Clay Miner.* **54**, 748–760.

Ottner, F., Gier, S., Kuderna, M. & Schwaighofer, B. (2000). *Results of an inter-laboratory comparison of methods for quantitative clay analysis. Appl. Clay Sci.* **17**, 223–243.

Parrish, W. (1965). Editor. *X-ray Analysis Papers*, 2nd ed. Eindhoven: Centrex Publishing Company.

Pawley, G. S. (1980). *EDINP, the Edinburgh powder profile refinement program. J. Appl. Cryst.* **13**, 630–633.

Pawley, G. S. (1981). *Unit-cell refinement from powder diffraction scans. J. Appl. Cryst.* **14**, 357–361.

Peplinski, B., Kleeberg, R., Bergmann, J. & Wenzel, J. (2004). *Quantitative phase analysis using the Rietveld method – estimates of possible problems based on two interlaboratory comparisons. Mater. Sci. Forum*, **443–444**, 45–50.

Popa, N. C. (1998). *The (hkl) dependence of diffraction-line broadening caused by strain and size for all Laue groups in Rietveld refinement. J. Appl. Cryst.* **31**, 176–180.

Raven, M. D. & Self, P. G. (2017). *Outcomes of 12 years of the Reynolds Cup quantitative mineral analysis round robin. Clays Clay Miner.* **65**, 122–134.

Reynolds, R. C. (1985). *Newmod, a computer program for the calculation of one-dimensional diffraction patterns of mixed-layered clays.* Hanover, USA.

Reynolds, R. (1989). *Quantitative mineral analysis of clays*. In *CMS Workshop Lectures 1*, edited by D. R. Pevear & F. A. Mumpton, pp. 4–37. Boulder: The Clay Minerals Society.

Reynolds, R. C. (1994). *Wildfire, a computer program for the calculation of threee-dimensional powder X-ray diffraction patterns for mica polytypes and their disordered variations.* Hanover, USA.

Reynolds, R. C. & Hower, J. (1970). *The nature of interlayering in mixed-layer illite-montmorillonites. Clays Clay Miner.* **18**, 25–36.

Rietveld, H. M. (1969). *A profile refinement method for nuclear and magnetic structures. J. Appl. Cryst.* **2**, 65–71.

Rowles, M. R., Styles, M. J., Madsen, I. C., Scarlett, N. V. Y., McGregor, K., Riley, D. P., Snook, G. A., Urban, A. J., Connolley, T. & Reinhard, C. (2012). *Quantification of passivation layer growth in inert anodes for molten salt electrochemistry by in situ energy-dispersive diffraction. J. Appl. Cryst.* **45**, 28–37.

Scarlett, N. V. Y. & Madsen, I. C. (2006). *Quantification of phases with partial or no known crystal structures. Powder Diffr.* **21**, 278–284.

Scarlett, N. V. Y., Madsen, I. C., Cranswick, L. M. D., Lwin, T., Groleau, E., Stephenson, G., Aylmore, M. & Agron-Olshina, N. (2002). *Outcomes of the International Union of Crystallography Commission on Powder Diffraction Round Robin on Quantitative Phase Analysis: samples 2, 3, 4, synthetic bauxite, natural granodiorite and pharmaceuticals. J. Appl. Cryst.* **35**, 383–400.

Scarlett, N. V. Y., Madsen, I. C., Evans, J. S. O., Coelho, A. A., McGregor, K., Rowles, M., Lanyon, M. R. & Urban, A. J. (2009). *Energy-*

dispersive diffraction studies of inert anodes. *J. Appl. Cryst.* **42**, 502–512.

Scarlett, N. V. Y., Madsen, I. C., Pownceby, M. I. & Christensen, A. N. (2004). *In situ X-ray diffraction analysis of iron ore sinter phases*. *J. Appl. Cryst.* **37**, 362–368.

Scarlett, N. V. Y., Madsen, I. C. & Whittington, B. I. (2008). *Time-resolved diffraction studies into the pressure acid leaching of nickel laterite ores: a comparison of laboratory and synchrotron X-ray experiments*. *J. Appl. Cryst.* **41**, 572–583.

Scarlett, N. V. Y., Pownceby, M. I., Madsen, I. C. & Christensen, A. N. (2004). *Reaction sequences in the formation of silico-ferrites of calcium and aluminum in iron ore sinter*. *Metall. Mater. Trans. B*, **35**, 929–936.

Schmitt, B., Brönnimann, C., Eikenberry, E. F., Gozzo, F., Hörmann, C., Horisberger, R. & Patterson, B. (2003). *Mythen detector system*. *Nucl. Instrum. Methods Phys. Res. A*, **501**, 267–272.

Smith, D. K. (1992). *Particle statistics and whole pattern methods in quantitative x-ray powder diffraction analysis. Adv. X-ray Anal.* **35**, 1–15.

Smith, D. K., Johnson, G. G., Scheible, A., Wims, A. M., Johnson, J. L. & Ullmann, G. (1987). *Quantitative X-ray powder diffraction method using the full diffraction pattern*. *Powder Diffr.* **2**, 73–77.

Snyder, R. L. & Bish, D. L. (1989). In *Modern Powder Diffraction*, edited by D. L. Bish & J. E. Post, pp. 101–142. Washington DC: Mineralogical Society of America.

Stephens, P. W. (1999). *Phenomenological model of anisotropic peak broadening in powder diffraction*. *J. Appl. Cryst.* **32**, 281–289.

Stinton, G. W. & Evans, J. S. O. (2007). *Parametric Rietveld refinement*. *J. Appl. Cryst.* **40**, 87–95.

Stutzman, P. E. & Leigh, S. (2000). Proceedings of the Twenty-Second International Conference on Cement Microscopy, 11–13 September 2000, Quebec City, Canada. https://cemmicro.org/publications/.

Styles, M. J., Rowles, M. R., Madsen, I. C., McGregor, K., Urban, A. J., Snook, G. A., Scarlett, N. V. Y. & Riley, D. P. (2012). *A furnace and environmental cell for the in situ investigation of molten salt electrolysis using high-energy X-ray diffraction*. *J. Synchrotron Rad.* **19**, 39–47.

Taylor, J. C. (1991). *Computer programs for standardless quantitative analysis of minerals using the full powder diffraction profile*. *Powder Diffr.* **6**, 2–9.

Taylor, J. C. & Rui, Z. (1992). *Simultaneous use of observed and calculated standard profiles in quantitative XRD analysis of minerals by the multiphase Rietveld method: the determination of pseudorutile in mineral sands products*. *Powder Diffr.* **7**, 152–161.

Taylor, R. M. & Norrish, K. (1966). *The measurement of orientation distribution and its application to quantitative X-ray diffraction analysis*. *Clay Miner.* **6**, 127–142.

Toraya (2016*a*). *A new method for quantitative phase analysis using X-ray powder diffraction: direct derivation of weight fractions from observed integrated intensities and chemical compositions of individual phases. J. Appl. Cryst.* **49**, 1508–1516

Toraya (2016*b*). *A new method for quantitative phase analysis using X-ray powder diffraction: direct derivation of weight fractions from observed integrated intensities and chemical compositions of individual phases. Corrigendum. J. Appl. Cryst.* **50**, 665.

Toraya, H. & Tsusaka, S. (1995). *Quantitative phase analysis using the whole-powder-pattern decomposition method. I. Solution from knowledge of chemical compositions*. *J. Appl. Cryst.* **28**, 392–399.

Treacy, M. M. J., Newsam, J. M. & Deem, M. W. (1991). *A general recursion method for calculating diffracted intensities from crystals containing planar faults*. *Proc. R. Soc. London Ser. A*, **433**, 499–520.

Ufer, K., Kleeberg, R., Bergmann, J., Curtius, H. & Dohrmann, R. (2008). *Refining real structure parameters of disordered layer structures within the Rietveld method*. *Z. Kristallogr.* Suppl. **27**, 151–158.

Ufer, K., Kleeberg, R., Bergmann, J. & Dohrmann, R. (2012). *Rietveld refinement of disordered illite-smectite mixed-layer structures by a recursive algorithm. II: powder-pattern refinement and quantitative phase analysis*. *Clays Clay Miner.* **60**, 535–552.

Ufer, K., Roth, G., Kleeberg, R., Stanjek, H. & Dohrmann, R. (2004). *Description of x-ray powder pattern of turbostratically disordered layer structures with a Rietveld compatible approach*. *Z. Kristallogr.* **219**, 519–527.

Ufer, K., Stanjek, H., Roth, G., Dohrmann, R., Kleeberg, R. & Kaufhold, S. (2008). *Quantitative phase analysis of bentonites by the Rietveld method*. *Clays Clay Miner.* **56**, 272–282.

Wang, X., Li, J., Hart, R. D., van Riessen, A. & McDonald, R. (2011). *Quantitative X-ray diffraction phase analysis of poorly ordered nontronite clay in nickel laterites*. *J. Appl. Cryst.* **44**, 902–910.

Warren, B. E. (1941). *X-ray diffraction in random layer lattices*. *Phys. Rev.* **59**, 693–698.

Webster, N. A. S., Madsen, I. C., Loan, M. J., Knott, R. B., Naim, F., Wallwork, K. S. & Kimpton, J. A. (2010). *An investigation of goethite-seeded $Al(OH)_3$ precipitation using in situ X-ray diffraction and Rietveld-based quantitative phase analysis. J. Appl. Cryst.* **43**, 466–472.

Webster, N. A. S., Pownceby, M. I. & Madsen, I. C. (2013). *In situ X-ray diffraction investigation of the formation mechanisms of silico-ferrite of calcium and aluminium-I-type (SFCA-I-type) complex calcium ferrites*. *ISIJ Int.* **53**, 1334–1340.

Westphal, T., Füllmann, T. & Pöllmann, H. (2009). *Rietveld quantification of amorphous portions with an internal standard – mathematical consequences of the experimental approach*. *Powder Diffr.* **24**, 239–243.

Williams, R. P., Hart, R. D. & van Riessen, A. (2011). *Quantification of the extent of reaction of metakaolin-based geopolymers using X-ray diffraction, scanning electron microscopy, and energy-dispersive spectroscopy*. *J. Am. Ceram. Soc.* **94**, 2663–2670.

Yuan, H. & Bish, D. (2010). *NEWMOD+, a new version of the NEWMOD program for interpreting X-ray powder diffraction patterns from interstratified clay minerals*. *Clays Clay Miner.* **58**, 318–326.

Zevin, L. & Viaene, W. (1990). *Impact of clay particle orientation on quantitative clay diffractometry*. *Clay Miner.* **25**, 401–418.

Zevin, L. S. & Kimmel, G. (1995). *Quantitative X-ray Diffractometry*. Springer-Verlag New York, Inc.

Zhao, Y., Von Dreele, R. B., Shankland, T. J., Weidner, D. J., Zhang, J., Wang, Y. & Gasparik, T. (1997). *Thermoelastic equation of state of jadeite $NaAlSi_2O_6$: an energy-dispersive Rietveld refinement study of low symmetry and multiple phases diffraction*. *Geophys. Res. Lett.* **24**, 5–8.

International Tables for Crystallography (2019). Vol. H, Chapter 3.10, pp. 374–384.

3.10. Accuracy in Rietveld quantitative phase analysis with strictly monochromatic Mo and Cu radiations

L. León-Reina, A. Cuesta, M. García-Maté, G. Álvarez-Pinazo, I. Santacruz, O. Vallcorba, A. G. De la Torre and M. A. G. Aranda

3.10.1. Introduction

Most industrial materials are multiphase systems and the accurate determination of their phase assemblage is key to understanding their performances. There are different approaches to carrying out quantitative phase analysis (QPA; see Chapter 3.9); however, nowadays, the Rietveld method is the most widely employed methodology for QPA of crystalline materials (Madsen *et al.*, 2001; Scarlett *et al.*, 2002), including cements (Stutzman, 2005; León-Reina *et al.*, 2009; Chapter 7.12).

The factors affecting the accuracy and precision of Rietveld quantitative phase analysis (RQPA) results can be gathered into three main groups: (i) instrument related, (ii) sample-preparation related and (iii) data-analysis protocol(s). The Rietveld method is a standardless methodology which uses the crystal-structure descriptions of each crystalline component to calculate its powder pattern. For this reason, the correct choice of crystal-structure description for each phase in multiphase materials is key (Zevin & Kimmel, 1995; Madsen *et al.*, 2001, 2011). The influence of the instrument type on RQPA has previously been evaluated (Madsen *et al.*, 2001) and the main conclusion was that neutron and synchrotron powder diffraction yielded the best results owing to larger irradiated volumes and also to the minimization of microabsorption effects.

High-energy (short-wavelength) X-rays contribute (i) to minimize absorption and microabsorption effects, (ii) to the measurement of a higher number of Bragg peaks and (iii) to increase the irradiated volume of the specimen. Figs. 3.10.1(*a*) and 3.10.1(*b*) show the irradiated volumes bathed by X-rays when using flat samples for Mo and Cu radiations in transmission geometry, and Fig. 3.10.1(*c*) shows the irradiated volume for Cu in reflection mode (Cuesta *et al.*, 2015). Mo radiation combined with a flat sample in transmission geometry allows an irradiated volume of close to 100 mm^3; meanwhile, for Cu radiation (flat samples in reflection and transmission geometries) the irradiated volumes are close to 5 mm^3 (Cuesta *et al.*, 2015). In this context, it is worth mentioning that the absorption correction for flat-

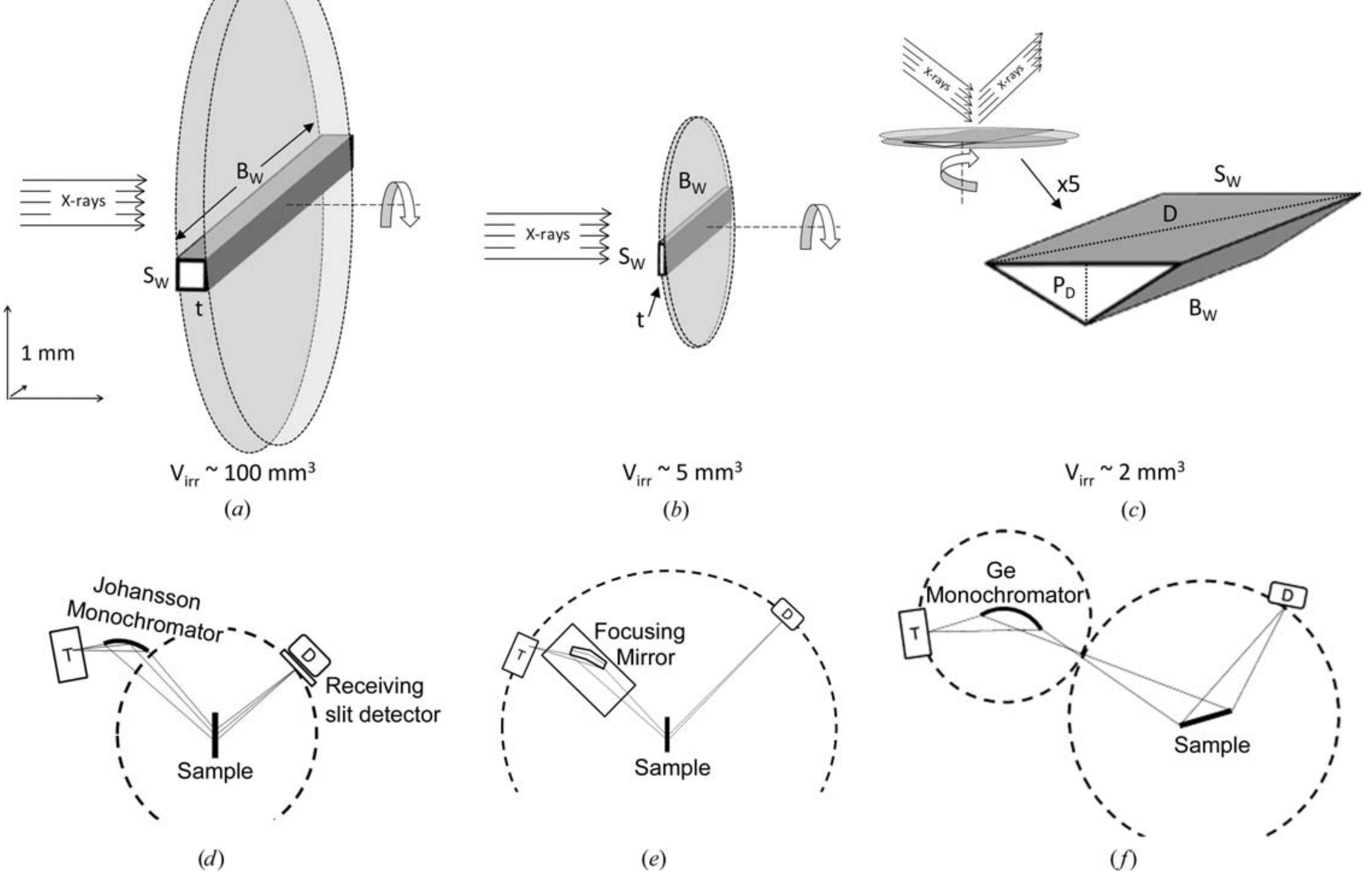

Figure 3.10.1
Irradiated volume for a flat sample holder in transmission mode using (*a*) Mo radiation and (*b*) Cu radiation, and (*c*) reflection mode using Cu radiation. Diffraction-geometry sketches: (*d*) transmission geometry with primary monochromator, (*e*) transmission geometry with focusing mirror and (*f*) reflection geometry with primary monochromator. [Reprinted from Cuesta *et al.* (2015) with permission from Cambridge University Press.]

Copyright © 2019 International Union of Crystallography

Table 3.10.1

Cambridge Structural Database (CSD)/Inorganic Crystal Structure Database (ICSD) reference codes for all phases used for Rietveld refinements in this work and the linear absorption coefficients for the wavelengths used

Phase	Chemical formula	CSD/ICSD refcode	μ (cm^{-1}), Cu $K\alpha_1$, λ = 1.5406 Å	μ (cm^{-1}), Mo $K\alpha_1$, λ = 0.7093 Å	μ (cm^{-1}), λ = 0.7744/0.4959 Å	Reference
Glucose	$C_6H_{12}O_6$	Glucsa10	12	1	1.3/—	Brown & Levy (1979)
Fructose	$C_6H_{12}O_6$	Fructo11	12	1	1.3/—	Kanters *et al.* (1977)
α-Lactose monohydrate	$C_{12}H_{22}O_{11}\cdot H_2O$	Lactos10	12	1	1.3/—	Fries *et al.* (1971)
Xylose	$C_5H_{10}O_5$	Xylose	12	1	1.2/—	Hordvik (1971)
Gypsum	$CaSO_4\cdot(H_2O)_2$	151692	141	16	22/—	De la Torre *et al.* (2004)
Quartz	SiO_2	41414	92	10	11/2.9	Will *et al.* (1988)
s-Anhydrite	$CaSO_4$	16382	219	24	31/—	Kirfel & Will (1980)
i-Anhydrite	$CaSO_4$	79527	219	24	31/—	Bezou *et al.* (1995)
Zincite	ZnO	65120	285	244	—/89.1	Albertsson *et al.* (1989)
Calcite	$CaCO_3$	80869	194	22	27/7.3	Maslen *et al.* (1995)
$SrSO_4$	$SrSO_4$	22322	299	187	40/—	Garske & Peacor (1965)

sample transmission geometry is conceptually similar to that for flat-plate reflection geometry, but the length of the scattered beam path has to be properly defined. The corresponding equation is given in section A5.2.5 of Egami & Billinge (2003).

It must also be noted that Mo radiation has a major drawback when compared with Cu radiation. The λ^3 dependence of diffraction intensity favours the use of Cu radiation by a factor of 10.2. Thus, a detector receives approximately ten times as many diffracted X-ray photons with Cu than with Mo (this calculation neglects the different fractions of photons lost in the diffractometer optical paths). This fact can be partially overcome in modern X-ray detectors by increasing the counting time for patterns collected with Mo radiation without reaching prohibitively long times.

As discussed in Chapter 3.9, there are many factors that affect the accuracy and precision of QPA results. It must be recalled that accuracy is the agreement between the analytical result and the true value, and precision is the agreement between results for analyses repeated under the same conditions. Precision may be further divided into repeatability, the agreement between analyses derived from several measurements on the same specimen, and reproducibility, the agreement including re-preparation, re-measurement and data re-analysis of the same sample. Since the largest sources of errors in RQPA are experimental, sample preparation is key, as the reproducibility of peak-intensity measurements is mainly governed by particle statistics (Elton & Salt, 1996). It is generally accepted that the diffraction intensities have to be collected with an accuracy close to ±1% to obtain patterns that are suitable for good RQPA procedures (Von Dreele & Rodriguez-Carvajal, 2008). Milling the sample to reduce the particle size is an approach that should be exercised with care to avoid peak broadening or amorphization (Buhrke *et al.*, 1998). In order to improve particle statistics, a very common practice is to continuously spin the sample during data collection. A much less developed approach is to use high-energy, highly penetrating laboratory X-rays.

Another important issue in the QPA of mixtures is the limit of detection (LoD) and the limit of quantification (LoQ). In this context, the LoD can be defined as the minimal concentration of analyte that can be detected with acceptable reliability (Zevin & Kimmel, 1995), *i.e.* for which its strongest (not overlapped) diffraction peak in the powder pattern has a signal-to-noise ratio larger than 3.0. The 'reliability' criterion is flexible and may be defined by regulatory agencies, as is mainly the case for active pharmaceutical ingredients. Evidently, the LoD can be reduced (improved) by increasing the intensity of the X-ray source, for example using synchrotron radiation. In this context, the LoQ can be defined as the minimum content of an analyte that can be determined with a value at least three times larger than its standard deviation and determined to an acceptable reliability level. For RQPA, this type of approach can be straightforward, although the accuracy for minor phases may be quite poor.

The main aim of the study described here was to test whether the use of high-energy Mo radiation, combined with high-resolution X-ray optics, could yield more accurate RQPA than well established procedures using Cu radiation. In order to do so, three sets of mixtures with increasing amounts of a given phase (the spiking method) were prepared and the corresponding RQPA results were evaluated with calibration curves (least-squares fits) and quantitatively by statistical analysis based on the Kullback–Leibler distance (KLD; Kullback, 1968). The three series were (i) crystalline inorganic phase mixtures with increasing amounts of an inorganic phase, (ii) crystalline organic phase mixtures with increasing amounts of an organic compound and (iii) a series with an increasing content of amorphous ground glass. This last series is the most challenging case because the amorphous content is derived from a small overestimation of the internal standard employed. Amorphous content determination is important for many industries, including cements, glasses, pharmaceuticals and alloys.

3.10.2. Compounds and series

3.10.2.1. *Single phases*

Table 3.10.1 provides information about the phases used in this work. Further details can be found in the original publication (León-Reina *et al.*, 2016). All of the mixtures were prepared by grinding the weighed phases by hand in an agate pestle and mortar for 20 min to ensure homogeneity.

3.10.2.2. *Crystalline inorganic series*

A constant matrix of calcite (C), gypsum (Gp) and quartz (Q) was prepared. Six samples with known increasing amounts of insoluble anhydrite (i-A) were then produced and were labelled CGpQ_*x*A, where *x* repesents the target i-A content: 0.00, 0.125, 0.25, 0.50, 1.0, 2.0 or 4.0 wt%.

3.10.2.3. *Crystalline organic series*

A constant matrix of glucose (G), fructose (F) and lactose (L) was prepared. Six samples with known increasing amounts of xylose (X) were then produced and labelled GFL_*x*X, where *x* represents the target X content: 0.00, 0.125, 0.25, 0.50, 1.0, 2.0 or 4.0 wt%.

3.10.2.4. *Variable amorphous content series*

A constant matrix of calcite (C) and zincite (Z) was prepared. Five samples with increasing contents of amorphous ground glass (Gl) were then prepared. The elemental composition of the ground glass is given in García-Maté *et al.* (2014). The mixtures were labelled CZQ_*x*Gl, where *x* indicates 0, 2, 4, 8, 16 or 32 wt% Gl. The amorphous content was determined by adding ~20 wt% quartz (Q) as an internal standard.

3.10.3. Analytical techniques

All phases and mixtures were studied with Mo $K\alpha_1$ (transmission geometry) and Cu $K\alpha_1$ (reflection geometry) monochromatic radiation. Table 3.10.1 shows the X-ray linear absorption coefficients for all of the phases, as microabsorption is always a concern in RQPA. A microabsorption correction was not applied in this work, but readers must be aware that this effect, if relevant, is one of the greatest source of inaccuracy in RQPA (Madsen *et al.*, 2001; Scarlett *et al.*, 2002). All of the phases were also characterized by scanning electron microscopy (see Fig. 3.10.2).

3.10.3.1. *Mo $K\alpha_1$ laboratory X-ray powder diffraction (LXRPD)*

Mo $K\alpha_1$ powder patterns were collected in transmission geometry in constant irradiated volume mode, in order to avoid any correction of the measured intensities, on a D8 ADVANCE (Bruker AXS) diffractometer (188.5 mm radius) equipped with a Ge(111) primary monochromator, which gives monochromatic Mo radiation (λ = 0.7093 Å). The X-ray tube operated at 50 kV and 50 mA. The optics configuration was a fixed divergence slit (2°) and a fixed diffracted anti-scatter slit (9°). A LYNXEYE XE 500 µm energy-dispersive linear detector, optimized for high-energy radiation, was used with the maximum opening angle. Using these conditions, the samples were measured between 3 and 35° 2θ with a step size of 0.006° and with a total measurement time of 3 h 5 min. The flat samples were placed into cylindrical holders between two Kapton foils (Cuesta *et al.*, 2015) and rotated at a rate of 10 revolutions per minute during data collection. Moreover, the absorption factor of each sample was experimentally measured by comparing the direct beam with and without the sample (Cuesta *et al.*, 2015). The amount of sample loaded (which determines the height of the cylinder) in the holders was adjusted to obtain a total absorption (μt) of ~1, which corresponds to an absorption factor of ~2.7 or 63% of direct-beam attenuation. For the organic samples this criterion was not followed as it would lead to very thick specimens. In this case, the maximum holder thickness was used (1.7 mm).

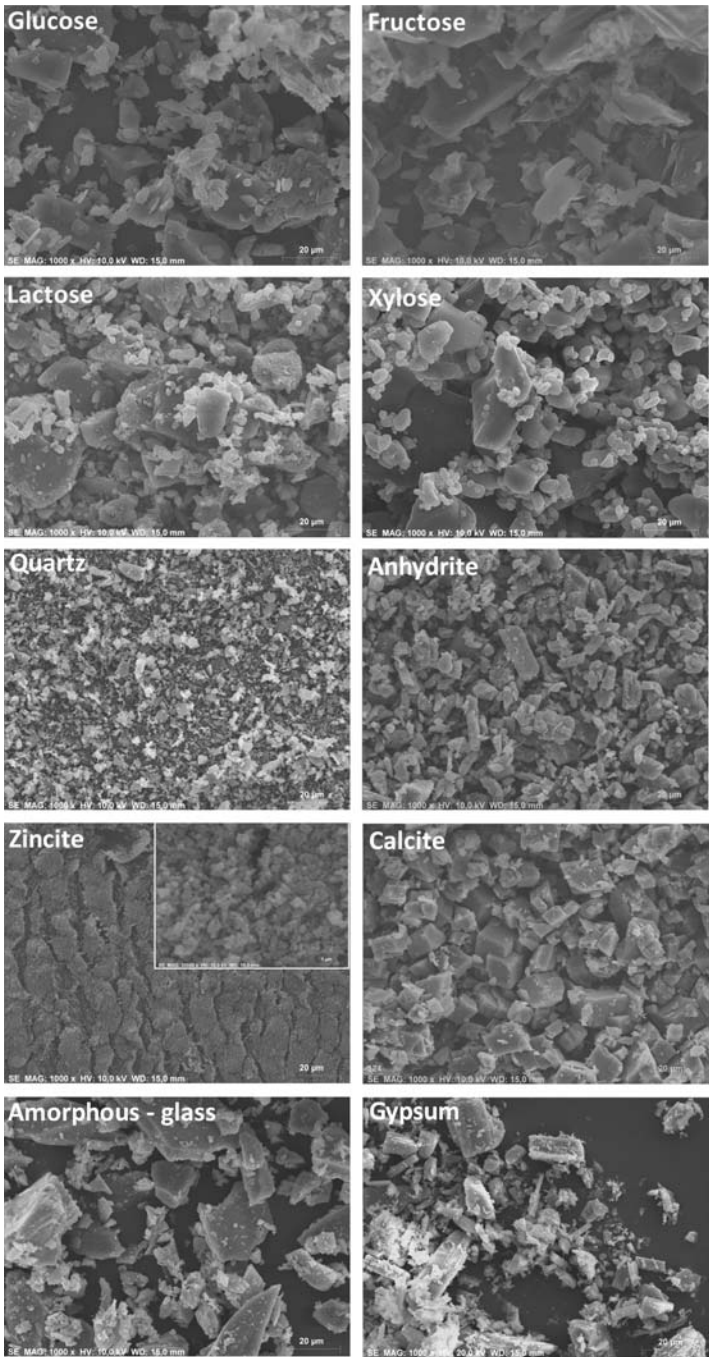

Figure 3.10.2
Scanning electron microscopy micrographs for the studied phases (×1000). The inset in the zincite micrograph shows the powder at higher magnification (×20 000).

3.10.3.2. *Cu $K\alpha_1$ laboratory X-ray powder diffraction (LXRPD)*

Cu $K\alpha_1$ powder patterns for exactly the same samples were recorded in reflection geometry ($\theta/2\theta$) on a X′Pert MPD PRO (PANalytical B.V.) diffractometer (240 mm radius) equipped with a Ge(111) primary monochromator, which gives monochromatic Cu radiation (λ = 1.54059 Å). The X-ray tube was operated at 45 kV and 40 mA. The optics configuration was a fixed divergence slit (0.5°), a fixed incident anti-scatter slit (1°), a fixed diffracted anti-scatter slit (0.5°) and an X′Celerator RTMS (real-time multiple strip) detector operating in scanning mode with the maximum active length. Using these conditions, the samples were measured between 6.5 and 81.5° 2θ with a step size of 0.0167° and a total measurement time of 2 h 36 min. The flat samples were prepared by rear charge of a flat sample holder in order to minimize preferred orientation and were rotated at a rate of 10 revolutions per minute.

The lowest analyte content samples, CGpQ_0.12A and GFL_0.12X, were measured three times using both radiations, Mo $K\alpha_1$ and Cu $K\alpha_1$, for a precision (reproducibility) assessment. Therefore, regrinding and reloading of the mixtures in the sample holder was carried out prior to every measurement.

3.10.3.3. *Transmission synchrotron X-ray powder diffraction (SXRPD)*

Powder patterns for the lowest analyte content samples, CGpQ_0.12A and GFL_0.12X, were also measured using synchrotron radiation. SXRPD data were collected in Debye–Scherrer (transmission) mode using the powder diffractometer at the ALBA Light Source (Fauth *et al.*, 2013). The wavelength, λ = 0.77439 (2) Å, was selected with a double-crystal Si(111) monochromator and was determined using the NIST SRM640d Si standard (a = 5.43123 Å). The diffractometer is equipped with a MYTHEN-II detector system. The samples were loaded into glass capillaries 0.7 mm in diameter and were rapidly rotated during data collection to improve the diffracting-particle statistics. The data-acquisition time was 20 min per pattern to attain a very good signal-to-noise (S/N) ratio over the angular range 1–35° 2θ. Three patterns, taken at different positions along the capillaries, were collected for each sample.

SXRPD data for the amorphous content series, CZQ_*x*Gl, were also measured at the ALBA Light Source. The experimental setup was the same as described above but the working wavelength was λ = 0.49591 (2) Å.

3.10.4. Powder-diffraction data analysis

All powder patterns were analysed by the Rietveld method using the *GSAS* software package (Larson & Von Dreele, 2000) with the pseudo-Voigt peak-shape function (Thompson *et al.*, 1987) for RQPA. The refined overall parameters were phase scale factors, background coefficients (linear interpolation function), unit-cell parameters, zero-shift error, peak-shape parameters and preferred-orientation coefficient, when needed. The March–Dollase preferred-orientation adjustment algorithm was employed (Dollase, 1986). The modelling direction must be given as input for the calculations. In this case, the directions for the different phases were taken from previous studies. Alternatively, this direction can be extracted from the pattern from an analysis of the differences between observed and calculated intensities for non-overlapped diffraction peaks. The crystal structures used are reported in Table 3.10.1.

In order to provide a single numerical assessment of the performance of each analysis, a statistic based on the KLD distance was used (Kullback, 1968). This approach was previously used to evaluate the accuracy of RQPA applied to standard mixtures (Madsen *et al.*, 2001; Scarlett *et al.*, 2002; León-Reina *et al.*, 2009). Both phase-related KLD distances and absolute values of the Kullback–Leibler distance (AKLD) were calculated. Accurate analyses are mirrored by low values of AKLD.

The overall amorphous content was determined from the internal standard methodology approach (De la Torre *et al.*, 2001; Aranda *et al.*, 2012) with quartz as an internal standard [using isotropic atomic displacement parameters (ADPs) of 0.045 and 0.0087 Å^2 for Si and O, respectively]. If the original sample contains an amorphous phase, the amount of standard will be overestimated in RQPA. From the (slight) overestimation of the standard, the amorphous content of the investigated sample can be derived (De la Torre *et al.*, 2001). The important role of the values of the ADPs in the results of RQPA mainly in amorphous content determinations using the internal-standard method has been discussed previously (Madsen *et al.*, 2011).

3.10.5. Crystalline single phases

All of the single phases were selected according to several parameters, such as relevance to selected applications, purity, particle size of the powder and preferred orientation. In order to check the suitability of the crystal structures used, all of the phases were first studied using powder diffraction with Mo $K\alpha_1$ radiation. These preliminary studies were of special interest for organic phases, as the CIF files obtained from the Cambridge Structural Database (CSD) did not contain the atomic displacement parameters (ADPs). For lactose and fructose, the ADPs were obtained from the original publications and were introduced manually into the *GSAS* control file. For glucose and

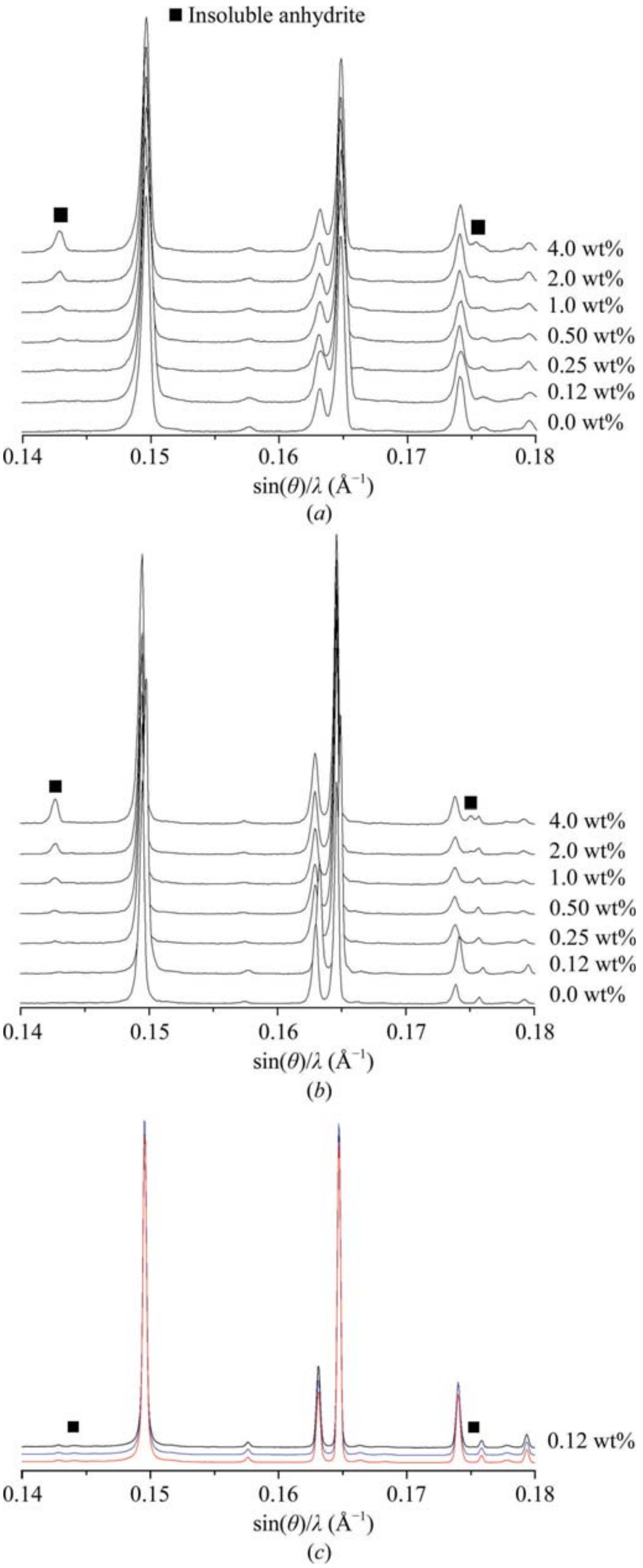

Figure 3.10.3

(*a*) Raw Mo $K\alpha_1$ powder patterns for the inorganic series composed of a constant matrix of calcite, gypsum and quartz, and increasing amounts of insoluble anhydrite (peaks highlighted with a solid square). (*b*) Raw Cu $K\alpha_1$ powder patterns for the same inorganic series. (*c*) Raw SXRPD patterns for CGpQ_0.12A collected at three different positions of the capillary (red, black and blue traces). The intensity values in (*c*) have been artificially offset to show the three different patterns.

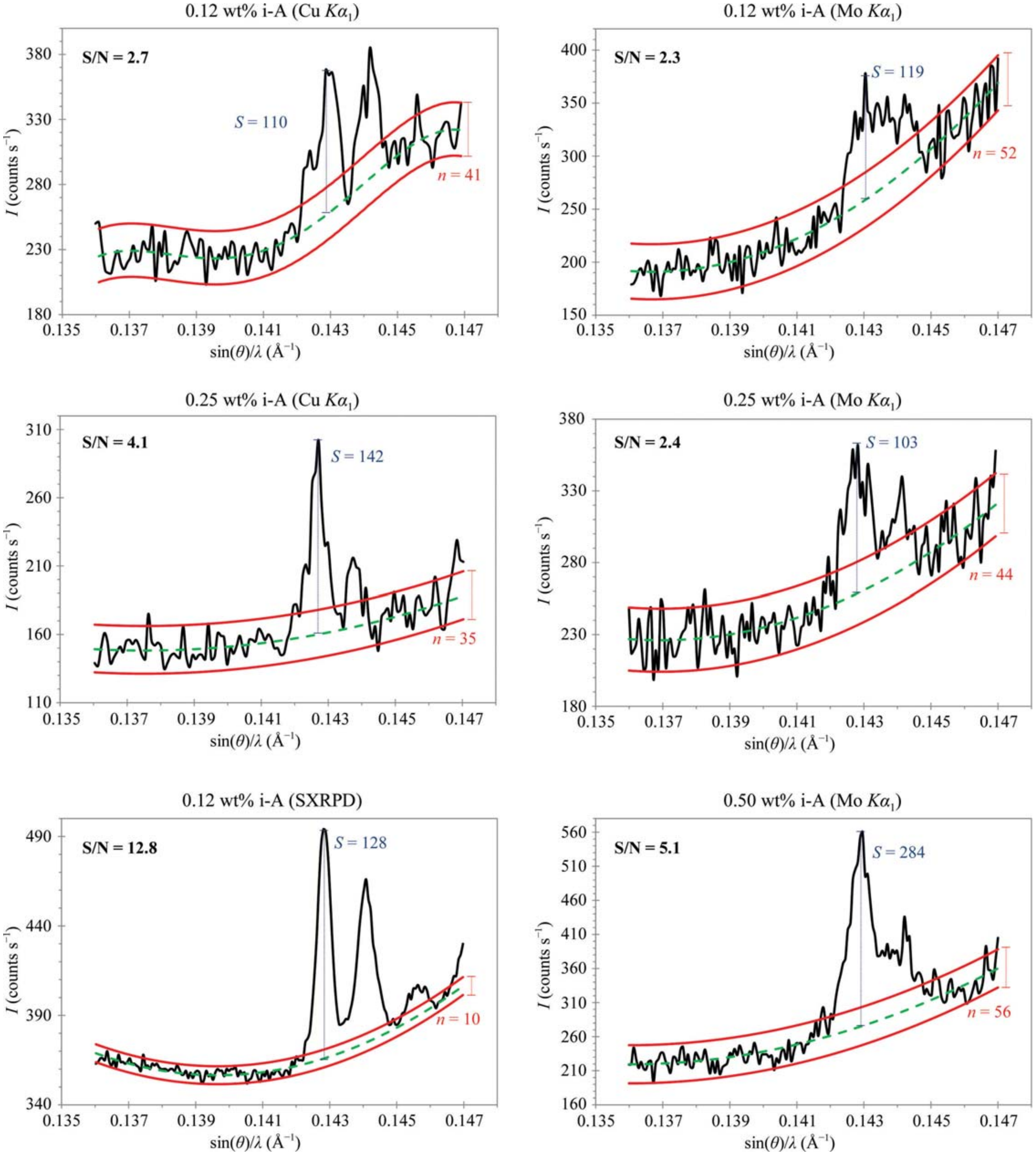

Figure 3.10.4

Selected region of the powder patterns showing the main diffraction peak of insoluble anhydrite for the low-content samples to investigate the limit of detection. Top left: Cu $K\alpha_1$ pattern for CGpQ_0.12A. Middle left, Cu $K\alpha_1$ pattern for CGpQ_0.25A. Bottom left, SXRPD pattern for CGpQ_0.12A. Top right, Mo $K\alpha_1$ pattern for CGpQ_0.12A. Middle right, Mo $K\alpha_1$ pattern for CGpQ_0.25A. Bottom right, Mo $K\alpha_1$ pattern for CGpQ_0.50A. The main peak of anhydrite, $(\theta)/\lambda = 0.143$ Å^{-1}, is located at 25.4, 11.6 and 12.7° 2θ for Cu $K\alpha_1$, Mo $K\alpha_1$ and synchrotron radiations, respectively. The peak at $\sin(\theta)/\lambda = 0.1445$ Å^{-1} is due to the soluble anhydrite from gypsum (constant content in all the samples). The very tiny peak at $\sin(\theta)/\lambda = 0.1457$ Å^{-1}, which is slightly visible only in the SXRPD pattern, arises from $SrSO_4$ (0.39 wt%) from gypsum.

xylose, the ADP values were not reported in the original publications. Hence, they were obtained from the fits to the Mo $K\alpha_1$ patterns for the single phases. Three groups of isotropic ADPs were refined: those for O, C and H atoms. The final ADP values are given in León-Reina *et al.* (2016) as well as the R_F values before and after optimization, showing the improvements in the fits. For RQPA of all of the mixtures the ADPs were kept fixed.

Preferred orientation was modelled by the March–Dollase algorithm along the [001] axis for both glucose and lactose. Since microparticle sizes and distributions for different phases may result in some sample-related effects, such as preferred orientation, microabsorption and 'rock-in-the-dust/graininess' effects, all powders were characterized by scanning electron microscopy (SEM). Fig. 3.10.2 shows SEM micrographs for all of the phases. All inorganic samples were single phases except for gypsum and insoluble anhydrite. The impurity-phase contents for these two samples were reported in León-Reina *et al.* (2016).

Both organic and inorganic phases were also measured using Cu $K\alpha_1$ radiation in reflection mode. As expected, a transparency effect was observed in the Cu $K\alpha_1$ patterns for organic samples (Buhrke *et al.*, 1998).

3.10.6. Limits of detection and quantification

LoD and LoQ are two important quantities in the validation of any analytical method. LoD/LoQ are terms that are used to describe the smallest concentration of an analyte that can be reliably detected/assessed by an analytical procedure, as discussed in Section 3.10.1. In techniques such as Rietveld analysis, the approach of having a powder pattern with its strongest (not overlapped) diffraction peak with an S/N ratio of larger than 3.0 is not straightforward because the full powder pattern is evaluated.

Fig. 3.10.3 shows Mo $K\alpha_1$ and Cu $K\alpha_1$ raw patterns for the inorganic series with increasing amounts of insoluble anhydrite (labelled with solid squares) and Fig. 3.10.4 shows the strongest diffraction peak for i-A in the mixtures containing 0.123 wt% anhydrite (CGpQ_0.12A) and 0.25 wt% anhydrite (CGpQ_0.25A) to evaluate the limits of detection in the conditions reported in Section 3.10.5. For CGpQ_0.12A, both laboratory powder patterns yielded peaks with S/N ratios lower than 3.0 (top panels in Fig. 3.10.4). For CGpQ_0.25A, the Cu $K\alpha_1$ pattern yielded a clear peak with S/N = 4.1; therefore, it can be concluded that the LoD for insoluble anhydrite with this radiation in this mixture is slightly lower than 0.2 wt%. For Mo $K\alpha_1$ radiation, the CGpQ_0.25A and CGpQ_0.50A samples yielded patterns with peaks with S/N ratios of 2.4 and 5.1, respectively. Hence, it can be concluded that the LoD for i-A with this radiation in this mixture is quite close to 0.3 wt%.

The LoQ for i-A in this matrix was also studied. Three Mo $K\alpha_1$ and Cu $K\alpha_1$ patterns were collected for CGpQ_0.12A. For the three Mo $K\alpha_1$ patterns, the average analysis result for i-A was 0.28 (2) wt%, but the accuracy of the obtained value is poor, as the expected value was 0.12 wt%. Similarly, the average value for the analyses of three Cu $K\alpha_1$ patterns was 0.24 (2) wt%. The RQPA results are given as supporting information in León-Reina *et al.* (2016). It was concluded that i-A can be quantified in this mixture at the level of 0.12 wt%, but with a relative error close to 100%. If the 'acceptable reliability' criterion in the analysis is taken into consideration, the LoQ value would be close to 1.0 wt% in order to have a relative associated error lower than 20%.

CGpQ_0.12A was also studied by SXRPD. Fig. 3.10.3(*c*) shows the SXRPD patterns collected at three different positions of the capillary, which were almost identical, and Fig. 3.10.4 (bottom left) shows the main diffraction peak of anhydrite. The S/N ratio for the strongest diffraction peak of anhydrite was 12.8 and hence the limit of detection for i-A with synchrotron radiation in this matrix is below 0.10 wt%.

To quantify the accuracy of the analyses, the KLD methodology was used. The AKLD values for each analysis as well as the KLD values for i-A are reported in León-Reina *et al.* (2016). The synchrotron analyses clearly had better accuracy than those using laboratory radiation. Moreover, the Mo $K\alpha_1$ radiation analyses were slightly better than those obtained using Cu $K\alpha_1$ radiation.

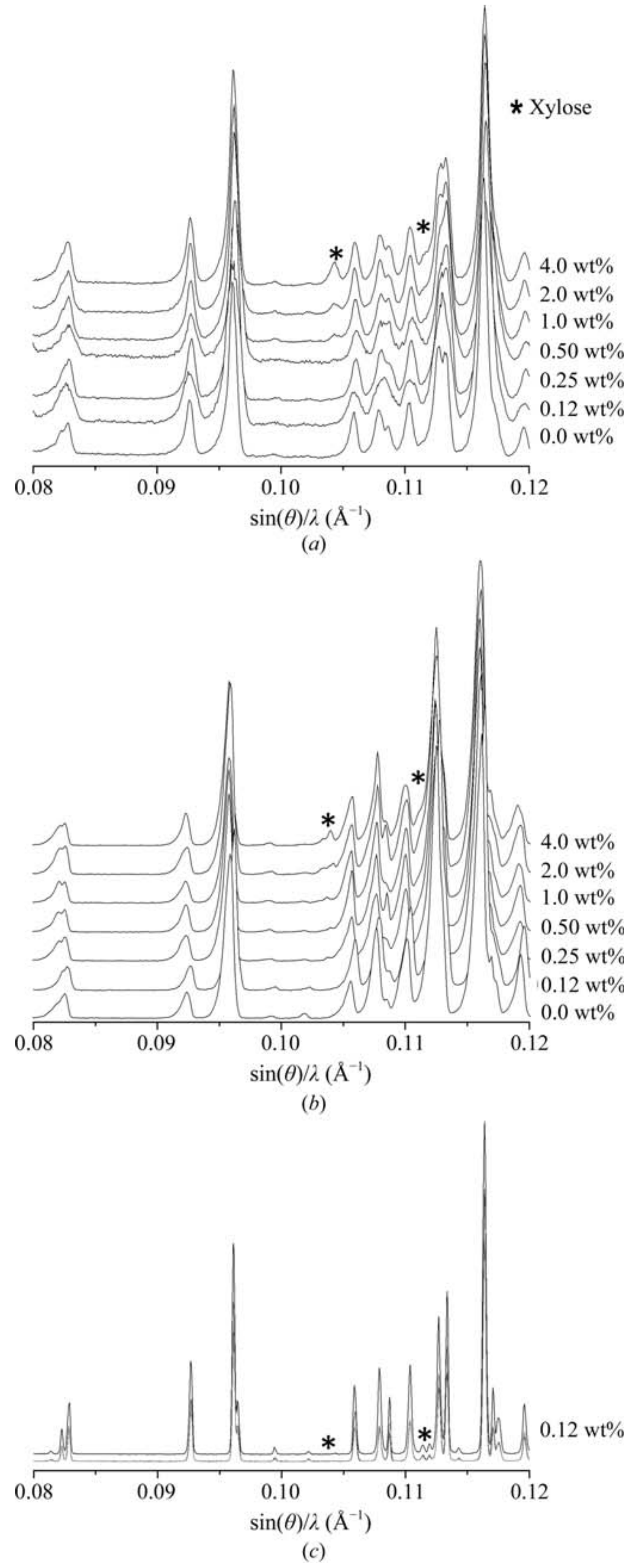

Figure 3.10.5
(*a*) Raw Mo $K\alpha_1$ powder patterns for the organic series composed of a constant matrix of glucose, fructose and lactose, and increasing amounts of xylose (peaks highlighted with an asterisk). (*b*) Raw Cu $K\alpha_1$ powder patterns for the same organic series. (*c*) Raw SXRPD patterns for GFL_0.12X collected at three different positions of the capillary (as collected).

Table 3.10.2
Rietveld quantitative phase analyses for the crystalline inorganic mixtures measured with Cu $K\alpha_1$ and Mo $K\alpha_1$ radiations

Weighed amounts (wt%) are also shown for comparison. Absolute values of the Kullback–Liebler distance (AKLD) for each mixture and the KLD value for i-anhydrite are also included. Trm, transmission; rfl, reflection.

	CGpQ_0.0A			CGpQ_0.25A			CGpQ_0.50A		
Phases	wt%	Mo trm	Cu rfl	wt%	Mo trm	Cu rfl	wt%	Mo trm	Cu rfl
C	32.9	32.6 (1)	30.4 (2)	32.8	32.0 (1)	33.6 (1)	32.7	33.2 (1)	32.8 (1)
Gp	31.7	31.7 (1)	34.5 (1)	31.7	32.5 (1)	31.6 (1)	31.6	30.1 (1)	30.7 (1)
Q	34.2	34.6 (1)	33.7 (1)	34.1	33.9 (1)	33.0 (1)	34.0	34.6 (1)	34.2 (1)
s-A	0.8	0.66 (3)	0.76 (5)	0.8	0.77 (4)	0.78 (5)	0.8	0.97 (3)	1.15 (5)
$SrSO_4$	0.4	0.44 (4)	0.70 (6)	0.4	0.44 (4)	0.67 (5)	0.4	0.39 (4)	0.56 (5)
i-A	—	—	—	0.28	0.42 (3)	0.42 (4)	0.52	0.71 (3)	0.71 (4)
AKLD sum		0.0089	0.0605		0.0198	0.0235		0.0295	0.0180
(i-A) KLD					−0.001	−0.001		−0.002	−0.002

	CGpQ_1.0A			CGpQ_2.0A			CGpQ_4.0A		
Phases	wt%	Mo trm	Cu rfl	wt%	Mo trm	Cu rfl	wt%	Mo trm	Cu rfl
C	32.5	32.8 (1)	32.6 (2)	32.2	31.3 (1)	31.4 (1)	31.6	31.2 (1)	31.8 (1)
Gp	31.5	30.4 (1)	30.7 (1)	31.1	32.1 (1)	32.3 (1)	30.5	30.7 (1)	30.5 (1)
Q	33.8	34.1 (1)	33.8 (1)	33.5	33.5 (1)	32.6 (1)	32.8	32.8 (1)	32.0 (1)
s-A	0.8	1.03 (4)	1.11 (5)	0.7	0.54 (3)	0.58 (5)	0.7	0.67 (3)	0.77 (4)
$SrSO_4$	0.4	0.43 (4)	0.68 (5)	0.4	0.48 (4)	0.68 (6)	0.4	0.45 (4)	0.63 (5)
i-A	1.02	1.23 (3)	1.17 (5)	2.02	2.05 (4)	2.38 (9)	4.02	4.30 (8)	4.33 (9)
AKLD sum		0.0214	0.0152		0.0218	0.0358		0.0095	0.0156
(i-A) KLD		−0.002	−0.001		0.000	−0.003		−0.004	−0.003

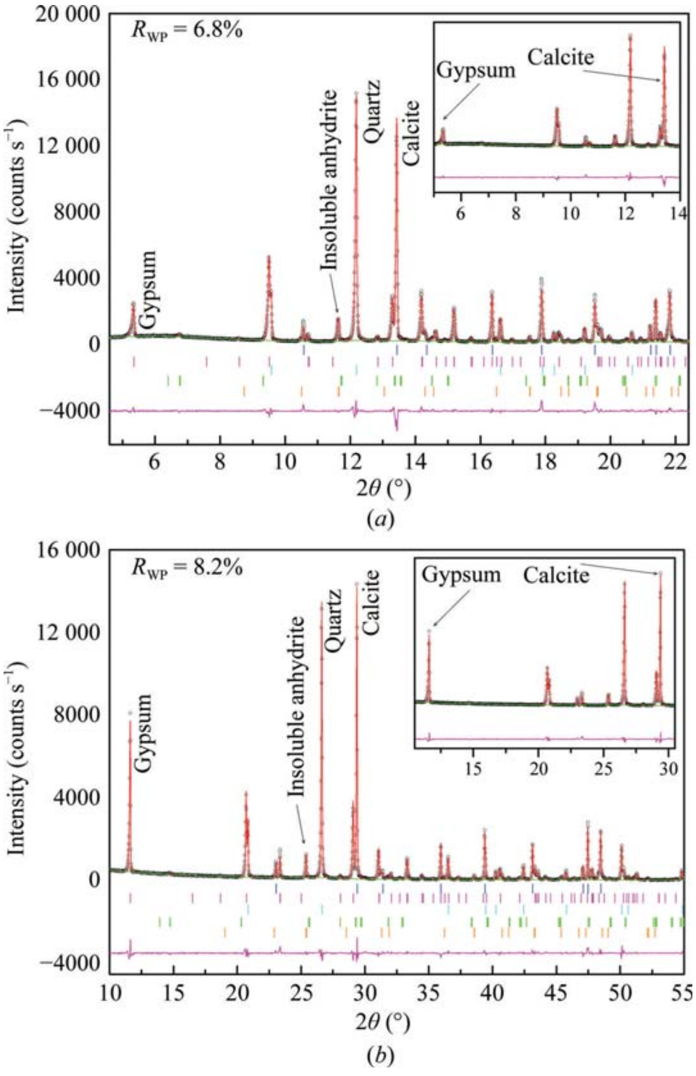

Figure 3.10.6
Selected range of the Rietveld plots for CGpQ_4.0A: (*a*) Mo $K\alpha_1$ and (*b*) Cu $K\alpha_1$ patterns. The inset highlights the effect of preferred orientation for gypsum and calcite.

Fig. 3.10.5 shows Mo $K\alpha_1$ and Cu $K\alpha_1$ raw patterns of the organic mixtures with increasing amounts of xylose. The strongest powder-diffraction peak for xylose in the GFL_0.12X patterns (with both Mo and Cu radiations) was not observed. The corresponding peak was observed in the GFL_0.25X patterns. Therefore, the LoD can be established as close to 0.25 wt%. The analysis results for xylose in GFL_0.25X were reported in León-Reina *et al.* (2016). These values showed that the results from Mo $K\alpha_1$ powder diffraction were slightly more accurate.

The LoQ for xylose was also studied. Once again, three Mo $K\alpha_1$ and Cu $K\alpha_1$ patterns were collected for GFL_0.12X. The average value for the analysis of the three Mo patterns was 0.18 (8) wt%. Similarly, the average result for the analyses of three Cu patterns was 0.34 (6) wt%. Full RQPA results are reported in the supporting information of León-Reina *et al.* (2016). The LoQ for xylose in this mixture for the two radiations can be established as close to 0.12 wt%. Indeed, if one applies an ‘acceptable reliability’ criterion, the LoQ would be much higher at above 1 wt%. The output of this study was that Cu $K\alpha_1$ radiation yielded a slightly less accurate result than that obtained from the Mo $K\alpha_1$ data.

GFL_0.12X was also studied by SXRPD in a rotating glass capillary in transmission mode. Fig. 3.10.5(*c*) shows SXRPD patterns for GFL_0.12X collected at three different positions of the same capillary. The powder patterns showed quite different peak ratios. It is important to bear in mind that filling a glass capillary with organic compounds is sometimes not easy due to electrostatic charge effects. For this reason, the phase ratio within the part of capillary bathed by the X-rays might not be the same as that of the sample under study. The behaviour observed in Fig. 3.10.5(*c*) could be explained by inhomogeneous capillary filling. Hence, in this case, the RQPA results are unreliable. Even in ‘well behaved’ samples, inhomogeneous filling of small capillaries could result in problems. Readers should be aware of this, and the authors strongly recommend that at least three patterns should be collected along the capillary and superimposed. If there is inhomogeneous filling the patterns will differ, and extreme care has to be exercised when filling capillaries in order to minimize this problem.

3.10.7. Increasing inorganic crystalline phase content series

Table 3.10.2 reports the RQPA results for six inorganic mixtures with increasing amounts of i-A measured with Mo $K\alpha_1$ (transmission) and Cu $K\alpha_1$ (reflection). The Rietveld plots of the mixture with 4 wt% i-A are shown in Fig. 3.10.6. For most of the samples, the AKLD values (see Table 3.10.2) for Mo $K\alpha_1$ radiation are slightly smaller than the corresponding values obtained for Cu $K\alpha_1$ radiation. For this reason, we can conclude that the Mo $K\alpha_1$ analyses are slightly better than those derived using Cu $K\alpha_1$ radiation.

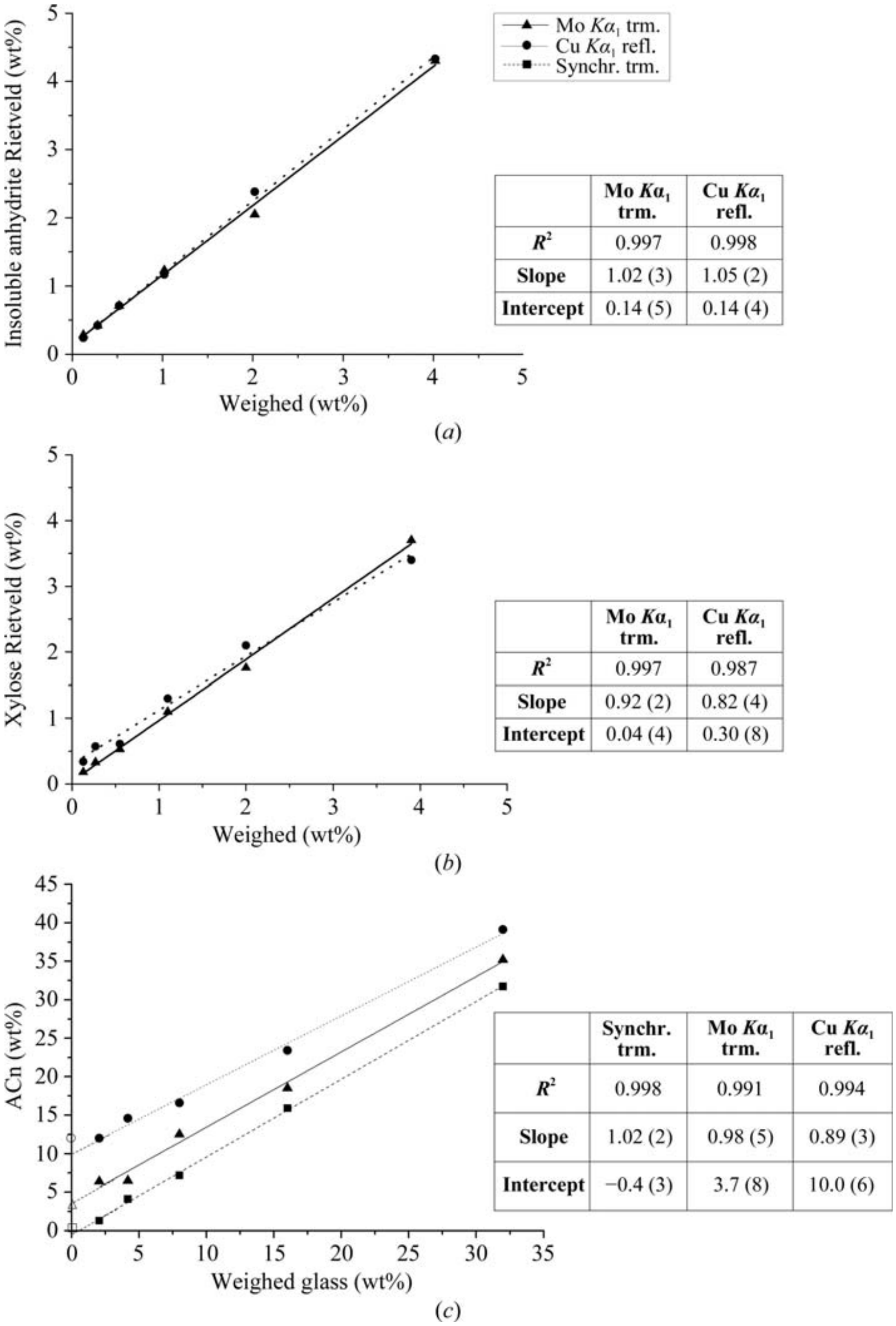

	Mo $K\alpha_1$ trm.	Cu $K\alpha_1$ refl.
R^2	0.997	0.998
Slope	1.02 (3)	1.05 (2)
Intercept	0.14 (5)	0.14 (4)

	Mo $K\alpha_1$ trm.	Cu $K\alpha_1$ refl.
R^2	0.997	0.987
Slope	0.92 (2)	0.82 (4)
Intercept	0.04 (4)	0.30 (8)

	Synchr. trm.	Mo $K\alpha_1$ trm.	Cu $K\alpha_1$ refl.
R^2	0.998	0.991	0.994
Slope	1.02 (2)	0.98 (5)	0.89 (3)
Intercept	−0.4 (3)	3.7 (8)	10.0 (6)

Figure 3.10.7

Rietveld quantification results for (*a*) the insoluble anhydrite series (within an inorganic crystalline matrix), (*b*) the xylose series (within an organic crystalline matrix) and (*c*) the ground-glass series (within an inorganic crystalline matrix) as a function of the weighed amount of each phase. Open symbols represent the derived amorphous contents in the mixtures without any added glass. The results of the least-squares fits are also shown.

On the other hand, calcite and gypsum presented preferred orientations, with the axes being [104] and [010], respectively. This effect was modelled using the March–Dollase algorithm. Preferred orientation makes the $0l0$ reflections for gypsum have higher intensities in the Cu $K\alpha_1$ patterns, and smaller intensities in the Mo $K\alpha_1$ patterns, than those calculated from the crystal structure (see insets in Fig. 3.10.6). As a consequence, the refined values for flat samples in reflection and transmission geometries were smaller and larger than 1.0, respectively (Cuesta *et al.*, 2015). Although preferred orientation is present in all patterns, the Cu $K\alpha_1$ patterns were recorded in reflection geometry (flat samples), while the Mo $K\alpha_1$ measurements were collected in transmission (also flat samples). This results in opposite diffraction intensity changes and points towards another (possible) fruitful use: joint refinement of these two types of patterns to counterbalance the effects of preferred orientation in RQPA.

Fig. 3.10.7(*a*) shows the quantified i-A contents (wt%), as determined by the Rietveld methodology, as a function of the weighed i-A amount. The two R^2 values for the fits are very close to 1.00, and the intercept values are very close to zero, showing the appropriateness of the Rietveld methodology for quantifying crystalline materials. Furthermore, the slopes of the calibration curves are also 1.00 in both cases. Consequently, this study allows it to be concluded that RQPA for crystalline inorganic phases using powder-diffraction patterns collected using Mo $K\alpha_1$ radiation yields results that are as accurate as those obtained from the well established method using Cu $K\alpha_1$.

3.10.8. Increasing crystalline organic phase content series

Table 3.10.3 shows RQPA results for six mixtures prepared with G, F, L and an increasing amount of X measured with Mo $K\alpha_1$ (transmission) and Cu $K\alpha_1$ (reflection). In general, the values obtained using both radiations are quite similar to the weighed values. The AKLD values and the KLD values for the xylose phase are also reported in Table 3.10.3. The AKLD values from Mo $K\alpha_1$ and Cu $K\alpha_1$ radiations are relatively similar. The main problem for RQPA of organic mixtures measured in reflection geometry is related to the low X-ray absorption of the samples and the transparency effects that lead to poor peak shapes and even some split peaks in the powder patterns, as discussed previously (León-Reina *et al.*, 2016).

Fig. 3.10.7(*b*) shows the quantified xylose contents (wt%) as determined by the Rietveld methodology as a function of the weighed amount of xylose added to the mixtures. The results were plotted to obtain the calibration lines with increasing content of the analyte. Both plots gave R^2 values close to 1.0. However, the slope values were 0.92 and 0.82 for Mo $K\alpha_1$ and Cu $K\alpha_1$ radiations, respec-

Table 3.10.3
RQPA for the crystalline organic mixtures measured with Cu $K\alpha_1$ and Mo $K\alpha_1$ radiations

Weighed amounts (wt%) are also shown for the sake of comparison. Absolute values of the Kullback–Liebler distance (AKLD) for each mixture and the KLD value for xylose are also included. Trm, transmission; rfl, reflection.

	GFL_0.0X			GFL_0.25X			GFL_0.50X		
Phases	wt%	Mo trm	Cu rfl	wt%	Mo trm	Cu rfl	wt%	Mo trm	Cu rfl
G	33.4	33.8 (1)	33.5 (3)	33.3	33.6 (1)	33.1 (2)	33.2	32.3 (2)	33.5 (2)
F	33.5	31.7 (1)	32.7 (3)	33.4	32.3 (1)	34.3 (2)	33.3	32.1 (2)	33.4 (2)
L	33.1	34.5 (1)	33.7 (3)	33.0	33.7 (1)	32.0 (2)	33.0	35.0 (3)	32.5 (2)
X	—	—		0.27	0.33 (4)	0.57 (9)	0.55	0.53 (8)	0.61 (9)
AKLD sum		0.0362	0.0150		0.0216	0.0231		0.0410	0.0096
(X) KLD		—	—		−0.001	−0.002		0.000	−0.001

	GFL_1.0X			GFL_2.0X			GFL_4.0X		
Phases	wt%	Mo trm	Cu rfl	wt%	Mo trm	Cu rfl	wt%	Mo trm	Cu rfl
G	33.0	34.7 (1)	33.6 (2)	32.7	32.2 (1)	31.5 (2)	32.0	32.8 (1)	33.6 (2)
F	33.1	32.6 (1)	33.7 (2)	32.8	31.7 (1)	34.4 (2)	32.2	30.7 (1)	32.5 (2)
L	32.8	31.6 (2)	31.4 (2)	32.5	34.3 (1)	32.0 (2)	31.8	32.9 (1)	30.5 (2)
X	1.1	1.10 (5)	1.3 (1)	2.0	1.76 (5)	2.1 (1)	3.9	3.70 (5)	3.4 (2)
AKLD sum		0.0338	0.0280		0.0363	0.0339		0.0361	0.0372
(X) KLD		0.000	−0.002		0.003	−0.001		0.002	0.005

Table 3.10.4
Rietveld quantitative phase analyses of the CQZ_*x*Gl mixture, where quartz (Q) is the internal standard, to derive amorphous content (am), obtained from SXRPD, Mo $K\alpha_1$ and Cu $K\alpha_1$ patterns

Absolute values of the Kullback–Liebler distance (AKLD) for each mixture and the KLD value for the amorphous content are also included. Trm, transmission; rfl, reflection.

	Weighed			Synchrotron trm				
Mixture	C wt%	Z wt%	Gl wt%	C wt%	Z wt%	Am wt%	AKLD sum	Am KLD
CZQ_0Gl	50.01	49.99	0.00	49.9 (1)	49.6 (1)	0.4 (1)	0.0050	—
CZQ_2Gl	48.98	48.96	2.05	49.7 (1)	49.0 (1)	1.3 (1)	0.0169	0.009
CZQ_4Gl	47.93	47.91	4.17	47.9 (1)	47.6 (1)	4.5 (1)	0.0066	−0.003
CZQ_8Gl	46.00	46.00	7.99	46.6 (1)	45.9 (1)	7.5 (1)	0.0120	0.005
CZQ_16Gl	41.99	41.99	16.01	42.0 (1)	41.6 (1)	16.4 (1)	0.0079	−0.004
CZQ_32Gl	34.00	34.00	31.99	34.0(1)	33.7 (1)	32.3 (1)	0.0061	−0.003

	Mo $K\alpha_1$ trm					Cu $K\alpha_1$ rfl				
Mixture	C wt%	Z wt%	Am wt%	AKLD sum	Am KLD	C wt%	Z wt%	Am wt%	AKLD sum	Am KLD
CZQ_0Gl	47.5 (1)	49.0 (1)	3.5 (1)	0.0358	—	47.2 (1)	40.8 (1)	12.0 (1)	0.1305	—
CZQ_2Gl	45.9 (1)	47.7 (1)	6.4 (1)	0.0679	−0.023	47.4 (1)	40.6 (1)	12.0 (1)	0.1440	−0.036
CZQ_4Gl	46.5 (1)	47.0 (1)	6.5 (1)	0.0422	−0.019	45.8 (1)	39.7 (1)	14.6 (1)	0.1641	−0.052
CZQ_8Gl	42.6 (1)	44.8 (1)	12.5 (1)	0.0832	−0.036	45.3 (1)	38.1 (1)	16.6 (1)	0.1522	−0.058
CZQ_16Gl	39.9 (1)	41.7 (1)	18.5 (1)	0.0475	−0.023	40.9 (1)	35.8 (1)	23.4 (1)	0.1388	−0.061
CZQ_32Gl	31.7 (1)	33.1 (1)	35.2 (1)	0.0635	−0.031	32.2 (1)	28.7 (1)	39.1 (1)	0.1403	−0.064

tively. Slope values close to 1.0 mirror accurate analyses. Furthermore, the *y*-intercept values were 0.04 and 0.30 for Mo $K\alpha_1$ and Cu $K\alpha_1$ radiations, respectively. A *y*-intercept value close to 0.0 mirrors accurate analyses. Hence, it can be concluded that slightly more accurate analyses are obtained for Mo $K\alpha_1$ powder diffraction in transmission when compared with Cu $K\alpha_1$ powder diffraction in reflection for organic crystalline samples.

3.10.9. Increasing amorphous content series within an inorganic crystalline phase matrix

Fig. 3.10.8 shows Mo $K\alpha_1$ (transmission), Cu $K\alpha_1$ (reflection) and SXRPD (transmission) raw patterns for the mixtures with increasing amounts of glass. It is important to highlight that the increase in the background due to the glass is very modest even for ∼32 wt% of glass. Table 3.10.4 shows the RQPA of these mixtures, prepared with C, Z and an increasing amount of Gl, for the three radiations. The glass-free sample may contain amorphous material from the employed phases. Hence, we used the SXRPD data to calculate a correction factor for quartz to yield zero amorphous content for the glass-free sample (León-Reina *et al.*, 2016).

The linear fit to the amorphous content values obtained using SXRPD was very good, $R^2 = 0.998$, with the slope being 1.00 within the errors (see Fig. 3.10.7*c*). This plot also shows the quantified amorphous contents, in weight percentage, as a function of the amount of added ground glass, measured with Mo $K\alpha_1$ and Cu $K\alpha_1$ radiations. Open symbols indicate the derived amorphous contents obtained with the internal-standard method in the mixture without any added glass, CZQ_0Gl. Both R^2 values are quite close to 1.00, showing the consistency of the internal-standard methodology. However, the slope values were 0.98 and 0.89 for Mo $K\alpha_1$ and Cu $K\alpha_1$ radiations, respectively. Furthermore, the *y*-intercept values were 3.7 and 10.0 for Mo $K\alpha_1$ and Cu $K\alpha_1$ radiations, respectively. Again, slope values close to 1.0 and *y* intercepts close to 0.0 mirror accurate analyses. It must also

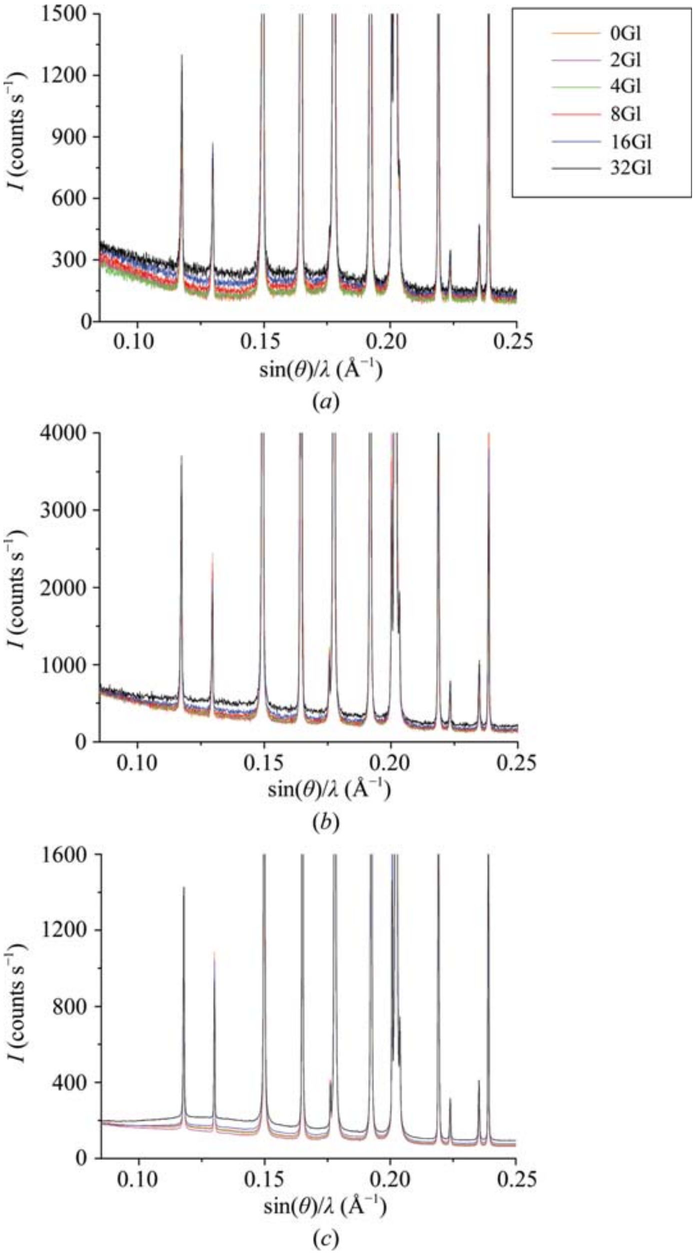

Figure 3.10.8
Raw powder patterns for the amorphous-material-containing series composed of a constant matrix of calcite and zincite, and increasing amounts of ground glass. Quartz was added as internal standard. (*a*) Mo $K\alpha_1$, (*b*) Cu $K\alpha_1$ and (*c*) SXRPD radiations. The intensities of the patterns have been rescaled to highlight the contributions of the glass to the background.

be pointed out that for the Mo $K\alpha_1$ analyses the value from the measurement of the Gl-free sample, 3.5 wt%, matches the value from the *y* intercept of the plot, 3.7 wt%, very well. Meanwhile, there is a much larger discrepancy for the similar Cu-based analyses, 12.0 and 10.0 wt%, respectively, which is quite far from zero. Hence, it is concluded that the amorphous contents derived from Mo $K\alpha_1$ data are more accurate than those derived from Cu $K\alpha_1$ data. However, it is not possible to reliably quantify amorphous contents below ~8–10 wt% from Mo $K\alpha_1$ and Cu $K\alpha_1$ diffraction data (see Table 3.10.4) with the internal-standard method.

On the contrary, SXRPD reliably allows quantification of amorphous contents down to ~2 wt% for this relatively simple mixture. In addition, the AKLD and the KLD values reported in Table 3.10.4 demonstrate that the synchrotron analyses are indeed much better than the laboratory analyses.

3.10.10. Conclusions

(i) We have thoroughly studied the limit of detection for a well crystallized inorganic phase in an inorganic compound matrix. We have determined the following LoDs for insoluble anhydrite: ~0.2 wt%, ~0.3 wt% and lower than 0.1 wt% for Cu $K\alpha_1$, Mo $K\alpha_1$ and synchrotron radiations, respectively. We conclude that the LoD is slightly better for Cu $K\alpha_1$ than for Mo $K\alpha_1$ because the λ^3 dependence of the diffraction intensity, with similar acquisition times, yielded slightly better signal-to-noise ratios in the Cu patterns. Of course, detector efficiencies also play a role in the measured signal-to-noise ratios.

(ii) We have also studied the limit of quantification for a well crystallized inorganic phase using laboratory X-ray powder diffraction. This phase could be quantified at the level of 0.12 wt% in stable fits with repeatable outputs and good precision. However, the accuracy of these analyses was quite poor, with relative errors close to 100%. Only contents higher than 1.0 wt% yielded analyses with relative errors lower than 20%.

(iii) The Rietveld quantitative phase analysis results from high-resolution Mo $K\alpha_1$ powder diffraction (transmission geometry) and high-resolution Cu $K\alpha_1$ powder diffraction (reflection geometry) were quite similar for a series of crystalline inorganic phase samples. We inferred the validation of the Mo-based analyses procedure from this initial study, as it yielded results very close to well established high-resolution Cu radiation analyses (see Fig. 3.10.7*a*). From the comparison of the AKLD values for the two types of analyses, it was demonstrated that the Mo $K\alpha_1$ analyses were slightly better than those using Cu $K\alpha_1$.

(iv) Comparison of the results obtained from Mo-based and Cu-based patterns for a series of crystalline organic phase mixtures showed that the Mo $K\alpha_1$ analyses gave slightly more accurate values. This conclusion was drawn because the calibration curve obtained from Mo patterns with increasing content of xylose gave an R^2 value closer to 1.0, a slope closer to 1.0 and an intercept value close to 0.0 (see Fig. 3.10.7*b*). The slightly poorer results from Cu $K\alpha_1$ analyses are very likely to be due to the transparency effects in reflection geometry.

(v) Comparison of the results obtained from Mo $K\alpha_1$ and Cu $K\alpha_1$ patterns for a series containing increasing amounts of amorphous glass also indicated that the Mo-based analyses were slightly more accurate than the corresponding Cu $K\alpha_1$ analyses. This conclusion was drawn because the obtained calibration curve from the Mo data has (1) a slope closer to 1.0, (2) a smaller amorphous value for the glass-free sample and (3) a closer agreement between the intercept from the least-squares fit and the determined amorphous value for the glass-free sample (see Fig. 3.10.7*c*). The AKLD analysis confirmed this outcome. Furthermore, the results from synchrotron data have the best accuracy, as shown by the calibration plot and the AKLD analysis.

Finally, we conclude that for the challenging quantification analyses studied here, the results derived from high-energy Mo $K\alpha_1$ patterns were slightly more accurate than those obtained from Cu $K\alpha_1$ patterns. We justify this conclusion based on the larger tested volume for Mo $K\alpha_1$ analyses, which led to better statistics/accuracy in the recorded powder-pattern intensities. The minimization of microabsorption in the Mo $K\alpha_1$ transmission data is very likely to be an additional factor in the improved accuracy.

This chapter is based on an article *Accuracy in Rietveld quantitative phase analysis: a comparative study of strictly monochromatic Mo and Cu radiations* by León-Reina *et al.* [(2016), *J. Appl. Cryst.* **49**, 722–735]. The work was supported by Spanish MINECO through BIA2014-57658-C2-2-R, which is co-funded by FEDER, and BIA2014-57658-C2-1-R research grants. Funding from Junta de Andalucía (grant P11-FQM-07517) is also acknowledged. We thank CELLS-ALBA (Barcelona, Spain) for providing synchrotron beam time on the BL04-MSPD beamline. All raw powder-diffraction data files underlying this work can be accessed at Zenodo at https://doi.org/10.5281/zenodo.1291900 and used under the Creative Commons Attribution license.

References

Albertsson, J., Abrahams, S. C. & Kvick, Å. (1989). *Atomic displacement, anharmonic thermal vibration, expansivity and pyroelectric coefficient thermal dependences in ZnO. Acta Cryst.* B**45**, 34–40.

Aranda, M. A. G., De la Torre, Á. G. & León-Reina, L. (2012). *Rietveld quantitative phase analysis of OPC clinkers, cements and hydration products. Rev. Mineral. Geochem.* **74**, 169–209.

Bezou, C., Nonat, A., Mutin, J.-C., Christensen, A. N. & Lehmann, M. S. (1995). *Investigation of the crystal structure of γ-$CaSO_4$, $CaSO_4$·$0.5H_2O$, and $CaSO_4$·$0.6H_2O$ by powder diffraction methods. J. Solid State Chem.* **117**, 165–176.

Brown, G. M. & Levy, H. A. (1979). *α-D-Glucose: further refinement based on neutron-diffraction data. Acta Cryst.* B**35**, 656–659.

Buhrke, V. E., Jenkins, R. & Smith, D. K. (1998). *A Practical Guide for the Preparation of Specimens for X-ray Fluorescence and X-ray Diffraction Analysis.* New York: Wiley.

Cuesta, A., Álvarez-Pinazo, G., García-Maté, M., Santacruz, I., Aranda, M. A. G., De la Torre, Á. G. & León-Reina, L. (2015). *Rietveld quantitative phase analysis with molybdenum radiation. Powder Diffr.* **30**, 25–35.

De La Torre, A. G., Bruque, S. & Aranda, M. A. G. (2001). *Rietveld quantitative amorphous content analysis. J. Appl. Cryst.* **34**, 196–202.

De la Torre, Á. G., López-Olmo, M., Álvarez-Rua, C., García-Granda, S. & Aranda, M. A. G. (2004). *Structure and microstructure of gypsum and its relevance to Rietveld quantitative phase analyses. Powder Diffr.* **19**, 240–246.

Dollase, W. A. (1986). *Correction of intensities for preferred orientation in powder diffractometry: application of the March model. J. Appl. Cryst.* **19**, 267–272.

Egami, T. & Billinge, S. J. L. (2003). *Underneath the Bragg Peaks. Structural Analysis of Complex Materials.* Amsterdam: Pergamon.

Elton, N. J. & Salt, P. D. (1996). *Particle statistics in quantitative X-ray diffractometry. Powder Diffr.* **11**, 218–229.

Fauth, F., Peral, I., Popescu, C. & Knapp, M. (2013). *The new material science powder diffraction beamline at ALBA synchrotron. Powder Diffr.* **28**, S360–S370.

Fries, D. C., Rao, S. T. & Sundaralingam, M. (1971). *Structural chemistry of carbohydrates. III. Crystal and molecular structure of 4-O-β-D-galactopyranosyl-α-D-glucopyranose monohydrate (α-lactose monohydrate). Acta Cryst.* B**27**, 994–1005.

García-Maté, M., Santacruz, I., Cuesta, A., León-Reina, L., Aranda, M. A. G., Baco, I., Morin, V., Walenta, G., Gartner, E. & De la Torre, A. G. (2014). *Amorphous content determination in calcium sulfoaluminate related materials by external and internal standard methodologies. Adv. Cem. Res.* **27**, 417–423.

Garske, D. & Peacor, D. R. (1965). *Refinement of the structure of celestite $SrSO_4$. Z. Kristallogr.* **121**, 204–210.

Hordvik, A. (1971). *The crystal and molecular structure of α-xylose. Acta Chem. Scand.* **25**, 2175–2182.

Kanters, J. A., Roelofsen, G., Alblas, B. P. & Meinders, I. (1977). *The crystal and molecular structure of β-D-fructose, with emphasis on anomeric effect and hydrogen-bond interactions. Acta Cryst.* B**33**, 665–672.

Kirfel, A. & Will, G. (1980). *Charge density in anhydrite, $CaSO_4$, from X-ray and neutron diffraction measurements. Acta Cryst.* B**36**, 2881–2890.

Kullback, S. (1968). *Information Theory and Statistics*, pp. 1–11. New York: Dover.

Larson, A. C. & Von Dreele, R. B. (2000). *General Structure Analysis System (GSAS).* Los Alamos National Laboratory Report LAUR 86-748.

León-Reina, L., De la Torre, A. G., Porras-Vázquez, J. M., Cruz, M., Ordonez, L. M., Alcobé, X., Gispert-Guirado, F., Larrañaga-Varga, A., Paul, M., Fuellmann, T., Schmidt, R. & Aranda, M. A. G. (2009). *Round robin on Rietveld quantitative phase analysis of Portland cements. J. Appl. Cryst.* **42**, 906–916.

León-Reina, L., García-Maté, M., Álvarez-Pinazo, G., Santacruz, I., Vallcorba, O., De la Torre, A. G. & Aranda, M. A. G. (2016). *Accuracy in Rietveld quantitative phase analysis: a comparative study of strictly monochromatic Mo and Cu radiations. J. Appl. Cryst.* **49**, 722–735.

Madsen, I. C., Scarlett, N. V. Y., Cranswick, L. M. D. & Lwin, T. (2001). *Outcomes of the International Union of Crystallography Commission on Powder Diffraction Round Robin on Quantitative Phase Analysis: samples 1a to 1h. J. Appl. Cryst.* **34**, 409–426.

Madsen, I. C., Scarlett, N. V. Y. & Kern, A. (2011). *Description and survey of methodologies for the determination of amorphous content via X-ray powder diffraction. Z. Kristallogr.* **226**, 944–955.

Maslen, E. N., Streltsov, V. A., Streltsova, N. R. & Ishizawa, N. (1995). *Electron density and optical anisotropy in rhombohedral carbonates. III. Synchrotron X-ray studies of $CaCO_3$, $MgCO_3$ and $MnCO_3$. Acta Cryst.* B**51**, 929–939.

Scarlett, N. V. Y., Madsen, I. C., Cranswick, L. M. D., Lwin, T., Groleau, E., Stephenson, G., Aylmore, M. & Agron-Olshina, N. (2002). *Outcomes of the International Union of Crystallography Commission on Powder Diffraction Round Robin on Quantitative Phase Analysis: samples 2, 3, 4, synthetic bauxite, natural granodiorite and pharmaceuticals. J. Appl. Cryst.* **35**, 383–400.

Stutzman, P. (2005). *Powder diffraction analysis of hydraulic cements: ASTM Rietveld round-robin results on precision. Powder Diffr.* **20**, 97–100.

Thompson, P., Cox, D. E. & Hastings, J. B. (1987). *Rietveld refinement of Debye–Scherrer synchrotron X-ray data from Al_2O_3. J. Appl. Cryst.* **20**, 79–83.

Von Dreele, R. B. & Rodriguez-Carvajal, J. (2008). *Powder Diffraction: Theory and Practice*, edited by R. E. Dinnebier & S. J. L. Billinge, pp. 58–88. Cambridge: Royal Society of Chemistry. https://doi.org/10.1039/9781847558237-00058.

Will, G., Bellotto, M., Parrish, W. & Hart, M. (1988). *Crystal structures of quartz and magnesium germanate by profile analysis of synchrotron-radiation high-resolution powder data. J. Appl. Cryst.* **21**, 182–191.

Zevin, L. S. & Kimmel, G. (1995). *Quantitative X-ray Diffractometry*. New York: Springer-Verlag.

International Tables for Crystallography (2019). Vol. H, Chapter 4.1, pp. 386–394.

4.1. An overview of currently used structure determination methods for powder diffraction data

K. Shankland

4.1.1. Introduction

The two chapters that follow this one deal in detail with reciprocal- and real-space methods of crystal structure determination from powder diffraction data (SDPD). The purpose of this chapter is to provide an overview and summary of the wide variety of methods that are available for SDPD; no single method is discussed in great depth, and the reader should refer to the subsequent chapters for fuller descriptions of the main methodologies.

The paucity of structural information contained in a powder diffraction data set, relative to a single-crystal data set, means that considerable ingenuity may be required to determine structural models that can serve as starting points for subsequent Rietveld refinement. The most significant issues for SDPD method development are (*a*) the relatively small number of structure amplitudes that are measured in the powder experiment (typically several hundred) compared with the several thousand of a typical single-crystal experiment; and (*b*) accidental reflection overlap, particularly at larger diffraction angles (smaller *d*-spacings) where each individual peak in the diffraction pattern no longer equates to a single reflection intensity. Furthermore, those reflection intensities that are well determined rarely extend to atomic resolution. It therefore comes as no surprise that conventional direct methods of structure determination developed for single-crystal experiments do not normally perform well with intensities extracted from powder diffraction data using simple profile fitting. Rather, it is adaptations of direct methods that are specifically tailored to powder diffraction data, or methods that incorporate a significant amount of prior information about the structure under study, that have come to dominate the field of SDPD. For particularly complex or challenging structure determinations, it is often a combination of analytical methods (*e.g.* powder diffraction and electron microscopy, or powder diffraction and nuclear magnetic resonance, NMR) that is required to solve the crystal structure.

This introduction to the limitations of powder diffraction data inevitably contains some generalizations, to which there are a great many exceptions. For example, many materials (typically those containing heavy atoms in high-symmetry systems) scatter strongly to high resolution; many neutron-diffraction experiments using powder samples may be able to access Bragg diffraction peaks at atomic resolution because of the lack of a form-factor fall-off with diffraction angle; many synchrotron-based powder diffractometers possess extremely good instrumental resolution that allows closely spaced reflections to be resolved, even at high diffraction angles. Nevertheless, the intrinsic limitations of powder diffraction data, imposed by the collapse of the three dimensions of reciprocal space onto the single dimension of a powder diffraction pattern, are such that SDPD is rarely as straightforward as its single-crystal equivalent.

4.1.2. Methods used in SDPD

The origins of SDPD can be traced to the first half of the 20th century, with the structures of many simple crystalline materials (such as rock salt) being determined from powder diffraction data. In the late 1940s, Zachariasen (1948) solved the structures of several uranium salts using an essentially trial-and-error approach, establishing the principle of varying atomic positions and comparing the resultant calculated reflection intensities with those observed in the diffraction data. The 1960s saw the first applications of direct and Patterson methods in the field, and the

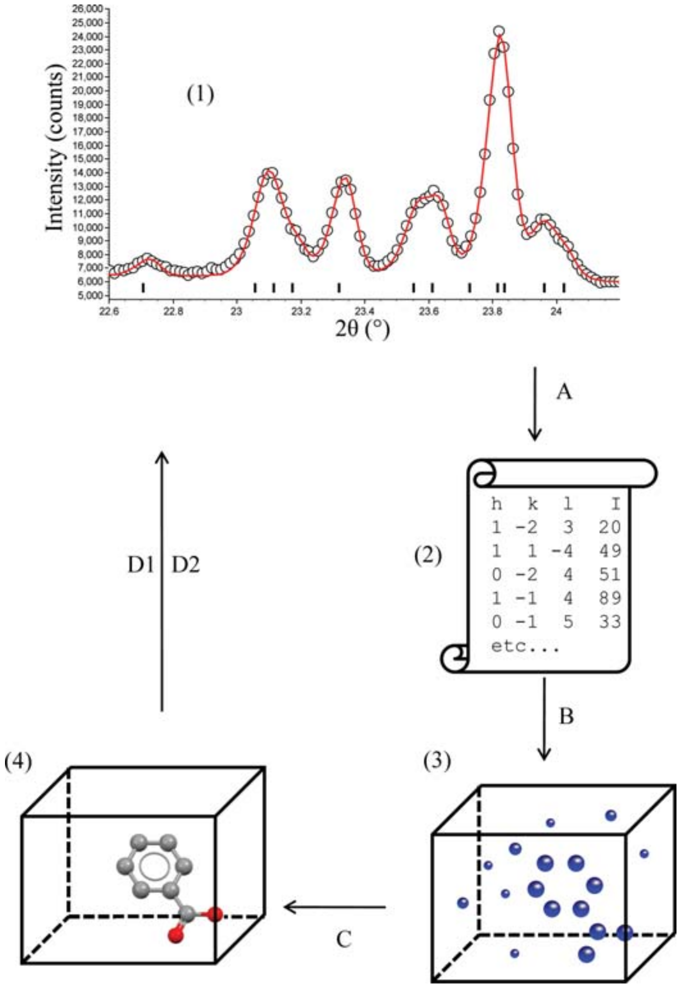

Figure 4.1.1
A generalized scheme for structure determination from powder diffraction data. A powder diffraction pattern (1) consists of a series of observed intensities (open circles) as a function of angle. The calculated intensities (red line) can be obtained either from a structure-independent Pawley or LeBail-type fit (A) to the data, or from a structure-dependent Rietveld-type fit (D1) to the data. Model-independent fits can be used to extract a list of reflection intensities (2) from the data and once phases have been assigned (B) to the structure amplitudes, a density map can be calculated (3). The structure (4) can then be identified (C) from the map and used as the basis of a Rietveld-type fit (D1) to the pattern in order to refine the structure. Alternatively, a structural fragment (4) may be identified and incorporated (D2) into a Pawley or LeBail-type fit in order to extract a more accurate set of reflection intensities for subsequent use in step B. In the global optimization approach to SDPD, a trial structural model (4) is constructed using a molecular model and the known unit cell, and assessed using a Rietveld-type fit (D1) to the pattern.

Copyright © 2019 International Union of Crystallography

Table 4.1.1
Some representative examples of structures solved using the methods described in this chapter

Section	Name	Formula	Space group	V (Å^3)	Z′	No. of non-H atoms	Radiation	Notes
4.1.3	Cimetidine	$C_{10}H_{16}N_6S$	$P2_1/c$	1281.5	1	17	Synchrotron	(*a*)
4.1.3	Ortho-xylene	C_8D_{10}	$P2_1/a$	634.4	1	18	Neutron	(*b*)
4.1.4	Amodiaquinium dichloride dihydrate	$C_{20}H_{24}ClN_3O^{2+}\cdot 2Cl^-\cdot 2H_2O$	$P2_1/c$	2283.6	1	29	Laboratory	(*c*)
4.1.5	ITQ-22	$Si_{16}O_{34}$ (unique)	*Pbam*	6939.8	1	50	Synchrotron	(*d*)
4.1.6	(*S*)(+)-Ibuprofen	$C_{13}H_{18}O_2$	$P2_1$	1246.0	2	30	Synchrotron	(*e*)
4.1.7	Strontium sulfate	$Sr^{2+}SO_4{}^{2-}$	*Pnma*	307.2	1	6	Synchrotron	(*f*)
4.1.8	Hen egg-white lysozyme	129 residues	$P4_32_12$	238240	1		Synchrotron	(*g*)
4.1.9	Lithium triflate	$Li^+CF_3SO_3{}^-$	$P2_1/c$	495.3	1	9	Laboratory	(*h*)
4.1.10	IM-5	$Si_{18}O_{36}$ (unique)	*Cmcm*	16536.4	1	54	Synchrotron/ electron	(*i*)
4.1.11	Boc-(2*R*,3*S*)-$\beta^{2,3}$-HVal(α-Me)-(2*R*,3*S*)-$\beta^{2,3}$-HAla(α-Me)-(2*R*,3*S*)-$\beta^{2,3}$-HLeu(α-Me)-OBn]	$C_{32}N_3O_6H_{53}$	$P2_12_12_1$	3466.2	1	41	Laboratory	(*j*)
4.1.12	(*R*,*S*,*R*,*S*)-2,6,10,14-Tetramethyl-1,5,9,13-tetra-azacyclohexadecane-4,8,12,16-tetraone	$C_{16}H_{28}N_4O_4$	$I\bar{4}$	904.4	0.25	6	Laboratory	(*k*)
4.1.13	Clarithromycin	$C_{38}H_{69}NO_{13}$	$P2_12_12$	4367.5	1	51	Synchrotron	(*l*)
4.1.13	Ponsin SH3.2	67 residues, 36 water molecules	$P2_12_12_1$	62225	1	580	Synchrotron	(*m*)
4.1.14	Chlorothiazide dimethylformamide solvate	$C_6H_6ClN_3O_4S_2\cdot 2(C_3H_7NO)$	$P2_1/c$	3942.3	2	54	Laboratory	(*n*)
4.1.14	Cyclohexene oxide	$C_6D_{10}O$	$P\bar{1}$	268.9	1	19	Neutron	(*o*)
4.1.15	Remacemide acetate	$C_{17}H_{21}N_2O^+\cdot C_2H_3O_2{}^-$	$P2_1/c$	1806.3	1	24	Synchrotron	(*p*)
4.1.16	Capsaicin	$C_{18}H_{27}NO_3$	$P2_1/c$	1707.7	1	22	Synchrotron	(*q*)
4.1.17	Zeolite-A	$Na_{96}Al_{96}Si_{96}O_{384}\cdot 150H_2O$ (cell)	$Fm\bar{3}c$	14811	1		Laboratory	(*r*)
4.1.17	IM-5	$Si_{24}O_{47}$ (unique)	*Cmcm*	16573	1	71	Synchrotron/ electron	(*s*)
4.1.17	Verapamil hydrochloride	$C_{27}H_{39}N_2O_4{}^+Cl^-$	$P\bar{1}$	1382	1	34	Laboratory	(*t*)
4.1.17	Tetracaine hydrochloride	$C_{15}H_{25}N_2O_2{}^+Cl^-$	$P\bar{1}$	822.3	1	20	Synchrotron	(*u*)
4.1.17	Paclitaxel (refined from SX model)	$C_{47}H_{51}NO_{14}$	$P2_12_12_1$	8659.8	2	124	Laboratory	(*v*)
4.1.18	α-L-Glutamic acid	$C_5H_9NO_4$	$P2_12_12_1$	638.1	1	8	Laboratory	(*w*)

Notes: (*a*) Cernik *et al.* (1991). (*b*) Ibberson, Morrison & Prager (2000). (*c*) Altomare *et al.* (2012). (*d*) Corma *et al.* (2003). (*e*) Rius (2011). (*f*) Burger *et al.* (1998). (*g*) Basso *et al.* (2010). (*h*) Lightfoot *et al.* (1993). (*i*) Baerlocher, Gramm *et al.* (2007). (*j*) Brenner *et al.* (2002). (*k*) Seebach *et al.* (1997). (*l*) Noguchi *et al.* (2012). (*m*) Margiolaki *et al.* (2007). (*n*) Fernandes *et al.* (2007). (*o*) Ibberson *et al.* (2006). (*p*) Markvardsen *et al.* (2002). (*q*) Shankland *et al.* (2010). (*r*) Grosse-Kunstleve *et al.* (1997) (topology search). (*s*) Baerlocher, McCusker & Palatinus (2007) (histogram matching). (*t*) Florence *et al.* (2009) (torsion-angle restrictions). (*u*) Nowell *et al.* (2002) (intermolecular distance restraints). (*v*) Harper *et al.* (2005). (*w*) Lanning *et al.* (2000).

advent of the Rietveld method (Rietveld, 1969) established not only the *de facto* procedure for structure refinement, but also laid the foundation of the Pawley and LeBail approaches for decomposition of powder diffraction patterns into individual reflection intensities. From the early 1990s onwards, significant effort has been expended in developing methods for SDPD and these have been reviewed on a regular basis – see, for example, Meden & Radosavljevic Evans (2015). Implementation of these methods has been greatly facilitated by advances in computing power that have allowed the automation of trial-and-error-type methods and also the use of increasingly complex direct-methods-type approaches.

For simplicity, in the sections that follow we assume the use of X-ray radiation sources and the determination of corresponding electron-density maps, though many of the methods described are equally applicable to neutron diffraction and electron diffraction. Fig. 4.1.1 summarizes several key generic steps in the SDPD process and representative examples of structures solved using the methods described below are presented in Table 4.1.1.

4.1.3. Conventional direct methods of structure determination

One of the most powerful features of direct methods of crystal structure determination is that they do not require any *a priori* knowledge of the connectivity or coordination of any of the atoms in the structure. Rather, such connectivity is derived from the electron-density map that is generated at the end of the process of assigning phases to the structure amplitudes. As such, direct methods can be brought to bear on diffraction data collected from crystalline materials of known and unknown composition; indeed, it is not uncommon for the composition and three-dimensional structure of a material under examination to differ significantly from a chemist's expectations. As the density map is the Fourier transform of a set of structure factors, the quality and interpretability of the map are a reflection of the accuracy (in terms of amplitude and phase angle) and resolution of those structure factors. For a typical single-crystal experiment, the quality of the map is not normally of concern, derived as it is from thousands of well defined structure amplitudes collected to sub-ångström resolution. With a typical powder diffraction experiment however (for the reasons mentioned in Section 4.1.1), map quality and interpretability are major issues. Accordingly, many early attempts at crystal structure determination from powders focused on collecting very high quality diffraction data with a view to extracting a set of structure amplitudes that could be input into one of the many standard direct-methods packages available at the time. Key to the success of this approach is the ability to extract a sufficient number of accurate structure amplitudes to near-atomic resolution; for powder diffraction experiments, this is a non-trivial task.

The crystal structure determination of the monoclinic form *A* of the anti-ulcer drug cimetidine (Table 4.1.1) is a good example of a moderately complex molecular crystal structure solved in this manner (Cernik *et al.*, 1991). Usable powder diffraction data were collected to 70° 2θ ($d_{\min} = 1.273$ Å; $\lambda = 1.4599$ Å) at Station 8.3 of the Daresbury synchrotron-radiation source. The presence of the sulfur atom aids structure determination by contributing strongly to Bragg scattering at high 2θ, and 561 intensities were extracted, with 204 rejected as unobserved. Even so, conventional direct-methods programs failed to yield a recognizable structure; the structure was eventually solved by taking the top 17 peak positions of the best E map returned by *SIR* (Burla *et al.*, 1989) and then applying several cycles of Fourier synthesis and least-squares refinement using the *CRYSTALS* package (Watkin *et al.*, 1985). Interestingly, a retrospective examination of the best initial E map showed that all the non-hydrogen-atom locations were in fact present in the map, but they had not been located by the automatic peak-search routines. This is not surprising: medium-resolution E maps, generated from small numbers of (not particularly accurate) structure factors, lack the clarity required to make atom assignment straightforward.

The significance of cimetidine as an early exemplar of SDPD is twofold: (*a*) as a molecule of pharmaceutical interest, it alerted the industry to the fact that powder diffraction had a structural utility that went beyond the 'fingerprinting' of physical forms; (*b*) aside from the use of synchrotron radiation, the structure determination used an entirely conventional approach. It also served to highlight some of the obvious limitations of applying unmodified single-crystal tools to powder diffraction data, and it is unsurprising that most successes using this standard approach have come either with relatively simple structures, with structures that contain strongly scattering atoms, or with high-resolution neutron-diffraction data (Ibberson *et al.*, 1997; Ibberson, Yamamuro & Matsuo, 2000; Ibberson, Morrison & Prager, 2000).

Some effort has been put into devising strategies for collecting powder diffraction data that are more 'single-crystal-like'. These include the exploitation of texture in samples (McCusker *et al.*, 2001) and inducing differential thermal expansion in crystals (Shankland *et al.*, 1997; Brunelli *et al.*, 2003). These approaches aim to overcome the reflection overlap problem experimentally and have been shown to work well, but have yet to make a substantial impact in terms of structure determination and their use cannot yet be described as routine.

4.1.4. Modified direct methods of structure determination

The extensive modifications that have been applied to adapt standard direct methods of structure solution to the specifics of powder diffraction data are dealt with in Chapter 4.2 and are only briefly considered here. Important gains in performance are achieved mainly by incorporating structural information obtained during the phasing process into the intensity-extraction stage. For example, consider two closely overlapping reflections $\mathbf{h}$ and $\mathbf{h}'$ that appear as a single peak in a powder diffraction pattern. In the absence of any prior information, only the summed intensity $I_{\mathbf{h}} + I_{\mathbf{h}'}$ is extracted in the powder pattern decomposition process, and this intensity is split equally between the two contributing reflections for an attempt at a direct-methods solution. Once a partial structure has been identified from this trial, it can be used to calculate a more probable partitioning of the observed intensities, based on the calculated values. This modified partitioning can then be used as the starting point for a more accurate decomposition of the pattern and the newly extracted intensities fed into another (hopefully improved) attempt at direct-methods solution (Altomare *et al.*, 2009). Important gains have also been realized using strategies devised to overcome the limitations of Fourier maps generated from powder diffraction data, with impressive results (Altomare *et al.*, 2012, 2013). Most importantly, modified direct methods of the type exemplified by the *EXPO* software package (Altomare *et al.*, 2013) are applicable to a broad range of problems that include inorganic, organic and organometallic structures using diffraction data collected on standard laboratory instrumentation, as well as high-resolution synchrotron instruments.

4.1.5. The direct-methods sum function

The direct-methods modulus sum function, S, is an example of a particular implementation of direct methods that is well suited to powder diffraction data (Rius, 1999). The value of the function S should be a maximum for the correct set of structure-factor phases and, as such, its use in structure determination requires an effective maximization process (Rius, 1993). Both a modified tangent formula and a fast Fourier transform (FFT) approach to function maximization have been used; the latter has also been combined with a 'Shake-and-Bake'-type approach (Rius & Frontera, 2007). As implemented in the *XLENS* program, distributed as part of the *Fullprof* suite (Rius, 1999; Rodriguez-Carvajal, 2013), the sum function has been used to solve a range of structures from powders, but has found particular utility in the solution of challenging framework-type structures such as ITQ-22 (Corma *et al.*, 2003).

4.1.6. The Patterson function

The Patterson function, $P(\mathbf{u})$, has one main advantage over conventional direct methods in the context of structure determination: it is calculated using only squared values of the observed structure amplitudes, $|F_{\mathbf{h}}|^2$, as coefficients and thus no phasing is required. Its biggest disadvantage is that the peaks in the resultant Patterson map represent interatomic vectors in the crystal structure rather than atomic positions. The map for a structure containing N atoms is 'crowded' with $N^2 - N$ non-origin peaks and is therefore difficult to interpret, usually with only vectors between any heavy atoms present showing up clearly. Interpretation issues are particularly acute with low-resolution maps derived from powder data and they have been addressed using sharpened Patterson functions (*e.g.* with $|E_{\mathbf{h}}|^2$ coefficients), maximum entropy (David, 1990) and the symmetry minimum function (Estermann, 1995). The Patterson function has also been used to improve the accuracy of individual intensities obtained from the partitioning of overlapped reflections prior to the application of direct methods (Estermann & Gramlich, 1993). Despite the elegance of many of the Patterson-based structure determination methods, they have not been widely used for SDPD purposes recently, having been largely superseded by both modified direct methods and global-optimization strategies. However, the introduction of Patterson-type direct methods (Rius, 2011) may well signal a renaissance. In this approach, a sum function, S_P, is maximized using a Patterson-function tangent formula that considers overlapping reflections in the phasing process and so is well suited to both powder and single-crystal diffraction data. The structure determination of the $(S)(+)$ form of ibuprofen from synchrotron powder diffraction data ($d_{\min}$ = 1.1 Å; Rius, 2011) is a convincing demonstration of the effectiveness of this approach.

4.1.7. Resonant (anomalous) scattering

Whilst anomalous-scattering techniques are very well established in the field of single-crystal protein structure determination, their use in the context of powder diffraction appears at first glance to be counterintuitive, as Friedel pairs **h** and −**h** overlap *exactly* in a single powder line. Nevertheless, ingenious methods for exploiting differences in the average intensity $\overline{I}(\lambda_i)$ of a powder line as a function of more than one wavelength have been used in combination with maximum-entropy methods to solve the orthorhombic structure of $SrSO_4$ (Burger *et al.*, 1998). The requirement for a source of incident X-rays that can be tuned to wavelengths suitable for the atoms in the sample being studied restricts such experiments to being performed at synchrotron sources.

4.1.8. Isomorphous replacement

Isomorphous replacement is a well established method for the solution of protein crystal structures. In this approach, heavy atoms are introduced into a structure with a consequent effect upon the reflection intensities. There is an assumption that this introduction does not affect the scattering from the native (*i.e.* original, unmodified) structure and that the heavy atoms occupy sites within the structure previously occupied by, for example, lighter ions or solvent molecules. Differences in scattering between the derivative and native structures are therefore attributable to the heavy atoms, and maps computed using these differences can be used to directly obtain the heavy-atom locations. These locations are then used to calculate likely phase angles for the native structure factors, with the most reliable estimates coming from measurements where more than one derivative structure has been prepared and measured. An excellent example of the application of this approach to powder diffraction data is given by determination of the secondary structure of hen egg-white lysozyme (Basso *et al.*, 2010), obtained using diffraction data collected from the native protein plus its gadolinium and holmium derivatives.

4.1.9. Maximum-entropy methods

The process of constrained entropy maximization (*i.e.* maximizing a function of the form $-\sum_{i=1}^{n} p_i \log p_i$, subject to a set of constraints) can be applied to Fourier-type maps where p_i is the pixel density at some point within the map and the constraints are such that an inverse Fourier transform must regenerate the original input structure amplitudes and phases used to generate the map. As the entropy-maximization process results in a modified electron-density map, the inverse Fourier transform also returns amplitudes and phases for structure factors *that were not part of the original input* (Fig. 4.1.2). The quality of these so-called *extrapolated* structure factors can be evaluated by the use of likelihood functions that assess the level of agreement between calculated and observed amplitudes. Entropy maximization and associated likelihood calculations form the basis of a distinct approach to structure determination from powders that is embodied in the *MICE* computer program (Gilmore *et al.*, 1991; Bricogne, 1991). This program has been successfully applied to a number of powder structure problems (Gilmore *et al.*, 1991; Tremayne, Lightfoot, Mehta *et al.*, 1992; Tremayne, Lightfoot, Glidewell *et al.*, 1992) but the approach has not been widely adopted; entropy maximization is computationally demanding and it is only relatively recently that computing power has advanced to the point where calculations can be run on timescales that are competitive with other approaches. Entropy maximization has also been used in combination with Rietveld refinement in structure completion. A good example is provided by the crystal structure determination of the steroid prednisolone succinate (Nishibori *et al.*, 2008). The initial structure solution, returned from a genetic-algorithm global-optimization procedure, had the succinate side chain incorrectly oriented; subsequent omit-type maximum-entropy maps were used to determine the correct orientation, permitting successful refinement.

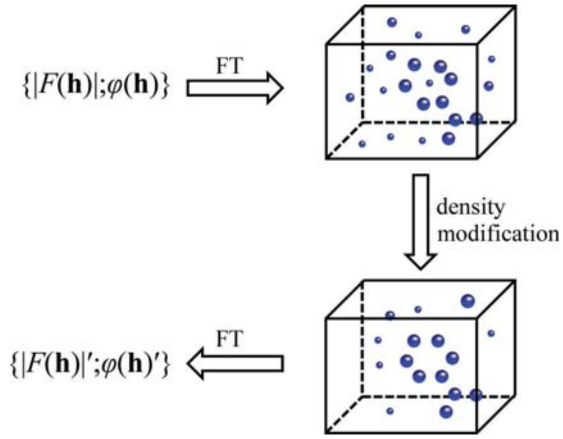
$\{|F(\mathbf{h})|;\varphi(\mathbf{h})\}$
FT
density modification
FT
$\{|F(\mathbf{h})|';\varphi(\mathbf{h})'\}$

Figure 4.1.2
A set of structure factors is Fourier transformed to yield a density map. Once the map is modified (*e.g.* by entropy maximization, histogram matching or charge flipping) the inverse transform returns a modified set of structure factors. Note that the size of the two sets need not necessarily be equal.

4.1.10. Charge flipping

The iterative charge-flipping algorithm (Oszlányi & Sütő, 2008; Palatinus, 2013) has been used extensively in single-crystal structure determination (Palatinus & Chapuis, 2007) and has also been adapted for use in a powder diffraction context (Baerlocher, McCusker & Palatinus, 2007). In common with direct methods of structure determination, it attempts to reconstruct electron density directly from structure amplitudes. Furthermore, it exploits the fact that most of the unit cell is characterized by very low electron density, whilst the regions of high electron density (corresponding to atoms) occupy only a very small part of the cell. The standard charge-flipping algorithm is relatively straightforward and does not require a knowledge of crystallographic symmetry. A set of observed structure amplitudes is assigned random starting phases; unobserved amplitudes are additionally assigned a magnitude of zero. The electron-density map calculated from the structure factors is modified by changing the sign of (*i.e.* 'flipping') any density points that lie below a certain threshold value, δ. A Fourier transform of this modified map returns a new set of structure factors whose phases are assigned to the corresponding observed structure amplitudes. This updated set of observed structure factors is then used in the next iteration of the process and the cycle is repeated until convergence, which is assessed by an R factor that compares observed amplitudes with amplitudes returned by the Fourier transform of the 'flipped' map. Note that there is no map interpretation involved until the algorithm has converged. The process is normally carried out in the complete unit cell (*i.e.* $P1$ symmetry; the true space-group symmetry is determined or confirmed subsequent to the actual structure solution) and typically only the δ threshold parameter needs to be adjusted across problems. As might be expected for a method that relies heavily on the use of modification of electron density, charge flipping performs well with atomic resolution data and data where the structure amplitudes are well determined. As such, and similarly to conventional direct methods, it does not perform particularly well (by default) with the majority of powder diffraction data sets. Modified charge-flipping procedures for powder data have been suggested and demonstrated; see, for example, the structure of zeolite catalyst IM-5 (Baerlocher, Gramm *et al.*, 2007) or the implementation of charge flipping incorporating tangent refinement (Coelho, 2007). Charge flipping has been used in combination with histogram matching (Baerlocher, McCusker & Palatinus, 2007) and also with maximum-entropy methods to improve the imaging of structural disorder in density maps (Samy *et al.*, 2010) and to optimize *SUPERFLIP* (Palatinus & Chapuis, 2007) input parameters for powder diffraction problems (Sisak *et al.*, 2012).

4.1.11. Molecular envelopes

Restrictions on the possible location of atoms within the unit cell, that can aid in automated searches and model-building approaches, can be obtained by correctly phasing a few strong, low-index reflections. These phased reflections are used to generate surfaces (formally, periodic nodal surfaces) within the unit cell that define an envelope into which the atoms of the structure must fit. The process of phasing the reflections is not straightforward but can be highly effective (McCusker *et al.*, 2001; Brenner *et al.*, 1997, 2002) in restricting possible solutions and benefits from the fact that low-index reflections in powder diffraction are those that are least likely to suffer from accidental reflection overlap.

4.1.12. Model building

Manual model building can be considered to be an optimization method, where chemical knowledge and crystallographic experience are used in place of automated trial and error. A model is constructed and placed in the unit cell to give a suitable starting point for a Rietveld refinement, using the agreement between the observed and calculated powder patterns as a guide to correctness. During model construction and placement, various factors may be taken into consideration, including: (*a*) molecular symmetry and special positions, *e.g.* the centre of symmetry of a benzene molecule may be coincident with a crystallographic centre of symmetry; (*b*) functional groups, *e.g.* carboxylic acid groups frequently form hydrogen-bonded dimers with other carboxylic acid or amide groups. Many specific examples of model building may be found in the literature (Seebach *et al.*, 1997; Freyhardt *et al.*, 1996). Although near-exhaustive automated searches have largely replaced this manual approach, it may still have a role to play in particularly complex cases and when the quality of the powder data is especially poor, such as is frequently the case with polymeric materials.

4.1.13. Molecular replacement

Molecular replacement (Rossmann, 1990) is a well established method for the solution of protein crystal structures. In this approach, an unknown structure is solved by placing a model of a closely related structure (typically >30% sequence identity, but this figure is constantly reducing as methods improve) in the unit cell of the unknown structure and then performing a series of discrete rotation and translation searches, aimed at maximizing the agreement between calculated and observed Patterson functions. The search problem is aided by the fact that *intramolecular* vectors in the map depend only upon the orientation of the model; once the best orientation of this model within the unit cell is found, it is used in a translation search to find the best agreement with the *intermolecular* vectors in the map. At this point, the optimal location of the model within the cell has been found and a structure refinement can be attempted. Most modern programs for molecular replacement now use likelihood-based rotation and translation functions (McCoy *et al.*, 2005; Storoni *et al.*, 2004). Encouragingly for powder diffraction, molecular replacement does not require atomic resolution data. It has been applied mainly to the problem of protein structure determination from powder diffraction data; an excellent example is that of the second SH3 domain of ponsin, solved using *MOLREP* (Vagin & Teplyakov, 2010) with high-quality synchrotron data that exploited anisotropic peak shifts to improve the quality of the extracted structure amplitudes (Margiolaki *et al.*, 2007). However, it has also been applied in the context of small molecule crystallography. For example, after initial direct-methods attempts from synchrotron powder diffraction data failed, the crystal structure of form I clarithromycin was solved by molecular replacement using a molecule derived from the form 0 structure (Noguchi *et al.*, 2012). The basis for this attempt was the observation that the molecular conformation of the clarithromycin moiety in previously reported crystal structures showed little structure-to-structure variance. Intensities were extracted from the powder data using *EXPO2009* (Altomare *et al.*, 2013) and the molecular replacement performed using *MOLREP* and data to 3 Å resolution.

The use of molecular replacement tools developed for single-crystal data (Scapin, 2013) does not always prove to be effective in the case of protein structure determination from powder diffraction data (Doebbler & Von Dreele, 2009*b*). In such circumstances, modified versions of programs developed specifically to solve small-molecule structures from powder data (see Section 4.1.14) can be used to good effect. By performing simultaneous translation/rotation searches of a known model inside the cell of the unknown structure, solutions can be obtained for sizeable problems, *e.g.* hen egg-white lysozyme (Doebbler & Von Dreele, 2009*a*). Whether applied to proteins or small molecules, the extent of the similarity between the known and unknown structures is key to the success of molecular replacement; if the model structure has a considerably different shape from that of the unknown, then the chances of obtaining a solution that can be used as a starting point for refinement are low.

4.1.14. Global optimization

The molecular replacement approach just outlined for protein structure determination from powder diffraction data may be considered to be a subset of the global-optimization procedures described in detail in Chapter 4.3. In this larger class of methods, a structural model is adjusted within the previously determined unit cell of the crystal structure under investigation, but the position and orientation of the model are adjusted simultaneously. There is no general requirement that the model is held rigid, *i.e.* a molecular conformation does not need to be known in advance. The problem of finding the best agreement between the observed and calculated intensities is that of locating the global minimum on an agreement-factor (*e.g.* $R_{\rm wp}$ or χ^2) hypersurface, whose dimensionality equals the number of structural variables in the problem. For example, in the case of a molecular organic crystal structure, these variables (or degrees of freedom) are typically: 3 to describe the position of the molecule in the unit cell, 3 to describe its orientation and n to describe the number of freely rotating torsion angles in the molecule. Such hypersurfaces encompass a multitude of stationary points and locating the global minimum is a non-trivial exercise. A plethora of approaches, including simulated annealing, genetic algorithms, evolutionary algorithms, random searches, grid searches, particle swarm and the hybrid Monte Carlo method, have been applied in the context of SDPD; these methods and their application to structural problems in powder diffraction have been comprehensively reviewed (*e.g.* David & Shankland, 2008; Harris, 2012; David *et al.*, 2002; Shankland *et al.*, 2013). Atom positions can be optimized as independent variables, but the more usual practice is to make use of prior information about the system under study, *e.g.* a description of molecular connectivity, or the coordination state of a metal ion. Obtaining this information is not generally a serious impediment. Where there are ambiguities in the model being optimized, multiple trials using distinct starting models can be used to decide upon the correct description. Alternatively, it is also possible to use maximum-likelihood methods to defer a precise description of certain components of a starting model until such time as the main component of the model has been correctly located in the unit cell. This is discussed more fully in Section 4.1.15 and Chapter 4.3.

4.1.15. Maximum-likelihood methods

Figures of merit used to assess the level of the agreement between the observed and calculated intensities in global-optimization methods are generally predicated on the assumption that the model under investigation is a complete and accurate description of the contents of the asymmetric unit. There are, however, many reasons why this assumption may not hold during a structure solution; for example, hydrogen atoms may have been omitted from the input model and only isotropic temperature factors used to describe the vibrational behaviour of atoms. Such relatively minor approximations will not normally prevent successful structure solution, but more substantial omissions from the input model will. Typical scenarios for the latter situation would be the deliberate omission of a molecular counter-ion or some solvent of crystallization from an input model in order to reduce the dimensionality of the problem search space. In their absence, calculated intensities cannot match the observed intensities and, as a consequence, the structure cannot be solved. The maximum-likelihood approach to structure solution does not ignore the omitted fragments; rather (whilst not adjusting them in the optimization) it treats their scattering contribution as a 'blur' that is randomly distributed throughout the unit cell. This effectively adds an uncertainty to the *calculated* intensities that has to be taken into consideration by the figure of merit along with the usual uncertainties in the observed intensities (Markvardsen *et al.*, 2002; Favre-Nicolin & Cerny, 2004*a*). A major advantage of this approach is that it allows complex multi-fragment structures to be solved in a sequential manner by global optimization.

4.1.16. Local minimization

It is also possible to use local-minimization methods, such as quasi-Newton or conjugate gradient, to locate the global minimum on a given hypersurface. In this approach, the use of a large number of minimizations, each starting from a different random point, compensates for the very low probability that any single minimization will terminate in the global minimum. This approach has the twin advantages of speed and simplicity, and has been demonstrated to be at least competitive with simulated annealing in the cases of solving the structures of famotidine and capsaicin from powder diffraction data (Shankland *et al.*, 2010). Simplex optimization (Nelder & Mead, 1965) can be used in a similar fashion, but requires many more function evaluations and can be slow to converge. A local-minimization approach has also been adopted in the *TALP* program (Vallcorba *et al.*, 2012) and has been used to solve a number of molecular crystal structures, including several from a test suite of laboratory-based powder diffraction data (Florence *et al.*, 2005).

4.1.17. Active use of prior information for particular structural classes

It is possible to tailor structure determination strategies to a particular class of materials in order to improve the chances of solving an unknown structure belonging to that class. Such tailoring works best where the class contains well defined structural motifs; for example, protein structure determination procedures exploit the fact that regions of α-helix and β-sheet can generally be quickly identified in an electron-density map. In the area of powder diffraction, a good example comes from the study of zeolites and zeolite-like materials, where a clearly defined framework topology (*e.g.* faujasite, mordenite) is expected in any electron-density map that corresponds to a likely solution. These electron-density maps may be searched passively (*i.e.* assign atoms to peaks in the map and then see what, if any, topology is evident) or actively (*i.e.* the map is searched for particular topologies). The computer program *FOCUS* (Grosse-Kunstleve *et al.*, 1997), which implements both types of search, has been applied successfully to the determination of several framework structures (see Chapter 4.6) (Smeets *et al.*, 2013) and has also been adapted to utilize three-dimensional electron-diffraction data when available (Smeets *et al.*, 2015).

The histogram-matching method (Yong *et al.*, 1990) also exploits features that are characteristic of particular classes of materials. The histogram in question is an electron-density probability distribution that captures the commonality (*e.g.* distribution of atom types, interatomic distances and angles) of different structures belonging to a particular class of materials. Originally utilized as an aid to phase determination and refinement in the field of protein crystallography (Zhang & Main, 1990), it seeks to modify the distribution of electron density in a map of the structure under investigation such that it matches that of an idealized histogram. It is important to realize that obtaining a match is a necessary, but not a sufficient, condition in the identification of the correct structure, *i.e.* there are many *incorrect* maps that still match the ideal histogram (Zhang, 2003). Nevertheless, obtaining a match is a highly effective constraint on a solution and it has been used in SDPD in order to improve the partitioning of the intensities of overlapping reflections. Specifically, after the process of histogram matching has resulted in modification of the electron-density map, a Fourier transform will return modified structure factors that are likely to be a more accurate representation of the true structure amplitudes. The reference histogram can be obtained from the electron-density map of a known structure belonging to the same class of materials, ideally obtained with approximately the same resolution as the unknown structure (Baerlocher, McCusker & Palatinus, 2007).

In the case of global optimization of molecular structures, the initial model is constructed using well characterized bond lengths and angles derived from the large ensemble of previously determined molecular crystal structures. Information about the distribution of torsion angles within molecular structures is also present in this ensemble and can, in principle, be used to restrict the search space that needs to be explored in the global-optimization step. A trivial example is that of an acyclic amide bond, where partial double-bond character results in a planar group, with the *trans* configuration [$R-\mathrm{C}(=\mathrm{O})-\mathrm{NH}-R' \simeq 180^\circ$] being observed much more frequently than the *cis* configuration. As such, the torsion angle of this bond can be treated as a fixed ($\tau = 180^\circ$) entity, removing one degree of freedom from the search problem. The *Mogul* molecular-geometry knowledge base (Bruno *et al.*, 2004), derived from the Cambridge Structural Database (CSD), is an invaluable tool for the quick and efficient retrieval of torsion-angle distributions for particular molecular motifs within the structure of interest. Only rarely does an observed distribution allow a particular torsion angle to be restricted to a narrow range, but large areas of space can often be safely eliminated from the global search. Any derived distribution information must be used with care, as applying excessive weight to such distributions will tend to exclude the possibility of solving structures that do not conform to expectation values. The utility of this particular approach to SDPD has been demonstrated (Florence *et al.*, 2009) but only recently has it been fully explored, with promising results, against a test suite of more than 100 molecular organic crystal structures (Kabova *et al.*, 2017).

The *IsoStar* knowledge base of intermolecular interactions (Bruno *et al.*, 1997) present in the CSD permits the rapid evaluation of probable distance and angle distributions for specified search motifs, and these distributions can be used actively in SDPD. A simple example is that of the $R-\mathrm{NH_3}^+\cdots\mathrm{Cl}^-$ motif found in many hydrochloride salts, where the $\mathrm{N}^+\cdots\mathrm{Cl}^-$ distance can be restricted to 3.2 Å on the basis of over 1000 observations in the CSD. Again, the utility of employing such restrictions has been demonstrated in isolated cases (Nowell *et al.*, 2002), but has yet to make a significant impact on SDPD in general.

Solid-state NMR has also been used in combination with powder diffraction in the structure determination of, for example, zeolites (Brouwer *et al.*, 2005) and molecular organic materials (Harper *et al.*, 2005; Dudenko *et al.*, 2013; Middleton *et al.*, 2002). Beyond the obvious application of determining Z' for a crystal structure, solid-state NMR chemical shift tensor data can yield detailed three-dimensional information that can, for example, be used in combination with computational modelling to generate more accurate or constrained models for subsequent optimization or refinement.

Further discussion of the use of supplementary information in the context of SDPD can be found in Chapter 4.4.

4.1.18. Combined figures of merit

In trial-and-error-type solution approaches such as global optimization, it may be advantageous to include in the figure-of-merit calculation terms other than those that are based purely on diffraction data. The most obvious additional contribution is an energetic one: the global minimum in the diffraction hypersurface is expected to be coincident with a minimum in the crystal energy landscape. Several computer programs for SDPD [*e.g.* *Endeavour* (Putz, 2001), *ORGANA* (Brodski *et al.*, 2005), *FOX* (Favre-Nicolin & Cerny, 2004*b*)] implement such a multi-objective approach and 'Pareto optimization' of the figures of merit has been successfully applied to problems in inorganic (Putz *et al.*, 1999) and organic structure determination (Pop *et al.*, 2002). The combined figure of merit, C, is often calculated as a simple weighted sum $\alpha\mathrm{FOM}_{\mathrm{Energy}} + (1-\alpha)\mathrm{FOM}_{\mathrm{Diffraction}}$ with α as a variable in the range 0–1 depending upon the desired relative weighting. The energy terms employed are usually relatively straightforward to calculate (*e.g.* Lennard-Jones type), the main restrictions being (*a*) the availability of suitable parameter sets for the particular system under investigation and (*b*) the computational cost associated with the evaluation of each new trial structure. The logical extension of this approach in which α is set to 1 equates to crystal-structure prediction (CSP), discussion of which lies outside the scope of this chapter. However, it is worth noting that when CSP returns multiple structures with very similar crystal lattice energies, a *post hoc* comparison of calculated powder patterns with experimental powder data can be a useful indicator of predictive power. In any such comparison, it must be remembered that predicted structures at 0 K will generate powder patterns that may, at first glance, appear to differ substantially from those collected at room temperature as a result of the effects of thermal expansion upon the unit cell. CSP-derived structures can also be of value in finalizing the details of structures solved from powder diffraction data; see, for example, hydrogen-atom positioning in the crystal structure determination of a simple 1:1 co-crystal (Wu *et al.*, 2013).

References

Altomare, A., Camalli, M., Cuocci, C., Giacovazzo, C., Moliterni, A. & Rizzi, R. (2009). *EXPO2009: structure solution by powder data in direct and reciprocal space. J. Appl. Cryst.* **42**, 1197–1202.

Altomare, A., Cuocci, C., Giacovazzo, C., Moliterni, A. & Rizzi, R. (2012). *COVMAP: a new algorithm for structure model optimization in the EXPO package. J. Appl. Cryst.* **45**, 789–797.

Altomare, A., Cuocci, C., Giacovazzo, C., Moliterni, A., Rizzi, R., Corriero, N. & Falcicchio, A. (2013). *EXPO2013: a kit of tools for phasing crystal structures from powder data. J. Appl. Cryst.* **46**, 1231–1235.

Baerlocher, C., Gramm, F., Massüger, L., McCusker, L. B., He, Z., Hovmöller, S. & Zou, X. (2007). *Structure of the polycrystalline zeolite catalyst IM-5 solved by enhanced charge flipping. Science*, **315**, 1113–1116.

Baerlocher, C., McCusker, L. B. & Palatinus, L. (2007). *Charge flipping combined with histogram matching to solve complex crystal structures from powder diffraction data. Z. Kristallogr.* **222**, 47–53.

Basso, S., Besnard, C., Wright, J. P., Margiolaki, I., Fitch, A., Pattison, P. & Schiltz, M. (2010). *Features of the secondary structure of a protein molecule from powder diffraction data. Acta Cryst.* D**66**, 756–761.

Brenner, S., McCusker, L. B. & Baerlocher, C. (1997). *Using a structure envelope to facilitate structure solution from powder diffraction data. J. Appl. Cryst.* **30**, 1167–1172.

Brenner, S., McCusker, L. B. & Baerlocher, C. (2002). *The application of structure envelopes in structure determination from powder diffraction data. J. Appl. Cryst.* **35**, 243–252.

Bricogne, G. (1991). *A multisolution method of phase determination by combined maximization of entropy and likelihood. III. Extension to powder diffraction data. Acta Cryst.* A**47**, 803–829.

Brodski, V., Peschar, R. & Schenk, H. (2005). *Organa – a program package for structure determination from powder diffraction data by direct-space methods. J. Appl. Cryst.* **38**, 688–693.

Brouwer, D. H., Darton, R. J., Morris, R. E. & Levitt, M. H. (2005). *A solid-state NMR method for solution of zeolite crystal structures. J. Am. Chem. Soc.* **127**, 10365–10370.

Brunelli, M., Wright, J. P., Vaughan, G. R. M., Mora, A. J. & Fitch, A. N. (2003). *Solving larger molecular crystal structures from powder diffraction data by exploiting anisotropic thermal expansion. Angew. Chem. Intl Ed.* **42**, 2029–2032.

Bruno, I. J., Cole, J. C., Kessler, M., Luo, J., Motherwell, W. D. S., Purkis, L. H., Smith, B. R., Taylor, R., Cooper, R. I., Harris, S. E. & Orpen,

A. G. (2004). *Retrieval of crystallographically-derived molecular geometry information. J. Chem. Inf. Comput. Sci.* **44**, 2133–2144.

Bruno, I. J., Cole, J. C., Lommerse, J. P. M., Rowland, R. S., Taylor, R. & Verdonk, M. L. (1997). *IsoStar: a library of information about nonbonded interactions. J. Comput. Aided Mol. Des.* **11**, 525–537.

Burger, K., Cox, D., Papoular, R. & Prandl, W. (1998). *The application of resonant scattering techniques to ab initio structure solution from powder data using $SrSO_4$ as a test case. J. Appl. Cryst.* **31**, 789–797.

Burla, M. C., Camalli, M., Cascarano, G., Giacovazzo, C., Polidori, G., Spagna, R. & Viterbo, D. (1989). *SIR88 – a direct-methods program for the automatic solution of crystal structures. J. Appl. Cryst.* **22**, 389–393.

Cernik, R. J., Cheetham, A. K., Prout, C. K., Watkin, D. J., Wilkinson, A. P. & Willis, B. T. M. (1991). *The structure of cimetidine ($C_{10}H_{16}N_6S$) solved from synchrotron-radiation X-ray powder diffraction data. J. Appl. Cryst.* **24**, 222–226.

Coelho, A. A. (2007). *A charge-flipping algorithm incorporating the tangent formula for solving difficult structures. Acta Cryst.* A**63**, 400–406.

Corma, A., Rey, F., Valencia, S., Jordá, J. L. & Rius, J. (2003). *A zeolite with interconnected 8-, 10- and 12-ring pores and its unique catalytic selectivity. Nat. Mater.* **2**, 493–497.

David, W. I. F. (1990). *Extending the power of powder diffraction for structure determination. Nature (London)*, **346**, 731–734.

David, W. I. F. & Shankland, K. (2008). *Structure determination from powder diffraction data. Acta Cryst.* A**64**, 52–64.

David, W. I. F., Shankland, K., McCusker, L. B. & Baerlocher, C. (2002). Editors. *Structure Determination from Powder Diffraction Data*, 2nd ed. Oxford University Press.

Doebbler, J. A. & Von Dreele, R. B. (2009*a*). *Application of molecular replacement to protein powder data from image plates. Acta Cryst.* D**65**, 348–355.

Doebbler, J. A. & Von Dreele, R. B. (2009*b*). *Macromolecular powder diffraction: structure solution via molecular replacement. Z. Kristallogr.* Suppl. **30**, 33–37.

Dudenko, D. V., Williams, P. A., Hughes, C. E., Antzutkin, O. N., Velaga, S. P., Brown, S. P. & Harris, K. D. M. (2013). *Exploiting the synergy of powder X-ray diffraction and solid-state NMR spectroscopy in structure determination of organic molecular solids. J. Phys. Chem. C*, **117**, 12258–12265.

Estermann, M. A. (1995). *Solving crystal-structures with the symmetry minimum function. Nucl. Instrum. Methods Phys. Res. Sect. A*, **354**, 126–133.

Estermann, M. A. & Gramlich, V. (1993). *Improved treatment of severely or exactly overlapping Bragg reflections for the application of direct methods to powder data. J. Appl. Cryst.* **26**, 396–404.

Favre-Nicolin, V. & Cerny, R. (2004*a*). *A better FOX: using flexible modelling and maximum likelihood to improve direct-space ab initio structure determination from powder diffraction. Z. Kristallogr.* **219**, 847–856.

Favre-Nicolin, V. & Cerny, R. (2004*b*). *FOX: Modular approach to crystal structure determination from powder diffraction*. In *European Powder Diffraction Epdic 8. Mater. Sci. Forum*, **443–444**, 35–38.

Fernandes, P., Shankland, K., Florence, A. J., Shankland, N. & Johnston, A. (2007). *Solving molecular crystal structures from X-ray powder diffraction data: the challenges posed by gamma-carbamazepine and chlorothiazide N,N,-dimethylformamide (1/2) solvate. J. Pharm. Sci.* **96**, 1192–1202.

Florence, A. J., Bardin, J., Johnston, B., Shankland, N., Griffin, T. A. N. & Shankland, K. (2009). *Structure determination from powder data: Mogul and CASTEP. Z. Kristallogr.* Suppl. **30**, 215–220.

Florence, A. J., Shankland, N., Shankland, K., David, W. I. F., Pidcock, E., Xu, X., Johnston, A., Kennedy, A. R., Cox, P. J., Evans, J. S. O., Steele, G., Cosgrove, S. D. & Frampton, C. S. (2005). *Solving molecular crystal structures from laboratory X-ray powder diffraction data with DASH: the state of the art and challenges. J. Appl. Cryst.* **38**, 249–259.

Freyhardt, C. C., Lobo, R. F., Khodabandeh, S., Lewis, J. E., Tsapatsis, M., Yoshikawa, M., Camblor, M. A., Pan, M., Helmkamp, M. M., Zones, S. I. & Davis, M. E. (1996). *VPI-8: a high-silica molecular sieve with a novel 'pinwheel' building unit and its implications for the synthesis of extra-large pore molecular sieves. J. Am. Chem. Soc.* **118**, 7299–7310.

Gilmore, C. J., Henderson, K. & Bricogne, G. (1991). *A multisolution method of phase determination by combined maximization of entropy and likelihood. IV. The ab initio solution of crystal structures from their X-ray powder data. Acta Cryst.* A**47**, 830–841.

Grosse-Kunstleve, R. W., McCusker, L. B. & Baerlocher, C. (1997). *Powder diffraction data and crystal chemical information combined in an automated structure determination procedure for zeolites. J. Appl. Cryst.* **30**, 985–995.

Harper, J. K., Barich, D. H., Heider, E. M., Grant, D. M., Franke, R. R., Johnson, J. H., Zhang, Y. G., Lee, P. L., Von Dreele, R. B., Scott, B., Williams, D. & Ansell, G. B. (2005). *A combined solid-state NMR and X-ray powder diffraction study of a stable polymorph of paclitaxel. Cryst. Growth Des.* **5**, 1737–1742.

Harris, K. D. M. (2012). *Powder diffraction crystallography of molecular solids. Top. Curr. Chem.* **315**, 133–177.

Ibberson, R. M., McDonald, P. J. & Pinter-Krainer, M. (1997). *The crystal structure determination of dimethylsulphide by high-resolution neutron powder diffraction. J. Mol. Struct.* **415**, 259–266.

Ibberson, R. M., Morrison, C. & Prager, M. (2000). *Neutron powder and ab initio structure of ortho-xylene: the influence of crystal packing on phenyl ring geometry at 2 K. Chem. Commun.* pp. 539–540.

Ibberson, R. M., Yamamuro, O. & Matsuo, T. (2000). *Crystal structures and phase behaviour of acetaldehyde-d4: a study by high-resolution neutron powder diffraction and calorimetry. J. Mol. Struct.* **520**, 265–272.

Ibberson, R. M., Yamamuro, O. & Tsukushi, I. (2006). *The crystal structures and phase behaviour of cyclohexene oxide. Chem. Phys. Lett.* **423**, 454–458.

Kabova, E. A., Cole, J. C., Korb, O., Williams, A. C. & Shankland, K. (2017). *Improved crystal structure solution from powder diffraction data by the use of conformational information. J. Appl. Cryst.* **50**, 1421–1427.

Lanning, O. J., Habershon, S., Harris, K. D. M., Johnston, R. L., Kariuki, B. M., Tedesco, E. & Turner, G. W. (2000). *Definition of a 'guiding function' in global optimization: a hybrid approach combining energy and R-factor in structure solution from powder diffraction data. Chem. Phys. Lett.* **317**, 296–303.

Lightfoot, P., Mehta, M. A. & Bruce, P. G. (1993). *Crystal structure of the polymer electrolyte poly(ethylene oxide)3:$LiCF_3SO_3$. Science*, **262**, 883–885.

McCoy, A. J., Grosse-Kunstleve, R. W., Storoni, L. C. & Read, R. J. (2005). *Likelihood-enhanced fast translation functions. Acta Cryst.* D**61**, 458–464.

McCusker, L. B., Baerlocher, C., Grosse-Kunstleve, R., Brenner, S. & Wessels, T. (2001). *Solving complex zeolite structures from powder diffraction data. Chimia*, **55**, 497–504.

Margiolaki, I., Wright, J. P., Wilmanns, M., Fitch, A. N. & Pinotsis, N. (2007). *Second SH3 domain of ponsin solved from powder diffraction. J. Am. Chem. Soc.* **129**, 11865–11871.

Markvardsen, A. J., David, W. I. F. & Shankland, K. (2002). *A maximum-likelihood method for global-optimization-based structure determination from powder diffraction data. Acta Cryst.* A**58**, 316–326.

Meden, A. & Radosavljevic Evans, I. (2015). *Structure determination from powder diffraction data: past, present and future challenges. Cryst. Res. Technol.* **50**, 747–758.

Middleton, D. A., Peng, X., Saunders, D., Shankland, K., David, W. I. F. & Markvardsen, A. J. (2002). *Conformational analysis by solid-state NMR and its application to restrained structure determination from powder diffraction data. Chem. Commun.* pp. 1976–1977.

Nelder, J. A. & Mead, R. (1965). *A simplex method for function minimization. Comput. J.* **7**, 308–313.

Nishibori, E., Ogura, T., Aoyagi, S. & Sakata, M. (2008). *Ab initio structure determination of a pharmaceutical compound, prednisolone succinate, from synchrotron powder data by combination of a genetic algorithm and the maximum entropy method. J. Appl. Cryst.* **41**, 292–301.

Noguchi, S., Miura, K., Fujiki, S., Iwao, Y. & Itai, S. (2012). *Clarithromycin form I determined by synchrotron X-ray powder diffraction. Acta Cryst.* C**68**, o41–o44.

Nowell, H., Attfield, J. P., Cole, J. C., Cox, P. J., Shankland, K., Maginn, S. J. & Motherwell, W. D. S. (2002). *Structure solution and refinement of tetracaine hydrochloride from X-ray powder diffraction data. New J. Chem.* **26**, 469–472.

Oszlányi, G. & Sütő, A. (2008). *The charge flipping algorithm. Acta Cryst.* A**64**, 123–134.

Palatinus, L. (2013). *The charge-flipping algorithm in crystallography. Acta Cryst.* B**69**, 1–16.

Palatinus, L. & Chapuis, G. (2007). *SUPERFLIP – a computer program for the solution of crystal structures by charge flipping in arbitrary dimensions. J. Appl. Cryst.* **40**, 786–790.

Pop, M. M., Goubitz, K., Borodi, G., Bogdan, M., De Ridder, D. J. A., Peschar, R. & Schenk, H. (2002). *Crystal structure of the inclusion complex of beta-cyclodextrin with mefenamic acid from high-resolution synchrotron powder-diffraction data in combination with molecular-mechanics calculations. Acta Cryst.* B**58**, 1036–1043.

Putz, H. (2001). *Structure solution from powder diffraction data by a combined global optimization of several cost functions: problems and perspectives*. In *European Powder Diffraction Epdic 7. Mater. Sci. Forum*, **378–381**, 53–58.

Putz, H., Schön, J. C. & Jansen, M. (1999). *Combined method for ab initio structure solution from powder diffraction data. J. Appl. Cryst.* **32**, 864–870.

Rietveld, H. M. (1969). *A profile refinement method for nuclear and magnetic structures. Acta Cryst.* **2**, 65–67.

Rius, J. (1993). *Derivation of a new tangent formula from Patterson-function arguments. Acta Cryst.* A**49**, 406–409.

Rius, J. (1999). *XLENS, a direct methods program based on the modulus sum function: its application to powder data. Powder Diffr.* **14**, 267–273.

Rius, J. (2011). *Patterson-function direct methods for structure determination of organic compounds from powder diffraction data. XVI. Acta Cryst.* A**67**, 63–67.

Rius, J. & Frontera, C. (2007). *Application of the constrained S-FFT direct-phasing method to powder diffraction data. XIII. J. Appl. Cryst.* **40**, 1035–1038.

Rodriguez-Carvajal, J. (2013). *FullProf Suite*, http://www.ill.eu/sites/fullprof/php/reference.html.

Rossmann, M. G. (1990). *The molecular replacement method. Acta Cryst.* A**46**, 73–82.

Samy, A., Dinnebier, R. E., van Smaalen, S. & Jansen, M. (2010). *Maximum entropy method and charge flipping, a powerful combination to visualize the true nature of structural disorder from in situ X-ray powder diffraction data. Acta Cryst.* B**66**, 184–195.

Scapin, G. (2013). *Molecular replacement, then and now. Acta Cryst.* D**69**, 2266–2275.

Seebach, D., Matthews, J. L., Meden, A., Wessels, T., Baerlocher, C. & McCusker, L. B. (1997). *Cyclo-beta-peptides: structure and tubular stacking of cyclic tetramers of 3-aminobutanoic acid as determined from powder diffraction data. Helv. Chim. Acta*, **80**, 173–182.

Shankland, K., David, W. I. F. & Sivia, D. S. (1997). *Routine ab initio structure determination of chlorothiazide by X-ray powder diffraction using optimized data collection and analysis strategies. J. Mater. Chem.* **7**, 569–572.

Shankland, K., Markvardsen, A. J., Rowlatt, C., Shankland, N. & David, W. I. F. (2010). *A benchmark method for global optimization problems in structure determination from powder diffraction data. J. Appl. Cryst.* **43**, 401–406.

Shankland, K., Spillman, M. J., Kabova, E. A., Edgeley, D. S. & Shankland, N. (2013). *The principles underlying the use of powder diffraction data in solving pharmaceutical crystal structures. Acta Cryst.* C**69**, 1251–1259.

Sisak, D., Baerlocher, C., McCusker, L. B. & Gilmore, C. J. (2012). *Optimizing the input parameters for powder charge flipping. J. Appl. Cryst.* **45**, 1125–1135.

Smeets, S., McCusker, L. B., Baerlocher, C., Mugnaioli, E. & Kolb, U. (2013). *Using FOCUS to solve zeolite structures from three-dimensional electron diffraction data. J. Appl. Cryst.* **46**, 1017–1023.

Smeets, S., McCusker, L. B., Baerlocher, C., Xie, D., Chen, C.-Y. & Zones, S. I. (2015). *SSZ-87: a borosilicate zeolite with unusually flexible 10-ring pore openings. J. Am. Chem. Soc.* **137**, 2015–2020.

Storoni, L. C., McCoy, A. J. & Read, R. J. (2004). *Likelihood-enhanced fast rotation functions. Acta Cryst.* D**60**, 432–438.

Tremayne, M., Lightfoot, P., Glidewell, C., Harris, K. D. M., Shankland, K., Gilmore, C. J., Bricogne, G. & Bruce, P. G. (1992). *Materials chemistry communications. Application of the combined maximum entropy and likelihood method to the ab initio determination of an organic crystal structure from X-ray powder diffraction data. J. Mater. Chem.* **2**, 1301–1302.

Tremayne, M., Lightfoot, P., Mehta, M. A., Bruce, P. G., Harris, K. D. M., Shankland, K., Gilmore, C. J. & Bricogne, G. (1992). *Ab initio structure determination of $LiCF_3SO_3$ from X-ray powder diffraction data using entropy maximization and likelihood ranking. J. Solid State Chem.* **100**, 191–196.

Vagin, A. & Teplyakov, A. (2010). *Molecular replacement with MOLREP. Acta Cryst.* D**66**, 22–25.

Vallcorba, O., Rius, J., Frontera, C. & Miravitlles, C. (2012). *TALP: a multisolution direct-space strategy for solving molecular crystals from powder diffraction data based on restrained least squares. J. Appl. Cryst.* **45**, 1270–1277.

Watkin, D. J., Carruthers, J. R. & Betteridge, P. W. (1985). *CRYSTALS User Guide.* Chemical Crystallography Laboratory, University of Oxford, England.

Wu, H., Habgood, M., Parker, J. E., Reeves-McLaren, N., Cockcroft, J. K., Vickers, M., West, A. R. & Jones, A. G. (2013). *Crystal structure determination by combined synchrotron powder X-ray diffraction and crystal structure prediction: 1:1 L-ephedrine D-tartrate. CrystEngComm*, **15**, 1853–1859.

Yong, K., Zhang, J. & Main, P. (1990). *Histogram matching as a new density modification technique for phase refinement and extension of protein molecules. Acta Cryst* A**46**, 41–46.

Zachariasen, W. H. (1948). *Crystal chemical studies of the 5f-series of elements. I. New structure types. Acta Cryst.* **1**, 265.

Zhang, K. Y. J. (2003). *Multidimensional histograms for density modification. Methods in Enzymology*, Vol. 374, *Macromolecular Crystallography*, edited by C. W. Carter Jr & R. M. Sweet. San Diego: Elsevier.

Zhang, K. Y. J. & Main, P. (1990). *The use of Sayre's equation with solvent flattening and histogram matching for phase extension and refinement of protein structures. Acta Cryst.* A**46**, 377–381.

International Tables for Crystallography (2019). Vol. H, Chapter 4.2, pp. 395–413.

4.2. Solving crystal structures using reciprocal-space methods

A. Altomare, C. Cuocci, A. Moliterni and R. Rizzi

4.2.1. Introduction

The aim of this chapter is to provide the necessary theoretical background and the practical tools for solving crystal structures from powder-diffraction data using reciprocal-space (RS) methods.

RS methods are so called because they work in reciprocal space in the following general way:

(1) The unit-cell dimensions are assumed to be known or calculated and the space group is (in general, but not always, see Section 4.2.6) determined. There may be ambiguities with respect to the space group, in which case all possibilities may need to be explored. The unit-cell contents are also needed, but these can be approximate.
(2) The structure-factor moduli $|F_{\mathbf{h}}|$ associated with each reflection $\mathbf{h}$ are extracted from the experimental diffraction profile.
(3) The phases $\varphi_{\mathbf{h}}$ of structure factors $F_{\mathbf{h}} = |F_{\mathbf{h}}| \exp(i\varphi_{\mathbf{h}})$ are estimated by phasing methods which use the experimental moduli. This is the core of direct methods.
(4) Finally, an electron-density map is calculated using $T^{-1}[F_{\mathbf{h}}]$, the inverse Fourier transform of the structure factors, determined in terms of both moduli and phases.

Until about 25 years ago, powder-diffraction methods were mainly used for qualitative and quantitative analysis. Attempts to solve crystal structures using powder-diffraction data started for several reasons: improvements in diffraction experimental techniques (*e.g.* the availability of synchrotron sources) and the availability of more powerful computers made it feasible, and there is a need to know the crystal structure of materials of chemical, technological, biological, pharmaceutical and geological interest. Early structures were solved using software packages designed for single-crystal data. Later RS methods were modified and improved to deal with the specific problems that occur with powder data, making the solution process more straightforward (David *et al.*, 2002). Around the end of the last century, direct-space methods became a viable alternative to reciprocal-space methods.

The main differences between RS methods and direct-space methods are that RS methods are model-free and do not need prior structural information, but they require the extraction of the integrated intensities from the experimental powder-diffraction pattern; direct-space methods use some prior knowledge about the structure (in particular, information on the molecular geometry), but they do not need the integrated intensities. When it is not possible to predict anything about the structure, RS methods are the obligatory choice.

For single-crystal data, RS methods have numerous advantages: they are fast, reliable, easy to use and able to solve the structure of any type of compound – inorganic, organic or organometallic. Small- and medium-size structures up to small proteins can be solved provided that good-quality, complete data to about 1.1 Å resolution are available. In the case of powders, however, the solution process is not so straightforward because three-dimensional reciprocal space is collapsed into the one-dimensional experimental pattern. This unavoidable situation results in a loss of experimental information and has serious consequences: Bragg diffraction peaks overlap and the individual intensity associated with each reflection cannot be accurately determined. In addition, other effects can add to the problem: the background cannot be always unambiguously modelled; the presence of preferred orientation modifies the intensity ratios; and scattering decay at high diffraction angles and/or large peak overlap reduces the achievable limit of experimental resolution. The peak-overlap problem also causes a significant reduction in the number of statistically independent experimental observations contained in the diffraction profile (Altomare *et al.*, 1995; David, 1999). Thus we are very far from the conditions of well estimated observed structure-factor moduli at a resolution better than 1.1 Å; these are rarely attained, particularly in the case of conventional laboratory diffractometer X-ray data.

4.2.2. Intensity extraction for RS methods

RS methods require that the integrated intensities associated with each reflection in the experimental profile must be evaluated. The intensity-extraction process is usually carried out by one of the two following approaches: the iterative Le Bail method usually combined with a profile-fitting procedure, or the least-squares-based Pawley method (Pawley, 1981; see also Chapter 3.5). The Le Bail method can be improved by exploiting the following additional information: pseudotranslational symmetry (Altomare, Foadi *et al.*, 1996), preferred orientation (Altomare *et al.*, 1994; Altomare, Burla *et al.*, 1996), triplet invariant relationship estimation (Carrozzini *et al.*, 1997), the Patterson function (Altomare, Foadi *et al.*, 1998), and the location of a partial structure fragment (Altomare, Giacovazzo *et al.*, 1998). The problem of peak overlap is the major difficulty. Synchrotron data are less affected by this than laboratory data, but the problems of intrinsic peak broadening from the sample itself still remain. Different strategies, both methodological and experimental, have been adopted. The simplest (but still effective) one is to equipartition the intensity of a cluster of overlapping reflections among the single reflections belonging to the cluster, and preferred orientation can be exploited for decomposing overlapping peaks by combining information contained in diffraction patterns collected on sample oriented in different ways (Wessel *et al.*, 1999; Baerlocher *et al.*, 2004). In the case of anisotropic thermal expansion, multiple temperature measurements can be used for obtaining a better estimate of the individual reflection intensities (Shankland *et al.*, 1997; Fernandes, 2006). Despite great efforts to improve extraction procedures, whatever the method used to calculate them (Le Bail or Pawley), the experimental structure-factor moduli, especially of overlapping reflections, are not often well determined and errors of about 40% are quite common in good-quality laboratory X-ray data. Consequently, the phasing process using RS methods may be not always successful. A successful outcome strongly depends on the quality of the extracted structure-factor moduli and on the experimental resolution. Structure complexity and the compound type also play an important role. Organic structures are more difficult to solve because the rapid decay in scattering factors for

Copyright © 2019 International Union of Crystallography

light atoms with diffraction angle further limits the experimental resolution.

4.2.3. Direct methods

The aim of direct methods (DM) is contained in their name: to derive the phases of reflections *directly* from the observed integrated intensities, through mathematical relationships. DM theory is based on two main assumptions about the electron density $\rho(\mathbf{r})$:

(1) positivity: $\rho(\mathbf{r})$ is everywhere positive; and
(2) atomicity: $\rho(\mathbf{r})$ corresponds to discrete atoms.

Harker & Kasper (1948) first demonstrated that phase information can be retrieved *via* inequalities involving unitary structure factors $U_{\mathbf{h}}$ (see Section 4.2.7 for a definition of $U_{\mathbf{h}}$). Later Sayre (1952) derived Sayre's equation, an algebraic expression among structure factors, by using the relationship between $\rho(\mathbf{r})$ and its square:

$$F_{\mathbf{h}} = \frac{f_{\mathbf{h}}}{g_{\mathbf{h}} V} \sum_{\mathbf{h}'} F_{\mathbf{h}'} F_{\mathbf{h}-\mathbf{h}'}, \qquad (4.2.1)$$

where $f_{\mathbf{h}}$ and $g_{\mathbf{h}}$ are the scattering factors for the normal and squared electron density, respectively, V is the unit-cell volume and the summation spans the whole of reciprocal space. It was derived for structures of equal resolved atoms and applied to the centrosymmetric case, and leads to the following relationship, which involves the signs of the structure factors (Cochran, 1952; Zachariasen, 1952):

$$s(\mathbf{h}) \approx s(\mathbf{h}')s(\mathbf{h}-\mathbf{h}'), \qquad (4.2.2)$$

where $s(\mathbf{h})$ is the sign of reflection $\mathbf{h}$ (+ is 0° and − is 180°) and we are using $\approx$ to mean 'probably equals'. The likelihood that (4.2.2) is true increases with the magnitudes of the three associated structure factors. The sign relationships were used for solving centrosymmetric structures or centrosymmetric projections of noncentrosymmetric structures. The probabilistic form of (4.2.2) suggested that it could be of practical use.

The first important probabilistic approach was proposed by Wilson (1942, 1949). Centric and acentric probability distributions of structure-factor moduli were derived by assuming that the atomic positions are random variables uniformly distributed over the unit cell. The comparison between theoretical and observed distributions enables one to establish whether there is an inversion centre in the crystal structure.

4.2.3.1. *Normalized structure factors*

Direct methods do not work with structure factors directly but with normalized structure factors $E_{\mathbf{h}}$. The diffraction intensities $|F_{\mathbf{h}}|^2_o$ provided by X-ray diffraction experiments are on a relative scale and the normalization process corrects for this as well as the attenuation in intensity with diffraction angle *via* the formula

$$|F_{\mathbf{h}}|^2_o = K|F_{\mathbf{h}}|^2 = K|F^0_{\mathbf{h}}|^2 \exp(-2Bs^2), \qquad (4.2.3)$$

where K is the scale factor, $|F^0_{\mathbf{h}}|$ is the observed structure-factor amplitude on an absolute scale for atoms at rest, B is related to the average displacement parameter (assumed equal for all the atoms) and $s = \sin\theta/\lambda$. The values of K and B can be determined by the Wilson method (Wilson, 1942), in which the observed diffraction data are divided into ranges of s (s is almost constant in the range) and the expectation value of the intensity in each shell is calculated:

$$\left\langle |F_{\mathbf{h}}|^2_o \right\rangle_s = K\left\langle |F^0_{\mathbf{h}}|^2 \right\rangle_s \exp\left(-2B\langle s^2\rangle\right) = K\sum_s^0 \exp\left(-2B\langle s^2\rangle\right). \quad (4.2.4)$$

In the absence of any structural information $\sum_s^0 = \sum_{j=1}^N \left(f_j^0\right)^2$, computed by using the tabulated values of f_j for atoms at rest and for $s = \langle s^2\rangle^{1/2}$. From equation (4.2.4) we obtain

$$\ln\left(\frac{\left\langle |F_{\mathbf{h}}|^2_o \right\rangle_s}{\sum_s^0}\right) = \ln K - 2Bs^2. \qquad (4.2.5)$$

A plot of the left side of (4.2.5) *versus* s^2 should yield a straight line, for which the intercept with the vertical axis would give $\ln K$ (and hence K) and the slope would give the value of $-2B$ and hence B.

In practice, owing to structural regularities (the atoms are not randomly located in the unit cell), the experimental values used in equation (4.2.5) for deriving K and B do not fully satisfy the linear condition: the best evaluation of K and B is then usually obtained by calculating a least-squares line.

The scattering factor f_j varies with θ and the expected intensity is

$$\left\langle |F_{\mathbf{h}}|^2_o \right\rangle = \varepsilon(\mathbf{h}) \sum_{j=1}^N f_j^2, \qquad (4.2.6)$$

where $\varepsilon(\mathbf{h})$ is a statistical weight due to the space-group symmetry (Rogers, 1980). The expected intensity is thermal-motion and resolution dependent. This means that reflections measured at different θ values cannot be compared directly. In order to overcome this, normalized structure factors $|E_{\mathbf{h}}|$ can be calculated according to

$$|E_{\mathbf{h}}|^2 = \frac{|F_{\mathbf{h}}|^2_o}{\left\langle |F_{\mathbf{h}}|^2_o \right\rangle} = \frac{|F_{\mathbf{h}}|^2_o}{K\varepsilon(\mathbf{h})\sum_{j=1}^N \left(f_j^0\right)^2 \exp(-2Bs^2)}. \qquad (4.2.7)$$

It follows that

$$\left\langle |E_{\mathbf{h}}|^2 \right\rangle = 1 \qquad (4.2.8)$$

for all regions of θ. The E values are independent of the scattering angle θ and correspond to an idealized point-atom structure. The largest $|E_{\mathbf{h}}|$ reflections (the strong reflections) play a major role in the phasing process (not only in DM, but also in all RS methods).

The distribution of $|E_{\mathbf{h}}|$ values is different for centrosymmetric and noncentrosymmetric space groups (Wilson, 1942, 1949); the probability distribution functions are, respectively,

$$P_{-1}(|E|) = (2/\pi)^{1/2} \exp\left(-|E|^2/2\right) \quad \text{(centrosymmetric)}, \qquad (4.2.9)$$

$$P_1(|E|) = 2|E| \exp\left(-|E|^2\right) \quad \text{(noncentrosymmetric)}, \qquad (4.2.10)$$

which are independent of the structure complexity. These expressions can be used to identify the correct space group for single-crystal data, but are unusable for powder data because the distribution of $|E_{\mathbf{h}}|^2$ values is strongly dependent on the algorithm used to decompose the powder-diffraction pattern into single integrated intensities (Pawley or Le Bail) (Giacovazzo, 1996). Owing to the inherent tendency of the Le Bail algorithm to equipartition the overall intensity among the severely overlapping reflections, the distribution of the extracted integrated intensities will be biased towards the noncentric distribution. In contrast, Pawley-based methods often provide negative intensities for strongly overlapped reflections, and consequently generate a high percentage of extreme $|E|$ values. Furthermore, the distributions of the normalized structure-factor moduli can be strongly affected by pseudotranslational symmetry and by preferred-orientation effects. Information about these effects can be used *a priori* to perform a better powder-pattern decomposition, so improving the efficiency of DM (see Section 4.2.4).

4.2.3.2. *Structure invariants*

We now need the concept of structure invariants. A structure factor (whether normalized or not) referred to a new unit-cell origin $\mathbf{x}_0$ takes the form $E'_{\mathbf{h}} = E_{\mathbf{h}}\exp(-2\pi i\mathbf{h}\cdot\mathbf{x}_0)$, *i.e.*, the phase $\varphi_{\mathbf{h}}$ changes according to $\varphi'_{\mathbf{h}} = \varphi_{\mathbf{h}} - 2\pi\mathbf{h}\cdot\mathbf{x}_0$, while the modulus remains unchanged ($|E'_{\mathbf{h}}| = |E_{\mathbf{h}}|$). A basic question now arises: since the origin can be arbitrarily chosen and phase values depend on the chosen origin, how can DM derive phases directly from the observed diffraction moduli? From the moduli we can obtain information only on combinations of phases, which are the structure invariants: products of *n* structure factors which remain invariant whatever the origin. They may be written as

$$E_{\mathbf{h}_1}E_{\mathbf{h}_2}\ldots E_{\mathbf{h}_n} = |E_{\mathbf{h}_1}E_{\mathbf{h}_2}\ldots E_{\mathbf{h}_n}|\exp[i(\varphi_{\mathbf{h}_1}+\varphi_{\mathbf{h}_2}+\ldots+\varphi_{\mathbf{h}_n})]. \qquad (4.2.11)$$

Any invariant satisfies the condition that the sum of the indices is zero:

$$\mathbf{h}_1+\mathbf{h}_2+\ldots+\mathbf{h}_n=\mathbf{0}. \qquad (4.2.12)$$

Structure invariants do not change when the origin is moved by a general vector $\mathbf{x}_0$. In fact, because of condition (4.2.12), the product in equation (4.2.11) remains unchanged:

$$E'_{\mathbf{h}_1}E'_{\mathbf{h}_2}\ldots E'_{\mathbf{h}_n} \equiv E_{\mathbf{h}_1}E_{\mathbf{h}_2}\ldots E_{\mathbf{h}_n}. \qquad (4.2.13)$$

Simple structure invariants are:

(*a*) $n = 2$, $E_{\mathbf{h}}E_{-\mathbf{h}} = |E_{\mathbf{h}}|^2$ (doublet invariants);

(*b*) $n = 3$, $E_{\mathbf{h}}E_{\mathbf{k}}E_{-\mathbf{h}-\mathbf{k}} = |E_{\mathbf{h}}E_{\mathbf{k}}E_{-\mathbf{h}-\mathbf{k}}|\exp[i(\varphi_{\mathbf{h}}+\varphi_{\mathbf{k}}+\varphi_{-\mathbf{h}-\mathbf{k}})]$ (triplet invariants);

(*c*) $n = 4$, $E_{\mathbf{h}}E_{\mathbf{k}}E_{\mathbf{l}}E_{-\mathbf{h}-\mathbf{k}-\mathbf{l}} = |E_{\mathbf{h}}E_{\mathbf{k}}E_{\mathbf{l}}E_{-\mathbf{h}-\mathbf{k}-\mathbf{l}}|\exp[i(\varphi_{\mathbf{h}}+\varphi_{\mathbf{k}}+\varphi_{\mathbf{l}}+\varphi_{-\mathbf{h}-\mathbf{k}-\mathbf{l}})]$ (quartet invariants).

Hauptman & Karle (1953) laid the probabilistic foundations of DM. They first proposed the calculation of joint probability distributions from which the conditional distribution function $P(\Phi|\{R\})$ is derived, where Φ is a structure invariant and $\{R\} = \{|E_{\mathbf{h}}|\}$ is a suitable set of normalized structure-factor moduli. $P(\Phi|\{R\})$ enables us to estimate Φ given the set $\{|E_{\mathbf{h}}|\}$. The *nested neighbourhoods principle* formulated by Hauptman (1975) defines a rule for optimally selecting the $\{|E_{\mathbf{h}}|\}$ to be used for estimating Φ. A more general concept, *representation theory*, has been formulated by Giacovazzo (1977, 1980). For more details see Giacovazzo (1998, 2001, 2013) and Woolfson & Fan (1995).

4.2.3.3. *Triplet invariants*

Triplet invariants (or simply 'triplets') play a central role in DM. A probabilistic formula for estimating triplets was first given by Cochran (1955), who derived the following von Mises (1918) type of function:

$$P(\Phi_{\mathbf{h},\mathbf{k}}) = (1/L)\exp(G_{\mathbf{h},\mathbf{k}}\cos\Phi_{\mathbf{h},\mathbf{k}}), \qquad (4.2.14)$$

where $G_{\mathbf{h},\mathbf{k}} = (2/N^{1/2})|E_{\mathbf{h}}E_{\mathbf{k}}E_{-\mathbf{h}-\mathbf{k}}|$ for equal atoms and $G_{\mathbf{h},\mathbf{k}} = 2\sigma_3\sigma_2^{-1/2}|E_{\mathbf{h}}E_{\mathbf{k}}E_{-\mathbf{h}-\mathbf{k}}|$ for non-equal atoms, $\sigma_n = \sum_{j=1}^{N} Z_j^n$, L is a normalization term depending only on $G_{\mathbf{h},\mathbf{k}}$ and $\Phi_{\mathbf{h},\mathbf{k}} = \varphi_{\mathbf{h}}+\varphi_{\mathbf{k}}+\varphi_{-\mathbf{h}-\mathbf{k}}$. The trend of equation (4.2.14) is very similar to that of a Gaussian and, for different values of $G_{\mathbf{h},\mathbf{k}}$, $P(\Phi_{\mathbf{h},\mathbf{k}})$ is always a maximum when $\Phi_{\mathbf{h},\mathbf{k}} = \varphi_{\mathbf{h}}+\varphi_{\mathbf{k}}+\varphi_{-\mathbf{h}-\mathbf{k}} = 0$ ($\Phi_{\mathbf{h},\mathbf{k}} \simeq 0$ corresponds to positive triplets, $\Phi_{\mathbf{h},\mathbf{k}} \simeq \pi$ to negative triplets), that is $\varphi_{\mathbf{h}} = -\varphi_{\mathbf{k}} - \varphi_{-\mathbf{h}-\mathbf{k}}$. The distribution curves become increasingly sharp with increasing values of $G_{\mathbf{h},\mathbf{k}}$, *i.e.* the variance decreases. The consequence of this is that the estimate $\Phi_{\mathbf{h},\mathbf{k}} = 0$ is only reliable for large values of $G_{\mathbf{h},\mathbf{k}}$ and so only the phases of large normalized structure factors can be determined, in general, by DM. This is shown diagramatically in Fig. 4.2.1.

Representation theory, as proposed by Giacovazzo (1977, 1980), indicates how the information contained in all of reciprocal space can be used to improve the Cochran's estimate of $\Phi_{\mathbf{h},\mathbf{k}}$. The $P_{10}(\Phi_{\mathbf{h},\mathbf{k}})$ conditional probability distribution (Cascarano *et al.*, 1984) has a von Mises expression and explores reciprocal space by means of a ten-node figure. P_{10} is more powerful than Cochran's formula because of its simultaneous use of strong and weak $|E|$ values, enabling one to estimate negative triplets as well.

4.2.3.4. *How direct methods work*

DM carries out the following main steps (see Fig. 4.2.1):

(1) *Normalization*. This process estimates the scale factor and the overall isotropic displacement factor, *B*; it normalizes the experimental structure-factor moduli and analyses the $\{|E_{\mathbf{h}}|\}$ distribution, which can assist with space-group determination.

(2) *Structure invariants*: The main structure invariants (*i.e.*, triplets) are calculated by considering the set of strong reflections and their Φ values are estimated.

(3) *Phasing process*: The phasing process has two parts: the assignment of initial phases to some or all of the normalized reflections, and the generation of new and/or refined phases.

Assignment of initial phases: There are two basic methods of assigning phases to reflections:

(*a*) Random values between 0 and 360° are assigned to reflections. This is the most common method.

The random approach for phasing was derived from the observation that it is possible to solve crystal structures by starting with a large set of phases (more than 40–50) even if they are very inaccurate (Viterbo, 2002).

(*b*) Some strong reflections are chosen for fixing the origin and, if necessary, the enantiomorph [see Rogers (1980) for details of this procedure]. If the number of these reflections is not enough to seed the phasing process, it is necessary to choose a larger number, which then constitutes the 'starting set'. The starting set is selected by a convergence procedure. In this procedure (Germain *et al.*, 1970) the reflections most strongly embedded in triplets are selected. It is a cyclic process that, step by step, eliminates the reflection with minimum $\langle\alpha_{\mathbf{h}}\rangle$ (and all the triplets in which the discarded reflection is involved), where $\langle\alpha_{\mathbf{h}}\rangle = \sum_j G_j D_1(G_j)$ and the summation is over the current triplets. G_j is the reliability of the *j*th triplet (see Section 4.2.3.3), $D_1(G_j) = I_1(G_j)/I_0(G_j)$, and $I_1(x)$ and $I_0(x)$ are the modified Bessel functions of order one and zero, respectively. The reflection with minimum $\langle\alpha_{\mathbf{h}}\rangle$ is retained only if it is necessary for fixing the origin or if it has already been included in the starting set. Towards the end of the process, the reflection with the smallest $\langle\alpha_{\mathbf{h}}\rangle$, *i.e.*, one that is uncorrelated (or weakly correlated) with those left in the set, is included in the starting set because it represents the link to reflections that have already been discarded. The convergence procedure is iterated until an optimum starting set of reflections has been obtained.

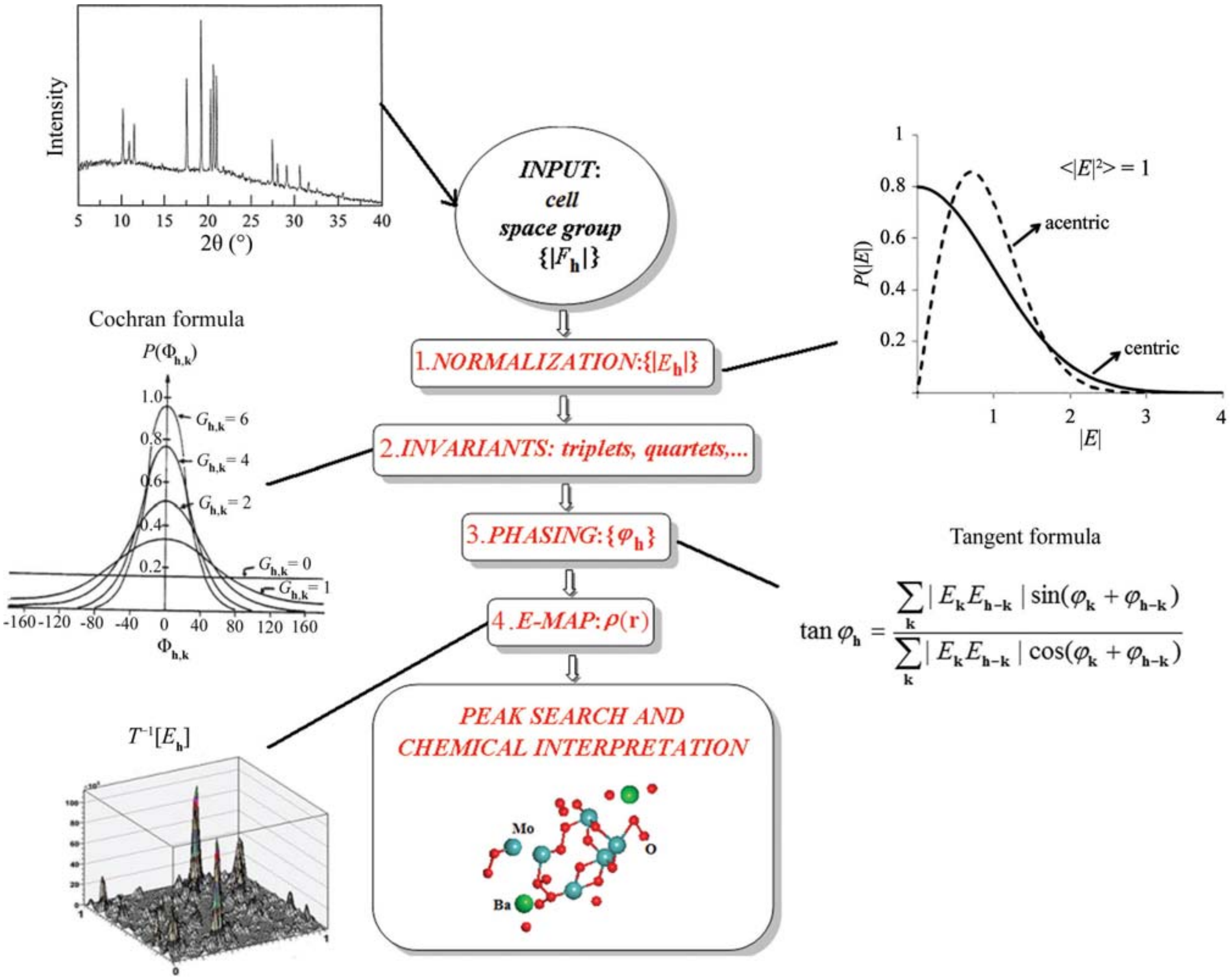
Intensity
5 10 15 20 25 30 35 40
2θ (°)
INPUT:
cell
space group
{|F_h|}
1.NORMALIZATION:{|E_h|}
2.INVARIANTS: triplets, quartets,...
3.PHASING:{φ_h}
4.E-MAP:ρ(r)
PEAK SEARCH AND CHEMICAL INTERPRETATION
Mo
O
Ba
Cochran formula
P(Φ_h,k)
1.0
0.8
0.6
0.4
0.2
G_h,k = 6
G_h,k = 4
G_h,k = 2
G_h,k = 0
G_h,k = 1
-160 -120 -80 -40 0 40 80 120 160
Φ_h,k
T⁻¹[E_h]
1
0.8
0.6
0.4
0.2
P(|E|)
<|E|²> = 1
acentric
centric
1 2 3 4
|E|
Tangent formula
tan φ_h = Σ_k |E_k E_h−k| sin(φ_k + φ_h−k) / Σ_k |E_k E_h−k| cos(φ_k + φ_h−k)

Figure 4.2.1
Flow chart for the DM procedure.

The choice of the starting set is fundamental, because the estimates of the rest of phases depend on it. If random phases are used, this step may not be required.

Starting-set phases can be assigned according to one of the two following approaches: symbolic addition (Karle & Karle, 1966), which associates algebraic symbols with phases, and multisolution methods based on magic integers (White & Woolfson, 1975), which give approximate numerical values.

Phase refinement and extension: The fundamental equation for this process is the tangent formula (Karle & Hauptman, 1956), which both calculates the phases of strong reflections and refines them by exploiting triplet relationships as follows:

$$\tan\varphi_{\mathbf{h}}=\frac{\sum_{\mathbf{k}}|E_{\mathbf{k}}E_{\mathbf{h}-\mathbf{k}}|\sin(\varphi_{\mathbf{k}}+\varphi_{\mathbf{h}-\mathbf{k}})}{\sum_{\mathbf{k}}|E_{\mathbf{k}}E_{\mathbf{h}-\mathbf{k}}|\cos(\varphi_{\mathbf{k}}+\varphi_{\mathbf{h}-\mathbf{k}})}=\frac{T_{\mathbf{h}}}{B_{\mathbf{h}}}. \qquad (4.2.15)$$

The summations in (4.2.15) are over **k** reflections related to **h** and **h** − **k** *via* the triplet relationship. Equation (4.2.15) is probably the most widely used formula in direct methods; it derives the phase of **h**, *via* knowledge of the phases ($\varphi_{\mathbf{k}}$, $\varphi_{\mathbf{h}-\mathbf{k}}$) of (**k**, **h** − **k**) couples.

$\varphi_{\mathbf{h}}$ in (4.2.15) is the most probable value of the phase of **h**; the reliability of $\varphi_{\mathbf{h}}$ is assessed *via* the parameter $\alpha_{\mathbf{h}}$, given by

$$\alpha_{\mathbf{h}}=(T_{\mathbf{h}}^2+B_{\mathbf{h}}^2)^{1/2}. \qquad (4.2.16)$$

Many variants of the tangent formula have been proposed, *e.g.* by including suitable weights and quartet relationships in order to make it more stable or improve its radius of convergence.

In general, only those reflections having $|E|>1$ are phased.

(4) *Figures of merit:* The DM phasing process provides a large number of possible sets of phases. They are ranked by figures of merit (FOMs) aimed at evaluating their reliability. CFOM is a suitably weighted combination of different FOMs. Among the most widely used FOMs (Declercq *et al.*, 1979; Karle & Karle, 1966; Cochran & Douglas, 1957) are

$$\mathrm{ABSFOM}=\frac{\sum_{\mathbf{h}}\alpha_{\mathbf{h}}-\sum_{\mathbf{h}}(\alpha_{\mathbf{h}})_r}{\sum_{\mathbf{h}}\langle\alpha_{\mathbf{h}}\rangle-\sum_{\mathbf{h}}(\alpha_{\mathbf{h}})_r} \qquad (4.2.17)$$

and

$$R_\alpha=\frac{\sum_{\mathbf{h}}\left|\alpha_{\mathbf{h}}-\langle\alpha_{\mathbf{h}}\rangle\right|}{\sum_{\mathbf{h}}\langle\alpha_{\mathbf{h}}\rangle}, \qquad (4.2.18)$$

where $\alpha_{\mathbf{h}}$ is the parameter in equation (4.2.16) estimating the reliability of the most probable phase of reflection **h**; $\langle\alpha_{\mathbf{h}}\rangle$ is the expected value of $\alpha_{\mathbf{h}}$ and $(\alpha_{\mathbf{h}})_r$ is the expected value of $\alpha_{\mathbf{h}}$ when the phases are assumed to be randomly distributed. ABSFOM tends to be unity for phases giving $\langle\alpha_{\mathbf{h}}\rangle$ and zero for random phases. A good set of phases may give ABSFOM in the range 1.0–1.4. R_α should be a minimum for the correct set of phases.

$$\Psi_0 = \frac{\sum_{\mathbf{h}} \left| \sum_{\mathbf{k}} E_{\mathbf{k}} E_{\mathbf{h}-\mathbf{k}} \right|}{\sum_{\mathbf{h}} \left(\sum_{\mathbf{k}} \left| E_{\mathbf{k}} E_{\mathbf{h}-\mathbf{k}} \right|^2 \right)^{1/2}}, \qquad (4.2.19)$$

where the outer summations are over $\mathbf{h}$ for which $E_{\mathbf{h}}$ is small, ideally zero; the inner summations include the large structure factors for which the phases are being determined. Ψ_0 is expected to be small for a correct set of phases and also for random phases. The individual FOMs can be combined into (Woolfson & Fan, 1995)

$$\begin{aligned} \mathrm{CFOM} = {} & w_1 \frac{\mathrm{ABSFOM} - \mathrm{ABSFOM}_{\min}}{\mathrm{ABSFOM}_{\max} - \mathrm{ABSFOM}_{\min}} \\ & + w_2 \frac{(\Psi_0)_{\max} - \Psi_0}{(\Psi_0)_{\max} - (\Psi_0)_{\min}} \\ & + w_3 \frac{(R_\alpha)_{\max} - R_\alpha}{(R_\alpha)_{\max} - (R_\alpha)_{\min}}, \end{aligned} \qquad (4.2.20)$$

where max and min refer to the value for the phase set with the greatest and least FOM, respectively and w_1, w_2, w_3 are empirical weights usually set to 0.6, 1.2 and 1.2, respectively.

Improved formulations of FOMs and CFOM have been proposed (Cascarano *et al.*, 1987, 1992). CFOM is expected to be 1.0 for a correct set of phases. In the case of powder data, the uncertainty on the integrated intensities makes CFOM statistically meaningless (*i.e.*, CFOM can be 1.0 for a wrong set and far from 1.0 for the set corresponding to the correct solution). Classical FOMs, which are functions of $\{|E|\}$, can be misleading for powder data and are less effective that those for single-crystal data. A new figure of merit, an atom-matching-based FOM (AMB FOM), has recently been proposed (Altomare *et al.*, 2011*a*), coupled with a special decomposition procedure (Altomare *et al.*, 2003; Altomare *et al.*, 2004) (see Section 4.2.4.3). The procedure, which is based on the generation of a huge number of phasing trials and of corresponding *E*-map [see step (5)] structure models, aims to select a subset of candidate models to be submitted to a refinement procedure. Adopting a similarity criterion (*i.e.*, two structure models are considered to be similar if they share a high percentage of atoms), the AMB FOM re-groups similar trial models in batches. Then the batch leader is identified as the representative model of the batch and finally the most reliable batch leaders are selected.

(5) *E-map calculation*: The best phase set is used for calculating an electron-density map $\rho(\mathbf{r})$ *via* a Fourier synthesis for which the coefficients are the $|E_{\mathbf{h}}|$ values (an *E*-map):

$$\rho(\mathbf{r}) \simeq (1/V) \sum_{\mathbf{h}} |E_{\mathbf{h}}| \exp(i\varphi_{\mathbf{h}}) \exp(-2\pi i \mathbf{h} \cdot \mathbf{r}). \qquad (4.2.21)$$

The limited number of reflections used for the Fourier synthesis leads to truncation errors. The Fourier synthesis plays the role of a mathematical lens giving, *via* the *E*-map, the direct image of the electron-density distribution. The maxima in the map, located *via* a peak-search procedure, should correspond to positions of atoms in the unit cell. A chemical interpretation of the peak positions is performed by taking into account the cell content. In the case of powder-diffraction data, the poor significance of FOMs may lead to uninterpretable or unsatisfactory structure models. In this case, other phasing sets among those most highly ranked by figures of merit should be explored. Often more than one *E*-map is calculated.

Problems with direct methods using powder data are:

(1) Information about the presence or absence of an inversion centre in the crystal structure cannot be accurately derived *via* the statistical analysis of the normalized experimental structure-factor moduli.

(2) The *B* value can be meaningless, not only because of inaccuracy in the integrated intensities, but also because of truncation errors. Negative values are not uncommon and can be reset to a positive value.

(3) In the case of severely overlapping reflections, strong wrongly estimated reflections can be responsible for failure of the phasing process. In order to improve the phasing efficiency, a procedure based on the generation of numerous trials of pattern decomposition has been developed (Altomare *et al.*, 2003, 2004) (see Section 4.2.4.3).

(4) In the case of structures containing heavy atoms, non-negligible pseudotranslational effects often occur. The statistical analysis of $\{|E|\}$ can detect the presence of pseudotranslation and evaluate the mean fractional scattering power of atoms involved in pseudosymmetry (Cascarano *et al.*, 1985). The pseudotranslational symmetry information can be suitably exploited in the Le Bail decomposition process (see Chapter 3.5) in order to improve the estimates of the integrated intensities (Altomare, Foadi *et al.*, 1996) (see Section 4.2.4.1).

(5) Preferred-orientation (PO) effects are responsible for a distortion of the ratios of the integrated intensities. In order to avoid failures in phasing, correction functions for PO have been proposed (Dollase, 1986; Altomare *et al.*, 1994; Altomare, Burla *et al.*, 1996) (see Section 4.2.4.2).

Despite these limitations, DM are often able to provide the correct solution.

4.2.4. Improving data normalization

4.2.4.1. *Pseudotranslational symmetry*

Pseudotranslational symmetry effects occur when a non-negligible part of the electron density, say $\rho_p(\mathbf{r})$, satisfies a vector $\mathbf{u}$ that is not exactly equal to a crystallographic translation (Lipson & Woolfson, 1952; Rogers & Wilson, 1953; Buerger, 1956, 1959). In this case, the structure should be treated as the sum of a substructure $\rho_p(\mathbf{r})$ and of a superstructure $\rho(\mathbf{r}) - \rho_p(\mathbf{r})$. Pseudotranslational symmetry may be recognized by the statistical analysis of the normalized structure-factor moduli because, when present, a non-uniform value of the average normalized intensity is obtained, *i.e.*, equation (4.2.8) is violated. The fractional scattering power (FSP) of the atoms obeying pseudo-translational symmetry can be evaluated (Altomare, Foadi *et al.* 1996) *via*

$$\mathrm{FSP} = \left(\left\langle |E_{\mathbf{h}}|^2 \right\rangle - 1 \right) \Big/ (\beta_{\mathbf{h}} - 1), \qquad (4.2.22)$$

where $\beta_{\mathbf{h}}$ is proportional to the number of times that the algebraic congruence $\mathbf{h} \cdot \mathbf{R}_s \mathbf{u} \equiv 0 \,(\mathrm{mod}\ 1)$ is satisfied by varying s (where $\mathbf{R}_s$ is the sth rotational symmetry operator). $\beta_{\mathbf{h}}$ corresponds to a superstructure reflection if equal to 0, and to a substructure reflection if non-zero. The information gained from equation (4.2.22) may be used to correct the normalized structure factors, which can then be used as a starting point for programs based on the Le Bail algorithm to obtain more accurate extracted structure-factor moduli.

4.2.4.2. *Preferred orientation*

Preferred orientation (PO) occurs when crystallites are not completely randomly oriented in the specimen. It produces a distortion of the ratios of the integrated intensities and therefore weakens the power of DM. In order to avoid this problem, the integrated intensities corresponding to randomly oriented crystallites have to be retrieved. These values can be derived in different ways:

1. by exploiting the measurements of pole-density distributions (Bunge *et al.*, 1989);
2. by using the symmetrized harmonics method (Järvinen, 1993); or
3. by applying a mathematical correction to the structure-factor moduli (*e.g.*, Dollase, 1986; Altomare *et al.*, 1994; Altomare, Burla *et al.*, 1996).

Among several mathematical forms proposed for the correction of PO effects, the most widely used is the March–Dollase function (Dollase, 1986).

Using a statistical analysis of the normalized structure-factor moduli it is possible to detect the presence of preferred-orientation effects (under the hypothesis that the specimen has cylindrical symmetry) (Altomare *et al.*, 1994; Altomare, Burla *et al.*, 1996). In the case of PO, the condition (4.2.8) is violated and, in order to correct for it, the $O_{\mathbf{h}}$ function has been introduced for transforming the experimental $|E_{\mathbf{h}}|^2$ values into corrected $|E_{\mathbf{h}}|^2_{\rm corr}$ according to

$$|E_{\mathbf{h}}|^2_{\rm corr} = |E_{\mathbf{h}}|^2 O_{\mathbf{h}}^{-1}. \qquad (4.2.23)$$

$O_{\mathbf{h}}$ is given by a von Mises distribution:

$$O_{\mathbf{h}} = \exp(G_{\rm PO}\cos 2\gamma), \qquad (4.2.24)$$

where $G_{\rm PO}$, to be estimated, represents the strength of the PO effect and γ is the angle between reflection **h** and the preferred-orientation direction. This approach uses the following steps:

1. a full pattern decomposition capable of estimating the experimental $\{|F_{\mathbf{h}}|\}$;
2. the normalization of the structure-factor moduli; and
3. the selection of the first n strongest reflections ($10 \le n \le 30$) in the low $\sin\theta/\lambda$ range. For each reflection, **k**, selected, the following additional steps are performed:
    - (*a*) Reciprocal space is divided into cones having common vertices and axes (*i.e.* vertices at the origin of the reciprocal space and axes [**k**] = [*hkl*]). The regions between two cones (*i.e.* a shell) have approximately equal volumes in order to contain, on average, equal numbers of reflections. The reflections **h** belonging to a shell form an approximately constant γ angle with **k**.
    - (*b*) For each shell, the $\langle|E|^2\rangle$ value is calculated. In the case of PO, this value is expected to be strongly different from 1.0. The trend of $\langle|E|^2\rangle$ *versus* γ is considered.
    - (*c*) Least-squares methods are used for evaluating the von Mises distribution in (4.2.24) best fitting the experimental $|E_{\mathbf{h}}|^2$ values according to (4.2.23).
    - (*d*) The plane **k** characterized by the largest value of $G_{\rm PO}$ is selected as the PO direction.
    - (*e*) New values of $|E_{\mathbf{h}}|^2_{\rm corr}$ are obtained.

The presence of preferred orientation in a pattern is not always obvious to the eye and, if undetected, can prove fatal to any structure-solution process. Undetected preferred orientation tends to concentrate electron density in a plane (for plate-like crystals) or in a line (for needles). The above statistical analysis can rationalize the effects of such patterns in the electron density, and provide evidence that preferred orientation is present. It is generally better to re-prepare the specimen to eliminate or reduce preferred orientation, rather than to deal with a distorted data set.

4.2.4.3. *Systematic decomposition*

After normalization, the reflections are sorted according to their $|E|$ values and only those larger than a threshold are actively used in the phasing process. Procedures have been proposed that aim to improve the quality of the extracted integrated intensities when the standard decomposition step fails to provide the correct solution. They are based on systematic variation of the normalized structure-factor moduli of clusters of severely overlapping reflections (Altomare *et al.*, 2003). The clusters containing the reflections that are expected to play a minor role in DM applications, *i.e.*. those for which no constituent reflection falls among the largest reflections, are not considered. This approach uses the Le Bail decomposition and carries out a systematic partition of the overall intensity of each of *ndoub* doublets of reflections, in three different ways, giving rise to $N_{\rm trials} = 3^{ndoub}$ decompositions. A doublet consists of a cluster of two overlapped reflections (no other reflection overlaps them); two reflections **h** and **k** are considered to overlap if

$$|2\theta_{\mathbf{h}} - 2\theta_{\mathbf{k}}| < {\rm th}_{\rm ov}{\rm FWHM}_{\mathbf{h}}, \qquad (4.2.25)$$

where ${\rm th}_{\rm ov}$ is a suitable threshold (usually in the range 0.1–1.0) and ${\rm FWHM}_{\mathbf{h}}$ is the full width at half maximum of the peak associated with the reflection **h**. If *ndoub* is large, a huge number of decompositions are to be performed. A consistent reduction of this number can be obtained by using linear error-correcting codes (Altomare *et al.*, 2004). For each decomposition trial, DM phasing is carried out and, by using a suitable figure of merit, the correct solution is recognized among the large number of trials (Altomare *et al.*, 2011*a*).

4.2.5. Patterson methods

The Patterson function $P(\mathbf{u})$ is the self-convolution of the electron density $\rho(\mathbf{r})$ in the cell (Milanesio & Viterbo, 2011):

$$P(\mathbf{u}) = \rho(\mathbf{r}) * \rho(-\mathbf{r}) = \int_V \rho(\mathbf{r})\rho(\mathbf{r}+\mathbf{u})\,{\rm d}\mathbf{r}. \qquad (4.2.26)$$

Its name is due to Patterson (1934), who proposed a mathematical expression for $P(\mathbf{u})$ in terms of Fourier synthesis of the observed $|F_{\mathbf{h}}|^2$ values:

$$P(\mathbf{u}) = T^{-1}[|F_{\mathbf{h}}|^2] = (1/V)\sum_{\mathbf{h}} |F_{\mathbf{h}}|^2 \exp(-2\pi i\mathbf{h}\cdot\mathbf{u}). \qquad (4.2.27)$$

$P(\mathbf{u})$ has a great advantage with respect to $\rho(\mathbf{r})$: it is easily calculated from the available experimental structure-factor moduli, and no phase information is required. Maxima occur in $P(\mathbf{u})$ if both $\rho(\mathbf{r})$ and $\rho(\mathbf{r} + \mathbf{u})$ are different from zero. This happens if **u** is an interatomic vector. The heights of the $P(\mathbf{u})$ maxima are proportional to the products of the atomic numbers of atoms involved in **u** and to the multiplicity of **u** (the multiplicity tells us how many times **u** occurs). The $P(\mathbf{u})$ maxima consist of N^2 peaks; N of them overlap and give rise to a strong origin peak, corresponding to the vector from each atom to itself; the remaining $N(N-1)$ peaks are distributed in the unit cell.

The interpretation of $P(\mathbf{u})$ is clearly more difficult than $\rho(\mathbf{r})$: Patterson peaks are broader, more numerous and usually overlap. These problems occur in both single-crystal and powder data, but they are more critical in the case of powder X-ray diffraction data: errors in integrated intensity estimates and truncation effects are responsible for the presence of very broad peaks, some of them false or misplaced from correct positions, making the Patterson map less easily interpretable than one from single-crystal data. The removal of the origin peak (using $|E_{\mathbf{h}}|^2 - 1$ as a Fourier coefficient) as well as the use of alternative coefficients such as $|E_{\mathbf{h}}|^2$, $|E_{\mathbf{h}}||F_{\mathbf{h}}|$ or $(|E_{\mathbf{h}}|^3|F_{\mathbf{h}}|)^{1/2}$ aim to sharpen the Patterson map and improve its interpretability.

The most traditional approach for interpreting the Patterson map is based on the use of Harker sections (Harker, 1936), which contain interatomic vectors $\mathbf{u}_{\mathrm{H}i} = \mathbf{r} - C_i\mathbf{r}$ ($C_i\mathbf{r} = \mathbf{R}_i\mathbf{r} + \mathbf{T}_i$, $\mathbf{R}_i$ and $\mathbf{T}_i$ are the rotational and translational components, respectively, of the ith symmetry operator of the space group) between an atom and its symmetry equivalents. In the case of structures with only a few heavy atoms, the Patterson peaks involving heavy atoms are usually dominant in the map and easily identified. By inspection of the Harker sections, it is possible to determine the heavy-atom positions from which the remaining light atoms can be located by Fourier synthesis using the observed structure-factor moduli and the phases calculated from the heavy atoms.

The use of the symmetry minimum function (SMF) or image-seeking minimum function (IMF) (Buerger, 1959) is based on automatic analysis of the Patterson map (Sheldrick, 2008), and is more effective than the manual inspection of Harker sections (Estermann & David, 2002). An example of the successful application of the SMF to powder data is given by Burla *et al.* (2007).

A different approach has been developed by Rius (Rius, 2002, 2011; Rius *et al.*, 1999, 2000, 2007; Rius & Frontera, 2007). In this context, a major role is played by the direct-methods modulus sum function used as a target function for refining phases of structure factors (Rius, 2002):

$$S'(\Phi_S) = \int_V P'(\mathbf{u})P(\mathbf{u}, \Phi_S)\,\mathrm{d}\mathbf{u}, \qquad (4.2.28)$$

where $P'(\mathbf{u})$ is the Patterson map without the origin peak, $P(\mathbf{u}, \Phi_S)$ is the calculated Patterson map where Φ_S is the set of phases of the strong reflections (those with the largest $|E|$ values). $S'(\Phi_S)$ should be a maximum for the true phases. The subtraction of the origin peak in $P'(\mathbf{u})$ enables weak reflections (reflections with the smallest $|E|$ values) to play an active role in the $S'(\Phi_S)$ maximization. The phases refined by maximizing $S'(\Phi_S)$ are considered to be the most probable ones and they are used for calculating the electron-density map. The method for maximizing $S'(\Phi_S)$ has also been optimized to refine the intensities of severely overlapping reflections with accidental overlap (Rius *et al.*, 2000). Other approaches have been developed for refining phases by maximizing S': the S'-TF tangent formula (Rius, 2002); the S-FFT approach which applies, in parallel mode, the tangent formula, and the fast Fourier transform (FFT) algorithm (Rius *et al.*, 2007). For powder data the use of the S_c-FFT procedure (Rius & Frontera, 2007) combining the S-FFT procedure with real-space constraints is similar to the *Shake-and-Bake* approach (Weeks *et al.*, 1993). A new type of direct methods, called Patterson-function DM, have also been developed that use the Patterson function of the squared structure directly (Rius, 2011) instead of the modulus function. It is based on the maximization of the S_P Patterson-function sum function:

$$S_P = 2\sum_{\mathbf{h}} \frac{I_{\mathbf{h}} - \langle I\rangle}{N} G_{-\mathbf{h}}(\Phi_S), \qquad (4.2.29)$$

where the summation is over the number of experimentally available reflections (strong and weak), $I_{\mathbf{h}}$ is the intensity of reflection $\mathbf{h}$ which, in the case of overlap, is obtained by the equidistribution of the overall intensity of the overlap cluster to which $\mathbf{h}$ belongs, $\langle I\rangle$ is the average intensity taken over all non-systematically absent reflections and $G_{-\mathbf{h}}(\Phi_S)$ is the calculated structure-factor amplitude of the squared structure. S_P has been optimized with the Patterson-function tangent formula using a variant of the S-FFT algorithm.

4.2.5.1. *The use of the Patterson function for estimating integrated intensities*

Patterson-function information has been used to improve the estimates of the integrated intensities of reflections. David (1987) proposed two approaches based on:

(1) maximization of the entropy of the Patterson function, subject to the constraints of measured intensities, and

(2) squaring of Patterson map using the squaring method of Sayre (1952).

Alternatively, the FIPS (fast iterative Patterson squaring) procedure can be used (Estermann *et al.*, 1992; Estermann & Gramlich, 1993). This adopts the squaring method, and has the following steps:

(1) A $P(\mathbf{u})$ map is calculated. The intensities of the strongly overlapping reflections are derived by equipartitioning the cluster intensity.

(2) A modified Patterson map $P^M(\mathbf{u})$ is derived by setting to zero any negative values in $P(\mathbf{u})$ and squaring the positive ones.

(3) New integrated intensities are obtained *via* the inverse Fourier transform of $P^M(\mathbf{u})$.

(4) The new intensity values are shifted away from the originally equipartitioned ones. The shifts are usually in the right direction but, in the majority of cases, they are too small with respect to the true amounts. In an attempt to obtain a distribution of intensity containing both small and large values, the shifts are exponentially increased by an empirical extrapolation. The intensities of non-overlapping reflections remain unchanged.

The previous cycles are repeated until convergence is attained.

A similar procedure (Altomare, Foadi *et al.*, 1998) carries out the following steps:

(1) Reduction of the effects of the origin peak: The intensities of the points of the Patterson map corresponding to the origin peak and belonging to a sphere with radius 2 Å are multiplied by an empirical value set to 0.7.

(2) Modification of the $P(\mathbf{u})$ map *via* a truncation criterion: The intensities of the pixels in the map having a density less than $\langle P\rangle + \sigma/n$ are set to zero. $\langle P\rangle$ is the average value of the Patterson density, σ is the standard deviation of the map and n is the current cycle number [see step (5)]. In this way, in the first cycle only the main peaks in the Patterson map are taken into account, then weak peaks are also considered.

(3) Inversion of the modified Patterson map: New integrated intensity values are obtained under the constraint that the overall observed intensity of clusters of overlapping reflections must be unchanged.

(4) Restoration of the single reflection intensities and assignment of new intensities to overlapping reflections. These intensities are used as a starting point for a new full-pattern-decomposition process according to the Le Bail algorithm (Le Bail *et al.*, 1988; Chapter 3.5).

(5) The intensities extracted in the previous step are now used and steps (2)–(4) are repeated.

4.2.6. Charge flipping

The charge-flipping (CF) method was devised by Oszlányi & Sütő (2004) for single-crystal data and successively improved (Oszlányi & Sütő, 2005, 2007, 2008, 2011); it has also been adapted to powder-diffraction data (Wu *et al.*, 2006; Baerlocher *et al.*, 2007). In its many variants it has been applied to a wide range of crystallographic problems: structure solution from single-crystal data; powder-, neutron- and electron-diffraction data; periodic and aperiodic structures; quasicrystals; and protein heavy-atom substructures. It is a dual-space iterative method switching back and forth between real and reciprocal space. Charge flipping needs the unit-cell parameters and the set of the experimental structure-factor moduli; neither the chemical composition nor symmetry information is required. It is based on the following steps:

(1) Random phases (satisfying the Friedel's law: $\varphi_{-\mathbf{h}} = -\varphi_{\mathbf{h}}$) are assigned to the observed structure-factor moduli $|F_{\mathbf{h}}|$ expanded to space group $P1$. Unobserved moduli are set to zero, except for $F(\mathbf{0})$ which is initially set to zero and allowed to change freely in the phasing process. The inverse Fourier transform of the structure factors is calculated to provide the starting electron density $\rho(\mathbf{r})$.

(2) $\rho(\mathbf{r})$ is modified into $g(\mathbf{r})$ by reversing (flipping) the sign of the density of all pixels with densities below a given (small) threshold positive value δ. The value of δ is a fraction of a typical light-atom peak and is the only parameter of the algorithm. The optimal choice of δ is critical because it determines the computational cost and the quality of the solution. It depends on the grid size used for calculating the density, the data resolution, the displacement parameters, and the types of atoms present in the cell. Some procedures have been proposed for evaluating the proper value of δ. The *a priori* determination of δ is a problem that has not been completely solved.

(3) The Fourier transform of $g(\mathbf{r})$ is carried out and the corresponding structure factors $G_{\mathbf{h}}$ are calculated.

(4) The phases of $G_{\mathbf{h}}$ are combined with the experimental $|F_{\mathbf{h}}|$ amplitudes.

(5) The new structure factors $F_{\mathbf{h}}$ are inverted to calculate a new electron-density map.

(6) The process is repeated from step (1) until convergence, or the requisite number of iterations has been carried out, or the system converges.

Figures of merit have been chosen for recognizing, in an automatic way, that the solution has been found and the process can stop (Oszlányi & Sütő, 2008).

CF is extremely simple and easily implemented. It works well at atomic resolution (better than 1.2 Å in the case of organic compounds, 1.6 Å for heavy-atom structures). As it is a method based on Fourier transforms, it is sensitive to data completeness (removing strong reflections from the data set is particularly harmful). An important aspect of CF is the handling of symmetry. No symmetry information is required and the method solves the structure in space group $P1$. The symmetry, which is encoded in the experimental amplitudes, is estimated from the analysis of the full electron density. This is an important advantage, making the structure solution insensitive to possible ambiguities in the determination of the space group. On the other hand, the density produced by CF is randomly shifted and the origin of the space group must be located. However, small deviations from a higher symmetry cannot be always accurately detected (*i.e.*, when all the heavy atoms match a higher symmetry and only a few light atoms break the symmetry).

Improvements to CF have been developed in relation to the treatment of weak reflections (reflections with small observed moduli) (Oszlányi & Sütő, 2005). This is introduced as a variant involving step (3): the new procedure identifies the weak reflections, and for them the amplitudes of $G_{\mathbf{h}}$ (and not the observed moduli) are retained and the phases are shifted by $\pi/2$.

In order to overcome the requirement for complete high-resolution data, new approaches have been proposed based on:

(*a*) the combination of classical CF with a maximum-entropy-optimized Patterson map to assign intensities to missing reflections (Palatinus *et al.*, 2007);

(*b*) the incorporation of the tangent formula of classical direct methods to create a modified iteration scheme (Coelho, 2007); and

(*c*) a variant of the basic algorithm in which an extended shell of freely floating reflections is combined with the iterative scheme. (The amplitude of a freely floating reflection is unconstrained and can evolve freely as the algorithm progresses.) This is known as the 'averaged alternating reflections' (AAR) scheme (Bauschke *et al.*, 2002, 2004) and uses significantly fewer data than are normally required (Oszlányi & Sütő, 2011).

As in other methods, the application of CF to powder data suffers from the inaccuracy of the extracted reflection intensities. If the reflection overlap is not too severe, the experimental structure-factor moduli values are reliable and the success of structure solution by CF is comparable to the single-crystal case. However, as the reflection overlap increases, the quality of the extracted intensities decreases and electron-density maps obtained by CF become unreliable, although they are not always completely wrong. One modification of the standard CF procedure for powder data is based on the concept that the ratios of $|G_{\mathbf{h}}|$ can be used for repartitioning the overall intensities of groups of overlapping reflections. This approach was first applied by Wu and co-workers (Wu *et al.*, 2006). They equipartitioned the overall intensity of a group of overlapping reflections to obtain the observed structure-factor moduli $|F_{\mathbf{h}}|$ used in step (1). In order to overcome the dependence upon the equipartitioned $|F_{\mathbf{h}}|$ values, a histogram-matching and repartitioning-based method has been proposed (Baerlocher *et al.*, 2007). The approach starts from the basic idea that correct and incorrect solutions can often be distinguished by the shape of the histogram of the electron-density map. After a certain number of cycles (defined by the user), the histogram-matching procedure modifies the values of the current density $\rho^{n}(\mathbf{r})$ so that the histogram of the modified density matches the expected one. The Fourier transform of the new density $\rho^{n\mathrm{HM}}(\mathbf{r})$ produces the structure factors $F_{\mathbf{h}}^{\mathrm{HM}}$ corresponding to the modified $\rho^{n}(\mathbf{r})$. Since $\rho^{n\mathrm{HM}}(\mathbf{r})$ has been improved by histogram-matching, $F_{\mathbf{h}}^{\mathrm{HM}}$ should also be improved with respect to $F_{\mathbf{h}}$ and, in particular, the ratios of the new amplitudes should be closer to the true ones. The new ratios are used for repartitioning the overall intensity of a group of overlapping reflections and obtaining new structure factors $F_{\mathbf{h}}^{\mathrm{new}}$ according to

$$F_{\mathbf{h}}^{\mathrm{new}} = F_{\mathbf{h}}^{\mathrm{HM}} \left(\frac{\sum |F_{\mathbf{h}}|^2}{\sum |F_{\mathbf{h}}^{\mathrm{HM}}|^2} \right)^{1/2}, \qquad (4.2.30)$$

where the summations run over reflections within an overlapping group. In the case of an individual reflection

$$F_{\mathbf{h}}^{\rm new} = F_{\mathbf{h}}^{\rm HM} \frac{|F_{\mathbf{h}}|}{|F_{\mathbf{h}}^{\rm HM}|}, \qquad (4.2.31)$$

that is, $|F_{\mathbf{h}}^{\rm new}| = |F_{\mathbf{h}}|$ and the phase of $F_{\mathbf{h}}^{\rm HM}$ is combined with the experimental amplitude of $F_{\mathbf{h}}$. In the case of overlapping reflections, the overall intensity of the overlapping group corresponds to the total experimental intensity, but the individual amplitudes within the group are modified.

The $F_{\mathbf{h}}^{\rm new}$ values are used as input to the next iteration cycle; the algorithm continues and the sequence of n cycles followed by histogram matching is repeated until convergence has been reached.

The reference histogram, provided by the user according to the chemical composition of the compound to be studied, describes the expected distribution of the electron density but does not locate the density in the unit cell. This adaptation of CF to powders has been successfully applied to solving different kinds of structures (Baerlocher *et al.*, 2007).

CF can be used not only as a structure-solution method, but also as a structure-completion method. In this case, the starting phases are not random but correspond to the partial structure model (Oszlányi & Sütő, 2005).

4.2.7. Maximum-entropy methods

Bricogne (1984) gave the theoretical basis for using maximum entropy (ME) for solving the phase problem, first for single-crystal data (Bricogne & Gilmore, 1990; Gilmore *et al.*, 1990) and successively for electron, powder (Bricogne, 1991; Gilmore *et al.*, 1991) and macromolecular data [see Gilmore (1996) for a general review]. ME methods (MEM) were found to be more robust than traditional DM in the case of structure solution using incomplete data sets, low-resolution data or intensities affected by errors (Gilmore, 1996).

If a discrete probability distribution is considered, given by a set of M probabilities $P = \{p_1, p_2, \ldots, p_M\}$, the relative entropy H of the distribution is

$$H = -\sum_{j=1}^{M} p_j \log(p_j/m_j), \qquad (4.2.32)$$

where $\{m_j\}$ are probabilities corresponding to prior knowledge. The goal of MEM is the determination of P by the maximization of H, subject to constraints which are expressed as expectation values representing knowledge derived from experiments or hypotheses.

This can be placed in a crystallographic context by replacing the discrete probabilities in equation (4.2.32) by normalized pixels in a trial electron-density map; the map is then subjected to constrained entropy maximization in which the constraints are the structure factors used to generate that map. The ME approach is based on the following steps (Gilmore, 1996; Gilmore *et al.*, 1999):

(1) The structure factors $|F_{\mathbf{h}}|$ are normalized and the corresponding unitary structure-factor moduli $|U_{\mathbf{h}}|$ are calculated *via*

$$|U_{\mathbf{h}}| = k|F_{\mathbf{h}}| \Big/ \sum_{j=1}^{N} f_j \exp(-B \sin\theta/\lambda). \qquad (4.2.33)$$

(2) A basis set $\{H\}$ is selected; it consists of phased reflections (*i.e.*, defined by the rules on origin and enantiomorph, see Rogers, 1980); let $\{K\}$ be the disjoint set of unphased reflections. The basis reflections in $\{H\}$ define the root node of the MEM phasing tree; their amplitudes and phases are exploited as constraints at the entropy-maximization step.

(3) $\{H\}$ is enlarged *via* an algorithm of optimum second-neighbourhood extension (Gilmore *et al.*, 1990) involving some strong non-phased reflections to which permuted phase values are given. Each possible phase choice creates a node that is subjected to constrained entropy maximization; the addition of reflections to $\{H\}$ leads to a huge generation of tree nodes (*i.e.*, 2^{nc} in the case of nc centric reflections, with possible phase values 0 and π, or $\pm\pi/2$; 4^{na} in the case of na acentric reflections, if four possible values of phases are considered: $\pm\pi/4$ and $\pm3\pi/4$). The likelihood function (Bricogne, 1984) is used as a suitable figure of merit; the log-likelihood gain (LLG) is able to recognize and discard nodes corresponding to wrong phase assignments (Gilmore *et al.*, 2002). It is a measure of the reliability of the phase prediction performed *via* the entropy-maximization process. Since no estimate of LLG standard deviations is available, the criterion of the highest LLG value for the selection of the nodes could be inadequate. In order to avoid this drawback, an analysis of the LLG values using the Student *t* test is performed (Shankland *et al.*, 1993) for selecting the best 8–16 nodes.

(4) The permutation-likelihood analysis procedure described in step (3) is iterated until a plausible structure model is obtained or the likelihood values begin to decrease.

The main problems related to MEM are a non-negligible computing time, due to the large number of solution trials generated, and difficulties that may arise in interpreting the results. Let us consider n nodes, p reflections and m degrees of freedom for each reflection to which permuted phases are assigned; nm^p phase sets are generated and subjected to constrained entropy maximization. In order to reduce the number of nodes in the MEM tree, error-correcting codes are used that ensure both an efficient phase permutation and a great decrease of the number of sets of phases (Gilmore *et al.*, 1999, 2002).

MEM have been suitably adapted for solving structures from powder data. The LLG can be calculated by considering or excluding the contribution of overlapping reflections (the preferred choice considers them). Entropy maximization coupled with likelihood can also predict the best assignment of integrated intensities of overlapping reflections (Dong & Gilmore, 1998; Gilmore *et al.*, 2002). In addition to the conventional phases, the method uses some angles, called pseudophases, which are introduced for describing the integrated intensities of the overlapping reflections. Let a given overlap contain m_a acentric and m_c centric reflections. The net intensity, I, is

$$I = \sum_{i=1}^{m_a} p_i(A_i^2 + B_i^2) + \sum_{i=m_a+1}^{m_a+m_c} p_i C_i^2, \qquad (4.2.34)$$

where p_i is the multiplicity of reflection i, A and B are the real and imaginary parts of an acentric structure factor, and C is the structure-factor component for centric reflections. The problem is one of determining the A, B and C coefficients in equation (4.2.34). It is useful to re-phrase this problem in terms of hyperphases. To do this we define the overlap as a vector $\mathbf{F}$ in an n-dimensional space R^n (Bricogne, 1991) as

$$\mathbf{F} = \begin{bmatrix} p_1^{1/2}A_1 \\ p_1^{1/2}B_1 \\ p_2^{1/2}A_2 \\ p_2^{1/2}B_2 \\ \vdots \\ p_{m_a}^{1/2}A_{m_a} \\ p_{m_a}^{1/2}B_{m_a} \\ \vdots \\ p_m^{1/2}C_m \end{bmatrix}, \tag{4.2.35}$$

where $n = 2m_a + m_c$ is the number of degrees of freedom, and $m = m_a + m_c$ is the number of reflection moduli under the overlap. $\mathbf{F}$ can be visualized as a hypersphere in R^n. A total of $m - 1$ splitting angles $\psi_{j,j=1,m-1}$, $0 \le \psi \le \pi/2$, which are called *pseudophases*, define a point on the positive unit hypersphere.

This is best seen *via* an example: consider an overlap of net intensity $I^{1/2}$ comprising two acentric reflections and one centric reflection. The radius of the hypersphere is $R = ||\mathbf{F}|| = I^{1/2}$. Defining R_1, R_2 and R_3 as the individual intensities of these three reflections, then

$$\begin{aligned} R' &= R\sin\psi_1, \quad 0 \le \psi_1 \le \pi/2, \\ R_1 &= R'\cos\psi_2, \quad 0 \le \psi_2 \le \pi/2, \\ R_2 &= R'\sin\psi_2, \\ R_3 &= R\cos\psi_1. \end{aligned} \tag{4.2.36}$$

The angles ψ_1 and ψ_2 are the two *pseudophases*; once they are known the individual intensities of the reflections are determined. It is then necessary to derive the associated phase angles to fully characterize the overlap, and this is the process of determining *hyperphases*. The whole partitioning of the overlap problem is now defined exclusively in terms of angles.

If m reflections overlap in a cluster, $m - 1$ pseudophases are considered. Permuted values belonging to the range $[0, \pi/2]$ are assigned to them. The phasing process aims to determine both the pseudophases and the conventional phases (this is known as hyperphases determination). Each possible choice of pseudophases and conventional phases defines a node in the MEM tree, subjected to constrained entropy maximization [see point (3)]. LLG analysis is performed in two steps by considering firstly the pseudophases and then the conventional phases. Statistical criteria are adopted for the selection of the pseudophases followed by the analysis of conventional phases.

4.2.8. Optimization of the structure model

In the case of powder data, the model derived from $\rho(\mathbf{r})$ calculated after the phasing process is often far from being a chemically reasonable one: some peaks are isolated, false peaks occur, some other positions are misplaced from the true ones, the chemical labels associated with peaks according to their intensities in the map may be roughly estimated, and atoms are missing. In serious cases the very approximate model cannot be refined by the Rietveld method (Rietveld, 1969; McCusker *et al.*, 1999) which, because of its modest convergence rate, needs a good starting model in order to provide a reliable refined structure. However, in many cases, despite the approximate starting point, the application of structure-optimization techniques leads to the correct model, or more generally to a reliable model appropriate for the final Rietveld refinement. Therefore, optimization of the model of the structure is sometimes a necessary step in the solution process (Altomare *et al.*, 2011*b*). We will now analyse the main tools for improving the model quality. Their efficiency often increases if they are suitably combined.

4.2.8.1. *Fourier recycling (FR)*

Starting from the available model supplied by RS methods, the structure factors $F_{\mathbf{h}c}$ can be calculated:

$$F_{\mathbf{h}_c} = \sum_{j=1}^{N} f_j^o \exp\left(-B_j \frac{\sin^2\theta_{\mathbf{h}}}{\lambda^2}\right) \exp(2\pi i \mathbf{h}\cdot\mathbf{r}_j) = |F_{\mathbf{h}}|_c \exp(i\varphi_{\mathbf{h}_c}), \tag{4.2.37}$$

where the overall isotropic displacement factor derived from the Wilson plot is associated with each atom. A Fourier synthesis is computed by using the $\varphi_{\mathbf{h}_c}$ phase values and the coefficients $|F_{\mathbf{h}}|_o$ (observed Fourier) or $(|F_{\mathbf{h}}|_o - |F_{\mathbf{h}}|_c)$ (difference Fourier) or $(2|F_{\mathbf{h}}|_o - |F_{\mathbf{h}}|_c)$ (summation of observed and difference Fouriers). The use of Fourier-map calculations is common and effective with single-crystal data for locating missing atoms (*e.g.*, the difference Fourier map is used for locating hydrogen atoms). A weighting scheme in the Fourier synthesis is usually used for two main reasons: minimizing the mean-square error in the electron density due to the errors in phases, and reducing the extent to which the electron-density map calculated using partial structure phases is biased towards the partial structure itself. In particular, Sim weights (Sim, 1960), which require that a well localized fraction of the structure is known, can also be applied when the number of missing atoms is not exactly determined (Altomare *et al.*, 2006).

In case of powders, we cannot expect the same behaviour because of the uncertainties in the $|F_{\mathbf{h}}|_o$ values. However, the Fourier-map techniques work quite well in many cases, especially if the following strategies are adopted:

1. $(2|F_{\mathbf{h}}|_o - |F_{\mathbf{h}}|_c)$ Fourier-map coefficients are used.
2. In order to improve the $|F_{\mathbf{h}}|_o$ estimates for overlapping reflections, the overall observed intensity of each cluster of overlapping reflections is partitioned in proportion to the calculated intensity of each reflection according to

   $$|F_{\mathbf{h}}|_n^2 = \frac{\sum_{\mathbf{k}} I_{\mathbf{k}o}}{\sum_{\mathbf{k}} I_{\mathbf{k}c}} |F_{\mathbf{h}}|_c^2, \tag{4.2.38}$$

   where $|F_{\mathbf{h}}|_n$ is the new modified $|F_{\mathbf{h}}|_o$, the summation is over the reflections belonging to the cluster, and $I_{\mathbf{k}o}$ and $I_{\mathbf{k}c}$ are the individual observed and calculated integrated intensities, respectively:

   $$I_{\mathbf{k}o} = m_{\mathbf{k}} LP_{\mathbf{k}} |F_{\mathbf{k}}|_o^2, \quad I_{\mathbf{k}c} = m_{\mathbf{k}} LP_{\mathbf{k}} |F_{\mathbf{k}}|_c^2, \tag{4.2.39}$$

   where $m_{\mathbf{k}}$ is the reflection multiplicity and $LP_{\mathbf{k}}$ is the Lorentz–polarization factor.
3. $|F_{\mathbf{h}}|_n$ is a better estimate of the partition than the original $|F_{\mathbf{h}}|_o$ value (although not much better if the model is very approximate), but it is biased by the current model and its use can sometimes prevent the complete recovery of the missing atoms.
4. The Fourier recycling technique is combined with weighted least-squares refinement (Altomare *et al.*, 2006) and with electron-density-map modification for resolution bias (Altomare, Cuocci, Giacovazzo, Kamel *et al.*, 2008; Altomare, Cuocci, Giacovazzo, Moliterni & Rizzi, 2008; Altomare, Cuocci *et al.*, 2009; Altomare *et al.*, 2010*a*,*b*).

4.2.8.2. *Weighted least-squares (WLSQ) refinement*

A least-squares refinement procedure using the integrated intensities can be used for refining an approximate structural model in order to make it more suitable for the final Rietveld refinement. It is based on the minimization of the residual

$$\sum_{\mathbf{h}} w_{\mathbf{h}}(I_{\mathbf{h}o} - I_{\mathbf{h}c})^2, \tag{4.2.40}$$

where the summation is over the number of reflections and $w_{\mathbf{h}}$ is a suitable weight, which is now described. It is important to realize that the optimization approach described here is preliminary, and not an alternative to the Rietveld method, which remains the most appropriate technique for refining a structural model from powder data. David (2004) has demonstrated a substantial equivalence between the results obtained from the Rietveld method and those from properly correlated integrated intensities extracted using the Pawley refinement (Pawley, 1981; Chapter 3.5). If the observed intensity estimates are reliable, the Rietveld method and the minimization procedure *via* (4.2.40) are comparable (Prince, 1981). Unfortunately, the $I_{\mathbf{h}o}$ values are not very well determined. This problem can be bypassed by using the overall intensities of clusters of overlapping reflections (in addition to the single intensities of non-overlapping reflections) in (4.2.40) instead of the individual observed intensities, because the cluster intensity is less affected by errors than the individual intensities within that cluster (Giacovazzo, 1998). This approach has the advantage that the observations are more reliable, but the disadvantage that the summation is over the number of overlapping clusters. This last number is smaller (sometimes much smaller, depending on the degree of overlap) than the number of reflections and, consequently, the ratio of the number of observations to the number of parameters for refinement decreases. The number of parameters to be refined is often large (*e.g.* when the crystallographic fractional coordinates and the isotropic displacement factors are varied). The use of the cluster intensity is more suitable for small structures.

If all the reflections are considered in (4.2.40), it is helpful to weight them in a suitable way. The following weighting scheme is able to take into account the lack of accuracy of the single reflection intensities (Altomare *et al.*, 2006):

$$w_{\mathbf{h}} = w_{1\mathbf{h}} w_{2\mathbf{h}}, \tag{4.2.41}$$

where

$$w_{1\mathbf{h}} = 1/[1 + 4(m_{\mathbf{h}} LP_{\mathbf{h}} |F_{\mathbf{h}}|_o)^2] \tag{4.2.42}$$

$$w_{2\mathbf{h}} = w_{a\mathbf{h}} w_{b\mathbf{h}} \tag{4.2.43}$$

$$w_{a\mathbf{h}} = \exp[-0.5(\sin\theta_{\mathbf{h}}/\lambda)^2] \tag{4.2.44}$$

$$w_{b\mathbf{h}} = (\mathrm{I}_{\mathbf{h}o}/\mathrm{I}'_{\mathbf{h}o})^{1/2} \tag{4.2.45}$$

$$I'_{\mathbf{h}o} = \sum_{\mathbf{k}} (1 - q^2_{\mathbf{kh}}) I_{\mathbf{k}o}, \tag{4.2.46}$$

where the summation is over the number of reflections $\mathbf{k}$ that overlap with $\mathbf{h}$ [see equation (4.2.25) for the numerical definition of overlap], including $\mathbf{h}$ itself:

$$q_{\mathbf{kh}} = |2\theta_{\mathbf{k}} - 2\theta_{\mathbf{h}}|/\mathrm{FWHM}_{\mathbf{h}}. \tag{4.2.47}$$

$w_{1\mathbf{h}}$ is used in order to avoid the least-squares calculation being dominated by the largest intensities. $w_{2\mathbf{h}}$ decreases with: (*a*) increasing $\theta_{\mathbf{h}}$ (it is more difficult to model overlaps and background in the high-angle regions of the experimental pattern), and (*b*) an increasing number of reflections overlapping with $\mathbf{h}$ ($I'_{\mathbf{h}o}$ increases, on average, when the number of overlapping reflections in a cluster increases). If the reflection is single, then $w_{2\mathbf{h}} = 1$, if it overlaps with other reflections the value of $w_{2\mathbf{h}}$ depends on the intensities of the neighbouring reflections: *i.e.*, if $I_{\mathbf{h}o}$ is large and the intensities of the reflections that overlap with $\mathbf{h}$, $I_{\mathbf{k}o}$, are small, then $w_{2\mathbf{h}} \simeq 1$; on the other hand $w_{2\mathbf{h}} \simeq 0$ if $I_{\mathbf{h}o}$ is small and the $I_{\mathbf{k}o}$ intensities are large.

The use of $w_{\mathbf{h}}$ in (4.2.40) is able to drive refinements towards an effective convergence. $w_{2\mathbf{h}}$ can also be used in (4.2.38) in order to reduce the model dependence on the data partition equation. Equation (4.2.38) is changed accordingly:

$$|F_{\mathbf{h}}|_n^2 = w_{2\mathbf{h}} |F_{\mathbf{h}}|_o^2 + \frac{\sum_{\mathbf{k}} (1 - w_{2\mathbf{k}}) I_{\mathbf{k}o}}{\sum_{\mathbf{k}} (1 - w_{2\mathbf{k}}) I_{\mathbf{k}c}} (1 - w_{2\mathbf{h}}) |F_{\mathbf{h}}|_c^2. \tag{4.2.48}$$

The partition in (4.2.48) is based on the following rationale: if $|F_{\mathbf{h}}|_o$ is well estimated (*i.e.*, $w_{2\mathbf{h}}$ is ~1), $|F_{\mathbf{h}}|_n$ differs only slightly from $|F_{\mathbf{h}}|_o$; on the contrary, if $w_{2\mathbf{h}} \simeq 0$, $|F_{\mathbf{h}}|_n$ is proportional to $|F_{\mathbf{h}}|_c$.

Cycles of least-squares minimization followed by $(2|F_{\mathbf{h}}|_o - |F_{\mathbf{h}}|_c)$ Fourier-map calculations are able to refine the current model towards the correct solution by discarding false positions and moving misplaced atoms towards their true positions (see the example in Section 4.2.9.4). A good strategy for balancing partition improvement and model dependence is to move from (4.2.48) to (4.2.38) ($w_{2\mathbf{h}} \simeq 0$) in the last cycles of the procedure, when the model is approaching the correct solution and the partitioning according to $|F_{\mathbf{h}}|_c$ is more effective.

4.2.8.3. *Resolution bias modification (RBM)*

After the phasing process, the electron-density map is obtained by Fourier synthesis. Ideally, this summation is over an infinite data set. In practice, the summation is finite because the measured experimental domain of the reciprocal space is finite. As a consequence, series-truncation errors can distort the map: negative values occur, peak intensities are distorted, peaks are broadened and surrounded by positive and negative ripples, and the combination of peaks and ripples moves peaks away from their true positions. Resolution bias effects, which are negligible at atomic resolution and critical when the resolution is >1 Å, are an additional source of error which combines with uncertainties in the intensities and phases.

The problem is particularly severe in case of organic compounds for which the data are usually far from atomic resolution. In fact, the rapid decay of the scattering factors of light atoms makes the high-2θ-angle region of the experimental pattern poorly informative. The resolution bias modification (RBM) method modifies the electron-density map in order to reduce the resolution bias effects and better locate peaks. This new approach works in direct space (Altomare, Cuocci, Giacovazzo, Kamel *et al.*, 2008; Altomare, Cuocci, Giacovazzo, Moliterni & Rizzi, 2008), reciprocal space (Altomare, Cuocci *et al.*, 2009) and with an appropriate combination of the two (Altomare *et al.*, 2010*a*). We will describe the *RBM* direct-space method. The procedure is based on two main steps:

(1) Determining a resolution bias correction function and applying it to the electron-density map (which we will call MAP). The correction function is evaluated as follows:
   (*a*) One single atom (*i.e.*, an atom belonging to the most frequent species in the unit cell) is located at the unit-cell origin and the displacement factor provided by the Wilson method is associated with it.

(*b*) The corresponding structure factors are calculated (up to the current resolution) and then used as coefficients in a Fourier synthesis.

(*c*) The resulting map consists of a main peak domain (MD) and a ripples domain (RD).

(*d*) The intensities $I_{\rm RD}$ of pixels belonging to the RD are normalized to $I_{\rm RDN}$ values in order to avoid dependence on chemical species:

$$I_{\rm RDN} = I_{\rm RD}/I_{\rm MD0},$$

where $I_{\rm MD0}$ is the maximum intensity of the main peak.

(*e*) For each peak in the electron-density map MAP, $I_{\rm RDN}$ is multiplied by the maximum value of the peak and then subtracted from the intensities of pixels not belonging to the main peak domain.

(2) Each main peak is described by the best-fit Gaussian function.

The new modified map, consisting of a summation of Gaussian-like peaks, has improved features: it is well resolved with better positioned peaks and reduced ripple contributions.

RBM, combined with the WLSQ-FR procedure, is able to optimize partial and poor models even at resolutions >1 Å (see the example in Section 4.2.9.5). The RBM strategy strongly increases the probability of a successful solution of organic compounds by RS methods.

More recently, the COVMAP approach has been proposed (Altomare *et al.*, 2012*a*) for completing and adjusting an approximate structure model. It was inspired by a mathematical technique for the evaluation of the covariance and/or the correlation between two points of an electron-density map (Altomare *et al.*, 2012*b*). COVMAP modifies the electron-density map corresponding to the imperfect model by considering some basic connectivity rules in order to pick up the missing atomic positions. Combined with RBM and WLSQ-FR procedures, it is able to provide the correct solution even when starting from a very rough model with few well-located atom positions and a large number of misplaced ones. These results encouraged the authors to propose the RAMM method (Altomare, Cuocci, Moliterni & Rizzi, 2013), which skips the phasing process by direct methods and starts from a fully random structure model. Cycles of combined RBM–COVMAP–WLSQ-FR procedures drive the random model to the correct solution. The RAMM method opens the way for a new RS solution approach, which avoids the direct phasing step and has a central role in structure-model optimization tools working in reciprocal and direct space.

4.2.9. Software packages for powder solution

One of the reasons for the increasing interest and progress in solving crystal structures from powder-diffraction data is the availability of sophisticated software packages in which constantly evolving theories are implemented. Computer programs based on RS methods include:

(1) *POWSIM* (Peschar *et al.*, 2002), which is a traditional DM package, properly modified for treating overlapping reflections.

(2) *XLENS* (Rius, 2013) uses the S-FFT phasing procedure (Rius *et al.*, 2007; Rius & Frontera, 2007). This has been recently optimized by an innovative Patterson-function DM approach (Rius, 2011) and is able to solve powder structures from good-quality diffraction patterns.

(3) *MICE* (Gilmore & Bricogne, 1997; Gilmore & Nicholson, 1994) is a maximum-entropy likelihood program, strengthened by the use of error-correcting codes for phase permutation (Gilmore *et al.*, 1999), and is able to solve structures resistant to traditional DM.

(4) *SUPERFLIP* (Palatinus & Chapuis, 2007) is able to solve crystal structures (including aperiodic structures, incommensurately modulated structures and quasicrystals from X-ray and neutron diffraction data) by application of the charge-flipping algorithm. Structure solution from powder-diffraction data is supported by combining the methodology with a histogram-matching procedure.

(5) *EXPO* (Altomare, Camalli *et al.*, 2009; Altomare, Cuocci, Giacovazzo *et al.*, 2013) is a software package for solving structures by DM. In addition, *EXPO* is uniquely able to carry out the complete structure-solution process: indexing, determination of the space group, *ab initio* structure solution or, alternatively, solving the structure by direct-space techniques, and finally refining by the Rietveld method.

The remainder of this section will focus on examples using *XLENS*, *SUPERFLIP* and *EXPO*. Extensive and detailed descriptions are given for the examples using *EXPO*. Full details on the use of the software can be found in the *EXPO* manual.

4.2.9.1. *Example of structure solution by XLENS*

The Patterson-function DM approach implemented in the *XLENS* program (Rius, 2013) was successfully applied to the crystal structure of (*S*)-(+)-ibuprofen (Freer *et al.*, 1993; Rius, 2011) (see Fig. 4.2.2). It consists of two symmetry-independent molecules in the asymmetric unit forming a cyclic hydrogen-bonded dimer with the chemical formula $C_{26}H_{16}O_4$. The structure is monoclinic (a = 12.4627, b = 8.0251, c = 13.5293 Å, β = 112.9509°) with space group $P2_1$, $2\theta_{\max} \simeq 54^\circ$, 1009 reflections, with a resolution of 1.10 Å. Data were collected at the Swiss Light Source using the Mythen-II microstrip one-dimensional detector at λ = 1.00097 (3) Å. There are 26 C and 4 O atoms in the asymmetric unit.

XLENS processed the integrated intensities, estimated by the program *DAJUST* (Vallcorba *et al.*, 2012) *via* whole-pattern least-squares refinement, and provided atomic distances accurate enough to enable the molecule to be identified in Fourier maps. Twenty-five different trials were attempted, of which 7 were

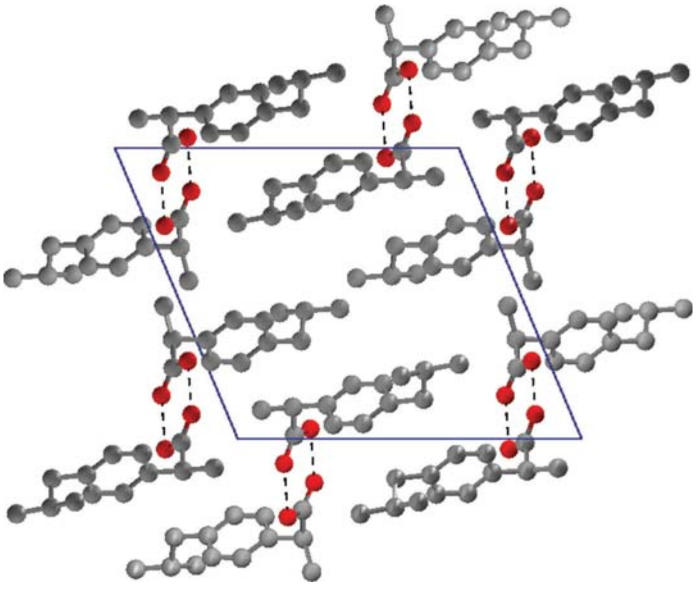

Figure 4.2.2
Crystal structure of (*S*)-(+)-ibuprofen solved by *XLENS*.

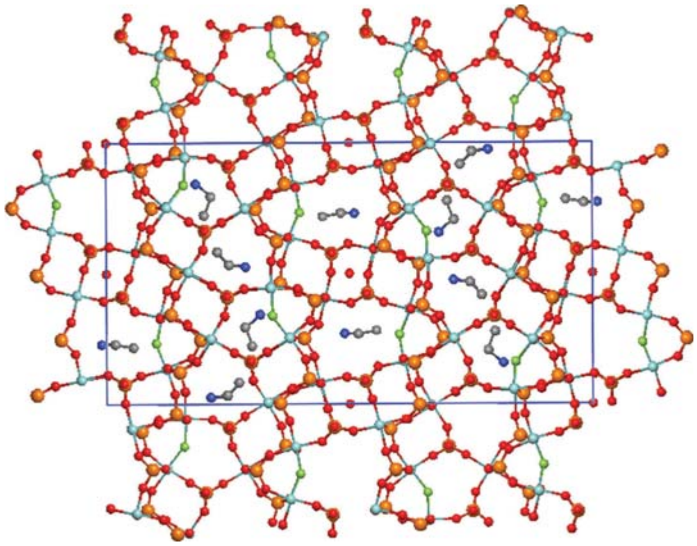

Figure 4.2.3
Crystal structure of the zeolite ZrPOF-EA solved by *SUPERFLIP*.

successful. All correct solutions led to the complete structural model.

4.2.9.2. *Example of structure solution by SUPERFLIP*

As an example of structure solution by the powder charge-flipping (pCF) algorithm (Oszlányi & Sütő, 2004; Baerlocher *et al.*, 2007) as implemented in the program *SUPERFLIP*, we consider the open-framework zirconium phosphate, $[(C_2H_7NH)_8(H_2O)_8][Zr_{32}P_{48}O_{176}F_8(OH)_{16}]$ (denoted ZrPOF-EA). Details of the experimental conditions and crystallographic information are given by Liu *et al.* (2011): orthorhombic (a = 6.165, b = 19.955, c = 37.062 Å), space group *Pbam*, 2θ experimental range 2–40°, with 6681 reflections measured to a resolution of 0.73 Å. The data were collected on the Swiss–Norwegian Beam line at the ESRF in Grenoble, France with λ = 0.50095 Å. There are 8 Zr, 12 P, 2F, 3N, 6 C and 42 O atoms in the asymmetric unit (some of them on special positions and/or with fractional occupancy).

Zirconium phosphate materials have been extensively investigated because they have important applications in the fields of ion exchange, catalysis, photochemistry and biotechnology. The structure of ZrPOF-EA is complicated (see Fig. 4.2.3): there are 3-, 4-, 5-, 6-, 7-, and 8-ring units in the structure, and these form small one-dimensional channels parallel to the c (7-ring) and a (8-ring) axes. Open-framework structures with 7- and 8-ring channels appear to be relatively rare.

The pattern was decomposed into single integrated intensities assuming first the space group $Pmc2_1$ and then the pCF algorithm in *SUPERFLIP* was applied. The interpretation of the resulting electron-density map yielded the positions of 16 zirconium, 23 phosphorus and 55 oxygen atoms. This model, with the missing bridging oxygen atoms inserted, was subjected to Rietveld refinement using the program *XRS-82* (Baerlocher, 1982).

A series of difference-electron-density maps led to the location of the missing P atom, the terminal O atoms and the non-framework species. Atoms bridging between two Zr atoms were assigned as F. The refinement was completed in the space group *Pbam*.

4.2.9.3. *The input file for a default run of EXPO*

To run *EXPO*, an input file containing minimal crystallographic information must be prepared. A typical example is shown in Fig. 4.2.4 for the solution of the structure of clomipramine hydrochloride, $C_{19}H_{23}ClN_2{\cdot}HCl$ (Florence *et al.*, 2005). The input file name is `clomipramine.exp`; `.exp` represents the default extension of the *EXPO* input file, which is an ASCII file created by the user by using the *EXPO* graphical interface or *via* a standard editor. The input file contains *commands*, which are identified by the % character preceding the command name, and *directives*, which are used as subcommands with no special character preceding them. Looking at the `clomipramine.exp` file, we have:

```
%structure clomipramine
%job laboratory X-ray data
%data
pattern clomipramine.xy
wavelength 1.54056
cell 15.514 8.610 14.035 90 96.93 90
spacegroup P 21/c
content (C19H23ClN2·HCl)4
%continue
```

Figure 4.2.4
Default input file for *EXPO* for the structure of clomipramine.

The command `%structure` followed by *name* (clomipramine), which specifies the output file names, where the program stores its main results.

The command `%job` is an optional character string to specify the job title.

The command `%data` is the most important one and contains the directives that provide the required minimal information for *EXPO*:

(1) The directive `pattern` is followed by the name of the file containing the observed diffraction pattern; different file formats are allowed. In case of clomipramine, the profile file is an ASCII text file containing values of 2θ and intensities in separate columns;
(2) The directive `wavelength` specifies the wavelength used in ångstroms. Laboratory X-ray data are the default choice, as in case of clomipramine; if synchrotron or neutron data are used, an additional directive `synchrotron` or `neutron` has to be introduced, respectively;
(3) The directives `cell` and `spacegroup` provide the obvious information. Because *EXPO* is able to determine the cell parameters and the space group, these directives can contain the information derived by *EXPO*;
(4) The directive `content` gives the atomic content of the unit cell.

The last command, `%continue`, allows the program to continue in a default way through the *ab initio* structure-solution process, performing in sequence normalization, structure-invariant estimation, the phasing process, E-map calculation and optimization of the structure model.

4.2.9.4. *An example of model optimization by EXPO for an inorganic compound*

In the case of heavy-atom inorganic structures, RS methods are usually able to locate the heavy atoms quite well, but the positions of the light atoms are more difficult to find. Some light atoms are often missing or misplaced from their true positions. The use of difference Fourier maps may be convenient, but is often insufficient to provide the complete model. We consider here the example of chromium chromate tetrachromate, Cr_8O_{21} (Norby *et al.*, 1991). The relevant data are: triclinic (a = 5.433, b =

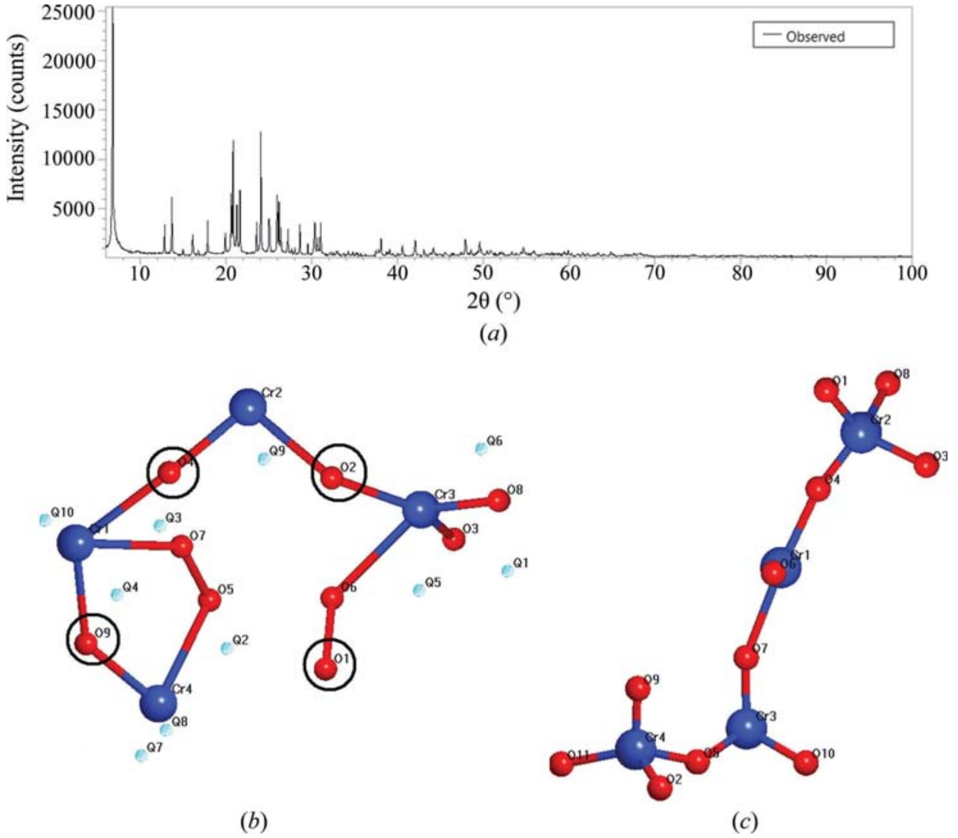

Figure 4.2.5

Structure solution for chromium chromate tetrachromate, Cr_8O_{21}: (*a*) the powder pattern; (*b*) the DM structure model; (*c*) the model optimized by the automatic *EXPO* WLSQ-FR procedure.

6.557, c = 12.117 Å, α = 106.36, β = 95.73, γ = 77.96°), $P\bar{1}$, 2θ experimental range 6–100°, 1130 reflections, resolution 0.91 Å; good-quality laboratory X-ray data (λ = 1.39222 Å); 39% of independent observations in the pattern calculated using the algorithm of Altomare *et al.* (1995); 4 Cr and 11 O atoms in the asymmetric unit. Starting *EXPO* with the experimental pattern (shown in Fig. 4.2.5*a*), the cell parameters, the space group and the unit-cell content information, DM are able to phase the structure. The solution with the first ranked CFOM phases the 293 largest reflections with a 9.8° average phase error. The DM Fourier map supplies the structure model for the asymmetric unit shown in Fig. 4.2.5(*b*), where, in addition to positions labelled as chromium (blue) and oxygen (red), those labelled Q (light blue) correspond to ghost atoms whose intensities in the electron-density map do not allow reasonable chemical label assignment. The structure appears not to be completely solved. In fact, a comparison with the true model indicates that, neglecting the 10 uninterpretable Q peaks, the 4 Cr peaks are all well positioned. However, only 4 of the 9 O peaks (circled in Fig. 4.2.5*b*) are reasonably located, with distances from the true positions less than 0.6 Å. The WLSQ-FR procedure described in Section 4.2.8.2 and implemented in *EXPO* for the automatic solution of inorganic structures is successful in this case: its application provides the model shown in Fig. 4.2.5(*c*) corresponding to the complete structure with an average distance of Cr and O peaks from the true atom positions of 0.16 Å.

It is worth highlighting that the Cr atoms are polyhedrally coordinated: Cr1 is octahedrally coordinated, and Cr2, Cr3 and Cr4 are tetrahedrally coordinated. If the polyhedral coordination information is available *a priori*, the POLPO method (Altomare *et al.*, 2000; Giacovazzo *et al.*, 2002) can be used as an alternative to the WLSQ-FR procedure for completing the model. The POLPO method is a hybrid approach – a reciprocal- and direct-space method, which exploits the DM solution and requires additional information (the polyhedral coordination type and expected atom–atom distances). It starts only with the reliable cation positions obtained by DM and generates several complete structure models according to a Monte Carlo scheme, all of which are compatible with the available polyhedral information. The model corresponding to the best figure of merit (the agreement between the observed and calculated diffraction profile is calculated here) is then selected. POLPO is able to successfully solve the Cr_8O_{21} structure by starting only from the four Cr positions of Fig. 4.2.5(*b*).

4.2.9.5. *Example of model optimization by EXPO for an organic compound*

As previously discussed, organic structures are usually resistant to attempts at solution by RS methods. In the case of organic compounds, *EXPO* automatically applies the RBM procedure to correct the electron-density map. We now examine the *EXPO ab initio* solution of clomipramine hydrochloride, $C_{19}H_{23}ClN_2{\cdot}HCl$ (Florence *et al.*, 2005), the input file for which is described in Section 4.2.9.3. Details are: monoclinic, $P2_1/c$ (a = 15.514, b = 8.610, c = 14.035 Å, β = 96.93°), 2θ experimental range 5–65°, 659 reflections, data resolution 1.43 Å, medium-quality laboratory X-ray data (λ = 1.5456 Å; see Fig. 4.2.6*a*), 43% of independent observations in the pattern (Altomare *et al.*, 1995), 2 Cl, 2 N and 19 C atoms in the asymmetric unit. The complete solution was not obtained in the first phasing set (ranked according to CFOM). The second set, however, provides the full model. An *a posteriori* analysis revealed that 209 reflections were phased with an average phase error of 29° in the first set, while 189 reflections were phased with an average phase error of 23° in the second set. It is very interesting to evaluate how the RBM optimization

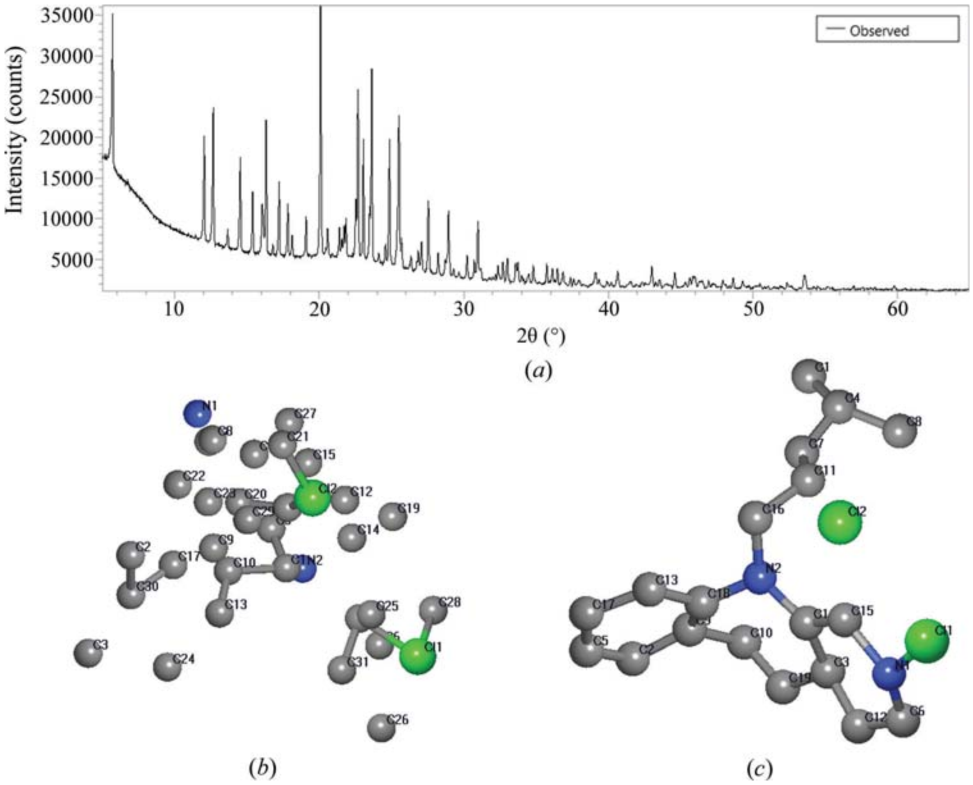

Figure 4.2.6
Structure solution for clomipramine hydrochloride, $C_{19}H_{23}ClN_2{\cdot}HCl$: (*a*) the powder pattern; (*b*) the DM structure model; (*c*) the model optimized by the automatic *EXPO* RBM procedure.

procedure worked: the DM Fourier map (*E*-map) is shown in Fig. 4.2.6(*b*) and the final model generated by RBM is shown in Fig. 4.2.6(*c*). The results are surprising:

(1) The uninterpretable model of Fig. 4.2.6(*b*) consists of 2 Cl, 2 N and 31 C peaks. (The number of peaks taken from the Fourier map is usually larger than the expected number of atoms in the asymmetric unit.) Only the 2 Cl peaks and 9 C peaks are close to the true positions at distances less than 0.6 Å. The average distance from the true coordinates is 0.33 Å and one of the quite well located C atoms has been labelled as N.

(2) The model of Fig. 4.2.6(*c*) is much improved and provides the solution. The incorrect assignments of atom type for C4 and N1 can be immediately corrected by using the user-friendly

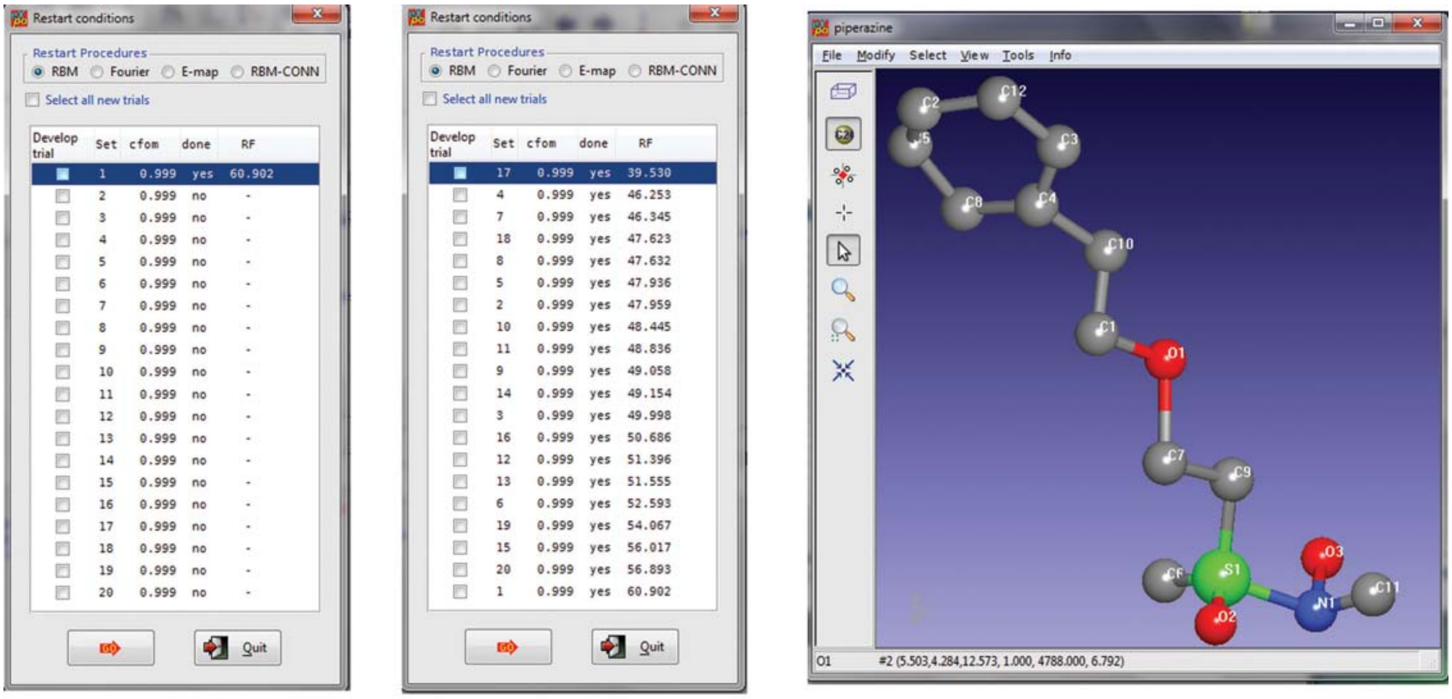
Restart conditions
Restart Procedures
● RBM ○ Fourier ○ E-map ○ RBM-CONN
☐ Select all new trials
GO
Quit
Restart conditions
Restart Procedures
● RBM ○ Fourier ○ E-map ○ RBM-CONN
☐ Select all new trials
GO
Quit
piperazine
File Modify Select View Tools Info
C2
C12
C5
C3
C8
C4
C10
C1
O1
C7
C9
O3
C6
S1
N1
C11
O2

Develop trial	Set	cfom	done	RF
☐	1	0.999	yes	60.902
☐	2	0.999	no	-
☐	3	0.999	no	-
☐	4	0.999	no	-
☐	5	0.999	no	-
☐	6	0.999	no	-
☐	7	0.999	no	-
☐	8	0.999	no	-
☐	9	0.999	no	-
☐	10	0.999	no	-
☐	11	0.999	no	-
☐	12	0.999	no	-
☐	13	0.999	no	-
☐	14	0.999	no	-
☐	15	0.999	no	-
☐	16	0.999	no	-
☐	17	0.999	no	-
☐	18	0.999	no	-
☐	19	0.999	no	-
☐	20	0.999	no	-

Develop trial	Set	cfom	done	RF
☐	17	0.999	yes	39.530
☐	4	0.999	yes	46.253
☐	7	0.999	yes	46.345
☐	18	0.999	yes	47.623
☐	8	0.999	yes	47.632
☐	5	0.999	yes	47.936
☐	2	0.999	yes	47.959
☐	10	0.999	yes	48.445
☐	11	0.999	yes	48.836
☐	9	0.999	yes	49.058
☐	14	0.999	yes	49.154
☐	3	0.999	yes	49.998
☐	16	0.999	yes	50.686
☐	12	0.999	yes	51.396
☐	13	0.999	yes	51.555
☐	6	0.999	yes	52.593
☐	19	0.999	yes	54.067
☐	15	0.999	yes	56.017
☐	20	0.999	yes	56.893
☐	1	0.999	yes	60.902

O1 #2 (5.503,4.284,12.573, 1.000, 4788.000, 6.792)

(*a*) (*b*) (*c*)

Figure 4.2.7
The ALLTRIALS procedure in *EXPO* for solving 1,4-bis-(2-phenethyloxy-ethanesulfonyl)-piperazine, $C_{24}H_{34}N_2O_6S_2$: (*a*) the phasing sets ranked according to CFOM; (*b*) the phasing sets ranked according to R_F; (*c*) the correct solution is automatically detected as set No. 17.

graphical tools of *EXPO*. The correct structure is suitable for Rietveld refinement.

4.2.9.6. *The ALLTRIALS tool in EXPO: exploring all the phase sets*

Once the data decomposition process has been carried out, the DM phasing process generates several trials which are ranked according to the combined figure of merit CFOM. The first 20 phasing trials are retained by *EXPO*; the one corresponding to the best CFOM is considered the most promising and the corresponding structure model is automatically submitted to the next optimization procedure. However, ranking the possible trials by CFOM quite often fails to find a solution in the case of powder-diffraction data, so all the available phasing sets have to be explored. The ALLTRIALS tool in *EXPO* does this automatically. For each of the 20 top-ranked trials by CFOM it carries out the solution process up to the final structure model, optimized according to the procedures described above, and shows the results graphically. For each final model, a reliability factor R_F is calculated, where

$$R_F = \frac{\sum \left| |F_{\mathbf{h}}|_o - |F_{\mathbf{h}}|_c \right|}{\sum |F_{\mathbf{h}}|_o}. \tag{4.2.49}$$

The model corresponding to the smallest R_F is automatically selected and displayed. As an example of an application of ALLTRIALS, the case of the 1,4-bis-(2-phenethyloxy-ethanesulfonyl)-piperazine $C_{24}H_{34}N_2O_6S_2$ structure (Florence *et al.*, 2005) is shown in Fig. 4.2.7. Details are: monoclinic, $P2_1/a$ (a = 13.442, b = 5.182, c = 19.796 Å, β = 108.74°) 2θ experimental range 4–65°, 464 reflections, with a resolution of 1.4 Å; medium-quality laboratory X-ray data (λ = 1.54056 Å); 48% of independent observations in the pattern (Altomare *et al.*, 1995); 1 S, 1 N, 3 O and 12 C atoms in the asymmetric unit. Fig. 4.2.7 shows the graphical display that supports the use of ALLTRIALS. In Fig. 4.2.7(*a*) the 20 stored sets of phases are listed and ranked according to CFOM; in this case, CFOM does not discriminate well between them, as none of the sets are significantly different from the best statistically expected value of unity. The top-ranked set of phases, which is automatically selected by the program to calculate the trial electron-density map, is not able to give the correct solution, so the use of CFOM alone has failed. Therefore, all the 20 phasing trials are processed and the solution process is carried out for each of them. *EXPO* automatically displays the view shown in Fig. 4.2.7(*b*), in which the sets are now ranked according to R_F. The lowest R_F trial here was ranked 17th by CFOM in Fig. 4.2.7(*a*). The corresponding complete structure solution is shown in Fig. 4.2.7(*c*). The wrong chemical assignments for O3 and C6 can be easily recognized and corrected using graphical options in *EXPO*. The structure models corresponding to the other phasing sets can be checked, and it can be verified that the best solution corresponds to the model shown in Fig. 4.2.7(*c*).

4.2.9.7. *Graphical tools in EXPO*

A user-friendly graphical interface supports all the principal procedures of the *EXPO* program, and can be used to visualize and to check the various steps of the solution process and to modify the default choices performed by the program. Some graphical tools are particularly useful for completing and validating the final model supplied by the program:

(1) Displaying crystal packing.
(2) Locating hydrogen atoms (these are ignored in the structure-solution process): *EXPO* can use geometrical criteria to add hydrogen atoms to the final structural model in an automatic way or by selecting the carbon type (tertiary C—H, secondary CH_2, primary CH_3, ethylenic $=CH_2$, acetylenic $\equiv CH$, aromatic C—H).
(3) Searching for hydrogen bonds and short non-bonded contacts: these are particularly useful for validating organic structures, and can be automatically found and displayed.
(4) Building coordination polyhedra: if polyhedrally coordinated atoms are present in the structure, the polyhedra can be automatically built and their drawing options modified.

4.2.10. Conclusions

RS methods, the best choice for the solution of small- and medium-sized crystal structures from single-crystal diffraction data, can be modified to solve structures from powder data as well. In particular, the phasing process and procedures for optimization of the structural model are key in dealing with the problems arising from peak overlap. RS methods also have the great advantage of requiring little starting information: the experimental pattern, the cell parameters, the space group and the chemical formula. They do not need a structural model. Their dependence on the quality of experimental pattern, in particular on the peak resolution, is a serious limitation, which can be overcome in many cases. Of course, the use of synchrotron radiation is always advantageous and is preferable. Progress to date enables us to state that, in general, medium-quality conventional laboratory diffractometer X-ray data with a resolution better than 1.4 Å can be successfully used for solving inorganic as well organic compounds by RS methods. Structures with around 30 non-hydrogen atoms in the asymmetric unit can be solved *ab initio*. The development of new sophisticated methodologies and software packages is ongoing.

References

Altomare, A., Burla, M. C., Cascarano, G., Giacovazzo, C., Guagliardi, A., Moliterni, A. G. G. & Polidori, G. (1996). *Early finding of preferred orientation: applications to direct methods. J. Appl. Cryst.* **29**, 341–345.

Altomare, A., Caliandro, R., Cuocci, C., da Silva, I., Giacovazzo, C., Moliterni, A. G. G. & Rizzi, R. (2004). *The use of error-correcting codes for the decomposition of a powder diffraction pattern. J. Appl. Cryst.* **37**, 204–209.

Altomare, A., Caliandro, R., Cuocci, C., Giacovazzo, C., Moliterni, A. G. G. & Rizzi, R. (2003). *A systematic procedure for the decomposition of a powder diffraction pattern. J. Appl. Cryst.* **36**, 906–913.

Altomare, A., Camalli, M., Cuocci, C., Giacovazzo, C., Moliterni, A. & Rizzi, R. (2009). *EXPO2009: structure solution by powder data in direct and reciprocal space. J. Appl. Cryst.* **42**, 1197–1202.

Altomare, A., Cascarano, G., Giacovazzo, C. & Guagliardi, A. (1994). *Early finding of preferred orientation: a new method. J. Appl. Cryst.* **27**, 1045–1050.

Altomare, A., Cascarano, G., Giacovazzo, C., Guagliardi, A., Moliterni, A. G. G., Burla, M. C. & Polidori, G. (1995). *On the number of statistically independent observations in a powder diffraction pattern. J. Appl. Cryst.* **28**, 738–744.

Altomare, A., Cuocci, C., Giacovazzo, C., Kamel, G. S., Moliterni, A. & Rizzi, R. (2008). *Minimally resolution biased electron-density maps. Acta Cryst.* A**64**, 326–336.

Altomare, A., Cuocci, C., Giacovazzo, C., Maggi, S., Moliterni, A. & Rizzi, R. (2009). *Correcting electron-density resolution bias in reciprocal space. Acta Cryst.* A**65**, 183–189.

Altomare, A., Cuocci, C., Giacovazzo, C., Moliterni, A. G. G. & Rizzi, R. (2006). *Powder diffraction: the new automatic least-squares Fourier recycling procedure in EXPO2005*. *J. Appl. Cryst.* **39**, 558–562.

Altomare, A., Cuocci, C., Giacovazzo, C., Moliterni, A. & Rizzi, R. (2008). *Correcting resolution bias in electron density maps of organic molecules derived by direct methods from powder data*. *J. Appl. Cryst.* **41**, 592–599.

Altomare, A., Cuocci, C., Giacovazzo, C., Moliterni, A. & Rizzi, R. (2010*a*). *The dual-space resolution bias correction algorithm: applications to powder data*. *J. Appl. Cryst.* **43**, 798–804.

Altomare, A., Cuocci, C., Giacovazzo, C., Moliterni, A. & Rizzi, R. (2010*b*). *The dual-space resolution bias correction in EXPO2010*. *Z. Kristallogr.* **225**, 548–551.

Altomare, A., Cuocci, C., Giacovazzo, C., Moliterni, A. & Rizzi, R. (2011*a*). *Advances in the EXPO2009 systematic decomposition procedure: an atom-matching-based figure of merit*. *J. Appl. Cryst.* **44**, 448–453.

Altomare, A., Cuocci, C., Giacovazzo, C., Moliterni, A. & Rizzi, R. (2011*b*). *Obtaining models suitable for Rietveld refinement: the EXPO2011 techniques*. *Z. Krystallogr.* **226**, 869–881.

Altomare, A., Cuocci, C., Giacovazzo, C., Moliterni, A. & Rizzi, R. (2012*a*). *COVMAP: a new algorithm for structure model optimization in the EXPO package*. *J. Appl. Cryst.* **45**, 789–797.

Altomare, A., Cuocci, C., Giacovazzo, C., Moliterni, A. & Rizzi, R. (2012*b*). *Covariance and correlation estimation in electron-density maps*. *Acta Cryst.* A**68**, 244–255.

Altomare, A., Cuocci, C., Giacovazzo, C., Moliterni, A., Rizzi, R., Corriero, N. & Falcicchio, A. (2013). *EXPO2013: a kit of tools for phasing crystal structures from powder data*. *J. Appl. Cryst.* **46**, 1231–1235.

Altomare, A., Cuocci, C., Moliterni, A. & Rizzi, R. (2013). *RAMM: a new random-model-based method for solving ab initio crystal structures using the EXPO package*. *J. Appl. Cryst.* **46**, 476–482.

Altomare, A., Foadi, J., Giacovazzo, C., Guagliardi, A. & Moliterni, A. G. G. (1996). *Solving crystal structures from powder data. II. Pseudotranslational symmetry and powder-pattern decomposition*. *J. Appl. Cryst.* **29**, 674–681.

Altomare, A., Foadi, J., Giacovazzo, C., Moliterni, A. G. G., Burla, M. C. & Polidori, G. (1998). *Solving crystal structures from powder data. IV. The use of the Patterson information for estimating the |F|'s*. *J. Appl. Cryst.* **31**, 74–77.

Altomare, A., Giacovazzo, C., Guagliardi, A. & Moliterni, A. G. G. (1998). *Solving crystal structures from powder data: the use of a molecular fragment*. *Mater. Sci. Forum*, **278–281**, 289–293.

Altomare, A., Giacovazzo, C., Guagliardi, A., Moliterni, A. G. G. & Rizzi, R. (2000). *Completion of crystal structures from powder data: the use of the coordination polyhedra*. *J. Appl. Cryst.* **33**, 1305–1310.

Baerlocher, Ch. (1982). *The X-ray Rietveld System (XRS-82)*, Laboratory of Crystallography, ETH Zurich.

Baerlocher, C., McCusker, L. B. & Palatinus, L. (2007). *Charge flipping combined with histogram matching to solve complex crystal structures from powder diffraction data*. *Z. Krystallogr.* **222**, 47–53.

Baerlocher, C., McCusker, L. B., Prokic, S. & Wessel, T. (2004). *Exploiting texture to estimate the relative intensities of overlapping reflections*. *Z. Kristallogr.* **219**, 803–812.

Bauschke, H. H., Combettes, P. L. & Luke, D. R. (2002). *Phase retrieval, error reduction algorithm, and Fienup variants: a view from convex optimization*. *J. Opt. Soc. Am. A*, **19**, 1334–1335.

Bauschke, H. H., Combettes, P. L. & Luke, D. R. (2004). *Finding best approximation pairs relative to two closed convex sets in Hilbert spaces*. *J. Approx. Theory*, **127**, 178–192.

Bricogne, G. (1984). *Maximum entropy and the foundations of direct methods*. *Acta Cryst.* A**40**, 410–445.

Bricogne, G. (1991). *A multisolution method of phase determination by combined maximization of entropy and likelihood. III. Extension to powder diffraction data*. *Acta Cryst.* A**47**, 803–829.

Bricogne, G. & Gilmore, C. J. (1990). *A multisolution method of phase determination by combined maximization of entropy and likelihood. I. Theory, algorithms and strategy*. *Acta Cryst.* A**46**, 284–297.

Buerger, M. J. (1956). *Partial Fourier syntheses and their application to the solution of certain crystal structures*. *Proc. Natl Acad. Sci. USA*, **42**, 776–781.

Buerger, M. J. (1959). *Vector Space*. New York: Wiley.

Bunge, H. J., Dahms, M. & Brokmeier, H. G. (1989). *The determination of integrated intensities from polycrystalline samples with preferred orientation*. *Crystallogr. Rev.* **2**, 67–86.

Burla, M. C., Caliandro, R., Carrozzini, B., Cascarano, G. L., De Caro, L., Giacovazzo, C., Polidori, G. & Siliqi, D. (2007). *The revenge of the Patterson methods. III. Ab initio phasing from powder diffraction data*. *J. Appl. Cryst.* **40**, 834–840.

Carrozzini, B., Giacovazzo, C., Guagliardi, A., Rizzi, R., Burla, M. C. & Polidori, G. (1997). *Solving crystal structures from powder data. III. The use of the probability distributions for estimating the |F|'s*. *J. Appl. Cryst.* **30**, 92–97.

Cascarano, G., Giacovazzo, C., Camalli, M., Spagna, R., Burla, M. C., Nunzi, A. & Polidori, G. (1984). *The method of representations of structure seminvariants. The strengthening of triplet relationships*. *Acta Cryst.* A**40**, 278–283.

Cascarano, G., Giacovazzo, C. & Guagliardi, A. (1992). *Improved figures of merit for direct methods*. *Acta Cryst.* A**48**, 859–865.

Cascarano, G., Giacovazzo, C. & Luic, M. (1985). *Direct methods and superstructures. I. Effects of the pseudotranslations on the reciprocal space*. *Acta Cryst.* A**41**, 544–551.

Cascarano, G., Giacovazzo, C. & Viterbo, D. (1987). *Figures of merit in direct methods: a new point of view*. *Acta Cryst.* A**43**, 22–29.

Cochran, W. (1952). *A relation between the signs of structure factors*. *Acta Cryst.* **5**, 65–67.

Cochran, W. (1955). *Relations between the phases of structure factors*. *Acta Cryst.* **8**, 473–478.

Cochran, W. & Douglas, S. (1957). *The use of a high-speed digital computer for the direct determination of crystal structures. II*. *Proc. R. Soc. Lond. Ser. A*, **243**, 281–288.

Coelho, A. A. (2007). *A charge-flipping algorithm incorporating the tangent formula for solving difficult structures*. *Acta Cryst.* A**63**, 400–406.

David, W. I. F. (1987). *The probabilistic determination of intensities of completely overlapping reflections in powder diffraction patterns*. *J. Appl. Cryst.* **20**, 316–319.

David, W. I. F. (1999). *On the number of independent reflections in a powder diffraction pattern*. *J. Appl. Cryst.* **32**, 654–663.

David, W. I. F. (2004). *On the equivalence of the Rietveld method and the correlated integrated intensities method in powder diffraction*. *J. Appl. Cryst.* **37**, 621–628.

David, W. I. F., Shankland, K., McCusker, L. B. & Baerlocher, Ch. (2002). Editors. *Structure Determination from Powder Diffraction Data*. Oxford University Press.

Declercq, J. P., Germain, G. & Woolfson, M. M. (1979). *On the application of phase relationships to complex structures. XVII. When MULTAN fails*. *Acta Cryst.* A**35**, 622–626.

Dollase, W. A. (1986). *Correction of intensities for preferred orientation in powder diffractometry: application of the March model*. *J. Appl. Cryst.* **19**, 267–272.

Dong, W. & Gilmore, C. J. (1998). *The ab initio solution of structures from powder diffraction data: the use of maximum entropy and likelihood to determine the relative amplitudes of overlapped reflections using the pseudophase concept*. *Acta Cryst.* A**54**, 438–446.

Estermann, M. A. & David, W. I. F. (2002). *Patterson methods in powder diffraction: maximum entropy and symmetry minimum function techniques*. In *Structure Determination from Powder Diffraction Data*, edited by W. I. F. David, K. Shankland, L. B. McCusker & Ch. Baerlocher, pp. 202–218. Oxford University Press.

Estermann, M. A. & Gramlich, V. (1993). *Improved treatment of severely or exactly overlapping Bragg reflections for the application of direct methods to powder data*. *J. Appl. Cryst.* **26**, 396–404.

Estermann, M. A., McCusker, L. B. & Baerlocher, C. (1992). *Ab initio structure determination from severely overlapping powder diffraction data*. *J. Appl. Cryst.* **25**, 539–543.

Fernandes, P. (2006). *Advanced strategies for determining organic crystal structures from powder diffraction data.* PhD thesis, University of Strathclyde, Glasgow, Scotland.

Florence, A. J., Shankland, N., Shankland, K., David, W. I. F., Pidcock, E., Xu, X., Johnston, A., Kennedy, A. R., Cox, P. J., Evans, J. S. O., Steele, G., Cosgrove, S. D. & Frampton, C. S. (2005). *Solving molecular crystal structures from laboratory X-ray powder diffraction data with DASH: the state of the art and challenges*. *J. Appl. Cryst.* **38**, 249–259.

Freer, A. A., Bunyan, J. M., Shankland, N. & Sheen, D. B. (1993). *Structure of (S)-(+)-ibuprofen*. *Acta Cryst.* C**49**, 1378–1380.

Germain, G., Main, P. & Woolfson, M. M. (1970). *On the application of phase relationships to complex structures. II. Getting a good start*. *Acta Cryst.* B**26**, 274–285.

Giacovazzo, C. (1977). *A general approach to phase relationships: the method of representations*. *Acta Cryst.* A**33**, 933–944.

Giacovazzo, C. (1980). *The method of representations of structure seminvariants. II. New theoretical and practical aspects*. *Acta Cryst.* A**36**, 362–372.

Giacovazzo, C. (1996). *Direct methods and powder data: state of the art and perspectives*. *Acta Cryst.* A**52**, 331–339.

Giacovazzo, C. (1998). *Direct Phasing in Crystallography*. Oxford: IUCr/Oxford University Press.

Giacovazzo, C. (2001). *Direct Methods*. In *International Tables for Crystallography*, Volume B, *Reciprocal space*, 2nd ed., edited by U. Shmueli, ch. 2.2, pp. 210–234. Dordrecht: IUCr/Kluwer Academic Publishers.

Giacovazzo, C. (2013). *Phasing in Crystallography: A Modern Perspective*. Oxford: IUCr/Oxford University Press.

Giacovazzo, C., Altomare, A., Cuocci, C., Moliterni, A. G. G. & Rizzi, R. (2002). *Completion of crystal structure by powder diffraction data: a new method for locating atoms with polyhedral coordination*. *J. Appl. Cryst.* **35**, 422–429.

Gilmore, C. J. (1996). *Maximum entropy and Bayesian statistics in crystallography: a review of practical applications*. *Acta Cryst.* A**52**, 561–589.

Gilmore, C. J. & Bricogne, G. (1997). *MICE computer program*. *Methods Enzymol.* **277**, 65–78.

Gilmore, C. J., Bricogne, G. & Bannister, C. (1990). *A multisolution method of phase determination by combined maximization of entropy and likelihood. II. Application to small molecules*. *Acta Cryst.* A**46**, 297–308.

Gilmore, C., Dong, W. & Bricogne, G. (1999). *A multisolution method of phase determination by combined maximization of entropy and likelihood. VI. The use of error-correcting codes as a source of phase permutation and their application to the phase problem in powder, electron and macromolecular crystallography*. *Acta Cryst.* A**55**, 70–83.

Gilmore, C. J., Henderson, K. & Bricogne, G. (1991). *A multisolution method of phase determination by combined maximization of entropy and likelihood. IV. The ab initio solution of crystal structures from their X-ray powder data*. *Acta Cryst.* A**47**, 830–841.

Gilmore, C. J. & Nicholson, W. V. (1994). *The MICE computer program, and its application to direct phase determination for powders, electron diffraction and macromolecules*. *Trans. Am. Crystallogr. Assoc.* **30**, 15–27.

Gilmore, C. J., Shankland, K. & Dong, W. (2002). *A maximum entropy approach to structure solution*. In *Structure Determination from Powder Diffraction Data*, edited by W. I. F. David, K. Shankland, L. B. McCusker & Ch. Baerlocher, pp. 233–251. Oxford University Press.

Harker, D. (1936). *The application of the three-dimensional Patterson method and the crystal structures of proustite, Ag_3AsS_3, and pyrargyrite, Ag_3SbS_3*. *J. Chem. Phys.* **4**, 381–390.

Harker, D. & Kasper, J. S. (1948). *Phases of Fourier coefficients directly from crystal diffraction data*. *Acta Cryst.* **1**, 70–75.

Hauptman, H. (1975). *A new method in the probabilistic theory of the structure invariants*. *Acta Cryst.* A**31**, 680–687.

Hauptman, H. & Karle, J. (1953). *Solution of the Phase Problem. I. The Centrosymmetric Crystal*. ACA Monograph No. 3. Pittsburgh: Polycrystal Book Service.

Järvinen, M. (1993). *Application of symmetrized harmonics expansion to correction of the preferred orientation effect*. *J. Appl. Cryst.* **26**, 525–531.

Karle, J. & Hauptman, H. (1956). *A theory of phase determination for the four types of non-centrosymmetric space groups 1P222, 2P22, 3P12, 3P22*. *Acta Cryst.* **9**, 635–651.

Karle, J. & Karle, I. L. (1966). *The symbolic addition procedure for phase determination for centrosymmetric and non-centrosymmetric crystals*. *Acta Cryst.* **21**, 849–859.

Le Bail, A., Duroy, H. & Fourquet, J. L. (1988). *Ab-initio structure determination of $LiSbWO_6$ by X-ray powder diffraction*. *Mater. Res. Bull.* **23**, 447–452.

Lipson, H. & Woolfson, M. M. (1952). *An extension of the use of intensity statistics*. *Acta Cryst.* **5**, 680–682.

Liu, L., Yang, J., Li, J., Dong, J., Šišak, D., Luzzatto, M. & McCusker, L. B. (2011). *Ionothermal synthesis and structure analysis of an open-framework zirconium phosphate with a high CO_2/CH_4 adsorption ratio*. *Angew. Chem. Int. Ed.* **50**, 8139–8142.

McCusker, L. B., Von Dreele, R. B., Cox, D. E., Louër, D. & Scardi, P. (1999). *Rietveld refinement guidelines*. *J. Appl. Cryst.* **32**, 36–50.

Milanesio, M. & Viterbo, D. (2011). *Solution and refinement of crystal structures*. In *Fundamentals of Crystallography*, 3rd ed., edited by C. Giacovazzo, pp. 417–511. Oxford: IUCr/Oxford University Press.

Mises, R. von (1918). *Über die 'Ganzzahligkeit' der Atomgewichte und verwandte Fragen*. *Phys. Z.* **19**, 490–500.

Norby, P., Christensen, A. N., Fjellvåg, H. & Nielsen, M. (1991). *The crystal structure of Cr_8O_{21} determined from powder diffraction data: thermal transformation and magnetic properties of a chromium-chromate-tetrachromate*. *J. Solid State Chem.* **94**, 281–293.

Oszlányi, G. & Sütő, A. (2004). *Ab initio structure solution by charge flipping*. *Acta Cryst.* A**60**, 134–141.

Oszlányi, G. & Sütő, A. (2005). *Ab initio structure solution by charge flipping. II. Use of weak reflections*. *Acta Cryst.* A**61**, 147–152.

Oszlányi, G. & Sütő, A. (2007). *Ab initio neutron crystallography by the charge flipping method*. *Acta Cryst.* A**63**, 156–163.

Oszlányi, G. & Sütő, A. (2008). *The charge flipping algorithm*. *Acta Cryst.* A**64**, 123–134.

Oszlányi, G. & Sütő, A. (2011). *A charge-flipping algorithm to handle incomplete data*. *Acta Cryst.* A**67**, 284–291.

Palatinus, L. & Chapuis, G. (2007). *SUPERFLIP – a computer program for the solution of crystal structures by charge flipping in arbitrary dimensions*. *J. Appl. Cryst.* **40**, 786–790.

Palatinus, L., Steurer, W. & Chapuis, G. (2007). *Extending the charge-flipping method towards structure solution from incomplete data sets*. *J. Appl. Cryst.* **40**, 456–462.

Patterson, A. L. (1934). *A Fourier series method for the determination of the components of interatomic distances in crystals*. *Phys. Rev.* **46**, 372–376.

Pawley, G. S. (1981). *Unit-cell refinement from powder diffraction scans*. *J. Appl. Cryst.* **14**, 357–361.

Peschar, R., Etz, A., Jansen, J. & Schenk, H. (2002). *Direct methods in powder diffraction – basic concepts.* In *Structure Determination from Powder Diffraction Data*, edited by W. I. F. David, K. Shankland, L. B. McCusker & Ch. Baerlocher, pp. 179–189. Oxford University Press.

Prince, E. (1981). *Comparison of profile and integrated-intensity methods in powder refinement*. *J. Appl. Cryst.* **14**, 157–159.

Rietveld, H. M. (1969). *A profile refinement method for nuclear and magnetic structures*. *J. Appl. Cryst.* **2**, 65–71.

Rius, J. (2002). *Solution of Patterson-type syntheses with the direct methods sum function.* In *Structure Determination from Powder Diffraction Data*, edited by W. I. F. David, K. Shankland, L. B. McCusker & Ch. Baerlocher, pp. 219–232. Oxford University Press.

Rius, J. (2011). *Patterson-function direct methods for structure determination of organic compounds from powder diffraction data. XVI. Acta Cryst.* A**67**, 63–67.

Rius, J. (2013). *XLENS*. Institut de Ciència de Materials de Barcelona, CSIC, Spain. Available at http://departments.icmab.es/crystallography/software.

Rius, J., Crespi, A. & Torrelles, X. (2007). *A direct phasing method based on the origin-free modulus sum function and the FFT algorithm. XII. Acta Cryst.* A**63**, 131–134.

Rius, J. & Frontera, C. (2007). *Application of the constrained S-FFT direct-phasing method to powder diffraction data. XIII. J. Appl. Cryst.* **40**, 1035–1038.

Rius, J., Miravitlles, C., Gies, H. & Amigó, J. M. (1999). *A tangent formula derived from Patterson-function arguments. VI. Structure solution from powder patterns with systematic overlap*. *J. Appl. Cryst.* **32**, 89–97.

Rius, J., Torrelles, X., Miravitlles, C., Ochando, L. E., Reventós, M. M. & Amigó, J. M. (2000). *A tangent formula derived from Patterson-function arguments. VII. Solution of inorganic structures from powder data with accidental overlap*. *J. Appl. Cryst.* **33**, 1208–1211.

Rogers, D. (1980). *Definition of origin and enantiomorph, and calculation of $|E|$ values*. In *Theory and Practice of Direct Methods in Crystallography*, edited by M. F. C. Ladd & R. A. Palmer, pp. 23–92. New York: Plenum Press.

Rogers, D. & Wilson, A. J. C. (1953). *The probability distribution of X-ray intensities. V. A note on some hypersymmetric distributions*. *Acta Cryst.* **6**, 439–449.

Sayre, D. (1952). *The squaring method: a new method for phase determination*. *Acta Cryst.* **5**, 60–65.

Shankland, K., David, W. I. F. & Sivia, D. S. (1997). *Routine ab initio structure determination of chlorothiazide by X-ray powder diffraction using optimised data collection and analysis strategies*. *J. Mater. Chem.* **7**, 569–572.

Shankland, K., Gilmore, C. J., Bricogne, G. & Hashizume, H. (1993). *A multisolution method of phase determination by combined maximization of entropy and likelihood. VI. Automatic likelihood analysis via the Student t test, with an application to the powder structure of magnesium boron nitride, Mg_3BN_3*. *Acta Cryst.* A**49**, 493–501.

Sheldrick, G. M. (2008). *A short history of SHELX*. *Acta Cryst.* A**64**, 112–122.

Sim, G. A. (1960). *A note on the heavy-atom method*. *Acta Cryst.* **13**, 511–512.

Vallcorba, O., Rius, J., Frontera, C., Peral, I. & Miravitlles, C. (2012). *DAJUST: a suite of computer programs for pattern matching, space-group determination and intensity extraction from powder diffraction data*. *J. Appl. Cryst.* **45**, 844–848.

Viterbo, D. (2002). *Solution and refinement of crystal structures*. In *Fundamentals of Crystallography*, 2nd ed., edited by C. Giacovazzo, pp. 413–501. Oxford: IUCr/Oxford University Press.

Weeks, C. M., DeTitta, G. T., Miller, R. & Hauptman, H. A. (1993). *Application of the minimal principle to peptide structures*. *Acta Cryst.* D**49**, 179–181.

Wessel, T., Baerlocher, C. & McCusker, L. B. (1999). *Single-crystal-like diffraction data from polycrystalline materials*. *Science*, **284**, 477–479.

White, P. S. & Woolfson, M. M. (1975). *The application of phase relationships to complex structures. VII. Magic integers*. *Acta Cryst.* A**31**, 53–56.

Wilson, A. J. C. (1942). *Determination of absolute from relative X-ray intensity data*. *Nature*, **150**, 151–152.

Wilson, A. J. C. (1949). *The probability distribution of X-ray intensities*. *Acta Cryst.* **2**, 318–321.

Woolfson, M. M. & Fan, H. F. (1995). *Physical and Non-Physical Methods of Solving Crystal Structures.* Cambridge University Press.

Wu, J., Leinenweber, K., Spence, J. C. H. & O'Keeffe, M. (2006). *Ab initio phasing of X-ray powder diffraction patterns by charge flipping*. *Nat. Mater.* **5**, 647–652.

Zachariasen, W. H. (1952). *A new analytical method for solving complex crystal structures*. *Acta Cryst.* **5**, 68–73.

International Tables for Crystallography (2019). Vol. H, Chapter 4.3, pp. 414–432.

4.3. Real-space methods for structure solution from powder-diffraction data: application to molecular structures

W. I. F. David

4.3.1. Introduction

Structure determination from powder-diffraction data (SDPD) is a significant crystallographic challenge. Determining the complete three-dimensional structure of a material from the single dimension of a powder-diffraction pattern is, *prima facie*, an uphill endeavour against a significant loss of information. Since 1990, however, considerable progress has been made in addressing this issue through the development of new algorithms, the availability of powerful structure-solution software and advances in powder-diffraction instrumentation. Prior to 1990, the recognized strength of powder diffraction was in the final refinement of a crystallographic model using the Rietveld method (Rietveld, 1969), in which a calculated diffraction pattern is compared with observed powder-diffraction data. However, the success of the Rietveld method depends on having an accurate starting model that is close to the correct structure, which can subsequently be obtained by standard least-squares minimization. For many materials, particularly organic molecular structures, this is often not the case and, in the absence of single crystals and with the availability only of powder samples, SDPD is the only method for directly obtaining the correct crystal structure.

The complexity of structures that can be refined from powder-diffraction data indicates the potential for the structure determination of equally complex systems. However, prior to 1990 attempts to solve structures from first principles would typically be limited to the stage of accurate lattice-parameter determination. Further progress towards structure solution was generally approached by searching structure databases for similar structures or by intuitive model building. Both approaches have been, and still are, successfully used for SDPD. The structural analyses of numerous high-temperature superconductor structures in the 1980s exemplified the strength of intuitive chemical crystallography combined with Rietveld analysis and established the power of powder diffraction to the chemistry, physics and materials-science communities. However, no automated procedure existed to move beyond unit-cell determination to space-group assignment and subsequent structure solution. Bricogne (1991) detailed the extent of the structure-factor information loss associated with the compression of the three-dimensional reciprocal lattice on to the one dimension of a powder-diffraction pattern. This loss is mathematically similar to the loss of phase information in a single-crystal experiment. However, while the phase loss associated with an individual single-crystal intensity is a single parameter, the hyper-phase permutations of N overlapping non-centrosymmetric powder-diffraction reflections runs to $2N - 1$ dimensions. Consequently, a modified direct-methods approach to solving crystal structures from powder-diffraction data appears to be a vast combinatorial challenge for all but the simplest structures. Despite this complexity, various maximum-entropy approaches have been developed and show significant promise (Gilmore *et al.*, 1991, 1993; David & Sivia, 2002). Direct-methods programs (Altomare *et al.*, 2009) have also been successfully developed for powder-diffraction data and are extensively discussed in Chapter 4.2.

Perhaps unsurprisingly, given the complexities of hyper-phase permutations, the breakthrough in SDPD followed a different route and generalized the intuitive model-building approach used previously in conjunction with the Rietveld method. While the work of Semenovskaya *et al.* (1985) indicated a putative algorithmic approach, it was the work of Lightfoot *et al.* (1993) and Harris *et al.* (1994) that paved the way for the development of SDPD. The successful solution of a molecular pharmaceutical crystal structure, the first structure determination from the powder-diffraction round-robin challenge in 1998 (Le Bail & Cranswick, 2001), along with an associated paper on the structure determination of three moderately complex pharmaceutical compounds (David *et al.*, 1998), established the potential of real-space methods for SDPD.

The process of SDPD has been compared with the challenge of walking through a maze; see Fig. 4.3.1(*a*). It is not always straightforward to complete the journey; how to reach the centre of the maze is never obvious at the beginning and multiple decisions must be taken sequentially to determine the most effective route to the solution. The decision to select real-space global-optimization methods as the structure-solution technique does reduce the number of decision points and complexity in the maze but also introduces additional prerequisites associated with the development of an initial structural model. This is illustrated in Fig. 4.3.1(*b*), which has two entrances to the structure-solution maze.

The first entrance involves the decisions associated with the sequential processes of sample preparation, experiment and initial analysis of the diffraction data. Introducing the second entrance highlights the fact that building the structural model can be undertaken in parallel and, indeed, independently of the initial diffraction experiment and analysis.

Preparation of the structural model is a sequence of processes that starts with determining the chemical formula. Generally, for molecular structures, this is already known, as for a new pharmaceutical polymorph. If the structure is only partly known (for example, the degree of hydration of a material) then additional physical measurements such as thermogravimetric analysis or more sophisticated minimization approaches such as maximum-likelihood methods (see Section 4.3.6) can be used to overcome this information loss. The molecular topology (connectivity) is again generally known beforehand. If there are uncertainties, then the best approach is to determine all the possible molecular topologies (which will usually be a small number) and test each topology in the structure-solution process. Molecular geometries, such as bond lengths, angles and dihedral angles, can be determined heuristically, but are best assessed by consulting a structural database such as the Cambridge Structural Database (Groom *et al.*, 2016).

Structure parameterization, both parameter selection and parameter range, can also be determined by chemical intuition or database screening (Bruno *et al.*, 2004). The parameterization itself is usually expressed in terms of molecular connectivity.

Copyright © 2019 International Union of Crystallography

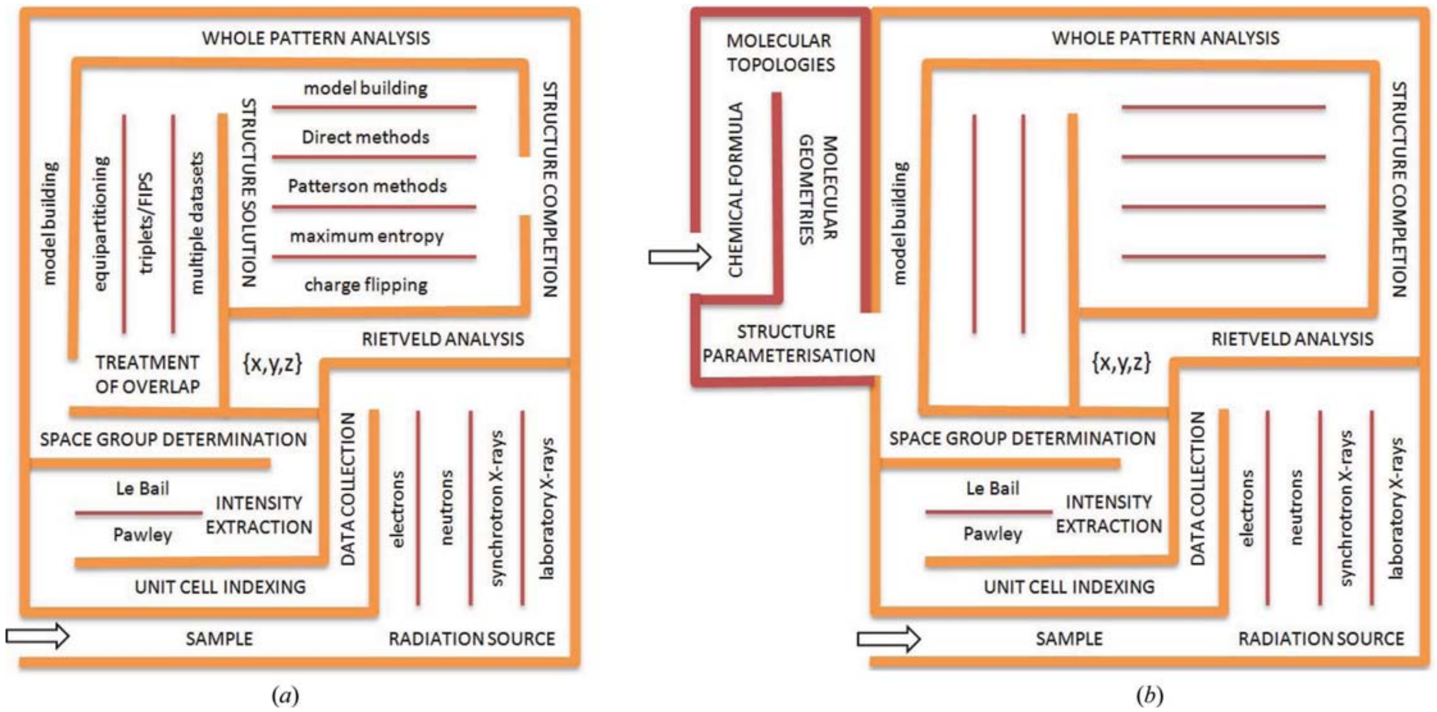
WHOLE PATTERN ANALYSIS
model building
Direct methods
Patterson methods
maximum entropy
charge flipping
STRUCTURE SOLUTION
STRUCTURE COMPLETION
model building
equipartitioning
triplets/FIPS
multiple datasets
TREATMENT OF OVERLAP
{x,y,z}
RIETVELD ANALYSIS
SPACE GROUP DETERMINATION
Le Bail
Pawley
INTENSITY EXTRACTION
UNIT CELL INDEXING
DATA COLLECTION
electrons
neutrons
synchrotron X-rays
laboratory X-rays
SAMPLE
RADIATION SOURCE
(a)
MOLECULAR TOPOLOGIES
CHEMICAL FORMULA
MOLECULAR GEOMETRIES
STRUCTURE PARAMETERISATION
WHOLE PATTERN ANALYSIS
model building
STRUCTURE COMPLETION
RIETVELD ANALYSIS
{x,y,z}
SPACE GROUP DETERMINATION
Le Bail
Pawley
INTENSITY EXTRACTION
UNIT CELL INDEXING
DATA COLLECTION
electrons
neutrons
synchrotron X-rays
laboratory X-rays
SAMPLE
RADIATION SOURCE
(b)

Figure 4.3.1

(*a*) The maze of strategies associated with the determination of crystal structures from powder-diffraction data (after Baerlocher & McCusker, 2002) and (*b*) the modified 'global-optimization' maze showing the double start point and simplification of the principal maze.

Early structure determinations used the procedure outlined by Arnott & Wonacott (1966). More recently, the *Z*-matrix approach has been adopted and programs such as *OpenBabel* (O'Boyle *et al.*, 2011) exist for converting molecular structures from common formats, such as CIF, to the *Z*-matrix formalism. The development of molecular models for the global-optimization methods of SDPD is discussed further in Section 4.3.3.2.

Returning to the experimental component of the structure-solution process, it is important to emphasise that careful sample preparation is essential for maximizing the success of a structure solution and for obtaining the best and most accurate crystal structure. For X-rays, capillary geometry is the geometry of choice as preferred-orientation effects are minimized. Careful measurements on laboratory X-ray diffractometers are quite sufficient for a significant proportion of molecular crystal structures (Florence *et al.*, 2005), but the improved resolution afforded by synchrotron X-ray diffractometers can help with the determination of more complex structures. Additionally, the rapid counting times available with synchrotron instrumentation mean that intermediate and transient phases may be observed during *in situ* experiments. Care, however, must be taken with synchrotron measurements, as the high fluxes can lead to radiation damage and sample degradation in organic materials. Molecular structures generally contain a significant amount of hydrogen and this, historically, has been an issue for neutron powder-diffraction measurements because of the concomitant high backgrounds associated with incoherent scattering from hydrogen. Deuteration is an option but introduces additional expense and synthesis complexity. This impasse has been significantly ameliorated by a new generation of instruments that include WISH (ISIS, http://www.isis.stfc.ac.uk/instruments/wish/wish-6465.html), POWGEN (SNS, http://neutrons.ornl.gov/powgen/), SuperHRPD (J-PARC, http://www.kek.jp/en/Facility/IMSS/MLF/KENS/BL08/) and D2b (ILL, https://www.ill.eu/instruments-support/instruments-groups/instruments/d2b/description/instrument-layout/). The visibility of hydrogen atoms in a neutron powder-diffraction experiment is an important benefit for determining the most accurate final structure, but also introduces the necessity of additional torsion angles, which further complicates the structure-solution process. Generally, if neutron powder-diffraction data are available, it is best to use X-rays in the first instance and, once the structure is solved, perform a combined structure refinement using the X-ray and neutron powder-diffraction data. The contrasting scattering factors in an X-ray and neutron powder-diffraction experiment mean that the successful fitting of both data sets may remove ambiguity and bring a higher degree of confidence to the accuracy of the final crystal structure.

After successful data collection, the next step is the determination of the unit cell of the unknown crystal structure. There are a number of different approaches that have been developed for autoindexing and these are extensively discussed in Chapter 3.4. The step following autoindexing is the fitting of the diffraction data. This not only further validates the correctness of the unit-cell assignment but also enables peak-shape and background parameters to be accurately determined. In the absence of a crystal structure, the intensities of the Bragg peaks must be treated as parameters to be refined. Two techniques, the Pawley and Le Bail methods (see Chapter 3.5), have been developed for this atom-coordinate-free profile refinement. It is at this point that the greatest care should be taken in fitting the diffraction pattern, as these methods will yield a better fit to the data than the final Rietveld refinement. Ideally, the unit-cell parameters, peak-width values and background polynomial coefficients should be fixed for all subsequent real-space structure determination attempts as well as the final Rietveld refinement.

Real-space structure-determination methods involve moving an atom or a set of atoms around a unit cell, determining whether the resulting fit to the diffraction data improves or worsens, and then deciding on whether to accept or reject the move.

Some real-space structure-determination programs, such as *DASH* (David *et al.*, 2006), use the extracted integrated intensities in addition to the diffraction profile for accelerated comparison between observed and calculated profiles (see Section 4.3.4.1); this requires evaluation of the integrated intensities covariance matrix, which is readily accessible using the Pawley method. Space-group determination is generally undertaken at the same time as initial profile fitting. The first space-group choice for profile refinement should be a space group of the appropriate Laue class having no systematic absences; these are $P\bar{1}$ (triclinic), $P2/m$ (monoclinic), $Pmmm$ (orthorhombic), $P4/m$ and $P4/mmm$ (tetragonal), $P\bar{3}$, $P\bar{3}1m$ and $P\bar{3}m1$ (trigonal), $P6/m$ and $P6/mmm$ (hexagonal), and $Pm\bar{3}$ and $Pm\bar{3}m$ (cubic).

Space-group determination is often undertaken by visual assessment of the systematically absent reflections and consultation of *International Tables for Crystallography* Volume A, Chapter 1.6. Automated space-group determination programs are also available, *e.g. ExtSym* (Markvardsen *et al.*, 2001, 2012), *DASH* (David *et al.*, 2006), *EXPO* (Altomare *et al.*, 2009) and *FOX* (Favre-Nicolin & Černý, 2004*a*,*b*), and give an accurate probabilistic ranking of the various extinction symbols using both present and absent reflections. Each extinction symbol is generally associated with more than one space group and chemical reasoning such as the presence or absence of a centre of symmetry from chirality considerations or an estimation of the number of molecules in a unit cell from volume considerations can reduce the number of potential options. If more than one space group is a plausible candidate, then multiple global-optimization runs with each potential space group should be performed. Space-group determination from powder-diffraction data is discussed more extensively in Chapter 3.4. The final Pawley or Le Bail fitting of the diffraction data should be performed using the final selection of space group(s). All the necessary diffraction information is then in place to proceed to the real-space structure-determination stage of the structure-solution process.

4.3.2. Real-space structure determination: a global-optimization extension of the Rietveld method

Real-space SDPD may be accurately described as a global Rietveld method. In both cases, a preliminary model is essential and the optimal structure is determined by minimizing the difference between the observed and calculated powder-diffraction patterns. The goodness of fit in real-space structure determination is the same as in standard Rietveld analysis, where the function that is minimized is either the least-squares function [with N, P and C, respectively, representing the number of observations, parameters and parameter constraints, and $w(i)$ is the statistical weight associated with observation i]

$$\chi^2 = S^2/(N-P+C),$$

where

$$S^2 = \sum_{i=0}^{N} w(i)\big[y_{\rm obs}(i) - y_{\rm calc}(i)\big]^2,$$

or the essentially equivalent weighted profile R factor, $R_{\rm wp}$,

$$R_{\rm wp} = \left(\frac{S^2}{\sum_{i=0}^{N} w(i) y_{\rm obs}(i)^2}\right)^{1/2}.$$

The ideal targets for χ^2 and $R_{\rm wp}$, for both real-space structure determination and Rietveld analysis, are, respectively, $\chi^2 = 1$ and the expected R factor, $R_{\rm exp}$,

$$R_{\rm exp} = \left(\frac{N-P+C}{\sum_{i=0}^{N} w(i) y_{\rm obs}(i)^2}\right)^{1/2}.$$

The equivalence between minimizing χ^2 and $R_{\rm wp}$ can be seen by noting that

$$\chi^2 = \left(R_{\rm wp}/R_{\rm exp}\right)^2.$$

The essential difference between real-space structure determination and the standard use of the Rietveld method is the range of convergence of the two techniques. The Rietveld method has been developed as a refinement procedure where the parameters chosen for the initial starting model are sufficiently close to the correct answer for a standard steepest-descents or equivalent minimization method to be adequate to obtain the structural parameters that correspond to an optimal fit between observed and calculated diffraction profiles. In other words, the initial starting parameters must be in the global minimum basin of the χ^2 hypersurface. Real-space structure determination, on the other hand, sets out to solve crystal structures from any randomly chosen set of structural parameters. As such, it is an optimization method that requires global-optimization algorithms. As stated previously, this implies that real-space structure determination is essentially a global parameter exploration version of the Rietveld method. The nature of the χ^2 hypersurface, which is discussed further in Section 4.3.4.2, is, however, extremely complex with multiple local minima. Given this complexity, the principal challenge in the development of real-space structure determination is the implementation of global-optimization techniques that efficiently and comprehensively explore the full structural parameter space that completely describes all chemically possible crystal structures. This goal requires the resolution of two distinct and significant issues. The first of these, the most efficient and compact description of the full structural parameter space, is discussed in Section 4.3.3.2. The second challenge, the optimal exploration of the full structural parameter space combined with the effective minimization of the goodness of fit between observed and calculated diffraction patterns, is discussed in Section 4.3.5.

4.3.3. Optimizing the process of real-space structure determination from powder-diffraction data

4.3.3.1. *Introduction*

Global optimization is a comprehensive and time-consuming procedure, and all possibilities for accelerating the search process should be explored. The choice of cost function and the metric for the comparison of observed and calculated diffraction data should be chosen to make the process as fast as possible without loss of accuracy. In the case of SDPD, the fastest, accurately representative cost function is the correlated integrated intensities goodness of fit, which is discussed in Section 4.3.4.1. Full-profile fitting is also commonly used and is (if fully optimized) less than an order of magnitude slower. Importantly, if full-profile fitting is being used, the refinement of parameters other than the essential structural parameters should be avoided. The inclusion in the real-space structure-determination process of the variation of lattice parameters, peak widths and background coefficients substantially reduces performance and convergence.

A number of different global-optimization algorithms have been developed and used for real-space structure determination. The majority of these algorithms are stochastic in nature and include simulated annealing, parallel tempering and genetic and evolutionary algorithms. Deterministic approaches have been explored to a lesser extent, but techniques such as the hybrid Monte Carlo method show significant promise. Other techniques, such as swarm and diffusion equation methods, have been discussed but not extensively explored. These methods have been summarized by David & Shankland (2008) and are discussed in more detail in Section 4.3.5.

The final significant factor in determining the performance of a global-optimization approach to real-space structure determination of molecular materials is the parameterization of the molecular structure. The shape, geometry and conformation of most molecules that can be tractably solved from powder-diffraction data are well known or can be constructed from structural databases. This can reduce the number of degrees of freedom from the maximum values of the 3*N* atomic coordinates of a molecule with *N* atoms to the six external degrees of translational and rotational freedom of the molecule and the often small number of internal torsional degrees of freedom. Although the building blocks of molecular structures are generally much more complicated than for many inorganic structures, the absence of an extended, connected framework for molecular structures (with the exception of polymeric materials) means that each independent molecule can be treated as an isolated entity. Molecules may be moved at random around the unit cell in the search for the correct crystal structure while maintaining the intramolecular connectivity and exploring the intramolecular geometry without any concern for all the possible permutations of extended framework connectivity.

4.3.3.2. *Parameterization of the molecular structure*

After the pioneering work of Arnott & Wonacott (1966), a number of formats have been developed to describe molecular structure. One common format for expressing molecular connectivity is the *Z*-matrix formalism developed for the *Gaussian* computer program (https://www.gaussian.com). The benefits of using a connectivity representation for molecular atomic coordinates are best illustrated by an example.

Consider the diuretic drug hydrochlorothiazide (Leech *et al.*, 2008), $C_7H_8ClN_3O_4S_2$, illustrated in Fig. 4.3.2(*a*). An atom in the molecule is selected to define the origin of the molecular coordinate system.

In hydrochlorothiazide, the best origin choice is the Cl atom. There are two criteria that are significant in this choice; firstly, the atom should ideally be part of a substantial inflexible component of the molecule that is close to the centre of the molecule, and second, the atom should be one of the stronger scatterers (for X-rays, this equates to one of the heavier atoms in the molecule). The reasons for these selection criteria will be discussed in Section 4.3.4.2.

The molecular coordinate system is described in terms of Cartesian coordinates. The *z* axis is chosen to align along the first molecular bond, Cl(1)—C(2); the *x* axis is defined to lie in the plane of the first three selected atoms, Cl(1), C(2) and C(3), and the *y* axis is perpendicular to both the *x* and *z* axes forming an orthogonal right-handed coordinate system. Full details of the molecular connectivity of the first five atoms are illustrated in Fig. 4.3.2(*b*) and shown symbolically in Table 4.3.1, where b_1, b_2, b_3 and b_4 denote the Cl(1)—C(2), C(2)—C(3), C(3)—S(4) and S(4)—O(5) bond lengths, respectively, φ_1, φ_2 and φ_3 are the bond angles Cl(1)—C(2)—C(3), C(2)—C(3)—S(4) and C(3)—S(4)—O(5), and τ_1, and τ_2 are the dihedral angles associated with the atom quartets Cl(1)—C(2)—C(3)—S(4) and C(2)—C(3)—S(4)—O(5).

Table 4.3.2 lists the full *Z*-matrix for hydrochlorothiazide using a slightly modified definition developed for *DASH* (David *et al.*, 2006) that illustrates generically all the required information to define the molecule confirmation.

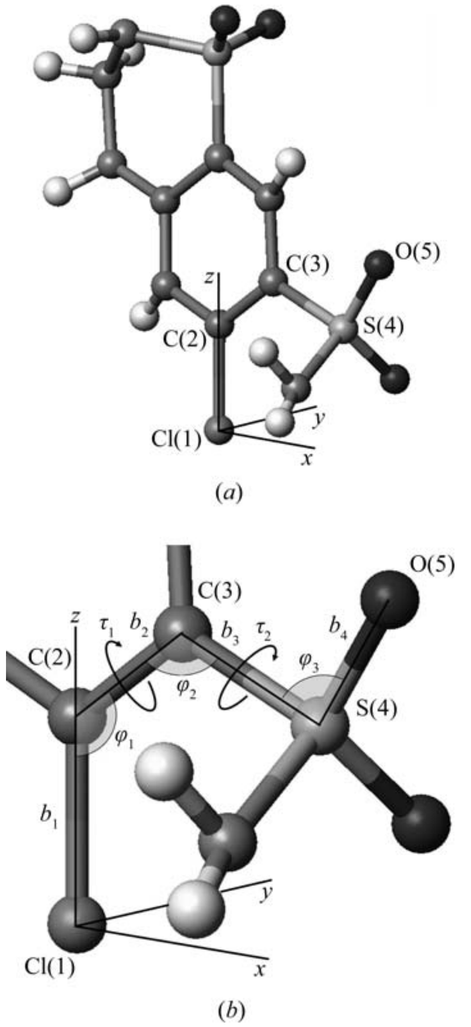

Figure 4.3.2
(*a*) The Cartesian molecular coordinate system for hydrochlorothiazide. The origin is located at the chlorine atom. (*b*) An expanded view around the origin of the molecular coordinate system highlighting the initial bond lengths, angles and dihedral angles in the *Z*-matrix of hydrochlorothiazide.

The rows shown in Table 4.3.2 define the full molecular connectivity. Each row has ten columns. The first denotes the atom type and columns 8, 9 and 10 indicate the atoms to which this atom is connected. Consider the first sulfur atom, which is atom number 4 in the list. It is 1.754 Å from atom 3, C(3), forms an angle with atom 3 and atom 2 [*i.e.* C(2)—C(3)—S(4)] of 124° and a dihedral angle of 1.07° involving the atom quartet Cl(1)—C(2)—C(3)—S(4). The remaining three columns, columns 3, 5 and 7, are flags indicating whether the bond length, angle or dihedral angle should be fixed (flag = 0) or varied (flag = 1). Inspection shows that all these flags are zero except for one, the dihedral angle listed in the fifth atom row. This corresponds to the dihedral angle, τ_2, and is the only dihedral angle in hydrochlorothiazide that can vary over a significant range of angles and is thus the only true torsion angle in the molecule (Fig. 4.3.2). All other dihedral angles and bond lengths and angles are chemically reasonable and close enough to their correct values to be fixed in the structure-solution process. This means that the global-optimization search only spans a seven-dimensional space corresponding to the six external degrees of freedom (three translational and three rotational) and one internal degree of torsional freedom, τ_2. This is the minimal number of degrees of freedom that fully describes the molecular flexibility. Other

Table 4.3.1
The symbolic representation of the initial bonds, angles and dihedral angles described in the *Z*-matrix of hydrochlorothiazide

See also Fig. 4.3.2(*b*)

Cl	0.000	0	0.000	0	0.000	0	0	0	0
C	b1	0	0.000	0	0.000	0	1	0	0
C	b2	0	$\varphi1$	0	0.000	0	2	1	0
S	b3	0	$\varphi2$	0	$\tau1$	0	3	2	1
O	b4	0	$\varphi3$	0	$\tau2$	1	4	3	2

Table 4.3.2
Z-matrix for hydrochlorothiazide

Cl	0.000	0	0.000	0	0.000	0	0	0	0
C	1.741	0	0.000	0	0.000	0	1	0	0
C	1.428	0	120.391	0	0.000	0	2	1	0
S	1.754	0	124.000	0	1.070	0	3	2	1
O	1.405	0	109.482	0	157.019	1	4	3	2
O	1.435	0	118.318	0	−120.792	0	4	5	3
N	1.626	0	106.173	0	−120.666	0	4	5	6
H	1.033	0	164.049	0	89.659	0	7	4	5
H	0.984	0	105.500	0	85.669	0	7	4	8
C	1.388	0	119.202	0	−179.183	0	3	4	2
C	1.378	0	121.165	0	175.853	0	10	3	4
S	1.744	0	120.301	0	−178.317	0	11	10	3
O	1.419	0	109.447	0	95.136	0	12	11	10
O	1.408	0	119.168	0	127.818	0	12	13	11
N	1.638	0	107.010	0	122.475	0	12	13	14
C	1.469	0	111.766	0	59.325	0	15	12	13
N	1.467	0	111.580	0	62.279	0	16	15	12
C	1.342	0	122.986	0	−34.217	0	17	16	15
C	1.366	0	117.139	0	−179.608	0	2	1	3
H	1.000	0	118.203	0	154.960	0	19	2	18
H	1.000	0	112.308	0	150.708	0	17	16	18
H	1.000	0	103.224	0	109.539	0	16	15	17
H	1.000	0	116.987	0	−138.243	0	16	15	17
H	1.000	0	111.677	0	135.240	0	15	12	16
H	1.000	0	120.285	0	160.635	0	10	3	11

approaches, such as that of the computer program *FOX* (Favre-Nicolin & Černý, 2004*b*), favour rather more flexible *Z*-matrices. Without this explicit connectivity obtained from an accurate knowledge of all intramolecular bonds and angles and the majority of intramolecular dihedral angles, all atoms would need to be moved independently of one another. Ignoring hydrogen atoms and noting that there would be three positional degrees of freedom associated with each non-hydrogen atom results in a 51-dimensional space. An indication of the probability of being able to tackle a global optimization in such a large parameter space is discussed in Section 4.3.4 and the probabilities of success are very low. Anti-bump and neighbour-avoiding random walks substantially reduce the search volume of this large hyperspace, but given that optimization complexity and time to solution increase exponentially with search-space dimensionality, it is evident that the *Z*-matrix and similar connectivity formalisms not only will lead to a massively improved rate of success but also represent the optimal parameterization of the molecular structure because they span the minimum number of parameter dimensions that contain all the chemically reasonable molecular locations and conformations.

4.3.4. The nature and magnitude of the global-optimization challenge

This section explores the nature and scale of the global-optimization challenge for real-space SDPD and highlights the efficiency of the bond-connectivity (*e.g.* the *Z*-matrix algorithm) approach for the solution of molecular crystal structures. Global optimization, by definition, involves full evaluation and a comprehensive exploration of the structure parameter space under investigation. In order to emphasize the effectiveness of the *Z*-matrix approach, it is worth stepping back and assessing the magnitude of the challenge if the chosen route were to move individual atoms independently around the unit cell.

Consider an organic molecular structure with N_A atoms (ignoring hydrogens) in each molecule. An estimate of the volume, V_c, of the unit cell is $V_c \simeq ZV_AN_A$ Å^3 (where Z is the number of molecules in the unit cell and $V_A \simeq 17$ Å^3 is a commonly considered approximate volume associated with a non-hydrogen atom in an organic crystal structure). Assuming that all the atoms are located on general positions (and this is often the case), the parameter space to be searched spans $3N_A$ dimensions. If an adequate solution is obtained when every atom is within a generous $r \simeq 1$ Å of a correct position, then the probability of finding an acceptable solution at random can be shown to be

$$\text{prob}_{\text{sol}} \simeq N_A!\left[r^3/N_A\left(V_A - V_{\text{EXC}}\right)\right]^{N_A}, \qquad (4.3.1)$$

where V_{EXC} is the excluded volume where atoms are forbidden to overlap. If atoms are placed randomly in the unit cell, then $V_{\text{EXC}} = 0$, whereas if solutions with overlapping atoms are forbidden then $V_{\text{EXC}} \simeq (1.4)^3$ Å^3, where 1.4 Å represents a typical interatomic distance. The $N_A!$ contribution in equation (4.3.1) allows permutation between all non-hydrogen atoms; in other words, each non-hydrogen atom must be at a non-hydrogen position, but not necessarily its correct position. This is a reasonable, common assumption and greatly increases (by a factor of $N_A!$) the probability of selecting $3N_A$ coordinates and obtaining a good solution at random. Equation (4.3.1) may be modified and simplified to give

$$\log_{10}(\text{prob}_{\text{sol}}) \simeq -N_A\left\{\log_{10}\left[\left(V_A - V_{\text{EXC}}\right)/r^3\right] + 0.43\right\}. \qquad (4.3.2)$$

For a molecule containing N_A = 5, 10 and 20 atoms, the solution probability values, with $V_{\text{EXC}} = (1.4)^3$ Å^3, are $10^{-7.9}$, $10^{-15.8}$ and $10^{-31.7}$, respectively. The likelihood of being within 1 Å of a correct solution is roughly 1 in 10^8 for the 5-atom molecule and vanishingly small for the 10- and 20-atom molecules. This correct solution can, however, be found if each random atom selection is within the radius of convergence of the global minimum in the $3N_A$-dimensional structural hyperspace. In Section 4.3.4.1, this radius of convergence, the extent of the global minimum basin, is shown to be similar to the spatial extent of an average interatomic vector peak in the Patterson function. Invoking the convolution theorem, this will be $r \simeq 2.0$ Å, which is about $2^{1/2}$ times larger than a typical atomic scattering-factor distribution. This doubling of the value of r leads to a very different set of probabilities when neighbour-avoiding solutions are considered. This is essentially the procedure adopted by Semenovskaya *et al.* (1985) in one of the earliest attempts at global optimization of real-space SDPD. For N_A = 5, 10 and 20 atoms with non-overlapping $V_{\text{EXC}} \simeq 2.7$ Å^3, the solution probability values are now 1 in ∼2500, 1 in $\sim 6 \times 10^6$ and 1 in $\sim 4 \times 10^{13}$. With 5- and 10-atom structures, it is feasible to consider the least-squares minimization of multiple neighbour-avoiding, semi-random atom configurations as a method of structure solution from powder-diffraction data. However, for larger structures this procedure is evidently not practical.

It is clear from equation (4.3.2) that the crucial factors in determining the probability of a successful structure determination are the number of atoms, N_A, and the excluded volume, $V_{\rm EXC}$, as both the typical radius of convergence, $r \simeq 2.0$ Å, and the approximate atom volume, $V_A \simeq 17$ Å^3, are essentially fixed quantities. The optimal approach to the issue of the excluded volume is (as discussed in Section 4.3.3.2) the use of molecular connectivity. Atoms within a molecule are not only forced to be apart but are optimally located apart by the use of chemically sensible and accurate bond lengths, angles and dihedral angles.

Moving from an individual-atom approach to a fully connected molecule also substantially reduces the dimensionality of the search space, as discussed in Section 4.3.3.2 where the selected example, hydrochlorothiazide, shows a lowering of search space dimensionality from $3N_A = 51$ to 7 dimensions. While it is straightforward to estimate the exponentially increased probability of structure-solution success from this reduction in dimensionality, it is less clear about the impact of the optimal excluded volume from the use of a *Z*-matrix or equivalent formalism. The discussion in Section 4.3.4.2 of success in the structure solution of the histamine H2-receptor antagonist, famotidine, $C_8H_{15}N_7O_2S_3$, (Shankland *et al.*, 2002) suggests that there is a very significant advantage. With 6 external and 7 internal torsional degrees of freedom ($N_{\rm DOF} = 13$), multiple random starts followed by direct least-squares minimization leads to a success rate of order 1 in 5000. Substituting this value into an appropriately modified version of equation (4.3.2),

$$\log_{10}({\rm prob}_{\rm sol}) \simeq -\tfrac{1}{3}N_{\rm DOF}\log_{10}\left[N_A\left(V_A - V_{\rm EXC}\right)/r^3\right], \qquad (4.3.3)$$

gives an estimated value of $V_{\rm EXC} \simeq 13.6$ Å^3 of the available 17 Å^3 compared with $V_{\rm EXC} \simeq 2.7$ Å^3 for the independent-atom search. Not only is the dimensionality of each search space substantially smaller when using a *Z*-matrix or equivalent molecular-connectivity formalism but the required fraction of the search space that must be explored is also greatly reduced.

Given the observed success rate for famotidine, the convergence hypersurface must only be ~5000 times smaller than the total 13-dimensional hypersurface. This corresponds, on average, to a fraction of around $0.5 \simeq (1/5000)^{1/13}$ for each degree of freedom. Remarkably, using molecular connectivity to reduce the size of the parameter space means that finding the hypersurface basin that contains the global minimum is essentially equivalent to tossing a coin for each external and internal degree of freedom. Correspondingly, increasing the number of degrees of freedom only increases the number of trials by a factor of around two. While this is a surprisingly small penalty to pay for increasing molecular complexity, it nevertheless means that the addition, for example, of ten more internal torsional degrees of freedom will lead to about a 1000-fold increase in minimization complexity. Increases in computer speed go some way to addressing this issue, but the principal gain can be had by parallelizing multiple structure-solution attempts. This strategy has been used for computer programs such as *DASH*, where *MDASH* (for multi-processors use on a single machine; Griffin *et al.*, 2009*a*) and the fully grid-enabled version *GDASH* (for very large calculations involving hundreds of processor cores; Griffin *et al.*, 2009*b*) have enabled complex structures to be solved on manageable timescales (Fernandes *et al.*, 2007). *FOXGrid*, a parallel version of the structure-solution program *FOX* (https://fox.vincefn.net/Manual/Fox.Grid) is also available.

In addition to the direct approach of utilizing multiple processors, additional stratagems for tackling more complex organic structures include the development of new global-optimization algorithms (see Section 4.3.5) and the reduction of the parameter exploration space. The latter strategy can be tackled using three different approaches: firstly, by restricting parameter ranges such as limiting torsion-angle values to those observed in structural databases, secondly, by limiting torsion angles and, more generally, molecular conformations by using additional structural information from other experimental data (such as NMR) and, thirdly, by completely removing parameters from the structural-solution process using maximum-likelihood methods; see Section 4.3.6.

4.3.4.1. *Interpretation of the least-squares cost function*

There is a close relationship between the best goodness-of-fit values obtained from a Pawley and a Rietveld refinement of a powder-diffraction pattern (David, 2004). The unnormalized goodness of fits

$$S^2_{\rm PAW} = \sum_{i=0}^{N} w(i)\left[y_{\rm obs}(i) - y_{\rm PAW}(i)\right]^2$$

and

$$S^2_{\rm RIET} = \sum_{i=0}^{N} w(i)\left[y_{\rm obs}(i) - y_{\rm RIET}(i)\right]^2$$

are related by the equation

$$S^2_{\rm RIET} = S^2_{\rm PAW} + S^2_{\rm CI}, \qquad (4.3.4)$$

where the correlated integrated intensities goodness of fit, $S^2_{\rm CI}$, is given by

$$S^2_{\rm CI} = \sum_{j}^{N_R}\sum_{k}^{N_R}\left(V^{-1}_{\rm PAW}\right)_{jk}\left[I_{\rm obs}(j) - I_{\rm calc}(j)\right]\left[I_{\rm obs}(k) - I_{\rm calc}(k)\right]. \qquad (4.3.5)$$

N_R is the number of statistically independent reflection peaks and $I_{\rm calc}(j)$ is the sum of the intensities contributing to each clump given by $I_{\rm calc}(j) = c\sum_{\{\mathbf{h}_j\}} m_{\mathbf{h}_j}\left|F(\mathbf{h}_j)\right|^2$, where c is a scale factor. This sum is over metrically exact (such as the 511 and 333 reflections) and accidentally very close reflections. The equivalence expressed in equation (4.3.4) has been discussed extensively by David (2004) and is illustrated in Fig. 4.3.3 by an analysis of the various goodness of fits obtained in the structure solution of the antipsychotic drug promazine hydrochloride. The associated normalized $\chi^2_{\rm CI}$ goodness of fit is given by

$$\chi^2_{\rm CI} = S^2_{\rm CI}/\left(N_R - P_S + C_S\right), \qquad (4.3.6)$$

where P_S and C_S are, respectively, the number of the structural parameters that are varied and the number of structural constraints.

The degree of overlap for adjacent reflections in equation (4.3.5) is evaluated statistically from the inverse of the integrated-intensity component of the correlation matrix, $V^{-1}_{\rm PAW}$, obtained from a Pawley analysis. The number of off-diagonal terms in this matrix is typically between one and two times the number of diagonal terms and thus the number of terms that must be evaluated for $S^2_{\rm CI}$ is roughly twice the number of reflections. Use of $S^2_{\rm CI}$ in the early days of real-space SDPD provided a substantial speed advantage. With increases in computer power, the advantages of an accelerated goodness-of-fit evaluation have become less necessary and many real-space global-optimization programs now use the weighted profile *R* factor, $R_{\rm wp}$, or the equivalent $\chi^2_{\rm Riet}$. With the appropriate storage of peak-shape and background functions, this typically results in only a factor of 3–4 decrease in the rate of goodness-of-fit evaluation.

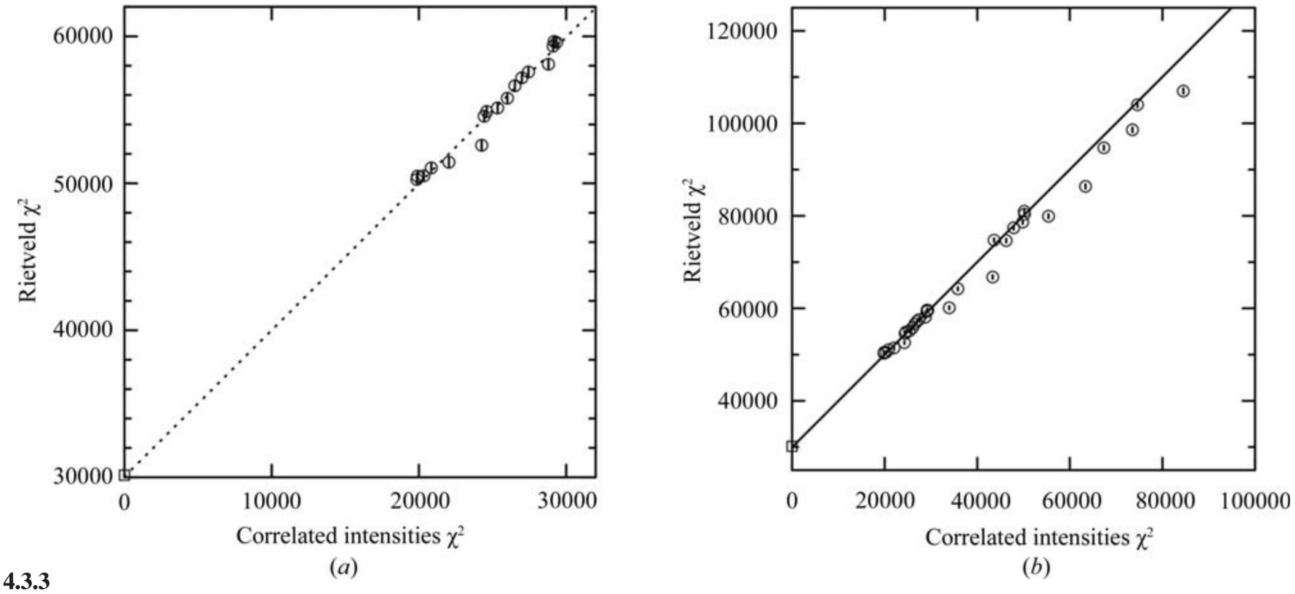

(*a*) (*b*)

Figure 4.3.3
The reported values for both $S^2_{\rm CI}$ and $S^2_{\rm RIET}$ in (*a*) the final stages of the structure-solution process for promazine hydrochloride. The dotted line is an intercept-only fit to these data (with a gradient of unity) and extrapolates to $S^2_{\rm PAW}$ to within statistical error. This provides experimental evidence of the equivalence $S^2_{\rm RIET} = S^2_{\rm PAW} + S^2_{\rm CI}$. (*b*) An extended plot of (*a*) showing that equivalence also holds well at earlier stages in the structure-solution process when the fit to the data is relatively poor.

The formal equivalence between minimizing either $\chi^2_{\rm Riet}$ or $S^2_{\rm CI}$ also sheds light on the nature of the real-space global-optimization process. The Patterson function is defined as the Fourier transform of the square of the structure-factor modulus:

$$P(\mathbf{u}) = \sum_{\mathbf{h}} \left|F(\mathbf{h})\right|^2 \exp(2\pi i\mathbf{h}\cdot\mathbf{u}) = \sum_{\mathbf{h}} F(\mathbf{h})F(\mathbf{h})^* \exp(2\pi i\mathbf{h}\cdot\mathbf{u})$$

(see Chapter 1.1). The Patterson function is the self convolution of the scattering density, $\rho(\mathbf{r})$; *i.e.* $P(\mathbf{u}) = \int_{V_c} \rho(\mathbf{r})\rho(\mathbf{u}+\mathbf{r})\,{\rm d}^3\mathbf{r}$. A more accessible and relevant understanding of this self-convolution is that the Patterson function is the set of interatomic vectors blurred by Debye–Waller factors and the atomic scattering distribution.

An important relationship in the theory of real-space structure determination may be obtained by invoking Parseval's theorem, which states that the scalar product of two functions in reciprocal space is exactly equivalent to the scalar product of the Fourier transforms of these two functions in real space.

If $P_1(\mathbf{u}) = \sum_{\{\mathbf{h}\}} |F_1(\mathbf{h})|^2 \exp(2\pi i\mathbf{h}\cdot\mathbf{u})$ and $P_2(\mathbf{u}) = \sum_{\{\mathbf{h}\}} |F_2(\mathbf{h})|^2 \exp(2\pi i\mathbf{h}\cdot\mathbf{u})$ then

$$\sum_{\{\mathbf{h}\}} \left|F_1(\mathbf{h})\right|^2 \left|F_2(\mathbf{h})\right|^2 = \int_V P_1(\mathbf{u})P_2(\mathbf{u})\,{\rm d}^3\mathbf{u}.$$

This may be extended to obtain the following equivalence for the unnormalized, unweighted integrated-intensity goodness of fit,

$$\begin{aligned} S^2_{\rm UWI} &= \sum_{\{\mathbf{h}\}} \left(\left|F_{\rm obs}(\mathbf{h})\right|^2 - \left|F_{\rm calc}(\mathbf{h})\right|^2\right)^2 \\ &= \int_V \left[P_{\rm obs}(\mathbf{u}) - P_{\rm calc}(\mathbf{u})\right]^2 {\rm d}^3\mathbf{u}. \qquad (4.3.7) \end{aligned}$$

In addition to $S^2_{\rm UWI}$ being the sum of the unweighted squares of the difference between the observed and calculated integrated intensities, it is also the integral over the difference between the observed and calculated interatomic vector maps (Patterson functions). This function is very similar to the function $S^2_{\rm CI}$, which accurately represents the minimization metric in the real-space structure-determination process. The only difference is the presence of the weight matrix, $(V^{-1}_{\rm PAW})$, in $S^2_{\rm CI}$. This has two consequences. The first concerns the on-diagonal terms, which are proportional to the inverse of the associated integrated intensity. This has the equivalent effect of sharpening the interatomic vector map features in the Patterson function by a factor of $\sim 2^{1/2}$. The second impact is from the off-diagonal terms. This is generally small for long *d*-spacing reflections but can be substantial at short *d*-spacings, where reflection overlap may become severe. In the limit of overlap, all reflections at a particular *d*-spacing will be completely overlapped. This is equivalent to forming a time-averaged pair distribution function where distance information is preserved but all directional information is lost. The goodness-of-fit functions in real-space structure determination will thus be smoother, and both inter- and intramolecular orientational information will be lost.

As a corollary, this real-space interpretation of severe overlap gives a clear rationale for the minimum *d*-spacing reflections to be used in the structure-solution process. A useful working criterion is to truncate the data at a point where the average separation between reflections is less than a fifth of the peak full width at half maximum. Assuming that the peak extent will be principally determined by strain broadening at short *d*-spacings leads to a $d_{\rm min}$ criterion of $\sim 2.7(\varepsilon N_{\rm AU})^{1/3}$, where $\varepsilon = \Delta d/d$ is the combined extent of the instrument resolution and strain broadening and $N_{\rm AU}$ is the number of non-hydrogen atoms in the asymmetric unit. ε will range from around 2×10^{-4} for sharply diffracting samples on synchrotron powder diffractometers to around 5×10^{-3} for samples with broader peaks on laboratory machines. The corresponding values for $d_{\rm min}$ for $N_{\rm AU}$ values of 20, 50, 100 and 500 are listed in Table 4.3.3 along with values of $\varepsilon = 2 \times 10^{-3}$ for good laboratory X-ray diffraction data.

Experience indicates that molecular structures may be solved using real-space SDPD alone if good diffraction data are available to a minimum *d*-spacing of ∼1.7 Å. This suggests that molecular structures with up to 50 atoms in the asymmetric unit may be solved from relatively poor diffraction data and up to 100 atoms for excellent laboratory data. This is a fair assessment of the potential of real-space structure determination from laboratory data alone, although the availability of additional informa-

Table 4.3.3
Estimated minimum *d*-spacing range extent (in Å) for structure solution for different complexities of molecular structures using low (5×10^{-3}), medium (2×10^{-3}) and high (2×10^{-4}) resolution instrumentation

	N_{AU}			
ε	20	50	100	500
5×10^{-3}	1.4	1.8	2.3	4.0
2×10^{-3}	0.9	1.3	1.6	2.7
2×10^{-4}	0.5	0.7	0.9	1.6

tion from, for example, NMR may extend these limits. The numbers for the very highest resolutions available with a combination of excellent sample and synchrotron powder diffraction suggest that very large structures may be successfully tackled, and this is indicated by the success of protein powder-diffraction measurements. However, the concomitant increase in structure complexity and, in particular, the combinatorial increase in torsion-angle conformations make real-space structure determination a difficult task without involving either new algorithm development or the use of ancillary information about inter- and intramolecular geometries from structural databases or additional experimental measurements.

Equation (4.3.7), with consideration of the impact of $(V_{\rm PAW}^{-1})$, gives a numerical assessment and clear picture of the impact of moving atoms around the unit cell in the process of real-space structure determination. This will be discussed further in Section 4.3.4.2.

4.3.4.2. *The chi-squared hypersurface*

In the remaining sections of this chapter, all references to structural parameters will be considered within the context of molecular-connectivity algorithms. The *Z*-matrix algorithm will be explicitly used and it will mostly be assumed that only the external rotational and translational and the internal torsional degrees of freedom will be adjusted. External orientation degrees of freedom may be described by either Euler angles or quaternions. For a comparison of the use of Euler angles and quaternions in crystallography, see Skone *et al.* (2013). The quaternion method (see Mackay, 1984) will be used in the remaining sections of this chapter.

Unsurprisingly, the initial selection of structural parameters in a real-space structure determination essentially never results in a structure that is close to the correct answer and the cost function (designated as χ^2 for convenience) is always much higher than the final value associated with the correct structure. In this section, the nature of the χ^2 hypersurface as a function of the various structural parameters is considered. The discussion principally focuses on the real-space structure determination of the histamine H2-receptor antagonist famotidine (Shankland *et al.*, 2002), $C_8H_{15}N_7O_2S_3$, using high-resolution synchrotron X-ray powder-diffraction data at 130 K at a wavelength of 0.85075 Å on the diffractometer ID31 at the ESRF, Grenoble. Famotidine adopts the space group $P2_1/c$ with lattice parameters $a = 17.652$, $b = 5.293$, $c = 18.256$ Å, $\beta = 123.56°$ and $V = 1421.6$ Å^3. The diffraction data were truncated at a minimum *d*-spacing of 1.75 Å. The molecule and crystal structure of famotidine are shown in Fig. 4.3.4. The seven internal torsion angles are shown in Fig. 4.3.4(*a*).

Fig. 4.3.5 shows the frequency distribution of $\chi^2_{\rm CI}$ values [equation (4.3.6)] of 10^6 randomly selected sets of structural parameters (six external and seven internal torsional degrees of freedom). Over 98% of $\chi^2_{\rm CI}$ values are very high.

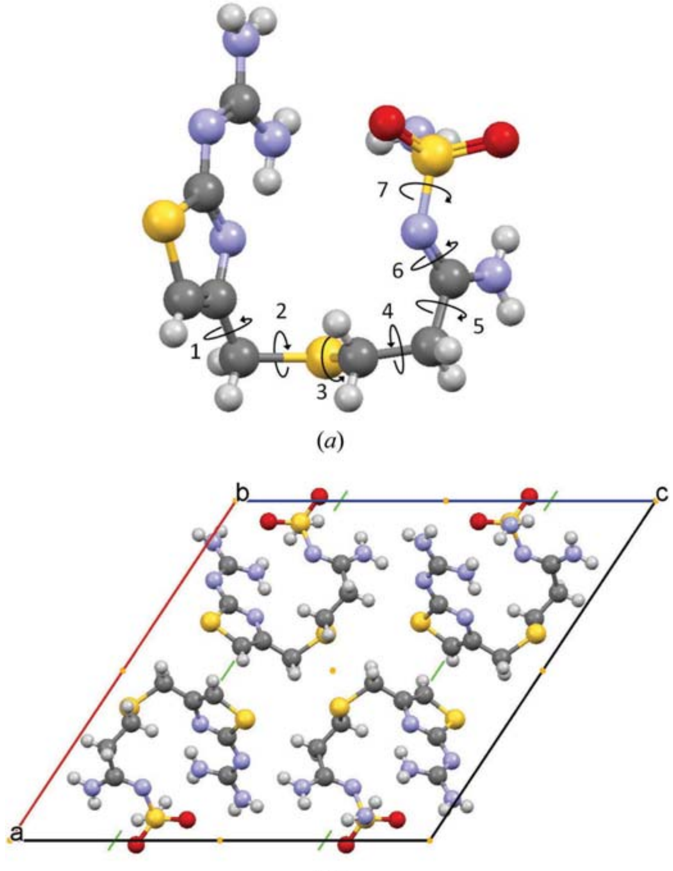

(*a*)

(*b*)

Figure 4.3.4
(*a*) The molecular structure and (*b*) the *b*-axis projection of the crystal structure of the polymorphic form B of famotidine. The seven internal torsion angles are enumerated in (*a*).

Fig. 4.3.6 gives an insight into this distribution of $\chi^2_{\rm CI}$ values. The two-dimensional section of the $\chi^2_{\rm CI}$ hypersurface shows $\chi^2_{\rm CI}$ as a function of *x* and *z* translational external degrees of freedom; all other parameters are set at the best refined values. Two sets of four deep minima are observed. The minima come in quartets because four different enantiomers are represented in this figure; all four deepest minima represent correct equivalent solutions that are illustrated in Fig. 4.3.6. There are a number of further significant features in this two-dimensional section of the $\chi^2_{\rm CI}$ hypersurface that merit further discussion.

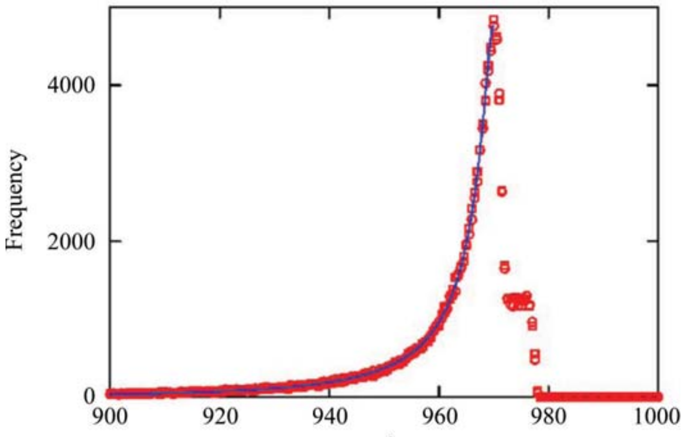

Figure 4.3.5
The $\chi^2_{\rm CI}$ frequency distribution for famotidine (form B).

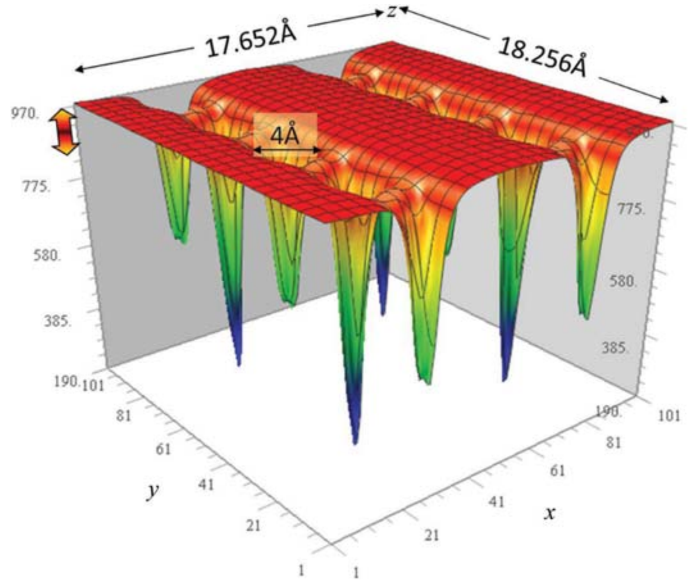

Figure 4.3.6
Two-dimensional section of the $\chi^2_{\rm CI}$ hypersurface showing the variation in $\chi^2_{\rm CI}$ as function of x and z translations.

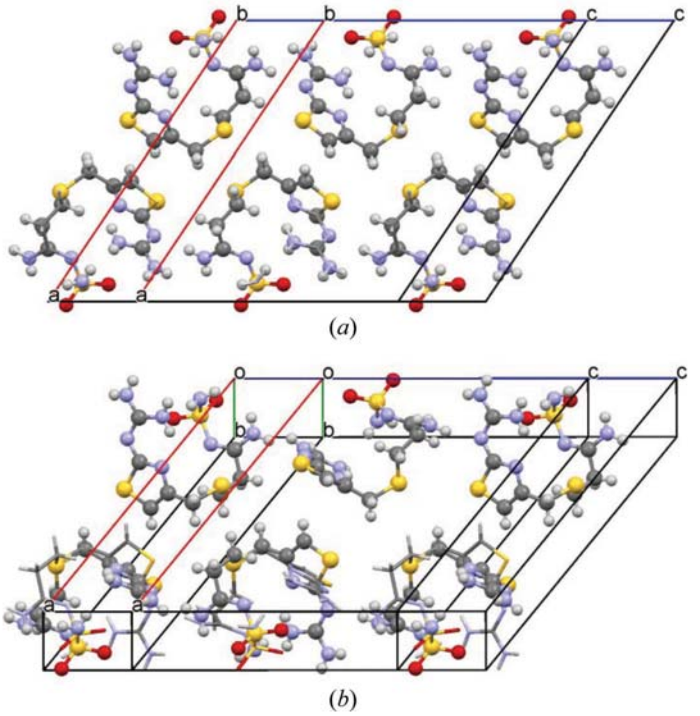

(*a*)

(*b*)

Figure 4.3.7
Comparison of the crystal structure shifted by z = 1/4 with the correct crystal structure of famotidine (form B). (*a*) The *b*-axis projections of the two structures are identical, implying that all $h0l$ reflections will be identical, and (*b*) an off-axis projection indicating the small differences in the crystal structure associated with the two deep fourfold-degenerate minima in Fig. 4.3.6.

Firstly, despite the fact that all the other 11 structural parameters are at their correct values, the majority of this surface is at high $\chi^2_{\rm CI}$ values equivalent to the highest observed with the random generated structures; see Fig. 4.3.5. The correct structure is never far away from a wrong solution that fits the diffraction data very badly. However, this top plateau is not reached for all the structural parameters. Later in this section it will be shown that the biggest $\chi^2_{\rm CI}$ changes are associated with the external rotational and translational parameters that involve the movement of the largest number of atoms and the greatest change in the number of interatomic vectors.

A second important point illustrated in Fig. 4.3.6 concerns the probability of choosing an x, z pair of coordinates at random and directly minimizing to the correct solution. The areas of each minimum are at least 4×4 Å^2 = 16 Å^2 out of a possible ~320 Å^2. With four degenerate correct and incorrect solutions, the probability of dropping into any of these minima will be greater than 0.4. Indeed, the flatness of the plateau suggests that there may be a 50:50 chance of obtaining the correct solution and that no other minima exist. This observation agrees with the discussion in Section 4.3.3 that the use of molecular connectivity in real-space structure determination costs an unexpectedly small factor of around two for each degree of freedom.

The third point of note in Fig. 4.3.6 is that the $\chi^2_{\rm CI}$ surface shows different behaviour as a function of the x and z translational coordinates. There is a substantially larger plateau region between solutions along the x coordinate, whereas the plateau is not reached along the z coordinate because of the presence of deep local minima between the global minima. Indeed, the four degenerate local minima are sufficiently deep to appear to be a relatively good fit to the data. The reason for this is illustrated in Fig. 4.3.7.

The local minima correspond to all the structural parameters being correct except for the z coordinate, which is shifted by 1/4. The corresponding incorrect structure (capped sticks in the figure) is superposed upon the correct structure (ball-and-stick model). The *b*-axis projection shown in Fig. 4.3.7(*a*) indicates an exact overlap in projection between the two structures, implying that all $h0l$ reflection intensities are the same for both. Given the short b axis, the $h0l$ reflections dominate the powder diffraction from long to intermediate d-spacings and, for low angles in particular, the calculated diffraction pattern for both correct and incorrect structures will be identical. Differences will only be seen at intermediate angles and even then these will be subtle as, from Fig. 4.3.7(*b*), it can be seen that half of the molecules (upper row) are coincident with one another and the other half (lower row) only differ by a mirror plane at y = 3/4. These pseudosymmetry features are commonly found in good but not correct solutions and, in molecular structures with two long axes, the optimal fitting of all low-angle reflections can lead to an unwarranted confidence in the crystal structure. All reflections up to the limit of data resolution should fit well before there can be confidence in the correctness of the structure. Checking this should be the final arbiter in determining the correctness of the structure, but even here, as illustrated in the example of famotidine, this may not be straightforward as the intramolecular geometry is correct in both cases and it is only a small number of interatomic distances (those between the upper and lower rows) that are wrong. Fortunately, these correct and incorrect solutions must occur with essentially equal probability and the best approach is to perform a sufficient number of structure-solution attempts to find the correct one. This has been discussed by Shankland *et al.* (2010), who successfully obtained the correct structure through multiple local minimizations.

Fig. 4.3.8 shows the distribution of $\chi^2_{\rm CI}$ obtained after minimizing 20 000 randomly chosen sets of parameters. This distribution is well-fitted to a log-normal distribution. When compared with the distribution of $\chi^2_{\rm CI}$ associated with randomly chosen structures (see Fig. 4.3.8*b*), the log–log scale reveals a number of significant details about the nature of the $\chi^2_{\rm CI}$ hypersurface. The log-normal distribution of minima (which appears as a quadratic function on a log–log scale) is shifted to significantly lower values than the $\chi^2_{\rm CI}$ values of the randomly selected structures. Indeed, the extrapolation of the latter distribution indicates that the

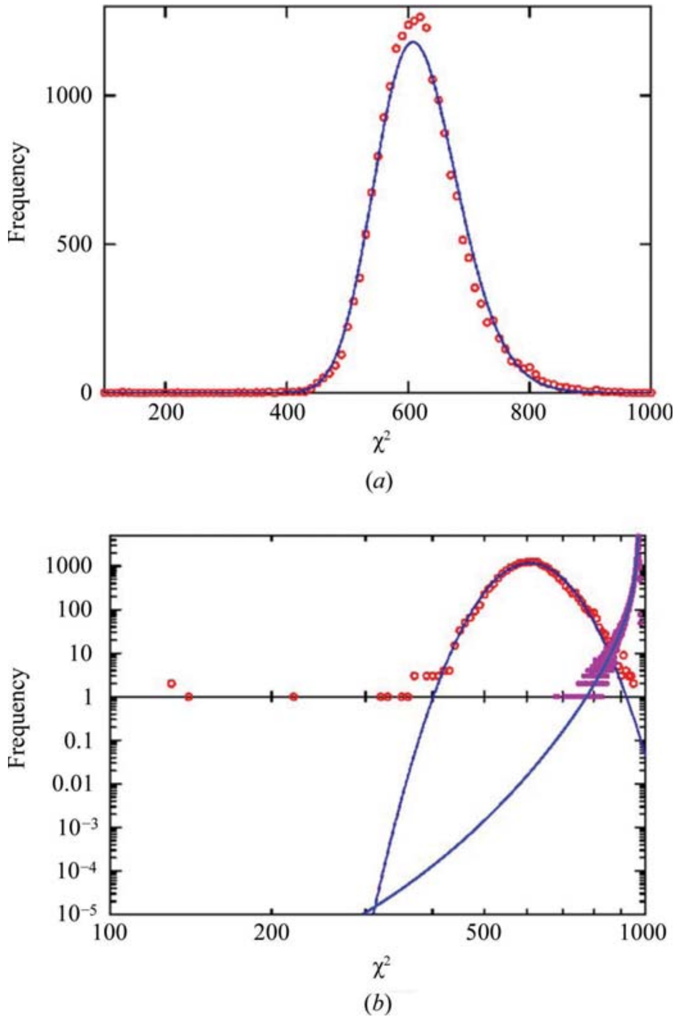

Figure 4.3.8

(*a*) The log-normal distribution of local minima obtained from steepest-descents minimization of 20 000 randomly selected famotidine form B crystal structures. (*b*) A log–log representation of the $\chi^2_{\rm CI}$ distributions of (i) random selected structures (purple points – fitted to an exponential distribution) and (ii) local minima (red points – fitted to a log-normal distribution). Note the small number of good and excellent $\chi^2_{\rm CI}$ values that depart from the log-normal distribution.

direct location of any of the many local minima is extremely improbable. As a consequence, efficient minimization is an essential component of any real-space structure-determination program. This, however, must be balanced with the requirement of escaping local minima, of which there are clearly a very large number that are substantially deeper than their immediate neighbourhood in the $\chi^2_{\rm CI}$ hypersurface. This conflict between efficient minimization and the need to escape local minima is the principal challenge facing a real-space global-optimization method. Many different approaches to this problem have been developed and are discussed in detail in Section 4.3.5.

The log–log scale in Fig. 4.3.8(*b*) also reveals that the tails of the frequency spectrum of the $\chi^2_{\rm CI}$ minima deviate from the log-normal distribution. There are deep minima that are distinct from the very large number of local minima that have $\chi^2_{\rm CI}$ values above 400. As discussed previously, all these minima are found to have some aspect of the correct solution either by translational pseudosymmetry or by correlated torsional mistakes that enable the strongly scattering components of the molecule (these are the sulfur atoms and rigid planar components in famotidine) to be located in approximately the correct position, while the weaker scattering components are not.

This is illustrated in Fig. 4.3.9, which shows three solutions that are correctly located with respect to both the translational and orientational external degrees of freedom. The structure corresponding to $\chi^2_{\rm CI}$ = 135 is the correct solution with the lowest goodness of fit. The structure with $\chi^2_{\rm CI}$ = 224 has only two carbon atoms that are substantially misplaced because of two correlated mistakes associated with neighbouring torsion angles. Again, the chemical differences between these two structures are small, as all the bond lengths and angles and the majority of torsion angles are correct. Given that both these structures look chemically sensible, care must be taken in ensuring that the correct structure has been found. The third solution ($\chi^2_{\rm CI}$ = 325) shown in Fig. 4.3.9 contains more incorrect torsion angles. Nevertheless, all the strongly scattering components of the molecule are correctly located, which, of course, must be the case for the $\chi^2_{\rm CI}$ value to be so low. It is interesting to conjecture that some of these solutions may represent metastable polymorphs; this could be tested using computational modelling techniques such as dispersion-force-corrected density-functional-theory geometry optimization.

Earlier in this section, it was noted that the global minimum was closely surrounded by regions of very high $\chi^2_{\rm CI}$. With all other parameters at their correct values, displacement of only the *x* coordinate by any value between 0.15 and 0.35 resulted in a $\chi^2_{\rm CI}$ value that was amongst the highest observed in the 10^6 random structure evaluations.

The *x*-coordinate shifted structure for $\Delta x = 1/4$ is shown in Fig. 4.3.10 and it is immediately clear why the agreement between the observed and calculated diffraction data is poor, as pairs of famotidine molecules are completely overlapped, leaving half the unit cell entirely devoid of any atoms and consequently totally absent of any scattering density.

Changing any of the translational or rotational external degrees of freedom has a significant impact on the $\chi^2_{\rm CI}$ goodness of fit because all the atoms are moved away from their correct positions. This impact may be quantified by investigating the changes in $\chi^2_{\rm CI}$ associated with different structural parameters during a real-space structure determination. Unsurprisingly, the effect of changing the other structural parameters (torsion angles, bond angles and bond lengths) is generally smaller, as fewer atom positions are altered in the process. This is illustrated in Fig. 4.3.11, which shows the r.m.s. fluctuation of $\chi^2_{\rm CI}$ in the initial stages of the structure solution of famotidine using *DASH* (David *et al.*, 2006). In addition to the six external and seven torsional degrees of freedom, four bond angles and six bond lengths are also allowed to vary. The logarithmic scale in Fig. 4.3.11 highlights

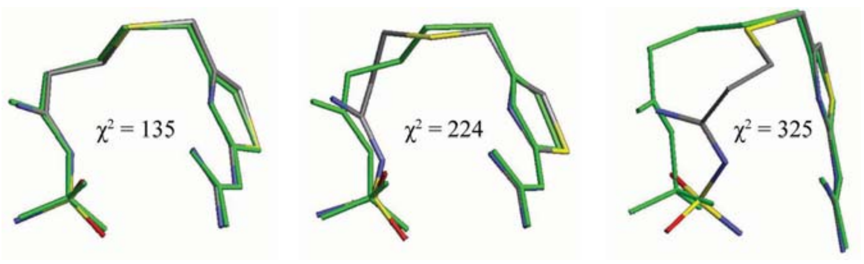

Figure 4.3.9

Three good solutions for the crystal structure determination of famotidine form B. All three solutions are correctly located with respect to both the translational and orientational degrees of freedom. The structure with $\chi^2_{\rm CI} = 135$ represents the correct solution. All the heavier atoms are essentially correctly located in the other two structures.

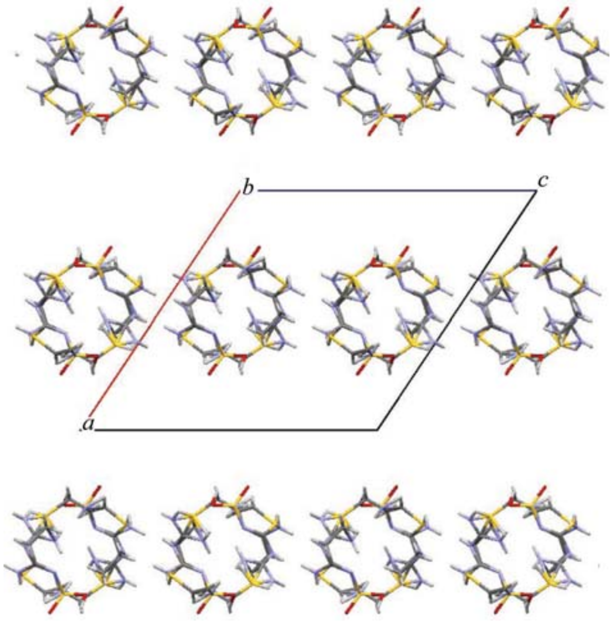

Figure 4.3.10
The crystal structure of famotidine form B associated with a $\Delta x = 1/4$ shift from the correct solution.

the substantial differences in the impact of the various structural parameters. The $\chi^2_{\rm CI}$ variations associated with bond-length variations are always small. This can be understood by recollecting the essential equivalence between $\chi^2_{\rm CI}$ and the volume integral of the square of the difference between observed and calculated interatomic vector maps; see Section 4.3.4.1. A single bond-length alteration only changes the interatomic vectors associated with two atoms, which is only a small fraction (approximately $1/N_A$) of the Patterson function. Moreover, the $\sim$2 Å blur associated with the real-space interpretation of $\chi^2_{\rm CI}$ [equation (4.3.6)] implies that small distance changes in interatomic vectors will have little impact on $\chi^2_{\rm CI}$ values. Indeed, fluctuations in $\chi^2_{\rm CI}$ from bond-length variations are never observed to be greater than 10 in Fig. 4.3.11 and therefore there is no advantage in including bond lengths as structural parameters in a structure solution, as they simply slow down the structure-solution process by introducing unnecessary additional $\chi^2_{\rm CI}$ evaluations.

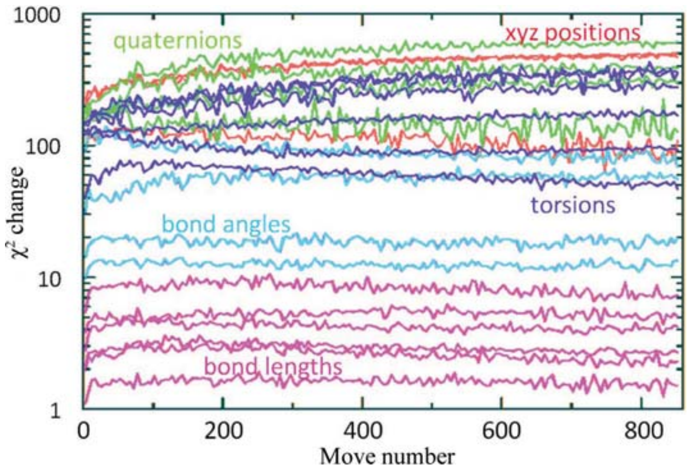

Figure 4.3.11
The move-by-move change in $\chi^2_{\rm CI}$ observed during a real-space structure-solution run for famotidine form B. Changes in orientation (quaternions) and location of the molecule have the largest effect on $\chi^2_{\rm CI}$. The effects of torsion angles, bond angles and bond lengths are progressively smaller.

It can be seen from Fig. 4.3.11 that bond angles produce greater $\chi^2_{\rm CI}$ changes than bond lengths, with values ranging from about 10 to about 100. Variations in key angles, such as the central C—S—C angle, will result in major alterations in the interatomic distances between opposite ends of the molecule and should be allowed to vary over the range of expected values if there is any significant bond-angle uncertainty. Most angles, however, are either adequately known or do not significantly alter the interatomic distances within a molecule and therefore need not be varied.

The remaining structural parameters, *i.e.* the translational and orientational external coordinates and internal torsion angles, can all have a major impact on the $\chi^2_{\rm CI}$ goodness of fit. Translational degrees of freedom change all the intermolecular interatomic vectors, while the orientational degrees of freedom alter both inter- and intramolecular interatomic vectors. It is thus to be expected (and is observed in the case of famotidine) that the orientational degrees of freedom, expressed in terms of quaternions, exhibit a slightly larger effect than the translational degrees of freedom. Key torsion angles, particularly those involving the central sulfur atoms, have an impact that is almost equivalent to the external degrees of freedom. Again, this can be understood in terms of the number of interatomic vectors that are changed. Torsion angles affect a subset of intra- and intermolecular interatomic vectors and, for this reason, generally have less impact than the orientational and translational coordinates. Indeed, the larger the fragment that is rotated on altering a torsion angle, the larger will be the change in $\chi^2_{\rm CI}$.

Parameters that should be included in a real-space global-optimization structure solution are those that have the potential to move a significant proportion of the crystal structure resulting in a change of a substantial fraction of the interatomic vectors by more than about 2 Å. These parameters are the external orientational and translational coordinates and the internal flexible torsion angles. The only significant addition to this set may be a key angle which possesses a range of possible values; it is important for the success of the structure solution that the angular range is limited to the range of possible values. Finally, varying known bond lengths and angles in a structure solution should be avoided, as including this only slows down the structure-solution process.

4.3.5. Global-optimization algorithms

The important issues for global optimization for real-space SDPD may be summarized as follows:

(1) Real-space structure determination may be regarded as a global Rietveld analysis where an initial, generally poorly fitting, structural model is proposed. With multiple iterations, the fit between observed and calculated diffraction data improves until excellent agreement is obtained and the resulting structure may be finally refined to obtain the correct crystal structure.

(2) For molecular crystal structures, the molecular connectivity (using the *Z*-matrix or equivalent formalism) provides an optimal method for defining the structural parameters that should be used in the global-optimization process.

(3) There are numerous local minima (greater than about 2^{N_P}) on the N_P-dimensional goodness-of-fit hypersurface. Any global-optimization program must be able not only to explore these minima but also escape false minima, some of which

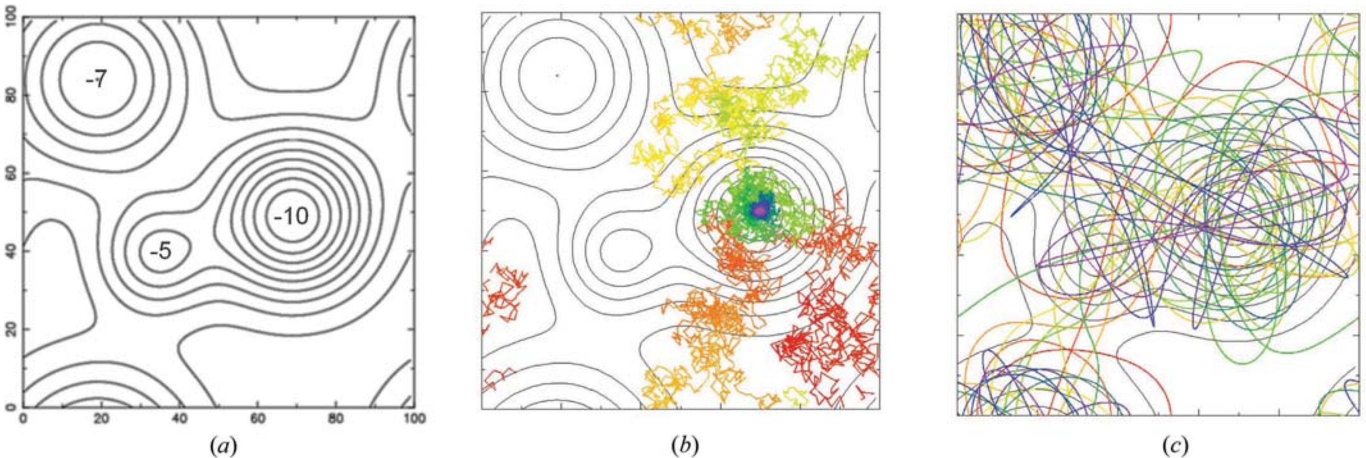

Figure 4.3.12
(*a*) A simple periodic potential-energy function constructed over a square cell. The maximum value of the potential energy is 0, with uniform contour levels shown. The function has three minima with values of −10, −7 and −5 at positions (70, 50), (20, 83) and (35, 40), respectively. (*b*) A simulated-annealing (SA) solution for the test function shown in (*a*). The SA run consists of 1000 moves and locates the global minimum. The figure highlights the random-walk nature of the SA algorithm. (*c*) A molecular-dynamics (MD) solution for the test function shown in (*a*). The MD run consists of 1000 steps and, significantly, all three minima are visited many times. The smooth trajectory is a consequence of the deterministic nature of MD equations of motion.

may appear to be excellent solutions and yet do not correspond to the correct crystal structure.

An effective global-optimization program for the real-space determination of molecular crystal structures must have properties that address all three of these issues. A wide range of programs and algorithms have been developed and these are discussed here.

Global-optimization programs can be broadly characterized as either stochastic (involving a substantial component of randomness in structural-parameter selection) or deterministic (involving a directed path from iteration to iteration for the structural parameters). The generic aspects of these conceptually very distinct algorithms are illustrated in Fig. 4.3.12, which shows the different search characteristics over a simple periodic function constructed over a square cell. (This could correspond to probing the full-range goodness-of-fit surface with two degrees of freedom.) In terms of understanding global-optimization algorithms, it is easier to consider the figure as representing a conceptually equivalent gravitational-potential-energy surface with the contours indicating depth rather than the goodness of fit.

Fig. 4.3.12(*b*) shows the trajectory followed by a simulated-annealing algorithm. This trajectory, which begins with red and follows the colours of the rainbow through to indigo, reaches the basin of the deepest minimum very quickly after around 100 moves. Direct downhill minimization at this point would lead to the correct solution. However, the algorithm can also enable the trajectory to leave the global minimum basin. It is this balance between the requirements of escaping false minima and efficiently reaching the global minimum that makes global optimization a difficult and often computationally expensive process. The trajectory in Fig. 4.3.12(*b*) essentially performs a random walk over a large area of high potential-energy values before finally settling into the global minimum. This search over high values is necessary if other deep minima are to be found. Of concern, however, is that this particular trajectory only samples a single minimum and this highlights the necessity of multiple attempts to reach the global minimum. Other stochastic processes such as genetic algorithms show a different behaviour from iteration to iteration. However, the time-averaged population of the energy landscape is similar, with a random distribution of attempts that are biased towards the best solutions and, as a consequence, the general issues discussed in this section also apply to these and other stochastic global-optimization algorithms.

The trajectory in Fig. 4.3.12(*c*), which is determined by a hybrid Monte Carlo (HMC) molecular-dynamics algorithm, shows an altogether different behaviour. Here, it is best to consider the trajectory in terms of the movement of a particle over the potential-energy surface. A position is selected at random and the particle is given an initial velocity vector and associated kinetic energy that is sufficient for it to move over the highest point on the surface. The particle trajectory is required to obey Hamilton's equations of motion for the combined kinetic and potential energies. The resulting trajectory must preferentially sample areas of lower potential energy, but also has sufficient total energy to escape these minima and explore the complete range of the potential-energy surface. Fig. 4.3.12(*c*) shows that the trajectory sampling is highly optimal, with the maximum amount of time spent within all the minima and with significant areas of high potential energy completely unexplored. The first observation means that there is a high probability that a significant fraction of deep minima will be visited in an HMC optimization, while the latter suggests that the particle dynamics introduce aspects of the search where high-potential-energy locations are not only not revisited but are never visited. These aspects of the deterministic trajectory and the stochastic trajectory are illustrated in Figs. 4.3.12(*c*) and (*b*), respectively, and are comparable with the difference between a downhill skier who can ski down into valleys and, without friction, ski straight back out again with a view to heading down the next valley, and a random walk that has the tendency to head in the right direction but can also waste time exploring unprofitable features. Unsurprisingly, the few studies of deterministic algorithms (Johnson *et al.*, 2002) all report a significantly improved performance. However, the implementation of stochastic algorithms such as simulated annealing and genetic algorithms is simpler, and they have been found to be effective in a wide range of structure solutions.

In the remainder of this section, the basic properties of the various search algorithms for real-space structure determination are presented along with a comprehensive list of references and examples of successful structure solutions.

4.3.5.1. *Stochastic search algorithms*

4.3.5.1.1. *Introduction*

The most widely used real-space global-optimization methods for the structure determination of organic compounds are stochastic in nature and can be colloquially described as a 'random walk through the good solutions'. Many different stochastic methods have been explored that include: simple Monte Carlo (Harris *et al.*, 1994), genetic algorithms (Shankland *et al.*, 1997*a*,*b*; Kariuki *et al.*, 1997; Harris *et al.*, 2004; Feng & Dong, 2007), evolutionary strategies (Chong & Tremayne, 2006) and particle swarm (Csoka & David, 1999), but it is simulated annealing (Andreev *et al.*, 1997; David *et al.*, 1998, Engel *et al.*, 1999; Putz *et al.*, 1999; Pagola & Stephens, 2010; Coelho, 2000; Favre-Nicolin & Černý, 2004*b*; David *et al.*, 2006) that is most widely used and that has had the largest impact. Its high level of success may be attributed to the fact that it is an effective, easy-to-use algorithm with relatively few control variables that can all be set automatically. Various modifications to the basic annealing scheme, such as parallel tempering (Earl & Deem, 2005), have been implemented (Favre-Nicolin & Černý, 2004*b*). Of the other stochastic algorithms, genetic algorithms in particular have been shown to be capable of delivering solutions of considerable complexity (Albesa-Jove *et al.*, 2004; Feng & Dong, 2007).

4.3.5.1.2. *Monte Carlo methods*

The Monte Carlo method (Metropolis, 1987) is an algorithm that involves repeated random sampling to simulate systems with many degrees of freedom – systems that are difficult to solve analytically. The first significant success (Harris *et al.*, 1994) in real-space SDPD implemented a random-walk Monte Carlo approach regulated by an acceptance criterion, originally proposed by Metropolis *et al.* (1953), that provides a statistical balance between downhill moves (χ^2 improvement) and uphill moves that can escape local minima. Specifically, the Metropolis criterion states that all downhill moves should be accepted, while uphill moves are accepted with a Boltzmann probability given by $\exp[-(\chi^2_{(k+1)} - \chi^2_{(k)})/T]$, where $\chi^2_{(k+1)}$ and $\chi^2_{(k)}$ are the goodness-of-fit values for iterations $(k+1)$ and (k), respectively, and the pseudo-temperature (denoted subsequently simply as temperature), T, is on a χ^2 scale. Harris *et al.* chose the temperature, T, so that around 40% of the uphill moves were accepted. The method was tested on the known crystal structure of p-$CH_3C_6H_8O_2NHNH_2$ and successfully used to solve the unknown crystal structure of p-$BrC_6H_4CH_2CO_2H$.

4.3.5.1.3. *Simulated-annealing methods*

Simulated annealing extends the Monte Carlo method by recognizing that in the early stages of global optimization it is important to accept worse solutions so that an extensive search may be made over parameter space, and that towards the end of the solution process there is little necessity for uphill moves as the targeted (hopefully global) minimum is approached. This change in the acceptance of uphill moves is effected by a slow lowering of the temperature, T, as the global-optimization process progresses. The method is called simulated annealing because the similarity with the physical process of annealing is a strong one with a number of important correspondences. The rate of cooling in a simulated-annealing optimization must, as with physical annealing, be considered with care to avoid quenching to a sub-optimal state. For annealing, this would be a kinetically stabilized state that is not thermodynamically stable; for simulated annealing, the corresponding state is a deep local (but not the global) minimum. Both the physical and computational processes generally have a phase transition that is marked by significant energy or χ^2 fluctuations and this stage in the annealing process must be treated with the greatest care. The earliest structure solutions using simulated annealing indicated the extended scope of the technique with the successful solutions of the crystal structure of the polymer electrolyte $LiN(SO_2CF_3)_2$ (Andreev *et al.*, 1996) and the molecular crystal structures of capsaicin, promazine hydrochloride and thiothixene (David *et al.*, 1998). The latter paper introduced a fast, automated simulated-annealing computer program that was the progenitor to *DASH* (David *et al.*, 2006). A significant number of simulated-annealing programs are available for use including *DASH* (David *et al.*, 2006), *FOX* (Favre-Nicolin & Černý, 2004*a*,*b*), *PowderSolve* (Engel *et al.*, 1999), *TOPAS* (Coelho, 2000), *WinPSSP* (Pagola *et al.*, 2017) and *Endeavour* (Putz *et al.*, 1999). The range of complexity of molecular structures that can be solved from powder-diffraction data alone using real-space SDPD techniques has been estimated to extend to around half of the molecular structures in the Cambridge Structural Database. A representative sample of solved structures has been reported by Florence *et al.* (2005), who determined 35 new structures. Three of the more complex structures are illustrated in Fig. 4.3.13. Perhaps the most impressive example to be solved to date using real-space SDPD is the simulated-annealing structure of the malaria pigment beta-haematin by Pagola *et al.* (2000); see Fig. 4.3.14.

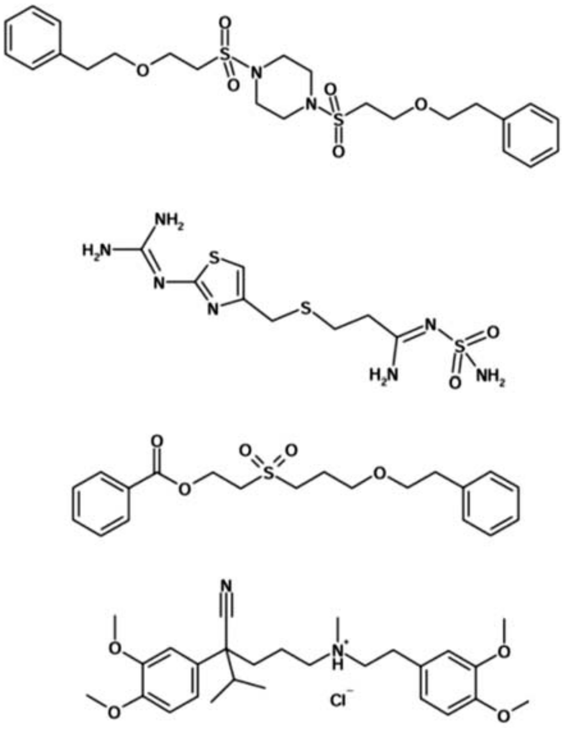

Figure 4.3.13
Molecular structures of 1,4-bis(2-phenethyloxyethanesulfonyl)piperazine, famotidine, 2-{[3-(2-phenylethoxy)propyl]sulfonyl}ethyl benzoate and verapamil hydrochloride.

The first step in a simulated-annealing procedure is the generation of an initial structure using a random set of parameters for both the external translational and orientational degrees of freedom and the internal torsion angles. One of the structural parameters, $p(i)$, is adjusted to a new value, $p'(i) = p(i) + \Delta p(i)$, and the diffraction pattern is recalculated. $\Delta p(i) = \mathrm{RAND}(-0.5{:}0.5)\Delta p_{\max}(i)$, where $\mathrm{RAND}(\ldots)$ is a random number between -0.5 and 0.5 and $\Delta p_{\max}(i)$ is the

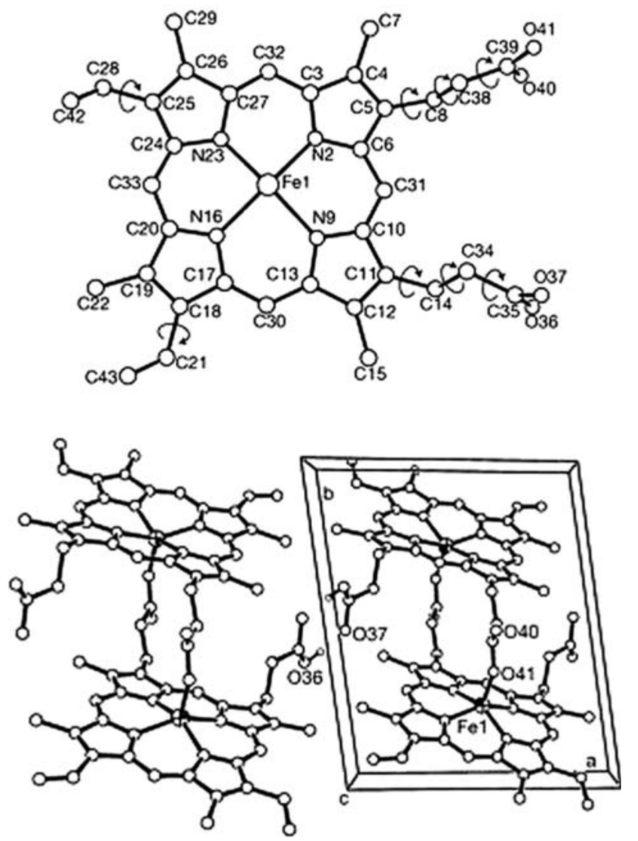

Figure 4.3.14

The molecular structure and crystal structure of the malaria pigment B-haematin. Reprinted by permission from Springer Nature (Pagola *et al.*, 2000).

magnitude of the maximum shift. This should initially represent the full extent of the range of the associated structural parameter. If the move represents an improvement, then the new structure is accepted. If the fit is poorer, then the new parameterization is not automatically rejected but is accepted with a Boltzmann probability of $\exp[-(\chi_1^2 - \chi_0^2)/T_0]$, where T_0 is the χ^2 'temperature', which is chosen so that a reasonable number of uphill moves are accepted. Consider the distribution of χ^2 values for famotidine illustrated in Fig. 4.3.5. In this case, it is highly probable that both χ_0^2 and χ_1^2 will be between ∼920 and ∼970. To ensure that there is an even probability of accepting an uphill move $\exp[-(\chi_1^2 - \chi_0^2)/T_0] \simeq \exp(-100/T_0) \simeq 0.5$, and so a good value for the initial temperature, T_0, would be ∼70. In other words, the initial temperature should approximate the χ^2 values of the initially randomly chosen structures. This effective temperature is maintained for $\sim 100N_p$ moves (where N_p is the number of parameters) with each parameter adjusted sequentially. The temperature is then lowered, which results in slightly fewer accepted uphill moves, and the procedure is repeated. A simple annealing schedule involves lowering the temperature by ∼2–5% each time.

In each simulated-annealing run, there is a transition from the sampling of only poor (high-χ^2) solutions to the sampling of both poor and good (low-χ^2) solutions. In the case of famotidine, the χ^2 values range from 990 to ∼750, corresponding to the onset of local minima; see Fig. 4.3.8(*a*). With a temperature of ∼70, the chance of a direct escape from the minimum is ∼1:30. Fortunately, there are intermediate plateaux and higher minima in the χ^2 hypersurface that permit escape from deep local minima. However, the observation of large χ^2 fluctuations is a signal to anneal more slowly. In general, a slow reduction in temperature through the high χ^2 fluctuation region of a simulated-annealing calculation generally leads to a much higher probability of reaching the global minimum and the resulting correct crystal structure.

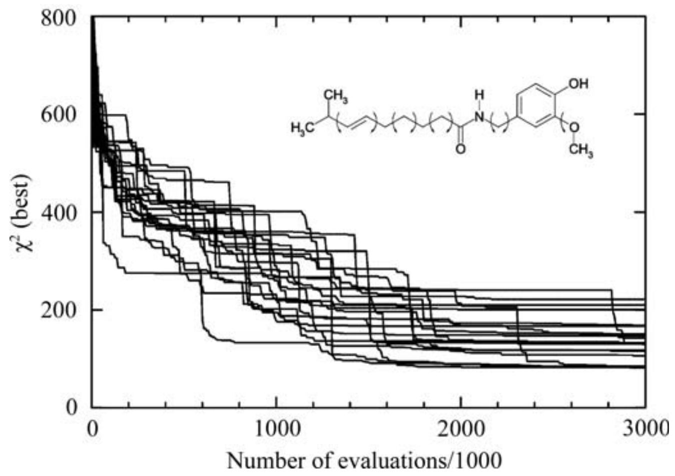

Figure 4.3.15

A plot of the best χ^2 values *versus* the number of χ^2 evaluations for the 20 simulated-annealing structure-solution attempts for capsaicin (after Shankland *et al.*, 2002). For comparison, see also Fig. 4.3.18.

A final consideration in the annealing protocol is the extent of the range, $\Delta p_{\max}(i)$, explored by each parameter shift. Initially, this range should explore the full parameter space. However, as the simulated-annealing process proceeds and good solutions are explored, this is inefficient. The best protocol is to ensure that the success rate for uphill moves remains around 0.5 as the temperature reduces. This reduction in parameter range is parameter dependent. For external translational and orientational parameters and significant torsion angles the reduction can be significant, while for torsion angles that do not change χ^2 significantly $\Delta p_{\max}(i)$ may not reduce at all. Additionally, when good solutions are obtained, there should be the option of direct downhill minimization. This can substantially speed up the final minimization and can be triggered automatically when χ^2 reaches a threshold; a good choice is when the ratio of Rietveld to Pawley χ^2 values is less than 5–10.

Despite these protocols, the stochastic nature of the simulated-annealing process means that structure solution is not guaranteed. Multiple runs are required. As shown in Fig. 4.3.15, if the observed success rate is low then the number of structure-solution attempts should be sufficiently high that at least 5–10 similarly low-χ^2 solutions are obtained, all corresponding to an excellent fit to the data. For a more general crystallographic discussion, see, for example, Brünger (1991).

4.3.5.1.4. *Parallel tempering*

While the underlying paradigm of simulated annealing is straightforward and readily understood, concerns about the choice of initial temperature and annealing schedule have led to the development and use of a closely related algorithm: parallel tempering. Here, as the name suggests, multiple constant-temperature runs are performed in parallel. Commonly, there are 5–10 temperatures, $T_1 < T_2 < \ldots < T_N$, where T_N is similar to the initial simulated-annealing temperature, T_0, and T_1 is a low temperature similar to the final expected χ^2 value. Few uphill moves are allowed for T_1 even when low-χ^2 values are obtained, while for T_N there is a relatively high probability of uphill moves even at the beginning of the structure-solution process. Thus the

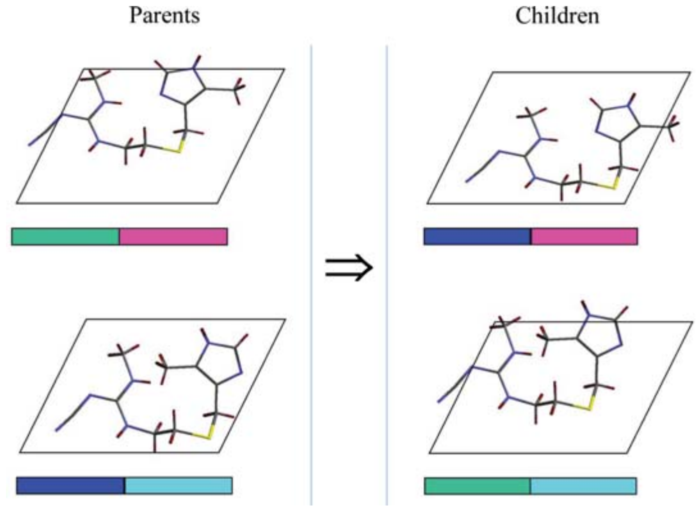

Figure 4.3.16
A single-point molecular crossover for cimetidine. In this simple example, each molecule is coded by only two genes, the leftmost one denoting the location of the central sulfur atom within the unit cell, the rightmost one denoting the torsion angle of the bond connecting the five-membered ring to the main chain. Note that after the crossover operation both children have inherited a position from one parent and a torsion angle from the other.

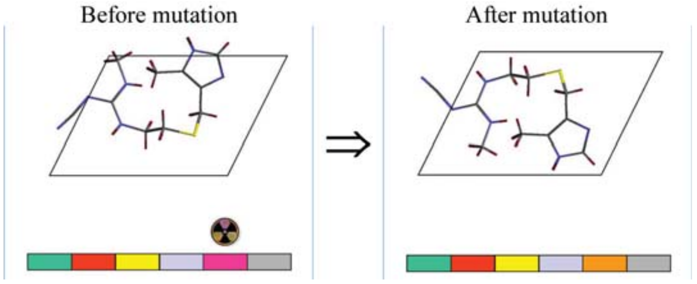

Figure 4.3.17
Mutation of a single gene influencing the orientation of a cimetidine molecule within the unit cell. A chance event (denoted by the mutation symbol) results in the value of a single gene changing to some new, random value. The result of this mutation is to turn the molecule upside down within the unit cell. In this way, new regions of space can be explored.

N temperatures together span the full range of criteria for accepting and rejecting moves.

The N parallel-tempering runs follow the same procedure as outlined in the previous section for a single temperature segment of a simulated-annealing run. Moves are always accepted if they lead to an improvement in the goodness of fit and are accepted with a probability $\exp\{-[\chi^2(k+1) - \chi^2(k)]/T_n\}$ for move $(k+1)$ at temperature T_n when the fit decreases. The temperatures T_n are chosen to follow a relationship of the form $T_{n+1} = \alpha T_n$ where $\alpha^N = T_N/T_1$.

The most significant aspect of parallel tempering is that moves may be swapped between different, normally adjacent, temperatures. After a set number of moves, which may be random, an exchange between the moves associated with T_n and T_{n+1} is performed with a probability given by $\min[1, \exp\{[\chi^2_n(k) - \chi^2_{n+1}(k)](T_n^{-1} - T_{n+1}^{-1})\}]$. This circumvents the need for an annealing protocol and is thus insensitive to the existence of high χ^2 fluctuations near the equivalent transition to the liquid–solid transition in a real annealing experiment. Parallel tempering was introduced in a crystallographic context by Falcioni & Deem (1999) and Earl & Deem (2005), and has been extensively and successfully utilized in the *FOX* program (Favre-Nicolin & Černý, 2004*b*).

4.3.5.1.5. *Genetic algorithms*

Genetic algorithms are the most familiar of a class of methods that imitate the process of natural evolution in order to find the global optimum of a given function (Goldberg, 1989). The algorithm relies on the collective learning over many generations of an initial population or set of populations of individuals. Each individual has a particular set of attributes, which in the optimization process correspond to various values of the structural parameters to be determined. The individuals, therefore, represent points in the space of potential solutions of the function under evaluation. The function values at the respective points represent the fitness of each individual within the population. With an initial random choice of individuals, adaptation then proceeds by means of selection, crossover and mutation. The selection process allows those individuals with a better fitness (lower χ^2 goodness of fit) to have more of an opportunity to reproduce compared with those individuals with a worse fitness (higher χ^2). The subsequent reproduction results from information exchange between individuals (crossover) combined with mutation of the resulting offspring. These offspring then replace the initial population and the process repeats until a high level of fitness is found for an individual in the population. Reaching the global minimum in the optimization process equates to finding the optimal individual (with parameters that describe the correct structure) for a particular ecological niche (fitting the calculated diffraction pattern to the observed powder-diffraction data).

The genetic-algorithm approach for SDPD may be explicitly described as follows: the molecular crystal structure is determined in terms of the N_τ internal torsional $\left(\tau_1, \tau_2, \ldots, \tau_{N_\tau}\right)$ and external translational (x, y, z) and orientational (q_1, q_2, q_3, q_4) quaternion coordinates. In genetic-algorithm terminology, this sequence $\left(x, y, z, q_1, q_2, q_3, q_4, \tau_1, \tau_2, \ldots, \tau_{N_\tau}\right)$ is a chromosome with genetic information that describes the molecular crystal structures; the individual parameters are the genes. Crossover and mutation processes are illustrated in a simple manner in Figs. 4.3.16 and 4.3.17 for the example of cimetidine.

In the first implementation of genetic algorithms for SDPD (Shankland *et al.*, 1997*a*,*b*; Csoka & David, 1999), crossover rates were typically in the range 80–90% (*i.e.* 80–90% of the parent population were selected for participation in crossovers) with an overall mutation rate of typically 5% (*i.e.* 5% of genes in the children were mutated). These children become the new generation and, after their fitnesses have been evaluated, the processes of selection, crossover and mutation are repeated. For complex structural-solution problems, populations can evolve over many thousands of generations before finally converging to the global minimum χ^2 value. As with simulated annealing and parallel tempering, good but false solutions may be obtained and therefore multiple attempts should be performed to ensure that the best structure has been obtained and that the correct structure may then be obtained after Rietveld analysis.

Unsurprisingly, given the complexities of evolution, there are many different opportunities for the optimization of genetic algorithms for real-space structure solution. Of particular note are the programs *EAGER* [Harris *et al.*, 1998, 2004; this program is based upon initial work (Kariuki *et al.*, 1997) that is contemporaneous with the work of Shankland *et al.* (1997*a*,*b*) and Csoka & David (1999)] and *GEST* (Feng & Dong, 2007). The latter paper gives a detailed description of algorithms and effective protocols for real-space SDPD using genetic algorithms. There are also a number of reviews of the subject (*e.g.* Harris, 2012).

4.3.5.1.6. *Differential evolution*

Differential evolution (Chong & Tremayne, 2006) can be regarded as a variant of genetic algorithms which self-regulates the region of the χ^2 hypersurface searched during each generation according to the extent of convergence of the population. In contrast to genetic algorithms in which the parameter values (chromosomes) of selected individuals are combined to create child structures, differential evolution uses the differences between individual chromosomes to create a child. Consequently, as the population converges and the genetic differences between individuals decrease, the region of the χ^2 hypersurface in which children are created also decreases. The evolution of a population of individuals is performed using a small number of operations, which makes differential evolution more straightforward to optimize and control than genetic algorithms. With differential evolution, child parameterizations are created from the parent using two main operations: mutation and recombination (which are analogous to the crossover operation in genetic algorithms). The two operations are controlled by separate control parameters designated K and F for recombination and mutation, respectively. These are independently assigned a value between 0 and 1 and thus differential evolution can be adapted to suit different types of optimization by using different combinations of K and F.

In common with genetic algorithms, the first step in differential evolution is the generation of a population of crystal structures using the usual random parameters. The population size is determined by the number of parameters and experience. Tremayne *et al.* (2009) have shown that, for a successful structure solution, the number of individuals in a population should be at least ten times the number of parameters. Similarly, it has been shown that setting $K = 1$ results in a rapid convergence, which generally will lead to a local minimum. However, setting $K = 0.99$ has been found to maintain a fast rate of convergence while reducing the probability of being trapped in a local minimum. The mutation constant, F, is usually set to a value between 0.4 and 0.7. Higher values reduce the probability of being trapped in a local minimum but increase the number of generations required to determine the correct crystal structure.

The search proceeds in a series of generations in which each parent, P, produces one child, C. To maintain genetic diversity, three new random individuals, R_1, R_2 and R_3, are selected to assist each new parent in the creation of a child which includes both recombination, $K(R_1 - P)$, to ensure the transferral of good parameter values and mutation, $F(R_2 - R_3)$, to avoid premature convergence. Specifically,

$$C = P + K(R_1 - P) + F(R_2 - R_3).$$

χ^2 is calculated for the child, C. If $\chi^2(C) < \chi^2(P)$, then the child replaces the parent as an active member of the population; otherwise the parent is retained. The lengths of the recombination and mutation vectors are determined by the distance between P, R_1, R_2 and R_3, As models cluster together, these distances decrease. During the initial generations, there is a high probability that P, R_1, R_2 and R_3 will range over a considerable region of the χ^2 hypersurface. Consequently, at the initial stages of global optimization, a child is likely to be created at a considerable distance from the parent. If the child is fitter than the parent, then the search rapidly moves to a distinctly different part of the χ^2 hypersurface, which means that it will be comprehensively explored in the initial stages of structure solution. Towards the end of the structure solution, when many models are clustered around what is hopefully the global minimum, there is a high probability that P, R_1, R_2 and R_3 will be clustered together near the minimum. The recombination and mutation vectors will be significantly shorter, increasing the probability that a child is created near the parent, thus allowing a controlled convergence towards the (global) minimum. As with all global-optimization strategies, it is essential to repeat many differential evolution runs to check for local minima and confirm that the global minimum has been reached.

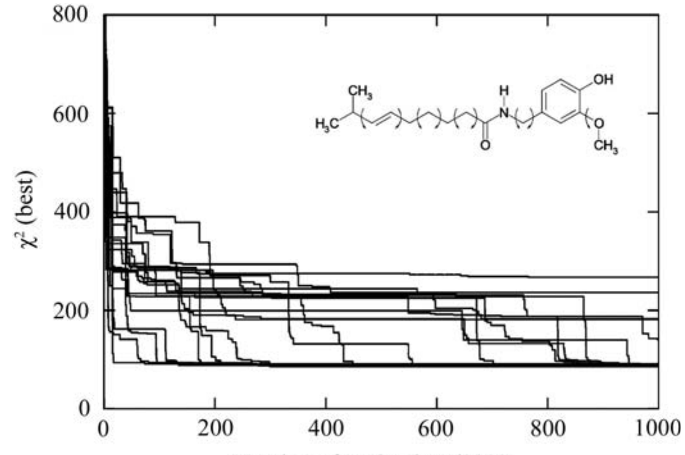

Figure 4.3.18
A plot of the best χ^2 values *versus* the number of χ^2 evaluations for the 20 hybrid Monte Carlo structure-solution attempts for capsaicin (after Shankland *et al.*, 2002). For comparison, see Fig. 4.3.15.

4.3.5.2. *Deterministic search algorithms*

4.3.5.2.1. *Introduction*

While stochastic techniques have been shown to be effective global-optimization methods, many other algorithms remain to be evaluated for SDPD and it is likely some of these will be more efficient and successful than the current techniques. One example is the hybrid Monte Carlo (HMC) algorithm that combines the key components of Monte Carlo (MC) and molecular dynamics (MD) approaches into a single algorithm.

4.3.5.2.2. *The hybrid Monte Carlo algorithm*

An extensive discussion of the HMC algorithm in the context of SDPD may be found in Johnston *et al.* (2002). HMC may be considered in terms of a particle that follows a trajectory determined by Hamilton's equations of motion in a hyperspace defined by a set of structural variables. The total energy of the particle at any point is equal to the sum of the kinetic energy and potential energy given by the goodness-of-fit target function. In theory, the total energy is conserved, but the use of finite time-step sizes in the numerical evaluation of the equations of motion means that this is not the case. To control this, a Metropolis acceptance criterion is used to determine whether to accept or reject the configuration at the end of a given molecular-dynamics trajectory. The trajectory either continues from the end point if it is accepted or returns to the previous start point if it is rejected. The effectiveness of the HMC algorithm has been convincingly demonstrated with the structure determination of capsaicin which, with a total of 15 degrees of freedom, represents a moderate challenge for SDPD. When compared with the default

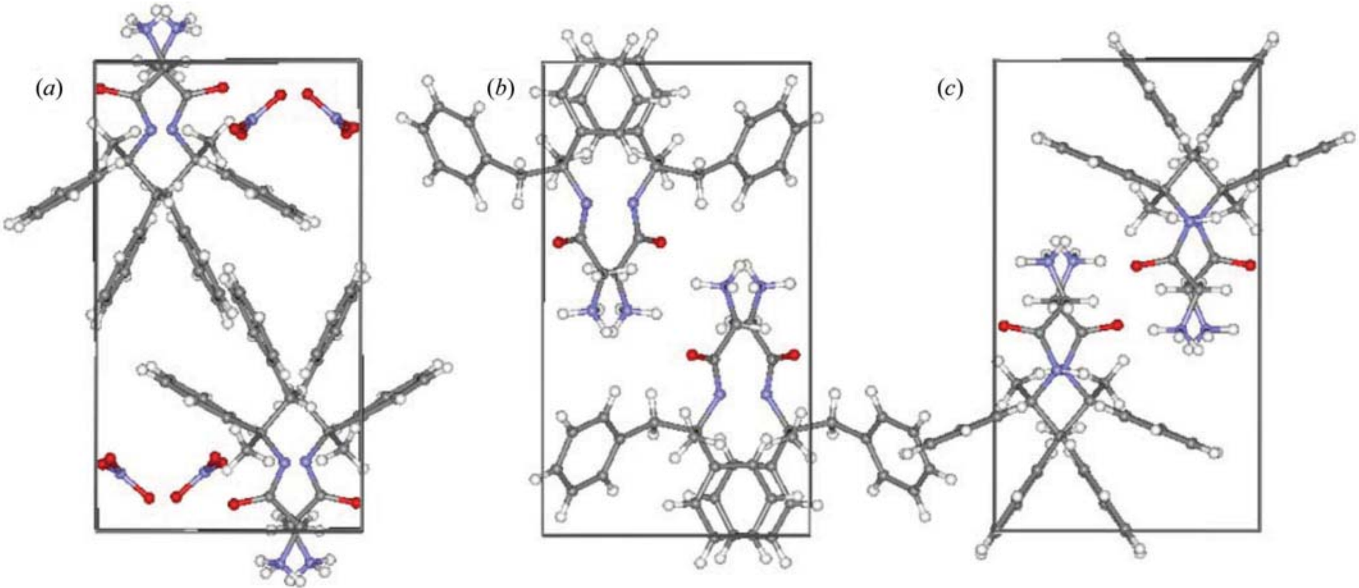

Figure 4.3.19
(*a*) The correct crystal structure of remacemide nitrate. (*b*) The best structure determination using a least-squares analysis to compare observed and calculated diffraction data with only the remacemide ion used in the structural model. Note that although the structural arrangement is completely incorrect, it is clear that the solution has resulted in an optimal correlation of observed and calculated electron density. Note in particular that the phenyl group maps closely onto the scattering density associated with the nitrate ion. (*c*) The best structure determination using a maximum-likelihood analysis to compare observed and calculated diffraction data with only the remacemide ion used in the structural model. The structure illustrated in (*c*) is enantioimetrically related to correct solution shown in (*a*). The agreement between the remacemide molecular position, orientation and conformation in (*a*) and (*c*) is as close as obtained in a standard least-squares analysis with the nitrate ion included.

implementation of simulated annealing in *DASH*, the HMC approach is a factor of 2 more successful in locating the global minimum over a series of 20 repeat runs. From a comparison of Figs. 4.3.15 and 4.3.18, it is evident that the hybrid Monte Carlo algorithm is also significantly more efficient, requiring on average an order of magnitude fewer χ^2 evaluations.

4.3.6. Using maximum-likelihood techniques to tackle incomplete structural models

4.3.6.1. *Introduction*

Solving crystal structures from powder-diffraction data is a significantly more difficult and less straightforward procedure than its single-crystal counterpart because of the loss of information associated with compressing the three-dimensional reciprocal lattice on to the one dimension of a powder-diffraction pattern with the corresponding inevitable overlap of Bragg reflections. The situation can be ameliorated and Bragg-peak intensities more easily extracted by explicitly using texture or methods such as differential thermal expansion (Brunelli *et al.*, 2003). However, discussion of these experimental methods is beyond the scope of this chapter. The incorporation of additional chemical information directly into the structure-solution process using both databases and complementary experimental techniques is discussed in Chapter 4.4. This section discusses the reverse situation, where there is a lack of chemical information, and highlights the effectiveness of maximum-likelihood methods.

4.3.6.2. *Working with incomplete structural models: maximum-likelihood methods*

In the previous section, the use of additional information to facilitate real-space structure solution was discussed. Specifically, constraining molecular conformation, through the active use of torsion-angle distributions derived from the Cambridge Structural Database and the intramolecular distance restraints derived from solid-state NMR measurements, was shown to accelerate structure solution and extend the range of complexity of structures that may be solved using real-space structure-determination techniques (Middleton *et al.*, 2002).

In this section, a complementary strategy is discussed where not all the structure is initially determined. Consider the case of a co-crystal or salt compound where there is more than one type of molecule in the crystal structure. It is possible, through the use of maximum-likelihood techniques, to account for and effectively ignore a significant structural component and yet determine precisely the location of all of the rest of the crystal structure. Take the specific case of the anti-convulsant agent remacemide nitrate ($C_{17}H_{21}N_2O^+ \cdot NO_3^-$). Markvardsen *et al.* (2002) showed that, although the nitrate group accounts for ~18% of the X-ray scattering, a real-space structure solution, based not on a conventional least-squares but on a maximum-likelihood optimization between observed and calculated diffraction data, yielded the correct location, orientation and torsion angles of the remacemide ion without any attempt to locate the nitrate ion; see Fig. 4.3.19.

The maximum-likelihood method is perhaps best explained by specific reference to this crystal structure. The remacemide and nitrate ions will be denoted as the fragment and blur, respectively, for the purposes of the discussion. Given that the objective of the maximum-likelihood approach is to determine only the remacemide fragment, the *a priori* presumption is that the scattering contribution of the blur is randomly distributed throughout the unit cell. In reciprocal-space terms, this means that the calculated structure factors are no longer a set of numbers but are instead represented by a multidimensional Gaussian distribution with a width that is determined by the magnitude of the random scattering associated with the blur. As a consequence, the scattering density of the nitrate ion is actively considered in structure-factor representation, even though its position is explicitly unknown. With a large unknown component, the Gaussian broadening will be large and the maximum-likelihood approach will lead to significantly different results than an equivalent least-squares analysis. As the blur scattering decreases, then the maximum-likelihood analysis becomes equivalent to least-squares analysis.

For further references on the use of maximum likelihood in crystallography, see, for example, McCoy (2004) and references therein. A full mathematical description of the maximum-likelihood formulation of powder-diffraction analysis, and particularly the discussion of overlapped and partially overlapped reflections, is beyond the scope of this article. A full discussion can be found in the paper by Markvardsen *et al.* (2002). Significantly, the analysis presented in the paper applies not only to structure determination but generally to structure refinement and Rietveld analysis.

References

Albesa-Jove, D., Kariuki, B. M., Kitchin, S. J., Grice, L., Cheung, E. Y. & Harris, K. D. M. (2004). *Challenges in direct-space structure determination from powder diffraction data: a molecular material with four independent molecules in the asymmetric unit*. *ChemPhysChem*, **5**, 414–418.

Altomare, A., Camalli, M., Cuocci, C., Giacovazzo, C., Moliterni, A. & Rizzi, R. (2009). *EXPO2009: structure solution by powder data in direct and reciprocal space*. *J. Appl. Cryst.* **42**, 1197–1202.

Andreev, Y. G., Lightfoot, P. & Bruce, P. G. (1996). *Structure of the polymer electrolyte poly(ethylene oxide)$_3$:LiN(SO$_2$CF$_3$)$_2$ determined by powder diffraction using a powerful Monte Carlo approach*. *Chem. Commun.* pp. 2169–2170.

Arnott, S. & Wonacott, A. J. (1966). *The refinement of the crystal and molecular structures of polymers using X-ray data and stereochemical constraints*. *Polymer*, **7**, 157–166.

Baerlocher, C. & McCusker, L. B. (2002). *The structure determination process*. In *Structure Determination from Powder Diffraction Data*, edited by W. I. F. David, K. Shankland, L. B. McCusker & Ch. Baerlocher, pp. 4–7. Oxford University Press.

Bricogne, G. (1991). *A multisolution method of phase determination by combined maximization of entropy and likelihood. III. Extension to powder diffraction data*. *Acta Cryst.* A**47**, 803–829.

Brunelli, M., Wright, J. P., Vaughan, G. R. M., Mora, A. J. & Fitch, A. N. (2003). *Solving larger molecular crystal structures from powder diffraction data by exploiting anisotropic thermal expansion*. *Angew. Chem. Int. Ed.* **42**, 2029–2032.

Brünger, A. T. (1991). *Simulated annealing in crystallography*. *Annu. Rev. Phys. Chem.* **42**, 197–223.

Bruno, I. J., Cole, J. C., Kessler, M., Luo, J., Motherwell, W. D. S., Purkis, L. H., Smith, B. R., Taylor, R., Cooper, R. I., Harris, S. E. & Orpen, A. G. (2004). *Retrieval of crystallographically-derived molecular geometry information*. *J. Chem. Inf. Comput. Sci.* **44**, 2133–2144.

Chong, S. Y. & Tremayne, M. (2006). *Combined optimization using cultural and differential evolution: application to crystal structure solution from powder diffraction data*. *Chem. Commun.* pp. 4078–4080.

Coelho, A. A. (2000). *Whole-profile structure solution from powder diffraction data using simulated annealing*. *J. Appl. Cryst.* **33**, 899–908.

Csoka, T. & David, W. I. F. (1999). *Structure determination from powder diffraction data by use of a swarm algorithm*. *Acta Cryst.* A**55** Supplement, P08.03.012.

David, W. I. F. (2004). *On the equivalence of the Rietveld method and the correlated integrated intensities method in powder diffraction*. *J. Appl. Cryst.* **37**, 621–628.

David, W. I. F. & Shankland, K. (2008). *Structure determination from powder diffraction data*. *Acta Cryst.* A**64**, 52–64.

David, W. I. F., Shankland, K. & Shankland, N. (1998). *Routine determination of molecular crystal structures from powder diffraction data*. *Chem. Commun.* pp. 931–932.

David, W. I. F., Shankland, K., van de Streek, J., Pidcock, E., Motherwell, W. D. S. & Cole, J. C. (2006). *DASH: a program for crystal structure determination from powder diffraction data*. *J. Appl. Cryst.* **39**, 910–915.

David, W. I. F. & Sivia, D. (2002). *Extracting integrated intensities from powder diffraction patterns*. In *Structure Determination from Powder Diffraction Data*, edited by W. I. F. David, K. Shankland, L. B. McCusker & Ch. Baerlocher, pp. 136–161. Oxford University Press.

Earl, D. J. & Deem, M. W. (2005). *Parallel tempering: theory, applications, and new perspectives*. *Phys. Chem. Chem. Phys.* **7**, 3910–3916.

Engel, G. E., Wilke, S., König, O., Harris, K. D. M. & Leusen, F. J. J. (1999). *PowderSolve – a complete package for crystal structure solution from powder diffraction patterns*. *J. Appl. Cryst.* **32**, 1169–1179.

Falcioni, M. & Deem, M. W. (1999). *A biased Monte Carlo scheme for zeolite structure solution*. *J. Chem. Phys.* **110**, 1754–1766.

Favre-Nicolin, V. & Černý, R. (2004*a*). *A better FOX: using flexible modelling and maximum likelihood to improve direct-space ab initio structure determination from powder diffraction*. *Z. Kristallogr.* **219**, 847–856.

Favre-Nicolin, V. & Černý, R. (2004*b*). *FOX: Modular approach to crystal structure determination from powder diffraction*. *Mater. Sci. Forum*, **443**, 35–38.

Feng, Z. J. & Dong, C. (2007). *GEST: a program for structure determination from powder diffraction data using a genetic algorithm*. *J. Appl. Cryst.* **40**, 583–588.

Fernandes, P., Shankland, K., Florence, A. J., Shankland, N. & Johnston, A. (2007). *Solving molecular crystal structures from X-ray powder diffraction data: the challenges posed by gamma-carbamazepine and chlorothiazide N,N-dimethylformamide (1/2) solvate*. *J. Pharm. Sci.* **96**, 1192–1202.

Florence, A. J., Shankland, N., Shankland, K., David, W. I. F., Pidcock, E., Xu, X., Johnston, A., Kennedy, A. R., Cox, P. J., Evans, J. S. O., Steele, G., Cosgrove, S. D. & Frampton, C. S. (2005). *Solving molecular crystal structures from laboratory X-ray powder diffraction data with DASH: the state of the art and challenges*. *J. Appl. Cryst.* **38**, 249–259.

Gilmore, C. J., Henderson, K. & Bricogne, G. (1991). *A multisolution method of phase determination by combined maximization of entropy and likelihood. IV. The ab initio solution of crystal structures from their X-ray powder data*. *Acta Cryst.* A**47**, 830–841.

Gilmore, C. J., Shankland, K. & Bricogne, G. (1993). *Applications of the maximum entropy method to powder diffraction and electron crystallography*. *Proc. R. Soc. London Ser. A*, **442**, 97–111.

Goldberg, D. E. (1989). *Genetic Algorithms in Search, Optimization, and Machine Learning*. Boston: Addison-Wesley.

Griffin, T. A. N., Shankland, K., van de Streek, J. & Cole, J. (2009*a*). *MDASH: a multi-core-enabled program for structure solution from powder diffraction data*. *J. Appl. Cryst.* **42**, 360–361.

Griffin, T. A. N., Shankland, K., van de Streek, J. & Cole, J. (2009*b*). *GDASH: a grid-enabled program for structure solution from powder diffraction data*. *J. Appl. Cryst.* **42**, 356–359.

Groom, C. R., Bruno, I. J., Lightfoot, M. P. & Ward, S. C. (2016). *The Cambridge Structural Database*. *Acta Cryst.* B**72**, 171–179.

Harris, K. D. M. (2012). *Powder diffraction crystallography of molecular solids*. *Top. Curr. Chem.* **315**, 133–177.

Harris, K. D. M., Habershon, S., Cheung, E. Y. & Johnston, R. L. (2004). *Developments in genetic algorithm techniques for structure solution from powder diffraction data*. *Z. Kristallogr.* **219**, 838–846.

Harris, K. D. M., Johnston, R. L., Kariuki, B. M. & Tremayne, M. (1998). *A genetic algorithm for crystal structure solution from powder diffraction data*. *J. Chem. Res.* pp. 390–391.

Harris, K. D. M., Tremayne, M., Lightfoot, P. & Bruce, P. G. (1994). *Crystal structure determination from powder diffraction data by Monte Carlo methods*. *J. Am. Chem. Soc.* **116**, 3543–3547.

Johnston, J. C., David, W. I. F., Markvardsen, A. J. & Shankland, K. (2002). *A hybrid Monte Carlo method for crystal structure determination from powder diffraction data*. *Acta Cryst.* A**58**, 441–447.

Kariuki, B. M., Serrano-González, H., Johnston, R. L. & Harris, K. D. M. (1997). *The application of a genetic algorithm for solving crystal structures from powder diffraction data*. *Chem. Phys. Lett.* **280**, 189–195.

Le Bail, A. & Cranswick, L. M. D. (2001). *Revisiting the 1998 SDPD Round Robin*. *IUCr Commission on Powder Diffraction Newsletter*, **25**, 7–9.

Leech, C. K., Fabbiani, F. P. A., Shankland, K., David, W. I. F. & Ibberson, R. M. (2008). *Accurate molecular structures of chlorothiazide* *and hydrochlorothiazide by joint refinement against powder neutron and X-ray diffraction data*. *Acta Cryst.* B**64**, 101–107.

Lightfoot, P., Mehta, M. A. & Bruce, P. G. (1993). *Crystal structure of the polymer electrolyte poly(ethylene oxide)$_3$:LiCF$_3$SO$_3$*. *Science*, **262**, 883–885.

McCoy, A. J. (2004). *Liking likelihood*. *Acta Cryst.* D**60**, 2169–2183.

Mackay, A. L. (1984). *Quaternion transformation of molecular orientation*. *Acta Cryst.* A**40**, 165–166.

Markvardsen, A. J., David, W. I. F., Johnson, J. C. & Shankland, K. (2001). *A probabilistic approach to space-group determination from powder diffraction data*. *Acta Cryst.* A**57**, 47–54.

Markvardsen, A. J., David, W. I. F., Johnston, J. C. & Shankland, K. (2012). *A probabilistic approach to space-group determination from powder diffraction data. Corrigendum*. *Acta Cryst.* A**68**, 780.

Markvardsen, A. J., David, W. I. F. & Shankland, K. (2002). *A maximum-likelihood method for global-optimization-based structure determination from powder diffraction data*. *Acta Cryst.* A**58**, 316–326.

Metropolis, N. (1987). *The beginning of the Monte Carlo method*. Los Alamos Science Special Issue, **125**, p. 130.

Metropolis, N., Rosenbluth, A. W., Rosenbluth, M. N., Teller, A. H. & Teller, E. (1953). *Equation of state calculations by fast computing machines*. *J. Chem. Phys.* **21**, 1087.

Middleton, D. A., Peng, X., Saunders, D., Shankland, K., David, W. I. F. & Markvardsen, A. J. (2002). *Conformational analysis by solid-state NMR and its application to restrained structure determination from powder diffraction data*. *Chem. Commun.* pp. 1976–1977.

O'Boyle, N. M., Banck, M., James, C. A., Morley, C., Vandermeersch, T. & Hutchison, G. R. (2011). *Open Babel; and open chemical toolbox*. *J. Cheminf.* **3**, 33–46.

Pagola, S., Polymeros, A. & Kourkoumelis, N. (2017). *WinPSSP: a revamp of the computer program PSSP and its performance solving the crystal structures of small organic compounds and solids of biological and pharmaceutical interest. J. Appl. Cryst.* **50**, 293–303.

Pagola, S. & Stephens, P. W. (2010). *PSSP, a computer program for the crystal structure solution of molecular materials from X-ray powder diffraction data*. *J. Appl. Cryst.* **43**, 370–376.

Pagola, S., Stephens, P. W., Bohle, D. S., Kosar, A. D. & Madsen, S. K. (2000). *The structure of malaria pigment beta-haematin*. *Nature*, **404**, 307–310.

Putz, H., Schön, J. C. & Jansen, M. (1999). *Combined method for ab initio structure solution from powder diffraction data*. *J. Appl. Cryst.* **32**, 864–870.

Rietveld, H. M. (1969). *A profile refinement method for nuclear and magnetic structures*. *J. Appl. Cryst.* **2**, 65–71.

Semenovskaya, S. V., Khachaturyan, K. A. & Khachaturyan, A. G. (1985). *Statistical mechanics approach to the structure determination of a crystal*. *Acta Cryst.* A**41**, 268–273.

Shankland, K., David, W. I. F. & Csoka, T. (1997*a*). *Crystal structure determination from powder diffraction data by the application of a genetic algorithm*. *Z. Kristallogr.* **212**, 550–552.

Shankland, K., David, W. I. F. & Sivia, D. S. (1997*b*). *Routine ab initio structure determination of chlorothiazide by X-ray powder diffraction using optimised data collection and analysis strategies*. *J. Mater. Chem.* **7**, 569–572.

Shankland, K., McBride, L., David, W. I. F., Shankland, N. & Steele, G. (2002). *Molecular, crystallographic and algorithmic factors in structure determination from powder diffraction data by simulated annealing*. *J. Appl. Cryst.* **35**, 443–454.

Shankland, K., Markvardsen, A. J., Rowlatt, C., Shankland, N. & David, W. I. F. (2010). *A benchmark method for global optimization problems in structure determination from powder diffraction data*. *J. Appl. Cryst.* **43**, 401–406.

Skone, G., Cameron, S. & Voiculescu, I. (2013). *Doing a good turn: the use of quaternions for rotation in molecular docking*. *J. Chem. Inf. Model.* **53**, 3367–3372.

Tremayne, M., Chong, S. Y. & Bell, D. (2009). *Optimisation of algorithm control parameters in cultural differential evolution applied to molecular crystallography*. *Front. Comput. Sci. China*, pp. 1–8.

International Tables for Crystallography (2019). Vol. H, Chapter 4.4, pp. 433–441.

4.4. The use of supplementary information to solve crystal structures from powder diffraction

A. J. Florence

4.4.1. General remarks

Structure determination by powder diffraction (SDPD) is an increasingly important element of structural investigations of a wide range of novel polycrystalline molecular materials including polymorphs (Chan *et al.*, 1999; Dinnebier *et al.*, 2000*a*; Florence *et al.*, 2008), salts (Stephenson, 2000; Lewis *et al.*, 2005; Antoniadis *et al.*, 2010), solvates (Pan *et al.*, 2005; Fernandes *et al.*, 2007; Chernyshev *et al.*, 2010) and co-crystals (Tremayne & Glidewell, 2000; Trask & Jones, 2005). This has been facilitated by access to high-quality synchrotron data and particularly the wide availability of modern laboratory powder diffractometers. Importantly, there is a wide range of powerful and user-friendly free and commercial software tools available for all stages of data analysis required for a successful SDPD study (Fig. 4.4.1).

Traditional direct-methods approaches used in single-crystal diffraction typically draw on thousands of individually measured reflection intensities in order to identify the positions of individual atoms within the unit cell. However, a high-resolution laboratory powder diffraction pattern may yield only a few hundred reliable reflection intensities as a result of peak overlap. Global-optimization methods accommodate the relative lack of diffraction intensity information by enabling additional non-diffraction data to be easily introduced into the structure-determination process. This supplementary information is typically in the form of chemical structure details, such as molecular geometry (bond lengths, angles) describing the atomic connectivity within the molecular fragments, or conformational constraints that have been derived from knowledge bases, calculation or measurement. This is of particular importance given the relative complexity of many molecular solids, including pharmaceuticals, in terms of the number of degrees of freedom that need to be resolved during the global-optimization process. Such structures may comprise large, flexible molecules and may have multiple fragments and/or $Z' > 1$ and/or disorder.

The fundamentals of global-optimization strategies for structure determination have been described elsewhere (Shankland & David, 2002) and a range of effective search methods has been implemented in various software packages [including *DASH* (David *et al.*, 2006); *EAGER* (Habershon *et al.*, 2003); *Endeavour* (Putz *et al.*, 1999); *ESPOIR* (Le Bail, 2001); *FOX* (Favre-Nicolin & Černý, 2002); *PowderSolve* (Engel *et al.*, 1999); *PSSP* (Stephens & Huq, 2002; Pagola *et al.*, 2017) and *TOPAS* (Coelho, 2000); for an extensive listing see for example Černý & Favre-Nicolin (2007)]. Indeed, armed with high-quality powder diffraction data (with good spatial and angular resolution) and an accurate description of the chemical composition of the sample (the molecular structure of all components and stoichiometry), global-optimization methods can routinely solve structures with significant structural complexity without recourse to additional constraints or restraints that encode other information sources. For example, the monoclinic $Z' = 2$ structure of chlorothiazide *N*,*N*-dimethyl formamide 2:1 solvate with six independent fragments equating to 36 external degrees of freedom was solved using simulated annealing against laboratory powder diffraction data (Fernandes *et al.*, 2007). However, structures containing 13 internal degrees of freedom have also been shown to present a considerable challenge to the global-optimization approach (Florence *et al.*, 2005*b*). Thus, in the context of solving complex structures *via* SDPD approaches, it is of particular interest to explore strategies that utilise additional information sources to supplement the available diffraction data and maximize the chances of success.

This chapter aims to highlight practical strategies where supplementary information can usefully contribute to maximizing the chances of successful structure determination across the workflow shown in Fig. 4.4.1. Whilst SDPD has been successfully applied to the study of a wide range of novel materials in recent years including inorganic (Deem & Newsam, 1989; Reinaudi *et al.*, 2000; Edgar *et al.*, 2002) and organometallic systems (Dinnebier *et al.*, 2000*b*; Ivashevskaja *et al.*, 2002; Mínguez Espallargas *et al.*, 2007) the focus here, driven by the author's experience, is on organic molecular structures containing large numbers of degrees of freedom and light, weakly scattering atoms. It is also worth considering how to confirm the accuracy of the global-optimization minimum and confirm that structures not only return a good graphical or statistical fit to the diffraction data but also are consistent with chemical knowledge (*i.e.* are chemically sensible). The aim is to obtain the best possible solution for input into a subsequent Rietveld refinement (Rietveld, 1969). Applications of potential-energy calculations will also be introduced. The use of high-quality X-ray diffraction data (either synchrotron or monochromatic laboratory capillary transmission data) is a prerequisite throughout a successful SDPD trial.

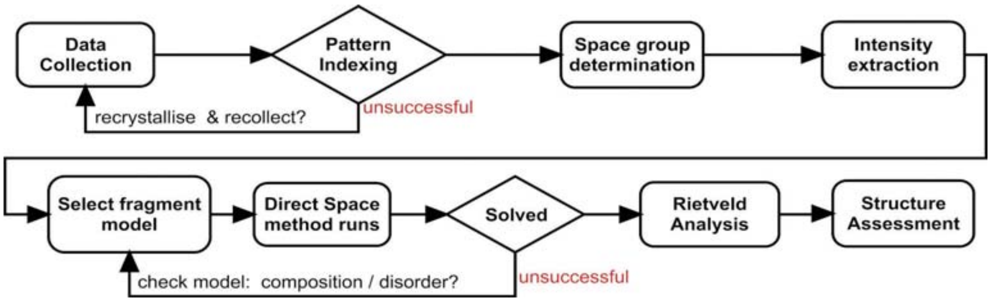

Figure 4.4.1
Key steps in crystal-structure determination from powder diffraction data (after Florence, 2009).

Copyright © 2019 International Union of Crystallography

Table 4.4.1
Comparison of molecular volumes for tetradecane-1,14-diol and carbamazepine from three different sources

Molecule	Simple summation estimation† (Å^3)	Hofmann average volume method‡ (Å^3)	*COSMO* volume§ (Å^3)	From room-temperature single-crystal structure¶ (Å^3)
Tetradecane-1,14-diol, $C_{14}H_{30}O_2$, CSD refcode: CAVDEI, monoclinic, $P2_1/n$, $Z' = 0.5$, $a = 4.976$ (1), $b = 5.197$ (1), $c = 27.955$ (3) Å, $\beta = 93.82$ (1)°	348	369.4	342.7	360.6
	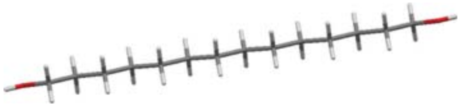			
Carbamazepine, $C_{15}H_{12}N_2O$, CSD refcode: CBMZPN01, monoclinic, $P2_1/c$, $Z' = 1$, $a = 7.529$, $b = 11.148$, $c = 15.470$ Å, $\beta = 116.17$°	348	304.0	283.1	291.3
	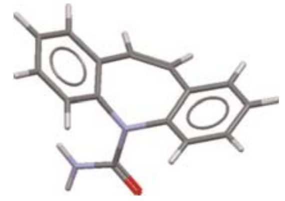			

† Using approximate volumes for C, N, O atoms of 18 Å^3 and H atoms of 2 Å^3. ‡ Using estimated atomic volumes for C, N, O and H atoms of 13.87, 11.8, 11.39 and 5.08 Å^3, respectively. § Calculated using *MOPAC2012* (Stewart, 2012) to carry out a semi-empirical geometry optimization with keywords PM3 EF MMOK GNORM=0.01 GEO-OK NOINTER XYZ. ¶ Carbamazepine form III (Reboul *et al.*, 1981); tetradecane1,14-diol (Nakamura & Sato, 1999).

4.4.2. Molecular models

4.4.2.1. *Molecular volume*

An accurate estimate of the molecular volume of all fragments to be included in a search is of value in SDPD. For indexing, a reliable estimate of the volume occupied by each molecule within the lattice provides an indication of the expected cell volume, informing the indexing process. This information also provides reassurance that the chemical composition and stoichiometry is consistent with a proposed unit cell and symmetry prior to carrying out global-optimization trials, or it can help to identify any discrepancies and avoid wasted effort. Approximate values are typically sufficiently reliable for this purpose, although with many different methods available for calculating molecular volume this can result in quite broad variation in numerical values (Bondi, 1964; Gavezzotti, 1983; Connolly, 1985; Rowland & Taylor, 1996; Preiss *et al.*, 2009; Glasser, 2011). Crystal-structure information for related structures such as polymorphs can be useful, and local crystal-structure databases or systems such as the Cambridge Structural Database (CSD; Groom *et al.*, 2016) are excellent resources in this regard. For additional sources applicable also to inorganic systems see also Kaduk (2007) and references therein.

By way of example, Table 4.4.1 highlights the molecular volumes for two molecular structures obtained using four straightforward techniques. The three estimates are based on: a simple summation of atomic volumes using approximate volumes for similarly sized C, N and O atoms of 18 Å^3 (Kempster & Lipson, 1972) and 2 Å^3 for H atoms; summation of average atomic volumes derived for each element from the CSD (Hofmann, 2002); a volume calculated using the semi-empirical package *MOPAC2012*; and lastly the volume per molecule extracted from the CSD entries for each structure. The estimates for the aliphatic diol tetradecane-1,14-diol are in relatively close agreement (±20 Å^3) with the experimental value. In contrast, the simple atom-volume summation significantly overestimates the volume for the fused-ring structure of carbamazepine by 57 Å^3. The Hofmann method is as simple to apply, but gives more reliable estimates than the previous method in both cases. The semi-empirical optimization-derived values, calculated in under 20 s from an optimization on a standard desktop PC, are also in good agreement with experiment for both molecules. It is also worth highlighting the need to use the information as an approximate guide rather than as a strict selection criterion. For carbamazepine, for example, the experimental value in Table 4.4.1 is from the monoclinic form-III polymorph, whereas the trigonal form-II (CSD refcode: CBMZPN03; Lowes *et al.*, 1987) structure returns a molecular volume of 318 Å^3 as a result of the presence of solvent-accessible voids within the structure (Cruz Cabeza *et al.*, 2007; Fabbiani *et al.*, 2007).

4.4.2.2. *Fragment model selection: bond length and angles*

Prior chemical information is routinely exploited in global-optimization approaches by directly introducing the atomic connectivity of molecular fragments, typically using an internal-coordinate description. This allows covalent bond lengths, bond angles and torsion angles to be defined and parameters for optimization to be flagged (Shankland & David, 2002). This usefully reduces the number of degrees of freedom required to describe the position of *n* independent atoms in an asymmetric unit to a single set of fractional coordinates and three Euler angles. It is of course essential to use accurate geometric parameters in the internal-coordinate description to avoid introducing errors at this stage – errors that will prevent the global optimization locating a model that accurately describes the observed diffraction data. Standard bond lengths and angles for many chemical groups are widely available from carefully measured experimental values from related crystal structures [see the tabulated values in Allen (2002) and Chapter 9.5 of Volume C (Allen *et al.*, 2006)] and from computational methods (see for example Fogarasi *et al.*, 1992; Stephenson & Liang, 2006; Stewart, 2013). Existing crystal structures of related structural fragments are therefore a convenient and commonly used source of information for directly generating a *Z*-matrix internal-coordinate description. Computational methods have also been used to generate the input molecular geometry. Form-I β-resorcylic acid was solved by simulated annealing using an

HF/6-31G(d,p) gas-phase global conformational minimum in which O—H and C—H distances were normalized to 0.9 and 0.95 Å, respectively, for the optimization against the X-ray diffraction data (Braun *et al.*, 2011). As bond lengths and angles are largely unaffected by crystal-packing forces, they are fixed at their known values during the search. Care should be exercised when building models based on crystal structures of related structural fragments that have significant differences in ionization or in the size of substituents because of the potential impact on covalent bond lengths and angles, respectively.

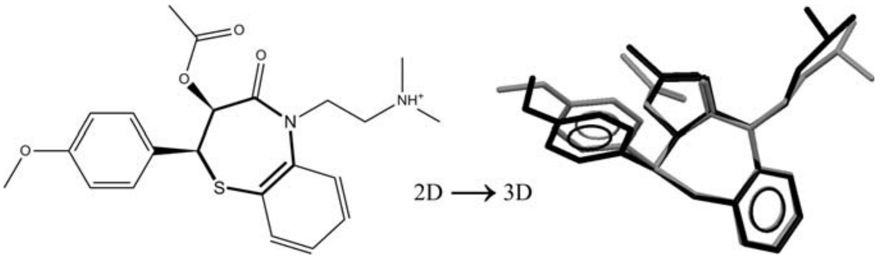

Figure 4.4.2
Automatic generation of reliable flexible-ring conformations in *Corina*. Left: 2D sketch of the diltiazem cation highlighting the 7-membered flexible ring. Right: overlay of the low-energy ring conformation produced from the sketch by *Corina* (grey) with the published single-crystal structure (black) (Kojić-Prodić *et al.*, 1984).

A number of software tools are also available that will automatically generate reliable three-dimensional (3D) coordinates from 2D sketches (see for example Sadowski *et al.*, 1994; Ebejer *et al.*, 2012). *Mercury* (Macrae *et al.*, 2008) also provides a set of convenient tools for editing molecular models, including editing groups or adding missing H atoms, to provide a reliable representation of the fragment. Regardless of the source of structural information used to build the molecular fragment model, it is important to check the accuracy of all input models to ensure that they are chemically sensible. In this regard, the *Mogul* (Bruno *et al.*, 2004) package contains a knowledge base of CSD-derived molecular geometries and provides a convenient and fast means of automatically checking the geometry of input molecular fragments.

4.4.2.3. *Flexible ring conformations*

Many small organic molecules contain flexible ring systems that have the potential to adopt alternative ring conformations, with the number of possible conformers increasing with the size of the ring (Cremer & Pople, 1975; Allen *et al.*, 1991, 1993; Brameld *et al.*, 2008). Closed rings are typically held fixed during the global-optimization search at a commonly observed (low-energy) conformation whilst the torsion-angle values in extended chains are allowed to vary. It is therefore useful to understand the conformational space that a given ring system can adopt during the assessment of the fragment geometry. This can be used to decide whether alternative conformers need to be considered in the global-optimization strategy.

Whilst the most commonly observed (or lowest-energy) conformer from database searches or conformational analysis will often be the correct conformation for a particular structure, flexible ring systems may of course also adopt higher-energy or less frequently observed conformations. For example, the tetrahydropyran ring in the crystal structure of 2,6-anhydro-*N*-methyl-D-glycero-D-ido-heptonamide (CSD refcode: LAFFAZ) adopts a twist-boat conformation in only this structure out of 21 related fragments in the CSD (Cottrell *et al.*, 2012). In this case, the initial selection of the most commonly observed or lowest-energy ring conformation would not result in a successful search. However, with access to suitable alternative models, such occurrences should not limit the ability to solve the structure. Also, high-speed parallelization of global-optimization methods allows different models to be tested with great efficiency (Griffin *et al.*, 2009).

In addition to using experimental data, there is a wide range of software packages that can be used to quickly assess ring conformations. *Corina* (Sadowski & Gasteiger, 1993; Sadowski *et al.*, 1994), for example, uses a set of structural rules and data tables with a simplified pseudo-force field to automatically generate multiple chemically reasonable low-energy ring conformations. Molecular structures can be drawn directly and converted from a 2D sketch *via* a graphical interface or entered *via* a standard 3D structure file format, including MOLFILE and PDB files. Conformations of the *S*,*S* diastereoisomer of diltazem were produced in *Corina* and compared with the conformation of the flexible 7-membered ring in the published crystal structure of diltiazem hydrochloride (CSD refcode: CEYHUJ01). Using a 10 kJ mol^{-1} cut-off value, two ring conformations were returned with the lowest-energy structure yielding an excellent match to the single-crystal structure with an r.m.s. deviation between all ring atoms of 0.055 Å (Fig. 4.4.2).

A different approach to individually testing distinct ring conformations is to search the conformational space of the flexible ring during the global optimization. This could be achieved by using slack constraints on ring bond lengths, enabling the search to access alternative arrangements (Černý & Favre-Nicolin, 2007). Also, for example, by removing the connecting bond altogether between the atoms C10 and C11 and opening the 7-membered dibenzazepine ring in carbamazepine, the two adjacent benzene substituents were allowed to rotate freely during the search (Fig. 4.4.3). Whilst this introduced two additional degrees of freedom, a completely unconstrained search of the ring's conformation space is performed. The final position and conformation of the ring is determined by fitting to the diffraction data. The trigonal $Z' = 1$ structure of carbamazepine

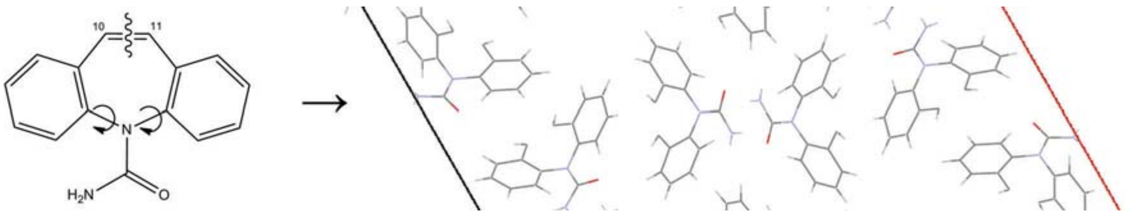

Figure 4.4.3
Determining ring conformation during global optimization using ring opening. The connectivity between C10 and C11 (highlighted) in the carbamazepine fragment model was removed and two additional torsion-angle variables around the N—C bonds were introduced (circular arrows).

form II can be solved in this way from laboratory powder diffraction data using simulated annealing. The structure was described using 9 degrees of freedom (3 position, 3 orientation and 3 torsion-angle parameters) and 100% of 50 simulated-annealing runs reached the target with 1×10^6 moves per run. The best solution returned an excellent final $\chi^2_{\rm profile}/\chi^2_{\rm Pawley}$ value of 2.1 (Florence *et al.*, 2005*b*) and the SDPD structure returned an r.m.s. deviation for all non-H atoms of 0.1 Å compared with the single-crystal structure.

4.4.2.4. *Torsion-angle constraints*

SDPD using global optimization has been shown to be highly effective in solving the crystal structures of highly flexible molecular systems with several variable torsion angles [*e.g.* atomoxetine hydrochloride: 6 torsions (Stephenson & Liang, 2006); telmistartan: 7 torsions (Dinnebier *et al.*, 2000*a*); famotidine: 9 torsions (Shankland & David, 2002); capsaicin: 11 torsions (David *et al.*, 1998); heptamethylene-1,7-bis(diphenylphosphane oxide): 12 torsions (Kariuki *et al.*, 1999); verapamil hydrochloride: 13 torsions (Florence *et al.*, 2005*b*)]. In the following sections, various strategies for increasing the probability of successfully solving crystal structures for flexible molecules are presented, focusing on the supplementary information on torsional flexibility and conformation that may be utilized when standard global-optimization approaches struggle.

4.4.2.4.1. *Crystal-structure-derived information*

For complex, flexible molecular structures the incorporation of prior chemical information in the form of torsion-angle constraints can be of considerable value. Their inclusion in the form of constraints does not reduce the number of degrees of freedom, but does reduce the extent of the search space that needs to be explored, focusing the search where the correct value is most likely to be found (Shankland *et al.*, 1998*a*). Ideally, methods for deriving and implementing torsional constraints should be straightforward, in order to facilitate their routine application in SDPD. Fortunately, this is readily tractable with the use of crystal-structure databases. In its simplest implementation, a torsion angle may be fixed at its most common value, *e.g.* fixing an H—N—C═O amide torsion to 180° based on an evaluation of amide groups in the CSD.

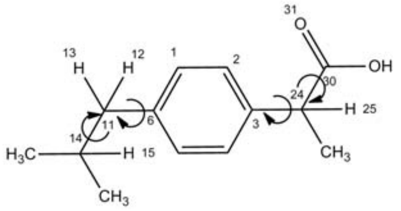

Figure 4.4.4
The structure of ibuprofen with flexible torsions highlighted (arrows).

For other groups it will be necessary to define a specific angular range for each flexible torsion angle based on conformational analysis of related crystal structures (Allen, 2002). A conformational analysis using semi-empirical energy calculations and CSD-based analysis of molecular conformations was used to obtain individual angular ranges for the four torsion angles in ibuprofen identified in Fig. 4.4.4 (Shankland *et al.*, 1998*b*). Four single-range torsion constraints (12—11—6—1 = 0–60°; 15—14—11—13 = 40–200°; 25—24—3—2 = −170–100°; 31—30—24—25 = 120–160°) were applied to the internal-coordinate description during a genetic algorithm search, increasing the frequency with which the global minimum was located in the structure solution of racemic ibuprofen using laboratory powder diffraction data (Shankland *et al.*, 1998*b*).

A simpler approach is to automatically extract modal torsion-angle constraints from the CSD using *Mogul* (Bruno *et al.*, 2004). Modal torsion constraints, in which multiple discrete ranges are defined for each torsion angle, offer a selective means of constraining a complex optimization problem. Individual torsion-angle values within crystal structures tend to form uni-, bi- or trimodal distributions and the conformation search space is restricted to one, two or three specific ranges. The common aliphatic fragment C—C—C—C returns a trimodal torsion-angle distribution with three distinct ranges separated by 120° (Fig. 4.4.5). Armed with such data for an unknown crystal structure, it is reasonable to assume that this torsion angle will adopt a value from within these ranges and constrain the search to sample only from within the trimodal distribution. An important caveat on the use of the CSD or other structural databases is the possibility

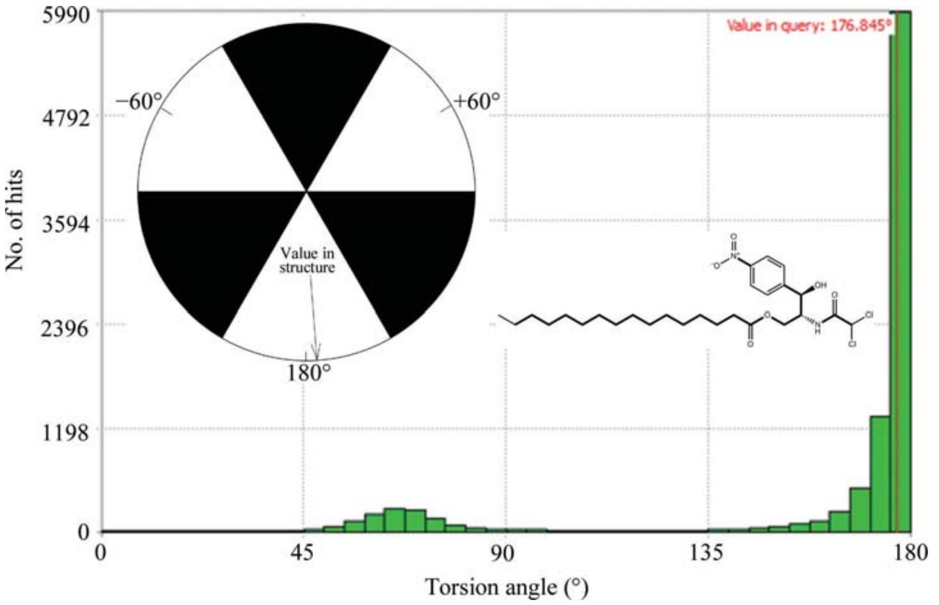

Figure 4.4.5
A trimodal torsion-angle distribution obtained from the CSD using *Mogul* for the C—C—C—C torsion in the query fragment (shown). All torsion values are mapped onto 0–180° (*x* axis) with the value in the query fragment being 176.8°. Inset: the associated trimodal search space in which the torsion-angle ranges shown in black are excluded from the search.

Table 4.4.2
Allowed ranges for the flexible torsion angles (τ1–13) identified in the verapamil cation using *Mogul* (from Florence *et al.*, 2009)

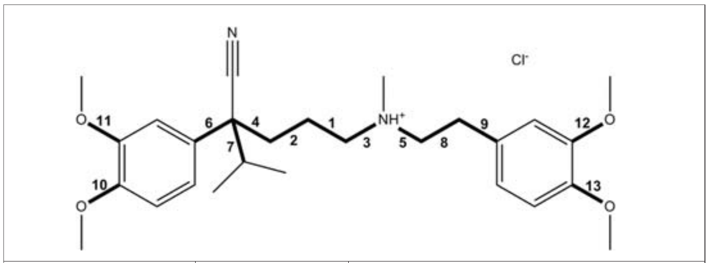

τ	Modal distribution type	Allowed torsion-angle search space (°)		
1, 2, 3, 4, 5, 7, 8	Trimodal	30–90	150–210	270–330
9	Bimodal	45–135	225–315	
6	Unimodal	0–360		
10, 11, 12, 13	Unimodal	−45–45		

that the actual value of any specific molecular torsion angle in the crystal structure being investigated may not lie within the ranges observed from other known structures. It is worth noting that where a simplex refinement is invoked at the end of each global-optimization run, angles outside this range may still be accessed (Florence *et al.*, 2009).

As the accessible conformational space around specific rotatable bonds in a flexible molecule may be influenced by steric effects from local functional groups, distributions based on a search of related molecular fragments will be most beneficial. An analysis of torsion-angle ranges in the compound verapamil hydrochloride (triclinic, $Z' = 1$, CSD refcode: CURHOM; Carpy *et al.*, 1985) highlights specific modal distributions for each of the torsions in the molecule (Table 4.4.2). This is a reasonably complex SDPD problem requiring 22 degrees of freedom (cation: 13 torsions plus 3 position plus 3 orientation; anion: 3 position), although with the availability of good-quality laboratory powder diffraction data (Florence *et al.*, 2005*b*) it is a useful test system for different SDPD approaches. The application of modal torsion-angle constraints to the effectiveness of an SDPD attempt reaching the target $\chi^2_{\rm profile}/\chi^2_{\rm Pawley}$ value (*i.e.* the global minimum) for verapamil hydrochloride was assessed using a simulated-annealing search algorithm (*DASH*: 800 runs, 2×10^7 moves, 0.01 cooling rate) against laboratory powder diffraction data in the range 3–42° 2θ (Florence *et al.*, 2009). Three separate trials were carried out: one in which the torsion values were fixed at the single-crystal conformation, a second in which all torsions were allowed to vary from 0 to 360° without restriction, and a third in which the torsions were restricted to the modal distributions shown in Table 4.4.2. As might be expected, owing to the simplification in the search by reducing the total number of degrees of freedom from 22 to 9, all of the fixed conformer runs reached the global minimum. The unrestricted and modal-constrained optimizations both had a lower success rate overall, consistent with the more complex search hypersurface being explored; however, they were essentially equally effective in reaching the target $\chi^2_{\rm profile}/\chi^2_{\rm Pawley}$ value, with 27 and 29 out of 800 runs respectively. The overall success rate is consistent with a previous SDPD study of verapamil hydrochloride (Florence *et al.*, 2005*b*). Notably when this approach was applied to a second complex SDPD problem (CSD refcode: XELBEV, $Z' = 2$, 30 degrees of freedom comprising 18 torsion, 6 position and 6 orientation; Florence *et al.*, 2009) the global minimum was only located from the runs including the modal torsion constraints (579/800 runs solved for the fixed single-crystal conformation; 0/800 solved for the unconstrained runs and 3/800 successfully solved for the modal torsion-angle constrained runs).

The implementation of the modal torsion distribution information in global-optimization searches has recently been further developed to include a modal distribution bias methodology (*DASH-v3.3*; CCDC Software Ltd/STFC, 2008). The modal distributions provide a statistical weighting for the selection of values included in the stochastic search. This method biases the selection of values used in the search towards highly populated regions of the torsion distribution but does not exclude any torsion angles. The application of the modal distribution bias in a SDPD study of verapamil hydrochloride [simulated-annealing search, laboratory powder data and fit range as per Florence *et al.* (2009)] showed a significant increase in the number of runs that reached the global minimum (24 out of 50; CCDC, 2015). This is an order-of-magnitude increase in the success rate of individual search runs compared with previous SDPD studies of this crystal structure and bodes well for tackling highly flexible molecules. Structure determination of this system was also assessed in the direct-space SDPD program *TALP* (Vallcorba *et al.*, 2012) and obtained the correct solution in 13 out of 100 runs, although it was noted that successful solution was dependent on the specific molecular model used and the search condition controls that were applied.

4.4.2.4.2. *Solid-state-NMR-derived information*

Solid-state NMR (SS-NMR) offers a powerful probe of structure and dynamics in molecular solids with numerous applications in materials and structural science (Brown & Spiess, 2001; Harris, 2004). SS-NMR can provide a wealth of crystallographically relevant information including determination of asymmetric unit, molecular symmetry and space group as well as information on disorder, molecular conformation and hydrogen bonding, and has been widely applied in studies of molecular crystals. In particular, SS-NMR techniques have been applied to conformational analysis of a range of flexible molecular molecules, revealing similarities and differences in the overall molecular conformations adopted in different polymorphic phases (Zell *et al.*, 2000; Hughes *et al.*, 2005). ^{13}C cross-polarization magic-angle-spinning (CPMAS) NMR was used to investigate the conformational differences between cimetidine in polycrystalline samples of three polymorphs and a monohydrate by measuring through-space interactions between atoms (Middleton

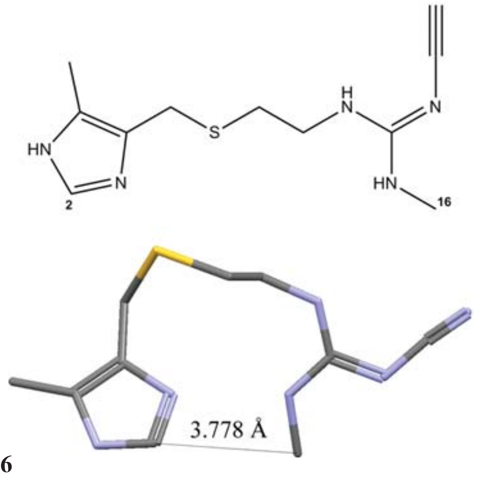

Figure 4.4.6
Top: structure of cimetidine molecule ^{13}C enriched at C2 and C16. Bottom: molecular conformation in the single-crystal structure of form-A cimetidine showing the equivalent C···C distance.

et al., 2000). By ^{13}C enrichment of the cimetidine at two sites (C2 and C16; Fig. 4.4.6) C···C separation distances were obtained describing the molecular conformations in each sample. The CPMAS NMR derived C2···C16 distance was 3.8 Å for form A compared with 3.778 Å in the published crystal structure (monoclinic, $P2_1/c$, CSD refcode: CIMETD).

The direct application of SS-NMR-derived torsion-angle information as constraints in SDPD has been demonstrated to excellent effect in a study of cimetidine form A using synchrotron diffraction data (Middleton *et al.*, 2002). The conformation of an ^{15}N labelled sample of cimetidine was determined in the form of four separate C···^{15}N through-space distances derived from rotational-echo double resonance (REDOR) NMR (Gullion & Schaefer, 1989; Gullion & Pennington, 1998). With SS-NMR-derived torsion-angle restraints applied, the performance of the search in locating the global minimum was significantly enhanced in terms of speed and reliability compared with a search with no torsional restraints. In effect, the application of the SS-NMR-derived torsion-angle information in this example simplified the global optimization to a more effective rigid-body search.

SS-NMR spectra simulated using the gauge including projector augmented wave (GIPAW) approach in combination with experimental SS-NMR data detailing two-dimensional correlations of ^{1}H and ^{13}C chemical shifts have been used to verify the accuracy of the structure of a 1:1 co-crystal of indomethacin and nicotinamide solved from powder diffraction data (Dudenko *et al.*, 2013). Hence, whilst in this case the SS-NMR-derived structural information was not utilized to direct the final refined crystal structure, such details can be helpful in providing independent confirmation that the structural model obtained is accurate.

4.4.2.5. *Intermolecular distance constraints*

The SDPD search space may also be reduced by introducing information describing intermolecular interactions between fragments in the structure. This can be done in the form of distance and/or angle restraints defining the contact between two fragments. For example, a CSD-derived distance restraint was applied to the $\mathrm{Cl^-}\cdots\mathrm{NH^+}$ separation (3 ± 0.3 Å) in SDPD attempts of verapamil hydrochloride. Although in this case it was not a prerequisite for successful structure solution given the quality of diffraction data available, the approach provides a useful tool in dealing with complex multicomponent crystal structures (CCDC, 2015). SS-NMR was used to identify hydrogen-bonding interactions between acetate and specific groups of the cortisone fragments in cortisone acetate polymorphs and was applied as a distance restraint in SDPD of form II (Harris, 2004). Another approach that has been applied in SDPD is to use energy penalties during the search to penalize nonsensical trial structures that have overlapping atoms (Stephenson & Liang, 2006). Whilst this can be effective in SDPD, such calculations are reliant on the accuracy of the energy calculation and also introduce a computational overhead on the overall SDPD process. A simple or 'anti-bump' cost function that uses minimum distance criteria only to avoid unlikely configurations has also been shown to be effective (Favre-Nicolin & Černý, 2002).

4.4.2.6. *H-atom location in structures solved from X-ray powder data*

As H atoms scatter X-rays very weakly, they often cannot be located independently in a structure determined from X-ray powder diffraction data. It is common practice therefore to fix H atoms in standard positions in the initial fragment model and retain these throughout the SDPD process (Fig. 4.4.1). With the application of appropriate Rietveld refinement strategies, reliable H-atom locations (*e.g.* for C—H bonds) can be achieved in the final structure. However, in many structures the orientation of N—H and O—H groups depends on intermolecular hydrogen-bonding interactions in the lattice. It is desirable therefore to ensure that a reliable, chemically sensible description of their locations is introduced into the final refinement. Following assessment of the crystal packing, this can be done manually by rotating the group defining the proton direction in order to satisfy the most probable hydrogen-bonding configuration.

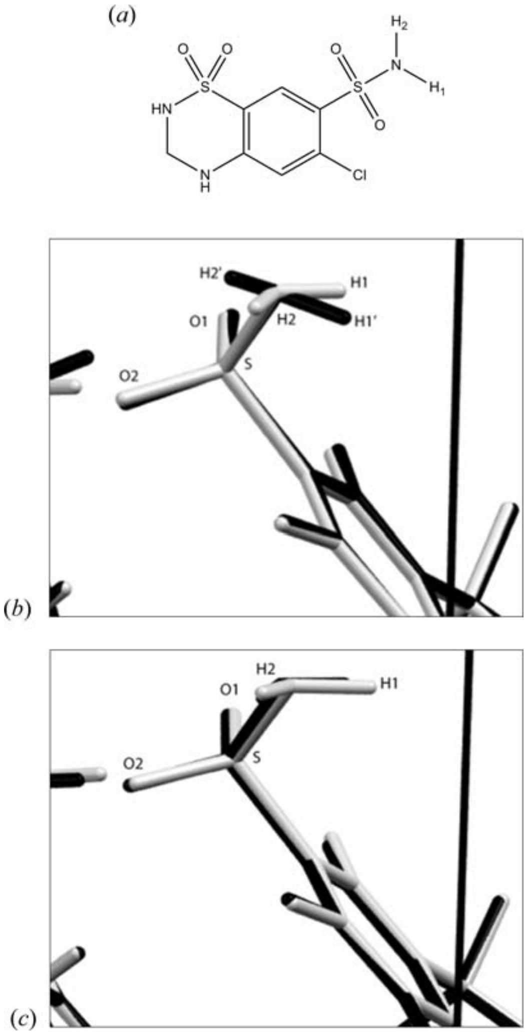

Figure 4.4.7
(*a*) Structure of hydrochlorothiazide (HCT) with H1 and H2 labelled; (*b*) overlay of HCT form-II SDPD (black) and single-crystal (grey) structures showing the discrepancy in N—H orientation around the N—S bond; (*c*) *CASTEP*-optimized SDPD (grey) and single-crystal (black) structures. From Florence *et al.* (2009).

Complementary experimental data can also contribute here. For example, ^{13}C tensor and ^{1}H/^{13}C correlation data were used to define the orientation of the five separate —OH groups in the SDPD structure determination of (+)-catechin 4.5-hydrate (Harper *et al.*, 2010). In an SDPD study of nimustine hydrochloride, the location of the protonation site on the pyrimidine ring was also successfully confirmed using SS-NMR (Beko *et al.*, 2012). This study also applied an energy minimization to all H-atom positions using the DREIDING/X6 force field prior to the final Rietveld refinement.

Once a global-minimum structure has been obtained, geometry-optimization calculations can be recommended where there is a particular interest in the reliable location of H atoms. The application of plane-wave density-functional theory (DFT) as a quantum-chemical aide in the accurate location of H atoms in organic crystals has been shown to be highly reliable in many cases and guidance on the practical application of these methods in this context is available (Deringer *et al.*, 2012). The thiazide diuretic hydrochlorothiazide has two hydrogen-bonded H atoms on a sulphonamide side chain and in the reported SDPD structure these had been positioned by manual rotation of the N—S bond to maximize contacts with surrounding H-atom acceptors (Fig. 4.4.7; Florence *et al.*, 2005*a*). First-principles DFT calculations in *CASTEP* (Clark *et al.*, 2005) significantly improved the accuracy of the orientation of the NH_2 group, showing excellent agreement with the locations identified from single-crystal diffraction (Florence *et al.*, 2009).

In a comprehensive analysis of 241 published crystal structures, dispersion-corrected DFT methods have been shown to reproduce experimental structures very accurately (van de Streek & Neumann, 2010). An energy-minimized r.m.s. Cartesian displacement (excluding H atoms) was used as an indicator of structural correctness: a correct structure obtained as the global minimum from a global-optimization search will correspond with an energy minimum to within less than 0.25 Å. In addition to assisting in the accurate location of H atoms, energy minimizations also have a useful application in the final assessment or validation of crystal structures and are a useful adjunct as part of an SDPD study.

4.4.2.7. *Crystal-structure prediction and crystal-structure solution*

Where it proves impossible to index a powder pattern, an SDPD attempt is halted and cannot progress to subsequent space-group assignment, intensity extraction or global optimization. Typically the researcher will seek to obtain better data, perhaps by recrystallization to remove any potential impurities or sharpen the diffraction peaks, or aim to recollect the data at a synchrotron. Given the advances made in the capability to predict crystal structures of molecular crystals *ab initio* (Day *et al.*, 2005, 2009), it is worth highlighting that crystal-structure prediction (CSP) can provide thermodynamically feasible model crystal structures. The crystal structure of form-I chlorothalonil was obtained by Rietveld refinement of the global-minimum lattice-energy structure from a CSP study against the experimental powder diffraction data (Tremayne *et al.*, 2004). In this case, the computational methods provided the structure in full, with the final refinement against the data confirming the veracity of the prediction. Hence, although crystal-structure prediction is not yet able to tackle large, flexible, multi-component pharmaceutical compounds as a matter of routine, just as advances in SS-NMR have extended the range of practical application in SDPD, computational methodologies for crystal-structure prediction and analysis show potential to become an increasingly powerful source of structural information.

4.4.3. Concluding remarks

Structure determination from powder diffraction data has progressed significantly over the last 15 years to the point where it can be viewed as a routine method for crystal-structure determination. Many structural problems can be tackled routinely where good-quality diffraction data and accurate molecular models are available. However, as the complexity of the structures investigated by SDPD increases, so the contribution of additional information becomes more valuable. With combined access to prior chemical knowledge, complementary analytical techniques and computational modelling techniques, the probability of success can be enhanced in increasingly challenging cases. The most appropriate approach to assist in a particular structural problem will often be case-specific and depend on several factors including available diffraction data quality, access to relevant chemical information, ability to utilize the information effectively within the search and the nature of the structure being investigated. However, with careful attention at each step of the SDPD process and with consideration for when supplementary information may be beneficial, the power of SDPD to solve complex, flexible, multi-component crystals with a high-degree of accuracy from the limited information content of a powder-diffraction pattern will continue to grow.

4.4.3.1. *Test data for SDPD*

As final remark, laboratory powder diffraction data for 35 compounds (Florence *et al.*, 2005*b*) are available for download from http://www.powderdata.net to allow interested readers to explore, test and compare different approaches to successful SDPD.

References

Allen, F. H. (2002). *The Cambridge Structural Database: a quarter of a million crystal structures and rising*. *Acta Cryst.* B**58**, 380–388.

Allen, F. H., Doyle, M. J. & Auf der Heyde, T. P. E. (1991). *Automated conformational analysis from crystallographic data. 6. Principal-component analysis for N-membered carbocyclic rings (N = 4, 5, 6): symmetry considerations and correlations with ring-puckering parameters*. *Acta Cryst.* B**47**, 412–424.

Allen, F. H., Howard, J. A. K. & Pitchford, N. A. (1993). *Symmetry-modified conformational mapping and classification of the medium rings from crystallographic data. I. Cycloheptane*. *Acta Cryst.* B**49**, 910–928.

Allen, F. H., Watson, D. G., Brammer, L., Orpen, A. G. & Taylor, R. (2006). *Typical interatomic distances: organic compounds*. In *International Tables for Crystallography*, Vol. C, *Mathematical, Physical and Chemical Tables*, edited by E. Prince, ch. 9.5, pp. 790–811. Chester: International Union of Crystallography.

Antoniadis, C. D., D'Oria, E., Karamertzanis, P. G., Tocher, D. A., Florence, A. J., Price, S. L. & Jones, A. G. (2010). *A computationally inspired investigation of the solid forms of (R)-1-phenylethylammonium-(S)-2-phenylbutyrate*. *Chirality*, **22**, 447–455.

Beko, S. L. D., Urmann, A., Lakatos, C., Glaubitz, C. & Schmidt, M. U. (2012). *Nimustine hydrochloride: the first crystal structure determination of a 2-chloroethyl-N-nitrosourea hydrochloride derivative by X-ray powder diffraction and solid-state NMR*. *Acta Cryst.* C**68**, o144–o148.

Bondi, A. (1964). *Van der Waals volumes and radii*. *J. Phys. Chem.* **68**, 441–451.

Brameld, K. A., Kuhn, B., Reuter, D. C. & Stahl, M. (2008). *Small molecule conformational preferences derived from crystal structure data. A medicinal chemistry focused analysis*. *J. Chem. Inf. Model.* **48**, 1–24.

Braun, D. E., Karamertzanis, P. G., Arlin, J. B., Florence, A. J., Kahlenberg, V., Tocher, D. A., Griesser, U. J. & Price, S. L. (2011). *Solid-state forms of β-resorcylic acid: how exhaustive should a polymorph screen be?* *Cryst. Growth Des.* **11**, 210–220.

Brown, S. P. & Spiess, H. W. (2001). *Advanced solid-state NMR methods for the elucidation of structure and dynamics of molecular, macromolecular, and supramolecular systems*. *Chem. Rev.* **101**, 4125–4156.

Bruno, I. J., Cole, J. C., Kessler, M., Luo, J., Motherwell, W. D. S., Purkis, L. H., Smith, B. R., Taylor, R., Cooper, R. I., Harris, S. E. & Orpen, A. G. (2004). *Retrieval of crystallographically-derived molecular geometry information*. *J. Chem. Inf. Comput. Sci.* **44**, 2133–2144.

Carpy, A., Léger, J.-M. & Melchiorre, C. (1985). *Structure of α-isopropyl-α-[(N-methyl-N-homoveratryl)-γ-aminopropyl]-3,4-dimethoxyphenyl-*

acetonitrile hydrochloride, verapamil, $C_{27}H_{38}N_2O_4{\cdot}HCl$. *Acta Cryst.* C**41**, 624–627.

CCDC (2015). *Solving the powder pattern of verapamil hydrochloride*. https://www.ccdc.cam.ac.uk/support-and-resources/ccdcresources/Verapamil_DASH.pdf

CCDC Software Ltd/STFC (2008). *DASH-v3.3 user guide*. The Cambridge Crystallographic Data Centre, Cambridge, UK.

Černý, R. & Favre-Nicolin, V. (2007). *Direct space methods of structure determination from powder diffraction: Principles, guidelines and perspectives*. *Z. Kristallogr.* **222**, 105–113.

Chan, F. C., Anwar, J., Cernik, R., Barnes, P. & Wilson, R. M. (1999). *Ab initio structure determination of sulfathiazole polymorph V from synchrotron X-ray powder diffraction data*. *J. Appl. Cryst.* **32**, 436–441.

Chernyshev, V. V., Kukushkin, S. Y. & Velikodny, Y. A. (2010). *Carvedilol dihydrogen phosphate propan-2-ol solvate from powder diffraction data*. *Acta Cryst.* E**66**, o613.

Clark, S. J., Segall, M. D., Pickard, C. J., Hasnip, P. J., Probert, M. I. J., Refson, K. & Payne, M. C. (2005). *First principles methods using CASTEP*. *Z. Kristallogr.* **220**, 567–570.

Coelho, A. A. (2000). *Whole-profile structure solution from powder diffraction data using simulated annealing*. *J. Appl. Cryst.* **33**, 899–908.

Connolly, M. L. (1985). *Computation of molecular volume*. *J. Am. Chem. Soc.* **107**, 1118–1124.

Cottrell, S. J., Olsson, T. S. G., Taylor, R., Cole, J. C. & Liebeschuetz, J. W. (2012). *Validating and understanding ring conformations using small molecule crystallographic data*. *J. Chem. Inf. Model.* **52**, 956–962.

Cremer, D. & Pople, J. A. (1975). *General definition of ring puckering coordinates*. *J. Am. Chem. Soc.* **97**, 1354–1358.

Cruz Cabeza, A. J., Day, G. M., Motherwell, W. D. S. & Jones, W. (2007). *Solvent inclusion in form II carbamazepine*. *Chem. Commun.* pp. 1600–1602.

David, W. I. F., Shankland, K. & Shankland, N. (1998). *Routine determination of molecular crystal structures from powder diffraction data*. *Chem. Commun.* pp. 931–932.

David, W. I. F., Shankland, K., van de Streek, J., Pidcock, E., Motherwell, W. D. S. & Cole, J. C. (2006). *DASH: a program for crystal structure determination from powder diffraction data*. *J. Appl. Cryst.* **39**, 910–915.

Day, G. M., Cooper, T. G., Cruz-Cabeza, A. J., Hejczyk, K. E., Ammon, H. L., Boerrigter, S. X. M., Tan, J. S., Della Valle, R. G., Venuti, E., Jose, J., Gadre, S. R., Desiraju, G. R., Thakur, T. S., van Eijck, B. P., Facelli, J. C., Bazterra, V. E., Ferraro, M. B., Hofmann, D. W. M., Neumann, M. A., Leusen, F. J. J., Kendrick, J., Price, S. L., Misquitta, A. J., Karamertzanis, P. G., Welch, G. W. A., Scheraga, H. A., Arnautova, Y. A., Schmidt, M. U., van de Streek, J., Wolf, A. K. & Schweizer, B. (2009). *Significant progress in predicting the crystal structures of small organic molecules – a report on the fourth blind test*. *Acta Cryst.* B**65**, 107–125.

Day, G. M., Motherwell, W. D. S., Ammon, H. L., Boerrigter, S. X. M., Della Valle, R. G., Venuti, E., Dzyabchenko, A., Dunitz, J. D., Schweizer, B., van Eijck, B. P., Erk, P., Facelli, J. C., Bazterra, V. E., Ferraro, M. B., Hofmann, D. W. M., Leusen, F. J. J., Liang, C., Pantelides, C. C., Karamertzanis, P. G., Price, S. L., Lewis, T. C., Nowell, H., Torrisi, A., Scheraga, H. A., Arnautova, Y. A., Schmidt, M. U. & Verwer, P. (2005). *A third blind test of crystal structure prediction*. *Acta Cryst.* B**61**, 511–527.

Deem, M. W. & Newsam, J. M. (1989). *Determination of 4-connected framework crystal structures by simulated annealing*. *Nature*, **342**, 260–262.

Deringer, V. L., Hoepfner, V. & Dronskowski, R. (2012). *Accurate hydrogen positions in organic crystals: assessing a quantum-chemical aide*. *Cryst. Growth Des.* **12**, 1014–1021.

Dinnebier, R. E., Sieger, P., Nar, H., Shankland, K. & David, W. I. F. (2000*a*). *Structural characterization of three crystalline modifications of telmisartan by single crystal and high-resolution X-ray powder diffraction*. *J. Pharm. Sci.* **89**, 1465–1479.

Dinnebier, R. E., Wagner, M., Peters, F., Shankland, K. & David, W. I. F. (2000*b*). *Crystal structure of the* $[(C_5H_4BMe_2)_2Fe]$*-4,4′-bipyridine polymer from high resolution X-ray powder diffraction*. *Z. Anorg. Allg. Chem.* **626**, 1400–1405.

Dudenko, D. V., Williams, P. A., Hughes, C. E., Antzutkin, O. N., Velaga, S. P., Brown, S. P. & Harris, K. D. M. (2013). *Exploiting the synergy of powder X-ray diffraction and solid-state NMR spectroscopy in structure determination of organic molecular solids*. *J. Phys. Chem. C*, **117**, 12258–12265.

Ebejer, J. P., Morris, G. M. & Deane, C. M. (2012). *Freely available conformer generation methods: how good are they?* *J. Chem. Inf. Model.* **52**, 1146–1158.

Edgar, M., Carter, V. J., Grewal, P., Sawers, L. J., Sastre, E., Tunstall, D. P., Cox, P. A., Lightfoot, P. & Wright, P. A. (2002). *Structure elucidation of a novel aluminum methylphosphonate,* $Al_3(CH_3PO_3)_2{\cdot}O{\cdot}(OH)_3$, *through a combination of X-ray powder diffraction, solid-state NMR spectroscopy, and computational energy minimization*. *Chem. Mater.* **14**, 3432–3439.

Engel, G. E., Wilke, S., König, O., Harris, K. D. M. & Leusen, F. J. J. (1999). *PowderSolve – a complete package for crystal structure solution from powder diffraction patterns*. *J. Appl. Cryst.* **32**, 1169–1179.

Fabbiani, F. P. A., Byrne, L. T., McKinnon, J. J. & Spackman, M. A. (2007). *Solvent inclusion in the structural voids of form II carbamazepine: Single-crystal X-ray diffraction, NMR spectroscopy and Hirshfeld surface analysis*. *CrystEngComm*, **9**, 728–731.

Favre-Nicolin, V. & Černý, R. (2002). *FOX, 'free objects for crystallography': a modular approach to ab initio structure determination from powder diffraction*. *J. Appl. Cryst.* **35**, 734–743.

Fernandes, P., Shankland, K., Florence, A. J., Shankland, N. & Johnston, A. (2007). *Solving molecular crystal structures from X-ray powder diffraction data: the challenges posed by gamma-carbamazepine and chlorothiazide N,N,-dimethylformamide (1/2) solvate*. *J. Pharm. Sci.* **96**, 1192–1202.

Florence, A. J. (2009). *The Solid State*. New York, London: Informa Healthcare.

Florence, A. J., Bardin, J., Johnston, B., Shankland, N., Griffin, T. A. N. & Shankland, K. (2009). *Structure determination from powder data: Mogul and CASTEP*. *Z. Kristallogr. Suppl.* **30**, 215–220.

Florence, A., Johnston, A., Fernandes, P., Shankland, K., Stevens, H. N. E., Osmundsen, S. & Mullen, A. B. (2005*a*). *Powder study of hydrochlorothiazide form II*. *Acta Cryst.* E**61**, o2798–o2800.

Florence, A. J., Shankland, K., Gelbrich, T., Hursthouse, M. B., Shankland, N., Johnston, A., Fernandes, P. & Leech, C. K. (2008). *A catemer-to-dimer structural transformation in cyheptamide*. *CrystEngComm*, **10**, 26–28.

Florence, A. J., Shankland, N., Shankland, K., David, W. I. F., Pidcock, E., Xu, X., Johnston, A., Kennedy, A. R., Cox, P. J., Evans, J. S. O., Steele, G., Cosgrove, S. D. & Frampton, C. S. (2005*b*). *Solving molecular crystal structures from laboratory X-ray powder diffraction data with DASH: the state of the art and challenges*. *J. Appl. Cryst.* **38**, 249–259.

Fogarasi, G., Zhou, X. F., Taylor, P. W. & Pulay, P. (1992). *The calculation of ab initio molecular geometries: efficient optimization by natural internal coordinates and empirical correction by offset forces*. *J. Am. Chem. Soc.* **114**, 8191–8201.

Gavezzotti, A. (1983). *The calculation of molecular volumes and the use of volume analysis in the investigation of structured media and of solid-state organic reactivity*. *J. Am. Chem. Soc.* **105**, 5220–5225.

Glasser, L. (2011). *Thermodynamics of condensed phases: formula unit volume,* V_m, *and the determination of the number of formula units, Z, in a crystallographic unit cell*. *J. Chem. Educ.* **88**, 581–585.

Griffin, T. A. N., Shankland, K., van de Streek, J. & Cole, J. (2009). *GDASH: a grid-enabled program for structure solution from powder diffraction data*. *J. Appl. Cryst.* **42**, 356–359.

Groom, C. R., Bruno, I. J., Lightfoot, M. P. & Ward, S. C. (2016). *The Cambridge Structural Database*. *Acta Cryst.* B**72**, 171–179.

Gullion, T. & Pennington, C. H. (1998). *Theta-redor: An MAS NMR method to simplify multiple coupled heteronuclear spin systems*. *Chem. Phys. Lett.* **290**, 88–93.

Gullion, T. & Schaefer, J. (1989). *Rotational-echo double-resonance NMR*. *J. Magn. Reson.* **81**, 196–200.

Habershon, S., Turner, G. W., Kariuki, B. M., Cheung, E. Y., Hanson, A., Tedesco, E., Albesa-Jove, D., Chao, M. H., Lanning, O. J., Johnston, R. L. & Harris, K. D. M. (2003). *Eager, computer program for structure solution from powder diffraction data*. Cardiff University and University of Birmingham.

Harper, J. K., Doebbler, J. A., Jacques, E., Grant, D. M. & Von Dreele, R. B. (2010). *A combined solid-state NMR and synchrotron X-ray diffraction powder study on the structure of the antioxidant (+)-catechin 4.5-hydrate*. *J. Am. Chem. Soc.* **132**, 2928–2937.

Harris, R. K. (2004). *NMR crystallography: the use of chemical shifts*. *Solid State Sci.* **6**, 1025–1037.

Hofmann, D. (2002). *Fast estimation of crystal densities*. *Acta Cryst.* B**58**, 489–493.

Hughes, C. E., Olejniczak, S., Helinski, J., Ciesielski, W., Repisky, M., Andronesi, O. C., Potrzebowski, M. J. & Baldus, M. (2005). *Probing structure in the polymorphic domain of the L-enantiomer of N-benzoylphenylalanine by means of 2D solid-state NMR spectroscopy and DFT calculations*. *J. Phys. Chem. B*, **109**, 23175–23182.

Ivashevskaja, S. N., Aleshina, L. A., Andreev, V. P., Nizhnik, Y. P., Chernyshev, V. V. & Schenk, H. (2002). *Dichlorobis(2-methylquinoline N-oxide-κO)zinc(II) from powder data*. *Acta Cryst.* C**58**, m300–m301.

Kaduk, J. A. (2007). *Chemical reasonableness in Rietveld analysis; organics*. *Powder Diffr.* **22**, 74–82.

Kariuki, B. M., Calcagno, P., Harris, K. D. M., Philp, D. & Johnston, R. L. (1999). *Evolving opportunities in structure solution from powder diffraction data – crystal structure determination of a molecular system with twelve variable torsion angles*. *Angew. Chem. Int. Ed.* **38**, 831–835.

Kempster, C. J. E. & Lipson, H. (1972). *A rapid method for assessing the number of molecules in the unit cell of an organic crystal*. *Acta Cryst.* B**28**, 3674.

Kojić-Prodić, B., Ružić-Toroš, Ž., Šunjić, V., Decorte, E. & Moimas, F. (1984). *Absolute conformation and configuration of (2S,3S)-3-acetoxy-5-(dimethylaminoethyl)-2-(4-methoxyphenyl)-2,3-dihydro-1,5-benzothiazepin-4(5h)-one chloride (dilthiazem hydrochloride)*. *Helv. Chim. Acta*, **67**, 916–926.

Le Bail, A. (2001). *ESPOIR: A program for solving structures by Monte Carlo analysis of powder diffraction data. Mater. Sci. Forum*, **378–381**, 65–70.

Lewis, G. R., Steele, G., McBride, L., Florence, A. J., Kennedy, A. R., Shankland, N., David, W. I. F., Shankland, K. & Teat, S. J. (2005). *Hydrophobic vs. hydrophilic: ionic competition in remacemide salt structures*. *Cryst. Growth Des.* **5**, 427–438.

Lowes, M. M. J., Caira, M. R., Lotter, A. P. & Van Der Watt, J. G. (1987). *Physicochemical properties and X-ray structural studies of the trigonal polymorph of carbamazepine*. *J. Pharm. Sci.* **76**, 744–752.

Macrae, C. F., Bruno, I. J., Chisholm, J. A., Edgington, P. R., McCabe, P., Pidcock, E., Rodriguez-Monge, L., Taylor, R., van de Streek, J. & Wood, P. A. (2008). *Mercury CSD 2.0 – new features for the visualization and investigation of crystal structures*. *J. Appl. Cryst.* **41**, 466–470.

Middleton, D. A., Le Duff, C. S., Peng, X., Reid, D. G. & Saunders, D. (2000). *Molecular conformations of the polymorphic forms of cimetidine from ^{13}C solid-state NMR distance and angle measurements*. *J. Am. Chem. Soc.* **122**, 1161–1170.

Middleton, D. A., Peng, X., Saunders, D., Shankland, K., David, W. I. F. & Markvardsen, A. J. (2002). *Conformational analysis by solid-state NMR and its application to restrained structure determination from powder diffraction data*. *Chem. Commun.* pp. 1976–1977.

Mínguez Espallargas, G., Hippler, M., Florence, A. J., Fernandes, P., van de Streek, J., Brunelli, M., David, W. I. F., Shankland, K. & Brammer, L. (2007). *Reversible gas uptake by a nonporous crystalline solid involving multiple changes in covalent bonding*. *J. Am. Chem. Soc.* **129**, 15606–15614.

Nakamura, N. & Sato, T. (1999). *1,14-Tetradecanediol*. *Acta Cryst.* C**55**, 1687–1689.

Pagola, S., Polymeros, A. & Kourkoumelis, N. (2017). *WinPSSP: a revamp of the computer program PSSP and its performance solving the crystal structures of small organic compounds and solids of biological and pharmaceutical interest. J. Appl. Cryst.* **50**, 293–303.

Pan, Z. G., Cheung, E. Y., Harris, K. D. M., Constable, E. C. & Housecroft, C. E. (2005). *A case study in direct-space structure determination from powder X-ray diffraction data: finding the hydrate structure of an organic molecule with significant conformational flexibility*. *Cryst. Growth Des.* **5**, 2084–2090.

Preiss, U., Slattery, J. M. & Krossing, I. (2009). *In silico prediction of molecular volumes, heat capacities, and temperature-dependent densities of ionic liquids*. *Ind. Eng. Chem. Res.* **48**, 2290–2296.

Putz, H., Schön, J. C. & Jansen, M. (1999). *Combined method for ab initio structure solution from powder diffraction data*. *J. Appl. Cryst.* **32**, 864–870.

Reboul, J. P., Cristau, B., Soyfer, J. C. & Astier, J. P. (1981). *5h-Dibenz[b,f]azépinecarboxamide-5 (carbamazépine)*. *Acta Cryst.* B**37**, 1844–1848.

Reinaudi, L., Leiva, E. P. M. & Carbonio, R. E. (2000). *Simulated annealing prediction of the crystal structure of ternary inorganic compounds using symmetry restrictions*. *J. Chem. Soc. Dalton Trans.* pp. 4258–4262.

Rietveld, H. M. (1969). *A profile refinement method for nuclear and magnetic structures*. *J. Appl. Cryst.* **2**, 65–71.

Rowland, R. S. & Taylor, R. (1996). *Intermolecular nonbonded contact distances in organic crystal structures: comparison with distances expected from van der Waals radii*. *J. Phys. Chem.* **100**, 7384–7391.

Sadowski, J. & Gasteiger, J. (1993). *From atoms and bonds to three-dimensional atomic coordinates: automatic model builders*. *Chem. Rev.* **93**, 2567–2581.

Sadowski, J. J., Gasteiger, J. & Klebe, G. (1994). *Comparison of automatic three-dimensional model builders using 639 X-ray structures*. *J. Chem. Inf. Model.* **34**, 1000–1008.

Shankland, K. & David, W. I. F. (2002). *Global optimization strategies*. In *Structure Determination from Powder Diffraction Data*, edited by W. I. F. David, K. Shankland, L. B. McKusker & C. Baerlocher, pp. 252–285. Oxford University Press.

Shankland, K., David, W. I. F., Csoka, T. & McBride, L. (1998*a*). *Structure solution of ibuprofen from powder diffraction data by the application of a genetic algorithm combined with prior conformational analysis*. *Int. J. Pharm.* **165**, 117–126.

Shankland, K., McBride, L., David, W. I. F., Shankland, N. & Steele, G. (2002). *Molecular, crystallographic and algorithmic factors in structure determination from powder diffraction data by simulated annealing*. *J. Appl. Cryst.* **35**, 443–454.

Shankland, N., Florence, A. J., Cox, P. J., Wilson, C. C. & Shankland, K. (1998*b*). *Conformational analysis of ibuprofen by crystallographic database searching and potential energy calculation*. *Int. J. Pharm.* **165**, 107–116.

Stephens, P. W. & Huq, A. (2002). *PSSP: An open source powder structure solution program for direct space simulated annealing. Trans. Am. Crystallogr. Assoc.* **27**, 127–144.

Stephenson, G. A. (2000). *Structure determination from conventional powder diffraction data: application to hydrates, hydrochloride salts, and metastable polymorphs*. *J. Pharm. Sci.* **89**, 958–966.

Stephenson, G. A. & Liang, C. (2006). *Structural determination of the stable and meta-stable forms of atomoxetine HCl using single crystal and powder X-ray diffraction methods*. *J. Pharm. Sci.* **95**, 1677–1683.

Stewart, J. J. (2013). *Optimization of parameters for semiempirical methods VI: More modifications to the NDDO approximations and re-optimization of parameters*. *J. Mol. Model.* **19**, 1–32.

Stewart, J. J. P. (2012). *MOPAC2012*. Stewart Computational Chemistry, Colorado Springs, USA. http://openmopac.net.

Streek, J. van de & Neumann, M. A. (2010). *Validation of experimental molecular crystal structures with dispersion-corrected density functional theory calculations*. *Acta Cryst.* B**66**, 544–558.

Trask, A. V. & Jones, W. (2005). *Crystal engineering of organic cocrystals by the solid-state grinding approach*. In *Organic Solid State Reactions*, edited by F. Toda, *Topics in Current Chemistry*, Vol. 254, pp. 41–70. Berlin: Springer-Verlag.

Tremayne, M. & Glidewell, C. (2000). *Direct-space structure solution from laboratory powder diffraction data of an organic cocrystal: 1,2,3-trihydroxybenzene–HMTA (1/1)*. *Chem. Commun.* pp. 2425–2426.

Tremayne, M., Grice, L., Pyatt, J. C., Seaton, C. C., Kariuki, B. M., Tsui, H. H. Y., Price, S. L. & Cherryman, J. C. (2004). *Characterization of complicated new polymorphs of chlorothalonil by X-ray diffraction and computer crystal structure prediction*. *J. Am. Chem. Soc.* **126**, 7071–7081.

Vallcorba, O., Rius, J., Frontera, C. & Miravitlles, C. (2012). *TALP: a multisolution direct-space strategy for solving molecular crystals from powder diffraction data based on restrained least squares*. *J. Appl. Cryst.* **45**, 1270–1277.

Zell, M. T., Padden, B. E., Grant, D. J. W., Schroeder, S. A., Wachholder, K. L., Prakash, I. & Munson, E. J. (2000). *Investigation of polymorphism in aspartame and neotame using solid-state NMR spectroscopy*. *Tetrahedron*, **56**, 6603–6616.

International Tables for Crystallography (2019). Vol. H, Chapter 4.5, pp. 442–451.

4.5. Solving and refining inorganic structures

R. Černý and V. Favre-Nicolin

4.5.1. The molecular/non-molecular and the organic/inorganic boundaries

An inorganic compound may be defined as a compound that does not correspond to the definition of organic compounds according to IUPAC (Rigaudy & Klesney, 1979). The separation of compounds by the inorganic/organic boundary is of minor importance for structure determination by diffraction methods. Even if the presence of only light elements in organic compounds decreases the diffraction contrast between atoms compared to the inorganic world, more important for diffraction is how the atoms build up larger building units and the crystal structure itself. Inorganic compounds usually do not contain isolated molecules. A molecular/non-molecular boundary is therefore relevant for the choice of a structure-determination method. Non-molecular compounds – also called extended solids – are constructed by bonds that extend ‘infinitely’ in three dimensions through a crystal. These non-molecular crystals usually crystallize with high symmetries and atoms often occupy special Wyckoff positions.

4.5.2. Modelling of non-molecular compounds

4.5.2.1. *Principles*

The modelling of non-molecular compounds is by nature complex; this is because they are extended solids, and therefore no obvious group of atoms (such as a molecule) can be isolated and used as a *building unit* (BU) for the entire structure (Fig. 4.5.1). This does not create a particular difficulty for *ab initio* structure-solution methods working entirely in reciprocal space (reciprocal-space methods, which we will abbreviate as RSMs). However, it becomes a problem for methods working entirely in direct space (direct-space methods or DSMs) and the use of *a priori* chemical knowledge about the compound. Any structure-solution algorithm working in direct space has to know how to define basic structural blocks of the crystal, BUs, which are then manipulated (optimized) by the algorithm. Moreover, the presence of high-order symmetries leads to a fragmentation of these BUs, as any group of atoms (*e.g.* an octahedron) can be located on a symmetry element, so that only a part of the atoms of a symmetry-constrained BU is truly crystallographically independent. Finally, the actual arrangement in space between BUs relative to the symmetry elements of the unit cell is *a priori* unknown.

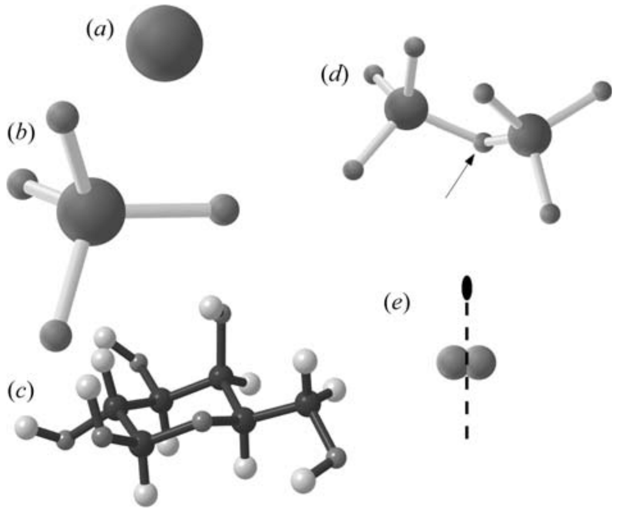

Figure 4.5.1
A non-molecular crystal can be described by primary building units (PBUs), which can be (*a*) isolated atoms, (*b*) coordination polyhedra, (*c*) molecules, or a more complex and flexible arrangement of secondary building units (SBUs). The choice of BUs is essential both to solving the structure and to ensuring that it is chemically and crystallographically sensible. One particular difficulty is identifying without *a priori* knowledge atoms (*d*) shared by several BUs or (*e*) a BU on a special position.

The basic principles to be followed when choosing the BU are the following:

(i) the model must describe the structure with as few parameters (degrees of freedom or DoF) as possible, so that the parameter space to explore is as small as possible;
(ii) the basic building units must allow the exploitation of any *a priori* chemical knowledge about the material, to provide an chemically unambiguous solution; and
(iii) all BUs must be constructed so that they can easily be linked to other BUs, in order to form an extended solid. This includes bonding with themselves in the presence of a symmetry element.

4.5.2.2. *Building units*

The choice of a BU is easy when isolated molecules or polyatomic ions are present in the crystal, such as in organic or coordination compounds where the molecules and ions are easily described by a finite number of internal coordinates (bonding distances, angles and torsion angles). A molecule or polyatomic ion is naturally a well defined BU that can be moved in the unit cell, and its conformation altered by modifying torsion angles. No sharing of atoms between the molecules or ions occurs.

The situation can become rather unclear when one tries to model the crystal structure of a non-molecular compound. The definition of a BU for a crystal such as Fe or NaCl is not unambiguous: should it be one atom, the first coordination sphere of each atom, a structural sheet of finite thickness, or the asymmetric unit? Pauling (1929) created the concept of BU when he defined coordination polyhedra for the description of structures, and stated Pauling’s rules. Coordination polyhedra, typically the first coordination spheres of selected atoms which will generate the whole inorganic crystal structure, can always be identified. These polyhedra will share corners, edges or faces in close-packed crystal structures and frameworks, but can also be chosen as isolated entities as in ionic crystals containing polyatomic ions. A wide range of polyhedra can be defined, and these are naturally described using bond distances, angles and torsion angles. The type of atomic coordination in non-molecular crystals can very often be predicted from their chemical formula, cationic valence state, the known structures of similar compounds and spectroscopic methods which are locally sensitive *e.g.* NMR, EXAFS, Mössbauer spectroscopy *etc*. The definition of BUs is easy for

Copyright © 2019 International Union of Crystallography

tetrahedral frameworks like zeolites, where the concept of primary building units (PBUs) and secondary building units (SBUs) is used (Meier & Olson, 1987). In the case of zeolites a PBU is a TO_4 tetrahedron (T being a tetrahedral atom), and SBUs are various fragments of the zeolite framework built from PBUs with the aim of using as few SBUs as possible (ideally just one) to build up the whole framework.

The concept of PBUs and SBUs may also be used for modelling an extended solid for structure-solution purposes using DSMs. In DSMs the PBUs are carefully selected from knowledge of the crystal chemistry of the compound under question, and are used as rigid or semi-rigid blocks which are then localized by a global-optimization algorithm within the crystal structure (unit cell) of the compound. The SBU may be used in the same way, *i.e.* as blocks constructed from a PBU or as additional information (restraints) in the global-optimization algorithm. Various SBUs are possible such as isolated polyhedral clusters, infinite polyhedral chains, sheets or frameworks.

A correct choice of PBU is important for the correct description of an *a priori* unknown structure, and may become decisive for the convergence of the global-optimization algorithm. We can distinguish three types of inorganic compounds from the point of view of PBU choice for structure determination:

Polyhedral compounds are mostly iono–covalent compounds (Pauling, 1929). The selection of a PBU is naturally a cation (but may also be an anion; see Krivovichev *et al.*, 2013) first coordination sphere. Examples are: salts, oxides, chalcogenides, halides, pnictides, silicates, complex and ionic hydrides, and also inorganic monomeric crystals like $Hf(BH_4)_4$ (Broach *et al.*, 1983) with isolated polyhedral PBUs.

Hybrid compounds are coordination polymers such as metal–organic frameworks (MOFs) (Tranchemontagne *et al.*, 2009) containing metal cations or their coordination polyhedra linked by molecular linkers as PBUs or SBUs, and also covalent organic frameworks (COFs) where the PBUs are simple molecular fragments like benzene rings connected by other molecular fragments of similar complexity (Côté *et al.*, 2005).

Close-packed compounds where the definition of the first coordination sphere polyhedron as a PBU is less evident. Examples are alloys and intermetallic compounds. The first coordination sphere polyhedra usually have a high number of vertices, such as in Frank–Kasper phases containing Kasper polyhedra (Frank & Kasper, 1958). In the case of quasicrystals the polyhedral clusters are themselves PBUs. In some cases the whole crystal is a PBU (nanoparticles). Modelling from free atoms seems to be more efficient in this case.

4.5.2.3. *Special positions and the sharing of atoms between building units*

When building a non-molecular crystal from the BUs, sharing of atoms between the BUs must be taken into account. Except in simple cases with small unit cells, the connectivity is *a priori* unknown. This is not a problem for RSMs, but in DSMs the global-optimization algorithm must be able to determine when BUs share corners, edges or faces, while also allowing BUs to move away from positions where they share atoms. A similar difficulty presents itself when an atom falls onto a special position and overlaps with its symmetry equivalents.

To cope with this, Deem & Newsam (1989) used a merging term in the cost function, which then evolved into a general and simple algorithm called the dynamical occupancy correction (DOC) by Favre-Nicolin & Černý (2002). For each proposed model, all atom positions in and near the asymmetric unit are generated, then for all unique atoms a neighbour table with all atoms closer than d_{min} (with d_{min} = 0.1 nm) is generated. The occupancy is then corrected as follows (Fig. 4.5.2):

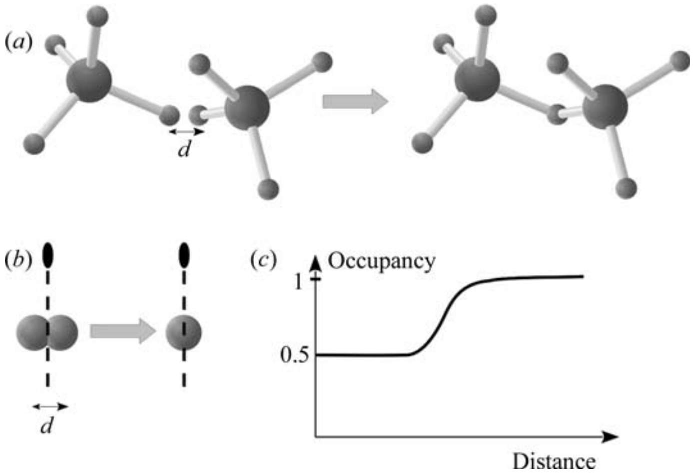

Figure 4.5.2
Ab initio structure-solution algorithms working in direct space must be able to automatically handle (*a*) atoms that are shared between individual building units and (*b*) atoms that are on special positions. In both cases, the algorithm can transform two overlapping atoms into a single one by (*c*) reducing the occupancy of the atoms when their distance apart falls below a threshold value. This 'dynamical occupancy correction' has the advantage of working without any *a priori* information, and is reversible.

$$\text{Occupancy}^{-1} = 1 + \sum_{\text{neighbours}} |d_{\min} - d_i|/d_{\min}. \qquad (4.5.1)$$

The sum is over all neighbours of the same atomic type. From this formula it is straightforward to see that if n atoms overlap ($d_i < d_{\min}$), the dynamical occupancy correction converges to $1/n$. After this correction has been applied, there will be n atoms with occupancy equal to or converging to $1/n$. Thus the algorithm for computing structure factors will use the correct electronic (or nuclear) density.

There are several advantages to this approach. It can handle any type of overlap (due to different BUs or symmetry-related) and allows a smooth transition (a progressive change of the occupancy) as the overlapping atoms get closer. Moreover, the atoms are not merged, so a direct-space algorithm can go back and forth between overlapping and non-overlapping atoms to search for the best solution.

The drawback of this approach is that it requires the calculation of a distance table between elements, which can take longer than the actual structure-factor calculation. Moreover, the ability to merge atoms also comes with a less obvious price: whenever it is used, there are too many atoms used to describe the unit-cell contents. Take, for example, a structure built from vertex-sharing octahedra: in this case the vertex atoms are shared between two octahedra, so that a description using only octahedra as a BU would use twice as many vertex atoms as necessary. This effectively increases the number of atoms, and thus both the number of parameters as well as the computing time for each trial structure. Even more important, looking at the three-dimensional model of the structure becomes challenging because of the high density of atoms in the unit cell (as long as the final solution has not been found, and the atoms are not perfectly overlapping). The recommendation is to switch off the DOC whenever possible, *i.e.* in the case of space groups having only general Wyckoff positions (fixed-point-free space groups): $P1$, $P2_1$, Pc,

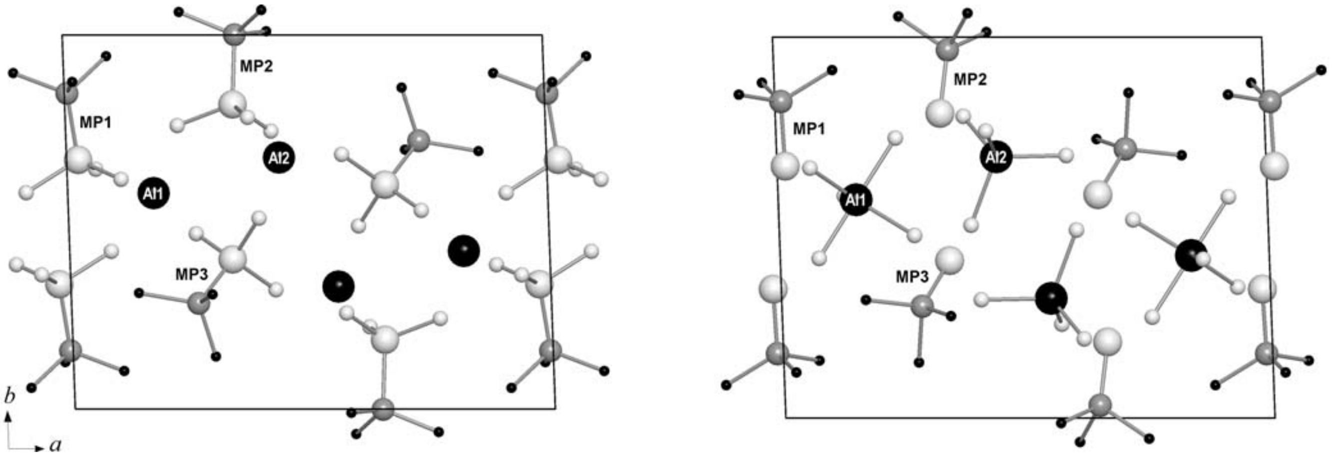

Figure 4.5.3
Modelling of the aluminium methylphosphonate structure using: (left) three H_3C-PO_3 blocks MP1–MP3 and two Al atoms, and (right) one AlO_5 trigonal bipyramid for Al1, one AlO_4 tetrahedron for Al2 and three H_3C-P groups MP1–MP3.

Cc, $P2_12_12_1$, $Pca2_1$, $Pna2_1$, $P4_1$, $P4_3$, $P3_1$, $P3_2$, $P6_1$, $P6_5$, and if no partly occupied sites are expected (see Section 4.5.2.4).

4.5.2.4. *Is there a need for precise unit-cell contents?*

The DOC can be an ideal tool to treat the uncertainty in unit-cell content and site occupancies. A good example is the hydrogen in interstitial hydrides like $NdNi_4MgH_{3.6}$ (Guénée *et al.*, 2003). When hydrogen is dissolved in the crystal lattice of an intermetallic compound, usually a great number of interstitial sites are partially occupied by H atoms, leading to an uncertainty in the total number of Wyckoff sites occupied by hydrogen. The DOC can easily treat this problem. The starting model for DSMs can contain more H atoms than needed for the correct structure. The excess H atoms are simply merged by the DOC. This means that when optimizing the structural model one does not need to specify at the beginning which Wyckoff sites (special or general) will be occupied by individual atoms, the connectivity between the BUs (such as sharing vertices between polyhedra) or even the exact chemical composition of the crystal. The only condition is that the starting model contains at least the correct number (or more) of independent BUs. Not only can excess atoms be merged by the DOC, but even whole BUs such as excess polyhedra!

This does not mean that the *a priori* knowledge of correct chemical composition may be underestimated when solving a crystal structure by DSMs. Direct-space modelling of relatively complex non-molecular structures can yield a relatively good fit for a wrong structure with the wrong chemical composition [see for example the case of $AZn_2(BH_4)_5$ (A = Li, Na) (Ravnsbaek *et al.*, 2009; Černý *et al.*, 2010)]. Such a structural model may have balanced interatomic forces as shown by density-functional theory (DFT) optimization, but it does not correspond to a stable polymorph under the given thermodynamic conditions. RSMs depend less on the correct knowledge of the chemical content of the unit cell, as they use it only for normalization of the structure-factor amplitudes and for interpretation of electron-density maps.

4.5.2.5. *Building units and the convergence of the DSM algorithm*

The choice of BUs often has an effect on the convergence of the global-optimization algorithm. A good example is the structure solution of aluminium methylphosphonate (Edgar *et al.*, 2002). For this material, individual PBUs were identified using ^{27}Al, ^{13}C and ^{31}P NMR spectra, which revealed the presence of three crystallographically inequivalent C-PO_3 units as well as two aluminium atoms in tetrahedrally and fivefold coordinated sites, respectively. From this *a priori* knowledge, two models were used to solve the structure (Fig. 4.5.3):

(i) using three H_3C-PO_3 blocks and two Al atoms (24 DoF, not counting the positions of H atoms);

(ii) one AlO_5 trigonal bipyramid, one AlO_4 tetrahedron and three H_3C-P groups (27 DoF, counting only five DoF for the H_3C-P groups since the H-atom positions cannot be found reliably).

In both cases the same structure was obtained. The inclusion of the H atoms and the use of an anti-bump cost function was very important in these optimizations, since it helped to differentiate C and O atoms, as well as (indirectly) P and Al, and therefore reduced the depth of local minima. Using the first model the solution required on average 0.7 million trials. The second model was much less successful during repeated runs (the distribution of the number of required trials to find the solution was wide, ranging from 0.3 to 16 million), even though it better exploited the NMR information on the aluminium coordination. This was because of the difficulty in finding the correct positions of the AlO_4 and AlO_5 groups, which are very similar from an electron-density viewpoint and almost isotropic so that their actual orientation is hard for the algorithm to pinpoint. In contrast, for the first model, two simple groups of identical building blocks (2 × Al and 3 × H_3C-PO_3) are used, where the Al and H_3C-PO_3 groups are easily distinguishable, anisotropic, and the invariance by permutation significantly reduces the parameter space to be explored. The role of the DoF (27 *versus* 24) is here less important than the nature of the PBUs.

4.5.2.6. *Random versus non-random DSM algorithms*

Once the BUs have been defined, several types of algorithms can be used to actually solve the structure:

(i) *Random, ergodic algorithms* such as the reverse Monte Carlo (RMC) or genetic algorithms (GAs) (see Chapter 4.3). These generate a very large number of trial structures by varying all the degrees of freedom and thus exploring the entire parameter space. This type of algorithm is thorough, but requires long computer running times. Additional chemical information applied in the choice of BUs and in the use of various cost functions based on coordination knowledge (anti-bump distances, crystal energy, bond-valence sums) is highly valuable in increasing the success rate of these algorithms.

(ii) *Topology-guided algorithms* (framework building). Where the type of crystal structure is known *a priori* (not just for the PBU, but also for the SBU) this kind of algorithm can be used. This approach is primarily used for framework compounds such as zeolites (Grosse-Kunstleve *et al.*, 1997) and MOFs (O'Keeffe & Yaghi, 2012; Tranchemontagne *et al.*, 2009) and in general for organometallic species (Masciocchi & Sironi, 2005) and the prediction of inorganic structures (Mellot Draznieks *et al.*, 2000).

(iii) *Crystal-chemistry guided algorithms*. These are based on quantum-chemistry calculations (Mercier *et al.*, 2006, 2007) or symmetry analysis (Evans *et al.*, 2003), and are useful for a very precise family of compounds where the structure is parameterized by a limited number of parameters. A good example is α-$Bi_2Sn_2O_7$, a 176-atom compound based on the pyrochlore structure (Evans *et al.*, 2003), which was solved from powder diffraction data by the symmetry analysis of superstructures based on a well described average structure. This approach can be particularly efficient for layered compounds, or when different polytypes are possible. An example of symmetry-guided refinement is parametric Rietveld refinement (Stinton & Evans, 2007) applied to the analysis of structural phase transitions (Müller *et al.*, 2010).

Crystal-chemistry knowledge can be used to accelerate the convergence of random algorithms by eliminating regions in the parameter space where the correct structure cannot exist. For example, the knowledge of the chemical composition and contents of the unit cell together with the space-group symmetry exclude some combinations of Wyckoff positions which cannot be occupied by a given atom type. This analysis is done *a priori* and is actively used in the random algorithm (Deng & Dong, 2011; Meredig & Wolverton, 2013) of DSMs, and can also be used in structure prediction with (Meredig & Wolverton, 2013) and without (Reinaudi *et al.*, 1998) the active use of diffraction data.

4.5.2.7. *The choice of the cost function in DSM algorithms*

A cost function based on additional chemical information in addition to the diffraction data should help the global-optimization algorithm in DSMs to find the global minimum of the diffraction-only cost function (see Chapter 4.3). In the case of non-molecular compounds, a simple anti-bump cost function penalizing the improbable atomic configurations provides the best results (Favre-Nicolin & Černý, 2002). Similarly, with DOCs the anti-bump cost function requires a time-consuming interatomic distances calculation, but the gain in the convergence of the optimization algorithm is more important than the time costs in most cases.

A cost function based on the crystal potential energy (for different types of the potential energy see Chapter 4.9) is a rigorous approach introducing additional exact information on the crystal structure besides the diffraction pattern. However, the calculations are highly time consuming unless simple potentials (mostly for ionic compounds) are selected. The improvement of the algorithm convergence is then comparable with a simple anti-bump cost function.

A cost function based on the calculation of bond-valence sums (BVSs) (Pannetier *et al.*, 1990) in iono–covalent crystals has a very narrow global minimum and a relatively flat hypersurface in parameter space. Because of this it is more useful for structure validation than for active use in global optimization.

Multiple cost functions may be used independently (Brodski *et al.*, 2005) or combined in one global cost function. The combination of different cost functions in one global optimization, known as Pareto optimization (Steuer, 1986), is yet to be evaluated in structure determination from powder diffraction. The weighting between individual cost functions depends on the complexity of the crystal structure, the quality of the powder diffraction data and crystallographers' experience.

4.5.3. Solving, refining and completing inorganic structures

4.5.3.1. *A general problem: poor quality powder data*

The *ab initio* structure determination of inorganic compounds often suffers from the low quality of powder data. Two common problems are line broadening and texture, which are typical problems for *in situ* studies. When it is isotropic, the line broadening just decreases the resolution of the powder pattern, and prevents the use of RSMs for structure solution. DSMs are then the only choice. Anisotropic line broadening due to the anisotropic crystallite size is a result of crystal growth (anisotropic growth conditions, anisotropic bonding in the crystal producing layered or columnar structures) or mechanical treatment of the sample (an extreme example is graphene production). A typical example of anisotropic line broadening due to anisotropic strain in the crystal is dislocation-induced line broadening. Anisotropic line broadening not only prevents the use of RSMs, but also complicates the profile modelling for DSMs. Texture is induced in inorganic samples either by sample preparation or by crystal-growth conditions as for *in situ* studies. The presence of texture in a standard powder diffraction experiment depends mostly on the shape anisotropy of grains in the sample, and it can be minimized by using Debye–Scherrer geometry in combination with an area detector (Ravnsbaek, Filinchuk, Černý & Jensen, 2010).

When working with DSMs, texture can be optimized jointly with the structural model. The first example of a successful structure solution on a strongly textured sample was for the high pressure phase of $NaBH_4$ ($BaSO_4$-type structure, $Pnma$, a = 7.2970 (11), b = 4.1166 (5), c = 5.5692 (7) Å at 11.2 GPa) (Filinchuk *et al.*, 2007). The preferentially oriented plane (h00) was identified and the magnitude of the texture optimized jointly with the positions of one Na atom and one BH_4 group.

4.5.3.2. *Indexing of multiphase samples*

The bottleneck of *ab initio* structural studies of new inorganic compounds is indexing the powder patterns, which is extremely challenging for multiphase samples. Solid-state-route synthesis produces samples which contain more than one phase; unreacted starting components can be present too. Modern methods of powder-pattern decomposition and indexing are needed and high-resolution powder diffraction data with high counting statistics are necessary in such cases. The correct indexing of the powder pattern of a new unknown compound is only possible after successful qualitative phase analysis of the sample. A successful indexing strategy for multiphase samples is 'decomposition-aided indexing', which utilizes *in situ* diffraction as a function of temperature (which is typically linearly dependent on time; this mode is known as 'T ramping') up to the decomposition/melting temperature of different phases (Černý & Filinchuk, 2011). This procedure allows the separation of diffraction peaks of individual phases (Fig. 4.5.4).

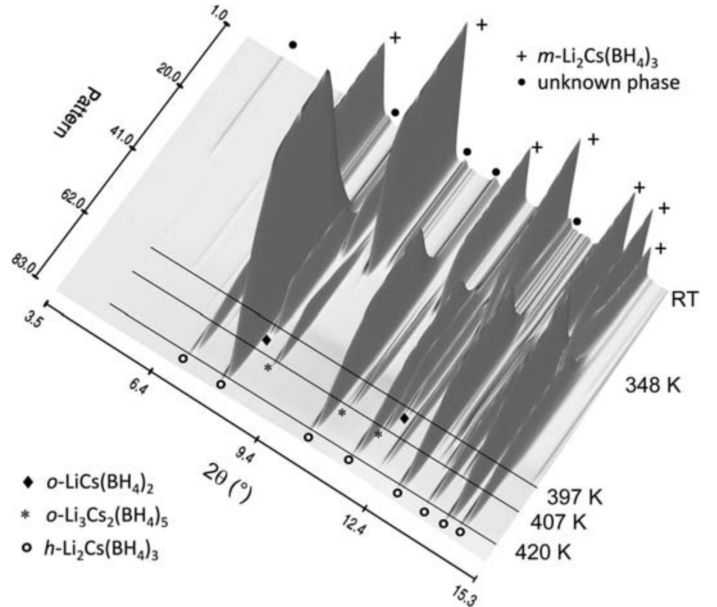

Figure 4.5.4
In situ synchrotron-radiation X-ray powder diffraction data as a function of temperature for a ball-milled sample of $LiBH_4$:$CsBH_4$ (2:1) (room temperature to 428 K, λ = 0.8210 Å). T ramping had to be used to attribute the observed peaks to individual phases and led to a successful indexing of the powder patterns. The letter in the name of each phase represents the crystal system: m for monoclinic, o for orthorhombic and h for hexagonal (Schouwink *et al.*, 2014).

4.5.3.3. *X-rays versus neutrons*

The choice of radiation used for powder diffraction experiments depends on many factors. The accessibility and price of the experiment (costs and time) are often the most important, in which case X-rays become the first choice. In the case of low-Z atomic structures, X-ray powder diffraction (XPD) may very well localize H atoms as hydrogen becomes a non-negligible X-ray scatterer, such as in $LiBH_4$ (Soulié *et al.*, 2002). The contribution of hydrogen to the X-ray intensity scattered by $LiBH_4$ is 26% while the contribution of deuterium to the neutron scattering by $LiBD_4$ is 52% (Filinchuk *et al.*, 2008). The precisions of the metal–hydrogen bond lengths obtained from XPD data are lower than those usually attained by neutron powder diffraction (NPD). Moreover, the positions of H atoms determined from X-ray diffraction data are displaced from the B atom along the B—H bond by ~0.08 Å because of displacement of the electron cloud, and by ~0.034–0.10 Å because of the libration motion of BH_4 groups, which is both temperature- and structure-dependent (Filinchuk *et al.*, 2008). Even charge densities in $LiBD_4$ have been reliably extracted from the synchrotron powder diffraction data using high counting statistics and maximum-entropy methods (Buchter *et al.*, 2011).

The arrangement of atoms in an inorganic compound may also show a small deviation from an arrangement with higher symmetry or shorter periodicity. Typical examples are metal hydrides. The deviation of metal-atom positions in a metal hydride from higher-symmetry positions is created by positioning H atoms in the matrix of metal atoms (it does not necessarily exist without hydrogen), which then becomes only slightly deformed. Because of the small deformation of the metal matrix and the low scattering power of hydrogen for X-rays, the splitting of peaks caused by lowering the symmetry is not very strong and the superstructure peaks are very weak in X-ray diffraction patterns; both are clearly visible only in neutron patterns. X-ray patterns with low background and high counting statistics are needed to detect the weak superstructure peaks. High angular resolution is necessary in both X-ray and neutron patterns to separate overlapping peaks and to detect the correct symmetry of the structure. The true symmetry can generally be revealed with confidence after successful indexing of the neutron powder diffraction pattern.

The high-temperature phase of $Y(BH_4)_3$ was determined from X-ray data as cubic [$Pm\bar{3}m$, a = 5.4547 (8) Å] and containing BH_4 tetrahedra rotationally disordered over two positions (Ravnsbaek, Filinchuk, Černý, Ley *et al.*, 2010). Only when NPD data were measured was the true cubic superstructure ($Fm\bar{3}c$, $2a$) with fully ordered BH_4 tetrahedra discovered (Fig. 4.5.5; Frommen *et al.*, 2010).

Interestingly, the only superstructure reflection (531) accessible within a typical XPD pattern (down to d = 1.4 $Å^{-1}$) has practically zero intensity, while it becomes the strongest reflection in the NPD pattern (Fig. 4.5.6).

Another example of a weak hydride superstructure is that of $Mg_6Co_2H_{11}$ (Černý *et al.*, 1992). An example of a strong pseudosymmetry of the metal lattice of a hydride is $LaMg_2NiH_7$ (Renaudin *et al.*, 2003).

4.5.3.4. *Chemical and positional disorder*

Chemical disorder is often observed in metal alloys where metal sites may have mixed occupancies. When the occupation of individual sites by different metals is not statistically random, it can be analysed provided that the scattering contrast between the

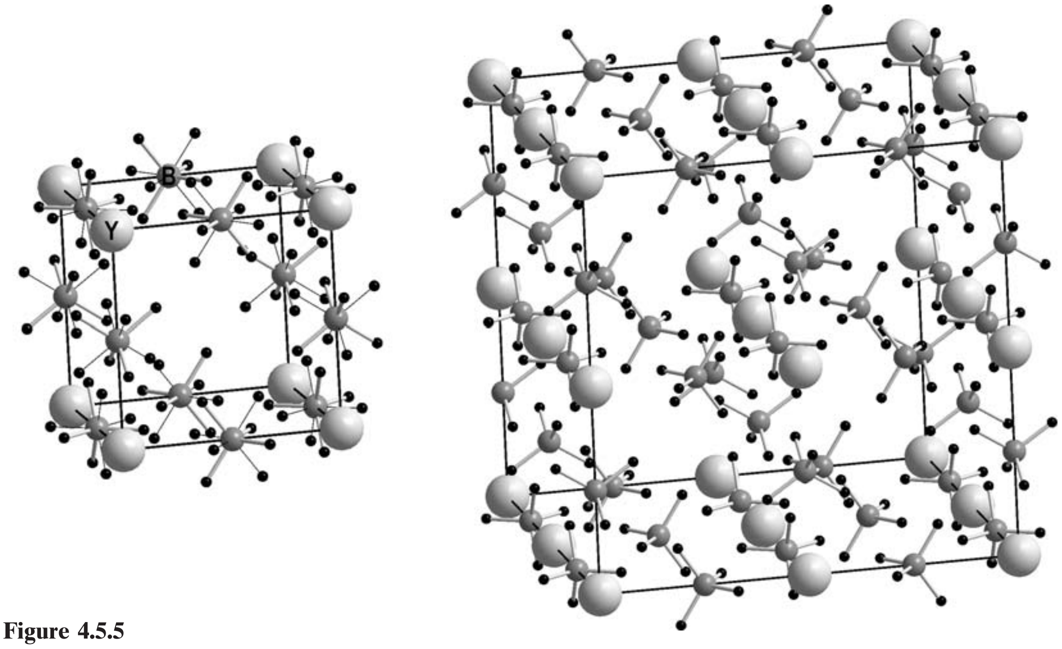

Figure 4.5.5
Yttrium borohydride appears to show positional disorder on the BH_4 groups when only XPD data are used (left: Ravnsbaek, Filinchuk, Černý, Ley *et al.*, 2010), but appears fully ordered when NPD data are also used (right: Frommen *et al.*, 2010). Reprinted from Frommen *et al.* (2010) with permission from Elsevier.

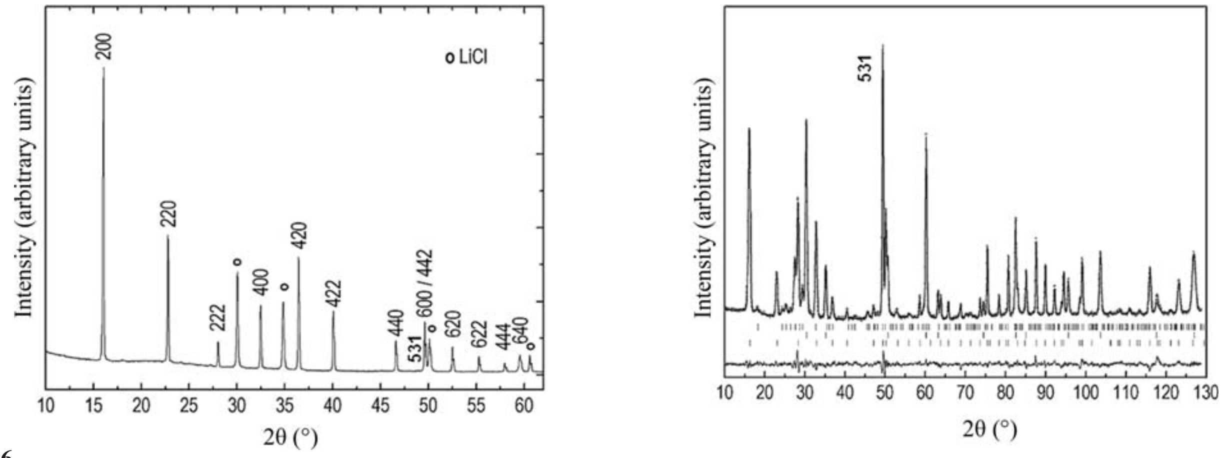

Figure 4.5.6
XPD (Cu $K\alpha_1$, left) and NPD (λ = 1.5558 Å, right) patterns for the high-temperature modification of yttrium borohydride. The peaks from LiCl are highlighted by open circles in the XPD pattern and the peak positions for the different refined phases are marked by tick marks in the NPD pattern: $Y(^{11}BD_4)_3$ (bottom), LiCl (middle) and $Li^{11}BD_4$ (top). The only superstructure reflection (531) which would allow the correct cubic lattice parameter to be detected has practically zero intensity in the XPD pattern, while it becomes the strongest reflection in the NPD pattern. Reprinted from Frommen *et al.* (2010) with permission from Elsevier.

metals is strong enough. Occupation can be quantified by either using the XPD and NPD data jointly or by resonant X-ray scattering. Note that for the case of n atomic species (including vacancies) on one Wyckoff site, one needs $n - 1$ diffraction patterns with different contrast between the scatterers in question.

Positional atomic disorder may show a local order (short-range order) which can be studied from the diffuse intensity of the scattered radiation. The diffuse scattering from polycrystalline samples may be studied by using the pair distribution function and Debye function (see Chapters 5.6 and 5.7) in direct space or RMC modelling in reciprocal space.

4.5.3.5. *Structure validation – theoretical issues*

Crystal structures solved from powder diffraction data must be validated. The first step is carried out in reciprocal space *via* the evaluation of how well the structural model explains the observed powder diffraction data. This is a necessary but not sufficient condition, as we see in Chapter 4.9; see also Section 4.5.2.4. There are a number of measures that can be used to evaluate this agreement, the most commonly used being the χ^2 and $R_{\rm wp}$ (Toby, 2006) values. However, these must be used with care. A good $R_{\rm wp}$ value will depend a lot on the quality and type of powder pattern recorded: 12% may be very good for a synchrotron powder pattern with very low noise, but would be very bad for neutron or laboratory data with a high background. It is also possible to compare the finally obtained $R_{\rm wp}$ to the value obtained using profile fitting (David, 2004). In practice, the best tool for evaluating the quality of the fit is still the eye of an experienced crystallographer (McCusker *et al.*, 1999).

The second step in the validation is the analysis of the crystal structure itself in direct space:

– Are there atoms ‘colliding with’ each other? If DSMs repeatedly find a global solution with atoms overlapping, an anti-bump penalty (see, for example, Favre-Nicolin & Černý, 2002) can be used to avoid this solution. Note that this should only happen if the quality of the powder pattern is low, and therefore includes insufficient information to ‘lock’ the DSM algorithm into the correct solution.

– Do the atomic environments make sense? A penalty based on bond-valence sum calculations (Pannetier *et al.*, 1990) can

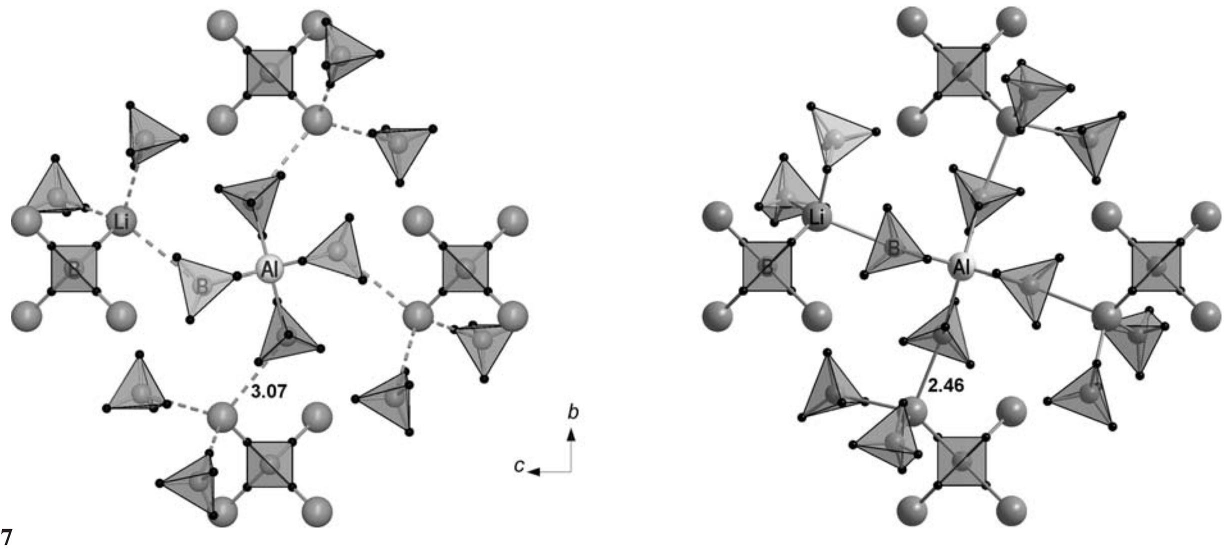

Figure 4.5.7
Structural model of $Li_4Al_3(BH_4)_{13}$ as solved from synchrotron XPD (left) and as corrected by DFT optimization (right). The Li–BH_4 contact changing the structure interpretation from ionic packing to a framework structure is 3.07 Å in the XPD structure (dashed) and 2.46 Å in the DFT structure (solid).

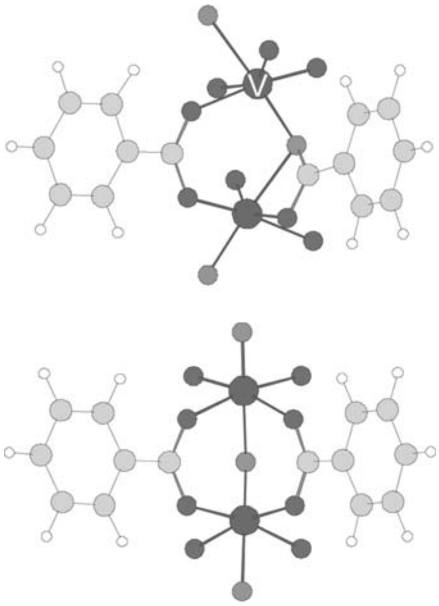

Figure 4.5.8
Structural fragment of a nanocrystalline inorganic–organic hybrid compound $VO(C_6H_5COO)_2$ (Djerdj *et al.*, 2009). The connectivity of VO_6 octahedra as proposed by DSM using synchrotron XPD (top) was corrected by DFT optimization (bottom).

pinpoint unlikely configurations. Again, if the valences are known *a priori*, they can be used as a criterion for the DSM optimization of the structure.

The third step should be a post-experiment optimization of the structure based on crystal energy minimization such as using DFT. This helps to validate new structures, locate light atoms (hydrogen) (especially when using high-pressure diffraction data) and even correct the symmetry and some structural details as shown by the following examples.

In the case of $Li_4Al_3(BH_4)_{13}$ (space group $P\bar{4}3n$) the DFT optimization (Lindemann *et al.*, 2010) of the experimental structure corrected the orientation of the complex anion $[Al(BH_4)_4]^-$ and so modified the bonding scheme in the structure from isolated complex ions $[(BH_4)Li_4]^{3+}$ and $[Al(BH_4)_4]^-$ to a three-dimensional framework structure. The corrected model was confirmed by the Rietveld refinement (Fig. 4.5.7).

A similar situation occurred for a nanocrystalline inorganic–organic hybrid compound $VO(C_6H_5COO)_2$ (Djerdj *et al.*, 2009), where the correct connectivity of VO_6 octahedron was revealed by DFT optimization of a structural model proposed by DSMs using synchrotron XPD (see Fig. 4.5.8).

The post-experimental DFT optimization of inorganic crystal structures allows the global minimum in Rietveld refinement to be reached, which is not easily done using only the diffraction data, and can be thus highly recommended. It is, however, important to keep in mind that *ab initio* calculations go beyond the validation of powder diffraction results. The DFT calculations may be a substitute for Rietveld refinement, and provide more accurate atomic positions. A variety of computer programs for theoretical calculations in the solid state are available, and most of them can be easily run on a PC. More details of the choices of computer programs can be found in a review from an Erice School in 2011 (Smrčok, 2011).

4.5.4. Examples

4.5.4.1. *Polyhedral compounds*

Metal oxides and salts are the most typical polyhedral compounds. Pauling's crystal-chemical rules are usually valid and allow for easy definition of PBUs. Typically, symmetry-guided algorithms are applied to this type of compound (Evans *et al.*, 2003). Although the use of DSMs is very beneficial for polyhedral compounds, one of the most complex polyhedral structures was solved *ab initio* from powder diffraction data using reciprocal-space techniques. This was a non-perovskite, $LaTi_2Al_9O_{19}$, which was originally solved with 60 atoms (Morris *et al.*, 1994) but was later shown to contain 31 atoms in the asymmetric unit (Kasunič *et al.*, 2011). Integrated intensities were extracted by Le Bail fit from a synchrotron powder pattern, and the structural model obtained by direct methods (*MULTAN84*; Main *et al.*, 1984) was then refined by Rietveld refinement (using *GSAS*). The structure was then revised based on BVS calculations and Rietveld refinement using the structural model from compounds with the same chemical composition.

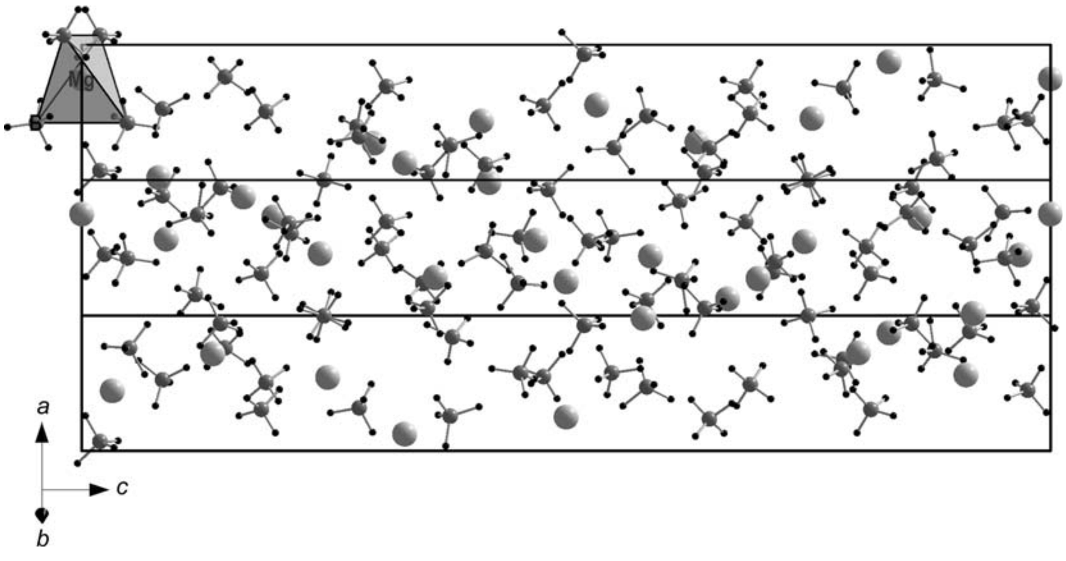

Figure 4.5.9
Structural model of $Mg(BH_4)_2$ as solved from XPD using a DSM (Černý *et al.*, 2007) and corrected by DFT optimization (Dai *et al.*, 2008) by incorporating the previously overlooked twofold axes of the space group $P6_122$, and finally refined against single-crystal data (Filinchuk *et al.*, 2009). The structure was modelled using five free Mg atoms and ten rigid tetrahedral BH_4 groups. Modelling using a super-tetrahedron $Mg(BH_4)_4$ (in grey) as an SBU did not improve the convergence of the DSM.

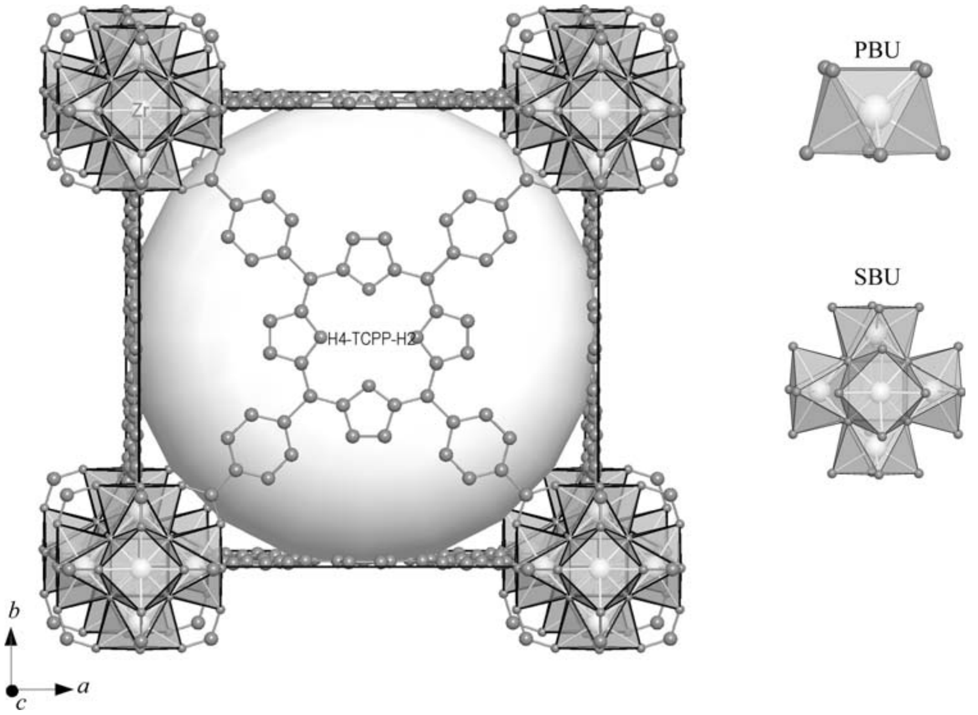

Figure 4.5.10
The crystal structure of MOF-525 (Morris *et al.*, 2012) built from the cuboctahedral SBU $Zr_6O_4(OH)_4$ connected by tetracarboxyphenylporphyrin (H_4-TCPP-H_2) linkers. H atoms are omitted for clarity. The SBU is built from six square-antiprismatic ZrO_8 PBUs. The resulting three-dimensional framework contains pores with a diameter of 20 Å, shown as a large sphere.

Zeolite structures are built from TO_4 tetrahedra as framework structures, and topology-guided algorithms for framework building are the most efficient for solving the structures of these compounds (see Chapter 4.6).

Magnesium borohydride $Mg(BH_4)_2$ (Černý *et al.*, 2007; Her *et al.*, 2007) can be also described as a polyhedral compound. Magnesium is tetrahedrally coordinated to four species which are, however, not single atoms but complex anions: $[BH_4]^-$ tetrahedra (Fig. 4.5.9). Starting from this complexity of anion, the advantage of modelling the structure from PBUs (magnesium coordination polyhedra) is lost, and better results are obtained from magnesium free atoms and the tetrahedral complex anion $[BH_4]^-$. Information on the cation coordination, which is *a priori* unknown but accessible from Raman and IR spectroscopies, may be used as an SBU in an antibump cost function.

This study is an excellent example of the power of both DSMs and RSMs in solving complex structures when well crystallized samples provide high-resolution powder diffraction data. With 55 atoms in the asymmetric unit, this compound represents one of the most complex structures ever solved from powder diffraction data. The correct structure was found independently by a DSM using the reverse Monte Carlo algorithm (Černý *et al.*, 2007) and by an RSM (Her *et al.*, 2007). In both cases high-resolution synchrotron data were required for indexing. In the DSM approach, the structure was modelled by five free Mg atoms and ten rigid tetrahedral BH_4 groups, and optimized jointly with synchrotron and neutron data. In the RSM approach, the structure was solved using only synchrotron data. The positions of Mg and B atoms were recognized in electron-density maps. In both cases the structure was refined by Rietveld refinement keeping the borohydride groups rigid. The difficulty in finding the correct orientation of BH_4 tetrahedra led to the overlooking of twofold axes in the $Mg(BH_4)_2$ space-group symmetry, which was originally identified as $P6_1$. The DFT optimization of the structural model (Dai *et al.*, 2008) suggested that the true symmetry was $P6_122$, which was then unambiguously confirmed by single-crystal X-ray diffraction (Filinchuk *et al.*, 2009). The fact that the structure solution was found independently by a DSM and an RSM in the lower Laue symmetry $6/m$ of the space group $P6_1$ rather than in the true Laue symmetry $6/mmm$ of the true space group $P6_122$ can also be understood by the presence of more degrees of freedom (*hkl* and *khl* are independent in $P6_1$) in $6/m$, which allowed for correction of systematic errors in the powder diffraction data (arising from grain statistics) of symmetry $6/mmm$.

A structure of similar complexity to $Mg(BH_4)_2$ can be solved even from low-resolution powder data provided that there is low noise in the data. This was the case for $Mn(BH_4)_2$ (Černý *et al.*, 2009) using an area detector and Debye–Scherrer geometry. The advantages of this setup, which allows *in situ* studies, are the simple sample environment and fast data collection, high data-collection rates, excellent time resolution, highly accurate measurements of diffracted intensities (good powder average) and a lower sensitivity to preferred-orientation effects. A combination of high counting rates with excellent reciprocal-space resolution provided by curved solid-state detectors (Mozzanica *et al.*, 2009) allows even more complex structures to be studied *in situ*. The use of a DSM was the only choice in the case of $Mn(BH_4)_2$, as the low-resolution powder pattern did not allow the extraction of reliable integrated intensities of overlapping reflections.

4.5.4.2. *Hybrid compounds*

Hybrid compounds are solved by various methods, but topology-guided algorithms are most specific to these types of compounds. Large MOF structures such as chromium terephthalate, MIL-101, having a cell volume of 702 000 $Å^3$, can be solved by topology-guided algorithms (Férey *et al.*, 2005). Zirconium MOF-525 is a good example of a successful application of such an algorithm to a hybrid compound (Morris *et al.*, 2012). The crystal is built from a zirconium(IV) cuboctahedral SBU, $Zr_6O_4(OH)_4$. This 12-connected SBU is then linked with 4-connected tetracarboxyphenylporphyrin (H_4-TCPP-H_2) linkers to make a three-dimensional MOF. On the basis of the connectivity of the BUs, initial structure matches were generated using nets that appear in the reticular chemistry structural resource (RCSR) (Ockwig *et al.*, 2005), a procedure that is frequently used to resolve COF structures (Côté *et al.*, 2007). Only three topologies in the RCSR combine 12,4-connected components. One was excluded because it incorporates tetrahedra, a geometry that is not accessible with the porphyrin BU. Another topology was excluded because the geometry of the 12-coordinate BU is not cuboctahedral. This allowed the identification of the only topology compatible with the local coordination in the BUs, which was then confirmed by Rietveld refinement, giving a cubic

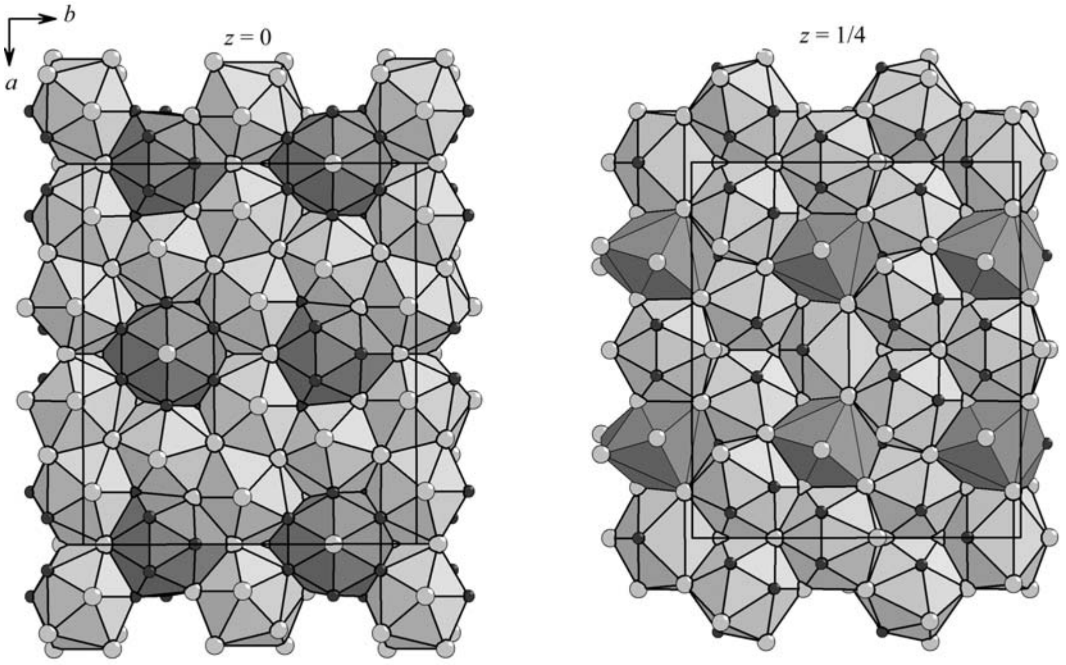

Figure 4.5.11
The crystal structure of the close-packed intermetallic phase MgIr (Černý *et al.*, 2004). The structure can be built from two layers perpendicular to the *c* axis situated at $z = 0$ and 1/4. The PBUs are then Ir-centred icosahedra (light grey) and Mg-centred Frank–Kasper polyhedra at $z = 0$ or Ir-centred polyhedra with a coordination number of 11 at $z = 1/4$ (dark grey). Owing to the difficulty in identifying the nature of the ligands in the polyhedra, modelling from isolated atoms was a better choice.

structure with cell volume of 7294 Å^3 containing pores 20 Å in diameter (Fig. 4.5.10).

4.5.4.3. *Close-packed compounds*

Topologically close-packed intermetallic phases are a difficult case for DSMs because of the complexity of BU choice. The compound MgIr contains 13 Ir and 12 Mg atoms in the asymmetric unit (Černý *et al.*, 2004). Its structure was originally solved from synchrotron XPD data using a DSM, and the structure was confirmed using single-crystal X-ray data. No additional information on the coordination of the Ir and Mg atoms was available, and the coordination number in close-packed phases can vary between 12 and 16. As a consequence, the structural model was built from isolated atoms (Fig. 4.5.11). The crystal structure was expected to be close packed, therefore the expected volume per atom was estimated to be 15–20 Å^3, giving between 250 and 330 atoms in the unit cell. In a final run (repeated many times) 13 Ir and 12 Mg free atoms were optimized simultaneously (75 DoF), and the same solution was always found in less than 5 min.

The final structure can be built from seven icosahedra centred on iridium with a different ratio between Mg and Ir atoms as ligands. Consequently, modelling with seven rigid icosahedra as PBUs was attempted, lowering the number of DoF to 42. Nevertheless, the convergence of this modelling was ~10 times slower, clearly owing to the fact that the icosahedra are not ideal (the central-atom-to-ligand distance varies between 2.45 and 3.52 Å) and owing to the problems with ligand identification. If the identification is carried out by the optimization algorithm using a random change ('swapping'), the DoF increases by 12 per icosahedron, and no associated increase in the optimization convergence was achieved.

References

Broach, R. W., Chuang, I. S., Marks, T. J. & Williams, J. M. (1983). *Metrical characterization of tridentate tetrahydroborate ligation to a transition-metal ion. Structure and bonding in Hf(BH$_4$)$_4$ by single-crystal neutron diffraction. Inorg. Chem.* **22**, 1081–1084.

Brodski, V., Peschar, R. & Schenk, H. (2005). *Organa – a program package for structure determination from powder diffraction data by direct-space methods. J. Appl. Cryst.* **38**, 688–693.

Buchter, F., Łodziana, Z., Remhof, A., Mauron, Ph., Friedrichs, O., Borgschulte, A., Züttel, A., Filinchuk, Y. & Palatinus, L. (2011). *Experimental charge density of LiBD$_4$ from maximum entropy method. Phys. Rev. B*, **83**, 064107.

Černý, R., Bonhomme, F., Yvon, K., Fischer, P., Zolliker, P., Cox, D. E. & Hewat, A. (1992). *Hexamagnesium dicobalt undecadeuteride Mg$_6$Co$_2$D$_{11}$: containing [CoD$_4$]$^{5-}$ and [CoD$_5$]$^{4-}$ complex anions conforming to the 18-electron rule. J. Alloys Compd.* **187**, 233–241.

Černý, R., Chul Kim, K., Penin, N., D'Anna, V., Hagemann, H. & Sholl, D. S. (2010). *AZn$_2$(BH$_4$)$_5$ (A = Li, Na) and NaZn(BH$_4$)$_3$: structural studies. J. Phys. Chem. C*, **114**, 19127–19133.

Černý, R. & Filinchuk, Y. (2011) *Complex inorganic structures from powder diffraction: case of tetrahydroborates of light metals. Z. Kristallogr.* **226**, 882–891.

Černý, R., Filinchuk, Y., Hagemann, H. & Yvon, K. (2007). *Magnesium borohydride: synthesis and crystal structure. Angew. Chem. Int. Ed.* **46**, 5765–5767.

Černý, R., Penin, N., Hagemann, H. & Filinchuk, Y. (2009). *The first crystallographic and spectroscopic characterization of a 3d-metal borohydride: Mn(BH$_4$)$_2$. J. Phys. Chem. C*, **113**, 9003–9007.

Černý, R., Renaudin, G., Favre-Nicolin, V., Hlukhyy, V. & Pöttgen, R. (2004). *Mg$_{1+x}$Ir$_{1-x}$ (x = 0, 0.037 and 0.054), a binary intermetallic compound with a new orthorhombic structure type determined from powder and single-crystal X-ray diffraction. Acta Cryst.* B**60**, 272–281.

Côté, A. P., Benin, A. I., Ockwig, N. W., O'Keeffe, M., Matzger, A. J. & Yaghi, O. M. (2005). *Porous, crystalline, covalent organic frameworks. Science*, **310**, 1166–1170.

Côté, A. P., El-Kaderi, H. M., Furukawa, H., Hunt, J. R. & Yaghi, O. M. (2007). *Reticular synthesis of microporous and mesoporous 2D covalent organic frameworks. J. Am. Chem. Soc.* **129**, 12914–12915.

Dai, B., Sholl, D. S. & Johnson, J. K. (2008). *First-principles study of experimental and hypothetical Mg(BH$_4$)$_2$ crystal structures. J. Phys. Chem. C*, **112**, 4391–4395.

David, W. I. F. (2004). *On the equivalence of the Rietveld method and the correlated integrated intensities method in powder diffraction. J. Appl. Cryst.* **37**, 621–628.

Deem, M. W. & Newsam, J. M. (1989). *Determination of 4-connected framework crystal structures by simulated annealing*. *Nature*, **342**, 260–262.

Deng, X. & Dong, C. (2011). *EPCryst: a computer program for solving crystal structures from powder diffraction data*. *J. Appl. Cryst.* **44**, 230–237.

Djerdj, I., Cao, M., Rocquefelte, X., Černý, R., Jagličič, Z., Arčon, D., Potočnik, A., Gozzo, F. & Niederberger, M. (2009). *Structural characterization of a nanocrystalline inorganic–organic hybrid with fiberlike morphology and one-dimensional antiferromagnetic properties*. *Chem. Mater.* **21**, 3356–3369.

Edgar, M., Carter, V. J., Tunstall, D. P., Grewal, P., Favre-Nicolin, V., Cox, P. A., Lightfoot, P. & Wright, P. A. (2002). *$Al_2(CH_3PO_3)_3$: Structure solution of a novel aluminium methylphosphonate using a new simulated annealing program and powder X-ray diffraction data*. *Chem. Commun.* **8**, 808–809.

Evans, I. R., Howard, J. A. K. & Evans, J. S. O. (2003). *α-$Bi_2Sn_2O_7$ – a 176 atom crystal structure from powder diffraction data*. *J. Mater. Chem.* **13**, 2098–2103.

Favre-Nicolin, V. & Černý, R. (2002). *FOX, 'free objects for crystallography': a modular approach to ab initio structure determination from powder diffraction*. *J. Appl. Cryst.* **35**, 734–743.

Férey, G., Mellot-Draznieks, C., Serre, C., Millange, F., Dutour, J., Surblé, S. & Margiolaki, I. (2005). *A chromium terephthalate-based solid with unusually large pore volumes and surface area*. *Science*, **309**, 2040–2042.

Filinchuk, Y., Černý, R. & Hagemann, H. (2009). *Insight into $Mg(BH_4)_2$ with synchrotron X-ray diffraction: structure revision, crystal chemistry, and anomalous thermal expansion*. *Chem. Mater.* **21**, 925–933.

Filinchuk, Y., Chernyshov, D. & Černý, R. (2008). *Lightest borohydride probed by synchrotron X-ray diffraction: experiment calls for a new theoretical revision*. *J. Phys. Chem. C*, **112**, 10579–10584.

Filinchuk, Y. E., Talyzin, A. V., Chernyshov, D. & Dmitriev, V. (2007). *High-pressure phase of $NaBH_4$: crystal structure from synchrotron powder diffraction data*. *Phys. Rev. B*, **76**, 092104.

Frank, F. C. & Kasper, J. S. (1958). *Complex alloy structures regarded as sphere packings. I. Definitions and basic principles*. *Acta Cryst.* **11**, 184–190.

Frommen, C., Aliouane, N., Deledda, S., Fonneløp, J. E., Grove, H., Lieutenant, K., Llamas-Jansa, I., Sartori, S., Sørby, M. H. & Hauback, B. C. (2010). *Crystal structure, polymorphism, and thermal properties of yttrium borohydride $Y(BH_4)_3$*. *J. Alloys Compd.* **496**, 710–716.

Grosse-Kunstleve, R. W., McCusker, L. B. & Baerlocher, C. (1997). *Powder diffraction data and crystal chemical information combined in an automated structure determination procedure for zeolites*. *J. Appl. Cryst.* **30**, 985–995.

Guénée, L., Favre-Nicolin, V. & Yvon, K. (2003). *Synthesis, crystal structure and hydrogenation properties of the ternary compounds $LaNi_4Mg$ and $NdNi_4Mg$*. *J. Alloys Compd.* **348**, 129–137.

Her, J.-H., Stephens, P. W., Gao, Y., Soloveichik, G. L., Rijssenbeek, J., Andrus, M. & Zhao, J.-C. (2007). *Structure of unsolvated magnesium borohydride $Mg(BH_4)_2$*. *Acta Cryst.* B**63**, 561–568.

Kasunic, M., Meden, A., Skapin, S. D., Suvorov, D. & Golobic, A. (2011). *Structure of $LaTi_2Al_9O_{19}$ and reanalysis of the crystal structure of $La_3Ti_5Al_{15}O_{37}$*. *Acta Cryst.* B**67**, 455–460.

Krivovichev, S. V., Mentré, O., Siidra, O. I., Colmont, M. & Filatov, S. K. (2013). *Anion-centered tetrahedra in inorganic compounds*. *Chem. Rev.* **113**, 6459–6535.

Lindemann, I., Ferrer, R. D., Dunsch, L., Filinchuk, Y., Černý, R., Hagemann, H., D'Anna, V., Lawson Daku, L. M., Schultz, L. & Gutfleisch, O. (2010). *$Al_3Li_4(BH_4)_{13}$: A new double-cation borohydride with a new structure*. *Chem. Eur. J.* **16**, 8707–8712.

McCusker, L. B., Von Dreele, R. B., Cox, D. E., Louër, D. & Scardi, P. (1999). *Rietveld refinement guidelines*. *J. Appl. Cryst.* **32**, 36–50.

Main, P., Germain, G. & Woolfson, M. M. (1984). *MULTAN84: A System of Computer Programs for the Automatic Solution of Crystal Structures from X-ray Diffraction Data*. University of York, England.

Masciocchi, N. & Sironi, A. (2005). *Structural powder diffraction characterization of organometallic species: the role of complementary information*. *C. R. Chim.* **8**, 1617–1630.

Meier, W. M. & Olson, D. H. (1987). *Atlas of Zeolite Structure Types*. London: Butterworths.

Mellot Draznieks, C., Newsam, J. M., Gorman, A. M., Freeman, C. M. & Férey, G. (2000). *De novo prediction of inorganic structures developed through automated assembly of secondary building units (AASBU method)*. *Angew. Chem. Int. Ed.* **39**, 2270–2275.

Mercier, P. H. J., Dong, Z., Baikie, T., Le Page, Y., White, T. J., Whitfield, P. S. & Mitchel, L. D. (2007). *Ab initio constrained crystal-chemical Rietveld refinement of $Ca_{10}(V_xP_{1-x}O_4)_6F_2$ apatites*. *Acta Cryst.* B**63**, 37–48.

Mercier, P. H. J., Le Page, Y., Whitfield, P. S. & Mitchell, L. D. (2006). *Geometrical parameterization of the crystal chemistry of $P6_3/m$ apatite. II. Precision, accuracy and numerical stability of the crystal-chemical Rietveld refinement*. *J. Appl. Cryst.* **39**, 369–375.

Meredig, B. & Wolverton, C. (2013). *A hybrid computational-experimental approach for automated crystal structure solution*. *Nat. Mater.* **12**, 123–127.

Morris, R. E., Owen, J. J., Stalick, J. K. & Cheetham, A. K. (1994). *Determination of complex structures from powder diffraction data: the crystal structure of $La_3Ti_5Al_{15}O_{37}$*. *J. Solid State Chem.* **111**, 52–57.

Morris, W., Volosskiy, B., Selcuk, D., Gándara, F., McGrier, P. L., Furukawa, H., Cascio, D., Stoddart, J. F. & Yaghi, O. M. (2012). *Synthesis, structure, and metalation of two new highly porous zirconium metal–organic frameworks*. *Inorg. Chem.* **51**, 6443–6445.

Mozzanica, A., Bergamaschi, A., Dinapoli, R., Gozzo, F., Heinrich, B., Kraft, P., Patterson, B. & Schmitt, B. (2009). *MythenII: A 128 channel single photon counting readout chip*. *Nucl. Instrum. Methods Phys. Res. A*, **607**, 250–252.

Müller, M., Dinnebier, R. E., Ali, N. Z., Campbell, B. J. & Jansen, M. (2010). *Direct access to the order parameter: parameterized symmetry modes and rigid body movements as a function of temperature*. *Mater. Sci. Forum*, **651**, 79–95.

Ockwig, N. W., Delgado-Friedrichs, O., O'Keeffe, M. & Yaghi, O. M. (2005). *Reticular chemistry: occurrence and taxonomy of nets and grammar for the design of frameworks*. *Acc. Chem. Res.* **38**, 176–182.

O'Keeffe, M. & Yaghi, O. M. (2012). *Deconstructing the crystal structures of metal-organic frameworks and related materials into their underlying nets*. *Chem. Rev.* **112**, 675–702.

Pannetier, J., Bassas-Alsina, J., Rodriguez-Carvajal, J. & Caignaert, V. (1990). *Prediction of crystal structures from crystal chemistry rules by simulated annealing*. *Nature*, **346**, 343–345.

Pauling, L. (1929). *The principles determining the structure of complex ionic crystals*. *J. Am. Chem. Soc.* **51**, 1010–1026.

Ravnsbaek, D., Filinchuk, Y., Cerenius, Y., Jakobsen, H. J., Besenbacher, F., Skibsted, J. & Jensen, T. R. (2009). *A series of mixed-metal borohydrides*. *Angew. Chem. Int. Ed.* **48**, 6659–6663.

Ravnsbaek, D. B., Filinchuk, Y., Černý, R. & Jensen, T. R. (2010). *Powder diffraction methods for studies of borohydride-based energy storage materials*. *Z. Kristallogr.* **225**, 557–569.

Ravnsbaek, D. B., Filinchuk, Y., Černý, R., Ley, M. B., Haase, D., Jakobsen, H. J., Skibsted, J. & Jensen, T. R. (2010). *Thermal polymorphism and decomposition of $Y(BH_4)_3$*. *Inorg. Chem.* **49**, 3801–3809.

Reinaudi, L., Carbonio, R. E. & Leiva, E. P. M. (1998). *Inclusion of symmetry for the enhanced determination of crystalline structures from powder diffraction data using simulated annealing*. *Chem. Commun.* pp. 255–256.

Renaudin, G., Guénée, L. & Yvon, K. (2003). *$LaMg_2NiH_7$, a novel quaternary metal hydride containing tetrahedral $[NiH_4]^{4-}$ complexes and hydride anions*. *J. Alloys Compd.* **350**, 145–150.

Rigaudy, J. & Klesney, S. P. (1979). Editors. *Nomenclature of Organic Chemistry*. IUPAC/Pergamon Press. ISBN 0-08022-3699.

Schouwink, P., Smrčok, L. & Černý, R. (2014). *Role of the Li^+ node in the Li-BH_4 substructure of double-cation tetrahydroborates*. *Acta Cryst.* B**70**, 871–878.

Smrčok, L. (2011). *Powder diffraction + computational methods*. In *Uniting Electron Crystallography and Powder Diffraction*, edited by U. Kolb, K. Shankland, L. Meshi, A. Avilov & W. David, pp. 165–172. Heidelberg: Springer.

Soulié, J. P., Renaudin, G., Černý, R. & Yvon, K. (2002). *Lithium borohydride $LiBH_4$*. *J. Alloys Compd.* **346**, 200–205.

Steuer, R. E. (1986). *Multiple Criteria Optimization: Theory, Computations, and Application*. New York: John Wiley & Sons, Inc.

Stinton, G. W. & Evans, J. S. O. (2007). *Parametric Rietveld refinement*. *J. Appl. Cryst.* **40**, 87–95.

Toby, B. (2006). *R factors in Rietveld analysis: how good is good enough?* *Powder Diffr.* **21**, 67–70.

Tranchemontagne, D. J., Mendoza-Cortés, J. L., O'Keeffe, M. & Yaghi, O. M. (2009). *Secondary building units, nets and bonding in the chemistry of metal-organic frameworks*. *Chem. Soc. Rev.* **38**, 1257–1283.

International Tables for Crystallography (2019). Vol. H, Chapter 4.6, pp. 452–464.

4.6. Zeolites

L. B. McCusker and Ch. Baerlocher

4.6.1. Introduction

Zeolites are a class of microporous aluminosilicate framework materials with diverse industrial applications (Cejka *et al.*, 2007). Whether they are used as catalysts, desiccants, adsorbents, ion-exchangers or hosts for nanoparticles, the key to the suitability of a zeolite for a specific purpose lies in its structure. In general, a zeolite consists of a relatively rigid, anionic and microporous framework structure constructed from corner-sharing TO_4 (T = Si, Al, P or any other tetrahedrally coordinated cation) tetrahedra. The pores form channels and/or cavities of molecular dimensions. Within these voids there are cations (organic or inorganic) that compensate for the negative charge of the framework and water or solvent molecules that fill the rest of the space. The inorganic cations are generally labile and can be exchanged to some extent; organic cations can usually be burned off leaving just protons in the zeolite; and the water or solvent can be removed by simple heating without destroying the framework structure. For many applications, the calcined (heat-treated) form is used, because the pores are then accessible to other molecules.

The Structure Commission of the International Zeolite Association evaluates new 4-connected framework structures as they are reported, and if the framework connectivity is new and the structure analysis is considered to be reliable, a three-letter framework type code is assigned. The most recent printed information on these framework types is given in the *Atlas of Zeolite Framework Types* (Baerlocher, McCusker & Olson, 2007), but for up-to-date information the reader is referred to the *Database of Zeolite Structures,* which is freely available at http://www.iza-structure.org/databases. The latter is updated each time new codes are approved. In the rest of this chapter, relevant framework-type codes will be indicated in bold in parentheses.

Of the 231 zeolite framework types officially recognized by March 2016, only about half of them (107) were determined from single-crystal X-ray diffraction data. Seven more were solved from single-crystal electron-diffraction data. The remaining 117 were solved in one way or another from powder diffraction data (Fig. 4.6.1). Indeed, most newly synthesized silicate-based zeolites, which are of particular interest for industrial applications, are polycrystalline. As a result, a variety of methods for solving zeolite structures from powder diffraction data have been developed over the years (Fig. 4.6.2). Initially, the only option available was model building by hand (67 framework types). However, as the quality of powder diffraction data improved and computing power increased, other approaches became feasible. These included modifying classical direct methods to accommodate the limitations of powder diffraction data (19 framework types), automating some of the principles used in model building in the computer programs *Focus* (22 framework types) and *ZEFSA II* (3 framework types), and adapting the charge-flipping algorithm to deal with overlapping reflections (6 framework types). Each of these approaches to solving the initial phase problem will be described in Section 4.6.2.

However, there is more to a zeolite structure than the connectivity of its framework. For example, where are the non-framework cations and molecules and how are they bonded? What happens to the geometry of the framework and the positions of the non-framework species upon calcination and/or ion exchange? Where are the isomorphously substituted cations (*e.g.* Ge) in the framework? These questions are generally answered during the course of the structure refinement process, which is described in Section 4.6.3.

4.6.2. Framework structure determination

When a novel zeolitic material is found or produced, the first question is what its framework structure looks like. Is it new?

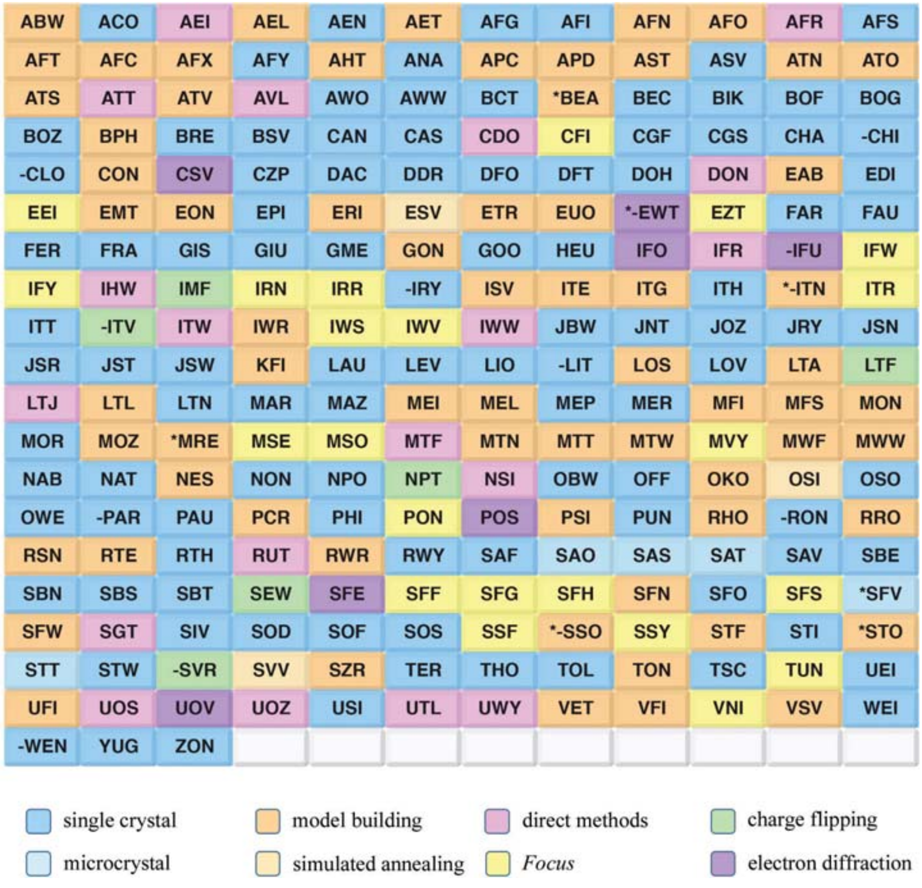

ABW	ACO	AEI	AEL	AEN	AET	AFG	AFI	AFN	AFO	AFR	AFS
AFT	AFC	AFX	AFY	AHT	ANA	APC	APD	AST	ASV	ATN	ATO
ATS	ATT	ATV	AVL	AWO	AWW	BCT	*BEA	BEC	BIK	BOF	BOG
BOZ	BPH	BRE	BSV	CAN	CAS	CDO	CFI	CGF	CGS	CHA	-CHI
-CLO	CON	CSV	CZP	DAC	DDR	DFO	DFT	DOH	DON	EAB	EDI
EEI	EMT	EON	EPI	ERI	ESV	ETR	EUO	*-EWT	EZT	FAR	FAU
FER	FRA	GIS	GIU	GME	GON	GOO	HEU	IFO	IFR	-IFU	IFW
IFY	IHW	IMF	IRN	IRR	-IRY	ISV	ITE	ITG	ITH	*-ITN	ITR
ITT	-ITV	ITW	IWR	IWS	IWV	IWW	JBW	JNT	JOZ	JRY	JSN
JSR	JST	JSW	KFI	LAU	LEV	LIO	-LIT	LOS	LOV	LTA	LTF
LTJ	LTL	LTN	MAR	MAZ	MEI	MEL	MEP	MER	MFI	MFS	MON
MOR	MOZ	*MRE	MSE	MSO	MTF	MTN	MTT	MTW	MVY	MWF	MWW
NAB	NAT	NES	NON	NPO	NPT	NSI	OBW	OFF	OKO	OSI	OSO
OWE	-PAR	PAU	PCR	PHI	PON	POS	PSI	PUN	RHO	-RON	RRO
RSN	RTE	RTH	RUT	RWR	RWY	SAF	SAO	SAS	SAT	SAV	SBE
SBN	SBS	SBT	SEW	SFE	SFF	SFG	SFH	SFN	SFO	SFS	*SFV
SFW	SGT	SIV	SOD	SOF	SOS	SSF	*-SSO	SSY	STF	STI	*STO
STT	STW	-SVR	SVV	SZR	TER	THO	TOL	TON	TSC	TUN	UEI
UFI	UOS	UOV	UOZ	USI	UTL	UWY	VET	VFI	VNI	VSV	WEI
-WEN	YUG	ZON									

Figure 4.6.1
The 231 framework type codes assigned by March 2016 and how their structures were solved. A '*' preceding a code indicates that the framework structure is disordered and a '-' that the 4-connected net is interrupted.

Copyright © 2019 International Union of Crystallography

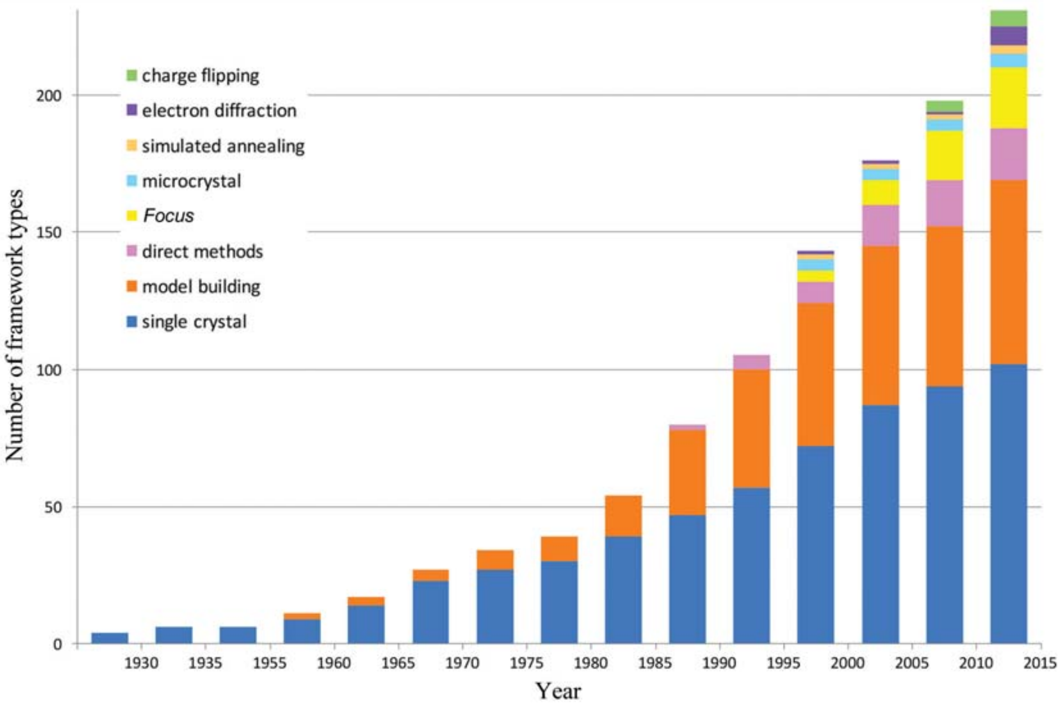

Figure 4.6.2
The evolution of methods used to solve zeolite framework structures.

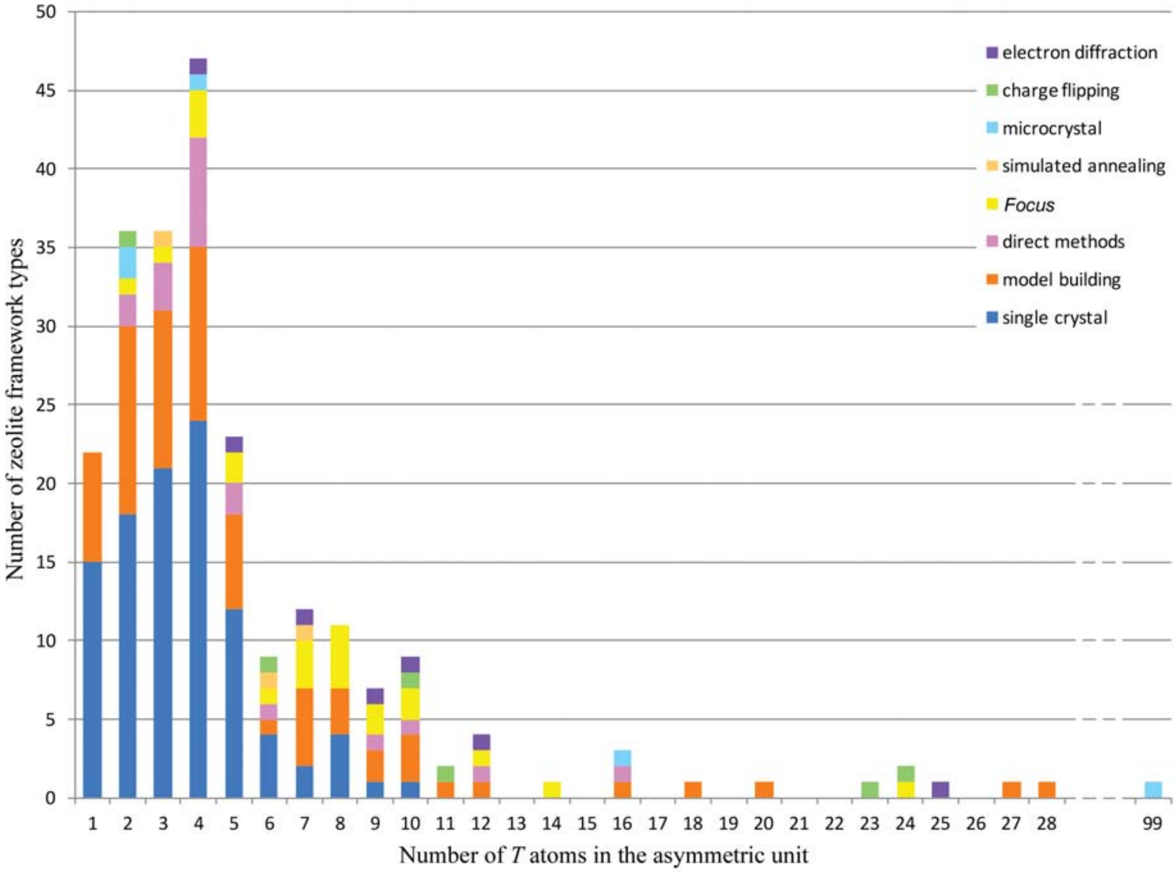

Figure 4.6.3
A histogram of the number of *T* atoms in the asymmetric unit for the 231 zeolite framework types, showing the methods used to solve their structures.

What kind of channel system does it have? If there are no single crystals available, X-ray powder diffraction techniques are usually applied to solve the initial phase problem and thereby establish the basic framework structure. There are different ways of viewing the complexity of a zeolite structure, but for the initial phasing process, the number of *T* atoms in the asymmetric unit is generally a good indicator, so these numbers are given along with the framework type code in the following sections. It is worth noting that 85% of the 231 framework types shown in Fig. 4.6.1 have 8 or fewer *T* atoms in the asymmetric unit (Fig. 4.6.3). These can generally be solved in a relatively straightforward manner. It is the last 15% that pose a challenge to powder diffraction techniques, and no single approach has emerged as being the best for these structures.

The normal approach for determining whether or not a new material has a known framework structure is to compare the measured powder diffraction pattern with those of all known zeolites. The simulated powder patterns for zeolites published by Treacy & Higgins (2007) or those available *via* the *Database of Zeolite Structures* can be used for this purpose. The latter have the advantage that they can be adjusted to reflect the peak shape and wavelength of the experimental pattern, but they must be generated and examined individually. The ICDD database of experimental powder diffraction patterns (http://icdd.com/products/), on the other hand, can be scanned automatically with a search/match routine, but the user must bear in mind that not all zeolites are present in this database, although efforts are underway to include them. This is why most synthesis laboratories have their own libraries, containing patterns taken from both experiments and the literature, for such searches. The low-angle reflections in a zeolite powder diffraction pattern are particularly sensitive to the extra-framework species in the pores (*e.g.* cations, water, organic structure-directing agent), so the initial comparison is best done in the mid- to high-angle region of the pattern. A new chemical composition may also alter the symmetry quite dramatically, and thereby obscure a structural relationship. In such cases, the identification of the unit-cell dimensions as discussed in the next section may help.

4.6.2.1. *Preliminary steps*

In order to progress to structure determination, the powder diffraction pattern must first be indexed, and this can be hindered by the presence of impurities. Because the synthesis conditions for zeolites only have to be changed very slightly in some cases to produce an entirely different zeolite, syntheses usually have to be optimized for a particular product. Even so, impurities cannot always be avoided. If the impurity can be identified, its diffraction pattern can be calculated and taken into account in the subsequent steps. However, if it is not identified, it is more difficult to judge which peaks belong to the phase of interest and which do not. The shapes of the peaks of the impurity phase are sometimes different enough from those of the majority phase to be distinguished (*e.g.* very sharp peaks from a salt or much broader peaks from a second zeolite phase that has crystallized under non-ideal conditions). If this is not the case and an impurity is suspected, the product from a second synthesis can be measured. It is unlikely that the amount of impurity will be identical in two independent syntheses, so the patterns can be compared to see if the relative intensities of a set of peaks differ in a consistent manner. Of course, scanning electron microscopy images can also be used to evaluate the purity of the material, and electron diffraction can also be used to facilitate indexing in difficult cases.

Once the unit cell has been established, the determination of the space group can be attempted. Systematic absences may be obscured by reflection overlap, so again electron diffraction may be useful to discriminate between the possible space groups. ^{29}Si magic angle spinning (MAS) NMR can also provide some useful information on the symmetry of pure SiO_2 materials, because there should be a signal for each crystallographically independent Si site with intensities corresponding to the multiplicities of the positions. Often several space groups have to be tried one at a time in the structure-determination procedure.

Once a unit cell and space group have been determined, the positions of the allowed reflections are known, and a profile fit, either LeBail (2005) or Pawley (1981), can be performed (see Chapter 3.5). Although it is generally relatively easy to define a peak-shape function that describes the profile of a single reflection in the pattern, it is not always easy to describe the whole pattern with this peak shape. The morphologies of zeolitic materials often exhibit extreme aspect ratios (*e.g.* long needles or thin platelets), and this leads to *hkl*-dependent (anisotropic) line broadening. In such cases, the *hkl* dependence (*e.g.* all 00*l* reflections are broader or sharper than the rest) must be determined and one or more anisotropic line-broadening parameters need to be refined.

The better the calculated diffraction pattern fits the experimental data, the more reliable the extracted reflection intensities. This is especially true for partially overlapping reflections, so for more complicated structures some extra effort at this stage can be worthwhile. Once a satisfactory profile fit has been achieved, structure solution can begin.

4.6.2.2. *Model building*

The classical approach to zeolite-framework structure determination is model building, and it is still used today in difficult cases where the more automated methods fail. The idea is to gather all the information known about the material from different characterization techniques (*e.g.* chemical analysis, thermogravimetric analysis, density determination, MAS NMR, IR spectroscopy, X-ray powder diffraction, electron microscopy) and to build a model that is consistent with all of these data. The powder diffraction pattern for this structural model is then calculated (using the peak-shape parameters determined in the previous step) and compared with the measured one. At this point it is the higher-angle data that are most important for the comparison, because the lower-angle (lower-resolution) data will be strongly affected by the presence of cations and molecules in the channels and cavities. If the fit looks promising, structure completion and refinement can be attempted (see Section 4.6.3). If it does not, the model needs to be modified and the procedure repeated.

One of the first zeolites to be synthesized in the laboratory was zeolite A (**LTA**, Breck *et al.*, 1956). The chemical composition was determined to be $NaAlSiO_4{\cdot}2.25H_2O$ and the density was 1.99 g cm^{-3}. Its powder diffraction pattern clearly indicated a cubic unit cell with $a \simeq 12.3$ Å and no systematic absences. By combining these pieces of information, the composition per unit cell could be estimated to be $|Na_{12}(H_2O)_{27}|[(Si,Al)_{24}O_{48}]$ [see McCusker *et al.* (2001) for a description of the |guest|[host] nomenclature recommended by IUPAC for microporous materials] with a total of 24 *T* atoms (12 Si and 12 Al) in a unit-cell volume of 1860 Å^3. Indeed, one of the characteristics of zeolite framework structures is that they normally have between 12 and 20 *T* atoms per 1000 Å^3. Adsorption experiments showed that only small molecules (with a kinetic diameter of less than 3.6 Å) could be adsorbed into the calcined material, and this indicated that the pore opening was probably an 8-ring (a ring formed by 8 corner-sharing TO_4 tetrahedra). This information alone was sufficient to deduce the framework structure, which has 8-rings arranged on the faces of a cube (Fig. 4.6.4). All 24 *T* atoms in the unit cell are related to one another by symmetry (*i.e.* it is a 1 *T* atom structure). If the strict alternation of the Si and Al atoms is also taken into account, the lattice parameter *a* must be doubled and the space group becomes $Fm\bar{3}c$.

A more recent and more complicated structure solved by model building is that of SSZ-59 (**SFN**, 8 *T* atoms, Burton *et al.*,

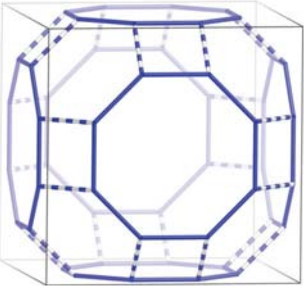

Figure 4.6.4
The framework structure of zeolite A (**LTA**) showing the 8-rings on the surfaces of the cubic unit cell and the linkages between them to form the *lta* cavity. Bridging O atoms have been omitted for clarity.

2003). In this case, it proved to be difficult to index the powder diffraction pattern satisfactorily. However, there was a strong reflection corresponding to a *d*-spacing of 2.51 Å, which was thought to be indicative of a 5 Å repeat distance. The adsorption capacity was very similar to that of UTD-1 (**DON**, 5 *T* atoms), which has one-dimensional 14-ring channels. Burton and co-workers therefore considered all framework structures with (1) 'butterfly units', which are typical of high-silica zeolites, (2) one-dimensional 10- or 12-ring channels and (3) 5 Å repeat distances along the channel.

This led to the frameworks **TON** (4 *T* atoms), **MTT** (7 *T* atoms) and **MTW** (7 *T* atoms). The concept of σ expansion (Barrer, 1978) between butterfly units to generate structures with 14-ring channels was then applied (Fig. 4.6.5). That is, the *T*–*T* linkage shared by neighbouring 'butterfly' units was replaced with a 4-ring. The idealized framework structures of the disordered zeolites ZSM-48 (***MRE**, 4 *T* atoms) and SSZ-31 (***STO**, 28 *T* atoms) are related to UTD-1 (**DON**) in a similar manner. Other variants of the expanded **MTW** framework in which layers were related by mirror planes rather than translation were also generated. The powder patterns calculated for these different models were quite distinct, and the measured pattern of SSZ-59 matched that of the expanded **MTW** framework very well. Subsequent Rietveld refinement (Rietveld, 1969) confirmed that this framework was the correct one.

It is obvious that model building is a time-consuming approach to structure solution that is strongly dependent upon the experience, ingenuity and patience of the model builder. Fortunately, alternatives have been developed over the last 20 years or so. These methods generally require computing power that was not available 30 years ago but is commonplace today. The high resolution of reflections in a powder diffraction pattern that can now be achieved at both laboratory and synchrotron sources has also contributed significantly to the development of several of these methods.

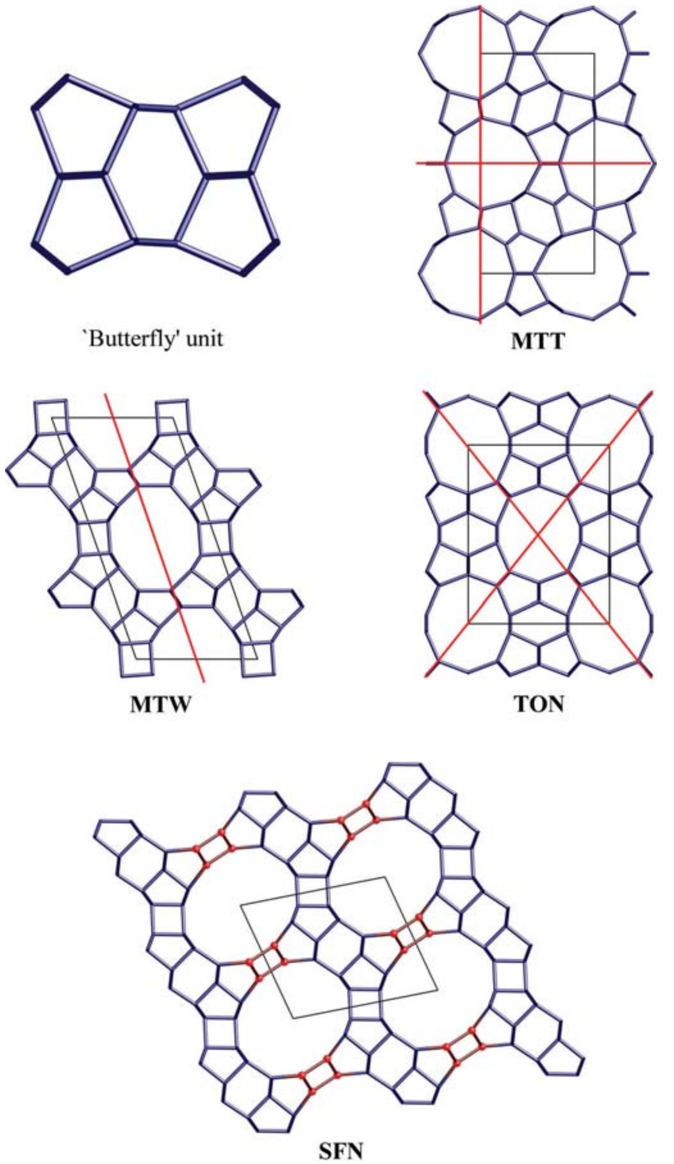

Figure 4.6.5
The 'butterfly' unit and projections of the three 10- and 12-ring framework types that have this unit, one-dimensional channels and a 5 Å repeat along the channel. The red lines indicate where a σ expansion could be applied between 'butterfly' units to create 14-rings. The *T*–*T* linkages along these lines would be expanded to 4-rings. The correct structure of SSZ-59 (**SFN**) is shown with the 4-rings resulting from the σ expansion of **MTW** highlighted.

Of course, an obvious way of advancing model-building technology is to use a computer algorithm to build the models and to test them against the measured data in an automatic manner. The first steps in this direction were taken by Deem & Newsam (1989). They used a simulated-annealing approach in which the cost function was based on pseudo-potentials for *T*–*T* distances, *T*–*T*–*T* angles and the number of *T*–*T* connections, which were derived from known zeolite structures. The unit cell, space group, the number of *T* atoms per unit cell and the number of unique *T* atoms were assumed to be known. This proof-of-principle study was developed further by Falcioni & Deem (1999) to include the powder diffraction pattern in the cost function, to introduce a biased Monte Carlo approach for the *T*-atom moves, and to incorporate parallel tempering into the annealing procedure. The latter allows the annealing scheme to be optimized by running several 'temperatures' in parallel and swapping between temperatures during the course of the simulated-annealing run. The program *ZEFSA II* was written by the same authors and can be downloaded without charge from http://www.mwdeem.rice.edu/zefsaII/. In addition to numerous known zeolites used by the authors to test the program, three novel structures, those of the aluminophosphate UiO-6 (**OSI**, 3 *T* atoms, Akporiaye *et al.*, 1996) the aluminosilicate ERS-7 (**ESV**, 6 *T* atoms, Campbell *et al.*, 1998) and the germanosilicate SSZ-77 (**SVV**, 7 *T* atoms, Earl *et al.*, 2008) were solved using this approach.

4.6.2.3. *Focus*

In model building, the powder diffraction pattern is used passively to check the resulting model. However, such data contain valuable structural information that might be harnessed to facilitate the model building. It was with this in mind that the program *Focus* (http://www.iza-structure.org/ under Other Links: Software) was devised (Grosse-Kunstleve *et al.*, 1997). It was reasoned that some of the ideas used in zeolite model building could be incorporated into a program to interpret electron-density maps generated using the diffraction data. A flowchart of the algorithm is shown in Fig. 4.6.6.

The structure-factor amplitudes extracted from the powder diffraction pattern are assigned random phases to generate an electron-density map. Because the phases are random, so is the map. Nonetheless, the program looks for a zeolite framework fragment in the peaks in the map, ignoring the heights of the peaks. It then takes the largest framework fragment it can find as a partial model and generates a new set of phases to combine with the measured amplitudes. This Fourier recycling procedure is then repeated until the phases converge or the maximum number of cycles is reached. It was found that alternating the largest framework fragment interpretation of the electron-density map with a more standard assignment of the heavier atoms to the larger peaks (but maintaining user-defined minimum distances between the different atom types) led to the fastest convergence, so that procedure is generally used. When the Fourier recycling procedure is finished, a new run is started with a new set of random phases.

Each time an electron-density map is produced, the program also searches for a complete 4-connected framework structure. If one is found it is classified and written to a file. The classification is based on coordination sequences (Brunner & Laves, 1971) rather than atomic coordinates, because the solutions may have different unit-cell origins. For each independent *T* atom in the framework, the number of next-nearest-neighbour *T* atoms (usually 4) is established. Then the number in the next shell of *T* atoms is counted (to a maximum of 12), and so on for ten shells. In most cases, these sets of coordination sequences are sufficient to distinguish one framework from another, but there are a few exceptions. Therefore, the vertex symbol (O'Keeffe & Hyde, 1997), which describes the smallest rings associated with the six tetrahedral angles of each *T* atom, is also used in the classification.

As the file of solutions grows, one usually dominates. It is found over and over again from different starting points. This is usually the correct framework structure and can be used as a starting point for structure completion and refinement (Section 4.6.3). As the number of independent *T* atoms in the framework increases, the number of possible solutions tends to decrease, so the histogram of the solutions for complex structures may consist of just a single result. Several examples of the application of the *Focus* method to structures of different complexities are described by Grosse-Kunstleve *et al.* (1999). One of the more recent applications was the solution of the structure of the borosilicate SSZ-56 (**SFS**, 14 *T* atoms) (Elomari *et al.*, 2009).

The *Focus* algorithm was recently adapted to work with electron-diffraction data. Tests showed that structure solution with such data, which may be incomplete or of poor quality, also benefits significantly from the additional chemical information (Smeets *et al.*, 2013).

4.6.2.4. *Direct methods*

Of course, the very powerful direct methods of structure solution developed originally for single-crystal data can also be applied to polycrystalline zeolites. However, it must be borne in mind that this approach relies heavily upon knowing which reflections are strong and which are weak, so the ambiguity arising from reflection overlap can have serious consequences. In simple cases, where reflection overlap is not too severe, a simple equipartitioning approach in the reflection-intensity extraction step can yield intensities of sufficient reliability to use single-crystal programs directly. This was done in the case of the high-silica zeolite Sigma-2 (**SGT**, 4 *T* atoms), for example (McCusker, 1988).

For more complex structures, where reflection overlap cannot be ignored, the computer programs *EXPO* (Altomare *et al.*, 2011) or *XLENS* (Rius & Frontera, 2007), which have been written specifically to work with powder diffraction data, are more likely to succeed. Examples include the structure of the germanosilicate IM-20 (**UWY**, 10 *T* atoms), which was solved using *EXPO* (Dodin *et al.*, 2010) and those of the germanosilicate ITQ-22 (**IWW**, 16 *T* atoms, Corma *et al.*, 2003) and the high-silica zeolite ITQ-32 (**IHW**, 9 *T* atoms, Cantin *et al.*, 2005), which were solved using *XLENS*.

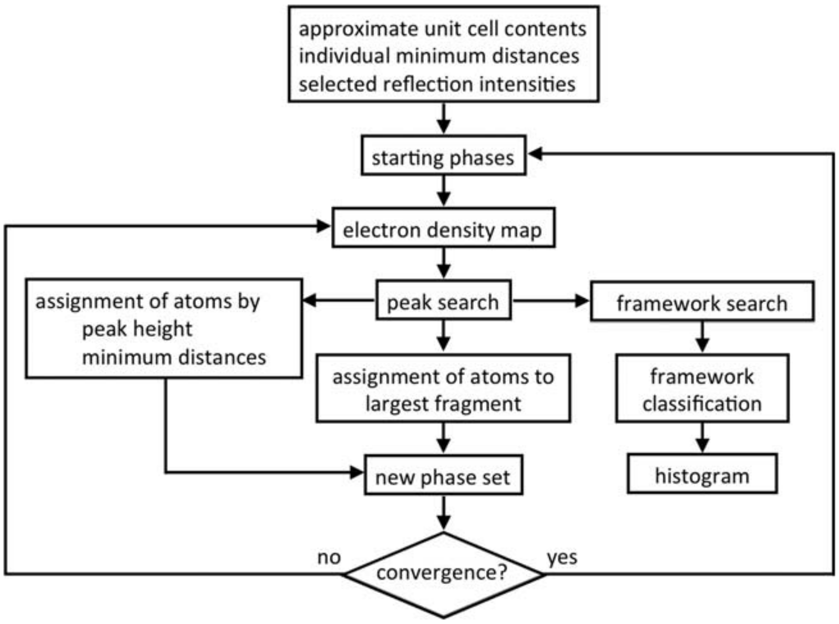
approximate unit cell contents
individual minimum distances
selected reflection intensities
starting phases
electron density map
assignment of atoms by peak height minimum distances
peak search
framework search
assignment of atoms to largest fragment
framework classification
new phase set
histogram
no
convergence?
yes

Figure 4.6.6
Flow chart of the *Focus* program.

4.6.2.5. *Charge flipping*

Model building is done in real space, whereas direct methods work with the diffraction data in reciprocal space. In the former, the diffraction pattern is used as a test of the correctness of the structure, while in the latter, chemical sense is used. In contrast, both diffraction data and chemical knowledge are used actively in the *Focus* algorithm. That is, it is a hybrid method working in both real and reciprocal spaces. Charge flipping, introduced for single-crystal data by Oszlányi & Sütő (2004, 2005) and adapted independently to powder diffraction data by Wu *et al.* (2006) and Baerlocher, McCusker & Palatinus (2007), is also a hybrid method. Its advantage over the *Focus* algorithm is that it is applicable to all types of materials, not just zeolites.

The algorithm is an elegantly simple one (Fig. 4.6.7). It begins in much the same way as *Focus*, by applying random phases to the extracted structure factors to generate a (random) electron-density map. Then instead of trying to interpret the map as

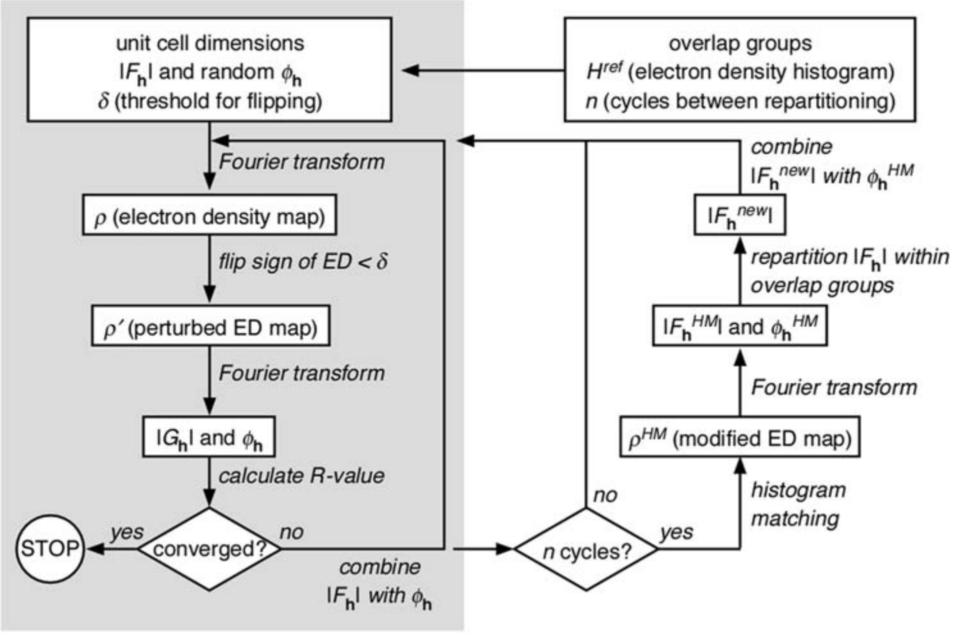
unit cell dimensions
$|F_h|$ and random ϕ_h
δ (threshold for flipping)
overlap groups
H^{ref} (electron density histogram)
n (cycles between repartitioning)
Fourier transform
ρ (electron density map)
flip sign of ED < δ
ρ' (perturbed ED map)
Fourier transform
$|G_h|$ and ϕ_h
calculate R-value
STOP
yes
converged?
no
combine $|F_h|$ with ϕ_h
no
n cycles?
yes
histogram matching
ρ^{HM} (modified ED map)
Fourier transform
$|F_h^{HM}|$ and ϕ_h^{HM}
repartition $|F_h|$ within overlap groups
$|F_h^{new}|$
combine $|F_h^{new}|$ with ϕ_h^{HM}

(*a*) (*b*)

Figure 4.6.7
Flow chart of the charge-flipping algorithm implemented in *Superflip*. (*a*) The original single-crystal algorithm, and (*b*) the modifications introduced to deal with powder diffraction data.

in *Focus*, the map itself is perturbed (in real space) by changing the sign of all densities below a user-defined threshold value (a small positive number). In essence, all negative electron densities, which are not physically meaningful, are made positive. A Fourier transform of this perturbed electron-density map yields a new set of structure-factor amplitudes and phases (reciprocal space). The new phases are assigned to the measured amplitudes and a new electron-density map is generated. In the single-crystal case, this procedure is repeated until the calculated amplitudes match the measured ones. For polycrystalline materials, however, some of the measured amplitudes are ambiguous, because of reflection overlap. The total intensity measured for each group of overlapping reflections (overlap group) is usually simply equipartitioned over the contributing reflections. In an attempt to improve this partitioning somewhat, an additional perturbation of the electron-density map based on histogram matching (Zhang & Main, 1990) was introduced into the powder charge-flipping algorithm in the program *Superflip* (Baerlocher, McCusker & Palatinus, 2007; Palatinus & Chapuis, 2007). The map is modified to match a histogram that reflects the chemical composition of the material (*i.e.* the number and height of the peaks in the map should correspond to the chemical formula), and the ratios of the structure-factor amplitudes obtained by Fourier transformation of this modified map are then used to repartition the measured intensity for each overlap group.

This approach is still quite new, but has already been used to solve six zeolite framework structures. A typical example is that of the aluminosilicate LZ-135 (**LTF**, 6 *T* atoms, McCusker *et al.*, 2009).

4.6.2.6. *Using additional information*

Even with all the methods described above at our disposal, some zeolite structures resist solution. In such cases, additional information is needed to supplement the powder diffraction pattern. Chemical knowledge is already used in *Focus* and *Superflip*, and in the more recent versions of *EXPO*, but there are also other possibilities.

In particular, partial phase information has proven to be a powerful enhancement. For example, the concept of a structure envelope (Brenner *et al.*, 1997), which is closely related to the molecular envelope used in protein crystallography, can be used to describe the pore system of a zeolite. Given the amplitudes and phases of just a few low-index reflections, such an envelope can be calculated. This periodic nodal surface (von Schnering & Nesper, 1991), which separates regions of high electron density from those of low electron density at a relatively low resolution, can be used to limit the parts of the unit cell in which the framework atoms are sought (Brenner *et al.*, 2002). Such an envelope can be enforced in both *Focus* and *Superflip*.

The phase information for the calculation of a structure envelope can sometimes be estimated from the powder diffraction data itself, but if a high-resolution transmission electron microscopy (HRTEM) image is available, the phases can be derived from the image (Hovmöller, 1992). This approach was used, for instance, in the solution of the very complex structure of the high-silica zeolite SSZ-74 (**-SVR**, 23 *T* atoms, Baerlocher *et al.*, 2008). In that case, the structure envelope was imposed in *Superflip* in real space (Fig. 4.6.8).

If the HRTEM images are of sufficiently high quality, more phase information can be extracted, and this can be included in the reciprocal-space part of any structure-solution algorithm. For TNU-9 (**TUN**, 24 *T* atoms), 258 phases were derived from three images, and only when these phases were included as starting phases in *Focus* could the structure be solved (Gramm *et al.*, 2006). In the case of IM-5 (**IMF**, 24 *T* atoms), starting phase sets were generated from an approximate model derived from HRTEM images. These phase sets (phases calculated from the model and then allowed to vary by a certain percentage in a random fashion) were then used as starting points for *Superflip* runs (Baerlocher, Gramm *et al.*, 2007).

Not only electron microscopy, but also electron-diffraction data can be used to supplement powder diffraction data. For example, in the case of the germanosilicate ITQ-37 (**-ITV**, 10 *T* atoms, Sun *et al.*, 2009), selected-area electron-diffraction patterns were used to pre-partition the overlapping reflections before the data were input to *Superflip*. It has also been shown that the phases obtained by applying two-dimensional (single-crystal) charge flipping to precession electron diffraction (PED) data are as reliable as those obtained from HRTEM images (Xie *et al.*, 2008). This means that the much simpler PED technique is a viable alternative to HRTEM for obtaining some starting phases to facilitate structure solution.

The fact that PED data can be used in this way led to a further development on the X-ray powder diffraction front. It was found that two-dimensional subsets of the reflection intensities extracted from a powder diffraction pattern could be used in much the same way (Xie, Baerlocher & McCusker, 2011). This 2D-XPD approach was tested on several very complex zeolite structures and then applied successfully to the novel

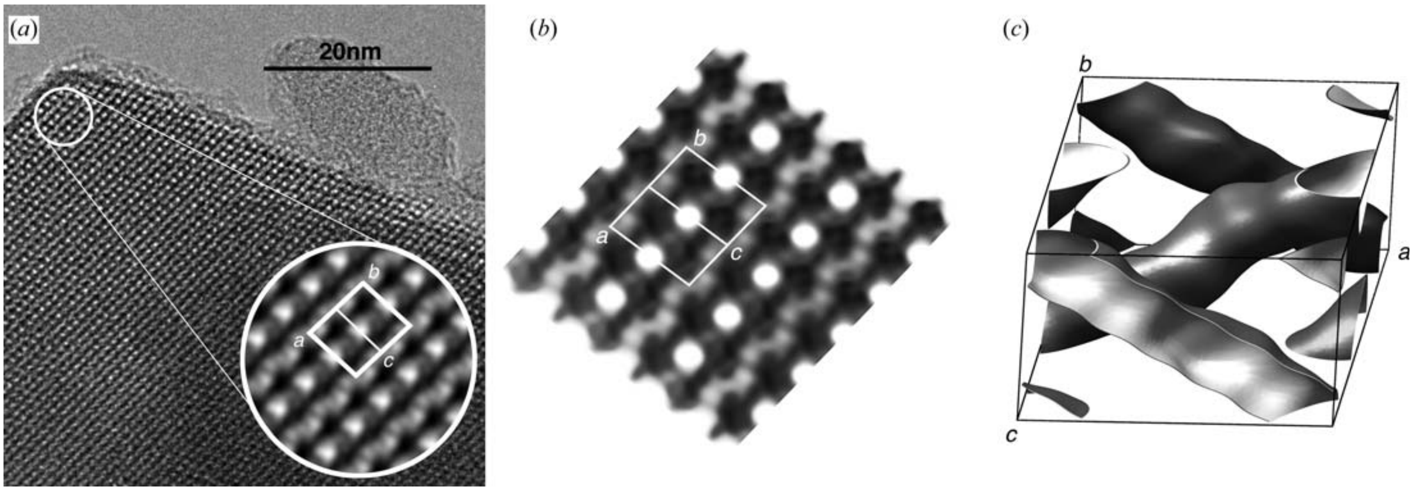

Figure 4.6.8
Structure envelope for SSZ-74. (*a*) HRTEM image of the [110] projection of SSZ-74 with a small section enlarged to show the unit cell. (*b*) Potential map for the [110] projection calculated from the 29 structure-factor amplitudes and phases derived from the image in (*a*). (*c*) A different orientation of a single unit cell showing the three-dimensional character of the structure envelope derived from (*b*) that was then used as input to *Superflip*. The darker side of the surface is where framework atoms would be expected.

borosilicate SSZ-82 (**SEW**, 11 *T* atoms, Xie, McCusker & Baerlocher, 2011).

4.6.3. Structure refinement

Although the determination of a zeolite's basic framework structure is often difficult, it is only the beginning of the story. The non-framework species have to be located, and then the whole structure has to be refined using the Rietveld method (Rietveld, 1969; McCusker *et al.*, 1999) to yield a chemically sensible structure that reproduces the measured diffraction pattern satisfactorily. In the following sections, a few aspects of structure refinement that are particularly relevant to zeolitic materials are discussed.

4.6.3.1. *Space-group ambiguity*

Zeolite framework structures tend towards high symmetry, but sometimes details of the framework geometry or the influence of non-framework species require that the space-group symmetry be reduced. This can be something simple, like the elimination of a centre of symmetry that causes an Si—O—Si linkage to have an unreasonable 180° angle or the elimination of a mirror plane that is incompatible with an ordering of framework atoms (*e.g.* the alternation of Al and P in an aluminophosphate). But it can also be quite complicated. For example, an aluminophosphate with the simple cubic sodalite framework type (**SOD**, 1 *T* atom) was synthesized using dimethylformamide as both the structure-directing agent and the solvent. This produced a material with the unit cell tripled in one direction and a noncentrosymmetric space group (Paillaud *et al.*, 2005). Similarly, the ideal framework structure of UTD-1 (**DON**) has only 5 *T* atoms in the asymmetric unit (space group *Cmcm*), but in the refined structure (space group *Pc*) there are 32 independent Si atoms (Wessels *et al.*, 1999). Chemically unreasonable interatomic distances are often an indication that a reduction in symmetry should be considered.

4.6.3.2. *Geometric restraints*

Although zeolites tend to diffract out to high angles and to have relatively high symmetries, their structures are also quite complex. As a result, the ratio of observations to parameters is usually very low. Fortunately, zeolite frameworks are generally constructed from atoms with well defined bond distances and angles, and this information can be used to advantage in the refinement process. By including known interatomic distances (*e.g.* Si—O, O···O and Si···Si) as geometric restraints (Waser, 1963; Baerlocher, 1993), the observation-to-parameter ratio can be improved. Furthermore, the restraints keep the structural model chemically sensible when the atomic positions are refined. It should be emphasized that these geometric restraints are simply used as additional information. The final structural model must fit both the X-ray powder diffraction profile and the geometric restraints.

Experience has shown that starting with a high weight on the geometric 'observations' at the beginning of the refinement keeps the framework structure reasonable while missing atoms are located and the other parameters find their minima. The weight can then be reduced to allow the atoms more freedom. If an assumption about the geometry is incorrect, it will not be possible to obtain a good fit to both the profile and the geometric restraints. To find the source of the problem, the weight of the restraints can be reduced to see which restraints deviate furthest from the prescribed distances and then to consider possible alternatives.

In such a restrained refinement, the geometric 'observations' are treated as a second data set, and the quantity minimized in the refinement is then

$$S = S_y + c_w S_G,$$

where S_y is the weighted difference between the observed and calculated diffraction patterns, S_G is that between the prescribed and calculated geometric restraints, and c_w is the factor used to weight the two data sets with respect to one another. The geometric restraints can also be used without any diffraction data (*i.e.* $S_y = 0$ and $c_w = 1$) to optimize the geometry of a new framework model. This is a quick and easy way of checking whether or not a framework model is geometrically viable, as there are always more known interatomic distances in a zeolite framework structure than there are positional variables. The distance least-squares program *DLS-76* (Baerlocher *et al.*, 1976) was written for this purpose.

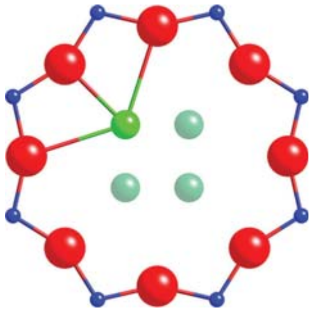

Figure 4.6.9
The disorder of the Na^+ ion (green) in the 8-ring of zeolite A (**LTA**). Only one of the four positions shown can be occupied at any one time.

4.6.3.3. *Disorder*

The cations and molecules in the pores of a zeolite framework structure rarely obey the high symmetry of the framework itself, and the result is that almost all zeolite structures are disordered in one way or another. For example, one of the Na^+ ion positions in zeolite A (**LTA**) lies off the centre of an 8-ring (Fig. 4.6.9) where it can coordinate to three O atoms of the framework. The symmetry of the framework would generate four equivalent positions in the 8-ring, but only one of these four can be occupied at any one time. In other words, these Na^+ ions are disordered with a maximum occupancy of 1/4. The disorder may be dynamic (*i.e.* the ion hops from one position to the next) or it may be static (*i.e.* the ions are arranged differently from unit cell to unit cell). The diffraction data cannot distinguish between these two possibilities.

The organic structure-directing agents (SDAs) used in many zeolite syntheses pose similar problems. A zigzag hydrocarbon chain of the SDA may lie across a mirror plane of the framework or a pentane ring may lie on a threefold axis, and this results in a cloud of electron density that is difficult to untangle into discrete atoms. However, if the geometry of the SDA is known, it may still be possible to interpret the electron-density cloud (see Section 4.6.3.4).

Another type of disorder can arise if an atom of the framework lies on a special position that forces the atom to adopt an unfavourable geometry. This is most often an O atom on a centre of symmetry. If this is the only ‘unhappy’ atom in the structural model, a reduction in the symmetry of the whole framework structure can be avoided by moving the atom off the special position to yield a more reasonable geometry and reducing its occupancy accordingly (*i.e.* adopting a disordered model).

4.6.3.4. *Locating non-framework species*

One of the key features of a zeolite structure is the location of the non-framework species in the pores. Although the framework structure itself defines the size, shape and dimensionality of the zeolite’s pore system, the cation positions are also important for catalytic, adsorption and ion-exchange applications. Furthermore, the location of the SDA is crucial to the understanding of the zeolite synthesis pathway. Fortunately, the phases calculated from the framework structure alone are usually sufficiently correct to generate interpretable difference electron-density maps, even from powder diffraction data. As in the single-crystal case, the difference map is biased towards the model because the phases from the model are assigned to the measured amplitudes that are used to calculate it. However, with powder diffraction data, a second bias is introduced because the amplitudes for overlapping reflections are also partitioned according to the model. This bias should always be borne in mind, but is not usually a problem.

With an approximately correct framework model, it is generally possible to get a good match to the measured powder diffraction pattern at high angles, but there will be large differences at low angles if the zeolite has not been calcined. That is, if there are species in the pores that have not yet been located, they will affect the low-angle (low-resolution) reflections most. Therefore, the measured and calculated patterns are best scaled to one another using only the high-angle ($d < 2.5$ Å) part of the pattern (Fig. 4.6.10). This will increase the discrepancy at low angle (and therefore the $R_{\rm wp}$ value), but these differences are real, so in fact cleaner maps are obtained (Fig. 4.6.11). If difference electron-density maps show significant peaks or holes at the positions of atoms already in the model, this is an indication that the scale factor and/or the background estimation need to be re-evaluated.

Interpretation of the peaks in the difference map is best done stepwise. The highest peaks with chemically sensible approaches to atoms already in the model are assigned first, and then another, improved difference map can be generated. This will generally allow cations and perhaps their immediate coordination spheres to be determined. As the peaks get weaker and more diffuse, however, the interpretation will become more difficult. At this point, information from other characterization techniques (in particular, chemical analysis, MAS NMR, thermogravimetric analysis, IR spectroscopy) and from related structures can be invaluable.

Locating a large organic SDA atom by atom can be very difficult, especially if there is disorder present. However, if the

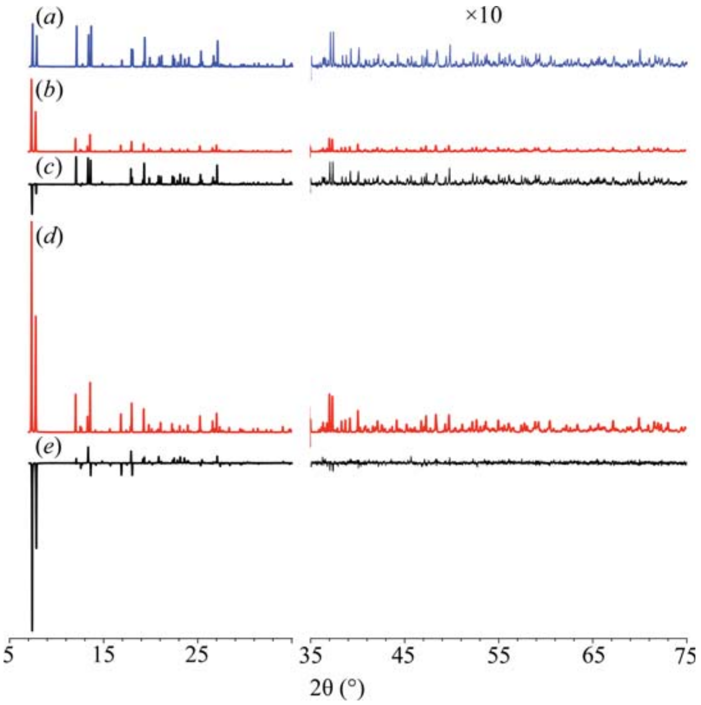

Figure 4.6.10
(*a*) The measured powder diffraction pattern for the silicoaluminophosphate SAPO-40 (**AFR**). (*b*) The powder diffraction pattern calculated for the framework structure of SAPO-40 using the scale factor calculated for the whole pattern, and (*c*) the difference between (*a*) and (*b*). (*d*) The powder diffraction pattern calculated for the framework structure of SAPO-40 using the scale factor calculated for the high-angle data only, and (*e*) the difference between (*a*) and (*d*). Note the much smaller differences in the high-angle region in (*e*) compared with (*c*). The 35–75° 2θ section of all diffraction patterns has been scaled up by a factor of 10 to show more detail.

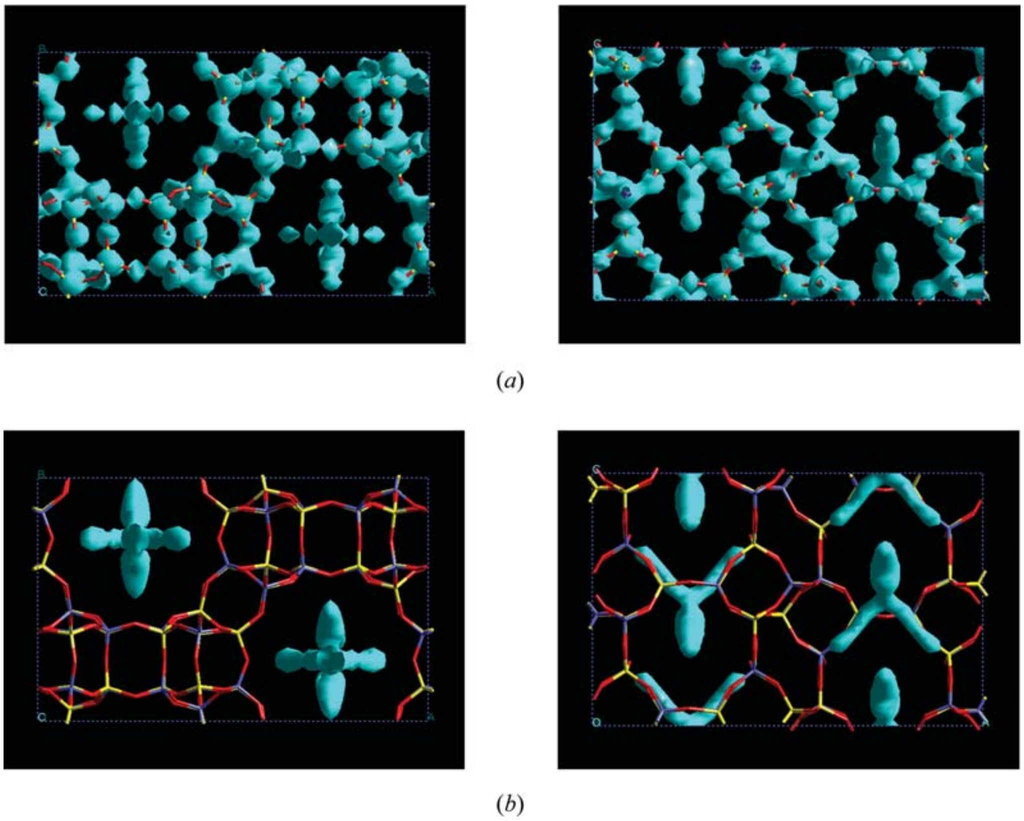

Figure 4.6.11
Difference electron-density maps (blue) calculated for SAPO-40 (**AFR**) along the [001] (left) and [010] (right) directions using (*a*) the scale factor calculated for the full diffraction pattern (Fig. 4.6.10*b*), and (*b*) the scale factor calculated for the high-angle data only (Fig. 4.6.10*d*). The framework structure has been overlaid to show the location of the pores. Note that in (*a*) there is more electron density on the framework atoms, which are already in the model, than in the pores, whereas only the electron density of the tetrapropylammonium ion in the pores is visible in (*b*).

geometry of the SDA is known and it is not too flexible, it can be added initially as a rigid body to get an approximate position and orientation, and then later refined using geometric restraints. The initial positioning of the SDA in the channels can be facilitated by applying a global-optimization algorithm like simulated annealing to test a large number of possibilities (Smeets *et al.*, 2016). Alternatively, computational chemistry can be used to estimate the best position of the SDA in the pores, and this can be used as a starting point for refinement. Geometric restraints should always be applied to keep the SDA bond distances and angles sensible. At least initially, ‘anti-bump’ restraints can be used to keep the atoms of the SDA a sensible distance away from those of the framework. It should be remembered that the SDA is an integral part of the synthesis process, and is unlikely to be randomly positioned in the structure. Although deciphering the atomic coordinates of an SDA may be a major undertaking, the effort can be rewarded with a unique insight into the synthesis process. Once all of the atoms have been included in the structural model, full Rietveld refinement with reduced weight on the geometric restraints can begin. It is at this point that details of the framework geometry become evident.

If the location of the SDA and/or solvent molecules proves to be too difficult, the material can often be calcined to remove these species, and then the empty framework structure can be refined. In our experience, the peaks in the diffraction pattern of the as-synthesized material are usually sharper, because the crystallites suffer somewhat during the removal of the non-framework species. However, the refinement of the framework structure alone may be easier. Of course, this means that the information about the role of the SDA in the synthesis process is lost.

4.6.3.5. *Rietveld refinement of SSZ-74*

The refinement of the structure of the zeolite SSZ-74 (**-SVR**, 23 *T* atoms, Baerlocher *et al.*, 2008) illustrates a number of the points made above. The structure was solved initially with *Superflip* using a structure envelope derived from an HRTEM image (see Section 4.6.2.6). The symmetry was ambiguous (*C*2/*c* or *Cc*), so *C*2/*c* was assumed to begin with. The initial model from *Superflip* had 11 Si atoms in the asymmetric unit forming an interrupted framework structure. However, there was a weak peak in the electron-density map that would complete a fully 4-connected net, so a twelfth Si atom was added at that position (Fig. 4.6.12*a*).

This structure yielded a good fit to the high-angle part of the diffraction pattern (R_F = 0.078, $R_{\rm wp}$ = 1.075, $R_{\rm exp}$ = 0.094, $R_{\rm res}$ = 0.018, where $R_{\rm res} = \{\sum_i w_i^2[d_i(\text{prescribed}) - d_i(\text{model})]^2/\sum_i w_i^2[d_i(\text{prescribed})]^2\}^{1/2}$, and a difference electron-density map was generated to locate the SDA [1,6-bis(*N*-methylpyrrolidinium)hexane] (Fig. 4.6.13). It was not clear how the SDA should be arranged in the electron-density cloud, so molecular modelling was used to get a starting model. This model (Fig. 4.6.12*b*) improved the fit to the diffraction pattern considerably (R_F = 0.065, $R_{\rm wp}$ = 0.189, $R_{\rm exp}$ = 0.094, $R_{\rm res}$ = 0.022). Then refinement of the framework geometry was started. However, the geometry of the twelfth atom was strained [Si(12)—O distances ranging from 1.62 to 1.67 Å, O—Si(12)—O angles ranging from 97.0 to 146.7°]. In an attempt to relieve this strain, the space group was reduced to *Cc* and the number of Si atoms increased to 24. Again the profile fit improved (Fig. 4.6.12*c*, R_F = 0.056, $R_{\rm wp}$ = 0.165, $R_{\rm exp}$ = 0.097, $R_{\rm res}$ = 0.014), but the distortion of the twelfth Si atom (now two Si positions) remained. In view of the fact that this Si position was not clear in the original solution from charge flipping, the

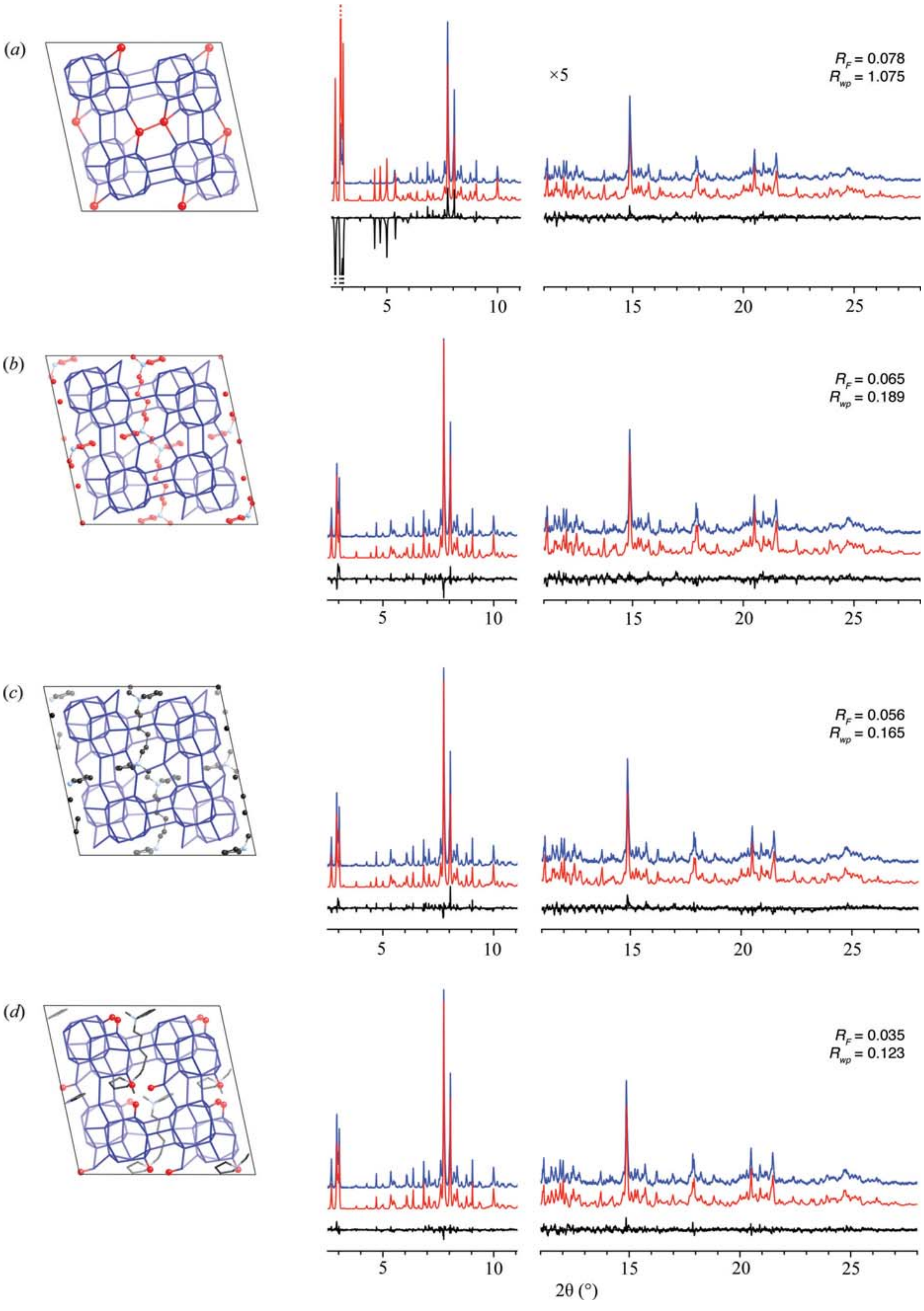

Figure 4.6.12
The structure completion and Rietveld refinement of SSZ-74 (**-SVR**). (*a*) The initial framework structure model in *C*2/*c* obtained from *Superflip* with a twelfth Si atom (highlighted in red) added to generate a fully connected net, and the corresponding profile fit. (*b*) The framework structure in *C*2/*c* with the SDA position and conformation obtained from molecular modelling. (*c*) The structure after reducing the symmetry to *Cc*. (*d*) The final structure with an ordered Si vacancy in the framework (terminal O atoms highlighted in red). Bridging framework O atoms have been omitted for clarity. The second part of each diffraction pattern has been scaled up by a factor of five to show more detail. The highest peak in (*a*) and the corresponding difference have been cut at 75% of the full height.

occupancy parameters of these two positions were refined. One of the two remained fully occupied, and the other disappeared. This resulted in an interrupted framework structure with 23 Si atoms in the asymmetric unit and an ordered Si vacancy, a distortion-free geometry, and an improved profile fit (Fig. 4.6.12*d*, $R_F = 0.035$, $R_{\rm wp} = 0.123$, $R_{\rm exp} = 0.097$, $R_{\rm res} = 0.009$). The ^{29}Si and ^{1}H MAS NMR spectra add further credence to this model. The former indicates the presence of an unusually high percentage of 3- rather than 4-connected Si atoms (Q^3 species) and the latter a strong signal that is consistent with a silanol/siloxy 'nest' (Koller *et al.*, 1995).

During the course of the refinement, the SDA molecule adjusted its position somewhat. This is not surprising, because the initial molecular modelling was performed with a fully connected framework structure, so the main SDA–framework interactions were steric in nature. However, with the Si vacancies, there are terminal O atoms that can be expected to interact more directly with the SDA, and indeed the N atoms of the two pyrrolidinium rings approach these terminal O atoms at hydrogen-bonding distances. That is, although the distances and angles of the SDA were restrained in the refinement, the molecule was able to adjust to a favourable conformation that makes chemical sense (Fig. 4.6.12*d*). No restraints on the SDA–framework distances were used. The final conformation was dictated by the diffraction data.

4.6.3.6. *Locating isomorphously substituted T atoms*

Perhaps one of the most challenging questions for a zeolite crystallographer is whether or not isomorphously replaced *T* atoms can be located. Even in a typical aluminosilicate, it is not always obvious where the Al atoms are. In only a few structures has a clear crystallographic ordering of these atoms been demonstrated (*e.g.* in zeolite A, the Al and Si alternate throughout the framework). In a more typical case, the Al will preferentially occupy certain positions, but the ordering is usually incomplete, and only the lengthening of the *T*—O distance [Si—O: 1.61 (1) Å; Al—O: 1.74 (1) Å] can be used to identify these sites and to estimate the Al content.

When the amount of the isomorphously substituted element falls below a certain level, its specific location in the framework structure usually remains a mystery. In some cases, however, a little insight can be gleaned. The most important factors that will determine whether or not a *T* atom site can be assigned to a particular element are (1) the amount of the substituted element in the framework, (2) the scattering power of the element with respect to that of the other *T* atoms (*i.e.* are they different enough?), (3) the ionic radius (*i.e.* can it be distinguished from other *T* atoms by bond distance?) and (4) the extent to which it is ordered. In some cases, anomalous dispersion can be used to advantage to enhance the contrast between an isomorphously substituted *T* atom and the others in the framework structure (Cox & Wilkinson, 1994).

Many attempts to locate Ti in titanosilicate **MFI**-type materials have been undertaken, for example, but no consensus has been found. The main problem in this case is that the amount of Ti is very low (Ti:Si *ca* 1:23) and it appears to be distributed over several of the 12 *T* sites. More success has been found in the realm of the germanosilicates ITQ-22 (**IWW**, 16 *T* atoms, Corma *et al.*, 2003) and SSZ-77 (14 *T* atoms, McCusker *et al.*, 2011), where the amount of Ge is significantly higher (Ge:Si *ca* 1:4.6 and 1:4.1, respectively) and Ge has a strong preference for double 4-rings in zeolite frameworks.

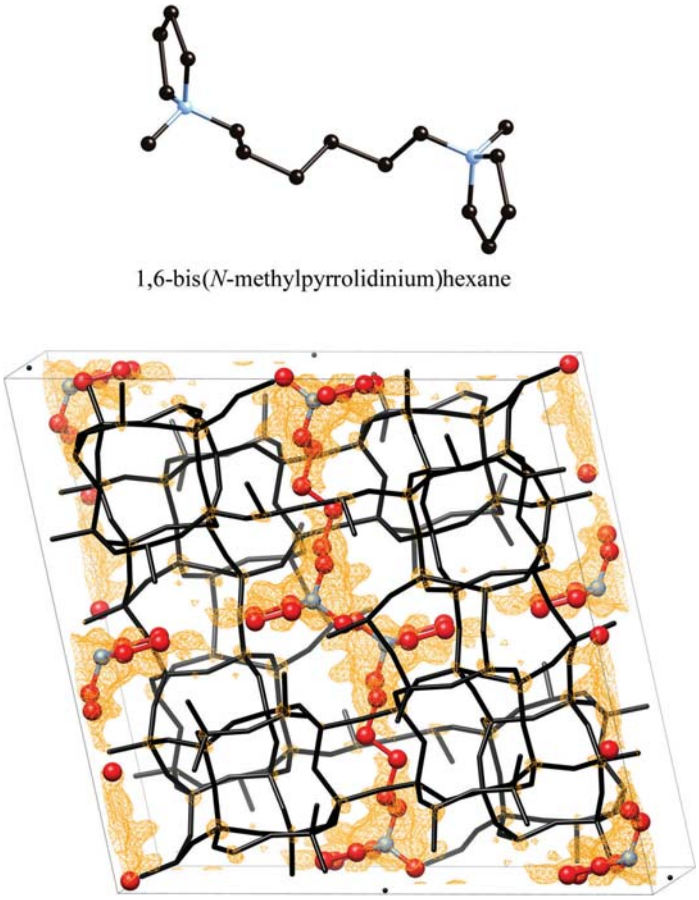

Figure 4.6.13
The structure-directing agent (SDA) used in the synthesis of SSZ-74 and the difference electron-density map (orange) generated from the pattern and model shown in Fig. 4.6.12(*a*). The framework structure (black) with the SDA position and conformation obtained from molecular modelling (N: blue, C: red) has been overlaid for comparison. Note that the SDA fits the electron-density cloud quite well.

A more indirect indication of where the Al is located in an aluminosilicate can be given by the positions of non-framework species (Pinar *et al.*, 2013). For example, metal cations can be exchanged for the protons in a calcined material, and they will be much easier to locate than the almost invisible H^+ ions. These cations can be expected to be associated with the framework O atoms that are bonded to the Al atoms. Similarly, a large molecule like pyridine can be adsorbed into a zeolite to probe where the protons (and thereby the Al) are located. These experiments can be expected to yield useful results as long as the Al is concentrated in specific positions and the associated O atoms are accessible to the cation or molecule used as a probe.

4.6.4. Conclusions

There are different levels of zeolite structure analysis that can be realized using powder diffraction data. In the simplest case, the positions of the reflections can be used to monitor unit-cell changes as a function of temperature, ion exchange or adsorption, or the peak widths to measure crystallite size. However, the structural information that lies in the intensities can also be deciphered by applying the methods outlined in this chapter. Whether the goal is to determine the framework structure of a new zeolitic material, to locate the non-framework species in the pores of a known framework structure, or to evaluate the most likely positions for isomorphously substituted framework cations, if the powder diffraction pattern contains the information, it can be extracted. The analysis of the structure of a polycrystalline zeolite is not necessarily easy or even straightforward, but it is possible, and the results are usually worth the effort.

References

Akporiaye, D. E., Fjellvag, H., Halvorsen, E. N., Haug, T., Karlsson, A. & Lillerud, K. P. (1996). *UiO-6: a novel 12-ring aluminophosphate structure solved by simulated annealing*. *Chem. Commun.* pp. 1553–1554.

Altomare, A., Cuocci, C., Giacovazzo, C., Moliterni, A. & Rizzi, R. (2011). *EXPO2011: a new package for powder crystallography*. *Powder Diffr.* **26**, S2–S12.

Baerlocher, Ch. (1993). *Restraints and constraints in Rietveld refinement*. In *The Rietveld Method*, edited by R. A. Young, pp. 186–196. Oxford University Press.

Baerlocher, Ch., Gramm, F., Massüger, L., McCusker, L. B., He, Z. B., Hovmöller, S. & Zou, X. D. (2007). *Structure of the polycrystalline zeolite catalyst IM-5 solved by enhanced charge flipping*. *Science*, **315**, 1113–1116.

Baerlocher, Ch., Hepp, A. & Meier, W. M. (1976). *DLS-76, a program for the simulation of crystal structures by geometric refinement*. Institut für Kristallographie, ETH Zurich, Switzerland.

Baerlocher, Ch., McCusker, L. B. & Olson, D. H. (2007). *Atlas of Zeolite Framework Types*, 6th revised ed. Amsterdam: Elsevier.

Baerlocher, Ch., McCusker, L. B. & Palatinus, L. (2007). *Charge flipping combined with histogram matching to solve complex crystal structures from powder diffraction data*. *Z. Kristallogr.* **222**, 47–53.

Baerlocher, Ch., Xie, D., McCusker, L. B., Hwang, S. J., Chan, I. Y., Ong, K., Burton, A. W. & Zones, S. I. (2008). *Ordered silicon vacancies in the framework structure of the zeolite catalyst SSZ-74*. *Nat. Mater.* **7**, 631–635.

Barrer, R. M. (1978). *Zeolites and Clay Minerals as Sorbents and Molecular Sieves*, p. 63. London: Academic Press.

Breck, D. W., Eversole, W. G., Milton, R. M., Reed, T. B. & Thomas, T. L. (1956). *Crystalline zeolites. I. The properties of a new synthetic zeolite, type A*. *J. Am. Chem. Soc.* **78**, 5963–5972.

Brenner, S., McCusker, L. B. & Baerlocher, Ch. (1997). *Using a structure envelope to facilitate structure solution from powder diffraction data*. *J. Appl. Cryst.* **30**, 1167–1172.

Brenner, S., McCusker, L. B. & Baerlocher, Ch. (2002). *The application of structure envelopes in structure determination from powder diffraction data*. *J. Appl. Cryst.* **35**, 243–252.

Brunner, G. O. & Laves, F. (1971). *Zum Problem der Koordinationszahl*. *Wiss. Z. Techn. Univ. Dres.* **20**, 387–390.

Burton, A., Elomari, S., Chen, C. Y., Medrud, R. C., Chan, I. Y., Bull, L. M., Kibby, C., Harris, T. V., Zones, S. I. & Vittoratos, E. S. (2003). *SSZ-53 and SSZ-59: two novel extra-large pore zeolites*. *Chem. Eur. J.* **9**, 5737–5748.

Campbell, B. J., Bellussi, G., Carluccio, L., Perego, G., Cheetham, A. K., Cox, D. E. & Millini, R. (1998). *The synthesis of the new zeolite, ERS-7, and the determination of its structure by simulated annealing and synchrotron X-ray powder diffraction*. *Chem. Commun.* pp. 1725–1726.

Cantin, A., Corma, A., Leiva, S., Rey, F., Rius, J. & Valencia, S. (2005). *Synthesis and structure of the bidimensional zeolite ITQ-32 with small and large pores*. *J. Am. Chem. Soc.* **127**, 11560–11561.

Cejka, J., van Bekkum, H., Corma, A. & Schüth, F. (2007). Editors. *Introduction to Zeolite Science and Practice*, 3rd revised ed. Amsterdam: Elsevier.

Corma, A., Rey, F., Valencia, S., Jorda, J. L. & Rius, J. (2003). *A zeolite with interconnected 8-, 10- and 12-ring pores and its unique catalytic selectivity*. *Nat. Mater.* **2**, 493–497.

Cox, D. E. & Wilkinson, A. P. (1994). *Powder diffraction studies using anomalous dispersion*. In *Resonant Anomalous X-ray Scattering*, edited by G. Materlik, C. J. Parks & K. Fischer, pp. 195–229. Amsterdam: Elsevier Science.

Deem, M. W. & Newsam, J. M. (1989). *Determination of 4-connected framework crystal structures by simulated annealing*. *Nature*, **342**, 260–262.

Dodin, M., Paillaud, J.-L., Lorgouilloux, Y., Caullet, P., Elkaim, E. & Bats, N. (2010). *A zeolitic material with a three-dimensional pore system formed by straight 12- and 10-ring channels synthesized with an imidazolium derivative as structure-directing agent*. *J. Am. Chem. Soc.* **132**, 10221–10223.

Earl, D. J., Burton, A. W., Rea, T., Ong, K., Deem, M. W., Hwang, S. J. & Zones, S. I. (2008). *Synthesis and Monte Carlo structure determination of SSZ-77: a new zeolite topology*. *J. Phys. Chem. C*, **112**, 9099–9105.

Elomari, S., Burton, A., Medrud, R. C. & Grosse-Kunstleve, R. (2009). *The synthesis, characterization, and structure solution of SSZ-56: An extreme example of isomer specificity in the structure direction of zeolites*. *Microporous Mesoporous Mater.* **118**, 325–333.

Falcioni, M. & Deem, M. W. (1999). *A biased Monte Carlo scheme for zeolite structure solution*. *J. Chem. Phys.* **110**, 1754–1766.

Gramm, F., Baerlocher, Ch., McCusker, L. B., Warrender, S. J., Wright, P. A., Han, B., Hong, S. B., Liu, Z., Ohsuna, T. & Terasaki, O. (2006). *Complex zeolite structure solved by combining powder diffraction and electron microscopy*. *Nature*, **444**, 79–81.

Grosse-Kunstleve, R. W., McCusker, L. B. & Baerlocher, Ch. (1997). *Powder diffraction data and crystal chemical information combined in an automated structure determination procedure for zeolites*. *J. Appl. Cryst.* **30**, 985–995.

Grosse-Kunstleve, R. W., McCusker, L. B. & Baerlocher, Ch. (1999). *Zeolite structure determination from powder diffraction data: applications of the FOCUS method*. *J. Appl. Cryst.* **32**, 536–542.

Hovmöller, S. (1992). *CRISP: crystallographic image processing on a personal computer*. *Ultramicroscopy*, **41**, 121–135.

Koller, H., Lobo, R. F., Burkett, S. L. & Davis, M. E. (1995). *SiO–⋯HOSi hydrogen bonds in as-synthesized high-silica zeolites*. *J. Phys. Chem.* **99**, 12588–12596.

Le Bail, A. (2005). *Whole powder pattern decomposition methods and applications: a retrospection*. *Powder Diffr.* **20**, 316–326.

McCusker, L. (1988). *The ab initio structure determination of sigma-2 (a new clathrasil phase) from synchrotron powder diffraction data*. *J. Appl. Cryst.* **21**, 305–310.

McCusker, L. B., Baerlocher, Ch., Burton, A. W. & Zones, S. I. (2011). *A re-examination of the structure of the germanosilicate zeolite SSZ-77*. *Solid State Sci.* **13**, 800–805.

McCusker, L. B., Baerlocher, Ch., Wilson, S. T. & Broach, R. W. (2009). *Synthesis and structural characterization of the aluminosilicate LZ-135, a zeolite related to ZSM-10*. *J. Phys. Chem. C*, **113**, 9838–9844.

McCusker, L. B., Liebau, F. & Engelhardt, G. (2001). *Nomenclature of structural and compositional characteristics of ordered microporous and mesoporous materials with inorganic hosts*. *Pure Appl. Chem.* **73**, 381–394.

McCusker, L. B., Von Dreele, R. B., Cox, D. E., Louër, D. & Scardi, P. (1999). *Rietveld refinement guidelines*. *J. Appl. Cryst.* **32**, 36–50.

O'Keeffe, M. & Hyde, S. T. (1997). *Vertex symbols for zeolite nets*. *Zeolites*, **19**, 370–374.

Oszlányi, G. & Sütő, A. (2004). *Ab initio structure solution by charge flipping*. *Acta Cryst.* A**60**, 134–141.

Oszlányi, G. & Sütő, A. (2005). *Ab initio structure solution by charge flipping. II. Use of weak reflections*. *Acta Cryst.* A**61**, 147–152.

Paillaud, J. L., Marichal, C., Roux, M., Baerlocher, Ch. & Chezeau, J. M. (2005). *Tripling of the unit cell volume of the non-centrosymmetric $AlPO_4$-SOD after dehydration: a structural study of a reversible process*. *J. Phys. Chem. B*, **109**, 11893–11899.

Palatinus, L. & Chapuis, G. (2007). *SUPERFLIP - a computer program for the solution of crystal structures by charge flipping in arbitrary dimensions*. *J. Appl. Cryst.* **40**, 786–790.

Pawley, G. S. (1981). *Unit-cell refinement from powder diffraction scans*. *J. Appl. Cryst.* **14**, 357–361.

Pinar, A. B., Gómez-Hortigüela, L., McCusker, L. B. & Pérez-Pariente, J. (2013). *Controlling the aluminum distribution in the zeolite ferrierite via the organic structure directing agent*. *Chem. Mater.* **25**, 3654–3661.

Rietveld, H. M. (1969). *A profile refinement method for nuclear and magnetic structures*. *J. Appl. Cryst.* **2**, 65–71.

Rius, J. & Frontera, C. (2007). *Application of the constrained S-FFT direct-phasing method to powder diffraction data. XIII*. *J. Appl. Cryst.* **40**, 1035–1038.

Schnering, H. G. von & Nesper, R. (1991). *Nodal surfaces of Fourier series: fundamental invariants of structured matter*. *Z. Phys. B Condens. Matter*, **83**, 407–412.

Smeets, S., McCusker, L. B., Baerlocher, Ch., Mugnaioli, E. & Kolb, U. (2013). *Using FOCUS to solve zeolite structures from three-dimensional electron diffraction data*. *J. Appl. Cryst.* **46**, 1017–1023.

Smeets, S., McCusker, L. B., Baerlocher, Ch., Xie, D., Zones, S. I. & Elomari, S. (2016). *Locating organic guests in inorganic host materials from X-ray powder diffraction data*. *J. Am. Chem. Soc.* **138**, 7099–7106.

Sun, J., Bonneau, C., Cantin, A., Corma, A., Diaz-Cabañas, M. J., Moliner, M., Zhang, D., Li, M. & Zou, X. (2009). *The ITQ-37 mesoporous chiral zeolite*. *Nature*, **458**, 1154–1157.

Treacy, M. M. J. & Higgins, J. B. (2007). *Collection of Simulated XRD Powder Patterns for Zeolites*, 5th revised ed. Amsterdam: Elsevier.

Waser, J. (1963). *Least-squares refinement with subsidiary conditions*. *Acta Cryst.* **16**, 1091–1094.

Wessels, T., Baerlocher, Ch., McCusker, L. B & Creyghton, E. J. (1999). *An ordered form of the extra-large-pore zeolite UTD-1: synthesis and structure analysis from powder diffraction data*. *J. Am. Chem. Soc.* **121**, 6242–6247.

Wu, J. S., Leinenweber, K., Spence, J. C. H. & O'Keeffe, M. (2006). *Ab initio phasing of X-ray powder diffraction patterns by charge flipping*. *Nat. Mater.* **5**, 647–652.

Xie, D., Baerlocher, Ch. & McCusker, L. B. (2008). *Combining precession electron diffraction data with X-ray powder diffraction data to facilitate structure solution*. *J. Appl. Cryst.* **41**, 1115–1121.

Xie, D., Baerlocher, Ch. & McCusker, L. B. (2011). *Using phases retrieved from two-dimensional projections to facilitate structure solution from X-ray powder diffraction data*. *J. Appl. Cryst.* **44**, 1023–1032.

Xie, D., McCusker, L. B. & Baerlocher, Ch. (2011). *Structure of the borosilicate zeolite catalyst SSZ-82 solved using 2D-XPD charge flipping*. *J. Am. Chem. Soc.* **133**, 20604–20610.

Zhang, K. Y. J. & Main, P. (1990). *Histogram matching as a new density modification technique for phase refinement and extension of protein molecules*. *Acta Cryst.* A**46**, 41–46.

International Tables for Crystallography (2019). Vol. H, Chapter 4.7, pp. 465–472.

4.7. Rietveld refinement

B. H. Toby

4.7.1. History

Powder diffraction was invented independently by Peter Debye & Paul Scherrer (1916) and Albert Hull (1917) for the purpose of descriptive crystal-structure determination, for materials where single-crystal specimens for materials were not available. Both groups and many others were successful in this work, but as the practice of single-crystal diffraction analysis improved, and structure refinement allowed quantitative structure determination to become routine, one of the key weaknesses of powder diffraction – the loss of information due to reflection overlap – became a major disadvantage. In the relatively few cases where structural refinement from powder diffraction was attempted, reflections that overlapped had to be discarded. Alternately, refinement software was created to treat the specific cases of groups of overlapped reflections for each structural study [for example, see Rietveld (1966)].

In the mid-1960s crystallographic analysis from powder diffraction was to see a major advance when the group of Bert Loopstra, Bob van Laar and later Hugo Rietveld at the Reactor Centre Netherlands in Petten considered the peak-overlap problem (van Laar & Schenk, 2018). Building on initial work in describing how peak widths changed for constant-wavelength (CW) neutron diffractometers (Cagliotti *et al.*, 1958) and 'profile decomposition' [using the nomenclature of Young (1993)] to determine intensities of overlapped reflections (van Laar, 1965), a method was developed for the fitting of crystallographic parameters, as well as experimental and sample parameters that dictate peak shapes (Rietveld, 1967). A computer program in ALGOL was later documented and distributed (Rietveld, 1969). The Petten group rapidly adopted this approach in their crystallographic work (Loopstra & Rietveld, 1969*a*,*b*). Rietveld would soon recast his code in the more widely used Fortran programming language and while that work was never reported in the literature, the code was widely distributed and used as the basis for the work of many others, for example the initial crystallographic fits to X-ray diffraction (Young *et al.*, 1977) and to pulsed-neutron diffraction data (Worlton *et al.*, 1976; Von Dreele *et al.*, 1982).

Several terms have been used to name this crystallographic method, such as 'profile refinement' and 'full-pattern fitting', but these unfortunately obscure the fact that the goal is crystallographic fitting rather than determination of peak shapes. In the words of Ray Young, an early adopter of this work, 'it was Rietveld who first worked out computer-based analytical procedures (quite sophisticated ones for the time, as it turned out) ... who put them in the public domain ... and who very importantly, freely and widely shared his computer program. It is for these reasons that the method is appropriately referred to now as 'the Rietveld method', or 'Rietveld refinement', or 'Rietveld analysis'.' (Young, 1993). Rietveld's method is general for all types of materials, could make use of intensities for even severely overlapped reflections as well as reflections with no intensity, and thereby made quantitative crystallographic analysis possible for materials that did not form single crystals, even when complex with low symmetry.

Rietveld implemented his analysis for only CW neutron diffraction, but did include treatment for magnetic scattering: the interaction between neutrons and unpaired electrons. His code also treated experimental complexities such as low-angle peak asymmetry (better described as axial divergence asymmetry), crystallite size broadening and preferred orientation. van Laar and others significantly improved the treatment of low-angle asymmetry some years later (van Laar & Yelon, 1984; Eddy *et al.*, 1986; Finger *et al.*, 1994). Initial use of CW neutrons simplified fitting, as these measurements usually offer very simple Gaussian peak shapes and also had the advantage that measurements are routinely made over a wide Q range ($Q = 2\pi/d = 4\pi\sin\theta/\lambda$). Subsequent work, fitting to X-ray diffraction data, required treatment of both Gaussian and Lorentzian broadening (Young *et al.*, 1977; Wiles & Young, 1981). Fitting to neutron time-of-flight (TOF) powder-diffraction data presented considerable technical challenges, since now one must correct for many wavelength-dependent effects, such as absorption and source flux (Worlton *et al.*, 1976; Von Dreele *et al.*, 1982; Albinati & Willis, 1982). Most significantly, TOF neutron diffraction peaks will have highly asymmetric shapes because of the rapid rise and slower bleed-off of neutrons leaving the spallation moderators. This peak shape changes considerably with wavelength, since the moderator 'shaping constant' changes with neutron energy (Jorgensen *et al.*, 1989), also see Chapter 3.3. While the equations and number of terms needed to describe TOF peak shapes are significantly more complex than those for CW X-rays and neutrons, recent work to decouple sample-dependent and instrument-dependent profile contributions greatly decreases the complexity of analysis of TOF data (Toby & Von Dreele, 2013, 2014). TOF data are often preferred as they can offer very high resolution coupled with great Q range.

When Rietveld analysis was initially applied, the method was questioned because the derived parameters, and in particular the standard uncertainties on these parameters, did not match results obtained from refinements using integrated intensities (Sakata & Cooper, 1979). The discrepancies between Rietveld results and those obtained from refinement based on intensities from peak integration were later explained as being due to the neglect of correlation information in the integrated peak approach (Prince, 1981). The same results are obtained with integrated intensities if the correlation information from the peak integration is carried forward into a second least-squares fit through use of a weight matrix, obtained from the covariance in the first fit. This adds considerable complexity to the process, since when independent observations are used in a fit, only the diagonal values in the weight matrix are non-zero; thus, the weights can be simplified as a list of values corresponding to each observation. Prince's masterful brief work continues to be relevant to those who argue over the proper way to fit a parametric equation to results from a series of crystallographic measurements, for example over a series of pressures or temperatures, since it shows the results are equivalent if performed with proper weighting.

The scope of materials studied with Rietveld analysis extends from the simplest chemical systems to phase analysis of very complex mixtures of Portland cement clinker (Morsli *et al.*, 2007).

Copyright © 2019 International Union of Crystallography

To the astonishment of many, Rietveld analysis can be applied to structural study of proteins (Von Dreele, 1999). Powder diffraction has even been used successfully to determine structures of proteins that were previously unknown (Von Dreele *et al.*, 2000; Margiolaki *et al.*, 2007).

Rietveld analysis requires too many computations to perform without computer software. A plethora of different computer codes for Rietveld analysis has been developed in the subsequent 40+ years (far too many to properly survey here), but some of the historically important codes are mentioned here. The original Fortran code from Rietveld served as the basis for many subsequent improvements and adaptations, but other programs are complete reimplementations and do not share any code from Rietveld. The adaptation of Rietveld's code by Hewat was widely distributed (Hewat, 1973). Likewise the *DBW* (later *DBWS*) code, which first implemented Rietveld analysis with laboratory X-ray data, was also widely used (Wiles & Young, 1981). The same is true for the *TOFLS* program, which first implemented Rietveld analysis for neutron TOF data (Von Dreele *et al.*, 1982).

At present, some of the most widely used packages for crystallographic analysis include: *Topas* (Coelho, 2007), *FullProf* (Rodríguez-Carvajal, 1993), *Jana* (Petricek *et al.*, 2006), and the *GSAS/EXPGUI* combination (Toby, 2001; Larson & Von Dreele, 2004). All functionality in *GSAS/EXPGUI* has been reimplemented in the new and more modern *GSAS-II* package, which also offers much greater functionality; citation of *GSAS-II* is growing exponentially (Toby & Von Dreele, 2013). In addition, there are also widely used programs devoted to a particular type of analysis or research community, for example the *MAUD* package is typically used for residual stress (better labelled as microstrain) or texture analysis (Lutterotti *et al.*, 1999) or the *RIETAN-FP* package, which implements maximum-entropy methods and includes documentation in Japanese (Izumi & Momma, 2007).

4.7.2. Rietveld *versus* single-crystal refinements

In contrast to a single-crystal refinement, where structural parameters are fitted to 'observed' structure factors, in a Rietveld fit one must describe all the items that affect the complete diffraction pattern. This requires that additional parameters must be added to the fitting model. These extra parameters predict the peak positions and describe the peak shapes, in addition to the structural parameters, which determine reflection intensities. The peak positions are directly determined by the lattice constants plus one or more correction terms, which vary with the type of instrument. Many factors influence the shapes of diffraction peaks: instrumental effects, crystallite size and residual strain broadening. In addition, Rietveld analysis must model both non-Bragg scattering effects, air scattering and other instrumental imperfections, as well as systematic corrections to the intensities and the background. This is in contrast to the single-crystal case, where these effects are removed as part of the data preprocessing.

Thus, the parameters needed in a Rietveld fit fall into four categories: (i) structural parameters, which include atom positions, occupancies and displacement parameters; (ii) lattice constants; (iii) instrumental parameters, which will differ for different types of measurements, but will usually be independent of the sample; and (iv) sample-dependent parameters that may depend on the specific specimen in use, because of treatment history and sample-preparation effects.

In contrast, a single-crystal refinement only fits the first set of parameters, the structural parameters. The other three categories of parameters add additional complexity to a Rietveld fit. Further, the structural information in a powder-diffraction data set is usually reduced relative to a single-crystal data set. One reason for this is the reflection overlap that occurs for powders but not single crystals. In addition, however, the total background scattering that is spread out over the full Ewald sphere in the single-crystal measurement becomes concentrated into a line in powder diffraction and thus becomes a larger and less separable contribution. Thus, with powders, intensity measurements are less accurate and it is usually harder to discern weak reflections. For this reason, where good-quality single crystals are available, structural studies using them are usually to be preferred.

Despite the advantages of single-crystal measurements, powder diffraction makes valuable contributions to structural science. This is because for many materials only polycrystalline samples can be produced; this is particularly true early in the materials discovery process. For other materials, the single crystals that are available may not be compositionally representative of the bulk phase or may be marred by effects such as twinning, which hinder accurate measurement of structure factors from single crystals. A powder-diffraction experiment is also often much simpler than a single-crystal one, particularly under extreme conditions. Finally, it should be noted that some of the additional parameters determined in a Rietveld fit are valuable for physical characterization of the specimen, and thus Rietveld fits are also commonly used for texture, microstrain and crystallite size measurements. Finally, powder diffraction usually provides much greater accuracy and precision for lattice-constant determination than does a routine single-crystal measurement. For all these reasons Rietveld analysis is a growing field.

4.7.3. Multiphase and multiple data set fitting

For early Rietveld fits, if a material contained a minor impurity phase, the regions of the powder pattern surrounding peaks from that impurity had to be excluded from the fit. However, this can only be done where an impurity has a very simple structure or is present at very small concentrations. A better practice is to include structural information for both phases in the model to obtain an optimal fit. This allows the relative abundance of each phase in the mixture to be quantified, since the scale factor for each phase is proportional to the number of unit cells of that phase in the specimen. This in turn allows the relative phase abundance to be stated in weight or mass units. Most modern Rietveld analysis codes allow multiple phases to be included in a fit. This is now used routinely for quantification of crystalline phases in a material, for example in cement clinker materials where more than ten component phases may be identified. Adding a known amount of a crystalline phase (as an internal standard) can be used to allow the Rietveld method to quantify amorphous content as well.

In order to take best advantage when multiple measurements are made on a single sample, the Rietveld method was adapted to fit a single model to multiple data sets. The most obvious use for this is to combine results from neutrons with those from X-rays. As an example, a particular synthetic jarosite contains both vanadium and hydrogen atoms; a combined X-ray single-crystal/neutron powder study provided accurate information about both atoms, despite the insensitivity of X-rays to the location of hydrogen atoms and the insensitivity of neutrons to the location of vanadium atoms (Grohol *et al.*, 2003). Neither data set alone was sufficient to fully elucidate the structure. It can also be advantageous to perform a combined refinement even where all data sets are collected with a single type of data. This is sometimes done where diffractometer settings will optimize resolution in different Q ranges or where temperature or preferred-orientation settings are used to separate overlapped reflections (Von Dreele *et al.*, 2000; Baerlocher *et al.*, 2004). Now that high-quality powder-diffraction patterns may be collected in fractions of a second, it becomes possible to use Rietveld analysis for parametric refinements to map out structural transitions, such as phase, lattice and order-parameter changes with temperature, chemical potential, time *etc*.

4.7.4. The mechanism of Rietveld fitting

The computations in a Rietveld fit require minimizing the weighted sum of the squares of differences between the observed powder-diffraction data points, $y_{\text{obs},i}$, at position Q_i and simulated measurements, $y_{\text{calc},i}$, computed from the combined structural, instrumental and experimental model. Thus the fitting function, S,

$$S = \sum_i w_i \left(y_{\text{obs},i} - y_{\text{calc},i}\right)^2,$$

is minimized, where w_i is the weight value for $y_{\text{obs},i}$, which is related to its standard uncertainty by $w_i = \sigma^{-2}(y_{\text{obs},i})$, where $\sigma(y)$ is the expected experimental uncertainty on observation y. The minimization has been done historically with Newton–Raphson least squares [see Chapter 8.1 in Volume C (Prince & Boggs, 2006)]. The Levenberg–Marquardt modification of the Newton–Raphson algorithm improves convergence when variables are highly correlated by emphasizing the diagonal terms in the Hessian matrix, which moves the minimization closer to a steepest-descent algorithm. The method of singular value decomposition can be used to re-parameterize refinements to utilize more a more orthogonal set of parameters, reducing correlation by removing underdetermined degrees of freedom (Mercier *et al.*, 2006). The more modern Broyden–Fletcher–Goldfarb–Shanno (BFGS) algorithm has also been proven to work well, though it only approximates the Hessian. Note that the covariance matrix, which is the inverse of the Hessian, is used to determine uncertainties on fit parameters once convergence is reached (Prince, 2004).

The $y_{\text{obs},i}$ values above are the experimental measurements, while the calculated measurement values, $y_{\text{calc},i}$, are computed using a sum over reflections *hkl* near the current data point using the computed structure factors, F_{hkl}, and peak profile functions, $P(Q_{hkl} - Q_i)$, by

$$y_{\text{calc},i} = B_i + I(Q_i) \sum_{hkl} m_{hkl} F^2_{hkl} O_{hkl} P(Q_{hkl} - Q_i), \tag{4.7.1}$$

where B_i is the background at the point; $I(Q_i)$ represents the product of the intensity adjustment terms, which will include a scale factor and Lorentz–polarization corrections and may include wavelength- or angle-dependent correction terms, such as absorption corrections, spectral corrections *etc*. The m_{hkl} term is the multiplicity of reflection *hkl*; O_{hkl} is an optional intensity adjustment due to preferred orientation; and Q_{hkl} is the location of reflection *hkl*. The structure factors, F_{hkl}, are computed from Fourier transform of the scattering from the unit cell using the standard relationship. The units used for Q are usually the as-collected units, which may be an angle or time-of-flight, and thus Q_{hkl} will be computed using Bragg's law and the lattice constants, but corrections to adjust for deviations of the recorded position from the true Bragg value are needed. Typical corrections may be a scalar, to correct for a 2θ zero offset term, or a more complex function, to account for specimen displacement and transparency in a Bragg–Brentano diffractometer, may be employed (Chapter 3.1). In the case of TOF diffraction, calibration constants are used to convert the time of flight to absolute units and *vice versa*.

4.7.5. Types of profile functions

Three different computational approaches have been used for generation of the profile function, $P(Q_{hkl} - Q_i)$:

(1) Use empirical functions that reproduce the experimentally observed peak shapes, in some cases using *ad hoc* curves derived directly from the actual experimental data.

(2) Use physically based terms that are parameterized to model physical phenomena such as strain or crystallite broadening in generalized and approximate equations. This is the most commonly implemented approach.

(3) The fundamental-parameters method computes a peak-shape function through the convolution of every aberration arising from the diffraction instrument and from the sample, usually in terms of physically meaningful values, though often some *ad hoc* adjustments are also needed (Cheary & Coelho, 1992).

Each of the previous approaches has its adherents, although empirical peak-shape methods are likely to introduce small systematic errors in lattice constants, since they do not properly account for shifts in diffraction peaks due to low-angle asymmetric peak broadening (Finger *et al.*, 1994; van Laar & Yelon, 1984; Eddy *et al.*, 1986). The fitted values from an empirical peak shape have no physical meaning, but both physically based parameters and fundamental parameters will provide terms that further characterize a sample, for example with crystallite size or strain information. Of the two methods, application of fundamental parameters requires much closer attention to the details of the experimental geometry, but can add extra rigour to a result by demonstrating that the entire experiment is behaving in an understood and reproducible manner (NIST, 2010).

4.7.6. Observed structure-factor estimates

Rietveld also addressed a second difficult algorithmic problem in his 1969 work. This was to produce a simple and stable method for estimating the intensities for each reflection in the diffraction pattern. Deconvolution methods are slow and leave an insolvable ambiguity for the apportioning of intensities from reflections that have very close positions and thus are completely unresolved. The approach used by Rietveld notes that, for every computed point in the pattern, a proportion of the intensity from each reflection can be determined from equation (4.7.1), which can be rewritten as

$$(y_{\text{calc},i} - B_i)/I(Q_i) = \sum_{hkl} C_{hkl,i} F^2_{hkl},$$

where $C_{hkl,i}$ accounts for all the correction terms and peak proportion, which have been computed for the refinement. This equation can be inverted to relate the structure factor to a sum over i points in the diffraction pattern:

$$F^2_{hkl} = \sum_i (y_{\text{calc},i} - B_i)/\left[I(Q_i) C_{hkl,i}\right].$$

Note that, in practice, $C_{hkl,i}$ drops to negligible values for data points more than a few peak widths from the peak centre, so that only points near the reflection need to be considered in this sum. This relationship can then be used to apportion the observed intensity into an estimate of the observed structure factors $F_{\text{obs},hkl}$ by applying the same ratios of intensity values as are applied to each of the computed structure factors using

$$F^2_{\text{obs},hkl} = \sum_i (y_{\text{obs},i} - B_i)/\big[I(Q_i)C_{hkl,i}\big].$$

Since the $C_{hkl,i}$ values are determined using the crystal-structure model, the accuracy of the structure-factor estimates is only as good as the quality of that model, but this is often the best estimate that can be made.

These estimated structure factors, $F_{\text{obs},hkl}$, are commonly used in two ways. As will be discussed later, an R factor can be computed with them to compare the agreement between the $F_{\text{obs},hkl}$ and F_{hkl} values and they can be used for Fourier map computations. Note that, owing to the approximate nature of the structure-factor estimation, in practice only the strongest few peaks in a difference Fourier computed from $(F_{\text{obs},hkl} - F_{hkl})$ will indicate missing or extra scattering material from the structural model. Weaker peaks in Rietveld Fourier maps are more likely to be spurious than those from single-crystal diffraction where structure factors are determined directly.

4.7.7. Estimating observed structure factors without a structure

The Rietveld method has been applied to the problem of estimating reflection intensities when no structural information is known in two different ways. Pawley developed an algorithm similar to the Rietveld fit where reflection intensities are treated as refinable variables in place of refining structural parameters (Pawley, 1981; Chapter 3.5). To do this requires special treatment for exactly and very nearly overlapped reflections. The covariance matrix from a Pawley fit can be used to estimate the uncertainty in intensity apportionment for overlapped reflections, which can be applied to speed up computations for iterative *ab initio* structure solution algorithms (David *et al.*, 2006; Stephens & Huq, 2002; Pagola & Stephens, 2010).

The alternative to the Pawley technique, known as the Le Bail intensity extraction method, is a clever adaptation of the Rietveld intensity estimation algorithm (Chapter 3.5). This algorithm applies the Rietveld intensity estimation algorithm in an unconventional way. First, the simulated diffraction pattern is computed with all F_{hkl} values arbitrarily set to unity. This provides a set of $F_{hkl,I}$ values that are independent of any structural model. With these $F_{hkl,I}$ values the $F_{\text{obs},hkl}$ values are computed as before. The algorithm is iterated by replacing the previous F_{hkl} values with the just-determined $F_{\text{obs},hkl}$ values. Each time this replacement is done and the intensity extraction algorithm is repeated, the agreement between the observed and simulated pattern improves and within a few cycles the changes become insignificant. This method also treats reflection intensities as arbitrary values (somewhat similar to the Pawley approach) but a steepest-descent-type fit is used for the $F_{\text{obs},hkl}$ values. Where reflections are completely overlapped, the Le Bail method will apportion intensity to reflections according to their relative multiplicities. Von Dreele later modified the Le Bail approach to use a partial structural model to compute the initial F_{hkl} values rather than set them to unity (Larson & Von Dreele, 2004). This will often converge faster and provide a more accurate apportionment for overlapped intensities when the structural model is fairly complete.

Reflection intensities from the Pawley or Le Bail methods are useful for *ab initio* crystal structure solution by real-space or reciprocal-space approaches (see Chapters 4.2 and 4.3). These methods can also be useful to model a single impurity phase in a mixture, where that phase has a known unit cell but an unknown structure, or where the phase is highly textured or occurs as too few grains to provide representative intensities. Thus, the fit proceeds where the peaks arising from the impurity phase are treated as having arbitrary intensities and are subtracted as best as possible from the pattern.

The Pawley or Le Bail method is also valuable as a method for obtaining starting values for non-structural parameters in a crystallographic fit or occasionally for sample characterization, where perhaps only peak-broadening terms are desired. To do this, one must first optimize the reflection intensities and then introduce additional non-structural parameters into the fit. Pawley refinements tend to be more stable than Le Bail fits because of the decoupling of the steepest-descent fit of intensities and the least-squares fit of the other parameters, but with care both methods do work. Many Rietveld practitioners will use a Le Bail or Pawley refinement to establish initial estimates for lattice, peak-shape and background parameters before exploring the details of the crystal structure. During the initial structural refinements, the non-structural parameters are fixed at these initial estimates, which speeds and simplifies the structural fitting process. In the final stages of the refinement, these fixed parameters are again re-optimized along with the structural parameters.

4.7.8. Agreement factors

An important question in crystallography is how to quantify the quality of the fit between the model and the data. For this purpose, agreement factors, such as R factors, are commonly used. To determine the quality of a Rietveld fit, many different quantities have been proposed (Toby, 2006). The same problem faces all these agreement factors: a single value is being used to measure the quality of fitting to the peak shape, peak positions and background, as well as intensity mismatch errors, where the last quantity is most crucial for understanding the quality of the structural model. Attempts have been made to adjust these agreement factors to remove the background from consideration, but this cannot be done rigorously and no mechanism can separate the peak-shape and position errors from the intensity disagreements.

Another disadvantage of all powder-diffraction agreement factors is that they cannot be interpreted on an absolute scale to determine the quality of a fit. This is in contrast to single-crystal refinements, where quantities such as R_{wF} will have a relatively small range of values and are commonly, though perhaps overly, used as a judge of the quality of the experimental fit.

The most commonly used term for gauging the quality of a Rietveld fit is the weighted-profile R factor, R_{wp},

$$R_{\text{wp}} = \left[\sum_j w_j (y_{\text{obs},j} - y_{\text{calc},j})^2 / \sum_j w_j y^2_{\text{obs},j}\right]^{1/2}.$$

The R_{wp} term is sometimes compared to the statistically expected R factor, R_{exp},

$$R_{\text{exp}} = \left[(j - \nu)/\sum_j w_j (y_{\text{obs},j})^2\right]^{1/2},$$

but this comparison is built into a statistical quantity called the reduced χ^2 (chi-squared), which is defined as

$$\chi^2 = \frac{1}{j - v}\sum_j w_j (y_{\text{obs},j} - y_{\text{calc},j})^2 = \left(\frac{R_{\text{wp}}}{R_{\text{exp}}}\right)^2.$$

In the above the number of data points is j and the number of refined parameters is v. Closely related to the reduced chi-squared is the goodness of fit (GOF), where $\text{GOF}^2 = \chi^2$.

The R_{wp} value is a good metric to follow the progress of a refinement and can be used to compare how well different models match the same set of experimental data, but the values have no meaning on an absolute scale. This is made clear by a thought experiment in which the same pattern is measured twice, but for one measurement the background is artificially increased. If a refinement is performed on both sets of data, fits that are equivalent will be obtained (other than a difference in the background parameters). However, a much lower R_{wp} value will be seen for the data set with a higher background, simply because the $\sum_j w_j y^2_{\text{obs},j}$ term is larger because of the extra background intensity multiplied by the large number of points in the pattern. Even though there will be a large difference in the R_{wp} values, there will be no significant difference in the actual fit quality.

The reduced χ^2 does have a statistical expectation value of unity, but still cannot be used on an absolute scale as a judge of refinement quality. The expectation value can be understood by noting that when data are properly weighted, w_j is the square of the reciprocal of the standard uncertainty, or $w_i = 1/\sigma^2(y_{\text{obs},j})$. In a statistically ideal fit, where all differences between the observed and simulated measurements are due only to statistical fluctuations, the standard uncertainty, $\sigma(y_{\text{obs},i})$, is the expectation value for $[\langle(y_{\text{obs},j} - y_{\text{calc},j})^2\rangle]^{1/2}$. Thus, $\chi^2 = 1$ when no systematic errors are present and $\chi^2 > 1$ with an imperfect model (or stated equivalently, with systematic errors in the data), but if $\chi^2 < 1$ occurs, then at least some of the uncertainties must be overestimated. Thus, χ^2 provides information about how far the model is from an ideal fit, but only if the uncertainty estimates are accurate.

The reason why the reduced χ^2 should not be used as an absolute measurement of the quality of a structural fit is because, given a model with a certain imperfection, the poorer the quality of the data set, the closer the χ^2 value will be to unity. Note that, improving the data-set quality by counting longer to reduce the statistical uncertainty will decrease the average $\sigma(y_{\text{obs},j})$ values, resulting in an increase in χ^2. Improving the sensitivity of the data set to imperfections in the model, for example by improving resolution, or by measuring the pattern over a wider Q range, will increase the average values of $|y_{\text{obs},j} - y_{\text{calc},j}|$, likewise increasing χ^2.

Nonetheless, when χ^2 is significantly different from unity, the reason for this should be understood. Visual review of a graph showing the observed and computed patterns and their difference (or even better, with these results normalized by the weighting values) will show if there is a poor fit to the reflection intensities (implying an inaccurate structure), in comparison with problems in fitting the background, peak shape or peak positions, or even the presence of an unfitted minor impurity phase.

One other sometimes useful type of R factor is called the Bragg R factor. This is computed from the estimated reflection intensities in a manner similar to that carried out for single-crystal fits. There are several versions of this R factor, but the most commonly published one is R_F,

$$R_F = \sum_{hkl}\left|F_{\text{obs},hkl} - F_{\text{calc},hkl}\right| / \sum_{hkl}\left|F_{\text{obs},hkl}\right|.$$

Similarly, R_F^2 can be computed using F^2_{hkl} values or occasionally R_I is computed from reflection intensities, I_{hkl}. For this reason the terms R_{Bragg} or R_{B} are ambiguous in comparison with R_F and R_F^2. This agreement factor does try to appraise the differences between observed and computed values due to imperfections in the structural fit, but non-structural problems in the fit can interfere with the determination of the structure factors, raising the Bragg R factors. On the other hand, the intensity-partitioning model biases the R factor towards providing lower values. Nonetheless, it does provide some information about the quality of the crystallographic fit, but it should be kept in mind that this value has no statistical validity and will be overly sensitive to minor discrepancies in the most intense reflections since it is unweighted.

4.7.9. Restraints and constraints in Rietveld refinement

Since powder data usually provide considerably fewer independent observations of the material's structure than would a single-crystal experiment, it is often impossible to follow the crystallographers 'rule of thumb' to have ten independent structure-factor observations for each refined parameter. While every data point in a diffraction pattern is a statistically unique observation and appropriate for use in a statistical test (such as the Student T test), the number of observations providing information about the structure is much smaller (Altomare *et al.*, 1995; Sivia, 2000). This will be of the order of the number of discernible peaks in the pattern, counting locations where reflections are located even where no peak intensity is observed. When the number of observations is lower than desired for a model, it is often wise to reduce the degrees of freedom in the model, either by simplification or by introduction of penalty functions that prejudice the model towards results that have been well established (for example, common bond distances and angles). This is also common practice when large complex structures, such as proteins, are fitted using single-crystal data.

Models can be simplified by the introduction of constraints. Each constraint replaces two or more parameters with a single new parameter, resulting in a model with fewer degrees of freedom. Some crystallographic examples of this include replacing the six atoms comprising the C atoms in a phenyl ring with an idealized hexagonal arrangement of the six atoms. If this rigid body is allowed to move and rotate freely, there will now be at most only six positional parameters (three rotations and three translations) in place of the 18 positional parameters needed to describe six independent atoms. Another example of a constraint is where a choice is made that atoms of the same type and in similar bonding environments will have approximately the same isotropic displacement parameters by using one refinable parameter for the set in place of a parameter for each of the similar atoms. Constraints are implemented in different ways in modern Rietveld codes, but the ability to constrain multiple parameters into a single one was available even in Hugo Rietveld's original code.

The use of restraints (sometimes misleadingly called soft constraints) effectively adds new 'observations' to the data set used in fitting. These 'observations' are not directly measured for the sample, but may be found statistically for a wide range of materials or from other *a priori* knowledge. Restraints provide a target value for some value derived from the refined parameters, for example a bond distance or bond angle. The fitting function, F, is then expanded by an extra set of terms,

$$F = \sum_i w_i (y_{\text{obs},i} - y_{\text{calc},i})^2 + \sum_j w_j (r_{\text{in},j} - r_{\text{fit},j})^2$$

where $r_{\text{in},j}$ is the input value for the restraint and $r_{\text{fit},j}$ is the value derived from the model. The w_j term usually incorporates both an uncertainty in the $r_{\text{in},j}$ value and a weighting factor. It is common to make weights as large as or even larger than the number of data points in a refinement in the initial stages of a fit, so that the $r_{\text{fit},j}$ values are not allowed to diverge far from their restraints. Different Rietveld codes offer differing types of restraint functions.

Both restraints and constraints introduce the crystallographer's preconceptions about the model into the fit and thus can conceal an unexpected result (see Chapter 4.9). Thus, it is important to test that constraints and restraints are indeed appropriate. Note that when restraints and constraints are needed, it is because the number or accuracy of the observations is not sufficient to discern the correct model from others that introduce deviations that we expect to be implausible. However, we would not expect these implausible results to agree with the data much better than the 'correct' one does. Thus, when the restraints and constraints are removed or relaxed in the model, the fit quality should improve slightly (since there are now more degrees of freedom), but not very significantly. Should a much better fit be obtained without the constraints or restraints, this model should be examined carefully for evidence that inappropriate assumptions have been made. As an example, if all O atoms in a complex oxide are constrained to have the same U_{iso} value, then there may not be any direct evidence that one of the O-atom sites is only half occupied. Only when the constraint is removed will the U_{iso} value for the overfilled site rise significantly above that of the average, since twice as much scattering density has been placed in the model than is actually present. Refining or fixing the occupancy as half-filled for that site will lead to a much more accurate model, although the impact on the agreement factors may be small.

4.7.10. The order in which to introduce parameters in a fit

One challenge for crystallographers learning to use the Rietveld method is to understand in what sequence parameters should be varied when performing the fit. With a well behaved model, it should not matter in what order parameters are added to the model, but in practice this is only true when all of the starting parameter values are reasonably close to the optimal ones. When an attempt is made to fit too many parameters at once the refinement can diverge. A good example would be attempting to fit a pattern where the lattice constants and scale factor are both far from the correct values. If both sets of parameters are refined together, then the least-squares refinement can result in an improved fit by reducing the scale factor to a value close to zero, since most of the peak intensity is computed in areas where little is observed. Once the scale factor has been set to a very small value, the fit quality becomes highly insensitive to the values of the lattice parameters, since the computed pattern now contains only tiny peaks. At this point, the lattice constants are likely to refine to unreasonable values, since they have so little impact on the refinement. Once that happens, the refinement can be deemed as diverged – it is unlikely to find the global minimum for the refined parameters no matter how many cycles of fitting are tried. With some computer programs, parameters can refine to values that cause the program to crash, for example negative lattice constants. In such cases, manual intervention is needed to reset the model to a better starting point or to change the order in which parameters are introduced. As an example, if the previous refinement is started by fixing the scale factor manually to a reasonable value, to bring observed and calculated intensities on to the same scale, and there is some overlap between the observed and computed peaks, it is usually possible to refine the lattice parameters alone to reach a reasonable fit. Once that is done, the scale factor can be added to the fit. However, it is far better to start with accurate lattice parameters, in which case the scale factor and lattice parameters *can* be refined together initially. Often the easiest way to derive accurate lattice parameters is to index the pattern (see Chapter 3.4).

The rule of thumb for adding parameters to a refinement is this: one should successively add parameters to the fit in an order such that each new parameter or set of related parameters will result in the largest improvement of the fitting function. (This is a cumbersome way of saying 'deal with the biggest errors first'.) The experienced user of Rietveld refinements will have an intuitive feeling for this by graphically examining the differences between the observed and computed diffraction patterns. Note that it is rarely necessary to remove parameters from a fit once added, except when high levels of correlation occur. Instrumental parameters are best determined by fitting to data for standards or at least well characterized materials with the current instrumental settings before attempting an unknown. The process of fitting sample and structural parameters is much simpler without needing to establish good starting values for instrumental parameters as well.

While no recipe will fit all projects, a rough guide for the order in which to add parameters is to start by refining the scale factor and background, and then confirm that the lattice parameters are close to correct. If not, adding them as well may cause the refinement to fail, so one can try the approach described above or correct them manually and repeat the previous refinement. It is often useful to add a specimen-displacement parameter at this point when using Bragg–Brentano data, as displacement is often the largest source of systematic error in the peak positions. Once the scale, background and lattice parameters are fitted reasonably well, one must check that the computed peak profiles are a reasonable approximation to the experimental ones; if not, this will need to be addressed before going any further. If the structural parameters are quite far off, it may be difficult to improve the peak shapes by refining them. Best practice is to characterize the instrument response function for a diffractometer with a standard having minimal size and microstrain broadening prior to initiating Rietveld analysis on a sample, so that only profile contributions from sample size and microstrain need be considered. However, when this is not done, the compendium of profile coefficients from Kaduk & Reid (2011) may serve as useful refinement starting point. Alternately, a Le Bail or Pawley fit can be used to concentrate on fitting the profile terms.

If the computed pattern falls off much more quickly with increasing Q than the observed data, it usually indicates that the atomic displacement parameters are too high. Likewise, very low displacement parameters will cause the computed pattern to have a more gradual decrease in intensities. Surface roughness and beam spillover are often the cause of anomalously low displacement parameters, so these effects need to be understood and eliminated. If either is true at this stage in the refinement, it may be best to refine a single overall U_{iso} or B_{iso} value for all atoms. However, if it appears that the discrepancies between the observed and computed patterns are largely independent of Q, optimization of displacement parameters may be deferred until later.

Once one has obtained reasonable values for the non-structural parameters previously discussed and the atomic displacement parameters are of the right order of magnitude, one can include the refinement of atomic coordinates. Start by adding only the atoms that contribute most to the pattern – high-multiplicity and high-Z atoms (for X-rays) or high-scattering-length atoms for neutrons. Once this is done, the movements of atoms should be reviewed by keeping track of bond distances and angles. Should these values move outside of a reasonable range, the refinement may be diverging. This can be addressed through introduction of bond-distance constraints with a high weight, to keep the structure from drifting off to something implausible. Once all atomic positions, consistent with symmetry constraints, have been refined, one then usually adds isotropic atomic displacement parameters ($U_{\rm iso}$ values) for individual atoms to the refinement, starting with atoms that have the greatest scattering power. In more complex structures it may be necessary to assign a single $U_{\rm iso}$ value to a group of atoms with similar mass and coordination.

It is worthwhile performing a refinement where all the isotropic displacement parameters ($U_{\rm iso}$'s) are refined freely even where this model has too many parameters for the number of observations. The reason for this is to look for individual $U_{\rm iso}$ values that differ significantly ($\gg 3\sigma$) from what would be expected either for similar materials under similar conditions or for other atoms in the material. Values of $U_{\rm iso}$ that are very small or negative may indicate that the model is under-representing the scattering density on that site, perhaps because the wrong type of atom has been placed there or partial occupancy has been incorrectly assumed. Large values of $U_{\rm iso}$ are of greater concern. These can indicate that too much scattering density is present in the model, perhaps as a consequence of unmodelled vacancies or incorrect site assignments *etc*. Note that when data are collected over a narrow Q range (common with Cu $K\alpha$ data), displacement parameters are usually not well determined and it is difficult to learn much from the $U_{\rm iso}$ values. Unless data are collected over a very wide Q range, it is usually impossible to refine occupancy factors and displacement parameters for the same site.

If a good fit is not obtained at this point, one should review a difference Fourier map to look for atom sites that are missing from the model. Preferred orientation or anisotropic broadening will sometimes produce large deviations between observed and computed intensities and a good crystallographic fit may be impossible without including appropriate terms in the model.

Once the crystallographic model has been fitted well to the data, one should ensure that all appropriate non-structural parameters (for example, the peak-shape parameters) are added to the refinement, if not done previously; likewise, the correction terms for diffractometer positioning calibration, for example, 2θ zero point or sample displacement *etc.*, should be included.

To complete the refinement, it is worthwhile to consider whether preferred orientation or anisotropic broadening may be present at a subtler level. Adding the appropriate terms to the model and seeing if the agreement improves significantly is a way to test for this. If significant improvement in $R_{\rm wp}$ or χ^2 is not seen, reset the terms to remove the correction and remove the parameters from the fit. Also, at the end of the fitting process, it is good to see whether restraints can be removed from the model, or at least whether their weights can be reduced significantly. With data of exceptional quality, one may even try anisotropic refinement for atoms that dominate the scattering.

It is very important to review the final Rietveld fit graphically, to visually identify and understand the sources of discrepancies between the fit and the observed pattern. It is common to try out many different options for treating remaining discrepancies. It is equally important to review the model for chemical plausibility (Kaduk, 2007*a*,*b*; Chapter 4.9). Past members of the IUCr Commission on Powder Diffraction have published an excellent guide to the practice of conducting and reporting a Rietveld refinement (McCusker *et al.*, 1999).

4.7.11. Examples

Several detailed tutorials on Rietveld fitting are provided with the *GSAS-II* software system (Toby & Von Dreele, 2013) at https://subversion.xray.aps.anl.gov/pyGSAS/trunk/help/Tutorials.html and http://bit.ly/GSASIItutorials. They include:

$Y_3(Fe_{0.58}Al_{0.42})_2(Al_{0.70}Fe_{0.30})_3O_{12}$ – an yttrium iron aluminium garnet using constant-wavelength neutron data collected on the D1a powder diffractometer at ILL, using a wavelength of 1.909 Å.

$Ca_5F(PO_4)_3$ – fluoroapatite using constant-wavelength laboratory X-ray powder data.

$PbSO_4$ – lead sulfate using combined neutron (D1a at ILL, λ = 1.909 Å) and laboratory Bragg–Brentano (Cu $K\alpha$ radiation) powder data. The neutron pattern was collected at low temperature and the X-ray pattern was collected at ambient conditions, so the lattice parameters differ for the two data sets.

$Na_2Ca_3Al_2F_{14}$ (NAC) – sodium calcium aluminium fluoride using data collected at ambient conditions using both synchrotron (11-BM, Advanced Photon Source) and TOF neutron data (POWGEN, Spallation Neutron Source). The sample contains a CaF_2 (unreacted starting material) impurity.

$CuCr_2O_4$ – a sequential refinement using multiple data sets collected from 7 to 300 K.

4.7.12. Conclusions

Rietveld analysis is a complex process, since it must fit structural, sample and instrumental terms, but it can provide results that cannot be obtained in other ways or values at their ultimate precision. Structural determination from single-crystal diffraction is usually preferred where appropriate specimens are available, but for many materials or measurement conditions powder diffraction is preferred. For this reason, use of Rietveld analysis is growing.

My knowledge of this field and its history has benefited greatly from a large number of gracious mentors, who took the time to talk or correspond with me during my younger years. These individuals include Drs David Cox, Judith Stalick, Robert Von Dreele, Frank Rotella, Jim Jorgensen, Alan Hewat, Ted Prince, Tony Santoro, Ray Young and many others; I cannot thank them enough. I also thank Dr Diane P. Toby for her efforts to help me write this more clearly. This work would not have been completed without the US Department of Energy (DOE) support of the Advanced Photon Source, an Office of Science User Facility operated for the DOE Office of Science by Argonne National Laboratory, through DOE Contract No. DE-AC02-06CH11357.

References

Albinati, A. & Willis, B. T. M. (1982). *The Rietveld method in neutron and X-ray powder diffraction. J. Appl. Cryst.* **15**, 361–374.

Altomare, A., Cascarano, G., Giacovazzo, C., Guagliardi, A., Moliterni, A. G. G., Burla, M. C. & Polidori, G. (1995). *On the number of statistically independent observations in a powder diffraction pattern. J. Appl. Cryst.* **28**, 738–744.

Baerlocher, C., McCusker, L. B., Prokic, S. & Wessels, T. (2004). *Z. Kristallogr.* **219**, 803–812.

Cagliotti, G., Paoletti, A. & Ricci, F. P. (1958). *Nucl. Instrum.* **3**, 223.

Cheary, R. W. & Coelho, A. (1992). *A fundamental parameters approach to X-ray line-profile fitting. J. Appl. Cryst.* **25**, 109–121.

Coelho, A. (2007). *TOPAS: General Profile and Structure Analysis Software for Powder Diffraction Data.* http://www.topas-academic.net/.

David, W. I. F., Shankland, K., van de Streek, J., Pidcock, E., Motherwell, W. D. S. & Cole, J. C. (2006). *DASH: a program for crystal structure determination from powder diffraction data. J. Appl. Cryst.* **39**, 910–915.

Debye, P. & Scherrer, P. (1916). *Phys. Z.* **17**, 277–283.

Eddy, M. M., Cheetham, A. K. & David, W. I. F. (1986). *Powder neutron diffraction study of zeolite Na ZK-4; an application of new functions for peak shape and asymmetry. Zeolites*, **6**, 449–454.

Finger, L. W., Cox, D. E. & Jephcoat, A. P. (1994). *A correction for powder diffraction peak asymmetry due to axial divergence. J. Appl. Cryst.* **27**, 892–900.

Grohol, D., Huang, Q. Z., Toby, B. H., Lynn, J. W., Lee, Y. S. & Nocera, D. G. (2003). *Powder neutron diffraction analysis and magnetic structure of kagomé-type vanadium jarosite. Phys. Rev. B*, **68**, 094404.

Hewat, A. (1973). *UKAERE Harwell Report RRL*, **73**, 897.

Hull, A. W. (1917). *Phys. Rev.* **10**, 661.

Izumi, F. & Momma, K. (2007). *Three-dimensional visualization in powder diffraction. Solid State Phenom.* **130**, 15–20.

Jorgensen, J. D., Faber, J., Carpenter, J. M., Crawford, R. K., Haumann, J. R., Hitterman, R. L., Kleb, R., Ostrowski, G. E., Rotella, F. J. & Worlton, T. G. (1989). *Electronically focused time-of-flight powder diffractometers at the intense pulsed neutron source. J. Appl. Cryst.* **22**, 321–333.

Kaduk, J. A. (2007*a*). *Chemical reasonableness in Rietveld analysis: organics. Powder Diffr.* **22**, 74–82.

Kaduk, J. A. (2007*b*). *Chemical reasonableness in Rietveld analysis: inorganics. Powder Diffr.* **22**, 268–278.

Kaduk, J. A. & Reid, J. (2011). *Typical values of Rietveld instrument profile coefficients. Powder Diffr.* **26**, 88–93.

Laar, B. van (1965). *Phys. Rev.* **138**, A584–A587.

Laar, B. van & Schenk, H. (2018). *The development of powder profile refinement at the Reactor Centre Netherlands at Petten. Acta Cryst.* A**74**, 88–92.

Laar, B. van & Yelon, W. B. (1984). *The peak in neutron powder diffraction. J. Appl. Cryst.* **17**, 47–54.

Larson, A. C. & Von Dreele, R. B. (2004). Report LAUR 86-748. Los Alamos National Laboratory, USA.

Loopstra, B. O. & Rietveld, H. M. (1969*a*). *The structure of some alkaline-earth metal uranates. Acta Cryst.* B**25**, 787–791.

Loopstra, B. O. & Rietveld, H. M. (1969*b*). *Further refinement of the structure of* WO_3*. Acta Cryst.* B**25**, 1420–1421.

Lutterotti, L., Matthies, S. & Wenk, H.-R. (1999). *MAUD: a friendly Java program for material analysis using diffraction. IUCr Commission on Powder Diffraction Newsletter*, Vol. 21, pp. 14–15.

McCusker, L. B., Von Dreele, R. B., Cox, D. E., Louër, D. & Scardi, P. (1999). *Rietveld refinement guidelines. J. Appl. Cryst.* **32**, 36–50.

Margiolaki, I., Wright, J. P., Wilmanns, M., Fitch, A. N. & Pinotsis, N. (2007). *Second SH3 domain of ponsin solved from powder diffraction. J. Am. Chem. Soc.* **129**, 11865–11871.

Mercier, P. H. J., Le Page, Y., Whitfield, P. S. & Mitchell, L. D. (2006). *SVDdiagnostic, a program to diagnose numerical conditioning of Rietveld refinements. J. Appl. Cryst.* **39**, 458–465.

Morsli, K., de la Torre, Á. G., Ángeles, G., Stöber, S., Cuberos, A. J. M., Zahir, M. & Aranda, M. A. G. (2007). *Quantitative phase analysis of laboratory-active belite clinkers by synchrotron powder diffraction. J. Am. Ceram. Soc.* **90**, 3205–3212.

NIST (2010). *Standard reference material 660b* LaB_6 *line position and line shape standard for powder diffraction.* US Department of Commerce, Gaithersburg, Maryland, USA.

Pagola, S. & Stephens, P. W. (2010). *PSSP, a computer program for the crystal structure solution of molecular materials from X-ray powder diffraction data. J. Appl. Cryst.* **43**, 370–376.

Pawley, G. S. (1981). *Unit-cell refinement from powder diffraction scans. J. Appl. Cryst.* **14**, 357–361.

Petricek, V., Dusek, M. & Palatinus, L. (2006). *Jana2006. The Crystallographic Computing System.* http://jana.fzu.cz/.

Prince, E. (1981). *Comparison of profile and integrated-intensity methods in powder refinement. J. Appl. Cryst.* **14**, 157–159.

Prince, E. (2004). *Mathematical Techniques in Crystallography and Materials Science*, 3rd ed. New York: Springer-Verlag.

Prince, E. & Boggs, P. T. (2006). *International Tables for Crystallography*, Vol. C, *Mathematical, Physical and Chemical Tables*, 1st online ed., pp. 678–688. Chester: International Union of Crystallography.

Rietveld, H. M. (1966). *The crystal structure of some alkaline earth metal uranates of the type* M_3UO_6*. Acta Cryst.* **20**, 508–513.

Rietveld, H. M. (1967). *Line profiles of neutron powder-diffraction peaks for structure refinement. Acta Cryst.* **22**, 151–152.

Rietveld, H. M. (1969). *A profile refinement method for nuclear and magnetic structures. J. Appl. Cryst.* **2**, 65–71.

Rodríguez-Carvajal, J. (1993). *Recent advances in magnetic structure determination by neutron powder diffraction. Physica B*, **192**, 55–69.

Sakata, M. & Cooper, M. J. (1979). *An analysis of the Rietveld refinement method. J. Appl. Cryst.* **12**, 554–563.

Sivia, D. S. (2000). *The number of good reflections in a powder pattern. J. Appl. Cryst.* **33**, 1295–1301.

Stephens, P. W. & Huq, A. (2002). *Trans. Am. Crystallogr. Assoc.* **37**, 125–142.

Toby, B. H. (2001). *EXPGUI, a graphical user interface for GSAS. J. Appl. Cryst.* **34**, 210–213.

Toby, B. H. (2006). *R factors in Rietveld analysis: how good is good enough? Powder Diffr.* **21**, 67–70.

Toby, B. H. & Von Dreele, R. B. (2013). *GSAS-II: the genesis of a modern open-source all purpose crystallography software package. J. Appl. Cryst.* **46**, 544–549.

Toby, B. H. & Von Dreele, R. B. (2014). *Powder Diffr.* **29**, S2–S6.

Von Dreele, R. B. (1999). *Combined Rietveld and stereochemical restraint refinement of a protein crystal structure. J. Appl. Cryst.* **32**, 1084–1089.

Von Dreele, R. B., Jorgensen, J. D. & Windsor, C. G. (1982). *Rietveld refinement with spallation neutron powder diffraction data. J. Appl. Cryst.* **15**, 581–589.

Von Dreele, R. B., Stephens, P. W., Smith, G. D. & Blessing, R. H. (2000). *The first protein crystal structure determined from high-resolution X-ray powder diffraction data: a variant of T3R3 human insulin–zinc complex produced by grinding. Acta Cryst.* D**56**, 1549–1553.

Wiles, D. B. & Young, R. A. (1981). *A new computer program for Rietveld analysis of X-ray powder diffraction patterns. J. Appl. Cryst.* **14**, 149–151.

Worlton, T. G., Jorgensen, J. D., Beyerlein, R. A. & Decker, D. L. (1976). *Nucl. Instrum. Methods*, **137**, 331–337.

Young, R. A. (1993). *The Rietveld Method*, edited by R. A. Young, pp. 1–38. Oxford University Press.

Young, R. A., Mackie, P. E. & von Dreele, R. B. (1977). *Application of the pattern-fitting structure-refinement method of X-ray powder diffractometer patterns. J. Appl. Cryst.* **10**, 262–269.

International Tables for Crystallography (2019). Vol. H, Chapter 4.8, pp. 473–488.

4.8. Application of the maximum-entropy method to powder-diffraction data

O. V. Magdysyuk, S. van Smaalen and R. E. Dinnebier

4.8.1. Introduction

Applications of the maximum-entropy method (MEM) to X-ray powder-diffraction data include the determination of accurate charge-density and spin-density distributions, localization of the missing atoms in incomplete structure models, and analysis of the modulation functions for aperiodic structures. In all these applications the MEM must overcome the limitations imposed by the reduced information content of powder-diffraction data as compared with single-crystal diffraction data. At the same time, great care should be taken not to apply the MEM outside its range of validity. Results obtained by the MEM should be carefully checked.

The electron-density distribution is related to the structure factors in X-ray diffraction by a Fourier transformation. This relationship is used in many applications of the MEM, and the most accurate analyses are based on the availability of a complete set of structure factors up to a certain high resolution. Single-crystal X-ray diffraction experiments provide accurate values for the amplitudes of, in principle, all the structure factors. Phases of these structure factors may be obtained from a structural model or other sources. The information obtained by X-ray powder-diffraction experiments is even more limited than the missing phase information in single-crystal diffraction data, owing to the projection of three-dimensional reciprocal space onto the one-dimensional 2θ axis and the resulting intrinsic and accidental peak overlap (Fig. 4.8.1). The latter effect increases with increasing size of the unit cell. The intensities of individual reflections *hkl* can still be extracted from powder-diffraction data, but their accuracy depends on the degree of overlap of reflections and on the quality of the powder pattern. Thus, powder averaging of the diffraction data strongly reduces its information content. The typical resolution of powder-diffraction data of $[(\sin\theta)/\lambda]_{\max} \simeq 0.6\ \text{Å}^{-1}$ prevents the determination of accurate electron densities by means of multipole refinements or Fourier transformation.

In neutron and X-ray scattering, the problem of the complex Fourier inversion of a limited set of noisy data has to be solved to determine the corresponding real-space scattering density. The electron (nuclear) density $\rho(\mathbf{r})$ in the unit cell of an ideal crystal is the inverse Fourier transform of an infinite number of structure factors $F(\mathbf{H})$:

$$\rho(\mathbf{r}) = \frac{1}{V}\sum_{\mathbf{H}} F(\mathbf{H})\exp\left(-2\pi i\mathbf{H}^T\cdot\mathbf{r}\right), \qquad (4.8.1)$$

where $\mathbf{H} = hkl$ is a reciprocal-lattice vector, V is the volume of the (direct) unit cell and $\mathbf{r} = (x, y, z)$ is the position vector of a point in direct space. The summation in equation (4.8.1) extends over the entire reciprocal lattice.

Most experiments provide a limited number of observed structure factors $F_{\rm obs}(\mathbf{H})$. Thus the summation runs over a finite number of Fourier amplitudes, and the Fourier transform is affected by series-termination errors (*e.g.* spurious peaks with positive densities that do not correspond to atoms in the structure, or local minima of unphysical negative densities). It has been shown that a Fourier map free from series-termination effects can be obtained by Fourier inversion of a complete set of structure factors up to at least $\sin(\theta)/\lambda = 6\ \text{Å}^{-1}$ (de Vries *et al.*, 1996; Roversi *et al.*, 1998; Mondal *et al.*, 2012), a resolution far beyond any realistic experimental resolution. Another disadvantage of the Fourier synthesis for computing electron densities is its inability to incorporate additional information about the density map, such as enforcing strict positivity of this map.

The concept of the entropy of a map of strictly positive values goes back to Shannon (1948*a*,*b*). The term ‘informational entropy’ refers to the mathematical similarities between this concept and the thermodynamic entropy. Maximizing the entropy of a map has become a powerful tool for solving reconstruction problems suffering from incomplete and/or noisy information. This method forms the basis for statistical mechanics and it plays an important role in the analysis of experimental data in a wide range of fields, such as astronomy, medicine, economics and condensed-matter physics. Ideally, the MEM gives a distribution that is consistent with the given information, is least biased with respect to missing information and does not introduce correlations in the results beyond those that are required by the data (French, 1978; Shore & Johnson, 1980, 1983; Gull & Skilling, 1984; Navaza *et al.*, 1983; Navaza, 1985, 1986; Livesey & Skilling, 1985). From the maps that fit the data, the criterion of maximum entropy (MaxEnt) selects the map with the least input information, thus giving the most probable result.

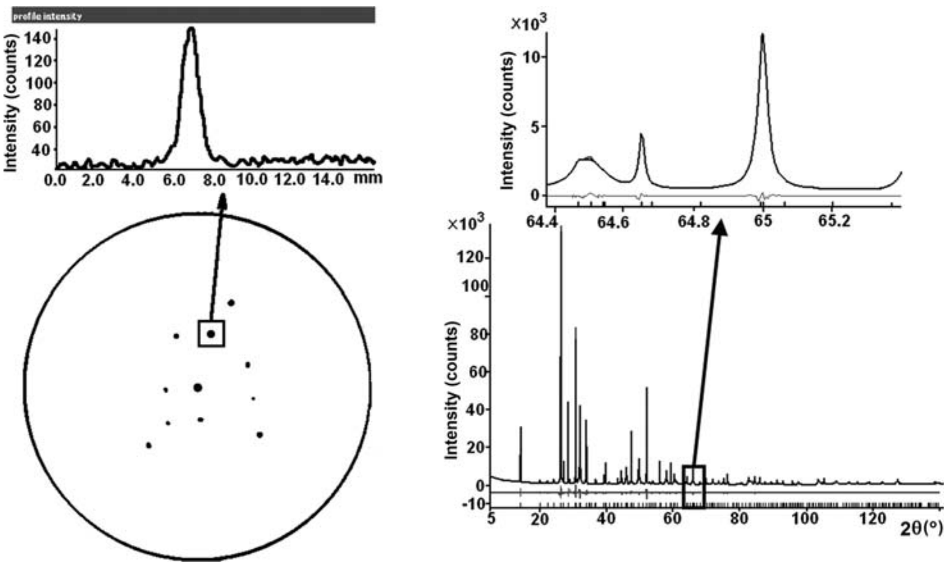

Figure 4.8.1
Single-crystal (left) and powder (right) X-ray diffraction data for Pb_3O_4. The powder-diffraction pattern includes overlapping reflections.

Copyright © 2019 International Union of Crystallography

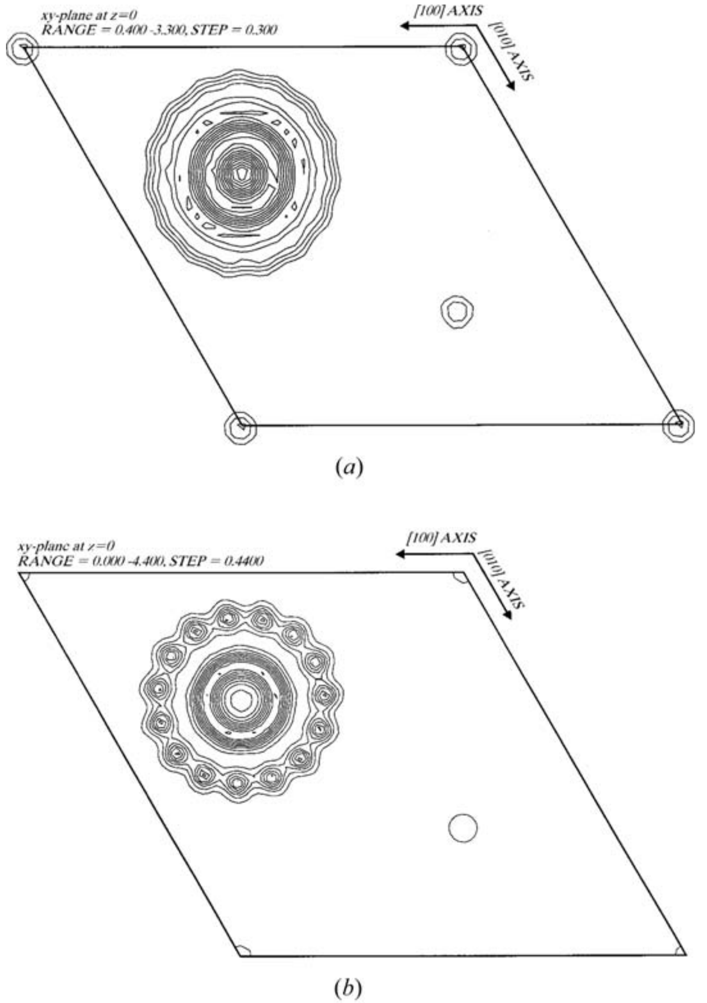

Figure 4.8.2
Electron-density distribution for threefold disordered pentamethylcyclopentadienyllithium (Li[$C_{10}H_{15}$], LiCp*). Shown are sections containing: (*a*) the planar fivefold ring in the Fourier map based on $F_{\rm obs}$, $\varphi^{\rm calc}$; (*b*) an MEM map based on $F_{\rm obs}$, $\varphi^{\rm calc}$ up to a resolution of $[\sin(\theta)/\lambda]_{\max} = 0.6$ Å^{-1} (from Dinnebier *et al.*, 1999).

The electron density in the unit cell is one type of map with strictly positive values, which thus has an entropy according to Shannon (1948*a*,*b*). The concept of entropy maximization was introduced into the field of crystallography to handle series-termination effects in Fourier maps. The MEM can successfully work with structure factors from powder diffraction for which $[\sin(\theta)/\lambda]_{\max} \geq 0.6$ Å^{-1}. Series-termination effects are much less prominent in MEM-optimized electron-density maps than in Fourier maps obtained with the same data. This is illustrated by application of both methods to the diffraction data of LiCp* (with structure-factor amplitudes $F_{\rm obs}$ and phases $\varphi^{\rm calc}$ calculated for a structure model with threefold disorder of the cyclopentadienyl ring; Dinnebier *et al.*, 1999). The electron density of the Fourier map exhibits almost cylindrical symmetry and individual atoms cannot be discerned (Fig. 4.8.2*a*), while the MEM electron density exhibits local maxima for each of the fifteen disordered positions of the methyl carbon atoms along the ring (Fig. 4.8.2*b*).

Another example is the electron-density distribution of Si (Fig. 4.8.3) calculated from powder X-ray diffraction data $F_{\rm obs}$ and phases $\varphi^{\rm calc}$ from a structure model (Sakata & Sato, 1990; de Vries *et al.*, 1996). The inverse Fourier transformation does show the atomic maxima, but it also contains severe series-termination effects within the regions of chemical bonds. On the other hand, the MEM applied to the same data but now using a procrystal electron density as prior or reference density clearly shows the electron density within the chemical bonds between the Si atoms. From Fig. 4.8.3, it follows that the Fourier map is not suitable for accurate charge-density analysis.

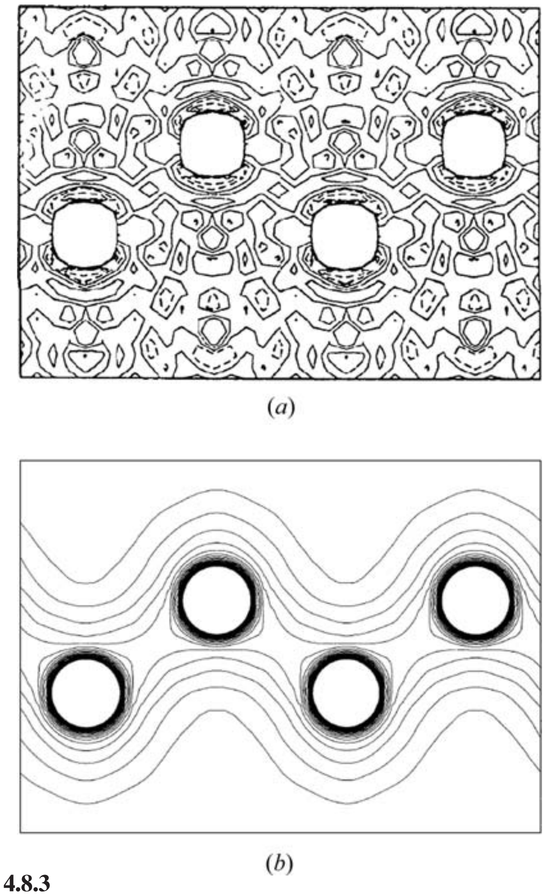

Figure 4.8.3
Electron-density distribution in the (110) plane of Si, calculated from powder X-ray diffraction data. (*a*) Inverse Fourier transform based on $F_{\rm obs}$, $\varphi^{\rm calc}$, contour level from −2.4 to 1.6 e Å^{-3} with step size 0.8 e Å^{-3} (from Sakata & Sato, 1990); (*b*) MEM electron density based on $F_{\rm obs}$, $\varphi^{\rm calc}$ (with procrystal prior); contour level from 0 to 2.5 e Å^{-3} with step size 0.1 e Å^{-3}. [Reprinted with permission from de Vries *et al.* (1996). Copyright (1996) American Physical Society.]

4.8.2. The principle of maximum entropy

The success of the MEM for deriving accurate electron-density (or nuclear-density) distributions from powder-diffraction data relies on the fact that these density maps are strictly positive. The entropy S of a discrete electron density is defined as

$$S = -\sum_{i=1}^{N_{\rm pix}} \left[-\rho_i + \rho_i^{\rm prior} + \rho_i \ln\left(\frac{\rho_i}{\rho_i^{\rm prior}}\right)\right], \qquad (4.8.2)$$

where the electron density is represented by its values $\rho_i = \rho(\mathbf{r}_i)$ on a sufficiently fine grid of $N_1 \times N_2 \times N_3 = N_{\rm pix}$ pixels over the unit cell, $\mathbf{r}_i$ being the position of pixel i. The grid must obey the crystal symmetry: each grid point must be transformed onto itself or onto another grid point by all symmetry operators. The values of $\rho_i^{\rm prior}$ define the prior (or reference) electron density. The prior density can be a constant function, thus called a flat or uniform prior. Alternatively, it can represent any desirable distribution of the available electrons over the unit cell.

Analysis of the electron-density distribution in the unit cell requires the determination of the values ρ_i at every point i of the grid. Of all possible electron-density maps only some are consistent with the measured diffraction data. The basic principle of the MEM is that the optimal image is defined to be the image with the maximum value of the entropy functional S, while one or more constraints of the type $C_j = 0$ ($j = 1, \ldots, N_C$) are fulfilled. The constraints should include at least one constraint involving the observed data. The technique of maximizing the entropy favours smooth maps, since the unconstrained maximum of S [equation (4.8.2))] is given by the prior density: $\rho(\mathbf{r}_i) = \rho^{\text{prior}}(\mathbf{r}_i)$.

4.8.3. Prior densities in MEM calculations

As part of Bayesian statistics, the MEM includes the so-called prior electron density ('prior' in short), equation (4.8.2). The prior is an essential part of the MaxEnt formalism, especially for powder-diffraction data. Fine features of the electron density, like the atomic charges or the distribution of the electron density within chemical bonds, are only revealed by the MEM if a sufficiently informative prior is employed (Zheludev *et al.*, 1995; Schotte *et al.*, 1995; de Vries *et al.*, 1996; Roversi *et al.*, 1998; Papoular *et al.*, 2002; Palatinus & van Smaalen, 2002; van Smaalen *et al.*, 2003; Buchter *et al.*, 2011). The same condition holds for MaxEnt reconstruction of extended X-ray absorption fine structure (EXAFS) analysis (Gull & Skilling, 1984).

The prior electron density is chosen to reflect as much as possible our state of knowledge about the true electron density. The best prior that can be obtained from a standard Rietveld refinement of powder-diffraction data is the thermally smeared electron density of the independent-atom model (IAM). The IAM density is a superposition of the spherically symmetric electron densities of free atoms convoluted with their thermal motion and placed at the positions in the structure model (Palatinus, 2003). An electron density constructed in this way is called a procrystal electron density [$\rho^{\text{IAM}}(\mathbf{r})$]. The IAM describes the major part of the electron density, but it does not fully account for the effects of bonding on the electron density. The deformation of the electron density due to the bonding is determined by the difference $\rho^{\text{MEM}} - \rho^{\text{IAM}}$ (van Smaalen *et al.*, 2003; Palatinus, 2003).

Recently, procrystal electron densities free from series-termination effects have been created by inverse Fourier transform of the structure factors calculated for an IAM or a multipole model up to a resolution of $\sin(\theta)/\lambda > 6.0$ Å^{-1} (Mondal *et al.*, 2012). An alternative method (Papoular *et al.*, 2002) is based on the evaluation of the electron density by means of an analytical Fourier transform, using the analytical approximation of the atomic form factors:

$$f_a\left(\frac{\sin\theta}{\lambda}\right) = \sum_{i=1}^{n} a_i \exp\left(-b_i \frac{\sin^2\theta}{\lambda^2}\right), \tag{4.8.3}$$

where a_i and b_i have been determined by comparison with the atomic wave functions, with $n = 5$ in Waasmaier & Kirfel (1995), and with $n = 6$ in Su & Coppens (1997) and Macchi & Coppens (2001).

For MEM calculations the atomic form factor in equation (4.8.3) should be expressed as a function of the diffraction vector $\mathbf{H}$ in the reciprocal crystal coordinates (Papoular *et al.*, 2002; Palatinus, 2003):

$$f_a(\mathbf{H}) = \sum_{i=1}^{n} a_i \exp\left(-\frac{b_i}{4}|\mathbf{H}|^2\right) = \sum_{i=1}^{n} a_i \exp\left(-\frac{b_i}{4}\mathbf{H}^T \boldsymbol{G}^* \mathbf{H}\right), \tag{4.8.4}$$

where $\boldsymbol{G}^*$ is the reciprocal metric tensor

$$G^*_{ij} = \mathbf{a}^*_i \cdot \mathbf{a}^*_j. \tag{4.8.5}$$

The anisotropic dynamic atomic form factor is defined as a convolution of the static atomic electron density with the anisotropic harmonic thermal motion of the atom (Palatinus, 2003), and is expressed in reciprocal space by multiplying the atomic form factor by the corresponding Debye–Waller factor that involves the displacement tensor $\boldsymbol{U}$ [*International Tables for Crystallography*, Volume B (Shmueli, 1996)]. This gives the anisotropic dynamic atomic form factor d_a,

$$d_a(\mathbf{H}) = \sum_{i=1}^{n} a_i \exp\left(-\frac{b_i}{4}\mathbf{H}^T \boldsymbol{G}^* \mathbf{H}\right) \exp\left(-2\pi^2 \mathbf{H}^T \mathbf{A}^* \boldsymbol{U} \mathbf{A}^* \mathbf{H}\right). \tag{4.8.6}$$

The matrix $\mathbf{A}^*$ is a diagonal matrix containing the lengths of the reciprocal-space basis vectors $\mathbf{a}^*_i$:

$$A^*_{ii} = \left|\mathbf{a}^*_i\right|^2; \quad A^*_{ij} = 0 \text{ for } i \neq j, \tag{4.8.7}$$

$$\begin{aligned} d_a(\mathbf{H}) &= \sum_{i=1}^{n} a_i \exp\left[-\mathbf{H}^T\left(\frac{b_i}{4}\boldsymbol{G}^* + 2\pi^2 \mathbf{A}^* \boldsymbol{U} \mathbf{A}^*\right)\mathbf{H}\right] \\ &= \sum_{i=1}^{n} a_i \exp\left(-\mathbf{H}^T \boldsymbol{M}_i \mathbf{H}\right), \end{aligned} \tag{4.8.8}$$

where $\boldsymbol{M}_i = [(b_i/4)\boldsymbol{G}^* + 2\pi^2 \mathbf{A}^* \boldsymbol{U} \mathbf{A}^*]$. The dynamic electron density of an atom is given by the Fourier transform of d_a:

$$\rho_a(\mathbf{r}) = |\boldsymbol{G}^*|^{1/2} \sum_{i=1}^{n} a_i \frac{\left|\boldsymbol{M}_i^{-1}\right|}{(2\pi)^{3/2}} \exp\left(-\mathbf{r}^T M_i^{-1} \mathbf{r}\right). \tag{4.8.9}$$

Finally, the procrystal electron density is obtained as the sum of atomic electron densities.

The prior density can be a constant (flat prior) with a value equal to the average electron density in the unit cell. Experience has shown that in the case of a uniform (flat) prior, the MEM-reconstructed electron density contains artifacts of larger magnitudes than the electron densities in bonding regions. Such MEM densities are thus not suitable for the investigation of the fine features of the electron densities. Use of a procrystal prior electron density reduces the artifacts and the resulting MEM-reconstructed electron density contains information about the redistribution of the electron density due to bonding and gives more accurate atomic charges.

Ongoing debates about the need to use a prior density in MEM calculations and about the type of prior density arise from misunderstandings of the role of the prior density in the procedure for applying the MEM for the determination of accurate charge-density distributions, and of the possibilities and limitations of the method. The prior density provides the correct estimate of the initial values of the structure factors of missing reflections and decreases the dynamic range of MEM calculations, thus making the MEM calculations numerically more stable.

The MEM reconstructions of the electron density of simple structures of Si and Be were initially performed with flat priors and revealed non-nuclear maxima in the electron density between the Si—Si and Be—Be bonds (Sakata & Sato, 1990; Iversen *et al.*, 1995). These non-nuclear maxima are not artifacts intrinsic to the MEM, but they represent low-level noise due to the use of a flat prior and a data set of limited resolution. They are not present in MEM electron-density maps calculated with procrystal densities (de Vries *et al.*, 1996). The sets of structure factors that were not measured (usually high-angle reflections) are extrapolated by the MEM to obtain the solution with the maximum entropy. Incorrect estimation of the non-measured structure factors by the MEM leads to the errors in the reconstructed MEM density. The prior information in the form of a procrystal electron density is a good estimate for the non-measured structure factors (Palatinus, 2003).

4.8.4. Crystallographic MEM equations

The basic equations and algorithms for MEM were developed in the field of image reconstruction for radio astronomy and were then adapted to different crystallographic problems (French, 1978; Collins, 1982; Collins & Mahar, 1983; Wilkins, 1983; Wilkins *et al.*, 1983; Navaza *et al.*, 1983; Bricogne, 1984; Navaza, 1985, 1986). In crystallographic applications of the MEM, the 'image' is the electron-density map and the data are structure factors of Bragg reflections. Here they will be considered for the case of X-ray powder-diffraction experiments. Since all MEM algorithms work with a discrete electron density, all MEM equations will be derived for the grid case and we will not use the analytical formalism. Readers who are interested in the analytical formalism should see Bricogne (1984) and Gilmore (1996).

The maximum-entropy criterion selects the electron-density map of maximum entropy among the maps that fulfil the constraints (Gull & Skilling, 1984). The data are supposed to be noisy with a Gaussian distribution of their estimated standard uncertainties (s.u.'s). Therefore the most probable solution is not the map corresponding to an exact fit to each reflection, but the map that satisfies the condition for so-called F constraints:

$$C_F = -\chi^2_{\rm aim} + \frac{1}{N_F}\sum_{i=1}^{N_F} w_i \left(\frac{|F_{\rm obs}(\mathbf{H}_i) - F_{\rm MEM}(\mathbf{H}_i)|}{\sigma(\mathbf{H}_i)}\right)^2 = 0, \tag{4.8.10}$$

where N_F is the number of observed structure factors $F_{\rm obs}(\mathbf{H}_i)$ with standard uncertainties $\sigma(\mathbf{H}_i)$; $F_{\rm MEM}(\mathbf{H}_i)$ is obtained by discrete Fourier transform of the current estimate of the charge density $\{\rho_i\}$. The standard version of the MEM employs $w_i = 1$ and $\chi^2_{\rm aim} = 1$.

The second constraint that is usually used in crystallographic applications of the MEM is the normalization of $\{\rho_i\}$ to the expected number of electrons, $N_{\rm el}$, in the unit cell of volume $V_{\rm UC}$:

$$C_N = N_{\rm el} - \frac{V_{\rm UC}}{N_{\rm pix}}\sum_{i=1}^{N_{\rm pix}} \rho_i = 0. \tag{4.8.11}$$

These constraints are chosen in a way that requires them to become zero when the conditions they represent are fulfilled. The amplitudes of the structure factors $F_{\rm obs}(\mathbf{H}_i)$ are determined experimentally and therefore each trial $\{\rho_i\}$ can be rejected or accepted based on its agreement with the experimental data.

The *unconstrained* maximum of the entropy [equation (4.8.2)] is given by $\rho_i = \rho_i^{\rm prior}$ for all points i. This means that the MEM reproduces the prior, which is indeed the best estimate for the electron density if data are not available. In particular, if only the total number of electrons per unit cell is known, the best estimate is a flat electron-density distribution.

Having N_C constraints, we should perform the constrained maximization of the entropy with respect to the $N_{\rm pix}$ values $\{\rho_i\}$. This optimization problem is solved by the application of the method of undetermined Lagrange multipliers λ_j (Palatinus, 2003):

$$Q(\{\rho_i\}) = S(\{\rho_i\}) - \sum_{j=1}^{N_C} \lambda_j C_j(\{\rho_i\}). \tag{4.8.12}$$

Differentiating the above equation with respect to ρ_i gives the condition

$$\frac{\partial Q}{\partial \rho_i} = \frac{\partial S}{\partial \rho_i} - \sum_{j=1}^{N_C} \lambda_j \frac{\partial C_j}{\partial \rho_i}. \tag{4.8.13}$$

Written explicitly for the two constraints C_F and C_N [equations (4.8.10) and (4.8.11)] and using the definition of entropy [equation (4.8.2)] we obtain

$$\frac{\partial Q}{\partial \rho_i} = -\ln\left(\frac{\rho_i}{\rho_i^{\rm prior}}\right) - \lambda_F \frac{\partial C_F}{\partial \rho_i} - \frac{V_{\rm UC}}{N_{\rm pix}}\lambda_N. \tag{4.8.14}$$

The maximum of Q follows from $\partial Q/\partial \rho_i = 0$ for all ρ_i, resulting in the formal solution for ρ_i,

$$\rho_i = \rho_i^{\rm prior} \exp\left(-\frac{V_{\rm UC}}{N_{\rm pix}}\lambda_N\right) \exp\left(-\lambda_F \frac{\partial C_F}{\partial \rho_i}\right), \tag{4.8.15}$$

where $\partial C_F/\partial \rho_i$ depends on all $\{\rho_i\}$. Substitution into the normalization condition [equation (4.8.11)] yields

$$\sum_{i=1}^{N_{\rm pix}} \rho_i^{\rm prior} \exp\left(-\frac{V_{\rm UC}}{N_{\rm pix}}\lambda_N\right) \exp\left(-\lambda_F \frac{\partial C_F}{\partial \rho_i}\right) = \frac{N_{\rm el} N_{\rm pix}}{V_{\rm UC}}. \tag{4.8.16}$$

The combination of equations (4.8.15) and (4.8.16) allows the elimination of the Lagrange multiplier λ_N. The final result for the normalized electron density is

$$\rho_i = \frac{N_{\rm el} N_{\rm pix}}{V_{\rm UC}} \rho_i^{\rm prior} \exp\left(-\lambda_F \frac{\partial C_F}{\partial \rho_i}\right) \Big/ \left[\sum_{i=1}^{N_{\rm pix}} \rho_i^{\rm prior} \exp\left(-\lambda_F \frac{\partial C_F}{\partial \rho_i}\right)\right]. \tag{4.8.17}$$

Equation (4.8.17) together with equation (4.8.10) gives a set of $N_{\rm pix} + 1$ nonlinear equations in the $N_{\rm pix}$ parameters $\{\rho_i\}$ and the Langrange multiplier λ_F. They cannot be solved analytically, because $\{\rho_i\}$ is included on both sides of equation (4.8.17).

4.8.5. MEM algorithms

Several iterative algorithms have been developed for solving the MEM equations (4.8.10) and (4.8.17). All approaches start with the prior density as zeroth-order approximation to the electron density:

$$\rho_i^{(0)} = \rho_i^{\rm prior}. \tag{4.8.18}$$

4.8.5.1. *Exponential modelling algorithm (Gull & Daniell, 1978; Collins, 1982; Collins & Mahar, 1983)*

The simplest algorithm is the exponential modelling algorithm (Gull–Daniell algorithm). For a small value of λ_F and starting with $n = 0$, the approximate solution $\{\rho_i^{(n)}\}$ of iteration n is used to evaluate the right-hand side of equation (4.8.17), thus providing the next estimate, $\{\rho_i^{(n+1)}\}$, for the electron-density map. The iteration is continued until convergence, *i.e.* until $\rho_i^{(n+1)} = \rho_i^{(n)}$ for all i. Then the value of λ_F is increased by a small amount, and iterations are again continued until $\rho_i^{(n+1)} = \rho_i^{(n)}$. The whole procedure is considered to be converged once the constraint equation (4.8.10) is fulfilled.

The Gull–Daniell algorithm in its initial form is known to be unstable, and several extensions have been proposed (Wu, 1997).

Significant improvement of this algorithm was achieved for the *ab initio* phasing of structure factors from single-crystal and powder-diffraction data (Bricogne & Gilmore, 1990; Gilmore *et al.*, 1990, 1991, 1999; Bricogne, 1988, 1991, 1993; Gilmore & Nicholson, 1994).

4.8.5.2. *Sakata–Sato algorithm (Sakata & Sato, 1990; Sakata et al., 1990, 1992, 1993; Kumazawa et al., 1995)*

This approach is similar to the Gull–Daniell algorithm, except that at each iteration step n not only the right-hand side of equation (4.8.17) is evaluated by substitution of $\{\rho_i^{(n)}\}$ for $\{\rho_i\}$, but also the prior density is replaced by $\{\rho_i^{(n)}\}$. The iterations commence with a fixed, suitably chosen value of λ_F. The iterations are considered to be converged once the constraint equation (4.8.10) is satisfied, *i.e.* when C_F drops below zero.

The Sakata–Sato algorithm implies that the prior is updated in every cycle, a procedure which violates the statistical principles at the foundation of the MEM. However, the algorithm has been shown to perform well in many applications, and thus is justified by the results rather than by a firm theoretical foundation (van Smaalen *et al.*, 2003).

The value of λ_F has an intricate effect on the iterations. The procedure does not converge for too large values of λ_F. Experience has shown that reliable MEM-optimized electron densities are only obtained if the value of the constraint [equation (4.8.10)] decreases in each step of the iteration. This can be achieved for sufficiently small λ_F, and the MEM-optimized electron density does not depend on the value of λ_F (Sakata & Sato, 1990; Kumazawa *et al.*, 1995). However, too small values of λ_F lead to very slow convergence, such that true convergence might not be reached within finite time. It is thus necessary to increase the value of λ_F after several iterations, or to employ the criterion of decrease of the value of the constraint at every cycle for automatic determination of an optimal value of λ_F (van Smaalen *et al.*, 2003).

4.8.5.3. *Cambridge algorithm (Bryan & Skilling, 1980, 1986; Burch et al., 1983; Skilling & Bryan, 1984; Gull & Skilling, 1987, 1999)*

The Cambridge algorithm for finding the map with the maximum entropy is based on Bayesian probability theory. Maximum probability that an electron-density map is the true electron density is attained for the density $\{\rho_i\}$ that maximizes the function

$$Q\big[\{\rho_i\}\big] = \alpha S\big[\{\rho_i\}\big] - C_F\big[\{\rho_i\}\big]. \tag{4.8.19}$$

Notice that the Lagrange multiplier λ_F of equation (4.8.12) is replaced by $1/\alpha$ here. The Cambridge algorithm involves a double iteration very similar to the Gull–Daniell algorithm (Section 4.8.5.1). Initially, for a large but fixed value of α the maximum of $Q[\{\rho_i\}]$ is determined by iteration over $\{\rho_i\}$. The value of α is gradually decreased, and at each value of α a new estimate of $\{\rho_i\}$ is obtained by iterative search for the maximum of $Q[\{\rho_i\}]$. The double iteration is converged once the constraint equation (4.8.10) is fulfilled. Probability theory provides a value for $\chi^2_{\rm aim}$ based on the data; its value usually is smaller than one.

The success of the Cambridge algorithm is rooted in the special iterative procedure for finding the maximum of $Q[\{\rho_i\}]$ for each given value of α. Unlike the Sakata–Sato algorithm, the Cambridge algorithm fulfils the formal requirements of the MEM approach, for example leading to an MEM-optimized electron density that better obeys the criterion $\partial Q/\partial \rho_i = 0$ than the Sakata–Sato algorithm does (van Smaalen *et al.*, 2003). Nevertheless, the MEM-optimized electron-density map is not necessarily better than the one obtained with the Sakata–Sato algorithm.

4.8.5.4. *Two-channel MaxEnt method (Papoular & Gillon, 1990; Zheludev et al., 1995; Papoular et al., 1996)*

The MEM requires a map with strictly positive values, as is provided by the electron density. Maps with both positive and negative values can be written as the difference between two strictly positive maps. The entropy can now be defined as the sum of entropies according to equation (4.8.2) of these two strictly positive functions. The concept of two-channel entropy was first introduced for reconstruction of the magnetization density from polarized neutron scattering data, whereby the two directions of the spin are represented by the two maps (Papoular & Gillon, 1990). The same formalism was used to reconstruct the deformation electron density, which has both positive and negative values (Papoular *et al.*, 1996). The deformation density $\Delta\rho(\mathbf{r})$ is written as the difference between two positive functions, ρ^+ and ρ^-, representing the densities of accumulation and depletion of electrons as compared to the IAM, respectively:

$$\Delta\rho(\mathbf{r}) = \rho^+(\mathbf{r}) - \rho^-(\mathbf{r}). \tag{4.8.20}$$

The entropy of the difference density is then defined as the sum of the entropies of $\rho^+(\mathbf{r})$ and $\rho^-(\mathbf{r})$,

$$\begin{aligned} S_{\Delta\rho} &= S_{\rho^+} + S_{\rho^-} \\ &= -\sum_{i=1}^{N_{\rm pix}} \left[-\rho_i^+ + \rho_i^{(\rm prior)+} + \rho_i^+ \ln\left(\frac{\rho_i^+}{\rho_i^{(\rm prior)+}}\right)\right] \\ &\quad - \sum_{i=1}^{N_{\rm pix}} \left[-\rho_i^- + \rho_i^{(\rm prior)-} + \rho_i^- \ln\left(\frac{\rho_i^-}{\rho_i^{(\rm prior)-}}\right)\right]. \end{aligned} \tag{4.8.21}$$

This entropy is maximized to obtain the MEM-reconstructed difference density $\Delta\rho_{\rm MEM}$. The input data consist of the difference structure factors $\Delta F = F_{\rm obs} - F_{\rm model}$. Any of the algorithms for MEM calculations described above can be modified for two-channel entropy calculations. The advantage of this approach is that the dynamic range of the map $\Delta\rho(\mathbf{r})$ is much smaller than the dynamic range of the electron density itself. The disadvantage of this formalism is that it introduces additional freedom in the form of two values (ρ_i^+ and ρ_i^-) representing the value of the map at pixel i. As a result, the two-channel entropy can suppress fine details in the reconstructed difference density. This problem can be partially solved by decreasing the stopping value of the constraints. So far, the two-channel algorithm has been tested exclusively on single-crystal diffraction data.

4.8.5.5. *Valence-only MaxEnt method (Roversi et al., 1998)*

This method aims for an accurate electron-density study at the last stage of structural analysis. The refined structural parameters are used to create a core electron-density fragment, which then is considered to be known and is not included in the MaxEnt optimization. Only the valence electron density is modified. This method relies on very precise knowledge of the atomic displacement parameters (ADPs), which is often not available. Any error in the ADPs leads to negative regions in the valence density, which cannot be accounted for by the MEM. So far, the valence-only algorithm has been tested exclusively on simulated single-crystal X-ray diffraction data.

4.8.6. Constraints in the MEM based on the measured intensities from powder-diffraction data

4.8.6.1. *F and G constraints*

Integrated intensities of individual Bragg reflections can be determined by powder diffraction for resolved reflections as well as for reflections without too severe overlap, employing one of the decomposition techniques for powder-diffraction data. These reflections can be used to define an F constraint [equation (4.8.10)] and the MEM may be applied in exactly the same way as for single-crystal diffraction data (Section 4.8.4).

Fig. 4.8.4 presents an example of decomposition of the intensities of overlapping reflections into individual reflections by a Le Bail fit (without a structural model; see Chapter 3.5) and by a Rietveld refinement (with a structural model) for $K_2C_2O_4$ (Samy *et al.*, 2010; Dinnebier *et al.*, 2005). Careful consideration of the Rietveld and Le Bail plots shows strong differences between peak fitting at $2\theta = 37.7^\circ$. Two reflections at $2\theta = 37.7^\circ$ are fully overlapped, and the Le Bail fit assigns equal intensities to both reflections. The Rietveld refinement assigns all experimental intensity to one Bragg reflection and zero intensity to the other, because the calculated structure factor of the latter is zero.

A simple two-peaks example (taken from Takata, 2008) of the decomposition of intensities of partially overlapped reflections allows us to consider in detail the Rietveld and Le Bail decomposition methods. The calculated diffraction pattern does not provide an exact description of the data points in Fig. 4.8.5 owing to the incomplete structure model. The peak area is proportional to the square of the structure-factor amplitude and thus the problem is reduced to finding the peak area. The observed peak area is easy to evaluate for an isolated peak. The fundamental idea of the procedure for extraction of intensities of individual reflections from partially and completely overlapped reflections is simple: instead of using the integrated intensities from a powder-diffraction pattern (like in single-crystal analysis), the entire information content of a powder pattern available in step-scanned intensity data is subjected to refinement using a least-squares procedure.

The diffracted intensity at each data point is distributed over the contributing reflections according to the calculated intensities of these reflections at that point:

$$Y_i^{\rm obs}(2\theta_j) = \frac{Y^{\rm obs}(2\theta_j)\,Y_i^{\rm calc}(2\theta_j)}{\sum_{i=1}^{N} Y_i^{\rm calc}(2\theta_j)}, \qquad (4.8.22)$$

where $Y^{\rm obs}(2\theta_j)$ is the observed diffraction intensity at scattering angle $2\theta_j$, which is split into contributions $Y_i^{\rm obs}(2\theta_j)$ from $i = 1, \ldots, N$ reflections (Fig. 4.8.5*b*). $Y_i^{\rm calc}(2\theta_j)$ is the calculated intensity of the ith reflection at $2\theta_j$; its value depends on the structure-factor amplitude of reflection i as well as on the profile function and distance between $2\theta_j$ and $2\theta_{hkl}$ (Fig. 4.8.5*a*; Rietveld, 1967, 1969). The observed structure-factor amplitude, $|F_{\rm obs}(\mathbf{H}_i)|^2$, of reflection i is obtained by summation of $Y_i^{\rm obs}(2\theta_j)$ over all $2\theta_j$ [equation (4.8.22)]. In the case of Rietveld decomposition, the calculated structure factors of the model are used in equation (4.8.22) to decompose overlapping reflections into contributions of individual reflections. This procedure results in strong bias by the (incomplete) model of the intensities and phases of individual reflections. The Le Bail fit works without a structure model. All calculated structure-factor amplitudes are initially given unit value, and the values of the integrated intensities are determined iteratively. Bragg reflections of unequal intensity are obtained by using the profile functions. For fully overlapping peaks, the intensities are partitioned equally (Le Bail *et al.*, 1988).

The observed structure-factor amplitudes can be used in MEM calculations in combination with reflection phases from the structural model. The MEM-reconstructed electron density is not necessarily accurate, because any technique of decomposition results in structure-factor amplitudes of individual reflections of limited accuracy that are possibly biased by the model. These

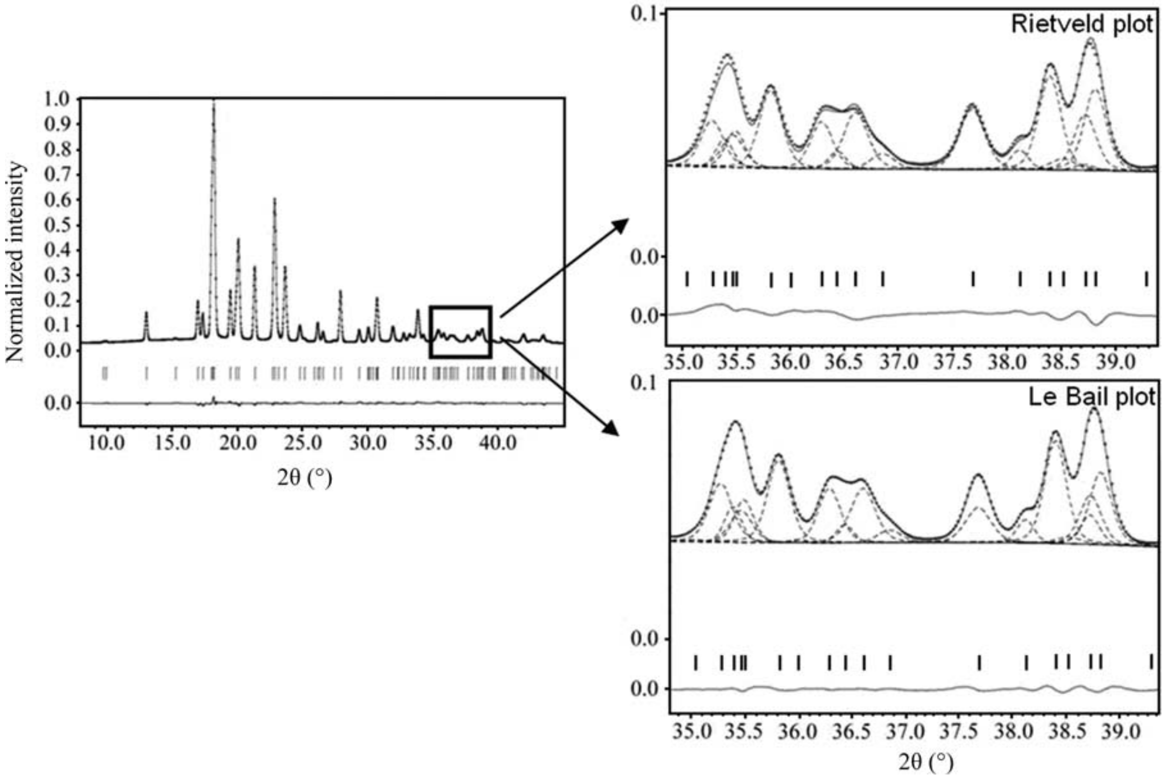

Figure 4.8.4

Dividing of the total intensity of the overlapping reflections into the contributions of individual reflections by Rietveld refinement (with a structural model) and by Le Bail fitting (without a structural model) for powder-diffraction data for $K_2C_2O_4$ (adapted from Samy *et al.*, 2010).

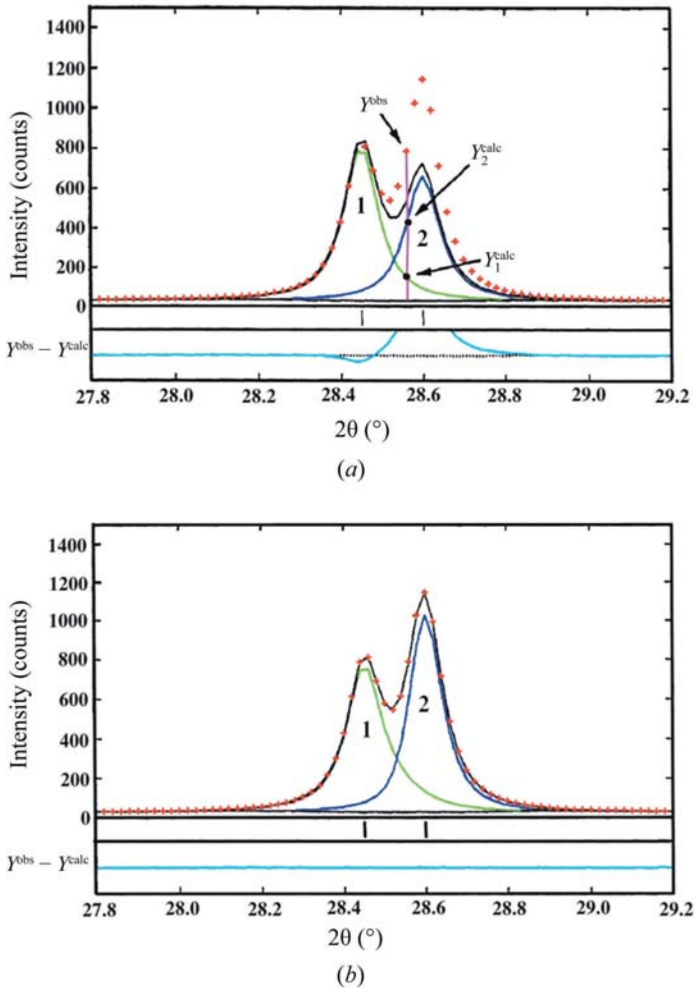

Figure 4.8.5
Observed intensity (points) as a function of the scattering angle, together with lines representing (*a*) the calculated intensity of the Rietveld refinement and (*b*) the intensities after decomposition according to equation (4.8.22) (from Takata, 2008).

uncertainties can be avoided by the use of so-called G constraints based on the integrated intensities of groups of overlapping reflections (Sakata *et al.*, 1990). G constraints can be easily incorporated into the Sakata–Sato algorithm, and are thus actively used in this algorithm.

G constraints are based on N_G groups of overlapping reflections. Group i has contributions of N_G^i reflections, resulting in a 'group amplitude' G^i equal to the square root of the integrated intensity and related to the structure-factor amplitudes through

$$G^i = \left[\sum_{j=1}^{N_G^i}\left(\frac{m_j}{\sum m_j}\left|F(\mathbf{H}_j)\right|^2\right)\right]^{1/2}, \qquad (4.8.23)$$

where m_j is the point-group multiplicity of reflection j. The summation runs over the symmetry-independent structure factors contributing to group i. The standard uncertainty of the group amplitude G_i follows as

$$\sigma(G^i) = \frac{1}{G^i}\left[\sum_{j=1}^{N_G^i}\left(\frac{m_j}{\sum m_j}\left|F(\mathbf{H}_j)\right|(\mathbf{H}_j)\right)^2\right]^{1/2}. \qquad (4.8.24)$$

The group amplitudes can be used in the G constraint in a similar way to the F constraint [equation (4.8.10)]:

$$C_G = -\chi^2_{\text{aim}}(G) + \frac{1}{N_G}\sum_{i=1}^{N_G} w_i\left(\frac{G^i_{\text{obs}} - G^i_{\text{MEM}}}{\sigma\left(G^i_{\text{obs}}\right)}\right)^2 = 0, \qquad (4.8.25)$$

where G^i_{obs} and $\sigma(G^i_{\text{obs}})$ are the group amplitude and standard uncertainty as obtained from the experiment, respectively, and G^i_{MEM} is computed from $F_{\text{MEM}}(\mathbf{H}_j)$ (Section 4.8.4) according to equation (4.8.23).

G constraints can be introduced into the MEM with aid of an additional Lagrange multiplier λ_G (see Section 4.8.4):

$$L = S - \lambda_N C_N - \lambda_F C_F - \lambda_G C_G. \qquad (4.8.26)$$

Experience has shown that a certain fraction of reflections must be available as F constraints in order for the MEM to converge to the correct electron-density distribution. Since the ratio of λ_F and λ_G is not known *a priori*, applications have used a single constraint with a single Lagrange multiplier λ_{FG} according to

$$L = S - \lambda_N C_N - \lambda_{FG} C_{FG} \qquad (4.8.27)$$

with the combined F and G constraint

$$C_{FG} = -\chi^2_{\text{aim}} + \frac{1}{N_{\text{all}}}\sum_{i=1}^{N_F} w_i\left(\frac{\left|F_{\text{obs}}(\mathbf{H}_i) - F_{\text{MEM}}(\mathbf{H}_i)\right|}{\sigma(\mathbf{H}_i)}\right)^2 + \frac{1}{N_{\text{all}}}\sum_{i=1}^{N_G} w_i\left(\frac{G^i_{\text{obs}} - G^i_{\text{MEM}}}{\sigma\left(G^i_{\text{obs}}\right)}\right)^2 = 0, \qquad (4.8.28)$$

where $N_{\text{all}} = N_F + N_G$ (Palatinus, 2003).

The formal solution of the MaxEnt equations then becomes [*cf.* equation (4.8.17)]

$$\rho_i = \frac{N_{\text{el}}N_{\text{pix}}}{V_{\text{UC}}}\rho_i^{\text{prior}}\exp\left[-\lambda_{FG}\left(\frac{\partial C_F}{\partial\rho_i} + \frac{\partial C_G}{\partial\rho_i}\right)\right] \times \left\{\sum_{i=1}^{N_{\text{pix}}}\rho_i^{\text{prior}}\exp\left[-\lambda_{FG}\left(\frac{\partial C_F}{\partial\rho_i} + \frac{\partial C_G}{\partial\rho_i}\right)\right]\right\}^{-1}. \qquad (4.8.29)$$

The implementation of G constraints in the Sakata–Sato algorithm is straightforward except for the computation of the derivative of the combined constraint, which is slightly more complicated than the calculation of the derivative of the F constraint.

4.8.6.2. *Constraints using 'partly phased' reflections for anomalous-scattering X-ray powder diffraction*

X-ray anomalous scattering from powders can be used for *ab initio* structure determination if at least two different data sets are available: one measured with a wavelength near the absorption edge of a chemical element contained in the sample and another measured with a wavelength far from the absorption edge. The corresponding Patterson map allows the localization of the resonant-scattering atoms. The phases of the resolved structure factors of centrosymmetric structures can be derived from this experiment. For noncentrosymmetric structures, two values remain for the phase φ_i of each reflection i. They can be written as $\varphi_i = \varphi_{0i} \pm \Delta_i$, where φ_{0i} and Δ_i are obtained from the experiment. This limited information from anomalous-scattering X-ray powder diffraction can be used in the MEM through the so-called A constraints for partly phased reflections (Burger & Prandl, 1999). Defining $A'^i = |F|\cos(\Delta_i)$ and $B'^i = |F||\sin(\Delta_i)|$, the A constraint is

$$C_A = -\chi^2_{\mathrm{aim}} + \frac{1}{N_A}\sum_{i=1}^{N_A}\left[\left(\frac{A'^i_{\mathrm{obs}} - A'^i_{\mathrm{MEM}}}{\sigma\left(A'^i_{\mathrm{obs}}\right)}\right)^2 + \left(\frac{B'^i_{\mathrm{obs}} - B'^i_{\mathrm{MEM}}}{\sigma\left(B'^i_{\mathrm{obs}}\right)}\right)^2\right]. \qquad (4.8.30)$$

4.8.6.3. *Prior-derived F constraints*

Experimentally, diffraction data are usually not available beyond $[\sin(\theta)/\lambda]_{\max}$ = 1.3 Å^{-1}. As discussed in Section 4.8.3, Fourier maps that are free from series-termination effects require all structure factors up to at least $[\sin(\theta)/\lambda]_{\max}$ = 6 Å^{-1}. Although much less severe, the MEM also suffers from series-termination effects if structure factors are incorporated of resolutions up to $[\sin(\theta)/\lambda]_{\max} \simeq 1.3$ Å^{-1}, even in cases where a procrystal prior is used. Since high-angle diffraction data are mainly determined by the core electrons, for which the procrystal prior is supposed to be a good estimate, it turns out that the calculated structure factors of the IAM are a better estimate for the high-order reflections than the value of zero that is implicit in using a resolution limit of 1.3 Å^{-1} or worse. Accordingly, the constraint in the MEM can be modified to include the so-called prior-derived F constraints (PDCs) based on calculated structure factors, $F_{\mathrm{prior}}(\mathbf{H}_i)$, of the prior structure model (Palatinus & van Smaalen, 2005):

$$\begin{aligned} C_{FG}^{\mathrm{PDC}} = {} & -\chi^2_{\mathrm{aim}} + \frac{1}{N_{\mathrm{all}}}\sum_{i=1}^{N_F} w_i\left(\frac{\left|F_{\mathrm{obs}}(\mathbf{H}_i) - F_{\mathrm{MEM}}(\mathbf{H}_i)\right|}{\sigma(\mathbf{H}_i)}\right)^2 \\ & + \frac{1}{N_{\mathrm{all}}}\sum_{i=1}^{N_G} w_i\left(\frac{G^i_{\mathrm{obs}} - G^i_{\mathrm{MEM}}}{\sigma\left(G^i_{\mathrm{obs}}\right)}\right)^2 \\ & + \frac{1}{N_{\mathrm{all}}}\sum_{i=1}^{N_{\mathrm{PDC}}} w_i\left(\frac{\left|F_{\mathrm{prior}}(\mathbf{H}_i) - F_{\mathrm{MEM}}(\mathbf{H}_i)\right|}{\sigma(\mathbf{H}_i)}\right)^2 = 0, \qquad (4.8.31) \end{aligned}$$

where the symbols have the same meaning as in equations (4.8.10) and (4.8.28), but $N_{\mathrm{all}} = N_F + N_G + N_{\mathrm{PDC}}$ and N_{PDC} is the number of reflections included in the PDC (third summation). The latter involve all reflections up to a high resolution of, for example, $[\sin(\theta)/\lambda]_{\max}$ = 2.5 Å^{-1}, which are not available in the experiment. Their standard uncertainties are made equal to the smallest standard uncertainty among the experimental data. While equation (4.8.31) is used for solving the MEM iterations [C_F is replaced by C_{FG}^{PDC} in equation (4.8.17)], the criterion for convergence is still based on constraints computed solely with the experimental data [equations (4.8.10) or (4.8.28)].

It has been shown for single-crystal diffraction data that a PDC with experimental data up to $[\sin(\theta)/\lambda]_{\max} \simeq 1.0$ Å^{-1} leads to good results. A single but unsuccessful application to powder X-ray diffraction data has been reported (Buchter *et al.*, 2011). However, the lack of success in that work might be related to the low data resolution of $[\sin(\theta)/\lambda]_{\max}$ = 0.6 Å^{-1} rather than to the use of powder-diffraction data instead of single-crystal diffraction data.

4.8.6.4. *Observed structure factors*

The structure factors for MEM calculations should be uniquely determined by the electron density. Anomalous scattering cannot be incorporated into this scheme, and experimental data have to be corrected for this effect. Furthermore, the precise scale of the observed structure factors and any extinction correction need to be known too. The MEM thus requires the availability of a structure refinement of reasonable quality, from which the magnitudes of these effects as well as the phases of the structure factors can be obtained to a good approximation. The refinement provides $F_{\mathrm{calc}}(\mathbf{H})$, which incorporate the effects of anomalous scattering as well as the scale factor (k_s) and a correction factor for extinction, (k_E).

The required corrections can be applied as follows (Bagautdinov *et al.*, 1998):

$$F^{\mathrm{elec}}_{\mathrm{obs}}(\mathbf{H}) = \frac{\left|F_{\mathrm{obs}}(\mathbf{H})\right|}{\left|F_{\mathrm{calc}}(\mathbf{H})\right|}\left[A^{\mathrm{elec}}_{\mathrm{calc}}(\mathbf{H}) + iB^{\mathrm{elec}}_{\mathrm{calc}}(\mathbf{H})\right], \qquad (4.8.32)$$

where $A^{\mathrm{elec}}_{\mathrm{calc}}(\mathbf{H})$ and $B^{\mathrm{elec}}_{\mathrm{calc}}(\mathbf{H})$ are the calculated real and imaginary parts of the structure factors without the contributions of anomalous scattering or extinction, *i.e.* they are the structure factors corresponding to the Fourier transform of the electron density of one unit cell.

4.8.7. Analysis of the electron-density distribution from powder-diffraction data

4.8.7.1. *Types of MEM-reconstructed electron-density distribution*

The principal application of the MEM to powder-diffraction data is the reconstruction of the electron (or nuclear) density distribution to investigate features not accounted for by a structure model or Fourier analysis. X-ray/neutron diffraction data carry information about the electron/nuclear density in the structure-factor amplitudes and phases extracted from the measured reflection intensities. This experimental information is used in the MEM *via* values for the observed structure factors $F_{\mathrm{obs}}(\mathbf{H})$ and their standard uncertainties $\sigma(\mathbf{H})$, and *via* the prior density distribution $\{\rho_i^{\mathrm{prior}}\}$ from Rietveld refinement.

The MEM can be applied to powder-diffraction data in several ways, which differ in the type of constraints, the way observed structure-factor amplitudes have been extracted from the data and the source of reflection phases (Fig. 4.8.6). The resulting density maps vary from completely biased by the structure model to model-free maps. A systematic investigation of the different maps has been carried out by Samy *et al.* (2010). Particularly noteworthy is the MEM electron-density map computed with F and G constraints with structure-factor amplitudes obtained by a LeBail fit and with phases from charge flipping. This type of map was first introduced by Samy *et al.* (2010), who showed that it provides a good description of the disorder in alkali-metal oxalates and carbonates. Following Samy *et al.* (2010), the different types of maps can be characterized as follows (Fig. 4.8.6).

(1) F_{calc}, φ^{calc}: the calculated structure factors (including phases), F_{calc}, are used as F_{obs} in the F constraint [equation (4.8.10)]. This MEM map is completely biased by the structure model, and should in principle reproduce it. Deviations from the model are usually found because of the limited resolution of the diffraction data and the resulting series-termination effects.

(2) F_{obs}, φ^{calc}: based on observed structure-factor amplitudes extracted from the data [equation (4.8.22)] with calculated structure factors from Rietveld refinement and phases calculated from the structure model. In the case of powder-diffraction data in particular, this MEM map is partially biased by the model, because calculated structure factors of the model are used to decompose overlapping reflections into contributions of individual reflections. This MEM map allows the localization of missing atoms in incomplete structure models, but it does not provide an accurate description of the electron- or nuclear-density distribution. The corresponding

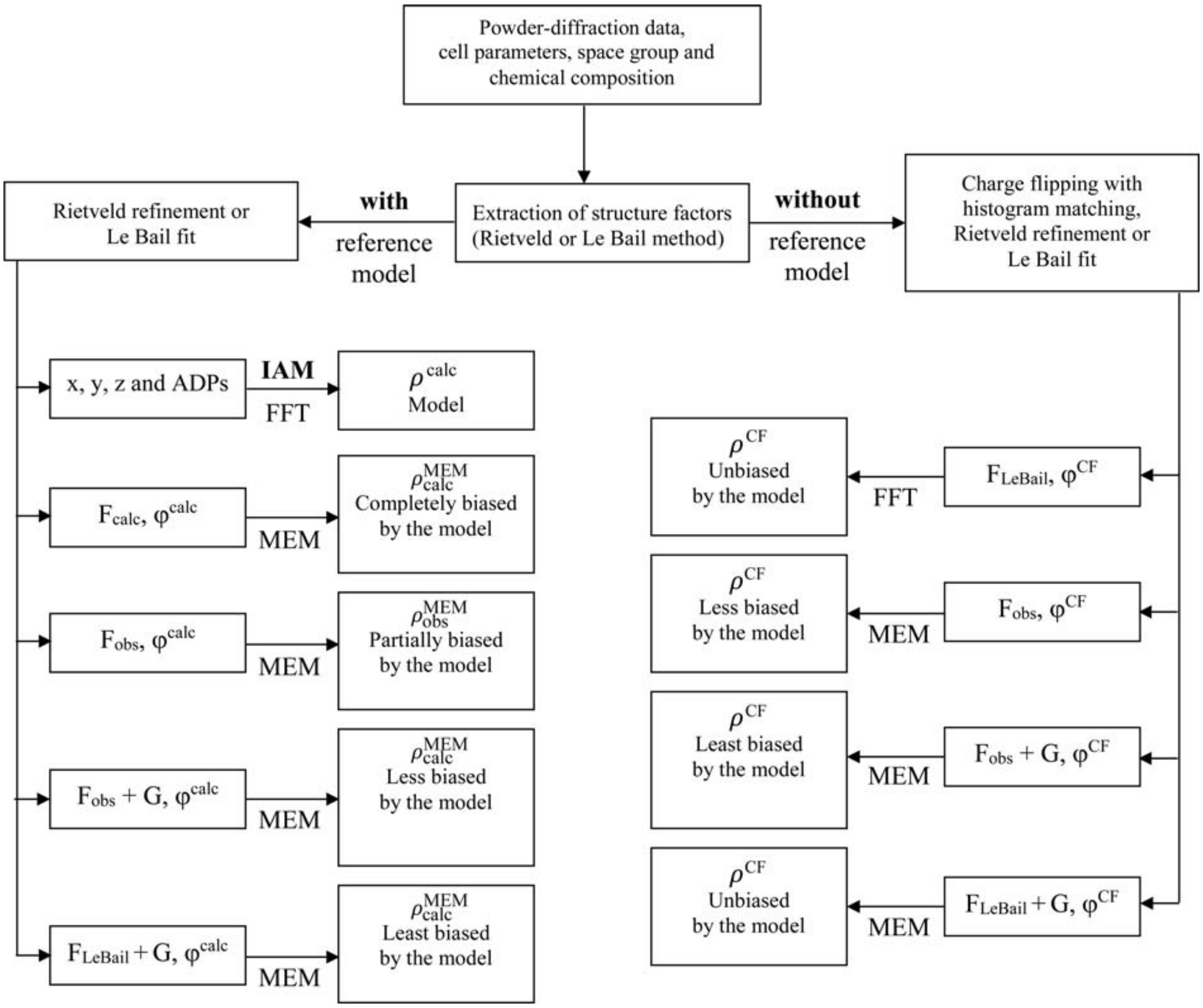
Powder-diffraction data, cell parameters, space group and chemical composition
Rietveld refinement or Le Bail fit
with reference model
Extraction of structure factors (Rietveld or Le Bail method)
without reference model
Charge flipping with histogram matching, Rietveld refinement or Le Bail fit
x, y, z and ADPs
IAM
FFT
ρ^calc Model
F_calc, φ^calc
MEM
ρ^MEM_calc Completely biased by the model
F_obs, φ^calc
MEM
ρ^MEM_obs Partially biased by the model
F_obs + G, φ^calc
MEM
ρ^MEM_calc Less biased by the model
F_LeBail + G, φ^calc
MEM
ρ^MEM_calc Least biased by the model
ρ^CF Unbiased by the model
FFT
F_LeBail, φ^CF
ρ^CF Less biased by the model
MEM
F_obs, φ^CF
ρ^CF Least biased by the model
MEM
F_obs + G, φ^CF
ρ^CF Unbiased by the model
MEM
F_LeBail + G, φ^CF

Figure 4.8.6

Flow chart of the procedure for reconstruction of the different MEM maps from powder-diffraction data. IAM – independent-atom model, FFT – fast Fourier transform (adapted from Samy *et al.*, 2010).

maps also often contain weak noise (areas with positive electron density that do not correspond to any atom in the structure), especially when a flat prior is used.

(3) $F_{\rm obs} + G$, $\varphi^{\rm calc}$: based on the observed structure-factor amplitudes as in (2), but with F constraints for resolved reflections and G constraints for groups of overlapping reflections; phases are calculated from the structure model. The corresponding MEM map is less biased by the model than in (2). It not only allows localization of missing atoms in incomplete structure models, but also the accurate analysis of electron-density distributions provided a procrystal density is used. When the number of G constraints is not too large (less than 20% of the reflections take part in G constraints), a flat prior can be used, but the corresponding MEM map then will suffer from noise.

(4) $F_{\rm LeBail} + G$, $\varphi^{\rm calc}$: based on observed structure-factor amplitudes extracted from the data [equation (4.8.22)] by Le Bail fit, with F constraints for resolved reflections and G constraints for groups of overlapping reflections; phases are calculated from the structure model. This MEM map is even less biased by the model than (3). Le Bail decomposition provides amplitudes of structure factors disregarding any structural information, and while individual amplitudes of reflections in a group of overlapping reflections might not be accurate, an accurate value is obtained for the group amplitude [equation (4.8.23)]. Therefore, $F + G$ constraints are the only reasonable option. Additionally, $F_{\rm LeBail}$ should be corrected for anomalous scattering.

(5) $F_{\rm obs}$, $\varphi^{\rm CF}$: based on $F_{\rm obs}$ [see (2)] with reflection phases, $\varphi^{\rm CF}$, obtained by charge flipping with histogram matching (Baerlocher *et al.*, 2007). The main limiting factors for this MEM map are the complexity of the crystal structure and the quality of the powder-diffraction data. In general, the correct determination of the phases of all reflections (including weak reflections) becomes more difficult with increasing complexity of the crystal structure. Using phases $\varphi^{\rm CF}$ from charge flipping is the method of choice for disordered structures, since the corresponding disordered structural model from Rietveld refinement is usually affected by the correlations between many refined parameters and needs to be verified.

(6) $F_{\rm obs} + G$, $\varphi^{\rm CF}$: based on measured structure-factor amplitudes for resolved reflections $F_{\rm obs}$ from Rietveld refinement with G constraints for group amplitudes of overlapping reflections, and phases $\varphi^{\rm CF}$ from charge flipping with histogram matching. This type of MEM map is less biased than (5) and thus provides a more stringent test of the structure model. A procrystal density representing an (incomplete) structure model can be used.

(7) $F_{\rm LeBail} + G$, $\varphi^{\rm CF}$: based on $F_{\rm LeBail}$ [see (4)] with F constraints for resolved reflections and G constraints for groups of overlapping reflections, and phases $\varphi^{\rm CF}$ [see (5)]. This MEM

map is unbiased by the model, since both structure-factor amplitudes and phases are extracted from the diffraction data without any structural information. The resulting density distributions can be considered as almost completely *ab initio* density distributions. This is a very useful type of MEM map for disordered structures, because it avoids any possible inaccurate modelling of the disorder. This MEM map is limited by the complexity of the crystal structure and the quality of the powder-diffraction data.

4.8.7.2. *MEM-based improvement of the structure model from charge flipping*

Charge flipping provides phases for the measured reflections along with an electron density that is basically a Fourier map (Oszlányi & Sütő, 2004, 2005; Palatinus, 2004; Wu *et al.*, 2006; Palatinus & Chapuis, 2007; Baerlocher *et al.*, 2007; Palatinus, 2013). As discussed in Section 4.8.7.1, the reflection phases resulting from the charge-flipping procedure can be employed in the MEM for generating an MEM electron-density map that shows significantly more details than the Fourier map obtained directly by charge flipping. As shown by Samy *et al.* (2010), the MEM based on $F_{\rm LeBail} + G$ constraints and $\varphi^{\rm CF}$ reflection phases may thus provide an *ab initio* determination of the details of disorder in crystal structures.

Samy *et al.* (2010) investigated two compounds with structural disorder. A good fit to the diffraction data was obtained in Rietveld refinements of structure models with 24-fold disorder of the oxalate ion in α-$Rb_2C_2O_4$, and with eightfold disorder of the carbonate group in α-Rb_2CO_3 (Fig. 4.8.7). While the disorder of the oxalate anions involves rotations about an axis perpendicular to the principal axis as well as different conformations through rotations of the carboxyl groups, the carbonate group has no internal degree of freedom and exhibits only orientational disorder (Dinnebier *et al.*, 2005).

The MEM electron densities based on F constraints with $F_{\rm calc}$ [type (1) in Section 4.8.7.1] provide the electron density corresponding to the disorder models. The MEM with F constraints based on $F_{\rm obs}$ with $\varphi^{\rm calc}$ [type (2) in Section 4.8.7.1] leads to a similar density but with distinct differences that can be described as a smoother distribution of the densities of the anions (Fig. 4.8.7). Three more MEM density maps of decreasing model bias are presented in Fig. 4.8.7 (*cf.* Section 4.8.7.1), all of which have similar appearances. These MEM density maps show that the major features of the disorder in these two compounds have been captured by the respective structure models. More interestingly, the high degree of similarity between the MEM electron density based on $F_{\rm obs}$ with $\varphi^{\rm calc}$ [type (2)] and that based on $F_{\rm LeBail} + G$ constraints with $\varphi^{\rm CF}$ [type (7)] demonstrates that the latter method may be used for *ab initio* determination of structural disorder from powder-diffraction data (Samy *et al.*, 2010). Of course, this conclusion can be directly applied to single-crystal X-ray diffraction data as well.

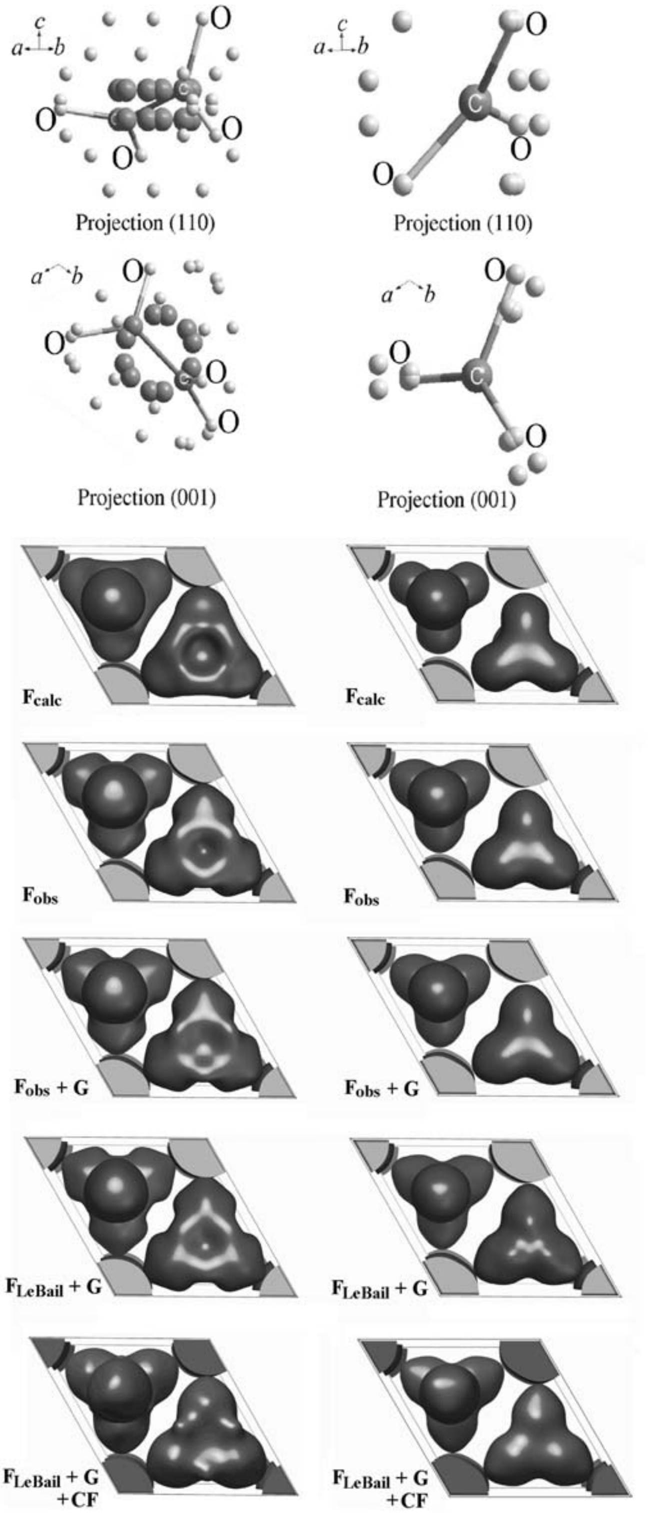

Figure 4.8.7
Structural model from Rietveld refinement and MEM electron densities of disordered α-$Rb_2C_2O_4$ (left) and α-Rb_2CO_3 (right). Contour level from 0.6 e Å^{-3} (adapted from Samy *et al.*, 2010).

4.8.7.3. *Combination of MEM and Rietveld refinement (REMEDY cycle)*

The MEM/Rietveld method has been developed as a method called the REMEDY cycle for improving structure models determined from X-ray powder-diffraction data (Takata *et al.*, 1995). It involves the alternate application of Rietveld refinement of a structure model and MEM calculations based on $F_{\rm obs}$ and $\varphi^{\rm calc}$ [type (2) map in Section 4.8.7.1], while in each cycle the MEM electron density is employed to generate an improved structure model (Fig. 4.8.8). In general, any combination of structure-factor amplitudes and phases could be used for this iterative procedure [types (2)–(4) in Section 4.8.7.1], but applications have mainly been restricted to type (2) MEM calculations with flat prior densities (Takata, 2008), although type (3) ($F_{\rm obs} + G$, $\varphi^{\rm calc}$) and type (4) ($F_{\rm LeBail} + G$, $\varphi^{\rm calc}$) MEM calculations with procrystal density usually lead to better results (Magdysyuk *et al.*, 2012).

As described by Takata (2008), the MEM/Rietveld method requires an initial structure model to start the iterative procedure

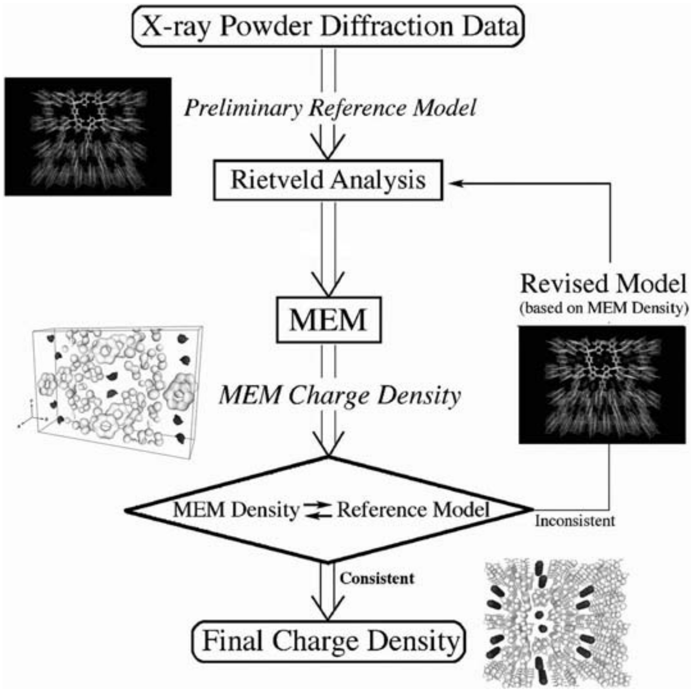

Figure 4.8.8

Flow chart of MEM/Rietveld method with structure refinement and MEM imaging of the charge density (adapted from Takata, 2008).

(Fig. 4.8.8). This model can be determined by any standard technique for structure solution from powder-diffraction data or it is known *a priori* (*e.g.* from similarities to related compounds). The initial model may be incomplete and the fit to the diffraction data attained with Rietveld refinement of the initial model may be poor. Based on this Rietveld refinement, $F_{\rm obs}$ amplitudes and $\varphi^{\rm calc}$ phases are obtained (Section 4.8.6.1), which are then used for the MEM calculations. The resulting MEM electron-density distribution allows for improvement of the structure model, *e.g.* by including newly located atoms. The improved model is then subjected to a second Rietveld refinement. The intensity repartitioning for overlapping reflections and phase assignment improves as the number of REMEDY cycles increases owing to improvements to the structure model and $F_{\rm calc}$, $\varphi^{\rm calc}$ values. In this way, MEM calculations and Rietveld refinement are alternately repeated (REMEDY cycles). Convergence is assumed if the R factors no longer decrease and no changes in the structural model can be detected.

One example of the successful application of the MEM/Rietveld method is the analysis of acetylene adsorption by a porous coordination polymer CPL-1 (Kubota *et al.*, 2006; Takata, 2008), which is shown in Fig. 4.8.9. Application of the MEM/Rietveld method has allowed the determination of small structural variations that depend on the filling fraction of acetylene molecules in the pores of the polymer (Takata, 2008).

The MEM/Rietveld method violates one of the principles of the MEM: strictly speaking, an iterative procedure, in which the result of the MEM is used as reference for the next cycle, is not allowed. On the other hand, one could argue that the improved structure model, as determined by application of the MEM, represents an independent new starting point for the Rietveld refinement and subsequent MEM calculations. In any case, the MEM/Rietveld method works, as demonstrated by many examples (Takata, 2008; Kato & Tanaka, 2016). The MEM/Rietveld method is more effective than Fourier synthesis for improving structural models owing to the higher signal-to-noise ratio of the former, as discussed elsewhere in this chapter.

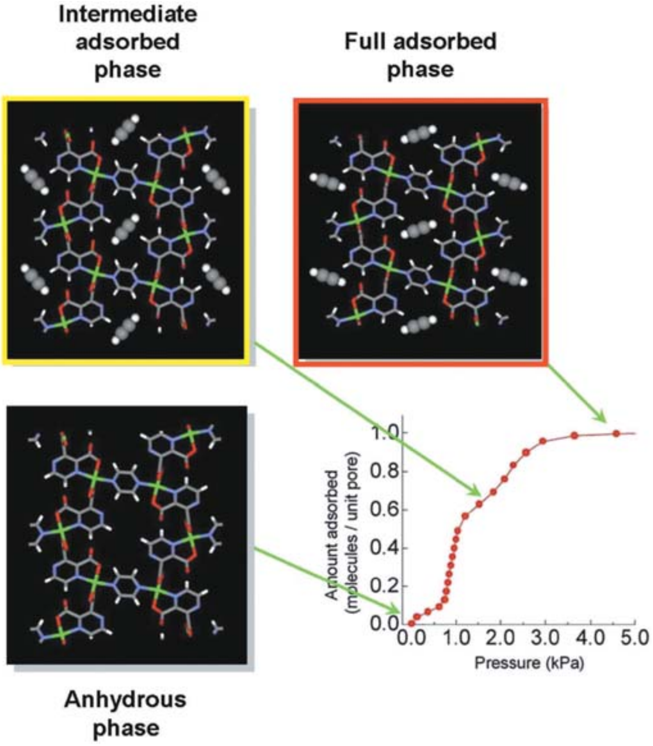

Figure 4.8.9

Acetylene adsorption isotherm and crystal structures of CPL-1 with adsorption of acetylene corresponding to the amount of adsorbed gas. Acetylene molecules are shown by the space-filling model; other molecules are shown as a wire model (from Takata, 2008).

The MEM/Rietveld method enables one to construct a detailed structure model on the basis of X-ray powder-diffraction data. In addition, at convergence and for diffraction data of sufficient resolution, the final MEM electron density may have the quality of showing features of chemical bonding (Kato & Tanaka, 2016; see Section 4.8.7.6).

4.8.7.4. *MEM-assisted structure solution by charge flipping*

As discussed in Section 4.8.7.2, reflection phases from charge flipping can be used for a complete *ab initio* determination of the electron density of ordered and disordered structures. The main limitation of charge flipping is the requirement of the availability of a complete data set up to a reasonable resolution (Palatinus *et al.*, 2007; Palatinus, 2013). If too many reflections are missing from the experiment, charge flipping will fail to solve the structure and the method of Section 4.8.7.2 cannot be applied.

An intrinsic property of the MEM is that it provides an estimate for the amplitudes and phases of the unmeasured structure factors (Sakata & Sato, 1990), thus the set of structure factors can be completed by MEM before applying the charge flipping for structure solution. This idea was used by Palatinus *et al.* (2007) to extrapolate the intensities of the missing reflections by optimizing the Patterson function, and subsequently use the computed structure factors together with experimentally measured reflections to enhance the ability of charge flipping to solve a crystal structure. The use of the MEM-optimized Patterson function was tested for the case of single-crystal diffraction data. In this way, it was possible to solve crystal structures from single-crystal X-ray diffraction data with approximately 50% coverage of reciprocal space. Although this method has not been tested for powder-diffraction data, it should be applicable to these data too.

Another way around the problem of incomplete data is the use of an approximate structure model for generating a non-random

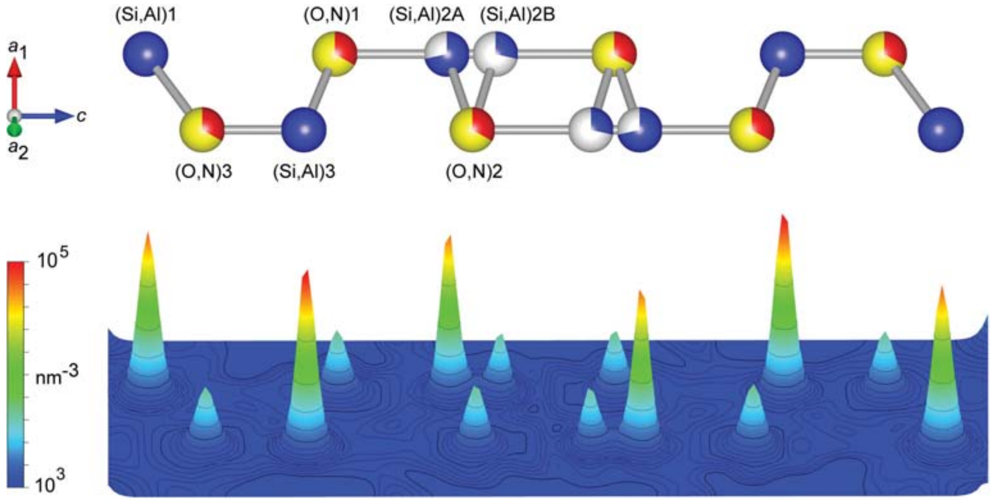

Figure 4.8.10
The top panel shows the (110) plane of the crystal structure of $SiAl_4O_2N_4$; red and yellow indicate fractional occupancies by oxygen and nitrogen, respectively; dark blue indicates the fractional occupancy of the (Si,Al)2A and (Si,Al)2B sites. The bottom panel gives a bird's-eye view of the MEM electron density on the (110) plane; (Si,Al)2A (fractional occupancy 0.72) clearly has more electrons than (Si,Al)2B (fractional occupancy 0.28). Reprinted from Banno *et al.* (2014), with permission from Elsevier. Corrected figure courtesy of Koichiro Fukuda.

set of starting phases for charge flipping (Šišak *et al.*, 2012). Since an approximate crystal-structure model is not necessarily available from external sources, it can be generated as the average of the structure models from the few best solutions of charge flipping applied to the incomplete data set. However, this model need not be close to the true model, because charge flipping applied to incomplete data may lead to a meaningless structure model that gives a good fit to the available data. Šišak *et al.* (2012) used the MEM to improve the set of starting phases of the approximate model, since the most reliable model will have the maximum value of the entropy of its electron density.

4.8.7.5. *Disorder and anharmonic atomic displacements*

Local maxima in the electron densities correspond to the positions of the atoms in ordered crystal structures. The MEM applied to diffraction data of partially ordered crystals leads to electron densities with local maxima of decreased magnitude for all partially occupied atomic sites. This feature has been nicely demonstrated in a series of studies on SiAlON compounds (Banno *et al.*, 2014). Fig. 4.8.10 shows part of the crystal structure with three independent (Si,Al) sites and three independent (O,N) sites. The site (Si,Al)2 is split into a pair of partially occupied sites with fractional occupancies of 0.72 for (Si,Al)2A and 0.28 for (Si,Al)2B. These unequal occupancies of the two sites of the split position are quantitatively reproduced in the MEM electron density (bottom part of Fig. 4.8.10). For the hydrogen-storage material KBH_4, an analysis by the MEM has revealed thermally activated orientational disorder of BH_4 groups (Bindzus *et al.*, 2015). The MEM combined with Rietveld refinements against X-ray powder-diffraction data has been used to locate extra-framework atoms in zeolites. This includes the determination of the locations of water molecules and potassium atoms in zeolite YNU-5 (Nakazawa *et al.*, 2017), the location of catalytically active Cu^{2+} in zeolite CHA (Andersen *et al.*, 2014) and absorbed water in faujasite (Perez *et al.*, 2017). Finally, the MEM has been used to determine the atomic distribution due to anharmonic displacements, including the identification of the diffusion pathways for Li^+-ion conduction in crystal structures or the absence thereof (Dietrich *et al.*, 2017; Monchak *et al.*, 2016). Employing the two-channel MEM with maps for atoms with negative and for atoms with positive scattering lengths, respectively, Monchak *et al.* (2016) have obtained a continuous volume of negative scattering density, demonstrating diffusion pathways for Li^+ ions in the superionic conductor $Li_{1.3}Al_{0.3}Ti_{1.7}(PO_4)_3$ (Fig. 4.8.11).

Atomic positions are also accessible through the nuclear-weighted X-ray maximum entropy method (NXMEM) introduced by Christensen *et al.* (2015). NXMEM defines nuclear scattering factors with the atomic pseudo-form factor equal to the number of electrons of the atom. Calculated structure factors of a good structure model are employed for the transformation of observed structure factors towards observed electron-weighted nuclear structure factors (Christensen *et al.*, 2015) in a procedure similar to the procedure for correcting observed structure factors for anomalous diffraction, extinction and scaling (Bagautdinov *et al.*, 1998; see Section 4.8.6.4). In this way, model bias is introduced into the MEM. The MEM and NXMEM have been employed to elucidate disorder and anharmonic displacements of the metal atoms in thermoelectric PbS, PbTe and SnTe as well as CsCl (Christensen *et al.*, 2015; Kastbjerg *et al.*, 2013; Sist *et al.*, 2016, 2017).

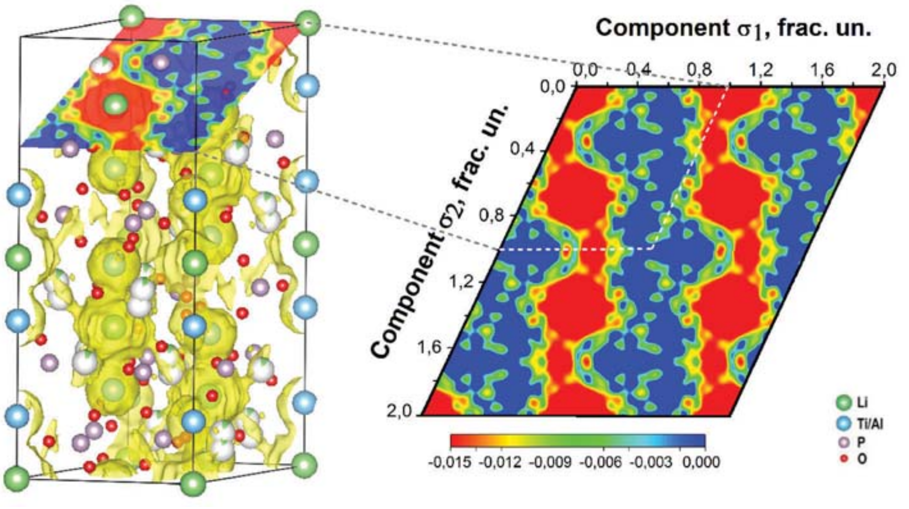

Figure 4.8.11
Crystal structure and MEM-reconstructed negative nuclear-density map of one unit cell of $Li_{1.3}Al_{0.3}Ti_{1.7}(PO_4)_3$, and the section $(01\bar{4})$ of this density. The axes in the right-hand panel are labelled with the values in fractional units (frac. un.) along the lattice directions denoted by σ_1 and σ_2. Reprinted with permission from Monchak *et al.* (2016). Copyright (2016) American Chemical Society.

4.8.7.6. *Accurate electron densities*

Initial applications of the MEM to single-crystal X-ray diffraction data have shown the importance of diffraction data sets being complete up to a resolution better than $[\sin(\theta)/\lambda]_{\max} = 1$ Å^{-1} if the determination of the electron density in chemical bonds is the goal (de Vries *et al.*, 1996; Takata & Sakata, 1996). These are the same requirements as the data have to fulfil for a multipole refinement (Gatti & Macchi, 2012). In X-ray powder diffraction, high-resolution data sets with $[\sin(\theta)/\lambda]_{\max} > 1.3$ Å^{-1} can be obtained with short-wavelength synchrotron radiation (Nishibori *et al.*, 2007; Momma *et al.*, 2013; Kato & Tanaka, 2016). Application of the MEM then may lead to electron densities that possess the quality of showing the reorganization of electron density within chemical bonds.

Integrated atomic charges can be determined from these MEM electron densities by topological analysis according to the quantum theory of atoms in molecules (QTAIM; Bader, 1990) of the experimental electron-density distribution. For the case of powder X-ray diffraction data for $LiBD_4$ this approach was successfully demonstrated by Buchter *et al.* (2011). Generation of accurate electron-density distributions may be impeded if too many reflections are available as *G* constraints, despite a formally high resolution of the diffraction data. This may happen in the case of heavy overlap of reflections, as it is an increasing problem for broad reflections and for structures of increasing complexity.

4.8.8. Extensions of the MEM

The principle of MaxEnt states that the most probable electron density is the one that maximizes the entropy [equation (4.8.2)], while fulfilling one or more constraints [*e.g.* the *F* constraint in equation (4.8.10)]. Straightforward application of the MaxEnt principle usually leads to noisy maps. Several extensions of the MEM have already been discussed in this chapter, all of which aim at a MEM that leads to a density distribution that is as informative as possible. They include the use of a non-uniform prior density [equation (4.8.2)], the use of prior-derived *F* constraints (Section 4.8.6.3), the use of static weights [equation (4.8.10)] and the selection of the point of convergence, $\chi^2_{\rm aim}$. The latter two aspects will be presented in more detail here. Finally, we will discuss the extension of the MEM to superspace for applications to aperiodic crystals (Section 4.8.8.3).

4.8.8.1. *Distribution of normalized residuals of the structure factors*

The experimental structure-factor amplitudes are not known exactly but deviate from their true values by an unknown amount. Assuming a Gaussian probability distribution for the difference between the measured and true values, the probability distribution is described by a single standard uncertainty σ_i or variance σ_i^2 for each structure-factor amplitude $|F(\mathbf{H}_i)|$.

For a sufficient number of independent reflections, one then expects a Gaussian distribution of the normalized residuals of the structure factors,

$$\frac{\Delta F(\mathbf{H}_i)}{\sigma(\mathbf{H}_i)} = \frac{F_{\rm obs}(\mathbf{H}_i) - F_{\rm MEM}(\mathbf{H}_i)}{\sigma(\mathbf{H}_i)}, \qquad (4.8.33)$$

if the $F_{\rm MEM}(\mathbf{H}_i)$ have been calculated from the MEM electron density. However, it was found (de Vries *et al.*, 1994; Jauch & Palmer, 1993; Palatinus & van Smaalen, 2002) that the distribution of the normalized residuals of the structure factors can deviate strongly from the Gaussian distribution. A few reflections (usually strong reflections at low angles) possess residuals of very large magnitudes, while the rest of the reflections are fitted almost exactly in order to fulfil the *F* constraint [equation (4.8.10) with $w_i = 1$ and $\chi^2_{\rm aim} = 1$]. The deviation from a Gaussian distribution of the residuals is reflected in the MEM electron density through the presence of non-physical features.

One possible solution to this problem was suggested by de Vries *et al.* (1994), who proposed so-called static weights, where weights are defined as proportional to some inverse integer power, $n = 2, 3, 4, \ldots$, of the length of the scattering vector [equation (4.8.10)]:

$$w_i = \frac{1}{|\mathbf{H}_i|^n}\left(\frac{1}{N_F}\sum_{i=1}^{N_F}\frac{1}{|\mathbf{H}_i|^n}\right)^{-1}. \qquad (4.8.34)$$

Both de Vries *et al.* (1994) and recent calculations on single-crystal X-ray diffraction by Hofmann *et al.* (2007) have shown $n = 4$ to be an optimal value. Another set of weights proposed by de Vries *et al.* (1994) is a weight proportional to an integer power of the structure-factor amplitude:

$$w_i = |F(\mathbf{H}_i)|^n\left(\frac{1}{N_F}\sum_{i=1}^{N_F}|F(\mathbf{H}_i)|^n\right)^{-1}. \qquad (4.8.35)$$

Static weights according to equation (4.8.34) are preferred for most applications. They ensure that the originally worst-fitting low-order reflections obtain a high weight in the modified *F* constraint, with the consequence of a much better approximation of the Gaussian distribution of the final distribution of residuals. Static weights according to equation (4.8.35) have been shown to lead to better results in the case of incommensurately modulated crystals (Section 4.8.8.3). This type of aperiodic crystals has many weak superlattice reflections including many appearing at low order, but which should be given small weights. Here, weights calculated according to (4.8.35) give high weights to the terms containing intense main reflections, most of which are of low order.

Another solution to the problem of a non-Gaussian distribution of residuals was proposed by Palatinus & van Smaalen (2002). They noted that the *F* constraint [equation (4.8.10)] is based on the second central moment of the distribution of $\Delta F(\mathbf{H})/\sigma(\mathbf{H})$. This allowed the introduction of the concept of generalized *F* constraints, or F_n constraints, which are based on the moment of order *n*:

$$\begin{aligned} C_{F_n} &= -\chi^2_{\rm aim} + \frac{1}{m_n({\rm Gauss})}\frac{1}{N_F}\sum_{i=1}^{N_F} w_i\left(\frac{|F_{\rm obs}(\mathbf{H}_i) - F_{\rm MEM}(\mathbf{H}_i)|}{\sigma(\mathbf{H}_i)}\right)^n \\ &= 0, \end{aligned} \qquad (4.8.36)$$

where $n = 2, 4, 6, \ldots$ is an even integer, and m_n(Gauss) is the value of the *n*th central moment of the Gaussian distribution. Several tests on selected examples showed that a generalized *F* constraint with $n = 4$ may lead to an improved distribution of residuals (Palatinus & van Smaalen, 2002).

4.8.8.2. *Stopping criterion*

The value of $\chi^2_{\rm aim}$ [equation (4.8.10)] does not influence the iterative procedure, since any constant in C_F drops out of its derivative with respect to any of the density parameters $\{\rho_i\}$ [equation (4.8.17)]. However, the value of $\chi^2_{\rm aim}$ determines the point of convergence through the criterion $C_F = 0$. It then directly gives the value of the sum of squares of reduced residuals [equations (4.8.10) and (4.8.33)]. Standard probability theory gives an expectation value of this sum of $\chi^2_{\rm aim} = 1$. Bayesian probability theory states that the model is biased towards the data, so that at convergence $\chi^2_{\rm aim} < 1$ (Gull & Skilling, 1999). These values not only assume a Gaussian distribution of the measurement errors in $F_{\rm obs}(\mathbf{H}_i)$, but they also assume that the estimated standard uncertainties $\sigma(\mathbf{H}_i)$ have been accurately obtained. This is not always the case. Straightforward application of the classical or Bayesian values of $\chi^2_{\rm aim}$ as a stopping criterion for the iterative procedure thus might lead to the fitting of noise in the data (when $\chi^2_{\rm aim}$ is too small) or to information in the data that is not fitted by the electron density (when $\chi^2_{\rm aim}$ is too large).

Based on these considerations, an empirical criterion for determination of the stopping criterion $\chi^2_{\rm aim}$ has been proposed (Hofmann *et al.*, 2007). This procedure involves a series of MEM calculations with different values of $\chi^2_{\rm aim}$. Visual inspection of the electron-density maps and the difference Fourier maps then allows the optimal value of $\chi^2_{\rm aim}$ to be determined. The difference Fourier map should contain features near atomic positions that are of similar magnitude to features outside bonds and atoms, thus showing them to be true noise. For the same $\chi^2_{\rm aim}$, the MEM electron-density map should show smooth isosurfaces and should be free from spurious maxima. Too-small values of $\chi^2_{\rm aim}$ violate the latter condition, while too-high values of $\chi^2_{\rm aim}$ give a difference Fourier map with clearly unfitted structure near the atoms. This procedure has worked well for several data sets. It could be shown that the optimal value of $\chi^2_{\rm aim}$ is related to the goodness of fit (GoF) of a multipole refinement using the same data by the relation $\chi^2_{\rm aim}$(optimum) = 0.68 × GoF (van Smaalen & Netzel, 2009).

4.8.8.3. *Generalization of MaxEnt algorithm to n dimensions (n > 3) and application to powder-diffraction data of aperiodic structures*

One aim of the application of the MEM in the field of superspace crystallography is to uncover the true modulations, and thus improve the structure model for aperiodic crystals (Papoular *et al.*, 1991; Steurer, 1991; Weber & Yamamoto, 1997; van Smaalen *et al.*, 2003; Palatinus & van Smaalen, 2004; Li *et al.*, 2011). Crystal structures of aperiodic crystals are described as periodic structures in (3 + d)-dimensional space, called superspace, where $n = 3 + d$ is the dimension of the space [*International Tables for Crystallography*, Volume C, Chapter 9.8 (Janssen *et al.*, 2006); van Smaalen, 2007]. Accordingly, aperiodic crystals are characterized by a generalized electron density $\rho_s(\mathbf{x}_s)$ in n-dimensional space. The MEM can be applied to the generalized electron density by the same formalism as described in this chapter. A discrete electron density is defined with $\rho_i = \rho_s(\mathbf{x}_i)$ where $\mathbf{x}_i$ are the coordinates of a grid of $N_{\rm pix} = N_1 \times \ldots \times N_{3+d}$ pixels over the superspace unit cell. Structure factors are the n-dimensional Fourier transform of $\rho_s(\mathbf{x}_s)$. With these two definitions, all equations of Sections 4.8.2–4.8.6 can directly be applied to superspace densities (van Smaalen *et al.*, 2003).

The MEM in superspace has only been applied to single-crystal X-ray diffraction data, but applications involving X-ray powder-diffraction data appear equally possible. It is actually a promising technique for structural analysis of powder-diffraction data of aperiodic crystals in those cases where only a limited number of the usually weak incommensurate superlattice reflections can be extracted from the powder-diffraction profile.

References

Andersen, C. W., Bremholm, M., Vennestrøm, P. N. R., Blichfeld, A. B., Lundegaard, L. F. & Iversen, B. B. (2014). *Location of Cu^{2+} in CHA zeolite investigated by X-ray diffraction using the Rietveld/maximum entropy method. IUCrJ*, **1**, 382–386.

Bader, R. F. W. (1990). *Atoms in Molecules: A Quantum Theory*. Oxford: Clarendon.

Baerlocher, C., McCusker, L. B. & Palatinus, L. (2007). *Charge flipping combined with histogram matching to solve complex crystal structures from powder diffraction data. Z. Kristallogr.* **222**, 47–53.

Bagautdinov, B., Luedecke, J., Schneider, M. & van Smaalen, S. (1998). *Disorder in the crystal structure of Cs_2HgCl_4 studied by the maximum entropy method. Acta Cryst.* B**54**, 626–634.

Banno, H., Hanai, T., Asaka, T., Kimoto, K. & Fukuda, K. (2014). *Electron density distribution and disordered crystal structure of 15R-SiAlON, $SiAl_4O_2N_4$. J. Solid State Chem.* **211**, 124–129.

Bindzus, N., Cargnoni, F., Gatti, C., Richter, B., Jensen, T. R., Takata, M. & Iversen, B. B. (2015). *Mapping the complete bonding network in KBH_4 using the combined power of powder diffraction and maximum entropy method. Comput. Theor. Chem.* **1053**, 245–253.

Bricogne, G. (1984). *Maximum entropy and the foundations of direct methods. Acta Cryst.* A**40**, 410–445.

Bricogne, G. (1988). *A Bayesian statistical theory of the phase problem. I. A multichannel maximum-entropy formalism for constructing generalized joint probability distributions of structure factors. Acta Cryst.* A**44**, 517–545.

Bricogne, G. (1991). *A multisolution method of phase determination by combined maximization of entropy and likelihood. III. Extension to powder diffraction data. Acta Cryst.* A**47**, 803–829.

Bricogne, G. (1993). *Direct phase determination by entropy maximization and likelihood ranking: status report and perspectives. Acta Cryst.* D**49**, 37–60.

Bricogne, G. & Gilmore, C. J. (1990). *A multisolution method of phase determination by combined maximization of entropy and likelihood. I. Theory, algorithms and strategy. Acta Cryst.* A**46**, 284–297.

Bryan, R. K. & Skilling, J. (1980). *Deconvolution by maximum-entropy, as illustrated by application to the jet of M87. Mon. Not. R. Astron. Soc.* **191**, 69–79.

Bryan, R. K. & Skilling, J. (1986). *Maximum entropy image reconstruction from phaseless Fourier data. Opt Acta Int. J. Opt.* **33**, 287–299.

Buchter, F., Lodziana, Z., Remhof, A., Mauron, Ph., Friedrichs, O., Borgschulte, A., Züttel, A., Filinchuk, Y. & Palatinus, L. (2011). *Experimental charge density of LiBD from maximum entropy method. Phys. Rev. B*, **83**, 064107.

Burch, S. F., Gull, S. F. & Skilling, J. (1983). *Image restoration by a powerful maximum entropy method. Comput. Vis. Graph. Image Process.* **23**, 113–128.

Burger, K. & Prandl, W. (1999). *A new type of constraint in the maximum-entropy method using ambiguous phase information from anomalous-scattering powder data. Acta Cryst.* A**55**, 719–728.

Christensen, S., Bindzus, N., Christensen, M. & Iversen, B. B. (2015). *Nuclear-weighted X-ray maximum entropy method – NXMEM. Acta Cryst.* A**71**, 9–19.

Collins, D. M. (1982). *Electron density images from imperfect data by iterative entropy maximization. Nature*, **298**, 49–51.

Collins, D. M. & Mahar, M. C. (1983). *Electron density: an exponential model. Acta Cryst.* A**39**, 252–256.

Dietrich, C., Weber, D. A., Culver, S., Senyshyn, A., Sedlmaier, S. J., Indris, S., Janek, J. & Zeier, W. G. (2017). *Synthesis, structural characterization, and lithium ion conductivity of the lithium thiophosphate $Li_2P_2S_6$. Inorg. Chem.* **56**, 6681–6687.

Dinnebier, R. E., Schneider, M., van Smaalen, S., Olbrich, F. & Behrens, U. (1999). *Disorder determined by high-resolution powder diffraction: structure of pentamethylcyclopentadienyllithium. Acta Cryst.* B**55**, 35–44.

Dinnebier, R. E., Vensky, S., Jansen, M. & Hanson, J. C. (2005). *Crystal structures and topological aspects of the high-temperature phases and decomposition products of the alkali-metal oxalates $M_2[C_2O_4]$ (M = K, Rb, Cs). Chem. Eur. J.* **11**, 1119–1129.

French, S. (1978). *A Bayesian three-stage model in crystallography. Acta Cryst.* A**34**, 728–738.

Gatti, C. & Macchi, P. (2012). *Modern Charge-Density Analysis*. Berlin: Springer.

Gilmore, C. J. (1996). *Maximum entropy and Bayesian statistics in crystallography: a review of practical applications. Acta Cryst.* A**52**, 561–589.

Gilmore, C. J., Bricogne, G. & Bannister, C. (1990). *A multisolution method of phase determination by combined maximization of entropy* *and likelihood. II. Application to small molecules. Acta Cryst.* A**46**, 297–308.

Gilmore, C., Dong, W. & Bricogne, G. (1999). *A multisolution method of phase determination by combined maximization of entropy and likelihood. VI. The use of error-correcting codes as a source of phase permutation and their application to the phase problem in powder, electron and macromolecular crystallography. Acta Cryst.* A**55**, 70–83.

Gilmore, C. J., Henderson, K. & Bricogne, G. (1991). *A multisolution method of phase determination by combined maximization of entropy and likelihood. IV. The ab initio solution of crystal structures from their X-ray powder data. Acta Cryst.* A**47**, 830–841.

Gilmore, C. J. & Nicholson, W. (1994). *The MICE computer program, and its application to direct phase determination for powders, electron diffraction and macromolecules. Trans. Am. Crystallogr. Assoc.* **30**, 15–27.

Gull, S. F. & Daniell, G. J. (1978). *Image reconstruction from incomplete and noisy data. Nature*, **272**, 686–690.

Gull, S. F. & Skilling, J. (1984). *Maximum entropy method in image processing. IEE Proc.* **131**, 646–659.

Gull, S. F. & Skilling, J. (1987). *Recent developments at Cambridge.* In *Maximum Entropy and Bayesian Spectral Analysis and Estimation Problems*, edited by C. R. Smith & G. J. Erickson, pp. 149–160. Dordrecht: Springer.

Gull, S. F. & Skilling, J. (1999). *MemSys5 User's Manual.* Maximum Entropy Data Consultants Ltd, Bury St Edmunds, UK.

Hofmann, A., Netzel, J. & van Smaalen, S. (2007). *Accurate charge density of trialanine: a comparison of the multipole formalism and the maximum entropy method (MEM). Acta Cryst.* B**63**, 285–295.

Iversen, B. B., Larsen, F. K., Souhassou, M. & Takata, M. (1995). *Experimental evidence for the existence of non-nuclear maxima in the electron-density distribution of metallic beryllium. A comparative study of the maximum entropy method and the multipole refinement method. Acta Cryst.* B**51**, 580–591.

Janssen, T., Janner, A., Looijenga-Vos, A. & de Wolff, P. M. (2006). *Incommensurate and commensurate modulated structures*. In *International Tables for Crystallography*, Vol. C, *Mathematical, Physical and Chemical Tables*, edited by E. Prince, pp. 907–955. Chester: International Union of Crystallography.

Jauch, W. & Palmer, A. (1993). *The maximum-entropy method in charge-density studies: aspects of reliability. Acta Cryst.* A**49**, 590–591.

Kastbjerg, S., Bindzus, N., Søndergaard, M., Johnsen, S., Lock, N., Christensen, M., Takata, M., Spackman, M. A. & Iversen, B. B. (2013). *Direct evidence of cation disorder in thermoelectric lead chalcogenides PbTe and PbS. Adv. Funct. Mater.* **23**, 5477–5483.

Kato, K. & Tanaka, H. (2016). *Visualizing charge densities and electrostatic potentials in materials by synchrotron X-ray powder diffraction. Adv. Phys. X*, **1**, 55–80.

Kubota, Y., Takata, M., Matsuda, R., Kitaura, R., Kitagawa, S. & Kobayashi, T. C. (2006). *Metastable sorption state of a metal–organic porous material determined by in situ synchrotron powder diffraction. Angew. Chem. Int. Ed.* **45**, 4932–4936.

Kumazawa, S., Takata, M. & Sakata, M. (1995). *On the single-pixel approximation in maximum-entropy analysis. Acta Cryst.* A**51**, 47–53.

Le Bail, A., Duroy, H. & Fourquet, J. L. (1988). *Ab-initio structure determination of* $LiSbWO_6$ *by x-ray powder diffraction. Mater. Res. Bull.* **23**, 447–452.

Li, L., Wölfel, A., Schönleber, A., Mondal, S., Schreurs, A. M. M., Kroon-Batenburg, L. M. J. & van Smaalen, S. (2011). *Modulated anharmonic ADPs are intrinsic to aperiodic crystals: a case study on incommensurate* Rb_2ZnCl_4*. Acta Cryst.* B**67**, 205–217.

Livesey, A. K. & Skilling, J. (1985). *Maximum entropy theory. Acta Cryst.* A**41**, 113–122.

Macchi, P. & Coppens, P. (2001). *Relativistic analytical wave functions and scattering factors for neutral atoms beyond Kr and for all chemically important ions up to* I^-*. Acta Cryst.* A**57**, 656–662.

Magdysyuk, O. V., Dinnebier, R. E., van Smaalen, S., Zykin, M. A., Kazin, P. E. & Jansen, M. (2012). *Reconstructions of electron density by the maximum entropy method from X-ray powder diffraction data based on incomplete and complete crystal structure models: a case study of apatites with different intercalated metal atoms. Z. Kristallogr.* **227**, 321–333.

Momma, K., Ikeda, T., Belik, A. A. & Izumi, F. (2013). *Dysnomia, a computer program for maximum-entropy method (MEM) analysis and its performance in the MEM-based pattern fitting. Powder Diffr.* **28**, 184–193.

Monchak, M., Hupfer, T., Senyshyn, A., Boysen, H., Chernyshov, D., Hansen, T., Schell, K. G., Bucharsky, E. C., Hoffmann, M. J. & Ehrenberg, H. (2016). *Lithium diffusion pathway in* $Li_{1.3}Al_{0.3}Ti_{1.7}(PO_4)_3$ *(LATP) superionic conductor. Inorg. Chem.* **55**, 2941–2945.

Mondal, S., Prathapa, S. J. & van Smaalen, S. (2012). *Experimental dynamic electron densities of multipole models at different temperatures. Acta Cryst.* A**68**, 568–581.

Nakazawa, N., Ikeda, T., Hiyoshi, N., Yoshida, Y., Han, Q., Inagaki, S. & Kubota, Y. (2017). *A microporous aluminosilicate with 12-, 12-, and 8-ring pores and isolated 8-ring channels. J. Am. Chem. Soc.* **139**, 7989–7997.

Navaza, J. (1985). *On the maximum-entropy estimate of the electron density function. Acta Cryst.* A**41**, 232–244.

Navaza, J. (1986). *The use of non-local constraints in maximum-entropy electron density reconstruction. Acta Cryst.* A**42**, 212–223.

Navaza, J., Castellano, E. E. & Tsoucaris, G. (1983). *Constrained density modifications by variational techniques. Acta Cryst.* A**39**, 622–631.

Nishibori, E., Sunaoshi, E., Yoshida, A., Aoyagi, S., Kato, K., Takata, M. & Sakata, M. (2007). *Accurate structure factors and experimental charge densities from synchrotron X-ray powder diffraction data at SPring-8. Acta Cryst.* A**63**, 43–52.

Oszlányi, G. & Sütő, A. (2004). *Ab initio structure solution by charge flipping. Acta Cryst.* A**60**, 134–141.

Oszlányi, G. & Sütő, A. (2005). *Ab initio structure solution by charge flipping. II. Use of weak reflections. Acta Cryst.* A**61**, 147–152.

Palatinus, L. (2003). PhD thesis. University of Bayreuth, Bayreuth, Germany.

Palatinus, L. (2004). *Ab initio determination of incommensurately modulated structures by charge flipping in superspace. Acta Cryst.* A**60**, 604–610.

Palatinus, L. (2013). *The charge-flipping algorithm in crystallography. Acta Cryst.* B**69**, 1–16.

Palatinus, L. & Chapuis, G. (2007). *SUPERFLIP – a computer program for the solution of crystal structures by charge flipping in arbitrary dimensions. J. Appl. Cryst.* **40**, 786–790.

Palatinus, L., Steurer, W. & Chapuis, G. (2007). *Extending the charge-flipping method towards structure solution from incomplete data sets. J. Appl. Cryst.* **40**, 456–462.

Palatinus, L. & van Smaalen, S. (2002). *The generalized F constraint in the maximum-entropy method – a study on simulated data. Acta Cryst.* A**58**, 559–567.

Palatinus, L. & van Smaalen, S. (2004). *Incommensurate modulations made visible by the maximum entropy method in superspace. Z. Kristallogr.* **219**, 719–729.

Palatinus, L. & van Smaalen, S. (2005). *The prior-derived F constraints in the maximum-entropy method. Acta Cryst.* A**61**, 363–372.

Papoular, R. J., Collin, G., Colson, D. & Viallet, V. (2002). *Direct imaging of fractional oxygen* O_δ *in Hg-based high-*T_c *superconductors. AIP Conf. Proc.* **617**, 204–226.

Papoular, R. J., de Boissieu, M. & Janot, C. (1991). In *Methods of Structural Analysis of Modulated Structures Quasicrystals*, edited by J. M. Perez-Mato, F. J. Zuniga & G. Madariaga, pp. 333–343. Singapore: World Scientific.

Papoular, R. J. & Gillon, B. (1990). *Maximum entropy reconstruction of spin density maps in crystals from polarized neutron diffraction data. Europhys. Lett.* **13**, 429–434.

Papoular, R. J., Vekhter, Y. & Coppens, P. (1996). *The two-channel maximum-entropy method applied to the charge density of a molecular crystal: α-glycine. Acta Cryst.* A**52**, 397–407.

Perez, C. A. C., de Resende, N. S., Salim, V. M. M. & Schmal, M. (2017). *Water interaction in faujasite probed by in situ X-ray powder diffraction. J. Phys. Chem. C*, **121**, 2755–2761.

Rietveld, H. M. (1967). *Line profiles of neutron powder-diffraction peaks for structure refinement. Acta Cryst.* **22**, 151–152.

Rietveld, H. M. (1969). *A profile refinement method for nuclear and magnetic structures. J. Appl. Cryst.* **2**, 65–71.

Roversi, P., Irwin, J. J. & Bricogne, G. (1998). *Accurate charge-density studies as an extension of Bayesian crystal structure determination. Acta Cryst.* A**54**, 971–996.

Sakata, M., Mori, R., Kumazawza, S., Takata, M. & Toraya, H. (1990). *Electron-density distribution from X-ray powder data by use of profile fits and the maximum-entropy method. J. Appl. Cryst.* **23**, 526–534.

Sakata, M. & Sato, M. (1990). *Accurate structure analysis by the maximum-entropy method. Acta Cryst.* A**46**, 263–270.

Sakata, M., Uno, T., Takata, M. & Howard, C. J. (1993). *Maximum-entropy-method analysis of neutron diffraction data. J. Appl. Cryst.* **26**, 159–165.

Sakata, M., Uno, T., Takata, M. & Mori, R. (1992). *Electron density in rutile (TiO_2) by the maximum entropy method. Acta Cryst.* B**48**, 591–598.

Samy, A., Dinnebier, R. E., van Smaalen, S. & Jansen, M. (2010). *Maximum entropy method and charge flipping, a powerful combination to visualize the true nature of structural disorder from in situ X-ray powder diffraction data. Acta Cryst.* B**66**, 184–195.

Schotte, K.-D., Schotte, U., Bleif, H.-J. & Papoular, R. J. (1995). *Maximum-entropy analysis of the cubic phases of KOH and KOD, NaOH and NaOD. Acta Cryst.* A**51**, 739–746.

Shannon, C. E. (1948*a*). *A Mathematical Theory of Communication. Bell Syst. Tech. J.* **27**, 379–423.

Shannon, C. E. (1948*b*). *A Mathematical Theory of Communication. Bell Syst. Tech. J.* **27**, 623–656.

Shmueli, U. (1996). Editor. *International Tables for Crystallography*, Vol. B, *Reciprocal Space*. Dordrecht: Kluwer Academic Publishers.

Shore, J. E. & Johnson, R. W. (1980). *Axiomatic derivation of the principle of maximum entropy and the principle of minimum cross-entropy. IEEE Trans. Inf. Theory*, **26**, 26–37.

Shore, J. E. & Johnson, R. W. (1983). *Comments on and correction to 'Axiomatic derivation of the principle of maximum entropy and the principle of minimum cross-entropy'. IEEE Trans. Inf. Theory*, **29**, 942–943.

Šišak, D., Baerlocher, C., McCusker, L. B. & Gilmore, C. J. (2012). *Optimizing the input parameters for powder charge flipping. J. Appl. Cryst.* **45**, 1125–1135.

Sist, M., Fischer, K. F. F., Kasai, H. & Iversen, B. B. (2017). *Low-temperature anharmonicity in cesium chloride (CsCl). Angew. Chem. Int. Ed.* **56**, 3625–3629.

Sist, M., Jensen Hedegaard, E. M., Christensen, S., Bindzus, N., Fischer, K. F. F., Kasai, H., Sugimoto, K. & Brummerstedt Iversen, B. (2016). *Carrier concentration dependence of structural disorder in thermoelectric $Sn_{1-x}Te$. IUCrJ*, **3**, 377–388.

Skilling, J. & Bryan, R. K. (1984). *Maximum entropy image reconstruction: general algorithm. Mon. Not. R. Astron. Soc.* **211**, 111–124.

Smaalen, S. van (2007). *Incommensurate Crystallography*. New York: Oxford University Press Inc.

Smaalen, S. van & Netzel, J. (2009). *The maximum entropy method in accurate charge-density studies. Phys. Scr.* **79**, 048304.

Smaalen, S. van, Palatinus, L. & Schneider, M. (2003). *The maximum-entropy method in superspace. Acta Cryst.* A**59**, 459–469.

Steurer, W. (1991). *Methods of Structural Analysis of Modulated Structures Quasicrystals*, edited by J. M. Perez-Mato, F. J. Zuniga & G. Madariaga, pp. 344–349. Singapore: World Scientific.

Su, Z. & Coppens, P. (1997). *Relativistic X-ray elastic scattering factors for neutral atoms Z = 1–54 from multiconfiguration Dirac–Fock wavefunctions in the 0–12 $Å^{-1}$ $\sin\theta/\lambda$ range, and six-Gaussian analytical expressions in the 0–6 $Å^{-1}$ range. Acta Cryst.* A**53**, 749–762.

Takata, M. (2008). *The MEM/Rietveld method with nano-applications – accurate charge-density studies of nano-structured materials by synchrotron-radiation powder diffraction. Acta Cryst.* A**64**, 232–245.

Takata, M. & Sakata, M. (1996). *The influence of the completeness of the data set on the charge density obtained with the maximum-entropy method. A re-examination of the electron-density distribution in Si. Acta Cryst.* A**52**, 287–290.

Takata, M., Umeda, B., Nishibori, E., Sakata, M., Saito, Y., Ohno, M. & Shinohara, H. (1995). *Confirmation by X-ray diffraction of the endohedral nature of the metallofullerene $Y@C_{82}$. Nature*, **377**, 46–49.

Vries, R. Y. de, Briels, W. J. & Feil, D. (1994). *Novel treatment of the experimental data in the application of the maximum-entropy method to the determination of the electron-density distribution from X-ray experiments. Acta Cryst.* A**50**, 383–391.

Vries, R. Y. de, Briels, W. J. & Feil, D. (1996). *Critical analysis of non-nuclear electron-density maxima and the maximum entropy method. Phys. Rev. Lett.* **77**, 1719–1722.

Waasmaier, D. & Kirfel, A. (1995). *New analytical scattering-factor functions for free atoms and ions. Acta Cryst.* A**51**, 416–431.

Weber, S. & Yamamoto, A. (1997). *Application of the five-dimensional maximum-entropy method to the structure refinement of decagonal $Al_{70}Mn_{17}Pd_{13}$. Philos. Mag. A*, **76**, 85–106.

Wilkins, S. W. (1983). *Statistical geometry. II. Numerical solution via the single pixel equation. Acta Cryst.* A**39**, 892–896.

Wilkins, S. W., Varghese, J. N. & Lehmann, M. S. (1983). *Statistical geometry. I. A self-consistent approach to the crystallographic inversion problem based on information theory. Acta Cryst.* A**39**, 47–60.

Wu, N. (1997). *The Maximum Entropy Method*. Springer Series in Information Science. Berlin: Springer.

Wu, J., Leinenweber, K., Spence, J. C. H. & O'Keeffe, M. (2006). *Ab initio phasing of X-ray powder diffraction patterns by charge flipping. Nat. Mater.* **5**, 647–652.

Zheludev, A., Papoular, R. J., Ressouche, E. & Schweizer, J. (1995). *A non-uniform reference model for maximum-entropy density reconstructions from diffraction data. Acta Cryst.* A**51**, 450–455.

International Tables for Crystallography (2019). Vol. H, Chapter 4.9, pp. 489–514.

4.9. Structure validation

J. A. Kaduk

4.9.1. Introduction

Just as there is no single measure of the quality of a Rietveld refinement, no one factor indicates the quality of a crystal structure derived from diffraction data. Statistical (Toby, 2006) and graphical measures are important, but chemical reasonableness can carry even more weight (McCusker *et al.*, 1999; Kaduk, 2007*a*,*b*). Much chemical knowledge is incorporated into structure-validation programs such as *PLATON* (Spek, 2003, 2009), which is at the core of the *checkCIF* system (Helliwell *et al.*, 2006), but many judgements of the validity and quality of a structure depend on the experience and expertise of the user. Knowledge of molecular geometry can be incorporated into Rietveld refinements by including restraints (soft constraints) and constraints into the refinement. In this chapter, thought processes and tools which can be applied during and after refinement to assess structural validity are discussed.

4.9.2. Statistical measures (with contributions from B. H. Toby)

In a Rietveld refinement, we fit a model to data; it is the model which is refined, not the data. The Rietveld algorithm optimizes the model function to minimize the weighted sum of squared differences between the observed and calculated intensity values. The most straightforward measure of the quality of the fit is the weighted profile *R* factor,

$$R_{\rm wp}^2 = \frac{\sum_i w_i (y_{oi} - y_{ci})^2}{\sum_i w_i y_{oi}^2}, \qquad (4.9.1)$$

in which y_{oi} are the observed intensities (data points), y_{ci} are the data points calculated from the model and w_i are the weights. Generally,

$$w_i = \frac{1}{\sigma^2(y_{oi})}, \qquad (4.9.2)$$

in which $\sigma(y_{oi})$ is the standard uncertainty (Schwarzenbach *et al.*, 1995, 1996) for the intensity. Other weighting schemes can be used, but when the errors are purely statistical in nature, it can be proven (Prince, 2004; David, 2004) that the smallest uncertainties in the fitted parameters are obtained with this weighting scheme.

If we have an ideal model, one that accurately predicts the true value of each y_{oi}, the average value of $(y_{oi} - y_{ci})^2$ will be equal to $\sigma^2(y_{oi})$, and the expected value of $w_i(y_{oi} - y_{ci})^2$ is unity. The fit (and thus the residual) that one would obtain with this ideal model is the best possible one that can be obtained, provided that the weights are correct. This 'best possible $R_{\rm wp}$' is a very useful concept, and is called the expected *R* factor, $R_{\rm exp}$. Using *N* as the number of data points and *P* as the number of refined parameters (Young, 1993),

$$R_{\rm exp}^2 = \frac{N - P}{\sum_i w_i y_{oi}^2}. \qquad (4.9.3)$$

A related statistical concept is the statistical quantity 'reduced chi squared', χ^2 (Toby, 2006). This is defined (Young, 1993) as

$$\chi^2 = \frac{1}{N - P} \sum_i \frac{(y_{oi} - y_{ci})^2}{\sigma^2(y_{oi})}. \qquad (4.9.4)$$

A little algebra shows that χ^2 can also be determined from the expected and weighted profile *R* factors:

$$\chi^2 = \left(\frac{R_{\rm wp}}{R_{\rm exp}}\right)^2. \qquad (4.9.5)$$

The single-crystal literature often uses the term goodness of fit (*S*), which is defined by $S^2 = \chi^2$. In powder diffraction, the convention is to report χ^2 rather than *S*.

During the refinement process, χ^2 (and $R_{\rm wp}$) starts out large when the model is poor and decreases as the model fits the data better. Least-squares refinement should never cause χ^2 to increase, but increases do sometimes occur when parameters are correlated. A small increase followed by a drop to a lower value in subsequent cycles of refinement is not a cause for concern, but a large increase during a refinement cycle is a sign of a problem.

If at any point $\chi^2 < 1$, the weights are wrong because the standard uncertainties are overestimated. This situation commonly occurs when the intensities have been scaled before refinement, such as when the data have been collected using a variable-divergence slit (all Rietveld programs assume fixed-slit intensities) and the uncertainties have not been calculated correctly. The standard uncertainty of a y_{oi} value is generally calculated as the square root of the number of counts (not counts s^{-1} or other count rates) at that point, and sometimes includes an additional contribution. Estimation of standard uncertainties can be difficult for detectors that do not directly count photons, such as charge-coupled detectors or image plates. Data from two-dimensional detectors are often on an arbitrary scale, and thus the statistical measures are not meaningful in an absolute sense. There are techniques for placing intensities on an absolute scale (Suortti *et al.*, 1985; Klug & Alexander, 1974), but they are not often used in powder diffraction. Getting the weights right is important. I have seen cases in which the weights were calculated incorrectly; this effectively discards data, resulting in a distorted structural model and incorrect chemical conclusions derived from it.

When χ^2 is close to unity, the errors in the fit are dominated by the statistical errors in the data. There is no guarantee that the model is correct (there may be many models that produce equivalent fits), but the data are not sufficient to support a more complex model. Many correct refinements have $1 < \chi^2 < 3$ (or even higher; see below), but under some circumstances models obtained with $\chi^2 > 30$ may provide accurate crystallographic results, and there is no general rule on what value of χ^2 is low enough. As will be discussed later, even refinements with χ^2 close to unity can have significant problems (that is, can be wrong).

When $\chi^2 \gg 1$, several situations are possible:

(i) The model is reasonable, but the standard uncertainties are underestimated.

(ii) The model is incomplete and/or the data contain systematic errors.

Copyright © 2019 International Union of Crystallography

(iii) The model is wrong.

Many fine studies are published with $\chi^2 \gg 1$, but the reasons for the poor fit must be understood and discussed.

An important test of the fit when $\chi^2 \gg 1$ is to compare the residuals from the Rietveld refinement with those obtained from a Le Bail (2008) or Pawley (1981) fit, in which the peak intensities are optimized without the constraint of a structural model (see Chapter 3.5). If the crystallographic fit is as good as the structureless fit, then features of the data such as profile shapes or background are not being modelled correctly. More detailed analysis is required to understand whether these errors are affecting the integrated intensities and thus the crystallographic results. If the structureless fit is good but the Rietveld fit is not, there are likely to be systematic crystallographic problems with the model. Often these can be discerned by considering the chemical reasonableness of the model, but sometimes the real chemical system is more complex than can be described by a conventional crystallographic model (for example, it might contain stacking faults and other types of imperfections). However, systematic errors in the data, such as preferred orientation or (more problematically) poor grain sampling, can produce a pattern that cannot be fitted well by a reasonable model.

Having a χ^2 value that is far from unity has a significant implication when interpreting the results from many modern Rietveld programs (Toby, 2006). The least-squares minimization allows the statistical uncertainty in the observations to be propagated to derive uncertainties in the refined parameters. These values are derived from the variance–covariance matrix, but these estimates are accurate only when $\chi^2 \simeq 1$ (Prince, 2004). Many (but not all, and not necessarily for all variables) Rietveld programs multiply the apparent standard uncertainties by the slope of the normal probability plot (discussed below in Section 4.9.3) to arrive at 'more accurate' estimates of the uncertainties. If the source of the error has a negligible correlation with the parameter in question (such as profile-shape errors and atomic coordinates), the 'corrected' uncertainty may be worse than the true uncertainty. On the other hand, if the systematic error is correlated with the parameter (such as intensity errors from beam spillover or a too-thin flat-plate specimen, which will correlate with the atomic displacement coefficients), the correction may not be large enough.

Most modern Rietveld programs compute other residuals, most of which I do not find useful in distinguishing bad refinements from good ones. Commonly calculated is the unweighted profile R factor,

$$R_p = \sum_i |y_{oi} - y_{ci}| / \sum_i y_{oi}. \qquad (4.9.6)$$

Since $R_{\rm wp}$ is the quantity minimized in the Rietveld refinement, and the weights are important, I do not find this quantity particularly useful. Some programs calculate $R_{\rm wp}$ both for the whole pattern and with the background subtracted. The background-subtracted version can occasionally be useful for assessing the quality of the fit to the peak intensities.

Single-crystal refinement residuals are based on the observed and calculated structure-factor amplitudes $F_o(hkl)$ and $F_c(hkl)$. While the $F_c(hkl)$ are computed directly from the structural model in a Rietveld refinement, the $F_o(hkl)$ are not directly measured because of the overlap of reflections in the powder pattern. One of the several great insights in the development of the Rietveld method (Rietveld, 1969) was the mechanism for estimating $F_o(hkl)$ by partitioning observed intensities according to the $F_c(hkl)$ values. The better the model, the better these estimates become. Using the extracted $F_o(hkl)$ and $F_c(hkl)$, approximations to the normal unweighted single-crystal R factors can be calculated (Young, 1993):

$$R(F) = \frac{\sum_{hkl} |F_o(hkl) - F_c(hkl)|}{\sum_{hkl} F_o(hkl)},$$
$$R(F^2) = \frac{\sum_{hkl} |F_o^2(hkl) - F_c^2(hkl)|}{\sum_{hkl} F_o^2(hkl)}. \qquad (4.9.7)$$

Since the $F_o(hkl)$ values are biased by the model, these residuals tend to be smaller than would be derived from a single-crystal data set, but they are useful for comparisons. The label $R_{\rm Bragg}$ is used in the Rietveld literature to refer to reflection-intensity-based residuals, but the term is ambiguous and is used to mean both $R(F)$ and $R(F^2)$. The best practice is to report both quantities so that there is no ambiguity.

There are differences of opinion on the utility of these various residuals, mainly arising from how they are computed. The easiest way to achieve a low χ^2 is to collect poor (noisy) data. The statistical errors in the data then swamp any errors in the model. A Rietveld refinement using noisy data will tend to have a low χ^2 but a high $R_{\rm wp}$. A similar situation arises when the background makes up a significant portion of the intensity, such as when a highly fluorescent specimen is measured. Counting for longer times increases the statistical precision of a diffraction measurement. As the total number of counts in the pattern increases, the $R_{\rm exp}$ decreases. Collecting better data will thus often increase the difference between $R_{\rm exp}$ and $R_{\rm wp}$ (although decreasing both of them), resulting in an increase in χ^2. Likewise, improved instrumental resolution is a good thing; it decreases the degree of peak overlap, resulting in more accurate integrated intensities and thus more accurate structural information. However, improved signal to noise and resolution often make imperfections in the model (particularly in the profile shapes) more obvious, resulting in increased refinement residuals. Synchrotron data are significantly better than laboratory patterns in both signal to noise and resolution, so we can often expect to see higher residuals from refinements using synchrotron data.

Statistical measures such as the F-test [see Volume C, Chapter 8.4 (Prince & Spiegelman, 2004)] are appropriate for comparing two different models compared with the same data, but are of little use in comparing one refinement with another (based on different data sets but assuming similar instrument configurations). With experience, each user develops a sense of what is an appropriate range for residuals for his/her types of problems and data. Whatever residual is used, the sources of the discrepancies in the fits must be understood and discussed in the report of the Rietveld refinement.

4.9.3. Graphical measures (with contributions from B. H. Toby and J. K. Stalick)

The statistical quality measures discussed in Section 4.9.2 provide overall measures of the quality of the Rietveld fit. Through graphical inspection of the discrepancies between the observed and calculated patterns, we can determine the nature of the disagreements, decide whether they are significant and how to adjust the model to minimize them, and judge whether any remaining systematic errors are likely to bias the fitted parameters. A good principle in carrying out a Rietveld refinement is 'deal with the sources of the largest errors first'. The best way to determine the origins of the greatest discrepancies in the fit is

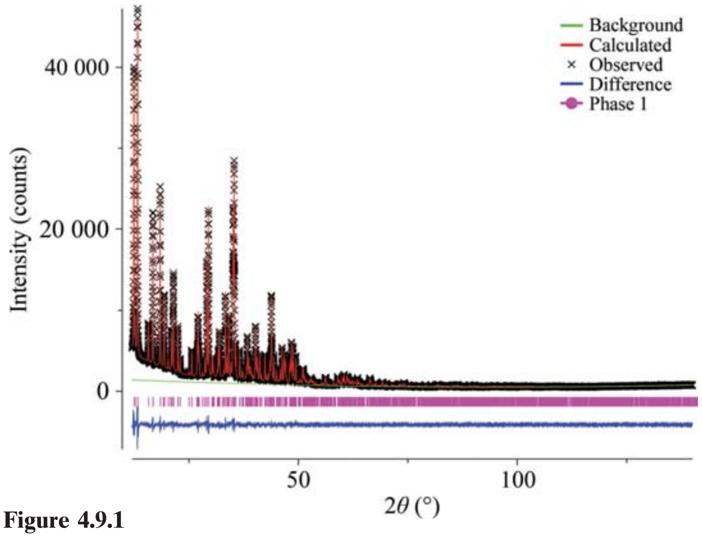

Figure 4.9.1
A 'Rietveld' plot from the refinement of calcium tartrate tetrahydrate. The observed data points are indicated by the black × symbols, the calculated pattern is represented by the red curve and the difference pattern (observed − calculated) is shown on the same vertical scale by the blue curve. The vertical tick marks indicate the reflection positions and the green curve is the background function.

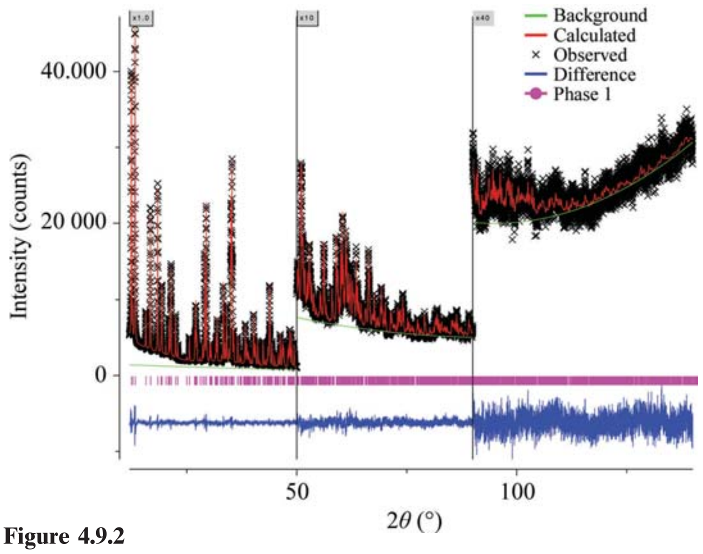

Figure 4.9.2
The calcium tartrate tetrahydrate Rietveld plot of Fig. 4.9.1 but with a variable vertical scale. The region from 50 to 90° has been multiplied by a factor of ten and the region above 90° by a factor of 40. Such changes in scale make it easier to judge the quality of the fit of the weaker peaks.

graphical examination of the observed and computed patterns. Detailed discussion of the physics and mathematics that give rise to various kinds of errors takes place in Chapters 3.1–3.3 of this volume. In this chapter, we concentrate on empirical advice.

Graphical inspection requires plotting the diffraction data on a range of scales and in a variety of formats. When evaluating one's own work this is not difficult, since Rietveld packages include plotting programs for this task. When reviewing published work this task is more difficult, since static figures in a paper cannot provide enough necessary detail. The incorporation of 'advanced figures' can facilitate evaluation enormously. Allowing reviewers and readers the ability to carry out graphical analysis of Rietveld results was one of the motivations for extending the CIF format to allow the exchange of observed and computed powder diffraction data (Toby, 2005). Many Rietveld packages allow the export of results in CIF. From these CIF files, utilities such as the *pdCIFplot* program (Toby, 2003) can be used for graphical inspection of the fits.

Although statistical measures can be discussed in abstract terms, graphical measures require looking at real plots. For this discussion, we will use the Rietveld refinement of the structure of calcium tartrate tetrahydrate (Kaduk, 2007*a*). The specimen was the sediment from the bottom of a wine bottle, and the pattern was collected on a Bruker D8 Advance diffractometer equipped with a VÅNTEC-1 position-sensitive detector (supplementary files kadu937.gsas and d8v3.prm). The initial structural model was taken from Hawthorne *et al.* (1982). The final residuals were $R_{\rm wp} = 0.0454$, reduced $\chi^2 = 3.336$, $R(F) = 0.0711$ and $R(F^2) = 0.0707$.

Rietveld results are most commonly displayed in a more-or-less standard format, generally referred to as the 'Rietveld plot' (Fig. 4.9.1). This type of plot displays the observed diffraction data as individual points, with the calculated pattern superimposed as a continuous line. The plot has vertical tick marks indicating the positions of the reflections. Also typically displayed is a difference plot (observed − calculated), generally on the same vertical scale as the observed and calculated plots. The difference curve tends to overaccentuate discrepancies in the most intense peaks, for which large deviations may be within the statistically expected levels. For this reason, it is preferable to plot intensities normalized by their uncertainties, $I/\sigma(I)$, which is sometimes referred to as a normalized Rietveld plot. In this mode, the plotted magnitudes of differences correspond directly to their contribution to $R_{\rm wp}$ and χ^2, and thus the influence that the discrepancies have on the fit. Having said this, it should be noted that the eye is not very good at integrating. A discrepancy of a few points at the top of a peak seems to be more significant than a small error in the background that extends over hundreds of points. The latter can have a much larger influence on χ^2. For this reason, the cumulative χ^2 plot, which will be introduced later, is useful for showing the true influence of discrepancies.

Although the static Rietveld plot generally found in a publication is useful for seeing the 'big picture', there is considerable detail that can only be seen when the information is viewed at several magnification scales. Thus, this plot is much more useful when it is 'live' (*i.e.* when it is possible to zoom in on details). More subtle features can then be discerned. To overcome the disadvantages of a static plot, a good practice is to vary the vertical scale in a publication figure to permit easier examination of the weak peaks (Fig. 4.9.2). Alternative ways of re-normalizing the plot to obtain greater sensitivity to the weak features are the (observed − calculated)/σ or 'error' plot (Fig. 4.9.3), the

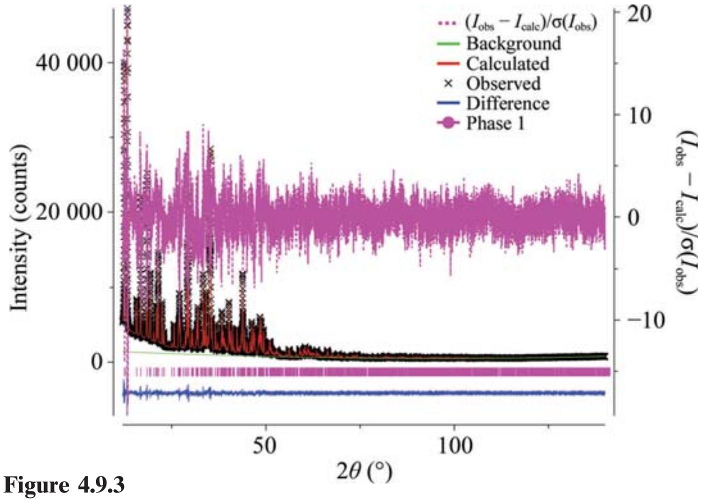

Figure 4.9.3
The calcium tartrate tetrahydrate Rietveld plot of Fig. 4.9.1 with an 'error' plot superimposed. The magenta curve (using the right-hand vertical scale) plots $(I_{\rm obs} - I_{\rm calc})/\sigma(I_{\rm obs})$ for each data point.

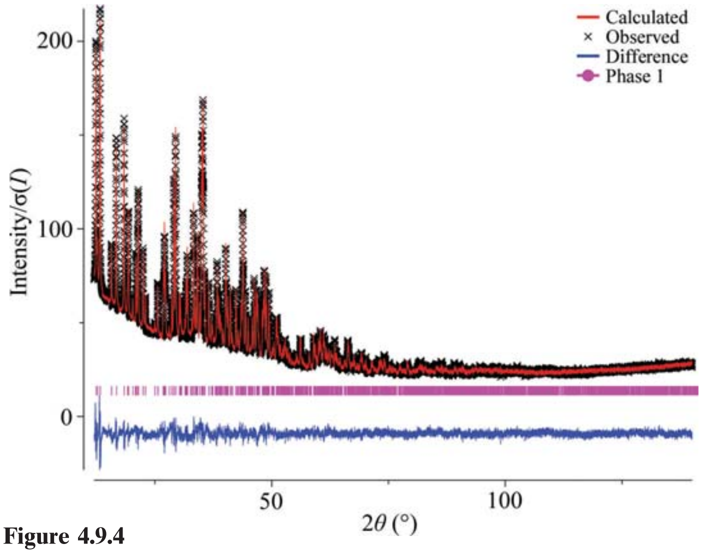

Figure 4.9.4
A normalized Rietveld plot for calcium tartrate tetrahydrate. The vertical axis in this plot is $I_{\rm obs}/\sigma(I_{\rm obs})$.

normalized Rietveld plot $I/\sigma(I)$ (Fig. 4.9.4) and the weighted Rietveld plot (Fig. 4.9.5). The weighted Rietveld plot is not commonly used, but I find it helpful because it is closer to the function that is minimized in the least-squares refinement. Such weighted plots also provide a vivid demonstration that the weak high-angle peaks are just as important to the least-squares refinement as the strong low-angle peaks (Figs. 4.9.6*a* and 4.9.6*b*; supplementary files kadu1536.gsas and iitd26.prm).

The cumulative χ^2 plot (Fig. 4.9.7; David, 2004) has advantages for highlighting the largest errors in the Rietveld fit. This function is simply the running average of the $[(\text{obs} - \text{cal})/\sigma]^2$ values. For an ideal fit, all points will be fitted with an average discrepancy of σ, so the cumulative χ^2 plot approximates a straight line with a slope of unity. For a non-ideal fit, regions that are poorly fitted will be highlighted by a sudden increase in the cumulative χ^2 values. The steps in Fig. 4.9.7 indicate (on zoomed examination) that the asymmetry of the strong low-angle peaks is not modelled particularly well. The integration contained in this type of plot highlights regions where smaller discrepancies over an extended range of the data degrade the fit. Smaller but extended discrepancies are much harder to discern in other types of plots. It is useful to review the reflection indices associated with an individual tick mark, as this simplifies the diagnosis of preferred orientation and anisotropic broadening.

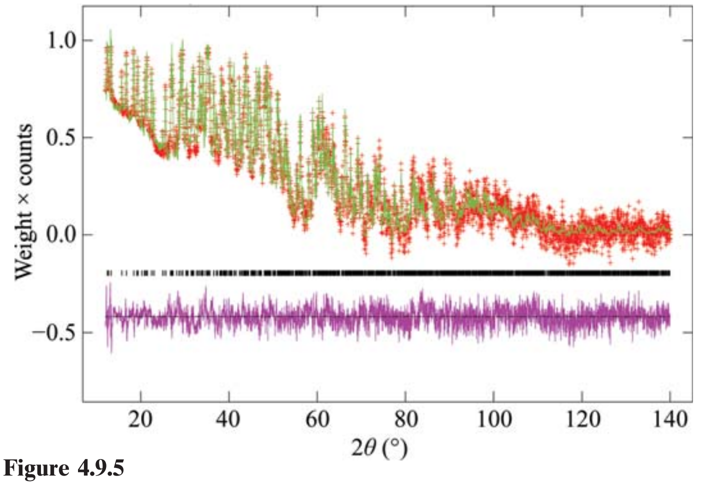

Figure 4.9.5
A weighted Rietveld plot for calcium tartrate tetrahydrate. The observed and calculated intensities are multiplied by the least-squares weights $1/\sigma^2(I_{\rm obs})$.

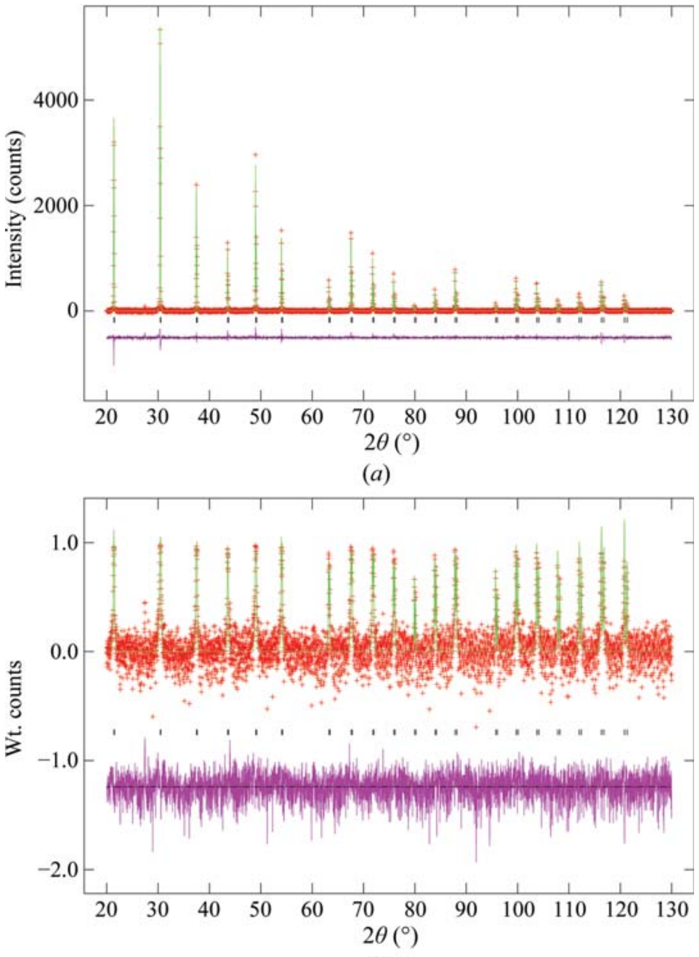

Figure 4.9.6
(*a*) A Rietveld plot from a refinement of NIST SRM 660a, $\rm LaB_6$. (*b*) The equivalent weighted Rietveld plot, making it clear that weak peaks are just as important as strong peaks.

The normal probability plot (Fig. 4.9.8) is useful for detecting systematic errors in the fit. To make this plot, the individual data points are sorted by $(\text{obs} - \text{cal})/\sigma$ and compared with the frequency of errors expected from a normal distribution. An ideal normal probability plot has a slope of unity and an intercept of zero. The example plot in Fig. 4.9.8 has a slope of 1.4928 and an intercept of 0.0296 (for the default region $\pm 2\sigma$). The slope of the normal probability plot is used internally in some least-squares programs to multiply the estimated standard uncertainties

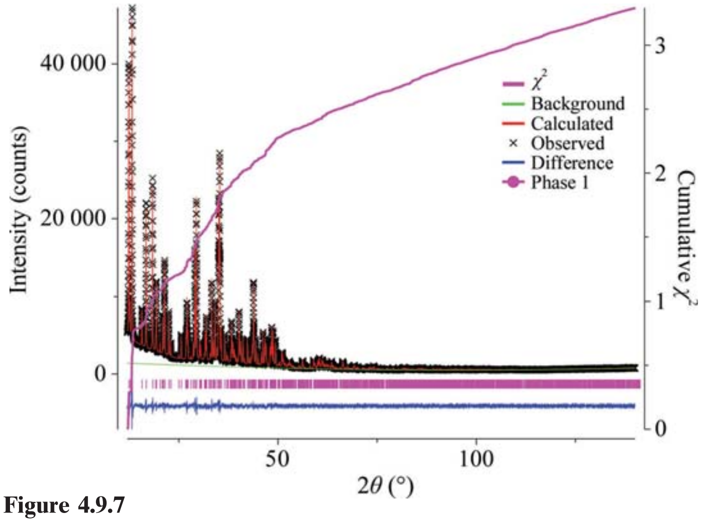

Figure 4.9.7
The calcium tartrate tetrahydrate Rietveld plot of Fig. 4.9.1 with the cumulative χ^2 plot superimposed in magenta.

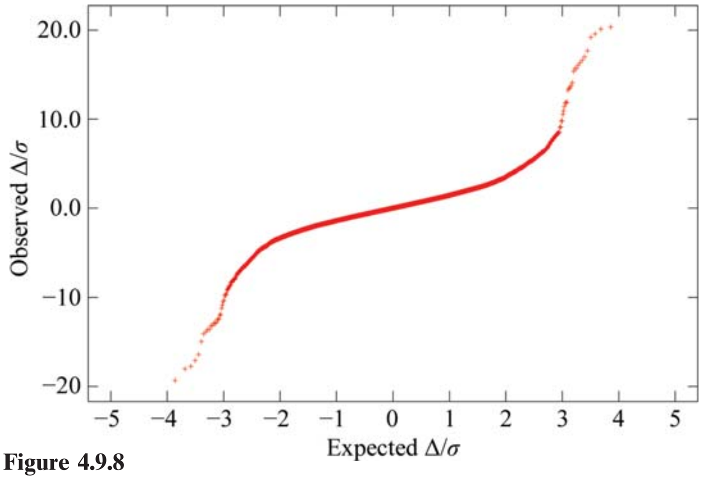

Figure 4.9.8
A normal probability plot from the refinement of calcium tartrate tetrahydrate.

obtained from the variance–covariance matrix to obtain a better estimate of the true uncertainties. An intercept far from zero suggests the presence of systematic errors, either in the data or the model.

The plots shown so far have been from the end of the refinement. It is also valuable to examine these plots periodically throughout the refinement to indicate which variables need to be considered next in the refinement. Examining the normal Rietveld plot at high vertical magnification, or the normalized (Fig. 4.9.9) or weighted (Fig. 4.9.10) plots, provides a check on the quality of the background fit. Away from the peaks, the calculated pattern should pass through the middle of the data points. The background should obviously not lie above the data points. The fits in Figs. 4.9.9 and 4.9.10 (after refinement of a scale factor and a three-term shifted Chebyshev polynomial background function) show that the background fitting needs to be improved. Additional background terms were added (up to nine) and the fit improved. For this case I ultimately chose to use a three-term shifted Chebyshev background function along with a diffuse scattering function to model the contributions of an apparently small amount of amorphous material in this sample. Display of the background function (shown in green in Figs. 4.9.1, 4.9.2, 4.9.3 and 4.9.7) is very helpful in assessing the quality of the fit.

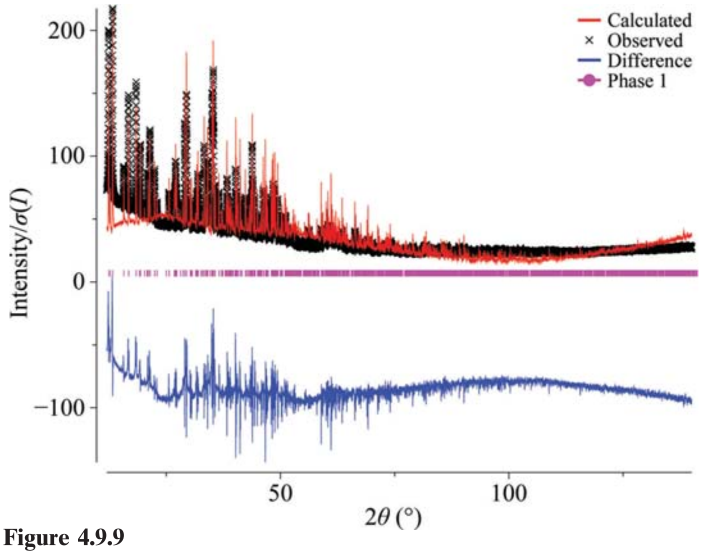

Figure 4.9.9
A Rietveld plot of calcium tartrate tetrahydrate after refinement of a phase fraction and a three-term shifted Chebyshev background function. The difference plot shows that a better background function is needed.

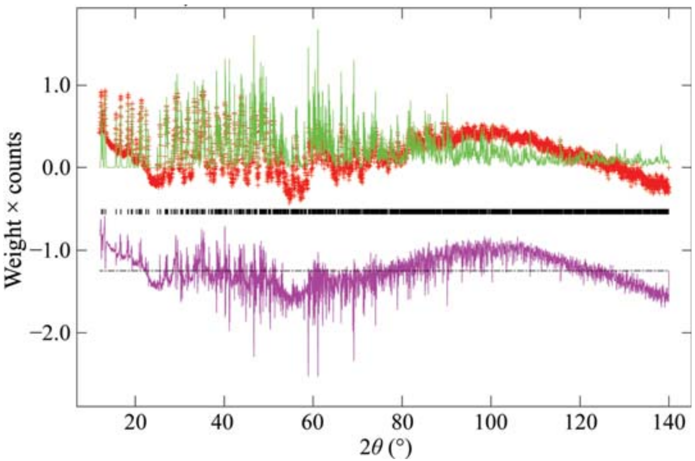

Figure 4.9.10
A weighted Rietveld plot of calcium tartrate tetrahydrate after refinement of a phase fraction and a three-term shifted Chebyshev background function. The difference plot shows that a better background function is needed.

A poorly fitted background most commonly affects the profile shape (especially the description of the peak tails), but can also affect the phase scaling factors and thus the quantitative analysis. This is particularly true for minor phases. When the background refines to a level that is too high and the profiles of the weak peaks become too wide, the phase fractions and thus the concentrations of minor phases will be over-represented. When the background is poorly fitted at high Q [where $Q = (2\pi)/d$], this same effect causes atomic displacement parameters to be overestimated, since higher-Q reflection intensities are undercounted. The influence of the background misfitting depends on the type of study, but usually does not affect the fractional atomic coordinates greatly. Crystallite size/strain analysis is often highly background dependent. In the current example, the background and diffuse scattering coefficients are highly correlated with each other, but are relatively independent of the structural and profile parameters.

It is highly advantageous to examine the computed background, which is best performed at high magnification with the background plotted against the observed data without normalization for uncertainty (which would cause the background to jump irregularly). Backgrounds from well crystallized samples in standard mountings are slowly varying and require only a few terms to fit well. This may not be true when special sample cells are used. Some programs include a $1/\sin 2\theta$ term, which describes air scattering well. A moderately common error is to use too many background terms in an attempt to fit medium-frequency features in the data. Such features can arise from amorphous components (which are better described using a diffuse scattering function) or the overlap of poorly modelled peak tails in clusters of peaks. Such fits point to deficiencies in the crystallographic and/or profile models. Attempting to fit such effects with more background terms can lead to serious errors in the structural model.

However, when too few terms are used the background function is not able to fit the observed changes in background with Q, leading to systematic errors in peak intensities and thus the crystal structure. A best practice is to use a small number of background terms in the initial stages of a refinement and to examine the fit graphically at regular intervals. In the final stages of refinement one can add more terms to see whether the fit is improved and (if so) that the changes in the background curve better match the observed background. It is also wise to check

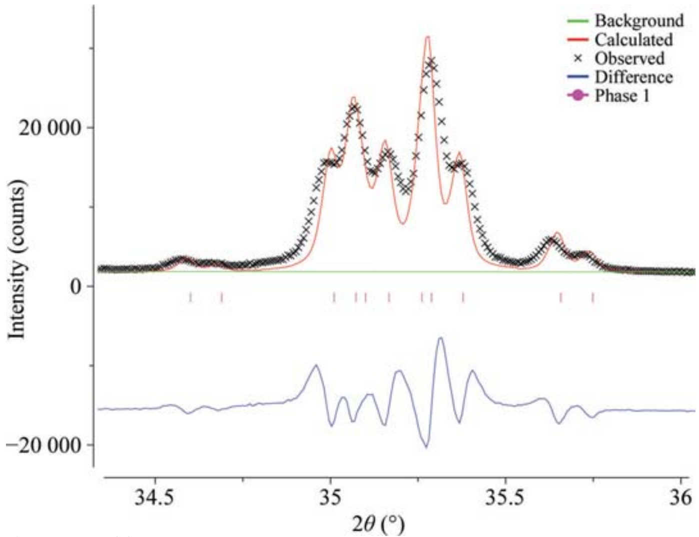

Figure 4.9.11
A small region of the calcium tartrate tetrahydrate Rietveld plot early in the refinement. The calculated peaks are not in the right places, so the conclusion was that the lattice parameters and the specimen displacement coefficient needed to be refined.

whether the structural model is altered by such changes to the background function.

The process of carrying out a Rietveld refinement requires continuous intimate interaction with the raw data, mainly through graphical tools. After the first few cycles of refinement (scale factor and three background terms), close examination of small regions of the pattern (Fig. 4.9.11) indicated that the peaks were not in the correct places. The main controls over the positions are the lattice parameters and the specimen displacement coefficient, so these were added to the refinement. Once the agreement of the calculated and observed peak positions was good (Fig. 4.9.12), it was clear that the calculated peak widths were too narrow. The appearance of the peaks is Lorenztian (Cauchy), suggesting that Lorentzian size and/or strain coefficients should be added to the refinement. The peak widths differ in this small region, suggesting that the broadening is anisotropic. Such anisotropy can arise from size and/or strain effects. In this case, the treatment of anisotropic strain broadening described by Stephens (1999) was used. (See also Chapters 5.1 and 5.2.)

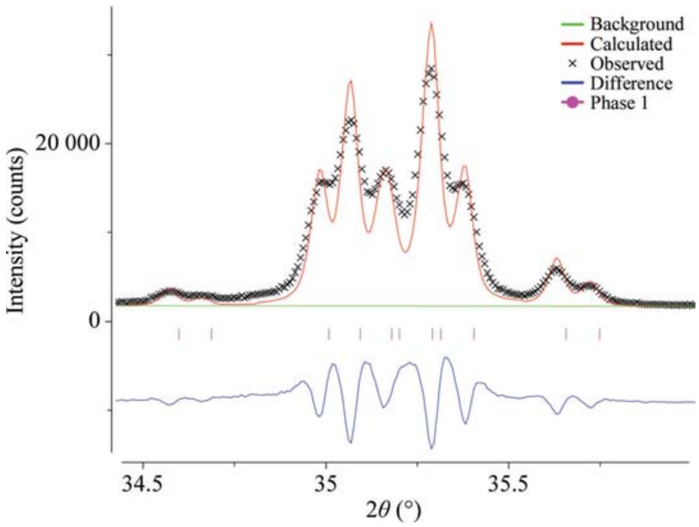

Figure 4.9.12
The same 34.5–36° region of the pattern of calcium tartrate tetrahydrate after refinement of the cell parameters and specimen displacement. The peak positions are now correct, but the profile coefficients need to be refined.

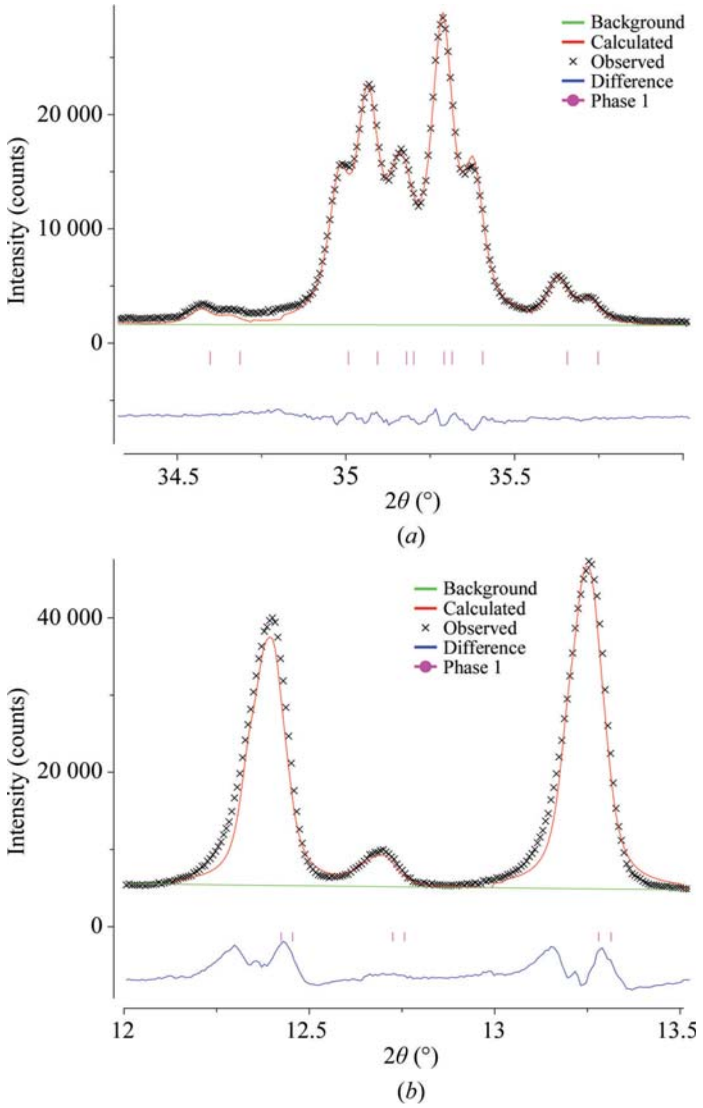

Figure 4.9.13
(*a*) The 34.5–36° region of the calcium tartrate tetrahydrate pattern after refinement of profile coefficients. The effects of the 1% peak cutoff can be seen on the peak tails. (*b*) The 12–13.5° low-angle region of the calcium tartrate tetrahydrate pattern. The profile asymmetry is not modelled well, suggesting that an asymmetry coefficient needs to be refined.

Once more cycles of refinement had been carried out, close examination of individual regions provided clear direction on how to improve the fit. Although the fit in the higher-angle regions was much better (Fig. 4.9.13*a*), the asymmetry of the low-angle peaks was not described correctly (Fig. 4.9.13*b*). The asymmetry of low-angle (and high-angle, but this is rarely observed) peaks arises mainly from instrumental effects, and results from axial divergence and flat-specimen contributions to the convolutions that determine profile shapes. Calcium tartrate tetrahydrate has fairly modest X-ray absorption, so we might expect an additional contribution to the asymmetry from transparency effects. Thus, one of the Finger–Cox–Jephcoat (Finger *et al.*, 1994; van Laar & Yelon, 1984) asymmetry parameters was added to the refinement.

An additional effect can be seen in Fig. 4.9.13(*b*), most clearly at $2\theta \simeq 13°$. All Rietveld codes limit the number of data points to which a reflection contributes (to save computer time). From the unit-cell and correction terms, the reflection position is known. Using this position and the profile shape, the data points to which this reflection contributes can be determined out to some limit. The limit is variously defined in terms of some fraction of the

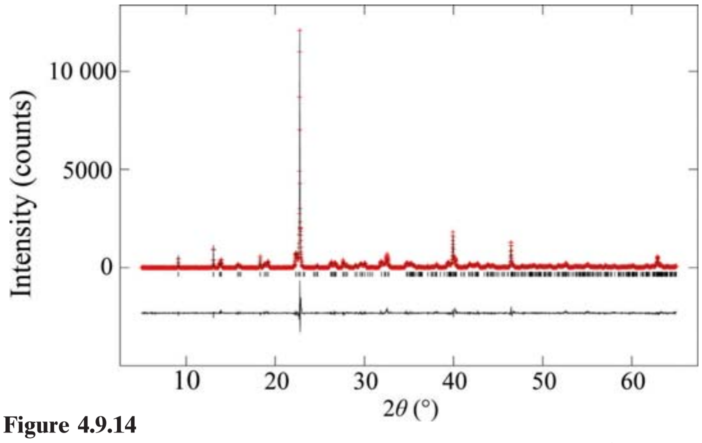

Figure 4.9.14
A full-scale Rietveld plot from the refinement of $Ba_3CaSb_2O_9$ (Rowda *et al.*, 2008) using synchrotron radiation before the impurity phases were identified and included in the refinement. The reduced χ^2 at this stage was 3.857.

maximum intensity or some multiple of the full width at half maximum (FWHM). In this case, each peak was assumed to contribute to data points down to 1% of the peak intensity; outside this range the peak contribution was zero. The result is an incomplete description of the tails of the strong peaks. To correct this, the peak cutoff was lowered to 0.5% of the peak intensity.

Additional types of deficiencies in the model can be determined by very close graphical inspection of the fit. Particularly important are observed peaks that are not accounted for by the model. The most common causes of such peaks are impurity phases and an incorrect cell/symmetry. Although the initial full-scale Rietveld plot (data) of the refinement of the 6H perovskite $Ba_3CaSb_2O_9$ (Rowda *et al.*, 2008) using synchrotron data appeared to be acceptable (Fig. 4.9.14), closer examination at zoomed scales (Fig. 4.9.15) revealed the presence of additional peaks. Some of these were resolved peaks, but others were shoulders on the strongest peaks. Searches for these peaks in the Powder Diffraction File indicated the presence of three impurity phases. Attempts to fit the multiphase data using a single-phase model resulted in structural distortions, which were eliminated by using a more complete model.

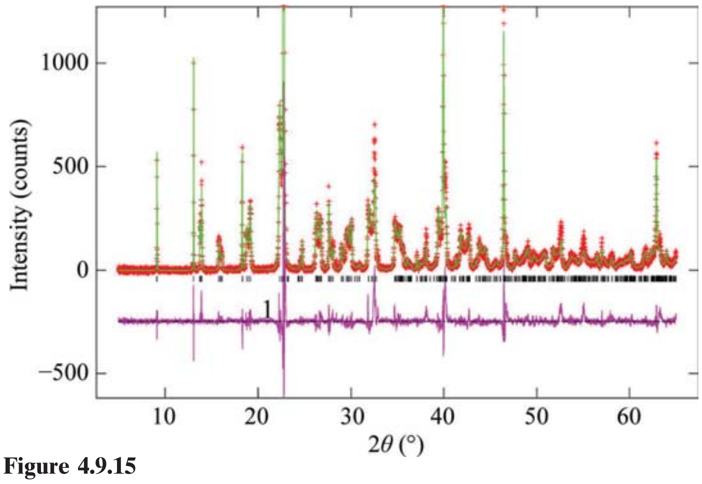

Figure 4.9.15
The plot of Fig. 4.9.14, zoomed in to the region under 1000 counts. The presence of impurity peaks is clear.

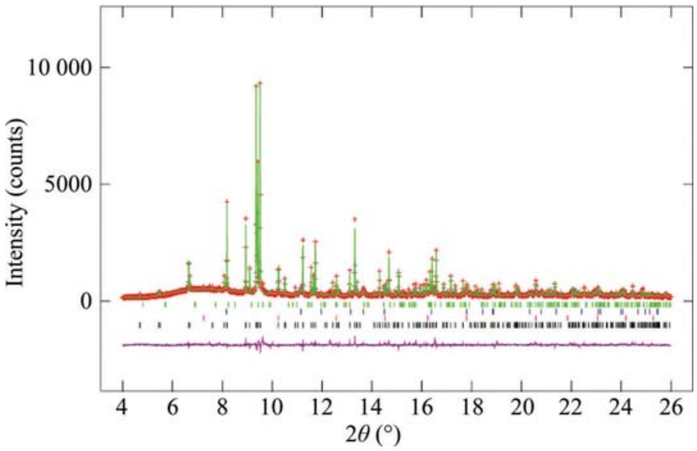

Figure 4.9.16
Full scale Rietveld plot of $(Ba_{1.25}Sr_{0.75})TiO_4$.

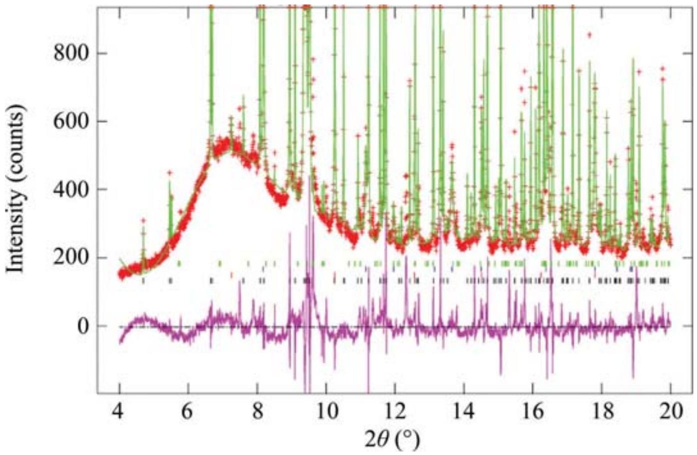

Figure 4.9.17
A portion of the plot of Fig. 4.9.16 zoomed in to the region under 1000 counts. Several weak peaks that are not accounted for by the current model are clear.

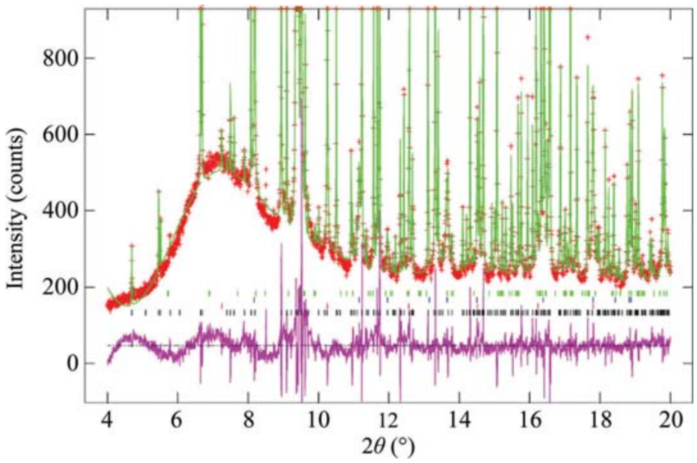

Figure 4.9.18
A portion of the Rietveld plot of $(Ba_{1.25}Sr_{0.75})TiO_4$ after the correct unit cell and structure had been identified. The new cell accounts for all of the weak peaks in Fig. 4.9.17.

The initial full-scale Rietveld plot (supplementary files ba2180.gsas and id100602.prm) of the refinement of the structure of $(Ba_{1.25}Sr_{0.75})TiO_4$ in *Pnma* with a = 7.48904 (3), b = 6.03638 (3), c = 10.32873 (5) Å and V = 466.928 (4) Å^3 appeared to be acceptable at full scale (Fig. 4.9.16), but closer examination (Fig. 4.9.17) showed the presence of extra peaks even after impurities had been identified. These peaks did not correspond to any known or chemically reasonable isostructural phase. They were added one at a time to the strong low-angle peaks as input to *DICVOL91* (Boultif & Louër, 1991), which repeatedly suggested the same primitive orthorhombic unit cell with $a = 2a$. Lattice matching led to the identification of a lowered symmetry $Pna2_1$ model that accounted for these weak peaks (Fig. 4.9.18)

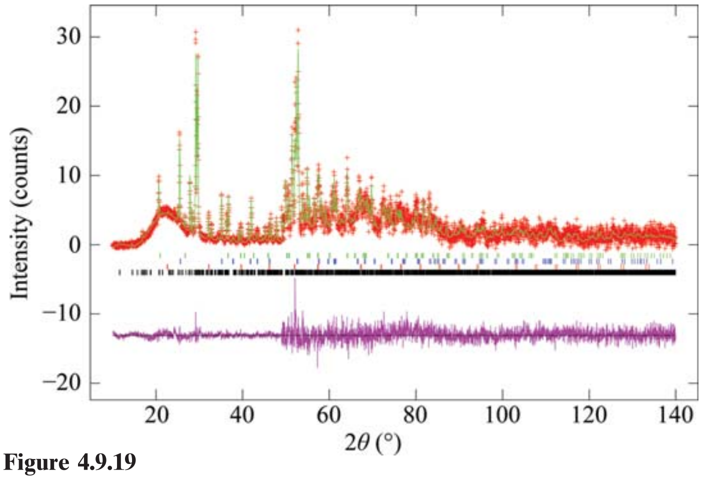

Figure 4.9.19
A Rietveld plot of $(Ba_{1.5}Sr_{0.5})TiO_4$ early in the refinement, with an incorrect unit cell for the major phase.

and was chemically reasonable. When confronted with a model that does not index a significant number of weak peaks (especially at low angles), it is often worthwhile to plot the reflection positions for the cell volume doubled in various ways (axis doubling as well as $2^{1/2} \times 2^{1/2}$ expansions of pairs of axes) to see whether these peaks can be explained by a subtle change of the symmetry.

The opposite problem, where a structural model is of too low symmetry, can also be encountered. As an example, initial refinement (supplementary files wong224.gsas and padv.prm) of the structure of $(Ba_{1.5}Sr_{0.5})TiO_4$ in $P2_1nb$ with $a = 6.0634$ (2), $b = 22.6066$ (9), $c = 10.4040$ (4) Å (as it was supposed to be isostructural to Ba_2TiO_4) yielded a reasonably good fit (Fig. 4.9.19), but there were chemically unreasonable features of the structure, and the cell predicted too many low-angle peaks which were unobserved (Fig. 4.9.20). Searches for extra symmetry yielded an aristotype having a cell with one third of the volume; this simpler model was more reasonable and yielded a better refinement.

The presence of a small number of unfitted peaks usually has only minor effects on the Rietveld refinement of the parameters of the major phase(s), particularly if the impurity peaks do not overlap those of the major phase significantly. Nonetheless, when a Rietveld analysis is completed, an important measure of quality is the fit of all of the peaks in the pattern. Often when the source of the problem becomes known, the problem turns out to be more profound than originally realized. The impurity phase may have large peaks which overlap those of the major phase(s) and the fit becomes skewed in trying to account for the spurious intensity. Exclusion of isolated peaks does not address this in any meaningful way, since the more serious problem of overlapping peaks is unresolved. Better results will be obtained when the impurity phase is included in the model (using a Le Bail or Pawley fit of the indexed impurity pattern) than by excluding the regions surrounding the impurity peaks.

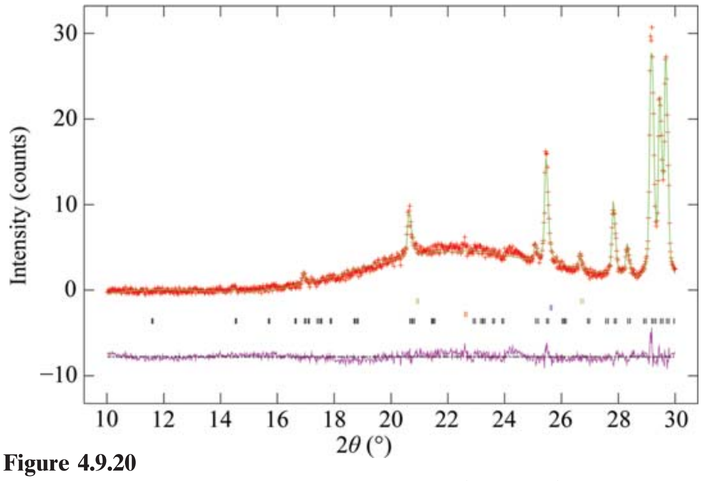

Figure 4.9.20
The low-angle portion of the Rietveld plot of $(Ba_{1.5}Sr_{0.5})TiO_4$, showing that the unit cell predicts many peaks which are not observed. The true unit cell had one-third of the volume of the cell used here.

In distinct contrast to the previous situation is the presence of calculated peaks that are not observed in the experimental pattern. No matter how small, this can only mean that the model structure is incorrect. One such example is the determination of the structure of '$BaCuO_2$', which was reported several times in the literature; unfortunately, in all cases there were calculated peaks with no observed intensity. This material (when prepared in air) was later found to contain carbonate ions (Aranda & Attfield, 1993).

4.9.4. Chemical reasonableness

Although statistical and graphical measures of the quality of the fit are important, the chemical reasonableness of the resulting structure carries even more weight (McCusker *et al.*, 1999). What do we mean by 'chemical reasonableness'? This is shorthand for saying that (with more than a million crystal structures determined) we have a good idea of normal values for bond distances, angles and other features of molecular geometry for most chemical systems. Structures refined by the Rietveld method should fall within these normal ranges. A proposal of remarkable geometry should be supported by more evidence than a routine Rietveld refinement. Chemical knowledge can be used in structure solution, refinement and analysis of results.

Our chemical knowledge is summarized in different ways for different classes of compounds. The repository of organic and organometallic crystal structures is the Cambridge Structural Database (CSD; Groom *et al*., 2016). We can perform our own analysis of any desired structural parameter using the tools in *ConQuest* and *Mercury* (Sykes *et al.*, 2011), or use the pre-created databases of intramolecular (Mogul; Bruno *et al.*, 2004) and intermolecular (GOLD) interactions supplied with the CSD. Inorganic crystal structures are archived in the PDF-4+/Linus Pauling File (Pearson's Crystal Data; Villars *et al.*, 1998; ICDD, 2012), the Inorganic Crystal Structure Database (Hellenbrandt, 2004) and CRYSTMET (White *et al.*, 2002). Our knowledge of inorganic bond distances is conveniently summarized in the bond-valence formalism (Brown & Altermatt, 1985; Brown, 1996, 2002) and tables of ionic radii (Shannon & Prewitt, 1969). Pearson's Crystal Data contains information about the distribution of interatomic distances between any pair of atom types, and similar histograms of interatomic distances derived from the Inorganic Crystal Structure Database are contained in the Build/Connectivity menu of the *Diamond* visualization software (Crystal Impact, 2013).

Ultimately, even though Rietveld refinements use powder diffraction data, we are still performing crystallography. Structure validation uses the same principles as those used for single-crystal studies, perhaps modified to account for the lower information content of powder data compared with single-crystal data.

4.9.4.1. *Organic compounds*

Validation of organic structures using the Cambridge Structural Database and the advanced statistical tools in *dSNAP* (Barr

Table 4.9.1
Average bond distances in a tartrate anion

Average of 136 examples from a *Mogul Geometry Check* using *Mercury* 3.0.1.

Bond	Distance (Å)
C3—C4	1.524 (21)
C3—O8	1.415 (27)
C4—O9	1.416 (27)
C2—C3	1.536 (26)
C4—C5	1.535 (25)
C2—O6	1.251 (19)
C2—O7	1.250 (23)
C5—O10	1.255 (21)
C5—O11	1.249 (18)

Table 4.9.2
Average bond angles in a tartrate anion

Average of 136 examples from a *Mogul Geometry Check* using *Mercury* 3.0.1.

Angle	Value (°)
O8—C3—C4	110.3 (23)
O9—C3—C4	110.3 (23)
C2—C3—C4	110.3 (36)
C3—C4—C5	110.2 (20)
C2—C3—O8	111.4 (25)
C5—C4—O9	111.3 (25)
O8—C2—C3	117.1 (17)
O7—C2—C3	117.3 (18)
O11—C5—C4	117.0 (22)
O10—C5—C4	117.6 (19)
O6—C2—O7	125.4 (16)
O10—C5—O12	125.3 (18)

et al., 2005) has been described in Barr *et al.* (2007). We can anticipate the development of additional statistical tools to make the job of structure validation easier. This section includes several examples of more traditional attempts to assess the quality of organic crystal structures.

4.9.4.1.1. *Calcium tartrate tetrahydrate*

The crystal structure of calcium tartrate tetrahydrate has been reported four times (Ambady, 1968; Hawthorne *et al.*, 1982; Boese & Heinemann, 1993; Kaduk, 2007*a*). The Rietveld refinement in Kaduk (2007*a*) provides a good test of the structural accuracy and precision that can be achieved using powder data.

Tartrate (Fig. 4.9.21) is a common anion and more than 400 crystal structures that contain it have been reported. The geometry of a tartrate ion is easily analysed using *Mercury* (Sykes *et al.*, 2011). For bond distances and angles (Tables 4.9.1 and 4.9.2), histograms (Figs. 4.9.22 and 4.9.23) and descriptive statistics are obtained. The standard uncertainty on a bond is typically 0.02 Å and that on a bond angle is 2°. The bonds and angles are quite well defined. Since the atom numbering is arbitrary, it is useful to group the distances, angles and torsions by topologically equivalent quantities. For torsion angles, averages are not as useful, but polar histograms (Fig. 4.9.24) are valuable for analysing the multimodal distributions of torsion angles.

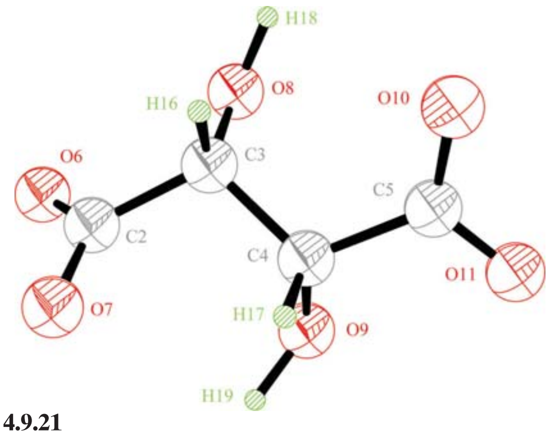

Figure 4.9.21
The structure of a tartrate anion.

This chemical information about bond distances and angles was incorporated into the refinement by the use of restraints. The restraints are treated as additional observations in the least-squares refinement; they are additional data items and the refinement will also attempt to minimize the weighted difference between the restraint target value and the value derived from the structure. I generally use the average from the Mogul/*Mercury* analysis as the restraint target value and use the standard deviation of the distribution as the uncertainty for the target value, sometimes modified by my experience with a particular

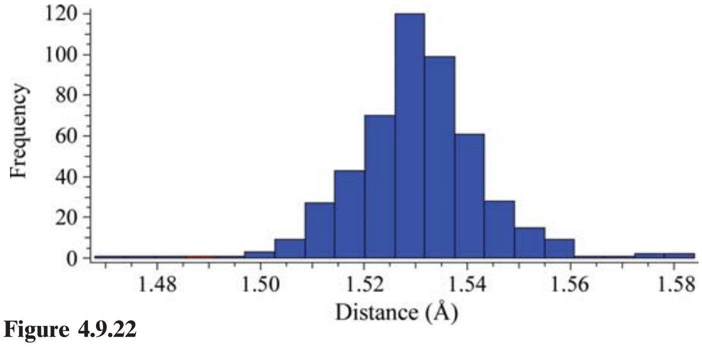

Figure 4.9.22
A *Mercury* plot of the distribution of the lengths of the central C3—C4 bond in tartrate anions.

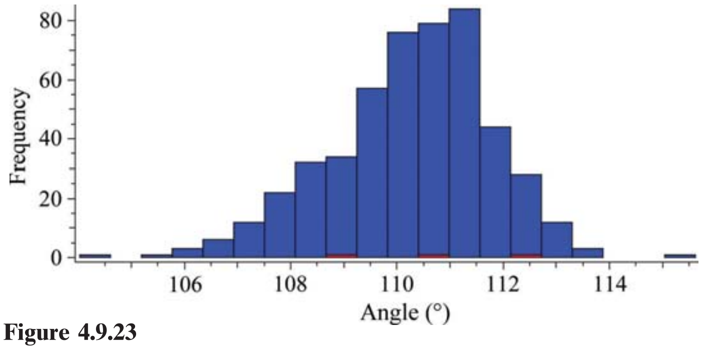

Figure 4.9.23
A *Mercury* histogram of the O8—C3—C4 bond angle in tartrate anions.

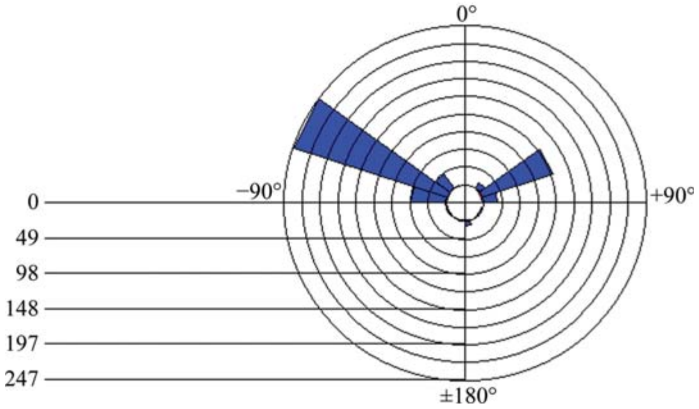

Figure 4.9.24
A *Mercury* polar histogram of the O8—C3—C4—O9 torsion angles in tartrate anions.

chemical system. The impact of each restraint is dictated by the restraint weighting factor divided by the square of the uncertainty.

Often a high weighting factor is used early in the refinement (a factor which may be as large as 1–2 orders of magnitude greater than the number of data points in the powder pattern), so that fitting to the restraints is as significant as fitting the data. As the refinement progresses the restraint weighting is gradually decreased. The best practice is for the restraint weights to be small (or even better, zero) in the final refinement; we want the results to be dominated by the data and not by our prior knowledge. There is currently some debate among crystallographers as to how the restraint weights should be documented. I prefer to report the fraction of the total χ^2 which is contributed by the restraints. For this calcium tartrate refinement, the restraint contribution was 1.1%.

There is often not sufficient information in an X-ray powder pattern to refine individual atomic displacement coefficients (informally called thermal parameters), and only with exceptional data can anisotropic displacement coefficients be refined successfully (and then only for the high-Z atoms). With less-than-ideal data, it is common to need to decrease the number of refined parameters. One good way to do this is to group $U_{\rm iso}$ values by similarity of environment or topology. A common isotropic displacement coefficient was refined for the tartrate C atoms, another for the tartrate O atoms and another for the O atoms of the four water molecules. The $U_{\rm iso}$ of each H atom was constrained to be 1.3 times that of the atom to which it is attached; this is essentially the riding model that is often used in single-crystal refinements.

The CSD does not currently report displacement coefficients, although they are being archived for incorporation into future releases of the database. We are thus faced with the problem of defining the initial values for $U_{\rm iso}$, and what to expect as reasonable values. For a known structure such as this one we can consult the original papers for the values (if they were reported at all). It might be necessary to consult deposited supplementary material. With experience, one can generally make reasonable guesses for the initial $U_{\rm iso}$. For this refinement, I used 0.02 Å^2 for calcium, 0.03 Å^2 for carbon and oxygen and 0.039 Å^2 for hydrogen. In refinements using X-ray powder data (especially laboratory data) it may be necessary to fix the $U_{\rm iso}$ values of at least some atoms (especially lighter atoms) to reasonable values. Sometimes the data do not support the refinement of displacement coefficients, especially if the angular range is limited. The $U_{\rm iso}$ values are often highly correlated with other parameters; for example, those of heavy atoms are correlated with the scale factor of the phase. Likewise, in refinements using data sets with extensive peak overlap at high angles there may be no clear information on the background intensity level. In this case, placing the background at different levels will change the refined $U_{\rm iso}$ values. In such a case, I may set the $U_{\rm iso}$ values to expected values and refine the background coefficients once. In subsequent refinements the $U_{\rm iso}$ values are refined. $U_{\rm iso}$ has no physical meaning if negative, but a value that is negative by less than 2–3 standard uncertainties is not significantly different from zero. One aspect of chemical reasonableness is to confirm that the $U_{\rm iso}$ values lie within the expected ranges; spurious values are likely to indicate quality problems with the data or the fit. Very large values indicate that too much scattering density is being placed at a site; it could be that an atom is not present at that location, that the site is disordered or that the site had a significant vacancy concentration. $U_{\rm iso}$ values of less than 2–3 standard uncertainties below zero can indicate that not enough scattering density is being placed on the site, perhaps because the wrong atom type has been assigned or perhaps because other areas of the structure are disordered, causing the scale factor to refine to a value that is too small. Many sources of experimental error, such as unmodelled preferred orientation, can give rise to very large or small $U_{\rm iso}$ values.

Another measure of reasonableness is the difference Fourier map. This electron-density map is calculated using the difference between the observed and calculated structure-factor amplitudes and the phases calculated from the current structure model. For X-rays, positive peaks indicate electron density which is 'in' the data but not yet in the model. Negative peaks (holes) indicate places where the model includes too much electron density. For neutrons, peaks indicate extra or missing scattering density; while most atoms have a positive scattering factor, a negative peak can represent too much of a positive atom or not enough of a negative atom. Difference maps calculated using powder data tend to be flatter than single-crystal difference maps because the F_o values for overlapping reflections are partitioned according to the F_c values and are thus biased by the model. Nevertheless, they are useful for locating missing atoms and assessing whether atom types have been assigned correctly. For such a 'complete' organic structure, the difference map should be flat, say to ± 1.0 e Å^{-3}. Difference maps for inorganic structures may exhibit larger peaks and holes, especially at special positions. Atoms at special positions often contribute to only some classes of reflections. Intensity errors at such reflections become relatively more important in the calculation of electron density at special positions.

Using high-quality powder data, it is sometimes (perhaps less than half of the time) possible to locate H atoms in the difference map, but it is rarely possible to refine their positions using X-ray powder data. When knowledge of the H-atom positions is an object of the structural study, neutron diffraction is the better technique, but samples with more than 10–25% of the atoms in the unit cell as H will usually require at least partial deuteration. The H-atom positions in calcium tartrate tetrahydrate were derived by a quantum-chemical geometry optimization with density functional theory (DFT) using *CASTEP* (Segall *et al.*, 2002) based on the refined heavy-atom positions and using the fixed experimental unit cell. For the final Rietveld refinement, the H atoms were fixed at their optimized positions and the heavy atoms were refined. In the absence of such a quantum calculation, it may be necessary to fix the H atoms at reasonable locations. It is always advisable to include the H atoms, even if their positions are only approximate. I have found that better residuals and more reasonable structures are obtained. At the very least, more accurate quantitative phase analyses are obtained. In this calcium tartrate tetrahydrate example, an excellent refinement was obtained (Kaduk, 2007*a*). The largest peak and hole in the difference Fourier map were 0.56 e Å^{-3} (1.22 Å from C5) and -0.51 e Å^{-3} (1.56 Å from O11), respectively.

Comparison of a refined structure with the universe of known organic crystal structures is most easily performed by reading the CIF into *Mercury* and executing *CSD System/Mogul Geometry Check*. In this case, most of the bond distances and angles, and all of the torsion angles, were found to be 'not unusual (enough hits)', indicating that they fall within the normally expected ranges. Three bond distances (C2—O6, C3—C4 and C5—O11) were found to be 'unusual (enough hits)'. The C3—C4 distance of 1.559 (4) Å is only 1.7 e.s.d.'s from the Mogul average of 1.524 (21) Å for this bond. Likewise, the C2—O6 and C5—O11 distances of 1.230 (4) and 1.287 (4) Å differ by 1.0 and 1.8 e.s.d.'s from the average carboxylate distance of 1.25 (2) Å indicated by Mogul. The two angles O7—C2—C3 and O11—C5—C4 of 113.9 (4) and 114.8 (4)° differ from the Mogul average value of 117.2 (20)° by 1.6 and 1.2 e.s.d.'s, respectively. The default *Geometry Check* tolerances are quite small, and all of these quantities lie well within the normal distribution of topologically equivalent parameters.

The Ca atom is eight-coordinate and its coordination is irregular. The Ca—O bond distances range from 2.35 to 2.53 Å, with an average of 2.45 (6) Å. The *Mercury CSD System/Mogul Geometry Check* indicated that there were 'not enough hits' for the Ca—O bonds, but a manual analysis of CaO_8 coordination spheres in the CSD (using *ConQuest*) indicated an average Ca—O distance of 2.48 Å. The Ca—O distance expected from the bond-valence formalism is also 2.48 Å. The sum of the Ca—O bond valences is 2.22, showing that the Ca atom is 'crowded'. The Mulliken overlap populations from the quantum calculation show that the bonds have significant covalent character.

A prominent feature of this (and many) crystal structures is hydrogen bonding. Analysis of the hydrogen-bond network is always a part of structure validation. Because the H-atom positions obtained from an X-ray Rietveld refinement are often not very accurate or precise, I tend to rely on analysis of the result from a DFT optimization of the refined crystal structure. *Mercury* provides a *Calculate/Graph Sets* tool for analysing the topology of hydrogen bonds, but its results often need to be corrected manually.

A good rule of thumb is that every hydrogen bond that can form does form. The presence or absence of expected hydrogen-bond patterns thus serves as a valuable check on the reasonableness of a structure, especially from an *ab initio* solution using powder data and before refinement. Both hydroxyl groups of the tartrate act as donors in very strong hydrogen bonds: O8—H18 to a solvated water molecule and O9—H19 to a coordinated carboxylate O atom. O9 also acts as an acceptor from a coordinated water molecule O12, but O8 does not act as an acceptor. Additional strong hydrogen bonds occur between the water molecules. Several weak hydrogen bonds also seem to be present, including ones that involve the two CH groups. The large amount of energy gained by the formation of these hydrogen bonds helps to explain the high bond-valence sum for calcium and the relatively high density of this compound (1.844 g cm^{-3}). The average density of compounds in the CSD containing only Ca, C, H and O atoms is 1.52 (40) g cm^{-3}.

It is instructive to compare the results from the Rietveld and previous single-crystal studies with respect to the accuracy and precision of the chemically interesting derived quantities. The lattice parameters are more precise and (I believe) more accurate than those of the single-crystal studies. The average relative precision of the lattice parameters derived from powder data in 2006 was 5×10^{-6}. The average relative precision of the single-crystal lattice parameters from 1968 is 2×10^{-3}, and the precision of those from 1982 and 1993 is 2×10^{-4}. The improvement in the single-crystal precision reflects improvements in instrumentation. Because powder diffractometers are optimized for resolution (single-crystal instruments can depend on the spatial resolution generated by the specimen), the lattice parameters from a Rietveld refinement will generally be more precise and accurate than those derived from a single-crystal data set. The use of area detectors in modern single-crystal work has resulted in improved precision of lattice parameters compared with these (they are determined using the positions of all of the reflections), but there is still a reason to carry out combined refinements using powder and single-crystal data sets. The improved precision of the lattice parameters from the powder data will propagate into improved precision of bond distances and angles, and thus more chemical insight. A difficulty is that today most single-crystal data sets are collected at low temperatures, while most powder data are collected under ambient conditions. The difference in temperature means that the lattice parameters will differ significantly. To carry out a combined refinement, the data sets need to be collected under the same conditions. All three single-crystal data sets were collected at room temperature, but the lattice parameters vary significantly. These differences may represent sample-to-sample variations, differences in the actual ambient temperatures or something as simple as a different value of the X-ray wavelength. The 1968 values were derived from photographic data, so it is easy to imagine that they might be systematically different from the diffractometer values. The powder values are closest to the 1982 determination.

To assess the accuracy of the Rietveld-derived bond distances, consider the two single-crystal determinations from 1982 and 1993. The apparent standard uncertainty of a C—C or C—O bond distance is 0.004 Å. The average standard uncertainty of the single-crystal bond distances is ~0.002 Å. As we might expect, the powder values are less precise than those obtained from single-crystal data. The powder bond distances differ by an average of 0.02 (2) Å from the single-crystal distances, and there is no systematic trend in the differences. The differences average three standard uncertainties but are well within the standard uncertainties of the Mogul-derived distributions. Although less precise, the powder-derived bond distances are accurate enough to answer most chemical questions (Kaduk & Partenheimer, 1997). The standard uncertainty of a Ca—O bond is ~0.005 Å, compared with 0.007 Å for the single-crystal distances; some bonds exhibit more variation than others between the two single-crystal determinations. There are no systematic differences between the individual powder and single-crystal Ca—O distances, and the average Ca—O distances are the same in all determinations.

The average difference between the powder and single-crystal bond angles is only 1.6 (11)°. The agreement among chemically equivalent angles is excellent, and all angles fall within the normal ranges indicated by Mogul. The average difference between the powder and single-crystal torsion angles is 1.3 (11)°. The agreement between the (unrestrained) torsions and the single-crystal values is excellent. Both the powder and single-crystal values fall within the normal ranges obtained from Mogul.

Deciding whether the displacement coefficients (thermal parameters) are reasonable can be a challenge, because the CSD does not currently include them (although they are now being archived and will be incorporated into the CSD in the future). Sometimes the displacement coefficients are included in the original publication, but more and more often they are relegated to supplementary material.

Displacement coefficients from Rietveld refinements often have a bad reputation, because they are often 'too low' or even negative (physically unreasonable). If the various systematic intensity errors at low angles (such as beam spillover and surface roughness) are minimized or modelled (or both), reasonable displacement coefficients can be obtained from Rietveld refinements.

The average $U_{\rm iso}$ value for Ca from the single-crystal refinements is 0.014 Å^2, compared with the value of 0.045 Å^2 from the Rietveld refinement. The average single-crystal values for the tartrate C atoms, tartrate O atoms and water O atoms are 0.017, 0.022 and 0.042 Å^2, respectively, compared with 0.041, 0.045 and 0.073 Å^2 from the Rietveld refinement. In this refinement, the $U_{\rm iso}$ values are actually larger than the single-crystal values. This was a powder specimen, so we might expect more disorder (static, dynamic or both) than in a carefully prepared single crystal. The refined $U_{\rm iso}$ values seem reasonable and increase confidence in the quality of the refinement. The U values in organic compounds generally vary smoothly with location in the molecule. *checkCIF* is particularly good at comparing the displacement coefficients of neighbouring atoms and generating alerts when one of them is unusual. Such anomalous U values are sometimes a sign of a misidentified atom.

Submitting a powder CIF to *checkCIF* often generates many pages of alerts, many of which do not represent real problems. In the future *checkCIF* will be improved to present alerts that are more appropriate to the type of study, but at present it is necessary for the author and editor to ‘filter’ these alerts. Submitting the CIF for this calcium tartrate tetrahydrate example yielded level-A alerts about isotropic non-H atoms in the major residue. Such alerts are expected, since we do not expect to refine anisotropic displacement coefficients using powder data. Many level-A alerts were generated about suspect O—H bonds. Since the H-atom positions were generated from a DFT calculation, the O—H distances are longer than those expected for the artificially shortened distances expected from a crystallographic refinement (Churchill, 1973). There were many level-C alerts about senseless standard uncertainties on interatomic distances involving H atoms. These are expected because the H-atom positions were not refined. There was a level-B alert that no absolute configuration information was given, and a level-C alert about a missing Flack parameter. Since the hkl and $\bar{h}\,\bar{k}\,\bar{l}$ reflections necessary to determine the absolute configuration always exactly overlap in a powder pattern, it is impossible to determine the absolute configuration using powder data! (*Note*: this test has since been disabled for powder CIFs.) There were a few level-G alerts, but these were either easily fixed or irrelevant for powder data.

4.9.4.1.2. *Guaifenesin*

The crystal structure of guaifenesin [3-(2-methoxyphenoxy)-1,2-propanediol; Fig. 4.9.25], a common expectorant, was first solved using synchrotron powder data (Kaduk, 2004; supplementary files guaifenesin.gsas and id101003.prm, CSD code PANKUL01). Almost simultaneously, the structure was solved using single-crystal data (Wang *et al.*, 2005; CSD code PANKUL) and then again later (Bredikhin *et al.*, 2009; CSD code PANKUL02). These three determinations under ambient conditions (along with the DFT-optimized structure) provide an excellent test of the quality that can be obtained using powder techniques.

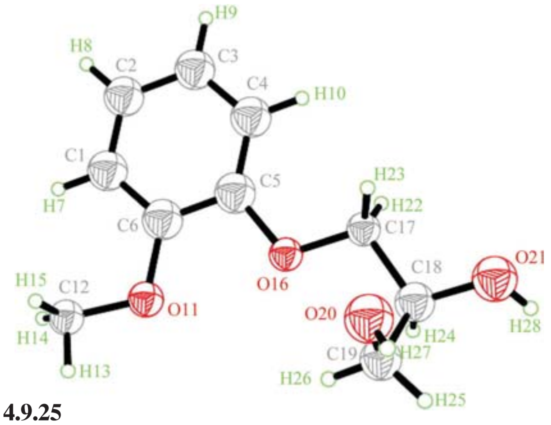

Figure 4.9.25
Refined molecular structure of guaifenesin.

Considering what is chemically reasonable can be important in the structure-solution process. It can make the task easier and save the crystallographer from reporting a wrong structure. The initial attempt to solve the structure using Monte Carlo simulated-annealing techniques used five torsion angles. A retrospective analysis of torsion angles in the CSD showed that the torsion angles involving the phenyl–oxygen bonds had very narrow distributions around 180°. These two torsions could have been fixed during the structure solution, making the problem smaller. In the CSD, the three torsion angles in the propyl side chain exhibit the normal *trans*/±*gauche* trimodal distributions. The structure could have been solved using $3 \times 3 \times 3 = 27$ rigid molecules instead of allowing the torsion angles to vary continuously. It is always worth carrying out such an analysis before structure solution, rather than after.

The initial model yielded a reasonable fit to the powder pattern, but the torsion angles were very far from the expected values. The $U_{\rm iso}$ value of the benzene-ring C atoms was much smaller than expected, while those of the side-chain heavy atoms became unreasonably large. Clearly this model was incorrect. These clues led me to consider other structural models, including different conformations of the propyl side chain. Eventually, a successful and much more reasonable model was derived.

Many common organic fragments are essentially rigid, and so can be described as rigid bodies in the Rietveld refinement. There is really no need to refine all of the structural parameters of a benzene ring. However, care must be taken when deciding whether to treat a fragment of a structure as a rigid body because some fragments (such as aromatic carboxylic acids; Kaduk *et al.*, 1998) are much more flexible than chemists commonly believe.

The final refinement of 56 variables using 8213 observations yielded the residuals $R_{\rm wp} = 0.1092$, $R_p = 0.0856$, $\chi^2 = 1.643$, $R(F) = 0.0931$ and $R(F^2) = 0.1179$. The refinement included a C_6H_4 rigid body and restraints on all of the bond distances and angles; the torsion angles were unrestrained. The restraints contributed 1.5% to the final χ^2. Several of the H atoms could be located in a difference Fourier map calculated without the H atoms. The largest peak and hole in the final difference Fourier map were 0.25 and −0.23 e Å^{-3}, respectively.

The *Mercury Mogul Geometry Check* output indicated that almost all of the bond distances and angles, and all of the torsion angles, fell within normal ranges. Only the C5—O16 and C6—O11 distances of 1.438 (1) and 1.438 (1) Å, respectively, were noted as ‘unusual (enough hits)’ (Figs. 4.9.26 and 4.9.27). These distances were subjected to restraints of 1.44 (1) Å. The Mogul averages for these distances are 1.371 (20) and 1.367 (16) Å, respectively. The angles C12—O11—C6 and C17—O16—C5 of 113.7 (3) and 114.1 (3)°, respectively, were noted as unusual (Figs. 4.9.28 and 4.9.29). These angles were subjected to restraints of 115 (3)°, and the Mogul averages are 117.6 (15) and 117.9 (19)°, respectively. The position of one of the torsion angles in the Mogul distribution is illustrated in Fig. 4.9.30. Changing these restraints to 1.37 (1) Å and 118 (3)°, as would be expected from Mogul, removed the geometry-check alerts. The statistical residuals were essentially unchanged. This serves as a good lesson that reasonable values should be used for geometrical restraints.

The *checkCIF* output contained many alerts about suspect bonds involving H atoms. Since the H atoms were reported in positions from the DFT calculation, the C/O—H bonds are longer than the crystallographically expected ones, and this alert

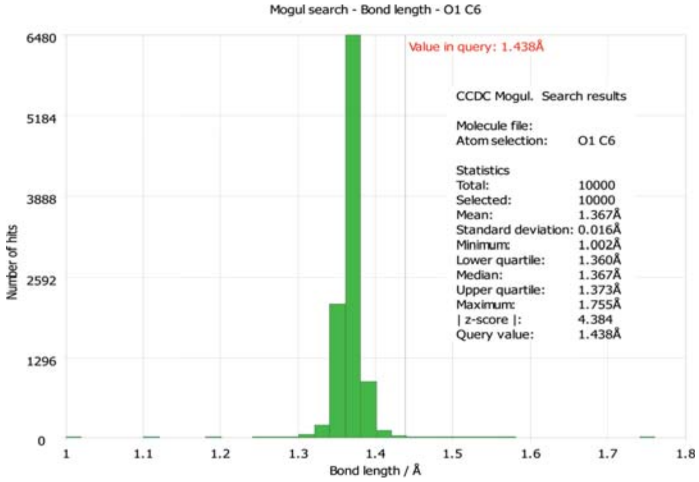

Figure 4.9.26
A *Mogul Geometry Check* histogram of the ‘unusual’ C5—O16 distance in guaifenesin, showing its position in the histogram of equivalent distances.

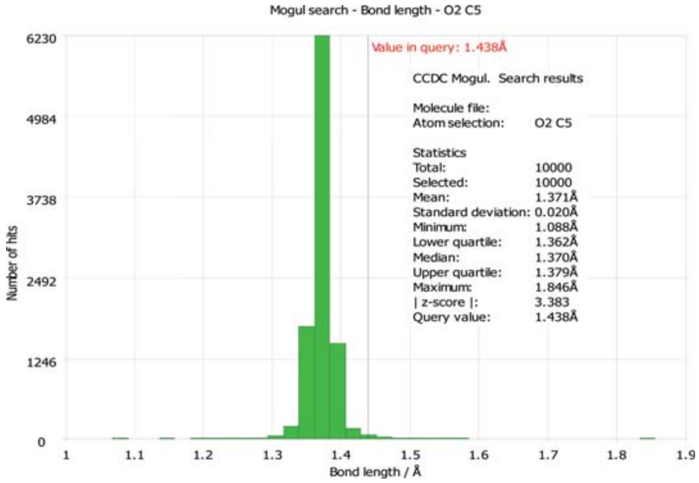

Figure 4.9.27
A *Mogul Geometry Check* histogram of the ‘unusual’ C6—O11 distance in guaifenesin, showing its position in the histogram of equivalent distances.

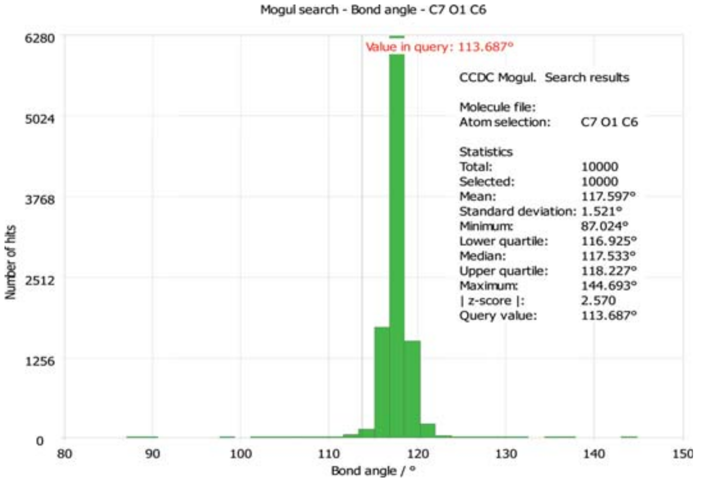

Figure 4.9.28
A *Mogul Geometry Check* histogram of the ‘unusual’ C12—O11—C6 angle in guaifenesin, showing its position in the histogram of equivalent angles.

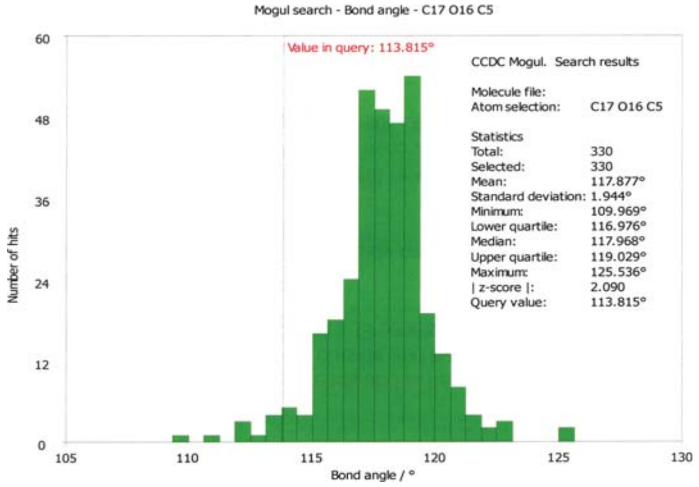

Figure 4.9.29
A *Mogul Geometry Check* histogram of the ‘unusual’ C17—O16—C5 angle in guaifenesin, showing its position in the histogram of equivalent angles.

is normal. *checkCIF* calculates different (and higher) standard uncertainties on the bond distances and angles. This difference is expected, as all of these quantities were subject to rigid-body constraints or restraints. It is best practice to report which geometrical quantities were subject to restraints, so that their significance can be evaluated by the reader.

A density-functional geometry optimization (with the unit-cell parameters fixed at the experimental values) using *Crystal09* (Dovesi *et al.*, 2005, 2009) resulted in a structure with no Mogul geometry check alerts. Examining the optimized structure using *checkCIF* resulted in no significant alerts.

Mogul geometry checks of the two single-crystal structures revealed no unusual geometrical features. The average differences between the bond distances, bond angles and torsion angles in these two structures are 0.004 (3) Å, 0.3 (2)° and 0.4 (3)°, respectively, and the differences are random. These two structures can be considered identical for all practical purposes. The average differences between the Rietveld and PANKUL02 bond distances, bond angles and torsion angles are 0.014 (9) Å, 1.0 (11)° and 1.7 (11)°, respectively, and the differences are random. The accuracy of the molecular geometry from the Rietveld refinement is good enough for most chemical purposes.

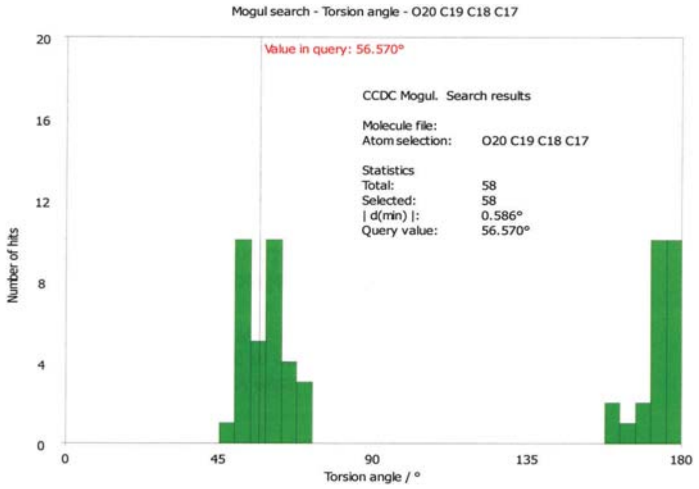

Figure 4.9.30
A *Mogul Geometry Check* histogram of the O20—C19—C18—C17 torsion angle in guaifenesin, showing its position in the histogram of equivalent angles.

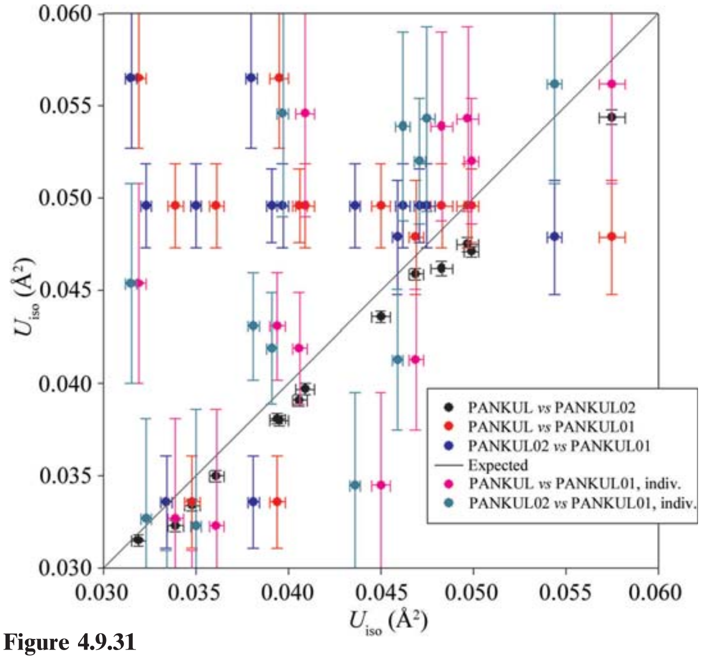

Figure 4.9.31
Comparison of the isotropic displacement coefficients for the powder (PANKUL01) and two single-crystal (PANKUL and PANKUL02) structures of guaifenesin.

Overlaying the DFT-optimized molecule with the Rietveld results yielded an r.m.s. difference in atom positions of 0.0345 Å. By far the largest differences were for the H atoms, as expected.

The *Mercury Calculate/Molecule Overlap* tool makes it easy to calculate the root-mean-square deviations between atomic positions in molecules. The r.m.s. differences between the powder structure PANKUL01 and the single-crystal structures PANKUL and PANKUL02 are 0.0392 Å (maximum 0.0603 Å) and 0.0434 Å (maximum 0.0755 Å), respectively. Visual overlays of the structures make them appear very similar. Changing the phenyl ether restraints to more reasonable values decreased these r.m.s. deviations to 0.0329 and 0.0348 Å, respectively.

The isotropic displacement coefficients of the C and O atoms from the Rietveld refinement are in good agreement with those determined from single-crystal data (Fig. 4.9.31), but their precision is nearly an order of magnitude worse. The main differences arise from the use of constraints on the U_{iso} values of the C atoms in the phenyl ring and in the propyl side chain in the Rietveld refinement. The agreement between the Rietveld and single-crystal U_{iso} values becomes better when they are allowed to refine individually. The agreement between the U_{iso} values in the two single-crystal refinements is excellent. With good powder data, we can reasonably expect accurate U_{iso} values from a Rietveld refinement, and obtaining such reasonable U_{iso} values is a good measure of the quality of the data and refinement.

When assessing the reasonableness of a structure or comparing structures, it is always worth examining the crystal structure as well as the molecular structure. The *Mercury Calculate/Structure Overlay* tool facilitates such comparisons. Although the heavy-atom positions in the two single-crystal structures of guaifenesin are identical, the positions of the hydroxyl protons differ (Fig. 4.9.32). The topology of the hydrogen-bond network is the same in both structures, but the locations of the protons in the hydrogen bonds (closer to one O atom or the other) differs. It is not clear what this difference means, although the structures are chiral. The hydroxyl proton positions of the Rietveld structure are the same as those in PANKUL02. Because the hydroxyl protons were located in a difference Fourier map and were confirmed by a DFT calculation, I believe that the PANKUL01/PANKUL02 hydroxyl groups are correct.

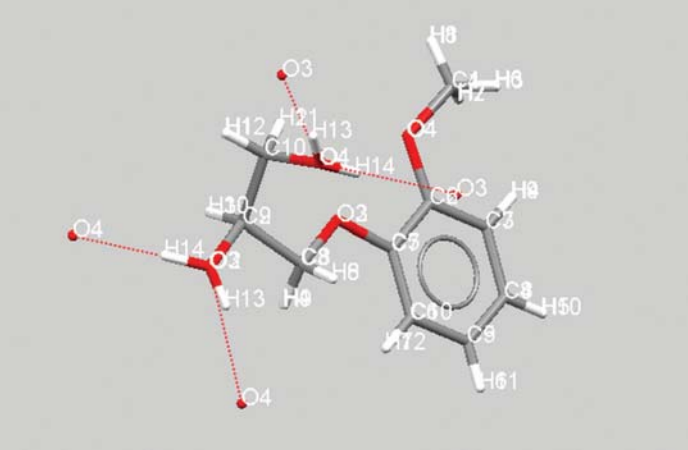

Figure 4.9.32
Mercury overlay of the two single-crystal structures (PANKUL and PANKUL02) of guaifenesin, showing the differences in the positions of the hydroxyl protons.

4.9.4.1.3. *Cobalt(II) acetate tetrahydrate,* $Co(C_2H_3O_2)_2(H_2O)_4$

The crystal structure of cobalt(II) acetate tetrahydrate was refined using single-crystal (the crystal was selected from the reagent used to generate the powder), laboratory and synchrotron X-ray powder data under ambient conditions using the same sample (Kaduk & Partenheimer, 1997; Kaduk, 1998). Refinements were carried out using individual data sets and in combination.

In the comparison of the various refinements, it is useful to compare bond distances and angles (Table 4.9.3), the root-mean-square deviations of the atoms (Table 4.9.4) and the displacement coefficients (Table 4.9.5). In this analysis, we will consider the *SHELXL* single-crystal refinement as the reference.

In the refinement using laboratory powder data, it was not possible to locate or refine the H-atom positions. They were fixed at the single-crystal locations with a common isotropic displacement coefficient. Restraints were desirable and necessary to obtain convergence, and their weight was decreased as the refinement progressed. It proved possible to distinguish the C—O and C═O bonds in the acetate ligand. The standard uncertainties on the bond distances were ~0.01 Å, compared with 0.001–0.002 Å in the single-crystal refinement. The average difference in the bond distances was 0.02 Å and that in the O···O distances was 0.08 Å. The average difference on the bond angles was 3° and the average r.m.s. displacement of the atoms was 0.07 Å.

The Co atom could be refined anisotropically using synchrotron data, and no restraints were necessary for stable refinement. It was still necessary to fix the H atoms at calculated positions. The standard uncertainties on the bond distances were ~0.005 Å. The standard uncertainties on the angles were ~0.2°, compared with 0.1° in the single-crystal refinements. The average differences in the bond distances, angles and O···O distances were 0.02 Å, 0.9° and 0.04 Å, respectively. The r.m.s. difference in the positions of the heavy atoms was 0.03 Å. The refinement using synchrotron powder data yielded excellent accuracy, with about half the precision of a single-crystal refinement.

In the joint refinement using two powder data sets, the Co atom was refined anisotropically and the remaining heavy atoms

Table 4.9.3
Bond distances (Å) and angles (°) in cobalt(II) acetate tetrahydrate (Kaduk & Partenheimer, 1997)

SC = single-crystal study.

Parameter	*SHELX* SC	*GSAS* SC	Laboratory powder	Synchrotron powder	Joint powder	Combined
Co—O1	2.098 (1)	2.100 (2)	2.092 (13)	2.129 (5)	2.132 (4)	2.101 (1)
Co—O3	2.122 (1)	2.124 (2)	2.114 (11)	2.142 (4)	2.138 (4)	2.122 (1)
Co—O4	2.092 (1)	2.087 (2)	2.050 (9)	2.071 (4)	2.095 (5)	2.091 (1)
O1—C1	1.275 (2)	1.276 (3)	1.294 (7)	1.297 (7)	1.295 (6)	1.276 (2)
O2—C1	1.247 (2)	1.243 (3)	1.233 (7)	1.238 (7)	1.240 (6)	1.242 (2)
C1—C2	1.500 (3)	1.503 (3)	1.504 (7)	1.501 (1)	1.514 (6)	1.503 (3)
O1—Co—O3	90.1 (1)	90.1 (1)	88.7 (4)	89.4 (2)	90.6 (2)	90.1 (1)
O1—Co—O4	90.7 (1)	90.6 (1)	89.1 (4)	90.8 (2)	90.8 (2)	90.6 (1)
O3—Co—O4	89.3 (1)	89.3 (1)	91.3 (4)	90.1 (2)	89.7 (2)	89.3 (1)
Co—O1—C1	125.9 (1)	126.4 (2)	129.7 (10)	125.1 (5)	124.5 (4)	125.5 (1)
O1—C1—O2	123.2 (2)	122.2 (2)	115.2 (14)	121.2 (8)	122.3 (6)	123.8 (2)
O1—C1—C2	117.2 (2)	118.2 (2)	122.6 (13)	116.5 (8)	116.3 (6)	117.1 (2)
O2—C1—C2	119.7 (2)	119.6 (2)	121.2 (13)	122.0 (8)	121.1 (6)	119.0 (2)
Hydrogen bonding O···O distances						
O1···H3A—O3	2.72	2.72	2.66	2.68	2.69	2.72
O2···H3B—O3	2.71	2.71	2.87	2.76	2.71	2.71
O2···H4B—O4	2.64	2.64	2.57	2.60	2.60	2.64
O4—H4A···O3	2.84	2.84	2.83	2.81	2.85	2.84

could be refined with individual isotropic displacement coefficients. Attempts to refine the C and O atoms anisotropically led to some non-positive-definite U tensors. The H-atom positions could be refined, subject to restraints. The $U_{\rm iso}$ values for the H atoms did not refine to reasonable values, so they were fixed at 0.06 Å^2. The accuracy and precision of the structural parameters were similar to those of the synchrotron refinement. Joint refinement using multiple powder data sets permitted the refinement of more structural parameters with good accuracy.

4.9.4.2. *Inorganic compounds*

The CSD and its associated software provide many tools which facilitate the validation of organic structures. The tools in the inorganic structural databases are not as well developed, so assessment of chemical reasonableness can be more indirect.

4.9.4.2.1. *The bond-valence method*

As crystallographic techniques developed, it became clear that there was a relationship between the length of a bond and its strength [see Brown (2002) and references therein]. We can consider the atomic valence V_i (the absolute value of the oxidation state) of the atom i in a crystal structure to be the sum of the individual bond valences,

$$V_i = \sum_j S_{ij}, \qquad (4.9.8)$$

and that the bond valence between atoms i and j is approximated by the two-parameter expression

$$S_{ij} = \exp\left(\frac{r_0 - r_{ij}}{B}\right), \qquad (4.9.9)$$

in which r_{ij} is the distance between atoms i and j, and r_0 and B are parameters that are chosen to ensure good agreement between the sums of bond valences and the atomic valences (formal charges or oxidation states) in a large number of well determined crystal structures. For many bond types, B is close to 0.37 Å. Brese & O'Keeffe (1991) determined these parameters for a large number of cation–anion pairs, and a current set of bond-valence parameters are maintained at http://www.ccp14.ac.uk/ccp/web-mirrors/i_d_brown/bond_valence_param by I. David Brown. Workers on a specific subset of compounds often determine more precise bond-valence parameters for their particular system (for examples, see Sidey, 2010, 2012; Krivovichev & Brown, 2001; Locock & Burns, 2004). It is frequently useful to incorporate the expected values for the bond distances in a particular cation–anion coordination sphere into Rietveld refinements as restraints.

4.9.4.2.2. *Hexaaquairon(II) tetrafluoroborate, [Fe(H$_2$O)$_6$](BF$_4$)$_2$*

A deposit (Kaduk, 2007*b*) isolated from a linear α-olefins plant (which used a BF$_3$ catalyst) yielded a nearly white crystalline powder when washed with methanol (supplementary files bagh09.gsas and d8v3.prm). The solid was moisture sensitive, so was protected from the atmosphere by a Kapton film attached to the sample holder with silicone grease.

The pattern could be indexed (*ITO12*; Visser, 1969) with a primitive orthorhombic unit cell with a = 7.686, b = 13.286, c = 5.376 Å and V = 548.95 Å^3. The cell accounted for 17 of the first 20 peaks (three weak peaks were unindexed), with a figure of merit of 34.4. This figure of merit is high enough that we can believe that there is some truth to the unit cell. The *ITO* output suggested that 'the cell is probably hexagonal, with a = 15.34 and c = 5.38 Å'. *ITO*'s suggestions of higher symmetry (based on the reduced form of the unit cell; Mighell &

Table 4.9.4
Root-mean-square density-weighted displacements (Å) of atoms in various refinements of cobalt(II) acetate tetrahydrate (Kaduk & Partenheimer, 1997)

SC = single-crystal study.

	SHELX SC	*GSAS* SC	Laboratory powder	Synchrotron powder	Joint powder	Combined
Co, C, O	—	0.006	0.07	0.03	0.03	0.007
H	—	0.18	0.006 (fixed)	0.006 (fixed)	0.45	0.19
All atoms	—	0.12	0.05	0.02	0.33	0.14

Table 4.9.5
Displacement coefficients (Å^2) from various refinements of cobalt(II) acetate tetrahydrate

SC = single-crystal study.

Atom	Displacement parameters	*SHELX* SC	*GSAS* SC	Laboratory powder	Synchrotron powder	Joint powder	Combined
Co	U_{11}	0.018 (1)	0.0190 (2)		0.015 (1)	0.014 (1)	0.019 (2)
	U_{22}	0.020 (1)	0.0194 (2)		0.017 (1)	0.018 (1)	0.019 (2)
	U_{33}	0.029 (1)	0.0308 (2)		0.026 (1)	0.027 (1)	0.030 (2)
	U_{23}	0.001 (1)	0.0007 (2)		0.003 (1)	0.002 (1)	0.0007 (2)
	U_{13}	−0.004 (1)	−0.0037 (2)		−0.012 (1)	−0.011 (1)	−0.0040 (1)
	U_{12}	0.000 (1)	0.0004 (2)		0.003 (1)	0.007 (1)	0.005 (2)
	U_{iso}	0.023 (1)	0.024	0.026 (2)	0.020	0.021	0.023
O1	U_{11}	0.023 (1)	0.022 (1)				0.022 (1)
	U_{22}	0.022 (1)	0.021 (1)				0.021 (1)
	U_{33}	0.047 (1)	0.047 (1)				0.047 (1)
	U_{23}	0.004 (1)	0.004 (1)				0.004 (1)
	U_{13}	−0.007 (1)	−0.006 (1)				−0.006 (1)
	U_{12}	−0.001 (1)	−0.001 (1)				−0.001 (1)
	U_{iso}	0.031 (1)	0.031	0.037 (3)	0.028 (2)	0.030 (1)	0.031
O2	U_{11}	0.038 (1)	0.040 (1)				0.040 (1)
	U_{22}	0.029 (1)	0.027 (1)				0.027 (1)
	U_{33}	0.056 (1)	0.058 (1)				0.057 (1)
	U_{23}	0.011 (1)	0.012 (1)				0.011 (1)
	U_{13}	−0.015 (1)	−0.016 (1)				−0.016 (1)
	U_{12}	−0.001 (1)	−0.002 (1)				−0.002 (1)
	U_{iso}	0.042 (1)	0.043	0.037 (3)	0.038 (2)	0.040 (2)	0.043
O3	U_{11}	0.022 (1)	0.022 (1)				0.022 (1)
	U_{22}	0.027 (1)	0.027 (1)				0.026 (1)
	U_{33}	0.037 (1)	0.038 (1)				0.037 (1)
	U_{23}	−0.006 (1)	−0.006 (1)				−0.007 (1)
	U_{13}	−0.004 (1)	−0.005 (1)				−0.005 (1)
	U_{12}	0.001 (1)	0.001 (1)				0.001 (1)
	U_{iso}	0.029 (1)	0.030	0.036 (4)	0.021 (2)	0.020 (1)	0.029
O4	U_{11}	0.027 (1)	0.028 (1)				0.027 (1)
	U_{22}	0.031 (1)	0.030 (1)				0.030 (1)
	U_{33}	0.038 (1)	0.040 (1)				0.040 (1)
	U_{23}	0.003 (1)	0.004 (1)				0.005 (1)
	U_{13}	−0.008 (1)	−0.007 (1)				−0.008 (1)
	U_{12}	−0.002 (1)	−0.004 (1)				−0.002 (1)
	U_{iso}	0.033 (1)	0.033	0.036 (4)	0.023 (2)	0.024 (1)	0.033
C1	U_{11}	0.028 (1)	0.029 (1)				0.029 (1)
	U_{22}	0.023 (1)	0.025 (1)				0.025 (1)
	U_{33}	0.034 (1)	0.033 (1)				0.033 (1)
	U_{23}	0.003 (1)	0.003 (1)				0.003 (1)
	U_{13}	0.002 (1)	0.004 (1)				0.004 (1)
	U_{12}	−0.001 (1)	−0.002 (1)				−0.001 (1)
	U_{iso}	0.028 (1)	0.029	0.037 (3)	0.035 (3)	0.035 (2)	0.029
C2	U_{11}	0.051 (1)	0.052 (2)				0.051 (2)
	U_{22}	0.027 (1)	0.026 (1)				0.026 (1)
	U_{33}	0.054 (2)	0.058 (2)				0.057 (2)
	U_{23}	−0.002 (1)	−0.000 (1)				0.002(1)
	U_{13}	−0.005 (1)	−0.006 (1)				−0.009 (1)
	U_{12}	−0.008 (1)	−0.008 (1)				−0.010 (1)
	U_{iso}	0.045 (1)	0.046	0.037 (3)	0.031 (3)	0.034 (2)	0.046
CH_3, H	U_{iso}	0.136 (11)	0.102 (8)	0.06	0.06	0.06	0.088 (6)
OH_2, H	U_{iso}	0.055 (4)	0.067 (5)	0.06	0.06	0.06	0.062 (4)

Rodgers, 1980; Stalick & Mighell, 1986) are correct often enough that they need to be taken seriously, but in this case the program was wrong.

Searching for matches to the reduced cells of both the orthorhombic and hexagonal unit cells in the ICSD using default tolerances yielded no hits. Widening the tolerances yielded what eventually turned out to be the correct structure model, but the actual process was more convoluted (Kaduk, 2007*b*). Similar searches for matches to the reduced cells in the NIST Crystal Data Identification File (Mighell & Himes, 1986) yielded a number of divalent-metal perchlorate and tetrafluoroborate hexahydrates, most of which were from the same paper (Moss *et al.*, 1961). The lattice constants were determined using a 9 cm diameter Debye–Scherrer camera, so it was uncertain whether the cells were hexagonal or pseudo-hexagonal, but I could be reasonably sure that the compound that I isolated was $Fe(BH_4)_2(H_2O)_6$.

$Fe(BH_4)_2(H_2O)_6$ was present in the Powder Diffraction File as entry 00-021-0427, and was reported to crystallize in $Pmn2_1$ with $a = 7.71$, $b = 13.54$, $c = 5.42$ Å: essentially the same cell as determined by *ITO*. The pattern did not look similar to the observed pattern (Fig. 4.9.33), but it is not a high-quality pattern, consistent with its 'blank' quality mark. The PDF entry lists $Mg(ClO_4)_2(H_2O)_6$ (West, 1935) as the prototype structure.

In the refinement, restraints of 2.12 (2) Å were applied to the Fe—O bonds. An analysis of all 59 $Fe^{2+}O_6$ coordination spheres in the CSD suggested a value of 2.10 (6) Å, and bond-valence calculations yielded 2.16 Å. In early refinements the BF_4 groups were modelled as rigid bodies, but in the final refinement the rigid bodies were replaced by restraints of 1.42 (1) Å on the B—F

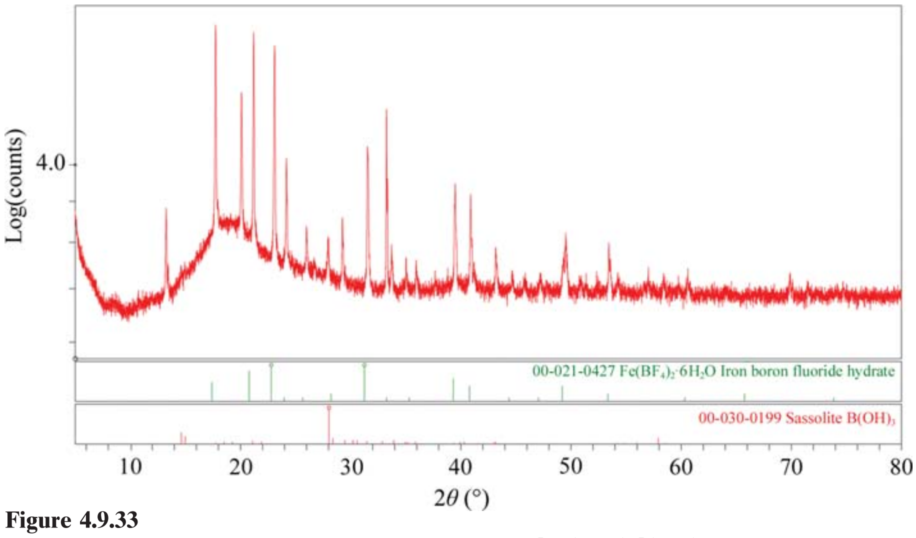

Figure 4.9.33

Comparison of the experimental powder pattern of $[Fe(H_2O)_6](BF_4)_2$ and the PDF entry 00-021-0427 reported for this compound. Sassolite was present as an impurity in the sample.

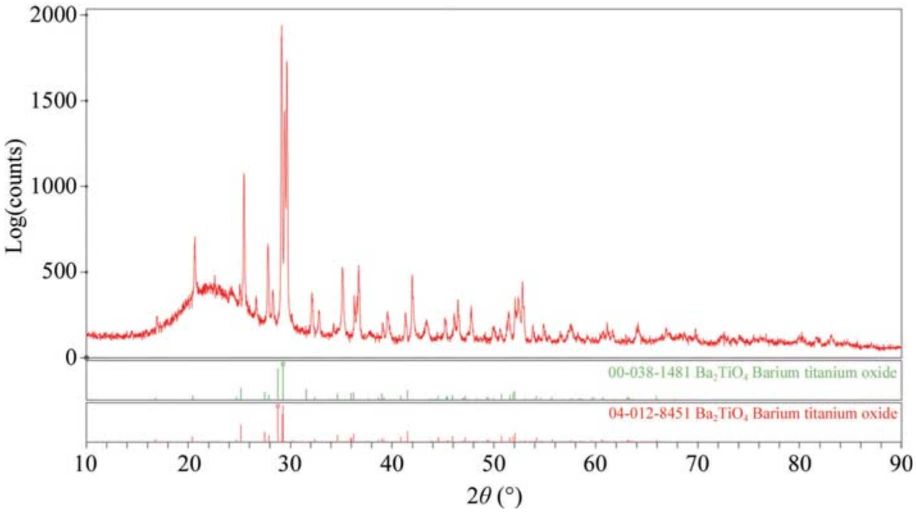

Figure 4.9.34

The observed pattern of $(Ba_{1.5}Sr_{0.5})TiO_4$ compared with the experimental and calculated PDF entries for Ba_2TiO_4. The sample had been blended with amorphous silica for grinding in a micronizing mill.

bond distances, along with F—B—F angle restraints. Analysis of 5546 hits for BF_4^- in the CSD suggested 1.36 (6) Å, bond-valence calculations suggested 1.39 Å, *International Tables for Crystallography* indicated 1.37 (7) Å and an analysis of tetrafluoroborates in the ICSD indicated 1.37 (3) Å. Since BF_4 anions are often disordered, exhibit large thermal motion (both of which lengthen the apparent bond distance) or both, I chose a larger value for the restraint.

The refinement yielded a geometrically reasonable structure. The $U_{\rm iso}$ values of the Fe and O atoms were 0.037 (2) and 0.056 (3) $Å^2$, respectively; these are higher than we might expect for an inorganic structure, but within the normal ranges. The $U_{\rm iso}$ values of the atoms in the two independent BF_4^- groups were uncomfortably large at 0.158 (6) and 0.092 (5) $Å^2$.

Most chemists know that, as a tetrahedral group, the tetrafluoroborate ion is often disordered statically or dynamically in crystal structures. We might therefore expect the $U_{\rm iso}$ values for the atoms in this group to be large, but how large is unreasonably large? Because BF_4^- is often the disordered counterion to a more chemically interesting cationic complex, there are fewer well defined structures of the BF_4^- ion than one might expect. Of the 67 structures of BF_4^- ions in the 2006/2 release of the CSD, 28% had missing displacement coefficients. For low-temperature (<200 K) structures the $U_{\rm iso}$ values for BF_4^- lie mainly in the range 0.02–0.06 $Å^2$, but some are as large as 0.12–0.16 $Å^2$. In room-temperature structures they are larger, generally ranging from 0.03 to 0.07 $Å^2$, but some are much higher. Checking the primary papers for the BF_4^- structures in the CSD suggested that the values of 0.16 and 0.09 $Å^2$ were not exceptionally high and thus were chemically reasonable.

The measurements of the physical properties of this compound and other divalent-metal tetrafluoroborates show that they all melt within 5 K of room temperature. Examination of the reported structures of compounds close to their melting points showed that the $U_{\rm iso}$ values of 0.16 and 0.09 $Å^2$ are not at all unreasonable for a structure determined within 5 K of the melting point. A knowledge of chemical reasonableness played a role at almost every point in the solution and refinement of the crystal structure of $Fe(BF_4)_2(H_2O)_6$, and shows how such knowledge contributed to the success of a Rietveld refinement.

4.9.4.2.3. *$(Ba_{1.5}Sr_{0.5})TiO_4$*

As part of a study aimed at understanding the details of the crystallography and crystal chemistry of the intermediate members of the $(Ba_{2-x}Ti_x)TiO_4$ solid-solution series (Kaduk, 2007*b*), a powder pattern (Fig. 4.9.34) was obtained that showed that $Ba_{1.5}Sr_{0.5}TiO_4$ (kindly supplied by W. Wong-Ng, NIST) was isostructural to orthorhombic Ba_2TiO_4 (supplementary files wong224.gsas and d8v3.prm). Orthorhombic β'-Ba_2TiO_4 crystallizes in $P2_1nb$, with a = 6.107 (1), b = 22.952 (4), c = 10.540 (2) Å (Günter & Jameson, 1984). The coordinates from Günter & Jameson (1984) were used as the initial structural model. The refined lattice parameters of $Ba_{1.5}Sr_{0.5}TiO_4$ were a = 6.0634 (2), b = 22.6606 (9), c = 10.4040 (4) Å. The refinement appeared to be excellent (Fig. 4.9.35). The residuals were $R_{\rm wp} = 0.1090$, $R_p = 0.0838$, $\chi^2 = 1.345$ and $R(F^2) = 0.1199$, but I was convinced that the structure was wrong.

The refinement of the atomic coordinates and other variables never converged, even with a damping factor of 9 (applying only one tenth of the calculated shift to the coordinates in each least-squares cycle). A refinement that does not converge is a sure sign that something is wrong with the model, the data or both. The stoichiometry derived from the fractional occupancies of the Ba/Sr sites was wrong. The difference between the 56 electrons of Ba and the 38 electrons of Sr is large enough that we should expect to get the fractional occupancies right, even when using laboratory X-ray data. The standard uncertainties of the fractional coordinates were exceptionally high, in the third decimal place for the cations and the second decimal place for the O atoms, and were higher than is reasonable. The $U_{\rm iso}$ value of the O atoms did not refine to a reasonable value, but this is not unusual in the presence of heavy atoms using X-ray data.

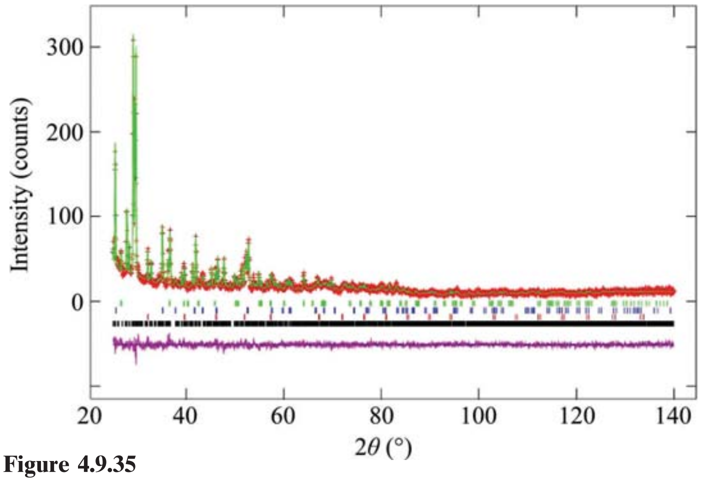

Figure 4.9.35
A Rietveld plot from an incorrect refinement of the structure of $(Ba_{1.5}Sr_{0.5})TiO_4$. The residuals were R_{wp} = 0.1090, R_p = 0.0838, χ^2 = 1.345 and $R(F^2)$ = 0.1199.

This combination of problems is often associated with wrong symmetry. The *MISSYM* program of the *NRCVAX* system (Le Page, 1987; this functionality is now incorporated into *checkCIF* and *PLATON* as *ADDSYM*) suggested the presence of a centre of symmetry at $\frac{1}{2}, \frac{1}{2}, \frac{1}{2}$ and thus that the space group was really *Pmnb*. This has the consequence that the six Ba/Sr sites, the three Ti sites and six of the O atoms are located on a mirror plane rather than a general position. Attempting to refine a structure in a space group with a symmetry that is too low can yield the symptoms observed here.

The appropriate atoms were moved manually to the special positions and the space group was changed. The resulting refinement was nearly as good as the first, with R_{wp} = 0.1011, R_p = 0.0851, χ^2 = 1.370 and $R(F^2)$ = 0.1424, but used only 61 variables instead of 85. (The Occam's razor principle of fewer variables is better is a good guide.) This refinement never converged; the shifts of the atom coordinates alternated between positive and negative, and never went to zero. The refined Ba/Sr composition was $Ba_{1.3}Sr_{0.7}$; closer to the known $Ba_{1.5}Sr_{0.5}$, but still disappointing. The U_{iso} values for the heavy atoms fell within normal ranges, but it was still not possible to refine the U_{iso} values for the O atoms. The standard uncertainties on the fractional coordinates were still too large: 0.001–0.004 for the heavy atoms and 0.003–0.012 for the O atoms. The most worrying feature was that many low-angle peaks were predicted for this fairly large unit cell, but were not observed. These would all have to be unobserved because of low intensity, rather that extinct by symmetry. This idea is built into the definition of the Smith–Snyder figure of merit for indexing (Smith & Snyder, 1979); a smaller unit cell which accounts for all of the peaks is favoured over a larger cell.

Another application of *MISSYM* (with larger than the default tolerances) suggested the presence of additional translational symmetry, with the translation vector $0, \frac{1}{3}, 0$. At this point I finally looked at the structure, and realized that β'-Ba_2TiO_4 was clearly a superstructure with its *b* axis three times that of a smaller unit cell. On searching for matches to the $a, \frac{1}{3}b, c$ cell in the NIST Crystal Data Identification File, I discovered that $(Ba_{1.5}Sr_{0.5})TiO_4$ is actually isostructural to K_2SO_4 and that I had been using a unit cell three times too large.

Restarting the refinement with coordinates based on those of K_2SO_4, I obtained an excellent refinement. The residuals were R_{wp} = 0.1115, R_p = 0.0864, χ^2 = 1.396 and $R(F^2)$ = 0.1565 and the model was chemically reasonable. The refinement of only 32 variables yielded a composition $Ba_{1.58}Sr_{0.42}$, which is acceptably close to the expected stoichiometry of $Ba_{1.5}Sr_{0.5}$. The U_{iso} value for Ba/Sr was 0.017 (1) Å^2, which is reasonable for a site occupied by disordered large cations. The U_{iso} value for Ti was a reasonable 0.013 (3) Å^2 and the U_{iso} value for the O atoms refined to 0.054 (7) Å^2; this is perhaps a little high for a ceramic, but the O atoms are bonded to Ba/Sr atoms which are disordered. The standard uncertainties on the Ba/Sr, Ti and O fractional coordinates were ∼0.0004, 0.0011 and 0.00*n*, respectively, which are about what I would expect for such a system. The interatomic distances (subject to restraints) and the O—Ti—O angles (free) were reasonable. All of the statistical, graphical and chemical measures suggested that the structure was (finally) correct.

4.9.4.2.4. *$(Ba_{1.25}Sr_{0.75})TiO_4$*

Another compound in the $(Ba_{2-x}Sr_x)TiO_4$ series was $(Ba_{1.25}Sr_{0.75})TiO_4$ (also kindly supplied by W. Wong-Ng, NIST). Given the trouble that was encountered with $(Ba_{1.5}Sr_{0.5})TiO_4$, synchrotron data were collected on the MR-CAT ID10 beamline at APS from a rotating capillary specimen using a wavelength of 0.4959 Å (supplementary files ba2180.gsas, wong224.gsas, id100602.prm and d8v3.prm). Starting from the $(Ba_{1.5}Sr_{0.5})TiO_4$ model yielded a reasonable refinement (49 variables): *Pnma*, *a* = 7.48904 (3), *b* = 6.03638 (3), *c* = 10.32873 (5) Å, *V* = 466.928 (4) Å^3, R_{wp} = 0.0847, R_p = 0.0621, χ^2 = 2.625. The refined stoichiometry was $Ba_{1.13}Sr_{0.87}TiO_4$. The U_{iso} values for Ba/Sr, Ti and O were 0.0245 (5), 0.0240 (16) and 0.066 (3) Å^2, respectively. The U_{iso} values for Ti and (notably) the O seemed a little too high, especially given the very good synchrotron data.

A full-scale Rietveld plot (Fig. 4.9.16) looked good, but an enlargement of the pattern (Fig. 4.9.17) revealed the presence of a number of weak peaks that were not accounted for by the model. Searches for the peaks (manually picked from the difference plot) against the Powder Diffraction File showed that they did not correspond to any known phase or to a new composition isostructural to a known phase. To test the hypothesis that the peaks were part of the pattern of the major phase, I added them one at a time to the strong peaks used to index the pattern using *DICVOL91* (Boultif & Louër, 1991). A feature of *DICVOL91* (and one that was overcome in later versions) was that it allowed no unindexed lines; this proved to be a useful feature for this problem. No matter which weak line I added, the program came up with the same primitive orthorhombic unit cell: *a* = 14.9760, *b* = 10.3177, *c* = 6.03666 Å, *V* = 932.77 Å^3. The *a* axis was twice what I had been using; this compound crystallized in a 2× supercell of the original cell. A search for matches to the reduced cell in the ICSD (with larger than default tolerances) yielded $(NH_4)_2BeF_4$, which crystallizes in Pna_12 (Srivastava *et al.*, 1999), the coordinates of which were used as the basis for a new refinement.

In addition to distance and angle restraints, chemical composition restraints were used in the refinement. Each of the four Ba/Sr sites was assumed to be fully occupied by a mixture of Ba and Sr. The restraint was that the unit cell contained 10.0 (3) Ba atoms and 6.0 (3) Sr atoms. Two of the sites were occupied mainly by Ba and the other two by Sr (Kaduk, 2007*b*). A major objective of the study was to determine how the Ba/Sr site occupancies changed as the overall composition varied.

A refinement of this model (90 variables) using combined synchrotron and laboratory patterns yielded an excellent refinement: R_{wp} = 0.0621, R_p = 0.0477, χ^2 = 1.561 and $R(F^2)$ = 0.0726. The largest peak and hole in the difference Fourier map were +1.75 and −2.15 e Å^{-3}, respectively. The refined lattice parameters were a = 14.97814 (5), b = 6.03634 (2), c = 6.03634 (2) Å and the space group was $Pna2_1$. *MISSYM* suggested that a centre of symmetry was present, but refinements in *Pnam* yielded poorer residuals and chemically less reasonable geometry; in this case the suggested extra symmetry was only approximate. The refined composition of the major phase was $Ba_{1.30}Sr_{0.70}TiO_4$, which was in good agreement with the expected formula. The $U_{\rm iso}$ values for Ba/Sr, Ti and O were 0.0141 (3), 0.0166 (11) and 0.0267 (20) Å^2, respectively, which were much more reasonable for a hard ceramic such as this. In this refinement, chemical reasonableness was important at almost every step in obtaining the correct structure.

4.9.4.2.5. *Mullite, $Al_{4.85}Si_{1.18}O_{9.77}$*

The refinement of a mullite supplied by Kyanite Mining Company (supplementary files kadu1286.gsas, kadu1328.gsas and d8v3.prm) provided a good example of many of the difficulties which can be involved in Rietveld refinement of an inorganic material (Kaduk, 2009). Several different approaches were used to validate the structure both during and after refinement.

A significant hurdle in beginning a Rietveld refinement can be deciding which structural model to use. The pattern of the major mullite phase was matched about equally well by several PDF entries. The PDF editors have extended the quality-mark system used for experimental patterns to calculated patterns and the structures from which they were derived. (The details of the quality-mark system are discussed in Chapter 3.7 of this volume.) The quality marks include * (no warning found during data evaluation), I (minor warning), B (significant warning), O (major warning), P (structure assigned by the editor based on a prototype) and H (hypothetical structure). I chose to begin the refinement with the coordinates from the 'star' quality pattern 01-074-4143 (Li *et al.*, 2004).

The mullite structure contains one fully occupied octahedral Al site and two partially occupied tetrahedral sites. Before refinement of the atom coordinates, the interatomic distances and angles were calculated, so that decisions could be made about how to incorporate chemical knowledge into the refinement. The octahedral Al1 was bonded to two O5 atoms at 1.90 Å and four O6 atoms at 2.04 Å. The tetrahedral Al2/Si3 was bonded to one O5 atom at 1.66 Å, two O6 atoms at 1.67 Å and one O7 atom at 1.67 Å. The tetrahedral Al4 was bonded to one O5 atom at 1.69 Å, two O6 atoms at 1.86 Å and one O8 atom at 1.48 Å. Based on experience and the bond-valence formalism (Brown, 2002), we know that 1.90 (2) Å is a reasonable value for an octahedral Al—O distance, 1.61 (2) Å is reasonable for a tetrahedral Si—O distance and 1.74 (2) Å is reasonable for a tetrahedral Al—O distance. The octahedral Al1 and tetrahedral Al4 sites could be confidently assigned as completely Al, but the composition of the Al2/Si3 site was not yet known. The current bond distance of 1.67 (2) Å was used in the initial restraint.

After refining the atom coordinates, the average Al2/Si3—O distance was 1.696 Å. Interpolating between the ideal tetrahedral Si—O and Al—O distances yielded an Al:Si ratio of 0.66:0.33. A constraint was set up to keep the Al:Si ratio at 2:1, but the total site occupancy was refined. Among potential refined parameters was the anisotropic size-broadening coefficient ptec. Refining this term rationally requires specifying (and thus knowing) a unique direction for the anisotropic broadening. Using *Mercury* to calculate the Bravais–Friedel–Donnay–Harker (BFDH) morphology (Bravais, 1866; Friedel, 1907; Donnay & Harker, 1937) expected from the crystal structure is often a good way of identifying the unique axis if it is not obvious from the symmetry.

The final refinement yielded the residuals $R_{\rm wp}$ = 0.0481, R_p = 0.0377, χ^2 = 1.533, $R(F)$ = 0.0183 and $R(F^2)$ = 0.0365. The restraints contributed 0.7% of the final χ^2. The largest peak and hole in the difference Fourier map were +0.33 (1.44 Å from two Al1 sites) and −0.38 e Å^{-3} (0.68 Å from Al1), respectively, so the map was acceptably flat. The slope and intercept of the normal probability plot were 1.141 and 0.0276, showing that any systematic errors were small.

The sample consisted of a mixture of phases, including 7.6 (1) wt% amorphous material (glass). In the absence of amorphous material, the bulk chemical analysis calculated from the phase concentrations and compositions can be compared with the measured bulk analysis for a valuable internal consistency check. In this case, such analysis would have to include an analysis of the glass in an electron microscope.

From the refined structural parameters, the composition of the mullite was calculated as $Al_{4.85}Si_{1.18}O_{9.77}$. The (unconstrained) sum of the positive charges in the unit cell was +19.28 and the sum of the negative charges was −19.54. The agreement was to ~1% of stoichiometric, which I considered acceptable. The ratio of the Al2 and Si3 occupancies was constrained, but the sum of the occupancies of Al2, Si3 and Al4 was not and was 1.008. As expected, either site 2/3 or 4 was occupied, but not both simultaneously (they are too close to each other).

The bond-valence sums were close to the expected values for Al1 (2.96), Al4 (2.94) and the O atoms (1.90, 2.10 and 1.96), but not for Al2/Si3. The differences from the expected values of 3 and 4 help to rationalize the multiple and partial occupancy of this site. The agreement of the bond-valence sums with their expected values is another way of saying that the bond distances fall within the normal ranges. The average deviation of the bond angles at the highly occupied metal sites was 2.2 (35)° and 7.2 (33)° for the less-occupied Al4 site.

The displacement coefficients of the atoms in mullite [Al/Si = 0.00932 (2), O = 0.0081 (4) Å^2], quartz [0.0156 (5) Å^2] and a silicon internal standard [0.0087 (5) Å^2] were quite reasonable for such rigid inorganic phases. With a large angular range of data and careful specimen preparation it is possible to obtain reasonable displacement coefficients even using laboratory X-ray powder data.

The refined mullite lattice parameters (space group *Pbam*) were a = 7.54718 (12), b = 7.70054 (12), c = 2.88546 (4) Å. A search of the ICSD for structures having reduced-cell parameters within 0.03 Å of these values yielded 24 aluminosilicate mullites. In almost all of these refinements the occupation of Al at the Al2 site was fixed at 1/2 and the Si occupancy was refined. This sample seemed to be a typical and chemically reasonable mullite, which is slightly richer in Al than average. The a lattice parameter corresponded to ~75 wt% Al_2O_3 and the cell volume to ~25% wt% SiO_2 according to the correlations in Deer *et al.* (1982). The refined composition is close to these values, providing another validation of the structure.

4.9.4.2.6. *6H perovskite $Ba_3CaSb_2O_9$*

The intial model for the crystal structure of the hexagonal 6H perovskite $Ba_3CaSb_2O_9$ determined using synchrotron powder data (Rowda *et al.*, 2008; discussed above in Section 4.9.3) had two worrying features. The two crystallographically independent Ba atoms had very different $U_{\rm iso}$ values: 0.0080 (9) and 0.0221 (9) Å^2. The angles around the octahedral Ca and Sb

Table 4.9.6

Average bond distances and angles from 26 experimental determinations of α-quartz compared with average values from 20 determinations in the ICSD

Parameter	Average experimental value	Average value from ICSD
Si—O (Å)	1.602 (12)	1.619 (12)
	1.595 (12)	1.599 (12)
O—Si—O (°)	110.83 (46)	111.15 (45)
	108.60 (18)	108.98 (32)
	108.67 (60)	108.27 (201)
	109.38 (74)	
Si—O—Si (°)	143.78 (60)	143.59 (45)

cations were very different from the expected 90/180°; normally these octahedra are quite rigid. These unusual structural features prompted an examination of the Rietveld plot, which led to the identification of 10.6 wt% face-centred cubic perovskite Ba_2CaSbO_6, 0.5 wt% CaO and 0.3 wt% BaO. Incorporating these impurity phases into the Rietveld refinement resulted in Ba U_{iso} values of 0.0239 (5) and 0.0228 (4) Å,^{2} and almost ideal octahedral geometry of the calcium and antimony cations. In the absence of the impurity phases, the model for the major phase had distorted to obtain the best fit to the powder pattern.

4.9.4.2.7. *Quartz*

As part of a study of cation-site occupancies in zeolite Y as a function of ion exchange (Kaduk, 2005), the structure of an α-quartz internal standard was refined 26 times using synchrotron powder data. From an individual Rietveld refinement, the standard uncertainties of the quartz lattice parameters were typically 0.00003 and 0.00004 Å for *a* and *c*, respectively. The averages of the 26 values were 4.9138 (8) and 5.4054 (4) Å at 300 K. The distributions corresponded reasonably to normal distributions. The standard uncertainty of an individual measurement of *a* was underestimated by a factor of 30 and that of *c* by a factor of 10 compared with those obtained by a true sampling of the population. To assess the accuracy (rather than the precision) of these results, the average values from 20 high-quality determinations from the ICSD were computed: a = 4.9130 (33) and c = 5.4037 (30) Å. The experimental values differed from these best values by less than one standard uncertainty.

The quantities of interest to a chemist, the bond distances and angles, were likewise accurate (Table 4.9.6). These results demonstrate that we can reasonably expect to measure bond distances to an accuracy of ~0.01 Å and angles to ~0.5° in favourable cases using powder data. This is a lower accuracy than is commonly supposed, but is sufficient for most chemical purposes.

4.9.5. Working by analogy

Lattice matching (reduced-cell searches) and comparison of formula types can be powerful and complementary techniques for phase identification and confirmation. Indeed, many thousands of structures have been assigned by the editors of Pearson's Crystal Data (Villars *et al.*, 1998) using just such 'prototyping' techniques. Searching for unit-cell and/or formula analogues can help to confirm the chemical reasonableness of a model and save the effort of *ab initio* structure determination.

The powder pattern of $Ba_5Zn_4Er_8O_{21}$ (supplementary files icdd124.gsas and padv.prm; now included in the Powder Diffraction File as entry 00-049-0598) could be indexed on body-centred tetragonal, end-centred orthorhombic and *C*-centred monoclinic unit cells with about the same high figures of merit. Searches for the formula type A4B5C8X21 in the ICSD and PDF showed that all examples of this formula crystallize in *I*4/*m*. The tetragonal cell was thus chosen, and a successful refinement was obtained in this space group.

Among the crystalline phases present in a black tar isolated from a pump seal in a refinery was PDF entry 00-022-0006, $Al_4H_2(SO_4)_7(H_2O)_{24}$ (supplementary file pak03.gsas). The crystal structure had not been reported, so a model had to be found in order to carry out a quantitative phase analysis by the Rietveld method. A search of the ICSD for the formula type A4B7X52 yielded only one hit, $Cr_4H_2(SO_4)_7(H_2O)_{24}$ (PDF entry 01-072-0981). Although the powder patterns did not resemble each other very well, the similarity of the metal charges and sizes, the common sulfate anions and the number of water molecules suggested that the two compounds might be isostructural. The Cr structure proved to be a suitable model for the Al compound (Kaduk, 2002).

Although it was easy to identify several iron oxides and hydrous oxides in a corrosion deposit from a pilot plant reactor that used a triflic acid catalyst, the major phase did not match any pattern in the Powder Diffraction File. The pattern (supplementary files simp08.gsas and padv.prm) of the major phase could be indexed in a *C*-centred orthorhombic unit cell with a = 18.6415 (14), b = 6.9291 (5), c = 6.5938 (5) Å. A reduced-cell search in the CSD yielded the hit $V^{2+}(CF_3SO_3)_2(H_2O)_6$, which proved to be a suitable isostructural model for Rietveld refinement (Kaduk, 1999).

Sometimes the process of lattice matching can be more convoluted. The pattern of a calcium salt of trimellitic acid (supplementary files barn133.gsas and d8v3.prm) could be indexed in a triclinic unit cell with a = 6.9419 (2), b = 7.0404 (2), c = 10.4125 (3) Å, α = 86.884 (3), β = 82.418 (2), γ = 69.531 (1)°. A reduced-cell search in the CSD (using a 3% tolerance on the volume) yielded (among others) the hit EKUNON, a cadmium salt of trimellitic acid, $Cd(HC_9H_3O_6)(H_2O)$. Substituting calcium for cadmium in the EKUNON structure model did not yield a good Rietveld refinement. The structure was then solved *ab initio*. Comparing the two structures showed that the chemical change had altered the relative magnitudes of the *a* and *b* axes. The compounds do turn out to be isostructural, but the interchange of the axes prevented success in the initial refinement.

4.9.6. Structure validation in general

The history of structure validation has focused on quantities derived from the fractional coordinates (distances, angles and torsions), but has on occasion extended to examination of the displacement coefficients (Harlow, 1996) and to the correction of space-group errors (Marsh, 1984, 1986, 1988, 1995, 1997, 1999, 2002, 2004; Marsh & Bernal, 1995; Marsh & Herbstein, 1983, 1988; Marsh *et al.*, 2002; Marsh & Schomaker, 1979, 1980, 1981; Baur & Kassner, 1992; Baur & Tillmanns, 1986; Herbstein, 1997; Herbstein & Marsh, 1982, 1998; Schomaker & Marsh, 1979).

Structures deposited in the Protein Data Bank are checked for the agreement of bond lengths and angles with standard values (Westbrook *et al.*, 2003). Validation of protein structures includes determining whether the backbone torsion angles φ and ψ in each residue lie in regions of a plot of φ against ψ that have favourable energy (Ramachandran *et al.*, 1963).

Much recent effort has been directed at the validation of protein structures. The set of tools included in *MolProbity*

(Lovell *et al.*, 2003; Davis *et al.*, 2007; Chen *et al.*, 2010) is noteworthy. Since protein refinements, like Rietveld refinements, ultimately suffer from a lack of data, validation tools have been developed (Zucker *et al.*, 2010) for protein structures in which the translation/libration/screw formalism has been used to model a large set of atoms acting as a rigid body.

The first steps towards the validation of protein structures were taken in the early 1990s (Richards, 1988; Brändén & Jones, 1990; Jones *et al.*, 1991; Laskowski *et al.*, 1993). The rapid growth in the number of structures deposited in the Protein Data Bank (Berman *et al.*, 2000) has permitted the development of more sophisticated tools for validation. These tools are summarized in the report of the X-ray Validation Task Force (VTF; Read *et al.*, 2011). Although the VTF states that the criteria are not necessarily applicable for the evaluation of structures derived from powder data, the report contains many ideas that are useful in general. The tools include evaluation of bond distances and angles, planarities and chiralities. The assumption that distributions of bond distances and angles are Gaussian is not necessarily true. Assessment of the protein backbone conformation involves analysis of torsion angles, and these are also important for validating side-chain conformations. It is crucial to include the H atoms so that all atom contacts can be evaluated. Analysis of underpacking and hydrogen bonds are also key parts of validation. The tools for structure-factor and electron-density validation and Wilson plots are not as relevant to powder structures, but should not be ignored.

Rietveld refinements often incorporate prior knowledge in the form of restraints and constraints. The quality of the resulting structure model will only be as good as the quality of the prior knowledge, which should be checked. It can be the case that what we think we know is not true. A correct structure model should permit the prediction of some parameters or properties that were not used in the refinement. If the model can successfully predict information that was not incorporated into the model, our confidence in the model is increased (Kleywegt, 2009).

Most constraints and restraints involve intramolecular quantities, but we should not neglect intermolecular features when validating a structure. There should be no bad contacts between atoms that are not covalently bonded, including H atoms. We can take clues from macromolecular crystallography, and expect that hydrophobic portions of molecules will pack together, hydrogen bonds will form, and positively and negatively charged regions of molecules will be close to each other.

A common way of testing the reasonableness of nonbonded contacts is to perform a conformational analysis of the molecule. Such conformational analyses tend to be performed *in vacuo*. This environment tends to result in more compact conformations than are typically observed in the solid state (see Taylor, 2011 and references therein) and so must be used with caution. For accurate comparison of nonbonded H–H distances, the bonded $X{-}H$ distances determined using X-ray diffraction need to be normalized (*Mercury Edit/Normalise Hydrogens*) to account for the artificially short distances derived in an X-ray experiment. Analysis of a large number of well determined structures in the CSD had yielded good values for the minimum expected nonbonded distances for a number of atom–atom pairs [see Table 2 in Taylor (2011)]. A statistical analysis of hydrogen bonds in the CSD has led to the logit hydrogen-bonding propensity (LHP) model (Galek *et al.*, 2007), which is useful in identifying and analysing likely and unusual hydrogen-bonding patterns.

The structure determination of 2,2-aziridinedicarboxamide (Podsiadło *et al.*, 2007) demonstrated the fact that that powder patterns can be insensitive to significant structural variations, and that geometrical tests can be crucial to determining the correct structure.

Table 4.9.7
R.m.s. differences Δ (Å) between the non-H atoms in experimental and DFT-optimized crystal structures of the citrate group in group-1 citrate salts

Cations	Reference	Experiment	R.m.s. Δ (Å)
H_3	CITRAC10	Single crystal	0.030†
$H_3(H_2O)_1$	CITARC	Single crystal	0.036†
Li_1H_2	LIHCIT	Single crystal	0.418†
$Li_1(H_2O)_1$	PIGPUQ	Single crystal	0.082‡
$Li_3(H_2O)_4$	FUQFUS	Single crystal	0.091‡
$Li_3(H_2O)_5$	CADJIA	Single crystal	0.101‡
Na_1H_2	New powder	Powder	0.261†
Na_1H_2	NAHCIT	Single crystal	0.040†
$Na_2H_1(H_2O)_{1.5}$	New single crystal	Single crystal	0.048§
Na_3	New powder	Powder	0.080†
$Na_3(H_2O)_2$	UMOGAE	Single crystal	0.068‡
$Na_3(H_2O)_{5.5}$	FATTID	Single crystal	0.192†
NaK_2	New powder	Powder	0.069†
K_1H_2	New single crystal	Single crystal	0.041†¶
$K_1H_2(H_2O)_2$	New single crystal	Single crystal	0.097†
K_2H_1	ZZZQRO01	Single crystal	0.038†
K_3	New powder	Powder	0.114§
$K_3(H_2O)_1$	ZZZHVI01	Single crystal	0.051†
Rb_1H_2	RBHCIT03	Single crystal	0.118‡
Rb_2H_1	New powder	Powder	0.118§
Rb_3	New powder	Powder	0.153‡
$Rb_3(H_2O)_1$	New powder	Powder	0.127‡
Cs_1H_2	New powder	Powder	0.387§
Cs_2H_1	New single crystal	Single crystal	0.121†
$Cs_3(H_2O)_1$	New single crystal	Single crystal	0.151†

† *Mercury* molecule overlay. ‡ Manual measurement in *Materials Studio*. § *Mercury* structure overlay. ¶ *CASTEP* geometry optimization.

A particularly powerful way of validating a crystal structure is to compare the experimental model with the results of a dispersion-corrected density-functional calculation (van de Streek & Neumann, 2010, 2014). Normal DFT calculations can also be used with a fixed unit cell. The r.m.s. deviation between the non-H-atom positions in the experimental and optimized structures is a good measure of the correctness of the experimental structure. Such calculations are useful for evaluating potential disorder, examining space-group ambiguities, correcting atom-type assignments and locating H atoms.

As part of a systematic study of group-1 citrate salts (Rammohan & Kaduk, 2018), the structures of known and new salts were optimized (using cells fixed at the experimental values) using DFT calculations. The r.m.s. deviation for the new powder structures was 0.22 Å (Table 4.9.7), while the r.m.s. deviation for the single-crystal structures was only 0.08 Å. (The single-crystal structure of trilithium citrate was excluded from the calculation of the average because the H atoms were not located in the original report and we could expect difficulty in determining the position of the light Li atom using X-ray data.) The accuracy of the powder structures does not seem to be as high as that of the single-crystal structures.

The deposition of raw data will make validation easier in the future.

4.9.7. *CheckCIF/PLATON*

The current state of the art for automated structure validation of small-molecule crystal structures is implemented in the *checkCIF/PLATON* web utility (https://checkcif.iucr.org/, http://journals.iucr.org/services/cif/checking/checkfull.html; Spek, 2009). Its use is required for all small-molecule structures published in IUCr journals, and is required or recommended by many other journals. Since most published crystal structures are determined using single-crystal data, the suite is geared to them. Powder crystallography is still crystallography (although performed with less information), so many of the tests are also applicable to powder structures. Some are not, however, and users submitting powder structures to *checkCIF* should be prepared to deal with some alerts which are not applicable.

Validation issues are divided into four categories:

(i) missing or inconsistent data,
(ii) indicators that the structure model may be wrong or deficient,
(iii) indicators that the quality of the results may be low,
(iv) cosmetic improvements, queries and suggestions.

The validation software assigns one of four severity levels (A, B, C or G) to detected issues. Level-A alerts indicate that there may be a serious problem, which should be resolved unless there is a scientifically acceptable explanation. Level-G alerts are general information and not necessarily errors. They indicate something unexpected, and can still point to serious problems that could not be analysed in detail on the basis of the available data. Currently, more than 460 validation tests have been implemented. Most tests result in a one-line message. Each test is associated with documentation explaining the problem, together with possible options to address it (http://journals.iucr.org/services/cif/datavalidation.html).

Most problems can be analysed and resolved using just the data available in the CIF. However, reflection data (as a structure-factor file, F_o/F_c in CIF format) are sometimes necessary. The listing of structure factors derived from a Rietveld refinement is less useful, so deposition of the raw powder data is required when submitting a powder structure to IUCr journals.

Of the more than 460 tests performed by *CheckCIF*/*PLATON*, some common and/or useful alerts for authors and editors deserve comment.

CELLV02. This checks that the standard uncertainty (s.u.) reported in the CIF (and generated by the Rietveld program) matches that calculated from the standard uncertainties on the lattice parameters reported in the CIF. Sometimes the difference is the result of rounding errors, but in other cases the difference is significant. Apparently Rietveld programs sometimes do not calculate this quantity correctly. A level-A alert is issued when the difference is more than 8 s.u.'s, a level-B alert when the difference is more than 4 s.u.'s and a level-C alert if the difference is more than 2 s.u.'s.

CELLZ01. This tests that the cell contents calculated from `_chemical_formula_sum` and `_cell_formula_units_Z` matches those calculated from the atom sites present in the `_atom_site_list` and the `_symmetry_information`. This is a surprisingly common alert, but is easily corrected by manual editing of the CIF generated by the Rietveld program

DENSD01. A related alert resulting from the error in molecular weight. Level-A, -B and -C alerts are issued if the ratio of the submitted crystal density and that calculated from the formula fall outside the ranges 0.90–1.10, 0.95–1.05 and 0.99–1.01, respectively.

FORMU01. Similarly, differences between the reported and calculated molecular weights can result in this alert concerning the `_chemical_formula_sum` and `_chemical_formula_moiety`.

PLAT080. A least-squares refinement converges when the shift/error value for each refined parameter is close to zero (within the tolerance established for convergence criteria). This test warns the user that the refinement has not converged. Because of correlations among parameters, it is never good practice to report results from a refinement that has not converged.

PLAT091 and **PLAT092**. These indicate that no wavelength was found in the CIF, and that the specified wavelength was not copper, molybdebum or silver radiation. (Valid alternatives are 'neutron' and 'synchrotron'.) When no wavelength is specified in the CIF, *checkCIF* defaults to molybdenum. For most powder experiments this is not appropriate, so it is wise for the user to manually edit the CIF to include the correct wavelength. Since the CIF is intended to be an archive of the experiment, in the long run it is worth including the correct wavelength.

PLAT094, **PLAT097** and **PLAT098**. These test for a report of the maximum and minimum densities in a difference Fourier map. Although not commonly reported (and generally smaller than expected from a single-crystal study because of the model bias of the $F_{\rm obs}$ values) they can be another useful measure of the quality of the refinement. I recommend their inclusion in the results of a powder study. Both the ratio of the maximum to the minimum densities and the absolute values can give clues about errors in the model (such as wrongly assigned atoms or systematic errors in the intensities).

PLAT110–115. These key tests examine the model for the presence of additional symmetry by the application of *ADDSYM*. Although a model too low in symmetry cannot generally be refined using powder data (the refinement tends to oscillate or diverge), these tests can be valuable in identifying the problem. Test 115 looks for the presence of noncrystallographic centres of symmetry and can be useful in identifying the presence of pseudosymmetry.

PLAT128–129. These test for nonstandard monoclinic settings and space-group names, respectively. Although some programs only know about standard settings, there may be valid scientific reasons for choosing a nonstandard space-group setting, particularly when the rules for defining the conventional or reduced cell conflict with a standard space-group setting. These alerts serve to indicate that some discussion of the choice of space group is warranted.

PLAT150–152. An alert is generated when the reported standard uncertainty on the cell volume differs from that calculated using the s.u.'s on the cell dimensions, or if the s.u. is not included at all. Some software packages do not calculate the s.u. on the cell volume correctly. The correct formula is given in Nardelli (1983).

PLAT155–158. These alerts concern low-symmetry unit cells. The convention for a (primitive triclinic) Niggli reduced cell is that $a < b < c$. There are two types of reduced unit cells: type 1, in which all angles are $<90^\circ$, and type 2, in which all angles are $\geq 90^\circ$. Mixed unit cells should not be reported. Unless there are special scientific reasons, the structure is best reported with reference to the reduced unit cell. The IUCr convention is that monoclinic cells should have $\beta > 90^\circ$, even though a cell with $\beta < 90^\circ$ could strictly speaking be considered correct.

PLAT161–163. These alerts indicate that standard uncertainties are missing on at least one x, y or z coordinate. Such alerts are common when some coordinates (such as those of H atoms or an atom fixed to define the origin) are fixed in the refinement. These alerts call for some discussion.

PLAT198. The temperature of the diffraction experiment (in K) should always be specified, even if it is ambient. Omission of the temperature is common, even in variable-temperature studies.

PLAT203–209 and **PLAT211–216**. These alerts concern anisotropic displacement coefficients. Since it is unusual to refine ADPs using powder data, the user can expect alerts about isotropic non-H atoms in the main residue. Even when using isotropic displacement coefficients, they should be positive. Tests for unusually shaped (prolate or oblate) ellipsoids are not generally relevant for powder structures unless ADPs have been refined.

PLAT220–221. These tests examine the isotropic equivalent displacement coefficients and so are directly relevant to powder structures. A larger than normal range of $U_{\rm iso}$ values can indicate that atoms have been incorrectly identified. The common practice of grouping $U_{\rm iso}$ values may reduce the usefulness of these tests.

PLAT230–234. These apply the Hirshfeld rigid-body test (Hirshfeld, 1976) to different classes of bonds. The idea behind these tests is that the most important intramolecular vibrational modes are generally torsional or angle-deformation modes. In comparison, bond-stretching modes have smaller amplitudes. Thus, we expect that bonds are relatively rigid and that the atoms at each end of the bond should have the same mean-square amplitudes of vibration along the bond. The displacement ellipsoids are then analysed to obtain the vibration amplitudes along each bond. When the two atoms have very different amplitudes, it can be a sign that something is wrong with the model.

PLAT241–244. We expect that an atom will have a similar displacement coefficient to its neighbours and to atoms in similar chemical environments. When the U value of an atom is unusually high or low compared with those of its neighbours, it is a sign that the model needs to be examined.

PLAT306–309. These test for unusual bonding of single atoms. Isolated O atoms are most likely to represent water molecules. It may be possible to locate the H atoms around these O atoms in a difference Fourier map, but the chances are less than 50:50. It is generally possible, however, to place the H atoms at least approximately by an analysis of O–X distances and deduce potential hydrogen-bonding patterns. Isolated metal atoms are generally a sign of misidentification of a halogen. Singly bonded metal atoms are very rare and are also a sign of a misidentified atom. An O atom that makes only a single bond is probably a sign of a missing H atom.

PLAT310. This test identifies very short contacts between atoms, which only become apparent after the application of symmetry to the asymmetric unit. It is a good reminder that as crystallographers we should examine not just intramolecular interactions but also intermolecular properties.

PLAT312–321. These tests flag unusual features of the local environment of C, N and O atoms, including the geometry and the number of attached H atoms. One of these alerts can be a sign of a misidentified atom.

PLAT330–332. These examine the C—C distances and the range of distances in phenyl rings. Since phenyl groups in Rietveld refinements are often described as rigid bodies, these tests may not be so useful.

PLAT340–342. These test the precision of the C—C bonds in structures with various sorts of heavy atoms. Since we can expect less precision using powder data, it is not unusual to encounter such alerts. They are still worth investigating.

PLAT350–374. These test whether many sorts of bonds are longer or shorter than normal. While (with the lower accuracy and precision of powder structures) we can expect occasional experimental values to lie on the tails of the normal distributions, true outliers are a sign that something is wrong with the model.

PLAT410–417. These test short H$\cdots$H contacts. Even though the H atoms are often placed in calculated positions, bad contacts suggest that there is something wrong with the structure model.

PLAT420–482. These examine real and potential hydrogen bonds. Generally, the presence of donors without acceptors or acceptors without donors is a sign that something is wrong. The geometrical criteria used in these tests are from Jeffrey (1997).

PLAT601–606. These tests examine any voids present in the structure. Except for nanoporous materials such as zeolites and metal–organic frameworks, we do not expect real crystals to contain empty space. Some voids may represent disordered solvent molecules, but others may represent real errors in the model. A paper reporting a structure with significant void volume should discuss the issue.

PLAT701. Bond distances in the CIF are cross-checked with the values calculated from the coordinates. Alerts are set at deviations of 3, 2 and 1 standard uncertainties. Small differences sometimes result from rounding, but larger differences often result from a mismatch between the id's of the symmetry codes for the space group as listed in one part of the CIF and the symmetry codes used in the specifications of the bonds in another part of the CIF. It is always wise to examine the list of bond distances and angles output by the CIF-generating program and prune out irrelevant values. Similar tests for standard uncertainties, angles, torsions and hydrogen bonds are carried out in **PLAT731–738**.

PLAT711–713. These test for problems with the atom labels for bonds, angles and torsions. When labels that are not in the coordinate list are found in bonds, angles and torsions, these alerts are issued. These are fairly common in CIFs from powder data.

PLAT751–758. These test for 'senseless' standard uncertainties on various geometrical quantitites. Such s.u.'s are senseless when the parameter has been the subject of a constraint or restraint. Application of constraints and/or restraints should always be indicated in tables of distances, angles, torsions and other parameters.

PLAT764. It is fairly common to take the list of geometrical parameters directly as written by the CIF-generating program. Often such lists contain more bonds *etc.* than are real or necessary. Manual trimming is generally necessary.

PLAT780. The atoms given in a CIF should form a connected set. Often a structure solution results in disconnected fragments. It is bad practice to accept this situation. Geometry listings become unwieldy if unconnected sets of atoms are used, and future users of the CIF will thank you if this is sorted out.

PLAT790. The centre of gravity of the molecule (or at least the main residue) should lie within the unit cell. Future users of the CIF will thank you if it does.

PLAT982–983. These test the resonant scattering terms f' and f'' against the values in *International Tables for Crystallography*. The use of characteristic radiation should not yield any alerts here, but it is fairly common for users of synchrotron radiation to neglect to include the appropriate terms for their wavelength. Although the errors in the resulting structure are generally small, they can be significant. It is always best practice to use the appropriate terms.

SHFSU01 (see **PLAT080**). Level-A, -B and -C alerts are issued when the value of `_refine_ls_shift/su_max` is greater than 0.20, in the range 0.10–0.20 and in the range 0.05–0.10, respectively. Final results need to come from a converged refinement, and any extraordinary measures that are needed to ensure such convergence need to be documented.

Permission from the International Centre for Diffraction Data to incorporate material from Kaduk (2007*a*,*b*, 2009) and Kaduk & Partenheimer (1997) is gratefully acknowledged. Work at MR-CAT was supported in part by funding from the Department of Energy under grant No. DEFG0200ER45811.

References

Ambady, G. K. (1968). *The crystal and molecular structures of strontium tartrate trihydrate and calcium tartrate tetrahydrate. Acta Cryst.* B**24**, 1548–1557.

Aranda, M. A. & Attfield, J. P. (1993). *$Ba_{44}Cu_{48}(CO_3)_6O_{87.9}$: the structure of ‘$BaCuO_2$’ from simultaneous X-ray and neutron powder diffraction. Angew. Chem. Int. Ed. Engl.* **32**, 1454–1456.

Barr, G., Dong, W., Gilmore, C. J., Kern, A., Parkin, A. & Wilson, C. C. (2007). *Using the Cambridge Structural Database to validate powder structures. Z. Kristallogr. Suppl.* **2007**, 209–214.

Barr, G., Dong, W., Gilmore, C. J., Parkin, A. & Wilson, C. C. (2005). *dSNAP: a computer program to cluster and classify Cambridge Structural Database searches. J. Appl. Cryst.* **38**, 833–841.

Baur, W. H. & Kassner, D. (1992). *The perils of Cc: comparing the frequencies of falsely assigned space groups with their general population. Acta Cryst.* B**48**, 356–369.

Baur, W. H. & Tillmanns, E. (1986). *How to avoid unnecessarily low symmetry in crystal structure determinations. Acta Cryst.* B**42**, 95–111.

Berman, H. M., Westbrook, J., Feng, Z., Gilliland, G., Bhat, T. N., Weissig, H., Shindyalov, I. N. & Bourne, P. E. (2000). *The Protein Data Bank. Nucleic Acids Res.* **28**, 235–242.

Boese, R. & Heinemann, O. (1993). *Crystal structure of calcium tartrate tetrahydrate, $C_4H_4O_6Ca(H_2O)_4$. Z. Kristallogr.* **205**, 348–349.

Boultif, A. & Louër, D. (1991). *Indexing of powder diffraction patterns for low-symmetry lattices by the successive dichotomy method. J. Appl. Cryst.* **24**, 987–993.

Brändén, C.-I. & Jones, T. A. (1990). *Between objectivity and subjectivity. Nature (London)*, **343**, 687–689.

Bravais, A. (1866). *Etudes Cristallographiques.* Paris: Gathier Villars.

Bredikhin, A. A., Gubaidullin, A. T., Bredikhina, Z. A., Krivolapov, D. B., Pashagin, A. V. & Litvinov, I. A. (2009). *Absolute configuration and crystal packing for three chiral drugs prone to spontaneous resolution: guaifenesin, methocarbamol and mephenesin. J. Mol. Struct.* **920**, 377–382.

Brese, N. E. & O’Keeffe, M. (1991). *Bond-valence parameters for solids. Acta Cryst.* B**47**, 192–197.

Brown, I. D. (1996). *VALENCE: a program for calculating bond valences. J. Appl. Cryst.* **29**, 479–480.

Brown, I. D. (2002). *The Chemical Bond in Inorganic Chemistry: The Bond Valence Model*, p. 12. Oxford University Press.

Brown, I. D. & Altermatt, D. (1985). *Bond-valence parameters obtained from a systematic analysis of the Inorganic Crystal Structure Database. Acta Cryst.* B**41**, 244–247.

Bruno, I. J., Cole, J. C., Kessler, M., Luo, J., Motherwell, W. D. S., Purkis, L. H., Smith, B. R., Taylor, R., Cooper, R. I., Harris, S. E. & Orpen, A. G. (2004). *Retrieval of crystallographically-derived molecular geometry information. J. Chem. Inf. Comput. Sci.* **44**, 2133–2144.

Chen, V. B., Arendall, W. B., Headd, J. J., Keedy, D. A., Immormino, R. M., Kapral, G. J., Murray, L. W., Richardson, J. S. & Richardson, D. C. (2010). *MolProbity: all-atom structure validation for macromolecular crystallography. Acta Cryst.* D**66**, 12–21.

Churchill, M. X. (1973). *Carbon–hydrogen and nitrogen–hydrogen distances assumed in, and determined from, recent X-ray diffraction studies on inorganic complexes. Inorg. Chem.* **12**, 1213–1214.

Crystal Impact (2013). *Diamond – Crystal and Molecular Structure Visualization*. http://www.crystalimpact.com/diamond.

David, W. I. F. (2004). *Powder diffraction: least-squares and beyond. J. Res. Natl Inst. Stand. Technol.* **109**, 107–123.

Davis, I. W., Leaver-Fay, A., Chen, V. B., Block, J. N., Kapral, G. J., Wang, X., Murray, L. W., Arendall, W. B. III, Snoeyink, J., Richardson, J. S. & Richardson, D. C. (2007). *MolProbity: all-atom contacts and structure validation for proteins and nucleic acids. Nucleic Acids Res.* **35**, W375–W383.

Deer, W. A., Howie, R. A. & Zussman, Y. (1982). *Rock Forming Minerals*, Vol. 1A, p. 745. Oxford: Geological Society of London.

Donnay, J. D. H. & Harker, D. (1937). *A new law of crystal morphology extending the law of Bravais. Am. Mineral.* **22**, 446–467.

Dovesi, R., Orlando, R., Civalleri, B., Roetti, C., Saunders, V. R. & Zicovich-Wilson, C. M. (2005). *CRYSTAL: a computational tool for the ab initio study of the electronic properties of crystals. Z. Kristallogr.* **220**, 571–573.

Dovesi, R., Saunders, V. R., Roetti, C., Orlando, R., Zicovich-Wilson, C. M., Pascale, F., Civalleri, B., Doll, K., Harrison, N. M., Bush, I. J., D’Arco, P. & Lunell, M. (2009). *CRYSTAL09 User’s Manual*. University of Torino, Italy.

Finger, L. W., Cox, D. E. & Jephcoat, A. P. (1994). *A correction for powder diffraction peak asymmetry due to axial divergence. J. Appl. Cryst.* **27**, 892–900.

Friedel, G. (1907). *Etudes sur la loi de Bravais*. *Bull. Soc. Fr. Miner.* **30**, 326–455.

Galek, P. T. A., Fábián, L., Motherwell, W. D. S., Allen, F. H. & Feeder, N. (2007). *Knowledge-based model of hydrogen-bonding propensity in organic crystals. Acta Cryst.* B**63**, 768–782.

Groom, C. R., Bruno, I. J., Lightfoot, M. P. & Ward, S. C. (2016). *The Cambridge Structural Database. Acta Cryst.* B**72**, 171–179.

Günter, J. R. & Jameson, G. B. (1984). *Orthorhombic barium orthotitanate, α'-Ba_2TiO_4. Acta Cryst.* C**40**, 207–210.

Harlow, R. L. (1996). *Troublesome crystal structures. Prevention, detection, and resolution. J. Res. Natl Inst. Stand. Technol.* **101**, 327–339.

Hawthorne, F. C., Borys, I. & Ferguson, R. B. (1982). *Structure of calcium tartrate tetrahydrate. Acta Cryst.* B**38**, 2461–2463.

Hellenbrandt, M. (2004). *The Inorganic Crystal Structure Database (ICSD) – present and future. Crystallogr. Rev.* **10**, 17–22.

Helliwell, J. R., Strickland, P. R. & McMahon, B. (2006). *The role of quality in providing seamless access to information and data in e-science; the experience gained in crystallography. Inf. Serv. Use*, **26**, 45–55.

Herbstein, F. H. (1997). *Recognizing the (false symmetry) triclinic (aP) to (true symmetry) centred monoclinic (mC) pathology. Acta Cryst.* B**53**, 968–975.

Herbstein, F. H. & Marsh, R. E. (1982). *Changes in space and Laue groups of some published crystal structures. Acta Cryst.* B**38**, 1051–1055.

Herbstein, F. H. & Marsh, R. E. (1998). *More space-group corrections: from triclinic to centred monoclinic and to rhombohedral; also from P1 to P−1 and from Cc to C2/c. Acta Cryst.* B**54**, 677–686.

Hirshfeld, F. L. (1976). *Can X-ray data distinguish bonding effects from vibrational smearing? Acta Cryst.* A**32**, 239–244.

ICDD (2012). *Powder Diffraction File*, edited by S. Kabekkodu. Newtown Square: ICDD.

Jeffrey, G. A. (1997). *An Introduction to Hydrogen Bonding*. Oxford University Press.

Jones, T. A., Zou, J.-Y., Cowan, S. W. & Kjeldgaard, M. (1991). *Improved methods for building protein models in electron density maps and the location of errors in these models. Acta Cryst.* A**47**, 110–119.

Kaduk, J. A. (1998). *Chemical accuracy and precision in structure refinements from powder diffraction data. Adv. X-ray Anal.* **40**, 352–370.

Kaduk, J. A. (1999). *Combining CDIF and PDF information in problem solving: crystal structure of a corrosion deposit, hexaaquairon(II) trifluoromethanesulfonate. Powder Diffr.* **14**, 166–170.

Kaduk, J. A. (2002). *Use of the Inorganic Crystal Structure Database as a problem solving tool. Acta Cryst.* B**58**, 370–379.

Kaduk, J. A. (2004). *Crystal structure of guaifenesin, 3-(2-methoxyphenoxy)-1,2-propanediol. Powder Diffr.* **19**, 127–132.

Kaduk, J. A. (2005). *Extraframework species in zeolite Y at nonambient conditions. Crystallogr. Rev.* **11**, 1–19.

Kaduk, J. A. (2007*a*). *Chemical reasonableness in Rietveld analysis; organics. Powder Diffr.* **22**, 74–82.

Kaduk, J. A. (2007*b*). *Chemical reasonableness in Rietveld analysis: inorganics. Powder Diffr.* **22**, 268–278.

Kaduk, J. A. (2009). *A Rietveld tutorial – mullite. Powder Diffr.* **24**, 351–361.

Kaduk, J. A., Golab, J. T. & Leusen, F. J. J. (1998). *The crystal structures of trimellitic anhydride and two of its solvates. Cryst. Eng.* **1**, 277–290.

Kaduk, J. A. & Partenheimer, W. (1997). *Chemical accuracy and precision in Rietveld analysis: the crystal structure of cobalt(II) acetate tetrahydrate. Powder Diffr.* **12**, 27–39.

Kleywegt, G. J. (2009). *On vital aid: the why, what and how of validation. Acta Cryst.* D**65**, 134–139.

Klug, H. P. & Alexander, L. E. (1974). *X-ray Diffraction Procedures for Polycrystalline and Amorphous Materials*, pp. 488–489. New York: John Wiley & Sons.

Krivovichev, S. V. & Brown, I. D. (2001). *Are the compressive effects of encapsulation an artifact of the bond valence parameters? Z. Kristallogr.* **216**, 245–247.

Laar, B. van & Yelon, W. B. (1984). *The peak in neutron powder diffraction. J. Appl. Cryst.* **17**, 47–54.

Laskowski, R. A., MacArthur, M. W., Moss, D. S. & Thornton, J. M. (1993). *PROCHECK: a program to check the stereochemical quality of protein structures. J. Appl. Cryst.* **26**, 283–291.

Le Bail, A. (2008). *The profile of a Bragg reflection for extracting intensities. Powder Diffraction: Theory and Practice*, edited by R. E. Dinnebier & S. J. L. Billinge, pp. 134–165. Cambridge: Royal Society of Chemistry.

Le Page, Y. (1987). *Computer derivation of the symmetry elements implied in a structure description. J. Appl. Cryst.* **20**, 264–269.

Li, J. F., Li, L. & Stott, F. H. (2004). *Crystallographical analysis of surface layers of refractory ceramics formed using combined flame spray and simultaneous laser treatment. J. Eur. Ceram. Soc.* **24**, 3129–3138.

Locock, A. J. & Burns, P. C. (2004). *Revised Tl(I)–O bond valence parameters and the structures of thallous dichromate and thallous uranyl phosphate hydrate. Z. Kristallogr.* **219**, 259–266.

Lovell, S., Davis, I., Arendall, W. B. III, de Bakker, P., Word, J., Prisant, M., Richardson, J. & Richardson, D. (2003). *Structure validation by Cα geometry: φ, ψ and Cβ deviation. Proteins*, **50**, 437–450.

McCusker, L. B., Von Dreele, R. B., Cox, D. E., Louër, D. & Scardi, P. (1999). *Rietveld refinement guidelines. J. Appl. Cryst.* **32**, 36–50.

Marsh, R. E. (1984). *The crystal structure of NH_4MnFeF_6: re-refinement in a higher symmetry space group. J. Solid State Chem.* **51**, 405–407.

Marsh, R. E. (1986). *Centrosymmetric or noncentrosymmetric? Acta Cryst.* B**42**, 193–198.

Marsh, R. E. (1988). *Two more space-group revisions. Inorg. Chem.* **27**, 2902–2903.

Marsh, R. E. (1995). *Some thoughts on choosing the correct space group. Acta Cryst.* B**51**, 897–907.

Marsh, R. E. (1997). *The perils of Cc revisited. Acta Cryst.* B**53**, 317–322.

Marsh, R. E. (1999). *P1 or P−1? Or something else? Acta Cryst.* B**55**, 931–936.

Marsh, R. E. (2002). *The space groups of point group C_3: some corrections, some comments. Acta Cryst.* B**58**, 893–899.

Marsh, R. E. (2004). *Space group Cc: an update. Acta Cryst.* B**60**, 252–253.

Marsh, R. E. & Bernal, I. (1995). *More space-group changes. Acta Cryst.* B**51**, 300–307.

Marsh, R. E. & Herbstein, F. H. (1983). *Some additional changes in space groups of published crystal structures. Acta Cryst.* B**39**, 280–287.

Marsh, R. E. & Herbstein, F. H. (1988). *More space-group changes. Acta Cryst.* B**44**, 77–88.

Marsh, R. E., Kapon, M., Hu, S. & Herbstein, F. H. (2002). *Some 60 new space-group corrections. Acta Cryst.* B**58**, 62–77.

Marsh, R. E. & Schomaker, V. (1979). *Some incorrect space groups in Inorganic Chemistry, Volume 16. Inorg. Chem.* **18**, 2331–2336.

Marsh, R. E. & Schomaker, V. (1980). *Potassium tetrachlorosulfatoborate: change in space group. Acta Cryst.* B**36**, 219–220.

Marsh, R. E. & Schomaker, V. (1981). *Some incorrect space groups: an update. Inorg. Chem.* **20**, 299–303.

Mighell, A. D. & Himes, V. L. (1986). *Compound identification and characterization using lattice-formula matching techniques. Acta Cryst.* A**42**, 101–105.

Mighell, A. D. & Rodgers, J. R. (1980). *Lattice symmetry determination. Acta Cryst.* A**36**, 321–326.

Moss, K. C., Russell, D. R. & Sharp, D. W. A. (1961). *The lattice constants of some metal-fluoroborate hexahydrates. Acta Cryst.* **14**, 330.

Nardelli, M. (1983). *PARST: a system of FORTRAN routines for calculating molecular structure parameters from results of crystal structure analyses*. *Comput. Chem.* **7**, 95–98.

Pawley, G. S. (1981). *Unit-cell refinement from powder diffraction scans. J. Appl. Cryst.* **14**, 357–361.

Podsiadło, M., Dziubek, K. & Katrusiak, A. (2007). *Pitfalls of data mining: triclinic polymorph of 2,2-aziridinedicarboxamide revisited. Acta Cryst.* B**63**, 118–123.

Prince, E. (2004). *Mathematical Techniques in Crystallography and Materials Science*, 3rd ed. New York: Springer.

Prince, E. & Spiegelman, C. H. (2004). *Statistical significance tests*. *International Tables for Crystallography*, Vol. C, *Mathematical, Physical and Chemical Tables*, ch. 8.4. Heidelberg: Springer.

Ramachandran, G. N., Ramakrishnan, C. & Sasisekharan, V. (1963). *Stereochemistry of polypeptide chain configurations. J. Mol. Biol.* **7**, 95–99.

Rammohan, A. & Kaduk, J. A. (2018). *Crystal structures of alkali metal (Group 1) citrate salts. Acta Cryst.* B**74**, 239–252.

Read, R. J., Adams, P. D., Arendall, W. B. III, Brunger, A. T., Emsley, P., Joosten, R. P., Kleywegt, G. J., Krissinel, E. B., Lütteke, T., Otwinowski, Z., Perrakis, A., Richardson, J. S., Sheffler, W. H., Smith, J. L., Tickle, I. J., Vriend, G. & Zwart, P. (2011). *A new generation of crystallographic validation tools for the Protein Data Bank. Structure*, **19**, 1395–1412.

Richards, F. M. (1988). *Public access to X-ray diffraction data. J. Comput. Aided Mol. Des.* **2**, 3–5.

Rietveld, H. M. (1969). *A profile refinement method for nuclear and magnetic structures. J. Appl. Cryst.* **2**, 65–71.

Rowda, B., Avdeev, M., Lee, P. L., Henry, P. F. & Ling, C. D. (2008). *Structures of 6H perovskites $Ba_3CaSb_2O_9$ and $Ba_3SrSb_2O_9$ determined by synchrotron X-ray diffraction, neutron powder diffraction and ab initio calculations. Acta Cryst.* B**64**, 154–159.

Schomaker, V. & Marsh, R. E. (1979). *The crystal structure of bis(tetraethylammonium) tetrachlorodioxouranate(VI): correction from P−1 to $P2_1/n$. Acta Cryst.* B**35**, 1094–1099.

Schwarzenbach, D., Abrahams, S. C., Flack, H. D., Prince, E. & Wilson, A. J. C. (1995). *Statisical descriptions in crystallography. II. Report of a working group on expression of uncertainty in measurement. Acta Cryst.* A**51**, 565–569.

Schwarzenbach, D., Abrahams, S. C., Flack, H. D., Prince, E. & Wilson, A. J. C. (1996). *Statistical descriptors in crystallography. Uncertainty of measurement.* http://ww1.iucr.org/comm/cnom/statdes/uncert.html.

Segall, M. D., Lindan, P. J. D., Probert, M. J., Pickard, C. J., Hasnip, P. J., Clark, S. J & Payne, M. C. (2002). *First-principles simulation: ideas, illustrations and the CASTEP code. J. Phys. Condens. Matter*, **14**, 2717–2744.

Shannon, R. D. & Prewitt, C. T. (1969). *Effective ionic radii in oxides and fluorides. Acta Cryst.* B**25**, 925–946.

Sidey, V. (2010). *On the accurate bond-valence parameters for the Sb^{3+}/O^{2-} ion pair. Acta Cryst.* B**66**, 307–314.

Sidey, V. (2012). *Exact solution of the bond-valence sum rule for a set of coordination shells. Acta Cryst.* B**68**, 318–320.

Smith, G. S. & Snyder, R. L. (1979). *F_N: a criterion for rating powder diffraction patterns and evaluating the reliability of powder-pattern indexing. J. Appl. Cryst.* **12**, 60–65.

Spek, A. L. (2003). *Single-crystal structure validation with the program PLATON. J. Appl. Cryst.* **36**, 7–13.

Spek, A. L. (2009). *Structure validation in chemical crystallography. Acta Cryst.* D**65**, 148–155.

Srivastava, R. C., Klooster, W. T. & Koetzle, T. F. (1999). *Neutron structures of ammonium tetrafluoroberyllate. Acta Cryst.* B**55**, 17–23.

Stalick, J. K. & Mighell, A. D. (1986). *Crystal Data, Version 1.0. Database Specifications.* NBS Technical Note 1229.

Stephens, P. W. (1999). *Phenomenological model of anisotropic peak broadening in powder diffraction. J. Appl. Cryst.* **32**, 281–289.

Streek, J. van de & Neumann, M. A. (2010). *Validation of experimental molecular crystal structures with dispersion-corrected density functional theory calculations. Acta Cryst.* B**66**, 544–558.

Streek, J. van de & Neumann, M. A. (2014). *Validation of molecular crystal structures from powder diffraction data with dispersion-corrected density functional theory (DFT-D). Acta Cryst.* B**70**, 1020–1032.

Suortti, P., Hastings, J. B. & Cox, D. E. (1985). *Powder diffraction with synchrotron radiation. I. Absolute measurements. Acta Cryst.* A**41**, 413–416.

Sykes, R. A., McCabe, P., Allen, F. H., Battle, G. M., Bruno, I. J. & Wood, P. A. (2011). *New software for statistical analysis of Cambridge Structural Database data. J. Appl. Cryst.* **44**, 882–886.

Taylor, R. (2011). *Short nonbonded contact distances in organic molecules and their use as atom-clash criteria in conformer validation and searching. J. Chem. Inf. Model.* **51**, 897–908.

Toby, B. H. (2003). *CIF applications. XII. Inspecting Rietveld fits from pdCIF: pdCIFplot. J. Appl. Cryst.* **36**, 1285–1287.

Toby, B. H. (2005). *Classification and use of powder diffraction data. International Tables for Crystallography*, Vol. G, edited by S. R. Hall & B. McMahon, pp. 117–130. Dordrecht: Springer.

Toby, B. H. (2006). *R factors in Rietveld analysis: how good is good enough? Powder Diffr.* **21**, 67–70.

Villars, P., Onodera, N. & Iwata, S. (1998). *The Linus Pauling File (LPF) and its application to materials design. J. Alloys Compd.* **279**, 1–7.

Visser, J. W. (1969). *A fully automatic program for finding the unit cell from powder data. J. Appl. Cryst.* **2**, 89–95.

Wang, Y., Li, M., Liu, L., Zhou, L. & Wang, J. (2005). *3-(2-Methoxyphenoxy)propane-1,2-diol. Acta Cryst.* E**61**, o1999–o2000.

West, C. D. (1935). *Crystal structures of some hydrated compounds, II. Z. Kristallogr.* **91**, 480–493.

Westbrook, J., Feng, Z., Burkhardt, K. & Berman, H. (2003). *Validation of protein structures for Protein Data Bank. Methods Enzymol.* **374**, 370–385.

White, P. S., Rodgers, J. R. & Le Page, Y. (2002). *CRYSTMET: a database of the structures and powder patterns of metals and intermetallics. Acta Cryst.* B**58**, 343–348.

Young, R. A. (1993). *Introduction to The Rietveld Method. The Rietveld Method*, edited by R. A. Young, pp. 1–38. Oxford University Press.

Zucker, F., Champ, P. C. & Merritt, E. A. (2010). *Validation of crystallographic models containing TLS or other descriptions of anisotropy. Acta Cryst.* D**66**, 889–900.

International Tables for Crystallography (2019). Vol. H, Chapter 4.10, pp. 515–521.

4.10. Use of CIF for powder diffraction data

B. H. Toby

4.10.1. Background

The Crystallographic Information Framework (originally named the Crystallographic Information File) was first adopted as a standard by the International Union of Crystallography in 1990 for the archive and exchange of structure factors and crystallographic results, as well as associated sample metadata (Hall *et al.*, 1991). Herein, the initially redundant term 'CIF file' will be used to describe a computer file containing information coded in this standard, while 'CIF' will refer to the standard itself. When CIF was initially developed, the text for a complete manuscript could also be placed in a CIF file, so that direct production of a journal article, including tables and figures, was possible from an ASCII computer file and this was soon used in production. Submission of the complete paper as a CIF file is an option for *Acta Crystallographica Section C*, and is required for *Section E*.

There are many critiques that could be aimed at CIF from a contemporary perspective, but it should be noted that it was developed at a time when the use of personal workstations or even email was not that widespread. Markup languages such as XML also arrived much later. CIF has evolved over the subsequent decades, benefiting from some of the ideas introduced in other standard formats, while largely maintaining compatibility with the initial format description.

Over a period that overlapped with the initial development of CIF, a subcommittee from the International Centre for Diffraction Data was developing yet another standard format for the exchange of raw powder diffraction data. While an initial format had been adopted, after the announcement of CIF it became clear that CIF was a better choice because of the superiority of the STAR (Self-defining Text Archive and Retrieval) syntax that CIF is based on, the well devised CIF dictionary (Hall, 1991), and the advantages of having powder diffraction and single-crystal crystallography use a common standard.

As will be described later, the CIF standard consists of a subset of STAR syntax, along with definitions for the labels associated with each set of values that will be specified in CIF files. These definitions, themselves formatted as a STAR file, are collected in a document referred to as a CIF dictionary. Thus, to accommodate powder diffraction in CIF, it was necessary to identify the additional types of values and data that would be needed and create definitions for them. Based on this work, a number of definitions were added to the core (general and single-crystal) CIF dictionary, since they would potentially be of multidisciplinary use, while others were placed in the newly created powder diffraction CIF dictionary, known as the pdCIF dictionary (Toby, 2005*a*). The initial comprehensive version of the pdCIF dictionary (version 1.0) was completed in 1997.

Subsequently, CIF has gone through several stages of development. The initial version was later structured through the addition of a set of rules called a data definition language (DDL), which provided an organizational context for the format and added some normalization rules to bring CIF closer to a relational database schema (DDL1.x). These rules were expanded to provide strict relational normalization with a second-generation DDL (DDL2.x). At the present time, powder diffraction CIF files may only be specified using DDL1.x, but macromolecular CIF files are specified using DDL2.x data names. A mixture of the two is needed for powder studies of macromolecular materials.

To make CIF even more versatile and add greater functionality, a next-generation DDL has been created (DDLm). Also, an augmented CIF standard (CIF2) was adopted in 2014. None of these revisions affect the validity of CIFs created using the initial CIF syntax and DDL1 dictionary. A backward-compatible DDLm compliant version of the pdCIF dictionary has been developed and approved, but further revisions are anticipated, which will allow powder diffraction to take advantage of the enhanced capabilities provided by DDLm.

4.10.2. A brief introduction to CIF

The reader is referred to *International Tables for Crystallography*, Vol. G, *Definition and Exchange of Crystallographic Data* (Hall & McMahon, 2005), for a comprehensive discussion of CIF and its associated dictionaries. However, a synopsis of CIF follows below for the purposes of discussion. Note that this is not intended to provide a complete description of the standard or its implementation, but it will help the novice powder diffractionist to understand how information is placed in a CIF file.

The most basic concept in CIF is that of a data name. CIF data names always begin with an underscore. The meaning and use of every defined CIF data name is spelled out in an entry in one of a series of separate files, called a CIF data dictionary. Each data name specifies something about the project stored in the CIF file, such as a lattice parameter or an author name. In the simplest CIF construct, files are populated with a value preceded by the data name to be associated with that value. A few examples are

```
_cell_volume   1811.00(5)
_cell_angle_gamma       120
_symmetry_cell_setting                  Hexagonal
_symmetry_space_group_name_H-M          "P 63/m m c"
```

A CIF data name and its associated value are together called a data item. Depending on how the data name is defined, the value can be a character string, a floating-point number or an integer. Values may include an uncertainty in parentheses. The use of quotation marks for strings is optional when the string contains no spaces. To specify a character string that spans multiple lines, one uses a different style of quoting:

```
_pd_proc_ls_background_function
;   GSAS Background function number 1 with 4 terms.
Shifted Chebyshev function of 1st kind
  1:  139.025    2:  -11.5408    3:  9.75652    4:  3.90497
;
```

The use of white space (blank spaces, tabs or new lines) to separate data names and values is required, but the use of more than one of these makes no difference, except within quoted strings. While it is expected that CIF data names will be defined in one of the existing CIF dictionaries, it is not an error to use an undefined data name. In fact, any CIF data name that begins with `_local_` is assumed to have a meaning only within the preparer's institution and should be ignored by others.

Copyright © 2019 International Union of Crystallography

CIF also allows a data name to be associated with a set of values. For this, a construct called a loop is used to specify a set of values, for example:

```
loop_
  _atom_site_label   _atom_site_fract_x
  _atom_site_fract_y   _atom_site_fract_z
Y1      0.125        0.0          0.25
O2     -0.02946(5)   0.05385(5)   0.15068(6)
```

A loop begins with the keyword `loop_` and is followed by one or multiple data names, most commonly more than one. In the example above, four data names are specified. Following the data names will be a number of data values that must be a multiple of the number of data names. Thus, each value is logically associated with each successive data name in a cyclic manner. The loop is terminated when another CIF data name or a CIF keyword such as `loop_` is encountered. Thus, in the example above, the values 'Y1' and 'O2' are associated with data name `_atom_site_label`. Further, the values specified in each group are also logically grouped so that the coordinates (0.125, 0.0, 0.25) are connected to the label 'Y1'. A loop can be envisioned as a data table with columns connected to each of the data names and as many rows as are specified. Note that formatting of loops is very flexible. The `loop_` keyword, the data names and the values must be separated by one or more white-space characters, but the placement of new lines is arbitrary. This means the table above could be specified equivalently with each value on a separate line, or with all eight values on a single line, or even as below:

```
loop_  _atom_site_label  _atom_site_fract_x
_atom_site_fract_y
_atom_site_fract_z
Y1
0.125        0.0          0.25
O2
   -0.02946(5)
    0.05385(5)
    0.15068(6)
```

Blank lines in a CIF file are ignored. Comments are also allowed. These have a hash mark (#) as the first non-blank character in the line. Comments are intended to assist a person reading through a CIF file, but not to convey meaning about the contents of the CIF file. The initial CIF standard specified that the maximum number of characters on a line could not exceed 80, but this was soon increased to 2048 characters.

There are two values with special meanings in CIF: a question mark (?) and an isolated period (.). A question mark indicates that a value has not been specified. The value ? commonly appears in templates for CIF to indicate a place where a value could be included. A value of . indicates that that value is undefined, inappropriate or, for a few specific cases, should be taken as the default. As an example, in a loop over author names, if ? is specified for an author's middle name, it would imply that the person preparing the CIF file did not know the information, while a value of . specifies that that author does not have a middle name.

Another requirement in CIF is the division of a file into logical units, called blocks. Before any data items are placed in a CIF file, a block must be started using a label that begins with the string `data_`, followed by an arbitrary set of non-blank characters, for example `data_block1`.

There must be a `data_` statement in the file before any data items are defined, but additional `data_` statements can appear later. The order in which CIF data items are specified in a data block is not significant, but the order in which groups of items are specified in a loop may be significant. Note that a data name can only appear once in a data block, since one could otherwise supply conflicting values for a given item.

As an example of block use, if one wishes to describe structures for two different chemical phases, one needs to specify multiple values for the lattice constants. If the data name `_cell_length_a` were to appear twice in a block, it would be ambiguous as to which phase would be associated with each value. Likewise, it would be unclear as to which atoms are associated with each phase. Thus, in order to describe two phases in a single file, each phase must appear in a separate data block to resolve this ambiguity. The CIF dictionary specifies that unit-cell lengths and angles (data names `_cell_length_` and `_cell_angle_`) may not be placed in a loop, so even in the case where cell parameters are determined for a large series of temperatures, each set of lattice parameters must be placed in a separate block. If there is a need to define a table of lattice parameters using a `loop_` construct, a new set of data names would need to be added to a CIF dictionary to allow this type of cell-parameter usage.

4.10.3. CIF usage for powder diffraction

The specific implementation of CIF to powder diffraction needs is discussed in detail in *International Tables for Crystallography*, Vol. G, *Definition and Exchange of Crystallographic Information*, where the CIF dictionary can be found in Chapter 4.2 and an explanation of the definitions and their use is found in Chapter 3.3. It should be noted that these definitions are expected to be used in combination with those found in the single-crystal CIF definitions in the core CIF dictionary (Vol. G, Chapter 4.2). The data names defined in the pdCIF dictionary begin with the four characters `_pd_`, while any other data name mentioned in this chapter can be assumed to be defined in the core dictionary. While CIF was initially devised as a mechanism to communicate the results from a crystallographic study, pdCIF was intended to also include and describe the raw and reduced powder data and the computed diffraction data, as will arise from a Rietveld refinement. For this reason, pdCIF includes a large number of data items to describe such metadata as the diffraction instrument configuration, the specimen preparation, and the data and analysis provenance.

CIF was initially envisioned to represent studies where each CIF block is completely self-defined, and where every block contains sample and instrumental information, structural results and the data (structure factors) used to obtain the results. However, one can envision single-crystal studies where a single structural model is obtained that cannot be incorporated into a single block, for example with a combination of X-ray and neutron single-crystal data sets. This need is rare. In powder diffraction, this paradigm of independence between data blocks is commonly violated, since a single sample can contain multiple phases, and likewise it can be good practice to combine different types of powder diffraction data sets in a single refinement. To introduce a mechanism to interrelate data blocks, pdCIF introduced a concept called a block pointer. The value for each block pointer is intended to be something that is highly unlikely to be duplicated and that can be assigned to every block, so that if data blocks are separated (which used to be a common practice), these references can still be resolved. The standard way of specifying a block pointer uses a date stamp, an instrument name and an author name, which is very likely to be a unique value.

The information that can be provided in a powder diffraction CIF file may be categorized by type, as is provided below. Note that there is no requirement that items from all categories be included in any one file.

(1) If a crystal structure model is included, then core CIF data items are used to specify the unit-cell constants, atomic coordinates *etc.*
(2) The IUCr allows the inclusion of a manuscript narrative in a CIF file with `_publ_` data items, although this usage is becoming less common.
(3) The powder diffraction instrument can be described using `_pd_instr_` data items.
(4) The instrument calibration process can be described using the `_pd_calib_` data items.
(5) The sample and specimen are described using core and `_pd_prep_`, `_pd_char_` and `_pd_spec_` data items.
(6) Measurement results (raw data) are included using the `_pd_meas_` data items.
(7) When the raw data are scaled or combined, or are reduced in some other fashion, there may be a set of `_pd_proc_` data items.
(8) When a pattern is simulated from a structural model, it will be included using the `_pd_calc_` data items.
(9) When a pattern is reduced to a set of diffraction peaks, for example to index the pattern, a table of peaks and intensities is determined, which can be included using the `_pd_peak_` data items. Note that a single peak can represent the superposition of multiple reflections that can arise from one or more chemical phases.
(10) After a diffraction pattern has been indexed, a table of reflections can be generated. The `_refln_` data items are used to specify reflection indices and intensities, along with `_pd_refln_` data items that define the phase giving rise to the reflection and/or interlink the peak and reflection tables.

Note that (6), (7) and (8) in the list above may be combined into a single loop when these data items all have the same number of values, but this is not always the case. Another useful point is that pdCIF can also have implied lists of values. As an example, when 2θ values are recorded with regular steps, it is preferable to spell out this relationship by specifying three single values, `_pd_meas_2theta_range_min`, `_pd_meas_2theta_range_max` and `pd_meas_2theta_range_inc`, rather than providing all the values with `_pd_meas_2theta_scan`.

4.10.4. Creation of pdCIF data files

Ideally, pdCIF files would be created and read by all commonly used powder diffraction software, but the community has been slow to adopt this standard and there are a considerable number of older computer programs still in common use that do not use it. Today, most common Rietveld programs read and write CIF files (both crystal structure and raw diffraction data). Most structure visualization programs will read and write crystal structures in CIF. The commonly used data-conversion programs *PowDLL* (Kourkoumelis, 2015) and *CMPR* (Toby, 2005*b*) currently read CIF files but do not write them. Even if a program reads and/or writes CIF files, there can still be pitfalls. Alternate choices of origin (origin 1 and 2 for some space groups) and non-standard space-group settings can still cause problems. A subtle problem which is sometimes encountered is that different programs list the symmetry operations in different orders. A consequence is that geometric quantities (bond distances, angles *etc.*) between symmetry-related atoms may differ among programs. The many conventions for reporting displacement coefficients can also cause problems, such as when one (B or U) is interpreted as the other (U or B). Overcoming such a situation can involve manual editing of the CIF file or the atom list in the Rietveld program. However, even in the absence of such software it can be fairly easy to create a rudimentary CIF file. As one example, it can be straightforward to convert an ASCII data file to a CIF file, assuming that an ASCII data file can be obtained that has the data in columns. When this is the case, one can add a short header to the file to obtain a valid CIF file. As an example, if one has a file that looks like this (2θ *versus* intensity),

```
     x        y_obs
  0.500      387.774
  0.501      413.941
  0.502      419.633
  0.503      418.683
  0.504      409.685
  ...
```

the file becomes a valid CIF file through the addition of two lines, as shown below: one with a `_data` keyword, to define a block, and the other with a `loop_` keyword, to add a loop header. (In fact, all this could be combined into a single line or spread out over more lines.)

```
data_CIF-example
loop_ _pd_meas_2theta_scan _pd_proc_intensity_total
       0.500      387.774
       0.501      413.941
       0.502      419.633
       0.503      418.683
       0.504      409.685
       ...
```

This editing can be done with any text editor that can edit and save an ASCII text file (such as *Wordpad* or *Textpad* on Windows, *Gedit* on Linux or *Textedit* on the Mac), but can also be done with the Cambridge Crystallographic Data Centre's (CCDC) *enCIFer* program (discussed in Section 4.10.6.1) (Allen *et al.*, 2004). There is, however, one limitation for the inclusion of diffraction data in this manner, which relates to uncertainties for intensity values. If the `_pd_meas_counts_total` data item is used, then the values are expected to have uncertainties following counting statistics (where the standard uncertainty is the square root of the intensity for larger intensity values). For `_pd_proc_intensity_total`, the standard uncertainties (s.u.'s) can be included with crystallographic notation, for example, 387.7 (9), or s.u. values can be entered with `_pd_proc_ls_weight`, but then as the inverse square of the s.u. values. At present, there is no way to specify directly in pdCIF a column of s.u. values.

Should the ASCII data file have extraneous columns, one can add a data name so that the column(s) will be ignored. A data name with the `_local_` prefix is perfect for this role.

```
data_CIF-example
loop_ _pd_meas_2theta_scan _pd_proc_intensity_total
      _local_unused1
#        x          y_obs    timestamp
       0.500      387.774    1001231
       0.501      413.941    1001247
       0.502      419.633    1001252
       0.503      418.683    1001267
       0.504      409.685    1001273
       ...
```

Note that it is also possible to add data to an existing CIF file by opening that file in a text editor and adding additional sections or by merging CIF files using *enCIFer*.

Creating a pdCIF file that describes, for example, the details of a Rietveld refinement is a more complex task because such a file should document the sample, the data collection and analysis methodology, the data, and the results. This requires a large number of CIF data items and considerable information that is not normally input to the analysis software. Template and example files, such as those found on the IUCr journals web site, http://journals.iucr.org/services/cif/powder.html, can be of value, but this will still be a rather time-consuming task to do manually. The *publCIF* utility, http://journals.iucr.org/services/cif/publcif/ (Westrip, 2010), can be very helpful.

Even if a Rietveld package creates a pdCIF file that includes all of the data and results, and provides a template with other data items for the user to include manually, this is still a less-than-optimal process. One reason is that a considerable amount of the information will be repeated for each fit, such as the descriptive information for a user's instrument. One would prefer not to insert such information manually for every study. Furthermore, it is common that, after one has completed a refinement and created a CIF file, a new idea for how the fit may be improved becomes clear. If the fit is improved, one would then like to merge the updated results with the previous CIF file rather than manually fill in the template again. The goal of a pdCIF export program for a Rietveld analysis program should be to document the results from the fit, as well as the original data and intermediates, such as the fitted pattern, since the graphical view of that can assist in determining the quality of the fit, as discussed further in Chapter 4.7 of this volume. Further, one should document the details of the data collection and sample processing, which are usually not input to the program. Also, since one may create several versions of the CIF file prior to the final publication of the study, one should be able to transfer this information easily, both between subsequent versions of the file and from one result to another where this information is shared. One program, *GSAS2CIF*, that was designed to facilitate this process has been discussed in the literature (Toby *et al.*, 2003). An even more streamlined approach has been implemented in the *GSAS-II* package, as will be presented below (Toby & Von Dreele, 2013).

4.10.5. Creating readers for pdCIF data files

One can find information from an individual pdCIF data file by opening the file with an ASCII text editor and browsing through it, though the *enCIFer* program provides more CIF-aware features that interpret the underlying CIF structure and links to the CIF dictionaries. However, in this era one would like information to simply flow between software packages, but this remains a work in progress for pdCIF, even though pdCIF is peerless as a powder diffraction data-exchange format.

Writing a program that will read a powder diffraction CIF file consists of two conceptually simple tasks.

First, one needs to parse the CIF file. This can be a trivial problem if someone else's code can be used to do this. The IUCr's website, http://www.iucr.org/resources/cif/software, lists a number of CIF software libraries that may be used for parsing CIF files. This author has had very good results with the well maintained *PyCifRW* package for Python programs (Hester, 2006). For C++ programming, the relatively recent *iotbx.cif* package may be of use (Gildea *et al.*, 2011). This package offers Python bindings as well, but programmers will probably find it easier to integrate *pyCifRW*, unless the large parent package to *iotbx*, *cctbx*, is already in use (Grosse-Kunstleve *et al.*, 2002).

Once the file is parsed, one needs to identify the data items that will needed. This is where pdCIF gets complex, since there is considerable flexibility in how data may be recorded to suit the many ways in which powder diffraction data are measured and processed. The most complex example of this occurs when extracting diffraction data from a CIF file. For that, one would need to look up the ordinate for the data (2θ, time of flight *etc.*), as well as at least one of several types of intensity data item. Below is an incomplete list of data items that may need to be checked.

4.10.5.1. *Ordinate*

The diffraction data are measured in terms of an independent variable that can be expressed in the original units or can be corrected and/or transformed to equivalent values. These are the CIF data names that can be used for recording this: `_pd_meas_2theta_scan`, `_pd_meas_time_of_flight`, `_pd_proc_2theta_corrected`, `_pd_proc_d_spacing`, `_pd_proc_recip_len_Q`; or the combinations of `_pd_meas_2theta_range_min`, `_pd_meas_2theta_range_max` and `_pd_meas_2theta_range_inc`; or likewise `_pd_proc_2theta_range_min`, `_pd_proc_2theta_range_max` and `_pd_proc_2theta_range_inc`.

One may combine several of these data names, although some do conflict (`_pd_meas_2theta_scan` and `_pd_meas_2theta_range_`, for example).

4.10.5.2. *Observed intensities*

The observed intensity values are recorded in one of several data names, which each have different meanings: `_pd_meas_counts_total`, `_pd_meas_intensity_total`, `_pd_proc_intensity_total` or `_pd_proc_intensity_net`. Note that standard uncertainties for the first (`_counts_`) data item are determined by Poisson statistics, but for the other data items σ can be indicated using crystallographic notation. Alternately, `_pd_proc_ls_weight` can be used to specify uncertainties (where the weight is $1/\sigma^2$).

4.10.5.3. *Background intensities*

There are several different values that can be specified for background measurements, such as `_pd_meas_intensity_background` and `_pd_meas_intensity_container`, which correspond to measurements with no scatterer and with an empty sample container, respectively. However, the most commonly used data item will be `_pd_proc_intensity_bkg_calc`, which represents the estimated background used in pattern fitting.

4.10.5.4. *Computed intensities*

The computed intensities can be recorded using `_pd_calc_intensity_net` or `_pd_calc_intensity_total`, which may have different scaling (as described in the pdCIF dictionary) and where the latter includes estimated background scattering.

Note that, when items appear together in a loop, this implies that the values are in correspondence. However, when items appear in separate loops this may not be true. As an example, if rebinning is used to change the point spacing, then `_pd_meas_2theta_scan` and `_pd_proc_2theta_corrected` are likely to have differing numbers of data points and should appear in different loops. Thus, these items would need to be grouped with (for example) `_pd_meas_intensity_total` and `_pd_proc_intensity_total`, respectively.

4.10.6. CIF software for powder diffraction

There are a large number of powder diffraction software packages that have some capability for reading and/or writing CIF files. No attempt will be made to provide a comprehensive review of all such implementations, but several programs are profiled here that provide novel capabilities and are available for all common computing platforms.

4.10.6.1. *enCIFer*

The *enCIFer* program (Allen *et al.*, 2004) was not the first general-purpose CIF editor and syntax checker to be published, but the CCDC has continued to maintain and improve this application as a service to the community, and it is the single most valuable application available for CIF creation, editing and browsing. The *enCIFer* application is oriented towards the CCDC's core audience of small-molecule crystallographers and includes simple molecular graphics. Nonetheless, the standard installation includes definitions for pdCIF data names. In addition to the editing of existing CIF files, it can be used to generate a CIF file from scratch or from a template, but can also be used to merge CIF files or to insert an ASCII data file into a CIF file where it can be provided with an appropriate `loop_` heading, as described in Section 4.10.4. It also provides a mechanism to validate the CIF file, establishing whether it is syntactically correct and can be used for submission to the IUCr's *checkCIF* utility for validation (see below) or to the CCDC for deposition to the Cambridge Structural Database. Unless a tool better suited to powder diffraction appears, anyone creating CIF files will find this a very useful utility to have.

4.10.6.2. *The IUCr publCIF application*

publCIF (Westrip, 2010) is an application designed for creating, editing and validating CIF files that are used for journal publication. It validates syntax and dictionary-defined data attributes through internal routines, and also provides an interface to the online *checkCIF* service of the IUCr. Access to the CIF dictionaries (both the definition of the item and valid data values) is particularly convenient, and the interface makes it easy to find entries causing an error, alert or warning. The graphical interface allows users to edit the CIF file, either in its raw ASCII form or as a formatted representation of a structure report. *publCIF* contains a number of convenient tools (such as spreadsheet representations of looped data), and provides access to options that facilitate the preparation of a structure report (databases of author details, experimental details, standard references *etc.*), along with tools for reference parsing, spell-checking, structure visualization and image management. *publCIF* was commissioned by the IUCr, and is available as free software for authors and as an in-house journal production tool, particularly for *Acta Crystallographica* Sections *C* and *E*.

4.10.6.3. *The IUCr checkCIF web application*

The IUCr runs a service called *checkCIF* where crystallographers can upload a CIF file for automated review at http://journals.iucr.org/services/cif/checking/checkfull.html. Use of this service is required as part of the editorial process for some journals. The *checkCIF* program validates the CIF file's syntax, as does *enCIFer*, but it also checks that the recommended fields are present. It also applies a number of consistency checks, including running the *PLATON* structural analysis program (Spek, 2003) and reporting indications of possible errors in the results, such as atoms located at improbably short distances from each other or the possible presence of higher-level symmetry. Currently, this service works best for the examination of discrete molecular rather than infinite structures and is best suited to organic and organometallic materials. Many of the alerts it reports are not appropriate for powder diffraction studies, but it still has value as it can catch a multitude of significant problems (see Chapter 4.9). The IUCr has determined that improvement of *checkCIF* for the review of powder diffraction crystallographic results would be beneficial, so it is hoped that the community will contribute to making this process even more valuable for the review of results.

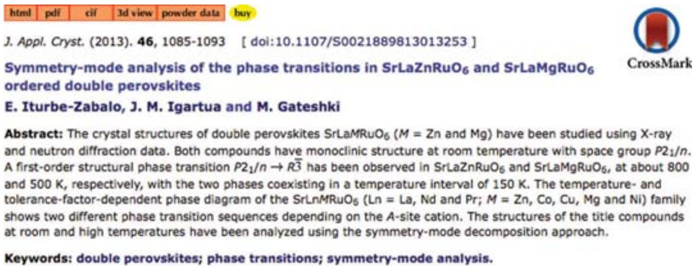

J. Appl. Cryst. (2013). **46**, 1085-1093 [doi:10.1107/S0021889813013253]

Symmetry-mode analysis of the phase transitions in $SrLaZnRuO_6$ and $SrLaMgRuO_6$ ordered double perovskites

E. Iturbe-Zabalo, J. M. Igartua and M. Gateshki

Abstract: The crystal structures of double perovskites $SrLaMRuO_6$ (M = Zn and Mg) have been studied using X-ray and neutron diffraction data. Both compounds have monoclinic structure at room temperature with space group $P2_1/n$. A first-order structural phase transition $P2_1/n \rightarrow R\overline{3}$ has been observed in $SrLaZnRuO_6$ and $SrLaMgRuO_6$, at about 800 and 500 K, respectively, with the two phases coexisting in a temperature interval of 150 K. The temperature- and tolerance-factor-dependent phase diagram of the $SrLnMRuO_6$ (Ln = La, Nd and Pr; M = Zn, Co, Cu, Mg and Ni) family shows two different phase transition sequences depending on the A-site cation. The structures of the title compounds at room and high temperatures have been analyzed using the symmetry-mode decomposition approach.

Keywords: double perovskites; phase transitions; symmetry-mode analysis.

Figure 4.10.1
An example of an IUCr Journals web page where powder diffraction data have been submitted with the publication. Note the 'powder data' button that appears at the top left of the figure; this allows these data to be downloaded as a pdCIF file or plotted.

4.10.6.4. *The IUCr pdCIFplot application*

The IUCr has a web application named *plotCIF* based on an older program, *pdCIFplot* (Toby, 2003; Westrip & Toby, 2013). Scientists can obtain graphical views of observed and computed powder diffraction patterns by uploading pdCIF files at https://publcif.iucr.org/services/tools/pdcifplot.php. This same capability has been integrated into the IUCr journals and can also be used to view diffraction patterns graphically, where pdCIF files are submitted along with manuscripts to supply data and fits. When the CIF file contains coordinates without actual data, the application invokes *PLATON* to compute a powder pattern from the coordinates. These plots are displayed interactively in a web browser using the JavaScript *Flot* package (http://www.flotcharts.org/), where users can manipulate the plot using the mouse and menus. When a contemporary article is viewed in *Acta Crystallographica* or *Journal of Applied Crystallography* and when powder diffraction data have been submitted, a 'powder data' button appears on the web page, as shown in Fig. 4.10.1. From that button, the data can be displayed or downloaded, with the user having considerable control over how the data are

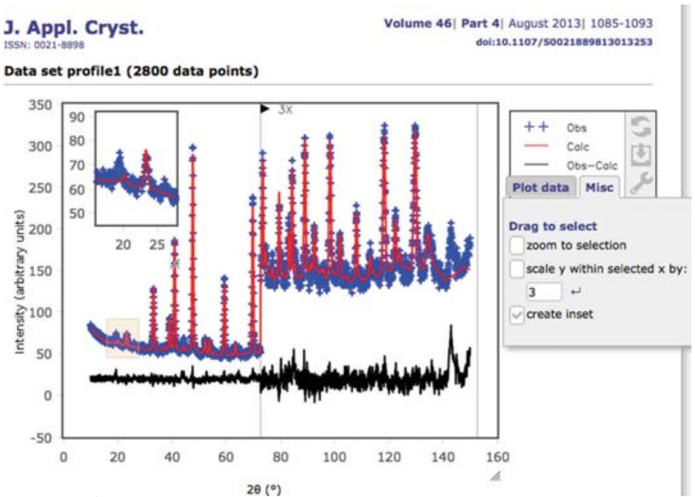

Figure 4.10.2
An example web-displayed *pdCIFplot* graphic for powder diffraction data from the article shown in Fig. 4.10.1, where sections of the plot have been magnified to show detail.

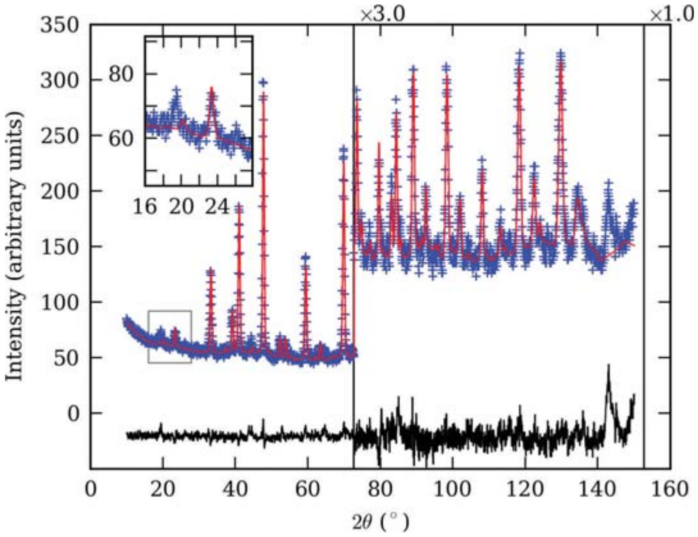

Figure 4.10.3
The publication-quality version of Fig. 4.10.2 from *pdCIFplot*. The generated figure is a bitmap file at 400 d.p.i.

displayed, as shown in Fig. 4.10.2. The generated graphic can also be exported as a high-resolution image, suitable for publication, as shown in Fig. 4.10.3. When coordinates are available in an article, the '3d view' button appears. This allows the structure to be plotted interactively in a web browser. A button within that web applet allows the generation and plotting or download of a simulated powder pattern.

4.10.6.5. *International Centre for Diffraction Data (ICDD) Genie application*

The *Genie* web submission application from the ICDD (http://www.icdd.com/websubmission/launch.html) shows how pdCIF can be integrated into the production process for the ICDD's Powder Diffraction File database. The *Genie* application is downloaded to the user's computer and runs in Java when the web launch link for the application is used. This provides an interactive program that can read and edit pdCIF files or build a pdCIF file from other input sources that provide raw data, a structural model and a peak or reflection table. The final pdCIF file created in *Genie* can then be submitted for editorial review by the ICDD for potential inclusion in the PDF database or for creation of a short publication in the journal *Powder Diffraction*. Alas, the final pdCIF file created in *Genie* cannot be saved locally by the user, thus limiting the utility of the application for other purposes.

4.10.6.6. *pdCIF creation in GSAS-II*

The *GSAS-II* crystallographic analysis program implements a very easy to use pdCIF file exporter that greatly simplifies the process of creating a CIF file (Toby & Von Dreele, 2013). After a refinement has been completed, the user may choose to export a CIF file of the project from a menu item (Export/Entire project as/Full CIF). This will include all data files and all phases that are interrelated. If a phase or data set is added to a project, but is not then utilized in a fit, that entry will be ignored. If the CIF file contains only one phase and one data set, a single-block CIF file will be created. Otherwise, a separate block will be used for each phase and each powder or single-crystal data set. Once the Full CIF menu item is invoked, the program will request, *via* a series of dialogue windows, those data items that are required for construction of the CIF block pointers, if this information has not already been input. This information includes the name of the author of the CIF file, atomic radii for searching distances and angles, and an instrument name for each data set, if that was not set by the instrument parameter file when the data were initially input. The values provided by the user are saved in the project file and are thus only input once.

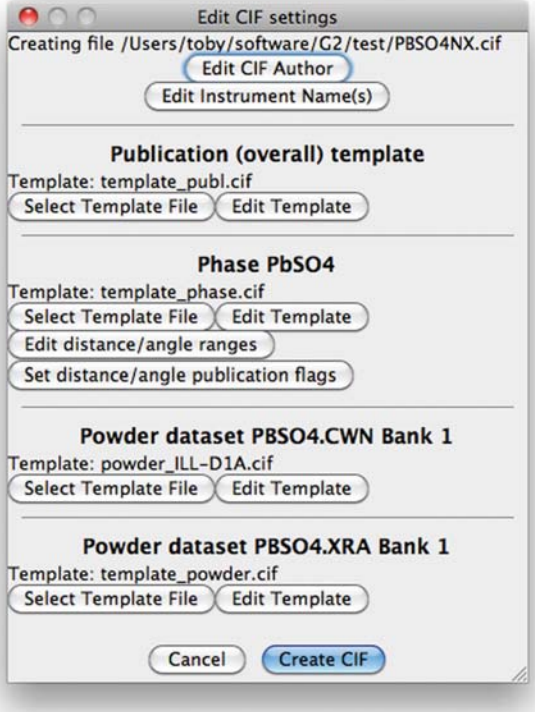
Edit CIF settings

Creating file /Users/toby/software/G2/test/PBSO4NX.cif

Publication (overall) template

Template: template_publ.cif

Phase PbSO4

Template: template_phase.cif

Select Template File
Edit Template
Edit distance/angle ranges
Set distance/angle publication flags

Powder dataset PBSO4.CWN Bank 1

Template: powder_ILL-D1A.cif

Powder dataset PBSO4.XRA Bank 1

Template: template_powder.cif

Figure 4.10.4
An example dialogue window from *GSAS-II* used in preparation of a CIF file. Each button on the window allows the user to edit information that will be included in the file.

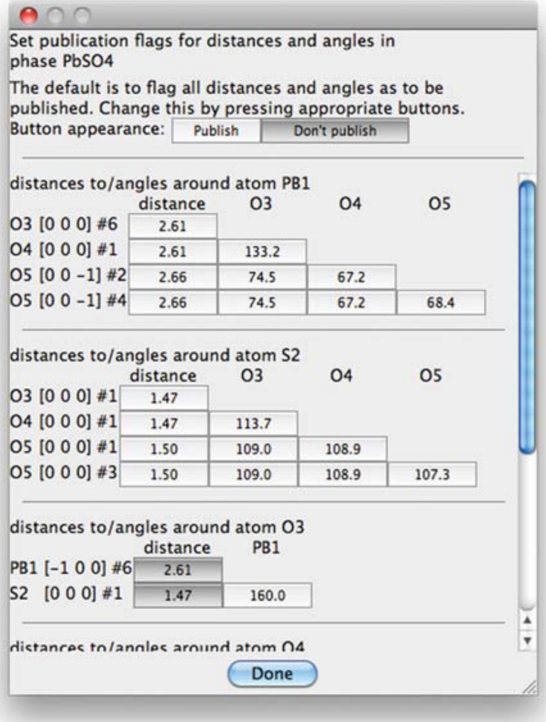
Set publication flags for distances and angles in phase PbSO4

The default is to flag all distances and angles as to be published. Change this by pressing appropriate buttons.

Button appearance:

distances to/angles around atom PB1

	distance	O3	O4	O5
O3 [0 0 0] #6	2.61			
O4 [0 0 0] #1	2.61	133.2		
O5 [0 0 −1] #2	2.66	74.5	67.2	
O5 [0 0 −1] #4	2.66	74.5	67.2	68.4

distances to/angles around atom S2

	distance	O3	O4	O5
O3 [0 0 0] #1	1.47			
O4 [0 0 0] #1	1.47	113.7		
O5 [0 0 0] #1	1.50	109.0	108.9	
O5 [0 0 0] #3	1.50	109.0	108.9	107.3

distances to/angles around atom O3

	distance	PB1
PB1 [−1 0 0] #6	2.61	
S2 [0 0 0] #1	1.47	160.0

distances to/angles around atom O4

Figure 4.10.5
An example dialogue window from *GSAS-II* used in the preparation of a CIF file, to edit the bond distances and angles for one phase.

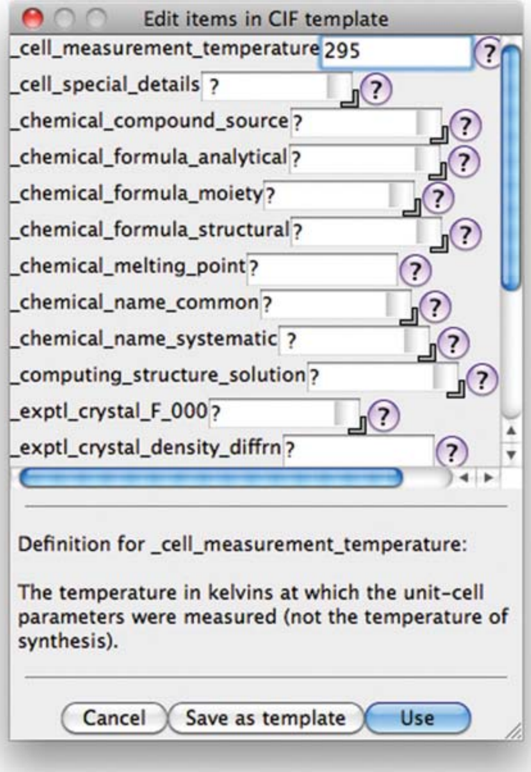

_cell_measurement_temperature 295
_cell_special_details ?
_chemical_compound_source ?
_chemical_formula_analytical ?
_chemical_formula_moiety ?
_chemical_formula_structural ?
_chemical_melting_point ?
_chemical_name_common ?
_chemical_name_systematic ?
_computing_structure_solution ?
_exptl_crystal_F_000 ?
_exptl_crystal_density_diffrn ?

Definition for _cell_measurement_temperature:

The temperature in kelvins at which the unit-cell parameters were measured (not the temperature of synthesis).

Figure 4.10.6
An example dialogue window from *GSAS-II* for editing the contents of a CIF template. Clicking on the help button (here labelled with '?') causes the definition for the selected data name to be shown at the bottom of the window.

Once this required information is input, a dialogue is presented, such as the example in Fig. 4.10.4. Note that each section of the CIF file has an associated template file. There is a default template for the overall section with publication information, and default templates for phases, powder diffraction data sets and single-crystal data sets. As this example shows, for each data set, if a default template is located that matches the name of the instrument (here ILL-D1A), that template is selected automatically. An alternative template file can be selected for use with the 'Select template file' button. For each phase, the 'Set distance/angle publication flag' button can be used to bring up an editing dialogue, as shown in Fig. 4.10.5, which can be used to set the publish/non-publish flag for bonding distances or angles. The 'Edit template' button opens a dialogue window, as shown in Fig. 4.10.6. This window allows information to be entered for each entry in the template, can show the dictionary definition and can save the information entered by the user, either in the *GSAS-II* project file or in a modified template file.

4.10.7. Conclusions

The pdCIF format for powder diffraction allows for the exchange of data, results and descriptive information in a facile manner. There is no other convenient mechanism for the exchange of this information. In contrast with single-crystal diffraction, where CIF is very widely used, at present this format has not been integrated into all commonly used powder diffraction software, but there are now many applications that do so for the benefit of all powder diffractionists.

The author is supported by the Advanced Photon Source, an Office of Science user facility operated for the US Department of Energy (DOE) Office of Science by Argonne National Laboratory, which is sponsored by the US DOE under contract No. DE-AC02–06CH11357. The author acknowledges Syd Hall and Brian McMahon for considerable input during the development process for the pdCIF dictionary.

References

Allen, F. H., Johnson, O., Shields, G. P., Smith, B. R. & Towler, M. (2004). *CIF applications. XV. enCIFer: a program for viewing, editing and visualizing CIFs. J. Appl. Cryst.* **37**, 335–338.

Gildea, R. J., Bourhis, L. J., Dolomanov, O. V., Grosse-Kunstleve, R. W., Puschmann, H., Adams, P. D. & Howard, J. A. K. (2011). *iotbx.cif: a comprehensive CIF toolbox. J. Appl. Cryst.* **44**, 1259–1263.

Grosse-Kunstleve, R. W., Sauter, N. K., Moriarty, N. W. & Adams, P. D. (2002). *The computational crystallography toolbox: crystallographic algorithms in a reusable software framework. J. Appl. Cryst.* **35**, 126–136.

Hall, S. R. (1991). *The STAR file: a new format for electronic data transfer and archiving. J. Chem. Inf. Model.* **31**, 326–333.

Hall, S. R., Allen, F. H. & Brown, I. D. (1991). *The crystallographic information file (CIF): a new standard archive file for crystallography. Acta Cryst.* A**47**, 655–685.

Hall, S. R. & McMahon, B. (2005). Editors. *International Tables for Crystallography*, Vol. G, *Definition and Exchange of Crystallographic Data*. Heidelberg: Springer.

Hester, J. (2006). *A validating CIF parser: PyCIFRW. J. Appl. Cryst.* **39**, 621–625.

Kourkoumelis, N. (2015). *PowDLL, a reusable .NET component for interconverting powder diffraction data. Recent developments, ICDD Annual Spring Meetings. Powder Diffr.* **28**, 137–148.

Spek, A. (2003). *Single-crystal structure validation with the program PLATON. J. Appl. Cryst.* **36**, 7–13.

Toby, B. H. (2003). *CIF applications. XII. Inspecting Rietveld fits from pdCIF: pdCIFplot. J. Appl. Cryst.* **36**, 1285–1287.

Toby, B. H. (2005*a*). *International Tables for Crystallography*, Vol. G, *Definition and Exchange of Crystallographic Data*, edited by S. R. Hall & B. McMahon, pp. 258–269. Heidelberg: Springer.

Toby, B. H. (2005*b*). *CMPR – a powder diffraction toolkit. J. Appl. Cryst.* **38**, 1040–1041.

Toby, B. H. & Von Dreele, R. B. (2013). *GSAS-II: the genesis of a modern open-source all-purpose crystallography software package. J. Appl. Cryst.* **46**, 544–549.

Toby, B. H., Von Dreele, R. B. & Larson, A. C. (2003). *CIF applications. XIV. Reporting of Rietveld results using pdCIF: GSAS2CIF. J. Appl. Cryst.* **36**, 1290–1294.

Westrip, S. P. (2010). *publCIF: software for editing, validating and formatting crystallographic information files. J. Appl. Cryst.* **43**, 920–925.

Westrip, S. & Toby, B. H. (2013). *plotCIF powder profiles*. https://publcif.iucr.org/services/tools/pdcifplot.php.

International Tables for Crystallography (2019). Vol. H, Chapter 5.1, pp. 524–537.

5.1. Domain size and domain-size distributions

M. Leoni

5.1.1. Introduction

With the continuous advancement of studies in the field of nanostructured materials, the non-destructive and accurate determination of the size of nanometric objects has become a real issue. Powder diffraction is one of the tools for obtaining this information, provided that we know the meaning of the result and the limits of the available analysis techniques.

A century ago, Scherrer (1918) identified a relationship between the breadth of a diffraction profile and the size of the corresponding domains. The definition of size is quite important here. In this context, the size is that of the smallest crystalline entities in the specimen (*domains* or *crystallites*) providing a coherent diffraction signal, but diffracting independently (and incoherently) of one another. The case of two non-connected regions contributing coherently to the intensity is therefore excluded. Another often-used definition for these domains is that of *primary particles*. In a microscope, they would represent the smallest independent crystalline areas of the specimen. Therefore, a domain can be quite different, for example, from a *particle* or a *grain*, as these objects may easily contain more than one domain. The X-ray diffraction techniques proposed here are unable to provide an estimation of the grain size: when microscopy is not an option, small-angle scattering as well as a graininess analysis of the diffraction rings can be viable alternatives. The differences between domain and grain, however, become faint for a colloid and in general for a nanocrystalline powder or aggregate: these are the major fields of application of diffractometric techniques, as the sizes that can be accessed are limited to the sub-micrometre range. Grain size can be estimated, under certain conditions, from the observation of relative intensity variations.

The Scherrer formula is the origin of line-profile analysis (LPA), the branch of diffraction devoted to the extraction of microstructure information from a pattern. The literature on LPA is vast: several techniques have been proposed over the years to allow for a more complete microstructural analysis and to remove most of the limitations of the original formulation by Scherrer. Those techniques have been developed with the goal of separating the various contributions to line-profile broadening: the variance method (Wilson, 1962), the Williamson–Hall method (Williamson & Hall, 1953), the Warren–Averbach technique (Warren & Averbach, 1950, 1952) and whole-powder-pattern modelling (Scardi & Leoni, 2002; Scardi *et al.*, 2010; see also Chapter 3.6) are probably the most important milestones there. With the advent of personal computers, some of the methods have lost their popularity and advantages; this is the case for the variance method, which is now only used sporadically (see *e.g.* Pantoja-Cortés *et al.*, 2012).

Nevertheless, most of the modern literature still presents quantitative results based on the original formalism – results that in most cases are either in disagreement with the underlying physics or are wrong on an absolute scale.

Peak broadening is the key in the determination of a size from a diffraction pattern. If we assume that our specimen is free from defects, the only parameters affecting this broadening are the instrument, the size and shape of the domains, and their distributions. The instrument limits the maximum size that can be reliably measured: domains larger than a few hundred nanometres can be considered as 'particles of infinite size' (Jones, 1938, 1941). All contributions to the broadening are folded into the observed line profile. In particular, if g describes the instrumental peak (*i.e.* a delta function broadened by all instrumental aberrations) and f the peak resulting from the specimen effects alone, then the function describing the whole profile h can be calculated as (Jones, 1938; Alexander, 1954; Klug & Alexander, 1974, and references therein)

$$h(x) = \int_{-\infty}^{\infty} f(y) g(x-y)\, \mathrm{d}y = f \otimes g(x). \qquad (5.1.1)$$

Exhaustive discussion on this issue can be found in, for example, Klug & Alexander (1974), Snyder *et al.* (1999) and Mittemeijer & Scardi (2004). Instrumental effects should be taken into due account when extracting the size contribution, as they might considerably alter the shape of the profiles; for a nanocrystalline powder, however, they can be negligible with respect to the size-related broadening and thus only small errors are made if they are not included. Unless otherwise specified, all derivations in the following will be done considering the instrumental effects as negligible, or properly taken into account, or removed.

Two approaches are available for the analysis of the size and size distribution: pattern decomposition (or fitting) and pattern modelling. In the first case, the information is obtained from some fitting parameter (no direct connection exists between the model and the data); in the latter case, a microstructure model is employed to simulate the peak profile and the model parameters are directly refined against the experimental data. The most common methods for the analysis are discussed here and the formulae for the simulation of the size-broadened profile are provided.

5.1.2. The Scherrer formula and integral-breadth methods

The Scherrer formula relates the full width at half maximum (FWHM) of a diffraction peak to an average domain size value: this apparently simple nature of the problem is the key to the success of the Scherrer formula and justifies its wide abuse. The original equation (Scherrer, 1918), paired with a more modern formalism, reads

$$h = 2\sqrt{\frac{\ln 2}{\pi}} \frac{\lambda}{\Lambda} \frac{1}{\cos \vartheta/2}, \qquad \mathrm{FWHM} = \frac{K_w \lambda}{\langle D \rangle \cos \theta_{hkl}}, \qquad (5.1.2)$$

where h is the FWHM, λ is the wavelength, Λ (now identified as $\langle D \rangle$ where $\langle\rangle$ indicates averaging) is the edge length of the cube-shaped domains (*Kriställchens*, as per Scherrer), ϑ (now called $2\theta_{hkl}$) is the diffraction (Bragg) angle and K_w is the so-called (half-width) Scherrer constant ($K_w \simeq 0.94$ in this case).

Neither of the two most frequent references to the Scherrer equation (Scherrer, 1918, 1922) actually contain any derivation of the formula. Scherrer himself suggests that it was presented in his *Habilitation* thesis (Scherrer, 1962). Fortunately, Scherrer's idea

Copyright © 2019 International Union of Crystallography

and the whole formalism has been reprised and extended by several authors (*e.g.* von Laue, 1926; Bragg, 1930; Jones, 1938; Patterson, 1939*a*,*b*; Wilson, 1962; Klug & Alexander, 1974; Langford & Wilson, 1978; Langford & Louër, 1996) and a derivation of equation (5.1.2), albeit with a whole range of Scherrer constants, can be found. Differences are in some cases just related to the definition of the size parameter. Even if a characteristic edge length can be the most obvious choice, the cube root of the domain volume V is often employed. For a cube this makes no difference, as $V^{1/3} = D$, whereas for a sphere of diameter D, for example, the cube root of the volume is $V^{1/3} = (\pi/6)^{1/3}D \simeq 0.806D$. Particular care should therefore be taken when choosing K_w.

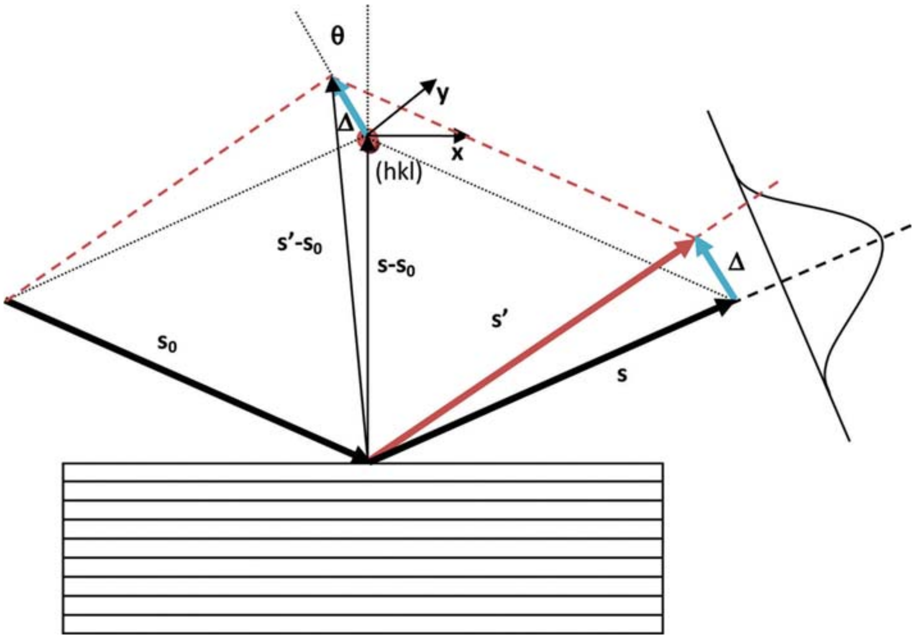

Figure 5.1.1
Geometry employed to derive the Scherrer equation.

The case of a small crystal of cubic shape and cubic lattice, on which the original Scherrer formula is based, will be shown here; the extension to different shapes and symmetries is straightforward and can be found in the cited literature. The powder-diffraction peak profile can be calculated by considering the object as a single crystal and integrating the corresponding intensity over all orientations in space. The diffracted intensity for a single crystal of cubic shape is (see *e.g.* von Laue, 1926; Jones, 1938; Warren, 1990)

$$I = I_e F^2 \frac{\sin^2\left[(\pi/\lambda)(\mathbf{s}-\mathbf{s}_0)\cdot N\mathbf{a}_1\right]}{\sin^2\left[(\pi/\lambda)(\mathbf{s}-\mathbf{s}_0)\cdot \mathbf{a}_1\right]} \frac{\sin^2\left[(\pi/\lambda)(\mathbf{s}-\mathbf{s}_0)\cdot N\mathbf{a}_2\right]}{\sin^2\left[(\pi/\lambda)(\mathbf{s}-\mathbf{s}_0)\cdot \mathbf{a}_2\right]} \times \frac{\sin^2\left[(\pi/\lambda)(\mathbf{s}-\mathbf{s}_0)\cdot N\mathbf{a}_3\right]}{\sin^2\left[(\pi/\lambda)(\mathbf{s}-\mathbf{s}_0)\cdot \mathbf{a}_3\right]}, \qquad (5.1.3)$$

where $\mathbf{s}_0$ and $\mathbf{s}$ are, respectively, the incident and diffracted beam, λ is the wavelength, N is the size of the cube in terms of numbers of cells along the three (real) directions $\mathbf{a}_1$, $\mathbf{a}_2$, $\mathbf{a}_3$, F^2 is the square modulus of the structure factor and I_e is the scattering intensity for an atom in electron units. The size of the cube is $\langle D\rangle = Na$. Here we are interested in the behaviour of the diffraction pattern near a Bragg spot. We consider therefore that $|(\mathbf{s}-\mathbf{s}_0)/\lambda| = 2\sin\theta_{hkl}/\lambda = d^*_{hkl}$ and we calculate the intensity in a point $(\mathbf{s}-\mathbf{s}_0+\Delta\mathbf{s})$ obtained by varying slightly the incident and diffracted beams. As we are in the neighbourhood of a Bragg spot, equation (5.1.3) can be modified to (see *e.g.* Warren, 1990)

$$I_{hkl} = I_e F^2 \frac{\sin^2\left(\pi N\Delta\mathbf{s}\cdot\mathbf{a}_1/\lambda\right)}{\sin^2\left(\pi\Delta\mathbf{s}\cdot\mathbf{a}_1/\lambda\right)} \frac{\sin^2\left(\pi N\Delta\mathbf{s}\cdot\mathbf{a}_2/\lambda\right)}{\sin^2\left(\pi\Delta\mathbf{s}\cdot\mathbf{a}_2/\lambda\right)} \times \frac{\sin^2\left(\pi N\Delta\mathbf{s}\cdot\mathbf{a}_3/\lambda\right)}{\sin^2\left(\pi\Delta\mathbf{s}\cdot\mathbf{a}_3/\lambda\right)}. \qquad (5.1.4)$$

To reduce the difficulties in integrating (5.1.4) over all orientations, we can replace each trigonometric ratio (leading to a peak with oscillatory tails) with a bell-shaped function having, for example, the same maximum and the same area (Gauss and Lorentz profiles were explored by von Laue). In the Gaussian case we have

$$\frac{\sin^2 Nx}{\sin^2 x} \rightarrow N^2\exp\left(-N^2x^2/\pi\right). \qquad (5.1.5)$$

Substituting equation (5.1.5) in equation (5.1.4) and considering the orthonormality of the $\mathbf{a}_i$ basis, we obtain

$$I_{hkl} = I_e F^2 N^6 \exp\left[-K\Delta s^2\right], \quad K = \pi\left(\frac{Na}{\lambda}\right)^2. \qquad (5.1.6)$$

We can now integrate equation (5.1.6) in reciprocal space [in place of equation (5.1.4)] and obtain the powder-diffraction intensity. Instead of rotating the crystal in space, we can integrate by varying the $\mathbf{s}$ vectors. Fortunately, the intensity is just concentrated in a small region close to the Bragg spots (according to the Laue equations) and we can thus substitute the integration in space by the integration over a small volume around them. The integration on a sphere can also be substituted by the integration over the plane tangent to it and orthogonal to $\mathbf{s}-\mathbf{s}_0$ with local axes $\mathbf{x}$ and $\mathbf{y}$ (Fig. 5.1.1). As the variation with respect to the Bragg condition is small, our $\Delta\mathbf{s}$ becomes $\Delta\mathbf{s} = \mathbf{x}+\mathbf{y}+\boldsymbol{\Delta}$ (see Fig. 5.1.1) and thus

$$\Delta s^2 = (x-\Delta\sin\theta_{hkl})^2 + y^2 + (\Delta\cos\theta_{hkl})^2. \qquad (5.1.7)$$

We now have

$$\begin{aligned} I_{hkl}(\Delta) &= I_e F^2 N^6 \exp\left(-K\Delta^2\cos^2\theta_{hkl}\right) \\ &\quad\times \int\limits_{-\infty}^{\infty} \exp\left(-K(x-\Delta\sin\theta_{hkl})^2\right)\,\mathrm{d}x \int\limits_{-\infty}^{\infty} \exp(-Ky^2)\,\mathrm{d}y \\ &= I_e F^2 N^6 \frac{\pi}{K}\exp\left(-K\Delta^2\cos^2\theta_{hkl}\right) \qquad (5.1.8) \end{aligned}$$

and thus the FWHM of this profile can be obtained as

$$\begin{aligned} \frac{I_{hkl}(0)}{2} &= I_{hkl}\left(\mathrm{FWHM}_{hkl}/2\right) = I_{hkl}(\Delta) \\ &= I_{hkl}(0)\exp\Big(-K\left(\mathrm{FWHM}_{hkl}/2\right)^2\cos^2\theta_{hkl}\Big), \qquad (5.1.9) \end{aligned}$$

from which

$$\mathrm{FWHM}_{hkl} = \frac{2(\ln 2/K)^{1/2}}{\cos\theta_{hkl}} = \frac{2(\ln 2/\pi)^{1/2}\lambda}{Na\cos\theta_{hkl}} = \frac{2(\ln 2/\pi)^{1/2}\lambda}{\langle D\rangle\cos\theta_{hkl}} = \frac{K_w\lambda}{\langle D\rangle\cos\theta_{hkl}} \qquad (5.1.10)$$

as originally obtained by Scherrer. Equation (5.1.10) assumes a simpler form if we analyse the problem in reciprocal space. In fact, we can note that

$$d^* = \frac{2\sin(2\theta/2)}{\lambda} \rightarrow \frac{\partial d^*}{\partial 2\theta} = \frac{\cos\theta}{\lambda} \rightarrow \mathrm{FWHM}^*_{hkl} = \frac{K_w}{\langle D\rangle}, \qquad (5.1.11)$$

where * is used to indicate quantities in reciprocal space.

Scherrer's result is mathematically exact when the diffraction profile is Gaussian: this does not mean it is also physically plausible, as it would correspond to the case where a certain domain shape leads to an equation like (5.1.4) but built with Gaussians in place of the trigonometric ratios. Moreover, different shapes are considered in the formalism just through K_w: the domain shape affects the profile shape, but the Gaussian approximation is still employed. An extra term could be added to the original formulation to take the instrumental broadening into account (Scherrer, 1922; von Laue, 1926; Alexander, 1954; Stokes, 1955):

$$h = 2\left(\frac{\ln 2}{\pi}\right)^{1/2} \frac{\lambda}{\Lambda}\frac{1}{\cos\vartheta/2} + b. \qquad (5.1.12)$$

The additivity of breadths depends on the shape of the profiles. According to equation (5.1.1), we have to consider a convolution of profiles: for instance, the breadth of the convolution of two Lorentzian profiles is the sum of the breadths, whereas for the Gaussian it is the root of the sum of the squared breadths. In equation (5.1.12), a Gauss approximation was employed to obtain the Scherrer formula, and now the instrumental broadening is added straight away as in a Lorentz approximation: the two hypotheses are therefore contrasting. However, considering the level of approximation involved in the derivation of the Scherrer equation and the limited effect of the instrumental profile, an approximation like equation (5.1.12) is still acceptable.

For a practical estimation of the size, equation (5.1.2) is usually preferred: in most cases the Scherrer constant is arbitrarily chosen (0.94 and 0.89, representing the cases of a cube and a sphere, are usually adopted), but problems arise in the evaluation of the FWHM. In fact, peaks can be partly overlapping and a background can be present, limiting the ability to isolate a peak from the pattern. The choice of the peak is also arbitrary: most publications show a tendency to employ the most intense peak or an isolated peak above $\sim 30^\circ$ in 2θ (where instrumental aberrations leading to peak asymmetry start to be less important). Unless size is the only source of broadening, different values for the apparent average domain size are obtained from different profiles.

This is therefore a very crude approach to determining the size of the coherently scattering domains, and to line-profile analysis in general. To avoid some of the problems related to the estimation of the FWHM, the integral breadth (IB) introduced by von Laue (1926) and extensively employed by Stokes & Wilson (1942, 1944) can be used. The IB is defined as the ratio between the peak area and the peak maximum intensity, and is therefore the width of a rectangular peak having the same intensity and area as the measured one. In reciprocal space the integral breadth for the *hkl* reflection is

$$\beta^*_{hkl} = \frac{1}{I_{hkl}(0)}\int\limits_{-\infty}^{\infty} I_{hkl}(s)\,\mathrm{d}s, \qquad (5.1.13)$$

where $s = d^* - d^*_{hkl}$. The integral breadth is related to the FWHM. In fact, we can take a unit area Gaussian,

$$G(s) = \frac{2[\ln(2)/\pi]^{1/2}}{\mathrm{FWHM}}\exp\left[-4\ln(2)\frac{s^2}{\mathrm{FWHM}^2}\right], \qquad (5.1.14)$$

and calculate the corresponding integral breadth:

$$\beta^* = \frac{1}{2[\ln(2)/\pi]^{1/2}/\mathrm{FWHM}} = \frac{\mathrm{FWHM}}{2[\ln(2)/\pi]^{1/2}}. \qquad (5.1.15)$$

The constant in equation (5.1.15) is exactly the same as that appearing in the original formula of Scherrer. Equation (5.1.2) can thus be rewritten in terms of integral breadth as

$$\beta^*_{hkl} = \frac{1}{\Lambda}, \quad \beta_{hkl} = \frac{K_\beta}{\langle D\rangle}\frac{\lambda}{\cos\theta_{hkl}}, \quad \beta^*_{hkl} = \frac{K_\beta}{\langle D\rangle}, \qquad (5.1.16)$$

where the new constant K_β takes the shape of the domains into account. The inverse of the integral breadth is sometimes defined as the *apparent size*. With the goal of calculating the integral breadth for some common shapes (including the cube already considered by several authors), the article by Stokes & Wilson (1942) provides some new ideas for calculating the intensity profile and opens the way to a new type of analysis based on a Fourier approach.

5.1.3. Fourier methods

In the Scherrer formula, and in general in the methods based on the integral breadth, just part of the information contained in the pattern is employed in the analysis. The information on the microstructure is coded into the whole shape of the peak, so the breadth can only give some order-of-magnitude estimate of the size. Fourier methods go further, and provide a description of the whole intensity profile in reciprocal space; not surprisingly, the Fourier formalism is also at the basis of the modern methods for line-profile broadening analysis.

5.1.4. The peak profile and the common volume function ('ghost')

Stokes and Wilson proposed a simple method for calculating the size-broadened line profiles and the corresponding integral breadths. The derivation, initially proposed for cubic lattices (Stokes & Wilson, 1942), was then seamlessly extended to the general case (Stokes & Wilson, 1944); the diffracted intensity for a row of scatterers of length T laying parallel to the $\langle hkl\rangle$ direction in reciprocal space can be written as (Wilson, 1962, equation 5 on p. 39)

$$I_{hkl}(s)\,\mathrm{d}s \propto \frac{1}{U}\int\!\!\int \frac{\sin^2(\pi T s)}{(\pi s)^2}\,\mathrm{d}y\,\mathrm{d}z\,\mathrm{d}s = \frac{1}{U}\int\!\!\int T^2\mathrm{sinc}^2(\pi T s)\,\mathrm{d}y\,\mathrm{d}z\,\mathrm{d}s, \qquad (5.1.17)$$

where $s = d^* - d^*_{hkl}$ ($S - S_{hkl}$ in the original notation), U is the unit-cell volume and the direction x is along the line of scatterers. The proportionality sign is used in equation (5.1.17) as constants and known functions of s are omitted in the derivation. By noting that the area of the peak is given by V/U, where V is the volume of the domain, the apparent integral-breadth size can easily be calculated as

$$\begin{aligned}\langle D\rangle &= \frac{1}{\beta^*_{hkl}} = \frac{I_{hkl}(0)}{V/U} = \frac{1}{V}\int\int T^2\,\mathrm{d}y\,\mathrm{d}z = \frac{1}{V}\int\int\int T\,\mathrm{d}x\,\mathrm{d}y\,\mathrm{d}z\\ &= \frac{1}{V}\int\limits_V T\,\mathrm{d}V. \end{aligned}\qquad (5.1.18)$$

According to Stokes & Wilson (1942), 'the reciprocal of the integral breadth [in reciprocal space] is the volume average of the thickness of the crystal measured perpendicular to the reflecting plane'. The integral in (5.1.18) can be conveniently rewritten as

$$(1/V)\int\int T^2\,\mathrm{d}y\,\mathrm{d}z = (1/V)\int\limits_{-\tau_{hkl}}^{\tau_{hkl}} V_{hkl}(L)\,\mathrm{d}L, \qquad (5.1.19)$$

where the function $V_{hkl}(L)$ is the self-convolution of the shape function of the domain (defined as unity inside the domain boundary and zero elsewhere), and it represents the volume common to the domain and its 'ghost' displaced by a quantity L along the *hkl* direction:

$$V_{hkl}(L) = \int\int (T - |L|)\,\mathrm{d}y\,\mathrm{d}z. \qquad (5.1.20)$$

From these definitions, it is clear that $V = V_{hkl}(0)$ and that $V_{hkl}(L) = V_{hkl}(-L)$. To simplify the notation, equation (5.1.20) is commonly assumed to be even (and employed for non-negative L), thus quite often L is found in place of $|L|$ in all expressions for the common volume function. The integration in (5.1.19) is limited to the distance τ_{hkl} where the common volume function (CVF) reaches zero. The geometrical interpretation of the CVF can be seen in Fig. 5.1.2.

Now, if we take the Fourier transform (FT) of the CVF, we obtain

$$\begin{aligned}&\int\limits_{-\tau}^{\tau} V_{hkl}(L)\exp(2\pi isL)\,\mathrm{d}L\\ &\quad= 2\int\limits_{0}^{\tau} V_{hkl}(L)\cos(2\pi sL)\,\mathrm{d}L + i\int\limits_{-\tau}^{\tau} V_{hkl}(L)\sin(2\pi sL)\,\mathrm{d}L\\ &\quad= 2\int\int\left(\int\limits_{0}^{\tau}(T-L)\cos(2\pi sL)\,\mathrm{d}L\right)\mathrm{d}y\,\mathrm{d}z + 0\\ &\quad= 2\int\int\left(T\int\limits_{0}^{\tau}\cos(2\pi sL)\,\mathrm{d}L - \int\limits_{0}^{\tau}L\cos(2\pi sL)\,\mathrm{d}L\right)\mathrm{d}y\,\mathrm{d}z\\ &\quad= \int\int\frac{\sin^2(\pi sT)}{(\pi s)^2}\,\mathrm{d}y\,\mathrm{d}z. \end{aligned}\qquad (5.1.21)$$

By comparing equations (5.1.17) and (5.1.21), we can conclude that the peak profile is related to the Fourier transform of the CVF:

$$\begin{aligned}I_{hkl}(s) &\propto \frac{1}{U}\int\limits_{-\tau}^{\tau} V_{hkl}(L)\exp(2\pi isL)\,\mathrm{d}L\\ &= \frac{2}{U}\int\limits_{0}^{\tau} V_{hkl}(L)\cos(2\pi sL)\,\mathrm{d}L\\ &\propto \frac{1}{U}\int\limits_{-1}^{1} V_{hkl}\left(\frac{L}{D}\right)\exp\left(2\pi is\frac{L}{D}\right)\mathrm{d}\frac{L}{D}\\ &= \frac{2}{U}\int\limits_{0}^{1} V_{hkl}\left(\frac{L}{D}\right)\cos\left(2\pi s\frac{L}{D}\right)\mathrm{d}\left(\frac{L}{D}\right). \end{aligned}\qquad (5.1.22)$$

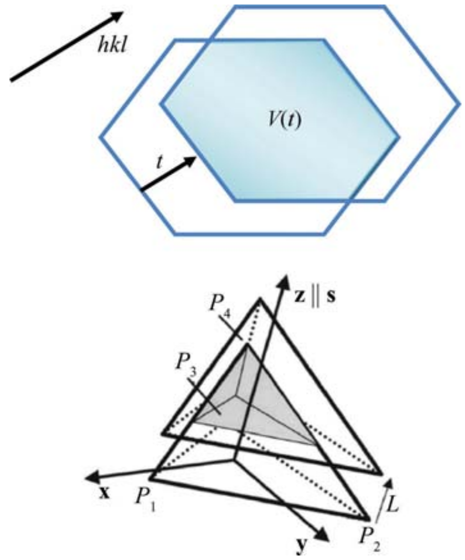

Figure 5.1.2
A domain and its ghost translated by a quantity L along *hkl*.

As can be seen, the limit of integration can be changed provided that the functions are defined consistently (see *e.g.* Adler & Houska, 1979). The normalized common volume function

$$A^S_{hkl}(L) = \frac{V_{hkl}(L)}{V_{hkl}(0)}, \qquad (5.1.23)$$

often referred to as the size Fourier term (or size Fourier coefficients), is traditionally used in place of the CVF in the description of line-profile broadening: the normalization is useful as it leads to unit-area peaks. Equation (5.1.22) can easily be rewritten in terms of $A^S_{hkl}(L)$. The size Fourier coefficients can also be employed to treat finite size effects in the total-scattering approach (Howell *et al.*, 2006).

The properties of the Fourier transform lead to an interesting result for the integral breadth (Bertaut, 1949*a*, 1950):

$$\beta^*_{hkl} = \frac{\int_{-\infty}^{\infty} I_{hkl}(s)\,\mathrm{d}s}{I_{hkl}(0)} = \frac{A^S_{hkl}(0)}{\int_{-\tau_{hkl}}^{\tau_{hkl}} A^S_{hkl}(L)\,\mathrm{d}L} = \left(\int\limits_{-\tau_{hkl}}^{\tau_{hkl}} A^S_{hkl}(L)\,\mathrm{d}L\right)^{-1}. \qquad (5.1.24)$$

This has important implications for practical size analysis using integral-breadth methods, as we can either work directly on the data (suitably represented in the correct space) or use the Fourier coefficients without actually calculating the profile. If we want to consider other broadening effects, working directly with the Fourier coefficients has undoubted advantages: in fact, the convolution theorem for the FT allows equation (5.1.1) to be written as

$$\begin{aligned}h(x) &= \mathrm{FT}^{-1}[\mathrm{FT}[h(x)]] = \mathrm{FT}^{-1}[\mathrm{FT}[f(x)]\cdot\mathrm{FT}[g(x)]]\\ &= f\otimes g(x),\end{aligned}\qquad (5.1.25)$$

where FT[x] and $\mathrm{FT}^{-1}[x]$ identify direct and inverse Fourier transformation. Convolution is thus transformed into a product in Fourier space and any additional broadening term k enters equation (5.1.22) as a multiplicative FT[k] element (*cf.* Paterson, 1952).

Equation (5.1.22) [together with equations (5.1.23) and (5.1.25)] can be used in two ways: we can simulate the profile *ab initio* and optimize the model parameters against the data, or we can extract the Fourier parameters directly from the data and try to work out the model parameters from them (see below). The first approach is the basis of the whole powder pattern modelling (Scardi & Leoni, 2002; Chapter 3.6), the second one is the basis of all Fourier methods of line-profile analysis, such as the Warren and Averbach method (Warren & Averbach, 1952; Paterson, 1952).

5.1.5. Common volume function for simple shapes

For simple shapes, the common volume function can be obtained in a simple closed form. For instance, the case of the sphere, obtained by Stokes & Wilson (1942), can be derived from the intersection of two circles (Fig. 5.1.3). In fact, the intersection of two spheres of diameter D is a lens (*i.e.* the sum of two equal spherical caps) with radius of the base r and height $(D - L)/2$ obtained by rotating the drawing of Fig. 5.1.3 around the segment connecting the centres of the circles. The volume of the lens is

$$V_{\rm lens}(L) = 2\pi \frac{h^2}{3}\left(3\frac{D}{2} - h\right) = \frac{\pi}{12}(D-L)^2(2D+L) = \frac{\pi D^3}{6} - \frac{\pi D^2 L}{4} + \frac{\pi L^3}{12} \tag{5.1.26}$$

and therefore the corresponding size Fourier coefficients read

$$A^s_{\rm sphere}(L) = \frac{V_{\rm lens}(L)}{V_{\rm lens}(0)} = \frac{\pi(D-L)^2(2D+L)/12}{\pi D^3/6} = 1 - \frac{3}{2}\frac{L}{D} + \frac{L^3}{2D^3}. \tag{5.1.27}$$

This function is analogous to the γ_0 function of Porod (1951), employed in the analysis of small-angle scattering data (see p. 12 of Guinier & Fournet, 1955). The size Fourier coefficients for the sphere reach zero at $L = \tau_{hkl} = D$ (τ_{hkl} is thus independent of hkl). We can immediately see [*cf.* equation (5.1.24)] that

$$\beta^* = \left(\int\limits_{-D}^{D} A^S_{\rm sphere}(L)\,{\rm d}L\right)^{-1} = \left[2\int\limits_{0}^{D}\left(1 - \frac{3}{2}\frac{L}{D} + \frac{L^3}{2D^3}\right){\rm d}L\right]^{-1} = \frac{4/3}{\langle D\rangle}. \tag{5.1.28}$$

Using the same approach we can also calculate the common volume of a hollow sphere that represents the case of a non-convex (not simply connected) object. Given a sphere of diameter D and a hole of diameter $d < D$, the common volume depends on the relative diameter and on the range of L. In particular, for $d < D/3$,

$$A^s_{\rm hollow}(L) = \begin{cases} 1 + \dfrac{3(d^2+D^2)L - 2L^3}{2(d^3 - D^3)} & 0 \le L \le d \\[2mm] \dfrac{4d^3 - (D-L)^2(2D+L)}{2(d^3 - D^3)} & d \le L \le (D-d)/2 \\[2mm] \dfrac{3(d^2-D^2)^2 - 16d^3L + 24d^2L^2 - 8L^4}{16(D^3 - d^3)L} & (D-d)/2 \le L \le (D+d)/2 \\[2mm] \dfrac{(D-L)^2(2D+L)}{2(D^3-d^3)} & (D+d)/2 \le L \le D, \end{cases} \tag{5.1.29}$$

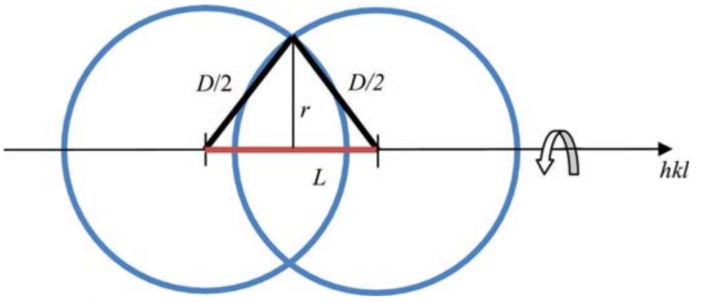

Figure 5.1.3
The intersection of two circles. The case of two spheres is obtained by rotating the system around the *hkl* axis.

whereas for $d \ge D/3$

$$A^s_{\rm hollow}(L) = \begin{cases} 1 + \dfrac{3(d^2+D^2)L - 2L^3}{2(d^3 - D^3)} & 0 \le L \le (D-d)/2 \\[2mm] \dfrac{3(D-d)(d+D)^2}{16(d^2+dD+D^2)L} & (D-d)/2 \le L \le d \\[2mm] \dfrac{3(d^2-D^2)^2 - 16d^3L + 24d^2L^2 - 8L^4}{16(D^3 - d^3)L} & d \le L \le (D+d)/2 \\[2mm] \dfrac{(D-L)^2(2D+L)}{2(D^3-d^3)} & (D+d)/2 \le L \le D. \end{cases} \tag{5.1.30}$$

The function is continuous, but defined over intervals: equation (5.1.29) reduces piecewise to the spherical case [equation (5.1.27)] when the inner diameter d is zero.

Things are more complex for any other (anisotropic) shape, as the CVF becomes a function of *hkl*. Taking the cube as an example, and working with a cubic lattice (Stokes & Wilson, 1942), the common volume for a displacement along $\langle h00\rangle$ is a prism with square base:

$$A^s_{\rm cube,100}(L) = 1 - (L/D) \tag{5.1.31}$$

with $\tau_{100} = D$, whereas for $\langle 111\rangle$ for example, we have

$$A^s_{\rm cube,111}(L) = \left(1 - \frac{L}{(3)^{1/2}D}\right)^3 \tag{5.1.32}$$

with $\tau_{111} = 3^{1/2}D$. The general equation for $h \ge k \ge l$ takes the form

$$A^s_{\rm cube,hkl}(L) = \left(1 - A\frac{L}{D}\right)\left(1 - B\frac{L}{D}\right)\left(1 - C\frac{L}{D}\right), \tag{5.1.33}$$

where $H = (h^2 + k^2 + l^2)^{1/2}$, $A = h/H$, $B = k/H$, $C = l/H$ and $\tau_{hkl} = D/A$. The formulae can be extended to the general lattice (lowest symmetry) by representing the *hkl* peak in the orthogonal frame defined by $\hat{\mathbf{e}}_1 \parallel \hat{\mathbf{a}}$, $\hat{\mathbf{e}}_3 \parallel \hat{\mathbf{c}}^*$ and $\hat{\mathbf{e}}_2 = \hat{\mathbf{e}}_3 \times \hat{\mathbf{e}}_1$ where $\hat{\mathbf{a}}$, $\hat{\mathbf{b}}$, $\hat{\mathbf{c}}$ and $\hat{\mathbf{a}}^*$, $\hat{\mathbf{b}}^*$, $\hat{\mathbf{c}}^*$ are, respectively, the direct- and reciprocal-lattice unit vectors (Giacovazzo *et al.*, 1991). From the metric tensor for the lattice,

$$\mathbf{G} = \begin{pmatrix} \mathbf{a}\cdot\mathbf{a} & \mathbf{a}\cdot\mathbf{b} & \mathbf{a}\cdot\mathbf{c} \\ \mathbf{b}\cdot\mathbf{a} & \mathbf{b}\cdot\mathbf{b} & \mathbf{b}\cdot\mathbf{c} \\ \mathbf{c}\cdot\mathbf{a} & \mathbf{c}\cdot\mathbf{b} & \mathbf{c}\cdot\mathbf{c} \end{pmatrix} = \begin{pmatrix} a^2 & ab\cos\gamma & ac\cos\beta \\ ab\cos\gamma & b^2 & bc\cos\alpha \\ ac\cos\beta & bc\cos\alpha & c^2 \end{pmatrix}, \tag{5.1.34}$$

we can compute the unit-cell volume:

Table 5.1.1

Coefficients for the calculation of the common volume function for a sphere, cube, tetrahedron and octahedron

Adapted from Scardi & Leoni (2001), assuming $H_0^c = 1$ and $\tau_{hkl} = DK_{hkl}$. See the text for the meaning of A, B, C. The errors present in Stokes & Wilson (1942) and Scardi & Leoni (2001) have been corrected.

			Tetrahedron		Octahedron	
Coefficient	Sphere	Cube	$A \geq B + C$	$A \leq B + C$	$A \geq B + C$	$A \leq B + C$
H_1^c	$-3/2$	$-(A + B + C)$	$-3(2^{1/2})A$	$-3(A + B + C)/(2^{1/2})$	$-3A/(2)^{1/2}$	$-3(A + B + C)/(8^{1/2})$
H_2^c	0	$AB + BC + CA$	$6A^2$	$3(A + B + C)^2/2$	$3(A^2 - B^2 - C^2)/2$	$-3[A^2 + (B - C)^2 - 2A(B + C)]/4$
H_3^c	1/2	$-ABC$	$-2(2^{1/2})A^3$	$-(A + B + C)^3/2(2^{1/2})$	$-[A^3 + 3A(B^2 + C^2) + 2(B^3 + C^3)]/2(2^{1/2})$	$(A^3 + B^3 + C^3 - 3ABC)/(2^{1/2})$
K_{hkl}	1	$1/A$	$1/(2^{1/2}A)$	$2^{1/2}/(A + B + C)$	$2^{1/2}/(A + B + C)$	$2^{1/2}/(A + B + C)$

$$\begin{aligned} V_c^2 &= \det(\mathbf{G}) \\ &= a^2b^2c^2\left(1 + 2\cos\alpha\cos\beta\cos\gamma - \cos^2\alpha - \cos^2\beta - \cos^2\gamma\right) \end{aligned} \tag{5.1.35}$$

and, through Cholesky decomposition, $\mathbf{G} = \mathbf{M}^{-1} \cdot (\mathbf{M}^{-1})^T$, the orthogonalization matrix $\mathbf{M}$. This will give us the general values for the A, B and C coefficients appearing in (5.1.33):

$$\begin{aligned} \begin{pmatrix} A \\ B \\ C \end{pmatrix} &= \frac{1}{|\mathbf{H}_{hkl}|}\mathbf{M} \cdot \begin{pmatrix} h \\ k \\ l \end{pmatrix} \\ &= d_{hkl}\begin{pmatrix} 1/a & 0 & 0 \\ -\cos\gamma/(a\sin\gamma) & 1/(b\sin\gamma) & 0 \\ a^*\cos\beta^* & b^*\cos\alpha^* & c^* \end{pmatrix} \cdot \begin{pmatrix} h \\ k \\ l \end{pmatrix}, \end{aligned} \tag{5.1.36}$$

where the modulus of the scattering vector is

$$\begin{aligned} |\mathbf{H}_{hkl}|^2 &= \begin{pmatrix} h & k & l \end{pmatrix}\mathbf{G}^{-1}\begin{pmatrix} h \\ k \\ l \end{pmatrix} \\ &= (h\mathbf{a}^* + k\mathbf{b}^* + l\mathbf{c}^*) \cdot (h\mathbf{a}^* + k\mathbf{b}^* + l\mathbf{c}^*) = \frac{1}{d_{hkl}^2} \\ &= \left[(ha^*)^2 + (kb^*)^2 + (lc^*)^2 + 2hka^*b^*\cos\gamma^* + 2hla^*c^*\cos\beta^* \right. \\ &\quad \left. + 2klb^*c^*\cos\alpha^*\right] \\ &= \frac{a^2b^2c^2}{V_c^2}\left[\frac{h^2\sin^2\alpha}{a^2} + \frac{k^2\sin^2\beta}{b^2} + \frac{l^2\sin^2\gamma}{c^2} \right. \\ &\quad + 2\frac{hk}{ab}(\cos\alpha\cos\beta - \cos\gamma) + 2\frac{kl}{bc}(\cos\beta\cos\gamma - \cos\alpha) \\ &\quad \left. + 2\frac{lh}{ac}(\cos\alpha\cos\gamma - \cos\beta)\right]. \end{aligned} \tag{5.1.37}$$

The values computed from equation (5.1.36),

$$\begin{aligned} A &= hd_{hkl}/a \\ B &= -hd_{hkl}\cos\gamma/(a\sin\gamma) + kd_{hkl}/(b\sin\gamma) \\ &= -A\tan\gamma + kd_{hkl}/(b\sin\gamma) \\ C &= hd_{hkl}a^*\cos\beta^* + kd_{hkl}b^*\cos\alpha^* + ld_{hkl}c^* \\ &= hd_{hkl}\frac{bc(\cos\alpha\cos\gamma - \cos\beta)}{V_c\sin\gamma} + kd_{hkl}\frac{ac(\cos\beta\cos\gamma - \cos\alpha)}{V_c\sin\gamma} \\ &\quad + ld_{hkl}\frac{ab\sin\gamma}{V_c}, \end{aligned} \tag{5.1.38}$$

must be then sorted in such a way that $A \geq B \geq C$. This replaces the sorting of Miller indices ($h \geq k \geq l$) proposed for the cubic case and still allows us to write $\tau_{hkl} = D/A$. In the cubic case ($a = b = c$, $\alpha = \beta = \gamma = 90°$), we have

$$d_{hkl} = \frac{a}{(h^2 + k^2 + l^2)^{1/2}} \tag{5.1.39}$$

and (5.1.38) reduces to the previously known result.

An analogous reasoning was employed by Popa & Balzar (2008) to obtain the CVF of an ellipsoid and that of an elliptical cylinder.

The integral breadth of the profile of a cube-shaped crystallite can be easily calculated from equation (5.1.33) as

$$\begin{aligned} \beta^* &= \left(\int_0^{D/A} 2A^S_{\text{cube},hkl}(L)\,\mathrm{d}L\right)^{-1} \\ &= \left[2\int_0^{D/A}\left(1 - A\frac{L}{D}\right)\left(1 - B\frac{L}{D}\right)\left(1 - C\frac{L}{D}\right)\mathrm{d}L\right]^{-1} \\ &= \frac{6h^3}{DH(6h^2 - 2hk + kl - 2lh)}. \end{aligned} \tag{5.1.40}$$

The common volume functions for a wide set of convex objects can be found *e.g.* in Stokes & Wilson (1942) (sphere and simple polyhedra), Lele & Anantharaman (1966) (triangular, square, hexagonal prisms and cylinder), Wilson (1969) (cylinders, prisms, hemispheres), Langford & Louër (1982) (cylinders), Vargas *et al.* (1983) (hexagonal prisms), Grebille & Bérar (1985) (convex polyhedra), Scardi & Leoni, 2001 (sphere, simple and general polyhedra, distributions of spheres and polyhedra) and Leonardi *et al.* (2012) (general case, fast numerical calculation). Patterson (1939*b*) and Allegra & Wilson (1983) give some hints on how to work with linearly transformed objects as well.

As a general rule, complex convex polyhedra can be decomposed into a finite number of simpler convex polyhedra [*cf.* Grebille & Bérar (1985) and Scardi & Leoni (2001)], leading to the general result that the common volume function for any convex polyhedron is a cubic function of L:

$$\begin{aligned} A^S_{hkl}(L) &= 1 + H_1\frac{L}{D} + H_2\left(\frac{L}{D}\right)^2 + H_3\left(\frac{L}{D}\right)^3 = \sum_{n=0}^{3} H_n\left(\frac{L}{D}\right)^n, \\ A^S_{hkl}(L \geq \tau_{hkl}) &= 0, \end{aligned} \tag{5.1.41}$$

where τ_{hkl}, H_1, H_2 and H_3 are functions of hkl. The coefficient $H_0 = 1$. Equation (5.1.41) is written in terms of a variable L normalized by a characteristic length D; a polynomial in the sole L can also be employed. Table 5.1.1 presents a collection of data for polyhedral shapes that can be observed, for example, in nanosized powders of cubic systems. Equation (5.1.38) can be used to calculate the (sorted) values of A, B, and C entering Table 5.1.1.

As shown by Leonardi *et al.* (2012), the CVF of a non-convex polyhedron can be calculated in a straightforward way by suitably considering the CVF of the hole with the correct sign. The function is still a cubic in L, but it is defined piecewise: however, once the CVF is known, all general calculations proposed here can also be applied to this case.

For some non-polyhedral shapes (notably for cylinders), the common volume function is not a cubic in L. In fact, as shown *e.g.* by Lele & Anantharaman (1966) and reprised by Langford & Louër (1982), the size Fourier term for a cylinder of diameter D and height H displaced by a quantity L along a direction hkl making an angle φ with the cylinder axis is

$$A^{S}_{\text{cylinder},hkl}(L) = (2/\pi)(1 - T\alpha)\Big[\arccos(\alpha) - \alpha\big(1-\alpha^2\big)^{1/2}\Big], \tag{5.1.42}$$

where $\alpha = (L/D)\sin\varphi$, $\Phi = \tan^{-1}(D/H)$ and $T = \tan\Phi/\tan\varphi$. The value of τ_{hkl} depends on φ: for $0 \le \varphi \le \Phi$, $\tau_{hkl} = H/\cos\varphi$, whereas for $\Phi \le \varphi \le \pi/2$, $\tau_{hkl} = D/\sin\varphi$. The calculation of the CVF in these cases cannot be easily generalized. The object can, however, be represented as a polyhedron with a large number of faces and the general approach of Leonardi *et al.* (2012), for example, can be employed for the calculation. We can observe a convergence of this solution with the analytical one when increasing the number of faces. For very small domains, the polyhedral approximation can be considered as physically more plausible than the corresponding continuum case, as the atomic nature of the atomic aggregate starts to play a role.

5.1.6. Calculation of the intensity profile for simple shapes

According to equation (5.1.22), the knowledge of the common volume function suffices to calculate the corresponding diffraction profile in reciprocal space. For a single sphere, the intensity profile assumes a particularly simple mathematical form (Wilson, 1962):

$$\begin{aligned} I_{\text{Wilson}}(s) &\propto 2\int_0^D A^S_{\text{sphere}}(L)\cos(2\pi sL)\,\mathrm{d}L \\ &= 2\int_0^D \left(1 - \frac{3}{2}\frac{L}{D} + \frac{1}{2}\frac{L^3}{D^3}\right)\cos(2\pi sL)\,\mathrm{d}L \\ &= \frac{3}{4}D\left(\frac{1 + 2\psi^2 - \cos 2\psi - 2\psi\sin 2\psi}{2\psi^4}\right) \\ &= \frac{3}{4}D\left(\frac{1 - 2\,\mathrm{sinc}\,2\psi + \mathrm{sinc}^2\psi}{\psi^2}\right) \\ &= \frac{3}{4}D\left(\frac{\psi^2 - \psi\sin 2\psi + \sin^2\psi}{\psi^4}\right), \end{aligned} \tag{5.1.43}$$

where $\psi = \pi sD$. The integral breadth of this profile gives a size value of

$$\begin{aligned} \beta^* &= \frac{1}{I_{\text{Wilson}}(0)}\int_{-\infty}^{\infty} I_{\text{Wilson}}(s)\,\mathrm{d}s \\ &= \frac{2}{I_{\text{Wilson}}(0)}\int_0^{\infty} I(s)\,\mathrm{d}s = \frac{4/3}{\langle D\rangle} \\ &\to \langle D\rangle = \frac{4}{3}\frac{1}{\beta^*} \end{aligned} \tag{5.1.44}$$

in agreement with the result previously found [*cf.* equation (5.1.28)]. The Scherrer constant is $K_\beta = 4/3$ if we deal with the diameter, and becomes almost unity $[(4/3)(\pi/6)^{1/3} = 1.0747]$ if we consider the cube root of the volume.

An interesting extension of equation (5.1.43) was proposed by Allegra & Wilson (1983): a linear transformation of the real space (or, analogously, of the domain shape) is reflected in a linear transformation of the reciprocal space by a factor R. If $(\mathbf{a}_1^*, \mathbf{b}_1^*, \mathbf{c}_1^*)$ is the basis of the reciprocal space for the transformed (non-regular) domain, p_a, p_b and p_c are the sizes of such a domain along these basis directions, p is the unique size parameter of the corresponding regular-shaped crystallite and $(h_1k_1l_1)$ are the Miller indices of the peak in the transformed lattice, then R can be defined as (Allegra & Wilson, 1983)

$$\begin{aligned} R &= \big[(h_1a_1^*)^2 + (k_1b_1^*)^2 + (l_1c_1^*)^2 + 2(h_1a_1^*)(k_1b_1^*)\cos\gamma^* \\ &\quad + 2(h_1a_1^*)(l_1c_1^*)\cos\beta^* + 2(k_1b_1^*)(l_1c_1^*)\cos\alpha^*\big]^{1/2} \\ &\quad \times \left\{p\Big[\big(a_1a_1^*q_h/p_a\big)^2 + \big(b_1b_1^*q_k/p_b\big)^2 + \big(c_1c_1^*q_l/p_c\big)^2\Big]^{1/2}\right\}^{-1} \\ &= \left(pd_{h_1k_1l_1}\big[(\sin\alpha_1 q_h/p_a)^2 + (\sin\beta_1 q_k/p_b)^2 + (\sin\gamma_1 q_l/p_c)^2\big]^{1/2}\right)^{-1}, \end{aligned} \tag{5.1.45}$$

where

$$\begin{pmatrix} q_h \\ q_k \\ q_l \end{pmatrix} = \begin{pmatrix} a_1^*h_1 & b_1^*k_1 & c_1^*l_1 \end{pmatrix} \begin{pmatrix} 1 & \cos\gamma^* & \cos\beta^* \\ \cos\gamma^* & 1 & \cos\alpha^* \\ \cos\beta^* & \cos\alpha^* & 1 \end{pmatrix}. \tag{5.1.46}$$

For instance, the diffraction intensity for an ellipsoid with axes p_a, p_b and p_c along the coordinates axes (a linear transformation of the sphere of diameter p) can be computed from (5.1.43) by replacing $\psi = \pi sD$ with $\psi_R = \pi sRD$.

It is possible to further generalize the result of equation (5.1.43) by using equation (5.1.41). The finite order of the polynomial allows integrating equation (5.1.22) by parts leading to (Wilson, 1962)

$$\begin{aligned} I(s) &\propto \frac{1}{U}2\Bigg\{\left[V(L)\frac{\sin(2\pi sL)}{2\pi s}\right]_0^{\tau_{hkl}} + \left[V'(L)\frac{\cos(2\pi sL)}{(2\pi s)^2}\right]_0^{\tau_{hkl}} \\ &\quad - \left[V''(L)\frac{\sin(2\pi sL)}{(2\pi s)^3}\right]_0^{\tau_{hkl}} - \left[V'''(L)\frac{\cos(2\pi sL)}{(2\pi s)^4}\right]_0^{\tau_{hkl}} \\ &\quad + \int_0^{\tau} V^{IV}(L)\frac{\cos(2\pi sL)}{(2\pi s)^4}\,\mathrm{d}L\Bigg\} \\ &= \frac{1}{U}\big[a_1\psi^{-2} + a_2\psi^{-2}\cos(2\psi) + a_3\psi^{-3}\sin(2\psi) \\ &\quad + a_4\psi^{-4}(1 - \cos(2\psi))\big] \\ &= \frac{V(0)}{U}\big[b_1\psi^{-2} + b_2\psi^{-2}\cos(2\psi) + b_3\psi^{-3}\sin(2\psi) \\ &\quad + b_4\psi^{-4}(1 - \cos(2\psi))\big], \end{aligned} \tag{5.1.47}$$

where $\psi = \pi s\tau_{hkl}$, $a_1 = -\tau_{hkl}^2 V'(0)/2$, $a_2 = \tau_{hkl}^2 V'(\tau_{hkl})/2$, $a_3 = -\tau_{hkl}^3 V''(\tau_{hkl})/4$ and $a_4 = \tau_{hkl}^4 V'''(\tau_{hkl})/8$. The b_i coefficients can be calculated as $b_i = a_i/V(0)$ and allow the description of the intensity using the size Fourier coefficients. The cubic nature of the CVF guarantees that the last integral in (5.1.47) is identically null. For the spherical case, we can easily see that $\tau_{hkl} = D$, $a_1 = \pi D^4/8$, $a_2 = 0$, $a_3 = \pi D^4/8$ and $a_4 = \pi D^4/16$ or $b_1 = 3D/4$,

$b_2 = 0$, $b_3 = 3D/4$ and $b_4 = 3D/8$, and equation (5.1.43) is recovered. Hints are given later in the chapter on the interpretation of some of these coefficients.

The simplification of equation (5.1.47) cannot be applied to a shape showing some odd trend in the Fourier terms [*e.g.* the cylinder discussed in equation (5.1.42)]: the integration in this case has to be done analytically (or numerically) *via* equation (5.1.22).

5.1.7. Meaning of the size Fourier coefficients: mean size and column-length distribution

An interpretation of the size Fourier coefficients and some insight into the possibility of extracting domain-size distribution information comes directly from the works of Bertaut (1949*a*,*b*, 1950) and Warren & Averbach (1950).[1] The form of the scattered intensity equation is the same as that of a set of linear lattices orthogonal to the diffraction planes: each scattering domain can thus be thought of as an ensemble of columns of cells oriented along the scattering direction and diffracting independently from the others.[2] The common volume function 'samples' those columns, quantifying those having the same length. For a given shape we can therefore build a column-length distribution (CLD) $p(M)$, such that $p(M)\,\mathrm{d}M$ gives the fraction of columns with a length between M and $M + \mathrm{d}M$. For instance, $p(M) = 2M/D^2$ for a sphere of diameter D. Without changing the formalism presented so far, Bertaut introduces the additional function

$$t(L) = A^S_{hkl}(L) \Big/ \left(- \frac{\partial A^S_{hkl}(L)}{\partial L} \bigg|_{L=0} \right). \tag{5.1.48}$$

This function leads to some remarkable results. In fact, we can see that

$$t(0) = \langle D \rangle \;\Leftrightarrow\; \langle D \rangle = \left(- \frac{\partial A^S_{hkl}(L)}{\partial L} \bigg|_{L=0} \right)^{-1}, \tag{5.1.49}$$

i.e. the initial slope of the Fourier coefficients is the average domain size. The value is not the same as the one that comes from the integral breadth evaluation. As the Fourier coefficients are normalized, this also represents the intercept of the initial slope tangent with the abscissa (Fig. 5.1.4). We also have

$$\int_{-\infty}^{\infty} t(L)\,\mathrm{d}L = \langle D^2 \rangle, \tag{5.1.50}$$

$$-\frac{\partial t(L)}{\partial L} = \int_L^{\infty} p(M)\,\mathrm{d}M \Leftrightarrow \frac{\partial A^S_{hkl}(L)}{\partial L} = -\frac{1}{\langle D \rangle} \int_L^{\infty} p(M)\,\mathrm{d}M, \tag{5.1.51}$$

$$\frac{\partial^2 t(L)}{\partial L^2} = p(L) \Leftrightarrow \frac{\partial^2 A^S_{hkl}(L)}{\partial L^2} = \frac{p(L)}{\langle D \rangle} \tag{5.1.52}$$

and thus the second derivative of the size Fourier coefficients is proportional to the CLD. It is worth stressing that the CLD is not the size distribution of the system: nothing can be said about the domains unless a proper modelling is done for the columns assembly.

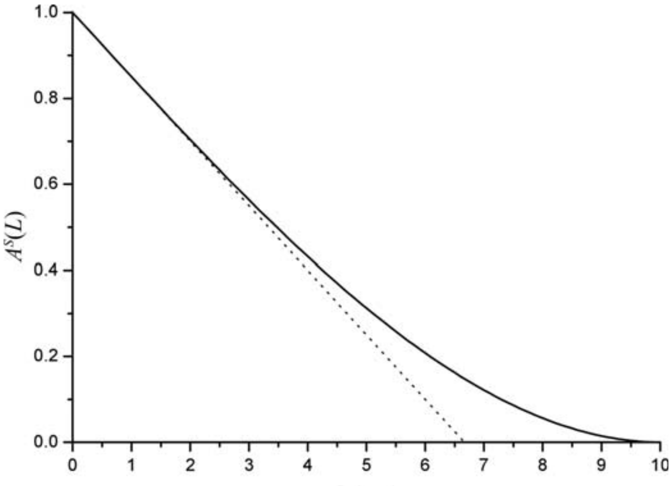

Figure 5.1.4
Size Fourier term for a sphere of 10 nm and tangent to the origin (initial slope).

For the sphere,

$$t(L) = \left(1 - \frac{3}{2}\frac{L}{D} + \frac{L^3}{2D^3} \right) \Big/ \left(\frac{3}{2D} \right) = \frac{(D-L)^2(2D+L)}{3D^2}, \tag{5.1.53}$$

$$\langle D \rangle = \left(- \frac{\partial A^S_{hkl}(L)}{\partial L} \bigg|_{L=0} \right)^{-1} = \left(\frac{3}{2D} \left(1 - \frac{L^2}{D^2} \right) \bigg|_{L=0} \right)^{-1} = \frac{2D}{3}, \tag{5.1.54}$$

$$p(L) = \langle D \rangle \frac{\partial^2 A^S_{hkl}(L)}{\partial L^2} = \frac{2D}{3} \times \frac{3L}{D^3} = \frac{2L}{D^2}. \tag{5.1.55}$$

A case where the CLD coincides with the size distribution (at least along one direction) is that of clays, as the domains are platelets with extended parallel faces (see *e.g.* Eberl *et al.*, 1996; Drits *et al.*, 1997).

The results of Bertaut place some restraints on the possible shape of a peak profile: it is in fact a misconception that peak profiles due to size contributions should be Voigtians. In fact, if we take the normalized Fourier transform of a Voigt function, $T_V(L)$ (Langford, 1978),

$$T_V(L) = \exp\left(-2\beta_C L - \pi^2 \beta_G^2 L^2\right), \tag{5.1.56}$$

where β_C and β_G are, respectively, the Cauchy and Gauss integral breadths, we obtain a column-length distribution $p_V(L)$,

$$p_V(L) = \left[4\left(\beta_C + \pi \beta_G^2 L\right)^2 - 2\pi\beta_G^2 \right] T_V(L). \tag{5.1.57}$$

Therefore, when $\beta_G \geq \beta_C (2\pi)^{1/2}$, $p_V(L)$ is negative for $0 \leq L \leq [\beta_G (2\pi)^{1/2} - 2\beta_C]/2\pi\beta_G^2$.

5.1.8. Extension of the Fourier approach to a size distribution

To what extent can the Scherrer formula be employed to the study of a real powder where a distribution of sizes is present? In 1955, Stokes wrote '*...It must be observed that this volume-average is all that we can find from measurements of breadths; we cannot find out anything about the distribution of sizes...*' (Stokes, 1955). In fact, the information on the distribution is contained in the whole profile and not in the breadth alone. Sixty years after the Scherrer equation, Langford & Wilson (1978) stated that '*. . . if there is a distribution of sizes, a modified Scherrer constant must be used*': however, the justification behind the use of a different Scherrer constant implies some *a priori* knowledge of the distribution.

---

[1] These authors state '*This important result has already been obtained by M. F. Bertaut by essentially the same method. The treatment given here is one developed by the authors before they were aware of Bertaut's work and it has been included here so as to present the particle size theory in the same notation used for distortion broadening.*' (Warren & Averbach, 1950).

[2] '*dans la méthode Debye–Scherrer un cristal est équivalent a un certain ensemble de réseaux linéaires et indépendants*' (Bertaut, 1950).

Several authors over the years have tried to propose a formalism to extract a size distribution from the diffraction data. The first milestone was the systematic work of Jones (1938), which among the several results shows that the size obtained from the integral breadth is the ratio of the fourth and third moments of the size distribution [Jones, 1938, equations (32)–(34)]. For a sufficiently large number of domains this results in

$$\langle D\rangle_{\rm IB}=\frac{\int_0^\infty p(D)D^4\,{\rm d}D}{\int_0^\infty p(D)D^3\,{\rm d}D},\quad \langle D\rangle_{\rm true}=\frac{\int_0^\infty p(D)D\,{\rm d}D}{\int_0^\infty p(D)\,{\rm d}D},\qquad(5.1.58)$$

where $\langle D\rangle_{\rm IB}$ and $\langle D\rangle_{\rm true}$ are, respectively, the size that we can measure *via* the integral breadth and the one that we would like to obtain. Jones obtained the arithmetic mean $\langle D\rangle_{\rm true}$ for a (non-physical) Gaussian distribution and for a Maxwellian one. The size obtained from the integral-breadth analysis is therefore a volume-weighted one. It can be also demonstrated that the size obtained from the Fourier analysis is an area-weighted one. The latter can be obtained as the ratio between the third and second moments of the distribution (Wilson, 1968):

$$\langle D\rangle_{\rm Fourier}=\frac{\int_0^\infty p(D)D^3\,{\rm d}D}{\int_0^\infty p(D)D^2\,{\rm d}D}.\qquad(5.1.59)$$

Therefore, if we know the two size values and we impose the type of distribution, we can obtain information on the first moment [see *e.g.* Krill & Birringer (1998) for the lognormal case].

A further discussion on the Fourier coefficients was presented by Smith (1976): with the intent of comparing the size measured from a transmission electron microscope (TEM) micrograph with that obtained from diffraction, he proposed the possibility of recovering the domain-size distribution directly from the column-length distribution, once the shape of the domain (and thus the common volume function) is known. Following Smith (1976), if the number of domains with sizes between A and A + dA is $G(A)$ dA and the number of columns with lengths between L and L + dL is given by $f(L, A)$dL, then the total number dN of columns with lengths between L and L + dL is

$${\rm d}N=p(L)\,{\rm d}L=\int\limits_{A_0(L)}^{\infty}f(L,A)G(A)\,{\rm d}A\,{\rm d}L,\qquad(5.1.60)$$

where $A_0(L)$ is the smallest A that can accommodate a column of length L. The column-length distribution $p(L)$, as seen previously [*cf.* equation (5.1.52)], is the second derivative of the Fourier coefficients. It is therefore possible, in principle, to obtain the size distribution $G(A)$ by suitably taking a derivative of the column-length distribution. Unfortunately the procedure, albeit correct from a mathematical point of view, can rarely be applied in practice for the estimation of the size distribution. It is in fact necessary to strip off the other sources of broadening and take a higher-order derivative of the (experimental) Fourier coefficients: noise can be a real issue with this (Le Bail & Louër, 1978).

A decade later, Rao & Houska (1986) started from the same point, but instead of extracting the size distribution from the CLD, they worked the other way round, deriving an approximate expression for $p(L)$ and using it to generate the size Fourier coefficients and build the profile. Vogel (1990) proposed a similar approach, based on the properties of the column-size distribution. To be a distribution, the CLD must in fact obey two simple rules:

$$\left.\frac{\partial^2A^S_{hkl}(L)}{\partial L^2}\right|_{L=0}=\left.\frac{p(L)}{\langle D\rangle}\right|_{L=0}=0,\qquad(5.1.61)$$

$$\lim_{L\to\infty}\frac{\partial^2A^S_{hkl}(L)}{\partial L^2}=\lim_{L\to\infty}\frac{p(L)}{\langle D\rangle}=0.\qquad(5.1.62)$$

A suitable class of functions possessing those two properties is of the type

$$A^S_{hkl}(L,D)=P(L/D)\exp(-L/D),\quad P(L/D)=\sum_{k=0}^{k_{\rm max}}a_kL^k\big/D^k.\qquad(5.1.63)$$

Vogel proposed two shapes for the function P above (identified as types I and II):

$$\text{I:}\quad a_0=1,\quad a_1=1/2,\qquad(5.1.64)$$

$$\text{II:}\quad a_0=1,\quad a_1=7/10,\quad a_2=1/5,\quad a_3=1/40.\qquad(5.1.65)$$

For spherical domains, the size distribution $H(D)$ compatible with the given CLD is proportional to

$$H(D)=\frac{\rm d}{{\rm d}L}\left.\left(\frac{1}{L}\frac{\partial^2A^S_{hkl}(L)}{\partial L^2}\right)\right|_{L=D}.\qquad(5.1.66)$$

The corresponding peak profile, obtained by Fourier transform, reads

$$I(x)=2D\sum_{k=0}^{k_{\rm max}}k!a_k{\rm Re}\big(u^{-k-1}\big),\quad u=1-2\pi ixD.\qquad(5.1.67)$$

If, according to (5.1.64), we set a_0 = 1 and $a_1=\frac{1}{2}$, we obtain a profile described as the sum of a Lorentzian and a squared Lorentzian:

$$I(x)=\big(1+4\pi^2x^2D^2\big)^{-1}+2\big(1+4\pi^2x^2D^2\big)^{-2}.\qquad(5.1.68)$$

The calculation of the profile for a polydisperse system is much simpler if we pass through the common volume function. The diffraction profile of an ensemble of scattering domains scattering incoherently with respect to one another is in fact the sum of the diffraction profiles from each of those domains. In turn, each domain contributes with a scattering power proportional to its volume (*i.e.* the number of scattering centres). For the *hkl* profile of a distribution of objects of shape *c*, we have

$$\begin{aligned}I_{c,hkl}(s)&\propto\frac{\int_0^\infty I_{c,hkl}(s,D)g(D)V_c(D)\,{\rm d}D}{\int_0^\infty g(D)V_c(D)\,{\rm d}D}\\&=\frac{\int_0^\infty I_{c,hkl}(s,D)w(D)\,{\rm d}D}{\int_0^\infty w(D)\,{\rm d}D},\end{aligned}\qquad(5.1.69)$$

where $g(D)$ is the size distribution function and where $I_{c,hkl}(s, D)$ and $V_c(D)$ are, respectively, the profile and the volume of the domain of shape c and size D. The weighting (or visibility) function $w(D) = g(D)V_c(D)$ is introduced: the larger the volume, the larger the contribution of the corresponding domain(s). If we now insert in equation (5.1.69) the explicit formula for the intensity profile of a single domain of shape c and size D, we obtain

$$
\begin{aligned}
I_{c,hkl}(s) &\propto \frac{\int_0^\infty \left(\int_{L=0}^{D/K_{hkl}} A^S_{c,hkl}(L,D)\exp(2\pi iLs)\,\mathrm{d}L\right) w(D)\,\mathrm{d}D}{\int_0^\infty w(D)\,\mathrm{d}D}\\
&\propto \frac{\int_{L=0}^\infty \left(\int_{D=LK_{hkl}}^\infty A^S_{c,hkl}(L,D)w(D)\,\mathrm{d}D\right)\exp(2\pi iLs)\,\mathrm{d}L}{\int_0^\infty w(D)\,\mathrm{d}D}\\
&\propto \int_{L=0}^\infty \left(\frac{\int_{D=LK_{hkl}}^\infty A^S_{c,hkl}(L,D)w(D)\,\mathrm{d}D}{\int_0^\infty w(D)\,\mathrm{d}D}\right)\exp(2\pi iLs)\,\mathrm{d}L
\end{aligned}
\tag{5.1.70}
$$

with $K_{hkl} = \tau_{hkl}/D$ (see Table 5.1.1). By introducing the Fourier coefficients $A^S_{hkl}(L)$ for the system of domains,

$$
A^S_{hkl}(L) = \frac{\int_{D=LK_{hkl}}^\infty A^S_{c,hkl}(L,D)w(D)\,\mathrm{d}D}{\int_0^\infty w(D)\,\mathrm{d}D},
\tag{5.1.71}
$$

we obtain an expression for the intensity analogous to that of a single domain [*cf.* equation (5.1.22)]:

$$
I(s) \propto \int\limits_{L=0}^{\infty} A^S_{hkl}(L)\exp(2\pi iLs)\,\mathrm{d}L.
\tag{5.1.72}
$$

5.1.9. Analytical distributions

In the general case, it is not possible to obtain the profile of a polydispersed system in closed form, as the existence of an analytical primitive for equation (5.1.72) cannot be guaranteed. It is, however, possible to find solutions both for the Fourier coefficients and for the profiles in some particular cases (Scardi & Leoni, 2001; Scardi *et al.*, 2006). For instance, the Fourier coefficients for a lognormal distribution of D defined as

$$
g_l(D) = \frac{1}{D\sigma_l(2\pi)^{1/2}}\exp\left[-\frac{(\ln D-\mu_l)^2}{2\sigma_l^2}\right]
\tag{5.1.73}
$$

with moments

$$
M_{l,n} = \exp\left(n\mu_l + \frac{n^2}{2}\sigma_l^2\right)
\tag{5.1.74}
$$

can easily be obtained as (Scardi & Leoni, 2001)

$$
\begin{aligned}
&A^S_{l,hkl}(L)\\
&\quad= \int_{D=LK_{hkl}}^\infty \sum\nolimits_{n=0}^3 \left(H^c_n\frac{L^n}{D^n}\right)D^3\frac{1}{D\sigma_l(2\pi)^{1/2}}\\
&\qquad\times \exp\left(-(\log D-\mu_l)^2/\left(2\sigma_l^2\right)\right)\mathrm{d}D\\
&\qquad\times\left[\int_0^\infty D^3\frac{1}{D\sigma_l(2\pi)^{1/2}}\exp\left(-(\log D-\mu_l)^2/\left(2\sigma_l^2\right)\right)\mathrm{d}D\right]^{-1}\\
&\quad= \sum_{n=0}^3 H^c_n\,\mathrm{erfc}\left[\frac{\ln(LK_{hkl})-\mu_l-(3-n)\sigma_l^2}{\sigma_l(2)^{1/2}}\right]\frac{M_{l,3-n}}{2M_{l,3}}L^n,
\end{aligned}
\tag{5.1.75}
$$

whereas the corresponding profile

$$
\begin{aligned}
I_{l,hkl}(s) \propto \int\limits_{L=0}^{\infty}\sum_{n=0}^{3} H^c_n\,\mathrm{erfc}\left[\frac{\ln(LK_{hkl})-\mu_l-(3-n)\sigma_l^2}{\sigma_l(2)^{1/2}}\right]\\
\times\frac{M_{l,3-n}}{2M_{l,3}}L^n\cos(2\pi Ls)\,\mathrm{d}L
\end{aligned}
\tag{5.1.76}
$$

can just be calculated *via* (fast) Fourier transform. Popa & Balzar (2002) and Ida *et al.* (2003) have proposed approximate expressions for the case of spherical domains. Popa & Balzar employed Gauss–Hermite quadrature, leading to a quite large error in the intensity for wide distributions. Ida *et al.* used a smart change of variables and employed Gauss–Legendre quadrature, obtaining a profile that closely resembles the true one.

An alternative to the lognormal is the gamma distribution, defined as

$$
\begin{aligned}
g_p(D) &= \frac{\sigma_p}{\mu_p\Gamma(\sigma_p)}\left(\frac{\sigma_pD}{\mu_p}\right)^{\sigma-1}\exp\left(-\frac{\sigma_pD}{\mu_p}\right),\\
\Gamma(x) &= \int\limits_0^\infty y^{x-1}\exp(-y)\,\mathrm{d}y,
\end{aligned}
\tag{5.1.77}
$$

with moments

$$
M_{p,n} = \left(\frac{\mu_p}{\sigma_p}\right)^n\frac{\Gamma(n+\sigma_p)}{\Gamma(\sigma_p)}.
\tag{5.1.78}
$$

The Fourier coefficients can easily be calculated as (Scardi & Leoni, 2001)

$$
A^S_{p,hkl}(L) = \sum_{n=0}^3 H^c_n\left(\frac{\sigma_p}{\mu_p}\right)^n\frac{\Gamma\left[\sigma_p+(3-n),K_{hkl}L\sigma_p/\mu_p\right]}{\Gamma(\sigma_p+3)}L^n.
\tag{5.1.79}
$$

An approximation of the corresponding line profile was proposed by Popa & Balzar (2002), who employed Gauss–Laguerre quadrature for the calculation. An analytical, albeit wrong, expression was obtained by Pielaszek (2004): its derivation lacks a proper volume weighting. The correct result can be found in Scardi *et al.* (2006) for any polyhedron having a common volume function described by equation (5.1.41). The intensity in this case reads

$$
\begin{aligned}
I_p(s;\mu_p,\sigma_p) = \frac{k(s)\mu_p\Phi^{-(3+\sigma)/2}}{4\psi^3K^3_{hkl}}&\left\{\frac{K_{hkl}\sigma_p(\Phi)^{1/2}}{(2+\sigma_p)}\right.\\
&\times\left[2(3H_3+K_{hkl}(2H_2+H_1K_{hkl}))\psi\cos\left((2+\sigma_p)\Theta\right)\right.\\
&\left.+\frac{K^2_{hkl}}{\psi}\Phi\left(\frac{3H_3\sigma_p}{1+\sigma_p}\left(\Phi^{\sigma/2}-\cos(\sigma_p\Theta)\right)-2H_1\psi^2\Phi^{\sigma/2}\right)\right]\\
&-2\left[\frac{K^2_{hkl}\sigma_p^2\Phi(3H_3+H_2K_{hkl})}{(2+\sigma_p)(1+\sigma_p)}\sin\left((1+\sigma_p)\Theta\right)\right.\\
&\left.\left.-2\psi^2(H_3+K_{hkl}(H_2+K(H_1+H_0K_{hkl})))\sin\left((3+\sigma_p)\Theta\right)\right]\right\},
\end{aligned}
\tag{5.1.80}
$$

where as usual $\psi = \pi s\tau_{hkl}$ and also $\Omega = 2\psi/(K\sigma)$, $\Theta = \tan^{-1}\Omega$ and $\Phi = 1+\Omega^2$. For the case of a lognormal distribution of spheres, equation (5.1.80) reduces to

$$
\begin{aligned}
I_{p,\mathrm{sphere}}(s;\mu,\sigma) = k(s)\frac{3\mu\sigma}{8\psi^4}&\left\{\frac{2\psi^2}{2+\sigma}+\frac{\sigma}{2+3\sigma+\sigma^2}\right.\\
&\times\left[1-\left(1+\left(\frac{2\psi}{\sigma}\right)^2\right)^{-\sigma/2}\cos\left(\sigma\,\mathrm{atan}\left(\frac{2\psi}{\sigma}\right)\right)\right.\\
&\left.\left.-2\psi\left(1+\left(\frac{2\psi}{\sigma}\right)^2\right)^{-(\sigma+1)/2}\sin\left((1+\sigma)\,\mathrm{atan}\left(\frac{2\psi}{\sigma}\right)\right)\right]\right\}.
\end{aligned}
\tag{5.1.81}
$$

5.1.10. Histogram (arbitrary) distributions

An analytical distribution is not always able to describe the observed profiles. In fact, the presence of a multimodal distribution or a complex arrangement cannot be excluded. The Fourier formalism proposed in equation (5.1.70) is still valid in this case. As shown by Leoni & Scardi (2004), the analytical distribution can be replaced by a histogram and the integration thus replaced with a sum over all histogram bins:

$$A^S_{hkl}(L) = \frac{\sum_{k=k_{hkl}}^{n} A^S_{c,hkl}(L, D_k) g(D_k) W_k D_k^3}{\sum_{k=k_{hkl}}^{n} g(D_k) W_k D_k^3},$$
$$\exists k_{hkl} : 1 \le k_{hkl} \le n, D_{\max(1, k_{hkl}-1)} \le L K_{hkl} \le D_{k_{hkl}}, \tag{5.1.82}$$

where n is the number of bins, D_k is the average size corresponding to the kth histogram bin, $g(D_k)$ is the number of domains of average size D_k and W_k is the width of the kth bin (*e.g.* equal to the difference of the D values of consecutive bins in a linear sampling). For a given L the sum runs from the first bin corresponding to a size not smaller than $L\tau_{hkl}$. Very high quality data and a reasonably small number of bins should be employed to avoid the extraction of information from the noise and from the background. Failure to do so often results in the appearance of an unphysical fraction of small domains that represents the contributions of a smooth background and of thermal diffuse scattering. In this case, we can either start the distribution at a larger size or, as suggested by Matěj *et al.* (2011), use Tikhonov regularization and/or a logarithmically sampled histogram to stabilize the algorithm.

An alternative was proposed by David *et al.* (2010), working directly in 2θ space and using the result of Wilson for a single sphere [equation (5.1.43)]: the global profile is simply the weighted sum of the profiles corresponding to each size component.

5.1.11. Example

The determination of the size of the domains in a ceria specimen is described here. The specimen was thoroughly characterized both by diffraction and transmission electron microscopy (Leoni *et al.*, 2004) and the corresponding powder-diffraction pattern is shown in Fig. 5.1.5. The data were collected on a Bragg–Brentano diffractometer showing quite a narrow and symmetrical instrumental profile using Cu $K\alpha$ radiation and a secondary graphite monochromator. The domains are spherical (*cf.* Leoni *et al.*, 2004) and the lattice is face-centred cubic, so most of the calculations can be done analytically. For the practical application of some of the formulae, the software *PM2K* (Leoni *et al.*, 2006) was used.

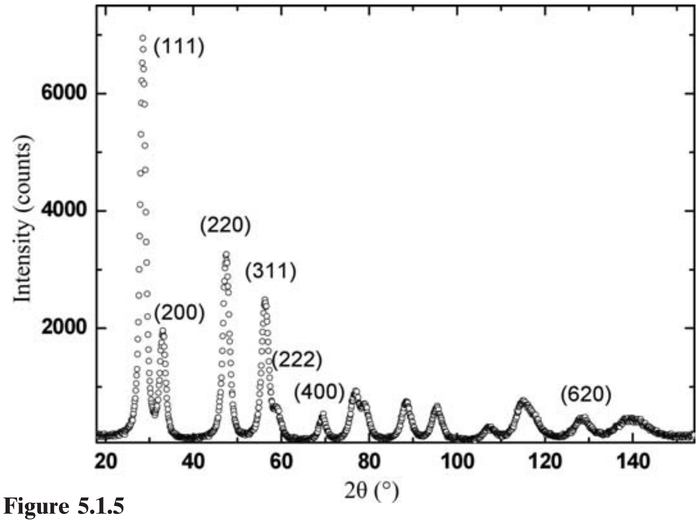

Figure 5.1.5
Nanocrystalline ceria pattern; the indices for some reflections are indicated.

The analysis will be done for the 111 and 200 reflections of ceria using several of the approaches proposed in this chapter. The analysis will be thus limited to the 2θ range 20–40°.

To apply the original Scherrer formula, we can estimate by eye (or using a ruler) the width of the 111 and 200 reflections, as in Fig. 5.1.6(*a*): this results in FWHM_{111} = 1.53° and FWHM_{200} = 1.68°. We cannot resolve the two emission components, we do not have any information on the instrumental effects and the estimation for the smaller peak is definitely more difficult. Scherrer analysis gives

$$\begin{aligned}\left.\frac{\langle D\rangle}{K_w}\right|_{111} &= \frac{\lambda}{\mathrm{FWHM}_{111}\cos\theta_{111}}\\ &= \frac{1.5406\times10^{-1}}{\dfrac{(29.28-27.75)^{\circ}\,\pi}{180^{\circ}}\cos\left(\dfrac{(29.28+27.75)/2^{\circ}}{2}\right)}\ \mathrm{nm}\\ &= 5.95\ \mathrm{nm},\\ \left.\frac{\langle D\rangle}{K_w}\right|_{200} &= \frac{\lambda}{\mathrm{FWHM}_{200}\cos\theta_{200}}\\ &= \frac{1.5406\times10^{-1}}{\dfrac{(33.89-32.21)^{\circ}\,\pi}{180^{\circ}}\cos\left(\dfrac{(33.89+32.21)/2^{\circ}}{2}\right)}\ \mathrm{nm}\\ &= 5.48\ \mathrm{nm}.\end{aligned} \tag{5.1.83}$$

The choice of the wavelength (an average value of 1.5406 Å was employed in this case) is definitely not critical. The two values are slightly different. We can also calculate the integral breadth of the profile, for example by fitting each peak with a couple of Voigt functions (to take the emission profile into account) and considering a linear Chebyshev polynomial background. The FWHM estimated in this way is smaller than the one estimated before (therefore the instrument plays some role, even if the effects cannot be easily seen). The integral-breadth analysis gives in this case (*cf.* Fig. 5.1.6*b*)

$$\left.\frac{\langle D\rangle}{K_\beta}\right|_{111} = \frac{1}{\beta_{111}} = \frac{1.5406\times10^{-1}}{\dfrac{13690.7}{7180.2}\dfrac{\pi}{180}\cos\left(\dfrac{28.5306^{\circ}}{2}\right)}\ \mathrm{nm} = 4.77\ \mathrm{nm}, \tag{5.1.84}$$

$$\left.\frac{\langle D\rangle}{K_\beta}\right|_{200} = \frac{1}{\beta_{200}} = \frac{1.5406\times10^{-1}}{\dfrac{3425.4}{1861.4}\dfrac{\pi}{180}\cos\left(\dfrac{33.0269^{\circ}}{2}\right)}\ \mathrm{nm} = 5.00\ \mathrm{nm}. \tag{5.1.85}$$

We see some differences between the values calculated with the two methods. However, we should remember the different definition of the Scherrer constant in the two cases.

We can also apply the Fourier formalism, using the known common volume function for the sphere. We show at the beginning the best fit of the model to the experimental data. For consistency, neither the instrumental contribution nor other sources of broadening were considered. Fig. 5.1.6(*c*) shows the modelling using the peak profile for a single sphere. It is clear that the oscillations present in the profile [*cf.* equation (5.1.43)] are

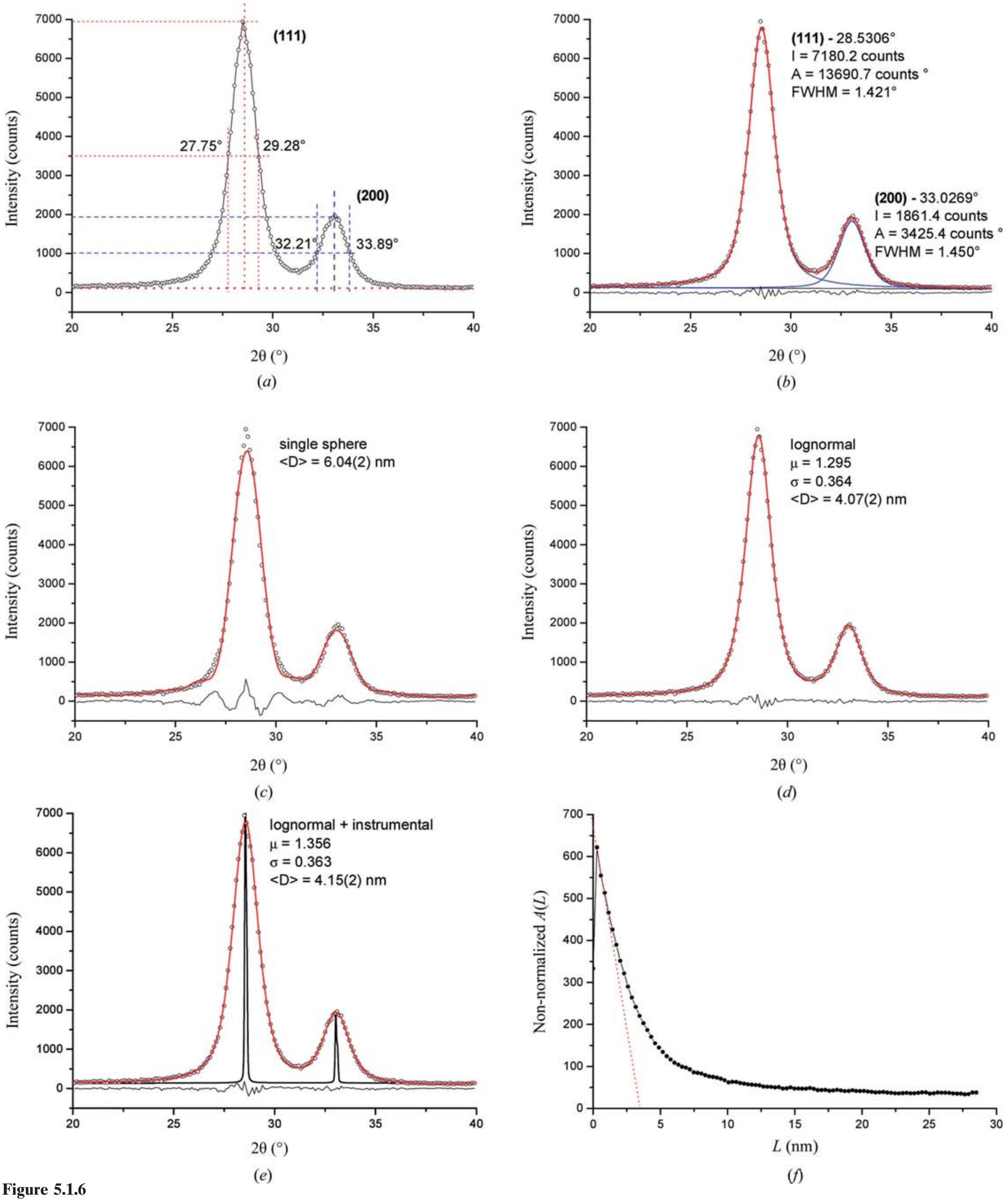

(*a*) (*b*) (*c*) (*d*) (*e*) (*f*)

Figure 5.1.6

Analysis of the 111 and 200 reflections of ceria: (*a*) calculation using the FWHM, (*b*) fit using Voigt functions: the single profiles are shown, (*c*) modelling as a single sphere, (*d*) modelling as a lognormal distribution of spheres, (*e*) comparison of the instrumental profile with the measured profile and modelling using a lognormal distribution of spheres, taking the instrumental contribution into account, and (*f*) cosine Fourier transform of the left side of the 111 peak. The difference between the data and the model is plotted at the bottom of (*b*)–(*e*).

not observed in the experimental pattern and do not allow for a perfect match. The size is highly overestimated. If we consider a lognormal distribution of size [Fig. 5.1.6(*d*) and equation (5.1.76)], we obtain a match quite similar to that of Fig. 5.1.6(*b*), but with a stronger physical meaning (the whole profile shape is compatible with the microstructure).

The instrument plays little role in this case. Fig. 5.1.6(*e*) shows the instrumental profile obtained by collecting the data for the

NIST SRM 660a (LaB_6) line-profile standard, fitting all reflections with pseudo-Voigt functions, parameterizing the profile parameters according to the Caglioti *et al.* (1958) equation and calculating the corresponding peak in the position of the ceria peaks and with a maximum intensity equal to that obtained from Fig. 5.1.6(*b*). The effect of this contribution on the value of the size can be seen at the second decimal place (see the ceria peaks modelling in Fig. 5.1.6*e*). The size value tends to become closer to the average one obtained by TEM (*cf.* Leoni *et al.*, 2004), but cannot reach it, as the other sources of broadening (notably strain) are not considered.

Fig. 5.1.6(*f*) shows what happens if we try to extract the Fourier coefficients from the data: to avoid any biasing introduced by the choice of the profile function, size Fourier coefficients were extracted from the (111) peak of ceria directly. The left tail of the (111) peak, remapped in $s = d^* - d^*_{hkl}$ space, was selected (this limits the problems with the emission-profile doublet). The position of the experimental point corresponding to the peak top ($2\theta = 28.5^\circ$) was chosen as d^*_{hkl}. The point at zero clearly does not follow the trend. This is one of the manifestations of the so-called ‘hook effect’: the causes are several and are all related to the choice of the centre of the peak and of the other (non-size) broadening sources. In our case, we selected the centre in a measured position and not where it was supposed to be. Moreover, the peak is still affected by the emission profile and the neighbouring 222 reflection. If we simply skip the first point, we can indeed calculate an initial slope tangent whose intercept provides an average size of 3.50 nm [which should correspond to an average diameter of 5.25 nm for a delta distribution if we take equation (5.1.54) into account].

References

Adler, T. & Houska, C. R. (1979). *Simplifications in the X-ray line-shape analysis. J. Appl. Phys.* **50**, 3282–3287.

Alexander, L. (1954). *The synthesis of X-ray spectrometer line profiles with application to crystallite size measurements. J. Appl. Phys.* **25**, 155–161.

Allegra, G. & Wilson, A. J. C. (1983). *Line profiles for a collection of identical crystals: effect of a linear transformation of shape. Acta Cryst.* A**39**, 280–282.

Bertaut, E. F. (1949*a*). *Etude aux rayons X de la répartition des dimensions des cristallites dans une poudre cristalline. C. R. Acad. Sci.* **228**, 492–494.

Bertaut, E. F. (1949*b*). *Signification de la dimension cristalline mesuree d'apres la largeur de raie Debye–Scherrer. C. R. Acad. Sci.* **228**, 187–189.

Bertaut, E. F. (1950). *Raies de Debye–Scherrer et repartition des dimensions des domaines de Bragg dans les poudres polycristallines. Acta Cryst.* **3**, 14–18.

Bragg, W. H. (1930). *The Crystalline State*. London: G. Bell & Sons.

Caglioti, G., Paoletti, A. & Ricci, F. P. (1958). *Choice of collimators for a crystal spectrometer for neutron diffraction. Nucl. Instrum.* **3**, 223–228.

David, W. I., Leoni, M. & Scardi, P. (2010). *Domain size analysis in the Rietveld method. Mater. Sci. Forum*, **651**, 187–200.

Drits, V. A., Srodon, J. & Eberl, D. D. (1997). *XRD measurement of mean crystallite thickness of illite and illite/smectite: reappraisal of the Kubler index and the Scherrer equation. Clays Clay Miner.* **45**, 461–475.

Eberl, D. D., Drits, V. A., Srodon, J. & Nüesch, R. (1996). *MUDMASTER: a program for calculating crystallite size distributions and strain from the shapes of X-ray diffraction peaks.* U.S. Geological Survey Open-File Report 96-171.

Giacovazzo, C., Monaco, H. L., Artioli, G., Viterbo, D., Ferraris, G., Gilli, G., Zanotti, G. & Catti, M. (1991). *Fundamentals of Crystallography*, 2nd ed., edited by C. Giacovazzo. New York: Oxford University Press.

Grebille, D. & Bérar, J. F. (1985). *Calculation of diffraction line profiles in the case of a major size effect: application to boehmite AlOOH. J. Appl. Cryst.* **18**, 301–307.

Guinier, A. & Fournet, G. (1955). *Small-Angle Scattering of X-rays*. New York: Wiley.

Howell, R., Proffen, T. & Conradson, S. (2006). *Pair distribution function and structure factor of spherical particles. Phys. Rev. B*, **73**, 1–7.

Ida, T., Shimazaki, S., Hibino, H. & Toraya, H. (2003). *Diffraction peak profiles from spherical crystallites with lognormal size distribution. J. Appl. Cryst.* **36**, 1107–1115.

Jones, F. W. (1938). *The measurement of particle size by the X-ray method. Proc. R. Soc. London Ser. A*, **166**, 16–43.

Jones, F. W. (1941). *Particle size measurement by the X-ray method. J. Sci. Instrum.* **18**, 157–158.

Klug, H. P. & Alexander, L. E. (1974). *X-ray diffraction procedures for polycrystalline and amorphous materials*, 2nd ed. New York: Wiley.

Krill, C. E. & Birringer, R. (1998). *Estimating grain-size distributions in nanocrystalline materials from X-ray diffraction profile analysis. Philos. Mag. A*, **77**, 621–640.

Langford, J. I. (1978). *A rapid method for analysing the breadths of diffraction and spectral lines using the Voigt function. J. Appl. Cryst.* **11**, 10–14.

Langford, J. I. & Louër, D. (1982). *Diffraction line profiles and Scherrer constants for materials with cylindrical crystallites. J. Appl. Cryst.* **15**, 20–26.

Langford, J. I. & Louër, D. (1996). *Powder diffraction. Rep. Prog. Phys.* **59**, 131–234.

Langford, J. I. & Wilson, A. J. C. (1978). *Scherrer after sixty years: a survey and some new results in the determination of crystallite size. J. Appl. Cryst.* **11**, 102–113.

Laue, M. von (1926). *Lorentz-Faktor und Intensitätsverteilung in Debye-Scherrer-Ringen. Z. Kristallogr.* **64**, 115–142.

Le Bail, A. & Louër, D. (1978). *Smoothing and validity of crystallite-size distributions from X-ray line-profile analysis. J. Appl. Cryst.* **11**, 50–55.

Lele, S. & Anantharaman, T. R. (1966). *Influence of crystallite shape on particle size broadening of Debye–Scherrer reflections. Proc. Indian Acad. Sci. Sec. A*, **64**, 261–274.

Leonardi, A., Leoni, M., Siboni, S. & Scardi, P. (2012). *Common volume functions and diffraction line profiles of polyhedral domains. J. Appl. Cryst.* **45**, 1162–1172.

Leoni, M., Confente, T. & Scardi, P. (2006). *PM2K: a flexible program implementing whole powder pattern modelling. Z. Kristallogr. Suppl.* **23**, 249–254.

Leoni, M., Maggio, R., Polizzi, S. & Scardi, P. (2004). *X-ray diffraction methodology for the microstructural analysis of nanocrystalline powders: application to cerium oxide. J. Am. Ceram. Soc.* **87**, 1133–1140.

Leoni, M. & Scardi, P. (2004). *Nanocrystalline domain size distributions from powder diffraction data. J. Appl. Cryst.* **37**, 629–634.

Matěj, Z., Matějová, L., Novotný, F., Drahokoupil, J. & Kužel, R. (2011). *Determination of crystallite size distribution histogram in nanocrystalline anatase powders by XRD. Z. Kristallogr. Proc.* **1**, 87–92.

Mittemeijer, E. J. & Scardi, P. (2004). *Diffraction analysis of the microstructure of materials*. Berlin: Springer Verlag.

Pantoja-Cortés, J., Sánchez-Bajo, F. & Ortiz, A. L. (2012). *A line-broadening analysis model for the microstructural characterization of nanocrystalline materials from asymmetric X-ray diffraction peaks. J. Phys. Condens. Matter*, **24**, 215301.

Paterson, M. S. (1952). *The effects of lattice imperfections on X-ray line broadening. J. Appl. Phys.* **23**, 499–500.

Patterson, A. L. (1939*a*). *The Scherrer formula for X-ray particle size determination. Phys. Rev.* **56**, 978–982.

Patterson, A. L. (1939*b*). *The diffraction of X-rays by small crystalline particles. Phys. Rev.* **56**, 972–977.

Pielaszek, R. (2004). *Analytical expression for diffraction line profile for polydispersive powders*. In *Applied Crystallography*, *Proceedings of the XIX CAC Conference*, edited by H. Morawiec & D. Stróż, pp. 43–50. Singapore: World Scientific.

Popa, N. C. & Balzar, D. (2002). *An analytical approximation for a size-broadened profile given by the lognormal and gamma distributions. J. Appl. Cryst.* **35**, 338–346.

Popa, N. C. & Balzar, D. (2008). *Size-broadening anisotropy in whole powder pattern fitting. Application to zinc oxide and interpretation of the apparent crystallites in terms of physical models. J. Appl. Cryst.* **41**, 615–627.

Porod, G. (1951). *Die Röntgenkleinwinkelstreuung von dicht gepackten kolloiden Systemen. 1. Teil. Kolloid Z.* **124**, 83–114.

Rao, S. I. & Houska, C. R. (1986). *X-ray particle-size broadening. Acta Cryst.* A**42**, 6–13.

Scardi, P. & Leoni, M. (2001). *Diffraction line profiles from polydisperse crystalline systems. Acta Cryst.* A**57**, 604–613.

Scardi, P. & Leoni, M. (2002). *Whole powder pattern modelling. Acta Cryst.* A**58**, 190–200.

Scardi, P., Leoni, M. & Faber, J. (2006). *Diffraction line profile from a disperse system: a simple alternative to Voigtian profiles. Powder Diffr.* **21**, 270–277.

Scardi, P., Ortolani, M. & Leoni, M. (2010). *WPPM: microstructural analysis beyond the Rietveld method. Mater. Sci. Forum*, **651**, 155–171.

Scherrer, P. (1918). *Bestimmung der Grösse und der inneren Struktur von Kolloidteilchen mittels Röntgenstrahlen. Nachr. K. Ges. Wiss. Goettingen Math.Phys. Kl.* pp. 98–100.

Scherrer, P. (1922). *Bestimmung der inneren Struktur und der Grosse von Kolloidteilchen mittels Rontgenstrahlen.* In *Kolloidchemie*, edited by R. Zsigmondy, pp. 387–409. Leipzig: Otto Spamer.

Scherrer, P. (1962). *Personal reminiscences.* In *Fifty years of X-ray diffraction*, edited by P. P. Ewald, pp. 642–646. Utrecht: N.V.A. Oosthoek's Uitgeversmaatschappij for the International Union of Crystallography.

Smith, W. L. (1976). *Crystallite shape and the Fourier analysis of diffraction line profiles. J. Appl. Cryst.* **9**, 187–189.

Snyder, R. L., Fiala, J. & Bunge, H. J. (1999). *Defect and Microstructure Analysis by Diffraction*. IUCr Monographs on Crystallography. New York: Oxford University Press.

Stokes, A. R. (1955). *Line profiles.* In *X-ray Diffraction by Polycrystalline Materials*, edited by A. H. Peiser, H. P. Rooksby & A. J. C. Wilson, pp. 409–429. London: The Institute of Physics.

Stokes, A. R. & Wilson, A. J. C. (1942). *A method of calculating the integral breadths of Debye–Scherrer lines. Math. Proc. Cambridge Philos. Soc.* **38**, 313–322.

Stokes, A. R. & Wilson, A. J. C. (1944). *A method of calculating the integral breadths of Debye–Scherrer lines: generalization to non-cubic crystals. Math. Proc. Cambridge Philos. Soc.* **40**, 197–198.

Vargas, R., Louër, D. & Langford, J. I. (1983). *Diffraction line profiles and Scherrer constants for materials with hexagonal crystallites. J. Appl. Cryst.* **16**, 512–518.

Vogel, W. (1990). *Size distributions of supported metal catalysts: an analytical X-ray line profile fitting routine. J. Catal.* **121**, 356–363.

Warren, B. E. (1990). *X-ray Diffraction*, 2nd unabridged ed. New York: Dover Publications.

Warren, B. E. & Averbach, B. L. (1950). *The effect of cold-work distortion on X-ray patterns. J. Appl. Phys.* **21**, 595–599.

Warren, B. E. & Averbach, B. L. (1952). *The separation of cold-work distortion and particle size broadening in X-ray patterns. J. Appl. Phys.* **23**, 497.

Williamson, G. K. & Hall, W. H. (1953). *X-ray line broadening from filed aluminium and wolfram. Acta Metall.* **1**, 22–31.

Wilson, A. J. C. (1962). *X-ray Optics*. London: Methuen.

Wilson, A. J. C. (1968). *On variance as a measure of line broadening in diffractometry: effect of a distribution of sizes on the apparent crystallite size. J. Appl. Cryst.* **1**, 194–196.

Wilson, A. J. C. (1969). *Variance apparent particle sizes for cylinders, prisms and hemispheres. J. Appl. Cryst.* **2**, 181–183.

International Tables for Crystallography (2019). Vol. H, Chapter 5.2, pp. 538–554.

5.2. Stress and strain

N. C. Popa

5.2.1. The importance of determining stress and the diffraction method

The determination of the elastic stress and strain state in polycrystalline samples is one of the oldest applications of the powder diffraction technique. Stress, which can be either residual or loading, can be beneficial or, in contrast, can provoke premature failures of manufacturing materials and machine parts. Consequently, determination of the stress and strain state is of major importance in engineering and technological applications and also in geology, mining and earth science.

There are several methods for investigating stress: mechanical, acoustic, optical and the diffraction of X-rays and neutrons, with the latter being the most appropriate for crystalline matter. The diffraction method is based on the variation in interplanar distance (*d*-spacing) caused by the strain induced by stress. There are two possible *d*-spacing variation effects that can be observed and measured by diffraction: peak shift and peak broadening. Peak shift is observed if the average strain on the irradiated sample volume (the macroscopic strain) differs from zero, while peak broadening is connected to the strain dispersion. There is a rich literature on these subjects. The comprehensive monographs by Noyan & Cohen (1987) and Hauk (1997) are strongly recommended for macrostrain peak shift, and the books by Wilson (1962) and by Warren (1969) for strain broadening.

5.2.2. Strain and stress in single crystals, elastic constants and transformations

The strain and stress are symmetrical tensors of rank 2. If $\mathbf{u}(\mathbf{r})$ is a small displacement of the point at position vector $\mathbf{r}$ in a single crystal, then the strain tensor is defined as

$$\varepsilon_{ij} = \frac{1}{2}\left(\frac{\partial u_i}{\partial x_j} + \frac{\partial u_j}{\partial x_i}\right) \quad (i, j = 1, 2, 3), \qquad (5.2.1)$$

where u_i and x_i are the components of $\mathbf{u}$ and $\mathbf{r}$ in an orthogonal coordinate system ($\mathbf{x}_i$, $i = 1, 2, 3$). The element σ_{ij} of the stress tensor is defined as the i component of the force acting on the unit area normal to the vector $\mathbf{x}_j$. For $i \neq j$ we have $\sigma_{ij} - \sigma_{ij} = 0$, otherwise the body rotates around the vector $\mathbf{x}_h = \mathbf{x}_i \times \mathbf{x}_j$. Thus, while the strain tensor is symmetrical by definition, the symmetry of the stress tensor is imposed by the mechanical equilibrium.

The magnitudes of the strain-tensor and stress-tensor elements are different in different reference systems. Let us consider another reference system ($\mathbf{y}_i$, $i = 1, 2, 3$) and denote by $\mathbf{a}(g)$ the Euler matrix transforming this system into ($\mathbf{x}_i$, $i = 1, 2, 3$),

$$\mathbf{x}_i = \sum_{j=1}^{3} a_{ij}(g)\mathbf{y}_j, \qquad (5.2.2)$$

$$\mathbf{a}(g) = \begin{pmatrix} \cos\varphi_1\cos\varphi_2 - \sin\varphi_1\sin\varphi_2\cos\Phi_0 & \sin\varphi_1\cos\varphi_2 + \cos\varphi_1\sin\varphi_2\cos\Phi_0 & \sin\varphi_2\sin\Phi_0 \\ -\cos\varphi_1\sin\varphi_2 - \sin\varphi_1\cos\varphi_2\cos\Phi_0 & -\sin\varphi_1\sin\varphi_2 + \cos\varphi_1\cos\varphi_2\cos\Phi_0 & \cos\varphi_2\sin\Phi_0 \\ \sin\varphi_1\sin\Phi_0 & -\cos\varphi_1\sin\Phi_0 & \cos\Phi_0 \end{pmatrix}. \qquad (5.2.3)$$

Here, the triplet $g = \varphi_1, \Phi_0, \varphi_2$ denotes the standard Euler angles, namely $\varphi_1 \in (0, 2\pi)$ is a rotation of the reference system ($\mathbf{y}_1, \mathbf{y}_2, \mathbf{y}_3$) around $\mathbf{y}_3$, resulting in ($\mathbf{y}_1', \mathbf{y}_2', \mathbf{y}_3$), $\Phi_0 \in (0, \pi)$ is the rotation of this system around $\mathbf{y}_1'$, resulting in ($\mathbf{y}_1', \mathbf{y}_2'', \mathbf{x}_3$), and, finally, $\varphi_2 \in (0, 2\pi)$ is the rotation of the last system around $\mathbf{x}_3$, resulting in ($\mathbf{x}_1, \mathbf{x}_2, \mathbf{x}_3$). Let us denote the strain and stress tensors in the system ($\mathbf{y}_i$, $i = 1, 2, 3$) by the Latin characters e_{ij} and s_{ij}, respectively. The transformations of the strain- and the stress-tensor elements in the coordinate-system transformation (5.2.2) are easily derived starting from the tensor definitions. For the strain tensor these are the following, with similar expressions being valid for stress:

$$\varepsilon_{ij} = \sum_{k=1}^{3}\sum_{m=1}^{3} a_{ik}a_{jm}e_{km}, \qquad (5.2.4a)$$

$$e_{km} = \sum_{i=1}^{3}\sum_{j=1}^{3} a_{ik}a_{jm}\varepsilon_{ij}. \qquad (5.2.4b)$$

The quantity observable in a diffraction experiment is the *d*-spacing variation along the reciprocal-lattice vector $\mathbf{H}(h, k, l)$ of unit vector $\mathbf{h}$,

$$[d(hkl) - d_0(hkl)]/d_0(hkl) = \Delta d/d_0 = -\Delta H/H_0 = \varepsilon_{hh} \equiv e_{hh}. \qquad (5.2.5)$$

To calculate this quantity from the strain-tensor elements ε_{ij} in ($\mathbf{x}_i$), we must define the reference system ($\mathbf{k}$, $\mathbf{l}$, $\mathbf{h}$) with the axis $\mathbf{k}$ in the plane ($\mathbf{x}_3$, $\mathbf{h}$) and normal to $\mathbf{h}$ and $\mathbf{l} = \mathbf{h} \times \mathbf{k}$. Describing the unit vector $\mathbf{h}$ by the polar and azimuthal angles (Φ, β), the connection between the ($\mathbf{k}$, $\mathbf{l}$, $\mathbf{h}$) and ($\mathbf{x}_i$) systems is

$$\begin{pmatrix} \mathbf{k} \\ \mathbf{l} \\ \mathbf{h} \end{pmatrix} = \mathbf{m}(\Phi, \beta)\begin{pmatrix} \mathbf{x}_1 \\ \mathbf{x}_2 \\ \mathbf{x}_3 \end{pmatrix}, \qquad (5.2.6)$$

$$\mathbf{m}(\Phi, \beta) = \begin{pmatrix} \cos\Phi\cos\beta & \cos\Phi\sin\beta & -\sin\Phi \\ -\sin\beta & \cos\beta & 0 \\ \sin\Phi\cos\beta & \sin\Phi\sin\beta & \cos\Phi \end{pmatrix}. \qquad (5.2.7)$$

A comparison of (5.2.6) with (5.2.2) allows the use of a transformation similar to (5.2.4*a*) to calculate ε_{hh},

$$\varepsilon_{hh} = \sum_{k=1}^{3}\sum_{m=1}^{3} m_{3k}(\Phi, \beta)m_{3m}(\Phi, \beta)\varepsilon_{km} = \sum_{k=1}^{3}\sum_{m=1}^{3} a_k a_m \varepsilon_{km}. \qquad (5.2.8)$$

Here, $(a_1, a_2, a_3) = (\cos\beta\sin\Phi, \sin\beta\sin\Phi, \cos\Phi)$ are the direction cosines of $\mathbf{h}$ in ($\mathbf{x}_i$). If the polar and azimuthal angles of $\mathbf{h}$ in ($\mathbf{y}_i$)

Copyright © 2019 International Union of Crystallography

are (Ψ, γ), then the direction cosines are $(b_1, b_2, b_3) = (\cos\gamma \sin\Psi, \sin\gamma \sin\Psi, \cos\Psi)$ and in place of (5.2.8) we have

$$e_{hh} = \sum_{k=1}^{3} \sum_{m=1}^{3} m_{3k}(\Psi, \gamma) m_{3m}(\Psi, \gamma) e_{km} = \sum_{k=1}^{3} \sum_{m=1}^{3} b_k b_m e_{km}. \quad (5.2.9)$$

Hereafter, we denote ε_{hh} and e_{hh} simply by $\varepsilon_{\mathbf{h}}$ and $e_{\mathbf{h}}$, respectively. We have $e_{\mathbf{h}} \equiv \varepsilon_{\mathbf{h}}$ as they define the same quantity.

In the limits of an elastically deformed body the stress and strain tensors are connected by the Hooke equations. To derive these equations, one starts from the elastic free energy per unit volume. The differential of this quantity is $\mathrm{d}F = \sum_{i=1}^{3} \sum_{j=1}^{3} \sigma_{ij}\, \mathrm{d}\varepsilon_{ij}$, and the Hooke equations are then

$$\sigma_{ij} = \frac{\partial F}{\partial \varepsilon_{ij}} \quad (i, j = 1, 2, 3). \quad (5.2.10)$$

As the magnitudes of the strain-tensor elements are small, the elastic free energy can be expanded in powers of these quantities, limiting the expansion to the second-order terms. As the terms of order zero and of order one are zero because F and σ_{ij} are zero when $\varepsilon_{ij} = 0$, we can write

$$F = \frac{1}{2} \sum_{i=1}^{3} \sum_{j=1}^{3} \sum_{k=1}^{3} \sum_{l=1}^{3} C_{ijkl} \varepsilon_{ij} \varepsilon_{kl}. \quad (5.2.11)$$

Here, C_{ijkl} are the stiffness elastic constants forming a fourth-rank tensor of 81 elements. As the strain tensor is symmetrical, the product $\varepsilon_{ij}\varepsilon_{kl}$ does not change if the indices i, j and k, l, as well as the pairs ij, kl, are permuted. The tensor C_{ijkl} can be chosen to have the same properties; as a consequence 21 independent constants remain for triclinic crystals, and their number decreases on increasing the Laue symmetry. By applying (5.2.10) to (5.2.11), one obtains

$$\sigma_{ij} = \sum_{k=1}^{3} \sum_{l=1}^{3} C_{ijkl} \varepsilon_{kl} \quad (i, j = 1, 2, 3). \quad (5.2.12)$$

There are nine equations in (5.2.12), but only six are independent because for every $i \neq j$ there are two equal strain and stress elements, respectively, and thus two identical equations. Inverting (5.2.12), we have

$$\varepsilon_{ij} = \sum_{k=1}^{3} \sum_{l=1}^{3} S_{ijkl} \sigma_{kl} \quad (i, j = 1, 2, 3), \quad (5.2.13)$$

where S_{ijkl} is a fourth-rank tensor of compliance elastic constants with exactly the same symmetry properties as the tensor of stiffness constants C_{ijkl}.

We can take advantage of the symmetry of the strain, stress and elastic constants tensors to introduce reduced indices defined as follows:

$$\begin{aligned} &11 \rightarrow 1, \quad 22 \rightarrow 2, \quad 33 \rightarrow 3, \quad 23 = 32 \rightarrow 4, \\ &\qquad 13 = 31 \rightarrow 5, \quad 12 = 21 \rightarrow 6. \end{aligned} \quad (5.2.14)$$

By using the reduced indices the strain and stress tensors are represented as vectors of dimension 6 and the elastic-constants tensors as symmetrical matrices of dimensions 6 × 6.

We then pass to the reduced-indices representation according to the convention described by Wooster (1973),[1]

$$\begin{aligned} &\varepsilon_{ij} = \varepsilon_{ji} \rightarrow \varepsilon_m \quad (m = 1, \ldots, 6), \\ &C_{ijkl} = C_{jikl} = C_{ijlk} = C_{klij} \rightarrow C_{mn} \quad (m, n = 1, \ldots, 6), \end{aligned} \quad (5.2.15)$$

and similarly for the stress tensor and compliance constants.

Accounting for (5.2.14) and (5.2.15), the transformations (5.2.4) for strain and for stress become

$$\varepsilon_i = \sum_{j=1}^{6} Q_{ij} e_j, \quad (5.2.16a)$$

$$e_i = \sum_{j=1}^{6} P_{ij} \varepsilon_j, \quad (5.2.16b)$$

$$\sigma_i = \sum_{j=1}^{6} Q_{ij} s_j, \quad (5.2.16c)$$

$$s_i = \sum_{j=1}^{6} P_{ij} \sigma_j. \quad (5.2.16d)$$

The matrices $\mathbf{Q}$ and $\mathbf{P} = \mathbf{Q}^{-1}$ of dimensions 6 × 6 in (5.2.16) can be expressed by another four matrices of dimensions 3 × 3 that are calculated from the elements of the Euler matrix (5.2.3),

$$\mathbf{Q} = \begin{pmatrix} \mathbf{L} & 2\mathbf{M} \\ \mathbf{N} & \mathbf{O} \end{pmatrix}, \quad (5.2.17a)$$

$$\mathbf{P} = \begin{pmatrix} \mathbf{L}^t & 2\mathbf{N}^t \\ \mathbf{M}^t & \mathbf{O}^t \end{pmatrix}, \quad (5.2.17b)$$

$$\left.\begin{aligned} &L_{kl} = a_{kl}^2, \quad M_{lk} = a_{li} a_{lj}, \quad N_{kl} = a_{il} a_{jl} \\ &O_{ij} = a_{kk} a_{ji} + a_{ki} a_{jk}, \; O_{kk} = a_{ii} a_{jj} + a_{ij} a_{ji} \end{aligned}\right\}, \; \left\{\begin{aligned} &i, j, k, l = 1, 2, 3 \\ &i \neq j \neq k \end{aligned}\right. . \quad (5.2.17c)$$

The following notation will be used:

$$(\rho_1, \ldots, \rho_6) = (1, 1, 1, 2, 2, 2), \quad (5.2.18)$$

$$(E_1, \ldots, E_6) = (a_1^2, a_2^2, a_3^2, a_2 a_3, a_1 a_3, a_1 a_2), \quad (5.2.19)$$

$$(F_1, \ldots, F_6) = (b_1^2, b_2^2, b_3^2, b_2 b_3, b_1 b_3, b_1 b_2). \quad (5.2.20)$$

Using this notation, the strain along the reciprocal-lattice vector (5.2.8) and (5.2.9) becomes

$$\varepsilon_{\mathbf{h}} = \sum_{j=1}^{6} E_j \rho_j \varepsilon_j, \quad (5.2.21a)$$

$$e_{\mathbf{h}} = \sum_{j=1}^{6} F_j \rho_j e_j. \quad (5.2.21b)$$

The free-energy expression (5.2.11) and the direct Hooke equations (5.2.10) and (5.2.12) become

$$F = \frac{1}{2} \sum_{m=1}^{6} C_{mm} \rho_m^2 \varepsilon_m^2 + \sum_{m=1}^{5} \sum_{n=m+1}^{6} C_{mn} \rho_m \rho_n \varepsilon_m \varepsilon_n, \quad (5.2.22)$$

$$\sigma_m = \frac{\partial F}{\partial \varepsilon_m} \quad (m = 1, 2, 3), \quad (5.2.23a)$$

$$2\sigma_m = \frac{\partial F}{\partial \varepsilon_m} \quad (m = 4, 5, 6), \quad (5.2.23b)$$

$$\left\{\begin{aligned} \sigma_m &= C_{m1}\varepsilon_1 + C_{m2}\varepsilon_2 + C_{m3}\varepsilon_3 \\ &\quad + 2C_{m4}\varepsilon_4 + 2C_{m5}\varepsilon_5 + 2C_{m6}\varepsilon_6 \quad (m = 1, 2, 3), \\ 2\sigma_m &= 2C_{m1}\varepsilon_1 + 2C_{m2}\varepsilon_2 + 2C_{m3}\varepsilon_3 \\ &\quad + 4C_{m4}\varepsilon_4 + 4C_{m5}\varepsilon_5 + 4C_{m6}\varepsilon_6 \quad (m = 4, 5, 6). \end{aligned}\right. \quad (5.2.24)$$

[The factor of 2 in the left-hand side of (5.2.23*b*) is due to the fact that for $i \neq j$ there are two contributions to the differential of the free energy, $\mathrm{d}F = \sigma_{ij}\mathrm{d}\varepsilon_{ij} + \sigma_{ji}\mathrm{d}\varepsilon_{ji} = 2\sigma_{ij}\mathrm{d}\varepsilon_{ij}$, and thus $\partial F/\partial\varepsilon_{ij} = 2\sigma_{ij}$.] The inverse Hooke equations obtained by solving (5.2.24) have exactly the same form except that the vectors ε_m and σ_m change places and the matrix **S** replaces **C**. From (5.2.24) it can be observed that the inversion relations between the matrices **C** and **S** are $\mathbf{S} = (\mathbf{C}')^{-1}$ and $\mathbf{C} = (\mathbf{S}')^{-1}$, where $\mathbf{C}'$ and $\mathbf{S}'$ are obtained by partitioning **C** and **S** into four 3 × 3 blocks multiplied as follows: the upper left block by 1, the upper right and bottom left by 2 and the bottom right block by 4. Once the relation between **C** and **S** has been established, the factor of 2 in (5.2.24*b*) can be dropped and the Hooke equations written unitarily as follows:

---

[1] Some of the literature uses a different convention, which is described in Nye (1957). The Wooster convention is preferred as it keeps the values of the tensor elements, and for symmetries higher than triclinic gives identical structures for the matrices **C** and **S**.

$$\sigma_i = \sum_{j=1}^{6} C_{ij}\rho_j\varepsilon_j \quad (i = 1, \ldots, 6), \qquad (5.2.25a)$$

$$\varepsilon_i = \sum_{j=1}^{6} S_{ij}\rho_j\sigma_j \quad (i = 1, \ldots, 6). \qquad (5.2.25b)$$

The matrices **C** for all Laue classes are given in Table 5.2.1. The matrices **S** have exactly the same structure. For a given Laue group the matrix **C** is found from the invariance conditions of the free energy (5.2.22) to the operations of this group.[2] This results in a system of 21 homogenous equations determining a number of linear constraints between the matrix elements and, consequently, a number of independent elastic constants specific to the Laue group. The simplest structure of **C** with many elements equal to zero is obtained if the crystal reference system ($\mathbf{x}_i$) is taken with $\mathbf{x}_3$ along the *n*-fold axis and $\mathbf{x}_1$ along the twofold axis normal to the *n*-fold axis for groups where this axis exists or in an arbitrary direction[3] for groups where this axis does not exist. On passing to the system $\mathbf{y}_i$, the Hooke equations and the single-crystal elastic constants change as follows:

$$s_i(g) = \sum_{j=1}^{6} C_{ij}(g)\rho_j e_j(g), \qquad (5.2.26a)$$

$$e_i(g) = \sum_{j=1}^{6} S_{ij}(g)\rho_j s_j(g), \qquad (5.2.26b)$$

$$C_{il}(g) = \rho_l^{-1}\sum_{j=1}^{6}\sum_{k=1}^{6} C_{jk}\rho_k P_{ij}(g)Q_{kl}(g), \qquad (5.2.27a)$$

$$S_{il}(g) = \rho_l^{-1}\sum_{j=1}^{6}\sum_{k=1}^{6} S_{jk}\rho_k P_{ij}(g)Q_{kl}(g). \qquad (5.2.27b)$$

Table 5.2.1
The matrix **C** for all Laue groups represented by specific constraints

An identical table can be written for the matrix **S**.

Symmetry (Laue groups)	Constraints	No. of independent elastic constants
$\bar{1}$	None	21
2/*m* (unique axis *c*)	$C_{14} = C_{15} = C_{24} = C_{25} = C_{34} = C_{35} = C_{46} = C_{56} = 0$	13
mmm	As for 2/*m*, plus $C_{16} = C_{26} = C_{36} = C_{45} = 0$	9
4/*m*	As for 2/*m*, plus $C_{36} = C_{45} = 0$, $C_{22} = C_{11}$, $C_{23} = C_{13}$, $C_{26} = -C_{16}$, $C_{55} = C_{44}$	7
4/*mmm*	As for 4/*m*, plus $C_{16} = 0$	6
$\bar{3}$	$C_{16} = C_{26} = C_{34} = C_{35} = C_{36} = C_{45} = 0$, $C_{22} = C_{11}$, $C_{23} = C_{13}$, $C_{24} = -C_{14}$, $C_{25} = -C_{15}$, $C_{46} = -C_{15}$, $C_{55} = C_{44}$, $C_{56} = C_{14}$, $C_{66} = (C_{11} - C_{12})/2$	7
$\bar{3}m$	As for $\bar{3}$, plus $C_{15} = 0$	6
Hexagonal Laue groups	As for $\bar{3}m$, plus $C_{14} = 0$	5
Cubic Laue groups	As for 4/*mmm*, plus $C_{13} = C_{12}$, $C_{33} = C_{11}$, $C_{66} = C_{44}$	3
Isotropic	As for cubic, plus $C_{44} = (C_{11} - C_{12})/2$	2

5.2.3. Strain and stress in polycrystalline samples

5.2.3.1. *Types of strains and stresses, and the strain/stress orientation distribution function*

A textured polycrystalline sample is formed from a large number of small single-crystal blocks with different orientations following a certain distribution called the *orientation distribution function* (ODF). The elastic strain and stress state of an individual crystallite is determined by the Hooke equations together with the boundary conditions. In a polycrystalline sample the boundary conditions are the result of the interaction of the crystallite with its neighbours, and this interaction depends on the crystallite shape and orientation. To describe both the texture and the strain/stress state of a polycrystalline sample two reference systems should be defined: one linked to the crystallite and the second to the sample. The crystallite reference system is ($\mathbf{x}_i$, $i = 1, 2, 3$) defined for every Laue group, as described in the previous section. The sample system ($\mathbf{y}_i$, $i = 1, 2, 3$) can be defined by using some prominent surfaces and directions resulting from the manufacturing process or given by the geometrical characteristics of the sample. In the most general case the strain and stress in a crystallite are not homogenous and are described by functions depending on the crystallite orientation *g* and on the position vector in the crystallite. Let us denote by $\mathbf{R}_k$ the position vector with respect to the sample system of the crystallite *k* with an orientation in the range (g, $g + \mathrm{d}g$). If **r** is the position vector of a point in this crystallite in the crystal reference system, then the elastic strain at this point in this system is $\varepsilon_i(\mathbf{R}_k + \mathbf{r}, g)$. Denoting the crystallite volume by V_k, the averaged strain in this crystallite is

$$\varepsilon_i(\mathbf{R}_k, g) = V_k^{-1}\int \varepsilon_i(\mathbf{R}_k + \mathbf{r}, g)\,\mathrm{d}\mathbf{r}. \qquad (5.2.28)$$

If N_g is the number of crystallites of orientation *g*, then the second average can be defined as

$$\varepsilon_i(g) = N_g^{-1}\sum_{k=1}^{N_g}\varepsilon_i(\mathbf{R}_k, g). \qquad (5.2.29)$$

Further, the third average can be defined by integrating (5.2.29) over the crystallites' orientations. Denoting the orientation distribution function (ODF) by $f(g)$, this average is

$$\overline{\varepsilon}_i = \iiint \mathrm{d}g\, f(g)\,\varepsilon_i(g). \qquad (5.2.30)$$

The functions $\varepsilon(g)$ are the *type-I* strains and the following differences define the *type-III*, *type-II* and *intergranular* strains:

$$\text{Type III: } \Delta\varepsilon_i(\mathbf{R}_k + \mathbf{r}, g) = \varepsilon_i(\mathbf{R}_k + \mathbf{r}, g) - \varepsilon_i(\mathbf{R}_k, g); \qquad (5.2.31)$$

$$\text{Type II: } \Delta\varepsilon_i(\mathbf{R}_k, g) = \varepsilon_i(\mathbf{R}_k, g) - \varepsilon_i(g); \qquad (5.2.32)$$

$$\text{Intergranular: } \Delta\varepsilon_i(g) = \varepsilon_i(g) - \overline{\varepsilon}_i. \qquad (5.2.33)$$

---

[2] Invariance to inversion is assured by the quadratic form.

[3] $\mathbf{x}_i = \mathbf{a}/a$ is appropriate in all cases if the twofold axis, when it exists, is taken along the unit-cell vector **a**.

The type-I strain, as well as its average, and the intergranular strain are macroscopic quantities. For simplicity, both the type-II and type-III strains are called *microscopic* strains, although the type-II strain is mesoscopic. Obviously, the following averages are zero:

$$V_k^{-1} \int \Delta\varepsilon_i(\mathbf{R}_k + \mathbf{r}, g)\,\mathrm{d}\mathbf{r} = 0, \tag{5.2.34a}$$

$$N_g^{-1} \sum_{k=1}^{N_g} \Delta\varepsilon_i(\mathbf{R}_k, g) = 0, \tag{5.2.34b}$$

$$\iiint \mathrm{d}g\, f(g)\,\Delta\varepsilon_i(g) = 0. \tag{5.2.34c}$$

The strain at the point **r** in the crystallite *k* of orientation *g* can be written as a sum of type-I, type-II and type-III strains,

$$\varepsilon_i(\mathbf{R}_k+\mathbf{r}, g) = \varepsilon_i(g) + \Delta\varepsilon_i(\mathbf{R}_k, g) + \Delta\varepsilon_i(\mathbf{R}_k+\mathbf{r}, g) \quad (i = 1, \ldots, 6). \tag{5.2.35}$$

Expressions similar to (5.2.28)–(5.2.35) can be written for any elastic strain or stress component in any reference system. In these expressions ε_i is, in fact, a placeholder for ε_i, e_i, σ_i or s_i.

Similarly to the texture, we can call $\varepsilon_i(g)$ the *strain/stress orientation distribution functions* (SODF). In contrast to the ODF, the average of the SODF over all variables is not unity but the *averaged macroscopic strain/stress* $\overline{\varepsilon}_i$. In general, both the averaged value and the intergranular strain/stress are necessary for a complete description of the macroscopic strain/stress state in a material. The intergranular strains/stresses have various origins such as elastic and plastic deformations, phase transformations, thermal treatments, mismatch of *d*-spacings in composite materials and differences in the coefficients of thermal expansion (Behnken, 2000). It is advantageous to group all of these elastic intergranular strains/stresses of different origins into only two terms, $\Delta\varepsilon_i^{\rm elastic}$ and $\Delta\varepsilon_i^{\rm plastic}$; the SODF can then be written as

$$\varepsilon_i(g) = \overline{\varepsilon}_i + \Delta\varepsilon_i^{\rm elastic}(g) + \Delta\varepsilon_i^{\rm plastic}(g). \tag{5.2.36}$$

The first two terms in the right-hand side of (5.2.36) represent the elastically induced part of the SODF, with the last term being the plastically induced part.

5.2.3.2. *The mean and variance of the observable strain, the peak shift and broadening*

According to (5.2.21*a*), the strain along **h** and its square in terms of the strain-tensor elements in the crystal reference system are the following:

$$\varepsilon_{\mathbf{h}}(\mathbf{R}_k + \mathbf{r}, g) = \sum_{i=1}^{6} E_i \rho_i \varepsilon_i(\mathbf{R}_k + \mathbf{r}, g), \tag{5.2.37}$$

$$\varepsilon_{\mathbf{h}}^2(\mathbf{R}_k + \mathbf{r}, g) = \sum_{i=1}^{6}\sum_{j=1}^{6} E_i E_j \rho_i \rho_j \varepsilon_i(\mathbf{R}_k + \mathbf{r}, g)\varepsilon_j(\mathbf{R}_k + \mathbf{r}, g). \tag{5.2.38}$$

The peak shift and the integral breadth caused by strain are obtained from (5.2.37) and (5.2.38), respectively, after substituting (5.2.35) and performing three averages. The first two averages are over **r** and over *k*, respectively, for a given orientation *g*. Taking account of (5.2.34*a*) and (5.2.34*b*), the following macroscopic quantities depending only on the crystallite orientation are obtained:

$$\varepsilon_{\mathbf{h}}(g) = \sum_{i=1}^{6} E_i \rho_i \varepsilon_i(g), \tag{5.2.39}$$

$$\varepsilon_{\mathbf{h}}^2(g) = \sum_{i=1}^{6}\sum_{j=1}^{6} E_i E_j \rho_i \rho_j \big[\varepsilon_i(g)\varepsilon_j(g) + \Delta_{ij}(g)\big], \tag{5.2.40}$$

$$\begin{aligned}\Delta_{ij}(g) = {}& \frac{1}{N_g}\sum_{k=1}^{N_g} \Delta\varepsilon_i(\mathbf{R}_k, g)\Delta\varepsilon_j(\mathbf{R}_k, g)\\ &+ \frac{1}{N_g}\sum_{k=1}^{N_g}\frac{1}{V_k}\int \mathrm{d}\mathbf{r}\,\Delta\varepsilon_i(\mathbf{R}_k + \mathbf{r}, g)\Delta\varepsilon_j(\mathbf{R}_k + \mathbf{r}, g).\end{aligned} \tag{5.2.41}$$

The third average is performed only over those crystallite orientations g^+ for which **h** is parallel to **y**, the unit vector of the scattering vector. This means that only crystallites with orientations fulfilling the Bragg reflection condition are considered. Under this constraint, the Euler matrix (5.2.3) can be written as

$$\mathbf{a}(g^+) = \mathbf{a}(\varphi_1^+, \Phi_0^+, \varphi_2^+) = \mathbf{m}^t(\Phi, \beta)\mathbf{n}(\omega)\mathbf{m}(\Psi, \gamma), \tag{5.2.42}$$

where **m** is given by (5.2.7), (Φ, β) and (Ψ, γ) are the polar and azimuthal angles of **h** in $(\mathbf{x}_i)$ and of **y** in $(\mathbf{y}_i)$, respectively, and where $\mathbf{n}(\omega)$ is a simple rotation matrix of angle $\omega \in (0, 2\pi)$. Now, by taking into account that the sample could be textured and denoting the (texture) pole distribution function by $p_{\mathbf{h}}(\mathbf{y}) = (1/2\pi)\int_{\mathbf{h}\|\mathbf{y}} \mathrm{d}\omega f(g^+)$, the average over g^+ of the observable strain ($n = 1$) and of its square ($n = 2$) are

$$\big\langle\varepsilon_{\mathbf{h}}^n(\mathbf{y})\big\rangle = (1/2\pi)\int_{\mathbf{h}\|\mathbf{y}} \mathrm{d}\omega\, f(g^+)\varepsilon_{\mathbf{h}}^n(g^+)/p_{\mathbf{h}}(\mathbf{y}). \tag{5.2.43}$$

This equation contains the texture pole distribution $p_{\mathbf{h}}(\mathbf{y})$ as a normalizing factor, which is not accessible to the diffraction measurements. This can be replaced by the *reduced pole distribution* $P_{\mathbf{h}}(\mathbf{y}) = (1/2)[p_{\mathbf{h}}(\mathbf{y}) + p_{-\mathbf{h}}(\mathbf{y})]$ because the peak positions for $-\mathbf{h}$ and **h** are not distinguishable. Therefore, in place of (5.2.43) we have

$$\begin{aligned}\big\langle\varepsilon_{\mathbf{h}}^n(\mathbf{y})\big\rangle P_{\mathbf{h}}(\mathbf{y}) &= \frac{1}{2}\left[\frac{1}{2\pi}\int_{\mathbf{h}\|\mathbf{y}} \mathrm{d}\omega\,\varepsilon_{\mathbf{h}}^n(g^+)f(g^+) + \frac{1}{2\pi}\int_{-\mathbf{h}\|\mathbf{y}} \mathrm{d}\omega\,\varepsilon_{\mathbf{h}}^n(g^-)f(g^-)\right]\\ &= \frac{1}{2\pi}\int_{\pm\mathbf{h}\|\mathbf{y}} \mathrm{d}\omega\,\varepsilon_{\mathbf{h}}^n(g^\pm)f(g^\pm).\end{aligned} \tag{5.2.43$'$}$$

Here, the significance of the ± symbol is the average of the two terms; the Euler matrix for $-\mathbf{h}\|\mathbf{y}$ is calculated using (5.2.42) with (Φ, β) replaced by $(\pi - \Phi, \beta + \pi)$. Now, substituting (5.2.39) and (5.2.40) into (5.2.43′), one obtains the following expressions for the *mean* [equation (5.2.44)] and for the *variance* [equations (5.2.45)] of the *observable* strain:

$$\langle\varepsilon_{\mathbf{h}}(\mathbf{y})\rangle P_{\mathbf{h}}(\mathbf{y}) = \sum_{i=1}^{6} E_i\rho_i \frac{1}{2\pi}\int_{\pm\mathbf{h}\|\mathbf{y}} \mathrm{d}\omega\,\varepsilon_i(g^\pm)f(g^\pm), \tag{5.2.44}$$

$$V_{\mathbf{h}}(\mathbf{y}) = \big\langle\varepsilon_{\mathbf{h}}^2(\mathbf{y})\big\rangle - \langle\varepsilon_{\mathbf{h}}(\mathbf{y})\rangle^2 = V_{\mathbf{h}}^M(\mathbf{y}) + V_{\mathbf{h}}^m(\mathbf{y}), \tag{5.2.45a}$$

$$\begin{aligned}V_{\mathbf{h}}^M(\mathbf{y}) = {}& \sum_{i=1}^{6}\sum_{j=1}^{6} E_i E_j \rho_i \rho_j\\ &\times \left[\begin{aligned}&P_{\mathbf{h}}^{-1}(\mathbf{y})(2\pi)^{-1}\int_{\pm\mathbf{h}\|\mathbf{y}} \mathrm{d}\omega\,\Delta\varepsilon_i(g^\pm)\Delta\varepsilon_j(g^\pm)f(g^\pm)\\ &- P_{\mathbf{h}}^{-2}(\mathbf{y})(2\pi)^{-2}\int_{\pm\mathbf{h}\|\mathbf{y}} \mathrm{d}\omega\,\Delta\varepsilon_i(g^\pm)f(g^\pm)\int_{\pm\mathbf{h}\|\mathbf{y}} \mathrm{d}\omega\,\Delta\varepsilon_j(g^\pm)f(g^\pm)\end{aligned}\right],\end{aligned} \tag{5.2.45b}$$

$$V_{\mathbf{h}}^m(\mathbf{y}) = \sum_{i=1}^{6}\sum_{j=1}^{6} E_i E_j \rho_i \rho_j \left[P_{\mathbf{h}}^{-1}(\mathbf{y})(2\pi)^{-1}\int_{\pm\mathbf{h}\|\mathbf{y}} \mathrm{d}\omega\,\Delta_{ij}(g^\pm)f(g^\pm)\right]. \tag{5.2.45c}$$

The mean determines the peak shift; the variance determines the peak breadth caused by strain. The variance has two components: the microstrain variance $V_{\mathbf{h}}^{m}(\mathbf{y})$ and the macrostrain variance $V_{\mathbf{h}}^{M}(\mathbf{y})$. The contributions to the peak shift of the second and of the third terms in (5.2.35) are zero because the averages of these terms over $\mathbf{r}$ and k, respectively, are zero. The peak shift is exclusively caused by type-I strain. Type-II and -III strains only contribute to the peak broadening. The broadening effect of microstrains is explained by correlations differing from zero appearing in (5.2.41); it can be observed that only correlations of strains of the same level are involved. Finally, macrostrain broadening is produced only by intergranular strain and, as will be seen later, can be considered to be a small correction of the microstrain broadening.

There is an alternative derivation of the peak shift and broadening, starting from (5.2.21b), giving the strain along $\mathbf{h}$ in terms of the strain-tensor elements in the sample reference system. The resulting mean and variance of the observable strain retain exactly the same structure as equations (5.2.44) and (5.2.45) with ε in the right-hand side[4] replaced by e and E_i replaced by F_i:

$$\langle\varepsilon_{\mathbf{h}}(\mathbf{y})\rangle P_{\mathbf{h}}(\mathbf{y}) = \sum_{i=1}^{6} F_i \rho_i \frac{1}{2\pi} \int_{\pm\mathbf{h}\|\mathbf{y}} \mathrm{d}\omega\, e_i(g^{\pm}) f(g^{\pm}), \qquad (5.2.44')$$

$$V_{\mathbf{h}}(\mathbf{y}) = \langle\varepsilon_{\mathbf{h}}^{2}(\mathbf{y})\rangle - \langle\varepsilon_{\mathbf{h}}(\mathbf{y})\rangle^{2} = V_{\mathbf{h}}^{M}(\mathbf{y}) + V_{\mathbf{h}}^{m}(\mathbf{y}) \qquad (5.2.45'a)$$

$$\begin{aligned} V_{\mathbf{h}}^{M}(\mathbf{y}) &= \sum_{i=1}^{6}\sum_{j=1}^{6} F_i F_j \rho_i \rho_j \\ &\times \left[\begin{aligned} &P_{\mathbf{h}}^{-1}(\mathbf{y})(2\pi)^{-1} \int_{\pm\mathbf{h}\|\mathbf{y}} \mathrm{d}\omega\, \Delta e_i(g^{\pm}) \Delta e_j(g^{\pm}) f(g^{\pm}) \\ &- P_{\mathbf{h}}^{-2}(\mathbf{y})(2\pi)^{-2} \int_{\pm\mathbf{h}\|\mathbf{y}} \mathrm{d}\omega\, \Delta e_i(g^{\pm}) f(g^{\pm}) \int_{\pm\mathbf{h}\|\mathbf{y}} \mathrm{d}\omega\, \Delta e_j(g^{\pm}) f(g^{\pm}) \end{aligned} \right] \end{aligned} \qquad (5.2.45'b)$$

$$V_{\mathbf{h}}^{m}(\mathbf{y}) = \sum_{i=1}^{6}\sum_{j=1}^{6} F_i F_j \rho_i \rho_j \left[P_{\mathbf{h}}^{-1}(\mathbf{y})(2\pi)^{-1} \int_{\pm\mathbf{h}\|\mathbf{y}} \mathrm{d}\omega\, \Delta_{ij}(g^{\pm}) f(g^{\pm}) \right]. \qquad (5.2.45'c)$$

For a given problem, the appropriate choice of one or the other alternative can save a significant amount of calculation.

The peak shift (5.2.44) can be also called the *strain pole distribution function*. The strain pole distribution is to the SODF what the pole distribution is to the texture, with an important difference: in the place of one distribution, six independent SODFs in a determined linear combination [equations (5.2.21)] are projected onto the space (Ψ, γ).

5.2.4. Determining the strain/stress by diffraction

5.2.4.1. *Determining the macrostrain/stress*

Although diffraction is able, in principle, to determine both the averaged strain/stress tensors $\overline{e}_i/\overline{s}_i$ as well as the intergranular strain/stress $\Delta e_i(g)/\Delta s_i(g)$, the principal aim for many decades was to determine only the averaged tensors. The determination was based on the supposition that the elastic strain and stress tensors $e_i(g)$, $s_i(g)$ in a crystallite are connected to the average tensors $\overline{s}_i$, $\overline{e}_i$ as follows (see, for example, Behnken, 2000):

$$e_i(g) = \sum_{j=1}^{6} S_{ij}^{\#}(g) \rho_j \overline{s}_j, \qquad (5.2.46a)$$

$$s_i(g) = \sum_{j=1}^{6} C_{ij}^{\#}(g) \rho_j \overline{e}_j. \qquad (5.2.46b)$$

Here, $S_{ij}^{\#}(g)$ and $C_{ij}^{\#}(g)$ are fourth-rank tensors describing the elastic behaviour of the crystallites in the polycrystalline materials, not necessarily the single-crystal compliance and stiffness tensors as in (5.2.26). Equations of type (5.2.46) are obtained if the plastically induced term in (5.2.36) is zero, and the elastically induced term of the strain/stress differs from zero only if the averaged stresses/strains differ from zero. If the equations (5.2.46) are valid, then the mean strain measured by diffraction can be expressed as

$$\langle\varepsilon_{\mathbf{h}}(\mathbf{y})\rangle = \sum_{j=1}^{6} R_j(\Psi, \gamma; \Phi, \beta) \overline{s}_j. \qquad (5.2.47)$$

The coefficients R_j are called *diffraction stress factors* and can be calculated analytically or numerically using (5.2.44) or (5.2.44′). Classical models such as those of Voigt (1928), Reuss (1929) and Kroner (1958) fit perfectly into this category. The average stresses can be obtained by fitting (5.2.47) to the measured data for a number of peaks and directions in the sample. For isotropic (non-textured) samples (5.2.47) becomes linear in $\sin^2\Psi$ and $\sin 2\Psi$, and is the basic equation of the traditional '$\sin^2\Psi$' method (Hauk, 1952; Christenson & Rowland, 1953). Most experimental data can be processed using this method, even if the sample has a weak texture.

For textured samples the relation between the peak shifts and $\sin^2\Psi$ becomes nonlinear. Analytical expressions can sometimes be found by approximating the texture pole distribution by δ functions in some prominent sample directions (Dölle, 1979). In general, this is a rough approximation, with numerical calculation of the diffraction stress factors being preferable. Many applications to thin films can be found in the review paper by Welzel *et al.* (2005).

Determination of the stress in a textured sample requires a prior, accurate determination of the texture. To eliminate this time-consuming step and to increase the accuracy of stress determination, Ferrari & Lutterotti (1994) proposed the inclusion of stress analysis in the Rietveld method, with the stress parameters being refined together with the texture spherical-harmonics coefficients and the structural parameters. Balzar *et al.* (1998) also used the Rietveld method with a Voigt-type formula implemented in *GSAS* by Larson & Von Dreele (2004) to determine the average strain tensor from multiple time-of-flight neutron diffraction patterns on Al/SiC composites.

The dependence of the measured strain on $\sin^2\Psi$ sometimes becomes strongly nonlinear, especially in metals after plastic deformation, and cannot be explained by the texture or by the stress-gradient effect. In general, equations (5.2.46) are too restrictive because they do not take the plastically induced part of the strain and stress into account. They must be replaced by the exact equations (5.2.26); in other words, the averaged strain and stress tensors and the whole intergranular strains and stresses must be considered. There are two possibilities for accounting for the whole intergranular stress. The first is to calculate the plastically induced part of the stress starting from models of the plastic flow of crystallites within a polycrystalline sample (Van Acker *et al.*, 1996). The second possibility is to construct the SODF $\varepsilon_i(g)$ by inverting the strain pole distributions $\langle\varepsilon_{\mathbf{h}}(\mathbf{y})\rangle$ measured for several peaks and in a large number of sample directions. No model is necessary to assume the elastic or plastic interactions of crystallites. In contrast, determination of the SODF for elastically loaded or plastically deformed samples gives essential information on the mechanisms of crystallite interactions.

---

[4] Remembering that $e_{\mathbf{h}} \equiv \varepsilon_{\mathbf{h}}$, in the left-hand side of (5.2.44′) and (5.2.45′) we have $\langle e_{\mathbf{h}}(\mathbf{y})\rangle^{n} \equiv \langle\varepsilon_{\mathbf{h}}(\mathbf{y})\rangle^{n}$.

To determine the SODF, Wang *et al.* (1999, 2001, 2003) and Behnken (2000) proposed an approach based on the representation of these functions by generalized spherical harmonics. These approaches presume prior determination of the ODF (texture) and of the peak positions considered as free parameters in pattern decomposition. Only isolated or weakly overlapping peaks can be used for accurate position determination, and a large part of the information contained in the diffraction pattern is then lost. To eliminate these drawbacks, Popa & Balzar (2001, 2014) proposed a variant of strain representation by generalized spherical harmonics that is appropriate for implementation in the Rietveld method.

In the following, three subjects concerning macrostrain/stress determination are developed: classical approximations for the macrostrain/stress in isotropic polycrystals and for isotropic polycrystals under hydrostatic pressure, and a spherical-harmonics analysis in the variant that can be implemented in Rietveld programs.

5.2.4.2. *Determining the microstrain*

The microstrain is part of the microstructure: it is the departure caused by the imperfections of a real polycrystal compared with an ideal polycrystal. The microstructure affects the profile of the diffraction peaks, and its study is then performed by *line profile analysis* (LPA) techniques. A historical overview of LPA techniques can be found in Langford (2004).

LPA is as old as powder diffraction itself, having its origin in the Scherrer equation (Scherrer, 1918). In terms of the physical quantities used today, the Scherrer equations for the constant wavelength and the time-of-flight diffraction methods are

$$\beta_H^D = \lambda/[D_V(\mathbf{h})\cos\theta_H] \text{ and}$$
$$\beta_H^D = \lambda_H^2/[2D_V(\mathbf{h})\sin\theta],$$

respectively. Here, θ_H and λ_H are the Bragg angle and wavelength, respectively, $D_V(\mathbf{h})$ is the *volume-averaged column length* along the reciprocal-lattice vector and β_H^D is the corresponding integral breadth of the diffraction line. During the two decades after the publication of the paper by Scherrer, diffraction phenomena that were not interpretable using his formula were observed, but only after 1940 were these understood and treated theoretically. Stokes & Wilson (1944) realized that peak broadening caused by strain may coexist with broadening due to the crystallite size, and that in reciprocal space the former increases linearly with the reflection order, while the latter is independent of this order. Consequently, considering a Gaussian for the distribution of the observable strain, the dependence of the strain breadth β_H^S on the strain variance [equation (5.2.45)] is

$$\beta_H^S = 2\tan\theta_H[2\pi V_{\mathbf{h}}(\mathbf{y})]^{1/2}, \qquad (5.2.48a)$$
$$\beta_H^S = \lambda_H[2\pi V_{\mathbf{h}}(\mathbf{y})]^{1/2}. \qquad (5.2.48b)$$

The sample peak profile is a convolution of the size and strain profiles, and the central problem of LPA is to separate the two contributions. Separation is possible owing to the different dependence of the breadth on the scanning variable. There are two kinds of methods for separation: *integral breadth methods*, which require models for the peak profiles, and *Fourier methods*, which do not require such models.

Based on the dependence of the size and strain breadths on the reflection order (Stokes & Wilson, 1944), Hall (1949) proposed an integral breadth method of separation known today as a *Williamson–Hall plot*. It consists of plotting $\beta_H^* = \beta_H\cos\theta_H/\lambda$ *versus* $d_H^* = m/d_h$, where m is the reflection order, d_h is the interplanar distance of the lattice planes (hkl) and β_H is the integral breadth of the experimental line profile corrected for the instrumental resolution. Presuming that $\beta_H = \beta_H^D + \beta_H^S$, which means that both the size and strain profiles are Lorentzian, we have $\beta_H^* = 1/D_V(\mathbf{h}) + (2\pi V_{\mathbf{h}})^{1/2} d_H^*$, and the crystallite size and strain variance are then obtained from the intercept and the slope of this line. Similar linear plots can be drawn for the Gauss sample profile and for the Voigt sample profile (Lorentz for size, Gauss for strain) if the coordinates (d_H^{*2}, β_H^{*2}) are used in place of (d_H^*, β_H^*).

Also based on Stokes & Wilson (1944), Averbach & Warren (1949) first proposed a Fourier method for separating the strain and size. According to these authors, the logarithms of the cosines of the Fourier coefficients of the sample line profile, which are the product of the size and strain Fourier coefficients, can be written as

$$\ln[A_n(m)] = \ln\left[A_n^D A_n^S(m)\right] = \ln(A_n^D) - 2\pi^2 n^2 m^2 V_{\mathbf{h}},$$

where n is the harmonic index and m is the order of reflection. More than two orders are rarely available. In a plot of $\ln(A_n)$ *versus* m^2 for different values of n, the slope and intercept give the strain variance and parameters connected with the crystallite size, respectively, namely the *area- and volume-averaged column lengths* and the *faulting probabilities*, if this is the case. Details can be found in Warren (1969).

Over the years, the Warren–Averbach method has been modified and improved, becoming a standard method in LPA; for details, see Langford (2004). Unfortunately, like the Williamson–Hall plot, this method has a serious limitation: it requires isolated diffraction peaks without overlaps, a condition that is rarely fulfilled.

Peak overlap is not an impediment to the integral breadth method called *whole powder pattern fitting* (WPPF) or *pattern decomposition*. WPPF aims to fit the whole diffraction pattern by using analytical functions for the peak profiles with at least one obligatory constraint: the breadth of a given peak is not a free, refinable parameter, but is calculated with a parameterized function depending on the scanning variable. For the strain breadth this function is (5.2.48*a*) or (5.2.48*b*), and one expects to have a parameterized expression describing the dependence of the strain variance on the directions in the crystal and sample. Such expressions for all Laue groups were recently derived by Popa & Lungu (2013) using the spherical-harmonics approach described below in Section 5.2.8. They have as classical limits the expressions of strain variance that are dependent only on crystal direction derived by Popa (1998) and independently by Stephens (1999), which are now implemented in all popular Rietveld programs.

5.2.5. Macrostrain/stress in isotropic samples: classical approximations

As stated in the previous section, if the aim of the diffraction experiment is determination of the averaged strain and stress tensors, the classical models of Voigt, Reuss and Kroner are good enough to process most experimental data. Moreover, the determination becomes a very simple routine if the sample is isotropic. The term ‘isotropic’ for a polycrystalline sample denotes the absence of a preferred orientation, which means that $f(g) = 1$. With regard to the elastic properties, such a sample is isotropic only on average; the behaviour of crystallites, with rare exceptions, is anisotropic. For this reason, it is appropriate to call this sample *quasi-isotropic*. As a consequence of isotropy, two averaged elastic constants specific to the model can be derived from the single-crystal elastic constants.

5.2.5.1. *The Voigt model*

According to Voigt (1928), the intergranular strain in the sample reference system is zero and the macroscopic strain tensor in the crystallite is thus identical to the averaged strain,

$$e_i(\varphi_1, \Phi_0, \varphi_2) = \overline{e}_i. \tag{5.2.49}$$

To find the averaged stress tensor in the same system, we substitute (5.2.49) into (5.2.26*a*) and integrate over Euler space. The integral acts only on the single-crystal stiffness tensor elements (5.2.27*a*) and can be calculated analytically. The averaged stress is

$$\overline{s}_i = \sum_{j=1}^{6} \overline{C}_{ij}^V \rho_j \overline{e}_j. \tag{5.2.50}$$

In (5.2.50) $\overline{C}_{ij}^V$ are the Voigt-averaged elastic stiffness constants for the isotropic polycrystal. They are calculated from the single-crystal stiffness constants as follows:

$$\overline{C}_{11}^V = \frac{(C_{11} + C_{22} + C_{33})}{5} + \frac{2(C_{12} + C_{13} + C_{23} + 2C_{44} + 2C_{55} + 2C_{66})}{15}, \tag{5.2.51a}$$

$$\overline{C}_{12}^V = \frac{(C_{11} + C_{22} + C_{33} - 2C_{44} - 2C_{55} - 2C_{66})}{15} + \frac{4(C_{12} + C_{13} + C_{23})}{15}. \tag{5.2.51b}$$

To find the peak shift for the Voigt model, equation (5.2.49) must be substituted into (5.2.44′). The integral in (5.2.44′) is trivial and one obtains

$$\langle \varepsilon_{\mathbf{h}}(\mathbf{y}) \rangle = \sum_{j=1}^{6} F_j \rho_j \overline{e}_j. \tag{5.2.52}$$

Equation (5.2.52) can be arranged to be similar to (5.2.47). By inverting (5.2.50) and substituting the resulting $\overline{e}_j$ in (5.2.52), this equation becomes

$$\begin{aligned}\langle \varepsilon_{\mathbf{h}}(\mathbf{y}) \rangle = {} & [F_1 \overline{S}_{11}^V + (F_2 + F_3)\overline{S}_{12}^V]\overline{s}_1 + [F_2 \overline{S}_{11}^V + (F_1 + F_3)\overline{S}_{12}^V]\overline{s}_2 \\ & + [F_3 \overline{S}_{11}^V + (F_1 + F_2)\overline{S}_{12}^V]\overline{s}_3 \\ & + 2(\overline{S}_{11}^V - \overline{S}_{12}^V)(F_4\overline{s}_4 + F_5\overline{s}_5 + F_6\overline{s}_6).\end{aligned} \tag{5.2.53}$$

In (5.2.53) $\overline{S}_{ij}^V$ is the compliance tensor obtained by inverting the stiffness tensor $\overline{C}_{ij}^V$,

$$\begin{aligned}\overline{S}_{11}^V &= (\overline{C}_{11}^V + \overline{C}_{12}^V)/[\overline{C}_{11}^V(\overline{C}_{11}^V + \overline{C}_{12}^V) - 2(\overline{C}_{12}^V)^2], \\ \overline{S}_{12}^V &= -\overline{C}_{12}^V/[\overline{C}_{11}^V(\overline{C}_{11}^V + \overline{C}_{12}^V) - 2(\overline{C}_{12}^V)^2].\end{aligned} \tag{5.2.54}$$

We can see from (5.2.52) or (5.2.53) that in the frame of the Voigt model of crystallite interactions the relative peak shift does not depend on the Miller indices, a fact that is frequently contradicted by experiment. The Reuss model gives such a dependence.

5.2.5.2. *The Reuss model*

In the hypothesis of Reuss (1929), the intergranular stress in the sample system is zero and thus

$$s_i(\varphi_1, \Phi_0, \varphi_2) = \overline{s}_i. \tag{5.2.55}$$

To find the averaged strain, equation (5.2.55) is substituted into (5.2.26*b*), which is integrated in Euler space, and one obtains

$$\overline{e}_i = \sum_{j=1}^{6} \overline{S}_{ij}^R \rho_j \overline{s}_j. \tag{5.2.56}$$

Here, $\overline{S}_{ij}^R$ are the Reuss-averaged compliance constants for the isotropic polycrystals. They are calculated from the single-crystal compliances with formulae similar to (5.2.51),

$$\overline{S}_{11}^R = \frac{(S_{11} + S_{22} + S_{33})}{5} + \frac{2(S_{12} + S_{13} + S_{23} + 2S_{44} + 2S_{55} + 2S_{66})}{15}, \tag{5.2.57a}$$

$$\overline{S}_{12}^R = \frac{(S_{11} + S_{22} + S_{33} - 2S_{44} - 2S_{55} - 2S_{66})}{15} + 4\frac{(S_{12} + S_{13} + S_{23})}{15}. \tag{5.2.57b}$$

Note that $\overline{S}_{ij}^R$ and $\overline{S}_{ij}^V$ are different. Also note that the stiffness constants $\overline{C}_{ij}^R$ obtained by inverting $\overline{S}_{ij}^R$ are different from $\overline{C}_{ij}^V$ defined previously.

To calculate the peak shift, there are two possibilities that should give identical results. According to Behnken & Hauk (1986), equations (5.2.55) and (5.2.27*b*) are substituted into (5.2.26*b*), (5.2.26*b*) is substituted into (5.2.21*b*), and the peak shift is then calculated with (5.2.44′), which becomes

$$\langle \varepsilon_{\mathbf{h}}(\mathbf{y}) \rangle = \sum_{i=1}^{6} F_i \rho_i \sum_{l=1}^{6} \overline{s}_l \sum_{j=1}^{6} \sum_{k=1}^{6} S_{jk} \rho_k \langle P_{ij} Q_{kl} \rangle.$$

Alternatively, according to Popa (2000), equation (5.2.55) is substituted into (5.2.16*c*), (5.2.16*c*) into (5.2.25*b*), and (5.2.25*b*) into (5.2.21*a*), and the peak shift is then calculated with (5.2.44), which becomes

$$\langle \varepsilon_{\mathbf{h}}(\mathbf{y}) \rangle = \sum_{i=1}^{6} E_i \rho_i \sum_{l=1}^{6} \overline{s}_l \sum_{j=1}^{6} S_{ij} \rho_j \langle Q_{jl} \rangle. \tag{5.2.58}$$

Obviously the last possibility, which is adopted here, is much cheaper computationally as there are only 36 average $\langle Q_{ij} \rangle$ to calculate in place of 1296 $\langle P_{ij} Q_{kl} \rangle$. Taking account of (5.2.17), (5.2.42) and (5.2.7), the integrals

$$\langle Q_{ij} \rangle = \frac{1}{2\pi} \int_0^{2\pi} \mathrm{d}\omega \, Q_{ij}(\varphi_1^{\pm}, \Phi_0^{\pm}, \varphi_2^{\pm}) \tag{5.2.59}$$

can be calculated analytically and one obtains

$$\langle Q_{ij} \rangle = \begin{cases} (3F_j - 1)E_i/2 + \delta_i(1 - F_j)/2 & \text{for } j = 1, 2, 3 \\ 3F_j E_i - \delta_i F_j & \text{for } j = 4, 5, 6 \end{cases} \tag{5.2.60}$$

$$(\delta_1, \ldots, \delta_6) = (1, 1, 1, 0, 0, 0).$$

Inserting (5.2.60) into (5.2.58) and rearranging the terms, the peak shift becomes

$$\langle \varepsilon_{\mathbf{h}}(\mathbf{y}) \rangle = (\overline{t}_s - \overline{s}_{\mathbf{y}})r_2/2 + (3\overline{s}_{\mathbf{y}} - \overline{t}_s)r_4/2, \tag{5.2.61}$$

Table 5.2.2
Quadratic and quartic forms for symmetries higher than triclinic

(*a*) Quadratic forms r_2.

Symmetry (Laue groups)	Quadratic form
$2/m$ (unique axis c)	$(S_{11}+S_{12}+S_{13})a_1^2 + (S_{12}+S_{22}+S_{23})a_2^2$ $+ (S_{13}+S_{23}+S_{33})a_3^2$ $+ 2(S_{16}+S_{26}+S_{36})a_1a_2$
mmm	$(S_{11}+S_{12}+S_{13})a_1^2 + (S_{12}+S_{22}+S_{23})a_2^2$ $+ (S_{13}+S_{23}+S_{33})a_3^2$
Tetragonal, trigonal, hexagonal Laue groups	$(S_{11}+S_{12}+S_{13})(a_1^2+a_2^2) + (2S_{13}+S_{33})a_3^2$
Cubic Laue groups	$S_{11}+2S_{12}$

(*b*) Quartic forms r_4.

Symmetry (Laue groups)	Quartic form
$2/m$ (unique axis c)	$S_{11}a_1^4 + S_{22}a_2^4 + S_{33}a_3^4 + 2(S_{23}+2S_{44})a_2^2a_3^2$ $+ 2(S_{13}+2S_{55})a_1^2a_3^2 + 2(S_{12}+2S_{66})a_1^2a_2^2$ $+ 4(S_{36}+2S_{45})a_1a_2a_3^2 + 4S_{16}a_1^3a_2 + 4S_{26}a_1a_2^3$
mmm	$S_{11}a_1^4 + S_{22}a_2^4 + S_{33}a_3^4 + 2(S_{23}+2S_{44})a_2^2a_3^2$ $+ 2(S_{13}+2S_{55})a_1^2a_3^2 + 2(S_{12}+2S_{66})a_1^2a_2^2$
$4/mmm$	$S_{11}(a_1^4+a_2^4) + S_{33}a_3^4 + 2(S_{13}+2S_{44})(a_1^2+a_2^2)a_3^2$ $+ 2(S_{12}+2S_{66})a_1^2a_2^2$
$4/m$	As for $4/mmm$, plus $4S_{16}(a_1^2-a_2^2)a_1a_2$
$\bar{3}m$	$S_{11}(a_1^2+a_2^2)^2 + S_{33}a_3^4 + 2(S_{13}+2S_{44})(a_1^2+a_2^2)a_3^2$ $+ 4S_{14}(3a_1^2-a_2^2)a_2a_3$
$\bar{3}$	As for $\bar{3}m$, plus $4S_{15}(a_1^2-3a_2^2)a_1a_3$
Hexagonal Laue groups	$S_{11}(a_1^2+a_2^2)^2 + S_{33}a_3^4 + 2(S_{13}+2S_{44})(a_1^2+a_2^2)a_3^2$
Cubic Laue groups	$S_{11}(a_1^4+a_2^4+a_3^4)$ $+ 2(S_{12}+2S_{44})(a_2^2a_3^2+a_1^2a_3^2+a_1^2a_2^2)$

where $\bar{t}_s$ is the trace of the averaged stress tensor and $\bar{s}_{\mathbf{y}}$ is the mean stress along **y**,

$$\bar{t}_s = \bar{s}_1 + \bar{s}_2 + \bar{s}_3, \qquad (5.2.62a)$$

$$\bar{s}_{\mathbf{y}} = F_1\bar{s}_1 + F_2\bar{s}_2 + F_3\bar{s}_3 + 2F_4\bar{s}_4 + 2F_5\bar{s}_5 + 2F_6\bar{s}_6. \qquad (5.2.62b)$$

The dependence of the peak shifts on the Miller indices is given by the factors r_2 and r_4, which are the quadratic and quartic forms, respectively, of the direction cosines a_i. For triclinic symmetry these factors are the following:

$$\begin{aligned} r_2 = {} & (S_{11}+S_{12}+S_{13})a_1^2 + (S_{12}+S_{22}+S_{23})a_2^2 \\ & + (S_{13}+S_{23}+S_{33})a_3^2 + 2(S_{14}+S_{24}+S_{34})a_2a_3 \\ & + 2(S_{15}+S_{25}+S_{35})a_1a_3 + 2(S_{16}+S_{26}+S_{36})a_1a_2, \end{aligned} \qquad (5.2.63)$$

$$\begin{aligned} r_4 = {} & S_{11}a_1^4 + S_{22}a_2^4 + S_{33}a_3^4 + 2(S_{23}+2S_{44})a_2^2a_3^2 \\ & + 2(S_{13}+2S_{55})a_1^2a_3^2 + 2(S_{12}+2S_{66})a_1^2a_2^2 \\ & + 4(S_{14}+2S_{56})a_1^2a_2a_3 + 4(S_{25}+2S_{46})a_1a_2^2a_3 \\ & + 4(S_{36}+2S_{45})a_1a_2a_3^2 + 4S_{24}a_2^3a_3 \\ & + 4S_{34}a_2a_3^3 + 4S_{15}a_1^3a_3 + 4S_{35}a_1a_3^3 \\ & + 4S_{16}a_1^3a_2 + 4S_{26}a_1a_2^3. \end{aligned} \qquad (5.2.64)$$

For higher symmetries, r_2 and r_4 can be derived from (5.2.63) and (5.2.64), taking Table 5.2.1 into account. They are given in Tables 5.2.2(*a*) and (*b*). The expressions in these tables are identical to those derived by Behnken & Hauk (1986) except for two Laue classes.

5.2.5.3. *The Hill average*

The Voigt and the Reuss models are two extreme cases of crystallite interactions that roughly describe the strain/stress state of isotropic polycrystalline samples. Hill (1952) observed that the real elastic constants are generally close enough to the arithmetic average of the constants calculated within the two models. Consequently, a very good description of the peak shift is obtained in practice by using the arithmetic average of the Voigt and Reuss peak shifts (5.2.53) and (5.2.61). Even better is to use a weighted average with the weight w ($0 < w < 1$) as a refinable parameter in a least-squares analysis (Popa, 2000):

$$\langle\varepsilon_{\mathbf{h}}(\mathbf{y})\rangle = w\langle\varepsilon_{\mathbf{h}}(\mathbf{y})\rangle^V + (1-w)\langle\varepsilon_{\mathbf{h}}(\mathbf{y})\rangle^R. \qquad (5.2.65)$$

5.2.5.4. *The Kroner model*

A model for crystallite interaction that is better than the Voigt or the Reuss model was proposed by Kroner (1958). According to Kroner, every crystallite is an inclusion in a continuous and homogenous matrix that has the elastic properties of the polycrystal. For the isotropic polycrystal, the strain on inclusion is

$$e_i(g) = \sum_{j=1}^{6}\left[\overline{S}_{ij}^R + t_{ij}(g)\right]\rho_j\bar{s}_j. \qquad (5.2.66)$$

In this expression, similar to (5.2.46*a*), the first term is the strain of the isotropic matrix given by (5.2.56). The second term is the strain induced in the crystallite by the matrix and is given by the theory of ellipsoidal inclusion of Eshelby (1957). The tensor $t_{ij}(g)$ accounts for the differences between the compliances of the inclusion and the matrix and has the property $\bar{t}_{ij} = 0$. To calculate the peak shift, (5.2.66) is substituted into (5.2.44′). Analytical calculations can only be performed for a spherical crystalline inclusion that has cubic symmetry. For the peak shift an expression similar to (5.2.53) is obtained but with different compliances. According to Bollenrath *et al.* (1967), the Voigt compliance constants in (5.2.53) must be replaced as follows:

$$\overline{S}_{11}^V \rightarrow \overline{S}_{11}^R + T_{11} - 2T_0\Gamma, \qquad (5.2.67a)$$

$$\overline{S}_{12}^V \rightarrow \overline{S}_{12}^R + T_{12} + T_0\Gamma, \qquad (5.2.67b)$$

$$T_0 = T_{11} - T_{12} - 2T_{44}, \qquad (5.2.67c)$$

$$\Gamma = a_2^2a_3^2 + a_1^2a_3^2 + a_1^2a_2^2. \qquad (5.2.67d)$$

The matrix compliances $\overline{S}_{11}^R$ and $\overline{S}_{12}^R$ are given by (5.2.57) for the case of cubic symmetry. The induced compliances T_{11}, T_{21} and T_{44} are also calculated from cubic single-crystal compliances by bulky algebraic expressions that have been reproduced in many papers: Bollenrath *et al.* (1967), Dölle (1979), Gnäupel-Herold *et al.* (1998) and Welzel *et al.* (2005).

5.2.5.5. *The ‘sin² Ψ’ method*

The peak-shift equations (5.2.53) and (5.2.61) can be arranged in the following form, which is convenient for experimental data processing:

$$\begin{aligned} \langle\varepsilon_{\mathbf{h}}(\mathbf{y})\rangle = {} & S_1(\bar{s}_1+\bar{s}_2+\bar{s}_3) + \tfrac{1}{2}S_2\bar{s}_3 \\ & + \tfrac{1}{2}S_2(\bar{s}_1\cos^2\gamma + \bar{s}_2\sin^2\gamma - \bar{s}_3 + \bar{s}_6\sin 2\gamma)\sin^2\Psi \\ & + \tfrac{1}{2}S_2(\bar{s}_4\sin\gamma + \bar{s}_5\cos\gamma)\sin 2\Psi. \end{aligned} \qquad (5.2.68)$$

The factors S_1 and S_2 are called *diffraction elastic constants*. For the models examined above they are the following:

$$\begin{aligned} &S_1 = \overline{S}^V_{12}, \quad S_2 = 2(\overline{S}^V_{11} - \overline{S}^V_{12}); && \text{Voigt} \\ &S_1 = (r_2 - r_4)/2, \quad S_2 = 3r_4 - r_2; && \text{Reuss} \\ &S_1 = \overline{S}^R_{12} + T_{12} + T_0\Gamma, && \\ &S_2 = 2(\overline{S}^R_{11} - \overline{S}^R_{12} + T_{11} - T_{12} - 3T_0\Gamma). && \text{Kroner (cubic)} \end{aligned} \tag{5.2.69}$$

Except for the Voigt model, the diffraction elastic constants are dependent on the Miller indices.

If we consider the peak shifts for γ and $\gamma + \pi$ at the same value of Ψ, equation (5.2.68) is split into two linear equations, one in $\sin^2\Psi$ and the other in $\sin 2\Psi$:

$$\begin{aligned} \langle\varepsilon_{\mathbf{h}}\rangle^+ &= \langle\varepsilon_{\mathbf{h}}(\Psi,\gamma)\rangle + \langle\varepsilon_{\mathbf{h}}(\Psi,\gamma+\pi)\rangle \\ &= 2S_1(\overline{s}_1 + \overline{s}_2 + \overline{s}_3) + S_2\overline{s}_3 \\ &\quad + S_2(\overline{s}_1\cos^2\gamma + \overline{s}_2\sin^2\gamma - \overline{s}_3 + \overline{s}_6\sin 2\gamma)\sin^2\Psi, \end{aligned} \tag{5.2.70a}$$

$$\begin{aligned} \langle\varepsilon_{\mathbf{h}}\rangle^- &= \langle\varepsilon_{\mathbf{h}}(\Psi,\gamma)\rangle - \langle\varepsilon_{\mathbf{h}}(\Psi,\gamma+\pi)\rangle \\ &= S_2(\overline{s}_4\sin\gamma + \overline{s}_5\cos\gamma)\sin 2\Psi. \end{aligned} \tag{5.2.70b}$$

Consequently, if the peak shifts for one or more peaks are measured as a function of Ψ in the range $(0, \pi/2)$ at γ and $\gamma + \pi$ for three fixed values of γ (for example 0, $\pi/4$ and $\pi/2$), the stress-tensor elements $\overline{s}_i$ can be determined from the intercepts and slopes of these lines. It is presumed that the single-crystal elastic constants are known and the diffraction elastic constants in equations (5.2.70) can be calculated following one of the models presented previously. This is the conventional '$\sin^2\Psi$' method. Alternatively, equation (5.2.68) can be used in a least-squares analysis or implemented in the Rietveld codes. If diffraction patterns measured at a number of points (Ψ, γ) are available, then the stress-tensor elements $\overline{s}_i$ can be refined together with the structural and other parameters.

5.2.5.6. *Determining the single-crystal elastic constants*

The dependence of the diffraction elastic constants on the Miller indices can be exploited to find the single-crystal elastic constants from powder diffraction data. Indeed, let us presume that an axial, known stress $\overline{s}_3$ is applied to a polycrystalline sample. All other components of the stress tensor are zero and equation (5.2.68) then becomes

$$\langle\varepsilon_{\mathbf{h}}(\mathbf{y})\rangle = (S_1 + \tfrac{1}{2}S_2\cos^2\Psi)\overline{s}_3. \tag{5.2.71}$$

By measuring the peak shift for $\Psi = 0$ and $\Psi = \pi/2$, both S_1 and S_2 can be determined. If the measurement is repeated for many peaks, the single-crystal elastic constants can be calculated by minimizing the value of χ^2 calculated using the differences between the measured diffraction elastic constants and those calculated with one of the models presented above (except for the Voigt model). For a given Laue group, the number of measured diffraction peaks must be greater than the number of independent single-crystal elastic constants. A comparison of the single-crystal elastic constants determined in this way for aluminium, copper and steel (Gnäupel-Herold *et al.*, 1998) with those measured on single crystals using ultrasonic pulses proved the reliability of the diffraction method.

5.2.6. The hydrostatic state in isotropic polycrystals

A hypothesis that has only recently been examined in the literature (Popa, 2008) is that the intergranular strain in the crystallite reference system is zero and then

$$\varepsilon_i(\varphi_1, \Phi_0, \varphi_2) = \overline{\varepsilon}_i. \tag{5.2.72}$$

To obtain the strain tensor in the sample reference system, (5.2.72) is substituted into (5.2.16*b*); to obtain the stress tensor, (5.2.72) is substituted into (5.2.25*a*), and (5.2.25*a*) into (5.2.16*d*). We then have

$$e_i(g) = \sum_{j=1}^{6} P_{ij}(g)\overline{\varepsilon}_j, \tag{5.2.73a}$$

$$s_i(g) = \sum_{l=1}^{6} \rho_l\overline{\varepsilon}_l \sum_{j=1}^{6} P_{ij}(g)C_{jl}. \tag{5.2.73b}$$

To calculate the macroscopic strains and stresses, equations (5.2.73) are averaged in Euler space. Presuming an isotropic polycrystal, the average acts only on the matrix $\mathbf{P}$ and one obtains

$$\overline{P}_{ij} = \begin{cases} 1/3 & \text{if } i,j = 1,2,3 \\ 0 & \text{if } i \text{ or } j > 3. \end{cases} \tag{5.2.74}$$

The macroscopic strains and stresses are then the following:

$$\overline{e}_1 = \overline{e}_2 = \overline{e}_3 = \overline{e} = (\overline{\varepsilon}_1 + \overline{\varepsilon}_2 + \overline{\varepsilon}_3)/3, \ \ \overline{e}_4 = \overline{e}_5 = \overline{e}_6 = 0, \tag{5.2.75a}$$

$$\overline{s}_1 = \overline{s}_2 = \overline{s}_3 = \overline{s} = \frac{1}{3}\sum_{l=1}^{6} \rho_l\overline{\varepsilon}_l(C_{1l} + C_{2l} + C_{3l}), \ \ \overline{s}_4 = \overline{s}_5 = \overline{s}_6 = 0. \tag{5.2.75b}$$

The structure of equations (5.2.75) is specific for the strain/stress state in a sample under a hydrostatic pressure.

To calculate the peak shift, we insert (5.2.72) into (5.2.44) and obtain

$$\langle\varepsilon_{\mathbf{h}}\rangle = \overline{\varepsilon}_1 a_1^2 + \overline{\varepsilon}_2 a_2^2 + \overline{\varepsilon}_3 a_3^2 + 2\overline{\varepsilon}_4 a_2 a_3 + 2\overline{\varepsilon}_5 a_1 a_3 + 2\overline{\varepsilon}_6 a_1 a_2. \tag{5.2.76}$$

As expected, the peak shift is independent of the direction in the sample. Crystal symmetries that are higher than triclinic impose constraints on the strains $\overline{\varepsilon}_i$ that can be found by setting the invariance conditions of the peak shift (5.2.76) to these symmetry operations. Hence, for monoclinic $2/m$, $a_1 \to -a_1$ and $a_2 \to -a_2$ by a twofold axis along $\mathbf{c}$, and one then finds $\overline{\varepsilon}_4 = \overline{\varepsilon}_5 = 0$. The peak shifts for all Laue classes higher than triclinic are given in the l = 2 row of Table 5.2.6. These formulae can be easily implemented in the Rietveld codes with $\overline{\varepsilon}_i$ refinable parameters. In fact they have already been implemented in *GSAS* (profile #5), but the derivation presented in the *GSAS* manual (Larson & Von Dreele, 2004) is different, with the concrete connection between the refined parameters and the macroscopic hydrostatic strain and stress not being revealed.

The hydrostatic state can be also modelled presuming zero intergranular stress in the crystal reference system:

$$\sigma_i(\varphi_1, \Phi_0, \varphi_2) = \overline{\sigma}_i. \tag{5.2.77}$$

Substituting (5.2.77) into (5.2.16*d*) and also into (5.2.25*b*), which is further substituted into (5.2.16*b*), one finds

$$s_i(g) = \sum_{j=1}^{6} P_{ij}(g)\overline{\sigma}_j, \tag{5.2.78a}$$

$$e_i(g) = \sum_{l=1}^{6} \rho_l\overline{\sigma}_l \sum_{j=1}^{6} P_{ij}(g)S_{jl}, \tag{5.2.78b}$$

and averaging in Euler space one obtains

$$\overline{s}_1 = \overline{s}_2 = \overline{s}_3 = \overline{s} = (\overline{\sigma}_1 + \overline{\sigma}_2 + \overline{\sigma}_3)/3, \ \overline{s}_4 = \overline{s}_5 = \overline{s}_6 = 0, \quad (5.2.79a)$$

$$\overline{e}_1 = \overline{e}_2 = \overline{e}_3 = \overline{e} = \frac{1}{3}\sum_{l=1}^{6} \rho_l \overline{\sigma}_l (S_{1l} + S_{2l} + S_{3l}), \ \overline{e}_4 = \overline{e}_5 = \overline{e}_6 = 0. \quad (5.2.79b)$$

The peak shift is given by the same equation (5.2.76) but with $\overline{\varepsilon}_i$ calculated from $\overline{\sigma}_i$,

$$\overline{\varepsilon}_i = \sum_{j=1}^{6} S_{ij} \rho_j \overline{\sigma}_j. \quad (5.2.80)$$

The hypotheses (5.2.72) and (5.2.77) fully describe the hydrostatic strain/stress state in isotropic samples. Indeed, from the refined parameters $\overline{\varepsilon}_i$ or $\overline{\sigma}_i$ the averaged strain and stress $\overline{e}_i$ and $\overline{s}_i$ can be calculated, and also the intergranular strains and stresses $\Delta e_i(g)$ and $\Delta s_i(g)$, both of which differ from zero. Relations of the type (5.2.46) cannot be obtained from equations (5.2.72) and (5.2.77), but only those of the type (5.2.26). For this reason, a linear homogenous equation of the Hooke type between the averaged stress and strain cannot be established.

5.2.7. Calculating the macroscopic strain/stress using spherical harmonics

As discussed in Section 5.2.4, in many cases the classical models of crystallite interactions cannot explain the strongly nonlinear dependence of the diffraction-peak shift on $\sin^2\Psi$, even if the texture is accounted for. A possible solution to this problem is to renounce any physical model and to find the strain/stress orientation distribution functions (SODFs) by inverting the measured strain pole distributions $\langle \varepsilon_{\mathbf{h}}(\mathbf{y}) \rangle$.

Similar to the ODF (texture), the SODF can be subjected to a Fourier analysis by using generalized spherical harmonics. However, there are two important differences. The first is that in place of one distribution (the ODF), six SODFs are analysed simultaneously. The components of the strain or the stress tensor in the sample or in the crystal reference system can be used for analysis. The second difference involves the invariance to the crystal and sample symmetry operations. The ODF is invariant to both crystal and sample symmetry operations. In contrast, the six SODFs in the sample reference system are invariant to the crystal symmetry operations, but they transform similarly to equations (5.2.16) if the sample reference system is replaced by an equivalent system. Inversely, the SODFs in the crystal reference system transform like (5.2.16) if an equivalent system replaces this system and remain invariant to any rotation of the sample reference system. Consequently, for the spherical-harmonics coefficients of the SODF one expects selection rules that differ from those for the ODF.

In the literature, three different approaches based on the spherical-harmonics representation of the SODF have been reported: those of Wang *et al.* (1999, 2001, 2003), Behnken (2000) and Popa & Balzar (2001, 2014). Wang and co-workers represented the stress tensor in the sample reference system $s_i(g)$ by spherical harmonics. Consequently, the harmonic coefficients with $l = 0$ are the averaged stresses $\overline{s}_i$, but to calculate the averaged strains $\overline{e}_i$ coefficients with $l = 0, 2, 4$ are necessary. Behnken proposed the expansion of both $e_i(g)$ and $s_i(g)$ independently in spherical harmonics. In this case $\overline{e}_i$ and $\overline{s}_i$ are the coefficients with $l = 0$ of the two series, but the volume of calculations by least squares to find the harmonic coefficients is greater. Both Wang and Behnken used (5.2.44′) to calculate the strain pole distribution $\langle \varepsilon_{\mathbf{h}}(\mathbf{y}) \rangle$. When the calculation starts from the harmonic series of $s_i(g)$, the single-crystal compliances in the sample reference system appear in (5.2.44′) as supplementary factors to the SODF and ODF. Behnken performs the integrals (5.2.44′) numerically. Wang and co-workers used the spherical-harmonics representation of the ODF and the Clebsch–Gordon coefficients to express the product of the SODF, ODF and the single-crystal compliances in a series that is further integrated like the ODF for texture. Both Wang and Behnken only considered the case of cubic crystal symmetry and orthorhombic sample symmetry, and constructed the corresponding symmetrized spherical harmonics according to the invariance and non-invariance properties in Euler space. The third approach, reported by Popa & Balzar (2001, 2014), is similar to those of Wang and Behnken, but with an important distinction that makes the problem of the strain and stress determination equivalent to the texture problem, for which a solution had been implemented in the Rietveld method. This approach, which is described below, extends to any sample and crystal symmetry and is appropriate for implementation in the Rietveld method. It was implemented by Lutterotti in his Rietveld program *MAUD* (Lutterotti, 2010) and integrated into a system of ‘combined analysis’ by Chanteigner, as described in his book of the same title (Chateigner, 2010).

5.2.7.1. *Strain expansion in generalized spherical harmonics: the Popa and Balzar approach*

In the approach of Popa & Balzar (2001, 2014), the representation by spherical harmonics is performed on the product of the SODF and the ODF; that is, the SODF weighted by texture (WSODF). In this product, a strain-tensor component in the crystallite reference system is used for SODF. We then have

$$\varepsilon_i(\varphi_1, \Phi_0, \varphi_2) f(\varphi_1, \Phi_0, \varphi_2) = \sum_{l=0}^{\infty} \sum_{m=-l}^{l} \sum_{n=-l}^{l} c_{il}^{mn} \exp(im\varphi_2) P_l^{mn}(\Phi_0) \exp(in\varphi_1), \quad (5.2.81)$$

where the Legendre functions $P_l^{mn}(\Phi_0)$ are defined by equation (14.2) from Bunge (1982); denoting $x = \cos\varphi_0$ these are

$$P_l^{mn}(x) = \frac{(-1)^{l-m} i^{n-m}}{2^l (l-m)!} \left[\frac{(l-m)!(l+n)!}{(l+m)!(l-n)!}\right]^{1/2} (1-x)^{-(n-m)/2} \times (1+x)^{-(n+m)/2} \frac{d^{l-n}}{dx^{l-n}} [(1-x)^{l-m}(1+x)^{l+m}].$$

The functions P_l^{mn} are real for $m + n$ = even and imaginary for $m + n$ = odd, and have the following properties:

$$P_l^{mn\,*}(\Phi) = (-1)^{m+n} P_l^{mn}(\Phi), \quad (5.2.82a)$$

$$P_l^{nm}(\Phi) = P_l^{mn}(\Phi) = P_l^{-m,-n}(\Phi), \quad (5.2.82b)$$

$$P_l^{mn}(\pi - \Phi) = (-1)^{l+m+n} P_l^{-mn}(\Phi), \quad (5.2.82c)$$

$$\int_0^{\pi} P_l^{mn}(\Phi) P_{l'}^{mn\,*}(\Phi) \sin\Phi \, \mathrm{d}\Phi = \frac{2}{2l+1} \delta_{ll'}. \quad (5.2.82d)$$

The last equation says that the functions P_l^{mn} of different harmonics indices l are orthogonal. By using equation (5.2.82a) and taking into account that WSODFs are real functions, one obtains the following condition for the complex coefficients c_l^{mn}:

$$c_{il}^{-m,-n} = (-1)^{m+n} c_{il}^{mn\,*}. \quad (5.2.83)$$

The integral in Euler space of (5.2.81) gives $c_{i0}^{00} = \overline{\varepsilon}_i$, and thus the term $l = 0$ (the ground state) represents the hydrostatic strain/stress state of the isotropic polycrystal discussed in Section 5.2.6. The rest of the terms represent the deviation of the real strain/stress from the hydrostatic state of an isotropic polycrystal (the perturbation of the ground state). To calculate the peak shift, equation (5.2.44) with the integrand replaced by (5.2.81) is used. Further, the integral over the crystallites in Bragg reflection in (5.2.44) is performed using the following equation derived from equation (14.160) in Bunge (1982):

$$\begin{aligned}&\frac{1}{2\pi}\int_{\mathbf{h}\|\mathbf{y}} \mathrm{d}\omega \, \exp(im\varphi_2^+)P_l^{mn}(\Phi_0^+)\exp(in\varphi_1^+)\\ &\qquad = \frac{2}{2l+1}\exp(-im\beta)P_l^m(\Phi)\exp(in\gamma)P_l^n(\Psi). \qquad (5.2.84)\end{aligned}$$

In this equation P_l^m is the adjunct Legendre function (equation 14.39 in Bunge, 1982); denoting $x = \cos\Phi$ or $x = \cos\Psi$, this function is

$$\begin{aligned}P_l^m(x) = {}& \frac{(-1)^{l-m}}{2^l l!}\left(\frac{2l+1}{2}\right)^{1/2}\left[\frac{(l+m)!}{(l-m)!}\right]^{1/2}\\ &\times (1-x^2)^{-m/2}\frac{d^{l-m}}{dx^{l-m}}(1-x^2)^l.\end{aligned}$$

There is an obvious relation between the functions P_l^{m0} and P_l^m:

$$P_l^{m0}(\Phi) = P_l^{0m}(\Phi) = i^{-m}[2/(2l+1)]^{1/2}P_l^m(\Phi). \qquad (5.2.85)$$

By substituting (5.2.85) into equations (5.2.82) one obtains the following properties for P_l^m:

$$P_l^m(\Phi) = (-1)^m P_l^{-m}(\Phi), \qquad (5.2.86a)$$

$$P_l^m(\pi - \Phi) = (-1)^{l+m}P_l^m(\Phi), \qquad (5.2.86b)$$

$$\int_0^\pi P_l^m(\Phi)P_{l'}^m(\Phi)\sin\Phi \, \mathrm{d}\Phi = \delta_{ll'}. \qquad (5.2.86c)$$

Accounting for the properties of (5.2.84), (5.2.86*a*) and (5.2.86*b*), the resulting terms in the expression for the peak shift after integration over ω are rearranged to have only positive indices, and one obtains

$$\langle\varepsilon_{\mathbf{h}}(\mathbf{y})\rangle P_{\mathbf{h}}(\mathbf{y}) = \sum_{l=0}^{\infty}[2/(2l+1)]I_l^M(\mathbf{h},\mathbf{y}), \quad l = \text{even}, \qquad (5.2.87)$$

$$I_l^M(\mathbf{h},\mathbf{y}) = \sum_{i=1}^{6} E_i\rho_i t_{il}(\mathbf{h},\mathbf{y}), \qquad (5.2.88)$$

$$t_{il}(\mathbf{h},\mathbf{y}) = A_{il}^0(\mathbf{y})P_l^0(\Phi) + \sum_{m=1}^{l}\left[A_{il}^m(\mathbf{y})\cos m\beta + B_{il}^m(\mathbf{y})\sin m\beta\right]P_l^m(\Phi), \qquad (5.2.89)$$

$$\begin{aligned}A_{il}^m(\mathbf{y}) = {}& \alpha_{il}^{m0}P_l^0(\Psi) + \sum_{n=1}^{l}\left(\alpha_{il}^{mn}\cos n\gamma + \beta_{il}^{mn}\sin n\gamma\right)P_l^n(\Psi)\\ &(m = 0, \ldots, l). \qquad (5.2.90a)\end{aligned}$$

$$\begin{aligned}B_{il}^m(\mathbf{y}) = {}& \gamma_{il}^{m0}P_l^0(\Psi) + \sum_{n=1}^{l}\left(\gamma_{il}^{mn}\cos n\gamma + \delta_{il}^{mn}\sin n\gamma\right)P_l^n(\Psi)\\ &(m = 1, \ldots, l). \qquad (5.2.90b)\end{aligned}$$

The first observation about equation (5.2.87) is that, as for the texture ODF, it is impossible to determine the odd-l Fourier coefficients of the WSODF from measured pole figures. This is a consequence of the action of Friedel's law.

The coefficients α_{il}^{mn}, β_{il}^{mn}, γ_{il}^{mn} and δ_{il}^{mn} in (5.2.90*a*) and (5.2.90*b*) are obtained from the coefficients c_{il}^{mn} according to the corrected[5] Table 1 from Popa & Balzar (2001, 2014). Equations (5.2.88) to (5.2.90) are valid for triclinic sample and crystal symmetries, and for a given value of l the total number of coefficients is $6(2l+1)^2$. If the crystal and sample symmetries are higher than triclinic, the number of coefficients is reduced, with some coefficients being zero and others being correlated.

5.2.7.2. *The selection rules for all Laue classes*

To find the selection rules for all Laue classes, the invariance conditions to rotations are applied to the peak shift weighted by texture $\langle\varepsilon_{\mathbf{h}}(\mathbf{y})\rangle P_{\mathbf{h}}(\mathbf{y})$. As the terms with different l in (5.2.87) are independent, the invariance conditions must be applied to every I_l^M.

We begin with the selection rules imposed by the crystal symmetry. An r-fold axis along $\mathbf{x}_3$ transforms Φ, β, a_1, a_2 as follows: $\Phi \to \Phi$, $\beta \to \beta + 2\pi/r$, $a_1 \to a_1\cos(2\pi/r) - a_2\sin(2\pi/r)$ and $a_2 \to a_1\sin(2\pi/r) + a_2\cos(2\pi/r)$. By applying the invariance conditions to (5.2.88) one obtains a system of six linear equations:

$$t_{il}(\Phi, \beta + 2\pi/r, \mathbf{y}) = \sum_{k=1}^{6} f_{ik}(r)t_{kl}(\Phi, \beta, \mathbf{y}). \qquad (5.2.91)$$

These equations are just the transformations (5.2.16) for a particular value of r. Furthermore, if (5.2.89) is substituted into (5.2.91) one obtains a system of homogenous equations in A_{il}^m and B_{il}^m that has a nontrivial solution only for certain values of m. If, besides the r-fold axis in $\mathbf{x}_3$, there is a twofold axis along $\mathbf{x}_1$, then A_{il}^m and B_{il}^m must fulfil supplementary conditions resulting from the invariance of I_l^M to the transformations $\Phi \to \pi - \Phi$, $\beta \to -\beta$ and $(a_2, a_3) \to (-a_2, -a_3)$. The selection rules imposed by the crystal symmetry for the non-cubic Laue groups are given in Tables 4–7 and 9–12 in Popa & Balzar (2001, 2014). Note that coefficients belonging to different strain-tensor components are correlated, but only two coefficients are involved in all correlations. The threefold axis added on the long diagonal of the *mmm* and 4/*mmm* prisms to obtain the cubic groups $m\overline{3}$ and $m\overline{3}m$ introduces supplementary correlations between the coefficients A_{il}^m and B_{il}^m of the orthorhombic and tetragonal groups, respectively. These correlations involve more than two coefficients and are found by evaluating I_l^M in terms of the direction cosines a_i and setting the condition of invariance to the transformation $(a_1, a_2, a_3) \to (a_2, a_3, a_1)$. The supplementary correlations added to *mmm* and 4/*mmm* by the cubic threefold axis are given in Tables 13 and 14 in Popa & Balzar (2001, 2014).

One would expect the selection rules imposed by the sample symmetry to be identical to those for the texture of the same sample symmetry. Indeed, the invariance conditions that act directly on (5.2.90*a*) and (5.2.90*b*) are identical to the spherical-harmonics coefficients of the texture pole distribution [see, for example, Popa (2008)]. Hence, the selection rules in index n for the coefficients α_{il}^{mn}, β_{il}^{mn}, γ_{il}^{mn} and δ_{il}^{mn} are those from Table 2 in Popa & Balzar (2001, 2014).

5.2.7.3. *Generalized spherical harmonics of real type, and the WSODF index*

The coefficients α_{il}^{mn}, …, δ_{il}^{mn} fulfilling the selection rules are determined by fitting (5.2.87) truncated at $l = l_0$ to the experimental diffraction-peak shifts caused by strain. The fit can be performed directly using a regular least-squares program

---

[5] According to the corrigendum, a factor of 2 must be added to the right-hand sides of the equations.

Table 5.2.3
Assignment of functions $T_l^\nu(\Phi, \beta; \Psi, \gamma)$ to the coefficients g_{il}^ν

g_{il}^ν	$\leftarrow$	$T_l^\nu(\Phi, \beta; \Psi, \gamma)$
α_{il}^{mn}	$\leftarrow$	$\cos m\beta P_l^m(\Phi) \cos n\gamma P_l^n(\Psi)$
β_{il}^{mn}	$\leftarrow$	$\cos m\beta P_l^m(\Phi) \sin n\gamma P_l^n(\Psi)$
γ_{il}^{mn}	$\leftarrow$	$\sin m\beta P_l^m(\Phi) \cos n\gamma P_l^n(\Psi)$
δ_{il}^{mn}	$\leftarrow$	$\sin m\beta P_l^m(\Phi) \sin n\gamma P_l^n(\Psi)$

or, much more efficiently, by using a Rietveld-type program. Programs providing stabilized (smoothed) solutions are preferred. Furthermore, by using the fitted coefficients the whole macrostrain/stress state of the sample can be determined. For easy handling and coding of these operations, it is useful to define the *parameter vectors* and the *generalized spherical harmonics of real type* associated with these vectors.

Denoting the pair m, n by ν, $\nu \in [1, (2l + 1)2]$, and the coefficients $\alpha_{il}^{mn}, \ldots, \delta_{il}^{mn}$ by g_{il}^ν, the vectors of the parameters are

$$\begin{aligned}\mathbf{g}_{il} = (g_{il}^\nu) = (&\alpha_{il}^{0,0}, \alpha_{il}^{0,1}, \beta_{il}^{0,1}, \ldots, \alpha_{il}^{0,n}, \beta_{il}^{0,n}, \ldots, \alpha_{il}^{0,l}, \beta_{il}^{0,l}; \ldots \\ &\alpha_{il}^{m,0}, \alpha_{il}^{m,1}, \beta_{il}^{m,1}, \ldots, \alpha_{il}^{m,n}, \beta_{il}^{m,n}, \ldots, \alpha_{il}^{m,l}, \beta_{il}^{m,l}; \\ &\gamma_{il}^{m,0}, \gamma_{il}^{m,1}, \delta_{il}^{m,1}, \ldots, \gamma_{il}^{m,n}, \delta_{il}^{m,n}, \ldots, \gamma_{il}^{m,l}, \delta_{il}^{m,l}; \ldots) \\ &(m = 1, \ldots, l). \end{aligned} \tag{5.2.92}$$

The sequence of vector elements in (5.2.92) is imposed by the sequence of the sums over the harmonic indices m, n in (5.2.89) and (5.2.90), with n varying faster than m. Using (5.2.92), equations (5.2.89) and (5.2.90) become

$$t_{il}(\mathbf{h}, \mathbf{y}) = \sum_{\nu=1}^{(2l+1)^2} g_{il}^\nu T_l^\nu(\Phi, \beta; \Psi, \gamma), \tag{5.2.93}$$

with the functions T_l^ν being paired with the coefficients g_{il}^ν according to Table 5.2.3.

To find the set of real generalized spherical harmonics associated with $\mathbf{g}_{il}$ one starts from equation (5.2.81). The sums are rearranged to have only positive indices, with n varying faster than m; furthermore, we use (5.2.83) and the properties (5.2.82*a*,*b*,*c*) of the Legendre functions P_l^{mn}, which are replaced by the following real functions: $Q_l^{mn} = P_l^{mn}$ for $m + n$ = even and $Q_l^{mn} = iP_l^{mn}$ for $m + n$ = odd. Note that the properties (5.2.82*b*,*c*) of P_l^{mn} are transferred to Q_l^{mn},

$$Q_l^{-m,-n}(x) = Q_l^{m,n}(x); \quad Q_l^{-m,n}(x) = (-1)^{l+m+n} Q_l^{m,n}(-x).$$

Finally, by using (5.2.92) and Table 1 from Popa & Balzar (2001, 2014), equation (5.2.81) becomes

$$f(g)\varepsilon_i(g) = \sum_{l=0}^{\infty} \sum_{\nu=1}^{(2l+1)^2} g_{il}^\nu R_l^\nu(g). \tag{5.2.94}$$

Here, R_l^ν are the generalized spherical harmonics of real type, explicitly given in Table 5.2.4. For every l they form a complete and orthogonal basis in Euler space with the following orthogonality condition:

$$(8\pi^2)^{-1} \textstyle\iiint \mathrm{d}g \, R_l^\nu(g) R_{l'}^{\nu'}(g) = r_l^\nu \delta_{ll'} \delta_{\nu\nu'}. \tag{5.2.95}$$

Finally, R_l^ν and T_l^ν fulfil the following equation similar to (5.2.84):

$$\frac{1}{2\pi} \int_{\mathbf{h}\|\mathbf{y}} \mathrm{d}\omega \, R_l^\nu(\varphi_1^+, \Phi_0^+, \varphi_2^+) = \frac{2}{2l+1} T_l^\nu(\Phi, \beta; \Psi, \gamma). \tag{5.2.96}$$

The texture index was introduced by Bunge (1982) to obtain a measure of the texture strength. Similarly, we can introduce a *WSODF index* that should be defined as follows:

$$J = \sum_{i=1}^{6} (8\pi^2)^{-1} \textstyle\iiint \mathrm{d}g \, [f(g)\varepsilon_i(g)]^2 \Big/ \sum_{i=1}^{6} (\overline{\varepsilon}_i)^2. \tag{5.2.97}$$

Inserting (5.2.94), truncating, and taking account of (5.2.95) and that $g_{i0}^1 = \overline{\varepsilon}_i$, one obtains

$$J = 1 + \sum_{i=1}^{6} \sum_{l=2}^{l_0} \sum_{\nu=1}^{(2l+1)^2} r_l^\nu (g_{il}^\nu)^2 \Big/ \sum_{i=1}^{6} (\overline{\varepsilon}_i)^2. \tag{5.2.98}$$

Beside its role as a measure of the WSODF strength, the index can be used to find a stabilized solution for the strain parameters g_{il}^ν by minimizing the Lagrange function $\chi^2 + \lambda(J - 1)$ in place of χ^2.

5.2.7.4. *Determining the macrostrain/stress state of the sample*

Once the strain parameters g_{il}^ν have been determined, the whole macrostrain/stress state can be calculated. Hence, inserting (5.2.94) truncated at $l = l_0$ into (5.2.16*b*), one obtains the WSODF for e_i:

$$f(g)e_i(g) = \sum_{j=1}^{6} \sum_{l=0}^{l_0} \sum_{\nu=1}^{(2l+1)^2} R_l^\nu(g) P_{ij}(g) g_{jl}^\nu. \tag{5.2.99}$$

If (5.2.94) is inserted into (5.2.25*a*), and (5.2.25*a*) into (5.2.16*d*), one obtains a similar expression for the WSODF as for s_i, but with the vector $\mathbf{g}_{jl}$ being replaced by $\mathbf{g}'_{jl}$, which is defined as

$$(g')_{jl}^\nu = \sum_{k=1}^{6} C_{jk} \rho_k g_{kl}^\nu. \tag{5.2.100}$$

According to (5.2.30), to determine $\overline{e}_i$, equation (5.2.99) must be integrated in Euler space. Only terms with $l = 0$ and $l = 2$ can

Table 5.2.4
The real generalized spherical harmonics

g_{il}^ν	$\leftarrow$	$R_l^\nu(\varphi_1, x, \varphi_2); \quad x = \cos\Phi_0$	
α_{il}^{mn}	$\leftarrow$	$[\cos(m\varphi_2) + n\varphi_1) Q_l^{mn}(x) + (-1)^{l+n} \cos(m\varphi_2 - n\varphi_1) Q_l^{mn}(-x)]/2,$	$m + n = \text{even}$
		$[\sin(m\varphi_2 + n\varphi_1) Q_l^{mn}(x) - (-1)^{l+n} \sin(m\varphi_2) - n\varphi_1) Q_l^{mn}(-x)]/2,$	$m + n = \text{odd}$
β_{il}^{mn}	$\leftarrow$	$[\sin(m\varphi_2 + n\varphi_1) Q_l^{mn}(x) - (-1)^{l+n} \sin(m\varphi_2 - n\varphi_1) Q_l^{mn}(-x)]/2,$	$m + n = \text{even}$
		$[-\cos(m\varphi_2 + n\varphi_1) Q_l^{mn}(x) - (-1)^{l+n} \cos(m\varphi_2 - n\varphi_1) Q_l^{mn}(-x)]/2,$	$m + n = \text{odd}$
γ_{il}^{mn}	$\leftarrow$	$[-\sin(m\varphi_2 + n\varphi_1) Q_l^{mn}(x) - (-1)^{l+n} \sin(m\varphi_2 - n\varphi_1) Q_l^{mn}(-x)]/2,$	$m + n = \text{even}$
		$[\cos(m\varphi_2 + n\varphi_1) Q_l^{mn}(x) - (-1)^{l+n} \cos(m\varphi_2 - n\varphi_1) Q_l^{mn}(-x)]/2,$	$m + n = \text{odd}$
δ_{il}^{mn}	$\leftarrow$	$[\cos(m\varphi_2 + n\varphi_1) Q_l^{mn}(x) - (-1)^{l+n} \cos(m\varphi_2 - n\varphi_1) Q_l^{mn}(-x)]/2,$	$m + n = \text{even}$
		$[\sin(m\varphi_2 + n\varphi_1) Q_l^{mn}(x) + (-1)^{l+n} \sin(m\varphi_2 - n\varphi_1) Q_l^{mn}(-x)]/2,$	$m + n = \text{odd}$

have contributions that differ from zero. This is the consequence of the fact that the elements of the matrix **P** can be written as a linear combination of R_0^1 and R_2^ν combined with the orthogonality condition (5.2.95). There are 936 integrals of the type $w_{ijl}^\nu = (1/8\pi^2)\iiint \mathrm{d}g\, P_{ij}(g) R_l^\nu(g)$. Although an analytical calculation is possible, they were calculated numerically. Only 73 differ from zero. The macroscopic averaged strain tensor is as follows:

$$\begin{aligned}
\overline{e}_1, \overline{e}_2 &= (1/3)(g_{10}^1 + g_{20}^1 + g_{30}^1) + (1/30)(g_{12}^1 + g_{22}^1 - 2g_{32}^1)\\
&\mp (1/10/\sqrt{6})(g_{12}^4 + g_{22}^4 - 2g_{32}^4) - (1/5/\sqrt{6})g_{52}^6\\
&\pm (1/10)g_{52}^9 - (1/5/\sqrt{6})g_{42}^{11} \pm (1/10)g_{42}^{14}\\
&- (1/10/\sqrt{6})(g_{12}^{16} - g_{22}^{16}) \pm (1/20)(g_{12}^{19} - g_{22}^{19})\\
&- (1/5/\sqrt{6})g_{62}^{21} \pm (1/10)g_{62}^{24}, \qquad (5.2.101a)\\
\overline{e}_3 &= (1/3)(g_{10}^1 + g_{20}^1 + g_{30}^1) - (1/15)(g_{12}^1 + g_{22}^1 - 2g_{32}^1)\\
&+ (2/5/\sqrt{6})g_{52}^6 + (2/5/\sqrt{6})g_{42}^{11} + (1/5/\sqrt{6})(g_{12}^{16} - g_{22}^{16})\\
&+ (2/5/\sqrt{6})g_{62}^{21}, \qquad (5.2.101b)\\
\overline{e}_4 &= -(1/10/\sqrt{6})(g_{12}^3 + g_{22}^3 - 2g_{32}^3) + (1/10)g_{52}^8\\
&+ (1/10)g_{42}^{13} + (1/20)(g_{12}^{18} - g_{22}^{18}) + (1/10)g_{62}^{23}, \qquad (5.2.101c)\\
\overline{e}_5 &= -(1/10/\sqrt{6})(g_{12}^2 + g_{22}^2 - 2g_{32}^2) + (1/10)g_{52}^7\\
&+ (1/10)g_{42}^{12} + (1/20)(g_{12}^{17} - g_{22}^{17}) + (1/10)g_{62}^{22}, \qquad (5.2.101d)\\
\overline{e}_6 &= -(1/10/\sqrt{6})(g_{12}^5 + g_{22}^5 - 2g_{32}^5) + (1/10)g_{52}^{10}\\
&+ (1/10)g_{42}^{15} + (1/20)(g_{12}^{20} - g_{22}^{20}) + (1/10)g_{62}^{25}. \qquad (5.2.101e)
\end{aligned}$$

The elements of the macroscopic averaged stress tensor $\overline{s}_i$ have exactly the same expressions except that $\mathbf{g}_{jl}$ is replaced by $\mathbf{g}'_{jl}$ given by (5.2.100).

5.2.7.5. *Simplified ('short') harmonics representation of the peak shift, and the 'mixed' representation*

When it is not necessary to find WSODFs and the averaged strain and stress tensors are not of interest, one can choose a different representation for I_l^M with fewer parameters that corrects only for the line shifts caused by stress. For this reason we call this representation 'short', in contrast to the 'full' representation of I_l^M given by equations (5.2.88) and (5.2.93). Besides correcting for the line shifts, the 'full' representation provides the whole macrostrain/stress state of the sample.

To derive the 'short' representation, the quantities E_i in equation (5.2.88) and the angles (Φ, β) in equation (5.2.89) are replaced by the direction cosines a_i and one obtains

$$I_l^M(\mathbf{h}, \mathbf{y}) = \sum_{i=1}^{6} t_{il}(\mathbf{h}, \mathbf{y}) \rho_i j_{i2}(a_1, a_2, a_3), \qquad (5.2.102a)$$

$$t_{il}(\mathbf{h}, \mathbf{y}) = \sum_{\mu=1}^{\mu_l} C_{il}^\mu(\mathbf{y}) j_{\mu l}(a_1, a_2, a_3). \qquad (5.2.102b)$$

The functions $C_{il}^\mu(\mathbf{y})$ are linear combinations of $A_{il}^m(\mathbf{y})$ and $B_{il}^m(\mathbf{y})$, while $j_{\nu l}(a_1, a_2, a_3)$ are the following monomials of degree l in the variables (a_1, a_2, a_3):

$$j_{\mu l}(a_1, a_2, a_3) = a_1^{l_1} a_2^{l_2} a_3^{l_3} \quad (l_1 + l_2 + l_3 = l,\ l_i \geq 0). \qquad (5.2.103)$$

For a given value of the harmonic number l there are μ_l monomials. The complete set of monomials for l = 2, 4, 6 is given in Table 5.2.5.

Substituting (5.2.102*b*) into (5.2.102*a*) and taking into account that $j_{\nu l} j_{\mu l'} = j_{\lambda, l+l'}$, where $\lambda \in [1, \mu_{l+l'}]$, one obtains

Table 5.2.5
The monomials $j_{\mu l}(a_1, a_2, a_3)$ for l = 2, 4, 6

μ_l is the number of monomials for harmonic index l.

l, μ_l	Monomials
$l = 2$, $\mu_2 = 6$	$a_1^2, a_2^2, a_3^2, a_2a_3, a_1a_3, a_1a_2$
$l = 4$, $\mu_4 = 15$	$a_1^4, a_2^4, a_3^4, a_2^3a_3, a_2a_3^3, a_1^3a_3, a_1a_3^3, a_1^3a_2, a_1a_2^3, a_2^2a_3^2, a_1^2a_3^2, a_1^2a_2^2, a_1^2a_2a_3, a_1a_2^2a_3, a_1a_2a_3^2$
$l = 6$, $\mu_6 = 28$	$a_1^6, a_2^6, a_3^6, a_2^5a_3, a_2a_3^5, a_1^5a_3, a_1a_3^5, a_1^5a_2, a_1a_2^5, a_2^4a_3^2, a_2^2a_3^4, a_1^4a_3^2, a_1^2a_3^4, a_1^4a_2^2, a_1^2a_2^4, a_2^3a_3^3, a_1^3a_3^3, a_1^3a_2^3, a_1a_2^3a_3^2, a_1a_2^2a_3^3, a_1^3a_2a_3^2, a_1^2a_2a_3^3, a_1^3a_2^2a_3, a_1^2a_2^3a_3, a_1^4a_2a_3, a_1a_2^4a_3, a_1a_2a_3^4$

$$I_l^M(\mathbf{h}, \mathbf{y}) = \sum_{\mu=1}^{\mu_{l+2}} E_{\mu l}(\mathbf{y}) j_{\mu, l+2}(a_1, a_2, a_3). \qquad (5.2.104)$$

The functions $E_{\mu l}(\mathbf{y})$ are linear combinations of $C_{il}^\mu(\mathbf{y})$ and thus are linear combinations of $A_{il}^m(\mathbf{y})$ and $B_{il}^m(\mathbf{y})$. Consequently, according to (5.2.90) we have

$$E_{\mu l}(\mathbf{y}) = \eta_{\mu l}^0 P_l^0(\Psi) + \sum_{n=1}^{l} \left(\eta_{\mu l}^n \cos n\gamma + \zeta_{\mu l}^n \sin n\gamma\right) P_l^n(\Psi). \qquad (5.2.105)$$

Equations (5.2.104) and (5.2.105) are valid for triclinic crystal symmetry and for triclinic sample symmetry, respectively. If the crystal symmetry is higher than triclinic then (5.2.104) should be replaced by

$$I_l^M(\mathbf{h}, \mathbf{y}) = \sum_{\mu=1}^{M_{l+2}} E_{\mu l}(\mathbf{y}) J_{\mu, l+2}(a_1, a_2, a_3). \qquad (5.2.106)$$

Here, $J_{\mu,l}$ are homogenous polynomials of degree l in the variables a_1, a_2, a_3, invariant to the symmetry operations of the crystal Laue group, and M_l is their number. They are derived by setting these invariance conditions on the function $I_l^M(\mathbf{h}, \mathbf{y})$ expressed by (5.2.104) (Popa & Balzar, 2001, 2014). The polynomials for l = 2, 4, 6 are listed in Table 5.2.6 for all Laue classes. For sample symmetry higher than triclinic the coefficients $\eta_{\mu l}^n$ and $\zeta_{\mu l}^n$ in (5.2.103) follow the selection rules of the texture with the same sample symmetry. For non-cubic Laue groups these selection rules can be found, for example, in Table 3 in Popa (1992).

The number M_{l+2} in (5.2.106) must be equal to or smaller than the total number of functions A_{il}^m, B_{il}^m in (5.2.90); for crystal symmetry higher than triclinic it is frequently much smaller. For example, if the Laue class is $\overline{3}$ and l = 4, the total number of A_{il}^m, B_{il}^m is 18 (Table 6 of Popa & Balzar, 2001, 2014) but M_6 = 10; this means that there are 90 refinable parameters in place of 162. Unfortunately, it is not possible to obtain the WSODF and the averaged strain and stress tensors from the coefficients $\eta_{\mu l}^n$ and $\zeta_{\mu l}^n$.

Finally, it is possible to have a 'mixed' representation of the peak shift if I_l^M in (5.2.87) is taken as in the full representation for l = 0, 2 and as in the short representation for $l \geq 4$. In this mixed representation, besides correcting for peak shift, it is possible to calculate the averaged macroscopic strain and stress tensors $\overline{e}_i$ and $\overline{s}_i$, but not the WSODF for e_i and s_i. Like the full and the short representations, the mixed representation is implementable in Rietveld programs.

5.2.7.6. *Implementation in Rietveld codes*

In the practical applications reported to date by Behnken (2000), by Wang *et al.* (2001, 2003) and recently by Balzar *et al.*

Table 5.2.6
The complete set of polynomials $J_{\mu l}$ for $l = 2, 4, 6$ for all Laue groups

M_l is the number of polynomials in a complete set. In parts (*a*) to (*d*) the list in square brackets should be added to the complete set of polynomials for the dihedral Laue group to obtain the complete set of the cyclic Laue group. For cubic Laue groups in part (*e*), the sets are identical for some values of l and different for other l. Polynomials common to cubic Laue groups may also exist in the second case but they do not form a complete set, completeness being realized by adding the two different lists in square brackets.

(*a*) Laue groups *mmm* and 2/*m*.

l, M_l	Polynomials
$l = 2$, $M_2 = 3$ [4]	$a_1^2, a_2^2, a_3^2, [a_1a_2]$
$l = 4$, $M_4 = 6$ [9]	$a_1^4, a_2^4, a_3^4, a_2^2a_3^2, a_1^2a_3^2, a_1^2a_2^2, [a_1^3a_2, a_1a_2^3, a_1a_2a_3^2]$
$l = 6$, $M_6 = 10$ [16]	$a_1^6, a_2^6, a_3^6, a_1^4a_2^2, a_1^2a_2^4, a_1^4a_3^2, a_1^2a_3^4, a_2^4a_3^2, a_2^2a_3^4, a_1^2a_2^2a_3^2,$ $[a_1^5a_2, a_1a_2^5, a_1^3a_2^3, a_1^3a_2a_3^2, a_1a_2^3a_3^2, a_1a_2a_3^4]$

(*b*) Laue groups 4/*mmm* and 4/*m*.

l, M_l	Polynomials
$l = 2$, $M_2 = 2$	$a_1^2 + a_2^2, a_3^2$
$l = 4$, $M_4 = 4$ [5]	$a_1^4 + a_2^4, a_3^4, (a_1^2 + a_2^2)a_3^2, a_1^2a_2^2, [(a_1^2 - a_2^2)a_1a_2]$
$l = 6$, $M_6 = 6$ [8]	$a_1^6 + a_2^6, a_3^6, (a_1^4 + a_2^4)a_3^2, (a_1^2 + a_2^2)a_3^4, a_1^2a_2^2a_3^2,$ $(a_1^2 + a_2^2)a_1^2a_2^2, [(a_1^2 - a_2^2)a_1a_2a_3^2, (a_1^4 - a_2^4)a_1a_2]$

(*c*) Laue groups $\overline{3}m$ and $\overline{3}$.

l, M_l	Polynomials
$l = 2$, $M_2 = 2$	$a_1^2 + a_2^2, a_3^2$
$l = 4$, $M_4 = 4$ [5]	$(a_1^2 + a_2^2)^2, a_3^4, (a_1^2 + a_2^2)a_3^2, (3a_1^2 - a_2^2)a_2a_3,$ $[(a_1^2 - 3a_2^2)a_1a_3]$
$l = 6$, $M_6 = 7$ [10]	$(a_1^2 + a_2^2)^3, a_3^6, (a_1^2 + a_2^2)^2a_3^2, (a_1^2 + a_2^2)a_3^4,$ $(a_1^2 + a_2^2)(3a_1^2 - a_2^2)a_2a_3, (3a_1^2 - a_2^2)a_2a_3^3,$ $a_1^6 - 15a_1^4a_2^2 + 15a_1^2a_2^4 - a_2^6,$ $[(a_1^2 + a_2^2)(a_1^2 - 3a_2^2)a_1a_3, (a_1^2 - 3a_2^2)a_1a_3^3,$ $(3a_1^2 - a_2^2)(a_1^2 - 3a_2^2)a_1a_2]$

(*d*) Laue groups 6/*mmm* and 6/*m*.

l, M_l	Polynomials
$l = 2$, $M_2 = 2$	$a_1^2 + a_2^2, a_3^2$
$l = 4$, $M_4 = 3$	$(a_1^2 + a_2^2)^2, a_3^4, (a_1^2 + a_2^2)a_3^2$
$l = 6$, $M_6 = 5$ [6]	$(a_1^2 + a_2^2)^3, a_3^6, (a_1^2 + a_2^2)^2a_3^2, (a_1^2 + a_2^2)a_3^4,$ $a_1^6 - 15a_1^4a_2^2 + 15a_1^2a_2^4 - a_2^6,$ $[(3a_1^2 - a_2^2)(a_1^2 - 3a_2^2)a_1a_2]$

(*e*) Laue groups $m\overline{3}m$ and $m\overline{3}$ (cubic means these two groups).

l, M_l	Polynomials
$l = 2$, cubic $M_2 = 1$	$a_1^2 + a_2^2 + a_3^2 = 1$
$l = 4$, cubic $M_4 = 2$	$a_1^4 + a_2^4 + a_3^4, a_2^2a_3^2 + a_1^2a_3^2 + a_1^2a_2^2$
$l = 6$, cubic not complete	$a_1^6 + a_2^6 + a_3^6, a_1^2a_2^2a_3^2,$
$m\overline{3}m$ $M_6 = [3]$	$[a_1^4a_2^2 + a_2^4a_3^2 + a_3^4a_1^2 + a_1^4a_3^2 + a_2^4a_1^2 + a_3^4a_2^2]$
$m\overline{3}$ $M_6 = [4]$	$[a_1^4a_2^2 + a_2^4a_3^2 + a_3^4a_1^2, a_1^4a_3^2 + a_2^4a_1^2 + a_3^4a_2^2]$

(2010), the least-squares method was used to fit the calculated peak shifts to the measured peak shifts. As mentioned in Section 5.2.4, finding the peak shift presumes prior accurate determination of the peak positions. Because of peak overlap this can be accomplished for only a small number of peaks, and a large part of the information contained in the diffraction pattern is thus lost. As a consequence, a reasonably good set of data that could be processed using full representation of the peak shift may become a set only supported by a less powerful representation. This and other drawbacks are eliminated by implementing the peak-shift representation into Rietveld programs. All WSODF representations discussed previously are appropriate for such implementation.

5.2.7.7. *An application: determining the averaged macroscopic strain and stress tensors in a rolled uranium plate from time-of-flight neutron diffraction data*

An application of the WSODF model was reported quite recently by Balzar *et al.* (2010). The article is based on time-of-flight diffraction data measured on two identically shaped uranium plates on the SMARTS diffractometer at Los Alamos Neutron Science Center (LANSCE). One plate was cold-rolled in order to determine the residual strain and stress after plastic deformation; the second was annealed for use as a reference for the first one. With the sample mounted on an Eulerian cradle, measurements were performed for 18 specimen orientations, all with the cradle rotation angle fixed at 130° and for four scattering angles ($2\theta = \pm 98.4^\circ, \pm 81.6^\circ$), which gave 72 histograms in total. Separating 19 Bragg reflections in every histogram by pattern decomposition with peak positions as free parameters, 1368 experimental peak shifts become available. As the peak positions of the annealed sample were used as references, the strain/stress state reported by Balzar *et al.* (2010) is relative to the state of this sample. The texture was determined by *GSAS* (Von Dreele, 1997) and, surprisingly, the texture sample symmetry *mmm* expected for the cold-rolled sample was not confirmed, with the pole figures rather showing a triclinic symmetry. Consequently, the sample Laue group is $\overline{1}$, with the crystal Laue group being *mmm* (the space group of uranium is *Cmcm*). For numerical calculations an 'in-house' least-squares program without a stabilizer was adapted. As the sample and crystal symmetries were low, the number of parameters becomes too large at large l, and to avoid unreliable refined parameters the series (5.2.87) was interrupted at $l_0 = 4$. Inspection of the data set suggested using a mixed rather than a full representation of the peak shift. The expression used in least squares was then

$$\langle\varepsilon_{\mathbf{h}}(\mathbf{y})\rangle P_{\mathbf{h}}(\mathbf{y}) = 2\sum_{i=1}^{3} E_i T_0^1 g_{i0}^1 + \frac{2}{5}\sum_{i=1}^{6} E_i \rho_i \sum_{\nu\in[\nu]_i} T_2^\nu g_{i2}^\nu + \frac{2}{9}\sum_{\mu=1}^{10} E_{\mu2} J_{\mu6}.$$

All quantities have already been defined except for $[\nu_i]$. These are the ranges of the index ν for which $g_{i2}^\nu \neq 0$, thus representing the selection rules for these parameters. Looking in Table 9 from Popa & Balzar (2001, 2014) with the aid of (5.2.92), one finds $[\nu]_i = [1, 5] \cup [16, 20]$ for $i = 1, 2, 3$, $[\nu]_4 = [11, 15]$, $[\nu]_5 = [6,10]$ and $[\nu]_6 = [20, 25]$. The necessary values of $P_{\mathbf{h}}(\mathbf{y})$ were 'picked' from the *GSAS* output. There are 90 parameters for $l = 4$ with the role of ensuring a good fit and 48 for $l = 0, 2$, from which the averaged macroscopic strain and stress tensors were calculated using the expressions (5.2.101) and (5.2.102) and literature data for the single-crystal stiffness elastic constants. Taking $\mathbf{y}_1$ as the transverse direction, $\mathbf{y}_2$ as the rolling direction and $\mathbf{y}_3$ as the normal direction, these tensors are

$$\mathbf{e} = \begin{bmatrix} 1.55\,(22) & -5.41 & -6.16 \\ -5.41 & 6.42 & -0.19 \\ -6.16 & -0.19 & -1.05 \end{bmatrix} \times 10^{-4},$$

$$\mathbf{s} = \begin{bmatrix} 63\,(2) & -65 & -87 \\ -65 & 135 & -2 \\ -87 & -2 & 4 \end{bmatrix} \text{ MPa.}$$

The standard uncertainties, which are approximately constant for all tensor elements, are given in parentheses only for e_{11} and s_{11}. The tensile strain and stress in the rolling and transverse directions, with the former being much higher (approximately four times in strain and two times in stress), and a compressive strain in the normal direction accompanied by practically zero stress (within the limits of two standard deviations) confirm the expectations. Unexpected results before the experiment, but in concordance with the texture sample symmetry found from the measurements, are the strong, compressive shear components in both the strain and stress tensors. This may be caused by the slippage of rollers or/and the existence of a strong texture before rolling. Unfortunately, the texture before rolling was not investigated.

5.2.7.8. *Limitations of the spherical-harmonics approach and possible further developments*

The coefficients g_{jl}^{ν} from (5.2.93) refined in a least-squares program (Rietveld included) could be unreliable if the number of terms in the truncated series (5.2.87) is too large. One expects there to be a large number of terms in three cases: for low sample and crystal symmetry, if the peak shift is a strongly varying function in its arguments and if the strain/stress state is far from the ground state. For the approach presented here the ground state is the hydrostatic strain/stress state of an isotropic polycrystal. It is possible to derive at least two other spherical-harmonics representations of the WSODF having the Voigtian and the Reussian strain/stress state of an anisotropic polycrystal as a ground state, respectively.[6] Compared to the approaches of Wang *et al.* (1999) and Behnken (2000), these new representations will extend to any sample and crystal symmetry and will be implementable in Rietveld programs. The best representation from the hydrostatic, Voigtian and Reussian ground-state representations can be determined by trials. It must be noted that searching for representations with different ground states makes sense only because the corresponding series are interrupted. Finally, for low crystal and sample symmetries and strongly varying WSODFs the number of parameters may still remain large. It will then be useful to examine the possibility of finding a direct method to invert the strain pole distributions similar to the WIMW (Williams, Imhof, Matthies and Vienel) direct method used in texture analysis to determine the ODF from the texture pole distribution.

5.2.8. The spherical-harmonics approach to strain broadening

5.2.8.1. *Ignoring the macrostrain variance*

The strain diffraction line integral breadth in WPPF calculated with one of the equations (5.2.48) is proportional to the square root of the variance of the strain. According to equations (5.2.45) this quantity has two components: the microstrain variance $V_{\mathbf{h}}^{m}(\mathbf{y})$ and the macrostrain variance $V_{\mathbf{h}}^{M}(\mathbf{y})$. As in Section 5.2.7, the strain tensors on the right-hand side of these functions are defined in the crystallite reference system. As it is determined only by the intergranular strain, the macrostrain variance is small if the macrostrain/stress state is not too far from the hydrostatic state. Starting from the fact that the first term in the spherical-harmonics representation of intergranular strain has the harmonic index $l = 2$, it is easy to show that the macrostrain variance can be represented as a series of polynomials in a_1, a_2, a_3 beginning with degree 8, thus anticipating that the microstrain variance can be represented as a series of polynomials beginning with degree 4. The macrostrain variance has a contribution to the high-order terms (≥ 8) which is ignored in practice; thus, we can set $V_{\mathbf{h}}(\mathbf{y}) \simeq V_{\mathbf{h}}^{m}(\mathbf{y})$.

5.2.8.2. *The double-dependent anisotropic strain breadth (DDASB)*

The variance of microstrains $V_{\mathbf{h}}^{m}(\mathbf{y})$ is susceptible to analysis by generalized spherical harmonics similar to those developed previously for the peak shift [equation (5.2.44)]. The functions to be expanded in generalized spherical harmonics are the elements of the microstrain correlation matrix $\Delta_{ij}(g)$ defined by (5.2.41), weighted by the ODF. An expansion of $\Delta_{ij}(g)f(g)$ in generalized spherical harmonics similar to (5.2.81) but with the index i replaced by the pair ij is inserted in (5.2.45*c*). Following the derivation from Section 5.2.7.1 and ignoring the macrostrain variance, the variance of observable strains becomes

$$V_{\mathbf{h}}(\mathbf{y})P_{\mathbf{h}}(\mathbf{y}) = \sum_{l=0}^{\infty}[2/(2l+1)]I_l^m(\mathbf{h},\mathbf{y}) \quad (l = \text{even}), \tag{5.2.107}$$

$$I_l^m(\mathbf{h},\mathbf{y}) = \sum_{i=1}^{6}\sum_{j=1}^{6} E_i E_j \rho_i \rho_j t_{ijl}(\mathbf{h},\mathbf{y}), \tag{5.2.108}$$

$$\begin{aligned} t_{ijl}(\mathbf{h},\mathbf{y}) = {} & A_{ijl}^{0}(\mathbf{y})P_l^0(\Phi) \\ & + \sum_{m=1}^{l}\left[A_{ijl}^{m}(\mathbf{y})\cos m\beta + B_{ijl}^{m}(\mathbf{y})\sin m\beta\right]P_l^m(\Phi). \end{aligned} \tag{5.2.109}$$

Expressions similar to (5.2.90) can be written for the coefficients $A_{ijl}^{m}(\mathbf{y})$ and $B_{ijl}^{m}(\mathbf{y})$.

Although similar, there are important differences between the spherical-harmonics representations of $\varepsilon_i(g)$ and of $\Delta_{ij}(g)$. Firstly, the symmetrical tensor Δ_{ij} has 21 distinct elements while ε_i has only six, and thus the number of harmonic coefficients is much greater for the former. Secondly, the selection rules for $A_{ijl}^{m}(\mathbf{y})$ and $B_{ijl}^{m}(\mathbf{y})$ resulting from the crystal symmetry operations should be different from those for $A_{il}^{m}(\mathbf{y})$ and $B_{il}^{m}(\mathbf{y})$ for the problem of the peak shift. Finally, if the determination of the strain orientation distribution functions $\varepsilon_i(g)$ is frequently required, there is no practical interest in determining the function $\Delta_{ij}(g)$. Only the dependence on $\mathbf{h}$ and $\mathbf{y}$ of the strain broadening is required and, for this purpose, an alternative representation of $I_l^m(\mathbf{h},\mathbf{y})$ with a smaller number of parameters can be derived, similar to the 'short' representation of $I_l^M(\mathbf{h},\mathbf{y})$ for the peak shift. In this case, deriving the selection rules for $A_{ijl}^{m}(\mathbf{y})$ and $B_{ijl}^{m}(\mathbf{y})$ becomes useless.

To arrive at the 'short' representation of the strain variance, one replaces the quantities E_i in (5.2.108) and the angles (Φ, β) in (5.2.109) by the direction cosines (a_1, a_2, a_3). After replacement these equations become

$$I_l^m(\mathbf{h},\mathbf{y}) = \sum_{\nu=1}^{15} t_{\nu l}(\mathbf{h},\mathbf{y})\, j_{\nu 4}(a_1, a_2, a_3), \tag{5.2.110}$$

$$t_{ijl}(\mathbf{h},\mathbf{y}) = \sum_{\mu=1}^{\mu_l} C_{ijl}^{\mu}(\mathbf{y})\, j_{\mu}(a_1, a_2, a_3). \tag{5.2.111}$$

The functions $t_{\nu l}(\mathbf{h},\mathbf{y})$ in (5.2.110) are linear combinations of $t_{ijl}(\mathbf{h},\mathbf{y})$, while $C_{ijl}^{\mu}(\mathbf{y})$ in (5.2.111) are linear combinations of $A_{ijl}^{m}(\mathbf{y})$ and $B_{ijl}^{m}(\mathbf{y})$. Substituting (5.2.111) into (5.2.110), one obtains

---

[6] WSODF representations with Voigtian and Reussian ground states have been reported by Popa *et al.* (2014, 2015) and by Popa (2017), respectively.

$$I_l^m(\mathbf{h}, \mathbf{y}) = \sum_{\mu=1}^{\mu_{l+4}} E_{\mu l}(\mathbf{y})\, j_{\mu,l+4}(a_1, a_2, a_3). \qquad (5.2.112)$$

For crystal symmetries higher than triclinic the monomials in (5.2.112) should be replaced by symmetrized polynomials and we then have

$$I_l^m(\mathbf{h}, \mathbf{y}) = \sum_{\mu=1}^{M_{l+4}} E_{\mu l}(\mathbf{y})\, J_{\mu,l+4}(a_1, a_2, a_3), \qquad (5.2.113)$$

Equations (5.2.48), (5.2.107), (5.2.113) and (5.2.105) describe the dependence of the strain diffraction line breadth on both the crystal and sample directions. These equations are appropriate for implementation in WPPF programs, including Rietveld, if (5.2.107) is truncated, keeping a dependence on both **h** and **y**, but not increasing the number of refinable parameters too much; truncating at $l = 2$ may be a reasonable choice.

5.2.8.3. *The 'classical' limit of the DDASB*

If $\Delta_{ij}(g) = \overline{\Delta}_{ij}$, where $\overline{\Delta}_{ij} = \iiint \mathrm{d}g\, f(g)\, \Delta_{ij}(g)$, and the sample is isotropic, then in the right-hand side of equation (5.2.113) there is only the term with harmonic index $l = 0$. This condition is similar to (5.2.72) defining the hydrostatic macrostrain/stress state. The coefficients in (5.2.105) become constants and the strain variance is independent of sample direction. We then have

$$V_{\mathbf{h}} = \sum_{\mu=1}^{M_4} \eta_{\mu 0}\, J_{\mu,4}(a_1, a_2, a_3). \qquad (5.2.114)$$

This is the phenomenological model of strain broadening anisotropy reported by Popa (1998) and independently by Stephens (1999). This model is implemented today in all popular Rietveld programs. In *GSAS* (Larson & Von Dreele, 2004) to simultaneously process a number of diffraction patterns recorded in different sample directions, the same number of independent sets of Popa/Stephens model parameters are necessary (R. B. Von Dreele, personal communication), while only one set of strain broadening parameters of the DDASB model is required if this model was implemented in the Rietveld method.

This work was performed with financial support from the Romanian National Authority for Scientific Research through contract PCE 102/2011.

References

Averbach, A. L. & Warren, B. E. (1949). *Interpretation of X-ray patterns of cold-worked metal. J. Appl. Phys.* **20**, 885–886.

Balzar, D., Popa, N. C. & Vogel, S. (2010). *Strain and stress tensors of rolled uranium plate by Rietveld refinement of TOF neutron-diffraction data. Mater. Sci. Eng. A*, **528**, 122–126.

Balzar, D., Von Dreele, R. B., Bennett, K. & Ledbetter, H. (1998). *Elastic-strain tensor by Rietveld refinement of diffraction measurements. J. Appl. Phys.* **84**, 4822–4833.

Behnken, H. (2000). *Strain-function method for the direct evaluation of intergranular strains and stresses*. *Phys. Status Solidi A*, **177**, 401–418.

Behnken, H. & Hauk, V. (1986). *Berechnung der rontgenographischen Elastizitetskonstanten (REK) des Vielkristalls aus den Einkristalldaten fur beliebige Kristallsymmetrie. Z. Metalkd.* **77**, 620–626.

Bollenrath, F., Hauk, V. & Müller, E. H. (1967). *Z. Metallkd.* **58**, 76–82.

Bunge, H.-J. (1982). *Texture Analysis in Materials Science: Mathematical Methods*. London: Butterworths.

Chateigner, D. (2010). *Combined Analysis*. London/Hoboken: ISTE/Wiley.

Christenson, A. L. & Rowland, E. S. (1953). *X-ray measurement of residual stress in hardened high carbon steel. Trans. Am. Soc. Met.* **45**, 638–676.

Dölle, H. (1979). *The influence of multiaxial stress states, stress gradients and elastic anisotropy on the evaluation of (residual) stresses by X-rays. J. Appl. Cryst.* **12**, 489–501.

Eshelby, J. D. (1957). *The determination of the elastic field of an ellipsoidal inclusion, and related problems. Proc. R. Soc. Lond. A*, **241**, 376–396.

Ferrari, M. & Lutterotti, L. (1994). *Method for the simultaneous determination of anisotropic residual stresses and texture by X-ray diffraction. J. Appl. Phys.* **76**, 7246–7255.

Gnäupel-Herold, T., Brand, P. C. & Prask, H. J. (1998). *Calculation of single-crystal elastic constants for cubic crystal symmetry from powder diffraction data. J. Appl. Cryst.* **31**, 929–935.

Hall, W. H. (1949). *X-ray line broadening in metals. Proc. Phys. Soc. Lond. A*, **62**, 741.

Hauk, V. (1952). *Röntgenographische und mechanische Verformungsmessungen an Grauguss. Arch. Eisenhüttenwesen*, **23**, 353–361.

Hauk, V. (1997). *Structural and Residual Stress Analysis by Nondestructive Methods*. Amsterdam: Elsevier Science.

Hill, R. (1952). *The elastic behaviour of a crystalline aggregate. Proc. Phys. Soc. A*, **65**, 349–354.

Kroner, E. (1958). *Berechnung der elastischen Konstanten des Vielkristalls aus den Konstanten des Einkristalls. Z. Phys.* **151**, 504–518.

Langford, J. I. (2004). *Diffraction Analysis of the Microstructure of Materials*, edited by E. J. Mitemeijer & P. Scardi, pp. 3–13. Berlin: Springer.

Larson, A. C. & Von Dreele, R. B. (2004). *General Structure Analysis System (GSAS)*. Report LAUR 86-748. Los Alamos National Laboratory, USA.

Lutterotti, L. (2010). *Total pattern fitting for the combined size–strain–stress–texture determination in thin film diffraction. Nucl. Instrum. Methods Phys. Res. B*, **268**, 334–340.

Noyan, I. C. & Cohen, J. B. (1987). *Residual Stress: Measurement by Diffraction and Interpretation*. New York: Springer-Verlag.

Nye, J. F. (1957). *Physical Properties of Crystals*. Oxford University Press.

Popa, N. C. (1992). *Texture in Rietveld refinement. J. Appl. Cryst.* **25**, 611–616.

Popa, N. C. (1998). *The (hkl) dependence of diffraction-line broadening caused by strain and size for all Laue groups in Rietveld refinement. J. Appl. Cryst.* **31**, 176–180.

Popa, N. C. (2000). *Diffraction-line shift caused by residual stress in polycrystal for all Laue groups in classical approximations. J. Appl. Cryst.* **33**, 103–107.

Popa, N. C. (2008). *Powder Diffraction: Theory and Practice*, edited by R. E. Dinnebier & S. J. L. Billinge, ch. 12. Cambridge: Royal Society of Chemistry.

Popa, N. C. (2017). *Spherical harmonics analysis based on the Reuss model in elastic macro strain and stress determination by powder diffraction. J. Appl. Cryst.* **50**, 1735–1743.

Popa, N. C. & Balzar, D. (2001). *Elastic strain and stress determination by Rietveld refinement: generalized treatment for textured polycrystals for all Laue classes. J. Appl. Cryst.* **34**, 187–195.

Popa, N. C. & Balzar, D. (2014). *Elastic strain and stress determination by Rietveld refinement: generalized treatment for textured polycrystals for all Laue classes. Second corrigendum. J. Appl. Cryst.* **47**, 2113.

Popa, N. C., Balzar, D. & Vogel, S. C. (2014). *Elastic macro strain and stress determination by powder diffraction: spherical harmonics analysis starting from the Voigt model. J. Appl. Cryst.* **47**, 154–159.

Popa, N. C., Balzar, D. & Vogel, S. C. (2015). *Elastic macro strain and stress determination by powder diffraction: spherical harmonics analysis starting from the Voigt model. Corrigenda. J. Appl. Cryst.* **48**, 311.

Popa, N. C. & Lungu, G. A. (2013). *Dependence of the strain diffraction line broadening on (hkl) and sample direction in textured polycrystals. J. Appl. Cryst.* **46**, 391–395.

Reuss, A. (1929). *Berechnung der Fliessgrenze von Mischkristallen auf Grund der Plastizitätsbedingung für Einkristalle. Z. Angew. Math. Mech.* **9**, 49–58.

Scherrer, P. (1918). *Bestimmung der Grösse und der inneren Struktur von Kolloidteilchen mittels Röntgenstrahlen. Nachr. Ges. Wiss. Göttingen*, pp. 98–100.

Stephens, P. W. (1999). *Phenomenological model of anisotropic peak broadening in powder diffraction. J. Appl. Cryst.* **32**, 281–289.

Stokes, A. R. & Wilson, A. J. C. (1944). *The diffraction of X-rays by distorted crystal aggregates – I. Proc. Phys. Soc.* **56**, 174–181.

Van Acker, K., Root, J., Van Houtte, P. & Aernoudt, E. (1996). *Neutron diffraction measurement of the residual stress in the cementite and ferrite phases of cold-drawn steel wires. Acta Mater.* **44**, 4039–4049.

Voigt, W. (1928). *Lehrbuch der Kristallphysik*. Berlin, Leipzig: Teubner Verlag.

Von Dreele, R. B. (1997). *Quantitative texture analysis by Rietveld refinement. J. Appl. Cryst.* **30**, 517–525.

Wang, Y. D., Peng, R. L. & McGreevy, R. (1999). *High anisotropy of orientation dependent residual stress in austenite of cold rolled stainless steel. Scr. Mater.* **41**, 995–1000.

Wang, Y. D., Peng, R. L. & McGreevy, R. (2001). *A novel method for constructing the mean field of grain-orientation-dependent residual stress. Philos. Mag. Lett.* **81**, 153–163.

Wang, Y. D., Wang, X.-L., Stoica, A. D., Richardson, J. W. & Peng, R. L. (2003). *Determination of the stress orientation distribution function using pulsed neutron sources. J. Appl. Cryst.* **36**, 14–22.

Warren, B. E. (1969). *X-ray Diffraction*. Reading: Addison–Wesley.

Welzel, U., Ligot, J., Lamparter, P., Vermeulen, A. C. & Mittemeijer, E. J. (2005). *Stress analysis of polycrystalline thin films and surface regions by X-ray diffraction. J. Appl. Cryst.* **38**, 1–29.

Wilson, A. J. C. (1962). *X-ray Optics*, 2nd ed. London: Methuen.

Wooster, W. A. (1973). *Tensors and Group Theory for Physical Properties of Crystals*. Oxford: Clarendon Press.

International Tables for Crystallography (2019). Vol. H, Chapter 5.3, pp. 555–580.

5.3. Quantitative texture analysis and combined analysis

D. Chateigner, L. Lutterotti and M. Morales

5.3.1. Introduction

For many solids, the growth of single crystals with sufficiently perfect crystallinity is not easy to manage, and is sometimes impossible. On the other hand, a perfectly randomly oriented powder is often impossible to obtain, or may even be undesirable if the anisotropic character of the sample is to be maintained. Consequently, any nondestructive characterization technique (for example diffraction) faces the difficulty of analysing textured samples, which are in a state between a perfect single crystal and a perfect powder. Such 'real samples' are obtained by complex techniques (alignment under uniaxial pressure, magnetic or electric fields, thermal gradients, flux or substrate growth, and combinations of these), and sample preparation is often difficult and time consuming. Unfortunately, when samples are crystallographically oriented to benefit from the intrinsic anisotropic properties of the constituent crystals, many characterization techniques (*i.e.* Rietveld analysis; Rietveld, 1969) are not appropriate or require sample grinding. Very often this grinding is not acceptable, as in the case of rare samples (for example fossils or comets), when grinding modifies the physical properties of the samples themselves (residually stressed materials), or when grinding is simply not possible (thin films).

It then becomes crucial to quantitatively take the textured character of the measured samples into account, either independently of other parameters that are accessible to diffraction (phase content, stresses, particle sizes and shapes), as in quantitative texture analysis (QTA), or to take these parameters into account by refining them all together, as in the combined-analysis (CA) methodology.

In this chapter, we introduce the various aspects of QTA and describe the additional information that CA can yield for the full characterization of real materials. QTA is most commonly applied because the existence of texture often determines the characteristics of the sample.

5.3.2. Crystallographic quantitative texture analysis (QTA)

Even though QTA was developed in the 1960s, the current literature shows that some qualitative information can still be usefully obtained by the simple 'classical' scans used by diffractionists. Such classical scans can be the usual one-dimensional θ–2θ or ω scans (rocking curves) in reflection mode, using point or position-sensitive detectors, or even single images in transmission. We should not forget that such scans can provide (depending on the texture itself) very restricted textural information, which has been thoroughly discussed in Chateigner (2010). There is then *a priori* no justification for using such limited views of texture, particularly with the recent technical advancements in sources and detectors that make the rapid acquisition of full texture scans available.

5.3.2.1. *Orientation distribution (OD)*

5.3.2.1.1. *The orientation space H*

Defining the orientation of a crystal requires the location of at least two directions of the crystal in a macroscopic reference frame. The definition of two reference frames (Fig. 5.3.1), one linked to the sample, $K_A = (\mathbf{x}_A, \mathbf{y}_A, \mathbf{z}_A)$, or (**100**, **010**, **001**), and the other to each of the crystals in the sample, K_B, is thus required. In order to make these two frames coincident (Fig. 5.3.2), one needs three Euler angles, α_c, β_c, γ_c, forming a triplet called the orientation component $g = \{\alpha_c, \beta_c, \gamma_c\}$. The angles β_c and α_c determine the orientation of the [001]* crystallite direction in K_A and are called the co-latitude (or pole distance) and azimuth, respectively, while γ_c defines the location of another crystallographic

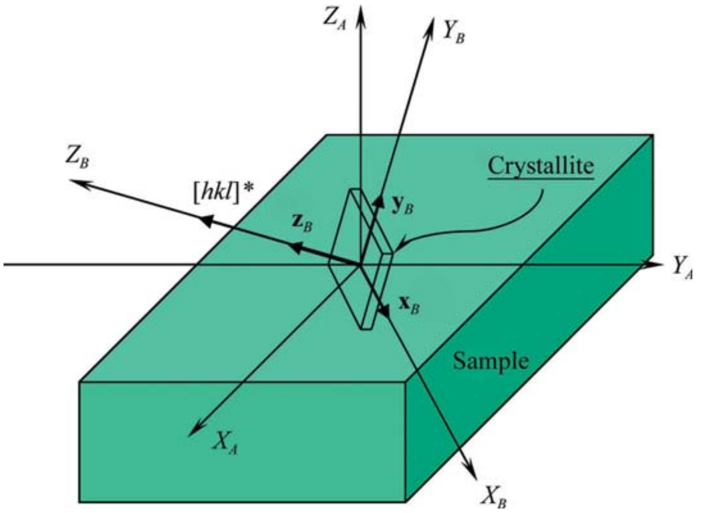

Figure 5.3.1
Crystal and sample reference frames $K_B = (\mathbf{x}_B, \mathbf{y}_B, \mathbf{z}_B)$ and $K_A = (\mathbf{x}_A, \mathbf{y}_A, \mathbf{z}_A)$. Only one crystallite is shown.

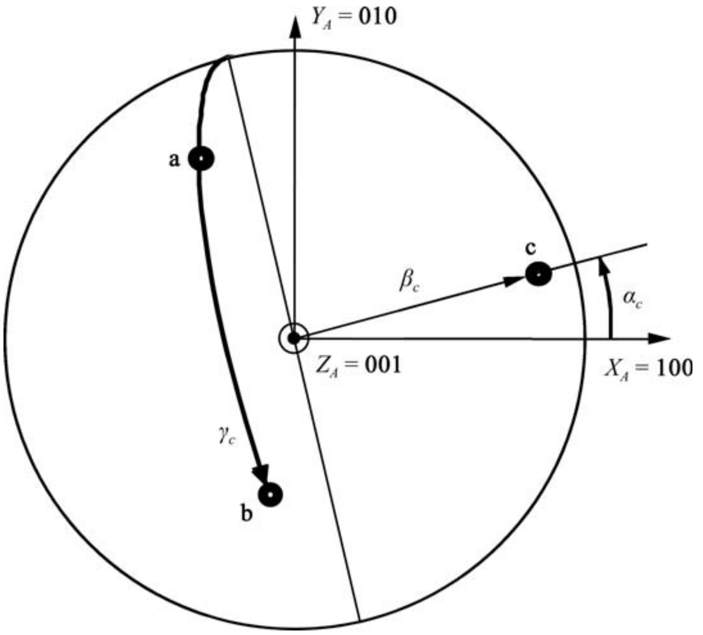

Figure 5.3.2
Definition of the three Euler angles α_c, β_c and γ_c that define the orientation of one crystallite frame $K_B = (\mathbf{a}, \mathbf{b}, \mathbf{c})$ of an orthogonal crystal cell in the sample coordinate system K_A. Note that **100**, **010** and **001** are not Miller indices but are vectors referring to an orthonormal frame aligned with K_A.

Copyright © 2019 International Union of Crystallography

direction, chosen as [010]* [in the (**a**, **b**) plane for orthogonal crystal cells].

The ensemble of all possible values of g defines the orientation space, or H space. Note that we use H here (rather than the usual 'G space' for QTA) after the description of orientation symmetry of Curien (1971). An infinite number of possibilities for the choice of Euler angles exist, but the two most commonly used are those of Roe–Matthies (Roe, 1965; Matthies *et al.*, 1987) and Bunge (Bunge, 1969). We use the former here, for which K_A is brought coincident to K_B by the operation g: $[K_A \mapsto K_B]$ using the three following rotations:

(i) rotation of K_A about the axis Z_A through the angle α_c: $[K_A \mapsto K'_A]$; associated rotation $g_1 = \{\alpha_c, 0, 0\}$,
(ii) rotation of K'_A about the axis Y'_A through the angle β_c: $[K'_A \mapsto K''_A]$; associated rotation $g_2 = \{0, \beta_c, 0\}$,
(iii) rotation of K''_A about the axis Z''_A through the angle γ_c: $[K''_A \mapsto K'''_A \parallel K_B]$; associated rotation $g_3 = \{0, 0, \gamma_c\}$.

Finally, we obtain

$$g = g_1\, g_2\, g_3 = \{\alpha_c, 0, 0\}\,\{0, \beta_c, 0\}\,\{0, 0, \gamma_c\} = \{\alpha_c, \beta_c, \gamma_c\}.$$

The choice of K_A has historically been dependent on the field of science. In metallurgy, in dealing with the rolling of metals and alloys (Coulomb, 1982), the normal to the rolling plane (ND), the rolling direction (RD) and its transverse (TD) are typically chosen. For geologists, the sample axes are aligned with respect to the lineation direction and foliation plane, with the track from the latter generally being aligned with the lineation on the pole figures (Wenk, 1985). The use of QTA in molluscan studies (Chateigner *et al.*, 2000) imposed the choice of a frame linked to the mollusc shell growth, margin and normal directions (**G**, **M** and **N**, respectively). In thin-film analyses (Chateigner & Erler, 1997), for which a heteroepitaxial relationship between the film and the underlying single-crystal substrate is generally desired, the sample frame is aligned with the main crystallographic directions of the substrate. In the case of unidirectional experimental environments such as magnetic fields (Morales *et al.*, 2003), fibre spinning, axial pressure (Wenk *et al.*, 1996), hot forging (Guilmeau *et al.*, 2003), spin coating (Ricote & Chateigner, 1999) and self-deposition in a liquid (Manceau *et al.*, 1998), the unique axis (of loading, field or spinning) is generally aligned with the $\mathbf{z_A}$ pole-figure axis. When a combination of several loads is applied, such as a magnetic field and a perpendicular thermal gradient (Durand *et al.*, 1995), the axis of one load is aligned with $\mathbf{z}_A$ while the other is parallel to $\mathbf{x}_A$ or $\mathbf{y}_A$. Using centrifugation, the axis of rotation of the centrifugation is not generally the axis along which the crystal orientation is forced (Gridi-Bennadji *et al.*, 2009), because the pressure axis resulting from centrifugation is radially distributed and is often placed along $\mathbf{z}_A$ in the pole figures, and there is no in-plane alignment in the sample.

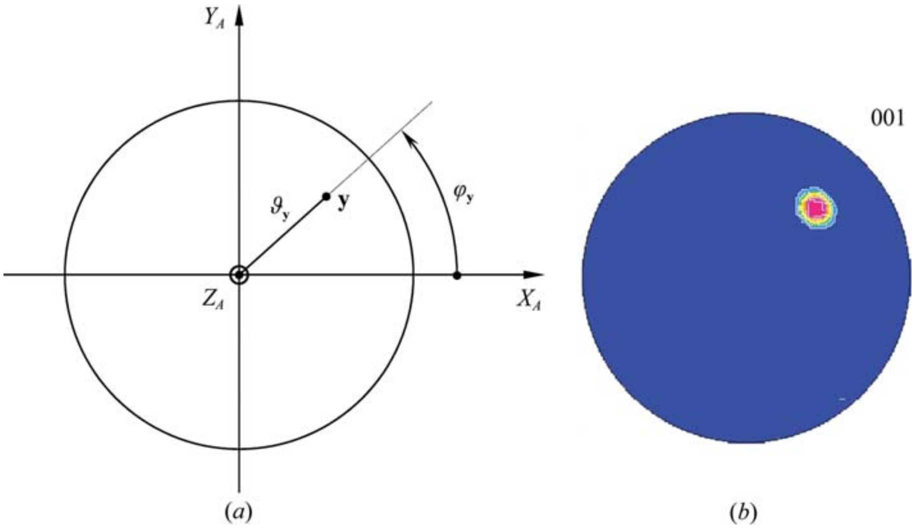

Figure 5.3.3
(*a*) $P_{\mathbf{h}}(\mathbf{y})$ diffraction pole figure for one crystallite. The direction **y** is associated with the [*hkl*]* vector. (*b*) Pole figure of a texture component centred on the previous **y**, with a Gaussian shape with 10° FWHM, for **h** = ⟨001⟩* of an orthorhombic crystal structure.

5.3.2.1.2. *The orientation distribution (OD) or orientation distribution function (ODF)*

Another concept is needed when dealing with an assembly of many crystals: the orientation distribution of crystallites (or OD), $f(g)$. This function, which can either be represented by an analytical function (ODF) or not (OD), represents the statistical distribution of the orientations of the crystallites in a polycrystalline aggregate. It is defined by

$$\frac{\mathrm{d}V(g)}{V} = \frac{1}{8\pi^2} f(g)\,\mathrm{d}g, \qquad (5.3.1)$$

where $\mathrm{d}g = \sin\beta_c\,\mathrm{d}\beta_c\,\mathrm{d}\alpha_c\,\mathrm{d}\gamma_c$ is the orientation element (Fig. 5.3.2) in the orientation space. The H space is constructed from the rotation groups of the crystallographic and sample symmetry (and the inversion centre in normal diffraction). V is the irradiated volume and $\mathrm{d}V(g)$ is the volume of crystallites which have an orientation between g and $g + \mathrm{d}g$.

$f(g)$ is consequently the volume density of crystallites oriented in dg. It is measured in m.r.d. (multiples of a random distribution) and normalized to the value $f_r(g) = 1$ for a sample without any preferred orientation (random). The $f(g)$ values are orientation distribution densities, and range from 0 (an absence of crystallites oriented in dg around g) to infinity (for some of the H-space values of single crystals). Since V is by definition 100%, the normalization condition of $f(g)$ over the whole orientation space is

$$\int\limits_{\alpha_c=0}^{2\pi} \int\limits_{\beta_c=0}^{\pi} \int\limits_{\gamma_c=0}^{2\pi} f(g)\,\mathrm{d}g = 8\pi^2. \qquad (5.3.2)$$

5.3.2.1.3. *Pole figures*

5.3.2.1.3.1. *Mathematical expression*

Pole figures, $P_{\mathbf{h}}(\mathbf{y})$, are representations of the distribution of a given **h** = ⟨*hkl*⟩* direction in K_A located in Y space (Fig. 5.3.3*a*). They represent the volume density of crystallites oriented in d**y**, *i.e.* between $(\vartheta_{\mathbf{y}}, \varphi_{\mathbf{y}})$ and $(\vartheta_{\mathbf{y}} + \mathrm{d}\vartheta_{\mathbf{y}}, \varphi_{\mathbf{y}} + \mathrm{d}\varphi_{\mathbf{y}})$,

$$\frac{\mathrm{d}V(\mathbf{y})}{V} = \frac{1}{4\pi} P_{\mathbf{h}}(\mathbf{y})\,\mathrm{d}\mathbf{y}, \qquad (5.3.3)$$

where V is the irradiated volume and $\mathrm{d}V(\mathbf{y})$ is the volume of crystallites which have an orientation with a direction **h** between **y** and **y** + d**y**, with $\mathrm{d}\mathbf{y} = \sin\vartheta_{\mathbf{y}}\mathrm{d}\vartheta_{\mathbf{y}}\mathrm{d}\varphi_{\mathbf{y}}$. The factor $1/4\pi$ arises from the normalization of the pole figures into distribution densities,

$$\int_{\varphi_{\mathbf{y}}=0}^{2\pi}\int_{\vartheta_{\mathbf{y}}=0}^{\pi} P_{\mathbf{h}}(\vartheta_{\mathbf{y}},\varphi_{\mathbf{y}})\sin\vartheta_{\mathbf{y}}\,\mathrm{d}\vartheta_{\mathbf{y}}\,\mathrm{d}\varphi_{\mathbf{y}} = 4\pi. \qquad (5.3.4)$$

Every pole figure of a random sample will exhibit the same density $P_{\mathbf{h}}(\mathbf{y})$ = 1 m.r.d., whatever the value of $\mathbf{y}$.

5.3.2.1.3.2. *Diffraction pole figures and orientation of planes*

At a Bragg angle corresponding to the $\{hkl\}$ planes and for a direction $\mathbf{y}$ of the sample, all of the planes such that $\mathbf{h}\|\mathbf{y}$ are in the diffraction condition, whatever their rotation around $\mathbf{y}$. Consequently, diffraction only probes a direction, not an orientation, and we need at least to determine the location of two directions of a plane to know its orientation. Diffraction only probes $P_{\mathbf{h}}(\mathbf{y})$, not $f(g)$ directly, and we need to measure at least several pole figures $P_{\mathbf{h}}(\mathbf{y})$ to determine $f(g)$.

Again, using normal diffraction Friedel's law applies and one cannot differentiate the diffracted intensity $I_{\mathbf{h}}$ from $I_{-\mathbf{h}}$. Consequently, the measured (reduced) pole figures are centrosymmetric and even objects, such that

$$\tilde{P}_{\mathbf{h}}(\mathbf{y}) = \tfrac{1}{2}[P_{\mathbf{h}}(\mathbf{y}) + P_{-\mathbf{h}}(\mathbf{y})]. \qquad (5.3.5)$$

5.3.2.1.3.3. *From diffraction measurements to pole figures and ODs*

Diffraction pole figures are usually measured using a four-circle diffractometer with regular increments in tilt (χ) and azimuth (φ) rotation axes, or in kappa geometry. Both reflection (Schulz, 1949*a*) and transmission (Schulz, 1949*b*; Field & Merchant, 1949) modes can be used, with point, one-dimensional or two-dimensional detectors, which can be either linear, flat or curved.

Prior to any measurement, it is necessary to know whether the data available from a given instrument can provide a correct OD characterization (*i.e.* how many pole figures are necessary and over which range each pole figure has to be measured) in order to permit an OD refinement. Helming (1992) addressed the question with the minimum pole-figure range, using the minimum pole density set concept of Vadon (1981). Such an approach defines as a necessary condition that the number and range of pole figures must be large enough such that any crystal orientation can be determined unambiguously. Using discrete data points, this requires that at least three projection paths $\tilde{\varphi}$ from pole figures pass through every OD cell. Complete OD coverage requires quite a large amount of data (typically 1300 measured points per pole figure, with several pole figures being necessary for low resolution using a 5° grid), which is nowadays accessible using multiple detectors.

The goniometer setting for each point can be described by three angles: ω, χ and φ. Additionally, if the diffraction point that we consider (the detector or pixel position) is outside the usual 2θ diffraction plane, another angle η is necessary along the Debye ring. We can define the resulting rotation matrix $\mathbf{R}$ as the product of the corresponding 3×3 matrices,

$$\mathbf{R} = -\boldsymbol{\Theta}\mathbf{H}\boldsymbol{\Omega}\mathbf{X}\boldsymbol{\Phi}, \qquad (5.3.6)$$

and the pole-figure angles can be obtained:

$$\begin{aligned}\cos\vartheta_{\mathbf{y}} &= R_{33},\\ \tan\varphi_{\mathbf{y}} &= R_{31}/R_{32}.\end{aligned} \qquad (5.3.7)$$

Depending on the experimental setup, various corrections have to be applied to the data. Localization corrections are those that transform the angular coordinates of the data from the diffractometer space S, where the scattered intensities are measured, to the space in which modelling occurs, for instance the pole-figure space Y (Bunge *et al.*, 1982; Heizmann & Laruelle, 1986; Heidelbach *et al.*, 1999; Chateigner, 2010). Also, depending on the sample itself, proper corrections for defocusing and background (Chernock & Beck, 1952; Gale & Griffiths, 1960; Holland, 1964; Feng, 1965; Tenckhoff, 1970; Couterne & Cizeron, 1971; Huijser-Gerits & Rieck, 1974), fluorescence, absorption and volume changes (Chateigner *et al.*, 1992, 1994*a*,*b*, 1995; Liu *et al.*, 2003) have to be carried out during sample rotations. The representation of pole figures is usually by stereographic (or equal-angular) projections. The main drawback of such a representation is that the density levels at the centre of the pole figures appear to be overrepresented compared with those near the equator. We then prefer to plot pole figures using Schmidt (or Lambert) projections (or equal-area projections), which offer representations with nearly equal surface elements at the centres and peripheries of pole figures (Kocks *et al.*, 1998).

After the previous corrections, one obtains the so-called diffraction (direct) pole figures, $I_{\mathbf{h}}(\mathbf{y})$. However, these depend on the porosity, crystalline state and other features of the sample, and to compare textures between samples the normalized pole figure $P_{\mathbf{h}}(\mathbf{y})$ has to be calculated.

Such normalization, calculations and refinements of the ODs using various algorithms are implemented in software such as the *Berkeley Texture* (*BEARTEX*) package (Wenk *et al.*, 1998), the *Preferred Orientation Package – Los Alamos* (*popLA*) package (Kocks *et al.*, 1994), the *LaboTex* texture-analysis software (Pawlik & Ozga, 1999) and the *MATLAB* toolbox for quantitative texture analysis (*MTEX*; Hielscher & Schaeben, 2008). The last is freeware. Two other programs, *Material Analysis Using Diffraction* (*MAUD*; Lutterotti *et al.*, 1999) and the *General Structure Analysis System* (*GSAS*; Von Dreele, 1997; Larson & Von Dreele, 2000), are furthermore able to carry out Rietveld analysis on large sets of data, giving access to many more material characteristics.

5.3.2.1.3.4. *Pole-figure normalization*

If a given $I_{\mathbf{h}}(\mathbf{y})$ pole figure has been measured completely (all of the $\mathbf{y}$ values could be obtained), it can be normalized

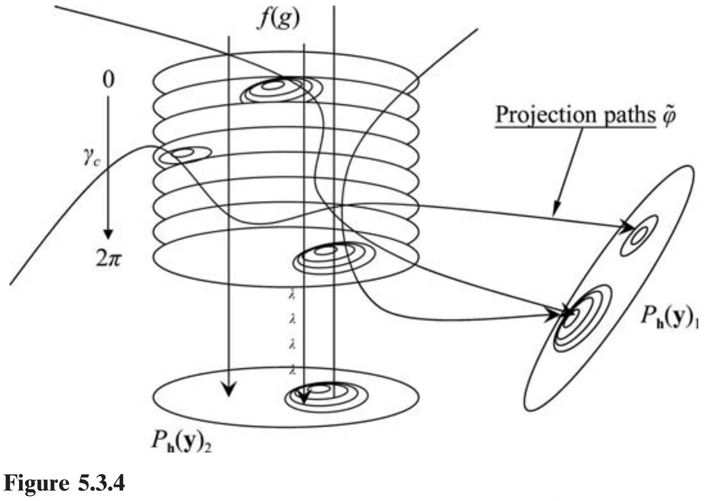
$f(g)$
0
γ_c
2π
Projection paths $\tilde{\varphi}$
λ
λ
λ
λ
$P_{\mathbf{h}}(\mathbf{y})_1$
$P_{\mathbf{h}}(\mathbf{y})_2$

Figure 5.3.4
Relationship between the three-dimensional object $f(g)$ and the pole figures $P_{\mathbf{h}}(\mathbf{y})$. Several OD boxes correspond to each pole figure cell, and each OD box is linked to several pole-figure cells.

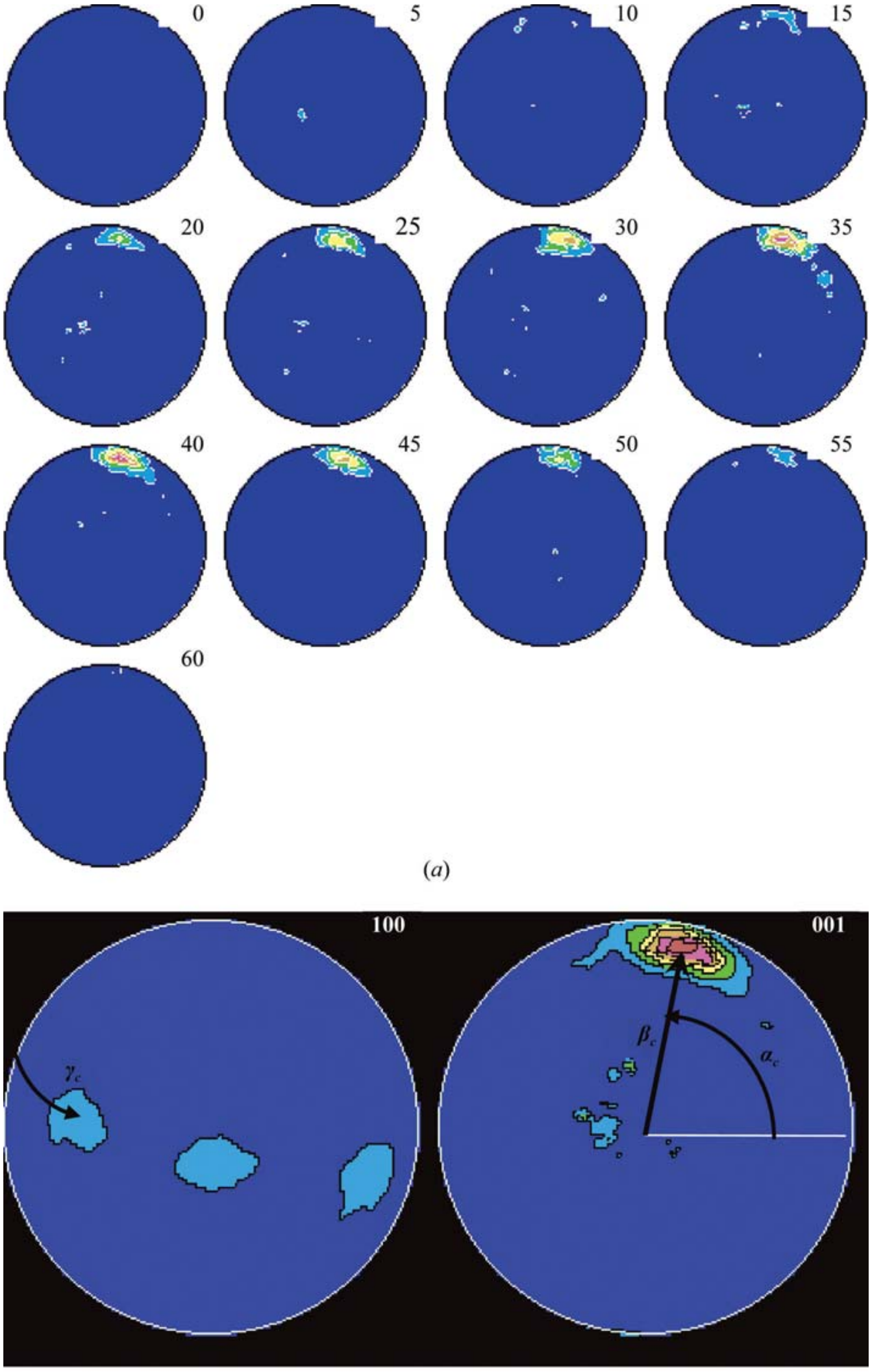

(*a*)

(*b*)

Figure 5.3.5
(*a*) An OD as γ_c sections and (*b*) as {100} and {001} pole figures.

directly. Since whatever the texture state of a given sample is (*i.e.* whether the sample exhibits a texture or is randomly oriented) the total intensity scattered by the sample $I^t_{\mathbf{h}}$ must be the same, the sum of all intensities $I_{\mathbf{h}}(\mathbf{y})$ collected on the hemisphere is the same, all other sample characteristics being constant:

$$I^t_{\mathbf{h}} = \int_{\varphi_{\mathbf{y}}=0}^{2\pi} \int_{\vartheta_{\mathbf{y}}=0}^{\pi/2} I_{\mathbf{h}}(\vartheta_{\mathbf{y}}, \varphi_{\mathbf{y}}) \sin\vartheta_{\mathbf{y}} \, \mathrm{d}\vartheta_{\mathbf{y}} \, \mathrm{d}\varphi_{\mathbf{y}}. \qquad (5.3.8)$$

One can then obtain the intensity $N_{\mathbf{h}}$ that would diffract from this sample for the $\mathbf{h}$ pole figure if it was randomly oriented,

$$N_{\mathbf{h}} = I^t_{\mathbf{h}} \Big/ \int_{\varphi_{\mathbf{y}}=0}^{2\pi} \int_{\vartheta_{\mathbf{y}}=0}^{\pi/2} \sin\vartheta_{\mathbf{y}} \, \mathrm{d}\vartheta_{\mathbf{y}} \, \mathrm{d}\varphi_{\mathbf{y}}, \quad (5.3.9)$$

which is necessary for calculation of the normalized pole figure (expressed in m.r.d. units),

$$P_{\mathbf{h}}(\mathbf{y}) = \frac{I_{\mathbf{h}}(\mathbf{y})}{N_{\mathbf{h}}}. \qquad (5.3.10)$$

However, experimental considerations mean that the pole figures are generally not measured completely, and the $N_{\mathbf{h}}$ factors are usually refined during the OD calculation (see Section 5.3.2.3.1).

5.3.2.2. *The fundamental equation of quantitative texture analysis*

Since a pole figure measures the distribution of only one direction type $\langle hkl \rangle^*$, it does not probe an orientation directly. Phrased differently, any rotation around this specific vector by an angle $\tilde{\varphi}$ results in the same diffracted intensity. From (5.3.1) and (5.3.3), one can obtain the fundamental equation of QTA,

$$P_{\mathbf{h}}(\mathbf{y}) = \frac{1}{2\pi} \int_{\mathbf{h}\parallel\mathbf{y}} f(g) \, \mathrm{d}\tilde{\varphi}, \qquad (5.3.11)$$

which represents the fact that each pole figure (which is a two-dimensional object) is a projection along a certain path $\tilde{\varphi}$ of the OD (a three-dimensional object) which depends on the crystal symmetry (Fig. 5.3.4). Each cell of a given pole figure will then be an average over several cells of the OD, and each cell of the OD will be measured by one or more cells from the pole figures. The larger the number of pole-figure cells that measure a specific OD cell, the more statistically reliable the measurement of this OD is. In practice, one has to measure the largest number possible of reliable (sufficiently intense) pole figures to define the OD with the best resolution available.

For instance, an OD of a hexagonal system represented by a series of γ_c sections (Fig. 5.3.5*a*) may reveal a maximum pole density for a γ_c value of 35°. The corresponding {100} and {001} pole figures (Fig. 5.3.5*b*) illustrate the meaning of γ_c in the pole-figure space for this single-component texture. In the {001} pole figure, the pole maximum is located at $(\varphi_{\mathbf{y}}, \vartheta_{\mathbf{y}}) = (\alpha_c, \beta_c) = (85°, 80°)$. Since γ_c locates the $\mathbf{b}$ axis, with this latter being represented by the {100} pole figure, $\gamma_c = 35°$ is the angle between the equator and $\mathbf{b}$ in this pole figure. Users should not be afraid to build a three-dimensional model of the unit-cell axes to assist in interpreting such pole figures.

Let us mention at this point that the pole figures that are obtained using normal diffraction methods are so-called reduced pole figures, $\tilde{P}_{\mathbf{h}}(\mathbf{y})$. Friedel's law requires that the measured pole figures are superpositions of $+\mathbf{h}$ and $-\mathbf{h}$ true pole figures. This fact (which is even the case for anomalous scattering in the case of centrosymmetric crystals) leads to the presence of 'ghost' phenomena (Matthies & Vinel, 1982; Matthies *et al.*, 1987). The true, unreduced or 'complete' pole figure is defined as

$$P_{\mathbf{h}}(\mathbf{y}) = \tilde{P}_{\mathbf{h}}(\mathbf{y}) + \tilde{\tilde{P}}_{\mathbf{h}}(\mathbf{y}), \tag{5.3.12}$$

in which $\tilde{\tilde{P}}_{\mathbf{h}}(\mathbf{y})$ is the nonmeasured part of the pole figures. We will not take account of this here since ghost suppression, if possible, would require anomalous diffraction and very intense beams. Instead, theoretically derived ghost-correcting approximations can be used. However, it should be strongly emphasized here that in the case of noncentrosymmetric crystal symmetry the ODF will not be determined completely.

5.3.2.3. *Resolution of the fundamental equation*

5.3.2.3.1. *Generalized spherical-harmonics expansion*

The solution proposed by Bunge & Esling (1982) consists of describing the OD and the pole figures as series of generalized spherical harmonics,

$$f(g) = \sum_{\lambda=0}^{\infty} \sum_{m=-\lambda}^{\lambda} \sum_{n=\lambda}^{\lambda} C_{\lambda}^{mn} T_{\lambda}^{mn}(g), \tag{5.3.13}$$

$$P_{\mathbf{h}}(\mathbf{y}) = \sum_{\lambda=0}^{\infty} \frac{4\pi}{2\lambda+1} \sum_{n=-\lambda}^{\lambda} k_{\lambda}^{n}(\mathbf{y}) \sum_{m=-\lambda}^{\lambda} C_{\lambda}^{mn} k_{\lambda}^{*m}(\Theta_{\mathbf{h}}\phi_{\mathbf{h}}). \tag{5.3.14}$$

(5.3.11) still holds, and in this approach one has to determine the C_{λ}^{mn} coefficients, which are the proportions of the respective $T_{\lambda}^{mn}(g)$ and depend on the texture, from the experiments. The $T_{\lambda}^{mn}(g)$ are known generalized spherical harmonics which depend on the crystal and texture symmetries. The series expands on both even and odd values of λ. In practice, the expansion on λ cannot be infinite and is limited to a value L, the maximum degree of series expansion, which fixes the angular resolution of the expansion. k_{λ}^{n} and k_{λ}^{*m} are spherical harmonics based on Legendre polynomials (Bunge & Esling, 1982). The angles $\Theta_{\mathbf{h}}$ and $\phi_{\mathbf{h}}$ are the spherical coordinates of the **h** direction in the crystal reference frame. The number of C_{λ}^{mn} coefficients and the extension L to which the series in (5.3.14) has to be expanded in λ are also dependent on the crystal and texture symmetries.

If a certain number of pole-figure values are measured for different crystallographic directions **h**, then a set of linear equations can be set up using (5.3.14) and solved. There are three commonly used methods to obtain the C_{λ}^{mn} coefficients.

The first method can be used only if complete pole figures are measured, in which case (5.3.14) can be written

$$P_{\mathbf{h}}(\mathbf{y}) = \sum_{\lambda=0}^{\infty} \sum_{n=-\lambda}^{\lambda} F_{\lambda}^{n}(\mathbf{h}) k_{\lambda}^{n}(\mathbf{y}) \tag{5.3.14a}$$

and

$$F_{\lambda}^{n}(\mathbf{h}) = \frac{4\pi}{2\lambda+1} \sum_{m=-\lambda=0}^{\lambda} C_{\lambda}^{mn} k_{\lambda}^{*m}(\Theta_{\mathbf{h}}, \phi_{\mathbf{h}}) \sum_{n=-\lambda}^{\lambda} F_{\lambda}^{n}(\mathbf{h}) k_{\lambda}^{n}(\mathbf{y}). \tag{5.3.14b}$$

Multiplying both sides of (5.3.14*a*) by $k_{\lambda}^{*m}(\mathbf{y})$ and integrating over the whole sphere then yields

$$\begin{aligned} F_{\lambda}^{n}(\mathbf{h}) &= \int P_{\mathbf{h}}(\mathbf{y}) k_{\lambda}^{*n}(\mathbf{y})\, \mathrm{d}\mathbf{y} \\ &= \int_{\vartheta_y}^{\pi} \int_{\varphi_{\mathbf{y}}}^{2\pi} P_{\mathbf{h}}(\vartheta_{\mathbf{y}}, \varphi_{\mathbf{y}}) k_{\lambda}^{*n}(\vartheta_{\mathbf{y}}, \varphi_{\mathbf{y}}) \sin\theta_{\mathbf{y}}\, \mathrm{d}\vartheta_{\mathbf{y}}\, \mathrm{d}\varphi_{\mathbf{y}}. \end{aligned} \tag{5.3.14c}$$

The first step of the procedure is to compute the quantities $F_{\lambda}^{n}(\mathbf{h})$ from (5.3.14*c*) using the measured pole-figure values. In the second step (transformation of coefficients), the system of linear equations (5.3.14*b*) solved for the variables C_{λ}^{mn} and $f(g)$ is determined.

The second method is used when it is not possible to measure complete pole figures and consequently the quantities in (5.3.14*c*) cannot be computed. In such a case, we refer the reader to Chapter 7 of Bunge & Esling (1982) for a complete exposition. The method also solves a system of linear equations to obtain the harmonic coefficients:

$$\sum_{\lambda=0}^{L} \sum_{m=1}^{M(\lambda)} \sum_{n=1}^{N(\lambda)} C_{\lambda}^{mn} \left[\alpha_{\lambda\lambda'}^{mm'} \zeta_{\lambda\lambda'}^{nn'} - \sum_{\mathbf{h}} \frac{a_{\lambda}^{mn}(\mathbf{h}) a_{\lambda'}^{m'n'}(\mathbf{h})}{P_{\mathbf{h}}} \right] = 0 \tag{5.3.14d}$$

and

$$P_{\mathbf{h}} = 2 \int_{B} [I_{\mathbf{h}}(\mathbf{y})]^2\, \mathrm{d}\mathbf{y},$$

where B is the measured range in the pole figure,

$$a_{\lambda}^{mn}(\mathbf{h}) = 2 \frac{4\pi}{2\lambda+1} \overset{\vdots}{k}{}_{\lambda}^{*m}(\Theta_{\mathbf{h}}, \phi_{\mathbf{h}}) \int_{B} I_{\mathbf{h}}(\mathbf{y}) \dot{k}_{\lambda}^{n}(\mathbf{y})\, \mathrm{d}\mathbf{y},$$

$$\zeta_{\lambda\lambda'}^{nn'} = 2 \int_{B} \dot{k}_{\lambda'}^{n'}(\mathbf{y}) \dot{k}_{\lambda}^{n}(\mathbf{y})\, \mathrm{d}\mathbf{y},$$

$$a_{\lambda\lambda'}^{mm'} = \frac{4\pi}{2\lambda+1} \frac{4\pi}{2\lambda'+1} \sum_{\mathbf{h}} \overset{\vdots}{k}{}_{\lambda}^{*m}(\Theta_{\mathbf{h}}, \phi_{\mathbf{h}}) \overset{\vdots}{k}{}_{\lambda'}^{*m'}(\Theta_{\mathbf{h}}, \phi_{\mathbf{h}}).$$

The third method uses the minimization procedure of (5.3.15) to refine the harmonic coefficients by a least-squares method, through which the $P_{\mathbf{h}}(\mathbf{y})$ are expressed using (5.3.14):

$$\sum_{\mathbf{h}} \oint [I_{\mathbf{h}}(\mathbf{y}) - N_{\mathbf{h}} P_{\mathbf{h}}(\mathbf{y})]^2\, \mathrm{d}\mathbf{y} = \min. \tag{5.3.15}$$

The integral is substituted by a summation over the entire measured range of the pole figures (complete or uncomplete).

For strongly textured samples, the harmonics formulation creates strong negative density values, in particular if the expansion is restricted to too low an L value (which unfortunately can be the case experimentally if insufficient pole figures can be measured), and has been proved to be less adequate than other discrete methods. Several methods have been developed to correct for this artifact, all of which force negative densities to zero (Wenk *et al.*, 1988). However, forcing densities to zero wherever they appear to be negative (if physically more reasonable) may appear to be a little arbitrary. This feeling may be reinforced by the fact that ghosts can also be positive, with these latter not being subject to the same 'correction' possibilities. However, one advantage of using a harmonic series is that it provides the necessary material for the simplest approximation of the mechanical property simulations with a limited number of coefficients to be refined (the C_{λ}^{mn} values). These coefficients can also be computed from the OD obtained by other methods.

Since $f(g)$ is a density, one should observe $f(g) \geq 0$ for all g values, or 'positivity'. From (5.3.5) we know that the measured or reduced pole figures are centrosymmetric, and as a consequence of (5.3.14) only the even-order coefficients can be determined by diffraction. On the other hand there are even and odd coefficients in $f(g)$, and two different ODs have then to be considered, depending on the parity of the λ terms,

$$f(g) = f^{e}(g) + f^{o}(g), \tag{5.3.16}$$

and here $f(g)$ and $f^o(g)$ are two unknowns, with the even part of the harmonic series $f^e(g)$ being the part that is accessible to normal diffraction; the odd part is measurable in certain cases using anomalous scattering. This phenomenon creates ghosts (negative, unphysical distribution densities) in the OD (Matthies, 1979; Matthies & Vinel, 1982), which are undesirable for a quantitative description of $f(g)$. An approximate 'ghost correction' by estimating the odd coefficients is more or less complicated in the harmonic formalism (Esling *et al.*, 1982). Some approaches for this correction have been developed such as the 'positivity method' (Dahms & Bunge, 1988; Wagner & Dahms, 1991) or the 'GHOST' and 'quadratic' methods (Van Houtte, 1983, 1991), all of which still permit some residual negative densities (see Section 5.3.2.3.8).

5.3.2.3.2. *Vector method*

This discrete method (Ruer, 1976; Ruer & Baro, 1977; Vadon, 1981) works in direct space. Here, $f(g)$ is represented by a vector called the 'texture vector' $\mathbf{f}_j$, $j = 1, \ldots, J$, with J the number of cells in which $f(g)$ is discretized. This number, of course, depends on the resolution of the measurement scans of the pole figures. Each pole figure is represented by $\mathbf{P}_i(\mathbf{h})$, $i = 1, \ldots, N$, with N being the number of cells of the pole figure. The fundamental equation of QTA becomes

$$P_i(\mathbf{h}) = [\boldsymbol{\sigma}_{ij}(\mathbf{h})]\mathbf{f}_j, \qquad (5.3.17)$$

in which $\boldsymbol{\sigma}_{\rm ij}(\mathbf{h})$ is a rectangular matrix. The fundamental problem therefore consists of finding the solution to the system of linear equations (5.3.17).

5.3.2.3.3. *WIMV method*

The WIMV approach [where WIMV is an acronym from Williams (1968), Imhof (1982) and Matthies & Vinel (1982)] is an iterative method which ensures a conditional ghost correction. It is based on the numerical refinement of $f(g)$ at step $n + 1$,

$$f^{n+1}(g) = \hat{N} \frac{f^n(g) f^0(g)}{\prod_{i=1}^{I} \left[\prod_{m=1}^{M_{\mathbf{h}i}} P^n_{\mathbf{h}_{im}}(\mathbf{y}) \right]^{1/IM_{\mathbf{h}i}}}, \qquad (5.3.18)$$

where the product extends over the I experimentally measured pole figures and the multiplicity is $M_{\mathbf{h}}$ for all the poles. $f^n(g)$ and $P^n_{\mathbf{h}}(\mathbf{y})$ represent the refined values of $f(g)$ and $P_{\mathbf{h}}(\mathbf{y})$ at the nth step, respectively. $\hat{N}$ is the normalization operation. The $P^n_{\mathbf{h}_{im}}(\mathbf{y})$ values are calculated at each cycle with (5.3.12). The first step in this procedure is to evaluate $f^0(g)$,

$$f^0(g) = \hat{N} \prod_{i=1}^{I} \left[\prod_{m=1}^{M_{\mathbf{h}i}} P^{\rm exp}_{\mathbf{h}_{im}}(\mathbf{y}) \right]^{1/IM_{\mathbf{h}i}}, \qquad (5.3.19)$$

in which $P^{\rm exp}_{\mathbf{h}}(\mathbf{y})$ represents the measured pole figures. The WIMV algorithm maximizes the so-called 'phon' (orientation background or minimum value of the OD which represents the randomly oriented fraction of the sample) and the texture sharpness. While in the previous methods of OD resolution low texture and crystal symmetries give rise to large amounts of data to store and long computation times, the WIMV approach does not depend greatly on these symmetries. Other methods have been derived from WIMV and they maintain the same iteration structure as depicted in (5.3.18); they are described in Sections 5.3.2.3.4, 5.3.2.3.5 and 5.3.2.3.6.

5.3.2.3.4. *Arbitrarily defined cells (ADC) method*

Essentially based on a WIMV-like algorithm (Pawlik, 1993), the ADC method uses projection tubes instead of projection paths. Each cell volume is then taken into account in the calculations, which gives a better smoothing scheme. A similar concept is also used in the EWIMV approach and is described in Section 5.3.2.3.6.

5.3.2.3.5. *Entropy-maximization method*

This method (Schaeben, 1988, 1991*a*,*b*) is based on the maximization of the texture 'disorder' or texture entropy, *i.e.* trying to obtain the maximum texture phon from a set of experiments. Following information theory (Shannon, 1948), the entropy estimator in texture can be described by

$$S = -\sum_i f(g_i) \ln f(g_i), \qquad (5.3.20)$$

which results in the iterative procedure

$$f^{n+1}(g) = f^n(g) \prod_{i=1}^{I} \prod_{m=1}^{M_{\mathbf{h}i}} \left[\frac{P_{\mathbf{h}}(\mathbf{y})}{P^n_{\mathbf{h}}(\mathbf{y})} \right]^{r_n/IM_{\mathbf{h}i}}, \qquad (5.3.21)$$

in which r_n is a relaxation parameter such that $0 < r_n < 1$.

5.3.2.3.6. *EWIMV method*

When the WIMV calculation is inserted into the Rietveld refinement procedure, it requires two additional steps:

(i) the extraction of the pole-figure or texture weights,

(ii) the interpolation of these weights to fit a regular grid (imposed by the original WIMV algorithm).

The latter yields non-optimized values of the OD, particularly for sharp textures and coarse irregular coverage of the OD. The entropy-modified WIMV (EWIMV) method has proved to be effective as an extension of the WIMV method (Lutterotti *et al.*, 2004; Morales *et al.*, 2002). In this latter the OD cell values are computed through an entropy iteration algorithm as in (5.3.21), with incorporation of the reflection weights $w_{\mathbf{h}}$:

$$f^{n+1}(g) = \hat{N} f^n(g) \prod_{h=1}^{I} \prod_{m=1}^{M_{\mathbf{h}i}} \left[\frac{P_{\mathbf{h}_{im}}(\mathbf{y})}{P^n_{\mathbf{h}_{im}}(\mathbf{y})} \right]^{r_n w_{\mathbf{h}}/IM_{\mathbf{h}i}}. \qquad (5.3.22)$$

$w_{\mathbf{h}}$ is introduced to take into account the different accuracy of the more intense and less overlapped reflections with respect to the smaller reflections, and is calculated analogously to the weight factors in the Rietveld analysis. In (5.3.22), the integration path is computed using a similar concept to the tube projection introduced by the ADC method (Section 5.3.2.3.4). In the case of EWIMV the projection for each integration point is calculated using all of the neighbouring cells in the OD to that in which the integration point falls, and the cell contribution is weighted using the reciprocal of the distance between the centre of the cell and the exact integration-point position. This has also a positive effect on smoothing out the noise from the OD and increases the experimental 'coverage' of the OD.

5.3.2.3.7. *Component method*

For very strong textures most of the orientation space cells have zero values, while a few cells exhibit very large distribution densities. In such cases the number of data to be acquired can be tremendously large and tends to an unacceptable limit. However, since the OD is described by a small number of orientations g, simple functions can be used to represent it, and the g values are easily handled. Let a specific texture component (Helming, 1992) centred at the orientation $g = g^c$ be represented by the model function $f^c(g)$. The total OD can be represented by

$$f(g) = F + \sum_c I^c f^c(g), \tag{5.3.23}$$

where the intensity I^c is the volume fraction of crystallites belonging to the component g^c of distribution $f^c(g)$, and F represents the volume fraction of randomly oriented crystallites. For consistency, the components have to respect the normalization conditions

$$F + \sum_c I^c = 1 \text{ and } \sum_c f^c(g) = 1. \tag{5.3.24}$$

The $f^c(g)$ components can be represented by any function, *i.e.* Gaussian, Lorentzian or elliptical distributions (Matthies *et al.*, 1987), that is normalized. Generally, two types of components are used: spherical (Matthies, 1980, 1982) and fibre (Matthies *et al.*, 1988). Each component may then have a Gaussian or Lorentzian character.

Spherical components are described by an orientation position g_0 in the OD space and a half-width at half-maximum, b, to characterize the shape of the distribution ($0 \leq b \leq 2\pi$). Taking $\tilde{\omega}$ as the angular distance between an orientation g and g_0, the Gaussian spherical component can be written as

$$f(g_0, b, g) = f(S, \tilde{\omega}) = N(S)\exp(S\cos\tilde{\omega}), \tag{5.3.24a}$$

with $0 \leq \tilde{\omega} = \tilde{\omega}\,(g_0, g) \leq \pi$, $0 \leq S \leq \infty$, $S = \ln 2/[2\sin^2(b/4)]$;

$$N(S) = [I_0(S) - I_1(S)]^{-1} \tag{5.3.24b}$$

is the normalization factor and $I_n(x)$ are the modified Bessel functions:

$$I_n(x) = \frac{1}{\pi}\int_0^{\pi} \exp[x\cos(t)]\cos(nt)\,\mathrm{d}t. \tag{5.3.24c}$$

Now the unreduced pole-figure value by integration using (5.3.9) becomes

$$P_{\mathbf{h}}(g_0, b, \mathbf{y}) = P(S, z) = N(S) I_0\left[\frac{S(z+1)}{2}\right]\exp\left[\frac{S(z-1)}{2}\right], \tag{5.3.25}$$

with $z = \mathbf{h} \cdot g_0 \cdot \mathbf{y}$.

Since the reduced pole figure is the measured one (Section 5.3.2.3.1), it must be computed as (using equation 5.3.5),

$$\bar{P}(S, z) = \frac{P(S, z) - P(S, -z)}{2}. \tag{5.3.26}$$

Similarly, for a Lorentzian spherical component

$$f(g_0, b, g) = f(t, \tilde{\omega}) = (1 - t^2)\frac{(1 + t^2)^2 + 4t^2\cos^2(\tilde{\omega}/2)}{[(1 + t^2)^2 - 4t^2\cos^2(\tilde{\omega}/2)]^2}, \tag{5.3.27}$$

where

$$\begin{aligned}
t &= \tau^{1/2} - (\tau - 1)^{1/2},\\
c &= \cos^2(b/4),\\
w &= (19c^2 - 34c + 19)^{1/2},\\
\tau &= \frac{2w}{3}\cos\left[\frac{1}{3}\cos^{-1}\left(\frac{-82c^3 + 240c^2 - 246c + 80}{w^3}\right)\right] + \frac{5 - 4c}{3},
\end{aligned}$$

and the unreduced pole-figure value becomes

$$P_{\mathbf{h}}(g_0, b, y) = P(t, z) = \frac{1 - t^4}{(1 - 2t^2 z + t^4)^{3/2}}. \tag{5.3.28}$$

A Gaussian-like fibre component is defined by two vectors ($\mathbf{h}_0$, $\mathbf{n}_0$) and the half-width b. $\mathbf{n}_0$ is the fibre direction in the sample coordinates and $\mathbf{h}_0$ is the fibre direction in the crystal coordinate system. Then,

$$f(\mathbf{h}_0, \mathbf{n}_0, b, g) = f(S, z) = \left[\frac{S}{\sinh(S)}\right]\exp(Sz), \tag{5.3.29}$$

in which z and S have been already defined for the Gaussian component. The unreduced pole figures can now be computed as

$$P(S, z_1, z_2) = \frac{S}{\sinh(S)} I_0\left[S(1 - z_1^2)^{1/2}(1 - z_2^2)^{1/2}\right]\exp(Sz_1z_2), \tag{5.3.30}$$

where

$$z_1 = \mathbf{h} \cdot \mathbf{h}_0, \quad z_2 = \mathbf{y} \cdot \mathbf{n}_0.$$

In the case of a Lorentzian fibre component, using the same definitions as for the Gaussian fibre component the equations are

$$f(\mathbf{h}_0, \mathbf{n}_0, b, g) = f(t_f, z) = \frac{1 - t_f}{(1 - 2t_f z + t_f^2)^{3/2}}, \tag{5.3.31}$$

where

$$\begin{aligned}
t_f &= R - (R^2 - 1)^{1/2},\\
R &= \frac{2^{2/3} - \cos(b/4)}{2^{2/3} - 1}
\end{aligned}$$

and the reduced pole figure is

$$\begin{aligned}
P(t_f, z_1, z_2) &= \frac{2}{\pi}\frac{1 - t_f^2}{(C - D)(C + D)^{1/2}} E\left(\frac{2D}{C + D}\right),\\
C &= 1 + t_f^2 - 2t_f z_1 z_2,\\
D &= 2t_f(1 - z_1^2)^{1/2}(1 - z_2^2)^{1/2}
\end{aligned}$$

and $E(k)$ is the complete elliptic integral of the second kind,

$$E(k) = \int_0^{\pi/2} (1 - k^2\sin^2\theta)^{1/2}\,\mathrm{d}\theta.$$

5.3.2.3.8. *Positivity and exponential harmonics*

In the positivity and exponential method the idea is to use and determine the odd coefficients that may ensure a positive $f(g)$. In the positivity method the even coefficients are not modified (as they are linked to the experimental pole figures) and the odd coefficients do not affect the computation. For a detailed description of the positivity algorithm, we refer to the original articles (Dahms & Bunge, 1988; Van Houtte, 1991). The goal of the algorithm is to determine the odd coefficients corresponding to an OD equal to (with sign inverted) the negative part of the OD found from the experimental data, $f_0(g)$,

$$C_\lambda^{mn} = -(2\lambda + 1)\int_{\forall g \in Z-} f_0(g) T_\lambda^{mn}(g)\,\mathrm{d}g, \tag{5.3.32}$$

where $Z-$ is the orientation space over which the $f_0(g)$ values are negative or lower than a given threshold α defining the OD background. Moreover, it has been recognized that most of the time there are a set of odd coefficients that are able to completely eliminate all negative parts of the OD, maintaining the even coefficients constant. Another way to ensure OD positivity (Van

Houtte, 1991) is to express it with functions that result in values that are always positive, such as exponentials with real function arguments $h(g)$. For instance, using $f(g) = \exp[h(g)] \geq 0$, (5.3.13) and (5.3.14) become

$$\exp[h(g)] = \sum_{\lambda=0}^{L} \sum_{m=1}^{M(\lambda)} \sum_{n=1}^{N(\lambda)} C_\lambda^{mn} T_\lambda^{mn}(g)$$
$$C_\lambda^{mn} = (2\lambda + 1) \textstyle\int \exp[h(g)] T_\lambda^{mn}(g)\,\mathrm{d}g. \qquad (5.3.33)$$

The first OD approximation is now obtained by the positivity method described above (or the GHOST version as described in Van Houtte, 1983). Calling this latter $f_0(g)$, the first approximation for $h_0(g)$ is imposed as

$$h_0(g) = \begin{cases} \ln[f_0(g)] & \text{if } f_0(g) > \alpha, \\ f_0(g) - \alpha + \ln\alpha & \text{if } f_0(g) \leq \alpha. \end{cases}$$

An iterative refinement is carried out using

$$h_{k+1}(g) = h_k(g) + \sum_{\lambda=0}^{L} \sum_{m=1}^{M(\lambda)} \sum_{n=1}^{N(\lambda)} \exp[-h_k(g)](C_\lambda^{mn} - C_{\lambda,k}^{mn}) T_\lambda^{mn}(g).$$

C_λ^{mn} are the initial coefficients obtained by the positivity or GHOST method and the $C_{\lambda,k}^{mn}$ before each iteration are computed using (5.3.14*b*) and the $h_k(g)$ values of the OD. A normalization of $h_k(g)$ is performed at each step. At the end the always-positive OD is computed as $f(g) = \exp[h_k(g)]$.

5.3.2.3.9. *Radon transform and Fourier analysis*

The fundamental equation of QTA (5.3.11) can be recognized as the Radon transform (Radon, 1986) of $f(g)$ as proposed by Schaeben & van den Boogaart (2003),

$$\mathscr{R}f(\mathbf{h}, \mathbf{y}) = \frac{1}{2\pi} \int\limits_{\tilde{\varphi}(\mathbf{h},\mathbf{y})} f(g)\,\mathrm{d}\tilde{\varphi}. \qquad (5.3.34)$$

The integration path $\tilde{\varphi}(\mathbf{h}, \mathbf{y})$ takes all of the equivalents of **h** into account, *i.e.* all of the rotations that represent the **h** multiplicity (such that $g\mathbf{h} = \mathbf{y}$). Because the Radon and the Fourier transforms are closely related, computationally efficient inversion formulas are available and $f(g)$ can be retrieved by fast Fourier inversion techniques. The biggest advantage is then that, unlike generalized spherical harmonics, both odd and even coefficients can be accessed from the inversion of the Radon transform.

5.3.2.4. *Inverse pole figures*

In a pole figure $P_\mathbf{h}(\mathbf{y})$ (5.3.11), all of the given **h** directions from all of the diffracting crystals are located using the **y** coordinates relative to K_A, the sample reference frame. In this way, one looks at only one of the equivalent **h** directions, and **y** varies in the pole figure. In some cases such as axially symmetric textures or when only some macroscopic directions **y** are of importance, it can be useful to represent which of the **h** directions align with the given **y**. For instance, one can aim to see which crystal directions are aligned with a uniaxial pressure axis ($\boldsymbol{\sigma}$). This time **y** is fixed ($\boldsymbol{\sigma}$, or Z_A if the pressure is applied along Z_A) and **h** varies, and an easy way to represent such a distribution of **h** directions *versus* **y** is an inverse pole figure, or $R_\mathbf{y}(\mathbf{h})$. Similarly to (5.3.9), one can calculate every inverse pole figure $R_\mathbf{y}(\mathbf{h})$ from $f(g)$,

$$R_\mathbf{y}(\mathbf{h}) = \frac{1}{2\pi} \int\limits_{\mathbf{y}\parallel\mathbf{h}} f(g)\,\mathrm{d}\overset{\approx}{\varphi}, \qquad (5.3.35)$$

in which $\overset{\approx}{\varphi}$ is an orientation path in $f(g)$ which takes account of the crystal symmetry. Inverse pole figures are represented in the crystal reference frame K_B (Fig. 5.3.6). Different sectors are equivalent by symmetry, from one for triclinic crystal symmetry to 24 for cubic symmetry. Only one sector is necessary to portray the unique information, and inverse pole figures are generally represented in the sector frame.

Similar to pole figures, inverse pole figures exhibit pole-density distributions. For instance, the inverse pole figure for the drawing axis of an aluminium wire shows that the ⟨111⟩ and ⟨001⟩ directions are the main alignment components, with a major ⟨111⟩

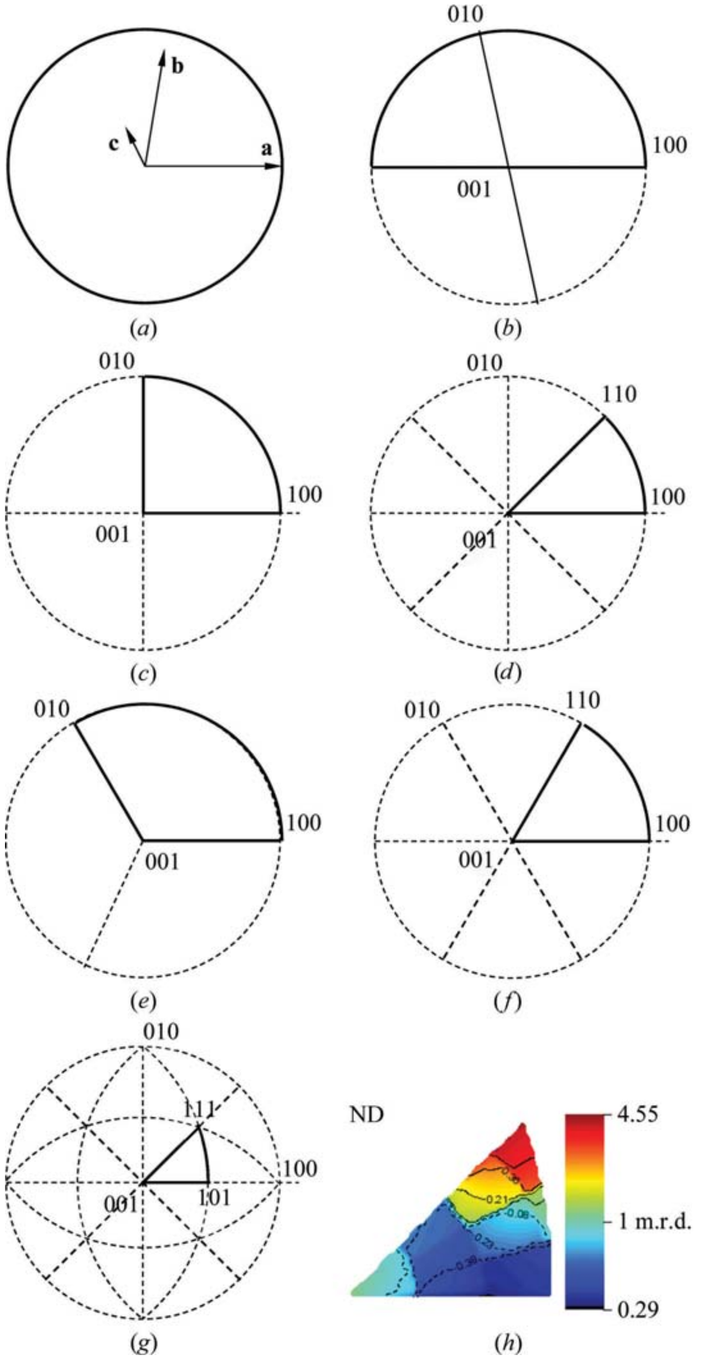

Figure 5.3.6
The inverse pole-figure sectors as a function of the crystal symmetry. The nonredundant sectors are indicated by bold edges. (*a*) Triclinic, (*b*) monoclinic (the *b*-axis unique setting has been used), (*c*) orthorhombic, (*d*) tetragonal, (*e*) rhombohedral using a hexagonal unit cell, (*f*) hexagonal and (*g*) cubic crystal systems. (*h*) An inverse pole figure for the drawing axis of an aluminium wire elaborated by cold drawing (linear density scale, cubic sector, equal-area projection).

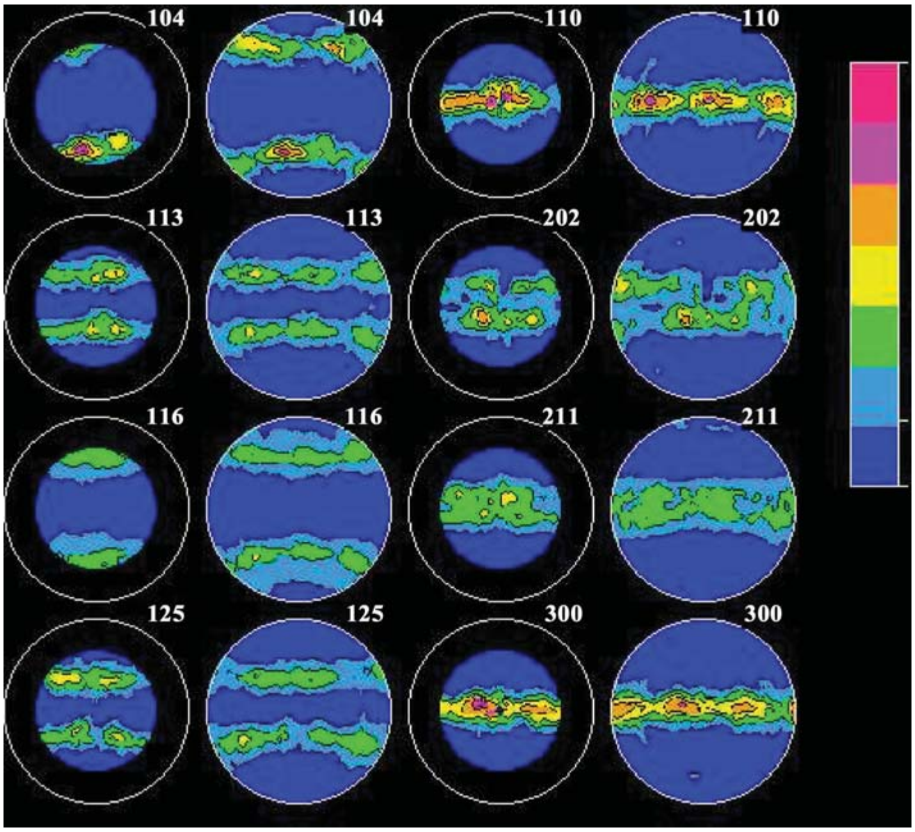

Figure 5.3.7
Visual examination of the OD refinement reliability using experimental and recalculated normalized {104}, {110}, {113}, {202}, {116}, {211}, {125} and {300} pole figures (in successive order). WIMV refinements are from *BEARTEX*. Linear density scale, equal angular projections. The sample is the calcite outer prismatic layer of the deep-ocean mussel *Bathymodiolus thermophilus*, maximum density 6.3 m.r.d., minimum density 0 m.r.d. Here, $\mathrm{RP}_{0.05}$ = 25% and RP_1 = 17%.

component, resulting from the gliding systems activated in the crystals (Fig. 5.3.6*h*).

5.3.2.5. *OD refinement reliability estimators*

As in Rietveld analysis, several factors are used to evaluate the reliability of the solution for $f(g)$. In most programs the RP_x factors are used,

$$\overline{\mathrm{RP}}_x = \frac{1}{I}\sum_i \sum_j \frac{\left|P^c_{\mathbf{h}_i}(\mathbf{y}_j) - P^o_{\mathbf{h}_{ii}}(\mathbf{y}_j)\right|}{P^o_{\mathbf{h}_i}(\mathbf{y}_j)}, \qquad (5.3.36)$$

where $\mathbf{h}_i$, $i = 1, \ldots, I$, are the measured pole figures, $\mathbf{y}_j$, $j = 1, \ldots, J$, are the measured points of the pole figures, a superscript 'o' indicates observed normalized values and a superscript 'c' indicates recalculated normalized values, $P_{\mathbf{h}_i}(\mathbf{y}_j)$ is the pole density at $\mathbf{y}_j$ on pole figure $\mathbf{h}_i$, and $x = 0, \varepsilon, 1, 10, \ldots$ is the criterion to estimate the accuracy *versus* the density level.

The value x is a criterion that is used to indicate the quality of the refinement for the low- and high-density levels. We use x = 0.05 to reveal the global quality and x = 1 to show this quality for density values higher than 1 m.r.d. However, RP factors depend on the texture strength since they are not weighted by the density level, and consequently make the comparison of refinement quality between samples ambiguous (Chateigner, 2005). In other words, one should compare the refinement quality with RP factors only for similar texture strengths and types. Working out reliability factors on individual pole figures helps to detect whether some pole figures are particularly badly reproduced after the refinement, in order to devise a correction strategy.

In order to avoid texture-strength dependence of the reliability factors, surface-weighted factors (Matthies *et al.*, 1987) and several arithmetic mean averaging schemes have been described (Chateigner, 2005). Bragg-like factors also can be calculated, either weighted by density levels or not (Chateigner, 2005). However, using full patterns, Rietveld-like analysis provides 'intensity-weighted' factors, which exhibit less overall variation with texture strength and are better indicators for comparing OD refinement quality among samples,

$$\mathrm{Rw}^z_x = \frac{\sum_{i=1}^{I}\sum_{j=1}^{J}\left[w^o_{ij} I^o_{\mathbf{h}_i}(\mathbf{y}_j) - w^c_{ij} I^c_{\mathbf{h}_i}(\mathbf{y}_j)\right]^2}{\sum_{i=1}^{I}\sum_{j=1}^{J}\left[w^z_{ij} I^z_{\mathbf{h}_i}\right]^2(\mathbf{y}_j)}\,\theta[x, P^o_{\mathbf{h}_i}(\mathbf{y}_j)], \qquad (5.3.37)$$

where

$$I^z_{\mathbf{h}_i}(\mathbf{y}_j) = P^o_{\mathbf{h}_i}(\mathbf{y}_j) N_{\mathbf{h}_i}$$

is the diffracted intensity, $N_{\mathbf{h}_i}$ is the refined normalizing factor,

$$w^z_{ij} = \frac{1}{[I^z_{\mathbf{h}_i}(\mathbf{y}_j)]^{1/2}}$$

is the diffracted intensity weight and

$$\theta(x, t) = \begin{cases} 1 & \text{for } P_{\mathbf{h}_i}(\mathbf{y}_j) > x, \\ 0 & \text{for } P_{\mathbf{h}_i}(\mathbf{y}_j) \le x. \end{cases}$$

Whatever the reliability factors, one of the best estimates of a physically reasonable solution remains visual (Fig. 5.3.7). If the OD has been satisfactorily refined, any pole figure recalculated from this OD should compare well with the experimental pole figure.

5.3.2.6. *Texture-strength factors*

Once $f(g)$ has been satisfactorily obtained, some factors can give an estimate of the overall texture strength. These factors are used to compare samples with the same crystal symmetries and similar texture components.

5.3.2.6.1. *Texture index*

5.3.2.6.1.1. *OD texture index*

The first overall texture-strength parameter is the so-called ‘texture index’ (Bunge, 1982; expressed in units of m.r.d.^{2}),

$$F^2 = \frac{1}{8\pi^2}\sum_i [(g_i)]^2 \Delta g_i, \qquad (5.3.38)$$

where Δg_i is the OD cell volume. This index varies from 1 (random powder) to infinity (perfect texture or single crystal). It represents the mean-square value of the OD. Using harmonics, this factor is calculated from the C_λ^{mn} coefficients:

$$F^2 = 1 + \sum_{\lambda=2}^{L}\left(\frac{1}{2\lambda+1}\right)\sum_{m=-\lambda}^{\lambda}\sum_{n=-\lambda}^{\lambda}|C_\lambda^{mn}|^2. \qquad (5.3.39)$$

5.3.2.6.1.2. *Pole-figure texture index*

To compare the texture strengths of different samples, the texture index associated with given pole figures may be used,

$$J_{\mathbf{h}}^2 = \frac{1}{4}\sum_i [P_{\mathbf{h}}(\mathbf{y}_i)]^2 \Delta \mathbf{y}_i, \qquad (5.3.40)$$

with $\Delta\mathbf{y} = \sin\vartheta_{\mathbf{y}}\Delta\vartheta_{\mathbf{y}}\Delta\varphi_{\mathbf{y}}$.

5.3.2.6.2. *Texture entropy*

The second overall texture strength parameter is a measure of the texture disorder, evaluated by the calculation of the entropy (Shannon, 1948),

$$S = -\frac{1}{8\pi^2}\sum_i f(g_i)\ln f(g_i)\Delta g_i. \qquad (5.3.41)$$

5.3.2.6.3. *Pole-figure and ODF strengths*

Both OD and pole-figure indexes are expressed in units that are not homogeneous with distribution density units (m.r.d.). To help with comparison and interpretation, it is more convenient to compare the square roots of these values, *i.e.* the OD and pole-figure strengths, respectively (Kocks *et al.*, 1998),

$$F = (F^2)^{1/2} \text{ and } J_{\mathbf{h}} = (J_{\mathbf{h}}^2)^{1/2}. \qquad (5.3.42)$$

The texture entropy can also serve as another texture-strength definition, called F_S:

$$F_S = [\exp(-S)]^{1/2}. \qquad (5.3.43)$$

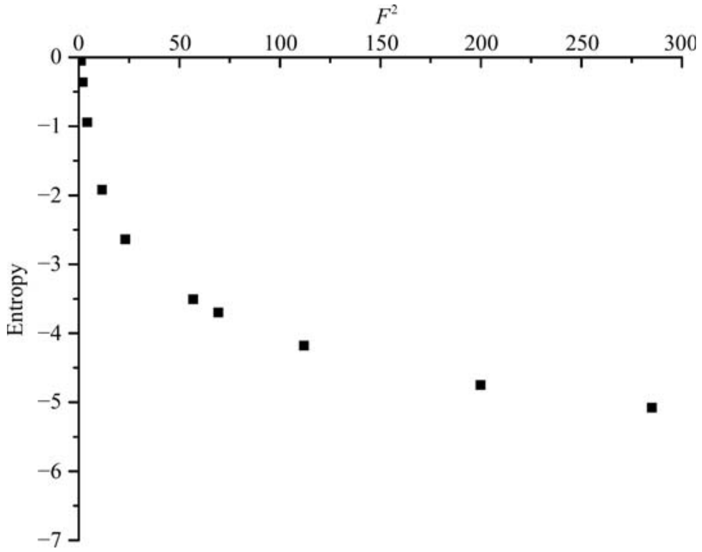

Figure 5.3.8
Entropy variation with texture index for modelled $f(g)$ functions.

5.3.2.6.4. *Correlation between F^2 and S*

From the definitions of F^2 and S, their variations are restricted to the $(1, \infty)$ and $(0, -\infty)$ domains, respectively. Entropy and texture index are correlated, but it is not possible to obtain a general analytical expression for this correlation, which depends on $f(g)$. To appreciate it, one can represent $f(g)$ functions as points in the (F^2, S) plane. In this plane there is a lower bound for $f(g)$, which can be visualized by the $f(g)$ functions of strongly textured samples with no random component (Fig. 5.3.8). This lower bound for the H space (Hielscher *et al.*, 2007) is defined by

$$S = -\ln F^2. \qquad (5.3.44)$$

No $f(g)$ function can be located below this bound, but *a priori* all of the space between it and the S = 0 axis of this graph corresponds to possible $f(g)$ functions. For instance, an OD composed of two components, one very sharp and corresponding to part of the sample volume and the other random and corresponding to the remaining volume fraction, would be positioned at the point (300, −0.5). On the S = 0 axis only the point (1, 0) corresponds to a valid point for $f(g)$, since if S = 0 then F^2 is automatically 1 m.r.d.^{2}.

5.3.2.7. *Texture types*

5.3.2.7.1. *Random texture*

A random texture (or random sample) belongs to the $\infty\infty/m$ Curie (limit) group and is simply a name given to the texture exhibited by a sample that has no preferred orientation. Its crystallites are randomly oriented. The same number of grains are diffracting at any $\mathbf{y}$, and the orientation density for any point $\mathbf{y}$ in a given $\mathbf{h}$ pole figure is the same. Consequently, all crystalline $\{hkl\}$ planes are randomly oriented, and $P_{\mathbf{h}}(\mathbf{y})$ = 1 m.r.d. for any $\mathbf{h}$ and $\mathbf{y}$, *i.e.* all pole figures exhibit homogeneous 1 m.r.d. densities. In such a texture, each crystallite has three degrees of freedom (rotations around three orthogonal axes) to orient K_B relative to K_A. Consequently, all of the OD values correspond to $f(g)$ = 1 m.r.d. distribution densities, whatever the value of g.

However, in some samples only a fraction of the total volume, V_r, is randomly oriented; the rest, $V_c(g)$, is the oriented fraction volume with orientation component or components $f_c(g)$. The random part produces a background level in the OD, sometimes called ‘fon’ or ‘phon’, and one can decompose the OD as

$$f(g) = f_r + f_c(g), \qquad (5.3.45)$$

with the mandatory conditions $0 \le f_r \le 1$ and $f_r = \min[f(g)]$.

By integrating (5.3.1) and taking into account (5.3.35), one obtains

$$\frac{V_r + V_c(g)}{V}\frac{1}{8\pi^2}\oint [f_r + f_c(g)]\,\mathrm{d}g,$$

which verifies that

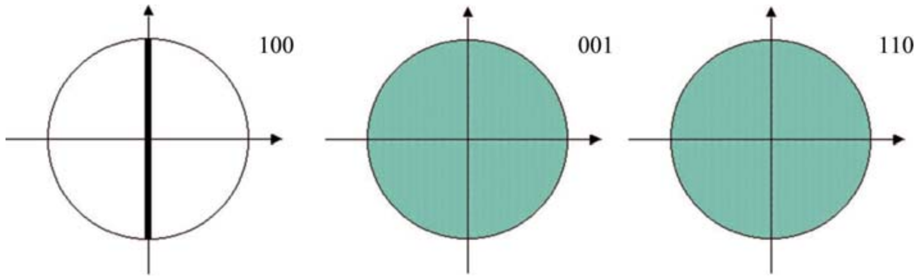

Figure 5.3.9
{100}, {001} and {110} pole figures of a planar texture in an orthorhombic crystal system. The rotation axis of the planar texture is with ⟨100⟩* directions perpendicular to X_A.

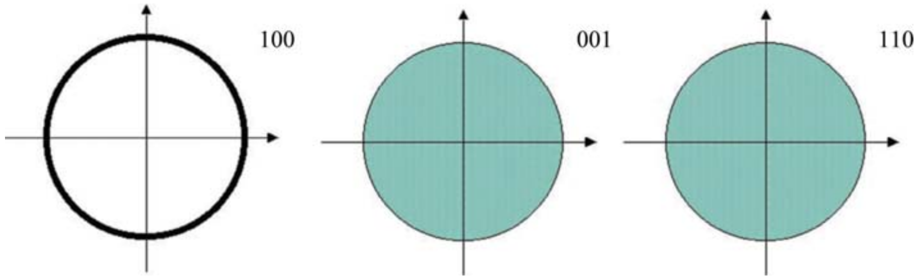

Figure 5.3.10
{100}, {001} and {110} pole figures of a cyclic-planar texture in an orthorhombic crystal system. The rotation axis of the cyclic-planar texture is with ⟨100⟩* directions perpendicular to Z_A.

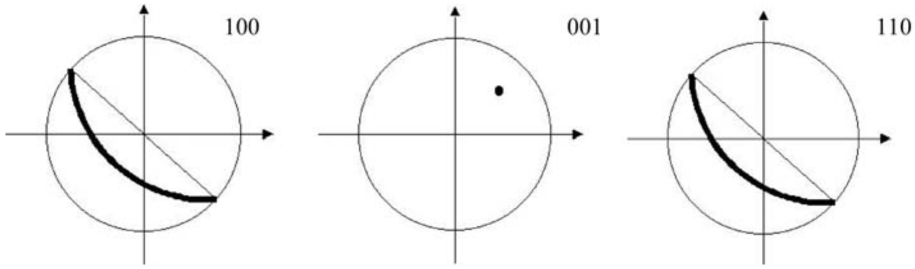

Figure 5.3.11
{100}, {001} and {110} pole figures of a fibre texture in an orthorhombic crystal system. The fibre axis is with ⟨001⟩* directions at ($\vartheta_{\mathbf{y}} = 45°$, $\varphi_{\mathbf{y}} = 45°$).

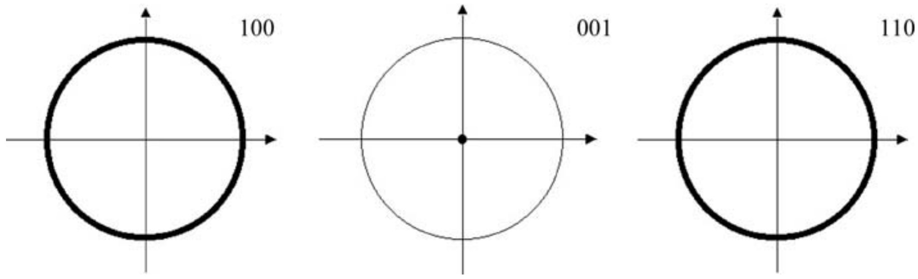

Figure 5.3.12
{100}, {001} and {110} pole figures of a cyclic-fibre texture in an orthorhombic crystal system. The fibre axis is with ⟨001⟩* directions along Z_A.

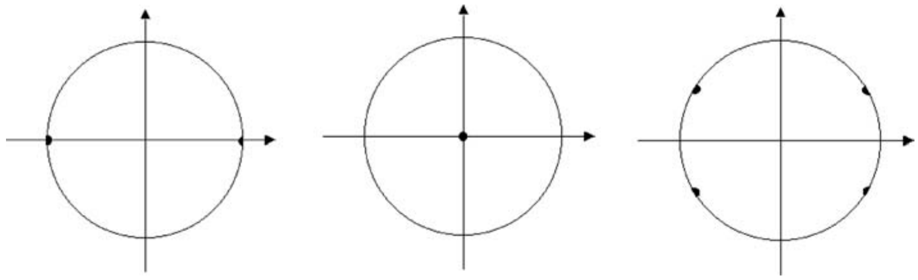

Figure 5.3.13
{100}, {001} and {110} pole figures of a three-dimensional texture in an orthorhombic crystal system, with ⟨001⟩* directions along Z_A and ⟨100⟩* directions along X_A.

$$V_r/V = f_r \text{ for the random part, and}$$
$$\frac{\mathrm{d}V_c(g)}{V} = \frac{1}{8\pi^2} f_c(g)\,\mathrm{d}g \text{ for the textured part.} \qquad (5.3.46)$$

This strictly means that the minimum value of the OD (*e.g.* f_r = 0.3 m.r.d.) defines the random volume fraction, *i.e.* 30% of the material is randomly oriented in this case.

5.3.2.7.2. *Planar textures*

This kind of texture is exhibited by samples in which the crystallites have two degrees of freedom to orient and belong to the $\infty\infty$ Curie group. One specific ⟨*hkl*⟩* direction family is allowed to rotate around one sample axis. The ⟨*hkl*⟩* directions are then located at random in a K_A plane perpendicular to the rotation axis. For instance, if the rotation axis is X_A with the direction family ⟨100⟩* of an orthorhombic crystal system (Fig. 5.3.9), the the ⟨100⟩* directions are then distributed in the (Y_A, Z_A) plane. However, since the other directions are at random around ⟨100⟩*, their pole figures remain quite homogeneous.

Of course, it is a special case that the rotation axis is along a major axis of the sample, and that the ⟨100⟩* (**a** axes) are the directions concerned. There could have been an inclined axis of rotation and reflections with a larger multiplicity, giving rise to more complex pole figures. Planar textures with the rotation axis around Z_A are called a 'cyclic-planar' texture (Fig. 5.3.10).

5.3.2.7.3. *Fibre textures*

If the crystallites lose another degree of freedom in their orientation (∞, ∞m, ∞/m, $\infty 2$ or ∞/mm Curie groups), they are forced to align one of their ⟨*hkl*⟩* directions with one direction **y** of K_A, with all other directions being at random around ⟨*hkl*⟩*. Such a texture is called 'fibre texture'. For instance, if all of the ⟨001⟩* directions from an orthorhombic crystal system are located along **y** = ($\vartheta_{\mathbf{y}} = 45°$, $\varphi_{\mathbf{y}} = 45°$) (Fig. 5.3.11), then the ⟨100⟩* and ⟨110⟩* directions will be located at random in a plane perpendicular to this **y**. As above, if the ⟨001⟩* directions are aligned with Z_A then the texture is called a 'cyclic-fibre texture' (Fig. 5.3.12). Such a texture has the ⟨100⟩* and ⟨110⟩* poles located on the periphery of the pole figures.

5.3.2.7.4. *Three-dimensional textures*

Samples composed of crystallites which have had no opportunity to orient themselves in K_A (zero degrees of freedom) will exhibit point poles for all of their pole figures. The pole figures will be similar to those of a single crystal. We call this a 'three-dimensional' or 'single-crystal-like' texture. For instance if the

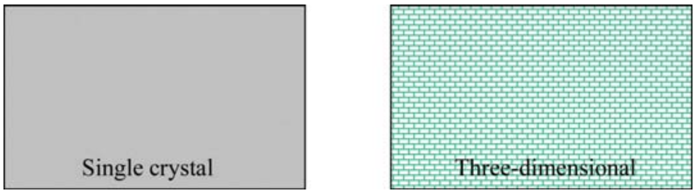

Figure 5.3.14
The difference between a perfect single crystal and a polycrystal with perfect three-dimensional crystallite orientations. The normalized pole figures should be identical.

$\langle 001\rangle^*$ directions are aligned with Z_A and the $\langle 100\rangle^*$ directions with X_A, the pole figures will look like those in Fig. 5.3.13, and the φ_y angles to which the $\langle 110\rangle^*$ poles are localized will depend on the b/a ratio of the orthorhombic structure.

One should avoid confusion between real single crystals and polycrystals exhibiting three-dimensional textures (Fig. 5.3.14). A single crystal, as usually understood in single-crystal crystallography, exhibits a 'mosaicity', itself composed of a mosaic spread and size. The mosaic spread is often measured using a so-called 'rocking curve', *i.e.* a limited view of the complete texture, and in this sense is a 'three-dimensional texture' with very small crystallite misorientation. The mosaic size represents the coherent domains (crystallites) of the mosaic in the single crystal. A perfect three-dimensional texture can correspond either to an ensemble of coherent domains with respective crystal reference frames perfectly parallel to one another (*i.e.* with no spread) but with no wave coherence between them, or to a large single crystal that diffracts as a single coherent domain. The diffracted intensity is much larger in the latter case and the direct pole figures will show very large intensities compared with the former. However, the normalized pole figures will be the same in both cases, as all effects other than crystal orientation are eliminated by normalization.

5.3.2.7.5. *Typical OD components*

Each of the previous texture types has corresponding OD descriptions as components of orientations, which can be represented, for example, using a Cartesian coordinate system for H space (Fig. 5.3.15) and isodensity surfaces for simplicity. An individual point g in this space represents an individual orientation located at $\{\alpha_c, \beta_c, \gamma_c\}$. A spherical component (b in Fig. 5.3.15) consists of concentric spheres with increasing radii for lower densities, with the level of these latter depending on the choice of the function representing the component. An elliptical component (c) shows an elongation in one or two directions (here along the α_c rotation axis). A tube around a given (α_c, β_c) couple that is elongated over the whole γ_c range represents a fibre texture with a fibre axis that is inclined with respect to the main K_A axis (a in Fig. 5.3.15). Isolated components respecting specific relationships between their coordinates can also exist; for instance, a tube around $\gamma_c = 0$ with $\alpha_c + \beta_c =$ constant (d in Fig. 5.3.15) or $\alpha_c^2 + \beta_c^2 =$ constant (e in Fig. 5.3.15).

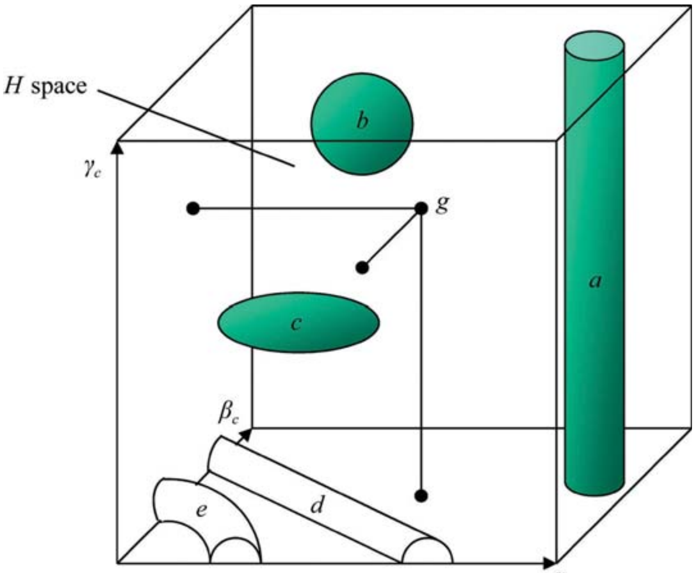

Figure 5.3.15
Isodensity surfaces representing isolated OD components in a Cartesian coordinate system in H space.

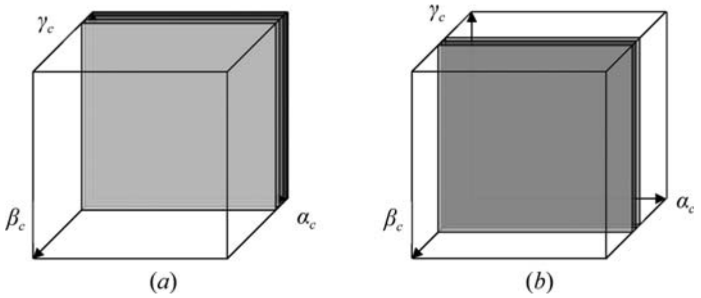

Figure 5.3.16
Several isodensity surfaces representing a cyclic-fibre OD (a) and a cyclic-planar OD (b) in H space.

For cyclic-fibre components $\beta_c = 0$ and α_c is distributed on 2π. In this configuration, a γ_c rotation or an α_c rotation have the same effect and the whole (α_c, γ_c) plane is filled by density (Fig. 5.3.16*a*). In a cyclic-planar texture (Fig. 5.3.16*b*), on the contrary, $\beta_c = 90^\circ$. However, in this case both α_c and γ_c are distributed on 2π, since the cyclic-planar axis Z_B is distributed in the (X_A, Y_A) plane and since all directions are at random Z_B. The result is an ODF representation that looks very similar to that of a cyclic-fibre texture, except for the coordinate of the high density levels along the β_c axis of rotation.

5.3.2.8. *Reciprocal-space mapping*

Reciprocal-space mapping (RSM) represents the localization of the momentum transfer in the sample reference frame (K_A). The momentum-transfer vector $\mathbf{q}$ is defined by

$$\mathbf{q} = (\mathbf{k}_o - \mathbf{k}_i),$$
$$\|\mathbf{q}\| = \frac{4\pi}{\lambda}\sin\theta = 2\|\mathbf{k}\|, \qquad (5.3.47)$$

in which $\mathbf{k}_i$ and $\mathbf{k}_o$ are the incident and outgoing wavevectors, respectively. The goal of RSM is then to locate a reciprocal vector, defined in reciprocal space $\mathbf{R}$, in a reference frame defined in the sample direct space. Since $\mathbf{q}$ is perpendicular to the diffracting plane (hkl), it is also parallel to the normal $\mathbf{h}$ of this latter. Consequently, RSM first determines the ensemble of $I_{\mathbf{h}}(\mathbf{y})$ diffracted intensities for the $\mathbf{y}$ orientations of a given reciprocal node corresponding to the extension of the Bragg peak $\mathbf{h}$ on the pole sphere. At this point one should notice that RSM is generally performed on strongly oriented samples such as epitaxial layers or single crystals. Each $\mathbf{y}$ set of measured orientations is then restricted in sample space on the pole sphere for a given $\mathbf{h}$. However, this does not avoid the measurement of a large number of points for each **h** to correctly describe the reciprocal-space node.

Secondly, one has to transform measured **y** directions of Y space to their corresponding values in R by multiplying them by the norm $\|\mathbf{q}\|$ of the **q** vector. This results in a set of $I_{\mathbf{h}}(\mathbf{q})$ values represented in K_A.

From the pole-figure definitions, the **q** coordinates are

$$\begin{aligned} q_{X_A} &= \frac{4\pi}{\lambda}\sin\theta\sin\vartheta_{\mathbf{y}}\cos\varphi_{\mathbf{y}} \\ q_{Y_A} &= \frac{4\pi}{\lambda}\sin\theta\sin\vartheta_{\mathbf{y}}\sin\varphi_{\mathbf{y}} \\ q_{Z_A} &= \frac{4\pi}{\lambda}\sin\theta\cos\vartheta_{\mathbf{y}}. \end{aligned} \qquad (5.3.48)$$

5.3.3. Magnetic quantitative texture analysis (MQTA)

5.3.3.1. *Magnetization curves and magnetic moment distributions*

The measurement of magnetic pole figures using neutron diffraction is sparsely documented and only a few attempts at refining magnetic ODs have been carried out to date (Birsan *et al.*, 1996), although knowledge of the anisotropic distribution of magnetic moments in a sample has been shown to be of crucial importance to predict macroscopic magnetic behaviours (Morales *et al.*, 2003). Anisotropic magnetic behaviour is usually probed using magnetization curves measured in only two perpendicular macroscopic directions of the sample, and is then intrinsically subjected to strong biases if the sample magnetic moment distribution does not respect some symmetry, adapted to the magnetization measurement (Fig. 5.3.17). Magnetic moment distribution characterization is thus a prerequisite for checking the validity of magnetization measurements for a given sample-measurement configuration.

Neutron diffraction is perfectly suited for the examination of macroscopic magnetic moment distributions, provided that one can measure the same sample with and without the application of an external magnetic field during the measurements (Chateigner *et al.*, 2010).

5.3.3.2. *Magnetic pole figures and magnetic ODs*

5.3.3.2.1. *Magnetic pole figures and ODs*

Using neutron diffraction, pole figures are composed of a nuclear (n; the usual crystallographic pole figures) and a magnetic (m) part in zero field or under the application of an external magnetic field **B**,

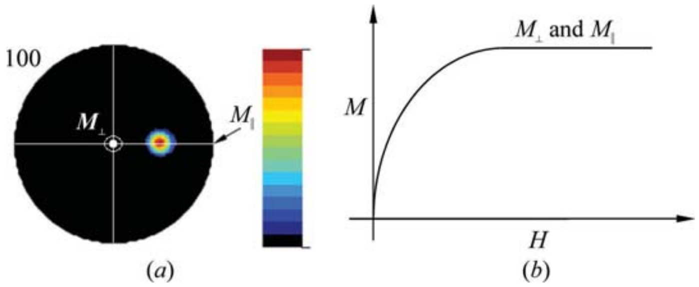

Figure 5.3.17
Illustration of a case for which a magnetization measurement in two perpendicular directions cannot reveal the macroscopic magnetic anisotropy. (a) Virtual distribution of the magnetic moments, with magnetic moments at 45° from both magnetization measurement directions, and (b) the corresponding magnetization curves.

$$\begin{aligned} I_{\mathbf{h}}(\mathbf{y}) &= I^n_{\mathbf{h}}(\mathbf{y}) + I^m_{\mathbf{h}}(\mathbf{y}), \\ I_{\mathbf{h}}(\mathbf{y},\mathbf{B}) &= I^n_{\mathbf{h}}(\mathbf{y},\mathbf{B}) + I^m_{\mathbf{h}}(\mathbf{y},\mathbf{B}). \end{aligned} \qquad (5.3.49)$$

For crystallites that are not free to rotate under **B**, for example in the solid state without phase transformation,

$$\begin{aligned} I^n_{\mathbf{h}}(\mathbf{y},\mathbf{B}) &= I^n_{\mathbf{h}}(\mathbf{y}), \ \text{hence} \\ I_{\mathbf{h}}(\mathbf{y},\mathbf{B}) &= I^n_{\mathbf{h}}(\mathbf{y}) + I^m_{\mathbf{h}}(\mathbf{y},\mathbf{B}). \end{aligned} \qquad (5.3.50)$$

This latter equation is of interest because it can serve for the determination of the magnetic part from an independent determination of the nuclear part, for example using X-ray diffraction. The application of a field **B** eventually induces a reorientation of magnetic moments in the sample, or magnetic polarization, which is seen using neutron diffraction as variations of intensities, $\Delta I^m_{\mathbf{h}}(\mathbf{y},\mathbf{B})$, in the pole figures, and (5.3.49) becomes

$$I_{\mathbf{h}}(\mathbf{y},\mathbf{B}) = I^n_{\mathbf{h}}(\mathbf{y},\mathbf{B}) + I^m_{\mathbf{h}}(\mathbf{y},0) + \Delta I^m_{\mathbf{h}}(\mathbf{y},\mathbf{B}). \qquad (5.3.51)$$

As for crystallographic QTA, total magnetic scattering normalized pole figures $[P^m_{\mathbf{h}}(\mathbf{y},\mathbf{B})]$, normalized magnetic scattering polarization pole figures $[\Delta P^m_{\mathbf{h}}(\mathbf{y},\mathbf{B})]$ and their respective magnetic ODs $[f_m(g,\mathbf{B})$ and $f^p_m(g,\mathbf{B})]$ have to respect normalization with their respective normalization factors (random intensities),

$$\begin{aligned} &\int_{\mathbf{y}} P^m_{\mathbf{h}}(\mathbf{y},\mathbf{B})\,\mathrm{d}\mathbf{y} = 2\pi, \\ &\int_{\mathbf{y}} \Delta P^m_{\mathbf{h}}(\mathbf{y},\mathbf{B})\,\mathrm{d}\mathbf{y} = 0, \\ &I^{n,r}_{\mathbf{h}} = \frac{\int_{\mathbf{y}} I^n_{\mathbf{h}}(\mathbf{y},\mathbf{B})\,\mathrm{d}\mathbf{y}}{\int_{\mathbf{y}}\mathrm{d}\mathbf{y}}, \\ &I^{m,r}_{\mathbf{h}} = \frac{\int_{\mathbf{y}} I^m_{\mathbf{h}}(\mathbf{y},\mathbf{B})\,\mathrm{d}\mathbf{y}}{\int_{\mathbf{y}}\mathrm{d}\mathbf{y}} = I^{m,r}_{\mathbf{h}}(\mathbf{y},0) = I^{m,r}_{\mathbf{h}}(\mathbf{y},\mathbf{B}), \\ &\int_g f_m(g)\,\mathrm{d}g = 4\pi^2, \\ &\int_g f^p_m(g)\,\mathrm{d}g = 0. \end{aligned} \qquad (5.3.52)$$

5.3.3.2.2. *Fundamental equations of MQTA*

Since two different magnetic scattering pole figures and ODs have been constructed, there are two corresponding fundamental equations:

$$P^m_{\mathbf{h}}(\mathbf{y},\mathbf{B}) = \frac{1}{2\pi}\int_{\mathbf{h}\|\mathbf{y}} f_m(g,\mathbf{B})\,\mathrm{d}\tilde{\varphi} \qquad (5.3.53)$$

for the total magnetic scattering, with $\tilde{\varphi}$ in general different from that of the crystallographic (nuclear) part since magnetic and nuclear cells can have different rotation groups, and

$$\Delta P^m_{\mathbf{h}}(\mathbf{y},\mathbf{B}) = \frac{1}{2\pi}\int_{\mathbf{h}\|\mathbf{y}} f^p_m(g,\mathbf{B})\,\mathrm{d}\tilde{\varphi} \qquad (5.3.54)$$

for the polarization part. Because the normalization of the polarization part requires us to work in the 'positive' and 'negative' spaces of the polarization pole figures, this latter equation is in fact composed of two parts:

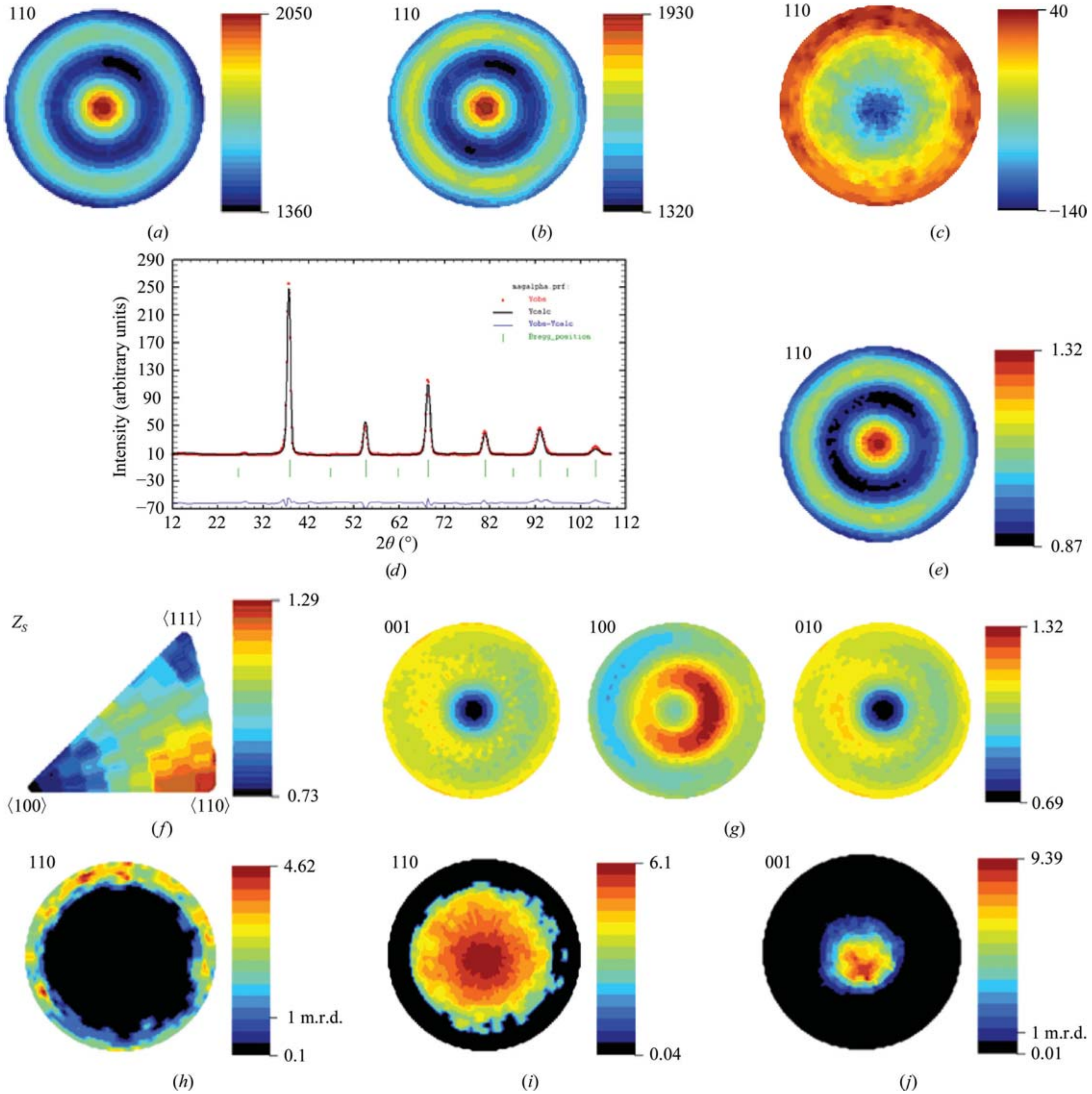

Figure 5.3.18

{110} pole figures at zero field (*a*), under 0.3 T (*b*) and the difference (*c*). (*d*) Fit of the sum of all diagrams at zero field using the orthorhombic magnetic subgroup in *FullProf*; (*e*) WIMV recalculated/normalized nuclear {110} pole figure. (*f*) Inverse nuclear pole figure for the cylinder sample-axis direction and (*g*) WIMV recalculated/normalized magnetic scattering contribution for the main orthorhombic axes. (*h*–*j*) Recalculated/normalized magnetic scattering polarization pole figures for the positive (*h*) and negative (*i*) parts of the difference pole figures, and the corresponding positive {001} magnetic scattering pole figure illustrating the magnetic moment reorientation (*j*).

$$\Delta P_{\mathbf{h}}^{m+}(\mathbf{y},\mathbf{B}) = \frac{1}{2\pi}\int\limits_{\mathbf{h}\parallel\mathbf{y}} f_m^{p+}(g,\mathbf{B})\,\mathrm{d}\tilde{\varphi},$$

$$\Delta P_{\mathbf{h}}^{m-}(\mathbf{y},\mathbf{B}) = \frac{1}{2\pi}\int\limits_{\mathbf{h}\parallel\mathbf{y}} f_m^{p-}(g,\mathbf{B})\,\mathrm{d}\tilde{\varphi}. \qquad (5.3.55)$$

The correct normalizations and determinations of the various orientation quantities accessible to neutron diffraction depend on many factors. The possibilities of observing neutron peaks without magnetic contributions and the initial magnetic and crystallographic orientation states of the sample (isotropic or anisotropic) have been discussed elsewhere (Chateigner *et al.*, 2010).

5.3.3.3. *An example*

Here, we illustrate magnetic quantitative texture analysis on an iron sample exhibiting magnetic saturation around 0.5 T (Chateigner *et al.*, 2010) that was initially not magnetized. Measurements were carried out on the D19 beamline at ILL first without and then with an applied magnetic field of 0.3 T, which is sufficient to partly reorient the magnetic moments. At zero field (Fig. 5.3.18*a*) the sample exhibits a strong signal with a moderate $\langle 110\rangle$ crystallographic texture. Under a 0.3 T field (Fig. 5.3.18*b*), the maximum of the $\{110\}$ experimental pole figure decreases significantly at the benefit of the pole-figure equator. This is coherent with a magnetic field applied along the sample cylinder axis (Z_A), with which magnetic moments tend to align, giving rise to more magnetic diffraction signal 90° to it. The difference $\{110\}$ pole figure illustrates this more explicitly (Fig. 5.3.18*c*), with negative differences at its centre and positive values on its equator. We then calculated the random magnetic contribution of the isotropic magnetic sample using *FullProf* (Fig. 5.3.18*d*), using the sum of all diagrams measured at all of the sample orientations, taking into account the resolution characteristics of the D19 instrument. This random magnetic contribution provides the possibility of decoupling nuclear and magnetic contributions at zero field: $I_h^n(\mathbf{y}, 0)$ and $I_h^m(\mathbf{y}, 0)$, respectively (Chateigner *et al.*, 2010). These latter pole figures were used to refine the corresponding ODs, $f_n(g)$ and $f_m(g)$, using the body-centred cubic crystal symmetry and the orthorhombic magnetic symmetries, respectively, and the WIMV algorithm in *BEARTEX* (Wenk *et al.*, 1998). The nuclear $\langle 110\rangle$ fibre texture (Fig. 5.3.18*e*) culminates at 1.32 m.r.d. [$f_n^{\max}(g) = 1.8$ m.r.d., $f_n^{\min}(g) = 0.61$ m.r.d., $F^2 =$ 1.03 m.r.d.^{2}, RP$_0$ = 1.42%], and the fibre axis is aligned with Z_A as the sole textured component (Fig. 5.3.18*f*). Since the easy-axis direction for magnetization in iron is $\langle 100\rangle$, the actual $\langle 110\rangle$ fibre does not correspond to an easy-magnetization configuration. Consequently, the total normalized magnetic scattering pole figures of the main magnetic unit-cell axes (Fig. 5.3.18*g*) do not show a strong reorientation of densities, and exhibit a maximum of only 1.32 m.r.d. on the pole figures, but a larger OD maximum value [$f_n^{\max}(g) = 2.3$ m.r.d., $f_n^{\min}(g) = 0.64$ m.r.d., $F^2 = 1.03$ m.r.d.^{2}, RP$_0$ = 0.24%].

From the magnetic scattering polarization pole figures we refined the magnetic polarization OD, $f_m^{p+}(g)$ and $f_m^{p-}(g)$. Since the magnetic scattering difference pole figures show positive and negative values, we divided them into positive and negative zones, $\Delta I_{\mathbf{h}}^{m+}(\mathbf{y}, \mathbf{B})$ and $\Delta I_{\mathbf{h}}^{m-}(\mathbf{y}, \mathbf{B})$, respectively, assigning zeros to the negative cells of $\Delta I_{\mathbf{h}}^{m+}(\mathbf{y}, \mathbf{B})$ and *vice versa*. From $\Delta I_{\mathbf{h}}^{m+}(\mathbf{y}, \mathbf{B})$ and $|\Delta I_{\mathbf{h}}^{m-}(\mathbf{y}, \mathbf{B})|$ we refined the magnetic scattering polarization ODs, $f_m^{p+}(g)$ [$f_m^{p+,\max}(g) = 93$ m.r.d., $f_m^{p+,\min}(g) =$ 0 m.r.d., $F^2 = 12.4$ m.r.d.^{2}, RP$_0$ = 6.83%] and $f_m^{p-}(g)$ [$f_m^{p-,\max}(g) =$ 6.1 m.r.d., $f_m^{p-,\min}(g) = 0.04$ m.r.d., $F^2 = 2.70$ m.r.d.^{2}, RP$_0$ = 0.00%] in *BEARTEX*, which yielded the normalized $\Delta P_{110}^{m+}(\mathbf{y}, \mathbf{B})$ and $|\Delta P_{110}^{m-}(\mathbf{y}, \mathbf{B})|$ pole figures (Figs. 5.3.18*h* and 5.3.18*i*, respectively). These latter clearly show the reoriented part of the magnetic signal, with a large density created in the centre of $|\Delta P_{110}^{m-}(\mathbf{y}, \mathbf{B})|$, indicating a departure of intensities in this area to reach the periphery of $\Delta P_{110}^{m+}(\mathbf{y}, \mathbf{B})$, both pointing towards magnetic moment alignment with Z_A. The maximum densities observed in these latter pole figures measure the strength of the intensity reorientations, as also seen from the texture indexes and OD maxima. Most importantly, since the diffracted signal reveals magnetic moments that are located 90° to it, one can search in this case for a reflection at this angle from [110], which is, for instance, 001 in this space group. The $\Delta P_{110}^{m+}(\mathbf{y}, \mathbf{B})$ (Fig. 5.3.18*j*) then directly reveals the distribution of reoriented magnetic moments, which in this case indicates a 9.4 m.r.d. density of reorientation. Interestingly, in this case one can see a slight but significant deviation of these magnetic moments with respect to Z_A ($\langle 110\rangle$ crystallographic fibre axis), probably owing to difficulty in controlling the application of the magnetic field.

5.3.4. Modelling of preferred orientation in the Rietveld method

The modelling of preferred orientation in diffraction patterns was originally developed to facilitate structure determination. The presence of an unrecognized preferred orientation can be fatal to structure solution. Texture is particularly present in easily cleaved materials or materials with anisotropic habits, and when the samples are prepared by anisotropic techniques. X-ray diffraction specimen preparation often introduces preferred orientations, which have been mostly considered as an undesirable phenomenon in Rietveld analysis.

When textures have not been removed successfully by careful grinding and packing, the remaining texture has to be modelled during the analysis. There are two types of texture treatments in Rietveld analysis. If the texture is simple (smooth, fibre type and not too severe), it can be modelled using analytical formulae. If it is more complex (several texture components, sharp pole figures) the treatment requires a quantitative texture analysis (the subject of Section 5.3.2). In this section the simplest texture corrections are described, but the best way to characterize texture effects is to carry out QTA inside the Rietveld approach. The texture is roughly modelled using three parameters:

(i) a texture axis linked to the sample symmetry (the normal to the sample surface for a flat sample in Bragg–Brentano geometry or the cylinder axis in Debye–Scherrer geometry),
(ii) the crystallographic direction $\mathbf{h}$, which tends to align with the previous axis, and
(iii) a texture strength (angular dispersion, texture factor *etc.*).

5.3.4.1. *Rietveld and March approaches*

The preferred orientations are modelled in the original equation of Rietveld by the March function (March, 1932) using the function $P_{\mathbf{h}}$,

$$P_{\mathbf{h}} = \exp(-G_1\alpha_{\mathbf{h}}^2) \qquad (5.3.56)$$

or

$$P_{\mathbf{h}} = G_2 + (1 - G_1)\exp(-G_1\alpha_{\mathbf{h}}^2), \qquad (5.3.57)$$

where G_1 and G_2 are refinable parameters and $\alpha_{\mathbf{h}}$ is the angle between the texture direction $\mathbf{h}$ and the scattering vector.

5.3.4.2. *March–Dollase approach*

Dollase proposed an improvement to the March approach using the following function (Dollase, 1986):

$$P_{\mathbf{h}} = \left[G_1^2\cos^2\alpha_{\mathbf{h}} + \left(\frac{1}{G_1}\right)\sin^2\alpha_{\mathbf{h}}\right]^{-3/2}. \qquad (5.3.58)$$

Originally, the March correction assumed a Gaussian distribution of the preferred-orientation axis of the individual crystallites about an axis. G_1 is a refinable parameter that now controls the distribution shape and is an index of the preferred-orientation strength ($0 < G_1 \leq 1$; $G_1 = 1$ for a random orientation).

This model provides

(i) a preferred-orientation model with minimum or maximum at $\alpha_{\mathbf{h}} = 0°$,
(ii) a symmetric and smooth evolution in the (0, 90°) $\alpha_{\mathbf{h}}$ range,
(iii) a single parameter to be fitted, and

(iv) the possibility of normalization of the orientation,

$$\int_0^{\pi/2} P_{\mathbf{h}} \sin\alpha_{\mathbf{h}}\, d\alpha_{\mathbf{h}} = 1. \qquad (5.3.59)$$

This latter property is important in order to keep the total diffracted intensity in a diffraction diagram constant whatever the distribution shape $P_{\mathbf{h}}$. A point that is often not realized is that the March–Dollase approach assumes cylindrical sample symmetry.

5.3.4.3. *Modified March–Dollase models*

More recently, Brosnan *et al.* (2006) proposed a modification of the March–Dollase approach by including a 'random' orientation factor,

$$P_{\mathbf{h}} = f\left\{\left[G_1^2\cos^2\alpha_{\mathbf{h}} + \left(\frac{1}{G_1}\right)\sin^2\alpha_{\mathbf{h}}\right]^{-3/2}\right\} + (1-f). \qquad (5.3.60)$$

In this model, it is expected that the factor f provides the random part, *i.e.* the volume of randomly oriented crystallites. However, it must be noted that this factor is linked to the component of orientation that is described by the formula. Since this only describes one orientation component, *i.e.* a specific $\mathbf{h}$ distributed in a given distribution around the normal to the sample, f is in fact only the volume fraction of crystallites that have their $\mathbf{h}$ direction in this distribution component, with $(1-f)$ being the volume fraction of crystallites that are not in this component (oriented differently) but are not necessarily randomly oriented. Let us give an example to illustrate this point: imagine a sample containing tetragonal crystallites with a single orientation component, for example with their c axes distributed in a Gaussian around the normal. In this case, if $f = 0.5$, 50% of the crystallites have [001] directions inside the Gaussian component. However, there is no information, for instance, about the orientation of the a axes around the orientation component. Thus, $(1 - f)$ does not mean that 50% of the crystallites are necessarily randomly oriented; the a axes may possibly be strongly oriented along one specific direction in the plane perpendicular to the c axes. The parameter f hence does not represent the orientation distribution function $f(g)$, and one should not confuse them.

A second modification (Zolotoyabko, 2009) focuses on the estimation of an orientation degree parameter η_Z, defined on the basis of the Dollase parameter G_1:

$$\eta_Z\,(\%) = \left[\frac{(1-G_1)^3}{1-G_1^3}\right]^{1/2}. \qquad (5.3.61)$$

The η_Z parameter tends to zero as G_1 values reach 1 and to 100% for $G_1 = 0$. It can easily be introduced in Rietveld programs and intrinsically contains the normalization condition of (5.3.59).

5.3.4.4. *Donnet–Jouanneaux function*

This model for preferred orientation is purely empirical, with a parameter D controlling the preferred orientation ($D = 0$ for a random orientation) (Jouanneaux, 1999):

$$P_{\mathbf{h}} = 1 + \frac{D\cos 2\alpha_{\mathbf{h}}}{1+(G-1)\sin^2\alpha_{\mathbf{h}}}. \qquad (5.3.62)$$

5.3.4.5. *Modelling by spherical harmonics (and exponential)*

Järvinen and others (Ahtee *et al.*, 1989; Järvinen, 1993) initially proposed the use of a harmonic method to model preferred orientation in Rietveld refinement for cylindrical sample symmetry. The idea was expanded by Popa (1992) to all sample symmetries and implemented by Von Dreele in *GSAS* (Larson & Von Dreele, 2000).

Equation (5.3.13) is utilized to compute the preferred-orientation effect on intensities as a function of the coefficients. The sample symmetry must be imposed depending on the kind of measurement that is performed. In general, with only one pattern in either Bragg–Brentano or Debye–Scherrer geometry, a cylindrical symmetry (fibre texture) for the sample should be used. The fibre axis will be normal to the surface of the sample for the Bragg–Brentano case and along the capillary axis for the Debye–Scherrer case. Spinning the sample along this fibre axis will ensure the correct symmetry for the sample in cases where it is not correct. When a static specimen with known rolling or shear texture is measured (preferably in multiple orientations), the appropriate noncylindrical sample symmetry should be used, and the angles relating the different orientations must be considered.

Another remark should be made on the use of spherical harmonics with the Rietveld method. All spherical-harmonics descriptions and implementations (the same is also true for discrete methods such as WIMV, EWIMV and ADC) in the case of monoclinic crystal symmetry work only in the c-axis unique (Mattheis & Wenk, 2009) setting.

Different approaches have been used to ensure an OD that is always positive. The approaches used to force a positive OD, such as those described by Van Houtte (1991), do not have an effect in this case as the even coefficients are the only ones that are used in preferred-orientation correction and are not affected by positivity or similar methods. Constraints to force positive texture-correction factors are already provided by the experimental pattern. Additional constraints may be added to force the OD to also have positive texture factors or to remain inside the measured bounds.

An alternative approach is to write the OD as $f(g) = \exp[h(g)]$ (in a similar fashion to the exponential-harmonic method of Van Houtte, 1991) and to expand the function $h(g)$ in terms of spherical harmonics. This will retain all of the symmetries of the OD and ensure an OD that is always positive. The problem is that the texture factors can no longer be calculated using (5.3.13) and should be evaluated by numerical integration over the OD using (5.3.11), and in the Rietveld least-squares method only the numerical derivative must be adopted.

5.3.4.6. *The use of standard functions (or texture components)*

An alternative model for preferred orientation is to use standard components. In the case of only one pattern, fibre components should be used or fibre sample symmetry as described in Section 5.3.2.3.7. To compute a pole-figure value or texture model for a general fibre component having a partial Gaussian and Lorentzian character, (5.3.29) and (5.3.31) can be used by integrating around the fibre axis.

5.3.4.7. *Remarks*

In most of the previous models, the formulations are only valid for axially distributed, single-component textures (with a cylindrical symmetry around the scattering vector, and for a Bragg–Brentano symmetric geometry), for which efficient corrections are obtained (O'Connor *et al.*, 1991; Capková *et al.*,

Table 5.3.1
Preferred-orientation (PO) modelling methods implemented in some Rietveld packages, and their capability to perform a full texture analysis (QTA) with determination of the OD from several patterns

Details are given in the form yes/no for PO correction/full QTA (OD refinement).

Software	*GSAS*	*FullProf*	*TOPAS*	*MAUD*	*Jana*	*BGMN*	*RIETAN*	*WinMprof*
March–Dollase	Yes/no	Yes/no	Yes/no	Yes/no	Yes/no	Yes/no	Yes/no	Yes/no
Donnet–Jouanneaux	No/no	No/no	No/no	No/no	No/no	No/no	No/no	Yes/no
Spherical harmonics	Yes/yes	No/no	Yes/no	Yes/yes	No/no	No/no	No/no	No/no
Exponential harmonic	No/no	No/no	No/no	Yes/yes	No/no	†/no	No/no	No/no
WIMV	No/no	No/no	No/no	Yes/yes	No/no	No/no	No/no	No/no
EWIMV	No/no	No/no	No/no	Yes/yes	No/no	No/no	No/no	No/no
Standard components	No/no	No/no	No/no	Yes/yes	No/no	No/no	No/no	No/no

† In this case an exponential-harmonics method is claimed, but the particular implementation does not ensure compatibility between pole-figure and OD values.

1993; Cerný *et al.*, 1995). They have been implemented in many Rietveld programs, and some of them allow the modelling of two or more texture components of this type. For all other textures, measurements and formalisms to resolve the texture are required, unless the conversion of the sample to powder is acceptable. Furthermore, one should take particular care regarding the geometry used for the measurements. The previous formulae describe the orientations in the sample reference frame, while measurements are carried out in the spectrometer frame. The relationships between the two frames are straightforward when using classical θ–2θ scans, but for any other measurements, such as rocking curves or the use of area detectors, for instance, prior localization corrections have to be made to locate the plane normals in the sample frame.

The previous models do not allow the description of texture either in terms of orientations or of distribution densities (expressed in m.r.d. units), based on the absence of OD calculations implying normalization. Also, many Rietveld-based programs offer preferred-orientation modelling capabilities, but do not always include OD refinement, *i.e.* not reaching the QTA stage (Table 5.3.1).

In particular, working on whole patterns became mandatory with the growing demand for the characterization of nanocrystalline samples. In such samples, the tremendous inter-phase and intra-phase overlaps prevent any correct QTA characterization if proper deconvolutions are not carried out. A Rietveld-like approach becomes mandatory, with the advantage of then being able to access other material characteristics such as residual stresses, phase amounts and line broadening. This is the subject of combined analysis.

5.3.5. Combined analysis: structure, texture, microstructure, stress, phase, layering and reflectivity analyses in a single approach

5.3.5.1. *Problems*

Analysis by the diffraction/scattering of X-rays is presently facing a major problem: the nondestructive characterization of samples with increasing complexity (thin or massive heterostructures, polyphase materials, hybrids *etc.*), including as many as possible of their characteristics (structure, texture, crystallite sizes). These real samples often exhibit optimized properties because of their anisotropy, and this creates some problems in data analysis.

Problem 1. Anisotropic samples exhibit diffraction diagrams depending on the sample orientation because of the presence of texture. Refinement of crystal structures requires a model for the texture, as shown in Section 5.3.4. Texture factors depend on sample orientation, whereas structure factors do not. Also, texture factors integrate to unity over the entire pole figure. This indicates that with a proper approach to the problem (exploiting the full texture analysis), texture and structure are completely uncorrelated and can easily be decoupled. Full (and sharp) texture can actually be used as an advantage in structure solution (Wessels *et al.*, 1999).

Problem 2. Anisotropy is induced during production (*e.g.* heteroepitaxy, uniaxial pressing *etc.*), along with residual stresses in the sample. The diffraction peaks are then shifted relative to their unstressed positions, which biases on the one hand structural determination (unit-cell parameters) and on the other hand QTA, since the peak positions vary with the necessary rotations of the sample for texture measurements. It is then necessary to analyse the residual stresses in order to determine both the structure and texture correctly. However, differently oriented crystallites do not deform identically under the same macroscopic stress thanks to their tensorial elastic properties (anisotropic if texture is present), and a mutual influence exists between texture and residual stresses. Thus, there is a need to analyse both texture and stress simultaneously to obtain more accurate values of each.

Problem 3. Samples can be composed of several layers of different phases, which then have to be characterized individually in terms of structure/texture/stress. Volume and absorption variations are not the same for a covered layer, a top film or a substrate, and have an effect on intensities measured at different 2θ and $\mathbf{y}$ positions. These variations, if unaccounted for, bias structural, quantitative and textural analyses. The corrections to be applied depend on the effective thicknesses of the layers and their absorption coefficients, and thus depend on the phase composition.

Problem 4. In polyphase materials (completely or partially crystalline), quantitative phase analysis (QPA) can be biased if texture is present, and a suitable model is necessary in the analysis. Simple models such as the March–Dollase model should be avoided. The texture should be fully accounted for or removed by suitable sample preparation.

Problem 5. All of these results (structure, QTA, QPA, residual stress analysis and layering) depend on the microstructural states, crystallite sizes and shapes (isotropic or anisotropic), crystalline defects (point, linear, planar or volumetric), composition variations and microstrains, which in turn will be correctly determined only if the other parameters are satisfactorily known. Let us take the example that crystallite size effects are revealed in the line broadening and are then decoupled from (for instance) texture, which induces only intensity variations. This working hypothesis is, however, only valid if no peak overlap occurs. Indeed, if overlap is present the separation of each individual line broadening will depend on the convoluted intensities, which in turn depend on the texture (and/or other intensity effects). In a multi-component line, it will become dangerous to separate the components without somehow constraining the intensities, which can be performed using both $F_{\mathbf{h}}$ and $f(g)$ information. Conversely, the correct estimation of each intensity for subsequent QTA requires the separation step, implying some knowledge of the broadening.

Problem 6. All of the previous determinations rely on an *a priori* knowledge of the exact material composition to be characterized. Unfortunately, compositions may vary from sample to sample, giving rise to incorrect assignments of parameters during refinement. For instance, we may have the same atoms distributed over multiple phases in an unknown way, or multiple atoms occupying the same crystallographic site in one or more phases. In such a case one needs to constrain the problem, using for instance elemental compositions from energy-dispersive X-ray spectroscopy (EDX) or X-ray fluorescence (XRF). Also, for a quantitative XRF or EDX analysis a precise knowledge of the phase concentrations is fundamental to estimate the matrix effect or absorption. Chemical analysis by EDX or XRF may benefit from a quantitative analysis by diffraction, as well as the reverse. Thus, there is a need for a combined analysis, either based on independent *in situ* or *ex situ* measurements of the same samples.

The question arises after this list of problems as to whether one could benefit from the anisotropy of the material, and/or from the multiple independent measurements necessary to carry out a complete characterization of the real material. Such an approach needs to take account of all the effects visible in the diffracted signal, to measure a sufficient number of independent data with different techniques when necessary, and perform a single fitting of the full data by either least-squares or other suitable methods.

5.3.5.2. *Intensity of a pattern and general scheme*

If we consider a sample composed of N_L layers (a bulk sample is then equivalent to a single layer of infinite thickness) and N_Φ phases distributed in the layers, the intensity of a single data point $\mathbf{y}_c$ at 2θ and η (see Section 5.3.2.1.3.3 for angle definitions) in a diffractogram measured at a given sample orientation $\mathbf{y}_S$ ($\mathbf{y}_S$ represents the sample orientation in the spectrometer space S, *i.e.* defined by the goniometer angles ω, χ and φ) can be calculated as the sum of all reflections contributing to that point for all phases in all layers,

$$\begin{aligned} y_c(\mathbf{y}_S,\theta,\eta) &= y_b(\mathbf{y}_S,\theta,\eta) \\ &\quad + I_0\sum_{i=1}^{N_L}\sum_{\Phi=1}^{N_\Phi}\frac{\nu_{i\Phi}}{V_{c\Phi}^2}\sum_{\mathbf{h}}\mathrm{Lp}(\theta)j_{\Phi\mathbf{h}}|F_{\Phi\mathbf{h}}|^2\Omega_{\Phi\mathbf{h}}(\mathbf{y}_S,\theta,\eta) \\ &\quad \times P_{\Phi\mathbf{h}}(\mathbf{y}_S,\theta,\eta)A_{i\Phi}(\mathbf{y}_S,\theta,\eta), \end{aligned} \qquad (5.3.63)$$

in which y_b is the background contribution, I_0 is the incident intensity on the sample, $\nu_{i\Phi}$ is the volumetric fraction of phase Φ in layer i, $V_{c\Phi}$ is the unit-cell volume of phase Φ, Lp is the Lorentz polarization factor, $j_{\Phi\mathbf{h}}$ is the multiplicity of line $\mathbf{h}$ for phase Φ, $|F_{\Phi\mathbf{h}}|$ is the modulus of the structure factor (including thermal vibrations) for line $\mathbf{h}$ of phase Φ, $\Omega_{i\Phi\mathbf{h}}$ is the profile function of line $\mathbf{h}$ for phase Φ, taking account of instrumental and sample broadenings, $P_{\Phi\mathbf{h}}$ is the preferred orientation (pole-figure value) of phase Φ and $A_{i\Phi}$ is an absorption factor which takes into account the experimental and sample geometries.

In a similar way, we can write the intensity of a measured point in a pattern for reflectivity and XRF or EDX. We will explicitly write the equations for the diffraction part, but the procedure can be extended to every technique for which a measured intensity can be written in terms of the parameters describing the sample. The overall weighted sum of squares, as in Rietveld joint refinements, can then be written as a weighted sum between different techniques, each measuring a certain number of patterns and with each pattern t composed of N_t measured points:

$$\mathrm{WSS} = \sum_{t=1}^{N_p} u_t \sum_{i=0}^{N_t} w_{it}(y_{itc} - y_{ito})^2. \qquad (5.3.64)$$

The weight w_{it} is usually related to the inverse of the measured intensity for point i of pattern t and is equal to the inverse of the square of the standard deviation. Each pattern t is weighted using the quantity u_t, which should be used to adjust the importance that we want to give to a particular technique or pattern with respect to the others.

The quantity WSS must be minimized to find the optimized parameters. The minimization can be performed through standard nonlinear least-squares methods or other minimization schemes depending on the particular models that are used and the efficiency of the algorithm for a given problem.

5.3.5.3. *Minimum experimental requirements*

This methodology requires a large amount of data, however, and to be practical requires rapid acquisition using, for example, multiple detectors. The first experiment using such an approach was carried out with X-rays on a thin film (Ferrari & Lutterotti, 1994) on a laboratory texture instrument using a scintillator detector. The first experiment of this kind using neutron TOF data (Lutterotti *et al.*, 1997) was performed on the General Purpose Powder Diffractometer (GPPD) at the Intense Pulsed Neutron Source (IPNS). Since then, the methodology has been used for various purposes (Chateigner *et al.*, 1998; Lutterotti *et al.*, 2002, 2004; Morales *et al.*, 2002, 2005; Ricote *et al.*, 2004; Guilmeau *et al.*, 2005).

The required diffractometer has to be equipped with four circles in order to correspond to a texture experiment, *i.e.* at least one tilt rotation χ, one azimuthal rotation φ, an incidence circle ω and a detection circle 2θ. One circle (one scanning movement) can be eliminated by using a linear detector on the 2θ arm. Another circle and scan can be saved by using bidimensional detectors.

5.3.5.4. *Theoretical implementation*

5.3.5.4.1. *Instrumental broadening calibration*

The spectrometer space is multidimensional, with each rotation axis possibly giving rise to defocusing or misalignment effects. Each of these aberrations has to be measured and corrected for. For instance, in dealing with goniometer misalignments (which should be minimized as much as possible by careful alignment of the instrument and the sample) one can model them to a certain extent in the computation by reproducing all effects of sample displacements, precession errors and angle offsets. The fitting of instrument- and sample-misalignment errors should only be used as a last resort, and a well performed experiment is obviously always preferred. Fig. 5.3.19 is an illustration of such aberrations measured on a KCl standard powder using a four-circle diffractometer and a curved position-sensitive detector (CPS 120 from Inel).

Three major effects are visible: peak broadening, peak shift and background variation.

Broadening occurs when the incident beam illuminates the sample surface, producing variations in the irradiated area and the apparent Bragg-angle values. These were originally called

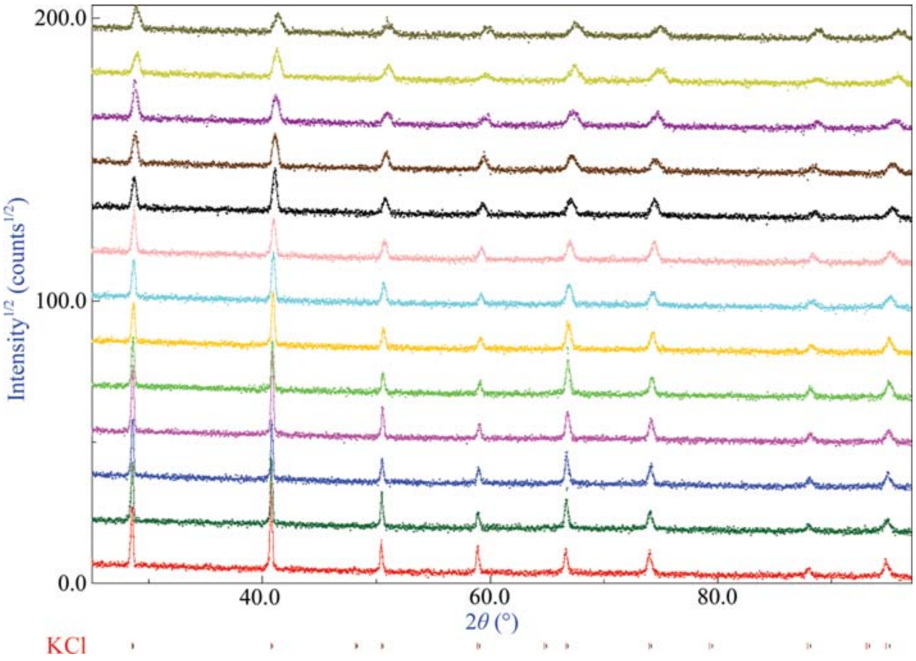

Figure 5.3.19
Illustration of the effects of defocusing and misadjustment on peak shapes and diffractometer resolution function. Measurements are on KCl powder. Diffractograms appear on top of each other from $\chi = 0°$ to $\chi = 60°$ in steps of 5° and were measured for $\omega = 20°$.

‘defocusing effects’, even if the experimental setup does not properly incorporate focusing optics (as in this case with the use of a parallel beam). They are dependent on the various angles of sample rotation.

When the sample tilt χ increases, the peaks broaden. For a square incident-beam cross section, the irradiated area on the flat sample is a rectangle at $\chi = 0°$ and becomes a parallelogram at $\chi > 0°$. The beam-footprint size then increases, giving rise to apparent θs and broadened peaks. For a bulk sample in symmetric reflection geometry the total integrated intensity remains constant whatever the value of χ (Schulz, 1949*a*). This implies that when using the full profile the defocusing effect is automatically taken into account since the total integrated area of the pattern is unchanged. However, at values of χ that are too large (typically >60°) the peak maxima decrease to values that are closer to the background, and even the integrated intensities are less reliable because of poorer counting statistics. This obviously depends on the instrumental setup, such as the detecting slit aperture, and can be partly compensated for by using larger counting times at larger χ values, but this always remains a compromise. For instance, increasing the detecting slit can provide a lower defocusing effect because of a larger integrating window, but as a result enhances the instrumental broadening and peak overlaps, and can prevent any microstructural analysis.

For a given diagram measured at ω, the peaks are broader at larger 2θ (Fig. 5.3.20). This effect is typical of flat specimen analyses; it does not occur, for instance, in transmission geometry using neutrons. For a given peak at 2θ, the full width at half maximum (FWHM) is smaller at larger ω angles owing to the smaller irradiated area of the sample. This effect also is typical of flat specimen analyses in reflection geometry and using a parallel beam.

In order to analyse the line broadening due to the characteristics of the sample, all of the various instrumental broadenings either have to be known from measuring the instrumental profiles using a standard sample with a known sample broadening or must be computed. The latter still requires the measurement of certain characteristics such as the tube focus.

A polynomial-like equation can then be used to represent the variations in the squared FWHM of the lines with the angles in a similar fashion to the Caglioti formula (Caglioti *et al.*, 1958),

$$\Delta_r \mathrm{FWHM}^2 = \sum_{u=0}^{U} p_{ru} r^u, \tag{5.3.65}$$

with r as a general rotation (χ, θ, $\tan\theta$, ω, $\eta, \ldots$) and with as many p_{ru} parameters as necessary, introducing them progressively in the refinement until they refine to negligible values.

5.3.5.4.2. *Peak-displacement errors*

Peak shifts arise from the misalignment of one or several of the rotation axes or sample displacement from the rotation centre. For instance, in Fig. 5.3.20 we clearly observe a 2θ peak shift for large χ values and this shift would not be the same at two different ω values. Depending on the experimental configuration, analytical formulae can be produced to fit these misalignments. If information about unit-cell parameters and/or residual strain are important, it is advisable to either have a perfectly aligned system or to use analytical formulae based on the geometrical features of the misalignment. Other empirical corrections are possible, based on polynomial fits or parametrizations per pattern, that are efficient for the correction of the peak position, but are more likely to cause a loss of positional information. These corrections are instrument dependent.

5.3.5.4.3. *Background fitting*

Furthermore, depending on many factors such as sample shape and absorption, the background B can also vary with the various angles of rotation. These variations have to be modelled, which is usually accomplished through a polynomial fit on all rotation axes,

$$\Delta_r B = \sum_{u=0}^{U} p'_{ru} r^u \tag{5.3.66}$$

or more complex functions such as Chebyshev polynomials (Larson & Von Dreele, 2000; Press *et al.*, 1988),

$$\Delta_r B = \sum_{u=0}^{U} p''_{ru} T_u(r^*), \qquad r^* = \frac{2(r - r_{\min})}{r_{\max} - r_{\min}} - 1, \tag{5.3.67}$$

where p'_{ru} and p''_{ru} are the factors to be determined. For Chebyshev polynomials the value of r must be substituted with r^* to be orthonormal, and $r_{\min}$ and $r_{\max}$ define the range of r.

Another option is to use an interpolated background which, instead of being applied to the original pattern (not advisable in Rietveld-like fitting), is applied to the residual pattern (the experimental data minus the computed profile) as in *MAUD* (Lutterotti, 2010). In this manner, the interpolation will not take intensity from the reflections as long as these are properly fitted.

In QTA with point detectors background subtraction is never easy; the evolution of background with rotation axes is not easily measured (because of defocusing from nearby peaks, for

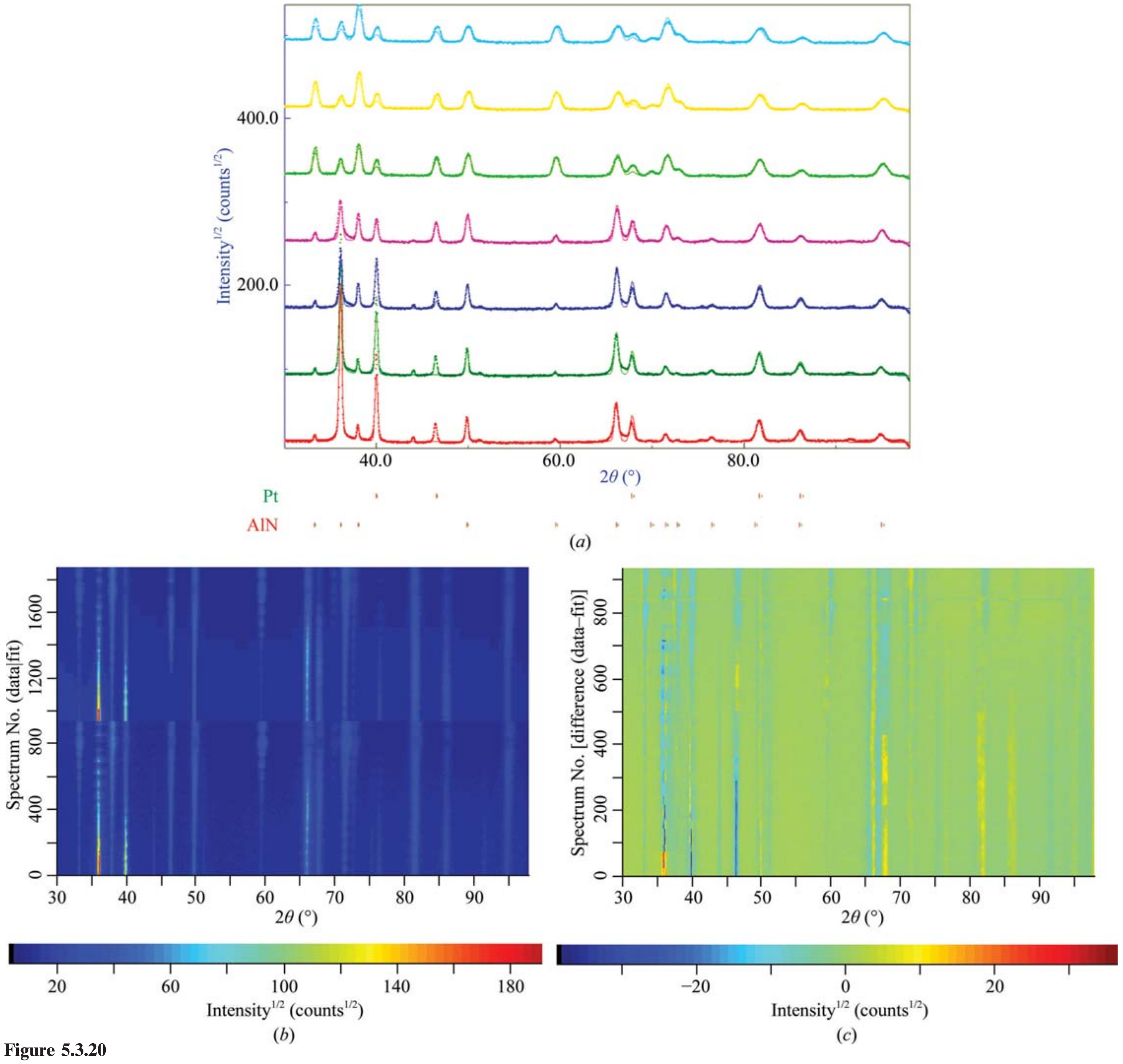

Figure 5.3.20

(*a*) Randomly selected diagrams (at increasing χ values and broadening due to defocusing from bottom to top) illustrating the quality of the fit, together with the textures of AlN and Pt. (*b*) Two-dimensional plots of the 936 experimental (lower half) and fitted (upper half) diagrams and (*c*) two-dimensional difference diagrams to reveal the errors.

instance) and is sample dependent. Here, one can see another advantage of full-profile analysis, where the background is not removed *a priori* but is modelled along with the reflection intensities.

5.3.5.4.4. *Reflection intensities*

Reflection intensities, as appearing in (5.3.63), depend mainly on the structure factors described elsewhere in this volume. Three different approaches are used to calculate them in the combined-analysis scheme.

The first approach calculates the structure factors from the atomic model with knowledge of the types and positions of the atoms in the unit cell. If an accurate crystal structure is not available for a particular phase, some information loss occurs (mainly phase concentrations and layer information), but we can still understand several other characteristics if at least an indexing of the phase is available. For most of the other properties (texture, stresses, anisotropic crystallite sizes and microstrains *etc.*) only the Laue group and an initial estimation of the unit-cell parameters are required. In this case, we can use the other two approaches.

The second approach starts from knowledge of the Laue group (or, better, the space group if available) and uses Le Bail or Pawley refinement for the intensities. In the case of Pawley refinement all of the reflection intensities become parameters to be refined (this is exactly equivalent to a whole-pattern fitting), and the exactly overlapped parameters should be treated as summed to achieve convergence. Normally this approach is rapid when the phase has a small number of reflections, but it becomes very difficult to carry out a fit when this number is very large. In this latter case the Le Bail approach is more efficient, and one can always switch to Pawley refinement just for the last iterations when the fitting is already satisfactory. These two methods are discussed in Chapter 3.5.

The third approach is a variant of the second, using an electron-density map (or a nuclear-density map for neutron diffraction) obtained from the extracted structure factors (using either one of the two methods mentioned above) at each iteration to calculate the intensities to be used in the fitting. This will force the structural intensities to be compatible with an electron-density map, providing a strong constraint for the severely overlapped peaks. It is assumed that by iteration the problem will converge toward the real electron-density map, but this cannot be ensured.

When associated with a strong texture of the sample, the second and third approaches can be used to obtain single-crystal-like structure factors that can be used to obtain the structure, as described by Wessels *et al.* (1999) and in a more recent variant in which texture and structure factors are extracted simultaneously from the same data (Lutterotti & Bortolotti, 2005; Grässlin *et al.*, 2015).

5.3.5.4.5. *Line profiles and sample broadening*

Profile functions are described as a convolution of two terms: the instrumental broadening and the sample broadening. In the combined approach we utilize the two explicitly separated contributions to perform refinement directly using the microstructural characteristics as parameters (Lutterotti & Scardi, 1990; Lutterotti & Gialanella, 1998; Lutterotti, 2010). If the instrumental broadening is known (see Section 5.3.5.4.1) we only need to refine the parameters concerning the sample broadening, and the best approach to ensure better convergence and more reliable results is to describe the sample broadening using physical quantities.

With respect to line-broadening theories, we note here that for this method we need equations and methods that allow computation of the sample-broadening profile from the microstructural characteristics and not the reverse.

These methods can be divided into two categories. The first category contains methods that describe the sample broadening using analytical functions, for which theory describes the variation of the parameters as a function of the scattering unit caused by the microstructural characteristics (Lutterotti & Scardi, 1990; Lutterotti & Gialanella, 1998). The second category does not impose analytical functions on the profile, but instead computes the profile directly from the crystallite size and microstrain distributions using the interference function (Lutterotti & Scardi, 1992), the Fourier transform (Ungár *et al.*, 2001; Lutterotti, 2010) or analytical approximations (Popa & Balzar, 2002). In the latter case it is the analytical shape of the distribution that is imposed. The crystallite and microstrain anisotropies, which cause anisotropy of the reflection broadenings, have been described previously by empirical formulae (Lutterotti & Scardi, 1990) or by taking into account the crystallographic symmetry restrictions (Popa, 1998), and can be coupled with the distribution-calculation method (Popa & Balzar, 2008).

In addition to crystallite sizes and microstrains, other microstructural characteristics have been included in the combined analysis as planar defects following Warren theory (Warren, 1969; Lutterotti & Gialanella, 1998) or turbostratic disorders (Ufer *et al.*, 2004; Lutterotti *et al.*, 2010); these are useful in the case of clay or graphitic materials.

5.3.5.4.6. *Texture computation*

The texture factors in (5.3.63) can be computed using one of the methods reported in Section 5.3.4 for Rietveld analysis, but only those associated with an OD computation, *i.e.* all but the empirical methods such as the March–Dollase and Donnet–Jouanneaux methods.

To ensure a physically meaningful texture analysis, two kinds of approach can be used in the combined analysis. The first is applicable when the pole figures can be computed through analytical functions containing the parameters to be refined. This is the case for the harmonic, exponential-harmonic and standard-components methods in Section 5.3.4. The implementation and the use of such methodologies is quite straightforward in the Rietveld framework.

A different case is the second approach (WIMV/EWIMV), in which there is no analytical function either to describe the OD or to compute the pole-figure values. This is performed through numerical integration using a discrete function with a very large number of unknowns. Therefore, by analogy to the electron-density case with structure factors, the method is to extract the texture values from patterns and use them to compute the OD, from which we can compute the texture value for the next Rietveld-like iteration step.

The extraction of the texture value (the difference between the random value and the measured value) can be performed using a modified Le Bail algorithm (Matthies *et al.*, 1997) working on the texture values instead of the structure factors. The resulting ‘experimental’ pole-figure values are used by the WIMV or EWIMV algorithms to compute the OD. After this, a final fitting of the patterns is performed using the quantities calculated from the OD as the texture values. In the case of WIMV an additional step is required before computing the OD, as WIMV requires the pole-figure data in a regular grid over the pole figures, and a cubic interpolation is used for this. On the other hand, EWIMV does not require such regular grids.

Much care is mandatory in using all of these methods in order to ensure that the measured data are sufficient to experimentally cover the entire OD. This can easily be checked using discrete methods such as WIMV/EWIMV, but not with others that may apparently work (output an OD) without having full coverage and thus with values for the uncovered part that depend on the assumptions made (for example, intrinsically when assuming an inappropriate specific texture symmetry as in the March–Dollase method or extrinsically when the unmeasured parts would have contained most of the texture information).

5.3.5.4.7. *Residual strains/stresses and evaluation of macroscopic tensors*

In the presence of residual stresses, diagrams measured at several tilt angles exhibit peak shifts that cannot be reproduced without correct modelling of the sample residual strains. These come from the macrostresses and microstresses in the sample and also depend on the crystallite orientations (ODs). There are two different methods to approach this problem in combined analysis. One makes use of elasticity theories and models the strains and thus the reflection shifts from the stresses; the other instead directly models the strains without any assumption about the relationship between strains and stresses.

In the first approach, defining $K_L = (X_L, Y_L, Z_L)$, a laboratory frame in which Z_L is coincident with the scattering vector, X_L lies in the plane defined by the incident and diffracted beams and is directed towards the detector, and $Y_L = (Z_L \times X_L)$, the deformation of the diffracting plane (direction 33 for the deformation tensor in K_L) is then

$$\begin{aligned}\overline{\varepsilon}_{33}^{L}(\overline{\sigma}; \mathbf{h}, \mathbf{y}) &= \frac{1}{4\pi\tilde{P}_{\mathbf{h}}(\mathbf{y})}\left[\int\limits_{\mathbf{h}\|\mathbf{y}} \varepsilon_{33}^{L}(\sigma; g) f(g)\,\mathrm{d}\tilde{\varphi} + \int\limits_{-\mathbf{h}\|\mathbf{y}} \varepsilon_{33}^{L}(\sigma; g) f(g)\,\mathrm{d}\tilde{\varphi}\right]\\ &\equiv S_{33kl}^{L}(\mathbf{h}, \mathbf{y})\overline{\sigma}_{kl}^{L}. \qquad (5.3.68)\end{aligned}$$

The crystallographic strain $\varepsilon_{33}^{L}(\sigma; g)$ depends on the macrostresses through the stress factor $S_{33kl}^{L}(\mathbf{h}, \mathbf{y})$ (Behnken & Hauk, 1991), and several schemes have been proposed to calculate it in the presence of texture using different averages over orientations as a theoretical basis. The most used are the Voigt (1928), Reuss (1929) and Hill (1952) models. In the Voigt case the stress factor does not depend on **h** and it imposes a linear behaviour in $\sin^2\psi$, whereas in the Reuss case it does not. The Voigt and Reuss models define upper and lower bounds, respectively, for the macrostresses, the macroscopic elastic constants (those of the real sample) and their average, but do not ensure the consistency of elastic properties (simultaneous stress and strain equilibria). Such consistency for elastic properties requires that the homogenized sample stiffness, $\langle C\rangle$, should be equal to the inverse of the homogenized compliance, $\langle S\rangle^{-1}$. Neither of the methods mentioned above meet this criterion. On the contrary, the geometric-mean approach guarantees such consistency.

Considering an ensemble of N grains, with each grain m having a volume fraction ν_m and with S_m being the single-crystal compliance tensor of the grain rotated in the sample reference frame, the arithmetic mean is then

$$\langle S\rangle_a^{-1} = \left[\sum_{m=1}^{N} \nu_m S_m\right]^{-1} \neq \sum_{m=1}^{N} \nu_m S_m^{-1} = \langle S^{-1}\rangle_a = \langle C\rangle_{\rm geo}, \qquad (5.3.69)$$

where the left-hand and right-hand sides correspond to the arithmetic averaging in the Reuss and Voigt hypotheses, respectively. Instead, for the geometric mean (Matthies & Humbert, 1993) the inversion property is guaranteed,

$$\begin{aligned}\langle S\rangle_{\rm geo}^{-1} &= \exp\left[-\sum_{m=1}^{N} \nu_m \ln S_m\right] = \exp\left[\sum_{m=1}^{N} \nu_m \ln S_m^{-1}\right]\\ &= \langle S^{-1}\rangle_{\rm geo} = \langle C\rangle_{\rm geo}\\ &\text{or}\\ \langle S\rangle_{\rm geo}^{-1} &= \left[\prod_{m=1}^{N} S_m^{\nu_m}\right]^{-1} = \prod_{m=1}^{N} S_m^{-\nu_m} = \prod_{m=1}^{N} (S_m^{-1})^{\nu_m}\\ &= \langle S^{-1}\rangle_{\rm geo} = \langle C\rangle_{\rm geo}. \qquad (5.3.70)\end{aligned}$$

Replacing the subscript m with the rotation g to bring the crystal tensor into the sample frame, using the explicit notation with four indices for the rank-4 compliance tensor and replacing the summation with the integral over H space, we obtain

$$\begin{aligned}&\langle S_{ijkl}\rangle_a = \int\limits_{H} S_{ijkl}^{0}(g) f(g)\,\mathrm{d}g, \quad S_{ijkl}^{0}(g) = \sum_{m,n,p,q=1}^{3} g_{mi}g_{nj}g_{pk}g_{ql}S_{mnpq},\\ &\langle S_{ijkl}\rangle_{\rm geo} = \langle(\ln S)_{ijkl}\rangle_a. \qquad (5.3.71)\end{aligned}$$

This modelling gives good estimates of the macroscopic elastic properties (Matthies & Humbert, 1995) and does not result in large calculation times, *i.e.* it is suitable for implementation in the routine combined algorithm to calculate the strain tensor inside the crystallite from the macrostresses of the sample.

Using (5.3.68), we make the hypothesis that the strains are constant inside the sample (the Voigt hypothesis), the macro elastic tensor is computed using the arithmetic mean of the stiffness and everything reduces to the analogous $\sin^2\psi$ method. If we consider the stresses in the sample to be constant, the elastic tensor is computed through the Reuss hypothesis or the average of the compliance tensor.

We examine here the interesting case of the geometric mean, where neither the stresses nor the strains are constant throughout the sample but vary as a function of grain orientation. This is the inverse problem with respect to the homogenization technique [equations (5.3.70) and (5.3.71)]. This case has been solved by Matthies and co-workers (Matthies *et al.*, 2001; Matthies & Vinel, 1994) in a two-step process. Let us first obtain the solution by using the geometric mean (GEO) method to directly compute the so-called pathGEO approximation. Writing the stress factor using the Reuss hypothesis,

$$\begin{aligned}S_{33kl}^{L}(\mathbf{h}, \mathbf{y}) &= {}^{\rm Reuss}S_{33kl}^{L,p}\\ &= \frac{1}{4\pi\tilde{P}_{\mathbf{h}}(\mathbf{y})}\left[\int\limits_{\mathbf{h}\|\mathbf{y}} S_{33kl}^{0}(g) f(g)\,\mathrm{d}\tilde{\varphi} + \int\limits_{-\mathbf{h}\|\mathbf{y}} S_{33kl}^{0}(g) f(g)\,\mathrm{d}\tilde{\varphi}\right]; \qquad (5.3.72)\end{aligned}$$

in analogy, the pathGEO approximation gives

$$\begin{aligned}S_{33kl}^{L}(\mathbf{h}, \mathbf{y}) &= {}^{\rm pathGEO}S_{33kl}^{L,p}\\ &= \exp\left\{\frac{1}{4\pi\tilde{P}_{\mathbf{h}}(\mathbf{y})}\left[\int\limits_{\mathbf{h}\|\mathbf{y}} S_{33kl}^{0}(g) f(g)\,\mathrm{d}\tilde{\varphi} + \int\limits_{-\mathbf{h}\|\mathbf{y}} S_{33kl}^{0}(g) f(g)\,\mathrm{d}\tilde{\varphi}\right]\right\}. \qquad (5.3.73)\end{aligned}$$

In the latter equation, we neglect the interaction of the matrix surrounding the crystallites. Adding it to the formulation, we obtain the final Bulk-PathGEO (BPG) formulation (Matthies & Humbert, 1995; Matthies *et al.*, 2001),

$$S^{L,\rm BPG} = \left[\left(\langle S\rangle_{\rm geo}^{L}\,{}^{\rm pathGEO}S^{L}\right)^{1/2}\right]^{\rm sym}, \qquad (5.3.74)$$

and we are interested in the $S_{33kl}^{L,\rm BPG}$ components of (5.3.68).

Another approach has been developed which does not consider the nature of the residual stresses and may be more appropriate in the case of plastic deformation or when pure elastic strains/stresses are not present. The method aims to use the Rietveld method to extract the crystallographic stresses in order to obtain the so-called stress orientation distribution function (SODF). Details can be found in Wang *et al.* (2000, 2003).

In combined analysis, a variant of this method is used that is more suitable for implementation in a Rietveld code. This variant (Popa & Balzar, 2001) considers that texture and stresses are always coupled by (5.3.68), and instead of using the SODF it defines a so-called WSODF (weighted-strain ODF) that is the product of the crystallographic OD and the SODF. This simplifies the formalism greatly and avoids the propagation of the errors present in the OD to the SODF (which is one of the problems of the original method). The WSODF (and similarly the SODF) is then expanded using spherical harmonics, and the right-hand side of (5.3.68) can be written in terms of harmonic coefficients to be refined. We refer the reader to the original paper for details of the symmetrization and implementation.

Table 5.3.2
Results obtained from combined analysis on an AlN/Pt/TiO_x/Al_2O_3/Ni(Co–Cr–Al–Y) stack

Standard deviations are given in parentheses for the last digit.

	AlN	Pt	Al_2O_3	Ni(Co–Cr–Al–Y)
Unit-cell parameters (Å)	a = 3.11203 (1), c = 4.98252 (1)	a = 3.91198 (1)	a = 4.7562 (6), c = 12.875 (3)	a = 3.569377 (5)
Effective layer (nm)	14270 (3)	1204 (3)	7790 (31)	∞
Isotropic mean crystallite size (Å)	2404 (8)	2173 (10)	150 (2)	7600 (1900)
Isotropic mean microstrain (r.m.s.)	0.001853 (2)	0.002410 (3)	0.008 (3)	0.00236 (3)
Biaxial macrostresses (MPa)	$\sigma_{11} = -1019$ (2), $\sigma_{22} = -845$ (2)	$\sigma_{11} = -196.5$ (8), $\sigma_{22} = -99.6$ (6)	Not fitted	$\sigma_{11} = -328$ (8), $\sigma_{22} = -411$ (9)
F^2 (m.r.d.^{2})	9.30	5.36	—	1.04
OD R factors (%)	R_w = 4.09, R_b = 4.41	R_w = 33.25, R_b = 26.63	—	R_w = 49.15, R_b = 37.38

5.3.5.4.8. *Absorption and layers*

Computation of the absorption is another important part of the approach, especially considering some samples that do not meet the requirements of standard computation (Bragg–Brentano: specimen completely intercepts the beam, homogeneity inside the volume, infinite thickness; Debye–Scherrer: cylindrical or spherical shape, sample inside the beam, light absorber). In the simple case of a thin film or multilayers we already have a heterogeneous sample and special treatment of the absorption correction is needed. Another case is an irregular shape or a strong absorber in Debye–Scherrer geometry.

For multilayers, a first implementation to correctly approach the problem in a Bragg–Brentano geometry (Lutterotti *et al.*, 1993) is aimed at phase analysis in the layers. For a more comprehensive absorption correction for a multilayer sample that includes all possible geometries and cases, Simek *et al.* (2006) developed a correction that depends only on the incident angle θ_i of the beam (with respect to the plane parallel to the layering and surface of the sample) and the exit angle θ_o,

$$A_{i\Phi} = \frac{\nu_{i\Phi}\sin\theta_i\sin\theta_o}{\overline{\mu}_i(\sin\theta_i+\sin\theta_o)}[1-\exp(-\overline{\mu}_i\tau_i W)]\prod_{k<i}\exp(-\overline{\mu}_k\tau_k W),$$

$$W = \frac{1}{\sin\theta_i}+\frac{1}{\sin\theta_o}, \qquad (5.3.75)$$

where $\overline{\mu}_i = \sum_{\Phi=1}^{N_\Phi}\nu_{i\Phi}\mu_{i\Phi}$ is the average linear absorption coefficient for layer i, $\mu_{i\Phi}$ is the absorption coefficient of phase Φ in layer i and τ_i is the thickness of layer i.

In the Debye–Scherrer geometry with either a strong absorber or an irregular sample shape, special care should be taken with the absorption computation. A general procedure has been developed (Xie *et al.*, 2004; Volz *et al.*, 2006) that represents the sample shape using the same harmonic expansion formulae as for the anisotropic crystallites (Popa, 1998) and uses a discretized integration of the beam path through the sample volume or a simplified path through the centre only (for computational speed; however, the shape refined is no longer representative of the sample).

5.3.5.5. *Implementation*

The combined-analysis software should allow the possibility of using X-ray (classical, synchrotron, monochromatic or energy dispersive, all scanning strategies and geometries, zero-dimensional, one-dimensional, flat and curved two-dimensional detectors) as well as neutron (thermal and TOF) or even electron data. It should be able to incorporate all formalisms corresponding to residual stress analysis (RSA), X-ray specular reflectivity, qualitative microstructure analysis, structure, QPA *etc.* and index diagrams for phase identification in an automatic approach [such as using the Crystallography Open Database (Grazulis *et al.*, 2009) or the Powder Diffraction File (Fawcett *et al.*, 2017)]. If the RSA of textured materials is of interest it should also offer tensor homogenization, openly accessing single-crystal tensors (Pepponi *et al.*, 2012). All of these requirement are actually met in the *MAUD* software (Lutterotti, 2010).

5.3.5.6. *Examination of a solution*

Using single-pattern refinement, a simple examination of the modelled and measured diagrams can suffice to detect refinement problems or refinement quality. When several hundreds of patterns are refined, such a comparison is cumbersome or simply impossible. One possibility to rapidly check whether the chosen

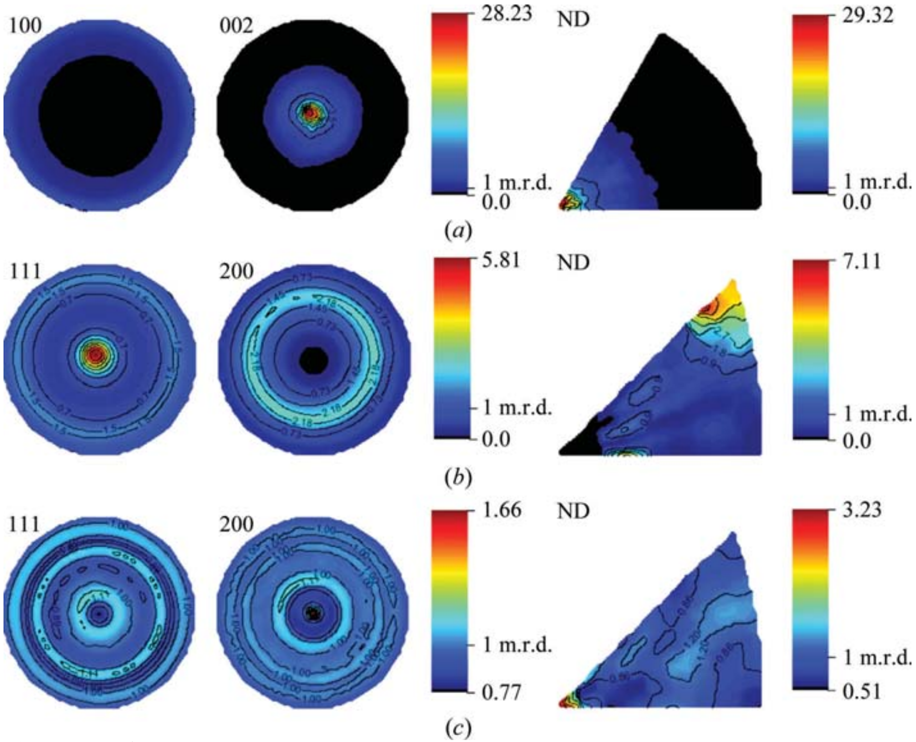

Figure 5.3.21
Low-index recalculated pole figures and Z_A inverse pole figures for the three textured phases of the stack. (*a*) AlN, (*b*) Pt, (*c*) Ni-based alloy. Equal-area density projections, linear density scale.

model is correct is to randomly select a small set of diffraction patterns to plot (Fig. 5.3.20*a*). However, such a method cannot prevent local strong discrepancies unless each diagram is examined in a laborious way. One can overcome this problem by plotting (for instance for an AlN/Pt/Al_2O_3/Ni alloy stack) all of the diagrams in a two-dimensional view (Fig. 5.3.20*b*), and completing the solution examination using two-dimensional residuals (Fig. 5.3.20*c*) in order to see where the main improvements to the model have to be carried out.

In such a case, combined analysis provides the characterization of the three ODs of Ni alloy, Pt and AlN, their respective biaxial residual stress states and structures. The layer thicknesses are also obtained with the crystallite isotropic sizes. The biaxial stress states are obtained using the geometric mean approach. All of the results are summarized in Table 5.3.2. These results were obtained within reliability factors of $R_{\rm w}$ = 24.12% and $R_{\rm exp}$ = 5.85% on 936 diagrams with a goodness of fit of 1.51.

The low-index pole figures of the three textured phases (Fig. 5.3.21) exhibit fibre textures with the fibre axis shifted slightly from the normal to the film plane Z_A. The substrate alloy shows the lowest texture strength; it is further increased in the Pt electrode and in the AlN film. This illustrates the electrical bias effect applied to the AlN orientation during sputtering, with a pronounced maximum of the {001} pole figure along Z_A of around 28 m.r.d. The Pt electrode exhibits a classical {111} orientation, with a slight tilt, while the Ni alloy is predominantly oriented with the {200} planes parallel to the sample plane. However, the corresponding inverse pole figures show that if AlN and Pt have a unique fibre orientation component, the Ni-alloy substrate also shows some minor fibre components.

The corresponding data for this example and many others can be found at http://www.ecole.ensicaen.fr/~chateign/formation/, together with some tutorials.

5.3.6. Conclusions

Classical quantitative texture analysis (and also residual stress, line broadening, phase composition *etc.*) becomes of questionable value for real samples that exhibit complex architectures with several phases and strong intra- and inter-phase peak overlapping. This is particularly true for poorly crystallized or nanocrystallized samples, for which line broadening is further enhanced. Proper deconvolution has to be carried out in such cases, which requires the use of full-pattern analysis in order to properly separate the various contributions to the diffraction diagrams (residual stresses, structure, phase content *etc.*). This can be elegantly achieved using the combined-analysis approach using X-rays, neutrons, electrons and *ad hoc* measurements.

References

Ahtee, M., Nurmela, M., Suortti, P. & Järvinen, M. (1989). *Correction for preferred orientation in Rietveld refinement. J. Appl. Cryst.* **22**, 261–268.

Behnken, H. & Hauk, V. (1991). *Berechnung der röntgenographischen Spannnungsfaktoren texturierter Werkstoffe – Vergleich mit experimentelle Ergebnissen. Z. Metallkde*, **82**, 151–158.

Birsan, M., Szpunar, A., Tun, Z. & Root, J. H. (1996). *Magnetic texture determination using nonpolarized neutron diffraction. Phys. Rev. B*, **53**, 6412–6417.

Brosnan, K. H., Messing, G. L., Meyer, R. J. Jr & Vaudin, M. D. (2006). *Texture measurements in ⟨001⟩ fiber-oriented PMN–PT. J. Am. Ceram. Soc.* **89**, 1965–1971.

Bunge, H.-J. (1969). *Mathematische Methoden der Texturanalyse*. Berlin: Akademie Verlag.

Bunge, H.-J. (1982). *Texture Analysis in Materials Science*. London: Butterworth–Heinemann.

Bunge, H.-J. & Esling, C. (1982). *Quantitative Texture Analysis*. Berlin: DGM Informationsgesellschaft Verlag.

Bunge, H.-J., Wenk, H.-R. & Pannetier, J. (1982). *Neutron diffraction texture analysis using a 2θ position sensitive detector. Textures Microstruct.* **5**, 153–170.

Caglioti, G., Paoletti, A. & Ricci, F. P. (1958). *Choice of collimators for a crystal spectrometer for neutron diffraction. Nucl. Instrum.* **3**, 223–228.

Capková, P., Peschar, R. & Schenk, H. (1993). *Partial multiplicity factors for texture correction of cubic structures in the disc-shaped crystallite model. J. Appl. Cryst.* **26**, 449–452.

Cerný, R., Valvoda, V. & Chládek, M. (1995). *Empirical texture corrections for asymmetric diffraction and inclined textures. J. Appl. Cryst.* **28**, 247–253.

Chateigner, D. (2005). *Reliability criteria in quantitative texture analysis with experimental and simulated orientation distributions. J. Appl. Cryst.* **38**, 603–611.

Chateigner, D. (2010). *Combined Analysis*. London/Hoboken: ISTE/Wiley.

Chateigner, D. & Erler, B. (1997). *Preferred orientations and epitaxial relationships of α-HgI_2 thin films on (001)-KCl and (001)-muscovite single crystals. Mater. Sci. Eng. B*, **45**, 152–161.

Chateigner, D., Germi, P. & Pernet, M. (1992). *Texture analysis by the Schulz reflection method: defocalization corrections for thin films. J. Appl. Cryst.* **25**, 766–769.

Chateigner, D., Germi, P. & Pernet, M. (1994*a*). *X-ray texture analysis of thin films by the reflection method: intermediate regime in defocusing corrections. J. Appl. Cryst.* **27**, 278–282.

Chateigner, D., Germi, P. & Pernet, M. (1994*b*). *X-ray texture analysis in films by the reflection method: principal aspects and applications. Mater. Sci. Forum*, **157–162**, 1379–1386.

Chateigner, D., Germi, P., Pernet, M., Fréchard, P. & Andrieu, S. (1995). *Fluorescence corrections in thin-film texture analysis. J. Appl. Cryst.* **28**, 369–374.

Chateigner, D., Hedegaard, C. & Wenk, H.-R. (2000). *Mollusc shell microstructures and crystallographic textures. J. Struct. Geol.* **22**, 1723–1735.

Chateigner, D., Lutterotti, L. & Hansen, T. (1998). *Quantitative phase and texture analysis on ceramics–matrix composites using Rietveld texture analysis. ILL Highlights*, **1997**, 28–29.

Chateigner, D., Ouladdiaf, B. & Léon, F. (2010). *Magnetic quantitative texture analysis using isotropic thermal neutron beams. Solid State Phenom.* **160**, 75–82.

Chernock, W. P. & Beck, P. A. (1952). *Analysis of certain errors in the X-ray reflection method for the quantitative determination of preferred orientations. J. Appl. Phys.* **23**, 341–345.

Coulomb, P. (1982). *Les Textures dans les Métaux de Réseaux Cubiques*. Paris: Dunod.

Couterne, J. C. & Cizeron, G. (1971). *Phénomène de défocalisation lié à la géométrie de la chambre de texture de Schulz et incidence sur l'intensité mesurée. J. Appl. Cryst.* **4**, 461–472.

Curien, H. (1971). *Les Groupes en Cristallographie*. In *Théorie des Groupes en Physique Classique et Quantique*, Vol. 2, edited by T. Kahan. Paris: Dunod.

Dahms, M. & Bunge, H.-J. (1988). *A positivity method for the determination of complete orientation distribution functions. Textures Microstruct.* **10**, 21–35.

Dollase, W. A. (1986). *Correction of intensities for preferred orientation in powder diffractometry: application of the March model. J. Appl. Cryst.* **19**, 267–272.

Durand, L., Kircher, F., Régnier, P., Chateigner, D., Pallerin, N., Gotor, F. J., Simon, P. & Odier, P. (1995). *Orientation of Y_2BaCuO_5 precipitates during unidirectional solidification of $Y_1Ba_2Cu_3O_{7-\delta}$ under a magnetic field. Supercond. Sci. Technol.* **8**, 214–218.

Esling, C., Muller, J. & Bunge, H.-J. (1982). *An integral formula for the even part of the texture function or 'the apparition of the fn and fω ghost distributions'. J. Phys. (Paris)*, **43**, 189–196.

Fawcett, T. G., Kabekkodu, S. N., Blanton, J. R. & Blanton, T. N. (2017). *Chemical analysis by diffraction: the Powder Diffraction File. Powder Diffr.* **32**, 63–77.

Feng, C. (1965). *Determination of relative intensity in X-ray reflection study. J. Appl. Phys.* **36**, 3432–3435.

Ferrari, M. & Lutterotti, L. (1994). *Method for the simultaneous determination of anisotropic residual stresses and texture by X-ray diffraction. J. Appl. Phys.* **76**, 7246–7255.

Field, M. & Merchant, M. E. (1949). *Reflection method of determining preferred orientation on the Geiger-counter spectrometer. J. Appl. Phys.* **20**, 741–745.

Gale, B. & Griffiths, D. (1960). *Influence of instrumental aberrations on the Schultz technique for the measurement of pole figures. Br. J. Appl. Phys.* **11**, 96–102.

Grässlin, J., McCusker, L. B., Baerlocher, C., Gozzo, F., Schmitt, B. & Lutterotti, L. (2015). *Advances in exploiting preferred orientation in the structure analysis of polycrystalline materials. J. Appl. Cryst.* **46**, 173–180.

Grazulis, S., Chateigner, D., Downs, R. T., Yokochi, A. F. T., Quirós, M., Lutterotti, L., Manakova, E., Butkus, J., Moeck, P. & Le Bail, A. (2009). *Crystallography Open Database – an open-access collection of crystal structures. J. Appl. Cryst.* **42**, 726–729.

Gridi-Bennadji, F., Chateigner, D., Di Vita, G. & Blanchart, P. (2009). *Mechanical properties of textured ceramics from muscovite–kaolinite alternate layers. J. Eur. Ceram. Soc.* **29**, 2177–2184.

Guilmeau, E., Chateigner, D. & Noudem, J. G. (2003). *Effect of the precursor powders on the final properties of hot-forged Bi2223 textured discs. Supercond. Sci. Technol.* **16**, 484–491.

Guilmeau, E., Chateigner, D., Noudem, J., Funahashi, R., Horii, S. & Ouladdiaf, B. (2005). *Rietveld texture analysis of complex oxides: examples of polyphased Bi2223 superconducting and Co349 thermoelectric textured ceramics characterization using neutron and X-ray diffraction. J. Appl. Cryst.* **38**, 199–210.

Heidelbach, F., Riekel, C. & Wenk, H.-R. (1999). *Quantitative texture analysis of small domains with synchrotron radiation X-rays. J. Appl. Cryst.* **32**, 841–849.

Heizmann, J. J. & Laruelle, C. (1986). *Simultaneous measurement of several X-ray pole figures. J. Appl. Cryst.* **19**, 467–472.

Helming, K. (1992). *Minimal pole figure ranges for quantitative texture analysis. Texture Microstruct.* **19**, 45–54.

Hielscher, R. & Schaeben, H. (2008). *A novel pole figure inversion method: specification of the MTEX algorithm. J. Appl. Cryst.* **41**, 1024–1037.

Hielscher, R., Schaeben, H. & Chateigner, D. (2007). *On the entropy to texture index relationship in quantitative texture analysis. J. Appl. Cryst.* **40**, 371–375.

Hill, R. (1952). *The elastic behaviour of a crystalline aggregate. Proc. Phys. Soc. A*, **65**, 349–354.

Holland, J. R. (1964). *Quantitative determinations and descriptions of preferred orientation. Adv. X-ray Anal.* **7**, 86–93.

Huijser-Gerits, E. M. C. & Rieck, G. D. (1974). *Defocusing effects in the reflexion technique for the determination of preferred orientation. J. Appl. Cryst.* **7**, 286–290.

Imhof, J. (1982). *The resolution of orientation space with reference to pole figure resolution. Textures Microstruct.* **4**, 189–200.

Järvinen, M. (1993). *Application of symmetrized harmonics expansion to correction of the preferred orientation effect. J. Appl. Cryst.* **26**, 525–531.

Jouanneaux, A. (1999). *WinMPorf: a visual Rietveld software. International Union of Crystallography Commission on Powder Diffraction Newsletter*, **21**, 13.

Kocks, U. F., Kallend, J. S., Wenk, H.-R., Rollet, A. D. & Wright, S. I. (1994). *popLA: Preferred Orientation Package – Los Alamos*. Technical Report LA-CC-89-18, Los Alamos National Laboratory, USA.

Kocks, U. F., Tomé, C. N. & Wenk, H.-R. (1998). *Texture and Anisotropy*. Cambridge University Press.

Larson, A. C. & Von Dreele, R. B. (2000). *General Structure Analysis System (GSAS)*. Los Alamos National Laboratory Report LAUR 86-748.

Liu, Y. S., Depre, L., de Buyser, L., Wu, T. B. & van Houtte, P. (2003). *Intensity correction in texture measurement of polycrystalline thin films by X-ray diffraction. Textures Microstruct.* **35**, 283–290.

Lutterotti, L. (2010). *Total pattern fitting for the combined size–strain–stress–texture determination in thin film diffraction. Nucl. Instrum. Methods Phys. Res. B*, **268**, 334–340.

Lutterotti, L. & Bortolotti, M. (2005). *Algorithms for solving crystal structure using texture. Acta Cryst.* A**61**, c158–c159.

Lutterotti, L., Chateigner, D., Ferrari, S. & Ricote, J. (2004). *Texture, residual stress and structural analysis of thin films using a combined X-ray analysis. Thin Solid Films*, **450**, 34–41.

Lutterotti, L. & Gialanella, S. (1998). *X-ray diffraction characterization of heavily deformed metallic specimens. Acta Mater.* **46**, 101–110.

Lutterotti, L., Matthies, S., Chateigner, D., Ferrari, F. & Ricote, J. (2002). *Rietveld texture and stress analysis of thin films by X-ray diffraction. Mater. Sci. Forum*, **408–412**, 1603–1608.

Lutterotti, L., Matthies, S. & Wenk, H.-R. (1999). *MAUD – Materials Analysis Using Diffraction*. http://maud.radiographema.com/.

Lutterotti, L., Matthies, S., Wenk, H.-R., Schultz, A. J. & Richardson, J. W. (1997). *Combined texture and structure analysis of deformed limestone from time-of-flight neutron diffraction spectra. J. Appl. Phys.* **81**, 594–600.

Lutterotti, L. & Scardi, P. (1990). *Simultaneous structure and size-strain refinement by the Rietveld method. J. Appl. Cryst.* **23**, 246–252.

Lutterotti, L. & Scardi, P. (1992). *Profile fitting by the interference function. Adv. X-ray Anal.* **35**A, 577–584.

Lutterotti, L., Scardi, P. & Tomasi, A. (1993). *Application of the Rietveld method to phase analysis of multilayered systems. Mater. Sci. Forum*, **133–136**, 57–62.

Lutterotti, L., Voltolini, M., Wenk, H.-R., Bandyopadhyay, K. & Vanorio, T. (2010). *Texture analysis of a turbostratically disordered Ca-montmorillonite. Am. Mineral.* **95**, 98–103.

Manceau, A., Chateigner, D. & Gates, W. P. (1998). *Polarized EXAFS, distance-valence least-squares modeling (DVLS), and quantitative texture analysis approaches to the structural refinement of Garfield nontronite. Phys. Chem. Miner.* **25**, 347–365.

March, A. (1932). *Mathematische Theorie des Regelung nach der Korngestalt bei affiner Deformation. Z. Kristallogr.* **81**, 285–297.

Matthies, S. (1979). *On the reproducibility of the orientation distribution function of texture samples from pole figures (ghost phenomena). Phys. Status Solidi B*, **92**, K135–K138.

Matthies, S. (1980). *Standard functions in the texture analysis. Phys. Status Solidi B*, **101**, K111–K115.

Matthies, S. (1982). *Form effects in the description of the orientation distribution function (ODF) of texturized materials by model components. Phys. Status Solidi B*, **112**, 705–716.

Matthies, S., Helming, K., Steinkopff, T. & Kunze, K. (1988). *Standard distributions for the case of fibre textures. Phys. Status Solidi B*, **150**, K1–K5.

Matthies, S. & Humbert, M. (1993). *The realization of the concept of a geometric mean for calculating physical constants of polycrystalline materials. Phys. Status Solidi B*, **177**, K47–K50.

Matthies, S. & Humbert, M. (1995). *On the principle of a geometric mean of even-rank symmetric tensors for textured polycrystals. J. Appl. Cryst.* **28**, 254–266.

Matthies, S., Lutteroti, L. & Wenk, H.-R. (1997). *Advances in texture analysis from diffraction spectra. J. Appl. Cryst.* **30**, 31–42.

Matthies, S., Priesmeyer, H. G. & Daymond, M. R. (2001). *On the diffractive determination of single-crystal elastic constants using polycrystalline samples. J. Appl. Cryst.* **34**, 585–601.

Matthies, S. & Vinel, G. W. (1982). *On the reproduction of the orientation distribution function of texturized samples from reduced pole figures using the conception of a conditional ghost correction. Phys. Status Solidi B*, **112**, K111–K114.

Matthies, S. & Vinel, G. W. (1994). *On some methodical developments concerning calculations performed directly in the orientation space. Mater. Sci. Forum*, **157–162**, 1641–1646.

Matthies, S., Vinel, G. W. & Helming, K. (1987). *Standard Distributions in Texture Analysis*, Vol. 1, edited by K. Helming. Berlin: Akademie Verlag.

Matthies, S. & Wenk, H.-R. (2009). *Transformations for monoclinic crystal symmetry in texture analysis. J. Appl. Cryst.* **42**, 564–571.

Morales, M., Chateigner, D. & Fruchart, D. (2003). *Texture and magnetocrystalline anisotropy analysis of an oriented ErMn$_4$Fe$_8$C powder sample. J. Magn. Magn. Mater.* **257**, 258–269.

Morales, M., Chateigner, D., Lutterotti, L. & Ricote, J. (2002). *X-ray combined QTA using a CPS applied to a ferroelectric ultrastructure. Mater. Sci. Forum*, **408–412**, 113–118.

Morales, M., Leconte, Y., Rizk, R. & Chateigner, D. (2005). *Structural and microstructural characterization of nanocrystalline silicon thin films obtained by radio-frequency magnetron sputtering. J. Appl. Phys.* **97**, 034307.

O'Connor, B. H., Li, D. Y. & Sitepu, H. (1991). *Strategies for preferred orientation corrections in X-ray powder diffraction using line intensity ratios. Adv. X-ray Anal.* **34**, 409–415.

Pawlik, K. (1993). *Application of the ADC method for ODF approximation in cases of low crystal and sample symmetries. Mater. Sci. Forum*, **133–136**, 151–156.

Pawlik, K. & Ozga, P. (1999). *LaboTex: The Texture Analysis Software for Windows.* http://www.labosoft.com.pl/.

Pepponi, G., Gražulis, S. & Chateigner, D. (2012). *MPOD: a Material Property Open Database linked to structural information. Nucl. Instrum. Methods Phys. Res. B*, **284**, 10–14.

Popa, N. C. (1992). *Texture in Rietveld refinement. J. Appl. Cryst.* **25**, 611–616.

Popa, N. C. (1998). *The (hkl) dependence of diffraction-line broadening caused by strain and size for all Laue groups in Rietveld refinement. J. Appl. Cryst.* **31**, 176–180.

Popa, N. C. & Balzar, D. (2001). *Elastic strain and stress determination by Rietveld refinement: generalized treatment for textured polycrystals for all Laue classes. J. Appl. Cryst.* **34**, 187–195.

Popa, N. C. & Balzar, D. (2002). *An analytical approximation for a size-broadened profile given by the lognormal and gamma distributions. J. Appl. Cryst.* **35**, 338–346.

Popa, N. C. & Balzar, D. (2008). *Size-broadening anisotropy in whole powder pattern fitting. Application to zinc oxide and interpretation of the apparent crystallites in terms of physical models. J. Appl. Cryst.* **41**, 615–627.

Press, W. H., Teukolsky, S. A., Vetterling, W. T. & Flannery, B. P. (1988). *Numerical Recipes in C*. Cambridge University Press.

Radon, J. H. (1986). *On the determination of functions from their integral values along certain manifolds. IEEE Trans. Med. Imaging*, **5**, 170–176.

Reuss, A. (1929). *Account of the liquid limit of mixed crystals on the basis of the plasticity condition for single crystal. Z. Angew. Math. Mech.* **9**, 49–58.

Ricote, J. & Chateigner, D. (1999). *Quantitative texture analysis applied to the study of preferential orientations in ferroelectric thin films. Bol. Soc. Esp. Ceram. Vidrio*, **38**, 587–591.

Ricote, J., Chateigner, D., Morales, M., Calzada, M. L. & Wiemer, C. (2004). *Application of the X-ray combined analysis to the study of lead titanate based ferroelectric thin films. Thin Solid Films*, **450**, 128–133.

Rietveld, H. M. (1969). *A profile refinement method for nuclear and magnetic structures. J. Appl. Cryst.* **2**, 65–71.

Roe, R.-J. (1965). *Description of crystallite orientation in polycrystalline materials. III. General solution to pole figure inversion. J. Appl. Phys.* **36**, 2024–2031.

Ruer, D. (1976). *Méthode vectorielle d'analyse de la texture*. Thesis. Université de Metz, France.

Ruer, D. & Baro, R. (1977). *A new method for the determination of the texture of materials of cubic structure from incomplete reflection pole figures. Adv. X-ray Anal.* **20**, 187–200.

Schaeben, H. (1988). *Entropy optimization in quantitative texture analysis. J. Appl. Phys.* **64**, 2236–2237.

Schaeben, H. (1991*a*). *Entropy optimization in quantitative texture analysis. II. Application to pole-to-orientation density inversion. J. Appl. Phys.* **69**, 1320–1329.

Schaeben, H. (1991*b*). *Determination of complete ODF using the maximum entropy method.* In *Advances and Applications of Quantitative Texture Analysis*, edited by H.-J. Bunge & C. Esling, pp. 109–118. Oberursel: DGM Informationsgesellschaft Verlag.

Schaeben, H. & van den Boogaart, K. G. (2003). *Spherical harmonics in texture analysis. Tectonophysics*, **370**, 253–268.

Schulz, L. G. (1949*a*). *A direct method of determining preferred orientation of a flat reflection sample using a Geiger counter X-ray spectrometer. J. Appl. Phys.* **20**, 1030–1033.

Schulz, L. G. (1949*b*). *Determination of preferred orientation in flat transmission samples using a Geiger counter X-ray spectrometer. J. Appl. Phys.* **20**, 1033–1036.

Shannon, C. E. (1948). *A mathematical theory of communication. Bell Syst. Tech. J.* **27**, 379–423.

Simek, D., Kuzel, R. & Rafaja, D. (2006). *Reciprocal-space mapping for simultaneous determination of texture and stress in thin films. J. Appl. Cryst.* **39**, 487–501.

Tenckhoff, E. (1970). *Defocusing for the Schulz technique of determining preferred orientation. J. Appl. Phys.* **41**, 3944–3948.

Ufer, K., Roth, G., Kleeberg, R., Stanjek, H., Dohrmann, R. & Bergmann, J. (2004). *Description of X-ray powder pattern of turbostratically disordered layer structures with a Rietveld compatible approach. Z. Kristallogr.* **219**, 519–527.

Ungár, T., Gubicza, J., Ribárik, G. & Borbély, A. (2001). *Crystallite size distribution and dislocation structure determined by diffraction profile analysis: principles and practical application to cubic and hexagonal crystals. J. Appl. Cryst.* **34**, 298–310.

Vadon, A. (1981). *Généralisation et optimisation de la méthode vectorielle d'analyse de la texture*. Thesis. Université de Metz, France.

Van Houtte, P. (1983). *The use of a quadratic form for the determination of non-negative texture functions. Textures Microstruct.* **6**, 1–19.

Van Houtte, P. (1991). *A method for the generation of various ghost correction algorithms – the example of the positivity method and the exponential method. Textures Microstruct.* **13**, 199–212.

Voigt, W. (1928). *Lehrbuch der Kristallphysik*. Leipzig: Teubner Verlag.

Volz, H. M., Vogel, S. C., Necker, C. T., Roberts, J. A., Lawson, A. C., Williams, D. J., Daemen, L. L., Lutterotti, L. & Pehl, J. (2006). *Rietveld texture analysis by neutron diffraction of highly absorbing materials. Powder Diffr.* **21**, 114–117.

Von Dreele, R. B. (1997). *Quantitative texture analysis by Rietveld refinement. J. Appl. Cryst.* **30**, 517–525.

Wagner, F. & Dahms, M. (1991). *Determination of complete ODFs with an optimized positivity method.* In *Advances and Applications of Quantitative Texture Analysis*, edited by H.-J. Bunge & C. Esling, pp. 101–108. Oberursel: DGM Informationsgesellschaft Verlag.

Wang, Y. D., Peng, R. L., Zeng, X. H. & McGreevy, R. (2000). *Stress-orientation distribution function (SODF) – description, symmetry and determination. Mater. Sci. Forum*, **347–349**, 66–73.

Wang, Y. D., Wang, X.-L., Stoica, A. D., Richardson, J. W. & Peng, R. L. (2003). *Determination of the stress orientation distribution function using pulsed neutron sources. J. Appl. Cryst.* **36**, 14–22.

Warren, B. E. (1969). *X-ray Diffraction.* Reading: Addison-Wesley.

Wenk, H.-R. (1985). *Preferred Orientation in Deformed Metals and Rocks: An Introduction to Modern Texture Analysis*. New York: Academic Press

Wenk, H.-R., Bunge, H.-J., Kallend, J. S., Lücke, K., Matthies, S., Pospiech, J. & Van Houtte, P. (1988). *Orientation Distributions: Representation and Determination.* In *Proceedings of the Eighth International Conference on Textures of Materials*, edited by J. S. Kallend & G. Gottstein, pp. 17–30. Warrendale: The Metallurgical Society.

Wenk, H.-R., Chateigner, D., Pernet, M., Bingert, J., Hellstrom, E. & Ouladdiaf, B. (1996). *Texture analysis of Bi-2212 and 2223 tapes and wires by neutron diffraction. Physica C*, **272**, 1–12.

Wenk, H.-R., Matthies, S., Donovan, J. & Chateigner, D. (1998). *BEARTEX: a Windows-based program system for quantitative texture analysis. J. Appl. Cryst.* **31**, 262–269.

Wessels, T., Baerlocher, C. & McCusker, L. B. (1999). *Single-crystal-like diffraction data from polycrystalline materials. Science*, **284**, 477–479.

Williams, R. O. (1968). *Analytical methods for representing complex textures by biaxial pole figures. J. Appl. Phys.* **39**, 4329–4335.

Xie, Y., Lutterotti, L. & Wenk, H.-R. (2004). *Texture analysis of ancient coins with TOF neutron diffraction. J. Mater. Sci.* **39**, 3329–3337.

Zolotoyabko, E. (2009). *Determination of the degree of preferred orientation within the March–Dollase approach. J. Appl. Cryst.* **42**, 513–518.

International Tables for Crystallography (2019). Vol. H, Chapter 5.4, pp. 581–600.

5.4. Thin films and multilayers

M. Birkholz

5.4.1. Introduction

Thin films and multilayers represent an important class of materials for science and technology. Their first applications were in the fields of mirrors and decorative coatings, which subsequently extended to surface finishing as required for hard coatings and high-tech optics. Further applications were found with the advent of nanotechnology in the areas of microelectronics, photonics and sensors, which all had a large impact on the development of thin films and their deposition techniques (Ohring, 2002). Thin films typically exhibit thicknesses between about 1 and some 10^4 nm, while their lateral extensions may range from a few micrometres to hundreds of metres. Depending on the intended use, thin films are either made of metals, inorganic compounds or organic compounds, or from biological molecules. Since the characterization of their structural properties is a highly relevant issue in thin-film development, the two fields have concomitantly evolved with technological progress (Holy *et al.*, 1999; Tolan, 1999; Fewster, 2003; Birkholz, 2006; Guinebretière, 2007; Daillaut & Gibaud, 2009; Boscherini *et al.*, 2010; Chateigner, 2010).

X-ray scattering techniques for the investigation of thin films and multilayers have mostly been derived from $\theta/2\theta$ powder diffractometry. Generally, polycrystalline thin films might simply be considered as thin-slab powder samples, and various aspects of their X-ray patterns can be understood from the previous chapters of this volume. Modifications are required, however, when the film thickness t becomes comparable to the inverse linear attenuation coefficient of the sample: $t \simeq 1/\mu$. Conventional powder diffraction then turns out to be the limiting case, where the sample thickness is usually much larger and $\mu t \gg 1$ is valid. If this is not the case, a large fraction of the beam intensity might be wasted in a conventional $\theta/2\theta$ scan. Experimental geometries have been introduced that differ from the conventional powder setup in order to exploit this otherwise lost intensity. In these techniques, the incident beam impinges at low incidence angles in order to extend the X-ray path within the layer.

Thin-film structural features of interest are the microstructural organization relating to the density of voids, the distribution of grain sizes and possible amorphous fractions (Mittemeijer & Scardi, 2004). In addition, nonrandom orientation distributions of the constituent crystallites typically occur, and characterizing such distributions requires a texture analysis (Bunge, 1982; Kocks *et al.*, 1998; Wenk & Van Houtte, 2004; Chateigner, 2010). Closely related to microstructure, texture and grain size is the state of internal stress (Hauk, 1997; Genzel, 2004, 2005). Moreover, all of these structural properties typically vary with film thickness, leading to pronounced depth gradients. X-ray investigations for determining this structural information are often required for adjusting the properties of the sample and for understanding the growth process. The present chapter will give a short overview of these techniques along with examples of their applications. The focus will be on polycrystalline materials; the field of single-crystalline or epitaxial layers will not be considered here and the interested reader is referred to Holy *et al.* (1999) and Fewster (2003) for this topic. Neutrons will also not be considered here, since neutron-scattering cross sections are too small to yield sufficient structural information for thin films and multilayers.

5.4.2. Effects of absorption

In contrast to conventional powder diffractometry, absorption effects play an important role in X-ray diffraction by thin films.

5.4.2.1. *Absorption factor*

The intensities $I_{\mathbf{h}}$ of diffraction peaks from thin films and multilayers are subject to the usual dependence on scattering angle 2θ *via* the Lorentz–polarization factor Lp, the structure factor F, the multiplicity m, the texture factor $T_{\mathbf{h}}$ *etc.* as outlined in previous chapters of this volume. $I_{\mathbf{h}}$ may be given by

$$I_{\mathbf{h}} = SCF\, m_{\mathbf{h}}\, T_{\mathbf{h}}\, Lp\, |F_{\mathbf{h}}|^2\, A_{\theta 2\theta}(t), \qquad (5.4.1)$$

where $\mathbf{h}$ represents the specific Bragg reflection hkl under consideration and SCF is a scaling factor that is dependent on physical constants and instrumental conditions such as scanning velocity *etc.* Most particular for diffraction from layers, however, is the form of the absorption factor A, which (i) is different from the usual one in $\theta/2\theta$ geometry and (ii) has to be adapted to the different scattering geometries used in thin-film work.

As outlined in Creagh & Hubbell [*International Tables for Crystallography*, Volume C (1999), Section 4.2.4], the intensity I_0 that enters the sample will be exponentially damped to $I_0 \exp(-2\mu l)$ after a path of $2l$, where μ is the linear attenuation coefficient. The inverse of μ can be regarded as a penetration depth for normal incidence $\tau_{1/e} = 1/\mu$, after which path the intensity has dropped to $1/e$ of its initial value. For many substances, attenuation coefficients of the order of 10^5 to 10^7 m^{-1} are obtained for Cu $K\alpha$ radiation or comparable wavelengths, corresponding to penetration depths of between 0.1 and 10 µm. Since these values are in the range of typical layer thicknesses, it is evident that absorption effects might significantly affect the Bragg reflections from the sample.

The situation typically encountered in a $\theta/2\theta$ scan is visualized in Fig. 5.4.1. For any X-ray beam travelling through the sample and scattering into the detector, the primary intensity is reduced by $\exp(-2\mu l)$. The reduction in intensity of the total X-ray beam

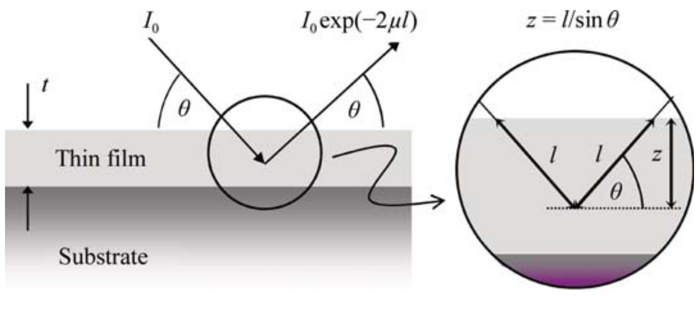

Figure 5.4.1
Schematic representation of absorption in a thin-film sample during a $\theta/2\theta$ scan.

Copyright © 2019 International Union of Crystallography

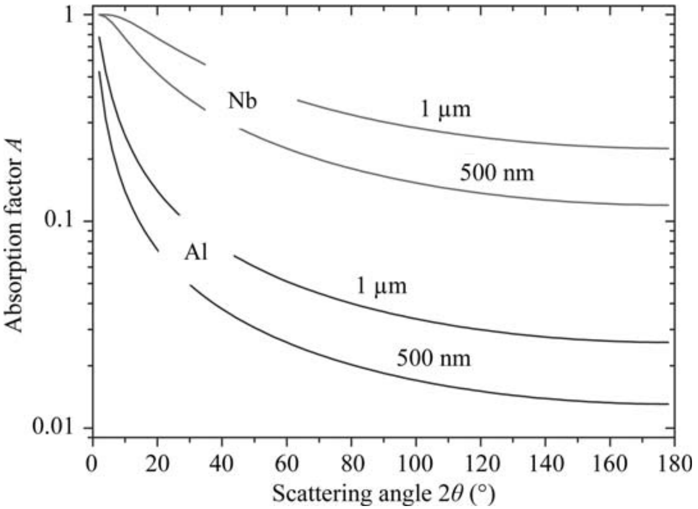

Figure 5.4.2
Absorption factor A for 500 nm and 1 µm Al and Nb films as function of 2θ.

derives from the sum over all beam paths within the limits 0 to $l_{\max}$,

$$\int_0^{l_{\max}} \exp(-2\mu l)\,\mathrm{d}l, \tag{5.4.2}$$

integration of which yields

$$\frac{1}{2\mu}\left[1-\exp\left(-\frac{2\mu t}{\sin\theta}\right)\right]. \tag{5.4.3}$$

The case of powder diffraction represents the limit of an infinitely thick sample, $t \to \infty$ or, equivalently, $t \gg 1/\mu$. In the latter case the well known result is $A = 1/(2\mu)$. In the following, the absorption factor A will be denoted by the ratio of the absorption for a sample of finite thickness to that for an infinitely thick sample:

$$A = \int_0^t \Big/ \int_0^\infty . \tag{5.4.4}$$

The application of this procedure yields the absorption factor of the $\theta/2\theta$ configuration:

$$A_{\theta 2\theta} = \left[1-\exp\left(-\frac{2\mu t}{\sin\theta}\right)\right]. \tag{5.4.5}$$

The subscript $\theta 2\theta$ has been added to indicate the measurement geometry. We will become acquainted with different A factors in the following for distinct instrumental configurations. The A factor is also denoted the thickness factor and it is seen to cause the measured intensity to decrease as a function of increasing scattering angle 2θ. In Fig. 5.4.2 the $A_{\theta 2\theta}$ factor is displayed for thin Al and Nb films of 500 nm and 1 µm thickness measured with Cu $K\alpha$ radiation, where use has been made of the material parameters $\mu = 1.31 \times 10^6$ m^{-1} for Al and 1.276×10^7 m^{-1} for Nb.

It can be realized from the plot that $A_{\theta 2\theta}$ is closer to unity the thicker the film or the larger μ is. Accordingly, the absorption factor depends on the product of these quantities and it will thus be denoted as the product μt in the following. This quantity derives from the two most important structural parameters of a thin film, which are its chemical composition and its thickness. The product μt is a dimensionless number and turns out to be the central parameter in X-ray investigations of thin films.

5.4.2.2. *Chemical phase identification*

As in powder diffraction in general, a typical task in thin-film analysis is the identification of chemical phases. The composition of the layers often has to be checked to ensure that the intended chemical phase has been successfully prepared. This may be done by measuring a diffraction pattern in a $\theta/2\theta$ powder-diffraction setup and comparing the Bragg-peak positions and intensities that are obtained with those of the phases that are expected, as listed in various crystallographic databases such as the Powder Diffraction File (PDF), the Inorganic Crystal Structure Database (ICSD), the Crystallography Open Database (COD) *etc.* (Chapter 3.7). Such comparison may be successful in identifying the chemical phase, but identification is often impeded by some of the specific phenomena observed in thin films. For instance, Bragg reflections may be:

(i) severely damped at higher scattering angles 2θ by the particular dependence of $A_{\theta 2\theta}$ on $\sin\theta$,
(ii) subject to strong broadening and subsequent overlap caused by small grain sizes,
(iii) modulated by a preferred crystallographic orientation (texture) such that one or a few reflections dominate the pattern, while others are missing, and/or
(iv) shifted from their usual $2\theta_0$ values because of residual stress.

Answering the question of what phases comprise the thin film may become very difficult in these cases. It may then become necessary to develop a thorough understanding of the microstructure of the sample and its underlying order parameters such as texture and strain. Again, the linear attenuation coefficient μ is of central importance for all of these tasks and should be determined at the beginning of any thorough X-ray study.

Most tables (such as those in Table 4.2.4.3 of Volume C of *International Tables for Crystallography*) specify the mass absorption coefficient μ_m, which is derived by dividing μ by the mass density,

$$\mu_m = \frac{\mu}{\rho}. \tag{5.4.6}$$

For a discussion of the physical causes of attenuation or absorption, the coefficient μ_m is advantageously further reduced to a cross section σ that is specified for a single atom. The normalization is achieved by multiplying by the atomic mass M and dividing by Avogadro's number N_A,

$$\sigma = \frac{\mu}{\rho}\frac{M}{N_A}, \tag{5.4.7}$$

leading to dimensions for σ of m^2 per atom.

If the linear absorption coefficient of a chemical compound is required, it must be derived from its density ρ and the sum over μ_m of the elements in the compound weighted by their mass fractions g_i/G. Here, g_i denotes the atomic mass of an element and $G = \sum g_i$ is the mass of the molecular unit. μ_m for a single element is then substituted by a sum over all elements in accordance with

$$\mu_m \to \sum_i \frac{g_i}{G}(\mu_m)_i, \tag{5.4.8}$$

Owing to the increase of μ_m with atomic number Z, the absorption coefficient of a compound or an alloy will in most cases be dominated by the heaviest elements in the sample.

It is a further feature of thin-film analysis that the calculated values $\mu_{\rm cal}$ are often found to be larger than those actually observed in the layer, $\mu_{\rm eff} < \mu_{\rm cal}$. This fact may sometimes be explained by porosity, which may affect $\mu_{\rm eff}$ through the inclusion of air or vacuum. In addition, the preparation of thin films in vacuum-based or wet-chemical processes may be accompanied by the inclusion of contaminants on inner surfaces, such as water, hydroxy groups, organic compounds *etc.*, that have a lower density than the main part of the film. However, the reverse situation $\mu_{\rm eff} > \mu_{\rm cal}$ can also occur. In plasma-assisted processes such as physical vapour deposition (PVD) or plasma-enhanced chemical vapour deposition (PECVD), for instance, sputter-gas atoms such as Ar may be included into the growing film. Depending on the processing parameters such as substrate bias *etc.*, the amount of Ar can rise to some at% so that μ may exceed the value calculated from the ideal film composition. The general statement can be made that for any calculation of μ according to (5.4.8) the real chemical composition of the layer has be checked carefully, as it may deviate from the intended one. Among other techniques, this may be performed by determining $A_{\theta 2\theta}$.

5.4.2.3. *Determination and interpretation of the product μt*

Because of its central role in X-ray analysis, the determination of the product μt should mark the start of every investigation of a thin film. This may be performed mathematically when μ and t are known from other sources. It may also be performed using X-ray techniques, and some approaches will now be presented.

A first technique relies on the appearance of a substrate Bragg reflection at scattering angle $2\theta_S$. If such a reflection is observed and can be measured in $\theta/2\theta$ scans, the integrated intensities for the uncoated and the coated sample $I_{S,{\rm unc}}$ and $I_{S,{\rm coa}}$ can be compared. The substrate peak of the coated sample will be damped by the absorption by the layer such that the intensities are related by

$$I_{S,{\rm coa}} = I_{S,{\rm unc}} \exp\left[-\frac{2(\mu t)_{\rm TF}}{\sin\theta_S}\right] \qquad (5.4.9)$$

since the X-ray beam has to traverse the thin film twice to appear as a diffraction peak of the substrate. The product $(\mu t)_{\rm TF}$ (where TF indicates thin film) of the film may then be calculated by rearranging (5.4.9) to obtain

$$(\mu t)_{\rm TF} = \frac{\sin\theta_S}{2}\ln\left(\frac{I_{S,{\rm unc}}}{I_{S,{\rm coa}}}\right). \qquad (5.4.10)$$

Use of this formula is straightforward: I_S is measured prior to and after the film deposition. It may also be applied to amorphous layers, since it makes use of a substrate reflection and does not rely on Bragg peaks from a polycrystalline layer.

These considerations can be extended to multilayer systems (see Fig. 5.4.3) that are built up from a stack of individual layers of different thicknesses and chemical compositions. In this case, the substrate is advantageously labelled by index J and assumed to be buried beneath $J-1$ layers, with the top layer being No. 1. It is evident that the intensity of a Bragg reflection from the jth layer is affected by the absorption of the layers above it. A modified absorption factor $A_{\theta 2\theta}^{\rm ML}$ (where ML indicates multilayer) then has to be introduced, which for the jth layer in a $\theta/2\theta$ scan becomes

$$A_{\theta 2\theta}^{{\rm ML},j}(2\theta) = \left\{1-\exp\left[-\frac{2(\mu t)_j}{\sin\theta}\right]\right\}\exp\left[-\sum_{p=1}^{j-1}\frac{2(\mu t)_p}{\sin\theta}\right]. \qquad (5.4.11)$$

Equation (5.4.11) can be compared with (5.4.5), with the second term describing the damping of beam intensities due to the upper layers.

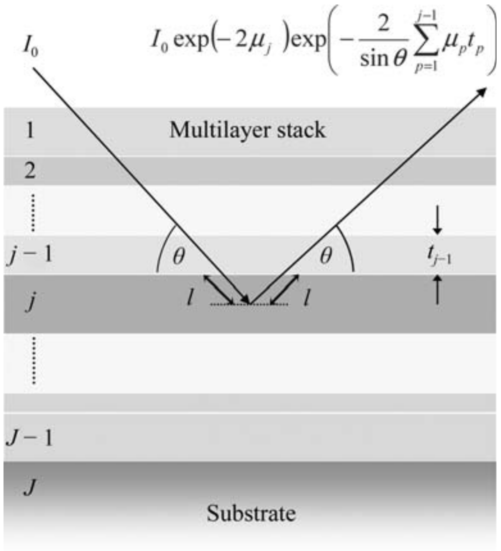
I_0
$I_0\exp(-2\mu_j\ )\exp\left(-\frac{2}{\sin\theta}\sum_{p=1}^{j-1}\mu_p t_p\right)$
1
Multilayer stack
2
$j-1$
θ
θ
t_{j-1}
j
l
l
$J-1$
J
Substrate

Figure 5.4.3
Schematics of absorption in a multilayer system.

Another technique for determining $(\mu t)_{\rm TF}$ uses harmonic reflections, the Miller indices of which are related by $(h_2k_2l_2) = n(h_1k_1l_1)$, with n being an integer. When the two reflections arise at θ_1 and θ_2 and have integrated intensities I_1 and I_2, the following expression may be derived from their ratio:

$$\left\{1-\exp\left[-\frac{2(\mu t)_{\rm TF}}{\sin\theta_1}\right]\right\} = \frac{I_1}{I_2}\frac{(Lp)_2}{(Lp)_1}\frac{F_2F_2^*}{F_1F_1^*}\left\{1-\exp\left[-\frac{2(\mu t)_{\rm TF}}{\sin\theta_2}\right]\right\}. \qquad (5.4.12)$$

From this equation, $(\mu t)_{\rm TF}$ can be solved numerically by inserting the measured intensities and calculating the other factors. Factors such as multiplicity *etc.* are no longer accounted for, since they are equal for harmonic reflections. $T_{\bf h} = 1$ can be used for ideal powder samples, but not for polycrystalline thin films. It is therefore highly advantageous that the term $T_{\bf h}$ vanishes here.

The main difference between this and the first technique is that the intensities stem from the thin film, while those in the previous technique come from the substrate. On the other hand, the structure must be known to obtain the structure factors $F_{\bf h}$. Another disadvantage of the technique is its limitation to harmonic reflections.

As an alternative, thin films with a thickness of less than about 100 nm may also be studied by X-ray reflectivity (XRR; see Section 5.4.6), from which the electron density ρ_e and the thickness t may be derived. Combining the value obtained for ρ_e with reliable assumptions on the layer stoichiometry generally allows the attenuation coefficient μ to be estimated, and finally μt.

If none of the aforementioned procedures can be applied, a numerical regression of the full diffractogram can be carried out. This task is denoted Rietveld refinement or whole-pattern fitting: see Chapters 4.7 and 3.6 in this volume, and Ferrari & Lutterotti (1994), Ribárik *et al.* (2001), Scardi & Leoni (2002), Lutterotti *et al.* (2004) and Apel *et al.* (2011). Some Rietveld programs that were initially developed for powder samples also allow the analysis of thin films.

Interesting conclusions may be drawn from the experimentally determined value for the product μt [$(\mu t)_{\rm exp}$]. The first relates to the film thickness t that can be obtained by dividing $(\mu t)_{\rm exp}$ by a reliable value for the absorption coefficient μ of the layer. It is a decisive advantage of X-ray techniques that the thickness may be

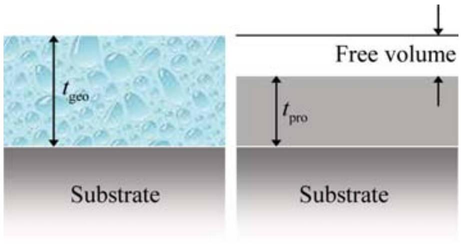

Figure 5.4.4
Visualization of geometrical thickness (left) and projected thickness (right). The difference between these accounts for the free volume of the layer.

determined without destroying the integrity of the sample, as is required for other methods such as profilometry or electron microscopy. To assess the obtainable accuracy and precision, one must be aware of any systematic variations in t caused by lateral inhomogeneity or surface roughness.

Other sources of systematic errors can be identified by decomposing the measured product μt into its constituent factors:

$$(\mu t)_{\mathrm{exp}} = \rho\mu_m t. \qquad (5.4.13)$$

Equation (5.4.13) clearly shows that systematic errors may stem from both ρ and μ_m. Possible errors in density (the term ρ_{bulk} is often used for macroscopic bulk material) may originate from voids and microcavities that are formed during growth. Inclusion of contaminants from the growth medium (mainly light elements) can also make the value of ρ_{bulk} larger than the density actually is.

On the other hand, (5.4.13) may be applied to quantitatively estimate the phenomena causing these systematic deviations. For example, the quantity $(\mu t)_{\mathrm{exp}}/(\rho\mu_m)$ can be denoted the projected thickness, t_{pro}, since it represents the thickness that a layer would have if it were free from voids and contaminants. The actual thickness, however, is the geometrical thickness t_{geo} that represents its geometrical height and may be determined by profilometry (see Fig. 5.4.4). A careful determination of both t_{pro} and t_{geo} may show a significant difference between these values, allowing conclusions to be drawn about the density of unintended phases within the layer.

5.4.2.4. *Phase inhomogeneities*

Deviations from a homogeneous chemical composition may arise in different variants in thin films. First, we consider a single-layer thin film containing P different crystalline phases, each having a weight fraction w_j/W. The sum over all phase weights w_j gives the total weight W of the film, $\sum_{j=1}^{P} w_j = W$.

The average mass attenuation coefficient $\overline{\mu}_m$ of phase mixtures is the sum over the μ_m coefficients of all phases weighted by their weight fraction,

$$\overline{\mu}_m = \sum_j \frac{w_j}{W}(\mu_m)_j. \qquad (5.4.14)$$

The average density, on the other hand, is the ratio of the sum over all phase weights and the total volume,

$$\overline{\rho} = \frac{1}{V}\sum_j w_j. \qquad (5.4.15)$$

The product of these quantities gives the average attenuation coefficient $\overline{\mu} = \overline{\rho\mu}_m$ of a mixed-phase sample, which replaces the term μ in the original formula for calculating the integral intensity of a diffraction pattern, resulting in

$$I_{\mathbf{h}j} = SCF\,Lp\,m_{\mathbf{h}j}\,T_{\mathbf{h}j}\,\frac{|F_{\mathbf{h}j}|^2}{V_{\mathrm{uc},j}^2}\,\frac{w_j}{\rho_j\overline{\mu}}\,A_{\theta2\theta}(t), \qquad (5.4.16)$$

where uc indicates unit cell, which describes the integral intensity of reflection **h** of phase j in a $\theta/2\theta$ diffractogram of a mixed-phase thin film.

Equation (5.4.16) shows that the reflection intensity depends on the weight fraction of the phase. This means that a $\theta/2\theta$ diffraction pattern of a polycrystalline phase mixture is strongly dominated by the compound containing elements with the highest Z values. The next important factor that may influence the application of (5.4.16) is the occurrence of a preferred orientation in the layer sample. This often occurs and may severely affect the integrated intensities gathered in a $\theta/2\theta$ scan, as shown by the $T_{\mathbf{h}}$ term in (5.4.16). In the case of strong sample texture, a quantitative determination of the chemical composition of the sample must be combined with an investigation of its texture. A whole-pattern fitting procedure should then be applied, such as that presented in Lutterotti *et al.* (2004).

In addition to phase mixtures, lateral phase inhomogeneities frequently occur in thin films. These may arise because of inhomogeneous deposition conditions during growth. Their effect often manifests itself as a radial inhomogeneity, where central areas of the sample are distinct from the areas at the substrate edges. However, this phenomenon can be exploited for the preparation of 'thin-film libraries', in which the composition and properties are systematically varied as a function of the sample position. Provided that lateral scanning techniques are available to probe the sample properties on appropriate length scales, the variation in properties can be correlated with the composition. This has recently been demonstrated by X-ray microdiffraction with a lateral resolution in the submillimetre range (Takeuchi *et al.*, 2002; Long *et al.*, 2009; Roncallo *et al.*, 2009). This allows the preparation of large thin-film libraries using a single sample and is an approach for high-throughput experimentation that is increasingly used in various fields of materials science.

5.4.3. Grazing-incidence configurations

As mentioned above, the inverse attenuation coefficient $1/\mu$ in many thin films is much larger than the film thickness, causing a large fraction of diffracted intensity in a symmetric $\theta/2\theta$ scan to stem from the substrate. Only a little structural information may then be gained from the sample, since the X-ray path is too short to deliver Bragg reflections with a sufficient peak-to-noise ratio.

X-ray diffraction techniques have thus been developed in which the primary beam enters the sample at very small angles of incidence. In its simplest variant this configuration is denoted grazing-incidence X-ray diffraction (GIXRD). The small incident angle causes the path travelled by the X-rays to significantly increase and the structural information contained in the diffractogram to stem primarily from the layer. The parafocusing geometry as applied in conventional powder diffractometry is not used in these experiments, and beam-shaping devices for parallel X-ray optics have to be used (see Chapter 2.1). Interestingly, the GIXRD technique allows depth-resolved structural information to be obtained by measuring diffraction patterns at different angles of incidence.

5.4.3.1. *Grazing-incidence X-ray diffraction (GIXRD)*

The experimental configuration in the GIXRD experiment is shown schematically in Fig. 5.4.5. The angle between the incoming beam and the sample surface is very small and amounts to only a few degrees or even less. It is generally denoted α. The incoming X-ray travels a maximum path of $l = t/\sin\alpha$ within the layer. A first criterion for a reliable choice of α is that the average path in the layer should be comparable to the inverse attenuation coefficient, *i.e.* $l \simeq 1/\mu$. This condition translates into the recommendation that $\alpha \simeq \arcsin(\mu t)$ should hold between the incidence angle and the product μt of the layer. Further restrictions have to be considered for α when α approaches the so-called critical angle. As in the symmetric $\theta/2\theta$ configuration, the wavevectors $\mathbf{K}_0$, $\mathbf{K}$ and the sample normal $\mathbf{s}_3$ all lie in the same plane in GIXRD and it is thus a coplanar configuration.

The measurement of the diffractogram is performed in such a way that the angle α is kept constant, while the detector is moved along the 2θ circle. However, the scattering angle 2θ again denotes the angle between the outgoing beam and the extension of the incoming beam. If the collected intensity is then plotted *versus* 2θ, Bragg reflections are found at comparable positions to those in a symmetrically measured pattern. In contrast to the latter, the angle between the outgoing beam and the sample surface is $2\theta - \alpha$ in a GIXRD experiment instead of θ as in a symmetrical scan.

The different measurement geometry has important consequences for the orientation of the scattering vector $\mathbf{Q}$ and the beam optics. In the symmetric $\theta/2\theta$ configuration the scattering vector $\mathbf{Q}$ is always parallel to the surface normal $\mathbf{s}_3$. The crystallographic lattice planes that give rise to an observed Bragg reflection are all oriented parallel to the substrate plane. In the grazing-incidence configuration, on the other hand, $\mathbf{Q}$ is neither parallel to $\mathbf{s}_3$ nor does its orientation remain constant. Rather, the orientation of $\mathbf{Q}$ changes over the course of the measurement, during which the scattering vector is tilted from the start position close to $\mathbf{s}_3$ towards an end position closer to the incoming beam $\mathbf{K}_0$. In the GIXRD configuration, reflections with distinct Bragg angles θ_{hkl} arise from lattice planes that are neither parallel to the substrate surface nor to each other. In the case of a random orientation of crystallites, as in a powder, a comparable pattern will be measured in both the symmetric and asymmetric configuration. For thin layers, however, where the structural parameters may sensitively depend on the film thickness and orientation, the different tilts of grain ensembles have to be considered in order to interpret the GIXRD patterns.

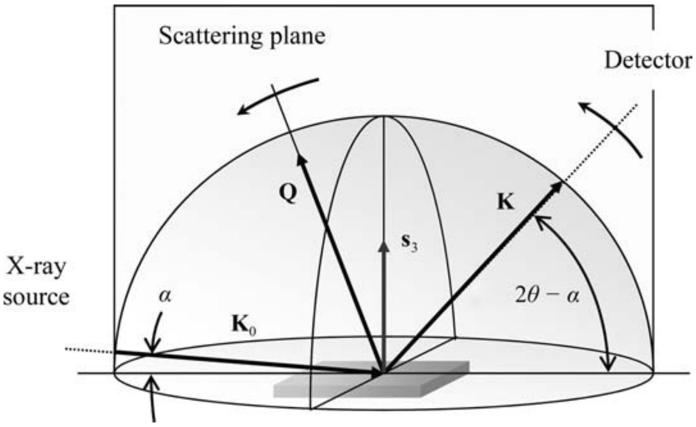

Figure 5.4.5
The geometry in grazing-incidence diffraction is characterized by a small incidence angle α that is kept constant during measurement.

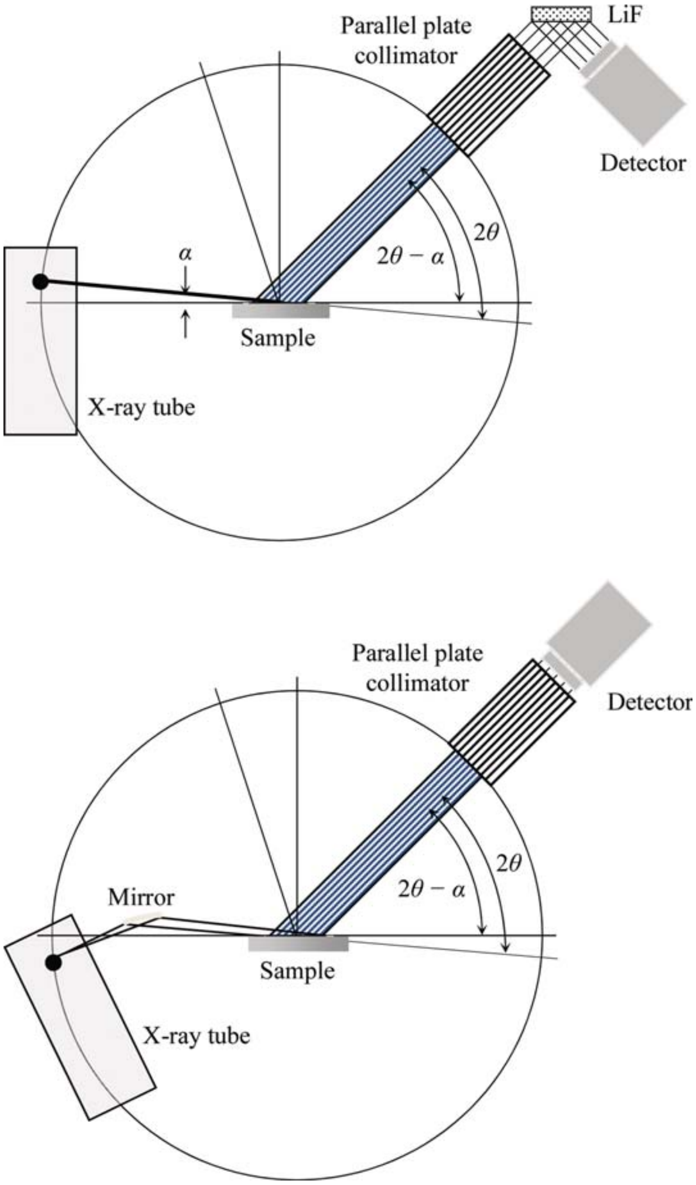

Figure 5.4.6
The two diffractometer configurations most frequently applied in GIXRD. The X-ray tube is operated in the line-focus mode. The drawing plane is the scattering plane.

The need for modified beam optics follows from the fact that the conditions of parafocusing geometry are not met in this asymmetric configuration. Because the incidence angle is fixed, the measuring circle and the focusing circle do not intersect throughout the whole scan, but only for a single point. Without taking special measures, the divergent beam leaving the X-ray tube and impinging on the sample would enter the detector unfocused. The solution to this problem is to run the diffractometer in parallel-beam mode. Fig. 5.4.6 displays the two different configurations that are in use when the tube operates in the line-focus mode. In the first setup (see Fig. 5.4.6*a*), the parallel fraction of the beam is collected on the secondary side by virtue of long collimator slits. Any remaining unparallel beam is subsequently cut off by a flat lithium fluoride crystal monochromator. The second (now widely used) parallel-beam setup, shown in Fig. 5.4.6(*b*), makes use of shaping the primary beam into a parallel bundle just after it has left the X-ray source. This can be achieved using laterally graded multilayer mirrors. A

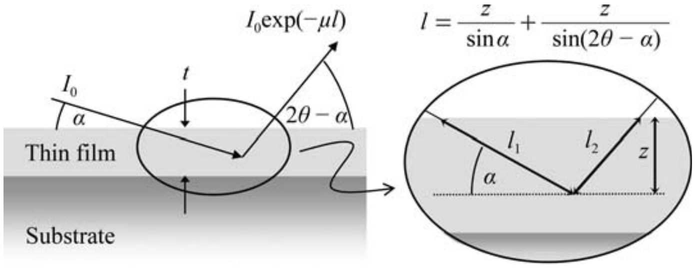

Figure 5.4.7
Schematics of the illuminated sample depth for the derivation of the absorption factor A_α in GIXRD.

sample rotation around the substrate normal or φ axis should be avoided in most GIXRD experiments, since this may cause extra broadening of reflections if the sample is not very precisely positioned. An average over many crystallites, which is the reason for φ spinning in symmetrical XRD, is already obtained in GIXRD through the illumination of many crystallites because of the flat entrance angle.

As a consequence of the particular beam course in GIXRD, the absorption factor A has a different form to that given in (5.4.4). The diffraction of the beam to a depth z is considered in Fig. 5.4.7 in order to derive the new absorption factor. A configuration factor k is now introduced to account for the beam path in the experiment. The factor k allows a general formulation of the absorption factor for any measurement configuration and, in general, it holds that

$$k = \frac{1}{\sin\alpha} + \frac{1}{\sin\beta}. \qquad (5.4.17)$$

It is easily seen for the symmetrical configuration that the factor becomes

$$k_{\theta 2\theta} = \frac{2}{\sin\theta}. \qquad (5.4.18)$$

For GIXRD, however, the more complex expression

$$k_\alpha = \frac{1}{\sin\alpha} + \frac{1}{\sin(2\theta - \alpha)} \qquad (5.4.19)$$

arises. The index α is used as subscript to k in order to characterize it as the appropriate GIXRD factor. The intensity scattered at depth z scales with $\exp(-\mu z/\sin\alpha)$ and $I_0/\sin\alpha$, since the incoming beam is attenuated and inclined. After being scattered, the intensity is attenuated in proportion to $\exp[-\mu z/\sin(2\theta - \alpha)]$,

$$\mathrm{d}P(z) = \frac{SCF \times I_0}{\sin\alpha}\exp\left\{-\mu z\left[\frac{1}{\sin\alpha} + \frac{1}{\sin(2\theta - \alpha)}\right]\right\}\mathrm{d}z. \quad (5.4.20)$$

Here, SCF is a constant that includes terms for the integrated intensity that are not considered in the following. The total scattered intensity follows from the integration over all depths,

$$P = \frac{SCF \times I_0}{\sin\alpha}\int\limits_0^t \exp(-\mu z k_\alpha)\,\mathrm{d}z = \frac{SCF \times I_0}{\mu}\frac{[1 - \exp(-\mu t k_\alpha)]}{k_\alpha \sin\alpha}. \qquad (5.4.21)$$

If P_∞ is used to represent the integrated intensity of a Bragg reflection of an infinitely thick sample, $P_\infty = SCF \times I_0/(\mu k_\alpha \sin\alpha)$ is obtained. As outlined at the beginning, the thin-film absorption factor A is obtained from (5.4.21) by division by P_∞. The GIXRD absorption factor A_α can accordingly be written as

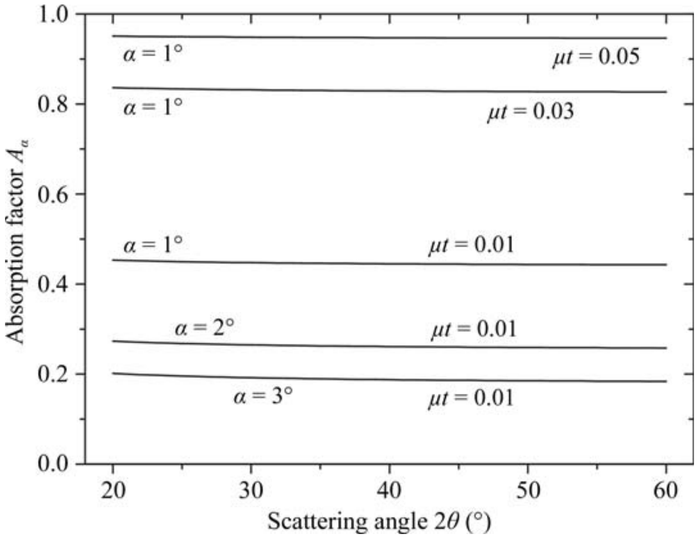

Figure 5.4.8
The absorption factor A_α in GIXRD geometry for various incidence angles α and values of the product μt.

$$A_\alpha = [1 - \exp(-\mu t k_\alpha)]. \qquad (5.4.22)$$

It is by this amount that a Bragg reflection from a thin-film sample is reduced in GIXRD geometry when compared with the intensity from an infinitely thick sample measured under the same conditions. The absorption factor A_α depends on the angles α and 2θ as well as on the product μt of the layer. Therefore, intensity corrections may only be performed when the latter is known and the same arguments as given in Section 5.4.2 hold with respect to the determination of μ, t or μt and the propagation of errors. In Fig. 5.4.8 some absorption factors A_α are displayed for various incidence angles α and values of μt. It can be seen that for all chosen combinations of α and μt the reduction of intensity is fairly constant over the 2θ range from 20 to 60°. This contrasts remarkably with the situation encountered in symmetric $\theta/2\theta$ diffractometry, for which the absorption coefficient $A_{\theta 2\theta}$ decreases significantly with increasing scattering angle 2θ. This different behaviour of A_α and $A_{\theta 2\theta}$ is caused by the different configuration factors k_α and $k_{\theta 2\theta}$ and demonstrates the versatility of GIXRD for the investigation of samples with low values of μt, such as thin films.

Fig. 5.4.9(*a*) displays the GIXRD pattern of a thin TiO_2 film prepared on a titanium-coated steel substrate measured with Cu $K\alpha$ radiation and an incidence angle of $\alpha = 1.8°$ for 2θ between 22 and 60° (Birkholz, Albers & Jung, 2004). Titanium dioxide occurs in a variety of phases, of which tetragonal rutile and anatase are the most common. In addition, thin TiO_2 films are often prepared as fully amorphous and are either transformed to crystalline phases *via* subsequent annealing steps or are used in the amorphous state when this is desired for the intended application. The optical index of refraction of different TiO_2 phases ranges from 2.2 to 2.8 and has the largest values for rutile films, the preparation of which either requires a minimum deposition temperature or high ion bombardment during film growth (Szczyrbowski *et al.*, 1999). Clearly, the peaks observed in Fig. 5.4.9(*a*) can be assigned to the rutile phase (PDF entry 00-021-1276), although the measured reflections are shifted to somewhat smaller 2θ angles. It turns out that the formation of the rutile phase at comparatively low temperatures is assisted by the high ion bombardment during the deposition process, which is also responsible for the intrinsic film stress indicated by the shift of the Bragg reflections. For comparison, the $\theta/2\theta$ pattern of the

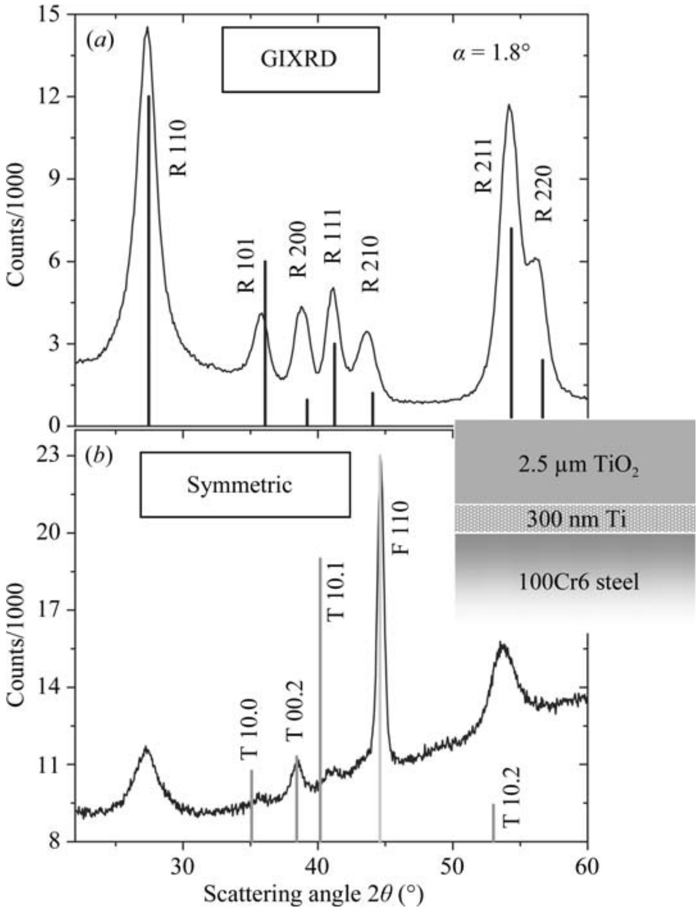

Figure 5.4.9
(*a*) GIXRD, $\alpha = 1.8°$, and (*b*) $\theta/2\theta$ diffraction pattern from the same TiO_2/Ti layer system on steel. Vertical lines indicate the positions of Bragg reflections *hkl* from rutile (R), titanium (T) and ferrite (F) according to the relevant entries in the Powder Diffraction File.

same film is also shown in Fig. 5.4.9(*b*). The symmetrically measured pattern is mainly characterized by the Bragg peaks of the steel substrate and the titanium interlayer, as is seen from the markers for the PDF entries 00-044-1294 for hexagonal-close-packed (h.c.p.) titanium and 0-006-0696 for body-centred cubic (b.c.c.) iron. Moreover, the $\theta/2\theta$ pattern of the same sample exhibits a pronounced background and a poorer signal-to-noise ratio owing to X-ray fluorescence from the iron substrate excited by the Cu $K\alpha$ radiation. For all but the lowest-angle peak, it is hard to decide whether the peaks stem from the substrate, the interlayer or the TiO_2 top layer. Many of the details of the rutile pattern obtained from the GIXRD measurement are completely buried under substrate and bottom-layer peaks in the symmetric $\theta/2\theta$ scan. This example convincingly illustrates the additional information that can be deduced from grazing-incidence diffraction for a thin-film sample.

The GIXRD technique that has just been outlined is also known under other names in the literature, such as grazing-incidence asymmetric Bragg diffraction (GIABD) and others.

5.4.3.2. *Penetration depth and information depth*

The growth of thin films is often associated with thickness-dependent evolutionary processes. For instance, the grain size may be observed to increase with increasing thickness, or the composition of distinct crystallographic phases may change either continuously or abruptly at a critical thickness. GIXRD studies may yield valuable experimental data on such property gradients by measuring a set of diffraction patterns $I(\alpha, 2\theta)$ under varying incidence angles α. However, transforming the measured structural information into a uniquely defined depth coordinate is not straightforward. The complexity of the problem is demonstrated by the existence of different concepts for the penetration depths τ of X-rays.

The first concept of intensity damping considers the depth $\tau_{1/e}$ as the characteristic quantity; this is the distance after which the X-ray beam is attenuated to $1/e$ of its initial value. In the case of GIXRD geometry this yields

$$\tau_{1/e} = \frac{\sin\alpha}{\mu}. \tag{5.4.23}$$

By virtue of the $1/e$ depth it is already possible to qualitatively understand distinct diffraction patterns obtained at different grazing angles α.

The disadvantage of the concept arises from the fact that $\tau_{1/e}$ may exceed the thickness t of the layer and should therefore be used with caution. Obviously, a useful depth definition for the ordering of structural information from different layer depths would have to include the film thickness t, or have the film thickness as a limiting value. These conditions are obeyed by the definition of the so-called average information depth $\overline{\tau}$. This quantity is calculated from the weighted sum of all beam paths that differ in the amount of damping that they suffer by diffraction at various depths. The exponential term, $\exp(-\mu z k)$, has the meaning of a weight function, while the integration is over all depths from the film surface to the interface with the substrate. The average information depth is of the general form

$$\overline{\tau} = \frac{\int_0^t z \exp(-\mu k z)\,\mathrm{d}z}{\int_0^t \exp(-\mu k z)\,\mathrm{d}z}. \tag{5.4.24}$$

Normalization is achieved by dividing the integral by the weight function. This expression is valid for all measuring configurations presented so far and may be adapted to the special configuration in use by inserting the appropriate configuration factor k. In the case of GIXRD, an information depth $\overline{\tau}_\alpha$ is calculated by inserting k_α from (5.4.19), obtaining

$$\overline{\tau}_\alpha = \frac{1}{\mu k_\alpha} + \frac{t}{1 - \exp(\mu t k_\alpha)}. \tag{5.4.25}$$

The appearance of the symbol τ in the context of a penetration depth is sometimes confusing in the literature. In some calculations it may be found as a term inserted for $1/\mu k$, where it has the meaning of an abbreviation. In addition to this, τ is frequently used when using $\overline{\tau}$ would be more appropriate.

In the limit of large incidence angles or small absorption, the average information depth approaches half the film thickness, $t/2$,

$$\lim_{\mu k \to 0} \overline{\tau} = \frac{t}{2}. \tag{5.4.26}$$

This limit corresponds to the situation in which the incident X-ray intensity is hardly damped at all over the whole thickness. In this situation, each partial layer of the film is almost equally illuminated and the measured diffraction information stems on average from the middle of the film. Bragg reflections measured at large α values would contain information from all depths.

5.4.3.3. *Depth-dependent properties*

The formalism discussed above can be developed for other depth-dependent properties such as the concentration of a chemical phase, the amorphous fraction, the crystallite size, microstrain or macrostress *etc*. If this depth-dependent property is denoted by $P(z)$, we realise that determining it by analysing a Bragg reflection yields a weighted average of this property $\overline{P} = \langle P(z)\rangle$, with the weight given by the attenuation of X-ray intensity. An attenuation length τ may be defined that allows $P(z)$ to be related to its average value by

$$\overline{P} = \frac{\int_0^t P(z)\exp(-z/\tau)\,\mathrm{d}z}{\int_0^t \exp(-z/\tau)\,\mathrm{d}z}. \tag{5.4.27}$$

A set of $\overline{P}_\alpha$ values under various incidence angles α can be determined by using the denominator (abbreviated by N_τ) and rewriting the equation using the Laplace transform $\mathcal{L}^t$, which for the GIXRD configuration results in

$$\overline{P}_\alpha = \frac{1}{N_\tau}\mathcal{L}^t[P(z), 1/\tau]. \tag{5.4.28}$$

$P(z)$ can be solved by inverting (5.4.28),

$$P(z) = (\mathcal{L}^t)^{-1}[N_\tau \overline{P}_\alpha(\tau), z], \tag{5.4.29}$$

but the result is highly dependent on the availability and reliability of $\overline{P}_\alpha$ data. Besides GIXRD, there are alternative techniques for collecting $\overline{P}_\alpha$ data. For instance, the scattering-vector technique was introduced by Genzel into the field of residual stress for elucidating stress gradients (Genzel, 1994, 2001). Another approach is to use synchrotron radiation, where the beam energy or wavelength can be varied. Birkholz proposed varying the information depth by using the strong variations of the product μt that occur at elemental absorption edges (Birkholz, 2007) and this has been applied to the determination of texture gradients (Birkholz *et al.*, 2008).

In a practical sense, inversion of the Laplace transformation is complicated by noisy and improperly spaced data in τ space. These cause instabilities in the numerical solution of (5.4.29) and may lead to physically meaningless results. A way to avoid this is to convert the equation into a polynomial equation and to use model parameters P_0, P_1, P_2, ... to compose the property function in real space:

$$P(z) = P_0 + P_1 z + P_2 z^2 + \ldots. \tag{5.4.30}$$

Equation (5.4.29) can be solved analytically by inserting the above expression, yielding

$$\overline{P}_\alpha = P_0 + P_1\left[\tau + \frac{t}{1+\exp(t/\tau)}\right] + P_2\left[2\tau^2 + \frac{t(t+2\tau)}{1+\exp(t/\tau)}\right] + \ldots. \tag{5.4.31}$$

This concept is mostly applied in the field of residual-stress analysis in thin films. However, a more appropriate expression for τ must be determined when very small incidence angles are approached, *i.e.* when α approaches the critical angle α_c, as will be seen in the following.

5.4.3.4. *Index of refraction for X-rays*

The energies of X-rays $h\nu$ by far exceed the resonance energies of intra-atomic excitations. Under this assumption, an expression may be derived for the refraction index of X-rays, showing that it deviates only little from unity, as indicated by

$$n = 1 - \rho_e \frac{\lambda^2 r_e}{2\pi}. \tag{5.4.32}$$

In this formula, ρ_e represents the density of electrons in the specimen and r_e is the classical radius of the electron: $r_e = 2.82 \times 10^{-6}$ nm. The rather small deviation is often denoted δ, leading to

$$n = 1 - \delta. \tag{5.4.33}$$

Table 5.4.1
Mass densities ρ, according to Weast (1986), electron densities ρ_e and critical angles α_c of some oxides used as optical coatings

Critical angles are given for Cu $K\alpha$ radiation.

Compound	ρ (g cm^{-3})	ρ_e (nm^{-3})	α_c (°)
Fused silica, SiO_2	2.20	662	0.216
Quartz, SiO_2	2.64–2.66	794–800	0.237–0.238
Anatase, TiO_2	3.84	1100	0.279
Rutile, TiO_2	4.26	1220	0.294
Nb_2O_5	4.47	1236	0.294
ZnO	5.61	1576	0.326
Amorphous Pr_2O_3	7.07	2040	0.352
SnO_2	6.95	1833	0.359
HfO_2	9.68	2437	0.399

The material constant δ is of the order of only 10^{-6} for wavelengths in the range $0.1 < \lambda < 0.2$ nm. The combination of these equations results in an expression for a monoatomic solid having ρ_a atoms per volume and a nuclear charge Z,

$$\delta = \rho_a (Z + f')\frac{\lambda^2 r_e}{2\pi}. \tag{5.4.34}$$

The scattering power of the Z electrons per atom has to be modified by adding the dispersion correction f'. Often, the real part of the susceptibility δ is expressed by the mass density ρ instead of the electron density ρ_e or atomic density ρ_a. For the general case of a solid composed of different component atoms having nuclear charges Z_i and atomic weights M_i, one obtains

$$\delta = \rho N_A \frac{\sum_i (Z_i + f_i')}{\sum_i M_i}\frac{\lambda^2 r_e}{2\pi}, \tag{5.4.35}$$

where the sums extend over all atoms in the unit cell.

In addition to the real part of the X-ray index of refraction, an imaginary part of the dielectric susceptibility β is needed to fully describe the deviation of n from unity. β is related to the attenuation coefficient μ *via*

$$\beta = \frac{\lambda}{4\pi}\mu. \tag{5.4.36}$$

This equation may be written in a comparable fashion to (5.4.35),

$$\beta = \rho N_A \frac{\sum_i f_i''}{\sum_i M_i}\frac{\lambda^2 r_e}{2\pi}, \tag{5.4.37}$$

where f'' is the imaginary anomalous dispersion factor.

Summarizing, the complex index of refraction for X-rays is given by

$$\hat{n} = 1 - \delta - i\beta. \tag{5.4.38}$$

Mass and electron densities ρ_e are given in Table 5.4.1 for a number of optical coatings, along with critical angles for Cu $K\alpha$ radiation, which is typically used for these studies.

5.4.3.5. *Total external reflection and critical angle*

The fact that $n < 1$ holds for X-rays has important consequences for the phenomenon of total reflection. This effect is generally encountered when electromagnetic radiation traverses a phase border. For optical wavelengths, total internal reflection can be observed in a medium surrounded by vacuum, where

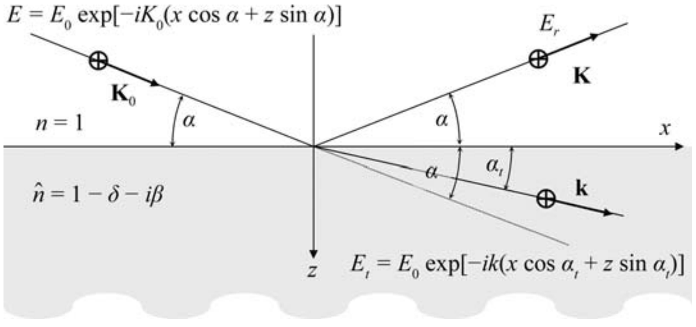
$E = E_0 \exp[-iK_0(x\cos\alpha + z\sin\alpha)]$
E_r
$\mathbf{K}_0$
$\mathbf{K}$
$n = 1$
α
α
x
$\hat{n} = 1 - \delta - i\beta$
α
α_t
$\mathbf{k}$
z
$E_t = E_0 \exp[-ik(x\cos\alpha_t + z\sin\alpha_t)]$

Figure 5.4.10
Electric field vectors **E** and wavevectors **K** and **k** of an electromagnetic plane wave at the surface of an illuminated sample (π polarization).

$n_{\rm med} > n_{\rm vac}$ holds. In X-ray optics, however, a beam impinging on the sample surface may become totally externally reflected, since $n_{\rm vac} > n_{\rm med}$ is valid. The critical angle α_c denotes the incidence angle below which the effect of total reflection will occur. It is described as a function of δ and β with the help of Fig. 5.4.10.

According to Snell's law of refraction, the sines of the incoming and outgoing angles are proportional to the indices of refraction of the two media at the interface at which the transition occurs. Since in X-ray terminology the beam angles are measured with respect to the sample surface and relative to the substrate normal in geometrical optics, the sine functions in Snell's law have to be substituted by cosines, and one arrives at

$$\frac{1}{\hat{n}} = \frac{\cos\alpha_t}{\cos\alpha}, \qquad (5.4.39)$$

where $\hat{n}$ is the index of refraction of the thin film or the substrate, and α_t and α are the angles of transmitted and incident beam, respectively. Both angles may be assumed to be very small such that the cosine functions may be approximated by $\cos x \simeq (1 - x^2/2)$ for $x \simeq 0$.

The transmission angle α_t in a case where absorption is fully neglected can be expressed as

$$\alpha_t = (\alpha^2 - 2\delta)^{1/2} \text{ for } \beta \simeq 0. \qquad (5.4.40)$$

Total reflection, *i.e.* $\alpha_t = 0$, will be observed for all angles of incidence for which the condition $\alpha^2 \leq 2\delta$ is fulfilled. The critical angle α_c is thus defined from this condition and it holds that

$$\alpha_c = (2\delta)^{1/2}. \qquad (5.4.41)$$

It may be estimated from the electron densities given in Table 5.4.1 that α_c takes values between 0.1 and 0.4° for Cu $K\alpha$ radiation.

When absorption is taken into consideration, α_t is described instead,

$$\alpha_t = (\alpha^2 - \alpha_c^2 - 2i\beta)^{1/2} \text{ for } \beta > 0, \qquad (5.4.42)$$

where the same approximations are made as above and α_c^2 has been inserted instead of 2δ. This angle can be developed into the sum of a real and an imaginary part,

$$\alpha_t = \mathrm{Re}(\alpha_t) + \mathrm{Im}(\alpha_t) = B_+ + iB_-, \qquad (5.4.43)$$

where the B_+ and B_- terms may be represented by the real and imaginary deviation of n from unity:

$$B_\pm^2 = \tfrac{1}{2}\Big\{\big[(\alpha^2 - \alpha_c^2)^2 + 4\beta^2\big]^{1/2} \pm (\alpha^2 - \alpha_c^2)\Big\}. \qquad (5.4.44)$$

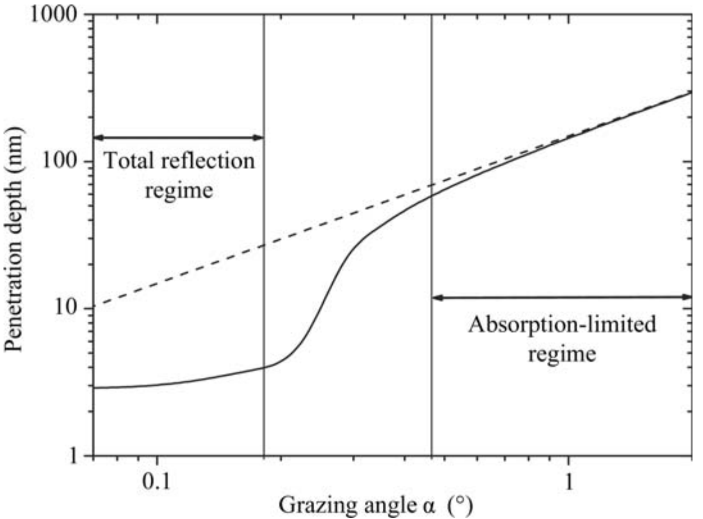

Figure 5.4.11
Penetration depth $\tau_{1/e}$ as function of incident angle α for TiO$_2$ and Cu $K\alpha$ radiation according to (5.4.45) (straight line) and (5.4.23) (dashed line).

For small incidence angles close to the critical angle, (5.4.45) describes the penetration depth $\tau_{1/e}$ better than (5.4.23):

$$\tau_{1/e} = \frac{\lambda}{4\pi B_-} = \frac{2^{1/2}\lambda}{4\pi}\Big\{\big[(\alpha^2 - \alpha_c^2)^2 + 4\beta^2\big]^{1/2} - (\alpha^2 - \alpha_c^2)\Big\}^{-1/2}. \qquad (5.4.45)$$

The penetration depths calculated using both equations [dashed line for equation (5.4.23) and straight line for equation (5.4.45)] are shown in Fig. 5.4.11.

The penetration depth $\tau_{1/e}$ can be divided into three ranges: the first has a grazing angle below the critical angle α_c with a nearly constant value of $\tau_{1/e}$, where $\tau_{1/e} \simeq \lambda/4\pi\alpha_c$ approximately holds. The second range lies above the critical angle α_c, where the penetration depth $\tau_{1/e}$ approaches the limit of $\mu/\sin\theta$, as given in (5.4.23) and as represented by the dashed line. The third (middle) range shows a transition in the vicinity of the critical angle between the two limiting cases. It is obvious that the sample may be monitored with respect to depths that differ by orders of magnitude by varying the incidence angle around α_c. For measurement settings of $\alpha < \alpha_c$, however, only structural information from the uppermost layer is collected.

The transition from (5.4.23) to (5.4.45) describes the effect of total reflection and absorption at very low incidence angles. The penetration depth given in (5.4.45) thus represents the required generalization given at the end of Section 5.4.3.3. By inserting (5.4.45) into equations (5.4.27) and (5.4.28), formulae to determine depth-dependent properties at incidence angles close to the critical angle α_c can be obtained.

Another aspect to be taken into account when using small incidence angles is the shift of reflections from their Bragg peak position θ_B, which increases as the angle of incidence α approaches the critical angle α_c (see Fig. 5.4.12). The shift $\Delta(2\theta)$ is written as

$$\begin{aligned}\tfrac{1}{2}\Delta(2\theta) &= \tfrac{1}{2}(2\theta - 2\theta_B) = \alpha - \mathrm{Re}(\alpha_t)\\ &= \alpha - B_+ \xrightarrow{\beta=0} \alpha - (\alpha^2 - \alpha_c^2)^{1/2}. \qquad (5.4.46)\end{aligned}$$

In the small-incidence-angle approximation and for negligible absorption, (5.4.46) becomes α for $\alpha < \alpha_c$ and $\alpha_c^2/2\alpha$ for $\alpha \gg \alpha_c$.

This effect has been studied in GIXRD experiments carried out on what was intended to be a thin film of γ-phase Fe$_2$O$_3$ for data-storage applications. By controlling the scattering depth through the variation of the incidence angle, the investigation

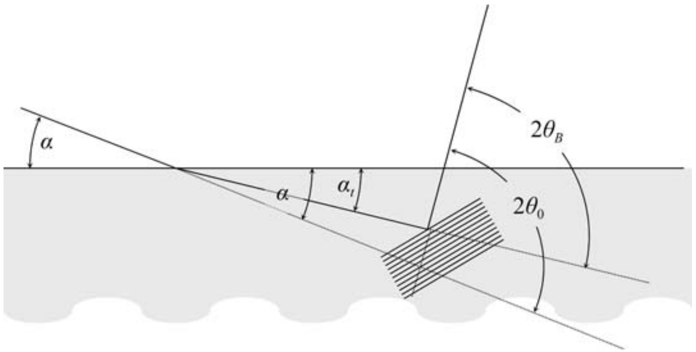

Figure 5.4.12
Schematic drawing for deriving the Bragg peak position shift in GIXRD due to the refraction of the incoming beam.

revealed a less-magnetizable layer of antiferromagnetic α-phase Fe_2O_3 on the film surface. The regression of the data to an appropriate fit function of the type in (5.4.27) allowed quantification of the thickness of the surface layer as 9 nm (Huang, 1990). Appropriate equations for the peak shift in a non-coplanar setup of asymmetric grazing-incidence diffraction have also been derived (Genzel, 2005).

5.4.3.6. *Use of synchrotron radiation*

The preference for a zero-divergent X-ray beam for grazing-incidence experiments is an important argument for using synchrotron radiation. Another reason, which holds in particular for thin films, where only a small scattering volume is active, is the high photon flux, which allows much faster recording of diffraction patterns than with conventional laboratory systems. Accordingly, thin-film studies are increasingly performed at synchrotron beamlines. Synchrotron radiation offers the additional advantage of delivering high-intensity radiation over a large spectral range that may be used in energy-dispersive or white-beam experiments. Based on these qualities, *in situ* investigations of thin-film growth have become possible, for which deposition chambers have been directly installed at synchrotron beamlines; one of the various examples is an energy-dispersive magnetron sputtering system, with which transparent conductive oxides have been investigated (Ellmer *et al.*, 2003).

The high intensity of synchrotron radiation may be a disadvantage when radiation-sensitive samples are under investigation. Organic layers are more prone to destruction by the beam (Beetz & Jacobsen, 2003) than inorganic layers. This effect should thus be considered in every synchrotron experiment; a basic understanding has been developed for protein crystals (Garman, 2010).

5.4.4. Thin-film textures and their depth dependence

The occurrence of texture is a ubiquitous phenomenon in polycrystalline thin films. It seems, in fact, that the preparation of an untextured layer is the exception rather than the rule. It is thus prudent to perform a texture analysis prior to any advanced structure investigation. To give only two reasons: the microstructure may be severely affected by the orientation distribution of crystallites, and also the texture state has to be considered for choosing appropriate grain-interaction models in residual-stress analysis.

Two kinds of texture typically occur in thin films. The first type is the fibre texture that has been identified in a large number of studies, where the fibre axis was typically found to coincide with the substrate normal $\mathbf{s}_3$. In this case, the crystallites have only one orientational degree of freedom: the angle of rotation around the fibre axis. Because of its widespread occurrence in thin films, it is also denoted as layer texture. The second type is biaxial texture, where the orientation of the crystallites is fixed along two directions in the sample reference frame (Chapter 5.3). This state can be regarded as a prelude to an epitaxial film into which the polycrystal would merge for perfectly aligned crystallites.

Thin-film textures may thus be investigated without using the full three-dimensional orientation distribution function (ODF) (a description of which is given in Chapter 5.3). For many cases, the investigation may be restricted to simplified methods such as the determination of texture factors $T_{\mathbf{h}}$, the measurement of pole figures of selected Bragg peaks, ω scans (rocking curves) or φ scans. A typical thin-film phenomenon that deserves consideration is the occurrence of texture gradients, *i.e.* the variation of texture strength with layer depth (Bonarski, 2006; Birkholz, 2007).

5.4.4.1. *Texture factors*

Texture factors $T_{\mathbf{H}}$ represent a straightforward approach to quantifying the degree of preferred orientation in a fibre-textured sample with fibre axis $\mathbf{H}$. The starting point of the calculation is the integrated intensity $I^m_{\mathbf{H}}$ of the measured reflection in a $\theta/2\theta$ pattern,

$$I^m_{\mathbf{H}} = SCF\, m_{\mathbf{H}}\, T_{\mathbf{H}}\, Lp\, |F_{\mathbf{H}}|^2 A_{\theta 2\theta}, \qquad (5.4.47)$$

where $A_{\theta 2\theta}$ is the absorption factor from the symmetric $\theta/2\theta$ setup [see equation (5.4.4)]. The meaning of $T_{\mathbf{H}}$ is that of a weight or concentration factor accounting for the enhancement of the *H*th reflection when compared with a powder sample. The latter is accounted for by $T_{\mathbf{H}} = 1$,

$$I^{\rm rand}_{\mathbf{H}} = SCF\, m_{\mathbf{H}}\, Lp\, |F_{\mathbf{H}}|^2, \qquad (5.4.48)$$

(where rand indicates ‘random’), which differs from (5.4.47) by the missing absorption factor $A_{\theta 2\theta}$, since this expression is valid for powder samples of infinite thickness ($\mu t \gg 1$).

In a second step, the sum of intensities $\sum_{\mathbf{h}} I_{\mathbf{h}}$ is calculated from all Bragg peaks observed in the 2θ range that is investigated. In order to remove the scaling factor, the sum is normalized to a fixed value such as 100, for instance, for both the thin-film pattern and the pattern of that would result from an ideally random orientation. The ratio $I_{\mathbf{H}}/\sum_{\mathbf{h}} I_{\mathbf{h}}$ is subsequently calculated for both patterns, and the texture factor $T_{\mathbf{H}}$ may be derived from

$$T_{\mathbf{H}} = \frac{I^m_{\mathbf{H}}/A_{\theta 2\theta}(\theta_{\mathbf{h}})}{\sum_{\mathbf{h}} I^m_{\mathbf{h}}/A_{\theta 2\theta}(\theta_{\mathbf{h}'})} \frac{\sum_{\mathbf{h}} I^{\rm rand}_{\mathbf{h}}}{I^{\rm rand}_{\mathbf{H}}}. \qquad (5.4.49)$$

The determination of $T_{\mathbf{H}}$ factors by measuring the integrated intensities and relating them to a model pattern offers a simple approach to obtaining a rough estimate of the degree of texture. It is for this purpose that texture factors are found widely in the literature. It has to be emphasized that the correct approach relies on the knowledge of the product μt for the layer, which enters *via* the absorption factor $A_{\theta 2\theta}$ of individual reflections into (5.4.49). Moreover, the method should be applied with caution, since misleading conclusions are easily drawn. For example, the preferred orientation has to be safely verified as a fibre texture with coinciding fibre axis $\mathbf{H}$ and substrate normal $\mathbf{s}_3$ and, moreover, the quantitative result may differ severely from that derived from a thorough harmonic analysis (Chapter 5.3).

5.4.4.2. *Pole-figure scans and analysis*

Measurements of pole figures $I_{\mathbf{h}}(\varphi, \psi)$ of single Bragg reflections, as is usual in ODF analysis, offer a more thorough approach to texture determination. The reader is thus referred to Chapter 5.3, in which the recording of pole figures and their analysis in the framework of harmonic analysis and appropriate methods is presented.

The texture strength is quantified in the harmonic method by the texture index J,

$$J = \frac{1}{4\pi} \sum_{l,\mu} (C_l^{\mu})^2, \tag{5.4.50}$$

which is the sum over the squared coefficients of the expansion coefficients of the ODF. This index might be the relevant condensate of a full harmonic analysis for the thin-film grower, since it gives a quantitative measure for texture optimization (Birkholz *et al.*, 2003).

In contrast to 'thick-sample' diffractometry ($\mu t \gg 1$), however, one has to consider the variation of information depth during the pole-figure measurement for thin films. The effect can be estimated by calculating the information depth τ according to equations (5.4.24) and (5.4.25) adapted to the actual configuration used by inserting the appropriate configuration factor k_ψ,

$$k_\psi = \frac{2}{\sin\theta\cos\psi}. \tag{5.4.51}$$

This can then be used to calculate the average information depth for ψ-tilted configurations:

$$\overline{\tau}_\psi = \frac{1}{\mu k_\psi} + \frac{t}{1 - \exp(\mu t k_\psi)}. \tag{5.4.52}$$

The influence of the tilt angle on the average information depth is shown in Fig. 5.4.13 for a set of thin $BaTiO_3$ films of various thickness and Cu $K\alpha$ radiation (μ = 0.10631 μm^{-1}). Layer thicknesses t of 0.5, 1 and 2 µm were chosen for the simulation and a reflection at $2\theta = 32°$ was investigated. The plot displays the general tendency that the average information depth $\overline{\tau}_\psi$ increases with increasing film thickness. It should be remembered that the limiting value is half the thickness, $t/2$, which would be attained for $\theta = 90°$. The value of $\overline{\tau}_\psi$ stays nearly constant close to zero tilt, but diminishes the closer the tilt angle approaches 90°. This is easily understood, since diffraction in the vicinity of $\psi = 90°$ is mainly due to layers from the utmost surface of the sample.

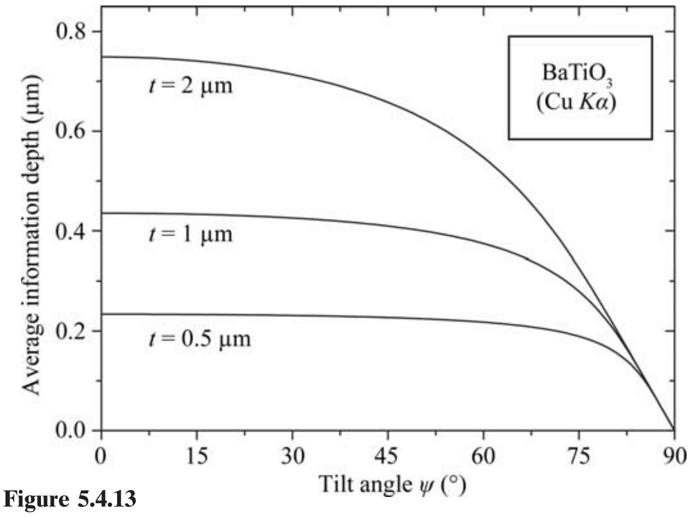

Figure 5.4.13
Average information depth $\overline{\tau}_\psi$ as a function of tilt angle ψ for a $2\theta = 32°$ reflection from thin $BaTiO_3$ films. Layer thicknesses were assumed as indicated in the figure.

It can be concluded from this example that a possible texture gradient would mainly affect the measurement for large tilt angles ψ. It is thus recommended that the variation of the information depth is estimated prior to the measurements. Depending on the result, it might be preferable to measure more pole figures with small $\psi_{\max}$ instead of a few pole figures with high $\psi_{\max}$. Otherwise, the measured pole-figure set would represent a mixture from various information depths (Bonarski *et al.*, 1998).

Pole figures are particularly clear for fibre-textured thin films, when the fibre axis $\mathbf{H}$ is oriented along the substrate normal $\mathbf{s}_3$. The measured intensity distribution $I_{\mathbf{H}}(\varphi, \psi)$ then becomes independent of the azimuth φ such that an intensity measurement for varying tilt angles $I_{\mathbf{H}}(\psi)$ contains the full orientation information. Two kinds of tilt-angle measurements may be performed: tilting in the scattering plane, which is denoted a ω scan, or tilting out of the scattering plane, which is denoted a ψ scan. The term 'rocking curve' is also frequently used for ω scans, since neither the X-ray source nor the detector are moved, but only the orientation of the sample is varied ('rocking the crystal'). The determination of FWHM values $\Delta\omega$ or $\Delta\psi$ may then serve as a quantitative measure for the degree of texture; this is a technique that is widely in use. However, defocusing corrections have to be applied to derive the crystallite orientation distribution from the intensity data (Vaudin, 1999).

Various model functions may describe the dependence of the intensity distribution $I_{\mathbf{H}}(\psi)$ on the tilt angle ψ (Bunge, 1982; Dollase, 1986). The analytical modelling may simply be performed by writing the texture factor as a function of ψ: $T_{\mathbf{H}} \rightarrow T_{\mathbf{H}}(\psi)$. It turns out that model functions of type $\cos^n \psi$ appear to be particularly suited for thin films (Birkholz, 2007; Birkholz *et al.*, 2008). They still have to be multiplied by the normalization factor N to include all crystal orientations in the irradiated volume. This results in an intensity distribution for a ψ-dependent texture factor,

$$T_{\mathbf{H}}(\psi) = \frac{n+1}{2\pi} \cos^n \psi, \tag{5.4.53}$$

in which n describes an order parameter which increases in value the more pronounced the fibre texture is. It may take any positive number, while a value of $n = 0$ accounts for a random orientation distribution. The strength of a fibre texture in the fibre pole is specified in intensity units of m.r.d. (multiples of the random distribution; Bunge, 1982; Chateigner, 2005). Applying a distribution function of the type given in equation (5.4.53) has the advantage that the parameter n directly corresponds to the m.r.d. value.

The intensity distribution for the fibre reflection then becomes

$$I_{\mathbf{H}}(\psi) = SCF\,\lambda^3\,Lp\,m_{\mathbf{H}}\,|F_{\mathbf{H}}|^2\,\frac{n+1}{2\pi}\cos^n\psi\,\frac{1}{2\mu}A_{\theta 2\theta}. \tag{5.4.54}$$

A fibre texture may be regarded as limiting the freedom of orientation of the crystallites in the out-of-plane direction, where the crystal orientation is given by the distribution function $I_{\mathbf{H}}(\psi)$. The orientation distribution in thin films may furthermore be limited to a quite small range of variation within the film plane, which is referred to as a twist and is denoted $\Delta\varphi$.

A quantitative determination of tilt may be performed in such cases by a ω scan of the fibre reflection $\mathbf{H}$ and deriving the tilt $\Delta\psi$ from the full-width at half-maximum (FWHM). This method,

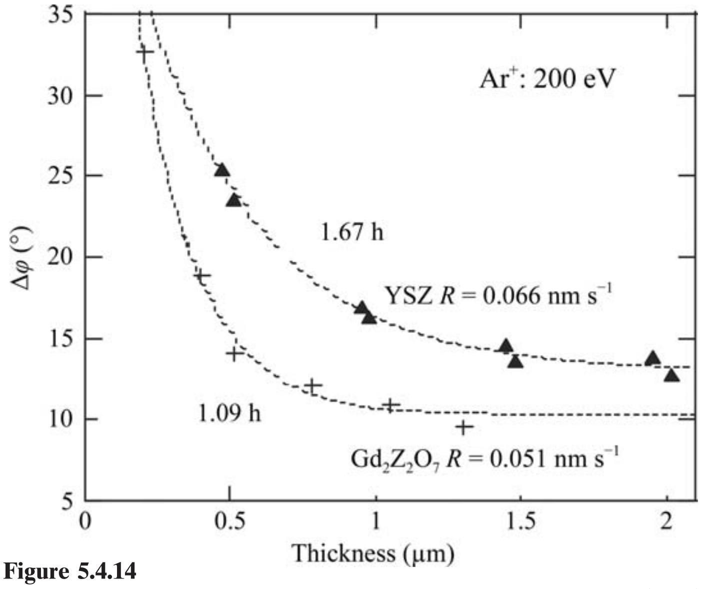

Figure 5.4.14
Thickness dependence of twist $\Delta\varphi$ for yttria-stabilized zirconia (YSZ) and $Gd_2Zr_2O_7$ films. Growth rates are indicated by R (see Iijima *et al.*, 2004).

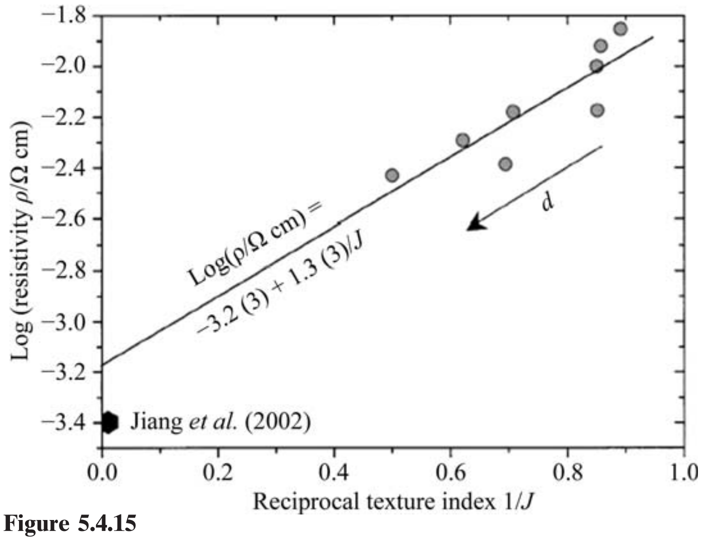

Figure 5.4.15
Resistivity of thin ZnO:Al films *versus* reciprocal texture index $1/J$ (Birkholz *et al.*, 2003).

however, will yield no information on $\Delta\varphi$. In most cases, another reflection $\mathbf{h}$ that exhibits a defined inclination with respect to the fibre reflection is measured for this purpose. The angle between the two crystallographic directions is then chosen as a constant tilt angle $\psi_t = \angle(\mathbf{h}, \mathbf{H})$ at which a rotational scan is performed within $0 \leq \varphi < 2\pi$. An intensity function $I_{\mathbf{h}}(\varphi)$ is obtained from this so-called φ scan, showing as many reflections $\mathbf{h}$ as the multiplicity $m_{\mathbf{h}}$ allows (for an example, see Fig. 5.4.14). A quantitative measure for the twist $\Delta\varphi$ is then derived from the FWHM of the reflections appearing in $I_{\mathbf{h}}(\varphi)$.

Important examples are found in thin-film technologies where a biaxial texture is required for suitable functioning of the device. One recent example is that of high-temperature superconductors (HTSCs), for which small twists and tilts can be achieved *via* clever choices of substrate and deposition process. These structural parameters directly control the superconducting currents through the scattering of Cooper pairs at grain boundaries. In yttrium barium copper oxide (YBCO) layers, for instance, quantification of the degree of texture has mainly been performed by determining $\Delta\omega$ and $\Delta\varphi$ for 103 reflections. The buffer layers for HTSC ribbon substrates are made from oxides such as MgO, CeO_2, yttria-stabilized Zr_2O_3 and $Gd_2Zr_2O_7$. The evolution of a biaxial texture in these buffer layers is supported by oblique deposition or ion-beam irradiation techniques (Iijima *et al.*, 2004; Arendt & Foltyn, 2004). In addition, the introduction of a $\{211\}\langle111\rangle$ copper-type texture into an amorphous precursor film has been demonstrated for yttria-stabilized zirconia in a combined process of oblique ion bombardment, oxidation and thermally induced crystallization (Berdahl *et al.*, 2003). The possibility of influencing the texture by ion-beam irradiation has long been recognized (Rauschenbach & Helming, 1989; Dong & Srolovitz, 1999; Birkholz, Genzel & Jung, 2004; Ellmer *et al.*, 2004), although the explanation of the effect is still controversial and under discussion.

5.4.4.3. *Texture gradients*

Thin-film textures have often been shown to exhibit pronounced depth dependence. It appears to be no exaggeration to state that whenever the effect is looked for, a gradient in preferred orientation is practically always found to occur in thin films. This phenomenon simply represents the fact that the thin-film deposition conditions change with increasing thickness. These changes are mainly related to the surface state and morphology upon which the growth processes occur, even when the thermodynamic conditions within the deposition chamber remain constant. Texture inhomogeneities may severely complicate the analysis, since pole figures become inconsistent owing to the variation of information depth during measurement [Bonarski *et al.*, 1998; Bonarski, 2006; see equation (5.4.52)].

Various techniques have been introduced for the experimental determination of texture gradients. The simplest one consists of preparing a set of samples under identical deposition conditions but of various thicknesses and measuring each sample separately (Birkholz *et al.*, 2000, 2001, 2003; Fenske *et al.*, 2005). The use of synchrotron-radiation sources allows *in situ* monitoring of selected Bragg peaks or even whole diffraction patterns during the deposition process, and valuable studies become possible with this tool (Tagliente *et al.*, 2001). However, this technique requires that the deposition system is connected to a synchrotron beamline and thus is only of limited use for most thin-film technologists. The most appealing approach for determining a texture gradient within a sample makes use of the procedures of depth monitoring by grazing-incidence techniques. By varying the incidence angle of the incoming beam, various depths of the sample are exposed to different X-ray intensities, and so is the diffracted beam.

An intensively investigated example of fibre-texture evolution is that of ZnO layers. ZnO and its derivatives may be used for various optoelectronic thin-film applications, among them the use of Al-doped ZnO for transparent electrodes in solar cells and liquid-crystal displays. Wurtzite-structured ZnO has been shown to exhibit an almost universal tendency to develop a *c*-axis layer texture during many different deposition processes (Kajikawa *et al.*, 2003; Kajikawa, 2006). In one of the few texture studies where the C_l^{μ} coefficients of the harmonic analysis were determined for thin-film samples, the texture index was found to be directly related to the resistivity of the ZnO:Al layers (Birkholz *et al.*, 2003). Fig. 5.4.15 shows the resistivity ρ of a set of eight ZnO:Al samples from a thickness series *versus* the inverse of the texture index, $1/J$, derived from the C_l^{μ} coefficients. A structure–function relationship could be established for the two parameters, relating the resistivity to the inverse texture index *via* $\rho = A\exp(B/J)$. According to a grain-boundary scattering model developed in this work, a value of $\rho = 6.9 \times 10^{-4}\,\Omega\,\mathrm{cm}$ was predicted for perfectly aligned ZnO:Al crystallites having $1/J = 0$. This value corresponds within the experimental margins of errors to one of the lowest resistivity values measured in a highly textured thin ZnO:Al film (Jiang *et al.*, 2002), shown as a black hexagon in the figure.

Preferred orientation has also been extensively investigated in semiconductor layers. Thin polycrystalline silicon films (poly-Si), as used for contacting the transistor-gate oxide in a metal–oxide–semiconductor field-effect transistor (a MOSFET), were shown to exhibit a pronounced layer texture, changing from an ($hh0$) preferred orientation observed at medium temperatures to ($h00$) at higher temperatures (Bisaro *et al.*, 1986; Wenk *et al.*, 1990). This effect was also observed for microcrystalline thin Si films intended for solar-cell applications, for which the depth dependence was accounted for by a power law, showing that the layer texture increased with $t^{1/6}$ (Birkholz *et al.*, 2000).

The concept of texture factors $T_{\mathbf{H}}$ offers a route to describing the depth dependence of a fibre texture by introducing a z dependence into $T_{\mathbf{H}}$, *i.e.*

$$T_{\mathbf{H}}(\psi) \rightarrow T_{\mathbf{H}}(\psi, z). \qquad (5.4.55)$$

In accordance with the arguments given in Section 5.4.3.3, it was shown in Birkholz (2007) that the tilt-angle-dependent intensity distribution given in (5.4.47) may then be expressed as

$$I_{\mathbf{h}}(\psi) = SCF\,\lambda^3\,Lp\,|F_{\mathbf{h}}|^2\,m_{\mathbf{h}}\,\frac{k}{2}\,\mathcal{L}^t(T_{\mathbf{h}}), \qquad (5.4.56)$$

where $\mathcal{L}^t(T_{\mathbf{h}})$ represents the finite Laplace transformation of the depth-dependent texture distribution function:

$$\mathcal{L}^t[T_{\mathbf{h}}(\psi, z)] = \int\limits_0^t T_{\mathbf{h}}(\psi, z)\exp(-\mu z k)\,\mathrm{d}z. \qquad (5.4.57)$$

This is the fundamental equation for describing the intensity distribution of a depth-dependent fibre texture. It directly represents the experimental result that is obtained by the thin-film diffractionist when measuring the intensity as a function of tilt ψ. The solution of the equation is not trivial and attempting it requires some assumptions to be made about the analytical form of $T_{\mathbf{h}}(\psi, z)$.

It is particularly useful to express the texture depth dependence through the order parameter n that was introduced in equation (5.4.53) for the $\cos^n \psi$ distribution of crystallite orientations. The increase in the texture strength may rather naturally be represented by a z-dependent index $n(z)$ increasing with thickness. In the simplest case, n is regarded as a first-order polynomial with the film growth starting at n_0 and continuously increasing by $n_1 z$ with sample thickness:

$$n \rightarrow n_0 + n_1 z. \qquad (5.4.58)$$

A solution to (5.4.57) was developed with this approach in Birkholz (2007). It makes use of a modified attenuation coefficient

$$M = \mu k - n_1 \ln(\cos\psi), \qquad (5.4.59)$$

by which the tilt-angle-dependent intensity distribution can be given in an analogous form to (5.4.54),

$$I_{\mathbf{H}}(\psi) = SCF\,\lambda^3\,Lp\,m_{\mathbf{H}}\,|F_{\mathbf{H}}|^2\,\tilde{N}\cos^{n_0}\psi\,\frac{k}{2M}\tilde{A}(t). \qquad (5.4.60)$$

Here, $\tilde{A}$ and $\tilde{N}$ represent the modified absorption and normalization factor, respectively:

$$\tilde{A}(t) = 1 - \exp(-Mt) = 1 - (\cos^{n_1 t}\psi)\exp(-\mu t k), \qquad (5.4.61)$$

$$\tilde{N} = \frac{1}{2\pi}\left[n_0 + n_1 t\left(\frac{1}{Mt} + \frac{1}{1-\exp(Mt)}\right) + 1\right]. \qquad (5.4.62)$$

These terms take the correct limiting values, *i.e.* $\tilde{A} \rightarrow A$ and $\tilde{N} \rightarrow (n_0 + 1)/(2\pi)$ for $n_1 \rightarrow 0$.

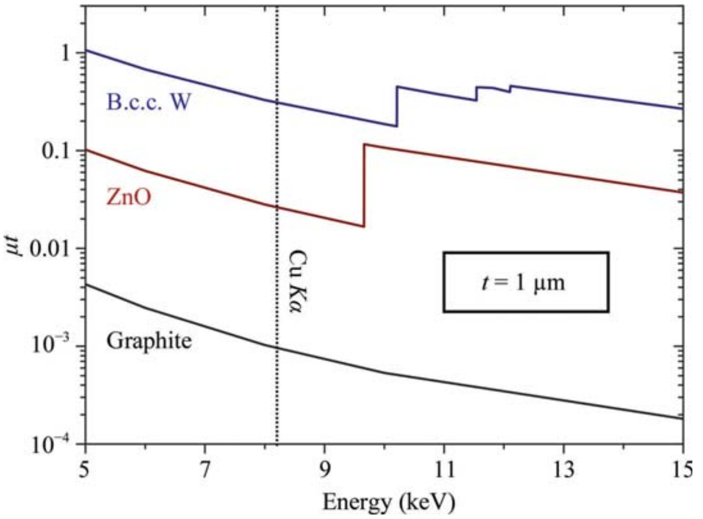

Figure 5.4.16

Variation of the products μt of representative thin-film materials having high, average and low electron densities in the X-ray energy range between 5 and 15 keV. The thickness of the films is assumed to be 1 μm (Birkholz, 2007).

A technique was presented in Birkholz *et al.* (2008) that allows the determination of texture gradients in a single sample by the use of 'coloured' X-ray probes. Instead of preparing a set of samples of different thickness, the information depth is varied by exploiting the dependence of the product μt on the X-ray wavelength. The procedure is particularly effective at the absorption edges of one of the elements forming the layer, where diffraction patterns can be recorded above and below the absorption edge. In general, the technique requires access to a synchrotron beamline, where, favourably, both powder diffraction and EXAFS experiments are routinely performed (Erko *et al.*, 2004). Fig. 5.4.16 shows the variation of the product μt of 1 μm-thin layers from examples of b.c.c. W, ZnO and graphite between 5 and 15 keV. A drastic change in μt by an order of magnitude is seen to occur at the Zn K edge at 9.67 keV. Measurements of ZnO 002 reflections in Birkholz *et al.* (2008) were thus performed at 8 and 10 keV, and texture gradients n_1 were found by this procedure to range from 0.03 to 0.3 m.r.d. nm^{-1}. These high values indicate a strong reconstruction of microstructure during growth, showing the significance of effective control of the texture during thin-film growth for engineering its properties. Collection of more data, such as n_1 values from other layer systems, would be of great interest in order to obtain a better understanding of the physical phenomena governing the evolution of texture, and the formalism presented in equations (5.4.54) to (5.4.62) offers a route to this approach.

5.4.5. Stress and strain analysis

The field of stress analysis by X-ray scattering techniques is outlined in Noyan *et al.* (1995), Hauk (1997), Welzel *et al.* (2005) and Birkholz & Genzel (2006), and in Chapter 5.2 of this volume. Here, only some remarks and references will be given with respect to the investigation of thin films and multilayers.

Remarkably high residual stresses $\sigma_{\rm RS}$ up to the GPa range may arise in thin films, stresses that are mainly caused by either (i) the difference in thermal-expansion coefficients of the substrate and layer or (ii) ion bombardment during plasma-assisted deposition processes. Residual stresses in thin films are anisotropic *par excellence*, *i.e.* a compressive (tensile) strain $\sigma_{\|}$ in the layer plane corresponds to a tensile (compressive) strain $\sigma_{\perp}$ along the substrate normal. The difference in interplanar spacing $\Delta d = (d - d_0)/d_0$ as measured in a symmetric $\theta/2\theta$ scan accounts for the strain $\varepsilon_{\perp}$ in the direction of the substrate normal and the experimentalist is asked to derive $\sigma_{\|}$ from it, since the state of residual stress, which is either compressive or tensile, is always indicated with respect to the in-plane stress $\sigma_{\|}$. The integral stress state may be determined without X-ray diffraction by measuring the bending of the sample and analysing it using the Stoney formula (Ohring, 2002), which works better the thinner the substrate.

A thorough investigation of residual stresses in thin films, however, requires the recording of a set of components of the strain tensor $\boldsymbol{\varepsilon}_{ij}$ by X-ray diffraction procedures, which may become a challenging task because of the occurrence of stress gradients and the interaction of stress and microstructure (texture and grain interaction). The presence of stress gradients and texture mean that the classical $\sin^2\psi$ method for stress analysis seldom yields reliable results for thin films. The scattering-vector method as used in single-crystal diffractometry was therefore introduced into the field by Genzel and combined with GIXRD in such a way that the variation of information depth may encompass the full thickness of a layer (Genzel, 1994, 2001). It was found that residual-stress gradients could be determined with a previously unattained precision by applying the technique to different hard coatings (Genzel & Reimers, 2003; Klaus *et al.*, 2006, 2008). A dedicated beamline has been commissioned at BESSY II, where residual stresses in thin films and near-surface layers in other materials may be investigated by virtue of energy-dispersive diffraction (Genzel *et al.*, 2007; Klaus *et al.*, 2009). In addition, a whole-pattern fitting program for Rietveld refinement against energy-dispersive synchrotron data has been developed for analysis (Apel *et al.*, 2011). This setup thus allows the experimenter to perform depth-resolved measurements with varying probe energies, as outlined above for determining texture gradients, and which has also been applied to the investigation of stress gradients (Wohlschlögel *et al.*, 2008).

In addition to the occurrence of stress gradients, the morphology may also have a pronounced effect on the residual-stress state. The underlying physical cause is easily understood, since the compliance C_{ij} or stiffness S_{ij} values with the elastic constants will not govern the stress alone, but the stress state will depend on the precise mechanical interactions of the crystallites, *i.e.* a grain-interaction model has to be included (Faurie *et al.*, 2009; Ortolani *et al.*, 2009). The best-established models are those of Voigt (1910) and Reuss (1929), which assume a constant strain or stress, respectively, to act between the crystallites. Both models seem to describe outlier cases, and reliable results for thin films have been obtained with the combined model of Hill (1952). In the case of polycrystalline layers, however, the effects of texture (Genzel, 2001, 2004; Birkholz, Genzel & Jung, 2004; Martinschitz *et al.*, 2009; Faurie *et al.*, 2011), anisotropic crystallite growth (Welzel *et al.*, 2003) and the occurrence of nanometre-sized crystallites (Birkholz, Albers & Jung, 2004; Kuru *et al.*, 2008), for which the mechanical properties may differ from macroscopic and mesoscopic materials, represent further challenges.

5.4.6. X-ray reflectivity (XRR)

It was shown in Section 5.4.3.4 that the X-ray index of refraction $\hat{n} = 1 - \delta - i\beta$ contains information on the density and chemical composition of the sample. In fact, the constants δ and β do not depend on the mass density, but on the electron density ρ_e. However, combining the knowledge of ρ_e with reliable assumptions allows interesting conclusions to be drawn about the sample composition.

Both the parameters δ and β may be determined from the measurement of the X-ray reflectivitiy (XRR), and this method has become an important characterization technique for thin films and multilayers (Daillaut & Gibaud, 2009). XRR does not rely on the diffraction of X-rays; rather it makes use of reflection and refraction like in optical ellipsometry, where the complex index of refraction is determined. The decisive distinction between the two methods is the radiation wavelength, which differs by about three orders of magnitude. Because of this, the associated phenomena may be observed only under very small incidence angles in the X-ray case. A further characteristic derives from the fact that the index of refraction n is smaller than unity for X-rays. Therefore, on passing from air into the film, the beam enters the less-dense optical medium, which is the opposite situation to that encountered in ellipsometry.

The use of XRR for the investigation of thin films has steadily increased in recent years. This development is rooted in the fact that the technique yields important information on structural quantities such as the depth-resolved electron density $\rho_e(z)$, the layer thickness t and the surface roughness. In addition, the sample may be amorphous and does not need to consist of crystalline matter, since the technique does not rely on diffraction.

5.4.6.1. *Reflectivity from a substrate*

XRR measurements are performed in a $\theta/2\theta$ mode, but in contrast to the conventional powder-diffraction setup the divergence of the incoming beam should be as low as possible. Experiments are thus preferably performed with a parallel-beam geometry as in GIXRD. In the following, the incidence and critical angles will be referred to as θ and θ_c instead of α and α_c as used in Section 5.4.3.

Firstly, the reflectivity from an uncovered substrate will be considered. For this purpose, the ratio of the reflected to incoming beam intensities I_R/I_0 should be calculated. The quotient is derived from the appropriate Fresnel coefficient by making use of the continuity of the tangential electric field component of the incident and reflected beam, giving

$$\frac{I_R}{I_0} = \left| \frac{\theta - (\theta^2 - \theta_c^2 - 2i\beta)^{1/2}}{\theta + (\theta^2 - \theta_c^2 - 2i\beta)^{1/2}} \right|^2. \qquad (5.4.63)$$

This expression is derived by equating $\sin\theta \simeq \theta$ *etc.*, as is allowed for small θ.

Equation (5.4.63) has two remarkable properties. Firstly, it yields a constant value of unity for $\theta < \theta_c$ and, on the other hand, it describes a very steep decrease for $\theta > \theta_c$. The latter effect becomes obvious when numerical values are inserted, such as a typical critical angle $\theta_c = 0.23^\circ$ (4×10^{-3} rad, $2\delta = 1.6 \times 10^{-5}$) and a vanishing absorption $\beta = 0$ is assumed. While $I_R/I_0 = 1$ then holds for all $\theta \leq 0.23^\circ$ because of total reflection, the intensity ratio declines by 3.5 orders of magnitude at $\theta = 2.3^\circ$ and, even more drastically, to a few 10^{-7} at $\theta = 4.6^\circ$. This means that a

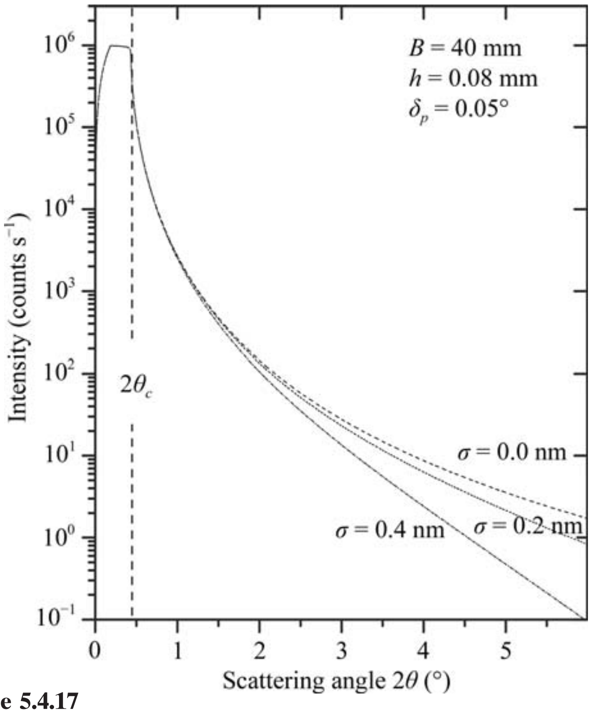

Figure 5.4.17
Simulation of an X-ray reflectivity scan from a quartz glass substrate of varying surface roughness σ probed by Cu $K\alpha$ radiation. δ_p and h represent the in-plane divergence and height of the beam, respectively, and B accounts for the in-plane extent of the sample.

dramatic intensity drop of almost seven orders of magnitude is observed in the range of scattering angles 2θ from 0.46 to 9.2°.

As an example, Fig. 5.4.17 displays the X-ray reflectivity of a fused silica substrate that was calculated using equation (5.4.63) for Cu $K\alpha$ radiation (using δ and β as given in Table 5.4.1). The region of total reflection up to θ_c and the steep decrease beyond can clearly be recognized. In an XRR experiment, the course of $I(2\theta)$ is measured in the vicinity of θ_c and the intensity curve is subjected to a numerical regression, from which the material constants δ, β and ρ_e are obtained.

So far, only an ideally smooth sample surface has been considered. It is evident, however, that any surface roughness will cause an even steeper decrease due to a loss of intensity scattered into the detector. The effect may be modelled by multiplying (5.4.63) by a factor $\exp(-\sigma^2 Q^2)$, which resembles a Debye–Waller factor. Here, σ accounts for the r.m.s. (root-mean-square) roughness of the surface and is given by

$$\sigma = \textstyle\int [z(x,y)^2 - \overline{z}^2]^{1/2}\,\mathrm{d}x\,\mathrm{d}y \Big/ \textstyle\int \mathrm{d}x\,\mathrm{d}y, \qquad (5.4.64)$$

where $\overline{z}$ represents the average height. Fig. 5.4.17 demonstrates the effect of surface roughness on the measured pattern by displaying the reflectivity curves of perfectly smooth fused silica and those with small r.m.s. roughnesses of 0.2 and 0.4 nm. Apart from the steeper decrease in intensity, rough surfaces also give rise to a diffuse component to the observed intensity. The reflectivity can thus be considered to be composed of a specular component and a diffuse component,

$$I(2\theta) = I_{\rm specular} + I_{\rm diffuse}. \qquad (5.4.65)$$

For high levels of surface roughness and at high scattering angles the diffuse component is similar in magnitude to the specular component and must be included. In many thin-film applications, however, it is sufficient to evaluate the XRR curve as being purely specular and to include the effects of surface roughness by modelling the Fresnel coefficient in combination with modified Debye–Waller factors.

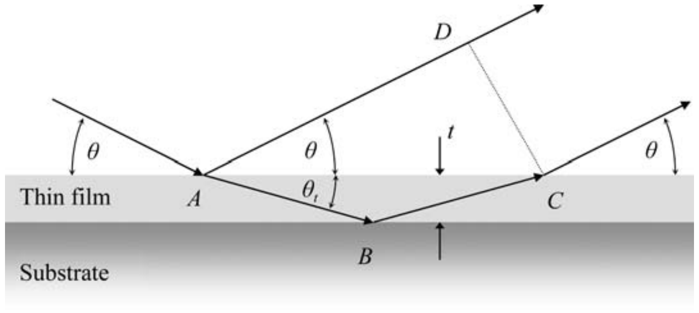

Figure 5.4.18
Scheme of reflected and refracted beams for deriving the phase difference Δ.

5.4.6.2. *Reflectivity of a single layer*

In addition to the steep intensity decline for $\theta > \theta_c$, the XRR pattern of a single-layer sample shows additional features caused by the interference of X-rays reflected at the layer surface and the film–substrate interface. This phenomenon is well known from optical ellipsometry, where it leads to characteristic intensity oscillations from which the layer thickness t may be deduced. Comparable intensity oscillations were first observed for X-rays by Kiessig in 1930 during his investigation of thin Ni films on glass. By using monochromatic X-rays, he observed intensity oscillations in the reflected pattern upon tilting the X-ray mirror in a static source–detector configuration (Kiessig, 1931*a*,*b*). These intensity oscillations were subsequently named Kiessig fringes.

A schematic drawing of the interfering beams is shown in Fig. 5.4.18. It can be seen that their phase difference is given by

$$\Delta = (AB + BC)n - AD, \qquad (5.4.66)$$

where n is the real part of the index of refraction, $n = 1 - \delta$. Since the incidence angle of the transmitted beam θ_t depends on both the critical angle θ_c and the incidence angle of the primary beam, it follows from $AB = BC = t/\sin\theta_t$ and Snell's law, $n = \cos\theta/\cos\theta_t$, that Δ is given by

$$\Delta = 2t\sin\theta_t \text{ or } \Delta \simeq 2t\theta_t = 2t(\theta^2 - \theta_c^2)^{1/2}. \qquad (5.4.67)$$

The phase difference has to be an integral multiple of the wavelength for constructive interference to occur, *i.e.* $\Delta = m\lambda$ should hold. This results in positions of the intensity maxima given by

$$\theta_m^2 = \theta_c^2 + \left(\frac{\lambda}{2t}\right)^2 m^2. \qquad (5.4.68)$$

This is the basic equation from which the thickness of a thin film may be determined by X-ray reflectivity. Its value is usually derived by fitting the reflectivity curve with the thickness t as a refinable parameter. The method is limited to a maximum value of about 100–200 nm, the precise value of which depends on the instrumental and sample properties such as beam divergence, possible bowing of the substrate, surface and interface roughness, and other factors that cause the smearing out of the sharp fringes that are required for the numerical regression. Fig. 5.4.19 displays an X-ray reflectivity curve of a 25 nm-thin Ta_2O_5 film on a glass substrate that was calculated using the XRR simulation program *RCRefSim* (Zaumseil, 2005).

The small 2θ spacing between fringe maxima is the main reason for requiring a preferably zero-divergent beam for XRR

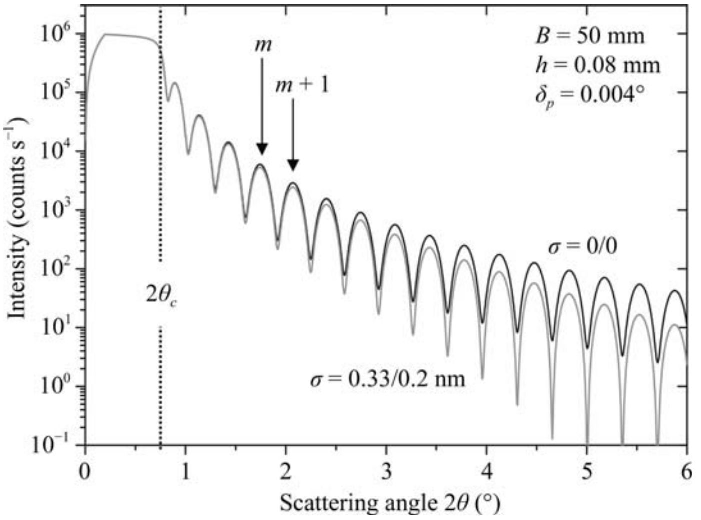

Figure 5.4.19
Simulated X-ray reflectivity of a Ta_2O_5 thin film, t = 25 nm, on a fused silica substrate recorded with Cu $K\alpha$ radiation. The upper curve is for a smooth surface and interface (black), while the lower curve is for 0.2 nm interface roughness and 0.33 nm surface roughness (grey).

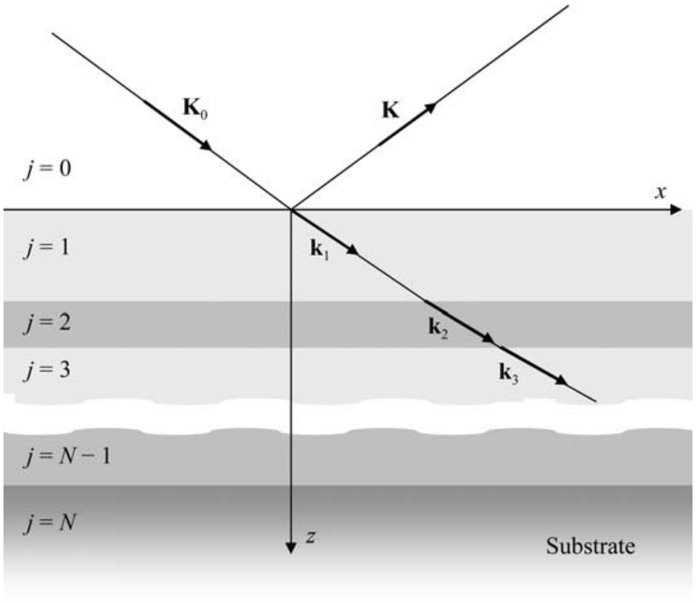

Figure 5.4.20
Notion of participating wavevectors of XRR of a multilayer system.

experiments. It is evident that fringing would not be observed if the divergence is comparable to the fringe separation. On the contrary: the smaller the beam divergence is, the thicker the layer may be for Kiessig fringes to be resolved. Like the high dynamic range in intensity that has to be dealt with in XRR, this constraint favours the use of synchrotron radiation. Dedicated XRR beamlines are thus available at synchrotron-radiation facilities that offer the possibility of recording XRR patterns within very short times. On the other hand, modern powder diffractometers can also be equipped with beam-shaping devices for parallel-beam experimentation, such as laterally graded multilayer mirrors (Chapter 2.1). Together, these developments made XRR a routine thin-film characterization technique that is widely in use, in particular for low-electron-density organic and biological materials (see, for example, Miller *et al.*, 2005; Birkholz *et al.*, 2006; Chen *et al.*, 2011). Detailed investigations of thin-film growth have also been carried out using this technique, revealing a wealth of structural information on density, roughness, molecular orientation *etc.* and their evolution during growth (Kowarik *et al.*, 2006; Hosokai *et al.*, 2010).

5.4.6.3. *Reflectivity of multilayers and superlattices*

In XRR measurements of multilayer systems, the incident-beam intensity will be reduced by the effects of reflection at interfaces and absorption in individual layers. The calculation of the reflected-beam intensity is based on the continuity condition of the tangential components of the electric fields and the conservation of tangential components of the wavevectors at the different interfaces. Parrat solved this task in 1954 during the investigation of surface-oxidation effects of metallic layers (Parratt, 1954).

A schematic of a multilayer system is depicted in Fig. 5.4.20. The layers are numbered in increasing order from the top to the bottom. In the matrix-technique approach (Gibaud & Hazra, 2000), the reflectivity of the multilayer system is described using reflection coefficients $r_{j,j+1}$,

$$r_{j,j+1} = \frac{k_{z,j} - k_{z,j+1}}{k_{z,j} + k_{z,j+1}}, \tag{5.4.69}$$

that contain the z wavevector components $k_{z,j}$ and $k_{z,j+1}$ in the two neighbouring media and account for the reflection of the incoming and the exiting beam at the j, $j + 1$ interface. A set of 2 × 2 matrices is introduced for each interface j, $j + 1$ and for each layer j, which are the refraction and transfer matrices $\boldsymbol{R}_{j,j+1}$ and $\boldsymbol{T}_j$, respectively. The product of all of these establishes the transfer matrix $\boldsymbol{M}$, with the ratio of the M_{12} and M_{22} components giving the amplitude of the multilayer reflectivity. Applying the procedure to a single-layer system results in an expression for the intensity of the reflected beam,

$$\frac{I_R}{I_0} = \frac{r_{0,1}^2 + r_{1,2}^2 + 2r_{0,1}r_{1,2}\cos 2k_{z,1}t}{1 + r_{0,1}^2 r_{1,2}^2 + 2r_{0,1}r_{1,2}\cos 2k_{z,1}t}, \tag{5.4.70}$$

that depends on the reflection coefficients of the air–film interface, $r_{0,1}$, and the film–substrate interface, $r_{1,2}$, according to (5.4.70). The ratio also accounts for the oscillation phenomena observed in Fig. 5.4.19 *via* the cosine term, which depends on the layer thickness t. The recursion scheme of the matrix technique allows it to be effectively integrated into computer code. Moreover, surface-roughness effects may also be included by multiplying the reflection coefficients by Debye–Waller-factor-like damping terms that contain the r.m.s. roughness of all individual j, $j + 1$ interfaces.

Analytical expressions for the reflectivity of multilayers with two and more layers become rather complicated, making it difficult to recognize the underlying physics. Instead of presenting the generalization of (5.4.70) to two-layer, three-layer systems and so on here, an example for a complex multilayer architecture is given. Fig. 5.4.21 displays a set of simulations from a thermal-barrier multilayer that comprises a stacking of oxide and metal layers, and small differences in the assumed architecture can be seen to cause substantial changes in the XRR pattern.

XRR may also uncover the inner architecture of periodic multilayers, which are also denoted as superlattices. These layer structures essentially comprise a stack of N pairs of layers of type A and B, where the thicknesses of individual layers t_A and t_B add up to the superlattice period $t_{\rm per}$,

$$t_{\text{per}} = t_A + t_B. \tag{5.4.71}$$

Such superlattices are fabricated for applications as so-called Bragg mirrors in light-emitting devices or as X-ray mirrors. The X-ray reflectivity curves of such multilayers have various characteristic features that are illustrated for the example of an X-ray mirror system in Fig. 5.4.22. The figure also displays the reflectograms of a 10 × (6 nm TiO_2/6 nm C) superlattice on an Si substrate that was again calculated using *RCRefSim* (Zaumseil, 2005). As for the single-layer system, a modified Bragg equation (5.4.53) may be derived describing the occurrence of the superlattice peaks by inserting t_{per} instead of t,

$$\theta_m^2 = \langle\theta_c\rangle^2 + m^2\left(\frac{\lambda}{2t_{\text{per}}}\right)^2, \tag{5.4.72}$$

where $\langle\theta_c\rangle$ is the average critical angle of the total superlattice. The thickness values for each individual layer A and B and the interface roughness σ_{AB} and σ_{BA} can be determined by fitting with the matrix formalism. The figure displays three different simulations with varying interface roughnesses. The difference between the large fringes is accounted for by (5.4.72), while the small fringing scales with the total thickness of the layer system, *i.e.* $1/(Nt_{\text{per}})$. Ideally, there are $N - 2$ small fringes between two adjacent superlattice peaks. It can be realized from the figure that for certain combinations of σ_{AB} and σ_{BA} every second maximum may vanish. This effect may be observed in superlattices having $t_A = t_B$ and is due to the destructive interference from X-ray beams reflected at the AB and BA interfaces.

Superlattices with large differences in electron density between individual layers can be used as X-ray mirrors. Typical material combinations are Mo/Si, V/C or La/B_4C and other systems with substantial ρ_e contrast. XRR also provides a sensitive tool for studying the surface oxidation of metals and other materials that are sensitive to surface oxidation. In fact, in his seminal study Parrat investigated a thin copper film on glass, where reliable agreement between the measured and simulated reflectivity could only be achieved by introducing a 15 nm-thin surface-oxide layer into the model (Parratt, 1954). The possibility that there may be an oxide layer on the top of a thin-film or multilayer system should routinely be considered when fitting measured reflectivity curves. Surface chemical reactions may also be studied by XRR.

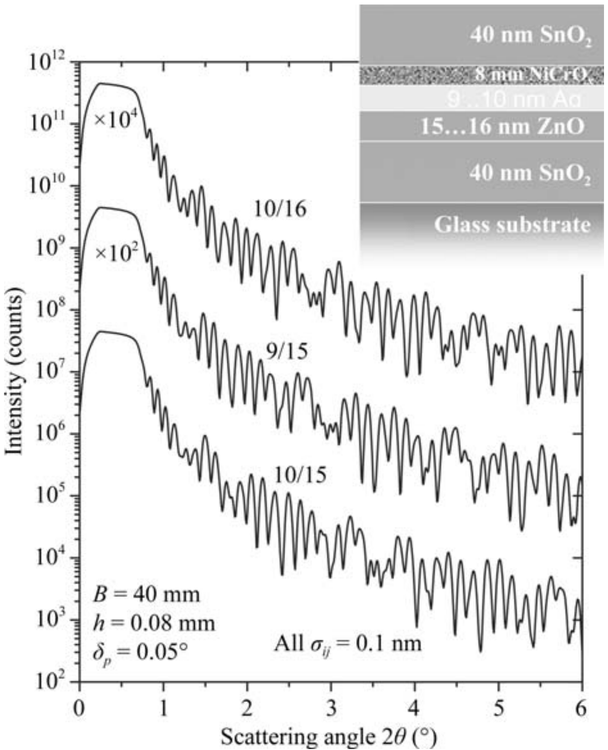

Figure 5.4.21

Simulated X-ray reflectivity patterns of barrier coating SnO/NiCrO$_x$/Ag/ZnO/SnO on glass recorded with Cu $K\alpha$ radiation. The numbers above each pattern indicate the thicknesses of the Ag and ZnO layers, respectively, in nanometres. Other thicknesses were kept constant.

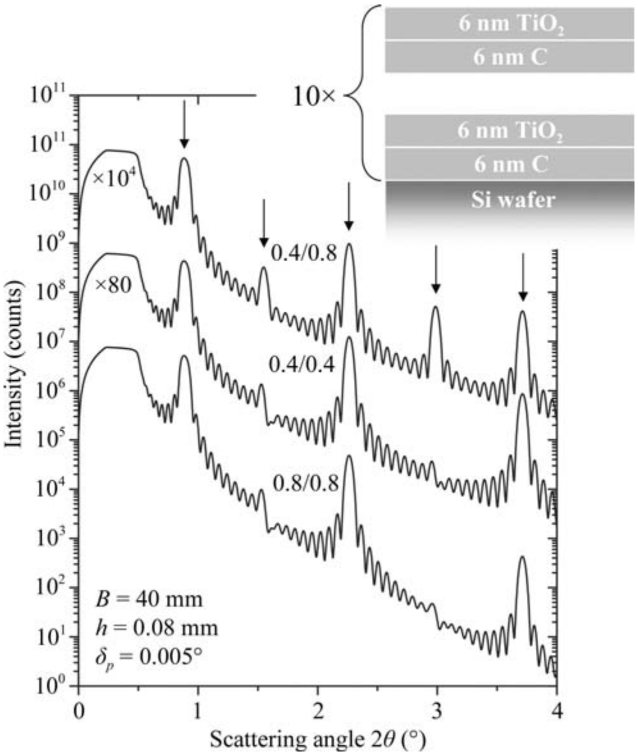

Figure 5.4.22

Simulation of X-ray reflectivity of a (TiO_2/C) superlattice on an Si wafer. The numbers above the pattern give the roughnesses of the TiO_2 and C layers, respectively, in nanometres. The substrate roughness was set to a constant 0.4 nm. Superlattice peaks are indicated by arrows.

5.4.7. Grazing-incidence X-ray scattering (GIXS)

In a GIXS experiment, a primary beam with momentum $\mathbf{K}_0$ impinges on the sample at a very small incidence angle, as in XRR. Again, the elastically scattered intensity with momentum vector $\mathbf{K}$, $|\mathbf{K}| = |\mathbf{K}_0| = 2\pi/\lambda$, is measured in a reflective configuration, but it is not the specular reflection alone that is measured by a point detector. Instead, the intensity in GIXS is collected by a two-dimensional detector screen, allowing scattering events for which the scattering vector $\mathbf{Q} = \mathbf{K} - \mathbf{K}_0$ deviates from the substrate normal to also be recorded. The incidence angle between the primary (scattered) beam and the substrate surface is generally denoted by α_i (α_f), while the azimuth of the scattered beam is indicated by $2\theta_f$. The two-dimensional intensity map is then given as a function of momentum-transfer coordinates Q_y and Q_z according to

$$\begin{aligned} Q_y &= \frac{2\pi}{\lambda}\sin\theta\cos\alpha_f\sin 2\theta_f, \\ Q_z &= \frac{2\pi}{\lambda}\sin\theta(\sin\alpha_i + \sin\alpha_f), \end{aligned} \tag{5.4.73}$$

where the projection of $\mathbf{K}_0$ to the sample surface is assumed to define the x axis. The method is often used with small scattering angles, and in this case is denoted as GISAXS. The analysis of the intensity patterns obtained is then performed within the conceptual framework developed for small-angle X-ray scattering (SAXS) (Chapter 5.8). The parameters to be derived are characterized by low momentum transfer and real-space extents that are much larger than the probing wavelength (Müller-Buschbaum, 2009). For thin films, for instance, the shape and size of the scattering entities in nanogranular films or nucleation layers have been investigated (d'Acapito & Zontone, 1999; Stangl *et al.*, 1999; Leroy *et al.*, 2003). This approach has also been extended to a grazing-exit configuration (GESAXS), where the scattering pattern in the $\alpha_f < \alpha_c$ range is monitored and the coherence of the radiation is employed (Pfeiffer *et al.*, 2004). Interesting results on the evolution of the microstructure of thin metal films during annealing have been obtained (Zhang & Robinson, 2007).

Experiments in a GIXS configuration meanwhile extend beyond the classical SAXS investigation, since diffraction peaks are often also observed and combined-analysis techniques have been developed to derive complete structural information from the measured intensity map. An important role in the development of the method has been played by diblock copolymers, owing to their pronounced tendency for forming self-assembled nanostructures such as, for instance, hexagonally perforated layers (Heo *et al.*, 2008). In general, GIXS is well suited for the investigation of organic thin layers (Jiang *et al.*, 2012).

5.4.8. Conclusions and perspective

To summarize, it is recommended that powder diffractionists start investigating a thin-film or multilayer by determining the product μt (or the set of products μt). Combining this result with knowledge of sample preparation will allow a critical estimation of the chemical composition and possible inhomogeneities. Subsequently, the texture and possible texture gradients should be investigated and, on the basis of these results, further microstructural properties such as the effective electron density, the extension of coherently scattering domains (the 'X-ray grain size') and residual stresses and their gradients can be examined. The results that are obtained will enable a basic understanding of the structure–function relationships operating within the sample and suggest possible ways to improve its properties. Most of the methods presented here will be helpful in this respect; it should be remembered, however, that a truly comprehensive picture becomes visible when different probing techniques are combined: either X-ray scattering methods only or in combination with other probes such as optical probes, ion beams, magnetic resonance *etc.*

It might be expected that the high rate of development of this field will continue and probably even increase in the next few years. A search for the combination of the terms 'X-ray diffraction' and 'thin film' in Google Scholar yielded an increase from about 6000 records in 2001 to more than 26 000 in 2017. It has thus become impossible to provide a complete overview of all the relevant developments in the field. In spite of this, I hope to have presented the most important aspects for the newcomer to the field as well as for the expert, and apologize if any of my colleagues feel that their work has been under-represented.

It seems that the unspoken programmatic goal of thin-film technology and analysis is to become capable of indicating the chemical nature and spatial position $r_i = (x_i, y_i, z_i)$, $i = 1, \ldots, N$, of every atom forming the layer *and* to describe how this set of data depends on the deposition conditions. Coming ever closer to this holy grail will pave the way to predicting the layer properties *in silico* with ever more accuracy. Although this goal has not been declared by any national or international agency or association, it represents an inherently crystallographic programme, since crystallography seeks the development of methods that allow the prediction of the properties of crystalline matter from the relative arrangement of their atomic constituents. It is obvious that the field of thin films and multilayers will develop in this direction, and perhaps will reach this target earlier than we expect today. The various X-ray powder-diffraction techniques that are in use and under development will continue to deliver indispensable contributions during this fascinating journey.

References

Apel, D., Klaus, M., Genzel, C. & Balzar, D. (2011). *Rietveld refinement of energy-dispersive synchrotron measurements. Z. Kristallogr.* **226**, 934–943.

Arendt, P. N. & Foltyn, S. R. (2004). *Biaxially textured IBAD–MgO templates for YBCO-coated conductors. MRS Bull.* **29**, 543–550.

Beetz, T. & Jacobsen, C. (2003). *Soft X-ray radiation-damage studies in PMMA using a cryo-STXM. J. Synchrotron Rad.* **10**, 280–283.

Berdahl, P., Reade, R. P., Liu, J., Russo, R. E., Fritzemeier, L., Buczek, D. & Schoop, U. (2003). *Oblique ion texturing of yttria-stabilized zirconia: the {211}⟨111⟩ structure. Appl. Phys. Lett.* **82**, 343–345.

Birkholz, M. (2006). *Thin Film Analysis by X-ray Scattering*. Weinheim: Wiley-VCH.

Birkholz, M. (2007). *Modelling of diffraction from fibre texture gradients in thin polycrystalline films. J. Appl. Cryst.* **40**, 735–742.

Birkholz, M., Albers, U. & Jung, T. (2004). *Nanocomposite layers of ceramic oxides and metals prepared by reactive gas-flow sputtering. Surf. Coat. Technol.* **179**, 279–285.

Birkholz, M., Darowski, N. & Zizak, I. (2008). *Profiling of fibre texture gradients in thin films by anomalous X-ray diffraction. Z. Kristallogr. Suppl.* **27**, 263–271.

Birkholz, M. & Genzel, C. (2006). *Thin Film Analysis by X-ray Scattering*, edited by M. Birkholz, pp. 239–295. Weinheim: Wiley-VCH.

Birkholz, M., Genzel, C. & Jung, T. (2004). *X-ray diffraction study on residual stress and preferred orientation in thin titanium films subjected to a high ion flux during deposition. J. Appl. Phys.* **96**, 7202–7211.

Birkholz, M., Selle, B., Conrad, E., Lips, K. & Fuhs, W. (2000). *Evolution of structure in thin microcrystalline silicon films grown by electron-cyclotron resonance chemical vapor deposition. J. Appl. Phys.* **88**, 4376–4379.

Birkholz, M., Selle, B., Fenske, F. & Fuhs, W. (2003). *Structure–function relationship between preferred orientation of crystallites and electrical resistivity in thin polycrystalline ZnO:Al films. Phys. Rev. B*, **68**, 205414.

Birkholz, M., Selle, B., Fuhs, W., Christiansen, S., Strunk, H. P. & Reich, R. (2001). *Amorphous-crystalline phase transition during the growth of thin films: the case of microcrystalline silicon. Phys. Rev. B*, **64**, 085402.

Birkholz, M., Zaumseil, P., Kittler, M., Wallat, I. & Heyn, M. P. (2006). *Structure of biomembrane-on-silicon hybrids derived from X-ray reflectometry. Mater. Sci. Eng. B*, **134**, 125–129.

Bisaro, R., Magariño, J., Proust, N. & Zellama, K. (1986). *Structure and crystal growth of atmospheric and low-pressure chemical-vapor-deposited silicon films. J. Appl. Phys.* **59**, 1167–1178.

Bonarski, J. T. (2006). *X-ray texture tomography of near-surface areas. Prog. Mater. Sci.* **51**, 61–149.

Bonarski, J. T., Bunge, H.-J., Wcislak, L. & Pawlik, K. (1998). *Investigation of inhomogeneous surface textures with constant information depth: Part 1: Fundamentals. Text. Microstruct.* **31**, 21–41.

Boscherini, F., Birkholz, M., Buffière, J.-Y., Chateigner, D., Fewster, P. F. & Heun, S. (2010). *X-ray techniques for advanced materials, nanostructures and thin films: from laboratory sources to synchrotron radiation. Nuclear Instrum. Methods Phys. Res. B*, **268**, 231–430.

Bunge, H.-J. (1982). *Texture Analysis in Materials Science.* London: Butterworth–Heinemann.

Chateigner, D. (2005). *Combined analysis: Structure–texture–microstructure–phase–stresses–reflectivity determination by X-ray and neutron scattering.* http://www.ecole.ensicaen.fr/~chateign/texture/combined.pdf.

Chateigner, D. (2010). *Combined Analysis.* London: ISTE.

Chen, C.-H., Málková, S., Cho, W. & Schlossman, M. L. (2011). *Configuration of membrane-bound proteins by X-ray reflectivity. J. Appl. Phys.* **110**, 102215.

Creagh, D. C. & Hubbell, J. H. (1999). *International Tables for Crystallography*, Vol. C, *Mathematical, Physical and Chemical Tables*, 2nd ed., Section 4.2.4, edited by A. J. C. Wilson & E. Prince, pp. 220–236. Dordrecht: Kluwer.

d'Acapito, F. & Zontone, F. (1999). *Grazing-incidence X-ray diffraction in the study of metallic clusters buried in glass obtained by ion implantation. J. Appl. Cryst.* **32**, 234–240.

Daillaut, J. & Gibaud, A. (2009). *X-ray and Neutron Reflectivity.* Berlin: Springer.

Dollase, W. A. (1986). *Correction of intensities for preferred orientation in powder diffractometry: application of the March model. J. Appl. Cryst.* **19**, 267–272.

Dong, L. & Srolovitz, D. J. (1999). *Mechanism of texture development in ion-beam-assisted deposition. Appl. Phys. Lett.* **75**, 584–586.

Ellmer, K., Mientus, R., Seeger, S. & Weiss, V. (2004). *Highly (001)-textured WS2-x films prepared by reactive radio frequency magnetron sputtering. Phys. Status Solidi A*, **201**, R97–R100.

Ellmer, K., Mientus, R., Weiss, V. & Rossner, H. (2003). *In situ energy-dispersive X-ray diffraction system for time-resolved thin-film growth studies. Meas. Sci. Technol.* **14**, 336–345.

Erko, A., Schäfers, F., Firsov, A., Peatman, W. B., Eberhardt, W. & Signorato, R. (2004). *The BESSY X-ray microfocus beamline project. At. Spectrosc.* **59**, 1543–1548.

Faurie, D., Castelnau, O., Brenner, R., Renault, P.-O., Le Bourhis, E. & Goudeau, P. (2009). *In situ diffraction strain analysis of elastically deformed polycrystalline thin films, and micromechanical interpretation. J. Appl. Cryst.* **42**, 1073–1084.

Faurie, D., Renault, P.-O., Le Bourhis, E., Chauveau, T., Castelnau, O. & Goudeau, P. (2011). *X-ray strain analysis of {111} fiber-textured thin films independent of grain-interaction models. J. Appl. Cryst.* **44**, 409–413.

Fenske, F., Selle, B. & Birkholz, M. (2005). *Preferred orientation and anisotropic growth in polycrystalline ZnO:Al films prepared by magnetron sputtering. Jpn. J. Appl. Phys.* **44**, L662–L664.

Ferrari, M. & Lutterotti, L. (1994). *Method for the simultaneous determination of anisotropic residual stresses and texture by X-ray diffraction. J. Appl. Phys.* **76**, 7246–7255.

Fewster, P. F. (2003). *X-ray Scattering from Semiconductors.* London: Imperial College Press.

Garman, E. F. (2010). *Radiation damage in macromolecular crystallography: what is it and why should we care? Acta Cryst.* D**66**, 339–351.

Genzel, C. (1994). *Formalism for the evaluation of strongly non-linear surface stress fields by X-ray diffraction performed in the scattering vector mode. Phys. Status Solidi A*, **146**, 629–637.

Genzel, C. (2001). *X-ray stress analysis in presence of gradients and texture. Adv. X-ray Anal.* **44**, 247–256.

Genzel, C. (2004). *Diffraction Analysis of the Microstructure of Materials*, edited by E. J. Mittemeijer & P. Scardi, pp. 473–503. Berlin: Springer.

Genzel, C. (2005). *X-ray residual stress analysis in thin films under grazing incidence – basic aspects and applications. Mater. Sci. Technol.* **21**, 10–18.

Genzel, C., Denks, I. A., Gibmeier, J., Klaus, M. & Wagener, G. (2007). *The materials science synchrotron beamline EDDI for energy-dispersive diffraction analysis. Nucl. Instrum. Methods Phys. Res. A*, **578**, 23–33.

Genzel, C. & Reimers, W. (2003). *Depth-resolved X-ray residual stress analysis in PVD (Ti, Cr) N hard coatings. Z. Metallkde*, **94**, 655–661.

Gibaud, A. & Hazra, S. (2000). *X-ray reflectivity and diffuse scattering. Curr. Sci.* **78**, 1467–1477.

Guinebretière, R. (2007). *X-ray Diffraction by Polycrystalline Materials.* London: ISTE.

Hauk, V. (1997). *Structural and Residual Stress Analysis by Nondestructive Methods.* Amsterdam: Elsevier.

Heo, K., Yoon, J., Jin, S., Kim, J., Kim, K.-W., Shin, T. J., Chung, B., Chang, T. & Ree, M. (2008). *Polystyrene-b-polyisoprene thin films with hexagonally perforated layer structure: quantitative grazing-incidence X-ray scattering analysis. J. Appl. Cryst.* **41**, 281–291.

Hill, R. (1952). *The elastic behaviour of a crystalline aggregate. Proc. Phys. Soc. A*, **65**, 349–354.

Holy, V., Baumbach, T. & Pietsch, U. (1999). *High-Resolution X-ray Scattering from Thin Films and Multilayers.* Berlin, Heidelberg: Springer-Verlag.

Hosokai, T., Gerlach, A., Hinderhofer, A., Frank, C., Ligorio, G., Heinemeyer, U., Vorobiev, A. & Schreiber, F. (2010). *Simultaneous in situ measurements of X-ray reflectivity and optical spectroscopy during organic semiconductor thin film growth. Appl. Phys. Lett.* **97**, 063301.

Huang, T. C. (1990). *Surface and ultra-thin film characterization by grazing-incidence asymmetric Bragg diffraction. Adv. X-ray Anal.* **33**, 91–100.

Iijima, Y., Kakimoto, K., Yamada, Y., Izumi, T., Saitoh, T. & Shiohara, Y. (2004). *Research and development of biaxially textured IBAD-GZO templates for coated superconductors. MRS Bull.* **29**, 564–571.

Jiang, X., Jia, C. L. & Szyszka, B. (2002). *Manufacture of specific structure of aluminum-doped zinc oxide films by patterning the substrate surface. Appl. Phys. Lett.* **80**, 3090–3092.

Jiang, Z., Li, X., Strzalka, J., Sprung, M., Sun, T., Sandy, A. R., Narayanan, S., Lee, D. R. & Wang, J. (2012). *The dedicated high-resolution grazing-incidence X-ray scattering beamline 8-ID-E at the Advanced Photon Source. J. Synchrotron Rad.* **19**, 627–636.

Kajikawa, Y. (2006). *Texture development of non-epitaxial polycrystalline ZnO films. J. Cryst. Growth*, **289**, 387–394.

Kajikawa, Y., Noda, S. & Komiyama, H. (2003). *Comprehensive perspective on the mechanism of preferred orientation in reactive-sputter-deposited nitrides. J. Vac. Sci. Technol. A*, **21**, 1943–1954.

Kiessig, H. (1931*a*). *Untersuchungen zur Totalreflexion von Röntgenstrahlen. Ann. Phys.* **402**, 715–768.

Kiessig, H. (1931*b*). *Interferenz von Röntgenstrahlen an dünnen Schichten. Ann. Phys.* **402**, 769–788.

Klaus, M., Denks, I. A. & Genzel, C. (2006). *X-ray diffraction analysis of nonuniform residual stress fields $\sigma_{ii}(\tau)$ under difficult conditions. Mater. Sci. Forum*, **524–525**, 601–606.

Klaus, M., Genzel, C. & Holzschuh, H. (2008). *Residual stress depth profiling in complex hard coating systems by X-ray diffraction. Thin Solid Films*, **517**, 1172–1176.

Klaus, M., Reimers, W. & Genzel, C. (2009). *Application of energy-dispersive diffraction to the analysis of highly inhomogeneous residual stress fields in thin film structures. Powder Diffr.* **24**, S82–S86.

Kocks, U. F., Tomé, C. N. & Wenk, H.-R. (1998). *Texture and Anisotropy: Preferred Orientations in Polycrystals and their Effect on Materials Properties.* Cambridge University Press.

Kowarik, S., Gerlach, A., Sellner, S., Schreiber, F., Cavalcanti, L. & Konovalov, O. (2006). *Real-time observation of structural and orientational transitions during growth of organic thin films. Phys. Rev. Lett.* **96**, 125504.

Kuru, Y., Wohlschlögel, M., Welzel, U. & Mittemeijer, E. J. (2008). *Non-ambient X-ray diffraction residual stress analysis of thin films: tracing nanosize-related effects on thermoelastic constants and identifying sources of residual stresses. J. Appl. Cryst.* **41**, 428–435.

Leroy, F., Eymery, J., Buttard, D., Renaud, G., Lazzari, R. & Fournel, F. (2003). *Grazing incidence X-ray scattering investigation of Si surface patterned with buried dislocation networks. Appl. Phys. Lett.* **82**, 2598–2600.

Long, C. J., Bunker, D., Li, X., Karen, V. L. & Takeuchi, I. (2009). *Rapid identification of structural phases in combinatorial thin-film libraries using X-ray diffraction and non-negative matrix factorization. Rev. Sci. Instrum.* **80**, 103902.

Lutterotti, L., Chateigner, D., Ferrari, S. & Ricote, J. (2004). *Texture, residual stress and structural analysis of thin films using a combined X-ray analysis. Thin Solid Films*, **450**, 34–41.

Martinschitz, K. J., Daniel, R., Mitterer, C. & Keckes, J. (2009). *Elastic constants of fibre-textured thin films determined by X-ray diffraction. J. Appl. Cryst.* **42**, 416–428.

Miller, C. E., Majewski, J., Gog, T. & Kuhl, T. L. (2005). *Characterization of biological thin films at the solid–liquid interface by X-ray reflectivity. Phys. Rev. Lett.* **94**, 238104.

Mittemeijer, E. J. & Scardi, P. (2004). *Diffraction Analysis of the Microstructure of Materials.* Berlin: Springer.

Müller-Buschbaum, P. (2009). *Applications of Synchrotron Light to Scattering and Diffraction in Materials and Life Sciences*, edited by M. Gomez, A. Nogales, M. C. Garcia-Gutierrez & T. A. Ezquerra, pp. 61–89. Berlin, Heidelberg: Springer.

Noyan, I. C., Huang, T. C. & York, B. R. (1995). *Residual stress/strain analysis in thin films by X-ray diffraction. Crit. Rev. Solid State Mater. Sci.* **20**, 125–177.

Ohring, M. (2002). *Materials Science of Thin Films: Deposition and Structure.* San Diego: Academic Press.

Ortolani, M., Azanza Ricardo, C. L. & Scardi, P. (2009). *Measurement of stress factors and residual stress of a film by in situ X-ray diffraction during four-point bending. J. Appl. Cryst.* **42**, 1102–1109.

Parratt, L. G. (1954). *Surface studies of solids by total reflection of X-rays. Phys. Rev.* **95**, 359–369.

Pfeiffer, F., Zhang, W. & Robinson, I. K. (2004). *Coherent grazing exit X-ray scattering geometry for probing the structure of thin films. Appl. Phys. Lett.* **84**, 1847–1849.

Rauschenbach, B. & Helming, K. (1989). *Implantation-induced texture. Nucl. Instrum. Methods Phys. Res. B*, **42**, 216–223.

Reuss, A. (1929). *Calculation of the flow limits of mixed crystals on the basis of the plasticity of monocrystals. Z. Angew. Math. Mech.* **9**, 49–58.

Ribárik, G., Ungár, T. & Gubicza, J. (2001). *MWP-fit: a program for multiple whole-profile fitting of diffraction peak profiles by ab initio theoretical functions. J. Appl. Cryst.* **34**, 669–676.

Roncallo, S., Karimi, O., Rogers, K. D., Lane, D. W. & Ansari, S. A. (2009). *An approach to high-throughput X-ray diffraction analysis of combinatorial polycrystalline thin film libraries. J. Appl. Cryst.* **42**, 174–178.

Scardi, P. & Leoni, M. (2002). *Whole powder pattern modelling. Acta Cryst.* A**58**, 190–200.

Stangl, J., Holý, V., Mikulík, P., Bauer, G., Kegel, I., Metzger, T. H., Schmidt, O. G., Lange, C. & Eberl, K. (1999). *Self-assembled carbon-induced germanium quantum dots studied by grazing-incidence small-angle X-ray scattering. Appl. Phys. Lett.* **74**, 3785–3787.

Szczyrbowski, J., Bräuer, G., Ruske, M., Bartella, J., Schroeder, J. & Zmelty, A. (1999). *Some properties of TiO_2 layers prepared by medium frequency reactive sputtering. Surf. Coat. Technol.* **112**, 261–266.

Tagliente, M. A., Falcone, R., Mello, D., Esposito, C. & Tapfer, L. (2001). *On the influence of carbon implantation on the structural properties of hard TiN coatings studied by glancing incidence X-ray diffraction. Nucl. Instrum. Methods Phys. Res. B*, **179**, 42–54.

Takeuchi, I., van Dover, R. B. & Koinuma, H. (2002). *Combinatorial synthesis and evaluation of functional inorganic materials using thin-film techniques. MRS Bull.* **27**, 301–308.

Tolan, M. (1999). *X-Ray Scattering from Soft-Matter Thin Films: Materials Science and Basic Research.* Berlin, Heidelberg: Springer-Verlag.

Vaudin, M. D. (1999). *Proceeding of the 12th International Conference on Textures of Materials*, edited by J. A. Szpunar, pp. 186–191. Ottawa: NRC Research Press.

Voigt, W. (1910). *Lehrbuch der Kristallphysik.* Leipzig: B. G. Teubner.

Weast, R. C. (1986). *Handbook of Chemistry and Physics*, 67th ed. Boca Raton: CRC Press.

Welzel, U., Leoni, M. & Mittemeijer, E. J. (2003). *The determination of stresses in thin films; modelling elastic grain interaction. Philos. Mag.* **83**, 603–630.

Welzel, U., Ligot, J., Lamparter, P., Vermeulen, A. C. & Mittemeijer, E. J. (2005). *Stress analysis of polycrystalline thin films and surface regions by X-ray diffraction. J. Appl. Cryst.* **38**, 1–29.

Wenk, H.-R. & Van Houtte, P. (2004). *Texture and anisotropy. Rep. Prog. Phys.* **67**, 1367–1428.

Wenk, H.-R., Sintubin, M., Huang, J., Johnson, G. C. & Howe, R. T. (1990). *Texture analysis of polycrystalline silicon films. J. Appl. Phys.* **67**, 572–574.

Wohlschlögel, M., Baumann, W., Welzel, U. & Mittemeijer, E. J. (2008). *Determination of depth gradients of grain interaction and stress in Cu thin films. J. Appl. Cryst.* **41**, 1067–1075.

Zaumseil, P. (2005). *RCRefSim: Rocking Curve and Reflectivity Simulation*. IHP, Frankfurt, Germany.

Zhang, W. & Robinson, I. K. (2007). *Grazing exit small angle X-ray scattering on grain formation in polycrystalline metal films. Z. Kristallogr.* **222**, 601–604..

International Tables for Crystallography (2019). Vol. H, Chapter 5.5, pp. 601–616.

5.5. Multigrain crystallography and three-dimensional grain mapping

H. F. Poulsen and G. B. M. Vaughan

5.5.1. List of symbols

2θ: Bragg diffraction angle.

$(\mathbf{x}_l, \mathbf{y}_l, \mathbf{z}_l)$: laboratory frame; $\mathbf{x}_l$ lies along the incident beam, $\mathbf{y}_l$ and $\mathbf{z}_l$ are perpendicular to the incident beam, laterally and vertically.

(x_l, y_l, z_l): position of the origin of a scattering event in the laboratory frame; the centre of mass of a diffracting crystal.

ω: rotation around $\mathbf{z}_l$

η: rotation around $\mathbf{x}_l$

$(x_\omega, y_\omega, z_\omega)$: rotated sample frame.

$\mathbf{\Omega}$, $\mathbf{X}$, $\mathbf{\Theta}$: rotation matrices of a generalized goniometer.

$\mathbf{\Gamma}$: total rotation matrix, $\mathbf{\Gamma} = \mathbf{\Omega X \Theta}$.

$(y_{\rm raw}, z_{\rm raw})$: detector coordinates on the face of the detector.

SC: spatial-distortion operator on the face of the detector.

$(y_{\rm det}, z_{\rm det})$: spatially corrected detector coordinates in the detector frame.

$(\varphi_x, \varphi_y, \varphi_z)$: right-handed detector tilts around $(\mathbf{x}_l, \mathbf{y}_l, \mathbf{z}_l)$.

$\boldsymbol{R}^X$, $\boldsymbol{R}^Y$ and $\boldsymbol{R}^Z$: detector rotation matrices corresponding to rotations of φ_x, φ_y and φ_z, respectively.

$\boldsymbol{R}$: total detector rotation matrix, $\boldsymbol{R}^X\boldsymbol{R}^Y\boldsymbol{R}^Z$.

$[y_{\rm det}(0), z_{\rm det}(0)]$: pixel coordinates for the incident ray passing through $(x_l, y_l, z_l) = (0, 0, 0)$.

P_y, P_z: pixel sizes on the detector face along $\mathbf{y}$ and $\mathbf{z}$.

$\mathbf{G}$: scattering vector (G vector)

$\mathbf{G}_l$, $\mathbf{G}_\omega$, $\mathbf{G}_\gamma$, $\mathbf{G}_s$, $\mathbf{G}_c$, $\mathbf{G}_{hkl}$: G vectors in the laboratory frame, ω frame, rotated frame, sample frame, Cartesian grain frame and reciprocal-lattice frame, respectively.

$\boldsymbol{S}$: rotation of the sample with respect to the goniometer rotation axes.

$\boldsymbol{U}$: rotation of a grain with respect to the sample.

$\boldsymbol{B}$: rotation between the Cartesian grain and reciprocal-lattice frames.

$(\mathbf{x}_c, \mathbf{y}_c, \mathbf{z}_c)$: Cartesian grain frame.

$(\mathbf{a}^*, \mathbf{b}^*, \mathbf{c}^*)$: reciprocal-lattice frame.

(hkl): Miller indices.

$(a, b, c, \alpha, \beta, \gamma)$; $(a^*, b^*, c^*, \alpha^*, \beta^*, \gamma^*)$: lattice parameters in direct and reciprocal space.

$\mathbf{y}$, $\mathbf{h}$, $\mathbf{v}$: unit G vectors in the sample, reciprocal-lattice and laboratory frames.

$\mathbf{u}$: scattering vector in the laboratory frame.

λ: wavelength of the incident radiation.

L: sample-to-detector distance.

$d_{\rm width}$, $d_{\rm height}$: detector width and height in pixels.

t: distance from the point of diffraction to the point of detection.

$\boldsymbol{g}$, $\boldsymbol{g}^*$: metric tensors expressing crystal-lattice size and orientation in direct and reciprocal space.

$(\varphi_1, \phi, \varphi_2)$: Euler angles.

$\mathbf{r}$, $\mathbf{n}$, φ: Rodrigues vector, its rotation axis and angle.

$\mathbf{q}$, $\mathbf{n}$, φ: quaternion, its rotation axis and angle.

$\boldsymbol{\varepsilon}$: strain tensor in direct space.

$(\mathbf{x}_d, \mathbf{y}_d, \mathbf{z}_d)$: basis in crystal coordinates for $\boldsymbol{\varepsilon}$.

$\boldsymbol{A}_0$, $\boldsymbol{A}$: matrices transforming the undeformed and deformed crystal coordinates to the laboratory frame.

$\boldsymbol{T}$: matrix characterizing the crystal deformation with respect to its initial state.

$\boldsymbol{\sigma}$: stress tensor.

$\beta_{\mathbf{k}}$: misorientation of a symmetry-equivalent direction with respect to the fundamental zone.

$\boldsymbol{g}$: $\boldsymbol{U}^{-1}$; sample rotation in Euler space.

5.5.2. Introduction

Conventionally, crystallography is based on either single-crystal or powder diffraction measurements. Such methods apply to two extremes of sample morphology: a homogeneous, mono-domain specimen, or an (ideally) mono-disperse and homogeneous powder comprising a huge number of isotropically oriented crystals. Unfortunately, the morphology of a sample is often a heterogeneous assembly of a finite number of poor crystals, perhaps even including several phases. While perturbative methods allow samples departing significantly from the ideal to be treated, many samples are still inappropriate for crystallographic characterization by these methods, leading to significant effort in sample preparation (see Chapter 2.10). In numerous cases, preparation of suitable single crystals is not possible, *e.g.* in relation to studies in extreme environments, studies involving first-order transitions or more generally cases where suitable crystallization conditions have not been found. In other cases, samples are extremely unstable, making it impossible to collect complete data sets. Structures are now routinely solved and refined from powder-diffraction data, but these structures are intrinsically less well determined than those from single crystals owing to the poorer data-to-parameter ratio and lack of redundancy, making them more prone to statistical and systematic errors. In particular, *ab initio* structure solution based on powder-diffraction data can be highly problematic for structures with more than about 40 atoms in the asymmetric part of the unit cell.

In the last decade, however, methods have been developed for treating polycrystalline specimens as ensembles of individual crystals, creating the possibility of rigorously characterizing such samples in terms of not just average properties, but of the distributions of those properties. In this way, crystallographic techniques developed for analysis of single-crystal data have been generalized to simultaneously characterize each of the crystals in the polycrystalline specimen. In particular, structure solution and refinement on multigrain data have been shown to be on a par with single-crystal work and superior to results from state-of-the-art powder diffraction (Vaughan *et al.*, 2004; Sørensen, Schmidt *et al.*, 2012). Other applications include reciprocal-space mapping (Jakobsen *et al.*, 2006), and characterization of size, strain and defect populations (Ungár *et al.*, 2010). In the following we shall refer collectively to these methods by the term *multigrain crystallography*.

Furthermore, methods such as three-dimensional X-ray diffraction (3DXRD) microscopy (Lauridsen *et al.*, 2001; Poulsen, 2004; Hefferan *et al.*, 2009; Bernier *et al.*, 2011) and diffraction contrast tomography (DCT) (Ludwig *et al.*, 2008, 2009) have emerged which enable 3D mapping of the morphology of the individual embedded crystals – known as grains – as well as 3D mapping of local crystallographic properties such as phase, crystallographic orientation and strain.

Copyright © 2019 International Union of Crystallography

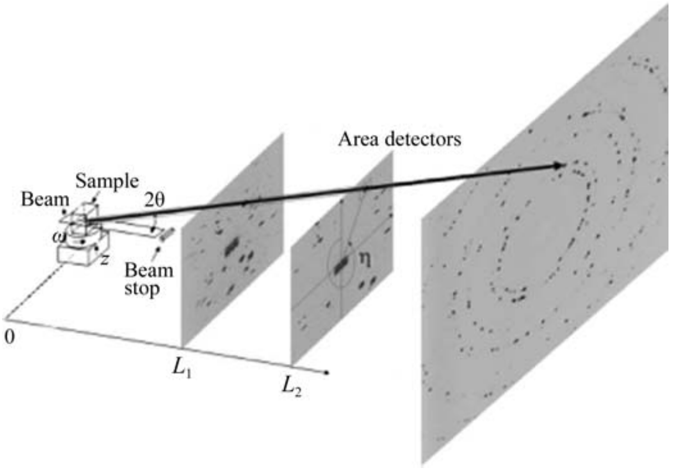

Figure 5.5.1
Sketch of the 3DXRD principle. The Bragg angle 2θ, the rotation angle ω and the azimuthal angle η are indicated for the diffracted beam arising from one grain of a coarse-grained specimen. The axes for the laboratory coordinate system are also shown.

Samples with up to 20 000 grains have been characterized in this way. Currently, the spatial resolution is at best 500 nm (Poulsen *et al.*, 2010). In the following we shall refer collectively to these methods by the term *3D grain mapping*.

Note that when using synchrotron radiation, data-acquisition rates are sufficiently rapid that all of the multigrain methods can be applied recursively during *in situ* studies. This implies a unique opportunity for materials scientists and geoscientists to directly visualize the structural dynamics at the grain level during processing. As examples of such work, studies have been made of nucleation (Offerman *et al.*, 2002; Iqbal *et al.*, 2005; West *et al.*, 2009), recrystallization (Schmidt *et al.*, 2004; Hefferan *et al.*, 2012), grain growth (Schmidt *et al.*, 2008; Hefferan *et al.*, 2009), stress evolution in grains at crack tips (Oddershede *et al.*, 2012) and the interaction of cracks with the 3D microstructure (King *et al.*, 2008). Such work has motivated the construction of dedicated 3D mapping instruments at a number of synchrotrons.

In the following sections, we report on the methodology behind these methods. Initially the experimental setup is presented and a rigorous formalism for the diffraction geometry is introduced. We then discuss methods for polycrystalline indexing and the work on multigrain crystallography is summarized. Next, the work on grain mapping is divided into two sections: centre-of-mass and stress mapping, and 3D grain and orientation mapping. The former type of mapping requires a simpler setup and the data acquisition can be faster, but for each grain only the centre-of-mass position (and the size, orientation and stress state) is determined. The latter types of routines provide a full volumetric mapping of the sample. These sections are followed by three sections of reference material on the representation of orientation space, the representation of strain and stress and on the topic of crystal symmetry for multigrain samples. Finally a short outlook is provided.

A comment on typography: vectors and quaternions are shown as bold, and matrices and tensors are shown as bold italic. (They are distinguishable by their subscripts.)

For a general introduction to the field of multigrain crystallography see also Sørensen, Schmidt *et al.* (2012). For grain mapping we also refer to Poulsen (2004) and Poulsen (2009). A comprehensive mathematical treatment of the geometry of 3DXRD is provided in Alpers *et al.* (2007).

5.5.3. Experimental setup

The setup for multigrain crystallography is identical to that typically used in modern single-crystal or powder crystallography, with a parallel incoming monochromatic beam, a fully illuminated sample in transmission geometry on an ω-rotary table and a 'far-field' 2D detector. Exposures are made during rotation in a manner identical to that used for single-crystal diffraction for equi-angular settings of ω with a step of $\Delta\omega$. As an option, x, y and z translations may be added, as well as additional rotations.

As sketched in Fig. 5.5.1, in a 3DXRD setup additional 2D detectors are added at different distances L from the centre of rotation. These are exposed either simultaneously (many detectors are semi-transparent to hard X-rays) or subsequently, thereby comprising a 3D detector. The added near-field detectors typically have a spatial resolution of 1 to 10 μm and are placed at distances of 2 to 20 mm from the sample. In comparison, the far-field detector typically has a resolution of 50 to 200 μm, with an L value in the range 20 to 50 cm. The high-resolution near-field detectors provide information on positional and orientational degrees of freedom, as well as detailed information about the grain morphology *via* the projections of the grain shape in the diffraction spots, while the latter probes the crystallography, including the potential strain degrees of freedom. Probing direct and reciprocal space simultaneously has several mathematical benefits; for example, it enables ray tracing of the diffracted beam, as illustrated in Fig. 5.5.1.

An example of a set of exposures obtained with this setup is provided in Fig. 5.5.2. Note that in the near-field images the spots are extended (comprising information on grain shape) and form no clear pattern on the detector, as their position is determined by Bragg's law as well as by the positions of the associated grains within the sample. In contrast, in the far-field image the spot sizes are instrumentally limited. Owing to L being much larger than

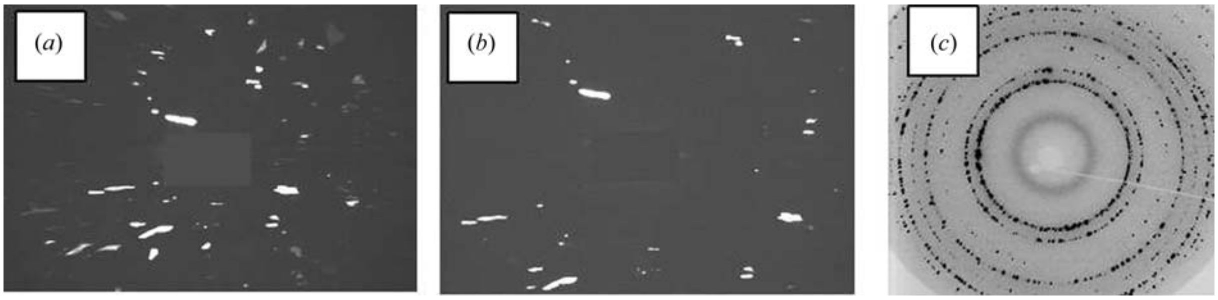

Figure 5.5.2
Typical 3DXRD data from a coarse-grained undeformed polycrystal. (*a*), (*b*) 'Near-field' exposures with high-spatial-resolution detectors (see Fig. 5.5.1) at distances of L = 4 and 8 mm, respectively. (*c*) A corresponding 'far-field' image made with the low-resolution detector at L = 400 mm and shown with inverted grey scale to improve visibility.

the displacement of the grains with respect to the centre of rotation, the positions of grains within the sample now make a small or even vanishing contribution to the positions of the spots, as is the case in conventional crystallography.

In a DCT setup only one near-field detector is used: this serves both to map grains and simultaneously to perform absorption or phase contrast tomography (Ludwig *et al.*, 2008, 2009).

5.5.4. Diffraction geometry

The algebra for associating diffraction observations with reciprocal space is well described for single crystals. The polycrystal case differs by the need for one extra coordinate system, since the sample and the grains are separate objects. In the following, equations describing a single scattering event are derived, first for the case of no detector tilt, then generalized to include such tilts.

The formalism below has served as a standard for the *FABLE* suite of programs (Schmidt *et al.*, 2009). [A closely related treatment can be found in Bernier *et al.* (2011)]. It is subject to the following basic assumptions:

(1) kinematical scattering;

(2) the beam divergence and the energy band width are neglected; and

(3) the relevant part of the sample is assumed to be fully illuminated at all ω settings.

When relevant, the single-crystal formalism of Busing & Levy (1967) is followed closely. However, the sign convention for ω used here is opposite to the one used there.

5.5.4.1. *The laboratory and rotated coordinate systems*

We first consider the basic setup shown in Fig. 5.5.1 with only one rotation axis, which is directed perpendicular to the incoming beam. In this case we define the laboratory system ($\mathbf{x}_l$, $\mathbf{y}_l$, $\mathbf{z}_l$) as having $\mathbf{x}_l$ pointing along the incoming beam, $\mathbf{y}_l$ transverse to it in the horizontal plane and $\mathbf{z}_l$ positive upwards, parallel to the ω rotation axis. Furthermore, ($\mathbf{x}_l$, $\mathbf{y}_l$) = (0, 0) along the ω rotation axis. The definition of $\mathbf{z}_l = 0$ is made by means of a reference beam of infinitesimal size.

In this system the direction of the diffracted ray can be parameterized by the Bragg angle 2θ and the azimuthal angle η, both defined in Fig. 5.5.1. Note that η is defined as positive in the clockwise (cw) direction when viewed along the beam direction from the sample towards the detector and η = 0 when pointing upwards (in the positive direction of $\mathbf{z}_l$). (For historical reasons, this is a left-handed system.)

Next, we define ω positive counterclockwise (ccw) when viewed along the z axis from the top of the instrument. Then

$$\begin{pmatrix} x_l \\ y_l \\ z_l \end{pmatrix} = \boldsymbol{\Omega} \begin{pmatrix} x_\omega \\ y_\omega \\ z_l \end{pmatrix} = \begin{pmatrix} \cos\omega & -\sin\omega & 0 \\ \sin\omega & \cos\omega & 0 \\ 0 & 0 & 1 \end{pmatrix} \begin{pmatrix} x_\omega \\ y_\omega \\ z_l \end{pmatrix}. \qquad (5.5.1)$$

The coordinates (x_ω, y_ω, z_l) refer to the rotated system, which is rigidly attached to the ω turntable. This coordinate system is identical to the sample system, unless the user wants to redefine the latter using a matrix $\boldsymbol{S}$ (see below).

We next consider a more generalized goniometer. Following Busing & Levy, we shall operate with three rotations, namely an outer ω-rotation stage (rotating around the z axis), a χ rotation and an innermost φ stage. The combined rotation is given by

$$\begin{pmatrix} x_l \\ y_l \\ z_l \end{pmatrix} = \boldsymbol{\Gamma} \begin{pmatrix} x_\omega \\ y_\omega \\ z_l \end{pmatrix} = \boldsymbol{\Omega}\mathbf{X}\boldsymbol{\Theta} \begin{pmatrix} x_\omega \\ y_\omega \\ z_l \end{pmatrix}. \qquad (5.5.2)$$

This definition can be used to handle, for example, a Eulerian cradle, a kappa goniometer or a double tilt above the ω axis. We shall leave the exact definition of $\mathbf{X}$ and $\boldsymbol{\Theta}$ to the user. We will assume that the ω rotation is used for scanning/oscillating during actual data acquisition and that this axis is perpendicular to the incident beam.

5.5.4.2. *Detector coordinate systems*

The detector read-out is in a pixel coordinate system. Different detector systems use different conventions for how to flip the image and where to put the origin. Here we define our own standard convention ($y_{\rm raw}$, $z_{\rm raw}$), which is used in equations below. This is a regular grid defined in pixels, as shown in Fig. 5.5.3. Other detector orientations (there are eight in total, considering the origin at any corner, and the detector viewed from the front or the back) may be treated by applying the appropriate unitary transformation matrix to the detector coordinates.

Hence, for the detector-plane normal parallel to the beam, $y_{\rm raw}$ is parallel to $\mathbf{y}_l$ and $z_{\rm raw}$ is parallel to $\mathbf{z}_l$. We define (0, 0) as corresponding to the centre of the pixel in the lower-right corner of the image. This implies that the border of the detection area will have half-integer values.

A spatial distortion, given by the operator SC, may be associated with the detector. We define ($y_{\rm det}$, $z_{\rm det}$) to represent the corrected system:

$$(y_{\rm det}, z_{\rm det}) = {\rm SC}[(y_{\rm raw}, z_{\rm raw})]. \qquad (5.5.3)$$

The detector-plane normal may be tilted with respect to the incoming beam. We define:

φ_x: tilt of detector around x (positive ccw around x: right-handed system);

φ_y: tilt of detector around y (positive ccw around y: right-handed system;

φ_z: tilt of detector around z (positive ccw around z: right-handed system).

Determining SC is typically performed by means of inserting a calibration grid in front of the detector.

Correspondingly we have the associated rotation matrices $\boldsymbol{R}^X$, $\boldsymbol{R}^Y$ and $\boldsymbol{R}^Z$:

$$\boldsymbol{R}^X = \begin{pmatrix} 1 & 0 & 0 \\ 0 & \cos\varphi_X & -\sin\varphi_X \\ 0 & \sin\varphi_X & \cos\varphi_X \end{pmatrix},$$

$$\boldsymbol{R}^Y = \begin{pmatrix} \cos\varphi_Y & 0 & \sin\varphi_Y \\ 0 & 1 & 0 \\ -\sin\varphi_Y & 0 & \cos\varphi_Y \end{pmatrix},$$

$$\boldsymbol{R}^Z = \begin{pmatrix} \cos\varphi_Z & -\sin\varphi_Z & 0 \\ \sin\varphi_Z & \cos\varphi_Z & 0 \\ 0 & 0 & 1 \end{pmatrix}. \qquad (5.5.4)$$

Furthermore, we use the convention that the detector system is rotated with respect to the laboratory system by[1]

$$\boldsymbol{R} = \boldsymbol{R}^X \boldsymbol{R}^Y \boldsymbol{R}^Z. \qquad (5.5.5)$$

We can now express the connection between a point on the detector as defined by pixel coordinates ($y_{\rm det}$, $z_{\rm det}$) and the corresponding point (x', y', z') in the laboratory system:

---

[1] Note that the order in which $\boldsymbol{R}^X$, $\boldsymbol{R}^Y$ and $\boldsymbol{R}^Z$ appear is important, even for relatively small tilts.

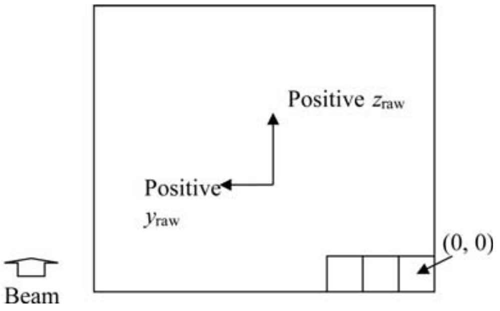

Figure 5.5.3
Definition of the detector pixel coordinate system (see text).

$$\begin{pmatrix} x' \\ y' \\ z' \end{pmatrix} = \begin{pmatrix} L \\ 0 \\ 0 \end{pmatrix} + \boldsymbol{R} \begin{pmatrix} 0 \\ P_y[y_{\text{det}} - y_{\text{det}}(0)] \\ P_z[z_{\text{det}} - z_{\text{det}}(0)] \end{pmatrix}. \qquad (5.5.6)$$

Here $[y_{\text{det}}(0), z_{\text{det}}(0)]$ are the pixel coordinates of the reference beam [the incident ray passing through $(x_1, y_1, z_1) = (0, 0, 0)$], P_y and P_z are the pixel size in the two directions, and L is the distance from the centre of rotation to the point where the incident ray hits the detector.

5.5.4.3. *Diffraction*

The scattering vector associated with the diffraction event is denoted $\mathbf{G}$. To describe its relationship with reciprocal space we need five Cartesian coordinate systems: the laboratory system, the omega system, the rotated system, the sample system and the Cartesian grain system. These are identified by subscripts l, ω, γ, s and c, respectively. The first three have already been defined. Hence, the scattering vector transforms as $\mathbf{G}_l = \boldsymbol{\Omega}\mathbf{G}_\omega = \boldsymbol{\Gamma}\mathbf{G}_\gamma$. (If there is only one rotation axis $\boldsymbol{\Gamma} = \boldsymbol{\Omega}$.)

The sample system is fixed with respect to the sample, as defined *a priori* by the experimentalist. As an example, in metallurgy the sample coordinates are typically defined by the rolling, transverse and normal directions of a rolled sheet (RD, TD and ND, respectively). The orientation of the sample on the ω turntable is given by the $\boldsymbol{S}$ matrix: $\mathbf{G}_\gamma = \boldsymbol{S}\mathbf{G}_s$. By default $\boldsymbol{S} = \boldsymbol{I}$, the identity matrix.

The crystallographic orientation of a grain with respect to the sample is represented by the matrix[2] $\boldsymbol{U}$, $\mathbf{G}_s = \boldsymbol{U}\mathbf{G}_c$, where index c refers to a Cartesian grain system. This system is fixed with respect to the reciprocal lattice $(\mathbf{a}^*, \mathbf{b}^*, \mathbf{c}^*)$ in the grain. We use the convention that $\mathbf{x}_c$ is parallel to $\mathbf{a}^*$, $\mathbf{y}_c$ is in the plane of $\mathbf{a}^*$ and $\mathbf{b}^*$, and $\mathbf{z}_c$ is perpendicular to that plane. Let $\mathbf{G}$ be represented in the reciprocal-lattice system by the integer Miller indices $\mathbf{G}_{hkl} = (h, k, l)^T$. The correspondence between the Cartesian grain system and reciprocal space is then given by the $\boldsymbol{B}$ matrix: $\mathbf{G}_c = \boldsymbol{B}\mathbf{G}_{hkl}$, with

$$\boldsymbol{B} = \begin{pmatrix} a^* & b^*\cos\gamma^* & c^*\cos\beta \\ 0 & b^*\sin\gamma^* & -c^*\sin\beta^*\cos\alpha \\ 0 & 0 & c^*\sin\beta^*\sin\alpha \end{pmatrix} \qquad (5.5.7)$$

and

$$\cos\alpha = \frac{\cos\beta^*\cos\gamma^* - \cos\alpha^*}{\sin\beta^*\sin\gamma^*}, \qquad (5.5.8)$$

Here $(a, b, c, \alpha, \beta, \gamma)$ and $(a^*, b^*, c^*, \alpha^*, \beta^*, \gamma^*)$ symbolize the lattice parameters in direct and reciprocal space, respectively.

With these definitions we have

$$\mathbf{G}_l = \boldsymbol{\Gamma}\boldsymbol{SUB}\mathbf{G}_{hkl}. \qquad (5.5.9)$$

At times it is relevant to operate with normalized scattering vectors instead. Let $\mathbf{u} = \mathbf{G}_l/||\mathbf{G}_l||$, $\mathbf{y} = \mathbf{G}_s/||\mathbf{G}_s||$ and $\mathbf{h} = \boldsymbol{B}\mathbf{G}_{hkl}/||\boldsymbol{B}\mathbf{G}_{hkl}||$. Then

$$\mathbf{u} = \boldsymbol{\Gamma}\boldsymbol{S}\mathbf{y} = \boldsymbol{\Gamma}\boldsymbol{SU}\mathbf{h} = \begin{pmatrix} -\sin\theta \\ -\cos\theta\sin\eta \\ \cos\theta\cos\eta \end{pmatrix}. \qquad (5.5.10)$$

For completeness, we mention that Bragg's law provides an alternative way to determine the norm of the G vectors. Using a formalism that includes 2π in the reciprocal-space definition, the corresponding equation for $\mathbf{h}$ is

$$\begin{pmatrix} h_1 \\ h_2 \\ h_3 \end{pmatrix} = ||\mathbf{G}||^{-1}\boldsymbol{B}\begin{pmatrix} h \\ k \\ l \end{pmatrix} = \frac{\lambda}{4\pi\sin\theta}\boldsymbol{B}\begin{pmatrix} h \\ k \\ l \end{pmatrix}. \qquad (5.5.11)$$

5.5.4.4. *Forward projection, no detector tilt*

Let the diffraction event take place at position (x_l, y_l, z_l) in the laboratory system and be associated with a certain orientation $\boldsymbol{U}$. Assume further we know $\mathbf{X}$ and $\boldsymbol{\Theta}$, the Bravais lattice, the lattice parameters (and therefore $\boldsymbol{B}$) and the X-ray wavelength. The task at hand is then to find the detector coordinates for the diffraction spot associated with a set of Miller indices $\mathbf{G}_{hkl}$.

We may proceed as follows. For each $\mathbf{G}_{hkl}$ first we find $\mathbf{G}_\omega$. The ω position at which the diffraction condition is fulfilled is then given by

$$\sin\theta = -\mathbf{u}_l = -[\boldsymbol{\Omega}\mathbf{G}_\omega]_l \qquad (5.5.12)$$

with $\sin\theta$ defined by Bragg's law. This is a quadratic equation for determination of ω given $\mathbf{G}_\omega$ and $\mathbf{h}$. The two possible solutions are

$$\cos\omega = \frac{ac \pm b(D)^{1/2}}{a^2 + b^2} \text{ and } \sin\omega = \frac{bc \mp a(D)^{1/2}}{a^2 + b^2}, \qquad (5.5.13)$$

where

$$a = \frac{G_{\omega,1}}{|G_\omega|}, \quad b = \frac{-G_{\omega,2}}{|G_\omega|}, \quad c = \frac{(\cos 2\theta) - 1}{[2 - 2\cos 2\theta]^{1/2}}$$
$$\text{and } D^{1/2} = a^2 + b^2 - c^2. \qquad (5.5.14)$$

Evidently the expression for c can be transformed in various ways.

Depending on ω range, none, one or two of these solutions may be real. Also note that (5.5.13) has to be interpreted carefully to obtain ω, because taking only the arccos or arcsin will not do. The proper value of ω has to be chosen to fulfil both equations.

Knowing $\boldsymbol{\Omega}$ we can compute $\mathbf{G}_l$ and $\mathbf{u}$. In the case of an *untilted* detector we have

---

[2] In the texture community it is customary to operate with $\boldsymbol{g} = \boldsymbol{U}^{-1}$. Note that this $\boldsymbol{g}$ is not related to the metric d$\boldsymbol{g}$ as defined in Section 5.5.9.

$$\begin{aligned}P_Y[y_{\rm det} - y_{\rm det}(0)] &= y_l - (L - x_l)\tan 2\theta \sin \eta \\ &= y_l + \frac{(L - x_l)\tan 2\theta}{\cos \theta} u_2 \\ &= y_l + \frac{(L - x_l)\lambda}{2\pi \cos 2\theta} G_{1,2}, \\ P_Z[z_{\rm det} - z_{\rm det}(0)] &= z_l - (L - x_l)\tan 2\theta \cos \eta \\ &= z_l + \frac{(L - x_l)\tan 2\theta}{\cos \theta} u_3 \\ &= z_l + \frac{(L - x_l)\lambda}{2\pi \cos 2\theta} G_{1,3}, \qquad (5.5.15)\end{aligned}$$

where L is the distance from the rotation axis to the detector.

5.5.4.5. *Forward projection with detector tilt and non-centred sample*

A number of different specifications for detector tilts exist. For reference, we introduce two of these below. The origins of the detector coordinate systems are defined in two different reference systems. In one case the origin has to be interpreted as the origin after tilting, while in the other case it is interpreted as the origin before tilting. In both cases we derive the equivalent of (5.5.15): an equation for determining the detector coordinates given a diffraction event in (x_l, y_l, z_l) and the G vector.

First, let us introduce some notation. The detector width and height in pixels are given by $d_{\rm width}$ and $d_{\rm height}$; the corresponding pixel sizes are denoted by P_y and P_z. The detector tilt angles are specified by the matrix $\boldsymbol{R}$ in (5.5.5). We want to compute the actual detector pixels $y_{\rm det}$ and $z_{\rm det}$ recording the diffraction, which takes place at $(x_l, y_l, 0)$ in the laboratory system. The unit directional vector $\mathbf{v}$, along which diffraction occurs, is given by

$$\mathbf{v} = \begin{pmatrix} \cos 2\theta \\ -\sin 2\theta \sin \eta \\ \sin 2\theta \cos \eta \end{pmatrix}. \qquad (5.5.16)$$

5.5.4.5.1. *Detector tilt specification I*

In this specification, the detector origin $[y_{\rm det}(0), z_{\rm det}(0)]$ is defined as the pixel in the tilted detector coordinate system that corresponds to the $(L, 0, 0)^T$ beam centre.

In the laboratory system, the diffracted beam thus hits the detector as expressed by

$$\begin{pmatrix} L \\ 0 \\ 0 \end{pmatrix} + \boldsymbol{R} \begin{pmatrix} 0 \\ P_Y[y_{\rm det} - y_{\rm det}(0)] \\ P_Z[z_{\rm det} - z_{\rm det}(0)] \end{pmatrix} = \begin{pmatrix} x_l \\ y_l \\ 0 \end{pmatrix} + t\mathbf{v}. \qquad (5.5.17)$$

We want to solve the three row equations in (5.5.17) for $y_{\rm det}$, $z_{\rm det}$ and t, the distance from the point of diffraction to the point of detection. The solution for t is

$$t = \frac{R_{11}(L - x_l) - R_{21} y_l - R_{31} z_l}{R_{11} v_1 + R_{21} v_2 + R_{31} v_3}, \qquad (5.5.18)$$

from which we find

$$\begin{aligned}&P_Y[y_{\rm det} - y_{\rm det}(0)] \\ &\quad = R_{12}[(x_l - L) + t v_1] + R_{22}(y_l + t v_2) + R_{32}(z_l + t v_3), \\ &P_Z[z_{\rm det} - z_{\rm det}(0)] \\ &\quad = R_{13}[(x_l - L) + t v_1] + R_{23}(y_l + t v_2) + R_{33}(z_l + t v_3).\end{aligned} \qquad (5.5.19)$$

5.5.4.5.2. *Detector tilt specification II*

In this case, the origin of the detector coordinate system $[y_{\rm det}(0), z_{\rm det}(0)]$ is specified within the laboratory system.

In the laboratory system, the diffracted beam thus hits the detector as expressed by

$$\boldsymbol{R} \begin{pmatrix} 0 \\ P_Y(y_{\rm det} - d_{\rm width}/2 + 1) \\ P_Z(z_{\rm det} - d_{\rm height}/2 + 1) \end{pmatrix} + \begin{pmatrix} L \\ y_{\rm det}(0) \\ z_{\rm det}(0) \end{pmatrix} = \begin{pmatrix} x_l \\ y_l \\ 0 \end{pmatrix} + t\mathbf{v}. \qquad (5.5.20)$$

From this equation we compute t by left-multiplication with the transpose of the first column vector of $\boldsymbol{R}$:

$$t = \frac{R_{11}(L - x_l) - R_{21}[y_{\rm det}(0) - y_l] - R_{31} z_{\rm det}(0)}{R_{11} v_1 + R_{21} v_2 + R_{31} v_3}. \qquad (5.5.21)$$

Left-multiplication with the transpose of the second and third column vectors of $\boldsymbol{R}$, respectively, yields

$$P_Y(y_{\rm det} - d_{\rm width}/2 + 1) = (R_{12}, R_{22}, R_{32}) \left(t\mathbf{v} + \begin{pmatrix} x_l - L \\ y_l - y_{\rm det}(0) \\ -z_{\rm det}(0) \end{pmatrix} \right) \qquad (5.5.22)$$

and

$$P_Z(z_{\rm det} - d_{\rm height}/2 + 1) = (R_{13}, R_{23}, R_{33}) \left(t\mathbf{v} + \begin{pmatrix} x_l - L \\ y_l - y_{\rm det}(0) \\ -z_{\rm det}(0) \end{pmatrix} \right), \qquad (5.5.23)$$

from which we obtain $(y_{\rm det}, z_{\rm det})$.

5.5.5. Indexing

An important simplification arises in the case where the diffraction pattern is composed of a set of primarily non-overlapping diffraction spots. Three examples of such data sets are shown in Fig. 5.5.2. In this case, polycrystalline indexing schemes can be applied readily (Lauridsen *et al.*, 2001).

The starting point for such schemes is peak-search routines, which identify the diffraction spots and determine their centre-of-mass positions in $(y_{\rm det}, z_{\rm det}, \omega)$ space, where $y_{\rm det}$ and $z_{\rm det}$ are the detector coordinates. Next, the directions of the corresponding diffracted X-rays are determined. In the case of the setup illustrated in Fig. 5.5.1, with several near-field detectors, ray tracing may be used. Alternatively or additionally, if acquiring data for a full 360° rotation in ω, Friedel pairs can be used (*e.g.* Ludwig *et al.*, 2009). In the case of far-field data, one may simply assume as a first approximation that all grains are positioned at the centre of rotation.

Assuming that the Bravais lattice of the material is known *a priori*, *e.g.* as the result of a traditional powder-diffraction analysis applied to the polycrystalline data (Vaughan *et al.*, 2004) or because the structure is known, we can associate each diffraction spot with a G vector. Indexing in this case means finding the orientation matrices of the grains in the sample and sorting the G vectors according to grain of origin. Following the presentation of the original polycrystalline indexing program *GRAINDEX* by Lauridsen *et al.* (2001), several alternative approaches have been proposed (Schmidt, 2014; Wright, 2011; Ludwig *et al.*, 2009; Bernier *et al.*, 2011; Sharma *et al.*, 2012). Some of these rely on the use of direct-space information on grain position, which is relevant for materials-science studies of coarse grain specimens but less so for crystallographic studies, where the size of the entire polycrystalline sample may be a few micrometres or less. For reasons of brevity, in the following we shall restrict ourselves to indexing based on orientation relationships between G vectors only.

In a triclinic system each G vector corresponds to one line in 3D orientation space. This line is known in different communities as the projection line, the fibre or the geodesic. Depending on the choice of representation of orientation space, the projection line may be straight or curved (see Section 5.5.11). Any point on this line is consistent with diffraction on the lattice planes defined by the G vector. The projection lines for all the G vectors belonging to a given grain will intersect in one point in orientation space. Hence, one indexing route is to project data into orientation space and search for intersections of lines. For other symmetry groups this route is complicated by the fact that orientation space maps onto itself under crystal symmetry operations. This implies that orientation space becomes tessellated into N regions of different sizes, with N being the number of symmetry operations (*e.g.* 24 for cubic). Furthermore, there will be N projection lines for each measurement (this is further explored in Section 5.5.11),

This approach of finding intersections is implemented in the *GrainSpotter* program (Schmidt, 2014) and has been shown to be very rapid. The complexity of the algorithm increases linearly with N, where N is the number of grains.

Alternatively, forward-simulation programs such as *GRAINDEX* calculate for each trial orientation the corresponding theoretical G vectors. These algorithms loop over orientation space and attempt at any given orientation to match the theoretical G vectors with experimental G vectors in the vicinity. Grains are defined mainly by a completeness criterion on the ratio between observed and expected G vectors. The program *ImageD11* (Wright, 2011), on the other hand, searches pairwise the list of G vectors, looking for those vectors with appropriate angular relationships for the structure under study. Candidate orientations thus generated are then tested against the remaining vectors, and orientations with many matches are retained.

In any case, once grains have been identified, subsequent filtering and optimization algorithms can be applied to fit the centre-of-mass grain positions, grain orientations and stress tensors using, for example, error estimation and outlier rejection (Oddershede *et al.*, 2010; Bernier *et al.*, 2011, Wright, 2011; Sharma *et al.*, 2012). The resulting combined algorithms are able to index as many as 3000 grains simultaneously. Furthermore, for each grain, the lattice orientations, lattice strain tensors and centre-of-mass coordinates may be determined to a precision that is better than 0.05°, 1×10^{-4} and 0.1 pixels, respectively.

The main limitation to the indexing techniques described above is spot overlap. The probability of spot overlap on the detector is determined by the number of grains illuminated, the texture of the sample, the size of the unit cell and – most critically – by the orientation spread of each grain. Experience shows that an overlap fraction of the order of 10% is acceptable for indexing, in the sense that overlapping spots are weeded out by the algorithms because of their erroneous positions and/or intensities. It follows that for typical samples of relevance to hard-materials science, one can aim to index up to a few thousand grains simultaneously, while for small molecules indexing of up to 100 grains is feasible (Sørensen, Schmidt *et al.*, 2012).

For generalizations towards indexing with larger degrees of spot overlap and for indexing of unknown Bravais lattices, see Sørensen, Schmidt *et al.* (2012).

5.5.6. Multigrain crystallography

The basic principle of multigrain crystallography is to extract quality data sets for each grain in the sample and then use existing single-crystal approaches for crystal solution and refinement. In the following we first assume that the sample is monophasic. In this case, as an alternative approach, data from different grains may be scaled and merged in order to create one single data set with increased redundancy. Next, we discuss generalizations to multigrain indexing of unknown multiphase materials.

5.5.6.1. *Monophase materials*

As for other crystallographic applications, the principal problem is to obtain the very accurate intensities necessary for precise structure refinement. Structure solution itself, whether by direct or real-space methods, is rather tolerant of noisy or even systematically faulty data. Structure refinement, however, is very sensitive to outliers, and for accurate structures to be refined they must be eliminated or appropriately down-weighted. In the following we discuss procedures for this filtering step, as described originally in Vaughan *et al.* (2004) and implemented in a series of programs (Vaughan, 2011).

The peaks are first filtered: peaks having too few or too many pixels, those near the rotation axis, those having peak intensities near the dynamic range of the detector and those not allowed by space-group symmetry are eliminated. Intensities are corrected for Lorentz and polarization factors. Additionally, it is possible to correct for lost intensity below the intensity threshold applied in the program by estimation of a peak-shape function from the measured data, either based on the extrapolation of an analytical fit, or *via* a learned empirical function. Correction for absorption is done grain-by-grain based on position within the sample.

If the data for each crystal in the sample are sufficiently redundant, it is possible to perform robust intra-crystal filtering based on equivalent statistics. The data can then be scaled by comparing the relative intensities of equivalent families, and a single data set can be produced by merging the data from all of the crystals, if appropriate. At each step outlier elimination must be carried out. As the outlier distributions are generally highly asymmetric, care must be taken regarding the central tendency indicator chosen for outlier elimination, with either the weighted mean, median or most-likely value (the mode of the histogrammed distribution) being the most appropriate depending on the data set.

The origins of the asymmetry in the intensity distribution are twofold. In particular, if a sample contains many crystals, peaks from other crystals will occur coincidentally near lattice points in reciprocal space occupied by reflections from the crystal in question. Those coming from unindexed crystals create a tail on the high side of the distribution. The tail on the low side of the distribution is due to imperfect treatment of the background. At present, backgrounds are estimated by using either the pixel-by-pixel through the image series median or minimum value. Neither is totally satisfactory, the first tending to overestimate, and the second to underestimate, the true value. In either case, the weakest peaks are the most affected.

By filtering and down-weighting outliers, it is possible to obtain symmetric distributions of equivalent intensities. The widths of these intensity distributions can then be used to more accurately determine the gain of the system, thereby making it possible to convert the measured intensities into counts, and produce proper weights.

Having carried out these steps, it is generally advantageous to use the set of filtered, weighted peaks to re-determine orientation matrices and global parameters, and to iterate through the procedure a second time in order to produce a final data set.

In the first iteration, it is preferable to filter with strict equivalence and statistical criteria in order to produce a data set for structure solution. If solution is successful, Fourier recycling and structure refinement can be carried out, with previously rejected peaks reconsidered at each step as merging parameters are improved. This is done by considering the *expected* value of structure factors, based on estimates of the crystal scale factors and the structure factors calculated by the current structure. Scale factors are thus refined iteratively along with the structure, with outlier rejection or down-weighting also carried out, until a satisfactory structure is obtained.

In order to illustrate the method and test its validity, Vaughan *et al.* (2004) performed an analysis and comparison of the structural results on cupric acetate monohydrate obtained by state-of-the-art high-resolution powder diffraction with the new multigrain crystallography approach. The quality of the two structures was compared with the high-quality structure determined from a single crystal. The final model refined from the polycrystal data gave R_1 of 0.057, and included positions and anisotropic mean-square displacement parameters of all non-H atoms. Furthermore, the H-atom positions of the water molecule could be located in the Fourier map and refined without geometric restraints.

It was not possible to refine the model to anywhere near the same level of detail from the powder data: no meaningful anisotropic displacement parameters for the carbon atoms could be obtained and H-atom positions could not be refined. Comparison of the multigrain structure and powder-diffraction structure with the single-crystal structure showed that the root-mean-square deviations of all positions were 0.0178 Å and 0.0350 Å, respectively. The comparison of the displacement parameters shows that the parameters obtained from multigrain refinement were about 10 times more accurate than the ones obtained from the powder-diffraction experiment. Furthermore, the deviations in bond distances are 2–3 times smaller for the multigrain crystallography structure compared with the powder-diffraction structure.

For an overview of multi-crystal crystallography, see Sørensen, Schmidt *et al.* (2012).

5.5.6.2. *Multiphase materials containing unknown phases*

A multigrain indexing algorithm for use with samples comprising an arbitrary number of known or unknown phases has been presented by Wejdemann & Poulsen (2016). No *a priori* crystallographic knowledge is required. The algorithm is for use with data acquired with a monochromatic beam and a conventional two-dimensional detector. Initially, candidate grains are found by searching for crystallographic planes, using a Dirac comb convoluted with a box function as a filter. Next, candidate grains are validated and the unit cell is optimized. The algorithm is validated by simulations. Simulations of 500 cementite grains and 100 reflections per grain resulted in 99.2% of all grains being indexed correctly and 99.5% of the reflections becoming associated with the right grain. Simulations with 200 grains associated with four mineral phases and 50–700 reflections per grain resulted in 99.9% of all grains being indexed correctly and 99.9% of the reflections becoming associated with the right grain. The main limitations are in terms of overlap of diffraction spots and computing time.

5.5.7. Centre-of-mass and stress mapping

The grain centres of mass (x_l, y_l, z_l) are obtained as fit parameters in the refinement of the orientation matrices, *via* the equations developed in Section 5.5.4. This suggests that these values may be used to make an approximate grain map with no additional input being necessary. In such maps, the grain boundaries are reconstructed *via* indirect methods. As a first approximation, boundaries can be inferred by Voronoi tessellation whereby the distances between grains are simply bisected. This procedure is demonstrated in Fig. 5.5.4, in which the grain boundaries reconstructed by Voronoi tessellation in one layer of a sample are shown. If the grain volumes can also be estimated from the intensities with 10% accuracy or better, this information can be included to improve the tessellation – the so-called modified Laguerre tessellation (Lyckegaard *et al.*, 2011). Laguerre maps have been shown to be more than 85% accurate in terms of voxel assignment to grains, and although the details of the grain boundaries are not characterized, the assignment of neighbouring grains is quite accurate (Lyckegaard *et al.*, 2011).

The generation of centre-of-mass grain maps has been implemented in programs such as *FitAllb* (Oddershede *et al.*, 2010), *ImageD11* (Wright, 2011) and the work by Bernier *et al.* (2011). The maps may be used as the starting point for more detailed reconstructions based on grain projections as described in Section 5.5.8, or used alone to give an approximate indication of the grain distribution.

The centre-of-mass algorithms typically involve fitting 12 parameters per grain: in addition to position and the lattice orientation, the six independent components in the average strain tensor for the grain are also determined. The combined indexing and centre-of-mass algorithms can be highly accurate, allowing the determination of crystallographic strain at the level of $\Delta d/d$

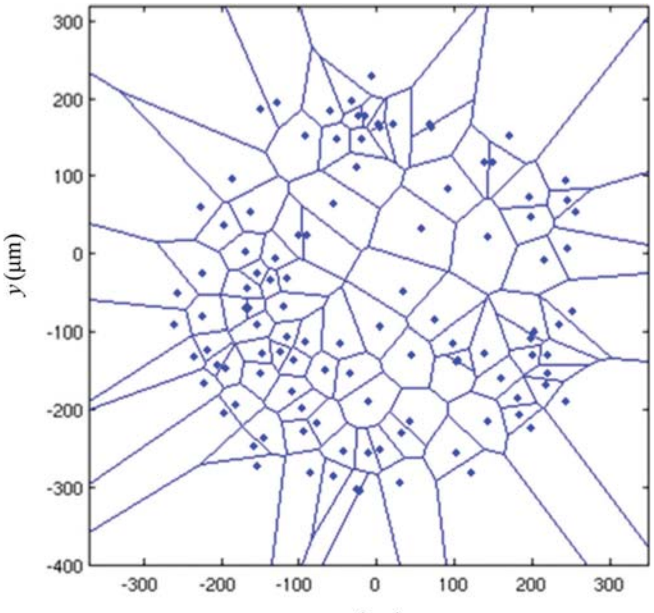

Figure 5.5.4
Grain areas reconstructed by Voronoi tessellation based on experimentally measured centres of mass (the points). In some cases two neighbouring grains have nearly identical centres of mass – an indication in this case of twinning. In an accurately reconstructed map, the measured grain centres will correspond to the centres of the reconstructed grains.

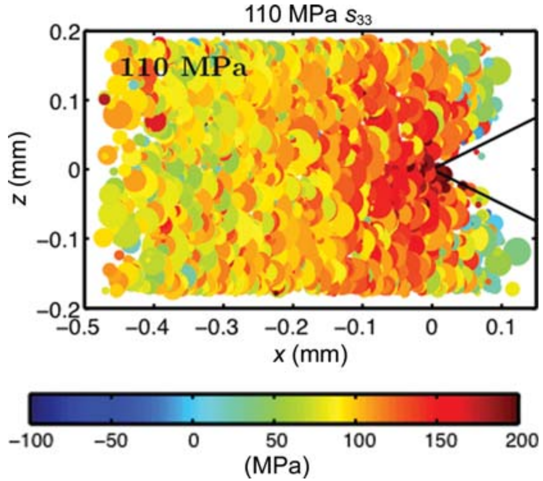

Figure 5.5.5
Stress map of 1750 grains around a notch in an Mg AZ321 sample during tensile deformation. Shown is the axial stress in each grain at an external load of 110 MPa colour coded according to the colour bar at the bottom. The figure represents a 2D projection of the 3D map. The diameters of the spheres represent the grain sizes. Reprinted from Oddershede *et al.* (2012), with permission from Elsevier.

$\simeq 10^{-4}$ and grain orientations to 0.5° precision (Margulies *et al.*, 2002; Martins *et al.*, 2004; Oddershede *et al.*, 2012; Bernier *et al.*, 2011). These properties imply that the method is well adapted to studies of grain rotations (*e.g.* Poulsen *et al.*, 2003). Furthermore, having determined the entire strain tensor for each grain, the corresponding stress tensor can be derived, using Hooke's law; see Section 5.5.10. Fig. 5.5.5 is an example of the application of such stress mapping. In practice this formalism is applicable up to 5–10% plastic deformation; at higher external loads the centre-of-mass algorithms tend to break down because of spot overlap.

5.5.8. 3D grain and orientation mapping

3DXRD microscopy and diffraction contrast tomography (DCT) enable relatively fast generation of large 3D grain maps and 3D orientation maps by use of tomographic reconstruction algorithms. The development of such algorithms is non-trivial, as the complexity in terms of the dimensionality and sheer size of the reconstruction space is much larger than for classical tomography. Another difference is that in 3DXRD and DCT the number of useful projections is given by the number of observable reflections and as such is intrinsically limited (Poulsen, 2004).

In the most general case, some or all of the grains may be smaller than the voxel size and as such the relevant representation is in terms of associating an orientation distribution function, ODF, with each voxel. This implies operating in a numerically very large six-dimensional solution space. Reconstruction algorithms for this case are not routinely available. In practice, focus has been on vector-field reconstructions, where each voxel is associated with one and only one orientation. However, even with this constraint, further simplifications may be required for computational reasons.

An important simplification is the case where the grains are both large in comparison to the voxel size and 'undeformed'; that is, the orientation spread within each grain is negligible. In this case the spatial and angular degrees of freedom are separate, and one may effectively reconstruct *grain maps* rather than orientation maps. Mathematically speaking, the task at hand in this case is to determine the 3D boundary network with as high a precision as possible.

Furthermore, if the diffraction spots do not overlap, one may initially index the various grains, and then reconstruct the 3D morphology of individual grains independently. Powerful methods from the field of discrete tomography can then be applied, allowing for reconstructions even in the case of very few projections (Alpers *et al.*, 2006; Batenburg *et al.*, 2010). The first 3D grain maps were of this kind (Fu *et al.*, 2003).

Another simplification for reconstructing both grains and orientations is the use of a line beam, *cf.* Fig. 5.5.1. In this case, 3D maps are generated by stacking independent reconstructions from a set of layers.

At the time of writing, orientation maps comprising up to 20 000 grains have been obtained. The spatial resolution is of the order 1–5 µm. Using synchrotron sources, the data-acquisition time for a full 3D map is typically of the order of a few hours.

Below we outline two popular approaches for reconstruction.

5.5.8.1. *Approach 1: Grain-by-grain volumetric mapping*

In this approach it is assumed that the grains have negligible orientation gradients. First, the orientations and centres-of-mass of the grains are found, *cf.* Section 5.5.7. Then the 3D shape of each grain is reconstructed. Owing to experimental uncertainties the shapes of the grains will not form a perfect 3D space-filling map, so the last step in the procedure is typically an optimization of the grain-boundary position based on standard image-analysis techniques such as smoothing or erosion/dilation. In practice, the presence of voids can be a concern when the aim is to reach a detailed description of boundary curvatures and triple-junction geometry.

Diffraction contrast tomography (*e.g.* Johnson *et al.*, 2008; Ludwig *et al.*, 2008; King *et al.*, 2008) is performed in this way, as are standard 3DXRD microscopy experiments. As an example of such work, Fig. 5.5.6 shows a grain map of a β-Ti sample reconstructed by the DCT algorithm.

5.5.8.2. *Approach 2: Orientation mapping by Monte Carlo optimization*

Classical transform algorithms are not well suited to handling vector-field reconstructions. Focus has therefore been on Monte Carlo based optimization routines. An example is the forward-

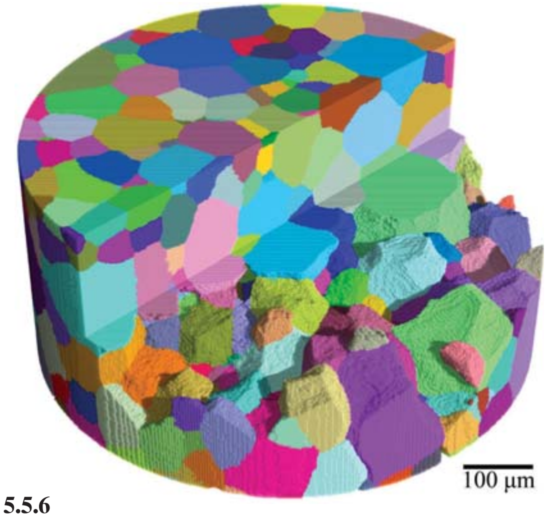

Figure 5.5.6
Rendition of the 3D grain structure in a cylindrical β-Ti specimen containing 1008 grains, as obtained by the DCT algorithm. From Ludwig *et al.* (2008).

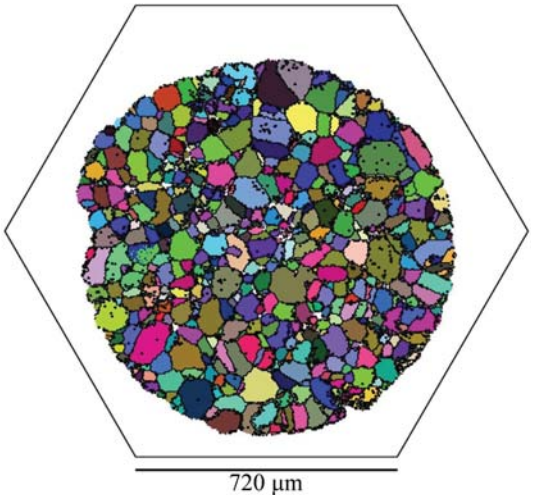

Figure 5.5.7
Map of one layer from a cylinder of high-purity nickel. The orientation (symbolized by colour) of each voxel element was fitted independently. Black lines in the map show edges separating voxels with more than a 2° misorientation. Reprinted from Hefferan *et al.* (2009), with permission from Elsevier.

projection software developed by Suter and collaborators (Hefferan *et al.*, 2009). This is a Monte Carlo Potts model layer-by-layer reconstruction method, where all voxels within the illuminated layer in the sample are free to take all orientations. Experimental work on high purity, well annealed nickel (Hefferan *et al.*, 2009) is reproduced here in Fig. 5.5.7. In this case, statistics on grain orientations, intra-granular misorientations, and nearest-neighbour grain misorientations were compared with statistics obtained from electron-microscopy data. The correspondence was excellent, and it was furthermore demonstrated that the orientation resolution with the setup at 1-ID at the Advanced Photon Source is of order 0.05°. Extensive 3D maps of this kind have been generated with a spatial resolution of 1–2 μm.

This algorithm can also be applied to deformed specimens, but is ultimately limited by the fact that the cross-talk between voxels is not considered. In order to provide a global optimization, it is of interest to reduce the size of configuration space by using known properties of the microstructure. More specifically, assume that prior information – arising for example from an indexing procedure based on far-field information – makes it possible to identify the number of grains, and for each grain determine an approximate average orientation and one voxel in the layer that belongs to this grain. Given these assumptions, Rodek *et al.* (2007) presented a forward-projection Monte Carlo algorithm, where the grains are 'grown' by allowing the following three basic operations:

(1) A voxel not yet assigned to a grain may be assigned to the grain and orientation of a neighbouring voxel.
(2) A labelled voxel may retain its association with a grain while its orientation is changed to an adjacent one in orientation space.
(3) A labelled voxel at a grain boundary may be associated with the grain and the orientation of a neighbouring voxel currently associated with another grain.

This approach was tested on a set of simulated microstructures typical of various degrees of deformation. As an example, in Fig. 5.5.8 the reconstruction of a microstructure with 22 grains and with an internal orientation spread within grains of up to 22° is shown. (In this reproduction it is difficult to see the orientation gradient within the grains.) It can be seen that the reconstruction is nearly perfect.

Finally we mention the *Grainsweeper* program (Schmidt *et al.*, 2008), which has generated a number of 3D grain maps of deformed specimens, for example in connection with 3D mapping of nucleation centres in Al (West *et al.*, 2009) and orientation gradients in 17% NaCl (Borthwick *et al.*, 2012).

5.5.9. Representation of crystallographic orientation

Crystallographic orientations can be expressed in numerous ways, as described in detail in the literature on texture (Kocks *et al.*, 1998; Randl & Engler, 2000). Traditionally four representations are used. The choice between these is non-trivial for numerical reasons. For algebra the natural choice is the 3 × 3 orthogonal matrix $\boldsymbol{U}$ or its inverse (transpose) $\boldsymbol{g}$, as defined above. For visualization and sampling, a representation by three parameters is preferable. The three alternatives are: Euler angles, Rodrigues vectors and unit quaternions. In the following we provide definitions and summarize the most important transforms and geometric properties for each of these representations.

Furthermore, we introduce a novel (fifth) representation based on bounding cubes, with superior numerical properties for some tasks.

5.5.9.1. *Euler angles (Bunge definition)*

Traditionally, orientations are parameterized by a set of Euler angles (φ_1, ϕ, φ_2), expressing sequential rotations around three axes, *cf.* Fig. 5.5.9. With the definitions of the angles as provided by Bunge (1969),

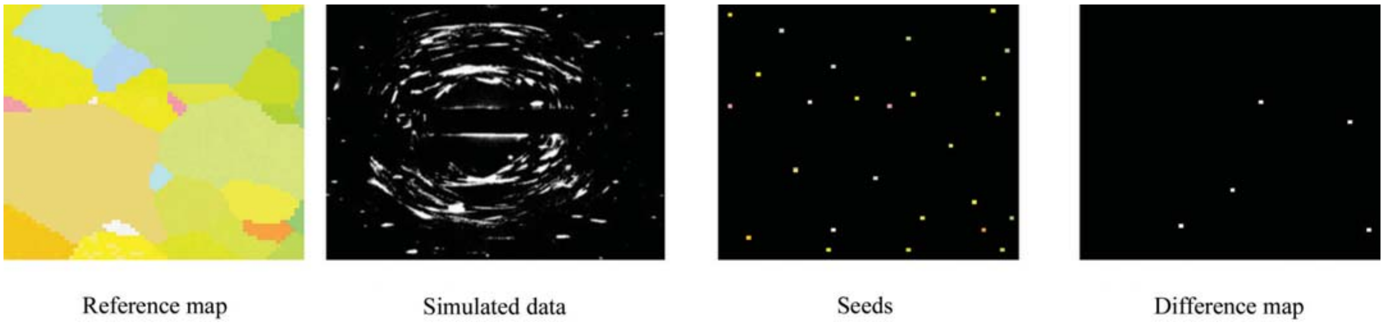
Reference map
Simulated data
Seeds
Difference map

Figure 5.5.8
Monte Carlo based reconstruction of a test case representing 20% deformed aluminium. From left to right: the reference map, with colours representing orientations; an example of the simulated data; the seeds used for the Monte Carlo reconstruction algorithm; and the difference between the reference and the reconstructed grain maps. Black voxels denote voxels correctly identified, white voxels represent mismatching ones. Adapted from Rodek *et al.* (2007).

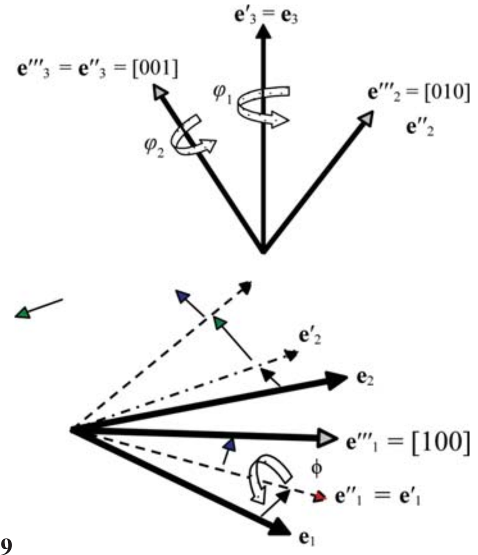

Figure 5.5.9
Definition of the Euler angles (φ_1, ϕ, φ_2) according to Bunge (1969). The sample system ($\mathbf{e}_1$, $\mathbf{e}_2$, $\mathbf{e}_3$) is rotated first around the third axis by φ_1, then around the new first axis $\mathbf{e}'_1$ by ϕ and finally around the new third axis $\mathbf{e}''_3$ by φ_2 to match the Cartesian grain system ($\mathbf{e}'''_1$, $\mathbf{e}'''_2$, $\mathbf{e}'''_3$). For cubic systems the latter set is identical to the reciprocal axes ([100], [010], [001]).

$$\boldsymbol{U} = \begin{bmatrix} c(\varphi_1)c(\varphi_2)-s(\varphi_1)s(\varphi_2)c(\phi) & -c(\varphi_1)s(\varphi_2)-s(\varphi_1)c(\varphi_2)c(\phi) & s(\varphi_1)s(\phi) \\ s(\varphi_1)c(\varphi_2)+c(\varphi_1)s(\varphi_2)c(\phi) & -s(\varphi_1)s(\varphi_2)+c(\varphi_1)c(\varphi_2)c(\phi) & -c(\varphi_1)s(\phi) \\ s(\varphi_2)s(\phi) & c(\varphi_2)s(\phi) & c(\phi) \end{bmatrix}. \tag{5.5.24}$$

Here we have used the shorthand c and s for cos and sin, respectively. The reverse relationship is given by

$$\begin{aligned} \varphi_1 &= -\arctan(U_{13}, U_{23}), \\ \phi &= \arccos(U_{33}), \\ \varphi_2 &= \arctan(U_{31}, U_{32}) \end{aligned} \tag{5.5.25}$$

Note that the two-argument inverse tangent $\arctan(x, y)$ computes $\arctan(x/y)$, but returns the correct angle by taking into account which quadrant (x, y) is in.

Calculating the compound rotation of two individual rotations is very cumbersome in the Euler-angle representation. This should be done using one of the other representations.

Sampling: Euler space is non-linear with singularities at $\phi = 0$ and π. In order to sample it uniformly, use of the metric d$\boldsymbol{g}$ is required (Bunge, 1969):

$$\mathrm{d}\boldsymbol{g}(\phi, \varphi_1, \varphi_2) = (1/8\pi^2)\sin\phi \;\; \mathrm{d}\phi \, \mathrm{d}\varphi_1 \, \mathrm{d}\varphi_2. \tag{5.5.26}$$

Projection lines: From a single diffraction event, only the direction of the scattering vector is probed. Measurements will be invariant to a rotation of the sample around this vector. The set of orientations that for given $\mathbf{y}$ and $\mathbf{h}$ fulfil $\mathbf{y} = \boldsymbol{U}\mathbf{h}$ constitutes a curve in orientation space, the so-called projection line for pole-figure inversion. It is evident from equation (5.5.24) that such lines are curved in Euler space.

5.5.9.2. *Rodrigues vectors*

The Rodrigues representation is in several ways more elegant and better suited for numerical work in connection with diffraction data (Neumann, 1991; Morawiec & Field, 1996; Kumar & Dawson, 2000). It is based on the fact that any rotation can be represented in a unique way by a rotation axis $\mathbf{n}$ and a rotation angle ϕ, defined on $[0, \pi]$. In the Rodrigues parameterization these are coupled in the definition of the Rodrigues vector (Frank, 1998):

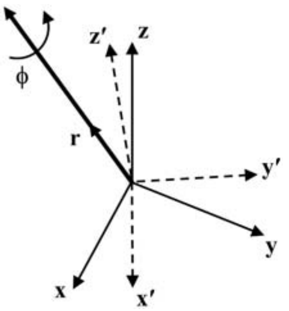

Figure 5.5.10
Definition of the Rodrigues vector $\mathbf{r}$. The coordinate system (x, y, z) is rotated around $\mathbf{n}$ by angle ϕ into (x', y', z'). $\mathbf{r}$ is parallel to $\mathbf{n}$: $\mathbf{r} = \mathbf{n}\tan(\phi/2)$.

$$\mathbf{r} = \tan(\phi/2)\mathbf{n}. \tag{5.5.27}$$

The definition is illustrated in Fig. 5.5.10.

The vector $\mathbf{r}$ can be treated as a vector in Euclidean space, with the exception of points with a rotation angle of π, which are represented by two opposite points in infinity. The axes of this space are colinear with those of the sample system in the sense that a vector $\mathbf{r} = (r_1, 0, 0)$ describes a rotation around the sample x axis.

The relationship to $\boldsymbol{g} = \boldsymbol{U}^{-1}$ is given by

$$g_{ij} = \sum_k \frac{1}{r_k r_k}\left[(1 - r_k r_k)\delta_{ij} + 2r_i r_j - 2\boldsymbol{\varepsilon}_{ijk} r_k\right], \tag{5.5.28}$$

where $\boldsymbol{\varepsilon}_{ijk}$ is the permutation tensor:

$$\boldsymbol{\varepsilon}_{ijk} = \begin{cases} +1 & \text{if } (i, j, k) \text{ is } (1, 2, 3), (2, 3, 1) \text{ or } (3, 1, 2), \\ -1 & \text{if } (i, j, k) \text{ is } (3, 2, 1), (1, 3, 2) \text{ or } (2, 3, 1), \\ 0 & \text{otherwise: } i = j \text{ or } j = k \text{ or } k = i. \end{cases} \tag{5.5.29}$$

The reverse relationship (determining $\mathbf{r}$ given $\boldsymbol{g}$) is given by

$$r_i = \sum_{j,k} \frac{\boldsymbol{\varepsilon}_{ijk} g_{jk}}{1 + \mathrm{Tr}(\boldsymbol{g})}, \tag{5.5.30}$$

where $\mathrm{Tr}(\boldsymbol{g})$ is the trace of $\boldsymbol{g}$. The result $\mathbf{r}_3$ of two rotations, first $\mathbf{r}_1$ and then $\mathbf{r}_2$, is

$$\mathbf{r}_3 = \frac{\mathbf{r}_1 + \mathbf{r}_2 - \mathbf{r}_1 \times \mathbf{r}_2}{1 - \mathbf{r}_1 \cdot \mathbf{r}_2}. \tag{5.5.31}$$

Sampling: The metric d_{ij} and the volume element dV are

$$d_{ij} = \frac{1}{(1 + r^2)^2}[(1 + r^2)\delta_{ij} - 2r_i r_j], \tag{5.5.32}$$

$$\mathrm{d}V = [\det(d_{ij})]^{1/2} = \frac{\mathrm{d}r_1 \, \mathrm{d}r_2 \mathrm{d}r_3}{1 + r^2}. \tag{5.5.33}$$

Evidently this leads to complications for $\mathbf{r} \to \infty$ (that is, for low crystal symmetry, *cf.* Section 5.5.11). On the other hand, for $\phi \to 0$ rotations become commutative. This is reflected in the fact that the metric becomes linear. As an example, for orientation distributions characterized by $\phi < 10^\circ$, the space is Euclidean within an accuracy of better than 1%.

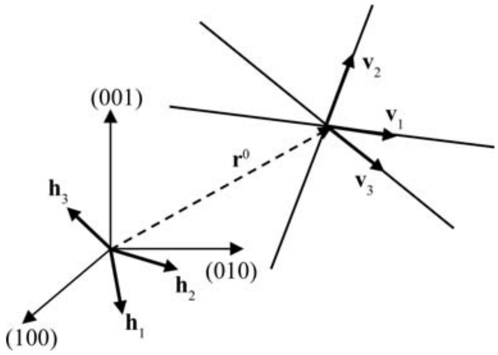

Figure 5.5.11

Symmetry of projection lines through point $\mathbf{r}^0$ in Rodrigues space. The directions of three normalized (h, k, l) vectors ($\mathbf{h}_1$, $\mathbf{h}_2$, $\mathbf{h}_3$) are marked. The associated projection lines pass through $\mathbf{r}^0$ with directions ($\mathbf{v}_1$, $\mathbf{v}_2$, $\mathbf{v}_3$).

Projection lines: A key fact is that the projection lines for pole-figure inversion are straight lines. Specifically, for a given set of vectors $\mathbf{h}$ and $\mathbf{y}$, the projection line is given by

$$\mathbf{r} = \mathbf{r}^0 + t\frac{\mathbf{h} + \mathbf{y}}{1 + \mathbf{h}\cdot\mathbf{y}}, \quad -\infty < t < \infty, \tag{5.5.34}$$

$$\mathbf{r}^0 = \frac{\mathbf{h} \times \mathbf{y}}{1 + \mathbf{h}\cdot\mathbf{y}} = \tan(\phi_0/2)\mathbf{n}, \tag{5.5.35}$$

where $\mathbf{r}^0$ is the rotation from $\mathbf{h}$ into $\mathbf{y}$ with the minimum rotation angle ϕ_0. The second term in equation (5.5.32) corresponds to an arbitrary rotation around the symmetric position $\mathbf{h} + \mathbf{y}$.

For $\phi \to 0$ the expression for the projection line simplifies to

$$\mathbf{r} = \frac{1}{2}(\mathbf{h} \times \mathbf{y}) + \frac{t}{2}(\mathbf{h} + \mathbf{y}). \tag{5.5.36}$$

As a first application of the Rodrigues-vector formalism let us address the following question: for a given orientation $\mathbf{r}^0$, what is the geometry of the projection lines observed?

The answer is illustrated in Fig. 5.5.11, where the full Rodrigues space is used. Assume that the detection geometry and intensity allow the observation of the set of reflections ($\mathbf{h}_1$, $\mathbf{h}_2$, …, $\mathbf{h}_N$). Then it follows that the associated projection lines are straight lines passing through $\mathbf{r}^0$ with the ith line pointing in the direction

$$\mathbf{v}_i = \frac{(\boldsymbol{I} + \boldsymbol{U})\mathbf{h}_i}{1 + \mathbf{h}_i'\boldsymbol{U}\mathbf{h}_i}. \tag{5.5.37}$$

As the expression conserves angles between vectors, the set ($\mathbf{v}_1$, $\mathbf{v}_2$, …, $\mathbf{v}_N$) is a rotation of the set ($\mathbf{h}_1$, $\mathbf{h}_2$, …, $\mathbf{h}_N$). In other words the projection lines associated with a given orientation exhibit the underlying crystal symmetry.

5.5.9.3. *Unit quaternions*

The theory of unit quaternions and their applications to orientations is well developed (Altmann, 1986; Conway & Smith, 2003; Kuipers, 1999; Morawiec, 2004; Meister & Schaeben, 2005). In this section we give only a skeletal development, providing the most relevant definitions.

5.5.9.3.1. *Quaternion basics*

A quaternion $\mathbf{q}$ is a 4-tuple (a, b, c, d) of real numbers. The product of two quaternions is defined by

$$(a_1, b_1, c_1, d_1)(a_2, b_2, c_2, d_2) = (a_3, b_3, c_3, d_3), \tag{5.5.38}$$

where

$$\begin{aligned} a_3 &= a_1a_2 - b_1b_2 - c_1c_2 - d_1d_2,\\ b_3 &= a_1b_2 + b_1a_2 + c_1d_2 - d_1c_2,\\ c_3 &= a_1c_2 - b_1d_2 + c_1a_2 + d_1b_2,\\ d_3 &= a_1d_2 + b_1c_2 - c_1b_2 + d_1a_2. \end{aligned} \tag{5.5.39}$$

Since the non-commutative multiplication is associative, we can use unambiguously the notation $\mathbf{pqr}$ for the product of the three quaternions $\mathbf{p}$, $\mathbf{q}$ and $\mathbf{r}$. Note also that (1, 0, 0, 0) is an identity element; *i.e.*, for any quaternion $\mathbf{q}$ we have $(1, 0, 0, 0)\mathbf{q} = \mathbf{q} = \mathbf{q}(1, 0, 0, 0)$.

The norm of the quaternion (a, b, c, d) is defined by

$$||(a, b, c, d)|| = (a^2 + b^2 + c^2 + d^2)^{1/2}. \tag{5.5.40}$$

It is often helpful to introduce the notation (a, $\mathbf{b}$), where $\mathbf{b}$ is the 3D vector (b, c, d), to abbreviate the quaternion (a, b, c, d). In this way, the conjugate of the quaternion $\mathbf{q} = (a, \mathbf{b})$ is defined as $\overline{q} = (a, -\mathbf{b})$. The conjugate of the product of two quaternions is the reversed product of their conjugates; *i.e.*, $\mathbf{q}_1\mathbf{q}_2 = \overline{q_2 q_1}$.

5.5.9.3.2. *Relation between unit quaternions and orientations*

The set of unit quaternions consists of quaternions whose norm is 1. They form SO(3), the 3-sphere in 4-space, similar to *e.g.* the Earth surface being a 2-sphere in 3-space. From this it follows that unit quaternion space is bounded, the product of two unit quaternions is a unit quaternion, and the conjugate of a unit quaternion is also a unit quaternion.

Every unit quaternion $\mathbf{q}$ defines an orientation, as it can be expressed as

$$\mathbf{q} = (a, \mathbf{b}) = [\cos(\varphi/2), \mathbf{n}\sin(\phi/2)], \tag{5.5.41}$$

where the unit vector $\mathbf{n} = \mathbf{b}/||\mathbf{b}||$ defines the axis and $\varphi = 2\arccos(a/||\mathbf{b}||)$ defines the angle of rotation. Note that $\mathbf{q}$ and $-\mathbf{q}$ define the same orientation. In fact, this mapping from SO(3) to orientation space (*i.e.*, Rodrigues space, Euler-angle space *etc.*) is a 2-to-1 mapping.

A particularly useful and elegant consequence of this approach is that the rotation represented by the unit quaternion $\mathbf{q}_1$ followed by the rotation represented by the unit quaternion $\mathbf{q}_2$ is the composite rotation represented by $\mathbf{q}_2\mathbf{q}_1$.

It follows from equations (5.5.27) and (5.5.41) that there is a gnomonic relationship between Rodrigues vectors and unit quaternions. This implies that one can go back and forth, *e.g.* for visualization in Rodrigues space and for calculations in quaternion space.

Via equation (5.5.41) we can compute for every unit quaternion $\mathbf{q}$ the corresponding $\mathbf{n}$ and φ, and thereby the corresponding Rodrigues vector, and *vice versa*.

The relationship from $\mathbf{q} = (a, b, c, d)$ to $\boldsymbol{U}$ is given by

$$\boldsymbol{U} = \begin{pmatrix} 2(a^2 + b^2) - 1 & 2(bc - ad) & 2(bd + ac) \\ 2(bc + ad) & 2(a^2 + c^2) - 1 & 2(cd - ab) \\ 2(bd - ac) & 2(cd + ab) & 2(a^2 + d^2) - 1 \end{pmatrix}. \tag{5.5.42}$$

The inverse relationship (determining $\mathbf{q}$ given $\boldsymbol{U}$) is, owing to the $\mathbf{q}$ and $-\mathbf{q}$ ambiguities, not uniquely defined. We give only one formula, which is appropriate if and only if $U_{11} + U_{22} + U_{33} \geq -1$:

$$
\begin{aligned}
a &= \frac{1}{2}(U_{11} + U_{22} + U_{33} + 1)^{1/2},\\
b &= \frac{1}{4a}(U_{32} - U_{23}),\\
c &= \frac{1}{4a}(U_{13} - U_{31})\\
d &= \frac{1}{4a}(U_{21} - U_{12}). \qquad (5.5.43)
\end{aligned}
$$

5.5.9.3.3. *Distance*

Following Alpers *et al.* (2007), we define the distance d between two orientations $\mathbf{q}_1$ and $\mathbf{q}_2$ by

$$d(\mathbf{q}_1, \mathbf{q}_2) = \min_{s_1, s_2 \in S} r(\mathbf{q}_1 s_1, \mathbf{q}_2 s_2), \qquad (5.5.44)$$

where S is the set of symmetry rotations given by crystal symmetry (see Section 5.5.11) and r is

$$r(\mathbf{q}_1, \mathbf{q}_2) = 1 - |a_3| = 1 - |\cos(\varphi_{12})|. \qquad (5.5.45)$$

In other words, the distance d is the minimal r when comparing all permutations of symmetry operations. For computing it is relevant to note that it is sufficient to loop over the symmetry operations once, as we can rewrite (5.5.44) to be

$$d(\mathbf{q}_1, \mathbf{q}_2) = \min_{s \in S} r\big((1, 0, 0, 0), s\mathbf{q}_2\overline{\mathbf{q}_1}\big). \qquad (5.5.46)$$

Usually in materials-science literature, the distance $d(\mathbf{q}_1, \mathbf{q}_2)$ is specified by the associated angle of disorientation, which is defined as that ϕ in the range $[0, 180^\circ]$ for which $\cos(\phi/2) = 1 - d$.

Sampling: Knowing that $a^2 + b^2 + c^2 + d^2 = 1$, a discretization by three parameters is possible. The ideal way to do so is not known to the presents authors. Alpers *et al.* (2007) and Kulshreshth *et al.* (2009) chose to sample in a regular grid over the components b, c and d in the interval $[-1, 1]$, allowing only values that satisfy $b^2 + c^2 + d^2 \leq 1$. This sampling leads to neighbouring voxel elements having misorientations that increases with the distance to $\mathbf{q} = (1, 0, 0, 0)$.

Projection lines: In unit-quaternion space the projection lines become circles. Following Meister & Schaeben (2005), the circle for a given set of $\mathbf{h}$ and $\mathbf{r}$ is defined by (under condition $\mathbf{h} \times \mathbf{r} \neq 0$) the two orthogonal unit quaternions $\mathbf{q}_1$ and $\mathbf{q}_2$,

$$\mathbf{q}_1 = \left(\cos(\phi/2), \frac{\mathbf{h} \times \mathbf{r}}{||\mathbf{h} \times \mathbf{r}||}\sin(\phi/2)\right), \quad \mathbf{q}_2 = \left(0, \frac{\mathbf{h} \times \mathbf{r}}{||\mathbf{h} \times \mathbf{r}||}\right), \qquad (5.5.47)$$

where ϕ is defined as the angle between $\mathbf{h}$ and $\mathbf{r}$, that is

$$||\mathbf{h} \times \mathbf{r}|| = 2\cos(\phi/2). \qquad (5.5.48)$$

With these definitions the circle is defined as

$$C(q_1, q_2) = \big\{q(t) = q_1 \cos t + q_2 \sin t\colon\ t \in [0, 2\pi]\big\}. \qquad (5.5.49)$$

5.5.9.4. *Bounding cubes*

The Rodrigues-vector representation has the advantage of straight projection lines, but the disadvantage of singularities and a rather complex formalism for adding orientations [equation (5.5.31)]. Unit quaternions, on the other hand, are not associated with singularities, and exhibit a very simple formula for addition, but the projection lines are circles [equation (5.5.49)].

In 2009, a new formalism was proposed by Kazantsev *et al.* (2009), which combines the superior properties of both representations. The representation is based on a gnomonic projection of SO(3) onto bounding cubes. In order to illustrate the concept, we initially reduce the dimension of the problem by one and consider the corresponding gnomonic projection of SO(2) – the unit sphere in conventional 3D space – onto a union of bounding squares. As illustrated in Fig. 5.5.12, the sphere can be inscribed by the boundary 3-cube, made up of six bounding squares. The sphere can be divided into six patches similar to **abcd**. By drawing straight lines from the origin O to the bounding squares, each point on the sphere is projected onto one and only one point in one of the bounding squares. The bounding squares can be unfolded, that is, mapped onto 2D space. The result is that $F_{\pm 1}$, $F_{\pm 2}$, $F_{\pm 3}$ constitute the unfolded 3-cube.

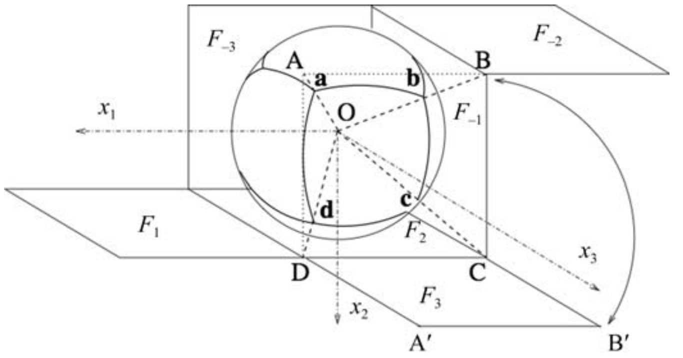

Figure 5.5.12
Three-dimensional illustration of the concepts of bounding squares. The bounding square ABCD (unfolded A′B′CD) is a gnomonic projection of patch **abcd** on the unit sphere centred at O (see text). From Kazantsev *et al.* (2009). Copyright IOP Publishing. All rights reserved.

For the actual problem at hand, SO(3) – the unit sphere in 4D space – is inscribed by the bounding 4D hypercube, made up of eight bounding cubes. The gnomonic projection maps SO(3) onto this union of eight bounding cubes, which again can be unfolded, that is, mapped onto 3D space. The result is that $F_{\pm 1}$, $F_{\pm 2}$, $F_{\pm 3}$, $F_{\pm 4}$ constitute the unfolded 4D hypercube. Given the 2-to-1 mapping of SO(3) on orientations, four bounding cubes are sufficient for representing orientation space.

If $\mathbf{Q} = (q_1, q_2, q_3, q_4)$ is a unit quaternion, let

$$q^{\max} = \max\big\{|q_1|, |q_2|, |q_3|, |q_4|\big\}. \qquad (5.5.50)$$

Then the gnomonic projection is defined by

$$Q \rightarrow (1/q^{\max})Q \in F_{\operatorname{sign}(qk)k}, \qquad (5.5.51)$$

where $F_{\operatorname{sign}(qk)k}$ is the boundary cube given by

$$q^{\max} = q_k \operatorname{sign}(q_k). \qquad (5.5.52)$$

This gnomonic projection (5.5.51) is closely related to the gnomonic projection from SO(3) onto Rodrigues space (5.5.41). This can envisioned as conventional infinite Rodrigues space being replaced by four finite 'versions of Rodrigues space': the bounding cubes. The metric properties are the same.

The projection lines in the bounding-cube representation are a collection of straight linear segments, bounded inside 4, 6 or 8 of the bounding cubes. Attention is required to keep track of the entry and exit of projection lines, but computationally efficient methods have been presented (Kazantsev *et al.*, 2009).

In conclusion, the virtue of the bounding-cube representation is that the singularity has been avoided, while the space is still 'linear'. As an example of an application, algebraic reconstruction algorithms for reconstructing orientation distributions functions (ODFs) can be made orders of magnitude faster in a 'linear' space, which has made it possible to reconstruct ODFs with an unprecedented angular resolution of 0.1°. In the future, the bounding-cube representation is expected to play a role in future algorithms for 3D reconstruction of grain and orientation maps.

5.5.10. Representation of elastic strain

For reference we provide a formalism for deriving the elastic strain tensor and – *via* Hookes law – the corresponding stress tensor.

5.5.10.1. *Definition of strain*

The strain is a perturbation of the local lattice. It is represented by a symmetric 3 × 3 matrix, the strain tensor, $\boldsymbol{\varepsilon}$. Notably, $\boldsymbol{\varepsilon}$ is defined in direct-space coordinates, not in reciprocal space. Hence for each position we define a Cartesian system with axes $(\hat{x}_d, \hat{y}_d, \hat{z}_d)$, with $\hat{x}_d$ parallel to **a**, $\hat{y}_d$ in the plane of **a** and **b**, and $\hat{z}_d$ perpendicular to that plane. By analogy with (5.5.7), the transformation between the crystal basis and the laboratory basis is given by a matrix:

$$\boldsymbol{A} = \begin{pmatrix} a & b\cos\gamma & c\cos\beta \\ 0 & b\sin\gamma & -c\sin\beta\cos\alpha^* \\ 0 & 0 & c\sin\beta\sin\alpha^* \end{pmatrix}. \tag{5.5.53}$$

Now chose a direct-space reference coordinate system and let $\boldsymbol{A}_0$ relate the undeformed Cartesian grain system to this reference, while $\boldsymbol{A}$ relates the deformed Cartesian grain system to the same reference. Furthermore, let $\boldsymbol{T}$ be given by

$$\boldsymbol{T} = \boldsymbol{A}\boldsymbol{A}_0^{-1}. \tag{5.5.54}$$

Then, by definition the strain tensor is

$$\boldsymbol{\varepsilon}_{ij} = \tfrac{1}{2}(\boldsymbol{T}_{ij} + \boldsymbol{T}_{ji}) - \boldsymbol{I}_{ij}, \tag{5.5.55}$$

where $\boldsymbol{I}$ is the identity matrix. This strain tensor, which is defined as the deformation of the lattice relative to the undeformed Cartesian grain system, is sometimes known as the linear Lagrangian strain tensor (Schlenker *et al.*, 1978).

With this general formalism, the relation between the diffraction geometry and the strain is *via* the metric $\boldsymbol{B}$, defined in (5.5.7). If $\boldsymbol{B}$ is known, $\boldsymbol{A}$ can be derived, from which follows $\boldsymbol{\varepsilon}$ by (5.5.54) and (5.5.55). Inversely, if $\boldsymbol{\varepsilon}$ is known, $\boldsymbol{T}$ can be obtained by rearranging (5.5.55); then $\boldsymbol{B}$ can be derived from $\boldsymbol{A} = \boldsymbol{T}\boldsymbol{A}_0$.

Note that the elastic strain tensor calculated above refers to the local Cartesian grain coordinate system. Under the assumption that the orientation of the grain does not change with the deformation, that is $\boldsymbol{U} = \boldsymbol{U}_0$, the strain tensor in the sample coordinate system is given by

$$\boldsymbol{\varepsilon}_{\rm sample} = \boldsymbol{U}\boldsymbol{\varepsilon}\boldsymbol{U}^T. \tag{5.5.56}$$

5.5.10.2. *Strain-to-stress conversion*

The strain tensor $\boldsymbol{\varepsilon}$ is related to the stress tensor $\boldsymbol{\sigma}$ by means of the stiffness tensor $\boldsymbol{C}$, which is a 6 × 6 symmetric matrix where the number of independent terms varies from 21 for triclinic to 3 for cubic space-group symmetry. The easiest way to convert from strain to stress is by writing $\boldsymbol{\varepsilon}$ and $\boldsymbol{\sigma}$ in the Mandel–Voigt notation:

$$\boldsymbol{\varepsilon}^{\rm MV} = \begin{pmatrix} \varepsilon_{11} \\ \varepsilon_{22} \\ \varepsilon_{33} \\ \sqrt{2}\varepsilon_{23} \\ \sqrt{2}\varepsilon_{13} \\ \sqrt{2}\varepsilon_{12} \end{pmatrix}, \quad \boldsymbol{\sigma}^{\rm MV} = \begin{pmatrix} \sigma_{11} \\ \sigma_{22} \\ \sigma_{33} \\ \sqrt{2}\sigma_{23} \\ \sqrt{2}\sigma_{13} \\ \sqrt{2}\sigma_{12} \end{pmatrix}. \tag{5.5.57}$$

We now define the orthogonal rotation matrix in the Mandel–Voigt frame as

$$\boldsymbol{U}^{\rm MV} = \begin{pmatrix} \boldsymbol{U}_1^{\rm MV} & \boldsymbol{U}_2^{\rm MV} \\ \boldsymbol{U}_3^{\rm MV} & \boldsymbol{U}_4^{\rm MV} \end{pmatrix}, \tag{5.5.58}$$

where

$$\begin{aligned} \boldsymbol{U}_1^{\rm MV} &= \begin{bmatrix} U_{11}^2 & U_{12}^2 & U_{13}^2 \\ U_{21}^2 & U_{22}^2 & U_{23}^2 \\ U_{31}^2 & U_{32}^2 & U_{33}^2 \end{bmatrix}, \\ \boldsymbol{U}_2^{\rm MV} &= \sqrt{2}\begin{bmatrix} U_{12}U_{13} & U_{11}U_{13} & U_{11}U_{12} \\ U_{22}U_{23} & U_{21}U_{23} & U_{21}U_{22} \\ U_{32}U_{33} & U_{31}U_{33} & U_{31}U_{32} \end{bmatrix}, \\ \boldsymbol{U}_3^{\rm MV} &= \sqrt{2}\begin{bmatrix} U_{21}U_{31} & U_{22}U_{32} & U_{23}U_{33} \\ U_{11}U_{31} & U_{12}U_{32} & U_{13}U_{33} \\ U_{11}U_{21} & U_{12}U_{22} & U_{13}U_{23} \end{bmatrix}, \\ \boldsymbol{U}_4^{\rm MV} &= \begin{bmatrix} U_{23}U_{32} + U_{22}U_{33} & U_{23}U_{31} + U_{21}U_{33} & U_{32}U_{21} + U_{31}U_{22} \\ U_{13}U_{32} + U_{12}U_{33} & U_{13}U_{31} + U_{11}U_{33} & U_{31}U_{12} + U_{32}U_{11} \\ U_{12}U_{23} + U_{13}U_{22} & U_{21}U_{13} + U_{23}U_{11} & U_{12}U_{21} + U_{11}U_{22} \end{bmatrix}. \end{aligned} \tag{5.5.59}$$

Then (5.5.57) can be rewritten as

$$\boldsymbol{\varepsilon}_{\rm sample}^{\rm MV} = \boldsymbol{U}^{\rm MV}\boldsymbol{\varepsilon}^{\rm MV}. \tag{5.5.60}$$

If the stiffness tensor, which is normally given in the Voigt notation, is now rescaled according to

$$\begin{aligned} C_{ij}^{\rm MV} &= C_{ij} \ \forall\ i,j \in \{1,2,3\}, \\ C_{ij}^{\rm MV} &= \sqrt{2}C_{ij} \ \forall\ i \in \{1,2,3\}, j \in \{4,5,6\}, \\ C_{ij}^{\rm MV} &= \sqrt{2}C_{ij} \ \forall\ i \in \{4,5,6\}, j \in \{1,2,3\}, \\ C_{ij}^{\rm MV} &= 2C_{ij} \ \forall\ i,j \in \{4,5,6\}, \end{aligned} \tag{5.5.61}$$

the conversion goes as

$$\boldsymbol{\sigma}^{\rm MV} = \boldsymbol{C}^{\rm MV}\boldsymbol{\varepsilon}^{\rm MV} \tag{5.5.62}$$

and

$$\boldsymbol{\sigma}_{\rm sample}^{\rm MV} = \boldsymbol{U}^{\rm MV}\boldsymbol{\sigma}^{\rm MV} = \boldsymbol{U}^{\rm MV}\boldsymbol{C}^{\rm MV}\boldsymbol{\varepsilon}^{\rm MV} = \boldsymbol{U}^{\rm MV}\boldsymbol{C}^{\rm MV}(\boldsymbol{U}^{\rm MV})^T\boldsymbol{\varepsilon}_{\rm sample}^{\rm MV}. \tag{5.5.63}$$

The reason for using the Mandel–Voigt notation rather than the traditional Voigt notation is that the former preserves the inner product of the tensor while the latter does not. This is of particular importance because in the elastic regime the work is defined as the inner product of $\boldsymbol{\sigma}$ and $\boldsymbol{\varepsilon}$.

5.5.11. Crystal symmetry in relation to multigrain samples

In texture literature one introduces both crystal and sample symmetry. For multigrain work – as for single grain work – there is no sample symmetry. The crystal symmetry operations associated with a given space group can be found in *International Tables of Crystallography*, Volume A (Aroyo, 2016).

Table 5.5.1
Irreducible part of Euler space for the seven Bravais classes

From Randl & Engler (2000).

Bravais class	ϕ_1	ϕ	ϕ_2
Cubic	[0, 360]	[54, 90]	[0, 90]
Tetragonal	[0, 360]	[0, 90]	[0, 90]
Orthorhombic	[0, 360]	[0, 90]	[0, 180]
Hexagonal	[0, 360]	[0, 90]	[0, 60]
Trigonal	[0, 360]	[0, 90]	[0, 120]
Monoclinic	[0, 360]	[0, 90]	[0, 360]
Triclinic	[0, 360]	[0, 180]	[0, 360]

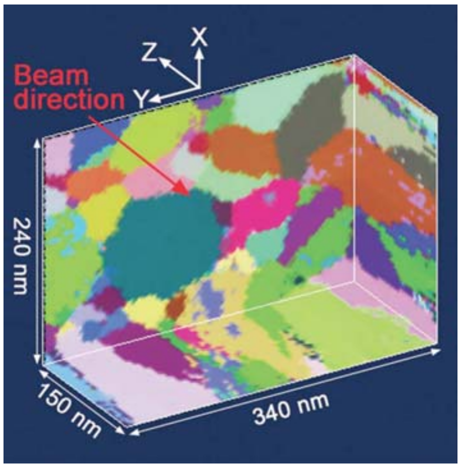

Figure 5.5.13
The TEM equivalent of 3DXRD orientation mapping. The 3D grain-orientation map comprises a subvolume of the fully reconstructed volume within a 150-nm-thick aluminium film specimen. The shades of grey represent different crystal orientations with a tolerance of 2°. The spatial resolution is estimated to be 1 nm. From Liu *et al.* (2011). Reprinted with permission from AAAS.

The crystal symmetry implies that orientation space is divided into a set of N equivalent subspaces, with N being half the number of symmetry operations in the Laue group (*e.g.* 48/2 = 24 for cubic systems; dividing by two allows for the fact that it is not possible to distinguish contributions to the intensity from grains in orientations related by a centre of symmetry). In order to simplify the description we identify one of the subspaces as the fundamental zone. Typically this is chosen to be the subspace around the origin, as this has superior geometric properties in comparison to the other subspaces, such as the orientation space being nearly flat. The output from programs typically refers to the fundamental zone.

5.5.11.1. *Fundamental zone*

The relevant ranges for the Euler representation are given in Table 5.5.1. Note that the threefold axis in cubic materials does not lead to subvolumes that have a rectangular shape in Euler space. The ϕ interval listed in Table 5.5.1 is the one that generates the smallest rectangular box comprising an irreducible volume.

The fundamental zone in Rodrigues space is centred around (0, 0, 0). The geometry of the fundamental zone for various symmetries is described by Morawiec & Fields (1996). The fundamental zone for unit quaternions is centred around (1, 0, 0, 0). The authors have not found a suitable reference to the geometry of the fundamental zone for various symmetries.

5.5.11.2. *Determining the orientation in the fundamental zone*

Given an arbitrary orientation we can determine all the symmetry-equivalent orientations. For each of these we derive the matrix $\boldsymbol{U}_k$. We then calculate the misorientation with respect to the identity matrix, that is, the misorientation with respect to the centre of the fundamental zone:

$$\beta_k = \cos^{-1}\left(\frac{Tr(\boldsymbol{U}_k) - 1}{2}\right). \tag{5.5.64}$$

The symmetry-equivalent orientation with the minimum β_k is the one that represents the fundamental zone.

5.5.11.3. *Use of symmetry-equivalent orientations for strain and stress characterization*

If the system under study is of monoclinic or higher symmetry in the undeformed state, then several different symmetry-equivalent versions of $\boldsymbol{U}$ can be used to describe the orientation of the grain relative to the sample frame. However, when the system is deformed we observe weak symmetry breaking in the lattice permutations. Consequently, in order to extract the evolution of the strain tensor for an individual grain, one must choose a well defined reference frame for the orientation, such that the lattice parameters do not permute from one strain level to the next. This is also important when comparing strain in neighbouring grains. This is done by choosing the symmetry-equivalent version of $\boldsymbol{U}$ that lies in the fundamental zone for each grain in the undeformed state, and then using this same $\boldsymbol{U}$ for all other strain states.

5.5.12. Discussion

In the formalism introduced above we have assumed the specimen to be monophasic. For known phases, extension to multiphase materials is conceptually straightforward, as multi-grain indexing and/or grain-mapping algorithms can be applied repeatedly, once for each phase. An example is the study of martensite formation in TRIP steels by Jimenez-Melero *et al.* (2011).

For grain mapping it may be advantageous to couple mapping based on diffraction contrast with absorption or phase-contrast tomography. Assuming that the density contrast between the phases is sufficient by such hybrid methods, one can first determine a phase map, which is then used as a constraint for the subsequent 3D grain or orientation map. An example of such work is the combined 3DXRD and microtomography study of natural chalk by Sørensen, Hakim *et al.* (2012). Based on existing knowledge, a catalogue of 11 possible phases was made to guide which minority phases to search for in the 3DXRD data.

The 3DXRD methodology has recently been applied to transmission electron microscopy (TEM). Using conical scanning dark-field microscopy in connection with a variant of the *GrainSweeper* reconstruction algorithm, orientation mapping with a spatial resolution in 3D of 1 nm had been demonstrated (Liu *et al.*, 2011). The first example of this was the mapping of a 150-nm-thick foil of nanocrystalline aluminium, see Fig. 5.5.13. The volume in the figure corresponds to a small fraction of the entire illuminated volume, which contained of the order of 1000 grains. However, the acquisition procedure used was slow in the sense that about 100 000 dark-field images were required. It is evident that one of the main limitations of the method (as in TEM tomography) is that it is restricted to electron-transparent foils.

H. F. Poulsen acknowledges support by the European Research Council and by the Danish Council for Independent Research *via* DANSCATT. G. B. M. Vaughan thanks the European Research Council, French Research Program (ANR) and the ESRF for support. The authors acknowledge J. Bernier for the derivations in relation to the strain-to-stress conversion, and S. Schmidt, H.O. Sørensen, J. Wright, W. Ludwig, A. King and J. Oddershede for discussions.

References

Alpers, A., Poulsen, H. F., Knudsen, E. & Herman, G. T. (2006). *A discrete tomography algorithm for improving the quality of three-dimensional X-ray diffraction grain maps. J. Appl. Cryst.* **39**, 582–588.

Alpers, A., Rodek, L., Poulsen, H. F., Knudsen, E. & Herman, G. T. (2007). *Discrete tomography for generating grain maps of polycrystals*. In *Advances in Discrete Tomography*, edited by G. T. Herman & A. Kuba, pp. 271–302. Secaucus: Birkhäuser.

Altmann, S. L. (1986). *Rotations, Quaternions, and Double Groups*. Oxford: Clarendon Press.

Aroyo, M. I. (2016). Editor. *International Tables for Crystallography*, Volume A, *Space-Group Symmetry*, 6th ed. Chichester: Wiley.

Batenburg, K. J., Sijbers, J., Poulsen, H. F. & Knudsen, E. (2010). *DART: a robust algorithm for fast reconstruction of three-dimensional grain maps. J. Appl. Cryst.* **43**, 1464–1473.

Bernier, J. V., Barton, N. R., Lienert, U. & Miller, M. P. (2011). *Far-field high-energy diffraction microscopy: a tool for intergranular orientation and strain analysis. J. Strain Anal. Eng. Des.* **46**, 527–547.

Borthwick, V. E., Schmidt, S., Piazolo, S. & Gundlach, C. (2012). *Quantification of mineral behaviour in 4 dimensions: grain boundary and substructure dynamics in salt. Geochem. Geophys. Geosyst.* **13**, 04057.

Bunge, H. J. (1969). *Matematische Methoden der Texturanalyse*. Berlin: Akademie Verlag.

Busing, W. R. & Levy, H. A. (1967). *Angle calculations for 3- and 4-circle X-ray and neutron diffractometers. Acta Cryst.* **22**, 457–464.

Conway, J. H. & Smith, D. A. (2003). *On Quaternions and Octonions: Their Geometry, Arithmetic, and Symmetry*. Natick: A. K. Peters.

Frank, F. C. (1998). *Orientation imaging. Metall. Trans. A*, **19**, 403.

Fu, X., Poulsen, H. F., Schmidt, S., Nielsen, S. F., Lauridsen, E. M. & Juul Jensen, D. (2003). *Non-destructive mapping of grains in three dimensions. Scr. Mater.* **49**, 1093–1096.

Hefferan, C. M., Li, S. F., Lind, J., Lienert, U., Rollett, A. D., Wynblatt, P. & Suter, R. M. (2009). *Statistics of high purity nickel microstructure from high energy X-ray diffraction microscopy. Comput. Mater. Contin.* **14**, 209–219.

Hefferan, C. M., Lind, J., Li, S. F., Lienert, U., Rollett, A. D. & Suter, R. M. (2012). *Observation of recovery and recrystallization in high-purity aluminum measured with forward modeling analysis of high-energy diffraction microscopy. Acta Mater.* **60**, 4311–4318.

Iqbal, N., van Dijk, N. H., Offerman, S. E., Moret, M. P., Katgerman, L. & Kearley, G. J. (2005). *Real-time observation of grain nucleation and growth during solidification of aluminium alloys. Acta Mater.* **53**, 2875–2880.

Jakobsen, B., Poulsen, H. F., Lienert, U., Almer, J., Shastri, S. D., Sørensen, H. O., Gundlach, C. & Pantleon, W. (2006). *Formation and subdivision of deformation structures during plastic deformation. Science*, **312**, 889–892.

Jimenez-Melero, E., van Dijk, N. H., Zhao, L., Sietsma, J., Wright, J. P. & van der Zwaag, S. (2011). *In situ synchrotron study on the interplay between martensite formation, texture evolution and load partitioning in low-alloyed TRIP steels. Mater. Sci. Eng. A*, **528**, 6407–6416.

Johnson, G., King, A., Honnicke, M. G., Marrow, J. & Ludwig, W. (2008). *X-ray diffraction contrast tomography: a novel technique for three-dimensional grain mapping of polycrystals. II. The combined case. J. Appl. Cryst.* **41**, 310–318.

Kazantsev, I. G., Schmidt, S. & Poulsen, H. F. (2009). *A discrete spherical X-ray transform of orientation distribution functions using bounding cubes. Inverse Probl.* **25**, 105009.

King, A., Johnson, G., Engelberg, D., Ludwig, W. & Marrow, J. (2008). *Observations of intergranular stress corrosion cracking in a grain-mapped polycrystal. Science*, **321**, 382–385.

Kocks, U. F., Tome, C. N. & Wenk, H. R. (1998). *Texture and Anisotropy*. Cambridge University Press.

Kuipers, J. B. (1999). *Quaternions and Rotation Sequences*. Princeton University Press.

Kulshreshth, A., Alpers, A., Herman, G., Knudsen, E., Rodek, L. & Poulsen, H. F. (2009). *A greedy method for reconstructing polycrystals from three-dimensional X-ray diffraction data. Inverse Probl. Imaging*, **3**, 69–85.

Kumar, A. & Dawson, P. R. (2000). *Computational modeling of F.C.C. deformation textures over Rodrigues' space. Acta Mater.* **48**, 2719–2736.

Lauridsen, E. M., Schmidt, S., Suter, R. M. & Poulsen, H. F. (2001). *Tracking: a method for structural characterization of grains in powders or polycrystals. J. Appl. Cryst.* **34**, 744–750.

Liu, H. H., Schmidt, S., Poulsen, H. F., Godfrey, A., Liu, Z. Q., Sharon, J. A. & Huang, X. (2011). *Three-dimensional orientation mapping in the transmission electron microscope. Science*, **332**, 833–834.

Ludwig, W., Schmidt, S., Lauridsen, E. M. & Poulsen, H. F. (2008). *X-ray diffraction contrast tomography: a novel technique for three-dimensional grain mapping of polycrystals. J. Appl. Cryst.* **41**, 302–309.

Ludwig, W., Reischig, P., King, A., Herbig, M., Lauridsen, E. M., Johnson, G., Marrow, T. J. & Buffière, J. Y. (2009). *Three-dimensional grain mapping by X-ray diffraction contrast tomography and the use of Friedel pairs in diffraction data analysis. Rev. Sci. Instrum.* **80**, 033905.

Lyckegaard, A., Lauridsen, E. M., Ludwig, W., Fonda, R. W. & Poulsen, H. F. (2011). *On the use of Laguerre tessellations for representations of 3d grain structures. Adv. Eng. Mater.* **13**, 165–170.

Margulies, L., Lorentzen, T., Poulsen, H. F. & Leffers, T. (2002). *Strain tensor development in a single grain in the bulk of a polycrystal under loading. Acta Mater.* **50**, 1771–1779.

Martins, R. V., Margulies, L., Schmidt, S., Poulsen, H. F. & Leffers, T. (2004). *Simultaneous measurement of the strain tensor of 10 individual grains embedded in an Al tensile sample. Mater. Sci. Eng. A*, **84–88**, 387–389.

Meister, L. & Schaeben, H. (2005). *A concise quaternion geometry of rotations. Math. Meth. Appl. Sci.* **28**, 101–126.

Morawiec, A. (2004). *Orientation and Rotations – Computations in Crystallographic Textures*. Berlin, Heidelberg: Springer.

Morawiec, A. & Field, D. P. (1996). *Rodrigues parameterization for orientation and misorientation distributions. Philos. Mag. A*, **73**, 1113–1130.

Neumann, P. (1991). *Representation of orientations of symmetrical objects by Rodrigues vectors. Textures Microstruct.* **14**, 53–58.

Oddershede, J. B., Camin, B., Schmidt, S. L. P., Mikkelsen, H. O., Sørensen, H. O., Lienert, U., Poulsen, H. F. & Reimers, W. (2012). *Measuring the stress field around an evolving crack in tensile deformed Mg AZ31 using three-dimensional X-ray diffraction. Acta Mater.* **60**, 3570–3580.

Oddershede, J., Schmidt, S., Poulsen, H. F., Sørensen, H. O., Wright, J. & Reimers, W. (2010). *Determining grain resolved stresses in polycrystalline materials using three-dimensional X-ray diffraction. J. Appl. Cryst.* **43**, 539–549.

Offerman, S. E., van Dijk, N. H., Sietsma, J., Grigull, S., Lauridsen, E. M., Margulies, L., Poulsen, H. F., Rekveldt, M. T. & van der Zwaag, S. (2002). *Grain nucleation and growth during phase transformations. Science*, **298**, 1003–1005.

Poulsen, H. F. (2004). *Three-Dimensional X-ray Diffraction Microscopy*. Berlin: Springer.

Poulsen, H. F. (2009). In *Advanced Tomographic Methods in Materials Research and Engineering*, edited by J. Banhart, pp. 249–277. Oxford University Press.

Poulsen, H. F., Ludwig, W., Laudridsen, E. M., Schmidt, S., Pantleon, W., Olsen, U. L., Oddershede, J., Reischig, P., Lyckegaard, A., Wright, J. O. & Vaughan, G. B. M. (2010). *4D characterization of metals by 3DXRD techniques.* In *Proceedings of the 31st Risø International Symposium on Materials Science*, edited by N. Hansen, D. Juul Jensen, S. F. Nielsen, H. F. Poulsen & B. Ralph, pp. 101–119. Roskilde: Technical University of Denmark.

Poulsen, H. F., Margulies, L., Schmidt, S. & Winther, G. (2003). *Lattice rotations of individual bulk grains. Acta Mater.* **51**, 3821–3830.

Randl, V. & Engler, O. (2000). *Introduction to Texture Analysis, Macrotexture, Microtexture and Orientation Mapping*. Boca Raton: CRC Press.

Rodek, L., Poulsen, H. F., Knudsen, E. & Herman, G. T. (2007). *A stochastic algorithm for reconstruction of grain maps of moderately* *deformed specimens based on X-ray diffraction. J. Appl. Cryst.* **40**, 313–321.

Schlenker, J. L., Gibbs, G. V. & Boisen, M. B. (1978). *Strain-tensor components expressed in terms of lattice parameters. Acta Cryst.* A**34**, 52–54.

Schmidt, S. (2014). *GrainSpotter: a fast and robust polycrystalline indexing algorithm. J. Appl. Cryst.* **47**, 276–284.

Schmidt, S., Nielsen, S. F., Gundlach, C., Margulies, L., Huang, X. & Jensen, D. J. (2004). *Watching the growth of bulk grains during recrystallization of deformed metals. Science*, **305**, 229–232.

Schmidt, S., Olsen, U. L., Poulsen, H. F., Sørensen, H. O., Lauridsen, E. M., Margulies, L., Maurice, C. & Juul Jensen, D. (2008). *Direct observation of 3-D grain growth in Al-0.1% Mn. Scr. Mater.* **59**, 491–494.

Schmidt, S., Vaughan, G. B. M., Wright, J., Sørensen, H. O., Oddershede, J., Suchet, G., Knudsen, E., Kieffer, J. & Götz, A. (2009). *FABLE*. http://sourceforge.net/projects/fable/.

Sharma, H., Huizenga, R. M. & Offerman, S. E. (2012). *A fast methodology to determine the characteristics of thousands of grains using three-dimensional X-ray diffraction. II. Volume, centre-of-mass position, crystallographic orientation and strain state of grains. J. Appl. Cryst.* **45**, 705–718.

Sørensen, H. O., Hakim, S., Pedersen, S., Christiansen, B. C., Balogh, Z. I., Hem, C. P., Pasarin, I. S., Schmidt, S., Olsen, U. L., Oddershede, J., Frandsen, C., Feidenhans'l, R. K. & Stipp, S. L. S. (2012). *Non-destructive identification of micrometer-scale minerals and their position within a bulk sample. Can. Mineral.* **50**, 501–509.

Sørensen, H. O., Schmidt, S., Wright, J. P., Vaughan, G. B. M., Techert, S., Garman, E. F., Oddershede, J., Davaasambuu, J., Paithankar, K. S., Gundlach, C. & Poulsen, H. F. (2012). *Multigrain crystallography. Z. Kristallogr.* **227**, 63–78.

Ungár, T., Ribárik, G., Balogh, L., Salem, A. A., Semiatin, S. L. & Vaughan, G. B. M. (2010). *Burgers vector population, dislocation types and dislocation densities in single grains extracted from a polycrystalline commercial-purity Ti specimen by X-ray line-profile analysis. Scr. Mater.* **63**, 69–72.

Vaughan, G. B. M. (2011). *Merge*. http://sourceforge.net/projects/fable/files/Merge.

Vaughan, G. B. M., Schmidt, S. & Poulsen, H. F. (2004). *Multicrystal approach to crystal structure solution and refinement. Z. Kristallogr.* **219**, 813–825.

Wejdemann, C. & Poulsen, H. F. (2016). *Multigrain indexing of unknown multiphase materials. J. Appl. Cryst.* **49**, 616–621.

West, S., Schmidt, S., Sørensen, H. O., Winther, G., Poulsen, H. F., Margulies, L., Gundlach, C. & Juul Jensen, D. (2009). *Direct non-destructive observation of bulk nucleation in 30% deformed aluminum. Scr. Mater.* **61**, 875–878.

Wright, J. P. (2011). *ImageD11*. http://sourceforge.net/projects/fable/files/ImageD11/.

5.6. X-ray diffraction from non-crystalline materials: the Debye model

S. Bates

5.6.1. Outline

In this chapter, the topic of X-ray diffraction from non-crystalline materials will be introduced. Many of the underlying principles behind this work were laid down in the early 1900s by pioneers such as Debye. Since that time, however, the primary focus of X-ray diffraction has been on crystalline materials and structure solution, and much of the early work on non-crystalline materials is not familiar to the diffraction scientist of today. As such, the topics in this chapter are presented at an introductory level from the perspective of an operator using X-ray powder diffraction as a tool to characterize non-crystalline materials.

As a first approximation, non-crystalline materials can be considered to be frozen glassy liquids, and the associated X-ray powder patterns will show a characteristic continuous pattern with a few broad, diffuse halos. There are, however, many diffraction phenomena and classes of materials that will give rise to broad, diffuse features in a measured powder pattern, for example non-crystalline, disordered crystals (Welberry, 2004) and mesophases [such as liquid crystals, plastic crystals or condis (conformationally disordered) crystals (Fu *et al.*, 1994; Chakravarty *et al.*, 2013)]. In each case, the diffuse diffraction contribution arises from a loss of molecular or atomic order. More precisely, diffuse scattering is generated when the local molecular or atomic order differs from the average state of the sample. Within a crystalline system, localized differences might be isolated defects, and for glassy systems, localized differences may relate to short-range order. When X-ray powder patterns exhibit diffuse scattering, this is often referred to as an X-ray amorphous contribution. Within this chapter, diffuse scattering will be used as the general descriptive term rather than X-ray amorphous when the source of the scattering is unknown.

Traditionally, continuous powder diffraction patterns generated by non-crystalline materials have been theoretically described using the Debye diffraction equation, which is based upon the idea of coherent scattering from single atom–atom pairs. This is an ideal starting point for non-crystalline materials, which all exhibit a common atomic level granularity. The bulk of this chapter will be directed towards the Debye diffraction equation and how to implement a Debye diffraction model to characterize experimentally observed continuous diffraction patterns.

In addition to sample-driven diffuse scattering, there are numerous experimental sources of diffuse, continuous X-ray scattering that can include air scatter, fluorescence, Compton scattering and *Bremsstrahlung* radiation. These will vary depending on the diffraction system and the elemental makeup of the sample. Although fluorescence and Compton scattering are both sample dependent and contain elemental information about the sample, for the purposes of diffraction analysis (*i.e.* structural analysis), these contributions along with the instrumental contributions are considered to be background contributions. As diffuse background contributions are essentially continuous like the non-crystalline diffraction component of interest, a critical component of robust analysis of non-crystalline powder patterns will be a data-normalization scheme that includes characterization of the diffuse background. A straightforward normalization procedure can be developed from the Debye diffraction equation and will be referred to as the Debye normalization. Data normalization is such an important part of the analysis of non-crystalline powder patterns that an understanding of the Debye diffraction equation is essential in determining when the Debye normalization can be applied and when it is not appropriate. With appropriate data normalization, non-crystalline powder patterns can be used for quantitative analysis, phase identification and even structural analysis. Because of the essentially continuous diffraction response, chemometric methods (Brereton, 1990; Deming *et al.*, 1988) such as variance and difference analysis along with partial least squares (PLS) and principal component analysis (PCA) become key tools for normalized non-crystalline powder pattern characterization.

5.6.2. Crystalline and non-crystalline: an introduction to the Debye model

The International Union of Crystallography has defined crystalline to refer to any solid that has 'an essentially discrete diffraction diagram' (International Union of Crystallography, 1992). By 'discrete' diffraction diagram it is implied that the measured X-ray diffraction pattern has well defined and resolved diffraction peaks. Inverting the definition, a non-crystalline system can be considered to have a diffraction diagram that is essentially continuous with no discrete diffraction features. The liquid state and solid state are the two high-density states of matter. Generally speaking, the crystalline state is considered to be the equilibrium state for solid forms while the non-crystalline state is considered to be the equilibrium state for liquid forms (Chaikin & Lubensky, 1995). As such, non-crystalline solid forms are usually considered to be metastable or unstable with respect to the underlying crystalline state (if there is one available). For the purpose of powder X-ray diffraction, which probes the average instantaneous local structure, the measured non-crystalline X-ray diffraction from either liquids or solids can be characterized using the same analytical methods. In the following sections, the term non-crystalline will be used to refer to high-density states that are either liquid or solid forms that exhibit an essentially continuous diffraction diagram.

In an ideal sense, the non-crystalline state is one that has the highest symmetry possible for a high-density form, where every atom is equivalent to every other atom in the system. Here 'symmetry' is being used in the mathematical sense where symmetry and entropy may increase together. From the perspective of X-ray diffraction, this ideal high-symmetry state (where every atom is essentially the same average atom) will appear continuous and isotropic on all length scales except the atomic length scale. On the atomic length scale, all ideal non-crystalline systems will exhibit an essential granularity that forms the basis of the characteristic non-crystalline powder pattern. This will be true for large molecular systems, small molecular systems and atomic systems. To achieve the ideal high-symmetry state, the system must be reduced to the common atomic level granularity. In reality, rigid structure within a single molecule and energetic interatomic bonding constraints will resist being deconstructed to a random atomic granularity (depending on the effective temperature of the system). The residual atomic level structure that resists being deconstructed breaks the local continuous symmetry and contributes a unique diffuse scattering component to the continuous powder pattern.

The Debye diffraction equation can be used to model the characteristic diffraction from residual local order based upon the coherent scattering between individual atom–atom pairs. Within the Debye diffraction model, the interference term describing the coherent diffraction intensity for a pair of atoms (A and B) can be written as

$$I(Q)_{\rm interference} = f_A f_B \,{\rm sinc}(Qd_{AB}).$$

The term Q represents the magnitude of the diffraction vector, $\mathbf{Q}$, which can be defined as $4\pi\sin(\theta)/\lambda$, where θ is half the diffraction angle 2θ and λ is the X-ray wavelength (for all calculations within this chapter the X-ray wavelength will be taken to be the mean Cu $K\alpha$ wavelength of approximately 1.5418 Å). Coherent interference is governed by the sinc function, which is defined as ${\rm sinc}(x) = \sin(x)/x$. The term f_A represents the individual atomic form factor of atom A and d_{AB} represents the atom–atom distance between atoms A and B. The coherent interference between diffraction contributions from each atom is represented by the sinc term. The total diffraction from a pair of atoms is then determined by applying the interference term above to every atom–atom combination (A–A, B–B, A–B and B–A) and summing the individual intensity terms:

$$I(Q)_{\rm atom\ pair} = f_A^2 + f_B^2 + 2f_A f_B \,{\rm sinc}(Qd_{AB}).$$

For self-scattering terms A–A and B–B, the distance is zero and the sinc term becomes 1.0.

To calculate the Debye diffraction response for a sample of interest, an atomic level model is required of the coherently related atoms and molecules that make up the sample. The interference term is then applied to every possible atom–atom pair and the resulting coherent intensities summed. Within the framework of the Debye equation, coherently related means atoms that have an essentially constant relative spatial relationship. For example, a single rigid molecule in a low-viscosity liquid might be in continuous motion during a diffraction measurement; however, the intramolecular atom–atom distances remain essentially constant. In this example, the atoms that make up the rigid groups of the molecule are considered to be coherently related for the Debye equation. As a second example, within a perfect single crystal, all the atoms exhibit essentially constant spatial relationships and will, therefore, all contribute to the coherent model. The Debye equation assumes that the coherent scattering from a single pair of atoms is an instantaneous process, with each atom–atom pair scattering independently of all other atom–atom pairs. The total diffraction response from the model sample is, therefore, the sum of the scattered intensities from each coherent atom–atom pair within the model.

In addition to atom coherency, the derivation of the Debye equation implicitly assumes that all orientations of a specific atom–atom pair with respect to the X-ray diffraction vector, $\mathbf{Q}$, are present in the sample. For many non-crystalline and crystalline powder samples this spherical symmetry requirement is satisfied. To help grasp the implicit spherical symmetry requirement within the Debye equation, it can be instructive to consider the application of the Debye equation to both a non-oriented crystalline powder sample and an ideal non-crystalline sample. For a non-oriented crystalline powder sample, within each single crystal, specific atom–atom pairs will be strongly oriented according to the inherent packing symmetry of the crystal. However, the same atom–atom pair will be randomly oriented when averaged throughout the powder sample over many thousands of individual crystals. As the Debye equation calculates the coherently scattered intensity from each individual atom–atom pair (and not the amplitude), the fact that the random orientation is between different crystals in the powder sample is irrelevant to the method. Non-crystalline systems naturally express long-range spherical symmetry with random atom–atom orientation both spatially and temporally. If we consider a specific atom–atom pair within a single molecule in a liquid, then because of the relatively rapid motion of molecules within a non-crystalline liquid from one instantaneous measurement to another, the molecule is likely to have a different orientation with respect to the diffraction vector. As the Debye equation calculates the instantaneous coherently scattered intensity from a specific atom–atom pair, the fact that the random orientation is a time average is also irrelevant to the method. The spherical symmetry requirement inherent in the Debye theory yields a total diffraction response that is also spherically symmetric, depending only on the radial magnitude of the diffraction vector $\mathbf{Q}$. The inherent symmetry of the Debye theory mirrors the inherent symmetry of a powder diffraction pattern collected on an ideally random crystalline powder sample. The relationship between powder patterns and the Debye diffraction response will be explored in later sections.

The Debye equation can in principle be used to calculate total diffraction responses from any material that exhibits random orientation either spatially or temporally, even if there is considerable instantaneous locally average order present. However, building representative atomic level models can be a challenge. To model crystalline systems, the atomic model must be large enough to naturally express the symmetry extinction rules, which often requires many thousands of atoms. For realistic non-crystalline materials, the challenge is to develop multiple instantaneous models sufficient to express conformational flexibility and variation in local packing arrangements (*i.e.* configurational entropy). This will also involve many thousands of atoms and can present a considerable computational challenge. In subsequent sections, the term 'locally average' order will be used to refer to a local ensemble of atom–atom distances that commonly occur within a sample. The averaging is performed over the time of the measurement and the volume of the sample with each atom–atom coherent diffraction event being local and instantaneous. Within a non-oriented crystalline powder, for example, the locally average order can be represented by the crystalline symmetry. For a non-crystalline material, the locally average order can be represented by an instantaneous cluster of molecules that commonly forms over the duration of the measurement.

The absence of any discrete features within a non-crystalline powder pattern is indicative of the absence of any average 'crystalline'-like order within the sample; *i.e.* macroscopically, the samples exhibit no specific average structure. However, the various halos and bumps that are observed in a non-crystalline powder pattern arise from the locally average order within the sample. For diffraction measurements, the specific atoms involved in the locally averaged order need not be chemically bound to each other, just spatially correlated. For organic molecules used as working examples within the following sections, the locally averaged order can arise from either intramolecular or intermolecular relationships. These form the internal and external terms of the Debye diffraction intensity sum. Organic molecules will typically have a well defined molecular structure, the rigid parts of which will give reproducible atom–atom distances within a non-crystalline sample. This represents the locally average intramolecular order. However, the observed average length scales of the intramolecular order will be limited by the length scale of commonly occurring structure (*e.g.* C—C bonds) within the molecule and its inherent conformational flexibility. In a non-crystalline system, a molecule is free to explore its available conformations without the constraints of periodicity; as such, molecular rigidity will directly influence the observed non-crystalline powder pattern.

The demands of high local packing density combined with the specific shape of organic molecules will often favour characteristic packing configurations (cybotaxis; Stewart, 1928). The atom–atom distances between molecules that exhibit specific local packing configurations represent the locally average intermolecular order. Because of the constraints of van der Waals type interactions between organic molecules, as a rule of thumb, intermolecular atom–atom distances are usually larger than 3.0 Å. For the Cu $K\alpha$ X-ray wavelength, 3.0 Å is approximately 30° 2θ. Thus, as a general rule, features observed in a non-crystalline powder pattern above about 30° 2θ arise from locally average intramolecular order. Features observed at angles lower than 30° 2θ can be due to either inter- or intramolecular order, but are typically due to local average intermolecular order.

5.6.3. Application of the Debye equation to a single molecule

The diffraction equations developed within this chapter will be based around the diffraction vector, **Q**, which defines a distance (magnitude) and direction in diffraction space. For non-crystalline materials, which will typically be isotropic in nature, diffraction space will be essentially spherically symmetric about the origin, and the variable of interest will be the magnitude of the diffraction vector Q. As expressed earlier, the magnitude can be written as $4\pi\sin(\theta)/\lambda$ or, using the Bragg transformation, the magnitude can be expressed as $2\pi/d$, where d is a characteristic distance within the sample. However, it must be pointed out that halos observed for non-crystalline materials do not follow Bragg's law and that the fundamental local distances in a non-crystalline sample can only be approximated through the use of the Bragg transformation. A rule of thumb (Guinier, 1994) suggests that a local distance x underlying an observed non-crystalline halo can be related to the Bragg d (calculated from the halo position) through the expression ($1.1d < x < 1.25d$). The exact nature of the relationship will depend on the local packing symmetry and the slope of the atomic form factor.

The Debye diffraction equation is a deceptively simple kinematic diffraction equation, being a sum over the scattered intensity from each atom–atom pair in the molecular model under study. However, the Debye equation expresses the total diffraction from a model sample and as such can give rise to complex calculated diffraction patterns that can be difficult to interpret from the perspective of Bragg or Laue diffraction. Furthermore, the formal application of the Debye equation requires detailed molecular/atomic models that fully express the structural features of interest.

The formal Debye diffraction intensity equation for a model of coherently related atoms can be written as (James, 1948)

$$I_D(Q) = \sum_{i=1}^{n} f_i^2 + 2\sum_{i,j=1,i\neq j}^{n} f_i f_j \sin(Qd_{ij})/(Qd_{ij}),$$

where the indices i and j run over all atoms in the model ($1 \rightarrow n$), f_j represents the individual atomic form factors, and d_{ij} is the atom–atom distance for each pair of different atoms i and j. The individual atomic form factors, f_j, implicitly depend on the magnitude of the diffraction vector, Q, and the X-ray wavelength used. The second term within the Debye equation is a weighted sinc function that generates the structural interference effects observed for coherently ordered systems. For large Q, the sinc function tends towards zero and the Debye equation reduces towards the independent coherent intensity function (James, 1948), which is the incoherent sum of the squared atomic form factors for all atoms i within the model. Although all atoms are scattering independently and incoherently with respect to each other, electrons within each atom are scattering coherently; hence the term 'independent coherent intensity':

$$I_{\rm ind}(Q) = \sum_{i=1}^{n} f_i^2.$$

As Q approaches zero, the Debye equation tends towards the coherent intensity function, which is the coherent sum of the atomic form factors for all atoms i within the model, squared:

$$I_{\rm coh}(Q) = \left(\sum_{i=1}^{n} f_i\right)^2.$$

The independent coherent intensity, $I_{\rm ind}(Q)$, scales with the number of atoms in the model system, while the coherent intensity, $I_{\rm coh}(Q)$, scales with the square of the number of atoms. At larger values of Q, the first term in the Debye equation is likely to dominate, and the scattered intensity from any model (sample) should approach the independent coherent intensity function. This is an important asymptotic behaviour at large Q that allows data measured on different samples and different X-ray instruments to be normalized to a common intensity framework, which is a required first step for robust analysis of measured non-crystalline powder patterns. The asymptotic high-angle behaviour of the Debye equation forms one aspect of the Debye normalization of measured powder patterns.

As Q approaches zero, the Debye equation collapses to the coherent intensity function that represents the maximum coherently scattered intensity when all atoms in the model are scattering in phase. This will typically only occur close to zero Q (the 000 reflection for crystalline materials) but may also occur at other Bragg-peak positions for simple atomic crystals (*e.g.* the 400 reflection for silicon).

For the purposes of exploring the Debye equation in more detail, the organic molecule mannitol ($C_6H_{14}O_6$) will be used as an initial example. The physical molecular structure used in the Debye model was extracted from a beta mannitol crystal structure [Cambridge Structural Database (CSD; Groom *et al.*, 2016) refcode DMANTL07 (Kaminsky & Glazer, 1997)] (see Fig. 5.6.1).

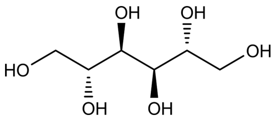

Figure 5.6.1
A chemical structure diagram for mannitol.

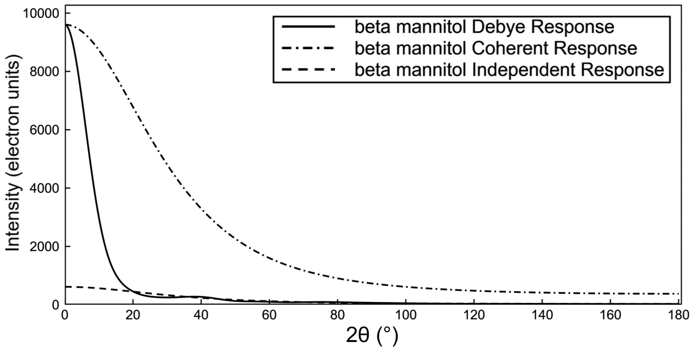

Figure 5.6.2
Calculated Debye diffraction response for a single mannitol molecule displayed with the coherent and incoherent diffraction responses. The *y* axis is in electron units.

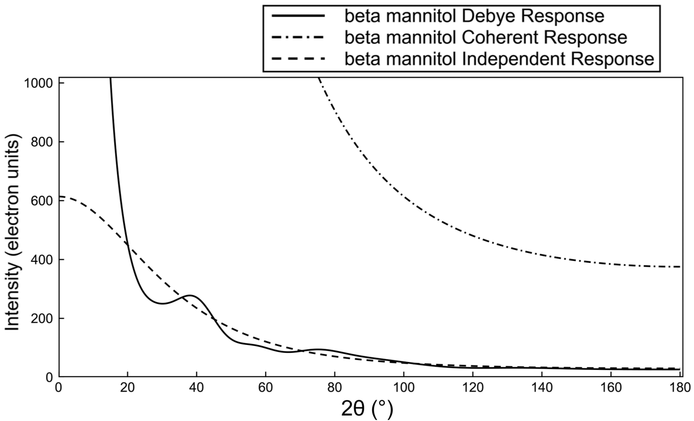

Figure 5.6.3
Zoomed-in view of Fig. 5.6.2 to show the oscillatory coherent diffraction response from a single mannitol molecule and the asymptotic high-Q behaviour approaching the independent coherent diffraction response.

Assuming that the non-crystalline sample of interest can be described as an ensemble of randomly packed non-interacting single mannitol molecules, and that the mannitol molecules are rigid (which, essentially, they are), then a single mannitol molecule is statistically representative of the locally average structure within the sample. This assumes that all molecules in the non-crystalline system scatter X-rays independently and incoherently with respect to each other, *i.e.* a complete absence of any intermolecular order. In principle, it might be expected that the Debye equation as applied to a single mannitol molecule should, therefore, give a reasonable description of the form of the expected diffraction response for the ideally random non-crystalline sample. In practice, as the Debye equation expresses the total diffraction response from any given molecular model, there are model-specific diffraction phenomena that have to be considered before a representative powder pattern can be calculated. In this mannitol example, the individual diffraction components generated by the Debye equation will be investigated from a rational and practical perspective. Figs. 5.6.2 and 5.6.3 show the calculated Debye diffraction response for a single mannitol molecule plotted against the independent, $I_{\rm ind}(Q)$, and coherent, $I_{\rm coh}(Q)$, diffraction functions. As a reality check, the $Q \to 0$ value for coherent intensity should tend towards the square of the number of electrons in a single mannitol molecule. Mannitol has 98 electrons per molecule giving a maximum coherent intensity response of 9604 electron units for a single molecule. The $Q \to 0$ value for the independent intensity should tend towards the sum of the squared number of electrons per atom. For $C_6H_{14}O_6$ this sum of squares is 614 electron units. The falloff in intensity observed in Fig. 5.6.3 for the independent diffraction function reflects the inherent Q dependence of the squared atomic form factors. For organic materials, the intensity falloff as a function of Q will be more severe than for inorganic materials.

Fig. 5.6.2 shows the $Q \to 0$ response for the Debye intensity function approaching the coherent diffraction function while Fig. 5.6.3 shows the asymptotic high-Q behaviour approaching the independent coherent diffraction response. The calculated Debye response has a dominating low-angle peak corresponding to the coherent scattering of all atoms in the model at small scattering angles. Measured diffraction patterns of organic molecular non-crystalline materials will typically exhibit a broad diffraction halo in the range of about 15.0 to 25.0° 2θ. This broad diffraction feature usually represents the highest diffraction intensity in the measured data. The continuously increasing diffraction intensity below about 60.0° 2θ observed in the calculated Debye response, Fig. 5.6.3, does not follow the intensity trend typically observed experimentally. While the calculated Debye diffraction response in Fig. 5.6.3 accurately represents the diffraction from a single mannitol molecule, it is not representative of a real bulk non-crystalline sample. The Debye diffraction model is a total diffraction model requiring that the sample be fully described within the associated molecular model. Following a thought experiment from James (1948), if the non-crystalline model is expanded from a single mannitol molecule to incorporate M random mannitol molecules with each molecule being incoherently related to every other molecule, then the sample diffraction response is simply the sum of the individual molecular Debye diffraction intensities over all M molecules:

$$I_{\rm sample}(Q) = M \times I_D(Q).$$

Within this model, the predicted intensity as $Q \to 0$ is simply $(M \times I_{\rm coh})$, which is incorrect. As with all molecular samples, the predicted intensity as $Q \to 0$ must be $M^2 \times I_{\rm coh}$. The missing intensity is due to the coherent diffraction contribution of all molecules in the physical sample at zero diffraction angle. For an ensemble of molecules in a solid continuum, the appearance of this low-angle coherent diffraction response is related to the physical ‘shape’ of the sample itself. The sample ‘shape’ is the physical bounding envelope containing all the randomly packed molecules. The role of ‘shape’ and molecular packing will be considered in more detail in Sections 5.6.11 and 5.6.12. For now, the ‘shape’ contribution is considered to be the small-angle scattering contribution from the physical sample. To continue the thought experiment, as a first approximation, the dominating low-angle Debye response can be taken to be related to the small-angle scattering response of a single free-standing molecule. A bulk non-crystalline sample will contain individual molecules embedded in an essentially isotropic continuum of electron density. As such, the small-angle scattering contribution from the physical shape of a single molecule will not be observed, being replaced by the small-angle scattering due to the bulk sample shape.

Various models have been proposed in an attempt to describe the dominating small-angle response (Debye, 1915; Guinier, 1994; James, 1948) in a manner that allows it to be mathematically removed from the calculated powder pattern. To remove the single-molecule small-angle X-ray scattering (SAXS) response within the spirit of the Debye equation, a molecular model would have to be generated containing many hundreds or thousands of randomly packed molecules, giving a volume large enough such that the ensemble SAXS response sharpens up and moves to lower angles. In this case, the calculated pattern more closely resembles measured non-crystalline powder patterns. However, it can be a challenge to generate a set of packed molecules that has an essentially random character and the computational overhead in applying the Debye equation can be significant for large molecular clusters. To provide a partial solution to the SAXS response based upon single-molecule models, Menke published a modification to the original Debye equation (James, 1948).

5.6.4. The Debye–Menke equation

To account for the high-density packing of complex molecules, Menke extended the Debye equation to include a molecular scattering function and a radial distribution function for each molecule (Menke, 1932). Following the review of the Menke extension as presented by James (1948), the molecular scattering function is expressed as

$$I_{\rm Menke}(Q)=\sum_{i=1}^{n}\sum_{j=1}^{n}f_i f_j \frac{\sin(Ql_{ci})}{Ql_{ci}}\frac{\sin(Ql_{cj})}{Ql_{cj}},$$

where l_{cj} is the distance of atom j from the defined origin of the molecular model. Although the Debye equation is independent of any real-space origin, when applying the Menke extension to the Debye equation, it is critical that the real-space origin of the atomic coordinates is coincident with the scattering centre of the model. The molecular scattering function essentially represents the coherent scattering from concentric shells of atoms about the defined molecular origin.

In Fig. 5.6.4, the Menke molecular scattering function for mannitol is plotted along with the calculated Debye response for a single mannitol molecule. The traditional Guinier small-angle scattering response (Guinier, 1994) for a radius of gyration, R_g, of about 2.78 Å is also displayed for comparative purposes:

$$I_{\rm Guinier}(Q)=I_0\exp\left(-Q^2R_g^2/3\right).$$

The Menke and Guinier scattering profiles are effectively similar descriptions of the small-angle scattering from a single free-standing mannitol molecule.

Traditionally, the shape-driven SAXS response for non-crystalline diffraction is subtracted from the Debye response, thus removing the central dominant component from the calculated diffraction profile. Although the extension to the Debye equation as originally presented by Menke included a radial probability distribution function in addition to the molecular scattering function, the Debye–Menke equation as used within this chapter can be expressed as

$$I_{\rm DM}(Q)=\left[\sum_{i=1}^{n}f_i^2+2\sum_{i,j=i,i\neq j}^{n}\frac{f_i f_j\sin(Qd_{ij})}{Qd_{ij}}\right]-\sum_{i=1}^{n}\sum_{j=1}^{n}f_i f_j\frac{\sin(Ql_{ci})}{Ql_{ci}}\frac{\sin(Ql_{cj})}{Ql_{cj}}.$$

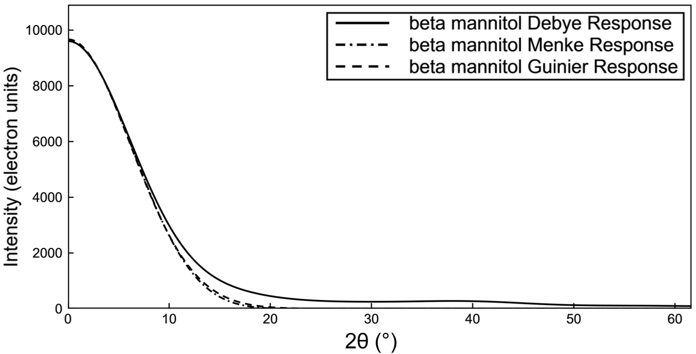

Figure 5.6.4
The Menke molecular scattering function displayed along with the Debye diffraction response and Guinier small-angle scattering response for a single mannitol molecule.

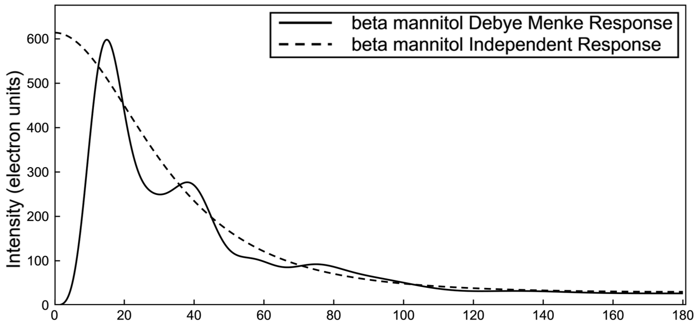

Figure 5.6.5
The diffraction response from a single mannitol molecule as calculated by the Debye–Menke equation displayed with the independent coherent scattering function.

The resulting Debye–Menke intensity function ($I_{\rm DM}$) for mannitol is shown in Fig. 5.6.5.

From Fig. 5.6.5, it can be seen that at large angles (high Q) the asymptotic form of the Debye–Menke intensity function approaches the independent coherent intensity function [$I_{\rm ind}(Q)$] while oscillating about that function. One component of the Debye normalization as applied to measured data is to scale all data to oscillate about the same independent coherent response at large measurement angles. The atomic composition of the sample and the X-ray wavelength used to collect the data will define the angular range required in order to observe the asymptotic high-angle behaviour. When using Cu $K\alpha$ X-rays, measurements will have to be made to relatively large 2θ angles in order to observe this asymptotic behaviour for organic systems. In Fig. 5.6.5, the calculations for mannitol were performed out to 180° 2θ and the oscillatory asymptotic behaviour of the Debye–Menke intensity function can be clearly observed. For many inorganic non-crystalline systems, the full asymptotic behaviour might not be observable when using Cu $K\alpha$ X-rays.

The relationship between the Debye–Menke intensity function ($I_{\rm DM}$) and the independent coherent intensity function ($I_{\rm ind}$) as displayed in Fig. 5.6.5 suggests a second aspect to the Debye normalization. The total diffraction intensity under the Debye–Menke curve (*i.e.* integrated intensity) approaches the integrated intensity for the independent coherent intensity function. This asymptotic integrated intensity behaviour again requires measurements out to high wavevectors in order to be approximately true and is related to the integrated intensity rules proposed by Vainshtein (1994). Following Vainshtein, the structural coherences that generate diffraction features are expressed in the summation over the various sine terms (Fourier terms). When averaged over a sufficient range in diffraction space, all the sine terms will tend to zero. As such, the total integrated intensity of X-rays scattered from a single molecular system should be a constant and independent of the structural details. In the absence of absorption, the constant is related to the atomic number density and illuminated volume of the sample. More specifically, with respect to the Debye equation, the structural interference terms are driven by weighted sinc functions. The integrated intensity of a sinc function is driven by the central halo, which is removed by the Menke correction. This suggests that if the central scattering component is ignored (which is realistic for samples greater than a few nanometres in size) and data are collected out to high enough diffraction angles, then the total integrated intensity for crystalline and non-crystalline materials of the same molecule should be the same and should approach the integrated intensity of I_{ind}. When applied to measured data, the instrumental intensity response (*e.g.* Lorentz and polarization factors) modifies the observed diffraction response, removing any absolute normalization possibility based upon the Debye equation. As such, a practical normalization procedure for measured data might require that each non-crystalline powder pattern be scaled such that the observed high-angle intensity asymptotically approaches (and oscillates about) a common intensity trend and that the data have common integrated intensity. This is a reasonable normalization procedure provided that the atomic compositions of the samples being studied are similar. Data normalization is such a critical component for the characterization of diffraction from non-crystalline systems that these rules of thumb will be investigated in more detail in Sections 5.6.7 to 5.6.10.

5.6.5. Verification of the Debye–Menke intensity function

The Debye–Menke intensity function (I_{DM}) for a single mannitol molecule, Fig. 5.6.5, shows a well defined low-angle halo at about 14.5° 2θ. In Fig. 5.6.6, the I_{DM} is plotted along with the full Debye intensity function, I_D, for mannitol; note that the dominant low-angle halo is not visible in I_D because of the huge SAXS contribution. Since the 14.5° halo is not visible in the full Debye intensity function, it may potentially be an artifact induced by subtraction of the Menke intensity due to the non-spherically symmetric mannitol. Using the Bragg relationship to convert this halo position to distance gives an effective interatomic spacing of about 6.1 Å. In order to verify whether this interatomic spacing is an inherent part of the mannitol molecular structure, a histogram of atom–atom pair distances within a mannitol molecule was determined and this is plotted in Fig. 5.6.6 along with I_{DM}.

To derive the histogram displayed in Fig. 5.6.6, each atom–atom distance d in the molecule is transformed to the corresponding diffraction-vector magnitude Q_d (*i.e.* $Q_d = 2\pi/d$) and expressed as a unitary Gaussian function with the standard deviation in Q of 0.01 and weight given by the atom-pair structure factor. The histogram is built up by accumulating all the unitary Gaussians for each atom–atom distance. The validity of using a Bragg transformation to relate single atom–atom distances to a position in diffraction space is questionable for non-crystalline systems but may provide a useful reference framework if used with care. The histogram as plotted essentially corresponds to the first-order coherent diffraction from a structure with characteristic distances defined by the individual atom–atom distances. The two primary halos observed at about 14.5 and 40.0° 2θ in I_{DM} are reproduced within the histogram, suggesting that they are characteristic features of a rigid mannitol molecule.

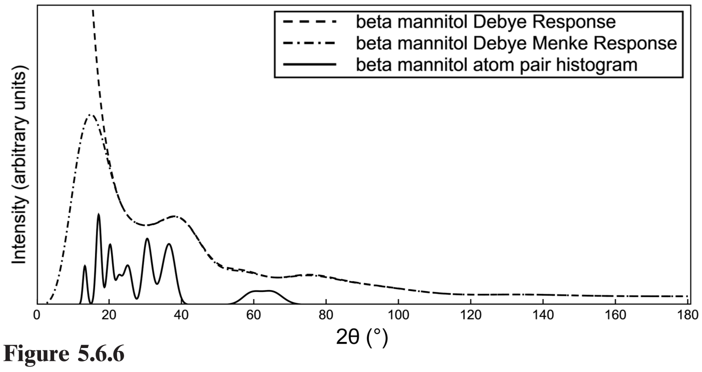

Figure 5.6.6
Overlay of the Debye and Debye–Menke response for mannitol with a weighted histogram of atom–atom pair distances within mannitol. The y axis is in arbitrary units.

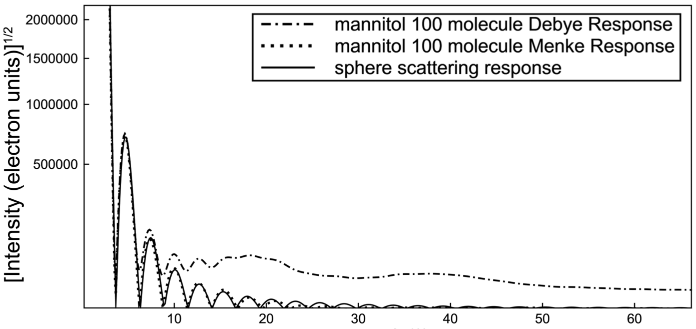

Figure 5.6.7
Calculated X-ray scattering responses for 100 mannitol molecules packed into a sphere of radius 1.71 nm. Note that the y axis is now the square root of the electron units to enhance the visibility of the small-angle scattering oscillations.

To further demonstrate that the Menke correction to the Debye equation removes the $Q \to 0$ small-angle scattering response arising from finite-sized molecular models, 100 mannitol molecules were 'randomly' packed into a sphere of radius 1.71 nm using the program *PACKMOL* (Martínez *et al.*, 2009). *PACKMOL* is a useful program for generating initial pseudo-random packing configurations for organic molecules and was used several times in the work described in this chapter whenever random packing configurations of a large number of molecules were required. To generate uniform high-density packing configurations, the model mannitol molecule is used without the attached hydrogen atoms. The small-angle scattering response from the packed sphere can be calculated using the sphere scattering formula:

$$I_{\mathrm{sphere}} = \left[3(\sin x - x\cos x)/x^3\right]^2,$$

where the variable $x = QR$, with R being the sphere radius. The Debye and Menke responses for the packed sphere of mannitol molecules and the calculated sphere scattering intensity are displayed in Fig. 5.6.7.

The Menke response as shown in Fig. 5.6.7 clearly exhibits extensive low-angle oscillations that extend out to diffraction angles greater than 20° 2θ. When the Menke response is compared with the calculated small-angle scattering response for a uniform sphere of radius 1.71 nm, the correlation is clearly visible. There are some differences between the sphere scattering and the Menke response at higher angles due to the granularity of the packed mannitol molecules and the lack of a smooth sphere surface. However, the correspondence is close enough to demonstrate further that the Menke response is an effective correction for small-angle scattering within the Debye model. (It should be mentioned that the Menke correction derives the small-angle scattering response in the Fraunhofer diffraction limit, which is an acceptable approximation for small clusters of molecules and in particular spherically symmetric samples.)

5.6.6. Background removal, intensity normalization and choice of X-ray optics

The analysis of non-crystalline powder patterns will typically require a different set of analytical tools than those employed for crystalline material analysis. The continuous nature of non-crystalline powder patterns makes them ideally suited to chemometric data analysis, which characterizes variance among individual data sets. As an additional consideration, being metastable (or unstable) solid forms, non-crystalline materials will change over time and will also change depending on the production pathway. This inherent variable nature further suggests that chemometric methods will be a primary analytical tool for the characterization of non-crystalline materials. A common requirement for the many chemometric approaches is appropriate data normalization. Normalization of a set of analytical data is an attempt to remove variances amongst the individual data sets that are spurious with respect to the analytical variance of interest. For powder diffraction measurements, spurious variances may include such variables as instrument intensity, instrument background, sample mass and sample packing density. Ideally, for chemometric analysis, the only unknown variability within the measured data after normalization should come from the intrinsic sample properties and not from the instrument or extrinsic sample variance.

The Debye equation suggests two fundamental intensity normalization approaches that can be applied to non-crystalline powder diffraction patterns. The first is that the total scattered analytical intensity from a sample should approach the integrated intensity under the independent scattering function. The second is that the high-angle data should asymptotically oscillate about the independent scattering curve. An additional practical constraint that may also be applied requires that the non-crystalline diffraction response should return to the instrumental baseline at low diffraction angles. The application of the constraint that forces the analytical signal to return to the baseline at low diffraction angles implicitly assumes that the non-crystalline sample being studied does not exhibit strong small-angle scattering from any micro-voids or internal density variation. As such, this final constraint, when used, should be applied with care.

Although the Debye equation suggests potential data normalization procedures, the traditional expression of the Debye equation is as raw diffraction intensity with no terms relating to how this diffraction response would appear as measured data. The appearance of the measured data will in part depend on the diffraction instrument configuration and geometry used. Each diffraction instrument will leave ‘fingerprints’ on the measured data that in principle have to be removed to enable full Debye modelling. Some of the fundamental instrumental contributions include diffuse background, angular resolution (peak width), intensity response and spectral purity. For non-crystalline material characterization, of greatest importance with respect to instrument optimization are well defined and smoothly varying background and intensity response functions. Ideally, the instrumental background should be low and the intensity response (diffraction signal) high. For ease of modelling, the instrumental spectral purity (energy resolution) should be as close to monochromatic as realistically possible. Because of the continuous nature of non-crystalline diffraction, the instrumental angular resolution is usually a secondary consideration.

Determining an instrumental background is typically a critical first step in employing data normalization procedures, as instrumental background intensity will not scale according to the same rules as the diffraction signal from a sample. As such, the instrumental background intensity must be either removed from the measured data or built into the intensity normalization procedure. Characterizing and/or removing instrumental background is a required data pre-processing step when dealing with powder patterns from non-crystalline samples. Because of the critical role played by instrumental background contributions in the analysis of non-crystalline data, the inherent instrumental background and its variability are key considerations in the choice of diffraction optics and geometry.

For crystalline X-ray diffraction, the instrumental intensity response function is usually expressed in terms of a Lorentz factor and polarization term. While the polarization term will be unchanged, the Lorentz factor as applied to the Debye equation differs from either the single-crystal or powder Lorentz terms. The differences arise from the inherent spherical integration that is implicit within the Debye equation and its continuous rather than discrete nature (James, 1948). For this initial discussion of data normalization, the role of the instrumental intensity response will not be considered. However, the instrumental intensity response and the differences in Lorentz factor will be discussed as part of the instrumental intensity modelling and advanced data normalization in Section 5.6.8.

In addition to the continuous nature of the diffraction response, non-crystalline materials are typically metastable and may exhibit variability and relaxation over the duration of the diffraction measurement. In order to observe the initial state of the non-crystalline sample, rapid data collection may, therefore, be required. The requirement for rapid data-collection capability should be balanced with the requirement for high count rates in the sample diffraction response and low instrument background. A good solution for laboratory measurements has proven to be a static or scanning position-sensitive detector (PSD) with diffracted-beam optics essentially open (relaxed). In this geometry, the powder diffraction data can be rapidly acquired in a series of loops or frames. A comparison of the powder patterns across the multiple loops or frames can be used to identify any propensity for physical or chemical instability over the duration of the measurement. The frames that show a consistent powder pattern can be summed to recover the high diffraction intensity required for robust analysis. Although open diffracted-beam optics can lead to significantly higher instrumental backgrounds, the simplicity of the X-ray optics tends to give a consistent and continuous background response that forms the basis of a more robust analysis.

At the present time, one of the most direct approaches to determining an instrumental background response is to measure a blank sample under the same conditions as the analytical sample. For reflection measurements, both the instrumental intensity response and background can be optimized by using offcut single-crystal low-background sample holders (*e.g.* silicon or quartz) with a shallow well. A suitable blank might be the holder itself or the holder plus a crystalline powder that has few reflections in the measurement range of interest. Ideally, the chosen crystalline ‘background’ sample should be of a similar atomic makeup to the analytical sample to minimize the impact of absorption differences. If a crystalline powder blank is used, then the Compton scattering, *Bremsstrahlung*, thermal diffuse scattering and defect scattering from the blank sample must be accounted for in order to isolate the pure instrumental background. The idea behind the blank sample measurement is to generate a continuous instrumental background response that

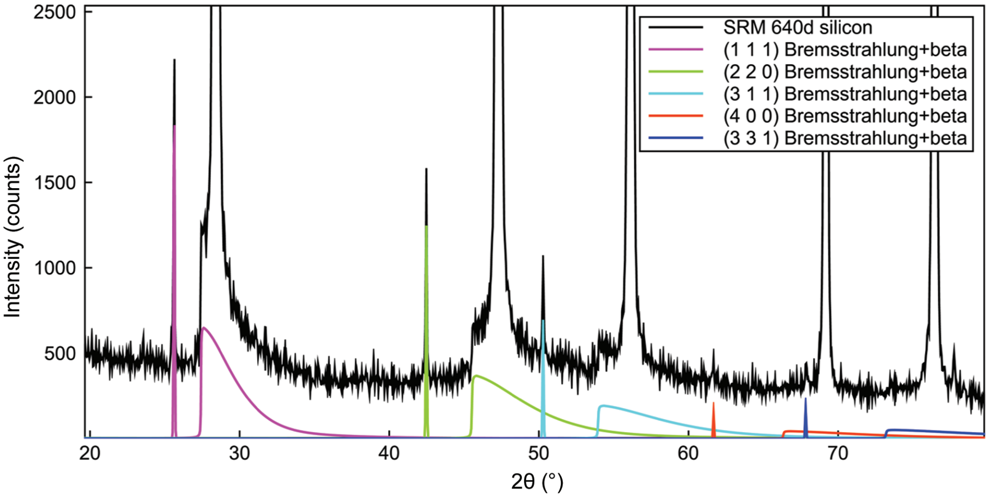

Figure 5.6.8

Measured Bragg–Brentano data for SRM 640d depicting the diffuse background and calculated *Bremsstrahlung* contributions. The individual calculated responses also include the Cu $K\beta$ Bragg peak from $K\beta$ X-rays that pass through the beta filter.

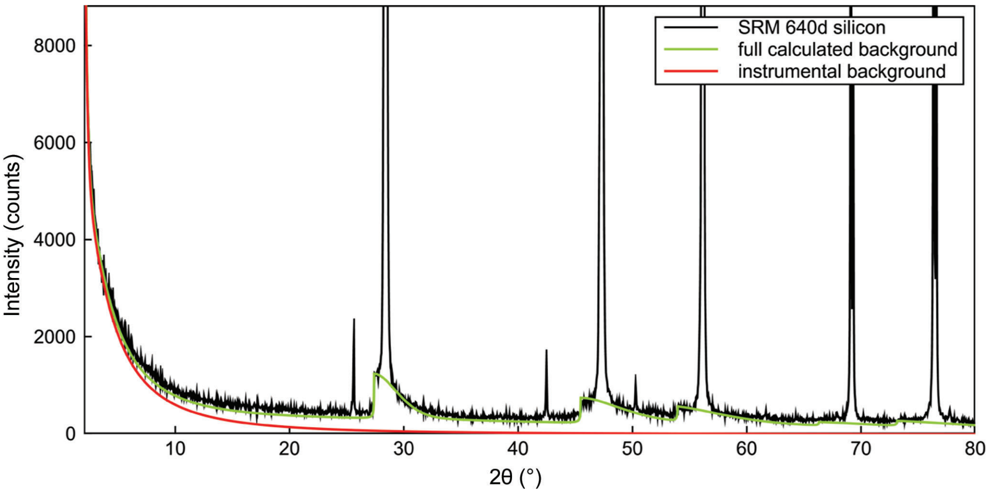

Figure 5.6.9

Measured Bragg–Brentano data for Si SRM 640d displayed with the calculated full background response including the instrumental contribution, *Bremsstrahlung*, thermal diffuse scattering and Compton scattering. The derived instrumental response is shown in red.

can be built into the intensity normalization procedure. For many reflection geometries, an empty low-background sample holder will give a suitable blank response that can be directly measured, but crystalline powder blanks have an additional advantage in that the crystalline peak intensities may also be used to track the instrumental intensity response function. As a general rule, it is not recommended that non-crystalline materials be used as holders for non-crystalline samples, as it can be difficult to isolate the non-crystalline holder pattern from the non-crystalline pattern of interest. For example, glass capillaries will often exhibit subtly different non-crystalline patterns from one capillary to another and may also give different patterns from one location to another on the same capillary.

An example of using a crystalline powder reference to extract the instrumental background is illustrated in Figs. 5.6.8 and 5.6.9 for NIST SRM 640d silicon. The data were collected using a Cu $K\alpha$ tube source on a diffractometer in Bragg–Brentano reflection geometry using a beta filter and open secondary optics; no active optical components (*e.g.* monochromator or mirror) were used. For this type of X-ray optics, scattering of *Bremsstrahlung* radiation contributes a significant intensity to the observed background level. *Bremsstrahlung* radiation is the continuous white X-ray background generated by all solid-anode X-ray sources, emitted by electrons during deceleration within the anode. Like synchrotron X-ray radiation, high-energy *Bremsstrahlung* is often plane polarized. For crystalline materials, the same crystalline planes that diffract the primary Cu $K\alpha$ X-rays will also diffract the white background continuum. As such, each crystalline Bragg peak will exhibit a characteristic *Bremsstrahlung* diffuse background (and Cu $K\beta$ peak). When a beta filter is used in the diffracted beam, the diffuse *Bremsstrahlung* background will exhibit a distinctive sharp step corresponding to the beta filter absorption edge. This background step can be used to identify the magnitude of the *Bremsstrahlung* diffuse component for each diffraction peak. In Fig. 5.6.8, the derived *Bremsstrahlung* contribution for each of the main crystalline Si peaks is presented along with the residual beta peak from the Cu $K\beta$ X-rays that pass through the beta filter. Because of the white radiation source, the *Bremsstrahlung* diffuse contribution becomes broader for peaks at higher diffraction angles. For the reflection Bragg–Brentano X-ray optical path used to collect the data in Fig. 5.6.8, the integrated intensity of the *Bremsstrahlung* contribution is approximately 7% of the total Bragg peak area. Although the diffuse *Bremsstrahlung* component is driven by the white background from the X-ray source and will be further modified by active X-ray optical components in the beam path, its appearance in the measured data is dependent on the coherent structure of the sample. As such, it is generally treated as a sample-dependent contribution to the diffuse scattering rather than an inherent instrumental background. An inspection of Fig. 5.6.8 suggests that once the *Bremsstrahlung* diffuse peaks have been removed, the measured background is essentially flat at about 300 counts. This flat background is, however, not the instrumental background as it is, for the most part, due to Compton scattering and thermal diffuse scattering from the Si powder sample. Individual modelling of Compton scattering will be discussed in Section 5.6.9, but the final theoretically calculated background response for powdered crystalline Si as measured using open Bragg–Brentano optics is shown in Fig. 5.6.9. The derived instrumental background contribution as depicted in Fig. 5.6.9 rapidly falls towards zero at large diffraction angles away from the main beam.

For characterization of crystalline powder samples, it is an accepted practice to routinely run validation standards in order to verify instrumental performance with respect to absolute peak positions, peak width, linearity and intensity (Cline, 1992; see also Chapter 3.1). For non-crystalline material analysis, routine validation standards should be run to verify both the instrumental background and instrumental intensity response. Although the powder silicon standard SRM 640d is not specifically recommended as either an intensity or background standard, it can be used to derive and validate continuous background and intensity response functions. Derivation of the instrumental intensity response is discussed in Section 5.6.8. Instrumental backgrounds for transmission measurements can be significantly higher than for reflection measurements, as the scatter of X-rays from the primary incident beam before the sample can pass through the sample and X-ray optics into the detector. A further diffuse component that may be observed for transmission measurements is X-ray scatter from any window or container materials that the incident X-rays pass through. For powder samples that can be prepared as free-standing films or wafers, then, in principle, the sample holder may require no window material or supporting material in the X-ray beam. For liquid or powder samples that cannot be prepared as free-standing solids, polymer films can be used to make a sandwich holding the sample, which is then mounted in standard transmission sample holders. To minimize these additional diffuse background components for transmission measurements, it is good practice to use thin (~3 μm) low-scattering polymer windows such as Etnom (Chemplex Industries) or Mylar (SPEX CertiPrep).

A worked example concerning data normalization for semi-quantitative analysis using transmission data is discussed in the following section.

5.6.7. Application of the Debye normalization to semi-quantitative analysis

As previously discussed, there are numerous sources of diffuse X-ray diffraction intensity that should ideally be removed before analysing non-crystalline powder patterns. However, for the specific case of semi-quantitative analysis of organic materials, many of the sample-dependent contributions will be very similar from sample to sample because of their similar elemental composition. Any small differences in the diffuse contribution from each phase of interest are likely to scale with the relative masses of each phase present in the sample (the validity of this assumption will be investigated below). With consistent and careful powder diffraction measurements using the same mass of sample each time, it may be possible to perform semi-quantitative analysis utilizing an instrumental background as measured on a blank sample. Within this chapter, semi-quantitative analysis refers to the determination of the relative masses of the phases of interest within a set of samples without using specially prepared calibration or validation standards. This is typically achieved by using full-pattern fitting and/or chemometric methods to characterize variance between individual data sets collected on an ensemble of samples. As a worked example, within this section, a series of sucrose lyophilizates with varying water content will be analysed to determine the residual water content. Each sample was isolated using thief sampling at different points within the final drying cycle. The water content is expected to vary with the time the sample spent in the final drying phase. More details of sample preparation and discussion of a full-pattern fitting method have been presented previously (Bates *et al.*, 2013); in this section, the same data will be analysed using an alternate chemometric variance technique to demonstrate the robustness of the Debye normalization.

The X-ray powder patterns were collected using a Rigaku SmartLab system in a transmission geometry using a convergent-incident-beam mirror and linear PSD (D'teX). The convergent beam was focused through an environmental cell onto the detector plane. In addition to the X-ray mirror and linear detector, the only other X-ray optics used for this measurement were passive slits to define the beam footprint and reduce parasitic background. The secondary (detector) optical path was essentially wide open, which gives a high but reproducible instrumental background and an instrumental intensity response function that is smooth and easy to model. The use of an environment cell to hold each sample was required because of the inherent instability of the lyophilizates with respect to temperature and humidity. Humidity is often a critical parameter requiring control when characterizing non-crystalline organics, as water is an effective plasticizer for these systems and can significantly accelerate both physical and chemical instability. In order to collect consistent powder patterns on the sucrose lyophile samples, the samples were mounted in a dry glove box ($\ll 0.3\%$ relative humidity) into an environmental cell which used double Etnom (Chemplex Industries) X-ray windows as a barrier to the ambient humidity. The double Etnom window allows about 1 h of sample stability, which is sufficient to collect multiple powder pattern frames.

The combination of the double Etnom environmental cell and open secondary optics gives a relatively high instrumental background that must be modelled out of the data to perform the semi-quantitative analysis. The background model was derived from a direct measurement of the empty environmental cell (blank). For each measured data set, the blank background and the measured sample data are scaled with respect to each other. The residual analytical data are then calculated by removing the scaled background from the scaled measured sample data. The relative scaling is performed to ensure that the integrated intensity of the residual analytical signal is a constant for all samples with the high-angle data asymptotically approaching the same signal level. For a more robust background model, the measured blank response should be corrected for absorption through the transmission sample. Any diffuse background components originating before the sample (*i.e.* air scatter) will have to pass through the sample before reaching the detector. For different sample thicknesses and packing densities, the absorption correction will be slightly different. To avoid an explicit absorption correction, a small linear damping term was applied to the blank response as an approximate absorption term. The degree of damping is a refinement variable along with the two scale factors in order to achieve consistent Debye normalization across all analytical data sets.

In this first approximation to Debye normalization, there are three variables: scale factors for the measured data and blank data, plus the degree of linear damping for the blank data. The conditions that define the correct solution are matching integrated intensity for the residual analytical data and asymptotic high-angle data (in order to converge correctly, an additional constraint requiring matching data at the low-angle background point may also be required). This approach to Debye normalization is simple enough to be routinely performed using Microsoft *Excel* or similar software. The integrated intensity normalization and high-angle asymptotic behaviour matching both implicitly assume that the same atom types and relative concentrations are present in all samples being studied. When the atomic compositions are very different between the various phases in the samples, then a bias is introduced into the subsequent analysis. Despite the potential for bias, the Debye normalization as presented here transforms the measured non-crystalline powder patterns into a suitable form for chemometric analysis.

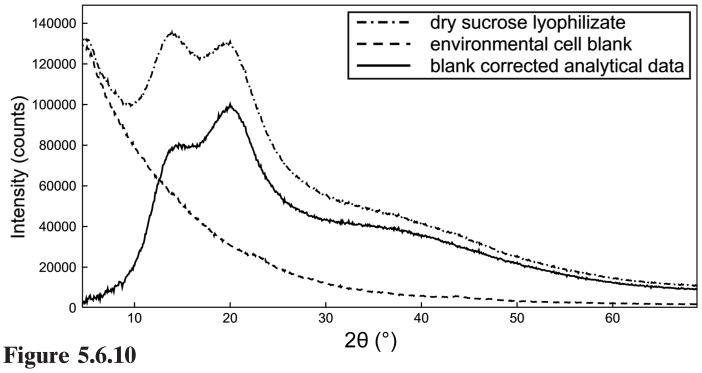

Figure 5.6.10
Measured non-crystalline powder pattern for a dry sucrose lyophilizate compared with the scaled blank background and resulting analytical signal.

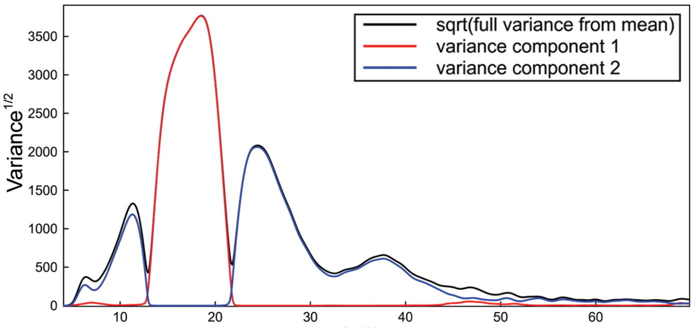

Figure 5.6.12
Square root of the full data ensemble variance from the mean display with two orthogonal principal variance components (expressed as real positive components).

Fig. 5.6.10 shows an example of the measured data for a dry sucrose lyophilizate compared with a scaled blank background and residual analytical signal. In Fig. 5.6.11, the resulting analytical data for dry and partially dry sucrose lyophilizates are compared to demonstrate the Debye normalization.

Visually, the two analytical data sets in Fig. 5.6.11 are similar with closely matching halo positions and relative intensities, but they are not the same. The difference between the two non-crystalline powder patterns is a result of the residual water content in the partially dry sample. For continuous and normalized data sets like those presented in Fig. 5.6.11, chemometric analysis provides a series of useful techniques for characterizing the variance between individual data files within an ensemble of data sets. There are a number of different variance-based chemometric techniques that could be employed to characterize the normalized data and extract the impact of residual water on the local sucrose structure (Brereton, 1990; Deming *et al.*, 1988). A simple approach that makes use of the Var.P(), Correl() and Solver() functions in Microsoft *Excel* is outlined below. The first step is to define principal variance components for the data ensemble. Taking N normalized observed powder patterns corresponding to different residual water contents, the mean and variance of the data ensemble can be defined as follows using *Excel* functions:

$$I_{\rm mean}(2\theta) = {\rm Average}\big[I_{\rm obs}(2\theta, 1)\ldots I_{\rm obs}(2\theta, N)\big],$$

$$\mathrm{SV}(2\theta) = \big\{{\rm Var.P}[I_{\rm obs}(2\theta, 1)\ldots I_{\rm obs}(2\theta, N)]\big\}^{1/2}.$$

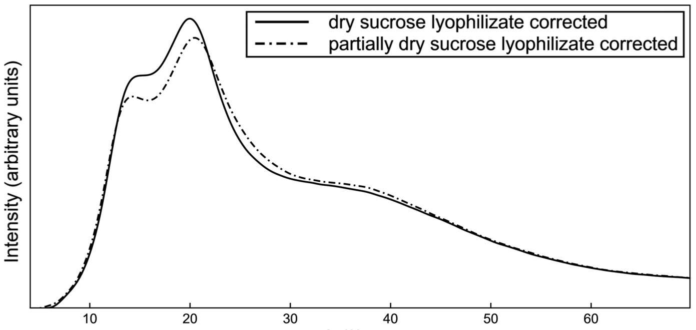

Figure 5.6.11
Normalized analytical data for dry and partially dry sucrose lyophilizates. Each analytical data set has the same integrated intensity and matching asymptotic behaviour towards 70° 2θ. An additional constraint of matching low-angle analytical signal was also imposed during the normalization.

The resulting square root variance [SV(2θ)] for the sucrose lyophilizates is presented in Fig. 5.6.12. Visual inspection of Fig. 5.6.12 indicates that the peak variance response occurs at about 18° 2θ. The position X of the peak variance response is used to define a correlation function for all variances with respect to the variance at X:

$$C(2\theta)|_X = {\rm Correl}\big[I_{\rm obs}(2\theta = X, 1)\ldots I_{\rm obs}(2\theta = X, N), \\ I_{\rm obs}(2\theta, 1)\ldots I_{\rm obs}(2\theta, N)\big].$$

The correlation function is expressed as a real positive variance component using the expression

$$\mathrm{VC}_X(2\theta) = \mathrm{SV}(2\theta)\big[C(2\theta)|_X - 1\big]/2.$$

In Fig. 5.6.12, the first real positive variance component as determined for X = 18° 2θ is plotted as variance component 1. Variance component 1 describes the central strong variance observed in the data but does not describe the complete observed variance. Using the residual variance, a second variance component can be defined using the strongest undescribed variance response at X = 24° 2θ. This second real positive variance component is plotted in Fig. 5.6.12 as variance component 2. The two variance components as displayed in Fig. 5.6.12 show no significant cross-correlation and are therefore essentially orthogonal with respect to each other and represent the principal variances within the data ensemble. The derived two-component model describes all the significant variance in the data ensemble.

The final step in the *Excel* chemometric model is to use the Solver() function in combination with the essentially orthogonal variance components to describe each of the individual normalized powder patterns. Each model powder pattern is constructed using

$$I_{\rm model}(2\theta) = I_{\rm mean}(2\theta) + \mathrm{SF}_1\mathrm{VC}_1(2\theta) + \mathrm{SF}_2\mathrm{VC}_2(2\theta),$$

where the SF_i terms are the individual variance component scale factors used as variables by the Solver() function to achieve the best fit to the individual normalized powder patterns. Within the standard Solver() model, the variance component scale factors must be allowed to assume positive or negative values. The best fit was determined using a full-pattern least-squares error minimization. The least-squares error to be minimized can be written as

$$\mathrm{LSE} = \sum_{2\theta}\big[I_{\rm obs}(2\theta) - I_{\rm model}(2\theta)\big]^2.$$

The resulting optimized scale factors give a quantitative measure of how far each powder pattern is displaced from the mean powder pattern. Each of the thief samples had independent residual water content analysis performed using an averaged KF (Karl Fisher) and IR absorption procedure allowing the opti-

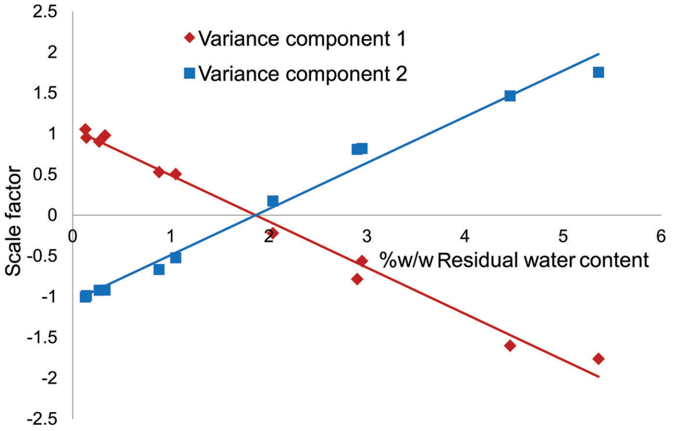

Figure 5.6.13
Scale factors for the variance principal components displayed in Fig. 5.6.12 plotted with respect to the known residual water content in *w*/*w* per cent. Note the essentially linear response over the region of interest.

mized scale factors to be plotted against determined residual water content; the reader is referred to the original reference (Bates *et al.*, 2013) for discussion of a more quantitative method.

The optimized scale factors shown in Fig. 5.6.13 for the variance components are essentially mirror images of each other, which further supports the conclusion that the normalized powder data represent a binary system. The scale-factor response is effectively linear within the region of interest down to the lowest residual water levels of less than 0.2%(*w*/*w*). This is a surprising level of sensitivity for a non-crystalline semi-quantitative method. Following the International Council for Harmonization of Technical Requirements for Pharmaceuticals for Human Use (ICH) guidelines Q2(R1) (ICH Harmonized Tripartite Guideline, 1994), the limit of detection, LOD, for the simple chemometric variance method can be determined using the slope of the response lines in Fig. 5.6.13 and the standard deviation of the response σ,

$$\mathrm{LOD} = 3.3\sigma/\mathrm{slope}.$$

For the data displayed in Fig. 5.6.13, the calculated LOD is about 0.75%(*w*/*w*) residual water in the sucrose lyophilizates.

From Fig. 5.6.13, scale factors of (1, −1) for the two orthogonal variance components allow the reconstruction of the 'driest' sucrose lyophilizate reference pattern and scale factors of (−2, 2) will reconstruct the 'wettest'. Setting the scale factors to say (−10, 10) will reconstruct a theoretical reference pattern for a lyophilizate with significant water content. A plot of the 'dry' sucrose lyophilizate with free water and the calculated 'wet' reference pattern is shown in Fig. 5.6.14. The calculated 'wet' sucrose reference as derived from the measured variance as a function of water content is significantly different from either the 'dry' sucrose or free-water powder patterns. The uniqueness of the calculated 'wet' reference pattern suggests that the residual water is combining with the sucrose to form a new solid/liquid phase with a different local structure than either water or non-crystalline sucrose. From a liquid-state perspective, the water is miscible within the non-crystalline sucrose at the molecular level. Miscibility at the molecular level essentially gives a single-phase system for each level of residual water content. However, across multiple samples with different residual water levels, a miscible system may also appear as a binary system. Whether the interaction between water and non-crystalline sucrose is a miscibility or solubility process, the chemometric analysis clearly demonstrates the binary nature of the sucrose:water system with no free water being observed.

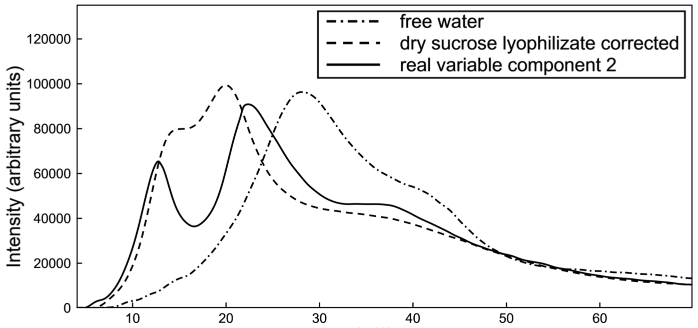

Figure 5.6.14
Normalized non-crystalline X-ray powder patterns for 'dry' sucrose, free water and a hypothetical 'wet' sucrose reference (variable component).

The miscibility behaviour of residual water within the lyophilized sucrose matrix is in part the reason why the simple chemometric analysis gives a linear response down to residual water contents of less than 0.2%(*w*/*w*). The X-ray measurements are picking up changes in the local 'dry' sucrose non-crystalline matrix induced by the miscibility/solubility. As such, the structural impact of each water molecule is magnified through the number of sucrose molecules involved in the local molecular interaction. These data demonstrate that the presence of even small amounts of residual water or solvent within an organic non-crystalline matrix can have significant consequences on the local structure if there is miscibility.

The lyophilized sucrose and residual water problem illustrates that with minimal data processing using Microsoft *Excel*, powder patterns collected on a laboratory X-ray diffraction instrument can be routinely used to study changes in local non-crystalline/glassy structure at the per cent level.

5.6.8. Correction for the instrumental intensity response

The appearance of powder diffraction data will be directly influenced by the diffraction instrument used to measure the data. For X-ray powder diffraction, the primary instrumental factors are background, angular resolution (peak width), spectral purity and intensity response function. In previous sections, the instrumental background and some aspects of spectral purity have been discussed. While the angular resolution is a critical parameter for the study of crystalline materials, for non-crystalline samples the instrumental intensity response function is more important. Ideally, the instrumental intensity response should be smoothly varying as a function of measurement angle and in addition should be straightforward to model analytically. With measured powder patterns for non-crystalline materials having an essentially smooth and continuous appearance, any discrete changes in the instrumental intensity response function will have a significant impact on the appearance of the measured data. Furthermore, structural characterization of non-crystalline powder patterns, whether through the use of pairwise distribution functions or direct analysis, requires that the instrumental intensity response be removed from the measured data, hence the requirement that the intensity response be relatively straightforward to model analytically.

For a laboratory X-ray powder system, the traditional analytical descriptions of the instrumental intensity response include the polarization correction, the Lorentz correction and relevant optical component corrections. For crystalline materials and powders, the Lorentz–polarization (LP) terms have been extensively discussed in various textbooks (*e.g.* James, 1948; Warren, 1990; Reynolds, 1989). The polarization term is essentially governed by the instrumental geometry, which is also affected by the choice of X-ray source and method of spectral resolution (*i.e.* monochromator). In contrast, the Lorentz factor depends on the type of sample being studied (for example, single-crystal, oriented powder or random powder) and the type of analysis being performed (for example, discrete peak intensity measurement or continuous total diffraction). For non-crystalline materials, the polarization factor remains unchanged from the traditional expression. The Lorentz factor, however, will follow a different form to that traditionally used for powder diffraction. The rationale behind the traditional Lorentz factor for powder measurements and how analysis of non-crystalline materials changes the required Lorentz factor is discussed later in this section.

One of the simplest X-ray optical systems to model with respect to the intensity response function and one that is available in most X-ray diffraction laboratories is the Bragg–Brentano reflection geometry. The Bragg–Brentano geometry is a symmetrical reflection geometry designed to measure X-ray powder patterns by scanning in a single radial direction in diffraction space (Q). The appropriate Lorentz factor for the Bragg–Brentano geometry is effectively a combination of two geometric terms that affect the measured diffraction intensity. The first geometric term, which is common to most diffraction measurements used to determine the Bragg peak intensity (*i.e.* its area), is often described as being related to the speed at which the diffraction measurement sweeps through the diffraction condition. For scans through single-crystalline peaks, this Lorentz term is traditionally expressed as $1/\sin(2\theta)$. The second geometric term is invoked for powdered materials consisting of numerous randomly oriented small crystals and expresses how the number of crystals contributing to the measured peak intensity changes as a function of measurement angle. Traditionally, this second Lorentz term is written as $1/\sin(\theta)$. Combining the two Lorentz terms together gives an intensity correction factor proportional to $1/[\sin(\theta)\sin(2\theta)]$, which is generally accepted as the default Lorentz factor when using Laue or Bragg diffraction theory to describe observed crystalline powder peak intensities. In contrast to Bragg and Laue diffraction theories, the Debye diffraction theory implicitly models the spherical symmetry present in ideal powders and non-crystalline materials, and the diffraction intensity is expressed as a continuous function in diffraction space. As such, the traditional Lorentz powder term is not required for either non-crystalline or crystalline powder data when used as continuous functions within a Debye diffraction model. More general derivations of the Lorentz term applicable to different diffraction geometries determine how the measurement volume in diffraction space intersects with the sample's diffracted intensity distribution. The impact of passive X-ray optical components such as slits and active components such as monochromators and mirrors on the measurement volume can be complex to describe accurately from first principles and the reader is referred to Zuev (2008), Kavanagh *et al.* (2012) and Fewster (2014) for more information.

The simplicity of the X-ray optics when coupled with the potential for low instrumental background makes Bragg–Brentano optics one of the more useful optical configurations for the characterization of non-crystalline materials, especially when used with a PSD to enhance count rate. Despite the simplicity of the Bragg–Brentano optics, suitable intensity standards are usually required in order to verify and refine the intensity response model. In the absence of non-crystalline intensity standards for X-ray diffraction, various crystalline materials are usually measured in order to track the instrumental intensity response as a function of measurement angle. In addition to the usual requirements for a powder diffraction intensity standard (random orientation and random particle statistics), the sample must produce a sufficient number of well defined free-standing diffraction peaks to cover the measurement range of interest (*i.e.* 2.0 to 150.0° 2θ for a laboratory Cu $K\alpha$ system). The difference between the calculated relative peak intensity and the observed relative peak intensity can be used to determine the instrumental intensity response. As the goal of the relative peak intensity study is to determine the instrumental contribution, the calculated crystalline peak intensities used should be raw unit-cell structure factors.

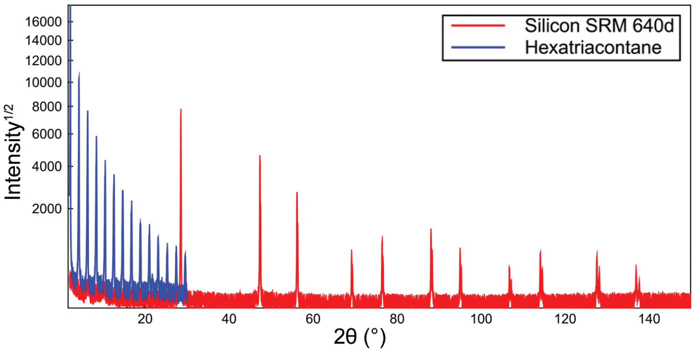

Figure 5.6.15
Measured powder patterns for an aligned hexatriacontane intensity reference and the silicon powder standard SRM 640d. Data were collected in Bragg–Brentano reflection geometry using a graphite diffracted-beam monochromator. The intensity is plotted on a square root scale.

Ideally, when measuring organic materials, the best practice is to use crystalline organic intensity standards to mimic the transparency and absorption sample effects. Hexatriacontane is one such organic crystalline material that can be used to map the instrumental intensity response for reflection measurements at low angles. When crystalline, the long-chain molecules are aligned to give a layered (plate-like) crystal structure with one large crystal unit-cell parameter (~48.4 Å) normal to the crystalline plates and two smaller unit-cell parameters (~7.42 and 5.57 Å) within the plane of the plates. When packed into a (top-loaded) reflection holder, the individual crystalline plates self-align (*i.e.* show preferred orientation) to create a sample that functions like an X-ray diffraction grating. The measured diffraction pattern for hexatriacontane out to 30° 2θ is shown in Fig. 5.6.15 on a square root scale. The first ten harmonic diffraction peaks from ~2.0 to ~21.0° 2θ are free standing and clearly visible. Being harmonics of the same diffraction planes, each peak will have the same theoretical structure factor (same number and type of coherently diffracting atoms). The variation of the observed peak intensity as a function of diffraction angle is a direct measure of the instrumental intensity response combined with the atomic form factor. An effective coherent atomic form factor can be readily calculated for hexatriacontane ($C_{36}H_{74}$) using values from atomic form-factor tables (Warren, 1990). The effective atomic form factor can also be approximated using a single carbon atom. When performing instrument intensity response calibration, the form of the Lorentz factor for specific calibration samples has to be allowed for. With the aligned hexatriacontane sample acting like a diffraction grating, the

Table 5.6.1
Analytical peaks for hexatriacontane (top) and silicon (bottom) listed by Miller index (*hkl*)

The atomic form factor squared has been normalized to 1 at $Q = 0$; values were derived from the tables in Warren (1990). The phase term is an intensity-modification term related to the ratio of in-phase and out-of-phase atoms for each reflection *hkl*. The Lorentz-difference column adjusts for the oriented nature of hexatriacontane, and the scale value for silicon is an arbitrary value to bring silicon into reference with hexatriacontane. The values in the column 'Final relative intensity', when scaled, should follow the observed peak areas (integrated intensity). The (511) silicon peak is overlapped with a weaker (333) peak, which has a multiplicity of 8. In this table the (511) multiplicity of 24 is used rather than an averaged value.

Miller index (*hkl*)	Effective atomic $(f)^2$	Multiplicity	Phase	Lorentz difference	Scale factor	Final relative intensity
(100)	0.9945	1	1	0.0182	1	55.264
(200)	0.9784	1	1	0.0363	1	28.166
(300)	0.9524	1	1	0.0545	1	19.276
(400)	0.9178	1	1	0.0726	1	15.002
(500)	0.8761	1	1	0.0907	1	12.581
(600)	0.8291	1	1	0.1091	1	11.051
(700)	0.7783	1	1	0.1273	1	10.093
(800)	0.7255	1	1	0.1455	1	9.475
(900)	0.6721	1	1	0.1637	1	9.091
(10 0 0)	0.6192	1	1	0.1818	1	8.882
(11 0 0)	0.5680	1	1	0.2000	1	8.803
(111)	0.5815	8	0.5	1	×	0.430
(220)	0.3671	12	1	1	×	0.227
(311)	0.3115	24	0.5	1	×	0.268
(400)	0.2586	6	1	1	×	0.644
(331)	0.2387	24	0.5	1	×	0.349
(422)	0.2157	24	1	1	×	0.193
(511)	0.2057	24	0.5	1	×	0.405
(440)	0.1929	12	1	1	×	0.432
(531)	0.1869	48	0.5	1	×	0.223
(620)	0.1789	24	1	1	×	0.233
(533)	0.1748	24	0.5	1	×	0.477

expected Lorentz factor for the observed peak intensities will more closely follow the single-crystal form [$\sim 1/\sin(2\theta)$] than the usual powder form {$\sim 1/[\sin(\theta)\sin(2\theta)]$} discussed previously.

With an aligned hexatriacontane sample, the instrumental intensity function can be followed out to about 30° 2θ using harmonic reflections. A second crystalline intensity standard is, therefore, required to map the instrument intensity response out to the higher angles used to study non-crystalline materials. While the silicon powder standard SRM 640d is not intended as an X-ray diffraction intensity standard, in practice the material can be used to map the variation in the instrumental intensity response as it gives eight peaks with self-consistent intensity out to 140° 2θ; see Fig. 5.6.15. Silicon will have a higher linear X-ray absorption coefficient than organic materials and as such will exhibit a subtly different 2θ intensity dependence. To offset the impact of absorption on the effective illuminated sample volume, the sample thickness can be kept to a minimum for all samples. For all reflection measurements presented within this chapter, offcut single-crystal silicon low-background sample holders were used with a 10 mm diameter and a depth of less than 0.1 mm.

For hexatriacontane, the harmonic peaks have the same unit-cell structure factor and multiplicity. To bring the powder silicon peak intensities towards an equivalent constant structure-factor response, the observed intensities for the silicon powder will have to be corrected for their individual multiplicities and ratio of in-phase and out-of-phase Si atoms within the unit cell. Table 5.6.1 contains a list of the analytical peaks for silicon and hexatriacontane along with approximate correction factors for the multiplicity plus the unit-cell phase correction. The final conversion factor in Table 5.6.1 includes the Lorentz-factor difference between hexatriacontane (aligned powder) and silicon (random powder). The effective squared atomic form factors in Table 5.6.1 for silicon and hexatriacontane have been normalized to 1 at $Q = 0$. Applying the correction factors and effective atomic form factors will give a series of observed peak intensities at different diffraction angles corresponding to a constant unit-cell structure factor for silicon and single unit-cell structure factor for hexatriacontane. The residual angular dependence of these observed peak intensities will be driven by the instrumental intensity response. The values in Table 5.6.1 should enable an instrumental intensity response function to be derived for any typical laboratory Bragg–Brentano system using Cu $K\alpha$ X-rays [with the effective atomic form factor squared derived from data presented by Warren (1990)].

To verify the general form of the instrumental intensity function, measured powder data for hexatriacontane and silicon were collected using two Rigaku SmartLab Bragg–Brentano systems with different detector configurations. The first system was configured with a graphite monochromator and a scintillation detector, while the second system used a beta filter plus a scanning PSD (D'teX). Peak heights were extracted from the four measured powder patterns and used to model the Lorentz factor. The traditional Lorentz factors and instrument intensity functions are defined for integrated peak intensities. However, for non-crystalline materials without discrete peaks, the instrument intensity function is used to remove the instrumental contribution point by point from the observed data. As such, the Lorentz factor and instrument intensity function of interest are continuous functions defined for every data point. To model this continuous function, peak heights are used for the silicon and hexatriacontane reference data rather than integrated peak intensities. To ensure consistency across the complete measured range, the individual observed peak profiles were fitted using the primary spectral components from a copper X-ray tube in order to isolate only the $K\alpha_1$ peak height. For crystalline reference material that gives instrumentally limited peak widths, the observed $K\alpha_1$ peak heights will be directly related to the 'final relative intensity' as presented in Table 5.6.1. For both detector systems, the inherent continuous Lorentz factor, L, was taken to be

$$L \simeq \frac{\cos^m(\theta)}{\sin^n(\theta)}.$$

The polarization term (with no monochromator) was taken to follow the traditional form

$$P = \frac{[1 + \cos^2(2\theta)]}{2}.$$

The continuous form of the Lorentz factor expressed above allows direct application of the calculated instrumental intensity response function to crystalline and non-crystalline samples as well as for Bragg/Laue and Debye modelling. Some idealized Lorentz terms for a reflection powder measurement are

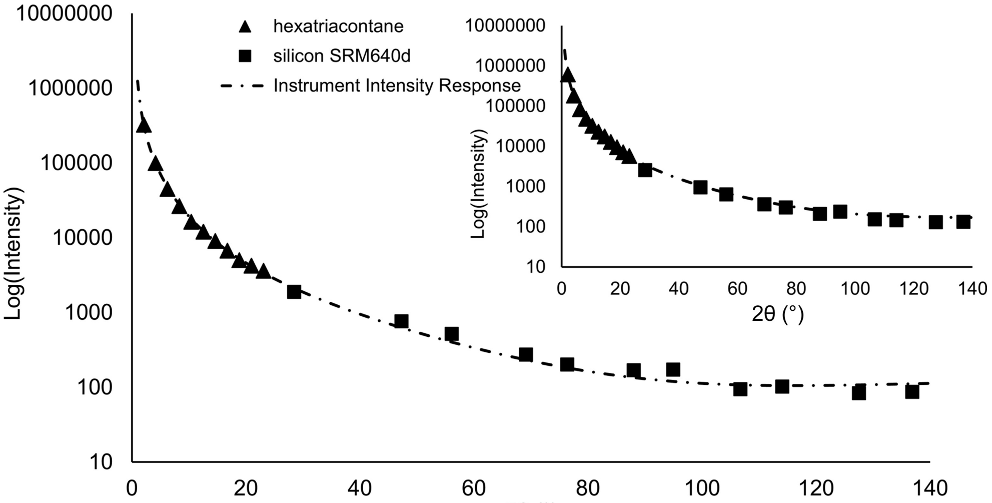

Figure 5.6.16
Reduced integrated peak intensities for hexatriacontane and Si SRM 640d plotted on a log scale with a derived analytical instrumental intensity response function using the core response function with m = 0.0 and n = 2.1. The main plot displays data collected using a scanning PSD while the inset displays data collected using a graphite monochromator.

$$L_{\text{non-crystalline}} \rightarrow \text{Debye} \simeq 1;\, n \rightarrow 0,$$

$$L_{\text{oriented powder}} \rightarrow \text{Bragg} \simeq 1/\sin(\theta);\, n \rightarrow 1,$$

$$L_{\text{random powder}} \rightarrow \text{Bragg} \simeq 1/\sin^2(\theta);\, n \rightarrow 2.$$

To determine the instrumental intensity response, the extracted peak heights for the reference crystalline hexatriacontane and silicon are first corrected by applying the final correction factors from Table 5.6.1 and then removing angular dependence due to the effective squared atomic form factors. An arbitrary scale factor was applied to the resulting silicon peak intensities to bring them into coincidence with the resulting hexatriacontane peak intensities. The 2θ intensity dependence of the corrected peak heights (see Fig. 5.6.16) was then modelled using the Lorentz and appropriate polarization factors. Least-squares minimization was performed using the Microsoft *Excel* Solver() function with m, n and a general scale factor as the primary variables. The overall fit to the observed intensity behaviour as displayed in Fig. 5.6.16 is good over about six orders of magnitude. The resulting minimized value for the sine power coefficient (n) was about 2.1 for both detector configurations: close to the ideal value of 2.0. The cosine power coefficient (m) was minimized to zero for both sets of data, indicating that the idealized Lorentz factors closely describe the observed instrumental intensity response.

The inherent Lorentz-factor difference between diffraction-peak raw unit-cell structure factors (Bragg) and peak intensities as calculated by the Debye equation can be illustrated for a hypothetical silicon nanocrystal, as shown in Fig. 5.6.17. Using the *Mercury* CSD 3.9 software package (Macrae *et al.*, 2008) to generate a packed 5 × 5 × 5 unit cell for silicon resulted in an atomic model of a silicon single-crystal nanocube with a cube axis of about 2.715 nm. The atomic nanocube was used as input for the Debye intensity calculation. The Bragg calculation used the unit-cell structure-factor intensity for each diffraction peak (hkl) and assigned a normalized Gaussian peak about the calculated Bragg position. The width of the Gaussian profile for each silicon peak was determined using the Scherrer equation:

$$\beta = K\lambda/D\cos(\theta).$$

The peak integral breadth (β) is expressed in radians and the crystal size parameter (D) was set to 3 nm. The Scherrer constant (K) was taken to be 0.88 and the X-ray wavelength was taken to be the mean Cu $K\alpha$ wavelength of 0.15418 nm.

The resulting Bragg intensity was divided by the $\sin^2(\theta)$ Lorentz-factor difference and scaled to account for the difference in the number of atoms in the crystalline unit cell and the complete nanocrystal. The peak-intensity variations as a function of 2θ for both the Debye- and Lorentz-corrected Bragg simulated powder patterns are essentially the same, confirming the inherent Lorentz-factor difference between the two theoretical diffraction approaches. There are, however, some notable differences in the nanocrystalline diffraction response as calculated by the two different methods. The Debye calculation, being a total diffraction calculation, will generate Laue interference effects (*Pendellösung* fringes) because of the finite size and flat surfaces of the single silicon nanocube.

The choice of an appropriate Lorentz term to describe the instrument intensity response depends on a number of factors that include instrumental geometry, sample symmetry and the theoretical framework being used to model the measured data. For the Bragg–Brentano optical configurations used in this study the ideal Lorentz factors were found to describe the instrumental response, and, as such, no formal Lorentz correction is required for measured data in order to transform them into the Debye reference frame. The absence of a Lorentz correction is another benefit to using Bragg–Brentano reflection configurations for routine analysis of non-crystalline materials.

It should be noted that, in addition to the Lorentz and polarization terms, the Bragg–Brentano optics have a low-angle intensity damping term arising from over-illumination of the sample. For a fixed-slit optical system, depending on the divergence slit size and sample size, at low enough incident angles onto the sample the incident-beam footprint will be larger than the sample size. As a consequence of the over-illumination, the

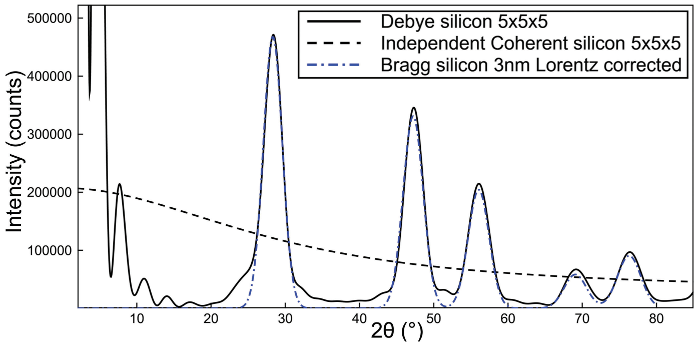

Figure 5.6.17
Calculated powder patterns for a ~3 nm silicon nanocube using both Debye and Bragg diffraction equations. The Bragg calculation has been scaled to account for the difference in the number of silicon atoms and modified by multiplying by the $\sin^2(\theta)$ Lorentz difference. The independent coherent limit for the full nanocube is shown for comparison.

sample will only intersect a small component of the full incident beam, thus reducing the observed diffracted intensity at lower angles. To minimize over-illumination, the powder measurements presented in this chapter were taken with narrow divergence slits (around 1/6°) with sample widths of 10 mm or more. Under these measurement conditions, significant intensity damping (>80%) due to over-illumination was limited to occur below about 9.0° 2θ. A complete instrumental intensity model requires that the low-angle over-illumination be described; however, owing to the nature of the Debye normalization procedure discussed in the following section, it is more important to describe accurately the high-angle intensity response.

5.6.9. The full Debye normalization procedure

After correcting for the instrumental intensity response, the full Debye normalization is applied to scale the measured X-ray diffraction intensity to an absolute electron-unit reference frame. For any structural characterization based upon non-crystalline powder patterns, this transformation from measured intensity to absolute electron units is a critical data pre-processing step. From a preliminary investigation of the Debye equation, two scattering limits were identified that can be used to normalize measured powder patterns:

(i) Coherent limit (all atoms in a model system scattering coherently – the coherent intensity function).
(ii) Independent limit (all atoms in a model system scattering independently – the independent coherent intensity function).

When the measured data have been transformed to electron units, a third scattering limit can be introduced:

(iii) Incoherent limit (Compton scattering – individual electron scattering).

For a particular model system, the coherent limit describes the maximum possible diffraction intensity from a material when all atoms are scattering coherently. After correcting for multiplicity, no diffraction peak intensity (including the sample SAXS peak) can exceed the coherent limit. The derivation of the coherent limit requires knowledge of the crystalline unit cell or the local coherent structure and is therefore dependent on the 'structure' of a material. The independent limit, however, is independent of the structure, as it is an atomic level scattering response that scales with the number of atoms. The independent limit is usually expressed with respect to the basic chemical unit (*e.g.* a single molecule) but can also be derived for a crystalline unit cell for absolute comparison with the coherent limit. The independent limit forms the mean scattering response from a model system and helps to define the total integrated scattering intensity expected from the model system. The total sample scattering intensity and its relationship with the independent limit is related to Vainshtein's conservation of diffraction intensity, which also predicts that the total integrated scattering intensity from a model system will be essentially independent of any 'structure' that might be present. The incoherent limit (Compton scattering) is a second structure-independent limit, depending only on the atomic makeup of a sample. The Compton scattering will also scale with the number of atoms in the model system, which allows a direct comparison with the independent limit based upon the same chemical unit or crystal unit cell.

Compton scattering represents the independent scattering from each of the electrons within a single atom (James, 1948). The quantum-level interaction that gives rise to Compton scattering removes energy from the incident X-rays, causing an increase in the X-ray wavelength for the emitted (scattered) X-ray. The wavelength shift increases as a function of scattering angle. The modification of the X-ray wavelength by the incoherent scattering process gives rise to the alternative term 'modified scattering response' (Warren, 1990). As with the atomic form factors, the Compton scattering response for different atoms has been tabulated, allowing a direct calculation of the incoherent limit for any crystalline or non-crystalline molecular model (*e.g.* Warren, 1990). When used for Debye normalization, however, an approximation can be used to derive the incoherent limit using the same atomic form factors as required to derive the coherent and independent limits. For an atomic model with n atoms, the approximate form can be expressed as

$$I_{\rm incoherent}(Q) \simeq \sum_i^n \frac{(Z_i - |f_i|^2/Z_i)}{B^3},$$

where Z is the total number of electrons within an atom and f is the atomic form factor. B represents the Briet–Dirac correction arising from individual electron 'recoil' when impacted by an incident X-ray. The recoil correction describes the change in X-ray wavelength. For Cu $K\alpha$ X-rays, B can be approximated by

$$B \sim 1 + 0.0744[\sin(\theta)/\lambda]^2.$$

The Briet–Dirac recoil correction can also be used to estimate the wavelength modification of the Compton scattering over the complete diffraction range for Cu $K\alpha$ X-rays. Out to 160°, the increase in wavelength is about 3%. This change is small enough that for many laboratory X-ray powder diffraction systems the Compton scattering will not be discriminated against by active optical components such as monochromators or mirrors in the diffraction beam path. As such, the incoherent limit can be used as a general lower limit to help scale measured data on an absolute electron scale; no real X-ray scattering intensity is expected to be observed below the Compton scattering limit. Despite the usefulness of Compton scattering as a scaling limit, the Compton scattering itself is one of the many diffuse X-ray scattering contributions to measured powder data and should typically be removed within a data pre-processing step in order to isolate the 'coherent' scattering response. Additionally, changes in the Compton scattering response can in principle be used for rudimentary elemental analysis.

To illustrate the full Debye normalization and transformation of measured data to electron units, glassy indomethacin will be used as a worked example. As noted earlier, the inherent continuous spherical symmetry introduces changes to the traditional Lorentz correction used for powder data when Debye modelling is to be performed. As such, for modelling non-crystalline materials and normalization *via* the Debye method, the working form of the LP factor (core instrument intensity response function) was taken to be

$$\mathrm{LP}_{\rm non\text{-}crystalline} \rightarrow \mathrm{Debye} \simeq \frac{\cos^m(\theta) \times [1+\cos^2(2\theta)]}{2\sin^{n-2}(\theta)}.$$

The instrument intensity function modelling performed in the previous section for two-reflection Bragg–Brentano systems returned values of $n \sim 2.1$ and $m \sim 0.0$. For the modelled Bragg–Brentano systems the Lorentz factor was, therefore, essentially removed from the instrument intensity function correction when powder data were to be used for Debye modelling or normalization. Fig. 5.6.18 displays a measured non-crystalline powder

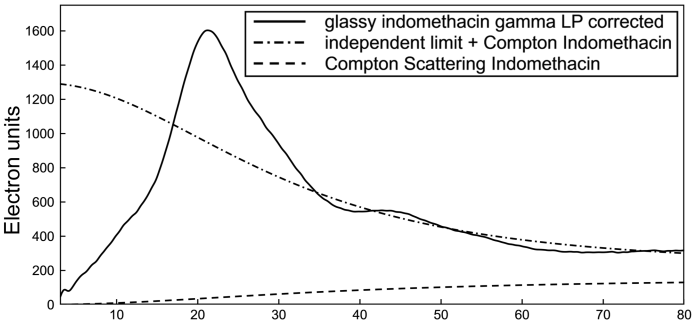

Figure 5.6.18
Non-crystalline powder pattern for glassy indomethacin after correction for the Bragg–Brentano instrument intensity response. The independent and incoherent limits as derived for a single indomethacin molecule are also displayed.

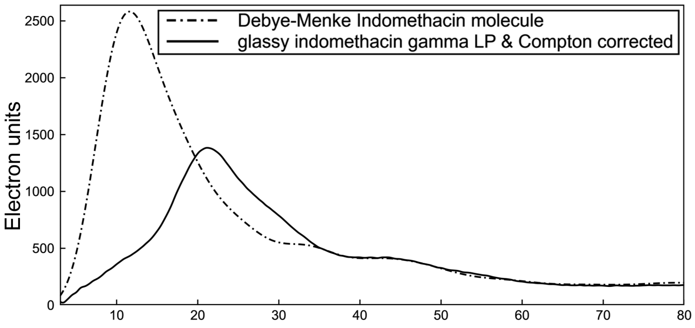

Figure 5.6.20
Non-crystalline indomethacin data after intensity correction and removal of the Compton response displayed with the Debye–Menke curve for a single indomethacin molecule.

pattern for indomethacin after correcting for the Bragg–Brentano instrument intensity response function as expressed above. The original crystalline powder sample was melted and quenched in a low-background Si sample holder to enable real-time measurement without disturbing the non-crystalline sample. The resulting indomethacin glass was stable enough for routine X-ray powder data collection.

The scaling of the intensity-corrected measured data to absolute electron units uses both the independent and incoherent limits as guides. No measured scattering should lie below the incoherent limit, and the combined independent and incoherent response becomes the asymptote for the high-angle data. In Fig. 5.6.18, a single indomethacin molecule was used to define the absolute electron scale. The scale of the incoherent limit (Compton scattering) will approach the number of electrons at large scattering angles, which is 186 for indomethacin ($C_{19}H_{16}NO_4Cl$).

The glassy indomethacin non-crystalline powder pattern was collected out to 80° 2θ, which is a larger angular range than often employed for organic crystalline systems. However, even with this extended range, it may be non-trivial to define exactly where the asymptotic oscillatory behaviour develops. In Fig. 5.6.18 it should be noted that the high-angle asymptote has been taken to be the independent limit plus the Compton scattering response.

For organic molecules, the higher-angle oscillatory behaviour (>30° 2θ for Cu $K\alpha$ X-rays) is most often due to the rigid atomic structure within a single molecule. Fortunately, for many organic systems, the molecule and the rigid structures that define the molecule are known. As an example, the structure for a single indomethacin molecule is shown in Fig. 5.6.19.

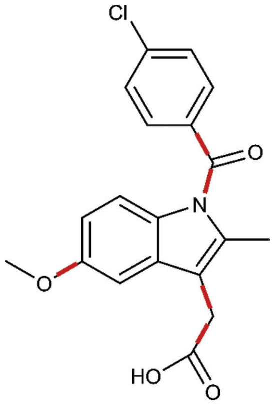

Figure 5.6.19
A single indomethacin molecule with the five significant torsion degrees of freedom indicated in red.

From a known molecular structure, the Debye–Menke calculation can be used to derive the expected high-angle response. In Fig. 5.6.20, the intensity-corrected non-crystalline powder pattern for indomethacin is displayed after correcting for Compton scattering. The calculated Debye–Menke response for a single indomethacin molecule is plotted with the corrected non-crystalline powder pattern. The observed data above about 30° 2θ closely follow the calculated Debye–Menke response, suggesting that scaling the intensity-corrected measured powder pattern to the independent and Compton scattering limits is an effective approach to transform the measured data to absolute electron units.

Below 30° 2θ, the calculated single-molecule curve diverges significantly from the measured non-crystalline powder pattern. Scattering arising from the longer-length-scale atom–atom distances within the molecule is heavily damped for the glassy solid of indomethacin. Damping of the scattering intensity expected for longer-length-scale atom–atom correlations has been observed for all organic molecular systems independent of molecule size or rigidity. The divergence between the calculated Debye–Menke response and observed data at low angles suggests that a single independent rigid molecule is not a complete model for the residual structure present within glassy indomethacin. A more robust model of glassy indomethacin including the impact of non-crystalline packing density on the low-angle Debye response will be investigated in Sections 5.6.12 and 5.6.13.

This worked example for glassy indomethacin not only demonstrates the use of Compton scattering and the independent limit as a means to transform measured powder patterns into electron units, but also suggests that the calculated rigid-molecule high-angle Debye response may provide a more robust transformation tool. This is especially true when using powder data not measured out to high enough diffraction angles in order to fully develop asymptotic behaviour with respect to the independent limit. Furthermore, as melt–quench glassy indomethacin can be reproducibly made in the laboratory, the sample may be used to verify and refine the derived high-angle instrument intensity response function. [Melt–quench indomethacin can be made directly in a low-background silicon holder by heating the holder to a few degrees above the melting point (~453 K for the gamma crystalline form). Once at temperature, powdered crystalline indomethacin added to the holder should immediately melt. When the holder is full of liquid indomethacin, the sample should be allowed to naturally cool to ambient temperature in a relatively dry atmosphere. Undisturbed glassy indomethacin should be stable for many months in the holder.]

5.6.10. Application of the Debye normalization procedure

For non-crystalline material analysis, normalization and background modelling procedures are two prerequisites for subsequent analysis, much like peak picking and profile fitting are prerequisites for the analysis of crystalline materials. A common application for organic non-crystalline materials is the characterization of powder patterns corresponding to materials produced under different conditions. Because of the metastability of non-crystalline solids, non-crystalline materials can be significantly affected by the choice of production processes and storage conditions, which may result in materials with very different physical and chemical properties. An appropriate normalization procedure allows a rational analysis of absolute variances between non-crystalline powder patterns that may be correlated with physical or chemical properties.

While the single-molecule Debye response can provide the basis for a robust normalization procedure, one of its challenges is the dependence on the molecular structure. In the non-crystalline state, the removal of crystalline packing constraints enables individual molecules to explore all energetically available molecular conformations. To assess the variance introduced by molecular conformation on the Debye response, a number of different energetically favourable conformations should be modelled. If the molecule of interest exhibits different crystalline polymorphs, then equilibrium molecular conformations can be extracted from the crystal structures without resorting to molecular modelling. As an example, indomethacin, which was used in the previous illustration of the Debye normalization procedure, has two relatively common crystal forms. The stable polymorph is gamma (CSD refcode INDMET; Kistenmacher & Marsh, 1972) and the metastable polymorph is alpha (CSD refcode INDMET02; Chen *et al.*, 2002). The gamma polymorph is triclinic ($P\bar{1}$) with a single unique molecule in the asymmetric unit, while the alpha polymorph is monoclinic ($P2_1$) with three unique molecules in the asymmetric unit. Between them, the two crystalline polymorphs contain four different equilibrium molecular conformations. In addition to the four crystalline molecular conformations, the molecular modelling program *SPARTAN* (Wavefunction, Inc., 2016) was used to minimize a generic indomethacin molecule *in vacuo* and in a water environment. In Fig. 5.6.21, the Debye–Menke curves for the four equilibrium molecular conformations and the two energy-minimized conformations are plotted along with Compton- and LP-corrected observed data for glassy indomethacin. All Debye–Menke curves displayed in Fig. 5.6.21 are similar, with the largest variance being at low angles for the larger atom–atom distances. Although indomethacin is a small organic molecule (about 322 Da), it exhibits five significant torsional degrees of freedom (see Fig. 5.6.19) allowing multiple molecular conformations. Despite the inherent molecular flexibility, the equilibrium and minimized conformations give calculated Debye curves that are essentially the same at higher diffraction angles ($>30^\circ\ 2\theta$). This behaviour reflects the robustness of short-distance atom–atom correlations within rigid molecular segments and supports the use of the high-angle Debye response as a suitable asymptotic limit for robust data normalization.

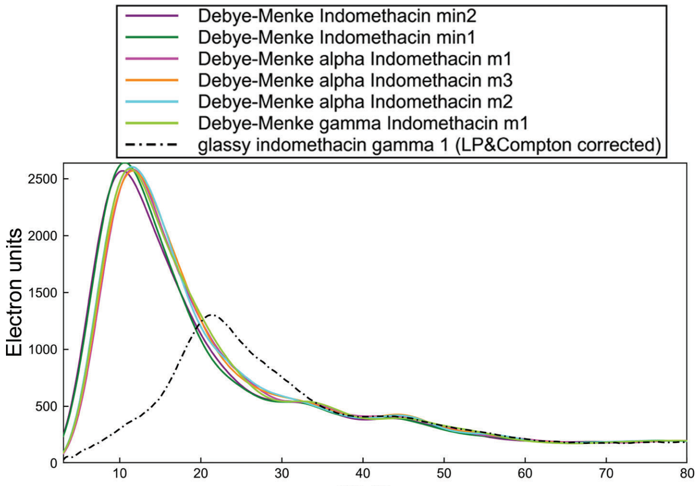

Figure 5.6.21
Non-crystalline indomethacin data after intensity correction and removal of the Compton response displayed with the Debye–Menke curves for different indomethacin molecular conformations.

With non-crystalline diffraction responses being essentially continuous in nature, chemometric variance-based data analysis procedures provide useful analytical methods for the investigation of production-induced difference between solid forms. With any variance-based analytical method, the spurious variances that might affect the analysis should be controlled. This requires well defined and well controlled experimental methodology. For example, the Bragg–Brentano reflection geometry is sensitive to sample presentation and requires a consistent flat and level sample with the sample surface aligned to the instrument reference surface. To investigate the impact of sample presentation for Bragg–Brentano reflection measurements, two different melt–quench procedures were performed using gamma indomethacin. In the first procedure, about 20 mg of powdered gamma indomethacin was mounted in a silicon low-background holder with a flat and level surface. The sample holder was then placed on a hotplate set to 453 K. Once the powder had completely melted, the holder was placed on the bench top and allowed to cool to ambient temperature. As the glassy indomethacin has a higher bulk density than the packed powder, the resulting sample surface was slightly lower than the instrument reference height. In the second preparation, the silicon low-background holder was heated to 453 K and 20 mg of powdered gamma indomethacin was slowly added. The sample holder was again placed on the bench top and allowed to cool to ambient temperature. The second preparation procedure produced a curved sample surface which was higher than the instrument reference height at the sample centre. The glassy form of indomethacin has a glass transition temperature, T_G, of about 309 K, about 10 to 15 K higher than the ambient measurement temperature. The resulting glassy indomethacin data are displayed in Fig. 5.6.22 after performing an LP correction and removal of the Compton response. After following the full Debye normalizing procedure, the principal difference between the two data sets occurs at the primary halo. The halo position remains unchanged but the second preparation technique gives a slightly higher intensity. Sample preparation techniques and sample masses require careful control to ensure robust variance analysis.

Glassy indomethacin can be made from either the alpha or the gamma crystalline polymorph. The gamma crystal form melts at about 434 K while the alpha crystal form melts at about 429 K. The glassy forms originating from both the alpha and gamma crystalline forms have the same glass transition temperature ($T_G \simeq 309$ K) when measured under the same conditions. Using both the alpha and gamma forms to make the glassy material allows investigation of two different potential production variances. The first is the effect of the melting point and the second is the effect of the starting crystalline form. For preparation from the gamma

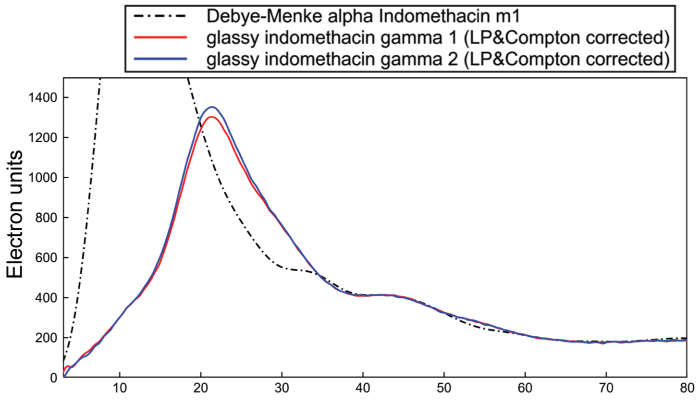

Figure 5.6.22
Non-crystalline indomethacin data collected for two sample-preparation methods after intensity correction (LP) and removal of Compton scattering. The Debye–Menke curve for a single indomethacin molecule is displayed for reference.

form, the hotplate was set to 453 K, while for the alpha form the hotplate was set to 448 K. Glassy samples were prepared using the level powder preparation technique investigated earlier. The resulting data are displayed in Fig. 5.6.23. Diffraction responses for the two glassy indomethacin samples are essentially the same and independent of production temperature and starting crystalline polymorph. The close agreement between the two glassy diffraction responses illustrates the reproducibility of the Debye normalization procedure when used in conjunction with controlled experimental conditions.

As a second comparative example, the glassy forms of (*R*,*S*)-ibuprofen (*R* + *S* racemic mixture) and *S*-ibuprofen were studied. The two crystal forms have very different melting points. (*R*,*S*)-ibuprofen melts at about 349 K while *S*-ibuprofen melts at about 325 K. The two crystal forms [(*R*,*S*) CCDC refcode IBPRAC (McConnell, 1974), (*S*) CCDC refcode JEKNOC10 (Freer *et al.*, 1993)] exhibit similar molecular packing and hydrogen-bonding relationships. The glassy forms of both *S*- and (*R*,*S*)-ibuprofen exhibit the same glass transition temperature of about 226.5 K and also exhibit the same change in heat capacity at T_G. The glassy forms were made as described previously, with the full, flat and level powder method using about 20 mg of material. The target hotplate temperature was about 20 K above the melt temperature. The ambient measurement conditions were between 65 and 70 K higher than the glass transition temperature; therefore, strictly speaking, the samples as measured were equilibrium super-cooled liquids and not glassy. Both super-cooled liquid samples were stable enough to collect high-quality diffraction data, with the *R*,*S* form being stable for extended periods of time. The molecular form of ibuprofen is displayed in Fig. 5.6.24 and the full Debye normalized (LP- and Compton-corrected) measured data are displayed in Fig. 5.6.25.

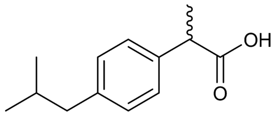

Figure 5.6.24
A chemical structure diagram for ibuprofen.

The observed non-crystalline X-ray powder diffraction (XRPD) data for *R*,*S*- and *S*-ibuprofen are very similar after Debye normalization. However, over multiple samples, the primary halo for the *S*-ibuprofen form appears to exhibit slightly increased intensity. The effect of this small intensity difference on the molecular packing description for ibuprofen will be investigated in Section 5.6.13.

While the indomethacin samples that were produced in different ways exhibited no significant variance in the non-crystalline diffraction response and the ibuprofen samples exhibited marginal differences, an example of a non-crystalline system that exhibits significant variability depending on the production method is simvastatin (Graeser *et al.*, 2008). When made through a melt–quench process, the non-crystalline form is stable for many months under ambient conditions. However, when made using cryo-grinding, re-crystallization begins within minutes of the system being exposed to ambient conditions. The melting point for simvastatin is about 412 K and the glass transition temperature of the melt–quench form about 305 K. The cryo-ground form exhibits a significantly broader glass transition event with an onset point about 10 K lower than that observed for the melt–quench material. Fig. 5.6.26 shows the measured powder patterns for the two different preparations of non-crystalline simvastatin after removing the instrumental background, applying the Debye normalization and subsequent removal of the Compton scattering. The data were collected in reflection Bragg–Brentano mode using a looping measurement to capture multiple frames. Only a single frame could be collected on the cryo-ground material before it began to re-crystallize, hence the slightly distorted profile. The resulting non-crystalline powder patterns both asymptotically approach the Debye–

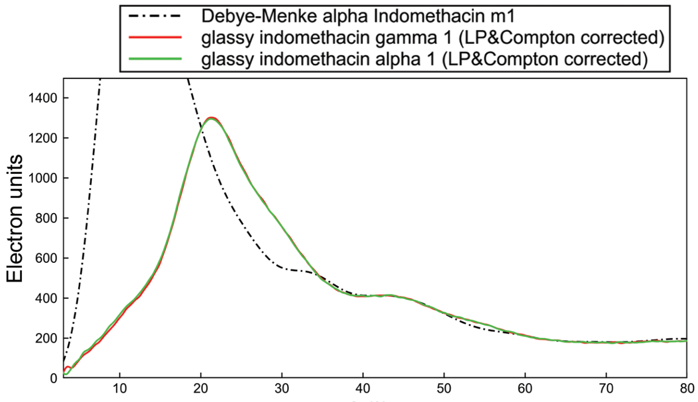

Figure 5.6.23
Non-crystalline indomethacin data collected for glasses prepared from alpha and gamma starting materials. The experimental data have been corrected for LP effects and Compton scattering. The Debye–Menke curve for a single indomethacin molecule is displayed for reference.

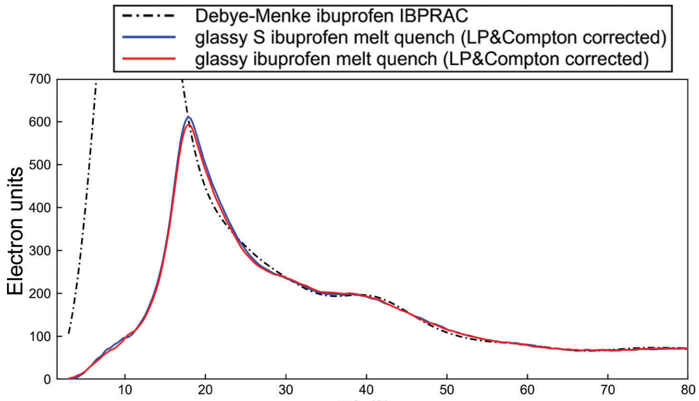

Figure 5.6.25
Non-crystalline ibuprofen data collected for glasses prepared from *R*,*S* and *S* crystalline starting materials. The experimental data have been corrected for LP effects and Compton scattering. The Debye–Menke curve for a single ibuprofen molecule is displayed for reference.

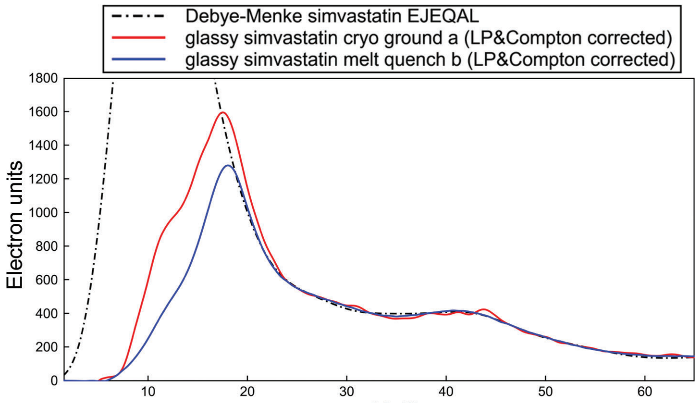

Figure 5.6.26
Normalized non-crystalline powder patterns for melt–quench and cryo-ground simvastatin displayed with the calculated Debye–Menke response for a single molecule of simvastatin.

Menke response at the highest measurement angles but have slightly different total diffraction intensities. As measured, the two powder patterns appear very similar, but after normalization significant differences become apparent. For the more stable melt–quench material, the primary low-angle halo moves to higher diffraction angles and more closely follows the independent limit. A similar trend relating material stability to X-ray diffraction profile shape has been observed using pair distribution function (PDF) analysis of API:polymer (where API is an active pharmaceutical ingredient) solid dispersions (see, for example, Velec *et al.*, 2005).

For non-crystalline sample preparation methods that are solvent based, residual solvent can distort the measured powder pattern in addition to changing the physical and chemical properties of the non-crystalline system. As explored in Section 5.6.7, low levels of residual solvent (<1%) can have a marked effect on the observed non-crystalline profile as a consequence of miscibility. The same is true of moisture picked up by the sample when exposed to ambient conditions. In this simvastatin example, both melt–quench and cryo-grinding are solvent-free sample preparation methods, so the observed differences in the non-crystalline powder patterns are associated with structural differences within the non-crystalline state rather than because of miscibility with a second component.

The normalized observed powder patterns for simvastatin, Fig. 5.6.26, are displayed with the Debye–Menke calculation for a single molecule. The molecular structure for simvastatin used for the Debye–Menke calculation as displayed in Fig. 5.6.27 was taken from the known crystal structure (CCDC refcode EJEQAL; Cejka *et al.*, 2003). As was observed for indomethacin, the higher-angle data corresponding to short distances within a single simvastatin molecule follow the calculated Debye–Menke response, but at low angles the observed data diverge significantly from the Debye–Menke calculation. The measured response for the melt–quench material more closely follows the higher-angle single-molecule Debye–Menke response from about 20° 2θ (less than about 4.4 Å) than the response for the cryo-ground material does. This suggests that the melt–quench material only exhibits local order related to the irreducible structures within a single simvastatin molecule. As pointed out above, close agreement between the observed non-crystalline data and the Debye–Menke response at higher angles and the damping of the low-angle halo both appear to be indicators of increased physical stability with respect to other non-crystalline forms of the same molecular entity. A more detailed analysis of the non-crystalline states of simvastatin and their related physical stabilities is in preparation. The origin of the low-angle difference between calculated and observed non-crystalline powder patterns and why certain materials diverge from the Debye–Menke response will be explored in Section 5.6.12.

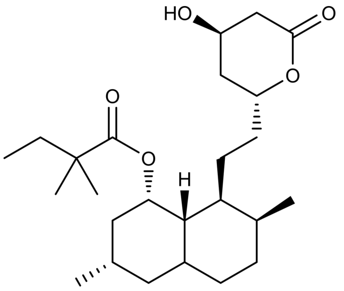

Figure 5.6.27
A chemical structure diagram for simvastatin.

5.6.11. Universal appearance of non-crystalline powder patterns

While modelling non-crystalline powder patterns within the spirit of the Debye method can be time-consuming and complex because a representative atomic level model is needed, some general observations can be made through direct inspection of normalized powder patterns. Pairwise distribution function (PDF) analysis (see Chapter 5.7) may also be used to provide direct analysis of measured non-crystalline powder patterns. One of the first observations when inspecting non-crystalline powder patterns is that the powder patterns appear visually similar to each other independent of the size, complexity or atomic composition of the constituent molecules. From the Debye–Menke theory, large rigid molecules should exhibit low-angle halos consistent with the long intramolecular distances present within the molecule. Furthermore, the nature of the X-ray measurement (*i.e.* the atomic form factor and Lorentz–polarization correction) should force these long-distance halos at low angles to have increased measured intensity relative to the shorter-distance halos. Yet, from the examples presented in this chapter, it is clear that the observed lower-angle response is significantly less than predicted. This loss of low-angle response forces the observed diffraction halos to lie within a narrow range of 2θ values. In Fig. 5.6.28, the normalized observed non-crystalline powder patterns for molecules of different levels of complexity and size are displayed together. The lowest-angle halo corresponds to melt–quench simvastatin, the middle halo is from melt–quench indomethacin and the higher-angle halo is for liquid

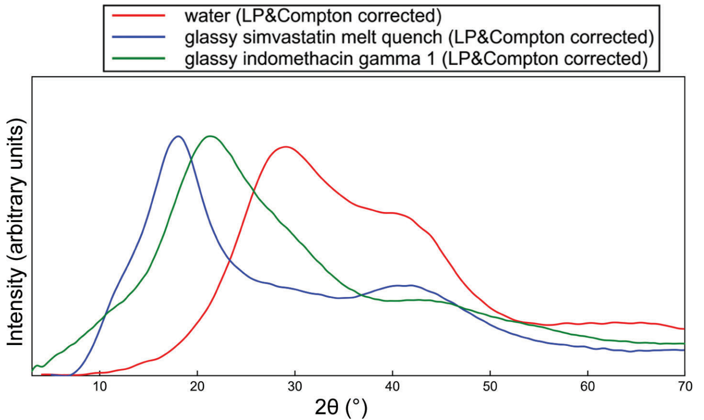

Figure 5.6.28
Normalized observed reflection powder patterns for simvastatin, indomethacin and water after full Debye normalization.

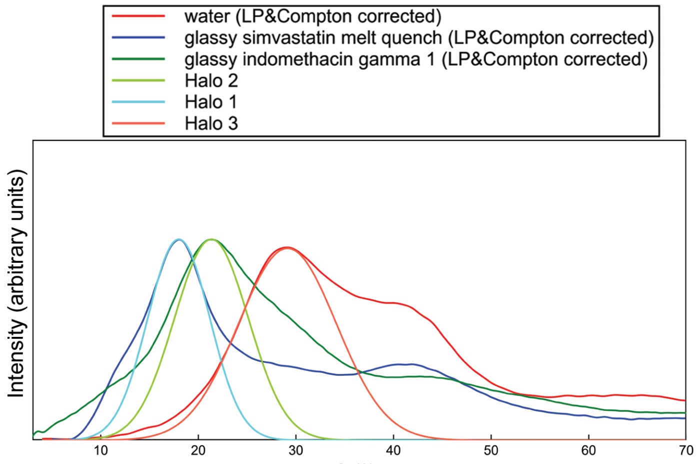

Figure 5.6.29
Normalized observed non-crystalline powder patterns (LP and Compton corrected) plotted with primary halo responses using a microstrain model with a microstrain variable of about 22%.

water. The data have been normalized to give similar halo peak intensities and are plotted on an arbitrary *y*-axis scale.

In addition to the absence of low-angle features, one of the most striking features of this plot is that the width of the primary halos increases as a function of the position of the halo. This is a common observation for molecular organic systems and can be considered to be a universal property of molecular glassy systems. A similar phenomenon of increasing peak width with increasing measurement angle is observed for crystalline diffraction peaks due to microstrain. Indeed, the universal feature of non-crystalline halo width can be described using a microstrain diffraction formula: integral breadth (2θ in radians) = $4\varepsilon\tan(\theta)$, where ε is the microstrain variable and takes a value of approximately 0.22 for non-crystalline halos. Calculated Gaussian profiles using the microstrain formula with a microstrain variable of about 22% are shown along with the normalized data in Fig. 5.6.29. The Gaussian heights and positions are taken directly from the primary halo in each normalized data set.

A more useful description of the universal halo width can be derived by describing random packing as an incremental type of disorder (*e.g.* random walk) and deriving an effective length scale of coherent order. Peak-broadening expressions have been derived by many authors (for example, Scherrer, 1918; Stokes & Wilson, 1944; Williamson & Hall, 1953; Warren & Averbach, 1950; Langford, 1980; Karen & Woodward, 1998) to address specific characterization needs. A general expression will be presented here that is amenable to many types of disorder including thermal vibration, point defects, microstrain and loss of long-range order. The general expression is based upon the Fourier-transform approximation for kinematic diffraction phenomena (Cowley, 1995; Guinier, 1994) and as such is based on the average atomic structure of a material. This is in direct contrast to the Debye theory, which is based upon the instantaneous local atomic structure. For simplicity, the average sample material in real space with respect to a spatial vector $\mathbf{r}$ will be considered to consist of a periodic lattice function $g(\mathbf{r})$, a generic atom type with electron-density function $\rho(\mathbf{r})$ and a bounding shape function $h(\mathbf{r})$ that limits the order length scale. A vector description based on $\mathbf{r}$ is used for real-space properties, as these properties may vary in different directions within the sample material. Along any single direction within the sample from an arbitrary origin, the average internal electron-density distribution can be mathematically described by

$$\text{directional electron density} \simeq [\rho(\mathbf{r}) * g(\mathbf{r})]h(\mathbf{r}),$$

where $*$ indicates convolution. The structure expression informs us that the atomic electron density appears around each lattice site and that the lattice is constrained to lie within a specific boundary. Applying a Fourier-transform convolution rule gives the diffraction amplitude from the model structure when the diffraction vector lies along the specific direction described by the structure expression,

$$\text{diffraction amplitude} \simeq [g(\mathbf{Q}) * h(\mathbf{Q})]\rho(\mathbf{Q}),$$

where $f(\mathbf{r}) \leftrightarrow f(\mathbf{Q})$ implies a Fourier transform. In the diffraction amplitude expression, the shape function is now convoluted with the lattice function, giving shape 'broadening' around every diffraction peak. In the amplitude expression, the atom contribution becomes a multiplicative constraining envelope limiting the diffraction amplitude as a function of $\mathbf{Q}$. Amplitude envelopes and intensity damping are the roles typically played by atomic form factors and unit-cell structure factors along with average vibrational disorder like the Debye–Waller thermal factor. The lattice, shape and atom functions are generic enough containers to hold a range of different physical structures. For example, the atom function could describe atoms, molecules, unit cells or supra-molecular structures. Essentially, any fundamental building block of a solid-state system can be substituted into the atom function. Any local atomic contributions not included within the average structure will give rise to diffuse scattering and are not described by this specific Fourier-transform approach. Local deviations from the average structure will be considered in more detail in Section 5.6.12.

This very simple diffraction amplitude expression allows the conceptual modelling of disorder affecting the lattice, the atoms and/or the bounding shape, and will be used throughout this chapter to explore different types of disorder. The utility of the Fourier-transform approach comes from the use of lattice, atom and shape functions that pass through the Fourier transform. Tables of Fourier-transform pairs can be found online (http://www.thefouriertransform.com/pairs/fourier.php; http://uspas.fnal.gov/materials/11ODU/FourierTransformPairs.pdf) and in a number of diffraction textbooks (Cowley, 1990; Guinier, 1994). Two common transform pairs that will be used to derive a peak-broadening expression are the infinite periodic lattice and the Gaussian function:

$$\begin{aligned}&\text{Periodic lattice with spacing } (d) \text{ in } \mathbf{r}\text{: } g(\mathbf{r})\\ &\quad\leftrightarrow \text{periodic lattice with spacing } (2\pi/d) \text{ in } \mathbf{Q}\text{: } g(\mathbf{Q}),\end{aligned}$$

$$\begin{aligned}&\text{Gaussian: } g(\mathbf{r}) = \left[\frac{1}{(2\pi)^{1/2}\sigma_r}\right]\exp\left[-\mathbf{r}^2/(2\sigma_r^2)\right]\\ &\quad\leftrightarrow \text{Gaussian: } g(\mathbf{Q})\exp\left[-(\mathbf{Q}\sigma_r)^2/2\right].\end{aligned}$$

What is important to note from the Gaussian pair is that a real-space Gaussian with a standard deviation of σ_r becomes a Gaussian in diffraction space with the inverse standard deviation of $(1/\sigma_r)$. Returning to the peak-broadening model, if on average over all crystalline regions in the system the finite-size shape effect is taken to be a Gaussian distribution with a standard deviation of σ_D, then the amplitude peak broadening will also be Gaussian in nature with a standard deviation of $(1/\sigma_D)$. As measurements are performed on diffraction intensity not amplitude, the standard deviation of the measured Gaussian peak broadening becomes: $1/(2^{1/2}\sigma_D)$.

With respect to non-crystalline molecular systems, the rigid structures within a molecule act like building blocks for the non-crystalline material. For a high-density system where molecules pack to minimize the free volume, the building blocks tend to exhibit a directionality driven by either intermolecular bonding constraints or the physical shape of the building block through van der Waals type short-range interactions. In addition, within a non-crystalline solid, molecular building blocks are also not able to occupy the same location in space at the same time. The combination of directionality and self-avoidance suggests that a self-avoiding and directed random walk might provide a realistic model as to the nature and consequences of random packing in a solid non-crystalline system made up from molecular building blocks. A directed self-avoiding random walk introduces a disorder that cumulatively increases for each subsequent block (step) along a specific packing direction. Cumulative disorder models have been used extensively to model diffraction from disordered systems [*e.g.* paracrystalline systems and disorder in clay minerals (Reynolds, 1989; Guinier, 1994, chapters 3, 6, 7 and 9)].

In the cumulative disorder model considered here, the nearest-neighbour relationship between two general molecules (the basic units) is used to define a packing direction **r** and an effective nearest-neighbour packing distance (the step). Projecting the packing distance out to longer distances along **r** creates the expectation of a simple periodic lattice $G(\mathbf{r})$. In reality, because of the random packing, as we proceed along the virtual lattice, each subsequent molecule is likely to be increasingly displaced from the ideal lattice point, creating the cumulative disorder. For a self-avoiding random walk, the standard deviation that describes the probability distribution of any specific molecule about the ideal lattice position is given by

$$\text{Standard deviation} = CN^{(1-X)},$$

where N is the step number away from the original molecule along the virtual lattice and C expresses how directed each random step is towards the preferred packing direction. For self-avoiding random walks X typically takes a value lying between 0.5 and 0.8 depending on the nature of the random walk. If we use a Gaussian probability distribution to describe the random step, then C is the standard deviation associated with the directional packing of nearest neighbours and $X = 0.5$.

In Fig. 5.6.30, a general directed random walk probability distribution is displayed, showing the cumulative uncertainty in the location of subsequent building blocks along the virtual lattice. The probability function describing the potential location of a specific molecule has been modelled as a unit-area Gaussian function. The sum over all the normalized Gaussian probability functions for all steps generates an effective probability distribution function for the building blocks as a function of distance from the chosen original block. The effective probability function is continuous at larger distances with unitary probability. For real systems, the continuous unitary probability corresponds to the effective molecular number density. It should be no surprise that the one-dimensional distribution function visually appears like a radial density distribution function for 'random' packing of solid spheres (Zernicke & Prins, 1927; Hosemann, 1951; Hosemann & Bagchi, 1962). The one-dimensional distribution function acts as an effective lattice within the Fourier diffraction derivation. This effective lattice is driven by the inherent shape of the molecule and is not necessarily related to any crystalline lattice. In real non-crystalline systems, the random packing will be three-dimensional in nature, the one-dimensional distribution being a simplification for strong molecular anisotropy.

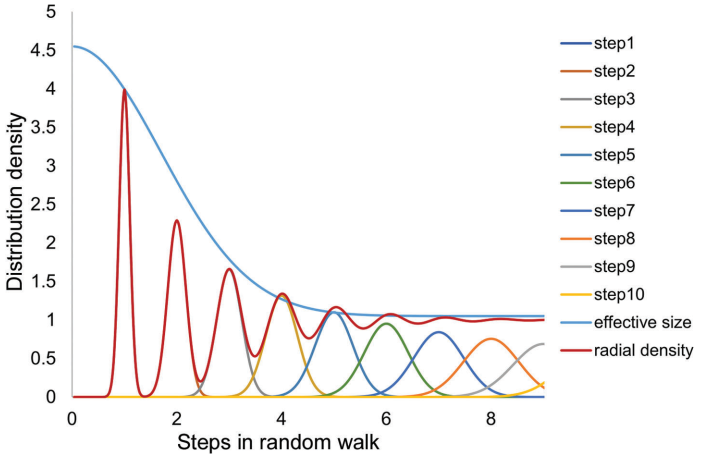

Figure 5.6.30
Cumulative disorder in the relative position of a building block as a function of steps away from the starting block. The sum of the individual probabilities appears like a radial distribution function typical of randomly packed spheres. The decay in the peaks of the sum gives an effective length scale over which spatial correlation occurs.

The cumulative incremental disorder as shown in Fig. 5.6.30 (the lattice) introduces an effective size that defines a region where some spatial correlation exists between building blocks. The effective size distribution illustrated in Fig. 5.6.30 is again based upon a Gaussian distribution to directly tie into the peak-broadening expression. The standard deviation of the Gaussian effective size function can be expressed as a number of steps, N_s, which can be converted to a physical size using the length of each step (*i.e.* the size of the building block), dN_s. This allows the diffraction amplitude peak broadening to be expressed as

$$\text{Random walk peak broadening standard deviation}\,(Q_p) = \sigma(Q_p) \cong \frac{1}{dN_s},$$

where N_s is the standard deviation of the effective size in number of steps and d is the effective step size given by the halo position $[d \simeq \lambda/(2\sin\theta)]$. The random-walk effective size, therefore, gives a size-broadening term that varies with the observed peak position. Using the random-walk size term, Fig. 5.6.29 can be re-created using a fixed N_s value. Fig. 5.6.31 shows the re-created plot using a value of $2^{1/2}N_s = 1$. The halo broadening observed for non-crystalline materials can therefore be described by a random packing procedure where the effective length scale of the coherent order is limited to nearest-neighbour distances alone. As such, universal halo widths observed for non-crystalline materials can be thought of as being the broadest peaks observable at any measurement angle for a one-dimensional molecular lattice. The Gaussian peak widths can be converted to a more traditional volume-averaged effective crystal size as described by the Scherrer equation [integral breadth (2θ in radians) $= K\lambda/(D_v\cos\theta)$] by noting that for $K = 0.95$, $D_v \simeq 2.225d \times 2^{1/2}N_s$.

For the derivation of the random-walk halo width, the nature of the solid-state building block is not defined. The block might be an entire molecule, or a rigid segment of a much larger molecule, or even atomic in nature. Whatever the individual building blocks, the model is based upon the hypothesis that there exists a characteristic spacing d that describes how the blocks are packed together. As a first approximation, that characteristic spacing has been derived from an observed halo posi-

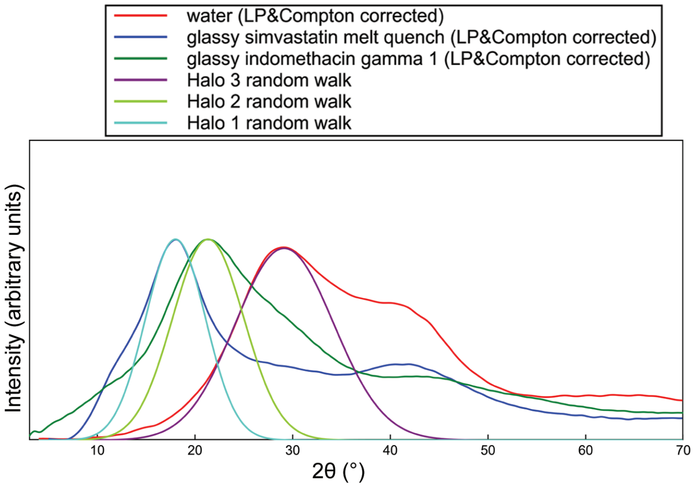

Figure 5.6.31
Normalized observed non-crystalline powder patterns (LP and Compton corrected) plotted with primary halo responses using a random-walk size model with $2^{1/2}N_s = 1$.

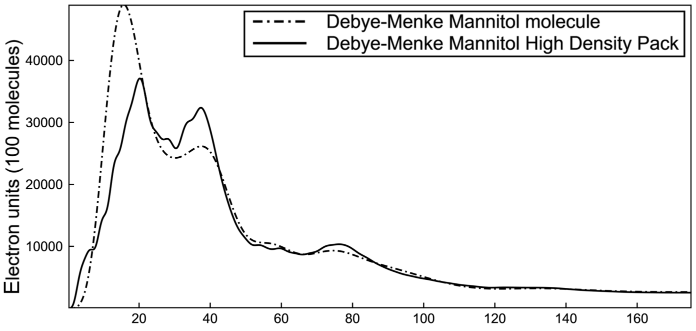

Figure 5.6.32
Debye–Menke response for mannitol compared with the mean simulated powder pattern for high-density randomly packed mannitol based upon multiple 100 molecule clusters generated using *PACKMOL*.

tion. Based upon the random-packing model, the observed non-crystalline universal halo width serves to signify that the solid-state building blocks are randomly packed and may not give any specific information on non-crystalline domain sizes or even molecular sizes. The observation that, in the non-crystalline solid state, the residual structure can be described by random packing of irreducible rigid building blocks is consistent with the high-symmetry description where ideally every atom (building block) becomes equivalent to every other atom (building block) within the system.

The self-avoiding random walk model proposed above is effectively a one-dimensional virtual lattice and implicitly assumes a preferred packing direction between neighbouring molecules. This preferred packing can appear in high-density systems driven by molecular shape or bonding constraints. This inherent asymmetry in local order can also be explicitly built within a general Debye model by constructing molecular models that show the expected preferred packing directions, although it can be challenging to construct models that effectively demonstrate randomness. A one-dimensional lattice model is an idealistic view of real non-crystalline materials and does not reflect their inherent spherical symmetry and isotropic nature. However, the Fourier-transform diffraction approach and lattice model provide useful insights into the nature of non-crystalline materials.

5.6.12. Steps towards an effective lattice model of high-density randomly packed materials

We have seen in the previous section how random packing in dense systems can lead to the natural formation of an effective lattice when the nearest-neighbour relationships between basic units have some directionality. Furthermore, the cumulative disorder associated with such a lattice can provide a framework for modelling the universal halo width phenomena of molecular non-crystalline systems. A second universal feature of molecular non-crystalline systems is the significant damping of scattering from longer-length-scale atom–atom correlations, which causes the observed diffraction intensity at lower angles to be significantly less than the predicted intensity from the Debye equation. One hypothesis is that the low-angle damping arises from conformational disorder. As an example, in Fig. 5.6.21, which shows the calculated Debye response from different low-energy and equilibrium conformations of a single indomethacin molecule, the variance in the low-angle response is larger than the variance in the higher-angle response. The low-angle variance reflects the conformation-induced changes in longer-distance atom–atom relationships. To allow for the conformational flexibility expected for non-crystalline systems, the Debye responses for the various possible conformations can be summed to give a single effective Debye response for an average molecule. While the higher-angle average response will remain relatively unchanged from a single molecule, the lower-angle response will be broadened and damped. Nevertheless, the conformation-induced low-angle intensity loss is not sufficient to describe the significant observed low-angle damping. Furthermore, the same intensity damping is also observed for small rigid molecules.

A second hypothesis is that low-angle intensity damping arises from the type of intermolecular packing present in the non-crystalline system. To investigate the role played by packing and packing density on the calculated Debye responses, a series of random dense packing studies was performed using rigid mannitol molecules. Mannitol molecules (with hydrogen atoms removed) can be readily packed to give a simulated high-density randomly packed system that allows the direct observation of the effect of packing on a calculated Debye response without the additional complexity of changes in conformation. *PACKMOL* was used to determine multiple packing configurations for mannitol with forced high and medium packing density. For the high-density packing, 100 mannitol molecules were constrained within a sphere radius of 15.75 Å with an allowed closest approach distance of 2.8 Å. For the medium-density packing, the sphere radius was expanded to 17.0 Å and the closest approach distance was set to 3.0 Å. Multiple packing configurations were generated using different random seeds, and the calculated powder patterns for each configuration were summed together to approximate a random system. The mean Debye response for the high-density packing exercise is displayed in Fig. 5.6.32 along with the Debye response of a single mannitol molecule. The mean high-density response displays some discontinuities due to the finite number of packing runs performed. A larger number of independent packing runs would be required in order to approach a smooth mean Debye response corresponding to an isotropic and random system. Nevertheless, the mean Debye response clearly demonstrates suppression of the lower-angle diffraction intensity. The high-density packing model was based upon a rigid mannitol molecule, which suggests that high-density molecular packing alone is a sufficient requirement to drive the observed low-angle intensity damping.

This exercise on mannitol dense packing is fully within the spirit of the Debye approach in that molecular models were constructed that naturally express the features of interest for the system under investigation. However, owing to the computational overhead imposed by this avenue of study, approximate forms of the Debye equation have been proposed (James, 1948; Menke, 1932; Warren, 1990) that can be applied without resorting to large-scale molecular models. One useful approximation is the introduction of a lattice function to describe molecular packing in bulk systems. In this approximation, the Debye function is applied to just the basic unit, and the lattice function takes care of the random packing. To investigate the relationship between the Debye diffraction equation and the Fourier lattice model, a simplified approach to a total diffraction model as outlined by Cowley (1990, chapter 5) will be followed. This approach makes use of the generalized Patterson function (the self-correlation function), which can be stretched to encompass the Debye formalism.

In the Patterson-function approach, the same expression used to determine the directional electron-density distribution in the previous section will be used. For this derivation, it will be assumed that the sample is large when compared with the molecule size and the length scale of local order. This allows the sample shape to be removed from the expression. As previously, the non-crystalline sample is assumed to be composed of basic units (molecules) that can be described by a three-dimensional electron-density function $\rho_0(\mathbf{r})$. Within the high-density non-crystalline state the average packing of the basic units is assumed to follow a four-dimensional 'lattice' function $g(\mathbf{r}, t)$, where t indicates time. Following Cowley, the electron-density distribution within the sample can be expressed as

$$\rho(\mathbf{r}, t) = \rho_0(\mathbf{r}) * g(\mathbf{r}, t).$$

This reflects a non-crystalline system where the basic unit has a specific electron-density distribution that is not time dependent but a packing function that may change over time. The general Patterson or self-correlation function becomes

$$P(\mathbf{r}, t) = [\rho_0(\mathbf{r}) * \rho_0(-\mathbf{r})] * [g(\mathbf{r}, t) * g(-\mathbf{r}, -t)].$$

Taking the Patterson function of the basic unit to be

$$P_0(\mathbf{r}) = \rho_0(\mathbf{r}) * \rho_0(-\mathbf{r})$$

and the distribution Patterson to be

$$G(\mathbf{r}, t) = g(\mathbf{r}, t) * g(-\mathbf{r}, -t),$$

then the general Patterson can be written as

$$P(\mathbf{r}, t) = P_0(\mathbf{r}) * G(\mathbf{r}, t).$$

One of the primary advantages of this approach is the direct Fourier-transform relationship between the Patterson function and the measured diffracted intensity: $P(\mathbf{r}, t) \leftrightarrow I_P(\mathbf{Q}, t)$. As such, the Patterson function can be experimentally determined. Applying the Fourier-transform convolution rule,

$$I_P(\mathbf{Q}, t) = \left|F_0(\mathbf{Q})\right|^2 \left|G(\mathbf{Q}, t)\right|^2,$$

where $P_0(\mathbf{r}) \leftrightarrow |F_0(\mathbf{Q})|^2$ and $G(\mathbf{r}, t) \leftrightarrow |G(\mathbf{Q}, t)|^2$ are direct Fourier-transform pairs.

The time variation is included within the general Patterson function for more liquid-like non-crystalline systems whose local intermolecular packing arrangements may change over the duration of a single measurement. However, X-ray diffraction measurements on the laboratory scale are usually considered to be instantaneous measurements. As such, the time dependence should more accurately be expressed as a time average over all instantaneous intensities. For a solid non-crystalline system, the local molecular-packing arrangements are considered to be static over the duration of a typical measurement. However, from point to point in a bulk sample, the packing arrangements may change. In this sense, the diffraction measurements on both liquid and solid non-crystalline samples are essentially configurational averages over many instantaneous diffraction events. For the basic unit, the configuration average can be expressed as an average over the rotational degrees of freedom θ and ϑ:

$$\langle P(\mathbf{r})\rangle = \langle \rho_0(\mathbf{r}, \theta, \vartheta) * \rho_0(\mathbf{r}, \theta, \vartheta) * g(\mathbf{r}, \theta, \vartheta) * g(\mathbf{r}, \theta, \vartheta)\rangle_{\theta,\vartheta}.$$

The configurational averaging as expressed above represents essentially the same spherical averaging as applied during the derivation of the Debye diffraction equation and gives a spherically symmetric Patterson function dependent on a single scalar distance.

In the random-walk example, the presence of an effective lattice was due to the preferred packing that occurs between nearest neighbours. This suggests that the angular symmetry of the basic unit will be reflected in the angular symmetry of the packing function. If, however, as a first approximation the symmetry relationship is broken between the basic unit and packing function, then the spherically averaged Patterson can be expressed as

$$\langle P(\mathbf{r})\rangle = \langle \rho_0(\mathbf{r}, \theta, \vartheta) * \rho_0(\mathbf{r}, \theta, \vartheta)\rangle_{\theta,\vartheta} * \langle g(\mathbf{r}, \theta, \vartheta) * g(\mathbf{r}, \theta, \vartheta)\rangle_{\theta,\vartheta}$$

which through the Fourier convolution relationship gives the diffraction intensity:

$$I_P(\mathbf{Q}) = \langle |F_0(\mathbf{Q}, \theta, \vartheta)|^2\rangle \langle |G(\mathbf{Q}, \theta, \vartheta)|^2\rangle$$

where $\langle \rho_0(\mathbf{r}, \theta, \vartheta) * \rho_0(\mathbf{r}, \theta, \vartheta)\rangle_{\theta,\vartheta} \leftrightarrow \langle |F_0(\mathbf{Q}, \theta, \vartheta)|^2\rangle$ and $\langle g(\mathbf{r}, \theta, \vartheta) * g(\mathbf{r}, \theta, \vartheta)\rangle_{\theta,\vartheta} \leftrightarrow \langle |G(\mathbf{Q}, \theta, \vartheta)|^2\rangle$ are direct Fourier transform pairs. The basic unit diffraction intensity is expressed as a spherically averaged self-correlation and is effectively the Debye diffraction intensity. This suggests that within the above approximations the total Debye diffraction intensity of a densely packed non-crystalline form can indeed be represented by a form that includes a lattice function:

$$I_D(Q) \sim I_{0,D}(Q) L_D(Q),$$

where $I_{0,D}(Q)$ is the usual Debye diffraction intensity from the basic unit and $L_D(Q)$ is the diffraction intensity due to an effective lattice. The effective lattice function is a spherically averaged diffraction intensity. During the derivation of the expression, in order to extract the effective lattice function from the basic unit Debye response, the symmetry relationship between the basic unit and the lattice function was broken. As a consequence of the loss of this symmetry relationship, the expression as derived is only rigorously applicable in cases when either the basic unit and/or the lattice function have spherical symmetry in real space. The same spherical symmetry constraints also apply to the Menke shape-correction term explored in Sections 5.6.4 and 5.6.5.

The most frequently referenced spherically symmetric lattice function with respect to the Debye diffraction model is the spherical exclusion zone. For both liquid and solid non-crystalline systems, due to the effectively instantaneous nature of the X-ray diffraction event, molecules (basic units) are not observed to occupy the same space during the diffraction event. As such, each basic unit has an effective exclusion zone around it that defines

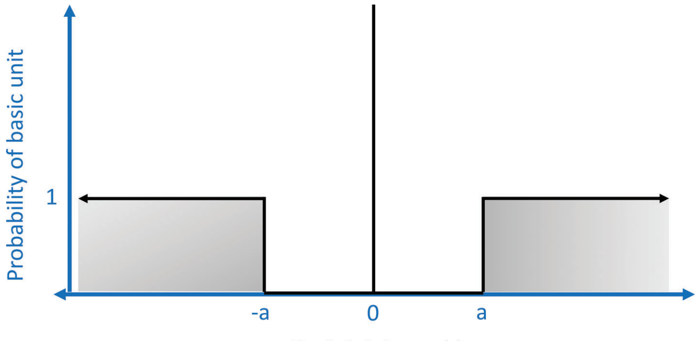

Figure 5.6.33
Schematic representation of a spherical exclusion zone centred on each basic unit.

the closest approach possible for neighbouring basic units. For molecular glasses, the exclusion zone is one of the sources of rigidity as the density increases. In Fig. 5.6.33, a schematic representation of the spherical exclusion zone is presented as a function of radial distance from the centre of a general basic unit. At the origin lies a delta function that places the central basic unit. For a distance of *a* around the central basic unit, there is zero probability of finding another basic unit. This defines the exclusion zone of radius *a*. Outside the exclusion zone the probability of finding another basic unit is unity in all directions and at all distances. In the exclusion-zone representation, there exists no short-range inter-unit order except for the exclusion zone itself.

The diffraction amplitude for a spherical exclusion zone of radius *a* with central delta function can be written as

$$G_{\rm SE}(Q) = 1 - \emptyset(Qa)$$

where $\emptyset(Qa)$, the sphere diffraction amplitude, is given by the usual expression,

$$\emptyset(Qa) = \frac{3[\sin(Qa) - (Qa)\cos(Qa)]}{(Qa)^3}.$$

The effective lattice function is now given by

$$L_{D,{\rm SE}}(Q) = |G_{\rm SE}(Q)|^2.$$

Fig. 5.6.34 shows the simulated impact of a spherical exclusion zone and the implied effective lattice on the calculated Debye–Menke response for mannitol (without hydrogen atoms). Sphere radii of 3.0, 2.5 and 2.0 Å were modelled, showing the increasing low-angle damping for increasing packing density (smaller exclusion-zone radii). For comparative purposes, the results for the high-density random packing exercise are also presented. The high-density packing fixed the closest approach between neighbouring mannitol molecules to be 2.8 Å, which is slightly larger than the molecular radius of gyration (~2.5 Å without hydrogen atoms). The exclusion-zone radii were chosen to bracket both the closest approach distance and the radius of gyration. Mannitol is essentially a linear molecule, yet the application of a spherical exclusion zone to the single-molecule Debye–Menke response provides a reasonable approximation as to the calculated Debye response from high-density randomly packed mannitol.

One of the primary goals of this chapter was to arrive at a theoretical diffraction framework that allowed the calculation of powder patterns for ideal molecular non-crystalline solids. Ideal non-crystalline solids are defined as exhibiting no short-range inter-atom order except for the rigid segments of the individual molecules (basic units). Based upon the mannitol example, the inclusion of a spherical exclusion zone and the implied effective lattice allow the Debye diffraction response for a single molecule to be extended to represent a densely packed ideal non-crystalline solid. Using this composite Debye approach, in principle, given a molecular entity or basic unit (dimer, trimer, unit cell *etc.*) the expected powder pattern for the corresponding ideal non-crystalline solid can be calculated.

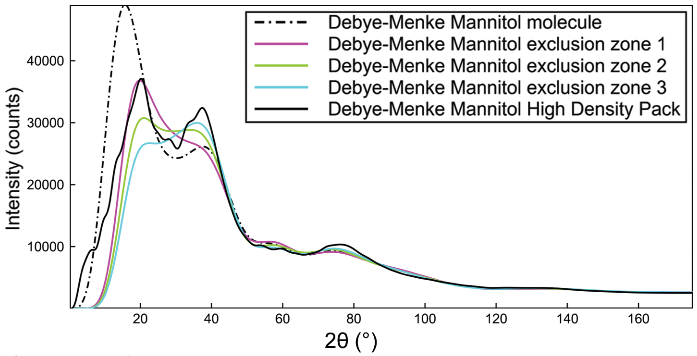

Figure 5.6.34
Effect on the calculated Debye–Menke single-molecule response for mannitol of a hard-sphere exclusion zone. Sphere radii of 3.0, 2.5 and 2.0 Å were chosen based upon the radius of gyration for mannitol. For comparative purposes, the calculated mean Debye–Menke response for the high-density random packing exercise is also displayed. Data have been scaled to 100 mannitol molecules (without hydrogen atoms).

Before considering practical examples of non-crystalline solids, it is instructive to extract the function form of $L_D(Q)$ directly from the calculated powder pattern for packed rigid mannitol molecules. From the observed powder diffraction intensity after full Debye normalization and transformation into electron units, the effective Debye lattice function can be derived by dividing by the Debye response for a single basic unit:

$$L_D(Q) \simeq I_{{\rm obs},D}(Q)/I_{0,D}(Q).$$

To extract the effective lattice function for the calculated response for the mannitol high-density random packing, the normalized observed diffraction intensity can be replaced by the Menke-corrected Debye response scaled to a single molecule. Using the Menke-corrected Debye response removes the shape effects of the small model size.

The extracted effective lattice function for the high-density packing exercise is shown in Fig. 5.6.35 along with the calculated effective lattice function for a spherical exclusion zone with radius 2.6 Å. The general shape and oscillatory nature are reproduced by the calculated function, but the magnitude of the oscillations is larger in the function extracted from the 100

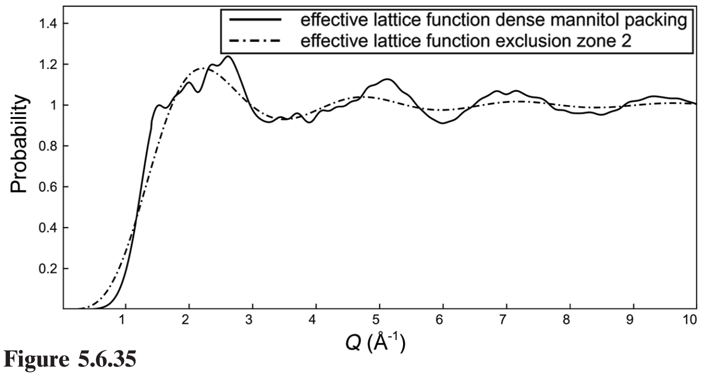

Figure 5.6.35
Extracted lattice function for high-density randomly packed mannitol compared with the theoretical lattice function derived from a spherical exclusion zone with a radius of 2.6 Å.

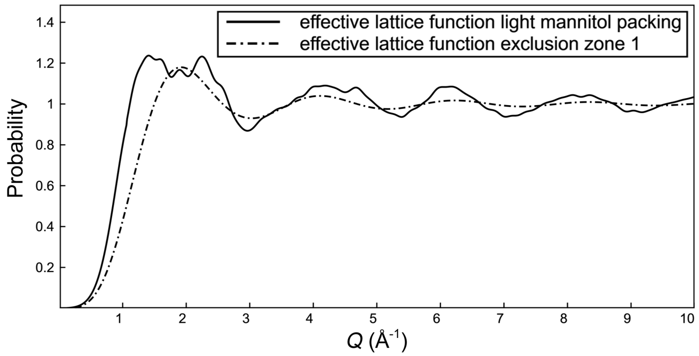

Figure 5.6.36
Extracted lattice function for low-density randomly packed mannitol compared with the theoretical lattice function derived from a spherical exclusion zone of 3.0 Å.

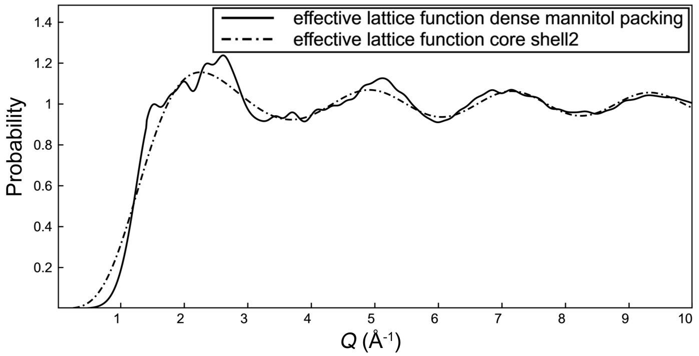

Figure 5.6.38
Extracted lattice function for high-density randomly packed mannitol compared with the theoretical lattice function derived from a three-sphere concentric exclusion zone.

randomly packed molecules. The closest approach distance was fixed for the high-density random packing to be 2.8 Å, which is similar to the displayed exclusion-zone radius.

Fig. 5.6.36 displays the equivalent effective lattice function extracted from the low-density mannitol packing exercise compared with the calculated lattice function derived from a spherical exclusion zone with radius 3.0 Å. During the low-density random packing of mannitol the nearest approach distance was set to 3.0 Å, which matches the radius of the displayed spherical exclusion zone lattice function. The general shape and oscillatory nature are reproduced by the calculated function but, as with the high-density packing, the magnitude of the oscillations is larger in the function extracted from the 100 randomly packed molecules.

Extracted lattice functions for the randomly packed low-density and high-density mannitol models are visibly more complex than the calculated lattice functions for spherical exclusion zones. Some of the additional complexity may come from the random-packing methodology and the limited sampling size, but overall the extracted data suggest a more complex packing. Within the Debye modelling methodology, any more complex packing model must maintain the inherent spherical symmetry. One approach to constructing more complex spherically symmetric effective lattice functions makes use of a core–shell-type of formulism as employed for small-angle scattering data modelling (for example, Pedersen, 1997). An example three-level core–shell model is illustrated in Fig. 5.6.37, which also breaks down the cumulative diffraction influence of the concentric spherical probability functions. When assembling the cumulative diffraction responses for the concentric spherical contributions, it is important to normalize the cumulative amplitude to be equal to unity as Q approaches zero.

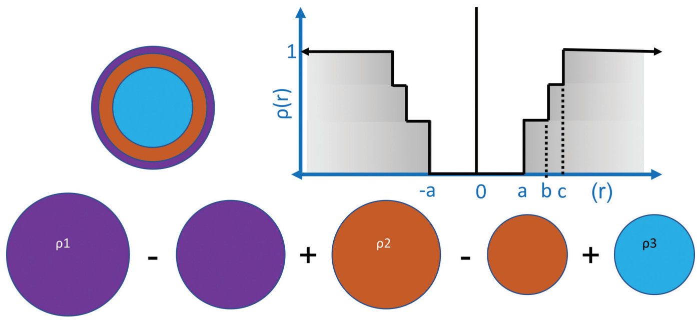

Figure 5.6.37
Schematic illustration of a spherical core–shell-type model to describe more complex exclusion zones and packing models for basic units.

Using the same formalism as for the spherical exclusion zone, the core–shell effective lattice function for the three-sphere model illustrated in Fig. 5.6.37 can be written as

$$G_{\rm SE}(Q) = \frac{1}{M_3}\Big\{1 - [\rho_1 V_1 Ø(Qc) + (\rho_2 - \rho_1) V_2 Ø(Qb) + (\rho_3 - \rho_2) V_3 Ø(Qa)]\Big\}$$

where V_1 is the spherical volume corresponding to exclusion distance c and M_3 is the normalizing constant:

$$M_3 = \rho_1 V_1 + (\rho_2 - \rho_1) V_2 + (\rho_3 - \rho_2) V_3.$$

The individual exclusion probabilities and distances were refined using the *Excel* Solver function in order to achieve the best fit between the calculated and extracted effective lattice functions. For the high-density mannitol random packing example, the best fit to the extracted effective lattice function using a three-sphere concentric lattice model is displayed in Fig. 5.6.38. The overall goodness of fit for the three-sphere lattice function is an improvement over the single spherical exclusion zone. For the high-density mannitol model, the molecular pair distribution and atomic pair distribution can be directly extracted from the molecular centres and atomic coordinates. The molecular pair distribution is displayed along with the three-sphere model in Fig. 5.6.39. The molecular pair distribution was calculated from a single random packing run using the coordinates of the molecular centres. The spiky nature of the pair distribution reflects the challenges of random packing for small sample sizes.

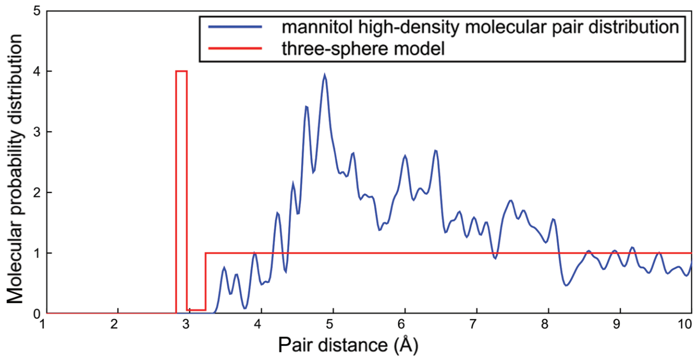

Figure 5.6.39
Molecular centre pair distribution extracted from high-density mannitol packing compared with a three-sphere effective lattice model. The three-sphere effective lattice model has an inner exclusion zone of radius 2.81 Å followed by a narrow high-probability zone of 0.15 Å corresponding to four molecular nearest neighbours.

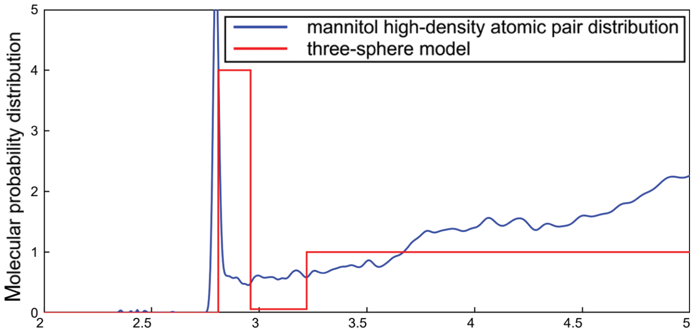

Figure 5.6.40
Normalized atom pair distribution extracted from high-density mannitol packing compared with a three-sphere effective lattice model. The atom pair distribution displays only intermolecular relationships.

The intermolecular nearest-neighbour distance for the high-density model is centred around 5 Å (consistent with known crystal structures) with an average coordination number of about 4. The molecular nearest-neighbour coordination number is reproduced in the three-sphere model, but the effective exclusion zone distance is clearly not related to intermolecular distances. In Fig. 5.6.40 a normalized atom pair distribution is displayed along with the three-sphere effective lattice model. The atom pair distribution was normalized by removing all intermolecular atom–atom distances and reducing to a molecular electron scale. The single strong intermolecular atom–atom distance (~2.8 Å) occurs at the same distance as the primary spherical exclusion zone. The nature of the high-density mannitol packing is clearly driven by the packing algorithm and the closest approach limit. Nevertheless, the model allows a demonstration of the utility of the effective lattice function method in combination with the Debye model.

5.6.13. Practical application of the effective lattice function determination

The glassy phase of indomethacin presents an instructive example of the step-by-step procedure used to determine an effective lattice function from measured data. The first prerequisite is that the measured non-crystalline XRPD response has to be normalized following the full Debye normalization. This includes a correction for both the instrumental background and the core instrument intensity response function, in addition to removal of the Compton scattering and any significant absorption or multiple-scattering contributions. Fig. 5.6.20 shows the full Debye normalization for glassy indomethacin where the high-Q response in the measured data follows the high-Q response of the molecular entity.

Once the measured data have been normalized, an appropriate basic unit for the effective lattice should be identified. Typically, the initial basic unit selected will be a single molecule. The effective lattice, as derived within the Debye approach, is based upon spherical symmetry. As such, any local ordering or specific chemical bonding should ideally be developed within the choice of basic unit. The selection of potential basic units can be partially automated using databases of common packing motifs, crystal structures of similar molecules and/or from molecular simulations. The choice of basic unit gives the appropriate Debye response function, $I_{0,D}(Q)$, with which to derive the effective lattice functions. For each basic unit, an effective lattice function, $L_D(Q)$, was extracted using iterative optimization of spherically symmetric core–shell models within the Microsoft *Excel* Solver module. The final 'best fit' core–shell lattice function was then combined with the corresponding calculated Debye response for the basic unit to determine a simulated glassy indomethacin response, which was compared with the original observed data. Each optimized solution consisting of a unique basic unit and corresponding core–shell lattice function was ranked according to how well the simulated glassy response matched the observed glassy response. The highest-ranking basic unit was a single molecule extracted from the known crystal structure of the alpha form. However, a basic unit consisting of the $P\bar{1}$ dimer extracted from the crystal structure of the gamma form also gave a good description of the observed data. Inspection of the derived core–shell lattice functions indicated that, for indomethacin, the dimer solution was not physically realistic. The effective lattice function corresponding to the highest-ranking single-molecule solution along with the 'best fit' core–shell model is shown in Fig. 5.6.41. The resulting core–shell lattice exhibits a well defined exclusion boundary at about 3.2 Å with an associated nearest-neighbour closest approach shell. The closest approach shell has an increased probability (number density) with a coordination number of about 1.2.

The fully normalized glassy indomethacin data are displayed in Fig. 5.6.42 along with simulated data sets derived from the single-molecule and $P\bar{1}$ dimer basic units. Both models provide an adequate fit to the observed data. This highlights a frequently encountered scenario when modelling non-crystalline materials, where a number of different models of local molecular order can describe the observed data. In practice, non-crystalline total diffraction data typically have lower information content than that observed for crystalline materials. As such, modelling non-crystalline materials requires strict limits with respect to the numbers of degrees of freedom used during any minimization procedure. The information content for non-crystalline diffraction data is encoded in the subtle changes in slope observed across the full diffuse continuous profile. To reveal the subtle changes in the diffuse halos requires a comprehensive data pre-

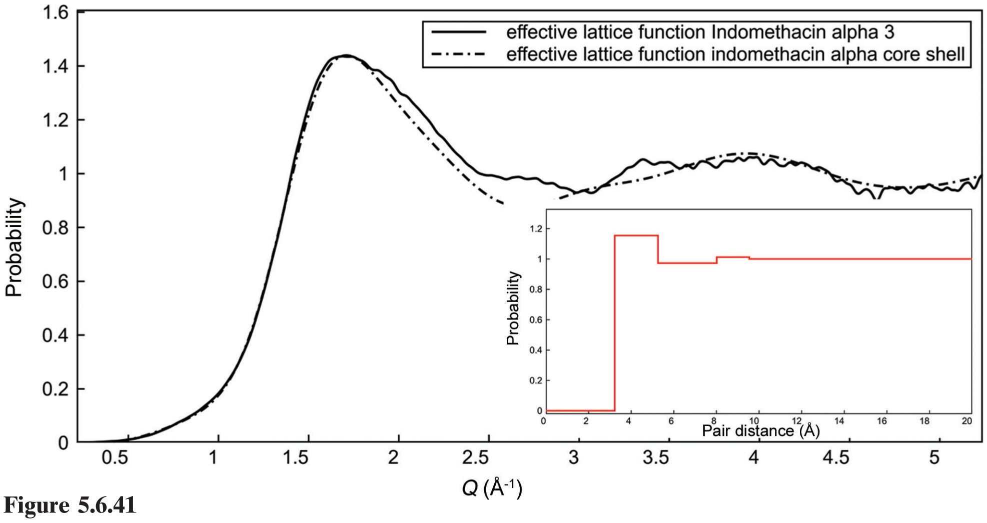

Figure 5.6.41
Effective lattice function for a single indomethacin molecule compared with the 'best fit' core–shell model (three-shell model) (inset).

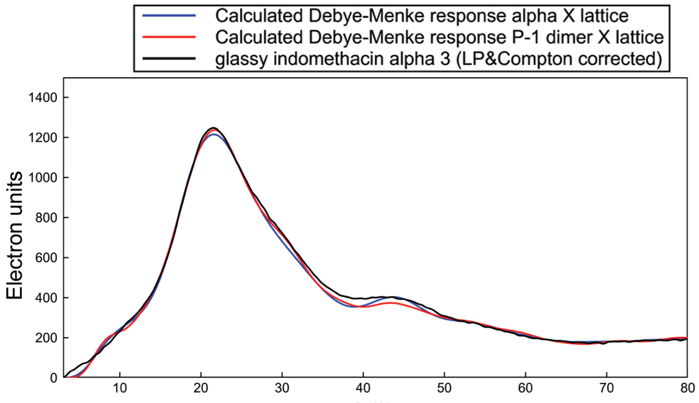

Figure 5.6.42
Fully normalized glassy indomethacin data (measured on the melt–quench alpha form) displayed with simulated data sets derived from single-molecule and dimer basic units.

treatment and normalization to remove as much of the instrument-driven variance as possible. The full Debye normalization procedure provides a robust and reproducible approach to the required data pre-treatment; however, to limit the degrees of freedom during modelling, the full Debye normalization should be performed prior to the modelling exercise and the resulting input data file taken as a fixed target. Furthermore, the choice of potential basic units should also be performed prior to the modelling procedure. Basic units are either selected from known crystal structures or built within molecular modelling/packing programs. For each selected basic unit, the only allowed variables during minimization are the radius of the spherical exclusion zone plus the weight and width of the subsequent concentric shells that define the packing model. For the 'best fit' indomethacin lattice function associated with a single-molecule basic unit, three concentric shells were used. The $P\overline{1}$ dimer basic unit required five concentric shells to achieve the same degree of fit to the observed data.

A comparison between the calculated Debye–Menke response for a single indomethacin molecule and the subsequent simulated data incorporating the core–shell lattice function, see Fig. 5.6.43, is instructive. As expected, both the Debye–Menke response and simulated data describe the observed high-angle diffraction features (above about 30° 2θ for Cu $K\alpha$ X-rays). The appearance of the primary halo at about 22° 2θ is driven by the exclusion zone around each molecule and the corresponding low-angle intensity damping. As observed with the mannitol random-packing models, the exclusion zone is related to nearest-neighbour electron-density closest approach distances and not explicitly related to intermolecular distances. As a consequence, for most linear or planar organic molecules, a common exclusion zone distance will be about 3.0 Å independent of molecular weight. This is in part the origin of the common primary halo positions for a wide range of organic molecular glassy materials. For the single-molecule basic unit, the exclusion-zone core radius was determined to be about 3.2 Å, which is consistent with single-molecule nearest-neighbour electron-density closest approach distances. For the $P\overline{1}$ dimer model, the required exclusion zone had a radius of about 3.1 Å, which was less consistent with closest approach distances for the larger basic unit. Molecular-dynamics simulation of glassy indomethacin (Xiang & Anderson, 2013) has indicated that, although the hydrogen-bonded dimers observed in the alpha and gamma crystalline polymorphs are present to a limited extent in the simulated glass, the molecular relationships are more complex with the appearance of extended hydrogen-bond chains. The extracted core–shell model is consistent with a complex local molecular environment which on average across a bulk glass reduces to an exclusion zone with weak nearest-neighbour correlation.

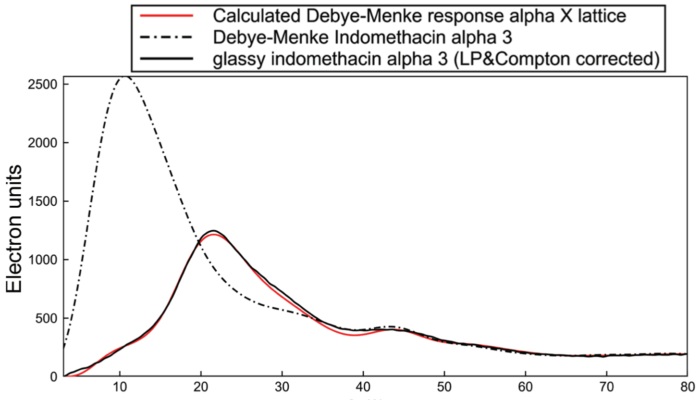

Figure 5.6.43
Fully normalized glassy indomethacin data (measured on the melt–quench alpha form) displayed with a simulated data set derived from a single-molecule basic unit and the corresponding Debye–Menke response.

An interesting example of effective lattice modelling that will be briefly discussed is that of simvastatin. Fig. 5.6.26 shows the two powder patterns collected on non-crystalline simvastatin prepared by melt–quench and cryo-grinding. These two non-crystalline forms of the same molecule exhibit significantly different physical stability with different glass transition and re-crystallization temperatures. After normalization, the two powder patterns are also observed to be significantly different in appearance. The powder pattern collected on the melt–quench data shows a shifting in the overall diffraction intensity towards higher angles while more closely following the calculated Debye–Menke curve at higher angles. As discussed previously, non-crystalline materials that generate powder patterns that closely follow the Debye–Menke curve have little in the way of local intermolecular order and approach the ideal non-crystalline symmetry state.

A relative shifting in diffraction intensity towards higher angles was also observed for simulated powder patterns generated from 100 randomly packed mannitol molecules. As the packing density is increased, the low-angle diffraction intensity is damped, and the primary halo intensity distribution is consequently shifted to higher angles. This is because of a reduction in the volume occupied by a single molecule and hence a reduction in the extent of the physical exclusion zone. Core–shell lattice

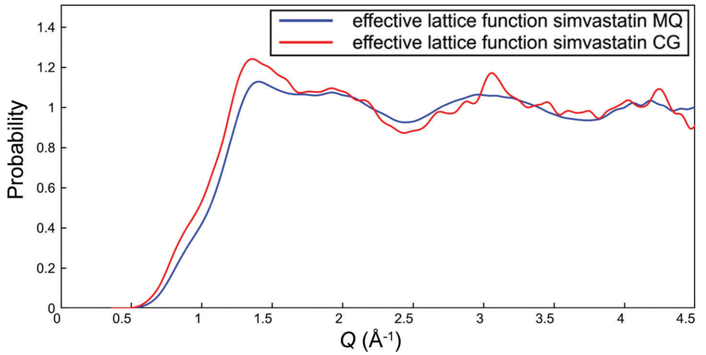

Figure 5.6.44
Effective lattice functions extracted from non-crystalline powder patterns measured on melt–quench (MQ) and cryo-ground (CG) simvastatin.

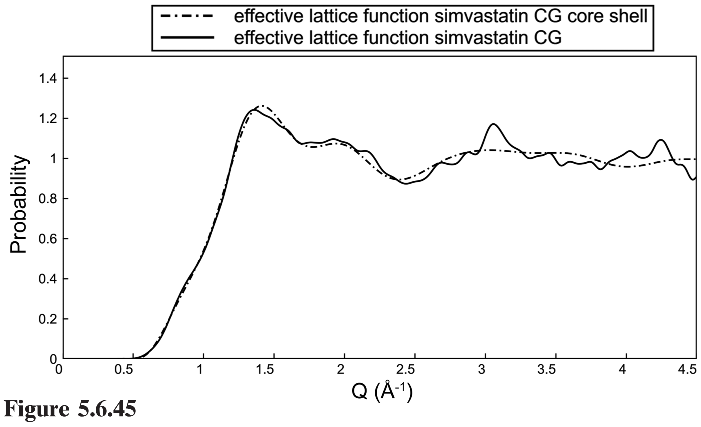

Figure 5.6.45
Core–shell lattice function fit to the effective lattice function for cryo-ground simvastatin.

function modelling can be performed on the simvastatin data to determine the difference in the exclusion zones for the melt–quench and cryo-ground materials. The extracted effective lattice functions are displayed in Fig. 5.6.44. The effective lattice function for the cryo-ground material exhibits significant noise due to the rapid data collection required to avoid re-crystallization.

The core–shell modelling was able to adequately describe both of the extracted lattice functions using a single-molecule basic unit and a core plus five concentric shells. The resulting fit to the effective lattice function extracted from non-crystalline cryo-ground data is shown along with the core–shell model data in Fig. 5.6.45.

The individual core–shell lattice models for the cryo-ground and melt–quench materials are displayed in Fig. 5.6.46. The general shape of the exclusion zone for the simvastatin materials exhibits a fuzzy boundary rather than the abrupt, well defined boundary observed for indomethacin. Outside the fuzzy exclusion zone, neither of the core–shell models exhibits a preferred molecular closest approach distance. The absence of significant intramolecular order except for an exclusion zone suggests that glassy simvastatin is close to an 'ideal' glassy system. The melt–quench simvastatin material exhibits a more restrictive exclusion zone than the cryo-ground material, as expected from the observed high-angle shift in the diffraction intensity. The resulting simulated data provide a good description of the observed data, describing all observed features of the non-crystalline profile for both cryo-ground and melt–quench materials.

While the change in the exclusion-zone profile between the cryo-ground and melt–quench materials is significant, the relationship between the exclusion zone and the packing density is more difficult to extract. As observed with the mannitol random-packing example, the extent of the exclusion zone is related to closest approach distances rather than the actual volume occupied by a single molecule. For the simvastatin example, the largest extent of the exclusion appears to increase from about 3.8 Å for the melt–quench material to about 4.0 Å for the cryo-ground material. This might be driven by a change in the average molecular conformation that forces the closest approach distance to change, or it might be related to an actual change in packing volume. Typically, changes in exclusion-zone profiles do not allow a direct modelling of molecular-packing differences but, as demonstrated for the simvastatin example, they can provide a measure of the change in physical stability between glassy forms of the same molecular entity.

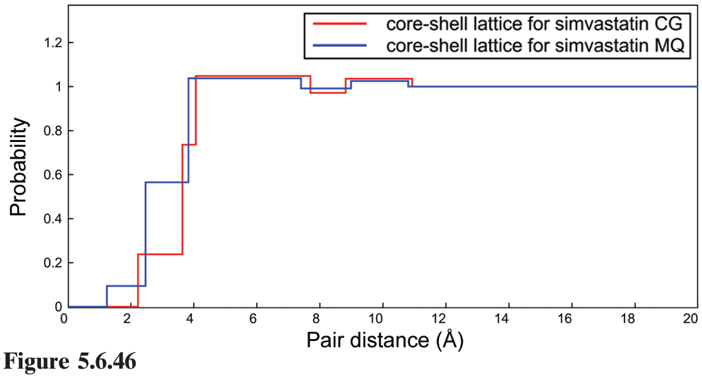

Figure 5.6.46
Core–shell lattice functions for cryo-ground and melt–quench simvastatin.

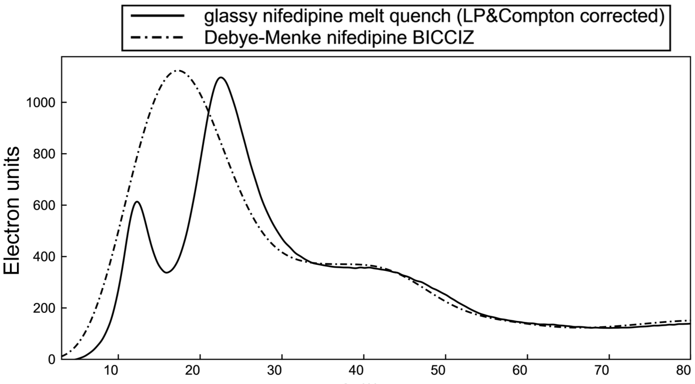

Figure 5.6.47
Fully normalized glassy nifedipine data (measured on a melt–quench glassy form) displayed with a single-molecule Debye–Menke response.

The previous examples (indomethacin and simvastatin) all exhibited weak low-angle halos in the corresponding non-crystalline diffraction patterns. In each case, the halo position was related to features within the individual molecular Debye diffraction profile rather than a specific intermolecular packing distance; see for example Fig. 5.6.43. The observed intensity of the smaller halo was, however, controlled by the specific molecular packing function. Nifedipine has been chosen as the last example in this section, as the glassy form exhibits two well defined diffraction halos within the total diffraction measurement that do not correspond to features in the individual molecular Debye response; see Fig. 5.6.47. The nifedipine molecule used for the Debye calculation was taken from the published crystal structure of the monoclinic polymorph (CCDC refcode BICCIZ; Triggle *et al.*, 1980). A molecular drawing is presented in Fig. 5.6.48.

The extracted effective lattice function and 'best fit' core–shell results are displayed in Fig. 5.6.49, and the corresponding simulated powder pattern is displayed in Fig. 5.6.50. The results clearly show that a five-shell spherical lattice model is able to fully describe both of the observed halos for glassy nifedipine. In addition to a well defined exclusion zone with a closest approach distance of about 3.15 Å, the derived lattice function is periodic in appearance, extending out to almost 20 Å. The overall periodic character of the core–shell lattice model suggests that a more

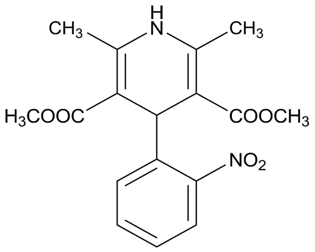

Figure 5.6.48
A chemical structure diagram for nifedipine.

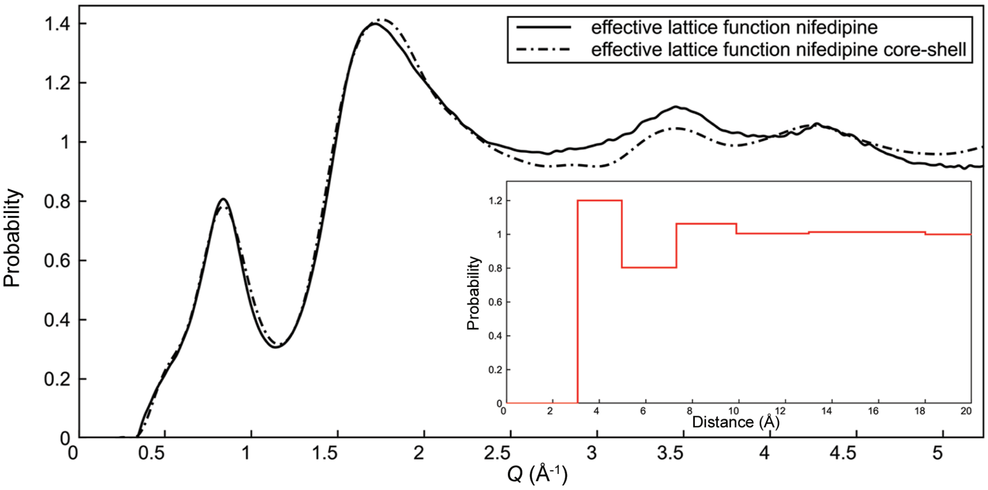

Figure 5.6.49
Effective lattice function for nifedipine extracted from measured glassy data plotted with the 'best fit' core–shell lattice model.

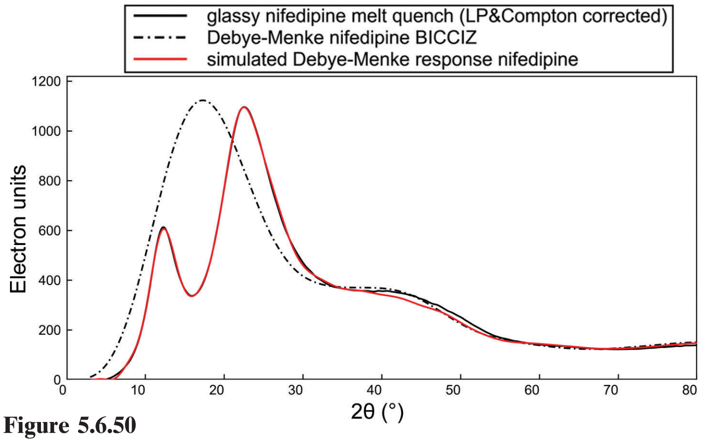

Figure 5.6.50
Fully normalized non-crystalline nifedipine diffraction response displayed with a simulated data set derived from a single-molecule basic unit with a core–shell lattice and the corresponding Debye–Menke response.

extensive local molecular order is driven by the characteristic shape of nifedipine and the associated preferred closest approach distances.

Although only a limited number of examples are presented in this section, the modelling results indicate that the total diffraction patterns from molecular non-crystalline systems can be adequately described using a single-molecule basic unit combined with a simple core–shell spherical lattice that describes the molecular exclusion zone and nearest-neighbour closest approach distances. However, the nifedipine core–shell results indicate that more extensive local order may be present within the glassy systems. The final section in this chapter explores modelling approaches for more extensive local order.

5.6.14. Debye diffraction models for larger molecular ensembles

The investigation of more extensive local ordering beyond what can be described by a spherical core–shell model will often require the simulation of total diffraction patterns from larger-scale molecular models. As with all total diffraction modelling using the Debye equation, the size and shape of the molecular cluster will be folded into the total diffraction response and may generate spurious results. As an example, in Fig. 5.6.17, the Debye total diffraction response calculated for a 3 nm silicon nanocrystal exhibited a series of weaker oscillations in addition to the expected diffraction peaks. The oscillations were generated by the sharp crystal surfaces of the nanocrystal atomic model. In previous sections, the spherically symmetric Menke correction has been used to remove molecular-shape effects from the Debye diffraction model. However, the Menke correction is a spherical approximation (similar to the Guinier small-angle scattering approximation) and will not fully compensate for molecular dimensionality and strong asymmetry in molecular shape. This was observed for the silicon nanocrystal example where the Menke correction did not remove the crystal-surface interference effects.

For larger-scale molecular models, an alternative Debye calculation procedure has been developed to avoid cluster size effects and to ensure representative sampling of the molecular model.

This approach is based upon the use of multiple spherical subsets (bubbles) extracted from the large-scale molecular model. As illustrated with the forced mannitol packing example, the shape effects from spherical molecular models can be fully removed by applying the Menke correction. To ensure a close-to-spherical electron-density distribution, each spherical subset must be wholly contained within the boundaries of the large-scale model. The radius of the spherical subset defines the effective coherence length of the Debye calculation. To explore different coherence lengths, a series of spherical radii can be used. Typically, spherical radii of 3.0 to 15.0 Å give sufficient coverage for non-crystalline materials. The number of spherical subsets selected and their location will be defined by the unique atomic environments that exist within the large-scale molecular model. If the molecular model is based upon a crystal structure, then each atom within the central asymmetric unit can be selected as a unique bubble centre. For large-scale randomly packed models, a reasonable approach is to select all atoms as unique bubble centres provided they are at least the spherical radius from the model boundary. A schematic representation of the bubble approach using multiple spherical subsets is shown in Fig. 5.6.51.

The core–shell lattice models for non-crystalline nifedipine indicated the presence of more extensive periodic local order

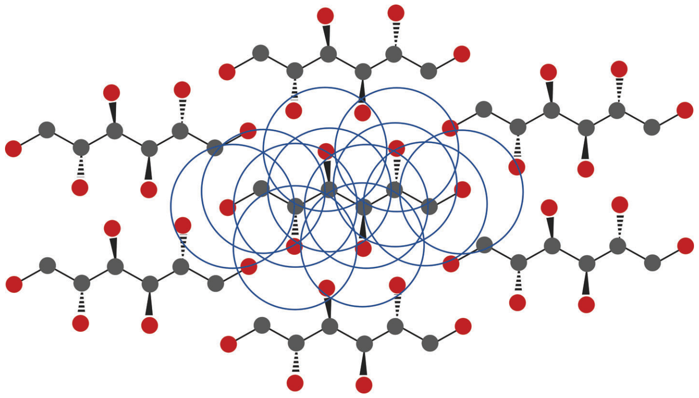

Figure 5.6.51
Schematic illustration of the multiple bubble Debye calculation approach using each atom for a single molecule of mannitol (without hydrogen atoms) as a unique bubble centre.

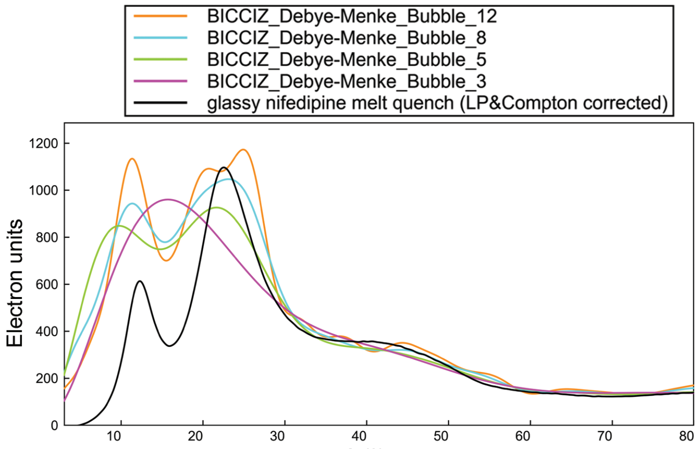

Figure 5.6.52
Total diffraction response for the Debye bubble calculation applied to the nifedipine crystal structure BICCIZ.

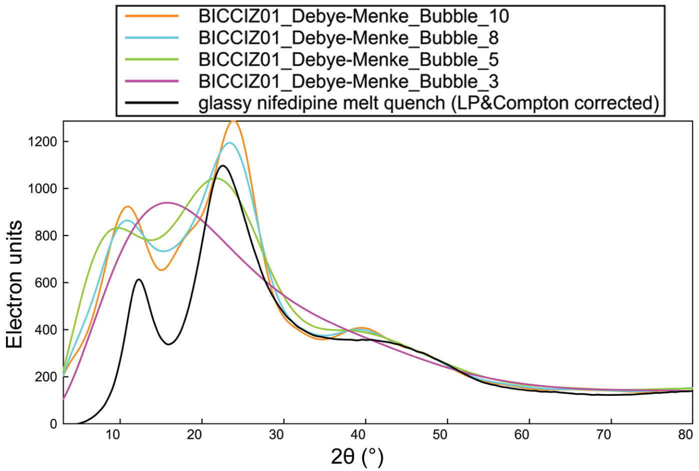

Figure 5.6.53
Total diffraction response for the Debye bubble calculation applied to the nifedipine crystal structure BICCIZ01.

than could be fully captured using a single-molecule packing model. To investigate the nature of the observed local order, the bubble Debye calculation approach was applied to large-scale crystalline models of nifedipine. The crystalline models were generated from the two known polymorphs of nifedipine (CCDC refcodes BICCIZ and BICCIZ01; Bortolotti *et al.*, 2011). Each model consisted of 5 × 5 × 5 unit cells; the smallest dimension was about 50 Å. For each molecular model, the atoms within the central asymmetric unit were taken as unique bubble centres. A series of Debye–Menke calculations was performed centred on the unique atoms and the total diffraction response was taken to be the sum of the individual Debye–Menke responses. The summation over multiple spherical subsets of the same radii gives a cluster-size response that can be removed by the Menke correction, giving a total diffraction response representative of the local molecular structure. To normalize the calculated total diffraction response from the bubble calculation, the high-angle diffraction response was scaled to match the single-molecule Debye–Menke response. The total diffraction results for the two nifedipine crystal structures are shown in Figs. 5.6.52 and 5.6.53 for bubble radii of 3, 5, 8, 10 and 12 Å (as indicated by _3 to _12 in the figure legends). For the small bubble radii, both crystal structures give a similar total diffraction response to the single-molecule Debye–Menke response. For larger bubble radii, both crystal structures develop a well defined low-angle halo similar in appearance to the experimentally observed data for non-crystalline nifedipine. The larger bubble radii as applied to the BICCIZ01 crystal structure also begin to develop the characteristic second higher-angle halo observed for non-crystalline nifedipine. The crystal structure BICCIZ gives a broader doublet in place of the higher-angle second halo and does not describe the observed data. For non-crystalline nifedipine, the core–shell lattice model indicated the presence of periodic local order and the Debye bubble calculation suggests that the periodic order might be related to the local molecular packing of the BICCIZ01 crystal structure.

The observation for nifedipine that the local order from a crystal structure is able to give a calculated total diffraction response that reproduces characteristic features observed in measured data from the non-crystalline material is not unusual. For many organic molecular non-crystalline systems, one of the associated crystalline polymorphs can be used as an initial model of non-crystalline local order. The relationships between crystalline and non-crystalline local order are beyond the scope of this introductory chapter and will be investigated in a subsequent publication.

5.6.15. Conclusions

The purpose of this chapter was to explore and introduce, at a basic level, X-ray diffraction from non-crystalline systems and to investigate the utility of the Debye diffraction approach as a tool for helping to characterize the measured diffraction data. Non-crystalline systems were defined to be high-density liquid or solid molecular systems that can be considered to be essentially isotropic and random with no long-range intermolecular order. Ideal non-crystalline systems represent the ‘high-symmetry’ ideal, where the only average interatomic order present will be due to rigid and irreducible fragments of individual molecules. X-ray powder diffraction measurements made on these types of systems give essentially continuous diffraction patterns characterized by a series of diffuse halos and an absence of any discrete diffraction peaks. Because of the continuous nature of non-crystalline diffraction, specific data-normalization and data-processing steps are required to transform the observed data into a suitable form for modelling.

For close-to-ideal non-crystalline systems, it was shown that total diffraction patterns calculated from a single molecule using the Debye theory should be representative of the measured high-angle diffraction response and can be used as an asymptote for data scaling. For systems where the molecular structure is unknown, the asymptote can be approximated by the independent coherent intensity, which is only dependent on the elemental makeup of the sample. For mixed or single-phase samples where the elemental makeup is similar (like organic systems) then the high-angle asymptote will be similar for all samples and data can be scaled to a common high-angle response. In practice, this Debye normalization step should only be applied when the measured background levels are similar from sample to sample or after suitable background modelling. The use of Debye normalization was illustrated using a model lyophile system where the sample masses and measurement conditions were carefully controlled to ensure a consistent background response. The Debye normalization was applied directly to the observed data, giving a self-consistent set of data that can be analysed using chemometric variance methods. Chemometric methods are often the method of choice for the characterization of non-crystalline systems and are particularly well suited to the quantitative analysis of multicomponent systems.

For more extensive total diffraction modelling, the measured data should be transformed into an instrument-free form that allows direct comparison with calculated Debye responses. The most critical data-processing step in this transformation was shown to be the modelling of instrumental background including sample-related contributions such as *Bremsstrahlung* and Compton scattering. After application of an appropriate background model, the background-free data were corrected to remove a calibrated instrument intensity response (*i.e.* a Lorentz–polarization correction was applied). Because of the nature of the Debye diffraction equation, the Lorentz correction as applied to non-crystalline data was shown to be different from the Lorentz corrections traditionally applied to single-crystal or powder diffraction data. With the measured total diffraction data transformed into an instrument-free form, calculated Debye diffraction patterns can be directly compared with the measured data to elucidate the nature of local molecular order present in the sample.

Within the spirit of Debye diffraction modelling, a suitable molecular model representing the sample of interest must first be generated. The Debye diffraction equation should then be applied iteratively to every atom–atom pair within the molecular model. However, for non-crystalline systems, the generation of a suitable molecular model that reflects the isotropic and random nature of the material can be challenging. As an alternative approach, the use of a single representative molecule and a spherically symmetric packing function or exclusion zone was explored. This modelling approach was based upon the observation that for ideal non-crystalline molecular systems, the only local atomic order would be due to the rigid sections of the molecular structure. For the majority of the examples presented in this chapter, the Debye diffraction response calculated for a single molecule when combined with the spherical core–shell-like packing function was able to describe the observed total diffraction data. This simplified approach to Debye diffraction modelling of non-crystalline systems is straightforward to employ for real-world modelling problems.

While examples of close-to-ideal non-crystalline systems can be found for larger flexible molecules (for example simvastatin), small-molecule systems with a well defined shape or strong directional bonding tend to exhibit more extensive local intermolecular order and require extended molecular models. For these larger-scale molecular models, the Debye bubble approach was introduced. The bubble algorithm was used to split the model into a series of spherical subsets. The total diffraction response from the individual subsets was then summed to give the total diffraction response of the system. The bubble approach allowed representative sampling of large-scale molecular models while limiting the effective diffraction coherence length and in addition gave a shape contribution that could be removed from the total diffraction calculation using the Menke correction. For systems exhibiting more extensive local order than can be described by the core–shell model, the Debye bubble approach applied to large-scale molecular models can be a practical approach to generating artifact-free total diffraction responses.

The motivation behind this work as applied to organic molecular solid forms was the investigation of relationships between local molecular order and long-term chemical/physical stability, in particular how changes in production conditions affect local order and long-term stability. These studies are continuing and will be the subject of a future publication.

I would like to thank Ting Xu, Harsh Shah and Rusha Sardhara from Long Island University, Arnold and Marie Schwartz College of Pharmacy, and Jeffrey Stewart from Triclinic Labs for X-ray diffraction data and constructive discussions during the preparation of this manuscript.

References

Bates, S., Jonaitis, D. & Nail, S. (2013). *Sucrose lyophiles: a semi-quantitative study of residual water content by total X-ray diffraction analysis. Eur. J. Pharm. Biopharm.* **85**, 184–188.

Bortolotti, M., Lonardelli, I. & Pepponi, G. (2011). *Determination of the crystal structure of nifedipine form C by synchrotron powder diffraction. Acta Cryst.* B**67**, 357–364.

Brereton, R. G. (1990). *Chemometrics: Applications of Mathematics and Statistics to Laboratory Systems*. Chichester: Ellis Horwood.

Cejka, J., Kratochvíl, B., Císarová, I. & Jegorov, A. (2003). *Simvastatin. Acta Cryst.* C**59**, o428–o430.

Chaikin, P. M. & Lubensky, T. C. (1995). *Principles of Condensed Matter Physics*, Vol. 1. Cambridge University Press.

Chakravarty, P., Bates, S. & Thomas, L. (2013). *Identification of a potential conformationally disordered mesophase in a small molecule: experimental and computational approaches. Mol. Pharm.* **10**, 2809–2822.

Chen, X., Morris, K. R., Griesser, U. J., Byrn, S. R. & Stowell, J. G. (2002). *Reactivity differences of indomethacin solid forms with ammonia gas. J. Am. Chem. Soc.* **124**, 15012–15019.

Cline, J. P. (1992). *NIST XRD standard reference materials: their characterization and uses. Proceedings of Accuracy in Powder Diffraction II*, NIST Spec. Publ. **846**, 68–74.

Cowley, J. M. (1990). *Diffraction Physics*, 2nd ed. Amsterdam: North-Holland.

Cox, P. J. & Manson, P. L. (2003). *γ-Indomethacin at 120 K. Acta Cryst.* E**59**, o986–o988.

Debye, P. (1915). *Zerstreuung von Röntgenstrahlen. Ann. Phys.* **351**, 809–823.

Deming, S. N., Michotte, Y., Massart, D. L., Kaufman, L. & Vandeginste, B. G. M. (1988). *Chemometrics: a Textbook*. Amsterdam: Elsevier.

Fewster, P. F. (2014). *A new theory for X-ray diffraction. Acta Cryst.* A**70**, 257–282.

Freer, A. A., Bunyan, J. M., Shankland, N. & Sheen, D. B. (1993). *Structure of (S)-(+)-ibuprofen. Acta Cryst.* C**49**, 1378–1380.

Fu, Y., Busing, W. R., Jin, Y., Affholter, K. A. & Wunderlilch, B. (1994). *Structure analysis of the noncrystalline material in poly(ethylene terephthalate) fibers. Macromol. Chem. Phys.* **195**, 802–822.

Graeser, K. A., Strachan, C. J., Patterson, J. E., Gordon, K. C. & Rades, T. (2008). *Physicochemical properties and stability of two differently prepared amorphous forms of simvastatin. Cryst. Growth Des.* **8**, 128–135.

Groom, C. R., Bruno, I. J., Lightfoot, M. P. & Ward, S. C. (2016). *The Cambridge Structural Database. Acta Cryst.* B**72**, 171–179.

Guinier, A. (1994). *X-ray Diffraction in Crystals, Imperfect Crystals, and Amorphous Bodies*. New York: Dover Publications.

Hosemann, R. (1951). *Die parakristalline Feinstruktur natürlicher und synthetischer Eiweisse. Visuelles Näherungsverfahren zur Bestimmung der Schwankungstensoren von Gitterzellen. Acta Cryst.* **4**, 520–530.

Hosemann, R. & Bagchi, S. N. (1962). *Direct Analysis of Diffraction by Matter.* Amsterdam: North-Holland.

ICH Harmonized Tripartite Guideline (1994). *Validation of analytical procedures: text and methodology Q2(R1).* [Published in the *Federal Register* (1995). **60**, 11260.]

International Union of Crystallography (1992). *Report of the Executive Committee for 1991. Acta Cryst.* A**48**, 922–946.

James, R. W. (1948). *The Optical Principles of the Diffraction of X-rays*, Vol. 2. London: G. Bell and Sons. Reprinted 1962.

Kaminsky, W. & Glazer, A. M. (1997). *Crystal optics of D-mannitol, $C_6H_{14}O_6$: crystal growth, structure, basic physical properties, birefringence, optical activity, Faraday effect, electro-optic effects and model calculations. Z. Kristallogr.* **212**, 283–296.

Karen, P. & Woodward, P. M. (1998). *Liquid-mix disorder in crystalline solids: $ScMnO_3$. J. Solid State Chem.* **141**, 78–88.

Kavanagh, A., McConvey, I., McCabe, J., Blade, H. & Cosgrove, S. (2012). *Amorphous pharmaceuticals – developing amorphous pharmaceuticals: opportunity and necessity. Am. Pharm. Rev.* **15**, 10.

Kistenmacher, T. J. & Marsh, R. E. (1972). *Crystal and molecular structure of an antiinflammatory agent, indomethacin, 1-(p-chlorobenzoyl)-5-methoxy-2-methylindole-3-acetic acid. J. Am. Chem. Soc.* **94**, 1340–1345.

Langford, J. I. (1980). *Accuracy of crystallite size and strain determined from the integral breadth of powder diffraction lines. Natl Bur. Stand. Spec. Publ.* **567**, 255–269.

Macrae, C. F., Bruno, I. J., Chisholm, J. A., Edgington, P. R., McCabe, P., Pidcock, E., Rodriguez-Monge, L., Taylor, R., van de Streek, J. & Wood, P. A. (2008). *Mercury CSD 2.0 – new features for the visualization and investigation of crystal structures. J. Appl. Cryst.* **41**, 466–470.

Martínez, L., Andrade, R., Birgin, E. G. & Martínez, J. M. (2009). *PACKMOL: a package for building initial configurations for molecular dynamics simulations. J. Comput. Chem.* **30**, 2157–2164.

Menke, H. (1932). *Rontgeninterferenzen an Flüssigkeiten (Hg, Ga, CCl_4). Phys. Z.* **33**, 593–604.

McConnell, J. F. (1974). *2-(4-Isobutylphenyl)propionic acid. Cryst. Struct. Commun.* **3**, 73–75.

Pedersen, J. S. (1997). *Analysis of small-angle scattering data from colloids and polymer solutions: modeling and least-squares fitting. Adv. Colloid Interface Sci.* **70**, 171–210.

Reynolds, R. C. (1989). *Diffraction by small and disordered crystals. Rev. Mineral. Geochem.* **20**, 145–181.

Scherrer, P. (1918). *Bestimmung der Grösse und der inneren Struktur von Kolloidteilchen mittels Röntgenstrahlen. Nachr. Ges. Wiss. Göttingen Math. Phys. Kl.* **1918**, 98–100.

Stewart, G. W. (1928). *Theory of X-ray diffraction in liquids. Phys. Rev.* **32**, 558–563.

Stokes, A. R. & Wilson, A. J. C. (1944). *The diffraction of X rays by distorted crystal aggregates – I. Proc. Phys. Soc.* **56**, 174–181.

Triggle, A. M., Shefter, E. & Triggle, D. J. (1980). *Crystal structures of calcium channel antagonists: 2,6-dimethyl-3,5-dicarbomethoxy-4-[2-nitro-, 3-cyano-, 4-(dimethylamino)-, and 2,3,4,5,6-pentafluorophenyl]-1,4-dihydropyridine. J. Med. Chem.* **23**, 1442–1445.

Vainshtein, B. K. (1994). Editor. *Fundamentals of Crystals: Symmetry, and Methods of Structural Crystallography*, Vol. 1. Berlin: Springer.

Velec, H. F., Gohlke, H. & Klebe, G. (2005). *DrugScore^{CSD} knowledge-based scoring function derived from small molecule crystal data with superior recognition rate of near-native ligand poses and better affinity prediction. J. Med. Chem.* **48**, 6296–6303.

Warren, B. E. (1990). *X-ray Diffraction*. New York: Dover Publications Inc.

Warren, B. E. & Averbach, B. L. (1950). *The effect of cold-work distortion on X-ray patterns. J. Appl. Phys.* **21**, 595–599.

Wavefunction, Inc. (2016). *Spartan'16*. Version 2.0.7. Wavefunction Inc., 18401 Von Karman Ave., Suite 370, Irvine, CA 92612, USA.

Welberry, T. R. (2004). *Diffuse X-ray Scattering and Models of Disorder.* IUCr/Oxford Science Publications.

Williamson, G. K. & Hall, W. H. (1953). *X-ray line broadening from filed aluminium and wolfram. Acta Metall.* **1**, 22–31.

Xiang, T. X. & Anderson, B. D. (2013). *Molecular dynamics simulation of amorphous indomethacin. Mol. Pharm.* **10**, 102–114.

Zernicke, F. & Prins, J. (1927). *Die Beugung von Rontgenstrahlen in Flüssigkeiten als Effekt der Molekülanordnung Z. Phys.* **41**, 84.

Zuev, A. (2008). *Instrumental contributions to the line profile in X-ray powder diffraction. Example of the diffractometer with Bragg–Brentano geometry.* In *Powder Diffraction: Theory and Practice*, edited by R. E. Dinnebier & S. J. L. Billinge. Cambridge: RCS Publishing.

International Tables for Crystallography (2019). Vol. H, Chapter 5.7, pp. 649–672.

5.7. Nanometre-scale structure from powder diffraction: total scattering and atomic pair distribution function analysis

S. J. L. Billinge

5.7.1. Introduction

In this chapter we develop the theory and describe the methodology for studying nanometre-scale structure in materials from 'powder diffraction' data. These methods are often referred to as 'total scattering' or atomic pair distribution function (PDF) analysis. In contrast to the case of crystals, it is not valid to use as a starting point the presumption of periodicity, leading as it does to the Bragg (Bragg, 1912) and Laue (Friedrich *et al.*, 1913) equations. Rather, as laid out in the introductory Chapter 1.1 of this volume, nanostructure results in diffraction intensities that are broad and diffuse rather than the sharp delta-function Bragg peaks of a well ordered crystal, and form part of what was traditionally thought of as the 'background' signal. The theoretical basis for calculating the scattering in this case is the Debye equation (Debye, 1915), which is derived herein. The formalism of correlation functions is also introduced; this comes from the atomic density of the material in real space. The Debye equation is related to the real-space pair correlation function through a Fourier transform, as shown first by Zernike & Prins (1927). Representing the data in real space can be highly intuitive, as well as being an appropriate representation for very diffuse signals which may be more sharply peaked in real space than in reciprocal space. The information content in the data is the same in reciprocal and real space, but how it is studied and what is learned from it can vary. Both approaches can be very valuable (Egami & Billinge, 2003, 2012). Enormous progress has been made in experimental techniques for studying nanomaterials from powders such that a revolution is taking place in this regard with high-throughput, time-resolved, spatially resolved and *in situ* studies now possible because of the high data acquisition rates that are made possible with new sources and methods. Advanced computation is also making data analysis quicker and modelling more powerful. This chapter aims to present the background theory in a rigorous but intuitive way. Some aspects of the experimentation are described to help understand issues and the current state of the art, but this is changing rapidly. Different approaches to modelling the data are then described.

5.7.1.1. *Types of nanostructure*

Any material that has structure whose coherence extends only on nanometre length scales can be thought of as nanostructured. The most obvious case is that of a discrete nanoparticle, which in the simplest case is a tiny nano-scale chunk of crystal. But this ignores an abundance of other possibilities. Nanoporous materials have been studied for some time, and are often referred to as mesoporous materials. These are bulk materials that have nano-sized holes in them. These holes may be empty, or may be themselves filled with confined liquids, molecules or nanoparticles. One of the most interesting emerging classes of material is that of bulk crystals that have an additional aperiodic component with nano-scale order (Billinge & Kanatzidis, 2004; Billinge, 2008; Young & Goodwin, 2011). These types of nanostructure are illustrated in Fig. 5.7.1.

Many of these materials have long been studied crystallographically, but have only revealed their nanostructure when studied using the total-scattering methods that are described in this chapter, or looked at in detail with nanometre-resolution spatially resolved probes such as atomic force (AFM), scanning tunnelling (STM) microscopies and electron and X-ray nanoprobes. In some of the most important cases the nanostructure is an important factor in determining the material properties, and only with its study can these material properties be understood.

According to the official US definition of nanotechnology (http://www.nano.gov/), structural dimensions should be between 1 and 100 nm to be considered a nanomaterial. According to this definition, particles with diameters of 100 nm are considered nanoparticles. At this size nanoparticles still scatter with Bragg peaks, albeit broadened because of finite size effects, and a total-scattering analysis is not really warranted. However, in many applications such as catalysis, it is the nanoparticles on the smaller end of the spectrum that have the most interesting properties. Total-scattering methods are the most powerful and widely used for such nanoparticles in the domain below 10 nm. The lower size boundary of 1 nm or 10 Å excludes small molecules and short-range structural correlations in most glasses and amorphous materials. These classes of materials are of great interest, but their study is not generally classified as nanotechnology, excepting the case of nanoparticles of short-range-ordered molecules. Folded proteins can definitely be considered as nanoparticles, with highly complex and interesting properties, but are too soft and of too low symmetry to be studied using total-scattering methods, at least at the time of writing.

Amorphous materials, although not considered as nanomaterials, are studied using total-scattering methods. In fact, the application of total-scattering methods to nanomaterials grew out of years of work on liquids and amorphous materials (Warren, 1934; Warren *et al.*, 1936; Franklin, 1950; Wright, 1998; Barnes *et al.*, 2003). It is probably fair to say that there now exists a synergy such that developments in the nano arena are feeding back again into work on the the structure of liquid and amorphous materials.

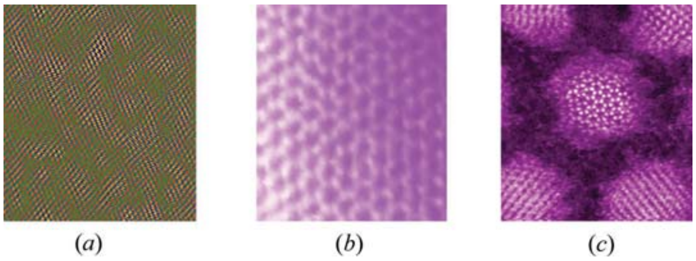

Figure 5.7.1
TEM images illustrating the variety in nanostructured materials: (*a*) Nanostructuring in a bulk material, (*b*) intercalation in a mesoporous host and (*c*) nanoparticles. Adapted from Billinge & Levin (2007).

Copyright © 2019 International Union of Crystallography

5.7.2. Scattering from nanostructures

5.7.2.1. *The Debye equation*

A number of textbooks describe the total-scattering and PDF technique (Warren, 1990; Klug & Alexander, 1974; Nield & Keen, 2001; Egami & Billinge, 2003; Dinnebier & Billinge, 2008; Egami & Billinge, 2012), but, except for the last one, the full derivation of the PDF equations is not reproduced clearly. It is worth following the derivation to gain a more complete understanding of the origin of features in the PDF. (The symbols and abbreviations used in this chapter are listed in Table 5.7.1.)

We start from the scattering amplitude from a set of i atoms at points $\mathbf{r}_i$. In the limit of kinematical scattering

$$\begin{aligned}\psi(\mathbf{Q}) &= \sum_i f_i(Q)\exp(i\mathbf{Q}\cdot\mathbf{r}_i)\\ &= \sum_i \psi_i. \qquad (5.7.1)\end{aligned}$$

This equation was justified in Chapter 1.1. In this equation the sum runs over every atom in the solid, $\mathbf{Q}$ is the scattering vector, $\mathbf{r}_i$ is the vector from the origin to the ith atom and $f_i(Q)$ is the atomic form factor of the ith atom; this equation serves to define ψ_i.

If the scattering from these atoms were totally incoherent, the total scattered intensity would be the sum of the intensities from each atom,

$$\begin{aligned}I_{\rm inc} &= \sum_i \psi_i^*\psi_i\\ &= \sum_i f_i^*(Q)f_i(Q)\\ &= \sum_\alpha N_\alpha f_\alpha^*(Q)f_\alpha(Q) \qquad (5.7.2)\\ &= N\sum_\alpha c_\alpha f_\alpha^*(Q)f_\alpha(Q)\\ &= N\langle f^2\rangle.\end{aligned}$$

In the lower versions of the equation we have changed the sum to be over α, which is now a sum over the different *species* of atoms in the sample with N being the total number of atoms and N_α being the number of atoms of type α; thus the concentration of species α is $c_\alpha = N_\alpha/N$. The asterisk indicates the complex conjugate and the angle brackets indicate a sample average, which is defined in detail in the equation.

Similarly, we can define the sample-averaged scattering power, $\langle f\rangle = \sum_\alpha c_\alpha f_\alpha$, and

$$\begin{aligned}\langle f\rangle^2 &= \frac{1}{N^2}\sum_{ij} f_j^* f_i\\ &= \sum_{\alpha\beta} c_\alpha c_\beta f_\alpha^* f_\beta. \qquad (5.7.3)\end{aligned}$$

Here we have dropped the Q dependence of the atomic scattering factors to simplify the notation, but the f's are understood to retain their Q dependence.

The full coherent scattering intensity, I_c, which contains the structural information, is given by $\psi^*\psi$,

$$\begin{aligned}I_c &= \sum_i\sum_j f_j^* f_i \exp[i\mathbf{Q}\cdot(\mathbf{r}_i-\mathbf{r}_j)]\\ &= \sum_{i,j} f_j^* f_i \exp(i\mathbf{Q}\cdot\mathbf{r}_{ij}), \qquad (5.7.4)\end{aligned}$$

which serves to define $\mathbf{r}_{ij}$. We can separate out the self-scattering, $i = j$, for which $\mathbf{r}_{ij} = 0$, which gives

Table 5.7.1
List of symbols and abbreviations used in this chapter

Note that there is a wide range of notations used in the literature for the same, or similar, functions, so it is important to check the precise definition of functions used in any given article. In particular, there is little overlap between nomenclature used in the community using PDF/RDF to study glasses and that used by those studying nanomaterials. Please see the article by Keen (2001) for more details on this.

Symbol	Definition
c_α	Concentration of atomic species α, or N_α/N
F_{hkl}	Crystallographic structure factor
$F(Q)$	Reduced total-scattering structure function
$f_i(Q)$	X-ray atomic form factor or scattering length of atom i in a sample; b_i for neutrons
$\mathscr{F}(r)$	Atomic pair distribution function, the inverse Fourier transform of the reduced total-scattering structure function
$G(r)$	Reduced atomic pair distribution function. Obtained from a sample when the SAS data is excluded: observed $G_{\rm obs}$ or calculated $G_{\rm calc}$
$I(Q)$	Scattering intensity diffracted by a sample: coherent I_c, incoherent $I_{\rm inc}$, distinct I_d, and small-angle $I^{\rm SAS}$ scattering intensity
N	Total number of atoms or scatterers in a sample, or of a specific type
N_α	Total number of atoms of element α in a sample
$\mathbf{Q}$	The diffraction vector: magnitude and direction of the momentum transfer in a scattering event
Q	Magnitude of the diffraction vector
$Q_{\rm min}$	Minimum value of Q in a measurement
$Q_{\rm max}$	Maximum value of Q in a measurement
r	Distance
$\mathbf{r}_{ij}$	The vector joining the ith and jth atoms
r_{ij}	The distance between the ith and jth atoms
$r_{\rm max}$	The maximum range the PDF is calculated over
r_{nn}	The distance between nearest neighbours in the material
$R(r)$, RDF	Radial distribution function
R_w	Residuals function used as a measure of 'goodness-of-fit' in PDF modelling
$S(Q)$	Total-scattering structure function, normalized scattering intensity of a sample
$S_{\alpha\beta}(Q)$	Partial structure function between atoms of atomic species α and β
$w(r_i)$	Statistical weighting factor for the ith point in r, *e.g.*, used in calculating R_w
Z	Atomic number for a sample species
$\gamma_0(r)$	Characteristic function of a nanoparticle. The auto-correlation function of the particle shape
$\rho(r)$	The atom-pair density, related to the PDF. Has units of inverse volume
ρ_0	Average number density of the material
$\rho_{\rm bulk}(r)$	The atomic pair density for an infinite solid
σ_{ij}^2	Correlated broadening term for pair of atoms i and j
$\psi(\mathbf{Q})$	Scattering amplitude

Abbreviation	Definition
ADP	Atomic displacement parameter. ADPs quantify the atomic distributions around their mean positions
AFM	Atomic force microscopy
CCD	Charge-coupled device
ePDF	Pair distribution function from electron diffraction data
EPSR	Empirical potential structure refinement
EXAFS	Extended X-ray absorption fine structure
PDF	Pair distribution function
RAPDF	Rapid acquisition pair distribution function
RMC	Reverse Monte Carlo
SAS	Small-angle scattering
STM	Scanning tunnelling microscopy
TEM	Transmission electron microscopy

$$\begin{aligned} I_c &= \sum_i f_i^* f_i + \sum_{i\neq j} f_j^* f_i \exp(i\mathbf{Q}\cdot\mathbf{r}_{ij}) \\ &= N\langle f^2\rangle + \sum_{i\neq j} f_j^* f_i \exp(i\mathbf{Q}\cdot\mathbf{r}_{ij}), \end{aligned} \qquad (5.7.5)$$

where we have used equation (5.7.2). This allows us to define a *distinct scattering intensity* for $i \neq j$ as

$$\begin{aligned} I_d &= I_c - N\langle f^2\rangle \\ &= \sum_{i\neq j} f_j^* f_i \exp(i\mathbf{Q}\cdot\mathbf{r}_{ij}). \end{aligned} \qquad (5.7.6)$$

We want an expression for the total-scattering structure function, $S(\mathbf{Q})$, which in the Faber–Ziman formalism (Faber & Ziman, 1965) is defined as $(I_c/N\langle f\rangle^2) - [\langle (f-\langle f\rangle)^2\rangle/\langle f\rangle^2]$. The second term in this definition is the Laue monotonic diffuse scattering that comes about because of the imperfect cancelation of intensity at the destructive interference condition when atomic sites are occupied by atoms of different scattering strength. It results in a monotonically decreasing background even in the case of perfectly coherent scattering, although of course it is absent in elemental materials.

To get $S(\mathbf{Q})$ from equation (5.7.4) we normalize by the total number of scatterers, N,

$$\frac{I_c}{N} = \langle f^2\rangle + \frac{1}{N}\sum_{i\neq j} f_j^* f_i \exp(i\mathbf{Q}\cdot\mathbf{r}_{ij}), \qquad (5.7.7)$$

and subtract the normalized self-scattering term to get

$$\frac{I_c}{N} - \langle f^2\rangle = \frac{1}{N}\sum_{i\neq j} f_j^* f_i \exp(i\mathbf{Q}\cdot\mathbf{r}_{ij}). \qquad (5.7.8)$$

Finally, we normalize by $\langle f\rangle^2$ to obtain

$$\frac{I_c}{N\langle f\rangle^2} - \frac{\langle f^2\rangle}{\langle f\rangle^2} = \frac{1}{N\langle f\rangle^2}\sum_{i\neq j} f_j^* f_i \exp(i\mathbf{Q}\cdot\mathbf{r}_{ij}). \qquad (5.7.9)$$

Thus,

$$\begin{aligned} S(\mathbf{Q}) - 1 &= \frac{I_c}{N\langle f\rangle^2} - \frac{\langle f^2\rangle}{\langle f\rangle^2} \\ &= \frac{I_d}{N\langle f\rangle^2} \\ &= \frac{1}{N\langle f\rangle^2}\sum_{i\neq j} f_j^* f_i \exp(i\mathbf{Q}\cdot\mathbf{r}_{ij}). \end{aligned} \qquad (5.7.10)$$

This expression yields precisely $S(\mathbf{Q}) - 1$ in terms of scattering from atoms in our sample and from measurable intensities.

For an isotropic sample, *e.g.* a powder of crystals or nanoparticles, we assume there to be a crystallite with every orientation with equal probability and we can take an orientational average. To do this we define the z axis as the direction of the $\mathbf{Q}$ vector, in which case, without loss of generality, we can express the dot product of $\mathbf{Q}$ with $\mathbf{r}_{ij}$, the vector separating atom i and atom j, as

$$\mathbf{Q}\cdot\mathbf{r}_{ij} = Qr_{ij}\cos\theta. \qquad (5.7.11)$$

The orientational averaging means that θ takes all values with equal probability. The measured intensity will therefore be proportional to the uniform average of the intensity over all orientations of the interatomic vector. To evaluate this we take the spherical integral of $\exp(i\mathbf{Q}\cdot\mathbf{r}_{ij})$,

$$\begin{aligned} \overline{\exp(i\mathbf{Q}\cdot\mathbf{r}_{ij})} &= \frac{\int_0^{2\pi} \mathrm{d}\phi \int_0^{\pi} \mathrm{d}\theta \exp(iQr_{ij}\cos\theta) r_{ij}^2 \sin\theta}{\int_0^{2\pi} \mathrm{d}\phi \int_0^{\pi} \mathrm{d}\theta\, r_{ij}^2 \sin\theta} \\ &= \frac{-2\pi r_{ij}^2 \left[\exp(iQr_{ij}\cos\theta)\right]_0^{\pi}}{4\pi r_{ij}^2 iQr_{ij}} \\ &= \frac{\left[\exp(iQr_{ij}) - \exp(-iQr_{ij})\right]}{2iQr_{ij}} \\ &= \frac{\sin(Qr_{ij})}{Qr_{ij}}. \end{aligned} \qquad (5.7.12)$$

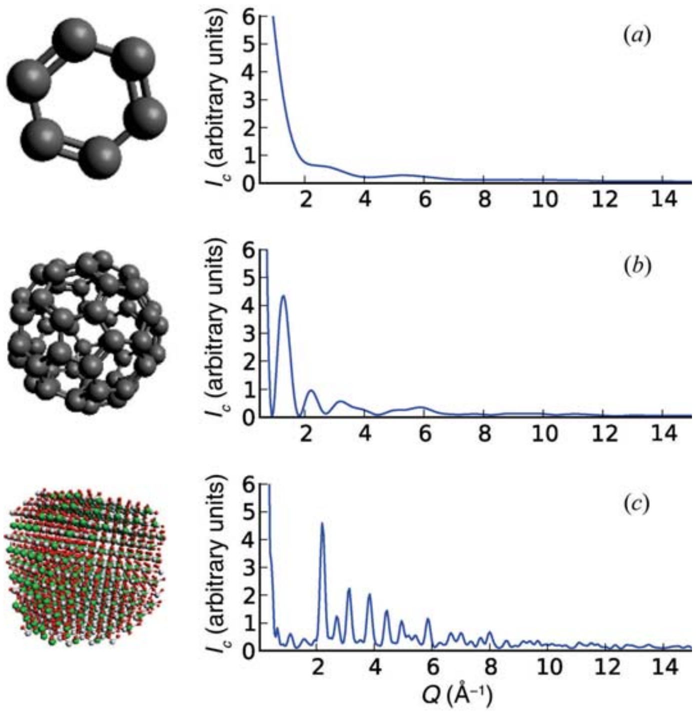

Figure 5.7.2
Scattering intensity calculated using the Debye function [equation (5.7.13)] for a number of discrete particles: (*a*) benzene, (*b*) fullerene C_{60} and (*c*) a $BaTiO_3$ nanoparticle. The intensities in part (*b*) are about ten times those in part (*a*) and the intensities in part (*c*) are about 10 000 times those in part (*a*).

Using this in equation (5.7.4) gives the average coherent scattering intensity, as expressed originally by the Debye (1915) equation,

$$I_c = \sum_{ij} f_j^* f_i \frac{\sin(Qr_{ij})}{Qr_{ij}}. \qquad (5.7.13)$$

Examples of the Debye function curves from some representative small clusters are shown in Fig. 5.7.2.

Bear in mind that the sum is over all atoms in the sample. This is quick to evaluate for molecules and small clusters, but computation is slow when the number of atoms becomes large. As discussed in Chapter 1.1, for the case of a crystal we can define a unit cell. In real space the full structure is the convolution of the unit-cell contents with the periodic lattice and the scattering is the product of the scattering from the unit cell and the lattice. The scattering from the unit-cell contents is just the Debye equation with the sum taken only over the atoms in the unit cell, none other than the crystallographic structure factor, F_{hkl}. The scattering from the lattice is simply a set of delta functions at the positions of the reciprocal-lattice points, so the observed scattering is a set of sharp Bragg peaks at the reciprocal-lattice points whose intensity is given by equation (5.7.4) taken over the contents of the unit cell. For noncrystalline (or far from crystalline) samples, this approximation is no longer a good one and the scattering is a continuous function given quantitatively by taking the sum over all the atoms in the sample, as done in equation (5.7.13).

5.7.2.2. *Correlation functions*

In 1927, Zernike & Prins (1927) first wrote down the scattering in terms of correlation functions of the density. At the atomic scale, the density is given by a set of delta functions at the positions of the atomic nuclei. The Fourier transform of the scattered X-ray intensity does not give the density directly but the autocorrelation function of the density, or the convolution of the density with itself. It still appears as delta functions but there are many more of them, at positions determined by taking the vectors joining every pair of atoms in the sample and moving them so their tails lie at the origin. This density–density autocorrelation function is therefore often referred to as the pair correlation function. In the case of powder diffraction the directions of the vectors are lost and the autocorrelation function becomes a distribution of delta functions on the distance axis at positions given by the separations of each atom. This is like taking all the pair vectors, with their tails at the origin, and rotating them to lie on top of each other, then placing a delta function at their tips. This is shown schematically in Fig. 5.7.3.

This is a histogram of interatomic distances, and this is where the name 'pair distribution function' comes from. Depending on the exact definition of the correlation function used, it may also have the dimensions of inverse volume, in which case it is referred to as the pair density function, although these terms are often applied somewhat loosely and non-rigorously. Some of the confusion that might result from the use in the literature of different correlation functions can be avoided by referring to the paper by Keen (2001), which defines rigorous transformations between some of the more commonly used variants.

We would like to find the precise relationship between the Debye equation and the correlation functions of Zernike & Prins (1927). If we normalize equation (5.7.13) by the number of scatterers and the mean scattering per atom and compare with equation (5.7.10) we get

$$S(Q) - 1 = \frac{1}{N\langle f\rangle^2} \sum_{i\neq j} f_j^* f_i \frac{\sin(Qr_{ij})}{Qr_{ij}}. \qquad (5.7.14)$$

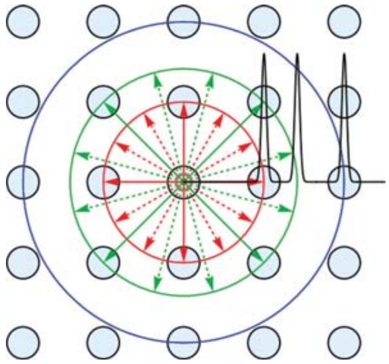

Figure 5.7.3

Schematic showing how the PDF is calculated. The origin is on a randomly selected atom in the sample. Spheres are then drawn (shown as circles in this 2D schematic) with all radii, and the number of atom centres in a differential annulus at that radius are counted and plotted as a histogram. If the structure were well ordered and the atoms stationary, the peaks would be sharp delta functions, but disorder and thermal motion broaden them into Gaussian-like peaks of finite width. In the plot the interatomic vectors are shown as solid arrows. The arrows drawn with dashed lines are the same length as the pair vectors and define the circle. The resulting partial RDF (referenced to the origin atom) is shown as the black line. The total PDF is the sum of the PDFs when each atom is taken in turn as the origin.

The quantity in the kernel of the Fourier transform that connects the scattering with the correlation functions is the reduced total-scattering structure function, $F(Q) = Q[S(Q) - 1]$, which is, using equation (5.7.14),

$$F(Q) = \frac{Q}{N\langle f\rangle^2} \sum_{i\neq j} f_j^* f_i \frac{\sin(Qr_{ij})}{r_{ij}}. \qquad (5.7.15)$$

The Q dependence of the X-ray form factors is problematic in the Fourier transform when there is more than one atomic species, since we do not know, *a priori*, the different Q dependencies of the different contributions to the scattering. It is convenient to remove the Q dependence of f by an approximate method. The form factors are assumed to be isotropic so depend only on Q and not $\mathbf{Q}$, which is a good approximation for scattering from core electrons in particular. We write $f(Q) = f(0)\tilde{f}(Q)$, where $\tilde{f}(Q)$ has the value 1 at $Q = 0$ and contains the Q dependence of the form factor, and $f(0)$ is given by the number of scattering electrons, which is generally taken to be the atomic number, Z, although for scattering from ions it is more appropriate to use the number of electrons on the ion rather than Z. The Morningstar–Warren approximation (Warren *et al.*, 1936) assumes that the Q-dependent part of the form factors can be well approximated by an average Q dependence, $\tilde{f}(Q) = (1/N_{\rm species}) \sum_\alpha c_\alpha \tilde{f}_\alpha(Q)$, where $N_{\rm species}$ is the number of different atomic species in the sample. In this case, the Q dependence, $\tilde{f}(Q)$, comes out of the double sums in equation (5.7.15) on the top and the bottom and cancels out. The f's that remain are Q-independent, and are normally replaced by the atomic number (modified by any anomalous scattering factors). Fig. 5.7.4 shows the form factors for Cd and Se. In the lower panel they are normalized and plotted on top of each other, with the average Q-dependent form factor plotted on top for comparison.

The same result holds for neutron scattering, where the f's are replaced by coherent neutron scattering lengths, b. These have no Q dependence and therefore the approximate method for removing the Q dependence is not needed. Errors introduced due to the Morningstar–Warren approximation will create aberrations in the PDF that mimic the effect of thermal factors (Billinge & Farrow, 2013) and in fits to the data will appear as a temperature-independent contribution to the refined atomic displacement factors.

A more precise determination of the X-ray PDF, at the possible cost of computational complexity, can be obtained by calculating the scattering intensity from a model using the Debye equation and Fourier transforming the result to obtain the PDF without approximation. Another approach, which combines the speed of real-space calculation but with increased accuracy, is to convolute the PDF obtained from the model, rather than deconvolute the data, with the atomic form factors. In this approach the PDF is calculated in real space, then each partial PDF is Fourier transformed individually to reciprocal space. These partial PDFs may then be multiplied by the product of the Q-dependent form factors in the pair, $f_\alpha(Q)f_\beta(Q)$, then properly weighted and recombined to yield the total $S(Q)$. This may then be fitted to the un-deconvoluted measured $S(Q)$ directly in reciprocal space, or, if preferred, these may both be Fourier

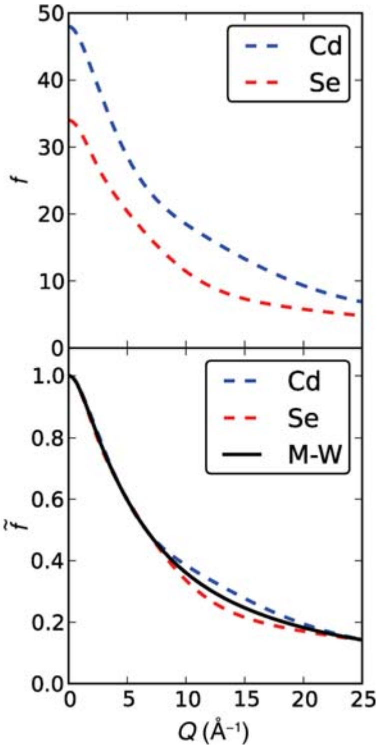

Figure 5.7.4
Atomic form factors and the Morningstar–Warren approximation for CdSe. The full form factors, $f(Q)$, for Cd and Se are shown in the top panel, and the form factors normalized to their value at $Q = 0$, comparing the Q dependence, are displayed in the bottom panel. The bottom panel also displays the Morningstar–Warren approximation for CdSe, labelled as 'M-W'.

transformed back to real space for fitting or visualization. In this case, the PDF will appear visually significantly broadened, since the peak width contains information about the size of the atom as well as the distribution of locations of the atomic centre. However, the information content is the same and the same result should be obtained through modelling, but without the uncertainty of the effects of the Morningstar–Warren approximation. More recently, a expansion to higher order allows a more accurate treatment of the approximation (Masson & Thomas, 2013), although in many cases the Morningstar–Warren approximation is rather good and is not the factor limiting the accuracy of models.

Now we want to consider the (inverse) Fourier transform of $F(Q)$. Because $F(Q)$ is an odd function, we use the sine-Fourier transform,

$$\mathscr{F}(r) = (2/\pi)\int_0^\infty F(Q)\sin(Qr)\,\mathrm{d}Q. \tag{5.7.16}$$

We choose the $2/\pi$ prefactor so that the direct sine transform has a prefactor of 1. Substituting equation (5.7.15) we get

$$\begin{aligned}\mathscr{F}(r) &= \frac{2}{\pi}\int_0^\infty \frac{1}{N\langle f\rangle^2}\sum_{i\neq j} f_j^* f_i \frac{\sin(Qr_{ij})}{r_{ij}}\sin(Qr)\,\mathrm{d}Q\\ &= \frac{2}{\pi N\langle f\rangle^2}\sum_{i\neq j}\frac{f_j^* f_i}{r_{ij}}\int_0^\infty \sin(Qr_{ij})\sin(Qr)\,\mathrm{d}Q\\ &= \frac{1}{N\langle f\rangle^2}\sum_{i\neq j}\frac{f_j^* f_i}{r_{ij}}[\delta(r-r_{ij})-\delta(r+r_{ij})]\\ &= \frac{1}{rN\langle f\rangle^2}\sum_{i\neq j} f_j^* f_i[\delta(r-r_{ij})-\delta(r+r_{ij})],\end{aligned} \tag{5.7.17}$$

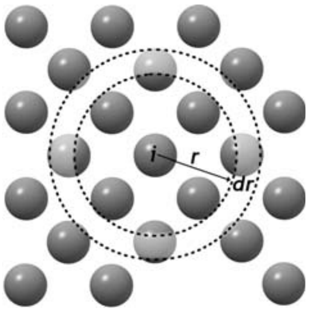

Figure 5.7.5
An illustration of the annulus used to calculate the coordination number. This is a 2D slice of a 3D spherical shell of thickness dr at distance r from an arbitrary origin atom.

which, if we confine ourselves to the positive axis only, is

$$\mathscr{F}(r) = \frac{1}{rN\langle f\rangle^2}\sum_{i\neq j} f_j^* f_i \delta(r-r_{ij}). \tag{5.7.18}$$

We can interpret $\mathscr{F}(r)$ in terms of the radial distribution function (RDF). The RDF, denoted $R(r)$, is defined for an elemental system such that for an arbitrary atom i at the origin $R_i(r)\,\mathrm{d}r$ gives the number of atoms in a shell of thickness dr at a distance r from that atom. This is illustrated in Fig. 5.7.5.

The total RDF is the scattering-length-weighted average of the partial RDFs over each atom taken at the origin. Thus, the integral of the RDF between two bounds, a and b, gives the number of atomic pairs per atom with separation within those bounds, N_{ab}. By inspection we see that equation (5.7.18) yields this behaviour if we multiply $\mathscr{F}(r)$ by r. For a solid with atomic species α we get

$$\begin{aligned}\int_a^b \mathscr{F}(r) r\,\mathrm{d}r &= \int_a^b \frac{1}{N\langle f\rangle^2}\sum_{i\neq j} f_j^* f_i \delta(r-r_{ij})\,\mathrm{d}r\\ &= \frac{1}{N\langle f\rangle^2}\sum_i\sum_{j\in S} f_j^* f_i\\ &= \frac{1}{\langle f\rangle^2}\sum_\alpha c_\alpha f_\alpha \sum_{j\in S} f_j^*,\end{aligned} \tag{5.7.19}$$

where S is the set of atoms with distance from atom i greater than a and less than b. In the case of just one atomic species, this reduces to

$$\begin{aligned}\int_a^b \mathscr{F}(r) r\,\mathrm{d}r &= (f^2/f^2)\sum_{j\in S} 1\\ &= N_{ab},\end{aligned} \tag{5.7.20}$$

as required. Thus,

$$\begin{aligned}\mathscr{F}(r) &= \frac{R(r)}{r}\\ &= 4\pi r\rho(r),\end{aligned} \tag{5.7.21}$$

where $\rho(r)$ is the atom-pair density. The second expression in equation (5.7.21) comes from the relationship between the RDF and the pair density. The pair density is defined such that $\int \mathrm{d}r\,\mathrm{d}\phi\,\mathrm{d}\theta\, r^2\sin(\theta)\rho(r) = \int R(r)\,\mathrm{d}r$, so that $4\pi r^2\rho(r) = R(r)$.[1]

---

[1] Historical note: The re-derivation of the PDF equations reproduced here was presented first in Farrow & Billinge (2009). Prior to that, in many papers the right-hand side of equation (5.7.16) was often incorrectly equated to the function $G(r)$, which is formally defined in equation (5.7.23), *i.e.* it was incorrectly written as $G(r) = (2/\pi)\int_0^\infty F(Q)\sin(Qr)\,\mathrm{d}Q$ (Egami & Billinge, 2003) but we see here that $(2/\pi)\int_0^\infty F(Q)\sin(Qr)\,\mathrm{d}Q = R(r)/r \neq G(r)$.

Rearranging equation (5.7.21) gives

$$\begin{aligned}\rho(r) &= \frac{\mathcal{F}(r)}{4\pi r}\\ &= \frac{1}{4\pi r^2 N\langle f\rangle^2}\sum_{i\neq j} f_j^* f_i \delta(r - r_{ij}).\end{aligned}\tag{5.7.22}$$

In reality, the scattering intensity in a PDF experiment, $I_c(Q)$ [equation (5.7.4)] is not measured to $Q = 0$ but to a minimum Q value because of the direct beam and the experimental setup. This means that in general the forward-scattering contributions are lost. We will consider the impact of this on the measured real-space function $\mathcal{F}(r)$. We rewrite the expression for the experimental $\mathcal{F}(r)$ as

$$\begin{aligned}\mathcal{F}(r; Q_{\min}) &= (2/\pi)\int\limits_{Q_{\min}}^{\infty} F(Q)\sin(Qr)\,\mathrm{d}Q\\ &= 4\pi r\rho(r) - (2/\pi)\int\limits_{0}^{Q_{\min}} F(Q)\sin(Qr)\,\mathrm{d}Q.\end{aligned}\tag{5.7.23}$$

Of course, we have a finite $Q_{\max}$ as well, but this will be disregarded during the following discussion, as the effects are well understood (Toby & Egami, 1992).

5.7.2.3. *Low-angle scattering intensity*

We will now consider a number of explicit examples to understand how the missing forward scattering affects the measured $\mathcal{F}(r; Q_{\min})$. This development makes explicit the connection between the equations of small-angle scattering and those of PDF analysis. We begin by considering the scattering from a large, uniform scatterer and gradually move to more realistic cases in steps.

First consider the RDF of an infinite scatterer of *uniform* density, ρ_0. Because the density is uniform the only scattering is in the forward direction (all the finite-Q scattering cancels) as a delta function at $Q = 0$: there is only small-angle scattering. In this case the scattering is infinite at $Q = 0$ and $F(0)$ is not well defined. We must therefore use a more rigorous description of the scattered intensity in this case. Since the scattering length is defined per atom, the scattering amplitude of a three-dimensional volume element $\mathrm{d}\mathbf{r}$ at position $\mathbf{r}$ is $\psi = \rho_0\langle f\rangle \exp(i\mathbf{Q}\cdot\mathbf{r})\,\mathrm{d}\mathbf{r}$. Then, for an infinite uniform scatterer, the intensity is given by

$$I_c(\mathbf{Q}) = \rho_0^2\langle f\rangle^2 \int\int \exp[i\mathbf{Q}\cdot(\mathbf{r}-\mathbf{r}')]\,\mathrm{d}\mathbf{r}\,\mathrm{d}\mathbf{r}',\tag{5.7.24}$$

where the integrals are over all space. Using this in equation (5.7.10) and integrating over Q first in equation (5.7.16) gives $\mathcal{F}(r) = 4\pi r\rho_0$, as expected. As a side note, using $I_c(Q) = 2\pi^2 N\langle f\rangle^2\rho_0\delta(Q)/Q$ gives the correct result, but we forgo this derivation for the one below, where we consider in detail the general case of an arbitrary scatterer.

To evaluate the scattered intensity for an arbitrary scatterer of uniform density we define a shape function $s(\mathbf{r})$ such that inside the shape $s = 1$ and outside the shape $s = 0$. For such a material,

$$I_c(\mathbf{Q}) = \rho_0^2\langle f\rangle^2 \int\int s(\mathbf{r})s(\mathbf{r}')\exp[i\mathbf{Q}\cdot(\mathbf{r}-\mathbf{r}')]\,\mathrm{d}\mathbf{r}\,\mathrm{d}\mathbf{r}'.\tag{5.7.25}$$

We redefine variables so that $\mathbf{r}'' = \mathbf{r} - \mathbf{r}'$ and $\mathrm{d}\mathbf{r}'' = \mathrm{d}\mathbf{r}$, in which case we have

$$\begin{aligned}I_c(\mathbf{Q}) &= \rho_0^2\langle f\rangle^2 \int\int s(\mathbf{r}')s(\mathbf{r}'+\mathbf{r}'')\exp(i\mathbf{Q}\cdot\mathbf{r}'')\,\mathrm{d}\mathbf{r}'\,\mathrm{d}\mathbf{r}''\\ &= \rho_0^2\langle f\rangle^2 \int \mathrm{d}\mathbf{r}''\exp(i\mathbf{Q}\cdot\mathbf{r}'')\int s(\mathbf{r}')s(\mathbf{r}'+\mathbf{r}'')\,\mathrm{d}\mathbf{r}'.\end{aligned}\tag{5.7.26}$$

The second integral is a self convolution, or autocorrelation, of the shape function. Let us define

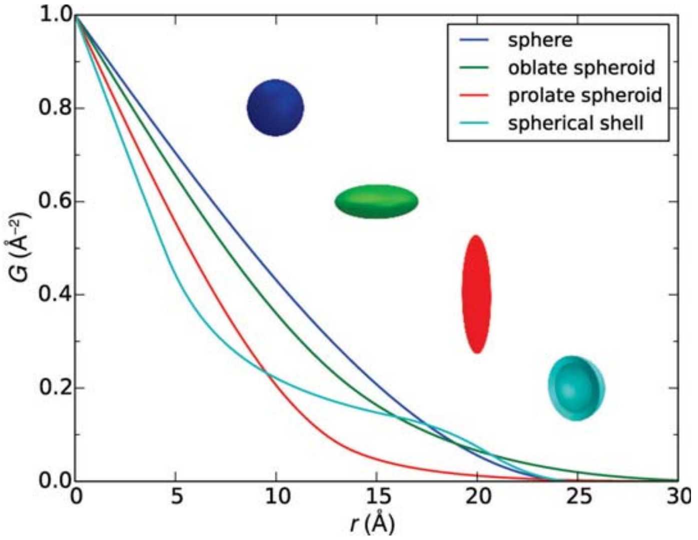

Figure 5.7.6
The nanoparticle form factors for a range of particle shapes.

$$\gamma_0(\mathbf{r}) = (1/V)\int s(\mathbf{r}')s(\mathbf{r}'+\mathbf{r})\,\mathrm{d}\mathbf{r}',\tag{5.7.27}$$

where $V = \int s(\mathbf{r})\,\mathrm{d}\mathbf{r}$ is the volume defined by the shape function. This $\gamma_0(\mathbf{r})$ is the characteristic function of the shape (Guinier *et al.*, 1955), and has been called the nanoparticle form factor in the PDF literature (Qiu *et al.*, 2005; Kodama *et al.*, 2006; Masadeh *et al.*, 2007). Defined as such, $\gamma_0(\mathbf{r})$ has the following properties:

$$\begin{aligned}\gamma_0(0) &= 1\\ \int\gamma_0(\mathbf{r})\,\mathrm{d}\mathbf{r} &= V.\end{aligned}\tag{5.7.28}$$

For reference, the nanoparticle form factor for a number of different particle shapes is shown in Fig. 5.7.6.

This definition and a convenient dropping of the double primes gives

$$I_c(\mathbf{Q}) = \rho_0^2\langle f\rangle^2 V\int\gamma_0(\mathbf{r})\exp(i\mathbf{Q}\cdot\mathbf{r})\,\mathrm{d}\mathbf{r}.\tag{5.7.29}$$

In analogy with the discrete case we want to convert this to equation (5.7.10), $S(\mathbf{Q}) - 1 = (I_c/N\langle f\rangle^2) - (\langle f^2\rangle/\langle f\rangle^2)$, and using the fact that $N = \rho_0 V$ we get

$$\begin{aligned}S(\mathbf{Q}) - 1 &= \frac{1}{N\langle f\rangle^2}\rho_0^2\langle f\rangle^2 V\int\gamma_0(\mathbf{r})\exp(i\mathbf{Q}\cdot\mathbf{r})\,\mathrm{d}\mathbf{r} - \frac{\langle f^2\rangle}{\langle f\rangle^2}\\ &= \rho_0\int\gamma_0(\mathbf{r})\exp(i\mathbf{Q}\cdot\mathbf{r})\,\mathrm{d}\mathbf{r} - \frac{\langle f^2\rangle}{\langle f\rangle^2}.\end{aligned}\tag{5.7.30}$$

The second term, $\langle f^2\rangle/\langle f\rangle^2$, is very small compared to the first term. It is of the order of unity, where the first term scales as $N = \rho_0 V$, and can safely be ignored in most cases.

Now we want to take the orientational average. This must be done with care as, in general, the orientation of the nanoparticle shape and the underlying structure are correlated. For example, the morphology of the particles (plates or needles) depends on easy growth directions of the underlying structure. As discussed by Gilbert (2008), this means that the shape function and the internal structure of the particle are not, in general, separable and it is not correct to get the scattered intensity by convoluting the reciprocal-space intensity with the Fourier transform of the characteristic function. Things are greatly simplified in the case where the underlying structure, or the nanoparticle shape, or both, are isotropic, or approximately so. Then we can denote the angle-averaged characteristic function as

$$\overline{\gamma_0(\mathbf{r})} = \gamma_0(r) = \frac{\int \mathrm{d}\phi \int \mathrm{d}\theta \sin(\theta) r^2 \gamma_0(\mathbf{r})}{\int \mathrm{d}\phi \int \mathrm{d}\theta\, r^2 \sin(\theta)}. \tag{5.7.31}$$

Using this and equation (5.7.12) we get

$$\begin{aligned} S(Q) - 1 &= \rho_0 \int\limits_0^\infty \mathrm{d}r \int\limits_0^{2\pi} \mathrm{d}\phi \int\limits_0^{\pi} \mathrm{d}\theta\, \overline{\gamma_0(\mathbf{r}) \exp(i\mathbf{Q}\cdot\mathbf{r})} r^2 \sin\theta \\ &= \rho_0 \int_0^\infty \mathrm{d}r \int\limits_0^{2\pi} \mathrm{d}\phi \int\limits_0^{\pi} \mathrm{d}\theta\, \overline{\gamma_0(\mathbf{r})}\overline{\exp(i\mathbf{Q}\cdot\mathbf{r})} r^2 \sin\theta \\ &= \rho_0 \int_0^\infty \mathrm{d}r \int\limits_0^{2\pi} \mathrm{d}\phi \int_0^{\pi} \mathrm{d}\theta\, \gamma_0(r) \frac{\sin(Qr)}{Qr} r^2 \sin\theta \\ &= \rho_0 \int_0^\infty \gamma_0(r) \frac{\sin(Qr)}{Qr} 4\pi r^2\, \mathrm{d}r. \end{aligned} \tag{5.7.32}$$

Since the particles have no preferred orientation in space, we have broken the average of the product in the first line into the product of the averages. This gives

$$F(Q) = \int\limits_0^\infty 4\pi\rho_0 r \gamma_0(r) \sin(Qr)\, \mathrm{d}r. \tag{5.7.33}$$

Noting that this is the direct sine-Fourier transform, we take the inverse transform to get

$$\begin{aligned} \mathscr{F}_u(r) &= (2/\pi) \int\limits_0^\infty F(Q) \sin(Qr)\, \mathrm{d}Q \\ &= 4\pi\rho_0 r \gamma_0(r), \end{aligned} \tag{5.7.34}$$

where the subscript u indicates that this result is for a solid of uniform density distribution, ρ_0.

Next we consider a macroscopic crystal. The difference in $F(Q)$ is at higher Q where, instead of complete cancellation of all the discrete intensity it appears at distinct reciprocal-lattice points as sharp Bragg peaks. Importantly, in the region of Q below the first Bragg peak, the distinct scattering is zero except at very low Q where small-angle-scattering region is reached. The *small-angle-scattering intensity*, $I^{\rm SAS} = I^{\rm SAS}_{\rm crystal}$ from the crystal is identical to that from the solid with uniform density, $I^{\rm SAS}_u$, *i.e.*, $I^{\rm SAS}_u = I^{\rm SAS}_{\rm crystal}$. In general the small- and wide-angle-scattering regions are well separated in Q and $I^{\rm SAS}$ decays to zero before $Q_{\rm min}$ is reached in the measurement. Thus,

$$\begin{aligned} \mathscr{F}^{\rm SAS}(r) &= (2/\pi) \int\limits_0^{Q_{\rm min}} F(Q) \sin(Qr)\, \mathrm{d}Q \\ &= \mathscr{F}_u(r) \end{aligned} \tag{5.7.35}$$

and therefore

$$(2/\pi) \int\limits_0^{Q_{\rm min}} F(Q) \sin(Qr)\, \mathrm{d}Q = 4\pi\rho_0 r \gamma_0(r). \tag{5.7.36}$$

We are now in a position to understand in detail the nature of the measured PDF $\mathscr{F}(r; Q_{\rm min})$. Substituting equation (5.7.36) into equation (5.7.23) we get

$$\mathscr{F}(r; Q_{\rm min}) = 4\pi r \rho(r) - 4\pi r \rho_0 \gamma_0(r). \tag{5.7.37}$$

This is similar to the definition of the PDF from equation (5.7.21), except that $\gamma_0(r)$ appears in an additional smoothly varying sloping baseline term.

Finally, we can express the important radial distribution function, $R(r) = 4\pi r^2 \rho(r)$, explicitly in terms of the experimentally accessible $G(r)$ as

$$\begin{aligned} G(r) &= \mathscr{F}(r; Q_{\rm min}) \\ &= \frac{R(r)}{r} - 4\pi r \rho_0 \gamma_0(r), \end{aligned} \tag{5.7.38}$$

and for completeness,

$$R(r) = r\big[G(r) + 4\pi r \rho_0 \gamma_0(r)\big]. \tag{5.7.39}$$

5.7.2.4. *Calculating $\mathscr{F}(r; Q_{\rm min})$ from models*

We can now consider the calculation of measured PDFs using equation (5.7.37) in a number of interesting limits.

5.7.2.4.1. *Calculating in real space for bulk crystals*

In the case of bulk crystals, the region of interest in the PDF is usually $r \ll D$, D being the smallest dimension across the crystal. In this region $\gamma_0(r) \approx 1$. Thus,

$$\begin{aligned} \mathscr{F}(r; Q_{\rm min}) &= G(r) \\ &= 4\pi r(\rho_{\rm bulk}(r) - \rho_0), \end{aligned} \tag{5.7.40}$$

which is the familiar definition of $G(r)$ in equation (5.7.37). The pair density function, $\rho_{\rm bulk}(r)$, is calculated from a model with periodic boundary conditions (Billinge, 1998; Proffen & Billinge, 1999; Farrow *et al.*, 2007) or from a box of atoms that is much larger in extent than the range of r of interest (McGreevy & Pusztai, 1988; Tucker *et al.*, 2007), using equation (5.7.22). The average number density ρ_0 is given by the number of atoms per unit volume, which in the case of crystals is the number of atoms in the unit cell divided by the unit-cell volume.

Equation (5.7.22) can be modified to account for peak broadening due to atomic vibrations and finite maximum Q. These modifications are discussed elsewhere (Proffen & Billinge, 1999; Egami & Billinge, 2012). The Debye–Waller approximation (Warren, 1990) for atomic motion holds rather well in most cases and the delta function is replaced by a Gaussian whose width is given by widths of the atomic displacement factors (ADPs) of each atom in the pair added in quadrature. If the atomic motion of near neighbours is correlated, the peak will be sharper as a result of motional correlations (Jeong *et al.*, 1999, 2003). If there are a large number of atoms in the model, such as in the big-box modelling approaches we describe below, the finite PDF peak widths are generally obtained by averaging over the atomic configuration in the box (or multiple configurations for better statistics) and no convolution is carried out. To account for termination effects in the Fourier transform of the data, the peak obtained by convoluting a Gaussian or sampling the configuration is convoluted with the Fourier transform of the termination function. If that is a simple cutoff the function convoluted is a sinc function.

5.7.2.4.2. *Calculating in real space for nanoparticles modelled as attenuated bulk crystals*

In this case $\rho_{\rm bulk}(r)$ is determined using a model of a bulk structure as described in Section 5.7.2.4.1. The pair density $\rho(r)$ in equation (5.7.37) is the function for the nanoparticle, which is approximated as $\gamma_0(r)\rho_{\rm bulk}(r)$ (Guinier, 1963). Thus,

$$\mathscr{F}(r; Q_{\rm min}) = 4\pi r \gamma_0(r)[\rho_{\rm bulk}(r) - \rho_0]. \tag{5.7.41}$$

This approach has been implemented in the *PDFgui* modelling program (Farrow *et al.*, 2007), for example, and used successfully on rather well ordered CdSe nanocrystals (Masadeh *et al.*, 2007; Yang *et al.*, 2013). The main shortcoming is that effects that cannot be incorporated in the average structure, such as surface relaxations or core–shell inhomogeneities, cannot be modelled this way.

If there is a distribution of nanoparticle sizes and shapes, the characteristic function $\gamma_0(r)$ can be replaced with an appropriately averaged characteristic function

$$\gamma(r) = \textstyle\int \gamma_0(r; R_1, R_2, \ldots) p(R_1, R_2, \ldots) \, \mathrm{d}R_1 \, \mathrm{d}R_2 \ldots . \qquad (5.7.42)$$

Here, $p(R_1, R_2, \ldots)$ is the normalized distribution of nanoparticle shapes parameterized by $R_1, \ R_2, \ldots$. For example, for spherical nanoparticles of radius R, $p(R_1, R_2, \ldots) = p(R)$, the distribution of nanoparticle radii. Finally, we replace equation (5.7.41) with

$$\mathscr{F}(r; Q_{\min}) = 4\pi r \gamma(r)[\rho_{\text{bulk}}(r) - \rho_0]. \qquad (5.7.43)$$

Great care should be taken to ensure that the result is unique when refining a number of nanoparticle morphology parameters beyond one or two.

5.7.2.4.3. *Calculating as the Fourier transform of the properly normalized Debye function*

This approach has been successfully used by a number of authors (Zhang *et al.*, 2003; Cervellino *et al.*, 2006; Farrow *et al.*, 2010). The $F(Q)$ function is evaluated using equation (5.7.15) and then Fourier transformed to obtain the desired real-space function. To account for thermal and zero-point motion in reciprocal-space calculations, equation (5.7.15) is replaced with a version that includes Debye–Waller effects,

$$F(Q) = \frac{1}{N\langle f\rangle^2} \sum_{i \neq j} f_j^* f_i \big[\exp(-\tfrac{1}{2}\sigma_{ij}^2 Q^2)\big] \frac{\sin(Qr_{ij})}{r_{ij}}. \qquad (5.7.44)$$

Here, σ_{ij}^2 is the correlated broadening factor for the atom pair (Proffen & Billinge, 1999; Thorpe *et al.*, 2002; Jeong *et al.*, 2003).

As we show here, for a quantitative comparison with measured data care must be taken with the Fourier transform so that it is carried out over the same range of Q as the experiment. The main drawback of the reciprocal-space approach is that it can be very slow compared to direct real-space calculation because of the long-range extent of the signal from each pair. It is generally preferred for smaller systems such as molecules or small clusters. However, as a result of recent algorithmic advances, the calculation of the Debye equation for larger systems can be greatly accelerated under certain circumstances (Cervellino *et al.*, 2006), although in these cases a real-space calculation of $G(r)$ is still often preferred.

Using this method, the termination effects coming from the finite Q range are implicity included provided that the Fourier transforms to obtain the model and data PDFs are terminated with the same $Q_{\min}$ and $Q_{\max}$ values. Note that it is important to select the right $Q_{\min}$ because of the effects of the small-angle scattering. This is not included in our definition of $G(r)$, and is not measured, but *is* included in the $G(r)$ obtained by Fourier tranforming the Debye equation unless it is explicitly excluded.

5.7.2.4.4. *Calculating in real space from discrete nanoparticle models*

In this case, equation (5.7.37) is used directly, where $\rho(r)$ is calculated from a finite model of the discrete nanoparticle using equation (5.7.22). The difficulty arises in determining a correct form for the baseline $-4\pi r\rho_0\gamma_0(r)$. Up until now, the shape of the baseline has been approximated using expansions of *ad hoc* mathematical functions (Korsunskiy & Neder, 2005; Neder & Korsunskiy, 2005; Korsunskiy *et al.*, 2007; Neder *et al.*, 2007). This is successful at approximating the behaviour of the baseline. As we showed here, the explicit form of the baseline may be calculated self-consistently from the characteristic function of the model or a measurement of the SAS. This is discussed in greater detail below.

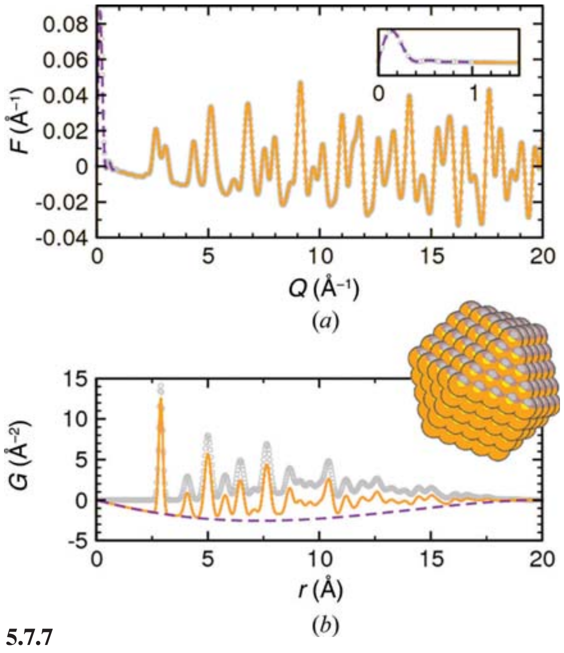

Figure 5.7.7

(*a*) The calculated diffraction pattern from a faceted 2 nm gold nanoparticle. The wide-angle X-ray scattering (WAXS) intensity is shown in gold and the small-angle X-ray scattering (SAXS) intensity is in purple. (*b*) Gold: the PDF of the gold nanoparticle obtained by Fourier transforming only the WAXS intensity shown in gold in (*a*). Purple: the PDF baseline that results from Fourier transforming the SAXS data shown in purple in (*a*). Grey: the RDF that is obtained if both the SAXS and the WAXS scattering are both Fourier transformed. Inset is the gold nanoparticle itself. All data are simulated.

If we have accurate small-angle-scattering data from the samples, from equation (5.7.37) we see that we can compute the PDF baseline from the measured SAS *via* a Fourier transform. This is illustrated in Fig. 5.7.7 for the case of a gold nanoparticle, which is shown in the inset. The simulated scattering signal calculated with the Debye equation is shown in the top panel, where the small-angle scattering is shown in purple and the wide-angle part in gold. In the lower panel, the gold curve is the Fourier transform of the gold data in the top panel (*i.e.*, the wide-angle data only). The dashed purple line that appears as a 'baseline' is the Fourier transform of the purple small-angle-scattering signal. Also plotted in grey is the function $R(r)/r$, which is the Fourier transform of the complete curve including small-angle and wide-angle data.

However, care must be exercised as the derivation assumes that the sample is made up of discrete nanoparticles. In general, clusters and aggregates of nanoparticles will form and small-angle-scattering signals from these structures on different length scales will be present and must be separated. Also, scattering-density fluctuations of any sort in the sample will affect the SAS signal, as discussed elsewhere (Cargill, 1971). None of these effects need be explicitly considered if the SAS signal is not used in the PDF definition, as in equation (5.7.37), although an alternative method is then required to determine the baseline.

The inclusion of SAS data has the potential to add significant value to any refinement of nanoparticle models from the PDF. Both small- and large-angle scattering contain information about the shape and size of nanoparticles, but this information is decoupled from the internal nanoparticle structure in the small-angle scattering. This same information is in the PDF, but it can be obscured by structural features, such as when the PDF prematurely attenuates because of a complex or amorphous surface structure. In this case the nanoparticle size obtained from SAS will be larger than the apparent nanoparticle size obtained from the PDF that reflects the size of the coherent core structure, which is sometimes called the crystallite size. Even without the inclusion of SAS data into PDF refinements, we can learn much from SAS analysis techniques. PDF nanoparticle refinements usually start with a simple model that includes atomic positions restricted by a shape. Therefore, PDF analysis can benefit from the various *ab initio* methods (Svergun & Stuhrmann, 1991; Chacón *et al.*, 1998) for determining the shape of a scatterer from the SAS.

Without the use of the small-angle intensity for determining $\gamma_0(r)$, we can consider approaches to determine it self-consistently from the model since it is the autocorrelation of the particle shape, which is directly available from the model itself by determining a 'shrink-wrapping' of the atomistic model. On the contrary, when the internal structure is well known, but the size and shape distribution of nanoparticles is not, then the characteristic function can be parameterized and refined to obtain the approximate nanoparticle dimensions, as was done by Masadeh *et al.* (2007).

5.7.2.5. *The extent of small-angle scattering*

We have considered the two asymptotic situations here of including or excluding all the SAS. If the SAS is retained in the intensity that is Fourier transformed, the resulting real-space function obtained is $4\pi r\rho(r) = R(r)/r$ [equation (5.7.18)]. Excluding it all results in $G(r)$ [equation (5.7.37)]. We now consider the possibility that some, but not all, of the small-angle scattering is included in the Fourier transform. This might occur in the case of very small nanoparticles, for example, when the SAS extends to wider angles. Here we estimate the circumstances under which a significant amount of small-angle intensity will appear in a wide-angle PDF experiment for the case of a sphere of uniform density. The scattered intensity is given by (Rayleigh, 1914)

$$I(Q) \propto \frac{9}{(QR)^6}[\sin(QR) - QR\cos(QR)]^2, \qquad (5.7.45)$$

where R is the radius of the sphere. By integrating this equation from 0 to $Q_{\min}$ and dividing by the total integrated intensity, we get an expression for the proportion of small-angle intensity above $Q_{\min}$ for a given nanoparticle diameter (Rayleigh, 1914):

$$\begin{aligned} i(x) = 1 - \frac{1}{2\pi r^5}\big[&(2x^4 - x^2 + 3)\cos(2x) \\ &+ x(x^2+6)\sin(2x) + 4x^5\mathrm{Si}(2x) - (5x^2+3)\big]. \end{aligned} \qquad (5.7.46)$$

Here, $x = Q_{\min}R$ and $\mathrm{Si}(x)$ represents the sine integral, $\mathrm{Si}(x) = \int_0^x \sin(x')/x'\,\mathrm{d}x'$. For a very small nanoparticle of radius 5 Å, we see that $i(5) < 0.01$, corresponding to $Q_{\min} \simeq 1$ Å^{-1}, which is typical for a rapid-acquisition PDF (RAPDF) (Chupas *et al.*, 2003) experiment, as very commonly carried out at synchrotron X-ray sources. Thus, for even quite small nanoparticles, practically all small-angle intensity is below $Q_{\min} = 1$ Å^{-1} and equation (5.7.37) is appropriate. However, care should be taken not to extend $Q_{\min}$ too low in Q in a measurement of a nanoparticulate system.

In the few-atom limit, such as the case of discrete small molecules, the small- and wide-angle scattering are not cleanly separated. To produce a complete real-space signal, one can approximate the small-angle scattering from a candidate structure model. This approach is commonly used in the study of small molecules in the gas phase (Hargittai & Hargittai, 1988). The Fourier transform of the estimated scattering approximates to $R(r)/r$, the nominal 'experimental' or 'modified' RDF. An equivalent method for obtaining the modified RDF from wide-angle scattering alone is to add a baseline estimated from a model structure to $\mathcal{F}(r, Q_{\min})$ (Ruan *et al.*, 2007). This approach has been successful for calculating $R(r)/r$ for many-atom nanoparticles.

5.7.2.6. *PDFs from structures with multiple elements*

The equations defined so far in Section 5.7.2 are given as double sums over all the atoms in the sample. It is often useful to separate these sums into partial sums over different atomic species in the material. The reason is that the prefactor for each term in the sum is $f_i^* f_j / \langle f \rangle^2$, which is the same for all pairs involving atoms of the same elements, allowing the prefactor to be pulled out of the partial sum over only those pairs. Thus, if we reconsider equation (5.7.14), for a compound,

$$\begin{aligned} S(Q) &= \frac{1}{\langle f \rangle^2}\left[\frac{1}{N}\sum_{i,j(i\neq j)} f_j^* f_i \frac{\sin(Qr_{ij})}{r_{ij}} + \langle f \rangle^2\right] \\ &= \frac{1}{\langle f \rangle^2}\left[\sum_{\alpha,\beta}\ \sum_{i\in\{\alpha\},j\in\{\beta\}(i\neq j)} \frac{f_\alpha^* f_\beta}{N}\frac{\sin(Qr_{ij})}{r_{ij}} + \langle f \rangle^2\right] \\ &= \frac{1}{\langle f \rangle^2}\left[\sum_{\alpha,\beta}\sum_{a,b}\frac{f_\alpha^* f_\beta}{N}\frac{\sin(Qr_{ij})}{r_{ij}} + \sum_{\alpha,\beta} c_\alpha c_\beta f_\alpha^* f_\beta\right] \\ &= \sum_{\alpha,\beta}\frac{c_\alpha c_\beta f_\alpha^* f_\beta}{\langle f \rangle^2}\left(\sum_{a,b}\frac{1}{N c_\alpha c_\beta}\frac{\sin(Qr_{ij})}{r_{ij}} + 1\right) \\ &= \sum_{\alpha,\beta}\frac{c_\alpha c_\beta f_\alpha^* f_\beta}{\langle f \rangle^2} S_{\alpha\beta}. \end{aligned} \qquad (5.7.47)$$

Here we have taken the double sum over all the atoms in the sample, and split it into partial sums over atom pairs between particular atom types. α denotes the set of atom types in the material, for example, if the material is an alloy of composition A_xB_{1-x}, then $\alpha = \beta = \{A, B\}$, and there are three partial sums over pairs of atom types, $\sum_{A,A}$, $\sum_{A,B}$ and $\sum_{B,B}$. Finally, we introduce the notation $\sum_{a,b}$ for brevity, defined in equation (5.7.47). The expression for $\langle f \rangle^2$ is taken from equation (5.7.3). This serves both to define the 'partial structure function',

$$S_{\alpha\beta} = \sum_{a,b}\frac{1}{N c_\alpha c_\beta}\frac{\sin(Qr_{ij})}{r_{ij}} + 1, \qquad (5.7.48)$$

and to show how the partial structure functions are combined to make the total. This definition is not unique, and is due to Faber & Ziman (1965). It has the nice feature that the partial structure functions have the same high-Q asymptotic behaviour as the total $S(Q)$, *i.e.*, they tend to unity, which means that it is straightforward to define their real-space equivalents, $\mathcal{F}_{\alpha\beta}(r; Q_{\min})$, by analogy with equation (5.7.23),

$$\mathcal{F}_{\alpha\beta}(r; Q_{\min}) = (2/\pi)\int\limits_{Q_{\min}}^{\infty} Q\big[S_{\alpha\beta} - 1\big]\sin(Qr)\,\mathrm{d}Q, \qquad (5.7.49)$$

which, following equation (5.7.23) and the discussion in Section 5.7.2.4, is simply

$$G_{\alpha\beta}(r) = (2/\pi) \int\limits_{Q_{\min}}^{\infty} Q\big[S_{\alpha\beta} - 1\big] \sin(Qr)\,\mathrm{d}Q. \qquad (5.7.50)$$

Here we can refer to $G_{\alpha\beta}(r)$ as the partial reduced pair distribution function. However, as discussed later in Section 5.7.5.1, when calculating pair distribution functions from models we need to know the relationship to the 'partial radial distribution function', $R_{\alpha\beta}(r)$, of the material. The full derivation requires use of equation (5.7.63), which allows partial sums to be taken in the real-space $R(r)$ function just as the case of the $S_{\alpha\beta}$ definition above. The full derivation is reproduced in Section 5.7.5.2, but for completeness we present the result here without derivation:

$$R(r) = \sum_{\alpha\beta} \frac{c_\alpha c_\beta f_\alpha f_\beta}{\langle f\rangle^2} R_{\alpha\beta}(r). \qquad (5.7.51)$$

5.7.2.7. *Differential structure functions*

Experimentally, $S_{\alpha\beta}$ is not accessible directly. However, it is possible to determine it using differential methods (Fuoss *et al.*, 1981; Waseda, 1984; Price & Saboungi, 1998). The approach of measuring close to an edge to get chemical information was first suggested by Shevchik (1977), with the first experimental demonstration making use of the newly available synchrotron radiation a few years later (Fuoss *et al.*, 1981). We rederive the equations here. Consider a situation where the distinct scattering intensity [equation (5.7.6)] is measured in two experiments which differ only in the sense that the scattering factor of one of the atom types changes from experiment 1 to experiment 2, *i.e.* we have $f_A(1) \neq f_A(2)$ and $\Delta f_A = f_A(2) - f_A(1)$. Now,

$$\begin{aligned}
\frac{I_d}{N} &= \langle f\rangle^2[S(Q) - 1] \\
&= \sum_{\alpha,\beta} c_\alpha c_\beta f^*_\alpha f_\beta S_{\alpha\beta} - \langle f\rangle^2 \\
&= c_A f^*_A \sum_\beta c_\beta f_\beta S_{A\beta} + \text{c.c.} + \sum_{(\alpha,\beta)\neq A} c_\alpha c_\beta f^*_\alpha f_\beta S_{\alpha\beta} \\
&\quad - c_A f^*_A \sum_\beta c_\beta f_\beta - \text{c.c.} - \sum_{(\alpha,\beta)\neq A} c_\alpha c_\beta f^*_\alpha f_\beta \\
&= c_A f^*_A \sum_\beta c_\beta f_\beta (S_{A\beta} - 1) + \text{c.c.} \\
&\quad + \sum_{(\alpha,\beta)\neq A} c_\alpha c_\beta f^*_\alpha f_\beta (S_{\alpha\beta} - 1), \qquad (5.7.52)
\end{aligned}$$

where c.c. denotes the complex conjugate. This form for I_d splits it into two sums; one involves A atoms and one does not. When we take the difference between the two measurements (1) and (2) the terms that do not involve A atoms cancel and we get

$$\begin{aligned}
\frac{\Delta I_d}{N} &= \frac{I_d(2) - I_d(1)}{N} \\
&= c_A^2[f^*_A(2) f_A(2) - f^*_A(1) f_A(1)](S_{AA} - 1) \\
&\quad + \left[c_A\big[f^*_A(2) - f^*_A(1)\big] \sum_{\beta\neq A} c_\beta f_\beta (S_{A\beta} - 1) + \text{c.c.}\right] \\
&= c_A^2 \Delta|f_A^2|(S_{AA} - 1) + \left[c_A \Delta f^*_A \sum_{\beta\neq A} c_\beta f_\beta (S_{A\beta} - 1) + \text{c.c.}\right].
\end{aligned} \qquad (5.7.53)$$

For neutrons, $f = b$ is real. For X-rays

$$f(Q, E) = f_0(Q) + f'(E) + if''(E), \qquad (5.7.54)$$

where $f_0(Q)$ is the non-resonant form factor and f' and f'' are the so-called anomalous scattering factors which have an effect at all wavelengths but which are only significant in the vicinity of an absorption edge. f' and f'' are connected by a Kramers–Kronig transform (Kronig, 1926; Kramers, 1927) and so are not independent. Values for f' and f'' may be calculated, at some computational expense, from relativistic quantum-mechanical calculations of atoms. They may also be measured directly by measuring X-ray absorption to find f'' over a sufficiently wide range of energies from below to above the absorption edge, and computing f' from the Kramers-Kronig transformation. If we assume that the difference between measurement (1) and measurement (2) is the incident X-ray energy, which is changed in the vicinity of an absorption edge for atom type A, we can define

$$\begin{aligned}
\Delta f &= [f_0 + f'(E_2)] - [f_0 + f'(E_1)] + i[f''(E_2) - f''(E_1)] \\
&= \Delta f' + i\Delta f'',
\end{aligned} \qquad (5.7.55)$$

and

$$\begin{aligned}
\Delta|f^2| &= [f_0 + f'(E_2)]^2 + f''^2(E_2) - [f_0 + f'(E_1)]^2 + f''^2(E_1) \\
&= [f'^2(E_2) - f'^2(E_1)] + 2f_0[f'(E_2) - f'(E_1)] \\
&\quad + [f''^2(E_2) - f''^2(E_1)] \\
&= \Delta f'^2 + 2\Delta f' f_0 + \Delta f''^2 \\
&\sim 2\Delta f' f_0,
\end{aligned} \qquad (5.7.56)$$

where for the last line it is assumed that $\Delta f'$ and $\Delta f''$ are small compared to f_0 and we can neglect terms of higher than linear order in the delta values. Below the absorption edge it is also true that $\Delta f'' \ll \Delta f'$ and it is a reasonable approximation to neglect $\Delta f''$. Finally, far from the absorption edges, true for the non-A-type atoms, f' and f'' themselves are small. Equation (5.7.53) can then be rewritten as

$$\begin{aligned}
\frac{\Delta I_d}{N} &= 2c_A^2 \Delta f'_A f_0^A (S_{AA} - 1) \\
&\quad + \left[c_A \Delta f'_A \sum_{\beta\neq A} c_\beta f_0^\beta (S_{A\beta} - 1) + \text{c.c.}\right] \\
&= 2c_A \Delta f'_A \sum_\beta c_\beta f_0^\beta (S_{A\beta} - 1)
\end{aligned} \qquad (5.7.57)$$

where now the sum over β includes atom-type A. This is now in a form where we can express it as a type of 'differential $S(Q)$' that is not a 'partial' that encodes correlations between atoms of two specified types, or a 'total' between all atom types, but an intermediate function that is between atom-type A and all the other atom types. We would like to define this 'differential structure function', $\Delta S = S_A$, such that it has the same asymptotic properties as all the Faber–Ziman structure functions already defined. Now, since $\langle f\rangle = \sum_\beta c_\beta f_0^\beta$,

$$\frac{\Delta I_d}{N} = 2c_A \Delta f'_A \left[\sum_\beta c_\beta f_0^\beta S_{A\beta} - \langle f\rangle\right], \qquad (5.7.58)$$

which, in analogy with equation (5.7.10) allows us readily to define S_A as

$$S_A = \frac{\Delta I_d}{N 2 c_A \Delta f'_A \langle f\rangle} + 1 \qquad (5.7.59)$$

and

$$S_A = \sum_\beta \frac{c_\beta f_\beta}{\langle f\rangle} S_{A\beta}. \qquad (5.7.60)$$

Equation (5.7.59) allows us to determine S_A experimentally, and equation (5.7.60) to express it in terms of partials, which can be calculated from models.

The differential structure function S_A is an experimentally accessible structure function that has chemical specificity. Explicitly, it contains the information about the positions of all the atoms surrounding atoms of type A. Since we defined it to have the same properties as all our other Faber–Ziman structure functions, we can use the same Fourier transform to obtain a corresponding real-space differential reduced pair distribution function $G_A(r)$,

$$G_A(r) = (2/\pi) \int\limits_{Q_{\min}}^{\infty} Q\big[S_A - 1\big] \sin(Qr)\,\mathrm{d}Q, \qquad (5.7.61)$$

which is the correlation function that yields the positions of all atoms around every atom of type A and is given by

$$G_A = \sum_{\beta} \frac{c_\beta f_\beta}{\langle f \rangle} G_{A\beta}. \qquad (5.7.62)$$

The desired differential may then be obtained by taking two measurements from the same sample but with two different incident energies, one close to (but just below) the absorption edge, and the other further below the edge (typically around 200 eV lower in energy).

For neutrons, the form factor (more commonly called the coherent scattering length and designated by b rather than f) depends on the isotopic composition of the element and may be varied for the A atoms in a sample by synthesising two samples with different isotopic compositions. The equations (5.7.59) and (5.7.60) are readily extended to the case of neutrons simply by replacing the f's with b's. The approach using isotopic substitution works very well, but synthesizing large quantities (preferred for neutron measurements) of isotopically enriched samples can be very expensive.

Finally, the poor person's way of doing the isotopically enriched experiment is to carry out two experiments on chemically similar compounds, where the assumption is made that the two samples have the same structure. We also note that non-diffraction-based methods can also provide valuable information here, such as extended X-ray absorption fine structure (EXAFS) (Teo, 1986; Lytle *et al.*, 1975) measurements.

5.7.3. Collecting data for total-scattering and PDF measurements

5.7.3.1. *Neutrons*

Neutrons for scientific studies are produced either at research reactors or at pulsed spallation neutron sources. The latter are generally the most useful for PDF analysis because of the presence of many short-wavelength epithermal neutrons in the spectrum and the vast majority of PDF studies to study disorder on crystalline materials are carried out at spallation sources. However, reactor neutrons also yield high-quality PDFs, especially from diffractometers that look at a hot moderator, such as D4 at the Institut Laue Langevin (ILL) in Grenoble, France.

Neutron powder diffractometers for PDF work are similar to those used for regular powder diffraction, and indeed early PDF work was done on regular powder diffractometers. Some special characteristics of the total-scattering measurement mean that now diffractometers optimized for this measurement are appearing. The time-of-flight diffractometer itself consists of a sample holder surrounded by fixed detectors.

In total-scattering measurements from crystals, a balance must be struck between Q-space resolution and intensity. Samples are generally held in cylindrical containers made of incoherently scattering materials such as vanadium. Other sample geometries are also used, for example, wide flat samples are used on SANDALS and NIMROD at the ISIS neutron source at Rutherford Appleton Laboratory in the UK, since most of the detectors on these instruments are in the forward-scattering direction. The secondary flight path is usually in the vicinity of 1–2 m. Low-angle detectors can be located further from the sample to help compensate for the inferior resolution in the forward-scattering direction. The vicinity of the sample is usually evacuated to reduce air scattering and to facilitate the use of sample environments such as cryostats and furnaces. Data consist of the histogram of neutrons that arrived at various time intervals after the generation of the incident pulse. The time-of-flight t over the path L translates into the neutron velocity, $v = L/t$, which gives the momentum $\hbar k = mv$. Thus t is inversely related to Q. To increase detected flux, as much solid angle as possible is filled with detectors. The modern trend is to use pixelated detectors to produce a three-dimensional data set: two dimensions for Q and the third dimension for t. At the time of writing some of the best instruments for PDF measurements are NPDF (Proffen *et al.*, 2002) at the Lujan Center at Los Alamos, NOMAD (Neuefeind *et al.*, 2012) at the spallation neutron source (SNS) at Oak Ridge National Laboratory, GEM (Williams *et al.*, 1997; Hannon, 2005), NIMROD (Bowron *et al.*, 2010) and the upgraded POLARIS (http://www.isis.stfc.ac.uk/instruments/polaris/) at the ISIS neutron source at the Rutherford Appleton Laboratory in the UK, and the NOVA, iMATERIA (Ishigaki *et al.*, 2009) and SPICA instruments at J-PARC/MLF in Japan (http://j-parc.jp/researcher/MatLife/en/instrumentation/ns.html). NIMROD has many detectors in the forward-scattering direction and is particularly suitable for studying complex liquids such as organics. It is especially designed for handling hydrogenated materials, although it has a low resolution. It also yields data over a wide range of Q, including the low-angle region, which may make it ideally suited to studying nanoparticles as discussed above in the theory section. Finally, as well as combining SAS and PDF into a single instrument, very good PDFs have been obtained from an inelastic neutron scattering spectrometer, ARCS (Bozin *et al.*, 2009) at SNS, meaning that PDF and inelastic neutron scattering from powders may be readily studied using a single instrument.

Additional fundamental requirements for the diffractometer are low backgrounds, stable detectors and detector electronics, stable beam monitors and a stable moderator. The low backgrounds are achieved primarily by excellent collimation and shielding, including a well shielded primary-beam dump, or 'get lost tube'. These modern instruments produce huge amounts of data requiring specialized data-reduction programs, which are well developed at this point, for example, *PDFgetN* (Peterson *et al.*, 2000) and *Gudrun* (Soper & Barney, 2011). Tools are also being developed as part of the Mantid project (http://mantid-project.org).

Diffractometers at reactor sources work quite differently. By way of example, D4 at ILL (Fischer *et al.*, 2002), on a hot moderator source, has a standard wavelength of 0.5 Å and detector banks cover a range from 2 to 140° that yields PDFs with $Q_{\max}$ = 23.6 Å^{-1}. Of particular interest at D4 is the very low background due to tight secondary collimation (after the sample and before the detectors). It was designed in part for detecting small differences in isotope-substitution measurements of glasses and liquids. To do this successfully, it is important to have extremely good count-rate stability and low backgrounds.

5.7.3.2. *X-rays*

Excellent PDFs may be obtained from nanomaterials using X-rays and this has become a widely used technique. Historically, PDFs with modest $Q_{\max}$ were obtained from laboratory sources with Mo or Ag sources. High real-space resolution PDFs were not thought to be feasible, even from higher-energy X-ray sources where the higher $Q_{\max}$ could be accessed, because the X-ray signal is strongly attenuated in this high-Q region because of the atomic form factor. This is indeed true, and neutrons are often preferred for high real-space resolution work for this reason. However, with the advent of high-energy synchrotron sources that produce an abundance of hard X-rays, it was demonstrated that sample-limited resolutions could be obtained even for quite challenging covalently bonded samples (Petkov *et al.*, 1999; Laaziri *et al.*, 1999; Petkov *et al.*, 2000; Jeong, Mohiuddin-Jacobs *et al.*, 2001). The experiments were slow and arduous, but with the advent of the rapid acquisition PDF (RAPDF) method (Chupas *et al.*, 2003) that utilizes two-dimensional (2D) detectors and a very high energy X-ray source, obtaining PDFs from X-rays has become straightforward and much more accessible.

Synchrotron sources with an electron energy of around 2.4 GeV or greater are preferred for PDF work on crystals and nanocrystals. The newer 'third-generation' sources such as the European Synchrotron Radiation Facility (ESRF) (Grenoble, France, http://www.esrf.eu/), the Advanced Photon Source (APS) (Argonne National Laboratory, Illinois, USA, http://www.aps.anl.gov/), SPRING-8 (Harima, Japan, http://www.spring8.or.jp/), NSLS-II (Brookhaven National Laboraotry, New York, USA, http://www.bnl.gov/ps/), Diamond Light Source (Rutherford Appleton Laboratory, Oxfordshire, UK, http://www.diamond.ac.uk/), Soleil (Saclay, France, http://www.synchrotron-soleil.fr/), PETRA-III (DESY Lab, Hamburg, http://petra3.desy.de/), MAX-IV (Sweden) and so on, feature high luminosity in addition to high intensity at high X-ray energies. Many scattering experiments that were formerly impossible or impractical are now feasible. Growth of the PDF technique has led to a number of beamlines operating or under construction at these sources that are optimized for PDF measurements, including at the time of writing, 11IDB and C at APS, XPD at NSLS-II, ID11 and ID15 at ESRF and XPDF at Diamond, although these designations tend to change with time because of facility upgrades and new construction. Current statuses can be found at facility websites. Good PDFs can also be obtained from laboratory X-ray sources with Mo or Ag anodes. The tradeoff is a significant reduction in intensity, which results in very long measurement times.

The primary respect in which modern synchrotron sources have revolutionized the PDF method is through the use of the RAPDF method, which is illustrated schematically in Fig. 5.7.8 and is extremely straightforward.

High-energy monochromatic X-rays from a synchrotron source are incident on the sample. A large-area 2D detector is placed orthogonal to the beam, in transmission geometry, and as close behind the sample as possible. The full diffraction pattern can be collected in a single frame that may be as short as around 30 ms. More often, multiple frames are collected with an integrated exposure time of a few seconds to a few minutes to get quality data to high Q. The geometry of the sample is sometimes pill-shaped and sometimes a capillary. The preferred diameter of the sample capillary or thickness of the pill depends on the scattering power of the sample for the incident X-ray energy. Normally 1 mm internal diameter (ID) capillary tubes are loosely filled with powder and mounted on a goniometer head or other support. For weakly scattering samples such as organics it may be preferable to use 2 mm ID tubes to increase the scattered intensity, albeit with a somewhat lower Q resolution of the measurement. For ease of handling and relatively weak scattering power, capillaries made of polyimide (sometimes called Kapton) tubing are often used. High-energy X-rays are very penetrating and it is rarely necessary to adjust the tube diameter to minimize absorption effects, although to increase the scattering signal from weakly scattering samples it is sometimes desirable to use larger diameter tubes, and to increase the Q-space resolution for strongly scattering samples it is possible to use smaller diameter samples too.

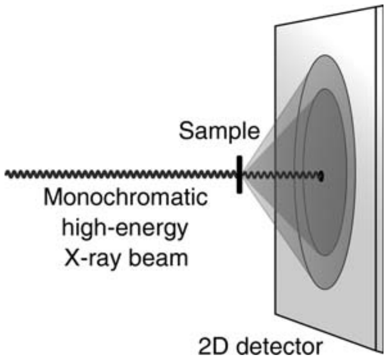

Figure 5.7.8
Schematic of the 2D detector and sample placement for a typical RAPDF measurement.

The capillary is often mounted with its long axis perpendicular to the beam, but may be mounted vertically or horizontally or at any other orientation, since the sample itself is an isotropic powder of micro- or nanograins. The final choice of orientation of the capillary will then depend on optimizing many experimental factors such as beam or measurement geometry or sample environment. Because of the horizontal polarization of the electric field of the X-rays at synchrotron sources, the detector is often scanned in the vertical plane when data are collected over a wide angular range. In this case a horizontal orientation of the capillary is more natural. The incident beam is often rectangular, or elongated in the horizontal plane if the source is a bending magnet or wiggler, and again a horizontal orientation may be preferred. Expediencies such as the best way to cool a sample with a flowing nitrogen cooler or a cramped environment in the instrument hutch at the sample position can all also affect the choice of orientation.

Overall, the RAPDF method is well adapted to experiments in special environments such as high temperature, high pressure, magnetic field or controlled gas environments. However, if a PDF over wide ranges of r is desired, then a higher Q-resolution measurement than is possible in the RAPDF geometry is needed. Similarly, if the X-ray energy is limited to a value much below 30 keV, for example when working at the absorption edge of low or intermediate Z or if using an Mo or Ag laboratory X-ray source, the available Q range in the RAPDF experiment will be very low and the RAPDF geometry is not preferred. In these cases the old-fashioned scanned-point-detection scheme, or a wide-angle 1D detector such as a strip detector, may be utilized. The experimental geometry could be Debye–Scherrer or Bragg–Brentano (Klug & Alexander, 1974). Roughly speaking, any powder-diffraction measurement carried out to sufficiently high Q can be used for a PDF measurement. One example is the high-

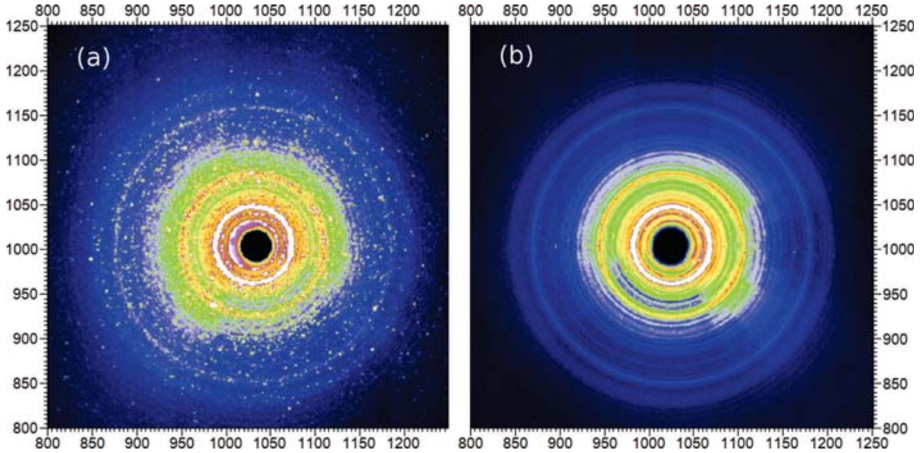

Figure 5.7.9
An example of the better powder average (reduced spottiness of the diffraction pattern) obtained when a sample with a poor powder average is spun. (*a*) Measured without spinning and (*b*) with spinning the capillary. The sample was a crystalline small-molecule organic sample.

resolution powder diffractometer currently at ID22 at ESRF, which has a bank of multiple analyser crystals (Fitch, 2004). It is mostly used for high-resolution powder diffraction for crystallographic analyses, but can also be used to good effect for PDF studies because the beamline can be operated with quite short wavelength X-rays. No special setup is required, but care should be taken to count for a long time in the high-angle region. Exactly how long is something that has to be assessed on a trial-and-error basis. It can be misleading to look at the counting statistics in individual bins in the high-Q region alone, since this depends on the bin width and the Fourier transform sums bins. In fact, the best way to assess this is to propagate the data all the way to the PDF, determine the $Q_{\max}$ that is desired and see whether the resulting PDF has a sufficient signal:noise ratio, then go back and count for longer if needed. Once this has been done for a particular experimental setup, it is then possible to judge directly by looking at the Q-space data. The high-resolution results in PDFs extend very far in r space, up to hundreds of nanometres for well ordered samples.

In terms of sample preparation for crystalline samples, the particle size should be small (<40 µm) and uniform. This may be accomplished by careful grinding in a mortar and pestle and sieving the sample through a 400 mesh sieve. Smaller particle sizes may be obtained by using a mechanical ball mill. This is particularly important to avoid spotty data. It can also help to reduce preferred orientation of grains (sometimes called texture) in the sample. It is less relevant for nanoparticulate samples that do not have large coherently scattering grains. Special difficulties can arise if the powder grains have a particularly oblate or prolate morphology. Oblate grains are generally not a problem in capillaries, but needle-like grains can become significantly orientationally ordered in a capillary if the sample size is too big. Gentle grinding often takes care of the problem, but samples containing needle-like grains could also be measured in the pill-shaped sample geometry described above to mitigate this problem.

Samples with crystallites that are too large produce ‘spotty’ diffraction patterns, which are easy to detect in a 2D diffraction pattern on an area detector (Fig. 5.7.9*a*). To mitigate this one can spin the capillary about its long axis, oriented perpendicular to the beam, which greatly improves powder statistics (Fig. 5.7.9*b*). In some sample environments spinning is not an option, but it may still be possible to wobble the sample, or gently rock it. Do so through as large an angular range as possible, but even a ±2° wobble during each exposure can help to improve the powder statistics a lot.

If the diffraction pattern from the spun or rocked sample is still spotty, it may be still be possible to recover a reasonably accurate PDF. For example, the 2D-to-1D integration also helps to average the intensity around the ring and the mean intensity of the spotty ring may not be so far from the ideal value. If a relatively small number of very bright spots are present within a more uniform ring of intensity it is possible to remove them by masking, or by taking the median intensity around the ring rather than the mean intensity during the integration step, which down-weights the contributions of the intense outlier spots. Of course it is better to remove the spottiness by better sample preparation where possible, as this removes uncertainty about how well the ‘work-around’ is working.

Loose powders may also be mounted in different geometries, such as in pill form supported with thin Kapton tape over the bottom and top surfaces. The Kapton tape is particularly important if the sample is to be cooled in a vacuum. Samples to be cooled may also be in Kapton capillaries. Uncovered powders rarely survive the pump down as air trapped between the grains forces its way out. Differential thermal contraction between the sample holder and the powder itself can also loosen a tightly packed powder. A small amount of grease, or Duco cement mixed with acetone, can also be mixed with a loose powder to stabilize it if the sample does not have to be recovered in its pristine state after the experiment. The scattering from the stabilizing agent is relatively weak and may be ignored in the subsequent data reduction in most cases.

5.7.3.3. *Electrons*

Some progress has been made recently in obtaining quantitatively reliable PDFs from electron-diffraction data measured on widely available laboratory electron microscopes. We refer to this electron-PDF as ePDF (Abeykoon *et al.*, 2012; Gorelik *et al.*, 2015) to differentiate from X-ray (xPDF) and neutron (nPDF) measurements. Application of ePDF methods to nanostructure determination is a relatively new development and practices and methods are likely to develop with time. However, we briefly describe here some aspects of the measurements that are pertinent for obtaining quantitative PDFs from nanosystems. An example of ePDF measurements from gold nanoparticles is shown in Fig. 5.7.10.

Apart from the strong scattering that leads to dynamical-scattering effects that distort the kinematical diffraction pattern needed for PDF work, electrons lend themselves naturally to a PDF analysis. Because of the strong scattering, a reasonable signal can be obtained from a small volume of sample in a very short time (*e.g.* 0.05 s). The study of amorphous thin films using electrons dates back to the pioneering work of Moss & Graczyk (1969) on amorphous silicon. Following this, a number of researchers collected similar data on amorphous thin films using energy filtering and various electron-detection methods

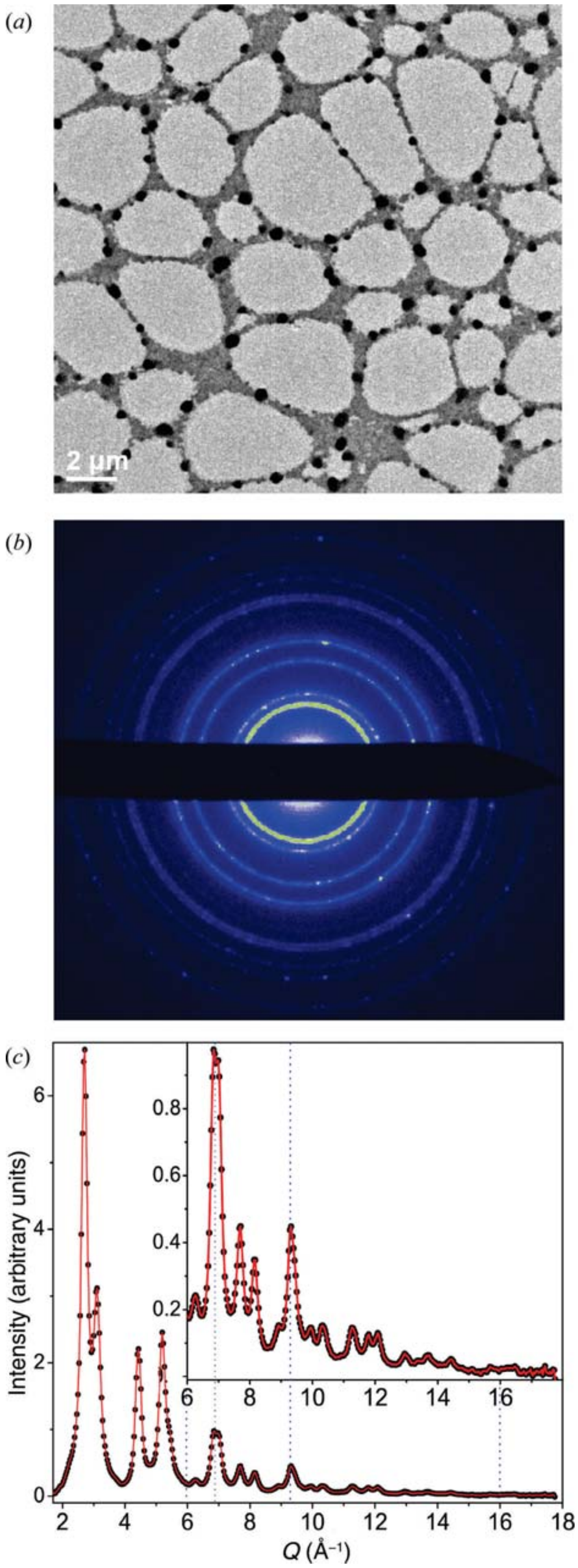

Figure 5.7.10
(*a*) TEM image of 100 nm Au nanoparticles (black dots) used for ePDF measurement. (*b*) Background-subtracted ED image of same region collected using 200 keV electrons. (*c*) 1D diffraction pattern obtained by integrating around the rings of intensity in (*b*). Adapted from Abeykoon *et al.* (2012) with permission from De Gruyter GmbH.

(Chaudhari *et al.*, 1972; Rudee & Howie, 1972; Gandais *et al.*, 1973; Cockayne & McKenzie, 1988; McBride *et al.*, 1999). Recently it has been shown that PDFs from nanomaterials can be obtained using electron diffraction that are sufficiently quantitatively reliable that they may be modelled using PDF modelling programs such as *PDFgui* (Abeykoon *et al.*, 2012). This study demonstrated the possibility of obtaining quantitatively accurate PDFs using standard laboratory transmission electron microscopes.

When collecting data for ePDF measurements, some issues require more careful consideration than for X-ray or neutron powder-diffraction measurements. Samples must be thin enough to avoid too much multiple scattering. For example, nanoparticles and films below 10 nm thickness are ideal. Because of the small sample volumes care must be taken to obtain a good powder average, which may be accomplished by taking multiple diffraction patterns from different parts of the sample, or rocking the sample. The camera length should typically be as short as possible. This may be set by adjusting electron-lens currents (Abeykoon *et al.*, 2015). A calibration of the camera length may be made by measuring a calibration sample of known lattice parameter. It is important to carry out the calibration measurements under precisely the same conditions, including all the lens currents, as the experiment on the sample itself. ePDFs may be collected using a standard CCD camera, although under certain circumstances an image plate may be preferred. The sample is usually supported on a weakly scattering membrane such as a holey carbon grid. The signal from the background may be measured from a region of the sample holder that contains no nanoparticles or film in the field of view. The use of an energy filter was at first thought to be essential, but has since been shown not to be (Abeykoon *et al.*, 2012). The perennial problem in electron diffraction, beam damage, is also true for ePDF but is manageable if handled correctly (Gorelik *et al.*, 2015).

5.7.3.4. *Q ranges and Q resolutions*

We briefly compare here the ranges of Q and the Q resolutions of these different sources and data-collection methods. Just to recap, collecting data over a wide Q range results in sharp peaks in the PDF and a high real-space resolution, at least from well ordered samples. On the other hand, the Q-space resolution affects the range in r over which the PDF extends. A lower-resolution measurement results in the PDF being attenuated by a resolution 'envelope' that diminishes the amplitude of the PDF peaks with increasing r. This is similar to the effects of nanocrystallinity. One should select the measurement geometry and source type that results in the best compromise of these factors (taking into account access to instrumentation, speed of measurement, penetration of special environments and so on) to extract the desired scientific result.

Historically, time-of-flight neutrons have been the probe of choice for the highest accuracy PDFs. At modern instruments PDFs can be collected over wide ranges of Q and with medium Q-space resolution, but adequate to get signals to hundreds of ångstroms in real space from well ordered samples. Neutrons also have the advantage that stronger peaks can be obtained from low-atomic-number materials, even when they are in a structure with high-atomic-number materials. The principal drawbacks are the large samples that are needed for neutron studies (typically grammes, although much smaller samples can now be studied with modern instruments), the relatively slow measurement times (typically hours per data set, although this is reduced to fractions of hours at modern sources) and the difficulty of accessing neutron beamtime due to oversubscription of the few available instruments. The principal advantages of RAPDF X-ray experiments at modern sources are the rapidity with which the data can be collected and the small sample sizes. Access to RAPDF X-ray instruments through general user programs can be limited, although this tends to be a less serious problem than for neutron instruments, which are more oversubscribed in general. In this geometry the Q resolution is low, which means even the most beautiful well ordered crystal appears nanocrystalline. The 'instrument resolution' damping can be corrected in modelling by calibrating against a well ordered sample measured in the same geometry, so this is not an insurmountable problem, but it means that the data are less accurate at determining the size and shape of the (coherent core of) the particles than higher Q-resolution data. However, a number of factors make the RAPDF approach currently the most widely used and most rapidly growing data-collection method. The ease of the experiments, small amount of sample that is required and high throughput (data can be collected in seconds, or less in favourable circumstances) make it a straightforward way to get high-quality PDFs. The open sample position coupled with the high energy of the incident X-rays also make this geometry straightforward for developing experiments in special environments such as low and high temperature, high pressure, and *in situ* reaction and flow cells. Such experiments can be done at neutron sources too, but are more difficult to engineer because of the relative inaccessibility of the sample position.

It is rare that information in PDFs is desired from the very high r region, but when it is, the highest Q-resolution measurements, and therefore PDFs extending over the highest range in r, can be obtained from high-resolution X-ray powder diffraction setups that nonetheless have a high incident X-ray energy. Examples are ID22 at the ESRF (formerly ID31) and XPD at NSLS-II, which may be used in RAPDF or high-resolution geometries. In high-resolution geometry data collection can be very slow, with one data set taking many hours to collect. This is not warranted unless data extending to high r are desired.

If a laborartory powder diffractometer with good flux and an Mo or Ag source is available, PDF experiments can be carried out using laboratory X-ray equipment. The great advantage of this is ease of access to the instrument: the user does not have to wait for access to a beamline through a slow proposal process. However, the data collection is much slower than in the RAPDF geometry and it can take an hour to many hours per data set, depending on the Q range of the measurement.

Finally, we mention ePDF, which is still under active development. This promises to be a very good way to obtain semi-quantitative PDFs very rapidly from very small amounts of sample on instruments that many laboratories have access to. We expect that this will become a powerful approach for quickly obtaining data from large numbers of samples, for example when screening samples during synthesis. Promising samples may then be subjected to more accurate xPDF and nPDF methods.

5.7.4. Data reduction

A detailed description of the processes for obtaining accurate PDFs from neutron, X-ray and electron diffraction data are beyond the scope of this chapter. Interested readers are referred to Chapter 5 of the book by Egami & Billinge (2012). The steps take a raw powder-diffraction pattern from an experiment, extract the coherent scattering cross section of the material and then correctly normalize it to absolute units (usually per atom) to obtain $S(Q)$, then $F(Q)$ and finally $G(r)$ as described in Section 5.7.2. Extra sources of scattering include scattering from a sample holder and other experimental components, air scattering, multiple scattering (*i.e.*, intensity from particles that have been scattered twice before reaching the detector), incoherent Compton scattering and fluorescence in the case of X-rays, and so on. There are also multiplicative aberrations to the data due to such things as sample absorption, detector response function *etc*. There are widely available computer programs for carrying out these tasks (Juhás *et al.*, 2013; Soper & Barney, 2011; Qiu *et al.*, 2004; Petkov, 1989; Jeong, Thompson *et al.*, 2001; Peterson *et al.*, 2000).

When attempting to extract coordination numbers directly from the data, or if modelling is to be carried out on an absolute scale, it is necessary to carry out an absolute normalization of the data, which is possible but requires care. The incident flux, the actual density of the sample powder or compress, the volume of the sample probed and so on must be known. It is more straightforward to do this from neutron-scattering data by the use of both upstream and downstream beam intensity monitors and comparing the loss in intensity with an incoherently scattering calibration sample, which may be a bar of vanadium (or, to be completely incoherently scattering, a vanadium–niobium alloy) of known dimension and density. It is much more difficult in the case of X-rays, where there is no such incoherently scattering calibration sample available. In this case, a careful measurement of the absorption of the sample, μt, where μ is the linear absorption coeffcient of the sample and t its thickness, using ion-chamber detectors before and after the sample can help a lot. μt may also be determined approximately from theoretical considerations, since values of μ are tabulated in *International Tables for Crystallography* Volume C, Table 4.2.4.3 for each element, and the thickness and powder packing fraction can be estimated. The values of μ depend on the X-ray energy and the value corresponding to the incident X-ray energy should be used. More details can be found in Egami & Billinge (2012). It is often not necessary to place the data onto an absolute scale, since an overall scale factor can be applied to any PDF calculated from a structural model when comparing it to the data.

The scattering functions $S(Q)$, $F(Q)$ and $G(r)$ have characteristic asymptotic properties that aid with the data-normalization process. In particular, $S(Q)$ approaches unity asymptotically in the high-Q range, and at $Q = 0$ becomes approximately equal to zero [in fact $S(0) = 1 - \langle Z^2\rangle / \langle Z\rangle^2$, where $\langle Z\rangle$ is the sample average of the number of electrons of each ionic species, which is often taken as the atomic number]. One of the normalization steps is to divide the diffraction data by the square of the mean scattering factor, $\langle f(Q)\rangle^2$. This division is done after additive contributions to the signal, such as sample container, fluorescence and Compton scattering, have been properly removed. Because of the asymptotic behaviour of $S(Q)$ in the high-Q regime, correction factors such as the powder packing fraction, sample volume and so on can be adjusted in an iterative way until this normalization works correctly, resulting in an $S(Q)$ that approaches one asymptotically at high Q. Most X-ray data-reduction programs allow for this kind iterative updating (Qiu *et al.*, 2004; Soper & Barney, 2011; Petkov, 1989; Jeong, Thompson *et al.*, 2001), and some automate it to some extent.

There is a good separation in frequency between the signal from the sample and the unwanted parasitic scattering, and it has recently been shown that a completely *ad hoc* approach can be taken for data corrections (Billinge & Farrow, 2013) in many cases whereby the aberrations in the data are determined automatically and removed without inputting information about their origin. This has resulted in a fully automated X-ray data-reduction program, *PDFgetX3* (Juhás *et al.*, 2013), which has been shown to produce PDFs of comparable quality to one of the established programs that implements all the corrections explicitly, *PDFgetX2* (Qiu *et al.*, 2004). This approach does not result in a PDF on an absolute scale, which is generally not a problem when modelling the data since an overall scale factor can be applied to the calculated PDF. In practice, our experience is that data sets collected at the same time (for example, a temperature series) and processed using *PDFgetX3* all appear with the same scale factor and features such as peak heights can be compared with each other even without modelling.

5.7.5. Extracting structural information

5.7.5.1. *Obtaining the PDF from a model*

Assume that we have a model for our sample that consists of a set of N atoms at positions $\mathbf{r}_i$ with respect to some origin. The model is built up as described in Section 5.7.2.2.

If we consider a crystalline single-element material, for example nickel, a typical neutron-sized sample contains in the vicinity of 10^{20} or more atoms. To properly calculate $R(r)$ we would therefore need to carry out a double sum over this many atoms, which is completely impractical. However, in practice accurate PDFs can be calculated from many fewer (and a practically small number of) atoms. First, we are generally only interested in calculating $R(r)$ over a relatively narrow range of r, say 20 Å. In this case, we would still need to put the origin on each of the 10^{20} atoms in turn to accurately represent the sample, but each time the sum need only be taken over atoms that lie within 20 Å of the origin atom, a volume that contains only 10^2–10^3 atoms. Second, the material in question may be crystalline. In this case, the total sample is made up of many equivalent unit cells which are periodically repeated in space (although it should be noted that in real crystals, the ideal of every unit cell being identical may not hold well). In this favourable situation we need only place the origin on each atom in the unit cell, since the equivalent atom in all the other unit cells has exactly the same atomic environment. This is now a computationally tractable problem: a double sum where the first sum is taken over the atoms in the unit cell (typically <100) and the second sum over all atoms within $r_{\max}$ of the origin atom, where $r_{\max}$ is the maximum extent over which the PDF is to be calculated. This is shown in Fig. 5.7.11.

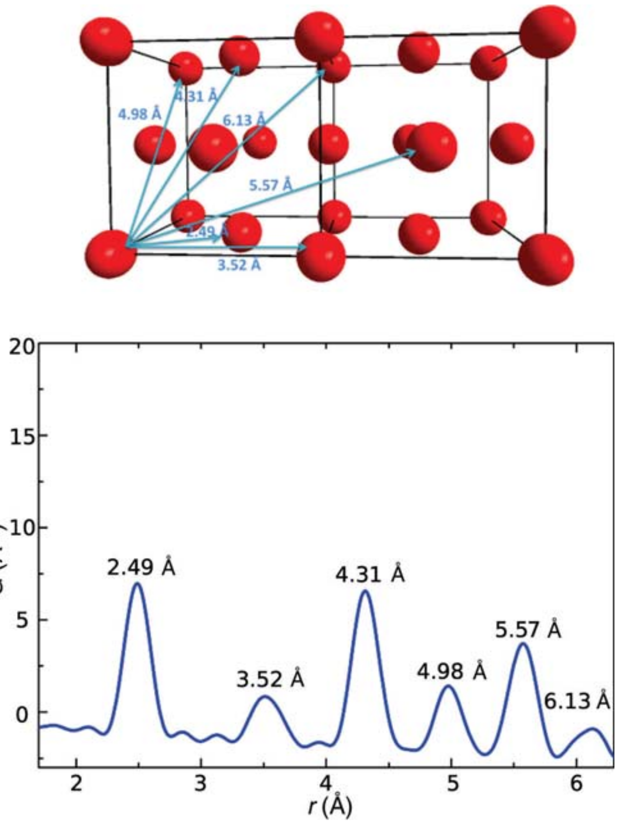

Figure 5.7.11
A schematic of the buildup of the PDF from the structural model for face-centred-cubic nickel. The top figure shows the bond distances of nearby atoms from a reference Ni atom at the corner. Its corresponding PDF is shown below.

Even in the case where the sample is nanocrystalline or amorphous, sufficient averaging over different possible configurations to replicate the measured PDF is in general possible with a much smaller number of atoms. For example, in typical big-box modelling approaches such as reverse Monte Carlo, boxes containing $\sim 10^4$ atoms are typical.

5.7.5.2. *PDFs from multi-element material*

When calculating the PDF from samples with multiple atomic species, we need an expression for the calculated radial distribution function expressed in terms of partial radial distribution functions between different atom types. In analogy to Section 5.7.2.6, when multiple elements are present in the sample we can write

$$\begin{aligned} R(r) &= \frac{1}{N\langle f\rangle^2}\sum_{i,j(i\neq j)} f_j^* f_i \delta(r-r_{i,j}) \\ &= \frac{1}{\langle f\rangle^2}\sum_{\alpha,\beta}\sum_{i\in\{\alpha\},j\in\{\beta\}(i\neq j)} \frac{f_\alpha^* f_\beta}{N}\delta(r-r_{i,j}) \\ &= \sum_{\alpha,\beta}\frac{c_\alpha c_\beta f_\alpha^* f_\beta}{\langle f\rangle^2}\left(\sum_{a,b}\frac{1}{Nc_\alpha c_\beta}\delta(r-r_{i,j})\right) \\ &= \sum_{\alpha,\beta}\frac{c_\alpha c_\beta f_\alpha^* f_\beta}{\langle f\rangle^2} R_{\alpha\beta}, \qquad (5.7.63) \end{aligned}$$

which serves to define

$$R_{\alpha\beta} = \frac{1}{Nc_\alpha c_\beta}\sum_{a,b}\delta(r-r_{i,j}). \qquad (5.7.64)$$

5.7.5.3. *Model-independent information from the PDF*

It is clear from this description that the PDF is a heavily averaged representation of the structure. First, directional information is lost. Second, it is a linear superposition of the local environments of many atoms. How can such a function contain any useful information at all? The reason is that, especially on very short length scales, the possible environments of particular atoms are very limited. In nickel, for example, all the atoms have the same number of neighbours (12) at the same nearest-neighbour distance, $r_{\rm nn}$ = 2.49 Å (Wyckoff, 1967). There is no intensity in $R(r)$ for $r < r_{\rm nn}$ and a sharp peak at $r_{\rm nn}$. This behaviour is very general and true even in atomically disordered systems such as glasses, liquids and gases. In such systems the second and higher neighbour distances are generally less well defined and the PDF peaks are broader. However, in crystals, because of the long-range order of the structure, all neighbours at all lengths are well defined and give rise to sharp PDF peaks (Levashov *et al.*, 2005). The position of these peaks directly gives the separations of pairs of atoms in the structure. If data are measured with high enough $Q_{\max}$, finding the position of a peak maximum will give the distance separating a pair of atoms in the material. If the structure is known well enough, the particular atoms contributing to that peak can also be deduced.

If a well defined PDF peak can be observed, we can determine the coordination number of the origin atom by integrating the intensity under that peak in the radial distribution function according to equation (5.7.20). For the case of Ni, when we construct our PDF we will therefore place 12 units of intensity at position r = 2.49 Å for each nickel atom placed at the origin. Since there are four Ni atoms in the unit cell this will be 48 units of intensity at this position (the weighting factor, $f_m f_n / \langle f \rangle^2$, is unity since there is only one kind of scatterer so $\langle f \rangle^2 = f^2$) and divide by N = 4 since we put four atoms, respectively, at the origin. Thus, integrating the first peak will yield 12, which is the coordination number of Ni. The same information can be obtained from multi-element samples if the chemical origin of the PDF peak and therefore the weighting factors are known. If, as is often the case, PDF peaks from different origins overlap this process may become complicated. As we discuss later, full-scale structural modelling largely overcomes the problem of PDF peak overlap, at least in crystalline materials.

As discussed, the PDF peaks are broadened from delta functions to Gaussian, or nearly Gaussian, shaped peaks. In cases where an atomic probability distribution function is non-Gaussian, for example if the atomic potential is multi-welled and atoms in the solid occupy each well in some disordered fashion, the PDF will reflect this and in principle this information can also be extracted from the PDF by an analysis of the PDF peak shape.

To summarize, there are three independent pieces of information which are contained in a PDF peak: its position gives the average separation of the pair of atoms in question; its integrated intensity yields the coordination number of that pair of atoms; and the width and shape of the peak gives the underlying atomic probability distribution.

5.7.5.4. *Modelling approaches*

In practice, the most information, and the most quantitatively reliable information, is obtained by fitting structural models to the data. The PDF is calculated from the model according to the method described in Section 5.7.5.1. Once the model PDF has been calculated it can be compared to a PDF derived from data to assess how good the structural model is. At this point it is typical to quantify the 'goodness-of-fit' with a suitably defined residuals function, often labelled as R_w. It may be defined in different ways, but a common definition is

$$R_w = \left(\frac{\sum_{i=1}^{n} w(r_i)[G_{\rm obs}(r_i) - G_{\rm calc}(r_i)]^2}{\sum_{i=1}^{n} w(r_i) G_{\rm obs}^2} \right)^{1/2}, \qquad (5.7.65)$$

where the w's are weights (often the inverse square of the data standard deviations) and $G_{\rm calc}$ and $G_{\rm obs}$ are the calculated and measured $G(r)$ functions, respectively.

Models may be compared with each other by comparing their goodness of fit. The model with the lower goodness-of-fit parameter is the better model if the difference is significant. The difference between models is significant if the difference in the goodness of fit exceeds the uncertainty in this parameter coming from the random errors in the data (Billinge *et al.*, 1991). The process of improving models may then be automated using a regression technique where model parameters are allowed to vary, subject to certain user-defined constraints, and these variations continue until a minimum is found for the goodness-of-fit parameter. An example of a converged fit is shown in Fig. 5.7.12.

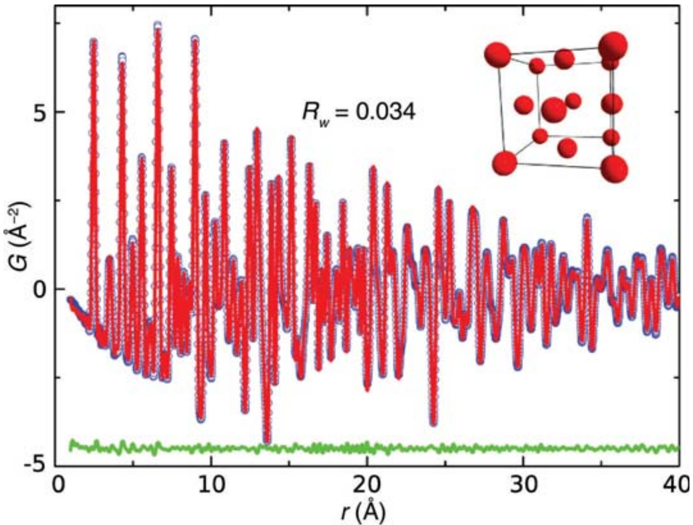

Figure 5.7.12
PDF fit of crystalline nickel. Blue circles and red curves correspond to experimental and calculated PDFs, respectively, with the green difference curve offset below. The inset shows the crystal-structure model.

Roughly speaking there are two different philosophies used for calculating models ('big-box' and 'small-box' modelling) and there are a wide range of different approaches used for the minimization procedure. The small-box approach for calculating the model is to specify the smallest possible unit cell that explains the structure and to calculate the PDF from this unit cell. Distributions in the atomic distances are accounted for by convoluting the resulting calculated PDF with Gaussian functions. The basic unit cell is periodically repeated in space as far as is necessary to calculate the PDF to the required $r_{\rm max}$.

The 'big-box' approach is to model the sample as a large box of atoms which is much larger than the range over which the PDF is to be calculated. In this approach the atomic distributions due to thermal motion are either explicitly included in the distribution of atom positions in the box or, if the box does not contain enough atoms to give smooth distributions, the convolution approach can be used, or the two approaches can be combined. As time goes on, the distinction between these modelling approaches is becoming somewhat blurred as the number of parameters in small-box models increases. It should be pointed out that once a structural model has been defined, both the scattering in Q space and the PDF can easily be calculated. Since the PDF is simply the Fourier transform of the total-scattering structure factor, the model could be fitted to the data in real or reciprocal space. Since the data are the same, each approach should yield the same information, but there is often debate about which approach is superior. Even though it is true that $S(Q)$ and the PDF contain the same information, there are some pertinent differences between the two representations and it turns out that, from a practical point of view, the two representations lend themselves to being modelled in different ways. Depending on the question being asked, the answer is often more accurately determined in one representation or the other.

5.7.5.4.1. *Small-box modelling*

The Rietveld full-profile fitting method (Rietveld, 1969) for extracting structural information from crystalline powder diffraction patterns revolutionized the use of powder diffraction for structure studies (Young, 1993), as discussed in detail elsewhere in this volume.

This approach has been applied in exact analogy but to the PDF (Billinge, 1998) in the programs *PDFFIT* (Proffen & Billinge, 1999) and more recently *PDFgui* (Farrow *et al.*, 2007). We highlight here the similarities and differences of this PDF fitting with conventional Rietveld fitting. The main similarity is that the model is defined in a small unit cell with atom positions specified in terms of fractional coordinates. The refined structural parameters are the same as those obtained from the Rietveld method (with a few additional structural parameters needed in the PDF). The main difference from the conventional Rietveld method is that the local structure is being fitted, which contains information about short-range atomic correlations. There is additional information in the data, which is not present in the average structure, about disordered and short-range ordered atomic displacements. To successfully model these displacements it is often necessary to use a unit cell that is larger than the crystallographic one. It is also a common strategy to introduce disorder in an average sense without increasing the unit cell. For example, in the case where an atom is sitting in one of two displaced minima in the atomic potential, its probability of being in either well is random, can be modelled as a split atomic position with 50% occupancy in each well. This is not a perfect approximation of the real situation but it is a very good aproximation, and is very useful as a first-order attempt at modelling the data.

This 'real-space Rietveld' approach is proving to be very useful and an important analysis approach for PDFs from crystalline and nanocrystalline materials. First, its similarity with the Rietveld method means that a traditional Rietveld-derived structure can be rapidly compared, quantitatively, with the PDF. This is an important first step in determining whether there is significant evidence for local distortions beyond the average structure. The Rietveld model is refined to the PDF without relaxing any of the symmetry constraints of the crystallographic model. The resulting fit can be assessed to look for significant deficiencies. In addition, the refined parameters can be compared directly with the results from the Rietveld fitting to make sure they are consistent. If evidence exists to suggest that local structural distortions beyond the average structure are present, these can then be incorporated in the PDF model. The second strength of the real-space Rietveld approach is the simplicity of the structural models, making it quick and straightforward to construct the structural models and making physical inferences from the models similarly quick and straightforward.

One piece of additional information in the PDF that cannot be determined from a conventional Rietveld refinement is information about motional correlations. Directly bonded near-neighbour atoms tend to move in phase with each other and their motion is positively correlated (Jeong *et al.*, 1999, 2003). This is illustrated in Fig. 5.7.13.

Because the PDF is a *pair* correlation function, if the motion of atoms is perfectly correlated (*i.e.*, they move together as if connected by a rigid rod) the PDF peak between those two atoms will be a delta function, even though the atoms are moving (Fig. 5.7.13*a*). On the other hand, if the motions of neighbours are completely uncorrelated, as if they were contained in separate boxes with solid walls (Fig. 5.7.13*b*), the width of the PDF peak between each pair would be broad and correspond to the Gaussian widths of each atomic probability distribution function added in quadrature. In general the situation is somewhere between these limits, crossing over to uncorrelated behaviour for widely separated neighbours (Fig. 5.7.13*c*). If the bond is very stiff, the relative motion of these neighbours with respect to each other can be quite small. For example, in covalent semiconductors the nearest-neighbour motion may be >80% correlated (Jeong *et al.*, 1999). The motion of far neighbours is uncorrelated: the motion of an atom at position *A* has no effect on the motion of atom at position *B* that is far from *A*. The thermal factor measured in a conventional crystallographic refinement is the uncorrelated one. This often reflects the softest bonds in the material. For example, in the semiconductor alloys it reflects the weak bond-bending forces. The stiff bond-stretching force can be measured from the correlated motion of the near neighbours, which is obtained directly from the width of near-neighbour peaks in the PDF.

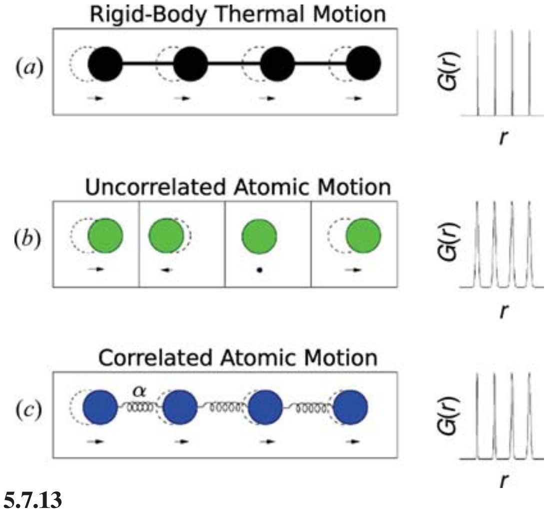

Figure 5.7.13
A schematic of three different motional correlations of atoms and their corresponding PDFs. (*a*) Completely correlated thermal motion, (*b*) uncorrelated thermal motion and (*c*) partially correlated thermal motion. Adapted from Jeong *et al.* (2003).

When local atomic displacements away from the average structure exist, and therefore significant diffuse scattering intensity is present in the scattering, a conventional Rietveld refinement becomes inadequate in principle. At this point a model is required that can fit both Bragg and diffuse intensities and that includes short-range ordered structures that are different from the average structure. This is readily done in real space where there is a natural separation in *r*, where it is now common to fit different models to explain the low-*r* region and the high-*r* region.

The approach was developed to study local structure in crystalline materials, but has found a natural extension to nanoparticles, clusters and nanoporous systems (Billinge & Kanatzidis, 2004; Masadeh *et al.*, 2007; Billinge, 2008).

5.7.5.4.2. *Big-box modelling*

In big-box modelling a model is created with often many tens of thousands of atoms in a box to simulate the solid. The PDF is then calculated from this model and compared to the measured PDF (of course the comparison can also be made in reciprocal space). Because of ergodicity, the temporal and ensemble averages of the ensemble of atoms in the real sample will give the same PDF. This may be used in the modelling since if the box contains enough atoms, the average PDF of those atoms can be used to simulate both static and dynamic disorder. Large boxes and/or multiple distinct configurations of the model are needed to get sufficient statistics on the calculated PDF to give a good agreement to the measured one.

Direct simulations of solids may also be done this way. For example, given an interatomic pair potential that gives the energy of pairs of atoms as a function of their separation, it is possible to put a large number of atoms in a box and to calculate the energy of the configuration. It is useful to then have a method to find the configuration that yields the minimum energy. This is a classic global-optimization problem and there are various algorithms for minimizing the energy. One of the most widely used is the Metropolis simulated annealing algorithm (Metropolis & Ulam, 1949). In the Metropolis algorithm, atom positions are allowed to vary in some random way. After each change the energy of the system is calculated using the specified potential-energy function. If a change reduces the energy of the system it is accepted. If it raises the energy of the system then it can be accepted or rejected. This decision is made randomly according to an underlying probability. It is this gambling aspect of the technique that gave it its name: the Monte Carlo algorithm. In simulated annealing the underlying probability governing whether a move is accepted is given by

$$P = \exp(-\Delta E/kT), \tag{5.7.66}$$

where ΔE is the change in energy, k is the Boltzmann constant and T is the 'temperature' of the system, which is initially set by the experimenter. When T is higher, more 'bad' moves are accepted and more of the energy landscape is probed by the simulation (it is easier to get out of local minima). The temperature can then be systematically lowered to guide the simulation into the global energy minimum. This is a widely used and powerful method in statistical physics and the computational technology is well developed (Binder & Heerman, 1992).

Clearly, Monte Carlo simulated annealing is a powerful approach to minimization of any parameterized function and is particularly applicable if there are a large number of parameters and a complicated parameter space. From this perspective, it lends itself to being applied to solving complicated structural problems, where the function to be minimized is not an energy but a residuals function. In this case there is no obvious reason why the underlying probability should be a Boltzmann distribution as in standard simulated annealing. However, in the absence of rigorous arguments justifying the adoption of another form for the probability distribution, and the extensive understanding that exists of the behaviour of simulated annealing with the Boltzmann distribution, this was the natural place to start. This approach is termed Reverse Monte Carlo (or RMC) following the pioneering work of McGreevy & Pusztai (1988), although there are some examples of similar approaches extending back to the 1960s (Kaplow *et al.*, 1968; Renninger *et al.*, 1974; Dmowski *et al.*, 1988).

The use of simulated annealing to minimize a residual function constitutes solving the 'inverse problem' of diffraction. The direct problem is: given a 3D arrangement of atoms, what is the diffraction pattern (or in this case the PDF)? The inverse problem is: given a PDF, what is the 3D structure that gave rise to it? The PDF data are the input to the inverse problem; the structural model is then fitted to the data by adjusting atom positions to minimize the residuals function. The problem is that, in general, the model is under-constrained, in which case there is not enough information in the data to yield a unique solution. This is the case of an ill-posed inverse problem. The great difficulty in all modelling, but big-box modelling in particular, is to know whether the resulting inverse problem is well posed or not. Despite this difficulty, it is still of value to model in this way. Any approach that provides physical insight and helps gain valuable understanding about the data is valid, as long as the conclusions drawn from the study are not overreached. Particular care should be taken to avoid overreach in more disordered systems, where the structural information is limited and there can be an enormous degeneracy in possible structural solutions consistent with the same data set. If one does not constrain the structural model in physically reasonable ways the structure solution is quite likely to be wrong and often unphysical (Keen, 1998).

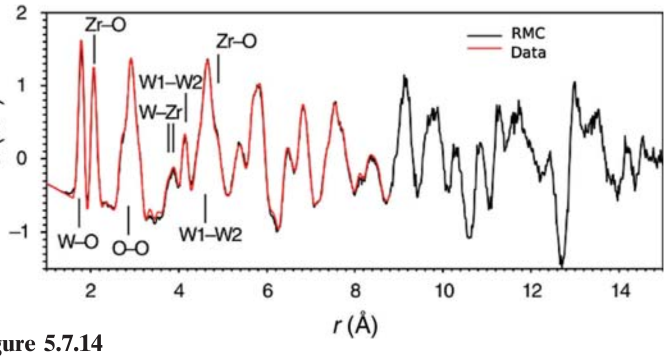

Figure 5.7.14
An example of an RMC refinement to the neutron total-scattering data of ZrW_2O_8. Reprinted with permission from Tucker *et al.* (2005). Copyright (2005) by the American Physical Society.

When faced with data from a crystalline material, a great deal is known about the structure from a conventional crystallographic analysis. It is clearly inefficient, and most probably disastrous, to specify the starting model by placing atoms randomly in the box and hoping that the correct crystal structure is found by random mutations of the model. In this case, a more conventional refinement is preferred where a well defined starting model is specified and this is allowed to distort randomly to fit the data. When a Monte Carlo algorithm is used for the regression the term 'RMC refinement' has been coined (Keen, 1998), distinguishing the approach from RMC modelling as described in the previous paragraph. An example of an RMC refinement is shown in Fig. 5.7.14.

As RMC modelling becomes more constrained (Tucker *et al.*, 2007) the distinction between small- and large-box modelling becomes somewhat cloudy; however, it is useful to distinguish the two approaches since in many people's eyes RMC equates to unconstrained RMC modelling with all its shortcomings.

For modelling local structure in crystalline systems, a number of powerful RMC refinement codes are emerging, mostly around the *RMCprofile* program (Tucker *et al.*, 2007), including a graphical user interface (http://www.rmcprofile.org). *RMCprofile* is good for incorporating additional constraints into the modelling; for example, it includes the Bragg profile in the fit for greatly improved reliability. A number of other RMC modelling and refinement codes are also freely available. Used mostly for disordered materials, *RMC++* is still under active development (http://www.szfki.hu/~nphys/rmc++/opening.html) (Evrard & Pusztai, 2005; Gereben *et al.*, 2007). As well as its special features for modelling nanoparticles using evolutionary algorithms, the *DISCUS* program (http://discus.sourceforge.net) also has an implementation of RMC (Proffen & Neder, 1997; Neder & Proffen, 2008). Other efforts include incorporating EXAFS data (Krayzman *et al.*, 2008, 2009) and prior chemical knowledge in the form of bond-valence sums (Norberg *et al.*, 2009) into big-box modelling schemes.

Empirical potential structure refinement (EPSR) (Soper, 1996, 2001, 2007) may be used for extracting structural information about solvation states of ionic and molecular complexes in solution. In general, multiple neutron liquid structure factors and PDFs with different kinds of deuteration are used in the

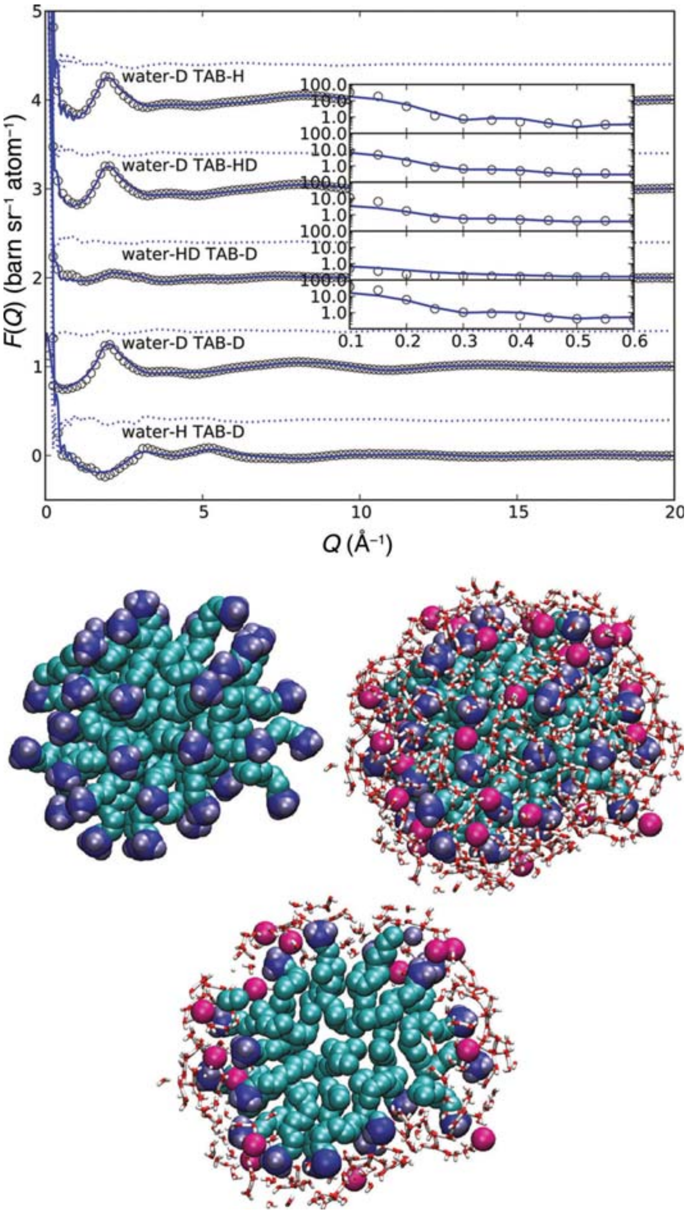

Figure 5.7.15

Total-scattering structure functions, with low-angle scattering (inset) from surfactant micelles of CTAB with different substitutions of hydrogen/deuterium. Representative structures are shown below: (top left) surfactant molecules, (top right) micelle surrounded by bromide counterions and water, and (bottom) a cross section with a width of 12 Å. Adapted from Hargreaves *et al.* (2011). Copyright (2011) American Chemical Society.

fitting. An excellent strategy for studying hydrogenated liquids and hydrogenated solute species is to preferentially deuterate different parts of the system and collect complementary data sets. The problem of collecting data from liquid systems containing hydrogen is also large, but largely solved, with the specially designed SANDALS and NIMROD diffractometers at ISIS. The modelling uses a big-box approach, but only a small number of parameters are refined: the parameters that define an interatomic potential between the atoms. A scheme is then used to refine the values of the potential parameters to give a good fit to all the data. This approach has proved to be very powerful in the study of complex liquids (Soper, 1996; Landron *et al.*, 2001; Hargreaves *et al.*, 2011). An example of EPSR fits to multiple different PDFs from differently deuterated samples of the surfactant CTAB, and the resulting structural models, are shown in Fig. 5.7.15.

Often something is known about the network connectivity of a structure and constraints can be introduced that maintain the network. Two such examples are geometric modelling (Wells *et al.*, 2002, 2004; Sartbaeva *et al.*, 2007) and a similarity constraint that ensures that every atom has the same local environment as every other atom (Cliffe *et al.*, 2010). Efforts are underway to use the advantages of modern object-oriented programming methods to modularize the process of building complexed models, and a complex modelling framework named *Diffpy-CMI* is under construction (http://diffpy.org). The modularity allows diverse fits to be built on the fly with great flexibility. The software has been released and has been a key component in a number of recent scientific studies where the modularity allowed modelling extension to be rapidly implemented (Jensen *et al.*, 2012; Tyrsted *et al.*, 2012; Farrow *et al.*, 2013; Yang *et al.*, 2013).

5.7.5.4.3. *Ab initio nanostructure solution from PDF data*

Outside the world of glasses and liquids, virtually all of the PDF modelling that has been done to date is refinement of a known (or guessed) starting model. However, crystal structures may be solved from powder diffraction data (David *et al.*, 2002). It was recently demonstrated that in some cases it is also possible to solve nanoparticle (Juhás *et al.*, 2006, 2008; Cliffe *et al.*, 2010) and crystal (Juhás *et al.*, 2010) structures directly from the PDF. The first structure solution from PDF data was achieved by developing a new regression algorithm that was based on a cluster-building approach, starting from small clusters and then building them up to form larger clusters. The algorithm competed clusters of the same size against each other to see which agreed best with the data. Well performing clusters could get 'promoted' to a higher division by adding one or more atoms. This league-table aspect gave rise to the name *LIGA* after the Spanish soccer leagues. The basic philosophy behind the new *LIGA* algorithm was that the PDF function is an *r*-dependent function. Any smaller sub-cluster of the total cluster must give PDF peaks that are consistent with the peaks in the lower-*r* region of the PDF. On the other hand, a sub-cluster that gives peaks in the wrong place must be wrong. Using the information contained in the PDF to guide the construction of trial models enormously reduces the search space for the global optimization, although the search space remains large. There are still many clusters and many incorrect sub-clusters that nonetheless are consistent with the low-*r* part of the PDF, so a backtracking method is required so that when promising but wrong clusters are built out, they can be taken apart again and rebuilt differently. Information in the PDF is again used when selecting 'bad' atoms to remove from the cluster, since atoms on the cluster may be scored based on how many incorrect distances they contribute to the PDF. The worst performing atoms are removed with higher probability. The algorithm is described in detail in Juhás *et al.* (2006), with all the implementational details described in Juhás *et al.* (2008). For structures with a high degree of self-similarity, such as high-symmetry C_{60}, there is a good match between the number of distinct peaks in the PDF and the number of atoms that need to be placed, and the algorithm worked very efficiently. For example, it found the solution to C_{60} from ideal data in less than a second, and from noisy data in a few minutes, on a laptop computer (Juhás *et al.*, 2006, 2008). The process for obtaining the structure solution is illustrated in Fig. 5.7.16.

More recently, the addition of one more constraint to the C_{60} problem, a similarity constraint that ensured that every atom had the same environment, allowed the structure to be solved *ab*

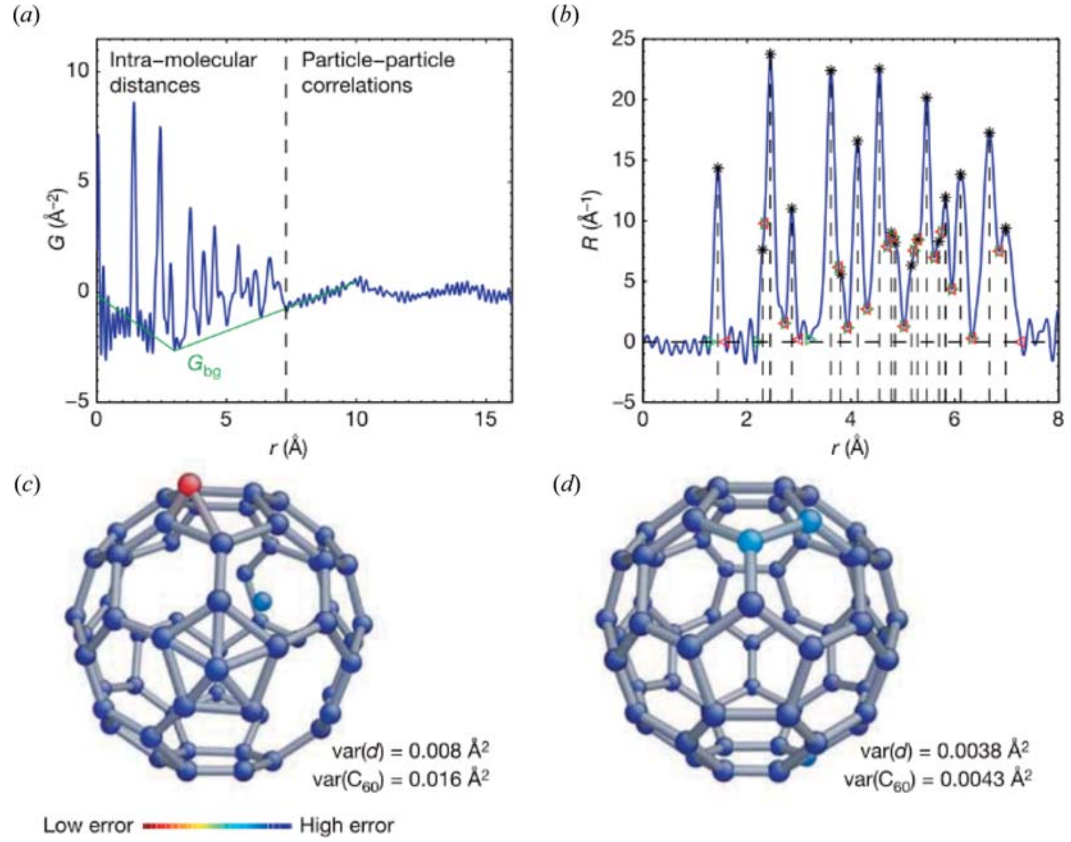

Figure 5.7.16
Structure solution of C_{60} from neutron PDF data using the *LIGA* algorithm (Juhás *et al.*, 2006). (*a*) The measured PDF, including intra- and intermolecular correlation functions. (*b*) The RDF of just the intramolecular part after removal of the intermolecular part. (*c*) Structural solution containing errors due to too strict adhherence to noisy data. Blue atoms contribute small errors and red ones high errors to the agreement. (*d*) The correct solution is obtained when the model is allowed to deviate from the strict intensities of the data, making it less susceptible to noise and resulting in the correct structure solution. Adapted from Juhás *et al.* (2006).

initio using simulated annealing (Cliffe *et al.*, 2010). This is an easier problem for the algorithm to solve than the original problem, where the structure was recreated from the data alone. The added constraint greatly reduces the search space of the solution space, showing the power of judicious addition of constraints in modelling. In fact, the symmetry of C_{60} is very high, and if the full symmetry of the molecule is known only two parameters need to be specified in order to solve its structure (David *et al.*, 1993). It is a thus a great example of the use of constraints in helping to solve nanostructure problems and gives hope that complex modelling will be successful in practice as well as just sensible in theory.

SJLB would like to acknowledge help in preparing the figures from Maxwell Terban, Chenyang Shi, Benjamin Frandsen and Kirsten Jensen, and Maxwell Terban for editorial help. This work was supported by the US Department of Energy Office of Science, Office of Basic Energy Sciences through through grant DE-SC00112704.

References

Abeykoon, A. M. M., Hu, H., Wu, L., Zhu, Y. & Billinge, S. J. L. (2015). *Calibration and data collection protocols for reliable lattice parameter values in electron pair distribution function studies*. *J. Appl. Cryst.* **48**, 244–251.

Abeykoon, A. M. M., Malliakas, C. D., Juhás, P., Božin, E. S., Kanatzidis, M. G. & Billinge, S. J. L. (2012). *Quantitative nanostructure characterization using atomic pair distribution functions obtained from laboratory electron microscopes*. *Z. Kristallogr.* **227**, 248–256.

Barnes, A. C., Fischer, H. E. & Salmon, P. S. (2003). *J. Phys. IV*, **111**, 59–96.

Billinge, S. J. L. (1998). In *Local Structure from Diffraction*, edited by S. J. L. Billinge & M. F. Thorpe, p. 137. New York: Plenum.

Billinge, S. J. L. (2008). *Nanoscale structural order from the atomic pair distribution function (PDF): there's plenty of room in the middle*. *J. Solid State Chem.* **181**, 1695–1700.

Billinge, S. J. L., Davies, P. K., Egami, T. & Catlow, C. R. A. (1991). *Deviations from planarity of copper-oxygen sheets*. *Phys. Rev. B*, **43**, 10340–10352.

Billinge, S. J. L. & Farrow, C. L. (2013). *Towards a robust ad-hoc data correction approach that yields reliable atomic pair distribution functions from powder diffraction data*. *J. Phys. Condens. Matter*, **25**, 454202.

Billinge, S. J. L. & Kanatzidis, M. G. (2004). *Beyond crystallography: the study of disorder, nanocrystallinity and crystallographically challenged materials with pair distribution functions*. *Chem. Commun.* pp. 749.

Billinge, S. J. L. & Levin, I. (2007). *The problem with determining atomic structure at the nanoscale*. *Science*, **316**, 561–565.

Binder, K. & Heerman, D. W. (1992). *Monte Carlo Simulation in Statistical Physics*, 2nd ed. Berlin: Springer-Verlag.

Bowron, D. T., Soper, A. K., Jones, K., Ansell, S., Birch, S., Norris, J., Perrott, L., Riedel, D., Rhodes, N. J., Wakefield, S. R., Botti, A., Ricci, M.-A., Grazzi, F. & Zoppi, M. (2010). *NIMROD: the near and InterMediate range order diffractometer of the ISIS second target station*. *Rev. Sci. Instrum.* **81**, 033905.

Bozin, E. S., Juhás, P., Zhou, W., Stone, M. B., Abernathy, D. L., Huq, A. & Billinge, S. J. L. (2009). *Atomic pair distribution function analysis from the ARCS chopper spectrometer at the spallation neutron source*. *J. Appl. Cryst.* **42**, 724–725.

Bragg, W. H. (1912). *X-rays and crystals. Nature (London)*, **90**, 219.

Cargill, G. S. (1971). *Influence of neglected small-angle scattering in radial distribution function analysis*. *J. Appl. Cryst.* **4**, 277–283.

Cervellino, A., Giannini, C. & Guagliardi, A. (2006). *On the efficient evaluation of Fourier patterns for nanoparticles and clusters*. *J. Comput. Chem.* **27**, 995–1008.

Chacón, P., Morán, F., Díaz, J. F., Pantos, E. & Andreu, J. M. (1998). *Low-resolution structures of proteins in solution retrieved from X-ray scattering with a genetic algorithm*. *Biophys. J.* **74**, 2760–2775.

Chaudhari, P., Graczyk, J. F. & Herd, S. R. (1972). *An electron microscope investigation of the structure of some amorphous materials. Phys. Status Solidi B*, **51**, 801.

Chupas, P. J., Qiu, X., Hanson, J. C., Lee, P. L., Grey, C. P. & Billinge, S. J. L. (2003). *Rapid-acquisition pair distribution function (RA-PDF) analysis*. *J. Appl. Cryst.* **36**, 1342–1347.

Cliffe, M. J., Dove, M. T., Drabold, D. A. & Goodwin, A. L. (2010). *Structure determination of disordered materials from diffraction data*. *Phys. Rev. Lett.* **104**, 125501.

Cockayne, D. J. H. & McKenzie, D. R. (1988). *Electron diffraction analysis of polycrystalline and amorphous thin films*. *Acta Cryst.* A**44**, 870–878.

David, W. I. F., Ibberson, R. M. & Matsuo, T. (1993). *High resolution neutron powder diffraction: a case study of the structure of C_{60}*. *Proc. R. Soc. London Ser. A*, **442**, 129–146.

David, W. I. F., Shankland, K., McCusker, L. B. & Baerlocher, C. (2002). Editors. *Structure Determination from Powder Diffraction Data*. Oxford University Press.

Debye, P. (1915). *Dispersion of Röntgen rays. Ann. Phys.* **46**, 809–823.

Dinnebier, R. E. & Billinge, S. J. L. (2008). Editors. *Powder Diffraction: Theory and Practice*. London: Royal Society of Chemistry.

Dmowski, W., Toby, B. H., Egami, T., Subramanian, M. A., Gopalakrishnan, J. & Sleight, A. W. (1988). *Short-range ordering due to displacements of thallium and oxygen atoms in superconducting $Tl_2Ba_2CaCu_2O_8$ observed by pulsed-neutron scattering*. *Phys. Rev. Lett.* **61**, 2608–2611.

Egami, T. & Billinge, S. J. L. (2003). *Underneath the Bragg Peaks: Structural Analysis of Complex Materials*. Oxford: Pergamon Press/Elsevier.

Egami, T. & Billinge, S. J. L. (2012). *Underneath the Bragg Peaks: Structural Analysis of Complex Materials*, 2nd ed. Amsterdam: Elsevier.

Evrard, G. & Pusztai, L. (2005). *Reverse Monte Carlo modelling of the structure of disordered materials with RMC++ : a new implementation of the algorithm in C++*. *J. Phys. Condens. Matter*, **17**, S1–S13.

Faber, T. E. & Ziman, J. M. (1965). *A theory of the electrical properties of liquid metals*. *Philos. Mag.* **11**, 153–173.

Farrow, C. L., Bediako, D. K., Surendranath, Y., Nocera, D. G. & Billinge, S. J. L. (2013). *Intermediate-range structure of self-assembled cobalt-based oxygen-evolving catalyst*. *J. Am. Chem. Soc.* **135**, 6403–6406.

Farrow, C. L. & Billinge, S. J. L. (2009). *Relationship between the atomic pair distribution function and small-angle scattering: implications for modeling of nanoparticles*. *Acta Cryst.* A**65**, 232–239.

Farrow, C. L., Juhas, P. & Billinge, S. J. L. (2010). *SrFit*. Unpublished.

Farrow, C. L., Juhás, P., Liu, J., Bryndin, D., Božin, E. S., Bloch, J., Proffen, T. & Billinge, S. J. L. (2007). *PDFfit2 and PDFgui: computer programs for studying nanostructure in crystals*. *J. Phys. Condens. Matter*, **19**, 335219.

Fischer, H. E., Cuello, G. J., Palleau, P., Feltin, D., Barnes, A. C., Badyal, Y. S. & Simonson, J. M. (2002). *Ann. Phys. N. Y.* **74**, s160.

Fitch, A. (2004). *J. Res. NIST*, **109**, 133.

Franklin, R. E. (1950). *The interpretation of diffuse X-ray diagrams of carbon*. *Acta Cryst.* **3**, 107–121.

Friedrich, W., Knipping, P. & Laue, M. (1913). *Interferenzerscheinungen bei Röntgenstrahlen*. *Ann. Phys.* **346**, 971–988.

Fuoss, P. H., Eisenberger, P., Warburton, W. K. & Bienenstock, A. I. (1981). *Application of differential anomalous X-ray scattering to structural studies of amorphous materials*. *Phys. Rev. Lett.* **46**, 1537–1540.

Gandais, M., Theye, M. L., Fisson, T. & Boissonade, J. (1973). *Structure studies by electron diffraction on amorphous Ge films*. *Phys. Status Solidi B*, **58**, 601–611.

Gereben, O., Jovari, P., Temleitner, L. & Pusztai, L. (2007). *J. Optoelectron. Adv. Mater.* **9**, 3021–3027.

Gilbert, B. (2008). *Finite size effects on the real-space pair distribution function of nanoparticles*. *J. Appl. Cryst.* **41**, 554–562.

Gorelik, T. E., Schmidt, M. U., Kolb, U. & Billinge, S. J. L. (2015). *Total-scattering pair distribution function of organic material from powder electron diffraction data. Microsc. Microanal.* **21**, 459–471.

Guinier, A. (1963). *X-ray Diffraction in Crystals, Imperfect Crystals, and Amorphous Bodies.* San Francisco: W. H. Freeman.

Guinier, A., Fournet, G., Walker, C. & Yudowitch, K. (1955). *Small-angle scattering of x-rays*. New York: John Wiley & Sons, Inc.

Hannon, C. (2005). *Results on disordered materials from the GEneral Materials diffractometer, GEM, at ISIS*. *Nucl. Instrum. Methods Phys. Res. A*, **551**, 88–107.

Hargittai, I. & Hargittai, M. (1988). Editors. *Stereochemical Applications of Gas-Phase Electron Diffraction*, 1st ed. New York: VHC Publishers.

Hargreaves, R., Bowron, D. T. & Edler, K. (2011). *Atomistic structure of a micelle in solution determined by wide Q-range neutron diffraction*. *J. Am. Chem. Soc.* **133**, 16524–16536.

Ishigaki, T., Hoshikawa, A., Yonemura, M., Morishima, T., Kamiyama, T., Oishi, R., Aizawa, K., Sakuma, T., Tomota, Y., Arai, M., Hayashi, M., Ebata, E., Takano, Y., Komatsuzaki, K., Asano, H., Takano, Y. & Kasao, T. (2009). *IBARAKI materials design diffractometer (iMATERIA)–Versatile neutron diffractometer at J-PARC. Nucl. Instrum. Methods Phys. Res. A*, **600**, 189–191.

Jensen, K. M. Ø., Christensen, M., Juhás, P., Tyrsted, C., Bøjesen, E. D., Lock, N., Billinge, S. J. L. & Iversen, B. B. (2012). *Revealing the mechanisms behind SnO_2 nanoparticle formation and growth during hydrothermal synthesis: an in situ total scattering study*. *J. Am. Chem. Soc.* **134**, 6785–6792.

Jeong, I. K., Heffner, R. H., Graf, M. J. & Billinge, S. J. L. (2003). *Lattice dynamics and correlated atomic motion from the atomic pair distribution function*. *Phys. Rev. B*, **67**, 104301.

Jeong, I., Mohiuddin-Jacobs, F., Petkov, V., Billinge, S. J. L. & Kycia, S. (2001). *Local structure of semiconductor alloys by high-energy synchrotron X-ray diffraction*. *Phys. Rev. B*, **63**, 205202.

Jeong, I., Proffen, T., Mohiuddin-Jacobs, F. & Billinge, S. J. L. (1999). *Measuring correlated atomic motion using X-ray diffraction*. *J. Phys. Chem. A*, **103**, 921–924.

Jeong, I.-K., Thompson, J., Proffen, Th., Turner, A. M. P. & Billinge, S. J. L. (2001). *PDFgetX: a program for obtaining the atomic pair distribution function from X-ray powder diffraction data*. *J. Appl. Cryst.* **34**, 536.

Juhás, P., Cherba, D. M., Duxbury, P. M., Punch, W. F. & Billinge, S. J. L. (2006). *Ab initio determination of solid-state nanostructure*. *Nature*, **440**, 655–658.

Juhás, P., Davis, T., Farrow, C. L. & Billinge, S. J. L. (2013). *PDFgetX3: a rapid and highly automatable program for processing powder diffraction data into total scattering pair distribution functions*. *J. Appl. Cryst.* **46**, 560–566.

Juhás, P., Granlund, L., Duxbury, P. M., Punch, W. F. & Billinge, S. J. L. (2008). *The Liga algorithm for ab initio determination of nanostructure*. *Acta Cryst.* A**64**, 631–640.

Juhás, P., Granlund, L., Gujarathi, S. R., Duxbury, P. M. & Billinge, S. J. L. (2010). *Crystal structure solution from experimentally determined atomic pair distribution functions*. *J. Appl. Cryst.* **43**, 623–629.

Kaplow, R., Rowe, T. A. & Averbach, B. L. (1968). *Atomic arrangement in vitreous selenium*. *Phys. Rev.* **168**, 1068–1079.

Keen, D. A. (1998). In *Local Structure from Diffraction*, edited by S. J. L. Billinge & M. F. Thorpe, p. 101. New York: Plenum.

Keen, D. A. (2001). *A comparison of various commonly used correlation functions for describing total scattering*. *J. Appl. Cryst.* **34**, 172–177.

Klug, H. P. & Alexander, L. E. (1974). *X-ray diffraction procedures for polycrystalline and amorphous materials*, 2nd ed. New York: Wiley.

Kodama, K., Iikubo, S., Taguchi, T. & Shamoto, S. (2006). *Finite size effects of nanoparticles on the atomic pair distribution functions*. *Acta Cryst.* A**62**, 444–453.

Korsunskiy, V. I. & Neder, R. B. (2005). *Exact model calculations of the total radial distribution functions for the X-ray diffraction case and systems of complicated chemical composition*. *J. Appl. Cryst.* **38**, 1020–1027.

Korsunskiy, V. I., Neder, R. B., Hofmann, A., Dembski, S., Graf, C. & Rühl, E. (2007). *Aspects of the modelling of the radial distribution function for small nanoparticles*. *J. Appl. Cryst.* **40**, 975–985.

Kramers, H. A. (1927). *La diffusion de la lumiere par les atomes. Atti del Congresso Internationale dei Fisici, Como*, **2**, 545–557.

Krayzman, V., Levin, I. & Tucker, M. G. (2008). *Simultaneous reverse Monte Carlo refinements of local structures in perovskite solid solutions using EXAFS and the total scattering pair-distribution function*. *J. Appl. Cryst.* **41**, 705–714.

Krayzman, V., Levin, I., Woicik, J. C., Proffen, Th., Vanderah, T. A. & Tucker, M. G. (2009). *A combined fit of total scattering and extended X-ray absorption fine structure data for local-structure determination in crystalline materials*. *J. Appl. Cryst.* **42**, 867–877.

Kronig, R. de (1926). *On the theory of dispersion of x-rays*. *J. Opt. Soc. Am.* **12**, 547–556.

Laaziri, K., Kycia, S., Roorda, S., Chicoine, M., Robertson, J. L., Wang, J. & Moss, S. C. (1999). *High-energy X-ray diffraction study of pure amorphous silicon*. *Phys. Rev. B*, **60**, 13520–13533.

Landron, C., Hennet, L., Jenkins, T. E., Greaves, G. N., Coutures, J. P. & Soper, A. K. (2001). *Liquid alumina: detailed atomic coordination determined from neutron diffraction data using empirical potential structure refinement*. *Phys. Rev. Lett.* **86**, 4839–4842.

Levashov, V. A., Billinge, S. J. L. & Thorpe, M. F. (2005). *Density fluctuations and the pair distribution function*. *Phys. Rev. B*, **72**, 024111.

Lytle, F. W., Sayers, D. E. & Stern, E. A. (1975). *Extended x-ray-absorption fine-structure technique. II. Experimental practice and selected results. Phys. Rev. B*, **11**, 4825.

McBride, W. E., Cockayne, D. J. H. & Goringe, C. M. (1999). *Reduced density function analysis using convergent electron illumination and iterative blind deconvolution*. *Ultramicroscopy*, **76**, 115–123.

McGreevy, R. L. & Pusztai, L. (1988). *Reverse Monte Carlo simulation: a new technique for the determination of disordered structures*. *Mol. Simul.* **1**, 359–367.

Masadeh, A. S., Božin, E. S., Farrow, C. L., Paglia, G., Juhás, P., Billinge, S. J. L., Karkamkar, A. & Kanatzidis, M. G. (2007). *Quantitative size-dependent structure and strain determination of CdSe nanoparticles using atomic pair distribution function analysis*. *Phys. Rev. B*, **76**, 115413.

Masson, O. & Thomas, P. (2013). *Exact and explicit expression of the atomic pair distribution function as obtained from X-ray total scattering experiments*. *J. Appl. Cryst.* **46**, 461–465.

Metropolis, N. & Ulam, S. (1949). *The Monte Carlo method*. *J. Am. Stat. Assoc.* **44**, 335–341.

Moss, S. C. & Graczyk, J. F. (1969). *Evidence of voids within the as-deposited structure of glassy silicon*. *Phys. Rev. Lett.* **23**, 1167–1171.

Neder, R. B. & Korsunskiy, V. I. (2005). *Structure of nanoparticles from powder diffraction data using the pair distribution function*. *J. Phys. Condens. Matter*, **17**, S125–S134.

Neder, R. B., Korsunskiy, V. I., Chory, C., Müller, G., Hofmann, A., Dembski, S., Graf, C. & Rühl, E. (2007). *Structural characterization of II-VI semiconductor nanoparticles*. *Phys. Status Solidi C*, **4**, 3221–3233.

Neder, R. B. & Proffen, T. (2008). *Diffuse Scattering and Defect Structure Simulations: A Cook Book Using the Program DISCUS*. Oxford University Press.

Neuefeind, J., Feygenson, M., Carruth, J., Hoffmann, R. & Chipley, K. K. (2012). *The Nanoscale Ordered MAterials diffractometer NOMAD at the spallation neutron source SNS*. *Nucl. Instrum. Methods Phys. Res. B*, **287**, 68–75.

Nield, V. M. & Keen, D. A. (2001). *Diffuse Neutron Scattering from Crystalline Materials*. Oxford University Press.

Norberg, S. T., Tucker, M. G. & Hull, S. (2009). *Bond valence sum: a new soft chemical constraint for RMCProfile*. *J. Appl. Cryst.* **42**, 179–184.

Peterson, P. F., Gutmann, M., Proffen, Th. & Billinge, S. J. L. (2000). *PDFgetN: a user-friendly program to extract the total scattering structure factor and the pair distribution function from neutron powder diffraction data*. *J. Appl. Cryst.* **33**, 1192.

Petkov, V. (1989). *RAD, a program for analysis of X-ray diffraction data from amorphous materials for personal computers*. *J. Appl. Cryst.* **22**, 387–389.

Petkov, V., Billinge, S. J. L., Shastri, S. D. & Himmel, B. (2000). *Polyhedral units and network connectivity in calcium aluminosilicate glasses from high-energy X-ray diffraction*. *Phys. Rev. Lett.* **85**, 3436–3439.

Petkov, V., Jeong, I., Chung, J. S., Thorpe, M. F., Kycia, S. & Billinge, S. J. L. (1999). *High real-space resolution measurement of the local structure of $Ga_{1-x}In_xAs$ using X-ray diffraction*. *Phys. Rev. Lett.* **83**, 4089–4092.

Price, D. L. & Saboungi, M.-L. (1998). In *Local Structure from Diffraction*, edited by S. J. L. Billinge & M. F. Thorpe, p. 23. New York: Plenum.

Proffen, Th. & Billinge, S. J. L. (1999). *PDFFIT, a program for full profile structural refinement of the atomic pair distribution function*. *J. Appl. Cryst.* **32**, 572–575.

Proffen, T., Egami, T., Billinge, S. J. L., Cheetham, A. K., Louca, D. & Parise, J. B. (2002). *Building a high resolution total scattering powder diffractometer - upgrade of NPD at MLNSC*. *Appl. Phys. A Mater. Sci. Process.* **74**, s163–s165.

Proffen, T. & Neder, R. B. (1997). *DISCUS: a program for diffuse scattering and defect-structure simulation*. *J. Appl. Cryst.* **30**, 171–175.

Qiu, X., Proffen, T., Mitchell, J. F. & Billinge, S. J. L. (2005). *Orbital correlations in the pseudocubic O and rhombohedral R phases of $LaMnO_3$*. *Phys. Rev. Lett.* **94**, 177203.

Qiu, X., Thompson, J. W. & Billinge, S. J. L. (2004). *PDFgetX2: a GUI-driven program to obtain the pair distribution function from X-ray powder diffraction data*. *J. Appl. Cryst.* **37**, 678.

Rayleigh, Lord (1914). *On the diffraction of light by spheres of small relative index*. *Proc. R. Soc. London Ser. A*, **90**, 219–225.

Renninger, A. L., Rechtin, M. D. & Averbach, B. L. (1974). *Monte Carlo models of atomic arrangements in arsenic-selenium glasses*. *J. Non-Cryst. Solids*, **16**, 1–14.

Rietveld, H. M. (1969). *A profile refinement method for nuclear and magnetic structures*. *J. Appl. Cryst.* **2**, 65–71.

Ruan, C.-Y., Murooka, Y., Raman, R. & Murdick, R. (2007). *Dynamics of size-selected gold nanoparticles studied by ultrafast electron nanocrystallography*. *Nano Lett.* **7**, 1290–1296.

Rudee, M. L. & Howie, A. (1972). *The structure of amorphous Si and Ge*. *Philos. Mag.* **25**, 1001–1007.

Sartbaeva, A., Wells, S. A., Thorpe, M. F., Božin, E. S. & Billinge, S. J. L. (2007). *Quadrupolar ordering in revealed from scattering data and geometric modeling*. *Phys. Rev. Lett.* **99**, 155503.

Shevchik, N. J. (1977). *Frequency modulated X-ray diffraction II. Structures of multi-element disordered systems*. *Philos. Mag.* **35**, 1289–1298.

Soper, A. K. (1996). *Empirical potential Monte Carlo simulation of fluid structure*. *Chem. Phys.* **202**, 295–306.

Soper, A. K. (2001). *Tests of the empirical potential structure refinement method and a new method of application to neutron diffraction data on water*. *Mol. Phys.* **99**, 1503–1516.

Soper, A. K. (2007). *Joint structure refinement of X-ray and neutron diffraction data on disordered materials: application to liquid water*. *J. Phys. Condens. Matter*, **19**, 335206.

Soper, A. K. & Barney, E. R. (2011). *Extracting the pair distribution function from white-beam X-ray total scattering data*. *J. Appl. Cryst.* **44**, 714–726.

Svergun, D. I. & Stuhrmann, H. B. (1991). *New developments in direct shape determination from small-angle scattering. 1. Theory and model calculations*. *Acta Cryst.* A**47**, 736–744.

Teo, B. K. (1986). *EXAFS: Basic Principles and Data Analysis*. New York: Springer-Verlag.

Thorpe, M. F., Levashov, V. A., Lei, M. & Billinge, S. J. L. (2002). In *From Semiconductors to Proteins: Beyond the Average Structure*, edited by S. J. L. Billinge & M. F. Thorpe, pp. 105–128. New York: Kluwer/Plenum.

Toby, B. H. & Egami, T. (1992). *Accuracy of pair distribution function analysis applied to crystalline and non-crystalline materials*. *Acta Cryst.* A**48**, 336–346.

Tucker, M. G., Goodwin, A. L., Dove, M. T., Keen, D. A., Wells, S. A. & Evans, J. S. O. (2005). *Negative thermal expansion in ZrW_2O_8: mechanisms, rigid unit modes, and neutron total scattering*. *Phys. Rev. Lett.* **95**, 255501.

Tucker, M. G., Keen, D. A., Dove, M. T., Goodwin, A. L. & Hui, Q. (2007). *RMCProfile: reverse Monte Carlo for polycrystalline materials*. *J. Phys. Condens. Matter*, **19**, 335218.

Tyrsted, C., Jensen, K. M. O., Bøjesen, E. D., Lock, N., Christensen, M., Billinge, S. J. L. & Iversen, B. B. (2012). *Understanding the formation and evolution of ceria nanoparticles under hydrothermal conditions*. *Angew. Chem. Int. Ed.* **51**, 9030–9033.

Warren, B. E. (1934). *X-ray diffraction study of carbon black*. *J. Chem. Phys.* **2**, 551–555.

Warren, B. E. (1990). *X-ray Diffraction*. New York: Dover.

Warren, B. E., Krutter, H. & Morningstar, O. (1936). *Fourier analysis of X-ray patterns of vitreous SiO_2 and B_2O_2*. *J. Am. Ceram. Soc.* **19**, 202–206.

Waseda, Y. (1984). *Novel Applications of Anomalous (Resonance) X-ray Scattering for Structural Characterization of Disordered Materials*. Berlin: Springer-Verlag.

Wells, S. A., Dove, M. T. & Tucker, M. G. (2002). *Finding best-fit polyhedral rotations with geometric algebra*. *J. Phys. Condens. Matter*, **14**, 4567–4584.

Wells, S., Dove, M. & Tucker, M. (2004). *Reverse Monte Carlo with geometric analysis - RMC+GA*. *J. Appl. Cryst.* **37**, 536–544.

Williams, W. G., Ibberson, R. M., Day, P. & Enderby, J. E. (1997). *GEM – general materials diffractometer at ISIS*. *Physica B*, **241–243**, 234–236.

Wright, A. C. (1998). *Glass Phys. Chem.* **24**, 148–179.

Wyckoff, R. W. G. (1967). *Crystal Structures*, Vol. 1, 2nd ed. New York: Wiley.

Yang, X., Masadeh, A. S., McBride, J. R., Božin, E. S., Rosenthal, S. J. & Billinge, S. J. L. (2013). *Confirmation of disordered structure of ultrasmall CdSe nanoparticles from X-ray atomic pair distribution function analysis*. *Phys. Chem. Chem. Phys.* **15**, 8480–8486.

Young, C. A. & Goodwin, A. L. (2011). *Applications of pair distribution function methods to contemporary problems in materials chemistry*. *J. Mater. Chem.* **21**, 6464–6476.

Young, R. A. (1993). *The Rietveld Method*. International Union of Crystallography Monographs on Crystallography, No. 5. Oxford University Press.

Zernike, F. & Prins, J. A. (1927). *Die Beugung von Röntgenstrahlen in Flüssigkeiten als Effekt der Molekülanordnung*. *Z. Phys.* **41**, 184–194.

Zhang, H. Z., Gilbert, B., Huang, F. & Banfield, J. F. (2003). *Water-driven structure transformation in nanoparticles at room temperature*. *Nature*, **424**, 1025–1029.

International Tables for Crystallography (2019). Vol. H, Chapter 5.8, pp. 673–696.

5.8. Scattering methods for disordered heterogeneous materials

A. J. Allen

5.8.1. Introduction and overview

5.8.1.1. *Amorphous and non-crystalline materials*

While powder diffraction and single-crystal diffraction have long comprised the standard means for determining the structure, phase and even the composition of solid materials, standard powder or single-crystal diffraction methods cannot be applied if no (or little) crystalline structure is present. The most obvious examples of amorphous and non-crystalline solid materials are glasses, polymers, various types of gel and sometimes thin films. A uniform amorphous material without structure at any length scale would not be very tractable to diffraction-based measurements of almost any kind. Fortunately, only a few (if any) materials amorphous over all length scales exist in nature. Most so-called amorphous materials contain some short-range order that can be elucidated, at least to some extent, by wide-angle liquid- or total-scattering methods increasingly available at synchrotron X-ray or neutron scattering facilities. Such methods are also applicable to poorly crystalline solids where defects and other heterogeneities disrupt any long-range order, and also to nanocrystalline materials where the crystal structure order is short range by definition (Bates *et al.*, 2006). Since wide-angle scattering (WAS) methods in general, and nanocrystalline materials in particular, are covered elsewhere in this volume (see Chapters 5.6 and 5.7), they will be discussed fairly briefly in this chapter. Here we will focus more on the disorder and heterogeneity at the microstructural level (from ∼10 Å to several μm), which pervades all material systems (including thin films) that are not uniform in structure and composition across all length scales.

5.8.1.2. *Disordered and heterogeneous (and multi-component) materials*

Fig. 5.8.1 presents examples of measurements possible for disordered and heterogeneous materials, together with the scale ranges applicable to the techniques discussed.

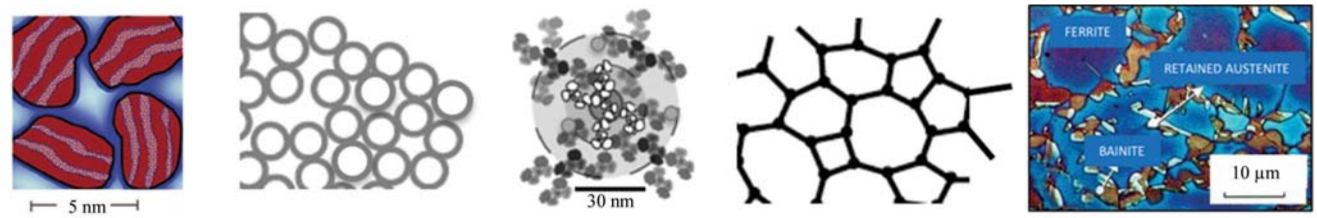

(*a*) C-S-H gel globules with internal structure (*b*) Colloidal dispersion (many possible length scales) (*c*) Fractal aggregate of C-S-H gel globules (*d*) Continuous random network (many possible length scales) (*e*) Phase transformations, defects and precipitates in an advanced steel

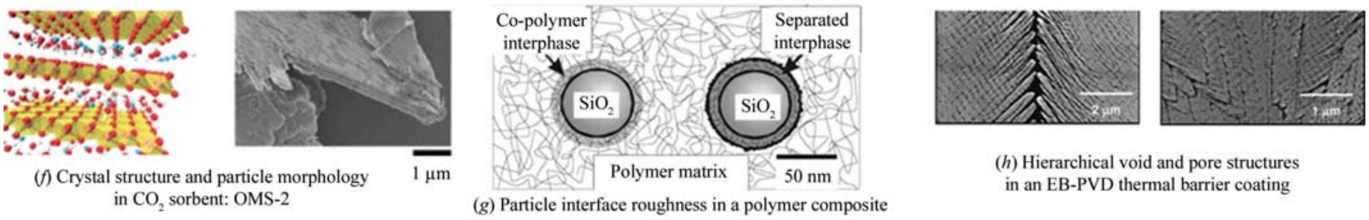

(*f*) Crystal structure and particle morphology in CO_2 sorbent: OMS-2 (*g*) Particle interface roughness in a polymer composite (*h*) Hierarchical void and pore structures in an EB-PVD thermal barrier coating

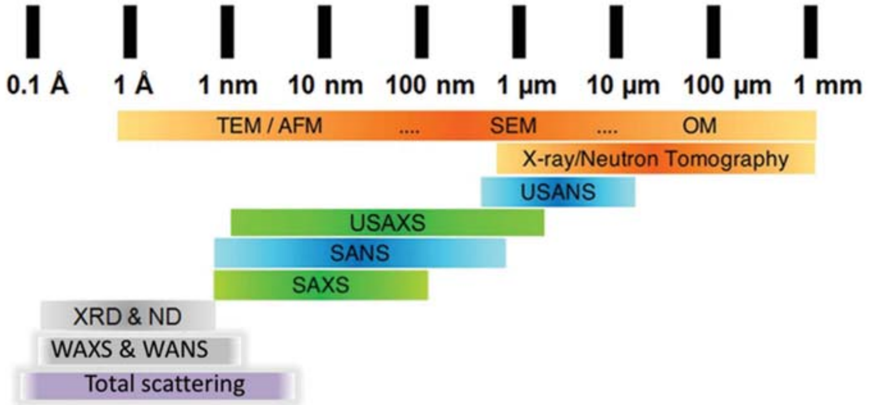

Figure 5.8.1

Examples of scattering methods applied to disordered, heterogeneous materials, together with the scale ranges of interest and the applicable scattering-based methods. Material examples: (*a*) calcium-silicate hydrate (C-S-H) gel globules in hydrating cement (Allen *et al.*, 2007); (*b*) colloidal particle dispersion (Bates *et al.*, 2006); (*c*) fractal aggregate of C-S-H gel globules (Jennings, 2000); (*d*) continuous random network [as (*b*)]; (*e*) complex microstructure of an advanced steel; (*f*) crystal layer structure and associated lamellar morphology of CO_2 solid sorbent, OMS-2 (Espinal *et al.*, 2012); (*g*) interphase-controlled interface surface roughness between particles and matrix in a polymer composite (Wilson *et al.*, 2007); and (*h*) void/pore structures in an electron-beam physical vapour-deposited (EB-PVD) thermal barrier coating (Renteria *et al.*, 2007). Techniques: TEM and SEM = transmission and scanning electron microscopy, AFM = atomic force microscopy, OM = optical microscopy (microscopies and imaging included for comparison); SAXS and SANS, USAXS and USANS = small-angle and ultra-small-angle X-ray and neutron scattering; XRD and ND = X-ray and neutron diffraction (structure determination); WAXS and WANS = wide-angle X-ray and neutron scattering (phase analysis, diffuse-scattering effects); and total scattering (atomic pair distribution function analysis).

Copyright © 2019 International Union of Crystallography

Table 5.8.1
Information on disordered or heterogeneous material systems using scattering methods

Abbreviations: GI-SAXS = grazing-incidence SAXS, NS-SANS = near-surface SANS, XRR = X-ray reflectivity, NR = neutron reflectivity.

Q-range, obtainable information (examples or applications)	SAXS, SANS	USAXS, USANS	GI-SAXS, NS-SANS	XRR, NR	WAXS, WANS	Total scattering
Minimum Q (Å^{-1})	10^{-3}	$< 10^{-4}$	10^{-3}	$\sim 10^{-1}$	1	~1
Maximum Q (Å^{-1})	1	1 or 10^{-3}	1	> 1	~5	> 40
Lattice spacings, crystal phases (precipitates/minority phases in alloys, CO_2 solid sorbents)					×	×
Mean particle or pore size, shape (colloids, porous rocks)	×	×	×	×		
Size distribution (precipitate nucleation, growth and coarsening)	×	×	×			
Pore or particle volume fraction (solution-mediated particle formation, cement hydration)	×	×				
Pore, particle or interface surface area and roughness (coating de-lamination, composite particle/matrix bonding)	×	×	×	×		
Composition, density of solid phases or layers (deposited dielectric films, clays, catalysts)	×	×	×	×	×	
Interparticle interactions (concentrated suspensions, gels)	×	×	×	×		
Particle or pore pair distribution function (concentrated suspensions, gels, fractal aggregates, cements)	×	×	×	×		
Local structure and atomic pair distribution function (quantum dots, nanoparticle internal crystal structures)					×	×

Many material systems exhibit heterogeneity and disorder, regardless of whether they contain components with crystal structure or not. As reviewed by several authors (*e.g.* Fratzl, 2003; Allen, 2005), obvious examples include nanoparticle (or small-particle) dispersions in liquid, cements and concretes, clays and minerals (including oil shales), porous solids of all kinds, thermal barrier coatings, nanocomposites, precipitates in metals and alloys, and even biological structures. Some more specific examples are given in Fig. 5.8.1 that demonstrate how the heterogeneous nature of a material may comprise a size distribution of discrete pores or particles, may comprise a network structure (as is frequently the case with polymers), or it may be hierarchical in nature, possibly exhibiting a fractal structure of some kind. The heterogeneity is usually disordered but, if not, coherent-diffraction hallmarks will be apparent that can be treated by an extension of crystal-diffraction principles to the microstructural ordering at coarser length scales. For a general disordered material system, small-angle scattering (SAS) methods can be applied (Kostorz, 1979), and these comprise the techniques most discussed in this chapter.

5.8.1.3. *Small-angle and wide-angle scattering tools*

As with all diffraction-based scattering techniques, the scattering intensity, as a function of the scattering-vector magnitude Q [where $Q = 4\pi \sin\theta/\lambda$, λ is the wavelength of the radiation used and 2θ is the scattering angle], is related to the Fourier transform of the structure or microstructure of interest. Whereas for powder or single-crystal diffraction the scattering forms the diffraction pattern associated with the particular crystal structure being investigated, for SAS/WAS the scattering can also be associated with the Fourier transform of the atomic density distribution within the sample. In the case of a disordered material system this relates to the mean microstructure arrangement averaged over the sampling measurement volume and measurement time. Small-angle X-ray and neutron scattering (SAXS and SANS) are becoming increasingly important methods for measuring the statistically representative, volume-weighted microstructures of disordered and heterogeneous material systems (Guinier & Fournet, 1955; Glatter & Kratky, 1982). Where possible, they should be used in conjunction with wide-angle X-ray or neutron scattering (WAXS and WANS) to provide quantitative phase information for the components of the heterogeneous system. Furthermore, total-scattering studies over an extended Q range, such as are possible at synchrotron X-ray beamlines or at pulsed neutron source facilities, can provide additional information on the local structure factor that defines any short-range order that may be present, and may also be used to determine, for example, the atomic pair distribution function inside diffracting nanocrystalline grains (Proffen *et al.*, 2003; Billinge & Levin, 2007; Keen & Goodwin, 2015). Total-scattering methods also supply information on thermal diffuse scattering from lattice vibrations. Thus, wide-angle and total-scattering methods should be used in conjunction with SAXS and SANS, and are discussed below for relevant situations, but our primary focus is on SAXS and SANS.

5.8.1.4. *Tabulated summary of quantitative information obtainable*

Table 5.8.1 summarizes the information obtainable from the techniques discussed in this chapter. While specific issues regarding the limitations and experimental uncertainties of the various techniques are discussed in the sections that follow, some general points can be made here. Most, but not all, scattering- and diffraction-based methods incorporate detectors that count events (*e.g.* scattered X-ray photons or neutrons) through associated electronic pulses of some kind. Thus, most statistical uncertainties in the measured intensities can be readily calculated and propagated through the data reduction (circular or sector-averaging of position-sensitive detector counts, blank-run-data subtraction, calibration and normalization, *etc.*). However, much of the data analysis and interpretation involves geometrical desmearing steps, separation of different scattering or diffraction phenomena, and Fourier transformations from the measured data in Q-space to structural and microstructural information in real space. Thus, it is critical that uncertainties and variation in the measured intensities remain sufficiently small so as not to introduce artifacts into the extracted structural information. Other sources of uncertainty in the structures and microstructures determined arise from finite resolution in Q, truncation effects due to the finite Q range considered, and the degree to which any one interpretative or model scheme is appropriate. These issues can play a particularly important role where different techniques are combined together for partially disordered material systems.

5.8.1.5. *Different notations*

The notation used in this chapter corresponds to that generally used in neutron scattering, although it is also increasingly used in X-ray scattering measurements carried out at X-ray synchrotron facilities. However, a different notation has also been associated with X-ray crystallography, especially small-angle X-ray scattering. See for example, Chapter 2.6 of *International Tables for Crystallography* Volume C (Glatter & May, 2006) and other texts (Guinier & Fournet, 1955; Glatter & Kratky, 1982). The principal difference in these earlier texts of relevance here is that h is used in place of Q, and $\mathbf{h}$ in place of $\mathbf{Q}$ when the direction of the scattering vector must be considered. (Note that q and $\mathbf{q}$ are also common notations corresponding to Q and $\mathbf{Q}$.) As is well covered in these earlier texts and *International Tables*, $\mathbf{h} = (2\pi/\lambda)(\mathbf{s} - \mathbf{s}_O)$, where $\mathbf{s}$ and $\mathbf{s}_O$ are unit vectors in the scattered and incident directions, respectively. Nowadays it is more common to see $\mathbf{Q}$ defined by $\mathbf{Q} = \mathbf{k} - \mathbf{k}_O$ where $\mathbf{k}$ and $\mathbf{k}_O$ are the scattered and incident wave vectors (of magnitude $2\pi/\lambda$).

5.8.2. Recommended measurement tools

All of the techniques discussed here utilize either X-rays or neutrons. We acknowledge the importance of light-scattering methods for the measurement of dilute, transparent, disordered systems at the micrometre scale. However, these techniques have limited applicability here, with the possible exception of dilute particulate suspensions, and they are well described elsewhere. Also, we acknowledge that increasingly sophisticated electron-scattering methods have become available with high-resolution transmission electron microscope (HRTEM), scanning TEM (STEM) and cryogenic sample-based (cryoEM) instrumentation. However, HRTEM, STEM or cryoEM facilities do not yet provide the Q range, signal-to-noise and intensity dynamic range capabilities required for SAS and total-scattering analysis. Nor do they provide the intensity calibration needed to determine the absolute scattering probabilities and the associated volume fractions or concentrations of scattering features. For these reasons, we confine our discussion to X-ray- and neutron-based methods. For X-rays, where X-ray photons interact with the atomic electron distribution, the scattering intensity increases as the square of the atomic number (Z) density. For neutrons, where the main scattering contribution comes from neutron interactions with the atomic nuclei, there is generally greater *relative* sensitivity to low-Z materials, but this depends on the specific elements and isotopes present. In fact, the neutron isotope effect allows scattering contrast variation studies (see Section 5.8.3.1.10) to be made by adjusting the isotope mix, for example, between H_2O and D_2O. Since the neutron has a magnetic moment, there is also a magnetic interaction with any atomic magnetic moments present, which can be exploited in magnetic scattering experiments (see Section 5.8.3.1.11).

5.8.2.1. *Small-angle scattering using a position-sensitive detector*

Fig. 5.8.2 shows the basic measurement geometry used in SAS measurements using a two-dimensional (2D) position-sensitive detector (PSD), together with typical reduced SAS data *versus* Q. A well collimated incident beam impinges on the sample, in which a small component of the beam is scattered out of the forward direction by small scattering angles, 2θ. Generally, the incident beam is monochromatic, or at least sufficiently so to be associated with a fixed wavelength, λ, and the optimum instrument geometry occurs when the incident and scattered angular resolutions are the same. In the case of SAXS (Guinier & Fournet, 1955; Glatter & Kratky, 1982), although the X-ray beam can be tightly collimated by the crystal optics, as much as possible of the incident and scattered flight paths need to be in vacuum or a non-scattering gas because air scattering attenuates the X-ray intensity significantly. For laboratory-based SAXS facilities, the energy, E, and λ are determined by the X-ray source used – usually either Cu $K\alpha$ (E = 8.048 keV, λ = 1.5418 Å) or Mo $K\alpha$ (E = 17.479 keV, λ = 0.7107 Å) X-rays. At X-ray beamlines at synchrotrons, λ can be selected over a wide range, with a resolution usually determined by the band pass of the monochromator crystal optics. Generally, for SAXS, the illuminated sample area is $\sim$0.5 mm but can be <0.1 mm at a synchrotron. The sample thickness depends on the material and the X-ray energy, but typically ranges from 0.01 mm (high Z, low E) to 1 mm (low Z, high E).

In the case of SANS, the linear relationship between neutron wavelength and neutron time-of-flight is exploited (Grillo, 2008).

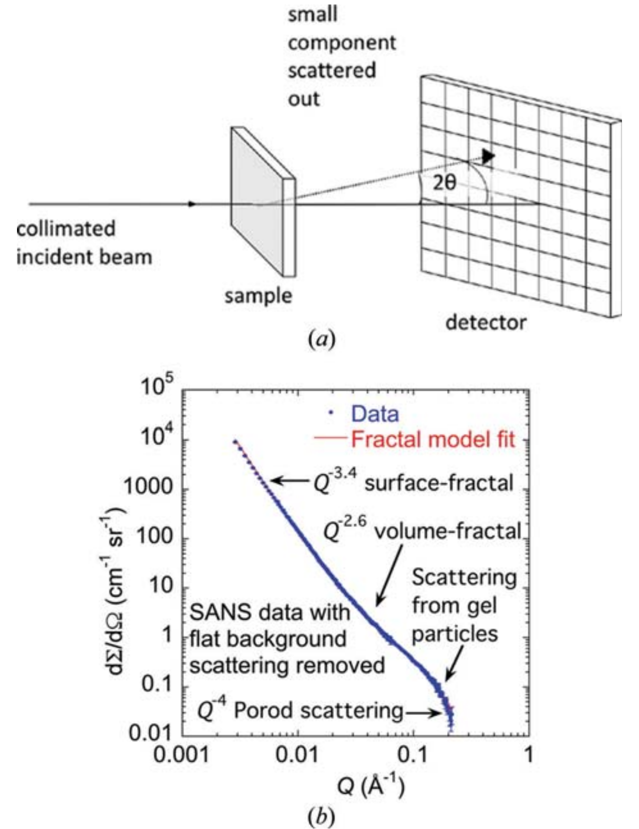

Figure 5.8.2
(*a*) Schematic of the basic measurement geometry for SAXS or SANS using a 2D PSD. The incident beam is monochromatic for SAXS and reactor-based SANS, and polychromatic for SANS at a pulsed source with energy/wavelength selection by time-of-flight. (*b*) Typical reduced and circularly-averaged SAS data with a fractal model fit (see Section 5.8.3.1.9). Vertical bars at each data point represent typical standard deviation uncertainties.

At a reactor-based neutron facility, λ is determined with typically 10 to 15% Δλ/λ resolution about a given value using a rotating helical velocity selector (only neutrons with a velocity, hence λ, along the incident direction within this band pass through the rotating helical path of the velocity selector). At a spallation neutron facility all neutrons are utilized in SANS measurements with λ for each time bin determined from the corresponding time of flight. In SANS, unlike SAXS, neutron waveguides are frequently used to collimate the neutrons as they travel from their effective source (fission or spallation) to an effective source slit at the exit of the last guide used. This aperture subtended at the sample position largely defines the incident-beam collimation, but the incident intensity decreases with the inverse square of the distance from this last guide to the sample position. The sample aperture (*i.e.* illuminated sample area) ranges from 5 to 20 mm with sample thicknesses ranging from 0.5 to 5 mm, depending on the material.

The 2D PSD measures the scattering intensity as a function both of the scattering angle, 2θ (hence Q), and the azimuthal angle about the incident-beam direction. Provided absolute intensity calibration is achieved (see Section 5.8.2.3) the objective in most SAXS or SANS measurements is to measure the differential scattering cross section, $\mathrm{d}\Sigma/\mathrm{d}\Omega$, as a function of Q. In this context, $\mathrm{d}\Sigma/\mathrm{d}\Omega$, for a given $\mathbf{Q}$, is defined as the scattering probability per unit incident flux and per unit sample volume of scattering into unit solid angle about the scattered beam direction associated with $\mathbf{Q}$. As in all diffraction processes, $\mathbf{Q}$ bisects the angle between the incident-beam direction and any given scattering direction (Fig. 5.8.2*a*). However, for small scattering angles, we note that this puts $\mathbf{Q}$ approximately in the sample plane. Thus, in the regular case of measurement transmission geometry, SAS primarily provides microstructural information within the sample plane, in a direction determined by the azimuthal direction of the scattering. When the microstructure within the sample is isotropic, or at least circularly symmetric about the incident-beam direction, data on the 2D PSD can be circularly averaged about the incident-beam direction and $\mathrm{d}\Sigma/\mathrm{d}\Omega$ can be expressed as a function of Q, rather than $\mathbf{Q}$. Indeed, the most common presentation of SAS data is in a three-column format of Q, $\mathrm{d}\Sigma/\mathrm{d}\Omega$ and the standard-deviation uncertainties in $\mathrm{d}\Sigma/\mathrm{d}\Omega$, together with the necessary metadata providing the measurement geometry, λ, Q resolution, sample thickness *etc.*, as well as details on the blank subtraction and the sample transmission. For SAXS or SANS with a 2D PSD, the standard-deviation uncertainties in $\mathrm{d}\Sigma/\mathrm{d}\Omega$ arise primarily from statistical uncertainties in the individual pixel detector counts. However, these must be propagated through the data-reduction software as the blank subtraction, intensity calibration and azimuthal or circular averaging steps are executed.

While data reduction to give $\mathrm{d}\Sigma/\mathrm{d}\Omega$ and data interpretation to model it are covered in more detail in later sections, we provide the basic theoretical basis for $\mathrm{d}\Sigma/\mathrm{d}\Omega$ here. At the fundamental level (Guinier & Fournet, 1955; Glatter & Kratky, 1982; Warren, 1990)

$$\frac{\mathrm{d}\Sigma}{\mathrm{d}\Omega}(\mathbf{Q}) = \frac{1}{V_S}\left|\int\limits_{V_S} \rho(\mathbf{r})\exp(i\mathbf{Q}\cdot\mathbf{r})\,\mathrm{d}^3\mathbf{r}\right|^2, \qquad (5.8.1)$$

where $\rho(\mathbf{r})$ is the spatial distribution of the coherent X-ray or neutron scattering-length density over the sampling volume, V_S. While this equation could be applied in most diffraction-based analyses, in SAS it is more conveniently expressed in terms of the material microstructure being studied. For an isotropic microstructure consisting of scattering particles of particle number density n_P (*i.e.*, the volume fraction $\Phi_V = n_P V_P$), the squared integral in equation (5.8.1) can be converted to give a single integral in the SAS-applicable form of the Debye equation:

$$\begin{aligned}\frac{\mathrm{d}\Sigma}{\mathrm{d}\Omega} &= n_P|\Delta\rho|^2 V_P \int\limits_0^\infty 4\pi r^2\gamma_0(r)\frac{\sin(Qr)}{Qr}\,\mathrm{d}r\\ &= n_P|\Delta\rho|^2 V_P^2 F_P^2(Q) S_P(Q),\end{aligned} \qquad (5.8.2a)$$

where $|\Delta\rho|^2$ is the scattering contrast factor between the particles and the surrounding medium, $\gamma_0(r)$ is the dimensionless atomic pair correlation function, V_P is the scattering particle volume, $F_P{}^2(Q)$ is the particle form factor, and $S_P(Q)$ is an interparticle structure factor containing information on the spatial relationship between the scattering particles. Here, we initially assume that $S_P(Q) = 1$ for a dilute population of uncorrelated particles, and we can write

$$F_P^2(Q) = \frac{1}{V_P}\int\limits_0^\infty 4\pi r^2\gamma_0(r)\frac{\sin(Qr)}{Qr}\,\mathrm{d}r$$

$$\text{where } \frac{1}{V_P}\int\limits_0^\infty 4\pi r^2\gamma_0(r)\,\mathrm{d}r = 1. \qquad (5.8.2b)$$

The particle form factor, $F_P{}^2(Q)$, can be expressed in terms of an assumed particle shape and/or real-space structure, *via* $\gamma_0(r)$, which decays to zero when r is greater than the maximum particle dimension, or it can be determined empirically from the data as a particle pair-distance distribution function (PDDF) (see Section 5.8.3).

Once again, we should mention a different convention frequently used in X-ray crystallography (Guinier & Fournet, 1955; Glatter & Kratky, 1982; Glatter & May, 2006). In this notation, a scattering intensity, $I(\mathbf{h})$ is used in place of $\mathrm{d}\Sigma(\mathbf{Q})/\mathrm{d}\Omega$ in equation (5.8.1) and the volume normalization is omitted. Similarly, $I(h)$ is used in place of $\mathrm{d}\Sigma/\mathrm{d}\Omega$ with the volume normalization omitted in equation (5.8.2*a*) *etc*. We use $\mathrm{d}\Sigma/\mathrm{d}\Omega$ as it is more readily related to what is actually measured in experiments, see Section 5.8.2.3.1.

Clearly, the measurement of $\mathrm{d}\Sigma/\mathrm{d}\Omega$ in a given Q regime requires sufficient Q resolution to gather the information potentially contained in the data. To cover a scale range of ∼10 Å to ∼0.1 mm, as is typical for conventional 2D SAXS or SANS, a corresponding Q range from ∼0.005 to ∼1 Å^{-1} is required, implying that several instrument configurations with different sample-to-detector distances (and corresponding incident-beam collimation) are required. In order to capture the microstructural information contained in the scattering profile, the Q resolution, defined by $\Delta Q/Q$, must be maintained for smaller Q values (larger scattering features). Also a correspondingly greater density of data points in Q is required if information is not to be lost. These requirements dictate tighter incident collimation and larger sample-to-detector distances for smaller Q values. However, the use of focusing optics at the more intense X-ray and neutron sources, coupled with new innovations in detector technology and the use of several 2D PSDs together, are opening up new possibilities in which SAXS or SANS data can be obtained across the whole Q range in one measurement, as discussed in Section 5.8.4.

Finally in this section, we discuss the requirements for 2D PSDs used in SAXS and SANS. Several technologies now exist for SAXS 2D PSDs: charge-coupled device (CCD) detectors, image plates and reverse-bias silicon-diode arrays are currently the most prominent types of X-ray 2D PSD (see Ponchut, 2006; Spieler, 2008). Several attributes need to be considered for SAXS applications: sensitive X-ray energy range, linear dynamic range in X-ray intensity, detector readout speed (this determines the cycling time, and hence time resolution of repeated measurements), spatial (pixel) resolution, signal-to-noise ratio, compactness and mass of overall detector system, and cost. All of these detector systems can be expensive, but they work well for X-ray energies up to ~12 keV. The detector efficiency generally declines for higher energies, but can be improved by increasing the thickness of the X-ray-sensitive materials. For SAXS, CCDs are compact, have reasonable linear dynamic range in intensity (14 to 16 bits), reasonable detector readout speed (a few seconds) and good spatial resolution (<100 µm pixel size), but can have significant dark-current noise that may limit application for weak scatterers. By comparison, image plates tend to be bulky and require more extensive cooling systems, can have better linear dynamic range in intensity (up to 18 bits) and have rather long readout times (~100 s) that severely limit time resolution, but have excellent spatial resolution (~10 µm pixel size) and low electronic backgrounds. SAXS 2D PSDs based on reverse-bias silicon-diode arrays or similar technologies currently present the best performance option (Eikenberry *et al.*, 2003).[1] They are light and compact, have excellent linear dynamic range in intensity (up to 20 bits), have very short detector readout speeds (a few milliseconds), acceptable spatial resolution for SAXS (<200 µm pixel size) and, as single-photon detectors, they exhibit zero dark current; but they are costly.

Development of 2D PSDs for SANS with good intensity dynamic range has progressed for several decades (Ibel, 1976; Glinka *et al.*, 1998) and continues, especially for new SANS instruments being installed at spallation neutron sources (Zhao *et al.*, 2010). Originally based on the absorption of neutrons in BF_3 gas, most SANS 2D PSDs now exploit the absorption of neutrons in ^{3}He gas (although the increasingly chronic shortage of ^{3}He is forcing renewed consideration of BF_3). In either case, neutron absorption results in a cascade of charged particles released in the gas close to the absorption site, and the resultant charge pulses registered on a 2D wire electrode array provide the intensity profile of the scattering intensity absorbed in the detector. The pixel resolution of SANS detectors is typically 5 to 10 mm. This is generally compatible with the larger scale of SANS instruments in general, but the detector pixel size subtended at the sample position must usually be taken into account in calculating the scattered-beam angular resolution. The dynamic intensity range of SANS 2D PSDs is more limited than for SAXS detectors (~14 bits). However, this limitation is partially mitigated for measurements at low Q where $d\Sigma/d\Omega$ is larger. This is because the larger SANS sample-to-detector distance, together with the correspondingly larger required collimation distance (between the source aperture at the exit of the last collimating neutron guide and the sample), very significantly reduce the measured scattering intensity at the detector. SANS 2D PSDs are very expensive, and there is a current need to develop new technologies, both for the new generation of SANS instruments at spallation neutron sources and to address a global shortage of ^{3}He.

5.8.2.2. *Ultra-small-angle scattering using crystal diffraction optics*

In conventional SAS with a 2D PSD the Q resolution is determined by the angular resolution associated with the incident and scattered beam geometries and also, especially for SANS, by the wavelength resolution. However, SAS measurements may also be made using Bonse–Hart crystal diffraction optics (Bonse & Hart, 1966; Long *et al.*, 1991). In this case, the Q resolution is defined by the band pass and Darwin width of the crystal optics used, and the resolution is decoupled from the source or sample apertures, and from the size of the point detector used. Because the minimum Q and Q resolution are significantly finer than possible with conventional SAS, lower Q values are accessible (corresponding to coarser feature sizes), and so the Bonse–Hart method is referred to as ultra-small-angle scattering (USAS, USAXS and USANS, corresponding to SAS, SAXS and SANS as described above).

Fig. 5.8.3(*a*) shows the configuration for a Bonse–Hart USAXS instrument. For both USAXS and USANS a pre-monochromated incident beam is passed through a pair of collimating crystals set to the Bragg condition for the appropriate wavelength. The X-rays or neutrons pass through the sample where small-angle scattering occurs, and then through a second pair of analysing crystals. The unscattered beam passes through both sets of crystal pairs (monoliths) when the analyser is also set to the appropriate Bragg condition. However, as the analyser is rotated away from this condition by a small angle 2θ, only X-rays or neutrons that have been scattered in the sample by the same angle satisfy the Bragg condition for the analyser monolith. Thus, a point detector placed after the analyser monolith can be used to measure the scattering intensity as a function of the analyser rotation angle, 2θ, to provide a scan of USAXS or USANS intensity *versus Q*, provided that the mechanical integrity and precision of the analyser angular rotation stage is sufficient for scanning the small angles involved. Because the Q range is scanned in a particular direction, the sample must be rotated azimuthally to obtain any anisotropic microstructural information. The fine Q resolution occurs only in the diffraction plane of the collimating and

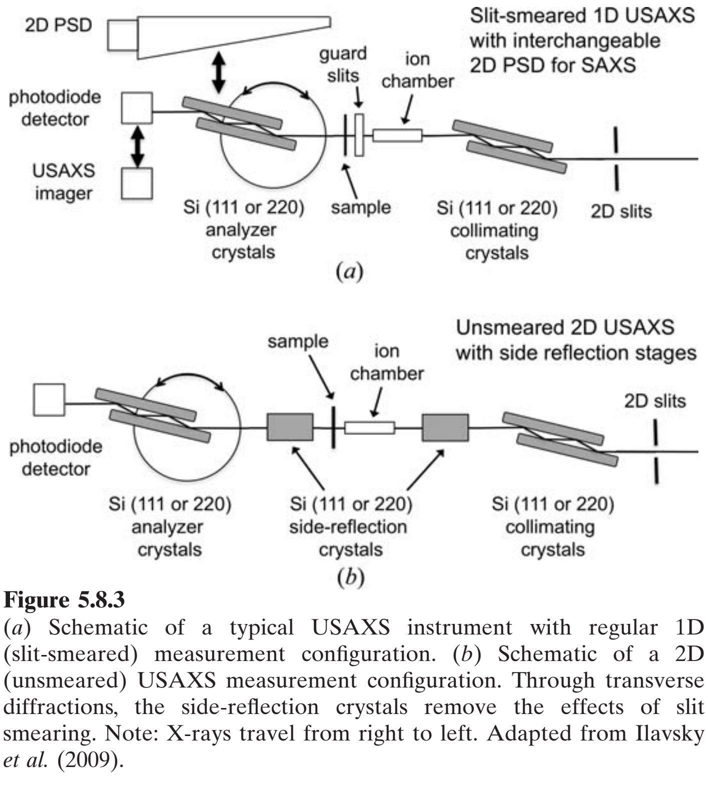
2D PSD
Slit-smeared 1D USAXS with interchangeable 2D PSD for SAXS
guard slits
ion chamber
photodiode detector
USAXS imager
Si (111 or 220) analyzer crystals
sample
Si (111 or 220) collimating crystals
2D slits
(a)
Unsmeared 2D USAXS with side reflection stages
sample
ion chamber
2D slits
photodiode detector
Si (111 or 220) analyzer crystals
Si (111 or 220) side-reflection crystals
Si (111 or 220) collimating crystals
(b)

Figure 5.8.3
(*a*) Schematic of a typical USAXS instrument with regular 1D (slit-smeared) measurement configuration. (*b*) Schematic of a 2D (unsmeared) USAXS measurement configuration. Through transverse diffractions, the side-reflection crystals remove the effects of slit smearing. Note: X-rays travel from right to left. Adapted from Ilavsky *et al.* (2009).

---

[1] Certain commercial materials, equipment and references are identified in this paper only to specify adequately experimental procedures. In no case does such identification imply recommendation by NIST nor does it imply that the material or equipment identified is necessarily the best available for this purpose.

analyser monoliths. In the transverse plane, the Q resolution is determined primarily by the angle subtended at the sample position by the detector aperture. This means that the data are intrinsically slit-smeared. While such data can be modelled directly by slit-smearing any model function, the data should be desmeared if they are to be compared with other SAS data measured with a 2D PSD. Fortunately, reliable iterative algorithms are available to accomplish this step, *e.g.* Lake (1967), *provided* that the statistical fluctuations in the data due to noise and other random uncertainties are small compared with genuine features in the scattering curve. If this is not the case, desmearing amplifies these effects, which then appear as artifacts in the desmeared data. In this situation, it is preferable to carry out slit smearing within any interpretation model being considered, and then fit this directly to the slit-smeared data without desmearing the experimental data.

Bonse–Hart USAXS and USANS instruments have developed along somewhat different lines because of the different challenges that have needed to be addressed for acceptable performance to be achieved with X-rays and neutrons. Initially, both USAXS and USANS instruments were developed simply to extend the minimum attainable Q range in SAS measurements to smaller values, and hence extend the microstructure characterization of heterogeneous systems to µm length scales. By combining USAS with SAS measurements it is possible to obtain statistically representative microstructure characterization over a scale range from 10 Å to several µm, while wide-angle scattering and other powder-diffraction methods provide information at the ångstrom scale. Much of the motivation for this comes from a growing realization that processes within material systems occur across length scales with nanoscale phenomena affecting microscale structure and *vice versa*.

USAXS instrumentation has been developed both for laboratory-based use and at synchrotron beamlines. Typically, the collimating and analyser monoliths are set up to accommodate four crystal reflections each. This provides an overall instrumental rocking curve with a full width at half maximum, FWHM, that is approximately equal to the Darwin width for the crystal reflection used [typically Si (111) or Si (220)] and rocking-curve tails that should be much steeper than the fall-off in the USAXS intensity from any sample. In practice, USAXS measurements are extremely sensitive to the state of the crystal surfaces in both monoliths, and careful polishing and etching are required to ensure that neither strain variation nor surface roughness introduce significant artifacts into the USAXS data. Features on the crystal surfaces inevitably contribute some scattering to the instrumental 'blank' runs, but this is not an issue provided such contributions are much less than the genuine USAXS intensity from samples of interest. The point detector is typically a photodiode. With appropriate supporting electronics, this can have a dynamic range in X-ray intensity of more than 10 decades. Thus, at a synchrotron beamline and with precautions to reduce parasitic background effects due to air scattering *etc.*, this is sufficient to measure the intensity profile over the incident beam at $Q = 0$, out into the full SAXS range discussed in the previous section with 2D PSDs in a single USAXS scan. Thus USAXS instruments at a synchrotron can be used in place of SAXS with a 2D PSD, although the signal-to-noise ratio of a well-set-up conventional SAXS instrument is usually better at high Q. The typical Q range of a synchrotron-based USAXS instrument is 0.0001 to 1 Å^{-1}, with the minimum Q also the Q resolution. At the lowest Q values scanned the increment in Q needs to be close to 0.0001 Å^{-1} in order to capture all of the available microstructure information. At larger Q values, the increment can be increased logarithmically to reduce the overall scan times (Ilavsky *et al.*, 2009).

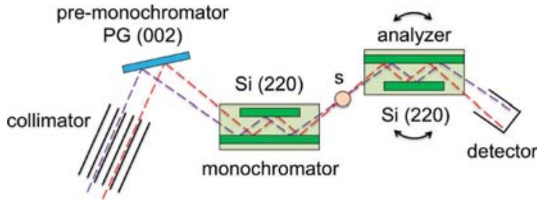

Figure 5.8.4
Schematic of typical USANS configuration at a reactor-based neutron source: s = sample, PG = pyrolitic graphite. Courtesy: J. Barker (NIST Center for Neutron Research).

The high brilliance of third-generation X-ray synchrotrons enables USAXS instrumentation to be developed and enhanced in several ways, some of which are discussed in later sections. However, one modified mode of operation should be mentioned here. While the standard USAXS configuration provides slit-smeared data, the slit smearing can be removed by inserting two transverse crystal pairs, one after the main collimating monolith, and the other before the analyser monolith. This 2D-USAXS configuration is shown in Fig. 5.8.3(*b*). While the USAXS scan still occurs in a single azimuthal direction of **Q**, the data are now unsmeared. Full anisotropic information for a sample can now be obtained by successive USAXS scans with different azimuthal sample orientations.

USANS can extend the SAS Q range to lower minimum Q values than USAXS. This is because the Darwin width of any given crystal's rocking curve for neutron diffraction is intrinsically narrower than for X-rays. However, for many years, the usefulness of USANS was severely limited because of low incident beam flux and the presence of high parasitic background scattering effects. One cause of the background was removed early on by having an odd number of Bragg reflections (usually three) in each crystal pair. This has the effect of removing the instrument from the direct path of parasitic (fast) neutrons coming from the source (Schwahn *et al.*, 1985). However, there remained a major parasitic background contribution, which was ultimately shown to arise from the high penetrating power of neutrons allowing multiple back reflections from the crystals in the collimating and analyser monoliths. In more recent years the problem has been solved by making cuts in the crystals and installing shielding inserts, or otherwise shielding out the contribution from crystal back reflections (Agamalian *et al.*, 1997). While the low incident neutron flux, with respect to X-rays, will probably always limit USANS to providing slit-smeared data in the low-Q regime only, the use of a pyrolitic graphite (PG) pre-monochromator that is convergent in the transverse plane increases the effective incident flux significantly without degrading the instrument performance. With these innovations, very acceptable USANS performance can now be achieved in a Q range from 0.00003 to ~0.005 Å^{-1}, depending on the sample (Barker *et al.*, 2005). This is sufficient to characterize microstructural length scales up to ~30 µm, while also providing overlap with conventional SANS instruments using a 2D PSD, especially with the recent introduction of neutron lenses, discussed in Section 5.8.4. A typical USANS instrument is shown schematically in Fig. 5.8.4. As with USAXS, a point detector is used for USANS, such as a BF_3 gas-filled counter. It must be well shielded against any fast neutron background, and requires sufficient intensity dynamic range to allow scans over the entire incident-beam profile.

5.8.2.3. *Data reduction and calibration of small-angle scattering data*

For all SAS measurements made using transmission geometry, the measured data must be corrected for sample transmission (absorption and other attenuation effects) and for background scattering effects, and then the data must be absolute-calibrated to obtain $d\Sigma/d\Omega$. To do this requires normalizing the scattering intensity to the incident-beam intensity using some monitor detector that provides a measure of the incident-beam intensity (monitor counts) without significantly attenuating it. The monitor counts are usually measured using an ion chamber for SAXS or a fission monitor detector for SANS. X-rays or neutrons, respectively, pass through each of these types of detector with only minimal loss of beam intensity. In the absence of multiple scattering, the sample transmission, T_S, is the ratio of the scattering intensity at $Q = 0$ when the sample is present to that at $Q = 0$ for the empty beam (blank), and is reduced from unity by sample absorption and by all processes in the sample that attenuate the beam *including* SAS. To obtain T_S accurately, the beam intensity is integrated over a region around $Q = 0$ to include the complete profile both of the incident beam (measured without the sample present) and of the transmitted beam measured through the sample.

5.8.2.3.1. *Reduction and calibration of 2D SAS data from a position-sensitive detector*

For a 2D PSD, the intensity, $I_C(i, j)$, in pixel (i, j), normalized to the incident beam and corrected for both electronic background and scattering background effects, is given by (Guinier & Fournet, 1955; Glatter & Kratky, 1982; Kline, 2006; Ilavsky, 2012)

$$I_C(i,j) = \left[\frac{I_S(i,j)}{M_S} - \frac{I_{\rm BGD}(i,j)}{M_{\rm BGD}}\right] - T_S\left[\frac{I_{\rm EB}(i,j)}{M_{\rm EB}} - \frac{I_{\rm BGD}(i,j)}{M_{\rm BGD}}\right], \qquad (5.8.3)$$

where $I_S(i, j)$, $I_{\rm BGD}(i, j)$ and $I_{\rm EB}(i, j)$ are the measured intensities for the sample, the electronic (beam off) dark current background and the empty beam runs, respectively; M_S, $M_{\rm BGD}$ and $M_{\rm EB}$ are the corresponding monitor counts for the incident beam, and T_S is the sample transmission, as defined above. The normalized $I_C(i, j)$ data then need to be calibrated and converted to $d\Sigma/d\Omega$. To do this, the position of the incident beam on the 2D PSD must be determined. This defines the PSD pixel for which $2\theta = Q = 0$. Using the instrument configuration geometry, the scattering angle and azimuthal angle for all other (i, j) pixels can be determined, and hence the corresponding $\mathbf{Q}_{ij}$. In order to complete the intensity calibration and convert the $I_C(i, j)$ or $I_C(\mathbf{Q}_{ij})$ to $d\Sigma/d\Omega$, we can apply from first principles the following relation:

$$\frac{d\Sigma}{d\Omega}(\mathbf{Q}_{ij}) = \frac{I_C(\mathbf{Q}_{ij})}{I_{\rm EB}(0)}\left(\frac{1}{T_{\rm SS}\tau_S\Delta\Omega}\right), \qquad (5.8.4)$$

where $I_{\rm EB}(0)$ is the incident-beam intensity at $Q = 0$ measured under the same conditions as for the sample, τ_S is the sample thickness and $\Delta\Omega$ is the solid angle subtended at the sample by one detector element. For SAS absolute intensity calibration purposes, the sample transmission, $T_{\rm SS}$ in equation (5.8.4), should *exclude* any incident-beam attenuation due to SAS itself. In most practical cases, $T_{\rm SS} \simeq T_S = I_C(0)/I_{\rm EB}(0)$, and the actual measured sample transmission, T_S, can be used in equation (5.8.4) in place of $T_{\rm SS}$. However, if significant multiple scattering is present, the measured $T_S < T_{\rm SS}$, and a multiple-scattering correction must be made (see Section 5.8.2.3.3).

Unfortunately, for most conventional SAS measurements using a 2D PSD, the detector does not have sufficient dynamic range to measure the incident-beam intensity and frequently it must be protected by a beam stop from damage due to exposure to the full incident-beam intensity during SAS measurements. To measure T_S, attenuators are required to protect the PSD during both the sample and empty beam measurements. Nowadays, the accepted best practice is to calibrate the attenuators, and simply multiply the right-hand side of equation (5.8.4) (using the measured T_S in place of $T_{\rm SS}$) by the inverse of the calibrated attenuation factor. However, the intensity calibration can also be carried out using a calibration standard sample. A 'primary' calibration standard may be used, calibrated using the primary (first-principles) relation described in equation (5.8.4) at a SAS instrument where the detector can indeed withstand the full incident-beam intensity. The SAS intensity is then measured at any other instrument for both the standard and the sample(s) of interest. The intensity factor required to put the standard's measured scattering intensity onto its known absolute scale is determined, and this same factor is then used to calibrate data from any 'unknown' sample. A recently established standard of this kind is the NIST Standard Reference Material SRM 3600, which is a SAXS intensity calibration standard based on glass carbon (Allen *et al.*, 2017). Alternatively, a 'secondary' standard can be used, such as a monodispersed silica sphere suspension of known volume concentration. The SAS data can be fitted using one of the models discussed in Section 5.8.3 such as the Guinier approximation, and the data calibrated from the fit result.

Finally, 2D PSD SAS data can be sector-averaged over an azimuthal range to give $d\Sigma/d\Omega$ as a function of $\mathbf{Q}$, where the $\mathbf{Q}$ direction is associated with the mean azimuthal angle of the sector. More usually, when the scattering is circularly symmetric about the incident-beam direction, the data are circularly averaged to give $d\Sigma/d\Omega$ as a function of Q.

5.8.2.3.2. *Reduction and calibration of 1D USAXS or USANS data*

For 1D USAS data, the 2D (i, j) indexing can be replaced from the outset by a 1D indexing of Q values, with the direction of $\mathbf{Q}$ defined by the plane of the instrument's diffraction optics and by the direction of scanning. In USAS measurements it is important that the scattering profile is measured over the centre of the rocking-curve peak in order to establish accurately where $Q = 0$. All other Q values are measured relative to this to give $I_C(Q)$ after applying a 1D form of equation (5.8.3). In both USAXS and USANS instruments, the detector has sufficient intensity dynamic range to measure the incident-beam intensity directly, so that $I_C(Q)$ can be converted to $d\Sigma(Q)/d\Omega$ using a 1D form of equation (5.8.4). For USAS measurements, $\Delta\Omega$ is the product of the angle subtended at the sample by the slit length in the direction transverse to the diffraction plane and the Darwin-based angular diffraction width in the diffraction plane. In the usual case of 1D USAXS or USANS, the calibrated $d\Sigma/d\Omega$ is slit-smeared and should be desmeared as described in Section 5.8.2.2.

5.8.2.3.3. *Corrections for multiple scattering and flat background*

A correction must be applied to the calibration when significant multiple-scattering effects are present. In the case of copious multiple SAS, there is significant broadening of the X-ray or neutron beam profile transmitted through the sample (*i.e.*, no unscattered beam survives passage through the sample). This situation is usually associated with a high concentration of strongly scattering coarse features, and a specialized analysis is required (Berk & Hardman-Rhyne, 1985, 1988). For the usual case, where the SAS remains distinguishable from the transmitted beam profile but where the total probability of small-angle scattering is greater than 5–10% of the incident beam, a more subtle correction suffices. Schelten & Schmatz (1980) developed a treatment of this situation that is still widely used at SANS facilities, but can also be applied to SAXS. In fact, any distortion of the scattering profile at low Q due to multiple scattering cannot easily be corrected. However, an intensity correction may be made that at least calibrates the intensity correctly for data at higher Q values. In this situation, T_S, measured simply from the ratio $I_C(0)/I_{\rm EB}(0)$, while remaining correct for subtracting out scattering from the blank in equation (5.8.3), is significantly underestimated for use in the calibration equation (5.8.4). It should be replaced with a corrected (larger) transmission, $T_{S\ \rm corr}$, which is obtained by integrating $I_C(Q)$ and $I_{\rm EB}(Q)$ from $Q = 0$ out to a Q value beyond which multiple scattering is negligible for the sample being studied. The ratio of the integrals then gives $T_{S\ \rm corr}$ [$= T_{\rm SS}$ in equation (5.8.4)].

Finally, many samples show flat background-scattering contributions in addition to the true SAS contribution. For X-rays, this arises from parasitic scattering contributions such as air scattering or scattering from the windows of the sample cell. For neutrons, incoherent flat background scattering results from the difference in the neutron interaction with a nuclide depending on whether the neutron and nuclear spins are parallel or anti-parallel. The average of the two cases gives rise to the coherent scattering on which SANS and ND are based. The spatially random fluctuations between the two cases leads to an incoherent flat background. For X-rays or neutrons, the flat background scattering should be subtracted out before applying the various interpretation models described in Section 5.8.3. If the flat background scattering is obvious at high Q, it can be directly subtracted out. If not, it can sometimes be determined by fitting the Porod scattering at high Q (see Section 5.8.3.1.2).

5.8.2.4. *Reflectivity, grazing-incidence small-angle scattering and diffraction*

All of the SAS methods discussed in previous sections assume transmission measurement geometry, but this precludes a major class of heterogeneous material systems of increasing technological importance: thin-film microstructures on a substrate. For such systems SAS and related measurements in reflection geometry are of interest. X-ray and neutron reflectivity (XRR and NR), where $\mathbf{Q}$ is perpendicular to the substrate, provide depth-dependent structural information for a thin film (Parratt, 1954). Grazing-incidence SAXS and SANS (GI-SAXS and GI-SANS), and, utilizing the high penetrating power of neutrons for thicker layers and coatings, near-surface SANS (NS-SANS) can provide microstructural information both as a function of film depth and within the plane of the film (Levine *et al.*, 1991; Hamilton *et al.*, 1996). Owing to the greater penetrating power of neutrons, NR and NS-SANS are more applicable to thicker coatings or to buried interfaces than are XRR or GI-SAXS, which are more applicable to thin films. The lower penetrating power of X-rays is frequently an advantage where information is sought on disordered or ordered structures within a film without the reflectivity or scattering data being affected by contributions from the substrate. Although NR and NS-SANS can provide important information in certain situations, thicker coatings *etc.* can usually be removed from the substrate for analysis, in section or in plane, using transmission geometry (at least with X-rays). However, thin films 10 Å to a few hundred ångstroms thick (which may or may not be disordered in nature) cannot usually be removed from the substrate, and must be studied with X-rays rather than neutrons. So, in this section, we concentrate on XRR and GI-SAXS.

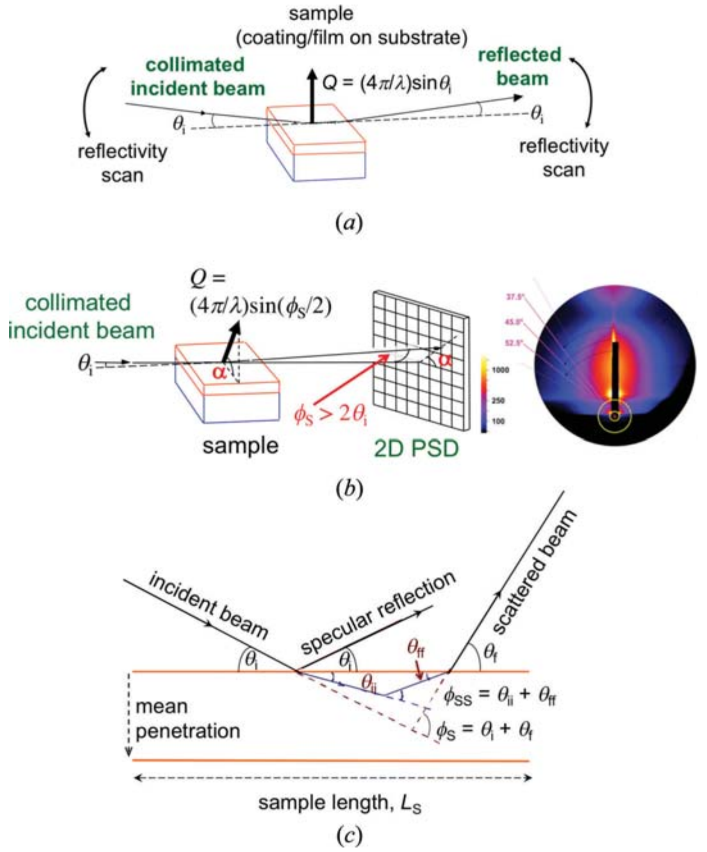

Figure 5.8.5
(*a*) Schematic of basic reflectivity measurement geometry for XRR or NR. (*b*) Schematic derived from Green *et al.* (2009) for GI-SAXS also showing typical 2D GI-SAXS data with sector averages. (*c*) Refraction and reflection geometries for GI-SAXS or NS-SANS, as discussed in the text.

Fig. 5.8.5(*a*) shows a schematic of the basic measurement geometry for XRR or NR, while Fig. 5.8.5(*b*) presents a corresponding schematic for GI-SAXS or NS-SANS. For specular reflectivity the direction of $\mathbf{Q}$ is perpendicular to the substrate plane and so information is obtained on through-thickness features, as well as effects due to surface roughness. In GI-SAXS or NS-SANS, components of $\mathbf{Q}$ are both perpendicular to the substrate ($\mathbf{q}_z$) and, depending on the azimuthal angle α, parallel to the substrate ($\mathbf{q}_y$). Thus, in-plane microstructure information is obtainable.

In reflectivity measurements, the intensity of the reflected beam is measured as a function of the incident angle, θ_i ($= \theta_r$). In a reflectivity scan the sample is rotated through θ_i angles from 0° to the maximum θ_r ($\theta_{r\rm MAX}$) for which a measurable reflected beam intensity can be detected, while the detector angle, $2\theta_r$, is rotated from 0° to $2\theta_{r\rm MAX}$. In principle, the reflectivity, $R(\theta_r)$, can be defined as $R(\theta_r) = I(\theta_r)/I(0)$, where $I(\theta_r)$ and $I(0)$ are the measured intensities of the reflected beam for θ_r and for 0°, respectively. In practice, the increasing length of the beam footprint on the sample for decreasing $\theta_i = \theta_r$ values results in a loss of reflected intensity once the footprint is longer than the sample dimension in the reflection plane, requiring a correction to be made for the consequent loss in intensity actually incident on the sample. Furthermore, for a well aligned sample geometry at $\theta_r = 0°$ the sample, seen edge-on, absorbs half of the incident beam while the other half of the incident beam does not impinge on the sample at all. Thus, direct measurement of $I(0)$ requires removal of the sample. Once corrected, $R(\theta_r) = 1$ for θ_i ($= \theta_r$) $< \theta_C$, where θ_C is the critical angle for total reflection given by $\theta_C = \lambda\{|\Delta\rho|/\pi\}^{1/2}$ and $|\Delta\rho|$ is the difference in scattering-length density across the reflecting interface. Corrected reflectivity data for $R(\theta_r)$ *versus* θ_r over sufficient angular range, and with sufficient angular resolution, must be obtained to capture the structural information associated with the thin-film layer(s). For practical purposes, laboratory-based X-ray sources can provide the required dynamic range in $R(\theta_r)$ for XRR measurements of films thicker than ~100 Å. For thinner films, measurements at least at a first-generation synchrotron are required, and it is usually necessary to determine the reflectivity curve from the surface of the bare substrate in order to correct for any substrate artifacts not associated with the thin-film structure of interest. Frequently, it is convenient to convert the θ_r values to Q [$= (4\pi/\lambda)\sin\theta_r$] and do further analysis on corrected data for $R(Q)$ *versus* Q, together with uncertainties in $R(Q)$.

In GI-SAXS or NS-SANS measurements the sample is oriented at a fixed grazing incident angle, θ_i, to the incident-beam direction ($\theta_i > \theta_C$ for scattering from within the film) and the data are collected using a 2D PSD as for conventional transmission geometry SAXS or SANS. Measurements can be made using different values of θ_i, and the different 2D scattering data analysed to determine how the film microstructure changes with depth. By reducing θ_i below θ_C, it can be established whether the microstructure that causes the scattering is within the film or is located on the surface. The location where the incident beam impinges on the sample (required for calculating where $Q = 0$ on the 2D detector), as well as the parasitic scattering contribution, can only be determined by moving the sample out of the beam. With the sample in place, both the incident beam and scattering that would be in the sample shadow as viewed from the 2D detector are occluded and unobservable. Also, the specularly reflected incident beam further obscures the data at low Q, and effectively increases the minimum observable Q. Refraction corrections must be applied to both the incident and scattered X-ray or neutron beam directions, and normalization to obtain $d\Sigma/d\Omega$ is complicated both by the complex effective sampling volume and the need to apply the distorted-wave Born approximation (DWBA) in the data reduction and analysis when multiple reflection and scattering contributions exist (Sinha *et al.*, 1988).

For a thick film of refractive index n, given by $n^2 = 1 - \theta_C^2$, Fig. 5.8.5(*c*) illustrates the situation for scattering in the refraction plane. For an external grazing-incidence angle θ_i, an external scattered grazing angle θ_f and apparent scattering angle φ_S ($= \theta_i + \theta_f$), measured outside the film, the corresponding angles inside the film are θ_{ii}, θ_{ff} and φ_{SS} ($= \theta_{ii} + \theta_{ff}$), where $\theta_{ii}^2 = \theta_i^2 - \theta_C^2$ and $\theta_{ff}^2 = \theta_f^2 - \theta_C^2$. For a finite azimuthal angle α, the outgoing scattered grazing angles are reduced to θ_2 and θ_{22} where $\theta_2 = \theta_f\cos\alpha$ and $\theta_{22}^2 = \theta_2^2 - \theta_C^2$. Refraction effects cause corresponding changes in the components of $\mathbf{Q}$. While the component parallel to the substrate, q_P, is the same inside or outside the film, *i.e.* $q'_P = q_P$, the component normal to the film, q_N, is changed by the refraction at the film boundary, so that inside the film $q'_N = q_N[\cos\theta_i(\sin\theta_{ii} + \sin\theta_{22})]/[\cos\theta_{ii}(\sin\theta_i + \sin\theta_2)]$ and Q' inside the film is given by $Q'^2 = Q^2 - q_N^2 + q'^2_N$, where Q is the apparent external value. The refraction causes all terms in the SAS expressions to change and for a thick film (where reflection from the film/substrate interface can be ignored) it can be shown that inside the film

$$\frac{d\Sigma'}{d\Omega'}(Q') = \left[\cot\theta_{ii} + \cot\theta_{22}\right]\left(\frac{\sin\theta_{22}}{\sin\theta_2}\right)\left(\frac{1}{T_S\sin\theta_{ii}}\right) \times \left[\frac{(\sin\theta_i + n\sin\theta_{ii})}{\sin\theta_i}\right]^2 \frac{d\Sigma}{d\Omega}(Q), \qquad (5.8.5)$$

where $T_S = 2[\exp(-\Sigma_T L_S) + \Sigma_T L_S - 1]/(\Sigma_T L_S)^2$ is the theoretical transmission of the sample film of length L_S along the beam direction and it is assumed that the film material has a total attenuation cross section of Σ_T. The value of Σ_T determines whether a film of thickness $\tau_{\rm film}$ can be considered thick or whether it must be treated as a thin film with the full DWBA formalism applied. The maximum penetration depth, $\zeta_{\max}$, measurable for a given scattering geometry is given by $\zeta_{\max} = L_S/[\cot\theta_{ii} + \cot\theta_{22}]$. However, the mean penetration depth $\zeta_{\rm mean} = \zeta_{\max}(1/\Sigma_T L_S)[2 + \Sigma_T L_S - (2/T_S)]$. While generally $\zeta_{\rm mean} \ll \zeta_{\max}$, the criterion for a thick film is that $\zeta_{\rm mean} \ll \tau_{\rm film}$.

5.8.2.5. *Wide-angle scattering and other methods for disordered structures*

As mentioned in Section 5.8.1, a heterogeneous material system may contain crystalline components even if the heterogeneous arrangement of those components is itself disordered. For the SAS and reflectivity measurements discussed in Section 5.8.2.4, a fully quantitative analysis is only possible if the elemental composition and density of each of the components are known. This information is required in order to determine accurately the $|\Delta\rho|^2$ contrast-factor term in equation (5.8.2*a*). Thus, wide-angle and powder-diffraction measurements that enable any component crystalline phases to be identified can play a critical role. General powder-diffraction characterization is covered elsewhere in this volume. However, when *in situ* studies of a disordered material undergoing some change in real time are of interest, the use of WAXS and WANS to monitor specific diffraction peaks associated with crystalline phases that may be present, even if only transitory in nature, can provide key information. Several combined SAXS/WAXS instruments have been developed at third-generation X-ray synchrotron-radiation sources to enable the simultaneous study of microstructure evolution and the appearance or disappearance of crystalline phases within the microstructure (Lai *et al.*, 2006).

Finally, some attention must be given to total-scattering methods that have evolved in recent years to interrogate the short-range or limited-range crystalline structure that can be encountered in disordered materials. These have evolved from earlier 'liquids amorphous' methods (mainly neutron-based) to quantify structure in materials with little or no crystalline structure, such as glasses (Price, 1999). However, these methods now extend to a wide range of nanocrystalline or poorly crystalline materials. The basis of such measurements is to collect contiguous data over a very large Q range with sufficient resolution and intensity throughout the Q range to quantify the degree and scale range of structure present. These requirements tend to confine such instruments to third-generation X-ray synchrotrons and pulsed-neutron-source facilities that can accommodate long beamlines. However, these instruments are now making significant progress in interrogating the whole range of disordered materials at the structural level (Billinge & Levin, 2007; see also Chapter 5.7).

For powder-diffraction studies, the coherent diffraction intensity, $I_{\rm coh}$, from an ensemble of N atoms is given by (Warren, 1990; Farrow & Billinge, 2009)

$$I_{\rm coh} = \sum_{i,j} b_j^* b_i \exp(i\mathbf{Q}\cdot\mathbf{r}_{ij}) = N\langle b^2\rangle + \sum_{i\neq j} b_j^* b_i \exp(i\mathbf{Q}\cdot\mathbf{r}_{ij}), \tag{5.8.6}$$

where b_i and b_j are the neutron scattering lengths or X-ray form factors per atom at sites i and j, respectively, $\mathbf{r}_{ij} = \mathbf{r}_i - \mathbf{r}_j$, b^* denotes a complex conjugate as a function of $\mathbf{Q}$, and $\langle b^2\rangle$ is the mean-square value of b_i or b_j. The total-scattering structure factor per atom, $S(\mathbf{Q})$, describes the scattering between the atoms in an ensemble, and is given by

$$S(\mathbf{Q}) = 1 + \frac{\sum_{i\neq j} b_j^* b_i \exp(i\mathbf{Q}\cdot\mathbf{r}_{ij})}{N\langle b\rangle^2}, \tag{5.8.7}$$

where $S(\mathbf{Q}) = 1$ for isolated atoms. We note that, for neutrons, b_i and b_j are isotropic and independent of Q for scattering from the nucleus. For X-ray scattering or magnetic neutron scattering from the atomic electron distribution a correction is required at high Q because of the finite size of the atom, but this can be neglected at least for the forward scattering. Thus, for an isotropic microstructure, the Debye relation that the orientational average of $\exp(i\mathbf{Q}\cdot\mathbf{r}_{ij})$ is equal to $\sin(Qr_{ij})/Qr_{ij}$ can be used to give

$$S(Q) - 1 = \left(\frac{1}{N\langle b\rangle^2}\right) \sum_{i\neq j} b_j^* b_i \left[\frac{\sin(Qr_{ij})}{Qr_{ij}}\right]. \tag{5.8.8}$$

The Q dependence can be removed from everything except for the sine term by using the reduced total-scattering structure factor, $S_{\rm RT}(Q)$, where

$$S_{\rm RT}(Q) = Q[S(Q) - 1] = \left(\frac{1}{N\langle b\rangle^2}\right) \sum_{i\neq j} b_j^* b_i \left[\frac{\sin(Qr_{ij})}{r_{ij}}\right]. \tag{5.8.9}$$

The sine Fourier transform of $S_{\rm RT}(Q)$ gives the real-space function $G(r)$, where

$$G(r) = (2/\pi) \int\limits_0^\infty S_{\rm RT}(Q) \sin(Qr)\,{\rm d}Q, \tag{5.8.10}$$

and by substituting equation (5.8.10) into equation (5.8.9), we get (for positive r)

$$G(r) = \left(\frac{1}{rN\langle b\rangle^2}\right) \sum_{i\neq j} b_j^* b_i \delta(r - r_{ij}), \tag{5.8.11}$$

where $\delta(x)$ denotes a Dirac delta function. It is clear that $G(r)$ is a pair density distribution function, as can be shown by considering the case of an ensemble of N identical atoms:

$$\int\limits_a^b G(r) r\,{\rm d}r = N_{ab} = \int\limits_a^b 4\pi r^2 n(r)\,{\rm d}r, \tag{5.8.12}$$

where N_{ab} is the number of atoms found between a radius $r = a$ and a radius $r = b$, measured from any one atom, and $n(r)$ is the atomic number density distribution measured similarly as a function of r, thus allowing a radial distribution function, $Y(r)$, to be defined by $Y(r) = 4\pi r^2 n(r)$.

Algorithms now exist to extract $G(r)$ *versus* r from measured $I_{\rm coh}$ data *versus* Q, *via* the derived $[S(Q) - 1]$ and $S_{\rm RT}(Q)$ functions (Juhás *et al.*, 2013). Fig. 5.8.6 shows both typical total-scattering $[S(Q) - 1]$ (model) data *versus* Q and the derived atomic pair distribution function, $G(r)$ *versus* r. In practice, the inverse Fourier sine transform of equation (5.8.10) has finite Q limits. In particular, there is always a finite minimum Q for which the scattering and hence $S(Q)$ can be measured. Loss of the non-measurable scattering contribution near $Q = 0$ leads to a subtraction from the calculated pair distribution function, $G(r)$, that can be associated with the scattering from structure at large r. In the case of a uniform bulk material microstructure, including many glasses, the subtracted component is simply related to the averaged atomic scattering-length density, n_0, applicable over large distances, and it can be shown that (Cargill, 1971; Farrow & Billinge, 2009)

$$G(r) = 4\pi r\big[n(r) - n_0\big]. \tag{5.8.13}$$

Disordered structures can be evaluated using equations (5.8.6)–(5.8.13) in the case of bulk materials. However, when the disordered elements themselves comprise an ensemble of nanocrystalline features, the $-4\pi r n_0$ term becomes more complex; this situation is discussed further in the next section.

Meanwhile, noise in the WAXS data at high Q can cause oscillatory artifacts to appear in the $G(r)$ function because of data truncation at a finite maximum Q. These can be removed by smoothing the data, but this still results in some loss of information in the extracted $G(r)$ function if the level of smoothing required either significantly exceeds that due to finite instrument resolution in Q, or it reduces peak intensities significantly more

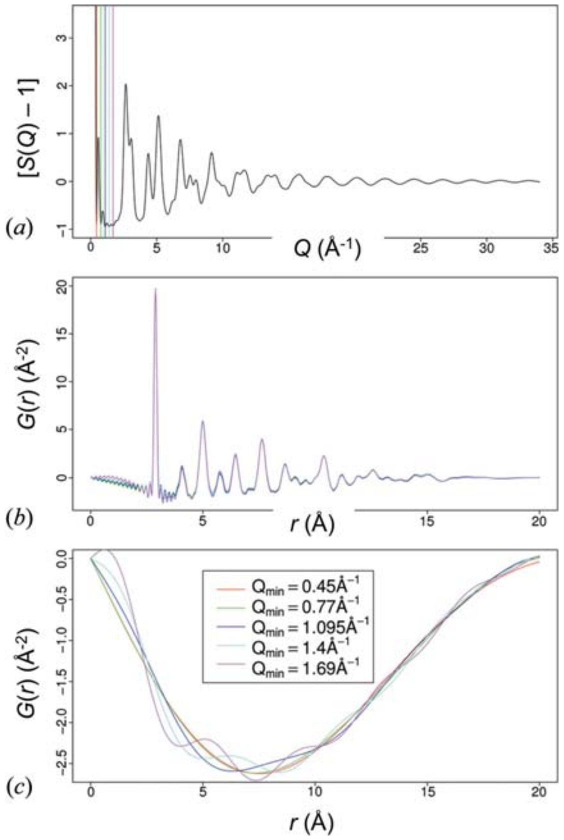

Figure 5.8.6

(*a*) Schematic of typical total-scattering $[S(Q) - 1]$ data *versus* Q for model Au core–shell nanoparticles. Choices of partition between small- and wide-angle scattering are marked by vertical lines. (*b*) The corresponding atomic pair density distribution function, $G(r)$, *versus* r, obtained *via* Fourier transform of wide-angle scattering data only, starting from various minimum Q values ($Q_{\rm min}$). (*c*) The Fourier transform of data in the SAS range from $Q = 0$ to $Q = Q_{\rm min}$ for various $Q_{\rm min}$. The $-4\pi r n_0$ term of equation (5.8.13) arising from the non-measurable scattering at $Q = 0$ is visible at low Q, but the rest of the function is related to $\gamma_0(r)$ described in Section 5.8.3.2 for nanoparticle scattering. Adapted from Mullen & Levin (2011).

than the Debye–Waller effect (see Section 5.8.3.3) of thermal diffuse scattering (Toby & Egami, 1992).

5.8.3. Quantitative analysis of disordered heterogeneous materials

In Section 5.8.2 we have set out the main experimental measurement techniques, the kind of data obtainable and how the data should be reduced to provide information on the sample material system of interest. In this section we consider how such data should be interpreted to quantify actual structural and microstructural parameters of interest for disordered material systems. It is not possible to cover every interpretative scheme in existence, but the main classes of interpretative schemes and models are reviewed to give a sense of the range of analyses possible.

5.8.3.1. *Interpretative models for analysis of SAS data*

5.8.3.1.1. *Guinier approximation*

Assuming any flat background scattering has been subtracted, the heterogeneous system is sufficiently disordered and dilute that the structure-factor term, $S(Q)$, in equation (5.8.2*a*) can be assumed to be unity and the inhomogeneities are approximately monodispersed in size and shape, perhaps the simplest interpretative approximation for SAS data is the Guinier approximation (Guinier & Fournet, 1955):

$$\frac{\mathrm{d}\Sigma}{\mathrm{d}\Omega} = \Phi_V|\Delta\rho|^2 V_P \exp\left(-\frac{Q^2R_G^2}{3}\right), \quad QR_G < {\sim}1, \qquad (5.8.14)$$

where R_G is the Guinier radius (mean radius of gyration) of the scattering features. For spherical particles or voids of radius R_P, $R_G^2 = 3R_P^2/5$ and $V_P = 4\pi R_P^3/3$. While the approximation is only valid for $QR_G < {\sim}1$, equation (5.8.14) clearly shows how the width of the scattering profile is inversely related to the size of the scattering features. We also note that the SAS intensity is proportional both to the volume fraction of scattering features present and to their individual mean volumes. Thus, SAS methods will be strongly volume-weighted over any size distribution of inhomogeneities that may actually be present.

5.8.3.1.2. *Porod scattering regime*

At high Q values the SAS intensity can be related to the specific surface area of the scattering features (Porod, 1951, 1952):

$$\frac{\mathrm{d}\Sigma}{\mathrm{d}\Omega} = \frac{2\pi|\Delta\rho|^2 S_V}{Q^4} + \mathrm{BGD}, \quad QR_G \gg 1, \qquad (5.8.15)$$

where S_V is the surface area per unit sample volume and BGD is any residual flat background scattering that needs to be considered at high Q where the true SAS scattering intensity is weak. Frequently, it is convenient to plot $Q^4\,\mathrm{d}\Sigma/\mathrm{d}\Omega$ *versus* Q^4 for high Q and fit a straight-line slope of gradient BGD and intercept $2\pi|\Delta\rho|^2 S_V$. (Note that this provides a means of determining the flat background, BGD.) Thus, just as equation (5.8.14) provides information on the volume fraction of the inhomogeneities in a disordered system, equation (5.8.15) provides the corresponding surface-area information – provided that the contrast factor, $|\Delta\rho|^2$, is known. Even when $|\Delta\rho|^2$ is not known, the ratio of the two front terms of these equations provides the surface area per unit volume of the individual inhomogeneities themselves, because $|\Delta\rho|^2$ cancels out.

5.8.3.1.3. *Scattering invariant*

The volume fraction of the inhomogeneous features giving rise to SAXS or SANS can be more generally related to the overall scattering through the so-called scattering invariant (Glatter & Kratky, 1982), which is essentially the SAS intensity integrated over all **Q**:

$$2\pi^2\Phi_V(1-\Phi_V)|\Delta\rho|^2 = \int\limits_0^\infty Q^2\frac{\mathrm{d}\Sigma}{\mathrm{d}\Omega}(Q)\,\mathrm{d}Q, \qquad (5.8.16)$$

where the integral is taken over all Q values (equivalent to scattering over a 4π solid angle). In principle, if $|\Delta\rho|^2$ is known, the volume fraction of the scattering features, Φ_V, can be determined independently of the specific morphology or disordered arrangement. Experimentally, the integrand on the right-hand side of equation (5.8.16) must usually be extrapolated beyond the measured Q range, both at low Q and at high Q where the Q^2-weighted SAS intensity is weak and a careful flat background subtraction must be made.

5.8.3.1.4. *Debye–Bueche model*

While many disordered material systems contain discrete particles or pores that comprise the inhomogeneities giving rise to SAS, this is not necessarily the case. For example, polymer blends may contain separate (non-mixing) phases separated by an interface that permeates throughout the sampling volume. Assuming the two phases (1 and 2) permeate the sampling volume randomly with a characteristic (Debye) length ξ, then it can be shown that the scattering is given by (Debye & Bueche, 1949)

$$\frac{\mathrm{d}\Sigma}{\mathrm{d}\Omega} = \frac{8\pi\xi^3\Phi_{1V}\Phi_{2V}|\Delta\rho|^2}{(1+Q^2\xi^2)^2}, \qquad (5.8.17)$$

where Φ_{1V} and Φ_{2V} are the volume fractions of the two phases ($\Phi_{1V} + \Phi_{2V} = 1$) and $|\Delta\rho|^2$ is the scattering contrast factor between phases 1 and 2. Assuming that $|\Delta\rho|^2$ is known, a Lorentzian function can be fitted to obtain ξ from the intensity variation in Q, then Φ_{1V} and Φ_{2V} determined from the absolute scattering intensity, together with the constraint that they must sum to unity. We also note that, in the limit of high Q, equation (5.8.17) gives Porod Q^{-4} scattering, and the surface area, S_v, so obtained can be related to the variables Φ_{1V}, Φ_{2V} and ξ determined by $S_v = 4\Phi_{1V}\Phi_{2V}/\xi$.

5.8.3.1.5. *Shape effects in the form factor*

As we have indicated, equations (5.8.14) and (5.8.15) provide working approximations for the scattering intensity at low Q and at high Q for a dilute population of randomly oriented scattering features. However, analytical expressions have been established for the scattering intensity at all Q for dilute populations of randomly oriented scattering features of specific shape that are also monodispersed in size and shape. For example, see Pedersen (1997). Here we summarize a few of the more significant generic expressions for $\mathrm{d}\Sigma/\mathrm{d}\Omega$ associated with scattering features of specific shape (also see Fig. 5.8.7):

(i) *Spheroidal features of orthogonal radii R_O, R_O, βR_O* (Shull & Roess, 1947; Roess & Shull, 1947):

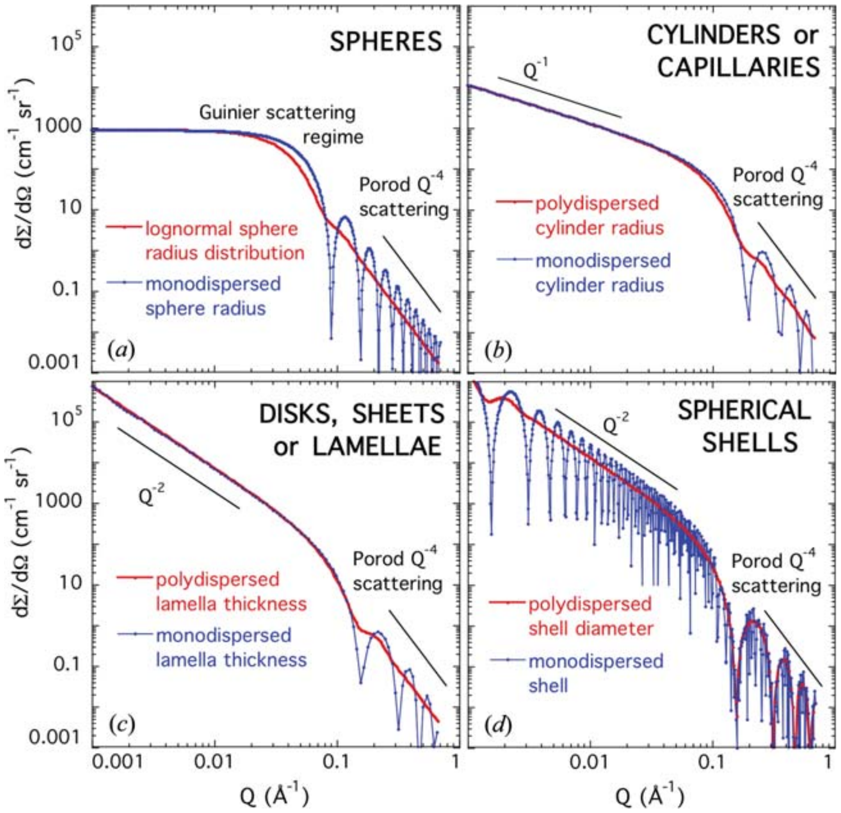

Figure 5.8.7

Characteristic SAS intensity profiles of ensembles of scattering features, both monodispersed and polydispersed in size. (*a*) Spheres of mean diameter 100 Å; (*b*) cylinders or capillaries of mean diameter 40 Å and length 4000 Å; (*c*) discs or lamellae of mean thickness 40 Å and diameter 4000 Å; and (*d*) spherical shells of mean diameter 4000 Å and fixed shell thickness 40 Å. Porod scattering and other characteristic power laws are indicated. Note that 20% polydispersity in size is sufficient to eliminate much of the Bessel-function oscillation found in the scattering from monodispersed features. Functions are derived using software developed by S. R. Kline of NIST Center for Neutron Research (Kline, 2006).

$$\frac{\mathrm{d}\Sigma}{\mathrm{d}\Omega} = \Phi_V|\Delta\rho|^2 V_P \frac{9\pi}{2}\int_0^1 \frac{\left[J_{3/2}(u)\right]^2}{u^3}\,\mathrm{d}X, \qquad (5.8.18)$$

where $V_P = 4\pi\beta R_O^3/3$, the ordinary Bessel function $J_{3/2}(u) = (2/\pi)^{1/2}(\sin u - u\cos u)/u^{3/2}$, $u = QR_O K(\beta, X)$, $K(\beta, X) = [1 + (\beta^2 - 1)X^2]^{1/2}$, $X = \cos\eta$, and η is the angle between the direction of **Q** and the βR_O axis of the spheroid. In the case of $\beta = 1$ we get for spherical features

$$\frac{\mathrm{d}\Sigma}{\mathrm{d}\Omega} = \Phi_V|\Delta\rho|^2 V_P \left[3\left(\frac{\sin(QR_O) - QR_O\cos(QR_O)}{(QR_O)^3}\right)\right]^2. \qquad (5.8.19)$$

The average intensity of the Bessel function oscillations in equations (5.8.18) and (5.8.19) can be approximated as a function of Q: in the small-Q regime by equation (5.8.14) where $R_G^2 = (2 + \beta^2)R_O^2/5$, and in the large-$Q$ regime by equation (5.8.15) where, for a spheroid,

$$S_V = \frac{3\Phi_V \chi_S}{R_O} \qquad (5.8.20a)$$

$$\chi_S = \frac{1}{2\beta}\left\{1 + \frac{\beta^2}{(1-\beta^2)^{1/2}}\ln\left[\frac{1 + (1-\beta^2)^{1/2}}{\beta}\right]\right\} \quad \beta \le 1, \qquad (5.8.20b)$$

$$\chi_S = \frac{1}{2\beta}\left\{1 + \frac{\beta^2}{(\beta^2-1)^{1/2}}\arcsin\left[\frac{(\beta^2-1)^{1/2}}{\beta}\right]\right\} \quad \beta \ge 1, \qquad (5.8.20c)$$

and we note that $\chi_S = 1$ for $\beta = 1$.

(ii) *Discs, sheets or laminar pores of diameter $2R_D$ and thickness τ_D, where $\tau_\Delta \ll 2R_D$* (Guinier & Fournet, 1955; Glatter & Kratky, 1982). Again, assuming a dilute ensemble of randomly oriented scattering features, it can be shown that

$$\frac{\mathrm{d}\Sigma}{\mathrm{d}\Omega} = \Phi_V|\Delta\rho|^2 V_P \int_0^1 \left| 2J_O\left(\frac{Q\tau_D X}{2}\right)\frac{J_1\left[QR_D(1-X^2)^{1/2}\right]}{QR_D(1-X^2)^{1/2}}\right|^2 \mathrm{d}X, \qquad (5.8.21a)$$

where $X = \cos\eta$ and η is the angle between the axis of the disc and the direction of **Q**, here $V_P = \pi R_D^2\tau_D$, and the spherical Bessel functions are given by $J_0(u) = \sin u/u$ and $J_1(v) = (\sin v - v\cos v)/v^2$. Equation (5.8.21*a*) is in fact valid for all values of τ_D and R_D, but for $\tau_D \ll 2R_D$ and neglecting the Bessel-function oscillations, the scattering intensity follows a Q^{-2} power law in the regime $R_D^{-1} \ll Q \ll 2\tau_D^{-1}$ and a Q^{-4} Porod power law for $Q \gg 2\tau_D^{-1}$. For near-infinitesimal τ_D, $\mathrm{d}\Sigma/\mathrm{d}\Omega$ is given by

$$\frac{\mathrm{d}\Sigma}{\mathrm{d}\Omega} = \Phi_V|\Delta\rho|^2 V_P\left[1 - \frac{J_1(2QR_D)}{QR_D}\right]\frac{2}{(QR_D)^2}, \qquad (5.8.21b)$$

where the spherical Bessel function $J_1(v) = (\sin v - v\cos v)/v^2$ and there is no Porod Q^{-4} scattering. The terminal slope $\simeq Q^{-2}$ for $Q \gg R_D^{-1}$. There is, however, a Guinier regime at low Q with $R_G^2 = R_D^2/2$.

(iii) *Cylinders, rods or capillary pores of radius r_C and length L, where $L \gg 2r_C$* (Guinier & Fournet, 1955; Glatter & Kratky, 1982):

$$\frac{\mathrm{d}\Sigma}{\mathrm{d}\Omega} = \Phi_V |\Delta\rho|^2 V_P \int\limits_0^1 \left| 2J_O\left(\frac{QLX}{2}\right) \frac{J_1\left[Qr_C(1-X^2)^{1/2}\right]}{Qr_C(1-X^2)^{1/2}} \right|^2 \mathrm{d}X, \tag{5.8.21c}$$

where $X = \cos\eta$ and η is the angle between the axis of the cylinder and the direction of $\mathbf{Q}$; here $V_P = \pi {r_C}^2 L$, and the spherical Bessel functions are given by $J_0(u) = \sin u/u$ and $J_1(v) = (\sin v - v\cos v)/v^2$. Again, equation (5.8.21c) is valid for all r_C and L, and is in fact mathematically identical to equation (5.8.21a). However, for $L \gg 2r_C$ and neglecting the Bessel-function oscillations, the scattering intensity follows a Q^{-1} power law in the regime $2L^{-1} \ll Q \ll r_C^{-1}$ and a Q^{-4} Porod power law for $Q \gg r_C^{-1}$. For near-infinitesimal r_C, $\mathrm{d}\Sigma/\mathrm{d}\Omega$ is given by

$$\frac{\mathrm{d}\Sigma}{\mathrm{d}\Omega} = \Phi_V |\Delta\rho|^2 V_P \left[\frac{2S_i(QL)}{QL} - \frac{\sin^2(QL/2)}{(QL/2)^2}\right], \tag{5.8.21d}$$

where $S_i(QL) = \int_0^{QL} (\sin u/u)\,\mathrm{d}u$. In this case, there is again no Porod Q^{-4} scattering and the terminal slope $\simeq Q^{-1}$ for $Q \gg 2L^{-1}$, but there is a Guinier regime at low Q with ${R_G}^2 = L^2/12$.

(iv) *Gaussian coil morphology (common in polymer science)* (Debye, 1947). SAS (especially SANS) has been applied to a myriad of situations in polymer science. It is not possible here to include all of the form factors of interest, and these have been reviewed elsewhere (Pedersen, 2000). Nevertheless, we include one generic case, common in polymer science, which is that of a polymer Gaussian coil with mean radius of gyration R_G and mean volume V_P:

$$\frac{\mathrm{d}\Sigma}{\mathrm{d}\Omega} = \Phi_V |\Delta\rho|^2 V_P \left\{ 2\frac{\left[\exp\left(-Q^2R_G^2\right) + Q^2R_G^2 - 1\right]}{Q^4R_G^4} \right\}. \tag{5.8.22}$$

In many practical polymer applications, it is convenient to re-write Φ_V and V_P in terms of the polymer molecular mass and density. It should be noted that for $QR_G \gg 1$, equation (5.8.22) predicts that $\mathrm{d}\Sigma/\mathrm{d}\Omega \simeq Q^{-2}$, similar to the power law found for the scattering from thin discs.

(v) *Core–shell particles* (Guinier & Fournet, 1955). Many SAS applications involve core–shell particles of one kind or another. These range from quantum-dot nanoparticles involving more than one component, through many systems where the scattering particles are coated with other organic or inorganic species, to the entire class of hollow particles (including micelles and vesicles). It is not feasible to cover all core–shell particle types here, but a generic example is given for guidance. Essentially, the SAS intensity for a core–shell particle is determined by considering it as an inner particle inside an outer particle. The form factor of the inner particle core with respect to the shell is summed coherently with the form factor of the outer particle with respect to the external medium. For a spherical core–shell particle of overall (shell) radius, $R_{\rm shell}$ and internal (core) radius, $R_{\rm core}$, with X-ray or neutron scattering-length densities $\rho_{\rm shell}$, $\rho_{\rm core}$ and ρ_O, respectively, for the shell, core and external (solvent) medium

$$\begin{aligned}\frac{\mathrm{d}\Sigma}{\mathrm{d}\Omega} &= \\ \frac{\Phi_V}{V_P}&\left| \left\{ 3V_C(\rho_{\rm core} - \rho_{\rm shell}) \frac{\left[\sin(QR_{\rm core}) - QR_{\rm core}\cos(QR_{\rm core})\right]}{(QR_{\rm core})^3} \right\} \right. \\ &\left. + \left\{ 3V_P\left(\rho_{\rm shell} - \rho_O\right) \frac{\left[\sin(QR_{\rm shell}) - QR_{\rm shell}\cos(QR_{\rm shell})\right]}{(QR_{\rm shell})^3} \right\} \right|^2,\end{aligned} \tag{5.8.23}$$

where Φ_V is the volume fraction of the overall particles of volume $V_P = 4\pi R_{\rm shell}^3/3$, and $V_C = 4\pi R_{\rm core}^3/3$. Equation (5.8.23) can be re-written in terms of the core volume and core volume fraction, or the shell volume and shell volume fraction, by re-scaling Φ_V and V_P appropriately. While the equations become more complex, the same basic principle applies to the scattering intensity from other core–shell particle shapes. For a hollow particle where $\rho_{\rm core} = \rho_O$, the inner particle is essentially subtracted from the outer particle in the form-factor term before squaring. In such a case where the shell thickness $\tau_{\rm shell} \ll R_{\rm core}$ (and $R_{\rm shell}$), equation (5.8.23) gives Q^{-2} scattering in the regime $R_{\rm core}^{-1} \ll Q \ll \tau_{\rm shell}^{-1}$. Note that this is the third scenario discussed in this section where Q^{-2} scattering is observed. Prior knowledge is needed in such scenarios to determine which one applies.

The characteristic SAS intensity as a function of Q is illustrated for several of the above scenarios in Fig. 5.8.7. The scattering from randomly oriented, monodispersed scattering features is compared with that from polydispersed scattering features of the same shape, where the FWHM of the size distribution is ~20%.

5.8.3.1.6. *Particle pair density distribution function (PDDF)*

All of the particle shapes considered in Section 5.8.3.1.5 model the scattering intensity *versus* Q as a Fourier transform of the scattering-particle (or feature) morphology. An alternative approach is to use an indirect Fourier transform method to extract the real-space function that gives rise to the scattering intensity (Glatter, 1977). This can then be interpreted in terms of the disordered scattering-feature morphology that may be present in the sample. For circularly symmetric small-angle scattering around the incident-beam direction, the particle pair density distribution function, PDDF or $p(r)$, is given by

$$p(r) = \frac{1}{2\pi^2} \int\limits_0^\infty \frac{\mathrm{d}\Sigma(Q)}{\mathrm{d}\Omega} Qr \sin(Qr)\,\mathrm{d}Q. \tag{5.8.24a}$$

Meanwhile

$$\frac{\mathrm{d}\Sigma(Q)}{\mathrm{d}\Omega} = 4\pi \int\limits_0^\infty p(r) \frac{\sin(Qr)}{Qr}\,\mathrm{d}r. \tag{5.8.24b}$$

We note that $p(0) = 0$, but

$$\frac{\mathrm{d}\Sigma(0)}{\mathrm{d}\Omega} = 4\pi \int\limits_0^\infty p(r)\mathrm{d}r = \Phi_V |\Delta\rho|^2 V_P. \tag{5.8.24c}$$

The inverse transform of equation (5.8.24a) is indirect in the sense that it must be carried out using an iterative inversion technique. Comparing equation (5.8.24b) with equation (5.8.2a), we note that the particle PDDF (which has units of $\mathrm{m}^{-2}\,\mathrm{sr}^{-1}$) is related to the atomic pair correlation function by $p(r) = n_P |\Delta\rho|^2 V_P r^2 \gamma(r) = \Phi_V |\Delta\rho|^2 r^2 \gamma(r)$. Comparison with equation

(5.8.16) indicates that $\gamma(0) = 1 - \Phi_V$, or for a dilute system $\gamma(0) = 1$. Meanwhile, the mean radius of gyration (or Guinier radius), R_G, of any particulate features present is given by

$$R_G^2 = \frac{\int_0^\infty p(r) r^2 \,\mathrm{d}r}{2\int_0^\infty p(r)\,\mathrm{d}r}. \tag{5.8.25}$$

The main advantages of using the PDDF method in SAS studies are that the scattering morphology can be modelled directly in real space and that the $p(r)$ function is essentially model-independent, so its use is tractable for a wide range of applications and analysis. Potential disadvantages are that (as with the scattering invariant) it is not possible to measure over the entire Q range required by the integral in equation (5.8.24*a*), so data must be extrapolated; and that the PDDF is affected by, and contains information on, any dispersion in the scattering feature size or shape. Whether it is preferable to model these effects in $\mathrm{d}\Sigma/\mathrm{d}\Omega$ *versus* Q or $p(r)$ *versus* r depends on the details of the scattering system.

5.8.3.1.7. *Size distribution analysis*

In the general case, SAS arises from scattering features that are not monodispersed in either shape or size. Frequently, it is not possible to distinguish polydispersity in shape from that in size as the SAS intensity profile is sensitive to variations in the dimensions of the scattering objects, whether coming from size or shape variation. For example, the scattering from a finite-width size distribution of spheroidal scattering objects with either $\beta < 1$ or $\beta > 1$ is identical to that from a different (broader) size distribution of spherical ($\beta = 1$) objects. In most cases, the shape of the scattering features can be inferred from prior information, and so it is a size distribution of entities of a given shape that is sought from the scattering data. There are in general two ways of accomplishing this, and these are now described.

(i) *Model size distributions*. One approach to size distribution analysis is simply to fit a size distribution, $\varphi_S(R_O)$, of an assumed functional form and average the scattering over the size distribution. For example, in the case of spheroidal scattering features, equation (5.8.18) becomes

$$\frac{\mathrm{d}\Sigma}{\mathrm{d}\Omega} = |\Delta\rho|^2 \int\limits_0^\infty \phi_V(R_O) V_P(R_O) \frac{9\pi}{2} \int\limits_0^1 \frac{[J_{3/2}(u)]^2}{u^3}\,\mathrm{d}X\,\mathrm{d}R_O, \tag{5.8.26}$$

where $V_P(R_O)$ is the volume of features of radius R_O. The advantage of fitting an assumed model size distribution is that various weighted-average sizes of interest can be extracted analytically from the result. To illustrate this, a lognormal size distribution can be assumed with minimum, mode, median and mean radii given by $R_{O\mathrm{min}}$, $R_{O\mathrm{mode}}$, $R_{O\mathrm{med}}$ and $R_{O\mathrm{mean}}$. If $A(R_O) = (R_O - R_{O\mathrm{min}})/(R_{O\mathrm{med}} - R_{O\mathrm{min}})$, $B_O = (R_{O\mathrm{med}} - R_{O\mathrm{min}})/(R_{O\mathrm{mode}} - R_{O\mathrm{min}})$, then

$$\phi_\mathrm{V}(R_O) = \frac{\Phi_V}{\{2\pi\ln(B_O)\}^{1/2}}\left(\frac{1}{R_O - R_{O\mathrm{min}}}\right)\exp\left\{\frac{-\{\ln[A(R_O)]\}^2}{2\ln(B_O)}\right\}, \tag{5.8.27}$$

and several useful parameters can be extracted from the size distribution analytically. For example: $R_{O\mathrm{mean}} = R_{O\mathrm{min}} + \{B_O{}^{1/2}(R_{O\mathrm{med}} - R_{O\mathrm{min}})\}$, the number-weighted mean radius, R_{ON}, is given by $R_{ON} = R_{O\mathrm{min}} + \{B_O{}^{-1/2}(R_{O\mathrm{mode}} - R_{O\mathrm{min}})\}$, and the surface area per unit sample volume of the distribution S_V, is given by $S_V = 3\Phi_V/R_{ON}$. Obviously, other model size distributions may be appropriate in given situations, and corresponding expressions can be used for these and similar ensemble averages. In general, a fitted model size distribution permits differences in a material system to be quantified as a function of differences in processing or other conditions, using a relatively small number of parameters.

(ii) *Size distributions using entropy maximization or other regularization.* An alternative approach to the least-squares fitting of a model function for the scattering-feature size distribution to the scattering data is to consider the contributions to the scattering intensity *versus* Q, from each histogram size bin within the size range of interest. In principle, the scattering contributions from each of the N size bins in a size distribution (assuming a given shape) can be treated as independent variables and fitted to the data by a least-squares method to determine the size distribution present. In practice, the large number of fitting parameters involved can make convergence to a unique solution, satisfying a good-fit χ^2 condition with respect to the measured data, difficult if not impossible. Furthermore, there is nothing to prevent unphysical negative regions from appearing in the fitted size distribution. Thus an additional constraint needs to be applied. Regularization methods link this second constraint to the minimum or required χ^2 condition *via* the use of a Lagrange multiplier. Two widely used additional constraints are either to require the size distribution to have maximum configurational entropy or to require that the size distribution is maximally smooth (free from oscillatory artifacts). In both cases, a major advantage is that the mathematical formulation is set up to ensure that the resulting size distribution is everywhere intrinsically positive.

The size distribution is assumed to extend over a finite scale range, associated with the SAS data, and to comprise a sufficiently large number of size intervals so as to capture the observable features in the size distribution. The size-interval increments are usually constant in linear size (relatively narrow population and a limited overall size range) or in logarithmic size (large dynamic range in the size of contributing features, and/or large range in the Q range investigated with constant $\Delta Q/Q$ resolution). Using similar notation as in previous sections, if $\varphi(R_i)$ is the value of the volume fraction distribution function for the ith size bin associated with size R_i (not necessarily R_O for a sphere or spheroid; any constant shape may be assumed), then the volume fraction in the ith size bin is $f_i = \varphi(R_i)\Delta R_i$ where ΔR_i is the width of the ith size bin. A configurational entropy, S_C, of the size distribution can then be defined in the convenient form

$$S_C = -\sum_{i=1}^{\mathrm{N}} \frac{f_i}{h}\log\left(\frac{f_i}{h}\right), \tag{5.8.28a}$$

where h is a baseline constant (or a default distribution, h_i), such that f_i/h is sufficiently large for Stirling's approximation to apply, *i.e.* $\log[(f_i/h)!] = (f_i/h)\log(f_i/h) - (f_i/h)$. (This is needed for all f_i of significance in the computing algorithm.) Note that the $\log(f_i/h)$ term implies that the f_i components are all positive. Entropy-maximization algorithms then find the histogram size distribution, f_i, hence the differential size distribution $\varphi(R_i)$, that meets the requirement

$$S_C - L_S\chi^2 = \text{a maximum}, \tag{5.8.28b}$$

where L_S is a Lagrange multiplier. Subject to the χ^2 requirement, analogous to the case in thermodynamics, the resulting maximum configurational entropy histogram distribution, f_i, is the most likely. However, because Bessel-function oscillations appear in the scattering from most assumed shapes for the scattering features, oscillations can still appear in the size distribution obtained, especially when this is a narrow distribution, despite applying the maximum entropy (*MaxEnt*) constraint (Potton *et al.*, 1988; Morrison *et al.*, 1992).

To find the smoothest size distribution consistent with the scattering data, it is necessary to define the roughness of the distribution, Z_C,

$$Z_C = \sum_{i=1}^{N} \left(f_{i+1} - f_i\right)^2 + f_1^2 + f_N^2, \qquad (5.8.29a)$$

and to satisfy the condition

$$Z_C + L_Z \chi^2 = \text{a minimum}, \qquad (5.8.29b)$$

where L_Z is another Lagrange multiplier.

Although frequently applied to obtain scattering-feature size distributions, this method, simply referred to as regularization in SAS analysis, was applied originally to optimize the PDDF $p(r)$ functions produced from SAS data *via* the indirect Fourier transform technique (Glatter, 1977, 1980). The maximum-entropy method has also been applied directly to derive PDDF $p(r)$ functions.

5.8.3.1.8. *Particle structure factor and interparticle interference effects*

With the exceptions of the scattering invariant and the Debye–Bueche approximation, our discussion so far has assumed that the SAS intensity arises from a dilute, disordered ensemble of discrete scattering features (particles or pores). In the terminology of equation (5.8.2*a*) this implies that the particle structure factor $S_P(Q)$ = 1. For many scattering morphologies, this assumption holds well for $\Phi_V < \sim 0.05$ (or 5%), although the effects of higher concentration are frequently neglected for $\Phi_V < \sim 0.10$. However, once the volume fraction of the scattering features is significantly above this, interparticle interference effects, as expressed in the particle structure factor $S_P(Q)$, can be significant. In general, it can be shown that (Guinier & Fournet, 1955)

$$S_P(Q) = 1 + n_P \int_0^{\infty} \left[g_P(r) - 1\right] \frac{4\pi r^2 \sin(Qr)}{Qr} \, \mathrm{d}r \qquad (5.8.30a)$$

and

$$g_P(r) = 1 + \frac{1}{2\pi^2 n_P} \int_0^{\infty} \left[S_P(Q) - 1\right] \frac{\sin(Qr)}{Qr} Q^2 \, \mathrm{d}Q, \qquad (5.8.30b)$$

where $g_P(r)$ is the dimensionless *particle* pair correlation function. Apart from the different normalization of equations (5.8.30*a*) and (5.8.30*b*) compared to equations (5.8.24*b*) and (5.8.24*a*), respectively, the slightly different form arises due to the exclusion volume around the centre of each scattering particle within which the centre of a neighbouring particle cannot approach. While this may not be strictly true for a population of voids or pores, it needs to be at least approximately true for a formalism assuming a concentrated population of discrete scattering features with well separated form-factor and structure-factor terms. It should also be noted that the actual radial distribution function for neighbouring particles, $Y_P(r)$, with units of m^{-1}, is given by $Y_P(r) = 4\pi r^2 n_P g_P(r)$.

In principle, equations (5.8.30*a*) and (5.8.30*b*) permit $g_P(r)$ and $Y_P(r)$ to be determined from an experimentally determined $S_P(Q)$, which in turn is extracted from $\mathrm{d}\Sigma/\mathrm{d}\Omega$ *versus* Q by dividing $\mathrm{d}\Sigma/\mathrm{d}\Omega$ by the known or assumed $n_P|\Delta\rho|^2 V_P^2 F_P^2(Q)$ or $\Phi_V |\Delta\rho|^2 V_P F_P^2(Q)$. The actual situation is complicated if any finite dispersion in the scattering feature size is present. The $S_P(Q)$ term in equation (5.8.2*a*) should then be replaced by $S_1(Q)$ where for a hard-sphere Percus–Yevick model (Percus & Yevick, 1958)

$$S_1(Q) = 1 + B_P(Q)\left[S_P(Q) - 1\right] \qquad (5.8.31a)$$

and

$$B_P(Q) = \left|\langle F_P(Q)\rangle\right|^2 \Big/ \left\langle \left|F_P(Q)\right|^2 \right\rangle. \qquad (5.8.31b)$$

Depending on how broad the size dispersion actually is, an interparticle interference may not be apparent in the scattering data. Nevertheless, the effects of high concentration [deviation of $S_P(Q)$ from 1] may still be significant.

5.8.3.1.9. *Fractal models*

Fractal scattering morphologies, despite generally being disordered in nature, are defined by their scale invariance and give rise to non-integral power laws in small-angle scattering. Examples of material systems incorporating fractal morphologies tractable for analysis by SAS methods abound, and include molecular sieves (Pauly *et al.*, 1999), dendrimers (Scherrenberg *et al.*, 1998), nanoparticle–polymer nanocomposites (Jouault *et al.*, 2009), aerogels (Emmerling & Fricke, 1992), crystallization phenomena (de Moor *et al.*, 1997), nanoparticle aggregates in flames (Hyeon-Lee *et al.*, 1998), Stober nanoparticle ensembles (Green *et al.*, 2003), cements and porous rocks (Allen, 1991), and asphaltene suspensions (Roux *et al.*, 2001). In some of these systems the solid phase, *e.g.* an assembly of nanoparticles, obviously forms the fractal morphology; in other systems, *e.g.* porous rocks, it may be the porous void network that constitutes the primary fractal morphology.

(i) *Mass- or volume-fractal morphologies.* In the case of a mass- or volume-fractal morphology, the mass and volume of the scattering features within a radius *r* of any one point in the morphology scales not with r^3, but with r^{D_V} where $D_V < 3$. The associated scattering power law can be shown to be Q^{-D_V}. For a contiguous scattering phase $D_V \geq 1$. $D_V = 1$ indicates a 1D chain structure and $D_V = 3$ indicates a space-filling phase with no fractal dependence. Thus $1 \leq D_V \leq 3$ for volume-fractal morphologies. However, $D_V = 2$ indicates a sheet-like structure, and $D_V < 2$ can be associated with a 2D fractal structure within an overall sheet-like morphology. So for three Euclidean dimensions $2 \leq D_V \leq 3$. Generally there is a maximum length scale, the correlation length ξ_V, over which volume-fractal scaling applies, and there is also a minimum length scale associated with the smallest scattering features that make up the fractal morphology. In the case of solid features of radius R_O, the minimum possible dimension for fractal scaling is the correlation hole radius, $R_C = 2R_O$, the minimum separation distance for centres of neighbouring particles. With a local packing fraction of η assumed within the correlation hole radius, and approximating the normalization to give extrapolation to Q = 0 consistent with a

Guinier approximation for the fractal structure (Freltoft *et al.*, 1986),

$$\frac{\mathrm{d}\Sigma}{\mathrm{d}\Omega} = \Phi_V|\Delta\rho|^2 V_P\left[\frac{\eta R_C^3}{R_O^3}\left(\frac{\xi_V}{R_C}\right)^{D_V} \times \left(\frac{\sin\left[\left(D_V-1\right)\arctan\left(Q\xi_V\right)\right]}{\left[1+(Q\xi)^2\right]^{\left(D_V-1\right)/2}\left(D_V-1\right)Q\xi_V}\right) + (1-\eta)^2\right]F^2(Q), \tag{5.8.32}$$

where Φ_V is the total volume fraction of the scattering features, here assumed to be spheres of volume $V_P = 4\pi R_O^3/3$ with scattering form factor $F^2(Q)$ that comprise the volume-fractal microstructure. The trigonometric terms refer to angles in radians and the arctangent angle is in the principal range from zero to $\pi/2$. This expression exhibits Q^{-D_V} scattering in the Q range $\xi_V^{-1} \ll Q \ll R_O^{-1}$, single-particle form-factor scattering in the range $Q \geq R_O^{-1}$ (including Porod Q^{-4} scattering for $Q \gg R_O^{-1}$), and the scattering Q-dependence 'tops out' for $Q \leq \xi_V^{-1}$. Volume-fractal SAS data can be fitted using this function with Φ_V, R_O, D_V, ξ_V and η as fitted parameters (plus a flat background term if needed). However, it must be emphasized that this can only be done if the data can be measured over a sufficient Q range and with sufficient Q resolution for the different scattering regimes indicated to be apparent in the data. If this condition is not met, other prior knowledge must be used to constrain the fitting parameters. Otherwise, equation (5.8.32) cannot result in convergence to a unique solution. This is particularly the case when other morphology components are present, such as surface-fractal scattering.

(ii) *Surface-fractal morphology*. Any rough interface between two phases exhibits the property that its measured surface area increases when additional roughness at finer length scales is included. Surface-fractal roughness occurs when a fixed exponent links the surface-area value to the inverse of the roughness scale considered. A true surface fractal involves roughness in all three dimensions with a convoluted surface topology that includes re-entry (doughnut-like) geometries. However, when the chord length across strands of the structure is comparable with the roughness scale being considered (Q^{-1}), SAS 'sees' this as a 3D structure, not as a rough 2D interface. For SAS applications, surface-fractal morphology is limited to an interface with self-affine 2D roughness that, otherwise, can be considered essentially planar in nature. Within this limitation, a surface fractal occurs when the number of surface elements of area $\Delta S(r)$ needed to cover an interface with roughness included down to a length scale r scales as r^{-D_S} where $D_S \geq 2$. We note that a smooth interface has $D_S = 2$. Once again, we assume that there is a maximum length scale or correlation length, ξ_S, over which the fractal roughness occurs, usually related to the size of the (large) features that possess the interface with fractal surface roughness. Generally, ξ_S can be associated with the geometrically smooth surface area, S_O. With these terms defined, a full expression for surface-fractal scattering can be derived using a generalization of Porod's law (Bale & Schmidt, 1984):

$$\frac{\mathrm{d}\Sigma}{\mathrm{d}\Omega} = \frac{\pi\xi_S^4|\Delta\rho|^2 S_O\Gamma\left(5-D_S\right)\sin\left[\left(3-D_S\right)\arctan\left(Q\xi_S\right)\right]}{\left[1+\left(Q\xi_S\right)^2\right]^{\left(5-D_S\right)/2} Q\xi_S}, \tag{5.8.33}$$

where $\Gamma(5 - D_S)$ refers to the Gamma function. When $D_S = 2$, equation (5.8.33) reduces to the Porod expression of equation (5.8.15). For a self-affine surface-fractal interface $2 \leq D_S \leq 3$, and the expression exhibits a $Q^{-(6-D_S)}$ power law for $Q \gg \xi_S^{-1}$. Again the scattering intensity 'tops out' for $Q \leq \xi_S^{-1}$. Unlike the approximate normalization at low Q provided by equation (5.8.32) for a volume-fractal morphology, the normalization at low Q provided by equation (5.8.33) for a self-affine surface-fractal morphology is exact. Equation (5.8.33) can be used fit to experimental data using three parameters: S_O, D_S and ξ_S. A further term like that used in equation (5.8.32) can be introduced to deal with the scattering at high Q. Alternatively, some other morphology such as volume-fractal scattering (power law between Q^{-2} and Q^{-3}) may take over from the steeply declining surface-fractal scattering (power law between Q^{-3} and Q^{-4}), and it may not be necessary to truncate the surface-fractal scattering at high Q. For a minimum roughness scale, R_O, where surface-fractal scaling applies, the fully rough surface area, S_{SF}, is related to the geometrically smooth surface area, S_O, by $S_{\mathrm{SF}} = S_O(\xi_S/R_O)^{(D_S-2)}$.

Particularly if volume- and surface-fractal morphologies coexist, it is essential that SAS data cover sufficient Q range (*e.g.*, $\xi_V^{-1} < Q < R_C^{-1}$ for a volume fractal) with sufficient Q resolution, and that sufficient parameter constraints based on prior knowledge be applied, to achieve convergence to a unique solution. In practice, fractal microstructures being hierarchical in nature, SAS data over three to four decades in Q, and perhaps eight or nine decades in intensity, are required. Despite these conditions, once an acceptable model paradigm is implemented, fractal models offer the advantage of combining single-feature scattering, dispersion effects and concentrated morphology issues into a single approach for fractal disordered systems.

In this and previous sections, we have considered physical microstructure models that produce the scattering observed. How well any one physical model can fit the data depends, at least to some extent, on how well the microstructure assumed approximates to that actually present. Unfortunately, while misfits should occur if the wrong model is assumed, they can also occur if the correct basic model is assumed but the actual situation is less idealized than the model implies, or if the data-point density and weighting *versus* Q make fitting of the SAS profile function mathematically ill-conditioned. One approach to addressing this situation is to develop a hierarchical nest of numerical fitting functions for SAS data that can achieve good and stable fits over a large Q range and for many situations. Having obtained a good fit, the SAS interpretation problem is then transferred to developing a credible physical interpretation of the mathematical fit parameters obtained. An obvious disadvantage is that the mathematical parameters can be misinterpreted. Nevertheless, one such approach that has met with considerable success in recent years, especially in the analysis of SAS data from polymer systems, is the 'unified fit' model developed by Beaucage (1995).

5.8.3.1.10. *Anomalous SAXS and contrast-variation SANS*

Intrinsic wide-angle and small-angle scattering intensities arise from the X-ray atomic scattering form factors, or the neutron nuclear scattering lengths (*i.e.*, b_i, b_j) for the various atomic species within a material. In diffraction, these are manifested in summations such as given in equation (5.8.6). In SAXS or SANS, the scattering contrast factors, $|\Delta\rho|^2$, derived from the scattering-length densities, determine the intrinsic strength of the scattering, as indicated in equation (5.8.2*a*). In many materials that are partially disordered and/or heterogeneous, several measurements involving both X-rays and neutrons may be desirable to determine the compositions, densities and phases of the components giving rise to the scattering. However, in both X-ray and neutron measurements, it is possible to vary the scattering lengths and contrast factors in order to interrogate the various scattering components within a single set of measurements. For WAXS and SAXS, this can be done at an X-ray synchrotron by varying the X-ray energy just below the absorption-edge energy for an atomic species present in a material of interest. For WANS and SANS, the neutron isotope effect is exploited by varying the isotope mix of one of the constituents present in the sample material, *e.g.*, H_2O/D_2O contrast variation. While these effects can be exploited in both diffraction and small-angle scattering, here we concentrate on SAXS and SANS.

(i) *Anomalous SAXS*. Just below the X-ray energy for resonant absorption by an atom of a given element (a characteristic absorption edge, obtainable from published tables, but also measurable at synchrotron sources by careful tuning of the X-ray energy using calibration absorption foils), the X-ray form factor, b_i, deviates significantly from its normal (non-resonant) value measured at X-ray energies far from an absorption edge (Thompson, 2009). Consequently, the X-ray scattering contrast factor $|\Delta\rho|^2$ applicable to SAXS measurements of any heterogeneous scattering features incorporating the given element also varies (anomalously) with the X-ray energy. Fundamental derivations of resonant-scattering contrast factors and their formal incorporation into the interpretation of anomalous SAXS (ASAXS) measurements are described in detail elsewhere (Cromer & Liberman, 1970; Hoyt *et al.*, 1984). For the purpose of ASAXS measurements of heterogeneities in disordered materials, it suffices to apply the following approximate relationship between the energy-dependent SAXS contrast factor, $|\Delta\rho(E)|^2$, and the X-ray energy, E, when this is below the absorption energy, E_0, by a few tens of eV:

$$\left|\Delta\rho(E)\right|^2 = |\Delta\rho|^2_{NR} + A_{E_0} \ln\left(\frac{E_0 - E}{E_0}\right), \qquad (5.8.34)$$

where $|\Delta\rho|^2_{NR}$ is the scattering contrast factor at X-ray energies far from the absorption edge and A_{E_0} is a scattering contrast constant for the specific material and absorption energy of interest. Note that the $\ln[(E_0 - E)/E_0]$ factor is strongly negative and ASAXS measurements must be made at $E < E_0$ because of the large decrease in sample transmission for $E > E_0$ as a result of the large increase in resonant X-ray absorption by the sample at $E = E_0$. While $|\Delta\rho|^2_{NR}$ is always positive, A_{E_0} is positive when the electron density is higher in the phase containing the element associated with the X-ray absorption edge, resulting in a decrease in scattering contrast with X-ray energy as the absorption-edge energy E_0 is approached from below. However, A_{E_0} is negative when the electron density is lower in the phase containing the X-ray-absorption-edge element, resulting in an increase in scattering contrast with X-ray energy as the absorption edge is approached from below. While ASAXS contrast variation with energy can be subtle, its careful measurement close to appropriate X-ray absorption edges can provide important insights into the composition and density of heterogeneities in disordered materials (Allen *et al.*, 2014).

(ii) *Contrast-variation SANS*. The strong isotope effect in neutron scattering lengths (Sears, 1992), together with the sensitivity of neutrons to hydrogen in hydrogenous materials, which are frequently disordered, makes these materials prime targets for investigation by contrast-variation SANS. Taking H_2O/D_2O contrast variation as an example, the neutron scattering-length density of H_2O is given by $\rho_H = -0.56 \times 10^{14}\,m^{-2}$, while for D_2O $\rho_D = +6.40 \times 10^{14}\,m^{-2}$. Since H_2O, HDO and D_2O are completely mixable at the atomic level, the scattering-length density of an H_2O/D_2O mix can be interpolated between these two end points for any molar mix of H_2O and D_2O. Furthermore, most solid hydrogenous materials have scattering-length densities between ρ_H and ρ_D. Thus, if the SANS is measured for a series of porous samples containing various H_2O/D_2O mixes in the pore water, the absolute-calibrated SANS intensity profile of $d\Sigma/d\Omega$ *versus* Q should remain the same as a function of D/H ratio, except that the absolute intensity across the Q range will follow a parabola in $|\Delta\rho|^2$, going to zero at the contrast match point where the scattering-length density in the pore water matches that of the solid phase. For a genuine two-phase system (one solid phase plus the pore fluid), the contrast match point can be found by plotting the square root of the intensity *versus* the molar fraction of D_2O, with negative values on the H_2O side of the estimated match point and positive values on the D_2O side. A straight-line fit then gives the match point as the intercept on the horizontal axis.

The situation is more complicated when more than one solid phase is present, as each solid phase has its own contrast-variation parabola with the pore fluid. The weighted sum of these parabolas is still a parabola, but now there is a contrast minimum with finite residual intensity (no one phase matched) at the minimum. If some of the solid phases have known composition and density, it may be possible to subtract these out, leaving a contrast-match curve for an unknown phase. Another complication occurs when the H_2O/D_2O exchange does not occur uniformly at all length scales. A decision must then be made as to which scale (and hence Q) to apply the contrast-variation analysis to. It is also possible to apply contrast-variation analysis to hydrogenous systems formed using various H/D isotope mixes, but care must be taken to ensure that the H/D exchange does not affect the reaction times which, despite the chemical equivalence of the hydrated and deuterated components, is not always the case. Despite these issues, SANS contrast-variation measurements play an important role in the investigation of heterogeneous and disordered materials, especially where a lack of crystallinity in one or more critical phases precludes many other diffraction-based analyses, as in the case of polymers or cements (Allen *et al.*, 2007).

5.8.3.1.11. *Magnetic SANS analysis*

As mentioned earlier in Section 5.8.2, neutrons, having a magnetic moment themselves, interact with atoms that also have a net magnetic moment. Much of what we know about magnetism or magnetic phenomena within materials has been discovered through magnetic neutron scattering and diffraction, *e.g.*, Ritter *et al.* (1997) (see also Chapter 2.8). Here, we add brief comments mainly regarding magnetic SANS analysis of heterogeneous magnetic materials. Even in a material containing atoms or molecules possessing net magnetic moments, there is no magnetic

SANS intensity if these magnetic moments are randomly oriented (although there may be a contribution to the incoherent flat background scattering). However, if magnetic ordering is present (ferromagnetic, antiferromagnetic, ferrimagnetic *etc.*), and if an axis of magnetic alignment is established, *e.g.* by applying a saturation magnetic field to align the atomic magnetic moments (or those of any magnetic domains present), an anisotropic magnetic SANS contribution can be measured. The magnetic SANS intensity varies as $\sin^2\alpha$, where α is the angle between the direction of the neutron magnetic moment and that of the sample (*i.e.*, that of the applied magnetic field). Analysis of the anisotropic intensity collected using a 2D PSD allows the anisotropic ($\sin^2\alpha$) magnetic SANS component to be separated from the (usually isotropic) nuclear SANS component.

Once the anisotropic nature of the magnetic SANS data is allowed for, the full set of analyses discussed previously in Section 5.8.3 can be applied, using the magnetic SANS contrast factors in place of the non-magnetic contrast factors, to model and quantify magnetic microstructures and heterogeneities that are present. Significant magnetic SANS studies have included precipitation phenomena in ferritic steels (Allen *et al.*, 1993; Mathon *et al.*, 2003), the magnetic structure of nanocrystalline iron (Wagner *et al.*, 1991), polarons in perovskites (De Teresa *et al.*, 1997) and flux-line lattice behaviour in superconductors (Yaron *et al.*, 1995; Riseman *et al.*, 1998). Magnetic SANS investigations have been made even more powerful by the development of polarized SANS instrumentation (SANSPOL) that uses supermirrors to provide significant polarization of the incident neutron beam (Zhao *et al.*, 1995). The spin-dependent scattering of polarized neutrons enables models for heterogeneous magnetic structures to be more finely tuned, as well as providing a better separation of the magnetic and non-magnetic scattering components in the experimental data (Heinemann & Wiedenmann, 2003; Mettus & Michels, 2015).

Finally, it should be mentioned that neutron-polarization analysis has been extended well beyond the magnetic SANS regime. Following the development of the neutron spin-echo technique by Mezei and others in the 1970s (Mezei, 1980), spin-echo SANS (SESANS) instruments have been designed to compare the neutron polarization before and after the sample position, and measure changes in the Larmor precession angle of the neutron polarization plane as neutrons traverse a sample. Although the analysis can be complex and goes beyond the scope of this chapter, this technique, which is applicable to all classes of sample systems, not just magnetic samples, can provide unique information on the dynamics of an ensemble system (including biological systems), as well as structural information over a length scale that overlaps with USANS (Rekveldt, 1996).

5.8.3.1.12. *Further analysis of X-ray reflectivity and GI-SAXS*

Some further discussion is warranted of disorder that can occur at surfaces and interfaces in materials, or within thin films:

(i) *Parratt function reflectivity profile* (Parratt, 1954). Assuming specular reflectivity $R(Q)$ *versus* Q data have been obtained and corrected as discussed previously, these can be analysed to give a density profile of a series of N thin-film layers on a substrate, together with a representation of the roughness/diffuseness associated with each film boundary. Assuming a scattering-length density $\rho(z)$ as a function of overall distance z below the mean position of the top surface of the whole sample,

$$\rho(z) = \rho_O + \sum_{m=1}^{N+1} \frac{(\rho_m - \rho_{m-1})}{2}\left[1 + \operatorname{erf}\left(\frac{z - z_m}{\sigma_m\sqrt{2}}\right)\right], \tag{5.8.35}$$

where $z_m = \sum_{k=1}^{m-1}\tau_k$, ρ_O is the scattering-length density above the top film layer (frequently $\rho_O = 0$ unless the film interfaces are buried in some other bulk material or are immersed in a liquid), ρ_m is the scattering-length density in the mth film layer, $\operatorname{erf}(x)$ is the error function, σ_m is the standard deviation of the roughness (or diffuseness) for the mth interface at the top of the mth film (where the first interface at $z_1 = 0$ defines the top of the whole assembly), and z_m is the mean location of the mth interface and is the sum of the thicknesses, τ_k, of each film above the mth interface and film. Note that the final $(N + 1)$th interface is with the substrate and z_{N+1} is the combined thickness of all of the films.

Practical refinement of the density profile by fitting the predicted reflectivity curve to experimental reflectivity data must take into account corrections not only for overall sample geometry but also for instrumental resolution corrections *etc.* However, the reflectivity curve $R(Q)$ for a series of thin films on a substrate, as described above, can in principle be compared to the Fresnel reflectivity curve, $R_F(Q)$, from a perfectly smooth, bare substrate of scattering-length density ρ_{N+1}, here denoted $\rho_{\rm SUB}$, by (Als-Nielsen, 2001)

$$\frac{R(Q)}{R_F(Q)} = \left|\frac{1}{\rho_{\rm SUB}}\int\limits_{-\infty}^{\infty}\exp(iQz)\left(\frac{{\rm d}\rho}{{\rm d}z}\right){\rm d}z\right|^2, \tag{5.8.36}$$

where the integral range must be extended out in both directions until $\mathrm{d}\rho/\mathrm{d}z = 0$.

Note that specular reflectivity studies can detect a rough or diffuse boundary between successive films, but cannot themselves differentiate between the two. This said, neutron contrast-variation methods may sometimes be used to interrogate the composition at an interface (Nelson, 2006). However, in most cases, non-specular reflectivity or GI-SAXS measurements must be used to investigate the nature of the disorder occurring at the film interfaces (or within films), or to characterize in-plane structures parallel to the substrate.

(ii) *Distorted-wave Born approximation (DWBA)*. In Section 5.8.2.4 the case of GI-SAXS or NS-SANS from a microstructure within a single thick film was discussed and the various refraction corrections considered. However, in the more general case of thin films where $\zeta_{\rm mean} \geq \tau_{\rm film}$, at least four different contributions to the scattering must be considered: (i) a single scattering event as discussed in Section 5.8.2.4; (ii) a single scattering event, followed by reflection from the film/substrate interface; (iii) reflection from the film/substrate interface, followed by a single scattering event; and (iv) as (iii) but with a further reflection from the film/substrate interface and possibly a further scattering event. To some extent component (i) can be separated from (ii) to (iv), corrected for refraction effects and interpreted using the Born approximation. However, for a full treatment of GI-SAXS data from thin films where components (ii) to (iv) cannot be ignored, distortions from the incident plane wave assumed in the Born approximation must be allowed for in what is effectively a superposition of the four components – hence, the use of the DWBA (Sinha *et al.*, 1988; Rauscher *et al.*, 1995). Because of this, the DWBA does not simply provide a modified form of $d\Sigma/d\Omega$ that takes into account all of the corrections involved, but it also modifies the form factors and structure factors associated with the underlying microstructural features within a film.

It is not practical to give a full exposition of the DWBA in the context of this chapter. Fortunately, it can be shown that the DWBA only has a significant effect for incidence and scattering grazing angles, θ_i and θ_2, close to the critical angle θ_C. Furthermore, software tools are now publicly available that address the analysis needs for most of the main cases of interest. We refer the interested reader to the various references and software available: Lazzari (2002), Babonneau (2010) and Korolkov *et al.* (2012), the last of which is focused on GI-SANS.

5.8.3.2. *Small-angle scattering effects on wide-angle scattering analysis*

In Section 5.8.2.5, it was pointed out that the determination of the real-space atomic pair density distribution function, $G(r)$, from wide-angle scattering (diffraction) is affected by the non-measurable scattering contribution close to $Q = 0$. For a macroscopic diffracting sample volume, the missing scattering is effectively at infinitesimal Q, and its absence from the Fourier transform integral of equation (5.8.10) results in the negative term $-4\pi r n_0$ appearing in the expression for $G(r)$. We now consider the case where the diffracting regions giving rise to the wide-angle scattering (whether internally crystalline or atomically disordered) are, themselves, randomly distributed particles of nanoscale size within a solid matrix or liquid medium. The finite size of the particles now contributes measurable small-angle scattering at low Q. If this is not measured, a more complex negative term appears in the expression for $G(r)$ determined from a Fourier transform of the total-scattering data measured in the wide-angle regime.

In general it can be shown that equation (5.8.13) for the atomic pair density distribution function, $G(r)$, can be modified to become (Cargill, 1971; Farrow & Billinge, 2009)

$$G(r) = 4\pi r\big[n(r) - \gamma_0(r)n_0\big], \qquad (5.8.37)$$

where $n(r)$ is the atomic number density distribution at all r with respect to any given atom, n_0 is the mean atomic number density and $\gamma_0(r)$ is the dimensionless atomic pair correlation function of equations (5.8.2*a*,*b*). While $\gamma_0(r)$ can be determined empirically from calibrated SAXS or SANS data, it can also be defined in terms of an individual small-angle scattering particle (Porod, 1951; Guinier & Fournet, 1955; Glatter & Kratky, 1982). Let $c(\mathbf{r})$ be a shape function with the property that $c(\mathbf{r}) = 1$ for $\mathbf{r}$ inside the particle and $c(\mathbf{r}) = 0$ for $\mathbf{r}$ outside the particle. Then for any given particle orientation

$$\gamma_0(\mathbf{r}) = \frac{1}{V_P}\int_0^\infty c(\mathbf{r})c(\mathbf{r}+\mathbf{r}')\,d\mathbf{r}' \text{ and } \int_0^\infty \gamma_0(\mathbf{r})\,d\mathbf{r} = V_P, \qquad (5.8.38)$$

where for randomly oriented particles, such as would give an isotropic microstructure, the orientational average of $\gamma_0(\mathbf{r})$ is $\gamma_0(r)$. For nanoscale small-angle scattering particles, we note that $\gamma_0(r) = 0$ for r greater than the largest chord dimension of the scattering particle. This gives the characteristic shape of the $G(r)$ component shown in Fig. 5.8.6(*c*) when scattering in the SAS regime ($Q < Q_{\min}$) is not measured in total-scattering measurements. However, when the total scattering is measured for a very dilute ensemble of nanoparticles, the $G(r)$ function itself becomes featureless for r greater than the largest chord length of the scattering particles, as has been demonstrated experimentally (Proffen & Kim, 2009). Meanwhile, we also note that when r is very much less than the maximum chord dimension of the particles, such as is always the case when the particles are macroscopic in size, $\gamma_0(r) = 1$ and equation (5.8.37) reverts to equation (5.8.13).

5.8.3.3. *Combining information from different methods*

Increasingly, several diffraction-based techniques are being used together to interrogate disordered or partially disordered material systems. A major example offered here is the combination of SAXS or SANS at low Q with diffraction-based total-scattering methods at larger Q, or wide-angle scattering. In order to account fully for the SAS contribution in total-scattering data, or simply to combine diffraction and SAS data, it is necessary to inter-calibrate the scattered and diffracted intensities between the techniques. In this connection, it is important to allow for the different conventions in normalizing the scattered or diffracted intensities.

In SAXS or SANS, the macroscopic differential scattering cross section, $d\Sigma/d\Omega$, is used to give the normalized intensity, as defined in Section 5.8.2. In diffraction, the coherent diffraction intensity, $I_{\rm coh}$, is used as defined in equation (5.8.6), with $I_{\rm coh}$ derived from a coherent sum of the diffraction amplitudes from all of the diffracting atoms sampled. In equation (5.8.6) it is assumed that the scattering is normalized to an incident beam comprising a plane wave of unit amplitude (hence unit intensity), and that the individual contributions to the scattered wave are also normalized per unit solid angle. Thus, the additional normalization required to convert $I_{\rm coh}$ to $d\Sigma/d\Omega$ is with respect to the sample volume and $d\Sigma/d\Omega = I_{\rm coh}/V_S$. However, whereas the SAS expressions are based on the assumption that the SAXS or SANS intensity is small compared with the incident-beam intensity, this assumption does not necessarily hold for WAXS or WANS.

In practice, the quantitative comparison of SAXS and SANS intensities with those of WAXS and WANS can be complicated by a number of factors. Crystalline structure factors summed over significant coherently diffracting sample volumes can lead to extinction effects that affect the Bragg diffraction peak intensities. Similarly, the peak intensities can also be affected by crystalline texture, or by the presence of stress and strain. All these issues are discussed in Chapters 5.2 and 5.3, but they are less likely to have a significant effect for a partially disordered material having weak diffraction peaks, which is of most interest here. Two effects that do influence any quantitative comparison of the small- and wide-angle scattering from disordered materials are those due to thermal diffuse scattering (WAXS, WANS, total scattering) and multiple scattering (SAXS and SANS).

Thermal diffuse scattering (TDS) reduces the intensity of the diffraction peaks measured in WAXS or WANS and redistributes it to the background scattering between the peaks. The functional form of the latter depends on the details of the material in question, and this can be further complicated in the case of disordered or partially disordered materials in the context of total-scattering measurements. However, the reduction in coherent Bragg peak intensity and its effect on the determination of $G(r)$ can be treated by a modification of equation (5.8.8) to allow for the effect of the Debye–Waller factor (Farrow & Billinge, 2009):

$$S(Q)-1=\left(\frac{1}{N\langle b\rangle^2}\right)\sum_{i\neq j} b_j^* b_i\left[\frac{\sin(Qr_{ij})}{Qr_{ij}}\right]\exp\left(-\frac{\sigma_{ij}^2 Q^2}{2}\right), \tag{5.8.39}$$

where σ_{ij}^2 is the correlated Debye–Waller broadening factor (in real space) for the *i–j*th atom pair. The σ_{ij}^2 term includes the expected Arrhenius dependence on the absolute temperature, T.

Multiple scattering in SAXS or SANS reduces the scattering intensity at the lowest Q values measured and redistributes the lost intensity to higher Q values. However, without correction, this effect can be masked by an incorrect sample transmission T_S, used in place of T_{SS}, in equation (5.8.4) for the intensity calibration. The multiple-scattering correction outlined in Section 5.8.2.3.3 must be applied before combining SAXS or SANS data with WAXS or WANS. Obviously, it is necessary to integrate the scattering intensity out to a Q value beyond which multiple scattering can be ignored. (A decrease in apparent intensity of one decade from that at $Q = 0$ suffices in most cases.) As indicated previously, this correction, alone, does *not* correct for the distortion in the SAS profile at low Q where multiple scattering is significant, but it *does* correct the calibrated $\mathrm{d}\Sigma/\mathrm{d}\Omega$ for all higher Q values. Multiple-scattering corrections that include correcting some of the distortions in the SAS profile at low Q have been treated by Schelten & Schmatz (1980).

Assuming that corrected absolute scattering intensities can be attained, there are strong advantages in comparing these for WAXS and WANS, SAXS and SANS across corresponding Q ranges for partially disordered systems, especially where spatial variations in composition exist. To achieve this, the X-ray and neutron measurements need to be made on samples that are as closely identical to each other as possible, although the sample thickness and volume for neutrons must frequently be larger than for X-rays. A ratio of the WAXS/WANS integrated diffraction peak intensities for corresponding Bragg peaks provides a test of the diffracting unit cell composition of the crystalline component of a partially disordered material. This is because the values of the b_i and b_j for different atoms in the corresponding summations of equation (5.8.6) for X-rays and neutrons are different, allowing the predicted structural composition of a crystalline phase to be tested against experiment. Meanwhile, the ratio of the calibrated SAXS/SANS intensities over corresponding Q ranges provides a similar test of the overall composition and density of heterogeneities within the microstructure, regardless of whether the solid phase is crystalline or amorphous. Again, this is because the contrast factor $|\Delta\rho|^2$ in equation (5.8.2*a*) is different for X-rays and neutrons (Thompson, 2009; Sears, 1992), depending on the composition and density both of the small-angle scattering heterogeneities and of the surrounding medium. The proportionality between the X-ray form factor and atomic number for X-ray scattering *versus* the strong isotope effect for neutron scattering can lead to very different sensitivities of X-rays and neutrons to different components in a disordered heterogeneous material system. This is particularly true when disordered hydrogeneous species are present, some bound into the solid matrix, not all of which is crystalline. Clearly, the use of H/D contrast methods in WANS and SANS discussed in Section 5.8.3.1.10 can be strongly complemented by a comparison between the X-ray and neutron intensities.

Finally, we note the importance of relating the WAXS and SAXS and/or WANS and SANS results. In previous sections, we have shown the importance of accounting for the small-angle scattering in total-scattering measurements of partially disordered material systems. With the added complications of needing to treat thermal diffuse scattering and other defect-related corrections to the scattering observed, the advantages of working independently with both the X-ray scattering form factors and contrast factors, and the corresponding neutron scattering-length densities and contrast factors, are that the entire interpretation scheme can be independently checked using two sets of scattering parameters. Again we emphasize the value of such an approach when hydrogenous components are present in a partially disordered heterogeneous material system.

5.8.4. Prospects for future development and recommended further reading

At the present time, rapid advances are taking place in the diffraction- and scattering-based analysis of partially disordered and heterogeneous materials. What follows is a very brief summary of some of the more promising current developments.

5.8.4.1. *Developments at X-ray synchrotron facilities*

New third-generation X-ray synchrotron facilities continue to come on line to serve the full range of diffraction- and spectroscopy-based techniques for investigating phenomena in new materials. Among these is the application of increasingly ambitious instrumentation using high X-ray energies for total-scattering analysis of nanocrystalline and disordered or partially crystalline materials over a large Q range (Petkov *et al.*, 2013). Instrumentation has also been developed to combine methods such as USAXS, SAXS and WAXS (including atomic pair density distribution analysis) to provide both microstructure and structure data for given samples within a single set of measurements (Becker *et al.*, 2010). Where possible, the X-ray energy range is being extended to higher energies to allow investigation of thicker or denser, more complex materials (Ilavsky *et al.*, 2012). At the same time, the increasingly higher X-ray fluxes available are allowing better time resolution and the more direct *in situ* studies of complex processes involving disordered materials. These instrumental developments include both bulk sample measurements using transmission geometry, and surface and thin-film measurements using a reflection geometry. As the need has increased for *in situ* studies of processes occurring within material systems, rather than just structural and microstructural measurements of materials under static conditions, so has interest in combining methods such as SAXS with techniques such as X-ray photon correlation spectroscopy (XPCS) to measure the equilibrium and non-equilibrium dynamics of phenomena occurring within materials (Zhang *et al.*, 2011). In this connection, the recent development of X-ray free-electron laser (FEL) coherent scattering (LCS) or fourth-generation X-ray sources is likely to play a major role in the future (Saldin *et al.*, 2011), as will the ongoing development of multi-bend achromat (MBA) diffraction-limited storage rings at synchrotrons (Tavares *et al.*, 2014). The coherent aspects of these new X-ray sources will affect all areas of X-ray scattering and diffraction. Specifically, the new sources will spur a much greater integration of structure and dynamics considerations for all classes of material, including disordered and heterogeneous materials.

For current information on and links to major X-ray facilities and instrumentation around the world please see http://www.lightsources.org/regions.

5.8.4.2. *Developments at steady-state and pulsed neutron sources*

While neutron fluxes are never likely to match those possible with X-rays, the high penetration ability in most materials, the absence of sample beam damage and the strong isotope effect for neutron scattering present major advantages for studies of disordered and heterogeneous materials. The magnetic properties of neutrons, and also their sensitivity to inelastic processes in materials, also provide important advantages. As pulsed (spallation) neutron sources have been developed around the world in recent years, the field of neutron powder diffraction has advanced significantly (Ibberson, 2009; Garlea *et al.*, 2010). The availability of long-pulse operations at an increasing number of locations together with the construction of long-flight-path instruments have enabled major advances in neutron total-scattering measurements and, to some degree, combination of WANS with SANS within the same instrument configuration (White *et al.*, 2010; Bowron *et al.*, 2010). Meanwhile, at steady-state (reactor-based) neutron sources, the greater availability of cold neutrons and the ability to achieve higher signal-to-noise ratios for SANS continue to make reactors the prime location for dedicated SANS measurement. Recent innovations in neutron optics such as neutron refractive lenses, new detector developments and the development of successful USANS instruments are resulting in new emerging SANS capabilities, such as the ability to measure in several instrument configurations at once (Frielinghaus *et al.*, 2009; Huang *et al.*, 2012). This will greatly reduce sample measurement times and improve the time resolution for *in situ* studies of material processes. Indeed, reactor-based SANS measurements continue to lead the exploration of *in situ* processes in polymer systems and other disordered materials (Eberle & Porcar, 2012).

For current information on and links to major steady-state reactor and pulsed source neutron facilities and instrumentation around the world please see http://www.neutron.anl.gov/facilities.html.

5.8.4.3. *Future prospects*

In closing we note that advanced technological materials development is increasingly concerned with harnessing complex phenomena in multi-component and heterogeneous material systems. The materials involved are frequently a hybrid mix of alloys, polymers and ceramics, intimately connected for the intended purpose of the overall system. Many of the material components are nanoscale and/or nanocrystalline in nature, or have poor crystallinity, or none. Even if not disordered with regard to crystalline structure, disordered distributions of heterogeneous elements are frequently present, and they may even govern performance. While many of the techniques and practices described elsewhere in this volume are appropriate for providing the needed characterization of new material systems, we have attempted in this chapter to focus on suitable methods for characterizing and measuring their more disordered aspects.

5.8.4.4. *Further reading*

Some selected textbooks relevant to the methods described in this chapter are listed below in chronological order.

Guinier, A. & Fournet, G. (1955). *Small-Angle Scattering of X-rays*. New York: John Wiley & Sons.

Kostorz, G. (1979). Editor. *Treatise on Materials Science and Technology*, Vol. 15, *Neutron Scattering*. New York: Academic Press.

Glatter, O. & Kratky, O. (1982). Editors. *Small-Angle X-ray Scattering*. London: Academic Press.

Feigin, L. A. & Svergun, D. I. (1987). *Structure Analysis by Small-Angle X-ray and Neutron Scattering.* New York: Plenum Press.

Brumberger, H. (1994, reprinted 2010). Editor. *Modern Aspects of Small-Angle Scattering*. *NATO Science Series*, Series C, *Mathematical and Physical Sciences*, 451. London: Springer.

Roe, R.-J. (1999). *Methods of X-ray and Neutron Scattering in Polymer Science.* Don Mills, ON, Canada: Oxford University Press (Canada).

Lindner, P. & Zemb, Th. (2002). Editors. *Neutron, X-ray & Light Scattering Methods Applied to Soft Condensed Matter*. Amsterdam: North Holland Delta Series.

Andersson, R. A. (2008). *Spin-echo Small-Angle Neutron Scattering Measurements.* Berlin, Heidelberg: Springer.

Borsali, R. & Pecora, R. (2008). Editors. *Soft Matter Characterization.* Berlin, Heidelberg: Springer.

Daillant, J. & Gibaud, A. (2009). Editors. *X-ray and Neutron Reflectivity: Principles and Applications*. *Lecture Notes in Physics* Vol. 770. Berlin, Heidelberg: Springer.

Egami, T. & Billinge, S. (2012). *Underneath the Bragg Peaks*. Oxford: Pergamon Press.

The SAS Portal web site, linked to the web site of the IUCr Commission on Small-Angle Scattering, includes a list of references and other educational links, not only for SAS methods, but also for general scattering methods relevant to heterogeneous materials in general – see http://smallangle.org/content/small-angle-scattering-bibliography.

References

Agamalian, M., Wignall, G. D. & Triolo, R. (1997). *Optimization of a Bonse–Hart ultra-small-angle neutron scattering facility by elimination of the rocking-curve wings*. *J. Appl. Cryst.* **30**, 345–352.

Allen, A. J. (1991). *Time-resolved phenomena in cements, clays and porous rocks*. *J. Appl. Cryst.* **24**, 624–634.

Allen, A. J. (2005). *Characterization of ceramics by X-ray and neutron small-angle scattering*. *J. Am. Ceram. Soc.* **88**, 1367–1381.

Allen, A. J., Gavillet, D. & Weertman, J. R. (1993). *SANS and TEM studies of isothermal M_2C carbide precipitation in ultrahigh strength AF1410 steels*. *Acta Metall. Mater.* **41**, 1869–1884.

Allen, A. J., Ilavsky, J., Jemian, P. R. & Braun, A. (2014). *Evolution of electrochemical interfaces in solid oxide fuel cells (SOFC): a Ni and Zr resonant anomalous ultra-small-angle X-ray scattering study with elemental and spatial resolution across the cell assembly*. *RSC Adv.* **4**, 4676–4690.

Allen, A. J., Thomas, J. J. & Jennings, H. M. (2007). *Composition and density of nanoscale calcium-silicate-hydrate in cement*. *Nat. Mater.* **6**, 311–316.

Allen, A. J., Zhang, F., Kline, R. J., Guthrie, W. F. & Ilavsky, J. (2017). *NIST Standard Reference Material 3600: absolute intensity calibration standard for small-angle X-ray scattering*. *J. Appl. Cryst.* **50**, 462–474.

Als-Nielsen, J. (2001). *Elements of Modern X-ray Physics.* New York: John Wiley & Sons.

Andersson, R. A. (2008). *Spin-Echo Small-Angle Neutron Scattering Measurements.* Berlin, Heidelberg: Springer.

Babonneau, D. (2010). *FitGISAXS: software package for modelling and analysis of GISAXS data using IGOR Pro*. *J. Appl. Cryst.* **43**, 929–936.

Bale, H. D. & Schmidt, P. W. (1984). *Small-angle X-ray-scattering investigation of submicroscopic porosity with fractal properties*. *Phys. Rev. Lett.* **53**, 596–599.

Barker, J. G., Glinka, C. J., Moyer, J. J., Kim, M. H., Drews, A. R. & Agamalian, M. (2005). *Design and performance of a thermal-neutron double-crystal diffractometer for USANS at NIST*. *J. Appl. Cryst.* **38**, 1004–1011.

Bates, S., Zografi, G., Engers, D., Morris, K., Crowley, K. & Newman, A. (2006). *Analysis of amorphous and nanocrystalline solids from their X-ray diffraction patterns*. *Pharm. Res.* **23**, 2333–2349.

Beaucage, G. (1995). *Approximations leading to a unified exponential/power-law approach to small-angle scattering*. *J. Appl. Cryst.* **28**, 717–728.

Becker, J., Bremholm, M., Tyrsted, C., Pauw, B., Jensen, K. M. Ø., Eltzholt, J., Christensen, M. & Iversen, B. B. (2010). *Experimental setup for in situ X-ray SAXS/WAXS/PDF studies of the formation and growth of nanoparticles in near- and supercritical fluids*. *J. Appl. Cryst.* **43**, 729–736.

Berk, N. F. & Hardman-Rhyne, K. A. (1985). *Characterization of alumina powder using multiple small-angle neutron scattering. I. Theory*. *J. Appl. Cryst.* **18**, 467–472.

Berk, N. F. & Hardman-Rhyne, K. A. (1988). *Analysis of SAS data dominated by multiple scattering*. *J. Appl. Cryst.* **21**, 645–651.

Billinge, S. J. L. & Levin, I. (2007). *The problem with determining atomic structure at the nanoscale*. *Science*, **316**, 561–565.

Bonse, U. & Hart, M. (1966). *Small angle X-ray scattering by spherical particles of polystyrene and polyvinyltoluene*. *Z. Phys.* **189**, 151–162.

Borsali, R. & Pecora, R. (2008). Editors. *Soft Matter Characterization.* Berlin, Heidelberg: Springer.

Bowron, D. T., Soper, A. K., Jones, K., Ansell, S., Birch, S., Norris, J., Perrott, L., Riedel, D., Rhodes, N. J., Botti, A., Ricci, M.-A., Grazzi, F. & Zoppi, M. (2010). *NIMROD: The Near and InterMediate Range Order Diffractometer of the ISIS second target station*. *Rev. Sci. Instrum.* **81**, 033905.

Brumberger, H. (1994, reprinted 2010). Editor. *Modern Aspects of Small-Angle Scattering*. *NATO Science Series*, Series C, *Mathematical and Physical Sciences*, 451. London: Springer.

Cargill, G. S. (1971). *Influence of neglected small-angle scattering in radial distribution function analysis*. *J. Appl. Cryst.* **4**, 277–283.

Cromer, D. T. & Liberman, D. (1970). *Relativistic calculation of anomalous scattering factors for X rays*. *J. Chem. Phys.* **53**, 1891–1898.

Daillant, J. & Gibaud, A. (2009). Editors. *X-ray and Neutron Reflectivity: Principles and Applications*. *Lecture Notes in Physics*, Vol. 770. Berlin, Heidelberg: Springer.

De Teresa, J. M., Ibarra, M. R., Algarabel, P. A., Ritter, C., Marquina, C., Blasco, J., García, J., del Moral, A. & Arnold, Z. (1997). *Evidence for magnetic polarons in the magnetoresistive perovskites*. *Nature*, **386**, 256–259.

Debye, P. (1947). *Molecular weight determination by light scattering*. *J. Phys. Colloid Chem.* **51**, 18–32.

Debye, P. & Bueche, A. M. (1949). *Scattering by an inhomogeneous solid*. *J. Appl. Phys.* **20**, 518–525.

Eberle, A. P. R. & Porcar, L. (2012). *Flow-SANS and Rheo-SANS applied to soft matter*. *Curr. Opin. Colloid Interface Sci.* **17**, 33–43.

Eikenberry, E. F., Bronnimann, Ch., Hulsen, G., Toyokawa, H., Horisberger, R., Schmitt, B., Schulze-Briese, C. & Tomizaki, T. (2003). *PILATUS: a two-dimensional X-ray detector for macromolecular crystallography*. *Nucl. Instrum. Methods. Phys. Res. A*, **501**, 260–266.

Egami, T. & Billinge, S. (2012). *Underneath the Bragg Peaks*. Oxford: Pergamon Press.

Emmerling, A. & Fricke, J. (1992). *Small-angle scattering and the structure of aerogels*. *J. Non-Cryst. Sol.* **145**, 113–120.

Espinal, L., Wong-Ng, W., Kaduk, J. A., Allen, A. J., Snyder, C. R., Chiu, C., Siderius, D. W., Li, L., Cockayne, E., Espinal, A. E. & Suib, S. L. (2012). *Time-dependent CO$_2$ sorption hysteresis in a one-dimensional microporous octahedral molecular sieve*. *J. Am. Chem. Soc.* **134**, 7944–7951.

Farrow, C. L. & Billinge, S. J. L. (2009). *Relationship between the atomic pair distribution function and small-angle scattering: implications for modeling of nanoparticles*. *Acta Cryst.* A**65**, 232–239.

Feigin, L. A. & Svergun, D. I. (1987). *Structure Analysis by Small-Angle X-ray and Neutron Scattering*. New York: Plenum Press.

Fratzl, P. (2003). *Small-angle scattering in materials science – a short review of applications in alloys, ceramics and composite materials*. *J. Appl. Cryst.* **36**, 397–404.

Freltoft, T., Kjems, J. K. & Sinha, S. K. (1986). *Power-law correlations and finite-size effects in silica particle aggregates studied by small-angle neutron scattering*. *Phys. Rev. B*, **33**, 269–275.

Frielinghaus, H., Pipich, V., Radulescu, A., Heiderich, M., Hanslik, R., Dahlhoff, K., Iwase, H., Koizumi, S. & Schwahn, D. (2009). *Aspherical refractive lenses for small-angle neutron scattering*. *J. Appl. Cryst.* **42**, 681–690.

Garlea, V. O., Chakoumakos, B. C., Moore, S. A., Taylor, G. B., Chae, T., Maples, R. G., Riedel, R. A., Lynn, G. W. & Selby, D. L. (2010). *The high-resolution powder diffractometer at the high flux isotope reactor*. *Appl. Phys. A*, **99**, 531–535.

Glatter, O. (1977). *A new method for the evaluation of small-angle scattering data*. *J. Appl. Cryst.* **10**, 415–421.

Glatter, O. (1980). *Determination of particle-size distribution functions from small-angle scattering data by means of the indirect transformation method*. *J. Appl. Cryst.* **13**, 7–11.

Glatter, O. & Kratky, O. (1982). Editors. *Small-Angle X-ray Scattering*. London: Academic Press.

Glatter, O. & May, R. (2006). *Small-angle techniques.* In *International Tables for Crystallography*, Vol. C, Chapter 2.6, pp. 89–112. Chester: International Union of Crystallography.

Glinka, C. J., Barker, J. G., Hammouda, B., Krueger, S., Moyer, J. J. & Orts, W. J. (1998). *The 30 m small-angle neutron scattering instruments at the National Institute of Standards and Technology*. *J. Appl. Cryst.* **31**, 430–445.

Green, D. L., Lin, J. S., Lam, Y.-F., Hu, M. Z.-C., Schaefer, D. W. & Harris, M. T. (2003). *Size, volume fraction, and nucleation of Stober silica nanoparticles*. *J. Colloid Interface Sci.* **266**, 346–358.

Green, M. L., Allen, A. J., Jordan-Sweet, J. L. & Ilavsky, J. (2009). *Annealing behavior of atomic layer deposited HfO$_2$ films studied by synchrotron X-ray reflectivity and grazing incidence small-angle scattering*. *J. Appl. Phys.* **105**, 103522.

Grillo, I. (2008). *Small-angle neutron scattering and applications in soft condensed matter.* In *Soft Matter Characterization*, edited by R. Borsali & R. Pecora, pp. 707–764. Berlin, Heidleberg: Springer Verlag.

Guinier, A. & Fournet, G. (1955). *Small-Angle Scattering of X-rays*. New York: John Wiley & Sons.

Hamilton, W. A., Butler, P. D., Hayter, J. B., Magid, L. J. & Kreke, P. J. (1996). *'Over the horizon' SANS: measurements on near-surface Poiseuille shear-induced ordering of dilute solutions of threadlike micelles*. *Physica B*, **221**, 309–319.

Heinemann, A. & Wiedenmann, A. (2003). *Benefits of polarized small-angle neutron scattering on magnetic nanometer scale structure modeling*. *J. Appl. Cryst.* **36**, 845–849.

Hoyt, J. J., de Fontaine, D. & Warburton, W. K. (1984). *Determination of the anomalous scattering factors for Cu, Ni and Ti using the dispersion relation*. *J. Appl. Cryst.* **17**, 344–351.

Huang, T. C., Gong, H., Shao, B. B., Wang, D., Zhang, X. Z., Zhang, K., Wei, J., Wang, X. W., Guan, X. L., Loong, C.-K., Tao, J. Z., Zhou, L. & Ke, Y. B. (2012). *Design of a new time-of-flight small-angle neutron scattering instrument at CPHS*. *Nucl. Instrum. Methods Phys. Res. A*, **669**, 14–18.

Hyeon-Lee, J., Beaucage, G., Pratsinis, S. E. & Vemury, S. (1998). *Fractal analysis of flame-synthesized nanostructured silica and titania powders using small-angle X-ray scattering*. *Langmuir*, **14**, 5751–5756.

Ibberson, R. M. (2009). *Design and performance of the new supermirror guide on HRPD at ISIS*. *Nucl. Instrum. Methods Phys. Res. A*, **600**, 47–49.

Ibel, K. (1976). *The neutron small-angle camera D11 at the high-flux reactor, Grenoble*. *J. Appl. Cryst.* **9**, 296–309.

Ilavsky, J. (2012). *Nika: software for two-dimensional data reduction*. *J. Appl. Cryst.* **45**, 324–328.

Ilavsky, J., Allen, A. J., Levine, L. E., Zhang, F., Jemian, P. R. & Long, G. G. (2012). *High-energy ultra-small-angle X-ray scattering instrument at the Advanced Photon Source*. *J. Appl. Cryst.* **45**, 469–479.

Ilavsky, J., Jemian, P. R., Allen, A. J., Zhang, F., Levine, L. E. & Long, G. G. (2009). *Ultra-small-angle X-ray scattering at the Advanced Photon Source*. *J. Appl. Cryst.* **42**, 1318–1320.

Jennings, H. M. (2000). *A model for the microstructure of calcium silicate hydrate in cement paste*. *Cem. Concr. Res.* **30**, 101–116.

Jouault, N., Vallat, P., Dalmas, F., Said, S., Jestin, J. & Boue, F. (2009). *Well-dispersed fractal aggregates as filler in polymer-silica nanocomposites: long-range effects in rheology*. *Macromolecules*, **42**, 2031–2040.

Juhás, P., Davis, T., Farrow, C. L. & Billinge, S. J. L. (2013). *PDFgetX3: a rapid and highly automatable program for processing powder diffraction data into total scattering pair distribution functions*. *J. Appl. Cryst.* **46**, 560–566.

Keen, D. A. & Goodwin, A. L. (2015). *The crystallography of correlated disorder.* *Nature*, **521**, 303–309.

Kline, S. R. (2006). *Reduction and analysis of SANS and USANS data using IGOR Pro*. *J. Appl. Cryst.* **39**, 895–900.

Korolkov, D., Busch, P., Willner, L., Kentzinger, E., Rücker, U., Paul, A., Frielinghaus, H. & Brückel, T. (2012). *Analysis of randomly oriented structures by grazing-incidence small-angle neutron scattering*. *J. Appl. Cryst.* **45**, 245–254.

Kostorz, G. (1979). Editor. *Treatise on Materials Science and Technology*, Vol. 15, *Neutron Scattering*, pp. 227–287. New York: Academic Press.

Lai, Y.-H., Sun, Y.-S., Jeng, U.-S., Lin, J.-M., Lin, T.-L., Sheu, H.-S., Chuang, W.-T., Huang, Y.-S., Hsu, C.-H., Lee, M.-T., Lee, H.-Y., Liang, K. S., Gabriel, A. & Koch, M. H. J. (2006). *An instrument for time-resolved and anomalous simultaneous small- and wide-angle X-ray scattering (SWAXS) at NSRRC*. *J. Appl. Cryst.* **39**, 871–877.

Lake, J. A. (1967). *An iterative method of slit-correcting small angle X-ray data*. *Acta Cryst.* **23**, 191–194.

Lazzari, R. (2002). *IsGISAXS: a program for grazing-incidence small-angle X-ray scattering analysis of supported islands*. *J. Appl. Cryst.* **35**, 406–421.

Levine, J. R., Cohen, J. B. & Chung, Y. W. (1991). *Thin film island growth kinetics: a grazing incidence small angle X-ray scattering study of gold on glass*. *Surf. Sci.* **248**, 215–224.

Lindner, P. & Zemb, Th. (2002). Editors. *Neutron, X-ray & Light Scattering Methods Applied to Soft Condensed Matter.* Amsterdam: North Holland Delta Series.

Long, G. G., Jemian, P. R., Weertman, J. R., Black, D. R., Burdette, H. E. & Spal, R. (1991). *High-resolution small-angle X-ray scattering camera for anomalous scattering*. *J. Appl. Cryst.* **24**, 30–37.

Mathon, M. H., de Carlan, Y., Geoffroy, G., Averty, X., Alamo, A. & de Novion, C. H. (2003). *A SANS investigation of the irradiation-enhanced α–α' phases separation in 7–12 Cr martensitic steels*. *J. Nucl. Mater.* **312**, 236–248.

Mettus, D. & Michels, A. (2015). *Small-angle neutron scattering correlation functions of bulk magnetic materials. J. Appl. Cryst.* **48**, 1437–1450.

Mezei, F. (1980). *Neutron Spin Echo*. *Lecture Notes in Physics*, Vol. 128. Berlin, Heidelberg: Springer.

Moor, P. E. A. de, Beelen, T. P. M., Komanschek, B. U., Diat, O. & van Santen, R. A. (1997). *In situ investigation of Si-TPA-MFI crystallization using (ultra-) small- and wide-angle X-ray scattering*. *J. Phys. Chem. B*, **101**, 11077–11086.

Morrison, J. D., Corcoran, J. D. & Lewis, K. E. (1992). *The determination of particle size distributions in small-angle scattering using the maximum-entropy method*. *J. Appl. Cryst.* **25**, 504–513.

Mullen, K. & Levin, I. (2011). *Mitigation of errors in pair distribution function analysis of nanoparticles*. *J. Appl. Cryst.* **44**, 788–797.

Nelson, A. (2006). *Co-refinement of multiple-contrast neutron/X-ray reflectivity data using MOTOFIT*. *J. Appl. Cryst.* **39**, 273–276.

Parratt, L. G. (1954). *Surface studies of solids by total reflection of X-rays*. *Phys. Rev.* **95**, 359–369.

Pauly, T. R., Liu, Y., Pinnavaia, T. J., Billinge, S. J. L. & Rieker, T. P. (1999). *Textural mesoporosity and the catalytic activity of mesoporous molecular sieves with wormhole framework structures*. *J. Am. Chem. Soc.* **121**, 8835–8842.

Pedersen, J.-S. (1997). *Analysis of small-angle scattering data from colloids and polymer solutions: modeling and least-squares fitting*. *Adv. Colloid Interface Sci.* **70**, 171–210.

Pedersen, J. S. (2000). *Form factors of block copolymer micelles with spherical, ellipsoidal and cylindrical cores*. *J. Appl. Cryst.* **33**, 637–640.

Percus, J. K. & Yevick, G. J. (1958). *Analysis of classical statistical mechanics by means of collective coordinates*. *Phys. Rev.* **110**, 1–13.

Petkov, V., Ren, Y., Kabekkodu, S. & Murphy, D. (2013). *Atomic pair distribution functions analysis of disordered low-Z materials*. *Phys. Chem. Chem. Phys.* **15**, 8544–8554.

Ponchut, C. (2006). *Characterization of X-ray area detectors for synchrotron beamlines*. *J. Synchrotron Rad.* **13**, 195–203.

Porod, G. (1951). *X-ray low angle scattering of dense colloid systems, part I*. *Kolloid Z.* **124**, 83–114.

Porod, G. (1952). *X-ray low angle scattering of dense colloid systems, part II*. *Kolloid Z.* **125**, 108–122.

Potton, J. A., Daniell, G. J. & Rainford, B. D. (1988). *Particle size distributions from SANS data using the maximum entropy method*. *J. Appl. Cryst.* **21**, 663–668.

Price, D. L. (1999). *Neutron scattering from disordered materials*. *J. Neutron Res.* **7**, 247–258.

Proffen, T., Billinge, S. J. L., Egami, T. & Louca, D. (2003). *Structural analysis of complex materials using the atomic pair distribution function – a practical guide*. *Z. Kristallogr.* **218**, 132–143.

Proffen, T. & Kim, H. (2009). *Advances in total scattering analysis*. *J. Mater. Chem.* **19**, 5078–5088.

Rauscher, M., Salditt, T. & Spohn, H. (1995). *Small-angle X-ray scattering under grazing incidence: the cross section in the distorted-wave Born approximation*. *Phys. Rev. B*, **52**, 16855–16863.

Rekveldt, M. T. (1996). *Novel SANS instrument using neutron spin echo*. *Nucl. Instrum. Methods Phys. Res. B*, **114**, 366–370.

Renteria, A. F., Saruhan, B., Ilavsky, J. & Allen, A. J. (2007). *Application of USAXS analysis and non-interacting approximation to determine the influence of process parameters and ageing on the thermal conductivity of electron-beam physical vapor deposited thermal barrier coatings*. *Surf. Coat. Technol.* **201**, 4781–4788.

Riseman, T. M., Kealey, P. G., Forgan, E. M., Mackenzie, A. P., Galvin, L. M., Tyler, A. W., Lee, S. L., Ager, C., Paul, D., Aegerter, C. M., Cubitt, R., Mao, Z. Q., Akima, T. & Maeno, Y. (1998). *Observation of a square flux-line lattice in the unconventional superconductor* Sr_2RuO_4. *Nature*, **396**, 242–245.

Ritter, C., Ibarra, M. I., De Teresa, J. M., Algarabel, P. A., Marquina, C., Blasco, J., Garcia, J., Oseroff, S. & Cheong, S.-W. (1997). *Influence of oxygen content on the structural, magnetotransport, and magnetic properties of* $LaMnO_{3+\delta}$. *Phys. Rev. B*, **56**, 8902–8911.

Roe, R.-J. (1999). *Methods of X-ray and Neutron Scattering in Polymer Science.* Don Mills: Oxford University Press (Canada).

Roess, L. C. & Shull, C. G. (1947). *X-ray scattering at small angles by finely-divided solids. II. Exact theory for random distributions of spheroidal particles*. *J. Appl. Phys.* **18**, 308–313.

Roux, J.-N., Broseta, B. & Deme, B. (2001). *SANS study of asphaltene aggregation: concentration and solvent quality effects*. *Langmuir*, **17**, 5085–5092.

Saldin, D. K., Poon, H. C., Bogan, M. J., Marchesini, S., Shapiro, D. A., Kirian, R. A., Weierstall, U. & Spence, J. C. H. (2011). *New light on disordered ensembles: ab initio structure determination of one particle from scattering fluctuations of many copies*. *Phys. Rev. Lett.* **106**, 115501.

Schelten, J. & Schmatz, W. (1980). *Multiple-scattering treatment for small-angle scattering problems*. *J. Appl. Cryst.* **13**, 385–390.

Scherrenberg, R., Coussens, B., van Vliet, P., Edouard, G., Brackman, J., de Brabander, E. & Mortensen, K. (1998). *The molecular characteristics of poly(propyleneimine) dendrimers as studied with small-angle neutron scattering, viscosimetry and molecular dynamics*. *Macromolecules*, **31**, 456–461.

Schwahn, D., Miksovsky, A., Rauch, H., Seidl, E. & Zugarek, G. (1985). *Test of channel-cut perfect crystals for neutron small angle scattering experiments*. *Nucl. Instrum. Methods Phys. Res. A*, **239**, 229–234.

Sears, V. F. (1992). *Neutron scattering lengths and cross sections*. *Neutron News*, **3**, 26–37.

Shull, C. G. & Roess, L. C. (1947). *X-ray scattering at small angles by finely-divided solids. I. General approximate theory and applications*. *J. Appl. Phys.* **18**, 295–307.

Sinha, S. K., Sirota, E. B., Garoff, S. & Stanley, H. B. (1988). *X-ray and neutron scattering from rough surfaces*. *Phys. Rev. B*, **38**, 2297–2311.

Spieler, H. (2008). *Semiconductor Detector Systems.* Oxford University Press.

Tavares, P. F., Leemann, S. C., Sjostrom, M. & Andersson, A. (2014). *The MAX IV storage ring project. J. Synchrotron Rad.* **21**, 862–877.

Thompson, A. (2009). Editor. *X-ray Data Booklet*. Publication PUB-490 Rev. 3. Berkeley: Lawrence Berkeley National Laboratory.

Toby, B. H. & Egami, T. (1992). *Accuracy of pair distribution function analysis applied to crystalline and non-crystalline materials*. *Acta Cryst.* A**48**, 336–346.

Wagner, W., Wiedenmann, A., Petry, W., Geibel, A. & Gleiter, H. (1991). *Magnetic microstructure of nanostructured Fe, studied by small angle neutron scattering*. *J. Mater. Res.* **6**, 2305–2311.

Warren, B. E. (1990). *X-ray Diffraction*. New York: Dover.

White, C. E., Provis, J. L., Proffen, T., Riley, D. P. & van Deventer, J. S. J. (2010). *Combining density functional theory (DFT) and pair distribution function (PDF) analysis to solve the structure of metastable materials: the case of metakaolin*. *Phys. Chem. Chem. Phys.* **12**, 3239–3245.

Wilson, K. S., Allen, A. J., Washburn, N. R. & Antonucci, J. M. (2007). *Interphase effects in dental nanocomposites investigated by small-angle neutron scattering*. *J. Biomed. Mater. Res. A*, **81**, 113–123.

Yaron, U., Gammel, P. L., Huse, D. A., Kleiman, R. N., Oglesby, C. S., Bucher, E., Batlogg, B., Bishop, D. J., Mortensen, K. & Clausen, K. N. (1995). *Structural evidence for a two-step process in the depinning of the superconducting flux-line lattice*. *Nature*, **376**, 753–755.

Zhang, F., Allen, A. J., Levine, L. E., Ilavsky, J., Long, G. G. & Sandy, A. R. (2011). *Development of ultra-small-angle X-ray scattering–X-ray photon correlation spectroscopy*. *J. Appl. Cryst.* **44**, 200–212.

Zhao, J. K., Gao, C. Y. & Liu, D. (2010). *The extended Q-range small-angle neutron scattering diffractometer at the SNS*. *J. Appl. Cryst.* **43**, 1068–1077.

Zhao, J., Meerwinck, W., Niinikoski, T., Rijllart, A., Schmitt, M., Willumeit, R. & Stuhrmann, H. (1995). *The polarized target station at GKSS*. *Nucl. Instrum. Methods Phys. Res. A*, **356**, 133–137.

International Tables for Crystallography (2019). Vol. H, Chapter 6.1, pp. 698–715.

6.1. Survey of computer programs for powder diffraction

C. J. Gilmore, J. A. Kaduk and H. Schenk

Table 6.1.1 lists currently available software for use in all areas of powder diffraction. It is based on the software database on the SINCRIS Information Server at http://www.cristal.org/DU-SDPD/nexus/iucr2/sincris-/index.htm supplemented by program references in chapters in this book and work carried out by Lachlan Cranswick before his untimely death. The latter can be found in Cranswick (2008) and on the CCP14 website at http://www.ccp14.ac.uk. CCP14 is curated in a minimal way by Professor Jeremy Cockcroft, who can be contacted at j.k.cockcroft@ucl.ac.uk.

We have used the following criteria for inclusion of programs in this list:

(1) The software must have a relevance to powder diffraction. Programs that only use single-crystal diffraction data have been excluded.

(2) The software must be current *i.e.* there must be a valid URL or a contactable author.

(3) Software that pre-dates the year 2000 and that seems to have no current user base has been excluded. Readers who need access to older programs can find details on the CCP14 website.

At the time of writing (March 2019) all the URLs in the table are active, but it is of course impossible to guarantee that this will not change quite rapidly.

The programs are listed in alphabetical order with a brief description of their use, a primary reference and a URL or contact e-mail address that should enable the reader to get easy access to the required software. The online version of this chapter is probably more convenient in this respect, since it allows the reader to search for specific program functions.

References

ACerS–NIST Phase Equilibria Diagrams Database (2013). CD-ROM database. The American Ceramic Society, Westerville, OH 43082, USA.

Akeroyd, F. A., Ashworth, R. L., Campbell, S. I., Johnston, S. D., Moreton-Smith, C. M., Sergeant, R. G. & Sivia, D. S. (1999). *Open GENIE reference manual.* Rutherford Appleton Laboratory Technical Report RAL-TR-1999-031. Rutherford Appleton Laboratory, Didcot, UK.

Allen, F. H., Johnson, O., Shields, G. P., Smith, B. R. & Towler, M. (2004). *CIF applications. XV. enCIFer: a program for viewing, editing and visualizing CIFs. J. Appl. Cryst.* **37**, 335–338.

Altermatt, U. D. & Brown, I. D. (1987). *A real-space computer-based symmetry algebra. Acta Cryst.* A**43**, 125–130.

Altomare, A., Burla, M. C., Giacovazzo, C., Guagliardi, A., Moliterni, A. G. G., Polidori, G. & Rizzi, R. (2001). *Quanto: a Rietveld program for quantitative phase analysis of polycrystalline mixtures. J. Appl. Cryst.* **34**, 392–397.

Altomare, A., Cuocci, C., Giacovazzo, C., Moliterni, A., Rizzi, R., Corriero, N. & Falcicchio, A. (2013). *EXPO2013: a kit of tools for phasing crystal structures from powder data. J. Appl. Cryst.* **46**, 1231–1235.

Aroyo, M. I., Perez-Mato, J. M., Orobengoa, D., Tasci, E., de la Flor, G. & Kirov, A. (2011). *Crystallography online: Bilbao Crystallographic Server. Bulg. Chem. Commun.* **43**, 183–197.

Babonneau, D. (2010). *FitGISAXS: software package for modelling and analysis of GISAXS data using IGOR pro. J. Appl. Cryst.* **43**, 929–936.

Baerlocher, Ch., Hepp, A. & Meier, W. M. (1976). *DLS-76, a program for the simulation of crystal structures by geometric refinement.* Institut für Kristallographie, ETH Zurich, Switzerland.

Baerlocher, Ch., Hepp, A. & Meier, W. M. (1977). *A Fortran program for the simulation of crystal structures by geometric refinement.* Institut für Kristallographie, ETH Zurich, Switzerland.

Baerlocher, Ch., McCusker, L. B., Meier, W. M. & Olson, D. H. (2003). *Database of Zeolite Structures*, http://www.iza-structure.org/.

Balzar, D. (1995). *BREADTH – a program for analyzing diffraction line broadening. J. Appl. Cryst.* **28**, 244–245.

Barr, G., Dong, W. & Gilmore, C. J. (2009). *PolySNAP3: a computer program for analysing and visualizing high-throughput data from diffraction and spectroscopic sources. J. Appl. Cryst.* **42**, 965–974.

Belsky, A., Hellenbrandt, M., Karen, V. L. & Luksch, P. (2002). *New developments in the inorganic crystal structure database (ICSD): accessibility in support of materials research and design. Acta Cryst.* B**58**, 364–369.

Bergmann, J. (2007). *EFLECH/INDEX – another try of whole pattern indexing. Z. Kristallogr. Suppl.* **2007**, 197–202.

Bergmann, J., Friedel, P. & Kleeberg, R. (1998). *BGMN – a new fundamental parameters based Rietveld program for laboratory X-ray sources, its use in quantitative analysis and structure investigations. IUCr Commission on Powder Diffraction Newsletter*, No. 20, pp. 5–8.

Bergmann, J., Le Bail, A., Shirley, R. & Zlokazov, V. B. (2004). *Renewed interest in powder diffraction data indexing. Z. Kristallogr.* **219**, 783–790.

Birkenstock, J., Fischer, R. X. & Messner, T. (2003). *BRASS 2003: The Bremen Rietveld Analysis and Structure Suite. Ber. DMG Beih. Eur. J. Mineral.* **15**, 21.

Boin, M. (2012). *nxs: a program library for neutron cross section calculations. J. Appl. Cryst.* **45**, 603–607.

Boultif, A. & Louër, D. (2004). *Powder pattern indexing with the dichotomy method. J. Appl. Cryst.* **37**, 724–731.

Bowden, M. E. (2000). *ConvX – data file conversion software for Windows. IUCr Commission on Powder Diffraction Newsletter*, No. 23, p. 21.

Brown, I. D. (1977). *Predicting bond lengths in inorganic crystals. Acta Cryst.* B**33**, 1305–1310.

Brown, I. D. (1996). *VALENCE: a program for calculating bond valences. J. Appl. Cryst.* **29**, 479–480.

Brückner, S. & Immirzi, A. (1997). *DEBVIN – a program for Rietveld refinement with generalized coordinates subjected to geometrical restraints. J. Appl. Cryst.* **30**, 207–208.

Bruno, I. J., Cole, J. C., Edgington, P. R., Kessler, M., Macrae, C. F., McCabe, P., Pearson, J. & Taylor, R. (2002). *New software for searching the Cambridge Structural Database and visualizing crystal structures. Acta Cryst.* B**58**, 389–397.

Bruno, I. J., Cole, J. C., Kessler, M., Luo, J., Motherwell, W. D. S., Purkis, L. H., Smith, B. R., Taylor, R., Cooper, R I., Harris, S. E. & Orpen, A. G. (2004). *Retrieval of crystallographically-derived molecular geometry information. J. Chem. Inf. Comput. Sci.* **44**, 2133–2144.

Bruno, I. J., Cole, J. C., Lommerse, J. P. M., Rowland, R. S., Taylor, R. & Verdonk, M. L. (1997). *IsoStar: A library of information about nonbonded interactions. J. Comput. Aided Mol. Des.* **11**, 525–537.

Canepa, P., Hanson, R. M., Ugliengo, P. & Alfredsson, M. (2011). *J-ICE: a new Jmol interface for handling and visualizing crystallographic and electronic properties. J. Appl. Cryst.* **44**, 225–229.

Casas-Cabanas, M., Reynaud, M., Rikarte, J., Horbach, P. & Rodríguez-Carvajal, J. (2016). *FAULTS: a program for refinement of structures with extended defects. J. Appl. Cryst.* **49**, 2259–2269.

(*continued on page* 713)

Copyright © 2019 International Union of Crystallography

Table 6.1.1
Software for powder diffraction

Program	Description	Function(s)	Reference(s)	URL or other source	Availability
ACerS–NIST Phase Equilibria Diagrams Database	Phase-equilibria diagrams	Database	ACerS–NIST Phase Equilibria Diagrams Database (2013)		Commercial
ADM	Software suite including device control, pattern evaluation, qualitative and quantitative phase analysis, indexing, lattice-parameter refinement, crystal-size evaluation, microstress analysis, profile analysis and pattern simulation	Phase analysis, indexing, lattice-parameter refinement, crystal size, stress, profile analysis, pattern simulation		http://www.RMSKempten.de/	Commercial
American Mineralogist Crystal Structure Database (AMCSD)	Online database that includes every structure published in *The American Mineralogist*, *The Canadian Mineralogist*, *European Journal of Mineralogy* and *Physics and Chemistry of Minerals*, as well as selected data sets from other journals	Minerals, database	Downs & Hall-Wallace (2003)	http://rruff.geo.arizona.edu/AMSamcsd.php	Free to use
ANAELU	Computer-based tools for inferring single-crystal structures and fibre textures from two-dimensional diffraction diagrams	Modelling, glasses	Fuentes-Montero *et al.* (2011)	http://www.esrf.eu/computing/scientific/ANAELU/Anelu_Page.htm	Free
ARITVE	Modelling of glass structures using the Rietveld method	Modelling, glasses	Le Bail (1995, 2000)	http://sdpd.univ-lemans.fr/aritve.html	Free
ATOMS	Structure visualization. Part of the *SHAPE* software package	Structure visualization	Shape Software, 521 Hidden Valley Road, Kingsport, TN 37663, USA	http://www.shapesoftware.com/	Commercial
AUTOFP	GUI for highly automated Rietveld refinement using an expert system algorithm based on *FULLPROF*	Rietveld refinement	Cui *et al.* (2015)	http://pmedia.shu.edu.cn/autofp	Free
AUTOX	Autoindexing multiphase samples; included with *VMRIA*	Indexing	Zlokazov (1995); Bergmann *et al.* (2004)	http://www.ccp14.ac.uk/ccp/web-mirrors/vmria	Free
AXES	Program for X-ray powder diffraction data evaluation, specially designed for peak-shape analysis and data preparation for Rietveld refinement in connection with *FULLPROF*	Data conversion, peak-shape analysis	Mändar *et al.* (1996)	http://www.ccp14.ac.uk/ccp/web-mirrors/axes/~hugo/axes/	Free for academic use
AXES-20B	Estimation of crystal size and shape. Links to a wide range of programs and includes a range of data-processing and display functions	Phase identification, data conversion, structure visualization, peak location, peak profiling, indexing	Mändar & Vajakas (1998); Mändar *et al.* (1999)	http://www.ccp14.ac.uk/ccp/web-mirrors/axes/	Free
Balls&Sticks	Structure visualization and animation	Structure visualization	Ozawa & Kang (2004)	http://www.toycrate.org/	Free
BALSAC	Construction, visualization and interactive analysis of crystal lattices	Structure visualization	K. Hermann, Fritz-Haber-Institut der MPG, Berlin, Germany	http://www.fhi-berlin.mpg.de/~hermann/Balsac/	Free
BEARTEX	Texture analysis in polycrystalline materials	Texture analysis	Wenk *et al.* (1998)	http://eps.berkeley.edu/~wenk/TexturePage/beartex.htm	Free

Program	Description	Function(s)	Reference(s)	URL or other source	Availability
BGMN	Fundamental parameters, Rietveld refinement and quantitative-analysis software	Fundamental parameters, Rietveld refinement, quantitative analysis	Bergmann *et al.* (1998)	http://www.bgmn.de/methods.html	Free
Bilbao Crystallographic Server	Variety of symmetry tools including space-group retrieval tools, Wyckoff positions of space groups and group–subgroup relations	Symmetry	Aroyo *et al.* (2011)	http://www.cryst.ehu.es/	Free
B-IncStrDB	Database of incommensurate structures	Database	Kroumova *et al.* (2005)	http://www.cryst.ehu.es/icsdb/	Free
Bond Valence Wizard	Predicts interatomic distances in crystals by the bond-valence method	Bond-length prediction	Orlov *et al.* (1998); Brown (1977)	http://orlov.ch/bondval/	Free
BRASS 2	Rietveld refinement, Fourier-map calculation and visualization software	Rietveld refinement, visualization	Birkenstock *et al.* (2003)	http://www.brass.uni-bremen.de/	Free
BREADTH	Analysis of diffraction line broadening	Line broadening	Balzar (1995)	http://www.du.edu/~balzar/breadth.htm	Free
Cambridge Structural Database	Database (including structures derived from powder data) with associated software and software suites; organics and organometallics	Database	Groom *et al.* (2016)	http://www.ccdc.cam.ac.uk/	Commercial
CaRine	Visualization of lattices, surfaces, interfaces and diffraction patterns	Visualization	C. Boudias & D. Monceau, 1989–2004, CaRIne Crystallography	http://carine.crystallography.pagesperso-orange.fr/	Commercial
CASTEP	Calculates the properties of materials from first principles	Physical properties	Segall *et al.* (2002)	http://www.castep.org/	Free for European academics
CCP14	Web page with links to powder diffraction software	Software database	Stephenson *et al.* (2006)	http://www.ccp14.ac.uk/	Free
cctbx	A set of basic programming tools for X-ray crystallography	Programming	Grosse-Kunstleve *et al.* (2002)	https://github.com/cctbx/cctbx_project	Free
CDASH	Runs *DASH* over a network of computers	Structure solution	Spillman *et al.* (2015)	https://www.ccdc.cam.ac.uk/Solutions/PowderDiffraction/Pages/DASH.aspx	Commercial
Celref	Program for refining the unit cell	Unit-cell refinement	Laugier & Bochu (2004)	http://www.ccp14.ac.uk/ccp/web-mirrors/lmgp-laugier-bochu/	Free
CHECKCELL	Indexing and space-group determination, links into *Crysfire*	Indexing, space-group determination		http://www.ccp14.ac.uk/tutorial/lmgp/chekcellb.htm	Free
checkCIF	Cif checking service	CIF		http://journals.iucr.org/services/cif/checking/checkfull.html	Free
Chemical Database Service (CDS)	EPSRC-funded access to a large number of scientific databases, including all the main crystallographic databases, to UK-based academics and students	Database	Fletcher *et al.* (1996)	http://cds.dl.ac.uk/	Free within UK
CIFTOOLS	Includes two programs: *pdCIFplot* to plot Rietveld results from pdCIF files, and *CIFEDIT* to create, browse through and edit CIF files	CIF		ftp://ftp.ncnr.nist.gov/pub/cryst/cif/	Free
Cinema:Debye-Scherrer	Interactive visualization of multi-data-set Rietveld analyses	Data visualization	Vogel *et al.* (2018)	https://github.com/cinemascience/cinema_debye_scherrer	Free

Program	Description	Function(s)	Reference(s)	URL or other source	Availability
CMPR	Displays diffraction data, manual and auto-indexing, and peak fitting	Data visualization, indexing, peak fitting	Toby (2005)	http://www.ncnr.nist.gov/xtal/software/cmpr/	Free
CMWP-fit	Determination of microstructural parameters from diffraction profiles	Profile fitting	Ribárik *et al.* (2001)	http://csendes.elte.hu/cmwp/	Free
CONEX	Angular calibration and averaging of two-dimensional powder diffraction patterns	Two-dimensional data	Gommes & Goderis (2010)	Available from the authors	Free
Conograph	Integrated system with a graphical user interface for indexing	Indexing	Esmaeili *et al.* (2017)	https://osdn.net/projects/conograph/releases/	Free
ConQuest	Software for searching the Cambridge Structural Database	Database searching	Bruno *et al.* (2002)	http://www.ccdc.cam.ac.uk/	Commercial
ConvX	Data-conversion program that can convert multiple files at once. Also possible to select a particular angular range to convert	Data conversion	Bowden (2000)	http://www.ccp14.ac.uk/ccp/web-mirrors/convx/	Free
Corina	Structure generator for drug-like molecules	Structure prediction	Molecular Networks GmbH, Nuremberg, Germany; Sadowski *et al.* (1994); Schwab (2010)	https://www.mn-am.com/products/corina	Commercial
CRISP	Uses crystallographic image processing to extract information from electron micrographs	Electron diffraction	Hovmöller (1992)	http://www.calidris-em.com/crisp.php	Commercial
CRYSCA	Crystal-structure calculations for flexible molecules	Structure prediction	Schmidt & Kalkhof (1997)	Available from the authors	
Cryscon	Allows conversion between several popular crystallographic file formats	Data conversion	Eric Dowry, Shape Software, 521 Hidden Valley Road, Kingsport, TN 37663, USA	http://www.shapesoftware.com/	Shareware
Crysfire	Automatic powder-pattern indexing	Indexing	Shirley (2002)	http://www.ccp14.ac.uk/tutorial/crys/, http://www.ccp14.ac.uk/ccp/web-mirrors/crys-r-shirley/	Free
CrystalDiffract	Data processing and visualization	Peak fitting	CrystalMaker Software Ltd, 5 Begbroke Science Park, Sandy Lane, Yarnton, OX5 1PF, UK	http://crystalmaker.com/crystaldiffract/index.html	Commercial
Crystal Maker X	Visualization, structure design, simulation and 3D printing package	Visualization, simulation	CrystalMaker Software Ltd, 5 Begbroke Science Park, Sandy Lane, Yarnton, OX5 1PF, UK	http://www.crystalmaker.com/	Commercial
Crystal Studio	Visualization including surfaces, interfaces, defects and simulation of diffraction data	Visualization, defects, data simulation	Crystalsoftcorp, PO Box 7006, Wattle Park, VIC 3128, Australia	http://www.crystalsoftcorp.com, http://www.crystal0studio.com/	Commercial
Crystallographica	A software toolkit for crystallography	Visualization, pattern simulation	Oxford Cryosystems (1997)	http://www.oxcryo.com/cg/	Free
Crystallography Open Database (COD)	Open-access database including predicted structures, covering organics, inorganics, metal–organics and minerals	Database	Grazulis *et al.* (2009)	http://www.crystallography.net/	Free

Program	Description	Function(s)	Reference(s)	URL or other source	Availability
CRYSTMET	Database of metals, alloys and intermetallics	Database	White *et al.* (2002); Toth Information Systems, Inc., 2045 Quincy Avenue, Ottawa, Ontario, K1J 6B2, Canada	https://cds.dl.ac.uk/cds/datasets/crys/mdf/llmdf.html	Free to UK academic users
DAJUST	Intensity extraction and space-group determination. Part of the *XLENS* package	Space-group determination, cell-parameter refinement, profile fitting, Le Bail method	Vallcorba *et al.* (2012)	https://departments.icmab.es/crystallography/news/42-pdsoftware	Free to non-commercial users
DANSE	General software for neutron scattering	Neutron scattering	Cummings *et al.* (2002)	http://wiki.cacr.caltech.edu/danse/index.php/Main_Page	Free
DASH	Software for solving crystal structures from X-ray powder diffraction patterns	Structure solution	David *et al.* (2006)	http://www.ccdc.cam.ac.uk/products/powder_diffraction/dash/	Commercial
Database of Zeolite Structures	Provides structural information on all of the zeolite framework types that have been approved by the Structure Commission of the International Zeolite Association (IZA-SC)	Database	Baerlocher *et al.* (2003)	http://www.iza-structure.org/databases/	Free
DataScan	Diffractometer automation hardware and software	Instrumentation, diffractometer control	Materials Data, Inc., 2551 Second Street, Livermore, CA 94550, USA	http://www.materialsdata.com/ds.htm	Commercial
Datasqueeze	Graphical interface for analysing data from two-dimensional X-ray diffraction detectors	Two-dimensional data analysis	Heiney (2002)	http://www.physics.upenn.edu/~heiney/datasqueeze/index.html	Free
DDM	Refinement using the Rietveld method or derivative difference minimization	Rietveld refinement, derivative difference refinement	Solovyov (2004)	https://sites.google.com/site/ddmsuite/	Free
Debussy 2.0	Analysis of powder diffraction data from nanocrystalline, defective and/or nonperiodic materials	Nanocrystalline and non-periodic materials, defects	Cervellino *et al.* (2015)	http://debussy.sourceforge.net/debussy/debussy.html	Free
DEBVIN	Rietveld refinement with the use of generalized coordinates	Rietveld refinement, polymers	Brückner & Immirzi (1997)	https://vdocuments.site/debvin-a-program-for-Rietveld-refinement-with-generalized-coordinates.html	Free
decryst	Software suite for structure determination from powder diffraction using the direct-space method	Structure solution	Liu (2018)	https://gitlab.com/CasperVector/decryst/	Free
Diamond	Crystal and molecular structure visualization and exploration	Structure visualization	Crystal Impact – K. Brandenburg and H. Putz GbR, Postfach 1251, D-53002 Bonn, Germany	http://www.crystalimpact.com/	Commercial
DICVOL	Automatic indexing	Indexing	Boultif & Louër (2004)	http://www.ccp14.ac.uk/ccp/web-mirrors/dicvol/	Free
DIFFaX	Simulation of powder diffraction patterns for faulted materials	Stacking faults, simulation	Treacy *et al.* (1991)	http://www.public.asu.edu/~mtreacy/DIFFaX.html	Free
DIFFaX+	A modified version of *DIFFaX* for the refinement of disordered stack materials	Refinement, disordered stack materials	Leoni *et al.* (2004)	Available from the author (matteo.leoni@unitn.it) on request	Free

Program	Description	Function(s)	Reference(s)	URL or other source	Availability
Diffpy-CMI	Python software for diffraction analysis and the study of the atomic structure of materials	Modelling	See https://www.diffpy.org/publications.html	http://diffpy.org	Free
DIFFRAC.EVA	Data processing, phase identification and quantitative analysis. Cluster analysis allows high-throughput screening	Profile fitting, cluster analysis, quantitative phase analysis	Bruker AXS GmbH, Oestliche Rheinbrueckenstr. 49, D-76187 Karlsruhe, Germany	https://www.bruker.com/products/x-ray-diffraction-and-elemental-analysis/x-ray-diffraction/xrd-software/eva/overview.html	Commercial
DIFFRAC.TOPAS	Profile and structure analysis (see *TOPAS*)	Profile analysis, Rietveld refinement	Bruker AXS GmbH, Oestliche Rheinbrueckenstr. 49, D-76187 Karlsruhe, Germany	https://www.bruker.com/products/x-ray-diffraction-and-elemental-analysis/x-ray-diffraction/xrd-software/topas.html	Commercial
DISCUS	Simulates defect structures and diffuse scattering, plus the simulation of perfect structures of non-crystalline materials	Defect structures, simulation	Proffen & Neder (1997, 1999)	https://www.xray.cz/ecm-cd/soft/xray/general/discus/discus/disfeat.html	Free
DLS-76	Structure refinement with distance constraints; part of *FOCUS*	Rietveld refinement	Baerlocher *et al.* (1976, 1977)	https://github.com/stefsmeets/focus_package, http://www.crystal.mat.ethz.ch/Software/index.html	Free
DRAWxtl	Open-source program for producing crystal-structure drawings	Visualization	Finger *et al.* (2007)	http://www.lwfinger.net/drawxtl/	Free
DRXWin	Diffraction data manipulation and qualitative analysis	Visualization, qualitative phase analysis, peak search	Vicent Primo Martín, El Instituto de Ciencia de los Materiales, Universitat de Valencia, Avda. Blasco Ibáñez, 13, 46010 Valencia, Spain	http://www.ccp14.ac.uk/ccp/web-mirrors/drxwin/drxwin/	Free
Dysnomia	Calculates electron and nuclear densities from observed structure factors by the maximum-entropy method	Electron and nuclear density calculations	Momma *et al.* (2013)	http://jp-minerals.org/dysnomia/en/	Free
Eager	Genetic algorithm for crystal structure solution from powder diffraction data	Structure solution	Harris *et al.* (2004)	Contact K. D. M. Harris	
EFLECH/INDEX	Whole-pattern indexing	Indexing	Bergmann (2007)	http://www.bgmn.de/indexpgm.html	Free
ELD	Quantitative information from electron-diffraction patterns	Electron diffraction	Calidris, Sweden	http://www.calidris-em.com/eld.php	Commercial
enCIFer	Viewing and editing CIF files	CIF editing	Allen *et al.* (2004)	https://www.ccdc.cam.ac.uk/Community/csd-community/encifer/	Free
Endeavour	Direct-space method for *ab initio* solution of structures from powder diffraction data by combined global optimization of pattern difference and potential energy	Structure solution	Putz *et al.* (1999)	http://www.crystalimpact.com/endeavour/	Commercial
EPCryst	Structure solution from powder diffraction data using models generated by an equivalent-position combination algorithm based on unit-cell content and space-group information	Structure solution	Deng & Dong (2011)	http://www.epcryst.com	Free
ESPOIR	Structure solution by Monte Carlo analysis of powder diffraction data	Structure solution	Le Bail (2001)	http://www.cristal.org/sdpd/espoir/	Free

Program	Description	Function(s)	Reference(s)	URL or other source	Availability
EXPGUI	Graphical interface for *GSAS*	Rietveld refinement, visualization	Toby (2001)	http://www.ncnr.nist.gov/programs/crystallography/software/expgui/	Free
EXPO2014	Structure-solution toolkit for phasing crystal structures from powder data	Structure solution	Altomare *et al.* (2013)	http://www.ba.ic.cnr.it/softwareic/expo/expo2014-installation/	Free for non-profit users
ExtSym	Space-group assignment. Bundled with *DASH* but can be obtained separately from Anders Markvardsen	Space-group determination	Markvardsen *et al.* (2001)	http://www.markvardsen.net/projects/ExtSym/main.html	Free
FABLE	Reads many X-ray detector image formats	Data processing	Schmidt *et al.* (2009)	http://sourceforge.net/projects/fable/	Free
FAULTS	Refinement of structures with extended defects, based on *DIFFaX*	Defect structures, simulation	Casas-Cabanas *et al.* (2016)		Free
FIT	Decomposition of powder diffraction patterns and profile analysis of pair correlation functions	Profile analysis, PDF analysis	Petkov & Bakaltchev (1990)	http://web.pa.msu.edu/people/petkov/software.html	Free for academic use
FIT2D	Calibration and correction of detector distortions, integration of two-dimensional data to a variety of one-dimensional scans, and one- and two-dimensional model fitting	Data analysis, visualization	Hammersley (1998, 2016); Hammersley *et al.* (1996)	http://www.esrf.fr/computing/scientific/FIT2D/	Free
FitAllb	Fitting centre-of-mass grain positions, orientation and elastic strain tensors	Strain	Oddershede *et al.* (2010)	https://sourceforge.net/p/fable/wiki/FitAllB/	Free
FitGISAXS	Modelling and analysis of grazing-incidence small-angle X-ray scattering data	GISAXS	Babonneau (2010)	https://www.pprime.fr/?q=en/node/1013; contact D. Babonneau, david.babonneau@univ-poitiers.fr	Free
FlexCryst	Program suite including crystal-structure prediction, structure determination and clustering	Structure prediction, structure determination	Hofmann & Apostolakis (2003)	http://www.flexcryst.com/html/home.pdf	Commercial
FOCUS	Automated structure determination of zeolites. Can use electron-diffraction data	Structure determination, zeolites	Grosse-Kunstleve *et al.* (1997)	https://github.com/stefsmeets/focus_package	Free
FOX	*Ab initio* structure determination using global-optimization algorithms, suitable for any type of crystal structure (organic, inorganic including automatic correction of special positions); can combine several data sets	Structure solution	Favre-Nicolin & Cerný (2002)	http://objcryst.sourceforge.net/Fox/	Free
FOXGrid	Structure solution using *FOX* with distributed computing	Structure solution	Rohlíček *et al.* (2007)	https://fox.vincefn.net/Manual/Fox.Grid	Free
FULLPAT	Full-pattern quantitative phase analysis merging the advantages of existing full-pattern fitting methods with the traditional reference intensity ratio method. Coded into Excel	Quantitative phase analysis	Chipera & Bish (2002)	http://www.ccp14.ac.uk/ccp/web-mirrors/fullpat/	Free
FULLPROF	Rietveld refinement and pattern matching	Rietveld refinement, pattern matching	Rodriguez-Carvajal (1990)	https://www.ill.eu/sites/fullprof/	Free
GDASH	Structure solution using grid computing	Structure solution	Griffin *et al.* (2009)	Contact Tom Griffin, tom.griffin@stfc.ac.uk	
GEST	Structure solution using a genetic algorithm	Structure solution	Feng & Dong (2007)	Contact Zhen Jie Feng, fengzhenjie@gmail.com	Free

Program	Description	Function(s)	Reference(s)	URL or other source	Availability
GETSPEC	Calculates the symmetry operators and special positions for any setting of any space group based on the Hall space-group symbol	Symmetry	Altermatt & Brown (1987)	http://www.ccp14.ac.uk/ccp/web-mirrors/i_d_brown/getspec/	Free
Gnu Xtal System	Set of portable crystallographic routines	Software development		http://xtal.sourceforge.net/	Free
GrainSpotter	Indexing grains in monophase crystalline materials	Indexing	Schmidt (2014)	https://sourceforge.net/p/fable/wiki/grainspotter/	Free
Gretep	Displacement-ellipsoid plot structure viewing and analysis. Part of the *LMGP* suite	Visualization	Laugier & Bochu (2004)	http://www.ccp14.ac.uk/tutorial/lmgp/#gretep, http://www.ccp14.ac.uk/ccp/web-mirrors/lmgp-laugier-bochu/	Free
GRINSP	Inorganic structure prediction	Structure prediction	Le Bail (2005)	http://www.cristal.org/grinsp/	Free
GSAS	Comprehensive system for the refinement of structural models to both X-ray and neutron diffraction data. Superseded by *GSAS-II*	Pattern fitting, structure solution, Rietveld refinement, visualization	Larson & Von Dreele (2004)	http://subversion.xray.aps.anl.gov/trac/EXPGUI	Free
GSAS-II	Open-source Python project that addresses all types of crystallographic studies, from simple materials through macromolecules, using both powder and single-crystal diffraction and with both X-ray and neutron probes	Pattern fitting, structure solution, Rietveld refinement, visualization	Toby & Von Dreele (2013)	https://subversion.xray.aps.anl.gov/trac/pyGSAS	Free
gsaslanguage	A language that provides input to and processes output from the *GSAS* package	Scripting	Vogel (2011)	http://code.google.com/p/gsaslanguage/	Free
GSASIIscriptable	Scripting interface for *GSAS-II*	Scripting	O'Donnell *et al.* (2018)	https://gsas-ii.readthedocs.io/en/latest/GSASIIscriptable.html	Free
GudrunN and *GudrunX*	Programs for correcting raw neutron and X-ray total-scattering data to differential cross sections	Data processing, neutron diffraction, total scattering	Soper & Barney (2011)	In-house software at ISIS	
HELIX	Simulation of helical diffraction	Powder-pattern calculation	Knupp & Squire (2004)	https://www.diamond.ac.uk/Instruments/Soft-Condensed-Matter/small-angle/SAXS-Software/CCP13.html	Free
Hypertext book of crystallographic space-group diagrams and tables	Space-group diagrams	Space-group information	Cockcroft (1999)	http://img.chem.ucl.ac.uk/sgp/	Commercial
ICDD Powder Diffraction File	Comprehensive powder database: PDF-4+, PDF-4 organics and PDF-2, plus derivatives	Database, phase identification	International Centre for Diffraction Data, 12 Campus Boulevard, Newtown Square, PA, 19073–3273, USA	http://www.icdd.com/	Commercial
IGOR Pro	Scientific data-analysis software	Data analysis	Kline (2006)	https://www.wavemetrics.com/products/igorpro	Commercial
ImageD11	Python codes for processing diffraction data from 2D detectors at the ID11 beamline at the ESRF	Data processing, neutron diffraction	Wright (2011)	http://sourceforge.net/projects/fable/files/ImageD11	Free
Inorganic Crystal Structure Database (ICSD)	Database of inorganic structures	Database	Belsky *et al.* (2002)	http://www2.fiz-karlsruhe.de/icsd_home.html	Commercial

Program	Description	Function(s)	Reference(s)	URL or other source	Availability
input4MAUD	Input of two-dimensional data into *MAUD*	Data conversion	Raue (2014)	http://kristall.uni-mki.gwdg.de/Docs/raue/input4MAUD/main.html	Free
International Tables Online	Online editions of all volumes of *International Tables for Crystallography*, including Volume A (*Space-Group Symmetry*), and an extensive symmetry database	Space-group information, database	*International Tables Online* (2019)	https://it.iucr.org	Commercial
iotbx.cif	Input, output and validation of CIFs	CIF	Gildea *et al.* (2011)	https://cci.lbl.gov/cctbx_docs/iotbx/iotbx.cif.html	Free
ISAACS	Interactive structure analysis of amorphous and crystalline systems	Structure analysis, amorphous materials	Le Roux & Petkov (2010)	http://isaacs.sourceforge.net	Free
IsoDEC	Calculation of diffraction elastic constants	Strain	Gnäupel-Herold (2012)	https://www.ncnr.nist.gov/xtal/software/isodec	Free
IsoStar	Information on intermolecular interactions derived from small-molecule crystal structures in the Cambridge Structural Database and from protein–ligand interactions observed in the Protein Data Bank (PDB)	Database	Bruno *et al.* (1997)	https://www.ccdc.cam.ac.uk/solutions/csd-system/components/isostar/	Commercial
ISOTROPY	Applies group-theoretical methods to the analysis of phase transitions in crystalline solids	Space-group determination	Stokes & Hatch (2002)	http://stokes.byu.edu/isotropy.html	Free web service
ITO	Powder-pattern indexing. Incorporated into many other packages, both free and commercial	Indexing	Visser (1969)	http://sdpd.univ-lemans.fr/ftp/ito13.zip	Free/commercial
JADE	Comprehensive powder diffraction data-processing suite. *JADE Standard* is available as perpetual license and *JADE Pro* as an annual subscription	Cluster analysis, data conversion, indexing, Le Bail fitting, Pawley fitting, peak location, peak profiling, phase identification, powder-pattern viewing, quantitative phase anaysis, Rietveld refinement, size–strain analysis	Materials Data, Inc. (2016)	http://www.materialsdata.com/products.htm; http://www.icdd.com/	Commercial
Jana2006	Analysis of incommensurate, modulated and composite structures, as well as standard Rietveld refinement	Le Bail fitting, Rietveld refinement, Fourier-map calculation and visualization, structure solution	Petříček *et al.* (2000); Dusek *et al.* (2001)	http://jana.fzu.cz/	Free
JEMS	Simulation of high-resolution TEM (HRTEM), CBED, PED and SAED patterns, and simulation of powder diffraction rings	Electron diffraction, simulation	Stadelmann (2003)	http://www.jems-saas.ch/Home/jemsWebSite/jems.html	Free for students
J-ICE	Visualization of crystallographic and electronic properties using *Jmol*	Visualization, data conversion	Canepa *et al.* (2011)	http://j-ice.sourceforge.net	Free
Jpowder	JAVA data viewer	Data visualization	Markvardsen *et al.* (2010)	https://sourceforge.net/projects/jpowder/	Free
KoalaRiet	Powder-pattern viewing, peak profiling and Rietveld refinement, fundamental parameters approach	Pattern visualization, peak fitting, Rietveld refinement	Cheary & Coelho (1996)	http://www.ccp14.ac.uk/	Free

Program	Description	Function(s)	Reference(s)	URL or other source	Availability
LABOTEX	Crystallographic texture analysis of rocks, semiconductors and superconductors, ceramics and composites, polymers, metals and alloys	Texture analysis	Pawlik & Ozga (1999)	http://www.labosoft.com.pl/	Commercial
LAPOD	Refinement of lattice parameters using optimal regression	Unit-cell refinement	Dong & Langford (2000)	http://www.ccp14.ac.uk/ccp/web-mirrors/powderx/lapod/	Free
LauePt	GUI for Laue-pattern simulation and analysis	Data analysis, simulation	Huang (2010)	http://www.ccp14.ac.uk/ccp/web-mirrors/xianrong-huang/	Free
MacDiff	Analysis and display of powder data on Macintosh platforms	Database, phase identification, data conversion	Petschick (2001)	http://www.geol-pal.uni-frankfurt.de/Staff/Homepages/Petschick/MacDiff/MacDiffInfoE.html	Free
MATCH!	Compares the diffraction pattern of the unknown to a database containing reference patterns; additional knowledge such as known phases, elements or density can also be used	Phase identification, quantitative phase analysis	Crystal Impact – K. Brandenburg and H. Putz GbR, Postfach 1251, D-53002 Bonn, Germany	http://www.crystalimpact.com/match/	Commercial
Materials Studio	Multipurpose suite	Indexing, model building, structure solution, visualization		http://accelrys.com/products/collaborative-science/biovia-materials-studio/	Commercial
MAUD	Rietveld-based program for combined analysis. Can be used to fit diffraction, fluorescence and reflectivity data collected using X-rays, neutrons or electrons	Data integration, indexing, space-group assignment, texture analysis, size–strain analysis, Rietveld refinement, quantitative phase analysis	Lutterotti *et al.* (1999)	http://maud.radiographema.eu/	Free
MCE-Marching Cubes	Interactive visualization of electron and other density maps, optimized for small molecules	Fourier-map calculation and visualization	Husák & Kratochvíl (2003)	https://sourceforge.net/projects/mce-marching-cube-eld/	Free
McMaille	Indexing using Monte Carlo methods	Indexing	Le Bail (2004)	http://www.cristal.org/McMaille	Free
Mercury	Statistical analysis of data from the Cambridge Structural Database, structure visualization and simulation of powder patterns	Structure visualization	Sykes *et al.* (2011)	http://www.ccdc.cam.ac.uk/products/mercury/	Free; commercial version has more functions
MINCRYST	Contains crystal-structure data for minerals	Database	Chichagov *et al.* (2001)	http://database.iem.ac.ru/mincryst/	Free
The Mineralogy Database	Includes information on the crystal structures, powder diffraction patterns, chemical composition, and physical and optical properties of minerals	Database		http://webmineral.com	Free
Mogul	Validation of bond lengths, angles and torsions against the Cambridge Structural Database	Structure validation	Bruno *et al.* (2004)	http://www.ccdc.cam.ac.uk/products/csd_system/mogul/	Commercial
MOPAC2016	Semi-empirical quantum chemistry calculations. *Mercury* has an interface to *MOPAC*	Structure validation, structure building	Stewart (2012)	http://openmopac.net	Free for academic use
Mstruct	Microstructure analysis using powder diffraction	Microstructure analysis	Matěj *et al.* (2014)	http://www.xray.cz/mstruct/	Free

Program	Description	Function(s)	Reference(s)	URL or other source	Availability
Multifit/Polydefit	Open-source IDL software package for data analysis of synchrotron-based plasticity, rheology or other time-dependent experiments	Texture analysis	Merkel & Hilairet (2015)	http://merkel.texture.rocks/Multifit-Polydefix/	Free
MultiRef	*MATLAB* framework for *GSAS*; Rietveld refinement of multiple powder diffractograms from *in situ*, scanning or diffraction tomography experiments	Rietveld refinement	Frølich & Birkedal (2015)	http://chem.au.dk/en/research/research-areas/inorganicchemistrymaterialschemistry/biological-and-bioinspired-materials/multiref/downloads/	Free
NanoPDF64	Software package for analysis of pair-distribution functions of nanocrystals, also capable of calculating theoretical powder diffraction patterns and pair-distribution functions for atomistic models of nanocrystals	PDF analysis	Skrobas *et al.* (2017)	http://www.unipress.waw.pl/nanopdf	Free
NEWMOD II	Modelling of interstratified layer structures	Powder-pattern calculation	Yuan & Bish (2010)	https://newmod-for-clays.com	Commercial
Nickel–Nichols Mineral Database	Mineral database	Phase identification	The Nickel–Nichols Mineral Database, Materials Data, Inc., 1224 Concannon Blvd, Livermore, CA 94550, USA; Nickel & Nichols (1991)	http://www.materialsdata.com/MINERALS.htm	Free
Nika	Open-source *Igor Pro*-based program for reduction of two-dimensional scattering data from area-detector small- and wide-angle scattering instruments. Can be used in transmission and grazing-incidence geometries	SAXS, WAXS	Ilavsky (2012)	https://usaxs.xray.anl.gov/software/nika	Free
NXS	Library for neutron cross-section calculations	Neutron diffraction	Boin (2012)	https://www.helmholtz-berlin.de/people/boin/nxs_en.html	Free
OpenBabel	Open-source chemistry toolbox, allowing users to search, convert, analyse or store data from molecular modelling, chemistry, solid-state materials, biochemistry or related areas	File conversion	O'Boyle *et al.* (2011)	http://openbabel.sourceforge.net/	Free
OpenGenie	Neutron-data analysis	Powder-pattern visualization	Akeroyd *et al.* (1999)	http://www.opengenie.org/Main_Page	Free
PASCal	Online tool for determining principal coefficients of thermal expansion and compressibilities using variable-pressure and variable-temperature lattice-parameter data	Strain	Cliffe & Goodwin (2012)	http://pascal.chem.ox.ac.uk	Free web access
PATE	*GSAS* powder-pattern extractor	Data conversion		http://www.ccp14.ac.uk/ccp/web-mirrors/scott-belmonte-software/pate/	Free
PCED3	Simulation of polycrystalline electron diffraction and phase identification	Electron diffraction, phase identification		http://www.unl.edu/ncmn-cfem/xzli/download	Free
PCOD	Open database of structures of inorganic compounds predicted or enumerated mainly using *ZEFSA II* or *GRINSP*	Phase identification, database		http://www.crystallography.net/pcod/	Free

Program	Description	Function(s)	Reference(s)	URL or other source	Availability
PDXL 2	Provides various analysis tools such as automatic phase identification, quantitative analysis, crystallite-size analysis, lattice-constants refinement, Rietveld analysis, *ab initio* structure determination and data clustering. Peak shapes can be modelled using a fundamental-parameters approach	Rietveld refinement, quantitative analysis, phase identification, structure determination	Rigaku (2014)	https://www.rigaku.com/en/service/software/pdxl	Commercial
PeckCryst	Molecular crystal structure determination from powder diffraction data using a particle swarm optimization algorithm	Structure solution	Feng *et al.* (2009)	Contact J. C. Zhang, jczhang@shu.edu.cn	Free
PLATON	Implements a large variety of standard geometrical calculations and tests (*e.g.* for missing symmetry, voids in the lattice *etc.*), and includes utilities for cell transformation and graphics. Used in *checkCIF*	Data conversion, space-group assignment, structure refinement, H-atom placement, structure validation, powder-pattern calculation, structure visualization	Spek (1998, 2003)	http://www.cryst.chem.uu.nl/platon/	Free
PM2K	Full-pattern fitting allowing microstructural investigation of nanocrystalline materials. Includes analysis of size broadening due to an analytical or to a generic (unconstrained) distribution of crystallites, the presence of dislocations, stacking faults and antiphase boundaries	Whole-powder-pattern modelling	Leoni *et al.* (2006)	Contact M. Leoni, matteo.leoni@unitn.it	Free for academic use
PolySNAP3	Clustering powder diffraction, XRF and spectroscopic data. Semi-quantitative analysis	Cluster analysis, phase analysis	Barr *et al.* (2009)	http://www.bruker.com/	Commercial
popLA	Pole-figure evaluation using the harmonic and WIMV methods	Texture analysis	Kocks *et al.* (1998)	http://lansce.lanl.gov/facilities/lujan/instruments/hippo/popLA.php	Free
Powder Cell	Represents the crystal structure and the corresponding powder pattern simultaneously. Translations and rotations of a preselected part of the asymmetric unit allow manipulation of the structure	Data conversion, powder-pattern calculation, powder-pattern viewing, Le Bail fitting, size–strain analysis, Rietveld refinement, quantitative phase analysis, structure visualization	Kraus & Nolze (1996)	http://powdercell-for-windows.software.informer.com/2.4/	Free
Powder3D	Multiple-pattern data reduction and graphical presentation. Part of *Materials Studio*	Data integration, data conversion, powder-pattern viewing, peak location	Hinrichsen *et al.* (2008)	https://www.fkf.mpg.de/4708688/Powder-3D-Software	Free
PowderX	Uses include plotting X-ray patterns, data smoothing, background subtraction, α_2-peak elimination, peak search, indexing, zero-angle error correction and data-format conversions	Data conversion, powder-pattern viewing, peak location, indexing	Dong (1999)	http://www.ccp14.ac.uk/ccp/web-mirrors/powderx/Powder/	Free
PowDLL	.NET dynamic link library used for interconversion between variable formats of X-ray powder diffraction files	Data conversion	Kourkoumelis (2005)	http://users.uoi.gr/nkourkou/powdll.htm	Free

Program	Description	Function(s)	Reference(s)	URL or other source	Availability
PRODD	Refinement of crystal and magnetic structures from powder diffraction data, can be used with time-of-flight and constant-wavelength neutron data as well as synchrotron X-ray data	Pawley fitting, Rietveld refinement, proteins	Wright (2004); Wright & Forsyth (2000); Wright *et al.* (2007)	http://www.ccp14.ac.uk/ccp/web-mirrors/prodd/~jpw22/	Free
PROFEX	A platform-independent open-source graphical user interface for the Rietveld refinement program *BGMN*. Reads and converts a variety of proprietary raw data formats	Rietveld refinement, data conversion	Doebelin & Kleeberg (2015)	http://profex.doebelin.org/	Free
Profil	Rietveld refinement and utilities. Can be used for organics and organometallics requiring restrained refinement	Unit-cell refinement, Rietveld refinement, Fourier-map calculation, visualization, data conversion	Cockcroft (1994)	http://img.chem.ucl.ac.uk/www/cockcroft/profil.htm	Free for academic use
publCIF	Editing, validating and formatting CIF files	CIF editing	Westrip (2010)	http://journals.iucr.org/services/cif/publcif/	Free
PyCifRW	Support for reading and writing of CIF files using Python, with optional validation against DDL dictionaries	CIF editing	Hester (2006)	https://pypi.org/project/PyCifRW/4.3/	Free
PyMOL	A comprehensive software package for rendering and animating 3D structures	Structure visualization		https://pymol.org/2/	Commercial
Quanto	Allows automatic estimation of the weight fraction of each crystalline phase in a mixture. The amorphous content can be estimated using the internal-standard method, and corrections for preferred orientation and microabsorption effects are available	Quantitative phase analysis	Altomare *et al.* (2001)	http://www.ic.cnr.it/	Free
RIETAN-FP	A package of programs for analysing crystal structures from X-ray and neutron powder diffraction data and visualizing the results in three dimensions, along with electronic-state calculations	Rietveld refinement, data conversion	Izumi & Momma (2007)	http://fujioizumi.verse.jp/download/download_Eng.html	Free
Rietica	Aids the creation and updating of Rietveld input files for and provides point-and-click control of the Rietveld program *LHPM*	Le Bail fitting, Rietveld refinement, visualization	Hunter (1998)	http://www.rietica.org/	Free
RMC++	Reverse Monte Carlo modelling of the structure of disordered materials, mainly using diffraction data, but additional information such as EXAFS data and different constraints can also be used	PDF analysis	Evrard & Pusztai (2005)	http://www.szfki.hu/~nphys/rmc++/opening.html	Free
RMCAW95	Uses the reverse Monte Carlo method for modelling both lattice and magnetic disorder in powder crystalline materials by direct calculation of the structure factor	PDF analysis	Mellergård & McGreevy (1999)	http://www.cristal.org/glasses/rmca/rmcaw95.html	Free

Program	Description	Function(s)	Reference(s)	URL or other source	Availability
RMCprofile	Built from the original *RMCA* code of McGreevy & Pusztai to determine the local structure of crystalline materials while still being capable of analysing disordered systems. Can be used to fit many data types (including total scattering, EXAFS, diffuse scattering) simultaneously	PDF analysis	Tucker *et al.* (2007)	http://www.rmcprofile.org	Free
ROCKJOCK	Quantitative analysis of mineralogical samples with or without using an internal standard by automatically fitting the sum of stored X-ray diffraction patterns of pure standard minerals to the measured pattern	Quantitative phase analysis, minerals	Eberl (2003)	http://pubs.er.usgs.gov/publication/ofr200378	Free
Siroquant	Comes with a comprehensive database of over 1800 phases. Phases from public sources such as the ICSD and AMCSD can also be added	Phase identification	Sietronics (2012)	http://www.siroquant.com	Commercial
SPEC	Software for the control of data acquisition. Includes *C-PLOT* for data display and analysis	Instrumentation	SPEC, Certified Scientific Software, PO Box 390640, Cambridge, MA, 02139-0007, USA	http://www.certif.com/	Commercial
STEREOPOLE	Analysis of X-ray diffraction pole figures, allowing experimental data to be compared graphically with simulated results, and epitaxic relationships between up to five different crystal layers to be evaluated	Texture analysis	Salzmann & Resel (2004)	http://www.if.tugraz.at/amd/stereopole/	Free
Struvir	Converts *STRUPLO* data files into Virtual Reality Modeling Language (VRML) for 3D visualization	Visualization	Le Bail (1996); Fischer (1985)	http://www.cristal.org/vrml/struvir.html	Free
SUPERFLIP	Structure solution from diffraction data using charge flipping. Can solve periodic structures, incommensurately modulated structures and the structures of quasicrystals from X-ray and neutron diffraction data	Structure solution	Palatinus & Chapuis (2007)	http://superflip.fzu.cz	Free
TOPAS and *TOPAS-Academic*	Nonlinear least-squares optimization programs written in C++, allowing users to easily modify program functionality to suit the problem at hand	Peak fitting, Le Bail fitting, Pawley fitting, Rietveld refinement, PDF analysis, indexing, structure solution, charge flipping, magnetic structures, stacking-fault analysis	Coelho (2018)	https://www.bruker.com/products/x-ray-diffraction-and-elemental-analysis/x-ray-diffraction/xrd-software/topas.html, http://www.topas-academic.net	Free
VALENCE	Calculates bond valences from bond lengths and *vice versa*. Can also calculate bond-valence sums and average bond lengths, and can determine bond-valence parameters from the bonding environments of various cations	Structure validation	Brown (1996)	http://netlib.ccp14.ac.uk/ccp/web-mirrors/valence	Free
VMRIA	Full-profile analysis of neutron-diffraction time-of-flight data for multiphase samples. Includes *Autox*	Rietveld refinement, indexing	Zlokazov & Chernyshev (1992); Zlokazov (2003)	http://www.ccp14.ac.uk/ccp/web-mirrors/vmria/	Free

Program	Description	Function(s)	Reference(s)	URL or other source	Availability
WinPLOTR	A graphical user interface for displaying powder patterns; part of *FULLPROF*	Powder-pattern viewing		http://www.cdifx.univ-rennes1.fr/winplotr/readme.htm	Free
WinPSSP	Uses direct-space methods to solve the crystal structures of small-molecule organic materials from X-ray powder diffraction data	Structure solution	Pagola *et al.* (2017)	http://users.uoi.gr/nkourkou/winpssp/	Free
WinXPow	Comprehensive package for data collection, profile fitting, indexing, and size–strain and crystallinity analysis	Phase identification, profile fitting, indexing, size–strain analysis, crystallinity	STOE & Cie GmbH, Hilpertstr. 10, D-64295 Darmstadt, Germany	https://www.stoe.com/product/software-powder-xrd/	Commercial
XDrawChem	Two-dimensional molecule drawing program for Unix operating systems	Model building	Herger (2002)	http://xdrawchem.sourceforge.net/	Free
xINTERPDF	Analysis of intermolecular pair-distribution functions of organic compounds from X-ray total-scattering data	PDF analysis	Shi (2018)	https://github.com/curieshicy/xINTERPDF	Free
XLENS	Uses Patterson-function direct methods instead of the modulus function. Well suited for handling powder diffraction data for organic compounds	Structure solution	Rius (2011, 2013)	https://departments.icmab.es/crystallography/software	Free for academic use
xPDFsuite	Suite of algorithms and software for pair-distribution-function analysis	PDF analysis	Juhás *et al.* (2013)	https://www.diffpy.org/products/xPDFsuite.html	Free for academic use
X'Pert HighScore Plus	Integrated powder-processing suite including profile fitting, structure solution, Rietveld refinement, quantitative analysis and cluster analysis	Cluster analysis, data conversion, indexing, Le Bail fitting, Pawley fitting, peak location, peak profiling, phase identification, powder-pattern viewing, quantitative phase analysis, Rietveld refinement, size–strain analysis	Malvern Panalytical BV, De Schakel 18, Kamer 50, Eindhoven, 5651 GH, Netherlands	https://www.malvernpanalytical.com/products/category/software/x-ray-diffraction-software/highscore-with-plus-option	Commercial
Xpowder	Identification, quantification and characterization of the crystalline components of solids, including natural minerals, artificial compounds and biological crystals	Phase identification	Quetzal Com S. L., La Carrera 5, 18110 HIJAR– Las Gabias, Granada, Spain	http://www.xpowder.com/	Commercial
XRD2DScan	Display and analysis of two-dimensional X-ray diffraction patterns collected with an area detector	2D data	Rodriguez-Navarro (2006)	http://www.ugr.es/~anava/xrd2dscan.htm	Free
XRDUA	Reconstruction of crystalline phase distribution maps from two-dimensional diffraction patterns collected by scanning and tomographic X-ray powder diffraction	Data processing, phase distributions	de Nolf (2014)	http://xrdua.ua.ac.be	Free
ZEFSA II	Zeolite structure solution using a biased Monte Carlo scheme	Structure solution, zeolites	Falcioni & Deem (1999)	http://www.mwdeem.rice.edu/zefsaII/	Free

Cervellino, A., Frison, R., Bertolotti, F. & Guagliardi, A. (2015). *DEBUSSY 2.0: the new release of a Debye user system for nanocrystalline and/or disordered materials. J. Appl. Cryst.* **48**, 2026–2032.

Cheary, R. W. & Coelho, A. A. (1996). *Programs XFIT and FOURYA.* CCP14 Powder Diffraction Library, Engineering and Physical Sciences Research Council, Daresbury Laboratory, UK.

Chichagov, A. V., Varlamov, D. A., Dilanyan, R. A., Dokina, T. N., Drozhzhina, N. A., Samokhvalova, O. L. & Ushakovskaya, T. V. (2001). *MINCRYST: a crystallographic database for minerals, local and network (WWW) versions. Crystallogr. Rep.* **46**, 876–879.

Chipera, S. J. & Bish, D. L. (2002). *FULLPAT: a full-pattern quantitative analysis program for X-ray powder diffraction using measured and calculated patterns. J. Appl. Cryst.* **35**, 744–749.

Cliffe, M. J. & Goodwin, A. L. (2012). *PASCal: a principal axis strain calculator for thermal expansion and compressibility determination. J. Appl. Cryst.* **45**, 1321–1329.

Cockcroft, J. K. (1994). *The PROFIL suite of programs.* Department of Crystallography, Birkbeck College, London, UK.

Cockcroft, J. K. (1999). *A hypertext book of crystallographic space-group diagrams and tables.* Birkbeck College, London, UK.

Coelho, A. A. (2018). *TOPAS and TOPAS-academic: an optimization program integrating computer algebra and crystallographic objects written in C++. J. Appl. Cryst.* **51**, 210–218.

Cranswick, L. D. (2008). *Powder Diffraction, Theory and Practice*, edited by R. E. Dinnebier & S. J. L. Billinge, pp. 494–570. Cambridge: Royal Society of Chemistry.

Cui, X., Feng, Z., Jin, Y., Cao, Y., Deng, D., Chu, H., Cao, S., Dong, C. & Zhang, J. (2015). *AutoFP: a GUI for highly automated Rietveld refinement using an expert system algorithm based on FullProf. J. Appl. Cryst.* **48**, 1581–1586.

Cummings, J., Aivazis, M., Samtaney, R., Radovitzky, R., Mauch, S. & Meiron, D. (2002). *A virtual test facility for the simulation of dynamic response in materials. J. Supercomput.* **23**, 39–50.

David, W. I. F., Shankland, K., van de Streek, J., Pidcock, E., Motherwell, W. D. S. & Cole, J. C. (2006). *DASH: a program for crystal structure determination from powder diffraction data. J. Appl. Cryst.* **39**, 910–915.

Deng, X. & Dong, C. (2011). *EPCryst: a computer program for solving crystal structures from powder diffraction data. J. Appl. Cryst.* **44**, 230–237.

Doebelin, N. & Kleeberg, R. (2015). *Profex: a graphical user interface for the Rietveld refinement program BGMN. J. Appl. Cryst.* **48**, 1573–1580.

Dong, C. (1999). *PowderX: Windows-95-based program for powder X-ray diffraction data processing. J. Appl. Cryst.* **32**, 838.

Dong, C. & Langford, J. I. (2000). *LAPODS: a computer program for refinement of lattice parameters using optimal regression. J. Appl. Cryst.* **33**, 1177–1179.

Downs, R. T. & Hall-Wallace, M. (2003). *The American Mineralogist Crystal Structure Database. Am. Miner.* **88**, 247–250.

Dusek, M., Petříček, V., Wunschel, M., Dinnebier, R. E. & van Smaalen, S. (2001). *Refinement of modulated structures against X-ray powder diffraction data with JANA2000. J. Appl. Cryst.* **34**, 398–404.

Eberl, D. D. (2003). *User's guide to RockJock – a program for determining quantitative mineralogy from powder X-ray diffraction data.* US Geological Survey Open-File Report 2003–78. US Geological Survey, Reston, VA, USA.

Esmaeili, A., Kamiyama, T. & Oishi-Tomiyasu, R. (2017). *New functions and graphical user interface attached to powder indexing software CONOGRAPH. J. Appl. Cryst.* **50**, 651–659.

Evrard, G. & Pusztai, L. (2005). *Reverse Monte Carlo modelling of the structure of disordered materials with RMC++: a new implementation of the algorithm in C++. J. Phys. Condens. Matter*, **17**, S1–S13.

Falcioni, M. & Deem, M. W. (1999). *A biased Monte Carlo scheme for zeolite structure solution. J. Chem. Phys.* **110**, 1754–1766.

Favre-Nicolin, V. & Cerný, R. (2002). *FOX, 'free objects for crystallography': a modular approach to ab initio structure determination from powder diffraction. J. Appl. Cryst.* **35**, 734–743.

Feng, Z. J. & Dong, C. (2007). *GEST: a program for structure determination from powder diffraction data using a genetic algorithm. J. Appl. Cryst.* **40**, 583–588.

Feng, Z. J., Dong, C., Jia, R. R., Deng, X. D., Cao, S. X. & Zhang, J. C. (2009). *PeckCryst: a program for structure determination from powder diffraction data using a particle swarm optimization algorithm. J. Appl. Cryst.* **42**, 1189–1193.

Finger, L. W., Kroeker, M. & Toby, B. H. (2007). *DRAWxtl, an open-source computer program to produce crystal structure drawings. J. Appl. Cryst.* **40**, 188–192.

Fischer, R. X. (1985). *STRUPLO84, a Fortran plot program for crystal structure illustrations in polyhedral representation. J. Appl. Cryst.* **18**, 258–262.

Fletcher, D. A., McMeeking, R. F. & Parkin, D. J. (1996). *The United Kingdom Chemical Database Service. J. Chem. Inf. Comput. Sci.* **36**, 746–749.

Frølich, S. & Birkedal, H. (2015). *MultiRef: software platform for Rietveld refinement of multiple powder diffractograms from in situ, scanning or diffraction tomography experiments. J. Appl. Cryst.* **48**, 2019–2025.

Fuentes-Montero, L., Montero-Cabrera, M. E. & Fuentes-Cobas, L. (2011). *The software package ANAELU for X-ray diffraction analysis using two-dimensional patterns. J. Appl. Cryst.* **44**, 241–246.

Gildea, R. J., Bourhis, L. J., Dolomanov, O. V., Grosse-Kunstleve, R. W., Puschmann, H., Adams, P. D. & Howard, J. A. K. (2011). *iotbx.cif: a comprehensive CIF toolbox. J. Appl. Cryst.* **44**, 1259–1263.

Gnäupel-Herold, T. (2012). *ISODEC: software for calculating diffraction elastic constants. J. Appl. Cryst.* **45**, 573–574.

Gommes, C. J. & Goderis, B. (2010). *CONEX, a program for angular calibration and averaging of two-dimensional powder scattering patterns. J. Appl. Cryst.* **43**, 352–355.

Grazulis, S., Chateigner, D., Downs, R. T., Yokochi, A. F. T., Quirós, M., Lutterotti, L., Manakova, E., Butkus, J., Moeck, P. & Le Bail, A. (2009). *Crystallography Open Database – an open-access collection of crystal structures. J. Appl. Cryst.* **42**, 726–729.

Griffin, T. A. N., Shankland, K., van de Streek, J. & Cole, J. (2009). *GDASH: a grid-enabled program for structure solution from powder diffraction data. J. Appl. Cryst.* **42**, 356–359.

Groom, C. R., Bruno, I. J., Lightfoot, M. P. & Ward, S. C. (2016). *The Cambridge Structural Database. Acta Cryst.* B**72**, 171–179.

Grosse-Kunstleve, R. W., McCusker, L. B. & Baerlocher, C. (1997). *Powder diffraction data and crystal chemical information combined in an automated structure determination procedure for zeolites. J. Appl. Cryst.* **30**, 985–995.

Grosse-Kunstleve, R. W., Sauter, N. K., Moriarty, N. W. & Adams, P. D. (2002). *The computational crystallography toolbox: crystallographic algorithms in a reusable software framework. J. Appl. Cryst.* **35**, 126–136.

Hammersley, A. P. (1998). *FIT2D reference manual.* ESRF Internal Report ESRF98HA01T. ESFR, Grenoble, France.

Hammersley, A. P. (2016). *FIT2D: a multi-purpose data reduction, analysis and visualization program. J. Appl. Cryst.* **49**, 646–652.

Hammersley, A. P., Svensson, S. O., Hanfland, M., Fitch, A. N. & Hausermann, D. (1996). *Two-dimensional detector software: from real detector to idealised image or two-theta scan. High Pressure Res.* **14**, 235–248.

Harris, K. D. M., Habershon, S., Cheung, E. Y. & Johnston, R. L. (2004). *A genetic algorithm for crystal structure solution from powder diffraction data. J. Chem. Res.* pp. 390–391.

Heiney, P. (2002). *Datasqueeze – program for analyzing 2D diffraction data, especially small-angle and powder diffraction.* PMB 252, 303 West Lancaster Ave, Wayne, PA, USA.

Herger, B. (2002). *XDrawChem.* Georgia Institute of Technology, Atlanta, USA.

Hester, J. R. (2006). *A validating CIF parser: PyCIFRW. J. Appl. Cryst.* **39**, 621–625.

Hinrichsen, B., Dinnebier, R. E., Rajiv, P. & Jansen, M. (2008). *Powder3D: a multi-pattern data reduction and graphical presentation software*, https://www.fkf.mpg.de/172766/Powder_3D.

Hofmann, D. W. M. & Apostolakis, J. (2003). *Crystal structure prediction by data mining. J. Mol. Struct.* **647**, 17–39.

Hovmöller, S. (1992). *CRISP: crystallographic image processing on a personal computer. Ultramicroscopy*, **41**, 121–135.

Huang, X. R. (2010). *LauePt, a graphical-user-interface program for simulating and analyzing white-beam X-ray diffraction Laue patterns. J. Appl. Cryst.* **43**, 926–928.

Hunter, B. (1998). *Rietica – A visual Rietveld program. IUCr Commission on Powder Diffraction Newsletter*, No. 20, p. 21.

Husák, M. & Kratochvíl, B. (2003). *MCE - program for fast interactive visualization of electron and similar density maps, optimized for small molecules. J. Appl. Cryst.* **36**, 1104.

Ilavsky, J. (2012). *Nika: software for two-dimensional data reduction. J. Appl. Cryst.* **45**, 324–328.

International Tables Online (2019). Chester: International Union of Crystallography.

Izumi, F. & Momma, K. (2007). *Three-dimensional visualization in powder diffraction. Solid State Phenom.* **130**, 15–20.

Juhás, P., Davis, T., Farrow, C. L. & Billinge, S. J. L. (2013). *PDFgetX3: a rapid and highly automatable program for processing powder diffraction data into total scattering pair distribution functions. J. Appl. Cryst.* **46**, 560–566.

Kline, S. R. (2006). *Reduction and analysis of SANS and USANS data using IGOR Pro. J. Appl. Cryst.* **39**, 895–900.

Knupp, C. & Squire, J. M. (2004). *HELIX: a helical diffraction simulation program. J. Appl. Cryst.* **37**, 832–835.

Kocks, U. F., Kallend, J. S., Wenk, H.-R., Rollett, A. D. & Wright, S. I. (1998). *popLA, Preferred Orientation Package – Los Alamos.* Report LA-CC-89–18. Los Alamos National Laboratory, NM, USA.

Kourkoumelis, N. (2005). *PowDLL: a reusable .NET component and XRD data interconversion utility*. http://users.uoi.gr/nkourkou/powdll/.

Kraus, W. & Nolze, G. (1996). *POWDER CELL – a program for the representation and manipulation of crystal structures and calculation of the resulting X-ray powder patterns. J. Appl. Cryst.* **29**, 301–303.

Kroumova, E., Luna, J. A., Madariaga, G. & Perez Mato, J. M. (2005). *The Bilbao Incommensurate Structures Database.* University of the Basque Country, Bilbao, Spain.

Larson, A. C. & Von Dreele, R. B. (2004). *General Structure Analysis System (GSAS).* Los Alamos National Laboratory Report LAUR 86–748, Los Alamos, USA.

Laugier, J. & Bochu, B. (2004). *LMGP – suite of programs for the interpretation of X-ray experiments.* ENSP/Laboratoire des Materiaux et du Genie Physique, Saint Martin d'Hères, France.

Le Bail, A. (1995). *Modelling the silica glass structure by the Rietveld method. J. Non-Cryst. Solids*, **183**, 39–42.

Le Bail, A. (1996). *VRML as a tool for exploring complex structures. Acta Cryst.* A**52**, C78.

Le Bail, A. (2000). *Reverse Monte Carlo and Rietveld modelling of the* $NaPbM_2F_9$ *(M = Fe, V) fluoride glass structures. J. Non-Cryst. Solids*, **271**, 249–259.

Le Bail, A. (2001). *ESPOIR: a program for solving structures by Monte Carlo analysis of powder diffraction data. Mater. Sci. Forum*, **378–381**, 65–70.

Le Bail, A. (2004). *Monte Carlo indexing with McMaille. Powder Diffr.* **19**, 249–254.

Le Bail, A. (2005). *Inorganic structure prediction with GRINSP. J. Appl. Cryst.* **38**, 389–395.

Le Roux, S. & Petkov, V. (2010). *ISAACS – interactive structure analysis of amorphous and crystalline systems. J. Appl. Cryst.* **43**, 181–185.

Leoni, M., Confente, T. & Scardi, P. (2006). *PM2K: a flexible program implementing whole powder pattern modelling. Z. Kristallogr. Suppl.* **2006**, 249–254.

Leoni, M., Gualtieri, A. F. & Roveri, N. (2004). *Simultaneous refinement of structure and microstructure of layered materials. J. Appl. Cryst.* **37**, 166–173.

Liu, Y. (2018). *decryst: an efficient software suite for structure determination from powder diffraction. J. Appl. Cryst.* **51**, 1237–1243.

Lutterotti, L., Matthies, S. & Wenk, H.-R. (1999). *MAUD: a friendly Java program for material analysis using diffraction. IUCr Commission on Powder Diffraction Newsletter*, No. 21, 14–15.

Mändar, H., Felsche, J., Mikli, V. & Vajakas, T. (1999). *AXES1.9: new tools for estimation of crystallite size and shape by Williamson–Hall analysis. J. Appl. Cryst.* **32**, 345–350.

Mändar, H. & Vajakas, T. (1998). *AXES – a software toolbox in powder diffraction. IUCr Commission on Powder Diffraction Newsletter*, No. 20, 31–32.

Mändar, H., Vajakas, T., Telsche, J. & Dinnebier, R. E. (1996). *AXES1.4 – a program for the preparation of parameter input files for FULLPROF. J. Appl. Cryst.* **29**, 304.

Markvardsen, A. J., David, W. I. F., Johnson, J. C. & Shankland, K. (2001). *A probabilistic approach to space-group determination from powder diffraction data. Acta Cryst.* A**57**, 47–54.

Markvardsen, A. J., Puphaiboon, K., Arjeneh, M., Shankland, K., Guest, H. L., Griffin, T. A. N., Badham, D. R. & Flannery, D. W. (2010). *Jpowder: a Java-based program for the display and examination of powder diffraction data. J. Appl. Cryst.* **43**, 1532–1534.

Matěj, Z., Kadlecová, A., Janeček, M., Matějová, L., Dopita, M. & Kužel, R. (2014). *Refining bimodal microstructure of materials with MSTRUCT. Powder Diffr.* **29**, S35–S41.

Materials Data Inc. (2016). *Jade 9.6.* Materials Data Inc., Livermore, CA, USA.

Mellergård, A. & McGreevy, R. L. (1999). *Reverse Monte Carlo modelling of neutron powder diffraction data. Acta Cryst.* A**55**, 783–789.

Merkel, S. & Hilairet, N. (2015). *Multifit/Polydefix: a framework for the analysis of polycrystal deformation using X-rays. J. Appl. Cryst.* **48**, 1307–1313.

Momma, K., Ikeda, T., Belik, A. A. & Izumi, F. (2013). *Dysnomia, a computer program for maximum-entropy method (MEM) analysis and its performance in the MEM-based pattern fitting. Powder Diffr.* **28**, 184–193.

Nickel, E. N. & Nichols, M. C. (1991). *Mineral reference manual.* New York: Van Nostrand Reinhold.

Nolf, W. de (2014). *XRDUA: crystalline phase distribution maps by two-dimensional scanning and tomographic (micro) X-ray powder diffraction. J. Appl. Cryst.* **47**, 1107–1117.

O'Boyle, N. M., Banck, M., James, C. A., Morley, C., Vandermeersch, T. & Hutchison, G. R. (2011). *Open Babel: an open chemical toolbox. J. Cheminformatics*, **3**, 33.

Oddershede, J., Schmidt, S., Poulsen, H. F., Sørensen, H. O., Wright, J. & Reimers, W. (2010). *Determining grain resolved stresses in polycrystalline materials using three-dimensional X-ray diffraction. J. Appl. Cryst.* **43**, 539–549.

O'Donnell, J. H., Von Dreele, R. B., Chan, M. K. Y. & Toby, B. H. (2018). *A scripting interface for GSAS-II. J. Appl. Cryst.* **51**, 1244–1250.

Orlov, I. P., Popov, K. A. & Urusov, V. S. (1998). *Program for predicting interatomic distances in crystals by the bond valence method. J. Struct. Chem.* **39**, 575–579.

Oxford Cryosystems (1997). *Crystallographica – a software toolkit for crystallography. J. Appl. Cryst.* **30**, 418–419.

Ozawa, T. C. & Kang, S. J. (2004). *Balls&Sticks: easy-to-use structure visualization and animation program. J. Appl. Cryst.* **37**, 679.

Pagola, S., Polymeros, A. & Kourkoumelis, N. (2017). *WinPSSP: a revamp of the computer program PSSP and its performance solving the crystal structures of small organic compounds and solids of biological and pharmaceutical interest. J. Appl. Cryst.* **50**, 293–303.

Palatinus, L. & Chapuis, G. (2007). *SUPERFLIP – a computer program for the solution of crystal structures by charge flipping in arbitrary dimensions. J. Appl. Cryst.* **40**, 786–790.

Pawlik, K. & Ozga, P. (1999). *LaboTex: the texture analysis software for Windows. Gött. Arb. Geol. Paläontol.* **Sb4**, 146–147.

Petkov, V. & Bakaltchev, N. (1990). *FIT, a computer program for decomposition of powder diffraction patterns and profile analysis of pair correlation functions. J. Appl. Cryst.* **23**, 138–140.

Petříček, V., Dušek, M. & Palatinus, L. (2000). *JANA2000, the crystallographic computing system.* Institute of Physics, Praha, Czech Republic.

Petschick, R. (2001). *MacDiff – a programme for analysis and display of X-ray powder diffractogrammes on Apple Macintosh platforms.* Johann Wolfgang Goethe-Universität Frankfurt am Main, Germany.

Proffen, Th. & Neder, R. B. (1997). *DISCUS: a program for diffuse scattering and defect-structure simulation. J. Appl. Cryst.* **30**, 171–175.

Proffen, Th. & Neder, R. B. (1999). *DISCUS, a program for diffuse scattering and defect structure simulations – update. J. Appl. Cryst.* **32**, 838–839.

Putz, H., Schön, J. C. & Jansen, M. (1999). *Combined method for ab initio structure solution from powder diffraction data. J. Appl. Cryst.* **32**, 864–870.

Raue, L. (2014). *input4MAUD: an efficient program for automatic two-dimensional diffraction image series input and/or batch refinement with MAUD. J. Appl. Cryst.* **47**, 2081–2085.

Ribárik, G., Ungár, T. & Gubicza, J. (2001). *MWP-fit: a program for multiple whole-profile fitting of diffraction peak profiles by ab initio theoretical functions. J. Appl. Cryst.* **34**, 669–676.

Rigaku (2014). *PDXL 2, Rigaku powder diffraction data analysis software*, Version 2.2. Rigaku Corporation, Tokyo, Japan.

Rius, J. (2011). *Patterson-function direct methods for structure determination of organic compounds from powder diffraction data. XVI. Acta Cryst.* A**67**, 63–67.

Rius, J. (2013). *XLENS.* Institut de Ciència de Materials de Barcelona, CSIC, Spain.

Rodriguez-Carvajal, J. (1990). *FULLPROF: a program for Rietveld refinement and pattern-matching analysis.* Abstracts of the Satellite

Meeting on Powder Diffraction of the XV Congress of the IUCr, Toulouse, France, pp. 127–128.

Rodriguez-Navarro, A. B. (2006). *XRD2DScan: new software for polycrystalline materials characterization using two-dimensional X-ray diffraction. J. Appl. Cryst.* **39**, 905–909.

Rohlíček, J., Hušák, M. & Kratochvíl, B. (2007). *FoxGrid – multi PC execution support for powder diffraction structure solution by Fox program. Acta Cryst.* A**63**, s242.

Sadowski, J., Gasteiger, J. & Klebe, G. (1994). *Comparison of automatic three-dimensional model builders using 639 X-ray structures. J. Chem. Inf. Comput. Sci.* **34**, 1000–1008.

Salzmann, I. & Resel, R. (2004). *STEREOPOLE: software for the analysis of X-ray diffraction pole figures with IDL. J. Appl. Cryst.* **37**, 1029–1033.

Schmidt, M. U. & Kalkhof, H. (1997). *CRYSCA. Program for crystal structure calculations of flexible molecules.* Clariant GmbH, Frankfurt am Main, Germany.

Schmidt, S. (2014). *GrainSpotter: a fast and robust polycrystalline indexing algorithm. J. Appl. Cryst.* **47**, 276–284.

Schmidt, S., Vaughan, G. B. M., Wright, J., Sørensen, H. O., Oddershede, J., Suchet, G., Knudsen, E., Kieffer, J. & Götz, A. (2009). *FABLE*, http://sourceforge.net/projects/fable/.

Schwab, C. H. (2010). *Conformations and 3D pharmacophore searching. Drug Discov. Today Technol.* **7**, e245–e253.

Segall, M. D., Lindan, P. J. D., Probert, M. J., Pickard, C. J., Hasnip, P. J., Clark, S. J. & Payne, M. C. (2002). *First-principles simulation: ideas, illustrations and the CASTEP code. J. Phys. Condens. Matter*, **14**, 2717–2744.

Shi, C. (2018). *xINTERPDF: a graphical user interface for analyzing intermolecular pair distribution functions of organic compounds from X-ray total scattering data. J. Appl. Cryst.* **51**, 1498–1499.

Shirley, R. (2002). *The Crysfire 2002 system for automatic powder indexing: user's manual.* The Lattice Press, Guildford, Surrey, England.

Sietronics (2012). *Siroquant*. Version 4. Sietronics, Canberra, Australia.

Skrobas, K., Stelmakh, S., Gierlotka, S. & Palosz, B. F. (2017). *NanoPDF64: software package for theoretical calculation and quantitative real-space analysis of powder diffraction data of nanocrystals. J. Appl. Cryst.* **50**, 1821–1829.

Solovyov, L. A. (2004). *Full-profile refinement by derivative difference minimization. J. Appl. Cryst.* **37**, 743–749.

Soper, A. K. & Barney, E. R. (2011). *Extracting the pair distribution function from white-beam X-ray total scattering data. J. Appl. Cryst.* **44**, 714–726.

Spek, A. L. (1998). *PLATON, a multipurpose crystallographic tool.* Utrecht University, Utrecht, The Netherlands.

Spek, A. L. (2003). *Single-crystal structure validation with the program PLATON. J. Appl. Cryst.* **36**, 7–13.

Spillman, M. J., Shankland, K., Williams, A. C. & Cole, J. C. (2015). *CDASH: a cloud-enabled program for structure solution from powder diffraction data. J. Appl. Cryst.* **48**, 2033–2039.

Stadelmann, P. (2003). *Image analysis and simulation software in transmission electron microscopy. Microsc. Microanal.* **9**, 60–61.

Stewart, J. J. P. (2012). *MOPAC2012.* Stewart Computational Chemistry, Colorado Springs, USA.

Stephenson, R., Cockcroft, J., Watkin, D. & Cernik, B. (2006). *The CCP14: freely available crystallographic software for academia (collaborative computational project number 14). Acta Cryst.* A**62**, s251.

Stokes, H. T. & Hatch, D. M. (2002). *ISOTROPY*. http://stokes.byu.edu/isotropy.html.

Sykes, R. A., McCabe, P., Allen, F. H., Battle, G. M., Bruno, I. J. & Wood, P. A. (2011). *New software for statistical analysis of Cambridge Structural Database data. J. Appl. Cryst.* **44**, 882–886.

Toby, B. H. (2001). *EXPGUI, a graphical user interface for GSAS. J. Appl. Cryst.* **34**, 210–213.

Toby, B. H. (2005). *CMPR – a powder diffraction toolkit. J. Appl. Cryst.* **38**, 1040–1041.

Toby, B. H. & Von Dreele, R. B. (2013). *GSAS-II: the genesis of a modern open-source all purpose crystallography software package. J. Appl. Cryst.* **46**, 544–549.

Treacy, M. M. J., Newsam, J. M. & Deem, M. W. (1991). *A general recursion method for calculating diffracted intensities from crystals containing planar faults. Proc. R. Soc. London Ser. A*, **433**, 499–520.

Tucker, M. G., Keen, D. A., Dove, M. T., Goodwin, A. L. & Hui, Q. (2007). *RMCProfile: reverse Monte Carlo for polycrystalline materials. J. Phys. Condens. Matter*, **19**, 335218.

Vallcorba, O., Rius, J., Frontera, C., Peral, I. & Miravitlles, C. (2012). *DAJUST: a suite of computer programs for pattern matching, space-group determination and intensity extraction from powder diffraction data. J. Appl. Cryst.* **45**, 844–848.

Visser, J. W. (1969). *A fully automatic program for finding the unit cell from powder data. J. Appl. Cryst.* **2**, 89–95.

Vogel, S. C. (2011). *gsaslanguage: a GSAS script language for automated Rietveld refinements of diffraction data. J. Appl. Cryst.* **44**, 873–877.

Vogel, S. C., Biwer, C. M., Rogers, D. H., Ahrens, J. P., Hackenberg, R. E., Onken, D. & Zhang, J. (2018). *Interactive visualization of multi-data-set Rietveld analyses using Cinema:Debye-Scherrer. J. Appl. Cryst.* **51**, 943–951.

Wenk, H.-R., Matthies, S., Donovan, J. & Chateigner, D. (1998). *BEARTEX: a Windows-based program system for quantitative texture analysis. J. Appl. Cryst.* **31**, 262–269.

Westrip, S. P. (2010). *PublCIF: software for editing, validating and formatting crystallographic information files. J. Appl. Cryst.* **43**, 920–925.

White, P. S., Rodgers, J. R. & Le Page, Y. (2002). *CRYSTMET: a database of the structures and powder patterns of metals and intermetallics. Acta Cryst.* B**58**, 343–348.

Wright, J. P. (2004). *Extraction and use of correlated integrated intensities with powder diffraction data. Z. Kristallogr.* **219**, 791–802.

Wright, J. P. (2011). *ImageD11*. http://sourceforge.net/projects/fable/files/ImageD11/.

Wright, J. P. & Forsyth, J. B. (2000). *PRODD profile refinement of diffraction data using the Cambridge Crystallographic Subroutine Library (CCSL).* Rutherford Appleton Laboratory Report RAL-TR-2000–012. Rutherford Appleton Laboratory, Didcot, UK.

Wright, J. P., Markvardsen, A. & Margiolaki, I. (2007). *Likelihood methods with protein powder diffraction data. Z. Kristallogr. Suppl.* **2007**, 27–32.

Yuan, H. & Bish, D. (2010). *NEWMOD+, a new version of the NEWMOD program for interpreting X-ray powder diffraction patterns from interstratified clay minerals. Clays Clay Miner.* **58**, 318–326.

Zlokazov, V. B. (1995). *AUTOX – a program for autoindexing reflections from multiphase polycrystals. Comput. Phys. Commun.* **85**, 415–422.

Zlokazov, V. B. (2003). *DELPHI-based visual object-oriented programming for the analysis of experimental data in low-energy physics. Nucl. Instrum. Methods Phys. Res. A*, **502**, 723–724.

Zlokazov, V. B. & Chernyshev, V. V. (1992). *MRIA – a program for a full profile analysis of powder multiphase neutron-diffraction time-of-flight (direct and Fourier) spectra. J. Appl. Cryst.* **25**, 447–451.

International Tables for Crystallography (2019). Vol. H, Chapter 7.1, pp. 718–736.

7.1. Macromolecular powder diffraction

I. Margiolaki

7.1.1. Introduction

The preparation of a powder sample is frequently observed, as microcrystalline powders are obtained for many proteins by batch precipitation (Von Dreele, 2003). The size of individual crystallites (~0.1–1 µm) in such precipitates is usually far too small for single-crystal diffraction studies, but it is (in many cases) ideal for powder diffractometry. In the last ten years, the use of powder data with macromolecules has gone from being an ambitious suggestion to a respectable method. To date, a series of experiments and data analyses has been carried out; these experiments establish the validity of the methodology (Von Dreele, 2003; Margiolaki & Wright, 2008; Karavassili & Margiolaki, 2016). Although methods for phasing and structure solution are still under development, molecular-replacement and structure-refinement methods are now mature enough for use by the more adventurous protein crystallographer. The solution of previously unknown structures described in this chapter shows how powder diffraction is already moving beyond 'demonstration' experiments and that the technique is ready to tackle genuine biological problems. It is fair to say that macromolecular powder diffraction has moved from an impossible dream to a reality, as exemplified by characterizing bulk pharmaceuticals, the molecular-replacement structure determination of the protein ponsin, the preliminary structural characterization of a Trinidadian virus which will not yield sizeable single crystals, the combination of powder-diffraction X-ray data with techniques such as cryo-electron microscopy (cryo-EM), and the combination of single-crystal data from micron-sized crystals with powder-diffraction data. Whilst it will obviously not seek to compete with single-crystal work for crystal structure analysis, macromolecular powder diffraction should be regarded as a technique that every crystallographer should know how to use. This chapter provides the necessary discussions of the theory, along with practical explanations and examples, all of which are useful for teaching. Tabulations are given of the total powder sample volume requirements in studies made so far, illustrated particularly with respect to the molecular weights of the proteins studied, where the amount required can increase significantly and/or where more detail is needed at the molecular level (Table 7.1.1); the instruments available at synchrotron sources worldwide (also Table 7.1.1); and software packages and their detailed capabilities (Table 7.1.2).

In this chapter, we cover the following:

1. methods for 'ideal powder' sample preparation;
2. synchrotron X-ray macromolecular powder diffraction (SXRPD) instrumentation options and measurements;
3. software suites commonly used;
4. a general survey of examples;
5. several highlighted case studies;
6. cases where combination with other methods, notably microcrystallography or electron microscopy (EM), is advantageous; and
7. some imaginative future prospects, including the use of electrons and X-ray lasers.

Particular emphasis is given throughout on cryo-cooling methods for protein powders for extending the sample's lifetime in the beam. Cryo-cooling techniques continually advance in order to reduce radiation-induced sample microstrains, which lead to severe peak broadening and loss of information owing to the high degree of reflection overlap. These advances are described in Section 7.1.4. Likewise, the use of the anisotropic changes in unit-cell parameters (usually evident with X-ray irradiation damage at synchrotron sources, even when cryo-cooled) allows more complete extraction of data; indeed, since peak overlap is increasingly severe at higher diffraction resolutions, this is a most important development for detailed work. Thus these two aspects of modern practice are discussed in detail (Watier *et al.*, 2009), as they are likely to be essential to practitioners facing increasingly challenging cases.

Powder diffraction is ideal for screening a large number of samples and current advances in this field are discussed in Section 7.1.5. During the last few years, there has been an evolution from single- to multiple-pattern fitting, leading to improvements in the data and resulting models, and we describe these in Section 7.1.6. Perhaps the most enticing goal for any crystallographer is to solve new structures, and Section 7.1.7 discusses the progress and prospects for powder diffraction in this area. Details of the application of the Rietveld method (Rietveld, 1969) and the use of stereochemical restraints as well as rigid bodies for the description of individual amino acids in the course of structure refinements are provided in Section 7.1.8. It is anticipated that the combination of powder diffraction with other experimental techniques, including X-ray microcrystallography, serial X-ray crystallography at free-electron lasers and electron diffraction (ED) methods will be highly advantageous, and related developments are discussed in Section 7.1.9. We end with some concluding remarks and a discussion of future prospects for the method in Section 7.1.10.

7.1.2. Sample preparation and handling

Preparation of suitable protein powder samples is considerably easier than that of high-quality single crystals. Protein powders are inherently 'perfect' for diffraction; the individual crystallites are of the right size (about 1 µm) and are almost completely strain free. Polycrystalline protein can be prepared directly by precipitation from solution, usually working at relatively high precipitant and/or protein concentrations in order to reach the precipitation zone limits (Asherie, 2004). To date, we have employed the salting-out procedure in batch mode for the preparation of several different polycrystalline protein samples, as shown in Fig. 7.1.1 (Margiolaki & Wright, 2008). The sample is preserved in an adequate amount of mother liquor or solvent to ensure that the protein powder does not dehydrate. Powders may also be prepared by simply grinding or pulverizing in their mother liquor a sufficient quantity of single crystals grown by conventional means. For example, Rotella *et al.* (2001) used a sonicator to prepare their samples, while Von Dreele hand-

Copyright © 2019 International Union of Crystallography

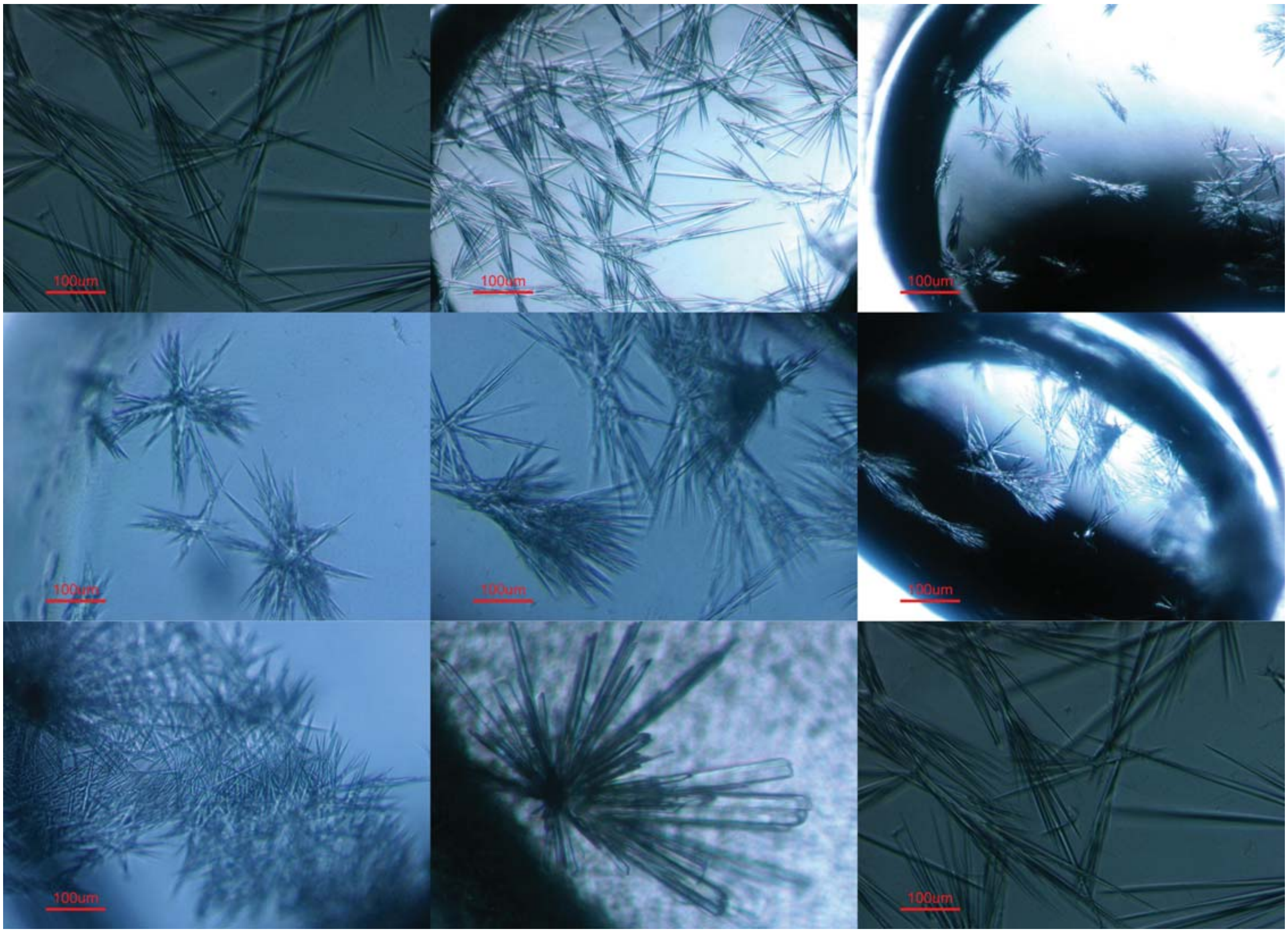

Figure 7.1.1
Optical-microscopy images of needle-shaped crystals of the nonstructural protein 3 (nsP3) macro domain of the Mayaro virus (MAYV) grown under different conditions (Papageorgiou *et al.*, 2010).

ground metmyoglobin (Von Dreele, 1999) and Zn insulin (Von Dreele *et al.*, 2000) crystals with an agate mortar and pestle. However, the application of pressure to protein crystals may result in different crystalline phases, as demonstrated by Von Dreele and co-workers (Von Dreele *et al.*, 2000). The resulting slurry is then loaded into a glass capillary and centrifuged in order to enhance packing of the protein crystals. Excess mother liquor is removed and the capillaries are sealed with wax to prevent protein dehydration.

Our high-angular-resolution synchrotron experiments typically use a 1.0 mm-diameter borosilicate or Kapton capillary (Von Dreele, 2006) that is illuminated over 2–6 mm of its length depending on the instrument; this specimen size uses approximately 5–15 mg of protein. Much smaller capillaries can be used on diffractometers equipped with either a charge-coupled device (CCD) or an image plate (IP); a 0.3 mm capillary requires only 0.02 mg of protein for the beam size normally used on these instruments. Alternatively, a small quantity of the slurry can be placed in a standard single-crystal loop, although dehydration of the sample is quite likely unless it is flash frozen. The amount of protein required is much less than 1 mg. In order to reduce the amount of sample required and avoid protein dehydration, Watier (2011) has employed Silson silicon-nitride membranes as alternative sample holders. The membrane window consists of a square silicon-nitride membrane in a square supporting frame. For synchrotron measurements at ID31 (ESRF) we chose a window size of 3 mm × 3 mm, slightly larger than our typical beam size of 2 mm × 1 mm. The window thickness was 500 nm (the available range is from 50 nm to 1000 nm). The sample was pipetted directly on top of the window. To avoid dehydration of the protein sample, a second Silson membrane was added on top and sealed with grease. This double silicon-nitride window allows collection while spinning (as with a capillary). A different approach was also proposed by Watier (2011) in order to collect synchrotron data on the smallest possible protein sample. The sample used corresponds to the nsP3 macro domain of the Mayaro virus, which forms needle-shaped crystals grown within single ‘urchins’ as shown in Fig. 7.1.2 (Papageorgiou *et al.*, 2010). In this case, a single urchin was loaded onto a micromesh grid holder 400 µm in diameter with a 25 µm opening (MiTeGen MicroMeshes). The urchin was kept hydrated with a humidity controller (Sanchez-Weatherby *et al.*, 2009) and data were collected using an area detector at the protein crystallography beamline ID14 (ESRF). We note that this setup is ideal for observation of the dynamic response of macromolecular crystals to changes in relative humidity (Dobrianov *et al.*, 2001; Hanson *et al.*, 2003), a field of great biotechnological importance (Salunke *et al.*, 1985; Kuntz & Kauzmann, 1974; Finney, 1979; Careri *et al.*, 1980; Blake *et al.*, 1983). Considering the very low amount of material, unexpectedly good diffraction patterns were observed

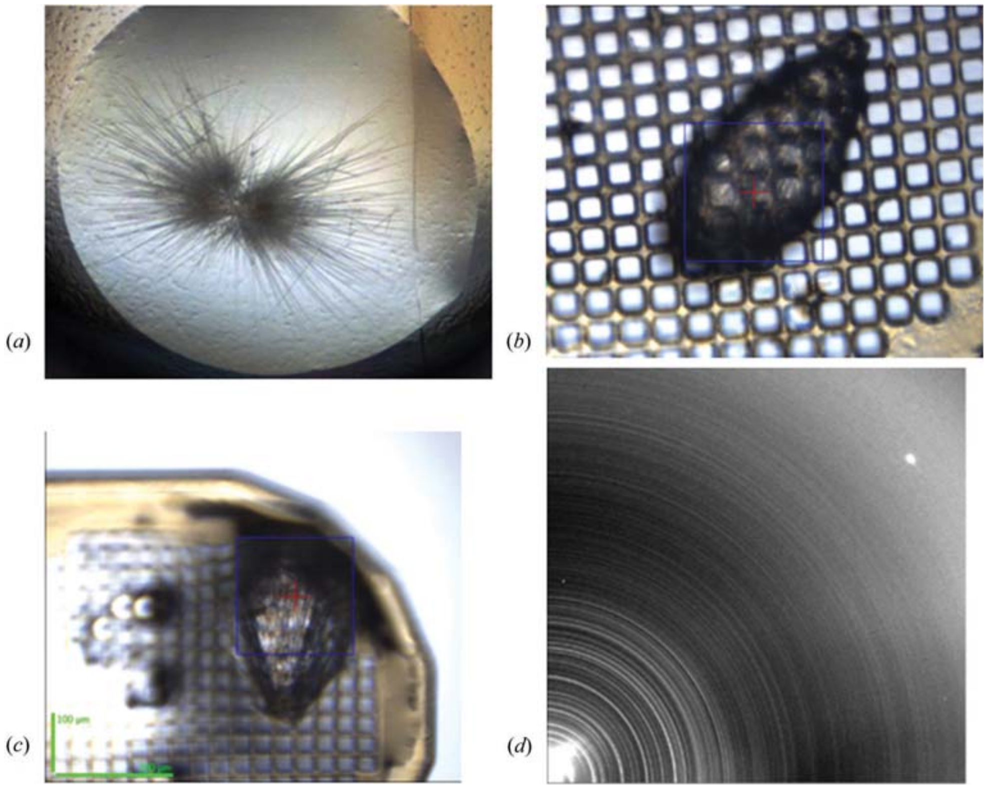

Figure 7.1.2
(*a*) A bunch of needle-shaped MAYV crystals as grown within single 'urchins'. (*b*, *c*) A single urchin was loaded onto a micromesh grid holder 400 μm in diameter with 25 μm openings (MiTeGen MicroMeshes). The urchin was kept hydrated with a humidity controller (Sanchez-Weatherby *et al.*, 2009) and (*d*) data were collected using an area detector at the protein crystallography beamline ID14 (ESRF) (Watier, 2011).

compared with the capillary-mode measurements (Fig. 7.1.2*d*) and therefore this method is considered as very promising for future protein powder experiments.

Finally, a different type of sample holder for in-house X-ray powder-diffraction (XRPD) analysis has recently been made and tested on lysozyme (Frankaer *et al.*, 2011). To collect as much signal as possible on in-house X-ray sources, the general principle behind the design is to support a thin film of protein crystallites with a relatively large surface area. The sample holder consists of a 1.0 mm-thick polycarbonate plate with a hole in it, either 4.5 or 3.0 mm in diameter, creating a sample-chamber volume of 16 or 7 μl, respectively. Metal-free polycarbonate was chosen to avoid a fluorescence signal from the sample holder. The sample is sealed by two pieces of Mylar foil, which are attached to the polycarbonate plate with either epoxy glue or double-sided adhesive tape. The use of an integrated pinhole reduced the background, and good signal-to-noise ratios were obtained from only 7 μl of sample, corresponding to approximately 2–3 mg of dry protein. The sample holder is further adaptable to X-ray absorption spectroscopy (XAS) measurements. Both XRPD and XAS at the Zn *K* edge were tested with hexameric Zn insulin.

7.1.3. Data collection

A crucial step in a protein powder experiment is the choice of the optimum instrument. While most of the early studies were limited to dedicated powder-diffraction instruments, it is becoming increasingly clear that a wider range of instrumental configurations can give additional useful information. A typical single-crystal synchrotron beamline should also give a good-quality powder pattern from a very small sample if the X-ray beam is focused at the detector surface. Once a sample is found to be microcrystalline, it is worthwhile to pursue an improved powder pattern. One of the main barriers appears to be the fact that the unit-cell volumes can be three orders of magnitude larger than those traditionally studied by powder methods. A particularly important question is the comparison of data-collection schemes with high-resolution analyser crystals on the one hand and multichannel position-sensitive detectors (one- and two-dimensional) on the other. Whereas the former configuration offers maximum angular resolution, the latter provides substantially higher data-collection rates, and therefore faster acquisition, allowing for studies of particularly radiation-sensitive systems. Data-collection strategies and data quality from different instruments of four main synchrotron sources (ESRF, APS, SPring8 and SLS) as well as laboratory instrumentation have been discussed (Margiolaki, Wright, Fitch *et al.*, 2007; Helliwell, 2012). Each instrumental configuration tested offers advantages in specific applications. While it is tempting to try to obtain the highest-angular-resolution data, a compromise is always forced upon us by the effects of radiation damage and the costs of producing large amounts of samples. In the process of screening extensive series of specimens under different conditions, the need

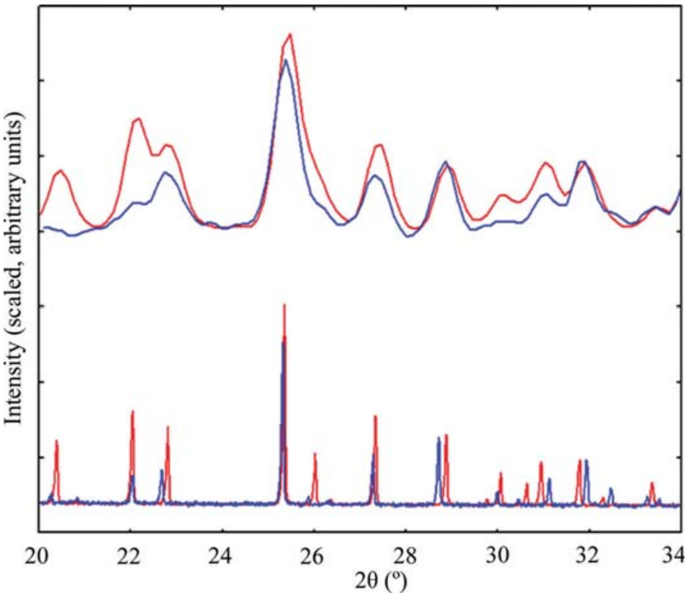

Figure 7.1.3
Low-angle region of powder-diffraction patterns from lysozyme samples. The lower and upper patterns correspond to analyser-crystal (ID31) and area-detector (BM01A) data, respectively. In these experiments, the intensities of certain low-angle reflections are modulated by varying the mean electron density of the solvent surrounding the protein molecules in the crystal *via* variations in the solvent composition. The red and blue spectra correspond, respectively, to samples soaked in solvents that have low and high electron density (Margiolaki & Wright, 2008).

Table 7.1.1
Synchrotron beamlines used for protein powder measurements and their key characteristics

Beamline	Detector type and energy range	Amount of sample required (protein precipitate)	Advantages, disadvantages and uses
ID14 – EH1 (ESRF)	Large two-dimensional detector (Quantum 210), E = 13.270 keV	1–5 µl (~1 crystallization drop)	Medium angular resolution, screening, initial indexing and phasing, fast acquisition, user friendly
ID11 (ESRF)	Two-dimensional detector (FReLoN camera), E = 25–140 keV	5–10 µl (several drops required)	Medium angular resolution, screening, ideal for tests of small amounts of samples and experimental configurations; complex to use
ID31 (ESRF)	Nine Si(111) analyser crystals each followed by a point detector [avalanche photodiode (APD) detectors], E = 5–60 keV	10–50 µl (batch crystallization is preferable as relatively large sample amounts are required)	High angular resolution, ideal for structure solution and refinement, robotic sample changer available, online data viewing and treatment software, user friendly, extensive use for protein powder diffraction
BM01B (ESRF)	Six Si(111) analyser crystals each followed by a point detector (NaI scintillation counters), E = 4–70 keV	10–50 µl (batch crystallization is preferable as relatively large sample amounts are required)	High angular resolution, structure solution and refinement
MS – X04SA (SLS)	Configuration 1: Five Si(111) analyser crystals each followed by a point-detector [NaI(Tl) scintillators–photomultipliers] Configuration 2: Modular (each module covering *ca.* 5° in 2θ) one-dimensional solid-state Si microstrip detector (MYTHEN II) covering 120° in 2θ E = 5–40 keV	10–50 µl 5–10 µl	High angular resolution (down to 0.002° in 2θ), ideal for structure solution and refinement, anomalous scattering Very fast acquisition time (down to 100 ms in continuous mode, down to 100 µs pump-and-probe mode), angular resolution dominated by capillary diameter (*ca.* 0.02° with a 0.3 mm capillary), ideal for time-resolved, dose-controlled structural analyses, robotic sample changer available.
BL40XU (SPring8)	Large Guinier-type camera, E = 8–17 keV	1–5 µl	High angular resolution, 1 m path length, structure solution and refinement, very fast data collection
17-BM (APS)	Two-dimensional detector (MAR345 and GE) offset vertically, E = 20 keV	1–5 µl	30 s data collection, medium angular resolution to ~2 Å d-spacing resolution
11-BM (APS)	12 Si(111) analyser crystals each followed by an $LaCl_3$ point detector, E = 12–36 keV	1–5 µl	High angular resolution, ideal for structure solution and refinement, robotic sample changer available

to collect patterns rapidly from small samples is more important than obtaining data suitable for structure refinement. The unit-cell parameters can normally be refined very precisely from a relatively small (<50) number of low-angle peaks. The use of a lower-angular-resolution instrument allows construction of phase diagrams and checking for ligand or heavy-atom binding to be carried out rapidly using small samples. When particularly interesting samples are identified during screening and a structure solution or refinement is to be attempted, it is of course vital to obtain the best possible data to increase the chances of success for the whole process. Here the analyser-crystal beamlines offer unparalleled instrumental resolution, which is very attractive in reducing the peak overlap (Fig. 7.1.3). In comparison, multichannel position-sensitive detectors, particularly those designed for larger unit cells, offer dramatically improved counting statistics. Ideally, both types of data set should be available in a combined refinement in order to exploit the advantages of each. The special characteristics of protein powders require development of instrumentation to take real advantage of the inherent sharpness of the diffraction patterns, while at the same time avoiding radiation-damage effects. From one point of view, this could be achieved using high-spatial-resolution two-dimensional area detectors designed to cover only the most useful part of the powder pattern (the low-2θ region) and by increasing the solid-angle coverage with increasing 2θ to give the best possible statistics. Table 7.1.1 lists the synchrotron beamlines used for such studies and their individual characteristics.

7.1.4. Cryo-cooling protein powder samples and microstructural effects

In a powder experiment, we sample a large number of very small crystals and the specimen will still be a powder even if some of the crystallites are broken (the typical size of the crystallites is approximately 0.1–1 µm). This has made powder methods extremely useful for the study of phase transitions and other phenomena that can ruin a fragile single crystal. If diffraction peaks are observed that are broader than the instrumental resolution, they can give some information about the microstructure of the sample. When there is a spread of cell parameters in the sample, a 'microstrain' broadening occurs and this has a larger effect at higher scattering angles. Assuming a Gaussian description of the diffraction peak widths parameterized *versus* 2θ as

$$\mathrm{FWHM}^2 = U\tan^2\theta + P/\cos^2\theta,$$

we gain the advantage that the parameters U and P can easily be related to the microstructure of the material [Larsen & Von

Dreele (2004), *GSAS* manual]. Strain broadening in real space gives $\Delta d/d$ as a constant, which can be related to the U parameter *via*

$$\text{strain} = \frac{\pi}{18000}[(8\ln 2)(U - U_{\rm i})]^{1/2}\%,$$

where $U_{\rm i}$ is the instrumental contribution. For particle-size broadening effects, the relationship is

$$\text{size} = \frac{18000K\lambda}{\pi(8\ln 2)^{1/2}P}\ \text{nm}.$$

When measured at room temperature, many proteins give diffraction peaks where the widths are limited only by the instrumental resolution. This indicates that the samples are extremely homogeneous, with all crystallites having the same unit-cell parameters. The truncation of the crystal lattice by a very small crystallite size also leads to a peak broadening which is similar over all of reciprocal space and is normally significant for crystallite sizes below about 1 µm. For structural refinements, the microstrain/size peak broadening increases at higher resolution (scattering angle) where the peak overlap is already more severe. Owing to the soft nature of the materials, the size broadening is often negligible. Crystallite sizes can be in the µm range so particle-size effects are often not pronounced. However, poor crystallinity, chemical inhomogeneity and changes induced by cryo-cooling often lead to peak broadening.

A typical protein powder sample loaded into a borosilicate capillary and mounted on the ID31 ESRF beamline (Fitch, 2004) at room temperature often cannot withstand more than two minutes exposure time owing to radiation damage. Thus, samples are translated periodically in order to expose a fresh part of the sample to the X-ray beam. When subsequent scans are collected from the same part of sample, radiation-damage effects are apparent in the observed gradual loss of peak intensities, peak shifts associated with alteration of lattice dimensions and an increase of the peak widths owing to the gradual loss of crystallinity. The suppression of radiation damage by cryo-cooling (Rodgers, 1997, 2001; Garman & Schneider, 1997) has meant that nowadays the majority of protein single-crystal structures are determined at low temperatures. For powder experiments, it is important to preserve sharp diffraction peaks and minimize peak overlaps; however, it is also useful to suppress radiation damage by cryo-cooling.

In an attempt to explore radiation damage, we initially investigated the freezing processes occurring in turkey egg-white lysozyme (TEWL) by collecting data while cooling and warming a powder sample (Margiolaki *et al.*, 2004, 2005). A phase transition in the protein structure is accompanied by freezing of the mother liquor, and leads to a broadening of the powder peaks.

In that particular case, the 'microstrain'-related peak-broadening parameter (%) was in agreement with the bulk overall contraction of the unit cell during freezing. Generating two-dimensional Fourier maps of the structure projected along the c axis gives a more direct view of the changes occurring upon freezing. Fig. 7.1.4 shows the Fourier map, which illustrates that the changes in intensity can be accounted for by a smoothing out of the electron density, which makes the apparent channel diameter seem larger. A more reasonable hypothesis for the contraction of the unit cell is that the formation of an ice phase in the bulk solvent leads to a rapid increase in the osmotic potential of the crystallization buffer. It is conceivable that this would lead to transport of liquid water out of the crystallites and would be manifested in a rapid contraction of the solvent channels and, by extension, the unit cell. While this explains the contraction, the changes in peak intensities are difficult to predict under those circumstances.

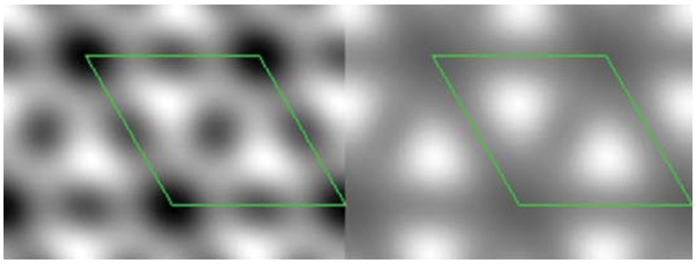

Figure 7.1.4
Projections of the electron density in the *ab* plane for TEWL at room temperature (left) and low temperature (right). The maps are constructed from the three reflections 100, 110 and 200, assuming that the phase angles do not change on passing through the freezing transition. The dark and light areas correspond to low and high electron density, respectively (Margiolaki *et al.*, 2004, 2005).

In order to find an optimized approach to cryo-cooling of powder samples, we have systematically varied the cryoprotectant type and concentration (Jenner *et al.*, 2007). With hen egg-white lysozyme (HEWL), it was shown that the unit-cell parameters of the microcrystals at low temperature are strongly affected by the addition of cryoprotectants. The changes in cell parameters were anisotropic and depended on the type of cryoprotectant molecule used. Also, the amount of induced peak broadening was found to be proportional to the change in unit-cell parameters caused by freezing; when there is less peak broadening, the unit cell was closer to the room-temperature cell. In all of these cases, the powder diagrams could be well accounted for by considering only a 'microstrain'-related peak-broadening term, meaning that the peak broadening arises mainly from having a distribution of unit-cell dimensions in the sample. Particle-size broadening effects were negligible in comparison. The increased sample size and use of a capillary to contain the powder sample means that the cooling rates are significantly lower for powders compared with single crystals in loops, and some challenges remain in finding ways to optimally cryo-cool microcrystalline samples. Moreover, in the case of HEWL, Rietveld analysis (Rietveld, 1969) showed significant differences compared with the room-temperature structure, with well defined regions of electron density being found that can be explained by bound cryoprotectant agent molecules (PEG 400) as shown in Fig. 7.1.5 (Margiolaki *et al.*, unpublished results).

Recently, a more efficient approach for cryo-cooling protein powders has been developed by our team. In this case, Kapton (polyimide) tubes are employed instead of borosilicate ones. It is well known that Kapton's high thermal conductivity (0.10 W m^{-1} K^{-1}) makes it ideal for use in dissipating and managing heat in electronic assemblies, and it is less fragile than glass (Von Dreele, 2006). Kapton tubes with an internal diameter of 1.0 mm (with a wall thickness of 0.025 mm) are usually selected. The optimum cryoprotecting agent and its concentration are protein dependent and are usually identified on a trial-and-error basis. The protein solution is then mixed with a relatively high concentration of the optimum cryoprotectant. The mixture is then transferred into the tube, which is cryo-cooled first using liquid nitrogen and later on, during data collection, by a nitrogen cryostream. In order to avoid formation of crystalline ice, rapid flash freezing of the sample is necessary, and is often unsuccessful. This problem has been partially solved by further reduction of the sample volume *via* insertion of a thinner tube

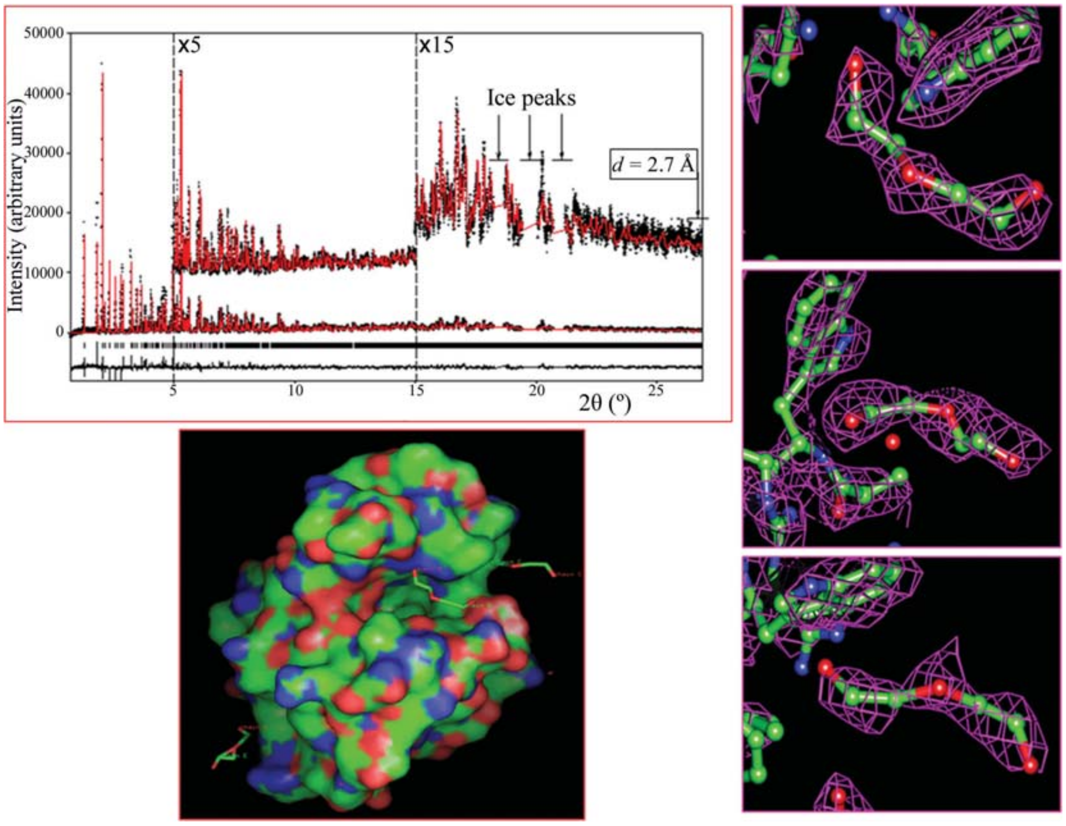

Figure 7.1.5

Upper left panel: The Rietveld fit for tetragonal HEWL at 100 K with a mixture of PEG 400 and methanol added for cryoprotection [λ = 1.250845 (23) Å, ID31, ESRF, *GSAS*: space group: $P4_32_12$, a = 78.31382 (6), c = 36.8870 (7) Å, $R_{\rm wp}$ = 6.74%, $R(F^2)$ = 9.66%]. Right panel: Perspective views of selected regions around three out of the four PEG chains of the total omit map at 2.7 Å resolution with the contour level at 1σ. Lower left panel: The refined molecular conformation of HEWL illustrated as a surface. The four additional PEG molecules identified to be bound on HEWL at 100 K are shown as cylinders.

(inner diameter 0.8 mm) inside the original one. This way, the resulting cylindrical annulus of the sample volume is reduced by a factor of three, allowing for an additional time delay in the cooling rate of the sample. As a result, faster and more uniform cooling can be obtained. This protocol led to the successful data collection for selected human insulin polymorphs (T3R3, T6) at 100 K to a d-spacing resolution limit of approximately 2.6 Å. The data resolution of the same insulin polymorphs at room temperature was approximately 3.5–4 Å. This demonstrates the substantial improvement of data quality at cryo-cooled conditions owing to the decrease of the atomic thermal motion and potential disorder of specific amino-acid regions. Electron-density maps computed from the measured structure factors and partially known structural models available from the Protein Data Bank (PDB; Berman *et al.*, 2003) (codes: 1fub, 1mso) displayed quality usually obtained from single-crystal measurements (Watier, 2011).

7.1.5. Crystal screening

Protein structure determination by X-ray crystallography is dependent on obtaining a good quality protein crystal suitable for diffraction data collection. Owing to this requirement, protein crystallization represents a key step in protein structure determination. Typical protein crystallization practice involves parallel setup and monitoring of a considerable number of individual protein crystallization experiments (Pusey *et al.*, 2005; Newman, 2011; Skarina *et al.*, 2014). Powder diffraction has been exploited as a technique for fingerprinting different crystalline substances and allows rapid phase identification and quantification of mixtures. High-resolution powder instrumentation is designed to obtain the sharpest possible peaks in reciprocal space and also to determine accurate peak positions. These features are complementary to area-detector single-crystal experiments, where the aim is normally to measure integrated intensities of diffraction peaks at the highest possible scattering angles in order to improve the direct-space resolution in an electron-density map. By exploiting the excellent reciprocal-space resolution of powder instruments, a variety of complementary studies can be carried out, studies which are typically more difficult to do with single crystals that are usually grown under a very specific set of conditions. Powder samples contain many millions of individual crystallites and give information about the bulk properties of a material; there is no question of whether a particular crystallite is representative of the whole sample. The first high-throughput demonstration study corresponded to the observation of the effect of pH and crystallization temperature on the tetragonal crystal form of HEWL (Basso *et al.*, 2005). We made accurate measurements of the evolution of the lattice parameters with pH, which is illustrated by the smooth anisotropic shifts in the peak positions in Fig. 7.1.6. The reproducibility of these results and the precision of the powder-diffraction data were verified by carrying out crystallization experiments at both 277 K and room temperature, where similar behaviour was observed.

Wherever microcrystalline proteins come into use as biomaterials or medicines, there will be an increasingly important role for powder diffraction to play. There are many benefits to using a crystalline form of an already known drug: it can allow better control over the release rate into the system by an optimization of the crystallite size and polymorphism, and it should also offer an extended shelf-life and a reduction in production costs (Yang *et al.*, 2003; Basu *et al.*, 2004; Havelund, 2009; Brader & Sukumar, 2005; Rabinow, 2004; Aguiar *et al.*, 1967; Bauer *et al.*, 2001). Microcrystalline forms of drugs tend to be slower acting, as the crystallites must dissolve before acting. Crystallite size and polymorphism both affect dissolution rates, and so they are important factors in understanding and characterizing formulations.

Our studies on microcrystalline human insulin (HI) and urate oxidase/rasburicase (Uox) (Collings *et al.*, 2010; Fili *et al.*, 2015; Karavassili *et al.*, 2017) suspensions using the powder-diffraction method have revealed a high degree of polymorphism upon variation of their physico-chemical environment (pH, ligand binding *etc.*). Even more important was our discovery of two new biologically active insulin–phenol complexes, which were later characterized *via* single-crystal methods (Norrman & Schluckebier, 2007). The effects of the ligands phenol and resorcinol on the crystallization of HI have been investigated as a function of pH. Powder-diffraction data were used to characterize several distinct polymorphic forms. A previously unknown polymorph with monoclinic symmetry ($P2_1$) was identified for both types of ligand with similar characteristics [the unit-cell parameters for the insulin–resorcinol complex were a = 114.0228 (8), b = 335.43 (3), c = 49.211 (6) Å, β = 101.531 (8)°] (Karavassili *et al.*, 2012). In a more recent study, HI was co-crystallized with two distinct phenolic derivatives, the organic ligands *meta*-cresol (*m*-cresol) and 4-nitrophenol (Valmas *et al.*, 2015). The formation of polycrystalline precipitates was then followed by means of structural characterization of the individual specimens in terms of unit-cell symmetry and dimensions employing both laboratory and synchrotron instruments. In both cases of ligands, two different polymorphs were identified, the first adopting the known trigonal symmetry ($R3$ space group) at higher pH values and a second of monoclinic symmetry (space group $P2_1$) with lattice parameters a = 87.4282 (5), b = 70.5020 (3), c = 48.3180 (4) Å, β = 106.8958 (4)°, the latter to our knowledge never observed before.

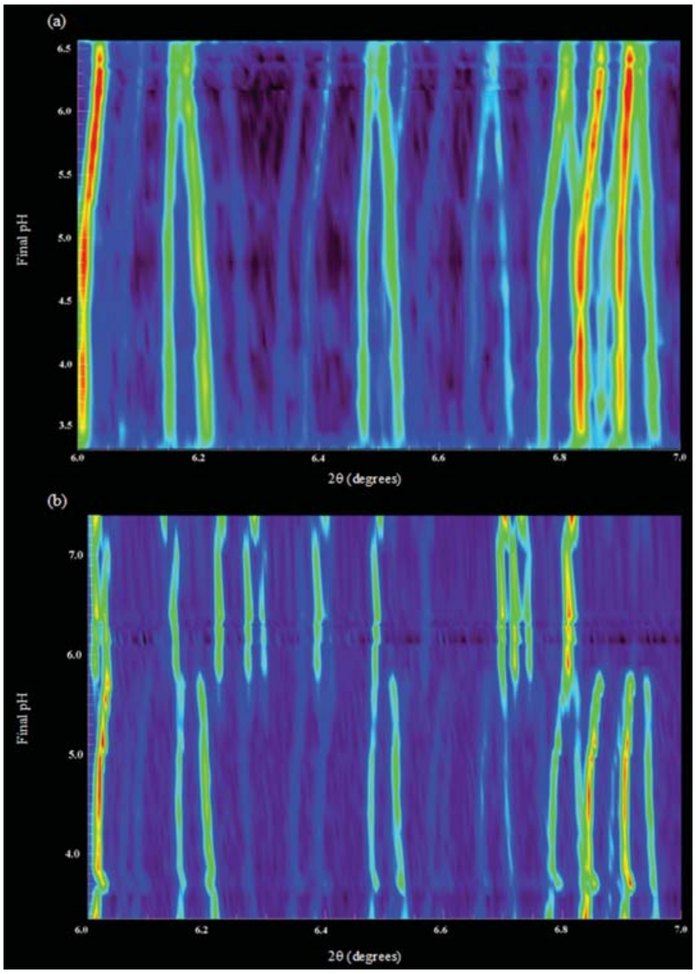

Figure 7.1.6
Colour representation of ID31 powder-diffraction data from the pH variation experiment, from pH 6.56 to 3.33, of HEWL crystallized at 277 K (*a*) and room temperature (*b*). At low temperature the tetragonal phase is favoured and a smooth anisotropic shift in the peak position is apparent (Basso *et al.*, 2005).

We note that the two new monoclinic polymorphs appear only at acidic environment (pH range: 5–6.3) using ligands such as phenol and specific derivatives such as *m*-cresol and 4-nitrophenol. On the other hand, the already known $P2_1$ phase, with lattice parameters a = 61.247, b = 61.739, c = 47.467 Å, β = 111.32° (PDB code: 1ev6), was previously detected at pH ~ 7 when insulin was co-crystallized with *m*-cresol, resorcinol (Smith *et al.*, 2000) or phenol (Derewenda *et al.*, 1989). The comparison between the known and novel isosymmetrical monoclinic forms, indicates, besides the larger unit-cell parameters, unusual crystal packing motifs for the new forms. The structurally known HI monoclinic polymorph (Smith *et al.*, 2000; PDB code 1ev6), consists of six molecules per asymmetric unit and 48% solvent content. According to the Matthews coefficient calculation (Matthews, 1968; Kantardjieff & Rupp, 2003), the $P2_1$ polymorph described by Valmas *et al.* contains 12 molecules per asymmetric unit and 39% solvent content (Matthews coefficient = 2.03 $\text{Å}^3\,\text{Da}^{-1}$). This large difference reveals a much denser crystal packing in the case of the novel monoclinic phase, which could be of great pharmacological importance. Structure solution of the novel polymorphs is currently in progress.

In the case of Uox, a key protein component of existing drugs (*i.e.* Fasturtec) that helps the body to eliminate uric acid (McGrath & Walsh, 2005; Wu *et al.*, 1992; Retailleau *et al.*, 2004, 2005), a previously unknown, biologically active polymorph was discovered when crystallization was performed in the absence of any chemical additives. Part of the current research within our group is devoted to the structural characterization of an extensive series of insulin–ligand complexes and Uox polymorphs prepared at different crystallization conditions (pH, ionic strength, crystallization agent) which are potential drug targets. Fig. 7.1.7 illustrates the tetrameric form of Uox co-crystallized with its inhibitor 8-azaxanthine (PDB code: 1r51) (Retailleau *et al.*, 2004).

There is a noticeable increase in the variety of protein powder data appearing in the literature for biological macromolecules systematically exhibiting difficulties in crystal growth. These include insect virus polyhedra, membrane proteins and amyloid-forming peptides. Polyhedra are naturally occurring protein crystals which form an armour coating around certain viruses. The crystals are extremely stable, shielding the virus particles from environmental damage and enabling them to survive in harsh environments over extended periods of time. Until a few years ago, the detailed atomic structures of the polyhedra remained unknown, in part because of the small size of the crystals. However, there have been several attempts at identifying the crystalline phases of different virus families including polyhedra (Anduleit *et al.*, 2005; Watier, 2011). Complete structural models have been subsequently solved *via* single-crystal diffraction by microcrystals with sizes smaller than 10 μm (Coulibaly *et al.*, 2007; Ji *et al.*, 2010; Evans *et al.*, 2011). Several data sets for

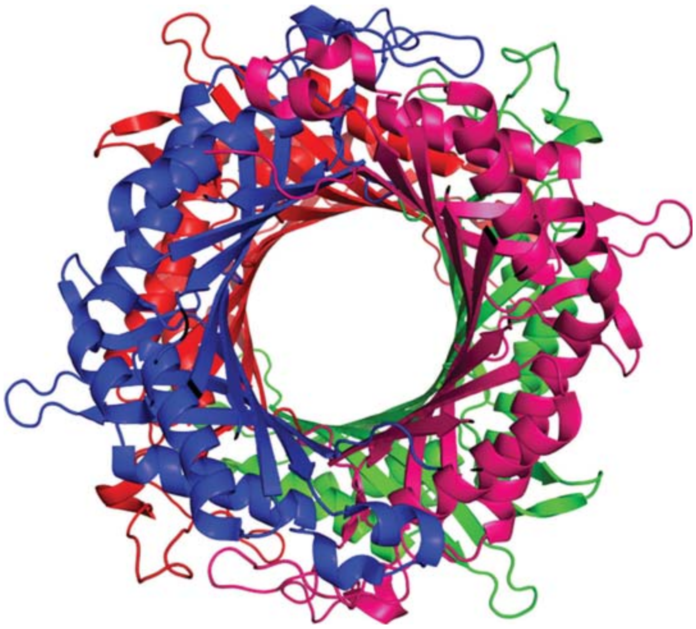

Figure 7.1.7
The tetrameric form of urate oxidase (Uox) co-crystallized with its inhibitor 8-azaxanthine (PDB code: 1r51, space group: $I222$, a = 81.30, b = 96.30, c = 105.60 Å) (Retailleau *et al.*, 2004; Collings *et al.*, 2010). The different colours correspond to four symmetry-related protein chains.

membrane proteins have been collected at various synchrotron sources and currently there are two published articles on the bacteriorhodopsin (bR) molecule from two-dimensional purple membrane crystals presenting mainly methodological developments for low-resolution phasing (Oka *et al.*, 2006; Dilanian *et al.*, 2011). Finally, there are several powder-diffraction studies of amyloid-forming peptides, mainly presenting identification of distinct crystalline phases (Balbirnie *et al.*, 2001; Bond *et al.*, 2003; Diaz-Avalos *et al.*, 2003; Inouye & Kirschner, 2006).

The possibility of using powder-diffraction data on microcrystalline protein samples for detection of ligands in protein–ligand complexes was illustrated by the studies of HEWL complexes with *N*-acetylglucosamine (NAG*n*, *n* = 1–6) oligosaccharides (Von Dreele, 2001, 2005). All of the protein powder-diffraction patterns in these studies showed extremely sharp Bragg peaks consistent with crystallites greater than 1 µm in size; the peaks were also devoid of line-broadening defects. The location of each NAG*n* could be found from difference-Fourier maps generated from structure factors extracted during preliminary Rietveld refinements. Full NAG*n*–protein structures were subjected to combined Rietveld and stereochemical restraint refinements and revealed binding modes for NAG*n* that depended on the length of the NAG oligosaccharide (Fig. 7.1.8). The series of refined powder structures is available in the Protein Data Bank *via* access codes 1ja2, 1ja4, 1ja6, 1ja7, 1sf4, 1sf6, 1sf7, 1sfb and 1sfg. These studies showed that powder diagrams can give interpretable electron-density maps for protein samples and showed unambiguously that a powder sample can be sufficient for structural analysis.

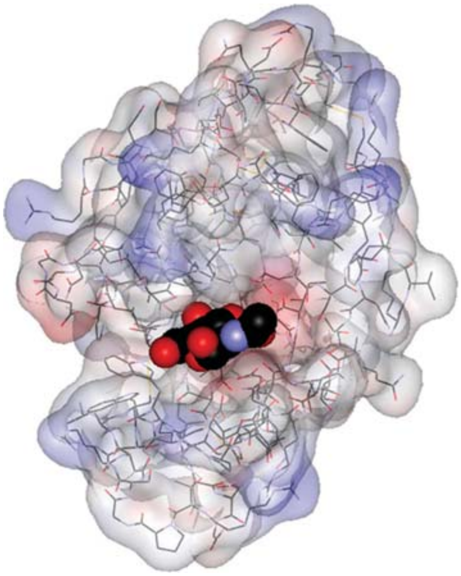

Figure 7.1.8
A view of the *N*-acetylglucosamine complex with HEWL as determined from high-resolution X-ray powder-diffraction data (Von Dreele, 2001, 2005).

7.1.6. Improvements in data quality *via* the use of multiple profiles

Powder data suffer from peak overlap. If this problem can somehow be circumvented (or at least reduced), we should be able to solve and refine larger structures more easily using powder methods. Changing the pattern of peak overlaps and collecting multiple data sets is one strategy for reducing the overlap problem. Varying the temperature of the sample for low-symmetry unit cells often leads to anisotropic thermal expansion, and therefore allows overlapped peaks to be untangled (Shankland *et al.*, 1997; Brunelli *et al.*, 2003). Similarly, if a sample can be prepared with a significant degree of preferred orientation, then overlapped peaks will have different intensities depending on the orientation of the sample (Dahms & Bunge, 1986; Bunge *et al.*, 1989; Cerny, 1996; Baerlocher *et al.*, 2004). Combining multiple data sets where either the cell parameters or the preferred orientation are different gives some information about the way in which the overlapped peaks should be partitioned. In order to benefit from anisotropic changes in unit-cell parameters for intensity extractions, the *PRODD* refinement program (Wright & Forsyth, 2000; Wright, 2004) was modified to allow a different set of unit-cell parameters to be used for each pattern in a multi-pattern Pawley fit (Pawley, 1981). A single list of Bragg-peak intensities is fitted to the profiles while an overall isotropic displacement coefficient and scale factor for each profile account for the bulk of the differences between the patterns. A Pawley refinement of myoglobin using high-resolution synchrotron data (λ = 0.413465 Å, BM16, ESRF) and *PRODD* illustrated the applicability of the method in cases of significant complexity and severe peak overlap (Wright, 2004). The integrated intensities that are extracted from the multi-pattern powder data are a considerable improvement over those that come from a single data set (Besnard *et al.*, 2007; Margiolaki, Wright, Fitch *et al.*, 2007) and are then useful for attempts at structure solution using single-crystal software packages. Care must be taken to ensure that the reflection intensities from the powder diagrams are corrected properly for Lorentz and multiplicity factors, and also that sensible error estimates are supplied. Error estimates on the extracted intensities are in principle difficult to determine properly.

Several studies demonstrate that the most significant improvements arise from the use of multiple data sets during intensity extraction (Besnard *et al.*, 2007) and/or structure refinements (Von Dreele, 2007; Basso *et al.*, 2005; Margiolaki, Wright, Wilmanns *et al.*, 2007). The unit-cell parameters are perturbed to alter the pattern of peak overlaps in the different patterns and reduce the overlap problem. Perutz (1954) used

Table 7.1.2

Software packages that allow extraction of reflection intensities including analysis of multiple profiles and calculation of error estimates

Software	Reference
GSAS	Larson, A. C. & Von Dreele, R. B. (2004). *General Structure Analysis System (GSAS)*. Los Alamos National Laboratory Report LAUR 86-748, Los Alamos, USA http://www.ccp14.ac.uk/solution/gsas/
TOPAS	Coelho, A. (2004). *TOPAS-Academic*. http://www.bruker-axs.de/topas.html Watier, Y. & Fitch, A. (2010). *Protein powder diffraction analysis with TOPAS. Mater. Sci. Forum Trans. Tech. Publ.* **651**, 117–129
PRODD	Wright, J. P. (2004). *Extraction and use of correlated integrated intensities with powder diffraction data. Z. Kristallogr.* **219**, 791–802 Wright, J. P., Markvardsen, A. & Margiolaki, I. (2007). *Likelihood methods with protein powder diffraction data. Z. Kristallogr.* Suppl. **26**, 27–32 http://www.ccp14.ac.uk/ccp/web-mirrors/prodd/~jpw22/

perturbations of the unit-cell parameters with single-crystal data in an early attempt to solve the phase problem by oversampling of reciprocal space. This approach was apparently abandoned owing to the development of other, simpler, phasing methods. Thus far, we have not attempted to exploit the intensity differences which come with the unit-cell changes for phasing, although in theory the oversampling method may still be applicable. Table 7.1.2 lists the software packages that allow extraction of reflection intensities including analysis of multiple profiles and calculation of error estimates.

7.1.7. Structure solution

If powder data contain enough information to refine the structure of a small protein, then it follows that the structure might also be solved from the same data. We are choosing an inclusive definition of 'solving' a protein structure in this context. The use of stereochemical restraints and introduction of prior knowledge, such as the amino-acid sequence, will be used to fill in missing information at high resolution. The first step in an analysis is the identification of cell dimensions and crystal symmetry. With high-resolution data, identification of cell dimensions is often straightforward. However, with poorer data, and particularly when the sample contains more than one crystalline phase, indexing can become a serious bottleneck. If the data appear reasonable and indexing does fail, then the most likely cause is the existence of more than one phase. Software has been developed for detecting the existence of secondary phases (David & Shankland, 2008). Whereas the inability to determine the correct unit cell makes structure solution impossible, some uncertainty in the correct space group is not an intractable problem, as each potential space group may be tested separately. Possible space groups are determined by examining diffraction patterns for systematically absent reflections. Severe ambiguities related to the correct space group may arise from the overlap of diffraction peaks, either accidental or as an unavoidable consequence of the crystal symmetry (*i.e.* the exact overlap of non-equivalent reflections in certain high-symmetry Laue groups). Determining absences for long *d*-spacing reflections is normally straightforward, but at shorter *d*-spacings reflection overlap makes it a much more subjective process. Choosing the space group with the fewest number of contributing reflections is a good pragmatic approach to resolving this problem. In the case of proteins, considerable help in space-group selection comes from their chiral nature, which limits the allowed space groups, and the well known frequency distribution of space groups (Andersson & Hovmöller, 2000). Some space groups can be eliminated from the beginning, since they require symmetries known to be absent in the molecule itself. For example, space groups with reflection or inversion symmetries cannot be observed for chiral molecules; thus, only 65 space groups of the possible 230 are allowed for protein molecules, which are almost always chiral. One of the most puzzling observations in protein crystallography is that the various space-group symmetries occur with striking non-uniformity. Earlier studies have shown that the observed frequencies for both two- and three-dimensional crystals can be explained by an entropic model. Under a requirement for connectivity, the favoured space groups are simply less restrictive than others, in that they allow the molecules more rigid-body degrees of freedom and can therefore be realized in a greater number of ways (Wukovitz & Yeates, 1995). In addition, over the past decade probabilistic approaches to space-group determination have been developed that remove the need for subjective judgements about the presence or absence of classes of reflections throughout the pattern (Markvardsen *et al.*, 2001; Altomare *et al.*, 2004). Knowing the most likely extinction symbol, it is usually a straightforward matter to pick the most likely space group. As such, these methods are particularly useful when dealing with systems of orthorhombic symmetry or higher, where the number of possible space groups (and settings) is relatively large.

Powder data can certainly be used to uncover new structural information at low or even modest resolution, and we expect to see this becoming a more common approach in the future. As water molecules have been seen in at least two refinements already (Margiolaki, Wright, Wilmanns *et al.*, 2007; Von Dreele, 2007), we can be confident that powder data will be sufficient to unravel new structural information.

7.1.7.1. *Molecular replacement*

In the molecular-replacement method (Rossmann, 1990), a model for a protein molecule is proposed based on known structures of proteins that have similar amino-acid sequences. This model is then oriented and positioned in the unit cell to match the experimental data for the unknown structure. In this era of structural genomics (Stevens *et al.*, 2001), the quality of the search models is expected to improve dramatically, so that molecular replacement using a powder diagram may be sufficient to confirm that a new protein is indeed similar to one that is previously known. Proteins are often found in a variety of different organisms with very similar amino-acid sequences, or are expressed with a few modified residues to investigate the effects these changes have on the protein. There are only six degrees of freedom to be determined per molecule in solving a structure by molecular replacement. The first three give the orientation and the second three give the position of the molecule with respect to the symmetry elements of the space group. Relatively low resolution data can often be used for molecular-replacement problems. A resolution of 6 Å can be sufficient and a cutoff of 3 Å is often applied. The solution of the structure of T3R3 insulin (Von Dreele *et al.*, 2000) was the first example of the molecular-replacement method using powder data (Fig. 7.1.9). In our own laboratory, we successfully used *MOLREP* (Vagin & Teplyakov, 1997) together with powder data for a variety of small proteins (consisting of 50–150 amino-acid residues). Integrated

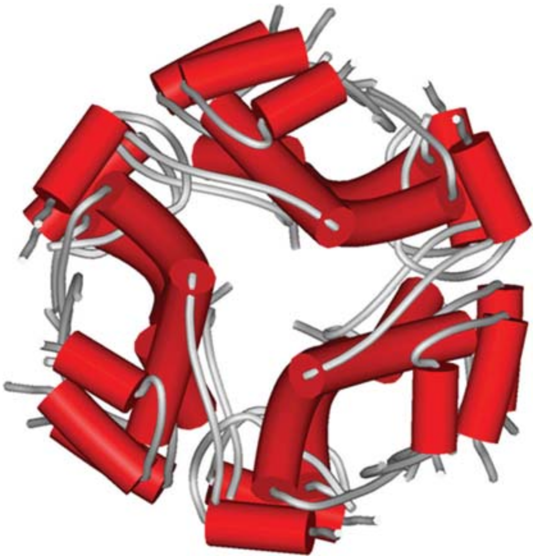

Figure 7.1.9
A schematic view down the *c* axis of the doubled-*c*-axis variant of the T3R3 Zn–insulin complex as determined from powder-diffraction data (Von Dreele *et al.*, 2000).

intensities are extracted (Wright, 2004) from the powder profile and then treated as if they came from a single crystal, ignoring the overlap problem. Fortunately, the molecular-replacement method tolerates errors in the input diffraction data as if they were due to errors in the model for the structure. In the cases of turkey (Margiolaki *et al.*, 2004, 2005) and hen (Basso *et al.*, 2005) egg-white lysozymes, there was a clear distinction between the best structure proposed by *MOLREP* and the second best, and in both cases the best structures were the correct positions and orientations for the molecule in the unit cell. After determining the position and orientation of a model for the protein molecule in the unit cell, it is of critical importance to be able to go through the structure and identify the regions that are different in the new protein compared with the initial model. A more recent example is the structure solution of the second SH3 domain (SH3.2) of ponsin *via* molecular replacement. The high quality of the extracted intensities from the measured profiles led to the unique determination of an unknown 544-atom protein structure (70 amino-acid residues) from powder data. The search model had 38% amino-acid sequence identity and was still sufficient for molecular replacement and model building based on electron-density maps calculated at 2.3 Å diffraction resolution. Fig. 7.1.10 illustrates the structure of the SH3.2 domain derived from powder diffraction (Margiolaki, Wright, Wilmanns *et al.*, 2007). Another example of a molecular-replacement-style approach is the use of phase angles or direct structural information from another technique, combined with data collected using powder-diffraction methods. Oka *et al.* (2006) have investigated the structure of purple membranes, which comprise two-dimensional crystals of bacteriorhodopsin trimers. They collected high-resolution synchrotron powder-diffraction data using a 1 m-path-length Guinier-type camera at beamline BL40B2 at SPring-8. By combining extracted intensities up to a resolution of 4.2 Å with phases from cryo-electron microscopy, they were able to produce an electron-density map. The data from the synchrotron improved the resolution for purple membrane compared with that attained previously with laboratory X-rays (intensities extracted up to ~7 Å) and opens up the possibility of studying these systems under a wider range of conditions. Moreover, Dilanian *et al.* (2011) proposed a novel method for treating highly overlapped reflections. They applied it to the structure of the bacteriorhodopsin (bR) molecule to a resolution of 7 Å using only powder-diffraction data obtained from two-dimensional purple membrane (PM) crystals.

Recently, we have extended our studies on the 160 amino-acid nsP3 protein macro domain of the Mayaro virus (MAYV), an emerging virus of South American tropical regions, by means of powder diffraction on microcrystalline precipitants. These results correspond to the first structural data existing in the literature since 1954 when the virus was isolated in Trinidad (Anderson *et al.*, 1957; Causey & Maroja, 1957). Comparison with known structures of sequence-homologous Chikungunya virus (CHIKV) macro domains (Malet *et al.*, 2009) indicate that MAYV adopts a trigonal/hexagonal structure associated with a looser molecular packing. The cell dimensions of MAYV are significantly altered in comparison to CHIKV and the unit cell is composed of six molecules and 58% solvent. Structure solution *via* the molecular-replacement technique and refinement of MAYV are currently in progress (Papageorgiou *et al.*, 2010).

Among hundreds of virus recombinant proteins isolated every year, considered as potential antivirus targets, several did not produce sizeable single crystals required for classical single-crystal X-ray diffraction studies. However, some of them produced microcrystals ideal for XRPD measurements. In certain cases, we have performed preliminary measurements validating the feasibility of the aforementioned approach especially concerning protease 3C of Coxsackie virus B3 (COXVB3) and Dengue virus (DENV) non-structural protein 5 (NS5) methyltransferase domain. In both cases, preliminary crystallization screens produced microcrystals and XRPD data were sufficient for polymorph identification for a specific crystallization condition (Fili *et al.*, 2016; Valmas *et al.*, 2017).

Finally, Doebbler & Von Dreele (2009) have shown that macromolecular structures can be solved *via* molecular replacement from powder-diffraction data collected not only on multi-analyser diffractometers but also on image plates. Diffraction peaks recorded on image plates are generally broader in line-width than those collected using an array of crystal-analyser detectors, but the image-plate data often allow the use of powder data to lower *d*-spacings. Owing to the high incidence

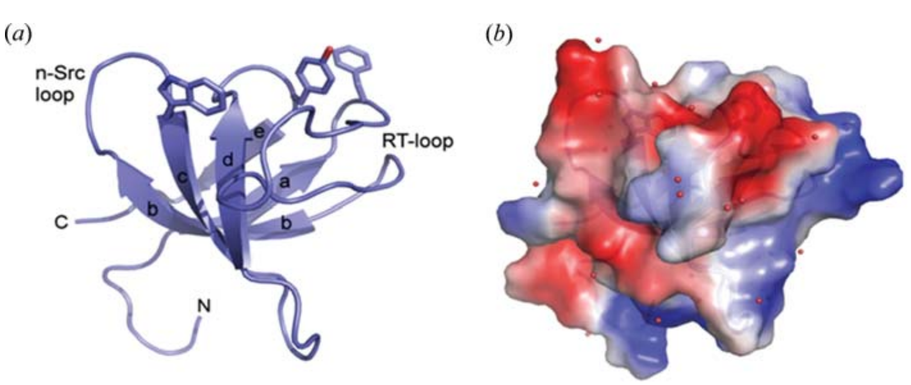

Figure 7.1.10
Powder-diffraction structure of the ponsin SH3.2 domain. (*a*) Ribbon representation of the SH3.2 domain indicating the secondary-structure elements of the domain. The main hydrophobic residues of the binding interface as well as the positions of the n-Src and RT loops are indicated. (*b*) Electrostatic potential representation of the domain, identifying additionally the water molecules as red spheres. This figure was generated using *PYMOL* (http://pymol.sourceforge.net/) (Margiolaki, Wright, Wilmanns *et al.*, 2007).

of reflection-intensity overlaps in powder patterns (which is especially evident for larger biological macromolecules), a multiple-diffraction-pattern Pawley refinement is necessary in order to distinguish intensity peaks. Von Dreele utilized various salt concentrations to produce small lattice distortions, which resulted in shifts of Bragg-peak positions in a suite of five powder-diffraction patterns. Using reflection structure-factor amplitudes obtained from this combined refinement, the structure of hen egg-white lysozyme was determined by molecular replacement using the 60% identical human lysozyme (PDB code 1lz1) as the search model. This work also expanded upon previous work by presenting a full-scale multi-species analysis combined with an investigation of the sensitivity with regard to discrimination between incorrect protein fold types. To test the limits of this technique, extension to higher-molecular-weight biological macromolecules is ongoing.

7.1.7.2. *The isomorphous-replacement method*

When there is no starting model available for a protein molecule, then we face the crystallographic phase problem. The isomorphous-replacement method (Perutz, 1956) determines the phases of X-ray reflections by comparing data from a series of crystals that contain different additive heavy atoms. This method was already in common use (prior to the application to proteins) for the determination of organic structures by comparing crystalline salts with differing cations or anions. The first application to proteins (Green *et al.*, 1954) was used to determine the signs of centric reflections in haemoglobin. In order to use the isomorphous-replacement method, one needs to collect data for a protein with and without the added heavy atom and to be able to measure and interpret the differences in the data due to the added atoms. Difficulties arise when the addition of the heavy atom perturbs the structure, leading to non-isomorphism and differences that can no longer be simply interpreted by a few atoms. With powder data, we can determine whether or not a particular heavy atom has formed a derivative by comparing the unit-cell parameters, which are normally perturbed by the addition of a heavy atom. In the case of a gadolinium derivative of hen egg-white lysozyme (HEWL) (Wright *et al.*, 2007), we prepared derivatives using different concentrations of Gd and also different pH values in order to alleviate the peak-overlap problem. Extracted intensities were then used to solve for the atomic positions of the Gd atoms using *SHELXD* (Usón & Sheldrick, 1999) and then refinement of the heavy-atom substructure and phasing were carried out using *Sharp* (La Fortelle & Bricogne, 1997). Similarly, in the case of a uranium derivative of porcine pancreatic elastase (PPE), a 240-amino-acid residue protein of 25.9 KDa molecular weight (Besnard *et al.*, 2007), the peak-overlap problem was reduced by comparing data sets that had been exposed to the X-ray beam for different amounts of time. The gradual changes in unit-cell parameters due to radiation damage changed the pattern of peak overlaps sufficiently so as to successfully deconvolute the overlapping diffraction peaks. The U atom is clearly visible in a difference Patterson map from native and derivative data sets, and phasing using *Sharp* proceeds to give a solvent mask which clearly and correctly delineated the protein and solvent regions (Wright *et al.*, 2007, 2008*a*,*b*). Recently, two heavy-atom derivatives of tetragonal HEWL (a gadolinium derivative and a holmium derivative) were crystallized at room temperature. Using synchrotron radiation, high-quality powder patterns were collected in which pH-induced anisotropic lattice-parameter changes were exploited in order to reduce the problem of overlapping reflections. The phasing power of two heavy-atom derivatives in a multiple-isomorphous-replacement (MIR) analysis enabled molecular structural information to be obtained up to approximately 5.3 Å resolution. At such a resolution, features of the secondary structure of the lysozyme molecule could be accurately located using programs for this purpose. In addition, the quoted resolution was sufficient to determine the correct hand of the heavy-atom substructure, which led to an electron-density map representing the protein molecule of proper chirality (Fig. 7.1.11) (Basso *et al.*, 2010).

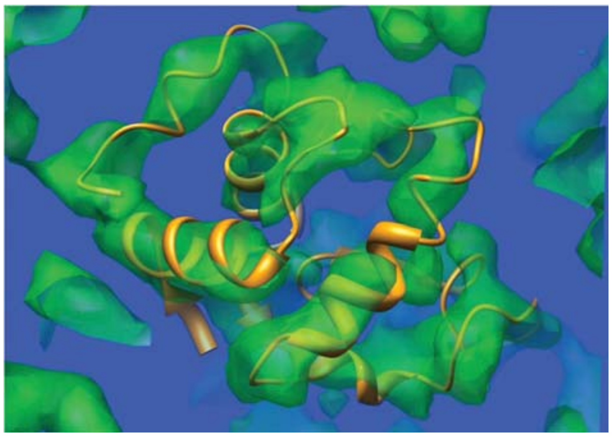

Figure 7.1.11
The electron-density map of HEWL (green) obtained from MIR data after density modification superimposed onto the known molecular structure (orange) obtained from the PDB (PDB code: 6lyt; Young *et al.*, 1993) (Basso *et al.*, 2010).

7.1.7.3. *Emerging powder phasing methods*

With single-crystal samples, the multiple-anomalous-dispersion (MAD) method has revolutionized the process of solving novel protein structures. Unfortunately, in powder experiments, the Friedel pairs hkl and $\bar{h}\bar{k}\bar{l}$ are always exactly overlapped, and so anomalous differences cannot be determined. Nevertheless, dispersive differences due to the variation in f' can be measured. The implications of this systematic overlap problem have been discussed by Prandl (1990, 1994), who reached the conclusion that phases can be determined for centric reflections using a single anomalous scatterer, but for acentric reflections at least two anomalously scattering species are required. Plöhn & Büldt (1986) have also considered the powder phasing problem and discuss the ways in which D_2O/H_2O substitution could be used for labelling with neutron data. The dispersive difference phasing methods were demonstrated by application to $SrSO_4$ by Burger *et al.* (1998), where the centric structure was solved using data near the Sr edge.

Helliwell *et al.* (2005) have collected data at the Ni edge for $Ni(SO_4){\cdot}6H_2O$ and determined optimal choices of wavelengths at the absorption edge. They indicate that the methods may also be applicable to microcrystalline protein samples. Work is in progress in our own laboratory, as well as in others, to exploit the dispersive differences that can be obtained by tuning the wavelength around an X-ray absorption edge for powder data. Helliwell and co-workers recorded high-quality synchrotron X-ray protein powder diffractograms (ID31, ESRF) from K_2PtBr_6 bound to lysozyme at 80 K to protect against X-radiation damage as much as possible and also to fix the K_2PtBr_6 heavy-atom-compound bound state (Helliwell *et al.*, 2010). With multiple-powder-pattern analysis, they then extracted individual reflection intensities and were thus able to show the presence of $PtBr_6^{2-}$ bound in lysozyme in $(F_o - F_c)$ Fourier omit maps at two binding sites. The wavelength-dispersive difference Patterson for the ID31 data at two wavelengths around the Br K edge and also the Pt L_{III} edge showed up binding site 1 in one of the six samples tested. In order to investigate the detailed binding behaviour they conducted single-crystal analyses with time-resolved freeze quenching after lysozyme-single-crystal soak times of 10, 90 and 170 min. Whilst the quick soaking of 10 minutes used in their first experiments at ID31 (ESRF) showed clear binding, there was a steady progression of increasing binding strength with increasing soak time. Thus, these time-resolved analytical-chemistry results show that further heavy-atom signal optimizations, and reproducible behaviour, are possible. The problem identified by Prandl (1990, 1994) for acentric reflections of using more than one anomalous-scatterer type can be approached instead *via* the method of 'solvent flattening'; test calculations in our laboratory with the MAD data of Peterson and co-workers (1996) using only the dispersive differences show that this can be effective in resolving a phase ambiguity (for this brominated oligonucleotide example) when only one anomalous scatterer is present. Recent experiments for extending their approach to the larger isomorphous and wavelength-dispersive signal cases of Ta_6Br_{12} as well as the non-ionic gadolinium chelate Gd(HP-D03A)($C_{17}H_{29}N_4O_7Gd{\cdot}1.3H_2O$) bound to lysozyme for powder experiments have been performed and data analysis is currently in progress. Overall, multiple-heavy-atom cluster compounds such as K_2PtBr_6 and Ta_6Br_{12} offer a way forward to solve *de novo* protein structures by powder diffraction as a complement to microcrystallography (Hedman *et al.*, 1985). Experience does suggest, however, that freezing a bulk lysozyme powder loaded with Ta_6Br_{12} is not as easy as freezing a single crystal soaked in Ta_6Br_{12}.

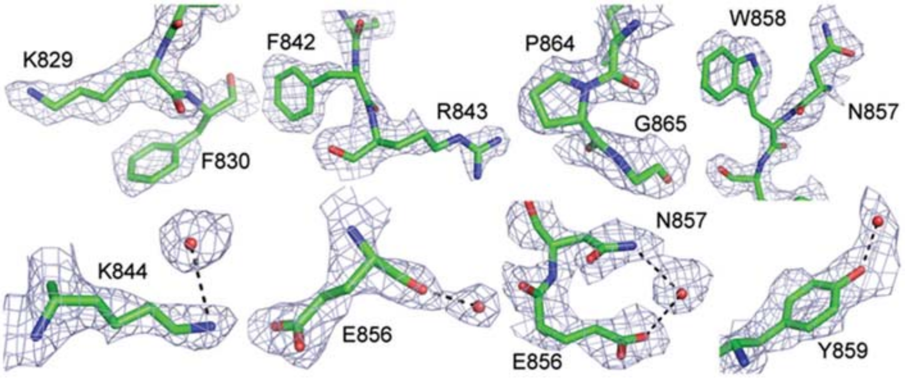

Figure 7.1.13
Selected regions of the final refined structural model of the second SH3 domain of ponsin in stick representation and the corresponding total omit map contoured at 1σ. This figure was generated using *PYMOL* (http://pymol.sourceforge.net/) (Margiolaki, Wright, Wilmanns *et al.*, 2007).

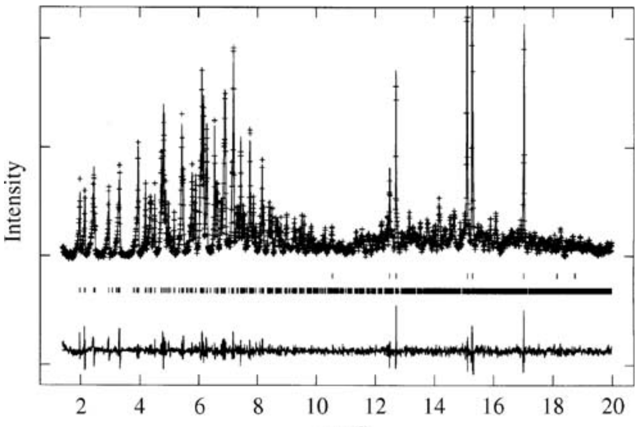

Figure 7.1.12
X-ray powder-diffraction profile from the final Rietveld refinement of whale metmyoglobin. Observed intensities are shown as crosses (+), calculated and difference curves as lines, and reflection positions for $(NH_4)_2SO_4$ and the protein as shown as vertical tick marks. The background intensity found in the refinement has been subtracted from the observed and calculated intensities for clarity (Von Dreele, 1999).

7.1.8. Structure refinement

7.1.8.1. *Stereochemical restraints*

In 1999, the first protein structure refinement using powder data was reported (Von Dreele, 1999) for metmyoglobin. High-angular-resolution synchrotron data from beamline X3B1 (λ = 1.14991 Å) at the National Synchrotron Light Source (NSLS), Brookhaven National Laboratory, USA, were used for the refinement (Fig. 7.1.12). A key characteristic of the powder profile was the observation of very sharp reflections associated with the highly crystalline protein sample. By combining a suite of stereochemical restraints with the measured diffraction profile, a successful refinement of the atomic positions of the 1260-atom protein was achieved (PDB code: 1f6h). In order to carry out this refinement, Von Dreele upgraded the *GSAS* (Larson & Von Dreele, 2004) software package in several ways. A suite of stereochemical restraints, as are normally used in low-resolution refinements with single-crystal data, was implemented with automatic recognition of atom and bond types for the standard amino-acid residues. A novel restraint was introduced to describe the two-dimensional pseudo-potential surface of a Ramachandran plot (Ramachandran *et al.*, 1963). Also, a Babinet's principle solvent correction was used to account for the disordered solvent within the crystal structure. The excellent Rietveld fit obtained was a breakthrough, showing for the first time that a crystal structure refinement could be carried out for a protein molecule from powder data.

Structure refinements can be significantly improved by the use of multiple data sets, provided there are not significant changes in the structure factors between the different data sets. Two independent investigations of HEWL showed that the use of multiple patterns associated with slightly different lattice parameters leads to enhanced extracted intensities and more robust structure refinements (Basso *et al.*, 2005; Von Dreele, 2007) using a modified version of *GSAS* which could account for small lattice strains in different patterns (Larson & Von Dreele, 2004). In our laboratory, we prepared a total of 44 different polycrystalline HEWL precipitates at 277 K and room temperature, and in the pH range between 6.56 and 3.33 (Basso *et al.*, 2005). High-resolution powder-diffraction data were collected at room temperature (λ = 1.249826 Å, ID31, ESRF). The anisotropic effect of pH of crystallization on the lattice dimensions of tetragonal HEWL shifts the peaks significantly and alleviates the peak-overlap problem. In order to try to quantify the improvements coming from the multiple-data-set approach, we selected four patterns across the range of pH for use in a multi-pattern Pawley (1981) refinement. Reflections with a reasonable signal-to-noise ratio could be observed visually in all data sets up to a maximum resolution of about 3.27 Å. We tried to find a way to quantify the resolution limit of these multi-pattern data sets by following the methodology described by Sivia (2000). The least-squares matrix from a multi-pattern Pawley refinement characterizes the data set, and the eigenvalue spectrum of this matrix is related to the effective error estimates on the extracted intensities (or linear combinations of intensities when peaks are overlapped). To provide easier comparison with single-crystal data-processing statistics, we computed the effective completeness for the combined data set as the fraction of 'peaks' having $I = \sigma(I)$ greater than some threshold. This analysis showed the significant improvement of the effective completeness as a result of the use of multiple profiles during intensity extraction. Von Dreele (2007) has proposed a computationally simpler scheme which also attempts to quantify the improvements arising from the use of multiple data sets, and can also be applied to Rietveld refinements. The same four histograms as used for the completeness analysis were employed in a multiple-data-set Rietveld refinement (Rietveld, 1969) in order to extract an average structural model for tetragonal HEWL using *GSAS* (Larson & Von Dreele, 2004). Some differences between diffraction patterns could be accounted for by allowing the solvent-scattering coefficients to differ for each one of the four histograms, following the observation that the largest observed differences in peak intensities were mainly at low angles. A more detailed description of this refinement can be found in Basso *et al.* (2005) and the model is deposited in the PDB with access code 2a6u. We found that this approach resulted in a much smoother and more robust refinement than previously experienced with single-pattern fits and produced a structural model with excellent stereochemistry. Von Dreele has also applied a multi-pattern approach to HEWL but using data sets obtained from an image plate and approaching single-crystal resolution limits ($d_{\min}$ ~ 2 Å). The patterns differ because of changes in salt concentration and radiation-induced lattice strains. Anisotropic changes in the unit cell are taken into account in all of these refinements using a special profile function implemented in *GSAS* (No. 5). Using this function, only one set of unit-cell parameters is refined, and those corresponding to the other patterns are related *via* a strain ($\Delta d/d$) of the reciprocal metric tensor elements. By selecting different combinations of data sets, Von Dreele refined three structural models and was able to add water molecules in each case (PDB codes: 2hs7, 2hs9 and 2hso). Many of these water molecules are conserved between the three models and have also been found in single-crystal structures. The stereochemistries of the resulting multiple-data-set models show significant improvements in comparison to previous single-pattern powder refinements.

In one of our most recent studies of the second SH3 domain of ponsin (Margiolaki, Wright, Wilmanns *et al.*, 2007), we exploited radiation-induced anisotropic lattice strains in a specially modified multi-pattern Pawley refinement, taking into consideration likelihood criteria for partitioning overlapped peaks (Wright *et al.*, 2007). The outcome of this analysis was a set of improved extracted intensities, in excellent agreement with single-crystal intensities later obtained by an independent experiment. The powder data were sufficient for the structure solution of the domain *via* the molecular-replacement method as described in Section 7.1.7.1. Maximum-likelihood refinement improved the phases to a level where we could trace the main-chain alterations,

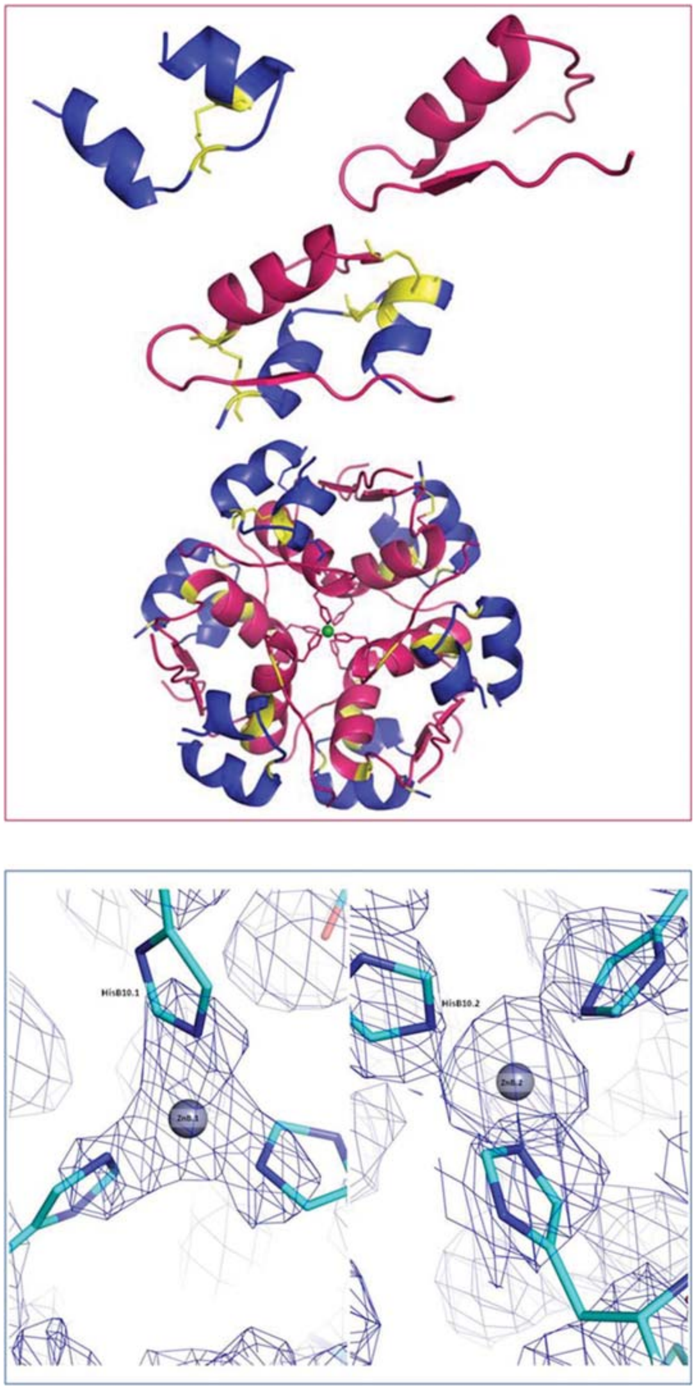

Figure 7.1.14
Upper panel: Powder-diffraction structure of the T6 bovine insulin (BI) hexamer. BI consists of two chains, A (21 amino acids) shown in blue and B (30 amino acids) shown in purple. Chain A contains a disulfide bond between two cysteines. The chains are held together by two disulfide bonds in order to form a monomer. Three monomers form the T6 hexamer shown. The Cα trace is viewed down the crystallographic threefold axis. The zinc ions are shown as red spheres. Each of two independent zinc ions is octahedrally coordinated by three histidine side chains shown in green. Because both zinc ions lie on the threefold axis, only one is visible in the drawing. Lower panel: Selected regions of the total omit map at 1σ clearly indicating the positions and coordination of the two zinc ions present in T6 BI. The map was computed at the initial stages of our analysis employing only the protein atoms (excluding all ligands) from the 2a3g PDB model (Smith *et al.*, 2005) and the extracted intensities from the seven-pattern combined Pawley fit. The map was computed using *SFCHECK*. The residues represented in green stick carbon atoms correspond to the final refined model and the red spheres represent the two independent zinc ions, which are octahedrally coordinated by three HisB10 side chains (Margiolaki *et al.*, 2013).

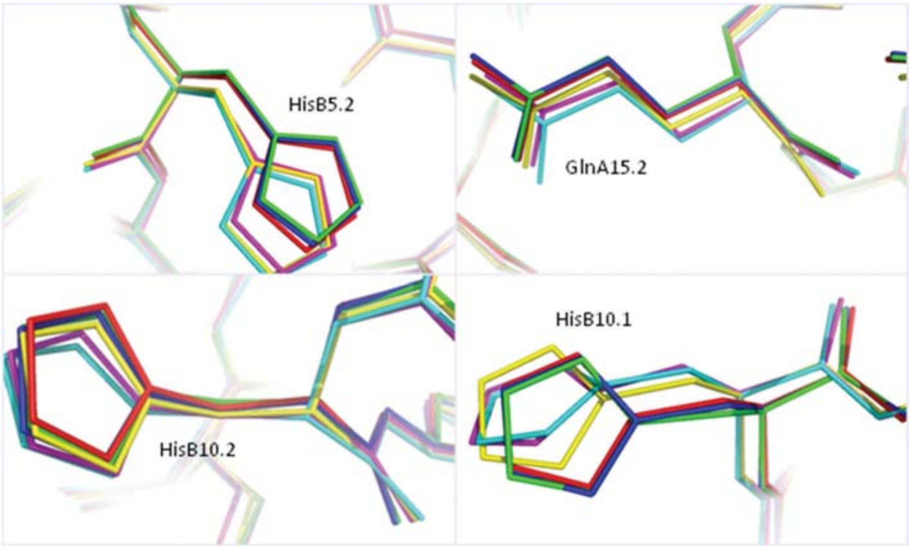

Figure 7.1.15
Evolution of selected amino acids along the protein chains during the Rietveld refinement procedure for T6 BI in *GSAS*. The amino-acid labels denote the residue type, amino-acid number in accordance with the 2a3g PDB model and monomer number (1 or 2). The red, green, blue, yellow, magenta, cyan and orange colours correspond to the refined model at subsequent stages of our analysis (Margiolaki *et al.*, 2013).

build additional residues where needed and eventually place the correct side chains along the sequence; a substantial result from powder-diffraction data. The protein conformation was refined in a multiple-data-set stereochemically restrained Rietveld analysis taking advantage of sample-induced anisotropic lattice strains. We further benefited from an approach combining multiple-data-set Rietveld analysis and periodical omit-map (Bhat, 1988) computation to reduce the bias of the final model, extending the resolution limits to levels comparable to single-crystal measurements, and even detecting several water molecules bound to the protein (Fig. 7.1.13). The benefits of the multi-pattern approach are perhaps most striking from the high quality of the computed omit map shown in Fig. 7.1.13.

7.1.8.2. *Rigid-body representation of amino-acid residues*

An efficient way of describing the structure of a protein has recently been implemented in *GSAS*, where each amino acid is represented by a flexible rigid body (FRB). The origin of each FRB is the location of the Cα atom and the orientation is described *via* a quaternion, thus requiring six adjustable parameters. The side chain of each amino acid has adjustable torsion angles and the orientations of the carbonyls (ψ angles) are also allowed variables for each FRB. All bond lengths and angles within each FRB are fixed at the ideal values. Restraints are then only needed for the interatomic distances and angles about the C—N coupling between amino acids along the polypeptide chain and for the torsion angles. This rigid-body model requires just over one-third of the number of refinable parameters in a full free-atom refinement, thus making it better suited for Rietveld refinement of proteins. This approach has been applied to SXRPD data (ID31, ESRF) of the T6 polymorph of bovine insulin. The number of parameters in the FRB refinement was 700, compared with the 1767 that would be needed for a free-atom refinement. Moreover, the use of idealized amino-acid bond lengths and angles in each FRB lowers the number of restraints from 1980 required for the free-atom refinement to just 400 for the FRB refinement. The refinement was robust, leading to convergence and a refined structural model of excellent stereochemistry in good agreement with the known single-crystal structure (PDB code: 2a3g). The structure is trigonal with three insulin dimers, where each monomer consists of two protein chains forming an hexamer, which is held together by two Zn atoms (Fig. 7.1.14). The correct positions and octahedral coordinations of both Zn atoms were immediately identified from total omit maps (Bhat, 1988) generated in the initial steps of our analysis and added to the structural model. The gradual evolution of selected side chains of individual amino acids during the refinement procedure is illustrated in Fig. 7.1.15 (Margiolaki *et al.*, 2013).

7.1.9. Related developments

Other techniques that seek alternatives to single-crystal structure analysis, and which are therefore interesting with respect to some aspects of this summary of macromolecular powder diffraction, are being developed. Obviously, the characterization of pharmaceutical samples which are absorbed by a patient in bulk form, such as insulin crystalline slurries, can only be characterized by powder diffraction. The alternatives to single-crystal analysis include methods that seek to work with a nanocrystal or even a single molecule, most notably at the new X-ray laser facilities. There are exciting developments with electron diffraction too, notably *via* the new precession-electron-diffraction technique. These developments are briefly summarized below.

The recent exciting results obtained at fourth-generation X-ray sources (X-ray free-electron lasers) demonstrated a method for structure determination where single-crystal X-ray diffraction ‘snapshots’ are collected from a fully hydrated stream of nanocrystals using femtosecond pulses from a hard-X-ray free-electron laser (Chapman *et al.*, 2011; Hunter *et al.*, 2011; Hunter & Fromme, 2011). They proved this concept with nanocrystals of photosystem I, one of the largest membrane-protein complexes. More than 3 000 000 diffraction patterns were collected in this study, and a three-dimensional data set was assembled from individual photosystem I nanocrystals (from 200 nm to 2 µm in size). The problem of radiation damage in crystallography was mitigated by using pulses briefer than the timescale of most damage processes. This certainly offers a new approach to structure determination of macromolecules that do not yield crystals of sufficient size for studies using conventional radiation sources or that are particularly sensitive to radiation damage. In 2012, Aquila and co-workers (2012) reported the first time-resolved femtosecond serial X-ray crystallography results related to light-induced changes of photosystem I–ferredoxin co-crystals observed at time delays of 5 to 10 µs after excitation. This technique opens the door to time-resolved structural studies of reaction dynamics in biological systems. Furthermore, protein crystallization in cells has been observed several times in nature. However, owing to their small size these crystals have not yet been used for X-ray crystallographic analysis. Koopman and co-workers prepared nanometre-sized *in vivo*-grown crystals of *Trypanosoma brucei* enzymes and applied the emerging method of free-electron-laser-based serial femtosecond crystallography to record interpretable diffraction data. This combined approach will open new opportunities in structural systems biology (Koopmann *et al.*, 2012).

On the other hand, the electron diffraction (ED) technique utilizes the electron beam generated by a transmission electron microscope (TEM) and thus measurements can be performed routinely. Electron diffraction and X-ray powder diffraction are remarkably complementary techniques. Electrons interact much more strongly with matter than X-rays, so a single-crystal electron-diffraction pattern can be obtained from a very tiny crystallite. The disadvantages that hindered the development of electron crystallography until recently were the strongly dynamical diffraction of electrons and the resulting non-trivial relation of the measured intensities to the structure-factor amplitudes. The precession-electron-diffraction (PED) technique, first described by Vincent & Midgley (1994), has already been employed for the structure solution of zeolites (McCusker & Baerlocher, 2013; Xie *et al.*, 2008) and other families of compounds including small pharmaceuticals (Dorset, 1995; Voigt-Martin *et al.*, 1997; Kolb *et al.*, 2007; Eddleston *et al.*, 2013). Diffraction experiments can be conducted on crystals with a diameter of the order of 50 nm. An individual particle of a powder sample can therefore be used as a single crystal for diffraction. PED data may be exploited in two different ways: (1) to identify weak reflections and (2) to estimate the phases of the reflections in the projection. The former is used to improve the partitioning of the reflection intensities within an overlap group and the latter to provide some starting phases for structure determination. Furthermore, the problems often stemming from a possible mixture of polymorphs in the powder sample can be overcome *via* ED methods by selecting individual crystals with the desired structure.

7.1.10. Concluding remarks

This chapter summarizes the advances of the macromolecular powder-diffraction method achieved during the last decade. Although developments of both experimental and computational aspects are still in progress, results obtained to date demonstrate that this is a technique ready to tackle genuine biological problems. The choice of the instrumental configuration is critical for obtaining the highest possible information from the collected profiles. The use of a lower-angular-resolution instrument allows construction of phase diagrams and checking for ligand or heavy-atom binding to be carried out rapidly using small quantities of powder sample. On the other hand, the analyser-crystal beamlines offer unparalleled instrumental resolution, which is very attractive in reducing the peak overlap. The unit-cell parameters are perturbed to alter the pattern of peak overlaps in the different data sets and reduce the overlap problem. Ultimately, in cases where this approach was used, it led to enhanced results in comparison to a single-pattern analysis.

High-throughput crystal screening requires a multivariate data-analysis strategy for fingerprinting in order to compare similarities and differences between the various patterns corresponding to different samples. A successful method used for the characterization of insulin microcrystals (Norrman *et al.*, 2006; Valmas *et al.*, 2015; Fili *et al.*, 2015) is principal component analysis (PCA) (Jolliffe, 1986; Wold *et al.*, 1987; Barr *et al.*, 2004). Several software packages are already available that have incorporated (among other methods) PCA for easy visualization of the total data variation of multiple powder-diffraction patterns. The aim of this method is to arrange a series of diffraction patterns into clusters based on their mutual similarities, allowing dominant patterns and major trends to be rapidly identified.

To date, data interpretation is performed *via* the combined use of software packages designed for powder diffraction as well as single-crystal diffraction data. Consequently, data analysis is often complex and time consuming, It is essential to improve the current algorithms in order to enhance and automate data analysis. For example, existing molecular-replacement (*MOLREP*/ *PHASER*) (Vagin & Teplyakov, 1997; McCoy *et al.*, 2007) and refinement (*REFMAC*) software (Murshudov *et al.*, 2011), which was initially designed for single-crystal data and is available from the *CCP4* suite (Collaborative Computational Project, Number 4, 1994), needs to be adapted for use with powder data by taking peak overlap into consideration. Algorithms for extracting reliable structural information from medium-resolution data (4.5–8 Å) are, as yet, still relatively scarce (Karmali *et al.*, 2009; Brunger *et al.*, 2009). However, this is expected to change as the gap between electron micoscopy and high-resolution X-ray diffraction is bridged.

According to statistical information provided in the PDB, 94 730 protein structures have been determined by means of X-ray diffraction to date. Some of these structures have been used for the development of drugs already available in the market for the treatment of diseases such as diabetes or HIV. Crystallization may be employed in order to formulate a protein–drug complex (Yang *et al.*, 2003; Basu *et al.*, 2004). Protein microcrystals have better stability and higher concentration than proteins in solution for storage and have a lower manufacturing cost compared with lyophilization. The polymorphism of the crystals has to be fully characterized in order to formulate a drug in solid form; this is mandatory for the drug's approval by health authorities. Powder diffraction is in this case the most suitable tool for the characterization of different polymorphs, as it provides information on numerous microcrystalline suspensions. Further advantages that are gained from the use of microcrystalline samples and powder-diffraction measurements include verification of the homogeneity and phase purity of the protein precipitates; the extraction of accurate lattice parameters, allowing direct observation of slight structure modifications; and exploitation of radiation- and sample-induced effects.

Finally, it is anticipated that the combination of powder diffraction with other experimental techniques, including X-ray microcrystallography of biological macromolecules (Hedman *et al.*, 1985; Evans *et al.*, 2011), serial X-ray crystallography at free-electron lasers (Hunter *et al.*, 2011) and electron-diffraction methods, could considerably enhance the structural characterization of materials employing nanocrystals.

The powder X-ray diffraction method applied to biological macromolecules is coming of age. It certainly has emerged out of the young-child phase to the teenager phase; various refinements of the method are needed, but to see this 'young adult' technique successfully emerging in its applications even thus far is delightful.

I am grateful to Professor A. N. Fitch, Dr J. P. Wright and Dr R. B. Von Dreele for their continuous input, advice and support during this project. In particular, the results and software packages produced by R. B. Von Dreele over the last decade led to the renaissance of the application of powder methods to proteins, an old idea which had not been exploited systematically in the past. I would like to thank six undergraduate students from the University of Bath who have worked with us for one year each: S. Basso, L. Knight, S. Dagogo, M. Jenner, I. Collings and L. Saunders, as well as our postdoctoral researcher, Y. Watier. I am also grateful to Professor J. R. Helliwell for the critical reading of this chapter and his advice for including practical information for non-experts in this scientific field. I am grateful to our collaborators Drs G. C. Fox, M. Norrman, G. Schluckebier, M. El Hajji, D. Beckers, T. Degen, F. Bonnete, M. Giffard, N. Papageorgiou, B. Canard, B. Coutard, M. Wilmanns, N. Pinotsis and K. Miura. I would like to thank Dr M. Schiltz and his group and especially Celine Besnard, for their help and collaboration. I would also like to thank my postgraduate/undergraduate group members at the University of Patras: Anastasia Giannopoulou, Fotini Karavassili, Eleni Kotsiliti, Marina Kalatha, Alexandros Valmas, Stavroula Fili, Konstantina Magiouf and Danae Lahana. I am grateful to the UNESCO and L'Oreal foundations for the International Fellowship for Women in Science (2010–2012). Part of this research has been co-financed by the European Union (European Regional Development Fund – ERDF) and Greek national funds through the Operational Program 'Regional Operational Programme' of the National Strategic Reference Framework (NSRF) – Research Funding Program: Support for research, technology and innovation actions in Region of Western Greece (Karatheodoris foundation). Since 2012, the EU FP7 REGPOT CT-2011- 285950 – 'SEE-DRUG' project and the companies NanoMEGAS, Novo Nordisk and PANalytical support the continuation of our work on macromolecular powder diffraction. Part of the research presented in this chapter has been co-financed by the following grants: (*a*) The International Atomic Energy Agency (CRP code: F12024), (*b*) The European Union (European Social Fund) and the Greek State under the 'ARISTEIA II' Action of the 'OPERATIONAL PROGRAMME EDUCATION AND LIFELONG LEARNING' and (*c*) The COST action (CM1306). Finally, we thank the ESRF, DESY and the SLS synchrotrons for provision of beam time. This chapter is dedicated to the memory of Dr Richard Kahn, an exceptional crystallographer, teacher and friend.

References

Aguiar, A. J., Krc, J., Kinkel, A. W. & Samyn, J. C. (1967). *Effect of polymorphism on the absorption of chloramphenicol from chloramphenicol palmitate. J. Pharm. Sci.* **56**, 847–853.

Altomare, A., Caliandro, R., Camalli, M., Cuocci, C., Giacovazzo, C., Moliterni, A. G. G. & Rizzi, R. (2004). *Automatic structure determination from powder data with EXPO2004. J. Appl. Cryst.* **37**, 1025–1028.

Anderson, C. R., Downs, W. G., Wattley, G. H., Ahin, N. W. & Reese, A. A. (1957). *Mayaro virus: a new human disease agent. II. Isolation from blood of patients in Trinidad. Am. J. Trop. Med. Hyg.* **6**, 1012–1016.

Andersson, K. M. & Hovmöller, S. (2000). *The protein content in crystals and packing coefficients in different space groups. Acta Cryst.* D**56**, 789–790.

Anduleit, K., Sutton, G., Diprose, J. M., Mertens, P. P., Grimes, J. M. & Stuart, D. I. (2005). *Crystal lattice as biological phenotype for insect viruses*. *Protein Sci.* **14**, 2741–2743.

Aquila, A. *et al.* (2012). *Time-resolved protein nano-crystallography using an X-ray free-electron laser. Opt. Express*, **20**, 2706–2716.

Asherie, N. (2004). *Protein crystallization and phase diagrams*. *Methods*, **34**, 266–272.

Baerlocher, C., McCusker, L. B., Prokic, S. & Wessels, T. (2004). *Exploiting texture to estimate the relative intensities of overlapping reflections. Z. Kristallogr.* **219**, 803–812.

Balbirnie, M., Grothe, R. & Eisenberg, D. S. (2001). *An amyloid-forming peptide from the yeast prion Sup35 reveals a dehydrated beta-sheet structure for amyloid. Proc. Natl Acad. Sci. USA*, **98**, 2375–2380.

Barr, G., Dong, W. & Gilmore, C. J. (2004). *PolySNAP: a computer program for analysing high-throughput powder diffraction data. J. Appl. Cryst.* **37**, 658–664.

Basso, S., Besnard, C., Wright, J. P., Margiolaki, I., Fitch, A. N., Pattison, P. & Schiltz, M. (2010). *Features of the secondary structure of a protein molecule from powder diffraction data. Acta Cryst.* D**66**, 756–761.

Basso, S., Fitch, A. N., Fox, G. C., Margiolaki, I. & Wright, J. P. (2005). *High-throughput phase-diagram mapping via powder diffraction: a case study of HEWL versus pH. Acta Cryst.* D**61**, 1612–1625.

Basu, S. K., Govardhan, C. P., Jung, C. W. & Margolin, A. L. (2004). *Protein crystals for the delivery of biopharmaceuticals. Expert Opin. Biol. Ther.* **4**, 301–317.

Bauer, J., Spanton, S., Henry, R., Quick, J., Dziki, W., Porter, W. & Morris, J. (2001). *Ritonavir: an extraordinary example of conformational polymorphism. Pharm. Res.* **18**, 859–866.

Berman, H., Henrick, K. & Nakamura, H. (2003). *Announcing the worldwide Protein Data Bank*. *Nat. Struct. Biol.* **10**, 980.

Besnard, C., Camus, F., Fleurant, M., Dahlström, A., Wright, J. P., Margiolaki, I., Pattison, P. & Schiltz, M. (2007). *Exploiting X-ray induced anisotropic lattice changes to improve intensity extraction in protein powder diffraction: application to heavy atom detection. Z. Kristallogr.* Suppl. **26**, 39–44.

Bhat, T. N. (1988). *Calculation of an OMIT map. J. Appl. Cryst.* **21**, 279–281.

Blake, C. C., Pulford, W. C. & Artymiuk, P. J. (1983). *X-ray studies of water in crystals of lysozyme. J. Mol. Biol.* **167**, 693–723.

Bond, J. P., Deverin, S. P., Inouye, H., el-Agnaf, O. M., Teeter, M. M. & Kirschner, D. A. (2003). *Assemblies of Alzheimer's peptides A25–35 and A31–35: reverse-turn conformation and side-chain interactions revealed by X-ray diffraction. J. Struct. Biol.* **141**, 156–170.

Brader, M. L. & Sukumar, M. (2005). US Patent 2005/0054818A1.

Brunelli, M., Wright, J. P., Vaughan, G. B. M., Mora, A. J. & Fitch, A. N. (2003). *Solving larger molecular crystal structures from powder diffraction data by exploiting anisotropic thermal expansion. Angew. Chem. Int. Ed.* **42**, 2029–2032.

Brunger, A. T., DeLaBarre, B., Davies, J. M. & Weis, W. I. (2009). *X-ray structure determination at low resolution. Acta Cryst.* D**65**, 128–133.

Bunge, H. J., Dahms, M. & Brokmeier, H. G. (1989). *The determination of integrated intensities from polycrystalline samples with preferred orientation. Crystallogr. Rev.* **2**, 67–86.

Burger, K., Cox, D., Papoular, R. & Prandl, W. (1998). *The application of resonant scattering techniques to ab initio structure solution from powder data using* $SrSO_4$ *as a test case. J. Appl. Cryst.* **31**, 789–797.

Careri, G., Gratton, E., Yang, P. H. & Rupley, J. A. (1980). *Correlation of IR spectroscopic, heat capacity, diamagnetic susceptibility and enzymatic measurements on lysozyme powder. Nature*, **284**, 572–573.

Causey, O. R. & Maroja, O. M. (1957). *Mayaro virus: a new human disease agent. III. Investigation of an epidemic of acute febrile illness on the river Guama in Pará, Brazil, and isolation of Mayaro virus as causative agent. Am. J. Trop. Med. Hyg.* **6**, 1017–1023.

Cerny, R. (1996). In *Proceedings of the 45th Annual Conference on Applications of X-ray Analysis*, Denver, 1996. *Adv. X-ray Anal.* **40**, 433–438.

Chapman, H. N. *et al.* (2011). *Femtosecond X-ray protein nanocrystallography. Nature*, **470**, 73–77.

Coelho, A. (2004). *TOPAS-Academic*. http://www.bruker-axs.de/topas.html.

Collaborative Computational Project, Number 4 (1994). *The CCP4 suite: programs for protein crystallography. Acta Cryst.* D**50**, 760–763.

Collings, I., Watier, Y., Giffard, M., Dagogo, S., Kahn, R., Bonneté, F., Wright, J. P., Fitch, A. N. & Margiolaki, I. (2010). *Polymorphism of microcrystalline urate oxidase from Aspergillus flavus. Acta Cryst.* D**66**, 539–548.

Coulibaly, F., Chiu, E., Ikeda, K., Gutmann, S., Haebel, P. W., Schulze-Briese, C., Mori, H. & Metcalf, P. (2007). *The molecular organization of cypovirus polyhedra. Nature*, **446**, 97–101.

Dahms, M. & Bunge, H. J. (1986). *Calculation of the normalization factor of incomplete pole figures by cubic extrapolation. Textures Microstruct.* **6**, 167–179.

David, W. I. F. & Shankland, K. (2008). *Structure determination from powder diffraction data. Acta Cryst.* A**64**, 52–64.

Derewenda, U., Derewenda, Z., Dodson, E. J., Dodson, G. G., Reynolds, C. D., Smith, G. D., Sparks, C. & Swenson, D. (1989). *Phenol stabilizes more helix in a new symmetrical zinc insulin hexamer. Nature (London)*, **338**, 594–596.

Diaz-Avalos, R., Long, C., Fontano, E., Balbirnie, M., Grothe, R., Eisenberg, D. & Caspa, D. L. D. (2003). *Cross-beta order and diversity in nano-crystals of an amyloid-forming peptide. J. Mol. Biol.* **330**, 1165–1175.

Dilanian, R. A., Darmanin, C., Varghese, J. N., Wilkins, S. W., Oka, T., Yagi, N., Quiney, H. M. & Nugent, K. A. (2011). *A new approach for structure analysis of two-dimensional membrane protein crystals using X-ray powder diffraction data. Protein Sci.* **20**, 457–464.

Dobrianov, I., Kriminski, S., Caylor, C. L., Lemay, S. G., Kimmer, C., Kisselev, A., Finkelstein, K. D. & Thorne, R. E. (2001). *Dynamic response of tetragonal lysozyme crystals to changes in relative humidity: implications for post-growth crystal treatments. Acta Cryst.* D**57**, 61–68.

Doebbler, J. A. & Von Dreele, R. B. (2009). *Application of molecular replacement to protein powder data from image plates. Acta Cryst.* D**65**, 348–355.

Dorset, D. L. (1995). *Structural Electron Crystallography*. New York: Plenum Press.

Eddleston, M. D., Hejczyk, K. E., Bithell, E. G., Day, G. M. & Jones, W. (2013). *Polymorph identification and crystal structure determination by a combined crystal structure prediction and transmission electron microscopy approach*. *Chem. Eur. J.* **19**, 7874–7882.

Evans, G., Axford, D., Waterman, D. & Owen, R. L. (2011). *Macromolecular microcrystallography. Crystallogr. Rev.* **17**, 105–142.

Finney, J. L. (1979). *The organization and function of water in protein crystals.* In *Water: A Comprehensive Treatise*, Vol. 6, edited by F. Franks, pp. 47–122. New York: Plenum Press.

Fili, S., Valmas, A., Christopoulou, M., Spiliopoulou, M., Nikolopoulos, N., Lichiére, J., Logotheti, S., Karavassili, F., Rosmaraki, E., Fitch, A., Wright, J. P., Beckers, D., Degen, T., Nénert, G., Hilgenfeld, R., Papageorgiou, N., Canard, B., Coutard B. & Margiolaki, I. (2016). *Coxsackievirus B3 protease 3C: expression, purification, crystallization and preliminary structural insights. Acta Cryst.* F**72**, 877–884.

Fili, S., Valmas, A., Norrman, M., Schluckebier, G., Beckers, D., Degen, T., Wright, J., Fitch, A., Gozzo, F., Giannopoulou, A. E., Karavassili, F. & Margiolaki, I. (2015). *Human insulin polymorphism upon ligand binding and pH variation: the case of 4-ethylresorcinol. IUCrJ*, **2**, 534–544.

Fitch, A. (2004). *The high resolution powder diffraction beam line at ESRF. J. Res. Natl Inst. Stand. Technol.* **109**, 133–142.

Frankaer, C. G., Harris, P. & Ståhl, K. (2011). *A sample holder for in-house X-ray powder diffraction studies of protein powders. J. Appl. Cryst.* **44**, 1288–1290.

Garman, E. F. & Schneider, T. R. (1997). *Macromolecular cryocrystallography. J. Appl. Cryst.* **30**, 211–237.

Green, D. W., Ingram, V. M. & Perutz, M. F. (1954). *The structure of haemoglobin. IV. Sign determination by the isomorphous replacement method*. *Proc. R. Soc. Lond. Ser. A*, **225**, 287–307.

Hanson, B. L., Schall, C. A. & Bunick, G. J. (2003). *New techniques in macromolecular cryocrystallography: macromolecular crystal annealing and cryogenic helium. J. Struct. Biol.* **142**, 77–87.

Havelund, S. (2009). US Patent 2009/0010854A9.

Hedman, B., Hodgson, K. O., Helliwell, J. R., Liddington, R. & Papiz, M. Z. (1985). *Protein micro-crystal diffraction and the effects of radiation damage with ultra-high-flux synchrotron radiation. Proc. Natl Acad. Sci. USA*, **82**, 7604–7607.

Helliwell, J. R. (2012). *The evolution of synchrotron radiation and the growth of its importance in crystallography. Crystallogr. Rev.* **18**, 33–93.

Helliwell, J. R., Bell, A. M. T., Bryant, P., Fisher, S., Habash, J., Helliwell, M., Margiolaki, I., Kaenket, S., Watier, Y., Wright, J. & Yalamanchilli, S. (2010). *Time-dependent analysis of K_2PtBr_6 binding to lysozyme studied by protein powder and single-crystal X-ray analysis. Z. Kristallogr.* **225**, 570–575.

Helliwell, J. R., Helliwell, M. & Jones, R. H. (2005). *Ab initio structure determination using dispersive differences from multiple-wavelength synchrotron-radiation powder diffraction data. Acta Cryst.* A**61**, 568–574.

Hunter, M. S., DePonte, D. P., Shapiro, D. A., Kirian, R. A., Wang, X., Starodub, D., Marchesini, S., Weierstall, U., Doak, R. B., Spence, J. C. & Fromme, P. (2011). *X-ray diffraction from membrane protein nanocrystals. Biophys. J.* **100**, 198–206.

Hunter, M. S. & Fromme, P. (2011). *Toward structure determination using membrane-protein nano-crystals and micro-crystals. Methods*, **55**, 387–404.

Inouye, H. & Kirschner, D. A. (2006). *X-ray fiber and powder diffraction of PrP prion peptides. Adv. Protein Chem.* **73**, 181–215

Jenner, M., Wright, J. P., Margiolaki, I. & Fitch, A. N. (2007). *Successful protein cryocooling for powder diffraction. J. Appl. Cryst.* **40**, 121–124.

Ji, X., Sutton, G., Evans, G., Axford, D., Owen, R. & Stuart, D. I. (2010). *How baculovirus polyhedra fit square pegs into round holes to robustly package viruses. EMBO J.* **29**, 505–514

Jolliffe, I. T. (1986). *Principal Component Analysis*. New York: Springer-Verlag.

Kantardjieff, K. A. & Rupp, B. (2003). *Matthews' coefficient probabilities: improved estimates for unit cell contents of proteins, DNA, and protein–nucleic acid complex crystals. Protein Sci.* **12**, 1865–1871.

Karavassili, F., Giannopoulou, A. E., Kotsiliti, E., Knight, L., Norrman, M., Schluckebier, G., Drube, L., Fitch, A. N., Wright, J. P. & Margiolaki, I. (2012). *Structural studies of human insulin cocrystallized with phenol or resorcinol via powder diffraction. Acta Cryst.* D**68**, 1632–1641.

Karavassili, F. & Margiolaki, I. (2016). *Macromolecular powder diffraction: ready for genuine biological problems. Protein Pept. Lett.* **23**, 232–241.

Karavassili, F., Valmas, A., Fili, S., Georgiou, C. D. & Margiolaki, I. (2017). *In quest for improved drugs against diabetes: the added value of X-ray powder diffraction methods. Biomolecules*, **7**, 63.

Karmali, A. M., Blundell, T. L. & Furnham, N. (2009). *Model-building strategies for low-resolution X-ray crystallographic data. Acta Cryst.* D**65**, 121–127.

Kolb, U., Gorelik, T., Kübel, C., Otten, M. T. & Hubert, D. (2007). *Towards automated diffraction tomography: part I – data acquisition. Ultramicroscopy*, **107**, 507–513.

Koopmann, R. *et al.* (2012). *In vivo protein crystallization opens new routes in structural biology. Nat. Methods*, **9**, 259–262.

Kuntz, I. D. Jr & Kauzmann, W. (1974). *Hydration of proteins and polypeptides. Adv. Protein Chem.* **28**, 239–345.

La Fortelle, E. & Bricogne, G. (1997). *Maximum-likelihood heavy-atom parameter refinement for multiple isomorphous replacement and multiwavelength anomalous diffraction methods. Methods Enzymol.* **276**, 472–494.

Larson, A. C. & Von Dreele, R. B. (2004). *General Structure Analysis System (GSAS)*, Los Alamos National Laboratory Report LAUR 86-748, Los Alamos, USA. http://www.ccp14.ac.uk/solution/gsas/.

McCoy, A. J., Grosse-Kunstleve, R. W., Adams, P. D., Winn, M. D., Storoni, L. C. & Read, R. J. (2007). *Phaser crystallographic software. J. Appl. Cryst.* **40**, 658–674.

McCusker, L. & Baerlocher, C. (2013). *Electron crystallography as a complement to X-ray powder diffraction techniques*. *Z. Kristallogr.* **228**, 1–10.

McGrath, B. M. & Walsh, G. (2005). Editors. *Directory of Therapeutic Enzymes*. Boca Raton: CRC Press.

Malet, H., Coutard, B., Jamal, S., Dutartre, H., Papageorgiou, N., Neuvonen, M., Ahola, T., Forrester, N., Gould, E. A., Lafitte, D., Ferron, F., Lescar, J., Gorbalenya, A. E., de Lamballerie, X. & Canard, B. (2009). *The crystal structures of Chikungunya and Venezuelan equine encephalitis virus nsP3 macro domains define a conserved adenosine binding pocket. J. Virol.* **83**, 6534–6545.

Margiolaki, I., Giannopoulou, A. E., Wright, J. P., Knight, L., Norrman, M., Schluckebier, G., Fitch, A. N. & Von Dreele, R. B. (2013). *High-resolution powder X-ray data reveal the T_6 hexameric form of bovine insulin. Acta Cryst.* D**69**, 978–990.

Margiolaki, I. & Wright, J. P. (2008). *Powder crystallography on macromolecules. Acta Cryst.* A**64**, 169–180.

Margiolaki, I., Wright, J. P., Fitch, A. N., Fox, G. C., Labrador, A., Von Dreele, R. B., Miura, K., Gozzo, F., Schiltz, M., Besnard, C., Camus, F., Pattison, P., Beckers, D. & Degen, T. (2007). *Powder diffraction studies for proteins: An overview of data collection approaches. Z. Kristallogr.* Suppl. **26**, 1–13.

Margiolaki, I., Wright, J. P., Fitch, A. N., Fox, G. C. & Von Dreele, R. B. (2004). *Synchrotron X-ray powder diffraction study of hexagonal turkey egg-white lysozyme. ESRF Scientific Highlights*, pp. 30–31.

Margiolaki, I., Wright, J. P., Fitch, A. N., Fox, G. C. & Von Dreele, R. B. (2005). *Synchrotron X-ray powder diffraction study of hexagonal turkey egg-white lysozyme. Acta Cryst.* D**61**, 423–432.

Margiolaki, I., Wright, J. P., Wilmanns, M., Fitch, A. N. & Pinotsis, N. (2007). *Second SH3 domain of ponsin solved from powder diffraction. J. Am. Chem. Soc.* **129**, 11865–11871.

Markvardsen, A. J., David, W. I. F., Johnson, J. C. & Shankland, K. (2001). *A probabilistic approach to space-group determination from powder diffraction data. Acta Cryst.* A**57**, 47–54.

Matthews, B. W. (1968). *Solvent content of protein crystals. J. Mol. Biol.* **33**, 491–497.

Murshudov, G. N., Skubák, P., Lebedev, A. A., Pannu, N. S., Steiner, R. A., Nicholls, R. A., Winn, M. D., Long, F. & Vagin, A. A. (2011). *Acta Cryst.* D**67**, 355–367.

Newman, J. (2011). *One plate, two plates, a thousand plates. How crystallisation changes with large numbers of samples. Methods*, **55**, 73–80.

Norrman, M. & Schluckebier, G. (2007). *Crystallographic characterization of two novel crystal forms of human insulin induced by chaotropic agents and a shift in pH. BMC Struct. Biol.* **7**, 83.

Norrman, M., Ståhl, K., Schluckebier, G. & Al-Karadaghi, S. (2006). *Characterization of insulin microcrystals using powder diffraction and multivariate data analysis. J. Appl. Cryst.* **39**, 391–400.

Oka, T., Miura, K., Inoue, K., Ueki, T. & Yagi, N. (2006). *High-resolution powder diffraction study of purple membrane with a large Guinier-type camera. J. Synchrotron Rad.* **13**, 281–284.

Papageorgiou, N., Watier, Y., Saunders, L., Coutard, B., Lantez, V., Gould, E. A., Fitch, A. N., Wright, J. P., Canard, B. & Margiolaki, I. (2010). *Preliminary insights into the non structural protein 3 macro domain of the Mayaro virus by powder diffraction. Z. Kristallogr.* **225**, 576–580.

Pawley, G. S. (1981). *Unit-cell refinement from powder diffraction scans. J. Appl. Cryst.* **14**, 357–361.

Perutz, M. F. (1954). *The structure of haemoglobin. III. Direct determination of the molecular transform. Proc. R. Soc. London Ser. A*, **225**, 264–286.

Perutz, M. F. (1956). *Isomorphous replacement and phase determination in non-centrosymmetric space groups. Acta Cryst.* **9**, 867–873.

Peterson, M. R., Harrop, S. J., McSweeney, S. M., Leonard, G. A., Thompson, A. W., Hunter, W. N. & Helliwell, J. R. (1996). *MAD phasing strategies explored with a brominated oligonucleotide crystal at 1.65 Å resolution. J. Synchrotron Rad.* **3**, 24–34.

Plöhn, H.-J. & Büldt, G. (1986). *The determination of label positions in membrane proteins by neutron and anomalous X-ray diffraction of powder samples. J. Appl. Cryst.* **19**, 255–261.

Prandl, W. (1990). *Phase determination and Patterson maps from multiwave powder data. Acta Cryst.* A**46**, 988–992.

Prandl, W. (1994). *Phase determination from X-ray powder diffraction data. II. Partial Patterson maps and the localization of anomalously scattering atoms. Acta Cryst.* A**50**, 52–55.

Pusey, M. L., Liu, Z. J., Tempel, W., Praissman, J., Lin, D., Wang, B. C., Gavira, J. A. & Ng, J. D. (2005). *Life in the fast lane for protein crystallization and X-ray crystallography*. *Prog. Biophys. Mol. Biol.* **88**, 359–386.

Rabinow, B. E. (2004). *Nanosuspensions in drug delivery. Nat. Rev. Drug Discov.* **3**, 785–796.

Ramachandran, G. N., Ramakrishnan, C. & Sasisekharan, V. (1963). *Stereochemistry of polypeptide chain configurations. J. Mol. Biol.* **7**, 95–99.

Retailleau, P., Colloc'h, N., Vivarès, D., Bonneté, F., Castro, B., El Hajji, M., Mornon, J.-P., Monard, G. & Prangé, T. (2004). *Complexed and ligand-free high-resolution structures of urate oxidase (Uox) from Aspergillus flavus: a reassignment of the active-site binding mode. Acta Cryst.* D**60**, 453–462.

Retailleau, P., Colloc'h, N., Vivarès, D., Bonneté, F., Castro, B., El Hajji, M. & Prangé, T. (2005). *Urate oxidase from Aspergillus flavus: new crystal-packing contacts in relation to the content of the active site. Acta Cryst.* D**61**, 218–229.

Rietveld, H. M. (1969). *A profile refinement method for nuclear and magnetic structures. J. Appl. Cryst.* **2**, 65-71.

Rodgers, D. (1997). *Practical cryocrystallography. Methods Enzymol.* **276**, 183–203.

Rodgers, D. (2001). *Cryocrystallography techniques and devices.* In *International Tables for Crystallography*, Volume F, *Crystallography of Biological Macromolecules*, edited by M. G. Rossmann & E. Arnold, ch. 10.2. Dordrecht: Kluwer.

Rossmann, M. G. (1990). *The molecular replacement method. Acta Cryst.* A**46**, 73–82.

Rotella, F., Duke, N., Giometti, C., Joachimiak, A. & Kaduk, J. (2001). Personal communication.

Salunke, D. M., Veerapandian, B., Kodandapani, R. & Vijayan, M. (1985). *Structural transformations in protein crystals caused by controlled dehydration. J. Biosci.* **8**, 37–44.

Sanchez-Weatherby, J., Bowler, M. W., Huet, J., Gobbo, A., Felisaz, F., Lavault, B., Moya, R., Kadlec, J., Ravelli, R. B. G. & Cipriani, F. (2009). *Improving diffraction by humidity control: a novel device compatible with X-ray beamlines. Acta Cryst.* D**65**, 1237–1246.

Shankland, K., David, W. I. F. & Sivia, D. S. (1997). *Routine ab initio structure determination of chlorothiazide by X-ray powder diffraction using optimised data collection and analysis strategies. J. Mater. Chem.* **7**, 569–572.

Sivia, D. S. (2000). *The number of good reflections in a powder pattern*. *J. Appl. Cryst.* **33**, 1295–1301.

Skarina, T., Xu, X., Evdokimova, E. & Savchenko, A. (2014). *High-throughput crystallization screening*. *Methods Mol. Biol.* **1140**, 159–168.

Smith, G. D., Ciszak, E., Magrum, L. A., Pangborn, W. A. & Blessing, R. H. (2000). *R_6 hexameric insulin complexed with m-cresol or resorcinol*. *Biochem. Biophys. Res. Commun.* **56**, 1541–1548.

Smith, G. D., Pangborn, W. A. & Blessing, R. H. (2005). *The structure of T6 bovine insulin. Acta Cryst.* D**61**, 1476–1482.

Stevens, R. C., Yokoyama, S. & Wilson, I. A. (2001). *Global efforts in structural genomics. Science*, **294**, 89–92.

Usón, I. & Sheldrick, G. M. (1999). *Advances in direct methods for protein crystallography. Curr. Opin. Struct. Biol.* **9**, 643–648.

Vagin, A. & Teplyakov, A. (1997). *MOLREP: an automated program for molecular replacement. J. Appl. Cryst.* **30**, 1022–1025.

Valmas, A., Fili, S., Nikolopoulos, N., Spiliopoulou, M., Christopoulou, M., Karavassili, F., Kosinas, C., Bastalias, K., Rosmaraki, E., Lichiére, J., Fitch, A., Beckers, D., Degen, T., Papageorgiou, N., Canard, B., Coutard, B. & Margiolaki, I. (2017). *Dengue virus 3 NS5 methyltransferase domain: expression, purification, crystallization and first structural data from microcrystalline specimens. Z. Kristallogr. Cryst. Mater.* **233**, 309–316.

Valmas, A., Magiouf, K., Fili, S., Norrman, M., Schluckebier, G., Beckers, D., Degen, T., Wright, J., Fitch, A., Gozzo, F., Giannopoulou, A. E., Karavassili, F. & Margiolaki, I. (2015). *Novel crystalline phase and first-order phase transitions of human insulin complexed with two distinct phenol derivatives*. *Acta Cryst.* D**71**, 819–828.

Vincent, R. & Midgley, P. (1994). *Double conical beam-rocking system for measurement of integrated electron diffraction intensities. Ultramicroscopy*, **53**, 271–282.

Voigt-Martin, I., Zhang, Z., Kolb, U. & Gilmore, C. (1997). *The use of maximum entropy statistics combined with simulation methods to determine the structure of 4-dimethylamino-3-cyanobiphenyl. Ultramicroscopy*, **68**, 43–59.

Von Dreele, R. B. (1999). *Combined Rietveld and stereochemical restraint refinement of a protein crystal structure*. *J. Appl. Cryst.* **32**, 1084–1089.

Von Dreele, R. B. (2001). *Binding of N-acetylglucosamine to chicken egg lysozyme: a powder diffraction study. Acta Cryst.* D**57**, 1836–1842.

Von Dreele, R. B. (2003). *Protein crystal structure analysis from high-resolution X-ray powder-diffraction data. Methods Enzymol.* **368**, 254–267.

Von Dreele, R. B. (2005). *Binding of N-acetylglucosamine oligosaccharides to hen egg-white lysozyme: a powder diffraction study*. *Acta Cryst.* D**61**, 22–32.

Von Dreele, R. B. (2006). *A rapidly filled capillary mount for both dry powder and polycrystalline slurry samples. J. Appl. Cryst.* **39**, 124–126.

Von Dreele, R. B. (2007). *Multipattern Rietveld refinement of protein powder data: an approach to higher resolution. J. Appl. Cryst.* **40**, 133–143.

Von Dreele, R. B., Stephens, P. W., Smith, G. D. & Blessing, R. H. (2000). *The first protein crystal structure determined from high-resolution X-ray powder diffraction data: a variant of T3R3 human insulin-zinc complex produced by grinding. Acta Cryst.* D**56**, 1549–1553.

Watier, Y. (2011). PhD thesis, Université de Grenoble & European Synchrotron Radiation Facility (ESRF, Grenoble), France.

Watier, Y. & Fitch, A. (2010). *Protein powder diffraction analysis with TOPAS. Mater. Sci. Forum Trans. Tech. Publ.* **651**, 117–129.

Watier, Y., Margiolaki, I., Wright, J., Fitch, A., Norrman, M. & Schluckebier, G. (2009). *Successful cryocooling of protein microcrystalline samples for powder diffraction. Acta Cryst.* A**65**, s320–s321.

Wold, S., Esbensen, K. & Geladi, P. (1987). *Principal component analysis. Chemom. Intell. Lab. Syst.* **2**, 37–52.

Wright, J. P. (2004). *Extraction and use of correlated integrated intensities with powder diffraction data. Z. Kristallogr.* **219**, 791–802.

Wright, J. P., Besnard, C., Margiolaki, I., Basso, S., Camus, F., Fitch, A. N., Fox, G. C., Pattison, P. & Schiltz, M. (2008*a*). *Molecular envelopes derived from protein powder diffraction data. J. Appl. Cryst.* **41**, 329–339.

Wright, J. P., Besnard, C., Margiolaki, I., Basso, S., Camus, F., Fitch, A. N., Fox, G. C., Pattison, P. & Schiltz, M. (2008*b*). *Molecular envelopes derived from protein powder diffraction data. ESRF Scientific Highlights (Structural Biology)*, pp. 61–62.

Wright, J. P. & Forsyth, J. B. (2000). *PRODD, Profile refinement of diffraction data using the Cambridge Crystallographic Subroutine Library*. Rutherford Appleton Laboratory Report RAL-TR-2000-012, Didcot, Oxon, UK.

Wright, J. P., Markvardsen, A. & Margiolaki, I. (2007). *Likelihood methods with protein powder diffraction data. Z. Kristallogr.* Suppl. **26**, 27–32.

Wu, X. W., Muzny, D. M., Lee, C. C. & Caskey, C. T. (1992). *Two independent mutational events in the loss of urate oxidase during hominoid evolution. J. Mol. Evol.* **34**, 78–84.

Wukovitz, S. W. & Yeates, T. O. (1995). *Why protein crystals favour some space-groups over others. Nat. Struct. Biol.* **2**, 1062–1067.

Xie, D., Baerlocher, C. & McCusker, L. B. (2008). *Combining precession electron diffraction data with X-ray powder diffraction data to facilitate structure solution. J. Appl. Cryst.* **41**, 1115–1121.

Yang, M. X., Shenoy, B., Disttler, M., Patel, R., McGrath, M., Pechenov, S. & Margolin, A. L. (2003). *Crystalline monoclonal antibodies for subcutaneous delivery. Proc. Natl Acad. Sci. USA*, **100**, 6934–6939.

Young, A. C. M., Dewan, J. C., Nave, C. & Tilton, R. F. (1993). *Comparison of radiation-induced decay and structure refinement from X-ray data collected from lysozyme crystals at low and ambient temperatures. J. Appl. Cryst.* **26**, 309–319.

International Tables for Crystallography (2019). Vol. H, Chapter 7.2, pp. 737–751.

7.2. Forensic applications of X-ray powder diffraction

D. F. Rendle

7.2.1. Introduction

7.2.1.1. *Background information*

X-ray powder diffraction (XRPD) as a method of chemical analysis was first described in a paper by Hull (1919), in which he stated the following:

> Every crystalline material gives a diffraction pattern; the same substance always gives the same pattern; in a mixture of substances each substance will produce its own pattern independently of the others, so that the diffraction pattern obtained will be the superimposed sum of the patterns that will be obtained by exposing each of the components separately for the same length of time. This law applies quantitatively to the intensities of the lines (provided the absorption is negligible for each of the components) as well as to their positions, so that the method is capable of development as a quantitative analysis.

Such diffraction patterns are a ‘fingerprint’ of the particular crystalline substance. However, as with human fingerprints, there must be a known standard with which to compare the unknown before the pattern can be of value (Marvin & Garbarino, 1953). These beautifully concise statements tell us all we need to know about the method, and today, almost 100 years after Hull’s publication, forensic analysts use XRPD with varying degrees of sophistication, for both qualitative and quantitative analysis, based upon those principles first stated by Hull.

Forensic science is the science that is used in a court of law, whether it be a criminal or civil court (Walls, 1974). Hans Gross (1847–1915), professor of criminology at the University of Prague, is generally recognized as one of its pioneers, and his classic publication *Handbuch fur Untersuchungsrichter* first appeared in 1893. The English translation, entitled *Criminal Investigation* (Gross, 1962), first appeared in 1906, and in it was stressed the help that science could give to the detective. Gross was a lawyer rather than a scientist, however, and did not contribute to the development of scientific methods. The greatest contributions in that field were probably those made or inspired by Edmond Locard (1877–1961) of the University of Lyon. His guiding principle, that ‘every contact leaves a trace’, known as Locard’s Exchange Principle, still figures prominently in lectures delivered on the subject of criminalistics.

So-called ‘contact traces’ appear in the traditional areas of forensic science, where the identification and comparison of trace quantities of material can help in the conviction or exoneration of a person suspected of involvement in a crime. Examples of contact trace materials include paint flakes, glass fragments, hair and fibres (natural and synthetic), slivers of metal, soils, building materials, plastics and polymers, stains of any description, cosmetics, explosives and gunshot residues, corrosion products, and loose powdered materials including drugs of abuse. The most important of comparisons is that between so-called ‘control’ and ‘suspect’ specimens. For example, in the case of a burglary in which the burglar has forced entry through a window, any paint flakes and glass fragments found on his outer clothing would constitute ‘suspect’ specimens and paint and glass specimens taken from the windowsill and pane by a crime scene investigator would be the ‘control specimens’.

Prior to the discovery of individual-specific ‘fingerprints’ of human DNA and subsequent forensic application of DNA fingerprints (Gill *et al.*, 1985), much time and effort was expended in the labour-intensive detection and analysis of such contact traces in attempts to prove, or disprove, links between a person suspected of involvement in a crime and the victim and/or crime scene. The advent of DNA profiling, however, meant that law-enforcement agencies now had at their disposal a means that would provide them with reliable, highly individual-specific evidence. Understandably, many of these agencies then began to rely heavily upon DNA evidence at the expense of the less individual-specific evidence generated by what were once known as classical contact trace materials. However, in the absence of material leading to the recovery of DNA, and of human finger marks, which are also individual-specific, the analysis and comparison of such trace materials once again becomes important, and one of the most useful and versatile methods for their analysis is X-ray powder diffraction. Some general articles describing the analysis of these materials and others by XRPD are available: Thatcher & Briner (1986), Fischer & Hellmiss (1989), Rendle (2000), Liberman (2000), Kügler (2003), Rendle (2003*a*,*b*), Heijnen *et al.* (2005), Kügler (2005), Kotrlý & Bezdička (2006), Abraham *et al.* (2007), Kotrlý (2007), Švarcová *et al.*, (2010) and Kotrlý (2011).

7.2.1.2. *Preservation of evidence*

The need for non-destructive methods of analysis in order to preserve evidence can be of great importance, although this requirement may vary from country to country or from state to state depending upon the prevailing criminal justice system. Even if preservation of the specimen for legal reasons is not required, non-destructive analysis means that the specimen may then be subjected to further complementary analyses. Most courts understand and accept that chemical analysis may occasionally result in destruction of a specimen, but in certain circumstances may insist on seeing the specimen that was analysed, and perhaps having that same specimen re-analysed by another scientist. In view of this, it is wise to use, where possible, a non-destructive analytical method as a matter of course, and XRPD meets this requirement admirably.

7.2.1.3. *Versatility*

XRPD probably ranks as one of the most versatile methods of instrumental analysis because it can be used to analyse any solid substance, crystalline or partially crystalline, whether it be organic, inorganic, metallic or a mixture thereof. Its main drawback is its lack of sensitivity; it is not a true trace technique. Although it is capable of analysing very small specimens, if one of the chemical components within the specimen is present at a low concentration, it may well go undetected. However, as long as the limitations of the method are known and understood, and it is used intelligently, XRPD will yield qualitative and quantitative results unrivalled by other techniques.

Copyright © 2019 International Union of Crystallography

7.2.1.3.1. *Drugs and toxicology*

Review articles (Clarke, 1962; Schmidt, 1962) indicate that some of the earliest published uses of XRPD methods in forensic science were in the 1950s (Huang & Jerslev, 1951; Huang, 1953), and concerned the analysis of drugs, specifically barbiturates. Unpublished work from the Toxicology Section of the Metropolitan Police Forensic Science Laboratory (London, UK) in the 1950s revealed that small-diameter Debye–Scherrer powder cameras were used to identify barbiturates (Jackson, 1977). The identification of barbiturates isolated from biological material was a difficult task for forensic chemists, and when more than one barbiturate was present it was almost impossible to isolate them in a pure enough state for melting points to be determined accurately. The problem was further complicated by the polymorphism (the ability of the same substance to crystallize in different forms) shown by many of these compounds, and by their tendency to form mixed crystals if two or more of them are present (Mesley *et al.*, 1968). Pinker (1952) indicated that XRPD had been used for barbiturate and general drug analysis some years earlier still, although no specific dates were given. A diffractometer was used in which the specimens covered thinly an area of about 6 mm^2 on a lead slide. The diffraction patterns were recorded on a moving strip of chart paper, and 16 patterns of drugs were shown. Further work on drug analysis (Marvin & Garbarino, 1953) using diffractometry was published, with reference to the importance of uniform specimen preparation, and a list of the perceived advantages and disadvantages of XRPD as an analytical method.

The analysis of opiates by XRPD methods was discussed even earlier than in those instances just described (Gross & Oberst, 1947; Oberst, 1938, 1943; Hubach & Jones, 1950), although in these cases the applications were not strictly forensic. Similarly, XRPD was used (Parsons, 1952) to identify cystine as the only constituent of a radiopaque renal calculus, and by Parsons & Beher (1955) to amass a collection of powder data on steroids, a project that was further extended (Parsons *et al.*, 1958). Barnes (1954) described in detail the powder method with particular emphasis on its use in the analysis of narcotics, and, in a co-authored paper, provided the first real collection of tabulated numerical XRD powder patterns of narcotics (Barnes & Sheppard, 1954). Cocaine and its substitutes were analysed by XRPD (Sullivan & O'Brien, 1970). Powder data for 17 local anaesthetics (Owen *et al.*, 1972), for some drugs, excipients and adulterants (Folen, 1975), and for piperidyl benzilates and related glycolates (Barrick *et al.*, 1977) have since been added to the Powder Diffraction File (ICDD, 2014). More recently Thangadurai *et al.* (2005) have emphasized the value of powder diffraction in the forensic analysis of a number of β-lactam, tetracycline and macrolide antibiotics.

In addition to identifying the precise chemical form of drugs (salt, base, acid), XRPD also provides information about the excipients (materials mixed with the drugs, both organic and inorganic) in drug seizures. In general these substances tend to be carbohydrates such as glucose, mannitol and occasionally sucrose, although a number of other more unusual compounds are sometimes encountered (Rendle, 2003*b*, 2004; Rendle & Connett, 1988; Ferguson *et al.*, 1991). The method has other important uses in forensic drug analyses, too, namely distinguishing between (*a*) polymorphic forms of drugs and excipients, (*b*) optically active and racemic forms of drugs, and (*c*) different hydrated forms of drugs and excipients. Barbiturates are prime examples of drugs with multiple polymorphic forms (Mesley *et al.*, 1968), whilst aspirin, ibuprofen and paracetamol (acetaminophen) have at least one polymorph each. Mannitol may appear as an excipient in drug/excipient mixtures in any one of three common polymorphic forms (α-, β- or δ-D-mannitol). Methylenedioxymethylamphetamine hydrochloride, commonly known as MDMA·HCl or ecstasy, is known to exist in a number of hydrated crystalline forms (Shulgin, 1986). The monohydrate of ecstasy has been encountered in drug seizures and its XRPD pattern has been identified and recorded (Rendle & Glazier, 2012). Gamma-hydroxybutyrate (GHB) is a sleep-inducing drug and has been used in cases of drug-facilitated sexual assault ('date rape'). Ferris & Went (2012) used XRPD to discriminate between four different salts of the drug. In a study on ecstasy and amphetamine seizures in Spain during 1995–2002, Pastor *et al.* (2003) used XRPD in conjunction with gas chromatography–mass spectrometry (GC-MS), high-performance liquid chromatography (HPLC) and Fourier transform infrared spectroscopy (FTIR) to identify the active drug components, excipients and precursors. Identification of *all* components in drug seizures is important from an intelligence aspect because chemical similarities between several seizures may indicate a common source of the drugs, *i.e.* one, as opposed to more than one, drug dealer (Rendle *et al.*, 2011). Synchrotron radiation was used to generate XRPD patterns for the comparison of a number of methamphetamine samples from different sources (Terada, 2005).

7.2.1.3.2. *Paint and pigments*

Forensic paint analysis 50 years ago usually meant identifying inorganic pigments, fillers and extenders (Heilman, 1960; Scott, 1969), but the growth of the organic pigment industry in the following years and the resultant increase in use of organic pigments in paint manufacture presented a new challenge for the analyst. Organic pigments are generally poorer scatterers of X-rays than their inorganic counterparts, yielding fewer diffraction data, and some organic pigments, because of their intense colouration, tend to be present in lower concentration than inorganic pigments in paints. In addition, the optimum particle diameter for pigments in paints is approximately 0.2–0.4 µm (200–400 nm) (Bentley & Turner, 1998), which may result in diffuse or broadened diffraction maxima. A general paper on pigment analysis (Kamarchik, 1980) appeared, and Curry *et al.* (1982) produced a list of the powder patterns of 71 organic pigments. These diffraction data enabled identification of pigments in paints, bearing in mind the comments above, and provided that their concentration in the paint was sufficiently high for detection by XRPD.

Decorative, automobile, tool and security paints contain resins, pigments and extenders. The pigments and extenders are usually crystalline, while the resins are not; thus paint may be described as a partially crystalline substance. Nonetheless, tiny paint flakes 0.1 mm^2 in area and weighing a few micrograms can yield diffraction patterns enabling comparison of control and suspect flakes. Under favourable circumstances the pigments and extenders may be identified as well, providing the forensic scientist with some means of assessing the evidential value of a positive match, should one occur. For example, white gloss paints rarely contain any other pigment than rutile, whereas red, blue, green or yellow paints may contain a variety of different pigments. Thus a match between diffraction patterns of white control and suspect paint flakes means far less than one between those of coloured paint flakes containing combinations of 'unusual' pigments and extenders. Polymorphism is not restricted to drugs and/or excipients, because titanium dioxide (the white paint pigment known as rutile) exists in two other ambient temperature forms – anatase and brookite, whilst calcium carbonate (another constituent of some paints) also has three main polymorphs: calcite, aragonite and vaterite.

7.2.1.3.3. *Pathology*

Establishment of the post-mortem interval (PMI) is a complex problem because of the number of intrinsic factors that may alter the normal course of post-mortem change, such as the age, sex, constitution, and previous physiological and pathological states of the subject, and external factors. XRPD parameters related to the degree of crystallinity of the mineral component (hydroxyapatite) in conjunction with biochemical analyses of long bones is suggested as a useful alternative for dating osseous remains (Prieto-Castelló *et al.*, 2007).

Much effort has been made to extract useful information from burned bone. Piga *et al.* (2009) suggested a method of determining the temperature and duration of burning of human remains in a forensic context, by application of XRPD to samples of human bone and teeth. Growth of hydroxyapatite crystallites was found to be a direct and predictable function of the applied temperature (473–1273 K) and duration of burning (0–60 min).

Crystallinity (the degree of long-range order) in bone mineral is increased markedly, at the expense of smaller, more disordered crystals of hydroxyapatite, as a result of diagenesis (the physical and chemical changes that occur in bone after burial) or heating (Rogers, Beckett *et al.*, 2010). This property is direction-dependent, however, and when determined by spectroscopic methods results in an average, which can be misleading. XRPD is capable of resolving direction-dependent characteristics, and demonstrates that recrystallization processes associated with heating and diagenesis produce hydroxyapatite crystallites with significantly different physical microstructures. This enables a distinction to be made between, for example, archaeological and contemporary bone specimens.

In a study of inter-species variation in bone mineral, Beckett *et al.* (2011) established significant differences between heated and unheated samples of human bone and bone from 11 other animal species using XRPD. The inter-species variation was measured in terms of the lattice parameters of calcium hydroxyapatite (bioapatite), its crystallinity and its thermal decomposition products upon heating to 1673 K. The characterization of bioapatite in this way has the potential to enable species identification, particularly in distinguishing human from non-human bone in cases of fragmented, burned and pulverized bone.

The ability to distinguish between cremated human remains (cremains) and other powdered materials of similar appearance can be of great importance (Bergslien *et al.*, 2008). In one instance, instead of cremating the bodies of deceased persons, the organization responsible dumped the bodies and provided the relatives with urns containing cement dust, silica and rock of any description.

A study of the composition of gallstones in patients in the age group 20–74 years (Nagpal *et al.*, 1982) revealed anhydrous cholesterol in 62% of calculi and the monohydrate in 46%. Calcium carbonate, identified as calcite and aragonite, was present in 23 and 8% of the calculi, respectively, and apatite (a general name for a series of calcium phosphates) was found in 38% of the calculi. Cholesterol crystals were also found, and identified by XRPD, in fluid from an intracranial cyst (Parsons & Bartone, 1961).

7.2.1.3.4. *Metals and alloys*

In most forensic science laboratories, metallic specimens would usually be analysed by X-ray fluorescence (XRF) or in the scanning electron microscope using energy-dispersive X-ray spectroscopy (SEM-EDS). These are elemental methods of analysis, however, and as such are incapable of distinguishing between the various crystalline phases that may occur in a metal or alloy. A number of counterfeit 500 yen coins (Hida *et al.*, 2001) were examined by a combination of XRPD and XRF with multivariate analysis. The presence of additional Bragg peaks in the powder patterns of nickel-plated coins and the shift in peak positions in patterns of the pressed coins, when compared to those of the genuine coins, enabled them to be classified as nickel-plated counterfeit, pressed counterfeit and genuine. An earlier XRPD study on brasses (Rendle, 1981) showed that useful discrimination was achievable between brass specimens containing α, β and $\alpha+\beta$ phases occurring as contact traces, and that the copper/zinc ratio within a single-phase α-brass could be estimated, in relative terms, with ease to ±1%.

7.2.1.3.5. *Soils and minerals*

Soil has long been regarded as potentially one of the most useful evidence types, but also as one whose provenance and significance has been one of the most difficult to gauge (Rawlins *et al.*, 2006). The soles of our footwear bear traces of what we have been standing in or on, which may in turn indicate where we have been. Similarly, vehicle tyres may carry traces of soil in addition to leaving behind their own characteristic tread marks in that soil. Not surprisingly, XRPD has been used widely for the analysis of soil traces because of the varying type and amounts of mineral content (Bebris, 2003; Ruffell & Wiltshire, 2004; Fitzpatrick & Raven, 2005; Melo *et al.*, 2008; Fitzpatrick *et al.*, 2009; Keaney *et al.*, 2009; Dawson & Hillier, 2010).

Adipocere is a post-mortem product which forms from body fat in the later stages of decomposition and its formation has the ability to slow or inhibit decomposition, so an understanding of the mechanism of its formation in grave soils is of interest to forensic scientists. Factors influencing adipocere formation include the type of grave soil in which the burial has taken place, and experiments with pig flesh buried in various types of soil were undertaken. Analysis of the soil types by XRPD (Forbes *et al.*, 2005) showed that certain types, including sand and silty sand, were able to accelerate adipocere formation when kept moist and in a temperate environment. Similar results were obtained in a more recent study (Durães *et al.*, 2010).

XRPD methods were used for soil and sediment analysis (Brown, 2006) following the exhumation of mass graves in NE Bosnia associated with the massacre of civilians in and around Srebrenica in July 1995. Bodies had been exhumed and transported from the original mass graves to a number of unknown secondary grave sites. An attempt was made to link the primary and secondary sites through soil and other analyses. On the basis of clast lithology, mineralogy, pollen and spore content, all secondary sites could be associated with matching primary sites.

A roadway embankment was constructed in 1995 with 60% fluidised bed combustion ash, 35% stoker ash and 5% class-F fly ash in West Lafayette, Indiana. Heaving of the embankment was observed during and after construction, and the pavement exhibited severe damage at several locations. Forensic XRPD and SEM studies (Yoon *et al.*, 2007) were used to compare the mineralogical phase composition of fresh samples and samples collected from the heaved embankment. Results indicated that the formation of ettringite [$Ca_6Al_2(SO_4)_3(OH)_{12}{\cdot}26H_2O$] led to the swelling of the embankment, which caused cracking of the pavement.

7.2.1.3.6. *Gunshot residues and explosives*

The most commonly used method for detecting and identifying gunshot residue in specimens obtained from skin is SEM-EDS, but this will not permit unequivocal identification of the compounds in such specimens. For example, whilst confirming the presence of lead, it cannot show whether it occurs in the metallic form, as lead oxide, or as lead sulfide – although it must be said that measurement of a Kikuchi pattern could make the identification unambiguous. Primer residues, gunshot residues from the barrel and gunshot residues emitted from the breech of a gun were analysed by XRPD and SEM-EDS (Tassa *et al.*, 1982). The residues were embedded in a thin film of petroleum jelly on a glass slide and analysed by diffractometry. Metallic lead was found to be the main constituent of all the residues tested. In the primer residues were found antimony, calcium silicide, lead sulfide, barium nitrate, barium aluminate and barium calcium silicate, all identified by XRPD. The residues from the barrel and breech were similar to each other, consisting mainly of lead with metallic copper. In some early work, Soldate & Noyes (1947) analysed explosives' constituents with XRPD, and Canfield & De Forest (1977) described a method for analysing and identifying a single crystal of explosive as small as 30 µm in diameter in an explosives residue, by means of a Gandolfi camera.

Beveridge *et al.* (1975) described a systematic procedure for the analysis of explosive residues, after detonating devices containing high and low explosives. The most useful techniques were reckoned to be microscopy, thin-layer chromatography (TLC), XRPD and infrared spectroscopy. Similar work is described in a more recent publication (Beveridge, 2010). The analysis of explosives by XRPD was also described in two papers (Abel & Kemmey, 1975; Higgs *et al.*, 1978). In the latter, although XRPD was used initially to analyse a substance thought to be a residue of explosives, it proved to be a corrosion product, thus removing the suspicion of explosives as having caused an airline disaster.

7.2.1.3.7. *Paper*

Forensic paper examination and analysis is usually associated with ransom notes, threatening letters, anonymous hate mail and wrappings from drug seizures (Heijnen *et al.*, 2005). The examination will more than likely be a comparison of paper from, for example, the ransom note with that found in a suspect's dwelling. XRPD or elemental analysis may be called for, but only after an initial examination by botanical or fibres experts. If the paper were white, for example, such an examination might include thickness and density measurement, observation of mesh marks and watermarks (if present), and maceration of a small sample in order to identify the type and number of each fibre present (Roe, 2012). If the paper were coloured, the dye(s) would be extracted and analysed by TLC. XRPD is used to identify the fillers present in the paper and it can also yield useful information about the crystallinity of the cellulose (Foner & Adan, 1983). A paper's mineral content depends upon its use and appearance. Newsprint and cheap copying paper usually have either no filler (cellulose only) or a clay mineral such as kaolinite, whereas other more expensive papers, of the type used in glossy magazines, have rutile or anatase as fillers. Causin *et al.* (2010) successfully discriminated between 19 different brands of general office paper ($80\ \mathrm{g\ m}^{-2}$) using a combination of XRPD and infrared spectroscopy.

7.2.1.3.8. *Plastics and polymers*

Plastics and polymers (Heilman, 1960; Turley, 1965), perhaps because of their appearance, are usually thought of as being noncrystalline, and in some cases this is true. However, the majority of the more common polymers and plastics are at least partially crystalline, and therefore lend themselves to analysis by XRPD. Plastics such as polyethylene and polypropylene, which find uses in a wide range of domestic and industrial goods, may have pigments added to them for colouration, and often exhibit a range of crystallinity. XRPD can be used to identify the pigments and the polymer, and provide an estimate of the percentage crystallinity. Causin *et al.* (2007) applied the method to the analysis of plastic bags used for packaging drugs. The polymer chains in the polyethylene bags were highly oriented, due to the manufacturing process, so two XRPD measurements were made, one parallel and one perpendicular to the long dimension of the bags. The relative intensities of the 110 and 200 peaks, together with the estimated degree of crystallinity, enabled discrimination between 33 white, matte, plastic bags.

7.2.1.3.9. *Miscellaneous*

Textile fibres are an example of material not usually analysed by XRPD, as other more appropriate techniques are available (Robertson & Grieve, 1999), but analyses have been undertaken on both single fibres (Lynch & Kerrigan, 1981) and pieces of cloth approximately 45 mm in diameter (Abraham *et al.*, 2007).

Cosmetics may occur as contact traces in cases of sexual assault, and the scientist may be asked to compare smears of face powder, eyeliner or lipstick on clothing belonging to the alleged assailant with control specimens owned by the victim. Ward (2000) describes an X-ray spectral database in which the energy-dispersive spectra of a wide range of materials (including cosmetics) are stored for such comparison cases. Abraham *et al.* (2007) demonstrated the use of XRPD in comparing control lipstick smears on glass slides with smears on clothing.

XRPD was used in conjunction with stable isotope profiling (SIP) and microscopy to analyse wooden safety matches (Farmer *et al.*, 2007) when an individual was suspected of attempting to burn materials potentially relating to a murder case. SIP and microscopy were used on the stems of the matches and XRPD to analyse the match heads. SIP showed the scene matches and seized matches to be different, which was confirmed by XRPD and microscopy.

A blue encrustation (Mann *et al.*, 1998) was found on the remains of three US servicemen listed as missing in action and repatriated from Vietnam after 28 years. The identification of the blue material was determined by XRPD and SEM-EDS and was found to be the mineral vivianite [$Fe_3(PO_4)_2{\cdot}8H_2O$]. The presence of this mineral provides information leading to a more complete understanding of taphonomic processes (those processes involved with fossilization).

Kasımiye Medresse is an important educational centre in the province of Mardin in south-eastern Turkey. There is a stain (Tuğ *et al.*, 2005) on the wall of Kasımiye Medresse, considered to be Sultan Kasım's blood. The stained and unstained parts of the wall were examined by XRPD. The unstained wall consisted solely of calcite, and the 'bloodstain' consisted of whewellite ($CaC_2O_4{\cdot}H_2O$) and weddellite ($CaC_2O_4{\cdot}2H_2O$) in addition to calcite. The stain appeared to be a dye made of herbal roots, with henna-containing whewellite mineral as a likely candidate for the 'bloodstain'.

Kela is a commercial rodenticide bait commonly used in Israel. It is made of wheat grains, which, according to its label, contain chlorophacinone. This product was involved in the death case (Azoury & Levin, 1998) of a man in which the victim's female companion was accused of assisting in his suicide and was subsequently convicted. Analysis of the wheat grains revealed zinc phosphide, the use of which is restricted to authorized exterminators only, instead of chlorophacinone. Zinc phosphide was identified using microscopic examination, SEM-EDS and XRPD.

When a firearm used to commit a crime has been disposed of in a body of water, determining the time since immersion may be of importance to the investigation. Adherent corrosion products on the slides of four different types of handguns were identified by SEM/EDS and XRPD (Wogan *et al.*, 2013) after the components had been immersed in (*a*) deionized water and (*b*) saline solution (separate experiments) for 180 d. However, utilizing a general approach in which surface area coverage of corrosion products is the sole consideration is not sufficient to determine the time since immersion. The results indicated possible corrosion mechanisms driving the process in high- and low-chloride environments, and showed the necessity of including the original firearm metal composition, rust composition and ion concentration in any models that attempt to elucidate the time since immersion of handguns.

7.2.1.4. *Variable specimen size*

Forensic specimens can range from the classical minute (microgramme) contact traces such as paint flakes, to large (kilogramme) quantities of illegal or restricted drugs, so the X-ray instrumentation must be capable of accommodating a range of specimen sizes, weights or volumes as well as specimen types.

7.2.1.5. *Contamination*

By their very nature, or the circumstances under which they are found, some forensic samples will be contaminated, and it is important for the analyst to recognize contamination as such, and not to mistake it for part of the true chemical makeup of the specimen. This will usually be evident upon microscopic examination of the original sample. Any contamination should be noted, however, as its presence may have particular significance when comparing control and suspect specimens.

7.2.1.6. *Identification versus comparison*

Forensic analyses can be categorized as follows: those simply requiring identification, and those requiring comparison of two or more samples in order to establish or preclude a common origin. For identification, a source of reference diffraction patterns is required. This may consist of a selection of 'standard' X-ray powder patterns produced in-house from pure, certified materials, or those contained in the comprehensive Powder Diffraction File, generated and marketed by the International Centre for Diffraction Data (ICDD, 2014). This file contains, at present, upwards of 700 000 powder diffraction patterns of single-phase organic, inorganic and metallic substances. Comparison cases need not *necessarily* require identifications, but it would be most unusual to make comparisons without identifications. Quantitative analysis (Madsen & Scarlett, 2008) may be attempted by either single-peak methods or by whole-pattern fitting, including the Rietveld method (Young, 1993).

7.2.1.7. *Complementary techniques*

In any analytical laboratory, the techniques available will be those dictated by the industry itself, such as pharmaceuticals, metallurgical, electronics, building construction, foodstuffs, polymers and plastics, geosurvey *etc*. A typical forensic science laboratory will not have the resources to attempt the kind of specialist analyses undertaken routinely by each of these major industries; nonetheless, its staff will be expected to cope with analyses of *all* kinds of material. Techniques available in a forensic science laboratory are likely to be dependent upon the type of evidence most frequently submitted for examination, and also upon the resident expertise. It is not surprising, therefore, that many forensic science laboratories will attempt to use the same instrumental technique for a variety of substances, even though it might not be the first choice for a given material, as long as it generates relevant analytical information.

Methods of drug analysis are traditionally solution based, even though a large proportion of samples submitted for analysis are solids. In a forensic science laboratory, routine methods of analysis such as spot tests and infrared spectroscopy (IR) (Bell *et al.*, 2012) are used initially to establish the type and number of drug(s) present in a specimen, such as heroin, cocaine, morphine or amphetamine. Combined, or hyphenated, techniques such as gas chromatography–mass spectrometry (GC-MS) and liquid chromatography–mass spectrometry (LC-MS) (Smith, 2005) and proton nuclear magnetic resonance (NMR) (Hays, 2005) are used for quantification.

A considerable amount of work on the identification of explosives and gunshot residues by XRPD has been undertaken (Abel & Kemmey, 1975; Beveridge *et al.*, 1975; Beveridge, 2010; Canfield & De Forest, 1977; Wolten *et al.*, 1977; Tassa *et al.*, 1982). However, explosives and narcotics can also be detected and analysed by, amongst other techniques, Raman spectroscopy (Sands *et al.*, 1998; Lacey *et al.*, 1996; Hayward *et al.*, 1995; Cheng *et al.*, 1995; Bell *et al.*, 2012; López-López *et al.*, 2012) and by ion mobility spectrometry (IMS) (Lawrence, 1987; Eiceman *et al.*, 2007). Development of some of these methods has been driven by the need to analyse drugs and explosives on site, at airports and seaports, without having to bring samples to a laboratory. Inorganic gunshot residues (primer residues) are normally analysed by scanning electron microscopy coupled with energy-dispersive spectrometry (SEM-EDS) (Wolten *et al.*, 1977), while organic residues (propellants) are analysed by chromatographic techniques (Lloyd, 1983; Laza *et al.*, 2007).

Techniques for examining paint flakes include visible light microscopy (Hamer, 1982), chemical tests (Castle, 1982) and SEM-EDS (Henson & Jergovich, 2001). Vehicle paint analysis in most laboratories is now undertaken using Fourier transform infrared spectroscopy (FTIR) because of the availability of comprehensive databases of automobile paint infrared spectra, one in North America known as PDQ (Paint Data Query) (Beveridge *et al.*, 2001), and one in Europe, known as EUCAP (European Collection of Automotive Paints). Use of these databases will not identify paint from one specific vehicle, but will narrow down the search to a manufacturer, a model and a year. Plastics and polymers can be identified by infrared spectroscopy (Heilman, 1960) and NMR, while metals and alloys are most readily analysed by XRF and SEM-EDS.

For particle identification, visible light microscopy used in conjunction with the McCrone *Particle Atlas* (McCrone & Delly, 1973) is a very useful alternative approach. Speed of analysis can be a critical factor, as can fitness for purpose, bearing in mind that XRPD provides information about the *compounds* present, and not just about the elemental composition.

7.2.2. Instrumentation

7.2.2.1. *Choice of instrumentation*

7.2.2.1.1. *Reflection or transmission diffractometry*

Most forensic science laboratories, if they have XRPD equipment, will have a powder diffractometer capable of operating in reflection or transmission mode, or both (Klug & Alexander, 1974; Jenkins & Snyder, 1996). Individual analysts may have a preference for one mode or the other, but it is wise to be familiar with the operation of both, as each has its own advantages and disadvantages. The correct choice of instrument for a given specimen is a matter of experience and also a reflection of the analyst's understanding of the equipment's capabilities. If a suspect specimen is very small, it must be compared with a control specimen of similar size. One should never compare the diffraction patterns of a small suspect specimen with that of a large control specimen, even if a considerable amount of control is available. A small specimen (a paint flake, a speck of unknown material, a sub-milligramme quantity of powder, scrapings from a surface, a sliver of metal) should be mounted as for transmission diffractometry, and larger quantities of powder, paper specimens and flat metallic specimens are ideal candidates for reflection geometry. Some small specimens may be analysed in reflection mode, but only if they are mounted on a zero-background substrate and appropriate small slits are selected.

7.2.2.1.2. *Scanning detector or stationary position-sensitive detector (PSD)*

Conventional powder diffractometers have detectors that scan at predetermined rates through an angular range selected by the analyst, and thus collect data sequentially. Stationary position-sensitive detectors amass the data over a fixed angular range, but simultaneously, resulting in rapid acquisition of data. This can be advantageous if, for example, the specimen is unstable, sensitive to light or to moisture, but one disadvantage of the PSD is that its angular resolution tends to be inferior to that of a scanning detector equipped with narrow receiving slits.

7.2.2.1.3. *One-dimensional or two-dimensional detector*

A further choice can be made, and that is to select a diffractometer that has a two-dimensional area detector (He, 2009), instead of the more common one-dimensional detector. Again, this choice will depend upon the type of specimen under examination – and one's budget, because two-dimensional detectors tend to be more expensive. The two-dimensional powder pattern generated can be much more informative in terms of crystallite size and preferred orientation effects than a one-dimensional pattern generated by a conventional reflection-geometry diffractometer.

7.2.2.1.4. *Energy dispersive X-ray diffraction (EDXRD)*

Energy dispersive X-ray diffraction, sometimes referred to as coherent X-ray scattering (CXRS), is an alternative to the usual angle-dispersive X-ray diffraction mode, in which a sample is irradiated with polychromatic white X-rays at a fixed scattering angle. An energy-dispersive detector is used to detect the wavelength of the scattered X-rays (Cook *et al.*, 2007; Sun *et al.*, 2010). Unlike conventional angle-dispersive XRPD equipment, it has no moving parts and it is a low-resolution technique that has its uses where a fixed geometry with penetrating X-rays is required, for example at luggage inspection facilities at airports and seaports (Harding & Harding, 2007). It would not be used in a forensic science laboratory for analysis of evidence, but more as a high-throughput screening technique to identify materials such as explosives and drugs concealed within items of luggage. Its chief disadvantage is the poor energy resolution obtained due to the limited energy resolution of the detector.

7.2.2.1.5. *Focal construct geometry*

An alternative to energy-dispersive X-ray diffraction for screening purposes is so-called focal construct XRPD. This comprises a simple novel geometry (Rogers, Evans *et al.*, 2010; Prokopiou *et al.*, 2014; Dicken *et al.*, 2014) that enables the measurement of diffractograms from polycrystalline materials through *linear translation* of a point detector. It is an angle-dispersive arrangement that is directed towards maximizing diffraction intensity at a measurement point, and has potential use as an alternative means of screening packages for illicit materials. The concept has been extended to the discrimination of liquids, in which a variety of liquids relevant to security inspection was analysed by focal construct technology, enabling discrimination of potential threat liquids (Prokopiou *et al.*, 2013).

7.2.2.2. *Choice of radiation*

The first choice in most laboratories would be Cu $K\alpha$ radiation (1.5418 Å), but if a large number of specimens are known to contain iron, iron oxides or salts of iron, Co $K\alpha$ radiation (1.7903 Å) should be used to remove the nuisance of fluorescent radiation, unless a diffracted-beam monochromator is fitted. Cobalt radiation represents an acceptable compromise between copper and chromium (2.291 Å) radiation. Unlike chromium radiation, which requires a vacuum, it is energetic enough to overcome absorption by the air. Its longer wavelength, relative to copper radiation, improves dispersion, enabling the resolution of low-angle diffraction peaks produced by organic specimens. With EDXRD used in its imaging capacity to locate and analyse materials concealed within baggage at ports of entry, radiation of higher energy is required. Items of baggage are examined in transmission mode, and incident-beam accelerating voltages tend to be of the order of 150 kV or higher (Harding & Harding, 2007; Dicken, Evans *et al.*, 2015; Dicken, Shevchuk *et al.*, 2015).

7.2.3. Technical procedures

7.2.3.1. *Variety and types of specimen encountered and specimen preparation*

In theory, any substance could be a forensic sample. A fundamental requirement for XRPD is that it must be crystalline, or something containing a crystalline substance. The following are some of the substances encountered in forensic casework: minerals, metals and alloys, paints, cosmetics, ointments, drugs and their excipients, papers, safe ballasts, detergents, pigments and dyes, plastics and polymers, abrasives, explosives, gunshot residues, soils, gemstones, automobile underseals, and building materials – plasters, putties, bricks, cements, mortars and concrete.

Specimen preparation for forensic analysis means disturbing the specimen as little as possible. Each sample should be treated on its merits and on the circumstances of its origin. It is good practice to examine the sample first using a low-power visible-light microscope to observe its physical characteristics. For example, if it is a powder, does it contain more than one component, is it contaminated, does its texture tell you anything? If it is a paint flake, how many layers are visible, are they coloured differently, can they be separated with ease? Do the nature and circumstances of the case dictate the way in which you should treat the sample? Is identification required, or merely a comparison of diffraction patterns? How much sample is available for analysis? Is non-destructive analysis absolutely essential, is the specimen required for other analytical techniques – if so, what is the best way of mounting the specimen?

7.2.3.2. *Specimen preparation – powders*

A good general reference for specimen preparation is that of Buhrke *et al.* (1998). Most routine diffraction work on powdered specimens is done in reflection mode. Each instrument manufacturer provides their own specimen holders, consisting of metallic discs with circular depressions machined to different depths to accommodate varying amounts of specimen. Other discs, known as zero-background holders (ZBHs), are made of a slice of silicon cut parallel to the 510 plane, which gives rise to no Bragg peaks in reflection mode. The sample is ground in an agate mortar, and is loaded into the metallic holders by top, back or by side loading (McMurdie *et al.*, 1986). Some silicon zero-background holders have a shallow depression machined in them, such that a small amount of powder may be loaded, but it is usual to take the flat surface, smear it with, *e.g.*, petroleum jelly, wipe it with a tissue and then sprinkle the small amount of the sample on the wiped surface. There will be sufficient adhesion to retain a thin layer of specimen after the excess is shaken off.

Specimens for transmission diffractometry may be mounted in one of three ways: as a thin planar specimen trapped between, *e.g.*, two polymer Kapton foils (8 µm; Spex-Certiprep, Stanmore, UK), or as a Debye–Scherrer cylindrical specimen in either a capillary tube, or as a minute specimen stuck on the end of a glass fibre with an adhesive such as rubber solution. The following procedure applies equally to organic and inorganic materials, with the exception of explosives, very hard abrasives, gemstones and single crystals, which for one reason or another should not be ground up: the coarse powdered sample is ground in a small agate mortar until the particle size is such that the resulting fine powder can be loaded easily into a 0.3 or 0.5 mm-diameter thin-walled glass capillary tube or sandwiched between Kapton foils. The foils are clamped between two metal rings, with a circular specimen aperture of typically 6 mm diameter. The specimen holder is spun in its own plane, which is presented perpendicular to the X-ray beam. For the Debye–Scherrer specimen, the filled tube is sealed with a flame and then mounted in modelling clay on a brass stub that fits in a standard ACA thread goniometer head, or on any stage suitable for the chosen diffractometer. The rod-like specimen is rotated about its long axis.

Large quantities (kilogrammes) of powder need to be sampled and subsampled prior to analysis, and the best way to ensure that the analytical specimen is truly representative of the bulk is to use a technique known as 'cone and quartering' (Buhrke *et al.*, 1998).

For microsamples of powder, for example those less than 1 mg in weight, a different approach may be used. The sample is carefully ground in an agate mortar as before, then a glass fibre (~0.05–0.1 mm in diameter) is dipped lightly in rubber solution and the end bearing the glue is rolled in the finely ground powder. The powder specimen is thus presented to the X-ray beam as a small-diameter cylinder. The main disadvantage here is that the beam has to pass through the adhesive and glass fibre as well as the specimen. Alternatively, a tiny ball of rubber solution (~0.5 mm diameter) can be rolled around in the powder with a needle, and the ball then speared with a thin glass fibre and mounted on the specimen stage. The glass fibre is rotated about its long axis as before.

Data are collected over an angular range appropriate to the specimen and radiation, in steps of 0.01–0.05° in 2θ.

7.2.3.3. *Specimen preparation – metals and alloys*

If the metallic specimen is of suitable dimensions, it may be placed directly on the sample stage of the diffractometer. If analysis of a large block of metal is required, a small sliver or a few filings will have to be removed, with a sharp scalpel or a clean needle file, respectively. One alloy, brass, is very common, and it occurs occasionally as a forensic sample (Rendle, 1981). Most metallic specimens need to be annealed before analysis, two common exceptions being aluminium and lead because, as relatively soft metals, any strains in them are quickly relieved at room temperature. Filings and slivers of brass, however, do require annealing in order to relieve strains within the specimen. This process ensures sharp, well defined diffraction peaks, enabling the measurement of accurate *d*-spacings. The tip of a glass Pasteur pipette is sealed in a Bunsen burner flame and the slivers or filings poured into the pipette. The part of the pipette containing the sliver or filings is then broken off and its open end sealed in a flame. The sealed tube is heated in a furnace to 773 K and slow-cooled to room temperature over 12–15 h. The sealed tube is removed from the furnace and broken open. The annealed sample is then poured out of the pipette, and the specimen, if filings, is sealed inside a thin-walled glass capillary tube as for a powder, or, if a sliver, is mounted on the end of a glass fibre with rubber solution, as for a paint flake, and placed on a diffractometer goniometer head or an equivalent sample spinner.

7.2.3.4. *Specimen preparation – monolithic (polycrystalline)*

A paint flake is a monolithic specimen, and usually consists of crystalline pigments and extenders (bulking agents such as talc and china clay) embedded in an amorphous resin. If the paint flake is multilayered, the layers can be separated and analysed individually, or analysed *in situ* if the X-ray beam is of a suitably small dimension (Kügler, 2003), otherwise the components identified by XRPD cannot be assigned to a specific layer. A glass fibre 0.05–0.1 mm in diameter is mounted in modelling clay on a brass stub. The end of the fibre is dipped lightly in rubber solution to leave a tiny deposit on the end of the fibre. The paint flake is picked up on the glued end of the fibre and teased into place with a needle probe so that it stands up on the tip of the fibre. If the flake is required for further analysis, such as analysis of the resins by pyrolysis–mass spectrometry (PyMS), water-soluble glue such as gum arabic should be used instead of rubber solution, so that the paint flake can be washed with water and removed from the fibre after XRPD analysis and prior to PyMS.

Other monolithic specimens are papers, plastics and polymers, and metallic slivers. Small specimens of these materials may be mounted and analysed by the same method as that described for paint flakes. Larger specimens of paper (Foner & Adan, 1983) may be mounted on aluminium mesh or a silicon ZBH using a suitable spray-mount adhesive. The substrate with the specimen is then placed directly in the diffractometer.

7.2.3.5. *Sample preparation – single crystal*

Single crystals of material that cannot, or should not, for a variety of reasons, be ground up are usually analysed in Gandolfi mode (Gandolfi, 1967). The reason could be that the crystal is explosive, too hard to grind (an abrasive material), too valuable (a gemstone), liable to change its crystalline form (polymorphism), or that its evidential value as a single crystal would be lost if it were crushed. XRPD data collected by a traditional point detector (one-dimensional) would not enable identification, and even data from a two-dimensional area detector may be difficult to interpret. Gandolfi mode, with its extra degree of rotational freedom for the specimen, generates a pseudo-powder pattern from a single-crystal specimen. The crystal (usually no larger than 0.5 mm in dimension) is mounted on the tip of a fine glass fibre (as for paint flakes) and placed on the Gandolfi stage.

In the case of gemstones it may be possible, if the stone has a fairly sharp culet, to mount it directly on modelling clay such that the culet just enters the X-ray beam. Powders such as barbiturates exist in many polymorphic forms, and it is known that some forms transform upon grinding into other crystalline modifications. A powdered barbiturate can be loaded directly (without grinding) into a thin-walled capillary tube, and the tube centred on the Gandolfi stage.

7.2.3.6. *Interpretation of results: identifications and comparisons, checking procedures*

When the samples have been submitted, together with details of the case circumstances, and the forensic diffractionist has collected all the diffraction data, he or she is then faced with interpreting the results. Most instrument manufacturers provide a copy of a database of powder patterns such as the ICDD Powder Diffraction File (ICDD, 2014) with their equipment, and appropriate data processing and search/match software, with some allowing the local user to input their own data collected from pure certified standard materials. This is a useful option, particularly where a lot of the submitted samples are of the same type and similar compositions are encountered on a frequent basis.

Many interpretations will be straightforward, with every diffraction peak in a pattern accounted for, but for every simple interpretation there will be at least two that are not easy, with unassigned or diffuse data. This is where additional information is often useful, for example the colour and/or the elemental composition of the specimen. The Boolean logic capabilities of the Powder Diffraction File enable one to incorporate such information within the search/match procedure. A successful, correct interpretation will depend upon the quality of the diffraction data, the interpretative skills and experience of the analyst, and also on the content and reliability of any databases that are used. It is incumbent on the analyst to ensure the quality of diffraction data by careful and consistent (in the case of control and suspect) specimen preparation, by choosing the most appropriate mode of diffractometer analysis, and by correct choice of instrumental parameters, *e.g.* radiation, filters/monochromators, slit size, beam collimator diameter, scan range, scan rate and step size. All interpretations should be checked by a second competent individual, preferably another diffractionist, before a technical report is produced. Quantitative analysis is possible on some specimens, but should be applied with caution. Forensic samples are rarely found as homogeneous and well ground powdered materials, with each component having similar particle size, no evidence of preferred orientation and similar absorption coefficients. Various methods of quantitative XRPD analysis, including Rietveld methods, are discussed by Madsen & Scarlett (2008).

7.2.3.6.1. *Use of the ICDD Powder Diffraction File and local databases*

The ICDD Powder Diffraction File (ICDD, 2014), produced and marketed by the International Centre for Diffraction Data, is recognized as *the* primary database for powder diffraction data. Both PDF-4+ (primarily inorganic) and PDF-4 Organics files are essential if powder diffraction analysis is to be one of the major analytical techniques used in a forensic science laboratory. The PDF contains within it a ‘forensic’ subfile, comprising approximately 4500 entries, of the patterns of compounds thought to be most relevant.

Most X-ray sections within forensic science laboratories will have their own local databases, usually built up over a period of time, when it becomes apparent what the most frequently encountered substances are. The laboratory must be careful to obtain pure, accredited specimens whose chemical composition is proven for producing standard diffraction patterns in-house. A specialized database of the powder patterns of forensically relevant substances complete with a search/match routine (Fischer & Goebel, 1984) was produced in 1984.

The most rapid and efficient approach is to use the locally generated standard powder patterns first, followed by the PDF forensic subfile, and then finally the whole PDF if there are still diffraction peaks unaccounted for.

7.2.3.7. *Data archives for statistical and reference purposes*

Once the interpretation has been completed and checked, and the report or statement written, the matter of filing and archiving the analytical results remains. The retention of case files, with all their information, is at the discretion of the local judicial system, and the seriousness of the crime will usually dictate the length of time for which the files are kept. Digital diffraction data tend to be archived automatically by the commercial software, but the retention of analytical interpretations will be a matter of local preference. It is a relatively simple task to set up and populate a spreadsheet with analytical results obtained from, for example, paint analyses or drug analyses, updating the spreadsheet at regular intervals, and this practice is highly recommended. In this way a useful reference system can be built up, and the data can be classified and cross-referenced in different ways. For example, paints can be classified as household, automobile, tool, security, each in terms of its colour. The household paints can be classified further as emulsion or enamel, gloss, undercoat or primer. Automobile paints can be listed under metallic or non-metallic finish. All paints can be re-classified according to their pigments, fillers and extenders.

Recording the results of drug analyses is of greatest benefit when the excipients, adulterants or impurities such as precursors and by-products of attempted syntheses are also included. A database of this kind may be searched easily and quickly, identifying mixtures of similar composition, possibly indicating a common source and providing, in a simple way, drugs intelligence. Powder diffraction patterns of prescription or over-the-counter drugs can be useful in identifying formulations. Paint flakes found on the clothing of the victim of a hit-and-run

Table 7.2.1
Statistics generated from a decade of drug analysis by XRPD

(*a*) Relative percentages of drug types analysed by XRPD over a period of ten years.

Drug	1980	1989
Heroin base	7	31
Heroin·HCl·H_2O	26	<1
Cocaine·HCl	21	29
Cocaine base	2	4
DL-Amphetamine sulfate	37	34
D- or L-Amphetamine sulfate	4	<1
Others	3	2

(*b*) Percentage of amphetamine, heroin base and cocaine·HCl seizures containing one or more of the carbohydrate excipients glucose, mannitol, lactose and sucrose analysed by XRPD over the period 1980–1989.

Drug	Glucose	Mannitol	Lactose	Sucrose
Amphetamine	87	46	10	2
Heroin base	23	12	2	1
Cocaine·HCl	42	35	15	<1

automobile accident can often lead, on forensic analysis and with the co-operation of the major automobile manufacturers, to the make, model and year of the car involved.

Household, garage or garden chemicals may be used in the commission of a crime, and it is of help to purchase quantities of the genuine articles as control samples and to acquire their powder diffraction patterns. These data will then form part of another database.

Keeping records of the type described can be very useful over a long period of time. Trends in drug usage may be revealed, together with trends in the use of excipients and adulterants (Table 7.2.1). Declining use of one drug may be counterbalanced by a rise in use of another (Rendle, 2004). Paint analyses may reveal a gradual replacement of older inorganic pigments by more modern organic pigments (Susich, 1950; Kamarchik, 1980; Curry *et al.*, 1982). Extenders and fillers in paints may change for economic reasons. Statistics like this, however simple, all serve as very useful background information for a court-going scientist.

7.2.3.8. *Continuity of evidence*

The chain of custody, evidentiary chain, or continuity of evidence is a crucial aspect of any forensic process. Items of evidence are submitted to the laboratory, in sealed, labelled exhibit bags, following strict rules in order to preserve the integrity of the items and their admissibility in court. Records of items requiring any chemical analysis must be kept in such a way that the movement and location of any item can be followed by an audit trail. Diffraction patterns must be labelled electronically such that they can be associated with one, and only one, specimen. Any samples submitted for analysis should be signed for, in the presence of the person who requests the analysis, and kept in a secure location until the analysis is complete. If the forensic science laboratory has a laboratory information management system (LIMS) that employs barcoding, then each new sample brought into the X-ray laboratory will be assigned a unique barcode which will remain with that sample and act as its identifier throughout the entire analytical process. Such systems can be expensive, however, and many laboratories still rely upon manual computer entries. This requires diligence on the part of staff, and rigorous adherence to protocol in order to prevent errors that may then be propagated through the evidentiary chain. It is perfectly within the right of the court to insist on seeing a printout of the laboratory logbook, in order to be convinced of the integrity of the whole analytical process.

Particular care is needed if the X-ray diffractometer has an automatic sample changer which has to be loaded manually, and in which a specific sample *must* be placed in a specific location. If a barcode system is in place then the likelihood of errors here is less, because the controlling software will detect a mismatch between the sample barcode and the barcode of its position on the holder. If manual loading is the norm, then each loading process should be witnessed by another X-ray diffractionist, and the signatures of both recorded as confirmation.

Continuity can be aided by removing one stage of the process, and that is by 'through the bag analysis'. Powdered materials, such as suspected illicit drugs, may be analysed, under certain circumstances, by diffractometry without removing the powder from its packaging (Rogers, 2012) (Fig. 7.2.1).

7.2.3.9. *Presentation of evidence to the court*

Procedures will vary from country to country, but in general the scientist can be expected to be questioned quite thoroughly by a well briefed counsel (Camp, 1979). The witness's academic and professional qualifications, or lack of them, are tackled first, thus establishing his or her credibility. Then counsel may ask how long they have worked as a forensic scientist and for how long in X-ray diffraction. Reference to the items analysed by XRPD follows, and the diffractionist may be asked to explain to the court, in layman's terms, how XRPD works. It is important to avoid scientific jargon, and development of a simple analogy is often the best approach.

Continuity of evidence will most certainly be questioned, with the analyst being asked if he or she is sure that the analytical results being reported are indeed those from the specimens submitted for analysis. Adherence to published quality-assurance procedures will also be queried. This will cover all specimen preparation procedures, the correct use of the X-ray instrument used for the analysis, correct computer entry of specimen details, unique labelling of diffraction patterns, and interpretation of the results. Any deviation from the laboratory's own published procedures, without very good reason, will be noted and used to undermine the validity of the work. The scientist may be asked to provide proof of validation of the XRPD method used in their laboratory, according to internationally recognized standards (Eckardt *et al.*, 2012).

Having got thus far, the diffractionist will be questioned on the results obtained from X-ray analysis of the evidential items, and the depth of questioning will depend upon whether or not counsel has a diffractionist briefing him or her. Questions on the suitability of XRPD for the analysis of the samples may be raised, and the analyst may be asked why he or she did not use another technique. It is here that the analyst must be aware of the alternative methods of analysis, and their pros and cons. As an expert witness, the analyst will usually be permitted to qualify his or her statements, and not be restricted to yes/no answers. The source of standard diffraction data may be queried, and it is advantageous to be able to say that one has used the most up-to-date database, such as the ICDD Powder Diffraction File (ICDD, 2014), in one's interpretations.

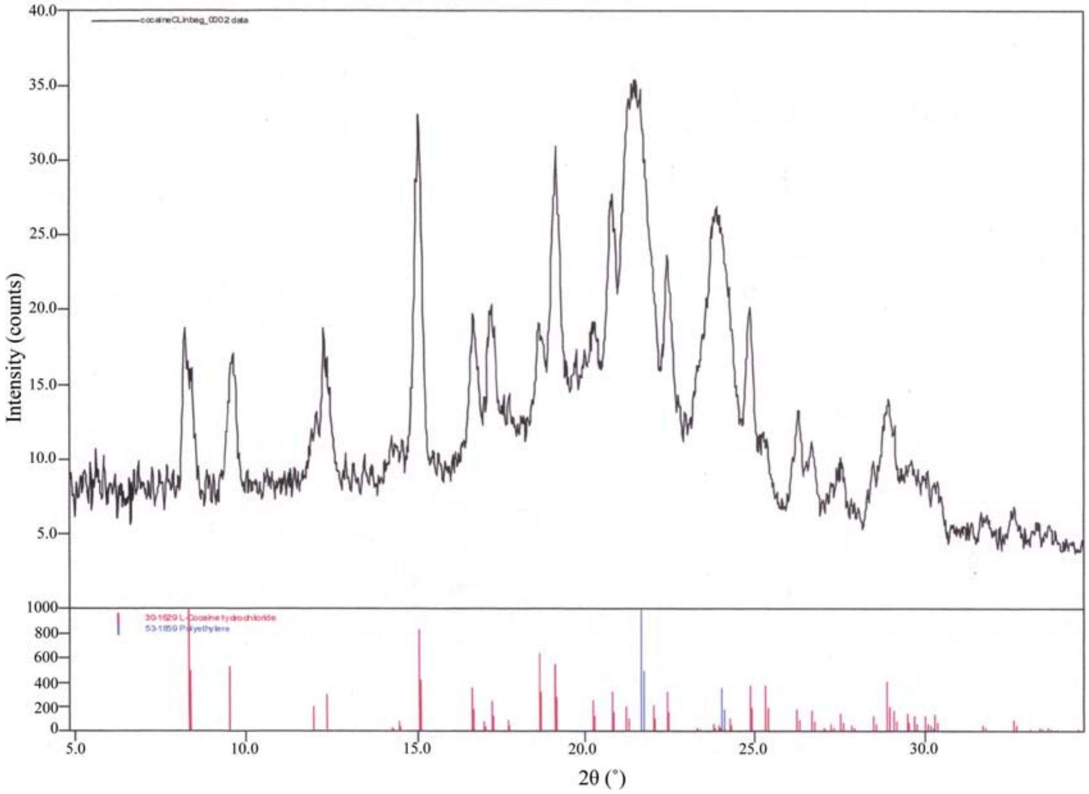

Figure 7.2.1
A powder pattern of cocaine hydrochloride (PDF No. 00-030-1629; red peaks in lower plot) acquired through a polyethylene bag (PDF No. 00-053-1859; blue peaks in lower plot). The pattern was acquired in 60 s using a Bruker D8 GADDS two-dimensional detector.

7.2.4. Examples of forensic casework involving the use of XRPD

7.2.4.1. *Criminal damage to an automobile*

A Porsche automobile belonging to a known criminal had been seized and impounded by the local police, pending charges against the man. However, evidence against the man was weak and charges were dropped. He was released and was allowed to reclaim his car. After a week he reported to the police that his car had gradually lost all power and he accused them of tampering with the engine.

The car was examined and oil from the sump was drained and filtered. A small amount of dark, very hard particles was found in the residue from the oil. A single particle was mounted on a glass fibre and rotated in Gandolfi mode using a Bruker D8 GADDS two-dimensional detector. Fig. 7.2.2 shows the particle, its two-dimensional XRPD pattern and its digitized pattern. The pattern is a match with that of silicon carbide (PDF No. 00-049-1428).

Under questioning, one of the police officers admitted to having removed the sparking plugs when the car was impounded, and to pouring valve grinding paste into the cylinders – hence the silicon carbide.

7.2.4.2. *Fatal road traffic accident*

A motorcyclist was killed in a head-on collision with an automobile. The driver of the car claimed that he had not seen the motorcyclist because he (the motorcyclist) had not had his headlight switched on. Other motorists who witnessed the accident said that the motorcyclist's headlight was definitely switched on.

Upon examining the motorcycle wreck, the headlamp bulb was found to be shattered. Microscopic examination of the bulb revealed traces of a pale yellow powder on the bulb filament and on the inside of the remains of the glass envelope. A very small amount of the powder was picked up with rubber solution on the end of a glass fibre and rotated in Debye–Scherrer mode using a

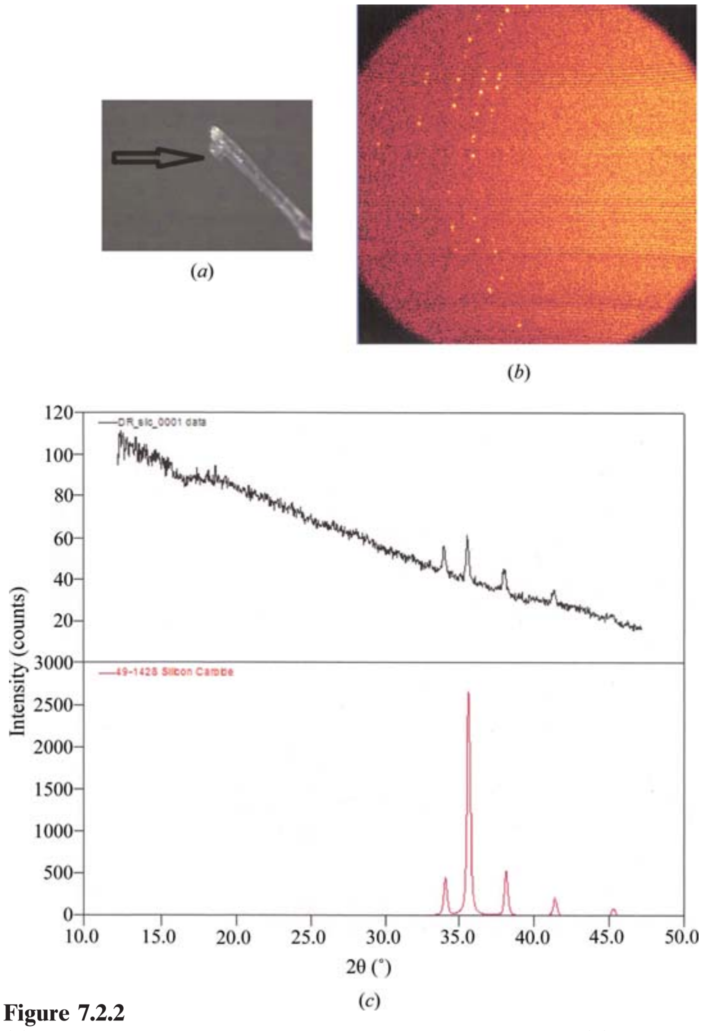

Figure 7.2.2
(*a*) A particle from vehicle oil mounted on a glass fibre, (*b*) the two-dimensional Gandolfi pattern and (*c*) the integrated digitized pattern (top) and PDF pattern (bottom) No. 00-49-1428 of silicon carbide (SiC).

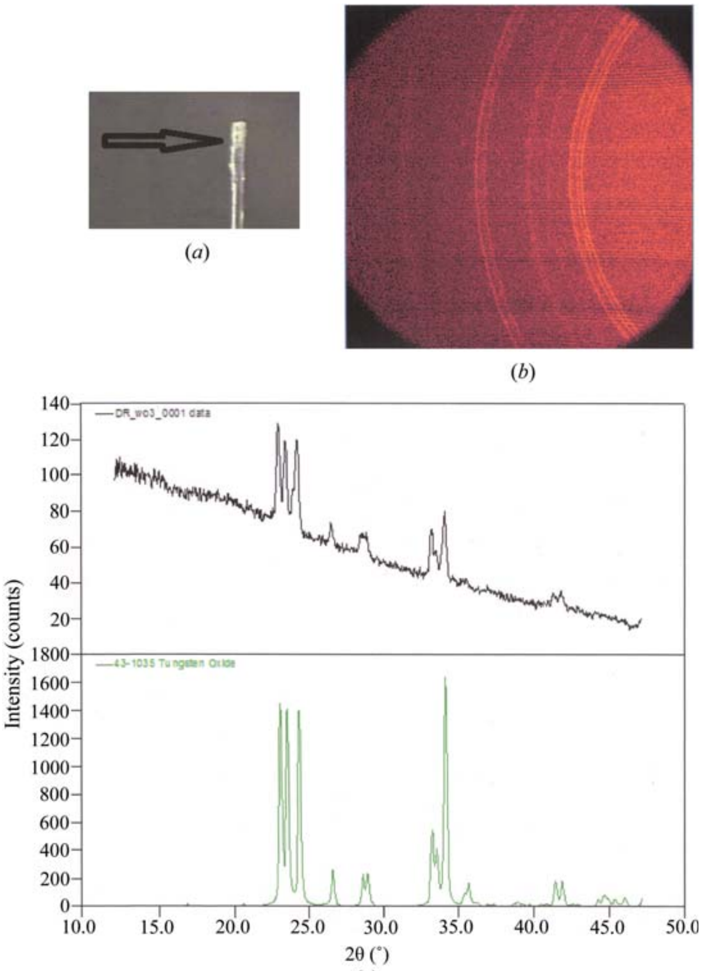

Figure 7.2.3
(*a*) Yellow powder particles glued to a glass fibre, (*b*) their two-dimensional Debye–Scherrer powder pattern and (*c*) the digitized powder pattern (top) and PDF pattern (bottom) No. 00-043-1035 of tungsten oxide (WO_3).

Bruker D8 GADDS two-dimensional detector. Fig. 7.2.3 shows the powder on the glass fibre, its two-dimensional XRPD pattern and its digitized pattern. The pattern is a match with that of tungsten oxide (WO_3) (PDF No. 00-043-1035).

The presence of tungsten oxide is proof that the headlight was switched on at the moment of impact. The tungsten filament was at white heat when the bulb was shattered and reacted with the oxygen in the atmosphere, forming tungsten oxide.

7.2.4.3. *Attempted murder?*

A young woman and her boyfriend had dinner together at his apartment. Later in the evening they argued and she went back to her own apartment, where she fell asleep. During the night she was violently ill and the next morning went to the local police station and accused her (now ex-) boyfriend of attempting to poison her. Samples of the food and wine consumed were collected by scenes-of-crime officers and sent for analysis. Two wine corks appeared to have some purplish solid residue and this was scraped off and ground thoroughly before examination by reflection geometry XRPD using a PANalytical X'Pert Pro diffractometer. A specimen was mounted for XRPD, and the result of a search/match using ICDD's PDF-4 Organics database was a match with the pattern for potassium bitartrate (PDF No. 02-075-1610).

This material is not poisonous. Tartaric acid occurs naturally in grapes and it reacts with potassium ions found in grape skins. Potassium bitartrate crystals are colourless ('wine diamonds') but can take on the colour of the wine. It would appear that the woman's illness had more to do with over-imbibing than to an attempt by her boyfriend to poison her.

7.2.4.4. *Synthesis of crack cocaine*

Crack cocaine is cocaine free base. It may be synthesised fairly simply by heating cocaine hydrochloride with sodium bicarbonate. If the synthesis is carried out carefully, the final products should be cocaine free base and sodium chloride. The presence of any additional compounds would indicate a poor synthesis.

A number of persons suspected of being in possession of controlled substances were arrested. All seizures were sent to the laboratory for analysis. Each produced a very similar powder diffraction pattern to the others, so the police had good reason to suspect that only one dealer was involved. One of the arrested gave information as to the location of the alleged dealer and the address was raided, a man taken into custody, and a large bag of white powder together with drugs paraphernalia taken for examination. Interpretation of the XRPD pattern of the powder from the suspected dealer's house, using the PDF-4+ database, revealed the presence of cocaine base (00-006-0153), sodium chloride (00-005-0628) and sodium bicarbonate (00-015-0700).

The composition of this powder was found to be very similar to those of each of the powders found on the people arrested. The presence of sodium bicarbonate indicated a rather careless synthesis, but in this instance its presence in both the stock supply, and in each of the individual seizures, constituted valuable information from a comparison viewpoint.

This evidence together with that supplied by other witnesses was sufficient to convict the dealer.

7.2.5. Summary

7.2.5.1. *Advantages and limitations of XRPD in forensic science*

The preceding paragraphs demonstrate that XRPD is a very useful technique to have for analysing solid materials that are either wholly or partially crystalline. Its advantages over some other analytical techniques are:

1. its ability to identify *compounds* rather than just elements or functional groups;
2. its non-destructive nature;
3. its versatility;
4. its ability to analyse mixtures of materials;
5. its ability to cope with microgramme to gramme-sized specimens, and single crystals;
6. its lack of need of special preparation for powder specimens – simple grinding is required;
7. its ability to distinguish polymorphs;
8. its ability to distinguish racemic materials from their optically active counterparts;
9. its ability to distinguish between a series of hydrated forms of a given compound; and
10. its ability to be both a qualitative and a quantitative method of analysis.

Disadvantages include the fact that one cannot analyse liquids or gases, and that XRPD is not generally a suitable technique for analysing amorphous materials, although there may be cases in which it can be useful. It is not a true trace technique; low levels of a substance in a mixture may go undetected.

The type or types of material one is called upon to analyse, and the kind of information desired, will dictate the analytical methods used, but if one is concerned mainly with solid specimens, XRPD has few rivals. In terms of cost, the original outlay for capital equipment items such as the X-ray generator and diffractometer can seem relatively high, but when one considers the expected lifetime of at least ten to fifteen years, it is very reasonable. Sealed X-ray tubes and specimen mounts are the main consumables, and neither liquid nitrogen nor liquid helium is required.

7.2.5.2. *Thoughts on the future*

The need for rapid results is a subject that is frequently raised at meetings between forensic scientists and the law-enforcement agencies they serve. As well as reducing turnaround times for laboratory analyses, the provision of scientific information *at the crime scene* can be extremely useful to the investigating officer. This is where truly portable equipment is required, and one such example provides both XRPD and XRF analysis on a 15 mg specimen (Inxitu, 2012). This device uses a microfocus X-ray tube with pinhole collimation and a solid-state CCD detector to acquire both the X-ray powder pattern and an XRF spectrum. Simultaneous acquisition of elemental composition helps narrow the range of compounds selected during a search/match procedure. A novel sample vibration chamber helps alleviate problems of preferred orientation within the specimen. Undoubtedly concerns will be raised as to the dangers of using X-rays at a crime scene, but the design of equipment such as that described above is such that there are no safety issues, as primary and scattered X-radiation are fully contained.

Miniaturization and portability of analytical equipment have long been goals both for forensic scientists and instrument manufacturers, and to a certain extent those goals have been achieved, but there is always a price to pay, and here it is in the quality of the resulting diffraction patterns. One should never expect the same quality of data from portable equipment as from laboratory-based diffractometers, but as long as the use of portable equipment is for quick identification purposes at a crime scene, for example, then this is quite acceptable. Equipment based upon energy-dispersive X-ray diffraction is an attractive option because of the absence of moving parts, but until solid-state detectors of suitable energy resolution are available, this mode of data collection will remain largely confined to that of screening duties.

There is currently sufficient variety in the design of laboratory powder diffractometers, which, with autosamplers and rapid data acquisition times, already guarantee fast turnaround times. There may be a demand for more two-dimensional area detectors in order to cope with minute powdered specimens or single crystals, and monolithic specimens exhibiting strong preferred orientation. Diffractometers capable of exploring the back-reflection region would be a useful addition, thus enabling accurate measurement of unit-cell parameters and hence discrimination between, for example, metallic specimens of closely similar composition, and solid solutions of minerals. Databases containing atomic coordinates, as well as powder patterns, for the most common materials will be sought after, as they would enable quantitative analysis by the Rietveld method for most specimens.

Most important of all, if a forensic science laboratory has XRPD equipment, retention of an XRPD expert is essential in order to maintain consistency in all aspects of the analytical process. Having a technician to maintain the instrument is essential, but the presence of an expert is needed for specimen preparation, choice of mode of analysis, interpretation of results and preparation of statements. The instrumental aspects of XRPD may become in time, as with many other analytical techniques, more 'black box' in nature, but the additional skills of an in-house expert will always be needed. Some laboratories may entertain the idea of providing a 'walk-up' service in XRPD, in which the person requesting the analysis is permitted to prepare the specimen themselves and mount it on the diffractometer, in order to economize on staff and time. This is false economy. It may be acceptable when the analytical technique is solution-based and the person has only to weigh out a specimen, dissolve it in solvent and place the solution in a vial (as for GC-MS). For XRPD analysis the practice should be discouraged for obvious reasons; specimen preparation is a crucial part of a successful analysis, and should be left to a full-time diffractionist.

The author wishes to acknowledge Professor K. D. Rogers and Dr S. Beckett for their helpful criticism during the preparation of this chapter. The comments and constructive suggestions made by the referees and the editors are also acknowledged.

References

Abel, J. E. & Kemmey, P. J. (1975). *Identification of explosives by X-ray diffraction*. Technical Report 4766, Research Laboratory, Picatinny Arsenal, Dover, New Jersey, USA.

Abraham, J. T., Shukla, S. K. & Singh, A. K. (2007). *Application of X-ray diffraction techniques in forensic science*. *Forensic Sci. Commun.* **9**, No. 2, April. http://www.fbi.gov/about-us/lab/forensic-science-communications/fsc/april2007/research/2007_04_research03.htm.

Azoury, M. & Levin, N. (1998). *Identification of zinc phosphide in a falsely labelled rodenticide bait. J. Forensic Sci.* **43**, 693–695.

Barnes, W. H. (1954). *Physical methods for the identification of narcotics, Part IIA. The X-ray diffraction method on powder*. *Bull. Narc.* **6**, No. 1 (January–April), 20–31.

Barnes, W. H. & Sheppard, H. M. (1954). *Physical methods for the identification of narcotics (contd.), Part IIB. X-ray diffraction powder data for eighty-three narcotics*. *Bull. Narc.* **6**, No. 2 (May–August), 27–68.

Barrick, J. C., Polk, D. E., Raman, R. V. & Giessen, B. C. (1977). *Forensic applications of X-ray diffraction. I: Differentiation of piperidyl benzilates and related glycolates by micro-X-ray diffraction*. *J. Forensic Sci.* **22**, 515–523.

Bebris, G. (2003). *Road dust mineral composition analysis with powder X-ray diffraction of unpaved roads*. *Proceedings of the 3rd European Academy of Forensic Science Meeting, Istanbul, Turkey*. *Forensic Sci. Intl*, **136**, Supplement 1, 106–107.

Beckett, S., Rogers, K. D. & Clement, J. G. (2011). *Inter-species variation in bone mineral behaviour upon heating*. *J. Forensic Sci.* **56**, 571–579.

Bell, S. E. J., Stewart, S. P. & Speers, S. J. (2012). *Raman spectroscopy of drugs of abuse*. In *Infrared and Raman Spectroscopy in Forensic Science*, edited by J. M. Chalmers, H. G. M. Edwards & M. D. Hargreaves. Chichester: John Wiley & Sons, Ltd. doi:10.1002/9781119962328.ch6.

Bentley, J. & Turner, G. P. A. (1998). *Introduction to Paint Chemistry and Principles of Paint Technology*, 4th ed., pp. 105–106. London: Chapman & Hall.

Bergslien, E. T., Bush, M. & Bush, P. J. (2008). *Identification of cremains using X-ray diffraction spectroscopy and a comparison to trace element analysis*. *Forensic Sci. Intl*, **175**, 218–226.

Beveridge, A., Fung, A. & MacDougall, D. (2001). *Use of infrared spectroscopy for the characterisation of paint fragments*. In *Forensic Examination of Glass and Paint: Analysis and Interpretation*, edited by B. Caddy, pp. 183–241. Taylor & Francis Forensic Science Series. London: Taylor & Francis.

Beveridge, A. D. (2010). *Forensic Investigation of Explosions*, 2nd ed. London: Taylor & Francis.

Beveridge, A. D., Payton, S. F., Audette, R. J., Lambertus, A. J. & Shaddick, R. C. (1975). *Systematic analysis of explosive residues*. *J. Forensic Sci.* **20**, 431–454.

Brown, A. G. (2006). *The use of forensic botany and geology in war crimes investigations in NE Bosnia*. *Forensic Sci. Intl*, **163**, 204–210.

Buhrke, V. E., Jenkins, R. & Smith, D. K. (1998). Editors. *A Practical Guide for the Preparation of Specimens for X-ray Fluorescence and X-ray Diffraction Analysis*. New York: John Wiley & Sons, Inc.

Camp, M. J. (1979). *Special problems in forensic materials analysis by XRD*. In *Advances in X-ray Analysis*, **22** (Proceedings of the 27th Annual Conference on Applications of X-ray Analysis, Denver, August 1–4, 1978), edited by G. J. McCarthy, C. S. Barrett, D. E. Leyden, J. B. Newkirk & C. O. Ruud, pp. 13–17. New York: Plenum Press.

Canfield, D. V. & De Forest, P. R. (1977). *The use of the Gandolfi camera as a screening and confirmation tool in the analysis of explosives residue*. *J. Forensic Sci.* **22**, 337–348.

Castle, D. A. (1982). *Pigment analysis in the forensic examination of paints. II. Analysis of motor vehicle paint pigments by chemical tests*. *J. Forensic Sci. Soc.* **22**, 179–186.

Causin, V., Marega, C., Carresi, P., Schiavone, S. & Marigo, A. (2007). *A quantitative differentiation method for plastic bags by wide angle X-ray diffraction for tracing the source of illegal drugs*. *Forensic Sci. Intl*, **168**, 37–41.

Causin, V., Marega, C., Marigo, A., Casamassima, R., Peluso, G. & Ripani, L. (2010). *Forensic differentiation of paper by X-ray diffraction and infrared spectroscopy*. *Forensic Sci. Intl*, **197**, 70–74.

Cheng, C., Kirkbride, T. E., Batchelder, D. N., Lacey, R. J. & Sheldon, T. G. (1995). *In situ detection and identification of trace explosives by Raman spectroscopy*. *J. Forensic Sci.* **40**, 31–37.

Clarke, E. G. C. (1962). *The isolation and identification of alkaloids*. In *Methods of Forensic Science*, Vol. 1, edited by F. Lundquist, p. 20. New York, London: Wiley Interscience.

Cook, E., Fong, R., Horrocks, J., Wilkinson, D. & Speller, R. (2007). *Energy dispersive X-ray diffraction as a means to identify illicit materials: a preliminary optimisation study*. *Appl. Radiat. Isot.* **65**, 959–967.

Curry, C. J., Rendle, D. F. & Rogers, A. (1982). *Pigment analysis in the forensic examination of paints. I. Pigment analysis by X-ray powder diffraction*. *J. Forensic Sci. Soc.* **22**, 173–177.

Dawson, L. A. & Hillier, S. (2010). *Measurement of soil characteristics for forensic applications*. *Surf. Interface Anal.* **42**, 363–377.

Dicken, A. J., Evans, J. P. O., Rogers, K. D., Greenwood, C., Godber, S. X., Prokopiou, D., Stone, N., Clement, J. G., Lyburn, I., Martin, R. M. & Zioupos, P. (2015). *Energy-dispersive X-ray diffraction using an annular beam*. *Opt. Express*, **23**, 13443–13454.

Dicken, A., Rogers, K., Godber, S., Prokopiou, D., Shevchuk, A., Tranfield, G. & Evans, P. (2014). *Validation study of a ray tracing simulator for focal construct geometry*. *Appl. Radiat. Isot.* **94**, 235–240.

Dicken, A., Shevchuk, A., Rogers, K., Godber, S. & Evans, P. (2015). *High energy transmission annular beam X-ray diffraction*. *Opt. Express*, **23**, 6304–6312.

Durães, N., Cortez, D., Algarra, M., Sánchez, F. G., Rodríguez-Borges, J. E., Bobos, I. & Esteves da Silva, J. C. G. (2010). *Comparison of adipocere formation in four soil types of the Porto (Portugal) district*. *Forensic Sci. Intl*, **195**, 168.e1–168.e6.

Eckardt, R., Krupicka, E. & Hofmeister, W. (2012). *Validation of powder X-ray diffraction following EN ISO/IEC 17025*. *J. Forensic Sci.* **57**, 722–737. doi:10.1111/j.1556-4029.2011.02025.x.

Eiceman, G. A., Schmidt, H. & Cagan, A. A. (2007). *Explosives detection using differential mobility spectrometry*. In *Counterterrorist Detection of Explosives*, edited by J. Yinon, pp 61–90. Amsterdam: Elsevier BV.

Farmer, N. L., Ruffell, A., Meier-Augenstein, W., Meneely, J. & Kalin, R. M. (2007). *Forensic analysis of wooden safety matches–a case study*. *Sci. Justice*, **47**, 88–98.

Ferguson, G., Kaitner, B., Connett, B. E. & Rendle, D. F. (1991). *Structure of the α-D-glucose–sodium chloride–water complex (2/1/1)*. *Acta Cryst.* B**47**, 479–484.

Ferris, T. J. & Went, M. J. (2012). *Synthesis, characterisation and detection of gamma-hydroxybutyrate salts*. *Forensic Sci. Intl*, **216**, 158–162.

Fischer, R. & Goebel, R. (1984). *Computer-aided X-ray diffraction identification of crystalline mixtures in forensic science investigations*. *J. Forensic Sci.* **29**, 155–162.

Fischer, R. & Hellmiss, G. (1989). *Principles and forensic applications of X-ray diffraction and X-ray fluorescence*. In *Advances in Forensic Science*, Vol. 2, *Instrumental Analysis and its Applications in Forensic Science*, edited by H. C. Lee & R. E. Gaensslen, pp. 129–158. Chicago: Year Book Medical Publishers Inc.

Fitzpatrick, R. W. & Raven, M. D. (2005). *Soil mineralogy and other properties in forensic investigations*. *Acta Cryst.* A**61**, c14. http://iucr2005.iucr.org/ms6.htm.

Fitzpatrick, R. W., Raven, M. D. & Forrester, S. T. (2009). *A systematic approach to soil forensics: criminal case studies involving transference from crime scene to forensic evidence*. In *Criminal and Environmental Soil Forensics*, edited by K. Ritz, L. A. Dawson & D. Miller, pp. 105–127. Heidelberg: Springer Science+Business Media BV.

Folen, V. A. (1975). *X-ray powder diffraction data for some drugs, excipients, and adulterants in illicit samples*. *J. Forensic Sci.* **20**, 348–372.

Foner, H. A. & Adan, N. (1983). *The characterisation of papers by X-ray diffraction (XRD): measurement of cellulose crystallinity and determination of mineral composition*. *J. Forensic Sci. Soc.* **23**, 313–321.

Forbes, S. L., Dent, B. B. & Stuart, B. H. (2005). *The effect of soil type on adipocere formation*. *Forensic Sci. Intl*, **154**, 35–43.

Gandolfi, G. (1967). *Discussion upon methods to obtain X-ray 'powder patterns' from a single crystal*. *Mineral. Petrogr. Acta*, **13**, 67–74.

Gill, P., Jeffreys, A. J. & Werrett, D. J. (1985). *Forensic application of DNA 'fingerprints'*. *Nature (London)*, **318**, 577–579.

Gross, H. (1962). *Criminal Investigation*, 5th ed. London: Sweet and Maxwell Ltd.

Gross, S. T. & Oberst, F. W. (1947). *Microanalysis of opiates by X-ray diffraction*. *J. Lab. Clin. Med.* **32**, 94–101.

Hamer, P. S. (1982). *Pigment analysis in the forensic examination of paints. III. A guide to motor vehicle paint examination by transmitted light microscopy*. *J. Forensic Sci. Soc.* **22**, 187–192.

Harding, G. & Harding, A. (2007). *X-ray diffraction imaging for explosives detection*. In *Counterterrorist Detection of Explosives*, edited by J. Yinon, pp. 199–235. Amstersdam: Elsevier BV.

Hays, P. A. (2005). *Proton nuclear magnetic resonance spectroscopy (NMR) methods for determining the purity of reference drug standards and illicit forensic drug seizures*. *J. Forensic Sci.* **50**, 1–19.

Hayward, I. P., Kirkbride, T. E., Batchelder, D. N. & Lacey, R. J. (1995). *Use of a fibre optic probe for the detection and identification of explosive materials by Raman spectroscopy*. *J. Forensic Sci.* **40**, 883–884.

He, B. B. (2009). *Two-dimensional X-ray diffraction.* New Jersey: John Wiley & Sons, Inc.

Heijnen, W., van de Craats, A., de Koeijer, J., Koomen, L. & Warmerdam, M. (2005). *Applications of XRD in forensic casework*. *Acta Cryst.* A**61**, c14–c15. http://iucr2005.iucr.org/ms6.htm.

Heilman, W. R. (1960). *Non-destructive infrared and X-ray diffraction analyses of paints and plastics*. *J. Forensic Sci.* **5**, 338–345.

Henson, M. L. & Jergovich, T. A. (2001). *Scanning electron microscopy and energy dispersive X-ray spectrometry (SEM/EDS) for the forensic examination of paints and coatings*. In *Forensic Examination of Glass and Paint: Analysis and Interpretation*, edited by B. Caddy, pp. 243–272. Taylor & Francis Forensic Science Series. London: Taylor & Francis.

Hida, M., Sato, H., Sugawara, H. & Mitsu, T. (2001). *Classification of counterfeit coins using multivariate analysis with X-ray diffraction and X-ray fluorescence methods*. *Forensic Sci. Intl*, **115**, 129–134.

Higgs, D. G., Jones, P. N., Markham, J. A. & Newton, E. (1978). *A review of explosives sabotage and its investigation in civil aircraft*. *J. Forensic Sci. Soc.* **18**, 137–159.

Huang, T.-Y. (1953). *The identification of barbiturates in forensic chemistry by the X-ray diffraction method*. *Dan. Tidsskr. Farm.* **27** (Suppl. 1), 7–58.

Huang, T.-Y. & Jerslev, B. (1951). *On the use of X-ray powder patterns for identification of barbiturates in forensic chemistry*. *Acta Pharmacol. Toxicol.* **7**, 227–230.

Hubach, C. E. & Jones, F. T. (1950). *Methadon hydrochloride optical properties, microchemical reactions, and X-ray diffraction data*. *Anal. Chem.* **22**, 595–598.

Hull, A. W. (1919). *A new method of chemical analysis*. *J. Am. Chem. Soc.* **41**, 1168–1175.

ICDD (2014). *PDF-4+ 2012 & PDF-4 Organics 2014 Databases*, edited by Dr S. Kabekkodu, International Centre for Diffraction Data, Newtown Square, PA, USA.

Inxitu (2012). (Now Olympus.) https://www.olympus-ims.com/en/xrf-xrd/mobile-benchtop-xrd/terra.

Jackson, J. V. (1977). Personal communication.

Jenkins, R. & Snyder, R. L. (1996). *Introduction to X-ray powder diffractometry*. In *Chemical Analysis*, Vol. 138. New York: John Wiley & Sons Inc.

Kamarchik, P. Jr (1980). *Quantitative crystalline pigment analysis by X-ray diffraction*. *J. Coat. Technol.* **52**, 79–82.

Keaney, A., Ruffell, A. & McKinley, J. (2009). *Geological trace evidence: forensic and legal perspectives*. In *Criminal and Environmental Soil Forensics*, edited by K. Ritz, L. A. Dawson & D. Miller, pp. 221–237. Heidelberg: Springer Science+ Business Media BV.

Klug, H. P. & Alexander, L. E. (1974). *X-ray Diffraction Procedures for Polycrystalline and Amorphous Materials*, 2nd ed., pp 389–391. New York: John Wiley & Sons Inc.

Kotrlý, M. (2007). *Using X-ray diffraction in forensic science*. *Z. Kristallogr.* **222**, 193–198.

Kotrlý, M. (2011). *Practical experience with powder XRD microdiffraction in forensic science field*. *Acta Cryst.* A**67**, C198–C199.

Kotrlý, M. & Bezdička, P. (2006). *X-ray powder diffraction in forensic practice*. http://www.xray.cz/xray/csca/kol2006/abst/kotrly.htm.

Kügler, W. (2003). *X-ray diffraction analysis in the forensic science: The last resort in many criminal cases*. In *Advances in X-ray Analysis*, Vol. 46 (Proceedings of the 51st Annual Conference on Applications of X-ray Analysis, Colorado Springs, 29 July – 2 August 2002), edited by T. C. Huang, V. E. Buhrke, J. V. Gilfrich, G. J. Havrilla, I. C. Noyan & R. L. Snyder, pp. 1–16. New York: Plenum Press. http://www.icdd.com/resources/axa/vol46/v46_01.pdf.

Kügler, W. (2005). *Application of X-ray diffraction in the Forensic Science Laboratory of Stuttgart, Germany*. *Acta Cryst.* A**61**, C14. http://iucr2005.iucr.org/ms6.htm

Lacey, R. J., Hayward, I. P., Sands, H. S. & Batchelder, D. N. (1996). *Characterisation and identification of contraband using UV resonant Raman spectroscopy*. Proceedings of the Photonics East SPIE Meeting, Boston, 18–22 November. *SPIE*, **2937**, 100–105.

Lawrence, A. H. (1987). *Detection of drug residues on the hands of subjects by surface sampling and ion mobility spectrometry*. *Forensic Sci. Intl*, **34**, 73–83.

Laza, D., Nys, B., De Kinder, J., Kirsch-De Mesmaeker, A. & Moucheron, C. (2007). *Development of a quantitative LC-MS/MS method for the analysis of common propellant powder stabilizers in gunshot residue*. *J. Forensic Sci.* **52**, 842–850.

Liberman, M. (2000). *U.S. customs laboratories*. In *Industrial Applications of X-ray Diffraction*, edited by F. H. Chung & D. K. Smith, pp. 677–685. New York: Marcel Dekker Inc.

Lloyd, J. B. F. (1983). *High performance liquid chromatography of organic explosives components with electrochemical detection at a pendent mercury drop electrode*. *J. Chromatogr.* **257**, 227–236.

López-López, M., Delgado, J. J. & Garcia-Ruiz, C. (2012). *Ammunition identification by means of the organic analysis of gunshot residues using Raman spectroscopy*. *Anal. Chem.* **84**, 3581–3585.

Lynch, B. J. & Kerrigan, G. C. (1981). *Identification of single fibres by X-ray diffraction in forensic analysis*. *X-ray Spectrom.* **10**, 196–197.

McCrone, W. C. & Delly, J. G. (1973). *The Particle Atlas Edition Two*, Vol. II, *The Light Microscopy Atlas*. Ann Arbor: Ann Arbor Science.

McMurdie, H. R., Morris, M. C., Evans, E. H., Paretzkin, B. & Wong-Ng, W. (1986). *Methods of producing standard X-ray diffraction powder patterns*. *Powder Diffr.* **1**, 40–43.

Madsen, I. C. & Scarlett, N. V. Y. (2008). *Quantitative phase analysis*. In *Powder Diffraction Theory and Practice*, edited by R. E. Dinnebier & S. J. L. Billinge. Cambridge: The Royal Society of Chemistry.

Mann, R. W., Feather, M. E., Tumosa, C. S., Holland, T. D. & Schneider, K. N. (1998). *A blue encrustation found on skeletal remains of Americans missing in action in Vietnam*. *Forensic Sci. Intl*, **97**, 79–86.

Marvin, B. & Garbarino, J. J. (1953). *The identification of barbiturates, narcotics, and patented specialties by X-ray diffraction*. *J. Crim. Law Criminol.* **44**, 525–530.

Melo, V. F., Barbar, L. C., Zamora, P. G. P., Schaefer, C. E. & Cordeiro, G. A. (2008). *Chemical, physical and mineralogical characterization of soils from the Curitiba Metropolitan Region for forensic purpose*. *Forensic Sci. Intl*, **179**, 123–134.

Mesley, R. J., Clements, R. L., Flaherty, B. & Goodhead, K. (1968). *The polymorphism of phenobarbitone*. *J. Pharm. Pharmacol.* **20**, 329–340.

Nagpal, K. C., Ghori, T. A. K. & Ali, S. Z. (1982). *X-ray diffraction studies of gall stones*. *Curr. Sci.* **51**, 814–815.

Oberst, F. W. (1938). *The determination of morphine in the urine of morphine addicts*. *J. Lab. Clin. Med.* **24**, 318–329.

Oberst, F. W. (1943). *Studies on the fate of heroin*. *J. Pharmacol. Exp. Ther.* **79**, 266–270.

Owen, J. T. R., Sithiraks, R. & Underwood, F. A. (1972). *X-ray powder diffraction data for seventeen local anaesthetics*. *J. Assoc. Off. Anal. Chem.* **55**, 1171–1174.

Parsons, J. (1952). *Radiopaque renal calculus identified as cystine by X-ray diffraction. Radiology*, **58**, 878–880.

Parsons, J. & Bartone, J. R. (1961). *Identification of cholesterol in fluid from an intracranial cyst by X-ray diffraction. Clin. Chem.* **7**, 477–481.

Parsons, J. & Beher, W. T. (1955). *X-ray diffraction powder data for steroids. Anal. Chem.* **27**, 514–517.

Parsons, J., Beher, W. T. & Baker, G. D. (1958). *X-ray diffraction powder data and index for the steroids. Henry Ford Hosp. Med. Bull.* **6**, 365–422.

Pastor, D., Rica, M. & Sogo, P. (2003). *Studies on 'Ecstasy' and amphetamine seizures in Spain over 1995–2002 using GC-MS, HPLC, FTIR and XRD*. Proceedings of the 3rd European Academy of Forensic Science Meeting, Istanbul, Turkey. *Forensic Sci. Intl*, **136**, Suppl. 1, 95.

Piga, G., Thompson, T. J. U., Malgosa, A. & Enzo, S. (2009). *The potential of X-ray diffraction in the analysis of burned remains from forensic contexts*. *J. Forensic Sci.* **54**, 534–539.

Pinker, R. H. (1952). *Forensic medicine: X-ray diffraction used in the identification of drugs*. *Ann. West. Med. Surg.* **6**, 595–599.

Prieto-Castelló, M. J., Hernández del Rincón, J. P., Pérez-Sirvent, C., Álvarez-Jiménez, P., Pérez-Cárceles, M. D., Osuna, E. & Luna, A. (2007). *Application of biochemical and X-ray diffraction analyses to establish the post-mortem interval*. *Forensic Sci. Intl*, **172**, 112–118.

Prokopiou, D., Rogers, K., Evans, P., Godber, S. & Dicken, A. (2013). *Discrimination of liquids by a focal construct X-ray diffraction geometry*. *Appl. Radiat. Isot.* **77**, 160–165.

Prokopiou, D., Rogers, K., Evans, P., Godber, S., Shackel, J. & Dicken, A. (2014). *X-ray diffraction with novel geometry. Nucl. Instrum. Methods Phys. Res. A*, **735**, 341–348.

Rawlins, B. G., Kemp, S. J., Hodgkinson, E. H., Riding, J. B., Vane, C. H., Poulton, C. & Freeborough, K. (2006). *Potential and pitfalls in establishing the provenance of earth-related samples in forensic investigations*. *J. Forensic Sci.* **51**, 832–845.

Rendle, D. F. (1981). *Analysis of brass by X-ray powder diffraction*. *J. Forensic Sci.* **26**, 343–351.

Rendle, D. F. (2000). *Forensic science: every contact leaves a trace*. In *Industrial Applications of X-ray Diffraction*, edited by F. H. Chung & D. K. Smith, pp. 659–675. New York: Marcel Dekker Inc.

Rendle, D. F. (2003*a*). *Use of X-rays in the United Kingdom Forensic Science Service*. In *Advances in X-ray Analysis*, Vol. 46 (Proceedings of the 51st Annual Conference on Applications of X-ray Analysis, Colorado Springs, 29 July – 2 August 2002), edited by T. C. Huang, V. E. Buhrke, J. V. Gilfrich, G. J. Havrilla, I. C. Noyan & R. L. Snyder, pp. 17–24. New York: Plenum Press. http://www.icdd.com/resources/axa/vol46/v46_02.pdf

Rendle, D. F. (2003*b*). *X-ray diffraction in forensic science*. *Rigaku J.* **19**, No. 2 and **20**, No. 1, 11–22.

Rendle, D. F. (2004). *Database use in forensic analysis*. *Crystallogr. Rev.* **10**, 23–28.

Rendle, D. F. & Connett, B. E. (1988). *Characterization of a glucose monohydrate/sodium chloride complex by X-ray diffraction methods. J. Forensic Sci. Soc.* **28**, 295–297.

Rendle, D. F. & Glazier, E. J. (2012). *Powder diffraction data for methylenedioxymethylamphetamine hydrochloride monohydrate (MDMA.HCl.H_2O, ecstasy hydrate). Powder Diffr.* **27**, 263–265.

Rendle, D. F., Rogers, K. D. & Beckett, S. (2011). *Ambient-temperature powder diffraction data for benzocaine hydrochloride and a monoclinic polymorph of benzocaine base. Powder Diffr.* **26**, 277–279.

Robertson, J. R. & Grieve, M. C. (1999). Editors. *Forensic Examination of Fibres*, 2nd ed. London: Taylor & Francis.

Roe, G. M. (2012). Personal communication.

Rogers, K., Evans, P., Rogers, J., Chan, J. & Dicken, A. (2010). *Focal construct geometry – a novel approach to the acquisition of diffraction data. J. Appl. Cryst.* **43**, 264–268.

Rogers, K. D. (2012). Personal communication.

Rogers, K. D., Beckett, S., Kuhn, S., Chamberlain, A. & Clement, J. (2010). *Contrasting the crystallinity indicators of heated and diagenetically altered bone mineral. Palaeogeogr. Palaeoclimatol. Palaeoecol.* **296**, 125–129.

Ruffell, A. & Wiltshire, P. (2004). *Conjunctive use of quantitative and qualitative X-ray diffraction analysis of soils and rocks for forensic analysis*. *Forensic Sci. Intl*, **145**, 13–23.

Sands, H. S., Hayward, I. P., Kirkbride, T. E., Bennett, R., Lacey, R. J. & Batchelder, D. N. (1998). *UV-excited resonance Raman spectroscopy of narcotics and explosives*. *J. Forensic Sci.* **43**, 509–513.

Schmidt, G. (1962). *Detection and estimation of barbituric acid derivatives*. In *Methods of Forensic Science*, Vol. 1, edited by F. Lundquist, pp. 455–457. New York, London: Wiley Interscience.

Scott, R. W. (1969). *Applications of X-ray diffraction in the paint industry*. *J. Paint Technol.* **41**, 422–430.

Shulgin, A. T. (1986). *The background chemistry of MDMA*. *J. Psychoactive Drugs*, **18**, 291–304.

Smith, F. P. (2005). Editor. *Handbook of Forensic Drug Analysis*. Burlington: Elsevier Academic Press.

Soldate, A. M. & Noyes, R. M. (1947). *X-ray diffraction patterns for identification of crystalline constituents of explosives*. *Anal. Chem.* **19**, 442–444.

Sullivan, R. C. & O'Brien, K. P. (1970). *X-ray diffraction studies of cocaine and its substitutes*. *Norelco Rep.* **17**, 1–6.

Sun, B., Li, M., Zhang, F., Zhong, Y., Kang, N., Lu, W. & Liu, J. (2010). *The performance of a fast testing system for illicit materials detection based on energy-dispersive X-ray diffraction technique*. *Microchem. J.* **95**, 293–297.

Susich, G. (1950). *Identification of organic dyestuffs by X-ray powder diffraction*. *Anal. Chem.* **22**, 425–430.

Švarcová, S., Kočí, E., Bezdička, P., Hradil, D. & Hradilová, J. (2010). *Evaluation of laboratory powder X-ray micro-diffraction for applications in the fields of cultural heritage and forensic science*. *Anal. Bioanal. Chem.* **398**, 1061–1076.

Tassa, M., Leist, Y. & Steinberg, M. (1982). *Characterization of gunshot residues by X-ray diffraction*. *J. Forensic Sci.* **27**, 677–683.

Terada, Y. (2005). *X-ray chemical analysis for forensic applications using synchrotron radiation*. *Acta Cryst.* A**61**, c15. http://iucr2005.iucr.org/ms6.htm.

Thangadurai, S., Abraham, J. T., Srivastava, A. K., Moorthy, M. N., Shukla, S. K. & Anjaneyulu, Y. (2005). *X-ray powder diffraction patterns for certain β-lactam, tetracycline and macrolide antibiotic drugs*. *Anal. Sci.* **21**, 833–838.

Thatcher, P. J. & Briner, G. P. (1986). *The application of X-ray powder diffraction to forensic science*. *Powder Diffr.* **1**, 320–324.

Tuğ, A., Alakoç, Y. D. & Hancı, İ. M. (2005). *An end to a rumour*. *Forensic Sci. Intl*, **153**, 156–160.

Turley, J. W. (1965). *X-ray diffraction patterns of polymers*. Chemical Physics Research Laboratory, The Dow Chemical Company, Midland, Michigan, USA.

Walls, H. J. (1974). *Forensic Science: An Introduction to Scientific Crime Detection*, 2nd ed. London: Sweet & Maxwell.

Ward, D. C. (2000). *Use of an X-ray spectral database in forensic science*. *Forensic Sci. Commun.* **2**, No. 3, July.

Wogan, M. E., Webster-Hoffmeyer, K. S. & Grgicak, C. M. (2013). *Corrosion behaviour of four handguns in aqueous environments: Corrosion product characterization and effects on estimating the time since deposition*. *Sci. Justice*, **53**, 363–370.

Wolten, G. M., Nesbitt, R. S., Calloway, A. R., Loper, G. L. & Jones, P. F. (1977). *Final report on particle analysis for gunshot residue detection*. Report ATR-77(7915)-3, Aerospace Corporation, El Segundo, CA, USA.

Yoon, S., Balunaini, U. & Prezzi, M. (2007). *Forensic examination of severe heaving of embankment constructed with fluidised bed combustion ash*. *Transp. Res. Rec. J. Transp. Res. Board*, Issue No. 2026, pp. 9–17. http://dx.doi.org/10.3141/2026-02.

Young, R. A. (1993). Editor. *The Rietveld Method*. IUCr Monographs on Crystallography, No. 5. Oxford University Press.

International Tables for Crystallography (2019). Vol. H, Chapter 7.3, pp. 752–758.

7.3. Materials for energy storage and conversion

M. A. Rodriguez

7.3.1. Introduction

Effective and efficient means of energy storage and conversion are critical to the day-to-day operation and security of a modern society. Hence, research and development in this field continues to expand due to the demands for clean, robust and sustainable sources of energy. This chapter is devoted to the use of X-ray diffraction in the field of energy storage and conversion; the examples presented herein are meant to be demonstrative with regard to the various fields of research discussed. These fields include fossil fuel, hydrogen storage, wind, solar and battery technologies. The aim of this chapter is to give the reader a sense of the impact X-ray diffraction analysis can have on their research efforts in the field of energy-related materials and processes. Suitable references are given throughout the chapter to encourage further investigation on specific topics of interest to the reader.

7.3.2. Fossil fuel

While fossil fuels are discussed in more detail in Chapter 7.11, they are worth mentioning in this chapter concerning energy storage and conversion because coal/petrochemical sources supply a majority of the world's energy.

Coal is one of the most common and inexpensive sources of energy on the planet. It is also responsible for significant pollution and carbon emission. The use of powder X-ray diffraction (PXRD) characterization of coals from mining locations can yield significant information. Coal characteristics such as the fraction of amorphous carbon, the aromaticity and crystallite size can all be derived from standard XRD analysis (Lu *et al.*, 2001; Sonibare *et al.*, 2010). The aromaticity (or ratio of aliphatic to aromatic rings) dictates the rank of a given coal, which correlates to the overall carbon content and thereby energy potential of the fuel. XRD coupled with other techniques can be used in a straightforward manner to characterize coal and asphaltenes (see Yen *et al.*, 1961). In addition, XRD characterizes the mineral reactions that occur during the combustion of coal in power-plant boilers (Gupta, 2007). Such reactions are critical for the understanding of slagging and fouling composites.

While the solid-state technique of PXRD typically has little to say about liquid-based petroleum fuels, the science of diffraction plays a critical role in analysis of materials employed by the petroleum industry (see Chapter 4.6 on zeolites and Chapter 7.11 on the petrochemical industry). Herein we touch only briefly on the zeolite-enabled process known as fluid catalytic cracking (FCC) and the important role that the science of diffraction plays in this field. FCC is a mainstay of modern petrochemical refineries (Vermeiren & Gilson, 2009) and the zeolite structures employed in this process enable this critical technology for gasoline refining. The zeolite employed in this process, typically type Y of the faujasite (FAU) family, is the active component of the catalyst used for the hydrocarbon-cracking reaction. The acidic sites of the zeolite confined within a porous cage-like structure enable the preferential reactivity of the gas oil feed to yield gasoline (Vermeiren & Gilson, 2009). Zeolites are convenient because they can be tuned to form materials with specialized reactivity for specific catalytic applications. However, in order to understand these materials and their properties, the structures must first be fully elucidated. This is where PXRD has a major impact. Structures are typically determined by single-crystal X-ray diffraction analysis. However, single crystals of many zeolite compounds cannot be grown to sufficient size to obtain adequate single-crystal data sets for structure solution. The use of powder XRD coupled with Rietveld structure refinement (Larson & Von Dreele, 2000; Toby, 2001; Rodriguez-Carvajal, 1993) is routinely employed for structure analysis of these cage-like crystal structures. The location of exchanged cations and reaction sites within the framework can be the information necessary for predicting the properties and performance of these compounds (Scherzer, 1989). The demand for ever-improved processing of fossil fuels continues to drive research and development of catalytic zeolites and other framework compounds at an ever-greater pace (Corma *et al.*, 2002). The employment of XRD for structural characterization of these materials is a critical tool in this field. The reader is referred to Chapter 4.6 on zeolites for more details of these important structures.

7.3.3. Hydrogen storage

XRD also plays an important role in research and development of materials for hydrogen storage. Cage-like frameworks similar to zeolites, but where the cage is expanded through the use of large (typically organic) linker molecules, are being investigated as fuel-storage media. These metal-organic frameworks (MOFs) have been targeted specifically for hydrogen storage because they are capable of storing many times their weight in hydrogen (H_2), where the gas is loosely attached to adsorption sites within the molecule but can be extracted again as H_2 (typically through heating). Materials development of these compounds relies heavily on structural determination *via* PXRD. For example, Luo *et al.* (2008) describe an yttria-based MOF in which the metal centres are linked by 1,3,5-benzenetricarboxylate molecules to generate a very large cage-like structure, preferentially suitable to H_2 storage. The authors demonstrate the use of Rietveld refinement from powder diffraction data coupled with difference-Fourier analysis to illuminate the H_2 gas adsorption sites within the framework. As hydrogen only scatters X-rays very weakly, D_2 was employed as the adsorption gas and neutron diffraction analysis was performed for H_2 molecule location within the MOF. Deuteration coupled with neutron scattering is common practice for the determination of hydrogen-bearing compounds. Other elegant studies of hydrogen-storage materials have been performed. For example, Riktor *et al.* (2007) employed synchrotron radiation to analyse release of H_2 gas from the compound $Ca(BH_4)_2$. The high brilliance of synchrotron radiation is amenable to *in situ* studies, which are able to collect data with sufficient speed and resolution to capture reaction behaviour (*e.g.* phase transitions and thermal decomposition) with incredible detail. Riktor *et al.* (2007), showed that the H_2 gas

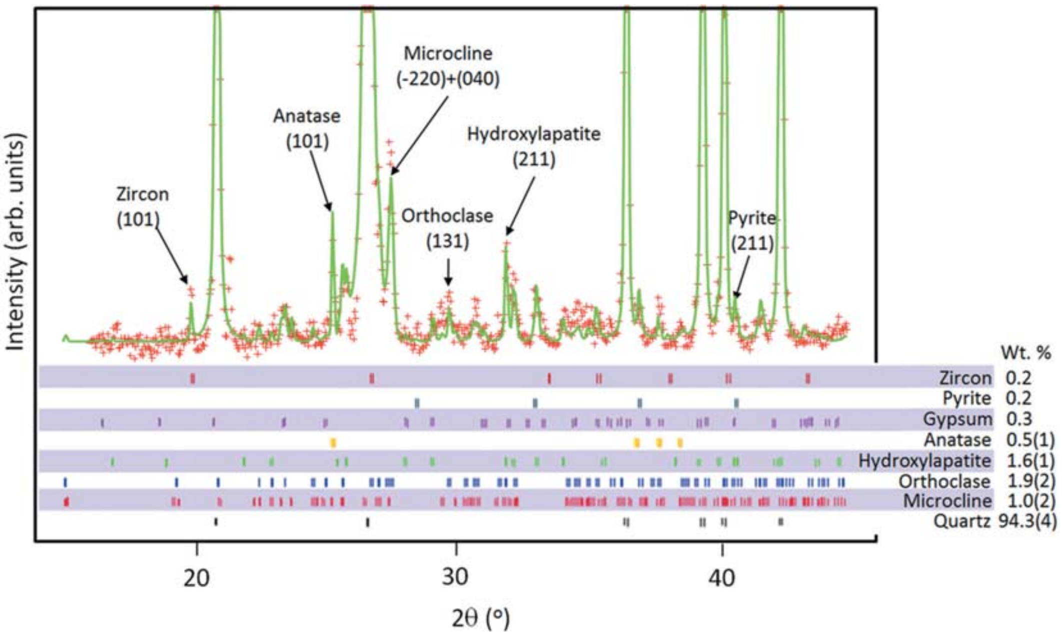

Figure 7.3.1
Multi-phase Rietveld refinement of a borehole specimen. The line shows the calculated pattern. Raw data points are shown as + symbols. Individual peaks for the trace phases are highlighted by arrows. Off-scale peaks are from quartz. Reflection tick marks for each phase are shown below the pattern. Quantitative weight % values for the phases are listed on the lower right of the plot. See Rodriguez *et al.* (2012). Copyright (2012) JCPDS – International Centre for Diffraction Data. Reproduced with permission.

release initiated upon conversion of the low-temperature γ-Ca(BH$_4$)$_2$ phase to the high temperature β-Ca(BH$_4$)$_2$ phase. Synchrotron sources also have the advantage of a tunable X-ray wavelength and are therefore not restricted to a fixed wavelength as dictated by the anode of a standard sealed-tube source. In this regard, synchrotron sources are often employed for atomic pair distribution function (PDF) analysis. This is because synchrotron sources can easily generate the hard X-ray wavelengths (*e.g.* <0.5 Å) that are necessary to achieve high momentum-transfer values (*i.e.* $Q_{\max} > 20$ Å^{-1}) in measured data sets (see Chupas *et al.*, 2003). PDF data are useful for characterizing nearest-neighbour distances between atomic species in a structure and can be beneficial for both crystalline and non-crystalline compounds. Chupas *et al.* (2007) demonstrated the use of synchrotron radiation to detect the presence of H_2 in $Mn_3[Co(CN)_6]_2 \cdot 3H_2$ by differential PDF analysis. This approach revealed how the H_2 molecules are bound within the porous framework, resulting in a more detailed understanding of how H_2 is stored and recovered from the material. While access to synchrotron facilities is often limited, well designed experiments can lead to significant knowledge of a material's behaviour. Chapter 2.2 in this volume is dedicated to synchrotron radiation and the reader is referred to that chapter for further details.

7.3.4. Wind

One of the critical aspects of green technologies such as wind and solar is the intermittent nature of the harvested energy, which dictates the necessity for energy storage. Wind farms have been employing a clever strategy for power storage through the use of compressed air energy storage (CAES), as outlined by Cavallo (2007). This method employs the use of underground caverns (man-made or naturally occurring). When the wind is active at a time of low power demand, a wind farm may choose to transfer power to an air compressor that pumps air into a cavern, thereby storing the energy in the form of pressure. The energy can be converted back to electricity by releasing the air pressure through a turbine. Careful characterization of cavern geology is important, especially with regard to the materials present in the access boreholes that are drilled deep into the ground to bridge the cavern to the surface (Rodriguez *et al.*, 2012). Quantitative characterization of the phases present as a function of depth is important information for assessing the impact of cyclic air pressure on the CAES station. Fig. 7.3.1 shows a Rietveld refinement for an eight-phase diffraction pattern obtained from a core-drill specimen. The identification of the phases was facilitated by employing X-ray fluorescence (XRF) for determination of the elemental composition (Rodriguez *et al.*, 2012). It is worth noting that the plot in Fig. 7.3.1 shows intensity for phases that are very close to the background level. The quartz peaks, which make up more than 90 wt% of the sample, go off-scale on the intensity axis. This allows the signals from the other minor or trace phases present to be seen more easily. One phase of critical importance for CAES functionality was FeS_2 (pyrite), because oxidation of this phase could alter the pH and mineralogy of the borehole. The phase analysis *via* Rietveld refinement revealed a very small weight fraction of pyrite at this borehole depth. In fact, the quantity was so small and confounded by peak overlap with other phases that its detection proved difficult without the supporting XRF analysis. Typical errors associated with phase quantification are in the 0.1 to 0.5 weight percent range, depending on the quality of the XRD data and the scattering behaviour of the quantified phase. This is one of the limitations of powder XRD. Detection and quantification of major, minor and trace phases *via* XRD analysis can give better insight into the functionality and possible issues that might impact CAES, a practical option for energy storage at large wind-farm facilities.

7.3.5. Solar

The challenge of solar technology is to efficiently convert photonic energy from sunlight into another form of energy, typically electricity. The solar cell is the quintessential building block of the industry, but materials science challenges still remain. The three best-known issues with photovoltaics are: (1) the influence of grain boundaries, (2) the electron affinity of

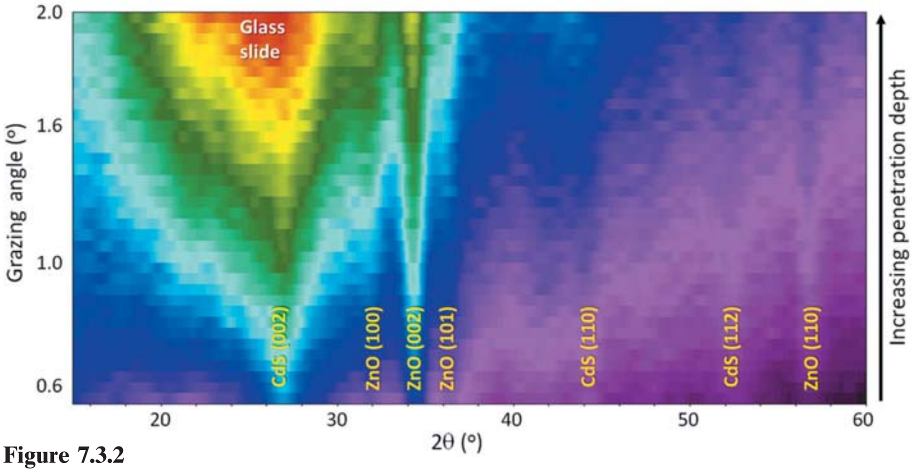

Figure 7.3.2
The GIXRD contour plot of a CdS/ZnO film deposited on a glass substrate. Increased grazing angle illustrates deeper penetration depth *via* detection of the broad amorphous peak from the substrate. (Data source: internal Sandia research, unpublished.)

absorbers and (3) the lack of clear understanding of point defects (Durose *et al.*, 2004). The fact that typical photovoltaic devices are of a thin-film nature often leads to analysis using grazing incidence X-ray diffraction (GIXRD) measurements (McCandless & Dobson, 2004; see also Chapter 5.4). GIXRD employs an 'asymmetric' diffraction condition where the film sample surface is set and fixed at a 'grazing angle' (GI) relative to the direct beam. GI values typically fall between 0.5 and 2° 2θ for Cu $K\alpha$ radiation and narrow-slit and/or parallel-beam optics are employed to reduce divergence. In this configuration, only the detector is scanned through the 2θ angle. The GI geometry enables preferential scattering from the film surface, thereby reducing the impact of the substrate. The benefit of GIXRD is offset by the difficulty posed by some samples that display significant preferential orientation. The assumption of a random grain distribution of the specimen guarantees that some of the crystallites will be in a diffraction condition for a given d-spacing of that phase, even when the grains must be *tilted* from the surface normal. When strong preferential orientation is present, this criterion breaks down. Fortunately, for many of the new nanomaterials being employed in solar cells, random orientation is more likely than for larger grained materials. Fig. 7.3.2 shows a series of diffraction patterns for CdS obtained using GIXRD. The CdS has been deposited as a film along with ZnO nanocrystallites upon a glass substrate. This contour plot shows 2θ on the x axis and incremental grazing angles on the y axis. Intensity, shown as a rainbow colour scale (purple = low counts, red = high counts), highlights the diffraction peaks as increasing intensity profiles with increased GI angle (*i.e.* penetration depth). Hence, this plot yields a qualitative depth profile for the film. The CdS (002) and ZnO (002) peaks are clearly detectable above the background level in this contour plot, especially at the lower GI angles; other peaks for these two phases are also observed. One can see the increase in the amorphous signal (broad peak centred at ~25° 2θ) when scans reach the higher GI angles (~1.6 to 2.0°). This indicates significant scatter from the glass substrate below the thin CdS film. Since the crystallite size-broadened nanocrystalline CdS (002) peak is significantly convoluted with the amorphous intensity from the glass substrate, a GI scan series can be of considerable help in discerning the CdS (002) peak presence in the sample. This is because one can look for the preferential detection of the surface film at lower GI angles, and then view this in context of the ever-increasing scatter from the glass as the GI angle increases. This adds confidence to the film detection.

Solar energy can also be employed for the cracking of CO_2 gas, to form CO and O_2. The subsequently synthesized CO gas can then be processed into hydrocarbon fuels *via* established syngas chemistry (Miller *et al.*, 2008). The high-temperature catalytic CO_2 cracking reactions are performed through a two-step electrochemical cycle that employs a reaction chamber where CO_2 gas can be exposed to an oxygen-starved material. One such material is an iron-doped zirconia ceramic (Coker *et al.*, 2012). The ceramic, isolated within the reaction chamber, can be heated *via* focused sunlight through a window on the reaction chamber (Miller *et al.*, 2008). At high temperatures (> 1473 K), Fe^{III} is reduced to Fe^{II} in the ceramic. The ceramic can then be cooled in an inert atmosphere to ~1373 K where CO_2 gas is bled into the chamber, re-oxidizing the ceramic by stripping the CO_2 of one of its oxygen atoms. This reactor system has been demonstrated in principle; however, understanding the science within the iron-doped zirconia ceramic has proven to be a challenge. The exact nature of the iron within the zirconia appears to influence the performance of the reactor. *In situ* high-temperature XRD has been performed in a mock reactor environment to monitor the changes in the zirconia catalyst material during heating and cooling in an inert atmosphere (Coker *et al.*, 2012). It is well known that Fe has a finite solubility in cubic ZrO_2 where the Fe may substitute at the Zr sites in the crystal structure (Davison *et al.*, 1988; Raming *et al.*, 2002). Iron substitution typically causes the cubic zirconia cell to contract. The use of *in situ* high-temperature PXRD has enabled the monitoring of an iron-saturated yttria-stabilized ZrO_2 (YSZ). Fig. 7.3.3 shows how the lattice parameter of this compound varies with heat treatment under an inert atmosphere (flowing helium). This sample was initially synthesized in air at 1773 K. There was a trace of haematite (Fe_2O_3) remaining in the powder, but the balance refined well as a cubic ZrO_2 with an initial room-temperature lattice parameter of a = 5.110 (3) Å. When *in situ* high-temperature PXRD was performed on this powder, typical linear thermal expansion behaviour occurs up to

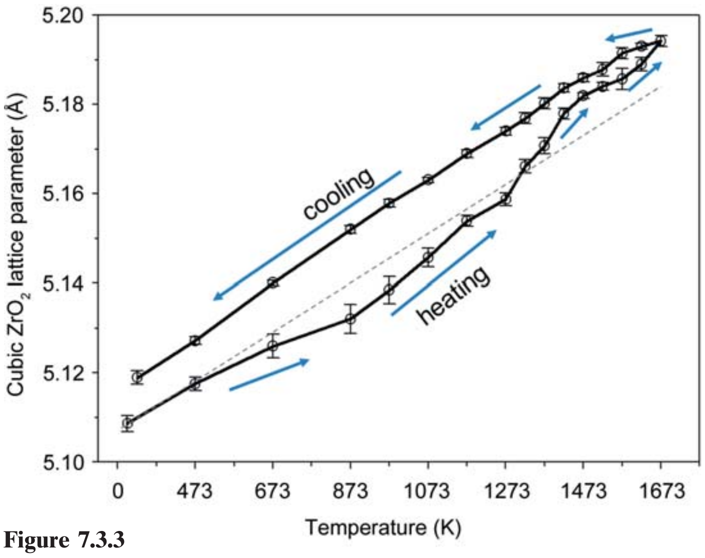

Figure 7.3.3
Lattice-parameter variation for an iron-doped YSZ heated/cooled under inert conditions. Figure reproduced with permission from Coker *et al.* (2012). Copyright (2012) JCPDS – International Centre for Diffraction Data. Reproduced with permission.

approximately 673 K (see Fig. 7.3.3). The dashed line in the figure represents the interpolated linear thermal expansion and serves as a guide to the eye for detecting behaviour that deviates from linearity. Above 673 K, upon heating one observes a drop below the linearity trend line. This observation suggests a subtle increase in iron solubility. It was noted that at this point in the diffraction data, the trace phase of Fe_2O_3 began to dissipate, possibly suggesting migration of the iron into the YSZ. However, upon further heating above 1273 K, one observes a more rapid change in slope, suggesting a *decrease* in iron solubility. At this point, wustite (FeO) was observed to form as a second phase, suggesting iron migration out of the ZrO_2. On cooling, the lattice shows a linear behaviour, suggesting that there is no variation in iron solubility, and inspection of the XRD pattern showed that the second phase of FeO persisted. The final lattice parameter of the cycled YSZ was a = 5.124 (3) Å, showing an increase of +0.014 Å from the initial cell dimension prior to heating. Subsequent reprocessing of the sample in an air environment to ~1773 K (not shown) can regenerate the more iron-soluble form of YSZ, returning it again to the initial state of high iron doping. Our ability to detect and monitor iron shuttling in and out of the ZrO_2 structure with temperature and atmospheric conditions has shed light on the understanding of the conditions within the ZrO_2 during the CO_2 splitting reaction. A point worth mentioning here is the sensitivity of XRD unit-cell parameters. Careful analysis can reveal changes in the unit-cell dimensions of the order of thousandths of ångstroms. As can be seen from Fig. 7.3.3, the error bars for each data point are in the 0.001–0.003 Å range. Hence, significant changes in cell dimensions of 0.005 Å are possible when employing well aligned powder diffraction instrumentation, and even greater precision is possible (down to the ±0.0005 Å range) for meticulous measurements.

7.3.6. Battery technology

There are many applications for XRD in the science of battery-based energy storage. Of particular interest are the chemical reactions, phase changes and morphological/microstructural variations that can occur at the anode and cathode inside the cell. Many of these characteristics can have significant impact on battery life, energy capacity and modes of failure. One example where the use of PXRD is paramount for cell design and fabrication has to do with the cathode of the lead–acid battery. Lead–acid battery technology has been in existence since the late 1800s and has proven to be the most successful rechargeable battery technology in history (Kurzweil, 2010; Lukic *et al.*, 2008). The use of PbO_2 as the cathode material makes sense in terms of economics and with regard to the simplicity of the cell design (where Pb is employed as the anode). The critical nature of the PbO_2 cathode is that it forms as the tetragonal β-PbO_2 phase, rather than the orthorhombic α-PbO_2 compound (Abaci *et al.*, 2000). This is because the α-PbO_2 phase displays a much lower electrical conductivity than the β-PbO_2 (almost an order of magnitude), as outlined by Mindt (1969). The synthesis procedure employed for generation of the PbO_2 cathode can have a major effect on which polymorph is formed, and detection and quantification of the α *versus* β phase fraction is straightforward from standard PXRD measurements (Abaci *et al.*, 2000). Such a clear tie between structure, property and performance allows for a means of process-quality control through a mechanistic understanding of battery function, all with a simple application of PXRD.

Li-ion battery technology benefits significantly from PXRD in a similar manner to other materials-science systems. The cathode tends to be the capacity-limiting factor in Li-ion cells, and therefore new compounds are under continual development. For example, Pouillerie *et al.* (2001) analysed various Mg-doped cathode compounds based on the $LiCoO_2$ layered structure. XRD analysis was performed in a 'post-mortem' fashion where batteries were first constructed with various cathode compounds, cycled (*i.e.* charged and discharged) and then disassembled for XRD analysis of the cathode material. This is a straightforward but time-consuming process. However, it is possible to obtain a great deal of information through this method. Pouillerie *et al.* (2001) have reported the impact of cycling on the performance of the battery by looking at the structural parameters of layered-$LiCoO_2$-type cathode compounds after just one cycle, and likewise after 500 cycles. Structural parameters such as lattice parameters, atom positions, site occupancies, crystallite size and microstrain can be derived from Rietveld structure refinement. Based on these results, it was determined that a small amount of Mg doping of these cathode materials reduced the fade (loss of capacity with cycling). Again, understanding of the Mg-site location, as determined by structure refinement, yielded the necessary mechanistic insight concerning the observation of improved performance. Pouillerie *et al.* (2001) found that Mg migrated from the Li site to the inter-slab site during cycling. The irreversible Mg migration aided the stability of the structure and reduced delamination of the cathode phase. These types of analyses prove much more informative than iterative trial-and-error processing. They illustrate the fundamental difference between the often slow, incremental improvement obtained by empirical approaches to the more mechanistic understanding of structure/property/performance relationships made possible in part through materials characterization.

One drawback of the 'post-mortem' technique is that one must assume that the disassembled material (such as cathode powder from a disassembled cell) represents what is present within the cell at the given state of charge (SOC). Electrochemical cells can display complex chemical reactions and in a sealed environment may form compounds that are unstable in air. Thus, disassembly of the battery and exposure to the environment may result in analysis of reaction products caused by air exposure. This is likely to prove confusing and even misleading in terms of the results and ultimate conclusions drawn from the analysis. Methods have been developed for the 'post-mortem' analysis of materials that display air sensitivity (see Rodriguez *et al.*, 2008). However, if one truly desires to obtain information regarding the chemical changes occurring within a battery, it would seem best to monitor these reactions *in situ* while simultaneously collecting the electrochemical cell response. Such *in situ* analyses have been performed (see Reimers & Dahn, 1992) and can yield much greater insight into battery performance because the structural data obtained *via* PXRD can be directly tagged to a simultaneous property measurement (*i.e.* SOC) and the results from each diffraction pattern can be viewed in context; that is, in comparison to the pattern before and the pattern after. The contextual aspect of the data set can be important for identification of experimental artifacts, and enables detection of trends in data while yielding the additional facet of property comparison. Fig. 7.3.4 shows such an *in situ* diffraction data set collected on the compound $Li_8Ni_5Co_2MnO_{16}$ (Boyle *et al.*, 1999). The figure shows the resulting PXRD patterns collected on this cathode material while the sample was charged, thus pulling Li out of the cathode material. The electrochemical cell was fabricated using poly-

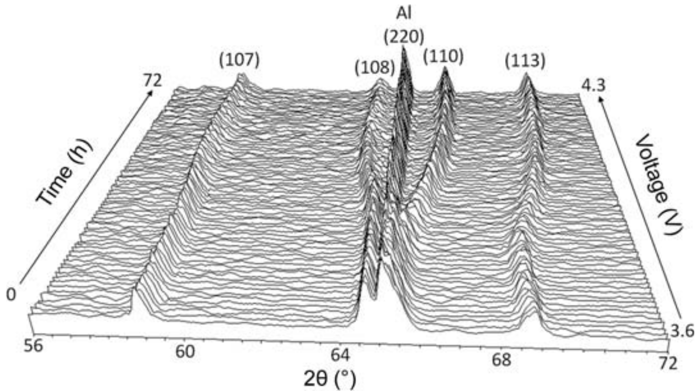

Figure 7.3.4
In situ XRD analysis of $Li_8Ni_5Co_2MnO_{16}$ during charging. The distortion of the unit cell during Li removal (charging) is manifest by shifting of peak positions in 2θ. The Al (220) peak is from the current collector and can serve as an internal standard. (Data source: internal Sandia research, unpublished.)

propylene plastic (see Rodriguez *et al.*, 1998). This ‘coffee bag’-type cell could be directly incorporated within the diffractometer. The results show peak-position shifts during charging. Only a limited 2θ range is shown in Fig. 7.3.4 because superpositions of other diffraction signals associated with different aspects of the cell (*i.e.* plastic, Li metal, separator *etc.*) can make analysis of the entire diffraction pattern difficult. The particular 2θ range shown here (56–72° 2θ) is useful because it is primarily composed of diffraction from the cathode, which is of interest in this experiment (Rodriguez *et al.*, 2000). As the cell is charged, the Li^+ ions are shuttled from the cathode to the anode (lithium metal). As the Li^+ ions are removed from the $Li_8Ni_5Co_2MnO_{16}$ cathode, the unit cell of this rhombohedral/hexagonal ($R\overline{3}m$) phase shows different behaviour for the *a* and *c* axes. The Miller indices for the individual peaks are labelled in the figure. The (107) and (108) peaks are particularly sensitive to the *c*-axis changes, while the (110) peak is strictly dependent on changes associated with the *a* axis. This is convenient because it allows for detection of changes in both axes for this structure. The (113) peak is affected by both *a* and *c* axes and perhaps serves as a good indication of the overall volume change in the cell. Lattice-parameter refinements of the initial unit cell (*i.e.* 0% SOC) indicate $a = 2.85$, $c = 14.19$ Å, $V = 99.80$ Å^3 and the final lattice parameters at 100% SOC (4.3 V) are $a = 2.80$, $c = 14.46$ Å, $V = 98.20$ Å^3. The implications of these results are that upon Li^+ removal, the *c* axis of the cathode material expands while the *a* axis shrinks, resulting in a net reduction in the unit-cell volume for the cathode material. This cell distortion is anisotropic at the scale of the individual crystallites. Note also that there is an aluminium (220) peak present throughout the entire pattern series. The Al is from the current collector and its presence is problematic due to overlap with the (110) peak profile. However, the Al (220) peak only overlaps the (110) peak from the cathode at the early stages of charging and the two peaks separate more as the sample reaches significant SOC voltages. Profile fitting easily deals with this overlap condition. As it turns out, the presence of the Al (220) peak can be helpful because it can be employed as an internal standard. This is because the *d*-spacing for the Al (220) peak should be unaffected by the charging process. As one can see in Fig. 7.3.4, the Al (220) peaks remain static in 2θ during the charging sequence. Methods for dealing with the convolution of *in situ* measurements have been addressed through the use of multivariate statistical analysis (MSA), which allows for the separation of large data sets into individual components, thereby reducing the complexity of the data set and separating reaction behaviour from the signal associated with static (inert) portions of the data set (Rodriguez *et al.*, 2007, 2010). This has proven to be a powerful technique for isolation of the dynamic behaviour within the *in situ* data collection.

A thermal battery is an electrochemical cell whose electrolyte takes the form of a solid-state salt (*e.g.* LiCl or KCl). The cell is fabricated with an anode, a cathode and a separator medium, and the salt electrolyte remains solid and inactive until the entire pile is heated. Upon heating, the electrolyte melts and the cell can be utilized as a power supply. These batteries are very useful when there is a need for an autonomous power supply with a long shelf-life that can be called upon at a moment’s notice to generate electrical power. PXRD can be employed in the analysis of these cells for phase identification of initial battery configurations as well as in cells that have undergone discharge (Wesolowski *et al.*, 2011; Griego *et al.*, 2012). Microdiffraction (μ-PXRD) has been performed on thermal battery cross sections to diagnose the phases present before and after cell discharge. The benefit of μ-PXRD (*e.g.* ∼500 μm spot size X-ray beam) is that diffraction data can be obtained spatially, thus giving an assessment of the phases present at reaction interfaces such as those which occur in battery stacks. Typically, thermal batteries are composed of layers of anode/separator/cathode; the electrochemical reaction front will begin at the anode/separator interface, and likewise at the cathode/separator interface, and progress outward toward the terminating outer surface of the anode or cathode. To monitor the electrochemical reaction, cells can be heated and then subsequently quenched at various locations on an SOC curve. Then cross sections of the battery stack can be made (*via* standard metrology preparation methods) and one can employ μ-PXRD measurements stepwise across the interface to study the phase changes. Fig. 7.3.5 is such a cross-sectional analysis using μ-PXRD. This specimen was a cell that was near full discharge. The figure shows 2θ on the *x* axis, scan number on the *y* axis (equivalent to the sample translation step) and intensity is shown as a colour contour (purple = low counts, red = high counts). The coloured lines running vertically indicate diffraction peaks. An optical image of the cross section is shown on the right of the μ-PXRD contour plot. Previous analysis on an unreacted sample (not shown) revealed that the anode material started as $Li_{13}Si_4$, the cathode was CoS_2 and the separator was MgO. Salts composed of Li and K cations with Cl and/or Br anions served as the electrolyte. As one can see from Fig. 7.3.5, the anode now contains the $Li_{12}Si_7$ phase, suggesting considerable loss of Li. Likewise, the cathode phase has changed to Co_9S_8, indicating loss of sulfur. There is a significant reaction product of Li_2S throughout the cathode and across a portion of the anode. It appears that there are two distinct regions in the reacted anode. One region, closer to the anode/separator interface, shows Li_2S along with Li_4SiO_4 and a relative deficiency of the $Li_{12}Si_7$ phase. The second region in the anode is further away from the anode/separator interface and is highlighted by the abrupt termination of the Li_2S phase. The region nearer the anode/separator interface may possibly be contaminated by oxygen, forming Li_4SiO_4. The MgO separator typically remains inert during discharge due to its unlikely chemical reduction. It seems more plausible that there was another source of oxygen present. It is also notable that the optical image, shown on the right side of the contour plot, shows cracks and fissures across the separator. Typically these cells are discharged under inert conditions. The observation of Li_4SiO_4 at the anode/separator interface may be consistent with loss of such inert conditions during discharge. It is worth

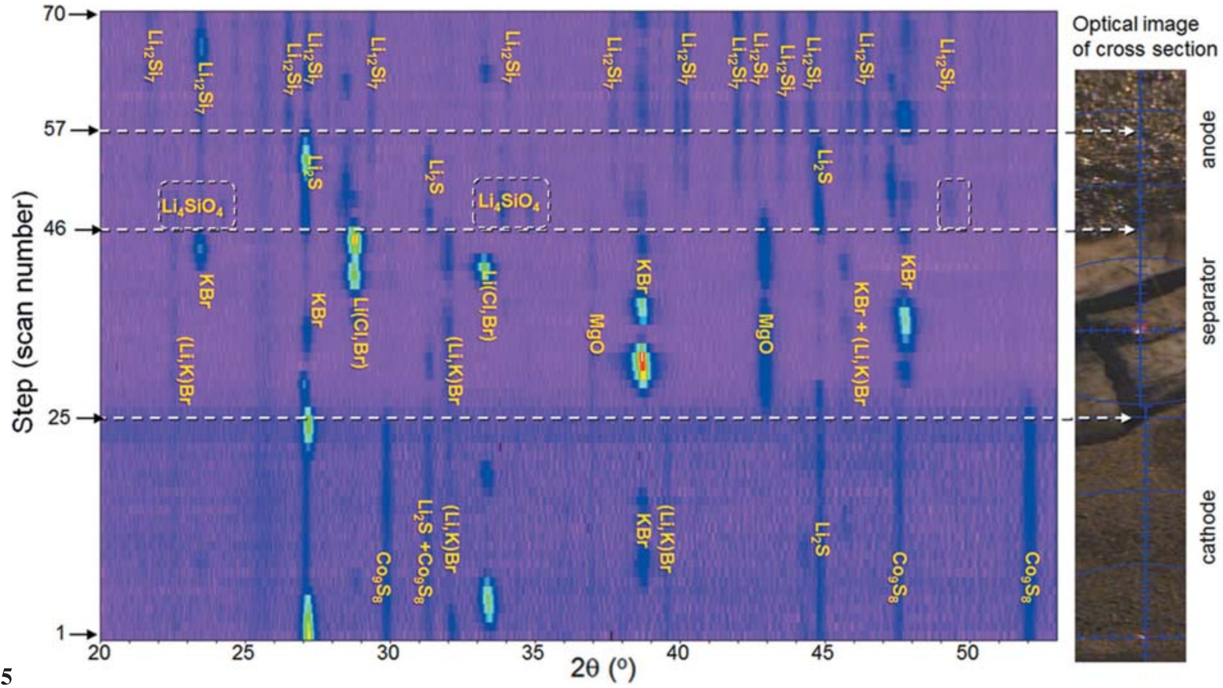

Figure 7.3.5

Contour plot showing spatial dependence of phases across a processed thermal battery. Regions separated by horizontal dotted lines indicate boundary interfaces between anode/separator/cathode sections. An optical image of the sample cross section is shown to the right of the contour plot. (Data source: internal Sandia research, unpublished.)

commenting about the discontinuous peak intensities for the alkali halide salts as one moves from cathode to separator to anode regions. For example, the KBr (220) peak at ~38.5° 2θ shows discrete intensity spikes at various steps across the contour map. This is an artifact of large grain size *versus* small beam size. As the X-ray beam becomes smaller, the fraction of illuminated crystallites is reduced as well. The small spot size impacts the statistical distribution of grain-orientation sampling as the diffraction experiment begins to approach a single-crystal condition. These data were collected with the use of an area detector, which improves sampling statistics by collecting more of the solid angle of the Debye cone. However, the electrolyte often contains large crystallites (> 100 µm) which, when encountered during the sequential step analysis of the small X-ray beam, would comprise a disproportionate fraction of the diffracted volume and lead to these spikes of intensity. The benefit of a spatially dependent analysis allows for easy diagnosis of this effect through visual inspection of the contour plot, and enables improved phase identification through merging of scans taken across different parts of the cross section so as to obtain a single, representative 2θ scan for each region (*e.g.* separator section). From this example, one can see the benefits of µ-PXRD for diagnostics and failure analysis for thermal-battery energy-storage devices.

Sandia National Laboratories is a multi-program laboratory managed and operated by Sandia Corporation, a wholly owned subsidiary of Lockheed Martin Corporation, for the US Department of Energy's National Nuclear Security Administration under contract DE-AC04-94AL85000. The author would like to thank James Griego for his aid in formatting aspects of this manuscript.

References

Abaci, S., Pekmez, K., Hökelek, T. & Yildiz, A. (2000). *Investigation of some parameters influencing electrocrystallisation of PbO_2*. *J. Power Sources*, **88**, 232–236.

Boyle, T. J., Ingersoll, D., Rodriguez, M. A., Tafoya, C. J. & Doughty, D. H. (1999). *An alternative lithium cathode material: synthesis, characterization, and electrochemical analysis of $Li_8(Ni_5Co_2Mn)O_{16}$*. *J. Electrochem. Soc.* **146**, 1683–1686.

Cavallo, A. (2007). *Controllable and affordable utility-scale electricity from intermittent wind resources and compressed air energy storage (CAES)*. *Energy*, **32**, 120–127.

Chupas, P. J., Chapman, K. W. & Lee, P. L. (2007). *Applications of an amorphous silicon-based area detector for high-resolution, high-sensitivity and fast time-resolved pair distribution function measurements*. *J. Appl. Cryst.* **40**, 463–470.

Chupas, P. J., Qiu, X., Hanson, J. C., Lee, P. L., Grey, C. P. & Billinge, S. J. L. (2003). *Rapid-acquisition pair distribution function (RA-PDF) analysis*. *J. Appl. Cryst.* **36**, 1342–1347.

Coker, E. N., Rodriguez, M. A., Ambrosini, A., Miller, J. E. & Stechel, E. B. (2012). *Using in-situ techniques to probe high-temperature reactions: thermochemical cycles for the production of synthetic fuels from CO_2 and water*. *Powder Diffr.* **27**, 117–125.

Corma, A., Díaz-Cabañas, M. J., Martínez-Triguero, J., Rey, F. & Ruis, J. (2002). *A large-cavity zeolite with wide pore windows and potential as an oil refining catalyst*. *Nature*, **418**, 514–518.

Davison, S., Kershaw, R., Dwight, K. & Wold, A. (1988). *Preparation and characterization of cubic ZrO_2 stabilized by Fe(III) and Fe(II)*. *J. Solid State Chem.* **73**, 47–51.

Durose, K., Asher, S. E., Jaegermann, W., Levi, D., McCandless, B. E., Metzger, W., Moutinho, H., Paulson, P. D., Perkins, C. L., Sites, J. R., Teeter, G. & Terheggen, M. (2004). *Physical characterization of thin-film solar cells*. *Prog. Photovolt. Res. Appl.* **12**, 177–217.

Griego, J. J. M., Rodriguez, M. A. & Wesolowski, D. E. (2012). *Phase transition behaviour of a processed thermal battery*. Report SAND2012–6312. Sandia National Laboratories, Albuquerque, New Mexico, USA.

Gupta, R. (2007). *Advanced coal characterization: a review*. *Energy Fuels*, **21**, 451–460.

Kurzweil, P. (2010). *Gaston Planté and his invention of the lead-acid battery–the genesis of the first practical rechargeable battery J. Power Sources*, **195**, 4424–4434.

Larson, A. C. & Von Dreele, R. B. (2000). *General structure analysis system (GSAS)*. Report LAUR No. 86-748. Los Alamos National Laboratory, New Mexico, USA.

Lu, L., Sahajwalla, V., Kong, C. & Harris, D. (2001). *Quantitative X-ray diffraction analysis and its application to various coals*. *Carbon*, **39**, 1821–1833.

Lukic, S. M., Cao, J., Bansal, R. C., Rodriguez, F. & Emadi, A. (2008). *Energy storage systems for automotive applications*. *IEEE Trans. Ind. Electron.* **55**, 2258–2267.

Luo, J., Xu, H., Liu, Y., Zhao, Y., Daemen, L. L., Brown, C., Timoefeeva, T. V., Ma, S. & Zhou, H.-C. (2008). *Hydrogen adsorption in a highly stable porous rare-earth metal-organic framework: sorption properties and neutron diffraction studies*. *J. Am. Chem. Soc.* **130**, 9626–9627.

McCandless, B. E. & Dobson, K. D. (2004). *Processing options for CdTe thin film solar cells*. *Solar Energy*, **77**, 839–856.

Miller, J. E., Allendorf, M. D., Diver, R. B., Evans, L. R., Siegel, N. P. & Stuecker, J. N. (2008). *Metal oxide composites and structures for ultra-high temperature solar thermochemical cycles*. *J. Mater. Sci.* **43**, 4714–4728.

Mindt, W. (1969). *Electrical properties of electrodeposited PbO_2 films*. *J. Electrochem. Soc.* **116**, 1076–1080.

Pouillerie, C., Perton, F., Biensan, Ph., Pérès, J. P., Broussely, M. & Delmas, C. (2001). *Effect of magnesium substitution on the cycling behaviour of lithium nickel cobalt oxide*. *J. Power Sources*, **96**, 293–302.

Raming, T., Winnbust, L. & Verwejj, H. (2002). *The synthesis and characterisation of mixed Y_2O_3-doped ZrO_2 and α–Fe_2O_3 nanosized powders*. *J. Mater. Chem.* **12**, 3705–3711.

Reimers, J. N. & Dahn, J. R. (1992). *Electrochemical and in situ X-ray diffraction studies of lithium intercalation in Li_xCoO_2*. *J. Electrochem. Soc.* **139**, 2091–2097.

Riktor, M. D., Sørby, M. H., Chłopek, K., Fichtner, M., Buchter, F., Züttel, A. & Hauback, B. C. (2007). *In situ synchrotron diffraction studies in phase transitions and thermal decomposition of $Mg(BH_4)_2$ and $Ca(BH_4)_2$*. *J. Mater. Chem.* **17**, 4939–4942.

Rodriguez, M. A., Boyle, T. J., Yang, P. & Harris, D. L. (2008). *A beryllium dome specimen holder for XRD analysis of air sensitive materials*. *Powder Diffr.* **23**, 121–124.

Rodriguez, M. A., Ingersoll, D. & Doughty, D. H. (2000). *In-situ X-ray diffraction studies on lithium-ion battery cathodes*. *Mater. Res. Soc. Symp. Proc.* **575**, 65–70.

Rodriguez, M. A., Ingersoll, D. & Doughty, D. H. (1998). *In-situ X-ray characterization of $LiMn_2O_4$: a comparison of structural and electrochemical behaviour*. *Mater. Res. Soc. Symp. Proc.* **496**, 275–285.

Rodriguez, M. A., Keenan, M. R. & Nagasubramanian, G. (2007). *In situ X-ray diffraction analysis of $(CF_x)_n$ batteries: signal extraction by multivariate analysis*. *J. Appl. Cryst.* **40**, 1097–1104.

Rodriguez, M. A., Kotula, P. G., Griego, J. J. M., Heath, J. E., Bauer, S. J. & Wesolowski, D. E. (2012). *Multivariate statistical analysis of micro-X-ray fluorescence spectral images*. *Powder Diffr.* **27**, 108–113.

Rodriguez, M. A., Van Benthem, M. H., Ingersoll, D., Vogel, S. C. & Reiche, H. M. (2010). *In situ analysis of $LiFePO_4$ batteries: signal extraction by multivariate analysis*. *Powder Diffr.* **25**, 143–148.

Rodriguez-Carvajal, J. (1993). *Recent advances in magnetic structure determination by neutron powder diffraction*. *Physica B*, **192**, 55–69.

Scherzer, J. (1989). *Octane-enhancing, zeolitic FCC catalysts: scientific and technical aspects*. *Catal. Rev. Sci. Eng.* **31**, 215–354.

Sonibare, O. O., Haeger, T. & Foley, S. F. (2010). *Structural characterization of Nigerian coals by X-ray diffraction, Raman and FTIR spectroscopy*. *Energy*, **35**, 5347–5353.

Toby, B. H. (2001). *EXPGUI, a graphical interface for GSAS*. *J. Appl. Cryst.* **34**, 201–213.

Vermeiren, W. & Gilson, J. P. (2009). *Impact of zeolites on the petroleum and petrochemical industry*. *Top Catal*. **52**, 1131–1161.

Wesolowski, D. E., Rodriguez, M. A., McKenzie, B. B. & Papenguth, H. W. (2011). *Low-hazard metallography of moisture-sensitive electrochemical cells*. *J. Microsc.* **243**, 197–205.

Yen, T. F., Erdman, J. G. & Pollack, S. S. (1961). *Investigation of the structure of petroleum asphaltenes by X-ray diffraction*. *Anal. Chem.* **33**, 1587–1594.

International Tables for Crystallography (2019). Vol. H, Chapter 7.4, pp. 759–766.

7.4. Powder diffraction in art and archaeology

G. Artioli

7.4.1. Introduction

The cultural heritage of mankind includes virtually all materials that humans have employed in their activities during prehistory and history, from the early use of natural organic and mineral compounds as tools for everyday survival to the modern sophisticated and highly symbolic use of technological-age materials in contemporary art. The materials pertaining to cultural heritage therefore potentially encompass most known compounds and their combinations, thus requiring the most advanced and powerful analytical and characterization tools. General targets are: (1) to define the nature and role of the materiality of the objects in relation to human activities, that is the past processes of manufacturing, transformation and use (Tite, 2001); (2) to reconstruct the original state of the materials and recognize the active and past degradation and alteration processes for conservation purposes (May & Jones, 2006); and (3) to establish the physical basis for appropriate interpretation of the intangible part of the cultural heritage (Bouchenaki, 2004).

Cultural-heritage investigations are broadly covered by archaeological science (or archaeometry) and conservation science. *Archaeometry*, a term largely used to describe the quantitative characterization of archaeological objects and processes (Tite, 1991), mainly deals with point (1) above, attempting to relate the materials to the associated past human activities. *Conservation science*, mostly related to curatorship, art history, museum conservation and restoration of art works, mainly deals with point (2) above; the main focus is preservation of heritage for future generations. In terms of the scientific techniques employed in the practical investigations of materials and the methodologies adopted, the two disciplines overlap considerably. Both sciences attempt to interpret cultural-heritage materials and objects (whether related to archaeology or art) as inserted into a timeline related to human activities, that is to understand the evolution of the materials from the raw natural sources, through the man-made production and transformation processes (often involving pyrotechnology), and their use, diffusion and consumption until their disposal, degradation or perhaps their conservation in cultural collections (Fig. 7.4.1). In short, science as applied to cultural-heritage studies is bound to define the present status of the material and the thermodynamics and kinetics of the processes acting on it in order to retrieve information on its past, and to optimize the methods for its preservation for future generations (Artioli, 2010*b*).

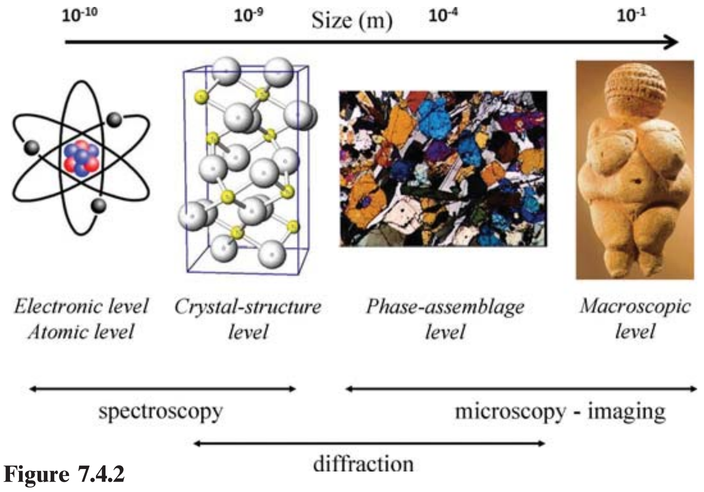

Figure 7.4.2
Different levels and scale of investigation of cultural-heritage materials. Diffraction is most suited to providing information at the crystal-phase level.

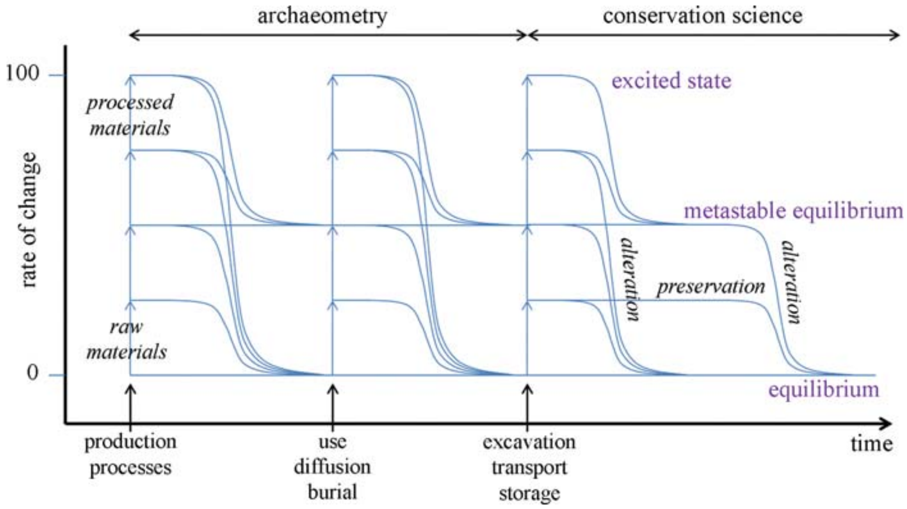

Figure 7.4.1
Rates of change in time for cultural-heritage objects and materials. Rapid changes may occur (*a*) at the manufacturing time of the object, when raw materials are processed and transformed into final objects, often by high-temperature processes, (*b*) during its lifetime (use, diffusion, change of environment and burial) and finally (*c*) during excavation and insertion into collections. Between these events, alteration tends to bring the object back to equilibrium with the environment, whereas conservation processes generally tend to preserve the object in the last metastable state reached during lifetime or burial (modified from Artioli & Angelini, 2011).

All scientific disciplines and available characterization techniques may to some extent contribute to cultural-heritage studies. However, diffraction proves to be invaluable because of its intrinsic sensitivity to crystalline solids. Provided that cultural-heritage materials may be probed at different levels and scales (Fig. 7.4.2), at a first approximation we may state that diffraction is the most important technique for probing materials at the 10^{-9}–10^{-3} m level, yielding information on the crystal phases and their structural arrangements at the atomic and molecular level, besides helping to define the size, shape and orientation of the crystallites. Each of these types of information is discussed in detail.

7.4.2. The information provided by diffraction

X-ray diffraction is the only routine technique in solid-state research that is intrinsically

Table 7.4.1
Mean penetration depth of different types of electromagnetic radiation or particle beams into common materials.

Material (density in g cm^{-3})	Soft X-rays (1 keV)	Cu $K\alpha$ (8 keV)	Hard X-rays (30 keV)	Thermal neutrons (25.3 meV)	Protons (2 MeV)	Electrons (30 keV)
Fe (7.87)	0.1 µm	4.2 µm	0.2 mm	8.3 mm	19.2 µm	2.1 µm
Quartz (2.64)	1.2 µm	0.1 mm	4.8 mm	3.5 cm	39.2 µm	6.2 µm
Bone (1.80)	1.3 µm	0.1 mm	4.9 mm	2.8 cm	46.5 µm	9.1 µm
Polypropylene (0.90)	5.9 µm	2.9 mm	4.7 cm	1.5 mm	74.6 µm	18.3 µm
Wood (0.59)	5.2 µm	2.0 mm	6.1 cm	5.2 cm	144.7 µm	27.9 µm

sensitive to the long-range order and symmetry in crystals. For 100 years since von Laue's discovery of the interaction between X-rays and crystals, it has allowed the analysis of crystal structures at the atomic and molecular level, providing the means of characterizing and interpreting the intimate nature of crystalline compounds from simple elemental and ionic solids to complex macromolecules. Because of the methodological advances and the versatility of present-day instrumentation, X-ray, neutron and electron-diffraction techniques are considered among the established basic tools for the analysis of materials. Traditionally, X-ray powder diffraction has been the technique of choice for the rapid and efficient identification of polycrystalline compounds, whereas single-crystal diffraction was and is the preferred technique for structure solution and analysis, although the recent advances in whole-pattern profile analysis (Dinnebier & Billinge, 2008) have considerably expanded the potential and applicability of powder diffraction. The power of powder diffraction, combined with the fact that the vast majority of archaeological and art materials are polycrystalline in nature, mean that powder techniques are universally employed in the field.

Diffraction techniques (Giacovazzo, 2011) in essence provide very basic information on the nature of the material, on its physical state, and on its atomic and chemical arrangement. This information includes: (1) the *phase identification and quantification* of crystalline compounds and complex polyphasic mixtures, (2) the *texture* and *orientation* of the crystalline phases, (3) the *atomic and molecular structure* of the phases involved, and (4) the physical *microstructural state* of the material in terms of crystallite size and accumulated strain. Fig. 7.4.3 schematically summarizes each one of the pieces of information that may profitably be used in cultural-heritage investigations. They will be discussed separately with reference to specific examples.

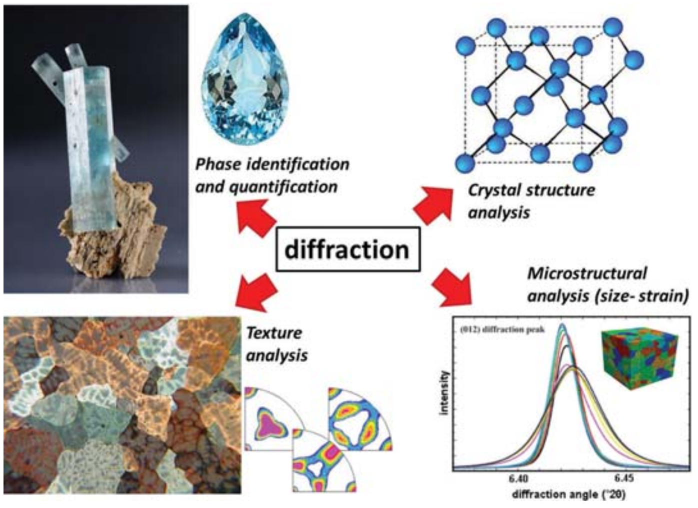
Phase identification and quantification
Crystal structure analysis
diffraction
Microstructural analysis (size- strain)
Texture analysis
(012) diffraction peak
intensity
6.40
6.45
diffraction angle (°2θ)

Figure 7.4.3
The main information on cultural-heritage materials provided by diffraction.

7.4.3. Phase identification and quantification

Whether we deal with pigments, archaeological ceramics, metals or stone tools, the first steps to understanding the nature of the compounds and the problems involved are invariably (1) a definition of the chemical system by elemental and chemical analysis and (2) the correct identification of the organic and inorganic crystalline phases present in the material by powder diffraction. When dealing with simple minerals or synthetic chemical precipitates, the identification of the crystalline phases is mostly a straightforward procedure, requiring good-quality diffraction measurements (most commonly X-ray powder-diffraction data) and appropriate search–match procedures within reference databases (ICDD Powder Diffraction File: http://www.icdd.com; ICSD – Inorganic Crystal Structure Database: http://www.fiz-karlsruhe.de/icsd.html; CSD – Cambridge Structural Database: http://www.ccdc.cam.ac.uk/Solutions/CSDSystem/Pages/CSD.aspx) (Bish & Post, 1989; Monaco & Artioli, 2011). However, cultural-heritage material can be varied (natural minerals, synthetic products, processed and treated materials, alteration and corrosion products, *etc.*) and potentially very complex. They are frequently polyphasic composites, and depending on the time that has elapsed between their production and their use, their original nature can be severely contaminated, degraded and altered. Phase identification therefore may be a very complicated process, requiring optimized measuring techniques and substantial experience for data interpretation.

From the experimental point of view, the most limiting factors for diffraction studies of cultural-heritage materials are the scarcity of available sample (if the object can be directly sampled) or the surface alteration and the treatment layers covering the original material (if the object cannot be sampled). Modern diffractometric techniques often allow direct non-invasive measurement of the object itself, although the depth of probing is closely related to the measuring conditions (energy of the probe, diffraction geometry *etc.*) and the nature of the material. Laboratory X-rays of course mostly probe just the surface layers of most materials, and bulk measurements must be performed with very energetic synchrotron hard X-rays or neutrons. Table 7.4.1 provides an indication of the mean penetration depth of different electromagnetic radiation or particle beams into matter. The selected diffraction geometry also has important consequences on the probed volume: surface layers (preservation treatments, protecting varnishes, corrosion layers, painting layers, glazes *etc.*) are conveniently explored with X-rays under glancing-angle conditions or through synchrotron microbeams (see, for example, the analysis of varnishes of ancient musical instruments: Echard & Lavédrine, 2008; Echard *et al.*, 2008); bulk analysis of the internal part of the objects is of course better performed using hard X-rays or neutrons (Kockelmann *et al.*, 2006). The powder-diffraction analysis of ancient Egyptian cosmetics contained in well-preserved sealed vessels (Martinetto

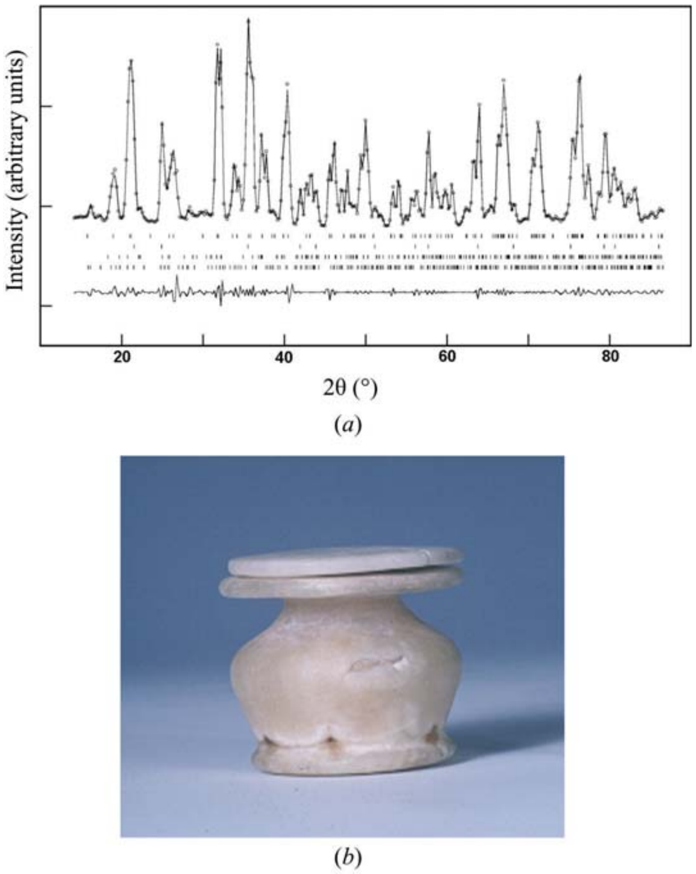

Figure 7.4.4
A neutron powder diffraction profile (*a*) of ancient Egyptian cosmetics contained inside a sealed vessel (*b*). Penetrating neutron beams allow phase identification of the material in a totally non-invasive mode (from Martinetto *et al.*, 2003).

et al., 2003) is a good example of phase identification through thick objects thanks to non-invasive penetrating neutron beams (Fig. 7.4.4).

One important aspect to be considered when working with extremely small quantities of powdered material or with microbeams that probe very small volumes of sample in a non-invasive way is the incomplete powder averaging of the diffraction signal, since the sample is far from an ideal polycrystalline sample having a large number of randomly oriented crystallites. In such cases, and also when using portable X-ray diffraction (XRD) probes, much caution should be taken in interpreting the data. If possible, repeated measurements through different directions in the sample should be performed when using point or linear detectors, and as much reciprocal space as accessible should be analysed when using two-dimensional detectors.

Besides phase identification, modern powder diffraction is a very powerful tool for the quantification of crystal phases in polyphasic mixtures (Madsen & Scarlett, 2008). Quantitative analysis applied to cultural-heritage materials is commonly used to characterize the phases relative to specific production processes, to trace the provenance of materials, to understand the details of the manufacturing techniques or to evaluate the degradation state of the object. If the phase quantification is carried out in great detail, the results may be used as a powerful discriminatory tool to distinguish apparently similar materials such as ancient mortars produced with slightly different raw materials and/or in different times (see, for example, Secco *et al.*, 2010; Artioli, 2010*a*). The statistical discriminant analysis performed on the phase quantities is analogous to that performed on chemical or isotopic tracers.

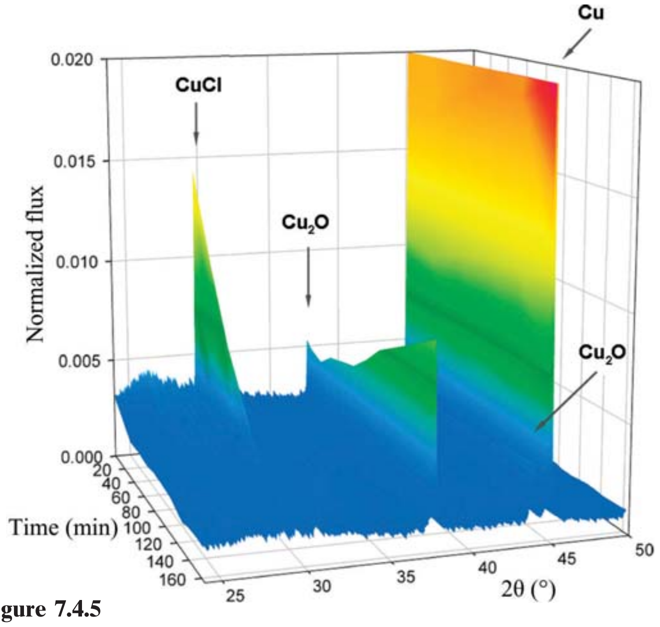

Figure 7.4.5
Synchrotron-based techniques have been used to evaluate corrosion-potential measurements as monitoring method for copper-based objects recovered from marine environments (from Adriaens & Dowsett, 2010). The extraction of chlorides from the corroded metal artifacts is required for conservation, since their presence will restart the corrosion process in very short times.

One interesting application is the *in situ* quantification of crystalline phases during the artificial treatment of the sample, for example under confined chemical conditions or at non-ambient pressure and temperature. Such *in situ* diffraction techniques require special sample-conditioning chambers and optimized experimental setups. These experiments yield crucial information on the kinetics of the processes, for example the determination of the rates of the corrosion processes in archaeological metals that are crucial for conservation purposes (Leyssens *et al.*, 2005). More specifically, synchrotron-based techniques have been employed to evaluate the use of corrosion-potential measurements as a visible monitoring method for copper-based objects recovered from marine environments (Fig. 7.4.5: Adriaens & Dowsett, 2008, 2010). High-temperature diffraction is also a very useful technique for assessing the phase transformations taking place during pyrotechnological processing. It has been successfully used to investigate cinnabar decomposition and the precipitation of silver particles in the lustre layer of medieval glazed ceramics (Pradell *et al.*, 2008), and in principle it could be used to assess directly the firing conditions of archaeological ceramics, for example by measuring *in situ* the reactivation temperature of the phase transformation. However, to date X-ray powder diffraction is mostly used at ambient conditions to check the products obtained by high-temperature firing of clays (Häusler, 2004).

7.4.4. Crystal structure analysis

Detailed knowledge of the crystal structure of heritage materials at the atomic or molecular levels is rarely required in routine investigations. However, for particular materials the atomic arrangement may provide the key to understanding the physicochemical properties and the reactivity of the phase. Pigment phases in paintings and frescoes are pertinent examples of important heritage materials that frequently require very detailed investigations to pinpoint the nature of the colouring mechanisms, the conservation state and their predicted variation in time. Advanced laboratory and synchrotron-based diffraction techniques are increasingly used in combination with complementary spectroscopic ones (especially X-ray absorption spectroscopy) in order to identify the pigments and their distribution in paint layers (see, for example, Welcomme *et al.*, 2007; Herrera *et al.*, 2008; Duran *et al.*, 2010), thus accessing information about the sub-surface layers and the pigment micro-spatial distribution (Cotte *et al.*, 2007, 2010). However, in complex cases the definition of the pigment and the complete understanding of its physico-chemical behaviour require knowledge of the atomic structure [see, for example, the case of Naples yellow (= lead antimonate); Dik *et al.*, 2005], and this can be a challenging task. Two classic examples involving rather complex crystal structures are the Maya blue and the Catalan blue pigments (Fig. 7.4.6).

Maya blue is the unusually stable typical blue colour present in Mayan frescoes and objects (Reyes-Valerio, 1993). Despite a large number of investigations, it has escaped full characterization for more than 50 years (Gettens, 1962), although it has long been recognized that it is a combination of an inorganic compound, the mineral palygorskite, and an organic part, the indigo molecule extracted from *Indigo sp.* plants. Ongoing investigations aimed at achieving a satisfactory model of the hybrid organo-clay complex include high-resolution transmission electron microscopy, proton-induced X-ray emission, X-ray absorption spectroscopy, Raman spectroscopy, thermal analysis and molecular modelling, beside a substantial number of structural studies (for a complete account, see Sanchez del Rio *et al.*, 2011, and references therein). Recent structure analysis by synchrotron X-ray and neutron diffraction clarified that the indigo molecule is indeed absorbed inside the zeolitic channels of the palygorskite clay, and that there is strong interaction between the organic molecule and the hosting framework. However, it is known that the palygorskite mineral system is invariably composed of at least two polymorphs, one orthorhombic and one monoclinic, that the structure may have extensive polysomatic defects (the palysepiole polysomatic series; Ferraris *et al.*, 2004), and therefore sepiolite impurities are frequently present. The real system is therefore substantially more complicated that the assumed models, and further work is required to sort the details of the pigment actually used in Mesoamerica.

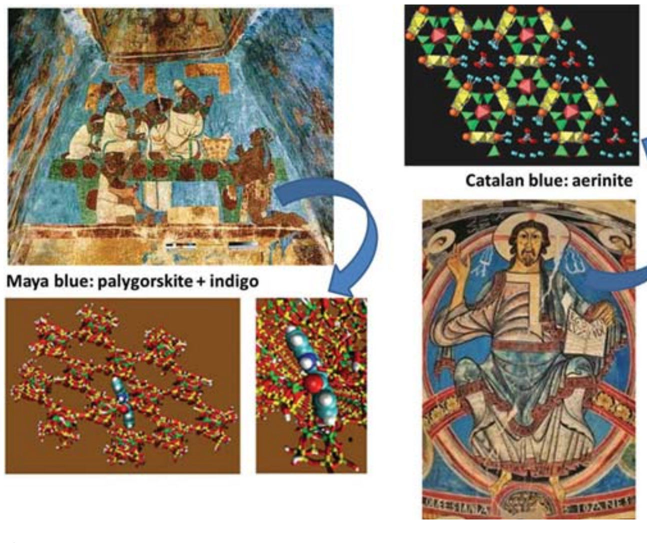

Figure 7.4.6
The crystal structure analysis of Maya blue (palygorskite) and Catalan blue pigments (aerinite) proved to be challenging tasks, both achieved through powder-diffraction analysis. Knowledge of the structural arrangements is fundamental in understanding their physico-chemical behaviour and pigmenting properties.

Catalan blue is also a very stable pigment, used in most Catalan Romanesque paintings between the 11th and 15th centuries. It has long been known to be essentially composed of the mineral aerinite, although its complex pyroxene-related structure remained unsolved until very recently (Rius *et al.*, 2004, 2009). In the aerinite case, synchrotron-radiation diffraction was pivotal not only in allowing the structure solution and subsequent refinement of the mineral, but also in determining the painting-layer stratigraphy with high spatial resolution of several church frescoes from the central Pyrenees, thus confirming the presence of aerinite-based pigments and therefore close artistic connections between Occitanian churches in the Pyrenees and the Catalan Romanesque paintings (Salvadó *et al.*, 2008).

7.4.5. Texture analysis

The inhomogeneous spatial distribution of crystallites in a sample implies an inhomogeneous distribution of Bragg intensity in the Debye rings. The measurement of the variation in intensity along the diffraction rings allows calculation of the so-called orientation distribution function (ODF) of the crystallites, that is, the function that statistically describes the crystallographic orientation of the crystals in the samples with respect to the sample orientation (Kocks *et al.*, 1998; Popa, 2008). Orientation distributions are generally represented graphically by means of pole figures in direct (*i.e.* the sample space) or inverse (*i.e.* the crystallographic space) space (Monaco & Artioli, 2011).

Since the shape and orientation of the crystallites in a solid depend on its thermo-mechanical history, the measurement of the crystallographic textural features of the sample (crystallographic texture analysis: CTA) is a powerful tool for determining the manufacturing process of an object: its application is especially important for archaeological and historical metals. The main technique universally used to interpret heritage metals is metallography (Scott, 1991), invasively performed by reflected-light optical microscopy on small polished and etched sections of the object's surface. CTA based on diffraction data has been proposed as a totally non-invasive alternative technique to conventional optical metallography (Artioli, 2007, 2010*b*, pp. 343–348). It should be noted that for metals and averagely absorbing materials, texture analysis performed with X-rays gives only a description of the surface layer of the sample, whereas the same analysis performed with deeply penetrating neutrons may yield a more appropriate interpretation of the bulk. Fig. 7.4.7 shows an example of the pole figures resulting from the full CTA analysis of a prehistoric copper axe; the data allow complete interpretation of the metallurgical processes employed to produce the object (Artioli *et al.*, 2003).

7.4.6. Microstructural analysis

A careful analysis of the profile shape of the diffraction maxima of a polycrystalline material and of their angular dependence can give information on the size distribution of the crystallites and on the presence of lattice strains. This is commonly referred to as microstructural analysis of the sample, and it describes the measured profile as the convolution of the sample-dependent effects with the instrumental contributions (Snyder *et al.*, 2000). Strain measurements, which are particularly important in the evaluation of residual stress present in industrial materials and engineering components, may also be profitably used to characterize cultural-heritage materials.

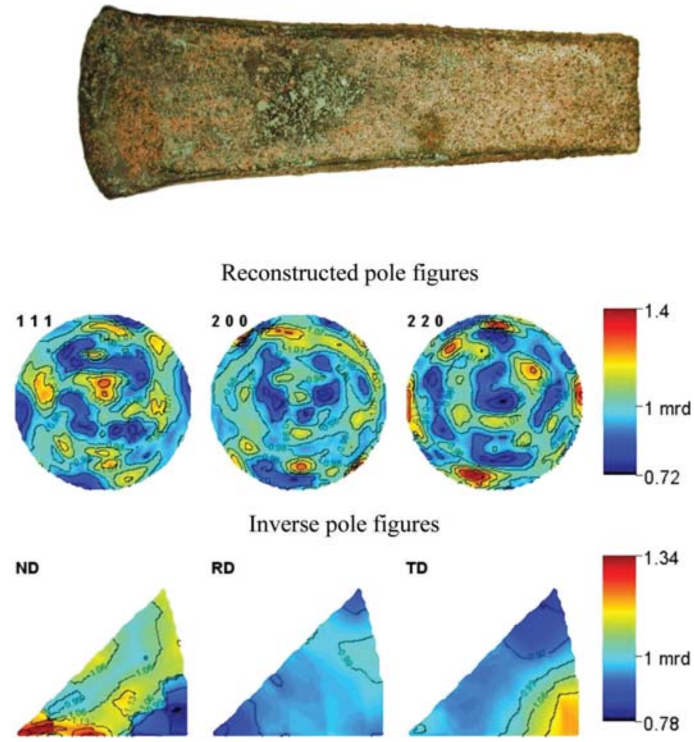

Figure 7.4.7
Recalculated and inverse pole figures for the Remedello copper axe from Tomb 102 (Artioli, 2007). The main recognizable features are weak 310 and 110 components of the fibre texture caused by mechanical working and the strong $\{100\}\langle 100\rangle$ cube recrystallization texture due to substantial thermal annealing.

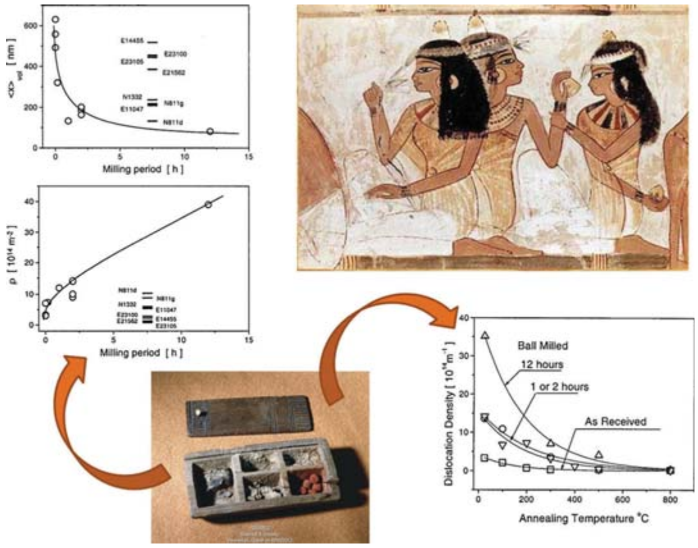

Figure 7.4.8
Detailed microstructural analysis of high-resolution synchrotron powder data of galena as the main ingredient in ancient Egyptian kohl (Ungar *et al.*, 2002, 2003). The archaeological samples are compatible with a controlled process that included grinding and thermal annealing, as inferred from the measured mean size and dislocation density in the crystallites of standard samples of galena prepared under controlled conditions. Reproduced with permission from Unger *et al.* (2002). Copyright (2002) AIP Publishing LLC.

The most illustrative example of microstructural analysis from the diffraction-peak broadening of heritage materials is the careful investigation of ancient Egyptian cosmetics performed by the joint Louvre–ESRF–CRNS group (Walter *et al.*, 1999; Tsoucaris *et al.*, 2001). In-depth analytical work performed by high-resolution synchrotron X-ray diffraction showed unequivocally that the large grain size and the significant particle strain of Egyptian kohl are related to hand grinding of galena particles (Fig. 7.4.8), whereas the small crystal size and lack of strain of Egyptian white pigments (mainly laurionite, hydrocerussite) are compatible with chemical precipitation (Martinetto *et al.* 2000, 2001; Ungar *et al.*, 2002, 2003). The careful control of the grinding and thermal annealing treatments of black galena, together with mixing with different proportions of white cerussite, allowed preparation of make-ups with specific colour shades and adhering properties. This neatly confirmed that the science and business of cosmetics started a long time ago (Martinetto *et al.*, 1999).

7.4.7. Present trends

It is appropriate to complete this brief overview with a few comments on present trends in the use of diffraction instrumentation and techniques applied to cultural-heritage materials.

(1) There is a general trend to produce and make use of portable instrumentation, either portable X-ray powder diffractometers or combined instruments performing diffraction and X-ray fluorescence analysis. A number of prototypes and a few commercial instruments are available on the market, the most successful ones applying instrumental technology similar to that selected for the Mars Science Laboratory (MSL Chemin Instrument: Yen *et al.*, 2012). This 'labs go to the museum' attitude (Artioli, 2010*b*) is equally welcomed by the manufacturers in search of novel markets and by cultural-heritage workers (museum curators, archaeologists, conservators *etc*.) who would like fast-access analyses in the most diverse situations: archaeological excavations, field surveys, wide screening of museum objects, outdoor architecture, monument characterization and the like. Although the trend is certainly positive, since it allows characterization of objects that cannot be taken to diffraction laboratories or sampled (for example statues, frescoes *etc.*), it should be stressed that the data obtained in non-standard laboratory conditions are frequently biased, especially for quantification purposes. Therefore the results from portable instrumentation are acceptable only as long as the approximate quality of most of the data obtained is recognized and the data are used accordingly. The danger is that low-quality, misleading or even wrong data may proliferate and be hard to contest should they enter the literature.

(2) In parallel to the fast development of laboratory diffraction instrumentation, large-scale facilities, especially synchrotron X-ray sources and neutron beams, are increasingly becoming available. In most cases access is provided by national and international institutions, so that their use is likely to expand among research groups.

Synchrotron facilities are being optimized for *microbeams* (Janssens & Van Grieken, 2004; Creagh, 2007; Bertrand *et al.*, 2012) and for simultaneous or combined two- and three-dimensional mapping of fluorescence, absorption and diffraction signals. The spatial correlation of the diffraction and spectroscopic signals is crucial in order to disentangle the presence of different compounds in complex polyphasic mixtures. These multi-spectral techniques yield complementary space-resolved information on chemical speciation and phase composition: they represent powerful tools for the characterization of cultural-heritage materials at the micron or sub-micron scale (Fig. 7.4.9), including for example metals (Friedman *et al.*, 2008; Young *et al.*,

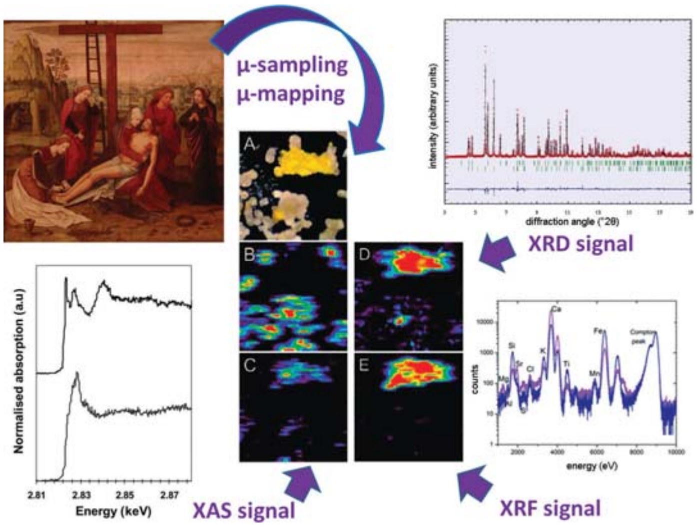

Figure 7.4.9
Schematic diagram showing the potential of simultaneous two-dimensional micro-mapping using synchrotron radiation to excite multiple signals. Combined interpretation of the maps allow extraction of information concerning the crystal phases from XRD, elemental chemistry from X-ray fluorescence and oxidation state of selected elements from X-ray absorption spectroscopy. (The scheme is not related to a single experiment, but rather a collage of pictures and data from various sources.)

2010; Young, 2012) and pigments (Cotte *et al.*, 2007, 2008, 2010; Dik *et al.*, 2008; Herrera *et al.*, 2009). Synchrotron-based experiments can also be combined with three-dimensional imaging (computed micro-tomography, μCT) and designed for the tomographic reconstruction of the diffraction signal (Bleuet *et al.*, 2008); the technique is defined as X-ray diffraction microtomography (XRD-μCT: De Nolf & Janssens, 2010; Artioli *et al.*, 2010; Valentini *et al.*, 2011) and it is an example of the increasing potential of the combination of diffraction and imaging techniques. Specific software is publicly available for the analysis of two-dimensional multi-spectral signals (*PyMCA – Python Multichannel Analyzer*: http://pymca.sourceforge.net/index.html; Solé *et al.*, 2007) and also for three-dimensional tomographic reconstructions using the diffraction signal (*XRDUA*: http://xrdua.ua.ac.be/; De Nolf & Janssens, 2010).

Thermal neutron beams, both from spallation sources and from steady-state nuclear reactors, by virtue of their penetration power (Table 7.4.1) are ideal for the analysis of large and thick objects. *Neutron imaging* is a leading technique for the internal visualization of art and archaeological objects (Lehmann *et al.*, 2005, 2010; Casali, 2006), and it is increasingly coupled with diffraction probing of the materials to obtain simultaneous complete information of phase composition and heterogeneous distribution of materials within the objects (van Langh *et al.*, 2011). Novel neutron-imaging techniques, sometimes called Bragg-edge imaging (Lehmann *et al.*, 2009), are being developed in order to enhance the phase sensitivity of the tomographic images (Kockelmann & Kirfel, 2006; Kockelmann *et al.*, 2006).

Both in the case of synchrotron microbeams and in the case of enhanced neutron imaging, it is expected that in the near future the powerful combination of imaging and diffraction will be a major tool in cultural-heritage research. Furthermore, synchrotron and spallation neutron beams allow experimental access to extended scattering space, so that the rapidly developing techniques based on pair-distribution functions (PDFs) that make use of total scattering for structure analysis can be efficiently employed (Welberry, 2004; Egami & Billinge, 2004). These techniques can equally be applied to crystalline and disordered materials and, although they have not yet been applied to cultural-heritage materials, they offer great potential for future contributions.

In honouring the past 100 years (1912–2012) as the period in which diffraction has developed into an important and mature characterization technique, we can not avoid recalling the huge instrumental developments that have occurred in the last decades. Should the technical and methodological developments proceed at the same pace, we will soon have many more tools available for the investigation of our past heritage.

As a final remark, it is advised that use of the cited diffraction techniques, from portable sources to advanced large-scale synchrotron radiation and neutron sources, are inserted into appropriate analytical protocols. Ranking the experimental operations in terms of increasing cost and manpower, the ideal analytical sequence involving diffraction might encompass: (*a*) a first qualitative step based on preliminary sampling and/or portable instrumentation; (*b*) a second quantitative step based on appropriate (micro)sampling, *in situ* analysis, and/or laboratory quantification; and (*c*) a third step exploiting experiments at large-scale facilities for improved data quality and access to non-standard instrumentation and techniques.

References

Adriaens, A. & Dowsett, M. (2008). *Time resolved spectroelectrochemistry studies for protection of heritage metals*. *Surf. Eng.* **24**, 84–89.

Adriaens, A. & Dowsett, M. (2010). *The coordinated use of synchrotron spectroelectrochemistry for corrosion studies on heritage metals*. *Acc. Chem. Res.* **43**, 927–935.

Artioli, G. (2007). *Crystallographic texture analysis of archaeological metals: interpretation of manufacturing techniques*. *Appl. Phys. A*, **89**, 899–908.

Artioli, G. (2010*a*). *Mineralogy and cultural heritage*. *Chimia*, **64**, 712–715.

Artioli, G. (2010*b*). *Scientific Methods and the Cultural Heritage*. Oxford University Press.

Artioli, G. & Angelini, I. (2011). *Mineralogy and archaeology: fatal attraction*. *Eur. J. Mineral.* **23**, 849–855.

Artioli, G., Cerulli, T., Cruciani, G., Dalconi, M. C., Ferrari, G., Parisatto, M., Rack, A. & Tucoulou, R. (2010). *X-ray diffraction microtomography (XRD-CT), a novel tool for non-invasive mapping of phase development in cement materials*. *Anal. Bioanal. Chem.* **397**, 2131–2136.

Artioli, G., Dugnani, M., Hansen, T., Lutterotti, L., Pedrotti, A. & Sperl, G. (2003). *Crystallographic texture analysis of the Iceman and coeval copper axes by non-invasive neutron powder diffraction*. In *La mummia dell'età del rame. 2. Nuove ricerche sull'uomo venuto dal ghiaccio*, Vol. 3, edited by A. Fleckinger, pp. 9–22. Collana del Museo Archeologico dell'Alto Adige, Folio Verlag, Bolzano.

Bertrand, L., Cotte, M., Stampanoni, M., Thoury, M., Marone, F. & Schoeder, S. (2012). *Developments and trends in synchrotron studies of ancient and historical materials*. *Phys. Rep.* **519**, 51–96.

Bish, D. L. & Post, J. E. (1989). Editors. *Modern Powder Diffraction*. *Reviews in Mineralogy*, Vol. 20. Chantilly: Mineralogical Society of America.

Bleuet, P., Welcomme, E., Dooryhée, E., Susini, J., Hodeau, J.-L. & Walter, Ph. (2008). *Probing the structure of heterogeneous diluted materials by diffraction tomography*. *Nat. Mater.* **7**, 468–472.

Bouchenaki, M. (2004). Editor. *Defining the intangible cultural heritage*. *Museum Int.* (Special issue) **56**, 1–197.

Casali, F. (2006). *X-ray and neutron digital radiography and computed tomography for cultural heritage*. In *Physical Techniques in the Study of Art, Archaeology and Cultural Heritage*, Vol. 1, edited by D. Bradley & D. Creagh, ch. 2, pp. 41–123. Amsterdam: Elsevier.

Cotte, M., Susini, J., Dik, J. & Janssens, K. (2010). *Synchrotron-based X-ray absorption spectroscopy for art conservation: looking back and looking forward*. *Acc. Chem. Res.* **43**, 705–714.

Cotte, M., Susini, J., Solé, V. A., Taniguchi, Y., Chillida, J., Checroun, E. & Walter, Ph. (2008). *Applications of synchrotron-based micro-*

imaging techniques to the chemical analysis of ancient paintings. *J. Anal. At. Spectrom.* **23**, 820–828.

Cotte, M., Welcomme, E., Solé, V. A., Salomé, M., Menu, M., Walter, Ph. & Susini, J. (2007). *Synchrotron-based X-ray spectromicroscopy used for the study of an atypical micrometric pigment in 16th century paintings*. *Anal. Chem.* **79**, 6988–6994.

Creagh, D. (2007). *Synchrotron radiation and its use in art, archaeometry, and cultural heritage studies*. In *Physical Techniques in the Study of Art, Archaeology and Cultural Heritage*, Vol. 2, edited by D. Bradley & D. Creagh. Amsterdam: Elsevier.

De Nolf, W. & Janssens, K. (2010). *Micro X-ray diffraction and fluorescence tomography for the study of multilayered automotive paints*. *Surf. Interface Anal.* **42**, 411–418.

Dik, J., Hermens, E., Peschar, R. & Schenk, H. (2005). *Early production recipes for lead antimonate yellow in Italian art*. *Archaeometry*, **47**, 593–607.

Dik, J., Janssens, K., Van Der Snickt, G., van der Loeff, L., Rickers, K. & Cotte, M. (2008). *Visualization of a lost painting by Vincent van Gogh using synchrotron radiation based X-ray fluorescence elemental mapping*. *Anal. Chem.* **80**, 6436–6442.

Dinnebier, R. E. & Billinge, S. J. L. (2008). Editors. *Powder Diffraction: Theory and Practice*. Cambridge: RCS Publishing.

Duran, A., Jimenez De Haro, M. C., Perez-Rodriguez, J. L., Franquelo, M. L., Herrera, L. K. & Justo, A. (2010). *Determination of pigments and binders in Pompeian wall paintings using synchrotron radiation – high-resolution X-ray powder diffraction and conventional spectroscopy – chromatography*. *Archaeometry*, **52**, 286–307.

Echard, J.-P., Cotte, M., Dooryhée, E. & Bertrand, L. (2008). *Insights into the varnishes of historical musical instruments using synchrotron micro-analytical methods*. *Appl. Phys. A*, **92**, 77–81.

Echard, J.-P. & Lavédrine, B. (2008). *Review on the characterisation of ancient stringed musical instruments varnishes and implementation of an analytical strategy*. *J. Cult. Herit.* **9**, 420–429.

Egami, T. & Billinge, S. J. L. (2004). *Underneath the Bragg Peaks: Structural Analysis of Complex Materials*. Oxford: Elsevier Science.

Ferraris, G., Makovicky, E. & Merlino, S. (2004). *Crystallography of Modular Materials*. IUCr Monographs on Crystallography, Vol. 15, pp. 259–262. Oxford Science Publications, Oxford.

Friedman, E. S., Brody, A. J., Young, M. L., Almer, J. D., Segre, C. U. & Mini, S. M. (2008). *Synchrotron radiation-based x-ray analysis of bronze artifacts from an Iron Age site in the Judean Hills*. *J. Arch. Sci.* **35**, 1951–1960.

Gettens, R. J. (1962). *Maya blue: an unresolved problem in ancient pigments*. *Am. Antiq.* **27**, 557–564.

Giacovazzo, C. (2011). Editor. *Fundamentals of Crystallography*. IUCr Texts on Crystallography, Vol. 15, 3rd ed. Oxford Science Publications.

Häusler, W. (2004). *Firing of clays studied by X-ray diffraction and Mössbauer spectroscopy*. *Hyperfine Interact.* **154**, 121–141.

Herrera, L., Cotte, M., Jimenez de Haro, M., Duran, A., Justo, A. & Perez-Rodriguez, J. (2008). *Characterization of iron oxide-based pigments by synchrotron-based micro X-ray diffraction*. *Appl. Clay Sci.* **42**, 57–62.

Herrera, L. K., Montalbani, S., Chiavari, G., Cotte, M., Solé, V. A., Bueno, J., Duran, A., Justo, A. & Perez-Rodriguez, J. L. (2009). *Advanced combined application of μ-X-ray diffraction/μ-X-ray fluorescence with conventional techniques for the identification of pictorial materials from Baroque Andalusia paintings*. *Talanta*, **80**, 71–83.

Janssens, K. & Van Grieken, R. (2004). Editors. *Non-destructive Microanalysis of Cultural Heritage Materials*. Comprehensive Analytical Chemistry Series, Vol. XLII. Amsterdam: Elsevier.

Kockelmann, W. & Kirfel, A. (2006). *Neutron diffraction imaging of cultural heritage objects*. *Archeom. Muhely*, **2**, 1–15.

Kockelmann, W., Siano, S., Bartoli, L., Visser, D., Hallebeek, P., Traum, R., Linke, R., Schreiner, M. & Kirfel, A. (2006). *Applications of TOF neutron diffraction in archaeometry*. *Appl. Phys. A*, **83**, 175–182.

Kocks, U. F., Tomé, C. N. & Wenk, H. R. (1998). Editors. *Texture and Anisotropy. Preferred Orientation in Polycrystals and their Effect on Materials Properties*. Cambridge University Press.

Langh, R. van, James, J., Burca, G., Kockelmann, W., Zhang, S. Y., Lehmann, E., Estermann, M. & Pappot, A. (2011). *New insights into alloy compositions: studying Renaissance bronze statuettes by combined neutron imaging and neutron diffraction techniques*. *J. Anal. At. Spectrom.* **26**, 949–958.

Lehmann, E., Frei, G., Vontobel, P., Josic, L., Kardjilov, N., Hilger, A., Kockelmann, W. & Steuwer, A. (2009). *The energy-selective option in neutron imaging*. *Nucl. Instrum. Methods Phys. Res. A*, **603**, 429–438.

Lehmann, E. H., Deschler-Erb, E. & Ford, A. (2010). *Neutron tomography as a valuable tool for the non-destructive analysis of historical bronze sculptures*. *Archaeometry*, **52**, 272–285.

Lehmann, E. H., Vontobel, P., Deschler-Erb, E. & Soares, M. (2005). *Non-invasive studies of objects from cultural heritage Nucl. Instrum. Methods Phys. Res. A*, **542**, 68–75.

Leyssens, K., Adriaens, A., Dowsett, M., Schotte, B., Oloff, I., Pantos, E., Bell, A. & Thompson, S. (2005). *Simultaneous in situ time resolved SR-XRD and corrosion potential analyses to monitor the corrosion on copper*. *Electrochem. Commun.* **7**, 1265–1270.

Madsen, I. C. & Scarlett, N. V. Y. (2008). *Quantitative phase analysis*. In *Powder Diffraction: Theory and Practice*, edited by R. E. Dinnebier & S. J. L. Billinge. pp. 298–331. Cambridge: RCS Publishing.

Martinetto, P., Anne, M., Dooryhée, E., Drakopoulos, M., Dubus, M., Salomon, J., Simionovici, A. & Walter, P. (2001). *Synchrotron X-ray micro-beam studies of ancient Egyptian make-up*. *Nucl. Instrum. Methods Phys. Res. B*, **181**, 744–748.

Martinetto, P., Anne, M., Dooryhée, E., Isnard, O. & Walter, P. (2003). *A non-destructive analysis by neutron diffraction inside make-up containers of ancient Egypt*. In *Molecular and Structural Archaeology: Cosmetic and Therapeutic Chemicals*, edited by G. Tsoucaris & J. Lipkowski. NATO Science Series II, Mathematics, Physics and Chemistry, Vol. 117, pp. 107–111. Dordrecht, Boston, London: Kluwer Academic Publishers.

Martinetto, P., Anne, M., Dooryhée, E., Tsoucaris, G. & Walter Ph. (2000). *A synchrotron X-ray diffraction study of Egyptian cosmetics*. In *Radiation in Art and Archaeometry*, edited by D. C. Creagh & D. A. Bradley, pp. 297–316. Amsterdam: Elsevier Science.

Martinetto, P., Dooryhée, E., Anne, M., Talabot, J., Tsoucaris, G. & Walter, P. (1999). *Cosmetic recipes and make-up manufacturing in ancient Egypt*. *Newsletter*, ESRF, April 1999, pp. 10–11.

May, E. & Jones, M. (2006). Editors. *Conservation Science*. Cambridge: RSC Publishing

Monaco, H. L. & Artioli, G. (2011). *Experimental methods in X-ray and neutron crystallography*. In *Fundamentals of Crystallography*, edited by C. Giacovazzo, Vol. 15, 3rd ed., ch. 5, pp. 301–416. IUCr Texts on Crystallography. Oxford Science Publications.

Popa, N. C. (2008). *Microstructural properties: Texture and macrostress effects*. In *Powder Diffraction: Theory and Practice*, edited by R. E. Dinnebier & S. J. L. Billinge, pp. 335–372. Cambridge: RCS Publishing.

Pradell, T., Molera, J., Pantos, E., Smith, A. D., Martin, C. M. & Labrador, L. (2008). *Temperature resolved reproduction of medieval luster*. *Appl. Phys. A*, **90**, 81–88.

Reyes-Valerio, C. (1993). *De Bonampak al Templo Mayor. El azul maya en Mesoamérica*. Coleccion América Nuestra, Vol. 40, pp. 1–157. Mexico City: Siglo XXI Editores.

Rius, J., Crespi, A., Roig, A. & Melgarejo, J. C. (2009). *Crystal-structure refinement of Fe^{3+}-rich aerinite from synchrotron powder diffraction and Mössbauer data*. *Eur. J. Mineral.* **21**, 233–240.

Rius, J., Elkaim, E. & Torrelles, X. (2004). *Structure determination of the blue mineral pigment aerinite from synchrotron powder diffraction data: the solution of an old riddle*. *Eur. J. Mineral.* **16**, 127–134.

Salvadó, N., Butí, S., Pantos, E., Bahrami, F., Labrador, A. & Pradell, T. (2008). *The use of combined synchrotron radiation micro FT–IR and XRD for the characterization of Romanesque wall paintings*. *Appl. Phys. Mater. Sci. Process.* **90**, 67–73.

Sanchez del Rio, M., Domenech, A., Domenech-Carbo, M. T., Vazquez de Agredos Pascual, M. L., Suarez, M. & Garcia-Romero, E. (2011). *The Maya blue pigment*. *Developments in Clay Science*, Vol. 3, ch. 18, pp. 453–481. Amsterdam: Elsevier.

Scott, D. A. (1991). *Metallography and Microstructure of Ancient and Historic Metals*. Los Angeles: The Getty Conservation Institute.

Secco, M., Artioli, G., Mazzoli, C., Gelichi, S., Cianciosi, A. & Piuzzi, F. (2010). *Archaeometrical studies on mortars from the Sachuidic Castle (Forni di Sopra, North-Eastern Italy): a tool for archaeological interpretation*. ISA2010, 38th International Symposium on Archaeometry, Tampa, Florida, 10–14 May 2010. Abst Vol. Poster N. 67, pp. 115–116.

Snyder, R. L., Fiala, J. & Bunge, H. J. (2000). Editors. *Defect and Microstructure Analysis by Diffraction*. Oxford University Press.

Solé, V., Papillon, E., Cotte, M., Walter, P. & Susini, J. (2007). *A multiplatform code for the analysis of energy-dispersive X-ray fluorescence spectra*. *Spectrochim. Acta Part B*, **62**, 63–68.

Tite, M. S. (1991). *Archaeological science – past achievements and future prospects*. *Archaeometry*, **31**, 139–151.

Tite, M. S. (2001). *Overview – materials study in archaeology*. In *Handbook of Archaeological Sciences*, edited by D. R. Brothwell & A. M. Pollard, pp. 443–448. Chichester: John Wiley & Sons.

Tsoucaris, G., Martinetto, P., Walter, P. & Lévêque, J. L. (2001). *Chemistry of cosmetics in antiquity*. *Ann. Pharm. Fr.* **59**, 415–422.

Ungar, T., Martinetto, P., Ribárik, G., Dooryhée, E., Walter, P. & Anne, M. (2002). *Revealing the powdering methods of black makeup in ancient Egypt by fitting microstructure based Fourier coefficients to the whole x-ray diffraction profiles of galena*. *J. Appl. Phys.* **91**, 2455–2465.

Ungar, T., Martinetto, P., Ribarik, G., Dooryhée, E., Walter, Ph., Anne, M. & Tsoucaris, G. (2003). *Microstructure determined by X-ray diffraction peak profile analysis: a fingerprint in archaeology*. In *Molecular and Structural Archaeology: Cosmetic and Therapeutic Chemicals*, edited by G. Tsoucaris & J. Lipkowski. NATO Science Series, Vol. 117, pp. 211–220. Netherlands: Springer.

Valentini, L., Dalconi, M. C., Parisatto, M., Cruciani, G. & Artioli, G. (2011). *Towards three-dimensional quantitative reconstruction of cement microstructure by X-ray diffraction microtomography*. *J. Appl. Cryst.* **44**, 272–280.

Walter, P., Martinetto, P., Tsoucaris, G., Breniaux, R., Lefebvre, M. A., Richard, G., Talabot, J. & Dooryhée, E. (1999). *Making make-up in Ancient Egypt*. *Nature*, **397**, 483–484.

Welberry T. R. (2004). *Diffuse X-ray Scattering and Models of Disorder*. Oxford University Press.

Welcomme, E., Walter, P., Bleuet, P., Hodeau, J., Dooryhée, E., Martinetto, P. & Menu, M. (2007). *Classification of lead white pigments using synchrotron radiation micro X-ray diffraction*. *Appl. Phys. A*, **89**, 825–832.

Yen, A. S., Bish, D. L., Blake, D. F., Vaniman, D. T., Treiman, A. H., Ming, D. W., Morris, R. V., Farmer, J. D., Downs, R. T., Chipera, S. J., Des Marais, D. J. & Chen, C. W. (2012). *Definitive mineralogy from the Mars Science Laboratory CheMin instrument*. 43rd Lunar and Planetary Science Conference, Abstract 2761. Houston: Lunar and Planetary Institute.

Young, M. L. (2012). *Archaeometallurgy using synchrotron radiation: a review*. *Rep. Prog. Phys.* **75**, 036504.

Young, M. L., Casadio, F., Schnepp, S., Pearlstein, E., Almer, J. D. & Haeffner, D. R. (2010). *Non-invasive characterization of manufacturing techniques and corrosion of ancient Chinese bronzes and a later replica using synchrotron X-ray diffraction*. *Appl. Phys. A*, **100**, 635–646.

International Tables for Crystallography (2019). Vol. H, Chapter 7.5, pp. 767–781.

7.5. Powder diffraction and pharmaceuticals

J. Bernstein and S. M. Reutzel-Edens

7.5.1. Introduction

X-ray powder diffraction (XRPD) plays an important, if not crucial, role in the pharmaceutical industry. In much of the world, the vast majority of pharmaceutical products are administered as solids in various forms – generally as tablets or capsules, but even in many cases when administered *via* inhalation, as suppositories, by parenteral injection or topically, the characterization and control of the solid-state properties of the active pharmaceutical ingredient (API) are of prime importance in the formulation of the final product. In this chapter, pharmaceutical solids will include crystalline materials (*i.e.* polymorphs, solvates, hydrates and co-crystals) as well as amorphous materials. As highlighted in Fig. 7.5.1, solid-state science and technology is applicable to virtually every aspect of the pharmaceutical industry and, as a principal tool in solid-state research, XRPD plays a key role in many aspects of that industry. In fact, X-ray powder diffraction is usually considered the 'gold standard' for the identification and characterization of pharmaceutical solid materials. This chapter will describe and provide examples of some of the important applications of powder diffraction in the various stages of pharmaceutical research and development, from initial identification of a potential API through the lifetime of a marketed product.

7.5.2. Some basic background and references

Because it has long been recognized as an important analytical tool for the identification and characterization of solids, a great deal has been written about the applications of X-ray powder diffraction in the pharmaceutical industry. The fundamentals of modern powder diffraction may be found in the classic text by Klug & Alexander (1974) and in more recent books by Jenkins & Snyder (1996*a*) and Lifshin (2008). Applications to the pharmaceutical industry are discussed, for instance, by Byrn *et al.* (1999), Bernstein & Henck (2000) and Ivanisevic *et al.* (2010), or in many of the chapters of the multi-authored volumes authored or edited by Hilfiker (2006), Hilfiker & von Raumer (2018) and Brittain (1999, 2009). The annual summaries by Brittain (*e.g.* Brittain, 2011) provide continuing examples of the application of X-ray powder diffraction to polymorphic and solvatomorphic pharmaceutical materials, either as a single analytical technique or, increasingly often, in combination with other analytical techniques – a strategy which is definitely to be encouraged.

The utility of powder diffraction in the pharmaceutical industry can be demonstrated by examining applications from the various stages of drug development, manufacturing and marketing, and establishing and protecting intellectual property. Owing to space limitations and the vast variety of problems that can be and have been tackled using XRPD, only a small selection is given here, with the intent that this snapshot can provide a picture of the central role of XRPD in the pharmaceutical industry.

7.5.3. Identification and characterization

7.5.3.1. *Polymorphs, salts, solvates, co-crystals*

The choice of the solid form of the API for a pharmaceutical product involves many facets of the discipline of organic solid-state chemistry (Pulacki *et al.*, 2010; Henck & Byrn, 2007). The selection of the solid form from among the possible salts, co-crystals, solvates and other solid forms of the drug, accompanied by knowledge of their physical properties, can reduce the development time to successful clinical trials, balance risk in subsequent pharmaceutical development and ultimately reduce the costs of making new drugs accessible to the patient. An understanding of the molecular structure of an active pharmaceutical ingredient (API) in the solid state and the use of a particular solid form can lead to better design and control of drug performance. Nowadays it is clearly understood that early engagement with the pharmaceutical development scientist on the identification of an optimal solid form and formulation during the drug-discovery stage can lead to significant benefits throughout the drug-development process. Solid forms such as different polymorphs of an API, hydrates or solvates, as well as salts, co-crystals and amorphous materials, including amorphous dispersions, need to be considered in this context. These different forms can show variations in the physical or chemical characteristics of a given API, such as solubility, bioavailability or stability. One of the most important benefits of early identification of solid forms is the potential for reducing pre-clinical candidate attrition and proceeding to *in vivo* studies more quickly; these studies can potentially demonstrate dose-limiting toxicity in order to establish acceptable and reproducible safety margins in

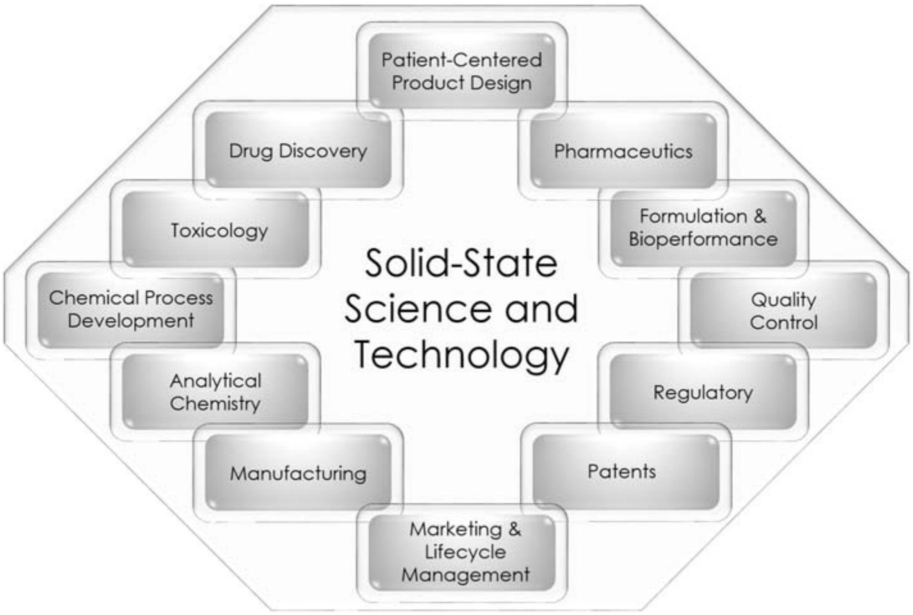
Solid-State Science and Technology
Patient-Centered Product Design
Drug Discovery
Pharmaceutics
Toxicology
Formulation & Bioperformance
Chemical Process Development
Quality Control
Analytical Chemistry
Regulatory
Manufacturing
Patents
Marketing & Lifecycle Management

Figure 7.5.1
Schematic highlighting the many areas across the pharmaceutical industry that are strongly impacted by solid-state science and technology.

pre-clinical toxicity studies. Timely identification of an optimal solid form can also minimize the need to change the solid form of an API during drug development, which in turn reduces costs of *in vitro* physicochemical studies and *in vivo* comparison studies. However, early optimization of the solid form of the API is just one aspect of a targeted drug-development strategy. Many other factors play an important role in whether or not a given API can be brought to the market successfully. It is clearly understood that crystalline materials exhibit properties that derive from both the molecular structure and from the arrangement of the molecules within the solid form; thus changes in the placement and/or interactions between the molecules resulting from a different solid-state structure usually have a direct impact on some or all of the properties of the particular solid (Grepioni & Braga, 2007). Today, solid-state chemists call upon a variety of different strategies when attempting to alter the chemical and physical properties of a given API; these typically include the formation of salts, co-crystals, polymorphs (including polymorphs of salts and co-crystals), amorphous materials (including amorphous dispersions), hydrates and solvates. Amorphous dispersions, where an amorphous API is embedded within a polymer matrix, also provide a viable solid-state route that sometimes leads to improved solubility and potentially improved bioavailability in comparison to the crystalline API. However, amorphous materials are inherently thermodynamically less stable than their crystalline counterparts, and thus are typically not the first solid form of a given API to be selected. Likewise, although thermodynamically metastable crystal forms of a given API usually have the potential benefit of being more water soluble relative to the thermodynamically stable crystal form at room temperature, these form(s) are typically not preferred in pharmaceutical development because of the risk of transformation into the stable form during pharmaceutical processing.

One primary route to a suitable solid form is the preparation of a salt, and it is estimated that over half of the medicines on the market are administered as salts (Stahl & Wermuth, 2002). However, a necessary criterion for this approach is that the API possesses a suitable ionizable site. Co-crystals, however, offer a different pathway, where any API, regardless of whether it is acidic, basic or non-ionizable, can potentially be co-crystallized with either an inert compound or one which can serve as an additional therapeutic agent. The efforts of the pharmaceutical industry over the last 15 to 20 years to invent new compounds to be used as APIs have led to more and more compounds with limited water solubility and bioavailability. It has been estimated that approximately 40% of marketed products and up to 75% of compounds under development are poorly water-soluble and belong to class 2 or class 4 of the biopharmaceutical classification system (Williams *et al.*, 2013). Class 2 compounds show low solubility and high permeability, whereas class 4 compounds exhibit low solubility and low permeability. Therefore, class 2 compounds are of particular interest in the context of salts and co-crystals (and amorphous dispersions), because improving the apparent solubility (a combination of dissolution and solubility) of a given material *via* formation of a co-crystal or salt may be a useful and successful strategy for improving bioavailability. Other properties of an API that could potentially be altered by forming a co-crystal or salt are the melting point, hygroscopicity, physical and chemical stability, filterability and colour, as well as crystallinity. It should be made clear that no one particular strategy improves the properties of all APIs. Each API must be examined and evaluated on a case-by-case basis in terms of molecular structure and the desired final properties (Amidon *et al.*, 1995). In addition, there is no guarantee that the particular property of interest will be altered, as we still lack the ability to predict the changes that might result in the properties of a compound due to a change in crystal form.

XRPD is the analytical tool that is most closely related to the crystal structure. The different solid forms of any given compound exhibit different X-ray powder diffraction patterns that be used to uniquely identify them. Structural information for solids can also be derived from powder X-ray diffractometry. Even upon identification and choice of a lead compound for further pharmaceutical development, it is usually highly advisable to survey the crystal-form landscape to get some idea of the number and characteristics of the polymorphs, solvates and hydrates that might exist for that compound. Such a survey can never be considered complete, especially in the early stages of development, since new crystal forms are often discovered, even serendipitously, well into development or even after launch (Hilfiker & von Raumer, 2018), but an appropriate screen can often provide crucial information about the ultimate choice of crystal form and the difficulties that might be encountered in obtaining that form consistently and robustly (Bernstein, 2019; Braga & Bernstein, 2007; Morris, 1999; Griesser, 2006; Byrn *et al.*, 1999).

Efforts to survey the crystal-form landscape as completely as possible also have important implications for intellectual-property rights. A familiarity with the landscape can extend the breadth of the intellectual property of the innovator; on the other hand, the development or discovery of new solid forms in the landscape can offer the opportunity to circumvent existing patent protection. In this regard, the continuing development of crystallization platforms is particularly noteworthy (Morissette *et al.*, 2004; Kumar *et al.*, 2007), and the availability of automatic sampling and measuring systems for X-ray powder diffraction (*e.g.* Beckers, 2008) has made it increasingly feasible as an efficient screening technique. While high-throughput screening techniques facilitate the survey of the crystal-form landscape, they are by no means routine. The choice of solvent, or solvent combinations, heating and cooling cycles, degree of supersaturation and a variety of other conditions lead to a virtually infinite array of possibilities. It is therefore crucial to develop strategies based on a preliminary assessment of solubility properties and also phase behaviours using techniques such as hot-stage microscopy and thermal methods [differential scanning calorimetry (DSC), thermogravimetric analysis (TGA)].

7.5.3.2. *Indexing*

An indexed powder pattern is a unique identifier of a solid material. While an XRPD pattern may be considered as the fingerprint for a particular solid, indexing its powder pattern does not, in itself, guarantee that the pattern is of a pure material. Ivanisevic *et al.* (2010) have provided an overview on how indexing can be used to generate structural information from XRPD patterns collected using standard laboratory X-ray equipment. Indexing is the process of determining the size and shape of the unit cell from the peak positions in the XRPD pattern. The term *indexing* is derived from the assignment of Miller index labels to individual peaks. Determining the lattice parameters of the unit cell from XRPD data requires knowledge of how to assign the Miller indices h, k, l to each diffraction peak. For a known material, this is done by comparing the data to those reported in the literature or found in a database such as the International Centre for Diffraction Data (ICDD) Powder

Diffraction File [PDF-4+ (2018); http://www.icdd.com], or to data generated from a known crystal structure from, for example, the Cambridge Structural Database [Groom *et al.* (2016); https://www.ccdc.cam.ac.uk]. The Miller indices relate the peak positions or *d*-spacings to the lattice parameters by an equation specific to the crystal system. The various indexing strategies and procedures are described in detail in Chapter 3.4.

Successfully indexing an XRPD pattern offers multiple benefits. If all of the peaks in the XRPD pattern are indexed using a single unit cell, this can be regarded as strong evidence that the sample contains a single crystalline phase. The unit-cell volume may then be calculated and if the chemical composition and therefore the molecular mass of the sample is known, the true density of the material can also be calculated accurately. Another important potential benefit of indexing a pattern is that it can be taken to show that an XRPD pattern is consistent with the structure determined by single-crystal X-ray diffraction, so that the two are representative of the same solid material. Examples of indexing programs and tools that are available either in the public domain or commercially and are widely used in the pharmaceutical field include *TREOR* (Werner *et al.*, 1985), *N-TREOR* (Altomare *et al.*, 2000), *X-CELL* (Neumann, 2003), *DICVOL* (Boultif & Louër, 2004), singular value decomposition (Coelho, 2003) and *TOPAS* (Bruker AXS, 2008).

7.5.3.3. *Crystal structure solution*

Crystal structure determination is a key component of studies relating the solid-state chemistry of drugs to their ultimate use in medicinal products. The connection between internal crystal structure, particle properties, processing and product performance, which collectively form the materials science tetrahedron (Sun, 2009), would be nearly impossible to draw without access to three-dimensional crystal structure information derived from X-ray diffraction. While single-crystal X-ray diffraction is unequivocally the most definitive and preferred technique for crystal structure determination, quite often suitable single crystals cannot be grown to sufficient size (of the order of ~100 µm) or quality for the classical approach to be taken. For example, rapid crystallization of metastable crystal forms, dehydration of hydrates and mechanical grinding, all common to the pharmaceutical industry, are capable of producing highly diffracting materials, but only as powders. In such cases, XRPD is increasingly used to solve the crystal structures of the component phases.

The determination of crystal structures from powder diffraction data, which is detailed in Part 4 of this volume, generally involves three steps: (1) indexing the peaks in the experimental pattern to determine the size and shape of the unit cell, along with the space-group symmetry; (2) using the diffraction peak intensities to generate a good approximation of the atomic positions in the crystal structure; and (3) refining (usually by the Rietveld method) the trial structure to fit the simulated XRPD pattern of the model to the full experimental powder pattern. Of all of the steps in the powder structure solution process, the initial determination of the lattice parameters tends to be the most problematic. Indexing solutions identified based on the molecular volume, cell volume and number of unindexed reflections (see Chapter 3.4) are therefore usually checked using either Le Bail (Le Bail *et al.*, 1988) or Pawley (Pawley, 1981) fitting (see Chapter 3.5). With input of the chemical structure, the unit-cell parameters and space group, trial crystal structures are next generated in direct or real space. Search algorithms, some implemented in commercially available programs, *e.g. DASH* (Shankland *et al.*, 2006), *TOPAS* (Coelho, 2000, 2003) and *PowderSolve* (Engel *et al.*, 1999), vary the positions, orientations and internal degrees of freedom of molecular fragments within a unit cell until a match between the simulated and experimental XRPD patterns is obtained. The resulting structure model, along with peak profile and background parameters, displacement parameters, zero-point error, and preferred orientation, are refined by the Rietveld method in the third and final stage to improve the accuracy of the structure solution, as shown for fexofenadine hydrochloride in Fig. 7.5.2.

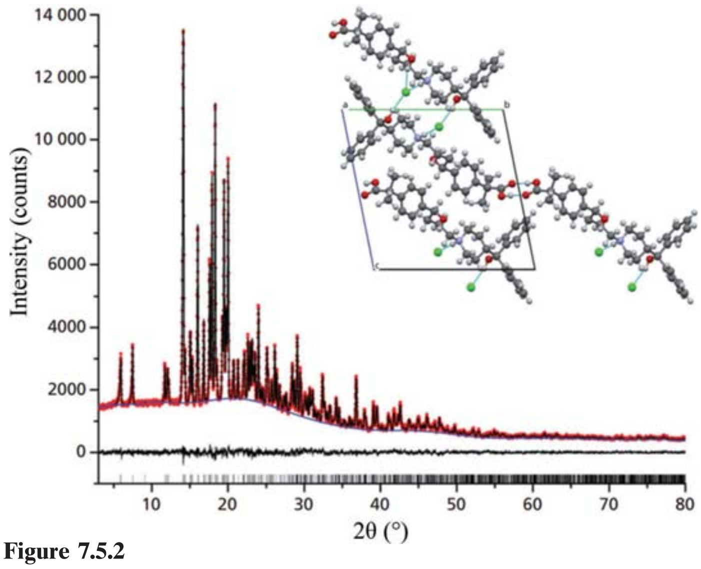

Figure 7.5.2
Profile plots for the Rietveld refinement of fexofenadine hydrochloride. Experimental data are shown as red dots, simulated data as a black line. The difference curve, along with tick marks representing the theoretical peak positions, are shown below. [From Brüning & Schmidt (2015) adapted with permission from John Wiley and Sons.]

The information that is inevitably lost when three-dimensional diffraction is compressed into a one-dimensional powder pattern generally increases the difficulty and uncertainty of structure solution from powders. Measures taken to ensure that the structure model is as accurate and precise as possible include carefully preparing highly crystalline, preferably phase-pure powders in thin-walled capillaries or between polymer films, and collecting data in transmission mode, while spinning the sample to both minimize preferred particle orientation effects and achieve good powder averaging (see Chapter 2.10). For the high accuracy needed for structure solution, the experimental diffraction pattern is typically measured over a wide 2θ range, usually up to 70 or 80°. The powder structure solution is assessed at the final Rietveld refinement stage (Chapter 4.7) by comparing its calculated powder pattern with the experimental pattern, the fit being qualitatively visualized by the difference curve (the black curve at the bottom of Fig. 7.5.2) and quantified by either a weighted powder profile R factor ($R_{\rm wp}$) or full profile χ^2. Dispersion-corrected density functional theory (DFT-D) energy minimization is often used to verify that crystal structure solutions are correct, given by a root-mean-square displacement (r.m.s.d.) of the atomic coordinates of 0.35 Å or less (van de Streek & Neumann, 2014).

7.5.4. Quantitation of mixtures by traditional and Rietveld methods

Given that the different solid forms (crystalline and amorphous) of a compound may perform differently in a drug product, validated quantitative methods may be required to ensure control of the manufacturing process. This is particularly the case when mixtures of forms known to have different chemical stabilities or physical properties that are relevant to drug product performance cannot be avoided. If a quantitative method is required, whether for quality control, process understanding or demonstrating patent infringement, X-ray powder diffraction can, under carefully controlled conditions, provide accurate quantitative information on *crystal form purity* (as distinguished from *chemical purity*). Quantitative phase analysis of crystal forms, as well as the assessment of the degree of crystallinity, by X-ray powder diffraction have been extensively reviewed (Jenkins & Snyder, 1996*b*; Stephenson *et al.*, 2001). Here we describe the basic elements of quantitative analysis by powder diffraction, highlighting applications in the pharmaceutical industry.

Quantitative phase analysis by X-ray powder diffraction is based on the assumption that the diffraction intensity for a component mixture is related to the proportion of each component in the mixture. The basic elements of quantitative analysis of powders from XRPD pattern intensities were initially outlined by Alexander & Klug in 1948. The general expression used for quantitative diffraction analysis of a two-component (α and β) system is

$$I_{(hkl)\alpha} = \frac{KX_\alpha}{\rho_\alpha[X_\alpha(\mu_\alpha^* - \mu_\beta^*) + \mu_\beta^*]},$$

where $I_{(hkl)\alpha}$ is the intensity of the *hkl* reflection of the α component, K is the proportionality constant given by physical parameters related to the experimental setup and specific to each *hkl* reflection, ρ_α and X_α are the density and weight fraction of component α, respectively, and $\mu_\alpha{}^*$ and $\mu_\beta{}^*$ are the mass attenuation coefficients of components α and β, obtained by dividing the linear attenuation coefficient, μ, by the component density. For the special case of polymorph mixtures or mixtures of crystalline and amorphous phases, where $\mu_\alpha{}^* = \mu_\beta{}^*$, the expression is simplified and the relative intensity of a given peak will be directly proportional to the phase concentration. For other physical mixtures, including formulations, where the mass attenuation coefficients of the analyte (α) and matrix (collectively described by β) are likely to be different, the relative peak intensity may not vary linearly with concentration. In cases where the elemental composition is known, $\mu_\alpha{}^*$ and $\mu_\beta{}^*$ may be calculated from published elemental mass attenuation coefficients. Although not extensively used in the pharmaceutical industry for quantitative phase analysis, this absorption method can be used to extract quantitative phase information, as has been demonstrated for carbamazepine (Suryanarayanan, 1989).

Traditional quantitative X-ray powder diffraction methods more usually rely on calibration curves constructed using internal standards, avoiding corrections based on mass attenuation coefficients. Internal-standard methods may be based on peak intensities (heights), relative peak-intensity ratios or integrated peak areas, and either individual peaks or whole patterns may be used to relate peak (or whole-pattern) intensities to the amount of each phase present. When examination of the diffraction patterns of the component phases reveals sufficient selectivity for a particular form, simple univariate quantification methods based on XRPD peak heights or areas may be appropriate. Whole-pattern methods, on the other hand, combine analysis of both Bragg diffraction and diffuse scattering, allowing for better definition of overlapping peak intensities, as well as improved background fitting. With whole-pattern methods, the diffraction patterns of the sample (unknown) and reference (component) phases are recorded as digitized intensity values, allowing the full diffraction pattern of the unknown to be reconstructed as a weighted sum of the diffraction patterns of the component phases. Multivariate chemometric techniques, including classical least-squares (CLS) regression, principal-component regression (PCR) and partial least-squares (PLS) regression, can be used to improve the correlation between predicted and measured compositions, as has been demonstrated for pharmaceutical compacts of theophylline (Moore *et al.*, 2009).

The Rietveld method (Rietveld, 1967), originally used for crystal-structure refinement, has evolved as an *ab initio* quantitative method for phase analysis. As in other whole-pattern methods, the Rietveld method involves point-by-point least-squares fitting of the entire experimental diffraction pattern with a calculated profile of a model constructed from known component phases. With the Rietveld method, however, the model of the diffraction pattern is first built, then matched to the experimental pattern by refining the lattice parameters, profile shape, scale factors, background coefficients, and in some cases the atomic positions and site occupancies, for each component phase. The scale factors defining the relative amounts of each component are adjusted to match the model to the experimental data until good agreement is obtained. Rietveld analysis, like other whole-pattern fitting methods, is a standardless method in the sense that it does not use a calibration curve, but it does require a structural model (lattice parameters, space-group symmetry, atomic positions, site occupancies) of each phase being analysed, from which a powder pattern can be simulated. Here it should be recognized that for pharmaceutical materials, single-crystal structure determination is often performed at low temperatures for increased accuracy, and it is becoming increasingly common to use 0 K structure models derived from *ab initio* crystal structure prediction calculations as inputs to Rietveld refinements. If low-temperature structures (or computed 0 K structures) are used, the possibility of unit-cell contraction, which will increase the scale factor, must be considered. In such cases, the unit cell, displacement parameters and scale factor will require adjustment in the refinement. An ICDD-sponsored round robin highlighted many of the challenges in quantitative phase identification using the Rietveld method, but demonstrated that in the hands of the experienced practitioner, accurate quantitative analysis (with errors of the order of 5–10%) is possible (Fawcett *et al.*, 2010). Shown in Fig. 7.5.3 is a successful application of the Rietveld method for the quantitative phase analysis of heat-treated carbamazepine (Antonio *et al.*, 2011). In this example, an improved fitting was achieved by accounting for a form-III phase impurity in a sample otherwise of form I.

To ensure that measured diffraction peak intensities (or areas) are proportional to the amounts of the different phases that are present, potential sources of error from the sample itself, the sample preparation and the instrument must be considered. The typically large unit cells and low symmetry of pharmaceutical compounds often lead to peak congestion. In drug product formulations, the dilution of the drug with large quantities of excipients and overlapping diffraction peaks can be especially problematic. Organic compounds tend to have low mass-absorption coefficients, leading to deep (of the order of mm) X-ray beam penetration into the sample, which can cause diffraction-line shifting. Diffraction peak intensities are strongly influenced by preferred crystallite orientation, packing density and the homogeneity of the sample. For hygroscopic materials, where the diffraction patterns change as a function of water

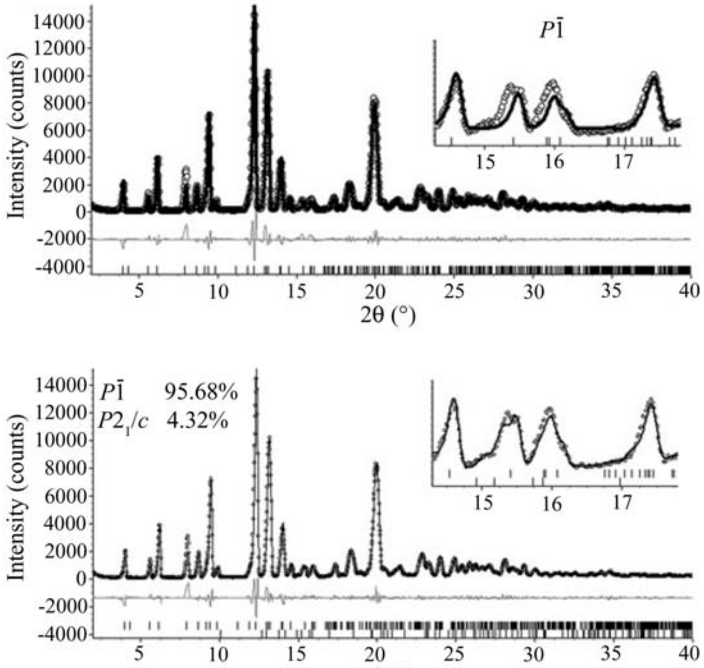

Figure 7.5.3
Profile plots of the Rietveld refinement of heat-treated carbamazepine, showing an improved fit over pure form I (space group $P\bar{1}$, top) obtained by modelling the X-ray powder diffraction pattern with ∼4% form III (space group $P2_1/c$) in form I (bottom) [from Antonio *et al.* (2011) with permission from John Wiley and Sons].

content, peak intensities may further depend on the relative humidity.

Quantitative diffraction methods depend upon obtaining an experimental powder pattern uncomplicated by the effects of preferred orientation, extinction, microabsorption, variable packing density and sample inhomogeneity. To avoid preferred orientation altogether requires sampling truly random orientations of crystallites, which can be difficult to achieve in practice. Common approaches to minimizing the effects of preferred orientation include collecting XRPD data in transmission geometry, particle-size reduction and sample back-filling. Whether or not preferred orientation has been minimized successfully can be determined by comparison of the experimental diffraction patterns to patterns of the components that have been calculated from single-crystal data, when available. Extinction and microabsorption effects will become negligible only when the particle size is sufficiently small. To this end, numerous techniques are available to reduce particle size; however, care must be taken to avoid phase transformations during comminution. In order to even out differences due to packing density, a specific sample weight and compaction pressure is often used to prepare samples for XRPD analysis. As sample homogeneity (sub-sampling) can also compromise the accuracy of quantitative analysis by XRPD, dry mixing and, in some cases, slurrying or sonicating in a non-solvent are used. For the latter method, the solvent of crystallization may be preferred for homogenizing solvates that are at risk of being desolvated or exchanged in suspensions of other solvents. Sample rotation is also generally recommended during XRPD analysis to improve counting statistics.

As with any quantitative assay, the validation of the XRPD method requires that range, specificity, linearity, accuracy, precision (repeatability) and ruggedness are demonstrated and the limit of quantitation (LOQ) and limit of detection (LOD) are firmly established. Range, specificity and linearity are demonstrated by a calibration curve. The LOQ and LOD are typically calculated according to the International Conference on Harmonization guidelines (ICH, 1996) as $10\sigma/S$ and $3.3\sigma/S$, respectively, where σ is the standard deviation from multiple measurements of the pure component (or a defined mixture of components) and S is the slope of the calibration curve. XRPD calibration models constructed for multivariate methods require the preparation of calibration samples, which must not only account for the multi-phase nature of the pharmaceutical system, but also be sufficiently robust to accommodate variability in the diffractograms. Method validation relies on prepared samples specifically not included in calibration data sets to evaluate accuracy, repeatability and intermediate precision, as well as to demonstrate laboratory-instrument comparability. Quality indicators for quantitative calibration models may include the correlation coefficient (R^2), the test-set validation coefficient (Q^2), the root-mean-squared error of estimation (RMSEE) and the root-mean-squared error of prediction (RMSEP). With the appropriate controls, XRPD methods have been developed with accuracy, precision and reliability rivalling, and in some cases exceeding, those of quantitative spectroscopic methods (Német *et al.*, 2010), positioning XRPD well as the gold standard for both qualitative *and* quantitative phase analysis of pharmaceutical materials.

7.5.5. Characterization of amorphous materials

As noted above, crystalline forms of a drug are generally preferred over amorphous forms, as they confer exquisite control over the physicochemical properties affecting drug product quality, safety and performance. However, when a material fails to crystallize, the only choice may be to proceed with an amorphous form. Additionally, with the ever-increasing number of poorly soluble new chemical entities in drug development, amorphous solids are increasingly being used in the hope of improving dissolution-rate-limited absorption. Amorphous forms designed to enhance bioavailability are commonly prepared, often in the presence of polymeric nucleation inhibitors, using techniques such as spray drying, lyophilization and melt extrusion. Amorphous or glassy phases may also be generated, albeit unintentionally, during high-energy processes such as milling or micronization, compaction and wet granulation (Yu, 2001). Crash precipitation or exposure of a drug crystal form to drying or storage conditions under which desolvation may occur has the potential to introduce disorder as well. Whether amorphous forms are encountered by default (when a substance is inherently noncrystalline), by design (when a substance is rendered amorphous through kinetic trapping) or by accident (when a substance is inadvertently rendered amorphous by mechanical or thermal stress), disorder can compromise the physical and chemical stability of solid drugs and is therefore important to understand and control (Ahlneck & Zografi, 1990).

X-ray powder diffraction has been widely used to assess crystallinity in pharmaceutical materials. Whereas crystalline phases possessing long-range order produce sharp Bragg diffraction peaks, X-ray amorphous materials are generally characterized by a raised baseline or 'halo' in their diffraction patterns. The characterization of sample crystallinity is complicated by the fact that amorphization or the loss of long-range order may occur under various processing or storage conditions throughout the bulk solid or predominantly at the surface of crystalline particles. As different types of disorder affect the physical and chemical properties of a drug substance in different

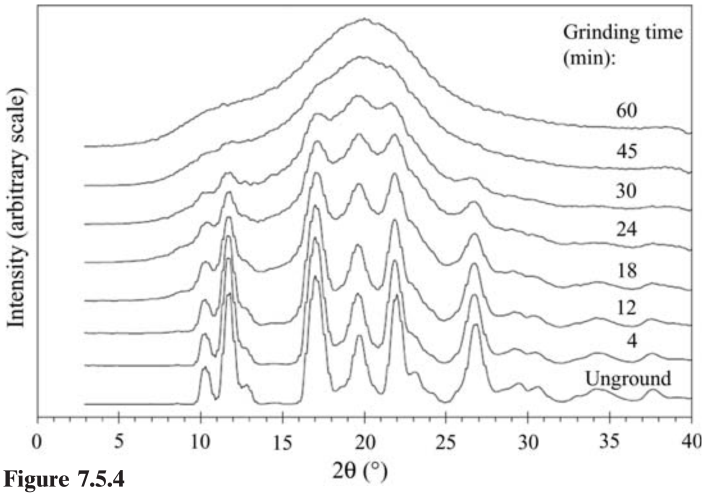

Figure 7.5.4

X-ray powder diffraction patterns of indomethacin, showing progressive loss of long-range order (crystallinity) with extended grinding. Within 60 min, a broad halo is formed as indomethacin is rendered X-ray amorphous. Reprinted by permission of Springer Nature from Bates *et al.* (2006). Copyright (2006).

ways and to different extents, the strategy used for characterization should account for the nature of the crystal imperfections or amorphous material.

It is important to distinguish here between, on the one hand, various types of disorder in a crystalline material that exhibits long-range order, and on the other hand an amorphous material. The distinction is described in detail in Giacovazzo *et al.* (2011). In the current context, for instance, the disorder of an aliphatic carbon chain in the pharmaceutically important compound ranitidine hydrochloride (Zantac) has been accounted for by a Rietveld refinement against synchrotron powder diffraction data (Huq & Stephens, 2003).

To assess the degree of crystallinity of a given sample accurately by accounting for the different types of disorder, partially ordered systems have been described using either ‘one-state’ or ‘two-state’ models (Hancock & Zografi, 1997). In the one-state model, amorphization is distributed throughout the bulk particles and domains are truly partially crystalline (Rani *et al.*, 2006). X-ray powder diffraction can be used to detect the accumulation of crystal defects that characterize partially crystalline one-state systems; however, other techniques, such as DSC or solid-state NMR spectroscopy, are commonly used in conjunction with XRPD to examine this type of disorder. In the two-state model, domains within a material are assumed to be either 100% amorphous or 100% crystalline and to coexist side-by-side in a physical mixture. The two-state model best characterizes surface amorphization as exemplified by indomethacin (Bates *et al.*, 2006), where the integrated intensity of background scattering in the diffraction pattern coming from the disordered (amorphous) phase increases at the expense of the diffraction peaks of the ordered (crystalline) phase upon continued grinding (Fig. 7.5.4).

By assuming that crystalline and amorphous components coexist as a phase-separated mixture (two-state model), partially crystalline materials may be simulated using physical mixtures of crystalline and amorphous reference materials with the extent of disorder in some cases being characterized by straightforward application of a calibration curve. Defining representative crystalline and amorphous standards can be difficult, however. Lattice defects are almost always present in crystalline materials, whether from the crystallization process or subsequent downstream processing (*e.g.* milling). Likewise, the background scattering of the amorphous phase will be affected by short-range order, which is not always easy to eliminate, and, in some cases component miscibility, which can cause the amorphous halo to change shape. In cases where the X-ray scattering pattern of multi-component amorphous systems cannot be described as a linear combination of the pure amorphous component diffraction patterns (Newman *et al.*, 2008), representative calibration samples may be generated by mixing the crystalline component with the combined amorphous matrix (Rumondor & Taylor, 2010). Once well defined crystalline and amorphous standards are in place, the degree of crystallinity may be determined by measuring either integrated diffraction peak intensities (or heights) or the intensity of amorphous scattering. Here, it is generally recognized that detecting the diffuse scattering of low levels of disorder in a mostly crystalline material is more difficult than detecting low levels of crystallinity (Bragg diffraction peaks) in an otherwise amorphous sample. Nonetheless, conventional X-ray powder diffraction has been used to quantify noncrystalline material down to levels of 5% with an absolute accuracy of ±3% (Byard *et al.*, 2005).

X-ray amorphous solids are characterized by the lack of Bragg diffraction peaks in their powder patterns, but the structure of these materials is not necessarily random. In fact, amorphous small-molecule materials often possess short-range order (less than 20–25 Å) extending to distances of the order of a few molecules or less. Traditional X-ray diffraction methods, which are powerful for identifying samples as X-ray amorphous and for characterizing the degree of crystallinity (long-range order) in partially crystalline materials, are of limited use for probing local (nanoscale) order in amorphous solids. However, atomic pair distribution function (PDF) analysis of powder diffraction data, which has long been used to study inorganic materials, has been applied to highly disordered and nanocrystalline pharmaceutical solids (Bates *et al.*, 2006), providing structural information that is otherwise inaccessible by the more established crystallographic techniques.

PDF is a total diffraction approach (the Bragg peaks and diffuse scattering are analysed together) used to study relationships between ordered and disordered systems by providing a fingerprint of interatomic distances, more specifically a weighted probability of finding two atoms separated by a distance r within a solid (Egami & Billinge, 2003). A PDF is generated by performing a Fourier sine transformation of the total scattering function $S(Q)$, the reduced structure-factor representation of a powder pattern measured in 2θ. As shown in Fig. 7.5.5 (Bøtker *et al.*, 2012), PDF data are generally presented as the probability, $G(r)$, of a given atom separation plotted as a function of distance r in Å. At sufficiently high resolution, interatomic distances may be accurately determined at each peak maximum in the PDF. Multiplying the amplitude of each peak with the corresponding distance further yields the number of atomic pairs separated by that distance.

The PDF analysis of crystalline, highly disordered and nanocrystalline pharmaceutical solids is illustrated for amlodipine besylate anhydrate (AH), dihydrate (DH) and milled (M) and quench-cooled (Q) samples in Fig. 7.5.5. Note the greater attenuation of the PDF trace of the Q material relative to the M material, which indicates a higher degree of disorder in the quench-cooled sample. These data, collected to 40° 2θ on a conventional laboratory diffractometer using low-resolution Cu $K\alpha$ radiation, were able to differentiate the local molecular-packing arrangements in the milled and quench-cooled amorphous samples, though they were not sufficiently accurate to

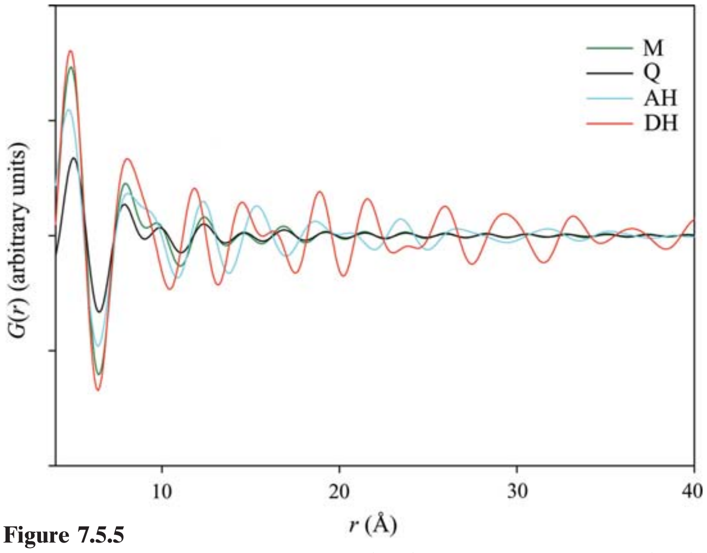

Figure 7.5.5
PDF traces of crystalline anhydrate (AH), crystalline dihydrate (DH), milled (M) and quench-cooled (Q) samples of amlodipine besylate [from Bøtker *et al.* (2012)].

relate the short-range order in the X-ray amorphous materials to structural features in the crystalline AH and DH forms.

To provide useful insights into local packing arrangements in noncrystalline materials across a wide range of *r* or at least to ensure that reliable fingerprints of amorphous pharmaceuticals are obtained, it is highly recommended that diffraction data used for PDF analysis are collected with low instrument background and good counting statistics to high momentum-transfer (*Q*) values. Synchrotron radiation can, of course, be used for this purpose (Billinge *et al.*, 2010); however, reliable high-resolution data are also achievable using laboratory diffractometers equipped with Ag or Mo sources (Dykhne *et al.*, 2011). With proper data collection, corrections (background scattering, sample absorption, polarization *etc.*) and normalization to account for instrument and sample effects, high-quality, physically meaningful PDF results can be obtained.

Interest in PDF analysis for the molecular-level characterization of pharmaceutical solids that are X-ray amorphous has grown rapidly in the pharmaceutical community. Applications range from fingerprinting amorphous forms (Dykhne *et al.*, 2011), following the evolution of structural disorder during processing and storage (Bates *et al.*, 2007) and characterizing the average particle size of nanocrystalline materials (Billinge *et al.*, 2010) to examining phase separation in amorphous dosage forms (Newman *et al.*, 2008). Another area of interest that relies on extracting detailed structural information is the identification of residual polymorphic 'memory', which can lead not only to batch-to-batch variability in materials rendered amorphous by milling, but also direct the crystallization of a particular polymorphic form from the amorphous state (Sheth *et al.*, 2005).

7.5.6. Quality control and regulatory aspects

The US Food and Drug Administration (FDA), recognizing that the presence of different crystalline forms has the potential to alter drug product quality and performance, have published guidance for setting acceptance criteria for new drug substances and drug products produced from them. The International Conference on Harmonization (ICH) Guidance on Q6A Specifications (ICH, 1999) specifically states that when physical-property differences between forms are shown to affect drug product performance, bioavailability or stability, the appropriate solid state should be specified. The choice of which analytical technique to use in support of setting material specifications is left to the applicant and will largely depend on identifying one that is both suitably discriminating and amenable to use in a quality-control (QC) setting. As a technique that is generally selective, relatively inexpensive and easy to implement, and allows for rapid and reliable analysis, XRPD is widely used in QC laboratories for the purpose of both fingerprinting incoming raw materials and release testing final products. It is generally accepted that when the manufacturing process for a drug substance consistently delivers a single solid-state form, qualitative 'identity' testing should be sufficient. However, in cases where a manufacturing process produces more than one solid-state form with the potential to affect drug product quality, safety or performance, validated quantitative methods may be required to ensure that the forms are produced in fixed proportion.

Today's regulatory environment has been further shaped by FDA guidance (ICH, 2009) advocating that quality be built into drug products by design as opposed to being tested into them. A key driving force for introducing new and efficient manufacturing technologies into the pharmaceutical industry was the appreciation that many process and product failures have resulted from poor understanding and control of crystallization processes. For a pharmaceutical crystallization process to consistently deliver a drug substance with the desired qualities, of which crystal form is paramount, the use of both process analytical technology (PAT) (Yu *et al.*, 2004) and quality by design (QbD) principles (Yu, 2008) has been encouraged. Online PAT tools are generally preferred as they allow for real-time process monitoring, and near infrared and Raman spectroscopy, in combination with chemometric methods, have increasingly been used for monitoring crystal form in pharmaceutical production settings. XRPD technology has also been developed for *in situ* monitoring of form evolution and has been successfully applied to both slurry conversion (Dharmayat *et al.*, 2006, 2008) and wet granulation (Davis *et al.*, 2003) processing. These applications have shown great promise for designing robust crystallization and formulation processes in the laboratory, but further development is needed to realize the full potential of online XRPD for providing continuous, real-time assurance of quality in commercial drug-substance and drug product manufacturing.

7.5.7. Creating and protecting intellectual property

Intellectual property rights are protected by patents. The patents on pharmaceuticals are among the most important and most valuable in modern society. Despite continuing debates about the relative costs and benefits of pharmaceutical patents, there is general agreement that the incentive for the invention and development of new drugs is intimately connected to the intellectual property protection afforded by the patent system.

Patents are granted for inventions and give the grantee exclusive rights over that invention – that is, the right to prevent others from making it, using it or selling it. A patent is a social contract: in return for granting the inventor those exclusive rights, the inventor must teach the public how to use his or her invention when those rights have expired. Two of the fundamental criteria for the granting of a patent are that the invention must be *novel* and it must be *non-obvious* to the hypothetical person 'skilled in the art' defined, for example, by the European Patent Office, as one who 'should be presumed to be a skilled practitioner in the relevant field of technology, who is possessed of average knowledge and ability and is aware of what was common general knowledge in the art at the relevant date'. Finally, it must have some *utility*.

Novelty and obviousness are terms that are debated in virtually every legal confrontation about crystal forms. As pointed out earlier (Bernstein, 2019; Bernstein & MacAlpine, 2018), by definition essentially every new solid form is novel. Furthermore, for any compound it is not obvious – and not possible to predict – how many different solid forms can be prepared or how to prepare any, as yet unknown, solid forms, and it is not possible to predict the properties of any, as yet unknown, solid forms. It is virtually impossible to provide specifics beyond that general statement since every compound is a new situation and every legal jurisdiction has its own rules, regulations, legal framework and case law, but the novelty and non-obviousness of crystal forms means that virtually every new crystal form is potentially a patentable entity.

Utility is considered differently by US and European patent examiners. In the US an invention meets the utility requirement if it is capable of being used and provides some identifiable benefit. In Europe utility is not a criterion for patentability; rather the invention must have some industrial applicability. In the current context it might be noted that a less stable crystal form might have greater solubility and hence higher bioavailability or more rapid physiological absorption than the corresponding stable form.

Because of the (albeit limited-term) market exclusivity they provide, the patents on crystal forms for many drugs are the linchpins of commercial success. The role of XRPD in defining the inventions for the preparation of a patent application and in the subsequent protection of the patent against alleged infringement is often crucial. As noted above, the XRPD pattern of a solid material is generally viewed as a fingerprint and is often considered to be the gold standard for characterizing solid materials. Therefore, many patents on solid forms contain XRPD patterns/data of the claimed form(s), either as the only characterizing physical or chemical data, or along with IR, Raman, solid-state NMR and/or DSC/TGA data for further characterization.

It is important to distinguish here between the major components of a patent. Following a general *background* leading up to the invention described in the patent, the inventors then provide the *specifications* that summarize how to make the invention. In the case of a patent for a pharmaceutical solid form, the specifications will describe in a general way how that solid form is made and how it may be identified and characterized. This is generally followed by specific *examples* that *teach* the detailed procedure for obtaining the solid form(s), that is, *enabling* the person of skill in the art to *practice* the invention. The examples will usually contain the analytical techniques and characterizing data for the solid form(s).

Following the specifications, the actual invention in a patent (for the present discussion, a solid form) is defined by the *claim(s)* that are listed separately from the specifications (usually at the end of the patent), or a general description of the invention. Since the claims actually define the invention, proof of infringement of the patent requires providing conclusive evidence that the alleged infringer has made, used or sold the invention as defined in the claim. Thus the framing and interpretation of claims on crystal forms is often a crucial issue in patent litigations. In spite of the order in which these sections are presented to the public, it is often enlightening to read the claims first in order to determine the nature of the invention.

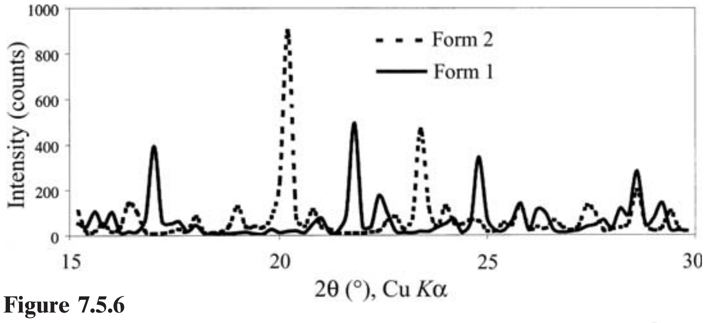

Figure 7.5.6
XRPD traces of the two pure forms of ranitidine hydrochloride [from Agatonovic-Kustin *et al.* (1999) with permission from Elsevier].

There is considerable freedom and hence considerable debate on how to present and define the XRPD pattern of a crystal form in a patent claim. Should the claim contain a graphical representation of the diffraction pattern or a complete or selected list of 2θ values (or equivalent *d*-spacings and intensities, relative or absolute)? If the graphical representation of the diffraction pattern is used to define the claim, then in the event of a litigation there will almost inevitably be contradictory views by the opposing expert witnesses on the comparison of the data for the allegedly infringing material with that claimed in the patent, including *inter alia* the preparation and handling of sample, methods and details of measurement, the work-up and presentation of data, *etc*. Similarly, for a selected list of 2θ values there will not always be a one-to-one correspondence between the number of peaks or the values they represent between the compared sets. Intensities (if given at all) may vary and the significance of differences in the precise values of the quoted peaks or lines in the XRPD pattern will be the subject of critique and debate.

A further point should be made here. We earlier made the distinction (see Section 7.5.4) between crystal-form purity and chemical purity. Here we note that there is a distinct and important difference between, on the one hand, the *polymorph identity* of a crystal form, *i.e.* the XRPD peaks that characterize that solid form, whether in isolation or in the presence of other solids and, on the other hand, the *polymorphic purity* of a particular sample, *i.e.* are there other solid forms of the same compound present and to what extent? A number of examples will serve to demonstrate some of the points raised here.

Fig. 7.5.6 shows the XRPD traces of the two polymorphic forms of ranitidine hydrochloride. This is an excellent demonstration of *polymorph identification* since the two major peaks in form 1 appear at 2θ values where there is a 'window' in form 2 and *vice versa*. Hence in a chemically pure sample of ranitidine hydrochloride there would be no difficulty in identifying which polymorph was present, or indeed if both were present.

In addressing the question of *polymorph purity*, the issue is whether a solid contains one form, and if not, how much of another particular form is present, either as the main component or as an 'impurity' of another solid form of the same compound. An example, wherein synchrotron XRPD achieved a limit of detection of 0.01 wt% of the minor component in salicylic acid–paracetamol mixtures (Gozzo, 2018), is given in Fig. 7.5.7

Chemists in general, and crystallographers in particular, are accustomed to comparing a list of peaks (in the current context XRPD peaks; in other cases IR, Raman or NMR peaks *etc*.) for the sample they are studying with those listed in the literature or in a patent. Rarely are all the peaks listed in a characterization. Rather, they are generally chosen by a person who is familiar with the material and the system of solids in which that material is

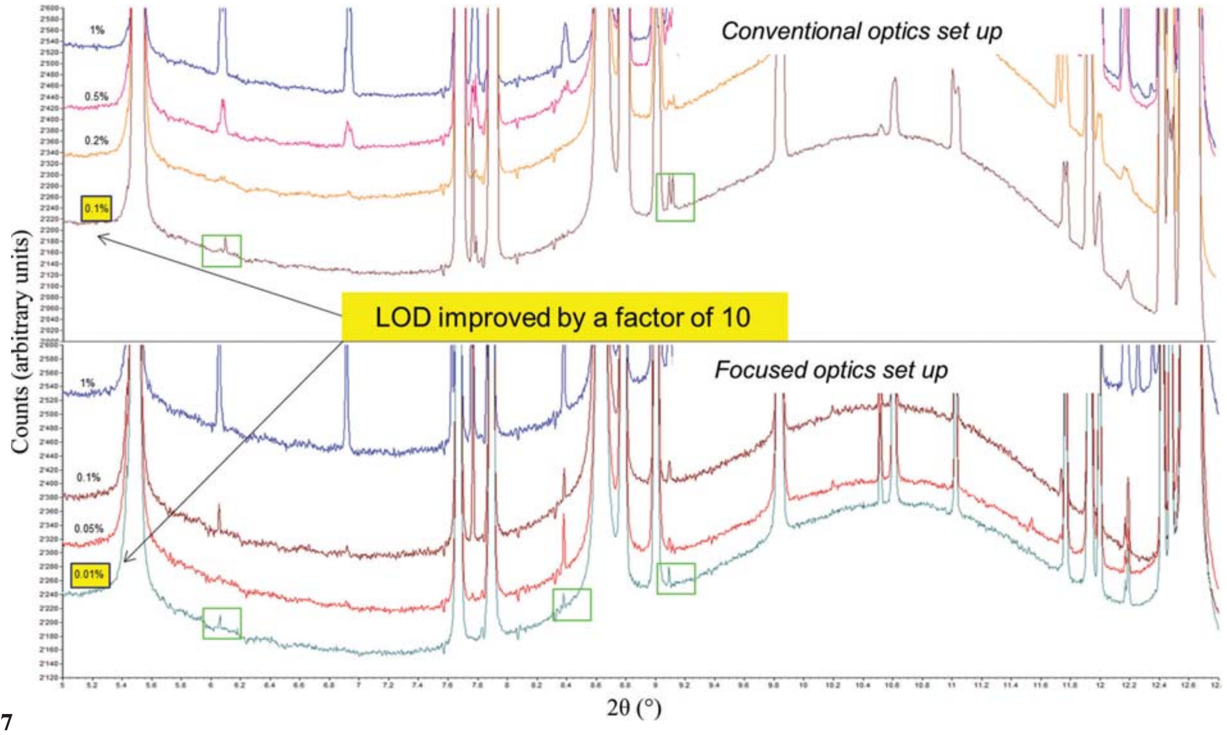

Figure 7.5.7
Synchrotron XRPD patterns of *ad hoc* mixtures of salicylic acid and paracetamol: the limit of detection of 0.1 wt% for the minor component achieved with a conventional optics setup was improved by a factor of 10 to 0.01 wt% with careful optimization of the beamline optics. From Gozzo (2018), with permission.

found, and represent what that person deems characteristic of that solid form. They need not be the most intense, but they generally represent what that person has come to recognize individually or collectively as representing that crystal form. For instance, in Fig. 7.5.6 one could easily imagine the choice of the two largest peaks in each of the traces as sufficient to define and distinguish between forms 1 and 2 of ranitidine hydrochloride, although certainly additional peaks might be added to the lists.

As noted above, when comparing experimentally determined peak positions with the published values, some peaks in the literature reference may not be present for the sample. The XRPD pattern of the sample will almost certainly contain many more peaks than the published list. Similarly, the comparison of two experimental XRPD traces will virtually never yield a perfect match. Peaks will not be in exactly the same position; some will be shifted slightly. The person carrying out the analysis will have to call upon experience with this kind of analytical reasoning as well as familiarity with the material in question in carrying out the comparison. This is often referred to as ‘fuzzy logic’, since it is not based on the digital yes/no or on/off logic of computers. However, it is a common reasoning process to practising chemists who routinely carry out such comparisons and analyses.

If the solid material is claimed using a list of peaks rather than an XRPD trace, then how many peaks should be included? Indeed, how many peaks are required to uniquely characterize a crystal form for a specific chemical entity? Should the claim(s) contain a maximum number of peaks, a minimum number of peaks, or is there some optimal number? Minimizing the number of peaks increases the risk that some other material (or even another crystal form of the same material) could have the same peaks (within experimental error), thus nullifying the novelty of the substance. On the other hand, defining the invented solid form in the claim by a large number of peaks may require finding all of them in allegedly infringing material, a task that becomes increasingly difficult as the number of peaks listed in the claim increases. This task is further complicated for *in situ* determination of infringing material at low concentrations and/or in the presence of excipients that may mask claimed peaks.

The patent literature reveals both extremes in the number of peaks claimed. An example at the minimalist end is the patent for one of the crystal forms of atorvastatin (Lipitor) (Briggs *et al.*, 2006), for which the first (independent) claim in the original patent in 1999 listed two peaks. The patent was re-examined in 2006 and the claim was reduced to one peak. On the other hand, a 2002 patent on a derivative of sildenafil (the active ingredient of Viagra) lists 99 peaks in the first – and only – claim (Harris *et al.*, 2006). The most intense peaks are not necessarily the most characteristic. Careful choice of the peaks included in the claim can make it difficult to challenge and can facilitate its enforcement.

The details of XRPD data vary widely in the patent literature. A survey conducted by Parker (2005) covering both the United States Patent and Trademark Office (USPTO) and the European Patent Office (EPO) for the period November 1988 – March 2005 is representative and illustrative of the situation. The numbers for the EPO (where relevant) are given in parentheses following those of the USPTO. The sample of 72 (27) patents chosen for review were selected from 42 for which ‘polymorphism’ appeared in the title, 100 reviewed of 3037 for which ‘crystalline’ appeared in the title, and 150 reviewed from 203 for which ‘crystalline’ and ‘drug’ appeared in the title. Twenty five (13) gave no data; 52 (21) recited XRPD characterization; the remainder cited another method or a combination of other methods. For those patents citing XRPD, 52 (16) contained numerical peak information, 9 (6) contained a figure with an XRPD trace, 12 (1) listed intensities, half of which were qualitative (*i.e.* s = strong, m = medium, w = weak, vw = very weak *etc.*), 6 (4) specify the radiation source and 1 (1) specifies the temperature and relative humidity. Twenty seven (5) of the patents listed ten peaks or fewer to define the crystal form, while 23 (11) designated ten or more peaks, and one designated 99 peaks. An additional datum of interest is the number of significant figures (SFs) associated with the numerical data: 25 (7) had peaks with one SF, 19 (5) with two SFs, 2 with 3 SFs, 3 (4) with four SFs and 1 with 5 SFs. The number of values listed varies from minimal to maximal. For instance, the first claim of US Patent 6,420,557 (Harris *et al.*, 2006) lists 99 peaks and intensities in the first (independent) claim for a specific crystal form, while the first (independent) claim of US Patent 5,969,156 (Briggs *et al.*, 2006) lists *either* of only two peaks as defining the invention. Current US case law suggests that the proof of literal infringement requires that most or all of the peaks listed *in a claim* be positively identified in the allegedly infringing material. This would seem to argue for including a minimum number of peaks in the claim, which again runs the risk of losing the novelty, since more than one material, or more specifically another solid form of the same material, may contain the same small number of peaks.

Since the claims define the invention, infringement must be proven by demonstrating that what is described in at least one of them has been copied. This case law was established in a case that also touches on a number of other aspects of the role played by powder diffraction in pharmaceuticals (Zenith Laboratories Inc., v. Bristol-Myers Squibb Co., 1994).

The antibiotic cefadroxil, marketed as a crystalline monohydrate claimed in US Patent No. 4,504,657 (the ’657 patent) issued in March 1985, is described in the patent in terms of its X-ray diffraction pattern, given as a list of 37 *d*-spacings and relative intensities in a table in the first claim with the leader ‘exhibiting essentially the following X-ray diffraction properties: . . . ’. The improvement of this substance over the earlier known material included greater stability and high bulk density, properties that enabled the production of smaller pills.

Prosecution of the ’657 patent was in fact quite lengthy, the original application dating from August 1979, and involved questions of similarities and differences in crystalline modifications.[1] The prior art included a 1973 patent (US Patent No. 3,781,282) (the ’282 patent) in which a modification of cefadroxil had also been prepared. This was termed the ‘Micetich form’ after one of the inventors. One of the questions surrounding the ’657 patent was whether the crystalline material described therein (known as the ‘Bouzard form’ or ‘Bouzard monohydrate’) was the same as or different from the ‘Micetich form’. In the end, the ’657 patent was granted, in essence recognizing the difference between the two.

In anticipation of the expiry of ’282 patent, there were attempts by generic pharmaceutical firms to make the Micetich form according to Example 19 in that patent in preparation for entering the market with the form that had gone off-patent. Those attempts invariably led to the Bouzard form, leading the companies involved to carry out experiments to claim *inherency* of the Bouzard form in the ’282 patent. Bristol-Myers’ (BM) explanation of these results included the role of unintentional seeding that tended to favour the formation of the Bouzard form rather than the Micetich form. A number of litigations ensued that involved these issues (*e.g.* Kalifarma, Inc. v. Bristol-Myers Company, 1989; Bristol-Myers v. United States International Trade Commission, 1989). In the former case, there was also a question of the identity of the various crystal modifications, determined mainly by powder X-ray diffraction, with conflicting opinions by various experts. There were many litigations and appeals. Many experiments were carried out and many issues arose in those cases. In the current context, the important point was that the X-ray powder pattern of the Bouzard form was indexed, showing that every line in the pattern could be accounted for by that crystal modification; this proved it was a unique and pure form.

The series of litigations continued over other issues, including the nature of crystal modifications (Zenith Laboratories, Inc. v Bristol-Myers Squibb Co., 1992, 1994). Zenith prepared and formulated a hemihydrate of cefadroxil, for which it submitted an abbreviated new drug application (ANDA) to the FDA. BM (now Bristol-Myers Squibb) contended that the FDA should require a much more extensive new drug application (NDA) for the hemihydrate, rather than approve it within the framework of the FDA monograph for the monohydrate. BM also alleged that the Zenith product converted to the monohydrate, thereby infringing the ’657 patent. BM’s theory of infringement was that the Zenith product converts to the Bouzard monohydrate after ingestion in the gullet and the stomach, as it is mixed with liquid. A US federal court found in favour of BM. Upon appeal, Zenith contended that the ’657 patent does not cover Bouzard-form crystals that might form momentarily in a patient’s stomach, and there were both legal and scientific grounds for the basis of that contention. One of the main points of contention was whether the XRPD pattern of the material found by BM in a patient’s stomach matched the claim of the Bouzard patent, as given in the table in Claim 1. Upon XRPD analysis following *in vivo* conversion, BM had identified 15 of the 37 diffraction lines cited in the claim. The court found that “Although the term ‘essentially’ recited in the claim permits some leeway in the exactness of the comparison with the specified 37 lines of the claim, it does not permit ignoring a substantial number of lines altogether”, and that “ . . . there was a failure of proof as to whether any crystals, assumed to form in the stomach from ingested cefadroxil . . . , literally infringe the ’657 claim”. On this basis, the appeals court reversed the lower court’s decision. One result of this decision is that many subsequent patent applications, including claims based on substances characterized by X-ray diffraction patterns and/or IR spectra, were framed in language that differs from that used in the ’657 patent; another result was that the claims (as opposed to the specifications) contain many fewer peaks, and only those that may be readily detected in the presence of other substances, such as excipients.

7.5.7.1. *Crystal habit*

As noted above, in the pharmaceutical industry XRPD may be employed in contexts other than solid-form identification or assessment of solid-form purity. One illustrative example dealt with the *crystal habit* of the widely used dipeptide artificial sweetener aspartame, marketed as Nutrisweet. In the original conventional manufacturing process, crystallization from aqueous solutions tended to produce needles with a diameter of 10 μm or less. The crystals were very fine, with large specific volume. These characteristics led to many problems in the filtration and drying processes, the formation of scale on reactor surfaces, and the high tendency to form a dust and hygroscopicity of the final product, which made it difficult to handle and unsuitable for use as a direct (*i.e.* table-top) sweetener (Kishimoto *et al.*, 1987; Ajinomoto Co., Inc., 1983).

Five crystal modifications of aspartame are known (Ajinomoto Co., Inc., 1983; Hatada *et al.*, 1985; Nagashima *et al.*, 1987; Tsuboi *et al.*, 1991; Kishimoto & Naruse, 1988; Furedi-Milhofer *et al.*, 1999). Many attempts were made to improve the quality of the

---

[1] See Kalifarma, Inc. v. Bristol-Myers Company (1989) for details of the history of the prosecution of the patent application.

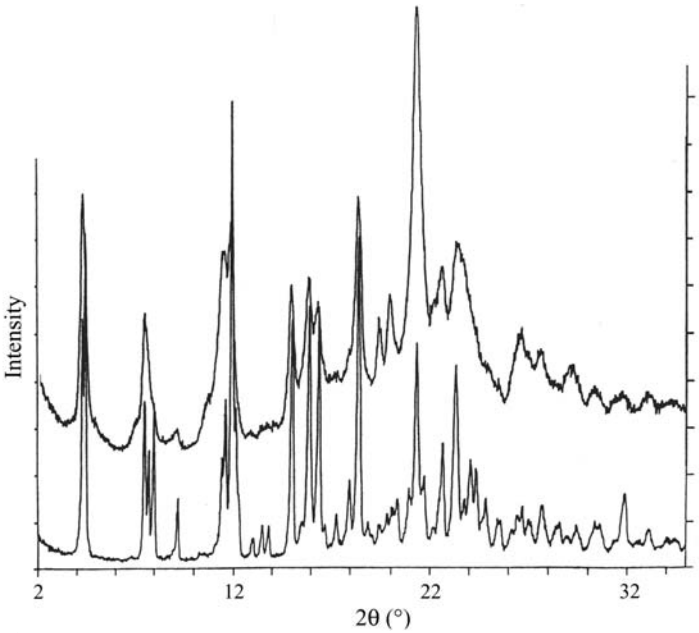

Figure 7.5.8
Comparison of the measured XRPD patterns for two different habits of aspartame. Upper, 'conventional' crystals; lower, 'bundle-like' crystals. [From Tarling (1991), with permission.]

crystals obtained from the conventional manufacturing process. The Japanese Ajinomoto Co. had a license to make aspartame and, as a result of 'intensive investigations to improve the workability (of the crystallization) step in the production . . . ', discovered that cooling aqueous solutions of aspartame without stirring led to 'bundle-like' aggregates of crystals (Kishimoto & Naruse, 1987). These crystals had significantly improved handling characteristics compared to the conventional crystals. This process was subsequently refined and led to an Ajinomoto European patent, granted in 1985.

In April 1992, the Opposition Division of the European Patent Office concluded that the bundle-like crystals were the same as the conventional crystals. In response to that decision, Ajinomoto presented a detailed study of the differences between the two (Tarling, 1992). The two types of crystals were *different habits* rather than polymorphs. The bundle-like crystals, produced without stirring, had a higher degree of crystal perfection than the conventional crystals produced with agitated stirring. The Tarling report identified some 'significant and reproducible differences' in a number of properties determined with a variety of analytical techniques. The differences formed the basis of the Ajinomoto response to the opposition, and included reproducible differences in the following properties: specific volumes, rate of dissolution, water content, density, solid-state NMR spectra, polarizing light spectroscopy and X-ray powder diffraction, as shown in Fig. 7.5.8.

For the latter, there are some slight differences in the peak positions, which was attributed to differences in water content and degree of internal crystal strain. There are some more obvious differences in relative intensities, including the position of the strongest peak. There are clear differences in the peak widths, which also reflect differences in the nature of the crystalline material obtained by the two methods; scanning electron microscopy, single-crystal X-ray diffraction (Hatada *et al.*, 1985; Kishimoto *et al.*, 1989) and crystal-habit modelling were used to determine the preferred orientation and to simulate the X-ray powder patterns of both forms to show a good comparison with the experimental data.

In May 1997, the Boards of Appeal of the European Patent Office set aside the 1992 opposition to the Ajinomoto patent (European Patent Office, 1997), and a New European Patent Specification was issued (Ajinomoto Co., Inc, 1998).

The ultimate value of a patent is judged by how well it can be defended against potential challengers and infringers. One important component of that process is how well the invention is defined, and XRPD can be the essential technique in defining the invention. If XRPD is the basis for defining and characterizing the invention, then determining a match between the invention and alleged infringing material is essential in that defence. We have noted above some of the pitfalls and difficulties in comparing a 'defining' XRPD pattern with that from an experimental sample. Increasingly sophisticated methods are being developed to make that comparison less subject to human judgement and more algorithm-based. While such developments are to be encouraged, there is a danger lurking in assigning a single number to a comparison of two sets of data, as courts naturally would like to do. Nevertheless, a great deal can be said for the ability of human beings to compare and recognize patterns, even in seemingly complex situations, and these judgements should remain an integral part of the intellectual property scene.

7.5.8. Counterfeit medicines

Counterfeit medicines are a global threat to public health. The US Food and Drug Administration (FDA, 2012) describes the situation.

> Counterfeit medicine is fake medicine. It may be contaminated or contain the wrong or no active ingredient. They could have the right active ingredient but at the wrong dose. Counterfeit drugs are illegal and may be harmful to your health. FDA takes all reports of suspect counterfeits seriously and, in order to combat counterfeit medicines, is working with other agencies and the private sector to help protect the nation's drug supply from the threat of counterfeits.

In order to give some direction to aid the prevention of counterfeiting of drugs, the FDA have published guidance for industry on (I) *Standards for Securing the Drug Supply Chain – Standardized Numerical Identification for Prescription Drug Packages*, (II) *Incorporation of Physical–Chemical Identifiers into Solid Oral Dosage Form Drug Product Anticounterfeiting*, and (III) *Drug Supply Chain Security Act Implementation: Identification of Suspect Product and Notification*, see https://www.fda.gov/Drugs/GuidanceComplianceRegulatoryInformation/Guidances/default.htm. In (II) the FDA pointed out that, for example, adding a physical–chemical identifier (PCID) to a nonfunctional tablet film coating is covered by this guidance, but adding a non-functional film coating that contains a PCID to a previously uncoated tablet involves manufacturing changes that are not covered by this guidance. Also the incorporation of a PCID into the packaging or labelling is not covered in this guidance. In addition, this guidance does not apply to manufacturing or formulation changes, made in conjunction with the addition of a PCID, that go beyond simply inserting the PCID into a blending or mixing operation. With that, the addition of a marker that can be used to identify counterfeit medicines, using for example spectroscopic or X-ray methods, is not a simple task.

Several incidents have proven that the US has a serious and growing problem with counterfeit medicines. In 2012, forged steroids killed 11 people and made another 100 sick (*The Economist*, 2012). In another example, vials puportedly of the cancer drug Avastin were shown not to contain the API. And in 2007–2008, 149 patients died from a contaminated batch of the blood thinner Heparin (*The Economist*, 2012). These cases and others have shown that powerful tools are required to identify counterfeit medicines reliably without adding special markers, as pointed out by the FDA guideline described above. Earlier we established that XRPD is a key analytical tool in the pharmaceutical industry. With powerful developments such as ultrafast detectors, Beckers (2008) has shown that laboratory-based XRPD equipment can be used to detect counterfeit tablets in intact blisters. Beckers reported studying commercially available tablets from European pharmacies and specially produced tablets for testing purposes. All tablets were contained within blister packs within a polymer cavity and aluminium lidding. XRPD measurements were performed with a diffractometer equipped with a focusing mirror and motorized high-throughput stage. The blister cards were mounted on a metal frame and the diffraction signals were measured in transmission mode. In other words, the measurement is non-invasive and non-destructive. But the escalating issue of counterfeit medicines demands new measures, including rapid and non-destructive analytical tools that are easy to use in the field by non-experts. Newly developed X-ray-based tools are among those which can be used in the field. Taylor (2009) has shown that portable X-ray diffractometers can be used to rapidly identify genuine and fake pharmaceuticals. The key is to equip the X-ray system with the correct X-ray pattern database for identifying pharmaceutical products. The instrument requires around 15 mg of loose powder to perform an analysis. This means that a tablet needs to be rendered into a powder for sample preparation, so such a measurement is destructive, a distinct disadvantage. The instrument does not contain any moving parts or variable parameters and requires about 2 to 3 minutes of acquisition time. The resulting diffraction pattern is then ready for processing with the software included. Other promising potential tools that can be used for identifying counterfeit medicines in the field are portable near-infrared and Raman spectrometers (O'Neil, 2012) and nano-encoding of individual tablets or pills (NanoGuardian, 2012).

Counterfeit medicines clearly also pose a serious threat to intellectual property (WHO, 2006; Fernandez *et al.*, 2008). Forged pharmaceutical products are not subject to regulatory supervision and, as noted above, at a minimum often lack therapeutic value or, much worse, may in fact threaten the health of the unwary or uninformed consumer. Thus, health officials as well as the holders of patent rights on drugs are on the watch for counterfeit pharmaceutical products. This is very much a cat-and-mouse game with the regulators and industrial watchdogs constantly improving methods of detection, while the counterfeiters attempt to match and outdo their sleuthing techniques with ever more sophisticated methods of copying. XRPD is an important part of the armoury on this economic and scientific battleground and is being used extensively in the efforts to detect forged products and prosecute the counterfeiters (Maurin *et al.*, 2007). A typical example is given in Fig. 7.5.9.

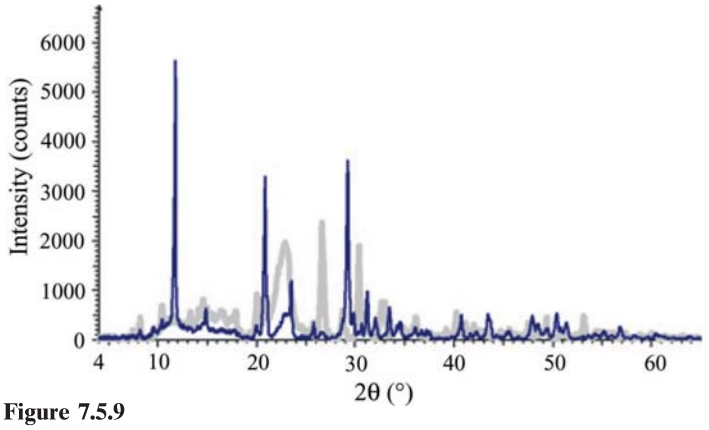

Figure 7.5.9
The comparison of diffraction patterns of a counterfeit 'Viagra' tablet and the original drug (shown as the thick lines in grey) taken with the coatings removed [from Maurin *et al.* (2007) with permission from Elsevier].

In this regard, it is worth pointing out that the limits of *in situ* detection for very low concentrations of a solid form or for 'polymorphic impurities' are constantly being extended. Yamada *et al.* (2011) have demonstrated the ability to detect crystalline substances in intact pharmaceutical tablets to a limit of quantification of 0.05% and a limit of detection of 0.02% using synchrotron powder diffractometry. A recent patent application claims the ability to detect a 'non-prevailing polymorph' (*i.e.* a polymorph impurity at a low concentration) at a concentration of 'even less than 0.005% by weight' (Brescello *et al.*, 2016; see also Cotarca, 2012).

7.5.9. Concluding remarks

XRPD plays a central role in virtually every aspect of research, development, production and market protection in the pharmaceutical industry. Some of the uses of XRPD, such as quality control, may be considered routine, but those are the measurements that determine whether a solid material passes inspection for purity or not. Considerable investment goes into each batch of API, but in addition to the financial consequences of a failed batch – or a failure to recognize a failed batch – the health of many people rests on robust and reliable test methods. In spite of the routine nature of some of the applications of XRPD in the pharmaceutical industry, there are constant demands to increase the sensitivity and selectivity of the analytical methods, prompting the development of cutting-edge and sophisticated technology. Indeed, many of the new initial practical applications of new technology in XRPD are to pharmaceutical problems, confirming the long-term symbiotic relationship between pure science and practical application in virtually every aspect of the pharmaceutical industry. Indeed, with industry increasingly relying on XRPD not only to aid in research and development, but also to establish and protect intellectual property rights and the pharmaceutical integrity of its products worldwide, it is certain that the role of XRPD in the pharmaceutical industry will continue to grow and expand.

References

Agatonovic-Kustin, S., Wu, V., Rades, T., Saville, D. & Tucker, I. G. (1999). *Powder diffractometric assay of two polymorphic forms of ranitidine hydrochloride*. *Int. J. Pharm.* **184**, 107–114.

Ahlneck, C. & Zografi, G. (1990). *The molecular basis of moisture effects on the physical and chemical stability of drugs in the solid state*. *Int. J. Pharm.* **62**, 87–95.

Ajinomoto Co., Inc. (1983). *Process for crystallizing α-L-asparatyl-L-phenyalanin-methyl ester*. New European Patent Specification 0 091 787 B2.

Ajinomoto Co., Inc. (1998). *Process for crystallizing α-L-asparatyl-L-phenyalanin-methyl ester*. European patent application 0 091 787 A1. Issued as European Patent Specification 0 091 787 B1 (04.09.85).

Alexander, L. & Klug, H. P. (1948). *Basic aspects of X-ray absorption in quantitative diffraction analysis of powder mixtures*. *Anal. Chem.* **20**, 886–889.

Altomare, A., Giacovazzo, C., Guagliardi, A., Moliterni, A. G. G., Rizzi, R. & Werner, P.-E. (2000). *New techniques for indexing: N-TREOR in EXPO*. *J. Appl. Cryst.* **33**, 1180–1186.

Amidon, G. L., Lennernaes, H., Shah, V. P. & Crison, J. R. (1995). *A theoretical basis for a biopharmaceutic drug classification: the correlation of in vitro drug product dissolution and in vivo bioavailability*. *Pharm. Res.* **12**, 413–420.

Antonio, S. G., Benini, F. R., Ferreira, F. F., Rosa, P. C. & Paiva-Santos, C. de O. (2011). *Quantitative phase analyses through the Rietveld method with X-ray powder diffraction data of heat-treated carbamazepine form III*. *J. Pharm. Sci.* **100**, 2658–2664.

Bates, S., Kelly, R. C., Ivanisevic, I., Schields, P., Zografi, G. & Newman, A. W. (2007). *Assessment of defects and amorphous structure produced in raffinose pentahydrate upon dehydration*. *J. Pharm. Sci.* **96**, 1418–1433.

Bates, S., Zografi, G., Engers, D., Morris, K., Crowley, K. & Newman, A. (2006). *Analysis of amorphous and nanocrystalline solids from their X-ray diffraction patterns*. *Pharm. Res.* **23**, 2333–2349.

Beckers, D. (2008). *Pharm. Manuf. Pack. Sources*, Spring 2008, pp. 82–85.

Bernstein, J. (2019). *Polymorphism in Molecular Crystals*, 2nd ed. In the press. Oxford University Press.

Bernstein, J. & Henck, J.-O. (2000). *Pharmaceuticals: development and formulation*. In *Industrial Applications of X-ray Diffraction*, edited by F. H. Chung & D. K. Smith, pp. 527–538. New York: Marcel Dekker.

Bernstein, J. & MacAlpine, J. (2018). *Pharmaceutical crystal forms and crystal form patents: novelty and obviousness.* In *Polymorphism in the Pharmaceutical Industry: Solid Form and Drug Development*, 1st ed., edited by R. Hilfiker & M. von Raumer. Wiley-VCH Verlag GmbH & Co. KGaA.

Billinge, S. J. L., Dykhne, T., Juhás, P., Božin, E., Taylor, R., Florence, A. J. & Shankland, K. (2010). *Characterization of amorphous and nanocrystalline molecular materials by total scattering*. *CrystEngComm*, **12**, 1366–1368.

Bøtker, J. P., Koradia, V., Rades, T., Rantanen, J. & Savolainen, M. (2012). *Atomic pairwise distribution function analysis of the amorphous phase prepared by different manufacturing routes*. *Pharmaceutics*, **4**, 93–103.

Boultif, A. & Louër, D. (2004). *Powder pattern indexing with the dichotomy method*. *J. Appl. Cryst.* **37**, 724–731.

Braga, D. & Bernstein, J. (2007). *Crystal polymorphism: challenges at the crossroads of science and technology*. In *Making Crystals by Design*, edited by D. Braga & F. Grepioni, pp. 293–314. Weinheim: Wiley-VCH Verlag.

Brescello, R., Cotarca, L., Smaniotto, A., Verzini, M., Polentarutti, M., Bais, G. & Rinkert Plaisier, J. (2016). *Method of detecting polymorphs using synchrotron radiation*. US Patent 9,513,237 B2, issued 6 December 2016.

Briggs, C. A., Jennings, R. A., Wade, R., Harasawa, K., Ichikawa, S., Minorara, K. & Nakagawa, S. (2006). *Crystalline (3R,5R)-7-[2-(4-fluorophenyl)-3-phenyl-4-(phenylcarbamoyl)-5-propan-2-ylpyrrol-1-yl]-3,5-dihydroxyheptanoic acid (atorvastatin)*. US Patent 5,969,156; re-examination certified Sept. 26, 2006.

Bristol-Myers Company v. United States International Trade Commission (1989). Gema, S. A. Kalipharma, Inc. Purepac Pharmaceutical Co., Istituto Biochimico Italiano Industria Giovanni Lorenzini, Institut Biochimique, S. A., and Biocraft Laboratories, Inc. (Dec. 1989) No. 89–1530. See also United States International Trade Commission, Investigation No. 337-TA-293.

Brittain, H. G. (1995). Editor. *Physical Characterization of Pharmaceutical Solids*. New York: Marcel Dekker.

Brittain, H. G. (1999). Editor. *Polymorphism in Pharmaceutical Solids*. New York: Marcel Dekker.

Brittain, H. G. (2009). Editor. *Polymorphism in Pharmaceutical Solids*, 2nd ed. New York: Informa Healthcare Press.

Brittain, H. G. (2011). *Polymorphism and Solvatomorphism in 2009*. *J. Pharm. Sci.* **100**, 1260–1279.

Bruker AXS (2008). *TOPAS V4: General profile and structure analysis software for powder diffraction data*. User's Manual. Bruker AXS, Karlsruhe, Germany.

Brüning J. & Schmidt, M. U. (2015). *The determination of crystal structures of active pharmaceutical ingredients from X-ray powder diffraction data: a brief, practical introduction, with fexofenadine hydrochloride as example*. *J. Pharm. Pharmacol.* **67**, 773–781.

Byard, S. J., Jackson, S. L., Smail, A., Bauer, M. & Apperley, D. C. (2005). *Studies on the crystallinity of a pharmaceutical development drug substance*. *J. Pharm. Sci.* **94**, 1321–1335.

Byrn, S. R., Pfeiffer, R. & Stowell, J. G. (1999). *Solid State Chemistry of Drugs*, 2nd ed. West Lafayette: SSCI Inc.

Coehlo, A. A. (2000). *Whole-profile structure solution from powder diffraction data using simulated annealing*. *J. Appl. Cryst.* **33**, 899–908.

Coelho, A. A. (2003). *Indexing of powder diffraction patterns by iterative use of singular value decomposition*. *J. Appl. Cryst.* **36**, 86–95.

Cotarca, L. (2012) *Novel high resolution XR-powder diffraction protocol for detection of API's polymorph contamination*. Oral presentation at 10th International Conference on Polymorphism and Crystallization, Prague, Czech Republic, 19–20 November 2012.

Davis, T. D., Morris, K. R., Huang, H., Peck, G. E., Stowell, J. G., Eisenhauer, B. J., Hilden, J. L., Gibson, D. & Byrn, S. R. (2003). *In situ monitoring of wet granulation using online X-ray powder diffraction*. *Pharm. Res.* **20**, 1851–1857.

Dharmayat, S., De Anda, J. C., Hammond, R. B., Lai, X., Roberts, K. J. & Wang, X. Z. (2006). *Polymorphic transformation of* L*-glutamic acid monitored using combined on-line video microscopy and x-ray diffraction*. *J. Cryst. Growth*, **294**, 35–40.

Dharmayat, S., Hammond, R. B., Lai, X., Ma, C., Purba, E., Roberts, K. J., Chen, Z.-P., Martin, E., Morris, J. & Bytheway, R. (2008). *An examination of the kinetics of the solution-mediated polymorphic phase transformation between α- and β-forms of* L*-glutamic acid as determined by online powder x-ray diffraction*. *Cryst. Growth Des.* **8**, 2205–2216.

Dykhne, T., Taylor, R., Florence, A. & Billinge, S. J. (2011). *Data requirements for the reliable use of atomic pair distribution functions in amorphous pharmaceutical fingerprinting*. *Pharm. Res.* **28**, 1041–1048.

Egami, T. & Billinge, S. J. L. (2003). *Underneath the Bragg Peaks: Structural Analysis of Complex Materials*. Oxford: Plenum.

Engel, G. E., Wilke, S. König, O., Harris, K. D. M. & Leusen, F. J. J. (1999). *PowderSolve – a complete package for crystal structure solution from powder diffraction patterns*. *J. Appl. Cryst.* **32**, 1169–1179.

European Patent Office (1997). Decision of 27 May 1997. Case Number T 0475/92–3.3.4. Application Number 833301951.6. Publication Number 0091787. IPC C07K 3/12.

Fawcett, T. G., Needham, F., Faber, J. & Crowder, C. E. (2010). *International Centre for Diffraction Data round robin on quantitative phase analysis of pharmaceuticals*. *Powder Diffr.* **25**, 60–67.

FDA (2012). http://www.fda.gov/Drugs/ResourcesForYou/Consumers/BuyingUsingMedicineSafely/CounterfeitMedicine/default.htm.

Fernandez, F. M., Green, M. D. & Newton, P. N. (2008). *Prevalence and detection of counterfeit pharmaceuticals: a mini review*. *Ind. Eng. Chem. Res.* **47**, 585–590.

Furedi-Milhofer, H., Garti, N. & Kamyshny, A. (1999). *Crystallization from microemulsions – a novel method for the preparation of new crystal forms of aspartame*. *J. Cryst. Growth*, **199**, 1365–1370.

Giacovazzo, C., Monaco, H. K., Artioli, G., Viterbo, D., Milanesio, M., Ferraris, G., Gilli, G., Gilli, P., Zanotti, G. & Catti, M. (2011). *Fundamentals of Crystallography*, 3rd ed., edited by C. Giacovazzo, ch. 4. Oxford University Press.

Gozzo, F. (2018). *The power of synchrotron x-ray diffraction for the characterization of pharmaceuticals*. *Pharm. Technol.* **42**, 18.

Grepioni, F. & Braga, D. (2007). Editors. *Making Crystals by Design – Methods, Techniques and Applications*. Weinheim: Wiley-VCH.

Griesser, U. J. (2006). *The importance of solvates*. In *Molecular Materials, Methods, Techniques, Applications*, edited by R. Hilfiker, pp. 211–234. Weinheim: Wiley-VCH.

Groom, C. R., Bruno, I. J., Lightfoot, M. P. & Ward, S. C. (2016). *The Cambridge Structural Database*. *Acta Cryst.* B**72**, 171–179.

Hancock, B. C. & Zografi, G. (1997). *Characteristics and significance of the amorphous state in pharmaceutical systems*. *J. Pharm. Sci.* **86**, 1–12.

Harris, L. J., Storey, R. A. & Wood, A. S. (2006). *Crystalline therapeutic agent*. US Patent 6,420,557.

Hatada, M., Jancarik, J., Graves, B. & Kim, S. H. (1985). *Crystal structure of aspartame, a peptide sweetener*. *J. Am. Chem. Soc.* **107**, 4279–4282.

Henck, J. O. & Byrn, S. R. (2007). *Designing a molecular delivery system within a preclinical timeframe*. *Drug Disc. Today*, **12**, 189–199.

Hilfiker, R. (2006). Editor. *Polymorphism in the Pharmaceutical Industry*. Weinheim: Wiley-VCH.

Hilfiker, R. & von Raumer, M. (2018). Editors. *Polymorphism in the Pharmaceutical Industry: Solid Form and Drug Development*, 1st ed. Wiley-VCH Verlag GmbH & Co. KGaA.

Huq, A. & Stephens, P. W. (2003). *Subtleties in crystal structure solution from powder diffraction data using simulated annealing: ranitidine hydrochloride*. *J. Pharm. Sci.* **92**, 244–249.

ICH (1996). *Validation of analytical procedures: Text and methodology Q2(R1), Harmonized tripartite guideline*. International Conference on Harmonization. http://www.ich.org/products/guidelines/quality/article/quality-guidelines.html.

ICH (1999). *Specifications: Test procedures and acceptance criteria for new drug substances Q6a, Harmonized tripartite guideline*. International Conference on Harmonization. http://www.ich.org/products/guidelines/quality/article/quality-guidelines.html.

ICH (2009). ICH guidance for industry *Q8(R2): Pharmaceutical development* - revision 2, November 2009. https://www.fda.gov/Drugs/GuidanceComplianceRegulatoryInformation/Guidances/.

Ivanisevic, I., McClurg, R. B. & Schields, P. J. (2010). *Uses of X-ray powder diffraction in the pharmaceutical industry*. In *Pharmaceutical Sciences Encyclopedia: Drug Discovery, Development, and Manufacturing*, edited by S. C. Gad, pp. 1–42. New York: John Wiley & Sons.

Jenkins, R. & Snyder, R. L. (1996*a*). *Introduction to X-ray Powder Diffraction*. New York: Wiley-Interscience.

Jenkins, R. & Snyder, R. L. (1996*b*). *Quantitative analysis*. In *Chemical Analysis: Introduction to X-ray Powder Diffractometry*, edited by J. D. Winefordner, ch. 13, pp. 355–387. New York: John Wiley & Sons.

Kalifarma, Inc. v Bristol-Myers Company (1989). No. pp. 88 CIV. 4640; 707 F. Supp. 741.

Kishimoto, S., Nagashima, N., Naruse, M. & Toyokura, K. (1989). *The 'bundle-like' crystals in aspartame crystallization*. *Process Technol. Proc.* **6**, 511–514.

Kishimoto, S. & Naruse, M. (1987). *The 'bundling' phenomenon in aspartame crystallization*. *Chem. Ind.* 16 February, p. 127.

Kishimoto, S. & Naruse, M. (1988). *A process development for the bundling crystallization of aspartame*. *J. Chem. Technol. Biotechnol.* **43**, 71–82.

Klug, H. P. & Alexander, L. E. (1974). *X-ray Diffraction Procedures for Polycrystalline and Amorphous Material*, 2nd ed. New York: John Wiley.

Kumar, L., Amin, A. & Bansal, A. K. (2007). *An overview of automated systems relevant to pharmaceutical salt screening. Drug Disc. Today*, **12**, 1046–1053.

Le Bail A., Duroy, H. & Fourquet, J. L. (1988). *Ab-initio structure determination of $LiSbWO_6$ by X-ray powder diffraction. Mater. Res. Bull.* **23**, 447–452.

Lifshin, E. (2008). *X-ray Characterization of Materials*. Weinheim: Wiley-VCH. (In German.)

Maurin, J. K., Pluciński, F., Mazurek, A. P. & Fijałek, Z. (2007). *The usefulness of simple X-ray powder diffraction analysis for counterfeit control–the Viagra example*. *J. Pharm. Biomed. Anal.* **43**, 1514–1518.

Moore, M. D., Cogdill, R. P. & Wildfong, P. L. (2009). *Evaluation of chemometric algorithms in quantitative X-ray powder diffraction (XRPD) of intact multi-component consolidated samples*. *J. Pharm. Biomed. Anal.* **49**, 619–626.

Morissette, S. L., Almarsson, Ö., Peterson, M. L., Remenar, J. F., Read, M. J., Lemmo, A. V., Ellisa, S., Cima, M. J. & Gardner, C. R. (2004). *High-throughput crystallization: polymorphs, salts, co-crystals and solvates of pharmaceutical solids*. *Adv. Drug Del. Rev.* **56**, 275–300.

Morris, K. R. (1999). *Structural aspects of hydrates and solvates*. In *Polymorphism in Pharmaceutical Solids*, edited by H. Brittain, pp. 125–182. New York: Marcel Dekker.

Nagashima, N., Sano, C., Kishimoto, S. & Iitaka, Y. (1987). *The characterization of various crystalline forms of aspartame (a dipeptide sweetener)*. *Acta Cryst.* A**43**, C54.

NanoGuardian (2012). http://www.nanoguardian.net/.

Németh, Z., Sajó, I. & Demeter, A. (2010). *Rietveld refinement in the routine quantitative analysis of famotidine polymorphs*. *J. Pharm. Biomed. Anal.* **51**, 572–576.

Neumann, M. A. (2003). *X-Cell: a novel indexing algorithm for routine tasks and difficult cases*. *J. Appl. Cryst.* **36**, 356–365.

Newman, A., Engers, D., Bates, S., Ivanisevic, I., Kelly, R. C. & Zografi, G. (2008). *Characterization of amorphous API:polymer mixtures using X-ray powder diffraction*. *J. Pharm. Sci.* **97**, 4840–4856.

O'Neil, A. (2012). *Counterfeit consumer products*. In *Infrared and Raman Spectroscopy in Forensic Science*, edited by J. M. Chalmers, H. G. M. Edwards & M. D. Hargreaves, pp. 515–559. Chichester: John Wiley & Sons, Ltd.

Parker, R. (2005). Personal communication to JB.

Pawley, G. S. (1981). *Unit-cell refinement from powder diffraction scans*. *J. Appl. Cryst.* **14**, 357–361.

PDF-4+ (2018). Edited by S. Kabekkodu. International Centre for Diffraction Data, Newtown Square, PA, USA.

Pulacki, M., Higgins, J. D., Kwong, E. & Templeton, A. C. (2010). *Strategies at the interface of drug discovery and development: early optimization of the solid state phase and preclinical toxicology formulation for potential drug candidates*. *J. Med. Chem.* **53**, 5897–5905.

Rani, M., Govindarajan, R., Surana, R. & Suryanarayanan, R. (2006). *Structure in dehydrated trehalose dihydrate–evaluation of the concept of partial crystallinity*. *Pharm. Res.* **23**, 2356–2367.

Rietveld, H. M. (1967). *Line profiles of neutron powder diffraction peaks for structure refinement*. *Acta Cryst.* **22**, 151–152.

Rumondor, A. C. & Taylor, L. S. (2010). *Application of partial least-squares (PLS) modeling in quantifying drug crystallinity in amorphous solid dispersions*. *Int. J. Pharm.* **398**, 155–160.

Shankland, K., Pidcock, E., van de Streek, J., David, W. I. F., Motherwell, W. D. S. & Cole, J. C. (2006). *DASH: a program for crystal structure determination from powder diffraction data*. *J. Appl. Cryst.* **39**, 910–915.

Sheth, A. R., Bates, S., Muller, F. X. & Grant, D. J. W. (2005). *Local structure in amorphous phases of piroxicam from powder X-ray diffractometry*. *Cryst. Growth Des.* **5**, 571–578.

Stahl, P. H. & Wermuth, C. G. (2002). Editors. *Handbook of Pharmaceutical Salts: Properties, Selection and Use*. Zürich: Verlag Helvetica Chimica Acta.

Stephenson, G. A., Forbes, R. A. & Reutzel-Edens, S. M. (2001). *Characterization of the solid-state: quantitative issues*. *Adv. Drug Del. Rev*. **48**, 67–90.

Streek, J. van de & Neumann, M. A. (2014). *Validation of molecular crystal structures from powder diffraction data with dispersion-corrected density functional theory (DFT-D)*. *Acta Cryst.* B**70**, 1020–1032.

Sun, C. C. (2009). *Materials science tetrahedron – A useful tool for pharmaceutical research and development. J. Pharm. Sci.* **98**, 1671–1687.

Suryanarayanan, R. (1989). *Determination of the relative amounts of anhydrous carbamazepine ($C_{15}H_{12}N_2O$) and carbamazepine dihydrate ($C_{15}H_{12}N_2O{\cdot}2H_2O$) in a mixture by powder X-ray diffractometry*. *Pharm. Res.* **6**, 1017–1024.

Tarling, S. E. (1991). Private communication to JB. See also http://www.vino.demon.co.uk/ppxrd/cefad.html.

Tarling, S. E. (1992). Declaration to European Patent Office regarding action of the Opposition Division dated 23rd April 1992 in relation to EP 0 091 787.

Taylor, P. (2009). *inXitu brings portable XRD analysis to pharma counterfeit fight*. *Securing Pharma*, 9 October 2009. http://www.securingpharma.com/40/articles/443/247.php.

The Economist (2012). *Bad medicine*. 13 October 2012. https://www.economist.com/international/2012/10/13/bad-medicine.

Tsuboi, M., Ueda, T. & Ikeda, T. (1991). *Use of a Raman microscope in conformational analysis of a peptide with polymorphism*. In *Proceedings of the Fourth European Conference on the Spectroscopy of Biological Molecules*, edited by R. E. Hester & R. B. Girling, Special Publication No. 94, pp. 29–30. London: Royal Society of Chemistry.

Visser, J. W. (1969). *A fully automatic program for finding the unit cell from powder data*. *J. Appl. Cryst.* **2**, 89–95.

Werner, P.-E., Eriksson, L. & Westdahl, M. (1985). *TREOR, a semi-exhaustive trial-and-error powder indexing program for all symmetries. J. Appl. Cryst.* **18**, 367–370.

WHO (2006). *Declaration of Rome, conclusions and recommendations of the WHO International Conference on Combating Counterfeit Medicines*, 18 February 2006. http://www.who.int/medicines/services/counterfeit/RomeDeclaration.pdf.

Williams, H. D., Trevaskis, N. L., Charman, S. A., Shanker, R. M., Charman, W. N., Pouton, C. W. & Porter, C. J. H. (2013). *Strategies to address low drug solubility in discovery and development. Pharmacol. Rev.* **65**, 315–499.

Yamada, H., Masuda, K., Ishige, T., Fujii, K., Uekusa, H., Miura, K., Yonemochi, E. & Terada, K. (2011). *Potential of synchrotron X-ray* *powder diffractometry for detection and quantification of small amounts of crystalline drug substances in pharmaceutical tablets*. *J. Pharm. Biomed. Anal.* **56**, 448–453.

Yu, L. (2001). *Amorphous pharmaceutical solids: preparation, characterization and stabilization*. *Adv. Drug Del. Rev*. **48**, 27–42.

Yu, L. X. (2008). *Pharmaceutical quality by design: product and process development, understanding, and control*. *Pharm. Res.* **25**, 781–791.

Yu, L. X., Lionberger, R. A., Raw, A. S., D'Costa, R., Wu, H. & Hussain, A. S. (2004). *Applications of process analytical technology to crystallization processes*. *Adv. Drug Del. Rev*. **56**, 349–369.

Zenith Laboratories, Inc. v Bristol-Myers Squibb Co. (1992). No. 91–3423; 1991 WL 267892 (D N.J.).

Zenith Laboratories, Inc. v Bristol-Myers Squibb Co. (1994). No. 92–1527; 19F. 3d 1418.

International Tables for Crystallography (2019). Vol. H, Chapter 7.6, pp. 782–792.

7.6. Selected applications of Rietveld analysis in the aluminium industry

F. R. Feret

7.6.1. Introduction

The Rietveld method has been used increasingly in the aluminium industry since the beginning of the 1990s. The initial applications were predominantly for the analysis of raw materials and selected products. During the intervening decades, its use has expanded to every stage of aluminium production and Rietveld analysis has now become a recognized analytical technique, applied routinely in bauxite exploration, reduction and fabrication processes. Typical applications of the Rietveld method in the aluminium industry at present are listed in Table 7.6.1. The number of crystalline phases determined summarizes usual industrial experience, and may vary among laboratories. The success rate of the method (understood as the accuracy and reliability of the information obtained) obviously depends on the matrix. The Rietveld method has replaced existing methodology in plant laboratories as a primary and universal method for the determination of the phase composition of electrolytic bath. Freeing the plant laboratory from older calibration-curve-based methods improves the reliability and accuracy of all determinations of mineralogical phase concentrations.

The conventional cavity-slide sample-preparation technique is the most commonly used for the application of the Rietveld method; however, briquetting dominates in the analysis of electrolytic bath. Cavity-slide sample preparation is a standard X-ray diffraction technique, which allows presentation of material for the analysis in the instrument. The finely ground sample material is packed into a cavity in a support (called a slide) in such a way that the sample material remains flat. Materials such as the electrolytic bath that do not have self-binding properties require addition of a binder prior to grinding. Briquetting involves use of a press (mostly hydraulic) to compress sample material into a mechanically stable briquette. In some plants, highly sophisticated automatic systems handle grinding and briquetting of a few hundred samples a day.

Rietveld analysis has not only replaced traditional X-ray diffraction calibration methods; it has also opened the door for new applications that were not previously possible. The use of the Rietveld method to characterize selected materials unique to the aluminium industry (for example bauxite, red mud, alumina, electrolytic bath, spent potlining and dross) has became routine. PANalytical's *X'Pert High Score Plus* software was used in the studies detailed here.

Table 7.6.1
Typical applications of the Rietveld method in the aluminium industry

Material	No. of phases	Sample type	Success rate
Bauxite	14–24	Cavity slide	Limited
Red mud	30–60	Cavity slide	Limited
Alumina	8	Cavity slide	Limited–high
Electrolytic bath	9–16	Briquette, cavity	High
Spent potlining	30–60	Cavity slide	Limited–high
Dross	10–20	Cavity slide	High
Intermetallics	> 20	Cavity slide	High

7.6.2. Bauxite

Aluminium-bearing minerals constitute a group of raw materials vital to the aluminium industry. Bauxite, a mixture of hydrated aluminium minerals, is the primary raw material used in the Bayer process (Habashi, 2005). Other materials of concern, such as clay, red mud and sand, are waste products. Clay is obtained during bauxite washing, whereas red mud and sand appear during the bauxite digestion process.

An accurate estimate of the quality of the bauxite that is being surveyed, mined and supplied is important to the efficient operation of a mine and a Bayer plant. Traditional methods used to determine bauxite phase composition are based on wet chemistry (WCh). They are relatively slow and require large supplies of chemicals as well as considerable space and manpower. Compared to wet chemistry, powder X-ray diffraction (PXRD) offers speed and a much lower cost of analysis, but is very often less accurate. Conventional tube-based X-ray diffraction is known to be seriously affected by the sample's amorphous content (Figs. 7.6.1 and 7.6.2). In the analysis of Fig.

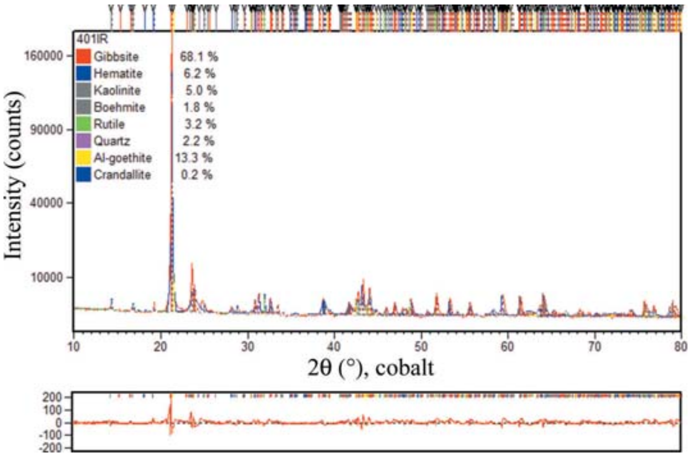

Figure 7.6.1
Example 1 of Rietveld refinement for bauxite.

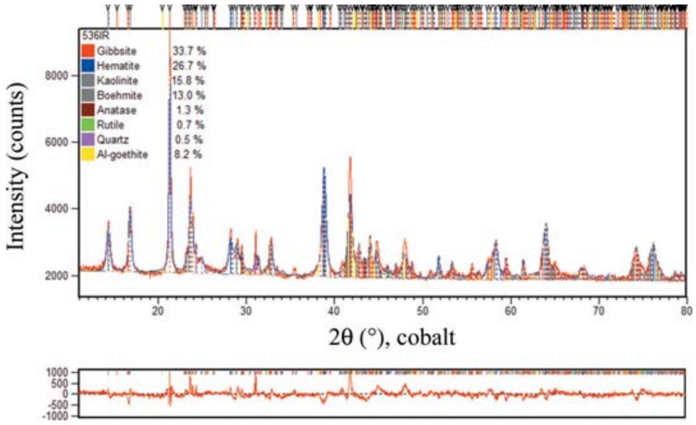

Figure 7.6.2
Example 2 of Rietveld refinement for bauxite.

Copyright © 2019 International Union of Crystallography

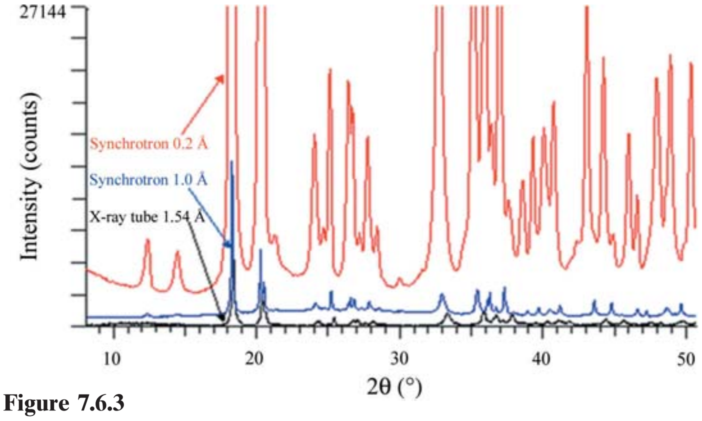

Figure 7.6.3
Comparison of diffractograms of BXT-12 from three sources. Red: synchrotron radiation, 0.2 Å; blue: synchrotron radiation, 1 Å; black: Cu *Kα* X-ray tube, 1.54 Å.

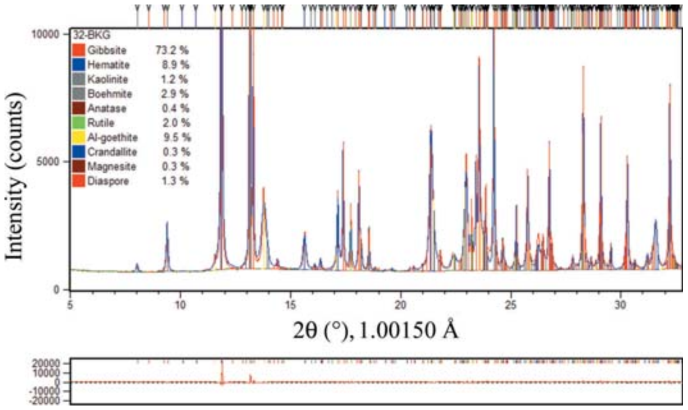

Figure 7.6.5
Rietveld refinement for BXT-02.

7.6.1, gibbsite is underestimated by approximately 8% and in Fig. 7.6.2 it is overestimated by the same amount with respect to WCh and mass-balance calculations. As a result of the low X-ray power, the limit of detection (LOD) of phase constituents is relatively high (Ni & Khalyapina, 1978). Not many studies of the application of Rietveld analysis to bauxite have been published (Bennett *et al.*, 1999). It was believed that synchrotron-radiation diffraction patterns with much better signal-to-noise ratios would help provide new information that cannot be obtained with X-ray tube instrumentation (Feret & See, 2010). It was also hoped that the diffractograms would facilitate detection of the amorphous content, which seriously plagues analysis of bauxite and red-mud material using conventional XRD.

The samples for the synchrotron experiments were ground to <325 mesh and packed into a thin-wall glass capillary (Feret & See, 2010). Diffractograms were recorded at the Japan Synchrotron Radiation Research Institute (JASRI) at wavelengths of 1.002 and 0.202 Å and covered 5–75° and 0–15° 2*θ*, respectively. The effect of the power of synchrotron radiation on a bauxite diffractogram can be appreciated in Fig. 7.6.3, which compares diffractograms of BXT-12 (Rio Tinto Alcan bauxite standard) from the 1 and 0.2 Å synchrotron and 1.54 Å Cu *Kα* radiation sources. The synchrotron diffractograms are not only much more intense, but the peak/background ratio and resolution are much higher than in the laboratory pattern. The 0.2 Å source diffractogram simply dwarfs the two other diffractograms by a large margin. All three features facilitate quantitative phase analysis. The first two peaks from kaolinite and boehmite are very well defined on the 0.2 Å source diffractogram.

In order to characterize all bauxite samples involved in the project, wet chemistry, BQuant (Kimmerle *et al.*, 1997), XDB Hungalu (Sajó, 1994), X-ray fluorescence (XRF) spectroscopy (Feret, 1993) and thermogravimetric analysis (TGA) determinations were carried out, in addition to Rietveld investigations.

Quantitative Rietveld results for Rio Tinto Alcan (RTA) bauxite reference materials using the 0.2 and 1 Å source diffractograms are presented in Figs. 7.6.4 and 7.6.5, respectively. In Table 7.6.2, major phase concentrations obtained for BXT-12 are compared. Gibbsite is to some extent overestimated and the boehmite concentration is underestimated using synchrotron radiation and the X-ray tube diffractograms. The boehmite concentration is lower from the 0.2 Å source diffractogram than from other sources. In contrast, Al-goethite (at 3.2%) is clearly confirmed in BXT-12 bauxite, while it is underestimated using the laboratory data. Anatase in Table 7.6.2 represents the sum of anatase and rutile.

Figs. 7.6.5 and 7.6.6 illustrate Rietveld results for BXT-02 and BXT-08, and confirm diaspore and ilmenite, respectively; these are impossible to quantify at these low levels using an X-ray tube diffractogram.

Apart from the phases appearing in Figs. 7.6.4–7.6.6, additional phases such as calcite, dolomite, magnetite, magnesite, chamosite, illite, muscovite, hausmanite, manganite, chabazite and others may also appear in small quantities, depending on the bauxite deposit.

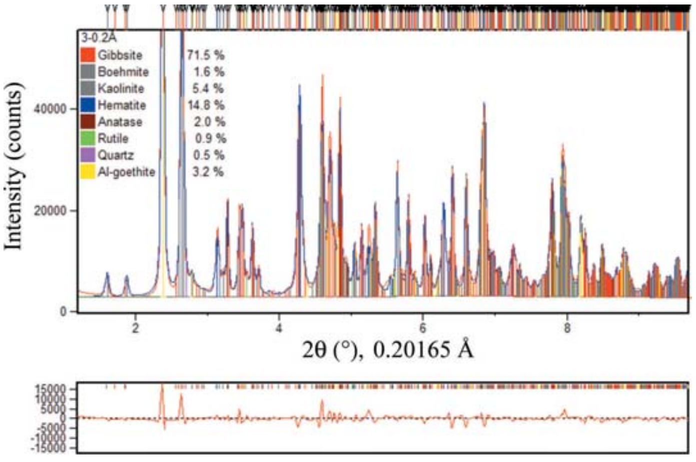

Figure 7.6.4
Rietveld refinement for BXT-12.

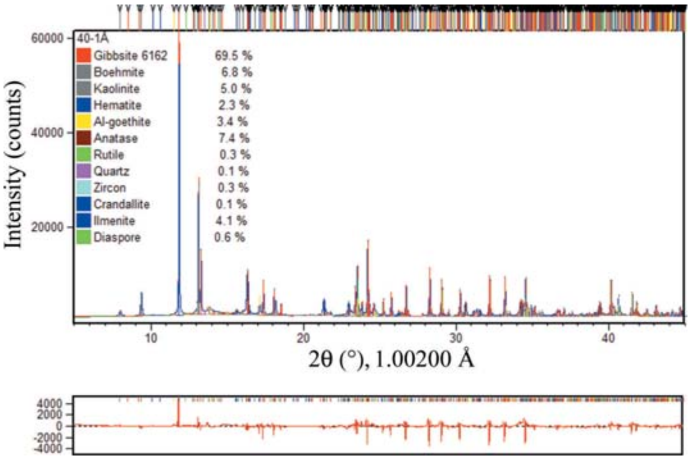

Figure 7.6.6
Rietveld refinement for BXT-08.

Table 7.6.2
Comparison of phase concentrations (wt%) for BXT-12

	Gibbsite	Boehmite	Kaolinite	Goethite	Haematite	Anatase	Quartz
Wet chemistry	69.5	3.0	5.9				
Mass balance	68.7	3.2	6.9	3.0	13.5	3.2	0.3
Rietveld (synchrotron radiation, 0.2 Å)	71.5	1.6	5.4	3.2	14.8	2.9	0.5
Rietveld (Cu X-ray tube)	71.2	2.4	5.9	1.2	15.7	3.2	0.4

When using an X-ray tube as the source, the concentrations of gibbsite are mostly overestimated by the Rietveld method (sometimes largely) with respect to WCh concentrations (Fig. 7.6.7). Most of the time, the main reason is underestimated boehmite, kaolinite and goethite concentrations. Because the Rietveld analysis normalizes the sum of all concentrations to 100%, increasing the content of the major constituent (gibbsite) compensates for the missing amorphous content. The correlation curve also demonstrates that the synchrotron diffractograms and XDB interpretations help to obtain the best correlation with WCh.

The Rietveld method using X-ray tube diffractograms tends to strongly underestimate kaolinite. This is evident from the XRF − WCh mass balance. The underestimation convincingly suggests that X-ray amorphous aluminosilicate must be present. In contrast to X-ray tube data, synchrotron data are much less affected by the amorphous content. The WCh and BQuant correlation for kaolinitic SiO_2 appears to be good, but this determination was modelled using Rio Tinto Alcan standards in which the total SiO_2 is relatively low. The XDB mass-balance calculations of the %SiO_2 in kaolinite,

$$\text{kaolinitic}\,SiO_2\,(\text{XDB}) = (\%SiO_2 - \%\text{quartz}),$$

provide the best fit with the WCh data.

The synchrotron study helped to validate the analytical methods employed for bauxite phase quantification and has changed our understanding of the bauxite matrix. Kaolinite and goethite, in particular, were already believed to be partially amorphous. However, contrary to past beliefs, even gibbsite and haematite may appear partially amorphous. The problem of bauxite amorphous content, although anticipated, was shown to have a profound effect on the quantification of selected phases using Rietveld and XDB methods and X-ray tube diffractograms. Simply, if a part of the bauxite matrix is X-ray amorphous, it will not contribute fully to a diffractogram. If several mineral contributions are missing on a diffractogram simultaneously, they can be quantified as a group, but not individually. The bauxite amorphous content, believed to be at the level of a few per cent, appears to be much higher than that.

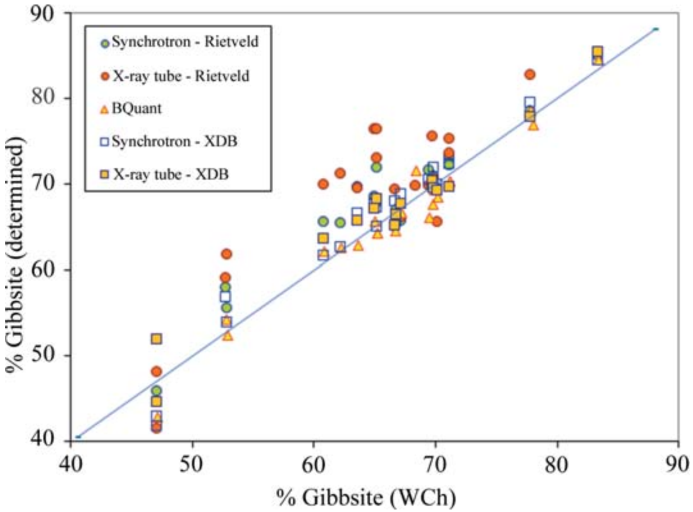

Figure 7.6.7
Comparison of gibbsite concentrations determined by different methods. %Gibbsite determined by various methods is compared with %gibbsite obtained from WCh analysis. The methods used are: synchrotron sample measurement with Rietveld-XRD interpretation; X-ray tube sample measurement with Rietveld-XRD interpretation; BQuant software, which uses XRF elemental composition and loss-of-mass data; synchrotron sample measurement with interpretation using XDB software; and X-ray tube sample measurement with interpretation using XDB software.

Despite high expectations, the synchrotron data did not allow phase concentrations equivalent to wet chemistry or mass-balance calculations to be obtained for several bauxites. Although powerful, synchrotron radiation by itself does not permit accurate quantification of amorphous phases. One of the methods described by Madsen & Scarlett (2008) must be used. On the other hand, synchrotron data, especially from the 0.2 Å source, resulted in a more detailed study on bauxite than conventional XRD.

7.6.3. Quantification of quartz in bauxite

Quartz is one of the important phase constituents of any bauxite and may vary from a small fraction to over 60% of the total SiO_2 concentration. At present, the most practical method of estimating quartz is by wet chemistry or using conventional XRD methods. Whether employing a direct or Rietveld approach, the XRD method is difficult, and not possible for small quartz concentrations because of severe line overlaps.

A new method devised for quantification of quartz in bauxite uses material calcined at 1273 K (Feret & Roy, 2002). This is an example of converting a difficult problem into one more easily solved by physical treatment. Major bauxite hydrated phases, such as gibbsite, boehmite, kaolinite and goethite, are entirely decomposed in the calcination process. The calcination proce-

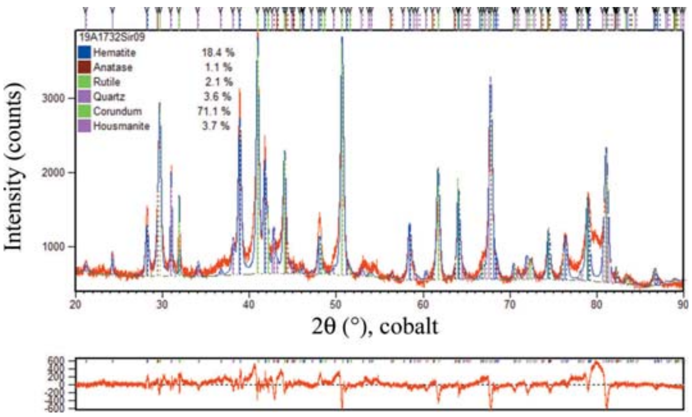

Figure 7.6.8
Rietveld quantification of calcined bauxite.

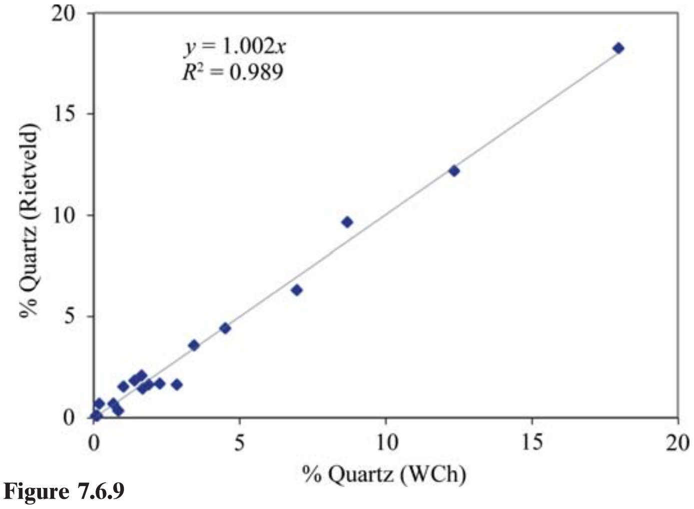

Figure 7.6.9
Comparison of % quartz determined by WCh and Rietveld methods.

dure converts kaolinite (the principal SiO_2 carrier) into amorphous material. In addition to the amorphous portion, there are just four major crystalline phases present in the calcined material: corundum, quartz, rutile and haematite (Fig. 7.6.8). Depending on the origin of the bauxite, some secondary phases (for example hausmanite, Mn_3O_4) can also occur. Corundum crystallizes from the decomposition products of major Al-bearing hydrates, mostly gibbsite and boehmite. Quartz in the calcined bauxite corresponds to the primary quartz occurring in the initial sample. Anatase is readily converted by heat into the more stable rutile at temperatures as low as 673 K. The amount of rutile in the calcined sample is the sum of the primary rutile and that resulting from anatase transformation. Rutile is employed as the internal standard. The haematite present is the sum of the primary haematite and haematite formed by goethite decomposition.

In order to determine the absolute quartz concentration, the quartz content from Rietveld analysis, quartz (R), needs to be corrected for various dilution effects in one single step, using the rutile as an internal standard. Employing one simple correction equation, the corrected quartz concentration, %quartz, is

$$\%\mathrm{quartz} = \mathrm{quartz}\ (\mathrm{R}) \frac{\mathrm{t.TiO_2}}{\mathrm{rutile}\ (\mathrm{R})}, \tag{7.6.1}$$

where $t.TiO_2$ is the total TiO_2 known from XRF, and rutile (R) is the rutile content from the Rietveld estimate. All of the Ti detected by bulk analysis is present as rutile. The accuracy of the quartz determination with the new method corresponds to that obtained by the conventional 'by difference' approach (Fig. 7.6.9). This approach is based on the total SiO_2 determined by XRF and kaolinitic silica (Si150) determined by WCh. The study also proves that SiO_2 determined in the low-temperature digestion process (Si150) is due to kaolinite and illite and not just due to kaolinite, as was previously believed. This fact has important implications for the plant processing of bauxite that contains illite.

7.6.4. Occurrence and characterization of Zn and Mn in bauxite

Zinc is one of the secondary elements occurring in Caribbean bauxite and the associated non-bauxitic material. It is generally believed that Zn in bauxite can either occur in gahnite ($ZnAl_2O_4$) or sphalerite (ZnS), or substitute for Fe in goethite. Manganese represents an appreciable impurity in Caribbean bauxites and is identified in diffractograms as lithiophorite $(Li,Al)MnO_2(OH)_2$. As Zn has been observed to increase with the MnO content, the objective of this study was to understand better the mineralogical nature of the Zn and Mn compounds. Data from 340 bauxite samples of different origins were assembled (Feret & See, 2006). It was found that Zn in bauxite could not possibly substitute for Fe in goethite or haematite (Fig. 7.6.10). Strong evidence was obtained that Zn occurs in the same compound as Mn. Application of the Rietveld method to characterize diffractograms and other XRD data suggest an aggregate, which we may call 'zincophorite' $Al(Zn_xMn_{1-x})O_2(OH)_2$. The x parameter could vary from 0.02 to 0.24. The concentration data corresponding to the group of samples investigated are given in Fig. 7.6.11.

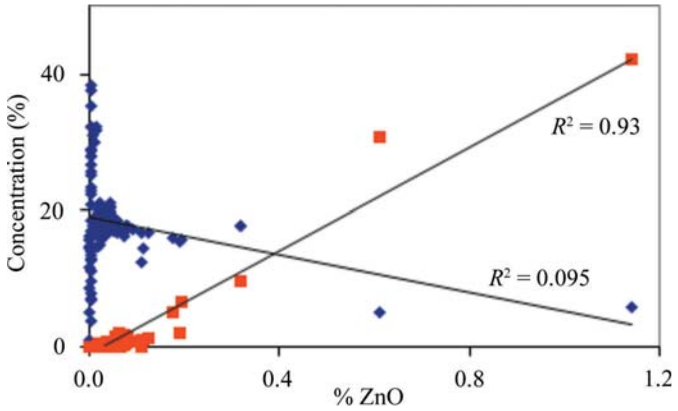

Figure 7.6.10
Correlation of ZnO *versus* MnO and Fe_2O_3 in bauxite. Red points represent MnO, blue points represent Fe_2O_3.

In Fig. 7.6.11, concentrations of ZnO are plotted against the concentrations of MnO and zincophorite. The correlation between the ZnO and MnO content is strong. Some points representative of zincophorite occur much below those of MnO at high ZnO concentrations. This is highly suggestive that a portion of lithiophorite might be amorphous.

7.6.5. Red mud (bauxite residue)

Red mud is the (semi-)solid waste product from the initial digestion of bauxite in caustic in the Bayer process. Storage, remediation and disposal of red mud represent significant challenges to a Bayer plant. The red colour arises from iron-containing compounds in the bauxite. Red muds consists of complex assemblages of minerals, and their analysis is a challenge.

Certain red-mud samples were analysed with synchrotron experiments (Feret & See, 2011). A dedicated control file containing all necessary crystallographic parameters was devel-

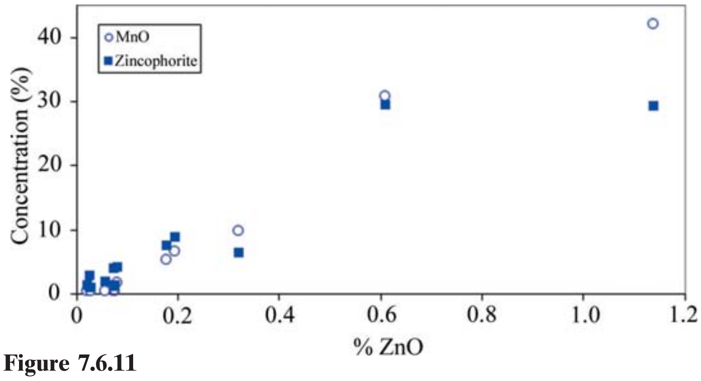

Figure 7.6.11
Correlation between ZnO and MnO and zincophorite in Jamaica bauxite.

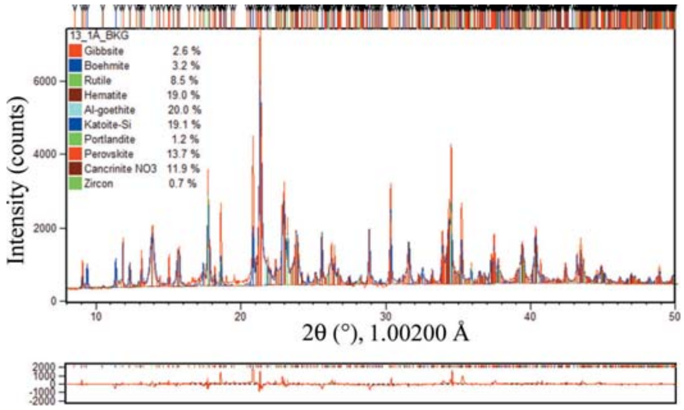

Figure 7.6.12
Example 1 of Rietveld refinement for red mud.

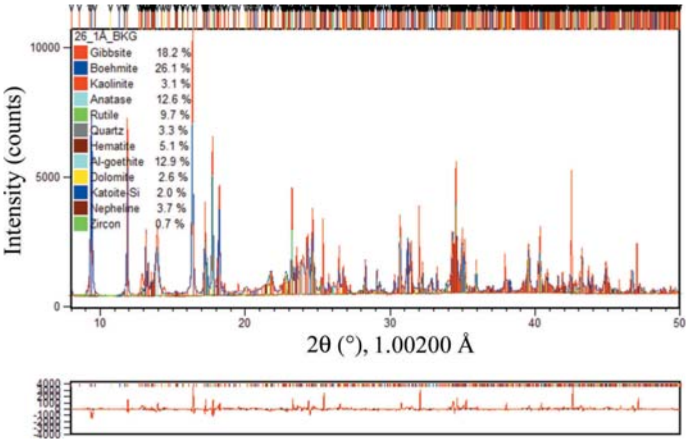

Figure 7.6.13
Example 2 of Rietveld refinement for red mud.

oped for quantification of 45 mineralogical phases in red mud. The maximum number of crystalline phases allowed during Rietveld refinement is limited in most commercial programs. Hence, the refinement was a tedious and time-consuming process beginning with phase confirmation and rejection, followed by Rietveld trials for a selected group of minerals. If a particular mineral was confirmed to be absent during the trial, it was replaced by another mineral. Given the large number of potential choices, most minerals determined with a concentration below 0.5% were rejected as unreliable. Concentrations of 28 different mineralogical phases in the red-mud matrix were determined: gibbsite, bayerite, boehmite, kaolinite, anatase, rutile, quartz, haematite, Al-goethite, sodalite, carnegieite, calcite, katoite-Si, brookite, ilmenite, portlandite, nepheline, perovskite, cancrinite-H_2O, cancrinite-CO_3, cancrinite-NO_3, cancrisilite, carbonate-hydroxyl-apatite, zircon, nosean, diaspore, lawsonite and schaeferite.

The phase-identification process followed by Rietveld refinement involved four different Al–Na silicates: sodalite ($Na_{8.08}Al_6Si_6O_{28.88}S_{0.98}$), cancrinite ($Na_{7.14}Al_6Si_6O_{31.6}$), cancrinite-$NO_3$ ($Na_{7.92}Al_6Si_6O_{31.56}N_{1.74}$) and nosean ($Na_8Al_6Si_6O_{28}S$).

The concentrations in Figs. 7.6.12 and 7.6.13 were reported by the Rietveld program and are overestimated owing to the X-ray amorphous portion of the sample material. In order to express the content of the crystalline phases more realistically, the sample amorphous content needed to be determined first.

Red mud is known to be partially amorphous. Selected phases such as haematite, quartz, rutile and anatase are considered to be crystalline in the red-mud matrix. However, phases such as sodalite or cancrinite account for only some of the aluminosilicates. Hence, one of the objectives of the study was to verify whether synchrotron radiation could characterize and quantify the amorphous phase(s). Initial Rietveld concentrations of the

Table 7.6.3
Summary of the phase composition of red mud

Mineral	Chemical formula	Maximum (%)	Minimum (%)
Gibbsite	$Al(OH)_3$	24.4	0.7
Bayerite	$Al(OH)_3$	4.0	3.6
Boehmite	$AlO(OH)$	41.3	3.6
Kaolinite	$Al_2Si_2O_5(OH)_4$	4.7	2.2
Anatase	TiO_2	13.5	2.5
Rutile	TiO_2	10.3	0.6
Quartz	SiO_2	4.9	0.2
Haematite	Fe_2O_3	66.2	0.6
Al-goethite	$(Fe,Al)_2O_3{\cdot}nH_2O$	57.5	1.7
Sodalite	$Na_{8.08}Al_6Si_6H_{1.92}O_{28.88}S_{0.98}$	22.5	1.8
Carnegieite	$Si_4Al_4Na_4O_{16}$	2.5	1.3
Calcite	$CaCO_3$	35.0	1.0
Dolomite	$CaMg(CO_3)_2$	2.5	1.5
Katoite-Si	$Ca_3Al_2(SiO_4,CO_3,OH)_3$	8.3	2.3
Brookite	TiO_2	5.4	3.1
Ilmenite	$FeTiO_3$	6.9	6.9
Portlandite	$Ca(OH)_2$	2.9	1.4
Nepheline	$NaAlSiO_4$	2.0	0.4
Perovskite	$CaTiO_3$	9.5	1.5
Cancrinite-H_2O	$Na_8(Al,Si)_{12}O_{24}(OH)_2{\cdot}2H_2O$	38.8	3.8
Cancrinite-CO_3	$(Na,Ca)_8(Al,Si)_{12}O_{24}(CO_3){\cdot}4H_2O$	9.1	8.6
Cancrinite-NO_3	$Na_{7.92}Si_6Al_6O_{31.56}N_{1.74}$	42.8	0.6
Cancrisilite-CO_3	$Na_{7.86}(AlSiO_4)_6(CO_3)(H_2O)_{3.3}$	4.6	4.6
Carbonate-hydroxyl-apatite	$Na_{0.8}Ca_{8.4}C_{2.4}P_{3.6}O_{23.6}$	4.8	4.8
Zircon	$ZrSiO_4$	1.0	0.0
Nosean	$Na_8Al_6Si_6O_{24}(SO_4)$	8.9	0.0
Diaspore	$AlO(OH)$	3.7	3.7
Lawsonite	$CaAl_2(Si_2O_7)(OH)_2(H_2O)$	13.0	4.3
Schaeferite	$(Na_{0.7}Ca_{2.3})(Mg_{1.85}Mn_{0.15})((VO4)_{2.88}(PO_4)_{0.12})$	17.2	17.2
X-ray amorphous part		33	0

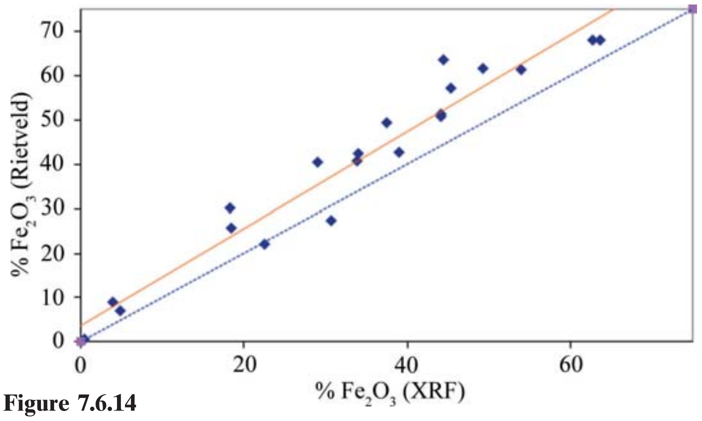

Figure 7.6.14
Correlation between XRF and Rietveld data for Fe_2O_3. The red solid line depicts the experimental correlation for %Fe_2O_3 as obtained by XRF and calculated from haematite and Al-goethite (Rietveld determined phases). The blue dotted line marks the theoretical correlation (45°).

crystalline phases allowed calculation of concentrations for major element oxides: Fe_2O_3, CaO and TiO_2. Then, estimation of the sample amorphous content was made using concentrations obtained from Rietveld estimated phases and determined by bulk XRF analysis. For some samples, the corresponding mass balances between XRF and Rietveld data suggest the occurrence of a significant quantity of amorphous material. Fig. 7.6.14 illustrates a correlation between XRF and Rietveld data for Fe_2O_3. The Fe_2O_3 concentrations from Rietveld analysis are clearly overestimated.

In red-mud samples, the average amount of the amorphous content was 18% and the maximum was 33%. With increasing amorphous content, the mass-balance deficit for Na, Al, Si and H_2O also increases. This indicates that a hydrated sodium aluminium silicate (resembling sodalite) makes up most of the amorphous content. Moreover, red mud is very complex in terms of the number and type of residual and/or neo-formed possible crystallographic phases that might occur. The cycles of phase identification, Rietveld phase quantification and mass-balance calculations were carried out for all samples several times. Mass-balance calculations provided feedback, triggering the beginning of a new cycle. In Table 7.6.3, a summary of the phase-composition range is given.

In spite of the time and effort put into the evaluation stage, the study clearly indicates that using high-quality synchrotron diffractograms is not enough to characterize the sample X-ray-amorphous content completely, and the true sample composition is not known. Differences among mass-balance estimates of the amorphous content for individual samples reflect the limited accuracy of the method.

7.6.6. Alumina

With red mud, the Bayer process produces a basic sodium aluminate solution, from which aluminium hydroxide is crystallized. The $Al(OH)_3$ is then calcined. Depending on the degree of calcination, metallurgical or ceramic grade aluminas are obtained. They differ with respect to the α-alumina content, by virtue of grindability, particle shape and size, impurity content, and other properties.

Application of PXRD in the analysis of alumina in the aluminium industry dates back to the 1960s. Special aluminas (non-metallurgical grades) have always presented a major challenge (Feret, 2000, 2012). Aluminas may have a variety of morphological forms (see Fig. 7.6.15) for which there are marked differences in relative intensities of their major XRD reflections (the preferred-orientation effect), as shown in Fig. 7.6.16. Comparing intensities (whether peak height or integrated) of selected reflections from a sample with those of a reference material may cause a serious analytical error. If the intensity of a selected reflection is compared to that from a reference standard for quantification, then the morphology of this standard must be the same as the unknowns.

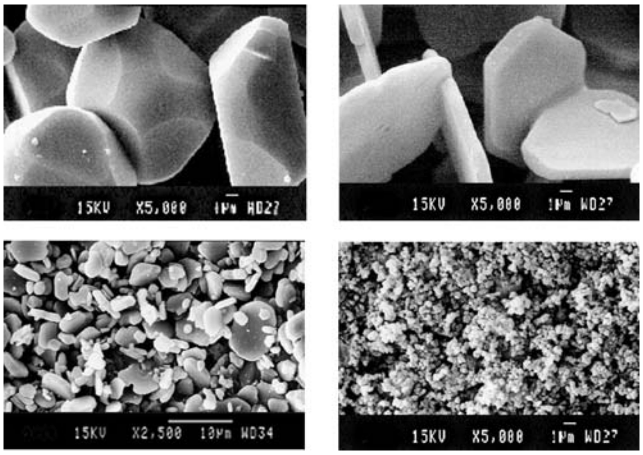

Figure 7.6.15
Examples of morphological forms of ceramic alumina.

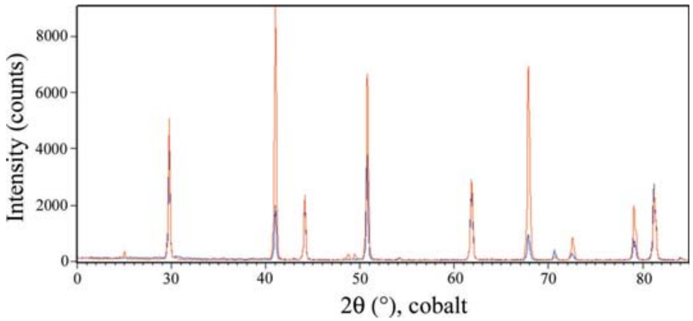

Figure 7.6.16
The superposition of the diffractograms from two ceramic aluminas of different morphology.

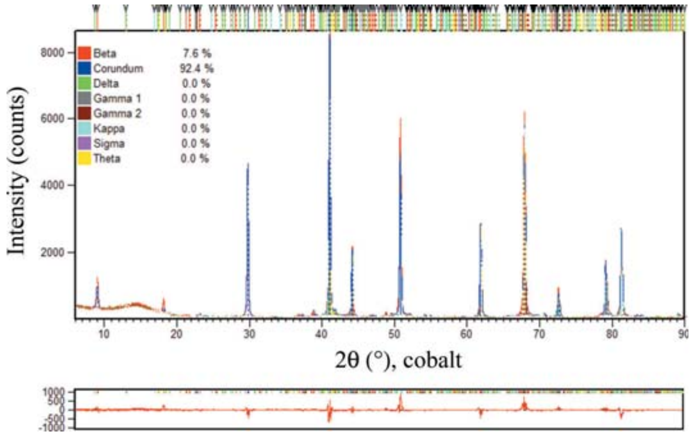

Figure 7.6.17
Example of Rietveld refinement for ceramic alumina.

The estimation of the content of so-called sub-alphas (sub-alphas are phases other than alpha, commonly called transition aluminas) is only possible using the Rietveld method. For the quantification of metallurgical and special aluminas, a dedicated

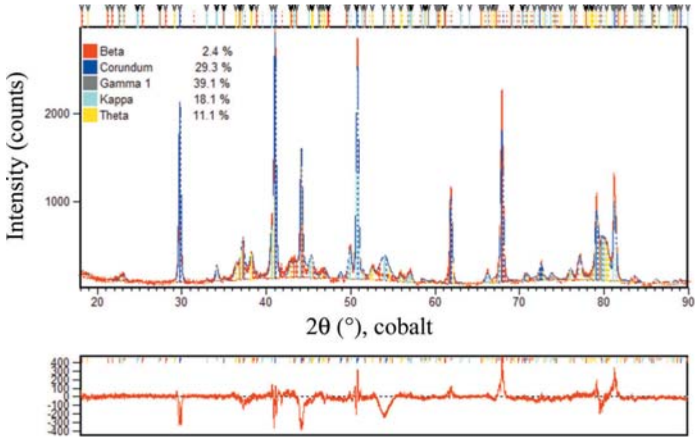

Figure 7.6.18
Example 1 of Rietveld refinement for a sub-alpha specimen.

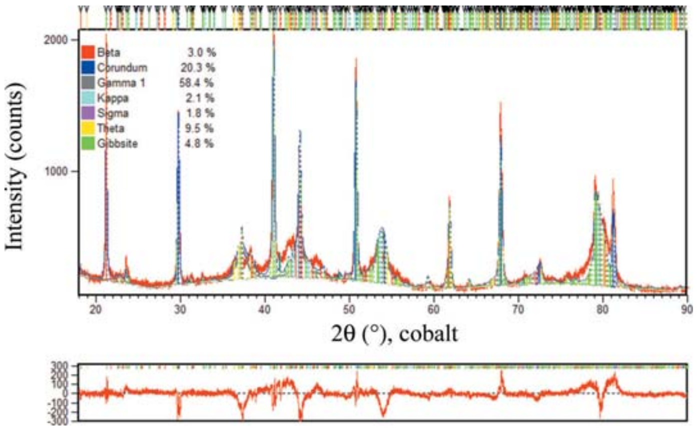

Figure 7.6.19
Example 2 of Rietveld refinement for a sub-alpha specimen.

Rietveld analytical program was written with structure data for eight alumina mineralogical phases: alpha, beta (β-Al_2O_3 = $Na_2O{\cdot}11Al_2O_3$), delta, gamma (two sets), kappa, sigma and theta, and also gibbsite. Figs. 7.6.17–7.6.19 show unique examples of the phase quantification in aluminas of various origin and phase composition using the Rietveld method.

7.6.7. Scrubber alumina

The alumina produced by the Bayer process is used as the feedstock in the Hall–Héroult process for producing metallic aluminium. The alumina is dissolved in molten cryolite, Na_3AlF_6, and electrolysed. AlF_3 and CaF_2 are added to decrease the melting point.

A dry scrubber is the most modern and efficient system generally used to prevent all discharge of pollutants from the aluminium plant. Gases from each pot are exhausted into the dry scrubber in which alumina is used to clean fluorine compounds from the pot gas, and the dust is collected in filter bags. Up to 99.8% of the overall fluorine is removed from the emissions.

Alumina from the dry scrubber, including bound fluorine mixed with dust, is called reacted alumina and is used in the pots as raw material. This recycling of fluorine in the dry scrubber reduces the need to purchase the fluorine materials necessary to operate the pots. Although total F is typically analysed by XRF or by table-top NMR, XRD is called upon periodically to verify an unusual content of reacted alumina or a mixture of alumina and AlF_3. Fig. 7.6.20 gives an example of such analysis. Because most of the sample material is X-ray amorphous, the Rietveld analysis gives an indication of distribution of AlF_3 and crystalline alumina phases.

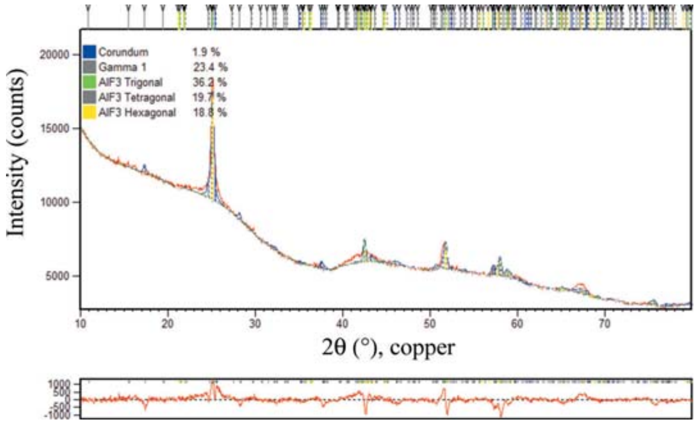

Figure 7.6.20
Rietveld analysis of reacted alumina.

7.6.8. Electrolytic bath

The characterization of the bath electrolyte for process control or for non-routine purposes is generally carried out using only two methods: a combined XRD and XRF method, or by wet chemistry. The wet-chemical methods were historically the first employed in bath-electrolyte characterization. These days, their role has mostly been reduced to certification and quality-control functions. Modern and very efficient industrial characterization of bath electrolyte for potroom process-control purposes involves instrumental XRF–XRD measurement. The instrument (often called potflux analyser or bath analyser) is employed for electrolyte characterization and determination of excess AlF_3 ($ExAlF_3$), bath ratio, Ca and undissolved Al_2O_3 (α-Al_2O_3) in the bath without or with additives. Natural bath standards are required in the instrument calibration.

Significant developments in the quantitative phase analysis of electrolytic bath have taken place in Alcan in recent years (Feret, 2007, 2008). The traditional equation used for controlling bath chemistry,

$$\%ExAlF_3 = 0.2424\%\text{chiolite} + K(\%CaF_2 - \%\text{fluorite}), \tag{7.6.2}$$

was critically examined and was no longer considered valid. Chiolite is $Na_5Al_3F_{14}$. The ($\%CaF_2 - \%$fluorite) term represents the $NaCaAlF_6$ compound, which is not the only Ca-cryolite occurring in bath. It was shown that calcium (in the form of CaF_2) plays a very important role in bath chemistry and is responsible for three major effects: the absorption of diffracted radiation, the formation of $NaCa_{1.5}AlF_7$ (which alters the bath chemistry) and the spectroscopic interference of $NaCa_{1.5}AlF_7$ over chiolite. The occurrence of two diverse Ca-cryolite ($NaCa_{1.5}AlF_7$ and $NaCaAlF_6$) phases in bath-electrolyte samples was identified as the reason for the experimental constant K being different from the theoretical K value of 0.717. Consequently, it was concluded that equation (7.6.2) does not correctly reflect the chemistry of plant samples. Moreover, equation (7.6.2) is sensitive to the crystallinity variation, which is related to the way the bath samples solidify. This situation compromised the control of plant

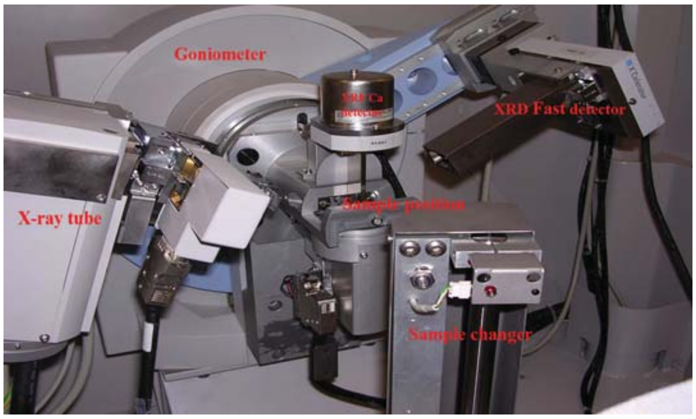

Figure 7.6.21
Hardware configuration of the bath analyser.

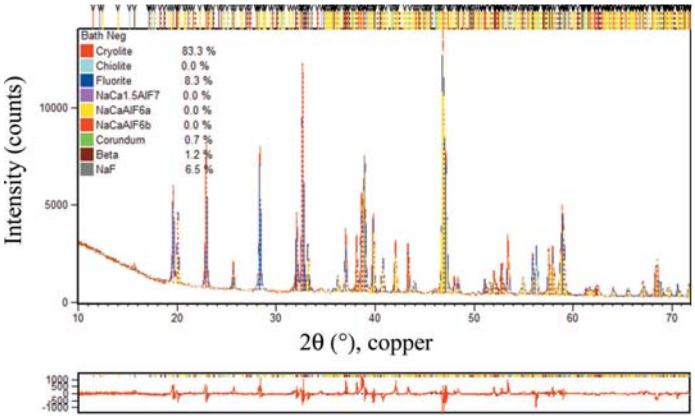

Figure 7.6.22
Rietveld refinement for a bath with negative $ExAlF_3$.

operations and did not allow plant efficiencies to be compared. Therefore, it had to be corrected.

For a successful Rietveld refinement, a good-quality diffractogram is required corresponding to the 10–72° 2θ angular range. Using a conventional diffractometer equipped with a scintillator detector, it takes approximately 1 h to obtain such a diffractogram. Obviously, such a long time would preclude implementation of the Rietveld method in real-time production in the plant laboratory. Therefore, the only possibility for a drastic shortening of the diffractogram acquisition time was introduction of a fast position-sensitive XRD detector (Fig. 7.6.21).

A dedicated control file was created for quantification of phases in bath electrolyte. The file is composed of crystallographic, physical and chemical data corresponding to phases known to occur in bath electrolyte such as cryolite, chiolite, fluorite, $NaCa_{1.5}AlF_7$, $NaCaAlF_6$ (α and β forms), $NaAl_{11}O_{17}$ (β-Al_2O_3), α-Al_2O_3, NaF and $LiNa_2AlF_6$ (Table 7.6.4).

Two other constituents – carbon and metallic aluminium – occasionally occur in bath specimens. Although they do not significantly affect the X-ray procedure, they pose a potential difficulty at the sample-preparation stage. Also γ-Al_2O_3 may occur at low content.

The Rietveld method gives concentrations of individual phase constituents that obviously allow calculation of total $ExAlF_3$. The $ExAlF_3$ is present in chiolite and two Ca-cryolite phases (Feret, 2007, 2008). The $ExAlF_3$ concentrations are calculated as follows:

$$\begin{aligned}\%ExAlF_3 = {} & a(\text{chiolite}) + b(NaCa_{1.5}AlF_7) + c(NaCaAlF_6)\\ & + d(NaF) + e(LiNa_2AlF_6),\end{aligned} \tag{7.6.3}$$

where a, b, c, d and e are stoichiometric constants.

Figs. 7.6.22 and 7.6.23 give examples of Rietveld refinement for bath samples. Fig. 7.6.24 shows the correlation between $ExAlF_3$

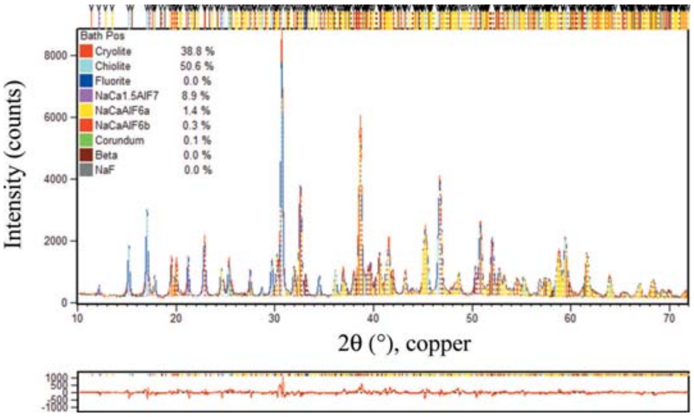

Figure 7.6.23
Rietveld refinement for a bath with positive $ExAlF_3$.

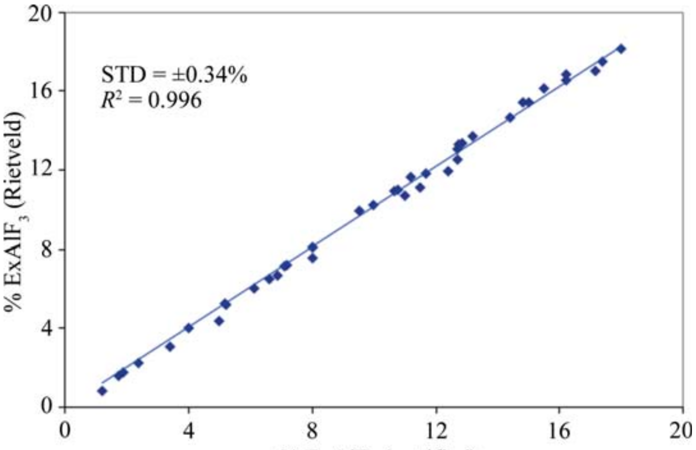

Figure 7.6.24
Bath standard samples: comparison of WCh and Rietveld concentrations for $ExAlF_3$. (STD = standard deviation.)

Table 7.6.4
Phases included in the Rietveld control file for electrolytic bath

No.	Phase identification	Chemical formula	$\%ExAlF_3$	Remarks
1	α-Alumina	Al_2O_3	0	Considered as contamination
2	Dissolved alumina	Al_2O_3	0	X-ray amorphous, not determined
3	β-Alumina	$NaAl_{11}O_{17}$	0	At low content, negative $ExAlF_3$
4	Calcium cryolite, α and β forms	$NaCaAlF_6$	27.44	At low content, positive $ExAlF_3$
5	Calcium cryolite	$NaCa_{1.5}AlF_7$	23.03	Bath with positive $ExAlF_3$
6	Cryolite	Na_3AlF_6	0	All baths
7	Chiolite	Na_5AlF_{14}	24.24	Bath with positive $ExAlF_3$
8	Fluorite	CaF_2	0	All baths
9	Villiaumite	NaF	−66.67	Bath with negative $ExAlF_3$
10	Li-cryolite	$LiNa_2AlF_6$	14.44	Li bath

Table 7.6.5
Comparison of Rietveld and standard method of analysis for electrolytic bath

Category	Rietveld method	Standard XRD
Zero-shift correction	Yes	Yes/no
Absorption correction	Yes	No
Line-overlap correction	Yes	No
Preferred-orientation correction	Yes	No
Amorphous-content correction	Yes	No
Full bath chemistry representation	Yes	No
Full crystallographic representation	Yes	No
Sensitivity to instrument instability	No	Yes
Particle-size effect	No	Yes
Need for bath standards	No	Yes
Need for calibration	No	Yes
Need for recalibration	No	Yes
Need for drift correction	No	Yes
Required level of expertise	Low	High

concentrations determined by WCh and the Rietveld method. Using Rietveld analysis, the $ExAlF_3$ concentrations determined for Alcan bath-electrolyte standard samples correspond very well with those determined by WCh. The standard deviation of the slope is ±0.34% and the repeatability established from analysis of the same sample is ±0.10%.

Until recently, wet chemistry was the only existing primary methodology used in the determination of $ExAlF_3$. At present, Rietveld can now be considered as another primary method used for this purpose. As Table 7.6.5 demonstrates, the Rietveld method of bath analysis offers many advantages over the conventional XRD method. In addition, using the bath-phase composition from the Rietveld method, one may calculate additional process parameters, for example the liquidus temperature.

7.6.9. Spent potlining (SPL)

Spent potlining (SPL) originates from the internal lining of the aluminium electrolysis cell and is composed of refractory bricks and carbon mixed up with electrolytic bath components (Pawlek, 2012) The SPL must be removed and replaced every few years of cell service. Globally, aluminium smelters produce in excess of 500 000 tonnes of SPL each year. As it is contaminated with fluorides and cyanides, SPL is classified as hazardous waste. In many cases, SPL is disposed of in landfill, but in several countries regulations require its neutralization. New processes that render the hazardous waste harmless have been developed. Whether prior to processing or after, the material composition needs to be known. The elemental composition is usually determined by XRF, but Rietveld analysis remains irreplaceable in phase-composition determination. The typical variation of the major phase constituents is very large and depends on an individual batch of material. Among the major mineralogical components one can name are carbon, graphite, cryolite, chiolite, fluorite, corundum, β-alumina, NaF, TiB_2, nepheline, quartz and albite. Analytical information is needed for the preparation of a balanced mixture of refractory, carbon and bath-input constituents to assure optimum performance of the neutralization process. Also, depending on the process, Rietveld analysis allows confirmation of the process effectiveness in the elimination of harmful F-containing phase constituents. For example, in the Alcan Low-Caustic Leach and Lime Process (LCLL), the finely ground SPL is leached with caustic to remove the fluorine, free and complexed cyanide, alumina and some silica into the leach liquor (Hamel *et al.*, 2009). Among the F-containing phases, only CaF_2 is left, which is neutral. After washing, the carbon-rich residue (Fig. 7.6.25) is a potential fuel or reducing material for metallurgical operations.

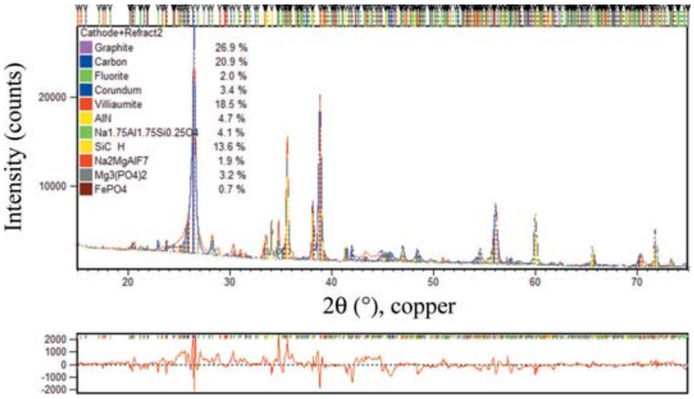

Figure 7.6.25
Rietveld refinement for SPL rich in carbon.

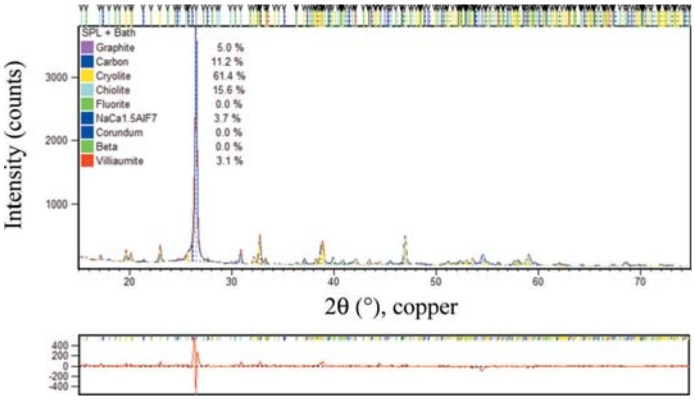

Figure 7.6.26
Rietveld refinement for SPL with bath.

Rietveld analysis not only provides qualitative and quantitative information on the nature of SPL, but also may help to quantify its commercial value before and after the neutralization process. In addition, valuable data such as the product's graphitization rate, estimation of the TiB_2 content (Fig. 7.6.26) and environmental risks are obtained.

7.6.10. Dross

Dross is the residual waste material produced from any process in which aluminium is melted and when the metal comes into contact with air. Dross usually comprises aluminium oxides, aluminium nitride, other metal oxides and minerals originating from scrap or contaminants (as salts) from melting furnaces (chlorides, sulfides, fluorides, phosphides, carbides), as well as metallic aluminium. The worldwide aluminium industry produces nearly five million tonnes of furnace waste each year and around 95% of this material is landfilled, costing the industry an estimated 80 000 000 US dollars. New regulation and spiralling costs are forcing the industry to consider alternatives.

Dross is usually crushed first. Then aluminium is separated from it to obtain aluminium dross residue, which is also known as non-metallic product (NMP). Other methods employed to separate Al metal from dross are known, and each requires information about the material content (Kevorkian *et al.*, 2013). Sodium-removal efficiency for chlorine and salt injection also

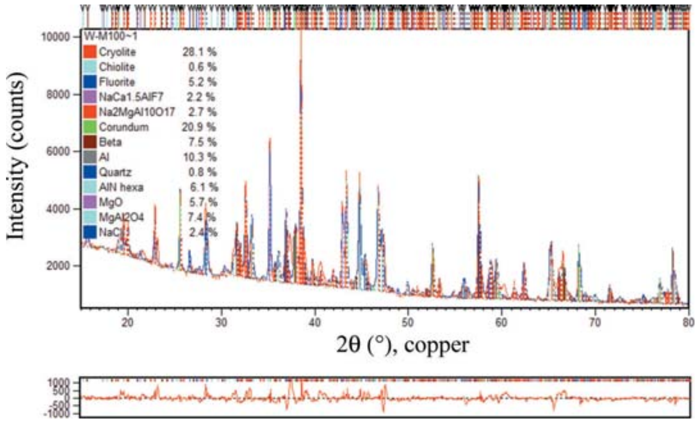

Figure 7.6.27
Example 1 of dross analysis.

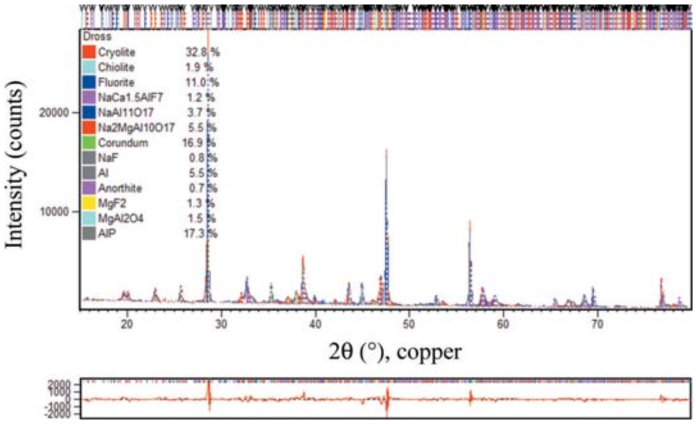

Figure 7.6.28
Example 2 of dross analysis.

requires monitoring. Figs. 7.6.27 and 7.6.28 give examples of dross analysis.

One of the difficulties with Rietveld analysis of dross is the constantly changing composition, as practically every furnace has different work parameters (Gomez *et al.*, 2008).

7.6.11. Discussion

As the aluminium-industry requirements for better process and quality control become more stringent, applications of the Rietveld method have been steadily increasing. From the technological beginning of aluminium manufacture (bauxite) to the final manufacturing processes, there is and will continue to be a place for Rietveld analysis. The choice of a suitable X-ray instrument will always depend on the price and performance ratio and will be dictated by a particular application. The advantage of XRD as an analytical instrument lies in the variety of characteristic parameters it can measure, simplicity of sample preparation and the ability to run the analysis of a series of samples in an automatic mode. Hence, XRD is capable of responding to today's laboratory demand for even greater flexibility and task multiplicity. Given the fact that future applications of the Rietveld method will be extended to materials such as new ceramics, environmental samples and composites, it is obvious that XRD will remain a universal and a very appealing analytical tool for the aluminium industry.

In addition to those materials that are mentioned in Table 7.6.1, there are others which are analysed more infrequently by the Rietveld method. Among them one can name fluorspar (CaF_2), AlF_3 and, recently, grey mud. The latter is predominantly composed of extremely oriented corundum crystals that precipitate from the electrolytic bath and cover the bottom of the electrolytic cell.

Accurate determination of Al_2O_3 distributed among various minerals is critically important for the industry, as it affects the material's commercial value and its process performance. It is ambitious to require Rietveld analysis using an X-ray tube diffractogram to become an accurate tool in the phase quantification of the majority of bauxites. Standard Rietveld software cannot consistently provide reliable concentrations of gibbsite, boehmite, Al-goethite or kaolinite (which are considered strategic) for most bauxite cases studied over the years. The major obstacle in the quantification process is the bauxite amorphous content, which originates not from one source, but from several sources simultaneously. There are numerous examples of bauxite diffractograms with missing representation of boehmite, kaolinite or Al-goethite, yet occurrence of these phases is confirmed by other methods. The total amorphous content of the bauxite matrix can obviously be quantified using the internal-standard method, but assigning its parts to individual mineralogical constituents is difficult or impossible employing XRD alone (see Madsen & Scarlett, 2008).

The use of synchrotron radiation is a powerful alternative to using radiation from an X-ray tube, but it is not a panacea. It facilitates the detection of amorphous material, but the glass capillary usually used to contain the specimen is itself amorphous. Nevertheless, synchrotron-radiation diffractograms offer substantial advantages over diffractograms from an X-ray tube – including higher count rates and improved signal-to-noise and peak-to-background ratios, and resolution. Whether using synchrotron radiation or an X-ray tube, a diffractogram is seldom a sufficiently complete representation of the mineralogical content of a bauxite sample. Gibbsite, being the most abundant phase and occurring with amorphous aluminium hydroxides, is the major victim of the Rietveld analysis of bauxite. Only very well crystallized bauxite from selected deposits can be successfully analysed, at least for certain mineralogical constituents. Diasporic bauxite shows a better chance for successful phase quantification (Nong *et al.*, 2007). New non-PXRD methods are emerging (*e.g.* mathematical modelling) (Kimmerle *et al.*, 1997), which erode some traditional applications of WCh and the Rietveld method.

Routine analysis of the phase composition of electrolytic bath for cell process control by the STARprobe method has recently been proposed (Wang *et al.*, 2011). The STARprobe does not require a laboratory and accelerates analysis. However, the STARprobe requires 4–5 min operator contact time per sample, does not apply to baths with negative $ExAlF_3$, or to baths with Li or Mg additives, is costly to use and provides results that are inferior in quality to the Rietveld method. The average XRD instrument lifespan in industry is 12–15 years, and that of the automatic sample-preparation equipment is much longer. The estimated cost per sample is therefore the lowest possible, despite high initial investment. Consequently, the STARprobe may remain a convenient, but more expensive, alternative to Rietveld in bath analysis.

This chapter contains material previously published in Feret (2013), which is reproduced with permission from JCPDS-International Centre for Diffraction Data. The author would like to express his gratitude to the management of the Arvida Research and Development Centre of Rio Tinto Alcan in

Jonquiere for permission to publish different parts of this material at various times. The editors of the volume are sincerely thanked for their suggestions for modifications to this chapter, and Ryan Provost is also thanked for providing diffractograms of dross and potlining for this review.

References

Bennett, F. R., Walker, G. S. & Aylmore, M. G. (1999). *A fundamental parameters based approach to the Rietveld quantitative phase analysis of bauxite*. Nabalco Development Laboratory, Report No. 99080. Brisbane: Queensland Government, Department of Science, Information Technology and Innovation (DSITI).

Feret, F. (1993). *Application of XRF in the aluminum industry*. *Advances in X-ray Analysis*, Vol. 36, edited by J. V. Gilfrich, T. C. Huang, C. R. Hubbard, M. R. James, R. Jenkins, G. R. Lachance & D. K. Smith, pp. 121–123. New York, London: Plenum Press.

Feret, F. (2000). *Determination of alpha and beta alumina in ceramic alumina by X-ray diffraction*. *Spectrochim. Acta B*, **55**, 1051–1061.

Feret, F. (2007). *Effect of Ca in characterization of bath electrolyte by the X-ray methods*. *Light Metals 2007*, pp. 373–377. Pittsburgh: The Minerals, Metals & Materials Society.

Feret, F. (2008). *Breakthrough in analysis of electrolytic bath using Rietveld-XRD method*. *Light Metals 2008*, pp. 343–346. Pittsburgh: The Minerals, Metals & Materials Society.

Feret, F. (2012). *Phase quantification of alumina using Rietveld-XRD analysis*. Travaux-Proceedings of ICSOBA 2012, Belem, Brazil.

Feret, F. (2013). *Selected applications of Rietveld-XRD analysis for raw materials of the aluminium industry*. *Advances in X-ray Analysis*, Vol. 57. Newtown Square: The International Centre for Diffraction Data.

Feret, F. & Roy, D. (2002). *Determination of quartz in bauxite by a combined X-ray diffraction and X-ray fluorescence method*. *Spectrochim. Acta B*, **57**, 551–559.

Feret, F. & See, J. (2006). *Occurrence and characterization of Zn and Mn in bauxite*. *Light Metals 2006*, pp. 41–46. Pittsburgh: The Minerals, Metals & Materials Society.

Feret, F. & See, J. (2010). *Analysis of bauxite by X-ray diffraction using synchrotron radiation*. Travaux-Proceedings of ICSOBA 2010, Zhengzhou, China.

Feret, F. & See, J. (2011). *Analysis of red mud by X-ray diffraction using synchrotron radiation*. Travaux-Proceedings of ICSOBA 2011, Goa, India.

Gomez, A., Lima, N. B. & Tenorio, J. A. (2008). *Quantitative analysis of aluminium dross by the Rietveld method*. *Mater. Trans.* **49**, 728–732.

Habashi, F. (2005). *A short history of hydrometallurgy*. *Hydrometallurgy*, **79**, 15–22.

Hamel, G., Breault, R., Charest, G., Poirier, S. & Boutin, B. (2009). *From the 'low caustic leaching and liming' process development to the Jonquiere spent potlining treatment pilot plant start-up, 5 years of process up-scaling, engineering and commissioning*. *Light Metals 2009*, pp. 921–926. Pittsburgh: The Minerals, Metals & Materials Society.

Kevorkian, V., Skapin, S. D. & Kovacec, U. (2013). *The nondestructive determination of the aluminum content in pressed skulls of aluminum dross*. *J. Met.* **65**, 284–293.

Kimmerle, F. M., Feret, F. & Feret, B. (1997). *BQuant: cost-effective calculations of bauxite mineralogy*. *Light Metals*, pp. 9–16. Pittsburgh: The Minerals, Metals & Materials Society.

Madsen, I. & Scarlett, N. (2008). *Quantitative phase analysis*. In *Powder Diffraction, Theory and Practice*, edited by R. E. Dinnebier & S. J. L. Billinge, ch. 11. London: The Royal Society of Chemistry.

Ni, L. P. & Khalyapina, O. B. (1978). *Physical-chemical properties of the raw materials and products of alumina production*. Alma-Ata: Izdatielstvo Nauka Kazakhskoi SSR.

Nong, L., Yang, X., Zeng, L. & Liu, J. (2007). *Qualitative and quantitative phase analyses of Pingguo bauxite mineral using X-ray powder diffraction and the Rietveld method*, *Powder Diffr.* **22**, 300–302.

Pawlek, R. (2012). *Spent potlining – update*. *Light Metals 2012*, pp. 1313–1318. Pittsburgh: The Minerals, Metals & Materials Society.

Sajó, I. (1994). *Powder diffraction phase analytical system Version 1.7, users guide*. Budapest: Aluterv-FKI Ltd.

Wang, X., Tarcy, G., Batista, E. & Wood, G. (2011). *Active pot control using Alcoa STARprobe^{TM}*. *Light Metals 2011*, pp. 491–496. Pittsburgh: The Minerals, Metals & Materials Society.

International Tables for Crystallography (2019). Vol. H, Chapter 7.7, pp. 793–803.

7.7. Mining and mineral processing

N. V. Y. Scarlett and D. L. Bish

7.7.1. Introduction

The history of mining and mineral processing effectively mirrors the history of civilization, and stone and metal have been mined since prehistoric times. Early mining involved the acquisition of native materials from close to the Earth's surface, whereas more complex excavation and subsequent metallurgical developments lent their names to the 'Three-Age System' of archaeological chronology (Heizer, 1962) developed by Christian Jürgensen Thomsen (1788–1865), which is still in common usage. The three ages are (i) the Stone Age, which lasted for approximately 3.4 million years, ending sometime between 4500 and 2000 BCE, (ii) the Bronze Age, which takes its name from the smelting of copper and tin together and occurred at various times in different parts of the world over a period from about 3600 to 300 BCE, and (iii) the Iron Age, the occurrence of which was similarly variable but extended from about 1300 BCE to 500 AD. The so-called 'Father of Metallurgy', Georg Agricola, published the volume *De re Metallica* (Agricola, 1912) in the 16th century, which detailed the technology of mining and metallurgical processing as it was understood at the time.

The modern 'resource sector' deals with the mining and processing of a range of nonrenewable resources in the mineral and energy streams. Many industries are connected with and dependent upon this sector, and much of society is subsequently reliant on the resulting products. Examples of some of these are given below.

(i) Building materials such as rocks (direct) and cement/bricks *etc.* (indirect; see Chapter 7.12 for more information on cement).

(ii) Steelmaking for use in civil engineering, transport, appliances, tools *etc.*

(iii) Ceramics, which are generally categorized as structural (*e.g.* bricks, tiles, pipes), refractories (*e.g.* furnace linings, crucibles), whiteware (domestic uses) and technical (*e.g.* biomedical implants, composite materials for aerospace applications). (See Chapters 7.8 and 7.9.)

(iv) Energy such as oil and natural gas, steaming and coking coal, coal seam methane gas and uranium (see Chapter 7.11).

(v) Agricultural applications such as the use of limestone to increase calcium content, to correct soil acidity and to provide calcium to animal and poultry feeds.

(vi) Glasses such as soda-lime glass (windows, drinking vessels), network glasses (fibre optics, solid-state storage media) and amorphous metals (achieved by rapid cooling from melt).

(vii) Precious metals and stones used for jewellery and other ornamentation.

(viii) Rare-earth elements used for electronics, batteries, magnets, lasers, alloys and catalysts.

The removal of nonrenewable resources from the Earth has potentially negative impacts on the environment that have resulted in the introduction of legislation across much of the world to mediate these effects. This has led to increased research in such areas as environmental management, site remediation and CO_2 sequestration.

Mining and mineral processing are concerned with the extraction of valuable metals and minerals from the earth and the separation of these minerals from the perceived wastes associated with them. There are several stages within these processes, and although details are generally specific to a particular ore body, there are several commonalities. Firstly, the ore body must be discovered. This is typically achieved by a process of exploration or prospecting. The ore body must then be assessed for quality and extent to determine the feasibility (physical and economic) of its recovery. If deemed to be feasible, the ore must then be physically extracted from the earth and treated in such a way as to make the valuable minerals accessible. At the conclusion of the life of a mining operation, the land must be regenerated or reclaimed for future use.

7.7.2. Use of powder diffraction in mining and mineral processing

By definition, mining and mineral processing rely upon mineral assemblages. Identifying, understanding and assessing these assemblages are vital to the successful extraction of the valuable resources. In this context, powder diffraction is particularly useful, as it allows a direct measurement of mineralogy rather than either inferring it from measured chemistry, spectroscopy or assessment *via* optical microscopy. Diffraction methods probe the crystal structural nature of solids, which is essentially the basis of the definition of minerals and other crystalline solids. Although spectroscopic methods, such as infrared or Raman, can be deployed remotely, they are derivative and are not directly related to crystal structure. Optical microscopy is labour-intensive, operator-dependent and severely impacted by sampling errors. This is particularly evident on the scale on which mining operations are conducted. Much of industry relies upon the measurement of bulk chemistry as a routine part of its operation and control. The measurement of bulk chemistry is relatively fast and convenient in an industrial environment. It can also be very accurate and precise. It can, however, only be partitioned into mineral phases based upon prescribed equations that cannot deal with the complex compositional variability that is inherent in many mineral suites. In addition, this approach does not have the ability to discriminate between polymorphs, *i.e.* materials with the same chemical composition but different crystal structures (and thus different physical properties). This approach is also highly dependent on representative sampling. An example of this type of calculation is the Bogue method (Bogue, 1929), which has long been an industry standard for the production of Portland cement (see Chapter 7.12). This method partitions the chemical analyses into individual phases (minerals) in a predetermined sequence based upon preset phase compositions. The greatest source of error in this method is the variability in the individual phase compositions, which has been confirmed by previous electron-probe microanalysis (Madsen & Scarlett, 1999), along with the exclusion of minor phases from the

Copyright © 2019 International Union of Crystallography

method (Taylor, 1989). Further discussion of the errors in these methods can be found in Madsen & Scarlett (1999) and references therein.

Electron-microscopy (EM) methods such as mineral liberation analysis (MLA; Gu, 2003) and QEMSCAN (Gottlieb *et al.*, 2000) have also been employed to determine mineralogy, but are still based upon phase calculations from microchemistry. EM methods can be accurate and precise, but involve labour-intensive sample preparation and relatively slow acquisition times. Even more so than with bulk chemical methods, sampling with EM methods is a significant issue, and it is often difficult to obtain an accurate representation of the true bulk chemistry. EM methods for the determination of mineralogy are also based on prior knowledge of phase chemistries, but can cope better with compositional variability. A significant advantage of EM methods is the parallel acquisition of spatial information, which can provide an indication of the mineral associations and degree of 'liberation', both of which can have a bearing on the separation techniques required for particularly valuable minerals.

Infrared (IR) and Raman spectroscopic techniques are becoming more common in the determination of mineralogy for mineral exploration. These techniques are appealing in that minimal sample preparation is required, data acquisition is rapid and the equipment can be portable. With appropriate equipment and a digital spectral database, this technique may be used in the laboratory, in the field (or with drill cores) or on a large scale during the acquisition of data for mineralogical maps. However, the low penetrating power of the IR beam makes it a surface-specific technique and it is therefore in essence semiquantitative (Madsen *et al.*, 2013). Raman spectroscopy is particularly susceptible to fluorescence effects, detracting from the general applicability of the method in the field. Although the signals in IR and Raman spectra are obtained directly, they must be calibrated against known library standards or independent data such as quantification *via* powder X-ray diffraction.

As emphasized above, powder diffraction has the potential to provide a direct measurement of the mineralogy of a sample. Such an analysis may take the form of a qualitative assessment where the component phases of a mixture are identified, it may be semi-quantitative based upon the relative peak heights (or integrated areas) of each of the phases giving a 'major, minor, trace'-style analysis, or it may be fully quantitative. Quantitative phase analysis (QPA) in this environment may be assessed with a high degree of precision, but there are many factors that determine the absolute accuracy of such measurements. These are discussed along with detailed methodologies in Chapter 3.9 of this volume. As with the other methods discussed above, powder-diffraction analysis may also be subject to sampling errors. However, modern inline, online and robotic systems have the potential to minimize these.

7.7.2.1. *Areas of applicability*

There are a number of operations in the mining and mineral processing industries where the application of powder diffraction can be beneficial. Traditionally, identification of the minerals present and estimation (or quantification) of phase abundances are the primary goals of X-ray powder diffraction. However, with the increased requirements to exploit ores that would not previously have been considered economical, detailed knowledge of crystal chemistry, crystallite size and amorphous content have become more important.

During the exploration stage, phase identification in drill cores is critical as an aid to the location of valuable ore bodies. An estimate of relative phase abundances is necessary to provide an assessment of ore grade and to determine the ease or otherwise of processing in order to make decisions regarding the economic feasibility of extracting the valuable minerals from an ore body. More detailed geometallurgical knowledge of the ore will determine the subsequent processing steps and will allow the most efficient choice of grinding regimes, reagents, waste separation and handling procedures, *etc.*

Knowledge of the mineralogy and chemistry of a system is vital at all processing points from the mine to the final product. Powder diffraction can serve as a valuable tool for determining the degree of concentration or separation during mineral dressing, the purity and form of mineral products during the extractive metallurgy phase, the quality of waste products that may be required for compliance with environmental legislation, and the quality control of the final product (for example iron-ore sinter, Portland cement, metal sheet *etc.*). Powder diffraction can also play an important role in the development of new processes and in the troubleshooting or optimization of existing processes.

7.7.3. Powder-diffraction methodology

7.7.3.1. *Equipment and data collection*

The data-collection strategies employed and the experimental setup used for diffraction measurements will depend wholly on the situation and the information required from the analysis. For example, equipment used in the field or plant will generally differ greatly from that used in the research laboratory. When choosing equipment and a data-collection strategy, consideration must be given to time-frame requirements, whether qualitative or quantitative analysis is required, the lower limits of detection required, whether or not detailed structural information is necessary, and whether the data collection must be static or dynamic. Detailed discussion of the types of instrumentation available and the options for data processing and analysis are given in Parts 2 and 3 of this volume and in other texts on the subject of diffraction in general (Chung & Smith, 1999; Cockcroft & Fitch, 2008; Klug & Alexander, 1974).

By far the most commonly used diffraction equipment in the mining and mineral processing context is the laboratory diffractometer employing an X-ray tube with a particular anode as the source. This instrument may be deployed in a variety of configurations for a range of situations, including process and quality control (on location in plants and at mine sites) and process development and optimization (within research facilities). Equipment specific to data collection in field environments will be discussed in Section 7.7.3.1.1 below. The data-collection parameters for each situation will very often be determined by the desired outcomes from the data obtained and established *via* prior research into the system under investigation. For example, routine 'scan and identify' data may generally be collected much more rapidly and at lower resolution than data required for quantitative phase analysis. However, prior research may be able to optimize the methodology so that more rapidly acquired, poorer quality data may be used for quantitative phase analysis within a restricted parameter set. Advanced radiation sources such as neutron and synchrotron facilities are generally the province of research applications. Thus, in the context of the subject of this chapter, they are usually restricted to the development phases of mineral process design and to fundamental

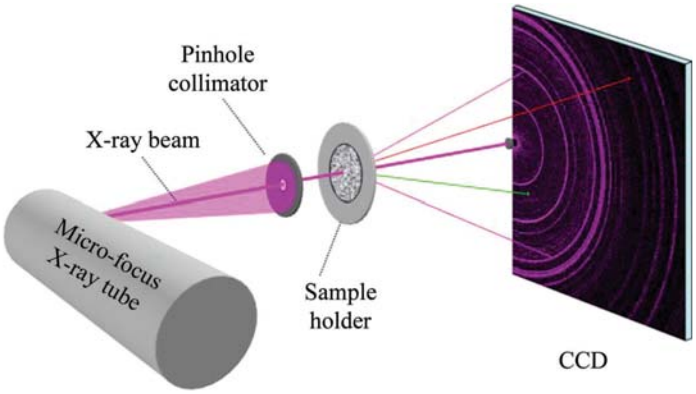

Figure 7.7.1
Overall geometry of CheMin (reproduced from Sarrazin, Blake *et al.*, 2005).

studies related to geological processes that may be of subsequent use in exploration operations.

7.7.3.1.1. *In-field diffraction*

Planetary exploration has been a driving force behind the development of truly portable, automated *in situ* powder X-ray diffraction (PXRD) instrumentation (Blake *et al.*, 1994; Vaniman *et al.*, 1991). Vaniman and co-workers described the potential for combined PXRD and X-ray fluorescence (XRF) for planetary surface analyses, with emphasis on the ability of PXRD to provide definitive mineral identification based upon crystal structure (*i.e. via* diffraction). They cited Mars as a 'good example of a planet where the capabilities of PXRD will be critical for adequate *in situ* surface exploration'. The goals of planetary exploration and exploration in the mining context are not dissimilar. The mineralogical analyses that help to locate and describe an ore body also provide information regarding the pressure and temperature conditions of formation necessary to establish the origin and provenance of a sample and the environmental history of a planet.

The CheMin instrument was developed as part of the NASA planetary exploration efforts and is an integral part of the scientific payload on the Mars Science Laboratory (Blake *et al.*, 2012; Sarrazin, Blake *et al.*, 2005). CheMin is a miniaturized PXRD/XRF instrument (Fig. 7.7.1) that uses transmission geometry and a low-power Co X-ray source to provide both XRF and PXRD data from a small vibrated powder sample. Energy-dispersive X-ray fluorescence spectra are collected by a two-dimensional charge-coupled device (CCD) detector that provides both spatial and energy resolution. Analysis of the two-dimensional distribution of CCD pixels impacted by characteristic X-ray photons (Co $K\alpha$ in this case) provides a two-dimensional diffraction pattern of the sample. These two-dimensional diffraction data can be integrated circumferentially to create a one-dimensional diffraction pattern that can be analysed by conventional methods, including Rietveld methods or other full-pattern methods such as *FULLPAT* (Chipera & Bish, 2002). The latter allows the analysis of both crystalline and amorphous materials.

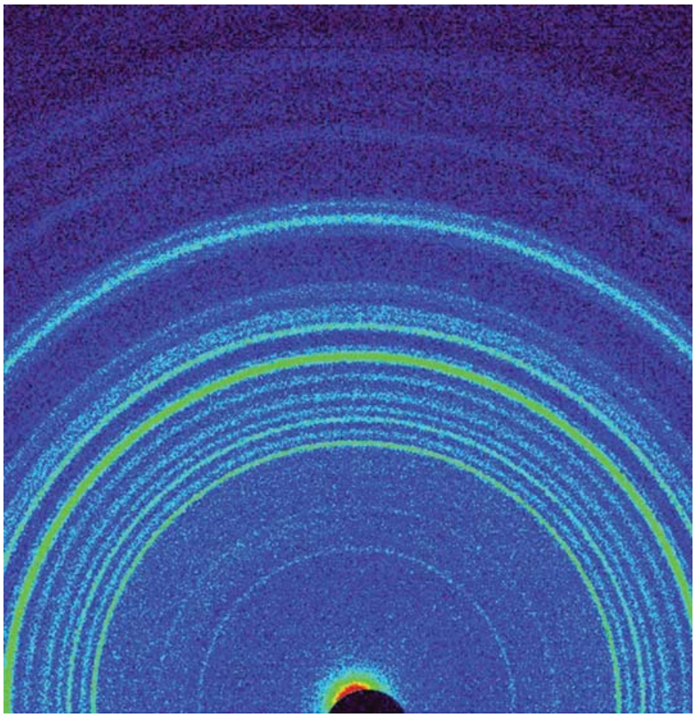

Figure 7.7.2
Two-dimensional X-ray diffraction pattern (Co $K\alpha$) of soil from the Rocknest aeolian bedform. This pattern is of scoop 5 and represents the sum of 63 half-hour frames. The black circle at the bottom of the image is the shadow of the beam stop.

The CheMin instrument is on board the Curiosity rover on the Mars Science Laboratory, which landed in Gale Crater on Mars on 5 August 2012. To date, the instrument has analysed 14 drilled samples and two scoop samples, along with several onboard standards. CheMin first analysed the <150 µm fraction of an aeolian bedform (*i.e.* a dune), which provided the first X-ray diffraction pattern obtained on another planet (Bish *et al.*, 2013, 2014). Fig. 7.7.2 shows the two-dimensional diffraction pattern for this material. Fig. 7.7.3 illustrates the results of Rietveld refinement using the one-dimensional data. The dune material, which consists of both fine-grained material of a global nature and more locally sourced coarser material, contained the typical basaltic minerals plagioclase, Fe-forsterite and two pyroxenes, with minor amounts of other silicate, oxide and sulfate minerals, most of which are

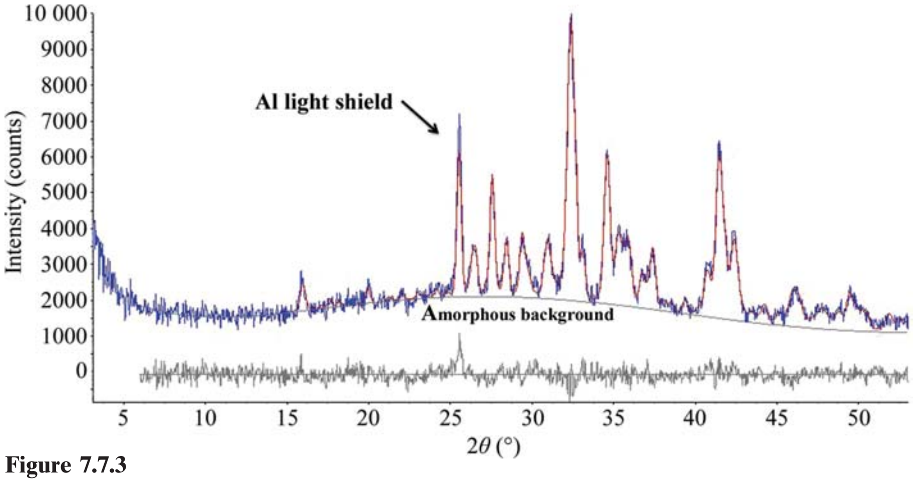

Figure 7.7.3
Conventional one-dimensional X-ray diffraction pattern derived from the data in Fig. 7.7.2. Observed data are in blue and the red plot represents the results of Rietveld refinement. The grey plot near the bottom represents the difference between observed and calculated patterns. Significant scattering contribution from amorphous components is visible in the 20–45° 2θ range. The unfitted intensity just above 25° 2θ is due to the aluminium light shield.

present near detection limits (Table 1 in Bish *et al.*, 2013). The dune material also contains considerable amorphous material (∼27%), and it is noteworthy that no hydrous crystalline components were identified. Independent evolved-gas analyses by the Sample Analysis on Mars (SAM) instrument on the Curiosity rover revealed several wt% H_2O in this sample, demonstrating that the amorphous component is hydrous. Subsequent PXRD analyses of two drill-hole samples of a mudstone revealed similar mineralogy, with the addition of a trioctahedral smectite, bassanite ($CaSO_4{\cdot}0.5H_2O$), considerable magnetite and little Fe-forsterite. The differences in mineralogy can be explained by the alteration of an Fe-forsterite-rich precursor to a mudstone containing magnetite and Fe-saponite. The successful demonstration of remote PXRD on another planet demonstrates the feasibility of performing PXRD in virtually any environment, with or without human intervention. In this case, the sky is no longer the limit.

One of the major difficulties in employing an *in situ* powder-diffraction instrument is that of sample preparation. An ideal powder-diffraction sample requires that effectively an infinite number of crystallites in all possible orientations be presented to the X-ray beam. This is not achieved in practice, but may be approximated by finely grinding and homogenizing the sample prior to data collection. *In situ* samples are likely to be coarse-grained and inhomogeneous. In order to overcome this requirement, the CheMin instrument uses a sonic vibrating sample holder that effectively increases the number of crystallites in the X-ray beam, thereby allowing the characterization of poorly prepared or oriented samples (Sarrazin, Chipera *et al.*, 2005). This development is of vital importance for an instrument designed to operate completely independently in a remote location (such as Mars).

The stimulus of space exploration often provides technology that ultimately yields benefits for terrestrial applications. Technologies developed for the CheMin instrument have been used in inXitu's (inXitu Inc., California; now owned and marketed by Olympus) portable transmission PXRD/XRF instrument (Terra), which is designed specifically for rock and mineral analysis in the field. It is self-contained with on-board software for producing conventional one-dimensional PXRD patterns and XRF spectra within minutes. The instrument is contained in a large suitcase and will operate for ∼4 h on a single charge. The transmission geometry of the instrument has been optimized using ray-tracing simulations to improve both resolution and intensity, and useful diffraction data can often be obtained in less than 5 min, making it a potentially powerful field exploration tool. The Terra instrument also uses the sonic vibration sample holder developed for CheMin, which allows the user to analyse poorly ground materials with ease. The Terra instrument can communicate wirelessly with an external computer, and data may thus be analysed in the field.

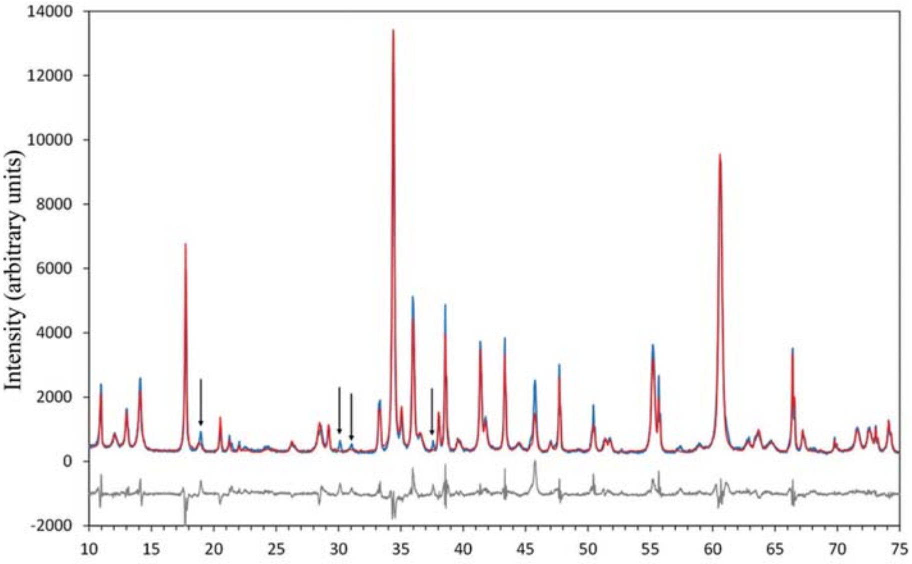

Figure 7.7.4
Diffraction pattern (Co *Kα* radiation) of nickel concentrate (blue) with calculated profile from a Rietveld refinement model (red) incorporating the following phases: pyrite, 17%; pentlandite, 51%; magnetite, 12%; magnesite, 5%; violarite, 3%; pyrrhotite, 3%; talc, 4%; hydrotalcite, 0.4%; lizardite, 4%; honessite, 1%. There are also several unmatched peaks indicating unidentified material in the sample (indicated by vertical arrows).

The CheMin instrument also spawned another PXRD/XRF instrument that is useful for *in situ* application. The Duetto instrument, also from inXitu (Chiari, 2008; Sarrazin *et al.*, 2008), was developed jointly with the Getty Conservation Institute specifically for non-invasive examinations of works of art. The Duetto instrument differs from CheMin and Terra primarily in the mode of sample presentation. Duetto operates in reflection rather than transmission mode to allow the examination of large objects *in situ*. The source and detector are as described previously for CheMin, but Duetto also includes an imaging camera for precise location of the area to be sampled. The Duetto instrument can potentially be used wherever sample preparation is not possible or desired, for example for the examination of rock faces or objects of art *in situ*.

Recently Hansford (2016) has proposed methodology suited to a simple, portable instrument of fixed geometry which exploits a method of selectively targeting a phase of interest within a sample. It is an energy-dispersive X-ray diffraction method based around the exploitation of coincidences of diffraction peaks and the ratios of different characteristic X-ray energies. It has potential for *in situ* or in-line use in situations where a particular phase is key to the application under investigation.

7.7.3.2. *Qualitative analysis*

Qualitative analysis in the context of powder diffraction primarily involves the identification of crystalline phases, such as minerals, in a multiphase sample, often referred to as the 'search–match' process. This is described in greater detail elsewhere in this volume (see Chapter 3.9), but usually involves the comparison of observed diffraction patterns with databases of known phases. Identification of the phases present is based on peak positions either alone or in combination with their relative intensities. The manufacturers of diffraction equipment often have proprietary software for this 'search–match' process (for example *PANalytical X'Pert Highscore* (PANalytical BV) and *EVA* (Bruker AXS)], as do the producers of licensed databases such as the ICDD PDF (Powder Diffraction File) products (Fawcett *et al.*, 2017) and the academic projects COD (Crystallographic Open Database; Downs & Hall-Wallace, 2003; Gražulis *et al.*, 2009, 2012, 2015; Merkys *et al.*, 2016) and PCOD (Predicted Crystallographic Open Database; Le Bail, 2005). Non-commercial software is also available (for example *LOGIC* and

CMPR from NIST and *MATCH*) but relies on access to an appropriate database. A Search–Match Round Robin (SMRR) was conducted in 2002 (Le Meins *et al.*, 2002) with the general finding that the expertise of the operator was one of the most important aspects of successful search–match, even when the elemental composition of the sample was known. However, knowledge of the origin of a sample, which allowed the selection of an appropriate PDF subset (organic, mineral, organometallic *etc.*), improved the success rate. The SMRR evaluated four different samples (geological, synthetic chemical, pharmaceutical and industrial processing plant), none of which contained more than four phases. Real geological samples, such as rocks, ores or concentrates, may be very complex and often contain considerably more than four phases, and in general it is recommended that as much information as possible (bulk and/or micro chemistry, origin *etc.*) be gathered about the sample to assist with phase identification. An illustration of this complexity is given in Fig. 7.7.4, which shows the diffraction pattern of a nickel concentrate with the calculated pattern from Rietveld refinement of a model containing ten minerals. Note that not all of the observed peaks are simulated by the model, indicating the presence of one or more unidentified materials.

7.7.3.3. *Quantitative analysis*

Quantitative phase analysis (QPA) often follows the identification process in diffraction analysis. Methods for performing QPA are described in detail in Chapter 3.9. As stated earlier, knowledge of phase abundance in geological samples is useful as part of the exploration process, in the assessment of ore grade and in determining the extent of separation processes in mineral dressing activities. Detailed QPA may also be of benefit during the research phases in order to understand the genesis, alteration, distribution and stability of minerals *etc.*, which may lead to improved processing options.

7.7.3.4. *Crystal structural analysis*

Mining productivity may be affected by the crystal structural features of individual minerals, such as substitutional solid solutions and strain. These may be assessed during the QPA stage of diffraction analysis, particularly if this is performed *via* the Rietveld method (Rietveld, 1969). Examples of such substitutions include Al-for-Fe substitutions in goethite (Fazey *et al.*, 1991), which limit the recovery of Al *via* the Bayer process, and the loss of silver by incorporation into jarosite (Dutrizac & Jambor, 2000), either *via* co-precipitation from hydrometallurgical solutions or by formation during the bioleaching of copper ores. Substitution and subsequent release of heavy metals from mine-waste dumps is also an important environmental issue (Benvenuti *et al.*, 1997). However, although QPA *via* the Rietveld method is a sensitive method for detecting minor changes in unit-cell parameters that result from chemical substitutions, those substitutions that involve trace elements will not generally be detected by diffraction methods.

7.7.3.5. *High-throughput and batch processing*

The ability to accumulate data rapidly in the field, in the plant or during time-resolved experimentation can result in extremely large data suites that may create data-processing and analysis challenges. To solve these challenges, batch-processing and cluster-analysis methods have been developed and applied in order to minimize analyses or to perform them in a semi-automated fashion.

7.7.3.5.1. *Cluster analysis*

Cluster analysis is an approach that facilitates the partitioning of large data sets into smaller subsets based on certain similarities between the component members. In the case of diffraction patterns, the partitioning may be carried out on the basis of the patterns alone or in combination with another property of the

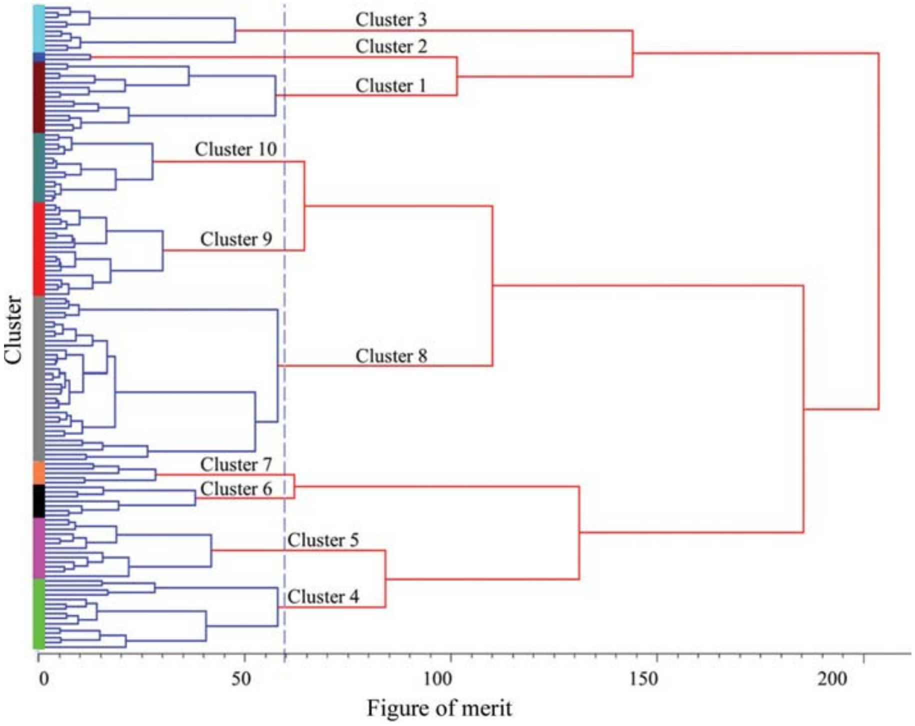

Figure 7.7.5
Dendrogram output from cluster analysis of the data suite collected during the decomposition of plumbojarosite. The vertical dotted line indicates the manually chosen cutoff point which determines the number of clusters into which the data are partitioned. The individual clusters are labelled and coloured using the same scheme as in Fig. 7.7.6.

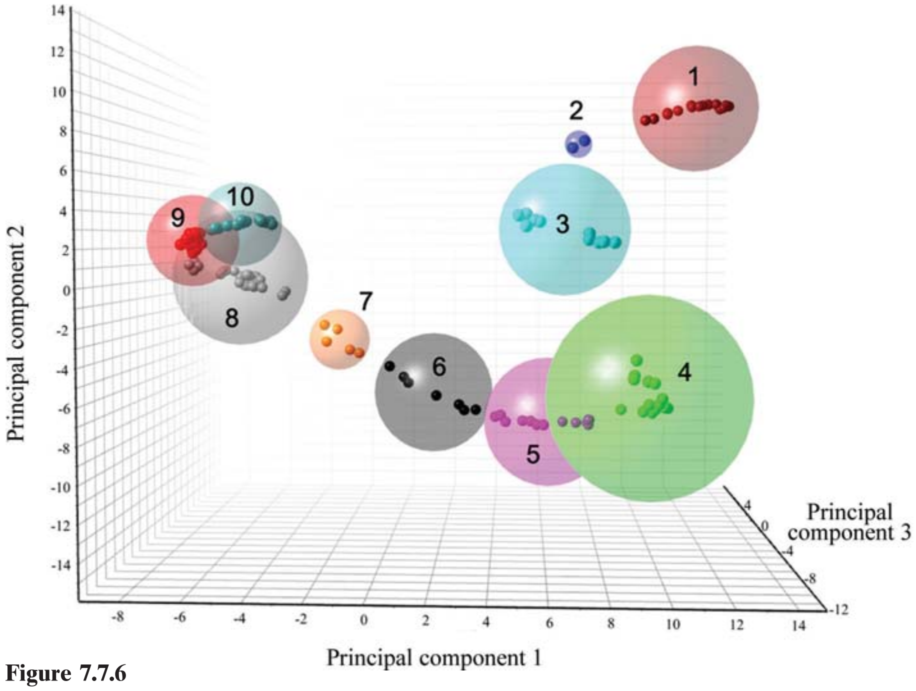

Figure 7.7.6
PCA output from cluster analysis of the data suite collected during the decomposition of plumbojarosite. The clusters are labelled and coloured in accordance with the dendrogram in Fig. 7.7.5.

samples (for example, chemical composition, processing conditions *etc.*). Agglomerative hierarchical cluster analysis begins by considering each member of a data set to be an independent cluster and then progressively merging them on the basis of their similarity. The output can be displayed as a dendrogram which shows the grouping of scans from a low (all scans independent) to a high (all scans contained in a single cluster) figure of merit (Fig. 7.7.5; see Chapter 3.8). Principal component analysis (PCA) may also be conducted as an independent method to assist with visualization and assessment of the quality of the clustering. The principal components of a data set are the directions within it where the variance is greatest. By re-framing the data to these principal components the dimensionality of the data set may be reduced. The position of each member of the data set may then be plotted within this framework as shown in Fig. 7.7.6. Further validation of the clustering may be achieved using techniques such as 'silhouettes' or 'fuzzy clustering' (Barr *et al.*, 2004*b*).

Cluster analysis has clear application in the areas of ore sorting and process control, where large numbers of samples may be assessed and grouped with respect to the desired parameters (for example, geological location, processing time/temperature, ratio of particular phases such as haematite/magnetite *etc.*). This methodology is also useful for partitioning the large data suites resulting from time-resolved experimentation. Fig. 7.7.7 shows an example of such clustering using a data set collected during the thermal decomposition of plumbojarosite (Madsen *et al.*, 2010). The accumulated diffraction patterns are viewed down the *z* axis and the plot has been partitioned according to the clustering shown in Figs. 7.7.5 and 7.7.6.

The most representative pattern from each cluster is reported with the results and may be analysed in detail according to the information required from the analysis (search–match, QPA, crystal structure analysis). An analytical method can then be developed that may be applied to other members of the cluster in a more automated fashion. Some available software packages will also denote the two most extreme patterns in each cluster and identify any outliers that do not fit within any subset of the data suite (König *et al.*, 2010). Software packages such as *Poly-SNAP* (Barr *et al.*, 2003, 2004*a*, 2009; Barr, Dong, Gilmore & Faber, 2004; Gilmore *et al.*, 2004) employ a similar range of clustering tools and can also perform automated, non-Rietveld QPA given an appropriate database of pure phases.

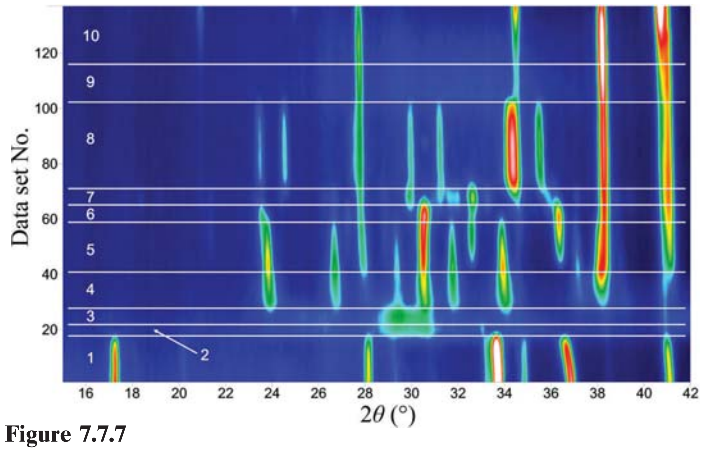

Figure 7.7.7
Accumulated laboratory PXRD patterns from the thermal decomposition of plumbojarosite. The data are represented as a three-dimensional plot with diffraction angle ($2\theta°$) along the *x* axis, data-set number along the *y* axis and intensity along the *z* axis. The white lines approximately delineate the identified clusters within the data suite and the numbers correspond to those in Fig. 7.7.6.

7.7.3.5.2. *Batch processing*

Batch processing is a method for automatically analysing multiple data sets, either sequentially or in parallel. In some instances a group of diffraction patterns must be analysed using identical starting parameters for either search–match or Rietveld analysis. In other cases, an evolving method must be employed to provide appropriate starting parameters for a continuous sequence of data with, for example, time, temperature or geographical distance as a variable. In the latter case, it may be useful to partition the entire data suite at the outset of the analysis in order to determine appropriate starting parameters based upon the most representative patterns from each group as determined by the clustering process (Section 7.7.3.5.1). Stinton & Evans (2007) devised a method of parametric Rietveld refinement that is a form of batch processing in which an entire suite of data is used simultaneously to refine a single evolving model. This allows the refinement of fewer independent variables and a reduction in the degree of uncertainty in parameters that remain constant for the entire suite. It is also possible *via* this technique to refine noncrystallographic parameters such as temperature and kinetic rate constants directly from the diffraction data. Such methodology requires the use of a Rietveld package such as *TOPAS* (Bruker AXS, 2009) that allows the inclusion of user-defined equations into its models without access to the source code.

7.7.4. Examples

7.7.4.1. *Exploration*

The presence of alteration envelopes around hydrothermal ore deposits is often used as a tracer in ore exploration. Traditional methods involve visual and optical microscopic evaluations, but mineralogical logging of drill samples by PXRD can supplement and provide more reliable and consistent analysis than these methods, many of which are operator-dependent (Hausen & Odekirk, 1991). PXRD analyses may be used during the mineral-mapping process to determine the nature and extent of the alteration halo around an ore body, and the *in situ* field-based methods described above have the potential to streamline and speed up such assessments. Hausen & Odekirk (1991) have described in detail the application of such a methodology to drill samples from gold-mining and copper-mining operations. PXRD analyses are also valuable for testing and verifying the results from other mineral-mapping techniques such as the airborne visible/infrared imaging spectrometer (AVIRIS; Rockwell *et al.*, 2006).

7.7.4.2. *Process control*

7.7.4.2.1. *Phosphate mineralogy*

Mintek of South Africa was one of the first organizations to employ real-time on-stream PXRD analysis for use with slurries in the phosphate industry (De Villiers *et al.*, 1983). Online analysis was developed to solve process-control problems that were not satisfied by the existing XRF-based instrumentation. The primary drawback of the XRF approach was an inability to analyse elements lighter than calcium, resulting from the absorption of fluorescent X-rays by the slurry medium (water). To compensate for these drawbacks, Mintek devised a PXRD instrument using Mo $K\alpha$ radiation to detect minerals containing phosphorus, silicon and fluorine in a $\sim$20 wt% solid slurry flowing at 2.5 l min^{-1}. This instrument provided good sampling, and the results were comparable to those provided by wet-chemical methods.

7.7.4.2.2. *Cement*

The US Geological Survey Mineral Commodity Summaries January 2017 lists world cement production for 2016 as $\sim$4.2 million metric tonnes (US Geological Survey, 2017). Cement is a key material for the building and construction industries across the world, and the quality of the final products made from cement is dependent upon the phases present in it and their relative abundances. Phase abundances are traditionally determined during cement production by optical microscopy or normative calculations from chemical analyses (*i.e.* the Bogue method discussed in Section 7.7.2 above).

PXRD is a more direct method of QPA for cement, and much development has been carried out by major diffraction-equipment manufacturers to improve the ease and accuracy of analysis. The approach taken generally incorporates high-throughput instrumentation using automatic sample changers, rapid detectors and automated Rietveld analysis (see, for example, Section 7.7.4.2.4). A different approach was developed through a collaboration between Australia's CSIRO (Commonwealth Scientific and Research Organisation) and Fuel & Combustion Technology Pty Ltd (FCT) (Madsen & Scarlett, 1999; Manias *et al.*, 2000, 2001; Manias, 2008; Scarlett *et al.*, 2001). The aim of this work was to design, construct, install and commission an online PXRD analyser capable of continuously monitoring phase abundances for use in process-plant control (Dhanjal *et al.*, 2006). The cornerstone of this analyser was the use of an Inel CPS 120 curved detector that allowed the simultaneous collection of 120° in 2θ of diffraction data, enabling rapid data collection with no moving parts. This latter feature is very desirable in the environment of an operating plant. This instrument is currently marketed by a subsidiary of FCT (FCT AcTech) under the name 'COSMA', which is an acronym for Continuous On-Stream Mineral Analyser. This instrument takes a continuous stream from either the clinker plant or cement mill and provides full QPA *via* the Rietveld method every minute. The development of the Rietveld method for this automated analysis involved a detailed description of all of the component phases within the material to be analysed. In the case of minor phases, this involved their separation from the bulk specimen in order to fully define their crystallographic parameters (Madsen & Scarlett, 1999). Such a methodology is complex and time consuming, and is inappropriate for the rapid-turnaround requirements of an on-stream instrument. However, with a consistent product such as cement, the parameter set being refined may be closely restricted or even fixed based on these phase definitions and therefore rapidly applied without the risk of analytical instability. The accuracy of such a method is dependent on the consistency of the phase chemistry of the samples. If any of the material inputs to the process change dramatically, the method must be adjusted to accommodate the changes in phase parameters. Although this instrument was originally designed for the cement industry, such an approach could be applicable in a variety of mineralogical contexts in the mining and process industries.

7.7.4.2.3. *Energy-dispersive diffraction (EDD)*

Obtaining a representative sample is one of the most important issues affecting the outcome of process control. One approach to improving online sampling is the use of higher-energy, more penetrating radiation (O'Dwyer & Tickner, 2007, 2008). O'Dwyer and Tickner developed a prototype instrument incorporating polychromatic radiation rather than the traditional monochromatic beam associated with most laboratory instruments (O'Dwyer & Tickner, 2006). Diffraction data resulting from the use of polychromatic radiation are typically presented as a function of energy rather than of diffraction angle. The basis of this 'energy-dispersive diffraction' experiment is still the satisfaction of Bragg's law,

$$\lambda = 2d\sin\theta, \qquad (7.7.1)$$

where λ is the wavelength of the incident radiation, d is the interplanar spacing of the diffracting phase and 2θ is the diffraction angle. The energy of the incident radiation is related to its wavelength *via*

$$E_{\rm keV} = \left(\frac{hc}{\lambda}\right)6.24\times10^{25} = \frac{12.4}{\lambda}, \qquad (7.7.2)$$

where $E_{\rm keV}$ is the energy of the incident radiation in keV, h is Planck's constant (6.626068×10^{-34} J s^{-1}), c is the speed of light (2.998×10^{8} m s^{-1}) and λ is the wavelength associated with this energy in ångströms. Rearrangement and substitution into Bragg's law allows the expression of energy in terms of d and diffraction angle:

$$E_{\rm keV} = \frac{6.2}{(d\sin\theta)}. \qquad (7.7.3)$$

O'Dwyer and Tickner's instrument was coupled with a simple linear regression calculation that effectively operated as a single-

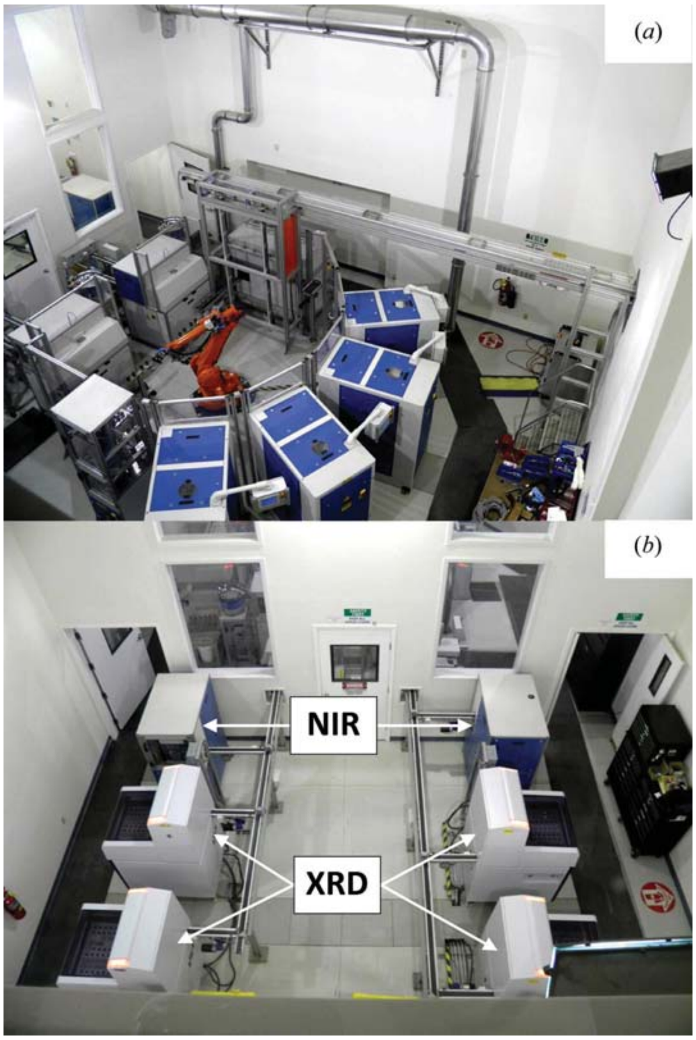

Figure 7.7.8
Automated PXRD–NIR installation at Freeport–McMoRan Copper and Gold Inc. (FCX) showing (*a*) the robotics sample-preparation laboratory and (*b*) the XRD–NIR laboratory. (Photograph courtesy of Freeport–McMoRan Copper and Gold Inc.)

peak method for QPA, developed from a ‘training suite’ of samples (O’Dwyer & Tickner, 2007). This is a simple and rapid approach to data analysis for an in-plant environment. More recently, however, it has been shown that EDD data may be quantified directly using a Rietveld refinement technique (Scarlett *et al.*, 2009) that improves the accuracy and applicability of this instrument.

7.7.4.2.4. *Freeport–McMoRan automated PXRD–NIR mineralogy laboratory*

A fully automated PXRD–NIR (near-infrared) installation was commissioned in 2009 for the international mining company Freeport–McMoRan Copper and Gold Inc. (FCX). The installation consists of two parts. The first is the robotics sample-preparation area (Fig. 7.7.8*a*) and the second is the analytical area containing four Bruker D4 Endeavour PXRD instruments and two ASD NIR units in Herzog automation cabinets (Fig. 7.7.8*b*). The design capacity of the laboratory is 500 PXRD mineralogy and approximately 800 NIR clay and alteration mineral analyses per day, and the system handles sample material from all mine operations, including blast holes, geological samples and speciality materials. The PXRD units perform 10 min data collections followed by 10 min Rietveld QPA using automated batch processing. The final Rietveld fit for every sample is checked by a mineralogist or technician. Results are reported automatically *via* a laboratory information system (LIMS).

Automated systems such as this must be carefully monitored to ensure that they are performing as expected. To ensure this, standard materials are analysed daily [including NIST corundum, laboratory ore standard (granite) and a blank (glass) to check for contamination]. A minimum of 5% of samples are replicated, and the pulverizing mills are checked daily to ensure that the proper particle size is produced.

7.7.4.3. *Research*

7.7.4.3.1. *Structure solution*

QPA *via* the Rietveld method is most easily obtained when the crystal structures of all component phases are known. In addition to the amounts of the component phases, Rietveld analyses have the potential to provide a wealth of crystal chemical data on the solid phases in a sample. These are powerful data that can also shed light on the mineral provenance and its relationship to other species, which have implications for understanding the genesis, extent and purity of ore bodies. Many mineral species are incompletely described owing to a lack of single crystals of suitable quality for structural determination. Recent advances in powder-diffraction methodology facilitate crystal structure solution from powder data [*i.e.* simulated annealing (Coelho, 2000) and charge flipping (Coelho, 2007; Oszlányi & Sütő, 2004, 2008)]. Detailed methodologies for structure solution are given in Part 4 of this volume.

7.7.4.3.2. *Environment*

The impact of mining and mineral processing activities on public health and the environment has been an increasingly important consideration in recent times. The detrimental effects of mining may include the clearance of land, erosion, a reduction in biodiversity, the contamination of ground and surface water, air pollution and greenhouse-gas emissions. In an effort to address these effects, many countries have implemented codes to ensure the rehabilitation of land, after the cessation of mining/extraction activity, to its original state or to other uses such as agriculture, industrial or residential purposes. In fact, environmental aspects are now one of the most important factors in determining the economic viability of mining a particular ore body (Jambor, 1994). As in the exploration process, an understanding of the mineralogy of solid gangue, mine waste and drainage effluents is essential for understanding the behaviour of these materials and their potential environmental impacts. X-ray powder diffraction is an invaluable tool for the direct identification of such mineralogy and as an adjunct to other characterization techniques.

One of the greatest environmental issues faced by active and abandoned mines is that of acid mine drainage (AMD). AMD occurs as a result of the exposure of sulfide minerals to oxygen and water. The most common of these minerals are pyrite and marcasite (both polymorphs of FeS_2). Oxidation of these minerals produces sulfuric acid and the precipitation of a range of ochreous deposits. These precipitates are deposited in rivers and streams and, together with the low-pH conditions accompanying the sulfuric acid, they have an impact on aquatic life. The acidic run-off often contributes to surface water and groundwater, lowering its pH. The original sulfide minerals often contain numerous trace elements (*e.g.* Mn, Zn, Co, Ni and Cu for Fe, and As and Se for S) that are also released into the environment upon weathering. Evidence of such release and precipitation is still apparent from ancient workings as described by Davis *et al.* (2000) in their study of the Rio Tinto system in the province of Huelva, southwestern Spain. According to them, this system is 'one of the most polluted fluvial-estuarine systems in the world and most likely has been so for thousands of years'. Phenomena similar to AMD may also occur naturally through the oxidation of sulfide-bearing soils and rocks (Schwertmann *et al.*, 1995).

Much research has been directed towards understanding and addressing the effects of AMD and the nature and origin of the precipitates formed. Some examples follow.

(i) Mineral samples from an area in the Sokolov Basin, Czech Republic, were characterized by Murad and Rojík using a combination of PXRD and chemical methods (Murad & Rojík, 2005). They found that variations in mine-drainage precipitate mineralogy can serve as indicators of pH and sulfate conditions, possibly indicating the genetic environment during precipitate formation. They used this detailed study as a means of relating other properties such as colour (which may be used for rapid assessment in the field or remotely) to mineralogy.

(ii) PXRD was used to confirm the mineralogy of samples used in a study of the geochemistry of bacterially-induced mineralization of mine-drainage precipitates (Kawano & Tomita, 2001).

(iii) Jambor *et al.* (2007) used PXRD to determine quantitative mineralogy in order to compute the neutralization potential (NP) of a selection of sedimentary, metamorphic and igneous extrusive rocks. These results have been compared with those from the Sobek method of static testing (Sobek *et al.*, 1978) for predicting the potential for AMD. The two methods were found to be in moderate agreement.

(iv) *In situ* diffraction studies of the stability of mine waste during dehydration–hydration reactions have been conducted using a purpose-built stage and control system (Peterson & Grant, 2005) in order to determine the controlling factors.

(v) Jarosite is an iron sulfate mineral found in ochreous deposits resulting from AMD, and it contributes to acidic run-off and increased metal mobility in these environments. It also forms during bioleaching and may act as a kinetic barrier to further reaction. *In situ* diffraction studies into the nucleation and crystallization of jarosite have been conducted (Brand *et al.*, 2012; Scarlett *et al.*, 2013)

One of the major environmental concerns facing mining operations is their production of greenhouse gases. Carbon dioxide is the most prevalent of these anthropogenic contributions to the Earth's atmosphere and has increased globally by about 100 p.p.m. (36%) over the last 250 years from around 278 p.p.m. in 1750 to 390 p.p.m. in 2011 (Stocker *et al.*, 2013). This increase has not been linear and the growth rate of CO_2 in the atmosphere has increased dramatically in the past 30 years. An increase of 50 p.p.m. from the pre-industrial era (prior to AD 1750) baseline was measured in the 1970s, with a further increase of 50 p.p.m. in the next 30 years. Between 1995 and 2000, atmospheric CO_2 increased by about 19 p.p.m., which is the highest average growth rate ever recorded.

In 1995, Lackner and co-workers proposed a method for the disposal of atmospheric CO_2 *via* the formation of stable carbonate minerals (Lackner *et al.*, 1995). They considered high-temperature and aqueous processing and investigated a range of common rocks rich in magnesium or calcium as suitable raw materials. A potential method for the implementation of this CO_2 sequestration is *via* the dissolution of silicates and precipitation of carbonates in mine tailings (Wilson, Dipple *et al.*, 2009). Mine tailings are particularly suited to this purpose as they are generally milled, which increases their surface area and accelerates mineral–fluid interactions. To some extent, this process occurs naturally, as demonstrated by Wilson and co-workers regarding the trapping and storage of atmospheric CO_2 in tailings from historic chrysotile mines at Clinton Creek, Yukon Territory and Cassiar, British Columbia. They used QPA from PXRD data to determine the mineralogy of the tailings in order to estimate the amount of CO_2 trapped within fine-grained, hydrous carbonate minerals (Wilson, Raudsepp & Dipple, 2009). The use of PXRD allows the various carbonate minerals to be distinguished and has an advantage over scanning electron microscopy (SEM) methods in its applicability to fine-grained, intergrown or hydrous minerals that may be affected by the electron beam. These findings indicate that it may be beneficial to promote the formation of secondary carbonate minerals at active mines in order to reduce or offset their net greenhouse-gas emissions.

7.7.5. Conclusions

From exploration to market to reclamation, the mining industry is reliant on detailed mineralogical knowledge of the materials with which it deals. The location of ore bodies can be determined from knowledge of the mineralogy of the surrounding landscape. The mode of extraction of valuable minerals or metals is determined by the assemblages in which they occur. The ease of processing and the final properties of marketable products are dependent upon the crystal chemistry of the starting materials. At all stages of production, quality control may be based around knowledge of the mineralogy of the intermediate products. New processing routes and modes of environmental protection and remediation can be developed through detailed understanding of the crystal structural nature of the minerals participating in the various reactions. Ultimately, the environmental history of the Earth and other planets may be ascertained by analysis of their mineralogy.

The level of detail of a PXRD analysis may vary from the simple identification of individual minerals to extensive structural studies probing the fine details of crystal structure at the atomic level. One of the most useful PXRD techniques relevant to the minerals industry is that of quantitative phase analysis. This technique finds application throughout all aspects of mineral processing and is now a routine tool in the field, the plant and the laboratory. PXRD is a powerful tool in its own right, but is greatly enhanced by association with other analytical techniques. For example, bulk chemical analysis can assist greatly with phase identification, and microanalysis *via* electron-beam techniques can indicate levels of chemical substitution within minerals. The modern analytical laboratory has a powerful array of techniques for the characterization of mineralogical specimens, but at its heart PXRD is based directly upon the structural nature of crystalline materials, and as such is the most fundamental 'fingerprinting' technique for assessing mineral assemblages.

The authors wish to thank Arnt Kern (Bruker AXS) and Douglas Allen (FCX) for details of the PXRD–NIR automated mineralogy laboratory.

References

Agricola, G. (1912). *De re Metallica*, translated and edited by H. C. Hoover & L. H. Hoover. New York: Dover.

Barr, G., Dong, W. & Gilmore, C. J. (2003). *PolySNAP: A computer program for the analysis of high-throughput powder diffraction data.*

University of Glasgow, Scotland. http://www.chem.gla.ac.uk/snap/PolySNAP_index.html.

Barr, G., Dong, W. & Gilmore, C. J. (2004*a*). *PolySNAP: a computer program for analysing high-throughput powder diffraction data. J. Appl. Cryst.* **37**, 658–664.

Barr, G., Dong, W. & Gilmore, C. J. (2004*b*). *High-throughput powder diffraction. IV. Cluster validation using silhouettes and fuzzy clustering. J. Appl. Cryst.* **37**, 874–882.

Barr, G., Dong, W. & Gilmore, C. J. (2009). *PolySNAP3: a computer program for analysing and visualizing high-throughput data from diffraction and spectroscopic sources. J. Appl. Cryst.* **42**, 965–974.

Barr, G., Dong, W., Gilmore, C. & Faber, J. (2004). *High-throughput powder diffraction. III. The application of full-profile pattern matching and multivariate statistical analysis to round-robin-type data sets. J. Appl. Cryst.* **37**, 635–642.

Benvenuti, M., Mascaro, I., Corsini, F., Lattanzi, P., Parrini, P. & Tanelli, G. (1997). *Mine waste dumps and heavy metal pollution in abandoned mining district of Boccheggiano (Southern Tuscany, Italy). Environ. Geol.* **30**, 238–243.

Bish, D. L. *et al.* (2013). *X-ray diffraction results from Mars Science Laboratory: mineralogy of Rocknest at Gale Crater. Science*, **341**, 1238932.

Bish, D. *et al.* (2014). *The first X-ray diffraction measurements on Mars. IUCrJ*, **1**, 514–522.

Blake, D. *et al.* (2012). *Characterization and calibration of the CheMin mineralogical instrument on Mars Science Laboratory. Space Sci. Rev.* **170**, 341–399.

Blake, D. F., Vaniman, D. T. & Bish, D. L. (1994). *A Mineralogical Instrument for Planetary Applications.* Lunar and Planetary Science Conference XXV, pp. 121–122. https://ntrs.nasa.gov/search.jsp?R=19940030902.

Bogue, R. H. (1929). *Calculation of the compounds in Portland cement. Ind. Eng. Chem. Anal. Ed.* **1**, 192–197.

Brand, H. E. A., Scarlett, N. V. Y. & Grey, I. E. (2012). *In situ studies into the formation kinetics of potassium jarosite. J. Appl. Cryst.* **45**, 535–545.

Bruker AXS (2009). *TOPAS v.4.2: General profile and structure analysis software for powder diffraction data*. Bruker AXS, Karlsruhe, Germany.

Chiari, G. (2008). *Saving art in situ. Nature*, **453**, 159.

Chipera, S. J. & Bish, D. L. (2002). *FULLPAT: a full-pattern quantitative analysis program for X-ray powder diffraction using measured and calculated patterns. J. Appl. Cryst.* **35**, 744–749.

Chung, F. H. & Smith, D. K. (1999). *Industrial Applications of X-ray Diffraction*, edited by F. H. Chung & D. K. Smith, pp. 13–35. Boca Raton: CRC Press. https://doi.org/10.1201/b16940-4.

Cockcroft, J. K. & Fitch, A. N. (2008). *Powder Diffraction: Theory and Practice*, edited by R. E. Dinnebier & S. J. L. Billinge, pp. 20–57. Cambridge: The Royal Society of Chemistry. https://doi.org/10.1039/9781847558237-00020.

Coelho, A. A. (2000). *Whole-profile structure solution from powder diffraction data using simulated annealing. J. Appl. Cryst.* **33**, 899–908.

Coelho, A. A. (2007). *A charge-flipping algorithm incorporating the tangent formula for solving difficult structures. Acta Cryst.* A**63**, 400–406.

Davis, R. A. Jr, Welty, A. T., Borrego, J., Morales, J. A., Pendon, J. G. & Ryan, J. G. (2000). *Rio Tinto estuary (Spain): 5000 years of pollution. Environ. Geol.* **39**, 1107–1116.

De Villiers, J. P. R., Ormrod, G. T. W. & Cole, A. E. (1983). *ICAM 81: Proceedings of the First International Congress on Applied Mineralogy*, edited by J. P. R. De Villiers & P. A. Cawthorn, pp. 435–442. Johannesburg: Geological Society of South Africa.

Dhanjal, S. K., Young, L. & Storer, P. (2006). *Automatic Control of Cement Quality Using On-Line XRD.* In *IEEE Cement Industry Technical Conference, 2006. Conference Record.* Piscataway: IEEE. https://doi.org/10.1109/CITCON.2006.1635726.

Downs, R. T. & Hall-Wallace, M. (2003). *The American Mineralogist crystal structure database. Am. Mineral.* **88**, 247–250.

Dutrizac, J. E. & Jambor, J. L. (2000). *Jarosites and Their Application in Hydrometallurgy. Sulfate Minerals: Crystallography, Geochemistry and Environmental Significance*, Vol. 40, edited by C. N. Alpers, J. L. Jambor & D. K. Nordstrom, pp. 405–452. Chantilly: Mineralogical Society of America.

Fawcett, T. G., Kabekkodu, S. N., Blanton, J. R. & Blanton, T. N. (2017). *Chemical analysis by diffraction: the Powder Diffraction File. Powder Diffr.* **32**, 63–71.

Fazey, P. G., O'Connor, B. H. & Hammond, L. C. (1991). *X-ray powder diffraction Rietveld characterization of synthetic aluminum-substituted goethite. Clays Clay Miner.* **39**, 248–253.

Gilmore, C. J., Barr, G. & Paisley, J. (2004). *High-throughput powder diffraction. I. A new approach to qualitative and quantitative powder diffraction pattern analysis using full pattern profiles. J. Appl. Cryst.* **37**, 231–242.

Gottlieb, P., Wilkie, G., Sutherland, D., Ho-Tun, E., Suthers, S., Perera, K., Jenkins, B., Spencer, S., Butcher, A. & Rayner, J. (2000). *Using quantitative electron microscopy for process mineralogy applications. JOM*, **52**, 24–25.

Gražulis, S., Chateigner, D., Downs, R. T., Yokochi, A. F. T., Quirós, M., Lutterotti, L., Manakova, E., Butkus, J., Moeck, P. & Le Bail, A. (2009). *Crystallography Open Database – an open-access collection of crystal structures. J. Appl. Cryst.* **42**, 726–729.

Gražulis, S., Daškevič, A., Merkys, A., Chateigner, D., Lutterotti, L., Quirós, M., Serebryanaya, N. R., Moeck, P., Downs, R. T. & Le Bail, A. (2012). *Crystallography Open Database (COD): an open-access collection of crystal structures and platform for world-wide collaboration. Nucleic Acids Res.* **40**, D420–D427.

Gražulis, S., Merkys, A., Vaitkus, A. & Okulič-Kazarinas, M. (2015). *Computing stoichiometric molecular composition from crystal structures. J. Appl. Cryst.* **48**, 85–91.

Gu, Y. (2003). *Automated scanning electron microscope based mineral liberation analysis: an introduction to JKMRC/FEI mineral liberation analyser*. *J. Miner. Mater. Charact. Eng.* **2**, 33–41.

Hansford, G. M. (2016). *Phase-targeted X-ray diffraction. J. Appl. Cryst.* **49**, 1561–1571.

Hausen, D. M. & Odekirk, J. R. (1991). *XRD mineralogic logging of drill samples from gold and copper mining operations. Ore Geol. Rev.* **6**, 107–118.

Heizer, R. F. (1962). *The background of Thomsen's three-age system. Technol. Cult.* **3**, 259–266.

Jambor, J. L. (1994). *Mineralogy of sulfide-rich tailings and their oxidation products. Short Course Handbook on Environmental Geochemistry of Sulfide Mine-wastes*, edited by J. Jambor & D. Blowes, pp. 59–102. Nepean: Mineralogical Association of Canada.

Jambor, J. L., Dutrizac, J. E. & Raudsepp, M. (2007). *Measured and computed neutralization potentials from static tests of diverse rock types. Environ. Geol.* **52**, 1019–1031.

Kawano, M. & Tomita, K. (2001). *Geochemical modeling of bacterially induced mineralization of schwertmannite and jarosite in sulfuric acid spring water. Am. Mineral.* **86**, 1156–1165.

Klug, H. P. & Alexander, L. E. (1974). *X-ray Diffraction Procedures*, 2nd ed. New York: John Wiley & Sons.

König, U., Hållstedt, J., Noreland, J., Vallo, K., Gobbo, L., Füllmann, T., Macchiarola, K. & Nieminen, J. (2010). *Using X-ray diffraction: in the hunt for cost and CO_2 reductions in the metal. Bergsmannen*, **3**, 7.

Lackner, K. S., Wendt, C. H., Butt, D. P., Joyce, E. L. & Sharp, D. H. (1995). *Carbon dioxide disposal in carbonate minerals. Energy*, **20**, 1153–1170.

Le Bail, A. (2005). *Inorganic structure prediction with GRINSP. J. Appl. Cryst.* **38**, 389–395.

Le Meins, J.-M., Cranswick, L. M. D. & Le Bail, A. (2002). *A Search-Match Round Robin. International Union of Crystallography Commission on Powder Diffraction Newsletter*, **27**, 32–33. http://www.mx.iucr.org/iucr-top/comm/cpd/Newsletters/no27jul2002/cpd27.pdf.

Madsen, I. C., Grey, I. E. & Mills, S. J. (2010). *In situ diffraction studies: thermal decomposition of a natural plumbojarosite and the development of Rietveld-based data analysis techniques. Mater. Sci. Forum*, **651**, 37–64.

Madsen, I. C. & Scarlett, N. V. Y. (1999). *Industrial Applications of X-ray Diffraction*, edited by F. H. Chung & D. K. Smith, pp. 415–440. Boca Raton: CRC Press. https://doi.org/10.1201/b16940-19.

Madsen, I. C., Scarlett, N. V. Y., Riley, D. P. & Raven, M. D. (2013). *Quantitative Phase Analysis Using the Rietveld Method. Modern Diffraction Methods*, edited by E. J. Mittemeijer & U. Welzel, pp. 283–320. Weinheim: Wiley-VCH. https://doi.org/10.1002/9783527649884.ch10.

Manias, C. G. (2008). *Real Time Mineralogical Analysis for Automated Control and Process Optimisation*. Automated Mineralogy 08, Brisbane, Australia. http://fct-actech.com/documents/20080820 Automated Mineralogy 2008rPaper Presentation _2.pdf.

Manias, C., Madsen, I. C. & Retallack, D. (2001). *Plant optimisation and control using continuous on-line XRD for mineral phase analysis. ZKG Int.* **54**, 138–145.

Manias, C., Retallack, D. & Madsen, I. C. (2000). *XRD for on-line analysis and control. World Cement*, **31**, 78–81.

Merkys, A., Vaitkus, A., Butkus, J., Okuli-Bè-Kazarinas, M., Kairys, V. & Gražulis, S. (2016). *COD::CIF::Parser: an error-correcting CIF parser for the Perl language. J. Appl. Cryst.* **49**, 292–301.

Murad, E. & Rojík, P. (2005). *Iron mineralogy of mine-drainage precipitates as environmental indicators: review of current concepts and a case study from the Sokolov Basin, Czech Republic. Clay Miner.* **40**, 427–440.

O'Dwyer, J. N. & Tickner, J. R. (2006). *A prototype energy-dispersive X-ray diffraction instrument for online mineralogical analysis.* Poster presentation at the 10th International Symposium on Radiation Physics, Coimbra, Portugal.

O'Dwyer, J. N. & Tickner, J. R. (2007). *Modelling diffractive X-ray scattering using the EGS Monte Carlo code. Nucl. Instrum. Methods Phys. Res. A*, **580**, 127–129.

O'Dwyer, J. N. & Tickner, J. R. (2008). *Quantitative mineral phase analysis of dry powders using energy-dispersive X-ray diffraction. Appl. Radiat. Isot.* **66**, 1359–1362.

Oszlányi, G. & Sütő, A. (2004). *Ab initio structure solution by charge flipping. Acta Cryst.* A**60**, 134–141.

Oszlányi, G. & Sütő, A. (2008). *The charge flipping algorithm. Acta Cryst.* A**64**, 123–134.

Peterson, R. C. & Grant, A. H. (2005). *Dehydration and crystallization reactions of secondary sulfate minerals found in mine waste: in situ powder-diffraction experiments. Can. Mineral.* **43**, 1171–1181.

Rietveld, H. M. (1969). *A profile refinement method for nuclear and magnetic structures. J. Appl. Cryst.* **2**, 65–71.

Rockwell, B. W., Cunningham, C. G., Breit, G. N. & Rye, R. O. (2006). *Spectroscopic mapping of the White Horse alunite deposit, Marysvale volcanic field, Utah: evidence of a magmatic component. Econ. Geol.* **101**, 1377–1395.

Sarrazin, P., Blake, D., Feldman, S., Chipera, S., Vaniman, D. & Bish, D. (2005). *Field deployment of a portable XRD/XRF instrument on Mars analog terrain. Adv. X-ray Anal.* **47**, 194–203. http://www.icdd.com/resources/axa/vol48/V48_27.pdf.

Sarrazin, P., Chiari, G. & Gailhanou, M. (2008). *A portable non-invasive XRD–XRF instrument for the study of art objects. Adv. X-ray Anal.* **52**, 175–186. http://www.icdd.com/resources/axa/vol52/V52_23.pdf.

Sarrazin, P., Chipera, S., Bish, D., Blake, D. & Vaniman, D. (2005). *Vibrating sample holder for XRD analysis with minimal sample preparation*. *Adv. X-ray Anal.* **48**, 156–164. http://www.icdd.com/resources/axa/vol48/V48_22.pdf.

Scarlett, N. V. Y., Grey, I. E. & Brand, H. E. A. (2013). *In situ synchrotron diffraction studies on the formation kinetics of jarosites. J. Synchrotron Rad.* **20**, 366–375.

Scarlett, N. V. Y., Madsen, I. C., Evans, J. S. O., Coelho, A. A., McGregor, K., Rowles, M., Lanyon, M. R. & Urban, A. J. (2009). *Energy-dispersive diffraction studies of inert anodes. J. Appl. Cryst.* **42**, 502–512.

Scarlett, N. V. Y., Madsen, I. C., Manias, C. & Retallack, D. (2001). *On-line X-ray diffraction for quantitative phase analysis: application in the Portland cement industry. Powder Diffr.* **16**, 71–80.

Schwertmann, U., Bigham, J. M. & Murad, E. (1995). *The first occurrence of schwertmannite in a natural stream environment. Eur. J. Mineral.* **7**, 547–552.

Sobek, A. A., Schuller, W. A., Freeman, J. R. & Smith, R. M. (1978). US Environmental Protection Agency Report EPA 600/2-78-054.

Stinton, G. W. & Evans, J. S. O. (2007). *Parametric Rietveld refinement. J. Appl. Cryst.* **40**, 87–95.

Stocker, T. F., Qin, D., Plattner, G.-K., Alexander, L. V., Allen, S. K., Bindoff, N. L., Bréon, F.-M., Church, J. A., Cubasch, U., Emori, S., Forster, P., Friedlingstein, P., Gillett, N., Gregory, J. M., Hartmann, D. L., Jansen, E., Kirtman, B., Knutti, R., Kumar, K. K., Lemke, P., Marotzke, J., Masson-Delmotte, V., Meehl, G. A., Mokhov, I. I., Piao, S., Ramaswamy, V., Randall, D., Rhein, M., Rojas, M., Sabine, C., Shindell, D., Talley, L. D., Vaughan, D. G. & Xie, S.-P. (2013). Technical Summary. In *Climate Change 2013: The Physical Science Basis. Contribution of Working Group I to the Fifth Assessment Report of the Intergovernmental Panel on Climate Change*, edited by T. F. Stocker, D. Qin, G.-K. Plattner, M. Tignor, S. K. Allen, J. Boschung, A. Nauels, Y. Xia, V. Bex & P. M. Midgley. Cambridge University Press.

Taylor, H. F. W. (1989). *Modification of the Bogue calculation. Adv. Cem. Res.* **2**, 73–77.

US Geological Survey (2017). *Mineral Commodity Summaries 2017*. US Geological Survey. https://pubs.er.usgs.gov/publication/70180197.

Vaniman, D. T., Bish, D. L. & Chipera, S. J. (1991). *In-Situ Planetary Surface Analyses: The Potential of X-ray Diffraction with Simultaneous X-ray Fluorescence*. *Lunar and Planetary Science XXII: Abstracts of Papers submitted to the Twenty-Second Lunar and Planetary Science Conference*, pp. 1429–1430. Houston: Lunar Planetary Institute.

Wilson, S. A., Dipple, G. M., Power, I. M., Thom, J. M., Anderson, R. G., Raudsepp, M., Gabites, J. E. & Southam, G. (2009). *Carbon dioxide fixation within mine wastes of ultramafic-hosted ore deposits: examples from the Clinton Creek and Cassiar chrysotile deposits, Canada. Econ. Geol.* **104**, 95–112.

Wilson, S. A., Raudsepp, M. & Dipple, G. M. (2009). *Quantifying carbon fixation in trace minerals from processed kimberlite: a comparative study of quantitative methods using X-ray powder diffraction data with applications to the Diavik Diamond Mine, Northwest Territories, Canada. Appl. Geochem.* **24**, 2312–2331.

7.8. Ceramic materials

W. Wong-Ng

7.8.1. Introduction

7.8.1.1. *Definition*

The term 'ceramics' is derived from the Greek word *keramikos*, which means 'burnt stuff' (Musikant, 1991), and was used originally to describe ware made from clay. After forming objects in clay, one can shape the material and harden it by firing at high temperatures to produce a ceramic which is relatively strong, hard and less permeable to fluids.

In the USA an extension of the meaning of 'ceramic' was authorized by the American Ceramic Society in the 1920s; chemically, clay is a silicate and it was proposed that the term 'ceramic' should be applied to all the silicate industries. This extended definition brought in glass, vitreous enamel and hydraulic cement. By a natural extension, the term 'ceramic' has since embraced all products made from fired clay, *i.e.* bricks and tiles, pipes and fireclay refractories, sanitaryware and electrical porcelain, as well as pottery tableware. Nowadays, the definition has been developed further into a broader term, so as to include in general inorganic, nonmetallic materials made from compounds of a metal and a nonmetal. Ceramics may be crystalline, partly crystalline or amorphous. They are formed by the action of heat and subsequent cooling. Ceramic materials tend to be strong in compression, but weak in shearing and tension. They are stiff and brittle. Most ceramic materials can withstand the chemical erosion that occurs in an acidic or caustic environment, and are nonconductors of heat and electricity, but their properties vary widely.

Ceramic materials can be subdivided into traditional and advanced ceramics. Traditional ceramics include clay-based materials. Advanced ceramics are tailored to have premium properties through the application of advanced materials science and technology to control the composition and internal structure. Advanced ceramic technology is often cited as an enabling technology: it enables engineers to design and build advanced systems for applications in fields such as the aerospace and automotive industries, and in consumer electronics.

7.8.1.2. *A brief history of ceramic development*

For detailed historical surveys of ceramic materials, readers can refer to *Kirk-Othmer Encyclopedia of Chemical Technology* (2007) and *The Britannica Concise Encyclopedia* (1994–2008). We will summarize the development of ceramics into what Norton called 'cycles in ceramic history' (Norton, 1978).

Since the dawn of humanity, use has been made of the plastic properties of clay for creating sculptures of humans and animals (known as early as the Paleolithic period). However, the practice of firing clay objects to make them hard, waterproof and fireproof became widespread only in the Neolithic period (about 5000 BC). Mastering ceramic production was one of the most important achievements of primitive people: the cooking of food in clay vessels made it possible to expand the range of edibles. The history of ceramics can be divided into alternating periods of activity and dormancy. These periods are:

The pre-Christian era – Ceramic ware was made largely from native clays, which produced a soft earthenware. Hand moulding and wheel throwing were usual. Glazes containing lead and tin were commonly used with a variety of colours. During this period ceramics were used largely in the household, but art ware was also produced.

The first 17 centuries of the Christian era – A great variety of pottery was made nearly everywhere, but most of it was earthenware. A giant step in pottery development took place in China. Earthenware was gradually refined to stoneware and finally to white translucent porcelain. Porcelain was introduced to Europe during Marco Polo's time around the thirteenth century.

Eighteenth-century Europe – Significant effort was made to duplicate Chinese porcelain. Vitreous pottery produced on the continent continued to be largely a hard porcelain body made of a kaolin–feldspar–quartz mixture, bisque-fired at low temperature and gloss-fired at a high temperature.

The nineteenth century – Germany invented the continuous-chamber kiln, a principle that had been used in China many years earlier, and of which Europeans were unaware. Towards the end of the 19th century electric power enabled the use of much higher temperatures.

The twentieth century to 1930 – Powerful electric furnaces enabled the making of silicon carbide, fused alumina and fused magnesia. Other changes included the increased use of gas and oil for kiln fuel, the invention of tunnel kilns and the use of electric motors for powerful forming machines.

The period from 1925 to the 1970s – Great gains in understanding the theories behind ceramic science were made due to the integration of multidisciplinary fields and the developments of a number of processing tools (high-temperature furnaces with even temperature distribution, isostatic pressing, slip casting, roller forming), analytical tools (in particular, powder-diffraction techniques), precise measurements of temperature, availability of phase diagrams, and the establishment of many ceramics-related conferences for information exchange.

The period from the 1970s to the present – Traditional ceramics production continued, but there has been a giant step towards the development of fine/advanced ceramics for modern industrial applications.

7.8.1.3. *Industrial aspects of fine ceramics/advanced ceramics*

In the past several decades there has been a rapidly growing interest in what are called fine, advanced or engineering ceramic materials. The Japanese industry, recognizing the economic potential of high-tech materials, had a systematic plan (blueprint) to develop new/fine ceramics in order to further its lead in the post-industrial age (Musikant, 1991). Fig. 7.8.1 shows the various areas that have been chosen for focus by Japan in a condensed format. The three concentric rings (reading from the centre outward) give the functions, properties and applications. The function labelled 'electric, magnetic' represents Japan's huge electronics industry and all the application areas in electronic devices in which Japan has been quite successful in the post-World War II era. The 'mechanical' function is directed largely to the automotive area. In the applications ring, the 'tool and jigs' item also contributes to low costs in automotive production, as ceramic tools have permitted an order of magnitude increase in speed in cutting and machining.

The transition from traditional to fine ceramics was only made possible by controlling the micro/mesostructure of ceramics, which in turn could not have been successful without sophisticated analytical tools, including powder diffractometers and electron microscopes. Fine ceramics have outstanding electrical properties, optical properties, abrasion resistance, heat resistance and/or corrosion resistance. Nowadays many ceramic companies apply such features in developing environmentally friendly automobile engines and industrial machinery, as well as other products, contributing to the betterment of society.

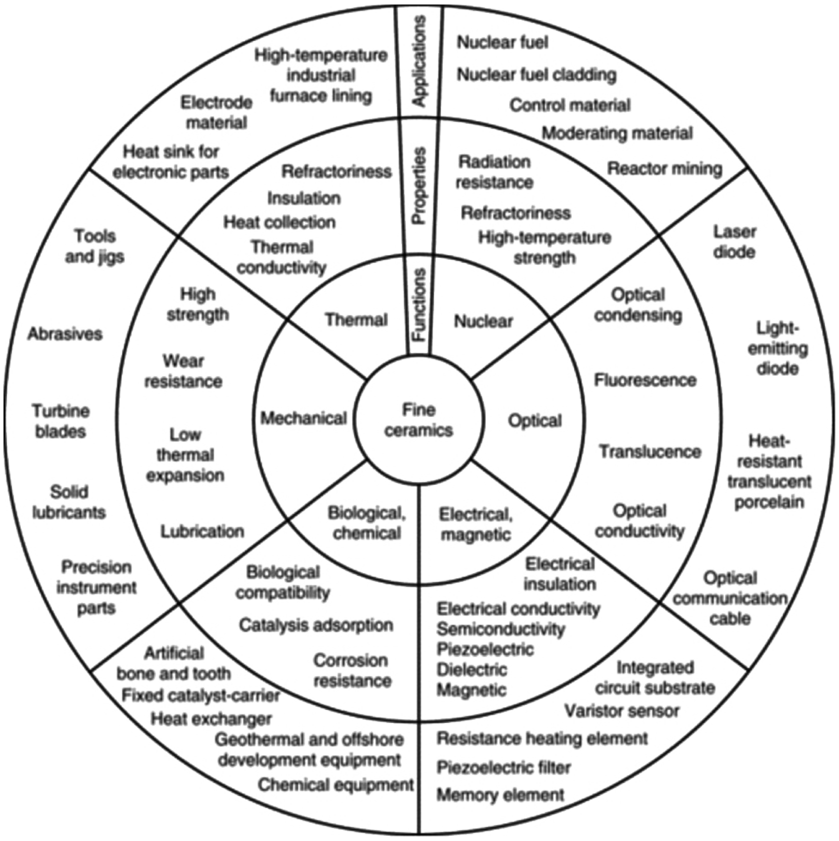
Applications
Properties
Functions
Fine ceramics
Thermal
Nuclear
Optical
Electrical, magnetic
Biological, chemical
Mechanical
Refractoriness
Insulation
Heat collection
Thermal conductivity
Radiation resistance
Refractoriness
High-temperature strength
Optical condensing
Fluorescence
Translucence
Optical conductivity
Electrical insulation
Electrical conductivity
Semiconductivity
Piezoelectric
Dielectric
Magnetic
Biological compatibility
Catalysis adsorption
Corrosion resistance
High strength
Wear resistance
Low thermal expansion
Lubrication
High-temperature industrial furnace lining
Electrode material
Heat sink for electronic parts
Nuclear fuel
Nuclear fuel cladding
Control material
Moderating material
Reactor mining
Laser diode
Light-emitting diode
Heat-resistant translucent porcelain
Optical communication cable
Integrated circuit substrate
Varistor sensor
Resistance heating element
Piezoelectric filter
Memory element
Chemical equipment
Geothermal and offshore development equipment
Heat exchanger
Fixed catalyst-carrier
Artificial bone and tooth
Precision instrument parts
Solid lubricants
Turbine blades
Abrasives
Tools and jigs

Figure 7.8.1
Fine/advanced ceramic areas for focus (Musikant, 1991). Reprinted by permission of the publisher (Taylor & Francis Ltd).

7.8.2. Categories of ceramics

Today's ceramics cover a wide range of materials. There are several common classifications of ceramics, depending on their type, chemical constituents and functionality. Chemically, they can be classified as oxides and non-oxides. In terms of their functionality, they can be classified broadly into electronic ceramics and structural ceramics. This chapter attempts to roughly classify them in terms of both applications and material types, namely, as art and archaeological ceramics, and as modern technical ceramics, with much emphasis on the latter. Hosts of other ceramics are still in various stages of development and production. The classification is simply an indication of the range of applications and the ceramic materials available.

7.8.2.1. *Art and archaeological ceramics*

Ceramics are known to laymen as the objects or the art that deals with the design and fabrication from dried clay. All types of earthenware, stoneware and porcelain are included in the term 'art ceramics'. Porcelain refers to wares that are fired at high temperatures and are to some extent translucent, while stoneware and earthenware (such as terracotta) are fired at lower temperatures and are opaque. The development of artistic ceramics involves the selection of clay and admixtures that make up the ceramic mass, the methods used to shape and fire the mass, and the methods used to treat and decorate the surface of the art work.

Ceramic artifacts, which are among the most common artifacts to be found at archaeological sites, play an important role in understanding the culture, technology and behaviour of people of the past. These artifacts are generally found in the form of small fragments of broken pottery called shards (or sherds). Processing of collected shards includes two main types of analysis: traditional and technical. Traditional analysis involves sorting ceramic artifacts, shards and larger fragments into specific types based on style, composition, manufacturing and morphology. The technical approach involves an examination of the phases and composition of ceramic artifacts and shards to determine the source of the material and the possible manufacturing site. Common techniques include powder X-ray diffraction and microscopic examinations.

7.8.2.2. *Modern technical ceramics*

Technical ceramics are categorized according to their modern usage, properties and applications:

7.8.2.2.1. *White ware*

White ware is a class of products that includes electrical and chemical technical porcelains and chinaware, and commonly used products such as fine dinnerware, wall tiles, pottery, dental porcelain and sanitary ware (Jones & Berard, 1993). White ware is usually manufactured from a mixture of minerals consisting of special clays, fluxing minerals (often feldspars) and finely ground quartz (SiO_2). This mineral mixture is shaped and then vitrified at high temperatures to produce a dense, hard material. An important step in the manufacturing of most white-ware products is the application of a glassy coating, called a glaze, to the product so as to seal the surface of the ceramic to prevent absorption of liquids and to increase the aesthetic appeal. Porcelain enamels are glassy coatings fused onto metals to provide corrosion protection and decoration. The fired colour is often white; hence the origin of the term 'white ware'.

7.8.2.2.2. *Structural clay products/building and construction materials (Jones & Berard, 1993)*

The structural clay products industry is concerned with the manufacture of bricks, construction tiles, floor tiles, vitrified sewer pipes, drain tiles *etc*. These products are usually manufactured from local natural mineral deposits such as shales, which are mineral mixtures rich in clays but with impurities. Durability and strength at low cost are keys to the success of these ceramic structural products.

The cement and gypsum industries are concerned with the production of the cements and plasters used in concrete, wallboards and other construction materials. They are produced by heat treatment of crushed raw materials to render them reactive with water to form a stone-like mass. In the cement industry, heat treatment is carried out in large rotary kilns. The major raw materials for the manufacture of cement are limestone, clays and aluminium-bearing minerials. Iron- and magnesium-bearing phases may also be present. Plaster is produced by gentle heating of gypsum ($CaSO_4{\cdot}2H_2O$) to drive off part of the natural chemical water.

7.8.2.2.3. *Machinery (Musikant, 1991)*

The ceramic applications in machinery are extremely demanding (Richerson, 1982). Heat-resistant structural materials such as Si_3N_4, SiC, cordierite ($2MgO{\cdot}2Al_2O_3{\cdot}5SiO_2$), mullite ($3Al_2O_3{\cdot}2SiO_2$) and ZrO_2 have found their way into ceramic machinery applications. Ceramic heat-engine components include internal parts of diesel engines, turbine blades, high-temperature bearings, external-combustion-engine components and ceramic heat exchangers. Other machinery applications include high-temperature transport rollers, and high-temperature gas and molten metal transport pipes.

Some ceramic parts can be fabricated to net shape or near net shape by appropriate densification methods. However, machining of some of the surfaces is required to meet dimensional tolerances, to achieve an improved surface finish or to remove surface flaws. Ceramic materials are often difficult and expensive to machine because of their high hardness and brittle nature. Machining must be done carefully to avoid brittle fracture of the component and the tool used must have a higher hardness than the ceramic being machined.

7.8.2.2.4. *Cutting tools*

Quality cutting tools must possess three characteristics: (1) high hardness and strength at high temperatures, (2) sufficient toughness (so that tools do not chip or fracture) and (3) high wear resistance to ensure long tool life (Schneider, 2009). The characteristics of modern ceramic cutting tools are a consequence of the intrinsic properties of the ceramics: high hardness at room and elevated temperature, high strength in compression, good chemical stability at high operating temperatures, and high thermal conductivity, which helps to reduce tip temperature. Cutting-tool materials have been improved with the introduction of Si_3N_4-based ceramics, SiC whisker-reinforced Al_2O_3, dense Al_2O_3–TiC materials, $Al_2O_3{\cdot}TiC$ and transformation-toughened ZrO_2 (discussed later in Section 7.8.3.3.4). Other examples of modern ceramics for cutting-tool applications are TiC, TiC·TiN, Si_3N_4, SiAlON, TiN cermet, cubic BN, WC coated with TiC, TiN, cubic BN and synthetic diamond.

7.8.2.2.5. *Nuclear applications (Musikant, 1991)*

The fission reactor consists of fissionable fuel, moderators that control the rate of fusion by absorbing neutrons and reflectors that minimize escape of neutrons out of the reactor. Nuclear fuel is a material that can be 'burned' by nuclear fission or fusion to derive nuclear energy. Most nuclear fuels contain heavy elements that are capable of nuclear fission. When these fuels are struck by neutrons, the nuclei of the heavy elements break apart, emitting more neutrons. The most common fissile nuclear fuels are uranium-235 (^{235}U) and plutonium-239 (^{239}Pu). For fission reactors, the fuel is usually based on the metal oxide (UO_2). Uranium nitride and carbide fuels have the advantages of higher heat conductivities and melting points. Because of the absence of oxygen in uranium carbide fuel as well as the ability to accommodate a ceramic coating (a ceramic–ceramic interface has structural and chemical advantages), uranium carbide is an ideal fuel candidate for certain gas-cooled fast reactors. Another essential element of the nuclear reactor is shielding. The shield prevents neutrons as well as gamma rays produced during the fission process from escaping into the environment. The various requirements of the shield can be met by the use of alternating layers, usually within a massive concrete structure. Some of the advanced ceramics useful for helping to provide these functions include reactor components (SiC, B_4C and Al_2O_3) and dosimeters (CaF_2, K_2SO_4, LiF).

7.8.2.2.6. *Electronic ceramics*

There are literally thousands of applications of advanced ceramics that depend on the interaction of the ceramics with applied electric or magnetic fields. While electronic properties are the main focus in these materials, in many cases additional mechanical- and thermal-property requirements must be met. We select 13 popular ceramic materials or applications for illustration.

7.8.2.2.6.1. Batteries and fuel cells

Two galvanic applications of conductive ceramics are in batteries and fuel cells (Jones *et al.*, 2012; Kordesch & Simader, 1996). A battery is a device that converts chemical energy into electricity. In its simplest form it consists of two metal or metal-oxide elements, called the anode and the cathode, immersed in a liquid or solid chemical compound called the electrolyte. Ion flow in the electrolyte is accompanied by a compensating movement of electrons from the anode; the electrons flow through an appropriate conductor to the cathode, and the electric circuit is complete. Batteries are abundant in modern life, especially finding use in portable appliances and motor vehicles. High-energy-density batteries based on sodium β-alumina have been developed for vehicular applications. β-Alumina has the formula $Na_2O{\cdot}11Al_2O_3$ and has a complicated structure consisting of spinel blocks sandwiching conduction planes in which Na^+ can rapidly migrate. A related structure is β''-alumina, $Na_2MgAl_{10}O_{17}$, where Mg^{2+} ions stabilize the structure and require additional Na^+ ions in the conduction plane for charge compensation. It is used as the solid electrolyte in the sodium–sulfur storage battery.

Fuel cells produce electric power in a similar way to a battery, except that power production is prolonged by supplying a gaseous or liquid fuel to the anode and air or oxygen to the cathode. Fuel cells have been developed for load-levelling in electric power plants, but they also may be used in motor vehicles. Of the several fuel-cell types, ceramics play key roles in the molten carbonate fuel cell (MCFC) and the solid oxide fuel cell (SOFC). In the MCFC, nickel-oxide ceramics serve as porous anodes for the molten salt (carbonate) electrolyte. In SOFCs, ceramics serve not only as the solid electrolyte (such as ZrO_2) but also as anodes and as conductive connections between adjacent cells (cobaltites, manganites and chromites of various transition metals).

7.8.2.2.6.2. Ceramic capacitors

Capacitors act as electrical buffers, diverting spurious electric signals and storing surges of charge that could damage circuits and disrupt their operation (Buchanan, 1986). A ceramic capacitor is a fixed capacitor with the ceramic material acting as the dielectric. It is constructed of two or more alternating layers of ceramic and a metal layer acting as the electrodes. The composition of the ceramic material defines the electrical behaviour and therefore the application of the capacitors, which are divided into several stability classes. Class-1 ceramic capacitors have high stability and low losses for resonant circuit applications. Examples are $MgNb_2O_6$, $MgTa_2O_6$, $ZnTa_2O_6$, $(ZnMg)TiO_3$, $(ZrSn)TiO_4$ and $Ba_2Ti_9O_{20}$. They have the lowest volumetric efficiency of the different types of ceramic capacitors. This is the result of the relatively low permittivity values (6 to 200 $\mathrm{F\,m^{-1}}$). Class-2 ceramic capacitors have high volumetric efficiency for buffer, by-pass and coupling applications. These are capacitors which have a dielectric with a high permittivity and therefore a better volumetric efficiency than class-1 capacitors, but lower reliability and stability. Class-3 barrier layer or semiconductive ceramic capacitors are capacitors which have a dielectric with a very high permittivity and therefore a better volumetric efficiency than class-2 capacitors. However, class-3 capacitors have poorer electrical characteristics, lower reliability and lower stability than class-2 capacitors. Barrier-layer ceramic capacitors are made of doped ferroelectric materials such as barium titanate ($BaTiO_3$).

7.8.2.2.6.3. High-temperature ceramic superconductors

High-temperature ceramic superconductors (abbreviated HTSs) are ceramic materials that behave as superconductors at unusually high temperatures. The first high-T_c superconductor was discovered in 1986 by IBM researchers Karl Müller and Johannes Bednorz (Bednorz & Müller, 1986), who were awarded the 1987 Nobel Prize in Physics 'for their important breakthrough in the discovery of superconductivity in ceramic materials' (Ford & Saunders, 2005). HTSs are type-II superconductors, and allow magnetic fields to penetrate their interior in quantized units of flux. The layered structure also gives a directional dependence to the magnetic field response. Whereas metallic superconductors usually have transition temperatures below 30 K, HTSs have been observed with transition temperatures as high as 160 K. The most studied high-temperature superconductors are the cuprate superconductors including yttrium barium copper oxide ($Ba_2YCu_3O_7$, famous as the first material to achieve superconductivity above the boiling point of liquid nitrogen), and $(Bi,Pb)_2Sr_2Ca_2Cu_3O_{10}$. Other high-$T_c$ cuprate superconductors include $La_{1.85}Ba_{0.15}CuO_4$, $HgBa_2Ca_2Cu_3O_x$ and $Ba_2RCu_3O_7$ (R = a lanthanide). The compound MgB_2 is also generally included with high-T_c materials. In recent years, a number of iron-based compounds [the iron pnictides SmFeAs(O,F), CeFeAs(O,F), LaFeAs(O,F)] have also been found to be superconducting at relatively high temperatures.

Two decades of intense experimental and theoretical research, with over 100 000 published papers on the subject, have reported many common features in the properties of high-temperature superconductors (Leggett, 2006), but so far there is no universally accepted theory to explain their properties. Ceramic superconductors and other unconventional superconductors differ in many important ways from conventional superconductors, such as elemental mercury or lead, which are adequately explained by the Bardeen–Cooper–Schrieffer (BCS) theory.

7.8.2.2.6.4. Ferroelectric ceramics

Ferroelectric materials belong to a subclass of pyroelectric materials. All ferroelectric materials are pyroelectric; however, not all pyroelectric materials are ferroelectric. Below a transition temperature called the Curie temperature, ferroelectric and pyroelectric materials are polar and possess a spontaneous polarization or electric dipole moment. This polarity can be reoriented or reversed fully or in part through the application of an electric field with ferroelectric materials. The direction of the spontaneous polarization conforms to the crystal symmetry of the material, while the reorientation of the spontaneous polarization is a result of atomic displacements. The magnitude of the spontaneous polarization is greatest at temperatures well below the Curie temperature and approaches zero as the Curie temperature is approached.

The phenomenon of ferroelectricity was discovered by J. Valasek (1921), who was investigating the dielectric properties of Rochelle salt ($NaKC_4H_4O_6{\cdot}4H_2O$). Barium titanate ($BaTiO_3$) was discovered to be ferroelectric in 1944 by von Hippel (1950) and is the most commonly encountered ferroelectric material. While there are over 250 materials that exhibit ferroelectric properties, some of the more common/significant materials include lead titanate, $PbTiO_3$, lead zirconate titanate (PZT) and lead lanthanum zirconate titanate (PLZT). Applications for ferroelectric materials include capacitors, non-volatile memory, piezoelectrics for ultrasound imaging and actuators, electro-optic materials for data-storage applications, thermistors, switches, oscillators and filters, and light deflectors, modulators and displays.

7.8.2.2.6.5. Glass ceramics

Glass ceramics are polycrystalline materials produced through crystallization of base glass (Montedo *et al.*, 2012). Glass ceramics are mostly produced in two steps, or what is referred to as a 'controlled crystallization' process: the glass is cooled and is then reheated in a second step, resulting in partial crystallization. These materials share many properties with both glasses and ceramics. Glass ceramics have an amorphous phase and one or more crystalline phases. They usually have between 30 to 90% crystallinity and yield an array of materials with interesting properties. A given glass ceramic may possess one or more of the following properties: zero porosity, high strength, toughness, translucency or opacity, pigmentation, opalescence, low or even negative thermal expansion, high temperature stability, fluorescence, machinability, ferromagnetism, high chemical durability, biocompatibility, bio-activity, ion conductivity, superconductivity, electrical isolation capabilities, low dielectric constant and loss, high resistivity, and high breakdown voltage. These properties can be tailored by controlling the base glass composition and by controlled heat treatment/crystallization of base glass. Considerable effort has been spent to obtain high-performance glass ceramics for potential applications in the medical, automotive and telecommunication applications (see Chapter 7.9).

7.8.2.2.6.6. Integrated-circuit packaging and substrates

In electronics manufacturing, integrated-circuit packaging is the final stage of semiconductor device fabrication, in which the small block of semiconducting material is encased in a supporting case that prevents physical damage and corrosion. The case, known as a 'package', supports the electrical contacts that connect the device to a circuit board. The earliest integrated circuits were packaged in ceramic flat packs (flat package): a rectangular or square package with leads parallel to base plane attached on two opposing sides of the package periphery. Flat packages were made of glass, ceramic and metal, and they could provide hermetic packaging for circuits, protecting them from moisture and corrosion; the military used them for many years because of their reliability and small size. In the area of commercial packaging, a ceramic pin-grid array (a ceramic substrate with pins arranged in a pin-grid array) is a type of packaging used for integrated circuits. Integrated circuits have also been developed for sensor applications in medical implants or other bioelectronic devices. In such biogenic environments, sealing strategies have to be planned to avoid corrosion or biogradation of the exposed semiconductor materials. As one of the few materials well established in complementary metal-oxide semiconductor (CMOS) technology, titanium nitride (TiN) has been found to be exceptionally stable and well suited for electrode applications in medical implants (Hämmerle *et al.*, 2002; Birkholz *et al.*, 2010).

7.8.2.2.6.7. Magnetic ceramics

Magnetic ceramics, or ferrites, are a very well established group of magnetic materials (Valenzuela, 1994; *Kirk-Othmer Encyclopedia of Chemical Technology*, 2007). They have the general chemical formula $M(\mathrm{Fe}_x\mathrm{O}_y)$, M representing metallic elements other than iron. Ferrites are complex materials because they combine two complex attributes: ceramic microstructure and ferromagnetism. Ceramic microstructure is formed as a result of physical-chemical processes such as solid-state sintering.

Commercially prepared magnetic ceramics are used in a variety of permanent magnet, transformer, telecommunications and information-recording applications. Many new and exciting applications, theories and preparation technologies are still under development. Three basic classes of ferrites are made into magnetic ceramic products: spinels, hexagonal ferrites and garnets. Spinels have the formula $M(\mathrm{Fe}_2\mathrm{O}_4)$, where M is usually a divalent cation such as Mn^{2+}, Ni^{2+}, Co^{2+}, Zn^{2+}, Cu^{2+} or Mg^{2+}. Because spinels are often cubic in structure, with no preferred direction of magnetization, they are 'soft' magnetically. The hexagonal ferrites have the formula $M(\mathrm{Fe}_{12}\mathrm{O}_{19})$, where M is usually Ba, Sr or Pb. The hexagonal crystal structure is complex, with a unique c axis. This is the easy axis of magnetization in the basic structure. Because the direction of magnetization cannot be changed easily to another axis, hexagonal ferrites are referred to as 'hard'. Garnet ferrites have the structure of the silicate mineral garnet and the chemical formula $M_3(\mathrm{Fe}_5\mathrm{O}_{12})$, where M is yttrium or a rare-earth ion. The garnet structure has tetrahedral, octahedral and dodecahedral (12-coordinated) sites. The net ferrimagnetism is thus a complex result of antiparallel spin alignments among the three types of sites. Garnets are also magnetically 'hard'.

7.8.2.2.6.8. Microwave communication ceramics

The recent progress in microwave telecommunication, satellite broadcasting and intelligent transport systems (ITSs) has resulted in an increasing demand for dielectric resonators (DRs), which are low-loss ceramic pucks used mainly in wireless communication devices (Fig. 7.8.2). Dielectric ceramics are commercially important as enabling materials for resonators, filters and other components in microwave communication systems (Sebastian, 2008; Vanderah, 2002). These ceramics have revolutionized the microwave wireless communication industry by reducing the size and cost of filter, oscillator and antenna components. The key properties required for a DR are high quality factor (Q), high relative permittivity and near zero temperature coefficient of resonance frequency, which are difficult to achieve simultaneously in a single material. Cohen (1968) performed the first extensive theoretical and experimental evolution of DRs using rutile ceramics (TiO_2) as the first microwave filter. The real breakthrough occurred in early 1970s when the first temperature-stable, low-loss $\mathrm{BaTi_4O_9}$ ceramics were developed by Masse *et al.* (1971). Later, $\mathrm{Ba_2Ti_9O_{20}}$ with improved performance was reported by Bell Laboratories (Plourde *et al.*, 1975). Extensive theoretical and experimental work followed. However, still only a limited number of useful dielectric ceramic materials are available. Today only two ceramic materials are optimized for 900-MHz-based station applications, one based on $\mathrm{ZrTiO_4}$ and the other based on $\mathrm{CaTiO_3}$–$\mathrm{NdAlO_3}$. For 2 GHz and higher, only the tantalite $\mathrm{Ba_3ZnTa_2O_8}$ has the required low dielectric loss. Many recent studies have been centred around pervoskites and pervoskite-like materials. The electronics industry is still searching for affordable new materials.

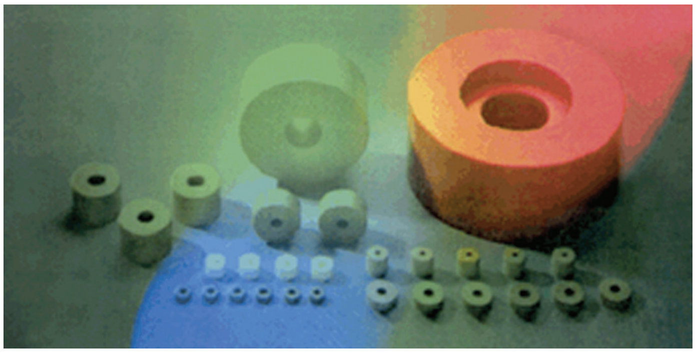

Figure 7.8.2
Dielectric resonators used in cellular base stations to store and transmit signals to handheld devices such as cell phones (Vanderah, 2002). Reproduced with permission from TCI Ceramics/National Magnetics Group.

7.8.2.2.6.9. Piezoelectric ceramics

The word piezoelectricity is derived from Greek, and means electricity resulting from pressure. Piezoelectricity was discovered in 1880 by French physicists Jacques and Pierre Curie (Curie & Curie, 1880). The piezoelectric effect is a reversible process and is understood as the linear electromechanical interaction between the mechanical and the electrical state in crystalline materials with no inversion symmetry. It has useful applications such as in the production and detection of sound, in the generation of high voltages, in electronic frequency generation, in microbalances, in ultrafine focusing of optical assemblies, and in fuel injector components.

The families of ceramics with pervoskite or tungsten-bronze structures that exhibit piezoelectricity include $\mathrm{BaTiO_3}$, $\mathrm{PbTiO_3}$, $\mathrm{Pb(Zr}_x\mathrm{Ti}_{1-x})\mathrm{O}_3$, $0 \le x \le 1$ (PZT), $\mathrm{KNbO_3}$, $\mathrm{LiNbO_3}$, $\mathrm{LiTaO_3}$, $\mathrm{Na_2WO_3}$, $\mathrm{Ba_2NaNb_5O_5}$, $\mathrm{Pb_2KNb_5O_{15}}$ and ZnO. More recently, there is growing concern regarding the toxicity of lead-containing devices. As a result, there is intense interest in non-lead-containing materials (Saito *et al.*, 2004), including $\mathrm{(K,Na)NbO_3}$ (with properties close to that of PZT), $\mathrm{BiFeO_3}$, $\mathrm{NaNbO_3}$, $\mathrm{Ba_4Ti_3O_{12}}$ and $\mathrm{Na_{0.5}Bi_{0.5}TiO_3}$.

7.8.2.2.6.10. Photovoltaics (solar cells)

The earth benefits from an impressive 125 000 TW of incident solar energy (Kippelen, 2007). While the future energy needs of the planet will likely be met with a combination of technologies, many believe that solar [in the form of photovoltaic (PV) cells] is the most efficient renewable energy source with the capacity to make a significant impact on global energy production. As a result, the race is on to push the performance of PV cells to a level where the total cost of the electricity generated is cheaper than that from carbon-based sources.

Most of the effort in PV cell fabrication is centred on thin-film deposition, rather than using wafer-based modules, as it uses less material and is much faster and simpler than the complex process of slicing, dicing and placing of silicon wafers. Manufacturers continue to experiment with various materials and refinements of the thin-film deposition process for solar cells based on silicon and other materials. The direct band-gap ceramic semiconductors cadmium telluride (CdTe), copper indium diselenide ($CuInSe_2$) and copper indium gallium diselenide alloy $Cu(InGa)Se_2$ have high optical absorption coefficients ($>10^5$ cm^{-1}) and are now emerging as the popular materials for the photoabsorption layer in thin-film photovoltaic (TFPV) cells. More than a dozen companies worldwide are already actively producing these cells.

7.8.2.2.6.11. Thermoelectric ceramics

The thermoelectric effect is the direct conversion of temperature differences to electric voltage and *vice versa*. A thermoelectric device creates a voltage when there is a different temperature on each side. Conversely, when a voltage is applied to it, it creates a temperature difference. These phenomena are known more specifically as the Seebeck effect (converting temperature difference to current), the Peltier effect (converting current to temperature difference) and the Thomson effect (conductor heating/cooling). The efficiency and performance of thermoelectric energy conversion or cooling is related to the dimensionless figure of merit (ZT) of the thermoelectric (TE) materials, given by $ZT = S^2\sigma T/\kappa$, where T is the absolute mean temperature, S is the Seebeck coefficient or thermoelectric power, σ is the electrical conductivity and κ is the thermal conductivity. Optimization of ZT is not a straightforward process because S, σ and κ are interrelated. Recent reports that relatively high ZT values (>1) are possible in both thin-film and bulk forms have revitalized interest in thermoelectric materials development (Tritt, 1996).

The stability of thermoelectric oxides at high temperature, their nontoxicity and their high oxidation resistance have made them highly relevant to waste-heat conversion applications. The low-dimensional cobaltates that include $NaCoO_x$, $Ca_2Co_3O_6$ and $Ca_3Co_4O_9$ (Shikano & Funahashi, 2003) exhibit the coexistence of large Seebeck coefficients and relatively low thermal conductivity. Consequently, considerable research has been conducted on thermoelectric oxides. Other examples being studied are $LaCoO_3$, $SrTiO_3$, Nb-doped $SrTiO_3$, $Zn_{0.98}M_{0.02}O$ (M = Ga, In, Al), the modulated layered cobalt oxides $Bi_2M_3Co_2O_8$ (M = Sr, Ca and Ba) and the Ruddleson–Popper phase $(SrTiO_3)_n(SrO)_m$ (Rowe, 2006). Research on thermoelectric oxide materials is ongoing, particularly in the nanostructured materials regime where simultaneous control of both the electric and phonon systems is important (Rowe, 2006).

7.8.2.2.6.12. Ceramic sensors

A sensor is a 'sensor element' including its physical packaging and external connections. A sensor element is a material or 'the fundamental transduction mechanism' that converts one form of energy into another. Some sensors may incorporate more than one sensor element (Buchanan, 1986; Smith, 2005). The terms sensor and transducer are often used synonymously. A transducer is a device that provides a usable output in response to a specified measurand, in which the measurand can be any physical, chemical or biological property or condition to be measured, and a usable output can be an optical, electronic or mechanical signal. Each sensor is different depending on its application. Oxide ceramics exhibit a number of special characteristics that make them particularly attractive for sensor applications. These include sensitivity to oxidizing and reducing gases or to temperature excursions. The following is a brief description of four types of sensors.

Physical sensors are materials that change their state and properties in a particular way while they are sensing physical changes. These includes changes in temperature, strain, force, pressure, displacement, position, velocity, acceleration, optical radiation, sound, flow rate, viscosity and electromagnetic fields. Three types of materials are in use: piezoelectric polymers, ceramics and composites. Piezoelectric sensors (quartz, ZnO, non-lead-containing piezoelectric materials) are used for applications including medical, aerospace, nuclear instrumentation and the automotive industry. Chemical sensors are used for the following measurands: ion concentration, chemical composition, rate of reactions, reduction–oxidation potentials and gas concentration. Application areas include the chemical-processing and fossil-fuel industries, and various environmental applications. Biosensors are sensors that respond to biologically produced substances, for example glucose, hormones and enzymes. Biological sensors are mainly of interest in health care and form an emerging trend in the diagnostic technology. Finally, thermistors, or thermally sensitive resistors, are electric resistors whose resistive properties vary with temperature. They are made of materials that have high temperature coefficients of resistance, where the temperature coefficient of resistance (TCR) of a material quantifies its change in resistance with temperature. Negative TCR, or NTCR, ceramics are materials whose electric resistance decreases as temperatures rise. These ceramics are usually spinel-based oxides of iron, cobalt and manganese that exhibit small-polaron conduction. NTCR thermistors are used as temperature sensors and as temperature-compensation resistors.

7.8.2.2.6.13. Ceramic varistors

A varistor is an electronic component with a 'diode-like' nonlinear current–voltage characteristic. The function of a varistor is to conduct significantly increased current when the voltage is excessive. Therefore, varistors are often used to protect circuits against excessive transient voltages by incorporating them into the circuit: when triggered, they will shunt the current created by the high voltage away from sensitive components.

Varistors are also known as voltage-dependent resistors. The most common type of varistor is the metal-oxide varistor (MOV). This contains a ceramic mass of zinc-oxide grains, in a matrix of other metal oxides (such as small amounts of bismuth, cobalt or manganese) sandwiched between two metal electrodes. The boundary between each grain and its neighbour forms a diode junction, which allows current to flow in one direction. The mass of randomly oriented grains is electrically equivalent to a network of back-to-back diode pairs, each pair in parallel with many other pairs. When a small or moderate voltage is applied across the electrodes, only a small current flows, which is caused by reverse leakage through the diode junctions.

7.8.2.2.7. *Optical ceramics or photonic ceramics*

Wide band-gap ceramic materials are transparent to light in the range of wavelengths near to or including the visible range, provided that they do not contain inhomogeneities, which can serve as scattering sites and which will reduce the transparency. Many ceramic materials, including single crystals, pore-free glasses and even pore-free single-phase polycrystalline ceramics, have found use as optically transparent materials in various forms from bulk solid-state components to high-surface-area forms such as thin films, coatings and fibres. The word 'photonics' is used to describe the collective optical properties of materials and the application of these properties to make useful devices. Such devices have found widespread use in the electro-optical field including: optical fibres for guided lightwave transmission, optical switches, laser amplifiers and lenses, hosts for solid-state lasers and optical window materials for gas lasers, and infrared (IR) heat-seeking devices for missile guidance systems and IR night vision.

Examples of optical materials can be divided into three areas, namely, transparent windows (Al_2O_3, MgF_2, ZnSe), mirror substrates (SiC and glass-ceramic Zerodur), and electro-optic materials (KH_2PO_4, $Ba_2NaNb_5O_{15}$ and $LiNbO_6$) (Musikant, 1991; Jones & Berard, 1993). Transparent polycrystalline electro-optic materials, such as PLZT ceramics, can be used for a variety of devices. An important photonic application of glass occurs in optical fibres that can carry a beam of light from one point to another without appreciable attenuation due either to absorption or to escape from the sides of the fibre. Lasers are devices capable of producing highly energetic beams of light having all waves in phase and of the same wavelength. These lasers are often made from specially doped glasses or single crystals such as Cr-doped Al_2O_3 (ruby lasers) or Nd-doped yttrium aluminium garnet (YAG lasers).

7.8.2.2.8. *Refractory ceramics*

Refractories are ceramic products manufactured for the purpose of withstanding the high-temperature corrosive conditions encountered in industrial furnaces and processing vessels. Refractories must have high melting temperatures, great strength, and resistance to heat, chemical attack and abrasive environments. Therefore refractories can be used in a furnace lining or other locations where they will be exposed to severe heating (Jones & Berard, 1993; McColm, 1983; Weimer, 1977).

Some examples of refractory materials are fireclay, silica, magnesite, chrome-magnesite, sintered alumina, beryllia, refractory cement, refractory coating and refractory concrete. Many of the metal carbide, nitride, silicide and boride materials are of considerable interest for structural and electronics applications because of their unique properties, including wear resistance (*e.g.* WC), high-temperature oxidation resistance (*e.g.* SiC and Si_3N_4), high hardness (*e.g.* B_4C), high toughness (*e.g.* Si_3N_4), resistance to attack by molten metals and glasses (*e.g.*TiB_2, BN and AlN) and unique combinations of properties such as high thermal conductivity/electrical insulation (*e.g.* AlN). Their structural applications have included heat-engine components, wear components, armour, corrosion-resistant crucibles (TiN_x, ZrN_x, HfN_x), cores of fuel elements of nuclear reactors (UC_x, ThC_x), high-temperature soldering (Mo_2C), protective coatings for rocket components, gas turbine blades (TiC_x) and high-temperature burners.

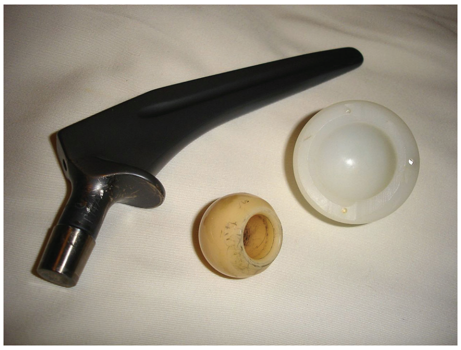

Figure 7.8.3
A titanium hip prosthesis, with a ceramic head and polyethylene acetabular cup for bone replacement/implant applications.

7.8.2.2.9. *Medical and bioceramics*

Today, advanced ceramics also find their way into the fields of medical and bioengineering. Prior to 1925, the materials used in implant surgery were primarily relatively pure metals. The 1930s marked the beginning of an era of better surgical techniques and also the first use of alloys such as Vitallium (Jones & Berard, 1993). In 1969 Hench (1991) and others discovered that various kinds of glasses and ceramics could bond to living bone (Hench, 1991; Yamamuro *et al.*, 1990). The final product was a new material which Hench called bioglass. This work inspired a new field called bioceramics.

Bioceramics and bioglasses are ceramic materials that are biocompatible. They are not the same as porcelain-type ceramic materials, but are closely related to either the body's own materials, or are extremely durable metal oxides that are inert in the body; at the other extreme are resorbable materials, which are eventually replaced by the materials which they were used to repair. Bioinert materials are non-toxic and non-inflammatory. These materials must be long lasting, resistant to structural failure and corrosion resistant; additionally, they must have a low Young's modulus to help prevent cracking of the material. Bioceramics are used in many types of medical procedures. There are in general two popular areas: the first area includes bone replacement/implants (Fig. 7.8.3 shows a titanium hip prosthesis, with a ceramic head and polyethylene acetabular cup), artificial joints (joint replacements are commonly coated with bioceramic materials to reduce wear and inflammatory response) and tooth implants. Common materials being used are Al_2O_3 (for implantation, wear surfaces) and hydroxylapatite (for bone material). A second area of application is as separators for biological components. Other examples of medical uses for bioceramics are in pacemakers, kidney dialysis machines and respirators (Kassinger, 2003). One potential use for bioceramics includes the treatment of cancer through the dispersion of drug-infused nanoparticles.

7.8.3. Applications of powder X-ray diffraction to the studies of ceramics

Applications of powder diffraction (using laboratory or synchrotron X-rays, neutrons or electrons) to the studies of selected categories of ceramics as listed above will be described according to the most relevant topics as listed in the three areas below. The general categories of subjects that are related to using powder diffraction in all categories of ceramics are:

(1) Phase characterization [phase identification; quantitative analysis; phase equilibria, crystal chemistry and crystal-

lography; phase evolution (films and bulk); phase transformation];

(2) Structure and microstructures (crystal structure; crystallite size; defects; residual stress measurements of ceramic components; texture/preferred orientation; thickness and roughness of ceramic films);

(3) Processing and performance (sintering/densification/grain growth; reaction mechanisms/sequence; kinetics and reaction rate; transformation toughening; degradation/corrosion of ceramics; crystallization of glass ceramics; microstructure evolution; and bulk modulus/compressibility determinations).

7.8.3.1. *Phase characterization*

7.8.3.1.1. *Phase identification*

Powder diffraction is a nondestructive technique that provides detailed information ranging from the phase identity to the detailed atomic structure of crystalline substances. It is a powerful tool in phase identification at various stages of ceramic manufacture, starting with the raw materials used to make ceramics, to advanced ceramic products. Many useful sources of information about diffraction theory and interpretation applied specifically to powder methods are available (Klug & Alexander, 1974; Cullity, 1978; Bish & Post, 1989; Zevin & Kimmel, 1995; Moore & Reynolds, 1997; Jenkins & Snyder, 1996; Cullity & Stock, 2001; Pecharsky & Zavalij, 2008; Clearfield *et al.*, 2008; Dinnebier & Billinge, 2008; Mittemeijer & Welzel, 2013). For most samples, the aim of the analysis is to identify the crystalline phases present. Even when other information is sought (*e.g.*, unit-cell calculations, quantitative determinations *etc.*), identification of the phase(s) is usually the first step in the study of both bulk and thin-film materials. Qualitative analysis involves the identification of a phase or phases in a specimen by comparison with reference patterns from available databases, and relative estimation of proportions of different phases in multiphase specimens by comparing peak intensities attributed to the identified phases. For example, the Powder Diffraction File (Fawcett *et al.*, 2017) consists of a very large set of reference patterns (with 398 726 inorganic data sets and 526 126 organic data sets in 2017) provided by the International Centre for Diffraction Data (ICDD, formerly known as JCPDS).

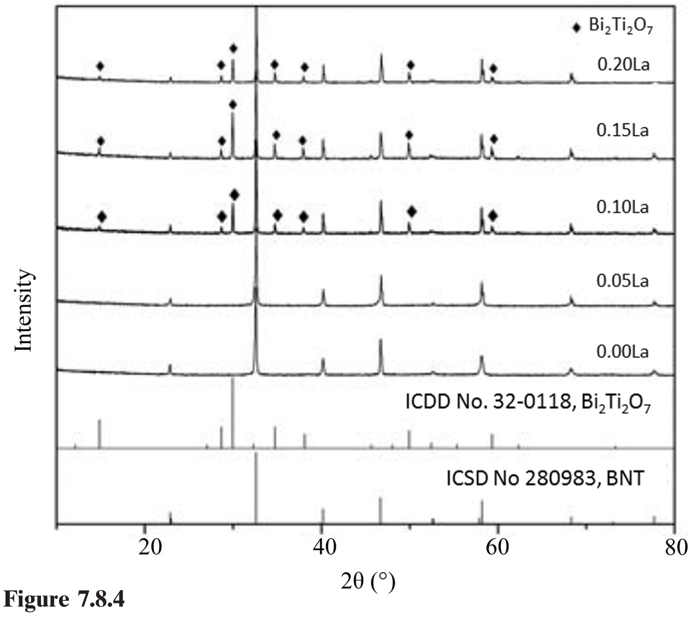

Figure 7.8.4
X-ray powder diffraction patterns of $(Bi_{0.5}Na_{0.5})_{1-1.5x}La_xTiO_3$ ceramics where x = 0, 0.05, 0.10, 0.15 and 0.20 (Eaksuwanchai *et al.*, 2013). Reprinted by permission of the publisher (Taylor & Francis Ltd).

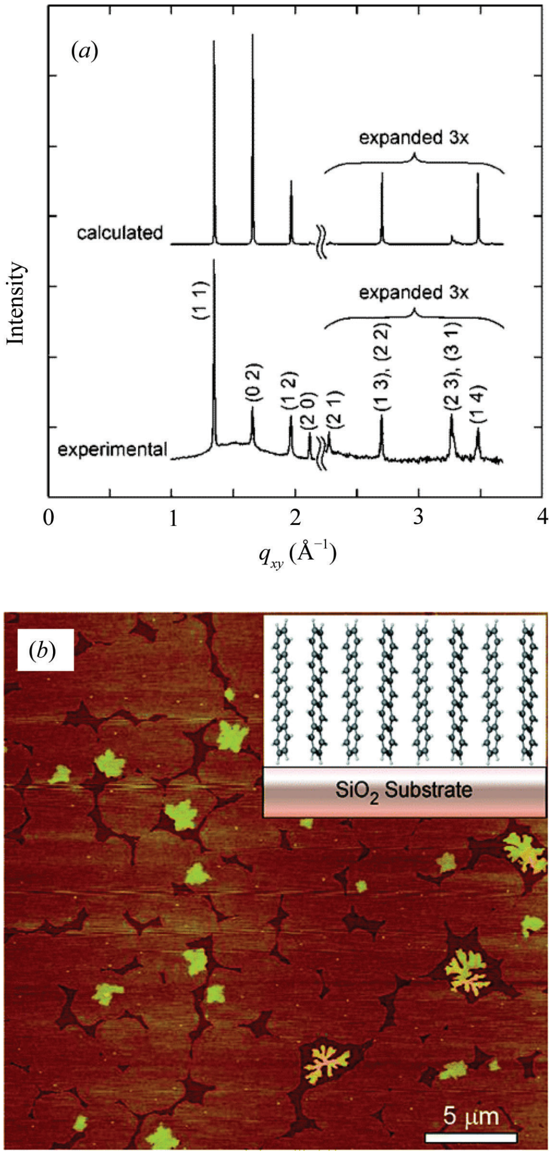

Figure 7.8.5
(*a*) A GIXD pattern (bottom) for a pentacene monolayer and a diffraction pattern (top) calculated for an energy-minimized crystal structure model based on the GIXD lattice parameters and the (001) layer motif of bulk pentacene as the starting point. (*b*) An atomic force microscopy (AFM) image recorded using a tapping mode and acquired in air under ambient conditions of monolayer-thick pentacene domains on a 3000 Å thick α-quartz film. Inset: The pentacene monolayer structure based on GIXD. Reprinted with permission from Fritz *et al.* (2004). Copyright (2004) American Chemical Society.

Often X-ray diffraction is used to characterize series of ceramic solid solutions to determine the homogeneity range of a single phase and to identify the presence of other impurity phases. As an example, $(Bi_{0.5}Na_{0.5})_{1-1.5x}La_xTiO_3$ (BNT) ceramics where x = 0, 0.05, 0.10, 0.15 and 0.20 were studied by Eaksuwanchai *et al.* (2012. These materials have potential applications as oxide thermoelectric compounds to directly convert heat to electricity or *vice versa*. Phase identification of these ceramics was carried out using the powder X-ray diffraction (XRD) technique (Fig. 7.8.4). The XRD patterns indicated that for La concentrations $x > 0.05$ all ceramic compositions contained a rhombohedral (or pseudo-cubic) BNT-based phase with formation of a secondary phase. Both the density and grain size of the ceramics decreased with increasing La content, and La-doped BNT ceramics became more electrically conducting despite the presence of a second phase in the matrix.

For phase identification of thin-film materials, the grazing-incidence X-ray and neutron diffraction (GID, GIXD, GIND) method allows the phase composition of a fabricated material to be probed as a function of depth from a surface (Tanner *et al.*, 2004). In brief, irradiation of a sample with an incident beam which is parallel and at a very low angle to the surface creates diffraction from the crystallites concentrated towards the surface. The depth of X-ray penetration is correlated with the incident angle; typical depth data can range from ~20 nm to approximately 10 µm. In other words, Bragg reflections only arise from the surface structure. An advantage of the grazing-incidence technique is that the electric field at the critical angle is amplified locally by a factor of four, making the signal stronger. A disadvantage is the limited in-plane spatial resolution. Typical applications for ceramic systems include studying changes in crystal structure influenced by deposition on top of a substrate, *e.g.* changes in the crystal form of TiO_2 (rutile *versus* anatase) towards the interface with metal substrates; and general characterization of ceramic layers deposited on a substrate with respect to phase identity, crystallite size and preferred orientation.

Grazing-incidence X-ray diffraction was used by Fritz *et al.* (2004) to show that a pentacene monolayer, grown on an amorphous ceramic α-quartz substrate [commonly used as a dielectric layer in organic thin-film transistors (OTFTs)], is crystalline. A preliminary energy-minimized model of the monolayer, based on the GIXD data, reveals that the pentacene molecules adopt a herringbone arrangement with their long axes tilted slightly from the substrate normal (Fig. 7.8.5). Although this arrangement resembles the general packing features of the (001) layer in single crystals of bulk pentacene, the monolayer lattice parameters and crystal structure differ from those of the bulk. Because carrier transport in pentacene OTFTs is likely to occur in the semiconductor layers near the dielectric interface, the discovery of a crystalline monolayer structure on amorphous SiO_2 has important implications for transport in OTFTs.

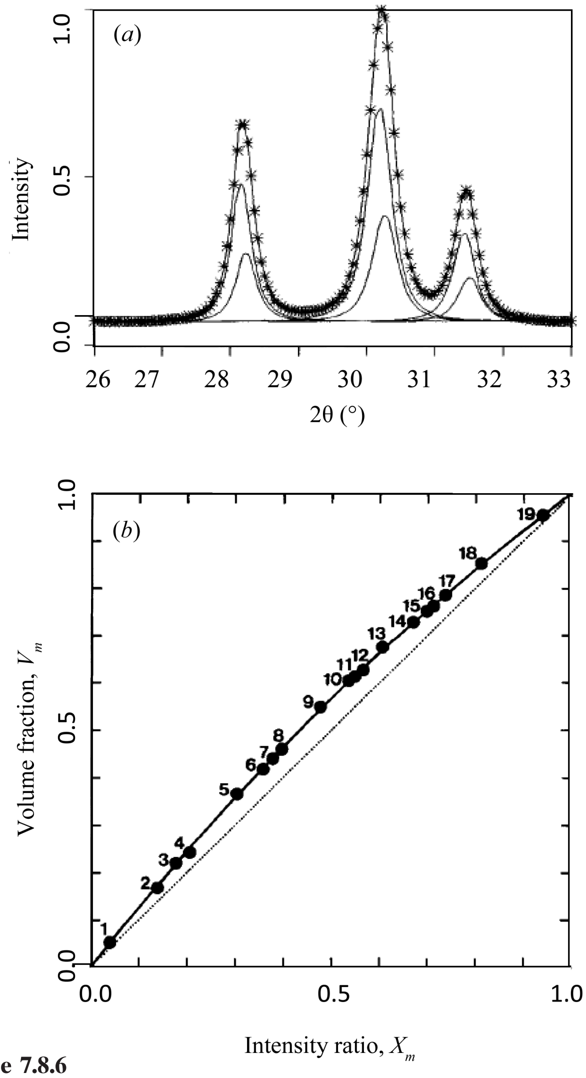

Figure 7.8.6
(*a*) Observed (*) and calculated profile intensities of monoclinic ($\bar{1}11$) (2θ = 28.2°) and (111) (2θ = 31.5°) and tetragonal (101) (2θ = 30.2°) reflections of sample No. 9. The $K\alpha$ and $K\alpha_1$ components of each reflection are also shown. (*b*) Volume fraction of monoclinic ZrO_z, V_m, *versus* intensity ratio, X_m, for the 19 samples. The intensity ratio (the polymorph method) underestimates the volume fraction of monoclinic ZrO_2. Reprinted with permission from Toraya *et al.* (1984). Copyright (1984) John Wiley and Sons.

7.8.3.1.2. *Quantitative analysis of phases*

Quantitative analysis using diffraction data usually refers to the determination of amounts of different phases in multiphase samples (see Chapter 3.9). All quantitative analysis requires precise and accurate determination of the peak positions and intensities of the diffraction pattern. Two general methods, the intensity-ratio method and the internal-standard method, have been used frequently for quantitative analysis. Rietveld refinement (Rietveld, 1969) also allows sophisticated quantitative treatments of phases present in a ceramic sample (Larson & Von Dreele, 2004; Rodríguez-Carvajal, 1993; Coelho, 2005). Since diffraction data are generally dependent on the systematics of the diffractometer and its data-collection system, application of quantitative methods that involve ratios of peak intensities requires careful calibration with well characterized standards.

As ZrO_2 is an important ceramic material, various quantitative analyses of this phase have been reported. In the classic paper by Toraya *et al.* (1984), a nonlinear calibration curve for volume fraction *versus* integrated intensity ratio was obtained for the monoclinic–tetragonal system by using X-ray powder pattern-fitting and pattern-decomposition techniques on 19 samples. They found that the pattern-decomposition technique can resolve the overlapping reflections into individual ones by a procedure similar to that of the pattern-fitting technique by disregarding the structure model (Parrish *et al.*, 1976). This technique was used to measure the integrated intensities of partially overlapping monoclinic ($\bar{1}11$) and (111) and tetragonal (101) reflections. Fig. 7.8.6(*a*) shows the pattern decomposition for one of the samples that exhibits the most striking partial overlap. The volume fractions of monoclinic ZrO_2 and intensity ratio X_m for the 19 samples are plotted in Fig. 7.8.6(*b*). Toraya *et al.* found that intensity-ratio method (Garvie & Nicholson, 1972) underestimates volume fraction of monoclinic ZrO_2. To suppress the error in X_m, the pattern-decomposition technique should be used. Schmid (1987) also obtained nonlinear calibration curves of weight fraction *versus* integrated intensity ratio for polymorphic mixtures of ZrO_2 by X-ray diffraction. Elshazly *et al.* (2011), by applying the modified Garvie and Nicholson method, were able to determine the monoclinic content of yttrium tetragonal zirconia biomaterials formed during a low-temperature aging process.

7.8.3.1.3. *Phase equilibria, crystal chemistry and crystallography*

Phase diagrams are critical research tools for many scientific disciplines including materials science, ceramics, geology, physics, metallurgy, chemical engineering and chemistry. Phase diagrams contain important information for the development of new materials, control of structure and composition of critical phases, and improvement of properties of technologically important materials. These diagrams often can be thought as 'road maps' for processing, as they provide the theoretical basis for the synthesis of materials. Applications of phase diagrams range from preparation of high-quality single crystals and single-phase materials to controlled precipitation of second phases and formation of melts.

As phase diagrams provide critical information for the scientific community, there are various world centres that are responsible for the compilation of these diagrams. For over 60 years, the American Ceramic Society (ACerS), in collaboration with NIST, has evaluated and published the *Phase Diagrams for Ceramists* series of compilations. Since the cooperative program between NIST and ACerS was formalized in 1982, computerization of data was established as a major goal to modernize the book products. More than 27 600 entries have been published in the CD-ROM product and in 21 book volumes. The continuous growth rate is about 500 new commentaries (with 1000 phase diagrams) per year. These products have provided high-quality phase-equilibrium data of ceramic phases to the technical community (ACerS–NIST Phase Equilibria Diagrams, 2018; https://www.nist.gov/srd/nist-standard-reference-database-31).

The preparation of an equilibrium phase diagram is a long process that requires a committed effort using a combination of methods (Carter, 1978; Roth & Vanderah, 2004). For example, to construct subsolidus phase diagrams, a number of compositions are prepared in the region of interest, followed by equilibration and determination of the phase assemblages present. Homogeneity regions and tie-lines connecting phases in equilibrium are determined by studying the evolution of these compositions as a function of time, temperature and pressure. The experimental methods for determining phase diagrams are generally divided into two types: static and dynamic. In the static methods, the temperature of the sample is held constant until equilibrium is attained. Quenching studies in combination with powder X-ray diffraction and petrographic microscopy for phase identification are essential for obtaining subsolidus phase diagrams. Dynamic techniques, including differential thermal analysis (DTA) and thermogravimetric analysis (TGA), are needed to obtain an indication of phase transitions, reactions and associated loss of volatiles such as oxygen. Electron-beam-based methods such as transmission electron microscopy (TEM) and scanning electron microscopy (SEM) are used to further define the microstructures of the experimental products, particularly of the crystalline phases. Quantitative micro-beam analytical techniques, including energy-dispersive X-ray analysis (EDS) or wavelength-dispersive methods (WDS), are used for the determination of the compositions of both the crystalline phases and the quenched liquid.

7.8.3.1.4. *Phase evolution*

As nanoceramics find important applications in many fields of modern electronics including medical appliances, there is an increasing need to understand the process of phase evolution of these materials. Quite often, combined use of several techniques such as *in situ* powder diffraction, the pair distribution function (PDF) approach (Billinge, 2004; see also Chapter 5.7), TEM and modelling has proved to be useful for understanding phase formation during crystallization as well as the local structure.

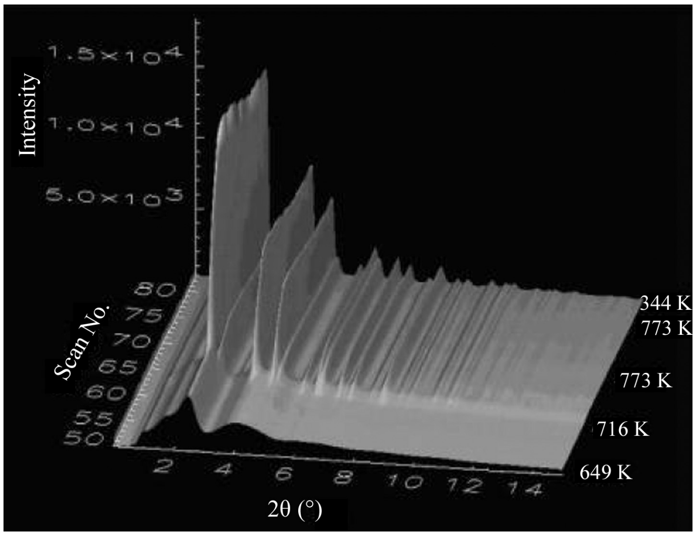

Figure 7.8.7
In situ XRD patterns demonstrating the phase transition from amorphous to cubic ZrO_2 in a reducing atmosphere. Reprinted with permission from Zhang *et al.* (2007). Copyright (2007) American Chemical Society.

High-temperature X-ray diffraction (HTXRD) is very useful for *in situ* studies to characterize phase evolution as a function of temperature. Pair distribution function (PDF) analysis and combined reverse Monte Carlo (RMC) simulation can also be used to study the details of local structure during the phase-evolution process. As an example, the amorphous-to-cubic crystallization of nano-ZrO_2 in a reducing environment was studied by *in situ* synchrotron X-ray diffraction (Zhang *et al.*, 2007). Rietveld analysis was performed to study the changes in crystallite size and lattice parameters as the cubic phase emerged. Fig. 7.8.7 illustrates *in situ* XRD patterns demonstrating the phase evolution from amorphous to cubic ZrO_2 in a reducing atmosphere. The PDF was obtained from the Fourier transformation of the normalized XRD patterns. A reverse Monte Carlo simulation was used to provide details of the local structure during the crystallization process as well as to calculate partial PDFs for Zr–Zr and Zr–O during the crystallization. It was found that the number of next-nearest neighbours of Zr remains at 12, whereas the number of O atoms as nearest neighbours of Zr increases from 6.7 to 7.3 as the material evolves from an amorphous into a cubic structure, suggesting the persistence of a high concentration of oxygen vacancies. These simulated atomic structures show that the local structure of the amorphous phase bears a resemblance to the short-range arrangement of cubic ZrO_2, consistent with the results of X-ray absorption near edge spectroscopy (XANES) at the Zr $L_{\rm II}$ and $L_{\rm III}$ edges. It was concluded that the amorphous-to-crystalline phase evolution is affected by the environment. Under an oxidizing environment, the amorphous phase crystallizes directly to tetragonal and subsequently to monoclinic zirconia.

In another example, phase evolution during firing of ceramic bodies from three different marine sediments was investigated as a function of temperature (Romero *et al.*, 2009). The mineralogical evolution was examined by XRD and revealed that quartz, which is a main crystalline phase in the original marine sediments, remains as a main phase in the sintered bodies in all three sediments. A glassy phase and new crystalline phases appear as result of different chemical reactions during firing. For

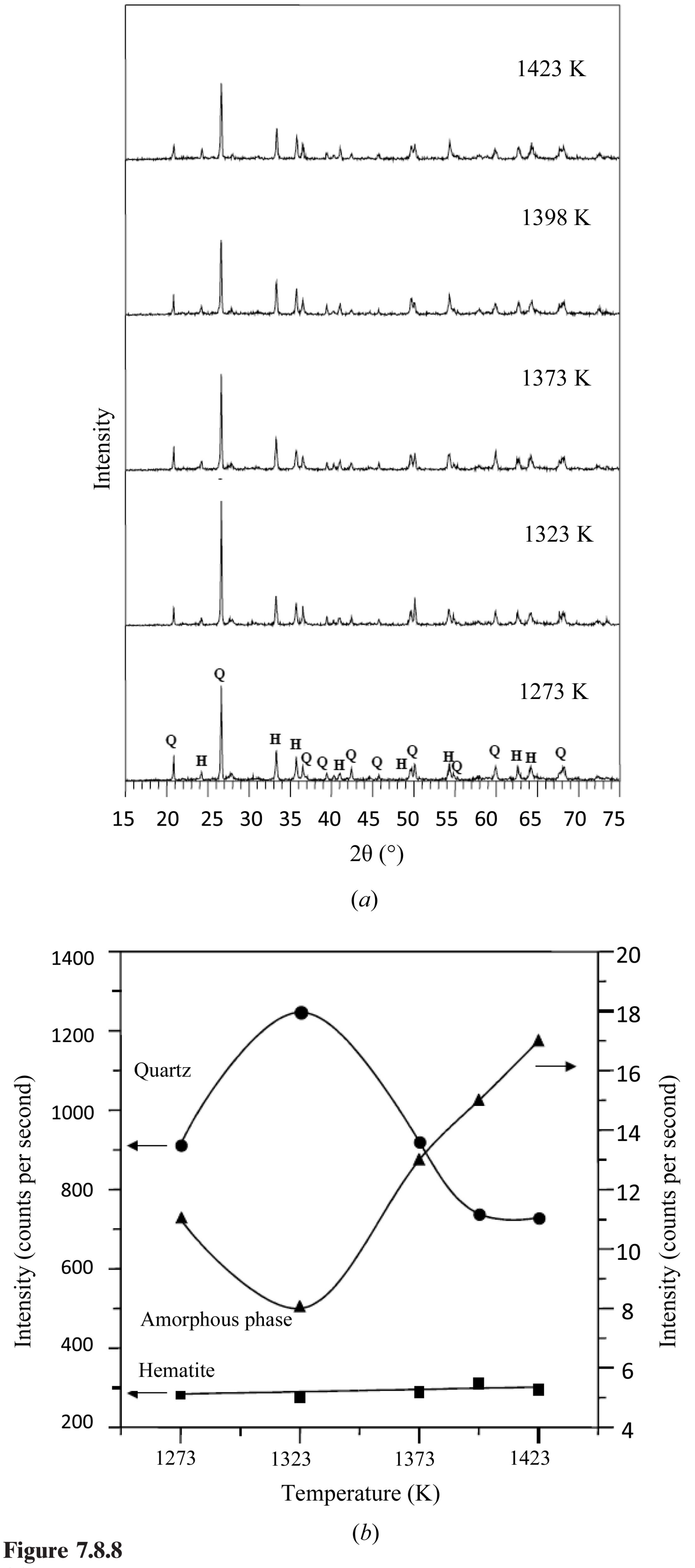

(*a*)

(*b*)

Figure 7.8.8

(*a*) XRD plots of astilleros sediment heat-treated in the range 1273–1423 K (Q quartz; H hematite). (*b*) Intensities of the (100) quartz reflection, (104) hematite reflection and amorphous phase as function of firing temperature in sintered Astilleros sediments. Reprinted with permission from Romero *et al.* (2009). Copyright (2009) Elsevier.

example, Fig. 7.8.8(*a*) shows the XRD pattern of one of the sediments (astilleros) heat-treated in the range 1273–1423 K. Fig. 7.8.8(*b*) plots the change in the amorphous phase by considering the background intensity at the position of the (100) quartz reflection. Although the amount of quartz undergoes a slight increase at the beginning of sintering process, it tends to decrease with heating temperature. The glassy phase shows an inverse behaviour. Increasing the sintering temperature gives rise to a partial dissolution of quartz grains and therefore the amount of glassy phase increases. Scanning electron microscopy (SEM) showed a homogeneous microstructure composed of pores, crystals and a ceramic matrix. Energy X-ray dispersive spectroscopy (EDS) analyses permitted differentiation of the crystalline phases previously identified by XRD from minor phases, which were not detected in the X-ray diffraction.

7.8.3.1.5. *Phase transformation*

The physical properties of technological ceramic materials are strongly dependent on their composition as well as their microstructure. The most efficient way of obtaining the desirable microstructure is *via* accurate control of phase transformations in these solids. The structure resulting from a solid-state phase transformation depends intimately on the crystallographic relationship between the Bravais lattices of the initial and product phases, on the elastic moduli of the separate phases, on the kinetics (or rate) of the transformation and on the processing environment.

Broadly speaking, a phase transition is the transformation of a thermodynamic system from one phase or state of matter to another. In solid-state processes, there are several different types of phase transformation. Multicomponent systems may not only involve a reorientation of the crystal lattice under consideration, but also some degree of atomic diffusion from the parent phase to the final sintered product. One example would be the transition from iron(II) oxide to iron(III) oxide. The formation of the product phase would be limited by the rate of diffusion of O atoms through the surface of the parent FeO layer. Alternatively, there are many phase transformations that are not limited by diffusion, but result simply from some form of thermomechanical instability of the crystal lattice, and may require a diffusionless structural transition from one crystallographic lattice to another. These displacive or diffusionless transformations are called martensitic, and typically involve a thermally induced shear of the unit cell constituting the Bravais lattice in the parent phase. Other types of solid-state transformation include: spinodal decomposition, in which a single phase is cooled and separates into two different compositions of that same phase; the transition between the ferromagnetic and paramagnetic phases of magnetic materials at the Curie point; and order–disorder transitions.

An example in Fig. 7.8.9 shows that a biphasic mixture of $CeNbO_{4+\delta}$ produced using solid-state synthesis techniques has undergone transformation in air to the tetragonal modification at 915 K (Skinner & Kang, 2003). This transformation process involves an initial oxidation stage where the overall stoichiometry increases to $\delta \simeq 0.38$. On cooling of the sample a single $\delta \simeq 0.25$ phase is produced. On repeating the thermal treatment with the now single-phase material, it was evident that no transformation to the $\delta \simeq 0.38$ phase occurred, but the tetragonal modification was observed at the same temperature as previously. Furthermore, the high-temperature tetragonal modification was found to be stable above 1023 K with an oxygen excess concentration corresponding to a stoichiometry of $CeNbO_{4.21}$.

7.8.3.2. *Structure and microstructure*

7.8.3.2.1. *Crystal structure*

Powder diffraction using X-ray, neutron, synchrotron and electron diffraction techniques (or any combination of these) has played a central role in structural analysis. Important advances in

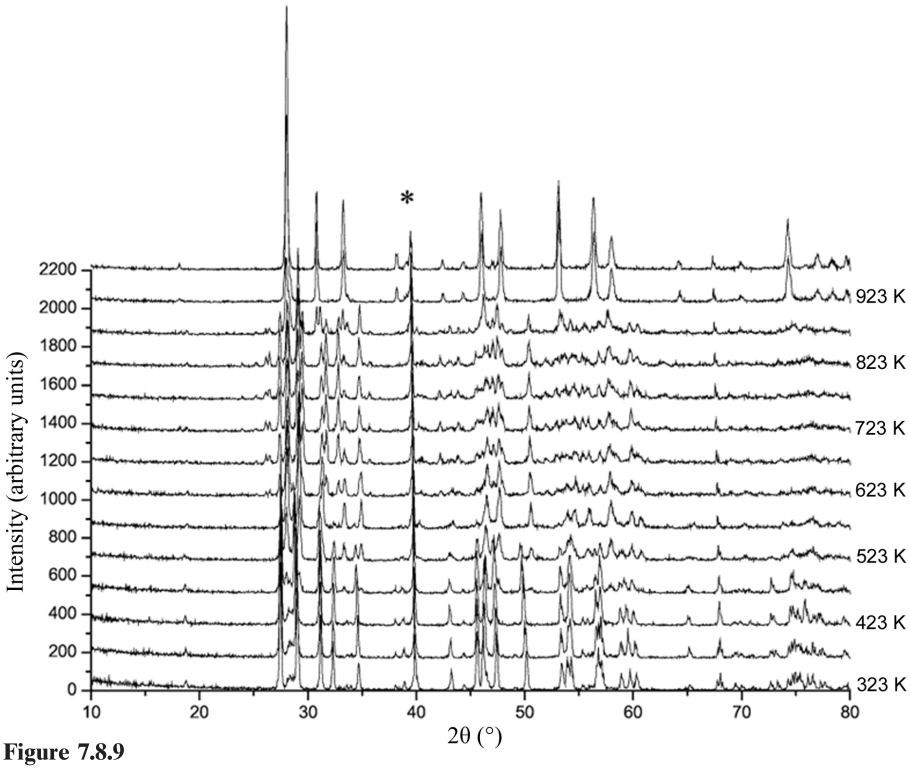

Figure 7.8.9
A series of HTXRD patterns for $CeNbO_{4+\delta}$. Reproduced from Skinner & Kang (2003). Copyright (2003) Elsevier Masson SAS. All rights reserved.

structural studies of ceramic materials of all classes were due to the renaissance of powder-diffraction techniques in the past several decades. By far the majority of these structures have been analysed using the Rietveld method (Rietveld, 1969; Larson & Von Dreele, 2004; Rodríguez-Carvajal, 1993; Coelho, 2005), a development which has greatly enhanced the power of powder-diffraction experiments. As the Rietveld technique is a refinement technique that requires a known structural model, the technique has its limitations. In recent years, tremendous development has been reported in terms of both the techniques and applications of *ab initio* powder structural solution (David *et al.*, 2002; see also Part 4 of this volume). The advancement of this technique is particularly important for ceramic materials in view of the fact that it is often difficult to grow single crystals of these. Even with the advances of synchrotron single-crystal diffraction, wherein one needs only crystals of micron size, the ability to solve the structure with an *ab initio* technique is extremely valuable. Other techniques that are useful for studying the local structure of a material include pair distribution function analysis (Billinge, 2004; Chapter 5.7) and extended X-ray absorption fine structure (EXAFS) (Koningsberger & Prins, 1988), which are important for local structure analysis for ceramic/nanoceramic materials.

Examples of successful ceramic structure studies using Rietveld refinement are abundant. In particular, using neutron diffraction, one can determine magnetic structures, where the magnetic spins also play a role in determining the overall structure (Vanderah *et al.*, 1997; Rodriguez *et al.*, 2005; Tachibana *et al.*, 2003). Vanderah *et al.* (1997) used low-temperature neutron powder diffraction to study the magnetic structure of a $Ba_4Fe_2Ti_{10}O_{27}$ phase which is a candidate microwave material for cellular communication applications. At room temperature this phase has an open-framework type structure with a monoclinic unit cell and space group *I*2/*m*. However, the magnetic structure exhibits $P12'$ symmetry and is illustrated in Fig. 7.8.10(*a*). The magnetic arrangement features two sets of collinear spins, (Fe1 + Fe4) and (*M*2 + *M*3) (where *M* denotes mixed Fe/Ti sites), with antiferromagnetic ordering within each set. The two sets correspond to the two types of polyhedra occupied by Fe^{3+}, as illustrated in Fig. 7.8.10(*b*). Segregation of the spins into two sets could be caused by the different types of exchange pathway permitted by the two polyhedral linkage patterns. The octahedral sites (*M*2 + *M*3) share edges, hence a pathway exists for direct Fe–Fe exchange in addition to 90° superexchange *via* shared oxygen sites. In contrast, the tetrahedral sites are vertex-linked, thus magnetic interactions occur *via* superexchange only.

Further examples of magnetic structure studies were illustrated by Rodriguez *et al.* (2005), using neutron powder diffraction. By combining Rietveld and pair distribution function analysis of the total neutron scattering data, they obtained the local and long-range structure of $La_{0.5}Ca_{0.5}MnO_3$ at room temperature and at 20 K. Tachibana *et al.* (2003) successfully used combined X-ray and neutron diffraction to study the influence of substitution ratio and oxygen partial pressure on the magnetic structure of an iron-substituted *Z*-type hexagonal barium ferrite, $Ba_3Co_{2-x}Fe_{24+x}O_{41}$ (x = 0–0.6).

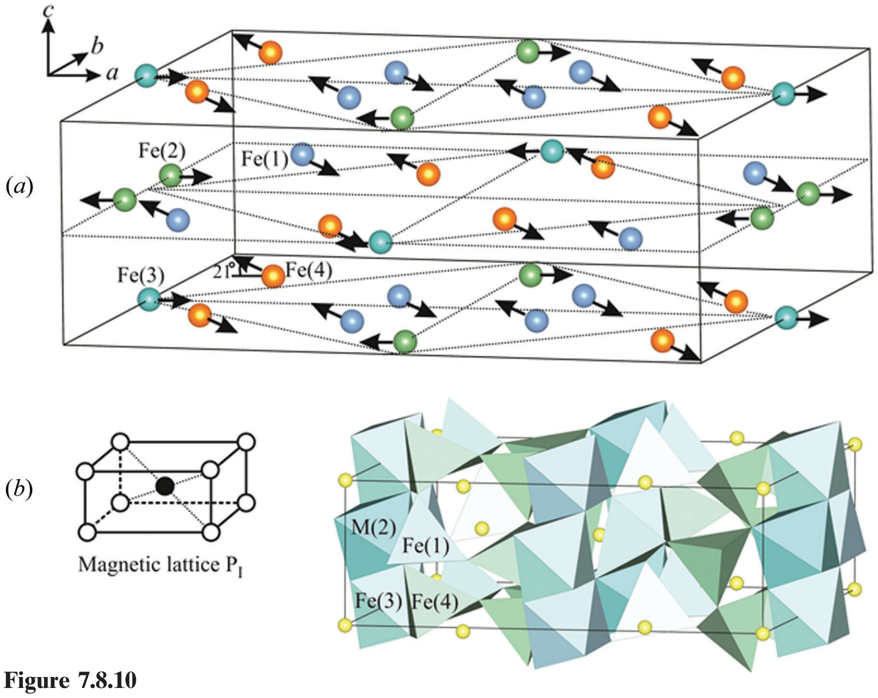

Figure 7.8.10
(*a*) Magnetic structure exhibiting $P12'$ symmetry for $Ba_4Fe_2Ti_{10}O_{27}$. (*b*) Two sets of magnetic ordering correspond to the two types of polyhedra occupied by Fe^{3+} in $Ba_4Fe_2Ti_{10}O_{27}$. Reproduced with permission from Vanderah *et al.* (1997). Copyright (1997) Elsevier.

7.8.3.2.2. *Crystallite size*

There are several diffraction approaches to studying the crystallite size of ceramic materials, ranging from traditional to new. Crystallite size is the size of a single crystal domain inside the particles or grains. A grain can be composed of several crystals. The size of the diffracting crystallites is often important in describing the reactivity of a ceramic material, because surface area increases with decreasing particle size (see Chapter 5.1). The Scherrer equation (Scherrer, 1918; Patterson, 1939) gives a first approximation of the value for this quantity:

$$L = K\lambda/(\beta\cos\theta),$$

where L is the mean crystallographic dimension in the same units as the wavelength λ, K is a constant near unity, β is the width of a peak at half height in radians and corrected for instrumental factors, and θ is the location of the peak. This equation was developed in 1918 to calculate nanocrystallite size (L) by X-ray diffraction of radiation of wavelength λ (nm) from measuring the full width at half maximum of peaks (β) in radians located at any 2θ in the pattern. The shape factor, K, can be 0.62–2.08 and is usually taken as about 0.89. However, the Scherrer equation may underestimate crystallite size, because it does not account for effects of atomic substitutions. A variety of factors can contribute to the width of a diffraction peak; besides crystallite size, the most important of these are inhomogeneous strain and instrumental effects. If all of these other contributions to the peak width were zero, then the peak width would be determined solely by the crystallite size and the Scherrer formula would apply. If the other contributions to the width are non-zero, then the crystallite size can be larger than that predicted by the Scherrer formula, with the 'extra' peak width coming from the other factors.

Monshi *et al.* (2012) provided a new approach to the use of the Scherrer equation, using a least-squares technique to minimize the sources of errors. The Scherrer equation shows systematically increased values of nanocrystallite size as d values decrease and 2θ values increase. Modified Scherrer equation plots of $\ln\beta$ against $\ln(1/\cos\theta)$ give the intercept of a least-squares regression line, $\ln = K\lambda/L$, from which a single value of L is obtained through all of the available peaks. They demonstrated this technique for a natural hydroxyapatite (HA) from bovine bone fired at 673, 873, 973, 1173 and 1373 K (Fig. 7.8.11) from which nanocrystallite sizes of 22.8, 35.5, 37.3 and 38.1 nm, respectively, were obtained; 1173 K was selected for biomaterials purposes. These results show that the modified Scherrer equation method is promising in nanomaterials applications and can distinguish between 37.3 and 38.1 nm by using the data from all of the available peaks.

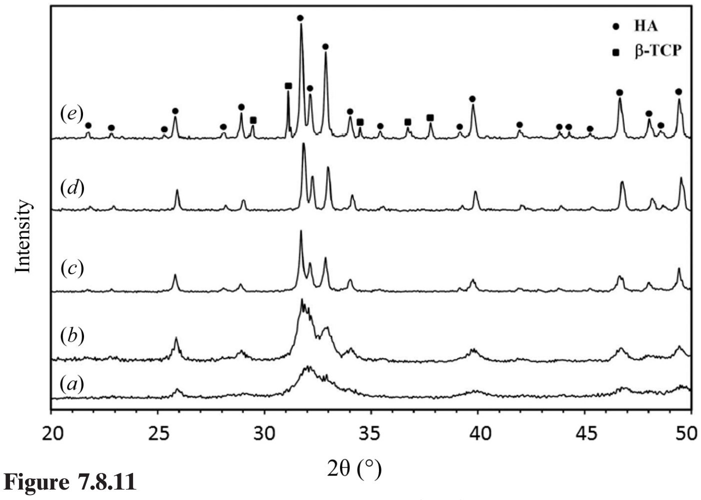

Figure 7.8.11
X-ray patterns of natural hydroxyapatite (HA) of bovine bone fired at (*a*) 673 K, (*b*) 873 K, (*c*) 973 K, (*d*) 1173 K and (*e*) 1373 K (Monshi *et al.*, 2012).

When the sample also contains residual strain, one can use the Williamson–Hall approach (Williamson & Hall, 1953) and the Warren–Averbach approach (Warren & Averbach, 1950). In recent years, the Rietveld refinement technique has been well developed to compute crystallite size and residual strain using known structural models (see Chapter 5.2). For example, Balzar & Popa (2002) proposed a model to yield complete texture-weighted strain and stress tensors as a function of crystallite orientation, and improved the size-broadened profile by a combination of Gaussian and Lorentzian functions.

7.8.3.2.3. *Imperfection (defects) in ceramics*

Defects in ceramics occur quite frequently and are partly responsible for various physical properties of ceramic materials, particularly their mechanical and electronic properties (Cai & Nix, 2016). The brittle fracture of ceramics limits their applications. The flaws that are produced during ceramic processing cannot be closely controlled; this leads to a large variability in the fracture strength of ceramic materials. The contaminants form flaws which eventually lead to crack formation. Crack propagation (perpendicular to the applied stress) is usually transgranular along cleavage planes. Common defects can be categorized in several types: 0D (zero-dimensional) point defects (atomic point defects, stoichiometric defects, non-stoichiometric defects and extrinsic defects), 1D defects (dislocations) and 2D defects (planar defects).

The following example illustrates the influence of sintering temperature and pressure on lattice defect structure (dislocation

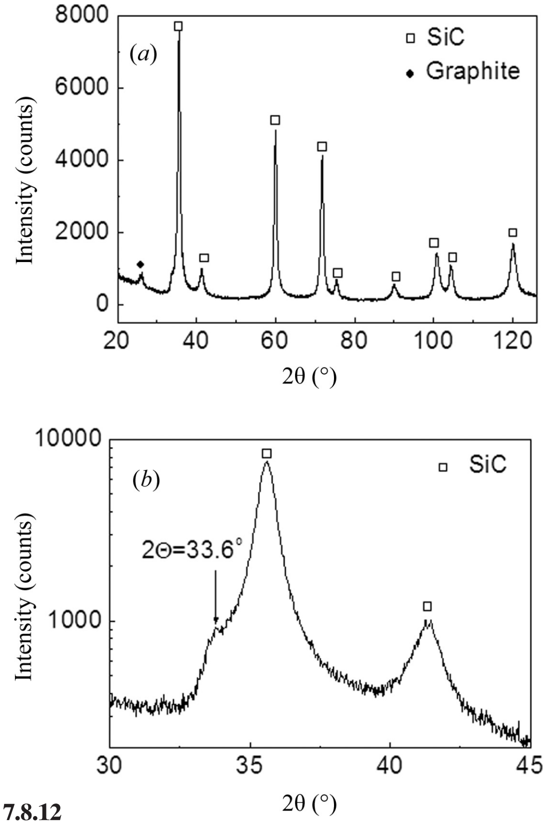

Figure 7.8.12
(*a*) X-ray powder pattern for the sample sintered at 2 GPa and 2073 K. (*b*) The X-ray diffraction pattern calculated for 10% twins for the 2θ range 30–45° (Gubicza *et al.*, 2007).

and planar fault densities and twins) and crystallite size in a series of sintered nanocrystalline SiC specimens by X-ray line profile analysis using the convolutional multiple whole profile (CMWP) fitting procedure (Gubicza *et al.*, 2007). The lattice defect structure and the crystallite size are determined as a function of pressure between 2 and 5.5 GPa for sintering temperatures in the range from 1673 to 2073 K. The X-ray powder pattern for the sample sintered at 2 GPa and 2073 K for the 2θ range between 30 and 45° is shown in Fig. 7.8.12(*a*). The X-ray diffraction pattern calculated for 10% twins is plotted in Fig. 7.8.12(*b*) for the 2θ range between 30 and 45°. The small peak at 33.6° is unambiguously related to planar faults. In the Williamson–Hall plots the FWHM values of the 111/222 and 200/400 reflection pairs are order-independent, indicating that line broadening is mainly caused by small crystallite size and/or planar faults. In summary, the sintering process results in an increase of the crystallite size. In the case of relatively small crystallite size values, *i.e.* less than about 20 nm, planar faults are the main lattice defects, while for crystallite sizes larger than 70 nm dislocations are more abundant.

7.8.3.2.4. *Residual stress measurements of ceramic components*

Residual stress is defined as 'the stress resident inside a component or structure after all applied forces have been removed'. Compressive residual stress acts by pushing the material together, while tensile residual stress pulls the material apart. Mechanical and thermal processes applied to a component during service may also alter its residual stress state. In general, compressive residual stress in the surface of a component is beneficial because it tends to increase fatigue strength and fatigue life, slow crack propagation, and increase resistance to environmentally assisted cracking. On the other hand, tensile residual stress in the surface of the component is generally undesirable as it decreases fatigue strength and fatigue life, increases crack propagation and lowers resistance to environmentally assisted cracking (Jones & Berard, 1993). Therefore, knowledge of the residual stress state is important to determine the actual loads experienced by a ceramic component.

Residual stresses can be characterized by the scale at which they exist within a material. Stresses that occur over long distances within a material are referred to as macro-stresses. Stresses that exist only locally (either between grains or inside a grain) are called micro-stresses. The total residual stress at a given location inside a material is the sum of all three of the following types of stresses:

(i) Type-I stresses: macro-stresses occurring over distances that involve many grains within a material.

(ii) Type-II stresses: micro-stresses caused by differences in the microstructure of a material and that occur over distances comparable to the size of the grain in the material. They can occur in single-phase materials because of the anisotropic behaviour of individual grains, or can occur in multiphase material as a result of the presence of different phases.

(iii) Type-III stresses: exist inside a grain as a result of crystal imperfections within the grain.

A number of different methods are available to measure residual stress; however, only a few are quantitative. X-ray diffraction is a nondestructive method which allows the measurement of residual stress in isolated spots spaced at distances as small as 100 μm apart. Neutron diffraction is an alternative nondestructive method which also allows measurement of residual stress in isolated spots. The choice between these two techniques depends on the design of the mechanical part to be tested.

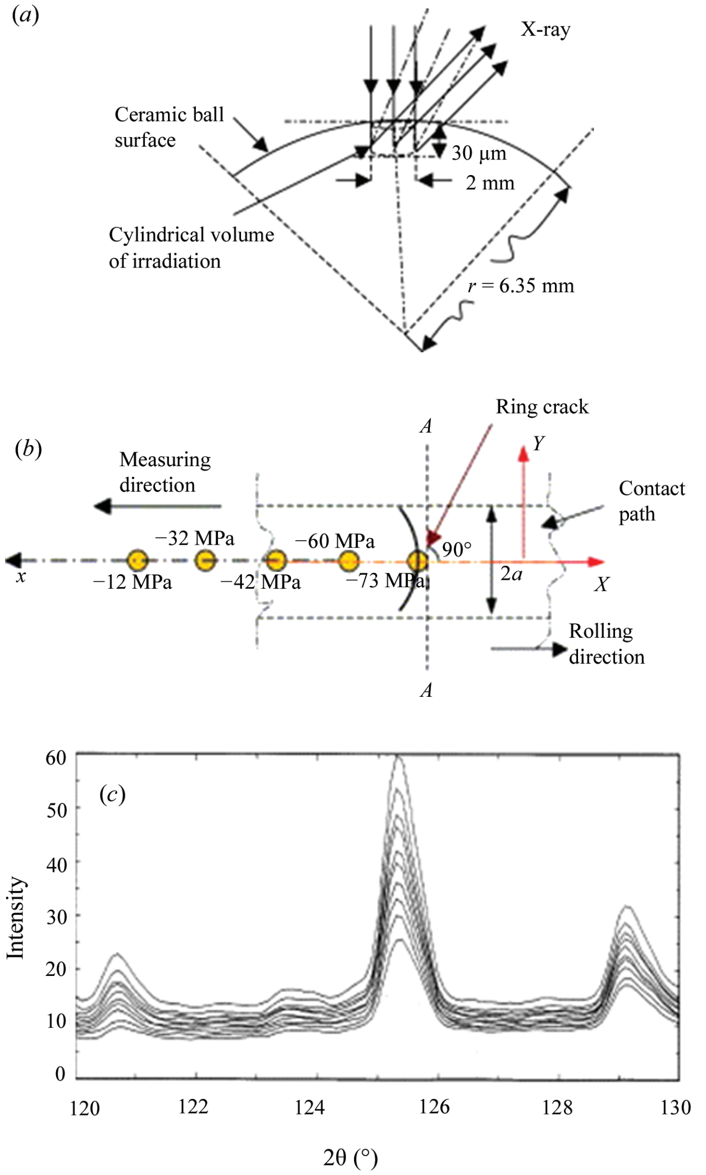

Figure 7.8.13

(*a*) A schematic of a Si_3N_4 ceramic ball cylindrical volume taken for residual stress measurement. Residual stress measurements were performed within the circle. (*b*) Measurement points and direction on the ball surface. (*c*) Ten measurements performed and averaged using data smoothing. Reproduced with permission from Khan *et al.* (2005). Copyright (2005) Elsevier.

The following example demonstrates X-ray residual stress measurement results of rolling contact fatigue on Si_3N_4 ceramic bearing elements with refrigerant lubrication using residual stress measurement testing methodology (Khan *et al.*, 2005). Analysing the relationship of residual stress with rolling contact fatigue is an important study which provides guidelines on the design, process and manufacturing of these elements. The rolling bearing elements were pre-cracked by inducing a ring crack and indents on the ball surface. The standard diffractometer method is called the two-exposure method (Cullity, 1978). Fig. 7.8.13(*a*) gives a schematic of the Si_3N_4 ceramic ball cylindrical volume taken for the residual stress measurements which were performed within the circle. Fig. 7.8.13(*b*) gives the measurement points and direction on the ball surface. Ten measurements were performed and averaged using data smoothing (Fig. 7.8.13*c*). The characteristic of this study was the small volume of irradiation. The X-ray beam penetrated sub-surface within the material to a depth

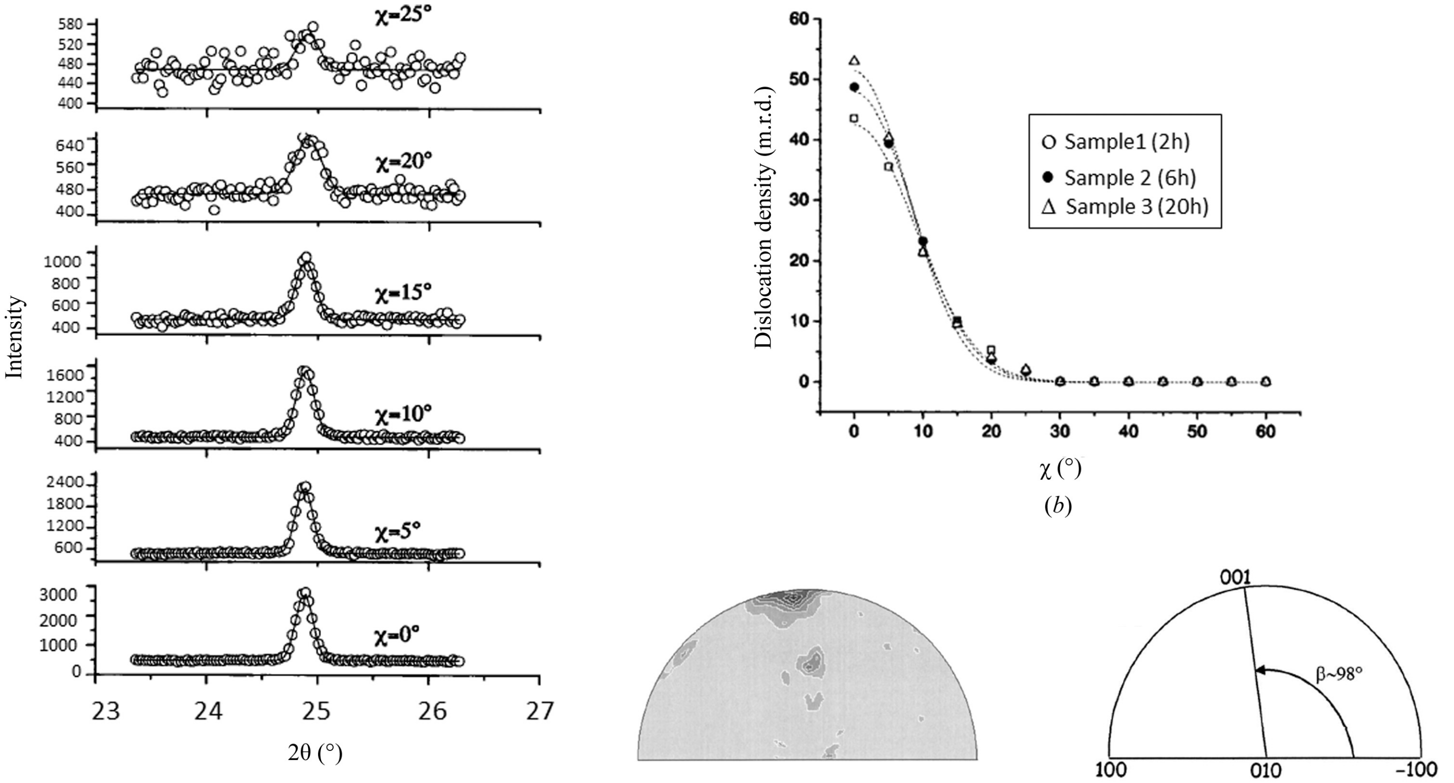

(*a*) (*b*) (*c*) (*d*)

Figure 7.8.14

(*a*) Experimental and Gaussian fitted profile of the {003} diffraction peak of $[Ca_2CoO_3]_{0.62}[CoO_2]$ for various χ angles. (*b*) χ-angle dependence of the distribution density of the RTGG samples. (*c*) Calculated {003} inversed pole figure of a sample with pressing duration time of 2 h that was derived from the ODF for the direction normal to the casting plane. (*d*) Inverse pole-figure scheme with crystallographic structure directions. Reproduced with permission from Guilmeau *et al.* (2005). Copyright (2005) AIP Publishing.

of 30 µm. Stress measurement was taken from a cylindrical volume of 0.0942 mm^3. Khan *et al.* found that low compressive residual stress values indicate a higher number of stress cycles attained, *i.e.*, the compressive residual stress values decreases with increase in stress cycles. A compressive residual stress value of −73 MPa near the ring crack and a comparatively lower value of −12 MPa on the contact indicate sub-surface crack initiation and propagation (Fig. 7.8.13*b*). The average fatigue spall ranged from 100 to 148 µm in depth. Within the spall area residual stress measurements suggest that compressive residual stress is relieved much faster in the region of sub-surface damage.

7.8.3.2.5. *Texture/preferred orientation*

In polycrystalline ceramic materials, the orientation of the crystallites is not usually distributed randomly, such as in an ideal powder specimen. In most cases, a preferred orientation of the crystallites with respect to the sample reference frame is present. Preferred orientation or texture of ceramics (Bunge, 1995) arises when there is a stronger tendency for the crystallites in a powder or a texture to be oriented more in one way, or one set of ways, than all others. An easily visualized case of preferred orientation in ceramics is that which results when a material with a strong cleavage or growth habit is packed into a specimen. Texture is responsible for many macroscopic properties of ceramic materials. For example, in the ceramic high-T_c superconductor materials, texturing of grains is important to improve the critical current density, J_c, by diminishing weak links. When the oxide grains are aligned, the current can go in one direction by utilizing adjacent layers of grains. Knowledge of the texture is an important factor in understanding the mechanical, physical or chemical behaviour of the material investigated.

Texture analysis is a diffraction technique in which the orientation distribution of the crystallites constituting a sample is determined (Bunge, 1995; Chapter 5.3). In X-ray diffraction analysis, the texture is determined from a set of pole figures. These pole figures are measured by recording the intensity distribution of a single reflection by tilting and rotating the sample over the orientation sphere. In this way the orientation distribution of a single reflection, and thus for a single lattice plane, is determined. When a set of pole figures for independent crystal orientations has been measured, the orientation distribution function (ODF) of the crystallites can be calculated.

An example of the study of the correlation of the texture of ceramic materials with enhanced properties can be illustrated by the state-of-the-art ceramic thermoelectric material $Ca_3Co_4O_9$ (Guilmeau *et al.*, 2005). $Ca_3Co_4O_9$ (or $[Ca_2CoO_3]_{0.62}[CoO_2]$) is a misfit layered oxide that has two monoclinic subsystems with identical cell parameters *a*, *c* and *β*, but different *b* (Masset *et al.*, 2000). The first subsystem consists of triple rock-salt layers of Ca_2CoO_3 in the *ab* plane while the second subsystem consists of a single CoO_2 layer, which has the CdI_2-type structure. This phase exhibits strong anisotropic thermoelectric properties in the *ab* plane. It is thought that the increased scattering of phonons at the interface of misfit layers leads to the lowering of the lattice thermal conductivity.

The texture analysis of highly grain-aligned ceramics of $Ca_3Co_4O_9$ prepared by the reactive-templated grain growth (RTGG) process that involved uniaxial pressing was examined by an quantitative texture-analysis technique using X-ray diffraction (fibre texture strength and crystallite size) as a function of pressing time. An X-ray diffraction pattern shows *c*-axis alignment of the tape-cast sample where platelets were aligned along the casting plane (only 00*l* peaks were observed); the (003) crystallographic planes for various χ angles (Fig. 7.8.14*a*) were used to study the orientation distribution of the *c* axes from the normal to the casting plane. After integration and renormalization of these peaks, the distribution of the orientation densities (inverse pole figure) (Fig. 7.8.14*b*) shows a strong centred pole as a sign of preferred orientation. The calculated {003} inversed pole figure of a sample with a pressing duration time of 2 h that was derived from the ODF for the direction normal to the casting plane is shown in Fig. 7.8.14(*c*). The texture increase is correlated with an enhancement of thermoelectric properties, and with larger electrical conductivity and power factor, as a function of pressing duration time.

7.8.3.2.6. *Thickness and roughness of ceramic films*

Structural characterization and determination of the thickness of ceramic thin films can be achieved with grazing-incidence X-ray diffraction (GIXD). Using the previous example of pentacene on an α-quartz substrate, GIXD yields a monolayer film thickness, 16.0 ± 0.6 Å (Fritz *et al.*, 2004).

X-ray reflectivity measurement is a nondestructive technique that provides microscopic information about the roughness, density profile and thickness of the layers that compose the thin film, and it offers advantages over ellipsometry in that precise information about the properties of buried layers can be obtained. The interface structure, thermal stability and densification of several ceramic ZrO_2 thin films [deposited from aqueous solution on Si(100) substrates] in the temperature range from room temperature to 1023 K in vacuum were measured by Ritley *et al.* (2000) using the high-temperature *in situ* X-ray reflectivity technique with a six-circle diffractometer. The reflectivity data for the ZrO_2 sample, as well as for a bare surface and self-assembled monolayers (SAMs) of an organic surface-covered Si substrate are shown in Fig. 7.8.15. Their detailed analysis showed that the growth rate of film is a nonlinear function of time in solution. The as-deposited films exhibit about 3 nm roughness and a density below that of bulk ZrO_2. Measurements in vacuum reveal decreasing film thickness, increasing film density and decreasing roughness upon annealing up to 1023 K. The densification saturates at the highest measured temperatures, presumably following evaporation of residual contaminants from the aqueous synthesis procedure. Above 473 K the SAM/ZrO_2 interface began to deteriorate, possibly due to interdiffusion. The ZrO_2 film structure obtained at the highest annealing temperatures persisted upon cooling to room temperature, and there was no visible evidence of stress-induced microstructural changes, such as peeling or cracking.

7.8.3.3. *Processing and performance*

7.8.3.3.1. *Sintering/densification/grain growth*

Sintering, which is based on atomic diffusion, is traditionally used for manufacturing ceramic objects from powders. Diffusion occurs in any material above absolute zero, but it occurs much faster at higher temperatures. In most ceramic sintering processes, the powdered material is subjected to high pressure and heated to a temperature below the melting point. The atoms in the powder particles diffuse across the boundaries of the particles, fusing the particles together and creating one solid piece. The different paths that the atoms take to get from one place to another are known as the sintering mechanisms. The six common mechanisms are: (1) lattice diffusion from a grain boundary, (2) grain boundary diffusion, (3) plastic deformation, (4) surface diffusion, (5) vapour transport and (6) lattice diffusion from the surface. Mechanisms (1) to (3) are densification mechanisms as atoms are moved from the bulk to the surface of pores, thereby eliminating porosity and increasing the density of the sample (Barsoum, 2003).

Sintering in practice is the control of both densification and grain growth. Sintering is effective when the process reduces the porosity and enhances properties such as strength, electrical conductivity, translucency and thermal conductivity. Densification is the act of reducing porosity in a sample thereby making it denser. Grain growth is the process of grain-boundary (GB) motion to increase the average grain size [a grain boundary is the transition area or interface between adjacent crystallites (or grains) of the same chemical and lattice composition]. Owing to the shifted positioning of the atoms in the GB, they have a higher energy state than the atoms in the crystal lattice of the grains. The driving force for densification is the change in free energy from the decrease in surface area and lowering of the surface free energy. Many properties benefit from both a high relative density

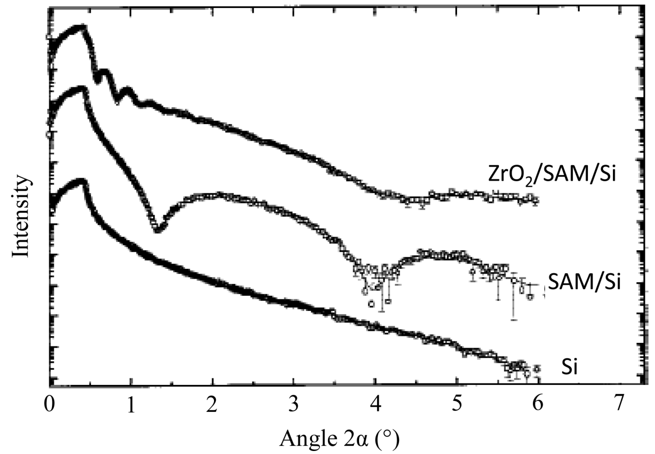

Figure 7.8.15
Measured and normalized X-ray reflectivity curves for a bare Si substrate, a SAM-terminated Si substrate and a ZrO_2/SAM/SiO_2/Si thin film with 26.8 nm ZrO_2. The curves have been offset for clarity. Reproduced with permission from Riley *et al.* (2002). Copyright (2002) John Wiley and Sons.

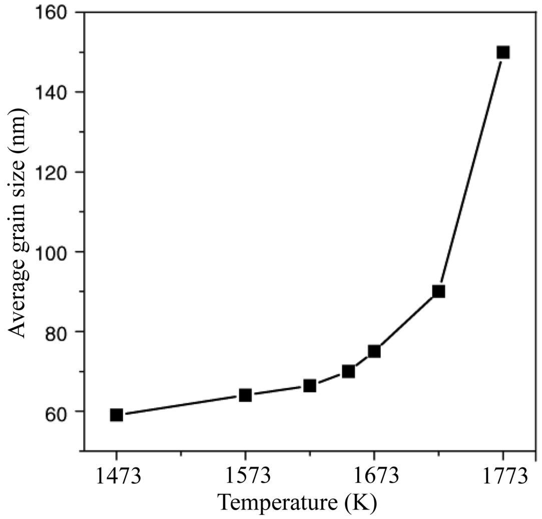

Figure 7.8.16
The average grain size of Al_2O_3 nanoceramics from an α-Al_2O_3 nanopowder with a mean particle size of 10 nm pressed at 1120 MPa as a function of the sintering temperature (with a fixed sintering time of 1 h). Reproduced with permission from Li & Ye (2006). Copyright (2006) John Wiley and Sons.

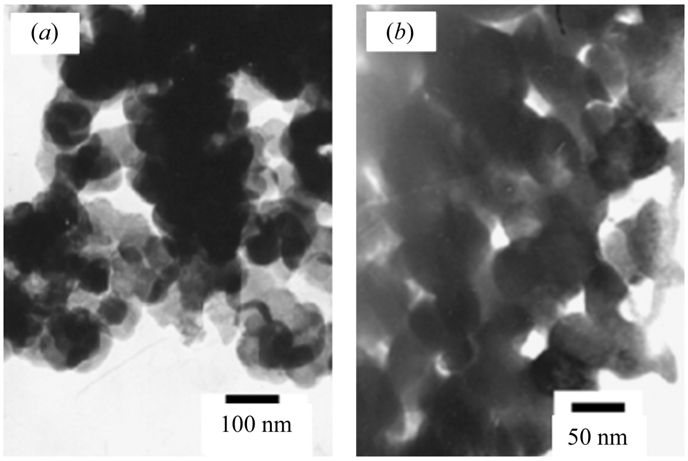

Figure 7.8.17
Transmission electron microscopy micrographs of Al_2O_3 nanoceramics from an α-Al_2O_3 nanopowder with a mean particle size of 10 nm pressed at 1120 MPa and sintered according to two different programmes: (*a*) sintering at 1723 K for 1 h and then at 1623 K for 34 h; (*b*) sintering at 1653 K for 1 h and then at 1603 K for 50 h. Reproduced with permission from Li & Ye (2006). Copyright (2006) John Wiley and Sons.

and a small grain size. Therefore, being able to control these properties during processing is of high technical importance.

In one study (Li & Ye, 2006), α-Al_2O_3 nanopowders with mean particle sizes of 10, 15, 48, and 80 nm (synthesized by the doped α-Al_2O_3 seed polyacrylamide gel method) were used to sinter bulk Al_2O_3 nanoceramics. It was found that the relative density of the Al_2O_3 nanoceramics increases with increasing compaction pressure on the green (unsintered) compacts and with decreasing mean particle size of the starting α-Al_2O_3 nanopowders. The Al_2O_3 nanoceramics with an average grain size of 70 nm (estimated from the corresponding X-ray peak broadening) and a relative density of 95% were obtained by a two-step sintering method. Fig. 7.8.16 shows that there was no fast grain growth observed in the second step of sintering below 1723 K. Transmission electron microscopy (TEM) micrographs showing the density and average grain size of the Al_2O_3 nanoceramics sintered by a two-step sintering method are shown in Fig. 7.8.17. It is seen that the average grain size of 70 nm in the Al_2O_3 nanoceramics sintered at 1653 K for 1 h and then sintered at 1603 K for 50 h (Fig. 7.8.17*b*) is smaller than that of the 90-nm Al_2O_3 nanoceramics sintered at 1723 K for 1 h and then sintered at 1623 K for 34 h (Fig. 7.8.17*a*). The densification and the suppression of the grain growth are achieved by exploiting the difference in kinetics between grain-boundary diffusion and grain-boundary migration (by the slower grain-boundary diffusion without promoting grain growth in second-step sintering).

7.8.3.3.2. *Reaction mechanisms/sequence*

In order to understand both the physical and chemical properties of ceramic materials, detailed knowledge of the reaction mechanisms that lead to phase formation of a desired ceramic phase is essential. Combined techniques such as powder diffraction, scanning electron microscopy (SEM), differential thermogravimetric analysis (DTA), nuclear magnetic resonance (NMR) and Raman spectroscopy have proved to be beneficial. Among these techniques, the *in situ* diffraction technique is indispensable. For ultra-fast ceramic reactions, in recent years, we can also use ultra-high-speed diffraction or synchrotron diffraction to study the reaction mechanisms. The following two examples illustrate the power of these state-of-the-art techniques.

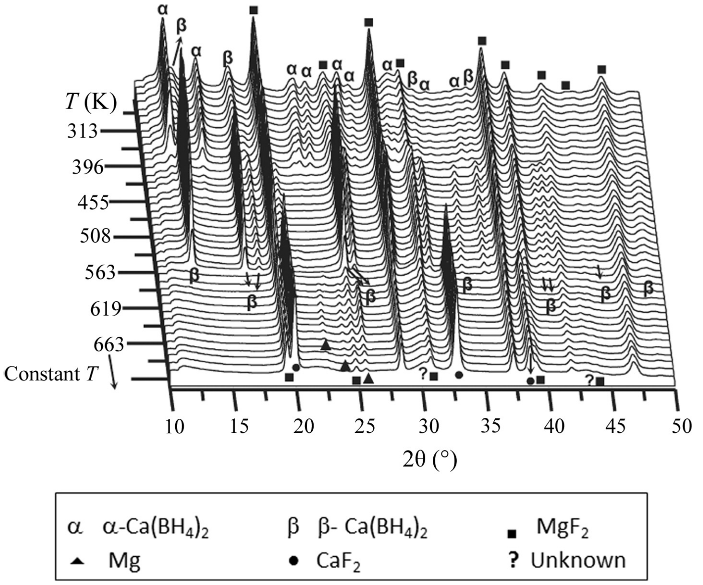

Figure 7.8.18
Synchrotron-radiation powder X-ray diffraction (SR-PXD) spectra of milled $Ca(BH_4)_2$–MgF_2 under a vacuum with the temperature programme of (i) heating from 298 to 663 K and (ii) dwelling at 663 K for 1 h. Reprinted with permission from Gosalawit-Utke *et al.* (2011). Copyright (2011) American Chemical Society.

The reaction mechanisms and kinetic properties of the $Ca(BH_4)_2$–MgF_2 reversible hydrogen storage process were studied by Gosalawit-Utke *et al.* (2011). The dehydrogenation and rehydrogenation reaction mechanisms were investigated by *in situ* time-resolved synchrotron-radiation powder X-ray diffraction (SR-PXD) and Raman spectroscopy. During dehydrogenation, the milled $Ca(BH_4)_2$–MgF_2 was heated to 663 K under a vacuum and held at 663 K for 1 h. Fig. 7.8.18 shows the SR-PXD patterns of milled $Ca(BH_4)_2$–MgF_2 with the temperature programmes of (1) heating from 298 to 663 K and (2) dwelling at 663 K for 1 h. At about 431 and 586 K, the polymorphic transformation from α- to β-$Ca(BH_4)_2$ and the melting of β-$Ca(BH_4)_2$ took place, respectively. At about 553 K the intensity of MgF_2 peaks decreased, indicating that the fluorine atoms in CaF_2 were obtained from MgF_2. Raman spectroscopy revealed the presence of CaB_6 together with amorphous α-boron. The dehydrogenation products were thus deduced to be CaF_2, CaB_6, Mg and α-B. The $Ca(BH_4)_2$–MgF_2 composite indicates kinetic destabilization and the reproducibility of hydrogen-storage capacities during cycling.

In situ neutron diffraction at 0.9 s time resolution was used by Riley *et al.* (2002) to determine the reaction mechanism during the self-propagating high-temperature synthesis (SHS) of Ti_3SiC_2 from furnace-ignited stoichiometric 3Ti + SiC + C mixtures. Ti_3SiC_2 is an important ceramic because of its unique properties of high melting point, good high-temperature strength, resistance to corrosion and oxidation, and high electrical and thermal conductivity, which are both ceramic and metallic in nature. The diffraction patterns indicate that the SHS proceeded in five stages: (i) preheating of the reactants, (ii) the $\alpha \rightarrow \beta$ phase transformation in Ti, (iii) pre-ignition reactions, (iv) the formation of a single solid intermediate phase in <0.9 s, and (v) the rapid nucleation and growth of the product phase Ti_3SiC_2. No amorphous contribution to the diffraction patterns from a liquid phase was detected and, therefore, it is unlikely that a liquid phase plays a major role in this SHS reaction. The intermediate phase is believed to be a solid solution of Si in TiC such that the overall stoichiometry is approximately 3Ti:1Si:2C. Lattice parameters and known thermal-expansion data were used to estimate the ignition temperature as 1196 ± 10 K (supported by the $\alpha \rightarrow \beta$ phase transformation in Ti) and the combustion temperature as 2593 ± 50 K.

Examples of studies of other reaction sequences/mechanisms include using combined X-ray diffraction and solid-state ^{29}Si and ^{27}Al magic-angle spinning NMR spectroscopies to monitor the initial formation of amorphous SiO_2, and to detect the formation of a noncrystalline mullite-like aluminosilicate which becomes crystalline at high temperatures (Mackenzie, 1997).

7.8.3.3.3. *Kinetics and reaction rate*

Diffraction techniques (particularly high-temperature setups) can be used to characterize ceramic reactions, including bulk materials and the interaction of ceramic films with buffer materials or substrates. Combining the diffraction technique with electron energy-loss spectroscopy/energy-dispersive spectroscopy (EELS/EDS) measurements and TEM, one can derive the kinetic rate laws and activation energies for the reactions. Examples include reaction kinetics of various classes of ceramic materials, such as formation of nanostructured silicon carbide (Wallis *et al.*, 2008), kinetic investigation of yttrium tetragonal zirconia biomaterials (Elshazly *et al.*, 2011), high temperature X-ray diffraction (HTXRD) study of reactions rates in the formation of ceramic Aurivillius phases (Peterson *et al.*, 2003), formation of one-dimensional hierarchical titania for enhanced reaction kinetics of photoanode materials of dye-sensitized solar cells (Qu *et al.*, 2010), optimized formation of magnesium ferrite (Paik *et al.*, 2005), formation of $CuInSe_2$ thin-film solar cells and reaction kinetics of the superconductor $Ba_2YCu_3O_{6+x}$ with CeO_2 (Cook *et al.*, 2007; Wong-Ng *et al.*, 2005).

The study of the reaction of the superconductor oxide $Ba_2YCu_3O_{6+x}$ with a buffer layer material, CeO_2, is illustrated (Cook *et al.*, 2007; Wong-Ng *et al.*, 2005). A $Ba_2YCu_3O_{6+x}$ film was deposited on CeO_2 pellets using a laser deposition technique. Sequential X-ray diffraction patterns of a $Ba_2YCu_3O_{6+x}$ pellet heat-treated at 1103 K for increasing cumulative time (min) are shown in Fig. 7.8.19. In most ceramic reactions, there is an interface between reacting phases. The overall process involves transport of material to the interface, reaction at the interface, and sometimes transport of reaction products away from the interface. For a reaction in which a compound is formed as the planar reaction layer, the rate of product formation is controlled by diffusion through the product layer. The reaction kinetics are expected to obey the parabolic rate rule $x = Kt^{1/2}$ (where x is the thickness of the reaction layer, t is the time and K is a constant related to the rate constant). The plots of intensity *versus* $t^{1/2}$ for the experiments at 1083 K are shown in Fig. 7.8.20. For the reaction products $Ba(Ce,Y)O_3$ (reflection 213) and BaY_2CuO_5 (reflection 131), the shape of the plots are rather similar. There is a straight-line portion for a relatively short reaction time period, and then the rate of change of intensity decreases. While the intensities of reflections from the products increase, the intensity of the reflection from the reactant, namely $Ba_2YCu_3O_{6+x}$, decreases. The intensity *versus* $t^{1/2}$ plots for the experiments at 1103 K are similar to those of 1083 K, except that at higher temperature the reaction progresses faster. For example, the reaction to form $Ba(Ce,Y)O_3$ was nearly complete at $t^{1/2} \sim 13.5$ min$^{1/2}$, while at 1083 K the corresponding time parameter was at 23 min$^{1/2}$. At 1063 K, the reaction was still occurring at $t^{1/2} = 60$ min $^{1/2}$. A bright-field image of a cross section of a sample provided information on the thickness of a monophasic

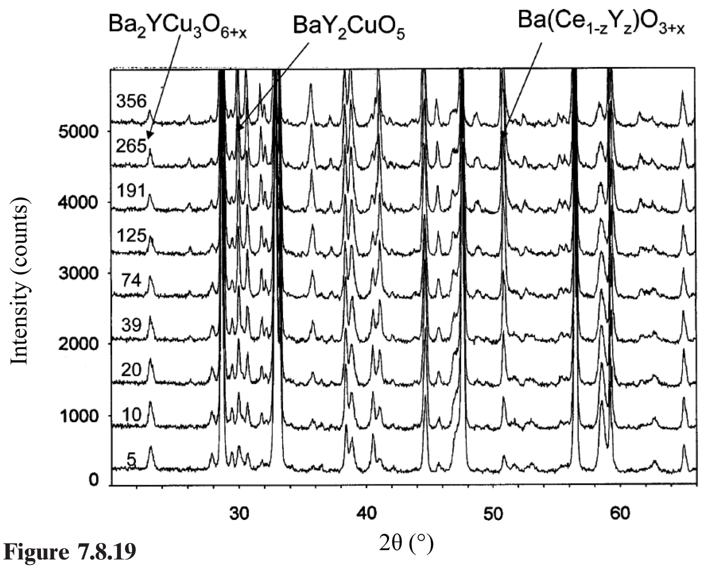

Figure 7.8.19
Sequential X-ray diffraction patterns of a $Ba_2YCu_3O_{6+x}/CeO_2$ pellet heat-treated at 1103 K for increasing cumulative time (in minutes). Reproduced with permission from Cook *et al.* (2007). Copyright (2007) Springer.

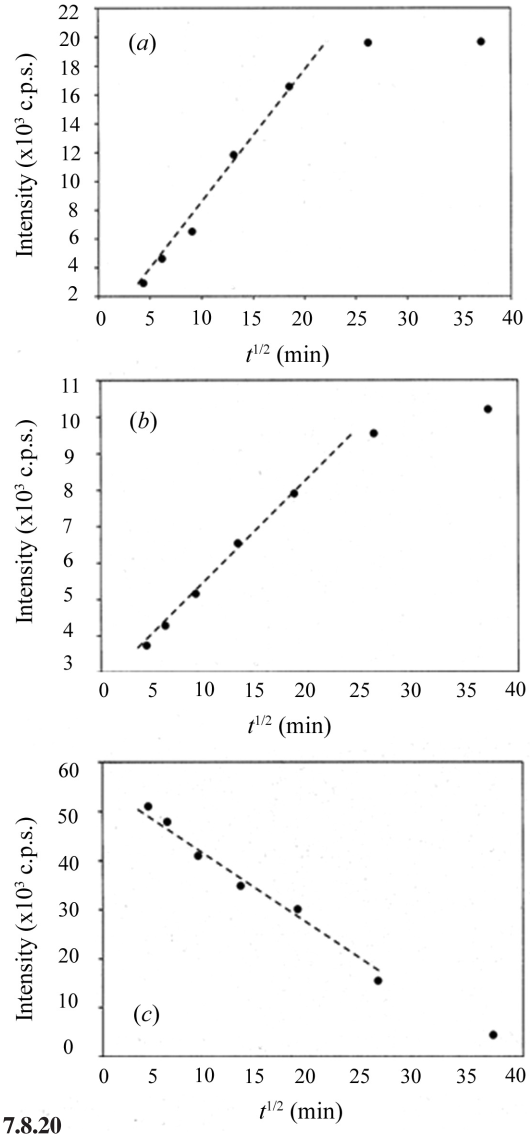

Figure 7.8.20
Plots of intensity *versus* time$^{1/2}$ (in minutes$^{1/2}$) for (*a*) $Ba(Ce_{1-z}Y_z)O_{3-x}$, (213), (*b*) BaY_2CuO_5 (131) and (*c*) $Ba_2YCu_3O_{6+x}$ (031) for a sample heat-treated at 1083 K. c.p.s. stands for counts per second. Reproduced with permission from Cook *et al.* (2007). Copyright (2007) Springer.

$Ba(Ce,Y)O_3$ reaction product layer. The fact that a monophasic product layer of $Ba(Ce,Y)O_3$ was formed adjacent to the CeO_2 suggests that the reaction occurred primarily by diffusion of Ba into the CeO_2. This process left behind products of BaY_2CuO_5 and CuO. One can deduce the K values at 1063 and at 1103 K. The activation energy ($E_{\rm act}$) for the reaction can be deduced to be 2.67×10^5 J mol^{-1} using the Arrhenius equation, $K1/K2 = [A\exp(-E_{\rm act}/RT_1)/A\exp(-E_{\rm act}/RT_2)]$, where A is a pre-exponential factor and R is the universal gas constant.

7.8.3.3.4. *Transformation toughening*

The traditional interest in the mechanical behaviour of ceramics is often related to their use as structural materials. Considerable effort has been expended to produce structural ceramics with enhanced toughness. In recent years, the applications have expanded to dental inlays, crowns and bridges. Toughening mechanisms that remain effective at high temperatures are still not totally understood. The toughening mechanisms include transformation toughening, toughening by a metallic particulate phase and fibre reinforcement. The most promising toughening mechanism for ceramic materials involves a phase transformation. Transformation toughening is based on the idea that a phase transformation can be stress-induced in a material in such a way that it decreases the driving force that is acting to propagate that cracks that are present, or that can form under stress in the material.

Although other materials such as alumina can be transformation-toughened, zirconia (ZrO_2) is the prototype material for this process. ZrO_2 is one of the most studied ceramic materials. It adopts a monoclinic crystal structure at room temperature and undergoes first-order phase transitions to tetragonal and cubic forms at higher temperatures. The volume expansion caused by the cubic-to-tetragonal-to-monoclinic transformation induces large stresses, and these stresses cause ZrO_2 to crack upon cooling from high temperatures. When the zirconia is blended with some other oxides, the tetragonal and/or cubic phases are stabilized, and the resulting material has superior thermal, mechanical and electrical properties. Effective dopants include magnesium oxide (MgO), yttrium oxide (Y_2O_3, yttria), calcium oxide (CaO) and cerium(III) oxide (Ce_2O_3) (Green *et al.*, 1989; Callon *et al.*, 2000). In some cases, the tetragonal phase can be metastable. If sufficient quantities of the metastable tetragonal phase are present, then an applied stress, magnified by the stress concentration at a crack tip, can cause the tetragonal phase to convert to monoclinic, with the associated volume expansion. This phase transformation can then put the crack into compression, retarding its growth, and enhancing the fracture toughness. This mechanism is known as transformation toughening. In Fig. 7.8.21, a crack and its surrounding transformation zone are shown schematically. The zone can be described as a large transformation inclusion that is constrained by the surrounding material. The transformation within the zone tries to make the zone larger, but this is opposed by the surrounding untransformed material (Callon *et al.*, 2000).

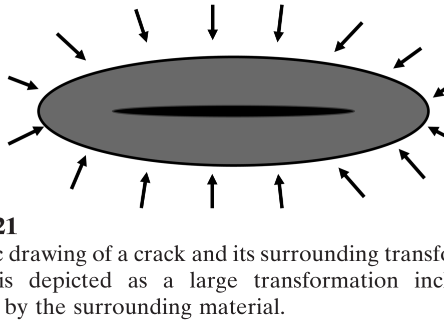

Figure 7.8.21
A schematic drawing of a crack and its surrounding transformation zone. The zone is depicted as a large transformation inclusion that is constrained by the surrounding material.

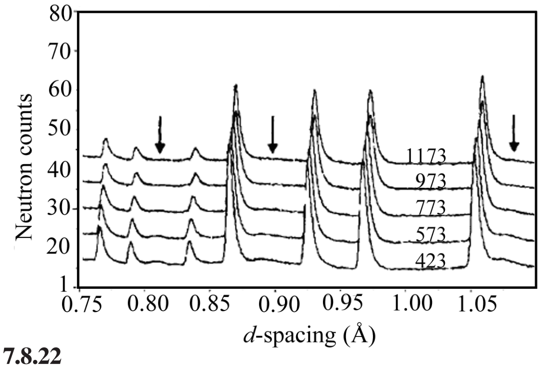

Figure 7.8.22
Comparison of neutron-diffraction profiles at 423, 573, 773, 973 and 1173 K for 8 mol% yttria-stabilized zirconia. The locations of low-temperature diffuse peaks are marked with arrows. Reproduced with permission from Gibson & Irvine (1996). Copyright (1996) Royal Society of Chemistry.

A comprehensive study of 8 mol% yttria-stabilized zirconia between 423 and 1273 K was carried out by Gibson & Irvine (1996) using high-temperature neutron powder diffraction and AC impedance spectroscopy. It was been demonstrated that the conductivity anomaly, which occurs at *ca* 923 K, is structural in origin. A sharp decrease in the activation energy for conduction of *ca* 0.2 eV was observed at *ca* 923 K. Additional broad, diffuse-scattering peaks were observed below 873 K in the neutron diffraction patterns (Fig. 7.8.22); above 923 K, the diffuse-scattering peaks disappeared. The low-temperature behaviour can be explained in terms of ordering of oxygen vacancy–(dopant) cation clusters to form microdomains, which are evidenced by the presence of diffuse-scattering peaks. At high temperature, the association of vacancies with defects breaks down, or randomizes, allowing vacancies to move more freely, as indicated by the decrease in activation energy for conduction. A discontinuity in the thermal-expansion coefficient (from neutron diffraction data) confirms the second-order nature of the transition.

7.8.3.3.5. *Degradation/corrosion of ceramics*

Corrosion is the local or extensive reaction of a material or component with a surrounding medium. Corrosion is a diffusion-controlled process. It occurs on exposed surfaces, and it degrades the useful properties of materials and structures including strength, appearance and permeability or impermeabilitiy to liquids and gases. Corrosion accelerates subcritical crack propagation under mechanical strain. Almost all environments are corrosive to some extent. For practical applications it is a matter of kinetics. The cost of corrosion to ceramics is enormous. McCauley (1995) discussed the fundamentals (corrosion by liquids, by gas, by solids; effects of porosity, surface energy, acid/base, thermodynamic/kinetics). Methods of corrosion analysis and test procedures are illustrated here with several examples.

Technical ceramics are relatively more stable than common metallic materials towards corrosion (except for the refractory carbides, silicides, nitrides and borides). When corrosion does occur in oxides, it is almost always a simple dissolution of the material or chemical reaction. A common example of corrosion protection in ceramics is the lime added to soda-lime glass to reduce its solubility in water. Normal glass forms sub-microscopic

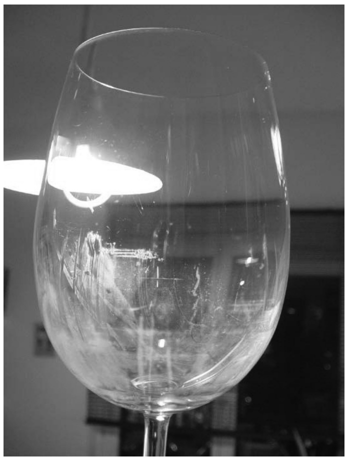

Figure 7.8.23
A wine glass plagued by 'glass disease'.

flaws when exposed to moisture. The corrosion of silicate glasses in aqueous solutions, which is known as 'glass disease', is governed by two mechanisms: diffusion-controlled leaching (ion exchange) and hydrolytic dissolution of the glass network. Fig. 7.8.23 shows a wine glass plagued by 'glass disease'.

Another example shows attack of a mullite refractory by glass. A mullite refractory was removed from the regenerator division wall of a soda-lime-silicate container glass furnace (McCauley, 1995). X-ray diffraction results showed that the mullite has completely converted to predominantly corundum and nepheline. The optical micrograph in Fig. 7.8.24 (with combined analysis from SEM/EDS) showed that the crystalline nepheline was embedded in a matrix of vitreous potassium titanium silicate. The potassium diffused into the refractory from glass batch impurities and the titanium was present in the original refractory in minor amounts.

Zirconia has also found wide application in dentistry because of its high mechanical strength and superior aesthetic properties (Kawai *et al.*, 2011). However, zirconia degradation caused by phase transformations occurring in a hydrothermal environment is of concern. In the study by Kawai *et al.* (2011), the phase transformation and microstructure of tetragonal zirconia polycrystals partially stabilized with yttrium oxide (Y-TZP) and alumina-toughened zirconia (ATZ) sintered at different temperatures were investigated. Using grazing-angle X-ray diffraction analysis, ATZ showed less phase transformation to the monoclinic phase than Y-TZP during hydrothermal treatment and this transformation appeared to occur to a depth of a few micrometres below the surface. Fig. 7.8.25 shows XRD patterns of zirconia by both the 2*θ*–*θ* method and the grazing-angle method (at 1 and 2°). At a higher sintering temperature the monoclinic phase content of ATZ was found to be less than that of Y-TZP (Fig. 7.8.26*a*,*b*). Examination by transmission electron microscopy (TEM) and studying of electron backscatter diffraction patterns indicated that the grain growth in ATZ was slightly suppressed compared with that in Y-TZP at higher sintering

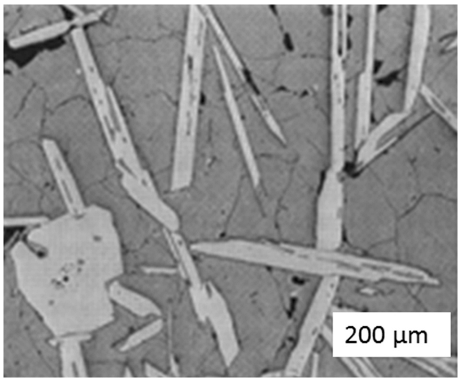

Figure 7.8.24
An optical micrograph (with combined analysis from SEM/EDS) showing the corrosion of a mullite refractory. Lighter areas are corundum and darker areas are nepheline (McCauley, 1995). Reprinted by permission of the publisher (Taylor & Francis Ltd).

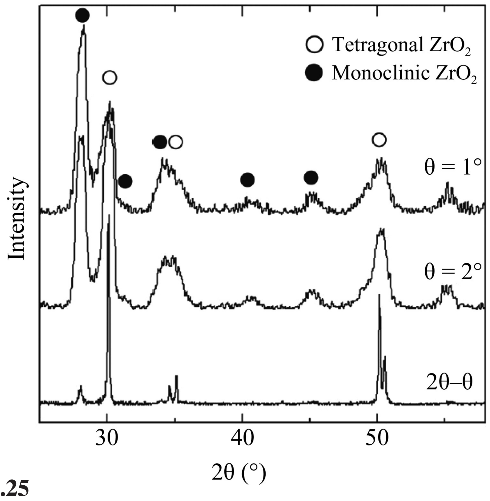

Figure 7.8.25
XRD spectra obtained by the 2*θ*–*θ* method and the grazing-angle method (at 1 and 2°). Zirconia was sintered at 1623 K and autoclaved for 3 days. Reproduced with permission from Kawai *et al.* (2011). Copyright (2011) The Japanese Society for Dental Materials and Devices.

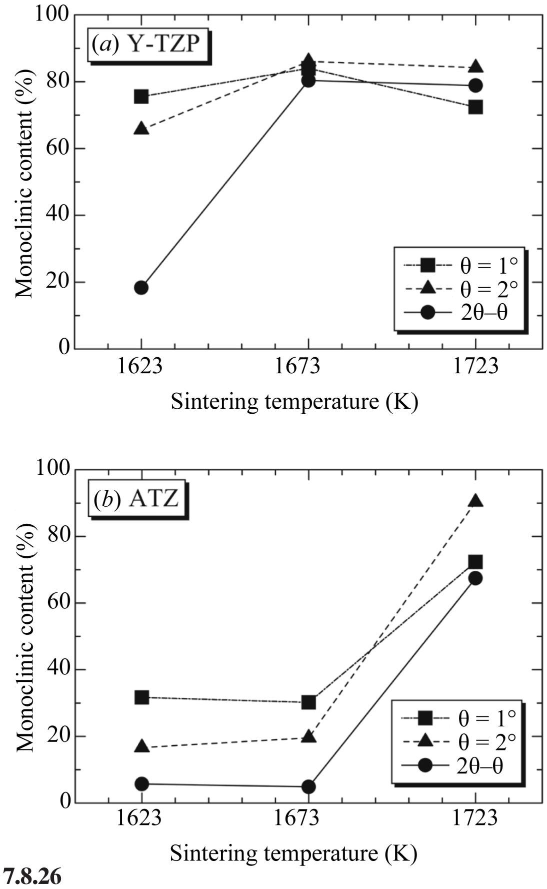

Figure 7.8.26
Monoclinic zirconia contents of (*a*) Y-TZP and (*b*) ATZ at different sintering temperatures. Reproduced with permission from Kawai *et al.* (2011). Copyright (2011) The Japanese Society for Dental Materials and Devices.

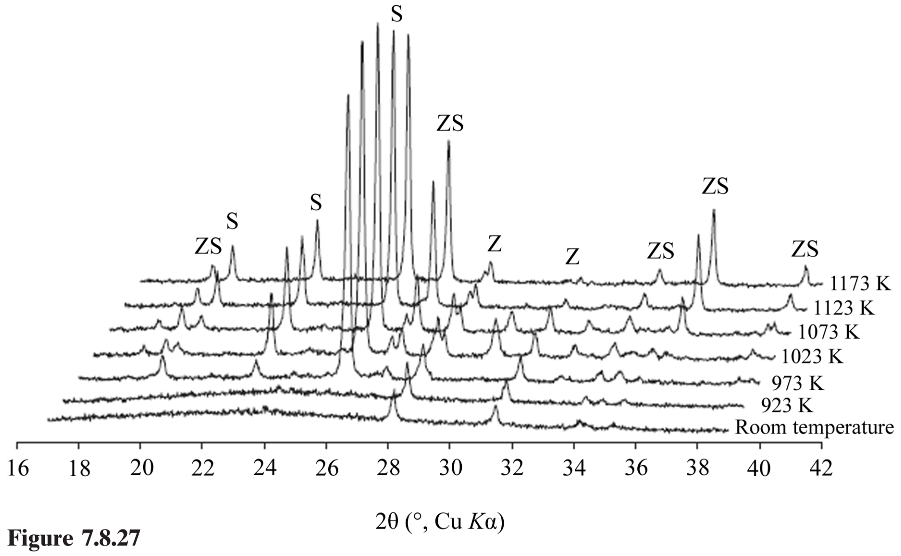

Figure 7.8.27
X-ray patterns recorded on a powdered sample of an LZSA glass ceramic with a composition of 16.9Li_2O–5.0ZrO_2–65.1SiO_2–8.6Al_2O_3 in the temperature range 923–1223 K (Montedo *et al.*, 2012). Peak labels: Z = ZrO_2, ZS = $ZrSiO_4$, S = spodumene.

temperatures. Therefore, alumina addition appears to suppress hydrothermal degradation to a larger extent than the addition of yttria.

7.8.3.3.6. *Glass ceramics (crystallization processes)*

Diffraction techniques, particularly *in situ* high-temperature diffraction techniques, are very valuable for studying glass-ceramic crystallization processes.

LZSA glass ceramics (Li_2O–ZrO_2–SiO_2–Al_2O_3) have been studied because of their beneficial thermal, mechanical and thermal properties (Montedo *et al.*, 2012). The crystallization sequence of an LZSA glass ceramic with a composition of 16.9Li_2O–5.0ZrO_2–65.1SiO_2–8.6Al_2O_3 was investigated using combined techniques of HTXRD, differential thermal analysis (DTA) and scanning electronic microscopy (SEM). X-ray patterns recorded on a powdered sample in the temperature range 923–1223 K are shown in Fig. 7.8.27. It is seen that at room temperature the material is essentially vitreous except for traces of zirconia (monoclinic ZrO_2). Crystallization of β-spodumene solid solution was found to commence at approximately 943 K. A pronounced acceleration was observed at temperatures above 998 K. Above 1023 K $ZrSiO_4$ crystallized as the major phase with the maximum amount reached at 1173 K. A wide variety of other glass-ceramic systems have been studied, *e.g.* the Li_2O–Al_2O_3–$n$$SiO_2$ (LAS) system, the MgO–Al_2O_3–$n$$SiO_2$ (MAS) system, the ZnO–Al_2O_3–$n$$SiO_2$ (ZAS) system and the MgO–SiO_2–Al_2O_3–K_2O–B_2O_3–F system (Ghasemzadeh *et al.*, 2011).

7.8.3.3.7. *Microstructure evolution*

The nondestructive (both neutron and synchrotron) small-angle-scattering technique has been used for many years to study the microstructure of intermetallic materials. In the past three decades, there has been an increase in the use of this technique. Details of the technique have been reported extensively elsewhere and will not be described here (Allen, 2005; see also Chapter 5.8). In brief, neutrons are an excellent nondestructive probe of microstructure because thermal neutron energies are very low and neutrons are not absorbed by most materials. Since the neutrons primarily interact with the nuclei of the atoms, the neutron beam is highly penetrating without disturbing the sample, so one can examine the bulk of the material, whereas X-ray and other techniques are more sensitive to surface phenomena.

Small-angle neutron scattering (SANS) techniques are used to study microstructural phenomena in the range 1 to 100 nm in size. Since these techniques cover a wide range of sizes, they are particularly useful in studies of ceramic processing and distributed damage in ceramics. Ceramics often have several microstructural components, such as residual voids from the sintering process, inclusions or impurities from starting materials, second phases, and microcracks or cavities from temperature and/or pressure treatments, as well as dislocations present in the material. All these effects result in small-angle neutron scattering signal. Beam-broadening theory and the SANS technique (Hardman-Rhyne *et al.*, 1984) allow us to study the microstructure development of ceramic materials in a nondestructive way. An example of the sintering of spinels ($MgAl_2O_4$) as a function of temperature is shown in Fig. 7.8.28. Although the spinel powders have been heated at 1603 K for 12 h, very little sintering has taken place, but sintering effects are apparent after only 3 h at 1773 K. The material is not fully sintered in that ε_b (the full width at half maximum of the direct beam, the blank) is much smaller than ε for the spinel at 1773 K.

7.8.3.3.8. *Bulk modulus/compressibility*

All ceramic materials can stretch, compress, bend, flex, shear, twist or deviate from their original unstressed shapes and dimensions when subjected to external forces or internal thermal stresses. The tendency of ceramic materials to deform is an important consideration in the design of any ceramic component whose operation depends on its ability to sustain loads or to maintain dimensions within specified tolerances: one needs to have information on the toughness of a ceramic material.

To estimate the toughness (K_{IC}) of a material quantitatively, it is necessary to know the value of Young's modulus (Y) for the solid. For ceramic materials, the latter parameter can be deter-

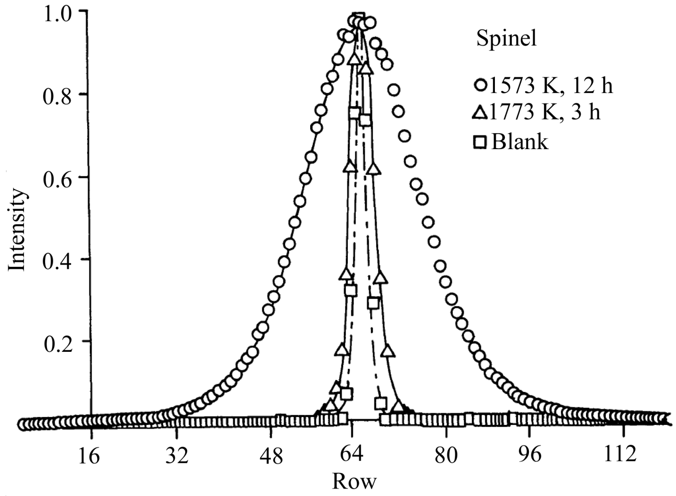

Figure 7.8.28
SANS spectra for a spinel ($MgAl_2O_4$) at λ = 0.9 nm. The circles represent the SANS spectra of the spinel with 12 h of heat treatment at 1573 K. After 3 h at 1773 K (triangles) the spinel is partially sintered but slight neutron-beam broadening can be seen compared with that of the direct beam (squares) (Hardman-Rhyne *et al.*, 1984).

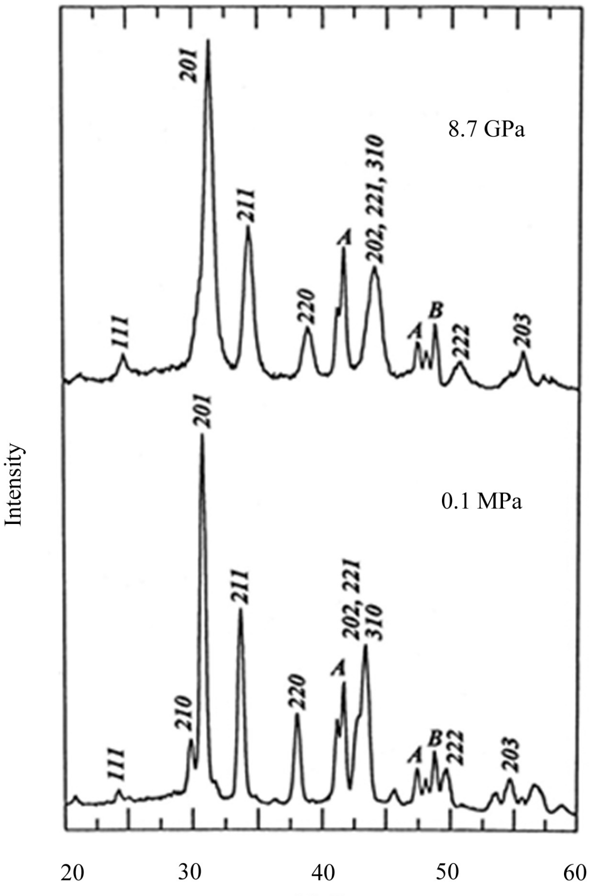

Figure 7.8.29
X-ray diffraction patterns of $BaNd_2CuO_5$ measured at 0.1 and 8.7 GPa. Reproduced with permission from Wong-Ng *et al.* (1995). Copyright (1995) International Centre for Diffraction Data.

mined from measurements of the bulk modulus, or its inverse, the compressibility, which can be determined by powder-diffraction techniques. K_{IC} is related to the Young's modulus, Y, by $K_{IC} = (Y/H)^{1/2}\ (L/C_0^{1.5})$. From indentation experiments, one can obtain the value of L (load), C_0 (indentation length) and H, the hardness. Y is in turn obtained from $Y = 3k(1 - 2\sigma)$, where k is the isothermal bulk modulus and σ is Poisson's ratio.

Powder-diffraction techniques also allow the lattice parameters to be evaluated at each state of compression. The isothermal equation of state can in turn be determined. If the compressibility dependence shows linear dependence, a first-order isothermal equation (the Bridgman equation) is usually used to compute the bulk modulus, $V = V_0 - (V_0/k)(P - P_0)$, where V is the volume, P is the pressure and k is the bulk modulus. The isothermal bulk modulus is then estimated using the thermodynamic relation $k = -V(\mathrm{d}P/\mathrm{d}V)_T$. It is possible to measure the bulk modulus of a ceramic material using a high-pressure measurement technique, which utilizes a diamond anvil high pressure cell (DAC) with energy-dispersive powder diffraction, as first developed at the National Bureau of Standards. The detailed history of its invention in the 1950s, its modification and its many applications have been described in a review article by Piermarini (2001) and the references cited therein. The DAC has been used with both conventional X-ray, synchrotron X-ray and neutron diffraction techniques. The compressibility and bulk modulus of many ceramic materials with different applications have been obtained using the DAC. Examples include zinc-blende solids (Cohen, 1985), tobermorite (a structural analogue of calcium silicate hydrates) (Oh *et al.*, 2012), β-boron (Nelmes *et al.*, 1993), $BaY_2Cu_3O_{6+x}$ (Block *et al.*, 1987), $Pb(N_3)_2$, $Ba(N_3)_2$, KN_3, TlN_3 and NaN_3 (Weir *et al.*, 1970).

Another example of this application is the study of $BaNd_2CuO_5$ (Wong-Ng *et al.*, 1995). A total of 221 data points were measured from ambient pressure up to about 8.7 GPa. The tetragonal unit-cell parameters for each pressure studied were obtained by indexing and performing least-squares refinements on the powder patterns (Fig. 7.8.29 shows two of the patterns, measured at 0.1 and 8.7 GPa). A linear least-squares fit of the volume compression of $BaNd_2CuO_5$ was obtained within a 99% confidence envelope along with uncertainties associated with pressure and volume. The equations of states for the tetragonal cell parameters, a, c and V are $a = -0.0139P + 6.700$, $c = -0.0125P + 5.807$, $V = -1.615P + 260.62$. A first-order Bridgman equation was used to compute the bulk modulus, k= 161.4 GPa. The Young's modulus, Y, was calculated to be 193.6 GPa, assuming a Poisson's ratio σ of 0.3.

7.8.4. Summary

Perhaps contrary to general public's perception of ceramics as primarily encompassing artwork, tableware, porcelain enamels, tiles and sanitary ware, ceramics cover a broad range of materials and applications. In this chapter, we have attempted to categorize these materials in terms of both their functions and applications, from traditional ceramics to modern advanced ceramics.

Powder diffraction has repeatedly been shown to provide the most critical and versatile tools for the characterization of many different aspects of ceramic materials. As many ceramic materials (regardless of their applications) exhibit similar features during processing and manufacturing (sintering and grain growth, texture, residual strain, microstructure evolution *etc.*), the applications of diffraction techniques have been demonstrated with selected representative applications.

In many cases, the combined use of powder diffraction (laboratory X-ray, synchrotron X-ray, neutron diffraction, electron diffraction) with other tools or specialized techniques (such as DTA,TGA, SEM, EDS, WDS, XANES, EXAFS, SANS, solid-state NMR, Raman spectroscopy, AC impedance spectroscopy, ellipsometry and modelling approaches) is either absolutely necessary or greatly beneficial for the characterization of the specific ceramic material at hand.

Although this chapter does not represent a complete range of the applications of powder diffraction to ceramics materials, it illustrates the typical types of studies and approaches that are pertinent to these diverse materials. It introduces some readers to the functions of ceramic materials in today's world, where many new applications continually being found. For more in-depth understanding of the theories behind various powder-diffraction applications, as well as more detailed descriptions of various applications of diffraction techniques to ceramic materials, other chapters of this volume should be consulted.

The author is grateful to the Fine Ceramics Office, Ministry of International Trade and Industry, Tokyo, for providing the chart on functions and applications of fine/advanced ceramics. The author also acknowledges Mississippi Valley Archaeological Center and Wikipedia, the Free Encyclopedia, for making available useful and relevant information.

References

ACerS–NIST Phase Equilibria Diagrams Database (2013). CD-ROM database. The American Ceramic Society, Westerville, OH 43082, USA.

Allen, A. J. (2005). *Characterization of ceramics by X-ray and neutron small-angle scattering*. *J. Am. Ceram. Soc.* **88**, 1367–1381.

Balzar, D. & Popa, N. C. (2002). *Improved modeling of residual strain/stress and crystallite size distribution in Rietveld refinement*. *Adv. X-ray Anal.* **45**, 152–157.

Barsoum, M. W. (2003). *Fundamentals of Ceramics*, ch. 10. *Series in Materials Science and Engineering*. Bristol, Philadelphia: Institute of Physics Publishing.

Bednorz, J. G. & Müller, K. A. (1986). *Possible high T_c superconductivity in the Ba-La-Cu-O system*. *Z. Phys. B*, **64**, 189–193.

Billinge, S. J. L. (2004). *The atomic pair distribution function: past and present*. *Z. Kristallogr.* **219**, 117–121.

Birkholz, M., Ehwald, K.-E., Wolansky, D., Costina, I., Baristiran-Kaynak, C., Fröhlich, M., Beyer, H., Kapp, A. & Lisdat, F. (2010). *Corrosion-resistant metal layers from a CMOS process for bioelectronic applications*. *Surf. Coat. Technol.* **204**, 2055–2059.

Bish, D. L. & Post, J. E. (1989). Editors. *Modern Powder Diffraction. Reviews in Mineralogy*, Vol. 20. Washington, DC: The Mineralogical Society of America.

Block, S., Piermarini, G., Munro, R. & Wong-Ng, W. (1987). *Advanced Ceramic Materials*, Vol. 2(3B), *Ceramic Superconductors*, edited by W. J. Smothers, pp. 601–605. Westerville: American Ceramic Society.

Britannica Concise Encyclopedia (1994–2008). Encyclopaedia Britannica, Inc.

Buchanan, R. C. (1986). *Ceramic Materials for Electronics: Processing, Properties, and Applications*. New York: Marcel Dekker, Inc.

Bunge, H. J. (1995). *Textures in ceramics*. *Textures Microstruc.* **24**, 1–12.

Cai, W. & Nix, W. D. (2016). *Imperfections in Crystalline Solids*. MRS-Cambridge Materials Fundamentals. Cambridge University Press.

Callon, G. J., Goldie, D. M., Dibb, M. F., Cairns, J. A. & Paton, J. (2000). *X-ray diffraction analysis of yttria stabilized zirconia powders produced by an organic sol-gel method*. *J. Mater. Sci. Lett.* **19**, 1689–1691.

Carter, G. C. (1978). *Applications of Phase Diagrams in Metallurgy and Ceramics*, Vol. 1, Proceedings of a workshop held at the National Bureau of Standards, Gaithersburg, MD, USA, 10–12 January 1977. Gaithersburg: NIST.

Clearfield, A., Reibenspies, J. & Bhuvanesh, N. (2008). *Principles and Applications of Powder Diffraction*. New York: Wiley-VCH.

Coelho, A. (2005). *TOPAS V3: General profile and structure analysis software for powder diffraction data*. User's Manual, Bruker AXS, Karlsruhe, Germany.

Cohen, S. B. (1968). *Microwave band pass filters containing high Q dielectric resonators*. *IEEE Trans. Microw. Theory Tech. MTT-16*, 1628–1629.

Cohen, M. L. (1985). *Calculation of bulk moduli of diamond and zinc-blende solids*. *Phys. Rev. B*, **32**, 7988–7991.

Cook, L. P., Wong-Ng, W., Schenck, P., Yang, Z., Levin, I. & Frank, J. (2007). *Kinetic studies of the interfacial reaction of the $Ba_2YCu_3O_{6+x}$ superconductor with a CeO_2 buffer*. *J. Electron. Mater.* **36**, 1293–1298.

Cullity, B. D. (1978). *Elements of X-ray Diffraction*. Reading, Massachusetts: Addison-Wesley.

Cullity, B. D. & Stock, S. R. (2001). *Elements of X-ray Diffraction*, 3rd ed. Upper Saddle River, New Jersey: Prentice Hall.

Curie, J. & Curie, P. (1880). *Development by pressure of polar electricity in hemihedral crystals with inclined faces*. *Bull. Soc. Miner. Fr.* **3**, 90–93.

David, W. I. F., Shankland, K., McCusker, L. B. & Baerlocher, Ch. (2002). *Structure Determination from Powder Diffraction Data. IUCr Monographs on Crystallography*, No. 13, Oxford Science Publications. ISBN 978-0-471-87547-5.

Dinnebier, R. E. & Billinge, S. J. L. (2008). *Powder Diffraction: Theory and Practice*. Cambridge: The Royal Society of Chemistry.

Eaksuwanchai, P., Jiansirisomboon, S. & Watcharapasorn, A. (2013). *Effect of lanthanum additive on electrical and thermal properties of bismuth sodium titanate ceramics*. *Integr. Ferroelectr.* **149**, 83–88.

Elshazly, E. S., El-Hout, S. M. & Ali, M. E.-S. (2011). *Yttria tetragonal zirconia biomaterials: kinetic investigation*. *J. Mater. Sci. Technol.* **27**, 332–337.

Fawcett, T. G., Kabekkodu, S. N., Blanton, J. R. & Blanton, T. N. (2017). *Chemical analysis by diffraction: the Powder Diffraction File^{TM}*. *Powder Diffr.* **32**, 63–71.

Ford, P. J. & Saunders, G. A. (2005). *The Rise of the Superconductors*. Boca Raton: CRC Press.

Fritz, S. E., Martin, S. M., Frisbie, C. D., Ward, M. D. & Toney, M. F. (2004). *Structural characterization of a pentacene monolayer on an amorphous SiO_2 substrate with grazing incidence X-ray diffraction*. *J. Am. Chem. Soc.* **126**, 4084–4085.

Garvie, R. C. & Nicholson, P. S. (1972). *Phase analysis in zirconia systems*. *J. Am. Ceram. Soc.* **55**, 303–305.

Ghasemzadeh, M., Nemati, A., Nozad, A., Hamnabard, Z. & Baghshahi, S. (2011). *Crystallization kinetics of glass-ceramics by differential thermal analysis*. *Ceram. Silik.* **55**, 188–194.

Gibson, I. R. & Irvine, J. T. S. (1996). *Study of the order–disorder transition in yttria-stabilised zirconia by neutron diffraction*. *J. Mater. Chem.* **6**, 895–898.

Gosalawit-Utke, R., Suarez, K., Bellosta von Colbe, J. M. B., Bösenberg, U., Jensen, T. R., Cerenius, Y., Minella, C. B., Pistidda, C., Barkhordarian, G., Schulze, M., Klassen, T., Bormann, R. & Dornheim, M. (2011). *$Ca(BH_4)_2$–MgF_2 reversible hydrogen storage: reaction mechanisms and kinetic properties*. *J. Phys. Chem. C*, **115**, 3762–3768.

Green, D. J., Hannink, R. H. J. & Swain, M. V. (1989). *Transformation Toughening of Ceramics*. Boca Raton: CRC Press.

Gubicza, J., Nauyoks, S., Balogh, L., Labar, J., Zerda, T. W. & Ungár, T. (2007). *Influence of sintering temperature and pressure on crystallite size and lattice defect structure in nanocrystalline SiC*. *J. Mater. Res.* **22**, 1314–1321.

Guilmeau, E., Itahara, H., Tani, T., Chateigner, D. & Grebille, D. (2005). *Quantitative texture analysis of grain-aligned $[Ca_2CoO_3]_{0.62}[CoO_2]$ ceramics processed by the reactive-templated grain growth method*. *J. Appl. Phys.* **97**, 064902.

Hämmerle, H., Kobuch, K., Kohler, K., Nisch, W., Sachs, H. & Stelzle, M. (2002). *Biostability of micro-photodiode arrays for subretinal implantation*. *Biomaterials*, **23**, 797–804.

Hardman-Rhyne, K., Berk, N. F. & Fuller, E. R. (1984). *Microstructural characterization of ceramic materials by small angle neutron scattering techniques*. *J. Res. NIST*, **89**, 17–34.

Hench, L. L. (1991). *Bioceramics: from concept to clinic*. *J. Am. Ceram. Soc.* **74**, 1487–1510.

Hippel, A. von (1950). *Ferroelectricity, domain structure and phase transitions of barium titanate. Rev. Mod. Phys.* **22**, 221.

Jenkins, R. & Snyder, R. L. (1996). *Introduction to X-ray Powder Diffractometry*. New York: John Wiley & Sons.

Jones, J. T. & Berard, M. F. (1993). *Ceramics, Industrial Processing and Testing*. Ames: Iowa State University Press.

Jones, K. S., Rudawski, N. G., Oladeji, I., Pitts, R. & Fox, R. (2012). *The state of solid-state batteries*. *Am. Ceram. Soc. Bull.* **91**, 26–31.

Kassinger, R. (2003). *Ceramics: From Magic Pots to Man-Made Bones* Brookfield: Twenty-First Century Books.

Kawai, Y., Uo, M., Wang, Y., Kono, S., Ohnuki, S. & Watari, F. (2011). *Phase transformation of zirconia ceramics by hydrothermal degradation*. *Dent. Mater. J.* **30**, 286–292.

Khan, Z. A., Hadfield, M., Tobe, S. & Wang, Y. (2005). *Ceramic rolling elements with ring crack defects – a residual stress approach*. *Mater. Sci. Eng. A*, **404**, 221–226.

Kippelen, B. (2007). *Organic photovoltaics*. *Opt. Photonics News*, **18**(10), 28–33.

Kirk-Othmer Encyclopedia of Chemical Technology (2007). 5th ed. Hoboken: Wiley Blackwell.

Klug, H. & Alexander, L. E. (1974). *X-ray Diffraction Procedures for Polycrystalline and Amorphous Materials*. New York, London, Sydney, Toronto: John Wiley & Sons.

Koningsberger, D. C. & Prins, R. (1988). *X-ray Absorption. Principles, Applications, Techniques of EXAFS, SEXAFS and XANES*. New York: John Wiley & Sons. ISBN 0-471-87547-3.

Kordesch, K. V. & Simader, G. R. (1996). *Fuel Cells and Their Applications*. New York: VCH.

Larson, A. C. & Von Dreele, R. B. (2004). *General Structure Analysis System (GSAS)*. Los Alamos National Laboratory Report LAUR 86-748, Los Alamos, USA.

Leggett, A. J. (2006). *What DO we know about high T_c? Nat. Phys.* **2**, 134–136.

Li, J. & Ye, Y. (2006). *Densification and grain growth of Al_2O_3 nanoceramics during pressureless sintering*. *J. Am. Ceram. Soc.* **89**, 139–143.

McCauley, R. A. (1995). *Corrosion of Ceramics*, pp. 135–137. New York: Marcel Dekker, Inc.

McColm, I. J. (1983). *Ceramic Science for Materials Technologies*. Glasgow: Leonard Hill.

Mackenzie, K. J. D., Shimada, S. & Aoki, T. (1997). *Thermal oxidation of carbothermal β'-sialon powder: reaction sequence and kinetics*. *J. Mater. Chem.* **7**, 527–530.

Masse, D. J., Pucel, R. A., Readey, D. W., Maguire, E. A. & Hartwig, C. P. (1971). *A new low-loss high-K temperature-compensated dielectric for microwave applications*. *Proc. IEEE*, **59**, 1628–1629.

Masset, A. C., Michel, C., Maignan, A., Hervieu, M., Toulemonde, O., Studer, F., Raveau, B. & Hejtmanek, J. (2000). *Misfit-layered cobaltite with an anisotropic giant magnetoresistance: $Ca_3Co_4O_9$*. *Phys. Rev. B*, **62**, 166–175.

Mittemeijer, E. J. & Welzel, U. (2013). *Modern Diffraction Methods*. Weinheim: Wiley-VCH.

Monshi, A., Foroughi, M. R. & Monshi, M. R. (2012). *Modified Scherrer equation to estimate more accurately nano-crystallite size using XRD*. *World J. Nano Sci. Eng.* **2**, 154–160.

Montedo, O. R. K., Hotza, D., de Oliveira, A. P. N., Meszaros, R., Travitzky, N. & Greil, P. (2012). *Crystallisation kinetics of a β-spodumene-based glass ceramic*. *Adv. Mater. Sci. Eng.* **2012**, 525428.

Moore, D. M. & Reynolds, R. C. (1997). *X-ray Diffraction and the Identification and Analysis of Clay Minerals*. Oxford University Press.

Musikant, S. (1991). *What Every Engineer Should Know About Ceramics*, edited by W. H. Middendorf, ch. 3, p. 32. New York: Marcel Dekker, Inc.

Muster, D. (1992). Editor. *Biomaterials Hard Tissue Repair and Replacement. European Materials Research Society Monographs*, Vol. 3. Amsterdam, New York: North-Holland. ISBN 0-444-88350-9.

Nelmes, R. J., Loveday, J. S., Allan, D. R., Besson, J. M., Hamel, G., Grima, P. & Hull, S. (1993). *Neutron- and X-ray-diffraction measurements of the bulk modulus of boron*. *Phys. Rev. B*, **47**, 7668–7673.

Norton, F. H. (1978). *Cycles in Ceramic History*. In *Ceramic Processing Before Firing*, edited by G. Y. Onoda Jr & L. L. Hench, pp. 3–9. New York: Wiley-Interscience.

Oh, J. E., Clark, S. M., Wenk, H. R. & Monteiro, P. J. M. (2012). *Experimental determination of bulk modulus of 14 Å tobermorite using high pressure synchrotron X-ray diffraction*. *Cem. Concr. Res.* **42**, 397–403.

Paik, J.-G., Lee, M.-J. & Hyun, S.-H. (2005). *Reaction kinetics and formation mechanism of magnesium ferrites*. *Thermochim. Acta*, **425**, 131–136.

Parrish, W., Huang, T. C. & Ayers, G. L. (1976). *Profile fitting: a powerful method of computer X-ray instrumentation and analysis*. *Trans. Am. Crystallogr. Assoc.* **12**, 55–74.

Patterson, A. L. (1939). *The Scherrer formula for X-ray particle size determination*. *Phys. Rev.* **56**, 978–982.

Pecharsky, V. & Zavalij, P. (2008). *Fundamentals of Powder Diffraction and Structural Characterization of Materials*, 2nd ed. Boston: Springer.

Peterson, M. S., Say, C. A., Speakman, S. A. & Misture, S. T. (2003). *High-temperature X-ray diffraction study of reaction rates in ceramics*. *Adv. X-ray Anal.* **46**, 226–231.

Piermarini, G. J. (2001). *High pressure X-ray crystallography with the diamond cell at NIST/NBS*. *J. Res. Natl Inst. Stand. Technol.* **106**, 889–920.

Plourde, J. K., Linn, D. F., O'-Bryan, H. M. & Thomson, J. (1975). *$Ba_2Ti_9O_{20}$ as a microwave dielectric resonator*. *J. Am. Ceram. Soc.* **58**, 418–420.

Qu, J., Li, G. R. & Gao, X. P. (2010). *One-dimensional hierarchical titania for fast reaction kinetics of photoanode materials of dye-sensitized solar cells*. *Energy Environ. Sci.* **3**, 2003–2009.

Richerson, D. A. (1982). *Modern Ceramic Engineering: Properties, Processing, and Use in Design*. New York, Basel: Marcel Dekker, Inc.

Rietveld, H. M. (1969). *A profile refinement method for nuclear and magnetic structures*. *J. Appl. Cryst.* **2**, 65–71.

Riley, D. P., Kisi, E. H., Hansen, T. C. & Hewat, A. W. (2002). *Self-propagating high-temperature synthesis of Ti_3SiC_2: I, Ultra-high-speed neutron diffraction study of the reaction mechanism*. *J. Am. Ceram. Soc.* **85**, 2417–2424.

Ritley, K. A., Just, K.-P., Schreiber, F., Dosch, H., Niesen, T. P. & Aldinger, F. (2000). *X-ray reflectivity study of solution-deposited ZrO_2 thin films on self-assembled monolayers: growth, interface properties, and thermal densification*. *J. Mater. Res.* **15**, 2706–2713.

Rodriguez, E. E., Proffen, Th., Llobet, A., Rhyne, J. J. & Mitchell, J. F. (2005). *Neutron diffraction study of average and local structure in $La_{0.5}Ca_{0.5}MnO_3$*. *Phys. Rev. B*, **71**, 104430.

Rodríguez-Carvajal, J. (1993). *Recent advances in magnetic structure determination by neutron powder diffraction*. *Physica B*, **192**, 55–69.

Romero, M., Andrés, A., Alonso, R., Viguri, J. & Rincón, J. Ma. (2009). *Phase evolution and microstructural characterization of sintered ceramic bodies from contaminated marine sediments*. *J. Eur. Ceram. Soc.* **29**, 15–22.

Roth, R. S. & Vanderah, T. A. (2004). *Solid State Ionics: The Science and Technology of Ions in Motion*, edited by B. V. R. Chowdari, H.-L. Yoo, G. M. Choi & J.-H. Lee, pp. 3–18. Hackensack: World Scientific Publishing Co.

Rowe, D. M. (2006). *Thermoelectrics Handbook: Macro to Nano*, ch. 35, *Oxide thermoelectrics*. Boca Raton: CRC Press.

Saito, Y., Takao, H., Tani, T., Nonoyama, T., Takatori, K., Homma, T., Nagaya, T. & Nakamura, M. (2004). *Lead-free piezoceramics*. *Nature*, **432**, 84–87.

Scherrer, P. (1918). *Bestimmung der Grösse und der inneren Struktur von Kolloidteilchen mittels Röntgenstrahlen*. *Göttinger Nachr. Gesell.* **2**, 98–100.

Schmid, H. K. (1987). *Quantitative analysis of polymorphic mixes of zirconia by X-ray diffraction*. *J. Am. Ceram. Soc.* **70**, 367–376.

Schneider, G. Jr (2009). *Chapter 1: Cutting Tool Materials*, American Machinist, October 2009. http://www.americanmachinist.com/cutting-tools/chapter-1-cutting-tool-materials.

Sebastian, M. T. (2008). *Dielectric Materials for Wireless Communication*. Oxford: Elsevier.

Shikano, M. & Funahashi, R. (2003). *Electrical and thermal properties of single-crystalline $(Ca_2CoO_3)_{0.7}CoO_2$ with a $Ca_3Co_4O_9$ structure*. *Appl. Phys. Lett.* **82**, 1851–1853.

Skinner, S. J. & Kang, Y. (2003). *X-ray diffraction studies and phase transformations of $CeNbO_{4+\delta}$ using in situ techniques*. *Solid State Sci.* **5**, 1475–1479.

Smith, R. L. (2005). *The Engineering Handbook*, 2nd ed., ch. 151, *Sensors and transducers*. Boca Raton: CRC Press.

Tachibana, T., Nakagawa, T., Takada, Y., Izumi, K., Yamamoto, T. A., Shimada, T. & Kawano, S. (2003). *X-ray and neutron diffraction studies on iron-substituted Z-type hexagonal barium ferrite: $Ba_3Co_{2-x}Fe_{24+x}O_{41}$ (x = 0–0.6)*. *J. Magn. Magn. Mater.* **262**, 248–257.

Tanner, B. K., Hase, T. P. A., Lafford, T. A. & Goorsky, M. S. (2004). *Grazing-incidence in-plane X-ray diffraction in the laboratory*. *Adv. X-ray Anal.* **47**, 309–314.

Toraya, H., Yoshimura, M. & Somiya, S. (1984). *Calibration curve for quantitative analysis of the monoclinic–tetragonal ZrO_2 system by X-ray diffraction*. *J. Am. Ceram. Soc.* **67**, C-119–C-121.

Tritt, T. M. (1996). *Thermoelectrics run hot and cold*. *Science*, **272**, 1276–1277.

Valasek, J. (1921). *Piezo-electric and allied phenomena in Rochelle salt*. *Phys. Rev.* **17**, 475–481.

Valenzuela, R. (1994). *Magnetic Ceramics*. Cambridge University Press.

Vanderah, T. A. (2002). *Talking ceramics*. *Science*, **298**, 1182–1184.

Vanderah, T. A., Wong-Ng, W., Huang, Q., Roth, R. S., Geyer, R. G. & Goldfarb, R. B. (1997). *Crystal structures and properties of $Ba_4Fe_2Ti_{10}O_{27}$ and $Ba_3Fe_{10}TiO_{20}$*. *J. Phys. Chem. Solids*, **58**, 1403–1415.

Wallis, K. L., Patyk, J. K. & Zerda, T. W. (2008). *Reaction kinetics of nanostructured silicon carbide*. *J. Phys. Condens. Matter*, **20**, 325216.

Warren, B. E. & Averbach, B. L. (1950). *The effect of cold-work distortion on X-ray patterns*. *J. Appl. Phys.* **21**, 595–599.

Weimer, A. W. (1977). Editor. *Carbide, Nitride and Boride Materials Synthesis and Processing*. London: Chapman & Hall.

Weir, C. E., Block, S. & Piermarini, G. J. (1970). *Compressibility of inorganic azides*. *J. Chem. Phys.* **53**, 4265–4269.

Williamson, G. K. & Hall, W. H. (1953). *X-ray line broadening from filed aluminium and wolfram*. *Acta Metal.* **1**, 22–31.

Wong-Ng, W., Piermarini, G. J. & Gallas, M. R. (1995). *X-ray diffraction study of $BaNd_2CuO_5$ at high pressures*. *Adv. X-ray Anal.* **38**, 741–747.

Wong-Ng, W., Yang, Z., Cook, L. P., Huang, Q., Kaduk, J. A. & Frank, J. (2005). *Chemical interaction between $Ba_2YCu_3O_{6+x}$ and CeO_2 at pO_2 = 100 Pa*. *Solid State Sci.* **7**, 1333–1343.

Yamamuro, T., Hench, L. L. & Wilson, J. (1990). Editors. *CRC Handbook of Bioactive Ceramics*, Vol II. Boca Raton: CRC Press. ISBN 0-8493-3242-7.

Zevin, L. S. & Kimmel, G. (1995). *Quantitative X-ray Diffractometry*, New York: Springer-Verlag.

Zhang, F., Chupas, P. J., Lui, S. L. A., Hanson, J. C., Caliebe, W. A., Lee, P. L. & Chan, S. W. (2007). *In situ study of the crystallization from amorphous to cubic zirconium oxide: Rietveld and reverse Monte Carlo analyses*. *Chem. Mater.* **19**, 3118–3126.

International Tables for Crystallography (2019). Vol. H, Chapter 7.9, pp. 828–833.

7.9. Applications in glass-ceramics

S. T. Misture

7.9.1. Introduction

Glass-ceramics find application in a broad range of technologies largely because they are easily processed to form crystalline solids with a wide range of grain sizes, grain morphologies and properties. Glass-ceramics are perhaps more correctly described as composites of crystalline and glassy phases with grain sizes ranging from nanometres to micrometres. The unique aspect of glass-ceramic processing is net-shape forming. During manufacture, the starting glass is melted and can be formed into a net or near-net shape using well known glass-forming techniques that produce full-density glasses. After shaping, the glass may then be subjected to an appropriate time–temperature excursion to induce partial or full crystallization, also called 'ceramization'. It should be noted that the crystallization of the glass begins from a full-density solid, which is a condition that cannot be achieved using traditional ceramics powder manufacturing techniques, and hence glass-ceramic microstructures are often considered superior to polycrystalline ceramic bodies that typically contain some fraction of closed porosity.

Our ability to control the phase assemblage and microstructure of glass-ceramics leads to a broad range of technological applications, with the ubiquitous example being transparent nano-grained cookware. Other examples include high-temperature ceramic-to-metal sealants used in commercial lighting, electrochemical devices, electronics packaging *etc*. In healthcare, glass-ceramics find application in dental restorations and for a range of biomedical devices, bone cements and the like.

7.9.1.1. *Devitrification*

Generically, 'glass-ceramics' include any composite material with a varying crystal-to-glass ratio, with the crystalline content approaching 100% in many cases. Glass-ceramic devices or components are typically fabricated in one of two ways: forming to net shape using glass-forming methods, or processed as powder to near-net shape. After forming, nucleation and crystallization is induced by an appropriate heat treatment to create a glassy matrix with crystalline grains. This process is called devitrification, although the term 'ceramization' is also often used. It is important to note that the glassy component may be small enough to ignore for most discussions of the microstructure–property relations in glass-ceramic bodies.

When using glass-forming methods, the advantage of the glass-ceramic method is the ability to form fully dense net-shape components without the need for traditional ceramic consolidation and sintering processes. However, it is often necessary to process glass-ceramics in powder or frit form to accommodate surface nucleation, as will be described in detail later. Crystallizing glass is a two-step process, understood as nucleation and growth, where both processes have strong temperature dependences. Nucleation is the clustering of atoms of some critical size so that the nucleus may either grow to become a crystal or redissolve. Nucleation rate shows a peak with temperature; initially it increases with temperature above some critical nucleation temperature, then after reaching a peak value the rate decreases at higher temperature as more and more nuclei redissolve. Crystal growth rates also show a peak with temperature, but of course growth of a crystal requires a stable nucleus and hence the onset of crystallization occurs at or above the onset of nucleation. In general, the nucleation and growth curves are separated in temperature. Nucleation generally occurs at lower temperatures and growth at higher temperatures, but both occur simultaneously over some temperature range. Often the nucleation and growth curves overlap extensively, but for some systems the nucleation and growth temperatures are well separated. Hence it is sometimes possible to study nucleation and crystallization as separate events.

Nucleation occurs *via* one of three mechanisms, two of which are understood as 'bulk' nucleation and the third of which is surface nucleation. The defining characteristic of 'bulk'-nucleated glasses is nucleation within the glass instead of at surfaces of the glass or at interfaces of the glass. The first of the bulk mechanisms is homogeneous nucleation induced by phase separation in the amorphous state. Many glasses undergo phase separation to form two or more amorphous phases either during cooling or during reheating as part of the devitrification cycle. Phase separation in the amorphous phase may be detected in the diffraction pattern as a change in the amorphous hump(s). Partitioning of the chemical elements in the glass into two or more new glass phases may result in one or more of the new glasses having a lower stability than the starting bulk glass. Unstable glassy phases then nucleate tiny seed crystals, which subsequently grow to produce crystallites.

Secondly, the use of bulk nucleating agents (for example some metals, ZrO_2 or TiO_2) is common to induce nucleation in homogeneous glasses that do not undergo phase separation.

Finally, surface nucleation is an alternative mechanism where low-energy surface sites nucleate crystals. The use of frit processing is common when taking advantage of surface nucleation, where the glass frit particle size can be easily controlled to define the surface-to-bulk ratio and hence the density of nuclei, and the number and size of crystals.

The maximum crystallite size is determined by the volume density of nuclei, because the crystal nuclei grow during an appropriate heat treatment. As crystals grow in the glass, they eventually impinge on one another or consume all of the necessary chemical components from the glass. Nano-grained, transparent glass-ceramics can be routinely processed by simply increasing the volume density of nuclei.

Of course not all materials may be fabricated using the glass-ceramic process, either because the composition cannot feasibly be melted to form a glass or because crystallization of the glass does not produce the desired crystalline phase. The complexities of the nucleation and crystallization process can often, however, be used to great advantage. Common devitrification processes include the following.

(i) The simple case of crystallization of the glass to form crystals of the same stoichiometry as the glass (referred to as stoichiometric crystallization).

(ii) Crystallization of phases that are of different chemistry to the parent glass, therefore changing the composition of the glassy matrix as crystallization proceeds.

Copyright © 2019 International Union of Crystallography

(iii) Crystallization of metastable phases that transform with time into stable crystalline phases, thus facilitating synthesis of the metastable or stable phase, depending upon the heat-treatment time–temperature profile.
(iv) Crystallization of more than one phase, either concurrently or sequentially.
(v) Crystallization of different phases at the surface and in the bulk.

Processes (ii)–(v) yield a glassy matrix with different chemistry and therefore different properties to the starting glass, showing how the formation of glass-ceramics is an elegant way to tune the properties of monolithic solids. By simply controlling the nucleation and time–temperature profiles for a glass of given composition, one may produce solids with vastly varied properties. Perhaps even more elegant is the use the glass-ceramic method to produce unusual microstructures, because the crystals may grow as spherulites, as plates or in other interesting morphologies (Pinckney & Beall, 2008). Therefore, the glass-ceramic method is a unique tool in the design and processing of materials.

7.9.1.2. *Applications of powder diffraction*

The use of powder diffraction in the study of glass-ceramics is well established, although only relatively few laboratories use *in situ* high-temperature neutron powder diffraction (NPD) or X-ray powder diffraction (XRD), which will be the focus of this chapter. Glass crystallization is often studied using thermal analysis, either differential scanning calorimetry (DSC) for glasses with lower crystallization temperatures, T_x, or differential thermal analysis (DTA) for those with higher T_x. Well established methods, described later, can be used to extract the reaction kinetics and therefore the energetics of the crystallization process. Thermal analysis methods do not, however, provide any information about the crystallite size, microstrain, crystallite orientation or phase content. In contrast, diffraction methods provide direct access to all of these characteristics from a single measurement.

7.9.2. Methods

Powder diffraction may be used to track the crystalline phase fraction using any of the several quantitative analysis procedures outlined in Chapter 3.9, including absolute quantification of the amorphous and crystalline content. Crystallite growth can be determined using the diffraction peak broadening (see Chapter 5.1) as the crystals grow from ~5 to 1000 nm, where ~1000 nm is the limit of the technique. The third important characteristic is crystallite orientation relative to surfaces for monolithic glasses. Many glasses display nucleation and oriented growth starting at the surface, and hence quantification of the crystallite orientation may be important. Pole-figure measurements and quantitative orientation distribution functions (see Chapter 5.3) may be used to understand the crystallite orientation and its link to properties.

7.9.2.1. *Time–temperature profiles*

Heat-treatment time–temperature profiles for glass-ceramics may be optimized by empirical means or by performing detailed kinetic studies that provide rate constants for the reaction. Both approaches may be undertaken using either pre-treated samples or *in situ* methods. For pre-treated samples, one generally heats the starting glass rapidly, for example by inserting a specimen into a preheated furnace. After a given time period, the specimen may be extracted and analysed with the confidence that the heating rate was indeed as fast as possible.

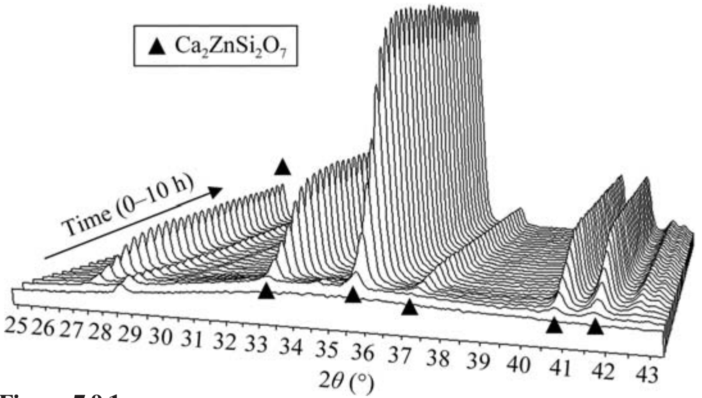

Figure 7.9.1
Three-dimensional view of isothermal *in situ* XRD data for the crystallization of $Ca_2ZnSi_2O_7$ from the glass at 1173 K.

In situ measurements provide a means of tracking crystallization as it happens, either in dynamic experiments in which the heating rate is constant or during isothermal holds. For dynamic measurements the XRD data are collected at fixed time increments while the sample continually heats or cools, and therefore obtaining a good signal-to-noise ratio can be a challenge. Modern one-dimensional detectors with remarkably fast data-collection times over small 2θ regions enable much improved experiments over point detectors. The same is of course true when comparing two-dimensional with one-dimensional detectors, with the ultimate experiment being a high-energy synchrotron experiment using two-dimensional detection. In our own laboratory, we routinely make reliable measurements in 2 s snapshots using one-dimensional detectors with sealed X-ray tube sources.

For isothermal measurements, the ideal experiment includes infinitely rapid heating to the target temperature. As noted earlier for pre-treated experiments, a good approximation to this condition is inserting the specimen into a preheated furnace. For *in situ* XRD, we may consider preheating the furnace and then inserting the sample to start the measurement. One of our own laboratory systems allows this type of measurement (Dolan *et al.*, 2003). The other option is to use the fastest heating rate possible, either in a metal strip XRD furnace or in an environmental furnace chamber. Metal strip heaters can reach the fastest heating rates, but true bulk heating furnaces may also achieve high heating rates, for example up to 600 K min^{-1} in one of our custom systems (Misture, 2003).

7.9.3. Qualitative analysis of devitrification

Qualitatively describing crystallization involves either non-isothermal or isothermal measurements of glasses defined by the following.

(i) The sample configuration: monolithic samples differ from frit or powder samples in their surface-to-bulk ratios, and therefore the extent of surface nucleation will differ among these sample configurations. Indeed, it is often straightforward to differentiate between bulk and surface nucleation using measurements of monolithic and powder samples.
(ii) The heating rate and/or the average heating rate (in the case of isothermal *in situ* measurements).
(iii) The nucleation hold time and temperature, if applicable.

Fig. 7.9.1 shows the simplest case of isothermal stoichiometric devitrification of a $Ca_2ZnSi_2O_7$ glass at 1173 K. From Fig. 7.9.1, we note that the amorphous hump that is initially present

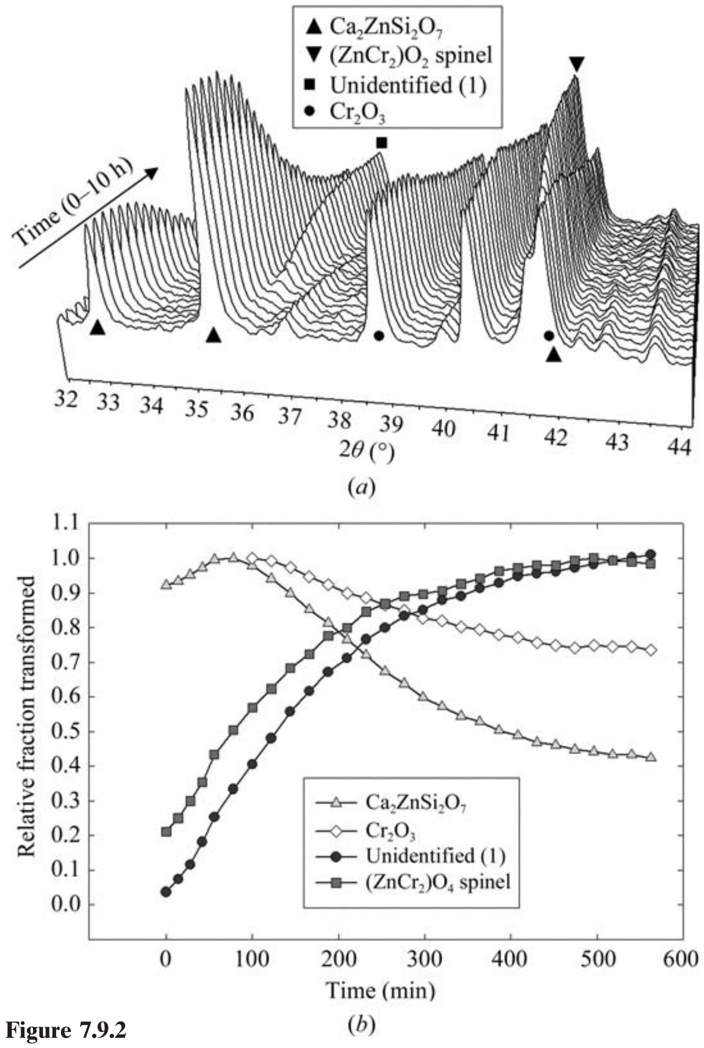

Figure 7.9.2
(*a*) *In situ* XRD isothermal data for a complex multiphase crystallization at 1223 K; (*b*) relative phase fractions of each component with time.

decreases in intensity as the crystalline $Ca_2ZnSi_2O_7$ phase grows over the course of ~200 min.

A more complex devitrification process is encountered with small changes in the initial glass composition away from $Ca_2ZnSi_2O_7$. Fig. 7.9.2 shows the *in situ* XRD data, where we note that the first XRD pattern contains peaks for $Ca_2ZnSi_2O_7$ and Cr_2O_3; in other words, these phases crystallized rapidly on heating to 1223 K. Two new phases crystallize over the course of the 10 h experiment, one of which is $ZnCr_2O_4$, which crystallizes at the expense of the $Ca_2ZnSi_2O_7$ phase. Clearly, a reaction between $Ca_2ZnSi_2O_7$ and Cr_2O_3 occurs to extract the zinc from the crystalline phase and therefore slowly eliminate the $Ca_2ZnSi_2O_7$ phase. A fourth phase begins to crystallize after about 1 h but was not successfully identified. Indeed, the issue of metastable phases in the study of glass-ceramics is of key importance, and one might expect to very often find diffraction patterns for high-temperature phases that have not been reported. It is possible in many cases to employ additional tools to identify the chemical composition of new phases and to prepare and characterize them separately. Some of our recent work has demonstrated this approach, where we have used *ab initio* structure solutions from powder-diffraction data to provide full structural data (Dolan & Misture, 2007). Of course, given the crystal structures, we can then perform Rietveld quantification to improve our analysis.

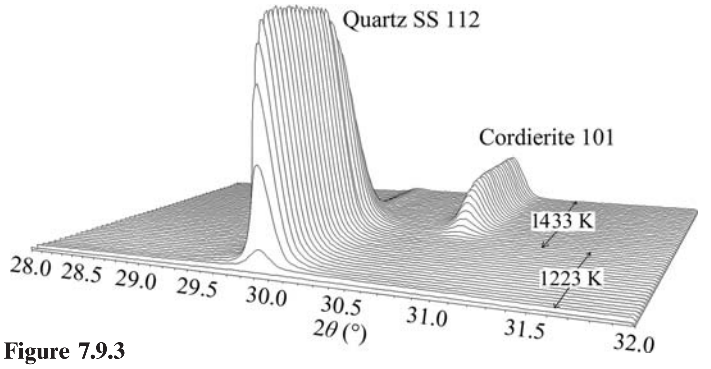

Figure 7.9.3
In situ XRD patterns for an $NiO{\cdot}MgO{\cdot}Al_2O_3{\cdot}SiO_2$ glass held isothermally at 1223 K for 1100 s to crystallize a β-quartz solid solution (SS) followed by heating to 1333 K to transform it to cordierite.

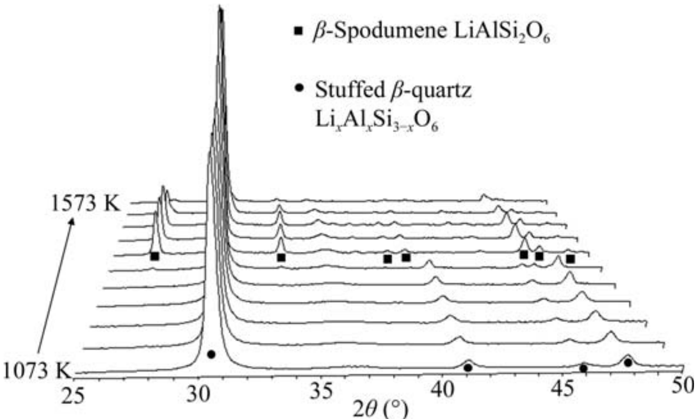

Figure 7.9.4
Example of a crystal-to-crystal conversion in Robax glass-ceramic. Temperature steps are 50 K between each XRD pattern.

Another example of the development of multiple phases is shown in Fig. 7.9.3, where we find complete conversion from β-quartz to cordierite during crystallization of $NiO{\cdot}MgO{\cdot}Al_2O_3{\cdot}SiO_2$ glasses (Miller & Misture, 2010). Fig. 7.9.3 shows the results for a sample held isothermally at 1223 K for 1100 s to crystallize β-quartz, followed by heating to 1333 K to transform the quartz to cordierite.

Finally, Fig. 7.9.4 shows an example of a crystal-to-crystal transformation. The glass is a commercial material manufactured by Schott Glass: Robax. Robax is a 'fully' crystalline glass-ceramic with a stuffed β-quartz crystalline phase, $Li_xAl_xSi_{3-x}O_6$. As shown in the *in situ* XRD patterns in Fig. 7.9.4, the β-quartz phase transforms to β-spodumene, $LiAlSi_2O_6$, near 1323 K (Sinton *et al.*, 2008). This result demonstrates the richness of options when processing glass-ceramics, where we may define the crystalline phases present by simply defining the time–temperature profile.

7.9.4. Kinetics analysis

7.9.4.1. *Theory*

The devitrification of glasses to form one or more crystalline phases is traditionally studied using the Kissinger analysis of thermal analysis heat-flow data, *i.e.* DSC or DTA. For diffraction data, we instead use the JMAK method, which is a more general approach that is easily applied. The JMAK method is named after Johnson and Mehl (Johnson & Mehl, 1939), Avrami (Avrami, 1939, 1940, 1941) and Kolmogorov (Kolmogorov, 1937), who described the isothermal transformation kinetics for nucleation and growth according to

$$x(t) = 1 - \exp(-kt^n), \qquad (7.9.1)$$

where x is the volume fraction transformed, t is the elapsed time, k is the rate constant and n is the Avrami exponent. The Avrami variables depend upon the type of nucleation and growth. For example, in the case of spherical crystals growing from homogenously distributed nuclei $k \simeq 1$ and $n = 4$ (Holand & Beall, 2002). The reader is referred to Hancock & Sharp (1971), who provide a set of ten theoretical rate equations with varied Avrami exponents as well as further detail regarding the interpretation of the Avrami exponents.

Equation (7.9.1) can be recast as $-\ln\{\ln[1 - x(t)]\} = \ln B + n\ln(t)$, and it is convenient to plot $\ln\{-\ln[1 - x(t)]\}$ *versus* $\ln(t)$ to extract the slope, n, as the Avrami exponent. The fraction transformed, $x(t)$, comes directly from the diffraction data, either using a simple measurement of peak heights or areas, or by more complex means including full absolute quantification to provide the quantity of all crystalline phases and the amorphous phase present.

To extract the fullest information from the analysis, one must measure the transformation rates at several temperatures (this is an isothermal approach) and then fit the rate constants (k) to the data in the form of an Avrami plot. Next, the rate constants can be used in an Arrhenius analysis to determine the temperature dependence of the reaction rates and therefore the activation energy for crystallization. An Arrhenius plot is typically shown as $\ln(k) = E_a/RT + \ln(A)$, where E_a is the activation energy for crystallization, R is the gas constant and A is the pre-exponential factor.

7.9.4.2. *Complexities in kinetics measurements*

From an experimental point of view, it is most common to measure changes in the XRD patterns after (or during) isothermal holds. Naturally, *post situ* XRD, optical microscopy or scanning electron microscopy (SEM) may be used to study individual samples after a specific heat treatment, but *in situ* analysis provides more information in a rapid and efficient manner. A drawback of isothermal measurements using *in situ* XRD is the uncertainty in the time = zero point, because of the finite heating rate experienced by the sample. However, this drawback is often mitigated by choosing temperatures where the extent of crystallization upon reaching the target temperature is insignificant, and hence the sample remains largely or fully amorphous to X-rays through at least the beginning of the first *in situ* XRD measurement. Therefore, the initial measurement provides a starting value for $x(t)$ that is zero or nearly zero, and/or $x(t)$ may be fitted to an exponential function to determine the fraction transformed at infinite time. Several examples follow to demonstrate the use of kinetics analysis.

7.9.4.3. *Kinetics analysis example 1: glass to single-phase crystal*

As discussed earlier, multi-component glasses may crystallize to form a single crystalline phase or multiple phases. An example of a complex glass crystallizing to form only one crystalline phase is EG9207, a sealing glass with an 'invert' composition (Dolan & Misture, 2007). Invert glasses contain a smaller fraction of network formers than other components and crystallize extensively, and in this example EG9207 contains only 25 mol% SiO_2, with 44 mol% alkaline-earth oxides, 15 mol% MgO and 16 mol% B_2O_3.

Fig. 7.9.5 shows the evolution of one of the XRD peaks for $Ba_2MgSi_2O_7$ as it crystallizes from a powdered glass (10 µm average particle size) isothermally at 1048 K. Fig. 7.9.5 shows clearly that the glass crystallizes over the course of roughly 900 s, and that measuring the XRD peak in 100 s increments is sufficient to provide 8–10 data points for the kinetics analysis.

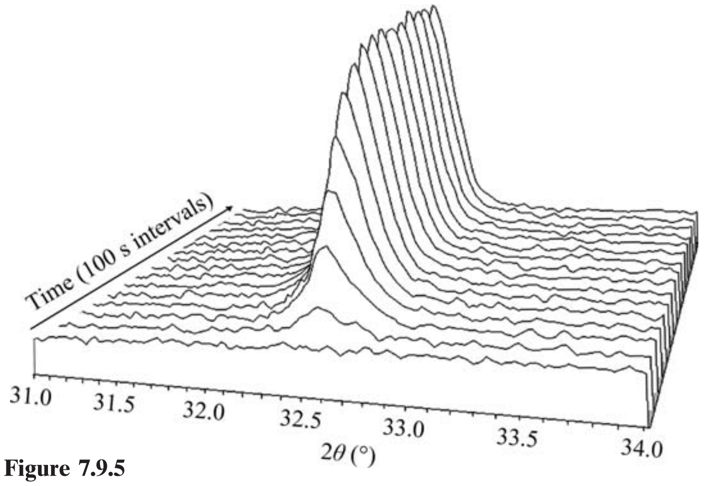

Figure 7.9.5
High-temperature XRD measurements of the crystallization of $Ba_2MgSi_2O_7$ from EG9207 glass.

Analysis of the kinetics started by extracting the peak areas from Fig. 7.9.5 and fitting an exponential function to the trend to obtain the fraction transformed, $x(t)$, *versus* time. The exponential fit provides $x(t)$ at $t \to \infty$ and is therefore a simple means of determining $x(t)$ at any t. The applicable rate equation for the process is first order, or $-\ln[1 - x(t)] = kt$. The Avrami plot is then drawn as $\ln(t)$ *versus* $\ln\{-\ln[1 - x(t)]\}$, and the slope of each Avrami plot for each isothermal measurement provides the rate constant, k. An Arrhenius plot can then be used to quantify the effects of temperature on crystallization rate, as shown in Fig. 7.9.6, the slope of which is E_a/RT, as noted earlier. For this particular glass composition, the activation energy is 281 ± 21 kJ mol^{-1}, which is typical for invert glasses (Pinckney & Beall, 2008).

Kinetics analysis provides some predictive capability and can be used to estimate the extent of crystallization at any arbitrary temperature after determining the rate constants. Fig. 7.9.7 shows the calculated crystallization rates for EG9207 glass at several temperatures, demonstrating the expected behaviour for a first-order reaction. Caution should be used, however, to ensure that extrapolations are not made beyond the bounds defined by the experimental determinations of rate constants; changes in mechanism and even additional phase transitions may occur, as shown earlier in Fig. 7.9.4.

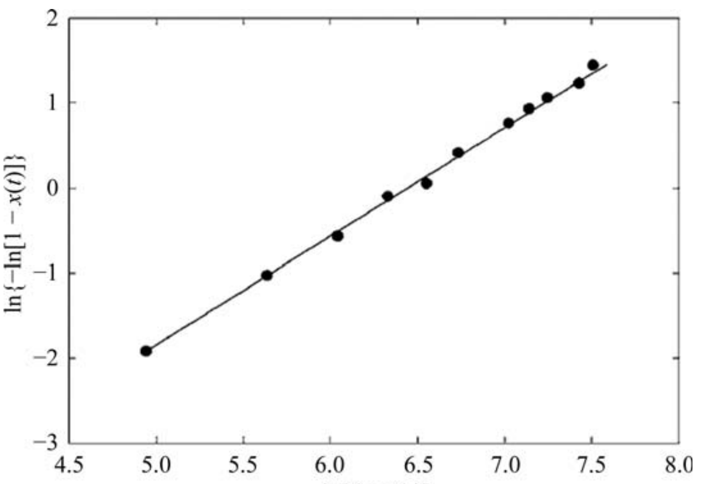

Figure 7.9.6
Avrami plot for crystallization extracted from Fig. 7.9.5.

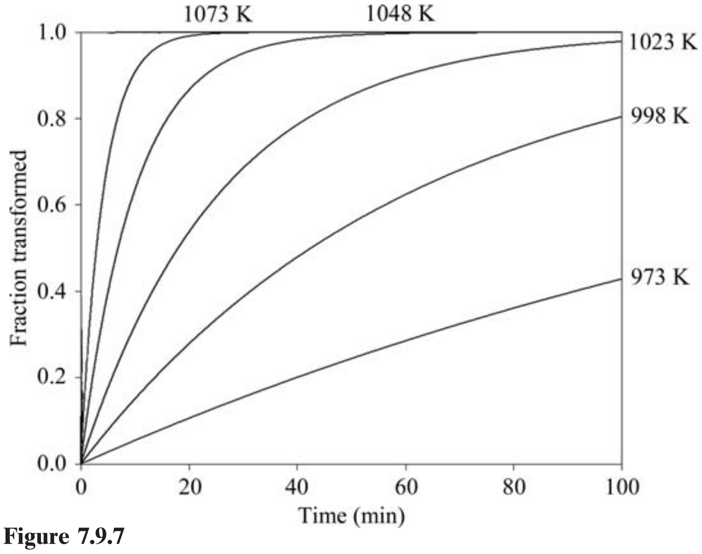

Figure 7.9.7
Crystallization rates for EG9207 glass calculated for several temperatures using the experimental rate constants.

7.9.4.4. *Kinetics analysis example 2: glass to crystal to crystal*

Extending the study shown in Fig. 7.9.3 to multiple temperatures enables full isothermal kinetics analysis of the conversion of a quartz solid solution to cordierite. The reader is referred to our complete description of the cordierite system for additional details (Miller & Misture, 2010), but in brief we show in Fig. 7.9.8 the Arrhenius plot for the crystallization of cordierite from the β-quartz phase for several glass compositions in the series. Crystallization of β-quartz occurs from the glass, and β-quartz then transforms to cordierite. The general JMAK approach allows us to directly extract the kinetics of both processes and a close examination of the reaction kinetics shows that the Avrami exponent (n value) is ~1.5 for both the glass → β-quartz and β-quartz → cordierite transformations. The value of n = 1.5 indicates that the transformation processes are diffusion-controlled with a nucleation rate of zero (Hancock & Sharp, 1971).

The initial crystallization of the glass to form β-quartz requires only ~600 kJ mol^{-1}. The activation energies calculated from the Arrhenius plot in Fig. 7.9.8 for the β-quartz → cordierite transition are between 800 and 850 kJ mol^{-1} across the compositional range, suggesting that the presence of additional nickel in the glass does not substantially change the rate-controlling steps of the reaction. Given that the Avrami exponent indicates a diffusional reaction path, we may surmise that the presence of nickel does not significantly alter the glass viscosity, density or other parameters that would affect diffusion rates.

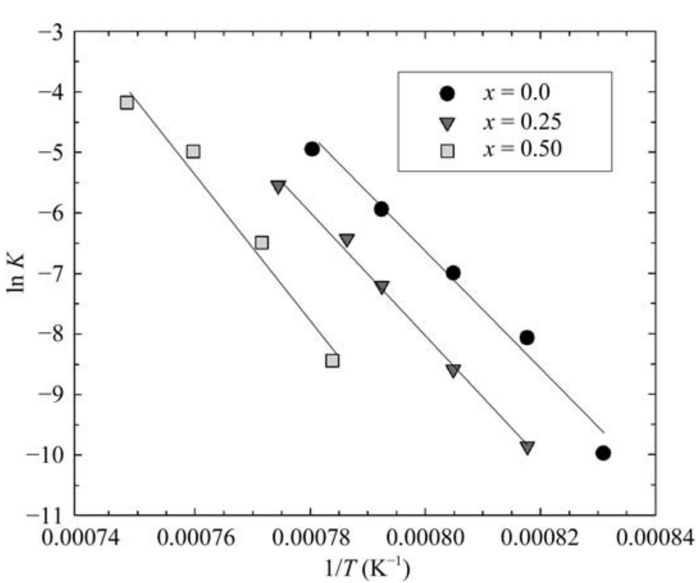

Figure 7.9.8
Arrhenius plot for the crystallization of cordierite in xNiO·(1 − x)MgO·2Al$_2$O$_3$·5SiO$_2$ glass for three different values of x. The corresponding activation energies for the transformation are 803 ± 60, 852 ± 37 and 1004 ± 117 kJ mol^{-1} for increasing values of x.

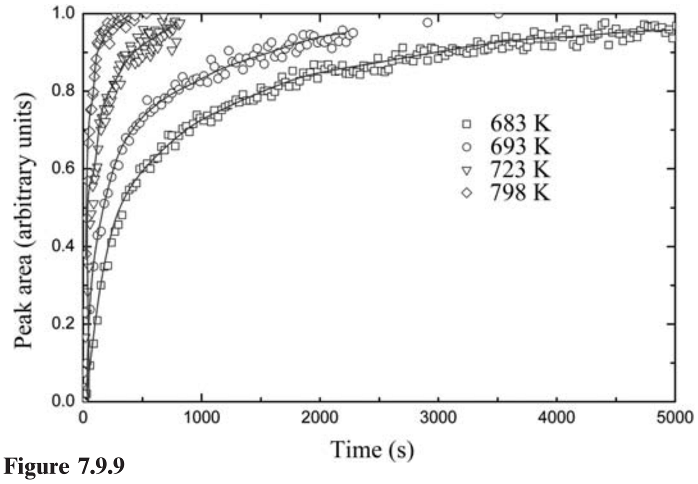

Figure 7.9.9
Reaction progress as reflected in XRD peak intensity *versus* time for the initial crystallization of 2Li$_2$O–SiO$_2$ glass.

An interesting opportunity in this reaction sequence is the ability to track the disappearance of the β-quartz phase and compare its kinetics with the kinetics of formation of cordierite. We found that the rate of disappearance of β-quartz matches the rate of growth of cordierite, confirming that the mechanism of transformation directly involves the conversion of β-quartz.

7.9.4.5. *Kinetics analysis example 3: effects of nucleation*

The final example provided relates to the nucleation treatment. Glasses of the orthosilicate composition, 2Li$_2$O–SiO$_2$, were studied using *in situ* XRD with rapid heating and data-collection rates, typically 20 s per XRD pattern (Wondraczek *et al.*, 2006). The phase progression is glass → unidentified crystalline phase (below 623 K) → Li$_4$SiO$_4$ (~773 K) → Li$_2$SiO$_3$ (~923 K). The initial crystallization is most sensitive to the nucleation treatment, and the kinetics were determined using multiple isothermal

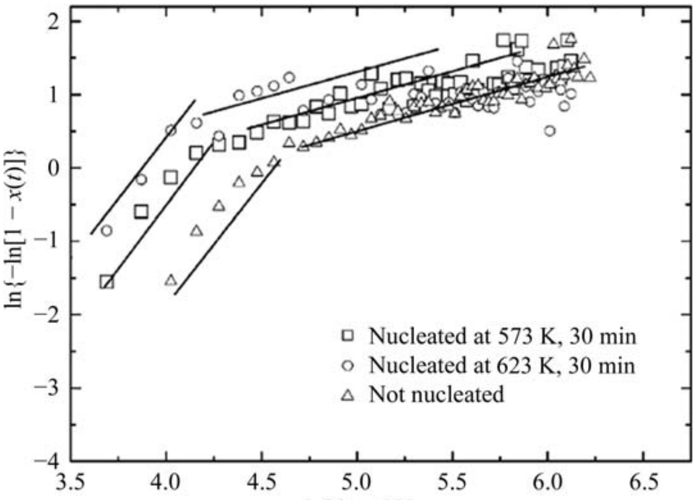

Figure 7.9.10
Effect of nucleation hold temperatures on crystallization of the glass, extracted from measurements paralleling those in Fig. 7.9.9.

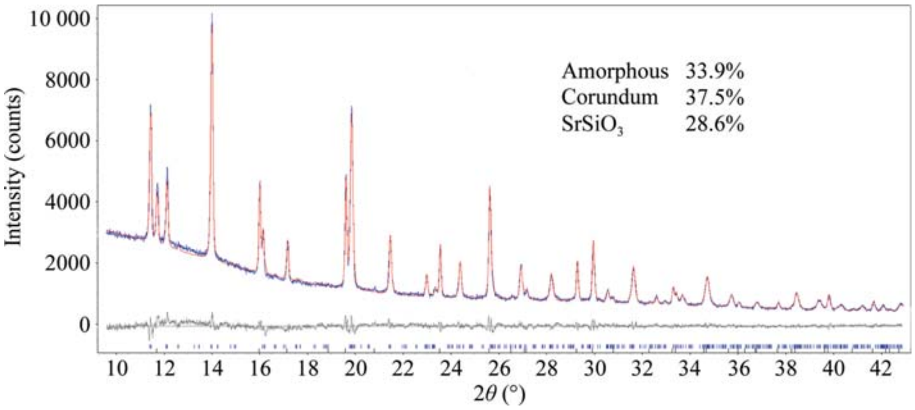

Figure 7.9.11
Rietveld fit of the XRD pattern of a partially crystallized glass, with an internal quantitative analysis standard, used to determine the remnant glass composition. Blue = observed profile, red = calculated profile, grey = difference profile.

measurements. Fig. 7.9.9 shows the growth rates which are used to generate the Arrhenius plot, yielding an activation energy of 90 kJ mol^{-1} for the transition.

To quantitatively determine the impact of nucleation, a set of nucleation experiments was performed by annealing the sample between 573 and 673 K for 30 min and then performing the isothermal high-temperature XRD experiment at 783 K. The results are shown in Fig. 7.9.10, which gives a clear indication that the extent of nucleation increases with temperature up to 623 K, which in turn increases the crystallization rate.

7.9.5. Remnant glass compositions *via* quantitative analysis

XRD has another interesting application in the area of glass-ceramics: absolute determination of the chemical composition of the remnant glass. Many glass-ceramics, in particular those used in ceramic metal sealing, rely on the complex interplay of glassy and crystalline phase components of the sealing material. In our laboratories, we have studied sealing glasses for solid oxide fuel cells extensively (Flügel *et al.*, 2007; Misture, 2008; Naylor *et al.*, 2013). In one case, for a glass containing ~60 mol% SiO$_2$, <10 mol% B$_2$O$_3$, 20 mol% SrO and 10 mol% Ga$_2$O$_3$, we found outstanding properties in the sealant, but because the sealant only crystallized to roughly 50 vol%, we endeavoured to synthesize and test the remnant glass itself.

The composition of the remnant glass phase after ~50% crystallization was determined using quantitative XRD analysis *via* the internal-standard Rietveld method. NIST SRM676 alumina quantitative analysis standard was mixed with the crystallized glass-ceramic and a powder-diffraction pattern was measured. Rietveld analysis of the pattern, shown in Fig. 7.9.11, provided the quantities of each phase (with their densities) as well as the quantity of the amorphous phase. A simple calculation then yielded the amorphous phase composition, which was prepared and tested successfully. The major crystalline phase is SrSiO$_3$, so we expected the remnant glass to be rich in boron. In fact, the original glass contained 10 mol% B$_2$O$_3$ and the remnant glass after partial crystallization was enriched to 18 mol%, markedly changing the properties of the glass.

7.9.6. Summary

Powder diffraction is a useful tool for analysis of the devitrification of glasses to form glass-ceramics. Unlike thermal-analysis methods, diffraction methods provide direct access to phase identity, phase quantities and phase-specific microstructural information, including crystallite size, microstrain and crystallite orientation. Isothermal kinetics analysis provides the crystallization activation energies and reaction rates, which are useful in the design and development of glass-ceramic preparation processes and in predicting the long-term behaviour at high temperature.

References

Avrami, M. (1939). *Kinetics of phase change I. General theory. J. Chem. Phys.* **7**, 1103–1112.

Avrami, M. (1940). *Kinetics of phase change II. Transformation–time relations for random distribution of nuclei. J. Chem. Phys.* **8**, 212–224.

Avrami, M. (1941). *Granulation, phase change, and microstructure. Kinetics of phase change III. J. Chem. Phys.* **9**, 177–184.

Dolan, M. D. & Misture, S. T. (2007). *Development of an improved devitrifiable fuel cell sealing glass. II. Crystallization behavior and structures of crystalline phases J. Electrochem. Soc.* **154**, B700–B711.

Dolan, M. D., Zdzieszynski, S. & Misture, S. T. (2003). *A high-temperature powder diffraction furnace. Adv. X-ray Anal.* **46**, 50–55. http://www.icdd.com/resources/axa/vol46/V46_07.pdf.

Flügel, A., Dolan, M. D., Varshneya, A. K., Zheng, Y., Coleman, N., Hall, M., Earl, D. & Misture, S. T. (2007). *Development of an improved devitrifiable fuel cell sealing glass. J. Electrochem. Soc.* **154**, B601–608.

Hancock, J. D. & Sharp, J. H. (1971). *Method of comparing solid-state kinetic data and its application to the decomposition of kaolinite, brucite, and BaCO$_3$. J. Am. Ceram. Soc.* **55**, 74–77.

Holand, W. & Beall, G. (2002). *Glass Ceramic Technology*. Westerville: American Ceramic Society.

Johnson, W. A. & Mehl, R. F. (1939). *Reaction kinetics in processes of nucleation and growth. Trans. Am. Inst. Min. Metall. Eng.* **135**, 416–441.

Kolmogorov, A. (1937). *On the statistical theory of crystallization of metals. Izv. Akad. Nauk. SSSR Ser. Mat.* **3**, 355–359.

Miller, M. E. & Misture, S. T. (2010). *Stoichiometric (Ni,Mg)-cordierite glass-ceramics. J. Am. Ceram. Soc.* **93**, 1018–1025.

Misture, S. T. (2003). *Large-volume atmosphere-controlled high-temperature X-ray diffraction furnace. Meas. Sci. Technol.* **14**, 1091–1098.

Misture, S. T. (2008). *Effects of hydrogen on the interactions of fuel cell sealing glasses with interconnect alloys. Powder Diffr.* **23**, 133–136.

Naylor, M. O., Jin, T., Shelby, J. E. & Misture, S. T. (2013). *Galliosilicate glasses for viscous sealants in solid oxide fuel cell stacks: part I: compositional design. Int. J. Hydrogen Energy*, **38**, 16300–16307.

Pinckney, L. R. & Beall, G. H. (2008). *Microstructural evolution in some silicate glass-ceramics: a review. J. Am. Ceram. Soc.* **91**, 773–779.

Sinton, C. W., Crawford, A., Seeger, J., Wondraczek, L., Deubener, J. & Misture, S. T. (2008). *High temperature reactions between soda–lime–silica glass and lithium aluminosilicate glass-ceramics. Glass Technol. Eur. J. Glass Sci. Technol. A*, **49**, 133–138.

Wondraczek, L., Deubener, J., Misture, S. T. & Knitter, R. (2006). *Crystallization kinetics of lithium orthosilicate glasses. J. Am. Ceram. Soc.* **89**, 1342–1346.

International Tables for Crystallography (2019). Vol. H, Chapter 7.10, pp. 834–842.

7.10. Industrial organic pigments

M. U. Schmidt

7.10.1. On organic pigments

Organic pigments are microcrystalline or nanocrystalline, coloured, highly insoluble organic compounds. There are two main chemical classes: hydrazone pigments (formerly called ‘azo pigments’) and heterocyclic pigments. Some examples are shown in Fig. 7.10.1.

Organic pigments are used industrially for the colouration of lacquers, coatings, polymers, paints, printing inks, toners, waxes *etc.* (Hunger & Schmidt, 2018). Their particle sizes are typically between 50 and 500 nm. In the application media, *e.g.* polymers, the pigments are not dissolved, but are finely dispersed. Thus, their crystal structures are maintained. At least 80% of industrially produced organic pigments are polymorphic, with most pigments having between three and six polymorphs. The number of polymorphic forms is as high as 11 for copper phthalocyanine, which is the most important pigment for blue shades in most applications. Five of the 11 polymorphs are industrially produced (*cf.* Fig. 7.10.3; Erk, 2012).

The polymorphic form depends on the conditions during synthesis, precipitation or crystallization. Additionally, the phase may change during heating as a dry powder, heating in suspension, solvent treatment, milling and storage.

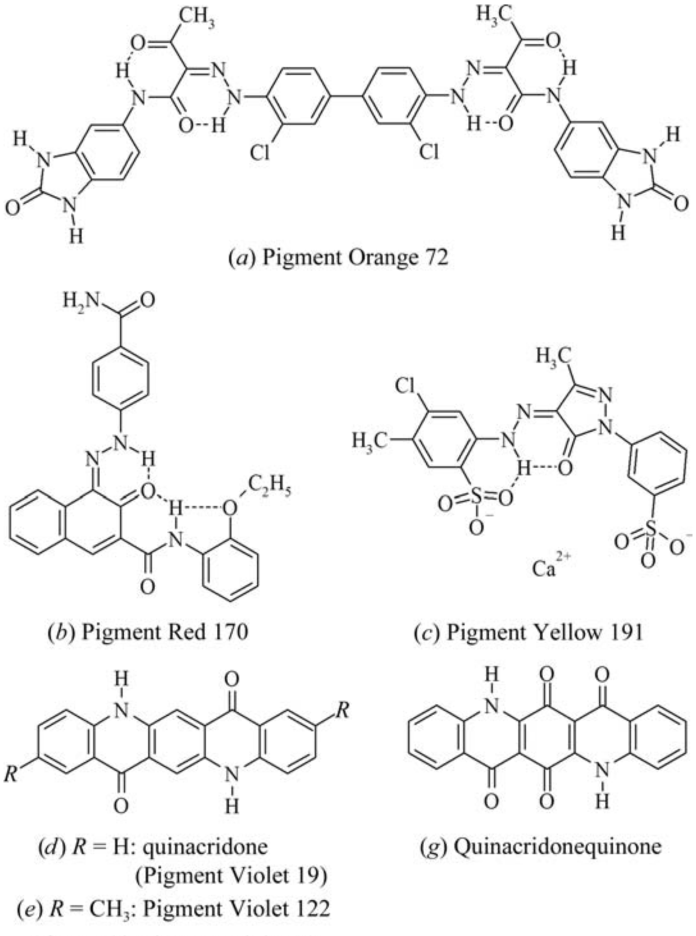
(*a*) Pigment Orange 72

(*b*) Pigment Red 170

(*c*) Pigment Yellow 191

(*d*) R = H: quinacridone (Pigment Violet 19)

(*e*) $R = CH_3$: Pigment Violet 122

(*f*) R = Cl: Pigment Violet 30

(*g*) Quinacridonequinone

Figure 7.10.1
Molecular formulae of some organic pigments mentioned in the text. Compounds (*a*)–(*c*) are hydrazone pigments.

As for inorganic pigments, the properties of organic pigments strongly depend on their crystal structures. For example, the bishydrazone compound Pigment Orange 72 (Fig. 7.10.1*a*) exhibits a red α-phase, an orange β-phase and dark brown γ- and δ-phases. Perylene pigments (Fig. 7.10.2*a*), which differ only in the lengths of the terminal alkyl or aryl chain, span the colour range from orange *via* red to black (Klebe *et al.*, 1989; Mizuguchi *et al.*, 2006). The crystal structure also has a strong effect on other properties such as thermal stability, photostability, fastness to solvents and colour strength (extinction coefficient). X-ray powder diffraction is routinely used for qualitative and quantitative phase analyses in research, development and quality control, as well as for resolving patent issues (see Section 7.10.2.1).

The particle size, the domain size, the lattice strain and the number and type of defects also have a strong influence on the properties of the pigment. For example, increasing the particle size of a yellow pigment leads to a pigment with a more orange hue, with reduced transparency and with improved hiding power, insolubility, photostability and heat fastness, but with a reduced molar colour strength. Reducing the particle size and/or increasing the number of lattice defects, *e.g.* by milling, leads to a deterioration in pigment fastness. X-ray powder diffraction is used to determine the domain size. The crystal structures of

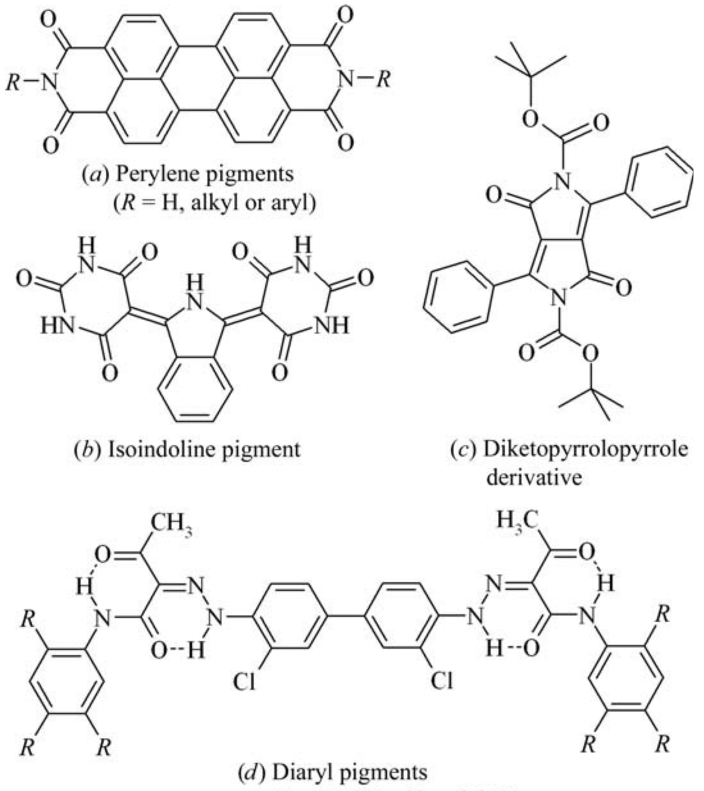
(*a*) Perylene pigments (R = H, alkyl or aryl)

(*b*) Isoindoline pigment

(*c*) Diketopyrrolopyrrole derivative

(*d*) Diaryl pigments ($R = H, CH_3, Cl$ or OCH_3)

Figure 7.10.2
Molecular formulae of some organic pigments, the crystal structures of which were determined from powder diffraction data. This book is printed using the diaryl pigment Pigment Yellow 174, which is a solid solution of molecules with R = o-CH_3 and R = o-CH_3, m-CH_3.

Copyright © 2019 International Union of Crystallography

organic pigments are usually highly anisotropic because they consist of generally planar, large molecules, which tend to arrange in chains, layers or stacks. Correspondingly, the particle morphology and the domain size can be strongly anisotropic as well.

Considerable effort has been invested in determining pigment crystal structures and in understanding their structure–property relationships. The growth of single crystals is generally hampered by the insolubility of the pigments in water and most solvents, even at elevated temperatures (373–573 K). Melting results in decomposition. Sublimation is only possible for some pigments (see, for example, Mizuguchi *et al.*, 2005; Senju *et al.*, 2005). Consequently, many of their crystal structures are determined by X-ray powder diffraction. Since pigment-producing companies were highly interested in obtaining knowledge of the crystal structures of pigments which had been produced for decades, industrial organic pigments were among the first organic crystal structures to be determined from powder data. The structures of several perylene compounds (Fig. 7.10.2*a*) and of an isoindoline pigment (Fig. 7.10.2*b*) were determined in about 1995 at BASF (Erk, 1995; Erk *et al.*, 2004), that of a diketopyrrolopyrrole derivative (Fig. 7.10.2*c*) in cooperation with Ciba–Geigy in 1996 (MacLean *et al.*, 2000), and that of the $\alpha^{\rm I}$-phase of quinacridone (Fig. 7.10.1*d*) and of a series of diaryl pigments (Fig. 7.10.2*d*) at Hoechst during 1994–1996 (Leusen, 1994; Schmidt, 1996; Paulus *et al.*, 2007; Schmidt, Dinnebier & Kalkhof, 2007). Many other structures have followed since then (see, for example, Schmidt & Dinnebier, 1999; Yatsenko *et al.*, 2001; Erk & Hengelsberg, 2003; Erk *et al.*, 2004; Schmidt *et al.*, 2005, 2006; Pidcock *et al.*, 2007; Schmidt, Brüning *et al.*, 2007; Schmidt, Buchsbaum *et al.*, 2007; Schmidt & Buchsbaum, 2008; Brüning *et al.*, 2009; Schmidt, Brühne *et al.*, 2009; Ivashevskaya *et al.*, 2009; Schmidt, van de Streek & Ivashevskaya, 2009; van de Streek *et al.*, 2009; Buchsbaum *et al.*, 2011; Bekö *et al.*, 2012; Gumbert *et al.*, 2016).

A considerable number of industrial pigments are nanocrystalline and have domain sizes below 20 nm, causing very broad reflections in the X-ray powder pattern. This is especially true for pigments synthesized by azo coupling in water because the pigments are fully insoluble in water and precipitate instantaneously during synthesis as fine, nanocrystalline powders.

Several pigments do not show Bragg peaks at all. In these instances, the local structure can be investigated using pair-distribution function analysis (see Chapter 5.7).

7.10.2. Main applications of X-ray powder diffraction to organic pigments (and other organic compounds)

The main applications are as follows.

(i) Qualitative phase analysis.
(ii) Quantitative phase analysis.
(iii) Determination of the domain size.
(iv) Structure determination from powder-diffraction data.
(v) Determination of the amorphous content.
(vi) Investigation of the local structures of nanocrystalline and amorphous organic compounds using pair-distribution function analyses.

For all applications, the X-ray powder diffractograms (also called 'powder patterns') should be measured in transmission mode in order to minimize preferred-orientation effects. The sample can be placed between polymer films or enclosed in a capillary. Usually, the diffractograms are measured using Cu $K\alpha_1$ radiation. A shorter wavelength is preferred for pair-distribution function (PDF) analyses in order to increase the resolution of the PDF curve.

7.10.2.1. *Qualitative phase analysis*

Qualitative phase analysis is used to identify the crystalline phases in a sample. The identification is generally made by comparison of the powder pattern to simulated or experimental X-ray powder patterns of known phases, or by a search in databases such as the Powder Diffraction File (Fawcett *et al.*, 2017). The phase analysis can also be performed in suspension, or in the final application, for example in coatings, if the pigment content is sufficiently high.

Applications include the following.

(i) The identification of polymorphic forms. Since the properties of the pigments strongly depend on the polymorphic form, it is essential to know which polymorphic forms are present in a given sample (Fig. 7.10.3). For the identification of polymorphs, X-ray powder diffraction is generally much more reliable and more sensitive than thermal methods or spectroscopic methods such as infrared or solid-state NMR spectroscopy. Qualitative phase analysis by X-ray diffraction is a routine tool in pigment research, development and quality control.
(ii) The identification of crystalline by-products and admixtures, *e.g.* other pigments or extenders such as $BaSO_4$.
(iii) The identification of pigments, for example in forensic investigations (see, for example, Curry *et al.*, 1982).
(iv) The identification of solid solutions. A mixture of chemically similar pigment molecules frequently crystallizes as a solid solution (mixed crystal) instead of forming a physical mixture of the crystals of the individual compounds. Such solid solutions may also exist in different polymorphic forms (Schmidt, Kempter *et al.*, 2002). The X-ray powder pattern of a physical mixture is the sum of the powder patterns of the

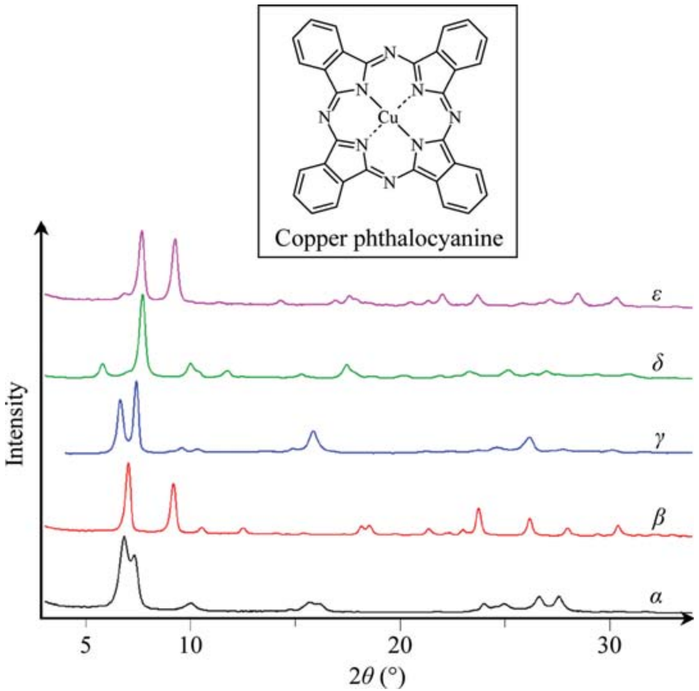

Figure 7.10.3
X-ray powder patterns of five polymorphs of copper phthalocyanine (Pigment Blue 15), which is the most important blue pigment. All five polymorphs are industrially produced. The patterns were recorded with Cu $K\alpha_1$ radiation. This book is printed with copper phthalocyanine (β-phase).

individual compounds, whereas a solid solution has a different powder pattern, with at least modified reflection positions and intensities. Several industrial pigments are sold as solid solutions, *e.g.* consisting of quinacridone and its methylated or chlorinated derivatives (Figs. 7.10.1*d* and 7.10.1*e* or Figs. 7.10.1*d* and 7.10.1*f*), or quinacridone and quinacridonequinone (Figs. 7.10.1*d* and 7.10.1*g*) (Hunger & Schmidt, 2018).

(v) The description of polymorphic forms in patents.

New polymorphic and pseudopolymorphic forms can be protected by patents. Patents are filed especially if the new crystal phases exhibit improved properties, for example for pigments with different shades or improved photostability, pharmaceuticals with improved bioavailability or better storage stability, or industrial intermediates with improved processability.

There are several industrial pigments which were or are protected only by patents on the polymorphic form, while the patent on the compound itself has expired. Examples include the γ-phase of Pigment Red 170 (Fig. 7.10.1*b*, Ribka, 1972) and the β-phase of Pigment Yellow 191 (Fig. 7.10.1*c*, Schmidt, Acs *et al.*, 2002). Similarly, many active pharmaceutical ingredients are protected for several additional years only by patents on their polymorphic form (Bernstein, 2007; see also Chapter 7.5).

A patent on a new polymorph usually contains either a figure showing the X-ray powder pattern or a listing of the characteristic reflections. However, powder data from patents should be regarded with caution. The data may be strongly affected by texture effects or by preferred orientation (expecially if the data are recorded in reflection mode). The pattern may display a mixture of polymorphs. It may contain reflections of organic or inorganic by-products, or even reflections arising from the sample holder. Lines may be shifted owing to measurement errors or owing to the formation of solid solutions *etc.* A given phase may be patented several times under different names, with different domain sizes or with different amounts of by-products, or a given phase name (*e.g.* 'phase III') may correspond to different polymorphs. An illustrative example for such 'phase chaos' is quinacridone (Fig. 7.10.1*d*). In the patent literature at least 14 phases are mentioned, which are called α, β, $\beta_{\rm I}$, γ, γ', $\gamma^{\rm I}$, $\gamma^{\rm II}$, $\gamma^{\rm III}$, $\gamma^{\rm IV}$, δ, Δ, two different ε-phases and at least one ζ-phase (Struve, 1958; Reidinger & Struve, 1958; Manger & Struve, 1958; Deuschel *et al.*, 1963; Schweizer, 1966; Hashizume *et al.*, 1970; Tyson & Schapiro, 1975; Toyo, 1976; Jaffe, 1988, 1989; Bäbler & Jaffe, 1993; Bäbler, 2001). All of the phases were characterized by X-ray powder diffraction. A closer look at the powder data for the individual phases reveals that β and $\beta_{\rm I}$ actually describe identical phases, and all of the γ-phases belong to only one crystallographic phase (γ). The phases described as 'δ' are either equivalent to the γ-phase or consist of a mixture of the γ-phase with a trace of the β-phase. Furthermore, the Δ-phase is the same polymorph as the γ-phase. The two ε-phases are actually both the γ-phase. The ζ-phase is apparently a mixture of at least three different phases (α, β and γ). To add to the confusion, the name 'α-phase' is actually used for two different phases, $\alpha^{\rm I}$ and $\alpha^{\rm II}$, which differ considerably from each other in their colours and in their X-ray powder patterns. Hence, a total of four phases remain ($\alpha^{\rm I}$, $\alpha^{\rm II}$, β and γ). For a review, see Paulus *et al.* (2007).

7.10.2.2. *Quantitative phase analysis*

Quantitative phase analysis is frequently used to determine the amounts of different polymorphic forms in a pigment sample. Applications include the following.

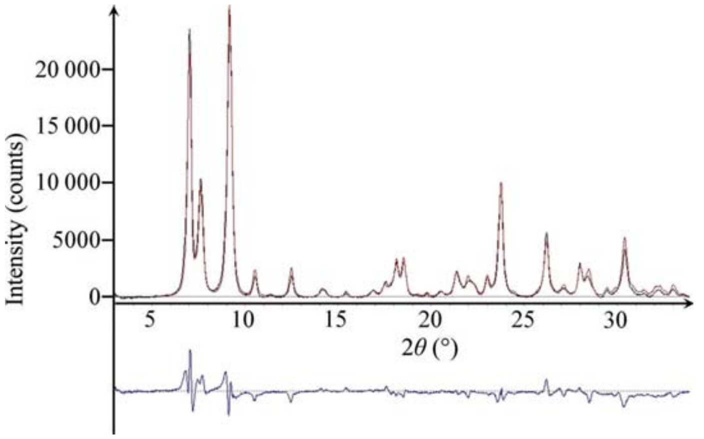

Figure 7.10.4
Quantitative phase analysis of a 70:30 mixture of the β- and the ε-phases of copper phthalocyanine (Pigment Blue 15) using the program *SiroQuant*. The data were measured with Cu $K\alpha_1$ radiation in transmission mode on a STOE Stadi-P diffractometer. The calculated ratio of the phases is 70.6 (±1.2)% β to 29.4 (±1.2)% ε. Courtesy of Martin Ermrich, Röntgenlabor Dr Ermrich, Reinheim, Germany.

(i) Optimization of synthesis and crystallization.
(ii) Quality control in production, especially for those pigments that are sold as a mixture of polymorphs.
(iii) Patent issues.

Quantitative phase analysis is additionally used for the quantification of different chemical entities in a mixture.

The methods for quantitative phase analysis are described in Chapter 3.9. The main methods used for organic pigments are as follows.

(i) Visual inspection of the diffraction pattern and comparison with reference patterns of mixtures with known composition.
(ii) Evaluation of the intensities of one or several non-overlapping reflections.
(iii) Quantitative Rietveld refinement.

The reliable quantitative phase analysis of organic pigments is frequently challenging because the small domain sizes result in broad reflections with high peak overlap. Additionally, most crystal structures are unknown; thus, is it not possible to simulate the powder patterns from single-crystal data. Furthermore, anisotropic peak broadening and texture effects have an influence on the powder pattern. Therefore, the use of a mixture series of the individual polymorphs to prove (and calibrate, if necessary) the results of a Rietveld refinement is generally recommended.

Most Rietveld programs can be used for quantitative phase analysis. Some programs, such as *SiroQuant* (Sietronics, 2013), are specially designed for phase quantification.

Fig. 7.10.4 shows an example of a quantitative Rietveld refinement using *SiroQuant*. The sample consisted of a 70:30 mixture of the β- and ε-phases of copper phthalocyanine. Powder patterns of the individual phases are shown in Fig. 7.10.3. All data were measured in transmission mode with Cu $K\alpha_1$ radiation on a STOE Stadi-P diffractometer. The crystal structural data were obtained from the Cambridge Structural Database (Groom *et al.*, 2016) [Refcode CUPOCY10 (Brown, 1968) and Refcode CUPOCY16 (Erk *et al.*, 2004)]. After background corrections, only the scale factors, lattice parameters, domain sizes and parameters for preferred orientation were refined. The atomic coordinates were left unchanged. Quantification was successful despite the broad peak widths of the sample. The Rietveld refinement calculates amounts of 70.6 and 29.4 (±1.2)% for the β

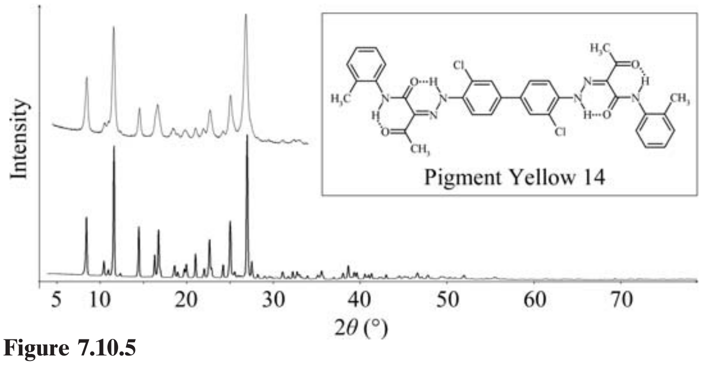

Figure 7.10.5
The effect of different domain sizes of Pigment Yellow 14. Top, the industrial product used in printing applications, with a domain size of about 40 nm. Bottom, sample recrystallized from dichlorobenzene at 453 K, with a domain size of about 500 nm. The data are laboratory data measured with Cu $K\alpha_1$ radiation in transmission mode on a STOE Stadi-P diffractometer.

and the ε modifications, respectively (R = 0.167). The domain sizes of the two phases were refined to τ = 65 nm for the β modification and τ = 52 nm for the ε modification.

7.10.2.3. *Determination of the domain size*

The widths and the shapes of the diffraction peaks in a powder pattern contain information on the domain sizes, on the lattice strain and on the number and type of defects. All features can be highly anisotropic. Industrial organic pigments generally have limited domain sizes, resulting in quite broad reflections. (This is especially true for the transparent pigments used in printing applications.) Typically, the domain sizes are between 20 and 100 nm (Fig. 7.10.5). In most cases, the data quality does not allow a separate determination of domain size, lattice strain and lattice defects. Often only the domain size is determined, which is regarded as a measure of the 'crystal quality' of the sample. (Frequently, the term 'crystallinity' is used to describe the domain size and/or the crystal quality. However, 'crystallinity' refers to the ratio of crystalline to amorphous content in a sample.) The domain size can either be calculated from the widths of individual non-overlapping reflections using the Scherrer formula (Chapter 5.1) or from the full profile using LeBail, Pawley or Rietveld refinements.

7.10.2.4. *Structure determination from powder-diffraction data*

7.10.2.4.1. *Procedure*

The information content of an X-ray powder pattern is limited, especially in the instance of poorly crystalline organic pigments. To compensate for this, the molecular geometry is used as additional information. An approximated or assumed molecular geometry is sufficient if the molecular flexibility, in particular torsions around single bonds, is taken into account. Further information could be provided by electron diffraction, solid-state NMR, IR or Raman spectroscopy.

The standard procedure for the determination of crystal structures of organic pigments and other molecular compounds from X-ray powder data consists of the following five steps.

(i) Measurement of a high-quality X-ray powder diffractogram in transmission mode.
(ii) Determination of reflection positions; indexing and determination of possible space groups.
(iii) Extraction of reflection intensities.
(iv) Structure solution, for example by real-space methods (see Chapter 4.3).
(v) Rietveld refinement.

The third step (extraction of reflection intensities) is crucial if the structure is to be solved by direct methods or charge flipping, but may be skipped in the case of real-space methods. Nevertheless, some real-space methods, such as *DASH* (David *et al.*, 2006), perform an extraction of reflection intensities to increase the calculation speed.

The most problematic step is still the indexing, *i.e.* the determination of the lattice parameters from the peak positions. The indexing fails if the powder has domain sizes that are too small or if it contains a mixture of different phases. In these cases the following approaches can be used.

(i) Modification of the syntheses and the crystallization conditions in order to obtain a single-phase powder and/or a powder with improved domain sizes.
(ii) Determination of the lattice parameters by electron diffraction (Gorelik *et al.*, 2009; Schmidt, Brühne *et al.*, 2009).
(iii) Searching for an isostructural derivative with improved domain sizes or known structure.
(iv) The prediction of possible crystal structures by global lattice-energy minimizations with free lattice parameters in various space groups. The minimizations can be performed by force-field or quantum-mechanical methods, or by combinations of these (Neumann *et al.*, 2008; Day *et al.*, 2009; Mörschel & Schmidt, 2014). In order to determine which of the predicted structures corresponds to the actual phase, the diffraction patterns are simulated for all low-energy structures and compared with the experimental pattern.

In difficult cases approaches (i)–(iv) have to be combined.

In all cases the structure is finally refined by the Rietveld method. Rietveld refinement also allows the location of missing atoms, *e.g.* counter-ions, water or solvent molecules. Generally, rigid bodies, constraints or restraints on the molecular geometry are applied in order to avoid chemically meaningless distortions of the molecules. Finally, if the quality of the data is good enough, a refinement of all atomic positions without restraints (except for H atoms) should be tried; if the atoms move only slightly, the structure can be considered to be correct. Alternatively, the correctness of the crystal structure can be proven by a quantum-mechanical lattice-energy minimization with a free unit cell (van de Streek & Neumann, 2014).

7.10.2.4.2. *Examples*

7.10.2.4.2.1. Pigment Red 57:1

Pigment Red 57:1 (Fig. 7.10.6) is used worldwide for printing newspapers, journals and books. This book is also printed with the β-phase of Pigment Red 57:1. The crystal structure of the α-phase (trihydrate) of Pigment Red 57:1 was solved by real-space methods from laboratory data measured in transmission mode (Bekö *et al.*, 2012). After indexing, the structure was solved with *DASH* (David *et al.*, 2006). The real-space search was performed with a flexible molecule, the counter-ion and two of the three water molecules, leading to in total 18 degrees of freedom. The third water molecule was located during the Rietveld refinement. Rietveld refinements were carried out with *TOPAS* (Coelho, 2018) using restraints on bond lengths, bond angles and planar groups. The refinement converged with a smooth difference curve (Fig. 7.10.6). In the same way, the crystal structures of the β-phase (monohydrate) and the γ-phase

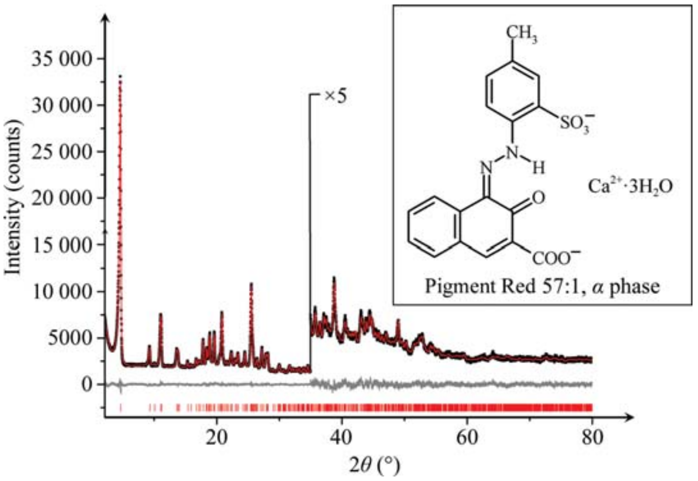

Figure 7.10.6
Rietveld refinement of Pigment Red 57:1 (α-phase, trihydrate). The experimental pattern is drawn as points and the calculated pattern as a solid line; the difference curve is shown at the bottom, with reflection positions as vertical lines. The data are laboratory data measured with Cu $K\alpha_1$ radiation in transmission mode on a STOE Stadi-P diffractometer. The space group is $P2_1/c$ with $Z = 4$, $a = 8.7613$ (5), $b = 5.8155$ (3), $c = 37.943$ (2) Å, $\beta = 90.883$ (3)°. R values: $R_{\rm wp} = 3.13\%$, $R_{\rm p} = 2.38\%$, $R_{\rm exp} = 2.48\%$ (values before background subtraction), $R'_{\rm wp} = 8.66\%$, $R'_{\rm p} = 7.89\%$, $R'_{\rm exp} = 6.85\%$ (after background subtraction); $\chi^2 = 1.264$.

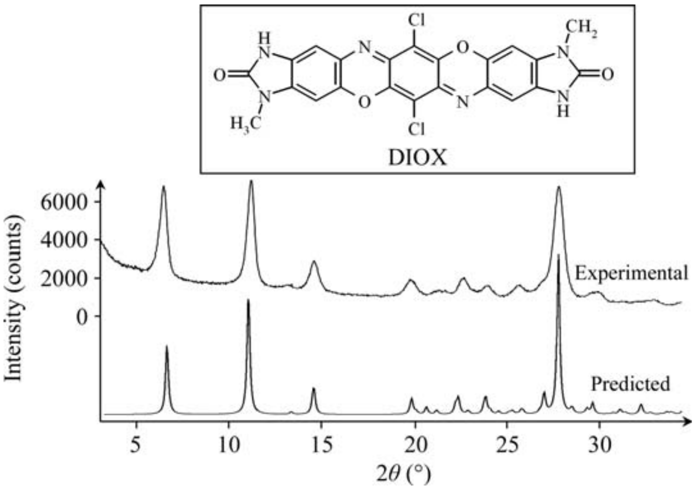

Figure 7.10.7
Structure solution of the nanocrystalline pigment DIOX. Top, experimental X-ray powder pattern (Cu $K\alpha_1$ radiation); bottom, simulated pattern of the predicted structure with energy rank 5, without any fit to the experimental data. The space group is $P\bar{1}$ with $Z = 1$, $a = 4.335$, $b = 8.419$, $c = 13.906$ Å, $\alpha = 106.95$, $\beta = 92.91$, $\gamma = 95.12°$, $V = 481.9$ Å^3. The difference between the simulated and experimental patterns is as small as for a misorientation of the molecule of about 1°.

(anhydrate) were determined. All three phases exhibit a double-layer structure, as is frequently observed in ionic molecular crystals. The nonpolar layer is formed by the phenyl and naphthalene fragments, whereas the polar/ionic layer contains the Ca^{2+} ions and the SO_3^-, COO^- and C=O groups, as well as the water molecules. Moisture-dependent and temperature-dependent X-ray powder diffraction investigations revealed that all phases can interconvert, depending on the temperature and relative humidity. These phase changes may result in a shift in the shade of red in printed newspapers depending on the weather conditions.

7.10.2.4.2.2. *Dioxazine pigment*

Crystal-structure predictions by lattice-energy minimizations were necessary to solve the structure of the nanocrystalline violet dioxazine pigment DIOX (Fig. 7.10.7). The compound is completely insoluble in water and all other solvents. Even in the best available solvents such as *N*-methylpyrrolidone or DMSO the solubility at about 473 K is below the detection limit of 10 µg l^{-1}. Correspondingly, all attempts at recrystallization failed. Sublimation was possible at 10^{-3} mbar (1 mbar = 100 Pa) and 623 K, but did not result in improved crystallinity. The best powder pattern of the β-phase is shown in Fig. 7.10.7 (top). From the line widths, a domain size of about 20 nm can be estimated. None of the powder patterns could be indexed. Possible crystal structures were predicted with the program *CRYSCA* (Schmidt & Kalkhof, 1997), starting from a very large set of random packings in various space groups with free lattice parameters. The lattice energy was optimized for all structures. After removing duplicate structures, X-ray powder diagrams were simulated for all low-energy structures and were compared with the experimental diagram. The packing with energy rank 5 showed a simulated powder diagram that was quite close to the experimental one (Fig. 7.10.7, bottom), indicating that this structure is very close to correct. The Rietveld refinement was challenging because the reflections were extremely broad. The correctness of the structure was finally proven some years later *via* the structure determination of an isostructural phase: if 50% of the CH_3 groups are replaced by C_2H_5 groups, a solid solution of CH_3 and C_2H_5 derivatives is formed. This solid solution exhibited excellent crystallinity. Its structure could be solved and refined without problems and confirmed the structure of the methyl derivative (Schmidt *et al.*, 2005).

7.10.2.4.2.3. *Pigment Red 170*

The structure of the nanocrystalline α-phase of Pigment Red 170 was solved *via* the crystal structure of an isostuctural methyl derivative with better crystallinity (Fig. 7.10.8). Indexing the powder pattern of the methyl derivative yielded the lattice parameters a^*, b^* and γ^*. Since 30 out of 33 low-angle reflections could be indexed with $hk0$, insufficient information was available to determine the remaining parameters c^*, α^* and β^*. The crystal system and the space group also remained unknown. The structure of the methyl derivative was solved by crystal-structure predictions in various space groups using the program *FlexCryst* (Hofmann & Apostolakis, 2003). Subsequently, the structure was refined against synchrotron data using the program *GSAS* (Larson & Von Dreele, 1994). The resulting structure of the methyl derivative was used as a starting model to refine the crystal structure of Pigment Red 170 from laboratory data (Schmidt *et al.*, 2006).

7.10.2.5. *Determination of the amorphous content*

A few organic pigments are sold as amorphous powders, which show no Bragg peaks in their X-ray powder diffractograms. Some other pigments are crystalline, but contain amorphous additives or extenders; for example, pigments used in offset printing can contain up to 30% of resin (which improves the dispersibility). The amorphous content in a sample can be analysed by different methods. The accuracy is generally improved by a calibration curve using mixtures of amorphous and crystalline compounds.

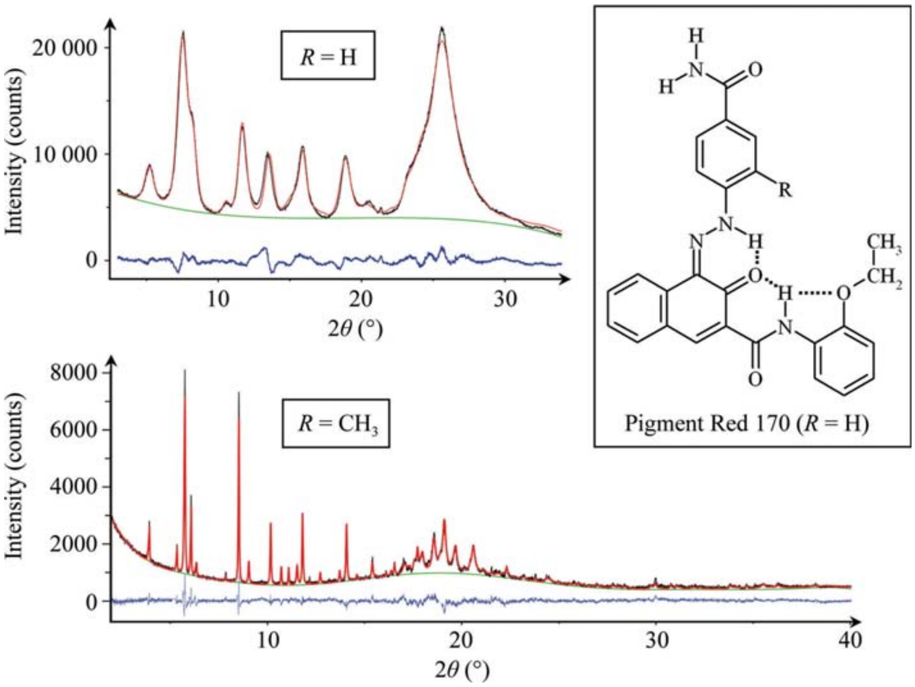

Figure 7.10.8

Structure determination of the nanocrystalline α-phase of Pigment Red 170 from powder data using an isostructural methyl derivative with improved crystallinity. Top, Rietveld plot of the α-phase of Pigment Red 170 (R = H); bottom, methyl derivative (R = CH_3). Experimental diffractograms are in black, the calculated diffractogram is in red, the background is in green and difference curves are in blue. Wavelengths were 1.5406 Å (Cu $K\alpha_1$) for Pigment Red 170 and 1.149914 Å (synchrotron radiation) for the methyl derivative. The space group is $P2_12_12_1$, with Z = 4, a = 23.960 (9), b = 23.234 (9), c = 3.887 (1) Å for Pigment Red 170 and a = 24.6208 (9), b = 22.8877 (9), c = 3.9388 (2) Å for the methyl derivative.

7.10.2.6. *Investigation of local structures of nanocrystalline and amorphous organic compounds using pair-distribution function analyses*

7.10.2.6.1. *General*

There is no sharp boundary between crystalline, nanocrystalline and amorphous states. In an amorphous sample the molecules can be ordered, despite the absence of Bragg reflections. For example, an organic compound with a domain size of 10 nm corresponding to about 5 × 5 × 5 unit cells with 500 molecules will not cause a single visible peak in the X-ray powder pattern; nevertheless, the molecules have a given conformation and form an ordered arrangement with a defined local structure.

Local structures in crystalline, nanocrystalline and amorphous organic compounds, including pharmaceuticals, agrochemicals, pigments and optoelectronic materials, can be investigated by pair-distribution function (PDF) analysis.

The pair-distribution function (also called the 'radial distribution function') represents the probability $G(r)$ of finding two atoms with an interatomic distance r. The PDF is weighted with the scattering power of the two atoms and is summed over all atom–atom pairs. The PDF contains intramolecular as well as intermolecular atom–atom distances. PDF curves are derived by Fourier transformations from carefully measured powder diffractograms. The method itself is explained in Chapter 5.7.

Applications to organic compounds include the following.

(i) The investigation of local structures and packing motifs in nanocrystalline and amorphous compounds.

(ii) The identification of polymorphic forms in nanocrystalline and amorphous compounds.

(iii) The investigation of the actual atomic and molecular arrangements in disordered structures.

(iv) To determine whether a powder is a co-crystal or a physical mixture of the individual compounds.

(v) The detection of crystal seeds in an amorphous powder. The commencement of crystallization is visible in the PDF at an earlier stage than in the powder diagram itself.

PDF analyses are widely used for inorganic compounds, for example glasses, liquids, amorphous or highly disordered materials, quasicrystals *etc.* (Neder & Proffen, 2009; Egami & Billinge, 2012). The application of PDF methods to organic compounds is at present (2018) in its infancy. The generation of a PDF curve from powder diffraction data is possible with programs such as *PDFgetX3* (Juhás *et al.*, 2013). The simulation of PDF curves from a structural model can be achieved, for example with *DISCUS* (Neder & Proffen, 2009), *RMCprofile* (Tucker *et al.*, 2007), *PDFgui* (Farrow *et al.*, 2007), *DiffPy-CMI* (Juhás *et al.*, 2015) or *TOPAS* (Coelho, 2018) (see Fig. 7.10.9). The full fitting of a structural model of an organic crystal structure to a PDF curve using restraints for bond lengths, bond angles and planar groups, such as in a Rietveld refinement, is nowadays becoming possible (Prill *et al.*, 2016).

7.10.2.6.2. *Example: nanocrystalline phase of Pigment Yellow 213*

Pigment Yellow 213 is an industrial hydrazone pigment used for automotive coatings. The compound exhibits two polymorphs (Fig. 7.10.10). The brown β-phase is obtained directly from the synthesis. Solvent treatment for 3 h at 423 K leads to the desired greenish-yellow α-phase. The crystal structure of the α-phase could be solved by a combination of X-ray powder diffraction, electron diffraction and lattice-energy minimizations (Schmidt, Brühne *et al.*, 2009). The molecules are almost planar and form a layer structure with an interlayer distance of 3.3 Å (Fig. 7.10.11).

The metastable β-phase is a nanocrystalline powder. The structures of both phases were investigated by PDF analyses. Powder patterns were carefully recorded with a short wavelength

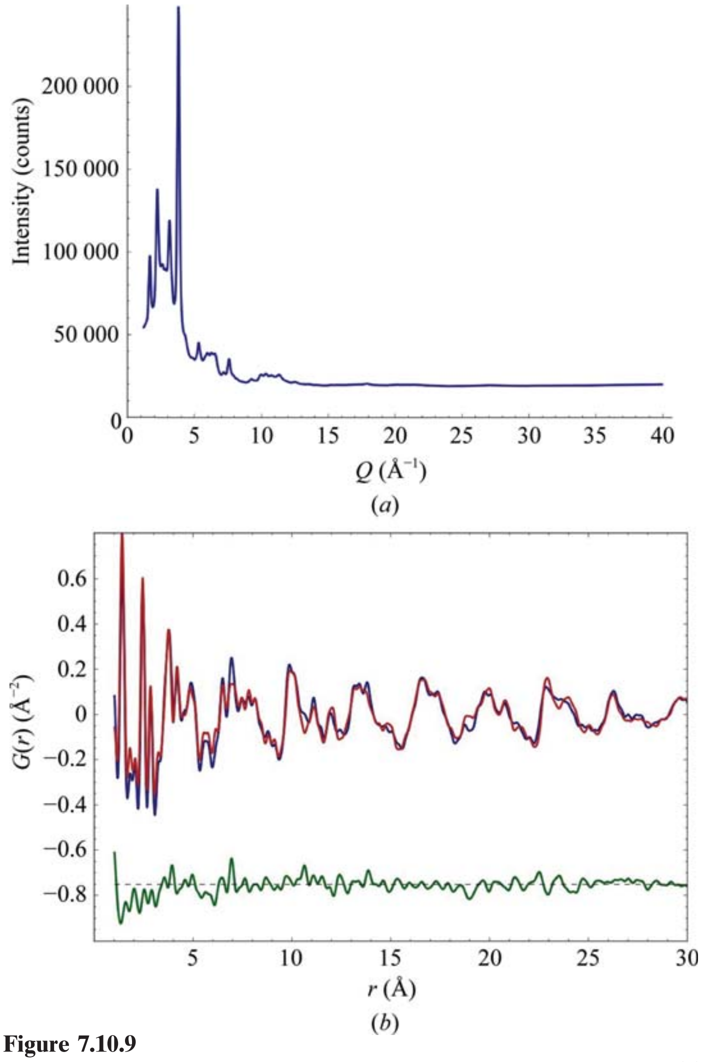

Figure 7.10.9
Pair-distribution function analyses of the β-phase of quinacridone. (*a*) Synchrotron X-ray powder pattern after normalization; λ = 0.2128 Å. (*b*) Comparison of the experimental PDF curve ($Q_{\max}$ = 19 Å^{-1}, blue) and the PDF simulated from the crystal-structure data (red). The difference curve is shown in green. The peak width was fitted with two parameters ($B_{\rm iso}^{\rm mol}$, $B_{\rm iso}^{\rm cryst}$) using the program *DiffPy-CMI*. The lattice parameters were refined. The atomic coordinates were not modified (Prill *et al.*, 2016). Note that the PDF curve is normalized in such a way that a value of $G(r)$ = 0 indicates an average probability, not a probability of zero.

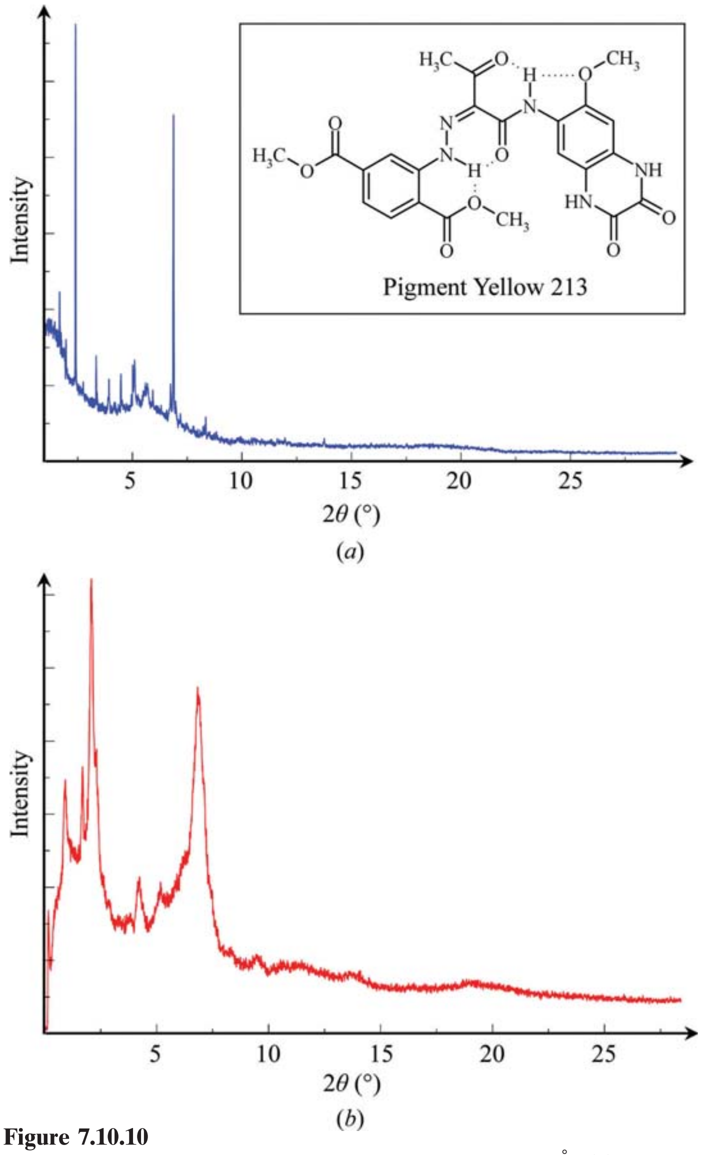

Figure 7.10.10
X-ray powder patterns of Pigment Yellow 213; λ = 0.40 Å. (*a*) α-phase, (*b*) β-phase.

(λ = 0.40 Å) over a large 2θ range. After background correction, normalization and Fourier transformation, the PDF curves were obtained (Fig. 7.10.12).

The PDF curve of the α-phase exhibits a regular sequence of maxima and minima with a periodicity of 3.3 Å. This regular feature is caused by the layer structure: atoms in neighbouring layers have distances of 3.3 Å. Interatomic distances of 3.3, 6.6, 9.9, 13.2, 16.5 Å *etc.* occur for many atom–atom pairs; this is reflected in the PDF. In other directions interatomic distances can adopt all values and do not lead to characteristic features in the PDF. At r values around 100 Å, the PDF curve still shows minima and maxima, which shows that the ordering length (domain size) in the stacking direction is much larger than 100 Å.

The PDF curve of the β-phase also shows this regular feature, as in the α-phase. Hence the molecules are also stacked (either in a layer structure or in a herringbone packing). The PDF curve of the β-phase vanishes at about 40 Å (4 nm); thus, the ordering length in the stacking direction is about 4 nm, which corresponds to stacks of 10–15 molecules only. This explains the absence of a sharp Bragg reflection at d = 3.3 Å in the X-ray powder pattern of the β-phase. From the width of the three low-angle reflections in the X-ray diffractogram the domain size in the lateral direction can be estimated as 100–200 Å, corresponding to the length and width of about ten molecules.

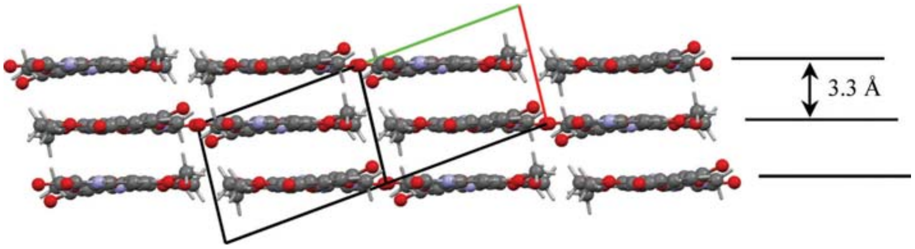

Figure 7.10.11
Crystal structure of the α-phase of Pigment Yellow 213 (Schmidt, Brühne *et al.*, 2009).

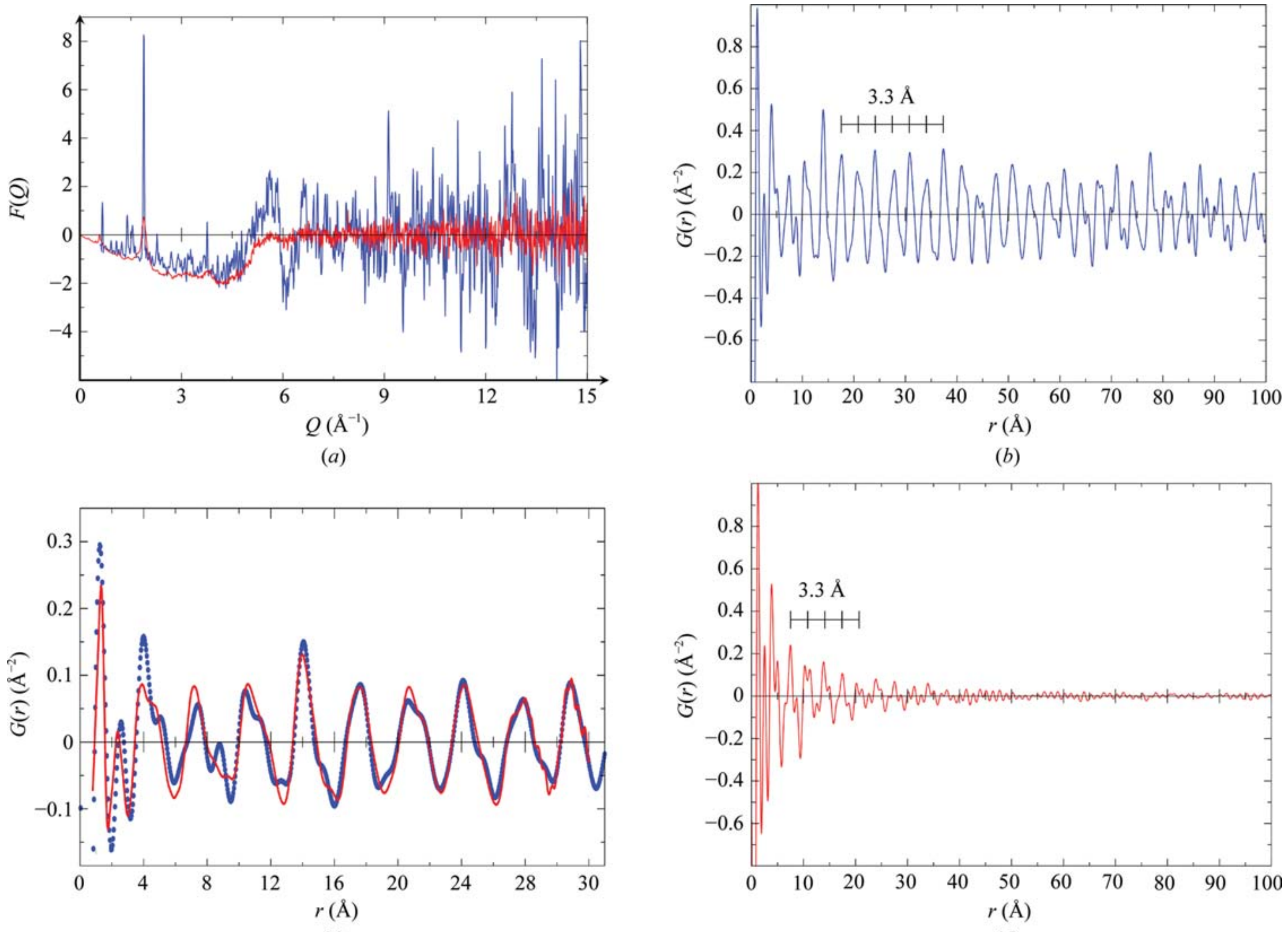

Figure 7.10.12

Pair-distribution function analyses of Pigment Yellow 213. (*a*) Synchrotron powder patterns after normalization with the α-phase in blue and the β-phase in red. $\lambda = 0.40$ Å, $Q_{\max} = 15$ Å^{-1}. (*b*) The PDF curve of the α-phase. (*c*) Comparison of the experimental PDF curve of the α-phase (blue) and the PDF simulated from the crystal-structure data for the α-phase (red). The peak width was fitted with two parameters (δ, φ); the lattice parameters and atomic coordinates were not modified. (*d*) PDF curve of the β-phase.

This example shows that a powder pattern of an almost amorphous compound, which seemed to contain no information at all, still contains valuable information on the local structure, for example on the molecular arrangement, and the domain size in different spatial directions.

References

Bäbler, F. (2001). *Gamma quinacridone pigment.* European Patent EP 1074587.

Bäbler, F. & Jaffe, E. E. (1993). *Modified gamma-quinacridone pigment.* European Patent EP 530143.

Bekö, S. L., Hammer, S. M. & Schmidt, M. U. (2012). *Crystal structures of the hydration states of Pigment Red 57:1. Angew. Chem. Int. Ed.* **51**, 4735–4738.

Bernstein, J. (2007). *Polymorphism in Molecular Crystals*. Oxford University Press.

Brown, C. J. (1968). *Crystal structure of β-copper phthalocyanine. J. Chem. Soc. A*, pp. 2488–2493.

Brüning, J., Alig, E., Meents, A., van de Streek, J. & Schmidt, M. U. (2009). *Structure determinations of three fluorescent organic pigments by powder diffraction and micro-crystal structure analysis. Z. Kristallogr.* **224**, 556–562.

Buchsbaum, C., Paulus, E. F. & Schmidt, M. U. (2011). *Crystal structures of thiazine-indigo pigments, determined from single-crystal and powder diffraction data. Z. Kristallogr.* **226**, 822–831.

Coelho, A. A. (2018). *TOPAS and TOPAS-Academic: an optimization program integrating computer algebra and crystallographic objects written in C++. J. Appl. Cryst.* **51**, 210–218.

Curry, C. J., Rendle, D. F. & Rogers, A. (1982). *Pigment analysis in the forensic examination of paints. I. Pigment analysis by X-ray powder diffraction. J. Forensic Sci. Soc.* **22**, 173–177.

David, W. I. F., Shankland, K., van de Streek, J., Pidcock, E., Motherwell, W. D. S. & Cole, J. C. (2006). *DASH: a program for crystal structure determination from powder diffraction data. J. Appl. Cryst.* **39**, 910–915.

Day, G. M. *et al.* (2009). *Significant progress in predicting the crystal structures of small organic molecules – a report on the fourth blind test. Acta Cryst.* B**65**, 107–125.

Deuschel, W., Gundel, F., Wuest, H. & Daubach, E. (1963). *Process for producing a modification of gamma 7,14-dioxo-5,7,12,14-tetrahydro-quinolino-(2,3-b) acridine.* US Patent 3074950.

Egami, T. & Billinge, S. J. L. (2012). *Underneath the Bragg Peaks: Structural Analysis of Complex Materials*, 2nd ed. Oxford: Elsevier.

Erk, P. (1995). Personal communication.

Erk, P. (2012). Personal communication.

Erk, P. & Hengelsberg, H. (2003). *The Porphyrin Handbook*, edited by K. M. Kadish, K. M. Smith & R. Guilard, Vol. 19, pp. 105–149. Amsterdam: Academic Press.

Erk, P., Hengelsberg, H., Haddow, M. F. & van Gelder, R. (2004). *The innovative momentum of crystal engineering. CrystEngComm*, **6**, 474–483.

Farrow, C. L., Juhás, P., Liu, J. W., Bryndin, D., Božin, E. S., Bloch, J., Proffen, T. & Billinge, S. J. L. (2007). *PDFfit2 and PDFgui: computer* *programs for studying nanostructure in crystals. J. Phys. Condens. Matter*, **19**, 335219.

Fawcett, T. G., Kabekkodu, S. N., Blanton, J. R. & Blanton, T. N. (2017). *Chemical analysis by diffraction: the Powder Diffraction File. Powder Diffr.* **32**, 63–71.

Gorelik, T., Schmidt, M. U., Brüning, J., Bekő, S. & Kolb, U. (2009). *Using electron diffraction to solve the crystal structure of a laked azo pigment. Cryst. Growth Des.* **9**, 3898–3903.

Groom, C. R., Bruno, I. J., Lightfoot, M. P. & Ward, S. C. (2016). *The Cambridge Structural Database. Acta Cryst.* B**72**, 171–179.

Gumbert, S. D., Körbitzer, M., Alig, E., Schmidt, M. U., Chierotti, M. C., Gobetto, R., Li, X. & van de Streek, J. (2016). *Crystal structure and tautomerism of Pigment Yellow 138 determined by X-ray powder diffraction and solid-state NMR. Dyes Pigm.* **131**, 364–372.

Hashizume, K., Miyatake, M., Shigemitsu, M., Kumano, I., Katsura, H. & Oshima, M. (1970). *Chinacridonpigment mit neuer Kristallmodifikation.* German Patent DE 1805266.

Hofmann, D. W. M. & Apostolakis, J. (2003). *Crystal structure prediction by data mining. J. Mol. Struct.* **647**, 17–39.

Hunger, K. & Schmidt, M. U. (2008). *Industrial Organic Pigments*, 4th ed. Weinheim: Wiley-VCH.

Ivashevskaya, S. N., van de Streek, J., Djanhan, J. E., Brüning, J., Alig, E., Bolte, M., Schmidt, M. U., Blaschka, P., Höffken, H. W. & Erk, P. (2009). *Structure determination of seven phases and solvates of Pigment Yellow 183 and Pigment Yellow 191 from X-ray powder and single-crystal data. Acta Cryst.* B**65**, 212–222.

Jaffe, E. E. (1988). *Process for the manufacture of a red gamma quinacridone with a yellow shade.* European Patent EP 267877.

Jaffe, E. E. (1989). *Modified beta-quinacridone pigment.* European Patent EP 305328.

Juhás, P., Davis, T., Farrow, C. L. & Billinge, S. J. L. (2013). *PDFgetX3: a rapid and highly automatable program for processing powder diffraction data into total scattering pair distribution functions. J. Appl. Cryst.* **46**, 560–566.

Juhás, P., Farrow, C. L., Yang, X., Knox, K. R. & Billinge, S. J. L. (2015). *Complex modeling: a strategy and software program for combining multiple information sources to solve ill posed structure and nanostructure inverse problems. Acta Cryst.* A**71**, 562–568.

Klebe, G., Graser, F., Hädicke, E. & Berndt, J. (1989). *Crystallochromy as a solid-state effect: correlation of molecular conformation, crystal packing and colour in perylene-3,4:9,10-bis(dicarboximide) pigments. Acta Cryst.* B**45**, 69–77.

Larson, A. C. & Von Dreele, R. B. (1994). *General Structure Analysis System (GSAS)*. Los Alamos National Laboratory Report LAUR 86–748.

Leusen, F. J. J. (1994). *Ab initio prediction of possible crystal structures.* Presentation at the 15th European Crystallographic Meeting ECM-15, Dresden, 28 August–2 September 1994. *Z. Kristallogr Suppl.* **8**, 161.

MacLean, E. J., Tremayne, M., Kariuki, B. M., Harris, K. D. M., Iqbal, A. F. M. & Hao, Z. (2000). *Structural understanding of a polymorphic system by structure solution and refinement from powder X-ray diffraction data: the α and β phases of the latent pigment DPP-Boc. J. Chem. Soc. Perkin Trans. 2*, pp. 1513–1519.

Manger, C. W. & Struve, W. S. (1958). *Organic pigments*. US Patent 2844581.

Mizuguchi, J., Hino, K. & Tojo, K. (2006). *Strikingly different electronic spectra of structurally similar perylene imide compounds. Dyes Pigm.* **70**, 126–135.

Mizuguchi, J., Sasaki, T. & Tojo, K. (2005). *Refinement of the crystal structure of 5,7,12,14-tetrahydro[2,3-b]-quinolinoacridine (γ-form), $C_{20}H_{12}N_2O_2$, at 223 K. Z. Kristallogr. New Cryst. Struct.* **217**, 249–250.

Mörschel, P. M. & Schmidt, M. U. (2014). *Prediction of molecular crystal structures by a crystallographic QM/MM model with full space-group symmetry. Acta Cryst.* A**71**, 26–35.

Neder, R. B. & Proffen, T. (2009). *Diffuse Scattering and Defect Structure Simulations: A Cook Book Using the Program DISCUS.* Oxford University Press.

Neumann, M. A., Leusen, F. J. J. & Kendrick, J. (2008). *A major advance in crystal structure prediction. Angew. Chem.* **120**, 2461–2464.

Paulus, E. F., Leusen, F. J. J. & Schmidt, M. U. (2007). *Crystal structures of quinacridones. CrystEngComm*, **9**, 131–143.

Pidcock, E., van de Streek, J. & Schmidt, M. U. (2007). *The crystal structure of Pigment Yellow 181 from laboratory powder diffraction data. Z. Kristallogr.* **222**, 713–717.

Prill, D., Juhás, P., Billinge, S. J. L. & Schmidt, M. U. (2016). *Towards solution and refinement of organic crystal structures by fitting to the atomic pair distribution function. Acta Cryst.* A**72**, 62–72.

Reidinger, A. D. & Struve, W. S. (1958). *Organic pigments.* US Patent 2844484.

Ribka, J. (1972). *Monoazopigment und Verfahren zu seiner Herstellung.* German Patent DE 2043482.

Schmidt, M. U. (1996). *Calculation and Prediction of Molecular Crystal Structures.* Presentation at the 17th Congress of the International Union for Crystallography. Abstract MS03.06.03.

Schmidt, M. U., Acs, A., Jung, R. & Schui, F. (2002). *New crystalline modification of C. I. Pigment Yellow 191 and manufacturing process thereof.* European Patent EP 1170338 A3.

Schmidt, M. U., Brühne, S., Wolf, A. K., Rech, A., Brüning, J., Alig, E., Fink, L., Buchsbaum, C., Glinnemann, J., van de Streek, J., Gozzo, F., Brunelli, M., Stowasser, F., Gorelik, T., Mugnaioli, E. & Kolb, U. (2009). *Electron diffraction, X-ray powder diffraction and pair-distribution-function analyses to determine the crystal structures of Pigment Yellow 213, $C_{23}H_{21}N_5O_9$. Acta Cryst.* B**65**, 189–199.

Schmidt, M. U., Brüning, J., Buchsbaum, C., Alig, E. & Fink, L. (2007). *Crystal-structure determination of the fluorescent bisazomethine pigment $C_{36}H_{26}N_4O_4$ from X-ray powder data. Z. Kristallogr.* **222**, 539–545.

Schmidt, M. U. & Buchsbaum, C. (2008). *Structure determination of 6,6′-bis(trifluoromethyl)thiazine-indigo from laboratory powder data and lattice-energy minimisation. Z. Kristallogr.* **223**, 418–423.

Schmidt, M. U., Buchsbaum, C., Schnorr, J. M., Hofmann, D. W. M. & Ermrich, M. (2007). *Pigment Orange 5: crystal structure determination from a non-indexed X-ray powder diagram. Z. Kristallogr.* **222**, 30–33.

Schmidt, M. U. & Dinnebier, R. E. (1999). *Combination of energy minimizations and rigid-body Rietveld refinement: the structure of 2,5-dihydroxybenzo[de]benzo[4,5]imidazo[2,1-a]isoquinolin-7-one. J. Appl. Cryst.* **32**, 178–186.

Schmidt, M. U., Dinnebier, R. E. & Kalkhof, H. (2007). *Crystal engineering on industrial diaryl pigments using lattice energy minimizations and X-ray powder diffraction. J. Phys. Chem. B*, **111**, 9722–9732.

Schmidt, M. U., Ermrich, M. & Dinnebier, R. E. (2005). *Determination of the structure of the violet pigment $C_{22}H_{12}C_{l2}N_6O_4$ from a non-indexed X-ray powder diagram. Acta Cryst.* B**61**, 37–45.

Schmidt, M. U., Hofmann, D. W. M., Buchsbaum, C. & Metz, H. J. (2006). *Crystal structures of Pigment Red 170 and derivatives, as determined by X-ray powder diffraction. Angew. Chem. Int. Ed.* **45**, 1313–1317.

Schmidt, M. U. & Kalkhof, H. (1997). *CRYSCA. Program for crystal structure calculations of flexible molecules.* Frankfurt am Main, Germany.

Schmidt, M. U., Kempter, P., Plüg, C. & Born, R. (2002). *Mixed crystals of benzimidazolonedioxazine derivatives.* European Patent EP 1201718.

Schmidt, M. U., van de Streek, J. & Ivashevskaya, S. N. (2009). *The first crystal structures of industrial laked yellow pigments determined by X-ray powder diffraction. Chem. Eur. J.* **15**, 338–341.

Schweizer, H. R. (1966). *Delta form of quinacridone pigment.* US Patent 3272821.

Senju, T., Hoki, T. & Mizuguchi, J. (2005). *2,9-Dichloro-5,12-dihydroquino[2,3-b]acridine-7,14-dione. Acta Cryst.* E**61**, o1061–o1063.

Sietronics (2013). *SiroQuant Rietveld program*, version 4.0. Sietronics Pty Ltd, Canberra, Australia.

Streek, J. van de, Brüning, J., Ivashevskaya, S. N., Ermrich, M., Paulus, E. F., Bolte, M. & Schmidt, M. U. (2009). *Structures of six industrial benzimidazolone pigments from laboratory powder diffraction data. Acta Cryst.* B**65**, 200–211.

Streek, J. van de & Neumann, M. A. (2014). *Validation of molecular crystal structures from powder diffraction data with dispersion-corrected density functional theory (DFT-D). Acta Cryst.* B**70**, 1020–1032.

Struve, W. S. (1958). *Organic Pigments.* US Patent 2844485.

Toyo (1976). Japanese Patent Sho51-11372.

Tucker, M. G., Keen, D. A., Dove, M. T., Goodwin, A. L. & Hui, Q. (2007). *RMCProfile: reverse Monte Carlo for polycrystalline materials. J. Phys. Condens. Matter*, **19**, 335218.

Tyson, R. S. & Schapiro, L. (1975). *Chinacridon-Pigmente und Verfahren zu ihrer Herstellung.* German Patent DE 2435219.

Yatsenko, A. V., Paseshnichenko, K. A., Chernyshev, V. V. & Schenk, H. (2001). *1-[(2-Nitrophenyl)hydrazono]-1H-naphthalen-2-one (Pigment Orange 2) from powder data. Acta Cryst.* E**57**, o1152–o1153.

International Tables for Crystallography (2019). Vol. H, Chapter 7.11, pp. 843–854.

7.11. Powder diffraction in the petroleum and petrochemical industries

J. A. Kaduk

7.11.1. Introduction

The petroleum industry is generally divided into two parts: exploration and production ('upstream'), and refining. Intimately associated with the refining business is the petrochemical industry. Together, refining and petrochemicals are generally referred to as 'downstream' operations. Given the huge scale and economic importance of the industry, probably more X-ray powder-diffraction measurements are made in it than in any other industry. Relatively few are published, given the highly proprietary nature of the information obtained. A comprehensive review of the applications of powder diffraction in the petroleum industry is impossible within any reasonable length, but a selection of recent representative examples are presented to illustrate the breadth of applications of powder diffraction in both the upstream and downstream sectors.

7.11.2. Exploration and production

The largest number of samples for X-ray diffraction (XRD) are analysed in support of exploration activities. Characterization of a single oil or gas well can easily involve hundreds of samples. Most of the analyses are considered routine, as they involve qualitative and quantitative phase identification. The analyses are not simple, however, because of the complex assemblies of minerals that are present in many rocks. The techniques and best practices described in other chapters of this volume should enable the analyst to carry out most such rock analyses. A strategy that is sometimes followed is to use a 'phase filter' (Morton *et al.*, 2001). This involves including in the input file of the Rietveld program all of the phases that might possibly be encountered in a particular set of samples. This could include 20–30 phases. The initial refinements involve only the scale factors of each phase. Those that refine to zero (or negative values) are fixed at zero, and subsequent refinements are used to examine the microstructural characteristics and concentrations of the phases that are actually present.

Generally, the powder-diffraction measurements in a geological study are a (small) part of a multi-technique investigation. A typical recent example is given in Glikson *et al.* (2010). Many samples of cuttings from drilling the well were examined to establish the stratigraphy and mineralogy of the formations. Most of the analysis was performed using electron microscopy, with powder diffraction serving to confirm mineral identifications and quantify their concentrations.

7.11.2.1. *Rock properties*

Characterizing the phases that are present is important not only in itself, but also for understanding the properties of the rock. Jiu *et al.* (2013) found that lacustrine shale reservoirs in the Zhanhua Depression consisted mainly of detrital minerals, carbonates and clay minerals. The detrital minerals included quartz and several feldspars. (Feldspar identification and quantification can be a real challenge, given the extensive peak overlap of these phases.) The carbonate minerals included calcite, dolomite and a small concentration of siderite. The clay minerals included a mixed illite/smectite, illite, kaolinite and chlorite. Quartz, feldspars and carbonates are considered to be the main brittle minerals in shale reservoirs (Hill & Nelson, 2000), so the bulk mineral analysis is important for predicting the fracture properties of the rocks in contemporary fracking operations.

The mudstones of the Belle Fourche and Second White Specks formations change with depth (Furmann *et al.*, 2014). These shales are composed of clay minerals (illite, kaolinite and chlorite), quartz, feldspar (albite), carbonates (calcite, dolomite and ankerite) and pyrite. The compositions are conveniently visualized in a ternary diagram of quartz + albite, carbonates and clays. The mineralogy correlates well with a 'ternary diagram' of macropores, mesopores and micropores. Mudstones containing >65 wt% quartz + feldspar are commonly more permeable than rocks with lower concentrations of these phases. Based on the quantified mineralogy, the brittleness of the rocks was calculated according to Jarvie *et al.* (2007) and Wang & Gale (2009).

7.11.2.2. *Clay mineralogy and the Reynolds Cup*

The most important part of a mineralogical analysis often lies in the clay minerals, for their identification and quantification can be used to assess the thermal history of the reservoir, and thus the nature of the petroleum which may be found in it. Analysis of the clay minerals using diffraction techniques is, however, the most difficult part of the analysis, because these minerals are often not ordered in three dimensions, and their layers are prone to intergrow. While it is often possible to 'force' crystalline models on these phases and obtain answers which are 'good enough' from a Rietveld refinement, such crystalline models are more of an approximation than they are for most phases, and special techniques are often required. These can include the PONCKS techniques described in Chapter 3.9, but special-purpose (non-Rietveld) software can be required. Such techniques will be facilitated by the inclusion of raw data patterns in the Powder Diffraction File (PDF; Chapter 3.7).

A renaissance in methods for clay mineral analysis dates from an inter-laboratory comparison (Ottner *et al.*, 2000). Since 2002, the Clay Minerals Society has sponsored seven Reynolds Cup challenges for mineral analysis (http://www.clays.org/Reynolds.html). The details of the methods used by the top finishers in the Third Reynolds Cup are documented in Omotoso *et al.* (2006).

Obtaining accurate phase identifications and quantifications required more effort than might be considered typical. Examination of the samples using optical and electron (with energy-dispersive spectroscopy) microscopes assisted in phase identification. Size fractionation (less and greater than 2, 6 or 20 µm, depending on the participant) helped to identify the clay minerals. Key to identifying the clay minerals were the usual treatments (air drying, magnesium and/or potassium exchange, ethylene-glycol intercalation, formamide intercalation and heating) and measurements of oriented specimens on glass slides. Additional treatments, such as washing with water, acid (to remove carbonates) and ethylenediaminetetraacetic acid (EDTA), can simplify analysis of the insoluble fractions.

Copyright © 2019 International Union of Crystallography

Patterns for quantitative analysis were generally collected from micronized specimens containing an internal standard. Most analyses were carried out by the Rietveld method. Key to the highest accuracy was comparison of the analysis calculated from the phase compositions and concentrations with that obtained by bulk chemical analysis. It was also important to use optimized structural models for the phases that were actually present, rather than 'random' models from a database.

7.11.2.3. *Gas hydrates*

Clathrate hydrates (or gas hydrates) are nonstoichiometric crystalline compounds formed by physical interactions (van der Waals forces) between a framework of hydrogen-bonded water molecules and guest molecules (Sloan & Koh, 2008; Atwood *et al.*, 1984). Three common structures designated I, II and H are known, mainly depending on the size of the molecular guest species. There is growing interest in gas hydrates for their potential application as a source of natural gas (Ji *et al.*, 2001), for deep-ocean CO_2 sequestration (Teng *et al.*, 1997) and for the recovery/separation of greenhouse gases from flue gas (Kang & Lee, 2000) because they can hold a large amount of gas in a small volume of solid hydrate phase.

The unexpected formation of gas hydrates during the production and transportation of natural gas is a severe problem (Kelland, 2006). Hydrate formation may block pipelines, creating a safety hazard (Ostergaard *et al.*, 2005). Accordingly, extensive work has been performed on inhibitors of gas-hydrate formation. Park *et al.* (2013) found that morpholine was a good inhibitor of methane hydrate formation and used powder diffraction to identify and quantify gas-hydrate phases.

7.11.2.4. *Corrosion deposits*

Corrosion-related failure of equipment which produces or transports hydrocarbon fuels can be catastrophic and newsworthy. A common task in an XRD laboratory is to characterize corrosion deposits (either pre-failure or post-failure) in an attempt to deduce the conditions that led to the corrosion and to prevent future failures.

The corrosion scale on a failed low-alloy Qinhuangdao–Shenyang natural gas pipeline consisted mainly of $FeCO_3$ (Shi *et al.*, 2014). Iron and Fe_3C from the uncorroded steel were also detected. No iron oxides were observed, as might be expected from the oxygen-free environment. The natural gas contained 2.27 mol% CO_2 and 2.58 mol% H_2O. Dry CO_2 cannot corrode steel; the presence of water is required. The siderite scale indicated that the corrosion was electrochemical in nature. The $FeCO_3$ was porous, so ion transport and pitting were facilitated once the siderite began to form.

Many well and pipeline deposits consist of mixtures of iron sulfides. Quantitative phase analysis, in conjunction with iron–sulfur phase diagrams, can provide detailed information on the conditions that led to the formation of the scale. The presence of the FeS polymorph mackinawite almost always indicates bacterial involvement in the corrosion.

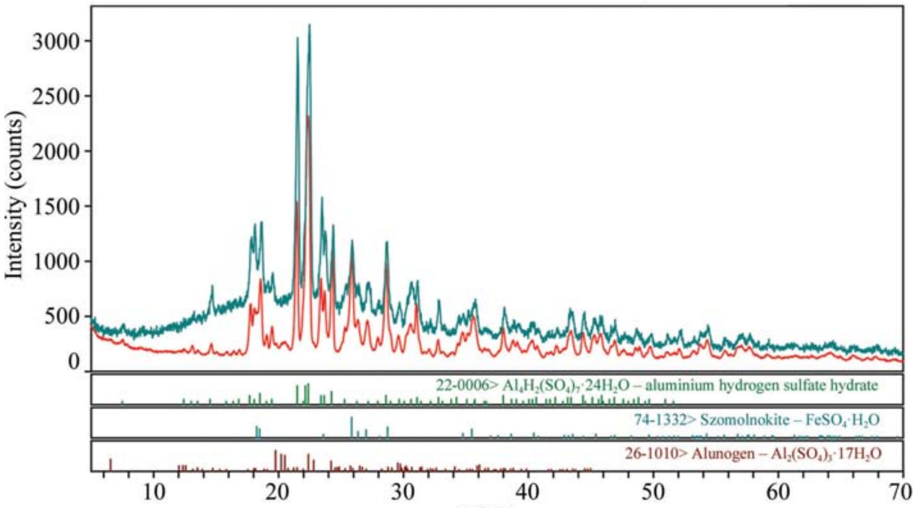

Figure 7.11.1
X-ray powder patterns of an alkylation-unit pump-seal deposit, both as received (green) and after removing the amorphous organic fraction by washing with acetone (red).

7.11.3. Refining and petrochemicals

7.11.3.1. *Corrosion deposits*

New phases are encountered remarkably often in support of the petroleum and petrochemical industries. These present both a problem (because their structures are not known and thus are harder to include in a Rietveld refinement) and also an opportunity to solve interesting new structures. The commercial value is generally not in the new structures themselves, but in understanding how/why these compounds came to be present in the sample.

7.11.3.1.1. $[Al(H_2O)_6][Al(H_2O)_5(SO_4)](H_3O)_2(SO_4)_5$

A black tar was recovered from a pump seal at a refinery alkylation unit. The process engineers were concerned that sulfuric acid had leaked into this pump, which had an aluminium housing. The powder pattern (Fig. 7.11.1) indicated that this tar contained the crystalline phases $Al_4H_2(SO_4)_7{\cdot}24H_2O$ (PDF entry 00-022-0006), szomolnokite, $FeSO_4{\cdot}H_2O$ (PDF entry 01-074-1332), and alunogen, $Al_2(SO_4)_3{\cdot}17H_2O$ (PDF entry 00-026-1010). The amorphous hydrocarbon present in the tar could be removed by washing with acetone. (Knowing how to deconstruct and separate samples is a useful skill.) At the time, the crystal structure of $Al_4H_2(SO_4)_7{\cdot}24H_2O$ had not been determined, so the structure had to be derived before the Rietveld quantitative analysis could be carried out.

The structure was solved by analogy using the formula type ANX in the Inorganic Crystal Structure Database (http://icsd.fiz-karlsruhe.de; Bergerhoff & Brown, 1987; Belsky *et al.*, 2002; Hellenbrandt, 2004). By the conventions of the ICSD, $Al_4H_2(SO_4)_7{\cdot}24H_2O$ has the formula type ANX = A4B7X52. At the time of this work, the ICSD contained only one entry with this formula type, that of $Cr_4H_2(SO_4)_7{\cdot}24H_2O$. Although the pattern of this chromium compound does not appear to match that of the aluminium compound very well (Fig. 7.11.2), the two compounds are in fact isostructural. Substituting Al for Cr in the reported structure (Gustafsson *et al.*, 1980) led to an excellent Rietveld refinement. Details of the refinement can be found in Kaduk (2002*a*). After the problem had been solved, a single-crystal structure of $Al_4H_2(SO_4)_7{\cdot}24H_2O$ was reported (Fischer *et al.*, 1996).

From the refined scale factors, the crystalline portion of the deposit contained 70 wt% $Al_4H_2(SO_4)_7{\cdot}24H_2O$, 22 wt%

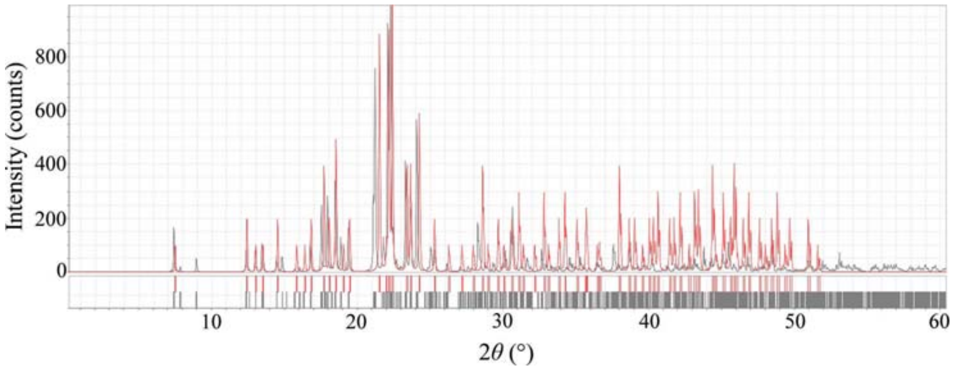

Figure 7.11.2
Comparison of the powder patterns of the isostructural compounds $Al_4H_2(SO_4)_7 \cdot 24H_2O$ (red) and ‘$(H_3O)_2Cr_4(SO_4)_7(H_2O)_{22}$’ (grey) = $Cr_4H_2(SO_4)_7 \cdot 24H_2O$.

$FeSO_4 \cdot H_2O$ and 8 wt% $Al_2(SO_4)_3 \cdot 17H_2O$. The Fe:S ratio calculated from these concentrations agreed well with the value of 0.27 determined by bulk chemical analysis. The Al:Fe and Al:S ratios of 2.02 and 0.45 were lower than the bulk values of 2.76 and 0.75, respectively. The conclusion was that the amorphous fraction of the tar contained Al. By combining the bulk chemical analysis with the Rietveld results, the true concentrations of these three phases in the whole deposit were 23, 7 and 3 wt%, respectively.

The most complete investigation of the $Al_2(SO_4)_3$–H_2SO_4–H_2O system (Taylor & Bassett, 1952) indicates that $Al_4H_2(SO_4)_7 \cdot 24H_2O$ is formed around 323–333 K at H_2SO_4:$Al_2(SO_4)_3$ ratios from 2.4 to 14.5, or acid-rich conditions. It was obtained by the slow transformation of $Al_2(SO_4)_3 \cdot 16H_2O$ or $Al_2H_2(SO_4)_4 \cdot 12H_2O$ and is metastable with respect to $Al_2(SO_4)_3 \cdot 14H_2O$. Apparently, sulfuric acid had leaked into the pump and reacted with both the aluminium housing and steel pump parts. The fact that the major phase is metastable with respect to other hydrated aluminium sulfates suggested that the corrosion was current and not a historical event. Accordingly, the recommendation was made to shut this unit down to repair the pump, rather than wait a few months for the scheduled shutdown and risk a catastrophic failure.

7.11.3.1.2. *$(NH_4)Fe(CO_3)(OH)_2$*

After the liquid-ammonia supply to a chemical plant was changed, deposits began to form in a liquid-ammonia heat exchanger. Such deposits reduce the efficiency of the exchanger, so identifying their nature (and thus their cause) had a significant impact on process economics. These deposits contained mixtures of phases, including PDF entry 00-022-0052, ‘$(NH_4)_2Fe(OH)_4(CO_3)_2(H_2O)$’ (Dvořák & Feitknecht, 1969). This compound had only been reported in one other reference (Erdös & Altorfer, 1976) as a corrosion product of carbon steel in aqueous solutions of ammonia and carbonic acid. Before the Rietveld quantitative analysis could be carried out, it was necessary to determine the structure of this compound.

The compound was prepared nearly phase-pure by the method of Dvořák & Feitknecht (1969). The powder pattern could be indexed in a *C*-centred orthorhombic unit cell with $a = 6.6154\ (6)$, $b = 12.0639\ (10)$, $c = 6.0263\ (5)$ Å. Default reduced-cell searches yielded no hits. Both from the process chemistry and the PDF entry, we could be reasonably sure that the compound contained carbon, hydrogen, nitrogen and oxygen. A search of the ICSD for compounds containing these elements and having *C*-centred orthorhombic unit cells yielded 25 hits, most of which could be discarded as they were cyanide complexes. Among the hits was ‘NH_4-dawsonite’, $(NH_4)Al(CO_3)(OH)_2$ (Iga & Kato, 1978), which had also been reported as a corrosion product by Erdös & Altorfer (1976). (Dawsonite is the sodium analogue.) The bulk chemical analysis reported by Dvořák & Feitknecht (1969) accounted for only 86.5% of the product, suggesting that their formulation was incorrect.

$(NH_4)Al(CO_3)(OH)_2$ proved to be a suitable starting model for $(NH_4)Fe(CO_3)(OH)_2$, the correct formulation of this phase (Fig. 7.11.3). Details of the refinement are given in Kaduk (2002*a*). Synthesis of $(NH_4)Fe(CO_3)(OH)_2$ requires CO_2 and H_2O, neither of which should have been present in the liquid-ammonia feed system. After careful examination of the system for leaks (and finding none), we concluded that these deposits were a startup problem (resulting from an incompletely cleaned pipeline) and not a failure of the system. After the initial formation the deposits did not return, confirming the conclusion.

7.11.3.1.3. *$(NH_4)Fe_2S_3$*

A deposit isolated from a refinery isomerization-unit pump screen contained several normal sulfide and oxide corrosion phases (Fig. 7.11.4), but the best match to the pattern of the major phase was rasvumite, KFe_2S_3. The presence of rasvumite would be very surprising, as there should be no potassium in a refinery stream, and none was detected by bulk chemical analysis. The jar containing the deposit smelled strongly of ammonia when it was opened. Ammonium and potassium ions are similar in size, and often form isostructural compounds. The infrared spectrum of the deposit was dominated by bands from NH_4^+ cations. Accordingly, the rasvumite structure was used as the initial model for the major phase, $(NH_4)Fe_2S_3$. The Rietveld refinement (Fig. 7.11.5)

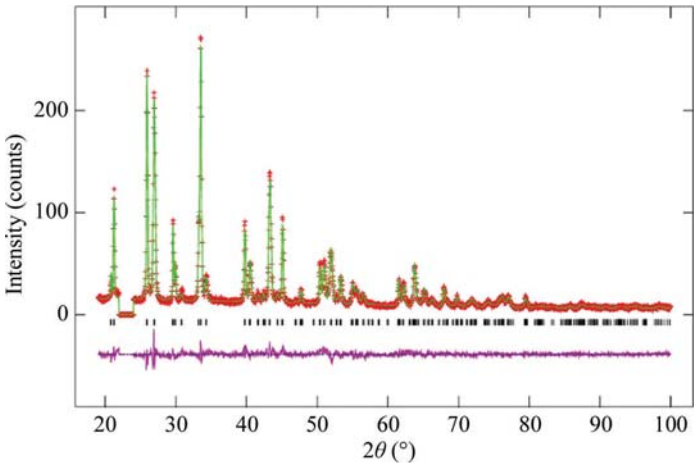

Figure 7.11.3
Rietveld refinement of $(NH_4)Fe(CO_3)(OH)_2$ based on the ‘NH_4-dawsonite’ model.

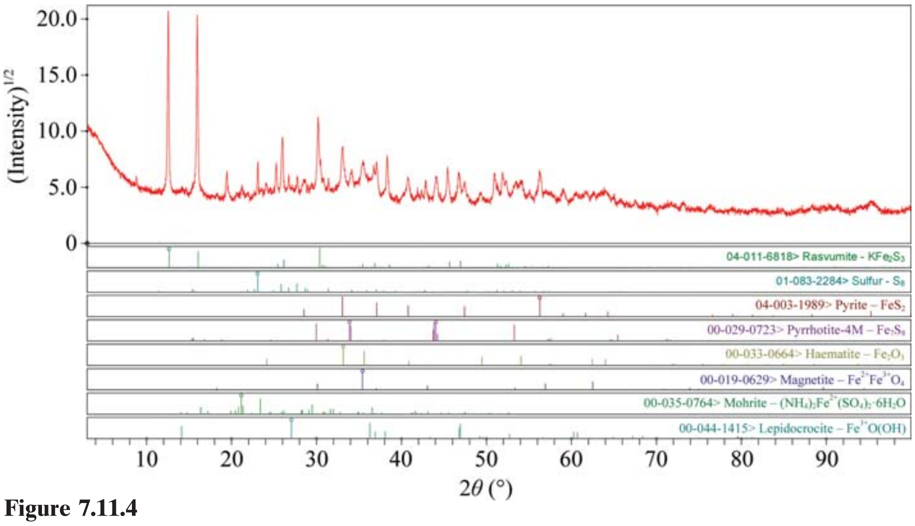

Figure 7.11.4
Powder pattern of a refinery isomerization-unit pump-screen deposit. The best match to the major phase was the chemically unreasonable KFe_2S_3.

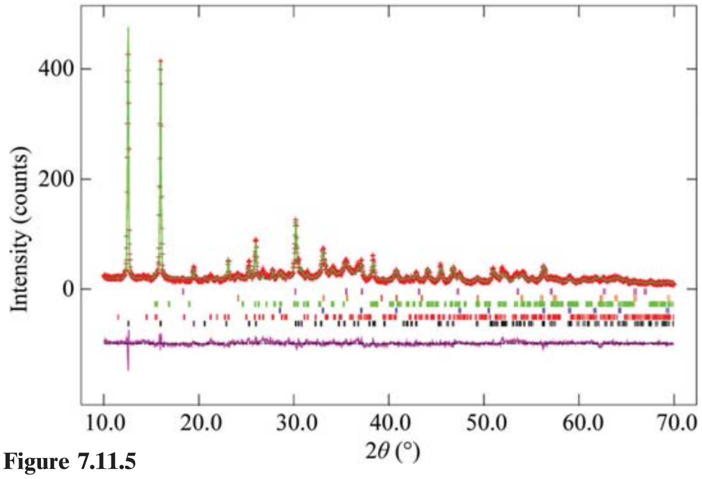

Figure 7.11.5
Rietveld refinement of the refinery isomerization-unit pump-screen deposit.

yielded the composition as 34.8 (3) wt% $(NH_4)Fe_2S_3$, 8.1 (3)% S_8, 10.4 (2)% pyrite (FeS_2), 5.0 (2)% pyrrhotite (Fe_7S_8), 30.6 (4)% magnetite (Fe_3O_4) and 11.0 (2)% haematite (Fe_2O_3). The deposit was not an unreasonable refinery corrosion deposit. The powder pattern and crystal structure of $(NH_4)Fe_2S_3$ are now included in the PDF as entry 00-055-0533.

7.11.3.2. *Catalysts*

Some of the preceding examples come from the 'upstream' (exploration and production) side of the petroleum industry. An important part of the work of most XRD laboratories in this industry is characterizing catalysts from the 'downstream' side (refining and chemicals). Such catalysts are often highly proprietary, but a few examples can be provided. Other examples are given in Medrud (2000) and Teller (2000).

7.11.3.2.1. *Quantitative analysis of zeolite catalysts*

ASTM method D5758-01 concerns the determination of the crystallinity of molecular sieves with the MFI framework type. It involves determining the integrated area of the 501/051/151/303/133 peak cluster (Fig. 7.11.6) and comparing it with the area from a reference sample. Similar methods exist for the FAU (D3906-03) and LTA (D5357-03) framework types. Although most zeolite quantitative analysis is currently performed using the Rietveld method, such peak-based methods have a role when high-volume and/or fast-turnaround analyses are necessary.

Zeolites and supported zeolite catalysts present special challenges for quantitative analysis. Everything about the procedures must be carefully controlled to achieve the highest accuracy and precision. The water content (and thus the unit-cell formula) varies with relative humidity, which must therefore be controlled. The equilibration time is often several hours, and often an overnight equilibration in a controlled-humidity chamber is required. The equilibration profile varies with framework type and composition, and must be determined experimentally for the system of concern.

Ion exchange (especially with high-*Z* metal cations) can change the absorption coefficient of the sample significantly. Since such methods rely on an external standard, it is important to calculate whether identical specimen volumes are illuminated in the exchanged specimen and the (generally metal-free) reference zeolite. It is possible to follow the ASTM method rigorously and obtain the wrong answer!

Any method should be qualified by making known mixtures of the reference zeolite and an appropriate support or amorphous phase. Blending of an MFI reference with γ-alumina can lead to microabsorption effects. These can be eliminated by micronizing the blend. Since micronizing requires a milling liquid, additional steps of removing the adsorbed liquid and re-equilibration are required. Certain large-crystallite Al-MFIs (ZSM-5) can be prone to preferred orientation and microabsorption, which can also be eliminated by micronizing and subsequent re-equilibration. Micronizing can change the amount and functional form of water absorption, and the supports (and internal standards!) can have a significant absorption capacity.

It is not rare for specimen preparation to change the as-received sample. The symmetry of the MFI can change from orthorhombic to monoclinic on grinding. Other phases can change polymorphs or be destroyed by grinding. The stability of each system of interest must be determined experimentally.

Even the data-processing method must be carefully controlled. The integrated areas are generally determined by profile fitting. We have found that we obtained more accurate and more precise

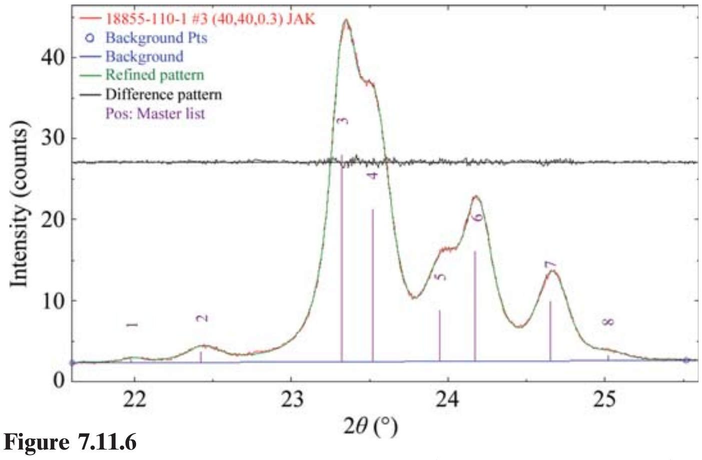

Figure 7.11.6
Profile fit of the 501/051/151/303/133 peaks (the five strongest peaks) to determine their integrated areas in ASTM method D5758-01 for the determination of the crystallinity of MFI molecular sieves.

integrated areas of the five strong peaks by including the three small peripheral peaks in the profile fitting. The shape of the profile can change the integrated areas. Even the background (which is generally assumed to be linear in this small region) can affect the resulting peak areas. Using 22–25° and 22.5–25° as background points can result in different integrated areas and thus quantitative analyses. Such data-processing issues are less of a problem when whole patterns are used in a Rietveld analysis, but background functions and structural models must be optimized and controlled.

Despite all of these cautions, with careful control of all steps of the analysis absolute accuracies of <0.2 wt% can be achieved for supported zeolite catalysts.

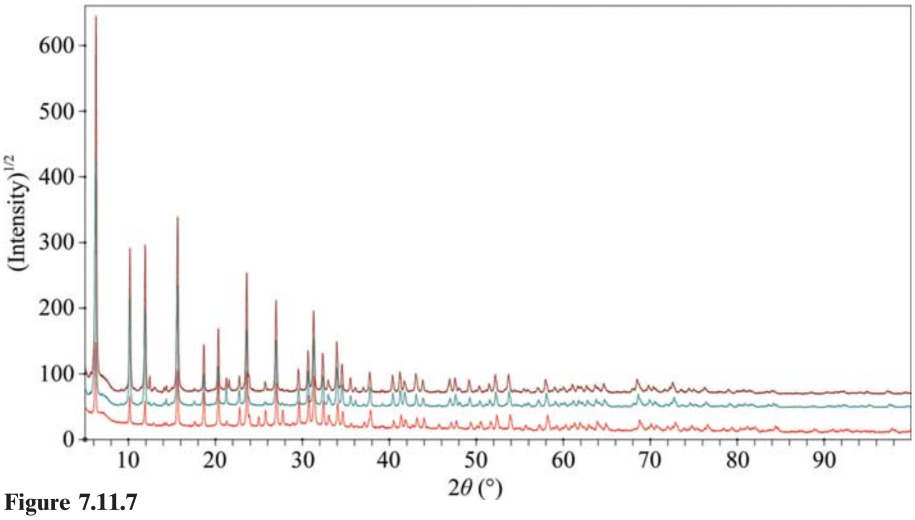

Figure 7.11.7
Patterns of Na-FAU measured under ambient conditions (red) and dehydrated both at 623 K (brown) and 298 K (green).

7.11.3.2.2. *Extraframework sites in Na-FAU*

Zeolites are crystalline aluminosilicates composed of corner-sharing tetrahedra joined into three-dimensional frameworks having pores of molecular dimensions. They are a subset of the larger class of molecular sieves. A pure silica framework is neutral. The presence of aluminium in the framework results in a negative framework charge, which is balanced by cations. These cations are relatively mobile and can be replaced using standard ion-exchange techniques. Faujasite (International Zeolite Association structure type FAU; Meier *et al.*, 1996) crystallizes in the cubic space group $Fd\bar{3}m$, with a lattice constant ranging from about 24.2 to 25.1 Å, depending on the framework aluminium concentration, cations and the state of hydration. There are 192 tetrahedral sites per unit cell. This zeolite is most conveniently visualized as being formed from 24-tetrahedra cuboctahedral units (sodalite cages) joined through hexagonal prisms (also known as double 6-rings). The structure can be viewed as the diamond structure, with the sodalite cages playing the role of C atoms and the double 6-rings the role of C—C bonds.

The pore structure is characterized by supercages approximately 12 Å in diameter with cavities which are linked through 12-ring windows of about 8 Å in diameter. These cages and pores permit access to quite large molecules, making this structure useful in catalytic applications. It is not much of an exaggeration to say that each drop of gasoline passes through this zeolite at least once.

The most commonly encountered faujasites are zeolite X (higher Al) and zeolite Y (lower Al). Zeolite Y is the most important catalytic zeolite, and is generally synthesized in the sodium form. Most of the catalysis of interest is acid catalysis, which requires replacing the sodium cations by protons, converting the sieve into the hydrogen form. This cannot be performed by direct ion exchange, since most H-faujasites are not acid stable. An indirect strategy is therefore used. Ammonium exchange is carried out, followed by calcination to decompose the NH_4^+ cations into ammonia and protons. In this way, highly crystalline H-FAU can be prepared. In some catalytic applications, it is desirable to incorporate metal cations into the sieve to modify the number and nature of the acid sites and to affect the diffusion of reactants and products. A detailed *in situ* study of extraframework species in FAU can be found in Kaduk (2005) (data files are available from the author on request).

The crystal structures of the hydrated Na-FAU LZ-Y52 starting material and the dehydrated material have been determined at both 623 and 298 K using *in situ* measurements on a laboratory diffractometer.

A sample of LZ-Y52 was packed into a 0.4 mm deep corundum holder. The X-ray powder pattern was first measured under ambient conditions on a PANalytical X'Pert Pro diffractometer equipped with a PIXcel position-sensitive detector and an Anton Paar HTK1200N furnace. The sample was heated to 623 K in vacuum (~3.2 × 10^{-5} mbar; 1 mbar = 100 Pa) and the pattern was re-measured *in situ*. The pattern was also measured after cooling to 298 K in vacuum. The faujasite crystal structure was refined by the Rietveld method using *GSAS* (Larson & Von Dreele, 2000).

By using the correlation of Fichtner-Schmittler *et al.* (1984) between the cubic lattice parameter and the framework Al concentration and the weight loss on dehydration, the formula of LZ-Y52 was the well known $Na_{56}Al_{56}Si_{136}O_{384}(H_2O)_{198}$. The powder pattern of the hydrated material differs from those of the dehydrated forms in subtle but important ways (Fig. 7.11.7), reflecting differences in the crystal structures.

The refinement of the structure of the hydrated zeolite is not particularly good (Fig. 7.11.8 and Table 7.11.1). Only some of the sodium cations can be located (as is typical for hydrated zeolites); the difference Fourier map is flat to ±0.7 e Å^{-3}. Site II′ is

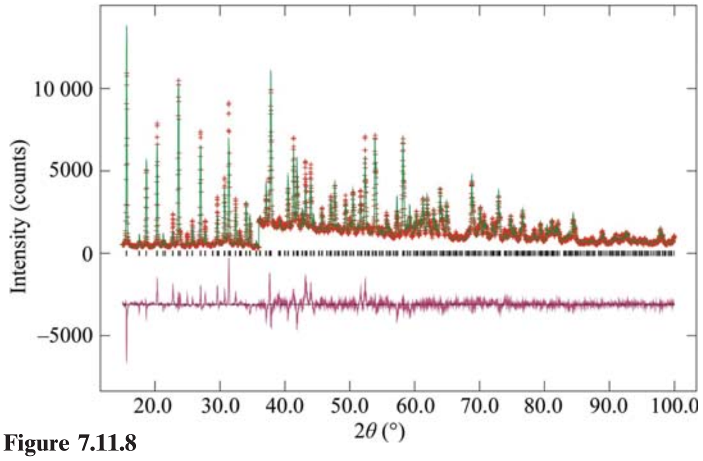

Figure 7.11.8
Rietveld refinement of hydrated Na-FAU under ambient conditions. The vertical scale has been enlarged by a factor of 5× for angles greater than 36°.

Table 7.11.1
Crystal structure of Na-FAU LZ-Y52

In each case, one value of U_{iso} was refined for all O atoms.

State	Hydrated, 298 K	Dehydrated, 298 K	Dehydrated, 623 K
File name	KADU1224.gsas	KADU1226.gsas	KADU1225.gsas
χ^2	10.04	3.626	2.939
a (Å)	24.7021 (4)	24.7616 (2)	24.8184 (3)
Si1/Al2, occupancies 0.71/0.29			
x	−0.03642 (11)	−0.03544 (5)	−0.03577 (6)
y	−0.12315 (13)	−0.12340 (7)	−0.12458 (6)
z	0.05357 (11)	0.05461 (5)	0.05511 (5)
U_{iso} (Å^2)	0.0113 (7)	0.0170 (4)	0.0220 (4)
O3 at 0, y, z			
y	−0.1070 (21)	−0.10884 (10)	−0.10771 (10)
z	0.10689 (21)	0.10873 (10)	0.10760 (10)
U_{iso} (Å^2)	0.0146 (11)	0.0231 (6)	0.0340 (6)
O4 at x, y, x			
x	0.00304 (23)	0.0374 (11)	0.0186 (10)
y	−0.13976 (30)	−0.14306 (15)	−0.14054 (16)
O5 at x, x, z			
x	−0.07262 (24)	−0.06934 (11)	−0.07407 (12)
z	0.02972 (30)	0.03298 (16)	0.03377 (18)
O6 at x, $-1/4 - x$, z			
x	−0.07213 (23)	−0.07327 (11)	−0.07058 (11)
z	0.07270 (35)	0.06715 (16)	0.06852 (16)
Na site I at 0, 0, 0			
U_{iso} (Å^2)	0.04	0.034 (2)	0.051 (2)
Occupancy	0.696 (18)	0.849 (9)	0.388 (8)
Na per cell	11	14	6
Na site I′ at x, x, x			
x	0.0671 (4)	0.0583 (4)	0.0525 (2)
Occupancy	0.554 (12)	0.241 (7)	0.528 (7)
Na per cell	18	8	17
Na site II′ at x, x, x			
x	0.1653 (2)	—	—
Occupancy	0.688 (15)		
Na per cell	22		
Na site II at x, x, x			
x	—	0.2316 (1)	0.2346 (1)
Occupancy		0.843 (8)	0.900 (7)
Na per cell		27	29

probably occupied by water molecules rather than sodium cations. The remaining sodium ions are disordered in the almost-liquid water that fills the large pores of this zeolite. Local ordering on the scale of a few unit cells results in distortion of the peak intensities. Attempts were made to use the solvent-flattening capability of *GSAS* (which is usually used for refining protein structures) to model this water, but the coefficients refined to values that were insignificantly different from zero and the refinements became unstable. Hydrated zeolites are difficult to describe using a purely crystalline model.

Better refinements were obtained for the dehydrated zeolite at both 298 and 623 K (Figs. 7.11.9 and 7.11.10) because there are no disordered water molecules. Almost all of the sodium cations could be located (49 and 52 sodium cations per cell at 298 and 623 K, respectively). They occupy sites I (double 6-rings), I′ (sodalite cage) and II (supercage) (Fig. 7.11.11), but the site occupancies are different at the two temperatures. In dehydrated Na-FAU site I is almost completely occupied by sodium at room temperature. At 623 K about half of these sodium cations move to site I′; the total number of cations in these two sites is nearly constant. Occupation of site I precludes occupation of two sites I′ (the sites are too close together for simultaneous occupancy), so the distribution of the cations reflects a subtle shift in the relative energies of the two sites at the two temperatures. The occupation of site II is nearly constant at the two temperatures. These results are in excellent agreement with other structure determinations of dehydrated Na-FAU.

Compared with the dehydrated form, Na I′ in hydrated LZ-Y52 is ~0.4 Å farther from the framework, indicating

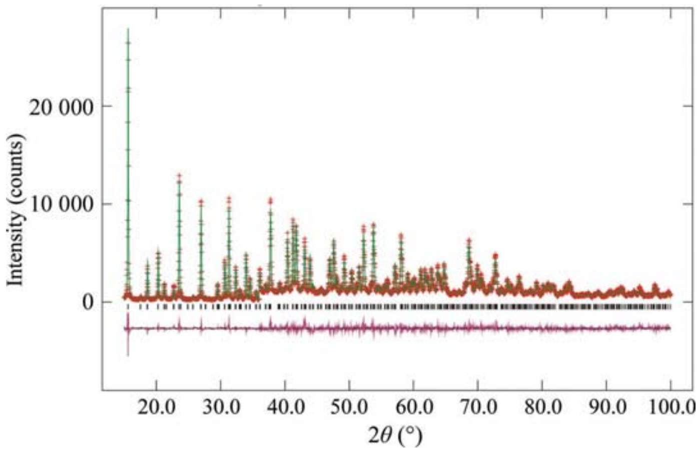

Figure 7.11.9
Rietveld refinement of dehydrated Na-FAU at 298 K in vacuum. The vertical scale has been enlarged by a factor of 5× for angles greater than 36°.

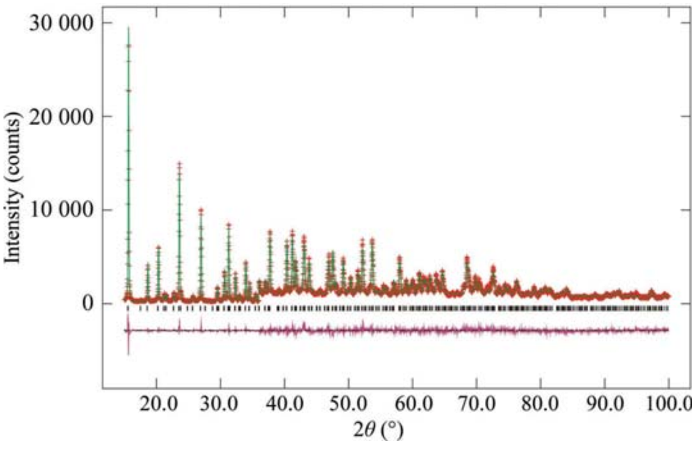

Figure 7.11.10
Rietveld refinement of dehydrated Na-FAU at 623 K in vacuum. The vertical scale has been enlarged by a factor of 5× for angles greater than 36°.

coordination to water molecules (Fig. 7.11.12). These water molecules occupy site II′, which is empty in the dehydrated zeolite. Site II is empty in the hydrated zeolite, showing that the remaining sodium cations are coordinated to water molecules ‘in solution’ in the large pores.

Table 7.11.2
Extraframework sites in Xe/Na-FAU at 20 K

Site	I′	II′	II	III	
x	0.0633 (5)	0.1637 (9)	0.2379 (4)	0.1901 (10)	0.3551 (9)
y	0.0633	0.1637	0.2379	−0.1099	−0.1051
z	0.0633	0.1637	0.2379	−0.1099	−0.1448 (9)
Occupancy	16 Na	10 Na	23 Na	5 Xe	2 Xe

Different cations occupy different sites at elevated (close to reaction) temperature and move differently when the sample is returned to ambient conditions (Kaduk, 2005). In a CaNa-FAU containing $Ca_{20}Na_{10}$ in the unit cell, hydrated calcium ions are approximately equally distributed over sites I′, II′ and II under ambient conditions. There is also a small population of hydrated calcium cations at site V. At 573 K there are large calcium populations at site I, and sites I′ and II are populated by a mixture of calcium and sodium. All of the cations were closer to the framework O atoms than under ambient conditions. On cooling to ambient conditions (and rehydrating) the cations move to positions that are not greatly different from their initial positions. A second calcium exchange to the composition $Ca_{27}Na_4$ led to very different cation locations at 573 K. Site I is vacant, but site I′ is half-occupied by calcium. Cation–cation repulsions preclude simultaneous occupation of sites I and I′. The remaining calcium cations occupy site II, and the sodium cations are displaced to the relatively unfavourable site II′.

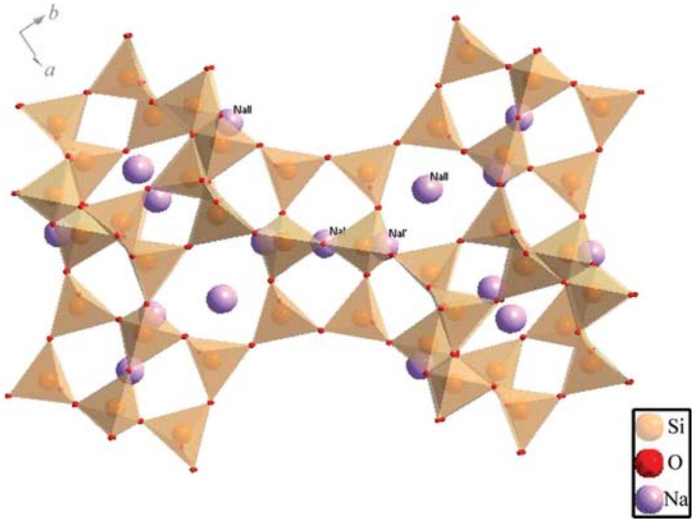

Figure 7.11.11
Positions of the sodium cations in dehydrated Na-FAU at 298 K.

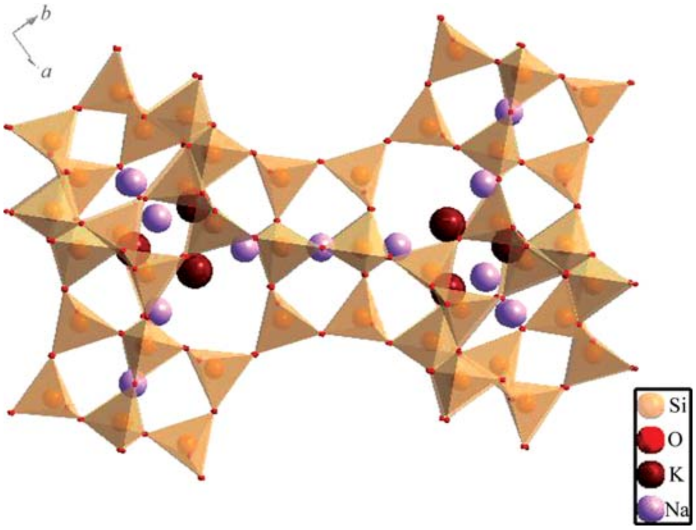

Figure 7.11.12
Positions of the sodium cations in dehydrated Na-FAU at 573 K. The sodium at site II′ is designated ‘K’ to distinguish it from the other sodium sites I and I′.

Barium cations occupy sites I′ and II, as well as an additional site in the supercages. In $La_{15}Na_{13}$ most of the lanthanum cations occupy site V, far away from the framework O atoms, and small lanthanum populations occupy sites I′, II and II′; the sodium cations also occupy site II′. At 573 K the great majority of the lanthanum cations occupy site I′, and the sodium cations are displaced to site II′. Unlike the calcium-exchanged FAU, the lanthanum cations tend to remain at their high-temperature positions on cooling and rehydration.

A zinc-edge resonant-scattering study (both under ambient conditions and *in situ* at 573 K) permitted determination of the zinc and sodium site occupancies in $Na_{13}Zn_{19}$-FAU. In the hydrated sample at ambient conditions the Zn cation occupy sites II′ and II, with the sodium cations at site I′. Electron density at the centre of the sodalite cage (site U) represents an O atom coordinated to the zinc. At 573 K the zinc cations move to sites I′ and II′, and the sodium cations are displaced to site II in the supercage.

Each cation moved differently between ambient and catalytic temperatures. To develop a valid structure–activity correlation, the correct structure (measured *in situ*) must be used.

7.11.3.2.3. *Xenon in Na-FAU*

^{129}Xe NMR is often used to study the diffusion and porosity of zeolites. An Xe atom is almost the same size as a methane molecule. To help understand the NMR results, and to provide some insight into how a methane molecule might interact with the FAU framework, a sample of commercial Na-FAU (LZ-Y52) was dehydrated carefully in a capillary attached to a vacuum line (Kaduk, 2002*b*). The sieve was cooled to room temperature and

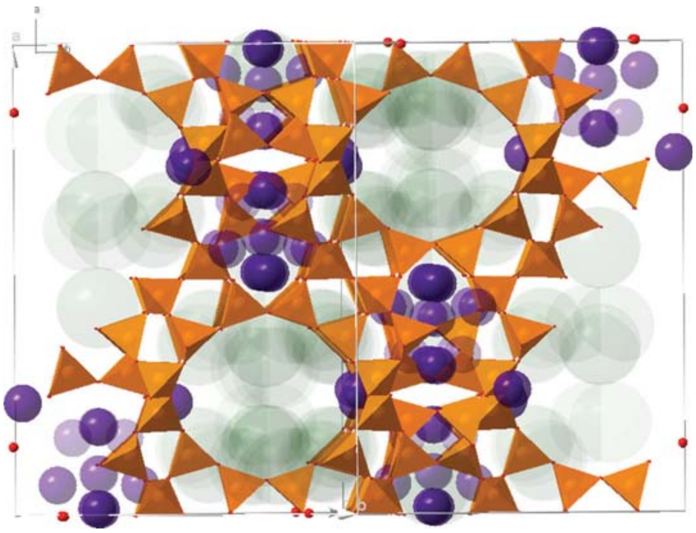

Figure 7.11.13
Extraframework xenon (and sodium) sites in Na-FAU at 20 K.

allowed to equilibrate with 1 atm xenon (1 atm = 101 325 Pa). The capillary was sealed and cooled to 20 K for measurement of the powder pattern. A total of 48 sodium cations per cell were located at sites I′, II′ and II (see Table V in Kaduk, 2005). Two additional extraframework sites, one near site III, a xenon van der Waals distance away from the framework O atoms, and another towards the centre of the supercage and a van der Waals distance away from site III, were found to be populated with Xe atoms (Table 7.11.2 and Fig. 7.11.13).

7.11.3.2.4. *CO_2 in Na-FAU*

The crystal structure of dehydrated Na-FAU with and without adsorbed CO_2 was determined at 4 K and at room temperature (RT) using neutron powder diffraction techniques (Wong-Ng *et al.*, 2013). Neutron diffraction data provided direct evidence that adsorption of CO_2 results in significant migration of the extraframework sodium cations in the zeolite structure. At 4 K, 45 of the apparent 76 CO_2 molecules per cell were located in two crystallographically independent sites bonding to the sodium cations (Na10) in the supercage site II. While the CO_2 molecule in the first site had a linear configuration, interacting with Na10 *via* one terminal O atom, the CO_2 molecule in the second site appeared to have a bent O—C—O configuration [148.3 (3)°], with both O atoms coordinating to two symmetry-related Na10 cations. Density-functional theory (DFT) total-energy calculations showed that the Na–CO_2 interaction slightly facilitates the bending motion of CO_2 by decreasing the energy cost for the 148.3 (3)° bond angle by ~0.2 eV per CO_2. However, this Na–CO_2 interaction is not sufficient to cause a 32° bond-angle distortion in CO_2 (an energy cost of ~0.66 eV per CO_2). Rotational disorder apparently plays a significant role here.

7.11.3.2.5. *Framework compositions*

One of the common zeolite analyses in an XRD laboratory is to calculate the framework composition from the refined lattice parameters. Correlations between the framework composition and the cell dimensions of carefully prepared samples are known for several common zeolite frameworks. Comparing the framework composition with the bulk chemical analysis easily yields estimates of the composition of amorphous and/or nonframework concentrations of heteroatoms.

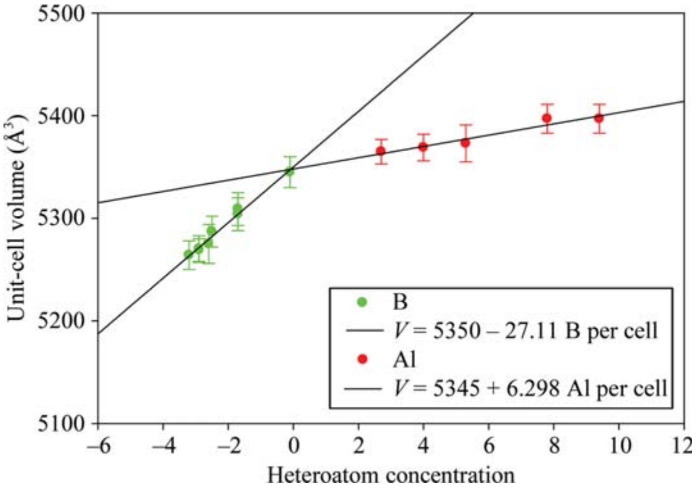

Figure 7.11.14
Unit-cell volume *versus* heteroatom concentration for B-MFI and Al-MFI molecular sieves (Meyers *et al.*, 1985).

Table 7.11.3
GSAS profile coefficients for fresh $(VO)_2P_2O_7$ catalyst and a catalyst that has been used for three years

State	Fresh	Used
File name	GOED05	GOED06
$(VO)_2P_2O_7$ (wt%)	95.17 (3)	100
V (Å³)	1231.4 (3)	1232.0 (4)
Profile *LX*	17.0 (2)	18.5 (3)
ptec(100)	4.9 (12)	−5.1 (19)
Size ∥ (Å)	370	630
Size ⊥ (Å)	480	450
S(400)	0	1.0(3)
S(040)	0	0
S(004)	0	0
S(220)	0.30 (4)	0.40 (6)
S(202)	0.14 (7)	0.19 (1)
S(022)	0	0
β-$VO(PO_3)_2$ (wt%)	3.6 (2)	—
α-$VOPO_4$ (wt%)	1.2 (2)	—

Three different correlations between the cubic lattice parameter of faujasite and the framework aluminium content have been reported (Kerr, 1989; Breck & Flanigen, 1968; Kerr *et al.*, 1978; Dempsey *et al.*, 1969; Fichtner-Schmittler *et al.*, 1984; Sohn *et al.*, 1986):

$$\begin{aligned}\text{Breck–Flanigen}\quad & N_{\rm Al} = 115.2(a - 24.191),\\ \text{Kerr–Dempsey}\quad & N_{\rm Al} = 112.1(a - 24.222),\\ \text{Fichtner-Schmittler}\quad & N_{\rm Al} = 107.1(a - 24.338).\end{aligned}$$

The analyst has to work with the customer to determine which correlation is most appropriate for the systems being studied.

Correlations for both Al-MFI and B-MFI are reported in Meyers *et al.* (1985). Updated to current nomenclature, these correspond to $V = 5345 + 6.298$ Al per cell and $V = 5350 - 27.11$ B per cell (Fig. 7.11.14). Similar correlations have been reported for mordenite (Olsson & Rollmann, 1977).

7.11.3.2.6. *$(VO)_2P_2O_7$*

Vanadyl pyrophosphate is used commercially as a catalyst for the selective oxidation of butane to maleic anhydride. Rietveld analyses of a fresh catalyst and a catalyst that had been used for three years (Table 7.11.3) demonstrated that the fresh catalyst

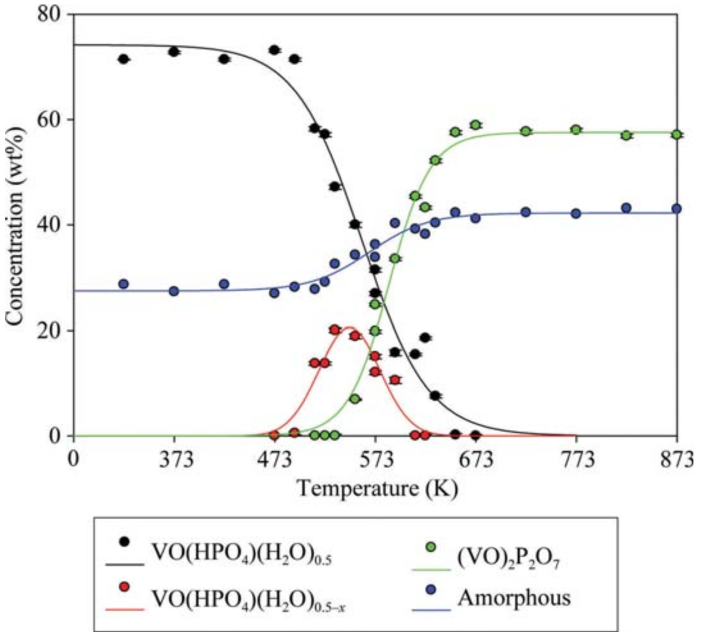

Figure 7.11.15
Phase concentrations during the calcination of a $VO(HPO_4)(H_2O)_{0.5}$ precursor to form $VO_2P_2O_7$.

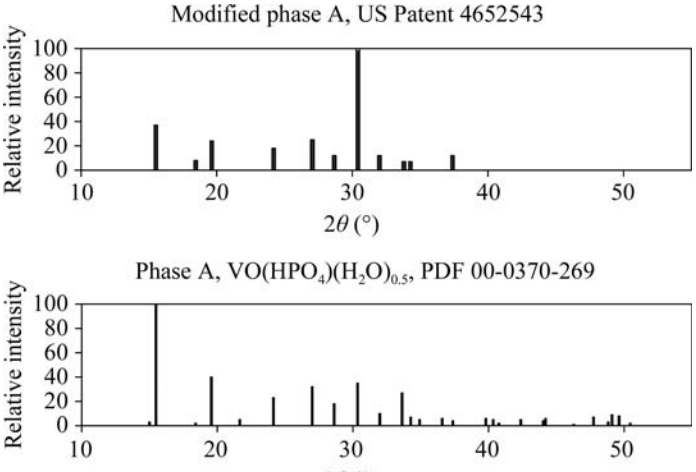

Figure 7.11.16
Powder patterns (as 2θ values and peak heights) of two morphologies of $VO(HPO_4)(H_2O)_{0.5}$. The differences in peak heights are the result of anisotropic size broadening.

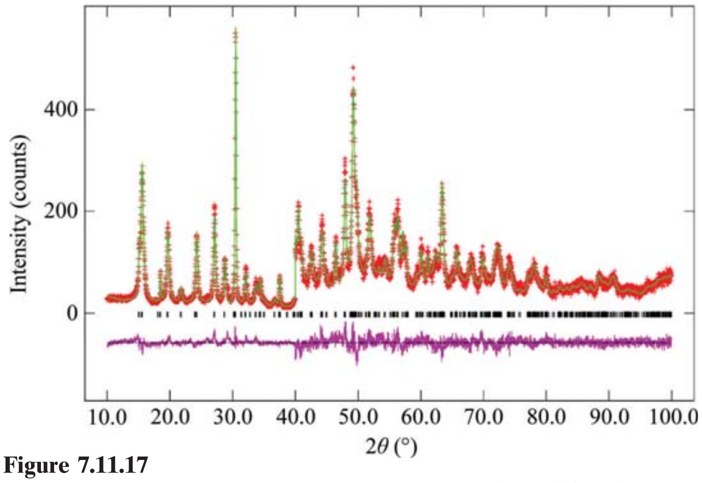

Figure 7.11.17
Rietveld refinement of ‘Modified Phase A’, $VO(HPO_4)(H_2O)_{0.5}$. The fixed published crystal structure model was used; anisotropic size-broadening profile coefficients account for the varying peak widths and peak heights compared with isotropic crystallites. The vertical scale has been magnified by a factor of 5× for angles greater than 40°.

contained small concentrations of two impurities: β-$VO(PO_3)_2$ and α-$VOPO_4$. The metaphosphate is a common impurity phase, while α-$VOPO_4$ indicated that the catalyst had been calcined under slightly oxidizing conditions. Its presence is detrimental, but both phases typically disappear in the first month of operation. Changes in the profile parameters indicated that the $(VO)_2P_2O_7$ had sintered only slightly in the three years of operation and that the anisotropic strain broadening had increased slightly.

Such catalysts are prepared by calcination of a $VO(HPO_4)(H_2O)_{0.5}$ precursor. *In situ* studies of the calcination confirmed that an intermediate phase occurred at intermediate temperatures (Fig. 7.11.15) and that the amount and nature of the amorphous phase changed during calcination.

Amoco Corporation obtained a patent for a ‘novel phosphorus–vanadium catalyst having a characteristic X-ray diffraction pattern’ (Edwards & Meyers, 1987). The composition of matter was defined by the stoichiometry $VO(HPO_4)(H_2O)_{0.5}$ and the characteristic powder pattern. The pattern exhibits some similarities in peak positions to that of $VO(HPO_4)(H_2O)_{0.5}$ (Fig. 7.11.16), but the relative peak heights of the two patterns are very different. A close examination of the pattern reveals that the peak broadening is highly anisotropic. A Rietveld refinement using a fixed structural model of $VO(HPO_4)(H_2O)_{0.5}$ (Leonowicz *et al.*, 1985) reproduced the observed pattern very well (Fig. 7.11.17) and demonstrated that there was no difference between the crystal structures of the two phases. There was thus no difference in the integrated intensities; anisotropic broadening caused the differences in peak heights. The refined profile coefficients indicated that the broadening was the result of size contributions, corresponding to plate-like grains averaging 170 × 840 × 840 Å. This morphology exposes more of the desirable {001} surface and thus explains the enhanced performance of the catalyst.

Table 7.11.4
Crystallite sizes for fresh and used vent-gas oxidation catalysts

Catalyst	Fresh	Used
File name	NUBE50	NUBE52
Cordierite, $Mg_2Al_4Si_5O_{18}$ (wt%)	89.0 (1)	90.2 (1)
V (Å^3)	1551.3 (2)	1551.9 (1)
Profile *LX*	1.8 (3)	1.9 (2)
Size (Å)	Large	Large
$(M,Zr)O_2$ (wt%)	11.0 (3)	9.6 (1)
a (Å)	4.9063 (69)	5.0557 (5)
Profile *LX*	430 (18)	76 (1)
Size (Å)	18	105
Pt (wt%)	—	0.21 (3)
a (Å)		3.9240 (31)
Profile *LX*		64 (1)
Size (Å)		125

7.11.3.2.7. *Vent-gas oxidation catalyst*

A vent-gas oxidation catalyst in a chemical plant consisted of an array of cordierite monolith bricks. These monoliths were coated with a stabilized cubic zirconia wash coat and impregnated with platinum (Fig. 7.11.18 and Table 7.11.4). While no crystalline platinum was detected in the fresh catalyst, it had sintered significantly during use. The cubic zirconia also sintered, while the cordierite monolith was essentially unchanged. If the zirconia particles are spherical, their average diameter can be estimated: diameter = 6/(density × BET area) (where BET = Brunauer–

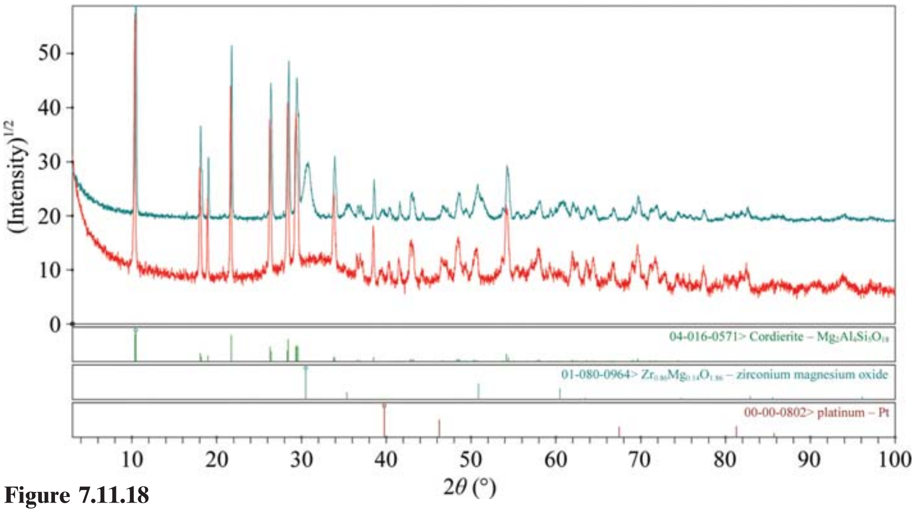

Figure 7.11.18
Powder patterns of a fresh (red) and used (green) vent-gas oxidation catalyst.

Emmett–Teller). These estimated diameters track the crystallite sizes calculated from the line broadening well.

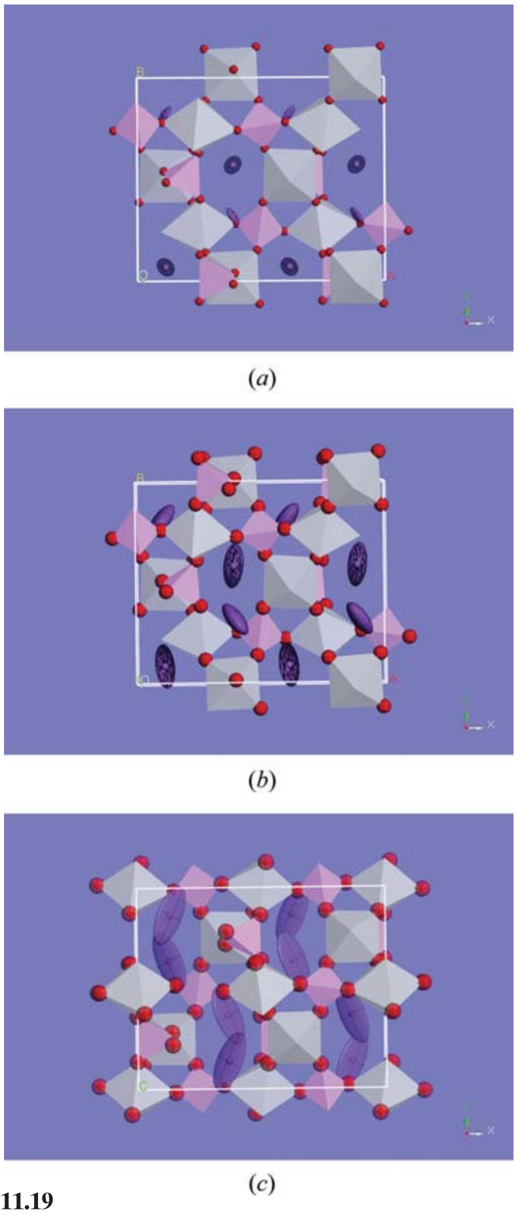

Figure 7.11.19
Crystal structure of $KTiOPO_4$ at 474 K (*a*) and 1174 K (*b*) (below the phase transition) and at 1324 K (*c*) (above the phase transition).

7.11.4. *In situ* studies

Even after several decades of experience, it is still true that *every* catalyst that we have studied under reaction conditions has had a different structure than under ambient conditions. A large part of catalyst research and development is the development of structure–activity correlations so that catalyst performance can be improved. Catalyst performance is (of course) measured under reaction conditions, but most analytical work is performed under ambient conditions. Developing a structure–activity correlation using the wrong structure is a bad business model, and is sure to limit the rate of catalyst development. It is virtually mandatory that *in situ* XRD studies be carried out, and XRD has an advantage over other analytical techniques in carrying out such studies. Such studies generally involve key intellectual property and are thus not often described in readily available publications.

A recent example of the importance of XRD to catalyst development is provided by US Patent 8697596 (Kaduk *et al.*, 2014) for metal-oxide catalysts for the conversion of lower alkane hydrocarbons, particularly for the ammoxidation of propane to acrylonitrile. The study was carried out under ambient conditions. The claims include a phase with the M1 crystalline structure, which has a unit-cell volume in the range 2250–2350 $Å^3$ and a crystallite aspect ratio in the range 0.7–2.0. The unit-cell volume is a proxy for changes in composition and subtle changes in the crystal structure of this phase. It does not take much of a structural change to significantly change the electronic properties at a catalyst site, so detailed structural studies of such catalysts provide the raw material for extensive quantum-chemical studies aimed at understanding the reactivity. The range of the aspect ratio of the crystallites reflects that crystallites that are too platy or needle-like yield poorer performance.

A noncatalytic example of an *in situ* study is the characterization of $KTiOPO_4$ (KTP) above and below the phase transition (Kaduk, 2000). The nonlinear optical properties of KTP have important applications in laser devices. KTP is used to generate 530 nm (green) light from 1060 nm infrared light produced by GaAs-pumped Nd/YAG solid-state lasers. KTP is also an ionic conductor, with large anisotropically enhanced conductivity along the [010] direction. This permits the synthesis of optical waveguides with reflecting walls parallel to (010).

KTP crystallizes in the orthorhombic space group $Pn2_1a$ at room temperature, and undergoes a high-temperature ferroelectric-to-paraelectric phase transition at 1207 K. KTP melts incongruently at 1343 K. Since KTP crystals are grown, and devices are fabricated, at temperatures near the phase transition, knowledge of the changes that occur at the transition would assist in the control of device properties.

Powdered KTP, prepared by solid-state synthesis from KH_2PO_4 and TiO_2, was pressed into pellets, and diffraction patterns were measured from 473 to 1323 K in flowing air using the 90° detector banks and the Miller furnace on the General Purpose Powder Diffractometer (GPPD) at the Intense Pulsed Neutron Source (IPNS) at Argonne National Laboratory. Patterns were measured in two sets of runs: one at a coarse temperature spacing to discern general features and a second closely spaced in temperature around the transition.

Neutron powder diffraction was used because the scattering contrast between the ions in KTP is well balanced (but is weighted towards titanium for X-rays) and because the transition temperature was not accessible on the single-crystal instrument at IPNS. The phase transition was crossed several times, and appeared to be reversible. No evidence of KTP decomposition was observed.

All data sets were first processed using the low-temperature $Pn2_1a$ model. The variation in the *a* and *c* lattice parameters was smooth, but there was a pronounced anomaly in the *b* lattice parameter at 1223 K. Given the uncertainties in the absolute temperature, this is close enough to the reported transition temperature of 1207 K to be identified with the phase transition.

Application of the *MISSYM* program from the *NRCVAX* system (Larson *et al.*, 1994) clearly indicated the presence of an additional *n*-glide perpendicular to *b* and a centre of symmetry. The transition is therefore analogous to that observed in $TlTiOPO_4$ at lower temperature using single-crystal techniques (Harrison *et al.*, 1990). Refinements using patterns collected below the transition were carried out in $Pn2_1a$ and those above the transition in *Pnna*.

In the KTP structure, alternating PO_4 tetrahedra and TiO_6 octahedra are linked by their vertices to form a two-dimensional network along the *a* and *b* axes, while the $(Ti1)O_6$ octahedra join

(P2)O_4 tetrahedra along *c*. The TiO_6 octahedra are linked together alternately *cis* and *trans* to form chains along [011] and $[01\bar{1}]$. The PO_4 tetrahedra are regular, while the TiO_6 octahedra are highly distorted, each containing one short (<1.75 Å) bond opposite a long bond (>2.10 Å) at room temperature. This distortion is believed to be the source of the large nonlinear optical coefficients of KTP. The potassium cations reside in channels parallel to [010] and [001], with windows defined by distorted hexagonal rings of O atoms.

In $Pn2_1a$ all of the atoms (two Ti atoms, two P atoms, two K atoms and ten O atoms) occupy general positions, while in *Pnna* the two independent Ti atoms occupy sites of 2 and $\bar{1}$ symmetry. The two P atoms remain independent and reside on twofold axes. The two independent K atoms become equivalent and occupy a general position. The ten O atoms reduce to five; in particular, the independent Ti—O—Ti chain O atoms O9 and O10 become equivalent.

The best measures of the phase transition are the metal–oxygen distances. The PO_4 tetrahedra remain virtually unchanged through the transition. The cations are intimately related to the physical properties of the material; replacing the potassium cations with sodium and rubidium lowers the melting temperature by >150 K.

The titanium coordinates change very little until the transition, when there is a sharp change to the high-temperature positions. The largest changes during the transition are in the *y* coordinates of the potassium cations; K1 moves nearly 0.7 Å and K2 by 0.3 Å to become equivalent. Changes in the Ti—O bond distances begin to occur at temperatures well below the transition temperature. At the transition, some changes in Ti—O distances are gradual (mostly involving Ti1), while others (principally involving Ti2) are sharp. To a good approximation, there are only low-temperature and high-temperature structures; intermediate structures are not observed.

In $Pn2_1a$ K1 is eight-coordinate and K2 is nine-coordinate, and the K—O distances span the normal range. In *Pnna* the single potassium is only five-coordinate and the distances are relatively short [according to bond-valence sum (BVS) calculations]. The anisotropic displacement coefficients of the potassium ions increase dramatically along *b* as the temperature increases (Fig. 7.11.19).

The phase transition appears to result not from a change in a single structural feature but from the sum of several smaller changes. The Ti—O and K—O distances begin to change at temperatures as low as 673 K, which is the result of both changes in the lattice parameters and potassium migration. At the transition, the accumulated changes are of sufficient magnitude to drive a sudden shift to the high-temperature structure. The transition is both displacive and second-order.

The observed structural changes are consistent with the changes in the optical and conduction properties and help to provide a firmer understanding of the properties of this complex structure. The practical significance of the work is to emphasize that high-quality single-domain crystals for device applications should be prepared at temperatures that are as low as possible to avoid imperfections caused by structural changes.

References

Atwood, J. L., Davis, J. E. D. & MacNicol, D. D. (1984). *Inclusion Compounds.* London: Academic Press.

Belsky, A., Hellenbrandt, M., Karen, V. L. & Luksch, P. (2002). *New developments in the Inorganic Crystal Structure Database (ICSD): accessibility in support of materials research and design. Acta Cryst.* B**58**, 364–369.

Bergerhoff, G. & Brown, I. D. (1987). *Inorganic Crystal Structure Database.* In *Crystallographic Databases*, edited by F. H. Allen, G. Bergerhoff & R. Sievers, pp. 77–95. Chester: International Union of Crystallography.

Breck, D. W. & Flanigen, E. M. (1968). *Synthesis and Properties of Union Carbide Zeolites L, X, and Y. Molecular Sieves*, edited by R. M. Barrer & B. Coughlan, pp. 47–61. London: Society of Chemical Industry.

Dempsey, E., Kuehl, G. H. & Olson, D. H. (1969). *Variation of the lattice parameter with aluminum content in synthetic sodium faujasites. Evidence for ordering of the framework ions. J. Phys. Chem.* **73**, 387–390.

Dvořák, V. & Feitknecht, W. (1969). *Sur les carbonates basiques de fer(III): II. Préparation, radiocristallographie et spectres IR du* $(NH_4)_2Fe_2(OH)_4(CO_3)_2{\cdot}H_2O$. *Helv. Chim. Acta*, **52**, 515–522.

Edwards, R. C. & Meyers, B. L. (1987). *Catalysts useful for the manufacture of maleic anhydride having a characteristic X-ray diffraction pattern.* US Patent 4652543.

Erdös, E. & Altorfer, H. (1976). *Zur Korrosion von unlegiertem Stahl und Aluminium in wässrigen Lösungen von Ammoniak und Kohlensäure – 1. Mitteilung: Korrosionsprodukte. Mater. Corros.* **27**, 611–618.

Fichtner-Schmittler, H., Lohse, U., Engelhardt, G. & Patzelová, V. (1984). *Unit cell constants of zeolites stabilized by dealumination determination of Al content from lattice parameters. Cryst. Res. Technol.* **19**, K1–K3.

Fischer, T., Kniep, R. & Wunderlich, H. (1996). *Crystal structure of dioxonium bis(tris(sulfato)dialuminate)sulfate docosahydrate,* $(H_3O)_2{\cdot}[Al_2(SO_4)_3]_2{\cdot}(SO_4){\cdot}22H_2O$. *Z. Kristallogr.* **211**, 469–470.

Furmann, A., Mastalerz, M., Schimmelmann, A., Pedersen, P. K. & Bish, D. (2014). *Relationships between porosity, organic matter, and mineral matter in mature organic-rich marine mudstones of the Belle Fourche and Second White Specks formations in Alberta, Canada. Mar. Pet. Geol.* **54**, 65–81.

Glikson, A. Y., Jablonski, D. & Westlake, S. (2010). *Origin of the Mt Ashmore structural dome, west Bonaparte Basin, Timor Sea. Aust. J. Earth Sci.* **57**, 411–430.

Gustafsson, T., Lundgren, J.-O. & Olovsson, I. (1980). *Hydrogen bond studies. CXXXIX. The structure of* $Cr_4H_2(SO_4)_7{\cdot}24H_2O$. *Acta Cryst.* B**36**, 1323–1326.

Harrison, W. T. A., Gier, T. E., Stucky, G. D. & Schultz, A. J. (1990). *The crystal of the nonlinear optical material thallium titanyl phosphate,* $TlTiOPO_4$, *above the ferroelectric to paraelectric phase transition. J. Chem. Soc. Chem. Commun.* pp. 540–542.

Hellenbrandt, M. (2004). *The Inorganic Crystal Structure Database (ICSD) – present and future. Crystallog. Rev.* **10**, 17–22.

Hill, D. G. & Nelson, C. R. (2000). *Reservoir properties of the Upper Cretaceous Lewis Shale, a new natural gas play in the San Juan Basin. AAPG Bull.* **84**, 1240.

Iga, T. & Kato, S. (1978). *Crystal structure of* NH_4*-dawsonite. J. Ceram. Soc. Jpn*, **86**, 509–512.

Jarvie, D. M., Hill, R. J., Ruble, T. E. & Pollastro, R. M. (2007). *Unconventional shale-gas systems: the Missipian Barnett Shale of north-central Texas as one model for thermogenic shale-gas assessment. AAPG Bull.* **91**, 475–499.

Ji, C., Ahmadi, G. & Smith, D. H. (2001). *Natural gas production by depressurization. Chem. Eng. Sci.* **56**, 5801–5814.

Jiu, K., Ding, W., Huang, W., Zhang, Y., Zhao, S. & Hu, L. (2013). *Fractures of lacustrine shale reservoirs, the Zhanhua Depression in the Bohai Basin, eastern China. Mar. Pet. Geol.* **48**, 113–123.

Kaduk, J. A. (2000). *Petroleum and petrochemicals. Industrial Applications of X-ray Diffraction*, edited by F. H. Chung & D. K. Smith, pp. 207–256. New York: Marcel Dekker.

Kaduk, J. A. (2002*a*). *Use of the Inorganic Crystal Structure Database as a problem solving tool. Acta Cryst.* B**58**, 370–379.

Kaduk, J. A. (2002*b*). *Non-traditional powder crystallography in the petrochemical industry. Adv. X-ray Anal.* **45**, 78–91.

Kaduk, J. A. (2005). *Extraframework species in zeolite Y at nonambient conditions. Crystallogr. Rev.* **11**, 1–19.

Kaduk, J. A., Brazdil, J. F., Bhattacharyya, A. & Paparizos, C. (2014). *Mixed metal oxide catalysts and catalytic conversions of lower alkane hydrocarbons*. US Patent 8697596 B2.

Kang, S.-P. & Lee, H. (2000). *Recovery of* CO_2 *from flue gas using gas hydrate: thermodynamic verification through phase equilibrium measurements. Environ. Sci. Technol.* **34**, 4397–4400.

Kelland, M. A. (2006). *History of the development of low dosage hydrate inhibitors. Energy Fuels*, **20**, 825–847.

Kerr, G. T. (1989). *Determination of framework aluminum content in zeolites X, Y, and dealuminated Y using unit cell size. Zeolites*, **9**, 350–351.

Kerr, G. T., Chester, A. W. & Olson, D. H. (1978). *Preparation of ultrahigh silicon faujasites by controlled-rate aluminum removal. Acta Phys. Chem.* **24**, 169–174.

Larson, A. C., Lee, F. L., Le Page, Y., Webster, M., Charland, J. P., Gabe, E. J. & White, P. S. (1994). *The NRCVAX Crystal Structure System, PC Version.* NRC Chemistry Division, Ottawa, Canada.

Larson, A. C. & Von Dreele, R. B. (2000). *General Structure Analysis System (GSAS).* Los Alamos National Laboratory Report LAUR 86-748.

Leonowicz, M. E., Johnson, J. W., Brody, J. F., Shannon, H. F. & Newsam, J. M. (1985). *Vanadyl hydrogenphosphate hydrates:* $VO(HPO_4)\cdot 4H_2O$ *and* $VO(HPO_4)\cdot 0.5H_2O$. *J. Solid State Chem.* **56**, 370–378.

Medrud, R. C. (2000). *Petroleum catalysts. Industrial Applications of X-ray Diffraction*, edited by F. H. Chung & D. K. Smith, pp. 257–285. New York: Marcel Dekker.

Meier, W. M., Oldon, D. H. & Baerlocher, C. (1996). *Atlas of Zeolite Structure Types*, 4th revised ed. London: Butterworth-Heinemann.

Meyers, B. L., Ely, S. R., Kutz, N. A., Kaduk, J. A. & van den Bossche, E. (1985). *Determination of structural boron in borosilicate molecular sieves via X-ray diffraction. J. Catal.* **91**, 352–355.

Morton, R. W., Simon, D. E., Gebel, J. F., Gislason, J. J. & Heald, R. L. (2001). *Applying the Rietveld method to mineral filled polyphenylene sulfide compounds. Adv. X-ray Anal.* **44**, 103–109.

Olsson, R. W. & Rollmann, L. D. (1977). *Crystal chemistry of dealuminized mordenites. Inorg. Chem.* **16**, 651–654.

Omotoso, O., McCarty, D. K., Hillier, S. & Kleeberg, R. (2006). *Some successful approaches to quantitative mineral analysis as revealed by the 3rd Reynolds Cup contest. Clays Clay Miner.* **54**, 748–760.

Ostergaard, K. K., Masoudi, R., Tohidi, B., Danesh, A. & Todd, C. (2005). *A general correlation for predicting the suppression of hydrate dissociation temperature in the presence of thermodynamic inhibitors. J. Pet. Sci. Eng.* **48**, 70–80.

Ottner, F., Gier, S., Kuderna, M. & Schwaighofer, B. (2000). *Results of an inter-laboratory comparison of methods for quantitative clay analysis. Appl. Clay Sci.* **17**, 223–243.

Park, S., Ro, H., Lee, J., Kang, H. & Lee, H. (2013). *Morpholine-induced thermodynamic and kinetic inhibitions on gas hydrate formation. Energy Fuels*, **27**, 6581–6586.

Shi, L., Wang, C. & Zou, C. (2014). *Corrosion failure of the L485 natural gas pipeline in* CO_2 *environment*. *Eng. Fail. Anal.* **36**, 372–378.

Sloan, E. D. & Koh, C. A. (2008). *Clathrate Hydrates of Natural Gases*, 3rd ed. Boca Raton: CRC Press.

Sohn, J. R., DeCanio, S. J., Lunsford, J. H. & O'Donnell, D. J. (1986). *Determination of framework aluminium content in dealuminated Y-type zeolites: a comparison based on unit cell size and wavenumber of IR bands. Zeolites*, **6**, 225–227.

Taylor, D. & Bassett, H. (1952). *The system* $Al_2(SO_4)_3$–H_2SO_4–H_2O. *J. Chem. Soc.* pp. 4431–4442.

Teller, R. (2000). *Petrochemicals: vitality of catalysts research. Industrial Applications of X-ray Diffraction*, edited by F. H. Chung & D. K. Smith, pp. 287–301. New York: Marcel Dekker.

Teng, H., Yamasaki, A., Chun, M. K. & Lee, H. (1997). *Why does* CO_2 *hydrate disposed of in the ocean in the hydrate-forming region dissolve in seawater? Energy*, **22**, 1111–1117.

Wang, F. P. & Gale, J. F. W. (2009). *Screening criteria for shale-gas systems. Gulf Coast Assoc. Geol. Soc. Trans.* **59**, 779–793.

Wong-Ng, W., Kaduk, J. A., Huang, Q., Espinal, L., Li, L. & Burress, J. W. (2013). *Investigation of NaY zeolite with adsorbed* CO_2 *by neutron powder diffraction. Microporous Mesoporous Mater.* **172**, 95–104.

International Tables for Crystallography (2019). Vol. H, Chapter 7.12, pp. 855–867.

7.12. Powder-diffraction characterization of cements

M. A. G. Aranda, A. G. De la Torre and L. León-Reina

7.12.1. An introduction to cements and types of cements

The term cement may be used for almost any type of binder, with chemistry ranging from fully organic to totally inorganic. The oldest organic 'cements' were made from plant extracts such as starch or latex. The oldest pure inorganic cements were based on muds and subsequently on gypsum plasters. This dual nature of cements may be exemplified by the 'bone cements' used for medical applications, which range from totally organic (mainly based on polymethyl methacrylate) to totally inorganic, *e.g.* based on calcium phosphates. However, in this work we will focus on inorganic oxide-based hydraulic binders for construction applications. In this case, the cements are used as poorly soluble but highly reactive powders in water. The initial suspension, usually named fresh cement paste, firstly undergoes setting, and on hardening yields the hardened cementitious matrix. The use of water for achieving the hardening results in the term 'hydraulic binders' to highlight that the reaction of cement with water yields the concrete used for modern construction, which can even harden under water.

The world yearly consumption of concrete (http://en.wikipedia.org/wiki/Concrete), which is based mainly on Portland cement (http://en.wikipedia.org/wiki/Portland_cement), is well over 6 km^3, or more than 2.5 tonnes per person. Furthermore, in spite of their universal use, Portland cements are one of the most environmentally contentious materials. The worldwide production of cement, at more than 2×10^9 tonnes per year, accounts for approximately 6% of total anthropogenic CO_2 production. X-ray powder diffraction (XRPD) has two main uses in the cement industry: firstly, for improving the performance of Portland cements by measuring the phase assemblage of clinkers and cements and by determining and quantifying the chemical reactions during hydration, and secondly, for investigating new types of eco-cements, which release less CO_2 in their fabrication processes or in their life-cycle balance.

In this chapter, we highlight the uses of powder diffraction related to cements with selected examples. Firstly, we focus our attention on its uses for analysing different types of Portland clinkers, cements and blended cements. In this section, online Rietveld refinement in Portland cement plants is also discussed. Secondly, the uses of powder diffraction to study the chemistry and mineralogy of other cementitious materials are also highlighted. These cementitious materials include calcium aluminate cements, calcium sulfoaluminate, belite calcium sulfoaluminate cements (also known as sulfobelite cements), alkali-activated binders and supersulfated cements. The uses of Rietveld quantitative phase analysis for studying cement hydration reactions are addressed. It is becoming very important in this context for the analysis of blended cements. Initially, calcite, pulverized fly ash (PFA), blast furnace slag (BFS) and pozzolane additions were investigated. All of these materials are now being used industrially, and research is mainly devoted to other residues and by-products that can be blended with Portland cements. Powder diffraction has a bright future as most of the techniques developed for ordinary Portland cement (OPC) can be used to analyse new eco-cements: mainly sulfobelite, alkali-activated fly ashes and alkali-activated slags. Finally, selected examples of the use of synchrotron and neutron powder diffraction for characterizing cementitious materials, including their formation and degradation, will be discussed.

The uses of powder diffraction for the characterization of cementitious materials span phase identification (from the line positions and relative intensities) to microstructural studies (from the line widths). However, there is no doubt that quantitative phase analysis is the most important use of powder diffraction for analysing cements in order to understand/predict their performance. Moreover, although several methodologies have been reported to attain this objective, today Rietveld quantitative phase analysis (RQPA) is by far the most used technique. Hereafter, we will mainly deal with the use of RQPA applied to cementitious materials.

7.12.2. Rietveld quantitative phase analysis of cements

Quantitative phase analysis based on powder diffraction has already been discussed in this volume (see Chapter 3.9). Details of Rietveld quantitative phase analysis are also included in that chapter. It is worth noting that Hugo Rietveld did not envisage this use (Rietveld, 2010) in his two seminal papers (Rietveld, 1967, 1969). Two initial studies established the basis of RQPA (Hill & Howard, 1987; Bish & Howard, 1988). RQPA was first applied to the analysis of a Portland clinker six years later (Taylor & Aldridge, 1993).

Guidelines for Rietveld studies have been provided by McCusker *et al.* (1999). There are also two excellent articles arising from a round-robin study on quantitative phase analysis by powder diffraction (Madsen *et al.*, 2001; Scarlett *et al.*, 2002). Later, the results of a specific round-robin study on RQPA of Portland cements were reported (León-Reina *et al.*, 2009) and two review articles have been devoted to the RQPA of anhydrous Portland cements (Le Saoût *et al.*, 2011) and Portland cements, blended Portland cements and their hydration products (Aranda *et al.*, 2012). Based on these papers and others, this section gives some insights into RQPA of cements. As the analyses are becoming very complex (for instance hydration reactions of blended cements), a lot of care has to be exercised to carry out the best possible analysis. Two steps are carried out: obtaining crystal-structure information on all the phases that are likely to be present, and data analysis.

7.12.2.1. *Obtaining crystal-structure information*

Descriptions of the structures of each phase present in a cement must be included in the Rietveld control file. A thorough compilation of cement phases has been reported by Taylor (1997). Two updated compilations of crystal structures for RQPA of Portland anhydrous cements and hydration products have recently been reported (Le Saoût *et al.*, 2011; Aranda *et al.*, 2012). Sometimes there is more than one structural description available in the literature for a given phase. In this case, one possible methodology for selecting the most appropriate crystal structure is to carry out two (or more) RQPAs with the two (or more)

Copyright © 2019 International Union of Crystallography

reported structural descriptions. The structure selected should be that which gives the best fit based on the R_F factor, which is hopefully linked to a more accurate quantification, ideally based on known mixtures of the phases of interest. In addition to the main phases, other phases must be identified by searching for the extra peaks in the experimental pattern in the Powder Diffraction File (PDF, http://www.icdd.com). Once the phase has been identified, the crystal structure can be exported as a CIF from the PDF entry, or from one of the structural databases AMCSD (American Mineralogist Crystal Structure Database; http://rruff.geo.arizona.edu/AMS/amcsd.php), ICSD (Inorganic Crystal Structure Database; http://www.fiz-karlsruhe.de/icsd.html), COD (Crystallography Open Database; http://www.crystallography.net) or Pearson's Crystal Data (http://www.crystalimpact.com/pcd), or from another more specialized database (see Chapter 3.7). Finally, and mainly for solid solutions, site-occupation factor(s) for a given crystal structure must sometimes be adapted to describe a given stoichiometry.

If the crystal structures are not known, quantification of these phases may be achieved using reference patterns as '*hkl* phases' (Taylor & Aldridge, 1993), for instance with the *SIROQUANT* software. This approach has subsequently been expanded (Scarlett & Madsen, 2006) and is used in the cement industry (Chapter 3.9).

7.12.2.2. *Data analysis*

Once a powder pattern as free as possible of systematic errors has been recorded, Rietveld analysis must be carried out with the appropriate program and the control file. It is worth noting that the strong peak overlap in cements makes the analysis of phase peak-shape parameters critical. Working in reflection geometry, specimen rotation increases the particle statistics but it does not minimize preferred orientation. Some cement phases show this effect, which must be corrected, usually with the March–Dollase algorithm (Dollase, 1986), by using the appropriate axis. The preferred-orientation axes for some cement phases are [010] for gypsum, [001] for portlandite, [001] for the AFm family (defined below), [104] for the calcite family, [$\bar{1}$01] for alite-M_3 and [100] for ettringite. Spherical harmonics can also be used to model preferred orientation, but the severe peak overlap limits their use.

Hereafter, standard cement nomenclature will be used, *i.e.* C = CaO, S = SiO_2, A = Al_2O_3, F = Fe_2O_3, M = MgO, $\underline{S}$ = SO_3, $\underline{C}$ = CO_2, H = H_2O, K = K_2O and N = Na_2O. Hence, typical Portland cement phases such as alite (Ca_3SiO_5), belite (Ca_2SiO_4), tricalcium aluminate ($Ca_3Al_2O_6$), calcium aluminoferrite ($Ca_4Al_2Fe_2O_{10}$), gypsum ($CaSO_4{\cdot}2H_2O$), anhydrite ($CaSO_4$) and calcite ($CaCO_3$) are abbreviated as C_3S, C_2S, C_3A, C_4AF, $C\underline{S}H_2$, $C\underline{S}$ and $C\underline{C}$, respectively. Many cement compounds are not pure, stoichiometric phases but may incorporate many ions (Taylor, 1997; Le Saoût *et al.*, 2011).

New phases that appear during hydration must also be taken into account. They may be crystalline, such as portlandite, $Ca(OH)_2$ or CH, or amorphous/quasicrystalline phases such as calcium silicate hydrate gel (C-S-H gel in cement nomenclature to highlight its variable chemical composition, which changes with hydrating time, overall water content and even with the type of initial cement). AFm and AFt phases should also be defined. AFm is an abbreviation for 'alumina, ferric oxide, mono-sulfate' or 'Al_2O_3–Fe_2O_3–mono'; AFt is a similar abbreviation but for 'tri-sulfate' or 'Al_2O_3–Fe_2O_3–tri'. The AFm phase refers to a family of hydrated calcium aluminates based on the hydrocalumite structure, $Ca_4Al_2(OH)_{12}{\cdot}[Cl(OH)]{\cdot}6H_2O$. The archetypal AFm phase is $C_3A{\cdot}CaSO_4{\cdot}12H_2O$ or $Ca_4Al_2(OH)_{12}{\cdot}[SO_4]{\cdot}6H_2O$, known as kuzelite, but Al can be partly replaced by Fe, and SO_4^{2-} can be partly or fully replaced by OH^-, CO_3^{2-} and other anions (Pöllmann, 2006). By far the most common AFt phase is ettringite, which has the stoichiometry $C_3A{\cdot}3CaSO_4{\cdot}32H_2O$, also written as $Ca_6Al_2(SO_4)_3(OH)_{12}{\cdot}26H_2O$.

Programs for RQPA are listed in Chapter 6.1, and Rietveld programs are also listed on the CCP14 web site (http://www.ccp14.ac.uk/solution/rietveld_software/index.html). *GSAS* (Larson & Von Dreele, 1994; Toby, 2001) and *FULLPROF* (Rodríguez-Carvajal, 1993; Roisnel & Rodríguez-Carvajal, 2001) are the most widely used packages in academia. Many other packages can also be used for RQPA, for example *TOPAS*, *BGMN*, *AUTOQUANT*, *PDXL* and *HighScore Plus*.

7.12.3. Phase quantification of Portland cements

The output of an RQPA study for a mixture of crystalline phases with known structures is a set of the corresponding phase scale factors. The phase weight fractions can be derived from the phase scale factors using some approximations and methodologies.

(i) The simplest approach is the approximation that the sample is composed only of crystalline phases with known structures. This approximation eliminates the need to measure the instrument calibration constant and the sample mass absorption coefficient, and the phase scale factors can be directly transformed to phase weight fractions (Hill & Howard, 1987). However, if the sample contains amorphous phases, and/or some amount of unaccounted-for crystalline phases, the reported weight fractions will be overestimated.

(ii) A second, more experimentally demanding approach is to mix the sample with a crystalline standard in a known amount. This standard must be free of amorphous content, or at least its non-diffracting content must be known. The internal-standard method, coupled with RQPA, was first used in 1988 (Bish & Howard, 1988). The accuracy of RQPA using the internal-standard method for measuring amorphous content has also been studied (De la Torre, Bruque *et al.*, 2001). This procedure has recently been employed for certifying a standard (Cline *et al.*, 2011)

(iii) To avoid complications that may arise from mixing an internal standard with the sample, it is possible to use an external-standard method. This approach requires recording two patterns under identical diffractometer configurations and conditions. RQPA based on this method was proposed by O'Connor & Raven (1988) and has recently been applied to anhydrous cements (Jansen, Stabler *et al.*, 2011) and cement pastes (Jansen, Goetz-Neunhoeffer *et al.*, 2012; Jansen, Neubauer *et al.*, 2012). This methodology, which is also known as the G-method or K-method, consists of determining the diffractometer constant with an appropriate standard and using that diffractometer constant and the mass attenuation coefficient of the sample to convert the phase scale factors to weight fractions. This is an important limitation of the method as the precise chemical analysis of the sample must be independently obtained, for instance by X-ray fluorescence, to calculate the overall absorption coefficient.

The main uses of Rietveld quantitative phase analysis for extracting information on OPC materials are given in Fig. 7.12.1. These uses can be directly extended to other cementitious materials.

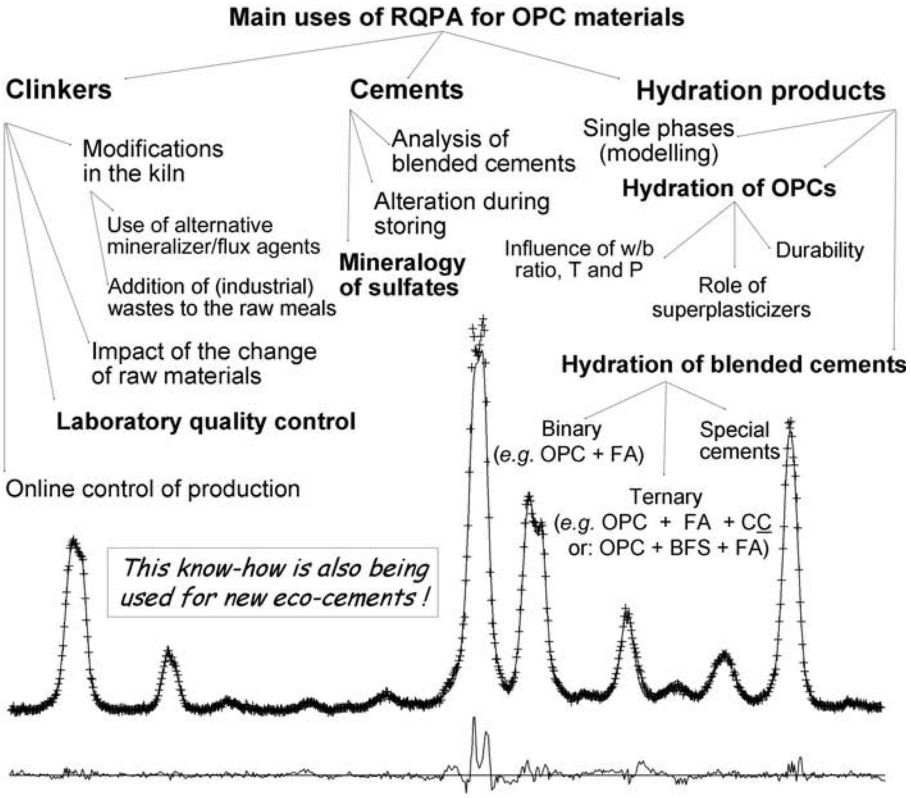
Main uses of RQPA for OPC materials
Clinkers
Modifications in the kiln
Use of alternative mineralizer/flux agents
Addition of (industrial) wastes to the raw meals
Impact of the change of raw materials
Laboratory quality control
Online control of production
Cements
Analysis of blended cements
Alteration during storing
Mineralogy of sulfates
Hydration products
Single phases (modelling)
Hydration of OPCs
Influence of w/b ratio, T and P
Durability
Role of superplasticizers
Hydration of blended cements
Binary (e.g. OPC + FA)
Special cements
Ternary (e.g. OPC + FA + CC or: OPC + BFS + FA)
This know-how is also being used for new eco-cements !

Figure 7.12.1
Main uses of Rietveld quantitative phase analysis for studying ordinary Portland clinkers, cements and hydration products. w/b is the water/binder ratio and 'raw meals' is a term used in the cement industry for raw material mixtures. [Reproduced with permission from Aranda *et al.* (2012).]

7.12.3.1. *Quantification of Portland clinkers*

The initial work on RQPA of a Portland clinker was published by Taylor & Aldridge (1993). Soon afterwards, other studies showed the advantages of this method, which does not require standards or calibration curves (Möller, 1995, 1998; Meyer *et al.*, 1998; Taylor *et al.*, 2000; Madsen & Scarlett, 2000). Initially, the studies were focused on OPC clinkers and were later expanded to different types of cements.

The main clinker phases are alite, belite and aluminate in white Portland clinkers and also ferrite in grey Portland clinkers. In addition, several other minor phases may be present: lime, periclase, arcanite, afthitalite and others. Two reviews of the phases present in OPC clinkers have been published (Le Saoût *et al.*, 2011; Aranda *et al.*, 2012). Several issues are discussed in these two reviews, including the selection of the alite polymorph, the implications of the Fe:Al ratio in ferrite quantification and the consequences of the existence of a solid solution in most clinker phases (resulting in small changes in the structure factors and densities of the analysed phases). As an example, Fig. 7.12.2 displays a selected region of the Rietveld plot for a typical commercial grey Portland clinker with the main peaks labelled. (This pattern and all the others displayed in this chapter were collected using strictly monochromatic Cu $K\alpha_1$ radiation. This is highly desirable to minimize peak overlap.) The inset in this figure shows the phase quantification under the first approximation stated above. (The sample is composed of 100% crystalline phases, which are all introduced in the Rietveld control file.)

The accuracy of RQPA of Portland clinker was investigated by De la Torre & Aranda (2003). The quantification of the amorphous/non-diffracting content in Portland clinkers has been a topic of research for a number of years. Suherman *et al.* (2002) carried out a thorough study using synchrotron and laboratory XRPD as well as internal- and external-standard approaches. Furthermore, selective dissolution and point-counting microscopy were also used with good results. The overall amorphous/non-diffracting contents for NIST reference clinker materials RM8486, RM8487 and RM8488 were ~6, ~11 and ~7 wt%, respectively. A subsequent analysis was dedicated to the study of the overall non-diffracting content in several commercial grey OPC clinkers and cements. The internal-standard method was used and an amorphous content close to 20 wt% was determined (Whitfield & Mitchell, 2003).

Another general use of RQPA is to study the role of mineralizing/flux agents in the kiln or the processing of industrial wastes in kilns by analysing the resulting clinker phase assemblage. The mechanism of action of the trace elements incorporated into the clinker is twofold depending on the amount of these elements (Herfort *et al.*, 2010).

(i) At low concentration, trace elements enter into the structure of the initial phases of the clinker as solid solutions (C_3Sss, C_2Sss, C_3Ass, C_4AFss).

(ii) At higher concentrations, the presence of new phases may be detected and quantified (Gineys *et al.*, 2011).

RQPA may help in both cases, initially by following the unit-cell variations of the solid solution(s) and secondly by quantification of the new phases. The implications of processing industrial waste(s) in Portland kilns have been studied by RQPA. As an example, this approach has been used to evaluate the effects of chromium and nickel additions to Portland clinker raw materials. The final goal was to better characterize the processing of galvanic sludge, which is the main hazardous solid waste produced by some metallurgical industries (Ferreira *et al.*, 2008).

7.12.3.2. *Quantification of Portland cements and blended cements*

Portland cements are formulated by adding a setting regulator to the Portland clinker. The sulfate phases added for this purpose may be gypsum or $C\underline{S}H_2$, hemihydrate $C\underline{S}H_{0.5}$ (also known as bassanite) and anhydrite $C\underline{S}$. Different types of Portland cements may have different additions, for instance calcite, $C\underline{C}$. Additionally, other highly amorphous materials may be added for blended cement and concrete production, such as BFS, PFA or pozzolane minerals. It must be kept in mind that these additions also contain some crystalline phases (for instance mullite or haematite) that must be quantified in blended cements. The reader is referred to the review of Aranda *et al.* (2012) for a full list of additional phases that may be present in blended Portland cements.

RQPA in OPCs can be used for a number of applications including (i) quantification of the crystalline phases in OPCs, (ii) to analyse the amount and role of sulfate-containing phases, (iii) to study the mineralogical phase assemblage in the materials used as addition(s) and (iv) to quantify all phases in blended OPCs, including the amorphous/non-diffracting content which is

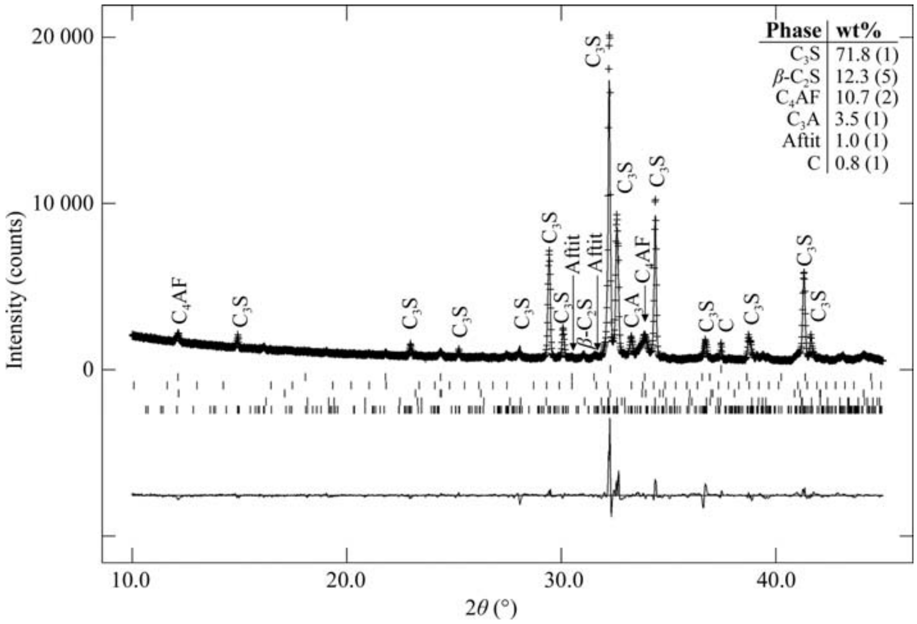

Phase	wt%
C_3S	71.8 (1)
β-C_2S	12.3 (5)
C_4AF	10.7 (2)
C_3A	3.5 (1)
Aftit	1.0 (1)
C	0.8 (1)

Figure 7.12.2
Selected region of a Rietveld plot using Cu $K\alpha_1$ radiation for a commercial grey Portland clinker with the main peaks labelled (Aftit stands for afthitalite). The RQPA result is shown in the inset.

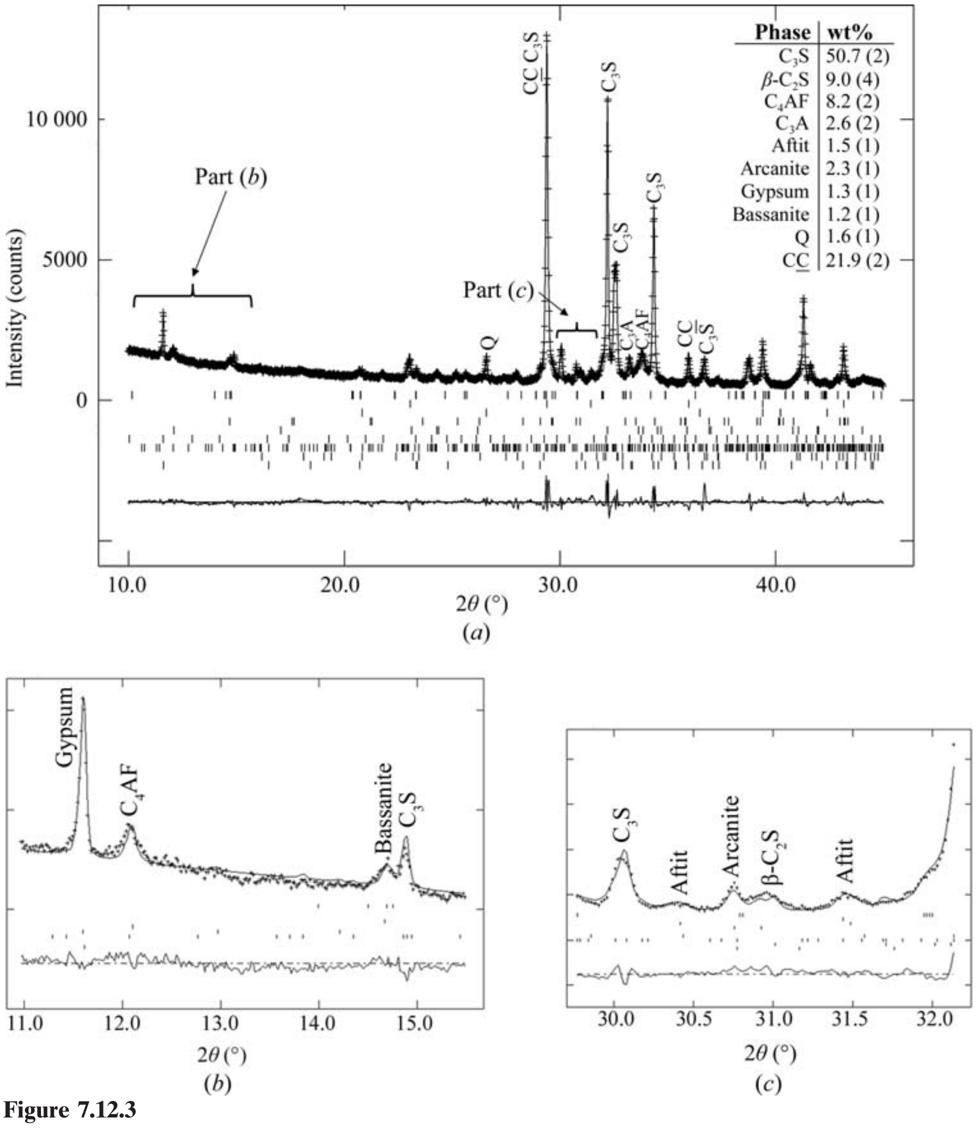

Phase	wt%
C_3S	50.7 (2)
β-C_2S	9.0 (4)
C_4AF	8.2 (2)
C_3A	2.6 (2)
Aftit	1.5 (1)
Arcanite	2.3 (1)
Gypsum	1.3 (1)
Bassanite	1.2 (1)
Q	1.6 (1)
$C\underline{C}$	21.9 (2)

(a)

(b)

(c)

Figure 7.12.3
(*a*) Selected region of a Rietveld plot using Cu $K\alpha_1$ radiation for a commercial Portland cement (CEM II/BL 32.5R) with the main peaks labelled. (*b*), (*c*) Enlarged regions highlighting characteristic diffraction peaks for minor content phases. Aftit and Q stand for afthitalite and quartz, respectively. The RQPA result is shown in the inset to part (*a*).

important in BFS and PFA additions. As an example, Fig. 7.12.3 displays a selected region of the Rietveld plot for a typical type-II commercial Portland cement (Jackson, 1998) with the main peaks labelled, where in addition to the clinker phases, gypsum, bassanite and calcite are also quantified.

Commercial OPCs contain sulfate carriers as setting regulators in variable amounts. Gypsum (or other calcium sulfates) is added to the clinker during the milling process, where it may partially dehydrate to bassanite or even to soluble anhydrite III. Owing to the different solubilities of these phases, it is important to be able to characterize the mineralogical composition of sulfate in a cement system to reach an optimal and reproducible setting (Seufert *et al.*, 2009). The use of RQPA to determine the amounts of gypsum, bassanite and anhydrite in OPC has been demonstrated (Madsen & Scarlett, 2000; Walenta & Füllmann, 2004). The mineralogy of the sulfate source, as well as its content, is very important for the fluidity, setting and hydration of mortars and concretes (Tang & Gartner, 1988; Rössler *et al.*, 2008).

Today, supplementary cementitious materials (SCMs) are widely used in concrete, either in blended cements or added separately in the concrete mixer. The use of silica-rich materials influences the amounts and kinds of hydrates formed and thus the volume, the porosity and finally the durability of these materials (Lothenbach *et al.*, 2011). Therefore, it is easy to understand that the mineralogical phase assemblage in different common additions has been intensely studied, including BFS, PFA, bottom ash, metakaolin and others (Kumar *et al.*, 2008; Korpa *et al.*, 2009; Gonçalves *et al.*, 2009; De Weerdt *et al.*, 2011; Narmluk & Nawa, 2011). Furthermore, RQPA has also been used to characterize other less common additions such as drinking-water treatment-plant sludge (Husillos Rodríguez *et al.*, 2010) and natural zeolites (Snellings *et al.*, 2010).

7.12.3.3. *Online quantification of Portland clinkers and cements*

A full discussion of the different types of analyses that can be carried out in the cement industry (offline, at-line, online and in-line) is beyond the scope of this work. Very briefly, offline and at-line analyses are characterized by manual sampling followed by discontinuous sample preparation, measurement and evaluation. On the other hand, online and in-line analyses permit continuous process control. Typical examples of each type are (i) offline, trace-element analysis and microscopy; (ii) at-line, CaO determination by wet chemistry; (iii) online, X-ray fluorescence (XRF) and laboratory X-ray powder diffraction; and (iv) in-line, prompt gamma neutron activation analysis. In addition to the use of XRF to monitor the elemental composition of the different materials, RQPA may be carried out online to provide mineralogical analyses of clinkers and cements. Other techniques that also provide mineralogical analysis, such as optical microscopy, cannot be easily implemented online, although they may yield very good offline results (Stutzman, 2012).

Online RQPA systems, where automatic data sampling is coupled to reproducible sample preparation (including milling and pressing in dedicated robot systems) and data collection in optimized powder diffractometers, is becoming widespread. After powder-diffraction data have been collected in a predefined 2θ range, resident automatic software carries out the analysis in a sequence of previously defined steps. It should be emphasized that the program computes what it is indicated in the control file(s), which is generally adapted to the specific sample (clinker or cement) in order to increase the accuracy of the analyses. Usually, each variable parameter has an upper and lower limit, which ensures the robustness and stability of the analysis. The reader is referred to Scarlett *et al.* (2001), Fullmann & Walenta (2003) and Paul *et al.* (2004) for further details. Finally, there is a review dealing with the analysis of building materials by powder diffraction in industry by Meier & Anderson (2012).

7.12.4. Quantification of other cementitious materials

There are many type of cementitious materials in addition to Portland cements. Here, we briefly discuss some important systems and give selected examples of powder-diffraction studies.

7.12.4.1. *Calcium aluminate cements*

The term calcium aluminate cements (CACs) covers a range of inorganic binders characterized by the presence of monocalcium aluminate ($CaAl_2O_4$, CA) as their main constituent. According to chemical composition, CACs are classified as (i) standard low alumina (36–42 wt% Al_2O_3 and 12–20 wt% Fe_2O_3 + FeO), (ii) low alumina, low iron (48–60 wt% Al_2O_3 and 1–3 wt% Fe_2O_3 + FeO), (iii) medium alumina (65–75 wt% Al_2O_3 and <0.5 wt% Fe_2O_3 + FeO) and (iv) high alumina ($\geq$80 wt% Al_2O_3 and <0.2 wt% Fe_2O_3 + FeO) (Pöllmann, 2012). This classification can be reduced to two groups: grey/black CACs and white CACs. Grey/black CACs consist mainly of CA, mayenite ($C_{12}A_7$), melilite [a gehlenite (C_2AS)–akermanite (C_2MS_2) solid solution], β-C_2S, pleochroite ($Ca_{20}Al_{32-x}Fe_xSi_xO_{68}$), ferrite ($C_4AF$), wüstite (FeO) and perovskite (CT). White CACs mainly contain CA, calcium dialuminate (CA_2) and α-alumina. Thus, some CACs may contain more than nine phases, and selective dissolutions to enrich minor phases are advisable to identify them. Furthermore, most of these phases are solid solutions, which may cause slight modifications in peak positions and relative intensities. Rietveld quantification is related to phase density and therefore the exact chemical compositions are needed even for minor phases. This phenomenon is especially relevant when analysing grey CACs, as iron can be distributed among different phases. For instance, CA may form a solid solution with iron ($CaAl_{2-2x}Fe_{2x}O_4$; Guirado & Galí, 2006). However, the use of laboratory XRPD is not advisable for refining the Al^{3+}/Fe^{3+} occupation factor(s). This ratio should be constrained to published values or determined by another technique(s), such as scanning electron microscopy with X-ray microanalysis. In any case, the unit-cell parameters must be optimized. The amount of iron in ferrite and pleochroite phases can also be variable. A detailed review of the mineralogy of these systems and a complete compilation of the crystal structures required to perform Rietveld refinement can be found in Pöllmann (2012) and Guirado & Galí (2006). Fig. 7.12.4 shows a selected range of a Rietveld plot for a grey CAC with the main peaks labelled and the RQPA result shown in the inset.

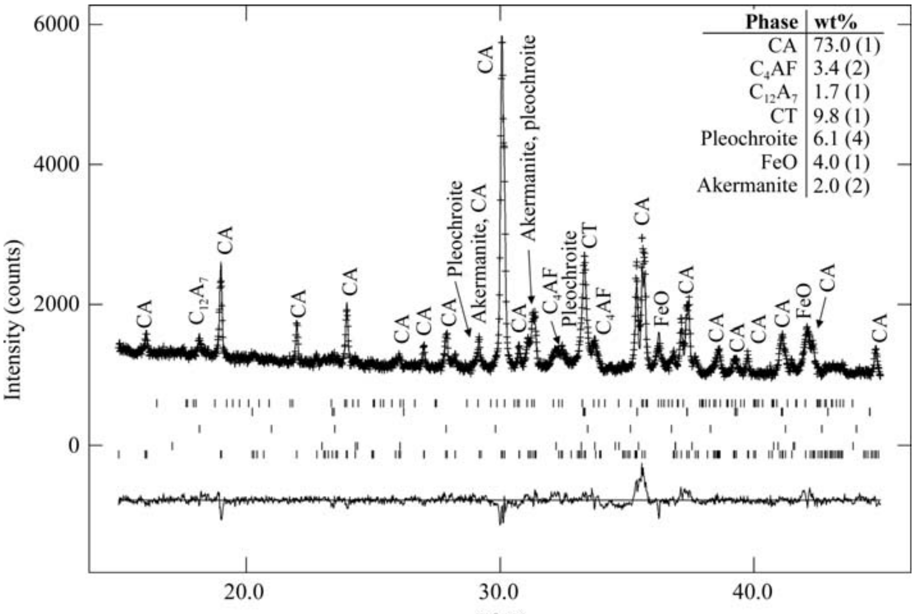

Figure 7.12.4

Selected region of a Rietveld plot using Cu $K\alpha_1$ radiation for a commercial calcium aluminate cement with the main peaks labelled. The RQPA result is shown in the inset.

7.12.4.2. *Calcium sulfoaluminate cements*

Laboratory-prepared calcium sulfoaluminate (CSA) cements have been known since the 1960s (Metha & Klein, 1965). Industrial cements based on this system were developed in the 1970s in China (Zhang *et al.*, 1999) and they are known as 'the third series cement of China'. CSA cements are characterized as containing high amounts of yeelimite, also called Klein's salt or tetracalcium trialuminate sulfate ($C_4A_3\underline{S}$). Two recent reviews of this type of cement have appeared (Juenger *et al.*, 2011; Aranda & De la Torre, 2013).

Binders based on CSA cements, or blended with OPC, are employed for quick repairs and pre-cast products or floor concrete applications. These binders have been used and standardized in China, and in spite of a lack of standards concerning these special cements, their manufacture has recently been started by several European companies (Álvarez-Pinazo *et al.*, 2012). Moreover, in recent years research on these cements has increased because of their low environmental impact, as the CO_2

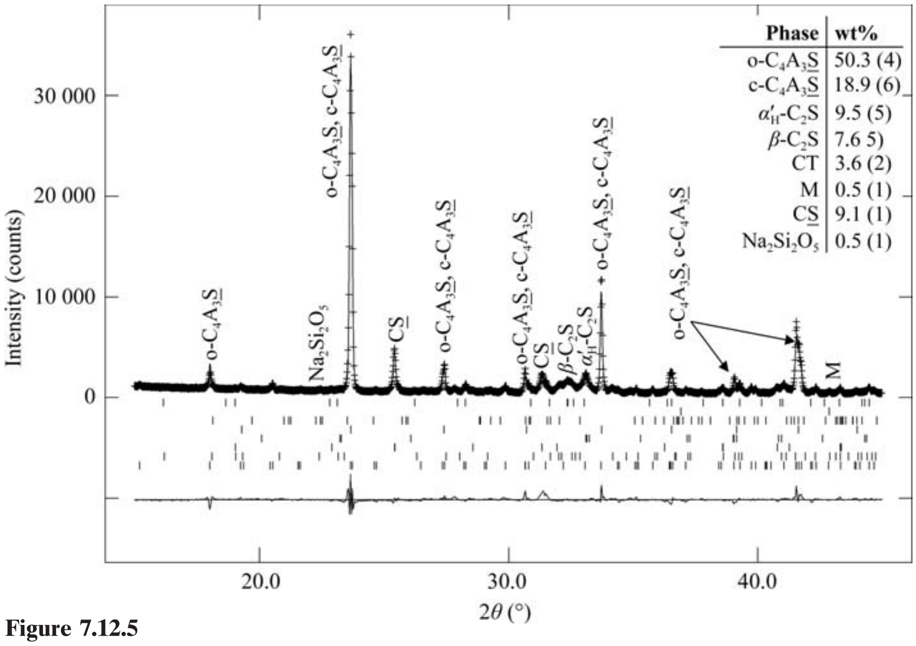

Figure 7.12.5

Selected region of a Rietveld plot using Cu $K\alpha_1$ radiation for a commercial calcium sulfoaluminate cement with the main peaks labelled. The RQPA result is shown in the inset.

emissions in their fabrication process are strongly reduced when compared to ordinary Portland cement production.

The raw material composition will determine the CSA clinker phase assemblage, containing $C_4A_3\underline{S}$ with other phases such as β-C_2S, ferrite, anhydrite, perovskite or gehlenite. Again, minor elements may form solid solutions. Recent work on yeelimite-containing cement matrices has reported several RQPAs for commercial cements (Álvarez-Pinazo *et al.*, 2012).

About 15–25 wt% sulfate carrier is interground with CSA clinker to tailor the setting time, strength development or volume stability of the final concrete. The most common sulfate carriers are gypsum, bassanite and anhydrite. On the other hand, the excess of anhydrite present in some CSA clinkers (formed in the clinkering process) is the less-soluble anhydrite II, which can be identified and quantified jointly with other sulfate carriers. Furthermore, ternary binders composed of OPC, CSA and anhydrite have also been studied by powder diffraction in order to determine the impact of variations of the OPC:CSA:$C\underline{S}$ ratio on the hydration process (Pelletier *et al.*, 2010). Fig. 7.12.5 shows, as an example, a selected region of a Rietveld plot for a commercial CSA clinker with the main peaks labelled and the RQPA results included as an inset.

7.12.4.3. *Calcium sulfobelite cements*

A new type of yeelimite-containing cement is emerging because of its environmental benefits. The term belite calcium sulfoaluminate (BCSA) is reserved for cements arising from clinkers with C_2S (belite) as the main phase and intermediate $C_4A_3\underline{S}$ contents. The most common formulation of BCSA clinkers, also known as sulfobelite, consists of β-C_2S, $C_4A_3\underline{S}$ and C_4AF (Janotka & Krajči, 1999; Adolfsson *et al.*, 2007). The lower CO_2 emission of this type of cement has been highlighted and its possible composition has been reviewed (Gartner & Macphee, 2011; Aranda & De la Torre, 2013).

Most BCSA clinkers contain ~55 wt% C_2S, ~25 wt% $C_4A_3\underline{S}$ and ~20 wt% C_4AF. These are iron-rich BCSA cements, also termed BCSAF. These binders develop high mechanical strengths at early ages because of the presence of yeelimite, which reacts rapidly with water to give ettringite. On the other hand, the reactivity of β-belite with water is very slow, and minor elements are included in the raw mixture to stabilize more reactive α-forms of C_2S (Gartner & Li, 2006; Cuberos *et al.*, 2010). Active sulfobelite cements have been successfully prepared in the laboratory (Cuberos *et al.*, 2010; Álvarez-Pinazo *et al.*, 2012). In these studies, the main goal was quantitative analysis using the RQPA methodology of α'_H-C_2S polymorph stabilization by borax addition. This polymorph hydrates much faster than β-C_2S. Fig. 7.12.6 shows Rietveld plots of an active BCSAF with 2.0 wt% B_2O_3 added as borax. The crystal structure of α'_H-C_2S doped with sodium and boron has been revised (Cuesta *et al.*, 2012) and better fits the α'_H-C_2S present in active sulfobelite cements.

7.12.4.4. *Materials with pozzolanic activity*

The term pozzolanic activity covers those reactions occurring between aluminosilicates and an alkaline solution, for instance lime and water. The use of aluminosilicates has an important sustainable impact as they are among the most abundant minerals at the surface of the Earth. As previously mentioned in Section 7.12.3.2, supplementary cementitious materials (SMCs) are used as active additions either to cements or concretes to give a pozzolanic reaction, yielding final materials with special properties (Snellings *et al.*, 2010). Alkali-activated binders are composed of a solid aluminosilicate powder mixed with an alkaline activation solution. The most common industrial sources are PFA from thermal plants and BFS from the pig-iron industry. The chemistry of the hydration processes is closely related to that of Portland cements blended with SMC materials and to alkali-activated binders, which will be introduced in the next section. Materials

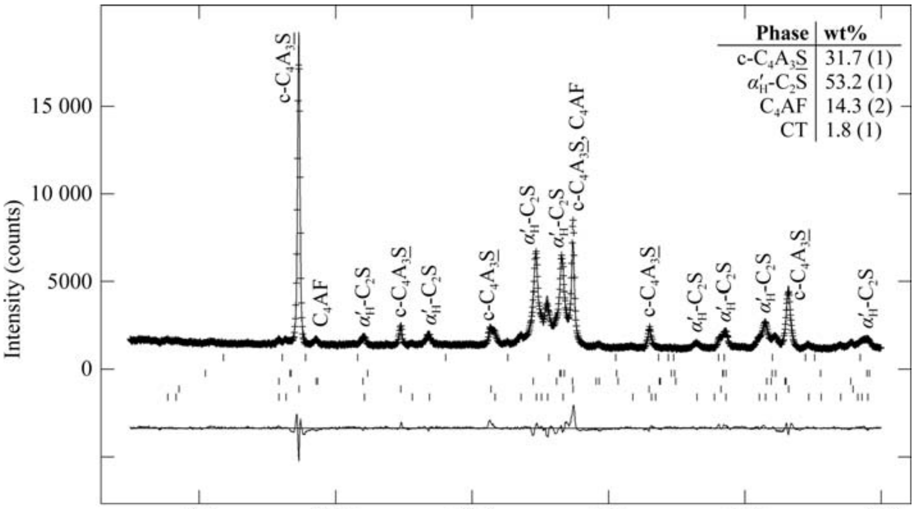

Figure 7.12.6

Selected region of a Rietveld plot using Cu $K\alpha_1$ radiation for a laboratory-prepared calcium sulfobelite cement with the main peaks labelled. The RQPA result is shown in the inset.

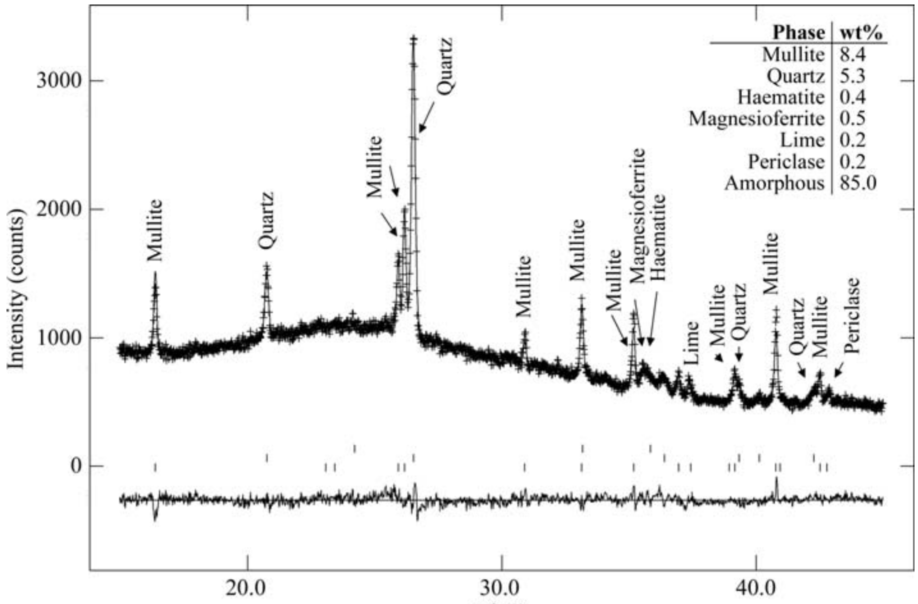

Figure 7.12.7

Selected region of a Rietveld plot using Cu $K\alpha_1$ radiation for a commercial pulverized fly ash. The RQPA result using the external-standard (G-) method is shown in the inset.

with pozzolanic activity should be fully characterized in order to understand and predict their final performance. Most of them are highly amorphous, containing some crystalline phases, such as mullite or haematite (Winburn *et al.*, 2000; Fernández-Jiménez *et al.*, 2006*a*). The quantification of the amorphous content in these materials can be approached by internal- or external-standard methods. Fig. 7.12.7 shows the Rietveld plot for a PFA with 85 wt% amorphous content, determined using the G-method with Si as an external standard. The initial direct Rietveld analysis, normalized to 100% of crystalline phases, gave 56.0 (3) wt% mullite, 35.2 (3) wt% quartz, 3.0 (2) wt% haematite, 3.4 (2) wt% magnesioferrite spinel, 1.0 (1) wt% lime and 1.5 (1) wt% periclase.

7.12.4.5. *Other cements*

There are several other alternative cement binders and there is not space here to treat all possible systems. However, some will be mentioned: supersulfated cements, partially prehydrated C-S-H-based binders and magnesium-based cements.

Supersulfated cements are generally composed of 70–90 wt% granulated BFS, 10–20 wt% calcium sulfate and <5 wt% of an alkaline activator, usually OPC or Portland clinker (Juenger *et al.*, 2011). Full mineralogical characterization of supersulfated cements by RQPA includes the quantification of amorphous and crystalline phases and the nature and content of the sulfate carrier (Adolfsson *et al.*, 2011). Granulated BFS with a high content of CaO, MgO and especially Al_2O_3 is suitable for the manufacturing of supersulfated binders and commonly contains very small amounts of crystalline phases. Gypsum and anhydrite are widely used as sulfate carriers, although bassanite or even secondary sulfate sources, such as phosphogypsum, may be added. With respect to the alkaline activator, there are some reports of the use of calcium or potassium hydroxide or sodium carbonate instead of OPC clinker. These materials are attracting attention as alternative, environmentally friendly binders with good durability in chemically aggressive environments. Moreover, there is a European Standard for supersulfated cements (EN 15743) which allows its use under specific conditions.

Celitement is a partially prehydrated C-S-H-based binder (Stemmermann *et al.*, 2010). This material is produced in two steps: crystalline α-C_2SH is first produced and is then interground with silica-rich filler. This step is essential to produce a reactive coating on the filler particles.

Magnesium-based cements are far from new: they were patented in 1867. These materials are composed of MgO which is hydrated with concentrated solutions of magnesium chloride (known as Sorel cements), magnesium sulfate or a soluble phosphate. All of these cements use MgO powders from the decarbonation of $MgCO_3$. The hydration reactions strongly depend on the microstructure and mineralogy of the MgO, which can be studied by laboratory XRPD jointly with other techniques such as scanning electron microscopy. Very recently, Novacem has presented a new approach to magnesium-based cementitious materials. The fundamental innovation consists of the extraction of MgO from magnesium silicate rocks by carbonation at high pressure. This binder is considered as a carbon-negative cement: not only are CO_2 emissions recycled back in the process, but also some atmospheric CO_2 may be absorbed (Gartner & Macphee, 2011).

7.12.5. Powder-diffraction studies on the hydration of cements

RQPA has been employed to investigate the hydration products of several types of cements, OPC and alternative cementitious materials. The hydration reactions have been studied in order to monitor the evolution of hydrous phases and to understand phase evolution, including the determination of the amorphous phase during the hydration reactions (Aranda *et al.*, 2012). The roles of several variables (water content, sulfate source and amount, role of admixtures and superplasticizers *etc.*) must be studied as they strongly influence mechanical strengths and chemical durability. A full discussion of the different systems that can be addressed is beyond the scope of this work. We highlight selected typical examples.

7.12.5.1. *Hydration studies of Portland cements and blended Portland cements*

Laboratory X-ray powder diffraction RQPA has been used to study the hydration reactions of commercial OPC in reflection (Scrivener *et al.*, 2004) and transmission (Mitchell *et al.*, 2006) geometries. Both methodologies allow the study of new phases arising during hydration; the results can be successfully compared to those obtained from thermal analysis and electron microscopy. It is important to underline the benefits of the transmission geometry as more particles are measured, which yields more reliable quantitative results along with a decrease in preferential orientation.

New phases appear during the hydration of OPCs. The mineralogy of the hydrate compounds is variable and it may depend upon the additions in blended cements (Matschei & Glasser, 2010). Many hydrate phases may be present in a given sample. A review of calcium silicate hydrates is given by Richardson (2008). The reader is referred to a review on OPC and RQPA for a list of phases that may be present in Portland

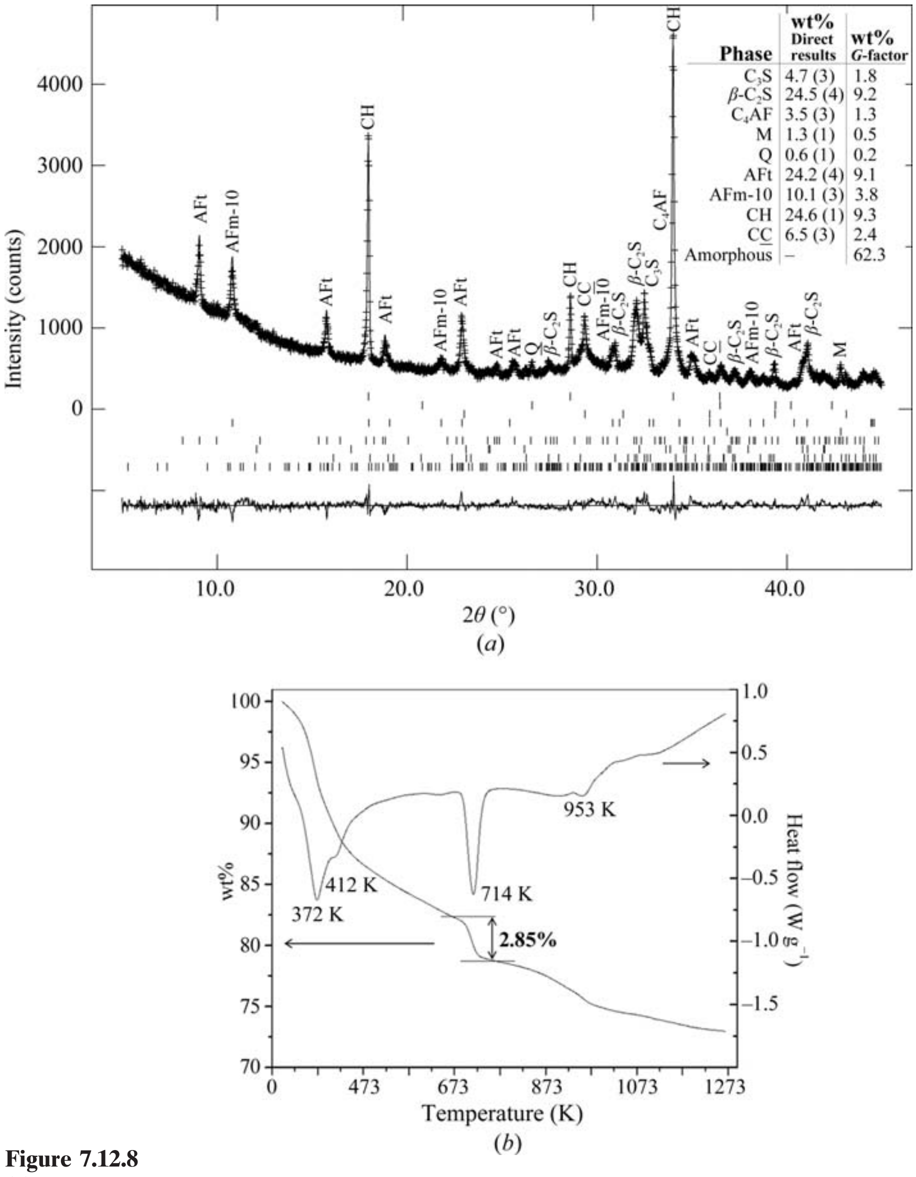

Phase	wt% Direct results	wt% G-factor
C_3S	4.7 (3)	1.8
β-C_2S	24.5 (4)	9.2
C_4AF	3.5 (3)	1.3
M	1.3 (1)	0.5
Q	0.6 (1)	0.2
AFt	24.2 (4)	9.1
AFm-10	10.1 (3)	3.8
CH	24.6 (1)	9.3
$C\underline{C}$	6.5 (3)	2.4
Amorphous	–	62.3

Figure 7.12.8

(*a*) Selected region of a Rietveld plot using Cu $K\alpha_1$ radiation for a hydrated Portland cement after 13 d. RQPA results, both direct and those obtained from the external-standard G-method, are shown as an inset table. (*b*) The thermal-analysis curves (thermogravimetric and differential thermal analysis) for this paste with the weight loss owing to portlandite, CH, highlighted.

cement pastes (Aranda *et al.*, 2012). Fig. 7.12.8(*a*) displays the Rietveld plot for an OPC hydrated sample showing a rich phase assemblage. This paste was fabricated with a water-to-cement weight ratio of 0.5 and hydrated for 13 d. The reactions were then stopped with acetone and the specimen was washed with ether. In addition to some remaining anhydrous cement phases, new crystalline hydrates appear, *e.g.* CH, AFt and AFm (see Fig. 7.12.8*a*). Additionally, a small amount of calcite arising from the carbonation of portlandite is also present. The peaks in the pattern are labelled to easily indentify each crystalline phase. In addition to the crystalline phases, a large amount of amorphous phase is measured by the G-method, which is mainly from the C-S-H gel. Finally, it is worth noting that accuracy of the analyses is always of the utmost importance. Fig. 7.12.8(*b*) shows the thermal-analysis data for this paste and the portlandite weight loss (2.85 wt%) indicates 11.7 wt% $C\underline{H}$ in the paste. This value is not far from that determined in the powder-diffraction analysis, 9.3 wt%, which indicates that the accuracy is within the region of ~2 wt%.

The process of the hydration of OPCs is commonly subdivided into several periods. These periods include early hydration and hydration after several days. The study of early and very early hydration processes is not easy using laboratory equipment and sometimes requires the use of temperature and humidity chambers (Scrivener *et al.*, 2004). The hydration of an OPC over 28 d has been studied by RQPA using the external- and internal-standard methods in order to determine the amount of amorphous content (Le Saoût *et al.*, 2007). The authors also studied the role of isopropanol in stopping the hydration reaction. The early hydration of cements has been also studied by laboratory XRPD using reflection geometry at defined temperatures and with different water:cement ratios (Hesse *et al.*, 2008, 2009). The heat flow measured by calorimetric experiments in the early hydration of OPCs was successfully compared with that calculated from RQPA results using the external-standard G-method (Jansen, Bergold *et al.*, 2011).

The hydration reactions of alkali-poor and alkali-rich OPCs have also been followed by RQPA. *In situ* laboratory XRPD for monitoring cement hydration has been used to study Portland cement clinkers consisting of alite and aluminate doped with different amounts of Na_2O (Wistuba *et al.*, 2007). Significant differences during early hydration have been measured as a consequence of the presence of syngenite when the alkali content is high.

The uses of RQPA to study hydration processes have been expanded from the hydration of model systems (Bellmann *et al.*, 2010) to blended cements and the role of admixtures and superplasticizers. RQPA has been used to analyse the hydration progress of cement pastes prepared by adding BFS and limestone powder (Hoshino *et al.*, 2006). Selective dissolution was employed to distinguish between the amorphous content coming from BFS and the newly formed C-S-H gel. A detailed study was carried out to quantitatively explain the effect of water curing on the compressive strengths of cement pastes containing PFA (Termkhajornkit *et al.*, 2006). A complete study using RQPA together with thermogravimetry, scanning electron microscopy and isothermal calorimetry was developed in order to understand the hydration mechanisms of ternary blended Portland cements containing fly ash and limestone powder (De Weerdt *et al.*, 2011). The authors studied the time evolution of all of the phases during hydration in order to understand the pozzolanic effect and the variations in chemical shrinkage. Furthermore, selective dissolution and RQPA have been employed to understand the effect of fly ash on the kinetics of OPC hydration at different curing temperatures (Narmluk & Nawa, 2011).

7.12.5.2. *Hydration studies of alternative cementitious materials*

It is not possible to describe in detail all of the studies on the hydration of alternative cementitious materials. Therefore, we give a summary of some selected research. RQPA has been applied to the hydration of cementitious materials such as CSA/

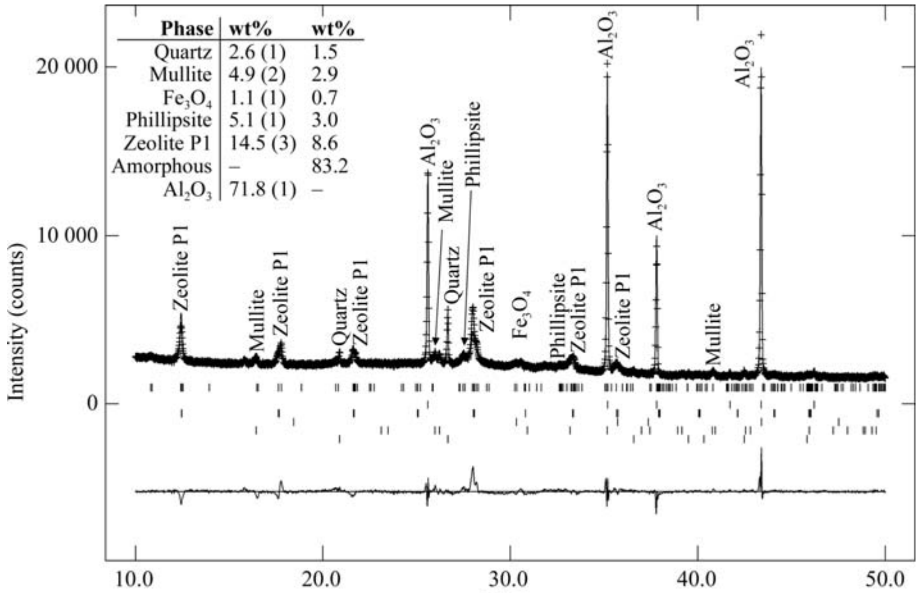

Figure 7.12.9
Selected region of a Rietveld plot using Cu $K\alpha_1$ radiation for an alkali-activated fly ash mixed with Al_2O_3 as an internal standard (weighed: 29.96 wt%) after 180 d of hydration. The RQPA results are given in the inset, with the first column being the direct analysis (normalized to 100% of crystalline phases including the standard) and the second column showing the analysis including the amorphous content and without the internal standard.

BCSA cements (Alesiani *et al.*, 2008; Cuberos *et al.*, 2010; Martín-Sedeño *et al.*, 2010; Morin *et al.*, 2011). These studies have confirmed the higher reactivity of the α-forms of C_2S and have determined the mechanism of hydration, as well as the influence of admixtures.

Alkali-activated cement hydration has also been characterized by RQPA jointly with other techniques (Criado *et al.*, 2007; Fernández-Jiménez *et al.*, 2006*b*). These studies not only quantify the crystalline zeolites formed during hydration as a function of the activator used, but also discriminate between the initial amorphous phases present in fly ashes and the sodium aluminosilicate gel formed as a consequence of activation. Fig. 7.12.9 shows a selected range of a Rietveld plot of an activated fly ash after 180 d of hydration mixed with α-Al_2O_3 as an internal standard to quantify the amorphous content. Activation was performed with a mixture of sodium silicate and sodium hydroxide ($SiO_2/Na_2O = 1.17$). Quantitative phase analysis, including amorphous content, is also shown as an inset to Fig. 7.12.9.

Laboratory XRPD has also been used to characterize the hydration products of the prehydrated C-S-H-based binder Celitement. The main hydration products of this type of cement are ettringite and C-S-H, and (as minor phases) AFm-type compounds (Gruskovnjak *et al.*, 2011). The hydration reactions of magnesium-based cement are complex, as several binary hydrated phases, such as $5Mg(OH)_2{\cdot}MgCl_2{\cdot}8H_2O$, may be present in the hydrated matrix (Ozer *et al.*, 2011). However, there is currently a dearth of applications of the RQPA methodology to these systems.

7.12.6. The use of synchrotron and neutron powder diffraction for studying cements

The first application of high-energy (λ = 0.442 Å) synchrotron X-ray powder diffraction (SXRPD) in Debye–Scherrer (transmission) configuration was for the accurate RQPA of a commercial OPC clinker (De la Torre, Cabeza *et al.*, 2001). The high-resolution nature of SXRPD allowed determination of the polymorphism of the phase without selective dissolution. Furthermore, the use of capillaries of 1.0 mm in diameter in the synchrotron study allowed a large amount of sample to be tested, which yielded reproducible diffraction intensities and thus accurate RQPA results. However, the expense of synchrotron measurement only allows its use for very special problems or for proof-of-principle experiments. The high-resolution data provided by synchrotron radiation established the coexistence of an alite phase in some commercial grey OPC clinkers for a range of magnesium contents (De la Torre *et al.*, 2005) and a change in alite crystal form as a function of the magnesium content (De la Torre *et al.*, 2008). Neutron powder diffraction (NPD) has also been used for the RQPA of clinkers (Pritula *et al.*, 2004). Furthermore, NPD, SXRPD and laboratory studies have been used to study the NIST reference clinker material RM8488 (Peterson *et al.*, 2006).

SXRPD (and NPD) has been used to study the crystal structures of selected phases in cements as well as relevant phase changes (and transitions) as a function of external variables including temperature, pressure, hydration, CO_2 partial pressure (carbonation), electrical field *etc.* We highlight some structural studies carried out using SXRPD for relevant cement phases (Yamazaki & Toraya, 2001; De la Torre *et al.*, 2002; Rapin *et al.*, 2002; Peterson *et al.*, 2004; Martucci & Cruciani, 2006; Garbev *et al.*, 2008; Mesbah *et al.*, 2011).

SXRPD has also been used, coupled to RQPA, for more demanding applications such as following *in situ* clinkering reactions at high temperatures (up to 1773 K). The preheated raw material is loaded into a platinum tube and high-energy synchrotron X-rays ($\lambda \simeq 0.30$ Å) are used to penetrate the holder and to obtain accurate intensities. This experimental procedure has been employed to study the clinkering reactions of belite cements (De la Torre *et al.*, 2007) and sulfobelite cements (De la Torre *et al.*, 2011).

SXRPD has also been widely used, coupled to RQPA, to characterize the hydration reactions of different types of cements. Early studies based on energy-dispersive low-resolution SXRPD are not reviewed here. RQPA based on *in situ* monochromatic SXRPD was used to monitor the evolution of hydrous phases during early hydration with a time resolution of 10 s (Weyer *et al.*, 2005). A related study but with lower time resolution (minutes) studied the hydration process in synthetic clinker phases (C_3A and C_4AF) and non-commercial OPCs (Merlini *et al.*, 2007). SXRPD has also been used to monitor the evolution of ettringite in a C_3A–gypsum synthetic mixture and in commercial OPCs during the first hours of hydration (Merlini *et al.*, 2008). *In situ* synchrotron RQPA has also been carried out to study the early hydration of class-A and -H oil-well Portland cements (Jupe *et al.*, 2007, 2008), active belite cement (Cuberos *et al.*, 2009), aluminium-rich belite sulfoaluminate cements (Martín-Sedeño *et al.*, 2010), and pozzolanic reactions in blended cements (Snellings *et al.*, 2010). Synchrotron radiation may also be used in more sophisticated types of characterization. For instance, high-energy synchrotron X-ray microdiffraction was used to quantify the orientation distribution of ettringite crystals. Diffraction images were analysed using the Rietveld method to obtain information on textures within thin slabs of mortars (Wenk *et al.*, 2009).

The composition and microstructural changes of cement pastes under a heating and cooling cycle have also been monitored by NPD. We highlight a study in which the heating rate, the state of the sample (block or ground) and the type of cement were varied (Castellote *et al.*, 2004). NPD was subsequently used to study the phase-composition changes of cement pastes during accelerated carbonation experiments (Castellote *et al.*, 2008). The same group used SXRPD to study the degradation over time of cement pastes, which was simulated by applying an electrical field (Castellote *et al.*, 2002).

SXRPD is very well suited for high-pressure studies, which are key to determining the bulk modulus values of relevant hydrate phases (Clark *et al.*, 2008; Oh *et al.*, 2011, 2012; Moon *et al.*, 2012). Energy-dispersive SXRPD was also used to study the hydration (hydrothermal) reactions of commercial oil-well cements, alone or with additions of silica flour and of corundum (Colston *et al.*, 2005; Meller *et al.*, 2007).

Finally, new techniques based on synchrotron radiation are emerging in which powder diffraction is combined with imaging tools in order to extract more information. For example, X-ray diffraction microtomography has been employed to study the hydration of Portland pastes (Artioli *et al.*, 2010; Valentini *et al.*, 2011) and of calcium sulfoaluminate pastes (Gastaldi *et al.*, 2012).

7.12.7. Conclusions and outlook

Powder diffraction coupled with Rietveld quantitative phase analysis is increasingly being used for the characterization of cementitious materials. Initially it was mainly used to measure anhydrous Portland clinkers and cements, but it is now used to analyse many types of hydrated products. RQPA is increasingly being used for studying the hydration reactions of blended cements. The number of residues and by-products (with different chemical and mineralogical compositions) that can be blended with Portland cements is large and expanding. In addition, research on new types of eco-cements is expanding rapidly. Here, powder diffraction has the brightest future, as most of the techniques developed for characterizing OPC samples are being adapted to analyse these new eco-cements.

However, as the complexity of the studied cementitious materials increases (some samples contain more than nine crystalline phases) the powder averaging for all phases becomes critical. Powder averaging may be increased by recording full two-dimensional patterns, but the current technology does not provide the highest-resolution powder patterns. An alternative approach is to use highly penetrating X-rays. Therefore, we expect molybdenum-radiation diffractometers to be used for the RQPA of very complex samples. However, peak overlap will be higher with Mo $K\alpha$ radiation than with Cu $K\alpha$ radiation as the powder pattern is compressed into a smaller range of 2θ (because the wavelength is shorter), so an incident-beam monochromator is needed to select only Mo $K\alpha_1$ radiation to minimize peak overlap. The effect of (possible) transparency issues should also be investigated. Mo $K\alpha$ incident-beam monochromator(s) coupled with fast detectors are likely to drive the next breakthrough in cement analysis.

Finally, we expect to see a large increase in the use of the external-standard method for hydration cement studies. This approach has two important advantages over the internal-standard method: (i) no dilution of low-content phases occurs and (ii) the possible interference of the standard with the hydration reactions is avoided.

Data for the studies described here are available from Zenodo (records 890585, 1027759 and 1147630).

This work was supported by Spanish research grant MAT2010-16213, which is co-funded by FEDER from the European Union.

References

Adolfsson, D., Menad, N., Viggh, E. & Bjorkman, B. (2007). *Hydraulic properties of sulphoaluminate belite cement based on steelmaking slags. Adv. Cem. Res.* **19**, 133–138.

Adolfsson, D., Robinson, R., Engström, F. & Björkman, B. (2011). *Influence of mineralogy on the hydraulic properties of ladle slag. Cem. Concr. Res.* **41**, 865–871.

Alesiani, M., Pirazzoli, I., Maraviglia, B. & Canonico, F. (2008). *NMR and XRD study on calcium sulfoaluminate cement. Appl. Magn. Reson.* **35**, 33–41.

Álvarez-Pinazo, G., Cuesta, A., García-Maté, M., Santacruz, I., Losilla, E. R., De la Torre, Á. G., León-Reina, L. & Aranda, M. A. G. (2012). *Rietveld quantitative phase analysis of yeelimite-containing cements. Cem. Concr. Res.* **42**, 960–971.

Aranda, M. A. G. & De la Torre, Á. G. (2013). *Sulfoaluminate cements.* In *Eco-efficient Concrete*, edited by F. Pacheco-Torgal, S. Jalali, J. Labrincha & V. M. John. Cambridge: Woodhead Publishing.

Aranda, M. A. G., De La Torre, Á. G. & Leon-Reina, L. (2012). *Rietveld quantitative phase analysis of OPC clinkers, cements and hydration products. Rev. Miner. Geochem.* **74**, 169–209.

Artioli, G., Cerulli, T., Cruciani, G., Dalconi, M. C., Ferrari, G., Parisatto, M., Rack, A. & Tucoulou, R. (2010). *X-ray diffraction microtomography (XRD-CT), a novel tool for non-invasive mapping of phase development in cement materials. Anal. Bioanal. Chem.* **397**, 2131–2136.

Bellmann, F., Damidot, D., Möser, B. & Skibsted, J. (2010). *Improved evidence for the existence of an intermediate phase during hydration of tricalcium silicate. Cem. Concr. Res.* **40**, 875–884.

Bish, D. L. & Howard, S. A. (1988). *Quantitative phase analysis using the Rietveld method. J. Appl. Cryst.* **21**, 86–91.

Castellote, M., Alonso, C., Andrade, C., Turrillas, X. & Campo, J. (2004). *Composition and microstructural changes of cement pastes upon heating, as studied by neutron diffraction. Cem. Concr. Res.* **34**, 1633–1644.

Castellote, M., Andrade, C., Alonso, C., Turrillas, X., Kvick, A., Terry, A., Vaughan, G. & Campo, J. (2002). *Synchrotron radiation diffraction study of the microstructure changes in cement paste due to accelerated leaching by application of electrical fields. J. Am. Ceram. Soc.* **85**, 631–635.

Castellote, M., Andrade, C., Turrillas, X., Campo, J. & Cuello, G. (2008). *Accelerated carbonation of cement pastes in situ monitored by neutron diffraction. Cem. Concr. Res.* **38**, 1365–1373.

Clark, S. M., Colas, B., Kunz, M., Speziale, S. & Monteiro, P. J. M. (2008). *Effect of pressure on the crystal structure of ettringite. Cem. Concr. Res.* **38**, 19–26.

Cline, J. P., Von Dreele, R. B., Winburn, R., Stephens, P. W. & Filliben, J. J. (2011). *Addressing the amorphous content issue in quantitative phase analysis: the certification of NIST standard reference material 676a. Acta Cryst.* A**67**, 357–367.

Colston, S. L., Barnes, P., Jupe, A. J., Jacques, S. D. M., Hall, C., Livesey, P., Dransfield, J., Meller, N. & Maitland, G. C. (2005). *An in situ synchrotron energy-dispersive diffraction study of the hydration of oilwell cement systems under high temperature/autoclave conditions up to 130°C. Cem. Concr. Res.* **35**, 2223–2232.

Criado, M., Fernández-Jiménez, A., De la Torre, Á. G., Aranda, M. A. G. & Palomo, A. (2007). *An XRD study of the effect of the SiO_2/Na_2O ratio on the alkali activation of fly ash. Cem. Concr. Res.* **37**, 671–679.

Cuberos, A. J. M., De la Torre, Á. G., Álvarez-Pinazo, G., Martín-Sedeño, M. C., Schollbach, K., Pöllmann, H. & Aranda, M. A. G. (2010). *Active iron-rich belite sulfoaluminate cements: clinkering and hydration. Environ. Sci. Technol.* **44**, 6855–6862.

Cuberos, A. J. M., De la Torre, Á. G., Martín-Sedeño, M. C., Moreno-Real, L., Merlini, M., Ordónez, L. M. & Aranda, M. A. G. (2009). *Phase development in conventional and active belite cement pastes by Rietveld analysis and chemical constraints. Cem. Concr. Res.* **39**, 833–842.

Cuesta, A., Losilla, E. R., Aranda, M. A. G., Sanz, J. & De la Torre, Á. G. (2012). *Reactive belite stabilization mechanisms by boron-bearing dopants. Cem. Concr. Res.* **42**, 598–606.

De la Torre, Á. G. & Aranda, M. A. G. (2003). *Accuracy in Rietveld quantitative phase analysis of Portland cements. J. Appl. Cryst.* **36**, 1169–1176.

De la Torre, Á. G., Bruque, S. & Aranda, M. A. G. (2001). *Rietveld quantitative amorphous content analysis. J. Appl. Cryst.* **34**, 196–202.

De la Torre, Á. G., Bruque, S., Campo, J. & Aranda, M. A. G. (2002). *The superstructure of C_3S from synchrotron and neutron powder diffraction and its role in quantitative phase analyses. Cem. Concr. Res.* **32**, 1347–1356.

De la Torre, Á. G., Cabeza, A., Calvente, A., Bruque, S. & Aranda, M. A. G. (2001). *Full phase analysis of Portland clinker by penetrating synchrotron powder diffraction. Anal. Chem.* **73**, 151–156.

De la Torre, Á. G., Cuberos, A. J. M., Álvarez-Pinazo, G., Cuesta, A. & Aranda, M. A. G. (2011). *In situ powder diffraction study of belite sulfoaluminate clinkering. J. Synchrotron. Rad.* **18**, 506–514.

De la Torre, Á. G., De Vera, R. N., Cuberos, A. J. M. & Aranda, M. A. G. (2008). *Crystal structure of low magnesium-content alite: application to Rietveld quantitative phase analysis. Cem. Concr. Res.* **38**, 1261–1269.

De la Torre, Á. G., Losilla, E. R., Cabeza, A. & Aranda, M. A. G. (2005). *High-resolution synchrotron powder diffraction analysis of ordinary Portland cements: phase coexistence of alite. Nucl. Instrum. Methods Phys. Res. B*, **238**, 87–91.

De la Torre, Á. G., Morsli, K., Zahir, M. & Aranda, M. A. G. (2007). *In situ synchrotron powder diffraction study of active belite clinkers. J. Appl. Cryst.* **40**, 999–1007.

De Weerdt, K., Haha, M. B., Le Saout, G., Kjellsen, K. O., Justnes, H. & Lothenbach, B. (2011). *Hydration mechanisms of ternary Portland cements containing limestone powder and fly ash. Cem. Concr. Res.* **41**, 279–291.

Dollase, W. A. (1986). *Correction of intensities for preferred orientation in powder diffractometry: application of the March model. J. Appl. Cryst.* **19**, 267–272.

Fernández-Jiménez, A., De la Torre, Á. G., Palomo, A., López-Olmo, G., Alonso, M. M. & Aranda, M. A. G. (2006*a*). *Quantitative determination of phases in the alkali activation of fly ash. Part I. Potential ash reactivity. Fuel*, **85**, 625–634.

Fernández-Jiménez, A., De la Torre, Á. G., Palomo, A., López-Olmo, G., Alonso, M. M. & Aranda, M. A. G. (2006*b*). *Quantitative determination of phases in the alkali activation of fly ash. Part II. Degree of reaction. Fuel*, **85**, 1960–1969.

Ferreira, A. V., Righi, A., Araujo, F. G. S., Espinosa, D. C. R. & Tenório, J. A. S. (2008). *Applications of the Rietveld method to quantify the crystalline phases of Portland cement clinker doped with nickel and chromium. Powder Diffr.* **23**, S42–S45.

Fullmann, T. & Walenta, G. (2003). *The quantitative Rietveld phase analysis in industrial applications. ZKG Int.* **56**, 45–53.

Garbev, K., Beuchle, G., Bornefeld, M., Black, L. & Stemmermann, P. (2008). *Cell dimensions and composition of nanocrystalline calcium silicate hydrate solid solutions. Part 1: synchrotron-based X-ray diffraction. J. Am. Ceram. Soc.* **91**, 3005–3014.

Gartner, E. M. & Li, G. S. (2006). *High belite sulfoaluminate clinker: fabrication process and binder preparation.* World Patent Application WO2006/018569 A2.

Gartner, E. M. & Macphee, D. E. (2011). *A physico-chemical basis for novel cementitious binders. Cem. Concr. Res.* **41**, 736–749.

Gastaldi, D., Canonico, F., Capelli, L., Boccaleri, E., Milanesio, M., Palin, L., Croce, G., Marone, F., Mader, K. & Stampanoni, M. (2012). *In situ tomographic investigation on the early hydration behaviors of cementing systems*. *Constr. Build. Mater.* **29**, 284–290.

Gineys, N., Aouad, G., Sorrentino, F. & Damidot, D. (2011). *Incorporation of trace elements in Portland cement clinker: thresholds limits for Cu, Ni, Sn or Zn. Cem. Concr. Res.* **41**, 1177–1184.

Gonçalves, J. P., Tavares, L. M., Toledo-Filho, R. D. & Fairbairn, E. M. R. (2009). *Performance evaluation of cement mortars modified with metakaolin or ground brick. Constr. Build. Mater.* **23**, 1971–1979.

Gruskovnjak, A., Lothenbach, B., Winnefeld, F., Münch, B., Figi, R., Ko, S.-C., Adler, M. & Mäder, U. (2011). *Quantification of hydration phases in supersulfated cements: review and new approaches. Adv. Cem. Res.* **23**, 265–275.

Guirado, F. & Galí, S. (2006). *Quantitative Rietveld analysis of CAC clinker phases using synchrotron radiation. Cem. Concr. Res.* **36**, 2021–2032.

Herfort, D., Moir, G. K., Johansen, V., Sorrentino, F. & Arceo, H. B. (2010). *The chemistry of Portland cement clinker. Adv. Cem. Res.* **22**, 187–194.

Hesse, C., Degenkolb, M., Gaeberlein, P., Goetz-Neunhoeffer, F., Neubauer, J. & Schwarz, V. (2008). *Investigations into the influence of temperature and w/c ratio on the early hydration of white cement. Cem. Int.* **6**, 68–78.

Hesse, C., Goetz-Neunhoeffer, F., Neubauer, J., Braeu, M. & Gaeberlein, P. (2009). *Quantitative in situ X-ray diffraction analysis of early hydration of Portland cement at defined temperatures. Powder Diffr.* **24**, 112–115.

Hill, R. J. & Howard, C. J. (1987). *Quantitative phase analysis from neutron powder diffraction data using the Rietveld method. J. Appl. Cryst.* **20**, 467–474.

Hoshino, S., Yamada, K. & Hirao, H. (2006). *XRD/Rietveld analysis of the hydration and strength development of slag and limestone blended cement. J. Adv. Concr. Technol.* **4**, 357–367.

Husillos Rodríguez, N., Ramírez, S. M., Varela, M. T. B., Guillem, M., Puig, J., Larrotcha, E. & Flores, J. (2010). *Re-use of drinking water treatment plant (DWTP) sludge: characterization and technological behaviour of cement mortars with atomized sludge additions. Cem. Concr. Res.* **40**, 778–786.

Jackson, P. J. (1998). *Portland cement: classification and manufacture.* In *Lea's Chemistry of Cement and Concrete*, 4th ed., edited by P. C. Hewlett, pp. 25–94. Amsterdam: Elsevier.

Janotka, I. & Krajči, L. (1999). *An experimental study on the upgrade of sulfoaluminatebelite cement systems by blending with Portland cement*. *Adv. Cem. Res.* **11**, 35–41.

Jansen, D., Bergold, S. T., Goetz-Neunhoeffer, F. & Neubauer, J. (2011). *The hydration of alite: a time-resolved quantitative X-ray diffraction approach using the G-factor method compared with heat release. J. Appl. Cryst.* **44**, 895–901.

Jansen, D., Goetz-Neunhoeffer, F., Lothenbach, B. & Neubauer, J. (2012). *The early hydration of ordinary Portland cement (OPC): an approach comparing measured heat flow with calculated heat flow from QXRD. Cem. Concr. Res.* **42**, 134–138.

Jansen, D., Neubauer, J., Goetz-Neunhoeffer, F., Haerzschel, R. & Hergeth, W. D. (2012). *Change in reaction kinetics of a Portland cement caused by a superplasticizer – calculation of heat flow curves from XRD data. Cem. Concr. Res.* **42**, 327–332.

Jansen, D., Stabler, C. H., Goetz-Neunhoeffer, F., Dittrich, S. & Neubauer, J. (2011). *Does ordinary Portland cement contain amorphous phase? A quantitative study using an external standard method. Powder Diffr.* **26**, 31–38.

Juenger, M. C. G., Winnefeld, F., Provis, J. L. & Ideker, J. H. (2011). *Advances in alternative cementitious binders. Cem. Concr. Res.* **41**, 1232–1243.

Jupe, A. C., Wilkinson, A. P., Luke, K. & Funkhouser, G. P. (2007). *Slurry consistency and in situ synchrotron X-ray diffraction during the early hydration of Portland cements with calcium chloride. J. Am. Ceram. Soc.* **90**, 2595–2602.

Jupe, A. C., Wilkinson, A. P., Luke, K. & Funkhouser, G. P. (2008). *Class H cement hydration at 180°C and high pressure in the presence of added silica. Cem. Concr. Res.* **38**, 660–666.

Korpa, A., Kowald, T. & Trettin, R. (2009). *Phase development in normal and ultra high performance cementitious systems by quantitative X-ray analysis and thermoanalytical methods. Cem. Concr. Res.* **39**, 69–76.

Kumar, S., Kumar, R., Bandopadhyay, A., Alex, T. C., Ravi Kumar, B., Das, S. K. & Mehrotra, S. P. (2008). *Mechanical activation of granulated blast furnace slag and its effect on the properties and structure of Portland slag cement. Cem. Concr. Compos.* **30**, 679–685.

Larson, A. C. & Von Dreele, R. B. (1994). Los Alamos National Laboratory Report No. LA-UR-86-748. Los Alamos, USA.

Le Saoût, G., Füllmann, T., Kocaba, V. & Scrivener, K. (2007). *Quantitative study of cementitious materials by X-ray diffraction/Rietveld analysis using an external standard.* In *Proceedings of the 12th International Congress on the Chemistry of Cement*, edited by J. J. Beaudoin, J. M. Makar & L. Raki. Ottowa: Cement Association of Canada.

Le Saoût, G., Kocaba, V. & Scrivener, K. (2011). *Application of the Rietveld method to the analysis of anhydrous cement. Cem. Concr. Res.* **41**, 133–148.

León-Reina, L., De la Torre, Á. G., Porras-Vázquez, J. M., Cruz, M., Ordonez, L. M., Alcobé, X., Gispert-Guirado, F., Larrañaga-Varga, A., Paul, M., Fuellmann, T., Schmidt, R. & Aranda, M. A. G. (2009). *Round robin on Rietveld quantitative phase analysis of Portland cements. J. Appl. Cryst.* **42**, 906–916.

Lothenbach, B., Scrivener, K. & Hooton, R. D. (2011). *Supplementary cementitious materials. Cem. Concr. Res.* **41**, 217–229.

McCusker, L. B., Von Dreele, R. B., Cox, D. E., Louër, D. & Scardi, P. (1999). *Rietveld refinement guidelines. J. Appl. Cryst.* **32**, 36–50.

Madsen, I. C. & Scarlett, N. V. Y. (2000). *Cement: quantitative phase analysis of Portland cement clinker. Industrial Applications of X-ray Diffraction*, edited by F. H. Chung & D. K. Smith, ch. 16. Boca Raton: CRC Press.

Madsen, I. C., Scarlett, N. V. Y., Cranswick, L. M. D. & Lwin, T. (2001). *Outcomes of the International Union of Crystallography Commission on Powder Diffraction Round Robin on Quantitative Phase Analysis: samples 1a to 1h. J. Appl. Cryst.* **34**, 409–426.

Martín-Sedeño, M. C., Cuberos, A. J. M., De la Torre, Á. G., Álvarez-Pinazo, G., Ordónez, L. M., Gateshki, M. & Aranda, M. A. G. (2010). *Aluminum-rich belite sulfoaluminate cements: clinkering and early age hydration. Cem. Concr. Res.* **40**, 359–369.

Martucci, A. & Cruciani, G. (2006). *In situ time resolved synchrotron powder diffraction study of thaumasite. Phys. Chem. Miner.* **33**, 723–731.

Matschei, T. & Glasser, F. P. (2010). *Temperature dependence, 0 to 40°C, of the mineralogy of Portland cement paste in the presence of calcium carbonate. Cem. Concr. Res.* **40**, 763–777.

Meier, R. & Anderson, J. (2012). *Industrial X-ray analysis of building materials. Rev. Miner. Geochem.* **74**, 147–165.

Meller, N., Hall, C., Kyritsis, K. & Giriat, G. (2007). *Synthesis of cement based $CaO–Al_2O_3–SiO_2–H_2O$ (CASH) hydroceramics at 200 and 250°C: ex-situ and in-situ diffraction. Cem. Concr. Res.* **37**, 823–833.

Merlini, M., Artioli, G., Cerulli, T., Cella, F. & Bravo, A. (2008). *Tricalcium aluminate hydration in additivated systems. A crystallographic study by SR-XRPD. Cem. Concr. Res.* **38**, 477–486.

Merlini, M., Artioli, G., Meneghini, C., Cerulli, T., Bravo, A. & Cella, F. (2007). *The early hydration and the set of Portland cements: in situ X-ray powder diffraction studies. Powder Diffr.* **22**, 201–208.

Mesbah, A., François, M., Cau-dit-Coumes, C., Frizon, F., Filinchuk, Y., Leroux, F., Ravaux, J. & Renaudin, G. (2011). *Crystal structure of Kuzel's salt $3CaO.Al_2O_3.1/2CaSO_4.1/2CaCl_2.11H_2O$ determined by synchrotron powder diffraction. Cem. Concr. Res.* **41**, 504–509.

Metha, P. K. & Klein, A. (1965). *Formation of ettringite by hydration of a system containing an anhydrous calcium sulfoaluminate. J. Am. Ceram. Soc.* **48**, 435–436.

Meyer, K. W., Neubauer, J. & Malovrh, S. (1998). *New quality control with standardless clinker phase determination using the Rietveld refinement. ZKG Int.* **3**, 152–162.

Mitchell, L. D., Margeson, J. C. & Whitfield, P. S. (2006). *Quantitative Rietveld analysis of hydrated cementitious systems. Powder Diffr.* **21**, 111–113.

Möller, H. (1995). *Standardless quantitative phase analysis of Portland cement clinkers. World Cem.* **26**, 75–84.

Möller, H. (1998). *Automatic profile investigation by the Rietveld method for standardless quantitative phase analysis. ZKG Int.* **1**, 40–50.

Moon, J., Oh, J. E., Balonis, M., Glasser, F. P., Clark, S. M. & Monteiro, P. J. M. (2012). *High pressure study of low compressibility tetracalcium aluminum carbonate hydrates $3CaO.Al_2O_3.CaCO_3.11H_2O$. Cem. Concr. Res.* **42**, 105–110.

Morin, V., Walenta, G., Gartner, E., Termkhajornkit, P., Baco, I. & Casabonne, J. M. (2011). *Hydration of a belite-calcium sulfoaluminate-ferrite cement: $Aether^{TM}$*. In *Proceedings of the 13th International Congress on the Chemistry of Cement*, Madrid, Spain.

Narmluk, M. & Nawa, T. (2011). *Effect of fly ash on the kinetics of Portland cement hydration at different curing temperatures. Cem. Concr. Res.* **41**, 579–589.

O'Connor, B. H. & Raven, M. D. (1988). *Application of the Rietveld refinement procedure in assaying powdered mixtures. Powder Diffr.* **3**, 2–6.

Oh, J. E., Clark, S. M. & Monteiro, P. J. M. (2011). *Does the Al substitution in C-S-H(I) change its mechanical property? Cem. Concr. Res.* **41**, 102–106.

Oh, J. E., Clark, S. M., Wenk, H. R. & Monteiro, P. J. M. (2012). *Experimental determination of bulk modulus of 14 Å tobermorite using high pressure synchrotron X-ray diffraction. Cem. Concr. Res.* **42**, 397–403.

Ozer, M. S., Ozturk, A. & Timucin, M. (2011). *Production and characterization of magnesium oxychloride cement bricks for fine polishing of porcelain stoneware tiles. Ind. Ceram.* **31**, 89–98.

Paul, M., Hornung, D., Enders, M. & Schmidt, R. (2004). *Process monitoring in a cement plant: the combination of optimized preparation procedures for clinker and cement and Rietveld analysis. Cem. Int.* **2**, 98–105.

Pelletier, L., Winnefeld, F. & Lothenbach, B. (2010). *The ternary system Portland cement–calcium sulphoaluminate clinker–anhydrite: hydration mechanism and mortar properties*. *Cem. Concr. Compos.* **32**, 497–507.

Peterson, V. K., Hunter, B. H. & Ray, A. (2004). *Tricalcium silicate t_1 and t_2 polymorphic investigations: Rietveld refinement at various temperatures using synchrotron powder diffraction. J. Am. Ceram. Soc.* **87**, 1625–1634.

Peterson, V. K., Ray, A. S. & Hunter, B. A. (2006). *A comparative study of Rietveld phase analysis of cement clinker using neutron, laboratory X-ray, and synchrotron data. Powder Diffr.* **21**, 12–18.

Pöllmann, H. (2006). *Syntheses, properties and solid solution of ternary lamellar calcium aluminate hydroxi salts (AFm-phases) containing SO_4^{2-}, CO_3^{2-} and OH^-. Neues Jahrb. Miner. Abh.* **182**, 173–181.

Pöllmann, H. (2012). *Calcium aluminate cements – raw materials, differences, hydration and properties. Rev. Miner. Geochem.* **74**, 1–2.

Pritula, O., Smrčok, L., Többens, D. M. & Langer, V. (2004). *X-ray and neutron Rietveld quantitative phase analysis of industrial Portland cement clinkers. Powder Diffr.* **19**, 232–239.

Rapin, J.-P., Renaudin, G., Elkaim, E. & Francois, M. (2002). *Structural transition of Friedel's salt $3CaO.Al_2O_3.CaCl_2.10H_2O$ studied by synchrotron powder diffraction. Cem. Concr. Res.* **32**, 513–519.

Richardson, I. G. (2008). *The calcium silicate hydrates. Cem. Concr. Res.* **38**, 137–158.

Rietveld, H. M. (1967). *Line profiles of neutron powder-diffraction peaks for structure refinement. Acta Cryst.* **22**, 151–152.

Rietveld, H. M. (1969). *A profile refinement method for nuclear and magnetic structures. J. Appl. Cryst.* **2**, 65–71.

Rietveld, H. M. (2010). Personal communication.

Rodríguez-Carvajal, J. (1993). *Recent advances in magnetic structure determination by neutron powder diffraction. Physica B*, **192**, 55–69.

Roisnel, T. & Rodríguez-Carvajal, J. (2001). *WinPLOTR: a Windows tool for powder diffraction patterns analysis. Mater. Sci. Forum*, **378–381**, 118–123.

Rössler, C., Eberhardt, A., Kučerová, H. & Möser, B. (2008). *Influence of hydration on the fluidity of normal Portland cement pastes. Cem. Concr. Res.* **38**, 897–906.

Scarlett, N. V. Y. & Madsen, I. C. (2006). *Quantification of phases with partial or no known crystal structures. Powder Diffr.* **21**, 278–284.

Scarlett, N. V. Y., Madsen, I. C., Cranswick, L. M. D., Lwin, T., Groleau, E., Stephenson, G., Aylmore, M. & Agron-Olshina, N. (2002). *Outcomes of the International Union of Crystallography Commission on Powder Diffraction Round Robin on Quantitative Phase Analysis: samples 2, 3, 4, synthetic bauxite, natural granodiorite and pharmaceuticals. J. Appl. Cryst.* **35**, 383–400.

Scarlett, N. V. Y., Madsen, I. C., Manias, C. & Retallack, D. (2001). *On-line X-ray diffraction for quantitative phase analysis: application in the Portland cement industry. Powder Diffr.* **16**, 71–80.

Scrivener, K. L., Füllmann, T., Gallucci, E., Walenta, G. & Bermejo, E. (2004). *Quantitative study of Portland cement hydration by X-ray diffraction/Rietveld analysis and independent methods. Cem. Concr. Res.* **34**, 1541–1547.

Seufert, S., Hesse, C., Goetz-Neunhoeffer, F. & Neubauer, J. (2009). *Quantitative determination of anhydrite III from dehydrated gypsum by XRD. Cem. Concr. Res.* **39**, 936–941.

Snellings, R., Mertens, G., Cizer, O. & Elsen, J. (2010). *Early age hydration and pozzolanic reaction in natural zeolite blended cements: reaction kinetics and products by in situ synchrotron X-ray powder diffraction. Cem. Concr. Res.* **40**, 1704–1713.

Stemmermann, P., Schweicke, U., Garbev, K., Beuchle, G. & Möller, H. (2010). *Celitement – a sustainable prospect for the cement industry. Cem. Int.* **8**, 52–66.

Stutzman, P. (2012). *Microscopy of clinker and hydraulic cements. Rev. Mineral. Geochem.* **74**, 101–146.

Suherman, P. M., van Riessen, A., O'Connor, B., Li, D., Bolton, D. & Fairhurst, H. (2002). *Determination of amorphous phase levels in Portland cement clinker. Powder Diffr.* **17**, 178–185.

Tang, F. J. & Gartner, E. M. (1988). *Influence of sulphate source on Portland cement hydration. Adv. Cem. Res.* **1**, 67–74.

Taylor, H. F. W. (1997). *Cement Chemistry*. London: Thomas Telford.

Taylor, J. C. & Aldridge, L. P. (1993). *Full-profile Rietveld quantitative XRD analysis of Portland cement: standard XRD profiles for the major phase tricalcium silicate (C_3S: $3CaO.SiO_2$). Powder Diffr.* **8**, 138–144.

Taylor, J. C., Hinczak, I. & Matulis, C. E. (2000). *Rietveld full-profile quantification of Portland cement clinker: the importance of including a full crystallography of the major phase polymorphs. Powder Diffr.* **15**, 7–18.

Termkhajornkit, P., Nawa, T. & Kurumisawa, K. (2006). *Effect of water curing conditions on the hydration degree and compressive strengths of fly ash–cement paste. Cem. Concr. Compos.* **28**, 781–789.

Toby, B. H. (2001). *EXPGUI, a graphical user interface for GSAS. J. Appl. Cryst.* **34**, 210–213.

Valentini, L., Dalconi, M. C., Parisatto, M., Cruciani, G. & Artioli, G. (2011). *Towards three-dimensional quantitative reconstruction of cement microstructure by X-ray diffraction microtomography. J. Appl. Cryst.* **44**, 272–280.

Walenta, G. & Füllmann, T. (2004). *Advances in quantitative XRD analysis for clinker, cements, and cementitious additions. Powder Diffr.* **19**, 40–44.

Wenk, H.-R., Monteiro, P. J. M., Kunz, M., Chen, K., Tamura, N., Lutterotti, L. & Del Arroz, J. (2009). *Preferred orientation of ettringite in concrete fractures. J. Appl. Cryst.* **42**, 429–432.

Weyer, H. J., Müller, I., Schmitt, B., Bosbach, D. & Putnis, A. (2005). *Time-resolved monitoring of cement hydration: influence of cellulose ethers on hydration kinetics. Nucl. Instrum. Methods Phys. Res. B*, **238**, 102–106.

Whitfield, P. S. & Mitchell, L. D. (2003). *Quantitative Rietveld analysis of the amorphous content in cements and clinkers. J. Mater. Sci.* **38**, 4415–4421.

Winburn, R. S., Grier, D. G., McCarthy, G. J. & Peterson, R. B. (2000). *Rietveld quantitative X-ray diffraction analysis of NIST fly ash standard reference materials. Powder Diffr.* **15**, 163–172.

Wistuba, S., Stephan, D., Raudaschl-Sieber, G. & Plank, J. (2007). *Hydration and hydration products of two-phase Portland cement clinker doped with Na_2O. Adv. Cem. Res.* **19**, 125–131.

Yamazaki, S. & Toraya, H. (2001). *Determination of positions of zeolitic calcium atoms and water molecules in hydrothermally formed aluminum-substituted tobermorite-1.1nm using synchrotron radiation powder diffraction data. J. Am. Ceram. Soc.* **84**, 2685–2690.

Zhang, L., Su, M. & Wang, Y. (1999). *Development of the use of sulfo- and ferroaluminate cements in China. Adv. Cem. Res.* **11**, 15–21.

International Tables for Crystallography (2019). Vol. H, Chapter 7.13, pp. 868–884.

7.13. Powder diffraction of superconductors

Qingzhen Huang

7.13.1. Introduction

In this chapter, we shall focus on the application of the powder-diffraction method to research on superconductivity, with an emphasis on using this method to obtain structural information. A great number of valuable research reports and review articles on this topic have been published in the past few decades and have been used as primary information sources in preparing this chapter. Because of space restrictions, however, only a limited number of these are given as references.

7.13.1.1. *Properties of superconductors*

Zero electrical resistance. Contrary to what happens in insulating, semiconducting and conducting materials, a superconductor in its superconducting state shows zero resistance to a flow of electrical current (Fig. 7.13.1*a*). T_c denotes the critical transition temperature below which the material transforms from a non-superconducting (NSC) state to the superconducting (SC) state.

Diamagnetism. Another distinguishing characteristic of superconductors is that they show diamagnetic behaviour below T_c. Figs. 7.13.1(*b*) and (*c*) show the critical field *versus* temperature diagrams for type-I and type-II superconductors, respectively (Lynn, 1990). For a type-I superconductor, the magnetic field is screened from the interior of the sample until a critical field H_c is reached; above H_c the superconductivity is quenched and the magnetic field penetrates uniformly into the material. For a type-II superconductor, when the applied magnetic field is less than the lower critical field H_{c1} it acts as a perfect diamagnet (like a type-I superconductor) and the field is screened from the interior bulk of the material, as shown in the SC1 region in Fig. 7.13.1(*c*). In the SC2 region above a critical field H_{c1}, the system is partially penetrated by the field and the material remains superconducting. The field increasingly penetrates the system as the applied field is increased, until finally above the second critical field H_{c2} the superconducting state is destroyed.

7.13.1.2. *A brief description of superconducting systems*

Kamerlingh Onnes (1911) first discovered superconductivity, observing that the direct current (DC) resistance of pure Hg metal droped to zero below 4.15 K. In the following years, superconductivity was found in elements, alloys, intermetallics and compounds. Bednorz & Muller (1986) reported the possible existence of a T_c of ~30 K in the La–Ba–Cu–O system. This was the first time that T_c was found to be higher than 23.2 K, previously reported for the best superconducting intermetallic Nb_3Ge thin films (Cadieu & Weaver, 1973). Since then, much effort has been devoted to superconductor research in many laboratories around the world, and hundreds of new superconductors with different structure types in different chemical systems have been successfully prepared. Cuprate high-temperature superconductors (HTSCs) are among the most interesting systems. A T_c of 93 K was found in the $YBa_2Cu_3O_{7-x}$ system (Wu *et al.*, 1987) and a T_c of 120 K was measured for the compound $Tl_2CaBa_2Cu_2O_{8+\delta}$ (Gao *et al.*, 1988). The highest T_c, 164 K, was observed in the $HgBa_2Ca_2Cu_3O_{8+x}$ system under pressure at 31 GPa (Gao *et al.*, 1994). Of the many non-Cu-containing superconducting systems, the Fe-based family has attracted recent interest for its high-T_c properties. In this family, the compound $NdFeAsO_{1-x}F_x$ has T_c = 55 K (Ren, Yang *et al.*, 2008). Selected superconducting systems and their years of discovery are given in Table 7.13.1. A few typical structure types are shown in Fig. 7.13.2.

The property of superconductivity relates closely to the structure type, chemical composition, the distribution of the atoms and/or ions in a material, and the temperature and pressure. Superconductivity can be shown by elements, alloys, intermetallics and chemical compounds with more complex compositions, and can be found in stoichiometric or nonstoichiometric materials.

Elements, alloys and intermetallics. Elemental superconductors can show type-I or type-II behaviour. The majority of the superconducting elements are members of the transition-metal series with a T_c as high as 9.3 K in Nb. Combinations of the transition elements with a number of other elements lead to the formation of superconducting alloys (with random atomic ordering) and intermetallic compounds [ordered crystallographically, such as Nb_3Ge (Fig. 7.13.2*a*) and MgB_2 (Fig. 7.13.2*c*)]. Fullerides (Gunnarsson, 1997; Buntar & Weber, 1996) are compounds with the general formula A_nC_{60} [the structure of an example with $n = 3$ is shown in Fig. 7.13.2(*b*)] and can become superconductors at high temperatures. The present record under pressure is held by Cs_3C_{60} with T_c = 40 K.

Transition-metal oxides with perovskite-like and layered structures (Figs. 7.13.2*e*, *f* and *g*). Oxide materials are strong type-II superconductors. Most superconducting oxides contain a transition metal. T_c's for transition-metal oxides range from low (T_c = 0.7 K for $SrTiO_{3-x}$) to above liquid-nitrogen temperature, such as for $HgBa_2Ca_2Cu_3O_{8+x}$, which has a T_c of 133 K (Antipov *et al.*, 1993). Cuprate HTSCs have played a central role in the scientific and technological development of superconductors. For other

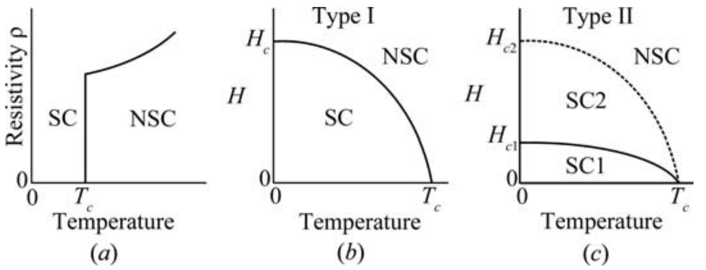

Figure 7.13.1
Definitions of superconductivity. (*a*) A superconductor shows zero resistance to a flow of current below T_c. The magnetic field *versus* temperature diagram for (*b*) a typical elemental type-I superconductor and (*c*) for a type-II superconductor. In regions SC in (*b*) and SC1 in (*c*) the material shows perfect diamagnetic behaviour and in the SC2 region the materials shows imperfect diamagnetic behaviour.

Copyright © 2019 International Union of Crystallography

Table 7.13.1
Selected superconducting elements, alloys, intermetallics, copper oxides, iron-based compounds and others

T = transition element, R = rare-earth element, Pn = pnictide, Ch = chalcogenide, A = alkali metal, M = alkaline-earth metal, Q = Group 15, 16 or 17 element.

Compound	T_c (K)	Space group, a, b, c (Å)	Year of discovery	System and chemical and structural features
Element, intermetallic and oxide superconductors reported before 1986				
Hg	4.1	$R\bar{3}m$, 3.458, 6.684	1911	Element/T_c (K): Be/0.03, Al/1.2, Sc/0.01, Ti/0.4, V/5.4, Zn/0.9, Ga/1.1, Zr/0.6, Mo/0.9, Tc/7.8, Ru/0.5, Cd/0.5, In/3.4, Sn/3.7, La/4.9, Hf/0.1, Ta/4.3, W/0.02, Re/1.7, Ir/0.1, Tl/2.4, Lu/0.1, Th/1.4, Pa/1.4, Am/1.0
Pb	7.2	$Fm\bar{3}m$, 4.949	1913	
Nb	9.3	$Im\bar{3}m$, 3.306	1930	
Nb_3Sn	18.1	$Pm\bar{3}n$, 5.291	1954	$T_{3+x}(Sb,Al,Ge)_{1-x}$ intermetallic
$Nb_3(Al_{0.75}Ge_{0.25})$	20–21	$Pm\bar{3}n$, 5.171	1966	
Nb_3Ge	23.2	$Pm\bar{3}n$, 5.168	1973	
NbO	1.4	$Fm\bar{3}m$, 4.210	1964	NaCl structure: T(O, C, N, S)/T_c (K): TiO/2.0, NbC/12, ZrS/3.3, NbN/17
$SrTiO_{3-x}$	0.7	$Pm\bar{3}m$, 3.905	1964	Perovskite: O-defect/mixed-valence
A_xWO_3	6	$Im\bar{3}$, 7.453	1965	Oxide: mixed-valence/A-defect
$Li_{1+x}M_xTi_2O_4$	13	$Fd\bar{3}m$, 8.405, $x \simeq 0$	1973	Spinel: mixed-valence/substitution
$Ba(Bi_{1-x}Pb_x)O_3$	13	$I4/mcm$, 6.060, 8.609, $x \simeq 0.3$	1975	Perovskite solid solution: substitution/mixed-valence
Copper-oxide superconductors with mixed-valence state and layer-stacking structure				
$(La_{1-x}Ba_x)_2CuO_4$	35	$I4/mmm$, 3.787, 13.288, $x \simeq 0.075$	1986	$(R_{1-x}M_x)_2CuO_4$: mixed-valence/substitution/Cu and R magnetic
$(Nb_{1-x}Ce_x)_2CuO_{4+y}$	30	$I4/mmm$, 3.780, 13.245, $x \simeq 0.15$	1987	$(Nb_{1-x}Ce_x)_2CuO_{4+x}$: mixed-valence/substitution/ electron-doping/Cu and R magnetic
$Sr_{1-x}Nd_xCuO_2$	40	$P4/mmm$, 3.930, 3.425, $x \simeq 0.14$	1991	M/R/Cu/O: mixed-valence/substitution
$Bi_2Sr_2CaCu_2O_8$	89	$Amaa$, 5.405, 5.401, 30.715	1988	$Bi_2Sr_2Ca_{n-1}Cu_nO_{2(n+2)}$: mixed-valence
$YBa_2Cu_3O_{7-x}$	95	$Pmmm$, 3.823, 3.886, 11.681, $x \simeq 0$	1987	$RM_2Cu_3O_{7-x}$: mixed-valence/O-defect and vacancy ordering/Cu and R magnetic
$Tl_2Ba_2Ca_2Cu_3O_{10}$	127	$I4/mmm$, 3.855, 29.318	1988	$Tl_2Ba_2Ca_{n-1}Cu_nO_{2(n+1)}$: mixed-valence
$HgBa_2Ca_2Cu_3O_{8+x}$	133	$P4/mmm$, 3.859, 12.695, $x \simeq 0.42$	1993	$HgBa_2Ca_{n-1}Cu_nO_{2(n+1)+x}$: mixed-valence/variable O-content
Fe-based and related superconductors containing edge-sharing TQ_4 tetrahedra				
YNi_2B_2C	17	$I4/mmm$, 3.509, 10.527	1994	RT_2B_2C intermetallic: R magnetic
YPd_2B_2C	23	$I4/mmm$, 3.710, 10.800	1994	RT_2B_2C intermetallic
YNiBC	0.8	$P4/nmm$, 3.566, 7.563	1994	RTBC intermetallic
$La_3Ni_2B_2N_3$	14.6	$I4/mmm$, 3.725, 20.517	1994	R/T/B/N intermetallic
$NdFeAsO_{1-x}F_x$	55	$I4/mmm$, 3.950, 8.537, $x \simeq 0.2$	2008	$RFePnO_{1-x}F_x$: mixed-valence/substitution/Fe and R magnetic
$NdFeAsO_{1-x}$	53.5	$I4/mmm$, 3.948, 8.545, $x \simeq 0.14$	2008	$RFePnO_{1-x}$: mixed-valence/O-defect/Fe and R magnetic
$Ba_{1-x}K_xFe_2As_2$	38	$I4/mmm$, 3.915, 13.294, $x \simeq 0.37$	2008	$M_{1-x}A_xFe_2Pn_2$: mixed-valence/substitution/Fe magnetic
$K_yFe_{2-x}Se_2$	32	$I4/m$, 8.731, 14.113, $x \simeq 0.36$, $y \simeq 0.8$	2010	$A_yFe_{2-x}Ch_{2-z}$: mixed-valence/substitution/Fe-vacancy ordering/Fe magnetic
LiFeAs	18	$P4/nmm$, 3.791, 6.364	2008	A_xFePn: mixed-valence/Fe magnetic
$Fe_yFeTe_{1-x}Se_x$	15	$P4/nmm$, 3.801, 5.993, $x \simeq 0.57$, $y \simeq 0.03$	2008	$Fe_yFeCh_{1-x}Ch'_x$: mixed-valence/substitution/Fe magnetic
LaFePO	5	$P4/nmm$, 3.941, 8.507	2008	RTPO
Other superconductors				
MgB_2	39	$P6/mmm$, 3.085, 3.520	2001	Borocarbides (TB, TB_2, T_2B, RB_6, RB_{12}, RTB_2, RT_3B_2, RT_4B_4 *etc.*)
$RbCs_2C_{60}$	33	$Fm\bar{3}m$, 14.555	1991	A_nC_{60} (n = 3, 4, 6)/C_{60} buckyball
$Na_xCoO_2 \cdot nH_2O$	4.3	$P6_3/mmc$, 2.822, 19.768, $x = 0.31$, $n = 1.25$	2004	Hydrated: mixed-valence
$MgC_{1-x}Ni_3$	8	$Pm\bar{3}m$, 3.813, $x \simeq 0.98$	2001	Antiperovskite/intermetallic
Sr_2RuO_4	1.5	$I4/mmm$, 3.871, 12.740	1994	Perovskite-derived n = 1 Ruddlesden–Popper phase
$Ba_{1-x}K_xBiO_3$	30	$Immm$, 12.130, 6.137, 8.663, $x \simeq 0.4$	1988	Perovskite: mixed-valence/substitution
$PuCoGa_5$	18	$P4/mmm$, 4.232, 6.768	2002	RTX_5 heavy fermion (UBe_{13}, AT_4X_{12}, CeT_2X_2, $CePt_3Si$, UGe_2): magnetic

References: Poole *et al.* (1988); Sleight *et al.* (1975); Sleight (1988); Stephens *et al.* (1991); Cava *et al.* (1988); Cava, Takagi, Batlogg *et al.* (1994); Cava, Takagi, Zandbergen *et al.* (1994); Schaak *et al.* (2003); Blaschkowski & Meyer (2003); Bud'ko & Canfield (2006); Ren & Zhao (2009); Buzea & Yamashita (2001); Zandbergen *et al.* (1994); Johnston (2010).

oxides, a T_c as high as 30 K has been found in $Ba_{1-x}K_xBiO_3$ (Cava *et al.*, 1988). A large proportion of high-T_c superconductors are copper oxides with layer-stacking structures that contain Cu in a mixed-valence state.

Fe-based systems and borocarbides with the $ThCr_2Si_2$-type structure. These constitute another important family of superconducting systems. T_c has been observed to be as high as 55 K in the $RFeAsO_{1-x}F_x$ (Fig. 7.13.2*i*) system (Ren & Zhao, 2009). These materials can be considered as interstitial derivatives of the $ThCr_2Si_2$-type structure in which the transition metal T is surrounded by four Q ions or atoms, forming conducting blocks of TQ_4 edge-sharing tetrahedra that alternate with charge-reservoir layers (metal layers or oxide blocks). The Q ions are elements belonging to Groups 14, 15 or 16. There are two major types of materials: (i) the nonstoichiometric Fe-based pnictides or chalcogenides; and (ii) the stoichiometric intermetallics and borocarbides [such as YPd_2B_2C: see Fig. 7.13.2(*h*)] with a T_c as high as 23 K (Cava, Takagi, Batlogg *et al.*, 1994).

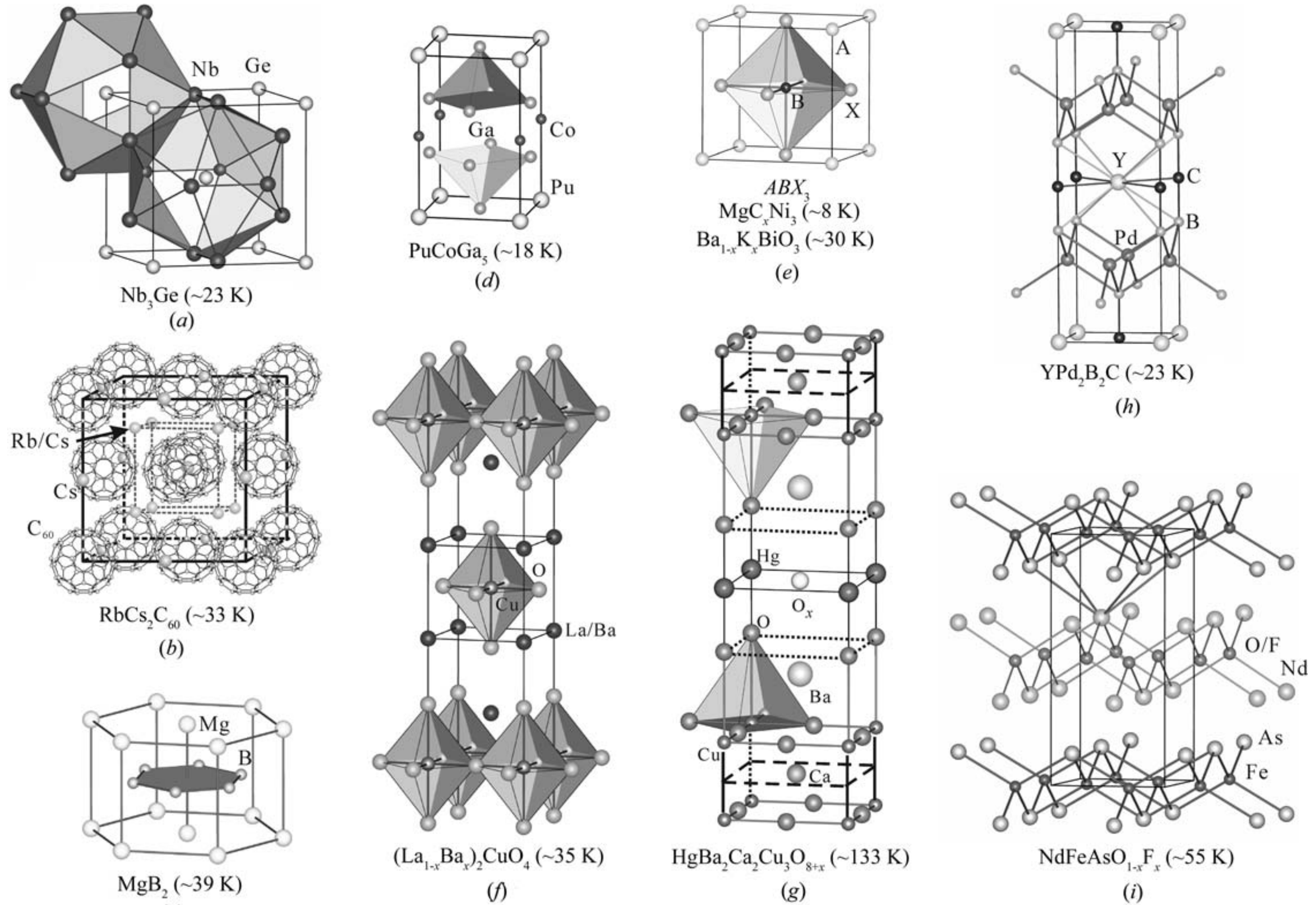

Figure 7.13.2

Typical structures for higher-T_c superconducting compounds shown in Table 7.13.1. The highest T_c reported in each system is given. (*a*) Nb_3Ge intermetallic; (*b*) $RbCs_2C_{60}$ 'buckyball'; (*c*) MgB_2 diboride; (*d*) the heavy-fermion superconductor $PuCoGa_5$; (*e*) intermetallic MgC_xNi_3 antiperovskite and $Ba_{1-x}K_xBiO_3$ perovskite; (*f*) $(La_{1-x}Ba_x)_2CuO_4$ perovskite-like layered cuprate; (*g*) $HgBa_2Ca_2Cu_3O_{8+x}$ layered copper oxide; (*h*) YPd_2B_2C borocarbide; (*i*) $NdFeAsO_{1-x}F_x$ iron-based layered compounds.

Heavy-fermion and magnetic superconductors. Heavy-fermion (HF) systems are stoichiometric lanthanide or actinide compounds whose qualitative low-temperature behaviour in the normal state closely parallels that of simple metals. The HF superconductors $PuCoGa_5$ (Fig. 7.13.2*d*) (Sarrao *et al.*, 2002) and $CeCu_2Si_2$ (Steglich *et al.*, 1979) contain disordered *f*-electron magnetic moments on Pu and Ce. At low temperature, a strong correlation between the *f*-electrons and conduction electrons develops, which results in effective masses for the conduction electrons that are one or two orders of magnitude larger than the free electron mass, and strong antiferromagnetic (AFM) spin correlations exist between the *f*-electron moments themselves. These correlations may condense into an ordered AFM state of heavy electrons, or lead to heavy-electron superconductivity, or lead to the coexistence of an AFM state and superconductivity under certain conditions. In a magnetic superconductor, the system contains transition-metal or rare-earth magnetic ions. The magnetic ions influence the superconducting properties more significantly than non-magnetic impurities. Long-range magnetic order may coexist with superconductivity; this has been found in cuprates (Lynn & Skanthakumar, 2001), borocarbides (Lynn *et al.*, 1997; Müller & Narozhnyi, 2001; Nagamatsu *et al.*, 2001; Nagarajan, 1997) and HF and Fe-based superconductors (Lynn & Dai, 2009; Lumsden & Christianson, 2010).

7.13.2. Advantages of structure analysis from powder diffraction

Obtaining structural information is one of the central issues in research on superconductivity. In general, X-ray and neutron powder diffraction (hereafter XPD and NPD, respectively) are the most convenient and powerful techniques for obtaining such information directly, and they are widely used in laboratories around the world. There are many important reasons for preferring powder over single-crystal analysis:

(*a*) In many systems it is almost impossible to grow single crystals of specified phases or compositions. Moreover, expensive equipment and a great deal of experience at crystal growing are needed.

(*b*) Superconducting compounds have small unit cells and high structural symmetry and, therefore, high-quality XPD and NPD data can often be obtained conveniently under different conditions. Rietveld structure refinement (Rietveld, 1969) and related methods of data analysis allow us to determine and to refine the crystal and magnetic structures, to detect phase transformations, and to identify the phases in polycrystalline samples.

(*c*) The study of powder samples is also convenient when special environmental conditions are required (low and high temperatures, high pressure *etc.*) and when diffraction, magnetization and resistivity measurements have to be done on the sample under such special conditions.

(*d*) For twinned systems where the structural distortions from higher-symmetry parent structures are not large, powder diffraction can allow for more unambiguous determination of the structures of the phase, because in single-crystal diffraction there may not be sufficient resolution to isolate the diffraction from a single twin.

The Rietveld method is a whole-pattern least-squares fitting method for extracting detailed crystal and magnetic structural information from XPD and NPD data. A detailed description was given by Young (1993); see also Chapter 4.7. The method uses directly the profile intensities obtained from measurements of the powder-diffraction pattern using either a fixed angle (energy-dispersive) or a fixed wavelength (angle-dispersive). Nuclear as well as magnetic structures can be refined, and a large number of successful refinements by this method have been reported. As an example, Von Dreele & Cheetham (1974) reported a refinement of 41 structure parameters, using NPD data, for $Ti_2Nb_{10}O_{29}$, which has the space group *Amma* and a unit-cell volume of 2178 Å^3. Experimentally, the Rietveld method is one of the most useful techniques for structural studies of superconductors.

7.13.2.1. *Comparison of XPD and NPD*

A good powder-diffraction pattern for structure determination and refinement using the Rietveld method should have a considerable number of independent Bragg reflections with strong intensities, precise peak positions with good resolution, and only small systematic errors.

The positions of the Bragg reflections are given by

$$2d_{hkl}\sin\theta = n\lambda, \tag{7.13.1}$$

where λ is the incident-beam wavelength, d are the distances between successive *hkl* planes and θ are the Bragg angles of reflections, and the intensitities I are proportional to the square of the structure-factor amplitudes $|F_{hkl}|$:

$$I \propto |F_{hkl}|^2. \tag{7.13.2}$$

For X-rays

$$F^2_{hkl} = \left|\sum f_j \exp(2\pi i)(hx/a_0 + ky/b_0 + lz/c_0)\right|^2 \exp(-2W), \tag{7.13.3}$$

where f_j is the atomic scattering factor of atom j, a_0, b_0 and c_0 are the unit-cell parameters and x, y, z are the fractional atomic coordinates.

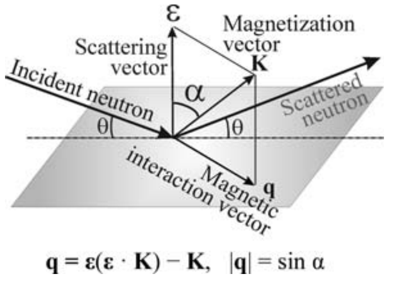

Figure 7.13.3
Definition of the vectors relevant in the evaluation of the magnetic structure factor. $\boldsymbol{\varepsilon}$ and $\mathbf{K}$ are unit vectors in the directions of the scattering and magnetic moment, respectively. The magnetic interaction vector $\mathbf{q}$ is always perpendicular to the scattering vector.

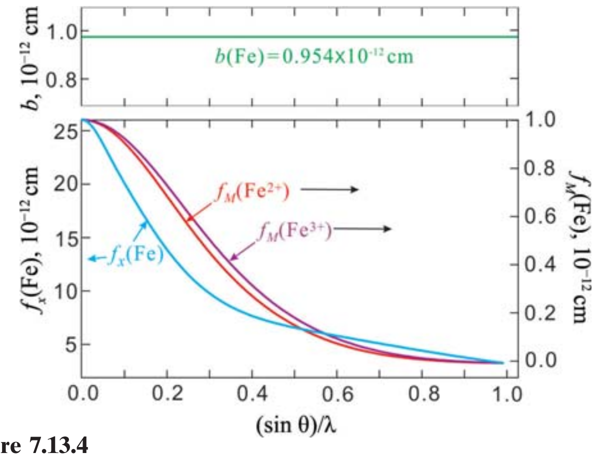

Figure 7.13.4
Angular dependence of the atomic scattering amplitudes of iron for X-rays [f_x(Fe)] and neutrons [b(Fe)], and of the magnetic form factors for Fe^{2+} [f_M(Fe^{2+})] and Fe^{3+} [f_M(Fe^{3+})]. The curves were calculated using the program *GSAS* (Larson & Von Dreele, 2004).

For neutrons

$$F^2_{hkl} = \left|\sum b_j \exp(2\pi i)(hx/a_0 + ky/b_0 + lz/c_0)\right|^2 \exp(-2W), \tag{7.13.4}$$

where b_j is the neutron scattering length for atom j.

For magnetic scattering

$$F^2_{hkl} = \left|\sum \mathbf{q}_j f_{Mj} \exp(2\pi i)(hx/a_0 + ky/b_0 + lz/c_0)\right|^2 \exp(-2W), \tag{7.13.5}$$

where $\mathbf{q}_j$ and f_{Mj} are the magnetic interaction vector and the magnetic form factor for atom j, respectively. $W = B(\sin^2\theta/\lambda^2)$ where B is the displacement parameter (Waller, 1923, 1926, 1927, 1928). The definition of $\mathbf{q}$ is indicated in Fig. 7.13.3.

In all the preceding formulas, the sums are over all the atoms in the unit cell of the structure. Fig. 7.13.4 is an example of the angular dependence of the atomic scattering amplitudes and magnetic form factors. The absolute values of the atomic scattering amplitudes for X-rays in the low-angle range of 2θ are considerably greater than those of neutrons, and this is reflected in the structure factors and in the magnitudes of the corresponding intensities of the Bragg peaks. However, the fact that the values of the atomic scattering amplitudes for neutrons remain constant as 2θ changes makes the neutron-diffraction intensities in the high-angle range comparable with those of low-angle reflections. This is an advantage when accurate measurements of displacement parameters are necessary, and to reduce correlation between displacement and occupancy parameters. The magnetic form factor for neutron diffraction is an angle-dependent parameter: its amplitude decreases with increasing θ. Most of the magnetic diffraction intensity, therefore, is found in the low-angle part of a diffraction pattern.

Another vitally important application of neutron diffraction is to study the magnetic structures and properties of materials. As shown in Fig. 7.13.3, the magnetic interaction vector is defined by

$$\mathbf{q} = \boldsymbol{\varepsilon}(\boldsymbol{\varepsilon} \cdot \mathbf{K}) - \mathbf{K}, \tag{7.13.6}$$

where the scattering factor $\boldsymbol{\varepsilon}$ is a unit vector in a direction perpendicular to the effective reflecting plane and the magnetization vector $\mathbf{K}$ is a unit vector in the direction of the atomic magnetic moment. Here we have $|\mathbf{q}| = \sin\alpha$, *i.e.* the magnetic structure factor F_{hkl} will be zero when $\boldsymbol{\varepsilon}_{hkl}$ is parallel to $\mathbf{K}$, which

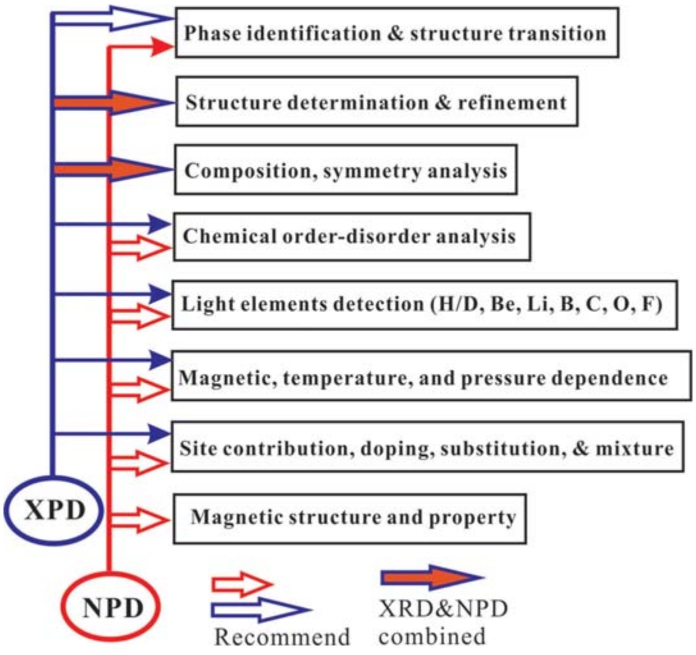
Phase identification & structure transition
Structure determination & refinement
Composition, symmetry analysis
Chemical order-disorder analysis
Light elements detection (H/D, Be, Li, B, C, O, F)
Magnetic, temperature, and pressure dependence
Site contribution, doping, substitution, & mixture
Magnetic structure and property
XPD
NPD
Recommend
XRD&NPD combined

Figure 7.13.5
Schematic representation of the choice of radiation recommended for powder-diffraction experiments to obtain different structural information in research on superconductivity.

means it is possible to find the direction of an ordered magnetic moment from NPD data.

7.13.2.2. *Choice of radiation*

In principle, the appropriate choice of the radiation used for powder-diffraction experiments depends on whether it will provide the required information on the structure. The examples in Table 7.13.1 show that superconductors and related compounds have a great variety of chemical compositions and structure types. This can make choosing the optimal technique rather complicated. For example, in many circumstances a compound consists of heavy and light elements or atoms with similar atomic numbers at the same site in a structure. In such cases, the use of X-ray diffraction may not be appropriate, since the light atoms cannot be easily located, and the technique is not the best for distinguishing atoms with similar atomic numbers. On the other hand, XPD offers the advantage of a resolution better than that achievable with even the best neutron diffractometer, and therefore can better detect the splitting of diffraction peaks that could indicate a phase transition. NPD is not able to distinguish between elements with similar neutron-scattering amplitudes located at the same site in a structure; however, it is essential for the study of magnetic materials. Choosing the most appropriate radiation for a powder-diffraction experiment in any particular case can be facilitated by analysis of Fig. 7.13.5, a schematic representation of the usefulness of XPD and NPD.

7.13.3. Analysis of the chemical and structural features of nonstoichiometric superconductors

Determining the chemical and structural features of a superconductor will require choosing the radiation (often more than one type), designing the data-collection conditions and obtaining good powder-diffraction data in order to obtain useful and reliable information for each particular case. Many superconductors are nonstoichiometric intermetallics, solid solutions or complex compounds. A common feature of these superconductors is that the superconducting property is a function of composition. For those superconductors, structure refinement using powder-diffraction data is used to determine the chemical formula and to study the relationships between T_c and composition. The intermetallic system $Nb_{3+x}Ge_{1-x}$ has its highest T_c of 23 K at $x = 0$. In the $BaPb_{1-x}Bi_xO_3$ solid-solution system, superconductivity was found in the composition range $0.05 < x < 0.3$ (Sleight *et al.*, 1975). The compound $HgBa_2Ca_2Cu_3O_{8+x}$ has the highest T_c of 133 K at the optimal composition $x = 0.42$. Moreover, for a compound having different structural modifications the powder-diffraction technique can be used to identify the structure of the superconducting phase. For example, the compound $La_{1.85}Ba_{0.15}CuO_4$ was found to have several modifications with different space groups, and their superconducting properties were studied (Axe *et al.*, 1989).

7.13.3.1. *Charge transfer and valence-state manipulation*

Charge transfer. It has been proved that charge transfer in high-T_c cuprate and Fe-based superconductors, and in many other nonstoichiometric superconducting systems plays a very important role in their superconducting properties. A schematic view in Fig. 7.13.6 shows a sketch of the charge transfer between the conducting and the charge-reservoir layers. The electron transfer changes the charge distribution in the structure and affects the superconductivity.

In general, it is believed that the CuO_2 plane is the conducting layer responsible for the superconductivity in copper-oxide superconductors. In the Fe-based and related superconductors having the $ThCr_2Si_2$-type structure, the conducting layer is considered to be the $T_{1-x}Q_4$ edge-sharing tetrahedral blocks that form a two-dimensional network (T is transition metal and Q is an element from Groups 15, 16 or 17). The atom T in the conducting layer may have a mixed valence state and may form covalent, semi-covalent or ionic bonds with the Q atoms. The concentration of charge carriers in the conducting layers varies when the formal charge of the transition metal T is varied. Near the conducting layer the reservoir layer acts as a charge donor to provide charge to the conducting layer. Electron transfer from the conducting layer to the charge-reservoir layer is known as 'hole doping' (on the right in Fig. 7.13.6) and moving electrons from the charge-reservoir layer to the conducting layer (on the left of Fig. 7.13.6) is known as 'electron doping'. The hole-type or electron-type charge carrier concentrations in the conducting layer are strongly related to the superconductivity. Typically, the cations in the conducting layers are transition metals that can exist in different valence states, and the cations in the

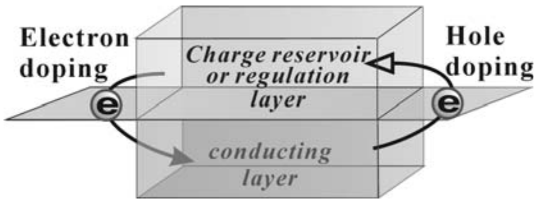

Figure 7.13.6
Schematic view of charge transfer between the conduction layer and the charge-reservoir layer in superconducting and related compounds. Electron transfer from the conducting layer to the charge-reservoir layer is known as 'hole doping' and movement of electrons from the charge-reservoir layer to the conducting layer is known as 'electron doping'.

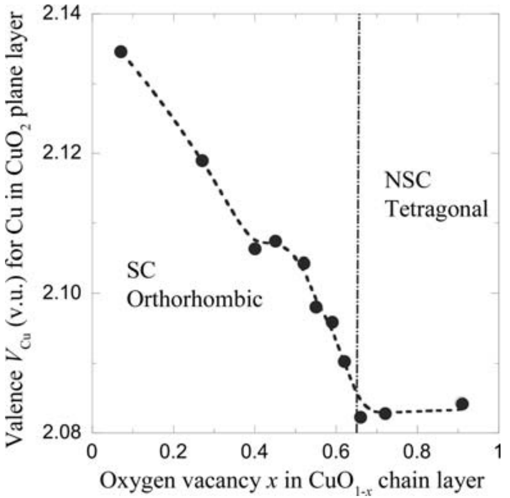

Figure 7.13.7
Calculated atomic valence for Cu in the CuO_2 plane layer *versus* oxygen content in the chain layer of $YBa_2Cu_3O_{7-x}$. The bond-distance data used in the calculation are based on the structure information reported by Jorgensen *et al.* (1990).

charge-reservoir layers are rare-earth elements, alkali metals and alkaline-earth metals that have a stable valence state.

The charge transformation can be achieved by adjusting the chemical composition through substitution, doping and vacancy introduction, and can be found indirectly by analysing the valence using bond distances.

Bond-valence analysis can be used to find evidence of charge transfer. In inorganic compounds, the valence of each atom is distributed between the bonds that it forms, and it is always possible to associate a valence with each bond in such a way that the sum of the bond valences around each atom is equal to its atomic valence (Brown, 1976, 2002; Brown & Altermatt, 1985). The valence for each bond can be calculated using

$$v_{ij} = \exp[(r_0 - r_{ij})/b], \qquad (7.13.7)$$

where r_0 is the bond-valence parameter, which is the hypothetical length of a bond of unit valence, v_{ij} is the bond valence and r_{ij} is the experimental (Brown & Altermatt, 1985) distance between atoms i and j; the constant b is 0.37. The total valence V_i for an atom i is the sum (over j) of the surrounding bond valences:

$$V_i = \sum_{j=1}^{j=n} v_j, \qquad (7.13.8)$$

where n is the number of bonds.

Example. It is very well known that the superconducting properties are strongly related to the oxygen content in the $YBa_2Cu_3O_{7-x}$ system. Jorgensen *et al.* (1990) reported the structure–property relationship for different levels of oxygen deficiency in this system with very detailed structure information obtained using NPD data. Fig. 7.13.7 shows the valence calculated using equation (7.13.8) for Cu in the conducting layer (CuO_2) as a function of the oxygen content x in the (CuO_x) layer. The behaviour is very similar to the variations of T_c as the oxygen vacancy x increases, with two plateaus being observed. In the range $0 < x < 0.35$, T_c decreases from 94 to 56 K, where the calculated valence for Cu, V_{Cu}, deceases from 2.135 to 2.108 valence units (v.u.). T_c was found to be constant with a value near 56 K for $0.35 < x < 0.45$, where a corresponding plateau is observed near V_{Cu} = 2.108. Then V_{Cu} drops rapidly to about 2.082 v.u. where T_c decreases from 56 K to zero near x = 0.65.

Cation substitution in superconducting oxides. After high-temperature superconductivity was discovered in the $(La,Ba)_2CuO_4$ system by Bednorz & Muller (1986), Takagi *et al.* (1987) confirmed that the superconducting phase $(La_{0.925}Ba_{0.075})_2CuO_4$ has the K_2NiF_4-type tetragonal structure with space group *I*4/*mmm* (No. 139) at high temperature (Fig. 7.13.8*a*), with atom positions ($La_{0.925}Ba_{0.075}$): 4*e* (0, 0, z); Cu: 2*a* (0, 0, 0); O1: 4*c* (0, $\frac{1}{2}$, 0) and O2: 4*e* (0, 0, z). There have been many studies concerning the role of cation substitution, oxygen vacancy and structural phase transitions in the high-T_c

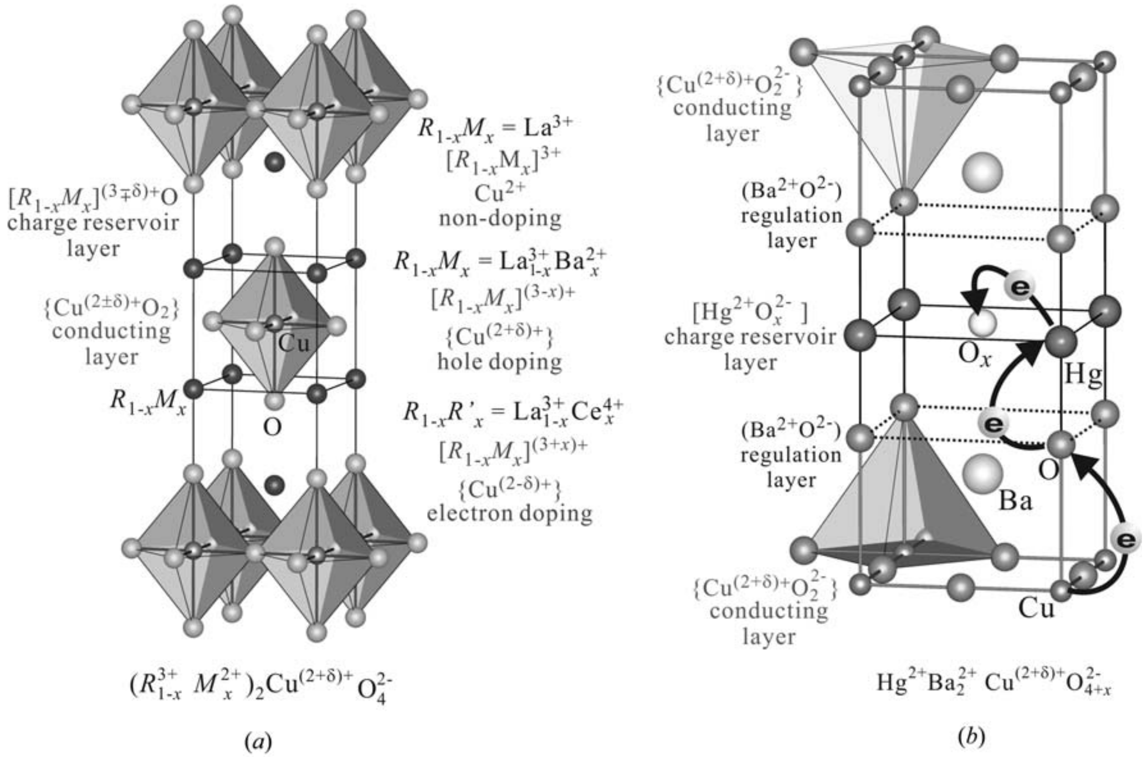
$R_{1-x}M_x$ = La^{3+}
$[R_{1-x}M_x]^{3+}$
Cu^{2+}
non-doping
$[R_{1-x}M_x]^{(3\mp\delta)+}O$
charge reservoir
layer
$R_{1-x}M_x = La^{3+}_{1-x}Ba^{2+}_x$
$[R_{1-x}M_x]^{(3-x)+}$
$\{Cu^{(2\pm\delta)+}O_2\}$
conducting
layer
$\{Cu^{(2+\delta)+}\}$
hole doping
Cu
$R_{1-x}M_x$
O
$R_{1-x}R'_x = La^{3+}_{1-x}Ce^{4+}_x$
$[R_{1-x}M_x]^{(3+x)+}$
$\{Cu^{(2-\delta)+}\}$
electron doping
$(R^{3+}_{1-x}\ M^{2+}_x)_2Cu^{(2+\delta)+}O^{2-}_4$
(*a*)
$\{Cu^{(2+\delta)+}O^{2-}_2\}$
conducting
layer
$(Ba^{2+}O^{2-})$
regulation
layer
$[Hg^{2+}O^{2-}_x]$
charge reservoir
layer
e
O_x
Hg
$(Ba^{2+}O^{2-})$
regulation
layer
e
O
Ba
e
$\{Cu^{(2+\delta)+}O^{2-}_2\}$
conducting
layer
Cu
$Hg^{2+}Ba^{2+}_2\ Cu^{(2+\delta)+}O^{2-}_{4+x}$
(*b*)

Figure 7.13.8
Schematic layer-stacking structures of (*a*) $(R_{1-x}M_x)_2CuO_4$ and (*b*) $HgBa_2CuO_{4+x}$ indicating the charge transfer between the reservoir and superconducting layers.

$(R_{1-x-y}M_xR'_y)_2CuO_{4-\delta}$ system, where R is a trivalent rare earth (La^{3+}, Nd^{3+}, Pr^{3+} . . .) and R' is tetravalent Ce^{4+}; M can be Ba^{2+} or Sr^{2+}.

The parent compounds La_2CuO_4 and Nd_2CuO_4 are semiconductors, and have valences of 3+, 2+ and 2− for the La/Nd, Cu and O ions, respectively. Superconductivity in these materials is induced by either holes or electrons in the charge-reservoir layer. This is accomplished by partial substitution of La^{3+} or Nd^{3+} at the 4e site with atoms of lower or higher valences, thus making the average formal valence of the site smaller or larger than 3+. Consequently, the formal Cu valence will be larger (hole doping) or smaller (electron doping) than 2+, respectively. More specifically, in the hole-doping case, substitution of Ba^{2+} for La^{3+} will cause an electron transfer from the adjacent CuO_2 conducting layers to the charge-reservoir layers, *i.e.* the oxidation state of copper will assume a value between 2+ and 3+. In fact, the compound $La_{1.85}Ba_{0.15}CuO_4$ becomes a superconductor below $T_c \simeq 30$ K by changing the formal valence of copper to 2.15+ instead of 2+. In the electron-doping case of $(Nd_{1-x}Ce_x)_2CuO_{4-\delta}$, the partial substitution of Ce^{4+} for Nd^{3+} and/or the presence of oxygen defects will generate an electron transfer from the reservoir to the conducting layers with consequent reduction of the copper formal valence from 2+ to between 2+ and 1+. Thus the superconducting compound $Nd_{1.845}Ce_{0.155}CuO_{3.93}$ (Izumi *et al.*, 1989) has the formal copper valence reduced to $Cu^{1.71+}$.

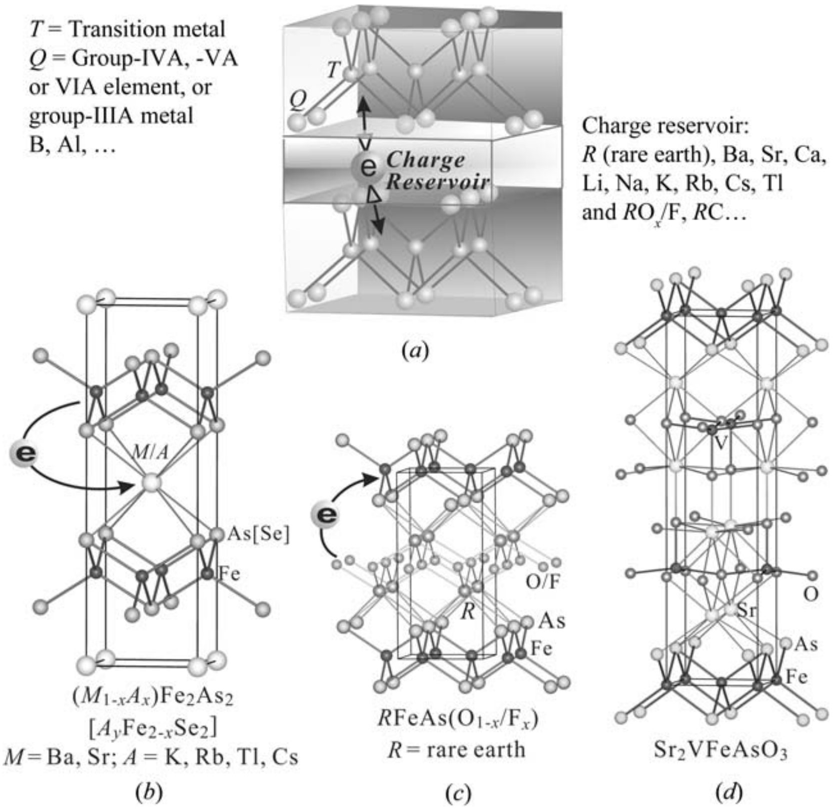
T = Transition metal
Q = Group-IVA, -VA or VIA element, or group-IIIA metal B, Al, …
T
Q
e Charge Reservoir
Charge reservoir: R (rare earth), Ba, Sr, Ca, Li, Na, K, Rb, Cs, Tl and ROx/F, RC…
(a)
e
M/A
As[Se]
Fe
(M1-xAx)Fe2As2
[AyFe2-xSe2]
M = Ba, Sr; A = K, Rb, Tl, Cs
(b)
e
O/F
R
As
Fe
RFeAs(O1-x/Fx)
R = rare earth
(c)
V
Sr
O
As
Fe
Sr2VFeAsO3
(d)

Figure 7.13.9

(*a*) Schematic view of electron transfer in Fe-based superconducting and related compounds. It is believed that the block of edge-sharing TQ_4 tetrahedra contributes to the superconductivity. (*b*) $AE_{1-x}A_xFe_2Pn_2$ (Rotter *et al.*, 2008) and $A_yFe_{2-x}Ch_2$, where AE are alkaline-earth metals and A are alkali metals; (*c*) RFeAs$O_{1-x}F_x$; and (*d*) phases, Sr_2MFePnO_3, where M = Sc, Ti, V.

Remarks. Choosing the proper radiation is key for determining the superconducting composition and the doping state (electron or hole doping). In the $(La_{1-x}Ba_x)_2CuO_{4-y}$ case, it is impossible to refine the ratio of La:Ba using XPD data because Ba and La have a similar atomic numbers ($Z_{Ba} = 56$ and $Z_{La} = 57$). However, using NPD data La and Ba can be distinguished well by Rietveld refinement because the neutron scattering amplitude of La ($0.827\ cm^{-12}$) is 57% larger than that of Ba ($0.525\ cm^{-12}$). However, the situation is more complex for the $(Nd_{1-x-y}Sr_xCe_y)_2CuO_{4+\delta}$ system, where three different elements occupy the same crystallographic site. The formal valence of copper can be larger or smaller than 2+, depending on the values of x, y and δ. Combined refinements using XPD and NPD data were able to determine the values x, y and δ as follows:

(i) Considering that Nd ($Z_{Nd} = 58$) and Ce ($Z_{Ce} = 60$) have similar atomic numbers Z, but quite different from that of Sr ($Z_{Sr} = 38$), and the amount of Ce in the compound is much less than the amount of Nd, the formula can be simplified to $[(Nd/Ce)_{1-x}Sr_x]_2CuO_{4-\delta}$ and x can be obtained from refinement using XPD data.

(ii) Fixing the x value obtained from step (i), the y value can be obtained from refinement using NPD data, where the difference in the neutron scattering amplitude between Ce ($0.484\ cm^{-12}$) and Nd ($0.769\ cm^{-12}$) is large.

(iii) The NPD data can be used to refine the oxygen vacancy δ, because O has a comparable neutron scattering amplitude ($0.525\ cm^{-12}$) to that of the cations.

Oxygen stoichiometry in superconducting cuprates and oxides. It is accepted that the oxygen stoichiometry dramatically affects the properties of HTSCs in most non-stoichiometric superconducting cuprates and oxides. In the $HgBa_2Ca_{n-1}Cu_nO_{2(n+1)+x}$ system, the parent compounds ($x = 0$) are all non-superconductors. When $x = 0.06$, the $n = 1$ compound $HgBa_2CuO_{4+x}$ has a T_c of 94 K (Fig. 7.13.8*b*) (Putilin *et al.*, 1993). The non-superconducting parent compound $HgBa_2CuO_4$ ($x = 0$) has Hg^{2+}, Ba^{2+}, Cu^{2+} and O^{2-}. By adding oxygen atoms to the HgO_x charge-reservoir layer, the formal copper valence is increased from Cu^{2+} to $Cu^{(2+\delta)+}$ and the compound becomes a hole-doped superconductor. In this system T_c has been found to be as high as 133 K (Antipov *et al.*, 1993; Chmaissem *et al.*, 1993) for the $n = 3$ compound $HgBa_2Ca_2Cu_3O_{8+x}$ with $x = 0.42$, *i.e.* the additional 0.42 oxygen atoms increase the formal copper valence from Cu^{2+} to $Cu^{2.26+}$.

Remarks: Compared with the metal atoms in these nonstoichiometric superconducting cuprates and oxides, oxygen is a light element and has a smaller X-ray scattering amplitude. Therefore, NPD data were needed to refine the oxygen occupancy, since the neutron scattering amplitude of O is similar to those of the metal atoms.

Cation and anion substitution in Fe-based superconductors. The Fe-based pnictide (Pn) and chalcogenide (Ch) families have Fe-containing layers in which the Fe atoms are coordinated by four pnictogen or chalcogen (Q) ions forming a block of FeQ_4 edge-sharing tetrahedra. The first superconductor observed in this system was LaFePO ($T_c = 5$ K), found by Kamihara *et al.* (2006). On replacing P by As, T_c increases to 26 K in the $LaFeAs(O_{1-x}F_x)$ system (Kamihara *et al.*, 2008). Soon after, a series of related superconductors were reported in the RFeAs$(O_{1-x}F_x)$ and RFeAsO_x systems with a maximum T_c of up to 55 K (Ren, Yang *et al.*, 2008; Ren, Che *et al.*, 2008).

Fe–Pn(Ch) compounds have high chemical and structural flexibility for a large variety of constituent elements. Like the high-T_c cuprates, where Cu has a mixed valence in the conducting

Table 7.13.2
Selected layered copper-oxide superconductors

n is the number of CuO_2 conducting layers per formula unit.

Formula	n	T_c (K)	Charge-reservoir unit	CuO_2 conducting layer and blocks
$Sr_{1-x}Nd_xCuO_2$	1	40	$[Sr_{1-x}Nd_x]$	CuO_2
$(R_{1-x}M_x)_2CuO_4$	1	35	$[R_{1-x}M_x\text{-}O_2\text{-}R_{1-x}M_x]$	CuO_2
$La_{2-x}M_xCa_{n-1}Cu_nO_{2n+1}$	1, 2	35, 60	$[(La,M)O\text{-}(La,Ca)O]$	$CuO_2\text{-}Ca\text{-}CuO_2$
$Nd_{2-x-y}Ce_xSr_yCuO_4$	1	28	$[Nd_{2-x-y}Ce_xSr_y\text{-}O_2\text{-}Nd_{2-x-y}Ce_xSr_y]$	CuO_2
$YBa_2Cu_3O_{7-x}$	3	90	BaO $[CuO_x]$ BaO	$CuO_2\text{-}Y\text{-}CuO_2$
$YBa_2Cu_4O_8$	4	80	BaO $[CuO_x]$ BaO	$CuO_2\text{-}BaO\text{-}CuO_2\text{-}Y\text{-}CuO_2\text{-}Y\text{-}CuO_2\text{-}BaO\text{-}CuO_2$
$HgBa_2Ca_{n-1}Cu_nO_{2n+2+x}$	1, 2, 3, 4, 5	94, 112, 133, 130, 100	BaO $[HgO_x]$ BaO	$CuO_2\text{-}Ca\text{-}CuO_2\text{-}Ca\text{-}CuO_2\text{-}Ca\text{-}CuO_2\text{-}Ca\text{-}CuO_2$
$Tl_{1-y}Ba_2Ca_{n-1}Cu_nO_{2n+3-x}$	1, 2, 3, 4, 5	50, 90, 110, 122, 117	BaO $[TlO_x]$ BaO	$CuO_2\text{-}Ca\text{-}CuO_2\text{-}Ca\text{-}CuO_2\text{-}Ca\text{-}CuO_2\text{-}Ca\text{-}CuO_2$
$Tl_{2-y}Ba_2Ca_{n-1}Cu_nO_{2n+4\text{-}x}$	1, 2, 3, 4	80, 110, 125, 113	BaO $[TlO_x\text{-}TlO_x]$ BaO	$CuO_2\text{-}Ca\text{-}CuO_2\text{-}Ca\text{-}CuO_2\text{-}Ca\text{-}CuO_2$
$Bi_2Sr_2Ca_{n-1}Cu_nO_{2n+4+x}$	1, 2, 3	22, 85, 110	SrO $[BiO_x\text{-}BiO_x]$ SrO	$CuO_2\text{-}Ca\text{-}CuO_2\text{-}Ca\text{-}CuO_2$
$(Pb_2Cu)Sr_2(Ca,Y)_{n-1}Cu_nO_{2n+4}$	1, 2	32, 70	SrO $[PbO_x\text{-}CuO_x\text{-}PbO_x]$ SrO	$CuO_2\text{-}(Y, Ca)\text{-}CuO_2$
$(Cu/C)_2Ba_2Ca_{n-1}Cu_nO_{2n+2}$	3, 4, 5	72, 117, 95	BaO $[(Cu/C)O\text{-}(Cu/C)O]$ BaO	$CuO_2\text{-}Ca\text{-}CuO_2\text{-}Ca\text{-}CuO_2\text{-}Ca\text{-}CuO_2\text{-}Ca\text{-}CuO_2$
$Cu_yBa_2Ca_{n-1}Cu_nO_{2n+3-x}$	3, 4	120, 117	BaO $[Cu_x]$ BaO	$CuO_2\text{-}Ca\text{-}CuO_2\text{-}Ca\text{-}CuO_2\text{-}Ca\text{-}CuO_2$

References: Cava (2000); Park & Snyder (1995); Hauck & Mika (1998); Tokura & Arima (1990); Parkin *et al.* (1988).

layers, the formal valence for iron can be adjusted from Fe^{2+} to $Fe^{(2\pm\delta)+}$ when electrons are transferred between the conducting and charge-reservoir layers, as shown in Fig. 7.13.9(*a*). Changing the valence state of Fe can be achieved by cation or anion doping. The layer or block between the blocks of $FeAs(Se)_4$ edge-sharing tetrahedra is the charge-reservoir unit: it can be a simple layer (Fig. 7.13.9*b*) or complex blocks (Figs. 7.13.9*c*, 7.13.9*d*). For the $Ba_{1-x}K_xFe_2As_2$ system shown in Fig. 7.13.9(*b*), the parent compound $BaFe_2As_2$ ($x = 0$) contains Ba^{2+}, Fe^{2+} and As^{3-} and is not a superconductor. Partial substitution of Ba^{2+} with the lower-valence cation K^{1+} will make the average formal valence for Fe larger than 2+ and the compound becomes a superconductor. In the $RFeAs(O_{1-x}F_x)$ system (Fig. 7.13.9*c*), the superconductivity can be introduced by electron doping when the formal valence for Fe is adjusted to be smaller than 2+ through partial replacement of F^{1-} with O^{2-}.

Remarks. As Ba has a higher atomic number than K but the neutron scattering amplitudes for Ba and K are very similar, XPD data should be better than NPD data for determining the K content in $(Ba_{1-x}K_x)Fe_2As_2$ compounds. On the other hand, neither XPD nor NPD data can be used to obtain the F content when replacing O by F in the $RFeAs(O_{1-x}F_x)$ system because of the small difference in both the numbers of electrons and the neutron scattering amplitudes for O and F.

7.13.3.2. *Modelling of layer structures*

Stacked layers are widely found in the structures of the cuprate superconductors and are used to explain the charge transfer. The structural features of the layered superconducting copper oxides and of related materials have been described in many reviews (Sleight, 1988; Tokura & Arima, 1990; Park & Snyder, 1995; Raveau *et al.*, 2013). Selected high-T_c copper-oxide systems with the stacking described below are shown in Table 7.13.2. These structures are formed by stacking layers of the conducting and intermediate layers. The intermediate layers can be charge-reservoir or 'regulation' layers. In the structures of $(R_{1-x}M_x)_2CuO_4$ and $HgBa_2CuO_{4+x}$, illustrated in Fig. 7.13.8, the CuO_2 plane is the conducting layer, and $(R_{1-x}M_x)O_y$ and HgO_x are the charge-reservoir layers. The BaO layer in $HgBa_2CuO_{4+x}$ is a regulation layer where the occupancies and valences of Ba and O remain unchanged. The structure is constructed by the following layer-stacking sequences:

$(R_{1-x}M_x)_2CuO_4$: $\{CuO_2\}_O$ $[R_{1-x}M_xO]_C$ $[R_{1-x}M_xO]_O$ $\{CuO_2\}_C$ $[R_{1-x}M_xO]_O$ $[R_{1-x}M_xO]_C$ $\{CuO_2\}_O \ldots$

$HgBa_2CuO_{4+x}$: $\{CuO_2\}_O$ $(BaO)_C$ $[HgO_x]_O$ $(BaO)_C$ $\{CuO_2\}_O$.

The chemical symbols enclosed in braces, square brackets and parentheses express the actual compositions of the conducting, charge-reservoir and regulation layers, respectively, and the subscripts *O* and *C* indicate whether the cation is located at the origin or at the centre, respectively, of the net of the layer. In $(R_{1-x}M_x)_2CuO_4$, the conducting CuO_2 layers sandwich the $R_{1-x}M_xO$ charge-reservoir layers in alternating stacking along the *c* axis. A few typical layer structures are illustrated in Fig. 7.13.10. Fig. 7.13.11 shows the stacking structure along the *c* axis of the $HgBa_2Ca_{n-1}Cu_nO_{2(n+1)+x}$ ($n = 1, 2, 3, 4, 5, 6$) series of superconductors. The structures can be constructed in the following way, where the charge-reservoir unit is shown in bold:

$\ldots\{CuO_2\}_O\,(Ca)_C\,\{CuO_2\}_O\,\mathbf{(BaO)_{\mathit{C}}\,[HgO_{\mathit{x}}]_{\mathit{O}}\,(BaO)_{\mathit{C}}}\,\{CuO_2\}_O\,(Ca)_C\,\{CuO_2\}_O\ldots$

Using the charge-reservoir unit as a centre, the CuO_2 and the Ca layers are stacked alternately along the *c* axis. The Ca layers

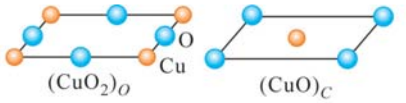

(*a*) Conducting layers

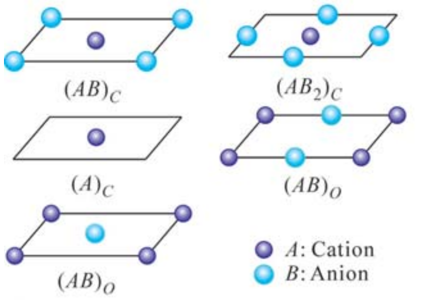

(*b*) Charge reservoir or regulation layers

Figure 7.13.10
Layers in copper-oxide high-T_c superconductors. (*a*) Typical conduction layers CuO and CuO_2 in cuprate families which are considered to be responsible for the superconductivity. (*b*) Selected layers that act as charge-reservoir or structure-regulation layers present in copper-oxide superconductors. The subscripts *O* and *C* indicate whether the cation is located at the origin or at the centre of the net of the layer, respectively. Selected examples for the reservoir layers are shown in Table 7.13.2.

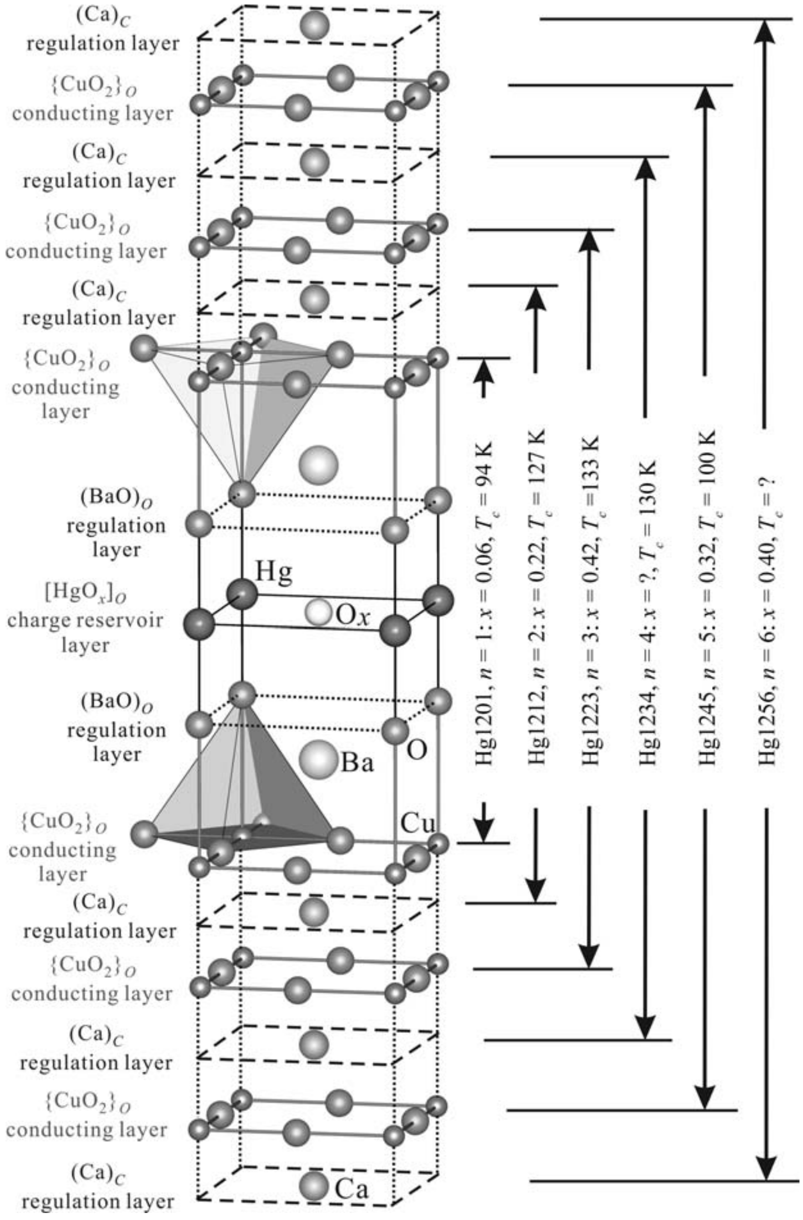
(Ca)$_C$ regulation layer
{CuO$_2$}$_O$ conducting layer
(Ca)$_C$ regulation layer
{CuO$_2$}$_O$ conducting layer
(Ca)$_C$ regulation layer
{CuO$_2$}$_O$ conducting layer
(BaO)$_O$ regulation layer
Hg
[HgO$_x$]$_O$ charge reservoir layer
Ox
(BaO)$_O$ regulation layer
Ba
O
Cu
{CuO$_2$}$_O$ conducting layer
(Ca)$_C$ regulation layer
{CuO$_2$}$_O$ conducting layer
(Ca)$_C$ regulation layer
{CuO$_2$}$_O$ conducting layer
(Ca)$_C$ regulation layer
Ca
Hg1201, n = 1: x = 0.06, T_c = 94 K
Hg1212, n = 2: x = 0.22, T_c = 127 K
Hg1223, n = 3: x = 0.42, T_c = 133 K
Hg1234, n = 4: x = ?, T_c = 130 K
Hg1245, n = 5: x = 0.32, T_c = 100 K
Hg1256, n = 6: x = 0.40, T_c = ?

Figure 7.13.11
Structure stacking along the c axis for the $\mathrm{HgBa_2Ca_{n-1}Cu_nO_{2(n+2)+x}}$ series of superconductors.

do not act as donors of charge carriers and only play the role of regulation layers for the geometric requirements of the structure. T_c depends on the oxygen content in the HgO_x charge-reservoir layer, and is strongly correlated with the number of $\mathrm{CuO_2}$ layers.

7.13.3.3. *Structural transformations*

Above T_c, a superconductor may be an electron insulator, a semiconductor or a metallic conductor. Changes in the electron-transport behaviour are in some cases accompanied by structural modifications due to structure distortions, chemical order–disorder and/or variations in composition. The different structures may belong to different crystal systems, or belong to the same crystal system but have different space groups; this can be determined by analysing the powder-diffraction pattern. Fig. 7.13.12 shows some examples of possible diffraction-peak positions calculated by considering only the primitive lattice. [Symmetry relations between space groups during structural distortions are discussed in *International Tables for Crystallography*, Volume A1 (2011).]

For data collection, the high resolution available for XPD (especially at a synchrotron) is beneficial for detecting the peak splittings that result from a small lattice distortion, and NPD has an advantage in measuring superstructure peaks where intensities come from small shifts of light elements.

Perovskite-like structure distortions. Superconductivity has been found in many compounds with perovskite-like structures. An ideal perovskite has the chemical formula ABX_3 with cubic $Pm\bar{3}m$ symmetry and with atomic positions A: 1a (0, 0, 0), B: 1b ($\frac{1}{2}$, $\frac{1}{2}$, $\frac{1}{2}$) and X: 3c ($\frac{1}{2}$, $\frac{1}{2}$, 0) [see Fig. 7.13.2(*e*)]. In practice it has been found that the perovskite structure exists if $0.75 \le p \le 1.0$, where

$$p = (r_A + r_X)/[2^{1/2}(r_B + r_X)];$$

p is Goldschmidt's tolerance factor (Goldschmidt, 1926) and r_A, r_B and r_X are the ionic radii (Shannon, 1976) of A, B and X, respectively. The A and B ions are located at the corners and at the centre of the cubic unit cell, respectively. The ions X are located at the centre of the six faces of the cubic cell and form an octahedron around the B cation. Each octahedron shares corners with the nearest neighbours. The distortion of the octahedra and/or their tilting results in different modifications of the ideal structure. Fig. 7.13.13 shows an example in which the octahedron at the centre and the four surrounding octahedra are rotated in opposite directions around the cubic c axis. Such rotations are responsible for a lowering of the symmetry from cubic to trigonal, tetragonal, orthorhombic or monoclinic (Glazer, 1972, 1975). The distortions can be temperature and/or composition dependent, as happens in the perovskite-like system $\mathrm{(La,Ba)_2CuO_4}$ (Axe *et al.*, 1989) as well as in $\mathrm{BaBi_{1-x}Pb_xO_3}$ (Cox & Sleight, 1976; Marx *et al.*, 1992).

Tetrahedral distortions. A structural transition due to polyhedral distortion is also present in Fe-based superconductors. As an example, the parent compound LaFeAsO of the $\mathrm{LaFeAsO_{1-x}F_x}$ superconductor has a structure with $P4/nmm$ symmetry and lattice parameters a_t = 4.03007 (9) Å and c_t = 8.7368 (2) Å at 175 K (Nomura *et al.*, 2008). The polyhedral distortion breaks the tetragonal symmetry below 155 K and the material becomes orthorhombic with $Cmma$ symmetry. The axes transformation from the tetragonal to the orthorhombic phase is $(a_o\ b_o\ c_o) = (110/\bar{1}10/001)(a_t\ b_t\ c_t)$, and the relation between the lattice parameters of the two phases is $a_o \simeq b_o \simeq 2^{1/2}a_t$ and $c_o \simeq c_t$. In this case, peak splitting and superlattice peaks will be present in the powder pattern.

Stoichiometry dependence and vacancy ordering. Order–disorder transitions can be induced by external forces (temperature and pressure) and/or internal forces (chemical composition). Chemical order–disorder is present in both the cuprate and Fe-based high-T_c superconducting families, as observed in the $\mathrm{YBa_2Cu_3O_{7-x}}$ and $\mathrm{K_xFe_{2-y}Se_2}$ systems.

The crystal structure and phase transition of $\mathrm{YBa_2Cu_3O_{7-x}}$ have been studied carefully with the Rietveld method, using both XPD and NPD data (Cava *et al.*, 1987; Jorgensen *et al.*, 1987, 1990). The results revealed the presence of oxygen vacancies in the $\mathrm{CuO_{1-x}}$ charge layer (see Fig. 7.13.14*a*) and the structure undergoes an orthorhombic $Pmmm$ to a tetragonal $P4/mmm$

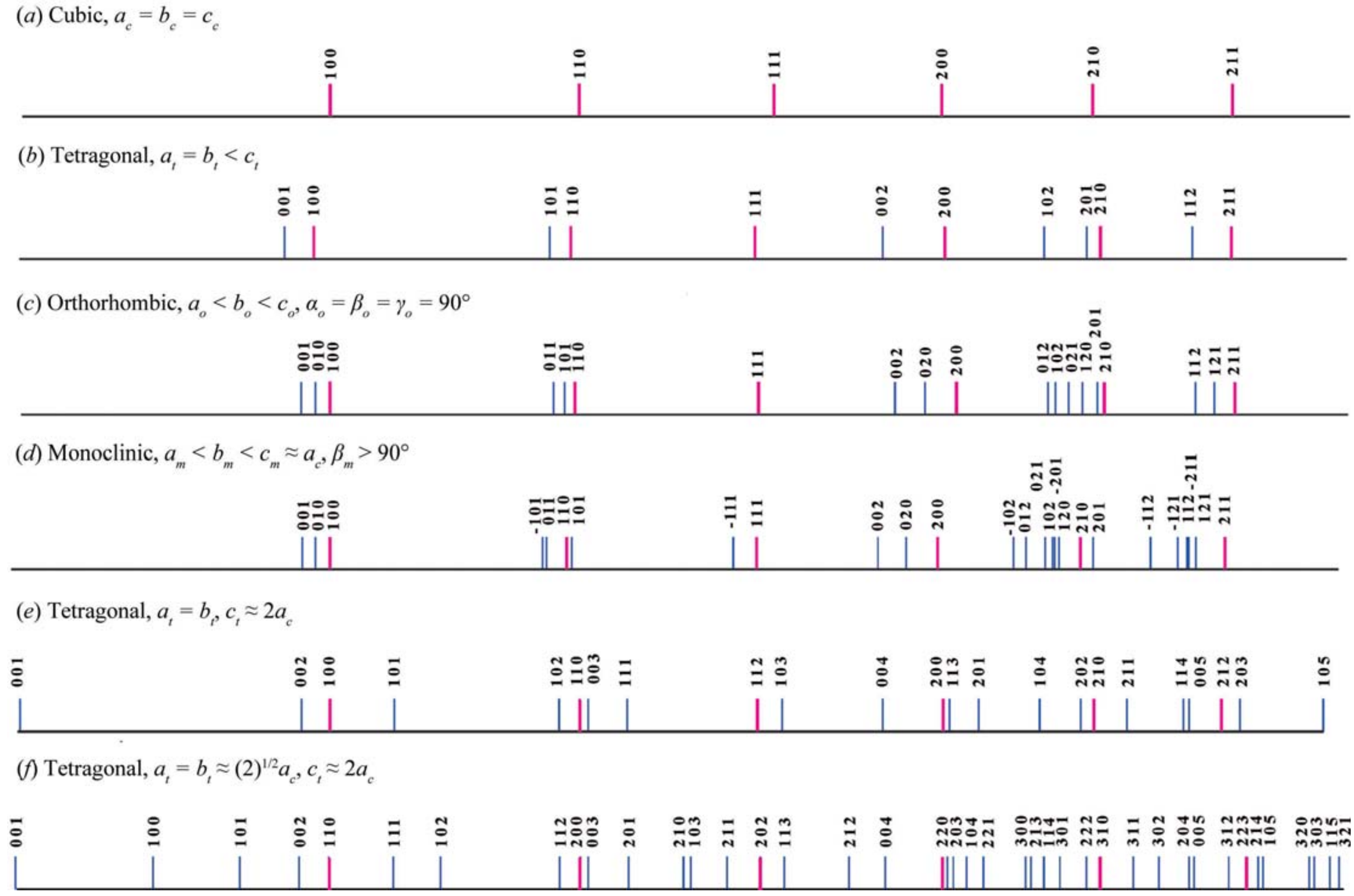

Figure 7.13.12
Schematic plot of the possible diffraction peaks with consideration of the primitive lattice only. The thick red lines are the reflections corresponding to a cubic lattice, and the thin blue lines are the reflections due to the peak splitting or the superlattice peaks. (*a*) Reflections from a simple cubic lattice; (*b*), (*c*) and (*d*) reflections from tetragonal, orthorhombic and monoclinic lattices, respectively. As a result of the lattice distortion, a cubic peak may be split into two or more peaks; in (*e*) and (*f*) reflections show the presence of peak splitting and also superlattice peaks (such as the peaks for *hkl* with *l* = odd) from the superlattice.

transition. The transition is induced by a change in the oxygen stoichiometry and is a function of temperature. The orthorhombic phase exists over the range $0 \leq x < 0.65$, with the oxygen vacancies along the *a* axis. The remaining oxygen atoms form chains along the *b* axis within square-planar CuO_4 motifs, coordinated in the *b*–*c* plane (Fig. 7.13.14*b*). The vacancies are disordered in the tetragonal phase ($x > {\sim}0.65$), thus destroying the Cu—O chains of the orthorhombic modification (Fig. 7.13.14*c*).

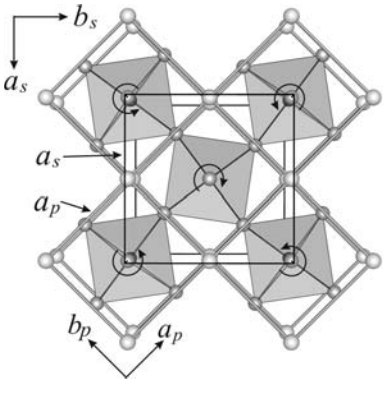

Figure 7.13.13
A structural transformation induced by a rotation of the octahedra in the perovskite structure. A projection along the *c* direction, showing that the rotation of the corner-shared octahedra is responsible for the symmetry change and for the formation of a superstructure in which $a_s = b_s = 2^{1/2}a_p$ and $c_s = c_p$, where a_p (= b_p = c_p) is the lattice parameter for the cubic perovskite and a_s, b_s and c_s are the parameters of the superlattice.

Structural transitions are observed due to the iron-vacancy ordering in the $A_xFe_{2-y}Se_2$ system. Guo *et al.* (2010) first reported a T_c of 31 K in $K_xFe_{2-y}Se_2$. Different iron-vacancy ordering models have been reported in compounds with *A* = K, Rb, Tl/Rb and Tl/K (Fig. 7.13.15). Structure analysis of the compound $K_{0.83(2)}Fe_{1.64(1)}Se_2$ (Bao *et al.*, 2011) using NPD data indicated that at 580 K the compound has the tetragonal $ThCr_2Si_2$-type structure (*I*4/*mmm*) with lattice parameters $a_{t1} = b_{t1} =$ 3.94502 (7) Å and c_{t1} = 14.1619 (4) Å. A long-range Fe-vacancy ordering occurs below 578 K (Fig. 7.13.15*b*), with a consequent structural transition from the *I*4/*mmm* phase (*t*1) to a tetragonal *I*4/*m* superstructure phase (*t*2) with parameters $a_{t2} = b_{t2} \simeq 5^{1/2}a_{t1}$ = 8.6929 (2) Å and $c_{t2} \simeq c_{t1}$ = 14.0168 (4) Å at 11 K. In this structure model the ideal composition should be KFe_4Se_5 where for every five possible Fe positions there is one vacancy. Another model for the long-range Fe-vacancy order [Fig. 7.13.15(*c*1)] was proposed by Fang *et al.* (2011) and Kazakov *et al.* (2011) for compounds with an ideal composition AFe_3Se_4. In this model, for every four possible Fe positions there is one vacancy and consequently the superlattice has orthorhombic symmetry with unit-cell parameters $a_o \simeq 2^{1/2}a_{t1}$, $b_o \simeq 2(2^{1/2})a_{t1}$ and $c_o \simeq c_{t1}$. The models in Figs. 7.13.15(*c*1) and 7.13.15(*c*2) are the two local configurations; they have the same symmetry and cannot be distinguished by Rietveld refinement. If the two configurations

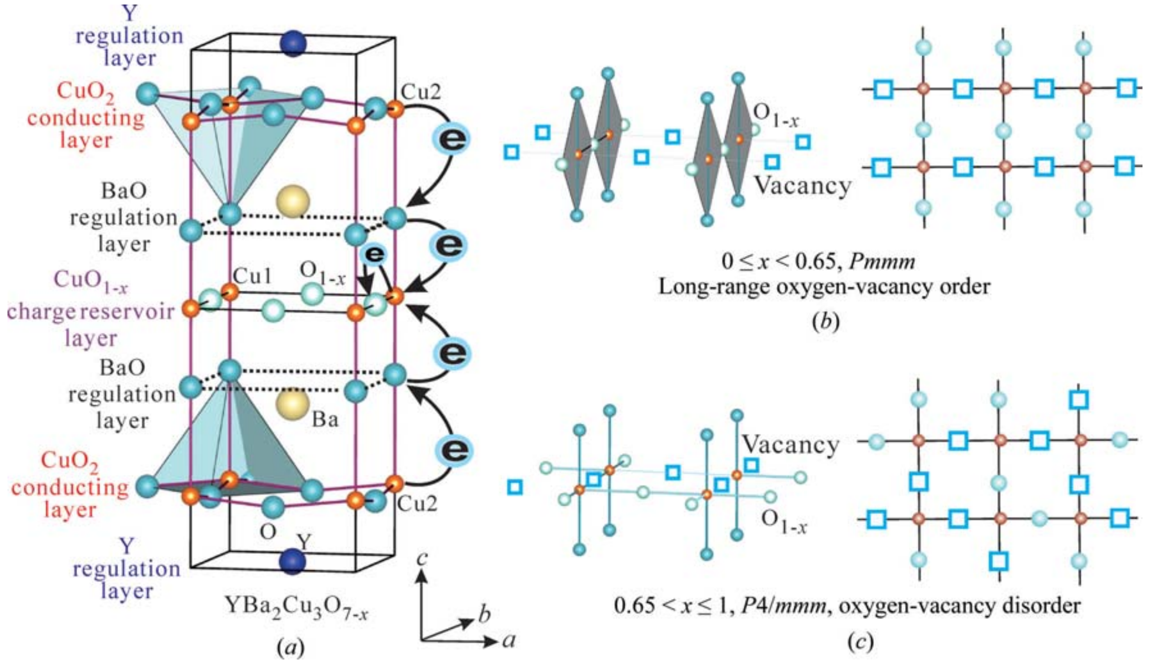

Figure 7.13.14
Structural transformation from tetragonal *P*4/*mmm* symmetry to orthorhombic *Pmmm* symmetry due to oxygen vacancy ordering in the CuO_{1-x} charge-reservoir layer. (*a*) Crystal structure of $YBa_2Cu_3O_{7-x}$. (*b*) The structure has orthorhombic symmetry when long-range oxygen-vacancy ordering occurs in the charge-reservoir layer, leaving the Cu in a CuO_4 square-planar configuration in which the Cu—O atoms form chains along the *b* axis of the unit cell. (*c*) In the range $0.65 < x \le 1$ the structure has tetragonal symmetry, in which the oxygen vacancies are disordered, thus fragmenting the one-dimensional Cu—O chains.

are present in equal amounts, one will get an average structure from powder diffraction. Therefore, the structure has an orthorhombic superlattice which is related to the tetragonal modification by the relations $a_o' \simeq b_o' \simeq 2^{1/2}a_{t1}$ and $c_o' \simeq c_{t1}$, as shown in Fig. 7.13.15(*c*).

Remarks. Since powder diffraction measures the average long-range-ordered structure, the local short-range-ordered structure might not be detected. In the $A_xFe_{2-y}Se_2$ system, the compositions of the compounds are very variable and the long-range Fe-vacancy ordering is achieved by diffusion in the solid state at a relatively low temperature. One cannot expect to reach a complete long-range Fe-vacancy order and a homogeneous distribution of vacancies in a bulk sample or a single crystal. The local structure, therefore, could be very complicated. The electron-diffraction method and/or pair distribution function (PDF) analysis can be used to obtain local structure information.

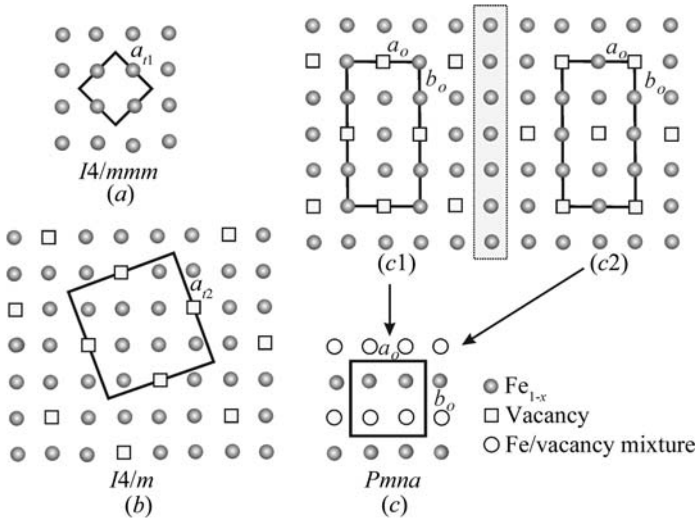

Figure 7.13.15
Possible vacancy-ordering arrangements in the Fe plane for $A_xFe_{2-y}Se_2$. (*a*) At high temperature the compound has no vacancies and forms the $ThCr_2Si_2$-type structure (*I*4/*mmm*). (*b*) One type of vacancy-ordering arrangement in the composition near $A_xFe_4Se_5$ where for every five Fe positions there is one vacancy. (*c*1), (*c*2) A proposed type of local vacancy-ordering configuration for the composition near $A_xFe_3Se_4$ where only three-quarters of the possible Fe positions are occupied (Fang *et al.*, 2011; Kazakov *et al.*, 2011). (*c*) In a powder-diffraction experiment, the pattern will show the average of the (*c*1) and (*c*2) domains resulting in an orthorhombic *Pmna* symmetry.

Substitution effects. In the $LaFeAs(O_{1-x}F_x)$ system, the parent compound ($x = 0$) has tetragonal *P*4/*nmm* symmetry at room temperature and an orthorhombic *Cmma* lattice at low temperature. However, the tetragonal *P*4/*nmm* phase is stabilized at low temperatures by partial replacement by fluorine for oxygen, *i.e.* by adjusting the dopant F concentration *x* (Zhao *et al.*, 2008; Huang *et al.*, 2008).

7.13.4. Magnetic order in superconductors and parent compounds

The interaction between superconductivity and magnetic properties is one of the most striking physical phenomena in this field. In a superconductor, in general, electrons can be in a superconducting state and/or in a magnetic state at low temperature. The study of the effects associated with the interaction between superconductivity and magnetism is a very active area of research for understanding the mechanism of superconductivity and whether superconductivity and magnetic order can coexist microscopically. Scientists have invested significant effort in investigating the magnetic properties of superconductors using different techniques, focusing on the high-T_c superconducting systems such the layered cuprates (Lynn & Skanthakumar, 2001; Niewa *et al.*, 2011), Fe-based compounds, borocarbides (Müller & Narozhnyi, 2001; de la Cruz *et al.*, 2008) and HF superconductors. Common features of the magnetic structures are:

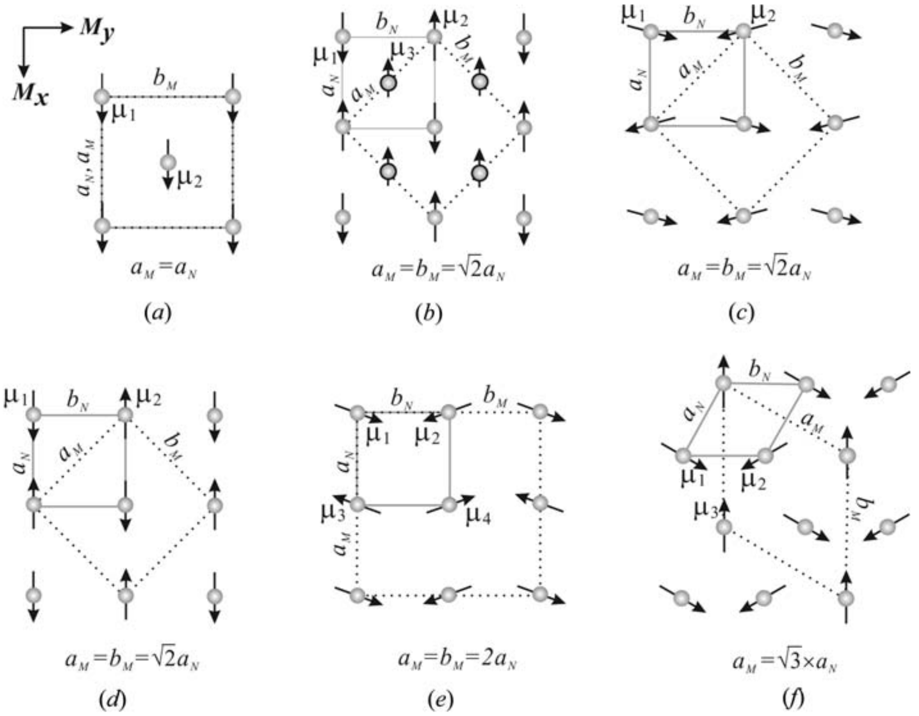

Figure 7.13.16

Representation of selected commensurate ferromagnetic and antiferromagnetic ordering schemes. Arrows show the magnitudes and directions of the moments. The crystallographic primitive unit cell is indicated by solid lines and the dotted lines show a possible magnetic unit cell. $a_N = b_N$ are the lattice parameters for the nuclear structure and a_M and b_M are those of the magnetic unit cell. (*a*) Ferromagnetic order; (*b*) a ferrimagnetic order; (*c*) a canted ferromagnetic order; (*d*) a collinear antiferromagnetic order; (*e*) a canted non-collinear antiferromagnetic order where both the $\mathbf{M}_x$ and $\mathbf{M}_y$ directions have antiparallel components; (*f*) an example of a triangular antiferromagnetic structure in hexagonal and trigonal crystals.

(i) Long-range antiferromagnetic ordering is present in some superconductors and related compounds containing rare-earth elements and/or transition metals.

(ii) In transition-metal compounds the ordering occurs at much higher temperatures and with considerably smaller moments than for compounds containing rare-earth elements. The ordering also occurs at much higher temperatures in compounds containing both types of elements.

(iii) Magnetic ordering is strongly correlated to chemical composition (including replacement and doping), crystal structure and superconductivity.

(iv) Magnetic ordering in some compounds containing rare-earth elements can coexist with superconductivity. It is questionable whether such coexistence can be present for transition metals located in the conducting layers.

NPD is essential for investigating magnetic materials, *e.g.* to determine the long-range order of magnetic structures and to measure the ordered magnetic moments (Cox, 1972).

7.13.5. Conclusions

Superconductivity can be shown by elements, alloys, intermetallics and chemical compounds of more complex compositions, and can be found in either stoichiometric or nonstoichiometric compounds. In general, the properties of superconductivity depend on the structure, *i.e.* the symmetry, the chemical composition, and the distribution of the atoms and/or ions in the structure under particular conditions (such as temperature, magnetic field and pressure). Powder diffraction has been widely and effectively employed to provide structural information and, combined with other tools or special techniques, to reveal the relationships between structure and superconductivity. As in many other research fields in materials science, powder diffraction is used to identify and to characterize the phase, to find the optimal composition, to study phase diagrams, and to determine the crystal and magnetic structures.

APPENDIX A7.13.1

The study of long-range magnetic order in superconductors

Magnetic properties have been described briefly by Borovik-Romanov *et al.* in Chapter 1.5 of *International Tables for Crystallography* Volume D (2013). Like crystal structures, the parameters of magnetic structures include the magnetic unit cell, the lattice, the magnetic moments, the symmetry elements and the space group. The moments can be arranged in parallel and antiparallel configurations, and the 14 Bravais lattices of classical crystallography become 36 magnetic lattices (Zamorzaev, 1957*a*,*b*). An additional element, 'antisymmetry', is produced by introducing the time (or current) reversal operator *R*, which acts in combination with a normal symmetry operation. With the antisymmetry element, and based on the symmetry of the 230 space groups, 1651 magnetic space groups (Shubnikov groups) have been derived [Shubnikov (1951); Belov *et al.* (1957); see also Chapter 3.6 in *International Tables for Crystallography* Volume A (Litvin, 2016)]. This section deals only with the basic magnetic crystallography related to investigations of long-range magnetic order in superconductors and in related materials, analysed using NPD.

A7.13.1.1. Commensurate magnetic ordering and primitive cells

The periodicity of a magnetic unit cell is consistent with the arrangement of the magnetic moments in addition to that of the atomic distribution. A schematic representation of the simplest types of ferromagnetic and antiferromagnetic moment arrangements (Fig. 7.13.16) helps to show the relationship between the

Table 7.13.3
Crystal systems, conventional coordinate systems and the 36 magnetic lattices in three dimensions

In the orthorhombic system, lattices with a different white lattice and location of black lattice (as indicated by the subscript) are shown in parentheses (see Section A7.13.1.2).

System	Symbol	Conventional coordinate system		Symbols of the 36 magnetic lattices	
		Restrictions on cell parameters	Parameters to be determined	White	White and black
Triclinic	a		$a, b, c, \alpha, \beta, \gamma$	aP	aP_s
Monoclinic	m	$\alpha = \gamma = 90°$	a, b, c, β	mP, mC	mP_b, mP_a, mP_C, mC_c, mC_a
Orthorhombic	o	$\alpha = \beta = \gamma = 90°$	a, b, c	oP, oI, oF (oC, oA)	oP_I, oF_s, oI_c (oP_C, oP_A) (oC_A, oA_C) (oP_c, oP_a) (oC_c, oA_a) (oC_a, oA_c)
Tetragonal	t	$a = b$, $\alpha = \beta = \gamma = 90°$	$a = b \neq c$	tP, tI	tP_c, tP_C, tP_I, tI_c
Trigonal	h	$a = b = c$, $\alpha = \beta = \gamma$	a, α	hR	hR_I
Hexagonal	h	$a = b$, $\alpha = \beta = 90°$, $\gamma = 120°$	a, c	hP	hP_c
Cubic	c	$a = b = c$, $\alpha = \beta = \gamma = 90°$		cP, cF, cI	cP_I, cF_s

unit cells of the nuclear and magnetic structures. For simplicity, only the *ab* plane in a tetragonal [(*a*)–(*e*)] and a hexagonal (*f*) structure is shown ($a_N = b_N$ are the nuclear and a_M and b_M are the magnetic unit-cell parameters).

Ferromagnetic ordering (Fig. 7.13.16*a*). Ferromagnetic order often involves only one kind of magnetic ion or atom and the spontaneous magnetization is uniform ($\boldsymbol{\mu}_1 = \boldsymbol{\mu}_2$), *i.e.* their magnetic moments have the same amplitude and are aligned parallel and in the same direction to each other. In this case, the magnetic structure has the same unit cell as the nuclear unit cell, *i.e.* $a_N = a_M$ and $b_N = b_M$. Therefore, it should be possible to index the magnetic reflections in an NPD pattern using the nuclear unit cell and the magnetic intensities will overlap with the nuclear peaks.

Ferrimagnetic ordering (Fig. 7.13.16*b*). In this example of ferrimagnetic order, all the moments have parallel alignment but have different amplitudes. The magnetic ions or atoms at the corners of the nuclear unit cell are aligned antiferromagnetically and have different moment amplitudes to the ones at the centre. The system has a net ferromagnetic moment $\boldsymbol{\mu} = \boldsymbol{\mu}_1 - \boldsymbol{\mu}_2 + \boldsymbol{\mu}_3 = \boldsymbol{\mu}_3$. The magnetic unit cell can be $a_M = 2a_N$ and $b_M = 2b_N$ or $a_M = b_M = 2^{1/2}a_N$ (indicated by dotted lines). In this case magnetic reflections corresponding to the magnetic superlattice should be observed in the NPD pattern.

Canted ferromagnetic ordering (Fig. 7.13.16*c*). The canted ferromagnetic order shown in the figure is a simple non-collinear structure generated by the tilting of the $\boldsymbol{\mu}_1$ and $\boldsymbol{\mu}_2$ moments. In this case the system possesses a net ferromagnetic moment; components in the $\mathbf{M}_x$ direction are ferromagnetic and the moment component in the $\mathbf{M}_y$ direction has an antiferromagnetic arrangement. The magnetic unit cell can be obtained by doubling a_N and b_N, or $a_M = b_M = 2^{1/2}a_N$ (dotted lines). The canted

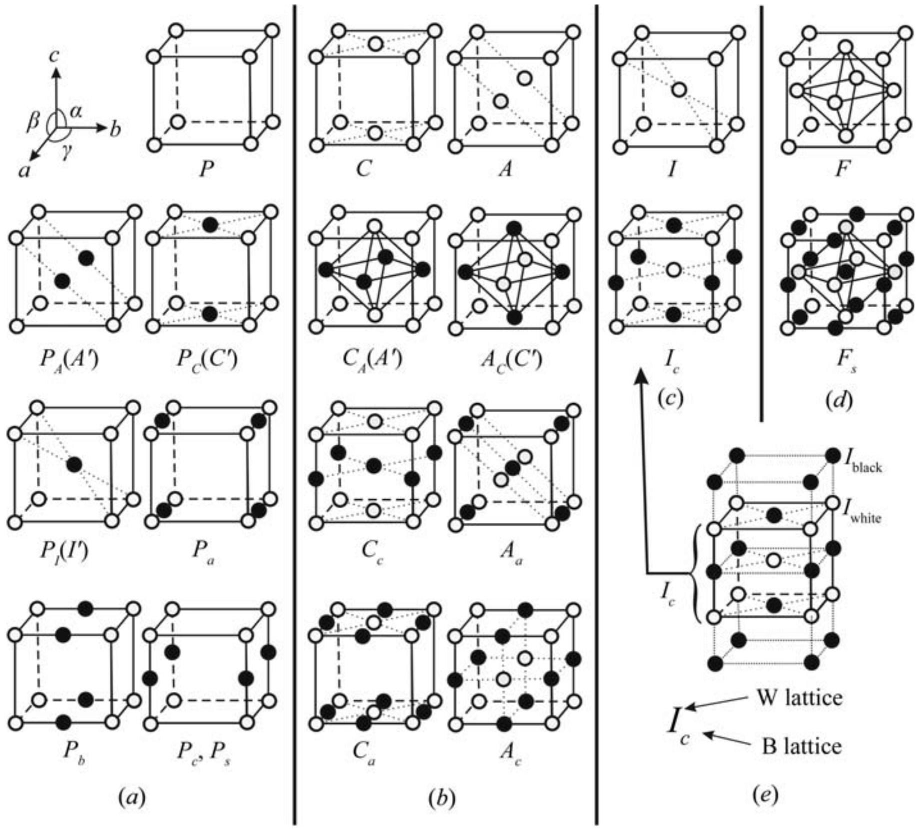

Figure 7.13.17
Types of magnetic lattices. The first row are the five white lattices *P*, *C*, *A*, *I* and *F*. The other white-and-black lattices can be constructed by combination of a white lattice with its corresponding black lattice, with the black lattice having its origin at the face centre or edge centre or body centre of the white lattice [indicated by the subscript, see (*e*)].

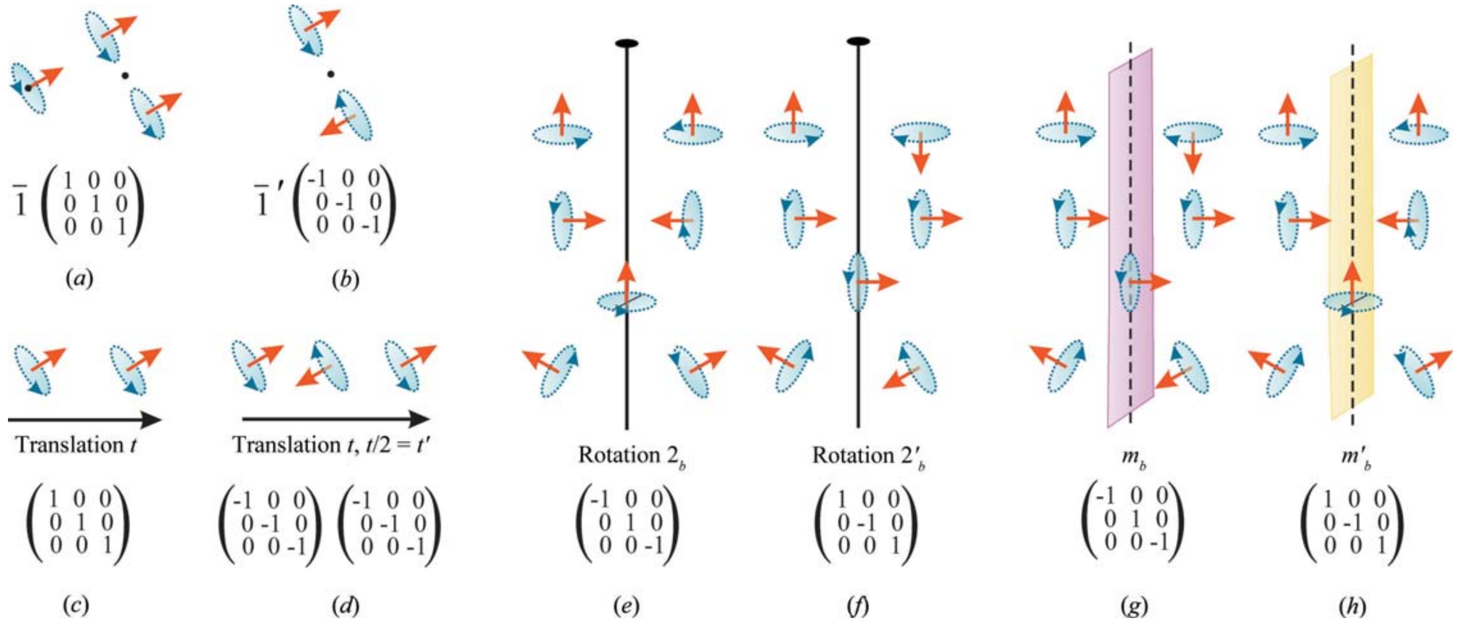

Figure 7.13.18

Selected magnetic symmetry and antisymmetry elements that Dannay *et al.* (1958) first applied to magnetic symmetry. (*a*) Inversion $\bar{1}$; (*b*) anti-inversion $\bar{1}'$; (*c*) translation *t*; (*d*) anti-translation *t*′; (*e*) rotation 2; (*f*) anti-rotation 2′; (*g*) reflection *m*; and (*h*) anti-reflection *m*′.

ferromagnetic moments have a ferromagnetic component and an antiferromagnetic component.

Collinear antiferromagnetic ordering. An example of collinear antiferromagnetic ordering is shown in Fig. 7.13.16(*d*). In this case there is only one type of ion (or atom), located in equivalent crystallographic positions and having equal moment amplitudes in an antiparallel orientation.

Canted antiferromagnetic ordering. Fig. 7.13.16(*e*) shows an example of a canted non-collinear antiferromagnetic order in which the moments tilt in such a way that both the $\mathbf{M}_x$ and $\mathbf{M}_y$ directions have antiparallel components. The magnetic unit cell has parameters that are double those of the nuclear unit cell.

A7.13.1.2. *The 36 magnetic lattices and 1651 Shubnikov groups*

The types of magnetic lattices are shown in Fig. 7.13.17. They are similar to the familiar crystal lattices in that they represent identical chemical entities, but the associated magnetic moments have the same amplitude and opposite orientation. The first row of the figure shows five types of white lattices: *P* (primitive), *C* (*C*-face centred), *A* (*A*-face centred), *F* (all-face centred) and *I* (body centred). All the white lattices represent ferromagnetic ordering of the moments. A white-and-black (W&B) lattice can be thought of as containing two lattices of the same type, one of which is termed 'white' and the other 'black'. The origin of the black lattice can be located at the centre of a face or at an edge, or at the body centre of the white lattice. For example, Fig. 7.13.17(*e*) indicates a white *I* lattice combined with a black *I* lattice with origin at *c*/2 of the white lattice, resulting in the W&B lattice I_c of Fig. 7.13.17(*c*). The W&B lattices are expressed by two-letter symbols in which the symbol (*P*, *C*, *A*, *I* or *F*) of the W lattice is followed by a subscript (*A*, *a*, *C*, *c*, *I* or *s*) which indicates the location of the origin of the black lattice. The capital subscript letters *A*, *C* and *I* indicate that the origin of the B lattice is at the *A*-face centre (0, *b*/2, *c*/2), *C*-face centre (*a*/2, *b*/2, 0) and at the body centre (*a*/2, *b*/2, *c*/2) of the white lattice, respectively. The lower-case subscript letters *a* and *c* indicate that the origin of the black lattice is at the centre of the *a* axis (*a*/2) and *c* axis (*c*/2) of the white lattice, respectively. For example, the lattice P_C is a combination of a *P* W lattice with a *P* B lattice with the origin at the *C*-face centre ($\frac{1}{2}$, $\frac{1}{2}$, 0) of the W lattice, while P_c indicates that the origin of the *P* B lattice is at *c*/2. These types of magnetic lattices, when applied to the seven crystal systems, give a total of 36 magnetic lattices, of which 14 are pure white and 22 are W&B lattices (see Table 7.13.3).

A7.13.1.3. *Magnetic symmetry and antisymmetry operations*

Magnetic symmetry elements include all the symmetry elements of the nuclear structure plus the corresponding antisymmetry elements that are produced by adding the time (or current) reversal operation *R*. Selected typical elements of symmetry and antisymmetry and their symmetry-operation matrices are shown in Fig. 7.13.18. The operation of an element of antisymmetry can be performed as a normal symmetry operation followed by a reversal in direction.

A7.13.1.4. *Magnetic reflection conditions for centred lattices*

Table 7.13.4 lists the possible neutron magnetic reflection conditions related to the magnetic lattices illustrated in Fig. 7.13.17. The results are obtained by evaluating the neutron magnetic structure factor for $F_{hkl} = 0$ and are confirmed by computations using the program *GSAS* (Larson & Von Dreele, 2004). The conditions for systematic extinctions of magnetic reflections for glide planes and screw axes were reported by Ozerov (1967).

Effects of spin orientation in magnetic structures. Fig. 7.13.3 is a schematic view of the definition of the vectors relevant to the evaluation of the magnetic structure factor. In addition to the magnetic reflection conditions for centred lattices, glides and screws, systematic absences can also be observed when the condition $F_{hkl} = 0$ occurs because the magnetic spin **K** is parallel to the scattering vector $\boldsymbol{\varepsilon}$ for a class of reflections *hkl*. In this case, the angle α between the scattering and the magnetization vectors is zero and, consequently, $|q| = \sin\alpha = 0$.

Ambiguous spin orientation. Shirane (1959) showed that ambiguous spin structures can be deduced from NPD data, and concluded that: (i) no information can be obtained about the spin

Table 7.13.4
Integral reflection conditions of centred magnetic lattices corresponding to Fig. 7.13.17

In the symbols for the W&B lattices, the first letter indicates the W lattice (P, C, A, I and F) and the subscript indicates the B lattice.

Type of magnetic lattice and origin for B lattice			Condition for *hkl* reflection	
W	W&B	Origin of B lattice	W lattices	W&B lattices
P				
	P_A	A-face centre, $(b + c)/2$		$k + l = 2n + 1$
	P_C	C-face centre, $(a + b)/2$		$h + k = 2n + 1$
	P_I	I (body) centre, $(a + b + c)/2$		$h + k + l = 2n + 1$
	P_a	a-axis centre, $a/2$		$h = 2n + 1$
	P_b	b-axis centre, $b/2$		$k = 2n + 1$
	P_c, P_s	c-axis centre, $c/2$		$l = 2n + 1$
C			$h + k = 2n$	
	C_A	A-face centre, $(b + c)/2$	$h + k = 2n$	$k + l = 2n + 1$
	C_c	c-axis centre, $c/2$	$h + k = 2n$	$l = 2n + 1$
	C_a	a-axis centre, $a/2$	$h + k = 2n$	$h, k = 2n + 1$
A			$k + l = 2n$	
	A_C	C-face centre, $(a + b)/2$	$k + l = 2n$	$h + k = 2n + 1$
	A_a	a-axis centre, $a/2$	$k + l = 2n$	$h = 2n + 1$
	A_c	c-axis centre, $c/2$	$k + l = 2n$	$l = 2n + 1$
I			$h + k + l = 2n$	
	I_c	c-axis centre, $c/2$	$h + k + l = 2n$	$l = 2n + 1$
F			h, k, l all odd or even	
	F_s	c-axis centre, $c/2$	h, k, l all odd or even	h, k, l all odd

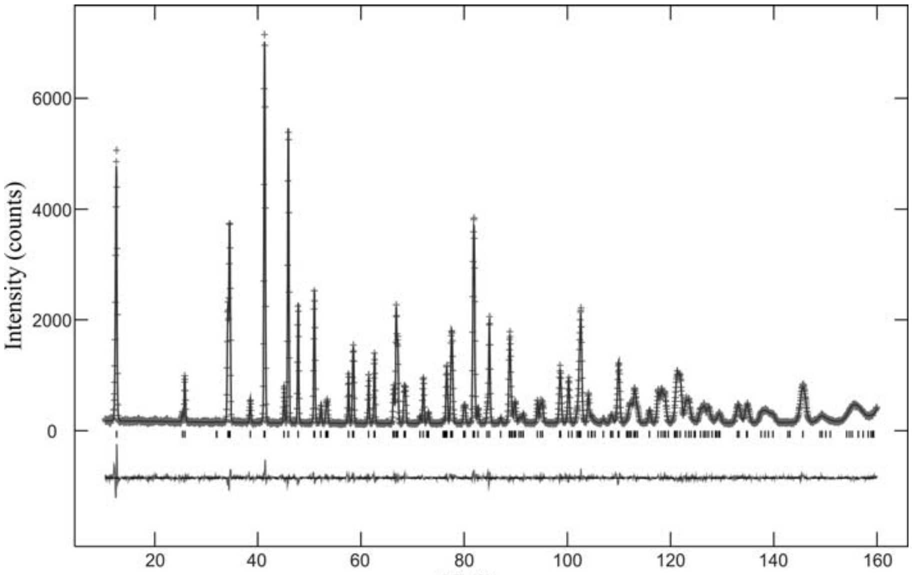

Figure 7.13.19
Observed (crosses) and calculated (solid line) intensities of neutron powder diffraction intensity data for the superconductor NaFeAs at 5 K. Possible Bragg positions are shown by vertical lines and the differences between the observed and calculated intensities are shown at the bottom of the figure.

direction if the symmetry is cubic; and (ii) in tetragonal and rhombohedral or hexagonal symmetries, the powder-diffraction intensities can only provide the angle between the spin direction and the unique c axis of the structure.

A7.13.1.5. An example of Rietveld refinement against NPD data for a superconductor

A plot of NPD intensity data for the superconductor NaFeAs (Li *et al.*, 2009) is given in Fig. 7.13.19. The data were measured on the BT-1 high-resolution powder diffractometer at the NIST Center for Neutron Research. A monochromatic neutron beam was produced using a Cu(311) monochromator (λ = 1.5403 Å) and three collimators with horizontal divergences of 15, 20 and 7′ full width at half-maximum (FWHM) before and after the monochromator, and after the sample. The crystal structure was refined using *GSAS* (Larson & Von Dreele, 2004). The raw data and the data-collection conditions in *GSAS* format are given in the supporting information as files NPD-NCNR_BT1 NaFeAs at 5K.gsas and NCNR-BT1_MonoCu311.inst, respectively. The initial structural model was obtained from the ICSD database (code 165997).

The author is grateful to the referee Dr Georg Roth for his very constructive comments and suggestions for the final version of this chapter. The author also acknowledges Dr J. K. Liang of the Institute of Physics, Chinese Academy of Science, Dr R. J. Cava of Princeton University, and Drs R. Erwen, J. W. Lynn, H. Wu and A. Santoro of the NIST Center for Neutron Research for helpful discussions.

References

Antipov, E. V., Loureiro, S. M., Chaillout, C., Capponi, J. J., Bordet, P., Tholence, J. L., Putilin, S. N. & Marezio, M. (1993). *The synthesis and characterization of the* $HgBa_2Ca_2Cu_3O_{8+\delta}$ *and* $HgBa_2Ca_3Cu_4O_{10+\delta}$ *phases*. *Physica C*, **215**, 1–10.

Axe, J. D., Moudden, A. H., Hohlwein, D., Cox, D. E., Mohanty, K. M., Moodenbaugh, A. R. & Xu, Y. (1989). *Structural phase transformations and superconductivity in* $La_{2-x}Ba_xCuO_4$. *Phys. Rev. Lett.* **62**, 2751–2754.

Bao, W., Huang, Q., Chen, G. F., Wang, D., He, J. & Qiu, Y. (2011). *A novel large moment antiferromagnetic order in* $K_{0.8}Fe_{1.6}Se_2$ *superconductor*. *Chin. Phys. Lett.* **28**, 086104.

Bednorz, J. G. & Muller, K. A. (1986). *Possible high-*T_c *superconductivity in the Ba–La–Cu–O system*. *Z. Phys. B Condens. Matter*, **64**, 189–193.

Belov, N. V., Neronova, K. N. & Smirnova, T. S. (1957). *Shubnikov groups*. *Sov. Phys. Crystallogr.* **2**, 311–322.

Blaschkowski, B. & Meyer, H.-J. (2003). *X-ray single crystal refinement and superconductivity of $La_3Ni_2B_2N_3$*. *Z. Anorg. Allg. Chem.* **629**, 129–132.

Borovik-Romanov, A. S., Grimmer, H. & Kenzelmann, M. (2013). *Magnetic properties*. *International Tables for Crystallography*, Volume D, *Physical Properties of Crystals*, edited by A. Authier, 2nd. ed., ch. 1.5, pp. 106–153.

Brown, I. D. (1976). *Bond valence theory: part I, a new twist to an old description of chemical bonding*. *J. Chem.* **53**, 100–101

Brown, I. D. (2002). *The Chemical Bond in Inorganic Chemistry: The Bond Valence Model*. IUCr Monographs on Crystallography, No. 12. IUCr/Oxford University Press.

Brown, I. D. & Altermatt, D. (1985). *Bond-valence parameters obtained from a systematic analysis of the Inorganic Crystal Structure Database*. *Acta Cryst.* B**41**, 244–247.

Bud'ko, S. L. & Canfield, P. C. (2006). *Magnetism and superconductivity in rare earth–nickel–borocarbides*. *C. R. Phys.* **7**, 56–67.

Buntar, V. & Weber, H. W. (1996). *Magnetic properties of fullerene superconductors*. *Supercond. Sci. Technol.* **9**, 599–615.

Buzea, C. & Yamashita, T. (2001). *Review of the superconducting properties of MgB_2*. *Supercond. Sci. Technol.* **14**, R115–R146.

Cadieu, F. J. & Weaver, J. S. (1973). *Superconductivity of stoichiometric Nb_3Ge*. *Bull. Am. Phys. Soc.* **18**, 704.

Cava, R. J. (2000). *Oxide superconductors*. *J. Am. Ceram. Soc.* **83**, 5–28.

Cava, R. J., Batlogg, B., Chen, C. H., Rietman, E. A., Zahurak, S. M. & Werder, D. (1987). *Oxygen stoichiometry, superconductivity and normal-state properties of $YBa_2Cu_3O_{7-\delta}$*. *Nature*, **329**, 423–425.

Cava, R. J., Batlogg, B., Krajewski, J. J., Farrow, R., Rupp, L. W. Jr, White, A. E., Short, K., Peck, W. F. & Kometani, T. (1988). *Superconductivity near 30 K without copper: the $Ba_{0.6}K_{0.4}BiO_3$ perovskite*. *Nature*, **332**, 814–816.

Cava, R. J., Takagi, H., Batlogg, B., Zandbergen, H. W., Krajewski, J. J., Peck, W. F., van Dover, R. B., Felder, R. J., Siegrist, T., Mizuhashi, K., Lee, J. O., Eisaki, E., Carter, S. A. & Uchida, S. (1994). *Superconductivity at 23 K in yttrium palladium boride carbide*. *Nature*, **367**, 146–148.

Cava, R. J., Takagi, H., Zandbergen, H. W., Krajewski, J., Peck, W. F., Siegrist, T., Batlogg, B., van Dover, R. B., Felder, R. J., Mizuhashi, K., Lee, J. O., Eisaki, H. & Uchida, S. (1994). *Superconductivity in the quaternary intermetallic compounds $LnNi_2B_2C$*. *Nature*, **367**, 252–253.

Chmaissem, O., Huang, Q., Antipov, E. V., Putilin, S. N., Marezio, M., Loureiro, S. M., Capponi, J. J., Tholence, J. L. & Santoro, A. (1993). *Neutron powder diffraction study at room temperature and at 10 K of the crystal structure of the 133 K superconductor $HgBa_2Ca_2Cu_3O_{8+\delta}$*. *Physica C*, **217**, 265–272.

Cox, D. E. (1972). *Neutron diffraction determination of magnetic structures*. *IEEE Trans. Mag.* **MAG-8**, 161–182.

Cox, D. E. & Sleight, A. W. (1976). Crystal structure of $Ba_2Bi^{3+}Bi^{5+}O_6$. *Solid State Commun.* **19**, 969–973. .

Cruz, C. de la, Huang, Q., Lynn, J. W., Li, J. Y., Ratcliff, W., Zarestky, J. L., Mook, H. A., Chen, G. F., Luo, J. L., Wang, N. L. & Dai, P. C. (2008). *Magnetic order close to superconductivity in the iron-based layered $LaO_{1-x}F_xFeAs$ systems*. *Nature*, **453**, 899–902.

Dannay, G., Corliss, L M., Donny, J. D. H., Elliott, N. & Hastings, J. M. (1958). *Symmetry of magnetic structure: magnetic structure of chalcopyrite. Phys. Rev.* **112**, 1917–1923.

Fang, M. H., Wang, H. D., Dong, C. H., Li, Z. J., Feng, C. M., Chen, J. & Yuan, H. Q. (2011). *Fe-based superconductivity with T_c = 31 K bordering an antiferromagnetic insulator in $(Tl,K)Fe_xSe_2$*. *Europhys. Lett.* **94**, 27009.

Gao, L., Huang, Z. J., Meng, R. L., Hor, P. H., Bechtold, J., Sun, Y. Y., Chu, C. W., Sheng, Z. Z. & Hermann, A. M. (1988). *Bulk superconductivity in $Tl_2CaBa_2Cu_2O_{8+\delta}$ up to 120 K*. *Nature*, **332**, 623–624.

Gao, L., Xue, Y. Y., Chen, F., Xiong, Q., Meng, R. L., Ramirez, D., Chu, C. W., Eggert, J. H. & Mao, H. K. (1994). *Superconductivity up to 164 K in $HgBa_2Ca_{m-1}Cu_mO_{2m+2+\delta}$ (m = 1, 2 and 3) under quasihydrostatic pressures*. *Phys. Rev. B*, **50**, 4260–4263.

Glazer, A. M. (1972). *The classification of tilted octahedra in perovskites*. *Acta Cryst.* B**28**, 3384–3392.

Glazer, A. M. (1975). *Simple ways of determining perovskite structures*. *Acta Cryst.* A**31**, 756–762.

Goldschmidt, V. M. (1926). *Die Gesetze der Krystallochemie*. *Naturwissenschaften*, **14**, 477–485.

Gunnarsson, O. (1997). *Superconductivity in fullerides*. *Rev. Mod. Phys.* **69**, 575–606.

Guo, J. G., Jin, S. F., Wang, G., Wang, S. C., Zhu, K. X., Zhou, T. T., He, M. & Chen, X. L. (2010). *Superconductivity in the iron selenide $K_xFe_2Se_2$* $(0 \leq x \leq 1.0)$. *Phys. Rev. B*, **82**, 180520.

Hauck, J. & Mika, K. (1998). *Structure families of superconducting oxides and interstitial alloys*. *Supercond. Sci. Technol.* **11**, 614–630.

Huang, Q., Zhao, J., Lynn, J. W., Chen, G. F., Luo, J. L., Wang, N. L. & Dai, P. C. (2008). *Doping evolution of antiferromagnetic order and structural distortion in $LaFeAsO_{1-x}F_x$*. *Phys. Rev. B*, **78**, 054529.

International Tables for Crystallography (2011). Volume A1, *Symmetry Relations Between Space Groups*, edited by H. Wondratschek & U. Müller, 2nd ed. Chichester: Wiley.

Izumi, F., Matsui, Y., Takagi, H., Uchida, S., Tokura, Y. & Asano, H. (1989). *Neutron and electron diffraction study of the electron-doped superconductor $Nd_{1.845}Ce_{0.155}CuO_{4-y}$*. *Physica C*, **158**, 433–439.

Johnston, D. C. (2010). *The puzzle of high temperature superconductivity in layered iron pnictides and chalcogenides*. *Adv. Phys.* **59**, 803–1061.

Jorgensen, J. D., Beno, M. A., Hinks, D. G., Soderholm, L., Volin, K. J., Hitterman, R. L., Grace, J. D., Schuller, I. K., Segre, C. U., Zhang, K. & Kleefisch, M. S. (1987). *Oxygen ordering and the orthorhombic-to-tetragonal phase transition in $YBa_2Cu_3O_{7-x}$*. *Phys. Rev. B*, **36**, 3608–3616.

Jorgensen, J. D., Veal, B. W., Paulikas, A. P., Nowicki, L. J., Crabtree, G. W., Claus, H. & Kwok, W. K. (1990). *Structural properties of oxygen-deficient $YBa_2Cu_3O_{7-\delta}$*. *Phys. Rev. B*, **41**, 1863–1877.

Kamerlingh Onnes, H. (1911). *Leiden. Commun.* 120b, 122b, 124c.

Kamihara, Y., Hiramatsu, H., Hirano, M., Kawamura, R., Yanagi, H., Kamiya, T. & Hosono, H. (2006). *Iron-based layered superconductor: LaOFeP*. *J. Am. Chem. Soc.* **128**, 10012–10013.

Kamihara, Y., Watanabe, T., Hirano, M. & Hosono, H. (2008). *Iron-based layered superconductor $La[O_{1-x}F_x]FeAs$ (x = 0.05–0.12) with T_c = 26 K*. *J. Am. Chem. Soc.* **130**, 3296–3297.

Kazakov, S. M., Abakumov, A. M., Gonzalez, S., Perez-Mato, J. M., Ovchinnikov, A. V., Roslova, M. V., Boltalin, A. I., Morozov, I. V., Antipov, E. V. & Van Tendeloo, G. (2011). *Uniform patterns of Fe-vacancy ordering in the $K_x(Fe,Co)_{2-y}Se_2$ superconductors*. *Chem. Matter*, **23**, 4311–4316.

Larson, A. C. & Von Dreele, R. B. (2004). *General Structure Analysis System (GSAS)*. Los Alamos National Laboratory Report LAUR 86–748. Los Alamos National Laboratory, USA.

Li, S. L., de la Cruz, C., Huang, Q., Chen, G. F., Xia, T.-L., Luo, J. L., Wang, N. L. & Dai, P. C. (2009). *Structural and magnetic phase transition in $Na_{1-\delta}FeAs$*. *Phys. Rev. B*, **80**, 020504.

Litvin, D. B. (2016). *Magnetic subperiodic groups and magnetic space groups*. *International Tables for Crystallography* Volume A, *Space-group symmetry*, 6th ed., edited by M. I. Aroyo, ch. 3.6. Chichester: Wiley.

Lumsden, M. D. & Christianson, A. D. (2010). *Magnetism in Fe-based superconductors*. *J. Phys. Condens. Matter*, **22**, 203203–203229.

Lynn, J. W. (1990). Editor. *High Temperature Superconductivity*. New York: Springer-Verlag Inc.

Lynn, J. W. & Dai, P. C. (2009). *Neutron studies of the iron-based family of high T_C magnetic superconductors*. *Physica C*, **469**, 469–476.

Lynn, J. W. & Skanthakumar, S. (2001). *Neutron scattering studies of lanthanide magnetic ordering*. *Handbook on the Physics and Chemistry of Rare Earths*, Vol. 31, edited by K. A. Gschneidner Jr, L. Eyring & M. B. Maple, pp. 313–348. Amsterdam: Elsevier Science BV.

Lynn, J. W., Skanthakumar, S., Huang, Q., Sinha, S. K., Hossain, Z., Gupta, L. C., Nagarajan, R. & Godart, R. (1997). *Magnetic order and crystal structure in the superconducting RNi_2B_2C materials*. *Phys. Rev. B*, **55**, 6584–6598.

Marx, D. T., Radaelli, P. G., Jorgensen, J. D., Hitterman, R. L., Hinks, D. G., Pei, S. Y. & Dabrowski, B. (1992). *Metastable behaviour of the superconducting phase in the $BaBi_{1-x}Pb_xO_3$ system*. *Phys. Rev. B*, **46**, 1144–1156.

Müller, K.-H. & Narozhnyi, V. N. (2001). *Interaction of superconductivity and magnetism in borocarbide superconductors*. *Rep. Prog. Phys.* **64**, 943–1008.

Nagamatsu, J., Nakagawa, N., Muranaka, T., Zenitani, Y. & Akimitsu, J. (2001). *Superconductivity at 39 K in magnesium diboride*. *Nature*, **410**, 63–64.

Nagarajan, R. (1997). *Superconductivity and magnetism in quaternary borocarbides*. *J. Low Temp. Phys.* **107**, 517–526.

Niewa, R., Shlyk, L. & Blaschkowski, B. (2011). *Rare-earth metal transition metal borocarbide and nitridoborate superconductors*. *Z. Kristallogr.* **226**, 352–384.

Nomura, T., Kim, S. W., Kamihara, Y. M., Hirano, M., Sushko, P. V., Kato, K., Takata, M., Shluger, A. L. & Hosono, H. (2008). *Crystallographic phase transition and high-T_c superconductivity in LaFeAsO:F*. *Supercond. Sci. Technol.* **21**, 125028.

Ozerov, R. P. (1967). *Systematic extinctions of reflections in coherent magnetic scattering of slow neutrons due to presence of symmetry and antisymmetry elements in collinear magnetic materials*. *Sov. Phys. Crystallogr.* **12**, 199–208.

Park, C. & Snyder, R. L. (1995). *Structures of high-temperature cuprate superconductors*. *J. Am. Ceram. Soc.* **78**, 3171–3194.

Parkin, S. S. P., Lee, V. Y., Nazzal, A. I., Savoy, R., Beyers, R. & La Placa, S. J. (1988). *$Tl_1Ca_{n-1}Ba_2Cu_nO_{2n+3}$ (n = 1, 2, 3): a new class of crystal structures exhibiting volume superconductivity at up to $\simeq$110 K*. *Phys. Rev. Lett.* **61**, 750–753.

Poole, C. P. Jr, Datta, T. & Farach, H. (1988). Editors. *Copper Oxide Superconductors*. New York: John Wiley & Sons, Inc.

Putilin, S. N., Antipov, E. V., Chmaissem, O. & Marezio, M. (1993). *Superconductivity at 94 K in $HgBa_2CuO_{4+\delta}$*. *Nature*, **362**, 226–228.

Raveau, B., Michel, C., Hervieu, M. & Groult, D. (2013). *Crystal Chemistry of High-T_c Superconducting Copper Oxides*, Vol. 15. Springer Science & Business Media.

Ren, Z. A., Che, G. C., Dong, X. L., Yang, J., Lu, W., Yi, W., Shen, X. L., Li, Z. C., Sun, L. L., Zhou, F. & Zhao, Z. X. (2008). *Superconductivity and phase diagram in iron-based arsenic-oxides $ReFeAsO_{1-\delta}$ (Re = rare-earth metal) without fluorine doping*. *Europhys. Lett.* **83**, 17002.

Ren, Z. A., Yang, J., Lu, W., Yi, W., Shen, X. L., Li, Z. C., Che, G. C., Dong, X. L., Sun, L. L., Zhou, F. & Zhao, Z. X. (2008). *Superconductivity in the iron-based F-doped layered quaternary compound $Nd[O_{1-x}F_x]FeAs$*. *Europhys. Lett.* **82**, 57002.

Ren, Z. A. & Zhao, Z. X. (2009). *Research and prospects of iron-based superconductors*. *Adv. Mater.* **21**, 4584–4592.

Rietveld, H. M. (1969). *A profile refinement method for nuclear and magnetic structures*. *J. Appl. Cryst.* **2**, 65–71.

Rotter, M., Tegel, M. & Johrendt, D. (2008). *Superconductivity at 38 K in the iron arsenide $Ba_{1-x}K_xFe_2As_2$*. *Phys. Rev. Lett.* **101**, 107006.

Sarrao, J. L., Morales, L. A., Thompson, J. D., Scott, B. L., Stewart, G. R., Wastin, F., Rebizant, J., Boulet, P., Colineau, E. & Lander, G. H. (2002). *Plutonium-based superconductivity with a transition temperature above 18 K*. *Nature*, **420**, 297–299.

Schaak, R. E., Klimczuk, T., Foo, M. L. & Cava, R. J. (2003). *Superconductivity phase diagram of $Na_xCoO_2{\cdot}1.3H_2O$*. *Nature*, **424**, 527–529.

Shannon, R. D. (1976). *Revised effective ionic radii and systematic studies of interatomic distances in halides and chalcogenides*. *Acta Cryst.* A**32**, 751–767.

Shirane, G. (1959). *A note on the magnetic intensities of powder neutron diffraction*. *Acta Cryst.* **12**, 282–285.

Shubnikov, A. V. (1951). *Symmetry and antisymmetry of finite figures*. *Izd. Acad. Sci. USSR (Moscow)*, pp. 3–172, 249–252.

Sleight, A. W. (1988). *Chemistry of high-temperature superconductors*. *Science*, **242**, 1519–1527.

Sleight, A. W., Gillson, J. L. & Bierstedt, P. E. (1975). *High-temperature superconductivity in the $BaPb_{1-x}Bi_xO_3$ systems*. *Solid State Commun.* **17**, 27–28.

Steglich, F., Aarts, J., Bredl, C. D., Lieke, W., Meschede, D., Franz, W. & Schäfer, H. (1979). *Superconductivity in the presence of strong Pauli paramagnetism: $CeCu_2Si_2$*. *Phys. Rev. Lett.* **43**, 1892–1896.

Stephens, P. W., Mihaly, L., Lee, P. L., Whetten, R. L., Huang, S. M., Kaner, R., Deiderich, F. & Holczer, K. (1991). *Structure of single-phase superconducting K_3C_{60}*. *Nature*, **351**, 632–634.

Takagi, H., Uchida, S., Kitazawa, K. & Tanaka, S. (1987). *High-T_c superconductivity of La–Ba–Cu oxide. II. Specification of the superconducting phase*. *Jpn. J. Appl. Phys.* **26**, L123–L124.

Tokura, Y. & Arima, T. (1990). *New classification method for layered copper oxide compounds and its application to design of new high T_c superconductors*. *Jpn. J. Appl. Phys.* **29**, 2388–2402.

Von Dreele, R. B. & Cheetham, A. K. (1974). *The structures of some titanium–niobium oxides by powder neutron diffraction*. *Proc. R. Soc. London A Math. Phys. Sci.* **338**, 311–326.

Waller, I. (1923). *On the question of the influence of thermal motion on the interference of X-rays*. *Z. Phys.* **17**, 398–408.

Waller, I. (1926). *The theory of X-ray reflection*. *Ann. Phys.* **384**, 261–272.

Waller, I. (1927). *The effect of the thermal motion of crystal atoms on intensity, position and sharpness of Roentgen spectral lines*. *Ann. Phys.* **388**, 153–183.

Waller, I. (1928). *About the generalized dispersion formula*. *Z. Phys.* **51**, 213–231.

Wu, M. K., Ashburn, J. R., Torng, C. J., Hor, P. H., Meng, R. L., Gao, L., Huang, Z. J., Wang, Y. Q. & Chu, C. W. (1987). *Superconductivity at 93 K in a new mixed-phase Yb–Ba–Cu–O compound system at ambient pressure*. *Phys. Rev. Lett.* **58**, 908–910.

Young, A. (1993). Editor. *The Rietveld Method*. IUCr Monographs on Crystallography, No. 5. New York: Oxford University Press Inc.

Zamorzaev, A. M. (1957*a*). *Generalization of Fedorov groups*. *Kristallografiya*, **2**, 15–20.

Zamorzaev, A. M. (1957*b*). *Generalization of Fedorov groups*. *Sov. Phys. Crystallogr.* **2**, 10–15.

Zandbergen, H. W., Jansen, J., Cava, R. J., Krajewski, J. J. & Peck, W. F. Jr (1994). *Structure of the 13 K superconductor $La_3Ni_2B_2N_3$ and the related phase LaNiBN*. *Nature*, **372**, 759–761.

Zhao, J., Huang, Q., de la Cruz, C., Li, S., Lynn, J. W., Chen, Y., Green, M. A., Chen, G. F., Li, G., Li, Z., Luo, J. L., Wang, N. L. & Dai, P. C. (2008). *Structural and magnetic phase diagram of $CeFeAsO_{1-x}F_x$ and its relation to high-temperature superconductivity*. *Nat. Mater.* **7**, 953–959.

International Tables for Crystallography (2019). Vol. H, Chapter 7.14, pp. 885–892.

7.14. Powder diffraction by minerals

R. Arletti, G. Cruciani and G. Ferraris

Unravelling the complexity and diversity of mineral structures is one of the most important topics in modern mineralogy. Knowledge of mineral composition, crystal structure, properties and occurrence is a source of inspiration and novel ideas not only for the Earth and planetary sciences, but also for materials science and modern technologies. These data have established a framework for developing the innovative concept of 'mineral evolution' (Hazen & Ferry, 2010), which focuses on changes in the composition, association, diversity and structural complexity of near-surface minerals through time on the Earth. An important advantage of the powder method over single-crystal methods is that the results might be more representative of the sample that is being investigated. In a single-crystal diffraction experiment, it is possible to obtain detailed information only on individual crystals, with all their individual particularities, which might differ substantially from one crystal to another. Instead, powder methods average over millions of crystallites and are thus more representative, for example, for a mineral species. In another very important respect, powder-diffraction methods allow the quantitative study of mineral mixtures, which is of primary importance for determining mineral paragenesis and investigating mixed crystals.

An understanding of mineral transformation processes (and of material transformations in general) is extremely important in several areas of earth and materials sciences.

Fig. 7.14.1 clearly indicates the strong increase in the number of scientific publications related to the study of minerals with X-ray powder diffraction in the last decade. The technical proficiencies of XRPD laboratories have developed strongly in the last few years, especially in relation to *in situ* powder-diffraction studies.

In situ investigations enable observation of the evolution of a material subjected to external perturbation (*e.g.* high temperature, high pressure, magnetic/electric fields *etc.*), as well as monitoring material processing (*i.e.*, crystallization, dehydration, catalytic reactions, Portland cement production and hydration, *etc.*). In order to fully capture the process dynamics, the measuring time needs to be shorter than the timescale of the process itself, allowing the collection of multiple snapshots at different stages. Thanks to the development of fast detectors, experiments at non-ambient conditions [*i.e.*, high temperature (HT) and high pressure (HP)] can be carried out in dynamic mode, enabling the recording of the sample evolution in time- or temperature-resolved conditions with a time resolution from minutes down to seconds. In recent decades, *in situ* powder-diffraction techniques based on synchrotron (or neutron) radiation have been successfully applied to study the process dynamics of transformations in minerals and their synthetic counterparts. The main advantages of time-resolved experiments are the possibility of gaining insights into transient and intermediate states of processes and to record non-quenchable structural modifications at conditions 'far from the equilibrium'.

In this chapter, we demonstrate how XRPD, alone or in conjunction with other methods, is a suitable technique for the structural characterization of minerals and their synthetic counterparts. Examples are presented in which powder diffraction is the main technique, together with case studies in which it is used in combination with other techniques. Many of the case studies involve rock-forming and hydrated minerals. Special emphasis is given to zeolites because these minerals – apart from being particularly complex and challenging in their structures – are also involved in many intriguing phenomena, as detailed later.

7.14.1. Powder diffraction and characterization of new mineral species

Searching for and characterizing new mineral species is a very active field in the mineralogical sciences, particularly in the sector of mineralogical crystallography and crystal chemistry. Sometimes even rare non-rock-forming minerals may be the basis for discovering and understanding unsuspected geological phenomena. A good example is the importance of the high-pressure silica phase coesite (Chopin, 1984) for the development of high-pressure metamorphic petrology. At the same time, the discovery of novel structural types that often occur in new minerals may offer inspiration for materials science (*e.g.* Ferraris & Merlino, 2005). The official list of mineral species approved by the Commission on New Minerals, Nomenclature and Classification (CNMNC) of the International Mineralogical Association (IMA) (http://nrmima.nrm.se/) includes some 5000 items. Apart from a very few cases (*e.g.* allophane, mercury, opal), minerals are crystalline materials and the procedures for submitting a proposal for the approval of a new mineral species (Nickel & Grice, 1998) require that the submitted data include a powder-

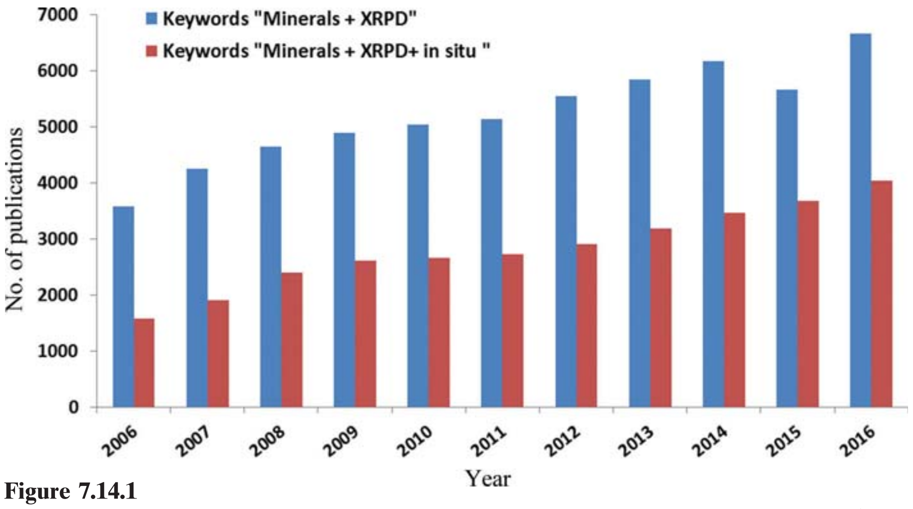

Figure 7.14.1
Number of publications related to studies carried out on minerals using XRPD per year (from Google Scholar).

Copyright © 2019 International Union of Crystallography

diffraction pattern suitable for later identification of the crystalline materials by searching specialized databases [*e.g.* the Powder Diffraction File (PDF), from the International Centre for Diffraction Data (ICDD), http://www.icdd.com/products/pdf4-minerals.htm, and RRUFF, http://rruff.info/].

In recent years, the IMA list of minerals has increased at a rate of about 100 new species per year, mainly because modern experimental methods (*e.g.* single-crystal diffraction using focusing X-ray optics or synchrotron radiation; electron diffraction tomography techniques; electron microprobe chemical analysis; electron backscatter diffraction) allow characterization of new mineral species from submicrometre-sized coherent domains of a single or mosaic crystal. In extreme cases, powder-diffraction data can also be acquired and recovered through: (i) the Gandolfi method, using either a specialist camera or a single-crystal diffractometer *via* a simulation routine; (ii) collapsing a three-dimensional (3D) single-crystal diffraction pattern to 1D; or (iii) calculating a powder-diffraction pattern from a crystal structure.

The lack of availability of large single crystals makes the use of powder-diffraction data for crystallographic characterization of new and rare minerals unavoidable, but it is also the best method for characterizing real minerals, as exemplified in the following case studies.

Anthoinite, $AlWO_3(OH)_3$, is available only as microcrystalline masses, and its layered triclinic structure was solved by applying *ab initio* methods to both X-ray and neutron powder-diffraction data, and then refined using the Rietveld method (Grey *et al.*, 2010).

The close similarities, both in chemical formulae and powder-diffraction patterns between the known pokrovskite, $Mg_2(CO_3)(OH)_2$, and the new mineral chukanovite, $Fe_2(CO_3)(OH)_2$, suggested a reliable starting model for the latter phase, which was successfully refined by the Rietveld method using synchrotron X-ray diffraction data (Pekov, Perchiazzi *et al.*, 2007).

Because of a complex pseudocubic twinning, the orthorhombic structure of lakargiite, $CaZrO_3$, could only be unravelled by combining single-crystal (cell parameters) and X-ray powder-diffraction data (solution and refinement) (Galuskin *et al.*, 2008).

The molybdoarsenates betpakdalite, natrobetpakdalite and obradovicite, as well as the molybdophosphates mendozavilite, paramendozavilite and melkovite, typically occur as coatings of minute, poor-quality and/or complexly twinned crystals. Comparative X-ray powder diffraction proved effective in identifying structurally related phases and obtaining refined cell parameters for those phases for which single-crystal studies could not be conducted (Kampf *et al.*, 2012).

Only curved and split crystals are known for gjerdingenite-Na, $(K,Na)_2Na(Nb,Ti)_4(Si_4O_{12})_2(OH,O)_4\cdot 5H_2O$, and gjerdingenite-Ca, $K_2Ca(Nb,Ti)_4(Si_4O_{12})_2(O,OH)_4\cdot 6H_2O$, two new mineral species of the labuntsovite group. Thus, their crystal structures were refined from X-ray powder-diffraction data starting from the coordinates of other members of the group (Pekov, Chukanov *et al.*, 2007).

Owing to the lack of suitable single crystals, the crystal structure of the new mineral jadarite, $LiNaSiB_3O_7(OH)$, was solved from laboratory powder-diffraction data and even the H atoms were located by applying *ab initio* optimization (Whitfield *et al.*, 2007).

Using synchrotron X-ray microdiffraction, diffraction patterns combining powder and single-crystal features can be obtained. Chladniite is a complex phosphate species belonging to the fillowite group first found in meteorites and recently also identified in a pegmatite from Córdoba (Argentina). Using the latter material and applying a synchrotron through-the-substrate microdiffraction technique to polished thin sections prepared on very thin glass substrates (0.1 mm), diffraction data were obtained with nearly single-crystal quality, allowing the crystal structure of chladniite to be solved (Vallcorba *et al.*, 2017).

Reflection overlap and peak-profile broadening in XRPD patterns can increase uncertainty in intensity determination and thus hinder structural studies, especially in relation to nanophases. In the field of structure determination, electron diffraction (ED) has recently been proved to be a perfect complementary tool to XRPD. While the potential use of ED for structure solution has been known for a long time (*e.g.* Rigamonti, 1936), its routine applicability has been severely hampered by the presence of marked dynamic effects and the high electron dose usually required to illuminate the sample, leading to rapid modification of the crystalline structure or complete amorphization. Nevertheless, high-resolution transmission electron microscopy (HRTEM) could access direct-space structural information down to a resolution of 0.8–0.5 Å from crystal nanodomains (Kisielowski *et al.*, 2008; Haider *et al.*, 1998). A breakthrough came with the use of precession electron diffraction (PED) to reduce the dynamic effects (Vincent & Midgley, 1994), paving the way for an increasing number of structure solutions obtained from PED data (*e.g.* Gemmi *et al.*, 2010; Palatinus *et al.*, 2013). A further step ahead was the recent development of automated diffraction tomography (ADT), allowing an automated procedure for 3D electron-diffraction data acquisition and processing (Kolb *et al.*, 2007, 2008). Electron-diffraction intensity data sets collected with ADT include large numbers of high-index reflections, which is highly advantageous for achieving a starting crystal-structure model (Mugnaioli *et al.*, 2009) that can be then used as input to refinements using XRPD data.

7.14.2. Mineral physics through *in situ* powder-diffraction experiments

7.14.2.1. *Thermoelastic behaviour of minerals*

A description of rock-forming minerals at the atomic scale is fundamental for the understanding the Earth's mineralogical composition and rheological properties. Another crucial issue for the progress of the Earth sciences is determining the stability of mineral phases under non-ambient conditions, *i.e.* understanding the structural modifications occurring in minerals subjected to pressures and temperatures comparable to the interior of the Earth. Transformations in Earth materials induced by pressure, as well as the combined effects of pressure and temperature, are the key to interpreting phenomena such as seismic discontinuities or the existence of elastic anisotropies in the deep Earth. Defining the full framework of dynamic processes therefore requires detailed studies of the structure, bonding and electronic properties of component minerals, and establishing the effects of extreme conditions on their physical and chemical properties. These aims are now achievable owing to the development of diamond anvil cell (DAC) techniques and *in situ* methods using synchrotron radiation. Recent structural studies indicate that the properties of many materials are strongly altered under deep Earth conditions, giving rise to transformations that cannot be ascertained from studies of the same materials at near-ambient conditions (Hemley *et al.*, 2000). These modifications include crystal-structure transformations (*i.e.*, reconstructive, displacive, order–disorder *etc.*), electronic changes (including spin-crossover, band structure, bonding and insulator–metal transitions) and magnetic transitions. The first experimental studies on minerals and rocks under HT and HP date back to the end of the eighteenth century in a series of melting and crystallization experiments. In the following centuries, a lot of progress was achieved and the impact on the earth sciences was enormous.

The lower mantle is the largest single region in the Earth's interior, and the definition of a thermoelastic model for deep-mantle minerals is of great interest (*e.g.* Chinnery *et al.*, 2000; Fiquet *et al.*, 2002; Andrault *et al.*, 2003; Merkel *et al.*, 2007; Kubo *et al.*, 2008). By the first half of the twentieth century, the presence of the main seismic discontinuity was established and linked to the phase transitions olivine–spinel and spinel–perovskite (Pv). For a long time, the $MgSiO_3$ perovskite was believed to be stable throughout the entire mantle, but, synchrotron powder-diffraction experiments (Murakami *et al.*, 2004; Iitaka *et al.*, 2004) indicated a phase transition at 125 GPa and 2500 K, corresponding to the D′′ seismic discontinuity, later established to be post-perovskite (pPv). The crystallographic models derived from the experiments showed that the pPv phase arises from the tilting of octahedral chains in the Pv structure. The pPv phase exhibits large structure anisotropy compared with the Pv phase. The transition is unquenchable to ambient conditions. The evolution of octahedral tilting upon compression is also a widely investigated topic in synthetic perovskites because of their interesting multiferroic (ferroelectric and ferromagnetic) properties. The contrasting HP behaviour of $A^{3+}B^{3+}O_3$ *versus* $A^{2+}B^{4+}O_3$ perovskites has attracted particular interest (*e.g.* Ardit *et al.*, 2010). Octahedral tilting is expected to increase in $A^{3+}B^{3+}O_3$ and decrease in $A^{2+}B^{4+}O_3$, thus leading to low- and high-symmetry phase transitions, respectively. Understanding the rheological properties of mantle minerals is necessary to follow the mechanism of solid-state convection in the Earth. The development of HP apparatus is required for quantitative studies of pressure strength and mantle rheology under challenging *in situ* conditions (Duffy, 2005). Advanced methods for measuring and interpreting lattice-strain anisotropy using XRPD have led to significant advances in the characterization of elastic anisotropy and texture development in materials of geological interest (Merkel, 2006; Singh, 2014).

Apart from the great interest in modelling the seismic behaviour of the Earth's lower mantle, an understanding of processes involving the crust and upper mantle is of fundamental importance. The extrapolation of equilibrium curves to the P–T conditions of the lower crust and upper mantle is an intriguing challenge, since these curves are sometimes quite inconsistent as regards the $\mathrm{d}P/\mathrm{d}T$ slope and absolute position, especially for reactions containing hydrous phases. For this reason, it is very important to collect thermophysical data [*i.e.*, data on the bulk modulus, $K_T = -V(\partial P/\partial V)_T$, and thermal expansivity, $\alpha = (1/V)(\delta V/\delta T)_P$] for high-pressure hydrous phases, which are stable in the lower crust and mantle regions, and calculate their equations of state (Grevel *et al.*, 2000; Welch & Marshall, 2001; Walter *et al.*, 2015).

7.14.2.2. *Negative thermal expansion in minerals*

The vast majority of solids expand when heated, a property that can create problems in some HT processes. However, certain materials exhibit negative thermal expansion (NTE) with volume contraction on heating, a phenomenon occurring, for example, in some metal oxides and zeolites (*e.g.* Marinkovic *et al.*, 2009; Leardini *et al.*, 2015). Detailed studies of these cases enable the development of new materials with coefficients of thermal expansion (CTE) equal to zero. NTE generally derives from cooperative or supramolecular structural mechanisms that prevail over the positive thermal expansion of interatomic bonds. These mechanisms include (i) transverse bond vibrations and libration; (ii) rigid unit modes (RUMs); (iii) phase transitions; (iv) cracking (Miller *et al.*, 2009); and (v) elastic recovery of transient deformations (Cruciani & Gualtieri, 1999). Understanding the mechanisms behind NTE behaviour is crucial for tailoring natural and synthetic materials to exhibit specific expansion properties. For instance, the creation (engineering) of overall zero thermal expansion (ZTE) materials can be achieved by using NTE parts as thermal-expansion compensators.

In situ XRPD coupled with Rietveld structural analysis is a powerful tool for quantifying and explaining the thermal expansion of materials. In the widely investigated field of porous materials, knowing the thermal-expansion coefficients of a particular zeolite is of paramount importance in many applications, including the prediction of possible mechanical issues in supported polycrystalline zeolitic membranes. Understanding the mechanisms governing heat-induced structural deformations is particularly crucial in, for example, aerospace technologies, microchips and optical devices.

Among the porous materials studied under HT, the pure silica zeolites and molecular sieves ITQ-1, ITQ-3, SSZ-23, ITQ-4, faujasite and ZSM-5 exhibit marked NTE (*e.g.* Woodcock *et al.*, 1999). Since NTE depends on lattice-dynamic effects, in zeolites it can be modified by the isomorphous substitution of heteroatoms in the framework. The dependence of NTE, and of thermal-expansion behaviour in general, on heteroatom substitution has been explored for zeolites sharing an MFI-type framework by *in situ* XRPD. It was demonstrated that the substitution of Si with metals enhances thermal contraction. HT-XRPD studies carried out on the metallosilicate molecular sieves Fe-silicalite-1 with different Si/Fe ratios (Si = 50, 75 and 100%) found that all the samples exhibited NTE in the temperature range 373–773 K with increasing strength as the Fe content rises (Bhange & Ramaswamy, 2010). The kind of heteroatom also affects the extent and strength of NTE in MFI topology (Bhange & Ramaswamy, 2007).

The NTE phenomenon has also been investigated for other minerals. For instance, cuprite (Cu_2O), besides being a mineral with a very small thermal-expansion coefficient, exhibits NTE in the temperature range 9–200 K, and then positive expansion up to the decomposition temperature (630 K). Synchrotron powder diffraction coupled with EXAFS showed that NTE effects observed in cuprite-type compounds depend on the transverse motion of the metal atoms perpendicular to the O–M–O linear bonds (Artioli *et al.*, 2006).

7.14.2.3. *Dehydration of nonporous minerals*

'Water' (more correctly, H_2O or OH^- or H^+) in minerals plays a crucial role in sustaining the geological activity of our planet by affecting melting relationships and influencing its rheology. Hence, considerable research has been carried out on the HT behaviour of hydrous mineral phases in order to understand the transport of H_2O into the Earth's interior (Nishi *et al.*, 2014; Shieh *et al.*, 2000). The water released by dehydration of a subducting oceanic slab strongly influences magmatic processes and plays an important role in seismic activity. For example, dehydration of serpentine minerals, formed from the alteration of ultramafic rocks (*i.e.*, igneous rocks with a very low silica content) and representing a major hydrous phase in the subducting oceanic plates, has attracted a lot of interest. The large amount of 'water' present in these phases (a serpentinized peridotite contains ~10% H_2O) is released in subduction zones when they break down into less-hydrated phases, thus leading to metasomatism in the overlying mantle (*e.g.* Scambelluri *et al.*, 2001, and references therein) and promoting partial melting in the mantle wedge, giving rise to arc magmatism (Ulmer & Trommsdorff, 1995). It has also been suggested that these reactions cause the seismicity observed in the subducting oceanic mantle, since dehydration may produce high pore pressures and embrittlement in lithospheric rocks (Dobson *et al.*, 2002). The stability field and dehydration rates of antigorite have been extensively studied both at ambient pressure (*e.g.* Cattaneo *et al.*, 2003) and high pressure (Perrillat *et al.*, 2005; Chollet *et al.*, 2011) to predict the depth at which fluid is released into subduction zones, indicating that serpentine dehydration is a possible explanation for intermediate-depth earthquakes.

7.14.2.4. *Dehydration and adsorption/desorption mechanisms in porous materials*

Zeolite dehydration mechanisms have been widely studied because the sorptive and catalytic properties exploited in industrial processes are typically activated by heating and are profoundly influenced by their structural behaviour at high temperature. A knowledge of the structural modifications induced by temperature and the definition of the stability field of these materials is of prime importance to assure their persistence and effectiveness in technological applications.

The development of *in situ* time- and temperature-resolved XRPD techniques, typically using synchrotron radiation, allows the process dynamics to be tracked for a continuous picture of the structural response of zeolites to dehydration. For instance, catching the short-lived 'pore-mouth breathing' motions provides information about the interplay between hydrogen bonding, thermal expansion and volume contraction in a framework structure. Monitoring $T{-}O{-}T$ angles during dehydration can provide information about the preferential diffusion path for H_2O molecules released through the channel system (Cruciani, 2006).

The thermal behaviour of natural and synthetic zeolites has been reviewed by several authors (Bish & Carey, 2001; Cruciani, 2006; Depmeier, 2009). In summary, upon heating, zeolites may undergo the following structural changes: (i) cell-volume contraction due to the removal of H_2O and/or templating organic molecules (dehydration and calcination); (ii) displacive or reconstructive phase transformation(s); (iii) breaking (and new formation) of $T{-}O{-}T$ bonds; (iv) NTE; (v) partial structural collapse with retention of some sorption properties; and (vi) structural breakdown. Among the principal factors, these effects are controlled by: (*a*) the Si/Al ratio, (*b*) the framework topology, and (*c*) the nature, number and coordination of extra-framework cations.

In addition to dehydration/rehydration dynamics, other processes such as adsorption/desorption of organic molecules by porous materials have been investigated in depth from a structural point of view through powder diffraction in recent years. Understanding the science behind adsorption processes and the interaction between adsorbent and adsorbate helps, for example, when designing sustainable water-remediation systems that exploit the capability of zeolites as adsorbing materials. An excellent example is represented by the structural studies performed by Martucci and co-workers (*e.g.* Martucci *et al.*, 2014) on high-silica zeolites used for the removal of organic pollutants (antibiotics and hydrocarbons) from waste water. It has been found that the adsorption of given organic molecules from aqueous solutions depends not only on the dimensions of the pore systems, but also on competition between the adsorbate and water, linked to the hydrophobicity of the zeolite in question.

7.14.2.5. *High-pressure (HP)-induced reaction/penetration in porous materials*

Recently it has been demonstrated through *in situ* X-ray/neutron powder-diffraction experiments that, in addition to HT, HP can also induce important structural changes in porous materials, modifying the accessibility of catalytic sites, and physical and chemical properties, and consequently feasible applications (Arletti *et al.*, 2003; Vezzalini *et al.*, 2014). In the experimental HP studies on zeolites, either 'pore penetrating' or 'non-penetrating' pressure-transmitting media (PTM) were used. The studies performed with 'non-penetrating' media highlighted that the HP-induced deformation mechanisms are controlled by tetrahedral tilting, which is strongly influenced by the framework type and composition, as well as by the extra-framework content.

The use of 'penetrating' media has been exploited in different pressure regimes to test a variety of effects of different media on microporous frameworks. It is known that compressing a zeolite with an aqueous solution can induce the pressure-induced hydration (PIH) effect (Lee *et al.*, 2002), which involves the penetration of additional H_2O molecules into the zeolite channels in response to the applied pressure. This phenomenon can be accompanied by abrupt volume expansion (*e.g.* Lee *et al.*, 2002) or, on the contrary, exhibit no cell volume expansion (*e.g.* Likhacheva *et al.*, 2006).

Not only H_2O penetration into zeolite cavities has attracted interest in recent years, but also the hyper-confinement of other guest molecules. It has been demonstrated that the confinement of organic molecules (*e.g.* ethylene, acetylene) inside zeolite channels can induce polymerization reactions, without the use of catalysts or activators (Santoro *et al.*, 2013).

The compression of zeolites in the absence of a medium or in the presence of a non-penetrating PTM is also used to induce pressure-induced amorphization (PIA). PIA is observed for a wide range of silicate structures and is characterized by important volume reductions, producing a new material denser than the corresponding crystalline and glass phases. Greaves *et al.* (2003) explored the time dependence and dynamics of zeolite amorphization generated by compression and found evidence for polyamorphism. This is the coexistence of different amorphous phases of the same composition but with different densities.

7.14.2.6. *Phase transitions and spontaneous strain in minerals*

Structural phase transitions are almost invariably accompanied by lattice strain arising from lattice distortions or relaxations on a macroscopic scale. Lattice distortions can represent the predominant driving force for a transition, as in ferroelastic transitions, or they can be a secondary response to some other driving mechanism. The excess energy deriving from a phase transition contains a component from elastic energy. The additional lattice strain (compared with the normal response of a crystal to changing temperature or pressure) associated with a phase transition is usually referred to as a spontaneous strain. Very accurate lattice distortion and strain measurements can be achieved using high-resolution powder diffraction, and provide valuable and detailed insights into the nature and mechanisms of a given phase transition. A quantitative thermodynamic analysis of spontaneous strain in ferroelastic minerals can be conveniently carried out within the theoretical framework of the Landau theory (Carpenter *et al.*, 1998).

Besides the early studies in minerals as reviewed by Carpenter *et al.* (1998), among the more recent examples of spontaneous-strain analysis combining high-resolution synchrotron and neutron powder diffraction with Landau theory is the work on (Ca,Sr)TiO_3 perovskite solid solutions, which exhibited a change in character from tricritical towards second order of the cubic–tetragonal phase transition (Carpenter *et al.*, 2006). Landau analysis applied to the pressure-induced phase transition from the rutile to the $CaCl_2$-structured polymorph of stishovite showed that the strain energy increased progressively as a function of pressure above the transition pressure, a trend compatible with a second-order transition and a dominant symmetry-breaking strain component (Andrault *et al.*, 2003).

As well as changes at the crystal-structure scale, phase transitions modify the microstructure of materials (*e.g.* twin domains), leading to anomalous mesoscopic features at domain boundaries. One important consequence of twin mesostructures is their modified transport properties relative to the bulk. Landau theory also provides a tool for the analysis of microstructures and mesostructures in ferroelastics (Salje *et al.*, 2005). An example that illustrates the relevance of lattice strain to mass transport properties is the transition from the ferroelastic (monoclinic) to the paraelastic (orthorhombic) phase in the ZSM-5 zeolite (a synthetic analogue of the mineral mutinaite), which is a widely employed material in catalysis and water-treatment processes. The spontaneous-strain analysis *via* Landau theory of high-resolution synchrotron powder-diffraction data collected *in situ* upon heating allowed assessment of the tricritical character of the phase transition. This might favour the formation and persistence of ferroelastic domains on a local scale even in the paraelastic phase, thus explaining the unusual and unexpected deformation field distribution observed in monoclinic ZSM-5 crystals (Ardit *et al.*, 2015).

7.14.2.7. *HT studies related to CO_2 sequestration*

The growing concerns over increasing greenhouse-gas emissions and the need to reduce atmospheric carbon dioxide (CO_2) concentrations explains the growing number of studies devoted to the development of technologies for CO_2 sequestration into mineral form. The synthesis of minerals *via* the reaction of CO_2 with Mg–Ca silicate rocks, or of hydrated Mg carbonates in aqueous solutions, offers attractive solutions for permanent safe storage of CO_2. Consequently, interest in assessing the thermal stability of the best-suited mineral phases has induced a large number of *in situ* HT-XRPD studies. Carbonates are clearly the most studied candidates (*e.g.* Ballirano *et al.*, 2010; Morgan *et al.*, 2015; Merlini *et al.*, 2016). Based on HT studies it has been demonstrated that some carbonates (*e.g.* nesquehonite, $MgCO_3{\cdot}3H_2O$) remain stable under the prevalent temperature conditions on the Earth's surface, even if their stability is also influenced by factors like pH_2O and pCO_2. Understanding the factors that influence the stability of these phases opens a path for developing methods for CO_2 sequestration *via* the synthesis of carbonates for industrial applications.

7.14.3. Minerals related to human health, the biosphere and planetary exploration

7.14.3.1. *Fibrous minerals*

There has been a large and growing interest in recent years in the identification and distribution of minerals characterized by a fibrous habit.

Fibrous minerals are aggregates of slender fibres, parallel, interlaced or radiating, with the fibres usually separable. The term 'asbestiform' refers to a special type of fibrous habit in which a mineral has longitudinal parting and can be split into individual fibres and fibrils of high tensile strength, flexibility and minor thickness. The term 'asbestos' also indicates a number of natural silicates characterized by high surface reactivity and strong biopersistence. Asbestos comprises amphiboles [riebeckite, $Na_2Fe_2^{3+}(Fe^{2+},Mg)_3Si_8O_{22}(OH)_2$, grunerite, $Fe_2Fe_5Si_8O_{22}(OH)_2$, antophyllite, $Mg_2Mg_5[Si_8O_{22}](OH)_2$, tremolite, $Ca_2Mg_5Si_8O_{22}(OH)_2$, and actinolite, $Ca_2(Mg,Fe)_5Si_8O_{22}(OH)_2$] and phyllosilicates [chrysotile–serpentine $Mg_6Si_4O_{10}(OH)_8$]. The fibre characteristics, in particular the habit, of these minerals are very different (see Fig. 7.14.2). According to the mineralogical community, 'fibre' is a textural term indicating that the material looks like and, more importantly, behaves as a fibre, so that it can curve and bend under force (Rossi *et al.*, 2016, and references therein).

Although there is enough scientific evidence that asbestos when inhaled may induce malignant lung diseases (Guthrie & Mossman, 1993; Mossman *et al.*, 1990; Bignon *et al.*, 1996; Martuzzi *et al.*, 1998; Oury *et al.*, 2014; Mastrantonio *et al.*, 2002; Kamp, 2009), there is still controversy in ranking the carcinogenicity of chrysotile asbestos with respect to amphibole asbestos (Bernstein *et al.*, 2013). As a matter of fact, all amphibole asbestos minerals are banned worldwide, whereas chrysotile is banned only in those countries where the ruling of the International Agency for Research on Cancer (IARC) is accepted (Collegium Ramazzini, 2010; Gualtieri *et al.*, 2017).

Owing to the hazardous nature of asbestos, exposure to it represents a serious health risk. Therefore, the identification and quantification of asbestos in bulk materials is crucial. Along with microscopy, X-ray powder diffraction is considered a reliable tool for characterization of bulk materials. The Rietveld method has been successfully applied for the quantitative determination of asbestos in bulk materials such as insulating cements, mixed asbestos–slag wools, contaminated soil and others (Gualtieri, 1999). Analyses by XRPD are usually performed to identify other fibrous minerals that can be confused with asbestos (Bloise *et al.*, 2014). The potential hazard from asbestos to the health of

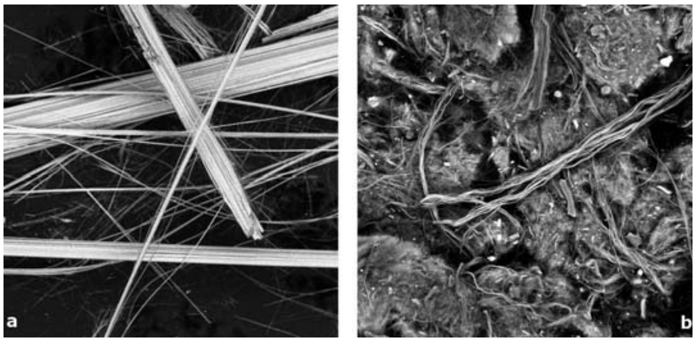

Figure 7.14.2
Habits of (*a*) amphibole asbestos (amosite) and (*b*) chrysotile asbestos. [Image courtesy of Professor Alessandro Gualtieri (University of Modena and Reggio Emilia, Italy) and Dr Alessandro Cavallo (University of Milano Bicocca, Italy)]

workers and public environmental issues during tunnel excavation in metamorphic formations, such as serpentinites, also require analytical procedures based on powder diffraction for an effective assessment of the presence of asbestos minerals (Ballirano *et al.*, 2008).

The elimination of asbestos-containing products from the environment has become a priority in many industrialized countries. It is now well established that asbestos-containing materials can be thermally transformed and recycled. In fact, when fired at temperatures higher than 1273 K, both serpentine or amphibole species transform into Mg–Fe silicates, which may be recycled at no cost in traditional ceramics (Gualtieri & Tartaglia, 2000). Thus, assessing the mechanism that controls the thermal decomposition of chrysotile at high temperatures has practical implications for the design of treatment plants and control of the firing processes of asbestos-containing materials.

Recently, research aimed at understanding the nature of the interaction of mineral fibres with biological systems and proposing a general model of fibre toxicity and/or pathogenicity has been carried out. The progress in synchrotron microdiffraction, μ-XRPD, allows improved understanding of the mechanisms of toxicity of these mineral fibres through the direct analyses of fibres found in the tissues of rats subjected to intraperitoneal/intrapleural injection of Union for International Cancer Control (UICC) chrysotile, UICC crocidolite and erionite-Na (Gualtieri *et al.*, 2017). The structural modifications observed through the collection of microdiffraction patterns, with special attention to the fibre crystallinity, allowed comparison of the biopersistence of the different phases, supporting the model of a lower biopersistence of chrysotile with respect to crocidolite; nevertheless, the formation of a silica-rich fibrous residue after the pseudo-amorphization of chrysotile could be responsible for the high cytotoxicity.

7.14.3.2. *Biominerals*

Biomineralization refers to the processes by which organisms form minerals and differentiates these phases from those formed by abiotic mineralization. The latter were the primary focus of Earth scientists over the last century, but the emergence of biogeochemistry and the urgent need to understand the past and future evolution of the Earth are moving biological mineralization into the forefront of various scientific fields, including the earth sciences (Weiner & Dove, 2003).

Furthermore, the study of biomaterials is a fascinating multidisciplinary field that crosses the boundary between basic and applied sciences. Knowledge of the mechanisms (fine-tuned by evolution over millions of years) used to produce materials perfectly fitting their functions enables development of new bio-inspired materials for use in modern technologies, such as bone implants or hybrid ceramic composites (Munch *et al.*, 2008; Xia & Jiang, 2008). Calcium carbonates are abundant building materials in nature (*e.g.* in mollusc shells, sea urchins and corals) and they also have many technological applications (*e.g.* as filler particles or coatings), making these minerals of great interest for biomimetic material synthesis. The mechanical properties of biominerals are often the result of a hierarchical construction employing organic components to regulate the precipitation of the inorganic phase (*e.g.* Mann, 2001). Recently, simple bio-inspired synthetic systems similar to biominerals were realized using charged polymer additives to induce hierarchical structuring of calcite, demonstrating how organic occlusions strongly affect the mechanism (Schenk *et al.*, 2012).

The advent of synchrotron radiation and the possibility of performing XRPD using micrometre and submicrometre spot sizes (μ-XRPD) represented a fundamental step for the study of these intriguing inhomogeneous, hierarchical materials. One of the first studies on biominerals was by DiMasi & Sarikaya (2004) on the orientation of crystals in the prismatic calcite layer and the nacre aragonite layer of a red abalone (Haliotis rufescens) shell. The exploitation of small-angle X-ray scattering (SAXS) (see Chapter 5.8) provides further information in the study of biominerals, such as grain size and shape. The coupling of μ-SAXS with μ-WAXS (wide-angle X-ray scattering) represents a powerful tool for investigating, for example, bone platelets. While μ-WAXS identifies the minerals and their crystallographic orientations in the bone, μ-SAXS reveals information about the morphology and orientation of the nanoplatelets. An example of the combined use of μ-SAXS and μ-WAXS was the investigation of bone formation in zebrafish, in which the authors observed a transition from amorphous to crystalline bone (Mahamid *et al.*, 2010).

7.14.3.3. *Mars mineralogy*

Curiosity and the other rovers (Sojourner, Spirit and Opportunity) have captured the public imagination since Sojourner safely landed on Mars in 1997. Although Sojourner and Spirit are no longer active, Curiosity still is (as of June 2018), providing a wealth of petrological, geochemical and mineralogical data that fascinate scientists and non-scientists alike. Curiosity landed at Gale Crater on 6 August 2012. The Mars Science Laboratory rover scooped samples of soil from the Rocknest Aeolian bedform in Gale Crater and the first non-terrestrial X-ray powder-diffraction pattern was collected. Analysis of the soil with the Chemistry & Mineralogy X-Ray Diffraction/X-Ray Fluorescence Instrument (CheMin) revealed the presence of plagioclase, forsteritic olivine, augite and pigeonite, with minor amounts of K-feldspar, magnetite, quartz, anhydrite, hematite and ilmenite (Bish *et al.*, 2014).

The use of μ-XRPD at synchrotron facilities is well known in the Earth sciences (Tamura & Kunz, 2015) and even hand-held X-ray powder diffractometers allowing identification of mineral phases in the field have been designed in the past, but only the miniature instrument of the Mars Science Laboratory (MSL; Sarrazin *et al.*, 2005) has attracted wide attention from scientists and the general public alike. The International Union of Crystallography (IUCr) and the International Astronomical Union sponsored the first International School/Workshop on Crystallography for Space Sciences organized by the Committee on Space Research (COSPAR), held in Puebla, Mexico, 17–29 April 2016. The aim of the workshop was to prepare participants for in-depth study of extra-terrestrial minerals, rocks and other interstellar particles, using *in situ* and remote analytical techniques.

References

Andrault, D., Angel, R. J., Mosenfelder, J. L. & Le Bihan, T. (2003). *Equation of state of stishovite to lower mantle pressures. Am. Mineral.* **88**, 301–307.

Ardit, M., Cruciani, G., Dondi, M., Merlini, M. & Bouvier, P. (2010). *Elastic properties of perovskite $YCrO_3$ up to 60 GPa. Phys. Rev. B*, **82**, 064109.

Ardit, M., Martucci, A. & Cruciani, G. (2015). *Monoclinic–orthorhombic phase transition in ZSM-5 zeolite: spontaneous strain variation and thermodynamic properties. J. Phys. Chem. C*, **119**, 7351–7359.

Arletti, R., Ferro, O., Quartieri, S., Sani, A., Tabacchi, G. & Vezzalini, G. (2003). *Structural deformation mechanisms of zeolites under pressure. Am. Mineral.* **88**, 1416–1422.

Artioli, G., Dapiaggi, M., Fornasini, P., Sanson, A., Rocca, F. & Merli, M. (2006). *Negative thermal expansion in cuprite-type compounds: a combined synchrotron XRPD, EXAFS, and computational study of* Cu_2O *and* Ag_2O*. J. Phys. Chem. Solids*, **67**, 1918–1922.

Ballirano, P., Andreozzi, G. & Belardi, G. (2008). *Crystal chemical and structural characterization of fibrous tremolite from Susa Valley, Italy, with comments on potential harmful effects on human health. Am. Mineral.* **93**, 1349–1355.

Ballirano, P., De Vito, C., Ferrini, V. & Mignardi, S. (2010). *The thermal behavior and structural stability of nesquehonite,* $MgCO_3.3H_2O$*, evaluated by in situ laboratory parallel-beam X-ray powder diffraction: New constraints on* CO_2 *sequestration within minerals. J. Hazard. Mater.* **178**, 522–528.

Bernstein, D. M., Dunnigan, J., Hesterberg, T., Brown, R., Velasco, J. A. L., Barrera, R., Hoskins, J. & Gibbs, A. (2013). *Health risk of chrysotile revisited. Crit. Rev. Toxicol.* **43**, 154–183.

Bhange, D. S. & Ramaswamy, V. (2007). *Thermal stability of the Mobil Five type metallosilicate molecular sieves – An in situ high temperature X-ray diffraction study. Mater. Res. Bull.* **42**, 851–860.

Bhange, D. S. & Ramaswamy, V. (2010). *Enhanced negative thermal expansion in MFI molecular sieves by varying framework composition. Microporous Mesoporous Mater.* **130**, 322–326.

Bignon, L., Brochard, P. & Pairon, L. C. (1996). *Mesothelioma: causes and fiber-related mechanism*. *Comprehensive Textbook of Thoracic Oncology*, edited by J. Aisner, M. C. Perry & M. R. Green, pp. 735–756. Baltimore: Lippincott, Williams and Wilkins.

Bish, D. L. *et al.* (2014). *X-ray diffraction results from Mars Science Laboratory: mineralogy of Rocknest at Gale Crater. Science*, **341**, 1238932–1.

Bish, D. L. & Carey, J. W. (2001). *Thermal behavior of natural zeolites*. In *Natural Zeolites: Occurrence, Properties, Applications*, edited by D. L. Bish & D. W. Ming. *Rev. Mineral. Geochem.* **45**, 403–452.

Bloise, A., Critelli, T., Catalano, M., Apollaro, C., Miriello, D., Croce, A., Barrese, E., Liberi, F., Piluso, E., Rinaudo, C. & Belluso, E. (2014). *Asbestos and other fibrous minerals contained in the serpentinites of the Gimigliano-Mount Reventino Unit (Calabria, S-Italy). Environ. Earth. Sci.* **71**, 3773–3786.

Carpenter, M. A., Howard, C. J., Knight, K. S. & Zhang, Z. (2006). *Structural relationships and a phase diagram for* $(Ca,Sr)TiO_3$ *perovskites. J. Phys. Condens. Matter*, **18**, 10725–10749.

Carpenter, M., Salje, E. & Graeme-Barber, A. (1998). *Spontaneous strain as a determinant of thermodynamic properties for phase transitions in minerals. Eur. J. Mineral.* **10**, 621–691.

Cattaneo, A., Gualtieri, A. F. & Artioli, G. (2003). *Kinetic study of the dehydroxylation of chrysotile asbestos with temperature by in situ XRPD. Phys. Chem. Mineral.* **30**, 177–183.

Chinnery, N., Pawley, A. R. & Clark, S. M. (2000). *The equation of state of lawsonite to 7 GPa and 873 K, and calculation of its high pressure stability. Am. Mineral.* **85**, 1001–1008.

Chollet, M., Daniel, I., Koga, K. T., Morard, G. & van de Moortèle, B. (2011). *Kinetics and mechanism of antigorite dehydration: Implications for subduction zone seismicity. J. Geophys. Res.* **116**, B04203–B04214.

Chopin, C. (1984). *Coesite and pure pyrope in high-grade blueschists of the Western Alps: a first record and some consequences. Contrib. Mineral. Petrol.* **86**, 107–118.

Collegium Ramazzini (2010). *Asbestos is still with us: repeat call for a universal ban. Arch. Environ. Occup. Health*, **65**, 121–126.

Cruciani, G. (2006). *Zeolites upon heating: factors governing their thermal stability and structural changes. J. Phys. Chem. Solids*, **67**, 1973–1994.

Cruciani, G. & Gualtieri, A. (1999). *Dehydration dynamics of analcime by in situ synchrotron powder diffraction. Am. Mineral.* **84**, 112–119.

Depmeier, W. (2009). *Some examples of temperature and time resolved studies of the dehydration and hydration behavior of zeolites and clathrates. Part. Part. Syst. Charact.* **26**, 138–150.

DiMasi, E. & Sarikaya, M. (2004). *Synchrotron x-ray microbeam diffraction from abalone shell. J. Mater. Res.* **19**, 1471–1476.

Dobson, D., Meredith, P. G. & Boon, S. A. (2002). *Simulation of subduction zone seismicity by dehydration of serpentine. Science*, **298**, 1407–1410.

Duffy, T. S. (2005). *Synchrotron facilities and the study of the Earth's deep interior. Rep. Prog. Phys.* **68**, 1811–1859.

Ferraris, G. & Merlino, S. (2005). Editors. *Micro and Mesoporous Mineral Phases*. *Rev. Mineral. Geochem.* **57**.

Fiquet, G., Guyot, F., Kunz, M., Matas, J., Andrault, D. & Hanfland, M. (2002). *Structural refinements of magnesite at very high pressure. Am. Mineral.* **87**, 1261–1265.

Galuskin, E. V., Gazeev, V. M., Armbruster, Th., Zadov, A. E., Galuskina, I. O., Pertesev, N. N., Dzierżanowski, P., Kadiyski, M., Gurbanov, A. G., Wrzalik, R. & Winiarski, V. (2008). *Lakargiite* $CaZrO_3$*: A new mineral of the perovskite group from the North Caucasus, Kabardino-Balkaria, Russia. Am. Mineral.* **93**, 1903–1910.

Gemmi, M., Klein, H., Rageau, A., Strobel, P. & Le Cras, F. (2010). *Structure solution of the new titanate* $Li_4Ti_8Ni_3O_{21}$ *using precession electron diffraction. Acta Cryst.* B**66**, 60–68.

Greaves, G. N., Meneau, F., Sapelkin, A., Colyer, L. M., ap Gwynn, I., Wade, S. & Sankar, G. (2003). *The rheology of collapsing zeolites amorphized by temperature and pressure. Nat. Mater.* **2**, 622–629.

Grevel, K. D., Nowlan, E. U., Fasshauer, D. W. & Burchard, M. (2000). *In situ X-ray diffraction investigation of lawsonite and zoisite at high pressures and temperatures. Am. Mineral.* **85**, 206–216.

Grey, I. E., Madsen, I. C., Mills, S. J., Hastert, F., Peterson, V. K. & Bastow, T. J. (2010). *A new type of cubic-stacked layer structure in anthoinite,* $AlWO_3(OH)_3$*. Am. Mineral.* **95**, 639–645.

Gualtieri, A. (1999). *The aid of X-ray powder diffraction to the characterization and treatment of asbestos containing materials. Period. Mineral.* **68**, 1–11.

Gualtieri, A. F., Bursi Gandolfi, N., Pollastri, S., Burghammer, M., Tibaldi, E., Belpoggi, F., Pollok, K., Langenhorst, F., Vigliaturo, R. & Dražić, G. (2017). *New insights into the toxicity of mineral fibres: a combined in situ synchrotron* μ*-XRD and HR-TEM study of chrysotile, crocidolite, and erionite fibres found in the tissues of Sprague-Dawley rats. Toxicol. Lett.* **274**, 20–30.

Gualtieri, A. & Tartaglia, A. (2000). *Thermal decomposition of asbestos and recycling in traditional ceramics. J. Eur. Ceram. Soc.* **20**, 1409–1418.

Guthrie, G. D. & Mossman, B. T. (1993). Editors. *Health Effects of Mineral Dust. Rev. Mineral.* **28**.

Haider, M., Rose, H., Uhlemann, S., Schwan, E., Kabius, B. & Urban, K. (1998). *A spherical-aberration corrected 200 kV transmission electron microscope. Ultramicroscopy*, **75**, 53–60.

Hazen, R. M. & Ferry, J. M. (2010). *Mineral evolution: Mineralogy in the fourth dimension. Elements*, **6**, 9–12.

Hemley, R. J., Mao, H. K. & Gramsch, A. (2000). *Pressure-induced transformations in deep mantle and core minerals. Mineral. Mag.* **64**, 157–184.

Iitaka, T., Hirose, K., Kawamura, K. & Murakami, M. (2004). *The elasticity of the* $MgSiO_3$ *post-perovskite phase in the Earth's lowermost mantle. Nature*, **430**, 442–445.

Kamp, D. W. (2009). *Asbestos-induced lung diseases: an update. Transl. Res.* **153**, 143–152.

Kampf, A. R., Mills, S. J., Rumsey, M. S., Dini, M., Birch, W. D., Spratt, J., Pluth, J. J., Steele, I. M., Jenkins, R. A. & Pinch, W. W. (2012). *The heteropolymolybdate family: structural relations, nomenclature scheme and new species. Mineral. Mag.* **76**, 1175–1207.

Kisielowski, C., Erni, R. & Freitag, B. (2008). *Object-defined resolution below 0.5 Å in transmission electron microscopy – recent advances on the TEAM 0.5 instrument. Microsc. Microanal.* **14**, 78–79.

Kolb, U., Gorelik, T., Kubel, C., Otten, M. T. & Hubert, D. (2007). *Towards automated diffraction tomography: Part I – Data acquisition. Ultramicroscopy*, **107**, 507–513.

Kolb, U., Gorelik, T. & Otten, M. T. (2008). *Towards automated diffraction tomography. Part II – Cell parameter determination. Ultramicroscopy*, **108**, 763–772.

Kubo, A., Kiefer, B., Shim, S. H., Shen, G., Vitali, G., Prakapenka, B. & Duffy, T. S. (2008). *Rietveld structure refinement of* $MgGeO_3$ *post-perovskite phase to 1 Mbar. Am. Mineral.* **93**, 965–976.

Leardini, L., Quartieri, S., Vezzalini, G. & Arletti, R. (2015). *Thermal behaviour of siliceous faujasite: Further structural interpretation of negative thermal expansion. Microporous Mesoporous Mater.* **202**, 226–233.

Lee, Y., Vogt, T., Hriljac, J. A., Parise, J. B., Hanson, J. C. & Kim, S. J. (2002). *Non-framework cation migration and irreversible pressure-induced hydration in a zeolite. Nature*, **420**, 485–489.

Likhacheva, A. Yu., Seryotkin, Y. V., Manakov, A., Goryainov, S. V. & Ancharov, A. I. (2006). *Non-hydrostatic compression of zeolite NaA in water medium: connection to anomalous conductivity. Z. Kristallogr.* **224**, 37–143.

Mahamid, J., Aichmayer, B., Shimoni, E., Ziblat, R., Li, C., Siegel, S., Paris, O., Fratzl, P., Weiner, S. & Addadi, L. (2010). *Mapping* *amorphous calcium phosphate transformation into crystalline mineral from the cell to the bone in zebrafish fin rays. Proc. Natl Acad. Sci. USA*, **107**, 6316–6321.

Mann, S. (2001). *Biomineralization. Principles and Concepts in Bioinorganic Materials Chemistry*. New York: Oxford University Press.

Marinkovic, B. A., Ari, M., de Avillez, R. R., Rizzo, F., Ferreira, F. F., Miller, K. J., Johnson, M. B. & White, M. A. (2009). *Correlation between AO_6 polyhedral distortion and negative thermal expansion in orthorhombic $Y_2Mo_3O_{12}$ and related materials. Chem. Mater.* **21**, 2886–2894.

Martucci, A., Braschi, I., Marchese, L. & Quartieri, S. (2014). *Recent advances in clean-up strategies of waters polluted with sulfonamide antibiotics: a review of sorbents and related properties. Mineral. Mag.* **78**, 1115–1140.

Martuzzi, M., Comba, P., De Santis, M., Iavarone, I., Di Paola, M., Mastrantonio, M. & Pirastu, R. (1998). *Asbestos-related lung cancer mortality in Piedmont, Italy. Am. J. Ind. Med.* **33**, 565–570.

Mastrantonio, M., Belli, S., Binazzi, A., Carboni, M., Comba, P., Fusco, P., Grignoli, M., Lavarone, I., Martuzzi, M., Nesti, M., Trinea, S. & Uccelli, R. (2002). *La mortalità per tumore maligno della pleura nei comuni italiani (1988–1997)*. Rapporti ISTISAN 02/12, 27 pp. Istituto Superiore di Sanita, Italy.

Merkel, S. (2006). *X-ray diffraction evaluation of stress in high pressure deformation experiments. J. Phys. Condens. Matter*, **18**, S949–S962.

Merkel, S., McNamara, A. K., Kubo, A., Speziale, S., Miyagi, L., Meng, Y., Duffy, T. S. & Wenk, H. R. (2007). *Deformation of (Mg,Fe)SiO_3 post-perovskite and D″ anisotropy. Science*, **316**, 1729–1732.

Merlini, M., Sapelli, F., Fumagalli, P., Gatta, G. D., Lotti, P., Tumiati, S., Abdellatief, M., Lausi, A., Plaisier, J., Hanfland, M., Crichton, W., Chantel, J., Guignard, J., Meneghini, C., Pavese, A. & Poli, S. (2016). *High-temperature and high-pressure behavior of carbonates in the ternary diagram $CaCO_3$-$MgCO_3$-$FeCO_3$. Am. Mineral.* **101**, 1423–1430.

Miller, W., Smith, C. W., Mackenzie, D. S. & Evans, K. E. (2009). *Negative thermal expansion: a review. J. Mater. Sci.* **44**, 5441–5451.

Morgan, B., Wilson, S. A., Madsen, I. C., Gozukara, Y. M. & Habsuda, J. (2015). *Increased thermal stability of nesquehonite ($MgCO_3.3H_2O$) in the presence of humidity and CO_2: implications for low-temperature CO_2 storage. Int. J. Greenh. Gas Control*, **39**, 366–376.

Mossman, B. T., Bignon, J., Corn, M., Seaton, A. & Gee, J. B. (1990). *Asbestos: scientific developments and implications for public policy. Science*, **247**, 294–301.

Mugnaioli, E., Gorelik, T. & Kolb, U. (2009). *'Ab-initio' structure solution from electron diffraction data obtained by a combination of automated diffraction tomography and precession technique. Ultramicroscopy*, **109**, 758–765.

Munch, E., Launey, M. E., Alsem, D. H., Saiz, E., Tomsia, A. P. & Ritchie, R. O. (2008). *Tough, bio-inspired hybrid materials. Science*, **322**, 1516–1520.

Murakami, M., Hirose, K., Kawamura, K., Sata, N. & Ohishi, Y. (2004). *Post-perovskite phase transition in $MgSiO_3$. Science*, **304**, 855–858.

Nickel, E. H. & Grice, J. D. (1998). *The IMA Commission on New Minerals and Mineral Names: procedures and guidelines on mineral nomenclature. Can. Mineral.* **36**, 913–926.

Nishi, M., Irifune, T., Tsuchiya, J., Tange, Y., Nishihara, Y., Fujino, K. & Higo, Y. (2014). *Stability of hydrous silicate at high pressures and water transport to the deep lower mantle. Nat. Geosci.* **7**, 224–227.

Oury, T. D., Sporn, Th. A. & Roggli, V. L. (2014). Editors. *Pathology of Asbestos-Associated Diseases.* Berlin: Springer.

Palatinus, L., Jacob, D., Cuvillier, P., Klementová, M., Sinkler, W. & Marks, L. D. (2013). *Structure refinement from precession electron diffraction data. Acta Cryst.* A**69**, 171–188.

Pekov, I. V., Chukanov, N. V., Yamnova, N. A., Zadov, A. E. & Tarassoff, P. (2007). *Gjerdingenite-Na and gjerdingenite-Ca, two new mineral species of the labuntsovite group. Can. Mineral.* **45**, 529–539.

Pekov, I. V., Perchiazzi, N., Merlino, S., Kalachev, V. N., Merlini, M. & Zadov, A. E. (2007). *Chukanovite, $Fe_2(CO_3)(OH)_2$, a new mineral from the weathered iron meteorite Dronino. Eur. J. Mineral.* **19**, 891–898.

Perrillat, J. P., Daniel, I., Koga, K. T., Reynard, B., Cardon, H. & Crichton, W. A. (2005). *Kinetics of antigorite dehydration: A real-time X-ray diffraction study. Earth Planet. Sci. Lett.* **236**, 899–913.

Rigamonti, R. (1936). *La struttura della catena paraffinica studiata mediante i raggi di elettroni. Gazz. Chim. Ital.* **66**, 174–182.

Rossi, M., Nestola, F., Ghiara, M. R. & Capitelli, F. (2016). *Fibrous minerals from Somma-Vesuvius volcanic complex. Mineral. Petrol.* **110**, 471–489.

Salje, E. K. H., Hayward, S. A. & Lee, W. T. (2005). *Ferroelastic phase transitions: structure and microstructure. Acta Cryst.* A**61**, 3–18.

Santoro, M., Gorelli, F. A., Bini, R., Haines, J. & van der Lee, A. (2013). *High-pressure synthesis of a polyethylene/zeolite nano-composite material. Nat. Commun.* **4**, 1557–1563.

Sarrazin, P., Blake, D., Feldman, S., Chipera, S., Vaniman, D. & Bish, D. (2005). *Field deployment of a portable X-ray diffraction/X-ray flourescence instrument on Mars analog terrain. Powder Diffr.* **20**, 128–133.

Scambelluri, M., Bottazzi, P., Trommsdorff, V., Vannucci, R., Hermann, J., Gòmez-Pugnaire, M. T. & Lòpez-Sànchez Vizcaino, V. (2001). *Incompatible element-rich fluids released by antigorite breakdown in deeply subducted mantle. Earth Planet. Sci. Lett.* **192**, 457–470.

Schenk, A. S., Zlotnikov, I., Pokroy, B., Gierlinger, N., Masic, A., Zaslansky, P., Fitch, A. N., Paris, O., Metzger, T. H., Cölfen, H., Fratzl, P. & Aichmayer, B. (2012). *Hierarchical calcite crystals with occlusions of a simple polyelectrolyte mimic complex biomineral structures. Adv. Funct. Mater.* **22**, 4668–4676.

Shieh, R., Mao, H., Hemley, R. J. & Ming, L. C. (2000). *In situ X-ray diffraction studies of dense hydrous magnesium silicates at mantle conditions. Earth Planet. Sci. Lett.* **177**, 69–80.

Singh, A. K. (2014). *Polycrystalline solids under nonhydrostatic compression: determination of strength from X-ray diffraction data. J. Phys. Conf. Ser.* **500**, 122005.

Tamura, N. & Kunz, M. (2015). *A concise synchrotron X-ray microdiffraction field guide for the Earth scientists. Bol. Soc. Geol. Mex.* **67**, 467–478.

Ulmer, P. & Trommsdorff, V. (1995). *Serpentine stability to mantle depths and subduction-related magmatism. Science*, **268**, 858–861.

Vallcorba, O., Casas, L., Colombo, F., Frontera, C. & Rius, J. (2017). *First terrestrial occurrence of the complex phosphate chladniite: crystal-structure refinement by synchrotron through-the-substrate microdiffraction. Eur. J. Mineral.* **29**, 287–293.

Vezzalini, G., Arletti, R. & Quartieri, S. (2014). *High-pressure-induced structural changes, amorphization and molecule penetration in MFI microporous materials: a review. Acta Cryst.* B**70**, 444–451.

Vincent, R. & Midgley, P. A. (1994). *Double conical beam-rocking system for measurement of integrated electron diffraction intensities. Ultramicroscopy*, **53**, 271–282.

Walter, M. J., Thomson, A. R., Wang, W., Lord, O. T., Ross, J., McMahon, S. C., Baron, M. A., Melekhova, E., Kleppe, A. K. & Kohn, S. C. (2015). *The stability of hydrous silicates in Earth's lower mantle: experimental constraints from the systems MgO–SiO_2–H_2O and MgO–Al_2O_3–SiO_2–H_2O. Chem. Geol.* **418**, 16–29.

Weiner, S. & Dove, P. M. (2003). *An overview of biomineralization processes and the problem of the vital effect*. In *Biomineralization*, edited by P. M. Dove, J. J. De Yoreo & S. Weiner. *Rev. Mineral. Geochem.* **54**, 1–30.

Welch, M. D. & Marshall, W. (2001). *High-pressure behavior of clinochlore. Am. Mineral.* **86**, 1380–1386.

Whitfield, P. S., Le Page, Y., Grice, J. D., Stanley, C. J., Jones, G. C., Rumsey, M. S., Blake, C., Roberts, A. C., Stirling, J. A. R. & Carpenter, G. J. C. (2007). *$LiNaSiB_3O_7(OH)$ – novel structure of the new borosilicate mineral jadarite determined from laboratory powder diffraction data. Acta Cryst.* B**63**, 396–401.

Woodcock, D. A., Lightfoot, P., Villaescusa, L. A., Díaz-Cabañas, M., Camblor, M. A. & Engberg, D. (1999). *Negative thermal expansion in the siliceous zeolites chabazite and ITQ-4: a neutron powder diffraction study. Chem. Mater.* **11**, 2508–2514.

Xia, F. & Jiang, L. (2008). *Bio-inspired, smart, multiscale interfacial materials. Adv. Mater.* **20**, 2842–2858.

Subject index

A constraints 479
Absolute phase abundances 349
Absorption 209, 257
    in *in situ* experiments 176
    in multilayers 577
    in multiphase samples 258
    in thin films 581
    neutron 220
Absorption corrections
    for anisotropic crystallites 577
    for multilayers 577
    in 2D diffraction 130
Absorption–diffraction method of phase analysis 345, 350
Absorption factor 581
Accuracy
    goniometer 34
    in neutron diffraction 94
    in quantitative phase analysis 350, 364, 374
    of phase analysis using electron diffraction 110
    of structural parameters 499
    of temperature measurements 155
Acid mine drainage 800
Actinolite 889
Active area of a detector 126
Active pharmaceutical ingredient 767
ADDSYM 506
Adipocere 739
Air scatter 15, 124, 131
Alignment 224, 230
Alite 856–857, 863
Alloys 739
ALLTRIALS 410
Alumina 787–788, 820
    NIST standard 236
Alumina-toughened zirconia 823
Aluminium acid sulfate 844
Aluminium industry, Rietveld analysis in 782
Amino acids, rigid-body representation of 731
Amlodipine besylate 772
Ammonium iron carbonate hydroxide 845
Ammonium iron sulfide, (NH$_4$)Fe$_2$S$_3$ 311, 845
Ammonium nitrate 335
Amorphous materials 649, 673, 767, 771
Amorphous phases 376, 382
    effect on data clustering 329
    in bauxite 783
    quantitative determination of 360, 838
Amoxicillin 311
Amphiboles 889
Analogue detectors 46
Analyser crystals 56–57
Analysis methods
    for artworks 796
    for planetary exploration 795
    in mining and mineral processing 793
    non-destructive 737, 743, 778, 796
    through-the-bag 745
Analytical standards 368
Anatase 586
Angular-dispersive diffraction, reaction cells for 194
Angular resolution 49, 57, 62
Anharmonic atomic displacements 484
Anhydrite 856–858, 860–861
Anisotropic peak broadening 445, 471
    in zeolites 454
Anisotropic strain broadening 259
Annealing 150, 153
Anomalous (resonant) scattering 62, 388, 479–480
Anomalous small-angle X-ray scattering 689
Anthoinite 886
Anti-bump cost function 438
Anti-bump restraints 460
Antiferromagnetic ordering 66
Antigorite 888
Antiphase domain boundaries 296
Antophyllite 889
Aperiodic structures 486
Apertures 40
Arbitrarily defined cells method of texture analysis 560
Archaeology 759, 805
Archaeometry 759
Area detectors 118, 125, *see also* two-dimensional detectors
    spatial resolution of 127
Art 759, 796, 805
Asbestos 889
Aspirin 333
Asymmetry in peak profiles 240, 257, 264, 465, 467
Atomic displacement parameters 10, 470, 498, *see also* Debye–Waller factors
    conventions for 517
    from electron-diffraction data 112
Atomic form factors 10, 253, 475
Atomic pair correlation function 676
Atomic resolution 402, 405
Atomic scattering factors 10, 253, 475
Attenuation, in neutron diffraction 69, 95
Attenuation coefficient 581
Auricupride, Cu$_3$Au 296
Automated diffraction tomography 886
Averaged alternating reflections (AAR) scheme 402
Averaged macroscopic strain/stress 541
Aviation engine valve deposit 310
Avrami plot 831
Axial direction 29
Axial divergence 40, 58, 227, 240, 257, 264
Azimuthal integration 9

Back-loading sample holders 206
Background 2, 15, 466, 469, 617
    corrections for, in small-angle scattering 679
    corrections for, in stress measurements 144
    fitting 285, 493, 573
    from extraneous sources 15
    in neutron diffraction 86
    in quantitative phase analysis 368
    information content in 15
    removal, for non-crystalline materials 623
Bacteriorhodopsin 725, 727
Ballistic guides 80
Barbiturates 738
Barium calcium antimonate 495, 507
Barium iron titanate 815
Barium magnesium silicate 831
Barium neodymium copper oxide 825
Barium strontium titanate 202, 495–496, 505–506
Barium titanate 591
Bassanite 857–858, 860–861
Batteries 181, 193–194, 755, 806
Bauxite 782
Bayer process 782, 785, 787–788, 797
Bayerite, Al(OH)$_3$ 352
Bayesian probability theory 477
Beam-path systems
    components 30
    hybrid 35
    multiple 35
    non-coplanar 35
Beam quality 36
Belite 856–857, 860
Bending magnets 52
Betpakdalite 886
Bias 480
Biaxial texture 590
Bioavailability 768
Bioceramics 810
Biomaterials 161
Biominerals 890
Bismuth sodium lanthanum titanate 811
Blended cements 857
Bogue method 793
Bond-valence analysis 503, 873
Bone mineral 739
Bonse–Hart optics 677
Bounding cubes 612
Bragg–Brentano geometry 27, 29, 124, 224, 628
Bragg-edge imaging 764
Bragg equation 2
Bragg *R* factor 469
Brass 739
Bravais-lattice determination 277
Bremsstrahlung 37, 71, 624
Bridgman anvils 157–158
Bridgman equation 825
Briet–Dirac correction 631
Brightness 36
Brilliance 36
Brindley correction for microabsorption 210, 258, 366
Bubble model for non-crystalline materials 645
Buckminsterfullerene 154
Building units 442
Bulk modulus 824
Bulk-solvent correction, flat 319

C test 328
Cadmium selenide, CdSe 17
Caesium thiocyanate 338
Calcite 362, 375–376
    magnesian calcite 309
Calcium aluminate 857
Calcium aluminate cements 859
Calcium aluminoferrite 856
Calcium cobaltate 818
Calcium sulfoaluminate cements 859
Calcium sulfobelite cements 860
Calcium tartrate tetrahydrate 491, 497
Calcium zinc silicate 829
Calibration 235, 241
Calinški–Harabasz test 328
Cambridge algorithm 477
Cambridge Structural Database (CSD) 313, 414, 434
Canted antiferromagnetic ordering 881
Canted ferromagnetic ordering 880
Capillaries 57, 215
    capillary reaction cells 190
    for high-temperature studies 150
Capillary optics 44
Capsaicin 391
Carbamazepine 435, 770
Carbon dioxide, sequestration of 801, 889
Cassiterite, SnO$_2$ 216
Catalan blue 762
Catalysis 754, 846
Cauchy function 263
CCP14 698
Cefadroxil 776
Cell parameters, *see* lattice parameters
Cements 799, 855
    hydration of 861
    nomenclature 856
    quantitative phase analysis 855
    variable-temperature study 152
Centre-of-mass mapping 607
Ceramic films 819
Ceramics 804
    defects in 816
    degradation of 822
    glass-ceramics 828
    in art and archaeology 805
    microstructure 824
    phase equilibria 813
    phase identification 811
    reaction mechanisms in 820
    stress in 817
    transformation toughening 822
    types of 805
Ceria 298, 534
Cerium niobate 814
Characteristic radiation 37
Charge-coupled device (CCD) detectors 48, 59, 107, 126, 128
Charge flipping 389, 402, 456, 482–483
Charge transfer, in superconductors 872
Chechevitsa anvils 158
checkCIF 500, 509, 519
Chemical reaction cells 189
Chemical reasonableness of a model 496

Chemometric data analysis 623, 626
Chi squared 469, 489
  cumulative plot 492
Chi-squared hypersurface 421
Chladniite 886
Chromium chromate tetrachromate 407
Chukanovite 886
CIF (Crystallographic Information Framework) 515
  data blocks 516
  data items 515
  data names 515
  metadata 516
  multiple data sets 516
  multiple phases 516
  standard uncertainties 517
Cimetidine 387
Clarithromycin 390
Clathrate hydrates 844
Clays 206, 356–359, 804, 843
Clomipramine hydrochloride 407
Close-packed compounds 443
Cluster analysis 325, 797
CMPR 517
Coal 752
Cobalt(II) acetate tetrahydrate 502
Cobalt vanadium oxide, $Co_3V_2O_8$ 184
Co-crystals 767–768
Coesite 885
Coherent diffraction intensity 682
Coherent elastic neutron scattering 68
Coherent scattering length density 68
Collimation 40, 53–55, 80
Collinear antiferromagnetic ordering 881
Column-length distribution 531
Combined analysis 555, 571
Combined figures of merit 392
Combi-optics 44
Common volume function 526, 528
Complementary metal–oxide–semiconductor (CMOS) detectors 48, 107
Compliance 594
Component method of texture analysis 560
Compound refractive lens 56
Compressed air energy storage 753
Compressibility 824
Compton scattering 19, 617, 631
Computer programs, *see* software
Cone and quartering technique 743
Configuration factor 586
Conograph 277
ConQuest 313
Conservation 759
Constraints 469
  in the maximum-entropy method 478
  torsion-angle 436
Contamination of evidence 741
Contrast-variation small-angle neutron scattering 689
Control rods 72
Convolution theorem 289
Convolutional multiple whole profile fitting 297
Conway's topograph 275
Coolants 153
Coordinate systems, for multigrain crystallography 603
Coordination polyhedra 410
Copper oxide, Cu_2O 299
Copper phthalocyanine 836
Copper(II)–Schiff base complex 279
Cordierite 832
Core–shell model for non-crystalline materials 641
Core–shell particles 685
Corina 435
Correlation matrix 326
Corrosion 202, 761, 822, 844
Corundum 347
Cosmetics 740
Cost functions 419, 445
  anti-bump 438
Counterfeit medicines 777
Counting detectors 46
Counting statistics 9, 94
Covariance matrix 467
COVMAP approach 406
Critical field 868
Critical grazing angle 55, 588
Critical temperature 868
Crocidolite 890
Cryogenic cooling 153, 721
Cryostats 153
Crysfire 278
Crystal chemistry, use in structure determination 445
Crystal habit 776
Crystal packing 410
Crystal screening for protein structure determination 723
Crystal seeds 839
Crystal-structure prediction 392, 439, 838
Crystallinity 837
  quantitative analysis of 145
Crystallite size 13, 267, 575
  in a vent-gas oxidation catalyst 852
  in ceramics 816
  in neutron diffraction 95
  measuring in reflection or transmission 147
  quantitative analysis of 145
Crystallization of glass-ceramics 828
Crystallization platforms 768
Crystallographic Information Framework (CIF) 515
Crystallographic orientation, representation of 609
Crystallography Open Database (COD) 320
CRYSTMET 318
Cultural heritage 759
Cumulative chi-squared plot 492
Cuprite 887
Curiosity rover 795
Curved detectors, pixel positions 122
Cyclic-fibre texture 565
Cyclic-planar texture 565

d_{hkl} values 3, 270
Darwin width 54–55
DASH 415, 419, 426
Data clustering 325, 797
  amorphous samples 329
  fuzzy clustering 333
  in quantitative phase analysis 361
  INDSCAL method 340
  software 342
  spectroscopic data 339
Data collection 235
  for electron diffraction 107
  for organic pigments 835
  for proteins 720
  for stress analysis 143
Data completeness, in high-pressure studies 161
Data definition language (DDL) 515
Data integration
  for electron diffraction 107
  for stress analysis 143
  for two-dimensional diffraction 128
  gamma 130
  two-theta 130
Data reduction 282
  algorithms 282
  for electron diffraction 107
  for high-pressure studies 167
  for two-dimensional diffraction 128
  in pair distribution function analysis 663
  in small-angle scattering 679
Data visualization 325, 329
  grand tour 331
  minimum spanning trees 331
  parallel-coordinates plots 330
  silhouettes 331
Databases 304
Debye–Bueche model 683
Debye cones 28
Debye equation 261, 619, 650, 676
Debye lattice function, effective 640
Debye–Menke equation 621
Debye–Menke intensity function 621
Debye model 18, 617
Debye rings 118
  spotty 37, 145, 191, 201, 661
Debye–Scherrer cones 7, 119
Debye–Scherrer geometry 26, 29, 58, 743, 746
  for non-ambient-temperature studies 154
  peak shifts in 265
Debye–Waller approximation 655
Debye–Waller factors 253, 475
  negative 258
Decafluoroquarterphenyl 279
Defocusing effects 134, 572
Deformation electron density 477
Deformation faults 295
Degradation of ceramics 822
Delaunay reduction 277
Dendrograms 327
Density-functional theory 439, 448, 501, 509, 769
Detection limit 128
Detective quantum efficiency 45, 127
Detector circle 29
Detector dead time 46, 84
Detector efficiency 83
Detector linearity 45
Detector position 121
Detector resolution 133
Detector scan 33
Detector space 121–123
Detectors 46
  active area 126
  angular resolution 49
  area 118, 125, 127
  charge-coupled device (CCD) 48, 59, 107, 126, 128
  complementary metal–oxide–semiconductor (CMOS) 48, 107
  counting (digital) 46
  detection limit 128
  dynamic range 128
  energy range of 127
  for electrons 107
  for *in operando* studies 175
  for *in situ* studies 175
  for neutrons 82, 87
  for pair distribution function analysis 63
  for synchrotron radiation 52
  for X-rays 45
  frame integration 130
  gas-filled proportional counters 47, 83, 87, 175
  integrating (analogue) 46, 128
  microchannel plate 88
  micro-gap 47
  multi-analyser crystal detectors 175
  multi-wire proportional counters 47, 83, 175
  neutron scintillators 175
  nonuniform response correction 129
  photon-counting 27, 47, 128, 176
  pixel size 126
  point 225
  position-sensitive 27, 56, 83, 225, 675, 677
  scintillation 46, 83, 88
  semiconductor 48, 83
  silicon micro-strip 48
  silicon pixel 48
  spatial correction 129
  spatial resolution 49
  static, for *in situ* studies 150
  strip detectors 175
  two-dimensional 8, 59, 127, 175
Devitrification 828–829
Diamond-anvil cells 159–160, 886
Diaryl pigments 835
DICVOL06 277
DICVOL91 276
Dielectric susceptibility 588
DIFFaX 295
Difference Fourier maps 404, 498
Differential evolution 429
Differential scattering cross section 253, 676
Differential structure functions 658
DIFFRAC.EVA 333
Diffraction cones 7, 119
Diffraction contrast tomography 601
Diffraction elastic constants 546
Diffraction geometry
  Bragg–Brentano 27, 29, 124, 224, 628
  Debye–Scherrer 26, 29, 154, 743, 746
  focal construct 742
  for multigrain crystallography 603
  Gandolfi 746

Diffraction plane 28
Diffraction power 104
Diffraction rings 118
Diffraction space 119
Diffraction stress factors 542
Diffraction vector 120
Diffraction-vector cones 120
Diffractometer circle 29
Diffractometer plane 118
Diffractometers
  alignment of 230
  at synchrotron sources 56
  Bragg–Brentano 27, 29, 124, 224, 628
  calibration of 241
  Debye–Scherrer 26, 58
  for energy-dispersive diffraction 59
  for engineering studies 88
  for residual stress studies 88
  Hart–Parrish design 58
  laboratory X-ray 224
  neutron 80, 84, 86, 91, 254
  portable 761, 763, 778
  synchrotron X-ray 56
Diffuse scattering 617
  elastic coherent 16
  inelastic coherent 18
  monotonic Laue 19, 68, 651
  thermal 18, 691
Digital detectors 46
Dioxazine pigment 838
Direct lattice 270
Direct methods 387–388, 396, 456
Direct-space methods 442
Dislocations 293
Disorder 446, 459, 484, 772
Disordered materials 673
Disordered structures 681
Distance between two orientations 612
Distance matrix 326
Distorted-wave Born approximation 690
Divergent refinements 470
Domain boundaries 296
Domain shape 292
Domain size 255, 292, 524
  apparent size 526
  Fourier methods 526
  from electron-diffraction data 112
  in organic pigments 837
  mean 531
Domain-size distributions 524
  analytical 533
  column-length distribution 531
  Fourier methods 531
  gamma distribution 533
  histogram model 534
  lognormal distribution 533
Domed hot stage 153
Donnet–Jouanneaux function 570
Double-dependent anisotropic strain breadth 552
Dross 790
Drugs 738
Dynamic high-pressure generation 157
Dynamic range 46, 128
Dynamical occupancy correction 443
Dynamical scattering 104

E-maps 399
EAGER 428
Earth materials 886
Effective Debye lattice function 640
EFLECH/INDEX 275
Eigenvalue analysis 327
Elastic coherent diffuse scattering 16
Elastic constants 538
  diffraction 546
  macroscopic 576
  single-crystal 546
  stiffness 539
Elastic strain, representation of 613
Electric fields, powder diffraction under 174
Electrochemical alloying 182
Electrochemical cells 181, 192, 196, 755
Electrolytic bath 788
Electron-density distributions 473, 480, 639
  accurate, from maximum-entropy method 485
  depth-resolved, in thin films 594
Electron-density maps
  from the maximum-entropy method 474
  modification 404
  non-nuclear maxima in 475
Electron detectors 107
Electron diffraction 102, 457
  calibration 107
  computer programs for 114
  data collection, integration and processing 107
  diffraction power 104
  dynamical scattering 104
  for proteins 732
  intensities 103
  kinematic approximation 104
  multiple-scattering effects 102
  nano-area 105
  pair distribution function analysis 113
  pattern geometry 103
  phase analysis 108
  phase identification 108
  precession electron diffraction 104
  preferred orientation in 112
  radiation damage 103
  sample preparation 106
  selected-area 105
  texture analysis 110
  time-resolved 103
  use of Powder Diffraction File 109
Electron energy filters 108
Electron lateral coherence length 105
Electron microscopy 105, 457
Emission profiles 228, 291
Empirical potential structure refinement 667
enCIFer 518–519
Endeavour 426
Energy conversion 752
Energy discrimination 46
Energy-dispersive diffraction 59, 254, 799
  peak profiles 266
  quantitative phase analysis 362
  reaction cells for 194
Energy-dispersive X-ray spectroscopy 572
Energy range of a detector 127
Energy resolution 46, 55
Energy storage 752
Engineering diffractometers 88
Entropy-maximization method of texture analysis 560
Environmental impact of mining and mineral processing 800
Epithermal neutrons 72
Equal-area projections 557
Equations of state 887
Equatorial divergence 40
Equatorial plane 28
Equipartition of peak intensities 283
Erionite-Na 890
Error-correcting codes 400, 403
Error plot 491
Estradiol 202
Ettringite 856, 863
Euler angles 609
Eulerian geometry 122
Evolutionary algorithms 391
Ewald construction 7
EWIMV method of texture analysis 110, 560
EXAFS 19
Excipients 738
Excitation error 104
Excluded volume 418
Exhaustive indexing methods 273
Expected *R* factor 468, 489
Experiment constant 348, 355
Explosives 740
EXPO 278, 406–407, 410, 456
Exponential harmonics method for texture analysis 561
Extended convolutional multiple whole profile fitting 297
Extended solids 442
External standard method 349
Extinction 209–211, 260, 480
Extinction length 261
Extinction symbols 416
Extrapolated structure factors 389

F constraints 476, 478, 480, 485
F_N criterion 271
Faber–Ziman formalism 651
Famotidine 391, 419, 421
Fast Fourier transform (FFT) methods 388
Fast iterative Patterson squaring (FIPS) 401
Fast neutrons 72
Faujasite 847, 849–850, 887
Fermi chopper 76
Ferrimagnetic ordering 880
Ferrite 857
Ferroelastic minerals 889
Ferroelectric ceramics 807
Ferroelectrics 177
Ferromagnetic ordering 880
Fexofenadine 769
FFT (fast Fourier transform) methods 388
Fibre texture 110, 565, 590
Fibrous minerals 889
Figures of merit 392, 398
  for indexing 271–272
Film cameras 26
Filters 40, 55
Fink search method 305
FIPS (fast iterative Patterson squaring) 401
Fixed-target X-ray sources 38
Flat detectors, pixel positions 121
Flat-foil specimens 213
Flat prior 475
Fluid catalytic cracking 752
Fluorescence 32, 37, 41, 125, 129, 572
Flux 36
Flux density 36
Focal construct geometry 742
Focus 455
FOMnew 280
Forensic science 737
  contact trace materials 737
  control specimen 737
  instrumentation 742
  specimen preparation 742
  suspect specimen 737
Forward problem 11
Fossil fuels 752
Fourier maps 404, 468, 473–474
Fourier methods for determining domain size 526
Fourier methods for determining domain-size distributions 531
Fourier recycling 404
Fourier synthesis 399
Fourier transforms 10, 12
FOX 419, 426
FOXGrid 419
Frame integration 130
Frame overlap 75
Framework building 445
Framework structures 452
Fraunhofer approximation 10
Free-electron lasers 197, 731
Freely floating reflections 402
Fresnel coefficient 594
Friedel pairs 253
Fructose 375
Frustrated magnetic systems 184
Fuel cells 806
Full-width-at-half-maximum (FWHM) 12, 58, 84, 127, 238, 263
FullProf 111, 278
Fundamental-parameters approach 12, 240, 265, 290
Fundamental zone 614
Fuzzy clustering 333, 798
Fzon 278

G constraints 478–479
GAIN 277
Gamma integration 130
Gamma test 328
Gandolfi mode 746
Gas-filled proportional counters 47, 83, 87

- Gas hydrates 844
- Gauge volume 88
- Gaussian fibre components 561
- Gaussian peak-shape functions 12, 240, 255, 263
- *GDASH* 419
- Gels 673
- Generalized F constraints 485
- Generalized spherical harmonics 549, 559
- Genetic algorithms 391, 428, 444
  - use in indexing 275
- *Genie* 520
- Geology 156, 753
- Geometric restraints 458
- *GEST* 428
- Ghost correction 560
- Gibbsite, $Al(OH)_3$ 352, 362
- Gjerdingenite-Ca 886
- Gjerdingenite-Na 886
- Glancing-angle X-ray diffraction 760
- Glass-ceramics 807, 828
  - crystallization 824, 828
  - devitrification 828
  - *in situ* studies 829
  - invert glasses 831
  - kinetics of formation 830
  - metastable phases 829–830
  - neutron powder diffraction 829
  - nucleation 828
  - phase separation 828
  - quantitative analysis 833
  - structure solution 830
- Glass disease 823
- Glass-forming methods 828
- Glasses 673
- Global optimization methods 275, 390, 424
- Glucose 375
- Gnomonic projection 612
- Göbel mirrors 27, 43
- Gold nanoparticles 656
- Goniometer accuracy 34
- Goniometer axes 32
- Goniometer circle 29
- Goniometer designs 32
- Goniometer geometry 122
- Goniometer precision 34
- Goniometers 225, 231
- Goodman & Kruskal's γ test 328
- Goodness of fit 109, 416, 419, 469
- Grain growth in ceramics 819
- Grain mapping 601
  - volumetric 608
- *GRAINDEX* 605
- Grand tour 331
- Granularity 37, 95, 201–202, 258, *see also* particle statistics
- Grazing-incidence diffraction 35, 213, 585, 754, 812
- Grazing-incidence small-angle scattering 680, 690
- Grazing-incidence X-ray scattering (GIXS) 597
- Grid-search method of indexing 275
- Ground glass 376
- Group amplitude 479
- Grunerite 889
- *GSAS* 466, 471
  - generation of CIFs 520
  - peak-shape functions 240, 247
  - preferred orientation 570–571
  - proteins 726, 729, 731
  - stress/strain studies 546, 553
  - texture analysis 557
- *GSAS2CIF* 518
- Guaifenesin 500
- Guinier approximation 683
- Guinier cameras 27
- Gull–Daniell algorithm 476
- Gunshot residues 740
- Gypsum 375, 855–858, 860–861

- Haematite 362
- Half cells, electrochemical 181
- Half-width-at-half-maximum (HWHM) 238
- Hanawalt search method 304
- Hard radiation 63
- Harker sections 401
- Harmonics 41, 82
- Hart–Parrish diffractometer design 58
- Hat function 12
- Heat treatment 150
- Heavy-fermion superconductors 870
- Height compensation 151
- Hen egg-white lysozyme 389, 722, 725, 728–729
- Hessian matrix 467
- Heterogeneous materials 673
- Hexaaquairon(II) tetrafluoroborate 503
- Hexatriacontane 628
- High-energy X-rays
  - advantages of 374
  - for capillary measurements 151
- High-pressure generation 157
- High-pressure studies 156
  - capillary reaction cells for 190
  - data corrections for 167
  - hydrostatic conditions 164
  - preferred orientation 164, 168
  - sample preparation 164
  - using neutron diffraction 166, 219
  - using synchrotron radiation 163
  - with variable temperature 160
- High-temperature studies 97, 150, 761
- High-throughput methods 325, 337, 742, 768, 797
- Hill average model for stress/strain determination 545
- Histogram matching 390–391, 402
- Homogenized compliance 576
- Hooke equations 539
- Hot stage, domed 153
- Humidity, control of 193
- Hybrid beam-path systems 35
- Hybrid compounds 443
- Hybrid Monte Carlo method 391, 429
- Hydrochlorothiazide 417
- Hydrogen atoms, location of 410, 415, 438, 446, 498
- Hydrogen bonding 410, 499, 509
- Hydrogen storage 196, 752, 820
- Hydrostatic pressure 164
- Hydrostatic state 546
- Hydrothermal reaction cells 196
- Hydroxyapatite 739, 816
- Hyperphases 404

- Ibuprofen 388, 406, 634
- Ideal powder 7, 26
- *ImageD11* 606
- Impurities 466, 468
  - effect on indexing 274
  - in zeolites 454
- *In operando* studies 150, 181, 193
- *In situ* crystallization 165
- *In situ* studies 150, 189, 602
  - absorption in 176
  - background minimization 16
  - batteries 755
  - catalysts 852
  - ferroelectrics 177
  - glass-ceramics 829
  - in art and archaeology 761
  - minerals 886
  - pharmaceuticals 778
  - quantitative phase analysis 361
  - using neutron diffraction 67, 89, 96
  - using synchrotron radiation 63
- Incident-beam monochromators 225
- Incoherent scattering 19
  - neutron 177
- Incomplete structural models 430
- Independent-atom model (IAM) 475
- Index-heuristics strategy 274
- Index of refraction 588
- Index permutation 274
- Index space 273
- Indexing 11, 270
  - basic equation for 271
  - effect of impurity peaks 274
  - figures of merit 271–272
  - geometrical ambiguities 272
  - in multigrain crystallography 605
  - methods 273, 275
  - of multiphase samples 445
  - of pharmaceuticals 768
- Indexing (*continued*)
  - of proteins 726
  - of zeolites 454
  - software for 275
  - using Pawley or Le Bail methods 286
- Individual differences scaling (INDSCAL) method 340
- Indomethacin 632, 642, 772
- Inelastic coherent diffuse scattering 18
- Information depth 587
- Informational entropy 473
- Inorganic compounds, structure determination 442
- Inorganic Crystal Structure Database (ICSD) 314
- Insertion devices 53
- Instrument calibration 241
- Instrument control software 31
- Instrument performance 238
- Instrument profile function 224
- Instrument response 240, 256, 627
- Instrumental peak broadening 256, 291, 526, 572
- Instrumental uncertainty 235
- Instrumentation
  - CheMin 795
  - COSMA 799
  - Duetto 796
  - for forensic science 742
  - for laboratory X-ray scattering 26
  - for mining and mineral processing 794
  - for two-dimensional diffraction 124
  - platform concept 28
  - portable instrumentation 795
  - Terra 796
- Insulin 724, 726, 731
- Integral breadth 255, 288, 524, 526, 541
- Integrating detectors 46, 128
- Intellectual-property rights 768, 773
- Intensity correction factors 11
- Intensity extraction 282, 284, 395
- Intensity normalization, for non-crystalline materials 623
- Intercalation 182
- Interface roughness 597
- Intergranular strain 540
- Intermetallic phases 450
- Intermolecular distance constraints 438
- Internal standard method 346, 350
- Internal standards 346, 466, 770
- International Centre for Diffraction Data (ICDD) 304
- Inverse pole figures 562
- Inverse problem 11
- Invert glasses 831
- Iron, texture analysis of 568
- Iron-based superconductors 869, 874
- Iron(II) oxide 814
- Iron(III) oxide 814
- Isocracker sludge 311
- Isomorphous replacement 389, 728
- Isotope incoherent scattering 68
- Isotopic substitution 66
- *ITO* 276

- Jadarite 886
- Jarosite 801
- JMAK method 830
- Johansson focusing optic 225
- Johnson–Vand search algorithm 305
- Joint Committee on Powder Diffraction Standards (JCPDS) 304

- $K\beta$ filters 40
- Kagomé systems 184
- Kapton 152, 213, 217, 722
- Kinematic approximation 104, 253
- Kinetic studies 94, 192
  - of glass formation 830
- Kirkpatrick–Baez mirror arrangement 56
- Kramers–Kronig relation 62, 658
- Kroner model for stress/strain determination 545

- Laboratory coordinates 119
- Lactose 375
- Lagrange multipliers 476
- Lakargiite 886

Lamp furnaces 152
Lanthanum barium copper oxide 873
Lanthanum calcium manganate 815
Lanthanum hexaboride, NIST standard 236
Lanthanum strontium copper oxide 338
Laplace transform 588, 593
Larmor diffraction 174
Lattice defects, in neutron diffraction 95
Lattice distortions 293
Lattice-energy minimization, organic pigments 837–838
Lattice parameters 5, 270
    accuracy and precision of 466, 499
    certified 236
    changes in 174
    for proteins 319
    from electron-diffraction data 111
    from Pawley and Le Bail methods 283–286
    refinement of 470
    standardized 316
Lattice planes 2
Laue equation 6
Laue monotonic scattering 19, 68, 651
Layer texture 590
Layered double hydroxides, intercalation of 192
Le Bail method 283–284, 395, 468, 478
Lead zirconate-titanate 177
Least-squares refinement 20, 109, 263, 405, 467
Levitation 219
Likelihood function 403
Limit of detection 379, 627, 771
Limit of quantification 379, 771
Line-profile analysis 288, 524, 543
Line-profile standards 291
Linear absorption coefficients 203, 257
Linear electron accelerators (LINACs) 71
Liouville's theorem 124
Liquid-helium cryostat 96
Liquid-metal-jet X-ray sources 39
Lithiated graphite 182
Lithium aluminium silicate, $LiAlSi_2O_6$ 830
Lithium-ion batteries 181, 196
Lithium nickel oxide, $LiNiO_2$ 182
Lithium silicate, Li_2SiO_3 832
Lithium silicate, Li_4SiO_4 832
Local minimization 391
Local structure 22, 617, 674
    of ceramics 813
    of organic pigments 839
Localization corrections 557
Locard's exchange principle 737
Lorentz corrections 130
Lorentzian fibre components 561
Lorentzian peak-shape function 12, 240, 255, 263
Low-temperature structures 150, 770

M_{20} figure of merit 271
Macromolecules 718
Macroscopic elastic constants 576
Macroscopic strain 541–543
Macroscopic stress 541–543
Magic angle spinning NMR 454
Magnesian calcite 309
Magnesium aluminate 824
Magnesium borohydride 449
Magnesium perchlorate hydrate, $Mg(ClO_4)_2 \cdot nH_2O$ 193
Magnetic ceramics 808
Magnetic fields
    diffraction under 174, 183
    pulsed 183
Magnetic form factors 69
Magnetic interaction vector 70
Magnetic lattices 881
Magnetic polarization 567
Magnetic polarization orientation distribution 567, 569
Magnetic pole figures 567
Magnetic quantitative texture analysis 567
Magnetic scattering 18, 66, 254, 465
Magnetic scattering lengths 69
Magnetic small-angle neutron scattering 689
Magnetic structure factor 254
Magnetic superconductors 870, 878–879
Magnetic symmetry 881
Magnetic systems, frustrated 184
Magnetoelectric materials 184
Magnon dispersion curves 18
Mail-in services 51, 67
Manganese, quantification in bauxite 785
Manganese oxide, antiferromagnetic ordering 66
Manganites, magnetic phase transtions in 185
Mannitol 619, 638, 640, 643
March–Dollase model 260, 377–388, 400, 569–570
March function 569
Mars, mineralogy of 890
Mass absorption coefficients 257, 582
Matrix-flushing method 347, 352
Matrix technique for reflectivity of multilayers 596
MAUD 110, 547, 571, 573, 577
Maximum-entropy methods 389, 403, 473
    Cambridge algorithm 477
    combined with the Rietveld method 482
    extensions of 485
    F constraints 476, 478, 480, 485
    G constraints 478–479
    Gull–Daniell algorithm 476
    nuclear-weighted X-ray 484
    phasing tree 403
    Sakata–Sato algorithm 477
    size-distribution analysis 688
    two-channel MaxEnt method 477
    valence-only MaxEnt method 477
Maximum-likelihood methods 391, 430
Maya blue 762
Mayaro virus 719, 727
McM$_{20}$ figure of merit 271
McMaille 278
MDASH 419
Mean domain size 531
Melkovite 886
Mendozavilite 886
Mercury 314
Merrill–Bassett diamond-anvil cell 160
Metadata 516
Metal–organic frameworks 449, 752
Metals 739
Metals data file (CRYSTMET) 318
Metamorphic petrology 885
Metastable phases, in glass-ceramics 829–830
Metric multidimensional scaling 328
Metropolis algorithm 20, 667
Mica 207
MICE 406
Microabsorption 209–210, 258
    Brindley method 210, 258, 366
    effect on quantitative phase analysis 366
Microchannel plate detector 88
Microdiffraction 119, 125, 128, 584, 756
Microfocus X-ray sources 38
Micro-gap detectors 47
Micronizing mills 205
Microreactors 190
Microscopic strain 541, 543
Microstrain 14, 267, 288
    induced by milling 205
Microstrain broadening 721
Microstructure 2, 288
    in art and archaeology 762
    in ceramics 824
    in proteins 721
    in thin films 594
Miller indices 3, 5, 252, 270
Mineral physics 886
Mineral processing 793
Minerals 156, 885
    deep-mantle minerals 887
    dehydration of 887
    ferroelastic 889
    fibrous 889
    in forensic analysis 739
    mineral evolution 885
    mineral paragenesis 885
    negative thermal expansion in 887
    new mineral species 885
    phase transitions in 885, 888
    polymorphism in 793
    porous 887–888
Minerals (*continued*)
    spontaneous strain in 888
    thermoelastic behaviour 886
    time-resolved experiments 885
Minimum spanning trees 331
Mining 793
Minkowski reduction 277
Mirrors 43, 55, 597
    for neutrons 77–80
    Göbel mirrors 27, 43
MISSYM 506
Mixed crystals 835
Modal torsion-angle constraints 436
Model building 390, 414
    for zeolites 454
Modified direct methods 388
Modified March–Dollase approach 570
Modified tangent formula 388
Modulus sum function 388, 401
Mogul 435
Mogul Geometry Check 498, 500
Molecular connectivity 417
Molecular coordinate system 417
Molecular envelopes 390
Molecular replacement 390, 726
Molecular structures 414
    parameterization of 417
Molecular symmetry, use in structure determination 390
Molecular volume 434
Monochromators 54, 225
    cooling of 55
    for neutrons 81
    higher-order reflections 54
    incident-beam 225
    multiple-reflection 42
    silicon crystal 55
    single-reflection 41
Monotonic Laue diffuse scattering 19, 68, 651
Monte Carlo methods 426, 444, 667
    for indexing 275
    for orientation mapping 806
Montel optics 43
MOPAC2012 434
Morningstar–Warren approximation 652
Morphology 206
Mosaic crystal 82
Mosaic spread 82
Mullite 507
Multi-analyser crystal detector 175
Multi-anvil presses 158
Multichannel analysers 60
Multi-component materials 673
Multiferroics 184
Multigrain crystallography 601
    centre-of-mass mapping 607
    coordinate systems 603
    crystal symmetry 613
    diffraction geometry 603
    indexing 605
    setup 602
    stress mapping 607
    use of synchrotron radiation 602
Multilayer mirrors 43
Multilayers 581
    absorption correction in 577
Multiphase samples
    in CIF 516
    indexing of 445
    refinements of 466
Multiple anomalous dispersion 728
Multiple-beam-path systems 35
Multiple data sets
    fitting 466
    for protein structure determination 725
    in CIF 516
Multiple scattering 210
    corrections for, in small-angle scattering 679, 692
    in electron diffraction 102, 113
Multiples of a random distribution (m.r.d.) 556
Multiplicity 8, 135, 144, 203, 253
Multivariate statistical analysis 756
Multivitamin supplement 312
Multi-wire proportional counters 83, 175

Mutinaite 889
Mythen position-sensitive detectors 59, 63

Nano-area electron diffraction (NAED) 105
Nanocrystalline organic pigments 839
Nanomaterials 649
Nanoparticles 649
    form factor 654
    gold 656
Nanoporous materials 649
Nanostructures 649
    self-assembled 598
Narcotics 738
Natrobetpakdalite 886
Negative Debye–Waller factors 258
Negative thermal expansion 887
Neodymium cerium copper oxide 874
Nested neighbourhoods principle 397
Neutron absorption 220
Neutron absorption cross section 257
Neutron activation 220–221
Neutron choppers 75
Neutron collimators 77, 80
Neutron detectors 82, 87, 675, 677
Neutron diffraction 66
    accuracy 94
    background reduction 86
    design of experiments 92
    for studying cements 863
    for studying glass-ceramics 829
    high-pressure studies 166
    high-temperature studies 97
    in art and archaeology 764
    in situ studies 96
    monochromators 81
    non-ambient-temperature studies 96
    opposed-anvil cells 219
    peak intensities 254
    precision 94
    quantitative phase analysis 67, 362
    reaction cells for 195
    resolution *versus* intensity 84
    sample containers 96, 218
    sample size 94, 218
    specimen preparation 218
    standards for 95
    structure factors 70, 254
    time-of-flight experiments 74, 465
    under a magnetic field 174
    under an electric field 174
    under applied stress 98
Neutron diffractometers 80, 91, 254
Neutron guides 77
    ballistic 80
    characteristic wavelength 79
Neutron mirrors 77–80
Neutron nuclear structure factor 254
Neutron scattering
    by different isotopes 220
    coherent elastic 68
Neutron scattering cross sections 66, 68, 220
Neutron scattering lengths 66, 68, 220
Neutron sources 70
    accelerator-based 71
    fission reactors 72
    for small-angle scattering 693
    moderators 74
    nuclear reactors 71
    pulse shape 265
    reactors 265
    spallation 71, 73, 265
Neutron velocity selectors 75
Neutrons
    attenuation of 69, 95
    epithermal 72
    fast 72
    magnetic scattering of 66
    polarized 82
    properties of 66–67
    refractive index for 68
    thermal 66, 72
NEWMOD 358
Nickel vanadium oxide, Ni$_3$V$_2$O$_8$ 184
Nifedipine 644
Niggli reduced cell 272
Non-ambient-temperature studies 150
    capillary reaction cells for 190
    under high pressure 160
    using neutron diffraction 96
Non-bonded contacts 410
Non-coplanar beam-path systems 35
Non-crystalline materials 617, 673
Non-destructive analysis 737, 743, 778, 796
Non-framework species 459
Non-invasive techniques 760
Non-molecular compounds, structure determination 442
Non-nuclear maxima in electron-density maps 475
Nonuniform response correction 129
Norbornene 278
Nordstrandite, Al(OH)$_3$ 352
Normal probability plot 492
Normalized Rietveld plot 491
Normalized structure factors 396
N-TREOR09 276
Nuclear coherent scattering lengths 254
Nuclear scattering 254
Nuclear-weighted X-ray maximum entropy method (NXMEM) 484
Nucleating agents 828
Nucleation of glass-ceramics 828

Obradovicite 886
Observed Fourier map 404
Octahedral tilting 887
Opposed-anvils presses 157–158, 219
Optical bench 28–30
Order parameter 591
Organic pigments 834
Organic pollutants 888
Orientation background 560
Orientation component 555
Orientation distribution 555–556
    magnetic 567
Orientation-distribution components 566
    elliptical 566
Orientation distribution function 540, 556
    stress 576
    weighted-strain 576
Orientation element 556
Orientation mapping 608
    by Monte Carlo optimization 608
    grain-by-grain volumetric mapping 608
Orientation relationships 139
Orientation space 555, 606
Oven heaters 152
Oxygen stoichiometry in superconductors 874

Paints 738
Pair distribution function analysis 16, 649
    big-box modelling 666
    buckminsterfullerene 154
    choice of wavelength 62
    data reduction 663
    detectors for 63
    in art and archaeology 764
    models for 665
    organic pigments 839
    pharmaceuticals 772
    rapid-acquisition 657, 660
    real-space Rietveld approach 666
    small-box approach 665
    structural information from 664
    using electrons 113, 661
    using neutrons 659
    using synchrotron radiation 660
    using X-rays 660
Paper 740
Parallel-beam instruments 30, 56
Parallel-coordinates plots 330
Parallel-plate collimators 40
Parallel tempering 427, 455
Paramendozavilite 886
Parameter space 273
Parametric refinements 9, 22, 361, 467
Pareto optimization 392
Parratt function reflectivity profile 690
Parseval's theorem 420
Partial structure function 657
Particle form factor 676
Particle pair density distribution function 685
Particle statistics 34, 37, 134, 144, 201, *see also* granularity
Particle structure factor 687
Partition equation 405
Patents 768, 773
Pathology 739
Pattern matching 326
Patterson function 388, 400
Pawley method 283–284, 395, 468
pdCIF 515
pdCIFplot 519
PDFgui 655
Peak asymmetry 240, 257, 264, 465, 467
Peak broadening 226, 524, 538
    crystallite size 267
    deformation faults 295
    dislocations 293
    domain size and shape 292
    in data from reaction cells 194
    instrumental 291, 526, 572
    microstrain 267
    strain 293, 541, 552
    twinning 295
Peak cutoff 495
Peak intensities 9, 345
    for neutron diffraction 254
    for X-ray diffraction 253
Peak overlap 8, 283–284, 395, 725
Peak positions 2, 252
Peak profiles 12, 236, 255, 263, 526
    for constant-wavelength radiation 263
    for neutron time-of-flight experiments 265–266
    for X-ray energy-dispersive experiments 266
    fundamental-parameters modelling 265
    instrumental contributions to 256
Peak shift 264–265, 538, 541, 550, 573, 589
Peak-shape functions 239, 301
    contributions to 240
    Gaussian 12, 240, 255, 263
    Lorentzian 240, 255, 263
    Pearson-VII 240, 255, 263
    pseudo-Voigt 240, 256, 263
    Voigt 240, 256, 264
Pearson-VII peak-shape function 240, 255, 263
Pearson's Crystal Data 316
Pearson's *r* coefficient 325
Pendellösung fringes 630
Penetration depth 587, 760
Pentacene 812
Periodic nodal surfaces 390
Perylene pigments 834
Petroleum and petrochemicals 752, 843
Pharmaceuticals 767
    amorphous materials 767, 771
    bioavailability 768
    co-crystals 767–768
    counterfeit 777
    crystal habit 776
    high-throughput screening 768
    in situ studies 778
    pair distribution function analysis 772
    polymorphs 767, 774
    quality control 773
    quantitative phase analysis 769
    salts 767–768
    sample preparation 771
    solubility 768
    solvates 767
    structure determination 769
Phase chaos 836
Phase constants 357
    Knudsen method 353
    standardless determination of 353
    Zevin & Kimmel method 353–354
Phase equilibria in ceramics 813
Phase identification 304
    ceramics 811
    in art and archaeology 760
    in thin films 582
    pharmaceuticals 767
    relative intensities 133

Phase identification (*continued*)
  using electron diffraction 108
  using two-dimensional diffraction 133
Phase inhomogeneities in thin films 584
Phase separation in glass-ceramics 828
Phase transitions 93, 97, 150, 156, 174
Phases with partial or no known crystal structures (PONKCS) 356
Phasing 397
Phosphates 799
Photographic film 27
Photon-counting detectors 27, 47, 128, 176
Photon energy 51
Photonic ceramics 810
Photovoltaics 753, 808
Phyllosilicates 889
Physical vapour deposition (PVD) 583
Piezoelectric ceramics 808
Pigments
  forensic analysis 738
  in art and archaeology 761
  industrial organic 834
  Pigment Orange 72 834
  Pigment Red 57:1 837
  Pigment Red 170 836, 838
  Pigment Yellow 191 836
  Pigment Yellow 213 839
Piston-and-cylinder press 157
Pixel position 121–122
Pixel size 49, 126
Planar texture 565
Planetary surface analysis 795
Plasma-enhanced chemical vapour deposition (PECVD) 583
Plastics 740
Platform concept 28
Plumbojarosite 798
PM2K 297
Point detectors 225
Point-spread function 127
Pokrovskite 886
Polarization 253
  of neutrons 82
  of synchrotron radiation 60
Polarization corrections 130
Polarization factor 241, 253
Pole density 136
Pole-density distributions 400
Pole-figure interpolation 139
Pole-figure space 557
Pole figures 136, 260, 556, 591
  inverse 562
  magnetic 567
  normalization of 557
  reduced 561
POLPO method 408
Polyamorphism 888
Polyhedral compounds 443
Polymers 673, 685, 740
Polymorphism
  in drugs 724, 738, 767, 774
  in macromolecules 724
  in minerals 793
  in organic pigments 834–835
PolySNAP 333
PONKCS method 356
Ponsin 390, 727, 730
Popa and Balzar approach to stress/strain determination 547
Porod scattering regime 683
Porous minerals 887–888
Portable X-ray diffraction equipment 761, 763, 778
Portland cements 856
Portland clinkers 857
Portlandite 856, 862
Position-sensitive detectors
  for neutrons 83
  for small-angle scattering 677
  for X-rays 27, 56, 225
  Mythen 59, 63
Positivity method for texture analysis 561
Potasssium titanyl phosphate 852
Powder, definition of 26
Powder diffraction CIF dictionary (pdCIF) 515
Powder Diffraction File (PDF) 305
  features of 307
  for electron-diffraction data 109
  forensic subfile 744
  quality marks 306
  sources and formats 306
Powder-pattern calculation, for proteins 319
PowderSolve 426, 769
PowDLL 517
POWSIM 406
Pozzolanic activity 860
Precession electron diffraction 104, 886
Precision
  goniometer 34
  in neutron diffraction 94
  in quantitative phase analysis 350, 364, 374–375
  of structural parameters 499
Prednisolone succinate 389
Preferred orientation 260, 284, 400, 471
  avoidance 206
  correction for 206
  effect on quantitative phase analysis 365
  in capillary reaction cells 191
  in cements 856
  in ceramics 818
  in electron diffraction 112
  in high-pressure studies 164, 168
  in neutron diffraction 95
  in proteins 725
  in semiconductor layers 593
  March–Dollase approach 260, 377–378, 400, 569–570
  modelling of 569
  spherical-harmonic approach 260
Pressure calibration 166
Principal-component analysis 329, 798
Prior-derived F constraints 480
Prior electron density 474–475
Prior information, use in structure determination 391
Probability distribution functions 396
Process analytical technology 773
ProcessDiffraction 110
Procrystal electron density 475
PRODD 725–726
Proportional counters 27, 46–47
Proportionality of a detector 46
Protein Data Bank (PDB) 318
Proteins 318, 718
  choice of wavelength 62
  powder-pattern calculation 319
  structure validation 508
Pseudoephedrine 312
Pseudophases 404
Pseudotranslational symmetry 399
Pseudo-Voigt peak-shape function 240, 256, 263
publCIF 519
Pulsed magnetic fields 183
Pump–probe experiments 63, 176
PyCifRW 518
Pyrotechnological processing 761

Q_{partial} figure of merit 271
Quadratic form 271
Qualitative phase analysis 796, 835
Quality control 342, 745, 773
Quantitative phase analysis 344
  absolute phase abundances 349
  absorption–diffraction method 345, 350
  accuracy 350, 364, 374
  background in 368
  batch processing 361
  calibration 356, 771
  cements 855
  ceramics 812
  corundum as a reference material 347
  crystallite-size issues 365
  data clustering 361
  disorder, treatment of 358
  disordered heterogeneous materials 683
  experiment constant 348, 355
  external standard method 349
  full-pattern fitting methods 348
  glass-ceramics 833
  in art and archaeology 760
Quantitative phase analysis (*continued*)
  in mining and mineral processing 797
  in situ studies 361
  in the aluminium industry 782
  internal standard method 346, 350
  matrix-flushing method 347, 352
  microabsorption 366
  non-crystalline materials 360, 625
  of phases with partial or no known crystal structures (PONKCS) 356
  organic pigments 836
  pharmaceuticals 769
  phase constant 349, 357
  precision 350, 364, 374–375
  preferred orientation 365
  reference intensity ratio method 347, 351
  relative phase abundances 350
  Rietveld-based methods 348, 352
  sample preparation 365
  spiking method 352
  standards 368–369
  systematic errors 364
  using electron diffraction 108, 110
  using energy-dispersive diffraction data 362
  using Mo or Cu radiation 374
  using neutron diffraction 67, 362
  using synchrotron radiation 376
  without Rietveld refinement 337
  zeolite catalysts 846
Quantitative texture analysis 555
  arbitrarily defined cells method 560
  component method 560
  entropy-maximization method 560
  EWIMV method 560
  exponential harmonics method 561
  fundamental equation for 558
  Gaussian fibre components 561
  Lorentzian fibre components 561
  magnetic 567
  positivity method 561
  reciprocal-space mapping 566
  spherical components 561
  tutorials 578
  using spherical harmonics 570
  vector method 560
  WIMV method 560
Quantum theory of atoms in molecules (QTAIM) 485
Quartet invariants 397
Quartz 202, 375, 508, 784, 832
Quasi-kinematic formalism 109
Quaternions 611
Quinacridone 835–836
Quinacridonequinone 836

R factors 468
  Bragg 469
  expected 468, 489
  weighted-profile 468, 489
Radial distribution function 653
Radiation damage 61, 103, 722
Radon transform 562
Raman spectroscopy 339, 342
RAMM method 406
Random texture 564
Ranitidine hydrochloride 774
Rapid-acquisition pair distribution function 657, 660
Rasvumite, KFe$_2$S$_3$ 311
Reaction cells
  electrochemical 196
  for angular-dispersive diffraction 194
  for neutron diffraction 195
  for solid–gas reactions 196
  humidity control 193
  hydrothermal 196
  large-volume 194
Reaction mechanisms in ceramics 820
Reciprocal lattice 4, 252, 270
Reciprocal space 4
Reciprocal-space mapping 123, 566
Red mud 785
Reduced chi squared 469, 489
Reduced pair distribution function 17
Reduced pole distribution 541
Reduced pole figures 561

- Reference electron density 474
- Reference intensity ratio method 347, 351
- Reflection sample holders 211
- Reflectivity 153, 594, 680
- Refraction matrix 596
- Refractive index 56, 588
  - for neutrons 68
- Relative intensities 133
- Relative phase abundances 350
- Reliability estimators for orientation distributions 563
- Remacemide nitrate 430
- REMEDY cycle 482
- Renewable energy sources 753
- Repartitioning method 402
- Repeatability 375
- Representation theory 397
- Reproducibility 375
- Residual strain 57, 575
- Residual stress 88, 575
- Resolution
  - angular 49, 62, 133, 174–175, 224, 485
  - energy 46, 55
  - of neutron diffractometers 84, 86, 93
  - spatial 49, 57, 62, 127
  - time 189
- Resolution bias modification 405, 408
- Resonant (anomalous) scattering 62, 388, 479–480
- Restraints 469, 497
- Reuss model for stress/strain determination 544
- Reverse Monte Carlo methods 444, 667
- Reversed figure of merit 272
- Reynolds Cup 370, 843
- Riebeckite 889
- Rietveld plot 491
  - normalized 491
  - weighted 492
- Rietveld refinement 19, 465
  - divergent 470
  - graphical assessment of fit 490
  - history of 465
  - order for refining parameters 470
  - statistical quality measures 489
  - using electron-diffraction data 111
- Rigid-body representation of amino acids 731
- Ring conformations 435
- *RMCprofile* 667
- Robax 830
- Rocking curve 33, 57, 591
- Rocks, properties of 843
- ‘Rocks in dust’ 204
- Rodrigues vectors 610
- Rotating-target X-ray sources 39
- Rutile 586, 889

- Sakata–Sato algorithm 477
- Sample (*versus* specimen) 26
- Sample changers 56
- Sample holders
  - back-loading 206
  - capillaries 215
  - flat foils 213
  - for neutron diffraction 96, 218
  - for proteins 719
  - levitation 219
  - reflection 211
  - sonic vibrating 796
  - transmission 213
  - zero-background 742–743
- Sample space 122
- Sample spinning 57, 205
- Sample stages 34
  - for non-ambient studies 150–151, 153
- Sample temperature 152
- Sampling statistics, *see* particle statistics
- Sayre’s equation 396
- Scan/covariance indexing method 273
- Scan modes 32
- Scattering contrast factor 676
- Scattering cross section, for neutrons 66, 68, 220
- Scattering invariant 683
- Scattering lengths, for neutrons 66, 68, 220
- Scattering plane 28
- Scattering vector 5, 120, 254
- Scattering-vector technique for thin films 588, 594
- Scherrer constant 267, 288
- Scherrer equation 13, 146, 255, 288, 524, 543
- Scintillation detectors 46, 83, 88
- Scott’s Moss Control Granules 202
- Scrubber alumina 788
- Search/match procedures 304
- Second-neighbourhood extension 403
- Seemann–Bohlin geometry 27
- Selected-area electron diffraction (SAED) 105
- Self-assembled nanostructures 598
- Semiconductor detectors 48, 83
- Series-termination effects 405, 473–474, 655
- Serpentine minerals 888
- Serpentinites 890
- S-FFT approach 401
- Shale 843
- Shape effects in small- and wide-angle scattering 683
- Shape factor 255
- Shape function 654
- Sharpened Patterson functions 388
- Shirley–Ishida–Watanabe (SIW) indexing 274
- Silhouettes 331
- Silicon 629
  - nanocrystalline 645
  - standard reference material 236
- Silicon carbide 817
- Silicon micro-strip detectors 48
- Silicon nitride 817
- Silicon pixel detectors 48
- Sim weights 404
- Simulated annealing 20, 391, 426, 455, 667
- Simvastatin 634, 643
- $\sin^2 \Psi$ method for stress/strain determination 545
- SINCRIS 698
- Single-crystal elastic constants 546
- Singular value decomposition 467
- *SIROQUANT* 357, 856
- Size distribution analysis 686
- Size Fourier term 527
- Small-angle neutron scattering 654, 673
  - background 679
  - calibration 679
  - contrast-variation 689
  - data reduction 679
  - fractal models 687
  - grazing-incidence 680
  - interparticle interference effects 687
  - magnetic 689
  - multiple scattering 679, 692
  - neutron sources 693
  - position-sensitive detectors 675, 677
  - shape effects 683
- Small-angle X-ray scattering 654, 673
  - anomalous 689
  - background 679
  - calibration 679
  - data reduction 679
  - fractal models 687
  - grazing-incidence 680, 690
  - interparticle interference effects 687
  - multiple scattering 679, 692
  - non-ambient studies 155
  - position-sensitive detectors 675, 677
  - shape effects 683
  - standard reference material 679
- Smear mounts 212
- Snell’s law of refraction 589, 595
- Sobek method 801
- Sodium parahydroxybenzoate 268
- Software 698
  - for data clustering 342
  - for electron diffraction 114
  - for indexing 275
  - for structure determination 406
- Soils 739
- Solar energy 753
- Solenoid magnets 183
- Solid solutions, organic pigments 835
- Solid-state NMR 437
- Soller collimators 40, 58, 81
- Solvent-accessible voids 434
- Space-group determination 416
  - ambiguity in 458
  - proteins 726
  - using Pawley or Le Bail methods 286
  - zeolites 454
- Spallation sources 71, 73, 265
- Spatial correction 129
- Spatial resolution 62
  - of a detector 49, 127
- Spearman’s rank order coefficient 325
- Specimen (*versus* sample) 26
- Specimen displacement 151, 211, 467, 470
- Specimen preparation 200, 415
  - for electron diffraction 106
  - for forensic science 742
  - for high-pressure studies 164
  - for neutron powder diffraction 218
  - for pharmaceuticals 771
  - for proteins 718
  - for quantitative phase analysis 365
  - for X-ray powder diffraction 200
  - in the aluminium industry 782
- Specimen transparency 265
- Spectral brightness 52
- Spectral reflection 43
- Spectroscopic data 339
- Spent potlining 790
- Spherical harmonics 547, 549, 559, 570
- Spiking method 352, 375
- Spin incoherent scattering 68
- Spinel 824
- Spodumene 824, 830
- Spontaneous strain, in minerals 888
- Spotty Debye rings 37, 145, 191, 201, 661
- Spray drying 208
- Squaring method 401
- Stacking disorder 358
- Standard reference materials (SRMs) 224, 235
  - certificates of analysis 235
  - for line profiles 291
  - for neutron diffraction 95
  - for non-crystalline materials 624
  - for quantitative phase analysis 369
  - for small-angle X-ray scattering 679
- Standard uncertainties 517
- STAR syntax 515
- Static high-pressure generation 157
- Static weights 485
- Stein’s unbiased risk estimate 326
- Step size 238
- Stereochemical restraints, in proteins 729
- Stiffness 594
- Stiffness elastic constants 539
- Stishovite 889
- Stopping criterion 485
- Storage rings 51
- Strain 256, 538
  - Hill average model 545
  - in cultural-heritage materials 762
  - in thin layers 593
  - intergranular 540
  - Kroner model 545
  - macroscopic 541–542
  - microscopic 541, 543
  - Popa and Balzar approach 547
  - Reuss model 544
  - $\sin^2 \Psi$ method 545
  - types I, II and III 540
  - Voigt model 544
- Strain broadening 256, 293
  - anisotropic 259
- Strain pole distribution function 542
- Strain/stress orientation distribution function 541, 547–549, 576
- Strain tensor 594, 613
- Strain-to-stress conversion 613
- Stress 140, 538
  - calculation of 144
  - data-collection strategies 143
  - data integration 143
  - equations for different stress states 142
  - fundamental equations 141
  - Hill average model 545
  - in ceramics 817

- Stress (*continued*)
  - in thin layers 593
  - Kroner model 545
  - macroscopic 541–542
  - neutron diffraction under uniaxial stress 98
  - peak evaluation 143
  - Reuss model 544
  - sin^2 Ψ method 545
  - Voigt model 544
- Stress gradients 594
- Stress mapping 607
- Stress–strain relations 140
- Strip detectors 175
- Strip heaters 152
- Stroboscopic experiments 92, 174, 176
- Strong reflections in structure determination 396
- Strontium sulfate, $SrSO_4$ 389
- Structure determination 386
  - bond lengths and angles 434
  - charge flipping 389
  - computational methods 434
  - crystal-chemistry guided algorithms 445
  - direct methods 387–388
  - direct-space methods 442
  - framework structures 388
  - genetic algorithms 444
  - glass-ceramics 830
  - global optimization 390
  - information from solid-state NMR 437
  - inorganic compounds 442
  - isomorphous replacement 389
  - local minimization 391
  - maximum-entropy methods 389, 483
  - maximum-likelihood methods 391
  - model building 390
  - molecular replacement 390
  - non-molecular compounds 442
  - organic pigments 837
  - Patterson method 388
  - pharmaceuticals 769
  - proteins 726
  - quality of powder-diffraction data 445
  - real-space methods 414
  - reciprocal-space methods 395
  - resonant-scattering methods 388
  - reverse Monte Carlo algorithms 444
  - software 406
  - strong reflections 396
  - topology-guided algorithms 445
  - trial-and-error methods 386
  - use of hydrogen bonding 390
  - use of molecular envelopes 390
  - use of molecular symmetry 390
  - use of prior information 391
  - use of synchrotron radiation 387
  - using model fragments 434
  - using Pawley or Le Bail methods 283, 286
  - using supplementary information 433
  - weak reflections 401–402
  - zeolites 391, 452
- Structure-directing agents 459
- Structure envelope 457
- Structure factors 395
  - extrapolated 389
  - for neutron diffraction 70, 254
  - magnetic 254
  - normalized 396
  - normalized residuals of 485
  - unitary 403
- Structure invariants 397
- Structure-optimization techniques 404
- Structure–property relationships, in organic pigments 835
- Structure refinement, proteins 729
- Structure validation 447, 489
  - proteins 508
- Substructure reflections 399
- Successive dichotomy indexing method 274
- Sucrose lyophilizate 627
- Sulfathiazole 342
- Sulfobelite cements 855
- Superconducting magnets 183
- Superconductors 868
  - alloys 868
  - borocarbides 869
  - ceramics 807, 821
  - elements 868
  - heavy-fermion 870
  - intermetallics 868
  - iron-based 869, 874
  - lanthanum barium copper oxide 873
  - layered structures 875
  - magnetic 870, 878–879
  - neodymium cerium copper oxide 874
  - oxygen stoichiometry in 874
  - properties of 868
  - structural transformations in 876
  - thin films 592
  - transition-metal oxides 868
  - types I and II 868
  - yttrium barium copper oxide 821, 873, 876
- *SUPERFLIP* 406–407, 457
- Superlattices, reflectivity of 596
- Supermirrors 80
- Superspace crystallography 486
- Superstructure reflections 399
- Surface roughness 209, 211, 258, 595
- *SVD-Index* 278
- Symmetric figure of merit 272
- Symmetrized harmonics method 400
- Symmetry
  - in multigrain crystallography 613
  - molecular 390
  - pseudotranslational 399
  - use of, in pole-figure interpolation 139
- Symmetry minimum function 388, 401
- Synchrotron radiation 51
  - advantages for structure determination 387
  - diffractometers for 56
  - for high-pressure studies 163
  - for quantitative phase analysis 376
  - for small-angle scattering 692
  - for studying cements 863
  - for wide-angle scattering 692
  - in art and archaeology 760, 763
  - *in situ* studies 752
  - instrumentation for proteins 720
  - optics 54
  - polarization 60
  - sample heating 61
  - stroboscopic experiments 174
  - studies of minerals using 886
  - thin films 588, 590, 596
  - tuning 54
  - use in bauxite analysis 783
  - use in multigrain crystallography 602
  - use in pair distribution function analysis 660

- *T* ramping 445
- Tangent formula 398
- Tartaric acid 747
- Temperature accuracy 155
- Temperature controllers 150
- Temperature gradients 150
- Temperature-resolved studies 150
- Terbium manganate, $TbMn_2O_5$ 185
- Terbium stannate, $Tb_2Sn_2O_7$ 185
- Tetrahedral tilting 888
- *TexPat* 110, 115
- Textiles 740
- Texture 260, 540, 542, 555
  - cyclic fibre 565
  - cyclic planar 565
  - fibre 110, 565, 590
  - in thin films 590
  - layer 590
  - planar 565
  - random 564
  - single-component 558
  - three-dimensional 565
- Texture analysis 136
  - data collection 138
  - data processing 138
  - entropy-maximization method 560
  - exponential-harmonics method 561
  - fundamental equations 137
- Texture analysis (*continued*)
  - in art and archaeology 762
  - in ceramics 818
  - magnetic quantitative 567
  - positivity method 561
  - quantitative 555
  - using electron diffraction 110
  - vector method 560
- Texture components 570
- Texture distribution function 593
- Texture entropy 564
- Texture factors 590
- Texture gradients 592
- Texture index 564, 591
- Texture strength 564, 591
- Thermal batteries 756
- Thermal diffuse scattering 18, 691
- Thermal expansion 155
- Thermal neutrons 66, 72
- Thermoelectric effect 809
- Theta zero angle 230, 232–233
- Thickness factor 582
- Thin films 581, 673, 680
  - data collection 119
  - phase inhomogeneities in 584
  - scattering-vector technique 588, 594
  - texture in 590
- Thin layers, stress and strain 593
- Three-dimensional grain mapping 601, 608
- Three-dimensional texture 565
- Three-dimensional X-ray diffraction microscopy 601
- Through-the-bag analysis 745
- Time-of-flight neutron diffraction 74, 465
  - diffractometers 85, 254
  - frame overlap 75
- Time-resolved experiments 63, 150, 189, 885
  - using electron diffraction 103
- Titanium oxide 586
- Titanium silicon carbide 820
- *TOPAS*
  - fundamental-parameters approach 224, 240
  - peak shapes in 247
  - pharmaceuticals 762
  - preferred orientation 571
  - proteins 726
  - simulated annealing 426
  - whole powder pattern modelling 297, 368
- Topographs indexing method 275
- Topology-guided algorithms 445
- Toroidal anvils 158
- Torsion angles 500
  - constraints 436
- Total external reflection 588
- Total scattering 2, 16, 649, 681
  - structure function 16
- Toxicology 738
- Transfer matrix 596
- Transfocators 56
- Transformation matrix 123
- Transition temperature, determination of 155
- Transmission electron microscopy 105, 457
- Transmission sample holders 213
- Tremolite 889
- *TREOR90* 276
- Trial-and-error methods 386
- Tricalcium aluminate 856
- Triplet invariants 397
- Tube tails 229
- Tuning of synchrotron radiation 54
- Turbostratic disorder 359, 575
- Turkey egg-white lysozyme 280, 722
- Twin mesostructures 889
- Twinning 295
- Two-channel MaxEnt method 477
- Two-dimensional detectors 8, 59, 125, 175, *see also* area detectors
  - spatial resolution of 127
- Two-dimensional diffraction 118
  - phase identification 133
- Two-theta integration 130
- Two-theta zero angle 230, 232–233
- Type-I, -II and -III strain 540
- Type-I and -II superconductors 868

Ultra-small-angle scattering 677
  instrumentation 678
Uncertainty, instrumental 235
Undulators 53
Unit quaternions 611
Unitary structure factors 403
Uranium 551
Urate oxidase 724
User facilities 51, 67, 156

Vacuum equipment for high-temperature studies 151
Valence-only MaxEnt method 477
Vanadyl pyrophosphate, $(VO)_2P_2O_7$ 310, 850
Vector method of texture analysis 560
Vent-gas oxidation catalyst 851
Verapamil hydrochloride 437
Vertical collimation 53
Voigt model for stress/strain determination 544
Voigt peak-shape function 240, 256, 264
von Mises distribution 400

Warren–Averbach method 289, 543
Wavelength, choice of 51, 61, 374
Weak reflections in structure determination 401–402
Weighted least-squares refinement 405
Weighted profile *R* factor 468, 489
Weighted Rietveld plot 492
Weighted-strain orientation distribution function 576
Weights 405, 465, 469, 489
  static 485
Whole powder pattern modelling 2, 282, 288, 290, 770
Wide-angle scattering 673, 681
  shape effects 683
Wigglers 53
WILDFIRE 359
Williamson–Hall plot 288, 543
Wilson method 396
WIMV method of texture analysis 560
Wind power 753
Wine diamonds 747
WinPLOTR 115, 278–279
WinPSSP 426
Wollastonite 209
WRIP20 figure of merit 272

X-CELL 278
XLENS 388, 406, 456
X-ray absorption spectroscopy, in art and archaeology 762
X-ray diffraction computed tomography 195
X-ray diffraction microtomography 764
X-ray free-electron lasers 197, 731
X-ray optics 39, 224
  for non-crystalline materials 623
  for two-dimensional diffraction 125
X-ray radiography 31
X-ray reflectivity 594, 690
  specular 577
X-ray sources 37
  fixed-target 38
  for two-dimensional diffraction 125
  free-electron lasers 197, 731
X-ray sources (*continued*)
  liquid-metal-jet 39
  microfocus 38
  performance of 39
  rotating-target 39
  synchrotrons 51

Young's modulus 824
Yttria-stabilized zirconia 823
Yttrium barium copper oxide 821, 873, 876
Yttrium managanate, YMn_2O_5 185

Z-matrix formalism 417, 434
ZEFSA II 452, 455
Zeolites 452, 752, 887
  catalysts 846
  template burning 191
  zeolite IM-5 390
Zeolitic membranes 887
Zernike–Prins correlation functions 652
Zernike–Van Cittert theorem 105
Zero-background holders 742–743
Zero-point correction 467
Zinc, quantification in bauxite 785
Zinc oxide 376, 592
Zirconia 812–813
  alumina-toughened 823
  degradation of 823
  thin films 819
  transformation toughening 822
  yttria-stabilized 823
Zirconium phosphate framework structure 407
Zone-indexing strategy 273